

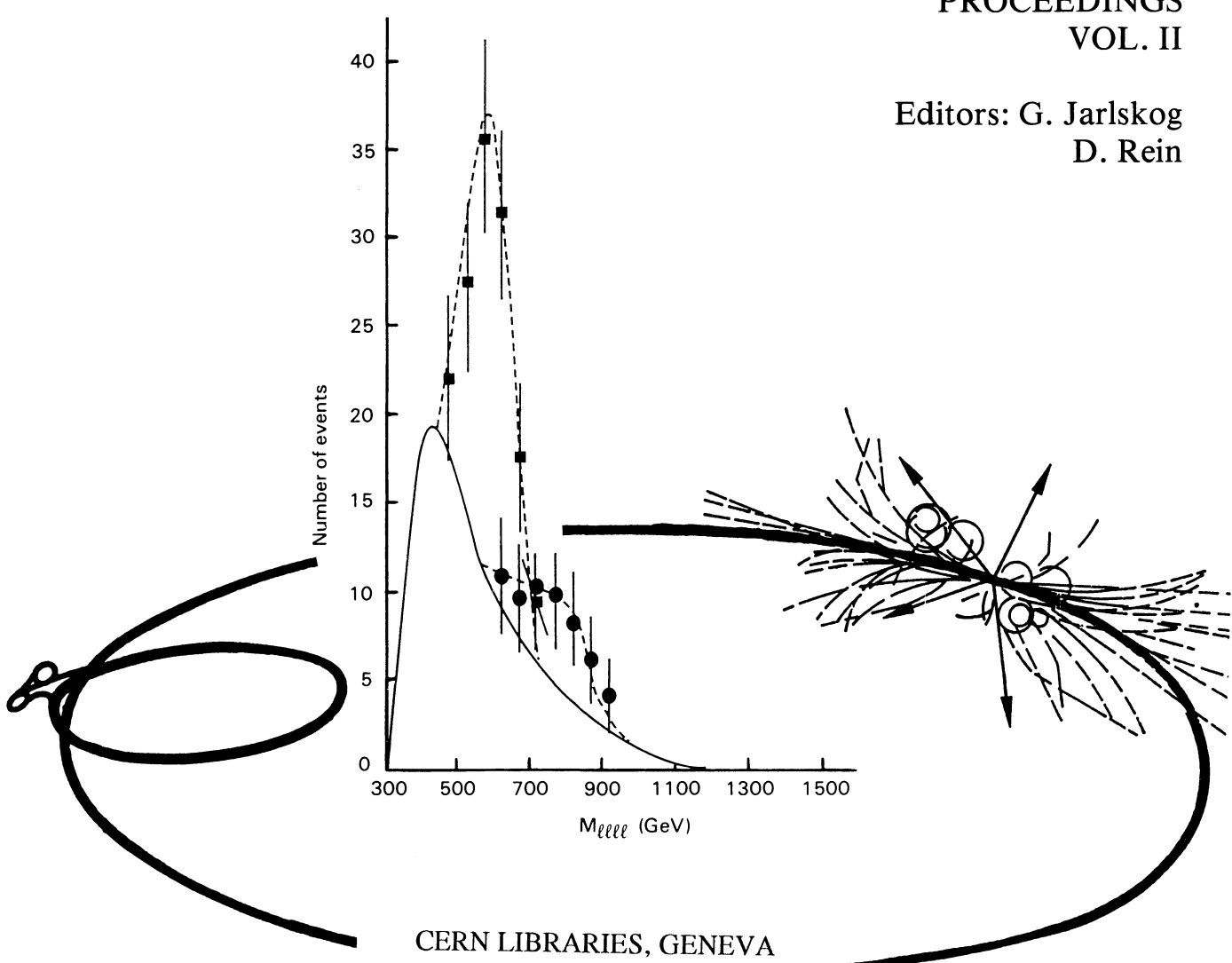
CERN 90-10
ECFA 90-133
Volume II
3 December 1990

EUROPEAN COMMITTEE FOR FUTURE ACCELERATORS

Large Hadron Collider Workshop

PROCEEDINGS
VOL. II

Editors: G. Jarlskog
D. Rein



CERN LIBRARIES, GENEVA



CM-P00075811

Aachen, 4-9 October 1990



© Copyright CERN, Genève, 1990

Propriété littéraire et scientifique réservée pour tous les pays du monde. Ce document ne peut être reproduit ou traduit en tout ou en partie sans l'autorisation écrite du Directeur général du CERN, titulaire du droit d'auteur. Dans les cas appropriés, et s'il s'agit d'utiliser le document à des fins non commerciales, cette autorisation sera volontiers accordée.

Le CERN ne revendique pas la propriété des inventions brevetables et dessins ou modèles susceptibles de dépôt qui pourraient être décrits dans le présent document; ceux-ci peuvent être librement utilisés par les instituts de recherche, les industriels et autres intéressés. Cependant, le CERN se réserve le droit de s'opposer à toute revendication qu'un usager pourrait faire de la propriété scientifique ou industrielle de toute invention et tout dessin ou modèle décrits dans le présent document.

Literary and scientific copyrights reserved in all countries of the world. This report, or any part of it, may not be reprinted or translated without written permission of the copyright holder, the Director-General of CERN. However, permission will be freely granted for appropriate non-commercial use.

If any patentable invention or registrable design is described in the report, CERN makes no claim to property rights in it but offers it for the free use of research institutions, manufacturers and others. CERN, however, may oppose any attempt by a user to claim any proprietary or patent rights in such inventions or designs as may be described in the present document.

ISSN 0007-8328
ISBN 92-9083-030-1

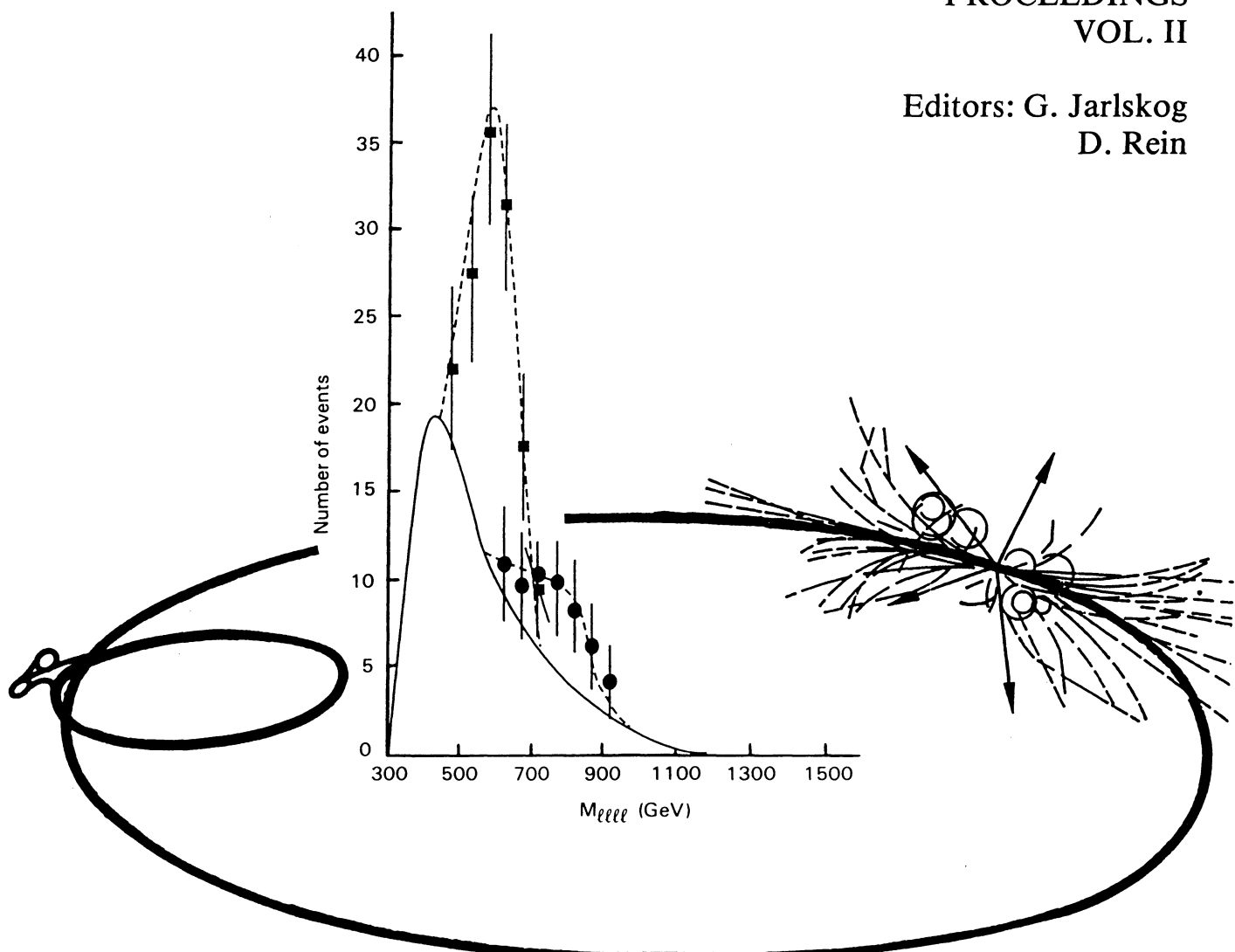
CERN 90-10
ECFA 90-133
Volume II
3 December 1990

EUROPEAN COMMITTEE FOR FUTURE ACCELERATORS

Large Hadron Collider Workshop

PROCEEDINGS
VOL. II

Editors: G. Jarlskog
D. Rein



Aachen, 4-9 October 1990



ABSTRACT

The aim of the LHC workshop at Aachen was to discuss the "discovery potential" of a high-luminosity hadron collider (the Large Hadron Collider) and to define the requirements of the detectors. Of central interest was whether a Higgs particle with mass below 1 TeV could be seen using detectors potentially available within a few years from now. Other topics included supersymmetry, heavy quarks, excited gauge bosons, and exotica in proton-proton collisions, as well as physics to be observed in electron-proton and heavy-ion collisions. A large part of the workshop was devoted to the discussion of instrumental and detector concepts, including simulation, signal processing, data acquisition, tracking, calorimetry, lepton identification and radiation hardness. The workshop began with parallel sessions of working groups on physics and instrumentation and continued, in the second half, with plenary talks giving overviews of the LHC project and the SSC, RHIC, and HERA programmes, summaries of the working groups, presentations from industry, and conclusions. Vol.1 of these proceedings contains the papers presented at the plenary sessions, Vol.2 the individual contributions to the physics sessions, and Vol.3 those to the instrumentation sessions.

SPONSORS

The workshop, which attracted roughly 500 participants including a sizeable group from industry, was organized by the European Committee for Future Accelerators and sponsored by the Commission of the European Communities, Deutsche Forschungsgemeinschaft, Deutscher Akademischer Austauschdienst, Bundesministerium für Forschung und Technologie, Philips Components, and CERN.



Volume I:	Plenary Sessions	
Volume III:	Instrumentation Working Groups	

CONTENTS

VOLUME II

PHYSICS WORKING GROUPS

A. Proton-Proton Collisions	1	A3. b physics	199
A1. Standard Model cross-sections	1	<i>Beauty at the LHC, G. Carboni et al.</i>	200
Standard Model cross-sections, <i>P. Nason</i>	2	Remarks on B-Physics with interactions of pp and e^+e^- , <i>A. Fridman, A. Snyder</i>	218
A new detector for small- p_t physics at LHC/SSC energies, <i>C. Da Via et al.</i>	6	Collider beauty physics at LHC, <i>S. Erhan et al.</i>	239
A fast and precise scintillating fiber tracking detector, <i>D. Bernard</i>	10	Possibilities for B-physics in fixed target mode at the LHC, <i>Y. Lemoigne, Y. Zolnierowski</i>	260
Total and elastic cross section, the experimental method, <i>G. Matthiae</i>	15	Fixed target physics at the SSC, <i>F. Grancagnolo</i>	277
Elastic scattering at LHC: a challenge to theory and experiment, <i>E. Leader</i>	22	Fixed target B physics at the LHC, <i>G. Fidecaro</i>	288
Detection of the tau-neutrino at the LHC, <i>K. Winter</i>	37		
Jets at the Large Hadron Collider, <i>P.T. Cox et al.</i>	50		
Production of direct photon at LHC and SSC, <i>P. Aurenche et al.</i>	69		
$\gamma\gamma$ production at LHC: a NLO order study of the "irreducible" background to $H^0 \rightarrow \gamma\gamma$, <i>P. Aurenche et al.</i>	83	A4. Top physics	295
Parton luminosities, W and Z cross sections and gauge boson pair production, <i>H. Kuijf et al.</i>	91	Summary and theoretical basis, <i>E. Reya et al.</i>	296
QCD corrections to Z pair production at LHC, <i>B. Mele et al.</i>	113	Top search: signal vs. background, <i>F. Cavanna et al.</i>	329
Heavy quark production at the LHC, <i>J.P. Guillet et al.</i>	116	Prospects for top search and top mass measurement, <i>G. Unal, L. Fayard</i>	360
A2. Event generators	129	Search for top decays to charged Higgs bosons, <i>M. Felcini</i>	414
Event generators for LHC, <i>F. Anselmo et al.</i>	130	Single top production: Wg fusion and top mass, <i>T. Moers et al.</i>	418
Structure functions, <i>H. Plotlow-Besch</i>	146		
Monte Carlo simulation of minimum bias events at the LHC energy, <i>G. Ciapetti, A. Di Ciaccio</i>	155	A5. Higgs physics	427
A comparison of bottom production in different event generators, <i>J.R. Cudell et al.</i>	164	The standard model Higgs at LHC: Branching ratios and cross-sections, <i>Z. Kunszt, W.J. Stirling</i>	428
Multi-jet event generators for LHC, <i>H. Kuijf et al.</i>	173	Experimental review of the search for the Higgs boson, <i>D. Froidevaux</i>	444
On the calculation of the exact $gg \rightarrow Zbb$ cross section including Z decay and b quark mass effects, <i>B. van Eijk, R. Kleiss</i>	183	Photon decay modes of the intermediate mass Higgs, <i>C. Seez et al.</i>	474
Vector boson production in association with jets, <i>W.T. Giele</i>	195	$HZ \rightarrow \gamma\gamma l^+l^-$. A possibility for an extremely high luminosity collider, <i>A. Grau et al.</i>	488
		Search for $pp \rightarrow H^0 \rightarrow Z^0 Z^0 \rightarrow \mu^+\mu^-\mu^+\mu^-$ at the LHC, <i>A. Nisati</i>	492
		Search for $H \rightarrow Z^*Z^* \rightarrow 4$ leptons at LHC, <i>M. Della Negra et al.</i>	509
		$H \rightarrow \tau^+\tau^-$ detection at LHC, <i>L. Di Lella</i>	530
		$H^0 \rightarrow \tau^+\tau^-$ detection at the LHC, <i>K. Bos et al.</i>	538
		Intermediate mass Higgs search	
		$pp \rightarrow Z(\rightarrow l^+l^-) + H(\rightarrow jj); W(\rightarrow l^\pm\nu) + H(\rightarrow jj)$ —Resolution and pile-up studies, <i>L. Poggioli</i>	547
		Tagging a heavy Higgs boson, <i>M.H. Seymour</i>	557
		A comparison of exact and approximate calculations of Higgs boson production at the LHC, <i>U. Baur, E.W.N. Glover</i>	570
		Testing the Higgs sector of the minimal supersymmetric standard model at LHC, <i>Z. Kunszt, F. Zwirner</i>	578

A6. Supersymmetry	605	B. Electron-Proton Collisions	829
Introduction, <i>G. Ridolfi et al.</i>	608	Kinematics and resolution at LEP x LHC, <i>J. Blümlein et al.</i>	830
Cascade decays of gluinos and squarks, <i>A. Bartl et al.</i>	615	LEP+LHC deep inelastic scattering: Structure functions	
Experimental aspects of gluino and squark searches, <i>C. Albajar et al.</i>	621	and final states, <i>G. Ingelman</i>	834
Neutralino and chargino production in association with gluinos and squarks, <i>H. Baer et al.</i>	654	Structure function measurement and QCD-tests at LEP X LHC,	
Charginos and neutralinos, <i>R. Barbieri et al.</i>	658	<i>J. Blümlein</i>	850
Sleptons, <i>F. Del Aguila et al.</i>	663	Extracting the gluon density from the longitudinal structure function,	
Broken R-parity, <i>P. Binetruy et al.</i>	666	<i>N. Magnussen, G.A. Schuler</i>	858
Detection of heavy stable exotics, <i>M. Drees, X. Tata</i>	676	Small -x physics at LEP x LHC, <i>J. Bartels, G.A. Schuler</i>	865
Signals for a superlight gravitino, <i>M. Drees, J. Woodside</i>	681	Electroweak radiative corrections at LEP + LHC, <i>H. Spiesberger</i>	888
		Leading log radiative corrections to deep inelastic scattering at	
		LEP/LHC, <i>J. Blümlein</i>	897
		Gluon extraction from charm and bottom production	
		at LEP/LHC, <i>K.J. Abraham et al.</i>	899
		Heavy quark physics in ep collisions at LEP+LHC, <i>A. Ali et al.</i>	917
		Single W and Z production at LEP/LHC, <i>U. Baur et al.</i>	956
		Searching for the Higgs in ep collisions at LEP/LHC,	
		<i>G. Grindhammer et al.</i>	967
		Contact interactions and new vector bosons at LEP/LHC, <i>F. Cornet,</i>	
		<i>H.-U. Martyn</i>	986
		Electroweak symmetry breaking by a strong sector at LEP LHC,	
		<i>D. Dominici, F. Feruglio</i>	1001
		Radiative corrections to deep inelastic scattering in the presence	
		of an additional Z' at LEP x LHC, <i>J. Blümlein et al.</i>	1010
		Excited leptons at LEP/LHC, <i>Ch. Berger et al.</i>	1014
		Leptoquark production at the LHC/LEP e-p collider, <i>N. Harnew</i>	1022
		Slepton-squark production and decay in ep collisions,	
		<i>A. Bartl et al.</i>	1033
		Prospects of supersymmetry searches at the LEP/LHC,	
		<i>M. Besançon</i>	1040
A7. New vector bosons	685	C. Heavy-Ion Collisions	1057
Introduction, <i>P. Chiappetta</i>	687	C1. Theoretical aspects	1057
Neutral E_6 gauge bosons at LHC, <i>M.C. Gonzales-Garcia, J.W.F. Valle</i>	689	Lattice QCD predictions for very hot nuclear matter, <i>B. Petersson</i>	1058
Z' from superstring-inspired E_6 models, <i>F. Del Aguila et al.</i>	698	Chiral phase transition at finite temperature and density,	
Z' into leptons, <i>P. Camarri et al.</i>	704	<i>A. Barducci et al.</i>	1069
Z' into jets, <i>J.P. Pansart</i>	709	General conditions in heavy ion collisions at the LHC, <i>U. Heinz et al.</i>	1079
WZ pair production in the left-right model, <i>D. Cocolicchio et al.</i>	710	Strangeness and antimatter production at the LHC, <i>P. Koch et al.</i>	1091
Production of W_R and W_L bosons from superstring-inspired E_6 models, <i>F. Aversa et al.</i>	717	The VENUS model for heavy ion collisions at LHC energies,	
W' signal and background at LHC, <i>F. Botterweck</i>	722	<i>K. Werner et al.</i>	1098
Production of vector bosons in the BESS model, <i>R. Casalbuoni et al.</i>	731	Results from VENUS 3.11 at LHC energies, <i>P. Cerello et al.</i>	1106
Isoscalers and excited bosons at LHC, <i>J.L. Kneur, G. Moustaka</i>	737	Results from PYTHIA at LHC energies, <i>M. Masera, L. Ramello</i>	1115
Mass discovery limits for new neutral gauge bosons from alternative symmetry breaking, <i>P. Chiappetta, M.C. Cousinou</i>	743	Results of the event generator FRITIOF, <i>U. Goerlach</i>	1123
Compositeness of Z^0, Z' at the LHC, <i>T. Medcalf</i>	752	Hadron production in nucleus-nucleus collisions at LHC energies in the dual parton Monte-Carlo model DTUNUC, <i>J. Ranft</i>	1127
		Background studies for dilepton experiments at the LHC, <i>P. Cerello</i>	1132
		Heavy quark resonances in heavy ion collisions:	
		from SPS to LHC, <i>F. Karsch</i>	1141
A8. Alternative symmetry breaking and exotica	757		
Introduction, <i>S. Dimopoulos, M. Lindner</i>	758		
Electroweak symmetry breaking and the TeV scale, <i>S. Dimopoulos, M. Lindner</i>	759		
$V_L V_L$ scattering: chiral Lagrangian approach, <i>A. Dobado et al.</i>	768		
WZ production from the BESS model, <i>R. Casalbuoni et al.</i>	786		
$W_L^\pm Z_L^0$ production at the LHC from the strongly interacting symmetry breaking sector—Experimental aspects, <i>I. Josa et al.</i>	796		
Compositeness, <i>E.N. Argyres et al.</i>	805		
Signatures for geometrical flavour interactions and B + L violation at the LHC, <i>J. Ellis et al.</i>	820		
Summary, <i>S. Dimopoulos, M. Lindner</i>	827		

Initial state scattering in nuclear Drell-Yan and J/ ψ production, <i>S. Gavin</i>	1154
Rates of thermal photons and lepton pairs in heavy ion collisions at LHC, <i>P. V. Ruuskanen</i>	1164
Dimuon background to thermal signatures in heavy ion collisions, <i>S. Gupta</i>	1174
Shadowing effect in heavy ion collisions at LHC energy, <i>C. Castorina, A. Donnachie</i>	1186
Minijet production in A+A at the LHC, <i>K.J. Eskola</i>	1195
Intermittency: an update with LHC in view, <i>J. Seixas</i>	1203
Cascading and intermittency, <i>I. Sarcevic</i>	1214
Coherent processes in heavy ion collisions at the LHC, <i>K.J. Abraham et al.</i>	1224
C2. Experimental aspects	1235
Experimental aspects of heavy ion physics at LHC energies, <i>H.J. Specht</i>	1236
Dilepton physics with ions at LHC, <i>P. Sonderegger</i>	1252
Remarks on hyperon detection at LHC, <i>E. Quercigh</i>	1261
Boson interferometry at RHIC and LHC (I), <i>D. Ferenc, G. Paic</i>	1264
D. Additional Papers for Volume III	1271
D2. Signal processing	1271
Vacuum microelectronics, <i>G.H. Grayer</i>	1272
The role of analogue circuitry in LHC/SSC triggering, <i>G.H. Grayer</i>	1279
D7. Muon identification	1289
Mass resolution for heavy Higgs particle search, <i>Th. Moers et al.</i>	1290



The Organizing Committee has the pleasure to thank one of the participants of this LHC Workshop at Aachen, Jan Hladky from the Czechoslovakian Academy of Sciences (CSAV) at Prague, for the charming artist's sketches of various Aachen sites he contributed to this Volume.

A: PROTON-PROTON COLLISIONS

Standard Model Cross Sections

P. Nason, convener

INFN, Gruppo Collegato di Parma

A1: STANDARD MODEL CROSS-SECTIONS

The working group on Standard Processes at the LHC was originally assigned the task of studying the cross sections for various standard processes of interest at the LHC. Two additional tasks were also assigned to this group: the measurement of the total and elastic cross section, and the study of the possibility for doing neutrino physics at the LHC. The group was therefore subdivided into a Total and Elastic cross section group, a Neutrino Physics group, and a Hard Processes group. The Hard Processes group was further subdivided into five subgroups, dealing with the structure functions, the physics of the intermediate vector bosons, the physics of direct photons, jets, and heavy quark production.

By its own nature, the group had to deal with all topics which were not considered central enough to require a single, dedicated working group, like the Higgs and Top searches, but on the other hand are very important in order to understand and model the physics at the LHC. Most of our work was the compilation of cross sections for everyday physics processes, with a considerable effort in trying to understand to what extent our present knowledge can be extrapolated to supercollider energies. Some processes that have impact on other areas of LHC physics have received particular attention. The $\gamma\gamma$ process, because of its importance as a background to an intermediate mass Higgs, was considered in detail. The cross sections for b and c production, which have an impact on the possibility of doing b physics and neutrino physics at the LHC, were also fully discussed, with much emphasis on the large amount of uncertainty that we have in their calculation. Some results of the working group are quite exciting, and stand by themselves as interesting physics topics. The limits on parton compositeness, arising both from jet and direct photon cross sections have considerable value, and certainly will be done at the LHC. A particularly interesting topic which was considered is the possibility of testing for anomalous couplings in the WWZ and $WW\gamma$ sectors, via WZ and $W\gamma$ detection. Both these topics have been fully discussed from an experimental point of view, at least at the level which is possible without a specific detector design. For the case of the $W\gamma$ process, the study of γ detection performed in the section on direct

photons was quite essential.

We have tried to clarify in which areas our knowledge is sound, and in which areas improvement is needed. We hope therefore that the work done in this study group will be a useful starting point for future studies.

Summary of the studies

Total and Elastic Cross Sections.

Conveners: A. Martin and G. Matthiae

Theorists: C. Bourrely, P. Gauron, E. Leader, A. Martin, B. Nicolescu, E. Predazzi, J. Soffer and T. T. Wu;

Machine experts: B. Jeanneret and W. Scandale;

Experimentalists: G. Bellettini, D. Bernard, J. Bourotte, M. Bozzo, T. Camporesi, R. Castaldi, C. Da Via, R. De Salvo, M. Haguenauer, R. M. Mondardini, G. Sanginetti, J. Timmermans, G. Tonelli, O. Ullaland and S. Zucchelli.

List of contributions:

- C. Da Via, R. De Salvo, M. R. Mondardini and J. Orear,
A new detector for small- p_t physics at LHC/SSC energies.
- D. Bernard,
A fast and precise scintillating fiber tracking detector.
- G. Matthiae,
Total and elastic cross section: the experimental method.
- E. Leader,
Elastic scattering at the LHC: a challenge to theory and experiment.

Neutrino Physics

Convener: K. Winter;

Theorists: A. De Rujula and A. B. Kaidalov;

Experimentalists: L. Camilleri, A. Capone, U. Dore, A. Ereditato, E. Fernandez, J. Gomez, P. F. Loverre, V. Palladino, F. Pietropaolo, L. Rolandi, R. Santacesaria, S. Schlenstedt and F. Vannucci.

List of contributions:

- K. Winter,
Detection of the tau-neutrino at the LHC.

Hard processes

Convener: P. Nason;

Theorists: P. Aurenche, M. Fontannaz, J. P. Guillet, H. Kuijf, T. Matsuura, B. Mele, L. Trentadue and D. Zeppenfeld;

Experimentalists: M. Bonesini, L. Camilleri, T. Cox, M. Kienzle-Focacci, P. Lubrano, M. Nessi, F. Nessi-Tedaldi, F. Pastore, M. Pepe, H. Plothow-Besch, M. Werlen and D. Wood.

List of contributions:

- Jets at the Large Hadron Collider.
P. T. Cox, J. P. Guillet, P. Lubrano, M. Nessi and F. Nessi-Tedaldi.
Cross sections for jet production, limits on parton compositeness and multi-jets.
- Production of direct photon at LHC and SSC.
P. Aurenche, M. Bonesini, L. Camilleri, P. Chiappetta, M. Fontannaz, J. P. Guillet, M. N. Kienzle-Focacci, M. Werlen.
Cross section for production of photon, with and without isolation cuts. Probing the gluon structure function at small values of x. Detailed discussion of photon detectability and backgrounds to the photon signal.
- $\gamma\gamma$ production at LHC: a NLO order study of the "irreducible" background to $H^0 \rightarrow \gamma\gamma$.
P. Aurenche, M. Bonesini, L. Camilleri, M. Fontannaz and M. Werlen.
Study of experimental cuts needed for separating the intermediate Higgs signal from the $\gamma\gamma$ background.
- Parton luminosities, W and Z cross sections and gauge boson pair production.
H. Kuijf, G. Martinelli, T. Matsuura, B. Mele, P. Nason, F. Pastore, M. Pepe,

A NEW DETECTOR FOR SMALL- P_t PHYSICS AT LHC/SSC ENERGIES

H. Plothow-Besch, L. Trentadue, D. Wood, D. Zeppenfeld.

Parton densities, W and Z cross sections and differential distributions, Drell-Yan pair production, Gauge boson pair production. Possibility of detecting deviations from the standard model three-vector-bosons couplings via WZ and $W\gamma$ production processes.

- QCD corrections to Z pair production at the LHC.

B. Mele, P. Nason and G. Ridolfi.

Results of a new calculation of strong radiative corrections to Z pair production processes.

- Heavy quark production at the LHC.

J. P. Guillet, P. Nason, H. Plothow-Besch.

Total and differential cross sections for the production of top, bottom and charmed hadron. Bottom and charm multiplicity in high p_\perp jets. Production of heavy quark at high p_\perp : the fragmentation function of the b quark.

presented by

Maria Rosa Mondardini

C. Da Via¹⁾, R. DeSalvo²⁾, M.R. Mondardini¹⁾ and J. Orear¹⁾

1) Cornell University, Ithaca, N.Y.

2) CERN/LAA Geneva, Switzerland

Abstract

Elastic pp (or $p\bar{p}$) scattering at microradian angles provides an absolute luminosity calibration as well as a measurement of the total pp (or $p\bar{p}$) cross section, the slope of the elastic scattering cross section with t (the square of the momentum transfer) and the ratio of real to imaginary scattering amplitudes. A detector is proposed which, given favourable beam design, can measure, at LHC/SSC energies, elastic scattering and small angle processes which are usually missed by a typical 4π detector. The proposed detector is made out of a scintillating fibers bundle. Light from these fibers is transported via fiber optics and read out with 2 Image Intensifiers and a Charge - Coupled Device (CCD). The active part of the detector is placed directly in the vacuum of the beam pipe and is moved by a high precision mechanism. Two couples of such detectors (symmetric in the horizontal or vertical plane) would be located along the beam pipe at symmetric positions respect to the interaction point.

1 The Detector

The proposed detector is shown schematically in Fig.1. The scattered particle travels $\sim 60\text{ mm}$ lengthwise along a bundle of $100\text{ }\mu\text{m}$ diameter scintillating fibers with 9 mm radius semi-circular cross section. Each fibre has an hexagonal cross section. The core of the fibers is a polystyrene based plastic scintillator with p-terphenyl as primary fluor and with $2000\text{ part per million}$ of 3HF (3-Hydroxy-Flavone, a yellow-green emitting waveshifter), surrounded by 12 mm PMMA cladding. 3HF is characterized by good radiation resistance (above 10 MRad), fast decay time (around $5 - 10\text{ nsec}$), and a large Stokes shift (poor self absorption and good attenuation length), properties which compensate for its poor scintillation efficiency ($\sim 36\%$). The front face of the fibers is Aluminum plated to enhance the light output, while the back face is glued to the light pipe. The entire bundle is sputtered with a heavy metal to slow outgassing (the same thing is done to the counter). The bundle is glued into a metal cradle with high vacuum grade epoxy and no material is foreseen on the front or bottom faces. The fibers are rotated at 1 degree from the beam axis to provide full efficiency and improve resolution by the method of center of gravity. Light from these fibers is transported by a bundle of non scintillating glass fibers to the readout system. The bundle is made out of $20\text{ }\mu\text{m}$ diameter glass fibers and has a 10 mm radius circular cross section. This

bundle traverses the flange between vacuum and air. The glass bundle vacuum seal is mounted on bellows and this allows the bottom of the bundle to be aligned parallel to beam by means of a set of three screws. Only half of the glass fibre bundle is used for piping the image coming from the active bundle to the read out chain. We take advantage of the remaining half to read out a backup scintillating counter which is housed behind the scintillating fibers bundle and covers the same solid angle (Fig.2). The counter is a $20 \times 10 \times 10$ mm scintillating plate with horns. The shape is such that it can fit with the counter located in the detector below to provide a position calibration.

2 Readout System

The readout chain is mounted directly on the conflat flange. It consists of two proximity-focused micro channel plate Image Intensifiers followed by a CCD. The Image Intensifiers are gated XX 1450 MCP intensifiers with S20 photocathode and P46 phosphore screen (DEP). The optical gain of each one is about 1000 ph/ph. The first Image Intensifier is used as a gate. Only at the moment of bunch crossing the potential of the input face of the MCP is raised to the operational value, allowing the free passage of photoelectrons through it. The second Image Intensifier can be used as a trigger: the charge collected in the phosphor screen can be extracted and this pulse can be used as a trigger for the data acquisition of the CCD. From the second II the light is transferred to the CCD by a taper. If the level trigger is satisfied, the event initially stored in the image zone is transferred on the memory zone and digitized. Otherwise, a fast clear ($1 \mu\text{sec}$) of the image zone is performed using the antiblooming electrodes [1].

3 Requirement on Machine Design

pp total cross section is expected to be about 110 mb at $\sqrt{s} = 16 \text{ TeV}$ [2]. According to this value, in order to measure the ρ value and to use the coulomb amplitude for normalization of $d\sigma/dt$ it is necessary to get to scattering angles smaller than $3 \mu\text{rad}$. The possibility of reaching this value does not depend only on the detector but primarily on the accelerator lattice. The machine parameters must be such that beam divergence at the scattering point be less than the minimum scattering angle to be measured. The values of the β function at the interaction point and at the detector position are the limiting factors and should be foreseen and studied at the stage of machine design. Assuming some values for the machine parameters and for the expected total cross section, it is possible to do some easy calculation that give an idea of these requirements.

We set our goal at reaching an angle $\Theta_{\min} = 2.5 \mu\text{rad}$, where the coulomb cross section would be ~ 4 times the nuclear cross section. We take the design normalized beam emittance of LHC of 3.8 mm mrad [3] ($\epsilon^* = \gamma\sigma^2/\beta^*$, β^* being the beta value at the interaction point and γ the energy in proton rest mass units). Our value of Θ_{\min} is smaller than the typical angular divergence of the beam at normal β values. We require a beam divergence $\Delta\Theta = 0.14\Theta_{\min}$, which is $0.35 \mu\text{rad}$. These assumptions give for β at the interaction point $\beta^* = 3.9 \text{ km}$. Then,

assuming our detector can go as close as 1 mm from the beam axis, an effective length $L_{eff} = 400 \text{ m}$ is required, implying at the detector the value $\beta_{det} = 40 \text{ m}$. These values would give also a beam spot size $\Delta x = 138 \mu\text{m}$, corresponding to a detector active zone at 7σ from the beam axis.

These calculations have been done assuming no beam scraping. Since our measurement will be done on a dedicated run, we can assume we will use a reduced emittance beam from SPS. The same calculations will then relax the beam specifications to $\beta^* = 1900 \text{ m}$, $\beta_{det} = 85 \text{ m}$ with a spot size $\Delta x = 140 \mu\text{m}$.

4 Future Operation

For easy testing, the prototype of this detector has been designed to fit the dimensions of already existing "Roman Pots", that have been used at Fermilab by the E710 collaboration. Experiment E710 has been the last experiment to measure elastic and total cross sections [4]. The experimental apparatus was located in one of the long straight sections at the Tevatron Collider and consisted of small drift chambers in "Roman Pots". Our detector will replace the "pot" and will be mounted on its support with the conflat flange. The support is provided with a high precision moving mechanism that can bring the bundle close to the circulating beam with a repositioning accuracy of $\sim 5 \mu\text{m}$ and an absolute location accuracy of $\sim 20 \mu\text{m}$. Both the pots and the experimental area are still available at Fermilab and a full chain of 4 detectors can be tested at Tevatron during next collider run (1992).

References

- [1] R. Ansorge et al., Nucl. Instr. and Meth. A265 (1988) 33.
- [2] M. Block et Al., Phys. Rev. D41, 978 (1990).
- [3] G. Brianti, CERN/AC/FA/90-03 LHC Note 134.
- [4] N. Amos et al., Nucl Phys. B16 (1990) 431-432.

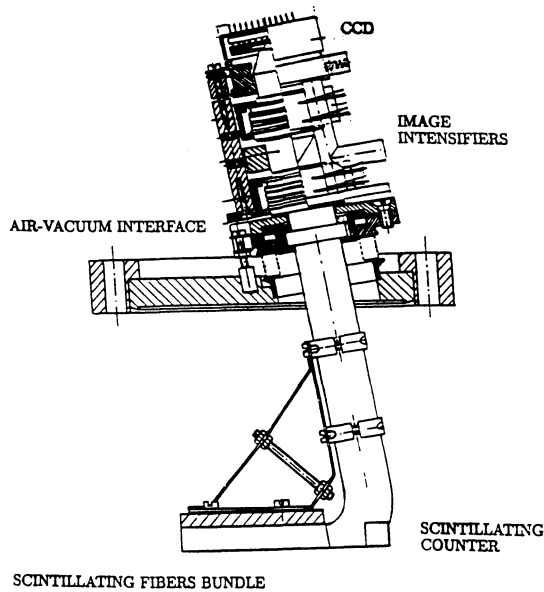


Fig. 1 Schematic view of the detector.

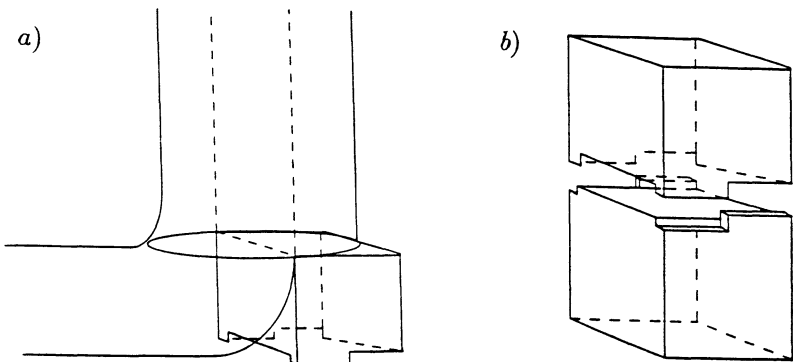


Fig. 2 a) The scintillating counter is housed behind the scintillating fibres bundle and is read out with half of the glass fibers bundle. b) The shape of the counter is such that it can fit with the counter located in the detector below to provide a position calibration.

A fast and precise scintillating fiber tracking detector

D. Bernard/Ecole Polytechnique, PALAISEAU, FRANCE

Abstract

A scintillating fiber tracking detector has been designed for the UA4-2 experiment. A high optical multiplexing factor allows the reading of hundreds of fibers with a few tens of photomultipliers. The tests of a prototype show that the efficiency after reconstruction is larger than 99% and that the resolution is better than $100\mu m$. This detector could be used close to a high energy high luminosity hadronic collider like LHC, thanks to its high rate capability.

1 Introduction

The experiment UA4 has measured the real part of the elastic amplitude at the SPS collider, at $|t| = 0$ and $\sqrt{s} = 546 GeV$ [1]. The measured value $\rho = 0.24 \pm 0.04$ was found higher than the predicted value of $0.11-0.13$ by 3 standard deviations. This astonishing result has lead to a lot of theoretical work and could be the indication of a new phenomenon in very high energy hadronic physics.

The UA4-2 experiment plans to perform a new measurement of ρ with an improved uncertainty. The statistical uncertainty will benefit from the increased luminosity since the commissioning of ACOL. The systematics will also be improved [2] with new optics giving access to the Coulomb region. The two coordinates of the scattered hadrons will then have to be measured with a precision of $100\mu m$. The charge division chamber which was measuring the transverse coordinate with a precision of $0.5mm$ [3] will then be replaced by a new detector. The specifications list for this new detector is the following:

- i) a resolution better than $100\mu m$
- ii) insensitivity to the beam peak-up
- iii) a good efficiency down to the bottom of the detector
- iv) resistance to radiation

A scintillating detector fulfills easily the last three requirements. The use of scintillating fibers provides the large segmentation needed for the required resolution.

In the following we present the principle of operation of the detector, its construction, the electronics, the computation of an optimal coding, and the choice of the parameters of the detector. Then the results of the beam test are given.

2 The principle of operation

The detector is made of a few planes ($n_{planes} = 8$ in our prototype) of parallel fibers with a diameter of $1mm$. The staggering of the planes (figure 1) provides the resolution σ : with a step of $1.2mm$, $\sigma = step/(n_{plane}\sqrt{12}) = 40\mu m$.

The fibers are read by photomultipliers (Cf. section 4). As the occupancy in the fibers is very low for an elastic event, they can be grouped on a small number of photomultipliers with a large multiplexing factor. The coding of the fibers onto the PM's is carefully chosen so that the probability that a real track fake a ghost track is minimized (Cf. section 5).

In our prototype, there are 50 fibers per plane, covering an area of $(60mm)^2$, and the 400 fibers are multiplexed on 40 photomultipliers. After an amplification, the signal is discriminated either on-line with a discriminator, or off-line after being digitized by an ADC. A fiber is considered as being hit if its photomultiplier is hit. A track is then simply reconstructed as a set of aligned fibers (figure 2).

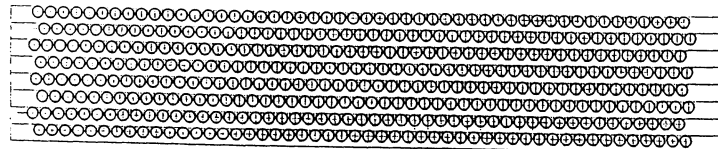


Figure 1: The staggering of the fibers.

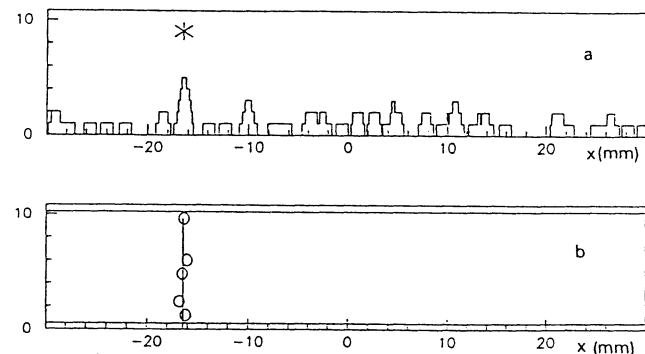


Figure 2: a) the projection on the horizontal plane of the hit fibers related to a given event. The * indicates the location of the drift chamber track. b) the reconstructed track and the associated fibers.

3 The construction of the prototype

We have chosen the Optecktron S-101-A fibers for their high number of photons (around 8 photo-electrons per millimeter ($\gamma e/mm$) after a S20 photocathode). Now-a-days many companies produce scintillating fibers¹. Several samples from various companies are under test.

The fibers were selected on their diameter, cut, polished, and tested with a radioactive source; they were then glued on an aluminum comb. The "V" shape (figure 3) of the comb centers the fibers independently on their diameter with a precision of $7\mu m$.

The planes were then glued together and the bottom of the detector was polished. The detector was then "knitted": each fiber was brought to its photomultiplier; the bundles were glued, cut, and polished. Then the bottom of the detector was aluminized.

4 The electronics

Small diameter — $1/2"$ — individual photomultipliers were chosen² for the absence of cross-talk. The size of the photocathode fits largely the size of a bundle of 10 fibers. A gain of 4.10^6 at 1000V provides a typical $10mV$ pulse when a minimum ionizing particle crosses a fiber at right angle. The signal is

¹Bicron, Kyowa, Nuclear Enterprises, Optecktron, Polivar.

²R647 from Hamamatsu

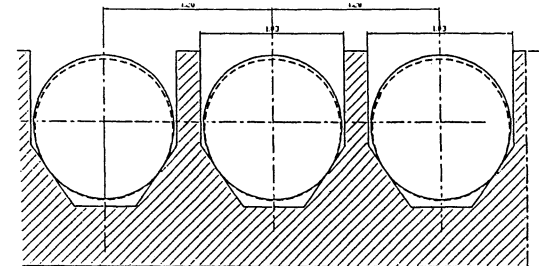


Figure 3: The schema of a comb.

The position of 2 fibers with different diameters is shown.

further amplified by a factor of 10 by a home made amplifier. Figure 4 shows the spectrum of the signal.³

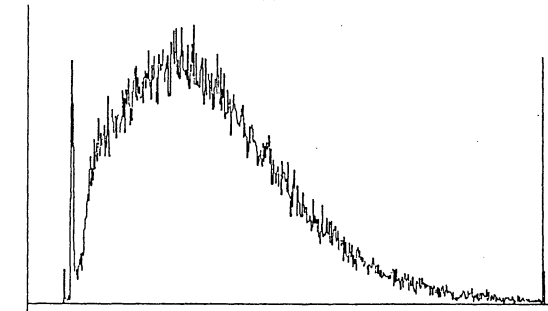


Figure 4: the spectrum of the signal of a photomultiplier reading one fiber. The fiber was exposed to a Sr^{90} source at a distance of 50cm. The trigger was formed from the signal of a photomultiplier at the other end of the fiber in coincidence with an external scintillator: $T = F_2.(Sc_1.Sc_2)$.

After calibration with a single photon peak, we find a mean value of $5.1 \gamma e$. In the beam test (section 7), the signal was discriminated; in the final experiment, it will be digitized to allow for a more detailed analysis.

5 The computation of an optimal coding

We call coding the assignment of the fibers to their photomultiplier. The map is chosen so that the set of photomultipliers illuminated by a given track do not simulate a ghost track in another part of the detector.

The fibers are numbered: $f_{i,j}, i=1, n_f, j=1, n_{plane}$ where n_f is the number of fibers per plane. We call a couple c_i the set of $2 * n_{plane}$ fibers belonging to the consecutive positions i and $i+1$.

For $i_1 = 1, n_f$ and $i_2 = 1, n_f$, with $|i_1 - i_2| > 1$, we compute the number n_{i_1, i_2} of the common photomultipliers of the couples c_{i_1} and c_{i_2} . The higher n_{i_1, i_2} , the higher the probability that a track going through the fibers of the couple c_{i_1} simulates a ghost track in the fibers of the couple c_{i_2} . We

³digitized by an ADC LRS 2249A

therefore form the distribution of the n_{i_1, i_2} . Let m be the maximum of the n_{i_1, i_2} , and $k(m)$ the number of occurence of $n_{i_1, i_2} = m$ (i.e. the content of the bin m). At a given value of m , we minimize $k(m)$ by a try-and-error method: we exchange the coding of two fibers; if $k(m)$ is unchanged or becomes smaller we keep the new coding; if $k(m)$ becomes worse we exchange the fibers back.

When $k(m)$ is zero m decreases by one unit, so we also minimize the value of m . A stable minimum is rapidly found — in a few million tries. We have shown that this procedure minimizes the probability that a track fakes a ghost track.

6 The choice of the parameters of the detector

The diameter of the fibers was chosen as a compromise between flexibility and efficiency. A diameter of 1mm was chosen providing about $6 \gamma e/mm$ after a path of 30cm in the fiber. With a step of 1.2mm and a sensitive area of $(60\text{mm})^2$ we have 50 fibers per plane. We now have to choose the number of planes and the number of photomultipliers: the higher n_{PM} and n_{plane} , the easier the separation of the track from the ghosts. This was studied with a MonteCarlo simulation.

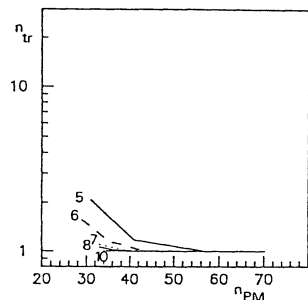


Figure 5: The number of reconstructed tracks as a function of n_{PM} .

The number of planes of fibers used in the simulation is indicated for each curve

The number of reconstructed tracks is shown in figure 5 as a function of n_{PM} and n_{plane} . Here at least $n_{plane} - 4$ aligned fibers were required to form a track. At high value of n_{PM} (above 40-50) the detector behaves very well: the number of reconstructed tracks is equal to the number of incident tracks. At lower value of n_{PM} the number of ghosts increases. We also see that at a given value of n_{PM} the number of ghosts decreases when n_{plane} increases.

The “coding capacity” clearly increases when the number of planes or the number of photomultipliers increases. The prototype was built with 8 planes of fibers and 40 photomultipliers.

7 The beam tests

The prototype was exposed to a $-70\text{GeV}/c$ pion beam in the X7 beam line at CERN in two three-days runs in june and july 1990. An external measurement of the position of the incoming particle was provided by a UA4 drift chamber [3], and the trigger was formed from a coincidence of counters. An hodoscope made of 6 scintillating fingers with a width of 5mm was placed after the detector.

The spectrum of the number of hit photomultipliers n_h shows a non Poissonian tail (fig 6a) which was not present in a previous cosmic test. The tail is depressed by a factor 5 by the requirement that no more than one finger is hit, so that it is likely to be due to the interaction of the pions in

the detector and/or to multitracks events — the depth of the detector being equivalent to 2% of an interaction lenght.

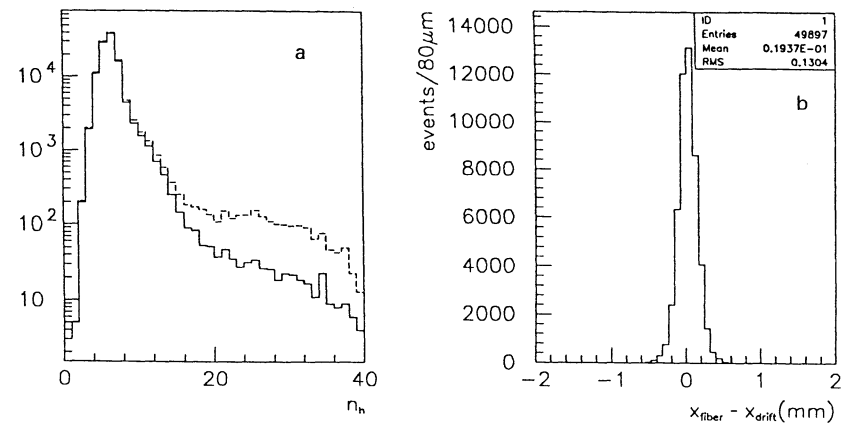


Figure 6: a) the distribution of the number n_h of hit photomultipliers.

(dashed curve: no cut; solid curve: finger cut (see text)).

b) the distribution of $x_{fiber} - x_{drift}$.

For each event the cut on the number l of aligned hit fibers was applied at the maximum of the histogram of figure 2. It was further asked that l be larger or equal to 2. The efficiency after reconstruction is estimated from the fraction of events having a track in the fiber detector compatible with the track in the drift chamber, and is found equal to 99.4%. The inefficiency is dominated by the contribution from the tail — actually in the n_h peak it is smaller than 10^3 .

An upper bound of the resolution is obtained from the width of the distribution of $x_{fiber} - x_{drift}$ (figure 6b). The resolution of the drift chamber in this test was of the order of $100\mu\text{m}$, including $70\mu\text{m}$ due to the time jitter of the trigger, so that the resolution of the fiber detector is lower than $100\mu\text{m}$, whereas the MonteCarlo study predicts $40\mu\text{m}$ for one track events.

8 Conclusion

A scintillating fiber tracking detector has been designed, built and tested for the UA4-2 experiment. It is fast and radiation hard; the ultimate resolution seems to be limited to $20 - 40\mu\text{m}$ by the diameter of high efficiency fibers — $(200 - 500\mu\text{m})$. All these features make this detector a particularly convenient tracking detector for an elastic and diffractive experiment close to a high energy high luminosity hadronic collider like LHC.

References

- [1] D. BERNARD et al., UA4 collaboration, Phys.Lett.B 198 (1987) 583.
- [2] CERN/SPSC 90-9, SPSC/P250.
- [3] J. BUSKENS et al., Nucl. Instr. and Meth., 207 (1983) 365.

TOTAL AND ELASTIC CROSS SECTION THE EXPERIMENTAL METHOD

G. MATTHIAE

Dipartimento di Fisica, Università di Roma II, *Tor Vergata*,
and
INFN, Sezione di Roma *Tor Vergata*

Introduction. A review of the experimental results on total cross section and elastic scattering at high-energy, up to $\sqrt{s} = 1.8$ TeV, is given by Denegri^[1] while the theoretical framework and present expectations at LHC were recently discussed by Leader^[2] and Martin^[3]. In this note we discuss only a few basic points on the experimental method and the requirements on the optics of the insertion.

An accurate measurement of the luminosity, as done at the ISR with the Van der Meer method, will not be possible at LHC. Therefore, the total cross section has to be measured with the luminosity independent method, as at the SPS Collider^[4] and at Fermilab^[5]. From the simultaneous measurement of low- t elastic scattering and of the rate of the inelastic events one obtains

$$\sigma_{tot} = \frac{16\pi}{1 + \rho^2} \frac{(dN_{el}/dt)_{t=0}}{N_{el} + N_{inel}} \quad (1)$$

where $(dN_{el}/dt)_{t=0}$ is derived by extrapolation of the differential elastic rate to $t = 0$. A precise knowledge of the parameter ρ which is the ratio of the real to the imaginary part of the amplitude in the forward direction is not needed because its numerical value is around 0.1 – 0.2 and, at least in first instance the aim is to measure σ_{tot} with an error of (3 – 4)%.

Elastic scattering at low- t . The technique of measuring elastic scattering is based on the use of high-resolution detectors placed inside "Roman pots" in an insertion with suitable optics. Elastic events are identified by detecting both scattered protons in coincidence and demanding the collinearity of their trajectories. The recently developed technique of the scintillating fibers was discussed in the ECFA study group and looks very promising^[6].

At low- t the differential cross section is usually described by the simple exponential e^{-bt} . At LHC we expect^[1] $b \approx 20 \text{ GeV}^{-2}$. In order to extrapolate dN_{el}/dt to the optical point by not more than about 10%, the minimum value of t should be $|t_{min}| \approx 5 * 10^{-3} \text{ GeV}^2$, which corresponds to $\vartheta_{min} \approx 10 \mu\text{rad}$, a very small angle indeed.

The basic requirements for an insertion to be suitable to the detection of elastic scattering are well known^[7] and can be summarised as follows. The displacement x at the detector is written (in either horizontal or vertical plane) as a function of the displacement x^* at the crossing point and of the scattering angle ϑ as

$$x = \sqrt{\beta/\beta^*} (\cos \Delta\psi + \alpha^* \sin \Delta\psi) x^* + (\sqrt{\beta^*\beta} \sin \Delta\psi) \vartheta \quad (2)$$

where β^* and β are the values of the betatron function at the crossing point and at the detector respectively. The phase advance of the betatron oscillations from the crossing to the detector is $\Delta\psi = \int ds/\beta(s)$ and $\alpha^* = -\frac{1}{2}(d\beta^*/ds)$. The beam size Δx and the beam angular divergence $\Delta\vartheta$ are written in terms of the emittance ϵ (defined at the one r.m.s. value) as $\Delta x = \sqrt{\epsilon\beta}$ and $\Delta\vartheta = \sqrt{\epsilon/\beta}$. The quantity $\sqrt{\beta^*\beta} \sin \Delta\psi$ represents the effective distance L_{eff} of the detectors from the crossing point.

The minimum distance of approach of the detectors to the beam axis is proportional to Δx , i.e. it can be written as $x_{min} = K\Delta x = K\sqrt{\epsilon\beta}$. At the SPS Collider it was empirically found $K \sim 20$. With a more sophisticated system of scraping^[8] one may hope to get a smaller value of K at LHC.

The minimum value of the scattering angle will then be

$$\vartheta_{min} = \frac{K\sqrt{\epsilon}}{\sqrt{\beta^*} \sin \Delta\psi} + \frac{\sqrt{\epsilon}(\cos \Delta\psi + \alpha^* \sin \Delta\psi)}{\sqrt{\beta^*} \sin \Delta\psi} \quad (3)$$

In order to reach a small ϑ_{min} , the first requirement is clearly that β^* should be large. One may then ask to have the β -function symmetric around the crossing point, i.e. $\alpha^* = 0$, and $\sin \Delta\psi = 1$, which implies $\Delta\psi = (2n + 1)\pi/2$ with n integer. This optics corresponds to a parallel to point focusing from the crossing point to the detectors. The beam size at the crossing, $\Delta x^* = \sqrt{\epsilon\beta^*}$, becomes irrelevant and in fact $\vartheta_{min} = K\Delta\vartheta^* = K\sqrt{\epsilon/\beta^*}$, i.e. the minimum detectable angle is K times the beam angular divergence at the crossing point. While this insertion is probably the ideal one for elastic

scattering, it might be difficult to implement at LHC because of the limited length of the straight sections which is fixed by the existing LEP tunnel.

A similar but alternative scheme consists of releasing both conditions $\sin \Delta\psi = 1$ and the $\alpha^* = 0$ and impose only the weaker condition $\cos \Delta\psi + \alpha^* \sin \Delta\psi \approx 0$. It should be noted that the first term in eq.(3) is the dominant one because of the presence of the factor K . This scheme would certainly allow greater flexibility in the design of the insertion^[8]. If, however, the first term in eq.(2) is not identically zero, we demand that it takes the same numerical value for both detector arms, otherwise the measurement of the scattering angle would be affected by the transverse size of the interaction region. An additional point is that with $\alpha^* \neq 0$, the phase space ellipse in the (x, x') plane at the crossing is not upright. This causes an increase of the angular divergence at the crossing $\Delta\vartheta^* = \sqrt{\epsilon(1 + \alpha^{*2})/\beta^*}$ which will deteriorate the momentum transfer resolution of the measurement of elastic scattering.

Another obvious requirement on the optics of the insertion is that the β -function at the position of the detectors should not be too small. In fact for practical reasons the minimum distance x_{min} of the edge of the detector from the beam axis should be at least 2 or 3 mm.

A study of a high- β insertion for LHC with $\alpha^* = 0$ was presented by Scandale^[9]. The β -value at the crossing is $\beta^* = 750$ m in both the horizontal and the vertical plane. With emittance $\epsilon = 2 * 10^{-10}$ m the size and angular divergence of the beam at the crossing are $x^* \simeq 0.4$ mm and $\Delta\vartheta^* = 0.5$ μ rads, respectively. The two proton beams cross each other at an angle of 2 mrad with a luminosity of about 10^{30} cm⁻²s⁻¹. The position of the detectors is at $\Delta\psi = \frac{1}{2}\pi$, about 200 m downstream of the crossing point, where $L_{eff} \simeq 60$ m. With $K = 20$ one finds $|t_{min}| \approx 5 * 10^{-3}$ GeV².

This insertion would be suitable for measuring σ_{tot} but the distance of the detectors from the beam axis is so small, $x_{min} \simeq \frac{1}{2}$ mm, that is not practical. The problem is that the value of β at the position of the detectors is too small. This has the unpleasant consequence that L_{eff} is too short, in fact quite smaller than the actual geometric distance of the detectors from the crossing point.

Two solutions could be envisaged. One could either release the requirement $\alpha^* = 0$, as already discussed above, or to adopt the scheme proposed for SSC^[10], where $\alpha^* = 0$ but the detectors are moved farther away from the

crossing at $\Delta\psi = 3\pi/2$ or $5\pi/2$. This may, however, cause some interference with the cryogenic system.

The momentum transfer resolution Δt is given in terms of the uncertainty $\Delta\vartheta$ on the scattering angle by

$$\Delta t = \sqrt{s |t|} \Delta\vartheta. \quad (4)$$

If the detectors have a very good spatial resolution, $\Delta\vartheta$ will be limited by the angular spread $\Delta\vartheta^*$ of the beams at the crossing point and given by $\Delta\vartheta = \Delta\vartheta^*/\sqrt{2}$. In that case, using the numerical values for the present high- β insertion^[9], one finds $\Delta t \simeq 6 * 10^{-3} \sqrt{|t|}$, which is a quite small, i.e. good, value. In fact $d\sigma/dt$ would change by less than 1% in a t bin equal to the resolution Δt .

The detector resolution Δx_{det} will also contribute to Δt . For the present insertion, with $L_{eff} \simeq 60$ m, the detector contribution would be the same as that due to the beam if $\Delta x_{det} = 30$ μ m. Such a resolution is attainable with present techniques, however, a larger value of L_{eff} would allow using detectors with more modest resolution. A safer design should aim at $L_{eff} \approx 200$ m and $\Delta x_{det} \approx 100$ μ m.

Measurement of N_{inel} . The measurement of the total inelastic rate N_{inel} requires a "fully inclusive" trigger and the identification of beam-beam events against beam-gas and beam-wall background. At present collider energies, a sizeable fraction of the inelastic events (about 15%) are of diffractive type, where a proton scattered at very small angles remains inside the vacuum pipe escaping detection and a few particles are emitted in the backward hemisphere in the angular region known as fragmentation region. Events of this kind can be observed only with a "single arm" trigger using telescopes of detectors which provide the reconstruction of the interaction vertex from the observed charged tracks.

We foresee to use at LHC the same technique which was employed at the SPS Collider by experiment UA4^[4] and at Fermilab by E710^[5]. Both experiments have covered about 3 pseudorapidity units extending down below $\eta_{max} \simeq y_{beam} - 1$. The fraction ΔN_{inel} of undetected inelastic events is estimated by extrapolating to the full solid angle.

If we assume that scaling in the fragmentation region, which is valid at present energies, will persist at the LHC, we find the results which are given in the following Table, together with information concerning UA4 and E710.

	$\sqrt{s}(TeV)$	y_{beam}	η_{min}	η_{max}	$\Delta\eta$	$y_{beam} - \eta_{max}$	ΔN_{inel}
UA4	0.55	6.4	2.5	5.6	3.1	0.8	1%
E710	1.8	7.5	3.8	6.5	2.7	1.0	2.5%
LHC	16	9.7	5.9	8.9	3.0	0.8	$\approx 1\%$

At LHC the pseudorapidity coverage should be at least from $\eta_{min} \simeq 5.9$ up to $\eta_{max} \simeq 8.9$. The corresponding range of production angles vary from 0.27 mrad up to 5.5 mrad. It is clear that in the high- β insertion, this interval of angles has to be left accessible to detection.

In practice the design of the detectors to measure N_{inel} will have to follow the final design of the insertion itself. The presence of quadrupoles near the crossing point, at a distance of only 10–20 m, will certainly affect the choice of the detectors and their location. In addition, the requirement of detecting tracks at angles of a few mrad might demand the use of some kind of "Roman pots" also for the measurement of the inelastic rate.

The conclusion is that, as the energy increases, not only the angles of elastic scattering but also the typical angles for measuring N_{inel} become smaller and the technical implications for the detectors and for the experimental layout require a careful study.

Elastic scattering at large-t. At LHC in the momentum transfer region above the diffraction peak one expects^[1] the presence of a "dip-bump" structure or a "shoulder" at $|t| \approx 0.4 \text{ GeV}^2$, followed by a more gentle decrease of $d\sigma/dt$ with perhaps a second "shoulder" or a discontinuity at larger t . The relevant parameters for the measurement of $d\sigma/dt$ in this region are the luminosity, the t -resolution and the rejection of the background of inelastic events.

The value of β^* affects both the luminosity and the momentum transfer resolution. In fact $L \sim 1/\beta^*$ and $\Delta t \sim \sqrt{|t|}/\sqrt{\beta^*}$. It is clearly desirable to design a high- β insertion with a tunable β^* in order to reach the best compromise between rate and experimental resolution. On the other hand, the luminosity of LHC is fortunately so high even in a high- β insertion that there will be no real problem of rate for $|t| \approx 1 \text{ GeV}^2$. In fact for the present high- β insertion^[9] with $L = 10^{30} \text{ cm}^{-2} \text{ s}^{-1}$ and assuming $d\sigma/dt = 10^{-29} \text{ cm}^2/\text{GeV}^2$ in the "dip" region^[1], one expects $\sim 2 * 10^3$ events/day in a t -bin of 0.05 GeV^2 . The momentum transfer resolution would be $\Delta t \approx 0.01 \text{ GeV}^2$, sufficient to observe the presence of a dip.

The interest of having also proton-antiproton collisions at LHC is dis-

cussed in the papers by Denegri^[1] and Leader^[2]. We only remark here that in the $\bar{p}p$ option, if the luminosity is $L = 10^{28} \text{ cm}^{-2} \text{ s}^{-1}$, about 200 events would be collected in a t -bin of 0.05 GeV^2 in the region of the "dip" during a running period of 10 days. This would be enough to study differences between the $p\bar{p}$ and the $\bar{p}p$ system.

The very high luminosity of the LHC machine might allow a study of $d\sigma/dt$ at large values of t . As a numerical example, with $L = 10^{34} \text{ cm}^{-2} \text{ s}^{-1}$ and assuming a t^{-8} dependence of the cross section at large- t , one would reach the level of ~ 1 event/(day* GeV^2) at $|t| \approx 15 \text{ GeV}^2$. The limitation will presumably come from the background of the inelastic events. An important reduction of this background can be achieved by exploiting the momentum dispersion which is provided by the machine elements present in the insertion. In the measurement of elastic scattering at the SPS Collider^[11], the "Roman pot" telescopes of UA4 provided at $|t| \approx 2 \text{ GeV}^2$, in addition to the angular correlation, also a momentum analysis with resolution which was better than 1%. This might, however, be not enough at much larger values of t .

Conclusions. The study done by the ECFA/LHC Working Group has shown that the measurement of σ_{tot} with the luminosity independent method is feasible at LHC with a precision of about 3% if a suitable high- β insertion is implemented. The present design by Scandale^[9] is the first step in this direction but requires additional tuning.

Elastic scattering can be measured up to large values of the momentum transfer, ($|t| \approx 15 \text{ GeV}^2$), in an insertion with variable β , by using telescopes of "Roman pots".

References

- [1] D. Denegri, Proceedings of this Conference, vol.I.
- [2] E. Leader, Proceedings of this Conference, vol.II.
- [3] A. Martin, Nuclear Physics B (Proc. Suppl.) 12 (1990) 1.
- [4] UA4 Collaboration, M.Bozzo et al., Phys. Lett. 147B (1984) 392.
- [5] E710 Collaboration, N.A.Amos et al., Phys. Lett. 243B (1990) 158.
- [6] C. Da Via', R. DeSalvo and M.R. Mondardini, Proceedings of this Conference, vol.II.
D. Bernard, Proceedings of this Conference, vol.II.
- [7] M. Haguener and G. Matthiae, Proceedings of the ECFA - CERN Workshop on the Large Hadron Collider in the LEP Tunnel, Lausanne 1984, vol. 1, pag. 303.
- [8] J.B. Jeanneret, Proceedings of this Conference, vol.II.
- [9] W. Scandale, Proceedings of this Conference, vol.II.
- [10] K. Goulianos et al., Report of Working Group 3 on Low p_t Physics at the SSC, CLNS 87/100, 1987.
- [11] UA4 Collaboration, M.Bozzo et al., Phys. Lett. 155B (1985) 197 and
R. Battiston et al., Nucl. Instr. and Methods, A238 (1985) 35.

Elastic Scattering at LHC: a challenge to theory and experiment.

Elliot Leader
Birkbeck College, Malet Street, London WC1E 7HX

1 Introduction

Elastic scattering experiments, looked at in the framework of QCD, will provide a powerful challenge to our understanding of the theory and will furnish information complementary to that which is obtained from Lepton-Hadron Deep Inelastic Scattering or from Large p_T Inclusive and Jet Reactions.

Traditionally, elastic scattering used to be considered in two kinematic regions: $\alpha)$ large p_T , meaning $|t| \gg$ a few times (nucleon mass) 2 , in which, prior to the parton model, very little could be said quantitatively, and $\beta)$ small $|t|$, meaning $0 \leq |t| \leq m_N^2$, in which a highly successful description of much data up to ISR energies was provided by Regge Theory or its more sophisticated offshoot Reggeon Field Theory. This success was marred by two features: the absence of a link to a more fundamental underlying theory and the failure of the model to correctly describe data on polarization type experiments.

With the advent of QCD there has to be a major change of perspective. QCD is characterized by a fundamental scale parameter $\Lambda_{QCD} \approx 150\text{ MeV}$ which divides the perturbative from the non-perturbative region. As a consequence elastic scattering should now be considered in three kinematic regions:

1. *Large p_T , i.e. $p_T^2 \gg m_N^2$.* This is the region where a direct perturbative approach should work. There is an age-old debate as to the relative importance of asymptotic-type Brodsky, Farrar, Lepage [1] type QCD diagrams, which lead to amazingly restrictive experimental predictions (especially for polarization-type measurements!), and the Landshoff [2] type diagrams which, naively, appear to dominate, but which intuitively were thought to be suppressed. With the advent of a beautiful new study by Botts and Sterman [3], this argument has been put onto a quantitative level. Predictions which hinge upon the deep properties of perturbative QCD should soon be available and must be tested experimentally.
2. *Medium t : $\Lambda_{QCD}^2 < |t| <$ few m_N^2 .* This is a region in which simple perturbative QCD is inadequate but in which certain non-perturbative effects can be handled by summing classes of Feynman graphs to all orders by use of integral equation techniques. There is a major programme of study under way led by Lipatov [4]. Preliminary results are

intriguing and seem to be providing a fundamental theoretical justification for a Reggeon Field Theory in which the parameters, instead of being put in by hand, (as was done when RFT was invented) are now related to basic QCD properties.

3. *Small t : $0 \leq |t| \leq \Lambda_{QCD}^2$.* This is the deeply non-perturbative region of QCD where nothing is known from actual QCD calculations. Nonetheless, and surprisingly, it is a region in which much can be said on the basis of general theorems which will hold provided that QCD is a ‘healthy’ field theory; which, it is hoped, it really is! It is here that new structure at $|t| = \Lambda_{QCD}^2$ may perhaps be found, linked to the transition between the perturbative and the non-perturbative regimes. And it is at $t = 0$ that there is a controversy raging as to the interpretation of the UA(4) measurement of the Real/Imaginary ratio [5] and the TEVATRON measurement of the total cross-section [6].

In the next Section we provide a very brief description of the theoretical approaches and issues involved in the three kinematic regions.

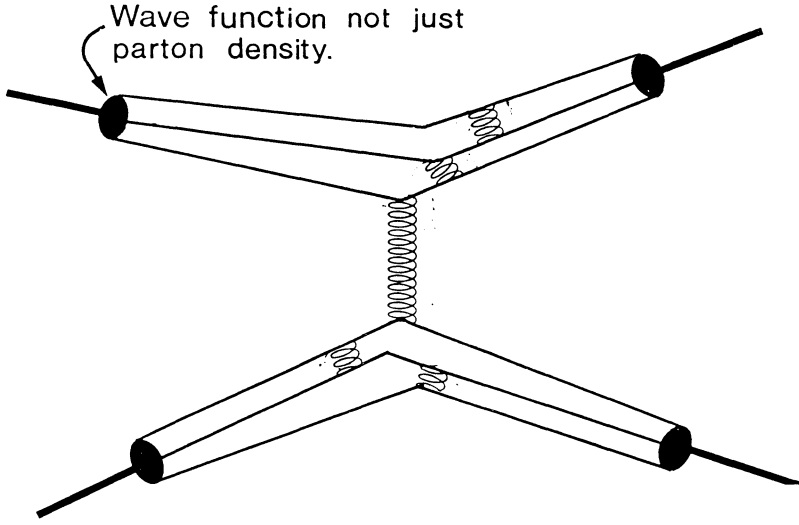
2 Theoretical Approaches

Our aim here is to provide only a *qualitative, heuristic* description of what mechanisms are expected to be important in the three kinematic regions introduced in Section 1.

2.1 Large p_T : $p_T^2 \gg m_N^2$

The original Brodksy, Farrar, Lepage [1] type diagrams which were supposed to dominate as $p_T^2 \rightarrow \infty$ and which lead to the ‘dimensional counting rules’ are shown at the top of the next page.

In these diagrams only one gluon connects the hadrons to each other and it provides a momentum kick between one quark from one hadron and one quark from the other hadron. Other gluons must then be exchanged between the quarks belonging to a *given* hadron so as to align their momenta to enable them to reform into the original hadron once again to produce an *elastic* scattering.



Note that one requires the actual *wave-function* of the hadron, not just a parton number density. Hence detailed studies of elastic scattering will tell us about the wave-function (a non-perturbative object) in the same way that large p_T inelastic experiments teach us the properties of $u(x)$, $d(x)$ etc. In the long run I suppose that the ultimate test of QCD will be the calculation of hadronic wave-functions. Thus experimental information is vital.

The Brodsky, Farrar, Lepage diagrams yield differential cross-sections for $pp \rightarrow pp$ or $\bar{p}p \rightarrow \bar{p}p$ of the form

$$\frac{d\sigma}{dt_{BFL}} = \frac{1}{s^{10}} f(\theta) \quad (1)$$

but because of the huge number of diagrams involved we do not know $f(\theta)$ accurately yet.

For large angles and energies below ISR the above behaviour seems roughly in agreement with data. But there is difficulty on several counts:

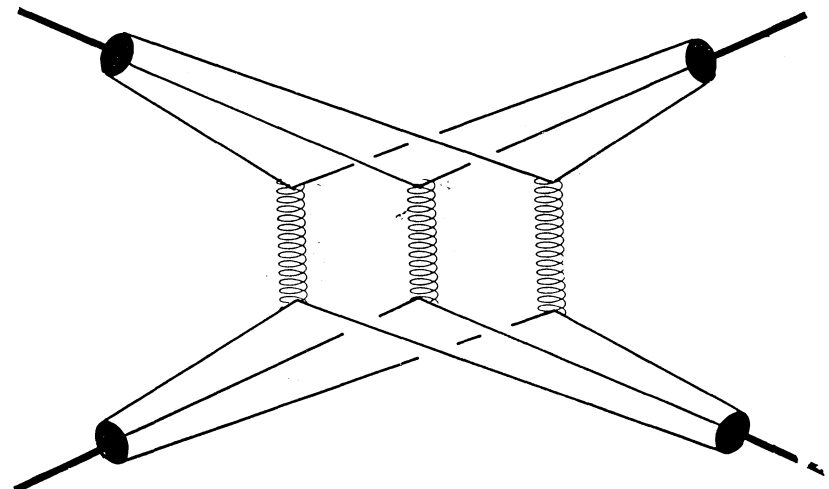
- Eqn (1) would imply, at fixed s , something like

$$\frac{d\sigma}{dt} \propto \frac{1}{s^{10-n}} \cdot \frac{1}{t^n} \quad (2)$$

which disagrees with higher energy data (see below).

- All its polarization predictions are wrong. One can escape by saying that the data is not yet at large enough p_T . (Data extends out to $p_T^2 \approx 7(GeV/c)^2$.)
- A careful study by Isgur and Llewellyn-Smith [7] shows that the bulk of the contribution from one of these diagrams at present energies and p_T values comes from regions where the q^2 carried by the propagators is not large, so that the perturbative treatment is unjustified.

On the other hand, Landshoff [2] had noticed that a diagram in which the momentum transfer is shared by three different gluons, as shown below,



leads to a cross-section that decreases less fast as s increases at fixed θ , than (1), so that at first sight it should dominate:

$$\frac{d\sigma}{dt_L} = \frac{1}{s^8} f(\theta) \approx \frac{c}{t^8} \quad \text{for } |t| \ll s \quad (3)$$

and, moreover, is in accord with data at ISR energies and beyond. Note that the fixed s behaviour is not compatible with (2).

But in the Landshoff diagram all the quarks are essentially on mass shell and are scattering like free particles. In that case, by analogy with QED, one expects the purely elastic scattering to be suppressed by 'gluon radiation'.

Recall that in QED

$$\left. \frac{d\sigma}{dt}(ee \rightarrow ee) \right|_{\text{BORN APPROX}} \neq 0 \quad (4)$$

yet

$$\left. \frac{d\sigma}{dt}(ee \rightarrow ee) \right|_{\text{EXACT}} = 0 \quad (5)$$

The latter is *not* a surprise. The exact result is zero also classically because you cannot accelerate an electron without emitting radiation.

In QCD you cannot radiate *free* gluons, but there will be an analogous effect involving the emission and re-absorption of gluons. This is referred to as Sudakov [8] suppression.

That such an effect will occur has long been suggested, but only recently has a detailed theoretical study emerged. Botts and Sterman [3] show that instead of (3) one should expect

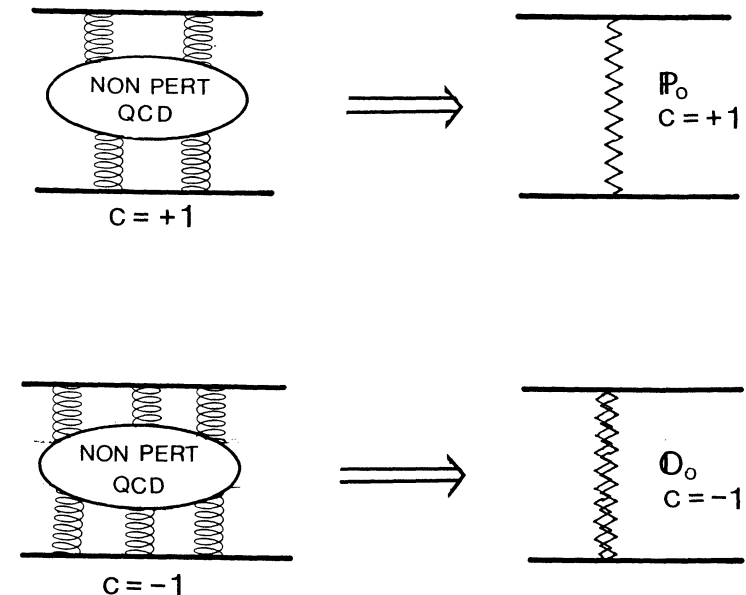
$$\frac{d\sigma}{dt_L} = \frac{c}{s^2 t^{7.66}} \quad (6)$$

which is very close to the dimensional counting behaviour given in (1). Again, a quantitative result for c is not yet available because of the complicated nature of the calculations.

Detailed experimental studies are important: i) to see whether the trend of the data is changing into the expected behaviour (6), and ii) because they would stimulate efforts to render the theory more quantitative.

2.2 Medium t : $\Lambda_{QCD}^2 \leq |t| \leq \text{few } (GeV/c)^2$.

Valiant efforts have been made by Lipatov [4] and collaborators to compute the non-perturbative 2 and 3 gluon exchange diagrams shown below, which are expected to be the key to the dynamics in this region.



It is almost proved that the 2 gluon exchange (which is $C = +1$) leads to an effective field theory in which the ‘quasi-particle’ that is exchanged is a complex object with variable spin $J = \alpha(t)$; namely a Reggeon referred to as the ‘bare Pomeron P_0 ’. It seems that

$$\alpha_{P_0}(t) = 1 + \epsilon_P(t) \quad (7)$$

where

$$\epsilon_P(t) = \left(\frac{4n_c \ln 2}{\pi} \right) \alpha_s(t) \quad (8)$$

where $n_c = 3$ is the number of colours.

Use of P_0 as the exchanged object in a Reggeon Field Theory is then tantamount to including the most important effects from 4, 6, 8...gluon exchange and will lead to a *crossing-even* scattering amplitude (i.e. a contribution which has the same value in $pp \rightarrow pp$ and $\bar{p}p \rightarrow \bar{p}p$) which is directly related to fundamental QCD parameters.

The case of 3 gluon exchanges is much more complicated. It contains both $C = \pm 1$. It appears that the $C = -1$ part leads to an effective field theory in which the exchanged quasi-particle is the ‘bare Odderon O_0 ’ whose spin is

$$\alpha_{O_0}(t) = 1 + \epsilon_O(t) \quad (9)$$

where $\epsilon_O(t)$ is not yet accurately known. Rough estimates, however, suggest the surprising result that $\alpha_{O_0}(t) > \alpha_{P_0}(t)$!

If we consider scattering amplitudes normalised so that

$$F = R + i\sigma \quad (10)$$

where σ is the total cross-section, then the single exchange of P_0 or O_0 (Born approximation) of course leads to amplitudes which grow faster with s than is permitted by unitarity, namely, for the even and odd (under crossing) amplitudes

$$F_+ \propto s^{\epsilon_P(t)} \quad F_- \propto s^{\epsilon_O(t)} \quad (11)$$

This behaviour would correspond to total cross-section growing like a power of s .

So it is essential to take the ‘field theory’ seriously, i.e. to include multi-pomeron and multi-oddron exchange. This is difficult and forms the central element of Lipatov’s research programme.

Of course there is a brute-force method of ensuring unitarity and that is simply to eikonalise the Born result. But in this approach there is no guarantee that one is not distorting the essential properties of the theory.

The $C = -1$, *crossing-odd* amplitude (i.e. contributing with opposite sign to pp and $\bar{p}p$) emerging from such an effective field theory offers fascinating prospects. It may turn out that even asymptotically

$$\left. \frac{d\sigma}{dt} \right|_{pp} \neq \left. \frac{d\sigma}{dt} \right|_{\bar{p}p} \quad (12)$$

The phenomenology of such an amplitude has been thoroughly investigated by Nicolescu [9] and by Donnachie and Landshoff [10] and others.

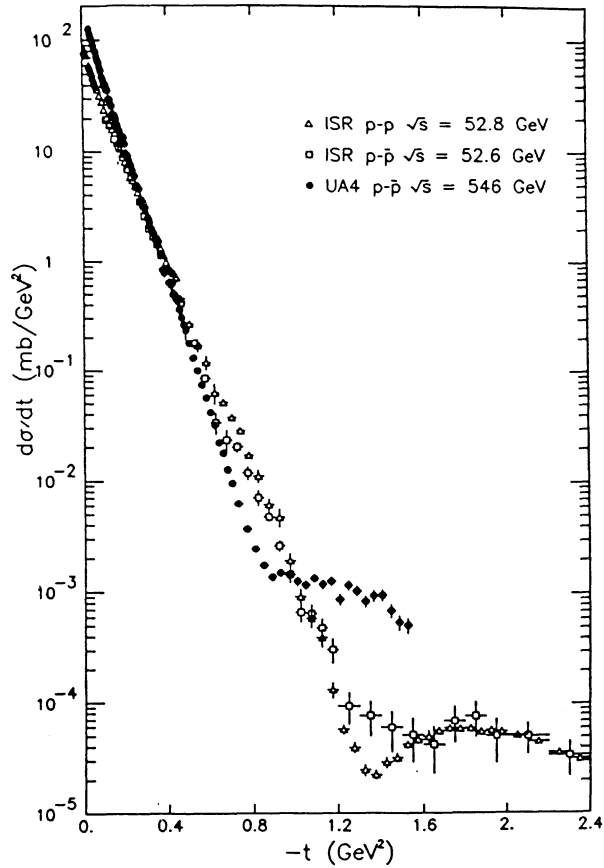
Regardless of the detailed calculations, certain general features must emerge from the theory, and can thus be looked for experimentally. Some examples:

1. The position of the diffraction dip t_{dip} should vary with s as

$$t_{dip} = \frac{c}{\ln^2 s} \quad (13)$$

Will this hold at LHC? Is there a change beyond the TEVATRON?

2. The ‘shoulder’: there is a big increase in $d\sigma/dt$ beyond t_{dip} between ISR and S $\bar{p}p$ S energies, which is possibly linked to O . Does this increase continue?
3. The most intriguing question of all. The figure on the next page compares the pp and $\bar{p}p$ differential cross-section at ISR energies and also shows $\bar{p}p$ at S $\bar{p}p$ S Collider energies. Is there a genuine difference between pp and $\bar{p}p$? Does this difference persist as the energy increases??



2.3 The forward direction and very small t : $|t| \leq \Lambda_{QCD}^2$

No real QCD calculations have been done in this highly non-perturbative region, but, if QCD is a ‘healthy’ field theory then one must have:

1. For both $p p$ and $\bar{p} p$

$$\sigma(s) \leq c \ln^2 s \quad \text{as } s \rightarrow \infty \quad (14)$$

(the Froissart bound)

2. The amplitude at $t = 0$ is an analytic function of s . It follows that the Real part of the amplitudes R_{pp} and $R_{\bar{p}p}$ are given by an integral over the cross-sections, but both $\sigma_{pp}(s)$ and $\sigma_{\bar{p}p}(s)$ are needed for each real part. The integrals run up to $s = \infty$ so one has to feed in an assumption as to what $\sigma(s)$ does as $s \rightarrow \infty$.

When one feeds in the Froissart behaviour

$$\begin{aligned} \sigma_{pp}(s) &\rightarrow c \ln^2 s \\ \sigma_{\bar{p}p}(s) &\rightarrow c \ln^2 s \end{aligned} \quad (15)$$

and in such a way that for the difference

$$\Delta\sigma \equiv \sigma_{\bar{p}p} - \sigma_{pp} \quad (16)$$

one assumes the conventional behaviour $\Delta\sigma \rightarrow 0$ like an inverse power of s , which is consistent with data up to the ISR region, one finds that $R_{\bar{p}p}$ at $\sqrt{s} = 546 \text{ GeV}$ is much smaller than the experimental result [5] of UA(4).

There is a very simple approximate (but reliable) way to see what the trouble is [11]. It utilises local consequences of the analyticity.

Take the amplitude normalisation given in (10) and define the mean cross-section

$$\bar{\sigma} \equiv \frac{1}{2} (\sigma_{\bar{p}p} + \sigma_{pp}) \quad (17)$$

and to avoid writing lots of π s, put

$$\eta \equiv \frac{2}{\pi} \ln^2 s \quad (18)$$

Then the rate of growth of $R_{\bar{p}p}(s)$ is governed by

$$\begin{aligned}\frac{dR_{\bar{p}p}}{d\eta} &= -\frac{\Delta\sigma}{2} + \frac{d^2}{d\eta^2} \left(\bar{\sigma} + \frac{\Delta\sigma}{3} \right) \\ &+ \frac{1}{3} \frac{d^4}{d\eta^4} \left(\bar{\sigma} + \frac{\Delta\sigma}{15} \right) \dots\end{aligned}\quad (19)$$

In the conventional picture $\Delta\sigma = 0$ and there is no 4th derivative. Then $R_{\bar{p}p}$ is too small at $\sqrt{s} = 546\text{GeV}$ by almost a factor of 2.

How can we make $R_{\bar{p}p}$ grow more rapidly beyond the ISR region?

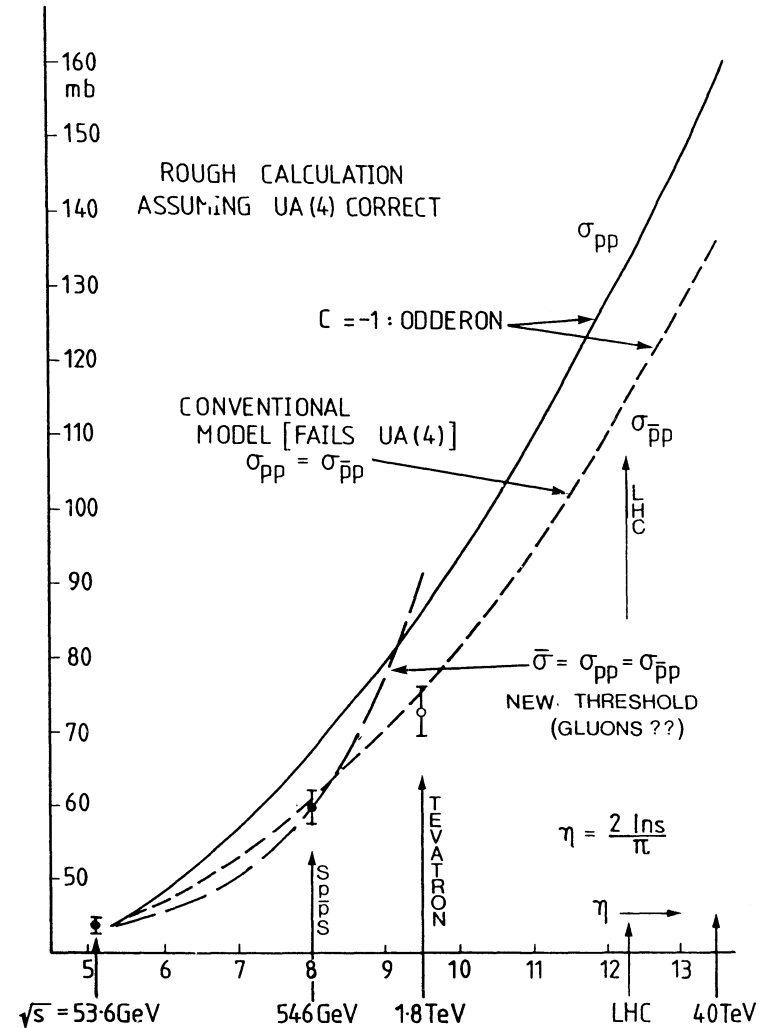
One method is to let $\bar{\sigma}(s)$ grow *faster* than $\ln^2 s$ beyond ISR (this could only be a temporary growth) so that there is a significant 4th derivative, and to keep $\Delta\sigma = 0$. There is a nice argument [12] linking this to the growing gluon density at very small x . But the trouble is that the large 4th derivative makes the cross-section too large at the TEVATRON!

A final possibility is to abandon $\Delta\sigma = 0$, as would be necessary if the Odderon ($C = -1$) amplitude becomes important at high energies, in which case one can fit *both* $R_{\bar{p}p}$ at $\sqrt{s} = 546\text{GeV}$ and the TEVATRON $\sigma_{\bar{p}p}$.

The Figure on the next page summarises the situation in the three cases of interest.

It should be clear that there are exciting questions begging for an experimental answer:

- Is the UA(4) measurement correct?
- Is the *interpretation* of the UA(4) result correct [13]?
- What is the value of ρ at TEVATRON and LHC energies?
- And the great challenge: Is $\sigma_{pp} = \sigma_{\bar{p}p}$ at LHC? Note that one might even expect a difference of $\approx 20\text{mb}$ at LHC according to the Figure.
- Is the TEVATRON hinting at something new? e.g. is $\sigma_{\bar{p}p}$ only growing like $\ln s$?



3 Summary

There has been great theoretical progress with QCD in trying to understand elastic scattering, at least at large and medium p_T values. More quantitative results will surely become available in response to experimental stimulus.

The major things that can be learnt from elastic scattering and some of the most challenging questions demanding an experimental answer are listed in the Table. In particular we emphasize the complementary nature of the information obtainable from elastic scattering and from inclusive and jet physics.

The rôle of elastic scattering studies.		
Kinematic Region	Measurements	Outcome
Large p_T : $p_T \gg m_N^2$	p_T dependence at fixed s ; s dependence at fixed θ . Does data begin to follow $d\sigma/dt \propto 1/s^2 t^{7.66}$?	Tests perturbative QCD. Yields information on hadronic wave function (not just parton densities).
Medium p_T : $\Lambda_{QCD}^2 \leq t \leq m_N^2$	s and t dependence of $d\sigma/dt$. Behaviour of dip and shoulder. Comparison of pp and $\bar{p}p$ data.	Tests more fundamental field theoretic aspects of QCD including some non-perturbative aspects. Tests relative importance of non-perturbative 2-gluon and 3-gluon effects.
Forward and small t : $ t \ll \Lambda_{QCD}^2$	Total cross-sections; ratio of real to imaginary parts of amplitudes. Comparison of pp and $\bar{p}p$ data.	Tests ultimate 'health' of QCD as a field theory (Analyticity, Froissart bound). Tests relation between deeply non-perturbative aspects of 2 and 3 gluon exchange. Teaches us about how the theory adjusts itself to respect unitarity.

Finally

UNIQUE
KEEP OPEN THE OPTION FOR
 $\bar{p}p$
SSC cannot compete!

References

- [1] Brodsky, S.J., and Farrar, G.R., *Phys. Rev. Lett.* **31** (1973) 1153; Lepage, G.P., and Brodsky, S.J., *Phys. Rev. D* **22** (1980) 2157.
- [2] Landshoff, P.V., *Phys. Rev. D* **10** (1974) 1024.
- [3] Botts, J. and Sterman, G., *Nucl. Phys.* **B325** (1989) 62
- [4] See: Lipatov, L., in *Perturbative QCD*, edited by Mueller, A.H., 1989 (World Scientific); Lipatov, L.N., *Preprint DESY 90-060*, May 1990.
- [5] UA(4) Collaboration, Bernard, D. *et al.*, *Phys.Lett.* **B198** (1987) 586.
- [6] E710 Collaboration, Amos, N. *et al.*, *CLNS Preprint 981*, to be published in *Phys.Lett.B*.
- [7] Isgur, N. and Llewellyn-Smith, C.H., *Nucl.Phys.* **B317** (1989) 526.
- [8] Sudakov, V.V., *Sov.Phys.-JETP* **3** (1956) 65.
- [9] See Gauron, P., Leader, E. and Nicolescu, B., *Phys.Lett.* **B238** (1990) 406.
- [10] Donnachie, A. and Landshoff, P.V., *Nucl.Phys.* **B244** (1984) 322.
- [11] Leader, E., *Phys.Rev.Lett.* **59** (1987) 1525.
- [12] Block, M., Fletcher, R., Halzen, F., Margolis, B. and Valin, P., *Phys.Rev.* **D41** (1990) 978.
- [13] Bourrely, C., Soffer, J. and Wu, T.T., *Phys.Lett.* **B196** (1988) 237.

DETECTION OF THE TAU-NEUTRINO AT THE LHC*

Klaus Winter

CERN, Geneva, Switzerland

1. Introduction

Following the discovery of the tau-lepton in e^+e^- collisions by M. Perl and collaborators [1], all evidence today favours the hypothesis that it is a sequential heavy lepton belonging to a third lepton family [2]. From measurements of the forward-backward angular asymmetry of tau produced in e^+e^- annihilations [3], [4]

$$e^+e^- \rightarrow \tau^+\tau^-$$

a value of the axial-vector neutral current coupling constant of $g_{a_\tau} = -0.45 \pm 0.05$ was deduced in agreement with $g_a = -1/2$ for the assignment of left-handed tau-leptons as the "down" state ($I_3 = -1/2$) of a weak isospin doublet. Hence, the most natural assignment of the "up" state ($I_3 = +1/2$) would be to a neutrino with the same lepton flavour, the tau-neutrino.

Further indirect evidence about the tau-neutrino can be obtained from leptonic tau decays [4], e.g.

$$\tau^- \rightarrow \mu^- \nu_\mu X$$

The muon energy spectrum has the familiar [2] Michel shape suggesting that the particle X is a spin $1/2$ particle. Its mass has been constrained to less than 35 MeV by analysing semi-leptonic tau-decays with multipion final states [5]. Hence, the particle X may be a neutrino. Is it a sequential neutrino, with a flavour property which distinguishes it from the electron- and the muon-neutrino? The possibility of a complete identity with ν_e or ν_μ can indeed be excluded. Searches for charged current neutrino-reactions which produce a tau-lepton

$$\nu N \rightarrow \tau^- X$$

have given negative results. A search in a beam dump experiment with ν_μ and ν_e at

CERN [6] excluded the identity $\nu_e = \nu_\tau$ by six standard deviations. A search in a muon-neutrino beam at FNAL [7] gave limits on the coupling constant of ν_μ and τ of 0.0021 and on the coupling constant of ν_e and τ of 0.073. Together with the lifetime and leptonic branching ratio measurements [3] [4], these results show that the tau-neutrino is distinct from ν_e and ν_μ .

Does the tau-neutrino exist as a particle? Surprisingly, this question cannot be answered by yes or no. Its existence can be proved by direct observation of the charged current reaction

$$\nu_\tau N \rightarrow \tau^- X.$$

All attempts to directly observe the reaction have failed up to now. Searches in so-called beam dump experiments have been performed at the 450 GeV CERN-SPS. In this type of experiment the proton beam is absorbed by a long block of copper [6]. Because of their strong absorption in copper, decays of long-lived mesons (π and K) are suppressed by a factor of $\sim 10^3$. Neutrinos from decays of short-lived charm-mesons (lifetime $\sim 3 \cdot 10^{-13}$ s) are not suppressed. Among the known decay channels there are semileptonic decays of the D meson ($c\bar{d}$) into ν_e and ν_μ and of the D_s -meson ($c\bar{s}$) into $\tau\nu_\tau$. The contribution of the latter channel which produces tau-neutrinos is too low at the CERN proton energy of 450 GeV to be detectable. At the 800 GeV Tevatron the situation would be slightly more favourable. However, the experiments [8] have been indefinitely deferred.

A new experiment [9] has been designed to detect the tau-neutrino at the 3 TeV proton accelerator UNK which is presently under construction at Protvino (Serpukhov) in the USSR. With the advent of high energy pp colliders (LHC and SSC) new possibilities have arisen which will be discussed in the following sections.

2. The Concept of Tau-Neutrino Detection

Previous experience with the detection of short-lived particles, e.g. of charm-mesons has shown that their identification by kinematics and by transverse momentum unbalance due to undetected neutrinos is not possible in the presence of a large background. The short lifetime itself is an unambiguous method to detect and to identify them. With a mean tau-neutrino event energy of 300 GeV at LHC we expect a mean decay path of ~ 1 cm. The majority of the tau decay modes (86%) produce a single

* Working group on neutrino physics: L. Camilleri, A. Capone, A. De Rujula, U. Dore, A. Ereditato, E. Fernandez, J. Gomez, A.B. Kaidalov, P.F. Lovere, V. Palladino, F. Pietropaolo, L. Rolandi, R. Santacesaria, S. Schlenstedt, F. Vanucci and K. Winter.

charged particle. The decay angle (kink) between the tau and the charged particle is small, about 1° on average and therefore difficult to detect. The decay length has a broad distribution because of the wide tau-neutrino energy spectrum. Because of the energy and momentum carried away in tau-decay by the ν_τ the energy of each tau-lepton and hence its lifetime in the rest system cannot be determined.

For the identification of a tau decay vertex we require instead a visible transverse decay length (kink) or a visible transverse impact parameter of a particle track with respect to the event vertex (figure 1).

Figure 2 shows the expected transverse decay length and impact parameter distribution with mean values of $\lambda_T = 243 \mu\text{m}$ and $\lambda_i = 65 \mu\text{m}$. These values are nearly invariant with respect to the spread of tau-neutrino energies. The transverse decay angle is large: a spectacular event with a $\tau \rightarrow \mu\nu_\mu\nu_\tau$ decay, simulated by Monte Carlo methods is shown in figure 3 [9]. It illustrates the basic concept.

Detection of short lived particles requires good space resolution ($\sim 20 \mu\text{m}$). There exist proven methods: emulsions, holographic bubble chambers or Silicon micro-strip detectors. Other detection techniques using e.g. a liquid argon drift chamber have also been investigated [10]. Because of the high muon flux (see Chapter 3) it is essential to have good time resolution ($\lesssim 10 \mu\text{s}$). This condition eliminates the emulsion and the bubble chamber as detectors. The CHARM II-Zeuthen Collaboration has been considering either Silicon micro-strip detectors or scintillating fibres [9], others have developed liquid argon drift chambers [10] for detecting the tau-neutrino. In Chapter 3, I am briefly describing the ν_τ beam and the expected ν_τ event rate in Chapter 4 the detector and in Chapter 5 the expected performance.

3. The Tau-Neutrino Beam

Tau neutrinos can be obtained from the production and decay of heavy quark flavors ($c\bar{c}, b\bar{b}$) in proton-proton collisions. The main source of ν_τ is the leptonic decay

$$D_s^+ \rightarrow \nu_\tau \tau^+, \quad \tau^+ \rightarrow \bar{\nu}_\tau + X$$

which is expected to occur with a branching ratio of $\sim 3\%$. The secondary ν_τ from τ decay has higher energy, on average 300 GeV at LHC energy, because of the Lorentz boost of the tau lepton in D_s decay, and is there dominating the expected event rate.

At the energy of fixed target accelerators (UNK, LHC, SSC) of $\sqrt{s} \sim 80 - 120 \text{ GeV}$ the cross section for D_s production can be safely estimated from results obtained at the ISR and at the $p\bar{p}$ colliders [9]. Using the collider mode of LHC, following a suggestion of A. De Rujula and R. Rückl [11], a ν_τ beam can be produced in $\sqrt{s} \approx 16 \text{ TeV}$ $p\bar{p}$ collisions.

The cross section dependence on \sqrt{s} and on the Feynman scaling variable x_F has been estimated by a scaling law approach [11], by the quark-gluon string model of Kaidalov et al. [12] and by the PYTHIA QCD Monte Carlo program. A very steeply rising x_F dependence at $x \sim 0$, like $1/x$ and a strong cross section increase with energy is predicted, with $\sigma(D_s^+) \sim \sigma(D_d^+) \sim \sigma(D_s^-) \sim 1 \text{ mb}$ at 16 TeV, a factor ~ 20 higher than in the fixed target mode at $\sqrt{s} \sim 120 \text{ GeV}$. These predictions must be subjected to experimental tests.

Figure 4 shows the energy spectrum of ν_τ at $\sqrt{s} = 16 \text{ TeV}$ as calculated by De Rujula, Fernandez and Gomez. Because of the energy imparted to the parent D_s mesons the angular distribution of the ν_τ flux is strongly peaked at small angles with respect to the proton direction (see figure 5). The luminosity, the ν_τ event rate for 10^7 s for a detector with a mass of 2 kg/cm^2 subtending an angular acceptance of $\pm 2.5 \text{ mrad}$, and the rate of ν_μ and ν_e induced reactions (from heavy quark decays) in a conventional detector with a mass of 6 kg/cm^2 is given in Table 1 for three different modes of operation: a gas jet with a density of $\rho \sim 4 \cdot 10^{14} \text{ nucleons/cm}^3$ and a beam dump receiving 10^{10} protons/s by slow ejection operate in the fixed target mode; for the beam-beam mode we have assumed a mean luminosity of $10^{34} \text{ cm}^{-2} \text{ s}^{-1}$ whereas the peak luminosity may be as high as $4 \cdot 10^{34}$. For comparison we also show the rate at a fixed target accelerator (UNK) with 10^{13} protons/s.

Table 1

Comparison of event rates in different operation modes at the LHC and at UNK.

Mode	$L(\text{cm}^{-2}\text{s}^{-1})$	$N(\nu_\tau)^4)$	$N(\nu_\mu)^5) = N(\nu_e)$
Beam-Beam	10^{34}	3800	80'000
Gas-Jet ¹⁾ (fixed target)	$2 \cdot 10^{33}$	25	500
Beam dump ²⁾ (fixed target)	$2 \cdot 10^{35}$	2500	50'000
UNK fixed target ³⁾	10^{38}	20'000	

1) $\rho(\text{jet}) \sim 4 \cdot 10^{14} \text{ nucleons/cm}^3$

2) slow ejection $10^{10} \text{ protons/s}$

3) slow ejection $10^{13} \text{ protons/s}$

4) target mass $\sim 2 \text{ kg/cm}^2$, $\Delta\theta \sim \pm 2.5 \text{ mrad}$, 10^7 s

5) target mass $\sim 6 \text{ kg/cm}^2$, $\Delta\theta \sim \pm 2.5 \text{ mrad}$, 10^7 s

Detecting τ decays in the leptonic decay $\tau \rightarrow \mu \nu_\mu \nu_\tau$ with a branching ratio of 17.8% and a detection efficiency (see Chapter 4) of $\epsilon \sim 30\%$ observation of the reaction $\nu_\tau N \rightarrow \tau X$ may be possible, except in the gas jet mode.

4. The Detector

We have considered two versions of a tau neutrino vertex detector using the fibre technique. In one version (see figure 6) the detector will consist of scintillating fibres of $20\mu\text{m}$ diameter oriented in the direction of the neutrino beam. The development of coherent bundles of glass capillaries filled with liquid scintillator is under way at CERN [13]. The read-out of the transverse image at the end face of the fibre target will be made using image intensifiers and CCD's following the development made for the UA2 scintillating fibre detector at CERN [14].

In the other version the detector would consist of alternating layers of live targets and micro strip detectors (Silicon or scintillating fibres) oriented perpendicular to the beam (figure 7). The (fibre) strip dimensions would again be $20\mu\text{m}$. Using the conventional impact parameter technique (see figure 1) the tau-lepton can be identified by its characteristic transverse impact parameter distribution with a mean value of $65\mu\text{m}$. In order to eliminate all prompt events a minimum impact parameter has to be required and it is expected that the efficiency of tau-lepton detection of this detector version is smaller than in the longitudinal fibre version. However, the effects of nuclear

fragments and evaporation nucleons are expected to affect the longitudinal fibre detector version more than the transverse (fibre) strip detector. The relative merits of the two detector versions have to be determined by a test experiment.

Detection with a liquid argon drift chamber has been investigated by Du Marchez, Nedelec and Vannucci [10]. They obtained a resolution of $\sigma \sim 60\mu$ in the drift direction (figure 8). However, there are problems with the resolution in the second view and with the two-track resolution. The time resolution of $\sim 100\mu\text{s}$ may cause problems with the muon flux.

The possible location of a detector at LHC has been studied by L. Camilleri (these proceedings). At a distance of $\sim 130 \text{ m}$ from the interaction point the beams are separated by 18cm . A detector of rectangular shape ($15\text{cm} \times 30\text{cm}$) may find space here. In intersection region 1 there is a possibility to install a large and massive detector for ν_μ and ν_e experiments at a distance of 500 m . The background due to hadrons and muons after magnetic deflection in the LHC magnet lattice and the possibility of passive shielding remain, however, to be calculated.

5. Background

Aiming at the detection of the reaction $\nu_\tau N \rightarrow \tau X$ the experiment must be designed for a situation in which the reaction may not occur at all or with reduced rate. A signal to background ratio of 10 to 1 must therefore be achieved.

Background produced by conventional neutrinos (ν_μ , ν_e) comes mainly from charm production :

$$\bar{\nu}_\mu N \rightarrow \mu^+ (\text{D}^- \rightarrow \mu^- + \text{neutrals}) X$$

$$\nu_\mu N \rightarrow \nu_\mu D \bar{D} X$$

$$\quad \downarrow \mu^- + \text{neutrals.}$$

A full simulation gives a background due to ν_μ and ν_e of $\sim 5\%$.

The efficiency for detection of a decay kink is $\sim 30\%$ [9]. It should therefore be possible to detect the tau neutrino.

6. Conclusions

Further work is required before an experiment can be planned. This work must be concerned with the detector, with its location and with the background of muons and the possibility to reduce it by passive or magnetic shielding.

References

- [1] M. Perl et al., Phys. Rev. Letters 35(1975)1489.
- [2] B.C. Barish, R. Stroynowski, Phys. Rep. 157(1988)1 .
- [3] T. Kamae, Proc. 24th Int. Conf. on High Energy Physics (Munich), Springer (R. Kotthaus, J.H. Kühn, editors) 1988, p. 156.
- [4] Particle Data Group, Phys. Lett. B204(1988)1 .
- [5] H. Albrecht et al., ARGUS, Phys. Lett. 202B(1988)149.
- [6] M. Talebzadeh et al., Nucl. Phys. B291(1987)503.
- [7] N. Ushida et al., Phys. Rev. Lett. 57 (1986)2897.
- [8] FNAL proposal E-636, E.S. Hafen et al. using a holographic bubble chamber (1980), and FNAL proposal E-646, A.E. Asratyan et al. ITEP preprint N133(1984) using emulsions.
- [9] Letter of intent "Detection of the ν_τ at UNK", 6 January 1989, CHARM II Collaboration (Brussels - CERN - Hamburg - Louvain - Moscow - Munich - Naples - Rome) and IHEP (Berlin, Zeuthen), and K. Winter, CERN-EP/89-182, Acta Physica Hungarica (in the press).
- [10] P. Astier et al. LPN HEP/8907(1990).
- [11] A. De Rujula, R. Rückl, ECFA 84-85/CERN 84-10. Vol. II, p.571 (Geneva 1984).
- [12] A.B. Kaidalov and O. Piskunova, Z. Phys. C30(1986)145 and preprint Moscow (1990).
- [13] A. Artamonov et al., Nucl. Instr. Methods (in the press) and CERN-EP/90-58.
- [14] R.E. Ansorge et al., UA2 Collaboration, Nucl. Instr. Methods A265(1988)33.

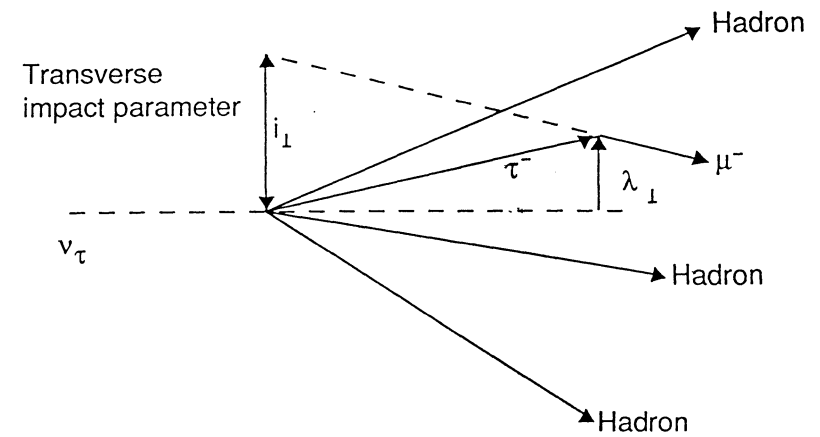


Figure 1
Illustration of the impact parameter technique.

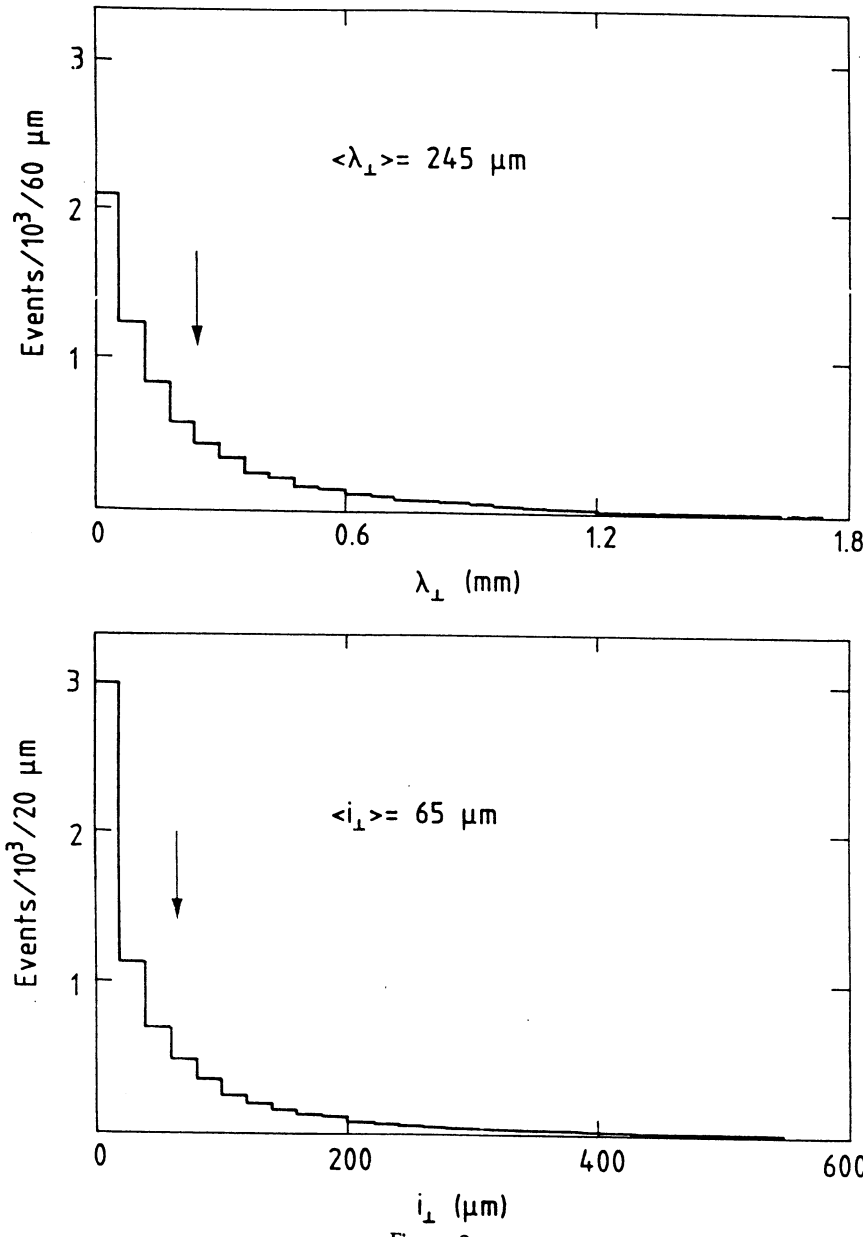


Figure 2

Distribution of transverse decay length and of transverse impact parameter of τ decays.

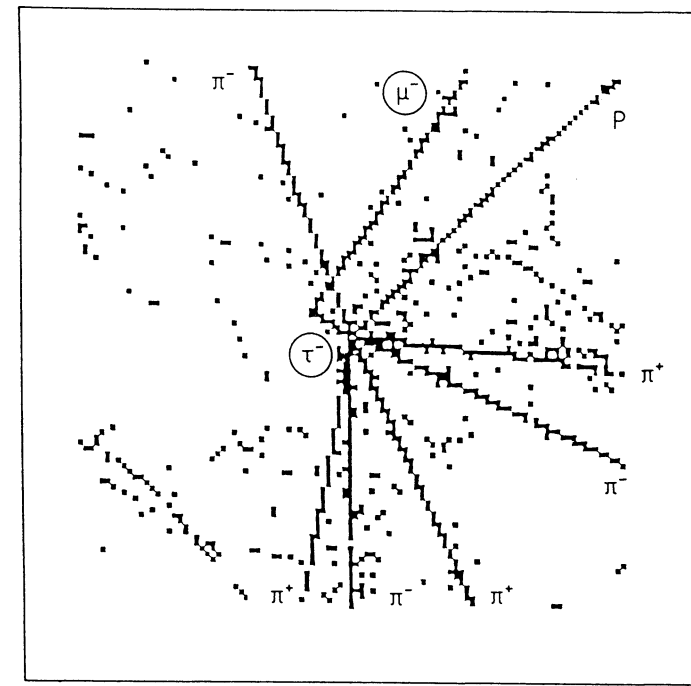


Figure 3

Simulated event of the type $\nu_\tau N \rightarrow \tau^- (\rightarrow \mu^- \bar{\nu}_\mu \nu_\tau) X$ in a 2 mm by 2 mm region of the longitudinal scintillating fiber ($20 \mu\text{m}$) detector [9]. The $\tau^- \rightarrow \mu^-$ decay kink is very spectacular in this event.

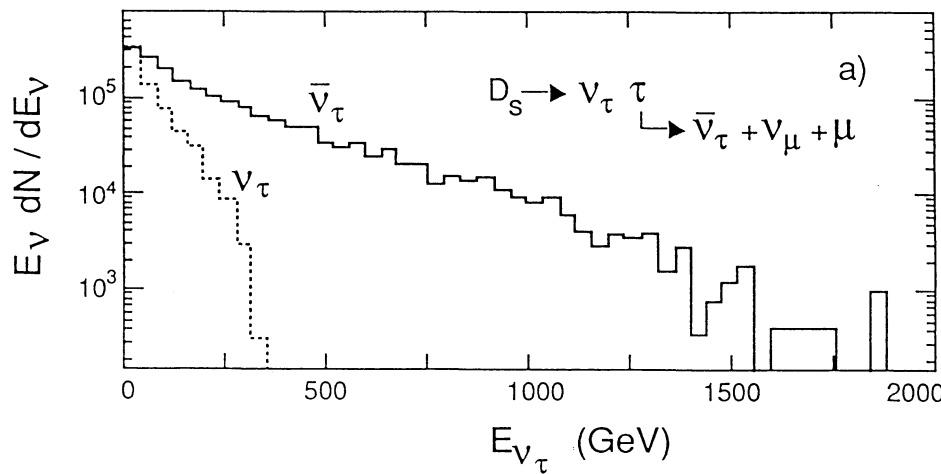


Figure 4
Tau-neutrino energy spectrum from D_s decay (De Rujula, Fernandez Gomez).

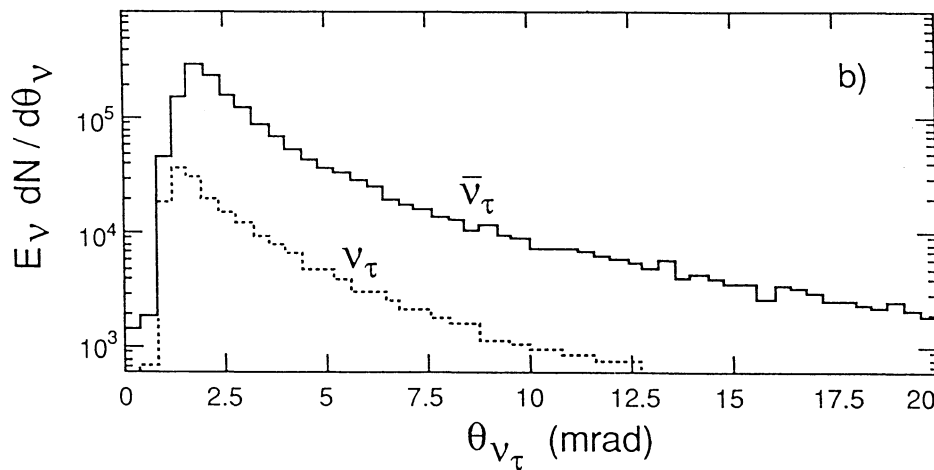


Figure 5
Angular distribution of ν_τ flux from D_s decay (De Rujula, Fernandez, Gomez).

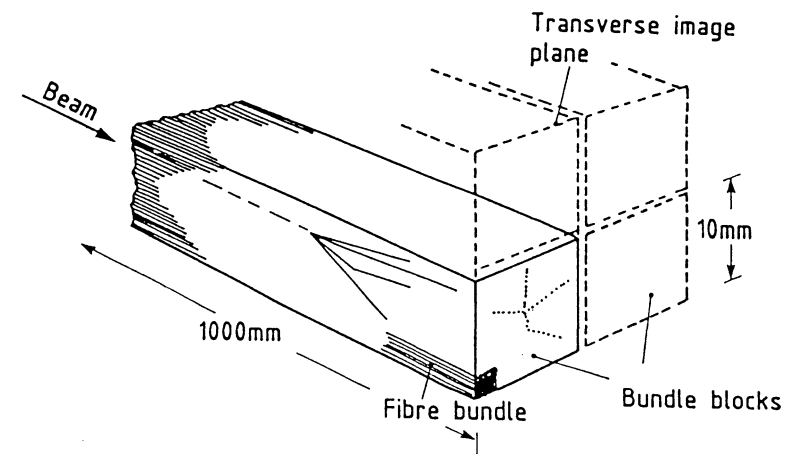


Figure 6
Schematic view of the longitudinal fibre target detector and read-out system [9].

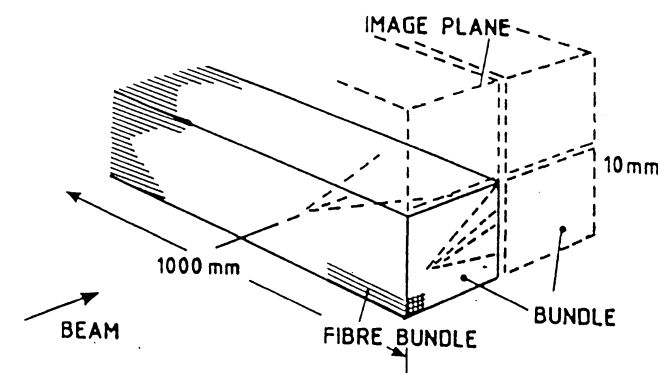


Figure 7
Schematic view of the transverse fibre detector [9].

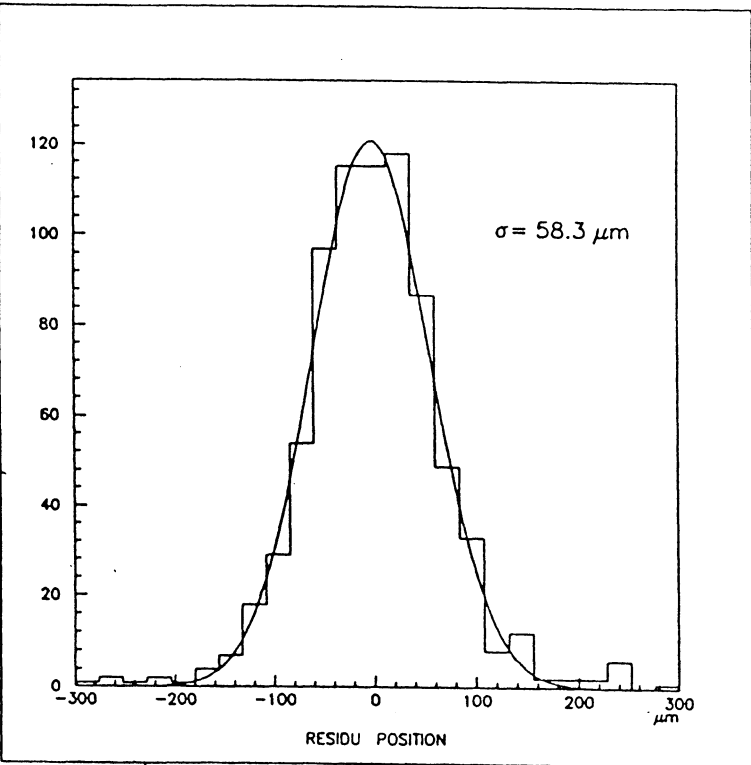


Figure 8

Resolution in drift direction in a liquid argon drift chamber (Du Marchez, Nedelec, Vannucci).

Jets at the Large Hadron Collider

P. T. Cox¹, J.-P. Guillet, P. Lubrano, M. Nessi, and F. Nessi-Tedaldi

PPE Division, CERN, CH-1211 Geneva 23, Switzerland²

1 Introduction

The Jet Subgroup of the Standard Model Cross-Section Working Group was set the task of tabulating high- p_T jet cross-sections in order to summarize the present expectations for such jet physics at LHC. Previous LHC studies [1,2,3] have also addressed this problem, and have included studies of jet physics using crude cell-level detector simulations, but the current studies concentrated on the jet cross-sections themselves, at the theoretical and Monte Carlo level, and ignored detector simulation completely. The topics which have been addressed in the current studies are grouped into four sections (2–5) below:

- Inclusive single-jet cross-sections (Calculational)
Section 2 gives a theoretical overview of the understanding of jets within QCD, as well as the results of several calculational studies based on the leading-logarithm (LL) and next-to-leading-logarithm (NLL) cross-sections at LHC. It is worthwhile emphasizing that even at the purely theoretical level, at greater than leading order there is some ambiguity in the definition of the object which will be called a jet, and this ambiguity must be resolved by adopting some convention.

- Inclusive single-jet cross-sections (Monte Carlo)
Section 3 examines Monte Carlo predictions for the inclusive-jet cross-section, and investigates how credible such predictions are likely to be at LHC.

- Limits on parton compositeness
In Section 4 is a short discussion of the use of inclusive-jet cross-sections as a probe of possible quark substructure, concluding with the limits on parton compositeness that may be expected from how such substructure would modify the QCD-jet spectrum.

- Multi-jet cross-sections
Finally Section 5 contains some results derived from a new calculation of multi-jet cross-sections.

Within each section there is some emphasis on how robust the results are to choice of: structure functions (s.f.), scale, higher-order effects, and jet definition.

¹The Rockefeller University, New York, NY 10021, USA.

²Bitnet: PTC, JGUILLET, LUBRANO, NESSI, NESSIF, @ CERNVM.CERN.CH

2 Inclusive-jet cross-sections (Calculational)

2.1 Formalism

Since it is not possible to fully describe an hadronic event within the framework of the fundamental strong-interaction theory (QCD), assumptions must be made in order to compare theory with experiment. In the case of the jets, it is assumed that the observed jet cross-sections and angular distributions closely follow those of the partonic ones. Then the hadronic cross-section can be written as the convolution of distribution functions $F_i^H(x, M^2)$ (soft part) with partonic cross-sections computed with the help of perturbative QCD (hard part). At the level of the Leading Logarithm (LL) approximation, the partonic cross-section is computed at order α_s^2 . A further step towards better understanding of jets has been made by the Next-To-Leading Log (NTLL) calculation: the hard part is evaluated at order α_s^3 . Such a computation has been performed by two groups [4,5], utilizing existing results on the $O(\alpha_s^3)$ matrix elements [6]. Schematically, for a jet with components (E, \vec{P}) , the cross-section can be written:

$$\begin{aligned} E \frac{d\sigma}{d^3\vec{P}} = & \sum_{i,j} \int_0^1 dx_1 \int_0^1 dx_2 F_i^H(x_1, M^2) F_j^H(x_2, M^2) \\ & \times \left(E \frac{d\hat{\sigma}}{d^3\vec{P}} \right)_{i,j \rightarrow \text{jet}} (x_1, x_2, \alpha_s(\mu^2), \mu^2, M^2, R). \end{aligned} \quad (1)$$

The partonic cross-section depends on:

- the renormalization scale (μ^2) (and not only via α_s),
- the factorization scale (M^2),
- the jet cone size (R).

Since physical quantities should not depend on these scales it follows that:

$$\mu^2 \frac{d}{d\mu^2} [E \frac{d\sigma}{d^3\vec{P}}] \simeq O(\alpha_s^4) \quad (2)$$

and

$$M^2 \frac{d}{dM^2} [E \frac{d\sigma}{d^3\vec{P}}] \simeq O(\alpha_s^4). \quad (3)$$

Note that the dependence on the scales μ and M is $O(\alpha_s^3)$ at the LL level, and hence at NTLL a reduced dependence on these scales is expected.

At the NTLL level, the jet cross-section depends on the definition of the jet (and on the cone size). In order to make predictions some jet definition must be chosen. The definition of Ellis, Kunszt and Soper [5], which is becoming standard, is adopted: Any hadron (η, ϕ) is in the cone of semi-aperture R centered on the jet axis (η_j, ϕ_j) if it fulfills the condition:

$$(\eta - \eta_j)^2 + (\phi - \phi_j)^2 < R^2. \quad (4)$$

The transverse energy E_{tj} of the jet is then:

$$E_{tj} = \sum_{i \in \text{cone}} E_{ti}. \quad (5)$$

The jet axis is defined by the weighted averages:

$$\eta_j = \frac{1}{E_{tj}} \sum_{i \in \text{cone}} E_{ti} \eta_i \quad (6)$$

$$\phi_j = \frac{1}{E_{tj}} \sum_{i \in \text{cone}} E_{ti} \phi_i. \quad (7)$$

2.2 Predictions

The above formalism has been applied to calculate jet cross-sections at LHC (pp at 16 TeV), to study the contribution from the various parton initiators, and to examine the dependence on rapidity, factorization scheme, jet-cone size, and choice of scale.

To reduce the amount of computer time required, the ‘*small cone*’ approximation has been made, in which only leading terms in R are kept. This approximation is valid in the range $R \leq 0.7$ [4]

For the LL and NTLL calculations, the two-loop running coupling constant $\alpha_s(\mu^2)$, evaluated at the scale μ^2 , was used. This is given by:

$$\alpha_s(\mu^2) = \frac{2\pi}{\beta_0 \ln(\mu^2/\Lambda^2)} \left(1 - \frac{\beta_1 \ln[\ln(\mu^2/\Lambda^2)]}{\beta_0^2 \ln(\mu^2/\Lambda^2)} \right) \quad (8)$$

with $\beta_0 = (11N)/6 - N_F/3$, $\beta_1 = (17N^2)/6 - (5N N_F)/6 - (C_F N_F)/2$, $N(N_F)$ being the number of colours(flavours) with $C_F = (N^2 - 1)/(2N)$. The parton distribution functions considered were:

- the three sets of DFLM [7] corresponding to $\Lambda = 0.160$ GeV, 0.260 GeV and 0.360 GeV,
- the two sets of HMRS³ [8]: B and E,
- the two sets of MT⁴ [9]: fit B1 and B2.

These fits have all been made in the NTLL approximation. The use, for LL calculation, of a two-loop α_s and NTLL distribution functions, may be criticized, but we think it more coherent since NTLL computations are available.

2.3 Results

2.3.1 Structure-function dependence and jet-initiators

Since the NTLL computation is very time consuming, only the LL calculation for $d\sigma/dE_t d\eta$ at $\eta = 0$ was performed for each of the seven structure-function sets. However, for each set the scale ($\mu = M$) was varied between $2E_t$ and $E_t/2$. The results are presented for HMRS-B in Table 1, and then just the most extreme of the results are shown: these are HMRS-E (Table 2) and DFLM-360 (Table 3); the other sets gave intermediate values. All results are summarized in Fig. 1, which shows, for the two extreme scale choices, the cross-section normalized to that obtained using HMRS-B. For HMRS-B the results were further separated into the different jet-initiator contributions (i.e. g, light quarks ($u, \bar{u}, d, \bar{d}, s, \bar{s}$), c (and \bar{c}), b (and \bar{b})), as shown in Fig. 2. The number of jets initiated by a gluon is very

³The higher value of Q^2 given in the HMRS tables is 10^6 .

⁴We assume a top mass of 100 GeV.

Table 1: LL jet cross-section at LHC using HMRSB structure functions.

E_t (GeV)	$d\sigma/d\eta dE_t _{\eta=0}$ (pb/GeV)		
	$\mu = M = E_t/2$	$\mu = M = E_t$	$\mu = M = 2E_t$
50	$0.478 \cdot 10^6$	$0.455 \cdot 10^6$	$0.425 \cdot 10^6$
75	$0.877 \cdot 10^5$	$0.797 \cdot 10^5$	$0.719 \cdot 10^5$
100	$0.250 \cdot 10^5$	$0.221 \cdot 10^5$	$0.194 \cdot 10^5$
150	$0.394 \cdot 10^4$	$0.337 \cdot 10^4$	$0.290 \cdot 10^4$
200	$0.101 \cdot 10^4$	$0.843 \cdot 10^3$	$0.712 \cdot 10^3$
300	$0.134 \cdot 10^3$	$0.110 \cdot 10^3$	$0.907 \cdot 10^2$
500	$0.889 \cdot 10^1$	$0.709 \cdot 10^1$	$0.573 \cdot 10^1$
800	$0.581 \cdot 10^0$	$0.454 \cdot 10^0$	$0.376 \cdot 10^0$
1000	$0.145 \cdot 10^0$	$0.111 \cdot 10^0$	$0.949 \cdot 10^{-1}$
2000	$0.953 \cdot 10^{-3}$	$0.808 \cdot 10^{-3}$	$0.711 \cdot 10^{-3}$

Table 2: LL jet cross-section at LHC using HMRSE structure functions.

E_t (GeV)	$d\sigma/d\eta dE_t _{\eta=0}$ (pb/GeV)		
	$\mu = M = E_t/2$	$\mu = M = E_t$	$\mu = M = 2E_t$
50	$0.315 \cdot 10^6$	$0.312 \cdot 10^6$	$0.301 \cdot 10^6$
75	$0.613 \cdot 10^5$	$0.579 \cdot 10^5$	$0.540 \cdot 10^5$
100	$0.183 \cdot 10^5$	$0.168 \cdot 10^5$	$0.153 \cdot 10^5$
150	$0.308 \cdot 10^4$	$0.273 \cdot 10^4$	$0.241 \cdot 10^4$
200	$0.824 \cdot 10^3$	$0.714 \cdot 10^3$	$0.621 \cdot 10^3$
300	$0.118 \cdot 10^3$	$0.996 \cdot 10^2$	$0.845 \cdot 10^2$
500	$0.859 \cdot 10^1$	$0.703 \cdot 10^1$	$0.582 \cdot 10^1$
800	$0.614 \cdot 10^0$	$0.491 \cdot 10^0$	$0.413 \cdot 10^0$
1000	$0.159 \cdot 10^0$	$0.125 \cdot 10^0$	$0.108 \cdot 10^0$
2000	$0.121 \cdot 10^{-2}$	$0.103 \cdot 10^{-2}$	$0.916 \cdot 10^{-3}$

Table 3: LL jet cross-section at LHC using DFLM ($\Lambda = 0.360$ GeV) s.f.

E_t (GeV)	$d\sigma/d\eta dE_t _{\eta=0}$ (pb/GeV)		
	$\mu = M = E_t/2$	$\mu = M = E_t$	$\mu = M = 2E_t$
50	$0.787 \cdot 10^6$	$0.686 \cdot 10^6$	$0.608 \cdot 10^6$
75	$0.126 \cdot 10^6$	$0.108 \cdot 10^6$	$0.922 \cdot 10^5$
100	$0.331 \cdot 10^5$	$0.279 \cdot 10^5$	$0.233 \cdot 10^5$
150	$0.473 \cdot 10^4$	$0.386 \cdot 10^4$	$0.318 \cdot 10^4$
200	$0.113 \cdot 10^4$	$0.907 \cdot 10^3$	$0.737 \cdot 10^3$
300	$0.138 \cdot 10^3$	$0.109 \cdot 10^3$	$0.873 \cdot 10^2$
500	$0.833 \cdot 10^1$	$0.645 \cdot 10^1$	$0.507 \cdot 10^1$
800	$0.514 \cdot 10^0$	$0.392 \cdot 10^0$	$0.306 \cdot 10^0$
1000	$0.125 \cdot 10^0$	$0.945 \cdot 10^{-1}$	$0.735 \cdot 10^{-1}$
2000	$0.825 \cdot 10^{-3}$	$0.619 \cdot 10^{-3}$	$0.468 \cdot 10^{-3}$

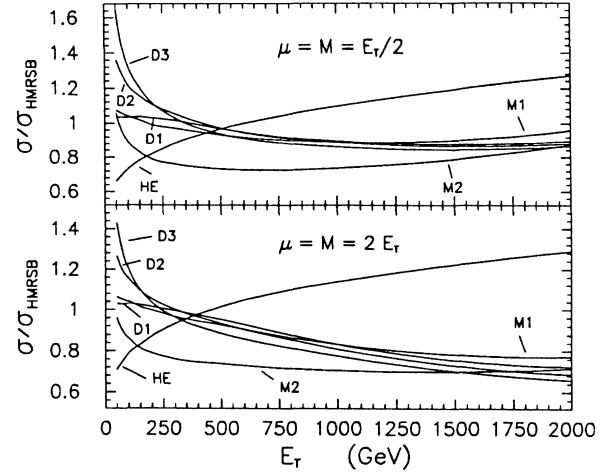


Figure 1: Leading-log jet cross-sections at LHC normalized to that using HMRS-B structure functions: HE = HMRS-E, D1 = DFLM (160 MeV), D2 = DFLM (260 MeV), D3 = DFLM (360 MeV), M1 = MT-B1, M2 = MT-B2.

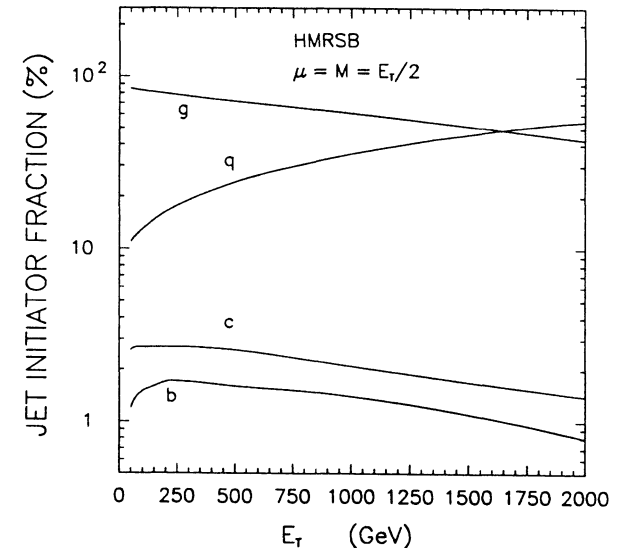


Figure 2: Fractional jet-initiator contributions to LL jet spectrum at LHC using HMRS-B structure functions.

large at small E_t due to the dominance of the gluon distribution at small x and the fact that the $gg \rightarrow gg$ contribution is about 100 times that of $gg \rightarrow q\bar{q}$. For larger values of E_t , the largest contribution is from light-quark initiators (especially valence quarks) because the valence distribution decreases less rapidly with x than the others. The number of jets initiated by c or b quarks is never large (even at large E_t) because in pp collisions there are no valence-valence contributions to produce sea quarks.

2.3.2 Rapidity dependence

The cross-section $d\sigma/d\eta dE_t$, integrated over E_t between $E_{t,\min}$ and $\sqrt{s}/2$, is computed for different values of η at the LL level, with $\mu = M = E_t/2$. We use the two sets of distribution functions B1 and B2 of MT in the \overline{MS} scheme. They have different behaviours at low x although both fit the existing data ($x > 0.03$). The results are given in Tables 4 and 5.

Table 4: LL incl. jet at LHC - MT fit B1 (\overline{MS} scheme)

$E_{t,\min}$ (GeV)	$d\sigma/d\eta$ (pb)			
	$\eta = 0$	$\eta = 1$	$\eta = 2$	$\eta = 3$
50	$0.717 \cdot 10^7$	$0.666 \cdot 10^7$	$0.522 \cdot 10^7$	$0.318 \cdot 10^7$
100	$0.616 \cdot 10^6$	$0.554 \cdot 10^6$	$0.388 \cdot 10^6$	$0.184 \cdot 10^6$
500	$0.676 \cdot 10^3$	$0.524 \cdot 10^3$	$0.196 \cdot 10^3$	$0.268 \cdot 10^1$
1000	$0.174 \cdot 10^2$	$0.114 \cdot 10^2$	$0.105 \cdot 10^1$	0
2000	$0.184 \cdot 10^0$	$0.653 \cdot 10^{-1}$	0	0

Table 5: LL incl. jet at LHC - MT fit B2 (\overline{MS} scheme)

$E_{t,\min}$ (GeV)	$d\sigma/d\eta$ (pb)			
	$\eta = 0$	$\eta = 1$	$\eta = 2$	$\eta = 3$
50	$0.641 \cdot 10^7$	$0.599 \cdot 10^7$	$0.480 \cdot 10^7$	$0.308 \cdot 10^7$
100	$0.505 \cdot 10^6$	$0.458 \cdot 10^6$	$0.331 \cdot 10^6$	$0.169 \cdot 10^6$
500	$0.542 \cdot 10^3$	$0.430 \cdot 10^3$	$0.170 \cdot 10^3$	$0.237 \cdot 10^1$
1000	$0.148 \cdot 10^2$	$0.100 \cdot 10^2$	$0.947 \cdot 10^0$	0
2000	$0.172 \cdot 10^0$	$0.619 \cdot 10^{-1}$	0	0

2.3.3 Factorization-scheme dependence

The factorization scheme (FS) is defined by the way collinear singularities are factorized in the distribution functions. To be consistent, we should have used LL distribution functions for LL calculation; in this case there would be no dependence on FS. The difference between factorization schemes at LL level is an artefact. On the contrary, if we use a NTLL calculation, the partonic cross-section is dependent on the FS. Since the MT distribution functions have been fitted using the DIS and \overline{MS} schemes, we can examine the difference at LL and NTLL level. Using set B1 of MT, we find only differences at the 5% level in $d\sigma/d\eta dE_t$ at $\eta = 0$, in the small cone approximation ($R = 0.7$), for E_t ranging from 100 to 2000 GeV.

2.3.4 Jet cone-size dependence

Since the LL cross-section is independent of R , effects due to the jet cone-size are expected to test the NTLL approximation in a non-trivial way. For three values of E_t , and HMRSB structure functions with $\mu = M = E_t/2$, Table 6 shows the dependence of the NTLL cross-section on the jet cone-size R . The results are

E_t (GeV)	$d\sigma/d\eta dE_t _{\eta=0}$ (pb/GeV)				
	$R = .1$	$R = .3$	$R = .7$	$R = 1.1$	$R = 1.3$
100	$0.156 \cdot 10^5$	$0.234 \cdot 10^5$	$0.321 \cdot 10^5$	$0.408 \cdot 10^5$	$0.484 \cdot 10^5$
1000	$0.828 \cdot 10^{-1}$	$0.120 \cdot 10^0$	$0.157 \cdot 10^0$	$0.196 \cdot 10^0$	$0.238 \cdot 10^0$
2000	$0.601 \cdot 10^{-3}$	$0.831 \cdot 10^{-3}$	$0.108 \cdot 10^{-2}$	$0.132 \cdot 10^{-2}$	$0.161 \cdot 10^{-2}$

plotted in Fig. 3. The NTLL result exhibits a logarithmic dependence on R and tends to $-\infty$ as R tends to zero. Note that the LL cross-section is independent of cone-size, being about a factor of 1.6 larger than the $R = 0.1$ NTLL values, and the same factor smaller than those for $R = 1.3$.

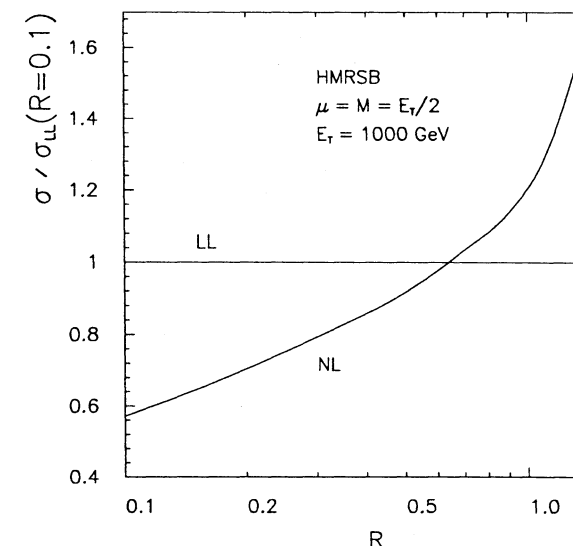


Figure 3: Dependence of NTLL inclusive-jet cross-section at LHC on jet-cone size R .

2.3.5 Scale dependence

Using DFLM ($\Lambda = 0.160 \text{ GeV}$) distribution functions at fixed E_t and R , Fig. 4 shows the dependence on $\mu = M$ between $E_t/4$ and $2E_t$ for NTLL and LL calculation. Note that the scale dependence is strongly reduced from 100% for LL calculation to 15% for NTLL, as already stressed in ref. [4,5].

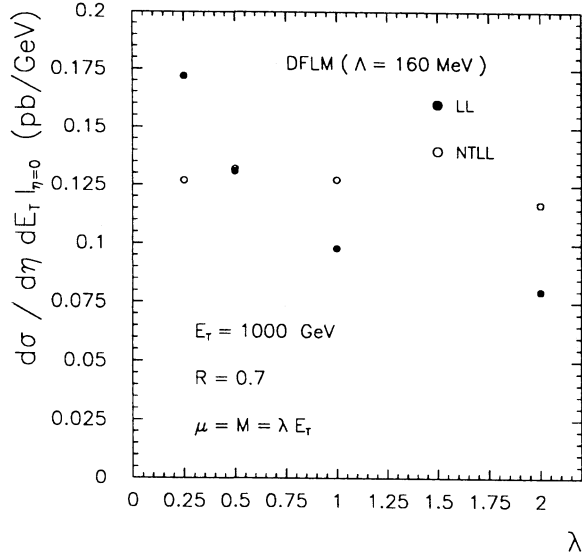


Figure 4: Dependence of LL and NTLL inclusive-jet cross-section at LHC on $\mu = M$.

3 Inclusive single-jet cross-sections (Monte Carlo)

Several Monte Carlo programs are being continually developed towards improved simulation of hadronic processes, generally using lower-energy data and data from electron machines to adjust the various phenomenological parameters which are required within these models in the absence of complete theoretical understanding. We have used PYTHIA 5.4 [12] to study the single-jet cross-section at LHC. A Monte Carlo like PYTHIA contains exact matrix elements for $2 \rightarrow 2$ partonic processes, and is hence expected to do at least as well as explicit $2 \rightarrow 2$ calculations in modelling the single-jet cross-section. At higher order the situation is less clear. It is of interest to investigate whether the parton-shower algorithms incorporated into several recent hadronic Monte Carlo programs effectively model jet production at next-to-leading order.

At current collider energies, $2 \rightarrow 2$ QCD-based Monte Carlo programs agree very well with the experimental single-jet data, as shown in Fig. 5 for data from

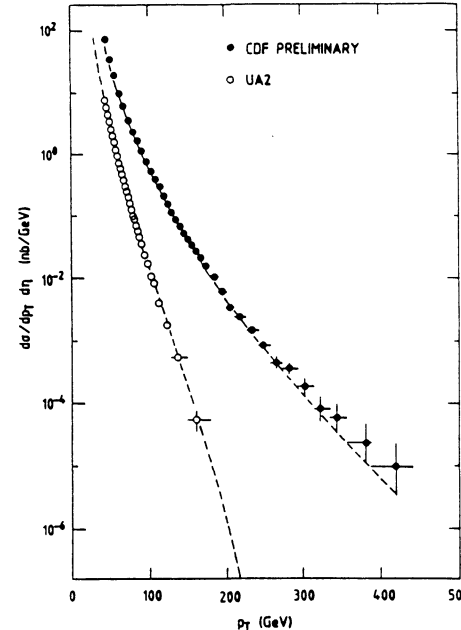


Figure 5: Single-jet inclusive spectra at $\eta = 0$ measured by UA2 ($\sqrt{s} = 630 \text{ GeV}$) and CDF ($\sqrt{s} = 1.8 \text{ TeV}$). The dashed lines are Monte Carlo predictions.

UA2 and CDF, together with curves based on such Monte Carlo calculations. Note that these are carefully tuned programs, run by the experimenters themselves [10,11], and before such tuning one would usually be content if a Monte Carlo agrees with experimental data within a factor of two or so. Within a Monte Carlo program simulating $2 \rightarrow 2$ QCD processes one is saved the real-world necessity of reconstructing jets from parton fragments since the properties of the hard-scattered partons are known. Thus the two primary outgoing partons (POPs) can be used to calculate a “jet” cross-section. In practice it is essential to fragment the partons and use some experimentally-based algorithm to reconstruct the jets just as must be done in the real world, in order to understand and model detector behaviour and inefficiencies. Running PYTHIA 5.4 at $\sqrt{s} = 630 \text{ GeV}$ for just $2 \rightarrow 2$ processes, without fragmentation of the POPs, and using default values for all other values in PYTHIA, yields a single-jet (POP) spectrum which is already in reasonable agreement with the UA2 corrected single-jet spectrum.

With such agreement in hand, we are free to extrapolate to LHC energies by running PYTHIA at $\sqrt{s} = 16 \text{ TeV}$. PYTHIA’s default parameters were used: these include EHLQ-1 [13] structure functions, $\Lambda = 0.20 \text{ GeV}$, α_S taken to be the 1st order running coupling constant, and $Q^2 = 1/2(m_{T_1}^2 + m_{T_2}^2)$. The resulting $2 \rightarrow 2$ spectrum is shown in as the solid line in Fig. 6. In the same figure the solid points show the theoretical LO spectrum as obtained using the methods discussed in Section 2, but with HMRS-B [8] structure functions. The “error” bars on the

theoretical points show the range obtained by varying $\mu = M$ from $E_t/2$ to $2E_t$. The agreement is encouraging, given the different structure-function sets used, but, as discussed above, expected.

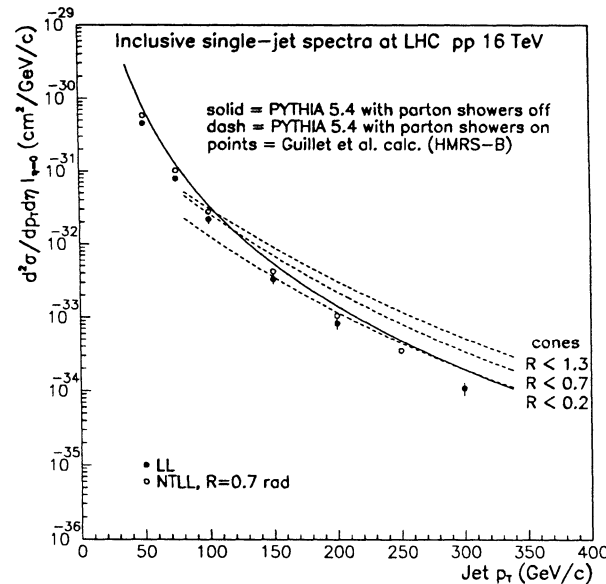


Figure 6: Inclusive jet spectra at LHC: the curves show results from PYTHIA using EHLQ-1 s.f. (solid = without, and dashed = with, parton-showering); the points were calculated by Guillet et al. using HMRS-B s.f. (solid = LL, open = NTLL).

Next the parton-showering algorithms available in PYTHIA were activated. Both initial-state and final-state parton showers occur. Within the Monte Carlo framework there still exist two POPs which can be directly considered as jets, but such an interpretation is no longer straightforward. As discussed in Section 2, some sort of jet definition is now essential. For these simple studies fragmentation of the final-state partons can still be avoided, and jet reconstruction can be based just upon these partons. The initial method considered all final-state partons lying within a cone of specific opening angle about an axis along the direction of the parent POP. The 4-momentum of the jet was taken to be the vector sum of the 4-momenta of each parton falling within the cone. It was quickly realized that the resultant 4-momentum of such a “space” cone, especially one of large opening-angle, is sensitive to distortion due to occasional low p_T but high-rapidity (y) partons which fall inside. A better algorithm is to use an “ $\eta - \phi$ ” cone relative to a POP; it was such considerations which motivated the use of such a cone in Section 2. The distribution of the variable R defined by:

$$R^2 = (\eta_{POP} - \eta_j)^2 + (\phi_{POP} - \phi_j)^2 \quad (9)$$

where j labels final-state partons, and POP is the nearer of the two parent POPs, is shown in Fig. 7a). A cone is defined by considering only partons for which R is below a given value, and hence the 4-momentum within the cone can be calculated. Figure 7b) shows how the pseudorapidity distributions of cones of increasing R gradually approach that of the POPs. The corresponding single-jet cone cross-sections are shown as the dotted curves in Fig. 6, for cone radii of 0.2, 0.7, and 1.3. In a real experiment, some p_T and $|\eta|$ cuts will be unavoidable. If the parton showers are restricted to the (optimistic) values $p_T > 0.1$ GeV/c and $|\eta| < 3.0$ the cone spectra are essentially unchanged. Allowing the final partons to fragment to hadrons hardly changes the cone spectra at all, although the required computer time is considerably increased. Finally, if the jet-axes are iterated until convergence (i.e. the POPs directions give just the 1st iteration jet directions) then the cone spectra become a little stiffer. Figure 6 also shows theoretical NTLL values using a cone of $R < 0.7$ rad. These values are slightly higher than the LL values but, as discussed in section 2, less sensitive to the values of input parameters. The spectrum from the Monte Carlo with parton showers is also higher than the leading-order spectrum.

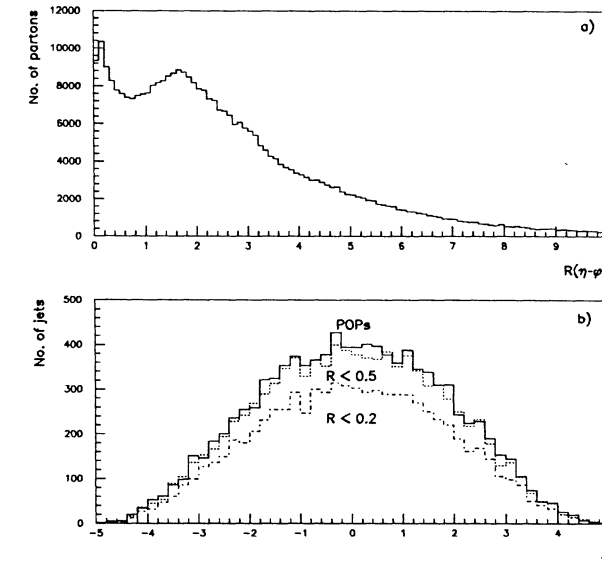


Figure 7: PYTHIA 5.4 results for 10000 QCD $2 \rightarrow 2$ events with jet $p_T > 75$ GeV/c at LHC: a) Distribution of $R(\eta - \phi)$; b) Pseudorapidity distributions for jets defined as cones of various maximum $R(\eta - \phi)$, and for the primary outgoing partons.

Figure 8 shows the leading-order single-jet spectrum up to jet p_T values around 3 TeV/c. The PYTHIA spectrum used the default values; the theoretical values are taken from Table 1 of Section 2, with the “error” bars once again showing the

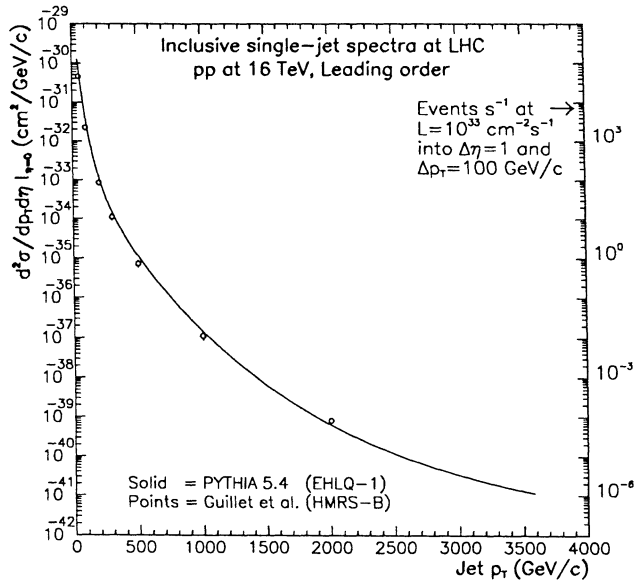


Figure 8: LO single-jet inclusive spectra at LHC from PYTHIA (solid) and Guillet et al. (points).

range obtained by changing the value $\mu = M$ from $E_t/2$ to $2E_t$. The agreement shows the insensitivity of the jet spectrum to choice of structure functions when examined over such a wide range of jet p_T , and the agreement between Monte Carlo and direct calculation. Figure 9 shows the results of a Monte Carlo calculation for pp at 16 TeV based directly on the leading-order $2 \rightarrow 2$ QCD matrix elements, using HMRS-B structure functions, but here divided into separate η ranges. Figures 8 and 9 also show single-jet event-rates for a jet p_T bin of 100 GeV and η bin of one unit, at an instantaneous luminosity of $10^{33} \text{ cm}^{-2} \text{s}^{-1}$. The kHz rate for jets of p_T around 100 – 200 GeV/c underlines the problematic background conditions with which experiments will have to contend while searching for rare physics signals. Jets of very high- p_T should be common; several jets of p_T around 2 TeV/c should occur per day.

4 Limits on parton compositeness

If quarks and leptons are bound states of a few fundamental objects (usually called preons), a hypothesis naively inspired by the Family Problem, then new physics beyond the Standard Model is to be expected [13]. Such constituents are expected to interact through a new strong gauge interaction (metacolour). Below a characteristic energy scale Λ_C , the new interaction becomes strong and

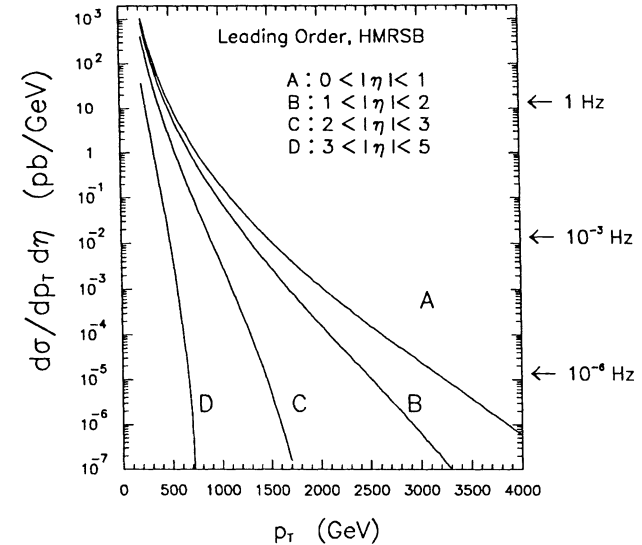


Figure 9: LO single-jet inclusive spectra at LHC from direct Monte Carlo of $2 \rightarrow 2$ QCD matrix elements, using HMRS-B structure functions.

binds preons into metacolour singlet states (i.e. quarks and leptons). Λ_C is of the order of magnitude of the energy required to dissociate them. Signals of compositeness would depend upon the subprocess energy \sqrt{s} available, relative to the characteristic scale Λ_C . At high energies ($s > \Lambda_C^2$) the familiar two-body parton-scattering contribution to the single-jet cross-section would be dominated in a spectacular way by multiple production processes. At lower energies tests of composite models rely on the behaviour of four-fermion contact interactions where the typical elastic interaction is mediated by the exchange of preon bound-states with masses of the order of Λ_C or by a metacolour gluon-exchange mechanism.

In the studies presented here we concentrate on the effect of a contact interaction in jet production, where the contact term modifies the cross-section for (anti)quark-(anti)quark scattering. This effect would be most apparent at high transverse momenta where valence-quark scattering dominates. The parton-level calculation uses a phase-space integration technique, performed through Monte Carlo generated events. The QCD matrix elements have been expanded including the contact terms following the parametrisation and notation of Ref. [13], with only light-quark compositeness, and no gluon compositeness, being considered. The usual choice of $g^2/4\pi = 1$ has been made for the coupling constant. The choice of the phase $\eta^{00} = \pm 1$ governing the interference terms between QCD and the new interaction is arbitrary, and results are shown for both cases. In Fig. 10 we present single-jet cross-sections for different choices of Λ_C and $\eta^{00} = \pm 1$ in

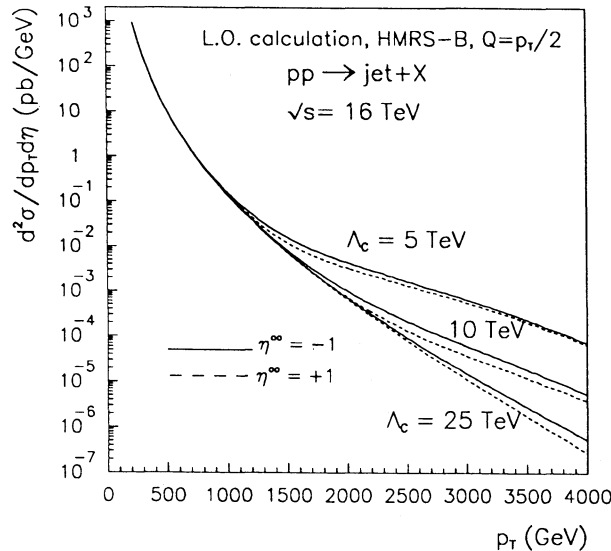


Figure 10: Inclusive jet cross-section $d^2\sigma/dp_T d\eta$ at $\eta = 0$ for several values of Λ_C , performed using HMRS-B s.f. and a scale $Q^2 = p_T^2/4$.

the case of pp scattering at $\sqrt{s} = 16 \text{ TeV}$ as a function of the parton transverse momentum p_T . The presence of the contact interaction terms increases the cross-section for higher values of transverse momentum, while leaving it unchanged at low p_T . In addition, because the \hat{u} and \hat{t} terms (Eq.(8.13) in Ref. [13]) are both negative, constructive interference enhances the cross-section for $\eta^{00} = -1$ relative to that with $\eta^{00} = +1$. These calculations have been performed using several quark and gluon distributions labelled DFLM⁵ [7], HMRS⁶ [8], MT⁷ [9], MRSB⁸ [14], and DO⁹ [15], in order to estimate the uncertainties introduced by the choice of structure-function set. The results shown are for the HMRS-B parton densities. A second systematic uncertainty in the calculation is introduced by the choice of the Q^2 scale, which influences not only the absolute scale but also the shape of the cross-section. A value $Q^2 = p_T^2/4$ has been arbitrarily chosen here. The two effects combine to yield an overall uncertainty on the cross-section shape of about 20%, with some p_T -dependence. To estimate what limits can be set on the compositeness scale at LHC, we show in Fig. 11 the effect on the cross-section of different values of Λ_C as a ratio to the pure QCD calculation $\Lambda_C = \infty$. The error

⁵with $\Lambda_{QCD} = 160 \text{ MeV}$.

⁶HMRSE: set E, HMRSB: set B.

⁷set S1 with $\Lambda_{QCD} = 212 \text{ MeV}$.

⁸set B' with $\Lambda_{QCD} = 228 \text{ MeV}$.

⁹with $\Lambda_{QCD} = 200 \text{ MeV}$.

bar in the figure reflects the statistical accuracy one would obtain in absence of a contact interaction after one year of running at $\mathcal{L} = 10^{33} \text{ cm}^{-2} \text{s}^{-1}$, i.e. with an integrated luminosity of $3 \times 10^4 \text{ pb}^{-1}$. In such a case, a limit $\Lambda_C < 13 \text{ TeV}$ can be set with a 95% confidence level. It is important to note that these results are

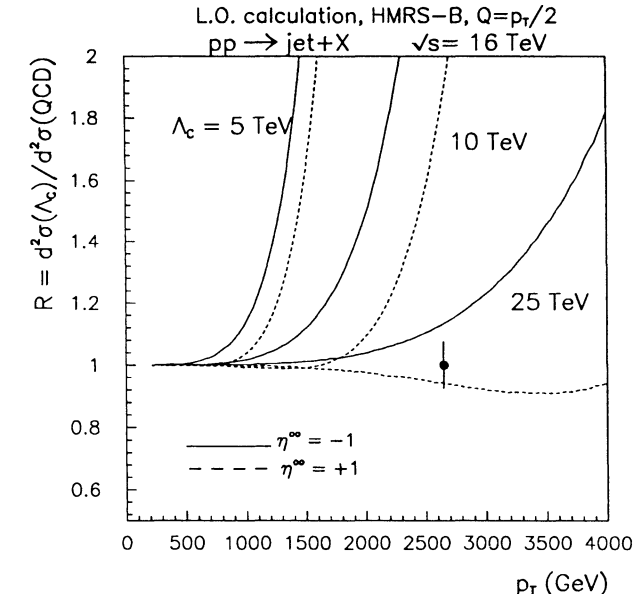


Figure 11: Ratio between parton-level calculations for different Λ_C values and the calculation for $\Lambda_C = \infty$, for HMRS-B s.f. and $Q^2 = p_T^2/4$. The error bar for the black circle gives the statistical accuracy that can be reached after 1 year of running at $\mathcal{L} = 10^{33} \text{ cm}^{-2} \text{s}^{-1}$.

valid only for the case of an ideal detector. Simulations based on realistic detector configurations, in which the response may not be linear, and resolution effects may be important, must still be performed. Even so, it is clear that measurement of the inclusive-jet cross-section at LHC energies should allow an increase by a factor of between 10 and 20 to the limit on the compositeness scale which is set currently by measurements of UA2 at the CERN Collider [10] and CDF at Fermilab [11].

5 Multi-jet cross-sections.

Multi-jet backgrounds at 16 TeV were estimated using a new calculation by H. Kuijf and F.A. Berends [16]. With respect to the previous work done by Z. Kunszt and W.J. Stirling [17] this new program provides the exact leading order (LO) calculation up to 5 jets production and good approximations up to 8 [18]. Both [16] and [17] have been shown to be in good agreement with existing Collider data up to 5 jets [19]. Figure 12 shows the inclusive p_T spectrum, $\frac{d\sigma}{dp_T}$, for four

jets events observed in the UA2 calorimeter. Each jet p_T enters the plot and only statistical errors are shown. Details of the analysis can be found in [19]. Briefly, the Monte-Carlo generated events were fragmented according to a Field-

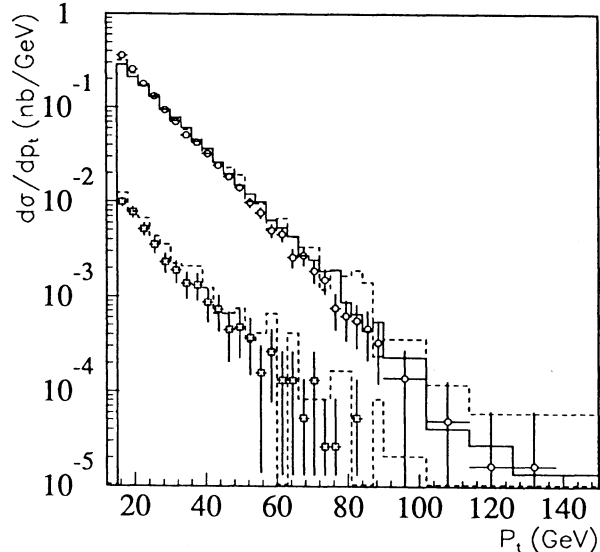


Figure 12: Uncorrected p_T spectra for 4- and 5-jet events. The data points are the UA2 data, only statistical errors are shown. The histograms represent the absolute prediction of the Kunszt-Stirling (solid) and Kuijf-Berends (dashed) calculations after full simulation of the calorimeter.

Feynman model, allowing for gluon radiation, and passed through a complete simulation of the UA2 detector, they were then analyzed in the same fashion as the data. The spectra generated agree quite well with the observed data. The acceptance-uncorrected integrated four-jets cross-section is $\sigma_4(\text{DATA}) = 1.31 \text{ nb}$, whereas the two QCD calculations predict $\sigma_4(\text{Kunszt - Stirling}) = 1.21 \text{ nb}$ and $\sigma_4(\text{Kuijf - Berends}) = 1.28 \text{ nb}$.

Motivated by the good agreement at lower energies we estimated multi-jet rates at the LHC. Since all the conclusions of [17] remain valid we will only concentrate on tabulating multi-jet cross-sections at the LHC energies. The following study is a pure parton level one: it does not include any fragmentation effect or detector smearing. More importantly it does not include any calorimeter “pile-up”, due to multiple interactions within the same bunch crossing, or “feed-down” effects where one, or more, jets in the event go undetected and a n-jet event is classified as a lower multiplicity event.

For this study the following parton level cuts were used to define a n-jet event:

$$E_{t,i} > 50 \text{ GeV} \quad i=1 \dots n$$

$$\begin{aligned} |\eta_i| &< 3.0 & i=1 \dots n \\ \theta_{ij} &> 30^\circ & \text{for any jet pair} \end{aligned}$$

The last condition is necessary to have well-separated partons and avoid collinear divergences. The structure-function set used was Duke-Owens (set 1); other sets (DO2, EHLQ, GR, MRSEB1 and MRSEB2) were also tried but the final conclusions are only weakly-dependent on structure functions. The Q scale was set to the maximum E_t in the event (i.e $Q^2 \equiv E_{t,\max}^2$). Table 7 summarizes the results for the multi-jet cross-sections.

Table 7 : Multi-jet cross-sections at LHC (nb)

m	EXACT	SPHEL	ESFAG
2	24020.	24200.	23600.
3	1150.	1170.	1110.
4	132.	163.	119.
5	13.4	18.5	14.04
6	-	2.3	-
7	-	0.35	-
8	-	0.034	-

The label EXACT refers to the exact calculation of the QCD matrix elements, whereas SPHEL and ESFAG are two approximations using different techniques[18]. For a typical integrated luminosity of 10^5 pb^{-1} the results of Table 7 translate from $\approx 2.4 \times 10^{12}$ 2-jet to $\approx 3 \times 10^6$ 8-jet events. Demanding the softest jet in each event to exceed 100 GeV in transverse energy results in $\approx 1.9 \times 10^{11}$ 2-jet and $\approx 6 \times 10^4$ 8-jet events. The inclusion of calorimeter “pile-up” and feed-down effects, however, could substantially modify these conclusions. Figure 13 shows the invariant mass spectra and the inclusive p_T spectra predicted for multi-jets at LHC energies. Each jet in the event enters the p_T plot. These spectra for 2- to 5-jet events were obtained using the exact QCD calculation.

6 Conclusions

It is evident that both single-jet and multi-jet rates will be enormous at LHC energies, and presumably these jets will be useful for various QCD tests (e.g. angular distributions) and for probing possible parton substructure, just as is done with the jets detected at present colliders. It appears that both theoretical calculations and Monte Carlo predictions of these cross-sections are in good agreement. Furthermore the reduced sensitivity to the various necessary parameter choices (structure functions, scale, etc.) of the theoretical NTLL calculations is particularly encouraging.

Further studies will of course be necessary to address the measurement of jets with realistic detector configurations. The importance of effects of detector resolution and response, and calorimetric hermeticity, cannot be overemphasized,

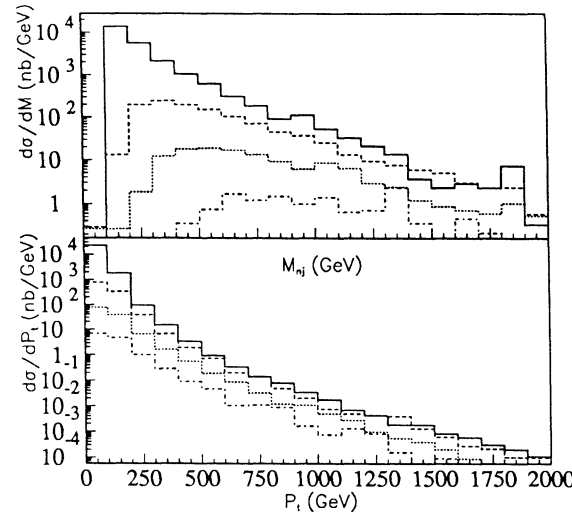


Figure 13: Invariant mass and inclusive p_T spectra for 2- to 5-jet events at the LHC.

as is already known from many previous studies. Furthermore, pile-up effects due to the high running luminosities will surely complicate an otherwise clear experimental situation.

References

- [1] T. Åkesson *et al.*, *Jets at the Large Hadron Collider*, and other contributions on jets, in Proc. of the ECFA-CERN Workshop on a Large Hadron Collider in the LEP Tunnel, Lausanne and Geneva, 21-27 March 1984, Vols. I and II, CERN 84-10.
- [2] T. Åkesson *et al.*, *Detection of jets with calorimeters at future accelerators*, and other contributions on jets, in Proc. of the Workshop on Physics at Future Accelerators, La Thuile (Italy) and Geneva (Switzerland), 7-13 January 1987, Vols. I and II, CERN 87-07.
- [3] *The feasibility of experiments at high luminosity at the Large Hadron Collider*, Ed. J. H. Mulvey, CERN 88-02.
- [4] F. Aversa, P. Chiappetta, M. Greco, and J.-P. Guillet, Phys. Rev. Lett. **65** (1990) 401.
- [5] S. Ellis, Z. Kunszt, and D. Soper, Phys. Rev. Lett. **64** (1990) 2121.
- [6] R. Ellis and J. Sexton, Nucl. Phys. **B269** (1986) 475.
- [7] M. Diemoz, F. Ferroni, E. Longo, and G. Martinelli, Z. Phys. **C39** (1988) 21.
- [8] P. Harriman, A. D. Martin, R. G. Roberts, and W. J. Stirling, Phys. Rev. **D42** (1990) 798.
- [9] J. G. Morfin and W.-K. Tung, preprint FERMILAB-Pub-90/74 (1990).
- [10] V. Cavassini (UA2 Collab.), in Proc. XXV Int. Conf. on High Energy Physics, Singapore 1990, Eds. K. K. Phua and Y. Yamaguchi
- [11] M. Dell'Orso (CDF Collab.), in Proc. XXV Int. Conf. on High Energy Physics, Singapore 1990, Eds. K. K. Phua and Y. Yamaguchi
- [12] Update of PYTHIA 4.8: H.-U. Bengtsson and T. Sjöstrand, Computer. Phys. Comm. **46** (1987) 43.
- [13] E. Eichten, K. Lane, and M. Peskin, Phys. Rev. Lett. **50** (1983) 811; E. Eichten, I. Hinchliffe, K. Lane, and C. Quigg, Rev. Mod. Phys. **56** (1984) 579; *erratum* Rev. Mod. Phys. **58** (1986) 1065.
- [14] A. D. Martin, R. G. Roberts, and W. J. Stirling, Mod. Phys. Lett **A4** (1989) 1135; Phys. Rev. **D37** (1988) 1161.
- [15] D. W. Duke and J. F. Owens, Phys. Rev. **D30** (1984) 49.
- [16] H. Kuijf, *Multiparton production at hadron colliders*, Thesis, Leiden University, in preparation.
- [17] Z. Kunszt and W. J. Stirling, *Multijet cross-sections in hadronic collisions*, in ref. [2].
- [18] H. Kuijf and P. Lubrano, *Multijet event generators for LHC*, these Proceedings.
- [19] P. Lubrano, *Jet physics with the UA2 detector*, in Proc. of the 4th Rencontre de Physique de la Vallee D'Aoste, La Thuile, March 18-24, 1990 (Editions Frontieres 1990).

Production of direct photon at LHC and SSC

P.Aurenche¹ M.Bonesini² L.Camilleri³ P.Chiappetta⁴ M.Fontannaz⁵
J.P.GUILLET⁶ M.N.Kienzle-Focacci⁷ M.Werlen⁸

presented by M.Werlen

1 Introduction

The production of prompt photon in hadronic collisions has been measured in a large domain, from fixed target at $\sqrt{s} = 20 \text{ GeV}$ to collider at $\sqrt{s} = 1.8 \text{ TeV}$, spanning the x_T range from about 0.02 to 0.7. For a recent compilation, see [1]. On the theoretical side, next to leading logarithm evaluations for inclusive photon [2] and more recently for photon + jet [3] are available. The phenomenology is quite advanced: in particular photon and deep inelastic data have been used to precisely constrain the gluon distribution for $x \geq 0.1$ [4]. Photon physics at super-collider energies has also been investigated in [5,6,7]. In this report, we try to evaluate the uncertainties in the predictions and study the background coming from jets and neutral hadrons as precisely as possible without a detailed knowledge of a final detector design.

Production of hadrons in proton-(anti)proton collisions with large transverse momentum is an important tool to test large angle scattering of proton constituents and to improve our knowledge of fragmentation functions. However π^0 production (and more generally neutral hadrons production) is a severe background to the real photon signal and its precise knowledge is crucial to pin down the existence of new particles such as $H^0 \rightarrow \gamma\gamma$ or any breaking of the standard model. On the theoretical side, next to leading order evaluations of single hadron [8] as well as jet [9,10] production at large p_T have been performed and are expected to substantially reduce the uncertainty on the choice of renormalization and factorization scales, as can be inferred from jet analysis [9].

In the following we make predictions for γ rates at $\sqrt{s} = 16 \text{ TeV}$ and $\sqrt{s} = 40 \text{ TeV}$ discussing, in some details, various theoretical uncertainties. We show that direct photons can be used to probe the gluon at values of x as low as those accessible at HERA, but at much higher Q^2 . We then discuss jet and π^0 production. As expected, the later is seen to overwhelm the prompt γ signal in the lower p_T range. Fortunately, various isolation criteria are shown to considerably reduce this hadronic background so that prompt γ can be reliably identified down to p_T values of 50 GeV/c.

¹LAPP,Annecy (AURENCH@FRCPN11)

²INFN,Milano (BONESINI@CERNVM)

³CERN (LLC@CERNVM)

⁴CPT,Marseille (CHIAPETA@FRCPN11)

⁵LPTHE,Orsay (FONTANNA@FRCPN11)

⁶CERN (JGUILLET@CERNVM)

⁷DPMC,Genève (FOC@CERNVM)

⁸IPN,Lausanne (MONICA@CERNVM)

2 Prompt photon signal

2.1 Inclusive cross section

At the Born level, only two subprocesses contribute to prompt photon production: the "QCD Compton" graph $qg \rightarrow \gamma q$, dominant in proton proton collisions and the annihilation diagram $q\bar{q} \rightarrow \gamma g$. Full next to leading logarithm (NLL) calculations $O(\alpha_s^2)$ are available [2]. The Born diagrams and examples of bremsstrahlung and higher order diagrams are shown in Fig. 1. NLL inclusive cross sections are given in table I with structure functions which are excellent fits to available direct photon data and high statistics deep inelastic scattering data [4]. In the calculation, the factorization scale and the renormalization scale have the same common value $Q = p_T/4$, which is found to lead to a good approximation of the optimized results (i.e. the results stable under local changes of scales). The Born term is given for completeness, although one should keep in mind the important scale dependence of such a term, which can be as much as 2.5 between $Q = p_T/4$ and $Q = 4p_T$.

2.2 Isolated cross section

In order to reject π^0 's, which are jet fragments, one needs to apply isolation cuts which will reduce the rate of the bremsstrahlung photons. A useful isolation cut introduced in the recent collider experiments defines a photon as isolated when in a cone R

$$R = \sqrt{\Delta\eta^2 + \Delta\phi^2} \quad (1)$$

around the photon, the accompanying energy

$$\epsilon' = \frac{E(\text{hadrons in cone})}{E_\gamma} \quad (2)$$

is smaller than some fraction ϵ . The cross sections for isolated photon with $R=0.1$ and $\epsilon = 15\%$ are also given on table I. These isolation criteria reduce the rate by about 20%.

The dependence of the cross sections as function of R for $\epsilon = 15\%$ is shown on Fig. 2 at $p_T = 100 \text{ GeV}/c$ and $y = 0$. Above R of 0.1, the dependence is small. All these results are based on an inclusive calculation where the constraints eqs. (1),(2) are implemented in an approximate way [14]. We have checked that they are in excellent agreement (better than 5%) with the results from the Monte Carlo program of Ref. [3]⁹.

The ϵ dependence is studied later in relation to π^0 production.

2.3 Rates

The rates, evaluated at a luminosity of $10^{33} \text{ cm}^{-2} \text{ s}^{-1}$ for $\Delta p_T = 100 \text{ GeV}/c$ and integrated in y between ± 1 , are shown in Fig. 3. Even with the low luminosity considered, the counting rate is very large: there are roughly 1 event/sec at $p_T = 100 \text{ GeV}/c$, 1 event/hour at $p_T = 600 \text{ GeV}/c$ and 1 event/day at $p_T = 1 \text{ TeV}/c$.

⁹This flexible code is not yet fully updated for LHC energies (no initial charm for example) and is more CPU intensive.

2.4 Scales and other theoretical uncertainties

The cross section at NLL can be written as

$$E \frac{d^3\sigma}{dp^3} = F(M) \otimes F(M) \alpha_s(\mu) (\sigma_{Born} + \frac{\alpha_s(\mu)}{\pi} R(\mu, M, \dots)) \quad (3)$$

where M is the factorization scale (structure function evolution) and μ the renormalization scale. When the same value is used for both, the common scale is denoted Q . In Fig. 4, we compare the predictions for the isolated cross section ($R=1, \epsilon = .15$) obtained from different scale choices. We plot, as a function of p_T , the ratio of the prediction with the scale $Q=p_T/4$ and $Q=4p_T$ to the optimized results obtained by applying the principle of minimum sensitivity to both the factorization and renormalization scales [11]. Over the whole p_T range the optimized predictions are the highest but the difference with the other scales is at most 25%. To an accuracy better than 10%, the predictions obtained with $Q = p_T/4$ are a good approximation to the optimized results, a feature already observed at the Tevatron energy.

Another source of uncertainties still concerns the higher order corrections. It is well known that the large corrections to the leading logarithm approximation are related at low p_T to the bremsstrahlung component associated to the configurations where a photon is found in the fragments of a jet. This component is similar to π^0 or single particle production at large p_T for which the NLL corrections have recently been calculated [8]. We assume that corrections to the bremsstrahlung contribution can therefore be reasonably approximated by the corrections to single hadron production where, in the calculation, the fragmentation of a parton into a hadron is replaced by the fragmentation of a parton into a photon. Including this corrected bremsstrahlung estimate in the usual NLL calculation, we find that the inclusive photon spectrum is increased by about 30% at $p_T = 20$ GeV/c and by a few % only in the TeV range. While these estimates require further work [12] to be put on a solid basis, they can be taken as an indication of the remaining theoretical uncertainties. It is amusing to note that these variations of the predictions are of the same order as those covered by the changes in the values of the scales discussed above.

Finally, we briefly illustrate the variation in the predictions due to different choices of structure functions by comparing the inclusive cross section of Table I at $\sqrt{s} = 16$ TeV with predictions based on set HMRSB [13] (table III). Not surprisingly there is perfect agreement in the medium and high p_T range which covers a measured domain of x . The most noticeable difference occurs at $p_T = 20$ GeV/c where the HMRSB rate is about 40% lower. This discrepancy probably reflects the differences in the assumed, but untested, extrapolations of the structure functions down to very low x values.

2.5 Gluon probe and QCD tests

Inclusive γ cross section probes the gluon in the domain $x \geq x_T e^{-y}$. The rapidity dependence of direct γ at low p_T is studied for two different gluon shapes:

$$xG(x, 2) \sim (1 - x)^4 \quad (4)$$

$$xG(x, 2) \sim \frac{1}{\sqrt{x}}(1 - x)^2 \quad (5)$$

These shapes are within the systematic uncertainties of existing direct photon and deep inelastic data [14]. As shown in table II, even if the absolute normalization is not precise, the shape of the rapidity distribution can be used to distinguish the standard form (eq. 4) from the singular form in $\frac{1}{\sqrt{x}}$. Indeed at the lower p_T values, the standard gluon leads to an essentially flat distribution whereas the singular one leads to a peak in the distribution, at $y=2.5$ to 3.0, moving inwards as p_T increases. At higher p_T values, the shape difference disappears. Rates in one day at $10^{33} \text{ cm}^{-2} \text{ s}^{-1}$ are given on Fig. 5 for a Δp_T of 5 GeV/c at $p_T = 80$ GeV/c, where as we will see later on, direct photon can be measured with a good calorimeter granularity. Statistical accuracy will be quite enough to distinguish the two shapes if the systematics as function of rapidity can be controlled to a few %.

At HERA, the gluon will be probed down to $x \approx 10^{-3}$ in the range $Q^2 \approx 10 \rightarrow 100 \text{ GeV}^2$ [15]. At LHC for instance, value of $p_T = 80$ GeV/c corresponds to $x \approx 10^{-3}$ and $Q^2 \approx 6 \cdot 10^3$ and $p_T = 2 \text{ TeV}/c$ corresponds to $x \approx 0.25$ and $Q^2 \approx 4 \cdot 10^6$. Combining measurements from both accelerators, the structure function evolution could therefore be tested over a large range.

2.6 Compositeness

Assuming the standard form [7]

$$\sigma_{\text{composite}} = (1 + (2p_T/\Lambda)^4)^2 \sigma_{\text{standard model}} \quad (6)$$

and integrating over $\Delta p_T = 500$ GeV/c and $\Delta y = 4$, with an integrated luminosity of 10^5 pb^{-1} (10^4 pb^{-1}) a scale of 6 TeV (4 TeV) can be probed. This is illustrated on Fig. 6, where the ratio of the number of events for a composite model vs the standard model is shown.

3 Background estimate and experimental feasibility

First, we will compare inclusive photon and jet production at LHC. Then we will evaluate the π^0 cross section.

3.1 Photon and jet cross sections

A comparison of inclusive photon and jet cross sections, is shown in table III and figure 7. Both are evaluated at next to leading order with the same structure function set HMRSB [13]. For the jet, the $O(\alpha_s^3)$ code from [9] has reduced the scale uncertainties to 23% varying $\mu = M$ from $p_T/4$ to $4p_T$ for $p_T = 100$ GeV/c. The dependence on the cone size for $R=0.7$ and 0.1 is also shown on the figure: the cross section with the larger cone size is roughly 75% higher. The table is produced with the same choice for both the renormalization and factorization scales of $Q = p_T/2$ for the jet (the stability region being around $Q = p_T$ for $R=0.1$ and $Q = p_T/2$ for $R=0.7$), and $Q = p_T/4$ for the photon. The ratio jet/γ varies

from $\sim 4.3 \cdot 10^3$ at $p_T = 50$ GeV/c to $\sim 8 \cdot 10^2$ at $p_T = 2$ TeV/c. What are the uncertainties on this ratio? Taking a p_T of 100 GeV/c, allowing the scales to vary between $p_T/4$ and $4p_T$ independently for the jet and the photon, this ratio varies from $2.8 \cdot 10^3$ to $4.7 \cdot 10^3$. Changing the cone size for the jet from $R=0.7$ to $R=0.1$, this ratio drops from $3.27 \cdot 10^3$ (see table III) to $1.82 \cdot 10^3$. There will also be a variation due to structure functions which we have not evaluated.

3.2 Inclusive π^0 production at LHC

The inclusive cross section for single hadron production at large transverse momentum:

$$H_1(k_1) + H_2(k_2) \rightarrow H_3(p) + X \quad (7)$$

is given by

$$\begin{aligned} E \frac{d\sigma}{d^3\vec{P}} &= \sum_{i,j,l} \int_0^1 dx_1 \int_0^1 dx_2 \int_{-(T+U)/S}^1 \frac{dx_3}{x_3^2} F_{P_i}^{H_1}(x_1, M) F_{P_j}^{H_2}(x_2, M) \\ &\times D_{P_i}^{H_3}(x_3, M_F) \left(P_l^0 \frac{d\hat{\sigma}}{d^3\vec{P}_l}(\mu, M, M_F, x_1, x_2) \right) \end{aligned} \quad (8)$$

where $F_P^H(x, M)$ and $D_P^H(x, M_F)$ are the structure and fragmentation functions evaluated at the scales M, M_F respectively. The partonic cross section $P_l^0 \frac{d\hat{\sigma}}{d^3\vec{P}_l}$ corresponding to the subprocess $P_i + P_j \rightarrow P_l + X$ has been evaluated up to $O(\alpha_s^3)$ [8]. We will use for the structure functions the set HMRSB ($\Lambda_{flavors} = 190$ MeV). Although the fragmentation function for quarks into pions is quite well constrained from $e^+ e^-$ data, collider results from ISR and SppS should give complementary information about the pion fragmentation function from gluons. The data from $e^+ e^-$, which are mainly sensitive to the fragmentation of quarks, indicate [18] that the BEP [16] parametrization has to be modified. We will use, for $Q_0^2 = 25$ GeV 2 :

$$\begin{aligned} D_u^{\pi^0}(z) &= D_d^{\pi^0}(z) = 0.55z^{-1.1}(1-z)^2 \\ D_{s,c}^{\pi^0}(z) &= D_{\bar{s},\bar{c}}^{\pi^0}(z) = (1+z)D_u^{\pi^0}(z) \\ D_g^{\pi^0}(z) &= 0.8z^{-1.2}(1-z)^{3.5} \end{aligned} \quad (9)$$

This parametrization describes correctly the data of the AFS collaboration [19]. The error on the fragmentation is estimated conservatively to be a factor of 2.

We will first discuss the magnitude of higher order corrections at LHC by comparing the Born expectation -using a running coupling constant evaluated within two loops - to $O(\alpha_s^3)$ calculations. For the common choice of scale $Q = p_T$ and $Q = p_T/2$, the next to leading order terms multiply the Born result by a factor 1.2 → 1.7 and 0.86 → 1.33 respectively, varying with p_T . The sensitivity to mass scales has been strongly reduced: the cross section $\frac{d\sigma}{dp_T dy}$ at $y=0$ varies by less than 20% from $Q = p_T/2$ to $Q = 2p_T$ whereas there is up to a factor 2 of uncertainty at Born level. The favored scale for which Born results are closest to next to leading estimates is $p_T/2$ [17]. The results are shown with this choice of scale on Table III.

3.3 Comparison with γ production.

As mentioned before, neutral hadron production is a severe background to prompt photon production. At LHC, as shown on table III (see also Fig. 8), the ratio of γ to π^0 production is below 10^{-2} at low p_T and reaches 1 around 1 TeV.

The importance of the π^0 production suggests another mechanism for direct γ production, namely through the vector meson dominance mechanism (VDM). Assuming a rate of ρ^0 production similar to π^0 production [18] and taking the usual value 1/200 for vector meson to γ coupling, it is seen that the VDM production represents about 45% of the QCD rate at $p_T = 20$ GeV/c and 15% at $p_T = 100$ GeV/c. Obviously VDM photons have the same characteristics as π^0 's and in particular they always appear as jet fragments while γ 's emitted through the usual QCD perturbative mechanism can also be produced in isolation. Therefore any isolation criterion which appreciably reduces the π^0 rate will also eliminate VDM photons.

One such "isolation" criterion, easy to implement in the inclusive calculations used here, concerns the energy surrounding the observed particle. More precisely, in the collinear fragmentation approximation, one obtains $\sigma(z)$ the rate of particle production for particles carrying more than a fraction z of the decaying parton energy (z is related to ϵ' defined in eq. (2) by $z = \frac{1}{1+\epsilon'}$) by substituting in eq. (8) $\int_{-T+U}^1 \frac{dx_3}{x_3^2} \frac{d\tau_3}{\tau_3^2}$ by $\int_z^1 \frac{dx_3}{x_3^2}$. We have not attempted to evaluate the production of isolated pions at next to leading order where the situation is more tricky since it involves 3 partons in the final state instead of 2. However, to approximately take into account the NLL corrections, we have evaluated the rates using the scales $Q = p_T/2$ which lead to a good approximation of the NLL spectrum as discussed in 3.2. We show in Fig. 8 the reduction factor for both the π^0 and the γ as a function of z , at $p_T = 100$ GeV/c. With $z=85\%$, the π^0 cross section is reduced by roughly two orders of magnitude while the photon rate drops by 50%. Above 1 TeV, the π^0 rate is reduced by one order of magnitude and the photon rate by 20%. This can be seen from table IV where both "isolated" photon and π^0 cross sections are shown. Then the theoretical background estimate is simply taken as the ratio of isolated π^0 to isolated γ . It goes down from $\sim 60\%$ at $p_T = 50$ GeV/c to $\sim 5\%$ at $p_T = 1$ TeV/c. The uncertainties on this estimate are probably a factor two mainly due to uncertainty in the fragmentation functions. This reduction seems sufficient to get a clean signal for photon production above p_T of 50 GeV/c.

3.4 Background from π^0 in direct γ

From the analysis of UA2 [20], the probability for a jet of $p_T \geq 12$ GeV/c to simulate a photon is estimated to be $3.5 \pm 0.5 \cdot 10^{-4}$ with isolation criteria based only on calorimetric information (granularity $\Delta\theta \times \Delta\phi = 10^\circ \times 15^\circ$, i.e. $\Delta\eta \times \Delta\phi \approx 0.20 \times 0.26$). Assuming a much better granularity at LHC ($\Delta\eta, \Delta\phi \approx 0.02 \rightarrow 0.03$ intended by Ref. [24]), a cut in the energy surrounding the particle as discussed in the previous section should be feasible. In practice, a conversion method such as used by R108 [21] or UA2 [22] is mandatory to measure the remaining background after an isolation cut rather than rely on simulations. The overlapping of minimum bias events (pile-up) will not affect this cut for high transverse momentum photons, as these events deposit a very low energy in the calorimeter. The rates are such

that for low p_T , one could afford to work at low luminosity.

The π^0 background has also been studied [23] assuming a tracking device. The fraction of π^0 not accompanied by charged tracks within a cone is shown in Fig. 10a as function of the half angle of the cone around the particle. This evaluation was made from an unweighted sample of jets with $p_T \geq 90 \text{ GeV}/c$ and $|\eta| \leq 3$ generated with PYTHIA 5.4. From the resulting limited π^0 statistics, a reduction of about two orders of magnitude seems to be feasible with a cone of less than 100 mrad half angle. Pile-up events may spoil the direct γ efficiency as indicated in Fig. 10b. Again, the γ rate is such (Fig. 3 and 5) at low p_T that the measurement can be made at low luminosity in order to reduce pile-up. At p_T of 500 GeV/c , as the ratio π^0/γ is less than 3 (table III), a reduction factor for π^0 of order 10 is sufficient and can be obtained with a cone of less than 40 mrad where the direct γ efficiency is less affected.

In the region of p_t below 100 GeV/c a further rejection against π^0 may be given by a tracking preshower detector. The detector parameters discussed in [24,25] have been used (Fig.11): a calorimeter having an interior radius of 1 meter and lateral cell size of the order of the Moliere radius $\Delta\eta \times \Delta\phi \approx 0.02 \times 0.02$ which gives a precision of $\sigma \approx 0.6 \text{ mm}$ for the center of gravity of the electromagnetic shower and a preshower detector of 0.7 meter radius with a conversion probability of 70% for each γ and a precision $\sigma \approx 0.25 \text{ mm}$. In order to keep the single γ efficiency greater than 90%, the two γ 's hypothesis is considered only if the distance between the two converted γ 's or the converted γ and the π^0 barycenter is greater than 3 times the shower width in the preshower ($\approx 3.5 \text{ mm}$). Under these conditions we calculate the probability to convert one or two γ 's of a π^0 and to distinguish it from a single shower configuration. The result is shown in Fig. 12: about 40% of the π^0 could be recognized at $p_T = 50 \text{ GeV}/c$. This figure depends on the radius of the preshower and could be significantly improved with a larger radius.

4 Summary and outlook

We have seen that the rate of prompt photon production is very high at LHC. Photons up to $p_T \simeq 2 \text{ TeV}/c$ could be observed with high luminosity. It is essential to apply isolation cuts to reduce the background to a tolerable level: therefore a very good electromagnetic and hadronic calorimetry is necessary. At low transverse momentum, the π^0 background is very important but good detector granularity associated with a tracking device allows stringent isolation cuts which considerably reduce this background (typically $signal/noise = 2$) so that the photon signal could reliably be extracted down to $p_T \simeq 50 \text{ GeV}/c$ at low luminosity.

The γ spectrum can be used to constrain the QCD parton distributions. In particular, the rapidity dependence up to $y \simeq 2.5$ (at $p_T \leq 100 \text{ GeV}/c$) would yield valuable information on the shape of the gluon spectrum in the range $x \geq 10^{-3}$, $Q^2 \geq 2500 \text{ GeV}^2$.

The theoretical uncertainties are highest in the low p_T range but never exceed 25%. A clear improvement would be the evaluation of higher order corrections to the bremsstrahlung component which we roughly estimate to increase the photon

spectrum by 20% at low p_T . The development of a fast Monte-Carlo program, at next to leading order, including the fragmentation of the partons into hadrons would be extremely useful.

References

- [1] P.Aurenche, M.R.Whalley, DPDG/89/04, RAL-89-106.
- [2] P.Aurenche, R.Baier, M.Fontannaz and D.Schiff, Nucl. Phys. **B297** (1988) 661.
- [3] H.Baer, J.Ohnemus and J.F.Owens, Phys. Rev. **D42** (1990) 61.
- [4] P.Aurenche, R.Baier, M.Fontannaz, J.F.Owens and M.Werlen, Phys. Rev. **D39** (1989) 3275.
- [5] M.Fontannaz, Proc. 4th INFN Eloisatron Project Workshop, Erice 1987, ed. by A.Ali, Plenum Press 1988, p 249.
- [6] A.Ali et al., ECFA 84/85, Vol.II, p469.
- [7] J.F.Owens, T.Ferbel, M.Dine, I.Bars, Snowmass 84, p218.
- [8] F.Aversa, M.Greco, P.Chiappetta and J.P.GUILLET, Nucl. Phys. **B327** (1989) 105.
- [9] F.Aversa, M.Greco, P.Chiappetta and J.P.GUILLET, Phys. Rev. Lett. **65** (1990) 401; F.Aversa, M.Greco, P.Chiappetta, J.P.GUILLET and L.Gonzales, CERN-TH-5710/90, to appear in Z. Phys. C.
- [10] S.D.Ellis, Z.Kunszt and D.E.Soper, Phys. Rev. Lett. **64** (1990) 2121.
- [11] P.M.Stevenson and H.D.Politzer, Nucl. Phys. **B277** (1986) 758.
- [12] work in progress
- [13] P.N.Harriman, A.D.Martin, W.J.Stirling and R.G.Roberts, Phys. Rev. **D42** (1990) 798.
- [14] P.Aurenche, R.Baier and M.Fontannaz, Phys. Rev. **D42** (1990) 1440.
- [15] J.Blümlein and G.A.Schuler, DESY 90-072.
- [16] R.Baier, J.Engels and B.Petersson, Z. Phys. **C2** (1979) 265.
- [17] P.Chiappetta, J.P.GUILLET et al., work in progress.
- [18] T.Sjöstrand, private communication.
- [19] T.Akesson et al., CERN/EP 89-98.
- [20] E.Lançon, Thesis, CEA-N-2549 (1988).
- [21] A.L.S.Angelis et al., Phys. Lett. **B94** (1980) 106.
- [22] R.Anvari et al., Z.Phys. **C41** (1988) 395.
- [23] F.Pastore, Dipt. di Fisica Nucl. e Teorica and INFN, Pavia and M.Pepe, CERN.
- [24] B.Aubert et al. CERN/DRDC/90-32.
- [25] D.J.Munday et al. CERN/DRDC/90-27.

p_T	LHC			SSC		
	Born	Inclusive	Isolated	Born	Inclusive	Isolated
20	.763 10 ³	.555 10 ⁴	.422 10 ⁴	.122 10 ⁴	.109 10 ⁵	.815 10 ⁴
50	.419 10 ²	.170 10 ³	.129 10 ³	.791 10 ²	.414 10 ³	.303 10 ³
80	.784 10 ¹	.250 10 ²	.191 10 ²	.161 10 ²	.670 10 ²	.490 10 ²
100	.339 10 ¹	.974 10 ¹	.748 10 ¹	.724 10 ¹	.272 10 ²	.200 10 ²
150	.698 10 ⁰	.168 10 ¹	.131 10 ¹	.161 10 ¹	.509 10 ¹	.376 10 ¹
200	.218 10 ⁰	.464 10 ⁰	.366 10 ⁰	.537 10 ⁰	.151 10 ¹	.112 10 ¹
300	.393 10 ⁻¹	.717 10 ⁻¹	.578 10 ⁻¹	.108 10 ⁰	.259 10 ⁰	.196 10 ⁰
500	.394 10 ⁻²	.602 10 ⁻²	.500 10 ⁻²	.131 10 ⁻¹	.261 10 ⁻¹	.203 10 ⁻¹
800	.375 10 ⁻³	.501 10 ⁻³	.432 10 ⁻³	.166 10 ⁻²	.283 10 ⁻²	.228 10 ⁻²
1000	.112 10 ⁻³	.141 10 ⁻³	.123 10 ⁻³	.601 10 ⁻³	.958 10 ⁻³	.782 10 ⁻³
1500	.940 10 ⁻⁵	.107 10 ⁻⁴	.961 10 ⁻⁵	.865 10 ⁻⁴	.123 10 ⁻³	.103 10 ⁻³
2000	.118 10 ⁻⁵	.125 10 ⁻⁵	.115 10 ⁻⁵	.197 10 ⁻⁴	.259 10 ⁻⁴	.222 10 ⁻⁴
3000	.278 10 ⁻⁷	.270 10 ⁻⁷	.255 10 ⁻⁷	.197 10 ⁻⁵	.235 10 ⁻⁵	.206 10 ⁻⁵

Table I: $d\sigma/dydp_T$ in pb/GeV at $y=0$, $Q = p_T/4$ for $p_T \rightarrow \gamma X$ at $\sqrt{s} = 16 TeV$ and $40 TeV$ using ABFOW structure functions [4]. The isolated criteria are $R=0.1$ and $\epsilon=15$.

p_T	γ	jet	$\frac{jet}{\gamma}$	π^0	$\frac{\pi^0}{\gamma}$
20	.351 10 ⁴	.219 10 ⁸	6.24 10 ³	.290 10 ⁶	8.25 10 ¹
30	.906 10 ³	.471 10 ⁷	5.21 10 ³	.449 10 ⁵	4.96 10 ¹
50	.135 10 ³	.583 10 ⁶	4.33 10 ³	.384 10 ⁴	2.85 10 ¹
75	.277 10 ²	.102 10 ⁶	3.68 10 ³	.511 10 ³	1.85 10 ¹
100	.856 10 ¹	.280 10 ⁵	3.27 10 ³	.119 10 ³	1.39 10 ¹
150	.153 10 ¹	.429 10 ⁴	2.80 10 ³	.143 10 ²	9.32
200	.432 10 ⁰	.107 10 ⁴	2.53 10 ³	.300 10 ¹	6.95
250	.159 10 ⁰	.354 10 ³	2.24 10 ³	.882 10 ⁰	5.57
500	.583 10 ⁻²	.906 10 ¹	1.55 10 ³	.149 10 ⁻¹	2.56
800	.499 10 ⁻³	.586 10 ⁰	1.17 10 ³	.690 10 ⁻³	1.38
1000	.139 10 ⁻³	.145 10 ⁰	1.04 10 ³	.142 10 ⁻³	1.02
1500	.106 10 ⁻⁴	.915 10 ⁻²	8.62 10 ²	.572 10 ⁻⁵	5.39 10 ⁻¹
2000	.123 10 ⁻⁵	.990 10 ⁻³	8.06 10 ²	.404 10 ⁻⁶	3.29 10 ⁻¹

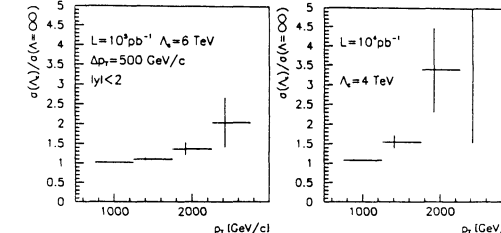
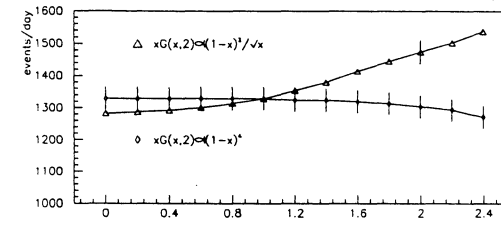
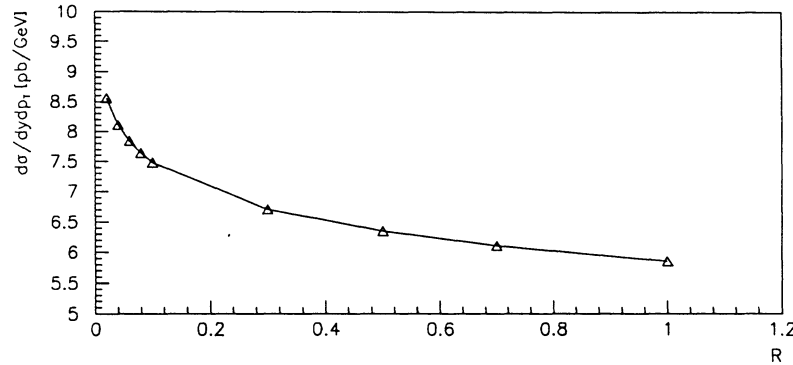
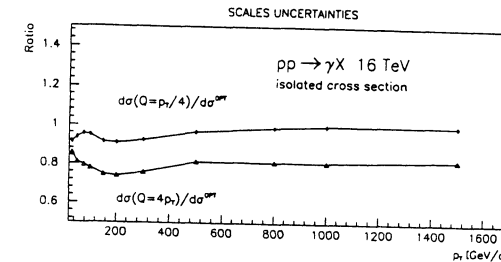
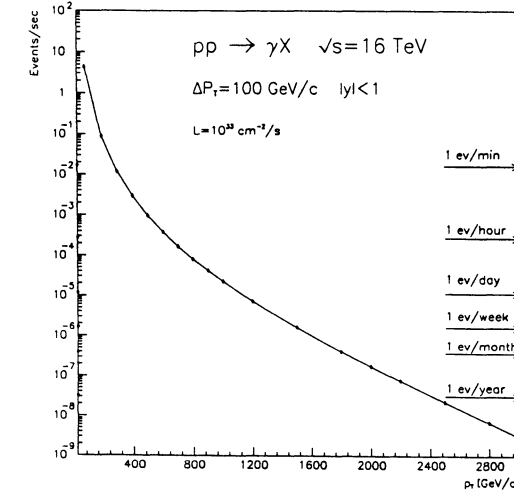
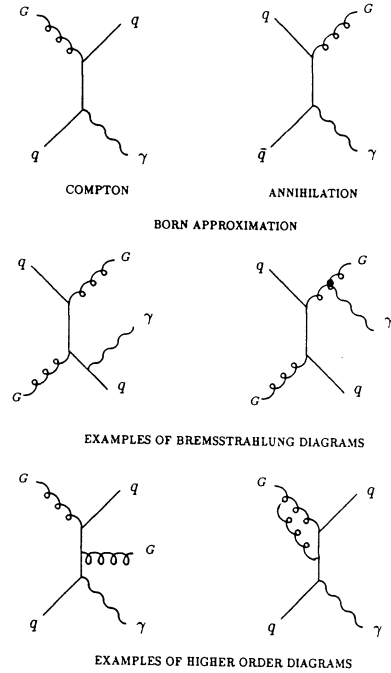
Table III: Comparison at $y=0$ of the inclusive cross sections $d\sigma/dydp_T$ in pb/GeV for γ , jet and π^0 production in pp at $16 TeV$, in the next to leading logarithm approximation, using HMRSB structure functions. The jet is defined with $R=0.7$ (calculations have been made in the small cone approximation which leads to an underestimate of $\sim 7\%$ [9]).

\sqrt{s}	$xG(x,2)$	p_T	y								unit
			0.	0.5	1.0	1.5	2.0	2.5	3.0	3.5	
16	$(1-x)^4$	50	.129	.129	.129	.127	.125	.123	.117	.104	10^3
16	$\frac{1}{\sqrt{x}}(1-x)^2$	50	.138	.139	.141	.145	.151	.158	.164	.158	10^3
16	$(1-x)^4$	100	.748	.748	.747	.743	.729	.686	.584	.393	10^1
16	$\frac{1}{\sqrt{x}}(1-x)^2$	100	.683	.691	.710	.740	.772	.779	.708	.504	10^1
16	$(1-x)^4$	500	50.0	49.9	48.3	41.6	26.8	8.96	.469		10^{-4}
16	$\frac{1}{\sqrt{x}}(1-x)^2$	500	41.4	41.8	41.7	37.2	24.7	8.36	.438		10^{-4}
40	$(1-x)^4$	50	.303	.301	.297	.292	.286	.280	.275	.266	10^3
40	$\frac{1}{\sqrt{x}}(1-x)^2$	50	.402	.401	.402	.405	.412	.424	.442	.463	10^3
40	$(1-x)^4$	100	.200	.199	.198	.194	.190	.186	.178	.164	10^2
40	$\frac{1}{\sqrt{x}}(1-x)^2$	100	.214	.215	.216	.220	.225	.233	.241	.238	10^2
40	$(1-x)^4$	500	2.03	2.03	2.03	1.99	1.84	1.47	.845	.231	10^{-2}
40	$\frac{1}{\sqrt{x}}(1-x)^2$	500	1.70	1.72	1.78	1.83	1.79	1.49	.889	.246	10^{-2}

Table II: Rapidity dependence of the isolated cross section $d\sigma/dydp_T$ in pb/GeV , $Q = p_T/4$ for two different gluon distributions.

p_T	γ	π^0	$\frac{\pi^0}{\gamma}$
20	.836 10 ³	.167 10 ⁴	2.00
30	.263 10 ³	.301 10 ³	1.14
50	.488 10 ²	.300 10 ²	6.15 10 ⁻¹
75	.115 10 ²	.449 10 ¹	3.91 10 ⁻¹
100	.390 10 ¹	.117 10 ¹	2.99 10 ⁻¹
150	.786 10 ⁰	.165 10 ⁰	2.10 10 ⁻¹
200	.241 10 ⁰	.390 10 ⁻¹	1.62 10 ⁻¹
250	.931 10 ⁻¹	.129 10 ⁻¹	1.39 10 ⁻¹
500	.402 10 ⁻²	.342 10 ⁻³	8.52 10 ⁻²
800	.375 10 ⁻³	.232 10 ⁻⁴	6.18 10 ⁻²
1000	.110 10 ⁻³	.586 10 ⁻⁵	5.32 10 ⁻²
1500	.888 10 ⁻⁵	.382 10 ⁻⁶	4.30 10 ⁻²
2000	.107 10 ⁻⁵	.409 10 ⁻⁷	3.82 10 ⁻²

Table IV: Comparison of "isolated" cross sections for γ and π^0 at $\sqrt{s} = 16 TeV$ with $z = E_{particle}/E_{parton} \geq 85\%$.



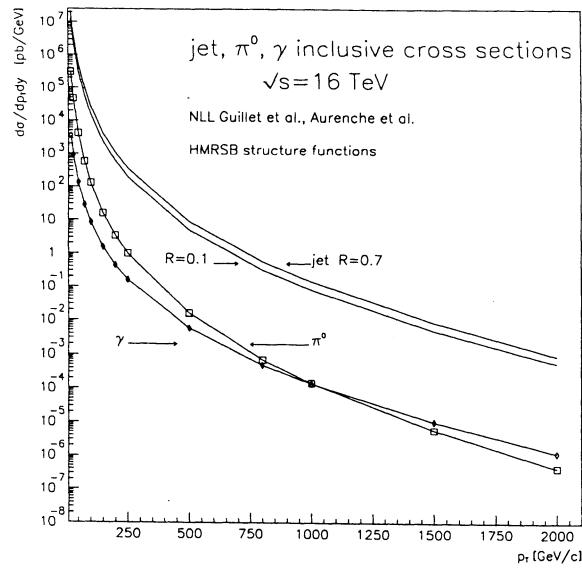


Figure 7: Comparison of jet, π^0 , γ inclusive cross sections at LHC at $y=0$.

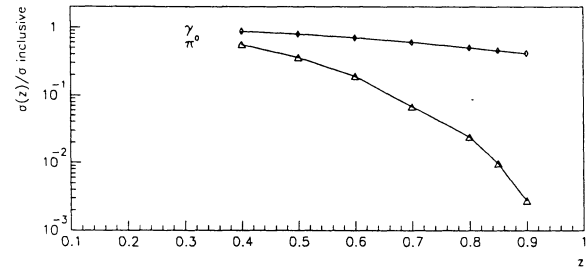


Figure 8: $\sigma(z)$ (see 3.3) relative to the inclusive cross section for γ and π^0 as a function of $z = \frac{E_\gamma \text{ or } \pi^0}{E_{\text{parton}}}$ at $p_T=100 \text{ GeV}/c$ and $y=0$.

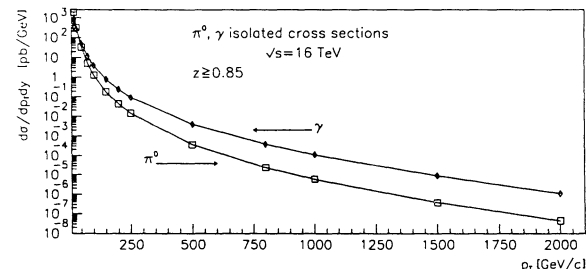


Figure 9: Comparison of γ and π^0 "isolated" cross section where the isolation is defined as $z = \frac{E_{\text{particle}}}{E_{\text{parton}}} \geq 85\%$.

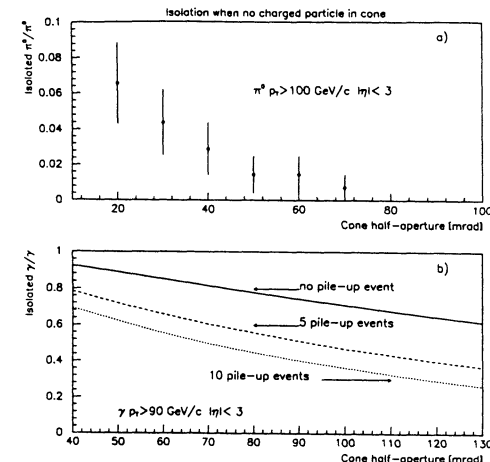


Figure 10: Fraction of π^0 (a) and γ (b) not accompanied by charged tracks within a cone as a function of the cone size.

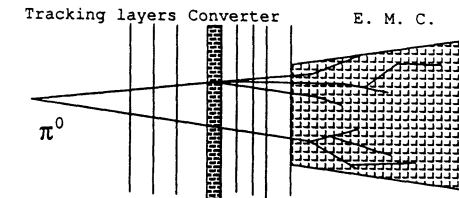


Figure 11: Schematic of $\pi^0 \rightarrow \gamma\gamma$ converted in the preshower detector and the electromagnetic calorimeter.

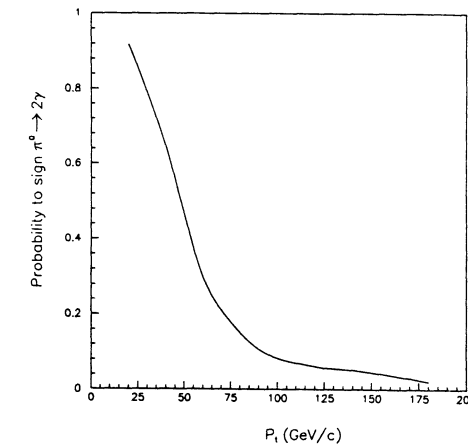


Figure 12: Probability to recognize a π^0 with the system of Fig. 11 (see 3.4).

$\gamma\gamma$ production at LHC: a NLO order study of the "irreducible" background to $H^0 \rightarrow \gamma\gamma$

P. Aurenche ¹, M. Bonesini ², L. Camilleri ³, M. Fontannaz ⁴
and M. Werlen ⁵

1 Introduction

Two photon reactions have been studied both experimentally and theoretically at SPS and collider energies [1]. At leading order two photons are produced through the Born diagram $q\bar{q} \rightarrow \gamma\gamma$ (fig. 1a). An important contribution of order α_s^2 is the diagram $gg \rightarrow \gamma\gamma$ (fig. 1b) with a quark loop in the box. Available next-to-leading order (NLO) calculations [2] include the bremsstrahlung contributions, where a photon is radiated collinearly from a final state parton such as $qg \rightarrow \gamma(g \rightarrow \gamma)$, $q\bar{q} \rightarrow \gamma(g \rightarrow \gamma)$ (fig. 1c) and higher order correction diagrams (fig. 1d). The bremsstrahlung contributions have been calculated in terms of the so-called "anomalous" quark and gluon fragmentation functions into a photon [3] : $D_{\gamma/q}(z, Q^2)$ and $D_{\gamma/g}(z, Q^2)$. As these functions behave as $\alpha/\alpha_s(Q^2)$, the relative diagrams are of the same leading order as $q\bar{q} \rightarrow \gamma\gamma$. Two photon production may be described by the pseudorapidity η_1 and transverse momentum p_{T_1} of the trigger gamma, while the second photon is described by the variable $z = -(\vec{p}_{T_1} \cdot \vec{p}_{T_2}) / |\vec{p}_{T_1}|^2$. At SPS energies the agreement between data and next-to-leading order calculation is quite good within the statistical errors. The predicted NLO cross sections as a function of p_{T_1} and η_1 for LHC energies ($\sqrt{s} = 16$ TeV) are shown in fig. 2a and 2b. The total cross section is dominated by the bremsstrahlung contributions, that can be reduced only with suitable cuts (see the following). The Box contribution is dominant with respect to the Born term at low p_T ($p_T \leq 40$ GeV) and the relative importance of the two is determined by the number of quarks included in the quark loop of the Box diagram, the use of leading log instead of next-to-leading log coupling constants ($\leq 50\%$), the shape of the assumed gluon structure function at small x ... At leading log (LL) the choice of the Q^2 scale to be used is arbitrary (a popular choice is $Q^2 = p_T^2$, the one

adopted here). At next-to-leading-log the choice is still arbitrary, but due to compensation between BORN+LL terms and NLO terms, the uncertainty in the total cross section is reduced. Fig. 3 shows the dependence of the total (Born) cross section as a function of the Q^2 scale, parametrized as $Q^2 = c \cdot p_T^2$. For the Born term only we have a big variation ($\sim 100\%$), that is reduced to $\sim 20\%$ for the total cross section. The uncertainty from the choice of the structure functions amounts to $\sim 20\%$, using common choices.

2 Intermediate mass $H^0 \rightarrow \gamma\gamma$

The main task facing LHC/SSC is to understand the mechanism of the electroweak symmetry breaking. As the Higgs mass is essentially unconstrained by low energy data, we must be ready to search for the Higgs in all mass ranges. A light Higgs ($M_H \leq 85$ GeV) can be found at LEP II before LHC/SSC take over, while a heavy mass Higgs ($M_H \geq 180$ GeV) has a clear signature through its $Z^0 Z^0$ or WW decays. The intermediate mass range ($85 \leq M_H \leq 180$ GeV) seems to be more problematical. The preferred decay into a pair of heavy quarks is buried under an overwhelming QCD two jet background. Only rare decay modes with a clean and distinctive signature (such as $H \rightarrow \gamma\gamma$) are worthwhile. For a Higgs lying below the WW threshold, the decay mode $H^0 \rightarrow \gamma\gamma$ may be detectable in spite of its small branching ratio ($\sim 10^{-3}$). This process has a clear signature: a pair of isolated high p_T gammas, no missing p_T and a minimal amount of hadronic debris.

The main backgrounds are due to the:

- $\gamma\gamma$ "irreducible" background (i.e. same final state as the signal) from $q\bar{q} \rightarrow \gamma\gamma$, $gg \rightarrow \gamma\gamma$ (see later for details)
- QCD two jet background

The large rate of QCD two jet events (10^8 more events with respect to 100 GeV Higgs decaying into $\gamma\gamma$ for a 2% mass bin in $M_{jet-jet}$) gives an appreciable fraction of events in which both jets simulate isolated e.m. showers. To have a QCD background significantly below the "irreducible" $\gamma\gamma$ one, a rejection factor of better than $\sim 10^4$ is required for single jets. Previous studies [4] show that a pure calorimetric rejection based on isolation cuts may not be sufficient. The e.m. calorimeter must have, in addition, good two shower separation to distinguish direct photons from energetic π^0 's.

¹LAPP, Annecy

²Sekzione INFN, Milano

³CERN, PPE Division, Geneve

⁴LPTHE, Orsay

⁵INPN, Lausanne

3 Two photons background to $H^0 \rightarrow \gamma\gamma$

The direct production of photon pairs is the most serious background for detecting $H^0 \rightarrow \gamma\gamma$. While various kinematical cuts can be applied to reduce the problem, the existence of events with two direct photons in the final state form an "irreducible" background to the desired signal [5]. As can be seen from fig. 2, at NLO the main contribution to the total $\gamma\gamma$ cross section is due to the bremsstrahlung terms (roughly an order of magnitude bigger than the Born or Box graphs). These events are characterized by the bremsstrahlung photon generally having a significantly lower p_T than the primary photon and being accompanied by parton fragments nearby. The bremsstrahlung contribution can therefore be reduced by requiring a p_T balance between the two photons and no hadronic activity near them. The reduction in the total $\gamma\gamma$ cross section, σ_{TOT} , and in $K' (= \sigma_{TOT}/(\sigma_{BORN} + \sigma_{BOX}))$ as a cut in z ($= p_{T2}/p_{T1}$) on the p_T balance is made tighter is shown in fig. 4a. Accepting only events with $z \geq z_{min} = 0.4$, the bremsstrahlung contribution can be reduced further by requiring that the separation between the bremsstrahlung photon and its parent parton $R = \sqrt{(\Delta\eta)^2 + (\Delta\phi)^2}$ be greater than a certain cut R_ϕ (fig. 4b) ("isolation"). Assuming : $R \geq R_\phi = 0.4$ and $z \geq z_{min} = 0.4$, we obtain a global correction factor to go from Box+Born terms to the full NLO cross section ~ 1.5 , with a weak dependence on the p_T and the pseudorapidity η of the trigger γ . Table I lists the Born and total cross sections with and without the z and R_ϕ cuts discussed above.

After having checked that at the Born and Box level the same results were obtained with the PYTHIA 5.4 Monte Carlo [6] as with the previous NLO computation, PYTHIA was used to generate $10^5 q\bar{q} \rightarrow \gamma\gamma$ and $gg \rightarrow \gamma\gamma$ events, to simulate the $\gamma\gamma$ background. Duke-Owens I structure functions were used and the Box diagram included only four light flavours. A correction factor ~ 1.5 was assumed throughout, to take into account the effects of higher order and bremsstrahlung corrections with the assumed R_ϕ , z_{min} cuts. The $H^0 \rightarrow \gamma\gamma$ signal was simulated with the same program for different values of the Higgs mass between 100 and 200 GeV. The energy and direction of photons were measured using gaussian resolution functions with :

- $\sigma_{VTX} = 6 \text{ cm}$
- $\sigma_\phi = .001 \text{ rad}$
- $\frac{\sigma(E)}{E} = \frac{10\%}{\sqrt{E}} + 1\%$

The assumed energy resolution corresponds to what can be achieved with a well designed conventional e.m. sampling calorimeter. In the Monte Carlo simulation the fragmentation of partons has been done with the Lund string model (default parameters) and 10 minimum bias events were superimposed to simulate event pileup. The following kinematical cuts were used for both signal and background

- $|\eta| \leq 3.0$
- $p_T(\gamma) \geq 20 \text{ GeV}$
- $R \geq R_\phi = 0.4$
- $z \geq z_{min} = 0.4$

The motivation for the first two cuts is that it seems unlikely that an LHC detector may have a high quality e.m. calorimetry in the forward direction and that the number of Higgs candidates with $p_T(\gamma) \leq 20 \text{ GeV}$ is low (the transverse energy distribution for Higgs photons peaks at $\sim m_H/2$). The last two cuts were used to reduce the amount of bremsstrahlung contributions to the total $\gamma\gamma$ cross section. A further cut on $|\cos\theta_{\gamma\gamma}^*| \leq 0.5$, where $\theta_{\gamma\gamma}^*$ is the photon angle in the $\gamma\gamma$ rest frame was used to enhance the Higgs signal (which is isotropic) with respect to the "irreducible" $\gamma\gamma$ background, which is forward peaked.

Fig. 5 shows the signal and "irreducible" $\gamma\gamma$ background cross sections for different values of m_H . In all the following considerations we have assumed a 3σ mass bin for both signal and background, to be more conservative. Assuming a peak luminosity of $10^{34} \text{ cm}^{-2} \text{ s}^{-1}$ for LHC, in a one year run an integrated luminosity of 10^6 pb^{-1} can be collected. In this case, the significance of $H^0 \rightarrow \gamma\gamma$ is shown as S/\sqrt{B} versus m_H in fig. 6.

4 Conclusions

A detailed NLO study of $\gamma\gamma$ production at LHC shows that this kind of background to an intermediate mass $H^0 \rightarrow \gamma\gamma$ can be reduced to a small level (i.e. $S/\sqrt{B} \geq 7$), assuming a good e.m. calorimetry and using appropriate "isolation cuts" to reduce the dominant bremsstrahlung contribution.

$p_T(\gamma_1)$ (GeV)	inclusive (total)	inclusive (Born)	isolated(total)
30	6.780	1.890	5.790
40	3.072	.752	2.020
50	1.610	.361	.875
70	.577	.114	.240
100	.181	$.317 \cdot 10^{-1}$	$.588 \cdot 10^{-1}$
120	$.970 \cdot 10^{-1}$	$.161 \cdot 10^{-1}$	$.282 \cdot 10^{-1}$
150	$.438 \cdot 10^{-1}$	$.687 \cdot 10^{-2}$	$.113 \cdot 10^{-1}$
200	$.149 \cdot 10^{-1}$	$.220 \cdot 10^{-2}$	$.338 \cdot 10^{-2}$

Table I: Comparison of the inclusive (with $p_T(\gamma_2) \geq 20$ GeV) and isolated ($z \geq 0.4$ and $R_\phi \geq 0.4$) cross sections $d\sigma/dp_T$ in pbarn/GeV in the pseudorapidity range $|\eta| \leq 3$.

References

- [1] C. De Marzo et al., Phys. Rev. **D42** (1990),748
C. Albajar et al., Phys. Lett. **B209** (1988),385
T. Akesson et al., Z. Phys. **C32** (1986),491
J. Badier et al., Phys. Lett. **164B** (1985),184
E. Bonvin et al., Z. Phys. **C41** (1989),591.
R. Ansari et al., Z. Phys. **C41** (1988),395.
- [2] P. Aurenche et al., Z. Phys. **C29** (1985),459.
- [3] E.L. Berger, E. Braaten, R.D. Field, Nucl. Phys. **B239** (1984),52.
C. H. Llewellyn-Smith, Phys. Lett. **79B** (1978),83.
- [4] D. M. Atwood et al., Berkeley 87,p. 728.
C. Barter et al., Snowmass 88,p. 98.
- [5] H. Baer, J.F. Owens, Phys. Lett **B205** (1988),377.
D.A. Dicus, S.D. Willenbrock, Phys. Rev. **D37** (1988),1801.
- [6] H. U. Bengtsson, T. Sjostrand, LU TP 86-22. (PYTHIA 5.3)
courtesy of T. Sjostrand (PYTHIA 5.4)

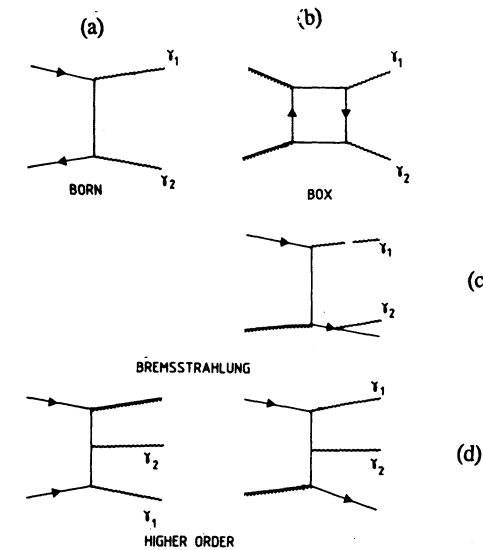


Fig. 1 Diagrams contributing to $\gamma\gamma$ production at NLO : a) Born, b) Box, c) bremsstrahlung, d) higher order

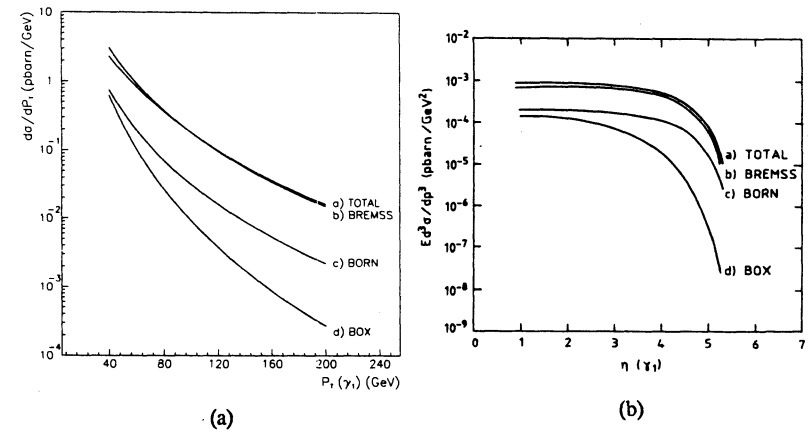


Fig. 2 NLO $\gamma\gamma$ cross sections as a function of (a) p_{t1} (assuming $|\eta_1| \leq 3.0$) and of (b) η_1 (assuming $p_{t1} = 50$ GeV for $p_{t2} \geq 20$ GeV)

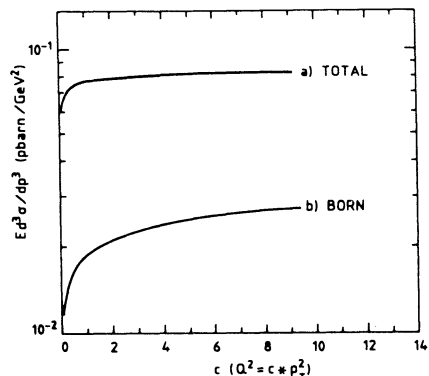


Fig. 3 Dependence of the total (Born) $\gamma\gamma$ cross section on the assumed Q^2 scale ($Q^2 = c p_t^2$) for $p_{t1} = 40 \text{ GeV}$ and $p_{t2} \geq 20 \text{ GeV}$

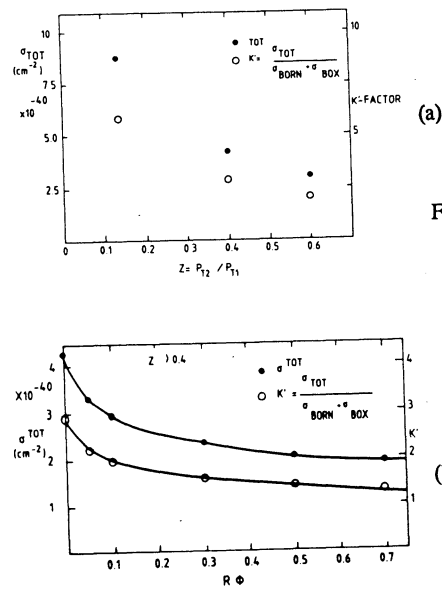


Fig. 4 Effect on the total cross section σ_{tot} (dots) and on the K' -factor (open circles) defined as $(\sigma_{tot}/(\sigma_{Born} + \sigma_{Box}))$ of (a) a z cut for $p_{t1} = 75 \text{ GeV}$, $|h_1| \leq 3.0$ and $p_{t2} \geq 20 \text{ GeV}$ and of (b) a separation cut R assuming also $z \geq 0.4$

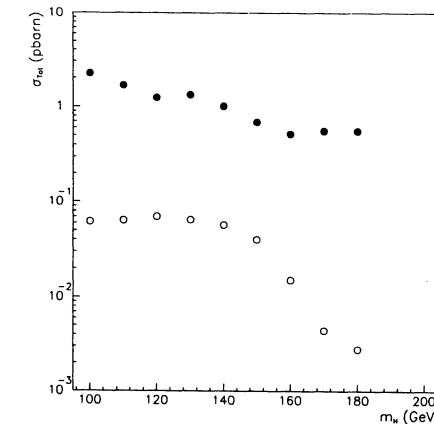


Fig. 5 Signal $H^0 \rightarrow \gamma\gamma$ (open circles) and "irreducible" $\gamma\gamma$ background (dots) cross sections versus m_{H^0}

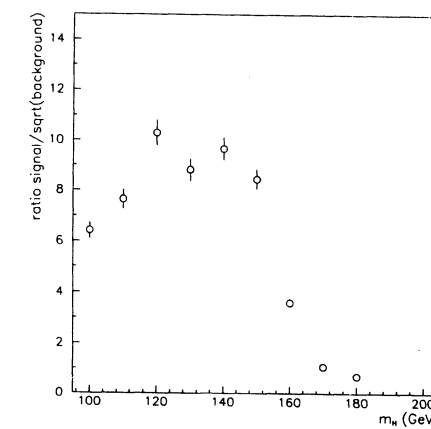


Fig. 6 Significance S/B of the $H^0 \rightarrow \gamma\gamma$ signal with respect to the "irreducible" $\gamma\gamma$ background versus m_{H^0}

PARTON LUMINOSITIES, W AND Z CROSS SECTIONS AND GAUGE BOSON PAIR PRODUCTION

Standard Model sub-group members on standard processes

H. KUIJF¹, G. MARTINELLI², T. MATSUURA³, B. MELE⁴, P. NASON⁵,
F. PASTORE⁶, M. PEPE⁷, H. PLOTHOW-BESCH⁷, L. TRENTADUE⁸,
D. WOOD⁹, D. ZEPPENFELD¹⁰

presented by H. PLOTHOW-BESCH

1. INTRODUCTION

Detailed studies on standard processes at the LHC and SSC have been performed. Recent parton luminosity evolutions are discussed. A summary on W and Z cross section calculations to second order in α_s are given. Gauge boson pair production has been investigated. It has been found that WZ and $W\gamma$ pairs are produced with high rates and nearly free of background. These channels are also very sensitive to anomalous couplings by about one order of magnitude better than LEP II. A summary of the Standard Model working sub-group on standard processes at the LHC is given on parton densities (Section 2), on total and differential W and Z production cross sections (Section 3) which also includes Drell-Yan production, and on gauge boson pair production (W^+W^- , $W^\pm Z^0$, Z^0Z^0 , $W^\pm\gamma$) (Section 4).

2. PARTON DENSITIES

G. Martinelli² and H. Plothow-Besch⁷

There are about 30 different sets of proton density functions from different authors [1,2,3] available today. Most of them, essentially the more recent ones, are next-to-leading order evolutions [2,3]. The older ones [1] are leading order evolutions only and its use

should be taken with some care, because most of them do not fit the recent low energy deep-inelastic lepton-nucleon data from NMC and BCMD [4]. This is not surprising because these data have not been available when the sets have been made. Theoretical predictions derived from evolutions of these older sets to small x values, where x is the momentum fraction of the parton in the nucleon, becoming important at LHC or SSC energies should be looked at with caution. This statement also holds for most of the new sets [2,3] when x values very much lower than present available data ($x > 0.07$) are used and when extrapolating to x ranges beyond the limits given by the authors ($x > \sim 10^{-4}$). The structure function distributions at $Q^2 = m_W^2$ for u and d valence quarks as well as for sea and gluon contributions are shown in Fig. 1a to 1d, respectively, as a function of x. It can be seen from these figures that there is a large spread in shape for the different sets in all contributions leading to different results in the cross section calculations.

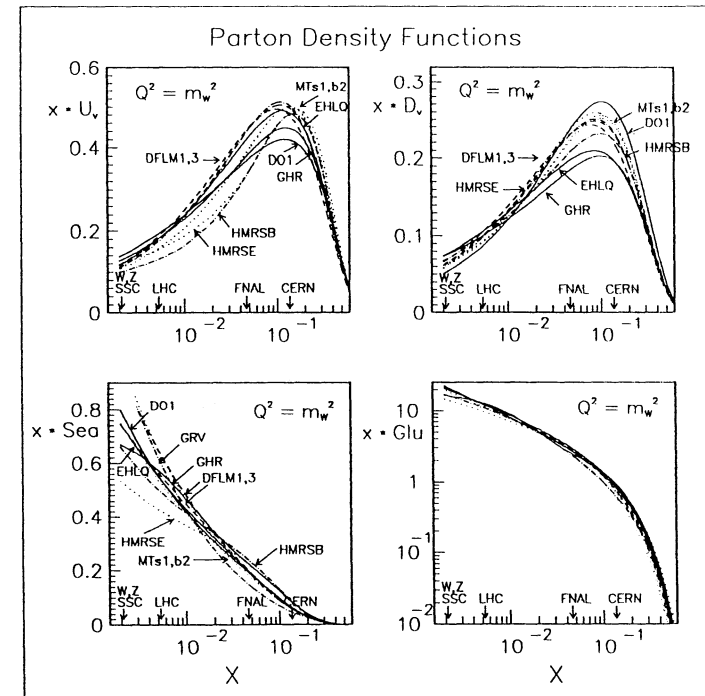


Figure 1
Different sets of structure functions
for a) u-valence b) d-valence c) sea d) gluon distributions

The ratio F_2^n/F_2^p at $Q^2 = m_W^2$ is shown in Fig. 2. This ratio mainly reflects the d/u ratio of valence quarks which gives the important contribution to the W and Z cross section calculations. Already from Fig. 2 we conclude that a large variation of the W and Z cross

¹ Instituut-Lorentz, University of Leiden, P.O.B. 9506, 2300 RA, Leiden, The Netherlands

² Dipartimento di Fisica, Università di Roma "La Sapienza" and INFN, Sezione di Roma, Italy

³ II. Institut für theoretische Physik, Universität Hamburg, 2000 Hamburg 50, Germany

⁴ CERN-TH, 1211 Geneva 23, Switzerland

⁵ INFN, Gruppo Collegato di Parma, Italy

⁶ Dipartimento di Fisica Nucleare e Teorica, Università di Pavia and INFN Sezione di Pavia, Italy

⁷ CERN-PPE, 1211 Geneva 23, Switzerland

⁸ Dipartimento di Fisica, Università di Parma and INFN, Gruppo Collegato di Parma, Italy

⁹ Laboratoire de l'Accélérateur Linéaire, Université de Paris-Sud, 91405 Orsay, France

¹⁰ Department of Physics, University of Madison, Wisconsin, WI 53706, USA

section at LHC or SSC energies can be expected from the different sets of structure functions. Since we go to smaller and smaller x ranges as we go higher and higher in \sqrt{s} , the cross section should be dominated by the sea-quark contributions which are the same for u and d quarks. Therefore uncertainties due to the different shapes of u and d quarks are expected to cancel. But, as can be seen from Fig. 1c, the differences in shape of the sea-quark distributions for the numerous sets are also large and become even larger as x decreases. This explains why the total W and Z cross sections have larger uncertainties as \sqrt{s} increases (see Section 3).

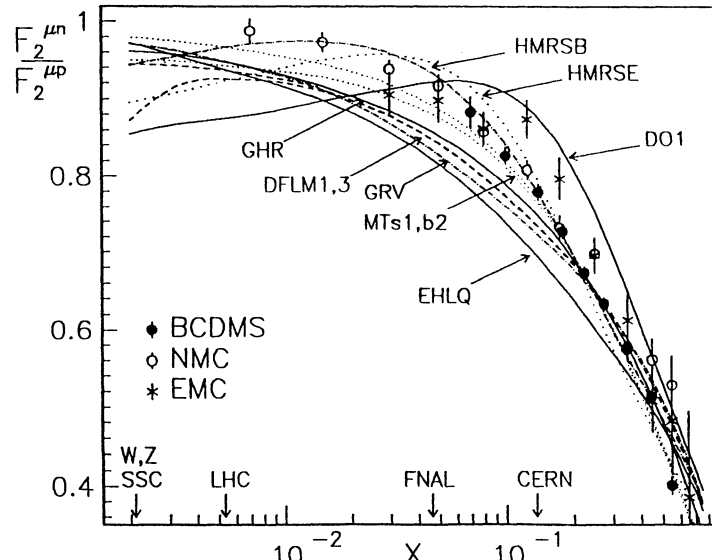


Figure 2

F_2^n/F_2^D ratio for different sets of structure functions

From Fig. 2 we also conclude that the older sets of structure functions, namely the Duke and Owens sets 1 and 2 and the sets of Eichten et al. do not fit the recent experimental data and should therefore be ignored for any physics process to be studied at LHC or SSC energies. Furthermore we conclude that the recent sets of parton densities, namely HMRSB and MTs1, could be preferred for all theoretical predictions involving structure functions, because they fit the present data best.

It also should be pointed out that new sets of structure functions will be extracted as soon as results from HERA will become available [5]. These data will probe parton densities at much higher values of Q^2 and much lower x ranges ($x > 10^{-4}$) than present data and therefore are expected to reduce the present uncertainties due to the large differences in the structure functions.

3. W AND Z PRODUCTION CROSS SECTIONS

In this Section we summarize the study on standard W^\pm and Z^0 and Drell-Yan production at LHC and SSC energies.

3.1 Total W and Z cross sections

T. Matsuura³ and H. Plothow-Besch⁷

The total W and Z cross sections have been calculated including full QCD corrections to order α_s [6] using mass values for the Intermediate Vector Bosons (IVBs) as given in Table 1 and the DFLM set of structure functions with the QCD scale factor $\Lambda_{\text{QCD}} = 260$ MeV [3]. In the calculation also partial QCD corrections to order α_s^2 in the DIS mass factorization scheme from Ref. [7] have been included. The missing parts in the second order calculation are the qg contribution and a complete $q\bar{q}$ calculation. The $q\bar{q}$ contribution has been calculated until now only in the so called "soft gluon limit". The problem of the exponentiation of these corrections has also been considered in Ref. [8]. With the inputs given above theory predicts the values as given in Table 1 for the total production cross sections of the W and Z bosons in pp collisions at $\sqrt{s} = 16$ TeV and 40 TeV.

Table 1: Theoretical predictions of the total W and Z cross sections

	DFLM $\Lambda_{\text{QCD}} = 260$ MeV	Range (nb)
$\sqrt{s} = 16$ TeV σ_W σ_Z	172.0 nb 51.6 nb	90.8 - 267.6 28.8 - 78.7
$\sqrt{s} = 40$ TeV σ_W σ_Z	304.5 nb 98.3 nb	126.5 - 777.2 42.2 - 231.0
$m_W = 80.2 \text{ GeV}/c^2, m_Z = 91.117 \text{ GeV}/c^2, \sin^2\theta_W = 0.230$		

The main theoretical uncertainties are due to structure functions, higher order corrections, the choice of the renormalisation scheme and the Q^2 scale dependence. The uncertainties due to the structure functions have been investigated. 14 different sets of proton density functions [1,2,3] obtained from leading or next-to-leading order calculations performed either in the $\overline{\text{MS}}$ or DIS regularisation scheme have been tested. These uncertainties are given in Table 1 indicated as "range" and amount to $\sim \pm 8\%$ at 630 GeV, $\sim \pm 12\%$ at 1.8 TeV, $\sim \pm 35\%$ at LHC and $\sim \pm 52\%$ at SSC energies. Fig. 3 shows the total W cross section as a function of the centre-of-mass energy, \sqrt{s} , for a

subset of structure functions (DFLM with $\Lambda_{\text{QCD}} = 160$ MeV to $\Lambda_{\text{QCD}} = 360$ MeV, MRSE', MRSB', HMRSE, HMRSB, MTs1 and MTb2) representing the minimal and maximal values as given in Table 1. Also indicated on the figure are the recent experimental measurements from the UA1, UA2 and CDF experiments [9] which agree well with theoretical expectations assuming a branching fraction of $\text{BR}(W \rightarrow \ell\nu) = 10.88\%$. The total Z cross section shows a very similar behaviour to the W cross section. Because of the large theoretical uncertainties, the use to the Z cross section as a luminosity monitor must be excluded. It is expected that new sets of structure functions which probe parton densities at lower x ranges ($x > 10^{-4}$) and much higher Q^2 values than present data, will reduce these uncertainties once results from HERA become available in the near future.

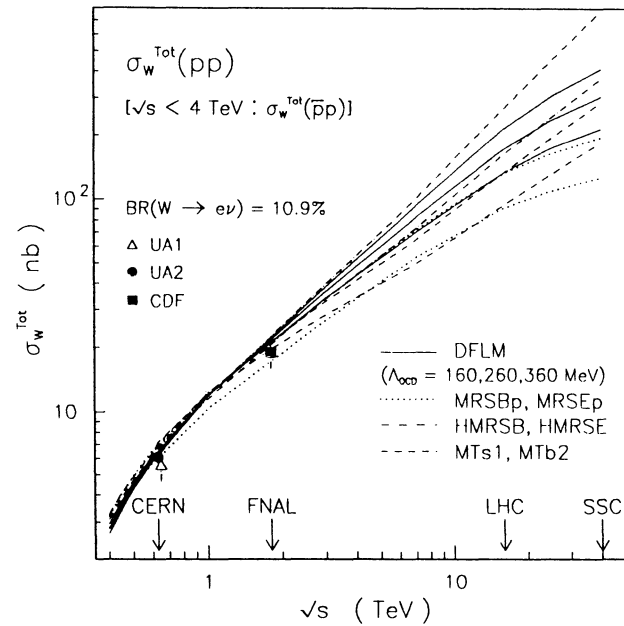


Figure 3
Total W cross section as a function of \sqrt{s}

A very recent complete second order QCD calculation [10] which has been performed in the $\overline{\text{MS}}$ mass factorization scheme show that at LHC and SSC energies the second order qg part is rather large and negative resulting in the fact that the total W and Z cross sections are slightly lowered compared to the numbers listed in Table 1. This new calculation has substantially reduced the uncertainties due to the Q^2 scale dependence. At $\sqrt{s} = 630$ GeV the remaining uncertainties amount to $\sim 5\%$ and increase to at most 15% at $\sqrt{s} = 40$ TeV for a variation of the scale Q by two orders of magnitude ($10 < Q < 1000$ GeV/c^2). The stabilizing effect of higher order contributions is nicely demonstrated in

Figs. 4a to 4d, where the total W cross sections at Born level (full line), first (dashed line) and second order (dotted line) QCD corrections are shown as a function of the mass factorisation or renormalisation scale Q (both scales are kept identical) at $\sqrt{s} = 0.630, 1.8, 16$ and 40 TeV, respectively.

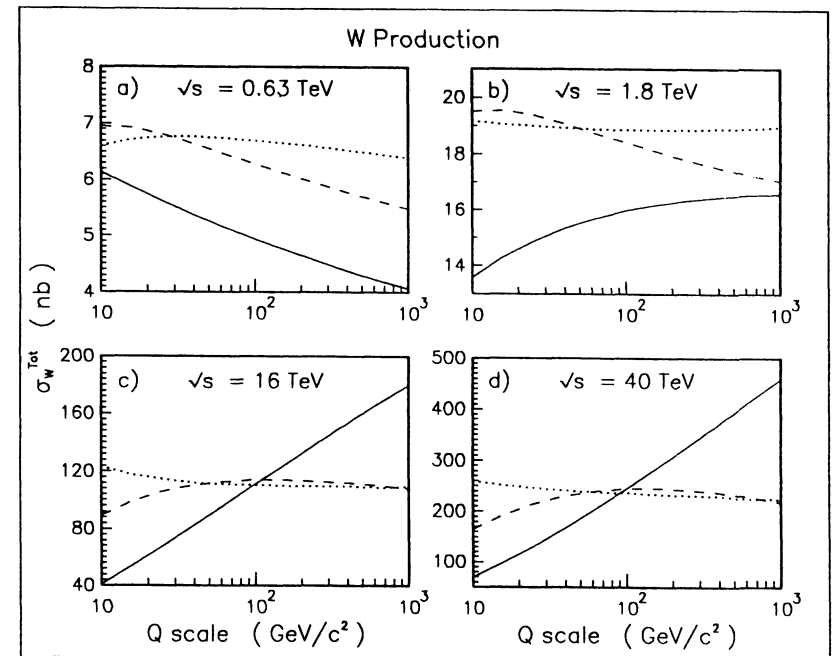


Figure 4
Total W cross section at Born level, 1st and 2nd order QCD corrections as a function of the scale Q at $\sqrt{s} = 0.630$ (a), 1.8 (b), 16 (c) and 40 TeV (d)

3.2 Differential W and Z cross sections, $d\sigma/dp_T$

H. Plothow-Besch⁷ and D. Wood⁹

In addition to the total cross sections for IVB production, the differential cross section in transverse momentum $d\sigma/dp_T$ has been studied. In particular, W's and Z's produced at high p_T are of interest. They are an abundant source of high p_T leptons and lepton pairs, and can constitute a background for new physics searches. In addition, it might prove difficult to trigger on W's produced near $p_T = 0$ because of the relatively low transverse momentum of the daughter leptons and the high rate of such events.

Consequently, the high p_T tail of the W spectrum might be the best place to measure the total W cross section.

The differential cross section $d\sigma/dp_T$ has recently been calculated in complete second order [11,12]. Programs to calculate $d^2\sigma/dp_T dy$ have been provided by the authors of Ref. [11] and were used to obtain all of the results which follow. One should make two notes of caution: (1) the calculations used do not include resummed contributions from multiple soft gluon radiation, which are important at very low p_T (≤ 20 GeV/c), and (2) for $p_T \leq 100$ GeV/c the calculations include contributions from the parton distributions at very low x values which are sometimes outside the stated ranges of validity for the structure function parametrizations.

Fig. 5a shows the prediction of $d\sigma_W/dp_T$ for seven sets of structure functions covering the full range of uncertainties. The variations among the different sets decrease at high p_T and are within about 25% at $p_T = 400$ GeV/c. Fig. 5b shows the effect of two different choices of factorization and renormalization scale, $Q^2 = M_W^2$ and $Q^2 = p_T^2$. The two prescriptions coincide at $p_T = M_W$ and the difference grows to about 30% at $p_T = 400$ GeV/c. The contribution from leading order ($O(\alpha_s)$) only is shown as well.

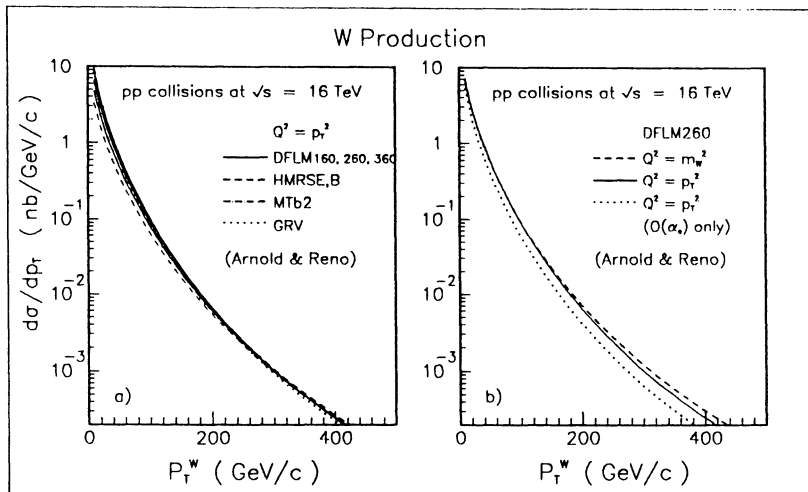


Figure 5

Differential W cross section as a function of p_T^W
(a) for different set of structure functions (b) for different choices of the Q^2 scale

Fig. 6a (6b) shows the integrated W (Z) cross section above the p_T thresholds on the abscissas. Assuming an LHC year of 10^5 pb $^{-1}$, one can read off the number of high

p_T bosons expects: 10^8 (10^7) W's above 150 GeV/c (250 GeV/c) yielding about 10^7 (10^6) $W \rightarrow \ell\nu$ events, where ℓ could be either an electron or a muon. Similarly, one predicts 10^8 (10^7) Z's above 100 GeV/c (230 GeV/c) yielding about $3 \cdot 10^6$ ($3 \cdot 10^5$) $Z \rightarrow \ell^+\ell^-$ events. The fractions of the total W (Z) cross section made up by high p_T bosons are summarized in Table 2 for several combinations of p_T threshold, structure functions, and scale. The variation in the fraction of high p_T W's is dominated by variations in the total cross section.

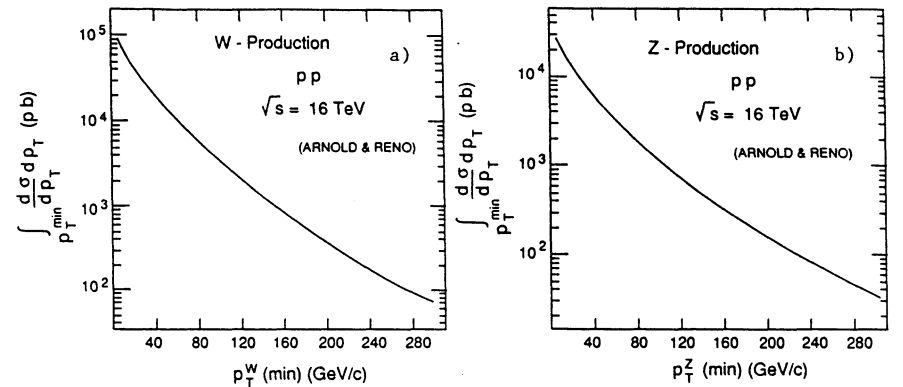


Figure 6
Integrated cross section as a function of p_T^W or p_T^Z threshold
(a) for W (b) for Z production

Table 2: Fraction of total W cross section above a p_T^W threshold

p_T^{\min} (GeV/c)	$\sigma^W(p_T > p_T^{\min})/\sigma^W$			
	Λ_{QCD} (GeV)	0.16	0.26	0.36
20		$3.5 \cdot 10^{-1}$	$3.3 \cdot 10^{-1}$	$3.2 \cdot 10^{-1}$
50		$1.0 \cdot 10^{-1}$	$0.9 \cdot 10^{-1}$	$0.9 \cdot 10^{-1}$
100		$2.3 \cdot 10^{-2}$	$2.0 \cdot 10^{-2}$	$1.7 \cdot 10^{-2}$
200		$2.9 \cdot 10^{-3}$	$2.4 \cdot 10^{-3}$	$2.0 \cdot 10^{-3}$
500		$8.4 \cdot 10^{-5}$	$6.4 \cdot 10^{-5}$	$5.0 \cdot 10^{-5}$
1000		$2.4 \cdot 10^{-6}$	$1.8 \cdot 10^{-6}$	$1.3 \cdot 10^{-6}$
1500		$1.5 \cdot 10^{-7}$	$1.2 \cdot 10^{-7}$	$0.8 \cdot 10^{-7}$

3.3 Drell-Yan Production

B. Mele⁴

The production of Drell-Yan has been studied at LHC energies. The differential cross section for the γ and Z contribution has been calculated as a function of the two lepton invariant mass, $m_{\ell\ell}$, where ℓ could be either an electron or a muon, using the DFLM sets of structure functions with $\Lambda_{QCD} = 260$ MeV. The result is shown in Fig. 7a. The Z resonance is clearly visible above the continuum. The integrated spectrum as a function of a minimal threshold on the two lepton mass is shown in Fig. 7b. For one LHC year of 10^5 pb^{-1} 1000 events with $m_{\ell\ell} > 950 \text{ GeV}/c^2$, 100 events with $m_{\ell\ell} > 1610 \text{ GeV}/c^2$, and still 10 events with $m_{\ell\ell} > 2450 \text{ GeV}/c^2$ are expected.

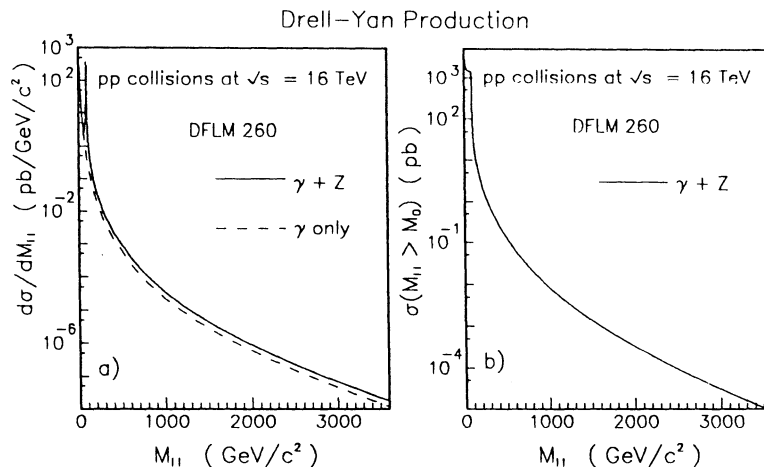


Figure 7

a) Drell-Yan production as a function of \sqrt{s}

b) Integrated Drell-Yan cross section as a function of $M(\ell^+\ell^-)$ pair threshold

4. GAUGE BOSON PAIR PRODUCTION

In this chapter we concentrate on the Standard Model (SM) physics impact from the *gauge boson pair* production. The physics potential of studies of electroweak *gauge boson pair* production was recognized long time ago [13]. At present colliders the process of gauge boson pair production is unfortunately below the kinematical limit. Therefore the rates of these potentially very interesting events resulting from the Vector Boson self-interactions predicted by the standard electroweak theory are too low to be observed. The present study of electroweak gauge boson pair production was triggered by some publications from the authors of Ref. [14] and [15].

4.1 Introduction

At LHC or SSC energies ($\sqrt{s} = 16 \text{ TeV}$ or 40 TeV , respectively) the production of single standard W^\pm 's and Z^0 's proceeds at a very high rate (i.e. $\sim 10^9 W$'s are produced for one year of data-taking at peak-luminosities of $\mathcal{L} = 10^{34} \text{ cm}^{-2}\text{s}^{-1}$ including the branching fraction for W decay into leptons). Because of this high rate the production of standard W^\pm 's and Z^0 's tends to be more important as a serious background to other interesting physics processes than as a signal for use in detailed physics studies.

On the other hand, detailed studies of W^+W^- , $W^\pm Z^0$, Z^0Z^0 , $W^\pm\gamma$ and $Z^0\gamma$ pair production are particular interesting as a test of the structure of the electroweak theory. These interactions are a manifestation of the non-abelian gauge symmetry on which the theory is based. In the SM there are important cancellations in the amplitudes for W^+W^- , $W^\pm Z^0$ and $W^\pm\gamma$ production which depend on the gauge structure of the WWV trilinear couplings ($V = Z^0$ or $V = \gamma$) [14,15]. The Z^0Z^0 and $Z^0\gamma$ reaction are *not* sensitive to these trilinear couplings, but could test non-standard interactions (i.e. compositeness of the gauge bosons). In addition, the rate of $W^\pm\gamma$ production is sensitive to the magnetic moment of the W boson. The lowest order Feynman diagrams for gauge boson pair production (W^+W^- , $W^\pm Z^0$, Z^0Z^0 and $W^\pm\gamma$) from $q\bar{q}$ annihilation are shown in Fig. 8.

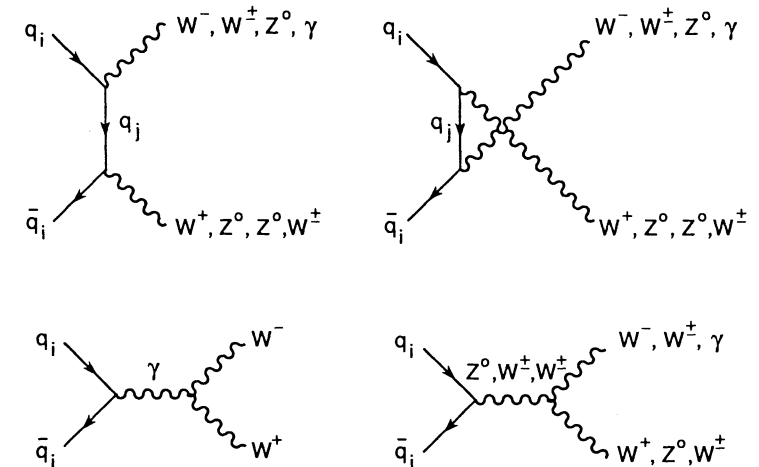


Figure 8
Lowest order Feynman diagrams for gauge boson pair production

In the approximation that the Vector Bosons are coupled to massless fermions the effective Lagrangian can be parametrized in terms of seven free parameters in case of $W^\pm Z^0$

production, which are g_1 , κ , λ , g_4 , g_5 , $\tilde{\kappa}$ and $\tilde{\lambda}$, and in terms of four free parameters in case of $W^\pm\gamma$ production, which are κ , λ , $\tilde{\kappa}$ and $\tilde{\lambda}$,

$$\begin{aligned}\mathcal{L}_{WWV} = & -g_V \{ i g_1 (W_{\mu\nu}^\dagger W^\mu V^\nu - W_\mu^\dagger V_\nu W^{\mu\nu}) \\ & + i \kappa W_\mu^\dagger V_\nu V^{\mu\nu} + \frac{i \lambda}{M_W^2} W_{\lambda\mu}^\dagger W^\mu V^\nu \lambda \\ & + i \tilde{\kappa} W_\mu^\dagger W_\nu \tilde{V}^{\mu\nu} + \frac{i \tilde{\lambda}}{M_W^2} W_{\lambda\mu}^\dagger W^\mu \tilde{V}^{\nu\lambda} \\ & - g_4 W_\mu^\dagger W_\nu (\partial^\mu Z^\nu + \partial^\nu Z^\mu) \\ & - g_5 \epsilon^{\mu\nu\rho\sigma} (W_\mu^\dagger \overset{\leftrightarrow}{\partial}_\rho W_\nu) Z_\sigma \},\end{aligned}$$

where V^μ represents either the Z or the photon fields, W^μ are the W fields, $g_V = e \cot\theta_W$ (WZ) or $g_V = e (W\gamma)$, where θ_W is the electroweak mixing angle and e is the proton charge. The following abbreviations are used: $W_{\mu\nu} = \partial_\mu V_\nu - \partial_\nu V_\mu$, $V_{\mu\nu} = \partial_\mu V_\nu - \partial_\nu V_\mu$, $\tilde{V}^{\mu\nu} = \frac{1}{2} \epsilon_{\mu\nu\rho\sigma} V^{\rho\sigma}$ and $(A \overset{\leftrightarrow}{\partial}_\mu B) = A(\partial_\mu B) - (\partial_\mu A)B$. Within the SM the couplings g_1 , κ and λ respect the discrete symmetries C and P, $\tilde{\kappa}$ and $\tilde{\lambda}$ are odd under P and even under C, g_4 respects P but is odd under C and, g_5 is odd under C and P, therefore within the SM $g_1 = \kappa = 1$ and $\lambda = \tilde{\kappa} = \tilde{\lambda} = g_4 = g_5 = 0$. In case of $W\gamma$ production g_1 is always fixed to unity by the electromagnetic gauge invariance and g_4 and g_5 are forbidden, the κ and λ terms are related to the magnetic dipole μ_W and electric quadrupole Q_W moments of the W , while $\tilde{\kappa}$ and $\tilde{\lambda}$ are related to the electric dipole d_W and magnetic quadrupole \tilde{Q}_W moments.

Any deviation of SM couplings, i.e. anomalous Vector Boson self-interactions leads to amplitudes which grow with energy. Therefore, deviations from the SM are more apparent at higher invariant masses of gauge boson pairs. To avoid violation of the unitarity bound anomalous couplings should not be assumed to be constant but have to be introduced as a form factor c which decreases at high invariant masses. This form factor $c(\hat{s}, q_W^2, q_V^2)$, which is a function of the square of the four-momenta of the three gauge bosons (WWZ or $WW\gamma$) is parametrized [14,15] as

$$c(\hat{s}, q_W^2 = M_W^2, q_V^2) = \frac{c_0}{(1 + \hat{s}/\Lambda^2)^n}$$

with $q_V^2 = M_Z^2$ (WZ) or $q_V^2 = 0$ ($W\gamma$), where n is chosen as the minimal value compatible with unitarity and Λ represents the scale at which new physics becomes important in the weak-boson sector, e.g. due to a composite structure of the W Boson. The form factor c vanishes when any of the four-momenta becomes large. The parameters of the form factor c has to be chosen such as to allow for an additional increase in the total cross section due to resonances in the vicinity of $\sqrt{\hat{s}} = \Lambda$, without conflicting with unitarity. In the following $n = 2$ and $\Lambda = 1$ TeV have been used throughout, if not stated differently. The sensitivity of the LHC and SSC to new physics in the weak-boson sector which manifests

itself in almost constant anomalous couplings at low energies ($\hat{s} < 1$ TeV) plus resonances at the scale Λ is studied without taking additional resonances into account. Therefore the quoted limits will be conservative.

4.2 Total cross sections for Intermediate Vector Boson pair production

B. Mele⁴ and H. Plothow-Besch⁷

The total cross section for Vector Boson pair production at lowest order has been calculated for the W^+W^- , Z^0Z^0 and $W^\pm Z^0$ channels using the DFLM set of structure functions with $\Lambda_{\text{QCD}} = 260$ MeV. The result is shown in Fig. 9 as a function of \sqrt{s} .

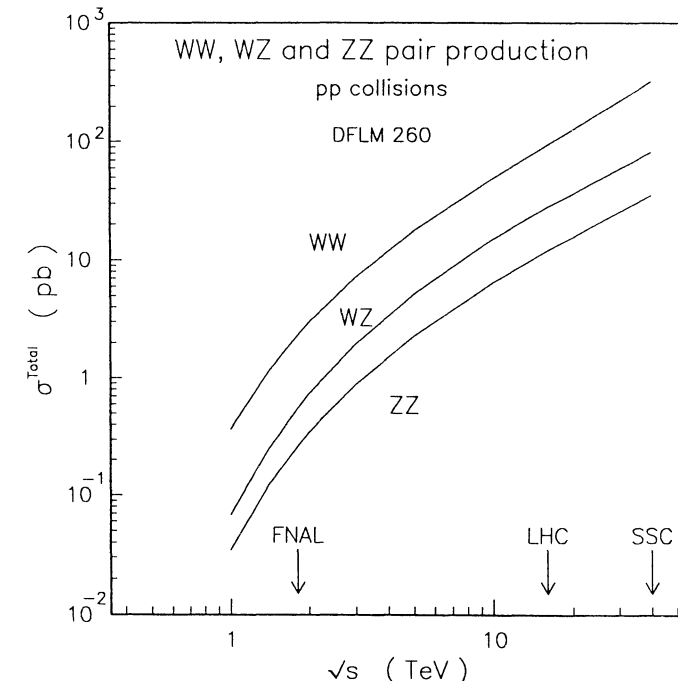


Figure 9
Total W^+W^- , Z^0Z^0 and $W^\pm Z^0$ pair production as a function of \sqrt{s}

For W^+W^- pair production a total cross section of $\sigma_{\text{Tot}}(W^+W^-) = 93.3$ pb at LHC and of 325.7 pb at SSC energies has been obtained. This channel is sensitive to the interplay in the s-channel among γ and Z^0 exchange and in the t and u channel to quark-exchange contributions. The absence of the Z^0 exchange term would give a strong rise of the total cross section with \sqrt{s} . LEP II will produce W^+W^- pairs close to its threshold ($\sqrt{s} = 180$ to 200 GeV) and can test anomalous couplings if the deviations from the

standard couplings are sufficiently large. This channel is very difficult to be seen at LHC or SSC energies, because it will be swamped by $t\bar{t}$ production followed by the subsequent decay of $t \rightarrow Wb$ which produces real W's at a 50 times higher rate (i.e. $\sigma(t\bar{t}) = 4.4 \text{ nb}$ for $m_{top} = 150 \text{ GeV}/c^2$).

The Z^0Z^0 pair production occurs at a rate of $\sigma_{Tot}(Z^0Z^0) = 12.0 \text{ pb}$ at 16 TeV and of 35.8 pb at 40 TeV. This channel is mostly interesting as a background process to the production and decay of a heavy Higgs boson. The yield of Z^0Z^0 pairs is smaller by about a factor 8 to 10 compared to W^+W^- pairs.

For $W^\pm Z^0$ pair production a total cross section of $\sigma_{Tot}(W^\pm Z^0) = 27.9 \text{ pb}$ at LHC and of 82.4 pb at SSC energies has been obtained. This channel is particular interesting (see Section 4.3), because it is easy to isolate compared to WW pair production, it is clean for testing the anomalous Vector Boson self-interactions and it allows to study the WWZ vertex alone (there is no contribution from a WW γ vertex).

The total cross section for $W^\pm\gamma$ pair production is of course formally infinite. Restrictions to specific kinematical regions remove the infrared divergence and allow to test the $WW\gamma$ vertex. Deviations from standard couplings can also be tested with high sensitivity (see Section 4.4).

4.3 $W^\pm Z^0$ pair production

H. Plothow-Besch⁷

In this Section we describe the study which has been performed at LHC energies on Intermediate Vector Boson pair production using the $W^\pm Z^0$ channel.

4.3.1 $W^\pm Z^0$ signal from Standard Model and background studies

To study in some detail the observability of the process $pp \rightarrow W^\pm Z^0 + X$ at the LHC a simulation program provided by the author of Ref. [14] has been used to obtain the results described in the following. Multi-jets from QCD production are produced with substantially higher cross section than the Vector Boson pairs. Therefore this background will swamp the purely hadronic signal from Vector Boson pair production. Also the W and Z cross sections with associated QCD production are well above the $W^\pm Z^0$ pair production. Therefore, in the analysis only WZ pairs with subsequent semileptonic decay of both, the W and the Z, leading to final states of three leptons and missing transverse momentum are considered. The leptons can be either electrons, muons or both giving a factor of 4 in rate.

For a realistic simulation of the process $pp \rightarrow W^\pm Z^0 + X$ a calorimeter resolution of $\Delta E/E = 15\%/\sqrt{E}$ for electromagnetic showers and of $\Delta E/E = 80\%/\sqrt{E}$ for hadronic showers

has been taken into account. The neutrino has been taken as a hadron and has been smeared with the hadronic resolution. Calorimetry coverage in the pseudorapidity range of $|\eta| < 2.5$ has been assumed. Kinematical cuts on the transverse momenta of the three outgoing leptons exceeding $25 \text{ GeV}/c$ have been applied. With these cuts a total cross section of 112.4 fb is obtained, where the leptonic branching fractions of $BR(W \rightarrow l\nu) = 10.88\%$ and of $BR(Z \rightarrow l^+l^-) = 3.36\%$ have been included and the electron, the muon and the e- μ channels have been taken into account. This cross section translates into a number of events of ~ 11000 for 10^5 pb^{-1} which corresponds to one year of running at peak-luminosities of $\mathcal{L} = 10^{34} \text{ cm}^{-2}\text{s}^{-1}$. This number is sufficiently large, even if one assumes peak-luminosities of only $10^{33} \text{ cm}^{-2}\text{s}^{-1}$, that one can afford efficiency losses which have not been taken into account yet. The total cross section for WZ pair production for different sets of structure functions is shown in Fig. 10 as a function of \sqrt{s} after the above cuts have been applied. The uncertainty in cross section due to these different sets is small and amounts to $\sim 15\%$ at LHC energies.

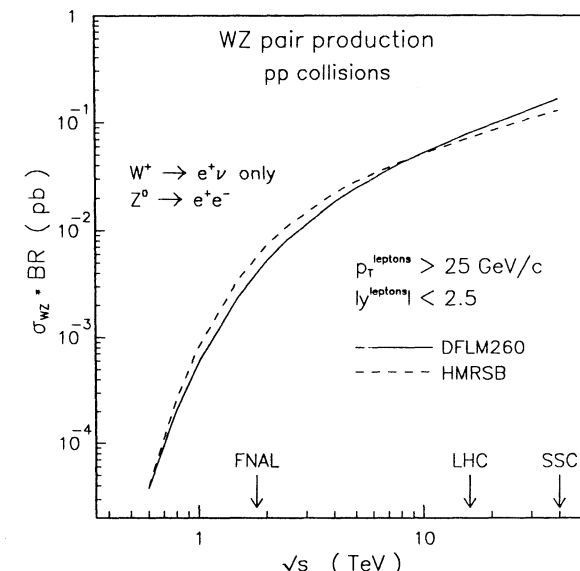


Figure 10
 $W^\pm Z^0$ pair production as a function of \sqrt{s} after cuts for different sets of structure functions

We have found that the signal is well above background by about one order of magnitude. The main background sources are expected from either $t\bar{t}$ with t or \bar{t} decaying semileptonically and one of the cascaded b's also decaying semileptonically, or from Z + jet (or Z + b) production with the Z $\rightarrow l^+l^-$ and the jet (b) fragments faking a lepton (electron or muon). The background from semileptonical t or b decays is already reduced by the kinematical cut of p_T^{leptons} exceeding $25 \text{ GeV}/c$ [16]. For the suppression of jets

faking the electron signature a rejection factor of $R = 10^4$ has been assumed, which is rather conservative compared to the rejection ($R > 5 \cdot 10^5$) obtained by the $p\bar{p}$ collider experiments UA2 and CDF. Taking into account the complexity of the events expected in an LHC environment this seems to be a reasonable assumption. Leptons from b decays are expected to be non isolated. Therefore an energy isolation requirement should reduce this background to a small amount. We have assumed a rejection factor of only $R = 5$, which again is very conservative because it could be as large as 50 depending on the detector performance. Background from $t\bar{t}$ production is much harder to be suppressed, because the subsequent $t \rightarrow Wb$ cascaded by $W \rightarrow \ell\bar{\nu}$ decays produces real, isolated leptons. The constraint that two leptons reconstruct to the Z mass, for which a rejection factor of 10 has been assumed, and an additional isolation requirement on one of the leptons from the b decay reduces this background well below the signal. Table 3 summarizes the expected signal and background rates assuming an integrated luminosity of 10^5 pb^{-1} .

Table 3: $W^\pm Z^0$ pair production, signal and background rates for 10^5 pb^{-1}

$\sqrt{s} = 16 \text{ TeV}$	$\sigma_{W^+Z^0} \cdot B_{\ell\nu}$	$\sigma_{W^-Z^0} \cdot B_{\ell\nu}$	$\sigma_{W^\pm Z^0} \cdot B_{\ell\nu}$	# events/year
$W^\pm Z^0$ $\downarrow \ell^+\ell^-$ $\downarrow \ell\nu$	62.6 fb	48.8 fb	112.4 fb	11240
$Z + \text{Jet(s)}$ $\downarrow \ell^+\ell^-$			3.0 fb	300
$Z + b$ $\downarrow \ell\bar{v}c$ $\downarrow \ell^+\ell^-$			5.5 fb	500
$t\bar{t}$ ($m_{top} = 130 \text{ GeV}/c^2$) $\downarrow \ell\bar{v}b$ $\downarrow \text{jets}$ [$t\bar{t}$ ($m_{top} = 150 \text{ GeV}/c^2$)]			$\leq 20 \text{ fb}$	≤ 2000
			$\leq 14 \text{ fb}$	≤ 1400
$ m_{\text{leptons}} < 2.5, p_T^{\text{leptons}} > 25 \text{ GeV}/c$				

4.3.2 $W^\pm Z^0$ anomalous couplings

As an example, the sensitivity to deviations from standard couplings has been tested by changing the parameter λ from its SM expectation ($\lambda = 0$) to $\lambda = 0.1$ and 0.04. The total cross section changes very little, but the shape of the total transverse mass distribution of the W and Z pair, M_T^{WZ} , is found to be very sensitive to anomalous couplings. This variable is easily accessed by experiment, because only well measured transverse variables are involved. The total mass M^{WZ} as proposed by Ref. [14] is less sensitive due to the ambiguity of the longitudinal momentum of the neutrino being unknown. The total transverse mass distribution M_T^{WZ} is shown in Fig. 11 for standard

couplings (full line), for $\lambda = 0.1$ (dashed line) and for $\lambda = 0.04$ (dotted line). If one defines as sensitivity to have at least 10 events integrated over all events above a certain transverse mass threshold, anomalous couplings can be tested up to $M_T^{WZ} = 1620 \text{ GeV}/c^2$ ($M_T^{WZ} = 1160 \text{ GeV}/c^2$) for $\lambda = 0.1$ ($\lambda = 0.04$) assuming 10^5 pb^{-1} .

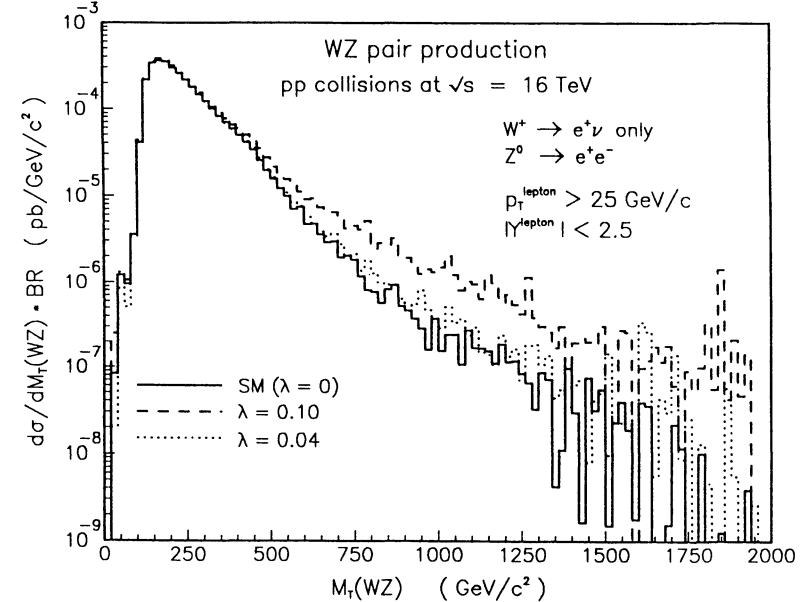


Figure 11
Transverse mass distribution of the W and Z pair, M_T^{WZ} , for standard ($\lambda = 0$) and anomalous couplings ($\lambda = 0.1$ and 0.04)

As a conclusion we have found that anomalous couplings could be tested to the 2 - 4% level, depending which coupling constant is considered, by comparing the shapes of the transverse mass spectrum of the WZ pair, a variable which is easily measurable by experiment and has no ambiguity due to the unknown longitudinal momentum of the neutrino. This gives about one order of magnitude better sensitivity than LEP II.

4.4 $W\gamma$ pair production

F. Pastore⁶ and M. Pepe⁷

In this Section we concentrate on $W^\pm\gamma$ production [17]. Here we study how well experiments at LHC will be able to observe this process and how sensitive would they be to deviations from Standard Model predictions.

4.4.1. Signal from Standard Model and background studies

In order to investigate the possibility to observe this process, we used a simulation program by D. Zeppenfeld. We selected final states containing two electromagnetic clusters in a calorimeter, the first due to the high p_T photon and the second to the electron coming from the $W \rightarrow ev$ decay. We neglected the hadronic and τ decay modes of the W since they will be overwhelmed by the QCD background. The $W \rightarrow \mu\nu$ decay is briefly discussed at the end of this section.

We used the leptonic branching fraction $BR(W \rightarrow \ell\nu) = 0.108$ in a framework in which $M_{Top} > M_W$. We assumed a realistic situation with an electromagnetic calorimeter energy resolution $\frac{\Delta E}{E} = \frac{13\%}{\sqrt{E}}$ and a calorimeter coverage of $|\eta| < 2.5$. The experimental technique is mainly based on the signature of the high p_T photon. Since a misidentified jet can fake a photon, we studied the effect of an isolation cut which requires no charged particles in a cone around the photon. The isolation reduces the background from jet production by a factor $\sim 10^4$ for $p_T^\gamma > 100$ GeV/c and $\geq 10^5$ for $p_T^\gamma > 200$ GeV/c [17].

We included the detector effects and applied the following selection criteria :

- $p_T^\gamma > 100$ GeV/c $|\eta_\gamma| < 2.5$
- $p_T^e > 25$ GeV/c $|\eta_e| < 2.5$

Fig. 12 shows the $W^+\gamma$ and $W^-\gamma$ production cross-sections as a function of \sqrt{s} after applying the previously defined cuts. The suppression of W^- with respect to W^+ production is due to the higher number of valence u with respect to d quarks inside the proton and to the finite rapidity window for the charged leptons. At LHC energies we expect a cross section of ~ 90.7 fb for $W^+\gamma$ and ~ 69.9 fb for $W^-\gamma$ giving a total of ~ 16000 events per year assuming one year of running at a luminosity of $\sim 10^{34}$ cm $^{-2}$ s $^{-1}$ adding both, the electron and the muon channel.

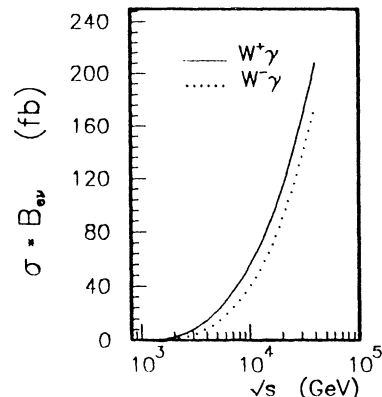


Figure 12
 $W^+\gamma$ and $W^-\gamma$ cross sections
as a function of \sqrt{s} after
applying the selection criteria
described in the text

The background is mainly due to two different sources: $W +$ jets and heavy flavour production (i.e. $b\bar{b} \rightarrow e\bar{v}c +$ jet), where the jet is misidentified as a photon.

1. The $W +$ jet(s) cross-section for $W \rightarrow ev$ with $p_T^{\text{jet}} > 25$ GeV/c and $|\eta_{e,\text{jet}}| < 2.5$ has been estimated (see Section 3.2) to be $\sigma \cdot B \sim 0.24$ nb ($\sigma \cdot B \sim 0.036$ nb) for $p_T^{\text{jet}} > 100$ GeV/c ($p_T^{\text{jet}} > 200$ GeV/c). Taking into account the rejection factors discussed above a background of ~ 24 fb (~ 0.36 fb) has been calculated.
2. The production of $b\bar{b} \rightarrow e\bar{v}c +$ jet in $|\eta| < 2.5$ and $p_T^{\text{jet}} > 100$ GeV/c has been studied using the Lund Monte Carlo [18]. We found that this cross section is ~ 8 nb. Taking into account the rejection factor for the photon and requiring an electron with $p_T^e > 25$ GeV/c this background reduces to ~ 0.1 fb for $p_T^\gamma > 100$ GeV/c and is completely negligible for $p_T^\gamma > 200$ GeV/c.

Table 4 summarizes the results for signal and background assuming an integrated luminosity per year of 10^5 pb $^{-1}$. A higher cut on p_T^γ clearly reduces the background contribution still keeping the signal at a significant level. If we apply stricter cuts requiring in addition $|M_T^{\text{ev}} - M_W| < 20$ GeV/c 2 , the signal is reduced to ~ 46.9 fb for $W^+\gamma$ and ~ 37.5 fb for $W^-\gamma$ corresponding to a total of ~ 8400 events.

Table 4
 $W^\pm\gamma$ signal and main background sources for different p_T^γ thresholds

	$p_T^\gamma > 100$ GeV/c		$p_T^\gamma > 200$ GeV/c	
	$\sigma \cdot B_{ev}$	# events/year	$\sigma \cdot B_{ev}$	# events/year
$W^\pm\gamma \rightarrow ev$	160.6 fb	16060	21.7 fb	2170
$W^\pm +$ jets $b\bar{b}X \rightarrow e\bar{v}c \rightarrow jets$	~ 24 fb 0.1 fb	2400 10	~ 0.36 fb	36 negligible

Table 5 : $W^+\gamma$ and $W^-\gamma$ cross-sections with $W \rightarrow \mu\nu$ for different values of the muon momentum resolution

α	$W^+\gamma \rightarrow \mu\nu$		$W^-\gamma \rightarrow \mu\nu$	
	$\sigma \cdot B_{\mu\nu}$	# events/year	$\sigma \cdot B_{\mu\nu}$	# events/year
0.001	21.9 fb	2190	16.5 fb	1650
0.003	13.8 fb	1380	10.1 fb	1010
0.005	10.5 fb	1050	7.4 fb	740

A similar analysis can be performed looking at $W \rightarrow \mu\nu$ decays with a similar event selection. The observable cross-section depends strongly on the muon momentum resolution. Under the assumption of $\Delta p_\mu/p_\mu = \alpha \cdot p_\mu$ the results for different values of α and $p_T^\gamma > 100 \text{ GeV}/c$ are shown in Table 5.

4.4.2. Signal for anomalous couplings

The presence of anomalies in the $WW\gamma$ vertex will yield an enhanced number of events at larger p_T^γ or large transverse masses of the $W\gamma$ system ($M_T^{W\gamma}$) similarly to the WZ pair production (see Section 4.3). The cross-section for the Standard Model and some representative choices of the parameters λ , κ and Λ are listed in Table 6 after the stricter selection criteria. The photon transverse momentum p_T^γ turns out to be a sensitive variable for different values of the parameters.

Table 6 : $W^\pm\gamma$ cross-sections for Standard Model and anomalous couplings

$\sigma_{W^\pm\gamma} \cdot B_{ev}$				
	$p_T^\gamma > 100 \text{ GeV}/c$		$p_T^\gamma > 200 \text{ GeV}/c$	
	$\Lambda = 1 \text{ TeV}$	$\Lambda = 2 \text{ TeV}$	$\Lambda = 1 \text{ TeV}$	$\Lambda = 2 \text{ TeV}$
S.M.	84.4 fb	84.4 fb	10.5 fb	10.5 fb
$\lambda = 0.02$	89.7 fb	94.8 fb	12.4 fb	16.4 fb
$\lambda = 0.05$	105.5 fb	135.0 fb	20.0 fb	42.7 fb
$\lambda = 0.10$	163.6 fb	269.3 fb	45.6 fb	133.3 fb
$\kappa = 1.5$	137.2 fb	172.4 fb	20.4 fb	37.4 fb

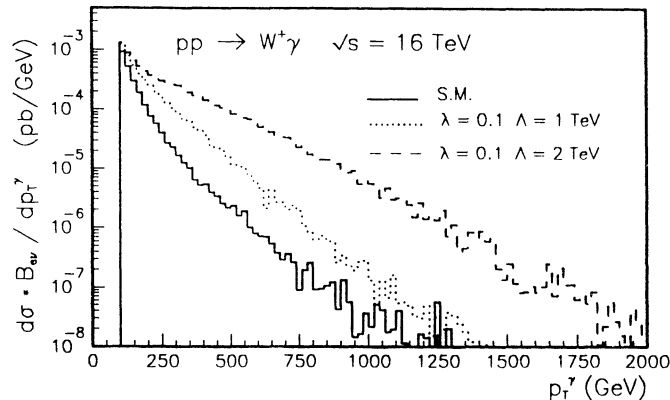


Figure 13

Photon transverse momentum distribution for $W^\pm\gamma$: anomalous couplings with $\lambda = 0.1$ and $\Lambda = 1$ (2) TeV compared to Standard Model predictions.

Fig. 13 compares the p_T^γ distribution for $\lambda = 0.1$ and $\Lambda = 1$ (2) TeV with the Standard Model expectations. Even in the case of $\Lambda = 1$ TeV the sensitivity to this anomalous coupling is up to $p_T^\gamma = 800 \text{ GeV}/c$. Fig. 14 shows the expected deviations in the p_T^γ distribution for different values of λ and $\Lambda = 1$ TeV.

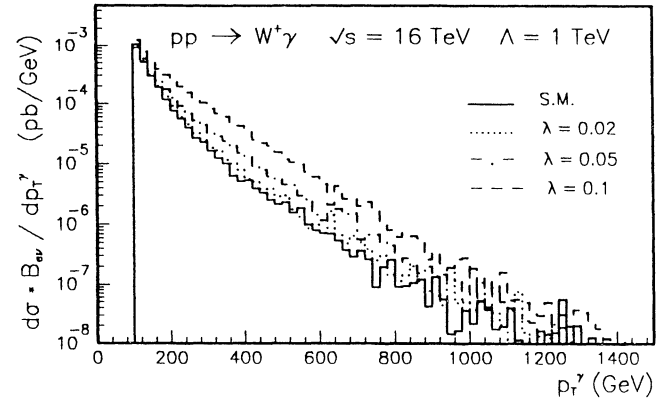


Figure 14

Expected deviations in the photon transverse momentum distribution for $W^\pm\gamma$ with different choices of λ and $\Lambda = 1$ TeV.

Another sensitive variable is the total transverse mass of the W and γ pair, $M_T^{W\gamma}$. Fig. 15 shows the expected deviations in the $M_T^{W\gamma}$ distribution when $\Lambda = 2$ TeV and $\kappa = 1.5$ or $\lambda = 0.1$. In this case the anomalous couplings can be tested up to a value $M_T^{W\gamma} \sim 2600 \text{ GeV}/c^2$ ($\sim 1700 \text{ GeV}/c^2$ if $\Lambda = 1$ TeV).

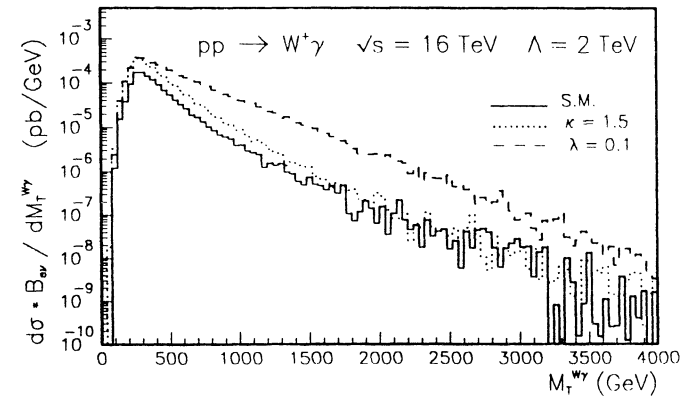


Figure 15

$W^\pm\gamma$ transverse mass distribution for $\kappa = 1.5$ or $\lambda = 0.1$ and $\Lambda = 2$ TeV compared to Standard Model predictions.

4.5 Conclusions

Gauge boson pair production is particularly interesting. Hadron colliders are capable of producing gauge boson pairs in both the charged and neutral channels. In pp collisions at LHC energies the structure of the WWZ (W γ) vertex can be studied by WZ (W γ) pair production. These channels allow to test the structure of the electroweak theory which predicts the existence of these Intermediate Vector Boson Self-Interactions.

Both, the W $^\pm Z^0$ and W $^\pm \gamma$ pair production are easily accessible by experiments after minor cuts. There is a clean signature, for W $^\pm Z^0$ three high p_T leptons and significant missing transverse momentum, while for W $^\pm \gamma$ one high p_T lepton, one very high p_T photon and missing transverse momentum are the dominant signatures. For an integrated luminosity of 10⁵ pb⁻¹ which corresponds to one year of running at $\mathcal{L} = 10^{34}$ cm⁻²s⁻¹ ~ 11000 W $^\pm Z^0$ events and ~ 16000 W $^\pm \gamma$ events are expected in the pseudorapidity range of | η | < 2.5 for both, the leptons and the photon, and transverse momenta in excess of 25 GeV/c for the leptons and of 100 GeV/c for photon. The main sources of background can be kept well below the ≤ 15% level of the signal.

The presence of anomalous couplings can be tested by comparing the shapes of the M_T^{WZ} or the M_T^{W γ} in case of WZ or W γ pair production, respectively, and in case of W $^\pm \gamma$ production also by comparing the behaviour at high values of the observed p_T ^{γ} with distributions from the Standard Model predictions. Gauge boson pair production of both, W $^\pm Z^0$ and W $^\pm \gamma$, allow tests of anomalous couplings up to a sensitivity of 2 - 4%. With 10⁵ pb⁻¹ of integrated luminosity mass ranges well above > 1600 GeV/c² can be tested which gives about one order of magnitude better sensitivity than LEP II. The different anomalous couplings can be distinguished using angular variables which would imply the measurement of the charge of the decay leptons. This statement needs more detailed studies, which have not been made yet.

In conclusion, the WZ and W γ pair production imply the following requirements on the lepton (electron and muons) identification for a detector at the LHC or SSC:

- a) moderate electron and good muon identification with lepton transverse momenta exceeding 20 GeV/c,
- b) good lepton isolation as an important implication for background suppression and
- c) determination of the charge of the leptons over a large pseudorapidity range.

5. CONCLUDING REMARKS

The Standard Model study group on standard processes has worked very successfully. The outcome of this study group results in an exciting physics topic such as *gauge boson pair* production which can be investigated at the LHC with high sensitivity up to masses exceeding the 1 TeV range.

REFERENCES

- [1] D.W. Duke and J.F. Owens, Phys. Rev. **D30** (1984) 49;
E. Eichten, I. Hinchliffe, K. Lane and C. Quigg, Rev. Mod. Phys. **56** (1984) 579;
M. Glück, E. Hoffman and E. Reya, Z. Phys. **C13** (1982) 119.
- [2] A.D. Martin, R.G. Roberts and W.J. Stirling, Phys. Lett. **206B** (1988) 327 and
Mod. Phys. Lett. **A4** (1989) 1135.
- [3] M. Diemoz, F. Ferroni, E. Longo and G. Martinelli, Z. Phys. **C39** (1988) 21;
P.N. Harriman, A.D. Martin, R.G. Roberts and W.J. Stirling, Durham Preprint,
DTP-90-04 (1990) and revised April 1990;
J. Morfin and W.K. Tung, FNAL-PUB-90-74;
J. Kwiecinski, A.D. Martin, R.G. Roberts and W.J. Stirling, DTP-90-46 (1990);
M. Glück, E. Reya and A. Vogt, Dortmund preprint, DO-TH-89/20 (1989).
- [4] BCMS Collaboration, A. C. Benvenuti et al., Phys. Lett. **237B** (1990) 529 and
Phys. Lett. **237B** (1990) 559;
EMC Collaboration, M. Arneodo et al., CERN - EP/89 - 121;
NMC Collaboration, D. Allasia et al., CERN - PPE/90 - 103.
- [5] J. Feltesse, Proceedings of the DESY Workshop on Physics at HERA,
DESY Hamburg 1987, Vol. 1, p. 33.
- [6] G. Altarelli et al., Nucl. Phys. **B246** (1984) 12 and Z. Phys. **C27** (1985) 617.
- [7] T. Matsuura and W.L. van Neerven, Z. Phys. **C38** (1988) 623;
T. Matsuura, S.C. van der Merck and W.L. van Neerven, Phys. Lett. **211B** (1988)
171 and Nucl. Phys. **B319** (1989) 570.
- [8] G. Sterman, Phys. Lett. **179B** (1986) 281 and Nucl. Phys. **B281** (1987) 310;
D. Appel, P. Mackenzie and G. Sterman, Nucl. Phys. **B309** (1988) 259;
S. Catani and L. Trentadue, Phys. Lett. **217B** (1989) 539, Nucl. Phys. **B327**
(1989) 323 and Cavendish Lab. preprint HEP 90/12 (submitted to Nucl. Phys. B).
- [9] UA1 Collaboration, C. Albajar et al., CERN - PPE/90 - 141;
UA2 Collaboration, J. Alitti et al., Z. Phys. **C47** (1990) 11;
CDF Collaboration, presented by T. Westhusing, Proc. of the 25th Rencontre de
Moriond on Z⁰ Physics, (1990), Editions Frontiers 1990, p. 423.
- [10] R. Hamberg, W.L. van Neerven and T. Matsuura, DESY/90-129 (1990).
- [11] P.B. Arnold, M.H. Reno, Nucl. Phys. **B319** (1989) 37.
- [12] R.J. Gonsalves, J. Pawłowski, C-F. Wai, Phys. Rev. **D40** (1989) 2245.
- [13] R.W. Brown, K.O. Mikaelian and D. Shadov, Phys. Rev. **D20** (1979) 1164;
E. Eichten, I. Hinchliffe, K. Lane and C. Quigg, Rev. Mod. Phys. **56** (1984) 579.
- [14] S. Willenbrock and D. Zeppenfeld, Phys. Rev. **D37** (1988) 1775;
U. Baur and E.W.N. Glover, FNAL-PUB-90/75-T.
- [15] U. Baur and D. Zeppenfeld, Nucl. Phys. **B308** (1988) 127.
- [16] A. Nisati, these proceedings.
- [17] presented by M. Werlen at the Aachen LHC workshop in the photon session.
- [18] H. U. Bengtsson and T. Sjöstrand, LU TP 86-22 (PYTHIA 5.3).

QCD corrections to Z pair production at LHC

B. Mele,¹ P. Nason² and G. Ridolfi³

Continuum ZZ pair production, arising in lowest order from the subprocess $q\bar{q} \rightarrow ZZ$, is one of the main backgrounds to a heavy Higgs signal at LHC and SSC [1]. As a consequence, it is particularly important to know the details of this process at high-energy pp colliders. In this note we briefly report on the results of a calculation of the QCD corrections of order α_S to the Z pair production total cross section in hadronic collisions [1]. We find that the corrections are positive in all the cases that we have considered, and are of the order of 20% to 30% of the total. The details of the calculation are described in ref. [2].

In Fig. 1 we plot the Z pair production total cross section as a function of the renormalization scale μ at LHC energy. The structure functions used are the DFLM set^[3] with $\Lambda_4 = 260$ MeV. We can observe that the scale dependence of the next-to-leading result is remarkably mild at LHC. For a comment on this issue, see ref. [2]. In Fig. 2 the cross section for Z pair production versus the centre-of-mass pp collision energy is shown for the same set of structure functions as before and for a value $\mu = 90$ GeV.

One can have an indication of the uncertainty related to our results by considering the variation in the total cross section coming from taking $\mu = 45, 90, 180$ GeV (keeping in mind that this cannot always be considered as a good estimate of the theoretical error due to $\mathcal{O}(\alpha_S^2)$ and higher order corrections).

In Table I we give cross sections (in pb) for Z pair production for energies of interest at various colliders, using the three sets of DFLM structure functions^[3] with $\Lambda_4 = 160, 260$ and 360 MeV, and the two sets of structure functions from ref. [4]. The scale μ is chosen equal to 90 GeV, and the errors quoted correspond to $\mu = 45$ and $\mu = 180$ GeV. Both the Born and the full (Born + $\mathcal{O}(\alpha_S)$) cross sections are shown. We can see that most of the uncertainty in the cross section comes from structure function dependence. The most extreme case is always given

by the HMRSE set, which is based upon EMC data. If we exclude this set, we find that at LHC energy the cross section ranges between 13.1 and 16.4 pb, while at the SSC it goes from 32.9 to 51.5 pb.

Table I

		DFLM160	DFLM260	DFLM360	HMRSE	HMRSB
$p\bar{p}$ $\sqrt{S} = 0.63$ TeV	Born	$0.0551^{+0.01}_{-0.007}$	$0.0475^{+0.01}_{-0.007}$	$0.0417^{+0.01}_{-0.007}$	$0.0682^{+0.01}_{-0.009}$	$0.0571^{+0.01}_{-0.008}$
	Full	$0.0693^{+0.005}_{-0.004}$	$0.0610^{+0.005}_{-0.004}$	$0.0542^{+0.005}_{-0.004}$	$0.0889^{+0.005}_{-0.005}$	$0.0766^{+0.005}_{-0.005}$
$p\bar{p}$ $\sqrt{S} = 1.8$ TeV	Born	$0.925^{+0.07}_{-0.06}$	$0.869^{+0.07}_{-0.06}$	$0.820^{+0.07}_{-0.06}$	$1.02^{+0.07}_{-0.04}$	$0.972^{+0.03}_{-0.07}$
	Full	$1.17^{+0.04}_{-0.04}$	$1.12^{+0.05}_{-0.04}$	$1.07^{+0.06}_{-0.05}$	$1.25^{+0.04}_{-0.04}$	$1.22^{+0.05}_{-0.04}$
pp $\sqrt{S} = 6$ TeV	Born	$3.00^{+0.07}_{-0.1}$	$3.02^{+0.05}_{-0.1}$	$2.99^{+0.02}_{-0.07}$	$3.01^{+0.1}_{-0.2}$	$3.29^{+0.1}_{-0.1}$
	Full	$3.97^{+0.08}_{-0.06}$	$4.06^{+0.1}_{-0.1}$	$4.06^{+0.1}_{-0.1}$	$3.80^{+0.06}_{-0.03}$	$4.21^{+0.09}_{-0.05}$
pp $\sqrt{S} = 16$ TeV	Born	$9.8^{+0.9}_{-1.1}$	10.7^{+1}_{-1}	11.4^{+1}_{-1}	$8.13^{+0.9}_{-1}$	9.75^{+1}_{-1}
	Full	$13.7^{+0.04}_{-0.08}$	$15.2^{+0.01}_{-0.02}$	$16.3^{+0.1}_{-0.1}$	$11.0^{+0.1}_{-0.1}$	$13.2^{+0.1}_{-0.08}$
pp $\sqrt{S} = 40$ TeV	Born	24.2^{+4}_{-4}	29.2^{+4}_{-5}	34.0^{+5}_{-5}	17.7^{+4}_{-3}	23.5^{+4}_{-4}
	Full	35.8^{+1}_{-1}	43.6^{+1}_{-1}	$50.8^{+0.7}_{-1}$	$25.6^{+0.9}_{-1}$	33.9^{+1}_{-1}
pp $\sqrt{S} = 100$ TeV	Born	48.6^{+12}_{-11}	64.6^{+14}_{-14}	82.2^{+17}_{-18}	36.8^{+10}_{-9}	53.2^{+13}_{-13}
	Full	77.4^{+3}_{-5}	103^{+3}_{-5}	131^{+3}_{-6}	56.3^{+3}_{-5}	81.3^{+3}_{-6}

References

- [1] Contribution to this report from the Higgs working group.
- [2] B. Mele, P. Nason and G. Ridolfi, preprint CERN-TH 5890/90 (1990).
- [3] M. Diemoz, F. Ferroni, E. Longo and G. Martinelli, *Z. Phys.* **C39**(1988)21; J. V. Allaby *et al.*, *Phys. Lett.* **197B**(1987)281.
- [4] P. N. Harriman, A. D. Martin, R. G. Roberts and W. J. Stirling, Preprint DTP-90-04.

¹CERN - Geneva, Switzerland

²INFN - Gruppo collegato di Parma, Italy

³INFN - Sezione di Genova, Italy

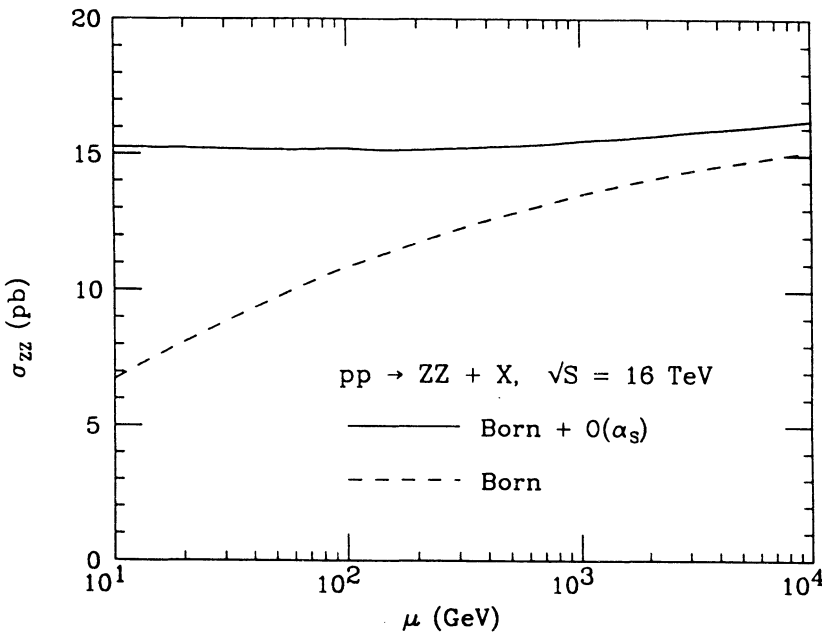


Fig. 1

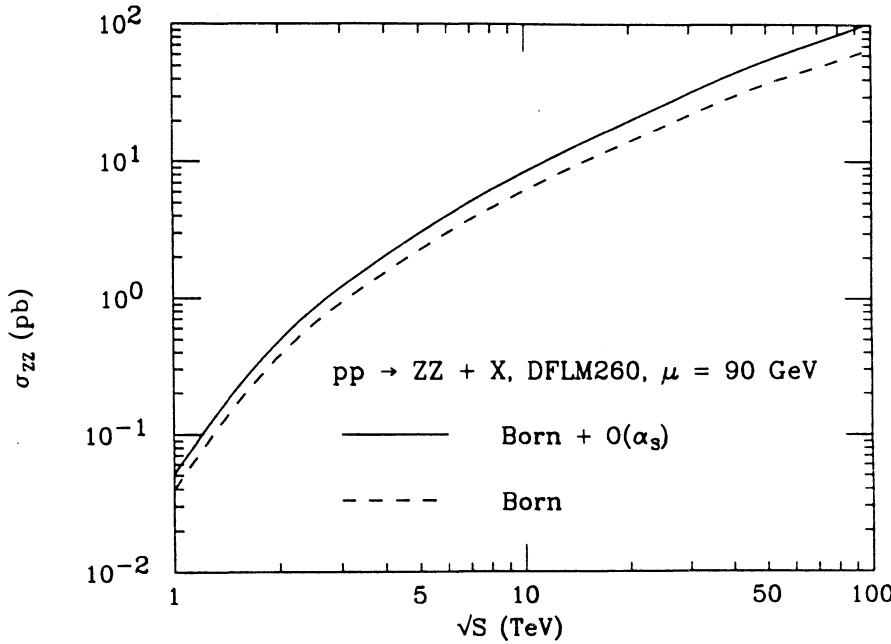


Fig. 2

Heavy Quark Production at the LHC

J. P. Guillet, P. Nason, H. Plothow-Besch

1. Introduction

At the LHC, top, bottom, and charm pairs are produced in large quantities, and they are important both for physics study and for understanding the background to other processes. If not discovered earlier at Fermilab, the LHC may be the first accelerator which will produce the top quark, and study its properties. There is the possibility to use the LHC for b physics studies. Furthermore, there are proposals to use the neutrinos coming from the decays of b and c quarks produced in large quantity in the LHC (as illustrated in the neutrino physics section of the report of this working group). Bottomed and charmed hadrons may also produce high momentum leptons, and therefore they always constitute a potential background to new physics.

The theory of hadronic production of heavy quarks is in reasonably good shape. Two groups^[1,2] have completed a calculation of the next-to-leading QCD corrections to the inclusive production of heavy quarks, and their results agree. These results can therefore be considered well established.

At supercolliders we distinguish three important regimes of heavy quark production:

- The production of a heavy quark with a mass of the order of a hundred GeV
- The production of relatively light ($m_Q \leq 5$ GeV) heavy quark, when $p_T \approx m_Q$ (the bulk of the production cross section comes from this kinematic region).
- The production of a relatively light quark ($m_Q \leq 5$ GeV) with transverse momentum much larger than its mass.

The first region is obviously relevant to top production. The second region is important both for b physics and to neutrino physics. The third region is relevant to the production of high p_T leptons, coming from high p_T b mesons. We will now illustrate cross sections and production properties of heavy quarks in these three cases.

DFLM260, $\sqrt{s} = 16$ TeV			
	$\mu = \frac{m_{\text{top}}}{2}$	$\mu = m_{\text{top}}$	$\mu = 2m_{\text{top}}$
Full	4.93 nb	4.34 nb	3.79 nb
Born	3.58 nb	2.84 nb	2.26 nb

Table I: Leading and next-to-leading top cross section for different scale choices.

2. Top production

In the regime of top production, fixed order QCD should give reasonable results. In table I we show the scale dependence of the total cross section for top production at the LHC. As one can see, the leading and next-to-leading results don't differ drastically, and the dependence upon the scale is substantially reduced, from 46% to 25% when next-to-leading corrections are included. We have computed the cross section for top production using different sets of structure functions, at 630 and 1800 GeV for $p\bar{p}$ collisions, and at 16 and 40 TeV at pp collisions. We have tried fourteen of the most used sets of structure functions^[3]. The cross section at LHC ranges from 3.3 to 4.8 nb, for $m_{\text{top}} = 130$ GeV and from 0.48 to 0.68 nb for $m_{\text{top}} = 200$ GeV. In table II we give the cross section for top production for three structure function sets. Finally, in fig. 1 we show the heavy quark total cross section as a function of the mass.

The differential distribution for top production at 16 TeV is shown in fig. 2. The main features of the production cross section is that the p_{\perp} is of the order of the mass, and the rapidity distribution has its typical bell shape.

3. Bottom and Charm cross sections.

Bottom and Charm cross section at the LHC and SSC are hardly calculable. One finds that fixed order perturbation theory is not well behaved, the next-to-leading term being as a rule of the order of the leading one. This behaviour is a consequence of the fact that the leading partonic cross section for gluon-gluon into

Total σ_{tt} in nb, $m_{\text{top}} = 130$ GeV			
	DFLM260	HMRSB	GRV
$p\bar{p}, 0.63$ TeV	$2.5 \cdot 10^{-4}$	$2.7 \cdot 10^{-4}$	$2.7 \cdot 10^{-4}$
$p\bar{p}, 1.8$ TeV	$2.23 \cdot 10^{-2}$	$2.33 \cdot 10^{-2}$	$1.95 \cdot 10^{-2}$
pp, 16 TeV	4.35	3.96	3.38
pp, 40 TeV	21.85	18.34	18.35
$m_{\text{top}} = 200$ GeV			
$p\bar{p}, 0.63$ TeV	$7.3 \cdot 10^{-6}$	$4.34 \cdot 10^{-6}$	$1.0 \cdot 10^{-5}$
$p\bar{p}, 1.8$ TeV	$1.9 \cdot 10^{-3}$	$2.2 \cdot 10^{-3}$	$1.9 \cdot 10^{-3}$
pp, 16 TeV	.636	.621	.489
pp, 40 TeV	3.89	3.50	3.17

Table II: Top cross sections at energies of interest for different sets of structure functions.

heavy quarks dies as a power of s , while the next to leading partonic cross section goes to a constant for large $s^{[1]}$. Because of this fact, the next-to-leading hadronic cross section is enhanced by a factor of the order of the maximum rapidity that the heavy quark may reach. This effect, already present at $SppS$ and Tevatron energies, becomes so strong at the LHC and SSC that one is no longer confident to be able to give a reasonable estimate of the cross section using fixed order perturbation theory. A further problem, which is intimately related to the one just mentioned, is the need to know the structure functions at very small values of x in order to be able to calculate b and c cross sections. Various cures have been proposed in order to solve this problems^[4,5,6], but they have not yet reached the level of being able to make a reliable prediction of the b cross section. For charm, the problem is complicated by the fact that the charm mass is too close to typical hadronic scales, and the strong coupling constant and the structure functions loose their meaning at these scales.

In this reports we certainly have not solved all these problems. Since some kind of prediction must be given, we have simply calculated bottom and charm cross section by using fixed order perturbation theory formulas, and varying as much as possible various parameter in order to assess the degree of uncertainty that one has.

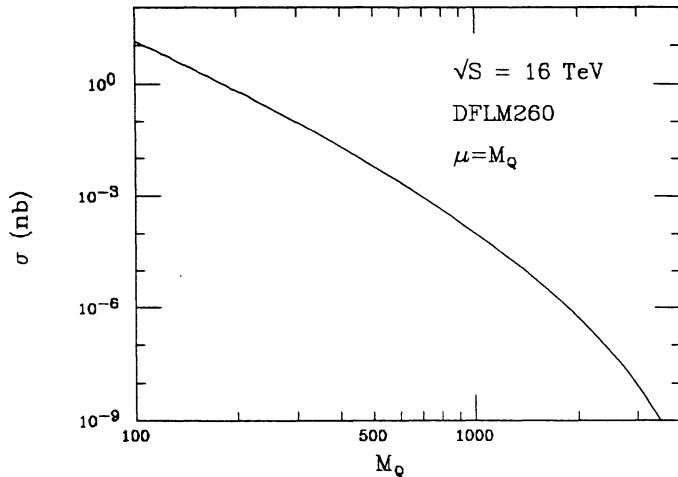


Fig. 1: Total cross section for the production of a heavy quark versus its mass at the LHC.

We have computed the cross section for b production using the sets of structure functions of ref. [3]. The range of variation of the cross section that we obtain in this way is $\sigma_{bb} = 0.1$ to 0.7 mb . The authors of ref. [7] calculate the b cross section from a completely different approach. They extrapolate their result on production of low mass hadrons to the production of b and c quarks. The authors themselves do not consider this procedure fully sound, as far as the prediction of the absolute rate is concerned. However, they claim that the energy dependence of the cross section should be well predicted by their model. Based upon the bottom cross section measured by the UA1 experiment^[8] they make a prediction of 0.1 to 0.7 mb for bottom cross section at LHC.

In fig. 3 we report the differential distribution for b production, including the next-to-leading corrections, using the structure function DFLM160 (which is the DFLM set having $\Lambda_{\text{QCD}}^{(4)} = 160 \text{ MeV}$, and the index (4) stands for four active flavours). The general features of the production distribution are a typical p_T of

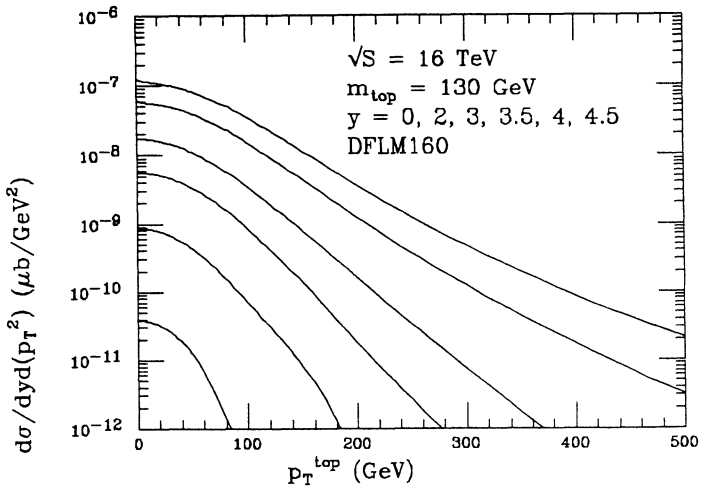


Fig. 2: Differential distributions for top production at LHC energy, for $m_{\text{top}} = 130 \text{ GeV}$.

the order of the heavy quark mass, and a rather flat rapidity distribution, which vanishes quickly near the last few units of rapidity available. We have found a considerable difference in shape in the predictions made with different sets of structure functions. There are also other sources of large uncertainties, like the choice of the scale and the mass of the b quark. The differential distributions we give should therefore be taken as a general indication.

Charm cross sections are even harder to predict than bottom cross sections. All the problems which are present for bottom are also there (and worse) for charm quarks. Furthermore, one more problem arises. The mass of the charm quark lies on the boundary of the Q^2 values at which it makes sense at all to talk about strong coupling constant and structure functions. We have estimated the charm total cross section by using two extreme approximations of the gluon structure function. We have used

$$xG(x) = 3(1-x)^5 \quad (3.1)$$

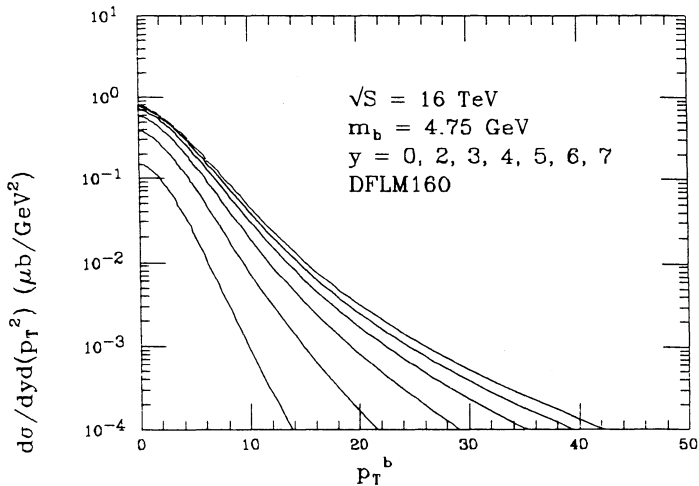


Fig. 3: Differential distributions for bottom production.

and

$$xG(x) = 1.35(1-x)^5x^{-0.5} \quad (3.2)$$

The two structure functions are plotted in fig. 4, together with the structure function DFLM260 at $Q^2 = 10, \text{GeV}^2$, extrapolated out of his range of validity. As one can see, the DFLM structure function is intermediate between the other two.

In fig. 5 we report the charm hadroproduction cross section in leading and next-to-leading accuracy for both models. The upper bound from ref. [9], at $\sqrt{S} = 0.63 \text{TeV}$ is also shown. We obtain a cross section between 3 and 150 mb at LHC energy (we remind the reader that inclusive production cross sections higher than the total cross section are possible, and they indicate that more than one charm pair is produced in each collision). The authors of ref. [7] give a prediction between 1 and 3 mb. The main features of the differential distribution one expects are, as usual, a transverse momentum of the b of the order of its mass, and a flat rapidity distribution, which vanishes quickly near the maximum rapidity region. In figs. 6

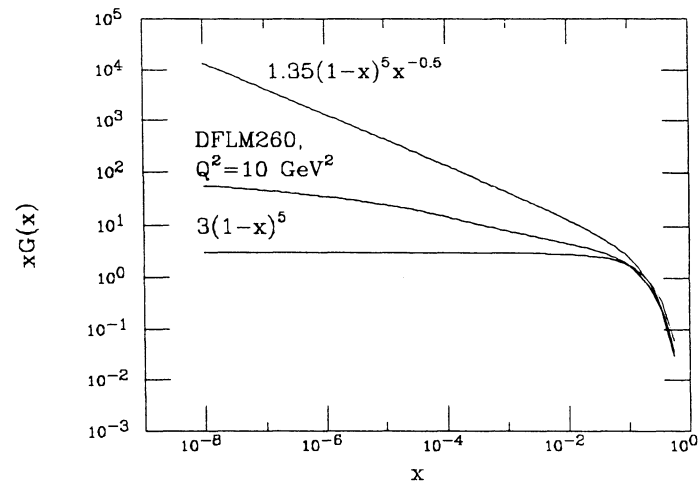


Fig. 4: Two extreme models of the gluon structure function at small Q^2 .

and 7 we give the rapidity and x_F distributions of charmed quarks, for the gluon structure function of eq. (3.1) and eq. (3.2). The x_F distributions are particularly interesting for the purpose of performing neutrino experiments at LHC. It is clear that most of the rate is concentrated at values of x_F around zero, and that most of the difference due to the gluon structure function arises from the different small x singularity of the two models.

4. Production of heavy quarks at large transverse momentum

Heavy quarks (b 's and c 's) start to behave as light hadrons in high p_\perp phenomena. The multiplicity of heavy quark in jets^[10], for example, grows very rapidly with the jet energy, as shown in fig. 8 (it does not depend upon \sqrt{S}). From the figure, we see that a 1 TeV jet contains a charmed pair about 50% of the time, and

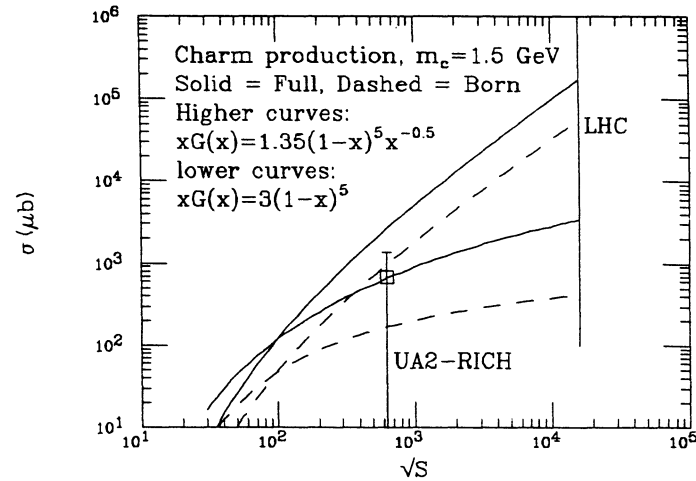


Fig. 5: Charm hadroproduction cross section in pp collisions versus the energy.

a bottomed pair about 10% of the time. Production of b and c quarks at very high transverse momenta cannot be described via conventional fixed order perturbation theory (e. g. order α_s^2 plus α_s^3 contributions). One should instead use a formalism which is more similar to the one employed for light hadrons inclusive production, where the cross section is given by the convolution of a parton cross section times a fragmentation function to go from the parton to the hadron. The cross section for heavy quark production becomes then a convolution of a cross section for parton production times a fragmentation function to go from a parton to the heavy quark, with the important difference that the fragmentation function for the production of a heavy quark is calculable from first principles^[11], while the fragmentation function for the production of a light hadron must be measured. In fig. 9 we plot the fragmentation function for finding a heavy quark in a 0.1 and 1 TeV jet with zero rapidity, at $\sqrt{S} = 16$ TeV. As one can see, in the case of a 0.1 TeV jet, a peak of the fragmentation function near $z = 1$ is still visible, while at 1 TeV it is completely gone. The two curves can be understood in terms of the superposition of different

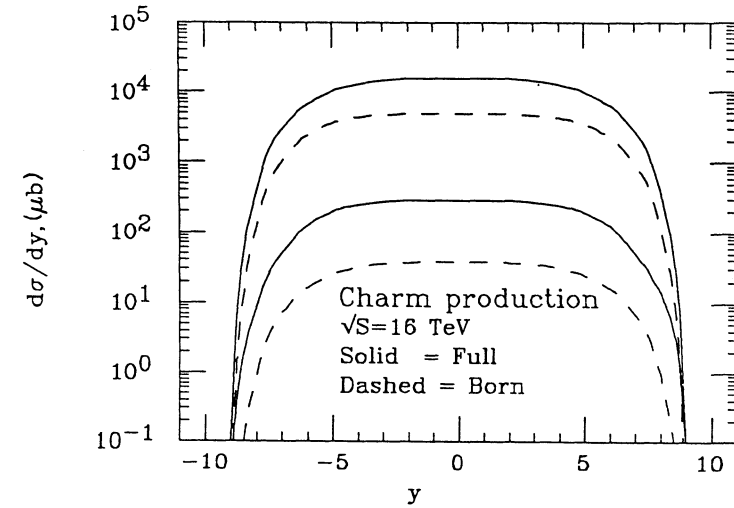


Fig. 6: Rapidity distribution of charmed quarks at the LHC. The lower curves are for the gluon density of eq. (3.1), and the higher curves for eq. (3.2).

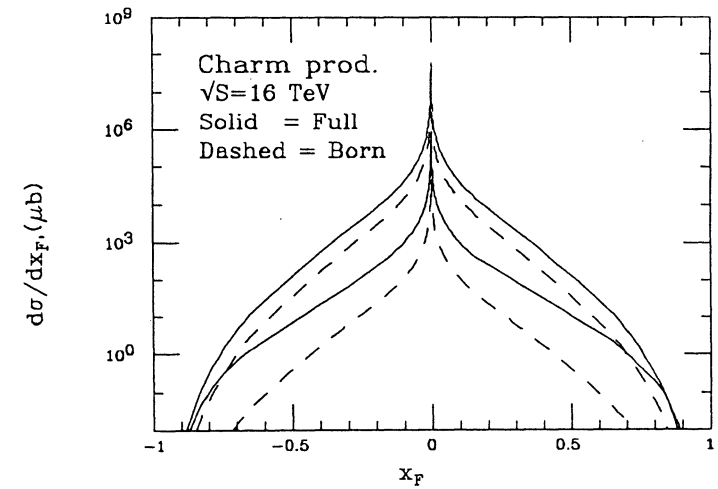


Fig. 7: x_F distribution of charmed quark at the LHC. The lower curves are for the gluon density of eq. (3.1), and the higher curves for eq. (3.2).

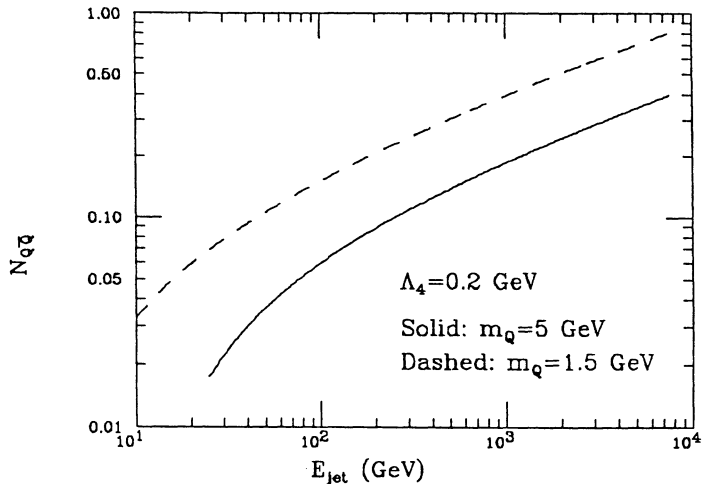


Fig. 8: Number of charmed and bottom pairs in a jet versus the energy.

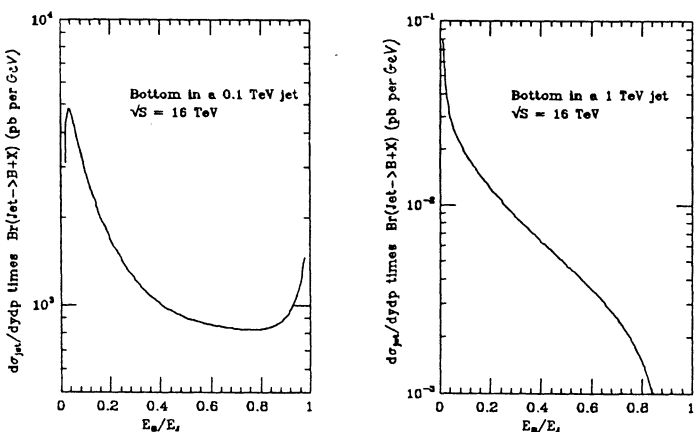


Fig. 9: The fragmentation function for finding a b quark in a 0.1 and 1 TeV jet.

production mechanism. The peak at $z = 1$ is due to direct production, where a b quark is directly produced by either gluon fusion, or by the scattering of an intrinsic heavy quark in one hadron with any parton in the other one. The peak at $z = 0$ arises instead because of the large number relatively soft gluons which are produced in high p_{\perp} phenomena, which can fragment into heavy quark pairs. For jets of 1 TeV forward peak has faded away. This is due to the fact that a very high energy heavy quark radiates a large amount of gluons, and therefore loses their longitudinal momenta.

5. Conclusions

We have found that the total and differential cross section for top production can be reliably calculated at supercollider energies. In contrast, the bulk of the cross section for b production is very difficult to calculate, due to theoretical problems related to the high energy limit (Regge limit, small x region, etc.). For c production the problem is even worse. Therefore, only estimates can be given, which differ widely according to the model one adopts, and to the assumptions one makes about the growth of structure functions at small x . Production of heavy quark at high transverse momentum can instead be calculated reliably, as long as one abandons the fixed order formalism. One must use instead a fragmentation function formalism, which is similar to the one used for standard inclusive production of light hadrons, with the difference that the fragmentation function for b quarks can be calculated explicitly.

REFERENCES

1. P. Nason, S. Dawson and K. Ellis, *Nucl. Phys.* **B303**(1988)607;
P. Nason, S. Dawson and K. Ellis, *Nucl. Phys.* **B327**(1989)49.
2. W. Beenakker et al., *Phys. Rev.* **D40**(1989)54;
W. Beenakker et al., DESY 90/064 (1990).
3. See references 1-3 of the section on Parton Luminosities, W and Z cross sections and gauge bosons pair production.
4. S. Catani, M. Ciafaloni and F. Hautmann, Cavendish-HEP 90/3, March, 1990.
5. R. K. Ellis, D. A. Ross, Fermilab-Pub-90/19-T.
6. E. M. Levin, M. G. Ryskin, Yu. M. Shabelski, A. G. Shuvaev, in preparation.
7. A. B. Keidalov and O. I. Piskounova, in preparation.
8. C. Albajar et al., *Phys. Lett.* **B213**(1988)405.
9. O. Botner et. al., *Phys. Lett.* **236B**(1990)488.
10. A. H. Mueller and P. Nason, *Nucl. Phys.* **B266**(1986)265.
11. B. Mele and P. Nason, *Phys. Lett.* **B245**(1990)635.

Event Generators for LHC

F. Anselmo¹, P.T. Cox², J.R. Cudell³, M. Della Negra³,
A. Di Ciaccio⁴, O. Di Rosa¹, B. van Eijk¹, D. Froidevaux³,
W.T. Giele⁵, R. Kleiss³, P. Lubrano³, R. Odorico⁶,
H. Plothow-Besch³, G. Polesello³, T. Sjöstrand³, G. Unal⁷

A2: EVENT GENERATORS

¹LAA Project, CERN, CH-1211 Geneva 23, Switzerland

²Rockefeller University, New York, NY, USA

³CERN, CH-1211 Geneva 23, Switzerland

⁴Università “Tor Vergata”, Rome, Italy

⁵FNAL, Batavia, IL, USA

⁶Università di Bologna and INFN, Bologna, Italy

⁷LAL, Université de Paris-Sud, Orsay, France

Abstract:

We give a survey of the event generators that may be used to predict pp collider physics at the LHC. The main program features are described, and also some of the known limitations are listed.

1 Introduction

The task of event generators is to describe, as accurately as possible, the experimental characteristics of physics processes of interest. The main applications are as follows.

- To give physicists a feeling for the kind of events one may expect/hope to find, and at what rates.
- As a help in the planning of a new detector, so that detector performance is optimized, within other constraints, for the study of interesting physics scenarios.
- As a tool for devising the analysis strategies that should be used on real data, so that signal-to-background conditions are optimized.
- As a method for estimating detector acceptance corrections that have to be applied to raw data, in order to extract the ‘true’ physics signal.

To write a good event generator is an art, not an exact science. It is essential not to trust blindly the results of any single event generator, but always to have several cross-checks. Further, an event generator cannot be thought of as an all-powerful oracle, able to give intelligent answers to ill-posed questions; sound judgement and

some understanding of the generator are necessary prerequisites for successful use. In spite of these limitations, the event generator approach is the most powerful tool at our disposal if we wish to gain a detailed and realistic understanding of physics at the LHC before the day when real data are available.

As the name indicates, the output of an event generator should be in the form of ‘events’, with the same average behaviour and the same fluctuations as real data. In generators, Monte Carlo techniques are used to select all relevant variables according to the desired probability distributions. The Monte Carlo approach ensures that the proper amount of randomness is included. Normally an ‘event’ is a list of all final state observable particles, i.e. hadrons, leptons, and photons, together with their momenta. The ‘event’ thus corresponds to what could actually be seen by an ideal detector. However, often one is only interested in the total energy and direction of a jet, rather than the detailed jet structure. Then a more crude event description, in terms of partons (\approx jets) and leptons, may be enough.

In principle, one must distinguish between an event generator and a numerical integration package for cross-sections: both can be used to evaluate the cross-section for a given process and for given cuts, but only the former gives the full multi-dimensional differential distribution of events within these cuts. In practice, this distinction is not always obvious for a large number of dedicated programs written to study one or a few specific processes: although the main application may be cross-section integration, only little additional effort is needed to generate simple ‘events’ which consist of a small number of outgoing partons and leptons. At the other end of the generator spectrum, there are large subroutine packages intended for general-purpose use, with many different processes included, and a full description of the production of all hadrons in an event. These packages contain many man-years of effort, and are generally better documented and supported than the smaller packages. It may be that they will dominate in the description below, although they need not be the best for all applications.

Programs still undergo rapid evolution: new processes are calculated and included; improved structure function parametrizations appear; aspects of parton showering, fragmentation and decay are gradually better modelled; and even the physics landscape changes (e.g., as a function of the currently favoured value for the top quark mass). The programs that will be used at LHC are likely to look rather different from those available today, which is why a too detailed study would be of limited use (unlike the e^+e^- event generators survey for LEP last year [1], on the eve of LEP startup). Further, it is not possible to view the event generators working group as separate from the seven other pp physics groups, which all have made extensive use of event generators as part of their specific physics studies. One may also find discussions of, and comparisons between, event generators in many of the recent studies on SSC physics, such as [2,3,4], and in the article [5].

The objective of the current report is not to repeat this work, but rather

- to give a survey of existing event generators, with an overview of what is included in them;
- to indicate known shortcomings, so that one may understand how seriously predictions should be taken; and
- to provide in-depth studies of a few specific topics, which serve to illustrate the status of programs.

In addition to the current report, the following papers appear as individual contributions to this working group.

- ‘Structure Functions’ by H. Plothow-Besch [6].
- ‘Monte Carlo Simulation of Minimum Bias Events at the LHC Energy’ by G. Ciapetti and A. Di Ciacio [7].
- ‘A Comparison of Bottom Production in Different Event Generators’ by J.R. Cudell, O. Di Rosa, I. ten Have, A. Nisati, R. Odorico and T. Sjöstrand [8].
- ‘Multi-jet Event Generators for LHC’, by H. Kuijf, P. Lubrano and V. Vercesi [9].
- ‘On the calculation of the exact $gg \rightarrow Z b\bar{b}$ cross section including Z decay and b quark mass effects’ by R. Kleiss and B. van Eijk [10].
- ‘Vector Boson Production in Association with Jets’ by W.T. Giele [11].

2 Overview of Event Generators

The perfect event generator does not exist. This reflects the limited understanding of physics in many areas. Indeed, a perfect event generator could only be constructed if everything were already known, in which case experiments would be superfluous. One therefore has to be satisfied with programs which are in reasonable agreement with already accumulated experience, theoretical and experimental, and which provide sensible extrapolations to higher energies. Since the ultimate goal is to look for new physics, it is also necessary to include the simulation of different alternative scenarios.

Given the complexity of the problem, the Monte Carlo approach allows a convenient subdivision into separate subtasks. Thus, to describe an event in full, one needs to consider the following components:

1. The hard scattering matrix elements. These define the process(es) under study, and are therefore at the core of the programs.
2. The structure functions. The differential cross-sections, which are to be simulated in the programs, are given as the products of structure functions and the hard scattering matrix elements above.
3. Final state radiation. Any partons in the final state may radiate. At high energies, this perturbative radiation is the main responsible for building up the structure of jets, with broad jet profiles and subjets.
4. Initial state radiation. The incoming partons may also radiate before the hard interaction, thus giving rise to additional jets close to the directions of the incoming hadrons.
5. Beam jets. Only one parton from each incoming hadron is assumed to participate in the hard interaction, and in the initial state showering. All the other partons act to produce the beam jets found along the directions of the original incoming hadrons.
6. Fragmentation and decays. Partons are not directly observable. Instead, once sufficiently removed from each other, they are fragmented into a collection of hadrons. Many of these hadrons are unstable, and subsequently decay.

Of course, this separation is very crude and schematic. Thus, one and the same $2 \rightarrow 3$ process might be described either in terms of a basic $2 \rightarrow 3$ matrix element, or in terms of a $2 \rightarrow 2$ hard scattering followed by final state radiation, or in terms of a $2 \rightarrow 2$ hard scattering preceded by initial state radiation. It is therefore important to join the different descriptions in a consistent manner, e.g. to avoid double counting.

The double counting issue is nontrivial, and in practice it has led to a split of the Monte Carlo program activity into two different approaches, which we will refer to as ‘parton showers’ (PS) and ‘matrix elements’ (ME), respectively.

In the ‘parton shower’ approach, it is customary to implement only the lowest order matrix elements, i.e. as a rule, basic $2 \rightarrow 2$ processes. Initial and final state radiation is added on to the basic scattering in the shower approach proper. The showers are assumed to be universal, i.e. the shower evolution is not allowed to depend on the details of the hard scattering, but only on the gross features: energies and flavours of incoming and outgoing partons, and an overall Q^2 scale for the hard scattering. The approximate nature is reflected in a limited accuracy for the rate of production of additional well-separated jets, but the internal structure of jets should be well modelled. It is feasible to add fragmentation and beam jets, and thus to generate realistic representations of the events produced in hadron colliders. In this category of programs, a large fraction of the total investment is in the common shower and fragmentation routines, while the effort needed to include yet another $2 \rightarrow 2$ process is modest, if only matrix elements are known and not too complex. Some of the programs of this kind therefore allow the simulation of many different processes.

The list of such event generators is fairly small. We are aware of the following programs:

- ISAJET, by Paige and Protopopescu, current version 6.36 [12].
- PYTHIA, by Bengtsson and Sjöstrand, current version 5.4 [13].
- HERWIG, by Marchesini and Webber, current version 5.0 [14].
- COJETS, by Odorico, current version 6.11 [15].
- DTUJET, by Ranft *et al.* [16].
- FIELDAJET, by Field *et al.* [17].
- The Fire-String program by Angelini *et al.* [18].
- FRITIOF, by Andersson *et al.*, current version 6.0 [19].

Without passing judgement on quality, the ordering above does reflect an element of quantity: ISAJET and PYTHIA clearly are more versatile than the others, while the latter four programs only cover QCD jets and minimum bias events.

The ‘matrix elements’ approach is represented by another class of programs. Here the emphasis is on the use of exact higher-order matrix elements. The analytic formulae in the programs are considerably more complicated, and the phase space generation machinery more advanced. The big investment here is in the matrix element calculation itself — usually these programs are written by the same people who calculated the matrix elements in the first place — and in selecting the kinematic variables in an efficient way. There is therefore less impetus for a common approach to many disparate processes. Since the precision aspect is important, it is not feasible to attach a simple, generic parton shower picture.

Normally, therefore, only a fixed (small) number of partons is generated. Since most modern fragmentation models are tuned to be attached at the end of the parton shower evolution, fragmentation and beam jet treatments also become less interesting. These programs therefore mainly generate parton configurations of ‘pencil jets’, rather than events as they may appear in a detector.

The number of matrix element programs is considerably higher than the number of parton shower programs: once a matrix element has been calculated, the Monte Carlo approach is usually the most convenient way to obtain physical cross-sections. Therefore many calculations are directly turned into programs. It is not possible in this report to give a complete list of all programs of this kind, some of which are publicly maintained and others which are not. Two programs contain matrix elements for widely different purposes:

- PAPAGENO, by Hinchliffe [20].
- EUROJET, by van Eijk *et al.* [21].

A few others will be mentioned in connection with the processes they simulate.

The parton shower and matrix element programs fill somewhat complementary functions. The former are convenient for exploratory work: it is fairly easy to simulate a new, postulated physics process in sufficient detail to establish experimental feasibility, and to try out the tools needed to separate signal from background. For high-precision measurements of an established process, on the other hand, one needs the higher order matrix elements. The matrix element programs are also more convenient for generating events within very specific phase space regions, since the cuts can be included from the start. With parton shower based programs it is necessary to generate more inclusive event samples and afterwards discard those events that do not fulfill the requirements, a procedure which can often be very inefficient.

2.1 Hard scattering subprocesses

Lists of subprocesses included in Monte Carlos are found in Tables 1 and 2. These tables should be read as follows. For ISAJET, PYTHIA and PAPAGENO, a ‘•’ indicates that the process is included and a ‘-’ that it is not. In the column ‘other PS’ (PS = parton shower programs) a ‘•’ indicates this is something found in most or all programs in this category, while a ‘H’ appears if only HERWIG includes it and a blank if no program does. In the column ‘other ME’ (ME = matrix element programs), an ‘E’ indicates a process included in EUROJET, and other letters indicate processes found in other programs, as explained further in the process-specific descriptions below.

The tables should be taken as indicative only, since there is a continuous evolution of many programs. For instance, the current EUROJET only contains a few processes, but a much expanded version is nearing completion and may be available by the time this appears in print; also, HERWIG has been expanded significantly since the beginning of this workshop. Furthermore, one and the same process may be treated differently in different programs. Below we will give some comments on a few of the processes, to illustrate the degrees of freedom open to Monte Carlo authors.

Table 1: Standard model physics processes included in the event generators studied. See text for program notation. ‘f’ stands for fermion, ‘V’ for W or Z , and ‘Q’ for heavy quark.

Process	ISAJET	PYTHIA	other PS	PAPA-GENO	other ME
QCD					
QCD jets	•	•	•	•	E, NJ
$q\bar{q}, gg \rightarrow t\bar{t}$	•	•	•	•	E
$qb \rightarrow q't$	-	•	H	-	
minimum bias	•	•	•	-	E
diffractive	•	•	-	-	
elastic	-	•	-	-	
Prompt photons					
$gg \rightarrow q\gamma, q\bar{q} \rightarrow g\gamma$	•	•	H	•	
$q\bar{q} \rightarrow \gamma\gamma$	•	•	-	•	
$gg \rightarrow \gamma\gamma$	-	•	-	•	
W/Z production					
$q\bar{q} \rightarrow V$	•	•	•	•	LD
$gg, q\bar{q} \rightarrow V(q, g)$	•	•	H	•	LD
$q\bar{q} \rightarrow VV, V\gamma$	•	•	-	•	BZ, BH
$q\bar{q}, gg \rightarrow VV(q, g)$	-	-	-	-	VV, BH
$gg \rightarrow VV, V\gamma$	-	-	-	-	GG
$q\bar{q} \rightarrow V^*V^*$	-	•	-	-	
$gg \rightarrow ZQ\bar{Q}$	-	•	-	•	LD
Standard model H^0 ($m_H \leq 800$ GeV)					
$q\bar{q} \rightarrow H^0$	•	•	-	-	
$gg \rightarrow H^0$	•	•	H	•	GG
$VV \rightarrow H^0$	•	•	H	•	BG
$q\bar{q} \rightarrow VH^0$	-	•	-	-	
$gg, gg, q\bar{q} \rightarrow H^0(q, g)$	-	•	-	-	HV
$H^0 \rightarrow VV$	•	•	H	•	BG, HV
$H^0 \rightarrow V^*V^*$	•	•	H	-	
$H^0 \rightarrow f\bar{f}$	•	•	H	-	
$H^0 \rightarrow gg$	•	•	-	-	
$H^0 \rightarrow \gamma\gamma$	•	•	H	-	
$H^0 \rightarrow \gamma Z^0$	-	•	-	-	
Standard model H^0 ($m_H \geq 700$ GeV)					
$VV \rightarrow VV$	•	•	H	-	BG
$gg \rightarrow VV$	-	-	-	-	GG

Table 2: Non-standard model physics processes included in the event generators studied. See text for program notation. In addition to notation for Table 1, ‘V’ stands for W' or Z' , ‘R’ for a horizontal boson, and ‘L’ for heavy lepton.

Process	ISAJET	PYTHIA	other PS	PAPA-GENO	other ME
Non-standard Higgs particles					
$q\bar{q}' \rightarrow H^+$	-	•	-	-	
$gb \rightarrow H^-t$	-	•	-	-	
$\gamma^*/Z^* \rightarrow H^+H^-$	-	•	-	-	
$t \rightarrow H^+b$	-	•	-	-	
$H^+ \rightarrow f\bar{f}'$	-	•	-	-	
Supersymmetry					
$q\bar{q}, gg \rightarrow \tilde{q}\tilde{q}$	•	-	-	•	UA, BT
$q\bar{q}, gg \rightarrow \tilde{g}\tilde{g}$	•	-	-	•	UA, BT
$qg \rightarrow \tilde{q}\tilde{g}$	•	-	-	•	UA, BT
$q\bar{q} \rightarrow \tilde{g}\tilde{V}$	•	-	-	-	UA
$qg \rightarrow \tilde{q}\tilde{V}$	•	-	-	-	UA
$\tilde{q}, \tilde{g}, \tilde{V}$ decays	-	-	-	•	UA, BT
New Gauge Groups					
$q\bar{q} \rightarrow V'$	-	•	-	-	
$VV \rightarrow V'$	-	-	-	-	
$V' \rightarrow f\bar{f}$	-	•	-	-	
$V' \rightarrow VV$	-	•	-	-	
$q\bar{q}' \rightarrow R \rightarrow q''\bar{q}'''$	-	•	-	-	
Fourth Generation					
$q\bar{q}, gg \rightarrow Q\bar{Q}$	•	•	-	•	
$V/V' \rightarrow Q\bar{Q}, L\bar{L}$	-	•	-	-	
$q\bar{q}' \rightarrow q''Q$	-	•	-	-	
Other Topics					
contact interactions	-	-	-	•	
axigluons	-	-	-	•	
leptoquarks	-	-	-	-	
strongly interacting V	-	•	-	-	E

2.1.1 QCD

Exact Born term cross-sections, for up to five jets in the final state, are available in the NJETS program of Kuijf and Berends (‘NJ’ of Table 1), see [9], which is the most advanced in this category. This program also contains approximate expressions for up to eight jets.

Complete loop calculations have been performed up to $\mathcal{O}(\alpha_S^3)$. These are implemented in the numerical integration programs of two groups [22], but no event generators exist.

Most programs only contain the lowest order Born term cross-sections for heavy flavour production. For top this may be sufficient, i.e. higher order contributions effectively contribute an overall K factor, but do not significantly change the production characteristics of top. However, at LHC energies, it is not correct to use only the Born term to estimate b or c production, since these quarks receive major higher order contributions, both by flavour excitation and by parton shower evolutions, see [8].

Minimum bias physics is discussed in section 2.4.

Even when diffractive and elastic scattering is included in programs, the treatment is fairly primitive, and likely to be insufficient for LHC physics. Several major features are missing, like high- p_\perp jet production in diffractive events.

2.1.2 Prompt photons

Complete next-to-leading order programs for prompt photon production are available from two groups [23], but both are intended for cross-section calculation rather than event generation. Leading order formulae are contained in many event generators. Some parton shower algorithms also include the emission of photons as part of the evolution.

The $gg \rightarrow \gamma\gamma$ graph contains a quark box. The cross-section is reasonably compact in the limit of vanishing quark mass, but very complex if the correct quark mass dependence is included. Therefore often the massless formulae are used, with the number of flavours suitably chosen. PYTHIA contains the full formulae as an option, but these then are numerically unstable in some regions of phase space, and therefore not easy to use.

2.1.3 W/Z production

The most complete W/Z ME program is the ‘Leiden-Durham W ’/VECBOS program (‘LD’ of Table 1), which contains the production of a V , i.e. a W or a Z , plus 0, 1, 2, 3 or 4 jets, see [11]. No loop corrections are available in this program, but analytical formulae exist up to complete second order in α_S [24]. Programs for the production of $V + V$ and $V + \gamma$ are also available, in [25] (‘BZ’ of Table 1) with special emphasis on the possibility of testing for anomalous couplings in triple gauge boson vertices. The production of a VV pair plus one additional jet is found in two programs: in VVJET [26] (‘VV’ of Table 1) and in [27] (‘BH’ of Table 1); the latter also contains matrix elements for a VV pair plus two jets. In all the programs above, subsequent V decays are included, with full angular correlations.

As in $\gamma\gamma$ pair production, VV pairs may also be produced from a gg initial state, via a quark box. The rates may be sizeable, thanks to the large value of the gluon structure functions at the small x values probed by LHC, and interference with the Higgs signal is of particular importance for Higgs searches. The program GGZZ simulates this process [28] (‘GG’ of Table 1).

The parton shower programs tend to give a fairly good description of V pro-

duction at current energies. However, the rate of high- p_\perp V production is not so well reproduced if the starting point is the $q\bar{q} \rightarrow V$ matrix element. One may instead use the $gg \rightarrow qV$ and $q\bar{q} \rightarrow Vg$ matrix elements, in which case at least one high- p_\perp jet is assured from the start, and then include showering to generate additional jets. This gives a better description at high $p_{\perp V}$, but cannot be used to describe inclusive V production, since the $2 \rightarrow 2$ matrix elements are divergent for $p_\perp \rightarrow 0$. The choice between the two descriptions therefore has to depend on the application. In ISAJET a special option is available, in which the $2 \rightarrow 2$ matrix elements have been regularized (by hand) in the limit $p_\perp \rightarrow 0$, and so a good description is obtainable over the whole p_\perp spectrum.

For intermediate mass Higgs background studies, the $Z + (Z^*/\gamma^*)$ (where $*$ denotes that the interesting configurations are those with the particle far off mass-shell) and $Zb\bar{b}$ channels are of particular interest. The latter process is calculated in [10], and is now included in a few generators, although still with an inefficient selection of phase-space points.

2.1.4 Standard model H^0

A single unified description of Higgs production and decay characteristics, valid for all Higgs masses, would be very complex. In practice, two different descriptions are in use in programs. For a reasonably light Higgs, and thereby a reasonably narrow one, the ‘signal’ and the ‘background’ graphs do not interfere significantly, so that it is possible to separate the process into Higgs production and Higgs decay. If the Higgs is heavy, this is no longer possible but, in this region, mainly the $VV \rightarrow H \rightarrow VV$ graphs are of experimental interest, and so only full interference with the $VV \rightarrow VV$ background need be included.

A light or intermediate mass Higgs is predominantly produced by $gg \rightarrow H$. The process $VV \rightarrow H$, i.e. properly $qq' \rightarrow q''q'''H$, also contributes. This process is included with the full matrix elements in HERWIG and PAPAGENO, but in ISAJET and PYTHIA only in the effective W approximation, an approximation which is known to be good for $m_H \gg m_W$. For $m_H < 2m_W$ the channel is switched off in ISAJET, while it is still on in PYTHIA, and here gives about a factor two too high a rate compared to the correct treatment.

In the description of Higgs decays, two new aspects have played a particular rôle in the current workshop. One is the introduction of running quark masses for couplings $H \rightarrow q\bar{q}$; this typically leads to a reduction of the quark partial widths by a factor of around 2. At intermediate Higgs masses, where the $H \rightarrow b\bar{b}$ decays dominate, some other branching ratios are enhanced by the same factor 2, notably $H \rightarrow \gamma\gamma$. Running quark masses are included in PYTHIA and HERWIG, but not in ISAJET. The other new aspect is $H \rightarrow V^{(*)}V^*$ decays, i.e. where one or both final state gauge bosons are significantly off mass-shell. Particularly interesting is the $H \rightarrow ZZ^* \rightarrow 4\ell$ decay. These decays are now found in ISAJET, PYTHIA and HERWIG.

For the heavy Higgs scenario, both ISAJET and PYTHIA rely fully on the effective W approximation for $VV \rightarrow VV$ matrix elements. In both programs the incoming V bosons are assumed longitudinally polarized, as are the outgoing in PYTHIA, while ISAJET includes all polarization combinations in the final state.

A more detailed description, based on exact matrix elements with full interference between all graphs that can yield VV plus two jets in the final state, is found in [29] ('BG' of Table 1); full angular correlations in the V decays are also included.

Finally, just as for the description of high- p_T V production, it may be convenient to have a description of a H recoiling against a jet; this is available in the program HVVJET [30] ('HV' of Table 1).

2.1.5 Non-standard Higgs particles

Very little effort has gone into scenarios with more Higgses than in the standard model — no event generators at all are available for an extended neutral Higgs sector. A charged Higgs, in the framework of the minimal supersymmetric extension to the standard model, is available in PYTHIA.

2.1.6 Supersymmetry

SUSY is an important area to be explored at LHC. Several different particles should be searched for, in particular squarks, gluinos and a host of gauginos. In the current workshop, the two main programs in this area are ISAJET and UA2SUSY. As the name indicates, the latter ('UA' of Table 2) is an upgrade of a dedicated program written inside the UA2 collaboration [31], which is described in more detail in [32]. A further program is found in [33] ('BT' of Table 2). In the current workshop, both for ISAJET and UA2SUSY, special emphasis has been put on a flexible and detailed modelling of all sequential decay chains predicted for different parameter sets of the Minimal Supersymmetric Standard Model.

Comparisons between ISAJET and UA2SUSY have been performed by the SUSY working group [32]. In general, good agreement is found; where disagreements exist, their origin is understood, and the effect on experimental signatures is kept under control.

2.1.7 New gauge groups

A number of different scenarios can give rise to new gauge particles, here denoted V' ($= Z^0$ or W'^{\pm}). In PYTHIA, vector and axial couplings of fermions to the V' have been left as free parameters; it is therefore possible to simulate most of the alternatives on the market by judicious choices. Couplings of a V' to the standard model gauge bosons can show a richer structure, and only a few of the possibilities are available here.

A specific model for a horizontal boson R , i.e. a boson which couples to generation number, has been included as a separate alternative in PYTHIA.

2.1.8 Fourth generation

With the current LEP limits on the number of light neutrino species, the prospects are slim for a standard fourth generation of fermions. Should there still be some interest in heavy standard quarks or leptons, the event generators are available, since only trivial extensions of the standard description of top are involved.

2.1.9 Other topics

The list of possible extensions to, or deviations from, the standard model is long, and only a few are found in Table 2. Among the most interesting ones are the prospects of a strongly interacting V sector, as could arise if the standard model Higgs were absent or, at least, much heavier than the 1 TeV mass scale directly probed. Some of the scenarios proposed in the literature have been implemented in PYTHIA.

2.2 Structure Functions

Knowledge of the proton structure functions is necessary for the calculation of any hard scattering cross-section. A community of people are involved in the analysis of data from current experiments, within the framework of perturbative QCD. The end result of these efforts is new structure function sets, with some region of validity in the (x, Q^2) plane. In the past, the number of sets available was fairly limited; for applications at the large Q^2 scales of LHC/SSC, only the EHLQ parametrizations [34] could be used, which is why these are still found as defaults in many programs.

More recently, the pace has picked up, and now new sets appear almost monthly. A review of, and comparison between, most of these is found in [6]. One conclusion is that many of the older sets do not do well when compared with current data, and therefore should no longer be used. Also some of the newer sets perform less well. In part, this is deliberate: given the large uncertainties involved, most authors do not provide one single 'best' set, but rather prefer to produce many different sets, which together are supposed to bracket the 'right' answer. The differences between these sets come from the correlation between the choice of Λ value (in α_s) and the choice of gluon structure function, from different assumptions about the behaviour of structure functions at low x , from different choices of s quark distributions at low Q^2 , etc.

Since all sets of structure functions are limited in validity to given x and Q^2 ranges (in particular, $x > 10^{-5}$ to 10^{-4} , depending on the set), their use for applications at LHC/SSC energies should be taken with some caution. Total cross-section calculations or integrated differential distributions (e.g. for top, b or c quark production) would be affected. To overcome the problem Monte Carlo authors have to introduce further assumptions themselves.

An additional element of disparity comes from the choice of order and renormalization scheme. The three main alternatives are leading order, next-to-leading order in the $\overline{\text{MS}}$ scheme, and next-to-leading order in the DIS scheme. For high precision measurements, it is essential to use the same conventions for matrix elements and structure functions, and here probably little confusion exists. The status may be less clear about the appropriate choice to use for parton shower based programs — while basically leading log, these programs do include some next-to-leading log contributions.

The main programming issue for structure functions is whether to use grids or parametrizations. In the former approach, the output of the evolution programs is stored directly as grids in the (x, Q^2) plane, and desired values can be obtained by interpolation in these grids. The drawback is that thousands of real numbers have

to be transferred to each new computer as external files, which makes programs a little less easily transportable. The advantage is that interpolation usually is fast. In the parametrization approach, smooth functions are fitted to the grid values, and subsequent use is based on these fits. This way the number of real values that characterize a structure function is significantly reduced — the most spectacular example is the very compact parametrizations by Morfin and Tung [35]. Such parametrizations can easily be included in the code of an event generator, and thus there are no transport problems. Since the evaluation typically involves logarithms and exponents, it may be significantly slower than in the grid interpolation approach, however.

2.3 Initial and Final State Showers

In the parton shower approach, a hard $2 \rightarrow 2$ scattering is convoluted with initial and final state radiation to build up multiparton final states. Of the two showering types, final state radiation is theoretically and experimentally well under control, while initial state radiation remains less well understood.

Final state showers are timelike: the two outgoing partons of a $2 \rightarrow 2$ scattering each has $m^2 = E^2 - \vec{p}^2 \geq 0$. An off-mass-shell parton may successively branch into partons of lower virtuality, until the mass-shell is reached. In leading log, the structure of allowed branchings $q \rightarrow qg$, $g \rightarrow gg$, and $g \rightarrow q\bar{q}$ is described by the standard Altarelli-Parisi evolution equations. The naive leading log parton shower picture is modified by coherence effects, which can be taken into account by the inclusion of angular ordering [36], i.e. not only are virtualities successively degraded, but so are the opening angles of branchings. Further details on the theory of timelike showers may be found in several reviews, e.g. [37,38].

On the experimental front, final state showers have been much studied in e^+e^- annihilation; since no initial state QCD showers appear in e^+e^- , and since the production graph is s -channel only, the analysis is simpler than in hadron collisions. The recent LEP results underline how well existing showering programs do, see e.g. [39,40]. It is seldom that disagreements between data and programs like JETSET (which is the program used for showering in PYTHIA) or HERWIG reach the 10% level. Even more importantly, with parameters tuned at LEP, programs also do a good job of describing data at lower energies, at PEP, PETRA and TRISTAN. Confidence in extrapolations to higher energies is therefore high.

Anytime one has to consider the hadronic decay of a colour singlet particle in hadron colliders, such as W , Z , H , etc., the e^+e^- experience is directly applicable, and predictive power high. In principle, questions could be raised whether colour exchange might take place between the partons of the decaying singlet particle and the partons of the underlying event; such effects could modify event topologies, but probably not drastically. When the hard process does not go through a colour singlet intermediate state, on the other hand, there are significant ambiguities in how to begin the shower evolution at high virtualities, such that the proper amount of multijet activity is obtained. Once a choice is made here, the subsequent evolution is again well under control.

Initial state radiation is considerably more difficult to model. The shower is initiated by a parton selected from structure functions at small Q^2 . This parton

may now branch, but in the branching only one daughter is timelike, whereas the other is spacelike, i.e. $m^2 < 0$. The timelike parton may develop a shower, very much like the final state radiation case, although typically with less allowed phase space and therefore less extensive. The spacelike parton may branch once again, to a new pair of one timelike and one spacelike daughter, etc. The sequence of spacelike daughters is terminated at the hard interaction: a $2 \rightarrow 2$ (QCD) process consists of two incoming spacelike partons and two outgoing timelike ones. In leading log language, the virtuality $Q^2 = -m^2$ of the sequence of spacelike partons is required to increase monotonically, and is constrained from above by the Q^2 scale of the hard interaction. In recent years, theoretical progress has been made in including coherence corrections to this picture [41]. The complexity of these corrections is such that no program includes all effects in full, however. HERWIG is the program that contains the most advanced machinery. It has still not been clarified exactly how big the differences are compared to the more simpleminded approaches in other programs.

2.4 Beam Jets

The description of beam jets, i.e. the physics of underlying events and minimum bias events, remains the least well understood aspect of Monte Carlo modelling of hadronic events. It is therefore possible to choose many possible approaches. One is simply to use a longitudinal phase space parametrization, as in COJETS and HERWIG, with parameters fitted to describe data. Another is to allow a variable number of parton-parton interactions to take place within one and the same hadron-hadron collision. This is done in ISAJET, PYTHIA and DTUJET, but along quite different lines in each. If, in the end, programs agree reasonably well, it is mainly because they have been tuned to the same data. For further discussions see [7].

Theoretical work on the structure of minimum bias events has been carried out in particular by Levin and Ryskin [42]. Their approach is also based on a multiple parton-parton interaction scenario. Compared to the models above, particular emphasis is put on saturation effects at small x . Saturation can arise when the local density of partons becomes so large that not only parton branchings but also parton recombinations have to be taken into account. This saturation is predicted to set in sooner than given by naive estimates, since a large fraction of the partons inside a proton are assumed to be concentrated in a few ‘hot spots’. If correct, naive extrapolations to LHC energies, as embodied in current event generators, may fail. Some first hints on the validity of the Levin-Ryskin model may come already with HERA. A more detailed description of the issues involved may be found in the report of the ep physics study group of this workshop [43].

2.5 Fragmentation and Decays

Fragmentation is a nonperturbative phenomenon, and as such is not yet understood from first principles. As with timelike parton showers, experience from e^+e^- annihilation helps constrain models significantly [39,40]. Three different main fragmentation schools exist: string (found in PYTHIA and FRITIOF), cluster (HERWIG) and independent (e.g. ISAJET, COJETS and EUROJET) fragmentation.

The former two are known to give good agreement with e^+e^- data over a wide range of energies, and are expected to work well also at higher energies, while the latter currently is not much used in e^+e^- (for a recent assessment of it see [44]). Differences between models are difficult to find in hadron collisions.

A majority of the particles produced in the fragmentation step are unstable and decay further. Almost all programs therefore include decay routines, more or less similar to each other. Decay data are taken from [45], where available, and according to the best understanding of the program author, where not. There are some differences in level of sophistication, with respect to inclusion of decay matrix elements and polarization information, but seldom does this give readily visible experimental consequences.

3 Concluding Remarks

3.1 Program Limitations

Already in the previous section, we have considered some of the uncertainties in our current understanding of physics at the LHC. Many more examples could certainly have been found.

Another class of uncertainties comes from the presence of bugs, i.e. programming errors, in event generators. Given the complexity of LHC simulation, almost all programs have bugs. Some of these simply are typographical errors, others are correct transcriptions of incorrect formulae in the literature (e.g., the $WZ \rightarrow WZ$ matrix elements in PYTHIA were incorrect for several years because the published formulae were not correct), others are programs that work at current energies but break down when run in single precision at LHC energies, and yet others are real mistakes by the programmer. Given the size of these generators, an error can lie dormant for a long time before being discovered. Even when discovered, errors need not be correctly corrected by the authors. Indeed, we saw three such examples during the workshop: the $gg \rightarrow \gamma\gamma$ matrix elements in PYTHIA, the $H \rightarrow \gamma\gamma$ partial width in ISAJET, and the $q\bar{q}, gg \rightarrow b\bar{b}$ matrix elements in HERWIG. In each of these cases, the first ‘corrections’ proposed by the authors did not solve the problem found by users, and repeated complaints were necessary to see some improvements in the situation. Errors that were more rapidly corrected are too numerous to be mentioned.

These examples do not imply a quality judgement on particular programs. Considering the size and complexity, there is no reason to say that event generators are any more error-prone than other comparable software. The message is rather that all critical studies should always be based on more than one event generator, and/or on analytical cross-checks of the generator results.

With the changing computer market, e.g. the emergence of RISC chips, one must also keep in mind that programs may need to be modified for maximum efficiency [9].

3.2 Summary

In this paper we have given an introduction to and overview of the LHC event generators currently available. As behooves a report of this kind, a heavy emphasis has been put on the unknown aspects. In particular, we have stressed the need for several independent cross-checks of crucial results.

However, one can also take another point of view: considering the number of years left before actual turn-on, the quantity and quality of LHC/SSC event generators are probably far superior to those available for any other major new accelerator at a corresponding stage of planning. We today have standard methods for turning the crank on any basic process (also including new hypothetical particles), to include initial and final state radiation, beam jets, fragmentation, etc., and to arrive at fairly realistic representations of what LHC events might look like. If the details may be a bit uncertain, the general picture of events at the LHC is still fairly clear. As experience from the Tevatron, LEP and HERA finds its way into programs, the quality should improve further. Needless to say, much continued work by event generator authors is necessary, not just to improve on the expected, but also to prepare for the unexpected.

References

- [1] ‘Z Physics at LEP 1’, eds. G. Altarelli, R. Kleiss, C. Verzegnassi, CERN 89-08, Vol. 3
- [2] ‘Physics of the Superconducting Super Collider 1986’, eds. R. Donaldson, J. Marx (1987)
- [3] ‘Experiments, Detectors, and Experimental Areas for the Supercollider’, eds. R. Donaldson, M.G.D. Gilchriese (World Scientific, Singapore, 1988)
- [4] ‘Proceedings of the Summer Study on High Energy Physics in the 1990s’, ed. S. Jensen (World Scientific, Singapore, 1989)
- [5] T. Sjöstrand, Z. Physik **C42** (1989) 301
- [6] H. Plothow-Besch, separate contribution in this section
- [7] G. Ciapetti, A. Di Ciaccio, separate contribution in this section
- [8] J.R. Cudell, O. Di Rosa, I. ten Have, A. Nisati, R. Odorico, T. Sjöstrand, separate contribution in this section
- [9] H. Kuijf, P. Lubrano, V. Vercesi, separate contribution in this section
- [10] R. Kleiss, B. van Eijk, separate contribution in this section
- [11] W.T. Giele, separate contribution in this section
- [12] F.E. Paige, S.D. Protopopescu, in ‘Physics of the Superconducting Super Collider 1986’, eds. R. Donaldson, J. Marx (1987), p. 320
- [13] H.-U. Bengtsson, T. Sjöstrand, Computer Physics Commun. **46** (1987) 43
- [14] B.R. Webber, G. Marchesini, Nucl. Phys. **B310** (1988) 461
- [15] R. Odorico, Computer Physics Commun. **32** (1984) 139, **59** (1990) 527
- [16] K. Hahn, J. Ranft, Phys. Rev. **D41** (1990) 1463
- [17] R.D. Field, G.C. Fox, R.L. Kelly, Phys. Lett. **119B** (1982) 439; R.D. Field, Nucl. Phys. **B264** (1986) 687
- [18] L. Angelini, L. Nitti, M. Pellicoro, G. Preparata, Phys. Rev. **D41** (1990) 2081

- [19] B. Andersson, G. Gustafson, B. Nilsson-Almqvist, Nucl. Phys. **B281** (1987) 289
- [20] I. Hinchliffe, personal communication
- [21] A. Ali, B. van Eijk, I. ten Have, Nucl. Phys. **B292** (1987) 1
- [22] F. Aversa, M. Greco, P. Chiappetta, J.P. Guillet, Z. Physik **C46** (1990) 253; S.D. Ellis, Z. Kunszt, D.E. Soper, Phys. Rev. Lett. **64** (1990) 2121
- [23] P. Aurenche, R. Baier, M. Fontannaz, D. Schiff, Nucl. Phys. **B297** (1988) 661; H. Baer, J. Ohnemus, J.F. Owens, Phys. Rev. **D42** (1990) 61
- [24] see 'Parton Luminosities, W and Z Cross Sections, and Gauge Boson Pair Production', H. Plothow-Besch *et al.*, this volume
- [25] U. Baur, D. Zeppenfeld, Nucl. Phys. **B308** (1988) 127; S. Willenbrock, D. Zeppenfeld, Phys. Rev. **D37** (1988) 1775
- [26] U. Baur, E.W.N. Glover, J.J. van der Bij, Nucl. Phys. **B318** (1989) 106
- [27] V. Barger, T. Han, J. Ohnemus, D. Zeppenfeld, Phys. Rev. **D41** (1990) 2782
- [28] J.J. van der Bij, E.W.N. Glover, Nucl. Phys. **B321** (1989) 561
- [29] U. Baur, E.W.N. Glover, Nucl. Phys. **B347** (1990) 12
- [30] U. Baur, E.W.N. Glover, Nucl. Phys. **B339** (1990) 38
- [31] UA2 Collaboration, J. Alitti *et al.*, Phys. Lett. **B235** (1990) 363
- [32] 'Experimental Aspects of Gluino and Squark Searches at the LHC', C. Albajar *et al.*, this volume
- [33] H. Baer, X. Tata, J. Woodside, Phys. Rev. **D42** (1990) 1450
- [34] E. Eichten, I. Hinchliffe, K. Lane, C. Quigg, Rev. Mod. Phys. **56** (1984) 579, **58** (1985) 1065
- [35] J.G. Morfin, W.-K. Tung, FERMILAB-PUB-90/74
- [36] A.H. Mueller, Phys. Lett. **B104** (1981) 161; B.I. Ermolaev, V.S. Fadin, JETP Lett. **33** (1981) 269
- [37] B.R. Webber, Ann. Rev. Nucl. Part. Sci. **36** (1986) 253
- [38] Yu.L. Dokshitzer, V.A. Khoze, S.I. Troyan, in 'Perturbative QCD', ed. A.H. Mueller (World Scientific, Singapore, 1989), p. 241
- [39] M. Jacob, CERN-TH.5821, to appear in the proceedings of the 25th International Conference on High Energy Physics (Singapore, 1990)
- [40] T. Sjöstrand, CERN-TH.5902/90
- [41] M. Ciafaloni, Nucl. Phys. **B296** (1987) 249; S. Catani, F. Fiorani, G. Marchesini, Nucl. Phys. **B336** (1990) 18
- [42] E.M. Levin, M.G. Ryskin, Phys. Rep. **189** (1990) 267
- [43] 'Small- x Physics at LEP/LHC', J. Bartels, G.A. Schuler, this volume
- [44] G. Bocchieri, R. Odorico, Nucl. Phys. **B345** (1990) 173
- [45] Particle Data Group, J. J. Hernández *et al.*, Phys. Lett. **B239** (1990) 1

STRUCTURE FUNCTIONS

H. PLOTHOW-BESCH
CERN - PPE, CH - 1211 Genève 23, Switzerland

1. INTRODUCTION

Knowledge of parton density functions is necessary for the calculation of the cross section of any hard scattering process. In this paper recent parton luminosity evolutions are presented and compared to each other (see Section 2). An attempt has been made to study the available sets of structure functions in view of their significance in comparison to existing low energy data from deep-inelastic lepton-nucleon scattering experiments and to W and Z cross section measurements at the CERN and the TEVATRON $\bar{p}p$ colliders. Estimates of W , Z , $b\bar{b}$, $t\bar{t}$ and Higgs production cross sections at LHC energies are given with a particular emphasis on the uncertainties due to structure functions (see Section 4).

2. THE DIFFERENT SETS OF PARTON DENSITY FUNCTIONS

The number of useful sets of parton density functions available today is about 30. The older ones are leading order evolutions only, like Duke and Owens (DO) sets 1 and 2 [1], Eichten, Hinchliffe, Lane and Quigg (EHLQ) [2] and Glück, Hoffman and Reya (GHR) [3]. Most of the sets, essentially all the more recent ones, are next-to-leading order evolutions, like Diemoz, Ferroni, Longo and Martinelli (DFLM) with $\Lambda_{\text{QCD}}^{[4]} = 160, 260, 360$ MeV and with $\Lambda_{\text{QCD}}^{[4]} = 300$ MeV for soft and hard gluon distributions [4], Martin, Roberts and Stirling (MRS) sets E' and B' [5], Harriman, Martin, Roberts and Stirling (HMRS) sets E and B [6], Kwiecinski, Martin, Roberts and Stirling (KMRS) sets B0 and B- [7], Morfin and Tung (MT) sets 1 to 6 [8] and finally Glück, Reya and Vogt (GRV) [9]. The different sets also differ in the renormalization scheme they use. The DFML series and most of the MT series, except MT set 5, are performed in the DIS renormalization scheme, whereas all the others are performed in the $\overline{\text{MS}}$ renormalization scheme. While all sets are made using four flavours in the initial state ($NF = 4$), the value of the QCD scale factor, $\Lambda_{\text{QCD}}^{[4]}$, ranges from 90 MeV to 400 MeV. As an example, the proton structure function distributions at the scale $Q^2 = m_W^2$ for u and d valence quarks as well as for sea and $gluon$ contributions are shown in Fig. 1a to 1d, respectively, as a function of x , where x is the momentum fraction of the parton in the nucleon. It can be seen from these figures that there is a large spread in shape for the different sets in all contributions leading to different results in the cross section calculations.

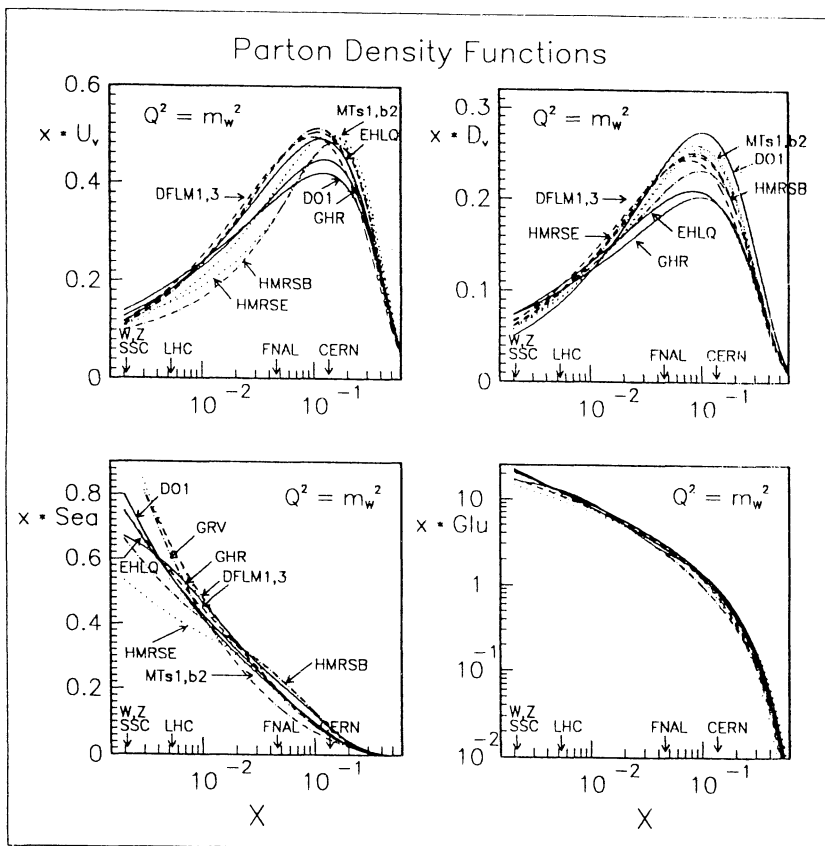


Figure 1
Different sets of structure functions
for a) u-valence b) d-valence c) sea d) gluon distributions

The d/u ratio of the valence quarks at $Q^2 = m_W^2$ is shown in Fig. 2.

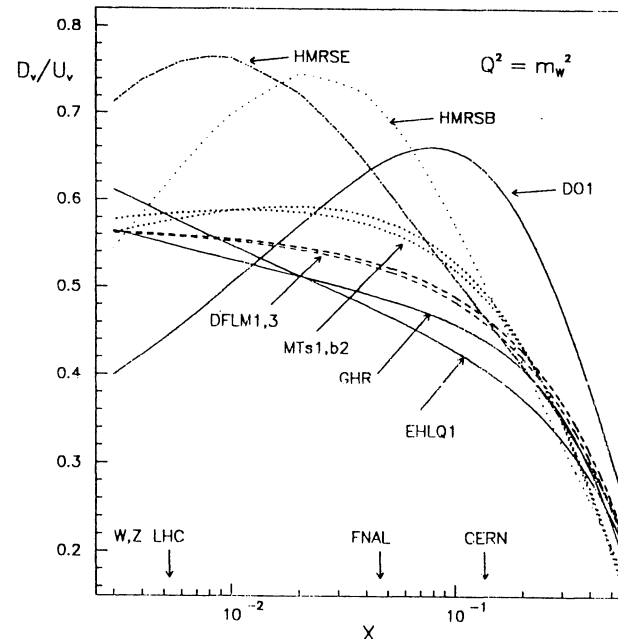


Figure 2
 d/u ratio for different sets of structure functions

The ratio F_2^n/F_2^p at $Q^2 = m_W^2$ is shown in Fig. 3. This ratio mainly reflects the d/u ratio of valence quarks which gives the important contribution to the W and Z cross section calculations. Already from Fig. 3 we conclude that a large variation of the W and Z cross section at LHC or SSC energies can be expected from the different sets of structure functions. Since we go to smaller and smaller x ranges as we go higher and higher in \sqrt{s} , the cross section should be dominated by the sea-quark contributions which are the same for u and d quarks. Therefore uncertainties due to the different shapes of u and d quarks are expected to cancel. But, as can be seen from Fig. 1c, the differences in shape of the sea-quark distributions for the numerous sets are also large and become even larger as x decreases. This explains why the total W and Z cross sections have larger uncertainties as \sqrt{s} increases (see Section 3).

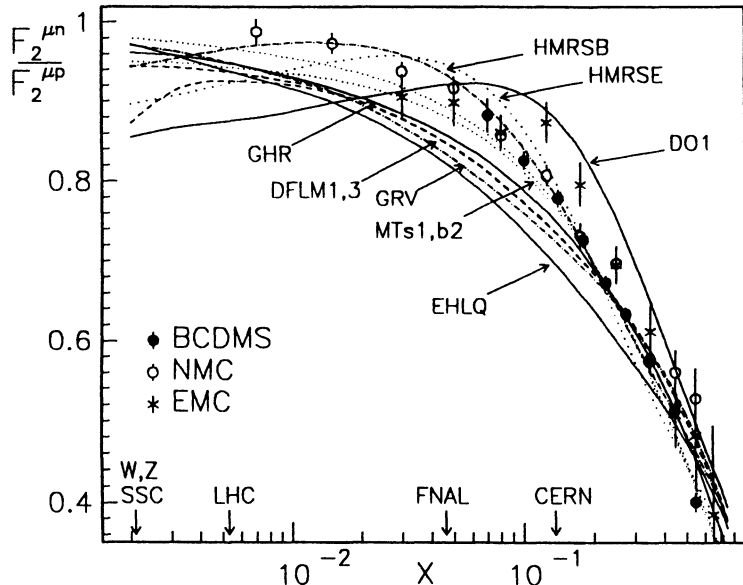


Figure 3

F_2^n/F_2^p ratio for different sets of structure functions

From Fig. 3 we also conclude that the use of the older sets of structure functions, namely the Duke and Owens sets 1 and 2 [1] and the sets of Eichten et al. [2], should be used with some care, because most of them do not fit the recent low energy deep-inelastic lepton-nucleon data from NMC and BCDMS [10]. This is not surprising because these data were not available when the sets were made. Therefore these sets should be ignored for any physics process to be studied at LHC or SSC energies. Furthermore we conclude that the recent sets of parton densities, namely HMRS set B and MT set 1, could be preferred for all theoretical predictions involving structure functions, because they fit the present data best.

Since all sets of structure functions are limited in validity to x and Q^2 ranges above a certain value ($x > 10^{-5}$ to 10^{-4} depending on the set), their use for applications at LHC/SSC energies, where small x values become important, should be taken with some caution. Total cross section calculations or integrated differential distributions (i.e. for top, b or c quark production) would be affected when extrapolating to x ranges beyond the limits given by the authors of the structure function sets. To overcome the problem Monte Carlo authors have to introduce further assumptions themselves.

It also should be pointed out that new sets of structure functions will be extracted as soon as results from HERA will become available [11]. These data will probe parton densities at much higher values of Q^2 and much lower x ranges ($x > 10^{-4}$) than present data and therefore are expected to reduce the present uncertainties due to the large differences in the structure functions.

3. UNCERTAINTIES OF DIFFERENT CROSS SECTIONS DUE TO STRUCTURE FUNCTIONS

The total W and Z cross sections have been calculated including full QCD corrections to order α_s [12] using mass values for the Intermediate Vector Bosons (IVBs) of $m_W = 80.2 \text{ GeV}/c^2$, $m_Z = 91.177 \text{ GeV}/c^2$ and $\sin^2\theta_W = 0.230$ and the DFLM set of structure functions with $\Lambda_{\text{QCD}}^{[4]} = 260 \text{ MeV}$ [4]. In the calculation also partial QCD corrections to order α_s^2 in the DIS mass factorization scheme from Ref. [13] have been included. Therefore rigorously speaking, only sets of structure functions evolved in the DIS scheme are appropriate to be used in the cross section calculation, and all cross section calculations which use sets of structure functions evolved in the $\overline{\text{MS}}$ renormalization scheme have an additional uncertainty due to the change in normalisation which is of the order of 1.5%. The missing parts in the second order calculation are the qg contribution and a complete $q\bar{q}$ calculation. The $q\bar{q}$ contribution has been calculated until now only in the so called "soft gluon limit". The problem of the exponentiation of these corrections has also been considered in Ref. [14]. With the inputs given above theory predicts the values as given in Table 1 for the total production cross sections of the W and Z bosons in $p\bar{p}$ collisions at $\sqrt{s} = 16 \text{ TeV}$.

The main theoretical uncertainties are due to structure functions, higher order corrections, the choice of the renormalisation scheme and the Q^2 scale dependence. The uncertainties due to the structure functions have been investigated. 14 different sets of proton density functions [1 - 9] obtained from leading or next-to-leading order calculations performed either in the $\overline{\text{MS}}$ or DIS regularisation scheme have been tested. These uncertainties are given in Table 1 indicated as "range" and amount to $\sim \pm 8\%$ at 630 GeV , $\sim \pm 12\%$ at 1.8 TeV , $\sim \pm 35\%$ at LHC and $\sim \pm 52\%$ at SSC energies. Fig. 4 shows the

total W cross section as a function of the centre-of-mass energy, \sqrt{s} , for a subset of structure functions (DFLM with $\Lambda_{\text{QCD}} = 160$ MeV to $\Lambda_{\text{QCD}} = 360$ MeV, MRSE', MRSB', HMRSE, HMRSB, MTs1 and MTb2) representing the minimal and maximal values as given in Table 1. Also indicated in the figure are the recent experimental measurements from the UA1, UA2 and CDF experiments [15] which agree well with theoretical expectations assuming a branching fraction of $\text{BR}(W \rightarrow l\nu) = 10.88\%$.

The total Z cross section shows a very similar behaviour to the W cross section. Because of the large theoretical uncertainties, the use of the Z cross section as a luminosity monitor must be excluded.

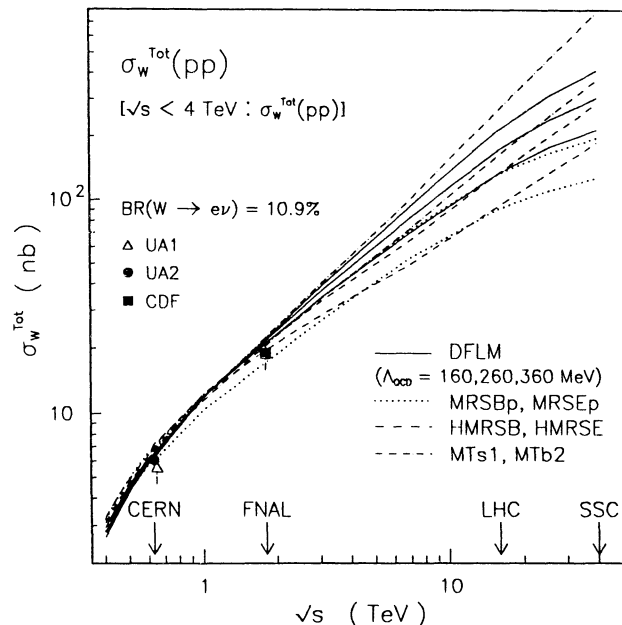


Figure 4
Total W cross section as a function of \sqrt{s}

A very recent complete second order QCD calculation [16] which has been performed in the $\overline{\text{MS}}$ mass factorization scheme show that at LHC and SSC energies the second order qg part is rather large and negative resulting in the fact that the total W and Z cross sections are slightly lowered compared to the numbers listed in Table 1. This new calculation has substantially reduced the uncertainties due to the Q^2 scale dependence. At $\sqrt{s} = 630$ GeV the remaining uncertainties amount to $\sim 5\%$ and increase to at most 15% at $\sqrt{s} = 40$ TeV for a variation of the scale Q by two orders of magnitude ($10 < Q < 1000$ GeV/c 2).

The cross sections for $b\bar{b}$ and $t\bar{t}$ production [17] up to next-to leading-order, α_s^3 , have been calculated at LHC and SSC energies for the same different sets of structure functions as above [1 - 9]. There are large uncertainties in the calculation of the $b\bar{b}$ production cross section. These uncertainties are related to the rather poor knowledge of the gluon structure functions at low x ($x \sim 10^{-3}$ to 10^{-4}) used as input at LHC/SSC energies. Furthermore they are related to the fact that for $2m_b/\sqrt{s} \ll 1$ fixed order perturbative QCD is not well behaved. Therefore it is questionable if perturbative QCD is applicable in this regime. For $m_b = 4.5$ GeV/c 2 the $b\bar{b}$ cross section varies from 0.1 mb to 1.1 mb as shown in Table 1. The $t\bar{t}$ production cross section has been calculated for two different values of the mass of the top-quark, $m_{\text{top}} = 130$ and 200 GeV/c 2 . The results for the DFLM set with $\Lambda_{\text{QCD}} = 260$ MeV as a reference, as well as the range obtained from the different sets are also given in Table 1.

Table 1: Uncertainties of different cross sections due to structure functions

$\sqrt{s} = 16$ TeV		
Process	DFLM $\Lambda_{\text{QCD}}^{[4]} = 260$ MeV	Range
W	172.0 nb	90.8 - 267.6 nb
Z	51.6 nb	28.8 - 78.7 nb
$b\bar{b}$ ($m_b = 4.5$ GeV/c 2)	535.6 μ b	112.5 - 1113.0 μ b
$t\bar{t}$ ($m_{\text{top}} = 130$ GeV/c 2)	4.4 nb	3.3 - 4.8 nb
$t\bar{t}$ ($m_{\text{top}} = 200$ GeV/c 2)	0.64 nb	0.59 - 0.68 nb
Higgs ($m_{\text{Higgs}} = 100$ GeV/c 2) ($m_{\text{top}} = 100$ GeV/c 2)	28.9 pb	16.3 - 33.8 pb
Higgs ($m_{\text{Higgs}} = 100$ GeV/c 2) ($m_{\text{top}} = 200$ GeV/c 2)	26.3 pb	14.8 - 30.6 pb
Higgs ($m_{\text{Higgs}} = 800$ GeV/c 2) ($m_{\text{top}} = 100$ GeV/c 2)	$8.9 \cdot 10^{-2}$ pb	$7.3 \cdot 10^{-2}$ - $10.4 \cdot 10^{-2}$ pb
Higgs ($m_{\text{Higgs}} = 800$ GeV/c 2) ($m_{\text{top}} = 200$ GeV/c 2)	$45.9 \cdot 10^{-2}$ pb	$37.4 \cdot 10^{-2}$ - $53.4 \cdot 10^{-2}$ pb

Also the cross section for Higgs production from gluon-gluon fusion [18] has been investigated at LHC and SSC energies using again the same different sets of structure functions [1 - 9] for two different top-quark masses, $m_{top} = 100$ and $200 \text{ GeV}/c^2$. The result for the DFLM set with $\Lambda_{QCD} = 260 \text{ MeV}$ as well as the range obtained from the different sets is also shown in Table 1. As an example, Fig. 5 shows the Higgs production for various sets of structure functions for $m_{top} = 200 \text{ GeV}/c^2$ as a function of m_{Higgs} .

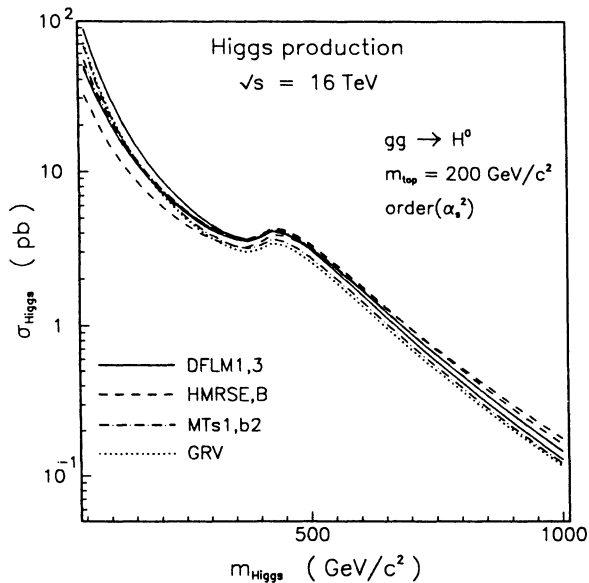


Figure 5

Higgs production cross section as a function of m_{Higgs}

5. CONCLUSIONS

About 30 different sets of structure functions are available today. The number is still growing. There is a release of a new set of structure functions nearly every three months. The existing data are not sufficient to reduce this large number to a fairly limited one. Hopefully if HERA gets into operation the number of sets gets reduced. This large number causes a substantial uncertainty in calculating cross sections at LHC/SSC energies.

One conclusion can be made which is that the older sets do not compare well to the current data. Therefore the older sets should be ignored for any physics process to be studied at LHC or SSC energies. Furthermore we conclude that two recent sets of parton densities, namely HMRS set B and MT set 1, could be preferred for all theoretical predictions involving structure functions, because they fit the present data best.

REFERENCES

- [1] D.W. Duke and J.F. Owens, Phys. Rev. **D30** (1984) 49.
- [2] E. Eichten, I. Hinchliffe, K. Lane and C. Quigg, Rev. Mod. Phys. **56** (1984) 579.
- [3] M. Glück, E. Hoffman and E. Reya, Z. Phys. **C13** (1982) 119.
- [4] M. Diemoz, F. Ferroni, E. Longo and G. Martinelli, Z. Phys. **C39** (1988) 21.
- [5] A.D. Martin, R.G. Roberts and W.J. Stirling, Phys. Lett. **206B** (1988) 327 and Mod. Phys. Lett. **A4** (1989) 1135.
- [6] P.N. Harriman, A.D. Martin, R.G. Roberts and W.J. Stirling, Durham Preprint, DTP-90-04 (1990) and revised April 1990.
- [7] J. Kwiecinski, A.D. Martin, R.G. Roberts and W.J. Stirling, DTP-90-46 (1990).
- [8] J. Morfin and W.K. Tung, FNAL-PUB-90-74.
- [9] M. Glück, E. Reya and A. Vogt, Dortmund preprint, DO-TH-89/20 (1989).
- [10] BCDMS Collaboration, A. C. Benvenuti et al., Phys. Lett. **237B** (1990) 529 and Phys. Lett. **237B** (1990) 559; EMC Collaboration, M. Arneodo et al., CERN - EP/89 - 121; NMC Collaboration, D. Allasia et al., CERN - PPE/90 - 103.
- [11] J. Feltesse, Proceedings of the DESY Workshop on Physics at HERA, DESY Hamburg 1987, Vol. 1, p. 33.
- [12] G. Altarelli et al., Nucl. Phys. **B246** (1984) 12 and Z. Phys. **C27** (1985) 617.
- [13] T. Matsuura and W.L. van Neerven, Z. Phys. **C38** (1988) 623; T. Matsuura, S.C. van der Merck and W.L. van Neerven, Phys. Lett. **211B** (1988) 171 and Nucl. Phys. **B319** (1989) 570.
- [14] G. Sterman, Phys. Lett. **179B** (1986) 281 and Nucl. Phys. **B281** (1987) 310; D. Appel, P. Mackenzie and G. Sterman, Nucl. Phys. **B309** (1988) 259; S. Catani and L. Trentadue, Phys. Lett. **217B** (1989) 539, Nucl. Phys. **B327** (1989) 323 and Cavendish Lab. preprint HEP 90/12 (submitted to Nucl. Phys. B).
- [15] UA1 Collaboration, C. Albajar et al., CERN - PPE/90 - 141; UA2 Collaboration, J. Alitti et al., Z. Phys. **C47** (1990) 11; CDF Collaboration, presented by T. Westhusing, Proc. of the 25th Rencontre de Moriond on Z^0 Physics, (1990), Editions Frontiers 1990, p. 423.
- [16] R. Hamberg, W.L. van Neerven and T. Matsuura, DESY/90-129 (1990).
- [17] P. Nason, S. Dawson and K. Ellis, Nucl. Phys. **B303** (1988) 607 and **B327** (1989) 49.
- [18] Z. Kunszt and W.J. Stirling, Higgs study group, these proceedings.

Monte Carlo Simulation of Minimum Bias Events at the LHC Energy

Guido Ciapetti¹ and Anna Di Ciaccio²

Dipartimento di Fisica, Università di Roma I¹ and Roma II²,
and INFN, Italy

1. - Introduction -

A good description of the soft hadronic interactions (so called minimum bias events) at the LHC energy is a necessary tool to do a realistic feasibility study of the experiments that must be able to disentangle possible rare physics processes from the bulk of proton-proton interactions.

In fact the pile-up of many soft interactions in the same trigger gate, due to the high luminosity and to the extremely short inter-bunch spacing, adds a non negligible level of noise on top of the interesting events, putting severe constraints on the level of background rejection that can be achieved in the analysis. Jet finding, isolation cuts, μ and electron identification will be affected by this noise, making a good simulation of the minimum bias events a mandatory task in the framework of a study group for possible experiments at this new collider.

The UA1/UA5 experimental data collected at the CERN SppS Collider working in a pulsed mode^[1,2] and the recent Fermilab Collider data (E735,CDF)^[3,4] have offered the possibility of studying low p_t interactions over a quite large interval in the center of mass energy from $\sqrt{s} = 0.2$ TeV up to $\sqrt{s} = 1.8$ TeV. In particular it has been observed that the main aspects of minimum bias events are well described in terms of quantities like the mean charged multiplicity $\langle n_{ch} \rangle$, the average transverse momentum $\langle p_t \rangle$ of charged particles and the scalar transverse energy ΣE_t . These quantities show an increase with the c.m. energy that can be very well reproduced by a linear $\log s$ dependence. Furthermore it has also been seen that the $\langle p_t \rangle$ for charged particles grows with the event mean charged multiplicity $\langle n_{ch} \rangle$. Such an increase is again a function of the c.m. energy. This last feature, together with the observation of a growing fraction of low transverse energy clusters with the c.m. energy, has been interpreted by some authors as due to the emergence of the jet phenomenon^[5].

During the past years various models, embedded in more general Monte Carlo programs, have been developed for the description of the minimum bias events^[6,7]. These models have been shown to be able to describe some general properties of soft hadronic interactions experimentally measured.

Therefore we have adopted the following procedure to simulate the minimum bias physics up to $\sqrt{s} = 16$ TeV (disregarding the difference between p - p and $p\bar{p}$ collisions):

- a) tune two of the existing generators of soft hadronic collisions (PYTHIA 5.3^[8], ISAJET 6.21^[9]) based on the experimental data in the interval $\sqrt{s} = 0.2+1.8$ TeV, trying to reproduce at the best the following quantities: the mean multiplicity $\langle n_{ch} \rangle$, the average $\langle p_t \rangle$, the average $\langle p_t \rangle$ versus multiplicity, the mean transverse scalar energy $\langle \Sigma E_t \rangle$ and the fraction of transverse energy clusters with $E_t > 5$ GeV.^(*)
- b) extrapolate to the LHC energy the value of the tuned parameters assuming a linear $\log s$ increase of the $\langle n_{ch} \rangle$ and of the $\langle p_t \rangle$ from $\sqrt{s} = 0.2$ TeV up to $\sqrt{s} = 16$ TeV.

2. - ISAJET tuning -

The ISAJET MINBIAS generator consists of a simple beam-jet fragmentation with no hard scattering and with the $\langle p_t \rangle$ constant as a function of the c.m. energy. To have a more realistic model we have mixed to these events a hard-scattering component with a cut-off on the minimum jet transverse energy E_t^{jet} . The E_t^{jet} cut-off and the relative fraction of the jet component have been tuned so that the total sample could reproduce reasonably well the main properties of the experimental data at the Collider energies.

With a fixed E_t^{jet} cut-off at 5 GeV and with a fraction of jet events increasing linearly with $\log s$ (9% at $\sqrt{s} = 0.2$ TeV, 17% at $\sqrt{s} = 0.9$ TeV and 32% at $\sqrt{s} = 16$ TeV) we have obtained a good agreement with the experimental values for $\langle n_{ch} \rangle$, $\langle p_t \rangle$ and $\langle p_t \rangle$ versus the event multiplicity.

3. - PYTHIA tuning -

The PYTHIA MINIMUM BIAS event generator has been implemented within the framework of the LUND Monte Carlo program.

The main feature of such a model is the idea that a minimum bias event is made out of multiple parton-parton interactions, with an average interaction rate given by perturbative QCD with a low p_t cut-off. Such a cut-off was chosen to be equal to 1.9 GeV/c to reproduce the average multiplicity values at the existing Collider energies. The remainder of the total cross-section is made up by low p_t events that are assumed consisting of two strings. The model allows a choice of three possibilities for the nature of the subsequent non-hardest interaction in an event. In particular to reproduce the behaviour of the $\langle p_t \rangle$ versus multiplicity we have made the following choice: 10% of

^(*) For these quantities a comparison with the results of a third generator, GENCL 1.3^[7], was also done. Without any tuning of this generator the $\langle n_{ch} \rangle$ and the $\langle p_t \rangle$ were reasonably well reproduced but not the dependence of the $\langle p_t \rangle$ from the event multiplicity.

quark-antiquark interactions and 90% of gluon-gluon interactions, of which 90% with "minimal" string length and 10% with "maximal" string length.

4. - Comparison of the data with model predictions -

Fig.1 and 2 show the mean charged multiplicity $\langle n_{ch} \rangle$ and the $\langle p_t \rangle$ in the pseudo-rapidity interval $|\eta| < 2.5$ as function of \sqrt{s} . The continuous line represents the result of a linear fit in log s to the data.

The general agreement between experimental data and the Monte Carlo predictions looks satisfactory. The extrapolated values at $\sqrt{s} = 16$ TeV range between 25 and 30 for the $\langle n_{ch} \rangle$ (5 to 6 charged particles per unit of pseudorapidity) and between 0.510 and 0.540 GeV/c for the $\langle p_t \rangle$.

The invariant cross-section for charged particles at $\sqrt{s} = 16$ TeV, averaged over the interval $|\eta| < 2.5$, is plotted in Fig.3 as a function of the transverse momentum and compared with data at lower energies.

In fig. 4 the $\langle p_t \rangle$ as function of the event multiplicity $\langle n_{ch} \rangle$ at $\sqrt{s} = 0.9$ TeV is compared with the ISAJET and PYTHIA results; again both generators are in good agreement with the data.

In fig. 5 the average transverse momentum versus the event charged multiplicity at $\sqrt{s} = 0.2$ and 0.9 TeV is compared with the Monte Carlo predictions at $\sqrt{s} = 16$ TeV. The distributions show a clear trend to start from a common $\langle p_t \rangle$ at lowest multiplicities and to rise remarkably with \sqrt{s} at high multiplicities. This behaviour has been studied in terms of a phase transition^[10,11] from a multiparticle state to a new state of quark-gluon plasma. An other possible explanation is the correlation with the observed abundant production of low transverse energy clusters^[5].

5. - Study of the pile-up -

At extremely high luminosities, like the ones expected at the LHC Collider, it will be unavoidable to pile-up several minimum bias events in the same trigger gate, adding a non negligible level of background to the response of the calorimeters. We have therefore investigated the influence of this background on physical quantities extracted from the calorimeters like the jet finding and the transverse energy isolation.

Pile-up events obtained adding up 10, 20, 30 minimum bias interactions (corresponding, for $\sigma_{inel} = 80$ mb and 15 ns of inter-bunch spacing, to luminosities $\mathcal{L} = 0.8, 1.6$ and $2.4 \cdot 10^{34}$ cm⁻²s⁻¹ respectively) were generated at $\sqrt{s} = 16$ TeV using our tuned version of ISAJET Monte Carlo. These events were then processed through an analysis program simulating a simple calorimeter geometry, covering a pseudorapidity range $|\eta| < 2.5$. The $\eta\text{-}\phi$ space was divided into cells of size $\Delta\eta \cdot \Delta\phi = 0.05 \times 0.05$.

Particles energies were smeared with the energy resolution of the calorimeter that was assumed to be $15\%/\sqrt{E}$ for electrons/photons and $50\%/\sqrt{E}$ for hadrons.

A jet-finding algorithm like the one used by the UA1 experiment^[12] was used to reconstruct jets with E_t^{jet} greater than a given threshold. The minimum E_t of the jet initiator was chosen to be equal at 1.5 GeV and $\Delta R = \sqrt{\Delta\Phi^2 + \Delta\eta^2} = 0.5$.

The simulation has been checked with the experimental data at $\sqrt{s} = 0.9$ TeV giving good results for the ΣE_t distribution and for the fraction of events with transverse energy clusters over a 5 GeV threshold.

Fig.6 shows the probability per event of finding a jet with transverse energy greater than a given E_t^{jet} value. As expected the jet finding probabilities increase remarkably with the number of pile-up events. For $n_{\text{pile-up}} = 30$ there is still a 1% probability of finding a fake jet with $E_t^{\text{jet}} > 70$ GeV, putting severe constraints on the smallest jet transverse energy accessible at the LHC Collider.

An important quantity for extracting rare signal from the bulk of proton-proton interactions is the so called isolation cut around the direction of a given particle. With this cut a ΣE_t smaller than a given value in a cone of radius $\Delta R = \sqrt{\Delta\Phi^2 + \Delta\eta^2}$, centred on the particle direction, is required^[13].

The minimum value of this cut depends again from the amount of pile-up events. To study the isolation we have considered cones of radius $\Delta R = 0.1$ and 0.3. For each event we have randomly selected a cone with the axis inside $|\eta| < 2.5$. Fig. 7a and fig. 7b show the probability of finding in $\Delta R = 0.1$ and 0.3 a sum of transverse energy greater than a certain threshold. For $n_{\text{pile-up}} = 30$ and $\Delta R = 0.1$ the minimum bias background gives, at 1% level, a contribution of ~ 6 GeV of transverse energy in the cone.

6. - Conclusions -

In this study we have given possible recipes for the minimum bias events simulation at the LHC energy. Two Monte Carlo generators, ISAJET and PYTHIA, have been tuned on the experimental data over the largest presently available range of c.m. energies. Their predictions have been extrapolated at $\sqrt{s} = 16$ TeV. Assuming a linear increase with $\log s$ for relevant quantities like $\langle n_{ch} \rangle$ and $\langle p_t \rangle$, both models seem to give reasonable results. An average charged multiplicity, per unit of pseudorapidity, of 5+6 particles and an average transverse momentum around 0.510+0.540 GeV/c is expected.

The effect of the pile-up of several minimum bias events in the same trigger gate was also investigated. Limits on the minimum jet transverse energy and on the minimum value of the isolation cut that can be used in the analysis of rare events have been derived.

- References -

- [1] C.Albajar et al.: Nucl.Phys. B335 (1990) 261.
- [2] G.J.Alner et al.: Z.Phys. C32 (1986) 153.
- [3] T.Alexopoulos et al.: Phys.Rev. D60 (1988) 1622.
- [4] F.Abe et al.: Phys.Rev. D61 (1988) 1819.
- [5] C.Albajar et al.: Nucl.Phys. B309 (1988) 405.
- [6] T.Sjöstrand and Maria van Zijl: Phys.Rev. D36 (1987) 2019.
- [7] G.J.Alner et al.: Nucl.Phys. B291 (1987) 445.
- [8] H.-U.Bengtsson and T.Sjöstrand, Comput.Phys.Commu. 46 (1987) 43.
- [9] F.Paige et S.Protopopescu, BNL-38034 (1986).
- [10] R.Hagedorn: Riv. Nuovo Cimento 6-10 (1983) 1.
- [11] L. van Hove: Phys.Lett. 118B (1982) 138.
R.Campanini: Nuovo Cimento Letters 44 (1985) 343.
- [12] G.Arnison et al.: Phys.Lett. B132 (1983) 214.
- [13] C.Albajar et al.:Z.Phys. C48 (1990) 1.

- Figure Captions -

Fig.1 Average charged multiplicity as a function of the c.m. energy for $|\eta| < 2.5$ and $p_t > 0.150 \text{ GeV}/c$.

Fig.2 Average transverse momentum for charged particles as a function of the c.m. energy for $|\eta| < 2.5$.

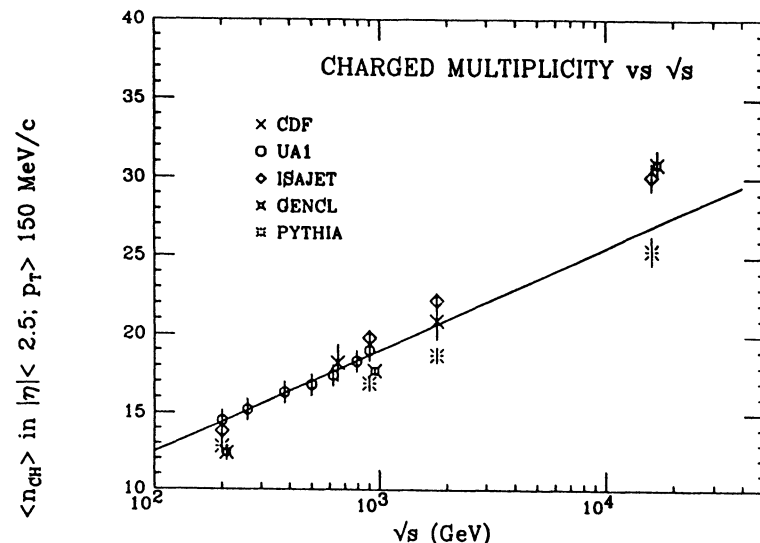
Fig.3 Inclusive invariant cross section for charged hadrons averaged over $|\eta| < 2.5$ as a function of the transverse momentum.

Fig.4 Average transverse momentum as a function of the charged particle multiplicity at $\sqrt{s} = 0.9 \text{ TeV}$. The data are compared with PYTHIA and ISAJET predictions.

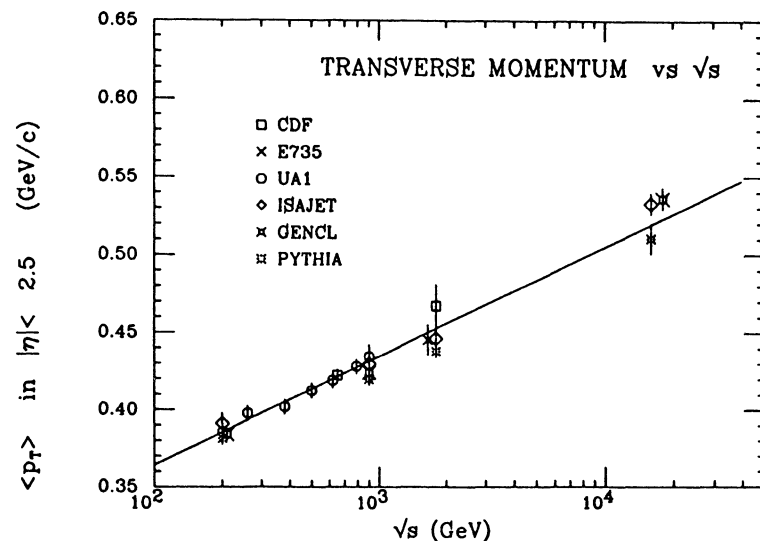
Fig.5 Average transverse momentum as a function of the charged particle multiplicity at $\sqrt{s} = 0.2, 0.9$ and 16 TeV .

Fig.6 Probability of finding a jet with $E_t > E_t^{\text{jet}}$ for 10, 20, 30 piled-up minimum bias events.

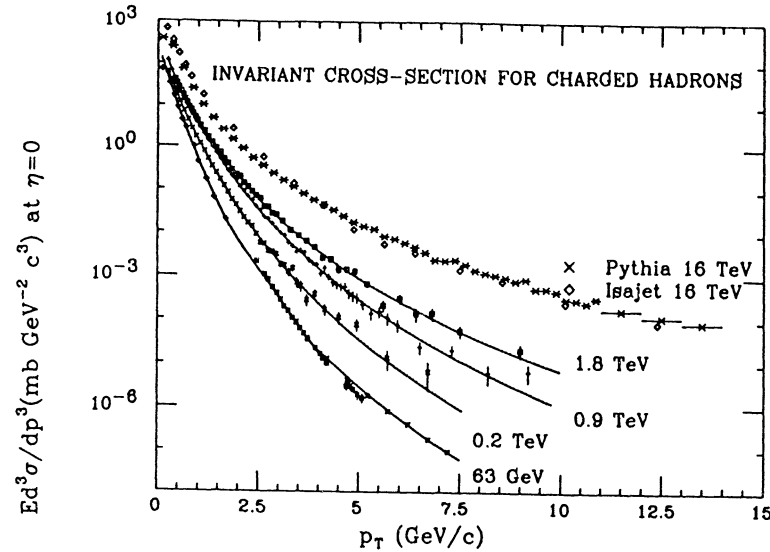
Fig.7 a); b) Probability of finding in a cone of radius $\Delta R = 0.1$ (0.3) a $\Sigma E_t > \Sigma E_t^{\text{thresh}}$.



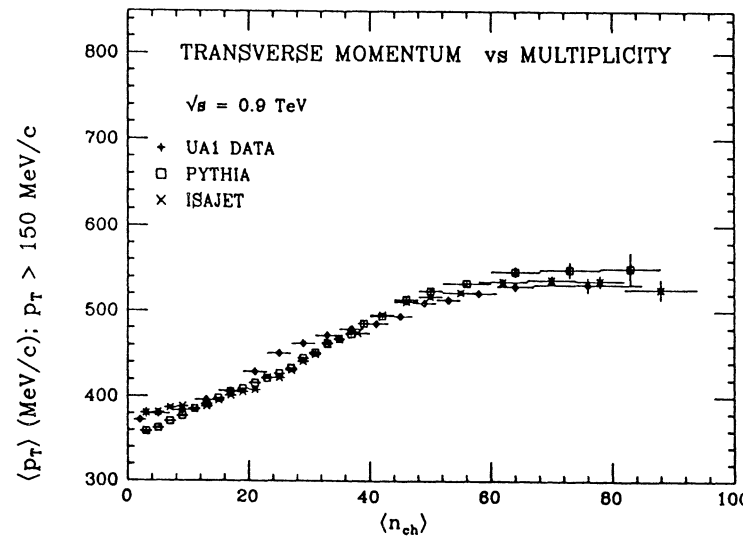
- Fig. 1 -



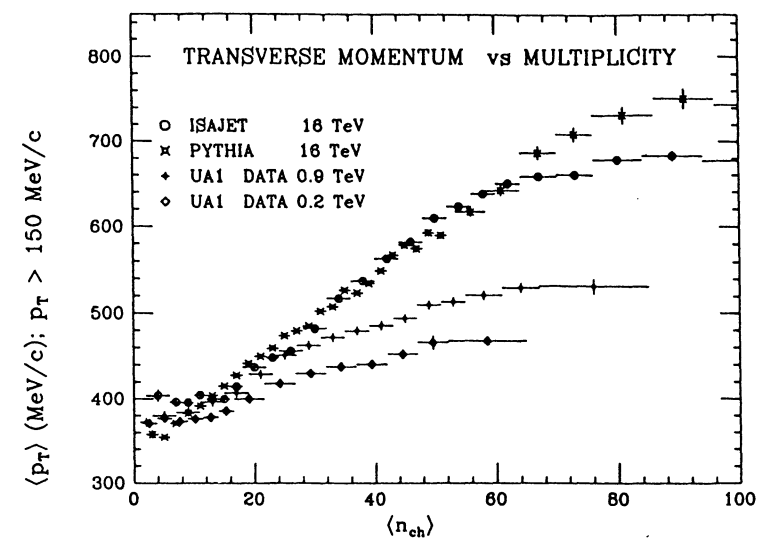
- Fig. 2 -



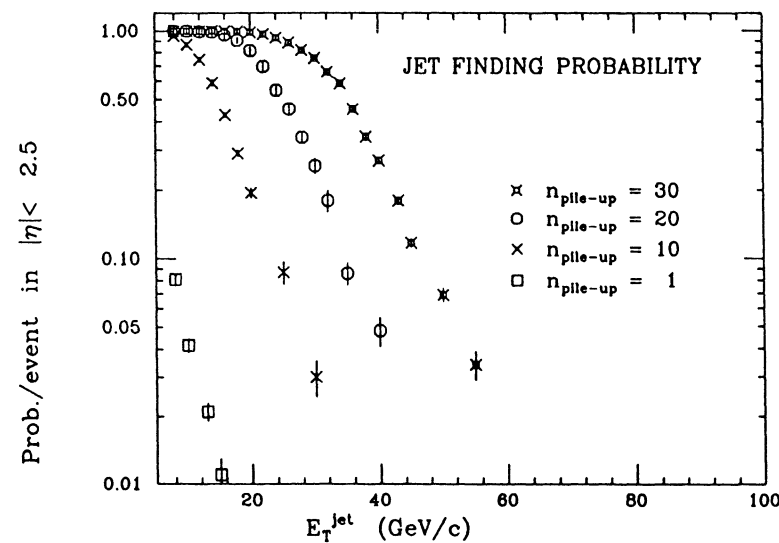
- Fig. 3 -



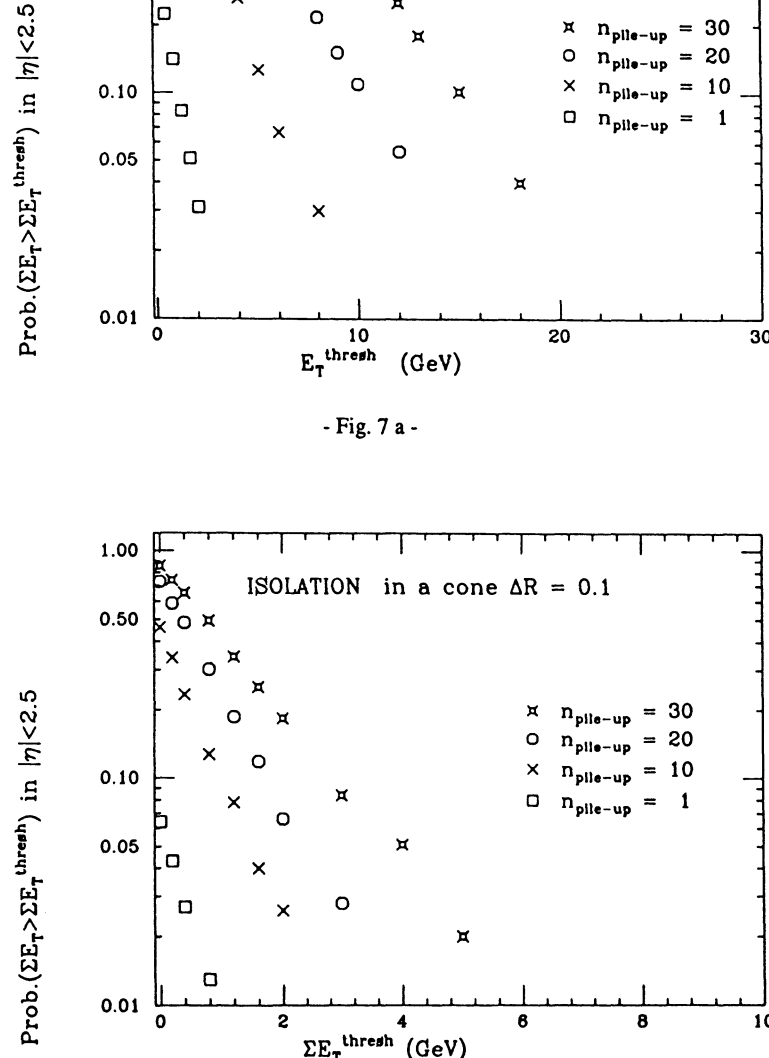
- Fig. 4 -



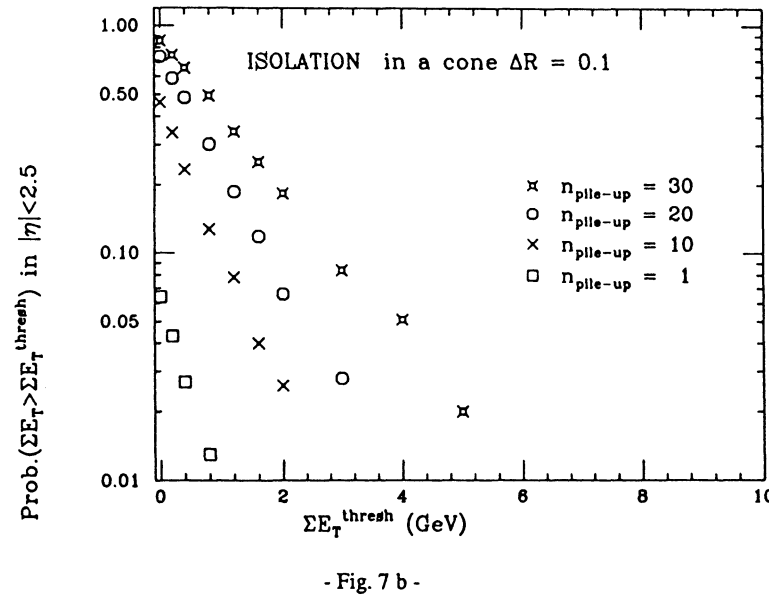
- Fig. 5 -



- Fig. 6 -



- Fig. 7 a -



- Fig. 7 b -

A Comparison of Bottom Production in Different Event Generators

J.R. Cudell¹, O. Di Rosa², I. ten Have³,
A. Nisati⁴, R. Odorico⁵, T. Sjöstrand¹

¹CERN, CH-1211 Geneva 23, Switzerland

²LAA Project, CERN, CH-1211 Geneva 23, Switzerland

³University of Glasgow, Glasgow, United Kingdom

⁴INFN, Rome, Italy

⁵Università di Bologna and INFN, Bologna, Italy

Abstract:

We study some of the uncertainties attached to the prediction of bottom production at LHC energies by comparing the answers of five different Monte Carlo event generators. The input parameters are set to be as close as possible, so that the resulting discrepancies are mostly due to different algorithms for perturbative QCD, fragmentation and decay. We show that the answers differ by at least a factor 3 after the perturbative description and 10 after fragmentation and decay.

The bottom quark is one of the main sources of prompt leptons at high energy hadron colliders. These leptons constitute a non-negligible background to planned LHC searches, for the top quark, Higgses, weak bosons, or more exotic particles. The optimization of experimental cuts requires the evaluation of this background via Monte Carlo simulations, and it is an important question to see how reliable the present event generation algorithms are.

It is well known that higher order corrections to b production are large. The exact $\mathcal{O}(\alpha_S^3)$ calculations [1] show enhancement factors of around 3, compared to the lowest order results, at LHC energies. In part this is due to the fact that higher orders include contributions for which a vector particle is exchanged in the t channel; these terms remain constant as the centre of momentum energy \sqrt{s} increases. An enhancement also comes from the rise of the gluon structure function at low x and from the big colour factors associated with $gg \rightarrow gg \rightarrow b\bar{b}g$. The size of yet higher order contributions is unknown.

Many of the event generators on the market do not make use of exact higher order matrix elements, but instead combine lowest order $2 \rightarrow 2$ hard scatterings with a parton shower picture for initial and final state radiation. Since both the exact matrix element and the parton shower approaches have limitations, it is interesting to see how well they compare, and also how big is the spread between programs of the same class.

We thus propose to compare five Monte Carlo simulations against one another and against the analytical results of Nason, based on [1]. The present study does not evaluate the uncertainties resulting from the input physical parameters,

Table 1: Physics input for the comparison of the various Monte Carlos.

parameter	value	exceptions
process	pp collisions	
\sqrt{s}	16 TeV	
structure functions	DFLM set 2 [2]	COJETS
α_s	1-loop, $n_f = 4$	HERWIG 4.6
$\Lambda_{QCD}(GeV)$	260 MeV	
α_s scale	$m_b^2 + p_T^2$	
m_b	4.75 GeV	
top quarks	assumed absent	

such as the quark masses or the structure functions, but concentrates on those discrepancies that are related to the different algorithms used. Accordingly, input parameters have been standardized as much as possible, as is summarized in Table 1.

The five Monte Carlo generators used are COJETS 6.11 [3], EUROJET [4], HERWIG 4.6 [5], ISAJET 6.24 [6] and PYTHIA 5.4 [7].

The last three use similar showering algorithms, in which the incoming partons at the hard scattering are evolved backward to the incoming hadrons, and the outgoing partons are evolved forward to the fragmentation region. Here the programs use distinct fragmentation algorithms, respectively cluster, independent and string fragmentation. Note that in its latest version, HERWIG uses a 2 loop expression for α_s with a Q^2 -dependent number of flavours. When appropriate, we shall quote the results of HERWIG 4.3, which is entirely comparable with ISAJET and PYTHIA in this respect.

COJETS proceeds from a different point of view, in which the parton showers are evolved forward from the protons to the hard scattering. This means that, contrary to the programs above, structure function parametrizations are only used at the initial low Q_0^2 scale where the showers are begun, with subsequent evolution calculated by the program itself. Since the evolution in COJETS is leading log, while DFLM contains next-to-leading corrections, utilization of DFLM with COJETS would lead to inconsistent results, which is why COJETS has been used with the leading log EHLQ set 1 [8] instead. COJETS uses independent fragmentation.

Finally, EUROJET is a matrix element Monte Carlo, which includes all $2 \rightarrow 2$ and $2 \rightarrow 3$ tree level diagrams. It does not include the loop corrections to $2 \rightarrow 2$ but, with a judicious choice of parton separation cutoffs, it is possible to reproduce the b rate of Nason *et al.* reasonably well. EUROJET contains no parton showering. It uses independent fragmentation.

In our comparisons, we choose to concentrate on inclusive p_T distributions at various stages of b production.

- Born level $q\bar{q}, gg \rightarrow b\bar{b}$ flavour creation results. Here only the hard scattering tree level cross-section enters, and thus all programs should agree.
- Results after the full perturbative QCD treatment, with shower or higher order matrix elements. Here one is sensitive to the QCD treatment, in particular to the details of the shower schemes.
- The muon distributions, which are sensitive to the full machinery, including fragmentation and decays.

Finally, we show that some related distributions can clearly distinguish between matrix element and shower Monte Carlos.

The results of the first, Born level, comparison are shown in Fig. 1. Results

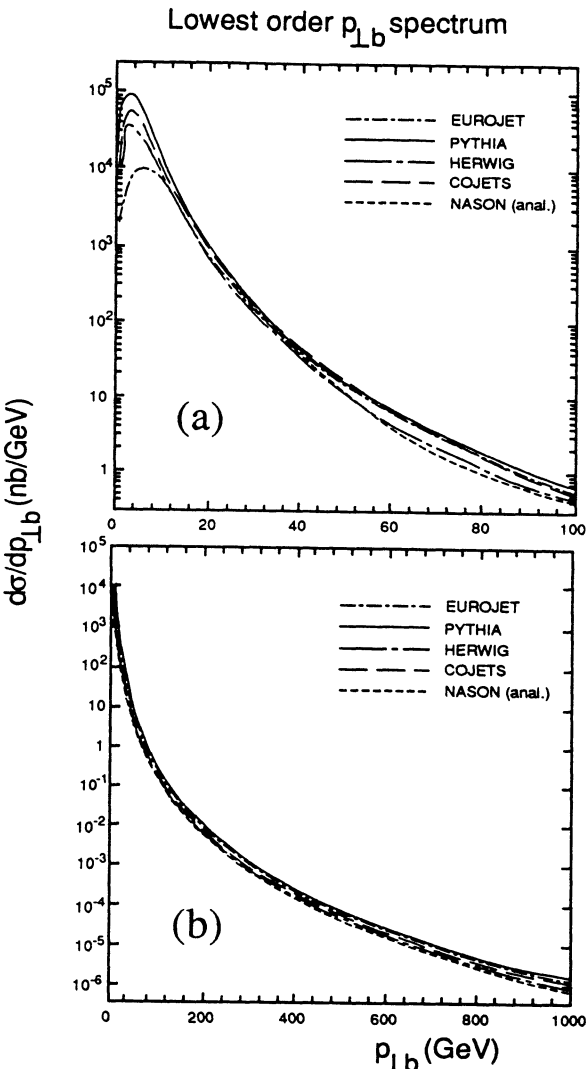


Figure 1: Inclusive $b + \bar{b}$ transverse momentum distribution for $2 \rightarrow 2$ flavour creation only ($q\bar{q} \rightarrow b\bar{b}$ and $gg \rightarrow b\bar{b}$) at (a) low and (b) high transverse momentum p_T .

are calculated using samples of roughly 10^4 events, except COJETS which uses much bigger statistics, and statistical fluctuations have been smoothed by hand. The differences between the lowest order calculations are understood as follows. HERWIG 4.6 and PYTHIA differ only because they are using 2 vs. 1 loop expressions for α_S : HERWIG 4.3 (after errors in the colour factors in that version have been corrected) is in perfect agreement with PYTHIA. Also the analytical curve is based on a 2-loop expression for α_S , and is in good agreement with HERWIG 4.6. The additional discrepancy between programs at low p_\perp is probably entirely related to structure functions: in this region many events are produced from partons which have x values below the stated region of validity of structure function parametrizations. In EUROJET the structure functions $f(x)$ are assumed to vanish in this x region, while PYTHIA extrapolates from the lower bound of the parametrizations under the assumption that $xf(x)$ is fix. Finally, as was pointed out before, COJETS uses leading-log evolved structure functions, and its results are thus similar to those obtained using EHLQ [8] in the other Monte Carlos.

The second test compares the $b + \bar{b}$ sample when the full perturbative QCD machinery is used in programs, Fig. 2. The parton shower curves include both flavour creation and flavour excitation, while the analytic curve and EUROJET take only flavour creation into account. The flavour excitation graphs $q + b \rightarrow q + b$ and $g + b \rightarrow g + b$ appear when branchings $g \rightarrow b\bar{b}$ are allowed to build up b structure functions inside the incoming hadrons. The $2 \rightarrow 3$ matrix elements include the contributions from initial $g \rightarrow b\bar{b}$ branchings, which is why it would be doublecounting also to include b structure functions in the matrix elements approach. At first glance, no doublecounting issues are involved in the parton shower approach, but actually the definition of heavy flavour structure functions is delicate [9], so that some doublecounting may still appear. Uncertainties are particularly important for $p_\perp \rightarrow 0$, where the naive cross-section is divergent. In the parton shower programs, flavour excitation gives a major contribution to the b cross-section, overshooting that of flavour creation by a factor 2 to 4.

One can see from Fig. 2 that various showering algorithms disagree by a factor 5 to 10. It is worth noting that the prediction of HERWIG 4.3 is in good agreement with that of PYTHIA, so that the discrepancy shown in the figure can be traced back to the use of a 2 loop expression in α_S . However, the parton shower programs cannot reproduce the analytical results of [1]. This is particularly obvious from Fig. 3, which shows the ratio of the full to the lowest order result: while the analytic formulae give a ratio that is essentially flat as a function of p_\perp , the shower programs give a ratio that tends to drop with p_\perp . There are two main reasons for the latter behaviour.

1. A b quark originally produced at a given p_\perp will be degraded towards a smaller p_\perp by final state gluon emission in the shower. Contributions from $b \rightarrow bg$ branchings also appear in the $2 \rightarrow 3$ matrix elements but, since at most one gluon may be emitted here, the true size of the effect is underestimated. In matrix element programs, the same effect could partly be taken into account by the proper choice of perturbative [10] and nonperturbative fragmentation function(s).
2. In the shower evolution, a gluon may branch into a $b\bar{b}$ pair. Again contributions of this type appear in the $2 \rightarrow 3$ matrix elements, but again the full shower description involves a larger number of gluons, and therefore an increased probability for one of them to branch into $b\bar{b}$ (see also [11]). Since the full energy of the original jet is shared between many partons, the additional production is concentrated towards smaller p_\perp .

Although the final answer is not at hand, there are good physics reasons to be

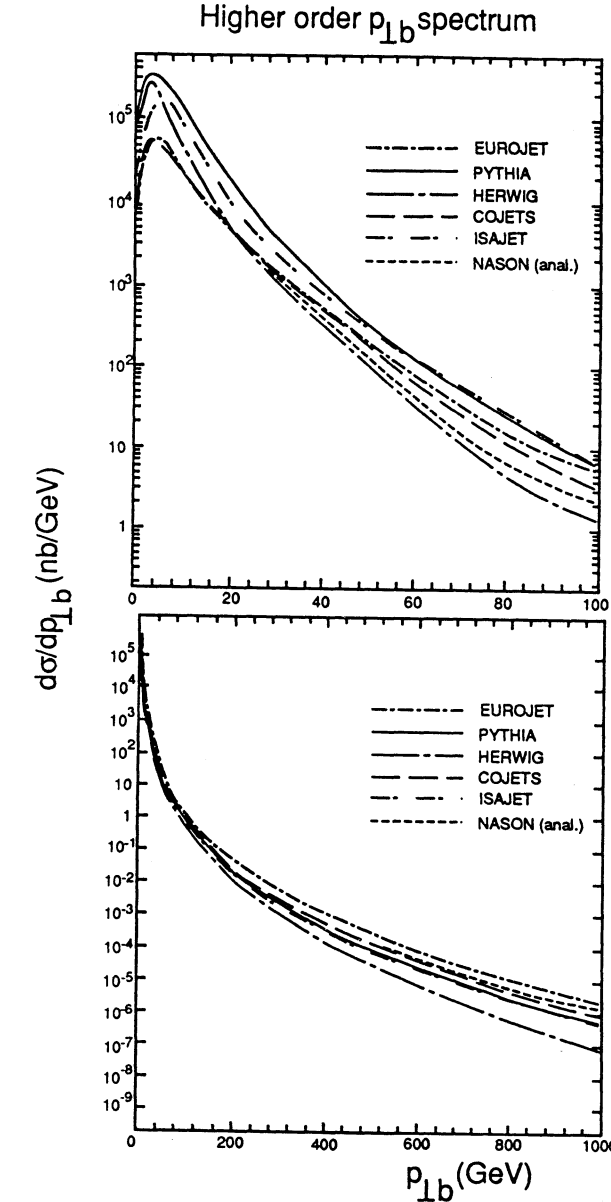


Figure 2: Inclusive $b + \bar{b}$ transverse momentum distribution after the full perturbative treatment, i.e. shower or higher order matrix elements, at (a) low and (b) high transverse momentum p_\perp .

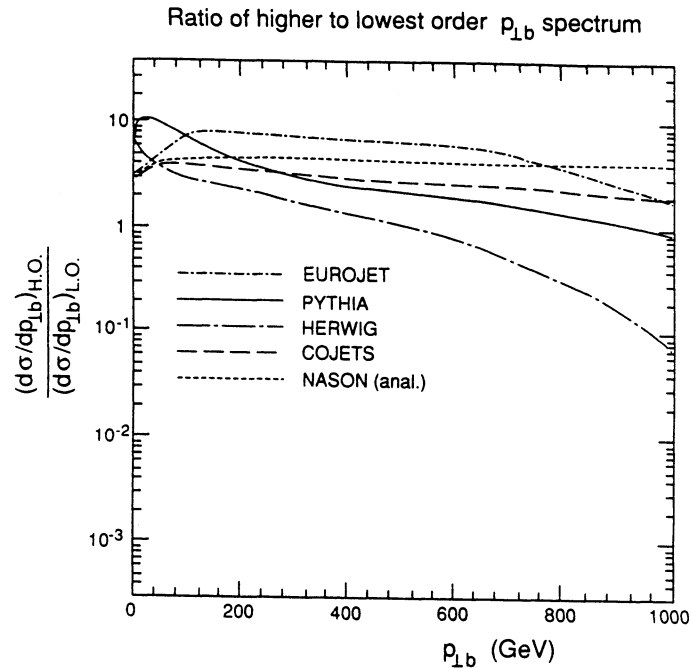


Figure 3: Ratio of the inclusive p_{\perp} distribution of $b + \bar{b}$ quarks in the full treatment, shower or higher order matrix elements, to those of lowest order flavour creation, i.e. the ratio of Figs. 2(b) and 1(b).

wary of the results of the $\mathcal{O}(\alpha_s^3)$ analytic calculations, and to believe that the ratio in Fig. 3 should indeed drop with p_{\perp} . However, the large spread between the shower programs indicates that, also in this approach, the answer is not well known.

Finally, we can also test the fragmentation and decay algorithms by looking at muon distributions. Fig. 4(a) shows the spectrum of the muons from primary b/\bar{b} decays, and again there is a disagreement, of about a factor 10 (the size of the statistical sample is not entirely appropriate to make this statement more precise). It is interesting to compare the primary μ spectrum of Fig. 4(a) with that of all the other muons produced in the shower, from charm and secondary b decays ($b \rightarrow c \rightarrow \mu$, $b \rightarrow \tau \rightarrow \mu$), Fig. 4(b). For the latter, the disagreement between the programs is slightly smaller, which leads to an interesting difference: while COJETS and PYTHIA predict most high- p_{\perp} muons to come from primary b decays, by a wide margin, HERWIG gives about equal importance to primary b decays and to the other sources. We do not know whether this comes from differences in the charm production in the shower or from differences in bottom and charm decays.

All the previous curves have been quite similar in shape, if not in magnitude.

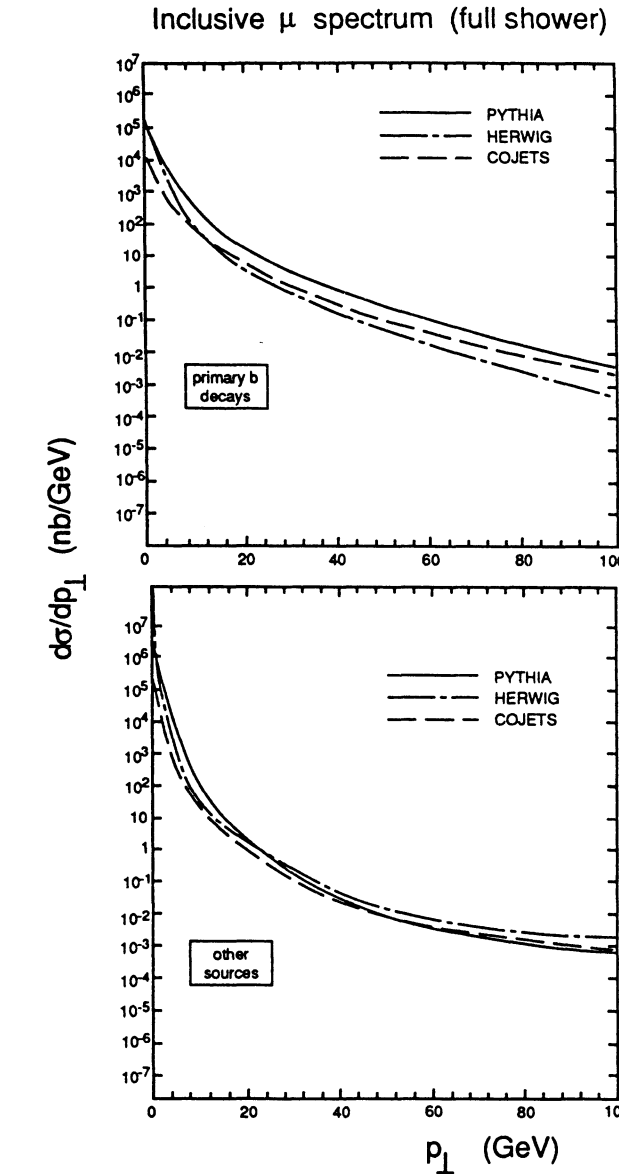


Figure 4: Inclusive muon p_{\perp} distributions, after full perturbative QCD, fragmentation and decay treatment. The direct muons from $b + \bar{b}$ are shown in (a), whereas (b) shows the muons coming from other sources (from secondary b decays, or from charm production).

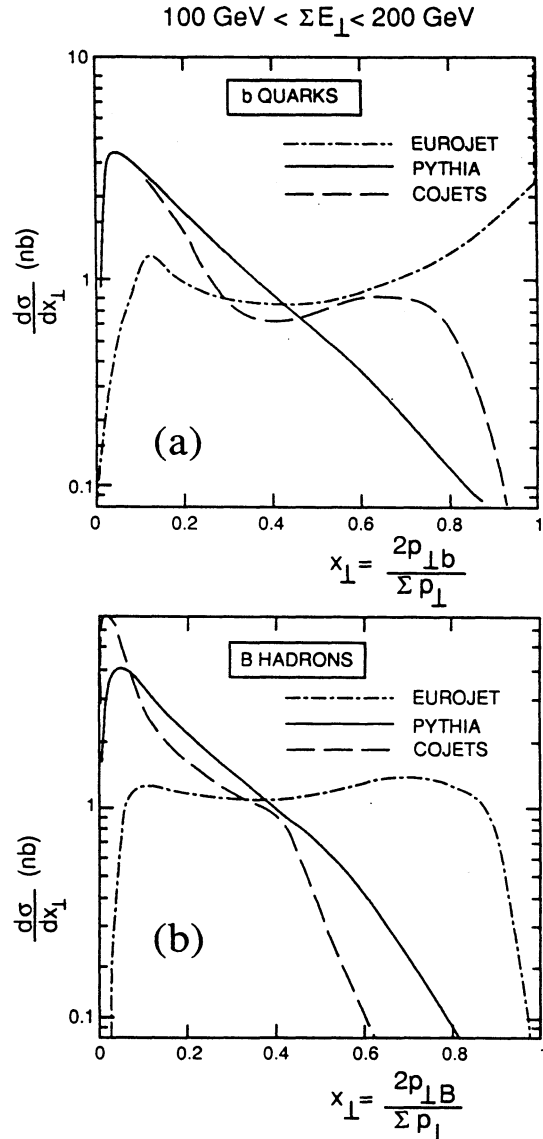


Figure 5: Inclusive transverse momentum fraction x_\perp for (a) $b + \bar{b}$ quarks after perturbative treatment and (b) bottom hadrons after fragmentation. The total (parton level) transverse energy of the event is constrained to lie between 100 and 200 GeV.

One can, however, find distributions which differ drastically. One of these is shown in Fig. 5. It gives the prediction of three Monte Carlos for the x_\perp distribution, first at the quark level, then at the hadron level. The $x_\perp = 2p_{\perp(b,B)} / \sum p_{\perp}$ variable tests both the perturbative description and the fragmentation. At the hard scattering level, for flavour creation, one has $x_\perp \equiv 1$, and also $2 \rightarrow 3$ matrix elements tend to be peaked near $x_\perp = 1$, cf. the EUROJET curve in Fig. 5(a). As noted above, in the shower description original b quarks are degraded in momentum due to gluon emission, and new $b\bar{b}$ pairs are created at smaller x_\perp values by gluon branchings; therefore the shower description gives an x_\perp spectrum concentrated at smaller values. Since the shower cutoff scale is higher in COJETS than in PYTHIA, more of the original peak at $x_\perp = 1$ survives; once fragmentation is included, Fig. 5(b), this peak disappears completely, however. If Figs. 5(a) and 5(b) are compared, one should also note that independent fragmentation gives a significant shift of the spectrum towards smaller x_\perp values, an effect that is almost absent in the string fragmentation picture.

In conclusion, even before considering ambiguities from the choice of scales or from structure functions, one has to realize that different theoretical and phenomenological estimates of the same background lead to uncertainties of the order of a factor 10, and that the actual shape of distributions can be very sensitive to the fragmentation description, i.e. to theoretically less well controlled parts of Monte Carlos. A minimum requirement on programs would be that they can describe existing data, both from $p\bar{p}$ colliders and from e^+e^- annihilation; in particular, LEP may be expected to contribute significantly to our current understanding.

The main lesson is that, currently, no single treatment of b production can be trusted on its own.

References

- [1] P. Nason, S. Dawson, R.K. Ellis, Nucl. Phys. **B327** (1989) 49
- [2] M. Diemoz, F. Ferroni, E. Longo, G. Martinelli, Z. Physik **C39** (1988) 21
- [3] R. Odorico, Computer Physics Commun. **32** (1984) 139, **59** (1990) 527
- [4] A. Ali, B. van Eijk, I. ten Have, Nucl. Phys. **B292** (1987) 1
- [5] B.R. Webber, G. Marchesini, Nucl. Phys. **B310** (1988) 461, **B330** (1990) 261
- [6] F.E. Paige, S.D. Protopopescu, in 'Physics of the Superconducting Super Collider 1986', eds. R. Donaldson, J. Marx (1987), p. 320
- [7] H.-U. Bengtsson, T. Sjöstrand, Computer Physics Commun. **46** (1987) 43
- [8] E. Eichten, I. Hinchliffe, K. Lane, C. Quigg, Rev. Mod. Phys. **56** (1984) 579, **58** (1985) 1065
- [9] F.I. Olness, W.-K. Tung, Nucl. Phys. **B308** (1988) 813
- [10] B. Mele, P. Nason, Phys. Lett. **B245** (1990) 635
- [11] A.H. Mueller, P. Nason, Nucl. Phys. **B266** (1986) 265

Multi-jet Event Generators for LHC

H. Kuijf

Instituut-Lorentz, University of Leiden, The Netherlands

P. Lubrano

PPE Division, CERN, CH-1211 Genève 23, Switzerland

V. Vercesi

INFN Sezione di Pavia, Pavia - Italy

I. Introduction

Multi-jet events will constitute a severe source of background for many of the new physics processes possibly accessible at the next generation of proposed hadron colliders. In this contribution we review the present status of multi-jet events generators. Because the Kunszt-Stirling generator [1] has been already discussed extensively in the past we will focus on a recent work [2] that, employing new techniques for the matrix element computation, allows the exact tree level calculation of the cross-section for the $2 \rightarrow m$ process, with m up to 5. New approximation techniques, allowing a sensible reduction in CPU time usage and the extension of m up to 8, will also be discussed. Finally, the program has been tested on several different computer frames (VAX, IBM 3090, APOLLO DN3500, APOLLO DN10000, SUNSPARC, DEC 5400, CRAY X-MP/48, CRAY Y-MP/48); a few comments about the portability of the code on the different systems will be made.

II. QCD Matrix Elements

This section deals with the evaluation of tree level matrix elements in QCD. Calculational details can be found in [2], here only the general ideas behind the exact calculation and the approximations considered will be discussed.

The matrix elements for $n \leq 6$, n being the global number of partons participating to the scattering, have been determined using the standard Feynman diagram technique. Each process had to be calculated independently. The $n = 6$ case (*i.e.* $2 \rightarrow 4$) was the last one that could be computed in this way [3]. The expressions for $\sum_{c,\lambda} |\mathcal{M}_n|^2$ were lengthy, required much computer time and did not lead to a deeper understanding of the dynamics of QCD matrix elements. In particular the soft gluon behaviour could not easily be inferred.

For higher n values new tools had to be introduced like the use of Weyl - van der Waerden spinors, the decomposition of the matrix elements in subamplitudes using the Chan Paton colour basis [4] and recursive techniques [5]. It was found that the general QCD matrix elements can be written as

$$\sum_{c,\lambda} |\mathcal{M}_n(P)|^2 = g^{2n-4} \sum_{c,\lambda} \left| \sum_{\text{perms}} F(T^a, N) K_F(P) \right|^2, \quad (1)$$

where the event P , a phase space point, is given as the explicit argument of $\sum_{c,\lambda} |\mathcal{M}_n|^2$. Each Feynman diagram in a scattering process is written as a colour part $F(T^a, N)$ which is a function of the fundamental representation matrices, T^a of the $SU(N)$ colour group, and a part called $\tilde{K}_F(P)$ which depends on momenta and helicities. Adding all the $\tilde{K}_F(P)$'s with the same $F(T^a, N)$ results in $K_F(P)$, a gauge invariant subamplitude. The full calculation consists of the determination of a number of $K_F(P)$'s. The \sum_{perms} denotes the sum over all the permutations of identical partons that change $F(T^a, N)$. Evaluating the square and summing over all colours eq. (1) results in a $N_P \times N_P$ colour matrix, where N_P is the above number of permutations.

The computer resources needed for Monte Carlo simulations increased drastically with n and several approximations to replace the exact calculations were proposed. To examine their validity the $n = 7$ case had to be fully evaluated. By introducing recursion relations in the number of gluons for the subamplitudes [5] it became possible to compute the numerically most important subprocess, the purely gluonic one, for $n = 7$ [6] and for $n = 8$ [7]. By rewriting the recursion relation one was even able to obtain exact expressions for the seven gluon subprocess [8]. This process, given by 2485 diagrams, cannot be calculated by traditional methods. The same recursion relation technique has been used to evaluate the two and four quark processes with an arbitrary number of gluons. Finally the six quark process was recalculated using a more systematic method to include extra gluons [9]. This completed the $n = 7$ case. Incorporating these calculations in a multi-jet event generator shows that one event, *i.e.* the sum over all possible subprocesses, takes about 7 seconds of CPU on a CRAY X-MP/48. This has to be compared with the 0.1 seconds for the $n = 6$ case. The difference is not only due to the extra gluon but also to the fact that there are many more parton subprocesses. Moreover for $n = 6$ analytic expressions are available, whereas for $n = 7$ they are not. The exact matrix elements are denoted by EXACT in the text below.

Currently available computers do not allow extensive studies of multijet backgrounds using the EXACT form of the matrix elements. Reliable approximation techniques have to be developed. In this respect the total cross section for m -jet production is considered.

$$\sigma_m(s) = \sum_{\text{Final}, i,j} \int \dots \int \frac{d\Phi dx_1 dx_2}{8x_1 x_2 s} \left\{ f_i^{H_1}(x_1, Q) f_j^{H_2}(x_2, Q) F_s F_c \sum_{c,\lambda} |\mathcal{M}_{m+2}|^2 \right\}. \quad (2)$$

The integrals are performed over the momentum fractions x_1 and x_2 of partons i and j for the hadrons H_1 and H_2 and $d\Phi$ is the accessible phase-space at a given parton CM energy squared $\hat{s} = x_1 x_2 s$. The $\sum_{\text{Final}, i,j}$ represents the sum over all possible parton processes. Conservation of charge and flavour is implicitly understood. F_s and F_c are the symmetry factor and the colour averaging factor.

Finally Q sets the QCD scale. Besides the exact calculation of the cross section using eq. (2) we consider the following approximations:

- SPHEL = Special helicity approximation.
Replace the \sum_{λ} in $\sum_{c,\lambda} |\mathcal{M}_n|^2$ by a sum over a limited set of helicity configurations where two partons have an helicity opposite to all the other helicities. For this specific combination short analytical expressions are known for all n .
- ESFAG and ESFAQ = Effective structure function approximation.

Replace the sum over the initial states by just one state and adjust the structure functions to account for the ones left out. In ESFAG this state is the gluon-gluon initial state. Effectively the $\sum_{i,j}$ is omitted and the $f^H(x, Q)$ become

$$f_{eff}(x, Q) = f_g(x, Q) + 4/9 \sum_q [f_q(x, Q) + f_{\bar{q}}(x, Q)], \quad (3)$$

where the sum runs over the quark flavours u, d, s and c. Likewise the sum $\sum_{i,j}$ is replaced by the $q\bar{q}$ term in ESFAQ, $q\bar{q}$ denote a quark and a antiquark of different flavour. In this case the effective structure function becomes

$$f_{eff}(x, Q) = 9/4 f_g(x, Q) + \sum_q [f_q(x, Q) + f_{\bar{q}}(x, Q)], \quad (4)$$

- MCHEL = Monte Carlo over helicity combinations.

Replace the \sum_{λ} in eq. (2) by $n_{\lambda} \times \sum_c |\mathcal{M}|^2$ for a random helicity combination, with n_{λ} the total number of helicity combinations. This Monte Carlo method is much slower than SPHEL and has other disadvantages as well [10], therefore no results for this approximation will be presented.

Based on the calculations described above, a multi-jet event generator program was written. The aim of this program, NJETS, is to predict multi-jet production rates and differential cross sections. Of interest in this respect is the computer resources that are needed to make production runs with NJETS. For the exact and some approximations the CPU-time needed to evaluate one event on the hadron level, *i.e.* the sum over all parton subprocesses, is given in Table 1. We see that SPHEL is very fast compared to the exact expressions. For five jets it is more than 5000 times faster. As a concluding remark we note that it is hard to predict how many events are needed to get reliable results for quantities like the total cross section. The number of events depends very much on the collider energy and the detector cuts imposed. In general a few thousand events that pass the phase-space cuts are the minimum.

III. Comparison with existing data

Both event generators (Kunszt-Stirling and Kuijf-Berends) have been shown to be in good agreement with existing multi-jets data from UA2. The details of the analysis can be found in [11]. Briefly, after generation, multi-jet events were fragmented

Table 1 : CPU Time per event in milliseconds of μ VAX 3500						
Method	nr. jets	0 quarks	2 quarks	4 quarks	6 quarks	Time/ev
EXACT	2	0.34	1.2	1.8	—	3.3
	3	0.56	11	19	—	31
	4	80	410	410	120	1000
	5	6300	30000	36500	2500	75000
SPHEL	2	0.61	2.1	5.8	—	8.5
	3	1.0	3.2	6.8	—	11.0
	4	3.0	5.8	9.1	—	17.9
	5	12.0	18.7	13	—	44
MCHEL	2	0.34	1.2	1.8	—	3.3
	3	0.56	11	19	—	31
	4	9.8	110	260	28	410
	5	230	2150	9300	330	12000

Table 1: CPU-time per event in milliseconds on a μ VAX 3500. This includes keeping statistics but not the determination of parton densities and filling the histograms.

using a Field-Feynman model allowing for gluon radiation. The events were then passed through a complete simulation of the UA2 calorimeter and analyzed in the same way as the data. The underlying event, from spectator quark interactions, was simulated by superimposing real minimum bias events to the hard-scattering. Many distributions were examined and found to be in good agreement with the measured spectra. As an example, Figure 1 shows the inclusive P_t spectrum for four- and five-jet events. Only statistical errors are shown and for each event every jet P_t enters the plot. The histograms represent the Monte Carlo absolute prediction. The acceptance uncorrected integrated four-jets cross-section, for the selection cuts of [11], is $\sigma_4(\text{DATA}) = 1.31 \text{ nb}$, whereas the two QCD calculations predict $\sigma_4(\text{Kunszt - Stirling}) = 1.21 \text{ nb}$ and $\sigma_4(\text{Kuijf - Berends}) = 1.28 \text{ nb}$. For the five-jet cross-section we obtained $\sigma_5(\text{Kuijf - Berends}) = 0.047 \text{ nb}$ and $\sigma_5(\text{DATA}) = 0.037 \text{ nb}$.

IV. Exact calculation versus approximation

The present study has been carried out on a μ VAX 3800 (about 1.5 times faster than the μ VAX 3500 mentioned above) using an equivalent of 1500 hours of CPU time in CERN units. Events were selected according to the following cuts:

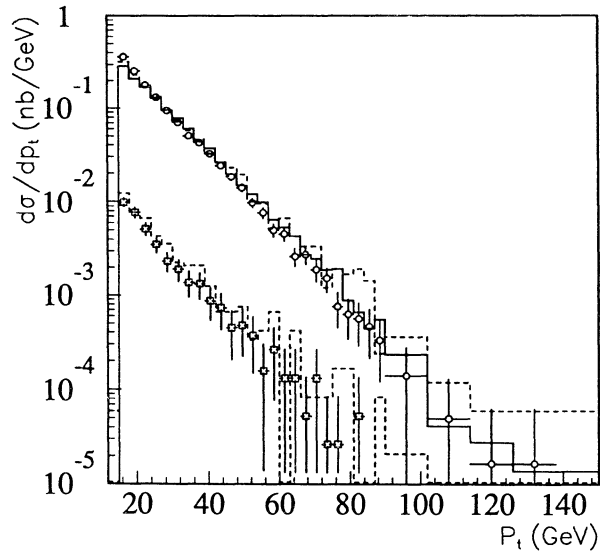


Figure 1: Uncorrected p_T spectrum for four- and five-jet events. The data points are the UA2 data (circles: four-jet events, squares: five-jet events). The histograms represent the absolute prediction of the Kunszt-Stirling (solid) and Kuijf-Berends (dashed) calculations after full simulation of the calorimeter.

$$\begin{aligned}
 E_{t,i} &> 50 \text{ GeV} & i=1\dots n \\
 |\eta_i| &< 3.0 & i=1\dots n \\
 \theta_{ij} &> 30^\circ & \text{for any jet pair}
 \end{aligned}$$

These demands require the outgoing partons to be well separated in phase-space and assure the validity of perturbative QCD avoiding collinear divergencies. The structure function set used was that of Duke-Owens (Set 1): other sets (D02, EHLQ, GRS, MRSEB1 and MRSEB2) have been used as well, however the final conclusions are insensitive to the choice of structure function set. An important parameter for the calculation is the QCD scale at which α_s is computed: this is especially true in the case of multi-jet events where more powers of α_s are involved in the calculation. In this work we have used $Q^2 \equiv E_{t,\max}^2$, where $E_{t,\max}$ is the largest jet transverse energy present in the event. Finally the centre-of-mass energy was chosen to be $\sqrt{s} = 16 \text{ TeV}$, the nominal energy of the proposed LHC design. Table 2 summarizes the results for the multi-jet cross-sections. In general

Table 2 : Multi-jet cross-sections at LHC (nb)

m	EXACT	SPHEL	ESFAG
2	$24020. \pm 112.$	$24200. \pm 112.$	$23600. \pm 108.$
3	$1150. \pm 16.7$	$1170. \pm 16.9$	$1110. \pm 15.1$
4	$132. \pm 4.4$	$163. \pm 7.2$	$119. \pm 5.8$
5	13.4 ± 1.4	18.5 ± 0.6	14.0 ± 0.5
6	-	2.3 ± 0.1	-
7	-	0.35 ± 0.04	-
8	-	0.034 ± 0.004	-

the two approximations considered here (SPHEL,ESFAG) are in fair agreement with the results obtained using the exact calculations of the matrix elements. For the two- and three-jet cases the differences are of the same order of magnitude of the statistical errors of the generation. Note that in general these errors are small, each generation set being made with $\approx 150K$ events. Only for the exact calculation of the five-jet cross-section and for seven- and eight-jet cross-sections using the SPHEL approximation the statistics was limited to $\approx 15K$ events, because of CPU time limits. The calculation of the EXACT five-jet cross-section alone used ≈ 600 hours of CPU time (CERN units).

For higher jet multiplicities the SPHEL approximation tends to overestimate the EXACT calculation: about 24% and 38% for four- and five-jet cross-sections respectively. The ESFAG approximation, on the other hand, is within 10% of the exact results in both cases. Table 2 suggests that multi-jet rates at LHC energies can be reliably estimated, even for very high jet multiplicities, using very fast approximation techniques.

Motivated by the good agreement for the absolute normalizations we have investigated whether also shapes of distributions could be correctly reproduced by approximate calculations. In particular we have focused on the invariant mass of the multi-jet system (M_{nj}) and the inclusive P_t spectrum. Figure 2 shows the invariant mass (a) and inclusive P_t spectrum (b) for multi-jet events at LHC. These spectra were obtained using the EXACT calculation. The ratio of the spectra obtained using the two approximations (SPHEL,ESFAG) to the EXACT results is shown in Figures 3 and 4. In all cases the deviation from a constant line (offsets from 1 are due to the different absolute normalizations) are small. At large P_t (or M_{nj}) the observed deviations could be due to a breakdown of the approximations, however these regions represent a very small portion of the phase-space and, given the limited statistics, a definite statement cannot be made. We conclude, therefore, that also the shapes of these distributions are successfully reproduced by the approximate calculations.

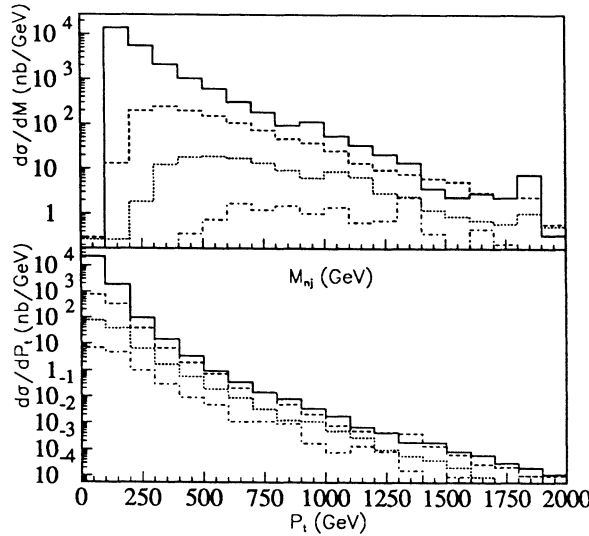


Figure 2: Invariant Mass (a) and inclusive P_t spectra of multi-jet events. The histograms represent the two-jet (solid), three-jet (dashed), four-jet (dotted) and five-jet (dashed-dotted) contributions.

V. Portability of the program on different computers

The new event generator has been tested on different computers, with a special emphasis devoted to high level workstations with RISC (Reduced Instruction Set Computer) architecture, which seem to be, in the near future, a promising source of low cost high CPU power. The main characteristics of those machines which are relevant for the work done can be summarized as follows:

- massive use of registers for temporary (local) calculations inside each program unit (dynamic allocation of variables)
- compilers which cope with the reduced instruction set by generating object code through a data flow analysis, to profit from the specific hardware architecture, *optimizing* in that way the CPU usage.

We found several problems linked to these characteristics, but we would like to stress from the beginning that nothing is peculiar to this particular generator, but all are common features that show up in programs which share the characteristics of having matrix-oriented tangled calculations. The first point we wish to make is that it is often implicitly assumed in writing Fortran code that variables have a static definition, *i.e.* the value of a certain memory location is saved across calls

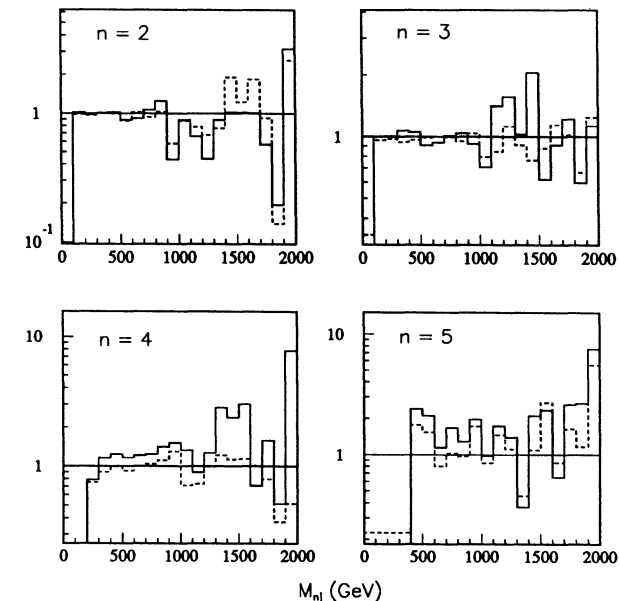


Figure 3: Invariant Mass ratios SPHEL/EXACT (solid histogram) and ESFAG/EXACT (dashed histogram).

to the specific program unit. This is not anymore true for computers based on microprocessors, or RISC based (nor it is true, by the way, for the CRAY Y-MP/48 and similar supercomputers), where the compiler tends to gain execution speed by allocating variables to registers. The primary effect is that if the program references these variables assuming that they are not on the stack, it will simply not run (usual problem is the "*memory access violation*" when a vector index is addressed in this way). So explicit SAVE statements, or reorganization of the program architecture are needed (introduction of COMMON blocks or use of calling sequences) to solve this problem and avoid wasting CPU time by forcing the static allocation. The second item is tightly related to the first one: in optimizing the code the compiler tries to minimize the series of operations that are redundant or could be ordered in a more efficient way. If the user code is not particularly suited to these compilers then optimization will not be feasible and the gain will be poor: in two particular cases we could not reach any level of optimization for the NJETS generator. It is clear that there is a strong correlation between the high level of complexity of the code and the way compilers deal with this. It is certainly true that RISC compilers need a lot more of debugging to cope with this complexity while keeping their efficiency, and it is already a great success for this simulation to run smoothly on several RISC machines. The advent of these compilers with data-flow capability for MIMD (Multi Instruction Multi Data) machines allows the

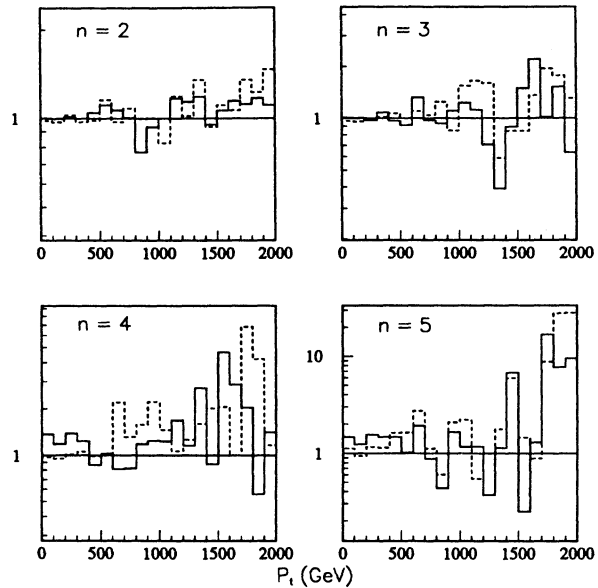


Figure 4: Inclusive P_t spectrum ratios SPHEL/EXACT (solid histogram) and ESFAG/EXACT (dashed histogram).

use of microparallelism inside each CPU (more than one instruction per cycle) and is particularly suited to these programs. Macroparallelism would of course require different coding, but is another interesting research line to be pursued.

It must be stressed that our conclusions are based on tests for the two jets EXACT calculations (for CPU time problems). The results were identical on any machine tested. The situation might become worse for more jets in the exact case as the matrix elements become more complicated. For most of the *approximations* the amount of jets is not important. We plan to complete our tests on 3,4 and 5 jets both in the exact and the approximated cases in the near future.

VI. Conclusion

Multi-jet event generators are available for background studies at the Large Hadron Collider. The exploitation of new techniques allows the calculation of the tree level exact cross-section up to 5 jets production. Fast event generators based on approximate calculations are also available and reproduce correctly the results of the exact calculation for both absolute normalization and shapes of distributions. They will allow background studies saving factors up to 1000 in CPU time, even to the highest possible jet multiplicities. A comparison with existing UA2 data on four- and five-jet events shows that these generators, with a realistic simulation of the

experimental setup, reproduce the data satisfactorily. Finally, the new program of Kuijf-Berends produces consistent results on many different computer frames, although the full optimization of modern compilers cannot be exploited. The experience gained in this work suggests that, with the present level of compilers and code analysers, much attention should be paid to the writing of the code of these simulations, if one really wants to exploit the full power of nowadays machines. It is important to remark that those simulations are an essential part of the LHC preparation work, and that the CPU time required is certainly one of the limiting factor in getting answers that are statistically meaningful.

References

- [1] Z. Kunszt, W.J. Stirling, Multijet cross-sections in hadronic collisions, in the Proceedings of the ECFA workshop in La Thuile, 1987, CERN 87-07.
- [2] H. Kuijf, Multiparton production at hadron colliders, Thesis, Feb. 1991.
- [3] J.F. Gunion and Z. Kunszt, Phys. Lett. **159B** (1985) 167.
Z. Kunszt, Nucl. Phys. **B271** (1986) 333.
J.F. Gunion and J. Kalinowski, Phys. Rev. **D34** (1986) 2119.
S.J. Parke and T.R. Taylor, Nucl. Phys. **B269** (1986) 410.
J.F. Gunion and Z. Kunszt, Phys. Lett. **176B** (1986) 163.
S.J. Parke and T.R. Taylor, Phys. Rev. **D35** (1987) 313.
- [4] F.A. Berends and W.T. Giele, Nucl. Phys. **B294** (1987) 700.
M. Mangano, S. J. Parke and Z. Xu, Nucl. Phys. **B298** (188) 653.
- [5] F.A. Berends and W.T. Giele, Nucl. Phys. **B306** (1988) 91.
- [6] R. Kleiss and H. Kuijf, Nucl. Phys. **B312** (1989) 616.
- [7] F.A. Berends, W.T. Giele and H. Kuijf, Phys. Lett. **232B** (1989) 266.
- [8] F.A. Berends, W.T. Giele and H. Kuijf, Nucl. Phys. **B333** (1990) 120.
- [9] F.A. Berends, H. Kuijf and B. Tausk, Processes with four and six quarks, in preparation
- [10] F.A. Berends and H. Kuijf, Jets at the LHC, to be published on Nuclear Physics
- [11] P. Lubrano, Jets physics with the UA2 detector, in the proceedings of the 4th Rencontre de Physique de la Vallee D'Aoste, La Thuile, March 18-24, 1990.
- [12] P.T. Cox et al., Jets at the Large Hadron Collider, These proceedings.

On the calculation of the exact $gg \rightarrow Z b\bar{b}$ cross section including Z decay and b quark mass effects

Bob van Eijk¹ and Ronald Kleiss²

¹Supported by the ‘Netherlands Organization for Scientific Research (NWO), the Netherlands and the CERN/LAA Project, Geneva, Zwitserland

²CERN, Genève

Abstract:

A calculation of the cross section for the process $gg \rightarrow Z b\bar{b}$ is presented. Comparisons are made with results from the PAPAGENO Monte Carlo.

Introduction

In the search for an intermediate-mass Higgs boson ($m_Z \leq m_H \leq 2m_w$) the decay channel $H \rightarrow Z^* Z^* \rightarrow 4$ leptons is relevant because of its potentially clear final state [1]. One of the possible backgrounds is provided by QCD processes that can also provide these leptons, in particular the production and decay of b quarks which with a probability of a few per cent [1] yield a stiff lepton with sufficient isolation to mimick a lepton from an (off shell) Z^* decay – note that whereas two leptons from an on-shell Z decay can easily be distinguished from the background by an invariant-mass constraint, this is not possible in the decay of an off-shell Z . Therefore the background process

$$\begin{aligned} g(k_1) & g(k_2) \rightarrow Z b(p_1) \bar{b}(p_2), \\ b(p_1) & \rightarrow l^- \bar{\nu}_l, \\ \bar{b}(p_2) & \rightarrow \bar{l}^+ \nu_l, \\ Z & \rightarrow l(l_1) \bar{l}(l_2), \end{aligned} \quad (1)$$

is of particular relevance (the additional background process $q\bar{q} \rightarrow Z b\bar{b}$ is expected to have a cross section smaller by about an order of magnitude). In order to estimate accurately the corresponding cross section after realistic experimental cuts it is important to implement both the angular correlations of the leptons from the Z decay as well as the effects of a nonzero b quark mass – after all, this is what makes the lepton isolation possible in the first place. In most currently used simulations a number of approximations to the exact result are made. In, for example, the PAPAGENO Monte Carlo [2] the b quark momenta are generated using a nonzero b quark mass: then, however, the matrix element is computed using the

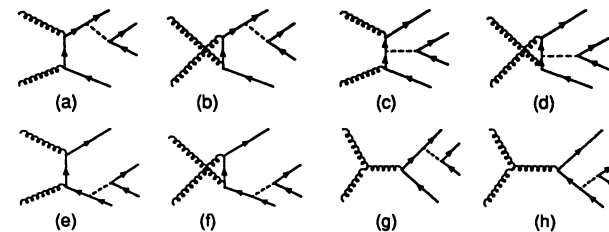


Figure 1: The Feynman diagrams for the process $gg \rightarrow Z b\bar{b}$. Diagrams (a), ..., (f) are the ‘abelian’ ones, diagrams (g), (h) the ‘nonabelian’ ones.

expression for massless quarks and unpolarized Z . Subsequently the Z is made to decay into a lepton pair assuming it has completely circular transverse polarization. In this way, mass effects of the b quarks as well as angular correlations of the leptons with the b quarks are subject to a possibly small but generally *unknown* bias: it follows that a comparison with the exact matrix element predictions is necessary to use such a MC program with confidence. Another important consequence of keeping a nonzero b quark mass m_b is that then there are no singularities in the amplitude: the total cross section is well-defined, and predictions can be made without having to rely on the flavour-excitation mechanism for b quarks with its attendant ambiguities.

The calculation

Here we describe the outline of such an exact calculation. The process (1) is described by eight Feynman diagrams depicted in fig.1.

Each diagram (i) ($i = a, b, \dots, h$) consists of a numerator part $N^{(i)}$ which contains the nontrivial spinor structure, a denominator part $D^{(i)}$ containing the propagator denominators (which are trivial to evaluate) and a prefactor $C^{(i)}$ with the strong coupling constants and the colour matrices. It is the complicated structure of the $N^{(i)}$ that makes the evaluation of the diagrams nontrivial: we have, for instance

$$\begin{aligned} N^{(a)} &= \bar{u}_{\lambda_b}(p_1) \left(v_b + a_b \gamma^5 \right) \gamma_\mu \left(\not{p}_b + \not{l}_1 + \not{l}_2 + m_b \right) \\ &\quad \times \gamma_\nu \epsilon_{\lambda_1}^\nu(k_1) \left(\not{k}_2 - \not{p}_2 + m_b \right) \gamma_\rho \epsilon_{\lambda_2}^\rho(k_2) v_{\lambda_b}(p_2), \\ D^{(a)} &= \left((p_1 + l_1 + l_2)^2 - m_b^2 \right) \left((k_2 - p_2)^2 - m_b^2 \right) \\ &\quad \times \left((l_1 + l_2)^2 - m_z^2 + i m_z \Gamma_z \right), \\ C^{(a)} &= ig_s^2 (T^{a_1} T^{a_2})_{c_1 c_2} \end{aligned} \quad (2)$$

where the chiralities $\lambda_{b,\bar{b}}$ of the b and \bar{b} quarks, and the helicities $\lambda_{1,2,e}$ of the gluons and leptons are indicated explicitly: the $v_{b,e}$ and $a_{b,e}$ are the vector and axial-vector

couplings of the b 's and the leptons to the Z . The Z propagator is represented by the appropriate Breit-Wigner; g_s is the strong coupling constant and the T are colour matrices with $a_{1,2}$ being the colour labels of the gluons, and $c_{1,2}$ those of the b and \bar{b} quarks.

The calculation is most easily done using *spinor techniques* which are described in a pedagogical manner in ref.[3]. Here, it is sufficient to note that the basic elements are spinor products: for two massless momenta k_1 and k_2 and helicity $\lambda = \pm$ (so that $u_\lambda(k_i) \equiv \frac{1}{2}(1 + \lambda\gamma^5)u_\lambda(k_i)$) we have

$$s_\lambda(k_1 k_2) \equiv \bar{u}_\lambda(k_1)u_{-\lambda}(k_2) = -s_\lambda(k_2 k_1) , \quad (3)$$

for a special choice of the overall complex phase of the spinors, which also leads immediately [3] to

$$\bar{u}_\lambda(k_1)\gamma^\mu u_\lambda(k_2) = \bar{u}_{-\lambda}(k_2)\gamma^\mu u_{-\lambda}(k_1) , \quad (4)$$

$$[\bar{u}_\lambda(k_1)\gamma^\mu u_\lambda(k_2)]\gamma_\mu = 2[u_\lambda(k_2)\bar{u}_\lambda(k_1) + u_{-\lambda}(k_1)\bar{u}_{-\lambda}(k_2)] , \quad (5)$$

and the explicit form of the spinor product:

$$\begin{aligned} s_+(k_1 k_2) &= (k_1^y + ik_1^z) \left[\frac{k_2^0 - k_2^z}{k_1^0 - k_1^z} \right]^{\frac{1}{2}} - (k_1 \leftrightarrow k_2) , \\ s_-(k_1 k_2) &= -s_+(k_1 k_2)^* , \\ |s_\lambda(k_1 k_2)|^2 &= 2(k_1 \cdot k_2) . \end{aligned} \quad (6)$$

Moreover, helicity conservation for massless fermions implies that

$$\bar{u}_\lambda(k_1)u_\lambda(k_2) = 0 . \quad (7)$$

The relevant ingredients for this particular computation are special representations for the gluon polarization vectors, and for the b quark spinors. For the gluon polarization ϵ with helicity λ we choose

$$\epsilon_\lambda^\mu(k_i) = \frac{\lambda}{\sqrt{2}} \frac{\bar{u}_\lambda(k_i)\gamma^\mu u_\lambda(r_i)}{s_{-\lambda}(k_i r_i)} , \quad (8)$$

so that in the ‘abelian’ diagrams (a), ..., (f)

$$\gamma_\mu \epsilon_\lambda^\mu(k_i) = \frac{\lambda \sqrt{2}}{s_{-\lambda}(k_i r_i)} [u_\lambda(r_i)\bar{u}_\lambda(k_i) + u_{-\lambda}(k_i)\bar{u}_{-\lambda}(r_i)] ; \quad (9)$$

here, r_i^μ is an arbitrary lightlike vector ($r_i^2 = 0$) not collinear with k_i^μ . Changing r_i^μ must leave the result unchanged and this provides an excellent sensitive test of the gauge-invariance of the result. For the massive spinor corresponding to the b quark we use a similar approach: for a b quark with momentum p_b (so that $p_b^2 = m_b^2$) and chirality $\lambda_b = \pm$ we replace in the amplitude

$$u_{\lambda_b}(p_b) \rightarrow \frac{1}{\sqrt{2(p_b \cdot q_b)}} (p_b + m_b) u_{-\lambda_b}(q_b) , \quad (10)$$

where again q_b^μ is an arbitrary lightlike vector. This choice leads to the desired result

$$\sum_{\lambda_b} u_{\lambda_b}(p_b) \bar{u}_{\lambda_b}(p_b) = p_b + m_b . \quad (11)$$

For the \bar{b} we replace m_b by $-m_b$. Again, in the spin-summed cross section, different choices for the q_b^μ should leave the result invariant.

Here it is worthwhile to note that by replacing in Eq.(10) the denominator by an appropriate factor also the production and decay of top quarks in the process $gg \rightarrow Zt\bar{t}$ can be correctly described, including the spin correlations of the top decay: in that case, the q_b^μ should be taken as the momentum of the charged lepton in the semileptonic decay. For b quarks, which tend to become depolarized since they hadronize before they decay the choice of q_b^μ is, as we have said, more arbitrary.

For the current describing the Z boson production and leptonic decay we note that it is the same in all the diagrams: it is given by

$$\begin{aligned} &\{\cdots(v_b + a_b\gamma^5)\gamma_\mu\cdots\}\bar{u}_{\lambda_e}(l_1)(v_e + a_e\gamma^5)\gamma^\mu u_{\lambda_e}(l_2) \\ &= 2(v_e - \lambda a_e)\{\cdots[(v_b + \lambda_e a_b)u_{\lambda_e}(l_2)\bar{u}_{\lambda_e}(l_1) \\ &\quad + (v_b - \lambda_e a_b)u_{-\lambda_e}(l_1)\bar{u}_{\lambda_e}(l_2)]\cdots\} . \end{aligned} \quad (12)$$

We can now implement Eqs.(9),(10) and (12) into the expressions for the ‘abelian’ graphs of fig.1(a), ..., (f) and note that the $N^{(i)}$ are then built up each out of ‘scalar’ structures that always have the form

$$F(\lambda_1, p_1, q, \lambda_2, p_2) \equiv \bar{u}_{\lambda_1}(p_1)(\not{q} + m_b)u_{\lambda_2}(p_2) , \quad (13)$$

where the $p_{1,2}^\mu$ are lightlike but the q^μ has a nonvanishing square q^2 . The function F can be evaluated as follows:

$$\begin{aligned} F(\lambda, p_1, q, -\lambda, p_2) &= m_b s_\lambda(p_1 p_2) , \\ F(\lambda, p_1, q, \lambda, p_2) &= \sigma_q s_\lambda(p_1 \hat{q}) s_{-\lambda}(\hat{q} p_2) , \\ \sigma_q &= \text{sign}(\hat{q}^0) , \quad \hat{q}^\mu = \sigma_q \tilde{q}^\mu , \\ \tilde{q}^\mu &= q^\mu - \frac{q^2}{2(q \cdot p_2)} p_2^\mu . \end{aligned} \quad (14)$$

For the ‘nonabelian’ graphs of fig.1(g), (h) we use the diagram manipulation of [4] to note that the numerator of diagram 1(g) is actually equal to the difference of the numerators of the diagrams 1(a) and 1(b), modulo a simple additional factor that does contain the gluon polarizations and the Z production-and-decay current, but no internal fermion propagators:

$$\begin{aligned} N^{(g)} &= -N^{(a)} + N^{(b)} + \tilde{N}^{(g)} \\ \tilde{N}^{(g)} &= -\bar{u}_{\lambda_b}(p_1)(v_b + a_b\gamma^5)\gamma_\mu \{ \not{q}_{\lambda_1}(k_1)\not{q}_{\lambda_2}(k_2) - \not{q}_{\lambda_2}(k_2)\not{q}_{\lambda_1}(k_1) \} v_{\lambda_b}(p_2) \\ &\quad \times \frac{1}{2}((p_1 + l_1 + l_2)^2 - m_b^2) \bar{u}_{\lambda_e}(l_1)(v_e + a_e\gamma^5)\gamma^\mu u_{\lambda_e}(l_2) . \end{aligned} \quad (15)$$

The additional term can be evaluated in a straightforward manner using the above spinor techniques. In this way the evaluation of the ‘nonabelian’ graphs is very efficient. In fact this manipulation is related to the ‘recursion relations’ discussed in ref.[6]. It should also be noted that each possible argument configuration in the function F occurs several times in the evaluation of the complete cross section, so that the F values can be stored in a lookup table, leading to an additional efficiency gain. Moreover, the structure of the resulting code is extremely systematic: in fact the FORTRAN source code has been obtained directly by computer algebra [5].

The colour summation of the squared helicity amplitudes is most simply carried out by treating the parts that are symmetric and antisymmetric in the colour labels of the two gluons separately: in the relatively simple colour structure we are dealing with here these do not interfere with each other, and the ‘nonabelian’ diagrams contribute only to the colour-odd part. The colour-even part is in fact (up to an overall constant) equal to the cross section for $\gamma\gamma \rightarrow Zb\bar{b}$.

Finally, a remark is in order on the helicity summation that has to be performed explicitly and numerically when one uses spinor techniques. For 2 incoming gluons, 2 massive b quarks and the massless lepton pair from the Z decay this leads to 32 distinct nonvanishing helicity amplitudes. The summation over these amplitudes can be speeded up by applying a *helicity Monte Carlo*: this consists of not considering the whole enumerated set of helicity combinations but instead a randomly chosen set: for n random choices of helicity combinations one evaluates the sum of the squared amplitudes and then multiplies the result by $32/n$. For $n \rightarrow \infty$ this yields the exact result. Note, however, that for $n = 32$ one does not necessarily obtain the exact result! The helicity Monte Carlo approach is appropriate to those cases where all helicity amplitudes are roughly of the same order of magnitude; in the present case it appears to work well enough.

Further information on the use of the above computation (available as file `ZBBAMP.FORTRAN` from **RONALD** at CERNVM) in the actual Higgs search environment can be found in [1].

Results and conclusions

We now present some numerical results. We have implemented the above calculation in the **EUROJET** Monte Carlo [7], which also allows for the fragmentation and decay of the b quarks (followed by additional c quark decay). The results are compared with those of the **PAPAGENO** program. Throughout we have used the Eichten et al. structure function set 1 [8], and a scale choice $Q^2 = m_Z^2$.

The most relevant quantity in this comparison is of course the total cross section. Whereas in our calculation this is a perfectly well-defined quantity since the b quarks are massive and no singularities arise anywhere in phase space, in the **PAPAGENO** case this is less trivial since the massless matrix element is employed. Singularities are avoided there because the kinematics are still massive also in that treatment - but as is well known such an approach leads to ambiguities in the final answer, as can be seen from the following example. One of the b propagators occurring in the cross section has a denominator of the form $(k_1 - p_1)^2 - m_b^2 = -2k_1 p_1$, which in the massless approximation is equivalent to $(k_1 - p_1)^2$ itself. Hence, a different *numerical* result is obtained from either the use of the dot product or of the momentum transfer squared: especially at small b transverse momentum this may become significant. Since the **PAPAGENO** expressions use the dot product form their result may be hoped to be accurate. We find

$$\begin{aligned} \sigma_{\text{tot}}^{\text{EUROJET}} &= 0.029 \text{ nb}, \\ \sigma_{\text{tot}}^{\text{PAPAGENO}} &= 0.022 \text{ nb}, \end{aligned} \quad (16)$$

in the gg channel. In **PAPAGENO** the additional $q\bar{q}$ channel adds another 10% to this. These two values are in rough but not completely satisfactory agreement (remember that this cross section is a background to a rather small signal). A small part of this discrepancy could be explained by the fact that the precise versions of the EHLQ set 1 structure functions used in the two calculations are

not completely identical. Another small effect can come from the slightly different b branching ratios that are used in **EUROJET** and **PAPAGENO**. But for the rest an effect of a finite b mass cannot be ruled out as yet. Note, however, that the omnipresent uncertainties in the choice of scale and structure functions allow for about 50% variation in the total cross section. Finally, we want to point out that in our calculation the $Z \rightarrow e^+e^-$ decay is an integral part of the matrix element, but that the cross section produced by **PAPAGENO** must always be multiplied by the $Z \rightarrow e^+e^-$ branching ration which we have taken to be 3.3%.

Next, we present in fig.2 the p_T spectrum of the Z . As expected the distribution is dominated by p_T values of the order of a fraction of m_Z . Note that for clarity we have scaled the **PAPAGENO** predictions down by a factor of 10. Apart from the overall normalization of the cross section the two spectra agree very well.

The same holds in fig.3 where we plot the transverse momentum of the leptons from the Z decay. There is a clear Jacobian peak around $m_Z/2$ as expected. Again, the results from **EUROJET** and **PAPAGENO** are quite similar, although in principle the exact prediction incorporates a different polarization density matrix (with nonzero off-diagonal elements) than the one employed by **PAPAGENO**, which assumes purely transverse polarization of the Z . As an illustration we have also plotted the result one would obtain by switching to a purely longitudinal polarization in **PAPAGENO** (this can trivially be done by replacing a subroutine call to `DECAY_Z` to `DECAY_ZL`). We have scaled this prediction down by a factor 2 for clarity. A slight difference is evident: as expected the Z ’s are still predominantly transverse.

In fig.4 the b quark transverse momentum is given: again the two curves are quite parallel, except for high p_T values. This is explained by the fact that in **PAPAGENO** we have had to suppress the Peterson fragmentation of the quarks. Note that for $p_T \gg m_b$ the spectra are expected to be identical: it is for small p_T that differences might show up.

Similar conclusions can be drawn from fig.5 where the p_T of the muons from the b quark decay is given.

Finally, in fig.6 we plot the opening angle between the electron tracks from the Z decay in the lab frame. It is this distribution that could provide information on the polarization of the Z . The longitudinal case appears to give a different distribution of the opening angles than the transverse case. This difference can be ascribed to the fact that in the longitudinal case the two leptons are preferentially produced at large angles to the Z direction of motion, so that their opening angle is more easily influenced by the boost to the lab frame than in the transverse case, where the leptons mostly come out at a relatively small angle to the Z direction. Consequently in the longitudinal case the opening angles are more easily pushed to small values ($\cos \theta \sim 1$). From comparison with the exact calculation we again conclude that any longitudinal Z component in the cross section is small.

We conclude that as far as event topologies are considered, programs like **PAPAGENO** which contain simplifying assumptions can safely be used in the simulation. Some care may have to be taken with events with low p_T of the b quarks, and therefore also with the results for the total cross section.

References

- [1] Higgs searches study group, these proceedings.
- [2] Papageno, Partonic Event Generator Version 3.10, I. Hinchliffe LBL - TH Division (unpublished).
- [3] R. Kleiss and W.J. Stirling, Nucl. Phys. **B262**(1985)235.

- [4] Z. Kunszt, unpublished.
 [5] M. Veltman, computer algebra program SCHOONSCHP.
 [6] F.A. Berends and W. Giele, Nucl. Phys. **B306**(1988)759.
 [7] B. van Eijk et al., EUROJET Monte Carlo, Nucl. Phys. **B292**(1987)1.
 Eurodec Version 3.1, B. van Eijk, Cern Program Library Long Write-Up
 W5048.
 Eurojet Version 3.1, F. Anselmo and B. van Eijk, Cern Program Library
 Long Write-Up W5048 (not yet released).
 [8] E. Eichten et al., Rev. Mod. Phys. **56**(1984)579, **E**: **58**(1985)1065.

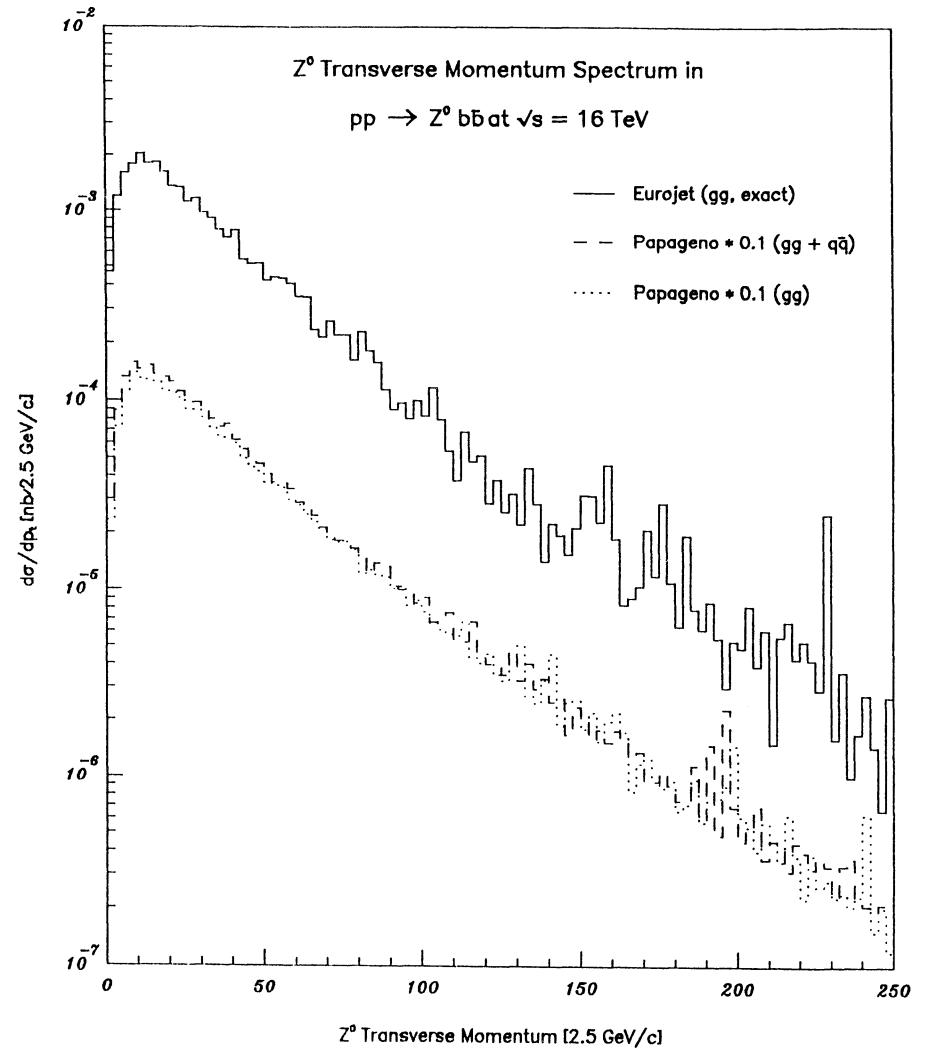


Figure 2: The Z^0 transverse momentum distribution.

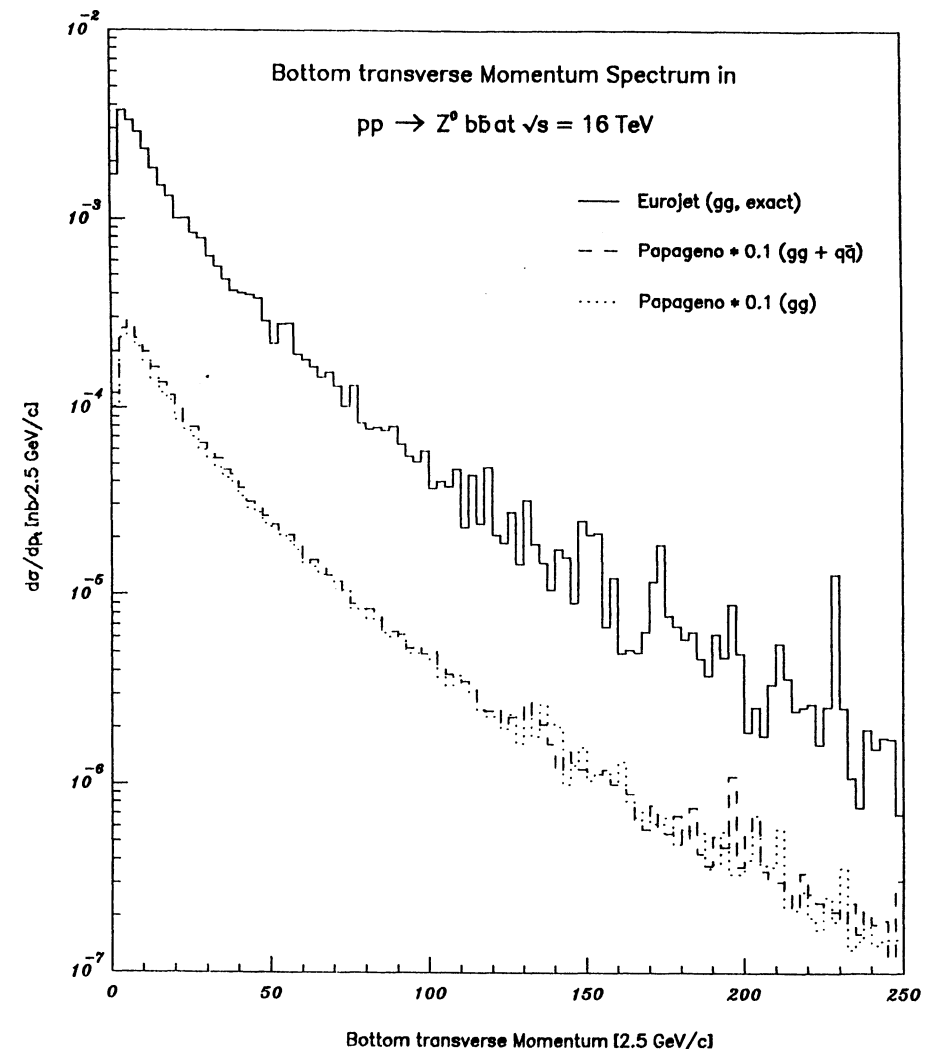
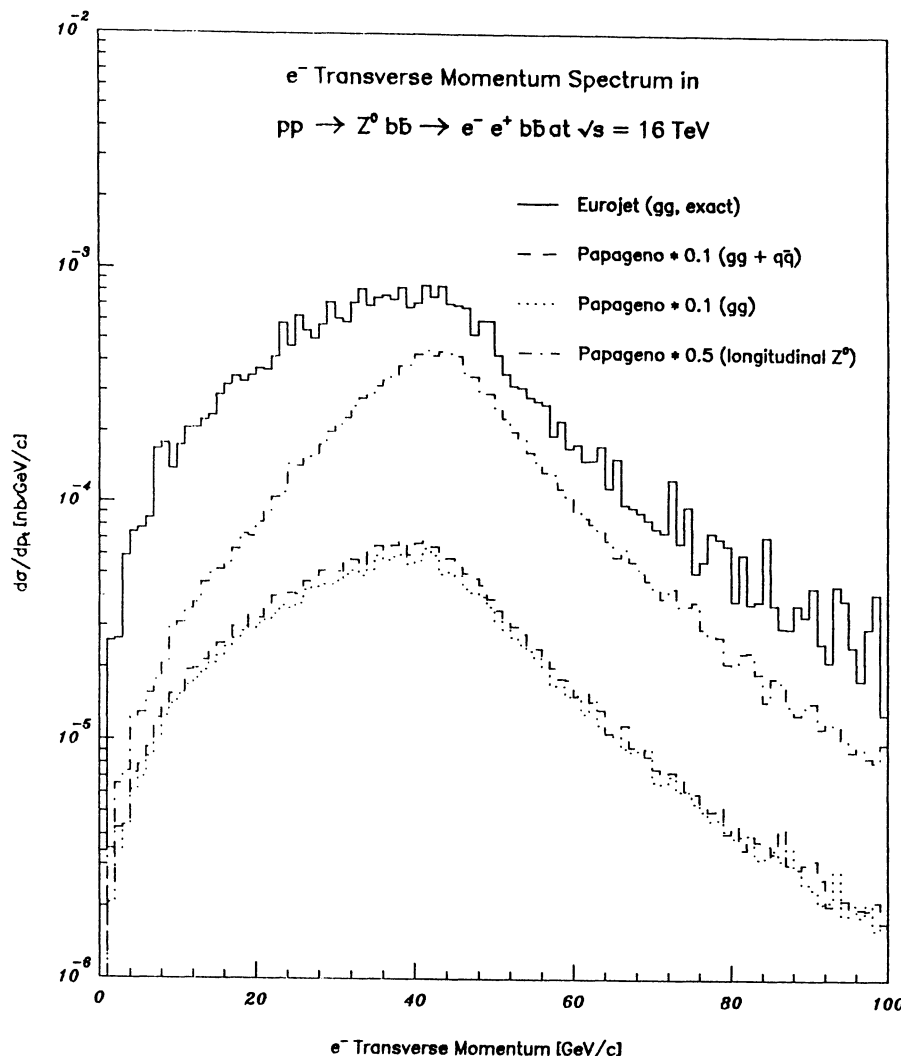


Figure 3: The e^\pm transverse momentum distribution.

Figure 4: The b quark transverse momentum distribution.

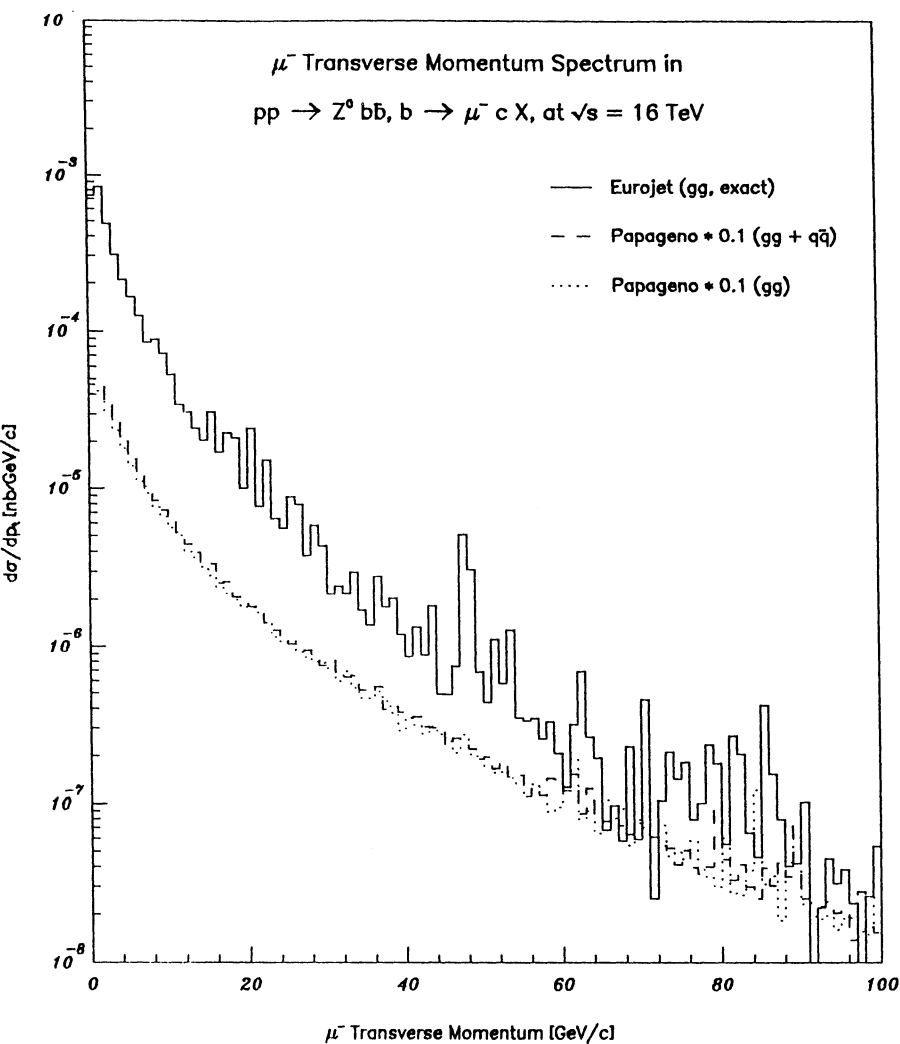


Figure 5: The transverse momentum distribution for μ^\pm from the b decay.

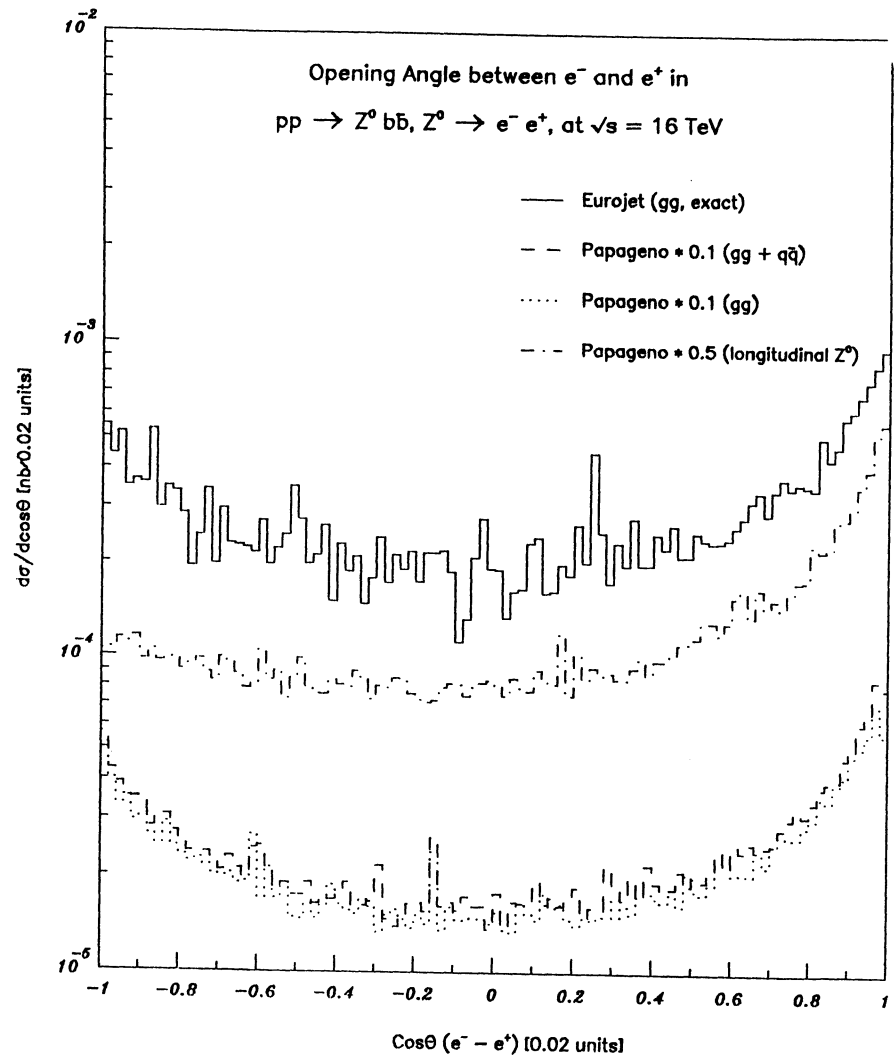


Figure 6: The opening angle between the e^+ and e^- tracks in the lab frame.

Vector Boson Production in Association with Jets

W.T. Giele¹

Fermi National Accelerator Laboratory²,
P.O.Box 500, Batavia, Illinois, USA.

Abstract:

In this contribution a short discussion is given on the calculation of the multiparton matrix elements relevant to the production $W/Z + 0, 1, 2, 3, 4$ jets, for more details see refs. [1,2]. Also discussed is the implementation of the matrix elements in the VECBOS program package together with a few numerical results.

1. Introduction

In the last years a lot of progress is made in the techniques to calculate multiparton treelevel matrix elements [1-9]. With these techniques it is possible to calculate the treelevel matrix elements with an arbitrary number of gluons attached to it by using recursive techniques [3]. The only limiting factor is the computer time needed to evaluate these matrix elements (see table 1). Two applications of these recursive techniques are the NJETS program [4] and the VECBOS program [2], the latter we will discuss in this contribution. The VECBOS program calculates the exact Born term cross sections for the production of a vector boson in association with up to 4 jets. These type of processes form a serious background to almost any new physics at hadron colliders. The two obvious examples are the top search and the Higgs search, though many other examples can be found such as non standard Z' decay, etc.

VECBOS is the successor of the LDW program. For one the $W + 4$ jets matrix elements are now included and secondly the old program code from the LDW program to evaluate the $W/Z + 0, 1, 2, 3$ jets was optimized which has lead to an improvement in the computer time needed to evaluate the matrix elements. The $Z + 4$ jets process is not yet build in.

The results from VECBOS have been compared to the HERWIG Monte Carlo [11] in great detail in ref. [10].

2. The calculation of the matrix elements

As mentioned in the introduction our ability to calculate treelevel multiparton matrix elements has increased dramatically in the last few years. In table 1 are given the number of different Feynman diagrams necessary to evaluate the Born cross section for the production of a vector boson accompanied by n jets. As is

¹In collaboration with F.A. Berends, H. Kuijf and B. Tausk, Instituut Lorentz, University of Leiden.

²Operated by Universities Research Association Inc. under contract with the United States Department of Energy.

n	number of diagrams	time/accepted event (in VAX 780 seconds)
0	1	0.042
1	2	0.081
2	12	0.39
3	74	4.2
4	640	66

Table 1: Number of contributing Feynman diagrams and time consumption in seconds (converted to VAX 780 units) per accepted event for the process $PP \rightarrow V + n$ jets.

clear from table 1 for the $n = 0, 1$ case (i.e. $V + 0, 1$ jet) one can use standard techniques to calculate the squared matrix elements. For $n = 2$ this becomes difficult [5] and for $n \geq 3$ virtually impossible.

The first useful method developed to calculate the multiparton processes was the CALKUL helicity method [6], which was later improved [7]. With this method compact expressions could be obtained for the matrix elements relevant the $V + 2$ jet cross section [8]. The helicity method can also be used to calculate the necessary matrix elements for $V + 3$ jets production [9], though the expressions thus obtained are long and not systematic. It is clear that using only the helicity method to extend the calculation to $V + 4$ jets would be an almost impossible task.

Instead a new method was developed in which one can add gluons to a basic process in a recursive way [3]. With this method compact expressions were obtained for the matrix elements necessary to calculate the $V + 0, 1, 2, 3$ jets [1], which lead to the LDW program. With the recursive method it became straightforward to extend the calculation to the matrix elements required to evaluate the $V + 4$ jets Born cross section [2]. These matrix elements, together with the old LDW matrix elements, were build into VECBOS.

In principle we could extend the calculation to include even more jets. But to get an reliable estimate for the $W + 4$ jets cross section we have to push computer resources already to the limit. In table 1 we see that the computer time needed to calculate one accepted event grows roughly with a factor of 10 when we include an additional jet, making the numerical evaluation of the $W + 5$ jets cross section impossible within an acceptable time frame.

The VECBOS program gives for each accepted event the final state momenta of the partons and the decay leptons from the vector boson together with the corresponding weight from the squared matrix elements. These can subsequently be used to calculate (differential) cross sections. Because we calculate the Born contribution to the exclusive jet cross section each outgoing parton momentum has to be identified with a jet axis momentum. This also means that the jet defining cuts translate back to the same cuts on the partons, which in turn ensures we stay well away from the singular regions in phase space (i.e. the soft and collinear regions). As a result the weights will not fluctuate too much and it is possible to get an estimate for the exclusive jet cross section. It is clear that we cannot make the jet too soft or the jet cone too small, this would result in large weights coming from the singular regions and it would be necessary to include the higher order effects. This point will be illustrated further in the next section.

$E_t^{\min} =$	50 GeV σ_n	50 GeV $R_{n/(n-1)}$	100 GeV σ_n	100 GeV $R_{n/(n-1)}$
1	58(1)	-	46.6(6)	-
2	41(1)	0.71(2)	15.2(7)	0.33(2)
3	20(1)	0.49(3)	4.7(2)	0.31(2)
4	7.5(6)	0.37(4)	1.29(8)	0.27(2)

Table 2: The cross section (in picobarn) and the ratio $R_{n/(n-1)}$ for $W + n$ jets production at LHC, for two E_t cuts of the jets (in brackets the estimate for the statistical error due to the numerical integration).

3. Numerical results

In table 2 we have used the VECBOS program to calculate the $W +$ jets cross section, with the W decay to $e^- \bar{\nu}$ and $e^+ \nu$ included. The used cuts for the charged leptons are: $E_t(l) > 50$ GeV, $|\eta(l)| < 2$, $\Delta R(jet, l) > 0.4$ and the missing transverse energy is required to be larger than 50 GeV. The jet defining cuts are: $E_t(j) > E_t^{\min}$, $|\eta(j)| < 3$ and $\Delta R(j, j) > 0.4$. The centre of mass energy is 16 TeV, the scale to evaluate the coupling constant was choosen to be $Q^2 = M_W^2 + < E_t(j) >^2$ (with $< E_t(j) >$ the average transverse momentum of the jets) and the MRSEB parametrizations of ref. [12] were used for the parton densities in the proton.

Also given in table 2 is the ratio $R_{n/(n-1)}$, which is the ratio of the $W + n$ jets over the $W + (n-1)$ jets cross section. This ratio can be used as an indicator to see whether the Born approximation makes sense with the used set of cuts. Naively one would expect this ratio to be a number of the order of the coupling constant. However if we make the jet defining cuts too loose (for example if we allow soft jets) this ratio will start to increase and one needs higher order corrections to get an reliable estimate for the cross section. This is demonstrated in table 2, we see that for jets with a minimum transverse energy of 50 GeV this ratio can be large. However increasing the minimal transverse momentum to 100 GeV reduces the ratio to a acceptable value (approximately 0.3 for $n=2,3,4$). This ensures us that we stay well away from the singular regions. Of course the uncertainty resulting from different scale choices Q^2 makes the calculation of the total cross section not very reliable, but with the 100 GeV cut we can reliably estimate all kinds of distributions. For the 50 GeV cut even the distributions resulting from the Born approximation would be doubtful.

4. Conclusions

In this contribution we have briefly discussed how the matrix elements relevant to the calculation of the Born cross section for vector boson production in association with jets were calculated. Also shown was that apart from the usual uncertainties one has with the tree level matrix elements (e.g. scale choice, stucture functions, etc) one must also be careful with the jet defining cuts. As an example it was demonstrated that with a minimum transverse energy cut of 100 GeV the cross section predictions with increasing number of jets behaves as expected. This in

contrast to the 50 GeV cut, where the behaviour is suspicious indicating we are too close to the singular region in phase space making the Born approximation doubtful.

Keeping the above described uncertainties in mind, these matrix element Monte Carlo's can be used as a powerful tool to estimate the background processes to many possible new physics signals at LHC.

References

- [1] F.A. Berends, W.T. Giele and H. Kuijf, Nucl. Phys. B321 (1989) 39;
F.A. Berends, W.T. Giele, H. Kuijf, R. Kleiss and W.J. Stirling, Phys. Lett. 224B (1989) 237.
- [2] F.A. Berends, W.T. Giele, H. Kuijf and B. Tausk,
FERMILAB-PUB-90-213-T/Leiden Preprint.
- [3] F.A. Berends and W.T. Giele, Nucl. Phys. B306 (1988) 759;
W.T. Giele, Ph.D thesis, University of Leiden (1989).
- [4] H. Kuijf, P.Lubrano and V. Vercesi, separate contribution in this section.
- [5] R.K. Ellis and R.J. Gonsalves, Proceedings of the Workshop on High Energy Physics, Eugene, 1985 (ed. D.E. Soper), pg. 287.
- [6] D. Danckaert et al., Phys. Lett. 114B (1982) 203;
F.A. Berends et al., Nucl. Phys. B206 (1982) 53; Nucl. Phys. B206 (1982) 61;
P. de Causmaecker, Ph.D. thesis, Leuven University, 1983;
F.A. Berends et al., Nucl. Phys. B239 (1984) 382; Nucl. Phys. B239 (1984) 395; Nucl. Phys. B264 (1986) 243; Nucl. Phys. B264 (1986) 265.
- [7] R. Kleiss, Nucl. Phys. B241 (1984) 235;
Z. Xu, Da-Hua Zhang and L. Chang, Tsinghua University Preprints, Beijing,
TUTP-84/4, TUTP-84/5, TUTP-84/6 and Nucl. Phys. B291 (1987) 392;
F.A. Berends, P.H. Daverveldt, R. Kleiss, Nucl. Phys. B253 (1985) 441;
R. Kleiss and W.J. Stirling, Nucl. Phys. B262 (1985) 235;
J.F. Gunion and Z. Kunszt, Phys. Lett. 161B (1985) 333.
- [8] S.D. Ellis, R. Kleiss and W.J. Stirling, Phys. Lett. 154B (1985) 435.
- [9] K. Hagiwara and D. Zeppenfeld, Nucl. Phys. B313 (1989) 560.
- [10] W.T. Giele, T. Matsuura, M.H. Seymour and B.R. Webber, FERMILAB-Conf-90/228-T;CAVENDISH-HEP-90/26, contribution to the proceedings of the 1990 Summer Study on High Energy Physics - Research Directions for the Decade, Snowmass, Colorado, June 1990.
- [11] HERWIG version 4.6, I.G. Knowles, G. Marchesini, M.H. Seymour and B.R. Webber.
- [12] A.D. Martin, R.G. Roberts and W.J. Stirling, Phys. Lett. 206B (1988) 327.

Beauty at the LHC

G. Carboni, J.B. Cheze, D. Denegri*, A. De Rújula*, S. Erhan, G. Fidecaro, A. Fridman,
 F. Grancagnolo, B. Jeanneret, S. Lammel, Y. Lemoigne, M. Lusignoli*, M. Masetti,
 M. Medinnis, A. Pich*, S. Petrarca, J. Prades, A. Pugliese, P. Schlein, H. Steger,
 Y. Zolnierowski and J. Zweizig.

A3: B PHYSICS

*) *Conveners.*

ABSTRACT

The LHC is expected to produce unprecedented amounts of pairs of beautiful particles. A high energy hadron collider is arguably the only machine sufficiently luminous to analyse CP violation in the B-sector, and to discover particles that are both charmed and beautiful. In a collider mode the main difficulty, that we discuss at length, is the extraction of the signal from the humongous backgrounds. We offer commentary on the comparison with a fixed target mode of operation and with other machines, such as e^+e^- Beauty-factories.

Organization

The various topics relevant to the analysis of beauty physics at future facilities are discussed here as separate contributions from the groups most directly involved in the various studies. An update of the standard theory of CP violation in the beauty sector, its predictions for the LHC and the fake asymmetries to be expected from the lack of particle-antiparticle symmetry of the initial state, as well as some new considerations concerning the production of $b\bar{c}$ states, are all discussed in the theoretical introduction. A. Fridman and collaborators have contributed detailed studies of the comparison of the physics potential of e^+e^- and pp colliders and the fixed target options of the latter. A crucial question is the feasibility of the search for CP-violation in the B realm in a collider mode. This is discussed in the form of a contribution devoted to a specific possibility of a collider experiment at the LHC. Three contributions discuss the potential of fixed target options at the LHC and the SSC.

Theory

A. De Rújula, M. Lusignoli, M. Masetti, A. Pich,
S. Petrarca, J. Prades, A. Pugliese, H. Steger.

1. Introduction and Motivation.

Once upon a time, Nicola Cabibbo summarized a talk [1] by showing a cartoon of a nuclear mushroom labelled “CP-violation” and two ostriches with their proverbially buried heads. In the caption they tell each other “we fully understand the weak interactions”. The situation has improved but the moral has not changed.

In the three-generation Standard Model, CP-violation originates from the single phase naturally occurring in the weak-quark-current Cabibbo-Kobayashi-Maskawa (CKM) matrix. The observations in the neutral kaon system, as well as all the limits gathered elsewhere, agree with the expectations: aren’t these grounds for total satisfaction? No. For one reason, we have no understanding of why nature has chosen the number and properties of fundamental fields *just so* that CP-violation may be possible, but only large enough to be observable, so far, in the kaon sector. Moreover, our empirical information on CP-*Violation* could hardly be more meager.

Most studies of CP-violation rely on the hope that the observable effects be much larger than the Standard Model (SM) would predict. The notable exception is CP-violation in the beauty analog to the $K_0\bar{K}_0$ system, wherein the SM predicts very large asymmetries in suitably chosen channels with, a price must be payed, low branching ratios. A dedicated e^+e^- collider may be incomparably clean, but access to the luminosity required for these studies is an unresolved problem, particularly in those cases that require the analysis of B_s^0 decays. In a pp collider, contrarily, the maximal luminosity would be too large to handle, but a reduced luminosity suffices to access the channels with large CP-odd effects, in which the fake asymmetries induced by the pp non-symmetric initial state are not expected to be an untractable problem. Similar considerations apply to relatively modest extracted or internal beams hitting a solid or a gas-jet target. In the no-longer-bearable scenario that the SM be correct, and if Higgs scalars are stubbornly sneaky, CP violation in the beauty sector may be the *only* novel and assured result of the LHC.

Let the CKM matrix be parametrized in the Maiani-Wolfenstein way:

$$V = \begin{pmatrix} V_{ud} & V_{us} & V_{ub} \\ V_{cd} & V_{cs} & V_{cb} \\ V_{td} & V_{ts} & V_{tb} \end{pmatrix} \simeq \begin{pmatrix} 1 & \lambda & A\lambda^3(\rho - i\eta) \\ -\lambda & 1 & A\lambda^2 \\ A\lambda^3(1 - \rho - i\eta) & -A\lambda^2 & 1 \end{pmatrix} \quad (1.1)$$

where $\lambda \simeq \sin \theta_C \simeq 0.22$, $|A| \sim 0.7 \rightarrow 1.1$ is determined from ratios of semileptonic B-decays, and $\eta \neq 0$ if CP is violated. Differences of rates that signal CP-violation are proportional to the small product $A^2\lambda^6\eta$, but the corresponding asymmetries (difference / sum) are enhanced in B-decay relative to K-decay by the fact that the decay widths involve CKM elements that are much smaller in the B realm ($|V_{cb}|^2$ or $|V_{ub}|^2 \ll |V_{us}|^2$).

The unitarity of the 3×3 CKM matrix implies, to leading order in λ , the relation:

$$V_{ub}^* + V_{td} \simeq \lambda V_{cb} \quad (1.2)$$

which can be simply visualized as a triangle in the complex plane. This is shown in fig. 1 where the triangle of (1.2) has been scaled by dividing its sides by λV_{cb} . In what follows the CP asymmetries are expressed in terms of the angles α , β , and γ of this unitarity triangle which, in absence of CP violation, degenerates into a segment along the real axis.

We concentrate on those CP-odd effects that are expected to be sizable and that are amenable to a fair theoretical treatment, namely the asymmetries [2] involving the decays of B^0 and \bar{B}^0 (or B_s^0 and \bar{B}_s^0) into a common final state f that is a CP-eigenstate. An example of the type of process one would like to observe is depicted in fig. 2. A pair consisting of a neutral and a charged B ($B^0 B^-$ or $\bar{B}^0 B^+$) is produced in a pp interaction. The nature of the newly born B^0 is determined by the charge of the companion charged B , that must be detected as a *tag* (the extent to which this gedanken tagging is realistic is discussed in Section 3). The B^0 (or \bar{B}^0) can decay directly to f , as in fig. 2a, or do it after the meson has been transmogrified into its antiparticle via the “mixing” process, as in fig. 2b. For the observable appearance of the final state f as a function of time, the interference between these two paths produces a deviation from an exponential decay law. If only a single amplitude contributes to the decay process, $|\bar{\rho}(f)| \equiv |A(\bar{B}^0 \rightarrow f)/A(B^0 \rightarrow f)| = 1$, and the modified decay law has the simple form:

$$\Gamma[B^0(t) \rightarrow f] \propto e^{-\Gamma t} \{1 - \text{Im}(\Lambda) \sin(\Delta M t)\}, \quad (1.3)$$

$$\Gamma[\bar{B}^0(t) \rightarrow f] \propto e^{-\Gamma t} \{1 + \text{Im}(\Lambda) \sin(\Delta M t)\}, \quad (1.4)$$

with $\text{Im}(\Lambda)$ a function of the CKM parameters. In some cases, such as those listed in Table 1, $\text{Im}(\Lambda) \simeq \sin(2\Phi)$, with $\pm\Phi$ one of the angles of the unitarity triangle.

Decay mode	CKM factor (Direct decay)	CKM factor (Penguin)	Exclusive channels	Φ
$b \rightarrow c\bar{s}s$	$A\lambda^2$	$-A\lambda^2$	$\bar{B}_d^0 \rightarrow J/\psi K_S, J/\psi K_L$	$\mp\beta$
$b \rightarrow s\bar{s}s$	-	$-A\lambda^2$	$\bar{B}_d^0 \rightarrow K_S \phi, K_L \phi$	$\mp\beta$
$b \rightarrow c\bar{c}d$	$-A\lambda^3$	$A\lambda^3(1 - \rho + i\eta)$	$\bar{B}_d^0 \rightarrow D^+ D^-, J/\psi \pi^0$	$\approx \mp\beta$
$b \rightarrow u\bar{u}d$	$A\lambda^3(\rho - i\eta)$	$A\lambda^3(1 - \rho + i\eta)$	$\bar{B}_d^0 \rightarrow \pi^+ \pi^-, p\bar{p}, \rho^0 \pi^0, \omega \pi^0$ $\bar{B}_s^0 \rightarrow \rho^0 K_S, \omega K_S, \pi^0 K_S, \rho^0 K_L, \omega K_L, \pi^0 K_L$	$\approx \pm\alpha$ $\approx \mp\gamma$

TABLE 1

CKM factors and relevant angle Φ for some B-decays into CP-eigenstates. Upper (lower) signs in the last column refer to CP-even (odd) final states, with the convention (1.4).

The b-quark is heavy enough, one hopes, to ascertain the underlying quark transition from the final states in a B-meson decay. The leading contributions to $b \rightarrow q' \bar{q}' q$ decay amplitudes are either “direct” (Fermi) or generated by gluon exchange (“penguin”). Although of higher order in the strong coupling constant, penguin amplitudes are logarithmically enhanced, due to the virtual W-loop, and are potentially competitive. Table 1 contains the CKM factors associated with the direct and penguin diagrams for different B-decay modes into CP-eigenstates (CKM unitarity and $m_b^2 \gg m_c^2, m_u^2$ imply that the phase of penguins is that of $V_{tb} V_{tq}^*$ ($q = d, s$) [3]). The $b \rightarrow c\bar{s}s$ quark decays are theoretically unambiguous: the direct and penguin amplitudes have the same weak phase $\sin(2\beta)$. Ditto for $b \rightarrow s\bar{s}s$, where only the penguin mechanism is possible. The $b \rightarrow c\bar{c}d$ and $b \rightarrow u\bar{u}d$ decay modes are not so simple, the two decay mechanisms have the same Cabibbo suppression (λ^3) and different weak phases, but the penguin amplitudes are down by $(\alpha_s/6\pi) \ln(m_W/m_b) \approx 3\%$: these decay modes can be used as approximate measurements of the angles of the unitarity triangle. We have not considered doubly Cabibbo-suppressed decay amplitudes, such as $b \rightarrow u\bar{u}s$, for which penguin effects can be important and spoil the simple estimates based on the direct decay mechanism.

Presumably the most realistic channels for the measurement of the angles $\Phi = (\beta, \alpha, \gamma)$ are $B_d^0 \rightarrow J/\psi K_S^0$, $B_d^0 \rightarrow \pi^+ \pi^-$, $B_s^0 \rightarrow \rho^0 K_S$, respectively. The first of these processes is no doubt the one with the cleanest signature and the most tractable background. Most of the following discussion refers to this mode of B decay.

2. Current constraints on the unitarity triangle.

To derive the present constraints on the angles of the unitarity triangle, we follow the analysis in [4], updating the experimental [5] and theoretical inputs. As in [4], we are conservative, and allow for generous error bars in the input parameters. The allowed region for the vertex in the (ρ, η) parameters defined in (1.1) is presently explained, and shown in fig. 3 for three different values of the top-quark mass, $m_t = 100, 140$ and 180 GeV.

We use [5] $|V_{cb}| = 0.044 \pm 0.009$. With $\lambda = \sin \theta_c = 0.221$, this implies $|A| = 0.90 \pm 0.18$. Three experimental inputs constrain the position of the ρ, η vertex:

- i) The constraint [5]

$$|V_{ub}/V_{cb}| = 0.09 \pm 0.04 \quad (2.1)$$

forces the point (ρ, η) to lie between the two (dashed) circles centered at the origin.

ii) The measured [6] $B^0 - \bar{B}^0$ mixing parameter, $x_d \equiv \Delta M/\Gamma = 0.66 \pm 0.11$, can be translated on information about the CKM-matrix, provided definite values are taken for m_t and $\xi_B \equiv |f_B \sqrt{|B_B|}|$ (which parametrizes the hadronic matrix element of the $\Delta B = 2$ four-quark operator between the B^0 and \bar{B}^0 mesons).

The actual size of ξ_B has been controversial for some time. Since the c and b quarks are quite heavy, many have used the infinite mass limit relation $f_B/f_D \sim \sqrt{m_c/m_b}$ to extrapolate the value of f_D (computed either via QCD-sum rules or lattice simulations) to the bottom-mass scale. Moreover, $B_B = 1$ has been usually assumed. But calculations of the bottom decay constant in the context of QCD-sum rules [7] [8] often result in $f_B \geq f_D$, also the prediction of recent lattice computations [9]. In a direct calculation [10] of the $B^0 - \bar{B}^0$ matrix element (i.e. ξ_B instead of f_B) a large value was also found, the result depending on the input b-quark “pole” mass. Using the presently favoured [8] value $m_b = (4.6 \pm 0.1)$ GeV, one obtains from [10] the range that we shall adopt:

$$\xi_B \equiv |f_B \sqrt{|B_B|}| = (1.7 \pm 0.4)f_\pi, \quad (2.2)$$

with which, assuming $B_B = 1$, lattice estimates also agree.

Using the experimental input [11] $\tau_b |V_{cb}|^2 = (3.5 \pm 0.6) \times 10^9 \text{ GeV}^{-1}$, the x_d -constraint forces the vertex (ρ, η) to the region between the two (dash-dotted) circles centered at the point $(1,0)$. The bigger circle corresponds to the smaller ξ_B .

iii) The third constraint is imposed by the measured CP-violating contamination [12] in the $K^0 - \bar{K}^0$ mixing matrix, $|\epsilon| = 2.27 \times 10^{-3}$. The main uncertainty here is the size of the hadronic matrix element of the $\Delta S = 2$ four-quark operator between the K^0 and \bar{K}^0 mesons, which is usually characterized by the so called B_K -parameter. Chiral symmetry arguments [13] [14] and QCD-sum rules calculations [14] [15] give B_K -values in the range $1/3$ to $1/2$. A value around $3/4$ is obtained [16] with $1/N_c$ -expansion techniques, and lattice calculations favour $B_K \sim 1$ [17]. We use

$$1/3 \leq B_K \leq 1. \quad (2.3)$$

The resulting allowed domain for the vertex (ρ, η) of the unitarity triangle is limited by the two hyperbolas (solid curves) in the figures. The smaller values of B_K correspond to bigger values of η .

The intersection of the three regions resulting from the constraints in i) ii) and iii) gives the final allowed domain (shaded area). The permissible values of the angles of the unitarity triangle can be read from the figure. For $90 \text{ GeV} \leq m_t \leq 200 \text{ GeV}$, we find:

$$-1 \leq \sin 2\alpha \leq 1, \quad (2.4a)$$

$$0.16 \leq \sin 2\beta \leq 1, \quad (2.4b)$$

$$-1 \leq \sin 2\gamma \leq 1. \quad (2.4c)$$

While nothing can be said at the moment on the expected size of $\sin 2\alpha$ and $\sin 2\gamma$, the magnitude of the CP-violating interference term is auspiciously guaranteed to be bigger than 0.16, for those asymmetries governed by $\sin 2\beta$. This lower bound depends on m_t . For $m_t = 100, 140$ and 180 GeV , the result is $\sin 2\beta \geq 0.16, 0.21$ and 0.24 , respectively.

3. Fake CP Violation in B Decays at pp Colliders

The initial state at a pp collider is not a CP eigenstate. The question arises that this CP-asymmetry could percolate, via “leading particle effects”, into the final state and

induce fake asymmetries mimicking CP violation in the B sector. This question has also been addressed by Fridman [18], whose treatment differs from ours in points of detail.

It must be vehemently emphasized from the very start that the physics connected to the details of the production of specific final states in high energy pp collisions is not understood to a depth sufficient to answer with confidence questions such as the fake asymmetries. An insufficiently uncommon attitude consists in believing results from Monte Carlo generators that are not trustworthy enough to address this type of question. Our attitude will be to use those generators, when unavoidable, to help establish extreme worst-case scenarios. Only in these extremes do the fake asymmetries turn out to size up with the true asymmetries expected in the Standard Model. To deal with the unlikely case that nature is equally extreme and perverse, and in an attempt to reach an empirical resolution of the problem, we discuss related measurable asymmetries that are expected to be exclusively “fake”, and their use as “background subtractions”.

Consider the gold-plated channel $B_d^0 \rightarrow K_S J/\psi$, followed by $K_S \rightarrow \pi^+ \pi^-$ and $J/\psi \rightarrow l^+ l^-$. The ideal case is that in which the second B is perfectly tagged, in the sense that the b or \bar{b} nature of its defining quark is established (this is possible for example for charged B’s flying long enough for their charged nature to be observed, for instance via their decay into a lepton the sign of whose charge is measured). Moreover, CP-conjugate b-flavoured hadron pairs must be produced in equal amounts, as in $e^+ e^-$ or $p\bar{p}$ collisions. The time-integrated asymmetry has in this ideal case the simple form:

$$A_{J/\psi K_S} = \frac{N(J/\psi K_S l^+) - N(J/\psi K_S l^-)}{N(J/\psi K_S l^+) + N(J/\psi K_S l^-)} = \frac{x_d}{1 + x_d^2} \sin 2\beta, \quad (3.1)$$

with $x_d/(1 + x_d^2) \approx 0.46$ the dilution factor due to the oscillation of the neutral B.

In a pp collider mode the ideal case may not be realistic. First, we must study the potential consequences of not knowing the precise identity of the tagging B-particle. The complication arises because, via their mixing, neutral B mesons may yield leptons of the “wrong” sign. Define the probability for an initially produced B^0 meson to decay as a \bar{B}^0 (or vice versa) by W (for the *Wrong* sign of the lepton) and let $R = 1 - W$ be its complement:

$$W = \frac{N(B^0 \rightarrow \bar{B}^0)}{N(B^0 \rightarrow \bar{B}^0) + N(B^0 \rightarrow B^0)} = \frac{N(\bar{B}^0 \rightarrow B^0)}{N(\bar{B}^0 \rightarrow B^0) + N(\bar{B}^0 \rightarrow \bar{B}^0)} = \frac{x^2}{2 + 2x^2}. \quad (3.2)$$

The possible semileptonic tags are $B^+ \rightarrow l^+ \nu_l X$ or $\bar{\Lambda}_b \rightarrow l^+ \nu_l X$ (fully efficient)¹, $B_d^0 \rightarrow l^+ \nu_l X$ (less efficient because of $B_d^0 - \bar{B}_d^0$ mixing) and $B_s^0 \rightarrow l^+ \nu_l X$ (inefficient: mixing is expected to be maximal). Because of this tag hierarchy, it is convenient to introduce the quantities:

$$\begin{aligned}\tilde{n}^+ &= N(B^+ \bar{B}_d^0) \text{Br}(B^+ \rightarrow l^+ \nu_l X) + N(\bar{\Lambda}_b \bar{B}_d^0) \text{Br}(\bar{\Lambda}_b \rightarrow l^+ \nu_l X), \\ \tilde{n}^- &= N(B^- \bar{B}_d^0) \text{Br}(B^- \rightarrow l^- \bar{\nu}_l X) + N(\Lambda_b B_d^0) \text{Br}(\Lambda_b \rightarrow l^- \bar{\nu}_l X), \\ \tilde{n}^0 &= N(B_d^0 \bar{B}_d^0) \times \frac{1}{2} [\text{Br}(B_d^0 \rightarrow l^+ \nu_l X) + \text{Br}(\bar{B}_d^0 \rightarrow l^- \bar{\nu}_l X)], \\ \tilde{n}_s &= N(B_s^0 \bar{B}_d^0) \text{Br}(B_s^0 \rightarrow l^+ \nu_l X), \\ \tilde{n}_{\bar{s}} &= N(\bar{B}_s^0 B_d^0) \text{Br}(\bar{B}_s^0 \rightarrow l^- \bar{\nu}_l X), \\ \tilde{n} &\equiv \tilde{n}^+ + \tilde{n}^- + 2\tilde{n}^0 + \tilde{n}_s + \tilde{n}_{\bar{s}},\end{aligned}\quad (3.3)$$

in terms of the numbers N of the various produced pairs. Up to an overall (and ultimately irrelevant) common factor, the number of decays into $J/\psi K_S l^+ X$ and $J/\psi K_S l^- X$ is obtained by combining (3.2) and (3.3), with the result:

$$\begin{aligned}N(J/\psi K_S l^+ X) &\propto \{\tilde{n}^+ + \tilde{n}^0 R_d + \tilde{n}_s R_s\} \left\{1 + \frac{x_d}{1+x_d^2} \sin(2\beta)\right\} \\ &+ \{\tilde{n}^0 W_d + \tilde{n}_{\bar{s}} W_s\} \left\{1 - \frac{x_d}{1+x_d^2} \sin(2\beta)\right\},\end{aligned}\quad (3.4a)$$

$$\begin{aligned}N(J/\psi K_S l^- X) &\propto \{\tilde{n}^- + \tilde{n}^0 R_d + \tilde{n}_{\bar{s}} R_s\} \left\{1 - \frac{x_d}{1+x_d^2} \sin(2\beta)\right\} \\ &+ \{\tilde{n}^0 W_d + \tilde{n}_s W_s\} \left\{1 + \frac{x_d}{1+x_d^2} \sin(2\beta)\right\}.\end{aligned}\quad (3.4b)$$

This corresponds to a time-integrated asymmetry:

$$\begin{aligned}A_{J/\psi K_S} &= \frac{N(J/\psi K_S l^+) - N(J/\psi K_S l^-)}{N(J/\psi K_S l^+) + N(J/\psi K_S l^-)} \\ &= \frac{\tilde{n}^+ - \tilde{n}^- + \frac{\tilde{n}_s - \tilde{n}_{\bar{s}}}{1+x_s^2} + \sin(2\beta) \frac{x_d}{1+x_d^2} (\tilde{n}^+ + \tilde{n}^- + \frac{2}{1+x_d^2} \tilde{n}^0 + \frac{\tilde{n}_s + \tilde{n}_{\bar{s}}}{1+x_s^2})}{\tilde{n} + \sin(2\beta) \frac{x_d}{1+x_d^2} (\tilde{n}^+ - \tilde{n}^- + \tilde{n}_s - \tilde{n}_{\bar{s}})},\end{aligned}\quad (3.5)$$

that would, in the half-ideal case of “perfect” tagging, simplify to:

$$A_{J/\psi K_S} = \frac{\tilde{n}^+ - \tilde{n}^- + \sin(2\beta) \frac{x_d}{1+x_d^2} (\tilde{n}^+ + \tilde{n}^-)}{\tilde{n}^+ + \tilde{n}^- + \sin(2\beta) \frac{x_d}{1+x_d^2} (\tilde{n}^+ - \tilde{n}^-)}.\quad (3.6)$$

¹ We denote by $\bar{\Lambda}_b$ any $\{\bar{b}\bar{q}\bar{q}'\}$ baryon that decays only weakly.

The asymmetry $A_{J/\psi K_S}$ does not vanish in the CP-conserving limit ($\beta = 0$) if \tilde{n}^+ differs from \tilde{n}^- , as it may be expected in a pp collision. To gauge the incidence of fake asymmetries it suffices to neglect in (3.5) the $\sin(2\beta)$ term in the denominator, and the terms containing x_s (the SM expectation is $x_s^2 \sim 80$ or larger). The asymmetry can then be simplified to read:

$$A_{J/\psi K_S} \approx a \cdot (F + \sin(2\beta)),\quad (3.7)$$

with

$$a \approx \frac{x_d}{1+x_d^2} \frac{1}{\tilde{n}} \left(\tilde{n}^+ + \tilde{n}^- + \frac{2}{1+x_d^2} \tilde{n}^0 \right) \approx \frac{2}{3} \frac{x_d}{1+x_d^2} \approx 0.30\quad (3.8)$$

the coefficient of $\sin(2\beta)$ in the true asymmetry and

$$F \equiv \frac{\tilde{n}^+ - \tilde{n}^-}{\frac{x_d}{1+x_d^2} (\tilde{n}^+ + \tilde{n}^- + \frac{2}{1+x_d^2} \tilde{n}^0)}\quad (3.9)$$

representing the “fake” addition to the true CP-odd parameter $\sin(2\beta)$.

We proceed to attempt to estimate F . The \bar{b} antiquarks may catch an incoming valence quark to result in more $\bar{b}u$ and $\bar{b}d$ than $b\bar{u}$ and $b\bar{d}$ mesons. Balancing this behaviour, more b baryons than antibaryons are to be expected. Unlike $\sin(2\beta)$, F should peak at large x_F and small p_T . Let $p_u = p_d$, p_s and p_Λ be the fragmentation probabilities (adding up to unity) for a \bar{b} quark to end up as B^+ , B^0 , B_s^0 and $\bar{\Lambda}_b$, in e^+e^- annihilation, wherein the leading particle effects are absent. To describe the difference between these probabilities and the corresponding ones in pp collisions (dubbed P) we introduce two parameters l_m and l_b (for mesons and baryons) implicitly defined via the following equations:

$$\begin{aligned}P(B^+) &= p_d(1 - l_m) + 2l_m/3, & P(B^-) &= p_d(1 - l_b), \\ P(B_d^0) &= p_d(1 - l_m) + l_m/3, & P(\bar{B}_d^0) &= p_d(1 - l_b), \\ P(B_s^0) &= p_s(1 - l_m), & P(\bar{B}_s^0) &= p_s(1 - l_b), \\ P(\bar{\Lambda}_b) &= p_\Lambda(1 - l_m), & P(\Lambda_b) &= p_\Lambda(1 - l_b) + l_b.\end{aligned}\quad (3.10)$$

For l_m and/or $l_b \neq 0$ the above particle-antiparticle asymmetries clearly yield a nonvanishing fake asymmetry F . Using PYTHIA Fridman [18] finds, for $p_T < 5$ GeV, $l_m \sim 1\%$; $l_b \sim 3\%$. Assuming $p_d = 0.38$, $p_s = 0.14$ and $p_\Lambda = 0.10$, these values correspond to $F \approx -3\%$. Our own estimates based on the HERWIG 5.0 generator [19] indicate even smaller fake asymmetries, but strongly depend on the choice of undecidable free parameters in the program. To illustrate a wide range of parameter space, we show in fig. 4a

the values of $A_{J/\psi K_S}$ for the case $\sin(2\beta) = 0$, as a function of l_m and l_b , both in the interval $0 \rightarrow 0.1$, keeping p_d , p_s and p_Λ at the values given before. For b-hadron decays the spectator model should hold, and we have in fig. 4a assumed

$$R_{\Lambda_b} \equiv \frac{\text{Br}(\Lambda_b \rightarrow l\nu_1 X)}{\text{Br}(B \rightarrow l\nu_1 X)} = 1. \quad (3.11)$$

To test the sensitivity to this assumption, we show in fig. 4b a similar plot using a value of $R_{\Lambda_b} \sim 0.37$, the measured result for charmed hadrons. The sensitivity to l_b and R_{Λ_b} is considerable: the role of semileptonic b-baryon decays is significant. In these plots we assumed an 8% probability of double versus single b-pair production [18], no doubt a pessimistically large choice (the single pair multiplicity is estimated to be less than $\sim 0.5\%$ in collider mode and $\sim 10^{-4}$ in fixed target mode). We did also neglect the possibility of distinguishing experimentally single from double pair production.

In fig. 4c we show F , defined in (3.9), for $R_{\Lambda_b} = 1$. F is very insensitive to l_m and may be as large as -14% for $l_m = 0$, $l_b = 0.1$. Such a large fake asymmetry may seriously hinder the search for a true CP-odd effect, but is difficult to imagine on fairly general grounds. A value $l_b = 0.1$ corresponds to a 10% probability of a b-quark spousing the original diquark in one of the incident protons. A typical LHC collider-mode event may have a particle multiplicity of ~ 100 or a $q + \bar{q}$ multiplicity of ~ 200 . It is hard to believe that in 10% of the cases the b-quark is the one to stick to the diquark. Complete satisfaction, however, may require more than educated guesswork, and we proceed to discuss two previous and one new empirical ways to tackle the problem of fake asymmetries:

i) Reconstruct and measure the decays of B^+ , B^- , B^0 , \bar{B}^0 , Λ_b and $\bar{\Lambda}_b$ produced in pp collisions, to obtain information on the parameters l_m and l_b [18]. This procedure involves absolute measurements of cross sections and is more sensitive to systematics than the (normalized) asymmetries are. Even without leading-particle effects \tilde{n}^+ , \tilde{n}^- and \tilde{n}^0 must be separately measured to extract the CP-odd effect. The method calls for an excellent vertex detector, and large statistics ($10^{10} \div 10^{11}$ b pairs per year), not a trivial task.

ii) The measurement and subtraction of asymmetries involving final states with opposite CP, e.g. $B \rightarrow J/\psi K_S$ and $B \rightarrow J/\psi K_L$ [20]. In this example

$$\begin{aligned} \Delta &\equiv A_{J/\psi K_S} - A_{J/\psi K_L} \\ &= 2 \sin(2\beta) \frac{x_d}{1+x_d^2} \left\{ \frac{\tilde{n}^+ + \tilde{n}^- + 2\frac{\tilde{n}^0}{1+x_d^2}}{\tilde{n}} + O\left(\left[\frac{\tilde{n}^+ - \tilde{n}^-}{\tilde{n}}\right]^2\right) \right\}. \end{aligned} \quad (3.12)$$

Again, one must measure \tilde{n}^+ , \tilde{n}^- and \tilde{n}^0 separately, and since K_L 's might often escape undetected, there are severe requirements on statistics.

iii) Express the fake contribution to the asymmetry in a channel where one may expect a large CP-odd effect in terms of asymmetries measured in channels wherein the putative effects are expected to be exclusively fake. As an example, consider our favorite “signal” channel $J/\psi K_S$, and the “fake” or calibration channels $D^+\pi^-l^+X$, $D^+\pi^-l^-X$, $D^-\pi^+l^-X$ and $D^-\pi^+l^+X$, for which the standard CP-odd effects are doubly Cabibbo suppressed ($\sin^2(\theta_C)$ in the amplitude). The relevant products of branching ratios [12] favourably compare with those in the $J/\psi K_S$ mode: $\text{Br}(B^0 \rightarrow D^-\pi^+) \times \text{Br}(D^- \rightarrow K^+\pi^-\pi^-) \approx 3 \cdot 10^{-4}$ versus $\text{Br}(B^0 \rightarrow J/\psi K_S) \times \text{Br}(J/\psi \rightarrow l^+l^-) \times \text{Br}(K_S \rightarrow \pi^+\pi^-) \approx 3 \cdot 10^{-5}$ (the reconstruction efficiency of D^- from the $K^+\pi^-\pi^-$ final state must also be compared with the product of those for $J/\psi \rightarrow l^+l^-$ and $K_S \rightarrow \pi^+\pi^-$). For the four possibilities of charge combinations we find:

$$\begin{aligned} N(D^+\pi^-l^+) &= \tilde{n}^+ R_d + \tilde{n}^0 \cdot (R_d^2 + W_d^2) + \tilde{n}_{\bar{s}} W_d W_s + \tilde{n}_s R_d R_s, \\ N(D^+\pi^-l^-) &= \tilde{n}^- W_d + 2\tilde{n}^0 R_d W_d + \tilde{n}_{\bar{s}} W_d R_s + \tilde{n}_s R_d W_s, \\ N(D^-\pi^+l^-) &= \tilde{n}^- R_d + \tilde{n}^0 \cdot (R_d^2 + W_d^2) + \tilde{n}_{\bar{s}} R_d R_s + \tilde{n}_s W_d W_s, \\ N(D^-\pi^+l^+) &= \tilde{n}^+ W_d + 2\tilde{n}^0 R_d W_d + \tilde{n}_{\bar{s}} R_d W_s + \tilde{n}_s W_d R_s. \end{aligned} \quad (3.13)$$

These may be combined into six asymmetries, three of which are linearly independent. Introduce the ratios:

$$\begin{aligned} A_1^{D\pi} &= (N(D^+\pi^-l^+) - N(D^-\pi^+l^-))/\tilde{n} \\ &= ((\tilde{n}^+ - \tilde{n}^-)R_d + (\tilde{n}_s - \tilde{n}_{\bar{s}})(R_d R_s - W_d W_s))/\tilde{n}, \\ A_2^{D\pi} &= (N(D^-\pi^+l^-) - N(D^+\pi^-l^-))/\tilde{n} \\ &= ((\tilde{n}^- - \tilde{n}^+)W_d - (\tilde{n}_s - \tilde{n}_{\bar{s}})(R_d W_s - W_d R_s))/\tilde{n}, \\ B_1^{D\pi} &= (N(D^+\pi^-l^+) - N(D^-\pi^+l^+))/\tilde{n} \\ &= (\tilde{n}^+ + \tilde{n}^0(R_d - W_d) + \tilde{n}_s R_s - \tilde{n}_{\bar{s}} W_s)(R_d - W_d)/\tilde{n}, \\ B_2^{D\pi} &= (N(D^-\pi^+l^-) - N(D^+\pi^-l^-))/\tilde{n} \\ &= (\tilde{n}^- + \tilde{n}^0(R_d - W_d) - \tilde{n}_s W_s + \tilde{n}_{\bar{s}} R_s)(R_d - W_d)/\tilde{n} \end{aligned} \quad (3.14)$$

and notice that only $A_1^{D\pi}$, $A_2^{D\pi}$ and $(B_1^{D\pi} - B_2^{D\pi})$ vanish for $\tilde{n}^+ = \tilde{n}^-$ and $\tilde{n}_s = \tilde{n}_{\bar{s}}$, but not $B_1^{D\pi}$ and $B_2^{D\pi}$ separately. The fake part F of the asymmetry in $J/\psi K_S$ decays can

be expressed in terms of asymmetries in the $D\pi$ decays of B mesons (expected to be pure "fakes") and of the mixing parameter x_d of the $B_d^0 - \bar{B}_d^0$ system:

$$\begin{aligned} F &= \frac{1}{x_d} \frac{A_1^{D\pi} + A_2^{D\pi}}{B_1^{D\pi} + B_2^{D\pi}} \\ &= \frac{1}{x_d} \frac{N(D^+\pi^-1^+) - N(D^-\pi^+1^-) - N(D^+\pi^-1^-) + N(D^-\pi^+1^+)}{N(D^+\pi^-1^+) - N(D^-\pi^+1^+) + N(D^-\pi^+1^-) - N(D^+\pi^-1^-)}. \end{aligned} \quad (3.15)$$

One may also express the total asymmetry for $J/\psi K_S$ in terms of the A 's, B 's, x_d and $\sin(2\beta)$:

$$A_{J/\psi K_S} = \frac{(A_1^{D\pi} + A_2^{D\pi}) + x_d \sin(2\beta) \cdot (B_1^{D\pi} + B_2^{D\pi})}{1 + x_d \sin(2\beta) \cdot (A_1^{D\pi} - A_2^{D\pi})}. \quad (3.16)$$

From this it is easy to calculate the asymmetry difference Δ of (3.12):

$$\Delta = 2x_d \sin(2\beta) \frac{B_1^{D\pi} + B_2^{D\pi} - (A_1^{D\pi})^2 + (A_2^{D\pi})^2}{1 - [x_d \sin(2\beta)(A_1^{D\pi} - A_2^{D\pi})]^2}. \quad (3.17)$$

It is therefore possible in the presence of fake asymmetries to measure the phase of the CKM matrix, even without measuring absolute cross sections. Naturally, the requirements on statistics are stiffer than for CP invariant initial states.

To conclude, we have argued (but not proven) that fake asymmetries induced by the leading-particle effects characteristic of a pp collider should not seriously hinder the search for CP violation in B decays. There are empirical ways to tackle the threat of forgery. The obvious one is to check the p_T - and x_F -independence of the potential signal. Another one is the search for asymmetries that (in the Standard Model) are not expected to reflect CP-violation. These asymmetries, if found not to vanish, can also be used to subtract the fake contribution to an honest-to-goodness CP-odd signal.

4. Search for B_c mesons

Besides CP violation in the beauty sector, there are other items of interest in b -physics: rare decays, $B_s \bar{B}_s$ mixing, etc. Many of these may be investigated at LEP, CESR or future e^+e^- Beauty factories before LHC starts operation at 23:59, Dec. 31st, 1997. An exception could be the discovery of long-lived particles containing two or more heavy quarks, such as mesons carrying both beauty and charm quantum numbers, no doubt the most promising example.

The spectrum of $b\bar{c}$ states can be predicted in potential models [21], that successfully describe the charmonium and bottomonium families. The lightest state is expected to be a $(\bar{b}c)$ pseudoscalar, B_c^+ , with a mass ~ 6.3 GeV. The first excited state, a vector meson, should be heavier by only $70 \rightarrow 100$ MeV: it would decay emitting a photon which, if detected, could help in identifying the subsequent weak B_c decay.

The decays of B_c^+ are of three types: spectator c quark, spectator \bar{b} , and $c\bar{b}$ annihilation. The total rate due to processes of the first class is expected to be equal to the decay rate for a B^+ (or B_d^0) meson. Contrarywise, the naive expectation should fail that the spectator-model prediction for the D decay rate correctly describe the rate of spectator \bar{b} decays, since the heavy (and less strongly bound) final B_s (or $B_{d,u}$) considerably reduces phase space: a $\sim 40\%$ suppression factor is expected [22]. Accepting the potential-model B_c decay constant ($f_{B_c} \simeq 570$ MeV), the annihilation contribution should be rather important. The three decay types contribute respectively 36%, 40% and 24% to the total rate; the lifetime is estimated to be similar to that of D^0 's, namely $\tau_{B_c} \simeq 4.4 \cdot 10^{-13}$ s.

A clear signature could be the decay $B_c^+ \rightarrow J/\psi \mu^+ \nu_\mu$, followed by $J/\psi \rightarrow \mu^+ \mu^-$. An estimate of the branching ratio is $0.03 \times 0.07 \simeq 2 \cdot 10^{-3}$, to be multiplied by four if the analogous electron channels are also observed. Complete reconstruction of the B_c mass would be possible in the decay $B_c^+ \rightarrow J/\psi \pi^+$, whose branching ratio is expected to be an order of magnitude below the previous one.

Predictions for B_c production cross section are very uncertain. For e^+e^- colliders, a naive nonrelativistic model [23] predicts a meagre 600 B_c^+ events in 10^7 s at the Z^0 peak with the project LEP luminosity $\mathcal{L} = 1.7 \cdot 10^{31} \text{ cm}^{-2} \text{ s}^{-1}$.

Existing estimates for pp interactions [24] depend on three unknowns: the probability $\lambda_c(\lambda_b)$ to produce a charmed (beautiful) quark pair in the fragmentation of a beauty (charm) quark and the probability μ for the c and \bar{b} to recombine in a B_c^+ . The guess in [24], corresponding to $\lambda_c \simeq 10 \cdot \lambda_b \simeq 0.04$ and $\mu \simeq 0.1$ is $\sigma(pp \rightarrow B_c^+ X) \simeq 5 \cdot 10^{-3} \sigma(pp \rightarrow b\bar{b} X)$.

To have a firmer estimate, HERWIG 5.0 [19] has been used. The result depends on parameters describing hadronization, in particular the probability of $c\bar{c}$ production in the non-perturbative splitting of a heavy colour-singlet cluster. Keeping this probability on the high side, within the constraints from ISR data, we obtain

$$\sigma(pp \rightarrow B_c^+ X) \leq 3 \cdot 10^{-4} \sigma(pp \rightarrow b\bar{b} X). \quad (4.1)$$

This result is much smaller than the guesstimate in [24], mainly because of the smaller $\mu \simeq 5 \cdot 10^{-3}$. One B_c^+ produced every $10^4 b\bar{b}$ pairs with at least $10^{10} b\bar{b}$ pairs produced in

one year in a *low luminosity* ($10^{31} \text{cm}^{-2}\text{s}^{-1}$) intersection at LHC energies [25], corresponds to one million B_c 's yearly produced. Even a tenth of this yield, not unthinkable within the uncertainties, should suffice to discover the B_c and to make a first study of its decays.

References

- [1] N. Cabibbo in *Proceedings of the XIII Rochester Conference*, Edited by Margaret Altson-Garnjost, Univ. of California Press, Berkeley, 1966.
- [2] A. Carter, A.I. Sanda, Phys. Rev. Lett. 45 (1980) 952; Phys. Rev. D23 (1981) 1567 ; I.I. Bigi and A.I. Sanda, Nucl. Phys. B193 (1981) 85.
- [3] D. London and R.D. Peccei, Phys. Lett. B223 (1989) 257.
- [4] C.O. Dib, I. Dunietz, F.J. Gilman and Y. Nir, Phys. Rev. D41 (1990) 1522.
- [5] F.J. Gilman, K. Kleinknecht and B. Renk, in 'Review of Particle Properties' (J.J. Hernández et al.), Phys. Lett. B239 (1990) III.61.
- [6] H. Albrecht et al. (ARGUS), Phys. Lett. B192 (1987) 245;
A. Bean et al. (CLEO), Phys. Rev. Lett. 58 (1987) 183.
- [7] S. Narison, Phys. Lett. B198 (1987) 104;
L.J. Reinders, Phys. Rev. D38 (1988) 947;
for a dissenting view, see C.A. Dominguez and N. Paver, Phys. Lett. B246 (1990) 493.
- [8] S. Narison, "QCD Spectral Sum Rules" (World Scientific Lecture Notes in Physics, Vol. 26), World Scientific, Singapore 1989.
- [9] C.R. Allton et al., Shep 89/90-11 (1990);
C. Alexandrou et al., PSI-PR-90-28 (1990);
E. Eichten, G. Hockney and H.B. Thacker, Fermilab-Conf-89/211-T (1989).
- [10] A. Pich, Phys. Lett. B206 (1988) 322.
- [11] F.J. Gilman and Y. Nir, SLAC-PUB-5198 (1990) to be published in Annual Review of Nuclear and Particle Science.
- [12] Particle Data Group (M. Aguilar-Benitez et al.), Phys. Lett. B239 (1990) 1.
- [13] J.F. Donoghue, E. Golowich and B.R. Holstein, Phys. Lett. B119 (1982) 412.
- [14] A. Pich and E. de Rafael, Phys. Lett. B158 (1985) 477.
- [15] N. Bilic, C.A. Dominguez and B. Guberina, Z.Phys. C39 (1988) 351, and references therein.
- [16] W.A. Bardeen, A.J. Buras and J.-M. Gerard, Phys. Lett. B211 (1988) 343.
- [17] S.R. Sharpe, Proc. 1989 Symposium on Lattice Field Theories (Capri, September 1989), eds. N. Cabibbo et al., Nucl. Phys. B (Proc. Suppl.) 17 (1990) 146, and references therein.
- [18] A. Fridman, CERN-EP/90-87 (1990).
- [19] G. Marchesini and B.R. Webber, Nucl. Phys. B310 (1988) 461; ibid. B330 (1990) 261.
- [20] V.D. Kekelidze, JINR-E2-88-460 (1988).
- [21] E. Eichten and F. Feinberg, Phys. Rev. D23 (1981) 2724;
S. Godfrey and N. Isgur, Phys. Rev. D32 (1985) 189;
S.S. Gershtein et al., Sov. J. Nucl. Phys. 48 (1988) 515.
- [22] M. Masetti, Rome "La Sapienza" University Thesis (September 1990);
M. Lusignoli and M. Masetti, to be published.
- [23] C.R. Ji and F. Amiri, Phys. Rev. D35 (1987) 3318.
- [24] V.V. Kiselev et al., Sov. J. Nucl. Phys. 49 (1989) 682;
S.S. Gershtein et al., IHEP preprint 89-214, 1989.
- [25] P. Nason in these Proceedings.

Figure Captions

- Fig. 1. The unitarity triangle serving to define the phases α , β and γ .
- Fig. 2. CP violation in tagged B decays, with the neutral B decaying into a CP-eigenstate f .
- Fig. 3. Constraints from $|V_{ub}/V_{cb}|$ (dashed circles), x_d (dot-dashed circles) and ϵ (solid hyperbolas) on the unitarity triangle of fig. 1, for $m_t = 100, 140$ and 180 GeV. The shaded region is allowed.
- Fig. 4. [a] The fake asymmetry $A = aF$ for $R_{\Lambda_b} = 1$ as a function of l_m and l_b . [b] The same for $R_{\Lambda_b} = 0.37$. [c] The fake contribution F to the asymmetry, for $R_{\Lambda_b} = 1$.

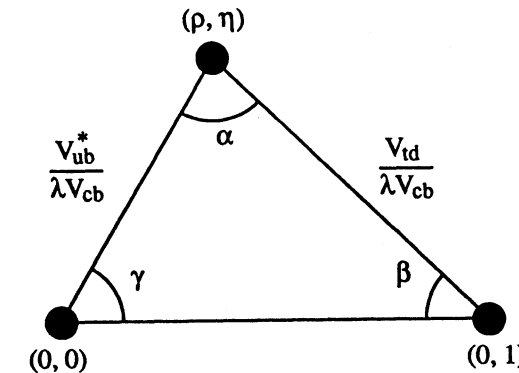


Fig. 1

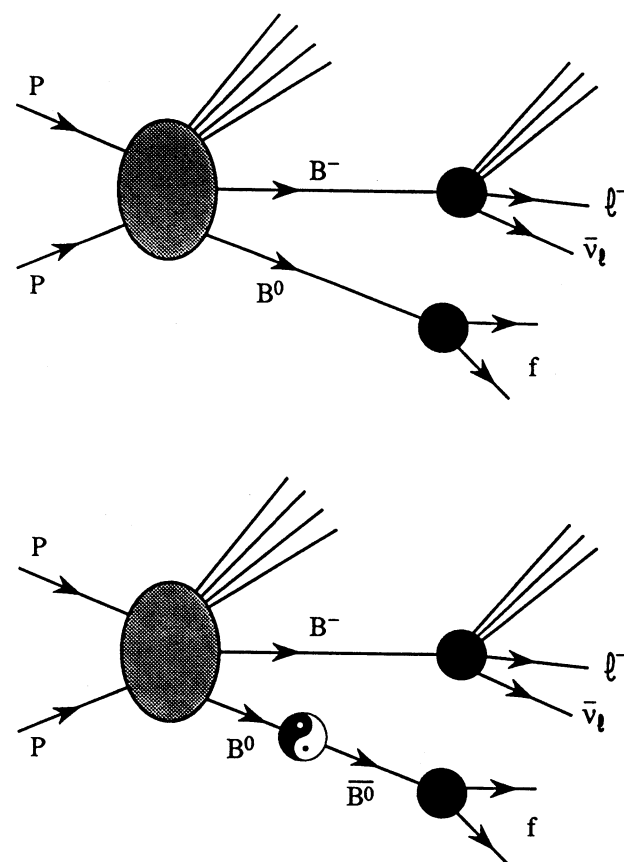


Fig. 2

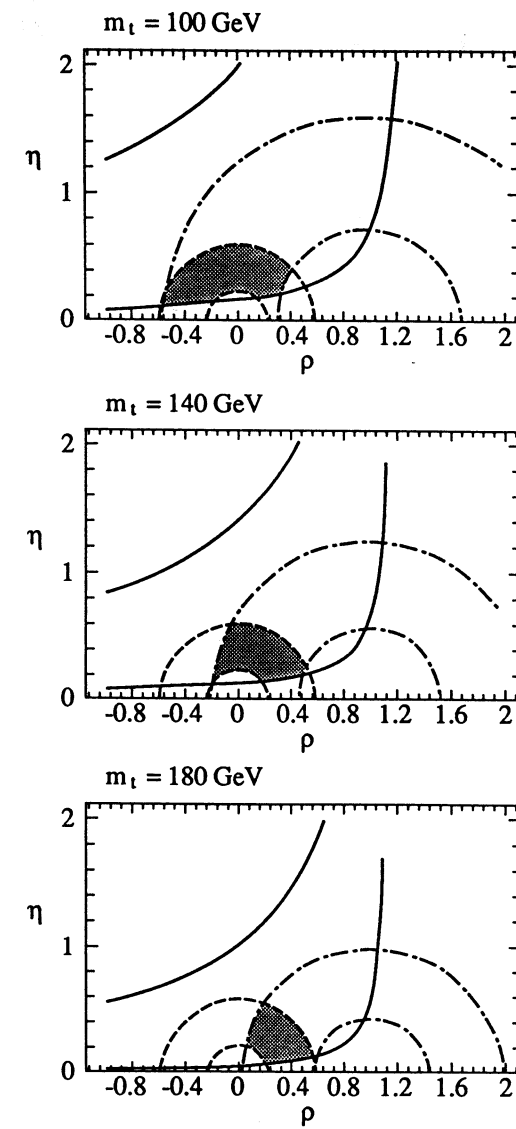
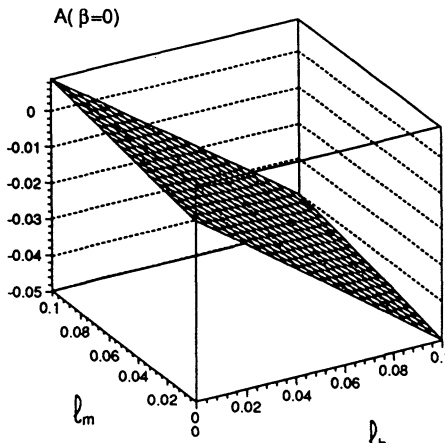
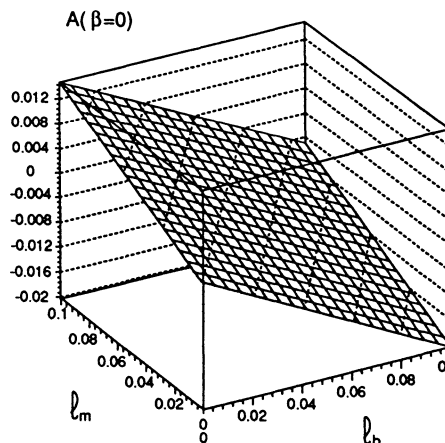


Fig. 3



(a)



(b)

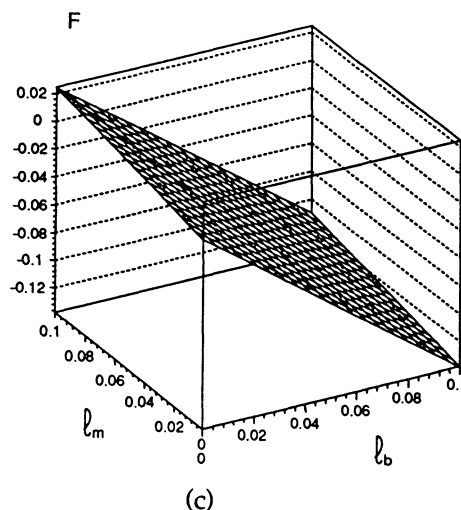


Fig. 4

Remarks on B-Physics with Interactions of $p\bar{p}$ and e^+e^- *

A. Fridman[†] and A. Snyder

*Stanford Linear Accelerator Center, Stanford University
Stanford, California 94309*

Abstract

We compare the B -physics that could be studied with $p\bar{p}$ or e^+e^- interactions. The $p\bar{p}$ colliders at cm energies of 16 TeV (LHC) and 40 TeV (SSC) as well as asymmetric e^+e^- colliders at the $\Upsilon(4S)$ cm energy are considered. In the case of $p\bar{p}$ interactions, we discuss the B production using $p\bar{p}$ colliders and a p beam with an external fixed target. For this preliminary comparison we explore the possibility of searching CP violation in the B_d^0 , $\bar{B}_d^0 \rightarrow J/\psi K_s^0$, $\pi^+\pi^-$ decays.

* Work Supported by the Department of Energy, Contact DE-AC03-763f00515
† LPHHE, Université de Paris VI et VII

1 - Introduction

In this note we briefly compare the B -physics that could be investigated with e^+e^- or pp interactions. During these last years the construction of B -factories has been envisioned¹⁻³ in order to increase the B statistics produced in e^+e^- collisions. In fact, a factor of ~ 100 in the statistics of the

$$e^+e^- \rightarrow \Upsilon(4S) \rightarrow B\bar{B}$$

events is under investigation¹.

On the other hand, several pp collider projects have also been under consideration: the Large Hadron Collider (LHC) at a cm energy of $\sqrt{s}=16$ TeV, and the Superconducting Super Collider (SSC) at $\sqrt{s}=40$ TeV. These colliders would have the advantage of being intense sources of B mesons although they do have some inconveniences (see below). For instance, the B mesons are produced in final state with large multiplicity, which will complicate the identification of B mesons.

Because of the importance of the B -physics^{1,4}, it is useful to discuss the various advantages of the e^+e^- and pp colliders. To this end, we will investigate the possibility of searching for CP violation in the B_d^0 decay. We consider the case where B_d^0 and \bar{B}_d^0 decay into a self-conjugated state, $f = \bar{f}$. Thus CP violation would mean that differences should be observed between the $B_d^0 \rightarrow f$ and $\bar{B}_d^0 \rightarrow f$ decay rates. For the present discussion we consider the following decays:

$$\begin{aligned} B_d^0, \bar{B}_d^0 &\rightarrow J/\psi K_s^0 \\ &\rightarrow \pi^+\pi^- \end{aligned}$$

The branching ratio of the $B \rightarrow J/\psi K_s^0$ was found to be $\sim 4 \times 10^{-4}$ with a $J/\psi \rightarrow l^+l^-$ decay rate of 14 % (Ref. 5). Theoretical models⁶ indicate that the $B \rightarrow \pi^+\pi^-$ branching ratio is expected to be of the order of $\sim 2 \times 10^{-5}$.

In the next section we discuss the theoretical aspects related to the measurement of CP violation^{7,8}. Section 3 considers the measurement possibilities of pp collisions. We essentially investigate the properties of generated events for the LHC and SSC colliders. For e^+e^- interactions (Section 4) we discuss the results obtained from the investigation of an asymmetric collider¹ (9×3.1 GeV²). Finally the discussion and conclusions are given in Section 5.

2 - The B_d^0, \bar{B}_d^0 decays

Because of mixing phenomena (and also because $f = \bar{f}$), the search for CP violation requires the tagging of the second B in each event. As usual, we consider that the tagging is given by the charge of the lepton (l) in the semileptonic decay ($B \rightarrow l^+X, \bar{B} \rightarrow l^-X, X$ meaning anything). This means that CP violation will be observed if

$$A = \frac{N_+ - N_-}{N_+ + N_-} \neq 0.$$

Here N_+ (N_-) represents the number of l^+fX (l^-fX) events in a given experiment. Fig. 1a gives the number of events, $N = N_+ + N_-$, necessary to detect a given asymmetry with three or five standard deviations. To obtain the real number of $B\bar{B}$ events, we must take into account the branching ratios as well as the efficiency for detecting the decay channels. Clearly the number of $B\bar{B}$ events needed for the analysis will be very important.

For pp interactions the B and \bar{B} are not produced in equal amount⁹, thus complicating the measurement of the A parameter (See below). However, the decay time distribution of $B_d^0, \bar{B}_d^0 \rightarrow f$ obtained with the lepton tagging can be used for searching CP violation¹⁰. The time-correlation function between the decay of the two B mesons is given by^{7,11}

$$\frac{d\sigma(l^\pm f)}{d\tau_l d\tau_f} = |T|^2 e^{-(n+\tau_f)} [1 \pm n \sin x(\tau_l - \tau_f)] \quad (1)$$

where $\tau_{l,f}$ are the decay times in units of B lifetimes and $x = \Delta M/\Gamma$ is a parameter describing the mixing (ΔM is the mass difference between the heavy and light B and Γ is their average width). As usual, we assume that there is no CP violation in the decay amplitude (T) and in the $B^0 - \bar{B}^0$ mixing. The quantity $n \equiv Im\lambda$ is responsible for the CP violation in the B^0 decay.

For the reactions considered here, simple expressions can be obtained for

$$\lambda = \eta \frac{\langle f | \bar{B}^0 \rangle}{\langle f | B^0 \rangle}$$

where

$$\eta \simeq \frac{V_{tb}^* V_{td}}{V_{tb} V_{td}^*} \simeq \frac{V_{td}}{V_{td}^*} = e^{2i\varphi_1}$$

is due to the $B^0 - \bar{B}^0$ mixing, V_{ij} being the CKM matrix elements⁷. For the

$B_d^0 \rightarrow J/\psi K_s^0$, the ratio of the amplitudes becomes

$$\frac{< f|\bar{B}^0 >}{< f|B^0 >} = \frac{V_{cb}^* V_{cs}}{V_{cb} V_{cs}^*} \simeq 1.$$

Hence,

$$\lambda = e^{2i\varphi_1}$$

Neglecting penguin diagrams for the $B_d^0 \rightarrow \pi^+ \pi^-$ decay, one obtains by a similar calculation

$$\lambda = \frac{V_{td} V_{ub}^*}{V_{td}^* V_{ub}} = e^{2i\varphi_2}.$$

Thus the measurement of the two decay channels will allow us to determine two angles ($\varphi_{1,2}$) present in the unitarity triangle of the 3×3 CKM matrix¹².

3 - pp interactions

There are essentially two methods for studying the $pp \rightarrow B\bar{B}X$ interactions. The first one consists of using the pp collider¹³, whereas the second method uses the interaction of a p beam with an external fixed target¹⁴. Table 1 compares the characteristics of the $B\bar{B}$ production in various accelerator cases. The total (σ_T) and $b\bar{b}X$ ($\sigma(b\bar{b})$) cross sections are theoretical predictions for the pp interactions¹⁵⁻¹⁷. The uncertainty is rather important for the $pp \rightarrow b\bar{b}X$ case¹⁷. Nevertheless it appears that σ_T and $\sigma(b\bar{b})$ are much larger in pp than in e^+e^- interactions (Table 1).

Table 2 presents the advantages and inconveniences of the various cases. Note that the number of $b\bar{b}X$ events per year ($10^7 s$) is much larger in the suggested pp interactions than in the e^+e^- collisions. For the LHC collider we use a luminosity of $10^{32} cm^{-2}s^{-1}$ so that two or more interactions per bunch crossing is unlikely. The average charged multiplicity $< n_c >$ (Ref. 18) and the $\sigma(b\bar{b})/\sigma_T$ values show, however, that it will not be easy to extract the B signal from the pp final state. In addition, the tremendous production rate (10^7 events per second for the SSC and LHC colliders) indicates that the triggering will be a major problem^{13,14}. For pp interactions, searching for CP violation by measuring the A parameter might have some complications because the B and \bar{B} are not produced in equal amount. The first effect is due to a combination of produced b or \bar{b} quarks with the u and d quarks contained in the beam particle (B^+ , B_d^0 or beauty-baryon). In this case the produced B mesons have a small transverse momentum ($p_T \leq 5$ Gev/c) and the number of B mesons is larger than the \bar{B} ones⁹. The second effect appears when the produced b and \bar{b} quarks have a large transverse momentum $p_T \gg 5$ Gev/c

(and hence the produced B mesons). For such p_T values the structure functions contribute mainly to the production of the u quarks. This leads to additional B^+ production and decreases the B_d^0 and B_s^0 in the final state¹⁹. To estimate the influence of the unequal B and \bar{B} amounts, we present in Fig. 1b, $A_m - A$ as a function of A , A_m being the measured asymmetry parameter

$$A_m = \frac{N_+(1 + \epsilon) - N_-}{N_+(1 + \epsilon) + N_-}.$$

Here ϵ is due to the unequal B and \bar{B} quantities, which are estimated to be in the $|\epsilon| = (2 - 10) \times 10^{-3}$ domain⁹. Note that the order of magnitude of $A - A_m$ is mainly important for small A values. In any case the ratio of B to \bar{B} production should be measured. This could be done, for instance, for the B^\pm by using their decay into states without CP violation.

In the following we investigate the possibility of identifying B mesons and in particular those that decay into the $J/\psi K^0$ and $\pi^+ \pi^-$ states. To this end, we use the PYTHIA Monte Carlo program²⁰. For each calculation we used about 2000 generated events. We first consider the pp collider and then the p interactions with a fixed target.

a) The collider

Table 3 presents the average momentum ($< p >$) and transverse momentum ($< p_T >$) of the produced B or \bar{B} for various θ_B limits. Here θ_B is the B or \bar{B} emission angle defined with respect to the beam direction ($0 \leq \theta_B \leq 90^\circ$). Table 3a (3b) corresponds to the LHC (SSC) project. We first notice that $< p_T >$ does not depend very much on the θ_B limit, whereas $< p >$ decreases strongly when the angular limit is increased. Apart from $< p >$ for $\theta_B > 0^\circ$, the calculated values for the LHC and SSC collider are nearly equal.

Smaller B momentum and wider emission angle may simplify detection of B mesons, but the number of $B\bar{B}$ events decreases. (The fraction of events with B or \bar{B} is $F(B) \simeq 30\%$ for $\theta_B > 20^\circ$, Table 3) As expected in large pp cm energy, a large amount of B and \bar{B} tend to be emitted with a relatively small opening angle θ_{BB} ($< \cos \theta_{BB} > \sim 0.5$ for $\theta_B > 0^\circ$). However, for $\theta_B > 20^\circ$ the $\cos \theta_{BB}$ distribution tends to become symmetric (see Table 3). This means that the detection of two B mesons in an event becomes more difficult. The study of the opening angle in the transverse plane (with respect to the beam direction) indicates that

$$f(160^\circ < \theta_{XY} < 180^\circ) \simeq 0.2$$

of the $B\bar{B}$ events have the B and \bar{B} produced back to back in the transverse plane

(Table 3). This percentage does not depend strongly of the θ_B limit. The back-to-back configuration simplifies the detection of the two B mesons, but it further reduces the statistics.

Table 4 presents the average momentum and transverse momentum of the charged unbiased tracks and those coming from the B decay. These values are calculated for $\theta > 0^\circ$, 1° , 20° where θ is the track emission angle with respect to the beam direction ($0 \leq \theta \leq 90^\circ$). In the general B decay case (for the LHC and SSC) we see that $\langle p \rangle$ and $\langle p_T \rangle$ of the unbiased tracks are nearly equal to the B decay tracks for $\theta > 1^\circ$, 20° . However, for the decay channels under discussion, the situation is different, particularly for the $B \rightarrow \pi^+\pi^-$. Here cuts on p or p_T of the charged decay tracks might decrease the background without doing much harm to the signal (see also Fig. 2).

For the $B^0 \rightarrow J/\psi K_s^0$ one has, in particular, to estimate the background due to the misidentification of outgoing particles. In any case the $J/\psi \rightarrow l^+l^-$ and $K_s^0 \rightarrow \pi^+\pi^-$ will be very efficient for reconstructing the B^0 decay and decreasing the background. One has also to estimate the branching ratio $B^0 \rightarrow J/\psi K_s^0\pi^0$ and to verify that this decay will not simulate the $B^0 \rightarrow J/\psi K_s^0$ channel, both decays can have an opposite CP violation sign. Reference (13) estimated that they will be able to reconstruct $3 \times 10^6 B_d^0 \rightarrow J/\psi K_s^0$ decays in one year (10^7 s) of running the SSC project with a luminosity of $10^{32} \text{ cm}^{-2}\text{s}^{-1}$. In addition, an efficient tagging method has to be investigated in order to search for CP violation.

The background for the $B \rightarrow \pi^+\pi^-$ case is more important because, among other things, the branching ratio of this decay is expected to be small ($\sim 2 \times 10^{-5}$). Fig. 2 presents the fraction of $B \rightarrow \pi^+\pi^-$ events left after taking only π^\pm having a transverse momentum larger than $p_T(\text{cut})$. The same figure also presents the fraction of $\pi^+\pi^-$ due to background as a function of $p_T(\text{cut})$. Here the background is only calculated from $B\bar{B}$ events. These curves are practically identical for the LHC and SSC cases. We see that by increasing $p_T(\text{cut})$, one decreases the background, whereas the number of $B \rightarrow \pi^+\pi^-$ events decreases much more slowly.

As an example, we present in Fig. 3 for the SSC case, the S/B ratio as a function of $p_T(\text{cut})$ for $\theta > 1^\circ$, and where the $\pi^+\pi^-$ mass is within ± 0.05 GeV of the B mass. Here S/B is the signal-to-background ratio obtained in a sample of $B\bar{B}$ events and found to be very small. Also shown is a curve where, in addition, we require that $\cos \theta_{\pi\pi} > 0.9$. Here, $\theta_{\pi\pi}$ is the angle between the two pions. Note from Fig. 3 that S/B increases with $p_T(\text{cut})$, whereas the fraction of $B\bar{B}$ events ($F(\theta)$ in this figure) does not decrease very much. For one year of running at the SSC project, $2 \times 10^6 B_d^0 \rightarrow \pi^+\pi^-$ decays could be reconstructed according to

reference (13). However, an efficient tagging method must also be envisioned for this case.

b) The fixed target

For the LHC (SSC) the interaction with a fixed target will occur at a rather low cm energy, $\sqrt{s} = 0.123$ TeV (0.193 TeV), although the momentum of the outgoing particles will be very large (Table 5). The small cm energy may lead to several advantages¹⁴, namely

- higher momentum of the outgoing tracks leads to a better momentum resolution because multiple scattering is decreased
- highest momentum of the produced B 's allows them to pass through a large microvertex device before decaying
- higher momentum of μ and e coming from the B decay may decrease the triggering difficulties
- lower multiplicity ($\langle n_c \rangle \simeq 20$) will decrease the background for the reconstruction of B meson.

Fig. 2 presents the fraction of $B \rightarrow \pi^+\pi^-$ events left after taking π^\pm with transverse momentum larger than $p_T(\text{cut})$. We see that $p_T(\text{cut})$ will be very useful for detecting the $B \rightarrow \pi^+\pi^-$ and will also increase the S/B ratio (similar to Fig. 3). The level of S/B is about one order of magnitude larger in the fixed target than for the collider (but still very small). However, the decay length of the B mesons are large for the fixed target experiment (See Table 5). This might help the reconstruction of B mesons and therefore improve the S/B ratio. The difficulty of the target experiment is mainly related to the small emission angle of the outgoing particles with respect to the beam line (Table 6). In addition, the large momentum of the tracks may also complicate the reconstruction and the measurement of the outgoing particles. A final consideration is that the construction of a p beam will require large efforts.

Table 1 - Some properties of the various accelerator possibilities for $B\bar{B}$ production. For pp interactions we consider the target (T) and the collider (C) cases. They are compared with e^+e^- possibilities, CESR and the new CESR and SLAC B factory projects (P). Note that the CESR (SLAC) project is a symmetric (asymmetric) collider. Here σ_T is the total pp or e^+e^- cross section, $\sigma(b\bar{b})$ is the $b\bar{b}X$ cross section, and L is the luminosity of the collider.

	\sqrt{s} TeV	L $cm^{-2}s^{-1}$	σ_T mb	$\sigma(b\bar{b})$ μb
LHC (T)	0.123	-	$\sim 50^{(16)}$	~ 2
SSC (T)	0.193	-	$\sim 58^{(b)}$	$2.5 - 10^{(14)}$
LHC (C)	16	10^{34} (a)	$\sim 110^{(16)}$	$\sim 200^{(17)}$
SSC (C)	40	10^{32} (13)	$\sim 100^{(13)}$	$\sim 500^{(13)}$
CESR	10.58 GeV	$3.6 \cdot 10^{31}$ (3)	$\sim 4 nb^{(3)}$	$1.2 nb^{(3)}$
CESR (P)	"	10^{34} (3)	"	"
SLAC (P)	"	$3 \cdot 10^{33}$ (1)	"	"

(a) G. Brianti, ECFA meeting at CERN in June 1990.

(b) This is the cross section used for calculating that obtained with a mixture of Be and Si, reference (14).

Table 2 - The advantages and inconveniences of the various cases. Same definitions and references as in Table 1 with $N(b\bar{b})$ representing the number of $b\bar{b}$ events. For pp interactions the $\langle n_c \rangle$ are calculated for non-diffractive events¹⁸. In the case of the LHC (C) we used a luminosity of $10^{32} cm^{-2}s^{-1}$ (see text).

	$\langle n_c \rangle$	$\sigma(b\bar{b})/\sigma_T$	$N(b\bar{b})/(10^7 s)$
LHC (T)	~ 17	$\sim 1/25 K$	$\sim 9.6 \cdot 10^9$
SSC (T)	~ 20	$\sim 1/8000$	$(1 - 5) \cdot 10^{10}$
LHC (C)	~ 80	$\sim 1/550$	$\sim 2 \cdot 10^{11}$
SSC (C)	~ 115	$\sim 1/200$	$\sim 5 \cdot 10^{11}$
CESR	~ 12	$1/4$	$4.3 \cdot 10^5$
CESR (P)	"	"	$1.2 \cdot 10^8$
SLAC (P)	"	"	$3.6 \cdot 10^7$

Table 3a - The Monte Carlo predictions of the average momentum (p) and the transverse momentum (p_T) of the B meson in the laboratory system (GeV/c) of the LHC collider for various θ_B limits. Here θ_B is the B emission angle with respect to the beam direction. We also give $\langle \cos \theta_{BB} \rangle$ and $\langle \cos \theta_{XY} \rangle$, where θ_{BB} and θ_{XY} are the $B\bar{B}$ opening angle in the laboratory system and in the transverse plane with respect to the beam direction, respectively. The parameter F denotes the fraction of B or \bar{B} , whereas f represents the fraction of $B\bar{B}$ events.

	$\theta_B \geq 0^\circ$	$\theta_B \geq 1^\circ$	$\theta_B \geq 20^\circ$
$\langle p \rangle$	124	64	26
$\langle p_T \rangle$	6.9	7.2	7.7
$F(\theta_B)$	100 %	~ 91 %	~ 36 %
$\langle \cos \theta_{BB} \rangle$	0.54	0.46	-0.05
$f(\theta_{BB} < 20^\circ)$	0.43	0.33	0.03
$f(160^\circ < \theta_{BB} < 180^\circ)$	0.03	0.04	0.07
$\langle \cos \theta_{XY} \rangle$	-0.25	-0.28	-0.29
$f(\theta_{XY} < 20^\circ)$	0.04	0.04	0.04
$f(160^\circ < \theta_{XY} < 180^\circ)$	0.17	0.18	0.19

Table 3b - Same as in Table 3a but for the SSC collider.

	$\theta_B \geq 0^\circ$	$\theta_B \geq 1^\circ$	$\theta_B \geq 20^\circ$
$\langle p \rangle$	180	70	27
$\langle p_T \rangle$	7.6	7.9	8.4
$F(\theta_B)$	100 %	~ 89 %	~ 41 %
$\langle \cos \theta_{BB} \rangle$	0.57	0.49	-0.06
$f(\theta_{BB} < 20^\circ)$	0.42	0.32	0.02
$f(160^\circ < \theta_{BB} < 180^\circ)$	0.03	0.03	0.04
$\langle \cos \theta_{XY} \rangle$	-0.19	-0.24	-0.31
$f(\theta_{XY} < 20^\circ)$	0.06	0.05	0.02
$f(160^\circ < \theta_{XY} < 180^\circ)$	0.15	0.16	0.17

Table 4a - The order of magnitude of the average momentum ($\langle p \rangle$) and transverse momentum ($\langle p_T \rangle$) for the unbiased charged tracks and for those coming from the B decay in GeV/c. The Monte Carlo calculations have also been done for tracks having an angle θ greater than 1 and 20 degrees with respect to the beam direction. The values correspond to the LHC collider.

		unbiased tracks	tracks from B or \bar{B}	tracks from $B \rightarrow \pi\pi$	tracks from $B \rightarrow \psi K_s$
All	$\langle p \rangle$	89	12	53	27
	$\langle p_T \rangle$	0.49	0.90	4.1	2.1
$\theta > 1^\circ$	$\langle p \rangle$	5.9	7.0	32	16
	$\langle p_T \rangle$	0.54	0.91	4.2	2.4
$\theta > 20^\circ$	$\langle p \rangle$	0.94	1.5	6.6	3.3
	$\langle p_T \rangle$	0.59	0.98	4.2	2.1

Table 4b - Same as in Table 4a but for the SSC collider.

		unbiased tracks	tracks from B or \bar{B}	tracks from $B \rightarrow \pi\pi$	tracks from $B \rightarrow \psi K_s$
All	$\langle p \rangle$	190	21	58	41
	$\langle p_T \rangle$	0.5	1.0	4.0	2.3
$\theta > 1^\circ$	$\langle p \rangle$	6.2	7.7	32	17
	$\langle p_T \rangle$	0.6	1.0	4.2	2.3
$\theta > 20^\circ$	$\langle p \rangle$	1.0	1.6	7.0	3.7
	$\langle p_T \rangle$	0.6	1.0	4.5	2.3

Table 5 - The average momentum (p) and transverse momentum (p_T) of the B meson in the laboratory system for the LHC and SSC target experiments (GeV/c). The θ_{XY} and the fraction f of $B\bar{B}$ events (same as in Table 3a and 3b) are also given in this table.

	LHC	SSC
$\langle p \rangle$	617	1165
$\langle p_T \rangle$	3.3	3.6
$\langle \cos \theta_{XY} \rangle$	-0.63	-0.55
$f(\theta_{XY} < 20^\circ)$	0.02	0.03
$f(160^\circ < \theta_{XY} < 180^\circ)$	0.42	0.35

Table 6a - Results for the target case in the LHC. The momentum and transverse momentum are given in GeV/c.

	unbiased tracks	tracks from B or \bar{B}	tracks from $B \rightarrow \pi\pi$	tracks from $B \rightarrow \psi K_s$
$\langle p \rangle$	165	67	306	151
$\langle p_T \rangle$	0.46	0.57	2.7	1.4
$\langle \cos \theta \rangle$	0.989	0.999	0.998	0.998

Table 6b - Same as in Table 6a but for the target experiment with the SSC.

	unbiased tracks	tracks from B or \bar{B}	tracks from $B \rightarrow \pi\pi$	tracks from $B \rightarrow \psi K_s$
$\langle p \rangle$	342	126	565	287
$\langle p_T \rangle$	0.47	0.60	2.8	1.4
$\langle \cos \theta \rangle$	0.991	0.999	0.999	0.999

4 - e^+e^- interactions

With a symmetric collider the $e^+e^- \rightarrow \Upsilon(4S) \rightarrow B_d^0\bar{B}_d^0$ reaction cannot be used to search for CP violation in the B^0 decay when $f = \bar{f}$ (Ref. 21). This is because the relative orbital momentum (L) between the outgoing B mesons is odd, yielding $A = 0$ (even in the presence of CP violation). However, time-dependent quantities obtained from formula (1) are still sensitive to CP violation in the B decay. Note that at the cm just above the $\Upsilon(4S)$ ($\sqrt{s} \simeq 10.72$ GeV), the $B\bar{B}^*$ or $\bar{B}B^*$ pair can be produced. Here, the even value of L between the $B\bar{B}$ in the $B\bar{B}\gamma$ final state would allow us to search for CP violation. However, the $B\bar{B}$ cross section at $\sqrt{s} \simeq 10.72$ GeV is much smaller than the $\Upsilon(4S)$ production cross section²².

We reiterate that even in the case of CP violation ($n \neq 0$) the number of l^+fX and l^-fX events are equal ($N_+ = N_- = N/2$) for the $\Upsilon(4S) \rightarrow B^0\bar{B}^0$ decay. However, by using formula (1) one obtains²³

$$\begin{aligned} N_{\pm}(\tau_l > \tau_f) &= \frac{N}{2} \left[1 \pm \frac{nx}{1+x^2} \right] \\ N_{\pm}(\tau_l < \tau_f) &= \frac{N}{2} \left[1 \mp \frac{nx}{1+x^2} \right] \end{aligned} \quad (2)$$

This means that a possible observation of differences between N_+ (or N_-) in the $\tau_l < \tau_f$ and $\tau_l > \tau_f$ regions would indicate CP violation in the B^0 decay^{23,24}. One could then obtain an estimate of n from the rate

$$\begin{aligned} r &= \frac{N_+(\tau_l > \tau_f) + N_-(\tau_l < \tau_f) - N_+(\tau_l < \tau_f) - N_-(\tau_l > \tau_f)}{N_+(\tau_l > \tau_f) + N_-(\tau_l < \tau_f) + N_+(\tau_l < \tau_f) - N_-(\tau_l > \tau_f)} \\ &= \frac{nx}{1+x^2} \end{aligned} \quad (3)$$

with a statistical error of

$$\frac{\Delta r}{r} = \frac{1}{\sqrt{2N}} \frac{1}{nx} \sqrt{(1+x^2)^2 - n^2x^2}$$

In e^+e^- symmetric colliders, the produced B or \bar{B} have very small momenta, leading to an average decay length of about 20 μm . Thus time-dependent measurements appear not to be possible.

With an asymmetric collider having an $\Upsilon(4S)$ cm energy, the decay length can be an order of magnitude larger than in the symmetric case²³. In this case

the $\Upsilon(4S)$ will move in the laboratory system while the B will travel in the same direction (but with a small emission angle with respect to the beam line). In principle we can measure the difference ΔR between the decay vertices. Strictly speaking, the τ_l, τ_f order in the $\Upsilon(4S)$ rest frame is not always equal to the decay vertex order in the laboratory system. The fraction of events that will have their proper time and their laboratory decay length ordering reversed is of the order of 2 % (Ref. 23). By neglecting this fraction as well as the B momentum in the $\Upsilon(4S)$ rest frame, we can relate ΔR with $\Delta = \tau_l - \tau_f$, namely

$$\Delta R \simeq \beta \gamma c \Gamma (\tau_l - \tau_f)$$

(β, γ are the parameters transforming quantities from the $\Upsilon(4S)$ rest frame to the laboratory system, Γ is the B^0 decay width) and then measure the $N_{\pm}(\tau_l > \tau_f)$ and $N_{\pm}(\tau_l < \tau_f)$ parameters.

With the above assumptions, one can also use the Δ distribution, which will be more efficient in searching the CP violation than the measurement of r (formula (3)). Indeed formula (1) can be transformed to^{23,24}

$$\frac{d\sigma(l^{\pm}f)}{d\Delta} = |T|^2 e^{-\Delta} [1 - n \sin x\Delta] \quad (4a)$$

$$\Delta = \tau_{l+} - \tau_f, \quad \tau_f - \tau_{l-} > 0$$

and

$$\frac{d\sigma(l^{\pm}f)}{d\Delta} = |T|^2 e^{-\Delta} [1 + n \sin x\Delta] \quad (4b)$$

$$\Delta = \tau_f - \tau_{l+}, \quad \tau_{l-} - \tau_f > 0.$$

Thus the comparison of these Δ (or decay length difference) distributions with a purely exponential distribution would be an efficient method of searching for CP violation.

As an example Fig. 3 presents the distributions of the decay length difference given in reference (1) between the meson decay into the $J/\psi K_s^0$ and that used for the tagging purpose. The curves are obtained using 6914 events generated with $x = 0.75$ and $n = -0.4$. The simultaneous fit of the two distributions shown in Fig. 3 (full lines) allows them to obtain $n = -0.408 \pm 0.023$, which is very close to the input value. In this framework the background has also been studied¹ by considering the following among the 6914 events

- having a hadron misidentified as a lepton to form a $J/\psi K_s^0$ candidate
- having both B decaying semileptonically and simulating $J/\psi \rightarrow l^+l^-$
- having $B \rightarrow J/\psi K_s^0 \pi^0$ simulating the $B \rightarrow J/\psi K_s^0$ channel, both decays having opposite CP violation signs.

The study of these channels leads to a background of $\sim 6\%$. With one year of running, reference (1) estimates that n could be measured to an accuracy of ± 0.07 .

The $B \rightarrow \pi^+\pi^-$ branching ratio is expected to be much smaller ($\sim 2 \times 10^{-5}$) than the above case. In addition, particle identification is necessary to decrease the background due to the $B \rightarrow \pi^\pm K^\mp$, K^+K^- which may simulate the $B \rightarrow \pi^+\pi^-$ decay. With a Cerenkov ring imaging detector (CRID) in the project of reference (1), it would be possible to decrease this background. To obtain 1000 events where one meson is decaying into the $\pi^+\pi^-$ and the other one in semileptonic decay, the project of reference (1) estimates that $\sim 4 \times 10^8 B\bar{B}$ would be necessary. The error of n will be now much larger, namely ~ 0.06 .

5 - Discussion and Conclusion

We see that the LHC and SSC colliders are very similar for studying B -physics. The high luminosity of the LHC project compensates partly the higher $pp \rightarrow b\bar{b}X$ cross section expected at the SSC cm energy. The ratio of the number of $B\bar{B}$ events between the SSC and the LHC is ~ 2.5 . Furthermore we note that for B mesons emitted with angles greater than 20° , the $\cos \theta_{B\bar{B}}$ distribution becomes symmetric ($\theta_{B\bar{B}}$ is the opening angle between the produced B mesons). This difficulty in identifying $B\bar{B}$ events might be overcome by studying the tracks in the transverse plane (transverse to the beam direction). In this case about $\sim 20\%$ of the $B\bar{B}$ events will appear back-to-back in the transverse plane. From the present discussion it appears that it will not be easy to detect the $B_d^0 \rightarrow \pi^+\pi^-$ channel because of the large background and the small value of signal to background.

The SSC letter of intent¹³ indicates that the large statistics of $B\bar{B}$ events should allow us to increase our knowledge concerning the B decays. However, to search for CP violation in the B^0 decay, the tagging of the other B is necessary as well as the measurement of the relative amount of B and \bar{B} production.

The experiment with a fixed target has many advantages¹⁴ but also some inconveniences. The fact that the particles are emitted with a small angle (with respect to the beam line) may complicate the momentum measurements of outgoing tracks, the identification of B mesons, and tagging purposes.

With an asymmetric collider the study of the $e^+e^- \rightarrow \Upsilon(4S) \rightarrow B\bar{B}$ reaction is much simpler than the $B\bar{B}$ production in pp collisions. The charged multiplicity

and the momentum of the outgoing particles are low in these e^+e^- interactions¹ thus allowing an easy identification of the charged particles. The search for CP violation in the B_d^0 decay can simply be done by measuring the length difference between the meson decaying into a given f state (here we consider states where $f = \bar{f}$) and that used for tagging purpose. The inconvenience, however, is that the number of $B\bar{B}$ per year for the SLAC project¹ (3×10^7) is not large, and in fact is much smaller than for the pp colliders ($\sim 5 \times 10^{11}$ at the SSC). However, the CP violation at the level assumed by the SLAC project could be investigated.

To summarize, we can say that the pp interactions at large cm energies (LHC and SSC) as well as the asymmetric e^+e^- collider (the SLAC project) might allow us to increase our understanding of B physics. Both approaches have advantages and inconveniences although the $B \rightarrow \pi^+\pi^-$ does not appear to be measurable in pp interactions. Nevertheless, the continuation of the present investigations will be of great interest for our future experiments.

Acknowledgments

It is a pleasure to thank E. Bloom, J. Dorfan and T. Sjostrand for useful discussions.

References

- 1) The Physics Program of a High-Luminosity Asymmetric B -Factory, SLAC-353 (1989);
- 2) Proposal for an Electron Positron Collider for Heavy Flavor Particle Physics and Synchrotron Radiation, PSI, PR-88-09, July 1988;
- 3) Prospects for a CESR B -Factory Upgrade, CLNS 89/962 (1989);
- 4) See, for instance, Justification for an Asymmetric B Factory, presented at the HEPAP Subpanel, J. Dorfan, March 8, 1990;
- 5) Particle Data Group, Phys. Letters, B239 (1990);
- 6) The $B \rightarrow \pi^+ \pi^-$ branching ratio is predicted to be $2.1 \times 10^{-3} |V_{ub}/V_{cb}|^2$ by M. Braun, B. Stech and M. Wirblel, Z. Phys. C34, 103 (1987). The V_{ij} are CKM matrix elements using here $|V_{ub}/V_{cb}| = 0.1$
- 7) I.I. Bigi and A.L. Sanda, Nucl. Phys. B281, 41 (1987);
- 8) I. Dunietz and J.L. Rosner, Phys. Rev. D34, 1404 (1986);
- 9) Remarks about CP Violation Measurements for B -Mesons Produced in pp Interactions, A. Fridman, CERN-EP/90-87 (1990);
- 10) Remarks about Measuring CP Violation Effects in B Decays, A. Boden and A. Fridman, UCLA-HEP-89-002 (1989);
- 11) See also the lectures "Mixing and CP Violation in the B -System", A. Fridman, CERN-EP/88-123 (1988);
- 12) C.O. Dib, I. Dunietz, F.J. Gilman and Y. Nir, Phys. Rev. D41, 1522 (1990);
- 13) Expression of Interest for a Bottom Collider Detector at the SSC, Letter of Intent (1990);
- 14) An Expression of Interest in a Super Fixed Target Beauty Facility at the SSC, Letter of Intent (1990);
- 15) G.J. Alner et al., Z. Phys. C32, 153 (1986);
- 16) M.M. Block and R.N. Cahn, Nucl. Phys. 188B, 143 (1987);
- 17) K.J. Foley et al., Proceedings of the Workshop on Experiments, Detectors, and Experimental Areas for the Supercollider, July 7-17, 1987, Berkeley; Private communications: R.K. Ellis (1989) and E.L. Berger (1990);
- 18) The $\langle n_c \rangle$ in Table 2 are calculated for non-diffractive events. See T. Sjostrand and M. van Zijl, Phys. Rev. D36, 2019 (1987);
- 19) For large p_T , the number of B^+ increases whereas the numbers of B_d^0 and B_s^0 decrease. The numbers are small but not equal, see 9.
- 20) H-U. Bengtsson and T. Sjostrand, Computer Phys. Comm. 46, 43 (1987);
- 21) I.I. Bigi and A.L. Sanda, Nucl. Phys. B193, 85 (1981);
- 22) The Need for a B -Factory, presented at the HEPAP Subpanel, N. Mistry, February 1990;
- 23) Estimate of the CP Violation Effects at the $\Upsilon(4S)$ Using Decay Length Differences, E. Bloom and A. Fridman, Report presented at the Snowmass meeting (1988);
- 24) R. Aleksan, J. Bartelt, P.R. Burchat and A. Seiden, Phys. Rev. D39, 1283 (1989);
- 25) Note that with formula (1) one has $N_-(\tau_l > \tau_f) = N_+(\tau_l < \tau_f)$ and $N_-(\tau_l < \tau_f) = N_+(\tau_l > \tau_f)$.

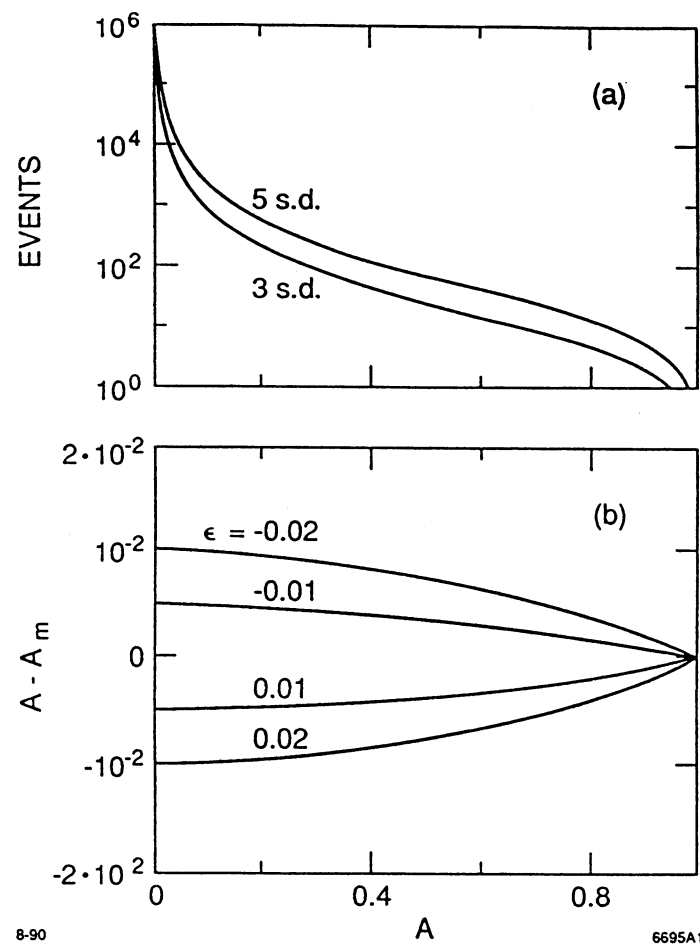


Fig 1 - a) The number of $B\bar{B} \rightarrow lfX$ events necessary to detect a given asymmetry A with 3 or 5 standard deviations. The curves are only valid for $A \leq 0.9$.
b) The $A - A_m$ as a function of A . Here A_m is the measured asymmetry due to CP violation effects and to the unequal amount of B and \bar{B} production. The latter case is described by the parameter $\epsilon \neq 0$ (see text).

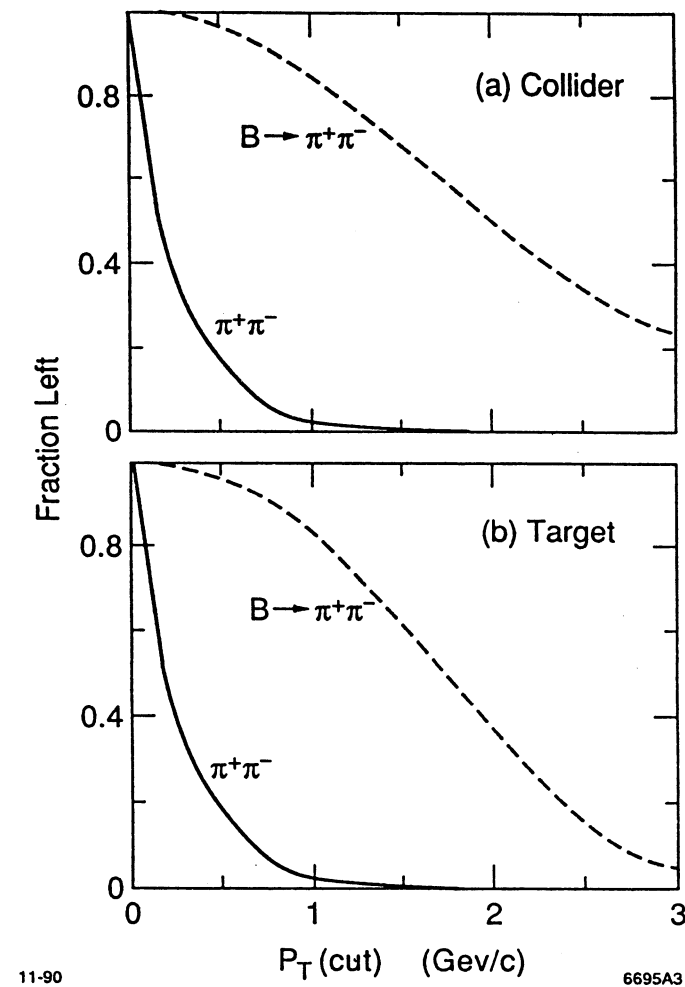


Fig. 2 - The fraction of $B \rightarrow \pi^+\pi^-$ and $\pi^+\pi^-$ background (see text) left after taking π^\pm having a momentum transfer greater than $p_T(\text{cut})$. The SSC collider and target are represented by (a) and (b), respectively.

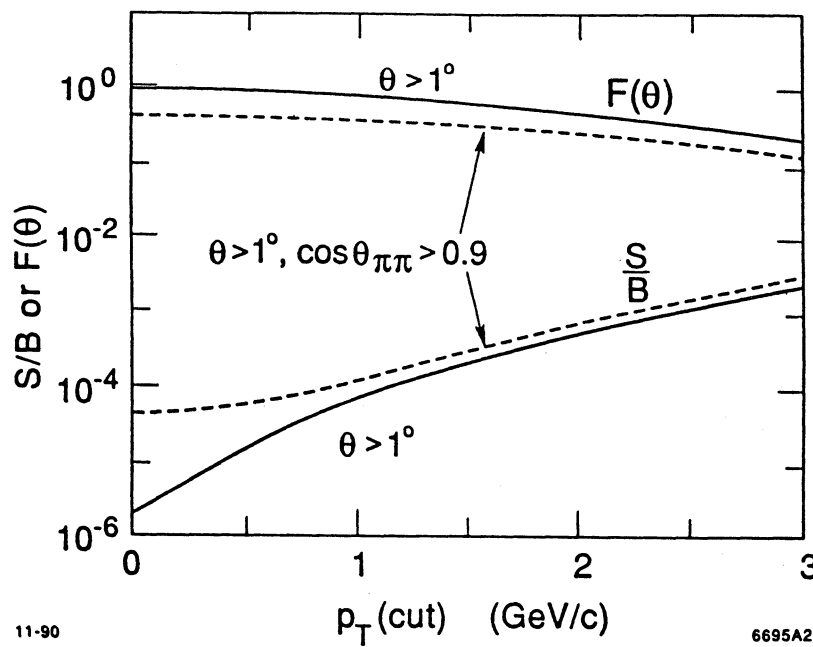


Fig. 3 - For the SSC collider the signal-to-background ratio (S/B) as a function of $p_T(\text{cut})$ for the $B \rightarrow \pi^+ \pi^-$ using also θ and $\theta_{\pi\pi}$ cuts (the two lower curves). Here θ is the angle of the π^\pm with respect to the beam direction while $\theta_{\pi\pi}$ is the opening angle between the two pions. The upper curves indicate the fraction of $B \rightarrow \pi^+ \pi^-$ ($F(\theta)$) passing the various cuts.

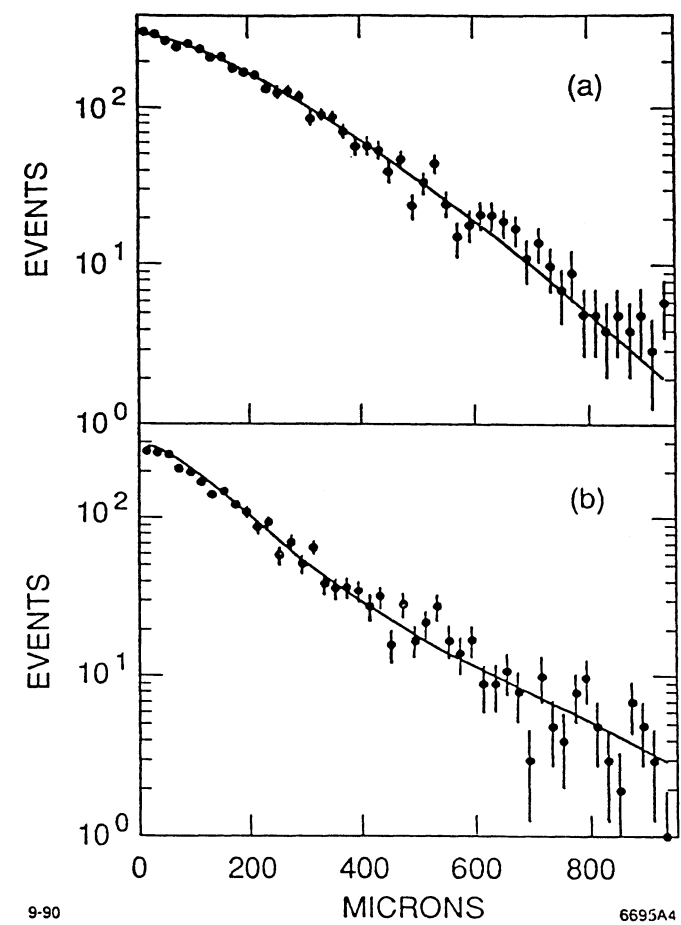


Fig 4 - The decay lenght difference between the meson decaying into the $J/\psi K_s^0$ and that used for the tagging purpose¹. The upper plot corresponds to $\tau_{l-} - \tau_f$, $\tau_f - \tau_{l+} > 0$ whereas the lower plot is obtained for $\tau_{l+} - \tau_f$, $\tau_f - \tau_{l-} > 0$.

Collider Beauty Physics at LHC

Samim Erhan, Michael Medinnis, Peter Schlein and John Zweizig

University of California^{*)}, Los Angeles, CA, U.S.A.

Abstract

How best to utilize the LHC B-Factory? Far above threshold in hadron colliders, the production of B-Mesons from gluon-gluon fusion is forward-backward peaked. The efficient detection of such systems is therefore best done with large aperture forward spectrometers and silicon microvertex detector planes perpendicular to the beam axis, similar to the geometry used in fixed-target experiments. Data acquisition can be triggered by real-time calculations on the silicon data. Results are given from a study of a possible Beauty experiment to measure CP-Violation at LHC.

1. INTRODUCTION

One of the most challenging and important problems in high energy experimental physics is how best to study rare decays of B particles (Beauty or Bottom) as a probe of possible new physics. The large cross section for $B\bar{B}$ production in hadronic interactions (e.g., 15 μ barn at Sp \bar{p} S-Collider and several hundred μ barn at LHC), coupled with sophisticated trigger processor techniques should make possible the acquisition of enormous samples of exclusive Beauty decays at hadron colliding-beam machines. In this document, we discuss a dedicated Beauty experiment for the Large Hadron Collider (LHC) which should make possible the study of CP-Violation effects in Beauty decay.

The experiment consists of a dedicated large aperture forward spectrometer with particle identification and electromagnetic calorimeter capability. There is a silicon strip microvertex detector with planes perpendicular to the beam axis, which operates in close proximity to the circulating beams. Data acquisition of the spectrometer is "triggered" by the results of real time calculations on the silicon data.

The desired aperture for such an experiment is suggested by Fig. 1, which shows the laboratory angular distribution of decay tracks from PYTHIA-generated B-Mesons produced primarily via gluon-gluon fusion¹ at $\sqrt{s} = 0.63$ and 16 TeV. The forward peaking results from the boost, due to the increasingly unequal energies of the interacting partons at higher collision energies. The striking difference between the angular distributions at $\sqrt{s} = 0.63$ and 16 TeV illustrate this dependence on collision energy. The dashed curves in Fig. 1 are for those events which have all decay track momenta larger than 200 MeV, and illustrate that most B mesons in the central region have decay tracks which have very low momenta.

It is evident from Fig. 1 that the detector must emphasize the forward direction. The maximum aperture which seems obtainable with a forward spectrometer which possesses uniformly planar geometry (all elements perpendicular to the beam axis, in the manner of fixed target experiments) is about 600 mrad. At the LHC, 72% of PYTHIA-generated $B\bar{B}$ events have all decay tracks of B or \bar{B} con-

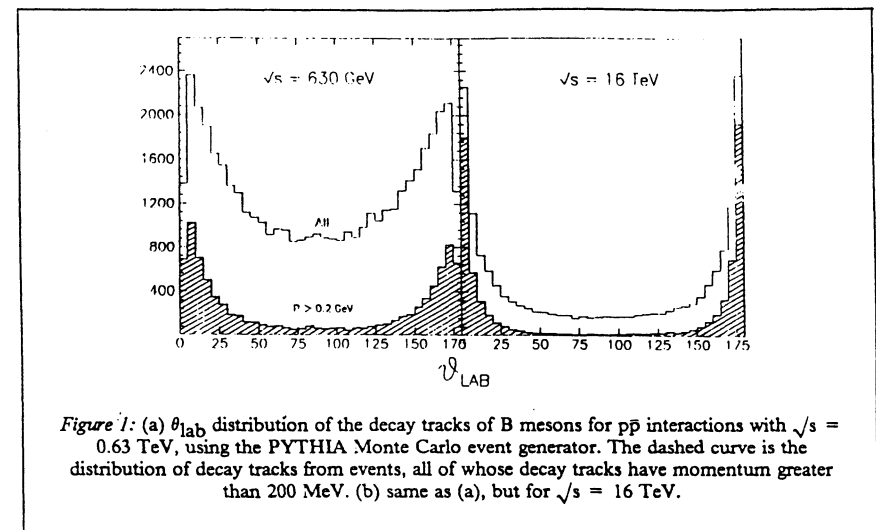


Figure 1: (a) θ_{lab} distribution of the decay tracks of B mesons for $p\bar{p}$ interactions with $\sqrt{s} = 0.63$ TeV, using the PYTHIA Monte Carlo event generator. The dashed curve is the distribution of decay tracks from events, all of whose decay tracks have momentum greater than 200 MeV. (b) same as (a), but for $\sqrt{s} = 16$ TeV.

tained in this aperture (about 32% have both B and \bar{B} contained).

Fig. 2 shows how the momenta of B-Meson decay tracks at both the LHC and the Sp \bar{p} S-Collider depend on laboratory angle. This plot allows us to understand the similarities between the track momenta at the two machines. In the angular range 100-600 mrad, the track momenta at LHC and Sp \bar{p} S are nearly the same, whereas in the angular range 10-100 mrad, tracks at LHC have roughly twice the momenta as at the Sp \bar{p} S. The necessary minimum angle can be defined as that which causes a loss of only 10% of the events whose decay tracks are fully contained in the 600 mrad aperture. At the LHC, this angle is approximately 2 mrad (at the Sp \bar{p} S, it is 10 mrad).

Fig. 3 shows the momentum distribution at the LHC of PYTHIA-generated B-Mesons. The shaded events are those, whose momentum vector lies within the 600 mrad aperture, and the solid events are those whose decay tracks are all within the 600 mrad aperture. The average momentum of the accepted B-Mesons is about 200 GeV, although this is greatly influenced by the long tail.

The LHC spectrometer which satisfies the aperture requirements discussed above and has the planar geometry required for minimal complexity and expense is shown in Fig. 4. The apparatus is described in Chapter 2. In the remaining chapters, questions of triggering, flavor tagging, event reconstruction and physics capabilities (B_s -Mixing and CP-Violation) are discussed.

^{*)} Supported by U.S. National Science Foundation Grant: PHY90-08221

¹ It has been pointed out by DeRujula [private communication] that the observed angular distributions may be even more sharply forward peaked than seen in Fig. 1, due to contributions from other than the low order QCD processes used in the generation of both PYTHIA and ISAJET.

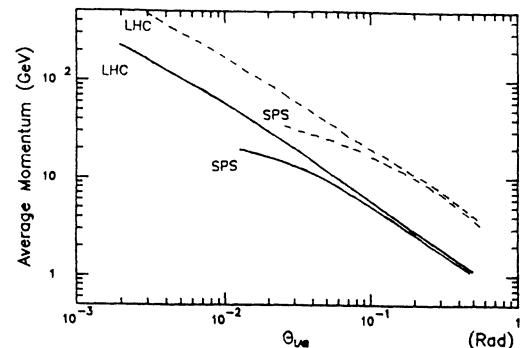


Figure 2: Mean B Decay Track Momentum vs. Laboratory Angle at LHC & Sp \bar{p} S. The mean momentum is evaluated for decay tracks of B -mesons which are generated at the two c.m. energies using the program ISAJET, and whose decay tracks are fully accepted in the 600 mrad aperture of the detector. The dashed curves are those momenta, below which 95% of all tracks occur.

We remark here that the apparatus shown in Fig. 4 is an outgrowth of the dedicated Beauty detector, known as P238, that we and our collaborators proposed² for the Sp \bar{p} S-Collider. This is of interest for several reasons: (a) For LHC R&D purposes, P238 was approved to test, and is presently running, a 43,000 channel silicon strip microvertex detector inside the Sp \bar{p} S vacuum pipe at 1.5 mm from the circulating beams. The observation of clean background-free events (discussed below) constitutes the first major step in demonstrating that the silicon trigger discussed in this document will actually work; (b) Because of the facts that significant R&D remains to be done for the LHC experiment and also that the first and second spectrometers of the LHC detector would also be optimal for the proposed Sp \bar{p} S experiment, the detector could be installed and tested at the Sp \bar{p} S, long before the LHC is completed. (c) Major Monte-Carlo calculations were performed in the preparation of the P238 proposal. Many of these calculations have been extended to the LHC experiment and are reported in this document. In cases where the LHC calculations have not yet been completed, reasonable extrapolations are made from the Sp \bar{p} S calculations.

2. APPARATUS

Fig. 4 shows the layout of one arm of the forward Beauty detector with aperture $2 < \theta < 600$ mrad. The vacuum pipe which contains the circulating beams passes through the various detector components. The vacuum chamber is constructed from aluminum in order to limit multiple scattering and interactions of small angle particles. There are three thin windows, one at $z \approx 0.3$ m, one at 4.8 m and one at 10 m. Conical sections with angles of 100 mr and 10 mr, respectively, connect the windows.

² Proposal P238, Study of Beauty Physics at the SPS-Collider with Real-Time Use of Silicon Microvertex Information, CERN-SPSC/88-33;

P238Add.1, Measurement of B_s Mixing, CERN-SPSC/89-43;

P238Add.2, Request For Collider Test of Silicon Microvertex Detector, CERN-SPSC/89-55;

P238Add.3, Further Comments on Collider Test of Silicon Microvertex Detector, CERN-SPSC/89-61.

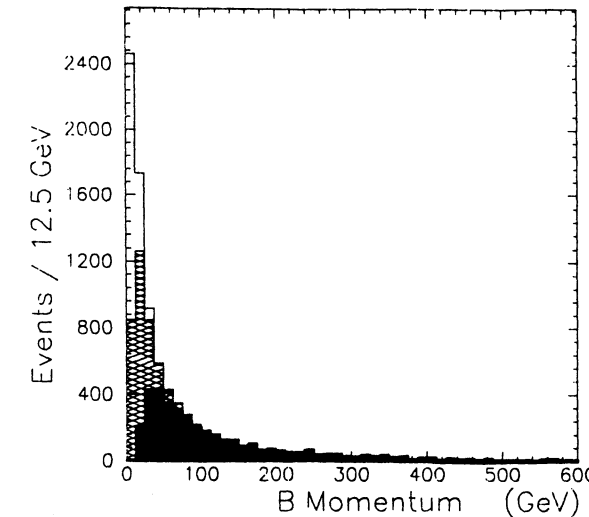


Figure 3: Momentum Distributions of B -Mesons at LHC. Unshaded: All B -mesons generated according to gluon-gluon fusion using PYTHIA; Shaded: Those with laboratory $\theta_B < 600$ mrad; Solid: Those B -meson events whose tracks are fully contained within a 600 mrad aperture are shown as the solid distribution. The B flight path is ≈ 7.5 mm per 100 GeV.

The last vacuum pipe section is conical with an angle of 2 mr.

Silicon-Strip Microvertex Detector: To match the forward spectrometer system, the microvertex detector has a geometry typical of fixed-target experiments with the silicon planes perpendicular to the circulating beams. The silicon microvertex detector system in Fig. 4 is installed at the center of the interaction region ($z = 0$) inside the vacuum chamber. The extended source size of the bunch crossing region and the need to minimize the extrapolation distance from measured track points in the silicon to an interaction vertex leads to a detector design in which the silicon planes are distributed along the intersection region with a spacing of 3 to 4 cm.

Fig. 5 shows a sketch of the 6-plane microvertex detector assembly which is currently running in intersection region LSS5 at the Sp \bar{p} S as an R&D project for LHC. It is known as P238. Each silicon plane in Fig. 5 contains eight 4.5 cm square detectors with single-sided³ readout, configured in four quadrants, with each quadrant containing one x and one y plane, separated in z by 2 mm. The planes are separated by 3.8 cm and are mounted on a Roman pot assembly, such that the upper and lower halves can be retracted to a safe position at 5 cm from the beams when there are beam manipulations. There is remote control of the vertical positioning (accurate to ± 25 μ m) which allows the detector assemblies to approach the beam line as close as 1.5 mm or less for data taking.

³ Silicon detectors with double sided (x,y) readout will be used in the full experiment.

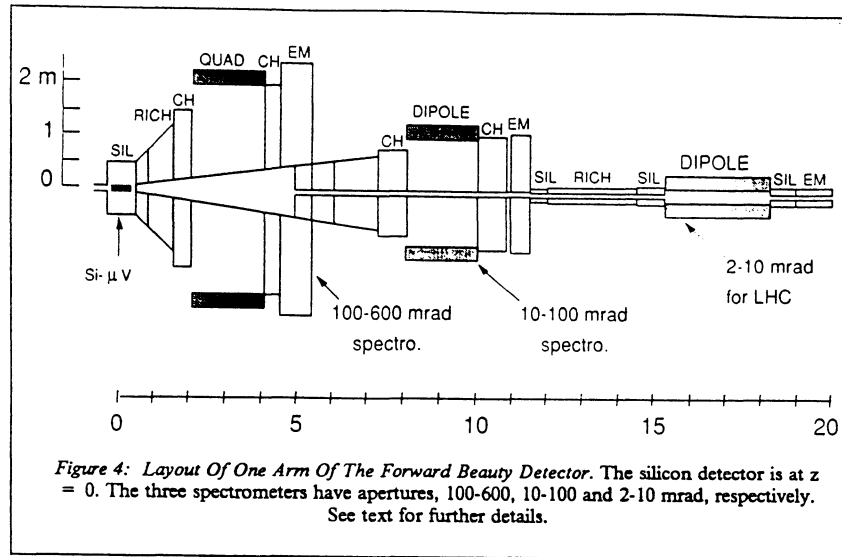


Figure 4: Layout Of One Arm Of The Forward Beauty Detector. The silicon detector is at $z = 0$. The three spectrometers have apertures, 100-600, 10-100 and 2-10 mrad, respectively. See text for further details.

A 200 μm thick aluminum window, which approximately follows the contours of the detectors, is used to provide shielding of the silicon detectors against RF pickup due to the passages of the beam bunches (a thinner aluminum window, with perhaps 100 μm thickness, will be used in a future installation). Collapse of these thin windows is avoided by having a secondary vacuum, in which the silicon detectors are found to function well, inside the Roman pots. The Roman pot, with its windows, also serves to isolate the main machine vacuum of the SppS from the effects of outgassing of materials in the silicon detector and eases the requirements on the materials used in the feedthroughs.

Fig. 6 shows a typical event recorded with the detector system 1.5 mm from the beam. Six x-detectors in one quadrant are shown, with the horizontal scale defined by the 896 strips times the pitch of 50 μm (total 4.48 cm). The vertical scale is defined by the 3.8 cm between planes. Only pulse heights larger than $4\sigma_{\text{noise}}$ are shown. Straight lines are drawn through the bases of the pulse heights.

The negligible background of event-unrelated hits in the silicon show that a large silicon strip detector centered on the interaction region can be run as close as 1.5 mm from the beam with minimal background. It is the single most important demonstration that the LHC experiment discussed in this document is indeed viable. Converting the silicon data to a trigger by means of powerful real time processing is a daunting but manageable task of digital engineering.

Spectrometers: The first spectrometer magnet, shown in Fig 4, is a normal-conducting quadrupole magnet with 2 m radius, 2m magnetic length and a pole tip field of 1.2 Tesla. T. Taylor of the LEP division at CERN suggested the use of such a large aperture quadrupole magnet as an alternative to large dipole spectrometer magnets with septum plates. A quadrupole magnet has several advantages: (a) the absence of septum plate material near the beam minimizes interactions of outgoing particles; (b) particles with angles between 10 and 100 mrad receive minimal bending inside the beam pipe before they emerge and enter spectrometer 2; (c) the negligible field at the position of the silicon detectors does not distort the straight tracks, thereby minimizing the complexity of the online trigger.

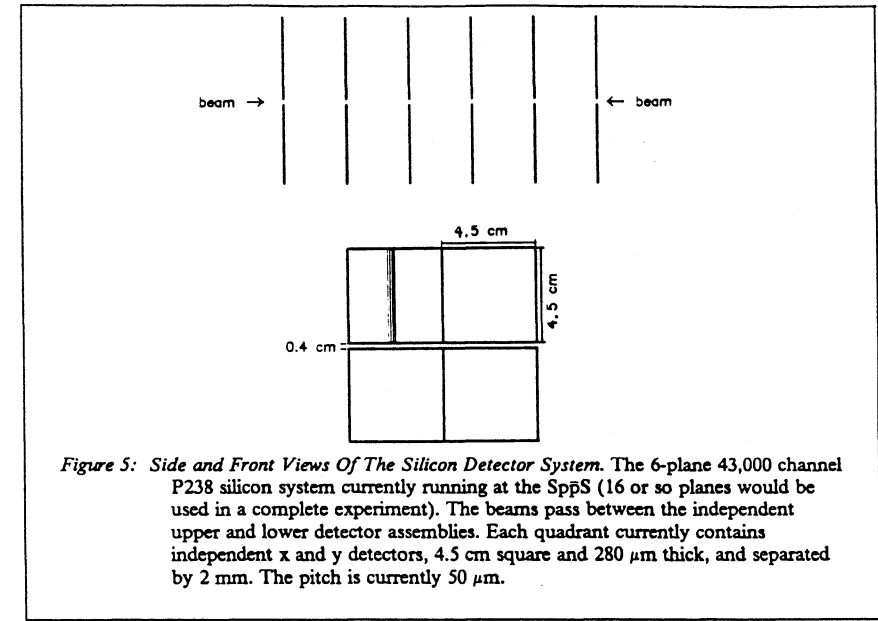


Figure 5: Side and Front Views Of The Silicon Detector System. The 6-plane 43,000 channel P238 silicon system currently running at the SppS (16 or so planes would be used in a complete experiment). The beams pass between the independent upper and lower detector assemblies. Each quadrant currently contains independent x and y detectors, 4.5 cm square and 280 μm thick, and separated by 2 mm. The pitch is currently 50 μm .

The second spectrometer contains a superconducting dipole with magnetic length of 2m, uniform magnetic field of 2.5 Tesla and no septum plate. The third spectrometer contains a smaller superconducting dipole magnet with equal but opposite field integral and no septum plate (An identical spectrometer, or at least magnets with similar field integrals, must be installed in the opposite arm for beam compensation).

In the P238 proposal, x-y pixel devices are used to match the two views of the silicon tracks and to aid in connecting these with tracks found in the spectrometers. A Silicon Pad Detector, with pixel size of $1 \times 1 \text{ mm}^2$, is installed inside the beam pipe at a distance of 35 cm from the center of the interaction region. Additional silicon detectors may also be mounted inside the beam pipe at points between $z = 0$ and the spectrometer windows.

The first detector elements after the vacuum windows in all spectrometers are Pixel Drift Chambers, in which the two-dimensional position of a track traversing the 20 mm thick gap is measured without ambiguity using sense wires strung in a direction approximately parallel to the outgoing tracks.

Wire chambers with jet-type drift cells are used to measure the position and direction of charged tracks before and after each magnet with a position resolution of 100 μm . There are a total of 80 samples per track in the chambers of spectrometer 1 and 128 samples per track in spectrometer 2. Spectrometer 3 has silicon tracking detectors (overall dimensions about ± 20 cm). The electromagnetic calorimetry should have energy resolution of, at least, $\sigma(E)/E = 4\%/\sqrt{E}$.

Particle identification is furnished offline with a system of liquid and gas Ring Imaging Cerenkov

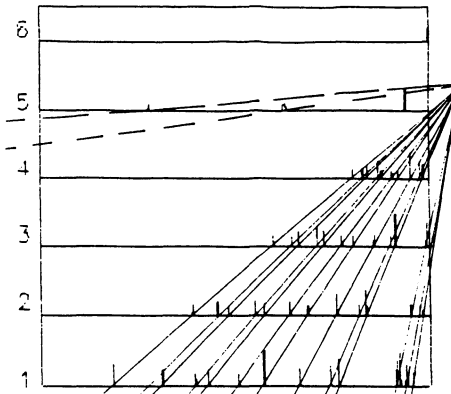


Figure 6: Silicon Event Recorded 1.5 mm from the Sp̄S-Collider Beams. One quadrant with six planes of y detectors are shown. There are 3.8 cm between planes and each detector is 4.8 cm wide. Pulse heights are shown if they are larger than 4σ noise. Lines are drawn by hand.

Counters.⁴ The RICH detectors are designed to identify all the hadrons from B decays as well as most of the leptons with momenta up to 20 GeV. Above 20 GeV, lepton identification is provided by the electromagnetic calorimeter. Each spectrometer has a C₆F₁₄ freon liquid radiator with 10 mm thickness, followed by a C₂F₁₂ freon gas radiator with 750 mm path length. Spectrometers II and III also have higher threshold CF₄ freon gas radiators with length 1.2 m.

3. TRIGGERING

Strategy: At the LHC, the ratio of a pp total inelastic cross section of about 70 mb and a b̄b production cross section of about 300 μ b is $\approx 230/1$ (compared with $\approx 3300/1$ at the Sp̄S). This defines the level of minimum bias suppression which is required. Much of this is accomplished in the on-line, Level-1 trigger, as discussed below. The remaining background can be suppressed by detailed topology studies in a "Level-2" parallel processor system and in offline analysis.

Because the silicon trigger algorithm is executed in real time, the silicon data must be read out in the shortest possible time. This leads us to "sparsify" on the detector and read out only digital information of the "hit" silicon strips. The overall strategy of the Level-1 trigger is to use the silicon digital information to search for events which are inconsistent with having a single vertex. This is clearly a much weaker condition than requiring the presence of a nearby secondary vertex. However, it is found that a sufficiently large suppression of the minimum bias background can be obtained to allow efficient transfer of accepted events to a "farm" of high performance parallel processors. The Level-1 algorithm,

described below, is sufficiently concise to allow straight-forward implementation in a hardware (data-driven) trigger processor.

Event Simulation: Since the effectiveness of the trigger in suppressing the minimum bias background events is such an important aspect of the proposed experiment, the problem has been studied in considerable detail. Using the CERN program GEANT, complete simulations were made of the silicon detector response to PYTHIA-generated minimum bias, inclusive Beauty and Charm events. The minimum bias events used in this study were found to agree well with UA5 results⁵ on minimum bias physics at the Sp̄S. Following this, a trigger algorithm was created and tuned to have the desired effects on these event samples, namely large suppression of minimum bias events with minimum suppression of Beauty events. Table 1 shows various quantities which characterize the event properties at LHC and Sp̄S. The table shows that the cluster density in a silicon quadrant approximately doubles at the LHC, which is a rather modest increase. Thus, a similar algorithm should also be adequate at LHC.

Table 1: Silicon Hits for Minimum Bias Events at LHC and Sp̄S-Collider^{*})

	LHC	Sp̄S
Average No. Clusters Per Quadrant	5.6	2.8
Average No. Strips Hit Per Quadrant	9.2	4.8
Cluster Width (Strips)	1.3	1.3
Point Resolution	7.6 μ m	7.6 μ m
First Vertex Resolution (see text)	0.8 mm	0.8 mm

^{*}) Silicon strip width is assumed to be 25 μ m. The silicon thickness is 250 μ m.

Trigger Algorithm: The general strategy of the trigger algorithm is then as follows:

- The geometric centers of strip clusters are taken as "points".
- Straight lines are found in at least three detector planes, with a road width of one silicon strip. Tracks which multiple scatter more than this (momentum ≈ 2 GeV or less) are not used in the trigger calculations.
- No x-y matching is performed in the online calculations. All calculations are performed using the x-z and y-z track projections.

⁴ R. Arnold et al., NIM A270 (1988)255; NIM A270 (1988)288;

T. Ypsilantis, CERN-EP/89-150; J. Seguinot, CERN-EP/89-92;

J. Seguinot et al., Reflective UV Photocathodes with Gas-Phase Electron Extraction; Solids, Liquids and Adsorbed Thin Films, CERN-EP/90-88; NIM A297 (1990) 133.

⁵ G.J. Alner et al. (UA5 Collaboration), Physics Reports 154 (1987) 247.

- The primary vertex is estimated by extrapolating all tracks to $x = 0$ or $y = 0$, respectively. A peak in the z-intercept distribution is taken as a First Vertex estimate (see Table 1). Tracks, whose projected impact parameters from this vertex are larger than 1 mm, are excluded (this tends to discard strange particle decay products or spurious tracks).
- A χ^2 is formed for the hypothesis that all impact parameter projections are zero (there is an independent sum over x-z and y-z tracks). A new vertex point is then found which minimizes the χ^2 . If the $\chi^2/\text{degree of freedom}$ is smaller than some cut value the event is rejected. If larger, an iteration process is carried out, in which two tracks with worst χ^2 contribution are rejected. Events which remain in poor agreement with the single vertex hypothesis are retained.

Trigger Performance and Expected Rates: The above Level-1 trigger algorithm, which was initially created and developed for the SppS, has been applied without fundamental modification to LHC events. Fig. 7 shows the fraction of minimum bias and two specific exclusive final states (accepted by the 600 mrad spectrometer) which survive the trigger algorithm, as a function of the χ^2 -cut value. A χ^2 cut of about 25 gives a suppression of 100 for minimum bias events while retaining between 20 and 40% of the B events (this depends on the B-decay product multiplicity). We have obtained a trigger efficiency of 1% for charm events and complete offline rejection of these events in our simulations for the SppS. At the LHC, the trigger efficiency should be $\approx 2\%$.

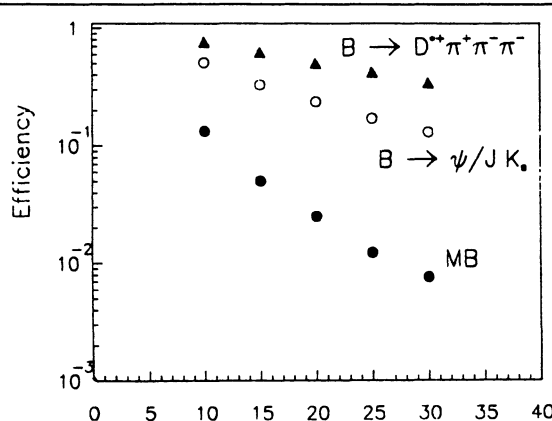


Figure 7: Trigger Efficiency vs. χ^2 -Cut Value. The fraction of events at the LHC which survive the Level-1 trigger algorithm. This quantity is shown for: (a) minimum bias events, (b) the exclusive final states $B \rightarrow D^+\pi^+\pi^-\pi^-$ and $B \rightarrow J/\psi K_S$.

In estimating the trigger rates, we assume a luminosity, $\mathcal{L} = 10^{31} \text{ cm}^{-2}\text{s}^{-1}$. Great demands are made on the data acquisition system and it seems prudent to initially evaluate the possibilities at this level. Radiation damage to the silicon system running in proximity to the beam is also a concern, to which we return in Chapter 7 when we consider the CP-Violation experiment. Assuming $\sigma_{\text{inelastic}} = 70 \text{ mb}$, $\sigma(\text{cc}) = 3.5 \text{ mb}$ and $\sigma(\text{bb}) = 300 \mu\text{b}$, and using Level-1 trigger efficiencies of 1/100, 1/50 and 1/8 (for inclusive B's), respectively, we find rates of 7.0 KHz, 0.7 KHz and 0.4 KHz, or a total of 8 KHz. With an event size of 200 Kbytes (including data from the electromagnetic calorimeter), we have a data rate of $\approx 1.6 \text{ Gbytes/sec}$ out of the Level-1 processor (This data rate can be reduced by having intelligent front end electronics, e.g., finding track segments in the various detectors, in parallel with the Level-1 "number crunching" on the silicon data) After the Level-1 decision, the events will be passed to a system of high performance parallel processors for the Level-2 trigger, in which a search will be made for events with multiple vertices. The Level-2 trigger implementation will require a (futuristic) system with about 800 50-MIPS processors to keep up with the Level-1 trigger rate, if an average of 0.1 sec per event is required to perform the Level-2 trigger calculation.

Pileup: Assuming that all detectors are gated at 100 ns, we note that 3.5% of all inelastic events will be accompanied by a second inelastic event within the gate (at $\mathcal{L} = 10^{31}$ and $\sigma_{\text{inelastic}} = 70 \text{ mbarn}$). Since these pileup events occur almost always in different 15 ns bunches, they can be eliminated by real-time calculations on signals from time-of-flight counters (outside the 600 mrad aperture). Such calculations will proceed in parallel with the silicon calculations.

Implementation with Data-Driven Trigger Processor: For each interaction, all detector information must be read out and stored in a pipeline until the Level-1 trigger decision is taken. In order to minimize the number of events which must be stored, the decision should be taken in the shortest possible time (15 μs or so). This can be accomplished with a data-driven trigger processor.⁶ The properties of such a processor are summarized as follows:

- No centralized control:** There is no CPU in the system. The processor consists of an array of function modules, in which the arrival of data at a module initiates its operation.
- Parallel:** Several data streams are processed in parallel. In our case, track finding in the silicon detectors is done in parallel in 8 identical processors (4 quadrants \times 2 views). Other parallelism can be intrinsic to the processor.
- Pipelined:** Several events are in the processor simultaneously. For example, with an interaction rate of 700 KHz and an event processing time of about 15 μs , about 10 events would be in the pipeline at a time.
- Synchronous:** All registers in the system are latched simultaneously by a 40 MHz central clock.

The operation of the entire modular structure of the processor is being emulated in software. A FORTRAN subroutine is written for each type of module, such that one subroutine call corresponds to one clock cycle, and the full system emulator provides an exact cycle by cycle description of the hardware. It is thus possible to precisely predict the operation of a given algorithm on any data set. For example, the average number of clock cycles per event can be determined or bottlenecks in the algorithm calculations can be located.

4. EVENT RECONSTRUCTION

The calculations described in this section were done for the SppS and have not yet been repeated for the LHC. However, the modest factor of two increase in silicon hits shown in Table 1, coupled with the decrease in multiple scattering, make it likely that similar reconstruction results will be found at the LHC. Software was written to reconstruct Monte-Carlo Beauty events which were generated using the program PYTHIA. Two types of Monte-Carlo event samples were studied: (a) a general or inclusive BB sample, in which B-mesons decay according to the "natural" B decay modes built into PYTHIA, and: (b) events in which all B's decay via a particular mode under study. In both cases,

⁶ W. Sippach et al., IEEE Trans. Nucl. Sci., 27 (1980) 578;
E.P. Hartouni et al., IEEE Trans. Nucl. Sci., 36 (1989) 1480;
B.C. Knapp, Proceedings of 4th Pisa Meeting on Advanced Detectors (1989), Nucl. Instr. & Meth. (in press - 1989)
J.G. Zweizig et al.(UA8 Collaboration); Nucl. Instruments & Methods A263 (1988)188.

PYTHIA generated an underlying event, similar in structure to a minimum bias event, in addition to the decay tracks from the B and \bar{B} states. Unit vectors describing track direction and position were obtained from a full silicon detector simulation using the program GEANT. Momentum measurement errors were simulated by randomly varying the generated Monte Carlo momentum vectors, in accordance with expected spectrometer resolutions.

Reconstruction software for exclusive final states proceeds in the following way. A vertex-finding algorithm consists of the repeated application of a vertex search among tracks that do not come from previously found vertices. For events with a desired vertex topology, the relevant invariant masses are calculated for all possible track combinations. In analyses done thus far, a minimum flight path of 0.5 mm has been required for the B-meson, making it possible to require transverse momentum balance with respect to the B direction of motion for each mass combination. This is found to greatly suppress combinatoric background under the B signal.

For the exclusive decay mode sample, events whose B-meson decay products are completely contained in the spectrometer aperture are passed through the trigger algorithm simulation software. The events which survive are passed through the reconstruction software in order to determine the reconstruction efficiency. Inclusive $B\bar{B}$ are passed through the same software chain used for the exclusive final state in order to determine the combinatoric background level.

It is found that the chief sources of combinatoric background to B-meson signals are: (a) those $B\bar{B}$ events which have similar topologies but which decay via modes other than the one under study; or (b) from the same mode, but where one or more tracks can not be uniquely assigned to the B decay vertex. For example, Fig. 8 shows the resulting invariant mass spectrum for the exclusive decay mode $B^0 \rightarrow D^* \pi \pi \pi$, with a background which is quite typical for exclusive decay modes which do not involve π^0 's. All expected combinatoric background is shown. We found that final states that contain J/ψ have very little background, due to the uniqueness of the dilepton in the final state.

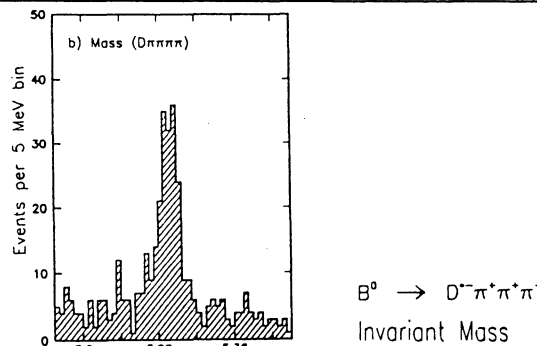


Figure 8: The expected B^0 signal in the channel: $B^0 \rightarrow D^{*-} \pi^+ \pi^+ \pi^-$, $D^{*-} \rightarrow D^0 \pi^-$, $D^0 \rightarrow K^+ \pi^+ \pi^- \pi^-$, after all D^{*-} and D^0 mass constraints, topology and transverse momentum balance cuts have been applied. The background shown is an estimate from all sources at the Sp \bar{p} S.

Measurement of B_s Lifetime: There is a mean distance of 2 cm between an event primary vertex and the nearest silicon plane. The experimental resolution in the measured proper time, t , is obtained by comparing the generated B-meson flight path with its reconstructed value for a large number of Monte-Carlo events. Using the relation $z = c t / m$, we find that the standard deviation in the proper time measurement is $\sigma(t)/t = 6.8\%$ at the Sp \bar{p} S, where the mean reconstructed B momentum is about 35 GeV (mean flight path about 2.5 mm). At LHC, the error in time measurement should be similar but smaller, because of the decrease in multiple scattering contribution at the mean momentum of 200 GeV and mean flight path of about 1.5 cm (and also because of possible improvements in algorithm and detector utilization).

Finally, we note that the proper time distribution expected at the Sp \bar{p} S is described by the empirical acceptance function, $A(t) = 4t^2/(1+4t^2)$ multiplied by e^{-t} (here, the proper time, t , is in units of mean life, τ). This was calculated for accepted B events which pass the trigger simulation and reconstruction software. At the LHC, we expect a similar acceptance function. Thus, the measured proper time distribution should be distorted very little for times longer than about one mean life.

5. FLAVOR TAGGING

To avoid the large event loss which arises from requiring full reconstruction of the tag-providing system, we advocate just using as tags, particles which are inconsistent with coming from the primary vertex. Thus the time-integrated probabilities for oscillation and non-oscillation of their source B's must be used to estimate the resulting mistagging. We come back to this point below.

The Use of Muon Tags: In order to understand the tagging possibilities using leptons, an analysis was made of LHC inclusive $B\bar{B}$ events, Monte-Carlo generated using PYTHIA. For 2571 $B\bar{B}$ events whose B decay products are fully contained in a 600 mrad spectrometer aperture, Fig. 9 shows the laboratory momentum of a muon from the accompanying \bar{B} plotted vs. its angle in the laboratory. The expected angular correlation between the μ and B directions is clearly visible and most muons are in the same hemisphere as the B.

7% of the events with a B-Meson reconstructed in the spectrometer are found to also have a muon in the spectrometer from the accompanying \bar{B} . Requiring the muons to have $p_t > 1.2$ GeV (necessary to suppress those muons from other sources) and $p < 100$ GeV (to allow RICH identification) leaves 6.4% of the events with a tag quality (good tags/all tags) of 74%.⁷ If electron tags are added, the fraction of tags would increase to twice this number. However, in both muon and electron cases, some additional cuts will be necessary to suppress background.

The Use of Kaon Tags: The possibility of using charged kaons as tags at the LHC has also been studied using PYTHIA-generated $B\bar{B}$ events. The overall strategy is to examine supplementary kaons in the spectrometer (those not associated with the reconstructed B). There are two major sources of such kaons. They either come from the accompanying \bar{B} meson or they come from the primary vertex. Those from the primary vertex have been estimated to be useful at lower energy colliders (Sp \bar{p} S and Tevatron) in tagging reconstructed B_s mesons. However, with the increased kaon production at the LHC, it is doubtful that they will lend much significance and we do not consider them here.

A K^\pm which contains the s-quark at the end of the $b \rightarrow c \rightarrow s$ chain uniquely identifies the flavor of its \bar{B} -meson at decay. However, there are many sources of mis-tagging, such as kaons which are produced from the ss sea or from a W^\pm in either the $b \rightarrow c$ or $c \rightarrow s$ transitions (which can have either sign). These are all accounted for, to some approximation, in the PYTHIA event generation and can be investigated by tabulating the supplementary kaons found in the spectrometer. For LHC events, 27% of the B-mesons in the spectrometer are found to have a tagging K^\pm with impact parameter greater than 3σ from the primary vertex. The correct charge was found in 80% of these tags.

⁷ If the p_t cut is increased to $p_t > 2.0$ GeV, the tag quality increases to 81.5%, although the tagging fraction decreases to 3.6%.

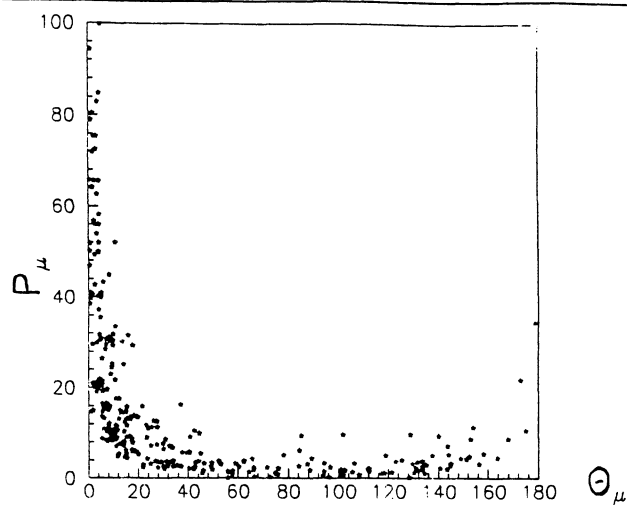


Figure 9: Lab. Momentum vs. Lab. Angle of Muons Accompanying an Accepted B at the LHC. The detected B is on the 0° side. The muons have $p_t > 1.2$ GeV.

Because the fraction of events tagged by either of these techniques is small, it will be advantageous to employ both techniques in parallel. 40% of all reconstructed B -Mesons can then be tagged with a tagging quality of 78%. Of course, these estimates depend greatly on the correctness of PYTHIA's hadronization scheme, which could be verified by measurements at existing hadron colliders.

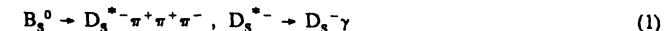
Dilution Effects: There are two types of dilution (decrease in statistical effectiveness) due to mistagging. One arises simply from using a tagging particle (kaon or lepton) which has the wrong sign because its source is extraneous. The other arises from the fact that the B (or \bar{B}) which provides the tagging particle may itself oscillate and thereby give the wrong sign tag. The estimates of mistagging given in the previous paragraphs are obtained with the use of a Monte-Carlo generator which does not have B -oscillation built into it. Thus the estimates are of the first type of mistagging. The relevant factor is not the "tag quality" referred to there, but rather the quantity $k_1 = (\text{good tag} - \text{bad tag})/(\text{good} + \text{bad})$. From the above discussions, we have for this dilution factor: $k_1 = 0.48$ and 0.60 , for muons and K^\pm , respectively.

To estimate the dilution factor, k_2 , from the second type of mistagging, due to the oscillation of the tag-providing B (or \bar{B}), we must use the time-integrated probabilities for oscillation and non-oscillation: $x^2/[2(1+x^2)]$ and $(2+x^2)/[2(1+x^2)]$, respectively. Here $x = \Delta M/\Gamma$ for the source B . Because the expected decay time dependences of the tagged- B (or \bar{B}) are of the general form $1 \pm a(t)$, it is explicitly shown in Chapter 6 on B_s -Mixing that the dilution factor multiplies the $a(t)$ term and is given by the weighted average of the quantity $1/(1+x^2)$ over the three types of tag-producing B 's according to their relative production frequency⁸ and their tag quality, k_1 . For lepton tags, a weighted average, of $[1/(1+x^2)]$ over B_u (40%), B_d (40%) and B_s (20%) is found to be: $k_2 \approx 0.67$, if we as-

sume x to be 0, 0.7 and 15, respectively, for the 3 cases. For K^\pm tags, however, we note that k_2 depends on the tag source, B_u , B_d or B_s . We estimate that the effective k_2 for K^\pm is 0.84. This leads to a net value for the dilution factor of ≈ 0.45 .

6. ANALYSIS OF B_s -MIXING (CP-Conserved)

The following is an analysis of a prototype mixing measurement in which exclusive final states of the B_s are reconstructed and the proper decay time of each event is measured. The effects of using electromagnetic calorimeter information in the reconstruction of the Reaction:



was studied in detail at the SpS energy, where the mean B_s momentum is 35 GeV. The signal/background ratio was found to vary from 4/1 for a calorimeter with resolution $\sigma(E)/E = 4\%/\sqrt{E}$ to 10/1 when $\sigma(E)/E = 0.5\%/\sqrt{E}$. The B_s reconstruction efficiency was found to vary from 29% for a $4\%/\sqrt{E}$ calorimeter to 43% for a $0.5\%/\sqrt{E}$ calorimeter. In our present estimates, we assume a 10% reconstruction efficiency. We assume that a b -quark has a 12% probability⁹ to combine with an s -quark to make a B_s -meson. This should allow, for example, for the loss of excited B_s which can decay into $B + K$. In addition, with the electromagnetic calorimetry, we would have the capability to detect $D^{*0} \rightarrow D^0 \gamma$ ($BR = 48\%$) for the first time, thereby opening the door to the study of entire new classes of final states.

Particular attention is paid in this chapter to the detection of a possible asymmetry in B_s and \bar{B}_s production due to valence quark effects in proton-proton interactions. This will later have relevance to the study of CP-Violation asymmetries. We first demonstrate that enormously large data samples will be available in such an experiment at the LHC. Table 2 tabulates the various efficiencies that influence the event yields for B_s . The yields are evaluated for an integrated luminosity, $\int \mathcal{L} dt = 200 \text{ pbarn}^{-1}$, which is necessary for a CP-Violation measurement, as discussed in Chapter 7.

As discussed in the latter part of this chapter, the total yield of 4.2×10^5 B_s events is about 800 times the minimum number necessary for a measurement of $\Delta M/\Gamma$ in B_s decay. Because this large yield is obtained for a final state with branching ratio less than 0.5% and a particularly small reconstruction efficiency (because of the single γ), it is easy to see that vast data samples of specific exclusive final states will be recorded during the course of a run to measure CP-Violation effects.

Phenomenology: With the $B^0 \leftrightarrow \bar{B}^0$ transitions allowed by second-order weak interactions, we have as the time-evolved state for an initial B^0 , expressed in terms of its mass eigenstates:

$$\psi(t) = [e^{-iM_1 t - \Gamma_1 t/2} |B_1\rangle + e^{-iM_2 t - \Gamma_2 t/2} |B_2\rangle] / \sqrt{2} \quad (2)$$

The probabilities to see $|B^0\rangle$ and $|\bar{B}^0\rangle$, starting from an initial $|B^0\rangle$ are obtained by expanding $|B_1\rangle$ and $|B_2\rangle$ in terms of the observed $|B^0\rangle$ and $|\bar{B}^0\rangle$ states and projecting out their amplitudes:

$$|< B^0 | \psi(t) >|^2 = e^{-\Gamma t} \cdot [1 + \cos(\Delta M t)] / 2 \quad (3)$$

$$|< \bar{B}^0 | \psi(t) >|^2 = e^{-\Gamma t} \cdot [1 - \cos(\Delta M t)] / 2 \quad (4)$$

In (3) and (4), $\Gamma = \Gamma_1 = \Gamma_2$, because of the large phase space available in B decay, and $\Delta M = M_1 - M_2$. As required, the sum of equations (3) and (4), $e^{-\Gamma t}$, describes untagged B_s decay. Integrating Eqs. (3) and (4) over time yields the rates for no-oscillation and oscillation referred to in Chapter 5.

If we assume that a B_s and its accompanying (tag-providing) \bar{B} decay independently and that only the time dependence of the B_s is measured, the expressions which describe the tagged time distributions are given by Eqs. (3) and (4) multiplied by the appropriate time-integrated decay rate for the

* P. Krawczyk, D. London & H. Steger, DESY-163 (Nov. 1988).

⁹ V. Khoze [private communication].

Table 2: B_s & \bar{B}_s Event Yields at the LHC

$6 \cdot 10^{10}$ $b\bar{b}$	using:	$\int \mathcal{L} dt = 200 \text{ pbarn}^{-1} (10^{31} \cdot 2 \cdot 10^7)$ $\sigma(b\bar{b}) = 300 \mu\text{b}$.
$7.2 \times 10^9 B_s$	$7.2 \times 10^9 \bar{B}_s$	0.12 = B_s Production
4.0×10^9	4.0×10^9	0.55 = 2-Arm Geometrical Acceptance
1.8×10^7	1.8×10^7	$4.5 \cdot 10^{-3}$ = Branching Ratios ($B_s \rightarrow D_s^+$, D_s^- and DK^- with $n\pi$) ($D_s^+ \rightarrow D_s^0 \gamma$) ($D_s^- \rightarrow K\bar{K}\pi$, $KK3\pi$, $K^0\bar{K}$)
1.2×10^7	1.2×10^7	0.70 = Live Time
5.2×10^6	5.2×10^6	0.42 = Trigger Efficiency ($D_s^+ 3\pi \rightarrow D_s^0 \gamma 3\pi$)
2.1×10^6	2.1×10^6	0.40 = Tagging Efficiency
2.1×10^5	2.1×10^5	0.10 = Reconstruction Efficiency (allowing for γ)
4.2×10^5		Total Reconstructed B_s and \bar{B}_s Events

Table 3: Joint Time-Integrated, Time-Dependent Rates(a,b,c)

Final State	Initial State $B\bar{B}_s$	Initial State $\bar{B}B_s$	Equal Sum
(1) $T^+ B_s(t)$	$(2+x^2) \cdot [1-\cos]$	$x^2 \cdot [1+\cos]$	$1-[1/(1+x^2)] \cdot \cos$
(2) $T^- B_s(t)$	$x^2 \cdot [1-\cos]$	$(2+x^2) \cdot [1+\cos]$	$1+[1/(1+x^2)] \cdot \cos$
(3) $T^+ \bar{B}_s(t)$	$(2+x^2) \cdot [1+\cos]$	$x^2 \cdot [1-\cos]$	$1+[1/(1+x^2)] \cdot \cos$
(4) $T^- \bar{B}_s(t)$	$x^2 \cdot [1+\cos]$	$(2+x^2) \cdot [1-\cos]$	$1-[1/(1+x^2)] \cdot \cos$

(a) To simplify the reading of this table, a common factor $e^{-\Gamma t}/(1+x^2)$ is suppressed in all terms in columns 2 and 3, as is the argument, ($\Delta M t$), from all cosine functions.

(b) The B or \bar{B} decay which provides the tagging particle is time-integrated. The B_s decay is time-dependent. Throughout this table, $x = \Delta M/\Gamma$ for the tagging B or \bar{B} , whereas the argument of the cosine function is for the B_s .

(c) In this table, the tagging particles are assumed to be secondary K^\pm or leptons. They give the flavor of the B or \bar{B} at time of decay (e.g., K^+ or ℓ^+ result from a B , whereas a K^- or ℓ^- result from a \bar{B}).

tag-providing \bar{B} . These products are shown in Table 3, for the four possible cases of tags T^+ and T^- (T^+ is a K^+ , μ^+ or e^+ , etc.) with B_s and \bar{B}_s , respectively, and for the two possible initial states. We note that Table 3 is true for each type of tag source and that, in practice, a weighted average over tag sources must be made.

Following the discussion on tagging in Chapter 5, we note that the B_s decay time distributions for Final States 1–4 in Table 3 have the following simple forms:

$$T^+ B_s \text{ or } T^- \bar{B}_s : A(t) \cdot e^{-t} \cdot [1 - K \cos(xt)] \quad (5)$$

$$T^+ \bar{B}_s \text{ or } T^- B_s : A(t) \cdot e^{-t} \cdot [1 + K \cos(xt)] \quad (6)$$

$$\text{Untagged } B_s \text{ or } \bar{B}_s : A(t) \cdot e^{-t} \quad (7)$$

In these formulae the mixing parameter, $x = \Delta M/\Gamma$ and t is the B_s proper lifetime in units of mean life, τ . K is the effective dilution factor which results from all types of "mis-tagging" and decreases the amplitude of the oscillation from the value it would have were the flavor of the decaying B always correctly determined. $A(t)$ is the acceptance function discussed in Chapter 4.

If the initial states $B\bar{B}_s$ and $\bar{B}B_s$ do not occur with equal probability (as may be the case in $p\bar{p}$ interactions and in $p\bar{p}$ interactions when the B_s are produced away from small Feynman- x), it may be seen from the entries in Table 3 that Final States 1 and 3 will have identical magnitudes for K (but opposite sign), and Final States 2 and 4 will also have identical values, but different from States 1 and

3. For example, if initial state $B\bar{B}_s$ has probability α and $\bar{B}B_s$ has probability $(1-\alpha)$, it can be seen that the experimental value of K should depend on α in the following way (for fixed value of x):

$$T^+ B_s \text{ or } T^+ \bar{B}_s : K^+ = \pm[-2\alpha + (1-2\alpha)x^2]/[2\alpha + x^2] \quad (8)$$

$$T^- B_s \text{ or } T^- \bar{B}_s : K^- = \pm[2(1-\alpha) + (1-2\alpha)x^2]/[2(1-\alpha) + x^2] \quad (9)$$

Fig. 10 shows how K depends on α for both types of final states and for $x = 0, 0.7$ and 10 , respectively. An observed value of K will, of course, be a weighted average over the three contributing values of x . The effective dilution factors for different types of tags can be directly measured by studying the tags which occur with B^\pm production.

Simulated Maximum Likelihood Analysis: Fig. 11 shows the results of a Monte-Carlo study of 5000 fully reconstructed and tagged B_s and \bar{B}_s mesons with measured proper decay time. According to the discussion in the previous paragraphs, the data should be described by the Eqs. (5) and (6). In order to demonstrate the expected statistical significance in the determination of x , τ and K with samples of various sizes, and to show how it depends on sample size and background, Monte-Carlo data samples were generated according to Eqs. (5-7) for each of the x values, 0.7, 5, 10 and 15 and subjected to joint maximum likelihood fits with x , τ and K as free parameters.

The value of K used in the generation was fixed at the relatively small value of 0.34 in an attempt to take RICH identification efficiency and a signal/background ratio of 4 into account. Since the background is mainly associated with B events, we assume for this analysis that it has an exponential

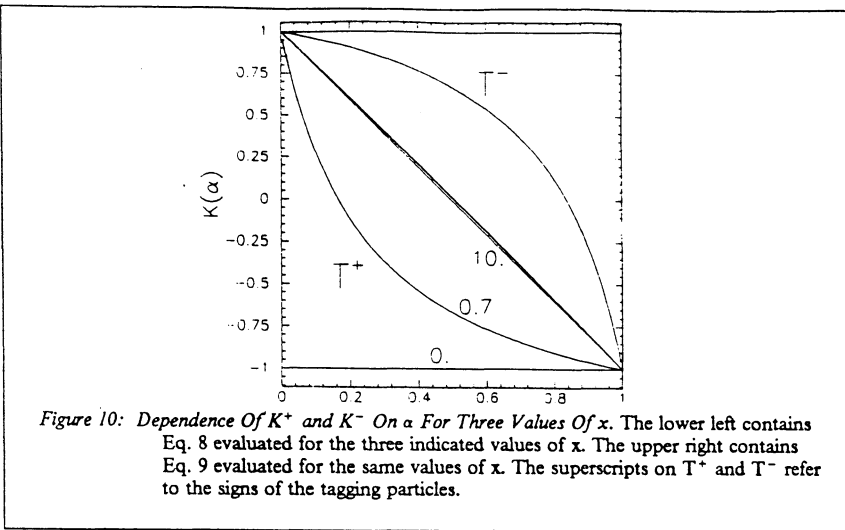


Figure 10: Dependence Of K^+ and K^- On α For Three Values Of x . The lower left contains Eq. 8 evaluated for the three indicated values of x . The upper right contains Eq. 9 evaluated for the same values of x . The superscripts on T^+ and T^- refer to the signs of the tagging particles.

proper time dependence with the same lifetime as the signal. With this assumption, the only effect of such a background is to further dilute the oscillation amplitude. A simultaneous maximum likelihood fit was then made to the entire data sample using the relevant equation for each event. The sum of $-\log \mathcal{L}$ for all events is minimized using the program MINUIT. The results are shown in Figs. 11 for all four values of x . The uniqueness of the likelihood maximum has been studied for a large number of independently generated samples of different sizes. A sample size of 1000 events typically gives an error in x of less than ± 0.1 . Sample sizes smaller than 500 events do not yield meaningful results.

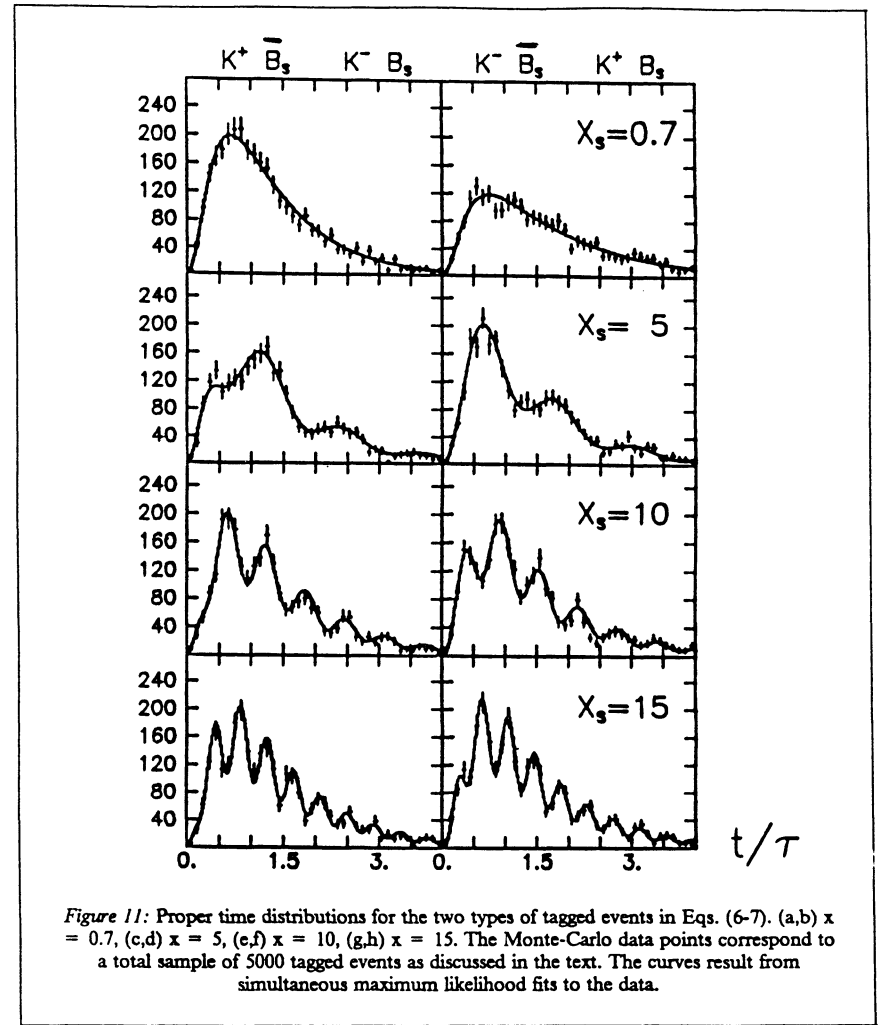


Figure 11: Proper time distributions for the two types of tagged events in Eqs. (6-7). (a,b) $x = 0.7$, (c,d) $x = 5$, (e,f) $x = 10$, (g,h) $x = 15$. The Monte-Carlo data points correspond to a total sample of 5000 tagged events as discussed in the text. The curves result from simultaneous maximum likelihood fits to the data.

7. SENSITIVITY OF CP-VIOLATION MEASUREMENTS

We have studied the sensitivity of the proposed apparatus to a measurement of a CP-Violation asymmetry in the decay:

$$B_d^0 \rightarrow J/\psi K_s^0 \quad (10)$$

$$\bar{B}_d^0 \rightarrow J/\psi K_s^0 \quad (11)$$

This may be thought of as a prototype of future CP-Violation measurements. Allowing for CP-Violation, the time dependences of the decay of B_d and \bar{B}_d into this CP eigenstate are:

$$N(B_d \rightarrow J/\psi K_s) \approx A(t) \cdot e^{-t} \cdot [1 - \sin(2\beta) \cdot \sin(xt)] \quad (12)$$

$$N(\bar{B}_d \rightarrow J/\psi K_s) \approx A(t) \cdot e^{-t} \cdot [1 + \sin(2\beta) \cdot \sin(xt)] \quad (13)$$

where t is the proper time measured from production, expressed in units of the B life time, β is an angle in the unitarity triangle and $x = \Delta M/\Gamma$ for the B (or \bar{B}) at production. $A(t)$ is the detector acceptance function referred to in Chapter 4.

These time dependences imply a time-dependent asymmetry in the decay: $(\bar{N} - N)/(\bar{N} + N)$. In order to measure this asymmetry, it is necessary to tag the flavor of the B at production using the techniques described in Chapter 5. Thus the inaccuracies inherent in the tagging must be taken into account and the observed asymmetry takes the form

$$A_{\text{obs}} = k_1 \cdot k_2 \cdot \sin(2\beta) \quad (14)$$

where k_1 and k_2 are the effective dilution factors which differ from unity due to imperfect tagging, as discussed in Chapter 5.

A Monte-Carlo study has been performed to determine the event sample size required to observe a given statistical significance in a measurement of a CP-Violation asymmetry. For example, Fig. 12(a,b) show the proper time distributions of 2100 Monte-Carlo examples each of Reactions 10 and 11, respectively, generated assuming $\sin(2\beta) = 0.20$, $x = 0.7$, a net dilution factor of 0.47 and our empirical acceptance function $A(t)$, referred to above. The curves shown are the result of a Maximum Likelihood fit for $\sin(2\beta)$ of Eqs. 12 and 13 jointly to the data in Figs. 12(a,b). The value found is $\sin(2\beta) = 0.176 \pm 0.044$ (4σ significance). Fig. 12(c) superimposes the two fitted curves from Figs. 12(a) and (b). The maximum deviation occurs at 2.2 mean lives, corresponding to a 90° argument in $\sin(xt)$ when $x = 0.7$.

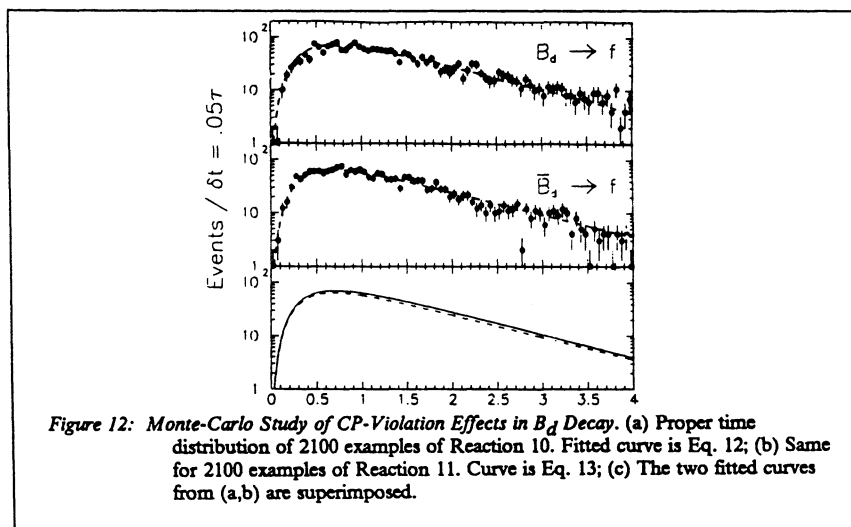


Figure 12: Monte-Carlo Study of CP-Violation Effects in B_d Decay. (a) Proper time distribution of 2100 examples of Reaction 10. Fitted curve is Eq. 12; (b) Same for 2100 examples of Reaction 11. Curve is Eq. 13; (c) The two fitted curves from (a,b) are superimposed.

Fig. 13 shows the total sample sizes of tagged B and \bar{B} required to observe a 3σ or a 4σ asymmetry effect as a function of $\sin(2\beta)$, when the net dilution factor is 0.47.

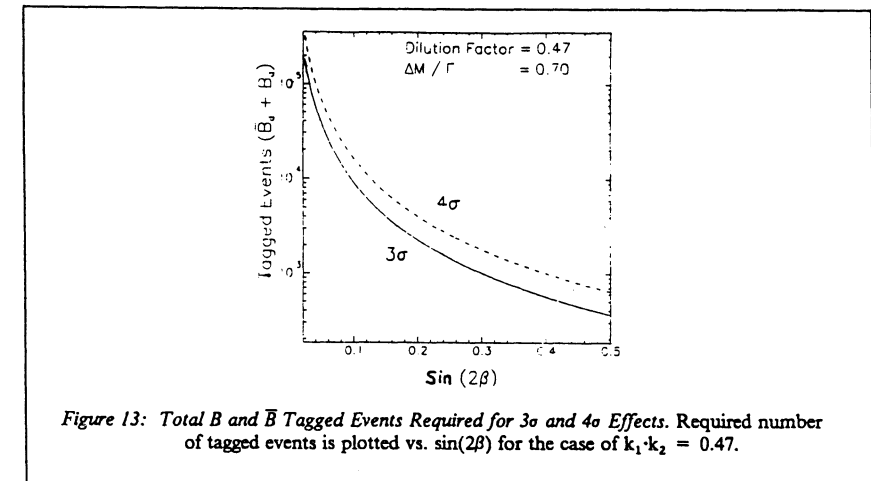


Figure 13: Total B and \bar{B} Tagged Events Required for 3σ and 4σ Effects. Required number of tagged events is plotted vs. $\sin(2\beta)$ for the case of $k_1 \cdot k_2 = 0.47$.

Table 4 gives a summary of the various factors which determine the event sample size available for a CP-Violation measurement at LHC. The estimates assume a $300 \mu b$ cross section for BB production and are given for an integrated luminosity, $\int \mathcal{L} dt = 200 \text{ pb}^{-1}$. Referring to Fig. 13, we can see that the 14,000 tagged events obtained in this run would permit a 3σ or more measurement of $\sin(2\beta)$ for values below 0.1. Similar results can be expected for other interesting final states, such as $B_d \rightarrow \pi^+ \pi^-$ and $B_s \rightarrow \rho K_s$.

In conclusion, a high-resolution forward spectrometer system coupled with a planar silicon detector and powerful trigger processor would allow exploitation of the LHC to study all facets of Beauty physics. Although some may feel that limiting the discussion to an operating luminosity of 10^{31} may be too conservative, we note that the very large quantities of data that must be examined in real time to isolate Beauty candidates probably saturate present and near-future technology with our present algorithm. However, the rapid pace of advances in detector and computer technology, and the further development of our triggering algorithm, will conceivably allow running at higher luminosities in the future.

We note as well that radiation damage¹⁰ to the silicon at high luminosities is not a fundamental limitation, although it will probably be necessary to regard the silicon detectors as expendable, at a cost which is quite tolerable, 300- 400 KSF, compared to the cost of the entire detector (about 25 MSF/arm for the LHC) and of running the machine.

¹⁰ Our preliminary estimates indicate that substantial radiation damage may occur during the course of a 100 pb^{-1} run and it may be necessary to replace the silicon once or twice during the course of a CP experiment.

Table 4: $B^0_d \rightarrow J/\psi K^0_s$ Event Yields at LHC

$6 \cdot 10^{10}$ $b\bar{b}$	using:	$\int \mathcal{L} dt = 200 \text{ pbarn}^{-1} (10^{31} \cdot 2 \cdot 10^7)$ $\sigma(b\bar{b}) = 300 \mu\text{b}$.
$2.4 \times 10^{10} B_d$	$2.4 \times 10^{10} \bar{B}_d$	0.40 = B_d Production
1.3×10^{10}	1.3×10^{10}	0.55 = 2-Arm Geometrical Acceptance
5.1×10^5	5.1×10^5	$3.9 \cdot 10^{-5} =$ Branching Ratios $B \rightarrow J/\psi K_s \rightarrow \ell^+ \ell^- \pi^+ \pi^-$
3.6×10^5	3.6×10^5	0.70 = Live Time
7.2×10^4	7.2×10^4	0.20 = Trigger Efficiency
2.9×10^4	2.9×10^4	0.40 = Tagging Efficiency
7.2×10^3	7.2×10^3	0.25 = Reconstruction Efficiency
1.4×10^4		Total Reconstructed $J/\psi K_s$ Events

Possibilities for B-Physics in fixed target mode at the LHC

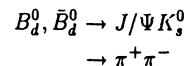
Y. Lemoigne¹ and Y. Zolnierowski²

CERN, Geneva, Switzerland

¹ DPHPE, Centre d'Etudes Nucléaires de Saclay
² INFN - Padova

1 - Introduction

We discuss some possibilities for B -physics at the Large Hadron Collider (LHC) operating in a fixed target mode (internal or external target). The main interest of such experiments, are the B -decay lengths of a few centimeters which are obtained in this mode of operation. Having in mind the possibility of searching for CP violation, we focus on the B_d^0 decay channels which are CP eigenstates like :



For CP violation studies with such CP eigenstates, the B -tagging with the B hadron produced in association is clearly necessary. Usually it is considered that the tagging is provided by the charge of the lepton l (μ, e) from the semileptonic decay $B \rightarrow l^+ X$, $\bar{B} \rightarrow l^- X$ (X meaning anything). However, other types of tagging, for instance the measurement of the charge of B mesons, could also be considered. This paper explains the choice of a fixed target mode, and gives some kinematical parameters specific to these interesting decays. We define a minimal scheme of an hypothetical experiment, to be able to perform Monte-Carlo simulations allowing us to estimate the possibilities of a jet target mode at the LHC in view of the physics goals to achieve.

2 - Why to use the LHC in a fixed target mode ?

The comparaison of the possibilities of the LHC (or the SSC) in the collider mode versus fixed target mode, as far as B physics is concerned, is given in another paper¹. In general, hadron accelerators are a powerful tool to observe particles containing heavy quarks owing to the fact that such particles have a measurable decay length. For many years, searches for charmed particles have been unsuccesfull at hadron machines, until detectors have not been used exploidiing this unique character of heavy quark particles. The pioneering work in that matter has been done by NA1, NA14 and NA32 at CERN, and E691 at FNAL.

The interaction with a fixed target (external or internal jet target) at the LHC will occur at a modest CM energy, $\sqrt{s} = 0.123$ TeV, but the momentum of the outgoing particles will be very large, due to the Lorentz boost (see table 1). The consequences are :

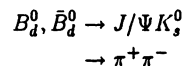
- The average decay length is about ten times longer in the fixed target mode than in the collider mode (see figure 1)

- The $B\bar{B}$ cross section at $\sqrt{s} = 0.123$ TeV is estimated to be of the order of $\sim 1 \mu\text{b}$. Thus an interaction rate of $2.10^7 / \text{sec}$ gives $4.10^9 b\bar{b}$ pairs produced per year (10^7 seconds).
- The B -decay products are collimated within a small angle around the beam line : the median angle for the B -decay charged products is of the order of 15 mrd. The vertex detector can then be much smaller than in the collider case and a good hermeticity can be achieved with a detector made of several planes of silicon microstrips of present day technology ($10 \times 10 \text{ cm}$ dimensions). The accuracy that can be obtained on the measurement of the decay length, and the ensuing separability between the primary and secondary vertex, is the main parameter to decide if the fixed target option is an interesting possibility, as it is this measurement which largely ensures the cleanliness of the B sample.
- The fixed target mode allows also to perform an experiment with a point-like source of B 's, for instance with the use of a jet target, which can be easily installed at a collider, or the use of an extracted beam, which is more complicated. In a jet target mode, the error on the determination of the primary vertex can be negligible, the decay length (and the lifetime measurement) is measurable in an unbiased way (see figure 2). In the analysis of the experiment, the finite B -decay length is used to isolate the heavy quark signal, by requiring that the 'decay' vertex lies a significant distance downstream the production vertex. The appropriate cut is not on the absolute vertex separation Δx , but rather on the quantity $N_\sigma = \Delta x / \sigma_z$, where N_σ is the number of standard deviations and σ_z is the error on the difference in the longitudinal coordinates of the production and 'decay' vertices. N_σ is more appropriate because it is independant of the Lorentz boost γ . Referring to figure 2 : $\Delta x = \gamma \beta c \tau$, where τ is the B -proper-time. But $\sigma_z = \sigma_{z2}$, if the error on the primary vertex is negligible(point-like target), then : $\sigma_{z2} \sim \sigma_z / \theta \sim 2\gamma \sigma_z$, where σ_z is the transverse error, independant of γ . Thus $N_\sigma = \Delta x / \sigma_z \sim \beta c \tau / \sigma_z$. A cut on N_σ should therefore lead to an unbiased sample for the measurement of the lifetime.
- Straight-line trajectories, a point-like target and a vertex detector with as little material as possible, are the minimal conditions which allow to consider an on-line trigger to select heavy quark particles, based on a secondary vertex. Events with tracks clearly not originating from the point-source, can be selected in this way. This could be the best method to accumulate the maximum number of B events in any decay channel.

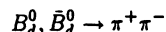
3 - Monte carlo studies

A comparaison has been made of B kinematics at the LHC and SSC colliders using ISAJET and PYTHIA (see table 1). The agreement in the results of the two programs has been verified. Figure 1 shows the distribution of decay length of the produced B (\bar{B}) as a function of the laboratory emission angle. From this figure we can see that the advantage of the fixed target versus the collider mode is lost, if a minimal angle of $\theta_B \geq 1^\circ$, is imposed. It is thus crucial to have this θ_{\min} dead-angle in the forward direction, in fact applied to the B -decay products, as small as possible.

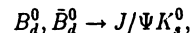
The studies considered mostly the two interesting decays :



Taking $\theta_\pi \geq 0.2^\circ$ (corresponding to a dead area of 36mm^2 at a distance of 1 meter from the target) for the $\pi^+ \pi^-$ decay mode, the B -decay length distributions are nearly equal for the LHC and the SSC, in fixed target mode (See figure 3). Some characteristic distributions for the



decay mode at the LHC (fixed target) are shown in figure 4 : The momentum distributions of the B 's and the π 's, the angular distribution and transverse momentum of the π 's. The large momenta of the π 's, allow us to neglect the multiple scattering through a material of the thin detector (Silicon). Figure 5 shows, for the decay:



the momentum and the angular distributions of the Ψ -decay μ 's, the momentum of the π 's from the K_s^0 , the decay length of the K_s^0 (there is a 45% probability that the K_s^0 decays before 5 meters).

4 - A possible scheme for a fixed target apparatus at the LHC

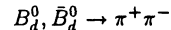
To calculate the experimental efficiencies and the B -decay length resolution, we need an approximate experimental set-up. The choices are (see figure 6) :

- A jet target³ which can be H_2 or *Cesium* the aim being the smallest area intersecting the proton beam (100 to $500 \mu\text{m}$). We have retained this option because of its technical simplicity which seems well suited with a machine at the beginning of operation. Thin targets like a W -wire in the halo of one beam can also be considered. We note also that the stability of the transverse position of the beam, which is intrinsic to this collider machine, can in fact allow a θ_{\min} angle smaller than thought-of at first look (see later).
- A telescope of Silicon microstrips as close as possible to the beam. We have simulated 10 two-coordinate planes, perpendicular to the beam direction and located from 50 to 450 cm from the target. There is no matter and no magnetic field around.
- Two magnets which are part of the system of bending magnets foreseen to bring together the two proton beams in the intersection region. A bending power of 5 Tm is convenient to keep the lower momentum particles from the B -decay, inside the first arm.
- We assume that π 's and K 's are identified in the two arms, with RICH detectors which discriminate π/K up to 350 GeV/c, i-e 80% of the π 's spectrum.
- An electromagnetic calorimeter identifies the electrons, photons and the π^0 (electron-tagging).
- A μ - filter completes the apparatus (J/Ψ trigger and μ -tagging).

The crucial problem is the determination of the minimal distance from the beam, acceptable for the silicon telescope. With a $\beta \sim 10m$ along the experimental zone (instead of $\beta \geq 30m$ foreseen), it could be possible to maintain the beam within $\sim 0.4\text{mm}$ from the central beam line, when crossing the silicon detector⁵. The two proton beams are also vertically separated by few millimeters, and do not interact with each other in this region.. In the horizontal plane, the two beams are separated by the first magnet behind the silicon detector ($\sim 10m$ downstream the target) but only by 18mm to minimize the dead zone in the downstream detectors. In such conditions, the silicon planes could be positioned at $\sim 1\text{mm}$ from the beam without too big damage : it is the distance used presently by the P238 group⁶ at the SPS collider. In the LHC case, the halo has been estimated⁵ to be $\sim 3.10^9$ at 6 standard deviations ($\sim 600\mu\text{m}$) from the central beam line. Thus at 10 standard deviations, the mean number of parasitic particles from the halo will be much lower than the contribution from the interactions themselves, but a careful design of the optic of the machine in this region is clearly necessary. Our Monte Carlo simulation uses a conservative distance of 1.5mm. Thus the geometric acceptance of the set-up will be from $\sim 1\text{mrd}$ to $\sim 100\text{mrd}$.

5 - Results from silicon detector simulation

We have tried to optimize the pitch of the microstrips of the silicon detector, giving the best accuracy on the longitudinal decay length. The study was done for the decay :



10 silicon microstrip planes (each with two coordinates) have been simulated, separated by 50 cm and starting 50 cm from the target and extending up to 450 cm. The area was 10 x 10 cm except a beam hole of 1.5 x 1.5 mm. We varied the pitch δ from 10 to 75 μm . The clusters resulting from the impacts of all the charged tracks are simulated in the Si-planes crossed. Enlargement of the cluster, wrong assignment of hits in the track reconstruction, as well as any degradation coming from the other tracks in the same event, have been taken in account before fitting the trajectories with straight lines to reconstruct the 'decay' vertex..

The program has been tested by simulating the response of the the microstrip silicon telescope previously used by the NA14 experiment⁴ (at $\sqrt{s} \sim 14 \text{ GeV}$). It was able to reproduce the main features of the secondary vertex reconstruction, in particular the observed longitudinal and transverse accuracy for a pitch of $\delta = 50 \mu\text{m}$ (see figure 7).

The accuracy we would obtain at the LHC is given at figure 7 : with a 10 μm pitch, the secondary vertex (in fact the decay length, if the error on the primary vertex is negligible), is longitudinally reconstructed with a standard deviation of $\sim 600 \mu\text{m}$, only two times the value measured by the NA14 experiment ($\sim 350 \mu\text{m}$ on the longitudinal coordinate). At the LHC however, the decay lengths will be more than 10 times larger than at the SPS, thus a big improvement is expected in event selection.

About 45% of the generated B_d^0 (or \bar{B}_d^0) have been reconstructed in the Si-microvertex detector by the program, and the geometrical acceptance varies only by $\sim 10\%$ when the decay length goes from zero to 10cm .

6 - Is an observation of B-CP violation possible at the LHC with a jet target ?

Before any observation of CP violation effects one has to :

- measure B_u^0, B_d^0 and B_s^0 production (and \bar{B}). This requires a good effective mass resolution (~ 50 to 100 MeV). This is not unreachable and existing fixed-target spectrometers have to be scaled up by a reasonable amount to obtain such a resolution.

- measure the lifetime and the branching ratios of the various species, in particular of the interesting modes ($\pi^+ \pi^-$ and $J/\Psi K_s^0$) : NA14 and NA32 have shown how to do that. Considering the signal to background ratio, Beauty detection at $\sqrt{s} = 123 \text{ GeV}$ is not very different from Charm detection at $\sqrt{s} = 14 \text{ GeV}$. Intrinsic lifetimes are of the same order.

- measure the mixing of particle and antiparticle, in particular of B_s^0 .

Assuming¹ a $b\bar{b}$ cross section of $\sim 1 \mu\text{b}$ at $\sqrt{s} = 123 \text{ GeV}$ and an interaction rate of 2.10^7 interactions/second (limitations from radiation damage and data acquisition) and for a running time of 10^7 sec, one gets $4.10^9 b\bar{b}$ pairs per year. Assuming that 40% of them hadronize in B_d^0 (\bar{B}_d^0) and with a branching ratio for the decay into $\pi^+ \pi^-$ estimated⁷ to $\sim 2.10^{-5}$, this gives $3.2 \cdot 10^4 B_d^0$ (\bar{B}_d^0) produced and decaying in $\pi^+ \pi^-$ per year.

Our simulations give a reconstruction probability (including secondary vertex reconstruction, geometrical and pattern recognition efficiency) of $\sim 40\%$: there are thus $1.3 \cdot 10^4$ interesting $\pi^+ \pi^-$ decays, which now have to be tagged by the semileptonic decay of the accompanying \bar{B} (B). With a branching ratio in leptons of 20% (electrons and muons), and an overall acceptance and pattern recognition efficiency of 38%, they are ~ 1000 tagged events which can be recorded in this decay mode.

The numbers are roughly the same for the $J/\Psi K^0$ channel. Thus ~ 1000 tagged events can be obtained, in such an experiment, in the two most promising modes.

There is also the possibility to use a Cesium target³ which is five times more favorable than for free protons, in terms of the fraction of $B\bar{B}$ events in the total interaction rate. A Tungsten wire could be also used but more precise studies have to be done to see if there is, in these cases, extra limitations with the electronics and the data acquisition rate.

What measurement of the CP-violation asymmetry A between particles and antiparticle (restricting the measurement to the first half period of an oscillation) is possible with three standard deviations? It can be shown² that, N being the number of available B_d (\bar{B}_d) events, the minimum value of A that could be resolved to S standard deviations is :

$$A_{\min} = S / \sqrt{(N + S^2)}$$

Therefore, with $N = 1000$, one can hope to observe an asymmetry of $A = 0.09$ with $S = 3$. An asymmetry of 0.12 can be resolved with 4 standard deviations,

and a minimal assymetry of 0.15 with 5 standard deviations. These numbers are estimated for one year of running time.

7 - Conclusion

A Monte Carlo done to simulate a fixed-jet-target B production experiment at the LHC, has been calibrated with the 'decay' vertex resolution obtained by a previous Charm production experiment at the SPS (NA14). This study shows that the limitations of fixed-target experiments in comparaison with the collider mode (relatively low $B\bar{B}$ cross sections, smaller average emission angle) do not invalidate the method : with a $10 \mu m$ pitch for Silicon microstrips, the decay length is longitudinally reconstructed with a standard deviation of $\sim 600 \mu m$, which is only two times the value measured by the NA14 experiment, but at the LHC the average decay lengths will be more than 10 times larger.

First estimates indicate the possibility to observe a CP violation asymmetry of the order of 10% in

$$\begin{aligned} B_d^0, \bar{B}_d^0 &\rightarrow J/\Psi K_s^0 \\ &\rightarrow \pi^+ \pi^- \end{aligned}$$

Clearly, more detailed investigations (general simulations of the apparatus, pattern recognition optimizations) and further Monte Carlo calculations are necessary.

We would like to thank Daniel Denegri for his encouragements and usefull discussions.

References

- 1) Fixed Target Versus pp Collider for B-Physics. A. Fridman et al., Large Hadron Collider Workshop - Aachen 1990;
- 2) SFT Beauty Facility at the SSC, Expression of Interest (1990), BCD at SSC, Expression of Interest (1990);
- 3) Internal Target Beauty Physics at the SSC, J. Rosen, Expression of Interest (1990);
- 4) NA14 Collaboration, M.P. Alvarez et al., Z. Phys. C47, 539 (1990)
Michel Primout : Thèse Université Paris XI - 1987 (unpublished)
Christophe Magneville : Thèse Université Paris XI - 1987 (unpublished)
- 5) B. Jeanneret : Private communication
- 6) P. Schlein : Private communication
- 7) Exclusive Non-Leptonic Decays of D^- , D_s^- , and B-mesons, M. Bauer et al., Z. Phys. C 34, 103 (1987)

Figure captions

Table 1 Comparaison of some experimental conditions in collider and fixed target mode (kinematics from ISAJET and/or PYTHIA); stars = quality of merit in each mode;

	Fixed target mode		Collider mode		
	LHC F-T	SSC F-T	LHC (coll)	SSC (coll)	
\sqrt{s} GeV	123	193	16000	40000	
$\sigma(B\bar{B})$	1 μ B	3 μ B	200 μ B	500 μ B	**
$\sigma(B\bar{B})/\sigma_{tot}$	1 / 50000 (H_2)	1 / 5000 ($Be+Si$)	1 / 500	1 / 200	*
$< n_{\text{charg.}} >$	18	20	80	115	
KINEMATICS					
$<p^B>$ GeV/c	560 GeV/c	967 GeV/c	146 GeV/c	270 GeV/c	
$<p^\pi(B \rightarrow \pi\pi)>$	275 GeV/c	475 GeV/c	72 GeV/c	137 GeV/c	
$<p^\mu(B \rightarrow \psi K)>$	192 GeV/c	315 GeV/c	49 GeV/c	86 GeV/c	
$<p^\pi(B \rightarrow \psi K)>$	93 GeV/c	155 GeV/c	24 GeV/c	42 GeV/c	
Ref. EXPERIMENT					
θ_{\min} experimental	This Set-up	"SFT"	"P238"	"BCD"	
	1 mrd	3 mrd	2 mrd	8 mrd	
$\Delta\Omega$	100 mrd	75 mrd	600x2 π mrd	750x2 π mrd	
KINEMATICS for Ref. Experiment:					
$<p^B>_{\theta>\theta_{\min}}$	510 GeV/c	480 GeV/c	* **	89 GeV/c	71 GeV/c
Median B-decay length	35 mm	45 mm		3.6 mm	4 mm
$<\theta^B>_{\theta>\theta_{\min}}$	0.6°	0.5°		17°	16°
$<p^B\text{-decays}>_{\theta>\theta_{\min}}$	52 GeV/c	48 GeV/c		9.8 GeV/c	8.3 GeV/c
$<\theta^B\text{-decays}>_{\theta>\theta_{\min}}$	1.5°	1.1°		22°	19°
$<p^\pi(B \rightarrow \pi\pi)>_{\theta>\theta_{\min}}$	250 GeV/c	235 GeV/c		39 GeV/c	31 GeV/c
$<p^\mu(B \rightarrow \psi K)>_{\theta>\theta_{\min}}$	183 GeV/c	155 GeV/c		32 GeV/c	24 GeV/c
PARTICLE IDENTIFICATION:					
P range	20 - 300 GeV/c		5 - 70 GeV/c		*
interaction/sec	$2 \cdot 10^7$	10^7	$10^6 (L \sim 10^{31})$	$10^7 (L \sim 10^{32})$	
$N(B\bar{B})/10^7 \text{ sec}$	$4 \cdot 10^9$	10^{10}	$\leq 10^{11}$	$5 \cdot 10^{11}$	**
TRIGGER:					
- Lepton	$p(e,\mu) > 100 \text{ GeV}/c$		*	$p_T(e,\mu) > 1 \text{ GeV}/c$	
- 2 nd vertex	possible if thin target		**	difficult : 1 st vertex not stable	
TAGGING:					
- Lepton/ ψ	hard lepton(s) : easier ?		*	soft lepton(s) : difficult !	
- Charge ($B^{+/}$)	possible ?		*	not easy !	

Fig.1) B decay length distributions for various θ_{\min}^B angles (see text). Fixed target mode, both for LHC and SSC, are compared with the collider mode (LHC only). Note that the units are arbitrary.

Fig.2) Description if the N_σ cut.

Fig.3) B-decay length distributions for various minimal angles imposed to the decay- π 's (θ_{\min}^π). Fixed target mode, both for LHC and SSC, are compared with the collider mode (LHC only). Note that the units are arbitrary.

Fig.4) Kinematics for LHC in fixed target mode :

a- Momentum distribution for the $B(\bar{B})$

b- Momentum distribution for the π 's from the $B(\bar{B})$ decays.

c- Angular distribution for the π 's from the $B(\bar{B})$ decays.

d- Transverse momentum distribution for the π 's from the $B(\bar{B})$ decays.

Fig.5) Kinematics for LHC in fixed target mode for the $J/\Psi K_s^0$ decay :

a- Momentum distribution of the μ from J/Ψ

b- Angular distribution of the μ from J/Ψ

c- Momentum distribution of the π from K_s^0

d- K_s^0 decay length distributions.

Fig.6) Scheme for an appropriate experimental set-up.

Fig.7) Secondary vertex reconstruction accuracy, as a function of the Silicon microstrip pitch (from 10 to 75 μ meter).

- Curve 1) shows the longitudinal accuracy for $B(\bar{B})$ production, computed for LHC fixed target (see text).

- Curve 2) shows the longitudinal accuracy for $D(\bar{D})$ production computed for the NA14 apparatus at their energy. The real accuracy obtained by this experiment is shown.

- Curve 3) shows the transversal accuracy computed for $B(\bar{B})$ production at LHC fixed target.

- Curve 4) shows the transversal accuracy for $D(\bar{D})$ production computed for the NA14 apparatus at their energy. The real accuracy obtained by this experiment is shown.

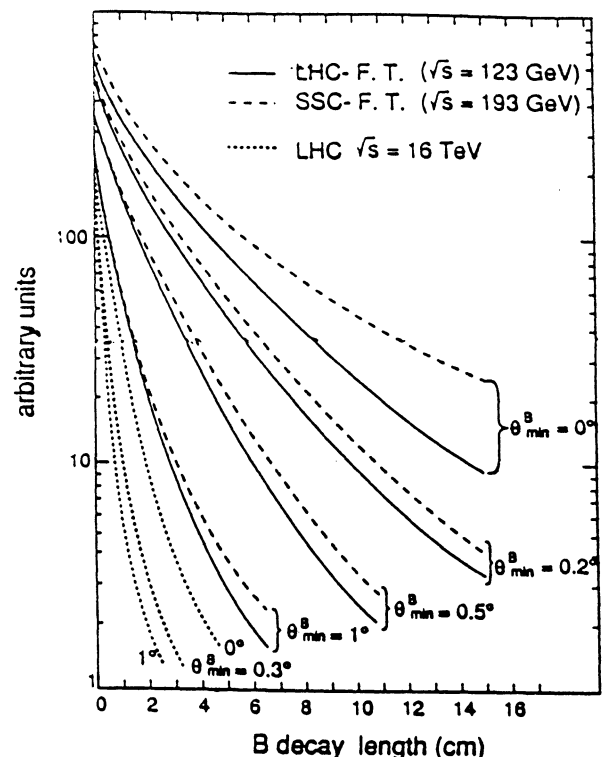


FIG. 1

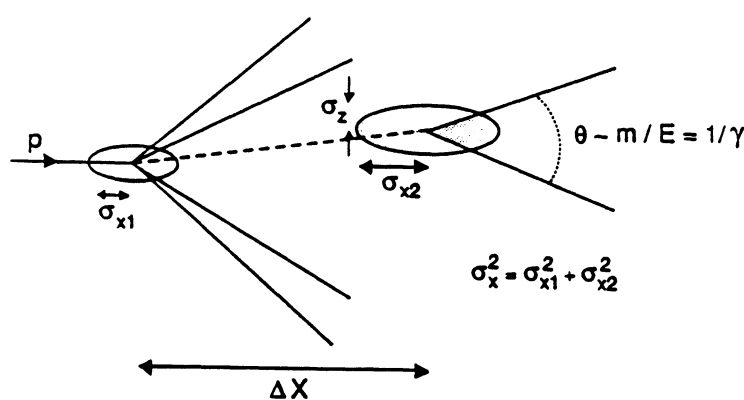


FIG. 2

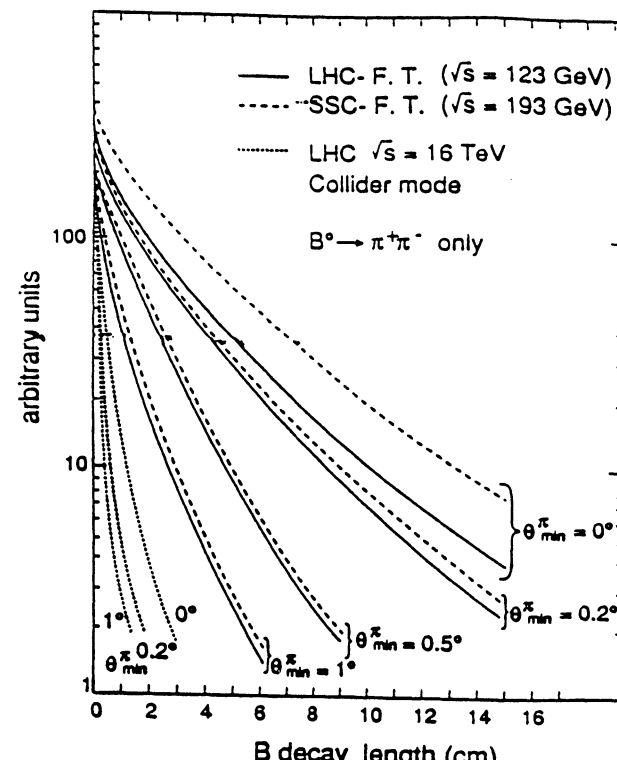
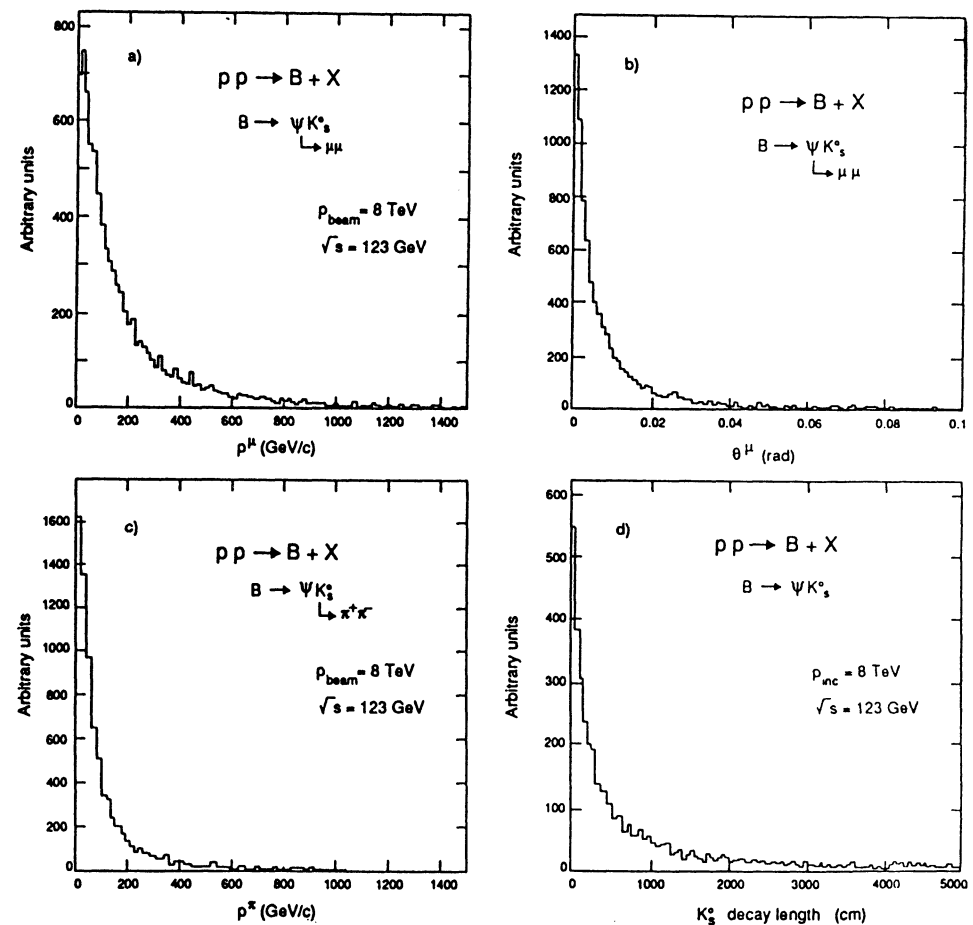
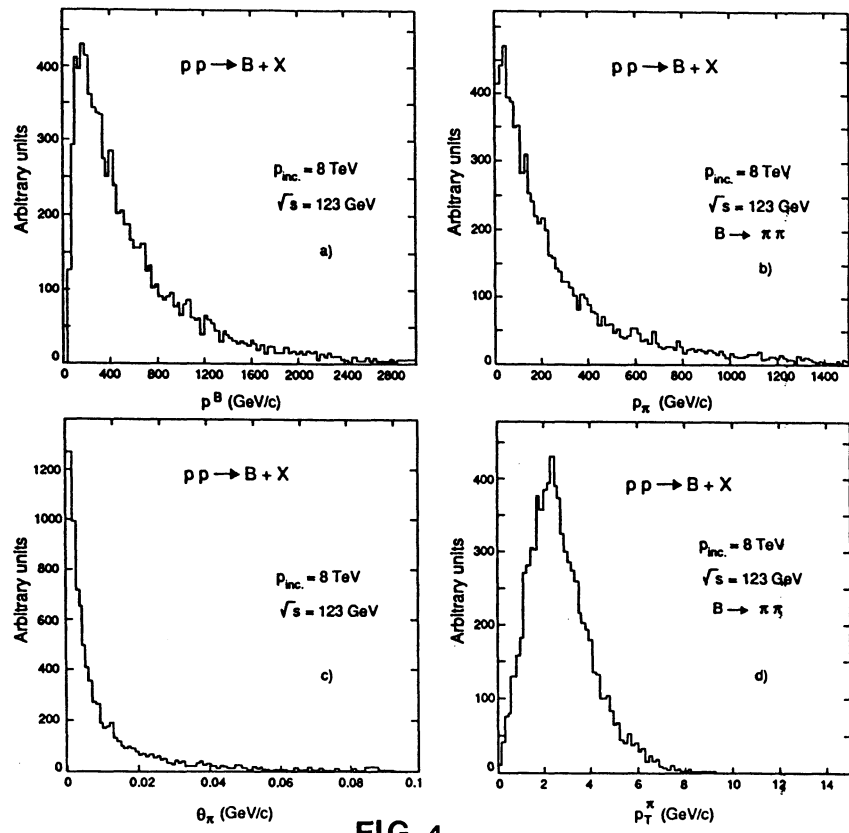


FIG. 3



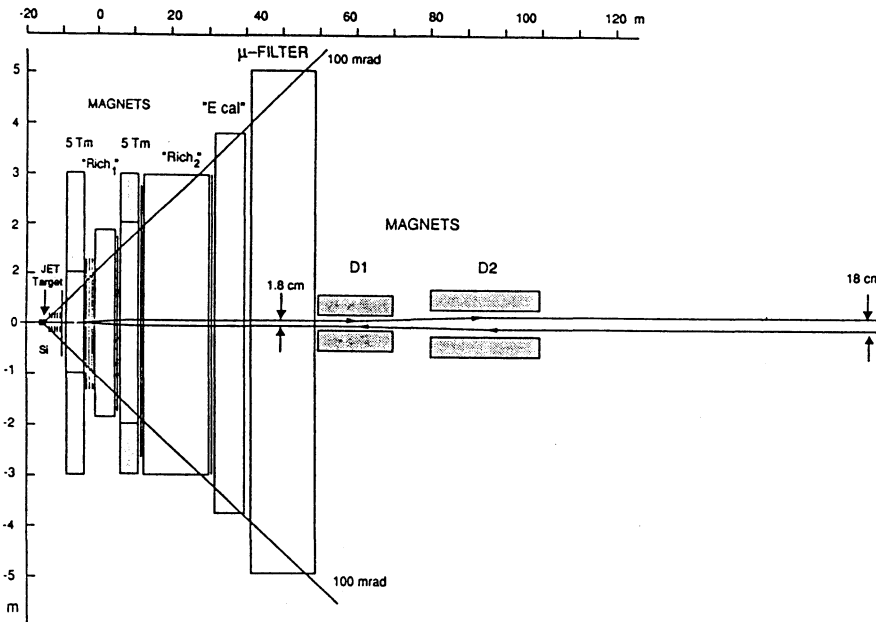


FIG. 6

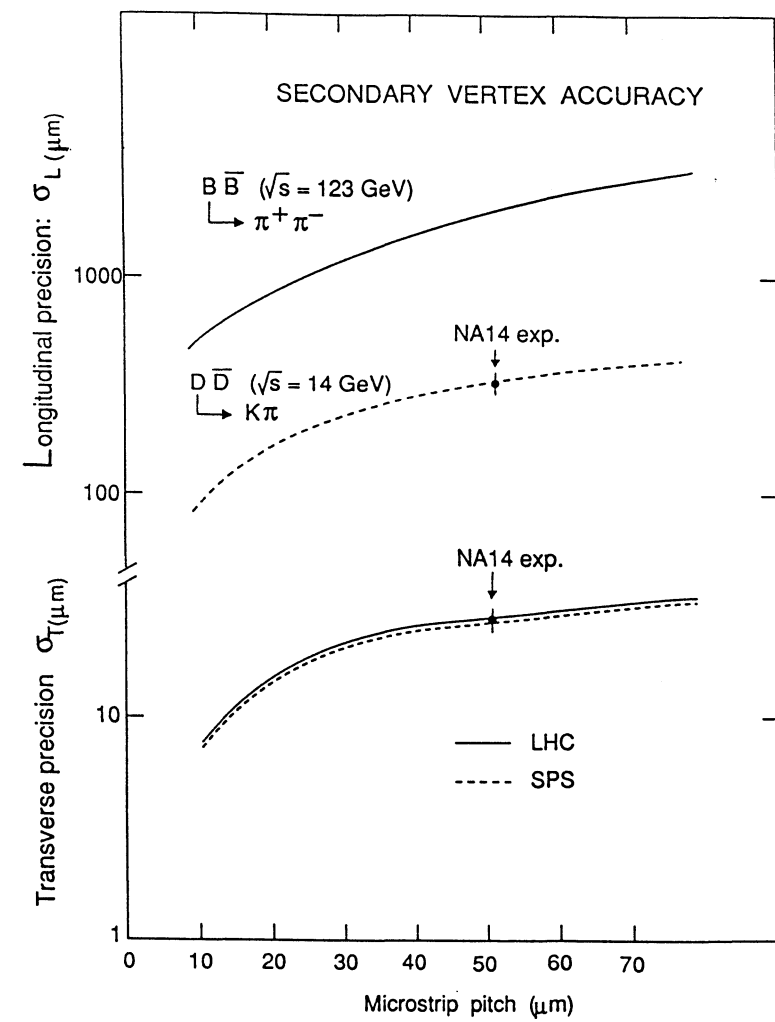


FIG. 7

FIXED TARGET PHYSICS AT THE SSC

F. Grancagnolo

INFN - Sezione di Lecce - Italia

ABSTRACT

This is an extract from the Expression of interest EOI14 for a Super Fixed Target Beauty Facility (SFT) at the Superconducting Super Collider to be built in Texas, USA.

we limit ourselves to the open geometry spectrometer which is the more general approach.

Among the topics that can be addressed with the large B statistics obtainable in the SFT are:

1. the measurement of the production of the heavy b quark and the attendant fragmentation and hadronization into the various B hadron species B_u , B_d and B_s ;
2. the measurement of the lifetimes of the various species;
3. the determination of the branching ratios for various decay modes;
4. the determination of the mixing of particle and antiparticle;
5. the observation of rare decay modes;
6. the detection and a precise measurement of CP violation effects.

2. FIXED TARGET VS COLLIDER EXPERIMENTS

2.1. Production Rates.

To obtain an estimate of the $pN \rightarrow BB$ production cross at $\sqrt{s}=193$ GeV we have used the third order (in α_s) calculations of K. Ellis et al. which predicts 2.5 to 10 μb total beauty cross section.

Assuming the heavy flavor production increases with atomic number of the target like A^1 , the beauty production cross section will be, for pSi, between 70 and 280 μb . Taking the total inelastic pN cross section at $\sqrt{s}=193$ GeV to be 38 mb and assuming an A dependence of $A^{0.72}$, we obtain a pSi total cross section of approximately 420 mb. Therefore, taking into account the thickness of the target (0.075 λ) one gets a production rate of $(1.3 \pm 5.2) \times 10^{-4} \bar{B}\bar{B}/\text{interaction}$. Therefore, at an interaction rate of 10^7 interactions/sec (this is essentially limited by the multiple interaction per bucket and by radiation damage), and for a running period of 10^7 sec (one year) one gets: $(1 \pm 5) \times 10^{10} \bar{B}\bar{B}/\text{year}$.

While this rate for $\sqrt{s}=193$ GeV pSi interactions is not as great as that expected in the hadron collider configuration $(2 \pm 5) \times 10^{11} \bar{B}\bar{B}/\text{year}$, there are aspects of the fixed target configuration which can lead to a greater fraction of the produced B's actually written to tape and eventually reconstructed. In addition, the fixed target configuration offers the unique opportunity of directly observing and measuring some significant fraction of the B's, an option that is available in no other experimental configuration. Thus, the factor of 10 in the yield per interaction between the SSC collider and the SSC fixed target mode becomes much less

1. INTRODUCTION

The 20 TeV Super Fixed Target B Physics Facility (SFT) contains two major components, the crystal channeling extraction/proton beam transport system and the fixed target beauty spectrometer.

We have considered two general approaches for the SFT spectrometer: open geometry and restrictive geometry. Open geometry gives large acceptance for a wide variety of decay modes and gives the opportunity of tagging, by observation of the second B decay in the event. However, the detector must deal with the full interaction rate. Restrictive geometry spectrometers emphasize rare low multiplicity decays and minimize rates in the detectors per interaction. This type of spectrometer offers simplicity of triggering and cleanliness of event reconstruction. Both approaches seem promising for a 20 TeV fixed target facility. In the sections that follow,

significant when the unique features, relative simplicity and relative economy of the fixed target experiment, are compared to the formidable challenges and expense of attempting a comparable B collider experiment.

2.2. B Momenta

One of the main points in favor of a fixed target configuration is the much higher momenta of the B's produced in the SSC fixed target interactions compared to those produced in the SSC collider configuration. There are several technical advantages which arise from this high momentum. The high momentum produces very long average decay lengths resulting in the unique situation (among all the options for doing B physics) where B's can pass through many microvertex planes before decaying. In SSC fixed target interactions, an average B will travel 9.5 cm before decaying and pass through approximately 30 silicon planes in the SFT microvertex detector. This allows the possibility of directly observing the B in these spectacular events, and determining whether it is neutral or charged (B_u or $B_{d,s}$). Furthermore, if a magnetic field is imposed on the silicon microvertex detector (an option under discussion), the sign of the charge of the B_u can be determined for a significant fraction of the B_u 's. Particle/antiparticle tagging is critical to CP violation measurements but is difficult in other experimental configurations because of the difficulty in determining the charge of the B's from reconstruction of all their secondary decay products. Observation of the charge of the parent B will replace the muon charge as the tag in the case of the $B_u \rightarrow \mu$ decays.

Another advantage of the higher momenta of the fixed target configuration is the better track resolution due to the smaller multiple scattering of B decay secondaries.

While it is true that the Lorentz expansion of the decay length is compensated for by the decrease in the average angle of secondaries from B decay such that the impact parameters of these secondaries remain of the same order of magnitude independent of the total center of mass energy, the multiple scattering of the B decay products becomes almost completely negligible in 20 TeV interactions. Thus, the ability to resolve secondary vertices improves. In addition, the negligible multiple scattering in Lorentz boosted 20 TeV events allows the use of more measurement planes leading to the opportunity mentioned above of directly observing the B's.

Higher momentum of the B's also makes possible tractable trigger strategies (in particular trigger strategies based on leptons). For example, muon triggers which depend on the separation of muons from hadrons become difficult if the muon momentum is too low (a muon shield cannot be made thick enough to range out hadrons effectively). The muon momentum is, in fact, low for producing a single muon trigger capable of collecting a large fraction of the B muonic decays in SSC collider events. No such problem exists in the SSC fixed target configuration where the mean and median lepton momenta are 280 GeV/c and 120 GeV/c respectively. The large lepton momentum also helps if an electron trigger is contemplated since distinguishing an electron from a hadron becomes progressively easier for both TRD's and calorimetry as the energy of the electron increases. These more powerful triggers have the advantage of minimizing the required data acquisition systems or on-line microprocessor farms, and the sometimes ignored advantage of reducing enormously the off-line computing load.

2.3. Multiplicity

Another aspect of fixed target events which makes detection and reconstruction of B's easier is the relatively low multiplicity of the events. At $\sqrt{s}=193$ GeV the average event is expected to contain approximately 23 charged tracks and 10 π^0 's. This is to be compared with an anticipated multiplicity of over a hundred in a $\sqrt{s}=40$ TeV pp collision. In addition, the B events themselves, at $\sqrt{s}=193$ GeV, have approximately the same low multiplicity (an average of 24 charged tracks). This low multiplicity greatly simplifies beauty triggers based on the hadronic characteristics of B events, as well as off-line reconstruction of B events.

2.4. Overall simplicity and today available technology

The detector components of the SFT themselves can be arranged in a simpler and more economical and effective way than the collider counterparts, even using today's technologies. In particular, the silicon microvertex detector can be a simple, planar arrangement leading to economies of effort and money in construction. The detector can be arranged so that the B decays occur inside itself at most 6 mm before a measurement plane, leading to excellent vertex resolution.

Finally, there is the obvious advantage that the size of a fixed target

beauty experiment is very modest because of the small solid angle that must be covered to capture the B decay products. The SFT spectrometer is designed to cover the 3+75 mrad forward cone. With this coverage, approximately 70% of all B's will have their decay products within the geometric acceptance of the spectrometer at $\sqrt{s}=193$ GeV. If we require that both B's in a given event have all decay products in the acceptance of the spectrometer, a geometric acceptance of 45% is obtained.

In Table I we summarize and compare the important global aspects of the various beauty hadroproduction options.

Table I

Important Parameters of Beauty Production
in Various Hadronic Experimental Configurations

	TeV Fixed Tgt	TeV I Collider	SSC Collider	SSC FixedTgt
Int Rate	$10^7\text{-}10^8/\text{sec}$	$10^5/\text{sec}^*$	$10^7/\text{sec}^{**}$	$10^7/\text{sec}$
$\sigma(pN \rightarrow B\bar{B})$	10nb	$20 \mu\text{b}$	200-500 μb	$2.5\text{-}10 \mu\text{b}$
$B\bar{B}/10^7 \text{ sec}$	$10^7\text{-}10^8$	4×10^8	$2 \times 10^{11}\text{-}5 \times 10^{11}$	$1 \times 10^{10}\text{-}5 \times 10^{10}$
$\sigma_T/\sigma(B\bar{B})$	*** 1.25×10^6	2.5×10^3	$2 \div 5 \div 10^2$	$7 \div 9 \times 10^2$
Multiplicity	≈ 15	≈ 45	$\sim \text{hundred}$	≈ 20
$\langle p_b \rangle$	143 GeV/c	38 GeV/c	51 GeV/c	635 GeV/c
$\langle p_B \rangle$	118 GeV/c	22 GeV/c	43 GeV/c	445 GeV/c
$\langle p_\mu \rangle$	32 GeV/c	13 GeV/c	36 GeV/c	280 GeV/c
Median B Decay Length	8mm	1.5mm	3mm	42 mm
Mean B Decay Length	16mm	4.7mm	13mm	95mm

* Present luminosity $\approx 10^{30} \text{ cm}^2 \text{ s}^{-1}$ for the Fermilab Collider. Presuming the injector upgrades and corresponding detector upgrades to take advantage of the higher luminosity, this may be increased to $5 \times 10^{31} \text{ cm}^2 \text{ s}^{-1}$.

** 10^7 interactions per second is taken as a limit for a high rate 4π B physics collider detector to avoid the problem of multiple high multiplicity events per bucket.

*** Taking into account the atomic number enhancement of the heavy flavor cross sections in heavy targets relative to the total cross section.

3. THE SPECTROMETER

The very important experimental advantages that an SSC fixed target configuration offers must be capitalized on by the design of the SFT spectrometer. The SFT spectrometer (Fig.1) is aimed at taking advantage of the following:

1. long B decay lengths to make direct observations of the B's and to facilitate better tagging;
2. high momentum of the B's and their decay products in the design of the silicon microvertex detector to make higher resolution measurements of the secondary vertices;
3. high momentum of the B's to design efficient, relatively simple triggers which can collect data samples rich in B events;
4. limited solid angle coverage required to capture all B decay products from both B's in a significant fraction of the events.

The SFT spectrometer is 70 meters long and 10 meters wide at its downstream end. The various components of the SFT include two large analysis magnets, a silicon microvertex detector, several stations of PWC wire and pad chambers, a RICH detector, an electromagnetic detector and a muon detector. Optional items under discussion are a 60 kG microvertex detector magnet which is under study for B_u tagging, and the use of silicon planes distributed along the beam to help extend the coverage to smaller angles.

The present design of the SFT calls for the two large aperture analysis magnets to be run with equal and opposite polarities to preserve initial angles in both bend and non-bend planes, simplifying trigger strategies and with the intent of minimizing the spectrometer transverse size.

The configuration of the SFT microvertex detector is similar to the planar silicon microvertex detectors in operation in several Fermilab fixed target experiments. The SFT microvertex detector will be operated as a live target, with the silicon planes providing the target material for the 20 TeV proton beam. The initial "target section" of the SFT microvertex detector consists of 90 planes of $5\text{cm} \times 5\text{cm}$, 200 micron double sided silicon detectors, spaced 6 mm apart for a total thickness of 4% of a nuclear interaction length and 19% of a radiation length. The silicon measurement planes in the target section will have strip widths of 25 microns. The target region silicon planes will be distributed over a length of 54 cm

The "tracking section" downstream of the target region of the microvertex detector will contain 30 additional 200 micron double sided measurement planes distributed over 1.2 meters (one every 4 cm). The second group of silicon detectors is positioned in this extended configuration to provide more lever arm for the measurement of secondaries. The downstream tracking section is 1.3% of an interaction length and 25% of a radiation length. The double sided planes will be 10cmx10cm and have 50 micron pitch.

The remaining components of the spectrometer are mostly standard as far as concepts and designs are concerned.

4. THE TRIGGER

The more prominent features of the B events that can be exploited for trigger purposes are:

1. the presence of a high p_t lepton (from the semileptonic B decays);
2. the presence of a high mass lepton pair (from the $B \rightarrow J/\Psi$ decays or the double semileptonic decays of the B and the \bar{B});
3. the large total transverse energy and individual track transverse p_t ;
4. the presence of secondary vertices.

The $B \rightarrow J/\Psi \mu\mu$ events are one of the most striking manifestations of beauty production in hadronic interactions and serve as the most powerful method to separate beauty events from the rest of the total cross section. The trigger strategy proposed here takes advantage of the special attributes of $B \rightarrow J/\Psi \mu\mu$ decays to produce a trigger with a large rejection of backgrounds, yielding an extremely favorable ratio of trigger to interactions.

In addition, the dimuons act as a starting point for the offline analysis, reducing the amount of reconstruction that must be performed on each recorded event and enabling excellent offline rejection of backgrounds since the observation of a J/Ψ from a secondary vertex unambiguously insures that an event contains a BB pair. We also emphasize here that $B \rightarrow J/\Psi$ decays are among the most interesting from the standpoint of searching for CP violation in B decay. There are several decay modes ($B \rightarrow J/\Psi + K_s^0$, $B \rightarrow J/\Psi \pi^+ \pi^-$, $B \rightarrow J/\Psi \phi$ for example) for which the final state is CP conjugate,

making them the most promising avenue to measuring CP violation.

The $B \rightarrow \mu + x$ semimuonic decays offer different challenges and opportunities. Two features of the $B \rightarrow \mu + x$ semileptonic decays are very different from the $B \rightarrow J/\Psi$ modes and are very important. First, as pointed out above, the charge of the muon "tags" the decaying B so that some knowledge is gained about its particle or antiparticle nature. This is important for both mixing and CP studies. In addition and most importantly, the $B \rightarrow \mu + x$ decays are far more copious than the $B \rightarrow J/\Psi \rightarrow \mu\mu$ decays. In events containing a BB pair, semimuonic decay will produce a muon approximately 23% of the time and approximately 42% of these muons will have a $p_t > 1.5$ GeV/c. Muons with a p_t this large are quite unusual; semileptonic decays of pions, kaons and charm produced in 20 TeV/c interaction contain muons with this magnitude of p_t in less than 1 interaction in 10^4 . Therefore, high p_t muons provide a distinctive signal on which to trigger.

Level I will require detection of one or more muons, as defined by the triple coincidence of an aligned set of pads in the projective pad geometry of three or more layers of Resistive Pad Chambers (RPC), embedded in the steel of the SFT muon detector. The minimum energy required for a muon to penetrate the SFT muon detector steel and produce a signal in the RPC's is 19 GeV in the central part of the acceptance and 15 GeV at wider angles. Studies of simulated $\sqrt{s}=193$ GeV events show that the probability for a minimum bias event containing a muon with more than 20 GeV from π or K decays in flight is of order 1-2%. A further reduction of the Level I trigger rate can be achieved by imposing a very rough minimum p_t requirement on the muons detected by the RPC's. In a scheme in which the accepted muon coincidences are defined by means of Programmable Logic Gate Arrays (PAL's), it is trivial to include only three-plane patterns consistent with a given p_t threshold. Although the p_t resolution achievable at this level is limited, it is adequate to provide the additional factor (two or three) required to fit the trigger rate comfortably within the Level II bandwidth. Alternatively, one can achieve the same goal by imposing a threshold on the total transverse electromagnetic energy of the event as determined by the SFT EM detector. Level I would be pipelined and would take less than a couple of hundred nanoseconds.

We plan to develop a Level II trigger for the SFT which would perform complete online tracking in a couple of microseconds. As presently planned,

this trigger level will increase the rejection of the total cross section by:

1. imposing the requirement that the muon have 1.0 to 1.5 GeV of transverse momentum and that several tracks with intermediate p_t be present in the event, thereby increasing the probability that the selected events contain high mass B hadrons;

2. examining the silicon microvertex detector for the presence of secondary vertices.

Given that the above two conditions can be applied independently of each other, it will be possible to optimize the signal to background ratio of the accepted events by tuning the parameters of the two requirements.

The overall rejection to be provided by the Level II trigger is about a factor of 50, an extremely modest requirement in view of the many different event features on which the trigger can operate. Given an expected input rate of the order of 5×10^4 events/s into Level II, one should think in terms of a processing time of about 2 microseconds, which would limit the dead-time to 10% even without the added complication of a pipelined system. We envisage reaching such a time performance while accomplishing a full track recognition by making use of associative memory pattern recognition.

In Table II below, the cumulative effect of all the acceptances, efficiencies and cuts on the muons from $B \rightarrow J/\Psi \rightarrow \mu\mu$ and $B \rightarrow \mu + x$ decays have been estimated using Monte Carlo estimates of the efficiencies of various detectors. The geometric acceptances in Table II have been calculated using PYTHIA for $B \rightarrow J/\Psi \rightarrow \mu\mu$ modes and semileptonic $B \rightarrow \mu + x$ modes.

Table II
 $B \rightarrow J/\Psi \rightarrow \mu\mu$ and $B \rightarrow \mu + x$
 Muon Acceptances and Efficiencies

	$B \rightarrow J/\Psi \rightarrow \mu\mu$	$B \rightarrow \mu + x$
<u>Level I</u>		
Geometric Acceptance for muon tracks (including steel attenuation)	0.85	0.87
Level I detector efficiencies	0.74	0.86
<u>Level II</u>		
Level II detector efficiencies	0.80	0.80
Multihadron and Secondary Vertex Requirements	0.70	0.70
Level II p_t cut efficiency for muons	0.95	0.42
Composite Acceptance/Eff. for single or dimuons triggers	0.33	0.18

The trigger rate reduction factors per interaction are shown in Table III below:

Table III
 Expected Trigger
 Suppression Factors
 per interaction

Trigger Level	DiMuon Trigger	Single Muon Trigger
I	$O(10^{-4})$	5×10^{-3}
II	10^{-1}	2×10^{-2}
I \times II	$O(10^{-5})$	$O(10^{-4})$

5. PROTON EXTRACTION BY BENT CRYSTAL CHANNELING

The extraction is initiated in the East Utility straight section of the SSC, just south of the East Campus.

The counterclockwise circulating proton beam is bent by 0.7 mrad with the first of a dogleg set of dipoles placed at the beginning of the straight section. After about 50 m, a 3 mm \times 3 mm transverse size and 3 cm long silicon channeling crystal is positioned. The crystal is bent so as to supply an effective 100 μ rads deflection to the portion of the beam which intercepts it and is channeled.

Approximately 200 m downstream of the crystal, where the channeled beam has been deflected by 20 mm, there is a set of 16 Lambertson magnets which leave the channeled beam undisturbed and bend back the unchanneled portion of the beam by 1.4 mrad into the last dipole of the dogleg set.

The beam transport which follows is the least innovative feature of the SFT and serves the only purpose of directing the beam to the spectrometer trying to avoid the muon vectors from the dumped beams.

As far as the process of crystal channeling is concerned, there are two main questions to be analyzed: one is the channeling efficiency and the other relates the difficulty of bringing the protons, in the desired quantity, onto the crystal.

Minor questions address: the difficulty of bending the crystal by only 100 μ rads (i.e. 3 μ m for a 3 cm crystal); the reproducibility of the crystal alignment; the flatness of the surface of the crystal (septum thickness);

the purity of the crystal and, possibly, the heating effects on the crystal.

Four are the main contributions to the dechanneling efficiency of a crystal. The first contribution is due to the multiple scattering of the beam off the electrons in the crystal. This is limited to about 4% given the high momentum of the beam and the short length of the crystal. The second contribution is due to the angular acceptance of the crystal. Also here the contribution is limited to about 4-5% given the critical angle of 1 μ rad and the angular spread of the beam (.4 μ rad). The bending dechanneling, which is the third contribution, is less than about 20% because of the very small bending angle, 100 μ rad, and therefore the very favourable ratio $p/R=0.67$ GeV/c/cm. The last contribution is due to the surface acceptance of the crystal. By taking into account the Thomas-Fermi radius for Si, one gets a cross sectional area of the crystal not available for channeling of about 16%.

The overall efficiency of channeling, therefore, is of the order of 65% after a single pass through the crystal. One can reasonably assume that, after many turns, a global efficiency of about 85% is reached.

More serious is the problem of the illumination of the crystal by the proton beam. Many strategies have been studied so far, starting from the obvious one of placing the crystal in the periphery of the beam halo and scraping off the desired amount of protons.

The current strategy relies on a two step procedure: first, create a high dispersion point, where the crystal is going to be placed, by changing the optics of the accelerator lattice next to the straight section and, secondly, create a halo in the beam by increasing the momentum of the off-momentum protons with a filtered rf noise, analogously to what has already been done at LEAR.

The combined effect should ensure the desired result.

FIXED-TARGET B-PHYSICS AT THE LHC

G. Fidecaro

CERN, European Organization for Nuclear Research,
Geneva, Switzerland

I. INTRODUCTION

Some preliminary work is presented here concerning the feasibility of a fixed-target experiment to search for CP violation in B-meson decay at the LHC. The initial purpose of this study was that of evaluating detection efficiency and background in the case of an experiment at the SPS (450 GeV) based on the detection of the well known CP-violating decay $B^0 \rightarrow J/\psi + K^0$ and of the semi-leptonic decay of the associated b-particle. As pointed out [1] at the March 1989 UNK (3 TeV) Workshop in Protvino, such a decay could be studied without a vertex detector, using well known detection techniques. As in principle higher intensity beams could be used in experiments without vertex detector, this might open the way to a search for CP violation at existing lower energy accelerators, like for example the SPS [2].

The present paper therefore deals with estimates and considerations at different energies, from SPS to UNK and LHC (8 TeV). The feasibility of a measurement of CP-violation in B-meson decay at the SPS does not seem limited by problems of identification of the CP-violating events, the three high- p_t muons and a K^0 signature being very characteristic of these events, or by luminosity. The main limitation might come from the expected high counting rate of detectors in an environment receiving very intense beams ($10^{11} \div 10^{13}$ protons/s). At the energy of the LHC, with a $b\bar{b}$ production cross-section three orders of magnitude larger, these environment problems could certainly be handled in a much easier way as correspondingly lower intensity beams would be necessary to get the same number of events.

As it is well known, fixed-target experiments have not been considered until now for the LHC. Purpose of this paper is also to point out the interest to have fixed-target facilities at the LHC for B-physics experiments. By the time LHC will be operating considerable progress will certainly have been

made in this field. However, almost certainly there will remain fundamental experiments still to be done, particularly in the domain of rare decays and, among these, experiments to search for CP-violating effects, which require luminosities not easily obtainable at e^+e^- colliders. A dedicated apparatus is considered here rather than a general purpose spectrometer, but with an open mind in this direction. Fixed-target experiments have already been considered for the SSC [3].

Reference will be made to more recent evaluations made at Dubna [4], at CERN [5] and in Pisa [6], and to theoretical papers presented in this session.

2. THE LHC AS A B-FACTORY

Purpose of the experiment would be the measurement of the asymmetry

$$\Lambda = \frac{(B^0 \rightarrow J/\psi + K_s^0) - (\bar{B}^0 \rightarrow J/\psi + K_s^0)}{(B^0 \rightarrow J/\psi + K_s^0) + (\bar{B}^0 \rightarrow J/\psi + K_s^0)}$$

which arises from the interference between the amplitude $B^0 \rightarrow J/\psi + K^0$ and, via mixing, the amplitude $B^0 \rightarrow \bar{B}^0 \rightarrow J/\psi + K^0$. This asymmetry is expected to be large 10–40 %. In addition, in the case of B^0 ϵ' is predicted to be large and ϵ small, contrary to the case of K^0 (see the talk by M. Lusignoli earlier in this session).

Assuming a branching ratio of $\sim 5 \times 10^{-4}$ (not well known) for the decay $B^0 \rightarrow J/\psi Y + K_S^0$, the fraction of B^0/\bar{B} ending in two muons and two charged pions via J/ψ and K_S^0 decay would be $\sim 2.3 \times 10^{-5}$. This fraction is further reduced to 2.6×10^{-6} by requiring the detection of tagging muons from the associated b decay (b-meson or b-hyperon), with a branching ratio of 0.11 for the semileptonic decay. Not much would be gained by turning attention to less rare B decays, because of the smaller asymmetry predicted. Furthermore, the $\sim 10\%$ loss of events produced by the detection of tagging muons is compensated by a better selection of the events.

In the case of a $10^{34} \text{ cm}^{-2} \text{ s}^{-1}$ luminosity e^+e^- b-factory (whose construction is still hypothetical) with 1 nb production cross-section one gets $\sim 10^8$ $b\bar{b}$ pairs in a 10^7 s year, corresponding to 260 CP-violating events. Assuming a 10% detection/reconstruction efficiency the experiment becomes marginal.

In the case of the SPS, the same number of CP-violating events would be produced by a $8.6 \times 10^8 \text{ s}^{-1}$ proton beam on a 1 cm thick tungsten target (assuming 1 nb production cross-section and A^4 scaling law). Proton beams four orders of magnitude larger are in principle available at the SPS.

By increasing the energy of the proton beam the production rate increases rapidly, as it can be seen in the following table which shows for existing or planned accelerators the intensity of the proton beam needed for the production of $10^{10} b\bar{b}$ pairs per year (1 year = 10^7 s) in a 1 cm thick W target, and the corresponding interaction rate.

Table 1				
	$P(\text{GeV}/c)$	$\sigma_W(\mu\text{b})$	Beam (s^{-1})	Int.rate (s^{-1})
SPS	450.	0.18	8.6×10^{10}	6.3×10^9
Tevatron	1000.	2.7	5.7×10^9	4.2×10^8
UNK	3000.	28.	5.5×10^8	4.1×10^7
LHC	8000.	110.	1.4×10^8	1.0×10^7
SSC	20000.	311.	5.0×10^7	3.6×10^6

The cross sections have been obtained from the Pythia Monte Carlo. These cross-sections are appreciably smaller than those used in the expression of interest for a Super Fixed-Target Beauty Facility at the SSC (1.4 μb vs. $2.5 \div 10 \mu\text{b}$ for pp collision at 20 TeV) [3].

One can see that luminosity-wise hadronic accelerators are by far superior to e^+e^- machines. However, the signal/background rate is orders of magnitude worst at proton machines.

Although it is not the purpose of this paper to compare fixed-target experiments with experiments performed in collider mode, it is worth pointing out that by increasing the beam energy p-tungsten cross-sections become equal to p-p cross-section (in collider mode) at approx. 10 TeV [6]. Pion beams have not been considered in spite of the somewhat larger cross-section for production of $b\bar{b}$ pairs because of their smaller intensity and because of the muon halo which accompanies these beams.

3. FIXED-TARGET FACILITIES AT THE LHC

Three possibilities have been envisaged. The use of a gas jet target, an internal solid target, and an extracted proton beam. The main limitation in all the three cases comes from the fact that fixed-target experiments are expected to coexist with collider mode experiments. Under this condition it is difficult to imagine how one could have more than 10^8 interactions/s in a jet or a solid internal targets, or extract more than 10^8 protons/s. Obviously in the case of LHC operation in fixed-target dedicated mode larger interaction rates would be permitted with internal targets, and more conventional techniques giving more flexibility could be used for beam extraction.

With a hydrogen gas jet target, density $\sim 3 \times 10^{14}$ atoms/cm², and a 10^{14} proton circulating beam one obtains a luminosity $\sim 3.3 \times 10^{32}$ cm⁻²s⁻¹ giving 2×10^9 b-pairs per 10^7 s year. The use of a heavier gas could make a jet target very attractive.

In the case of a W internal solid target one should be able to work at the 10^8 s⁻¹ interaction rate mentioned above. If this rate is reached one would get 10^{11} b-pairs in a 10^7 s year.

Following a suggestion by W. Scandale [7] one could use for beam extraction the same technique used for the LHC dump, provided a 0.7 mrad bent crystal having the required precision can be manufactured and used for the extraction of protons from the halo surrounding the circulating beam. In this case one of the three insertions reserved for LHC experiment should be dedicated to fixed-target experiments. It seems difficult to reach beam intensities much larger than 10^8 protons/s using a bent crystal.

An external proton beams obviously gives much more flexibility than internal targets, but with a smaller interaction rate. For example a vertex detector can be easily mounted on an external beam. In the case of an internal target a technique similar to that at present being investigated by P. Schlein and collaborators (see Schlein's talk in this session) could be used for a vertex detector.

4. EVENT SELECTION.

It appears from the simulation studies so far made [1,4,5,6] that the CP-violating events can be extracted by selecting muons having p_t larger than about 1 GeV/c and large momentum K⁰'s without great difficulty. The mass

of the B⁰/B̄⁰ should be reconstructed. At 450 GeV, if K⁰'s at an angular interval between 20 and 40 mrad and momentum larger than 50 GeV are selected, preliminary estimates give ~ 20 events/ 10^{10} b̄b pairs. Similar results have been obtained using a slightly different angular range for the K⁰'s and a slightly different momentum cut. However, there are indications that non-negligible factors could be gained by careful optimization work. At 8 TeV, working at an interaction rate of 10^8 s⁻¹, a simple extrapolation gives a few hundred events per year ($1 \text{ y} = 10^7 \text{ s}$).

Background coming from direct production of J/ψ accompanied by muons and Kaons seems negligible with the above mentioned cuts, though at 450 GeV random coincidences of particles produced in different events are much more disturbing than at 8 TeV.

The main source of background comes from events in which the tagging muon comes from a B→D decay as these muons have opposite sign. However, muons from B decay have larger p_t than muons from D decay and it appears possible to do a good selection on this basis. At 450 GeV/c this background could be of the order of 10%. Preliminary results give some indication that charm production should not contribute in an important way to the background

5. THE EXPERIMENTAL APPARATUS

Careful simulation studies have to be carried out before a proposal can be made, particularly on the target region. This region consists essentially of a very thick absorber made of light material, through which muons come out. A hole behind the target lets the non-interacting part of the beam go through. The hole could be replaced by a beam dump if a good solution was found. Kaons would come out through a conical opening covering the chosen angular interval (for example 20–40 mrad in the case of 450 GeV), with muons going out at larger angles. In principle, the absorber could be placed in a very strong magnetic field in such a way to prevent as much as possible charged particles from escaping through the conical hole. In the case of an LHC experiment using an internal target such a magnetic field would disturb the operation of the collider and could not be used. According to the preliminary design by Aleev et al [4] the same magnetic field would be used to measure the momentum of the muons.

Near the $t\bar{t}$ threshold the cross sections are affected by resonance production and Coulomb rescattering forces [8,9,10]. These corrections can be estimated in a simplified potential picture. The driving 1-gluon exchange potential is attractive if the $t\bar{t}$ pair is in a color singlet state and repulsive in a color-octet state

$$\begin{aligned}\sigma^{(1)}(gg \rightarrow t\bar{t}) &= \frac{2}{7} \sigma_B(gg \rightarrow t\bar{t}) |\Psi^{(1)}|^2 \\ \sigma^{(8)}(gg \rightarrow t\bar{t}) &= \frac{5}{7} \sigma_B(gg \rightarrow t\bar{t}) |\Psi^{(8)}|^2 \\ \sigma^{(8)}(q\bar{q} \rightarrow t\bar{t}) &= \sigma_B(q\bar{q} \rightarrow t\bar{t}) |\Psi^{(8)}|^2\end{aligned}\quad (1.5)$$

The Coulombic attraction leads to a sharp rise of the cross section at the threshold in the singlet channel, even if no resonances can be formed anymore, since the phase space suppression of the Born term $\sigma_B^0 \propto \beta_t$ is neutralized by the Coulomb enhancement of the wave function $|\Psi_1|^2 \propto \alpha_s/\beta_t$. In the octet channel, by contrast, the cross sections are strongly reduced by the Coulombic repulsion which effectively leads to an exponential fall-off of the cross sections $\sigma_8 \propto \exp[-\pi\alpha_s/6\beta_t]$ at the threshold. Due to the averaging over parton luminosities [10] the effects are less spectacular in pp than in e^+e^- collisions.

In going beyond pure QCD corrections, let us first note that the lowest order α_s^2 electroweak contributions, the Drell-Yan annihilation process (via γ and Z^0 exchange), would only be of significance if $m_t < M_Z/2$, what has experimentally been ruled out by LEP. Here we examine the next order electroweak contributions * $O(\alpha\alpha_s^2)$ to both the $q\bar{q} \rightarrow t\bar{t}$ and $gg \rightarrow t\bar{t}$ subprocesses and we give quantitative results for the corrections to the parton cross sections [11]. These corrections become important in the LHC range for two reasons: the large q^2 [= \hat{s} in the parton frame] and the large Yukawa coupling of the (virtual) Higgs bosons to the top quark.

The loop diagrams to the parton processes under consideration are shown schematically in Fig.6. The complete set is gauge invariant, IR finite, and also UV finite without renormalization of the strong coupling constant (only mass renormalization in the t -channel top propagator is required). This is different for pure electroweak processes where the corresponding vertex corrections are not gauge invariant and also not UV finite without coupling constant renormalization. A large fraction of the corrections is due to the Higgs boson H , together with its unphysical components Φ^\pm, χ in the R_ξ -gauge, that have Yukawa couplings $\sim m_t/M_W$ to the top quark.

Fig.7 shows the relative correction to the $q\bar{q} \rightarrow t\bar{t}$ cross section at the parton level. Due to the initial state correction from Z exchange they are flavor dependent, and the results of Fig.7 correspond to $q = u$. The difference to d -type quarks, however, is only marginal and not of numerical importance. The loop diagrams can be summarized in terms of an effective quark-gluon vertex with finite form factors $F_{V,A,M}(q^2)$,

$$= g_s \frac{\lambda_a}{2} [\gamma_\mu F_V + \gamma_\mu \gamma_5 F_A + (p - \bar{p})_\mu F_M + ..] \quad (1.6)$$

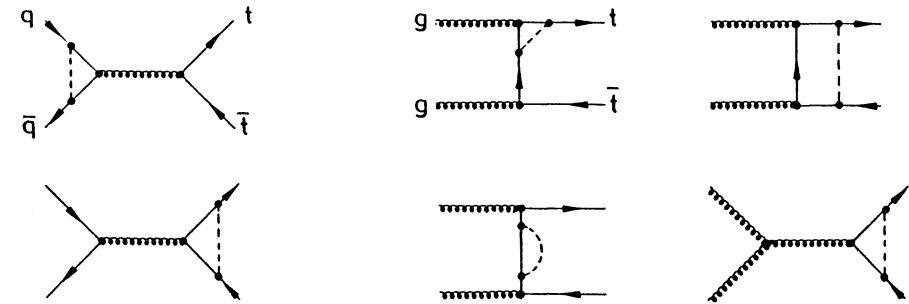


Fig.6. Generic diagrams genuine of electroweak corrections [broken line = W, Z, H].

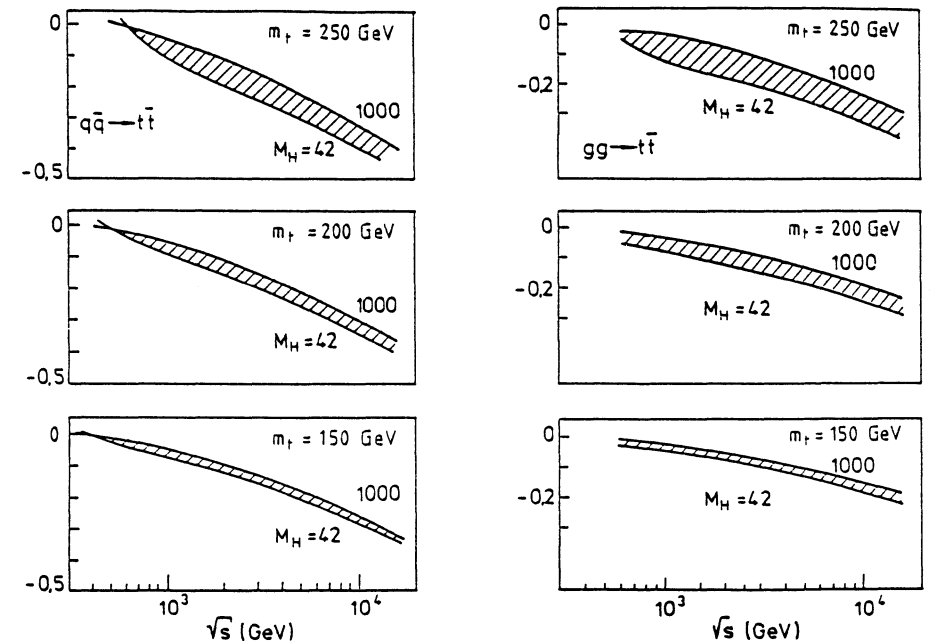


Fig.7./8. Relative electroweak corrections for the $q\bar{q}$ and $gg \rightarrow t\bar{t}$ fusion processes [\sqrt{s} = cms energy for the parton process].

As a result of the interference with the Born diagram, F_A does effectively not contribute to the 1-loop cross section. The magnetic term is much smaller in size than F_V and, not too close to the threshold where the corrections are large, practically negligible. Hence, the correction is essentially a t -independent correction factor to the differential as well as the integrated cross section. The increasing influence of the Higgs boson with increasing top mass m_t is reflected by the broadening of the area covered by the variation of M_H between 42 and 1,000 GeV.

A similar situation is encountered for the $gg \rightarrow t\bar{t}$ process. The box diagrams lead to a more complicated structure of the 1-loop terms and make the corrections depend also on the production angle. Fig.8 displays the relative correction to the differential parton cross section for transverse top production (in the parton cms). The variation with p_t , however, is rather smooth. The corrections become smaller in the forward direction and with higher top masses more sensitive to changes in p_t .

Summarizing, except for a small region close to the production threshold, the corrections are always negative and can become sizeably large, in particular if the top is very heavy. After convoluting the cross sections of the subprocesses with the parton distributions, a reduction of the Born cross section at a level of 10 to 20% is expected for $m_t \geq 200$ GeV.

1.2 Wg fusion to $t\bar{b}^*$

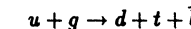
The interaction radius in the QCD gg fusion process shrinks with rising energy so that the cross section $\sigma(gg \rightarrow t\bar{t}) \sim \alpha_s^2/\delta$ [mod. log's] vanishes asymptotically. By contrast, the interaction radius in the weak fusion process [12] is set by the Compton wave length of the W boson and therefore asymptotically non-zero, $\sigma \rightarrow G_F^2 m_W^2/2\pi$. Folding this subprocess with the quark-gluon luminosities, the fall-off of the total cross section $\sigma(pp \rightarrow t\bar{b})$ is less steep than for the QCD fusion processes. As a result, the Wg fusion process will become dominant at large top quark masses ≥ 250 GeV, while being suppressed at masses of order 100 GeV by about two orders of magnitude. Nevertheless, as shown in detail in Fig.1b of the Introduction, more than 10^6 top quarks will be produced by this mechanism for any mass value at an integrated luminosity of $\int \mathcal{L} = 10^4 pb^{-1}$.

A close inspection of the diagrams in Fig.1a reveals immediately that the by far dominant part of the cross section is due to b exchange, with the b quark being near its mass shell. Since the b quark is almost collinear to the incoming gluon, this cross section is logarithmically enhanced $\sim \ln(m_t^2/m_b^2)$ over other mechanisms. This naturally suggests to approximate [12] the process by the subprocess $u + b \xrightarrow{W} d + t$ with the b -quark distribution generated perturbatively by gluon splitting employing massless evolution equations. The weak cross sections can be presented in a compact form,

$$\begin{aligned} \sigma(ub \xrightarrow{W} dt) &= \frac{G_F^2 m_W^2}{2\pi} \frac{(\hat{s} - m_t^2)^2}{\hat{s}(\hat{s} + m_W^2 - m_t^2)} \rightarrow \frac{G_F^2 m_W^2}{2\pi} \\ \sigma(d\bar{b} \xrightarrow{W} u\bar{t}) &= \frac{G_F^2 m_W^2}{2\pi} \left[1 + \frac{\hat{s}(2m_W^2 - m_t^2) - 2m_W^2 m_t^2}{\hat{s}^2} \right. \\ &\quad \left. - \frac{(2\hat{s} + 2m_W^2 - m_t^2)m_t^2}{\hat{s}^2} \log \frac{\hat{s} + m_W^2 - m_t^2}{m_W^2} \right] \rightarrow \frac{G_F^2 m_W^2}{2\pi} \end{aligned}$$

and identically the same expressions for the C -conjugate reactions.

The characteristics of the final states are displayed in Table 2 for the subprocess



at a top quark mass of 150 GeV. The final state d quark is emitted at a transverse momentum of $\sim m_W/2 = 40$ GeV that is characteristic for W exchange processes. The rapidity distribution has its maximum value at $|y| \approx 3.5$. Both observables can be exploited to tag this type of reaction [13]. The spectator \bar{b} quark, on the other hand, is characterized by a transverse momentum of $m_b \sim 5$ GeV and an average rapidity of $\sim \pm 1.6$ for events with positive/negative y . The top quark, finally, balances the transverse momentum of the d quark. It is emitted in the forward direction [which is defined by the tagged d quark]. Detailed distributions of the transverse momenta and the rapidities are shown in the experimental section. To illustrate the information that can be extracted from d tagging, we present, in addition to the symmetrized distributions, "one-sided" y values where the W is assumed to belong to the proton travelling in $+\hat{z}$ direction. [This case can approximately be realized by tagging the outgoing d quark.]

Top quarks are created in $u + g$ collisions, anti-top quarks in $d + g$ collisions where the absorption of a W^- transforms a \bar{b} quark to a \bar{t} quark. The naïve expectation from valence quark counting for the ratio of t and \bar{t} cross sections, $\sigma(u \rightarrow t) : \sigma(d \rightarrow \bar{t}) \sim 2 : 1$ is corroborated by a detailed analysis; in fact, the ratio turns out to be 2.1 for top quark masses of 150 GeV.

Table 2

m_t 150 GeV	Transv. momentum [GeV]		Rapidity		Rapidity (one-sided)	
	$d\sigma/dp_\perp = \text{max}$		$d\sigma/dy = \text{max}$		$d\sigma/dy = \text{max}$	
	$ug \rightarrow d(t\bar{b})$	$ub \rightarrow dt$	$ug \rightarrow d(t\bar{b})$	$ub \rightarrow dt$	$ug \rightarrow d(t\bar{b})$	$ub \rightarrow dt$
etc.	etc.	etc.	etc.	etc.	etc.	etc.
d quark	38	36	3.3	3.3	3.3	3.3
\bar{b} quark	5	—	0	—	—0.3	—
t quark	40	36	0	0	1.3	1.1

The approximate cross sections and distributions are compared with the complete $2 \rightarrow 3$ reaction in Table 2. The agreement is satisfactory [indeed, not only for the average values but also for the differential distributions]. As a result, the $2 \rightarrow 2$ process $u + b \xrightarrow{W} d + t$ etc. can be used for t production via Wg fusion in shower Monte Carlos as Pythia and Herwig.

As will be studied in the experimental section in more detail, there is a large background to the final states in Wg fusion from



production, one of the jets being emitted at small transverse momentum. The corresponding cross sections have been evaluated in the matrix element approach as well as in parton shower

Monte Carlos. The signal can only be isolated if the experimental resolution is so excellent that a peak in the $W + jet$ invariant mass distribution at the top mass can be seen.

Single top production in Wg fusion as well as single-lepton events in $q\bar{q}/gg$ fusion to $t\bar{t}$ pairs can be exploited to measure the top quark mass independently of any theoretical model. The W mass constraint $m_W^2 = (p_t + p_\nu)^2$ allows us to reconstruct the longitudinal ν momentum. There remains an ambiguity in the solution

$$p_{\nu L} = \frac{1}{2 \vec{p}_{\mu T}^2} \left[p_{\mu L} (m_W^2 + 2 \vec{p}_{\mu T} \vec{p}_{\nu T}) \pm E_\mu m_W \sqrt{m_W^2 + 4 \vec{p}_{\mu T} \vec{p}_{\nu T}} \right] \quad (1.8)$$

However, in most cases [$\approx 65\%$] the lower value is physically realized as may be proved by comparing the solutions with Monte Carlo analyses.

2. Top Quark Fragmentation *

The hadronization process of top quarks is complicated because strong and weak mechanisms are intimately intertwined. The incisive scale is set by the lifetime of the top quark [8], approximately given by

$$\tau_*^{-1} \approx 175 \text{ MeV} \times \left[\frac{m_t}{m_W} \right]^3 \quad (2.1)$$

for sufficiently heavy top masses in the SM decay $t \rightarrow b + W^+$. [Details will be discussed in the next section.] For $m_t \leq 100$ GeV the lifetime $\tau_* \geq \Lambda^{-1}$ is long enough to form non-perturbatively mesonic ($T_q = (t\bar{q})$) or baryonic (tqq) bound states. The perturbative gluon radiation at early times is followed by a small non-perturbative deceleration of the t hadron [14-17]. On the other hand, if $m_t \geq 100$ GeV, the decay is so rapid that hadrons cannot build-up anymore. The top quark is decelerated only by the early radiation of hard, non-collinear gluons [8].

Perturbative gluon radiation off heavy quarks is described to leading order by the non-singlet Altarelli-Parisi equation [18]. The solution for the t energy spectrum [scaled by the initial parton energy E]

$$\langle z \rangle_{PQCD} = \left[\frac{\alpha_s(E^2)}{\alpha_s(m_t^2)} \right]^{\frac{32}{3(3-2N_f)}} \quad (2.2)$$

reveals that only a small fraction of energy is radiated off for an initial energy $E \sim$ several m_t in the gg fusion process [$N_f = 5$]. For a top mass of 150 GeV and $\Lambda = 200$ MeV, the average $\langle z \rangle_{PQCD}$ falls from 0.92 to 0.90 when the initial parton energy rises from 500 GeV to 1 TeV. The angular distribution (Θ) and the energy distribution (ω) of the radiated gluon is approximately given by

$$dP_g = \frac{4\alpha_s}{3\pi} \frac{\Theta^2 d\Theta^2}{[\Theta^2 + \frac{1}{\gamma^2}]^2 + [\frac{\Gamma_t/\gamma}{\omega}]^2} \frac{d\omega}{\omega} \quad (2.3)$$

for a short-lived gluon radiation source accelerated to $\gamma = E/m_t$. The gluons accumulate on the surface of a cone with half-aperture $\Theta_c \sim \gamma^{-1}$ for a long-lived t and $\gamma^{-1} \sqrt{\gamma \Gamma_t/\omega}$ if the particle decays quickly. The spectrum has a maximum at $\omega \sim \Gamma_t/\gamma$ if Γ_t rises beyond the

confinement energy Λ . Below the maximum, the fragmentation function can be approximated by the simple leading log form [19]

$$D(z)_{PQCD} \propto \frac{1+z^2}{(1-z)^{1-\eta}} \quad \text{with} \quad \eta = \frac{16}{33-2N_f} \log \left[\frac{\alpha_s(E^2)}{\alpha_s(m_t^2)} \right] \quad (2.4)$$

This leading log form is improved by terms of order $\alpha_s \log(1-z)$ and $\alpha_s \log^2(1-z)$, generating a maximum in the energy distribution that is followed by a sharp fall-off when z approaches 1 [20].

For small top quark masses $m_t \leq 100$ GeV the t -hadron energy is derived by convoluting the perturbative spectrum with the non-perturbative fragmentation function so that

$$\langle z \rangle_t = \langle z \rangle_{NP} < z \rangle_{PQCD} \quad (2.5)$$

The non-perturbative deceleration is small for heavy top quarks. Adopting the Peterson et al. form for the fragmentation function [17] we find

$$\langle z \rangle_{NP} = 1 - \sqrt{\epsilon_t} \quad \text{with} \quad \sqrt{\epsilon_t} \approx 400 \text{ MeV}/m_t \quad (2.6)$$

The non-perturbative fragmentation function itself is strongly peaked near $z \simeq 1$.

For top quark masses $m_t \geq 100$ GeV the weak decay process $t \rightarrow b + W^+$ intercepts the fragmentation process [8]. t bound states do not form anymore, and small hadronization effects due to the beginning of string formation [so long as $m_t < (2Em_W^3)^{1/4}$] are shrouded by perturbative gluon radiation. Also the perturbative gluon radiation is cut-off for lack of time at $\omega \geq \Gamma_t/\gamma$. The top fragmentation is therefore described by a narrow peak at $z \simeq 1$, followed by the standard QCD continuum distribution.

After the decays of the top quarks in the gg fusion process, $t\bar{t} \rightarrow b\bar{b}W^+W^-$, the bottom quarks fragment independently of each other. Their color flux lines are connected to the gluonic remnants of the perturbative t and \bar{t} fragmentation processes [21].

3. Top Quark Decay in the Standard Model *

Based on the Standard Model, the lower limit of the top quark mass $m_t > 89$ GeV has been shifted to a level well above the real W threshold for the decay mode $t \rightarrow b + W$. In the 3-family SM the CKM matrix element of the (tb) coupling $V_{tb} = 0.9990 \pm 0.0004$ is well-known to be very close to unity [22]. As a result, the width of the top quark can be precisely predicted in the SM [8]:

$$\Gamma(t \rightarrow b + W^+) = \frac{G_F m_t^3}{8\sqrt{2}\pi} \left[1 - \frac{m_W^2}{m_t^2} \right]^2 \left[1 + 2 \frac{m_W^2}{m_t^2} \right] \quad (3.1)$$

The width approaches quickly the asymptotic form

$$\Gamma(t \rightarrow b + W^+) \rightarrow 175 \text{ MeV} \times \left[\frac{m_t}{m_W} \right]^3 \quad (3.2)$$

and the lifetime drops below 10^{-23} sec. This is illustrated in Fig.9. The final state consists of a b -quark jet plus a lepton pair or two other jets from the W decay which, being a color singlet system, fragment independently of the environment.

*V. Khoze and P. M. Zerwas

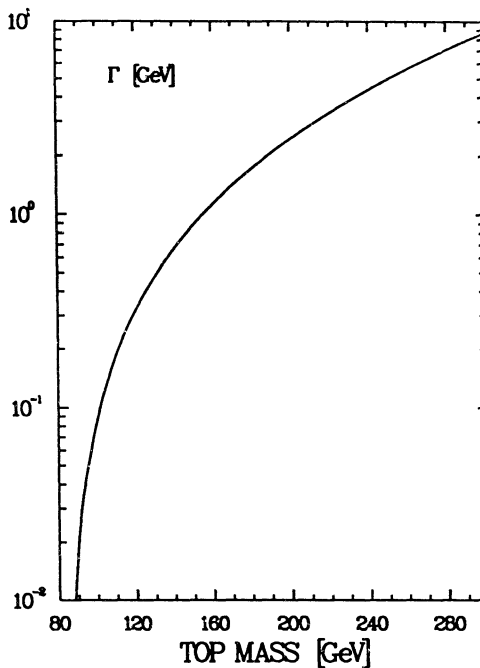


Fig.9. Width of the top quark in the Standard Model.

With rising top quark mass the W boson is emitted more and more frequently in a state of longitudinal polarization [23]. The ratio of longitudinal polarization to transverse polarization Γ_L/Γ_T rises from $1/2$ at the real W threshold to $2m_t^2/m_W^2$ asymptotically. If the decaying top quark is polarized with a degree \mathcal{P}_t , the charged l^+ lepton is emitted preferentially in the top spin direction with a probability $\frac{1}{2} [1 + \mathcal{P}_t \cos\vartheta]$.

The energy spectra of the leptons, and correspondingly the invariant (bl) mass, $\mu^2 = m^2(bl)/m_t^2$, are affected by the chirality of the (tb) charged weak current for moderate top masses. Assuming the charged lepton current to be of the well established $V - A$ form, the probability to observe a charged lepton of maximal energy $E_l = m_t/2$ vanishes for the conventional $V - A$ form of the (tb) current while it is non-zero for a speculative $V + A$ coupling. Equivalently, the distribution of the invariant (bl) mass is given by

$$\frac{1}{\Gamma} \frac{d\Gamma}{d\mu^2} \propto \begin{cases} \mu^2(1 - \mu^2) + \eta(1 - 2\mu^2) - \eta^2 & (V - A)_{tb} \text{ coupling (SM)} \\ \mu^2(1 - \mu^2) & (V + A)_{tb} \text{ coupling} \end{cases} \quad (3.3)$$

where $\eta = m_W^2/m_t^2$ and $0 \leq \mu^2 \leq 1 - \eta$. A deviation of the (tb) coupling from the $V - A$ structure of the SM would thus lead to a stiffening of the charged lepton spectrum.

Genuine electroweak corrections to the top quark decay are expected to be of order $G_F m_t^2/\pi^2$ while QED corrections, summed up and no energy and angular cuts applied, should be $O(\alpha/\pi)$.

QCD gluonic corrections, though being well under control, reduce the width nevertheless at a level of $\sim 10\%$. Furthermore, they distort the charged lepton spectrum of the W decay [24]. The correction to the width can be cast into a simple form

$$\Gamma = \Gamma_B \left[1 - \frac{2}{3} \frac{\alpha_s}{\pi} f \right] \quad (3.4)$$

with, for $m_b = 0$,

$$\begin{aligned} f = \mathcal{F}_1/\mathcal{F}_0 : \quad \mathcal{F}_0 &= 2(1 - \eta)^2(1 + 2\eta) \\ \mathcal{F}_1 &= \mathcal{F}_0 [\pi^2 + 2Sp(\eta) - 2Sp(1 - \eta)] + 4\eta(1 - \eta - 2\eta^2) \log \eta \\ &\quad + 2(1 - \eta)^2(5 + 4\eta) \log(1 - \eta) - (1 - \eta)(5 + 9\eta - 6\eta^2) \end{aligned}$$

In the mass range $m_t \geq 100$ GeV, the QCD correction amounts to

$$\delta_{QCD} \approx (3 \text{ to } 4) \alpha_s/\pi \quad (3.5)$$

The change of the lepton spectrum [described by a somewhat clumsy formula] may be taken from the literature directly [24].

4. Top Signals and Backgrounds *

A. General features of signals

The most promising top signals via $t \rightarrow bW$ decays are [25,26]

$$gg/q\bar{q} \rightarrow t\bar{t} \rightarrow b\bar{b}WW \rightarrow b\bar{b}l\nu jj \quad (4.1)$$

$$gg/q\bar{q} \rightarrow t\bar{t} \rightarrow b\bar{b}WW \rightarrow b\bar{b}l\nu\bar{\nu} \quad (4.2)$$

$$ug \rightarrow dt\bar{b} \rightarrow db\bar{b}W \rightarrow db\bar{b}l\nu \quad (4.3)$$

The essential ingredients in these signals are

i) Charged leptons with high p_T , usually isolated from accompanying hadrons.

ii) Neutrinos from $W \rightarrow l\nu$, giving high missing transverse energy \cancel{E}_T . In single-lepton cases, the transverse mass $m_T(l, \cancel{E}_T) = [2\vec{p}_T(l) \cdot \cancel{E}_T]^{1/2}$ has a Jacobian peak near $m_T = m_W$, smeared by measurement errors and other contributions to \cancel{E}_T .

iii) b and \bar{b} jets from $W \rightarrow t\bar{b}$. They have typically very high p_T with a Jacobian peak at $p_T(b) = (m_t^2 - m_W^2)/2m_t$ smeared by top transverse motion. For $m_t > 150$, this peak has $p_T(b) > 50$ [we use GeV units throughout]. The essential b -flavor can be tagged by a decay muon in the jet or by microvertex detection of displaced decay vertices.

iv) Jets from $W \rightarrow jj$, with high p_T (Jacobian peak at $p_T \sim \frac{1}{2}m_W$, smeared by W transverse motion); p_T is typically less than b -jets, for $m_t > 150$. Jet pairs have $m(jj) \sim m_W$.

B. Backgrounds with similar features

i) The largest QCD backgrounds are from b and c quark pairs:

$$QCD \rightarrow b\bar{b} \text{ (or } c\bar{c}) X \rightarrow \text{leptons} + \cancel{E}_T + \text{jets.} \quad (4.4)$$

*R. J. N. Phillips

For high- p_T leptons, $b\bar{b}$ dominates over $c\bar{c}$. [High- p_T production is similar, but b has harder fragmentation and harder lepton decay spectrum.]

The first step is to demand high $p_T(l)$: for $t\bar{t} \rightarrow lX$ signals we find

$$\begin{aligned} p_T(l) \geq 30 &: \text{ background/signal} \sim 40 \text{ (700) for } m_t = 150 \text{ (300)} \\ p_T(l) \geq 60 &: \text{ background/signal} \sim 5 \text{ (70) for } m_t = 150 \text{ (300)} \end{aligned} \quad (4.5)$$

Another step is to require isolation (e.g. sum of hadronic energy to be less than 8 GeV in a cone (ΔR) $^2 = (\Delta\eta)^2 + (\Delta\phi)^2 < 0.16$ about the lepton direction). This typically suppresses the background by a factor ~ 25 (50) for $p_T(l) \geq 30$ (60).

For single-lepton signals, we can require $m_T(l, \cancel{E}_T)$ to lie near m_W , e.g. $50 \leq m_T \leq 90$: This introduces a suppression factor ~ 20 .

For dilepton signals, we can require that the two leptons are not back-to-back e.g. $30^\circ < \Delta\phi(l_1, l_2) < 150^\circ$, since this background is strongly peaked near $\Delta\phi = 0^\circ$ and 180° while the $t\bar{t}$ signals are not.

This background contains two b -jets, but any high- p_T leptons are correlated with them, so they cannot fully fake this aspect of the signals.

ii) Genuine W production [27]:

$$pp \rightarrow W + \text{jets} \rightarrow l\nu + \text{jets} \quad (4.6)$$

This fakes the leptonic aspects of one-lepton signals [$p_T(l), \cancel{E}_T$ and $m_T(l, \cancel{E}_T)$]. But the accompanying jets are mostly less hard than those from $t \rightarrow bW$ and $W \rightarrow jj$. Furthermore, they have no peak at $m(jj) \simeq m_W$ and they rarely have b -flavor.

iii) Double- W production [28]:

$$pp \rightarrow WW + \text{jets} \rightarrow l_1 l_2 \nu \bar{\nu} + \text{jets} \quad (4.7)$$

This fakes the lepton side of two-lepton signals, but not the jets [see (ii)]. WW production by 4-parton scattering and event overlap are negligible compared to the direct process $q\bar{q} \rightarrow WW$.

iv) Drell-Yan electroweak dilepton production:

$$pp \rightarrow (\gamma^*, Z \rightarrow e^+ e^-, \mu^+ \mu^-) + \text{jets} \quad (4.8)$$

This gives isolated dileptons with a peak at $m(l_1 l_2) = m_Z$. The leptons always have the same flavor, \cancel{E}_T is small (from measurement errors etc.); for jets see (ii).

v) τ pair production:

$$pp \rightarrow (\gamma^*, Z \rightarrow \tau\bar{\tau}) + \text{jets} \quad (4.9)$$

τ decays give isolated leptons or jets plus \cancel{E}_T . The leptons can have any flavor (e or μ) but are relatively soft; there is no $m(l_1 l_2)$ constraint; \cancel{E}_T can be large. However, if we form the cluster transverse mass, from the cluster $c = l_1 + l_2$,

$$m_T^2 = \{[p_T^2(c) + m_c^2]^{1/2} + \cancel{E}_T\}^2 - (\vec{p}_T(c) + \vec{\cancel{E}}_T)^2$$

we get $m_T < m_Z$ [modulo measurement errors etc. contributing to \cancel{E}_T and off shell Z^*, γ^* tail].

C. Specific signals

i) $t\bar{t} \rightarrow 1 \text{ lepton} + (n \leq 4) \text{ jets}$.

The $b\bar{b}$ background requires lepton cuts. Requiring e.g. $p_T(l) > 50$ with $50 < m_T(l, E_T) < 90$ and lepton isolation probably suppresses this below the signal for $m_t < 300$ [see (B) above for numbers].

The $pp \rightarrow W + n \text{ jet}$ background * can be reduced but not removed by savage jet cuts. For $n \leq 3$ this background process has been available already for some time. The $n = 4$ case has recently been evaluated [27]. The many subprocesses can be classified according to the number of participating quarks: 2, 4 or 6 quarks. The two-quark subprocesses contain many gluons. It then becomes profitable to use a technique recursive in the number of gluons. For the other processes helicity amplitudes are calculated using the Weyl-van der Waerden spinor calculus. For the evaluation of the $W + n \text{ jet}$ cross section the MRSEB parton densities are used and M_W is taken as the QCD scale. The following cuts on the transverse energy E_T of the jets and the lepton, on the missing transverse energy, on the pseudorapidity η of the jets and the lepton and on the separation ΔR between two jets or between a jet and a lepton were applied to both the signal and the background calculation:

$$\begin{aligned} E_T^{\min}(j) &= E_T^{\min}(l) &= E_T^{\min}(\text{miss}) &= 50 \text{ GeV} \\ |\eta^{\max}(j)| &= |\eta^{\max}(l)| &= 3 \\ \Delta R^{\min}(j, j) &= \Delta R^{\min}(j, l) &= 0.4 \end{aligned}$$

The results are listed in Tables 3 and 4. Table 3 gives the total background process for $n = 1, \dots, 4$ jets and its division into quark subprocesses. It should be noted that the relevance of the four-quark processes increases with n . The six-quark process is still negligible.

In Table 4 the signal as obtained from [29] is given for various m_{top} values together with the background. If in the background only the events containing a $b\bar{b}$ are selected, the background effectively disappears.

Table 3

number of jets	$\sigma(pp \rightarrow W + n \text{ jets}) [\text{pb}]$			total
	2 quarks	4 quarks	6 quarks	
1	80	-	-	80
2	45	7.0	-	52
3	18	5.8	-	24
4	6.1	2.4	0.13	8.6

We can also search for the top signal as a peak above background, e.g. in the invariant mass distribution of jets in the hemisphere opposite to the trigger lepton [30].

*F. Berends

Table 4

m_{top} (GeV)	$\sigma(pp \rightarrow l\nu + n \text{ jets})$ [pb]		
	$\sigma(l\nu + 2 \text{ jets})$	$\sigma(l\nu + 3 \text{ jets})$	$\sigma(l\nu + 4 \text{ jets})$
100	37.9	7.9	0.48
110	34.0	10.7	1.27
120	29.8	11.4	1.72
130	25.4	11.6	2.10
140	21.5	11.4	2.28
150	18.3	11.2	2.38
160	15.7	10.7	2.40
170	13.4	10.2	2.41
180	11.1	9.82	2.48
190	9.22	9.38	2.49
200	7.51	8.81	2.51
background	52	24	8.6
with b tagging	0.087	0.24	0.17

ii) Electroweak $ug \rightarrow d\bar{b} \rightarrow$ isolated lepton + ($n \geq 3$ jets).

This channel becomes competitive for very heavy top, $m_t \geq 300$ as discussed in the previous section. The $b\bar{b}$ and $W +$ jets backgrounds are serious, as above. But here we have a new trick (see [13]); the b -jet from $t \rightarrow bW$ is expected to have the smallest rapidity among the high- p_T jets. With b identified and ν reconstructed (from E_T and $m(l\nu) = m_W$), we can construct the invariant mass $m(b\nu)$; the top signal can in principle be seen as a narrow peak above backgrounds in this mass distribution. Unfortunately this requires very accurate E_T measurements.

iii) $t\bar{t} \rightarrow 2$ isolated leptons + ($n \geq 2$ jets).

A lepton p_T cut brings the $b\bar{b}$ background in sight:

$$p_T(l), p_T > 40 : b\bar{b} \text{ background/signal} \sim 5 (50) \text{ for } m_t = 150 (300) \quad (4.10)$$

$\Delta\phi(l_1l_2)$ and isolation cuts (both leptons) then suppress this background.

The $\tau\bar{\tau}$ is then removed by $m_T(l_1l_2, E_T) > m_Z$.

The $WW +$ jets background remains, being similar to the signal in the lepton sector. Requiring 2 hard jets removes it: E.g. $p_T(j) > 50$ with $p_T(l), p_T > 25$ gives

$$\begin{aligned} \sigma(WWjj \rightarrow e\mu\nu\nu jj) &\sim 0.04 \text{ pb} \\ \sigma(t\bar{t} \rightarrow e\mu\nu\nu jj) &\sim 9 (1.5) \text{ pb for } m_t = 150 (300) \end{aligned} \quad (4.11)$$

This leaves a clean signal. Additional b -tagging is not necessary, but would make the signal extremely clean and help in reconstructing observed top events.

5. Non-Standard Model Decays

5.1 The Charged Higgs Decay Mode of the Top Quark *

Among possible extensions of the Standard Model the minimal supersymmetric model *MSSM* has received much attention [31]. For this model to be anomaly-free, two Higgs doublets must exist, generating altogether 5 physical particles. Two of the particles are charged, H^\pm , two scalars h, H and one pseudoscalar A [$CP=-1$] are neutral. At the tree level, the mass spectrum is restricted by the relations

$$\begin{aligned} m_{H^\pm}^2 &= m_W^2 + m_A^2 \\ m_{h,H}^2 &= \frac{1}{2} [m_Z^2 + m_A^2 \mp \sqrt{(m_Z^2 + m_A^2)^2 - 2m_Z^2 m_A^2 \cos^2 2\beta}] \leq m_Z^2 \end{aligned} \quad (5.1)$$

The angle $\tan\beta = v_2/v_1$ is given by the ratio of the vacuum expectation values of the Higgs fields which provide the masses to up and down quarks, respectively. In the *MSSM*, v_2/v_1 is expected [32] to acquire a value between 1 and $\sim m_t/m_b$. LEP analyses have set lower limits on the light neutral Higgs particles $m_A > m_h > 32$ GeV (for a summary see Ref.[33]). Lower limits on m_h restrict the parameter range of $[m_{H^\pm}, \tan\beta]$ to the areas shown in Fig.10.

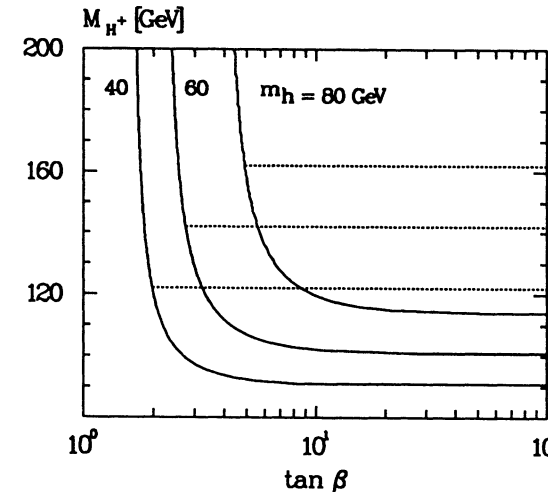


Fig.10. Allowed areas of $[m_{H^\pm}, \tan\beta]$ for given light scalar Higgs masses in the *MSSM*. [Below the dashed lines the decay mode $H^+ \rightarrow hW^+$ is kinematically forbidden.]

For a wide range of parameters the decay of top quarks to charged Higgs bosons $t \rightarrow b + H^+$ is kinematically allowed and, as a result of the large quark masses involved, the magnitude of the branching ratio is noticeable [8,31,34,35]. A comparison of the width

$$\Gamma(t \rightarrow b + H^+) = \frac{G_F m_t^3}{4\sqrt{2}\pi} \frac{p_H}{m_t} \left\{ \left[1 + \frac{m_b^2 - m_H^2}{m_t^2} \right] \left[\left(\frac{m_b}{m_t} \right)^2 \tan^2 \beta + \cot^2 \beta \right] + 4 \left(\frac{m_b}{m_t} \right)^2 \right\} \quad (5.2)$$

*P. M. Zerwas and J. Zunft

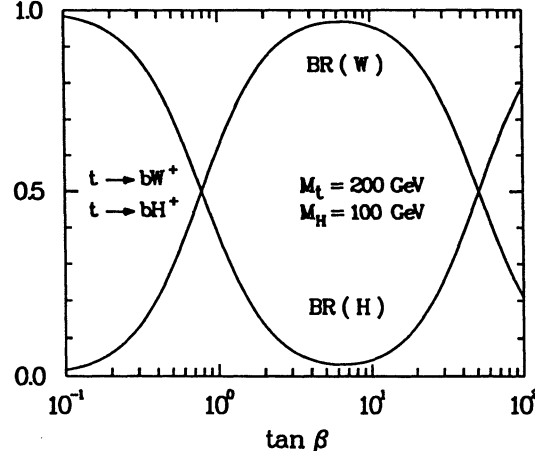


Fig.11. Branching ratios for top decays to W^+ and charged Higgs H^+ . The minimal value of $\tan\beta$ in the *MSSM* depends on the light Higgs mass and can be read off the previous figure.

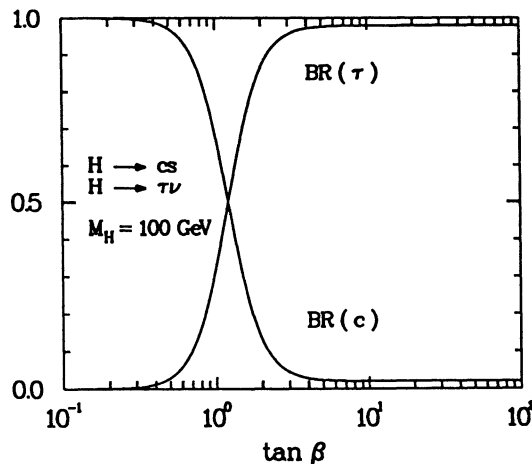


Fig.12. Branching ratios of charged Higgs decays for $m_{H^\pm} = 100$ GeV where the decay to W and light Higgs is kinematically forbidden. The lower limit for $\tan\beta$ in the *MSSM* can be read off Fig.10.

with the *SM* width in eq.(3.1) shows that in the physically interesting range of $\tan\beta$ the Higgs decay does not spoil the search strategies for top quarks based on the *SM* decay $t \rightarrow b + W^+$ [in contrast to models where $m_H < m_t < m_W$ is assumed [36]]. On the other hand, the branching ratio $\text{BR}(t \rightarrow b + H^+)$ is large enough to search for charged Higgs particles in top quark decays. This is illustrated quantitatively in Fig.11 for a top quark mass of 150 GeV and a Higgs mass of 100 GeV.

Charged Higgs bosons decay into heavy fermion pairs $H^+ \rightarrow \tau^+ \nu_\tau$ and $c\bar{s}$ as well as Wh final states if kinematically allowed [the areas in parameter space are restricted by the dashed lines in Fig.10]. The partial widths are given by

$$\begin{aligned}\Gamma(H^+ \rightarrow \tau^+ \nu_\tau) &= \frac{G_F m_\tau^2}{\sqrt{2}} \frac{m_H}{4\pi} \tan^2\beta \\ \Gamma(H^+ \rightarrow c\bar{s}) &= 3 \frac{G_F m_c^2}{\sqrt{2}} \frac{m_H}{4\pi} \left[\left(\frac{m_s}{m_c}\right)^2 \tan^2\beta + \cot^2\beta \right] \\ \Gamma(H^+ \rightarrow W^+ h) &= \frac{G_F m_H^3}{8\pi\sqrt{2}} \left(\frac{2p_W}{m_H}\right)^3 \cos^2(\beta - \alpha)\end{aligned}\quad (5.3)$$

with

$$\tan 2\alpha = \tan 2\beta \frac{m_H^2 + m_h^2}{m_A^2 - m_Z^2}$$

They add up to a small total width of less than $\mathcal{O}(0.1\text{MeV})$ so that the charged Higgs particles are very narrow in the parameter range relevant for top decays. The branching ratios are displayed in Fig.12 for $m_{H^\pm} = 100$ GeV. Except for low $\tan\beta$ and large m_{H^\pm} values, the leptonic $H^+ \rightarrow \tau^+ \nu_\tau$ decay mode is dominant.

For large $\tan\beta$ the τ decay mode is nearly exclusive, providing an excellent signature for charged Higgs decays. As a result, top decays into H^+ could manifest themselves through deviations of the semileptonic branching ratios $\text{BR}(t \rightarrow \mu^+, e^+)$ and $\text{BR}(t \rightarrow \tau^+)$ from the universal value 1/9 as prescribed by the real W decays in the Standard Model.

Addendum. Because of low rates and large backgrounds it is very difficult to search for direct $H^+ H^-$ pair production through the electroweak Drell-Yan mechanism in pp colliders. Besides the top decay to H^+ , associated production of top and charged Higgs $pp \rightarrow tH^-$, mediated by bg fusion, lends itself as a possible channel for charged Higgs search [35], in particular if $m_{H^\pm} > m_t$. However, the cross sections for the LHC are in the range of 1 to 10 pb, varying with the H^\pm mass and $\tan\beta$, so that it would be very difficult to detect the charged Higgs particles in this channel [37].

5.2 Supersymmetric Extension: Stop *

In supersymmetric (SUSY) extensions [38] of the Standard Model the two scalar partners of the left- and right-handed fermions give rise to a 2×2 mass matrix with off-diagonal elements proportional to the fermion mass considered. For all fermions, including the b -quark, this mixing is immaterial. For the heavy t quark however, it could become significant,

*E. Reya

leading, upon diagonalization, to a physical stop \tilde{t} mass eigenstate which might be *lighter* than m_t [39,40]. The mass matrix for the two states $\tilde{t}_{L,R}$ associated in chiral supermultiplets Q_L and \bar{T}_R with the left-handed $(t,b)_L$ quark doublet and the right-handed t quark singlet, follows straightforwardly from the soft SUSY breaking potential

$$V_{soft} \propto m_0 h_t A_t Q_L \bar{T}_R H_2 + m_0 (A_t - 1) \mu H_1 H_2 + m_Q^2 |Q_L|^2 + \dots \quad (5.4)$$

with the Higgs supermultiplets giving masses to "up" and "down" members, such as $m_t = |h_t v_2| [v_i = < H_i^0 >]$ and, as before, we define $\tan\beta = v_2/v_1$. In the simplest and most naïve model [$A_t = 2$, $\mu = 0$, $\cos 2\beta = 0$] one expects $m_t = |m_t - m_0|$ at the unification scale M_X , with the scalar-mass scale being $m_0 = m_{3/2} = \mathcal{O}(M_W)$ with the gravitino mass denoted by $m_{3/2}$. In general, however, the lightest stop mass $m_{\tilde{t}}$ depends on at least five SUSY parameters [38,41,42] m_0 , $M_{1/2}$, μ , A_t , $\tan\beta$. Also the gaugino mass $M_{1/2}$ enters via the coupled renormalization group equations used for the evolution from M_X down to M_W . Although these parameters are constrained by the correct $SU(2) \times U(1)$ breaking conditions, there is still enough freedom for not having $m_{\tilde{t}} < m_t$. A recent analysis [43], based on stringent astrophysical assumptions such as a SUSY solution to the dark matter problem, has shown that $100 < m_{\tilde{t}} < 300$ GeV. In view of this theoretically rather ambiguous and non-predictive situation, let us simply *assume* that $m_{\tilde{t}} < m_t$, and discuss the consequences of SUSY top decays as compared to the standard decay $t \rightarrow b + W$.

If $m_{\tilde{t}} < m_t$, the dominant SUSY decay of the top quark will be

$$t \rightarrow \tilde{t} + \tilde{\gamma}$$

where of course the lightest SUSY particle (LSP), the neutralino $\tilde{\gamma}$, must be light enough as well. (The purely hadronic decay mode $t \rightarrow \tilde{t} + \tilde{g}$ appears to be not relevant due to the present experimental large bound on the gluino mass $M_{\tilde{g}} \geq 100$ GeV). In this case the SUSY decay rate becomes competitive to the *SM* decay:

$$\frac{\Gamma(t \rightarrow \tilde{t} \tilde{\gamma})}{\Gamma(t \rightarrow bW)} \simeq \frac{8\sqrt{2}\pi\alpha}{9G_F M_W^2} \left(\frac{m_W}{m_t}\right)^2 \frac{(1 - m_t^2/m_t^2)^2}{(1 - M_W^2/m_t^2)^2 (1 + 2M_W^2/m_t^2)} \quad (5.5)$$

which holds for $M_{\tilde{\gamma}} \ll m_t$ [the factor in front being approximately 0.4]. This SUSY t -decay gives rise to very different signatures compared to the *SM* decay $t \rightarrow bW$ due to the primary missing energy associated with $\tilde{\gamma}$. This implies in turn also, for example, a softer lepton energy spectrum in comparison to the *SM*. Such differences, however, depend on the details of the various \tilde{t} decays [40,44-47] and in particular on unknown SUSY masses involved. The dominant decay modes will be

$$\tilde{t} \rightarrow b\tilde{W} \rightarrow b\bar{f}f'\tilde{\gamma} \quad \text{and} \quad \tilde{t} \rightarrow \tilde{b}W \rightarrow \tilde{b}\bar{\gamma}f\bar{f}'$$

with $f\bar{f}' = \nu_l l^+, u\bar{d}, c\bar{s}$, which give rise to a softer charged lepton energy spectrum and to a more pronounced transverse mass distribution [44,45] than in the *SM*. Even the 2-body flavor-changing decay

$$\tilde{t} \rightarrow c + \tilde{\gamma}$$

which proceeds via $b\tilde{b}\tilde{W}$ triangle graphs, could become competitive [45] if $m_{\tilde{t}} < M_W$ and the 4-body phase space is suppressed. In this case there will be no hard primary lepton in the final state.

Alternatively, if the LSP is a (scalar) sneutrino $\tilde{\nu}$, the dominant decay mode will be $\tilde{t} \rightarrow b\tilde{W} \rightarrow bl^+\tilde{\nu}$ [45,47]. In this case primary leptons are *always* present in the final state and their energy spectrum is rather hard.

To summarize, the typical signatures of SUSY t -decays are (i) larger missing energy and (ii) softer charged lepton spectra than in the *SM* t -decay. At present there are too many unknown SUSY parameters for conclusive analyses and unambiguous predictions. Therefore, the best strategy to search for these SUSY signals in top-decays would be to look for access events which are not compatible with the precise expectations for the *SM* decay $t \rightarrow bW$. On the other hand, the observation of a t quark conforming exactly to the *SM* expectations would serve to rule out light stops and/or neutralinos! A more detailed experimental feasibility study is presented in the SUSY Section of these proceedings.

6. Non-SM Quarks *

6.1 Fourth generation quarks

If a fourth generation of leptons and quarks (ν_L, L), (t', b') exists [48], the quark masses must exceed 89 GeV to escape the CDF bound [49] and the lepton masses must be of order $m_Z/2$ or greater in order to conform with the LEP data. The mass splittings are constrained by electroweak radiative corrections [50]

$$(m_{t'} - m_{b'})^2 + \frac{1}{3} (m_{\nu_L} - m_L)^2 + m_t^2 \leq (200 \text{ GeV})^2 \quad (5.6)$$

QCD production of $b'b'$ and $t'\bar{t}'$ pairs is similar to $t\bar{t}$; electroweak $t'b'$ production is suppressed relative to the tb case, however, since both quarks are heavy. If b' were lighter than t [51], it would be produced more copiously and it would be discovered first. Its probable decay mode $b' \rightarrow cW$ gives signals very similar to top; however, the lepton and neutrino distributions are different compared to $t \rightarrow bW$ (essentially interchanged), and this may eventually be discernible [52]. If $m_{t'} > m_b + m_W$, t' can decay by $t' \rightarrow b'W \rightarrow cWW$, so that $t'\bar{t}'$ production gives distinctive *four-W final states*. Different mass orderings and mass splittings lead to a variety of scenarios that we do not pursue in detail here; there are many similarities [30] to the standard $t\bar{t}$ scenario, but also significant differences do exist.

6.2 Exotic quarks

New quarks may be present below 1 TeV and they could be produced in this mass range at large hadron colliders as shown in the Summary. If they do not belong to standard families, they are called *exotic*. The simplest and most attractive possibility is a *new vector-like quark of charge $-\frac{1}{3}$* in each family. [The left and right-handed components of vector-like fermions have the same transformation properties under $SU(2)_L \times U(1)_Y$]. Such quarks [53] are present in many extensions of the Standard Model, for instance in extended gauge models, in models of spontaneous *CP* violation, etc. Present data constrain their masses little because their mixing with the standard quarks is naturally small. We discuss the possibility to detect such quarks at the LHC, assuming that the matter content of the theory is that of the minimal Standard Model plus this new fermion.

For a large range of the parameter space a new vector-like D quark will have similar signatures as the top quark. Its dominant decay is into a W plus a charge $\frac{2}{3}$ quark (typically

*F. del Aguila and R. J. N. Phillips

50 %) which looks like a top decay if we cannot determine the flavor of the final quark. However, D can also decay to Z or H (typically 25 % to each of them) plus a light quark. Therefore, although D should be searched for in the same final states as the top, its character will be determined by observing its neutral decay modes. The CDF lower limit $m_t > 89$ GeV applies approximately to m_D too. However, whereas the present analysis of neutral current data and LEP results (including radiative corrections) indicate $m_t < 200$ GeV, m_D has no upper bound.

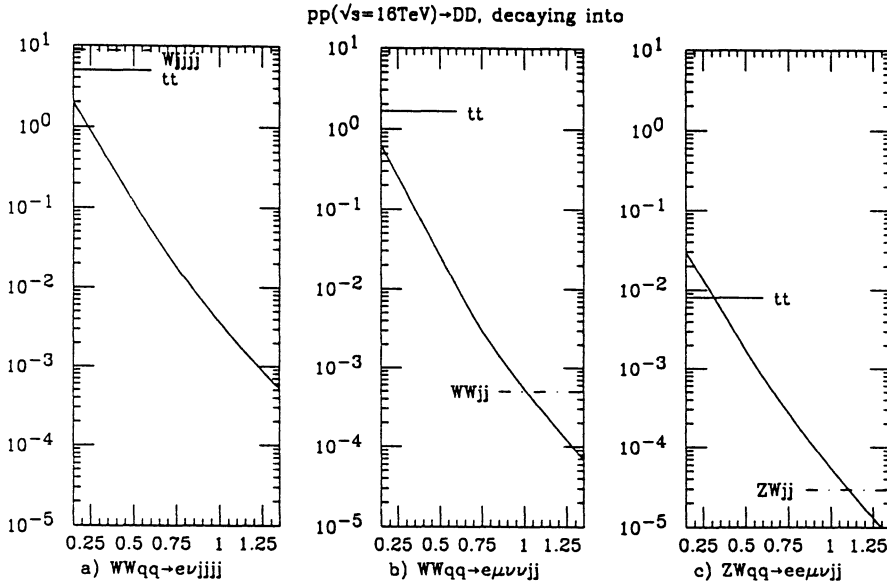


Fig.13. σ [pb] as a function of the D quark mass (in TeV). All transverse momenta ($l, j, \text{missing}$) are required to be > 50 GeV, whereas the top mass is equal to 200 GeV.

We have calculated the $pp \rightarrow D\bar{D}$ cross sections plus the decays into the most interesting channels, (a) $W^+W^-q\bar{q} \rightarrow e\nu jjjj$, (b) $e\bar{\mu}\nu\bar{\nu}jj$ and (c) $ZWq\bar{q} \rightarrow e\bar{e}\mu\nu jj$. The analysis is carried out at the parton level and the normalization is chosen as $\sigma(pp \rightarrow D\bar{D}) = \sigma(pp \rightarrow t\bar{t}) = 0.58\text{nb}$ for $m_D = m_t = 200$ GeV; this is in the middle of the QCD predictions. In all cases we require $p_{t,\text{missing}}^2 > 50$ GeV. We assume the $D\bar{D}$ decay fractions to be (a) $(\frac{1}{2})^2 \times 2 \times \frac{1}{9} \times 0.67$, (b) $(\frac{1}{2})^2 \times 2 \times (\frac{1}{8})^2$ and (c) $2 \times \frac{1}{4} \times \frac{1}{2} \times 0.034 \times \frac{1}{9}$ where the D decay fractions into W and Z are equal to $\frac{1}{2}$ and $\frac{1}{4}$, respectively. [We implicitly assume that the Higgs is lighter than the new D quark, and the D decay fraction into H is $\frac{1}{4}$.]

In channels (a) and (b), the $D\bar{D}$ signal is like $t\bar{t}$ but reduced by a factor $\frac{1}{4}$. The two cases are therefore difficult to distinguish if $m_t < 200$ GeV as expected. The horizontal lines marked $t\bar{t}$ in Fig.13 show the $t\bar{t}$ backgrounds for $m_t = 200$ GeV. [For other backgrounds and references see the $t\bar{t}$ discussions.]

In channel (c) the $t\bar{t}$ background enters via semileptonic b -decays; if we impose an additional mass cut $|m(e^+e^-) - m_Z| < 10$ GeV, the cross section is about 0.008 pb as shown in Fig.13. A further isolation cut (not shown) could reduce the $t\bar{t}$ background by a factor of 50, approaching the irreducible $pp \rightarrow ZWjj$ background which is estimated to be a few times 10^{-5} pb.

We conclude that the $t\bar{t}$ background (let alone other backgrounds) renders channels (a) and (b) unpromising, but that a $D\bar{D}$ signal should be detectable in the NC channel (c) up to $m_D \sim 400 - 500$ GeV for $\int \mathcal{L} = 10^4 \text{pb}^{-1}$, and eventually up to 700 GeV for a ten times larger integrated luminosity.

REFERENCES

- [1] M. Glück, J. F. Owens and E. Reya, Phys. Rev. D17 (1978) 2324; B. L. Combridge, Nucl. Phys. B151 (1979) 429.
- [2] M. Diemoz, F. Ferrari, E. Longo and G. Martinelli, Z. Phys. C39 (1988) 21.
- [3] M. Glück, E. Reya and A. Vogt, Z. Phys. C48 (1990) 471 and Proceedings of the 'Small-x' meeting, DESY, May 1990 (Nucl. Phys. B).
- [4] P. Nason, S. Dawson and R. K. Ellis, Nucl. Phys. B303 (1988) 607 and Nucl. Phys. B327 (1989) 49.
- [5] W. Beenacker, H. Kuijf, W. L. van Neerven and J. Smith, Phys. Rev. D40 (1989) 54; W. Beenacker, W. L. van Neerven, R. Meng, G. A. Schuler and J. Smith, DESY 90-064.
- [6] G. Altarelli, M. Diemoz, G. Martinelli and P. Nason, Nucl. Phys. B308 (1988) 724.
- [7] R. Meng, G. A. Schuler, J. Smith and W. L. van Neerven, Nucl. Phys. B339 (1990) 325.
- [8] I. Bigi, Y. Dokshitzer, V. Khoze, J. Kühn and P. Zerwas, Phys. Lett. B181 (1986) 157.
- [9] S. Güsken, J. H. Kühn and P. M. Zerwas, Phys. Lett. 155B (1985) 185.
- [10] V. Fadin, V. Khoze, JETP Lett. 46, 417 (1987); Yad. Fiz. 48 (1988) 487; V. Fadin, V. Khoze and T. Sjöstrand, CERN-TH 5687/90.
- [11] W. Beenakker, A. Denner, W. Hollik and T. Sack, MPI Report, in preparation.

- [12] S. Willenbrock and D. A. Dicus, Phys. Rev. D34 (1986) 155.
- [13] C.-P. Yuan, Phys. Rev. D41 (1990) 42.
- [14] Y. Azimov, L. Frankfurt and V. Khoze, Leningrad Report LNPI-222 (1976).
- [15] M. Suzuki, Phys. Lett. B71 (1977) 139.
- [16] J. D. Bjorken, Phys. Rev. D17 (1978) 171.
- [17] C. Peterson, D. Schlatter, I. Schmitt and P. M. Zerwas, Phys. Rev. D27 (1983) 105.
- [18] G. Altarelli and G. Parisi, Nucl. Phys. B126 (1977) 298.
- [19] Azimov et al., Yad. Fiz. 40 (1984) 777.
- [20] B. Mele and P. Nason, CERN-TH 5707/90;
Y. Dokshitzer et al., in preparation.
- [21] I. Bigi, V. Khoze, J. H. Kühn, T. Sjöstrand and P. M. Zerwas, in preparation.
- [22] F. Gilman and Y. Nir, SLAC-PUB-5198 (1990).
- [23] F. Gilman and R. Kauffman, Phys. Rev. D37 (1988) 2676.
- [24] M. Jezabek and J. Kühn, Nucl. Phys. B314 (1989) 1; *ibid.* B320 (1989) 20.
- [25] H. Baer, V. Barger, H. Goldberg and R. J. N. Phillips, Phys. Rev. D37 (1988) 3152;
H. Baer, V. Barger and R. J. N. Phillips, Phys. Rev. D39 (1989) 3310;
S. Gupta and D. P. Roy, Z. Phys. C39 (1988) 417.
- [26] H. Baer et al., Phys. Rev. D42 (1990) 54;
F. Halzen et al., Mod. Phys. Lett. A4 (1989) 1531;
R. Kleiss et al., Z. Phys. C39 (1988) 393, and further references therein.
- [27] F. A. Berends, W. T. Giele and H. Kuijf, Nucl. Phys. B321 (1989) 39;
F. A. Berends, W. T. Giele, H. Kuijf and B. Tausk, Fermilab-Pub-90/213-T.
- [28] D. Zeppenfeld, to be published.
- [29] R. Kleiss and W. J. Stirling, Z. Phys. C40 (1988) 419.
- [30] H. Baer, V. Barger, H. Goldberg and J. Ohnemus, Phys. Rev. D38 (1988) 3467;
S. Dawson and S. Godfrey, Phys. Rev. D39 (1989) 221.
- [31] J. F. Gunion, H. E. Haber, G. Kane and S. Dawson, *The Higgs Hunter's Guide* (Addison and Wesley 1990) and references quoted therein.
- [32] See the contribution by F. Zwirner [SUSY Group] to these proceedings.
- [33] F. Dydak, Proceedings, XXV. Intern. Conference on High Energy Physics, Singapore 1990.
- [34] V. Barger, J. L. Hewett and R. J. N. Phillips, Phys. Rev. D41 (1990) 3421.
- [35] A. C. Bawa, C. S. Kim and A. D. Martin, Z. Physik C 47 (1990) 75.

- [36] M. Felcini [UA1 Coll.], Proceedings, 8th Topical Workshop on Proton-Antiproton Collider Physics, Castiglione della Pescaia (Italia), 1989.
- [37] J. Zunft, contribution to this Workshop;
A. C. Bawa et al., contribution to this Workshop, based on Ref.[35].
- [38] For reviews see: H. P. Nilles, Phys. Rep. C110 (1984) 1;
H. E. Haber and G. L. Kane, Phys. Rep. C117 (1985) 75;
P. Nath, R. Arnowitt and A. H. Chamseddine, "Supersymmetry and Supergravity, Non-perturbative QCD", Vol. 208 of Lecture Notes in Physics (Springer, N. Y. 1984), 113;
L. J. Hall, *ibid.*, 197;
E. Reya, Proceedings of the XXIII. Intern. Conference on High Energy Physics, Berkeley 1986, ed. S. C. Loken (World Scientific, 1987), vol. I, 285 and references therein.
- [39] E. Cremmer, P. Fayet and L. Girardello, Phys. Lett. B122 (1983) 41.
- [40] J. Ellis and S. Rudaz, Phys. Lett. B128 (1983) 248.
- [41] L. E. Ibanez and C. Lopez, Nucl. Phys. B233 (1984) 511;
L. E. Ibanez, C. Lopez and C. Munoz, Nucl. Phys. B256 (1985) 218;
A. Bouquet, J. Kaplan and C. A. Savoy, Nucl. Phys. B262 (1985) 299.
- [42] C. Kounnas, A. Lahanas, D. Nanopoulos and M. Quiros, Nucl. Phys. B236 (1984) 438.
- [43] J. Ellis and F. Zwirner, CERN-TH 5460/89.
- [44] G. Altarelli and R. Rückl, Phys. Lett. B144 (1984) 126.
- [45] I. Bigi and S. Rudaz, Phys. Lett. B153 (1985) 335;
K. Hikasa and M. Kobayashi, Phys. Rev. D36 (1987) 724.
- [46] H. Baer and X. Tata, Phys. Lett. B167 (1986) 241.
- [47] H. E. Haber and G. L. Kane, in Ref.[38].
- [48] V. Barger, H. Baer, K. Hagiwara and R. J. N. Phillips, Phys. Rev. D30 (1984) 947.
- [49] CDF Collaboration, 25th Rencontre de Moriond, Les Arcs 1990 (pres. by K. Sliwa).
- [50] G. Altarelli, Proceedings, 1989 Int. Symp. on Lepton and Photon Interaction at High Energies, Stanford, ed. M. Riordan (World Scientific Pub. Co. 1990);
J. Ellis and G. L. Fogli, Phys. Lett. B232 (1989) 139 and CERN-TH 5817/90;
D. Haidt, DESY 89-073;
V. Barger, J. L. Hewett and T. G. Rizzo, Phys. Rev. Lett. 65 (1990) 1313;
P. Langacker, UPR-0435 T (1990);
F. Dydak, Proceedings, XXV. Int. Conference on High Energy Physics, Singapore 1990.
- [51] V. Barger et al., Phys. Rev. D30 (1984) 947.
- [52] V. Barger and R. J. N. Phillips, Phys. Rev. D41 (1990) 52.
- [53] F. del Aguila, E. Laermann and P. Zerwas, Nucl. Phys. B297 (1988) 1;
F. del Aguila, Ll. Ametller, G.L. Kane and J. Vidal, Nucl. Phys. B334 (1990) 1;
V.D. Angelopoulos et al., Nucl. Phys. B292 (1987) 59;
V. Barger, N. G. Deshpande and J. F. Gunion et al., Proc. of 1986 Snowmass Workshop;
V. Barger, N. G. Deshpande and K. Whisnant, Phys. Rev. D33 (1986) 1912.

TOP SEARCH AT THE LHC: SIGNAL VERSUS BACKGROUND

F. CAVANNA¹, D. DENEGRI² and T. RODRIGO³

Abstract

We discuss the various ways of searching for the t -quark at the LHC, concentrating on the expected Standard Model mass-range $100 \lesssim m_t \lesssim 250 \text{ GeV}/c^2$. Extensive simulations of the signal and of the expected backgrounds have been performed, the different techniques of reducing the backgrounds are discussed and the expected signal-to-background ratios in the main experimental channels are evaluated.

§. 1 - Introduction

In the past decade the t -quark has been systematically searched at e^+e^- and hadron colliders. Nevertheless the t -quark still escapes discovery; its "non-existence" would require a total overhaul of the Standard Model and is not plausible. All that makes the search for the t -quark one of the most urgent and compelling challenges in high energy physics.

The present lower limits on m_t are shown in fig.1.1.

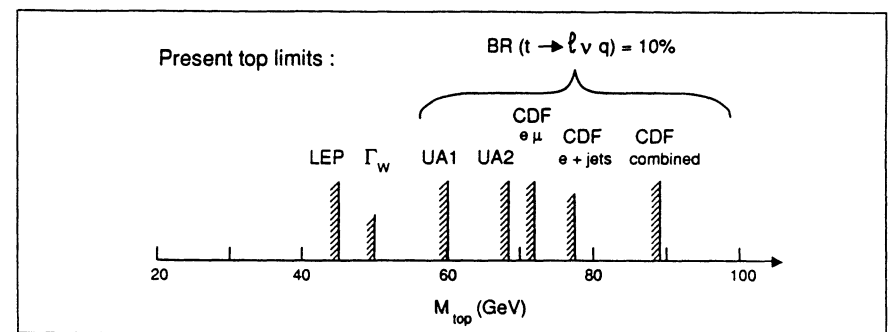


Fig.1.1 : Present lower limits on m_t from direct searches

The most stringent lower limits on m_t come from the $p\bar{p}$ collider experiments UA1, UA2 and CDF [1]. The CDF collaboration has recently set a lower limit of $m_t = 89 \text{ GeV}/c^2$ [2], i.e. above the W mass. The limits from LEP [3] and the Γ_W measurement [4] are independent of the assumed leptonic branching ratios $BR(t \rightarrow l\nu, b) \simeq 1/9$. On the other hand, an upper limit of $m_t \approx 200 \text{ GeV}/c^2$ is obtained combining, for example, the measurements of m_Z and m_W/m_Z with the electroweak radiative corrections to $\sin^2\theta_W$, which depends on the t -quark mass [5]. A comprehensive analysis of radiative corrections to all available electroweak data yields for the best fit $m_t \approx 130 \text{ GeV}/c^2$ [5].

The total integrated luminosity foreseen for the coming years at Fermilab ($\sim 200 \text{ pb}^{-1}$) should allow to explore the m_t range up to $\sim 150 \text{ GeV}/c^2$. Above this mass the discovery of t -quark is problematic because of limited statistics and larger backgrounds.

In terms of c.m. energy and luminosity, the LHC would allow to explore a large t -quark domain, with mass up to $\sim 1 \text{ TeV}/c^2$. In the m_t range expected from the Standard Model, namely $100 \lesssim m_t \lesssim 200 \text{ GeV}/c^2$, the production rates are very large. A precision measurement of the t -quark mass and of the decay branching ratios would be possible in this mass range, after a potential discovery in the $\gtrsim 150 \text{ GeV}/c^2$ region. Since the t -quark may be an important source of charged Higgs particles expected in the SUSY extension of the Standard Model [6], a precise measurement of the t -quark decay branching ratios is very important too. In conclusion the t -quark search is one of the most exciting issues at the LHC. Moreover, there is a compelling need to complete the fermion families, since

¹ LAPP, Annecy, France and CERN, Geneva, Switzerland

² DPhPE, CEN-Saclay, Gif-sur-Yvette, France

³ CERN, Geneva, Switzerland and CIEMAT, Madrid, Spain

the recent LEP neutrino count strongly suggests that the t -quark is the last quark one may expect.

We discuss here the results of an extensive simulation of t -quark production and of the main background sources. After a consistency check between the MonteCarlo and the theoretical cross sections [7],[8], the main t -quark signatures are considered, with the corresponding backgrounds. The aim is to define selection criteria allowing first observation of the t -quark at machine start-up, if not discovered by then, and to obtain clean samples for detailed studies (mass, BR's). A set of acceptance cuts are given for the "single lepton" and "di-leptons" t -quark decay modes. We also discuss the presence of additional (non-isolated) μ 's tagging the b 's produced in the t -quark decay as a further mean to improve signal to background ratios.

There is no detailed apparatus simulation in this study. We assume an el.m./had. calorimetric capability in the central rapidity region of $|\eta| \leq 1.5 \div 2.0$ and a minimal level of granularity ($\Delta\eta \times \Delta\phi \leq 0.1 \times 0.1$) is required for isolation purposes. We also assume the possibility of triggering on μ and e above a threshold of $\sim 30\text{GeV}/c$, but for muon tagging of b 's it would be desirable to have muon detection at $p_T^\mu \gtrsim 10\text{GeV}/c$, and a muon rapidity coverage $|\eta^\mu| \lesssim 2.5$. There is no specific requirements either on the lepton (μ and e) or on the jet resolutions¹. We try to avoid signal defining criteria depending on the missing transverse energy reconstruction.

The event generators used are EUROJET [9] and ISAJET [10] for the t -quark signal, and ISAJET and LDW [11] for the various background sources, $b\bar{b}$ production, $W + jets$ production, WW production, etc... .

§. 2 - Top production and decay

The t -quark production mechanisms and decay modes are reviewed in details elsewhere in these proceedings, [8]. We recall here only the basic features. In hadronic collisions the t -quark can be produced either via strong interaction or via electroweak interactions. In the mass range we want to explore,

$$100 \lesssim m_t \lesssim 250\text{GeV}/c^2,$$

the QCD contribution dominates with $t\bar{t}$ pair produced by $q\bar{q}$ and gg fusion. Next-to-the-leading order (NLO) contributions have been theoretically computed [7] and also partially parametrized in the MC generators.

The weak interactions contribute significantly only for a very heavy t -quark and become dominant above a mass of $\sim 300\text{GeV}/c^2$, fig.2.1.a. Among the weak mechanisms the dominant one is the W -gluon fusion, where a single t -quark is produced in a $t\bar{b}$ pair. In fig.2.1.a the theoretical $t\bar{t}$ and $t\bar{b}$ production cross sections [8] are given as a function of the t -quark mass and in fig.2.1.b the $t\bar{t}$ cross section at the LHC is compared with those at the SSC and the Tevatron [8]. For $m_t = 150\text{GeV}/c^2$, the production cross section at the LHC is larger than at Fermilab by a factor of ~ 300 . For the MC

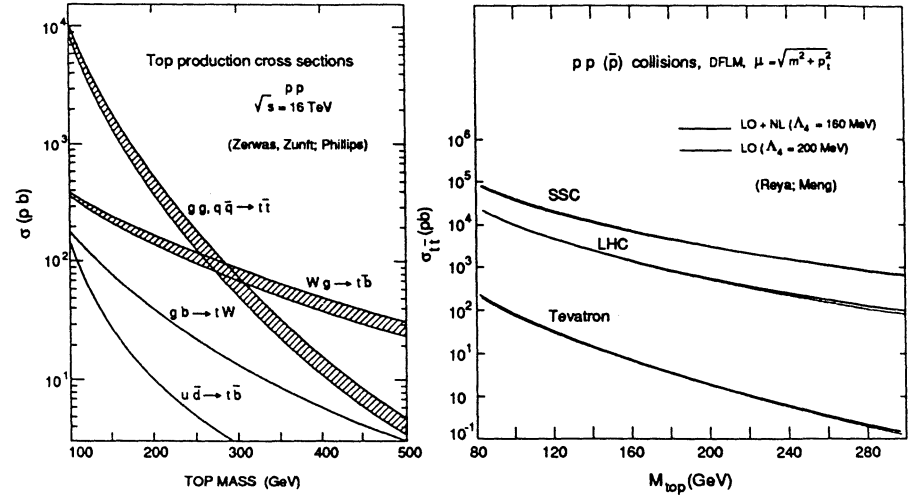


Fig.2.1 : Top quark production cross sections: theoretical calculations
(a) Strong and Electroweak processes at $\sqrt{s}=16\text{TeV}$, (b) $t\bar{t}$ cross sections at various c.m. energies

study we produced large samples of $t\bar{t}$ events, from pp collisions at $\sqrt{s} = 16\text{TeV}$, corresponding to different values of the t -quark mass ($100, 125, 150, 200, 300\text{ GeV}/c^2$). For $t\bar{t}$ production we employed EUROJET, and ISAJET as a test of consistency. The EUROJET MC explicitly incorporates matrix elements approximating the next-to-leading order contributions. For high p_T phenomena, this approach may be more reliable than the higher order contributions approximation via parton evolution schemes. A partial list of the $t\bar{t}$ Feynman diagrams (LO+NLO) included in the EUROJET simulation are shown in fig.2.2.

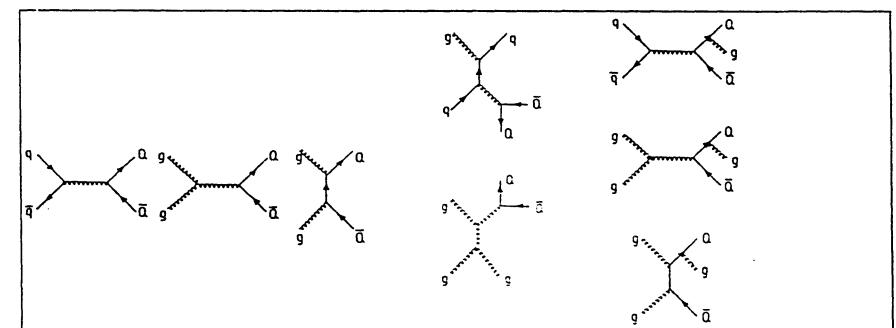


Fig.2.2 : Some of the Feynman diagrams for $t\bar{t}$ production (LO+NLO)
in the EUROJET Montecarlo

¹ Standard values for the electron and hadron energy resolution and for the muon momentum resolution are implicitly assumed, namely $\Delta E/E \approx 15\%/\sqrt{E}$ for electrons, $\Delta E/E \approx 80\%/\sqrt{E}$ for jets and $\Delta p/p \approx 10\%$ for muons

In order to reproduce the expected theoretical $t\bar{t}$ cross section, the NLO contribution can be tuned in the MC via a cut-off on the extra-jet p_T . Choosing a cut-off of $p_T^{\text{cut}} = 40 \text{ GeV}/c$, the agreement between the EUROJET simulation and theory is good (within $\simeq 20\%$) as it is shown in fig.2.3.a. In fig.2.3.b the variation of the $t\bar{t}$ cross section with energy (\sqrt{s}) and the comparison with the $\sqrt{s} = 16 \text{ TeV}$ theoretical calculation is also shown.

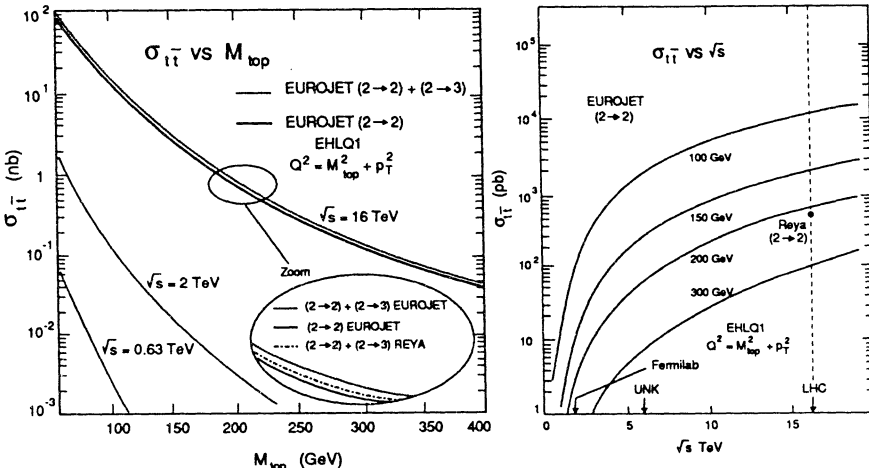


Fig.2.3 : Comparison between $t\bar{t}$ Montecarlo cross sections and theoretical reference calculations
(a) in terms of m_t , (b) in terms of c.m. energy

There are some uncertainties in the evaluation of these cross sections. They are due to the choice of the Structure Functions (SF) set and to the Q^2 scale. To evaluate these effects we generated several $t\bar{t}$ event samples, selecting different SF sets¹ or different Q^2 values². The $\sigma_{t\bar{t}}$ uncertainty due to structure functions is of the order of 20% for any m_t value in the $100 \div 200 \text{ GeV}/c^2$ range of mass, fig.2.4.a. The Q^2 uncertainty, on the other hand, introduces a 20 \div 30% variation of $\sigma_{t\bar{t}}$ in the same mass range, fig.2.4.b.

We consider as a default choice the EHLQ1 set [12] of Structure Functions and a Q^2 scale of $(p_T^2 + m_t^2)$.

2.1 - Top-quark decay and experimental signatures

In the Minimal Standard Model (MSM) framework there is only one t -quark decay mode:

$$t \rightarrow W b$$

(The W in the final state is on shell if $m_t > m_W + m_b$). If one extends the scheme to include charged Higgs, H^\pm , there is a possibility for a competitive t -decay mechanism

¹ The SF we used are DO1 and DO2 (Duke, Owens), EHLQ1 and EHLQ2 (Eichten et al.), GHR (Gluck et al.) and DFLM (Diemoz et al., not reported in the analysis).

² The Q^2 scale factors we considered are: $(p_T^2 + m_t^2)$, m_t^2 , $4(p_T^2 + m_t^2)$

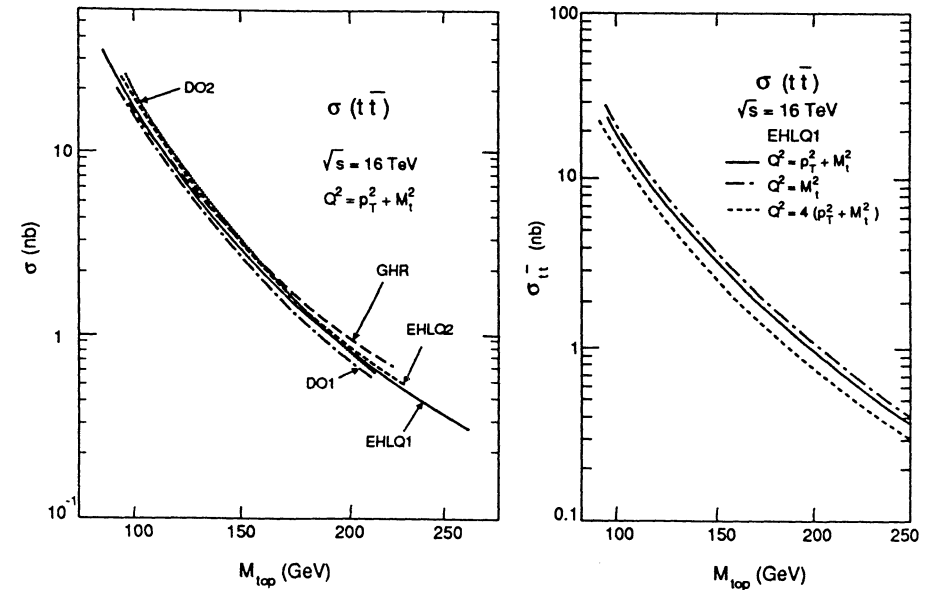


Fig.2.4 : Stability of the $t\bar{t}$ cross section as a function of:
(a) Structure Function variation, (b) Q^2 scale variation

of $t \rightarrow H^\pm b$. This channel, and the possibility to observe it, are described elsewhere in these proceedings [13], [14]. We consider here only the MSM option where $BR(t \rightarrow W b) = 1$.

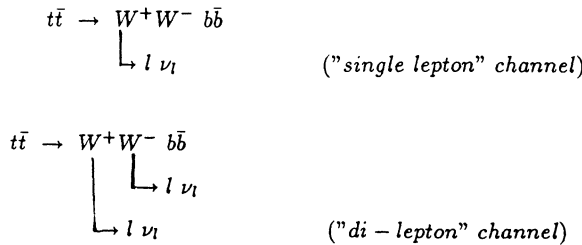
The total $t\bar{t}$ cross section for a t -quark in the $150 \div 200 \text{ GeV}/c^2$ range of mass is of the order of $\sim 1 \text{ nb}$. With an integrated luminosity of $\sim 10^4 \text{ pb}^{-1}$, i.e. one year of running (10^7 sec) with a luminosity of $L = 10^{33} \text{ cm}^{-2} \text{ s}^{-1}$, a very large annual production of $\sim 10^7 \text{ evts}$ is thus expected. Let us see how this statistics can be used to identify and select the t -quark signal.

The $t\bar{t}$ pair can give rise to several final state signatures, with each of the intermediate decay components ($W \bar{W} b \bar{b}$) having a hadronic or a (semi-)leptonic decay, producing in the latter case a (l, ν_l) pair with a branching ratio of $\approx 1/9$. Different search strategies can thus be developed, according to the number of final state leptons.

Although the statistics is largest in the purely hadronic $t\bar{t}$ decay mode,

$$t\bar{t} \rightarrow W^+ W^- b\bar{b} \rightarrow \geq 6 \text{ jets}$$

it is nonetheless overwhelmed by QCD multijets backgrounds, as it was shown at the La Thuile Workshop [15]. The solution is to look for leptonic signatures, where the leptons can come either from W or b decays. The W decay leptons are harder and well isolated and are thus the main topological signature. According to whether one or both W 's decay to a (l, ν) pair, we have "single" or "di"-lepton decay channels:



For the hard and isolated leptons from W decays, both electrons and muons can be considered. The b -decay leptons are usually softer and embedded in the b -jet; thus only muons are considered and we discuss this in the following as b -tagging.

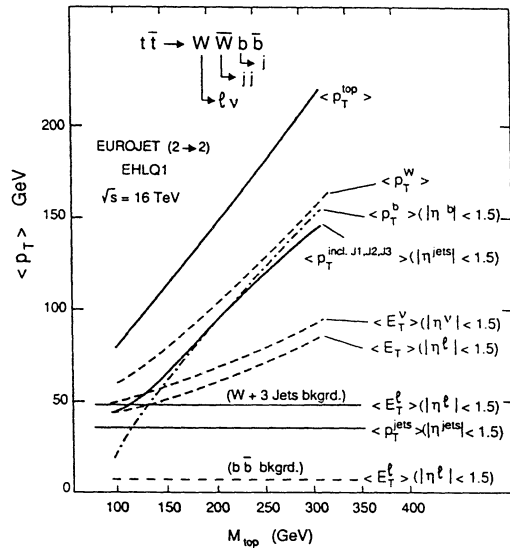


Fig.2.5 : Average p_T , (E_T) for t -quark and t decay products
Comparison with $\langle p_T \rangle$ levels from the major background sources

Multilepton (≥ 3) final states will clearly have lower backgrounds, but the loss of statistics is large, even at the highest LHC luminosity. Thus it is important to consider first the "single lepton" signature where the production rate is largest, and the first observation of the t -quark may occur at machine start-up. In this channel the background is also important and needs to be properly reduced. The "single-lepton" mode can also be used to determine directly m_t in a $t \rightarrow 3\text{jets}$ decay, without missing particle [14]. We discuss then the "di-lepton" channel which is much cleaner and is also suitable for detailed studies of the t -quark mass. A comparison of event rates in the single and di-lepton channels provides a way of measuring the t -decay branching ratios. Finally we consider the effect of b -tagging with additional muons, and the improvement in the S/B ratio it brings, particularly important in the "single lepton" mode.

The main features of the $t\bar{t}$ production kinematics at $\sqrt{s} = 16\text{TeV}$ are summarized in fig.2.5. It shows the m_t dependence of the average transverse momentum (or energy) of the t -parton and of its decay products, the W , the b -jet, the ν_l and l from W decay. The average p_T of the three leading jets from $t\bar{t} \rightarrow WWb\bar{b} \rightarrow l\nu + \text{jets}$ is also plotted. In the same plot, fig.2.5, the average p_T levels of the lepton and of the jets from the $W + 3\text{jets}$ background (where all jets are constrained to $E_T^{jet} \geq 20\text{GeV}$) are also shown, as well as the $\langle p_T^l \rangle$ for the $b\bar{b}$ background.

§. 3 - Isolated single-lepton top decay mode

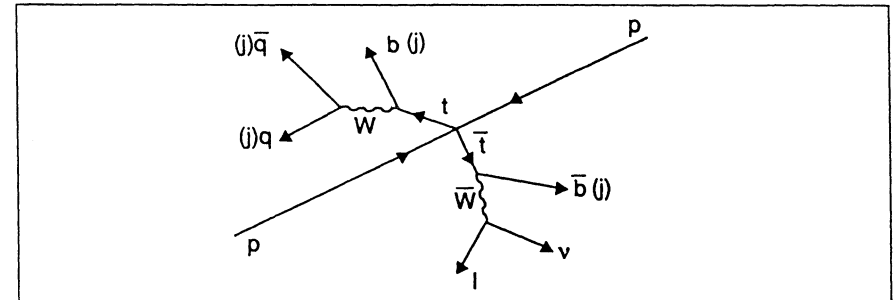


Fig.3.1 : Sketch of a $pp \rightarrow t\bar{t} \rightarrow W^+W^-b\bar{b} \rightarrow l\nu_l + \text{jets}$ final state in the pp center of mass

A schematic view of a pp interaction giving $t\bar{t}$ with an isolated single lepton is shown in fig.3.1. The final state signature is $t\bar{t} \rightarrow W^+W^-b\bar{b} \rightarrow l\nu_l + \text{jets}$. For $m_t = 150\text{GeV}/c^2$ the $t\bar{t}$ cross section is $\approx 0.5\text{nb}$, and the branching ratio in this channel BR_{sl} is:

$$BR_{sl} = 2 \times BR(W_1 \rightarrow l\nu) \times BR(W_2 \rightarrow q\bar{q}) \approx 2 \times 1/9 \times 2/3 = 0.148$$

where the factor 2 comes from the two W 's in the final state and we consider here electron or muon final states.

The main backgrounds in this t -quark search channel are:

- $b\bar{b}$ ($c\bar{c}$) $\rightarrow l\nu + \text{jets}$
- $W + \text{jets} \rightarrow l\nu + \text{jets}$
- $W^+W^- \rightarrow l\nu + \text{jets}$

In fig.3.2 we show the \sqrt{s} dependance of the signal and background cross sections over the Tevatron-UNK-LHC energy range. The $b\bar{b}$ background has a very large production cross section ($\sigma_{b\bar{b}} \approx 200\mu\text{b}$ for $\sqrt{s} = 16\text{TeV}$), with an uncertainty of almost an order of magnitude. The $t\bar{t}$ signal to $b\bar{b}$ background ratio (S/B) at production level

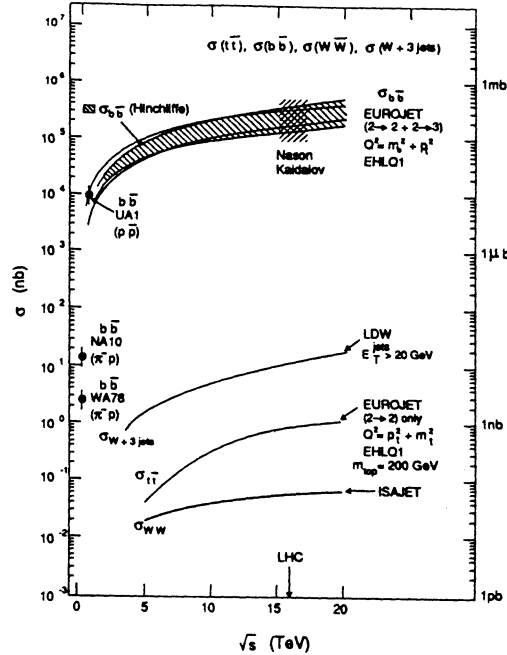


Fig.3.2 : $t\bar{t}$ cross section ($m_t=200\text{GeV}/c^2$) and the major background cross sections as a function of c.m. energy

is very unfavorable, $S/B \approx 10^{-6}$. Fig.3.2 also shows that the $W + \text{jets}$ background is much smaller, but still exceeds the signal by more than an order of magnitude, whilst the WW background is small and plays no significant role as long as $m_t \lesssim 250\text{GeV}/c^2$. Let us first explore ways of reducing the $b\bar{b}(g)$ background.

The transverse momentum p_T^Q distribution for both $(b+c)$ and t -quark production at $\sqrt{s} = 16\text{TeV}$ are shown in fig.3.3 [16]. The harder p_T spectrum of the t -quark ($p_T^t \sim m_t$) compared with the one of b -quark ($p_T^b \sim m_b$) suggests how to get rid of most of the background, by imposing a p_T cut on the lepton from the heavy quark decay. The lepton transverse momentum spectra have been carefully studied using both EUROJET and ISAJET. There is a good agreement in both the shape and magnitude of the distributions for the generated leptons from t -quark decay over a wide range of p_T^l , ($5 \leq p_T^l \leq 500\text{GeV}/c$). The differences noticed for the b -quark decay are understood, and we consider the ISAJET predictions (parton shower MC) more reliable in the case of b production.

Fig.3.4.a compares the the shape of the lepton p_T spectrum from b with the one from a t -quark decay, while fig.3.4.b compares the lepton pseudorapidity (η) distributions. From these figures it is obvious that a selection on hard and centrally-produced leptons strongly improves the S/B ratio. Accepting leptons in the central rapidity region ($|\eta| \leq 1.5$) and above a p_T threshold of $p_T^{thr} \geq 30\text{GeV}/c$ we get

$$S/B \sim 10^{-2} \quad (m_t = 150\text{GeV}/c^2)$$

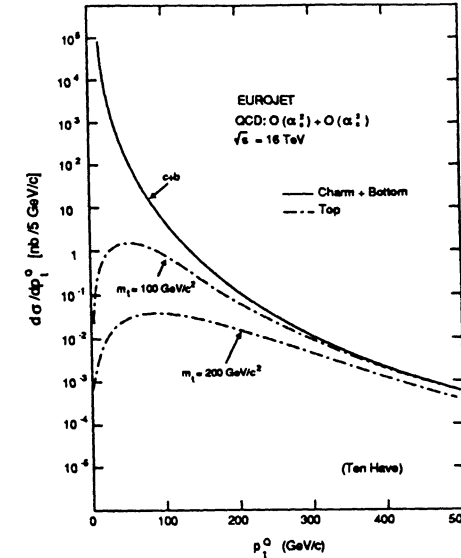


Fig.3.3 : Transverse momentum distributions for t -quark signal and $(b+c)$ -quark background

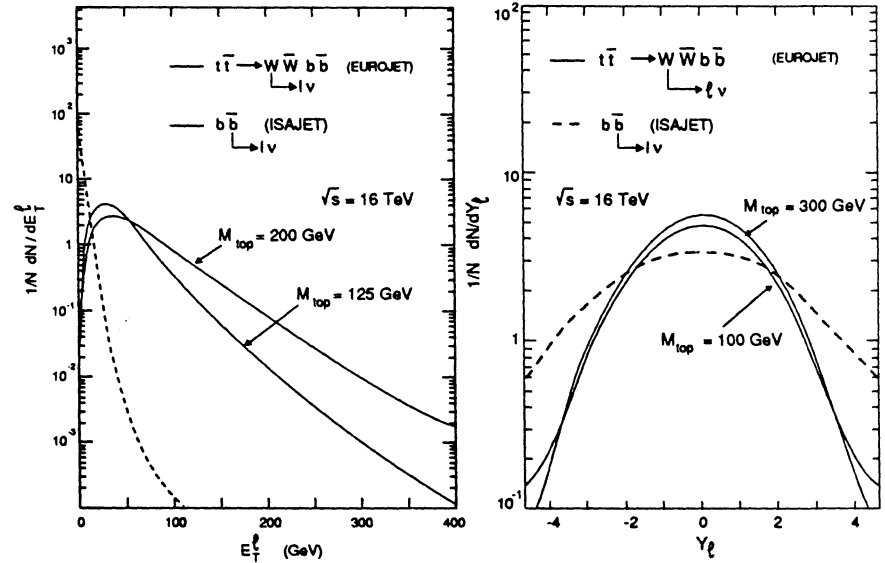


Fig.3.4 : $t\bar{t}$ signal and $b\bar{b}$ background lepton kinematics:
(a) The transverse momentum distribution, (b) the pseudorapidity distribution

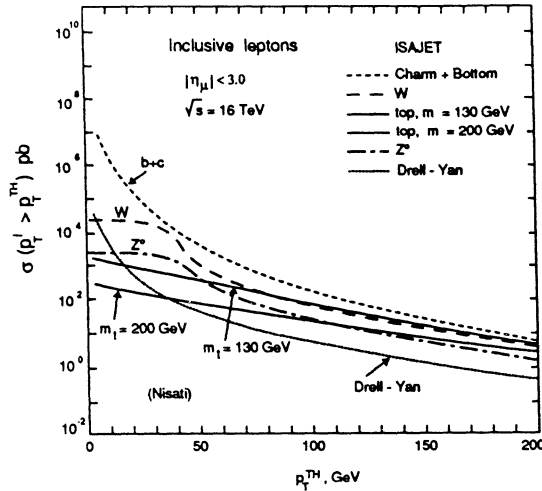


Fig.3.5 : Integrated single-lepton cross sections as a function of lepton transverse momentum threshold

A better background rejection can be obtained by increasing further the p_T^{thr} on the lepton, say up to $50\text{GeV}/c$, when $S/B \sim 10^{-1}$, or even higher, fig.3.5 [17]. Increasing the p_T threshold is, however, not the most economical way to suppress this background, and at low luminosity may be too costly in terms of production rate. A much more efficient way to further suppress the $b\bar{b}$ background is to ask for lepton isolation. As lepton isolation is a very important selection criterion, not only for t -quark physics, but also for the Higgs and for two-gauge boson ($WZ, W\gamma$) searches and studies, we discuss it in more detail.

3.1 - The Isolation Requirement

To define lepton isolation one has to measure the total transverse energy (ΣE_T) deposition in a cone of radius $\Delta R(\eta, \phi)$ around the lepton passing the p_T^{thr} cut. The lepton produced in a b decay, since the decay Q -value is small, cannot be much separated from the recoiling c -jet, thus the energy flow around the lepton is quite large. On the other hand, the large t -quark mass allows to produce a real W which recoils against the b -jet, and the lepton from the W decay is spatially well separated from any jet activity and thus isolated.

We have studied the dependence of the ΣE_T isolation distribution on the parameters ΔR and p_T^{thr} . Considering an ideal case without calorimeter resolution smearing, the cone size has been varied ($\Delta R = 0.7, 0.4, 0.2, 0.1$) for a fixed p_T^{thr} ($30\text{GeV}/c$), and the effect of increasing the p_T threshold with the same ΔR (0.4) has been studied, plotting the ΣE_T distribution for the $t\bar{t}$ sample and for the $b\bar{b}$ sample of MC events. No optimization of the parameters has been performed at this stage, since a detailed apparatus simulation would have been necessary. Rather, we looked for general indications on the necessary cone size (related to the calorimeter granularity) and to the

p_T threshold (related to the trigger threshold) compatible with the present expectations for an LHC detector (i.e. lepton trigger detection threshold at $\sim 30\text{GeV}/c$ and a granularity of the order of $\Delta\eta \times \Delta\Phi \simeq 0.05 \times 0.05$). Since the lepton isolation criterion is partly "apparatus dependent", our final background rejection factor is obtained by normalizing it to the measured and well understood lepton isolation from the UA1 t -quark search [1,18]. To separate efficiently leptons from $t\bar{t}$ and those from $b\bar{b}$ decay, the cone size should be large enough, since with decreasing cone size the lepton from the b decay becomes better and better isolated, as can be seen in fig.3.6. The cone must not be too large either, otherwise energy deposition from the underlying event and event pile-up becomes annoying, decreasing the efficiency on the t -quark signal.

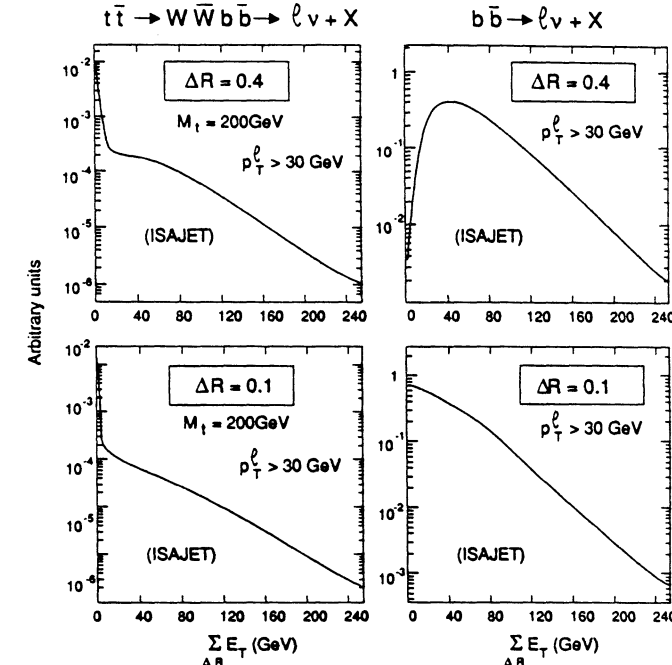


Fig.3.6 : Variation of the transverse energy deposition with the cone size, $t\bar{t}$ signal vs $b\bar{b}$ background - (a) cone size $\Delta R=0.4$, (b) cone size $\Delta R=0.1$

A cone of

$$\Delta R = 0.4$$

is a good compromise and a calorimeter granularity of $\Delta\eta \times \Delta\Phi \simeq 0.05 \times 0.05$ is adequate in this respect. The p_T^l dependance of the lepton isolation distribution shows, fig.3.7, that the higher is the p_T cutoff, the better is the signal to background separation. A threshold of

$$p_T^{thr} = 30 \div 40\text{GeV}/c$$

clearly provides a large isolation-rejection-factor, provided that events with $\Sigma E_T \lesssim 10\text{GeV}$ are selected. The ΣE_T distributions, using a cone size of $\Delta R = 0.4$ and a

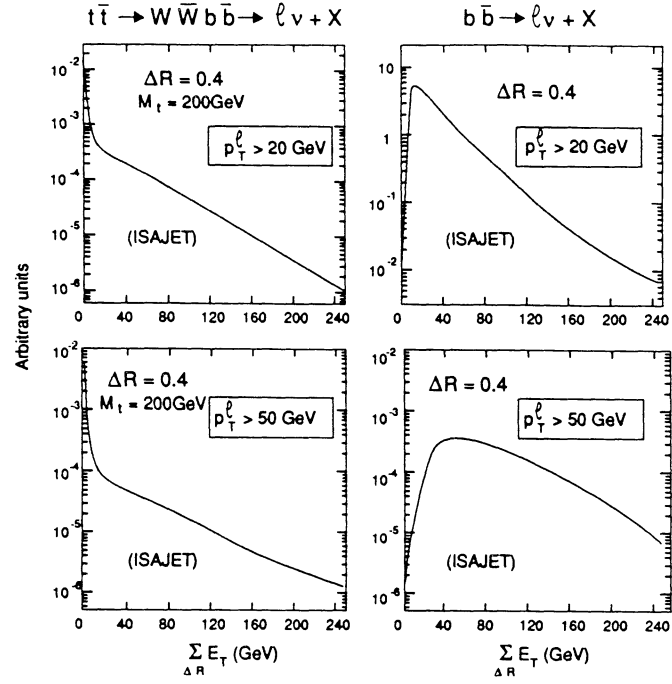


Fig.3.7 : Variation of the transverse energy deposition with the lepton p_T threshold,
 $t\bar{t}$ signal vs $b\bar{b}$ background - (a) $p_T^{lept} \geq 20 \text{ GeV}/c$, (b) $p_T^{lept} \geq 50 \text{ GeV}/c$

$p_T^{thr} = 30 \text{ GeV}/c$, for both the $t\bar{t}$ signal and the $b\bar{b}$ background are shown in fig.3.8. If we chose the isolation cut

$$\Sigma E_T \leq 10 \text{ GeV}$$

about 90% of the t -quark sample is kept, while only $\sim 3\%$ of the b sample survives the cut. This would ideally lead to a S/B rejection factor $RF_{iso} \approx 30$. If the p_T^{thr} cut is increased to $50 \text{ GeV}/c$, the rejection factor is $RF_{iso} \approx 50$.

However, as mentioned above, to be closer to real experimental conditions and more conservative, we rescaled this ideal MC RF_{iso} dependence as a function of p_T^{thr} to the measured UA1 experimental point at $p_T^{thr} \approx 10 \text{ GeV}/c$, fig.3.9. In this case the lepton isolation rejection factor is $RF_{UA1} \approx 10$ [18], while our MC study would give a $RF_{MC} \approx 15$. In the following we use RF_{iso} versus p_T^l from fig.3.9.

3.2 - The $b\bar{b}$ background

We have just seen that the most efficient ways to reject $b\bar{b}$ background is with a p_T^l threshold cut and with lepton isolation. With $p_T^l \geq 30 \text{ GeV}$ and $\Sigma E_T \leq 10 \text{ GeV}$ in a $\Delta R = 0.4$ cone ($RF \simeq 20$) we have:

$$S/B \sim 1/4 \quad \text{for} \quad m_t = 130 \text{ GeV}/c^2$$

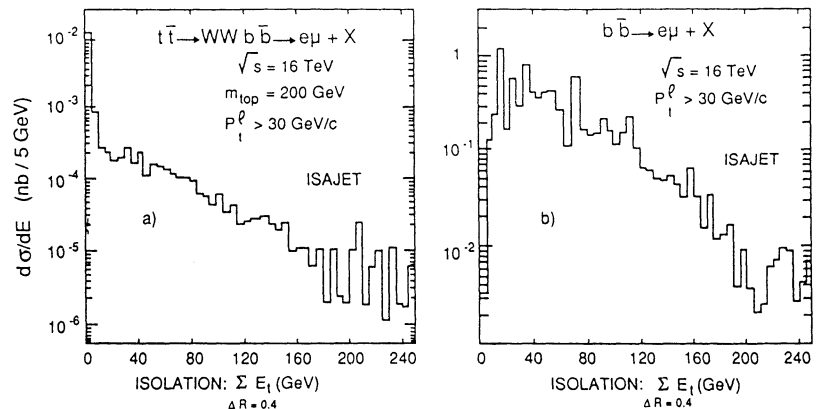


Fig.3.8 : The lepton isolation requirement. ΣE_T distributions for:
(a) $t\bar{t}$ signal, (b) $b\bar{b}$ background

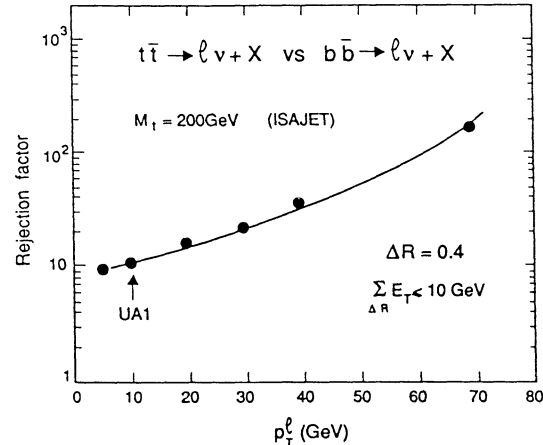


Fig.3.9 : Rejection factor from the isolation requirement
A realistic re-scaled behaviour as function of p_T^l threshold

For a higher lepton p_T cut, $p_T^{thr} = 50 \text{ GeV}/c$, the S/B gets larger than one, $S/B \sim 5$, for $m_t = 130 \text{ GeV}/c^2$ and is close to one for $m_t = 200 \text{ GeV}/c^2$.

In conclusion, the heavy flavour $b\bar{b}$ ($c\bar{c}$) background to the $t\bar{t}$ signal in the "single isolated lepton" channel can be reduced to an acceptable level by *Kinematical* \oplus *Isolation cuts* alone, with a $p_T^{thr} \gtrsim 50 \text{ GeV}/c$. If one employs a softer cut (i.e. $p_T^{thr} \approx 30 \text{ GeV}/c$), other ways may be used to improve the S/B ratio. For example, a jet-jet mass cut $M_{JJ} = m_W \pm \delta m_W$ can be used to enhance the t -quark signal relative to the non-resonant $b\bar{b}(g)$ background. A mass cut around the W mass, with $\delta m_W = \pm 20 \text{ GeV}/c^2$ gives a rejection factor of $RF_{JJ} \approx 3 \div 5$. Another possibility is

the azimuthal (Φ) angular correlation between the lepton and the hardest jet ($J1$) in the event. The large t -quark mass results in rather spherical $t\bar{t}$ final states, i.e. in a flatish $\Delta\Phi(l, J1)$ distribution, while the $b\bar{b}(g)$ events appear preferentially in "back-to-back" configurations, with a $\Delta\Phi(l, J1)$ distribution more strongly peaked around π . A rejection factor of $RF_{\Delta\Phi} \approx 3$ can be obtained by applying this kind of cut.

Combining thus *Kinematical* \oplus *Isolation* $\oplus M_{JJ} \oplus \Delta\Phi$ cuts with a lepton $p_T^{thr} = 30\text{GeV}/c$, the background from heavy flavours is definitely reduced below the signal, with $S/B \sim O(10)$.

We didn't consider up to now the further rejection which might be provided by a missing energy cut, because the E_T^M reconstruction requires a hermetic calorimeter, and at the LHC this might be difficult to achieve, especially at high luminosity. Clearly, if the calorimeter would allow an E_T^M measurement with a resolution $\delta E_T^M \approx 10 \div 20\text{GeV}$, the $b\bar{b}$ background could be suppressed just requiring a *Kinematical cut* $\oplus E_T^M$ cut. This is, however, rather unlikely, and the background rejection will heavily rely on lepton isolation; this requires then an adequate calorimeter granularity.

3.3 - The $W+jets$ background

The most dangerous background to the "single-isolated-lepton" channel is, however, represented by $W(\rightarrow l, \nu)$ production accompanied by jets, since in this case no lepton isolation or E_T^M cut can separate signal from background. A detailed study of this irreducible background has been performed, using a large MC event sample from the LWD generator¹. The present version of this MC program allows to generate W , from pp collision, with up to 3 jets from higher order QCD processes. Very recently a $W+4jets$ MC simulation [19] was made available; the comparison of this background with the t -quark signal in the single lepton mode is still under way.

As a consistency test, the LWD Montecarlo p_T^W distribution was compared with available experimental data at lower c.m. energies (W production at the SpS and TeVatron Colliders [20] and with the complete α_s^2 theoretical computation of Arnold and Reno [21]. The agreement is very good, as it is shown in fig.3.10.

At $\sqrt{s} = 16\text{TeV}$ we obtain a cross section of

$$\sigma(W + 3\text{jets}) \simeq 10\text{nb}$$

with $E_T^{jets} \geq 20\text{GeV}$. This cross section is a factor 5 \div 10 larger than the $t\bar{t}$ production cross section for m_t in the range of $150 \div 200\text{GeV}/c^2$, fig.3.11, and ways must be found to improve the S/B ratio.

The main handle to separate the $t\bar{t}$ signal from the $W+jets$ background, is provided by jets. Fig.3.12.a shows the normalized p_T^{jet} spectrum for signal and background. The t -quark inclusive p_T jet distribution is harder and has a turn-over at lower p_T^{jet} , whilst the bremsstrahlung distribution for the $W+3\text{jets}$ background process diverges as p_T^{jet} decreases. Moreover, the jets from t -quark decay are more central in rapidity, fig.3.12.b.

As far as the final-state lepton is concerned, some background suppression can be still obtained, in particular for a heavy t -quark, using a lepton p_T cut, thanks to the

¹ The LWD (Leiden-Wisconsin-Durham) is a higher order QCD matrix element Montecarlo generator described in [12].

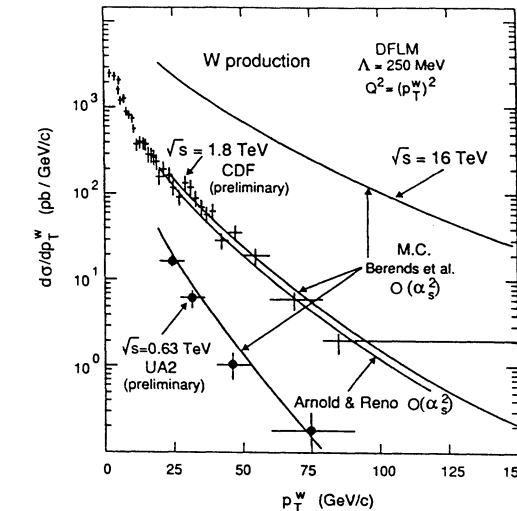


Fig.3.10 : Comparison of p_T^W distributions from the LWD MonteCarlo with experimental data

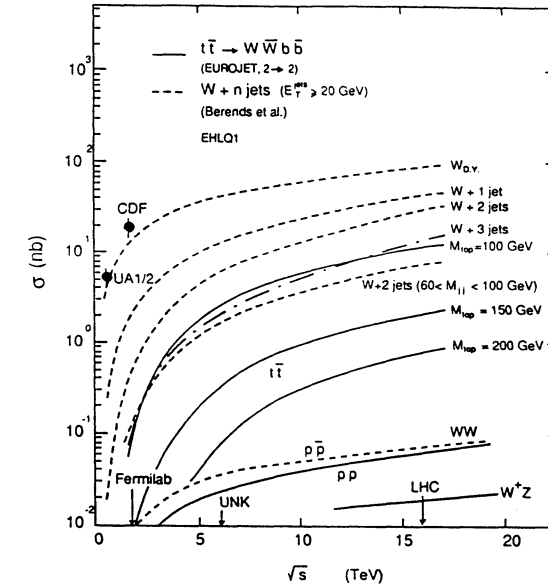


Fig.3.11 : $t\bar{t}$ signal for various m_t values vs $W+n\text{jets}$ and WW, WZ background total cross sections

harder signal W transverse momentum distribution, fig.3.13. For the $t\bar{t}$ production $\langle p_T^W \rangle \sim O(m_t) \sim 100\text{GeV}/c$, whilst $\langle p_T^W \rangle \sim 25\text{GeV}/c$ for the $W+jets$ production at the LHC, fig.2.5.

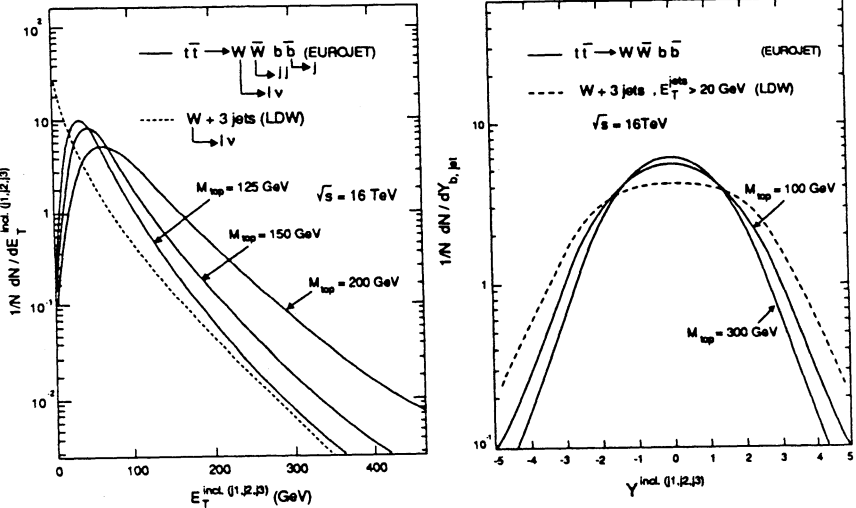


Fig.3.12 : $t\bar{t}$ signal and $W+jets$ background jet kinematics:
(a) the inclusive 3-jets p_T distribution, (b) the pseudorapidity distribution

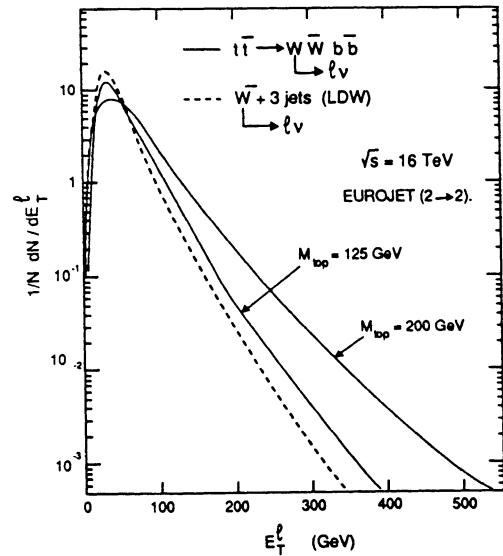


Fig.3.13 : $t\bar{t}$ signal and $W+jets$ background kinematics:
the lepton p_T distributions

An optimization study was carried out to find the most suitable set of kinematical cuts on p_T^{jets} , η^{jets} , p_T^{lept} and η^{lept} . A further cut was introduced to insure lepton

isolation and unambiguous jet counting, namely we asked for a minimal angular separation of $\Delta R = 0.4$ between any two jets, as well as between the lepton and all the jets.

Within the rapidity interval $-1.5 \leq \eta \leq 1.5$ the S/B ratio shows a pronounced maximum corresponding to

$$p_T^{thr}(jets) = 40 \text{ GeV}/c$$

The variation of the the S/B ratio with respect to the p_T^ℓ threshold is smoother and starts droping at:

$$p_T^{thr}(\text{lept}) \gtrsim 35 \text{ GeV}/c$$

Fig.3.14 shows the S/B behaviour as a function of p_T^{thr} for both lepton and inclusive 3-jets cuts.

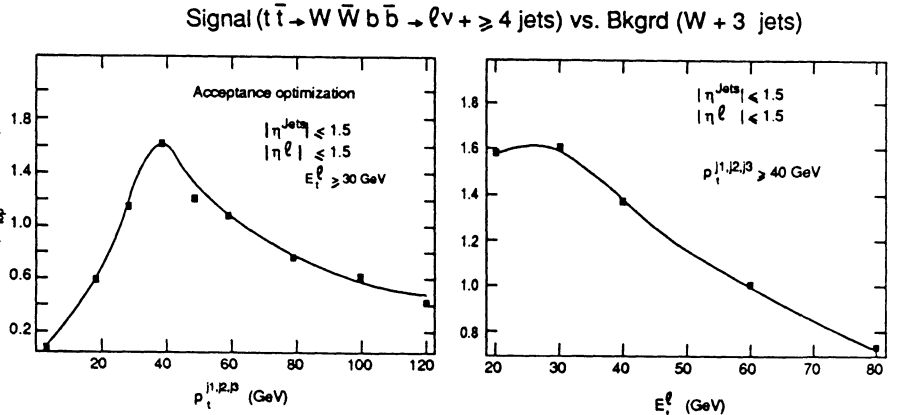


Fig.3.14 : Optimization of the $t\bar{t}$ signal to $W+jets$ background ratio:
(a) variation with the inclusive 3-jets p_T threshold, (b) variation with the lepton p_T threshold

As a result of the S/B optimization we find:

$$S/B \simeq 1.6 \quad (m_t = 150 \text{ GeV}/c^2)$$

with the lowest order ($2 \rightarrow 2$) $t\bar{t}$ signal sample. With the total sample of $(2 \rightarrow 2) \oplus (2 \rightarrow 3)$ MC events the signal to background separation is somewhat better. The best S/B ratio corresponds to $m_t \simeq 150 \text{ GeV}/c^2$ where the optimization study was performed:

$$S/B \simeq 2.$$

In conclusion, fig.3.15 shows the $t\bar{t}$ signal production cross section and the successive effects of the branching ratio (BR_{sl}) and of the lepton and jets acceptance cuts (A^{opt}),

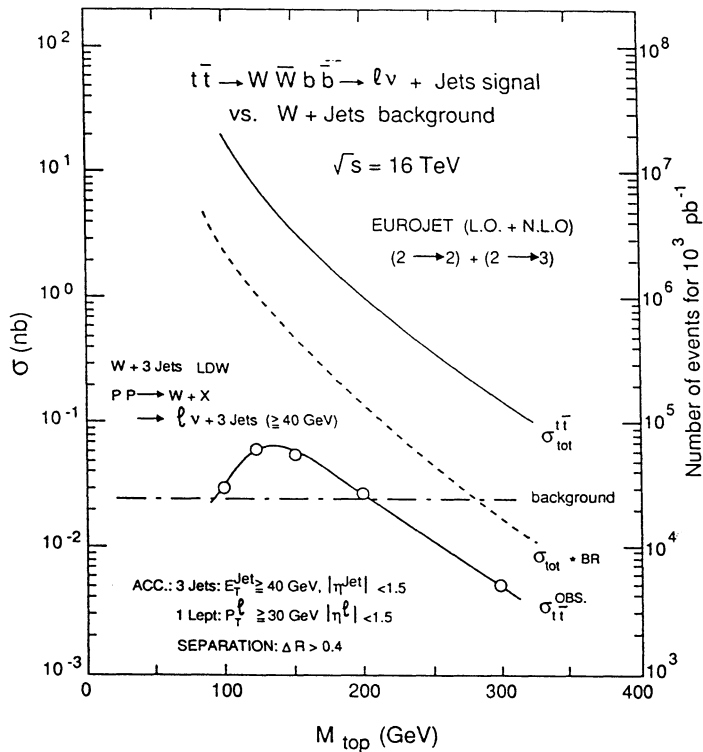


Fig.3.15 : $t\bar{t}$ cross section in the single-lepton channel and expected $W+jets$ background, after branching ratio reduction and acceptance cuts

as a function of the t -quark mass. The expected level of $W+3jets$ background after the same cuts is also shown in fig.3.15.

The annual rate of observable $t\bar{t}$ events corresponding, for example, to the "low" luminosity option, $L_{int} = 10^3 pb^{-1}$ would thus be:

$$N_{tt}^{OBS}(m_t = 150 GeV/c^2) = L_{int} \times \sigma_{tt} \times BR_{sl} \times A^{opt} \times \simeq 5 \times 10^4 \text{ evt}$$

This rate should be further reduced by the lepton and jet detection efficiencies (ϵ) of the apparatus. A conservative efficiency of $\epsilon \simeq 0.8$ can be assumed, and the rate of the observed events is thus reduced to $\sim 4 \times 10^4$ events per year. As just discussed, the $t\bar{t}$ signal is expected to be about twice the irreducible ($W+jets$) background, even without asking for other constraints, as the M_{JJ} correlation or the azimuthal $\Delta\Phi(l, J1)$ correlation, each of these having additional rejection factors of 2 to 3. In fig.3.16 the jet-jet from $W+jets$ invariant mass distribution is shown, for jets with $E_T^{jets} \geq 20 GeV/c^2$. A possible mass cut is also indicated in fig.3.16, it would provide a RF of about 3.

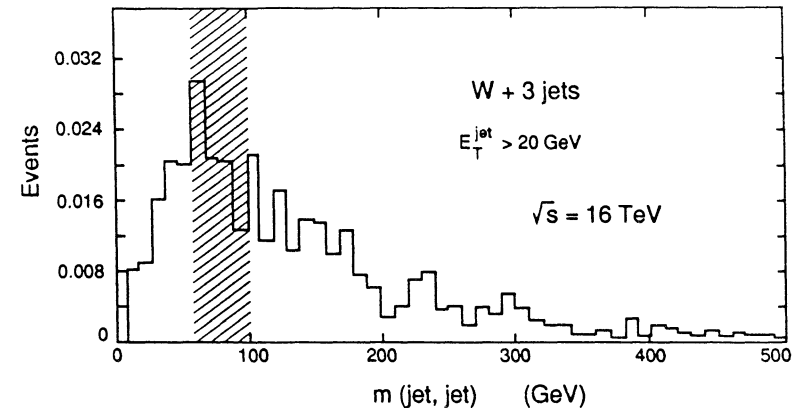


Fig.3.16 : Jet-jet invariant mass distribution for $W+3jets$ background, with $E_T^{jets} \geq 20 GeV$.

The other source of background we studied, from $b\bar{b}$ decay, can also be reduced by raising the p_T^l threshold or hardening the isolation cut.

This type of study would most probably allow the first observation of the t -quark at the LHC start-up with low luminosity. At a higher luminosity of $\sim 10^{33} cm^{-2}s^{-1}$, where $\sim 10^6 \text{ evts/year}$ should be produced, if we want to exploit this "single-isolated-lepton" mode for t -quark mass and decay branching ratio determinations, further substantial background suppression can be achieved, at the expense of efficiency, tagging the b -quarks by asking an additional lepton (muon) in the final state. We discuss this in section §.5.

§. 4 - Isolated di-lepton top decay mode

The experimental signature in this channel is the presence of two isolated and high transverse momentum leptons (e , μ) coming from W decays, as sketched in fig.4.1:

$$t\bar{t} \rightarrow W^+W^- b\bar{b} \rightarrow l\nu l'\nu + \geq 2 jets$$

The presence of b -jets in the event final state can also help in the separation of the signal from other sources of di-leptons from SM processes.

The physical backgrounds considered here are:

- $b\bar{b} \rightarrow l\nu l'\nu + jets$
- $W^+W^- \rightarrow l\nu l'\nu$
- $Z^0 + jets \rightarrow l\bar{l} + jets$
- $D.Y. + jets \rightarrow l\bar{l} + jets$

If we consider, for example, a t -quark with $m_t = 200 GeV/c^2$, a cross section of $\approx 4 \times 10^{-2} nb$ is expected in this isolated di-lepton mode, before any acceptance cut; the (e - μ) branching ratio $BR_{di-lept}$ is:

$$BR_{di-lept} = 2 \times BR(W_1 \rightarrow l_1\nu) \times BR(W_2 \rightarrow l_2\nu) = 2 \times 1/9 \times 1/9 = 0.025$$

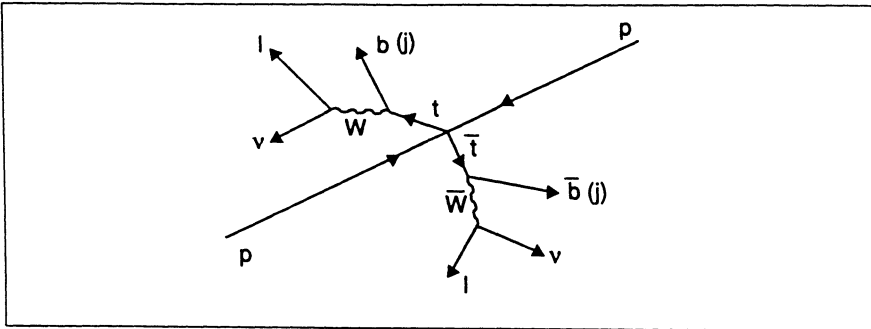


Fig.4.1 : Sketch of a $p\bar{p} \rightarrow t\bar{t} \rightarrow W^+W^- b\bar{b} \rightarrow l\nu l\nu + \geq 2 \text{jets}$ final state in the $p\bar{p}$ center of mass

and a factor 2 larger if we consider also e^-e^- and $\mu^-\mu^-$ pairs.

The t -quark signal and the $b\bar{b}$, WW , Z^0 and DY background processes have been studied using EUROJET and ISAJET generators. The various background cross sections as a function of the c.m. energy are compared with the t -quark signal in fig.3.2, §.3.1. As already mentioned, the $b\bar{b}$ production cross section at $\sqrt{s} = 16 \text{ TeV}$ is larger than the signal by a factor $\sim 10^6$, for $m_t = 200 \text{ GeV}/c^2$. The substantial uncertainty on the total $b\bar{b}$ cross section is, however, considerably reduced when considering high transverse momentum b -quark production. Electroweak WW pair production is lower than the t -quark signal by a factor ≈ 10 (for $m_t = 200 \text{ GeV}/c^2$); therefore it doesn't represent a major problem and is relevant only after the $b\bar{b}$ background has been sufficiently reduced (§.4.2). The last two processes, $Z^0 + \text{jets}$ and $DY + \text{jets}$, have to be considered for e^+e^- or $\mu^+\mu^-$ final states, but can obviously be avoided just asking for a mixed $e^- \mu^+$ lepton pair.

4.1 - The $b\bar{b}$ background in the isolated di-lepton channel

As already discussed in section §.3, the most efficient way to suppress the $b\bar{b}(g)$ background is to exploit the much harder p_T spectrum of the parent t -quark, fig.3.3, and thus of the decay lepton, fig.4.2.a. The suppression factor is much larger now, since the p_T^l threshold cut can be applied to both leptons. Fig.4.3 shows the inclusive di-lepton spectrum, integrated from a p_T^l threshold.

The effect of increasing the lepton p_T^l threshold, on both the signal and background is evident. The t -quark cross section becomes larger than the $b + c$ cross section, for any t -quark mass below $\approx 200 \text{ GeV}/c^2$, if one applies a cut:

$$p_T^{thr}(l_1, l_2) \gtrsim 100 \text{ GeV}/c \quad (|\eta^{l_1, l_2}| \leq 3)$$

(no isolation is required yet).

As already mentioned, the leptons from t -quark decay are more centrally produced. Fig.4.2.b shows the inclusive di-lepton $d\sigma/d\eta$ distribution for t -quark and b decays. A

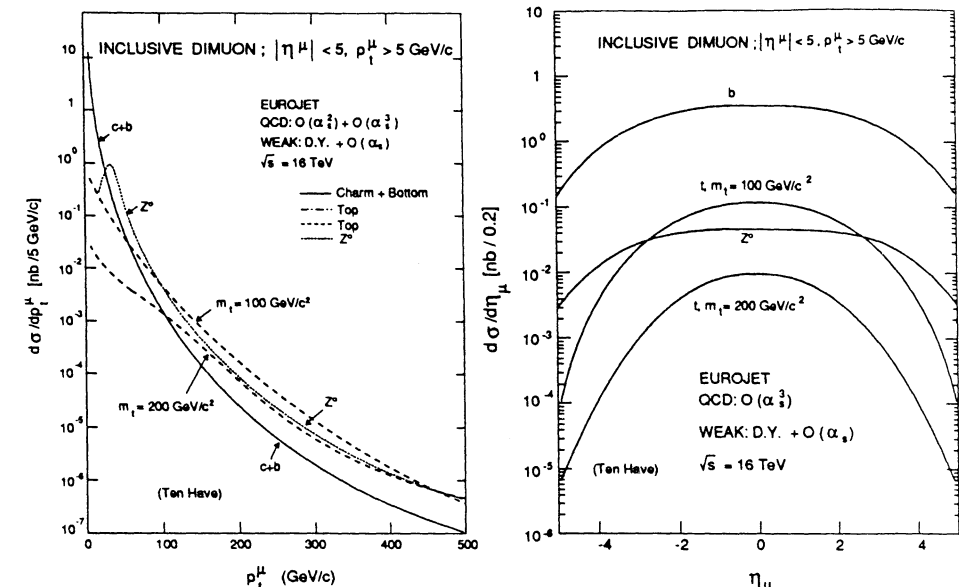


Fig.4.2 : $t\bar{t}$ signal and heavy flavours background differential cross sections as a function of:
(a) inclusive di-lepton, (b) inclusive di-lepton pseudorapidity

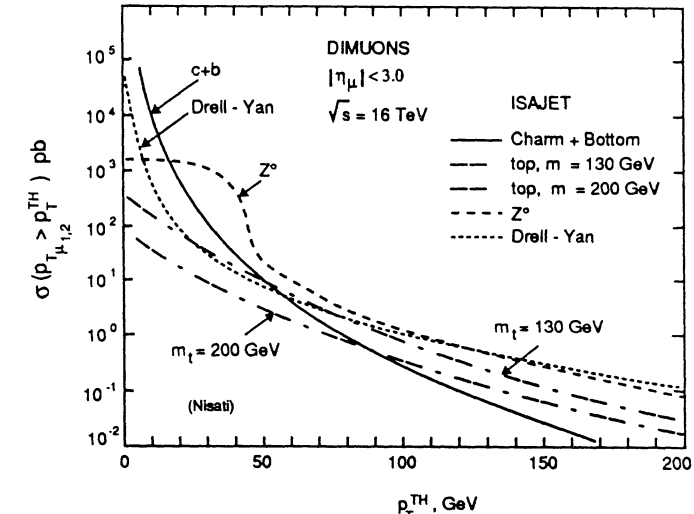


Fig.4.3 : $t\bar{t}$ signal and heavy flavours background integrated cross sections as a function of a lepton transverse momentum threshold

background rejection factor of $RF \approx 2 \div 3$ can be obtained selecting leptons in the central

region, $|\eta^{l_1, l_2}| \leq 1.5$. This rejection factor is obviously reduced if the lepton rapidity selection is applied after the high p_T lepton selection. A good signal to background separation can thus be obtained requiring just *Kinematical cuts* (p_T^l, η^l) on both leptons. The lepton p_T cut ($p_T^{thr} \gtrsim 100\text{GeV}/c$) implies, however, a severe loss of statistics on the signal sample, and may not be the most appropriate way of analysing data. Other ways to suppress backgrounds exist, less costly in terms of statistics. The lepton isolation criterion (already discussed in §.3.1), here applied to both leptons, can be used, as well as an azimuthal $\Delta\Phi$ angular correlation between the two leptons.

Fig.4.4 shows the angular separation, $\Delta\Phi$, of l_1 and l_2 in the transverse plane for the $t\bar{t}$ signal and for the $b\bar{b}$ background, after a $p_T^l \geq 30\text{GeV}/c$ cut.

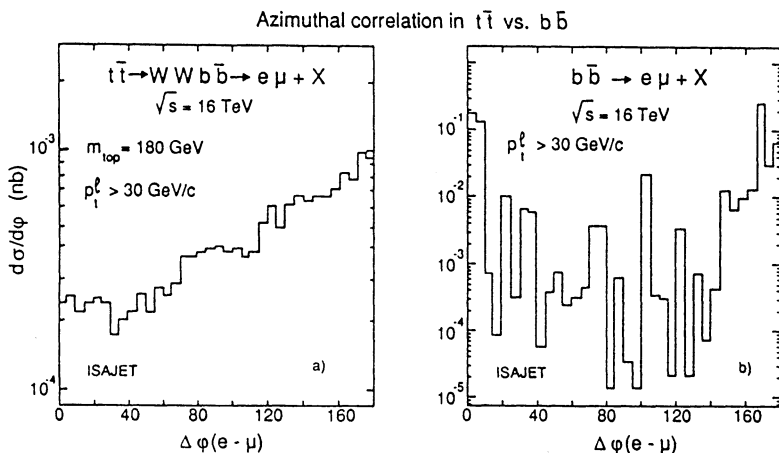


Fig.4.4 : The azimuthal $\Delta\Phi$ correlation between l_1 and l_2 , for the $t\bar{t}$ signal and for the $b\bar{b}$ background

The $\Delta\Phi$ distribution for $t\bar{t}$ production is peaked at $\Delta\phi = \pi$, but the peaking is not very pronounced as a consequence of the rather spherical $t\bar{t}$ final state. On the other hand, the leptons from the $b\bar{b}$ background are strongly correlated in $\Delta\Phi$, showing two very pronounced peaks around $\Delta\Phi = 0$ and π . These two peaks are due to the two main $b\bar{b}$ production mechanisms, namely the direct one from $q\bar{q}$, $(gg) \rightarrow b\bar{b}$ feeding the peak at $\Delta\Phi \simeq \pi$, and the higher order process of gluon splitting ($g \rightarrow b\bar{b}$) contributing mostly at $\Delta\Phi \simeq 0$. Selecting the events in the angular window

$$\pi/6 \leq \Delta\Phi(l_1, l_2) \leq 5/6 \pi$$

we can obtain a signal to background rejection factor of $RF \approx 5$, limiting the loss of t -quark statistics to $\leq 40\%$.

Lepton isolation is, however, the most powerful rejection criterion. Both leptons from $t\bar{t}$ are now isolated, while the leptons from the $b\bar{b}$ background are not. A strong background suppression is thus obtained:

$$RF_{di-lept}^{isol} = (RF_{sl}^{isol})^2 \simeq (10^2 \div 20^2)$$

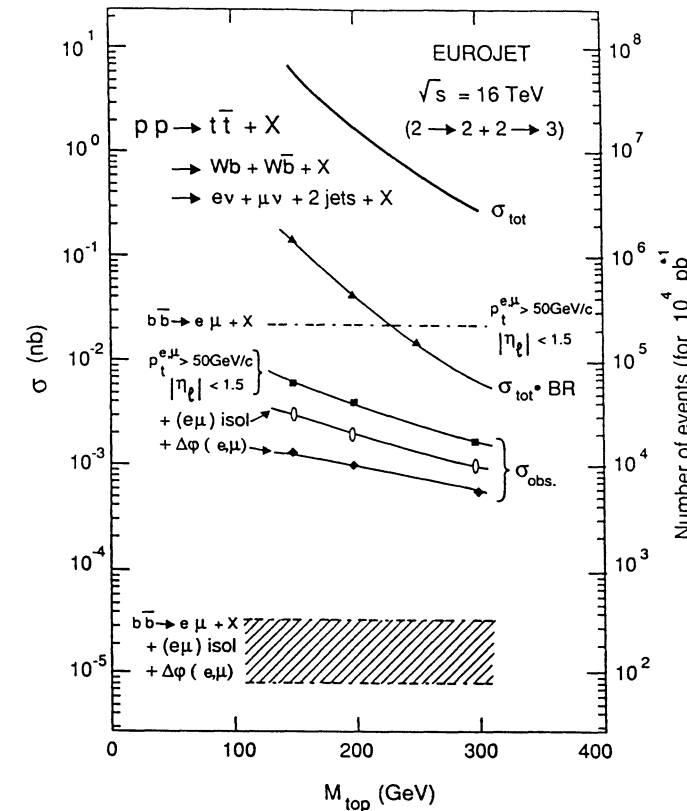


Fig.4.5 : $t\bar{t}$ cross section in the di-lepton channel and the expected $b\bar{b}$ background levels, after branching ratio reduction and acceptance cuts

if a $p_T^{thr} \approx 10 \div 30\text{GeV}/c$ is required on both leptons, fig.3.9,§.3.2. This large background suppression allows to lower p_T^{thr} (depending on m_t), thereby gaining substantially on signal statistics.

Combining thus *Kinematical* \oplus *Isolation* \oplus $\Delta\Phi$ cuts we can obtain a very clean sample of $t\bar{t} \rightarrow e\mu$ events, free of $b\bar{b}$ background. The observable $t\bar{t}$ signal, with two hard (for example $p_T^{l_1, l_2} \geq 50\text{GeV}/c$) and isolated ($\Sigma E_T \leq 10\text{GeV}$) leptons, when compared with the $b\bar{b}$ background, is at the level of

$$S/B \gtrsim 100 \quad \text{for} \quad 100 \lesssim m_t \lesssim 250\text{ GeV}/c^2$$

The reduction of the signal, due to the di-lepton branching ratio ($BR_{di-lept}$), to the kinematical acceptance (A^{kin}), to the isolation (A^{isol}) and angular ($A^{\Delta\Phi}$) acceptances, is shown in fig.4.5 as a function of t -quark mass. The $b\bar{b}$ background level, after the same set of cuts is also shown in fig.4.5. The band reflects the uncertainties on the $b\bar{b}$ cross section and on the effects of the cuts, as obtained comparing EUROJET and ISAJET.

The annual rate of observable isolated di-lepton $t\bar{t}$ events (with $p_T^l > 50\text{GeV}/c$), for an intermediate luminosity of $L_{int} = 10^4 \text{pb}^{-1}$, is:

$$N_{t\bar{t}}^{OBS} = L_{int} \times \sigma_{t\bar{t}} \times BR_{di-lept} \times A^{kin} \times A^{\Delta\Phi} \times A^{isol} = \\ \simeq 10^4 \text{ evts}$$

(We can assume a large lepton recognition efficiency, $\epsilon_l \simeq 0.9$ for each lepton, for $p_T^l \geq 50\text{GeV}/c$).

At the highest luminosity, $L \simeq 10^{34} \text{cm}^{-2}\text{s}^{-1}$, to compensate the loss of rejection power of the lepton isolation due to the pile-up, harder cuts on the p_T of the leptons can be used. With $p_T^{l_1, l_2} \simeq 100\text{GeV}/c$ in $|\eta^{l_1, l_2}| \leq 1.5$, combined with the azimuthal requirement on $\Delta\Phi(l_1, l_2)$ and no isolation cut, we still expect a signal to $b\bar{b}$ background ratio $S/B \sim 5$ and an annual rate again close to 10^4 evts. Requiring a third lepton tagging the b 's (section §.5), a further large rejection factor can be obtained. In any case this "two-(or three)-lepton" channel can be exploited for t -quark physics up to the highest luminosity envisaged. It provides good methods to determine m_t and is needed to measure the t -quark branching ratios.

4.2 - Jet multiplicity

A $t\bar{t}$ event property which can also be exploited, is the presence of b -jets (without tagging) in the final state. Jet activity in the $t\bar{t} \rightarrow WWb\bar{b} \rightarrow l\nu l\nu + \geq 2$ jets signal and $b\bar{b}(g)$ background events has been studied using ISAJET, which includes initial and final state gluon radiation. Jet reconstruction has been done using a standard jet algorithm and varying the cone in the jet definition. Cone sizes of $\Delta R = 0.7$ and $\Delta R = 0.4$ have been used, however, in what follows, for jet counting with $E_T^{jets} \geq 50\text{GeV}$, our jet definition includes $\Delta R = 0.7$ and an initiator above a $p_T \geq 10\text{GeV}/c$ threshold. An angular separation of $\Delta R = 1.0$ between leptons and jets is also demanded and the rapidity region is limited to $|\eta^{jets}| \leq 1.5$.

As the transverse energy of the reconstructed jet is correlated with the lepton transverse momentum through the p_T of the parton initially produced (t or b), the expected differences in terms of jet activity between $t\bar{t}$ and $b\bar{b}$ events become less important once hard p_T leptons are required, fig.4.6. Jet counting thus turns out not to represent a particularly efficient way of rejecting the background.

For large m_t ($\gtrsim 200\text{GeV}/c^2$), a satisfactory separation nevertheless can be obtained using kinematical cuts on the two hardest jets ($J1, J2$) in the event, if combined with kinematical cuts on the leptons, namely

$$p_T^{J1} \geq 75\text{GeV}/c \quad ; \quad p_T^{J2} \geq 50\text{GeV}/c$$

and a $p_T^l \geq 50\text{GeV}/c$ cut on both leptons, all in the central rapidity region. In these conditions the signal to background ratio is $S/B \gtrsim 1$ for a t -quark mass of $200\text{GeV}/c^2$, fig.4.3, without any isolation requirement or $\Delta\Phi$ azimuthal lepton correlation cut. Notice, however, that this background rejection procedure is not appropriate at $m_t \lesssim 150\text{GeV}/c^2$, since the b -jets from $t \rightarrow W b$ become soft, fig.2.5.

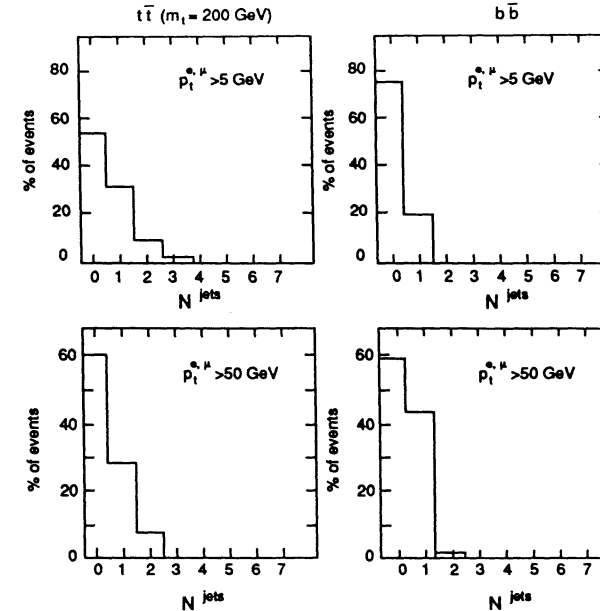


Fig.4.6 : Jet multiplicity in $t\bar{t}$ and $b\bar{b}$ events:
(a) low di-lepton p_T threshold, (b) higher di-lepton p_T threshold

4.3 - The electroweak W^+W^- background

Once the $b\bar{b}$ background has been reduced to a negligible level, the residual background comes from the electroweak W^+W^- pair production. As visible from fig.3.2 this background is not dangerous, since the $t\bar{t}$ production cross section is larger by a factor $\gtrsim 10$ for $m_t \lesssim 200\text{GeV}/c^2$. Applying the same Kinematical cuts as for the $b\bar{b}$ reduction, i.e. a $p_T^l \geq 50\text{GeV}/c$ on both leptons in the central rapidity region $|\eta| \leq 1.5$, an additional rejection factor of $RF \sim 2$ is obtained. The signal to background ratio is

$$S/B \gtrsim 20$$

for $m_t = 200\text{GeV}/c^2$. This background could presumably be further reduced requiring a minimal (hard and central) jet multiplicity.

4.4 - The Z^0 and Drell-Yan background

Up to now we considered the $e - \mu$ isolated-di-lepton channel. For isolated e^+e^- and $\mu^+\mu^-$ pairs from $t\bar{t}$, the $Z^0 + jets$ and Drell-Yan ($DY + jets$) production are possible backgrounds. A cut on the lepton-pair effective mass is now the best background rejection criterion; lepton isolation obviously cannot help. The background from $Z^0 + jets$ can be eliminated by an explicit l_1, l_2 mass cut around the Z^0 resonance. Assuming a moderate lepton momentum resolution, $\Delta p/p = 10\%$, only $\approx 21\%$ of the $t\bar{t}$ events ($m_t = 200\text{GeV}/c^2$) will satisfy a requirement of

$$m_{Z^0} - 3\sigma \leq M(l_1, l_2) \leq m_{Z^0} + 3\sigma$$

whilst the Z^0 reconstruction efficiency is $\approx 96\%$. Thus a rejection factor of the order of $RF = 10 \div 20$ can be obtained by the $m_Z \pm \delta m_Z$ cut, at no excessive expense for the signal. With $p_T^l \geq 50\text{GeV}/c$ the signal to the Z^0 background ratio is larger than one.

Drell-Yan production (investigated with ISAJET) is concentrated at low (l_1, l_2) invariant masses. A signal to background ratio close to one can be obtained just by requiring a $p_T^l \geq 30\text{GeV}/c$ cut on both leptons, and

$$M(l_1, l_2) > 20\text{GeV}/c^2 \quad (40\text{GeV}/c^2) \quad \text{for} \quad m_t = 130\text{GeV}/c^2 \quad (200\text{GeV}/c^2)$$

Selection cuts on the azimuthal correlations between leptons and jets, as described above, can further improve the S/B ratio for these e^+e^- , $\mu^+\mu^-$ channels, as well as a more stringent M_{l_1, l_2} cut. An efficient way to suppress both the $Z^0 + \text{jets}$ and $DY + \text{jets}$ background would be to apply a missing transverse energy cut, but a more practical way to reduce backgrounds in both the single and di-lepton channels, and in particular for e^+e^- and $\mu^+\mu^-$ final states, is to use b -tagging with muons, which we discuss next.

§. 5 - B-jet tagging with muons

The $t\bar{t}$ event yields in the single- and two-isolated-lepton channels are still large even after the appropriate kinematical and acceptance cuts to reduce the background were applied (10^4 to 10^5 events/year at $10^{33}\text{cm}^{-2}\text{s}^{-1}$). This makes it possible to further improve the signal to background ratio by requiring a (non-isolated), relatively low p_T muon in the final state coming from the b decay. In fact, b -tagging is necessary if we want to improve substantially the signal to background ratio in the "single-isolated-lepton" channel. Requiring an additional lepton is also an efficient way to reduce the background in the "isolated di-lepton" channel, in particular with e^+e^- or $\mu^+\mu^-$ final states; it also allows looser cuts on isolation and the azimuthal correlation. Asking for an additional muon in the event is also an efficient way to reduce the trigger rate one would have at high luminosity, especially in the single lepton mode.

Requiring a further lepton (muon) the statistics are rescaled firstly by a leptonic branching ratio ($BR \approx 1/9$), for both the t -quark signal and the $b\bar{b}$ background; a further reduction comes from the muon p_T detection threshold and from the geometrical acceptance (η^μ), both depending on m_t .

The inclusive p_T distribution for any muon (either from W or b decay) in a $t\bar{t}$ event is shown in fig.5.1. This spectrum has two contributions, the hard one from W decay and the soft one, strongly depending on m_t , from the b decay. In the isolated-single-lepton t -quark detection channel, the second lepton, selected without any isolation constraint, is then a mixture of hard p_T muons from the second W decay (this is the "isolated di-lepton" mode, discussed in section 4), and rather softer p_T muons from a b (or \bar{b}) decay.

The signal to $b\bar{b}$ background ratio, in the single isolated lepton channel, was $S/B_{b\bar{b}} \approx 1/4$ if one requires only Kinematical (l_1) \oplus Isolation (l_1) cuts, (for a $m_t = 150\text{GeV}/c^2$ and a $p_T^l \geq 30\text{GeV}/c$, §3). Requiring kinematical cuts on the second (non-isolated) lepton, $p_T^2 \geq 20\text{GeV}/c$, $|\eta^{l_2}| \leq 2.5$, this background can be further reduced and we have a $S/B \approx 5$ (see fig.4.3 and fig.3.9), whilst the event statistics is reduced by a factor ~ 30 (depends on m_t). A further improvements in the S/B ratio can always be obtained using a harder p_T^l cut on the isolated lepton, or the M_{JJ} cut and the $\Delta\Phi(l_1, J1)$ correlation, as discussed in §3.2. After these cuts the $b\bar{b}$ background is reduced to a negligible level ($S/B_{b\bar{b}} > 10$).

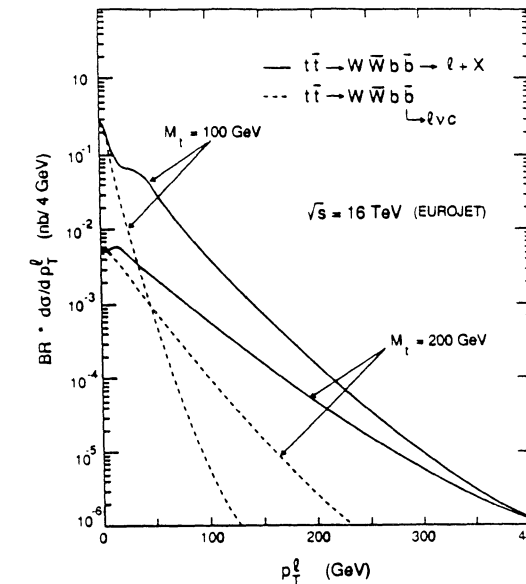


Fig.5.1 : Inclusive p_T spectrum for any lepton (muon) from $t\bar{t}$ prouction and decay
the muon p_T spectrum from b decay ($t \rightarrow Wb$) is shown explicitly

The main reason to ask for the presence of a second softer and non-isolated lepton in this final state is to reduce the more dangerous background from $W + \text{jets}$ to a more suitable level ($S/B_{W+jets} \approx 2$ in §3.3). Only processes like $q\bar{q} \rightarrow gW \rightarrow b\bar{b}W$ can generate a prompt second lepton in the $W + \text{jets}$ final state. However, the fraction of $Wb\bar{b}$ events in the $W + \geq 3\text{jets}$ is expected to be small, less than 5% [22]. Thus the $W + \text{jets}$ background to the " $t\bar{t} \rightarrow \text{single-isolated-lepton} + \text{non-isolated-muon}$ " signal should be at a $S/B > 20$ level, i.e. reduced below the $b\bar{b}(g)$ background. Note that when the tagged b comes from the same parent t -quark as the isolated lepton, the recoiling t -quark, fig.3.1, decaying to $Wb \rightarrow 3\text{jets}$ has no missing E_T associated with it. The t -quark mass can thus be directly reconstructed (see [14] in these proceedings).

The $WW \rightarrow l\nu + l\nu + X$ background to this di-lepton channel is not particularly dangerous since, as already mentioned, the WW production cross section is smaller (factor $\gtrsim 10$) than the $t\bar{t}$ cross section in the t -mass range we are considering.

In conclusion, the "single-isolated-lepton + muon" is an important channel. The muon tagging the b -quark is particularly helpful to suppress the $W + \text{jets}$ background. It works better at larger m_t ; for $m_t \lesssim 130\text{GeV}/c^2$ the p_T of the muon from the b -quark becomes rather soft, fig.5.1 and fig.5.2. To mantain good efficiency the tagging p_T^μ detection threshold should be smaller, $p_T^\mu \gtrsim 10\text{GeV}$. At high luminosity the second muon is also needed to reduce the trigger rate.

In the $t\bar{t} \rightarrow WWb\bar{b} \rightarrow ll'\nu\bar{\nu}b\bar{b}$ channel, the signal cross section, with a b -tagging muon is reduced by a $BR = 2/9$ and by a further factor (depending on m_t) corresponding to the third muon detection threshold, fig.5.2. The observable cross section, after

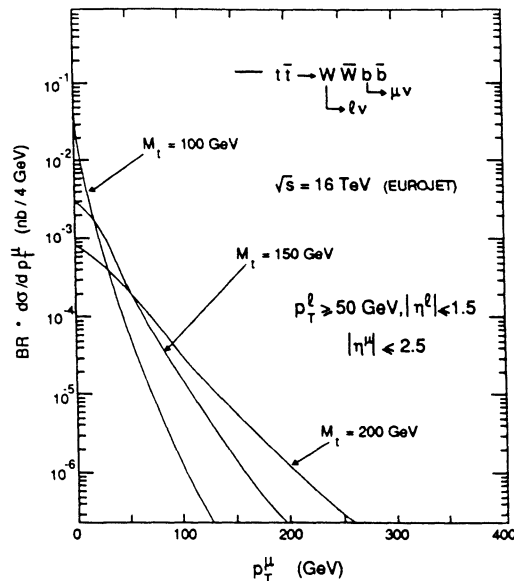


Fig.5.2 : p_T distribution of the (non-isolated) muon from b -quark ($t \rightarrow Wb$),
after cuts on the isolated lepton from W decay

kinematical cuts on the third lepton (like $p_T^\mu \geq 20\text{GeV}/c$, $|\eta^\mu| \leq 2.5$) and the cuts discussed in §.4.1 on the isolated di-leptons, is reduced by a factor ≈ 30 . The event rate, for $m_t = 200\text{GeV}/c^2$, is $\sim 0.5 \times 10^3 \text{evt/year}$ with a luminosity of $10^{33}\text{cm}^{-2}\text{s}^{-1}$. In this "3-lepton" channel there is no significant contamination from the background sources previously considered ($b\bar{b}(g)$, $W + \text{jets}$, $WW, Z + \text{jets}, DY + \text{jets}$). The known mechanisms yielding 3 leptons in final state, like $WZ \rightarrow l\nu ll$, fig.3.11, or $WZ \rightarrow l\nu \tau\tau \rightarrow l\nu ll$ and $WWW \rightarrow l\nu l\nu l\nu$, have very small cross sections ($< 10^{-5}\text{nb}$ after leptonic BR , [22]). Once the acceptance cuts are applied, the observable cross sections for these background becomes totally negligible in comparison with the $t\bar{t}$ signal.

In conclusion, the $t\bar{t}$ signal in the "tri-lepton" channel can be made essentially background-free and the production rates at $10^{34}\text{cm}^{-2}\text{s}^{-1}$ are large enough to afford it. As discussed in [14] this channel also allows one of the most precise determination of m_t . This channel is particularly important at high luminosity, when the isolation criteria become less efficient and reliable.

§. 6 - Conclusion

The search and study of the t -quark is one of the major issue at the LHC. The production cross section for $m_t \sim 150\text{GeV}/c^2$ is a factor of ~ 300 larger than at the Tevatron. At the nominal LHC luminosity the t -quark production rates will be very

large, of the order of 10^6 to 10^7evts/year for m_t in the expected SM mass range, $100 \lesssim m_t \lesssim 200\text{GeV}/c^2$. The basic handle to extract the t -quark signal is the observation of hard and central isolated leptons ($p_T^l \gtrsim 30$ to $50\text{GeV}/c$ in $|\eta^l| \lesssim 1.5$) from the $t \rightarrow Wb \rightarrow l\nu b$ decay.

The production rate is largest in the single-isolated lepton channel, $t\bar{t} \rightarrow l\nu + \text{jets}$. This channel may allow first observations of the t -quark at machine start-up and makes possible a direct determination of the t -quark mass, without missing particles. The $b\bar{b}(g)$ background can be reduced to a $S/B \sim O(10)$ level by a combination of p_T^l ($\gtrsim 30$ to $50\text{GeV}/c$) cuts and isolation cuts. The $W + \text{jets}$ QCD background is however reducible only to a $S/B \sim O(1)$ level by kinematical cuts alone. Tagging the b -quarks with an additional muon (in jet) improves very much this S/B ratio and allows to exploit this channel at high luminosity with an acceptable rate.

The two-isolated-leptons mode, $t\bar{t} \rightarrow WWb\bar{b} \rightarrow l\nu l'\nu b\bar{b}$, is much cleaner. The $b\bar{b}(g)$ background can be reduced to a $S/B \sim O(10 \div 100)$ level by a combination of p_T^l ($\gtrsim 30$ to $50\text{GeV}/c$) and isolation cuts on both the leptons. A $p_T^l \gtrsim 100\text{GeV}/c$ cut alone suffices to have $S/B \gtrsim 1$, thus allowing t -quark physics at the highest LHC luminosity envisaged. Additional (b -tagging) muons would provide very clean samples. Electroweak WW production is smaller than $t\bar{t}$ production, provided $m_t \lesssim 250\text{GeV}/c^2$, and thus should not represent a major difficulty. This isolated di-lepton channel is also important for m_t determination with little background. In conjunction with the "single-lepton" mode, it allows the measurement of the t -decay branching ratios.

Acknowledgements

We would like to acknowledge the important contributions to this work given by G. Sajot, I. TenHave and A. Nisati, and express our thanks for that. We are grateful to all the members of the "Top Working Group", in particular to R. Phillips, E. Reya and P. Zerwas for the helpful discussions and to L. Fayard for his co-operation. Some stimulating discussions with M. Mangano were also greatly appreciated. Special thanks go to the ECFA Workshop organizers for their enthusiasm and encouragement, in particular to G. Altarelli and P. Zerwas. We are grateful to C. Rigoni for her patience and competence in doing the figures of this article.

References

- [1] - C. Albajar *et al.* (UA1 Collaboration), *Z.Phys.* **C48** (1990), p. 1.
T. Akesson *et al.* (UA2 Collaboration), *Z.Phys.* **C46** (1990) p. 179.
- [2] - F. Abe *et al.* (CDF Collaboration), *Phys. Rev. Lett.* **64** (1990) p. 142, p. 147.
- [3] - K. Sliwa (CDF Collaboration), *Proc. 25th Rencontre de Moriond* on Hadronic Interactions, Les Arcs (1990), Editions Frontières, Gif-sur-Yvette.
- [4] - M.Z. Akrawy *et al.* (OPAL Collaboration), *Phys. Lett.* **B236** (1990) p. 364.
D. Decamp *et al.* (ALEPH Collaboration), *Phys. Lett.* **B236** (1990) p. 511.
P. Abreu *et al.* (DELPHI Collaboration), *Phys. Lett.* **B242** (1990) p. 536.
- [5] - C. Albajar *et al.* (UA1 Collaboration), preprint *CERN-PPE/90-141* (1990).
- [6] - P. Langacker, *Phys. Rev. Lett.* **63** (1989) p. 1920.
J. Ellis and G.L. Fogli, *Phys. Lett.* **B232** (1989) p. 139.
J. Ellis and G.L. Fogli, preprint *CERN TH/5862* (1990).
A. Blondel, preprint *CERN-EP/90-10* (1990).
- [7] - H.E. Haber, *SCIPIP 89/38* (Univ. Calif. Santa Cruz report) (1989).
V. Barger and R.J.N. Phillips, *Phys. Rev.* **D41** (1990) p. 301.
- [8] - P. Nason, S. Dawson and K. Ellis, *Nucl. Phys.* **B303** (1988) p. 607.
G. Altarelli *et al.*, *Nucl. Phys.* **B308** (1988) p. 724.
- [9] - E. Reya and P. Zerwas, this volume **ECFA LHC Workshop**, Aachen (1990).
W. Beenakker *et al.*, *DESY 90/064* (1990).
R.J.N. Phillips, this volume **ECFA LHC Workshop**, Aachen (1990).
H. Reithler *et al.*, this volume **ECFA LHC Workshop**, Aachen (1990).
- [10] - B. van Eijk, EUROJET Program, *CERN-EP/85-121* (1985).
A. Ali *et al.*, *Nucl. Phys.* **56** (1984) p. 579.
- [11] - F.E. Paige and S.D. Protopopescu, ISAJET Program, *BNL 38034* (1986).
- [12] - S.D. Ellis, R. Kleiss and W.J Stirling, *Phys. Lett.* **B154** (1985) p. 435.
F.A. Berends *et al.*, *Phys. Lett.* **B224** (1989) p. 237.
- [13] - E. Eichten *et al.*, *Rev. Mod. Phys.* **58** (1986) p. 1065.
- [14] - M. Felcini, this volume **ECFA LHC Workshop**, Aachen (1990);
PhD Thesis, Boston University, in preparation.
- [15] - L. Fayard and G. Unal, this volume **ECFA LHC Workshop**, Aachen (1990).
- [16] - G. Altarelli *et al.*, **ECFA LHC Workshop**, La Thuile (1987), Proc. Vol.1.
D. Froidevaux *et al.*, **ECFA LHC Workshop**, La Thuile (1987), Proc. Vol.1.
- [17] - I. TenHave, *Proc. 9th Eloisatron Workshop* on Perspective for New Detectors in Future Supercolliders, Erice (1989).
- [18] - A. Nisati, **ECFA LHC Workshop**, Aachen (1990), (*ECFA 90-133*) Proc. Vol.3.
- [19] - C. Albajar *et al.* (UA1 Collaboration), *Z. Phys.* **C37** (1988) p. 505.
- [20] - F.A. Berends, W.T. Giele and H. Kuijf, *Nucl. Phys.* **B233** (1990) p. 120.
- [21] - J. Alitti *et al.* (UA2 Collaboration), *Z. Phys.* **C47** (1990) p. 11.
T. Westhusing (CDF Collaboration) *Proc. 25th Rencontre de Moriond* on Z Physics, Les Arcs (1990), Editions Frontières, Gif-sur-Yvette.
- [22] - P.B. Arnold and M.H. Reno, *Nucl. Phys.* **B139** (1989) p. 37.
- [23] - M. Mangano, priv. communication.

PROSPECTS FOR TOP SEARCH AND TOP MASS MEASUREMENTS AT THE LHC

G. UNAL and L. FAYARD

Laboratoire de l'Accélérateur Linéaire, IN2P3-CNRS
et Université de Paris-Sud, F-91405 Orsay Cedex, France

I. INTRODUCTION

Last year gave us more information on the top mass m_{top} . From direct searches CDF^[1], at the Fermilab $\bar{p}p$ collider (Tevatron : $\sqrt{s} = 1.8$ TeV), analysing dilepton events in 4.4 pb^{-1} and assuming the minimal standard model decay $t \rightarrow bW$, set a limit $m_{top} > 89 \text{ GeV}/c^2$ at 95 % C.L. If a decay mode into a charged Higgs $t \rightarrow bH^+$ is also allowed, we know from SLC and LEP that^[2] $m_{top} \geq m_Z/2$. Within the minimal standard model, an analysis of the electroweak data including deep inelastic νN scattering, m_W measurement at $\bar{p}p$ colliders and precise measurements at LEP shows that the "most probable" value of the top mass is around $m_{top} = 130 \text{ GeV}/c^2$ and that it cannot be much larger than $200 \text{ GeV}/c^2$ ^[3]. Since the top cross-section at a 1.8 TeV $\bar{p}p$ collider is 100 times smaller for $m_{top} = 180 \text{ GeV}/c^2$ than for $m_{top} = 80 \text{ GeV}/c^2$, the luminosity required to discover the top at the Tevatron for $m_{top} = 180 \text{ GeV}/c^2$ will be $\sim 0.5 \text{ fb}^{-1}$ and the top can be discovered at the $\sqrt{s} = 16$ TeV proton-proton CERN Large Hadron Collider (LHC)^[4,5] which is expected to work at luminosities \mathcal{L} up to $2 \cdot 10^{34} \text{ cm}^{-2}\text{s}^{-1}$. The top production will be copious at the LHC : for $m_{top} = 130 \text{ GeV}/c^2$, the top cross-section is 200 times larger for a 16 TeV $p\bar{p}$ collider than for a 1.8 TeV $\bar{p}p$ collider. The top will be mainly produced through $t\bar{t}$ pairs.

It is clearly seen in figure 1 where are shown^[6] the different top productions : the strong interaction $t\bar{t}$ production is dominant for masses up to ~ 280 GeV/c² where $Wg \rightarrow t\bar{b}$ starts to be larger.

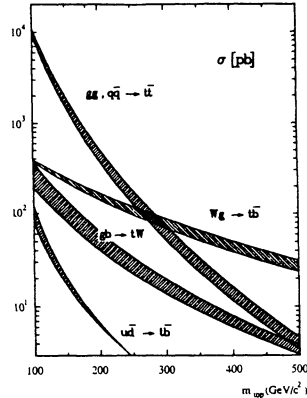


Fig. 1 : Different top cross-sections for pp collisions at $\sqrt{s}=16$ TeV^[6]

For $\mathcal{L} \sim 2 \cdot 10^{34}$ cm⁻² s⁻¹ with the time between crossings equal to 15 ns, the mean number of interactions $\langle n \rangle$ in each crossing of the bunches is ~ 20 . We will see that a large fraction of the top physics can be done at $\mathcal{L} \lesssim 10^{33}$ cm⁻² s⁻¹ where $\langle n \rangle \lesssim 1$: at this level there is no pile-up problem.

Recently, the next to leading QCD corrections to the $t\bar{t}$ cross-section have been computed^[7-9]. The cross-sections at the LHC used here are 4.6 nb for $m_{top} = 130$ GeV/c² and 0.7 nb for $m_{top} = 200$ GeV/c². They have typical uncertainties smaller than $\sim 40\%$ ^[10]. Such uncertainties imply that a precise measurement of the $t\bar{t}$ cross-section gives m_{top} with an error of $\sim \pm 15$ GeV/c² for $m_{top} \sim 200$ GeV/c². The error needed in order to match the precise measurements of LEP^[11-14] is smaller : an error $\Delta m_w \sim \pm 50$ MeV/c² corresponds to $\Delta m_{top} \sim \pm 5$ GeV/c². At this level of precision, the order α_s correction to the m_{top}^2 radiative correction contribution is needed^[15].

Sections II et III describe different searches of $t\bar{t}$ events using events containing one or several leptons and the m_{top} measurements achievable through these channels. In section IV, the $t\bar{b}$ production via the W -gluon fusion process will be studied. We will study two typical top masses $m_{top} = 130$ GeV/c² and $m_{top} = 200$ GeV/c² and in most of the paper we will assume the minimal standard model decay $t \rightarrow bW$ which gives a top width :

$$\Gamma \sim A \left(\frac{m_{top}}{m_W} \right)^3 \left(1 - \frac{m_W^2}{m_{top}^2} \right)^2 \left(1 + 2 \frac{m_W^2}{m_{top}^2} \right)$$

where $A = G_F \frac{m_W^3}{8\pi\sqrt{2}} \sim .17$ GeV/c². This gives a value $\Gamma \sim .5$ GeV/c² (resp $\Gamma \sim 2.5$ GeV/c²) for $m_{top} = 130$ GeV/c² (resp 200 GeV/c²). For top masses $m_{top} \gtrsim 100$ GeV/c², the lifetime is of the same order or smaller than the formation time of a top hadron. The top will then

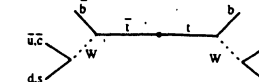
decay before hadronisation, but after gluon bremsstrahlung.

However, in section V, we will look at the effect of the existence of a charged Higgs which could be produced in the top decay.

II. $t\bar{t}$ EVENTS WITH $t \rightarrow b\ell\nu$

1. Signal and $W +$ jet background

In this section, we will study the channel $t\bar{t}$; $t \rightarrow b\ell\nu$, $\bar{t} \rightarrow 3$ jets.



Although the $t\bar{t}$ cross-section is large, the $W +$ jet background is also very important (proportionally more important at LHC than at the Tevatron).

Figure 2 shows the neutrino, charged lepton and b spectrum in the t decay obtained with the EUROJET Monte-Carlo^[16] here used at the lowest order. This Monte-Carlo with $\Lambda_{QCD} = .2$ GeV EHLQ structure functions^[17] will be used during all the paper for the top signal together with the PYTHIA Monte-Carlo^[18,19] used with the same structure functions. The Monte-Carlo cross-sections will be normalised to the next to leading cross-sections (see section I).

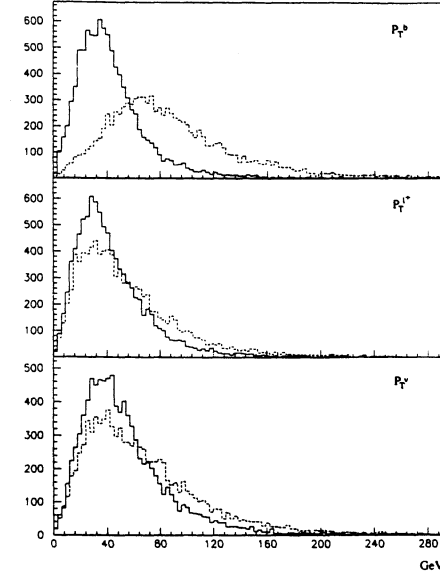


Fig. 2 : Transverse momentum distributions of the b, ℓ^+ and ν . Their average transverse momenta are 43, 44, 54 GeV/c (resp. 87, 56, 67 GeV/c) for $m_{top} = 130$ GeV/c². - Solid line (resp. $m_{top} = 200$ GeV/c² - dashed line).

Figure 3 shows $\frac{d\sigma^{top}}{dp_T^{top}}$ for the different Monte-Carlos. Their values are compared to the leading (dashed curve) and the next to leading (full curves) predictions^[20]. The agreement is good. Since the charged lepton and jets in the top decay are more central than those produced in $W + \text{jets}$ events we will require "central" lepton and jets : $|\eta'| < 1.5$, $|\eta^{\text{jet}}| < 2$. Three jets also are asked in the event in order to decrease the $W + \text{jets}$ background.

The detector simulation performed, which will be used in most of this paper consists in depositing the energy of the particles in small towers (typically $\Delta\varphi \sim \Delta\eta \sim .06$), without any showering with an energy resolution of $15\%/\sqrt{E} \oplus 1\%$ for electromagnetic particles and $50\%/\sqrt{E} \oplus 2\%$ for other hadrons.

The jets are then obtained collecting the energy in $\Delta R = (\Delta\eta^2 + \Delta\varphi^2)^{1/2} < .4$ around a local maximum. We can add some minimum bias pile-up events and then simulate all the possible luminosities. In most of the cases, we will consider that the time response of our "calorimeter" is smaller than 15 ns, the time between 2 LHC bunches^[21].

It has been checked in several cases that using GEANT^[22] with a calorimeter at a radius $R \sim 1$ m gives similar results. In particular, figure 4 shows the energy profile for jets of transverse energy greater than 25 GeV/c coming from top obtained with our crude simulation and with GEANT.

Table 1 shows the detected cross-section for various cuts. The EUROJET value is the $0(\alpha_s^2)$ value (\dagger). On table 1 for each top mass, the column corresponding to the PYTHIA Monte-Carlo gives larger observed cross-sections than the column of EUROJET, the effect being more important for $m_{top} = 130$ GeV/c² than for $m_{top} = 200$ GeV/c².

This is due to the additional jets radiated in PYTHIA, while in EUROJET $0(\alpha_s^2)$ there are only the jets produced in the top decay. We will use preferably PYTHIA, which is supposed to provide a more realistic simulation.

The $W + 3$ jets contributions are also shown on table 1. Two Monte-Carlo have been used : PYTHIA, a parton shower Monte-Carlo and LDW^[23,24], a matrix element Monte-Carlo.

It is clear that one obtains similar rates for $W + \text{jets}$ and top, even for $m_{top} = 200$ GeV/c² where the production cross-section is smaller^[25].

2. Other backgrounds

a) misidentified electrons

When the lepton is an electron, an important background to the electron + 3 jets signal comes from 4 jet events where one jet fakes an electron. The cross-section for having 4 jets of transverse momentum larger than 40 GeV/c with $|\eta| \leq 2$ has been computed to be ~ 200 nb with a QCD multijet matrix element^[26] Monte-Carlo and ~ 500 nb with PYTHIA.

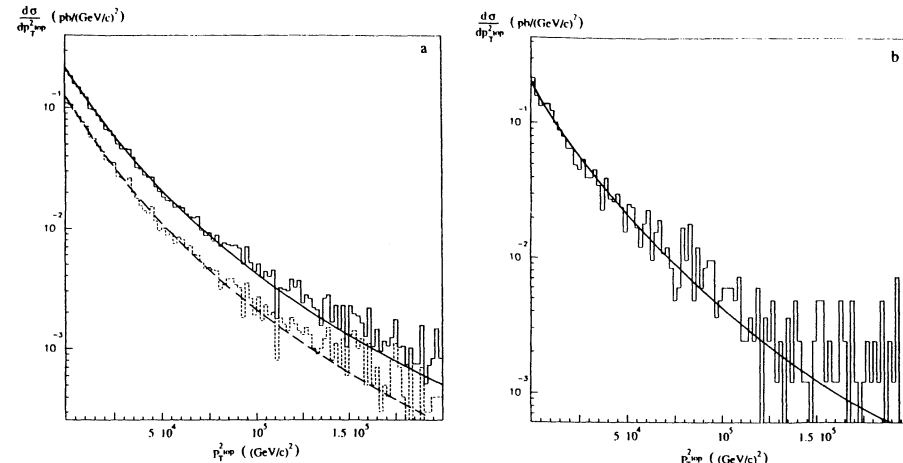


Fig. 3 : Comparison of the distributions of $\frac{d\sigma^{top}}{dp_T^{top}}$ for EUROJET (a) and PYTHIA (b) to the theoretical predictions^[20]. In figure (a) the lower histogram corresponds to $0(\alpha_s^2)$ simulation, the upper one to a mixture of $0(\alpha_s^2)$ and $0(\alpha_s^3)$.

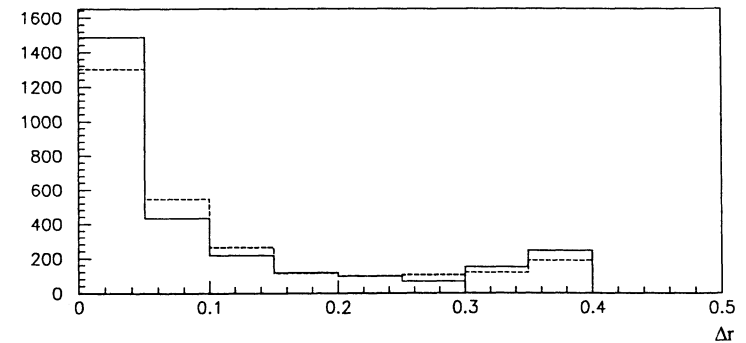


Fig. 4 : Energy profile for our simulation (full line) and for the GEANT simulation (dotted line) as a function of $\Delta r = (\Delta\eta^2 + \Delta\varphi^2)^{1/2}$.

(†) If we consider the $0(\alpha_s^3)$ EUROJET Monte-Carlo generated with a cut on p_T of the jet produced with the $t\bar{t}$ pair, $p_T > 5$ GeV/c, the values quoted in the second and third line of table 1 increase by $\sim 20\%$ for $m_{top} = 200$ GeV/c² and by a factor 2 for $m_{top} = 130$ GeV/c²

One sees that if we want to reach the level of the cross-sections of ~ 25 pb of the second line of table 1 one needs a rejection $R \sim 4(200 \div 500 \text{ nb}) / 25 \text{ pb} \sim (3 \cdot 10^4 \div 10^5)$ at luminosities $\mathcal{L} \leq 10^{33} \text{ cm}^{-2} \text{ s}^{-1}$. The rejection needed is ~ 5 times larger for $\mathcal{L} \sim 1.5 \cdot 10^{34} \text{ cm}^{-2} \text{ s}^{-1}$: this is because there is an additional four-jet cross-section made of two jets from one interaction and two jets from another interaction in the same bunch crossing. This additional cross-section is $\sim 20 \text{ nb}$ at $\mathcal{L} = 10^{33} \text{ cm}^{-2} \text{ s}^{-1}$ and $\sim 3 \mu\text{b}$ at $\mathcal{L} = 1.5 \cdot 10^{34} \text{ cm}^{-2} \text{ s}^{-1}$. If there was no additional pile-up of minimum bias events, this cross-section would be proportional to \mathcal{L} but the additional pile-up of minimum bias events increases the transverse momentum of the jets and this cross-section increases more rapidly than $\mathcal{L}^{[27]}$.

	$m_{top} = 130 \text{ GeV}/c^2$		$m_{top} = 200 \text{ GeV}/c^2$		$W + \text{Jets}$	
	EUROJET	PYTHIA	EUROJET	PYTHIA	LDW	PYTHIA
$p_T^\ell > 25 \text{ GeV}/c$ $p_T^{j1,j2,j3} > 25 \text{ GeV}/c$	150	278	40	62	52	83
$p_T^\ell > 40 \text{ GeV}/c$ $p_T^{j1} > 50 \text{ GeV}/c$ $p_T^{j2,j3} > 40 \text{ GeV}/c$	34	119	21	40	25	22
like above but the 3 jets in the electron opposite hemisphere	5	38	5.6	17	6.3	6.0

Table 1 : Observed cross-section (in pb) of top events and $W + \text{jets}$ events for different cuts. We have always $|\eta^\ell| < 1.5$, $|\eta^{jet}| < 2$. The cross-section corresponds to one type of lepton (e or μ) and an efficiency of 1.

This rejection R is the product of the rejection for jets faking electrons R_e and the rejection $R_{\not{p}_T}$ of a possible missing transverse momentum cut (multijet events have a smaller \not{p}_T than top events where there is one neutrino). We know from past $\bar{p}p$ experience^[28] that an electron rejection of 10^5 is possible.

The additional rejection one may get from a \not{p}_T cut will be smaller at LHC energies than it was at the CERN and Fermilab $\bar{p}p$ colliders because initial state jet bremsstrahlung is much more important at large \sqrt{s} . Figure 5 shows, as a function of the calorimeter coverage η^{max} , the percentage of events above a missing transverse momentum of $50 \text{ GeV}/c$ for PYTHIA two-jet events where two jets are asked to be central and with a transverse momentum larger than $100 \text{ GeV}/c$. The flat plateau at $\eta^{max} \gtrsim 5$ corresponds to the particles not measured by the calorimeter (neutrinos and muons). It is clear from curve b that the \not{p}_T rejection degrades at high luminosity. From curve a, we see that, even at low luminosity the rejection $R_{\not{p}_T}$ (ratio of curve c over curve a) is only a factor 5 for $\eta^{max} = 3$ increasing to ~ 50 for $\eta^{max} = 5$. The

small value of $R_{\not{p}_T}$ at $\eta^{max} \leq 4$ is due to jets escaping the acceptance of the calorimeter. This has been checked using 2-jet and 3-jet events generated with the EUROJET Monte-Carlo at the parton level. Results similar to those obtained with PYTHIA are found.

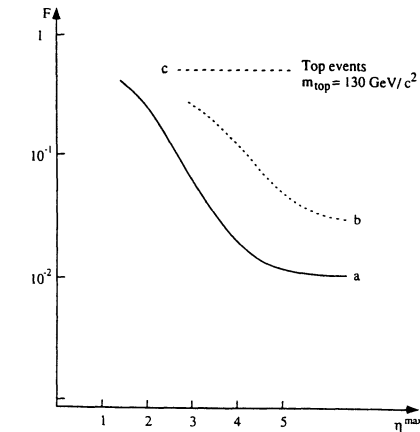


Fig. 5 : Fraction of events with $\not{p}_T > 50 \text{ GeV}/c$ as a function of the calorimeter coverage η^{max} . Curve a) corresponds to PYTHIA two-jet events with both jets central having $p_T > 100 \text{ GeV}/c$ and $|\eta| < .5$. Curve b) corresponds to the same events where 20 minimum bias have been superimposed ($\mathcal{L} \sim 2 \cdot 10^{34} \text{ cm}^{-2} \text{ s}^{-1}$).

b) $b\bar{b}$ events

Although $b\bar{b}$ events will be discussed in more detail in section III, we can note that it is a non negligible background to the single lepton channel. The cross-section of $b\bar{b}$ events with 1 jet and 1 lepton with $|\eta| < 2$ and with $p_T > 40 \text{ GeV}$ is $\sim 7 \text{ nb}$ from EUROJET. If we ask for 2 additional jets, we reduce this cross-section by a factor $\gtrsim 10$ (†) for luminosities smaller than few $10^{33} \text{ cm}^{-2} \text{ s}^{-1}$. An additional rejection of ~ 10 can be obtained with isolation (see section III.1). At this level even a small \not{p}_T rejection is sufficient to reduce the $b\bar{b}$ background below $t\bar{t}$.

3. Trigger

- The rate of inclusive muons with $|\eta^\mu| < 2, p_T^\mu > 40 \text{ GeV}$ is $\sim 10 \text{ Hz}^{[29,30]}$ at $\mathcal{L} \sim 10^{33} \text{ cm}^{-2} \text{ s}^{-1}$. It should then be relatively easy to have a muon + 3 jets trigger at luminosities up to $2 \cdot 10^{34} \text{ cm}^{-2} \text{ s}^{-1}$.
- The electron triggers are expected to be dominated by jets faking electrons. If we take the pessimistic 4 jet cross-section of $\sim 500 \text{ nb}$ quoted in section II. 2 and if we assume a rejection at the trigger of 10^2 including the electron rejection applied on each jet one obtains a trigger rate of $.5 \text{ Hz}$ at $10^{32} \text{ cm}^{-2} \text{ s}^{-1}$ and 5 Hz at $10^{33} \text{ cm}^{-2} \text{ s}^{-1}$.

(†) This value is the one found with PYTHIA. The value found by EUROJET is larger.

The trigger rate goes up to ~ 500 Hz at 10^{34} cm $^{-2}$ s $^{-1}$. It increases more rapidly than \mathcal{L} (see section II. 2)^[31]. In conclusion, electron + 3 jets trigger can be made at luminosities up to few 10^{33} cm $^{-2}$ s $^{-1}$ especially if the rejection at the trigger level is large (10^3 , or more...)

4. Multijet masses

a) Method

It is well known^[32] that one can try to reconstruct the top mass m_{top} in $t\bar{t}$ events, $t \rightarrow b\ell\nu$ doing invariant masses of jets of the associated \bar{t} .

This measurement is difficult because, on top of calorimeter calibration the definition of the jets used in the invariant mass is very important. In order to reduce the systematic uncertainties due to this effect, we need to have a very good understanding of the prescription used in order to include hadrons ("jet algorithm"). This is one of the reasons why in $p\bar{p}$ collisions it has been difficult to observe^[33,34] the intermediate vector bosons through their hadronic decays.

However in the \bar{t} decay, two of the jets are coming from the decay of a W and we may hope to reduce the systematic uncertainties in the measurement of m_{top} with this 3-jet invariant mass method by a renormalisation of the 2-jet invariant mass to m_W . Figures 6-8(a) show the invariant mass of each pair of two jets of $p_T > 40$ GeV/c in the hemisphere opposite to the electron (\dagger), the events being selected according to the third line of table 1 for PYTHIA $t\bar{t}$ and W + jet events (the average number of entries for an event in figures 6-8(a) is ~ 3.5 for W + jets and $t\bar{t}$, $m_{top} = 130$ GeV/c 2 and ~ 4 for $t\bar{t}$, $m_{top} = 200$ GeV/c 2).

In figures 6(a) and 7(a) one observes a clear peak near m_W corresponding to the invariant mass of the two jets from the W decay. Figures 6-8(b) show the invariant mass of 3 jets, two of the three jets selected in figures 6-8(a) by $|m_{jj} - m_W| < 20$ GeV/c 2 , the third one being a jet in the hemisphere opposite to the electron with $p_T > 50$ GeV/c. A clear peak around m_{top} appears in figures 6-7(b).

Special care has to be given to the b fragmentation. PYTHIA does not yet have gluon bremsstrahlung of the b quark in t decay before hadronisation into a B hadron. The standard PYTHIA fragmentation has to be modified^[19,35] into a "Peterson" fragmentation^[36] with an ϵ_b which simulates the b fragmentation observed at LEP^[37] in agreement with theoretical predictions^[38]. At this level we can note that the B's in EUROJET are also too hard.

It is clear from figures 6 and 7 that a signal of ~ 5 standard deviations at m_{top} in the three-jet invariant mass can appear for an integrated luminosity of ~ 30 pb $^{-1}$ even for $m_{top} \sim 200$ GeV/c 2 . At this time, one may note that the statistical errors of figure 6-8 where are shown the number of entries for a bin of 2 GeV an efficiency of 1 and for 10 3 pb $^{-1}$ does not correspond to what would be expected with 10 3 pb $^{-1}$. It corresponds to the statistical error due to the luminosity generated for each of the sets of Monte-Carlo events.

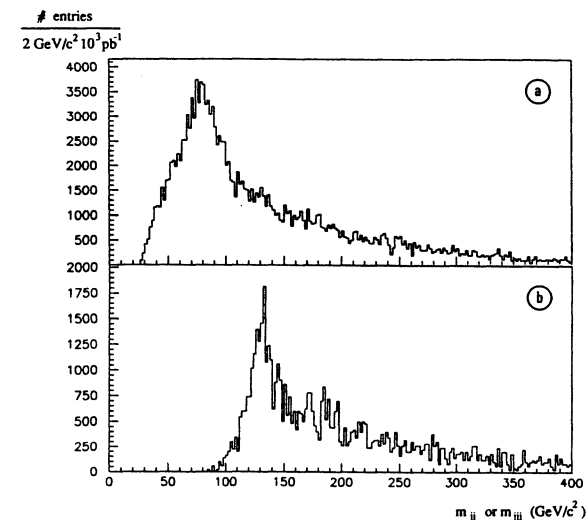


Fig. 6 : Two-jet (a) and three-jet (b) invariant mass distributions (see text) for $t\bar{t}$ events ; $m_{top} = 130$ GeV/c 2 .

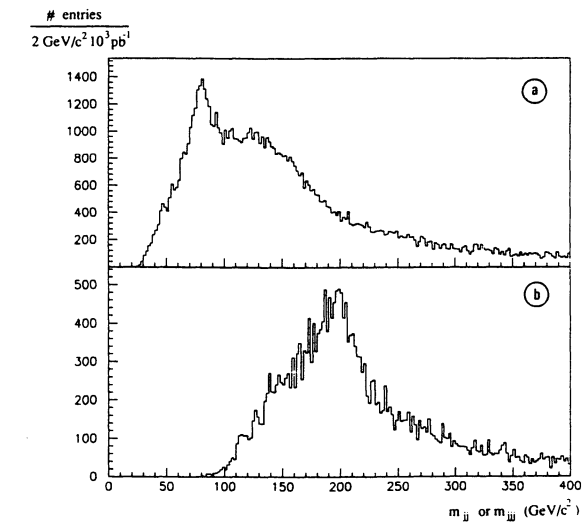


Fig. 7 : Like figure 6 but with $m_{top} = 200$ GeV/c 2 .

(†) We consider here just the case where $W \rightarrow e$; the case where $W \rightarrow \mu$ is identical.

This luminosity, for computer-time reasons is smaller than 10^3 pb^{-1} (this effect will be also present on most of the figures of this paper). For figures 6-8, the luminosity generated is $\sim 600 \text{ pb}^{-1}$ for $t\bar{t}$ events $m_{top} = 200 \text{ GeV}/c^2$, $\sim 30 \text{ pb}^{-1}$ for $m_{top} = 130 \text{ GeV}/c^2$ and $\sim 10 \text{ pb}^{-1}$ for $W + \text{jets}$ events. The luminosity is sufficient, since for $t\bar{t}$ events it is larger than the one required in order to observe the signal.

b) Tagging

The large combinatorial background which appears in the figures 6-7 can be reduced with two b's tagged by a microvertex detector (this tagging cannot be done by leptons because in this case there are neutrinos in final state and mass reconstructions are not possible).

Figure 9, assuming perfect b tagging (100 % efficiency and no misidentification), shows the reduction of this combinatorial background. The events are required to have two tagged b's with p_T above $50 \text{ GeV}/c$.

All other jets with $p_T > 40 \text{ GeV}/c$ in the hemisphere opposite to the electron are used to form the two-jet mass distribution. The top mass is obtained, after $|m_{jj} - m_w| < 20 \text{ GeV}/c^2$, by adding a jet tagged as b in the hemisphere opposite to the electron.

At this level, the background from $W + \text{jets}$ is strongly reduced and is much smaller than the signal.

One sees from figure 9 that :

- the combinatorial background (like the $W + \text{jet}$ or the misidentified electron background) is smaller than without b tagging.
- provided the b tagging can be done with a reasonable efficiency ($\gtrsim .5$) the statistical significance of the top signal is better than in figure 7, without b tagging.

c) W-mass constraint

The constraint of the W mass can be used globally to renormalize the top mass and to reduce the uncertainties in the jet energy scale, but can also be used event by event in order to improve also the resolution on the top mass, as shown in figure 10 compared to figure 7(b) (the events are selected with the same method as in figure 6-8(b), but the jet energies are corrected such that the two jets selected as "from W " give $m_{jj} = m_w$).

d) Systematic uncertainties

As shown before, the number of events in this channel is very large even for integrated luminosities of 10^2 pb^{-1} . Therefore, the error on the top mass measurement in this channel is expected to be limited by systematic uncertainties.

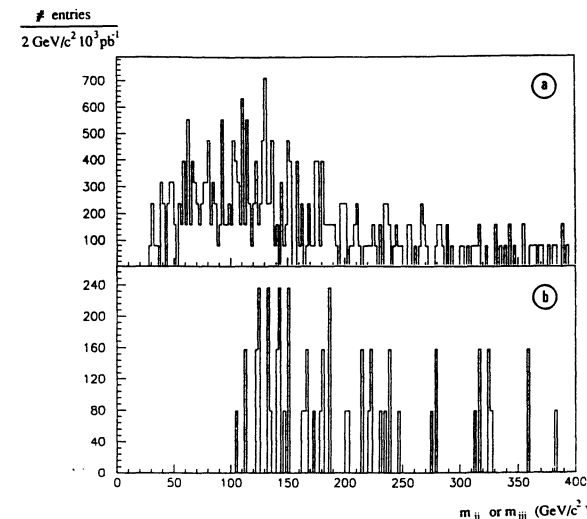


Fig. 8 : Two-jet (a) and three-jet (b) invariant mass distributions for $W + \text{jets}$ events.

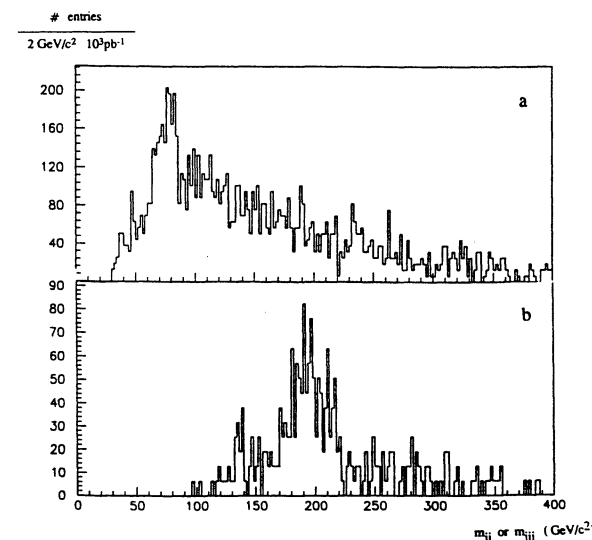


Fig. 9 : Two-jet (a) and three-jet (b) invariant masses assuming perfect b-tagging ($m_{top} = 200 \text{ GeV}/c^2$).

Using figure 7 and figure 10, one finds after the W-mass constraint $m_{top} = 198 \pm 1.5$ GeV/c^2 , the error being the statistical error of the Monte-Carlo generation (for 10^3 pb^{-1} , the statistical error on m_{top} is below $1 \text{ GeV}/c^2$).

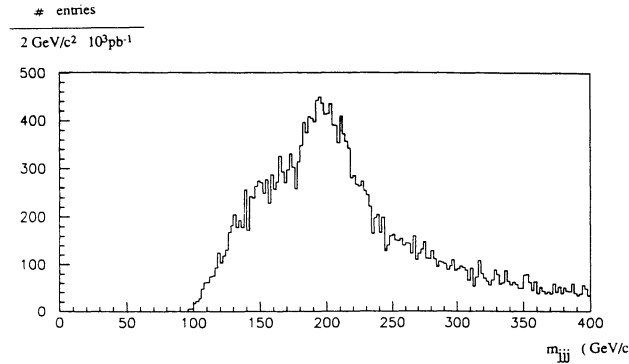


Fig. 10 : Three-jet mass after constraint of the two-jet mass to m_W ($m_{top} = 200 \text{ GeV}/c^2$).

After the constraint of the W-mass, the systematic uncertainties arise mainly from the uncertainties in the measurement of the b jet, which has a different nature and also a different energy compared to the jets from W. Such uncertainties are difficult to compute. In the following, we will investigate the possible uncertainties from b fragmentation, the initial state radiation, the underlying event, the cone algorithm used and from non linearities in the calorimeter response to jets. All these uncertainties are estimated by the PYTHIA Monte-Carlo program for a top mass of $200 \text{ GeV}/c^2$.

Uncertainties in the b fragmentation : the b fragmentation was changed^[39] in PYTHIA within the error band given by LEP^[37] results (see above). The change on the top mass (after constraint of the W-mass) is $\lesssim \pm 3 \text{ GeV}/c^2$.

Uncertainties in the initial state radiation : a change in the initial state radiation changes the shape of the combinatorial background and can also affect the energy flow in the jets from top decay. A modification of the PYTHIA parameters^[40] gives a change in the top mass $\lesssim 3 \text{ GeV}/c^2$.

Uncertainties in the underlying event : the underlying event gives a contribution in the jet energy and therefore an uncertainty in the underlying event will give an uncertainty on the jet mass measurement. This uncertainty was estimated by superimposing at the top event, minimum bias events from PYTHIA. If we change the number of minimum bias events superimposed from 1 to 5, the top mass changes by $\lesssim 3 \text{ GeV}/c^2$.

Cone algorithm : to estimate the effect of the cone algorithm used, we changed the cone size from .4 to .6 radians. This changes the top mass by $\lesssim 3 \text{ GeV}/c^2$.

Uncertainties in the calorimeter response to jets : we changed the e/π ratio of the calorimeter from 1 to 1.1 and we modified the response to low energy hadrons. This changes

the top mass by $\lesssim 4 \text{ GeV}/c^2$.

By adding the previous effects in quadrature, we obtain a total systematic uncertainty on the top mass of $\sim 8 \text{ GeV}/c^2$ (for $m_{top} \approx 200 \text{ GeV}/c^2$). Going to a smaller uncertainty will require a very good understanding of the calorimeter response and of the jet fragmentation : it will be a challenge for experimentalists.

5. Top mass measurement using $t \rightarrow b\ell\nu$

In this channel with only one neutrino, it is also possible to reconstruct the top mass with the electron-neutrino-jet mass $m_{e\nu j}$ where we have to use the jet which is most likely to be the b-jet.

In hadron colliders, the longitudinal component (p_z^ν) of the neutrino momentum cannot be measured while the transverse component can be obtained with the measurement of the missing transverse momentum (\vec{p}_T). However, the neutrino comes from the decay of a real W in electron-neutrino. Therefore p_z^ν can be estimated from \vec{p}_T and from the electron momentum using the constraint of the W mass (and neglecting the W width). There are in general two solutions for p_z^ν . We choose the one which has the smallest absolute value. This allows therefore to compute $m_{e\nu j}$ (†).

We have also to "select" the b-jet. This can be done by using the jet closest to the electron in ΔR to form $m_{e\nu j}$. The efficiency of this method can be increased if the b can be tagged.

In this simulation, \vec{p}_T is computed at the particle level with smearing of all energies, using a given calorimeter coverage in pseudorapidity (η_{max}).

The distributions of $m_{e\nu j}$ for $m_{top} = 130 \text{ GeV}/c^2$ and $200 \text{ GeV}/c^2$ are shown in figures 11 and 12 for $\eta_{max} = 4$ after the cuts $p_T^e > 40 \text{ GeV}/c$, $|\eta_e| < 1.5$, $\vec{p}_T > 40 \text{ GeV}/c$, at least 3 jets within $|\eta| < 2$ with $p_T^{jet} > 40 \text{ GeV}/c$.

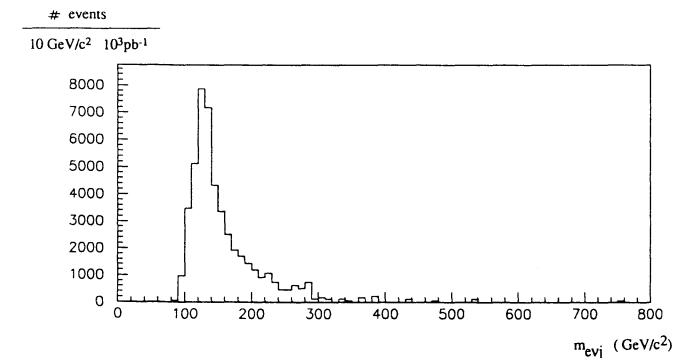


Fig. 11 : $e-\nu$ -jet mass distribution ; $m_{top} = 130 \text{ GeV}/c^2$

(†) The global efficiency of this method is $\sim 50 \%$ for $m_{top} = 200 \text{ GeV}/c^2$.

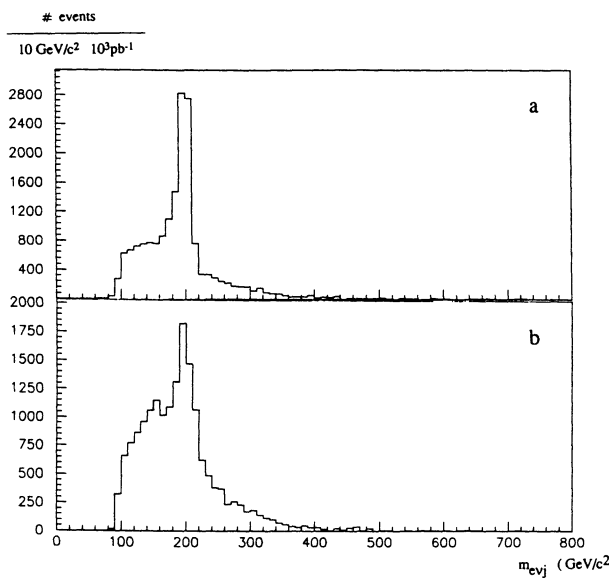


Fig. 12 : $e-\bar{\nu}$ -jet mass distribution (b) ; $m_{top} = 200 \text{ GeV}/c^2$. Figure a) shows the same mass where, instead of the reconstructed neutrino the generated neutrino was used.

The resolution on the top mass is dominated by the \vec{p}_T resolution and therefore, is very sensitive to the calorimetric coverage. If η_{max} goes from 4 to 3, the resolution on the top mass (for $m_{top} = 130 \text{ GeV}/c^2$) goes from 15 to 24 GeV/c^2 .

The systematic uncertainties on the top mass measurement are expected to be larger than with the previous method because this method uses \vec{p}_T measurement for which the uncertainties from the underlying event are larger. This method will also be used for the Wg -fusion process (see section IV) for which it is the only way to reconstruct the top mass.

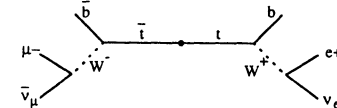
III. STUDY OF MULTI-LEPTON CHANNELS (TWO OR MORE LEPTONS)

In the previous section, we have shown that in the single lepton channel, using jet masses, the top signal can be extracted above the dominant background from $W +$ jet production. However, in this single lepton channel, it is difficult to get a very clean signal and it becomes more and more difficult at high luminosity ($\mathcal{L} \gtrsim 10^{33} \text{ cm}^{-2} \text{ s}^{-1}$). We will show in this section that the multileptons channels can be used to extract a clean signal (especially in the isolated electron and muon channel), even at high luminosity.

These channels can also be used to obtain a precise top mass measurement (the more precise measurement can be done in the 3 charged leptons channel) and we will also show that these multileptons channel can be used up to the maximal LHC luminosity with reasonable trigger rates.

1. Study of signal separation from the physical backgrounds in the isolated electron and muon channel.

In this channel we ask for one isolated electron and one isolated muon, as shown below :



The potential physical backgrounds are the following :

- * WW continuum ; $W \rightarrow e\nu_e$ $W \rightarrow \mu\nu_\mu$
- * $Z \rightarrow \tau\tau$; $\tau \rightarrow e\nu_e\nu_\tau$, $\tau \rightarrow \mu\nu_\mu\nu_\tau$
- * Wbb ; $W \rightarrow e\nu$, $b \rightarrow \mu$ or $\bar{b} \rightarrow \mu$
- * $b\bar{b}$; $b \rightarrow e\nu_e c$ $\bar{b} \rightarrow \mu\nu_\mu c$

To reduce these backgrounds, we can use the following variables :

- * p_T^e and p_T^μ
- * $\Delta\phi(e - \mu)$: angular separation in the transverse plane to take advantage of the top mass.
- * additional jets (we have the 2 jets from b in top events)
- * isolation : to reduce the backgrounds involving b decay(s) to lepton(s).

It is well known^[29] that with very strict cuts on $p_T^{e,\mu}$, the top signal is the dominant source of $e-\mu$ pairs (e.g. for $p_T^{e,\mu} \gtrsim 100 \text{ GeV}/c$ and $m_{top} = 200 \text{ GeV}/c^2$).

We can also combine some cuts on the variables described above in order to obtain very large ratio signal over background with reasonable acceptances for top ($\sim 10 \%$ for $m_{top} = 200 \text{ GeV}/c^2$).

The simulations used here are performed at the particle level, similar to those described in section II.1, with the same resolutions.

First, we apply a cut on $p_T^{e,\mu}$ at 25 or 50 GeV/c (asking also for $|\eta^e|$ and $|\eta^\mu|$ smaller than 1.5).

We obtain the following results for the signal and the backgrounds where the cross-

sections (including the semileptonic branching ratios) are given in pb :

	$t\bar{t}$ $m_{top} = 130$	$t\bar{t}$ $m_{top} = 200$	WW	$Z \rightarrow \tau\tau$	$Wb\bar{b}$	$b\bar{b}$ EUROJET	$b\bar{b}$ PYTHIA
$p_T^e, \mu > 25 \text{ GeV}/c$	30	6	0.25	0.2		340	
$p_T^e, \mu > 50 \text{ GeV}/c$	8	2	0.05	.01	.2	25	10

The Monte-Carlo programs used are :

EUROJET : for $t\bar{t}$ and $b\bar{b}$ (for $b\bar{b}$: $0(\alpha_s^2) + 0(\alpha_s^3)$)

PYTHIA : for $t\bar{t}$, $b\bar{b}$ ^[41], WW and $Wb\bar{b}$ (from $W +$ jets + parton shower)

LDW : for $Z \rightarrow \tau\tau$

For $t\bar{t}$, EUROJET and PYTHIA are in agreement. For $b\bar{b}$, there is a non negligible difference^[42] and both results are indicated.

EUROJET uses tree-level matrix element $0(\alpha_s^2)$ and $0(\alpha_s^3)$ (\dagger), and PYTHIA uses the $0(\alpha_s^2)$ matrix element with parton shower (including $b\bar{b}$ events produced in this parton shower).

From the previous number, we conclude that the dominant background is $b\bar{b}$. Therefore all other backgrounds are neglected in the following (if we use also lepton isolation for $Wb\bar{b}$, they are all below 2 % of the signal). From now on, we will use the cuts $p_T^e, p_T^\mu > 50 \text{ GeV}/c$.

In order to reduce $b\bar{b}$ background only with the leptons, we can use the variables described above :

* $e - \mu$ angular separation

$\Delta\varphi(e - \mu)$ is the separation between e and μ in the transverse plane. The distribution of this variable for the top signal and the $b\bar{b}$ background, simulated with EUROJET, are shown in figure 13.

For $b\bar{b}$, $\Delta\varphi(e - \mu)$ is close to 180° if the b 's are produced back-to-back because the b mass is small compared to their momentum ($\dagger\dagger$). We can have also a contribution at $\Delta\varphi \sim 0^\circ$, which is more important in PYTHIA, from a gluon splitting into $b\bar{b}$ which gives 2 b 's in the same direction.

For $t\bar{t}$, the tops are dominantly produced back to back in the transverse plane, but the top mass is large, and therefore, the leptons are not exactly back to back.

(\dagger) The main contribution comes from the $0(\alpha_s^3)$ part, generated with accompanying jets of $p_T > 5 \text{ GeV}$. The contribution of the $0(\alpha_s^2)$ part is ~ 8 times smaller.

($\dagger\dagger$) The PYTHIA distribution of $\Delta\varphi(e - \mu)$ is less strongly peaked at 180° .

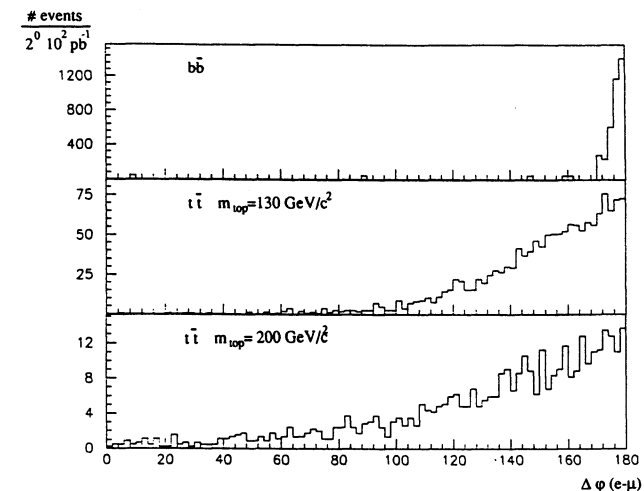


Fig. 13 : $\Delta\varphi(e - \mu)$ after $p_T^e, p_T^\mu > 50 \text{ GeV}/c$; no rapidity cut.

Finally, the following cut is used : $20^\circ < \Delta\varphi(e - \mu) < 160^\circ$. We obtain the following cross-sections :

$t\bar{t}$ $m_{top} = 130$	$t\bar{t}$ $m_{top} = 200$	$b\bar{b}$ EUROJET	$b\bar{b}$ PYTHIA
5 pb	1.5 pb	$.5 \pm .5 \text{ pb}$	$3 \pm .5 \text{ pb}$

At this level, we obtain comparable rates for the signal and the background.

* Energy isolation

We can also use the isolation. Indeed, the leptons from top decays are isolated and not the leptons from $b \rightarrow c\ell\nu$ (because the c jet is close to the lepton).

The effect of this isolation cut depends on the granularity of the calorimeter (related to the cone size which is used in order to compute the energy inside) and also on the pile-up.

The visible transverse energy (except the lepton) in a cone of .1 in ΔR around the lepton direction is shown in figure 14 for leptons from b and top with $p_T^{e,\mu}$ above 50 GeV/c without any pile-up effect.

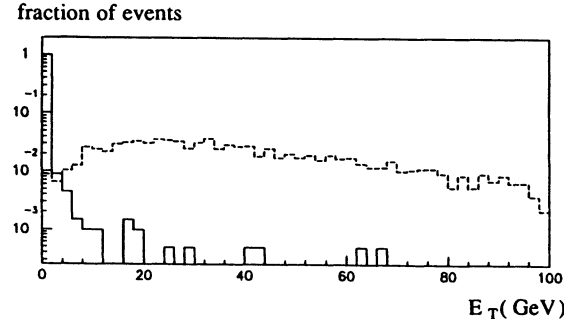


Fig. 14

Several studies have been made at the particle level^[25] and also after GEANT simulation^[43] and it has been shown that a rejection $\gtrsim 10$ per lepton from b with a top efficiency of $\sim 90\%$ is reachable with reasonable granularity of the electromagnetic calorimeter at $\mathcal{L} \simeq 10^{34} \text{ cm}^{-2} \text{ s}^{-1}$. Therefore in the following a factor 10 of rejection per lepton from b is assumed.

* Additional jets

We can also use additional jets in order to reduce the background. The rejection that we obtain for the $b\bar{b}$ background is different for EUROJET and PYTHIA. The more pessimistic is obtained with PYTHIA. If we require at least one additional jet with $p_T > 50 \text{ GeV}/c$, the rejection at $\mathcal{L} \sim 10^{33} \text{ cm}^{-2} \text{ s}^{-1}$ from EUROJET is ~ 10 , the rejection from PYTHIA is ~ 3 .

For 2 jets with $p_T > 50 \text{ GeV}/c$, the rejection from PYTHIA is ~ 10 and the efficiency for top is only $\epsilon \sim .5$. Therefore, we don't use jets to reduce $b\bar{b}$ background (we can have also problems with additional jets due to pile-up at large luminosities : $\mathcal{L} \gtrsim 10^{34} \text{ cm}^{-2} \text{ s}^{-1}$).

* Conclusion

In conclusion, if we require an isolated e and an isolated μ with $p_T^{e,\mu} > 50 \text{ GeV}/c$ $|\eta^{e,\mu}| < 1.5$ and $20^\circ < \Delta\varphi(e-\mu) < 160^\circ$, the signal from $t\bar{t}$ can already be seen above the background and the ratio signal/background is ~ 50 with a signal cross-section of $\sim 1 \text{ pb}$ for $m_{top} \sim 200 \text{ GeV}/c^2$.

This channel can therefore be used to obtain clean top signal with large statistics. The luminosity needed to discover a top with $m_{top} \sim 200 \text{ GeV}/c^2$ in this channel is around 5 to 10 pb^{-1} , corresponding to a few days at $\mathcal{L} = 10^{32} \text{ cm}^{-2} \text{ s}^{-1}$.

We note that this channel can also be used to search for a new heavy quark Q, assuming

$Q \rightarrow qW$. With 10^3 pb^{-1} (1 "year" of 10^7 s at $\mathcal{L} = 10^{32} \text{ cm}^{-2} \text{ s}^{-1}$) masses up to more than 500 GeV/c^2 can be reached : at this level of heavy quark cross-section the backgrounds considered above are still smaller than the contribution of the heavy quark, without even tightening the cuts on p_T^e , p_T^μ .

2. Other 2 lepton channels

a) Isolated e pairs or isolated μ pairs

The signal is the same as in the previous section (except that the branching ratio $BR(t\bar{t} \rightarrow ee) = \frac{1}{81}$ is only half of $BR(t\bar{t} \rightarrow e\mu) = \frac{2}{81}$).

The previous backgrounds exist also in this channel, with the same signal to background ratio, but we have also to take into account the additional backgrounds from Drell-Yan and Z which are the dominant sources of isolated electron (or muon) pairs^[29].

The Drell-Yan and Z backgrounds are estimated with PYTHIA (the γ^*/Z interference is taken into account). If we use the same cuts on the leptons as in the previous section ($p_T^e > 50 \text{ GeV}$, $|\eta^e| < 1.5$, $20^\circ < \Delta\varphi(\ell - \ell') < 160^\circ$) we find that the observed cross-section is $\sim 2 \text{ pb}$. The above cuts are in particular very efficient in order to reject $Z \rightarrow \ell\ell$ which is large : $\sigma(Z \rightarrow ee) \sim 1 \text{ nb}$ is reduced at the level of $\sim 2 \text{ pb}$.

If we want to reduce it even more the table below (for the ee channel) shows the observed cross-sections after a cut on the dilepton invariant mass, m_{ee} .

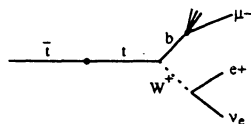
	$t\bar{t}$ $m_{top} = 130$	$t\bar{t}$ $m_{top} = 200$	DY and Z
$\sigma \times BR \times \text{acceptance}$ $m_{ee} > 115 \text{ GeV}/c^2$.25 pb	.75 pb	.8 pb
$m_{ee} > 150 \text{ GeV}/c^2$.12 pb	.5 pb	.3 pb

This gives signal/background ratio of ~ 1 to 4 which can be improved by requiring jets (an additional rejection of ~ 10 can be obtained with an efficiency $\sim 50\%$).

It is also possible to use the missing transverse energy to reduce the background with almost similar rejection and efficiency (provided the calorimetric coverage extends to ~ 4 in rapidity : see section II.2).

In conclusion, the top signal can also be seen in the ee and $\mu\mu$ channels. However, we have to use additional cuts compare to the $e\mu$ channel in order to reduce the Drell-Yan/Z background and therefore we can only improve the top statistics by $\sim 50\%$.

b) Isolated e and muon from b



This channel can also be used to extract a clean top sample where we ask for only one top decay to W ("top tagging" using a sort of "b tagging" by the non isolated muon). It is particularly useful for the search of non standard top decays. The background, mainly from $b\bar{b}$ and $Wb\bar{b}$ (see section V), is found to be small.

We could also consider the diagram shown above where a μ^+ replaces the e^+ . There is then an additional Z/Drell-Yan background, which is more difficult to get rid of than in section III.2 a), because we can only use softer cuts on the transverse momentum of the non-isolated muon from the b decay than for the isolated muon in the t decay and on the $\mu^- \mu^+$ invariant mass which in this case is bounded by m_{top} .

Figure 15 shows the transverse momentum of the muon from the b coming from the t (after asking that both W's have a semileptonic decay with $p_T^l > 50$ GeV), for $m_{top} = 200$ GeV/c 2 . This spectrum is of course much softer than those of figure 2.

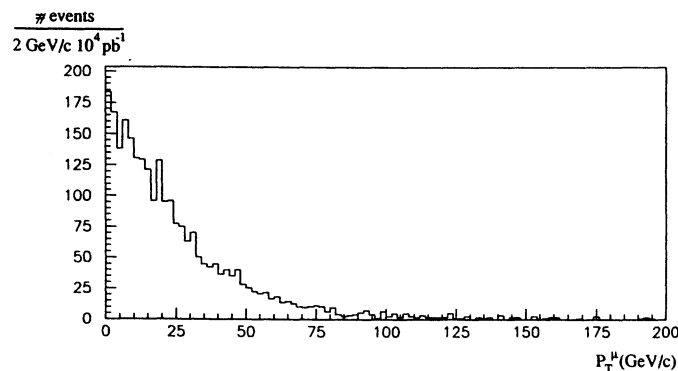


Fig. 15

3. Top mass measurements in the multilepton channel

a) In the channel $t \rightarrow e\nu b$; $b \rightarrow \mu$

The top mass measurement can be done using the jet masses in the hemisphere opposite to the electron ("b tagging" by muons) : see section II.4. We can also use the invariant mass of the isolated e and the non-isolated μ : see section III.3 d).

b) In the isolated electron and muon channels

There are two energetic neutrinos in the final state. Therefore, full mass reconstruction is not possible. More or less, all kinematical variables depend on the top mass and can be used to determine this mass. However, these kinematical variables depend also on the transverse momentum of the top (p_T^{top}), which has uncertainties (from higher order effects,...).

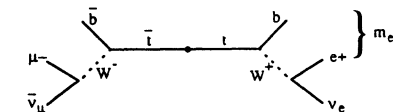
Therefore, to measure the top mass, we have to find a kinematical variable which is sensitive to the top mass and not too sensitive to the top momentum, in order to have the smallest systematic error from the uncertainties on p_T^{top} .

The best variables to measure the top mass are Lorentz invariants for which the dependence on p_T^{top} can only arise from an effect of the cuts used to define the sample (without cuts there is no dependence). For example, after the cuts exposed in the previous part ($p_T^{e,\mu} > 50$ GeV/c, $20 < \Delta\varphi(e - \mu) < 160^\circ$), the p_T of the leptons has a more important dependence with p_T^{top} than with the top mass.

Generally, if the cuts are not "too hard", (if the selected events are not in the high p_T tail of the p_T^{top} distribution), this effect is small and therefore the systematic error from the p_T^{top} uncertainties on the top mass measurement will be small.

We will now discuss two Lorentz invariants which can be used to determine the top mass : the electron-jet mass m_{ej} in section III.3.c) (†), and the dimuon mass $m_{\mu\mu}$ in section III.3.d), in the $e \mu^+ \mu^-$ channel (where we require a b decaying into a μ)

c) The electron-jet mass m_{ej}



m_{ej} is used to estimate m_{eb} . We have first to find the correct jet from the b. For this, we use the jet with p_T above 50 GeV/c closest to the electron in : $\Delta R = \sqrt{\Delta\eta^2 + \Delta\varphi^2}$.

However for high top mass, where the top decay becomes more isotropic, we are subject to confusion between the b and \bar{b} jets. Therefore, if the luminosity is sufficient ($\mathcal{L} \gtrsim 10^{33}$ cm $^{-2}$ s $^{-1}$) it is favourable to ask for \bar{b} decaying into a μ^+ , in order to reduce this problem.

We cannot however reduce the background from jets produced in association with the $t\bar{t}$ pair but, for high top masses, the b jet has a large p_T and can be more easily separated from most of the additional jets. We will do this from now on, the cuts being $p_T^{e,\mu,j} > 50$ GeV/c, $|\eta^{e,\mu}| < 1.5$, $|\eta^j| < 2$ and a tagged \bar{b} .

(†) We choose the electron-jet mass but the arguments are the same for the muon-jet mass.

The m_{ej} distribution is of course sensitive to the top mass, but also to the nature of the coupling of the top to the W (in the Standard Model, this coupling is V-A).

Figure 16 shows the m_{ej} distribution for $m_{top} = 200 \text{ GeV}/c^2$ with V-A and V+A couplings and also for $m_{top} = 211 \text{ GeV}/c^2$ with V-A coupling, estimated with EUROJET assuming perfect $\bar{b} \rightarrow \mu$ tagging (\dagger). The mean value for $m_{top} = 200 \text{ GeV}/c^2$ and V+A is equal to the mean value for $m_{top} = 211 \text{ GeV}/c^2$ and V-A.

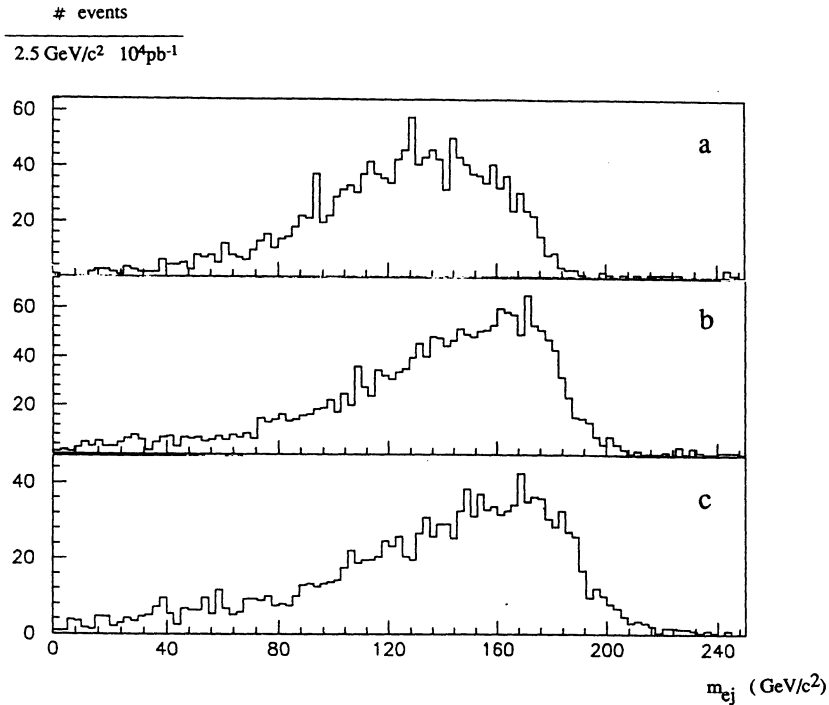
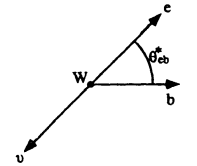


Fig. 16 : Distribution of m_{ej} for :

- a) $m_{top} = 200 \text{ GeV}/c^2$; V-A coupling $\langle m_{ej} \rangle \sim 125 \text{ GeV}/c^2$
- b) $m_{top} = 200 \text{ GeV}/c^2$; V+A coupling $\langle m_{ej} \rangle \sim 136 \text{ GeV}/c^2$
- c) $m_{top} = 211 \text{ GeV}/c^2$; V-A coupling $\langle m_{ej} \rangle \sim 136 \text{ GeV}/c^2$

A different way to illustrate this is to recompute from m_{eb} , $\cos\theta_{eb}^*$ calculated in the W rest frame^[44] where $\cos\theta_{eb}^*$ will be estimated from $\cos\theta_{ej}^*$.



$$\cos\theta_{eb}^* = \frac{1}{p_b^*} [E_b^* - 2 \frac{p_e \cdot p_b}{m_W}] \quad (p_e \cdot p_b \text{ is the Lorentz product of the 4-vectors})$$

where E_b^* , p_b^* are the b energy and momentum in the W rest frame :

$$E_b^* = \frac{1}{2m_W} (m_{top}^2 - m_W^2 - m_b^2)$$

If we neglect m_e and m_b , we have $2p_e \cdot p_b = m_{eb}^2$, $(m_{eb}^2 = (p_e + p_b)^2 = 2p_e \cdot p_b + m_e^2 + m_b^2)$, and $\cos\theta_{eb}^* = 1 - 2 \frac{m_{eb}^2}{m_{top}^2 - m_W^2}$. The 2 variables θ_{eb}^* and m_{eb} are therefore completely correlated.

To compute this variable, we have to use the top mass as input since we cannot recompute E_b^* (we cannot measure the W boost since there are 2 neutrinos in the final state).

If (and only if) the correct top mass is used as input, the $\cos\theta_{eb}^*$ values span exactly the [-1, +1] interval (if we do not take into account resolution and jet misidentifications effects). Of course, the $\cos\theta_{eb}^*$ shape is sensitive to the coupling of the top to the W.

Figure 17 shows the $\cos\theta_{ej}^*$ distributions for :

$m_{top} = 200 \text{ GeV}/c^2$ V - A	analysed with $m_{top} = 200 \text{ GeV}/c^2$
$m_{top} = 200 \text{ GeV}/c^2$ V + A	analysed with $m_{top} = 201$ (211) GeV/c^2
$m_{top} = 211 \text{ GeV}/c^2$ V - A	analysed with $m_{top} = 211 \text{ GeV}/c^2$

These distributions of $\cos\theta_{ej}^*$ and m_{ej} should allow us to measure both the top mass and the top coupling to the W by comparing their shapes and mean values. As noted above the average value of the m_{ej} or $\cos\theta_{ej}^*$ distributions does not allow us to disentangle a V-A $m_{top} = 211 \text{ GeV}/c^2$ and V+A $m_{top} = 200 \text{ GeV}/c^2$.

In order to do that, we have to see the differences in the shapes of figure 16b and 16c or the difference between the two curves of figure 17c. Since we use 3 leptons, in order to reduce the jet misidentification problem, we need $\mathcal{L} \gtrsim 10^{33} \text{ cm}^{-2} \text{ s}^{-1}$. However, the errors will be dominated by the systematic uncertainties on the jet measurements (see section II. for more details on systematics on jets) and a measurement of m_{top} independant of the coupling is clearly an experimental challenge.

(†) In reality, we have to take into account $\bar{b} \rightarrow \mu$ tagging efficiency related to the p_T^μ cut we will be able to apply in the real experiment (see figure 15).

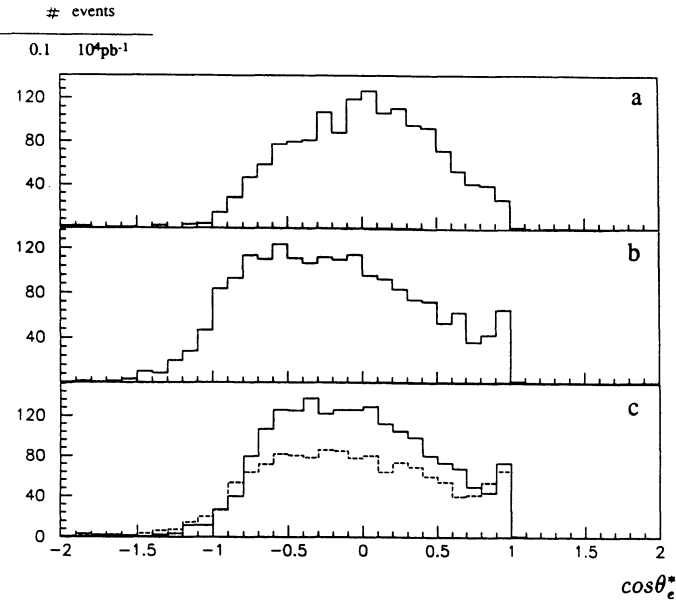
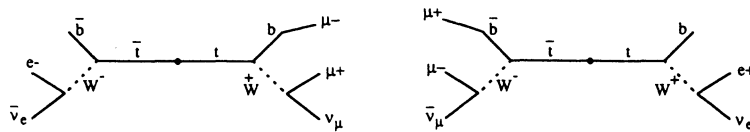


Fig. 17 : Distribution of $\cos \theta_{ej}^*$ for
 a) $m_{top} = 200 \text{ GeV}/c^2$; V-A coupling
 b) $m_{top} = 200 \text{ GeV}/c^2$; V+A coupling
 c) $m_{top} = 200 \text{ GeV}/c^2$; V+A coupling (full line)
 $m_{top} = 211 \text{ GeV}/c^2$; V-A coupling (dashed line)
 a) and b) are analysed with $m_{top} = 200 \text{ GeV}/c^2$; c) with $211 \text{ GeV}/c^2$

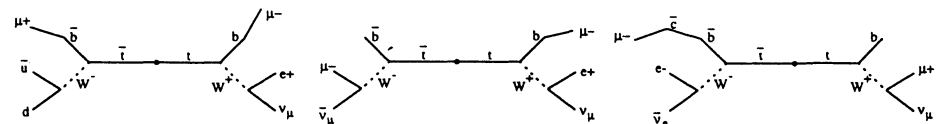
d) The dimuon mass $m_{\mu^+ \mu^-}$

We start from the $e^- \mu^+ \mu^-$ sample :



and we use now the $m_{\mu^+ \mu^-}$ mass to estimate the top mass^[46]. In the following (except in section III.3.g)), we assume the standard V-A coupling of the top to the W. The advantages of this method compared to m_{ej} , is that it uses only leptons and therefore the experimental systematics are small and it can work without any problem at high luminosity ($\mathcal{L} \sim 10^{34} \text{ cm}^{-2} \text{ s}^{-1}$).

The "good" decay modes (where both muons come from the same top) are indicated above, but we have also to take into account an "internal background" where both muons do not come from the same top. This "internal background" including leptonic decays of charm is given by :



The $e \mu^+ \mu^-$ events are selected by the following cuts :

- one isolated electron with $p_T > 50 \text{ GeV}/c$
 - one isolated muon with $p_T > 50 \text{ GeV}/c$
 - one other muon with $p_T > 25 \text{ GeV}/c$
- with $|\eta| < 1.5$

We assume a factor 10 of rejection (see section III.1) if we apply an isolation cut to a lepton from b. The dominant contribution comes from the "good" decays modes, but the other have to be taken into account because they induce tails in the $m_{\mu^- \mu^+}$ distribution.

The $m_{\mu^+ \mu^-}$ distributions for $m_{top} = 130 \text{ GeV}/c^2$ and $m_{top} = 200 \text{ GeV}/c^2$ are shown in figure 18 (simulated by EUROJET (†)).

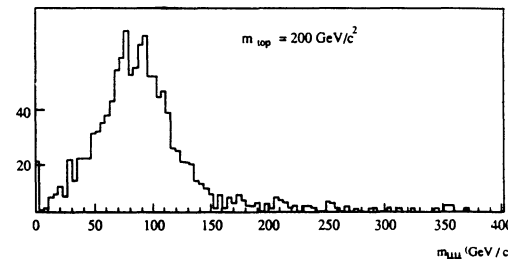
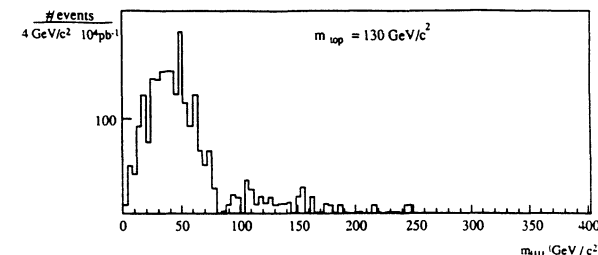


Fig. 18 : Distribution of the $\mu^+ \mu^-$ invariant mass in $e \mu^+ \mu^- t \bar{t}$ events (including "internal background").
 The lepton efficiency is taken to be equal to 1. $\langle m_{\mu \mu} \rangle \sim 55 \text{ GeV}/c^2$ (resp. $93 \text{ GeV}/c^2$) for
 $m_{top} = 130 \text{ GeV}/c^2$ (resp. $200 \text{ GeV}/c^2$).

(†) The events generated by Monte-Carlo correspond to $\sim 3000 \text{ pb}^{-1}$ (resp 20000 pb^{-1}) for $m_{top} = 130 \text{ GeV}$ (resp 200 GeV).

To obtain a clean measurement of the top mass in this channel, we have to control the background. The dominant background is WZ ($W \rightarrow e\nu, Z \rightarrow \mu\mu$) which is $\sim 3\%$ of the signal for $m_{top} = 200 \text{ GeV}/c^2$. The other backgrounds estimated with PYTHIA ($Zb\bar{b}$; $Z \rightarrow \mu\mu, b \rightarrow e$; or $Z \rightarrow ee, b \rightarrow \mu, \bar{b} \rightarrow \mu$ and $Wb\bar{b}, W \rightarrow e, b \rightarrow \mu, \bar{b} \rightarrow \mu$) are around or below 1 % of the signal (for $m_{top} = 200 \text{ GeV}/c^2$).

We conclude therefore, that there is no background problem for a precise top mass measurement in this channel. The statistical error achievable with this method (by using just the mean value of $m_{\mu^+\mu^-}$ to obtain the top mass) is shown below :

	$m_{top} = 130 \text{ GeV}/c^2$	$m_{top} = 200 \text{ GeV}/c^2$
G x BR x acceptance	.17 pb	.10 pb
# ev/year at $10^{33} \text{ cm}^{-2} \text{ s}^{-1}$	850	500
Stat. error on m_{top} for 1 year at $10^{33} \text{ cm}^{-2} \text{ s}^{-1}$ (10^4 pb^{-1})	$2.8 \text{ GeV}/c^2$	$4.5 \text{ GeV}/c^2$
Stat. error on m_{top} for 1 year at $10^{34} \text{ cm}^{-2} \text{ s}^{-1}$ (10^5 pb^{-1})	$.9 \text{ GeV}/c^2$	$1.4 \text{ GeV}/c^2$

with global lepton efficiency of 50 %^[47].

We will now investigate the possible systematic uncertainties :

- Uncertainty on the energy scale of leptons :

An uncertainty of 1 % in the energy scale (probably pessimistic, because this energy scale can be fixed by real Z's) will give a $\sim 1\%$ error on the top mass (only $\pm 2 \text{ GeV}/c^2$ for $m_{top} = 200 \text{ GeV}/c^2$).

- Uncertainties from p_T^{top} :

From the arguments exposed above we expect relatively small uncertainties but this has to be quantified. Figure 19 shows the mean value of $m_{\mu^+\mu^-}$ per 40 GeV/c bin of p_T^{top} for $m_{top} = 130 \text{ GeV}/c^2$ and $m_{top} = 200 \text{ GeV}/c^2$ and the cuts described above (†). The uncertainty on the top mass from this effect is most probably below $\sim \pm 2 \text{ GeV}/c^2$ (this corresponds to an uncertainty on p_T^{top} of 15 GeV/c).

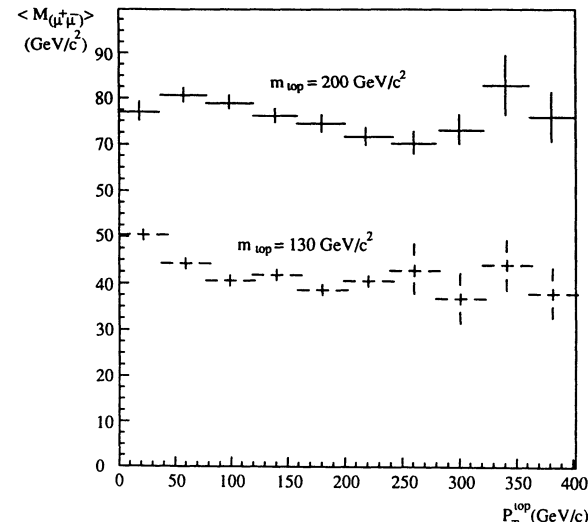


Fig. 19

- Uncertainties from the b fragmentation into muons :

For the b fragmentation, we can use the results from LEP^[37] which give $\langle x_b \rangle = 0.68 \pm 0.03$ in agreement with theoretical predictions^[38]. If we use this error as uncertainty on the b fragmentation, the resulting uncertainty on the top mass is around 2 to 3 %.

Finally, with 10^5 pb^{-1} , the error on the top mass is ± 2 (stat) ± 5 (syst) GeV/c^2 .

The systematic error due to the LEP measurement of $\langle x_b \rangle$ may decrease with more data but there are some additional theoretical errors^[48]. It should be a challenge for theorists to reduce them.

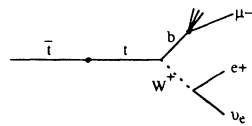
e) Other dilepton masses

In section III.3.d), we considered the $e\mu^+\mu^-$ sample where we looked at the $\mu^+\mu^-$ mass. There was for a top mass $m_{top} = 200 \text{ GeV}/c^2$, a cross-section of $\sim .08 \text{ pb}$ due to the diagram drawn on top of section III.3.d) (†). There is an easy way to gain a factor 2 in rate considering the $e\mu$ mass within the $e\mu^-\mu^-$ or $e\mu^+\mu^+$ events (the e coming from the decay of a W coming from the t decay, the muons coming from the other W and from the b associated to the electron). The cross-sections quoted above can be increased by ~ 1.7 going to $\sim .13 \text{ pb}$ if instead of the 50,50,25 GeV/c of the section III.3.d) the cuts 40,40,20 - still safe - are taken.

(†) The cross-section on the above table is $\sim .1 \text{ pb}$, larger than the $.08 \text{ pb}$ quoted here because in the table the "internal background" was taken into account.

(†) In this figure the internal $t\bar{t}$ background has been taken into account.

Using $e\mu$ events (no third muon asked), we can make the $m_{e\mu}$ invariant mass.



Compared to the 3 lepton channel used above for the mass measurement, this channel has the advantage that we gain a semileptonic branching ratio of the b but, if we want to reduce the $b\bar{b}$ and $Wb\bar{b}$ backgrounds (see section V.3), we may need to cut harder. For example, the seen cross-section with cuts $|\eta^{e,\mu}| < 1.5$, $p_T^e > 75 \text{ GeV}/c$, $p_T^\mu > 25 \text{ GeV}/c$ and $20^\circ < \Delta\varphi(e - \mu) < 100^\circ$, is $\sim .48 \text{ pb}$, a noticeable increase of cross-section. One sees in figure 20 that even with these harder cuts, the dependance of $m_{e\mu}$ (for $m_{top} = 200 \text{ GeV}/c^2$) as a function of p_T^{top} is small.

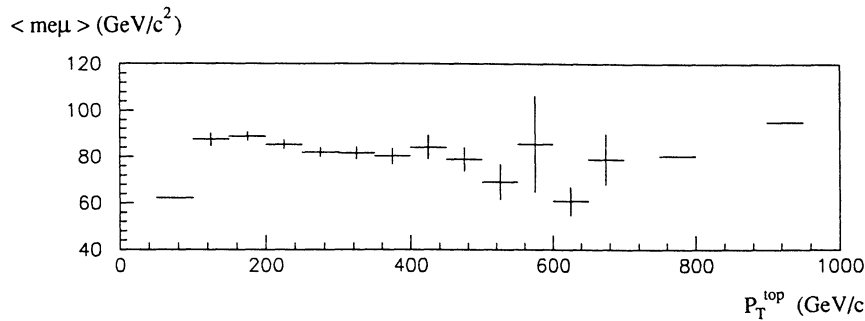


Fig. 20

There are other "internal" backgrounds in this channel : $e^\mp\mu^\pm$ with both leptons from W decay (one may note that here both leptons are isolated, which can be used in order to reduce this background), and $e^+\mu^+$ or $e^-\mu^-$ where the e is coming from the W decay of one top, the μ from the b decay of the other (if we measure the sign of the electron this background disappears).

f) Parenthesis on the tbW coupling

In section III.3.c), we looked at the distributions of $\cos\theta_{eb}^*$ and m_{eb} and we noticed that it was very difficult to measure the tbW coupling and the top mass : we needed to measure correctly the difference between the 2 curves of figure 17c. The jet definition and jet measurement was one of the problems. One may ask if it is easier with the $\mu^+\mu^-$ pair shown above. Unfortunately, there is some dilution of the shapes going from the b to the μ

and figure 21 shows that the $m_{\mu^+\mu^-}$ distribution of a $V+A$ $m_{top} = 200 \text{ GeV}$ events (obtained with slightly different cuts than above) is close to the distribution of $V-A$ $m_{top} = 215 \text{ GeV}$.

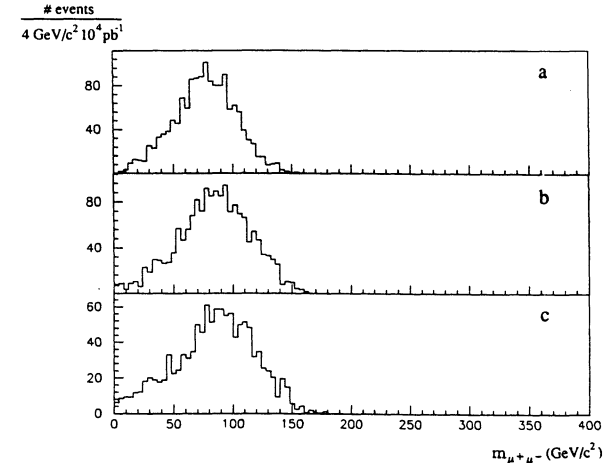


Fig. 21 : $\mu^+\mu^-$ invariant mass distributions for $e\mu^+\mu^-$ events (without any internal $t\bar{t}$ background)
a) $m_{top} = 200 \text{ GeV}/c^2$; $V-A$ coupling ($\langle m_{\mu\mu} \rangle \sim 77 \text{ GeV}/c^2$)
b) $m_{top} = 200 \text{ GeV}/c^2$; $V+A$ coupling ($\langle m_{\mu\mu} \rangle \sim 85 \text{ GeV}/c^2$)
c) $m_{top} = 215 \text{ GeV}/c^2$; $V-A$ coupling ($\langle m_{\mu\mu} \rangle \sim 85 \text{ GeV}/c^2$)

4. Background from fake electrons and trigger rates for the isolated $e - \mu$ channel

If we assume that the muon rate is dominated by b decays, the main background arises from fake electrons where $b \rightarrow \mu$ and the \bar{b} jet (or an other jet) fakes an electron. We have $\sigma(b\bar{b}; p_T^b > 50, |\eta| < 1.5, p_T^b > 50) \sim 3 \text{ nb}$ from EUROJET.

The signal cross-section with $p_T^{e,\mu} > 50 \text{ GeV}$ is around 3 pb. Therefore, we need a rejection against jets in the electron identification $\gtrsim \text{few } 10^3$ (at high luminosity, this rejection should be ~ 2 to 4 times greater because the pile-up increases the number of jets) much smaller than the one needed in section II.2. where only one electron was asked in the t decay.

We obtain trigger rates (if the rejection at the first and second level is assumed pessimistically to be $\sim 10^2$) of $\sim .3 \text{ Hz}$ at $\mathcal{L} = 10^{33} \text{ cm}^{-2} \text{ s}^{-1}$ and $3 \div 10 \text{ Hz}$ for $\mathcal{L} = 10^{34} \text{ cm}^{-2} \text{ s}^{-1}$. Therefore, this channel can probably work at the maximum LHC luminosity. There is no problem of fake electron background and trigger rate for the channels with $\gtrsim 3$ charged leptons.

5. Conclusions on the multilepton channels

The multilepton channels can be used to obtain a clean top signal (especially in the isolated electron-muon channel) with large statistics because we can work at $\mathcal{L} = 10^{34} \text{ cm}^{-2} \text{ s}^{-1}$. This allows precise top mass measurements. The best top mass determination can probably be done in the $e - \mu - \mu$ channel through the $m_{\mu^+\mu^-}$ distribution which gives a global error on m_{top} of $\sim 5 \text{ GeV}/c^2$ at $m_{top} = 200 \text{ GeV}/c^2$ for 10^5 pb^{-1} .

IV. W-GLUON PROCESS

1. Introduction

The dominant top production mechanism at LHC is the strong $t\bar{t}$ pair production, but for large values of the top mass, the single top production via the Wg fusion process^[49] competes with the $t\bar{t}$ process for very heavy top ($m_{top} \gtrsim 280 \text{ GeV}/c^2$). It gives special kinematics with a spectator quark at large rapidity. This allows to find the top decay products with simple kinematic criteria and therefore, a mass reconstruction without combinatorial background.

The Feynman diagrams, for the W -gluon fusion process are shown in figure 22 for the case of $t\bar{b}$ production. The cross-section for this single top production (including both $t\bar{b}$ and $\bar{t}b$) is shown in figure 1.

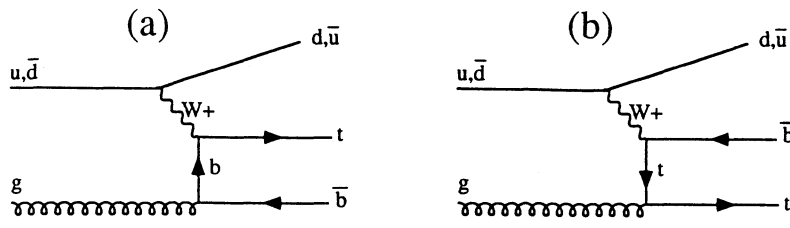


Fig. 22 : Feynman graphs for the W -gluon fusion process

It should be noted that this process can be used only for a heavy top and not for a new heavy quark from a hypothetical fourth generation.

2. Wg events

The signal will appear as a high p_T electron (or muon) associated with jets. The figure 23 shows the final state of the W^+ gluon fusion process if the t decays to $b^+ \nu_e$ through a real W . We will consider now only the electron channel $t \rightarrow W \rightarrow e$ but the analysis would be identical in the muon channel (except section IV.4.).

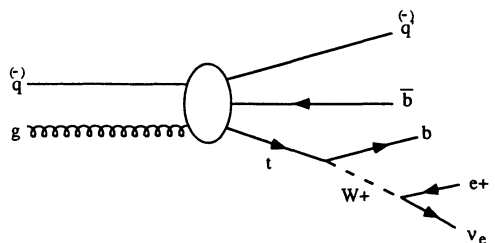


Fig. 23 : The final states of the W^+ -gluon process are shown

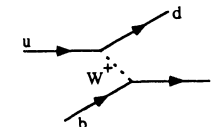
In the Wg fusion process, the propagator of the virtual W radiated by the incoming quark q is roughly $\frac{1}{p_T^2 + m_W^2}$, p_T being the transverse momentum of the W relative to the incident quark direction. Therefore, the p_T of the Wg (or the $t\bar{b}$) system is typically of $0(m_W)$ and is balanced by the p_T of the spectator quark q' . We see that this spectator quark has high p_T . This spectator jet is also produced at large rapidity and therefore could be "tagged"^[50] in a forward calorimeter. The other hard jet in the event is the b jet from the top decay because the top is heavy. For the same argument, this jet is produced in the central region. The last jet, from the \bar{b} , has a smaller p_T .

This allows us to determine the b jet from the top decay. In the two hardest jets of the event, the jet with smallest rapidity is most likely the b jet and the jet with largest rapidity is most likely the q' jet. The efficiency of this method, as will be shown, is very high.

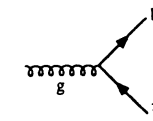
Because we have only one top in the event and because we look for a t decay into leptons in order to have a chance to see the signal, the only way to reconstruct the top mass is to use the neutrino (see section II.5.). Using the procedure described in section II.5. in order to find p_z^ν , all particles from top decay are completely specified and it is possible to reconstruct the top mass using the electron-neutrino-jet mass ($m_{e\nu j}$) where the jet is selected as described above. It was demonstrated for the Tevatron and SSC cases^[51] that this allows to separate the signal from the W +jet background, but without taking into account experimental resolutions.

3. Simulation of the signal

The simulation of the Wg process was done using the PYTHIA Monte-Carlo program^[19]. The full matrix element is not included but the simplified one :



the other part of the diagram (a) of figure 22 (the diagram (b) is neglected) is in some sense recovered by the "parton shower" evolution which is :



The results from PYTHIA for the kinematic properties of outgoing quarks, are in agreement with a parton Monte-Carlo^[52] which contains the full matrix element. The transverse momentum and the rapidity distributions of the spectator quark from PYTHIA are shown in figure 24. For the simulation, we use the same method and the same resolutions as for the previous channels, except for the calorimeter coverage. Because the spectator quark goes up to large rapidity, we will first assume a calorimetric coverage up to 5 in pseudorapidity. The simulation was performed for a top mass of $200 \text{ GeV}/c^2$, without pile-up effects ($\mathcal{L} \lesssim 10^{33} \text{ cm}^{-2} \text{ s}^{-1}$).

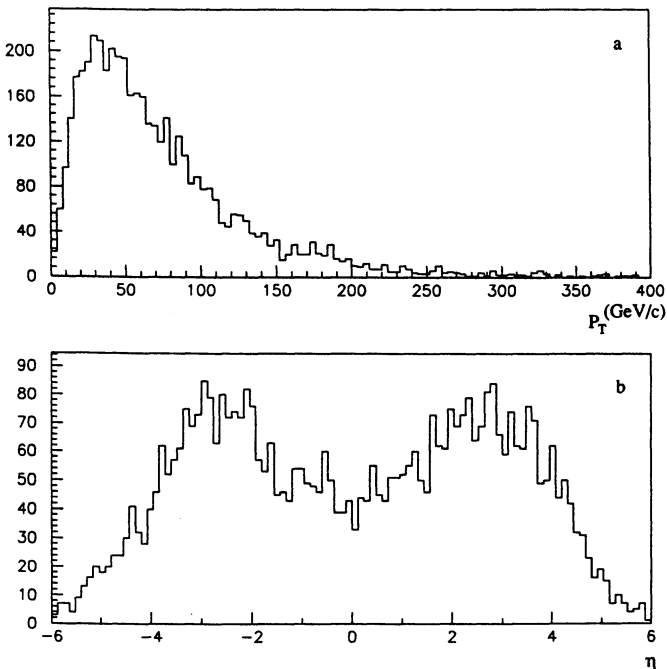


Fig. 24 : Distribution of the transverse momentum (a) and of the rapidity (b) of the spectator quark in W-gluon process.

The \not{p}_T is computed as the vectorial sum of the momenta of all detectable particles in the acceptance after smearing energy. The distribution of $\not{p}_T - p_T^\nu$ (where p_T^ν is the generated transverse momentum of the neutrino from W decay), is shown in figure 25.

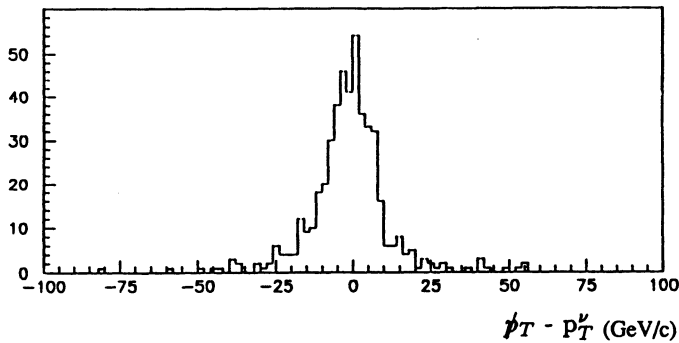


Fig. 25 : $\not{p}_T - p_T^\nu$ after a cut $\not{p}_T > 40$ GeV/c.

The following cuts are applied :

- $p_T^\nu > 40$ GeV with $|\eta^\nu| < 1.5$
- $\not{p}_T > 40$ GeV
- at least two reconstructed jets in the event with $p_T > 50$ GeV, within the calorimeter acceptance.

The b jet is then selected according the method exposed in the previous section (smallest rapidity), and the $m_{e\nu j}$ is computed after the estimation of p_z^ν . The distribution of $m_{e\nu j}$ for the signal ($m_{top} = 200$ GeV/c 2) is shown in figure 26a(†). The resolution on the mass is around 20 GeV/c 2 dominated by the resolution on the neutrino measurement. The high efficiency of this method to reconstruct the top can easily be seen with this distribution.

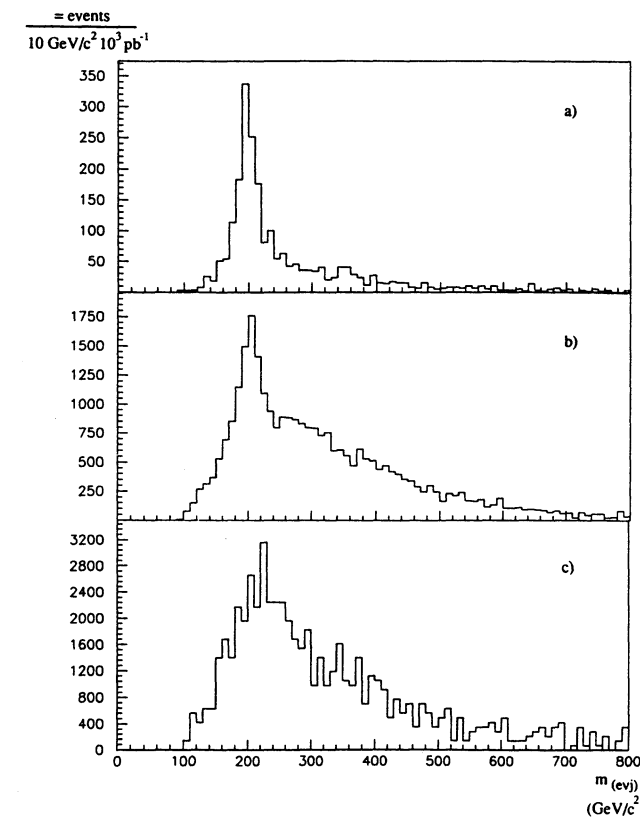


Fig. 26 : Distribution of the reconstructed $e\nu$ -jet mass for the W -gluon signal (a) and the $t\bar{t}$ (b) and W +jet (c) backgrounds.

(†) The events generated by Monte-Carlo correspond to ~ 600 pb $^{-1}$

The systematic errors on the mass measurement are expected to be the same as in section II.5.

4. Physical backgrounds

The dominant source of energetic isolated electrons associated with jets is the production of W+jet followed by the W decay into an electron. The dominant background is therefore the W+ $\geq 2j$ background. It was estimated using PYTHIA. The cross-section for W+2 jet production with $p_T > 40$ GeV/c is compatible with the result from the LDW Monte-Carlo program^[23] which contains the correct matrix element for the W+2 jet production.

We have also to consider the internal top background from the normal $t\bar{t}$ strong production which is dominant up to $m_{top} \sim 280$ GeV/c². This background was also estimated with PYTHIA.

The table 2 gives the results on the cross-section in pb for the Wg fusion signal and for the two background exposed above. The $m_{e\nu j}$ distributions for these backgrounds processes are shown in figure 26(b) and (c).

	$Wg \rightarrow t\bar{b}$ or $\bar{t}b$	$t\bar{t}$	$W + 2j$
Cross – section (including electron BR)	21	140	4300
$p_T^e > 40$ GeV/c $p_T^{\bar{b}} > 40$ GeV/c $p_T^{j_1} > 50$ GeV/c all masses $p_T^{j_2} > 50$ GeV/c	2.3	30	60
and $180 < m_{e\nu j} < 220$ GeV/c ²	0.95	6	8

Table 2 : Cross-section for W-gluon signal and background in pb. In the 1st line, the W + 2 jet cross-section has $p_T^{j_1}, p_T^{j_2} > 20$ GeV/c.

W + jets are the dominant background but with 10^3 pb⁻¹ (1 year at $\mathcal{L} = 10^{33}$ cm⁻² s⁻¹) the mass peak from the Wg signal can be seen with a statistical significance of :

$$\frac{\text{signal (Wg)}}{\sqrt{\text{background (W+2j)}}} \sim 10 \text{ (using an electron efficiency of 90 \%)}.$$

But at this level, it is not possible to distinguish the Wg signal from the $t\bar{t}$ process because $t\bar{t}$ gives also a peak at m_{top} . To separate the Wg signal from $t\bar{t}$, we have to use the rapidity of the spectator quark and the lower jet multiplicity in $Wg \rightarrow t\bar{b}$ events compared to $t\bar{t}$ events.

The distributions of the rapidity of the jet with the largest (in absolute value) rapidity $\eta^{max}(\dagger)$ and of the number of reconstructed jets with $p_T > 25$ GeV/c and $|\eta| < 5$ are shown in figures 27 and 28 ((a) for W-gluon events ; (b) for $t\bar{t}$) after all cuts described above including $180 < m_{e\nu j} < 220$ GeV/c² (for $t\bar{t}$, the events with two isolated leptons have been excluded).

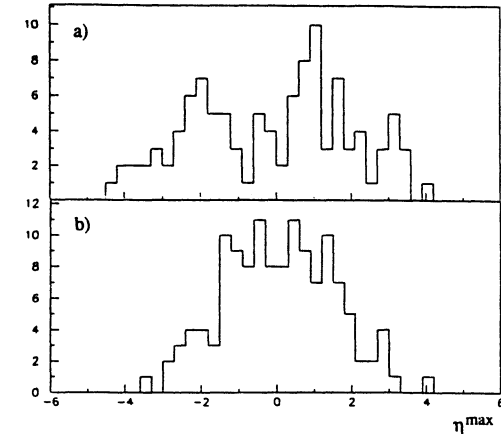


Fig. 27

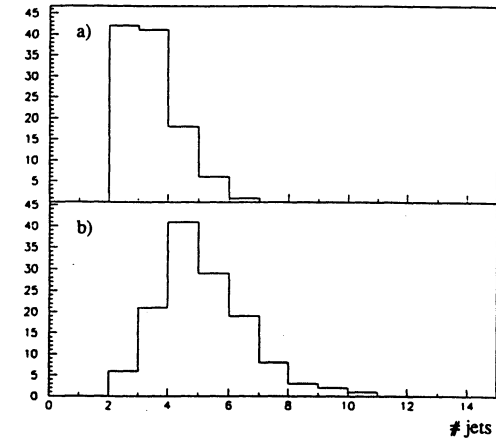


Fig. 28

(†) choosen among the two jets having the largest p_T

The following cuts are applied in order to separate the Wg fusion signal from the $t\bar{t}$ process :

- $\eta^{max} > 2$
- (number of jets with p_T above 25 GeV/c) ≤ 3

After these cuts, we obtain the following cross-sections for the signal and the backgrounds (in pb) :

	$Wg \rightarrow t\bar{b}$ or $\bar{t}b$	$t\bar{t}$	$W + 2j$
after all above cuts applied	.6	.6	17
after all above cuts and $180 < m_{e\nu j} < 220$ GeV	.3	.1	3

The $Wg \rightarrow t\bar{b}$ is now significantly above the $t\bar{t}$ process. The peak in the mass distribution can be seen above the background from $W + 2$ jets with a statistical significance of ~ 5 for 10^3 pb $^{-1}$ and an electron efficiency of 90 %, assuming a smooth background shape.

5. Background from fake electrons

In the previous section, we have considered only the backgrounds involving real electrons. Another potential background is the background from 3-jet events where one jet fakes an electron and with apparent missing transverse energy. What is the rejection that we need against this background ?

The cross section for 3-jet events in the acceptance ($p_T^j > 50$ GeV/c ; $|\eta^j| < 5$) is ~ 1500 nb $^{[26]}$.

If R_e is the rejection given by the electron identification and $R_{\not{p}_T}$ the rejection given by the \not{p}_T cut, the contribution of 3-jet events to the data sample is :

$$3 \times \frac{1500 \text{ nb}}{R_e R_{\not{p}_T}}$$

In order to obtain a contribution below the $W + 2$ jet background, we need $R_e R_{\not{p}_T} \geq$ few 10^5 . As shown before, if the calorimetric coverage is up to 5 in pseudorapidity $R_{\not{p}_T} \sim 20$ for $\mathcal{L} < 10^{33} \text{ cm}^{-2} \text{ s}^{-1}$ and therefore we need $R_e > 10^4$.

6. Trigger

a) electron channel

To select the Wg fusion signal we have to trigger on "electron" + 2 jets (with p_T above the previous cuts). The trigger rate is dominated by 3 jet events. Assuming a rejection of 10^2 at the trigger level the trigger rate is ~ 2 Hz for $\mathcal{L} = 10^{32} \text{ cm}^{-2} \text{ s}^{-1}$.

We conclude that for \mathcal{L} up to $10^{33} \text{ cm}^{-2} \text{ s}^{-1}$, we can trigger on this channel (we can note that for luminosities larger than $10^{33} \text{ cm}^{-2} \text{ s}^{-1}$ we will have the same increase of the trigger rate that was described in section II.3.).

b) muon channel

It should be easy (sic) to trigger on muon + 2 jets for luminosities up to $10^{33} \text{ cm}^{-2} \text{ s}^{-1}$ (see section II.3).

7. Influence of the calorimeter coverage

In the previous part we have assumed a calorimeter coverage up to 5 in η . We have redone the same analysis for a calorimeter coverage up to 4 and 3 in η .

The results in pb are shown below (they have to be compared to the values corresponding to a coverage up to 5, shown on the table at the end of section IV.3) :

	$Wg \rightarrow t\bar{b}$ or $\bar{t}b$	$t\bar{t}$	$W + 2j$
$ \eta < 4$ all masses $180 < m_{e\nu j} < 220$ GeV/c 2	.4 .14	.6 .1	12 1.5
$ \eta < 3$ all masses $180 < m_{e\nu j} < 220$ GeV/c 2	.3 .08	.6 .1	9 .8

For the Wg-fusion signal the acceptance decreases as the coverage decreases because the spectator quark escapes the acceptance. The ratio between the signal and the $W +$ jets is almost constant (the jets produced in association with the W are also at relatively large rapidities), but the separation with the $t\bar{t}$ internal background becomes more difficult because in $t\bar{t}$, the jets are in the central region and therefore the acceptance for the $t\bar{t}$ process is almost constant if the calorimeter coverage goes from 5 to 3 in η .

The separation of the Wg-fusion signal from the $t\bar{t}$ process is therefore more difficult and becomes not possible for a calorimeter coverage only up to 3 in η . If the calorimeter coverage decreases, the resolution on the mass is also affected because the \not{p}_T measurement is less precise, but it is not a dramatic effect because we require that the spectator quark is in the acceptance.

8. Conclusion

The Wg-fusion process cannot compete with the normal strong pair production for the discovery of the top and for a precise top mass measurement, in the case of $m_{top} \gtrsim 200$ GeV/c 2 .

This channel is also probably possible only at low luminosity (below $\mathcal{L} = 10^{33} \text{ cm}^{-2} \text{ s}^{-1}$).

It is however possible to extract the signal of this process from the background of W + Jets with a signal to background ratio around 1/10 and a statistical significance of 5 for 1 year at $10^{32} \text{ cm}^{-2} \text{ s}^{-1}$ in the electron + ≥ 2 jets channels. The separation from the $t\bar{t}$ process needs however a good apparatus with a calorimeter coverage up to 4 or 5 in η .

V. TOP DECAYS INTO A CHARGED HIGGS

1. Introduction

In the previous sections, we have assumed that the top decays only into W (real if $m_{top} > m_w + m_b$) as in the Minimal Standard Model. This is not necessarily true in extensions of the Standard Model. The most interesting case is a model with two Higgs doublets^[53], of which the Minimal Supersymmetric Standard Model (MSSM). In a model with two Higgs doublets, five Higgs fields are physical : 3 neutrals and 2 charged H^+ , H^- . In all these models, the charged Higgs sector depends on only two parameters : the charged Higgs mass m_{H^+} and $\tan\beta = \frac{v_2}{v_1}$; v_2 (resp v_1) is the vacuum expectation value of the Higgs doublet which couples to up (resp down) quarks (we consider only the models where one doublet is coupled to up quarks, and the other is coupled to down quarks(\dagger)).

We can have 4 possibilities :

- i) $m_{top} < m_{H^+}, m_w$
- ii) $m_{H^+} < m_{top} < m_w$
- iii) $m_w < m_{top} < m_{H^+}$
- iv) $m_{H^+}, m_w < m_{top}$

Since in this paper we consider top masses larger than m_w , we do not consider cases i) and ii). In the case iii), the top decays only into bW so we are back to what was studied in the previous sections. We will therefore limit ourselves in this part to case iv) where the decays $t \rightarrow bW^+$ and $t \rightarrow bH^+$ compete with each other.

We will also assume $m_{H^+} > m_w$ which is necessarily the case in the MSSM. In the framework of the MSSM, LEP results give $\tan\beta < .6$ or $\tan\beta > 1.6$ ^[54]. The actual LEP limit is $m_{H^+} > 36 \text{ GeV}/c^2$ ^[54], this will increase with LEP2, although the limit $m_{H^+} > m_w$ will be difficult to reach.

In the following, we will consider here the case $m_{top} > m_{H^+} > m_w$ and $m_{top} = 200 \text{ GeV}/c^2$.

The H^+ produced in the top decay can decay into $\tau\nu_\tau$ or $c\bar{s}$, depending on the $\tan\beta$ value.

$$\frac{BR(t \rightarrow bH^+)}{BR(t \rightarrow bW^+)} = \frac{p_{H^+}}{p_W} \times \frac{(m_b^2 + m_t^2 - m_{H^+}^2)(m_b^2 \tan^2 \beta + m_t^2 \cotan^2 \beta) + 4m_b^2 m_t^2}{m_w^2(m_t^2 + m_b^2 - 2m_w^2) + (m_t^2 - m_b^2)^2}$$

$$\frac{BR(H^+ \rightarrow \tau^+ \nu)}{BR(H^+ \rightarrow c\bar{s})} = \frac{p_\tau}{3p_c} \times \frac{m_\tau^2 \tan^2 \beta (m_{H^+}^2 - m_\tau^2)}{(m_s^2 \tan^2 \beta + m_c^2 \cotan^2 \beta)((m_{H^+}^2 - m_c^2 - m_s^2) - 4m_c^2 m_s^2)}$$

The top branching ratios to bW^+ and bH^+ for the $\tan\beta$ range $0.1 \rightarrow 100$ for $m_{top} = 200 \text{ GeV}/c^2$ and $m_{H^+} = 130 \text{ GeV}/c^2$ are shown in figure 29(a). For the "preferred" range of $\tan\beta$ values in the MSSM, ($1.6 \lesssim \tan\beta \lesssim 20$), the top decay into bW^+ dominates. The H^+ decay branching ratios for $m_{H^+} = 130 \text{ GeV}/c^2$ are shown in figure 29(b).

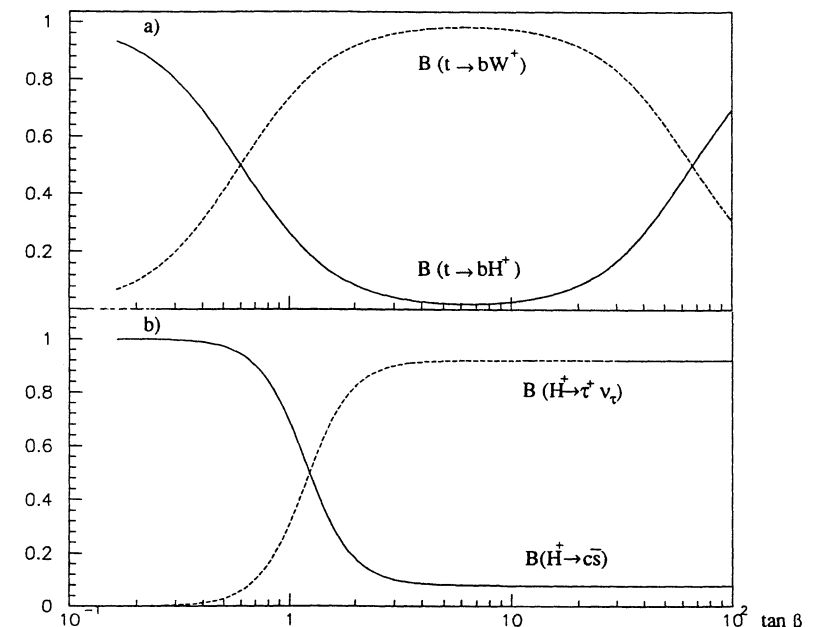


Fig. 29

In the following, we will discuss^[55,56] the two possible channels to see the top decay into a charged Higgs : e + jet channel if the H^+ decays into $c\bar{s}$ and the search for taus after top

(†) This is the model II of section IV.1. of reference 53

"tagging" if the H^+ decays into $\tau\nu_\tau$ (\dagger). We will also discuss a determination of the branching ratio of top to Wb by a comparison of single and two isolated lepton(s) rates.

One can note that for $\tan\beta$ between 10^{-2} and 10^2 the H^+ width :

$$\Gamma_{H^+} \sim \frac{G_F m_{H^+}}{4\pi\sqrt{2}} [3(m_s^2 \tan^2\beta + m_c^2 \cotan^2\beta) + m_\tau^2 \tan^2\beta]$$

is smaller than 5 GeV for $m_{H^+} \sim 130$ GeV and will therefore be neglected in the following (for $\tan\beta > 10^2$ or $\tan\beta < 10^{-2}$, Γ_{H^+} should not be neglected due to the $\tan^2\beta$ and $\cotan^2\beta$ terms).

2. Determination of $\text{BR}(t \rightarrow W)$: signal case

In this section, we will show that the comparison of the channels with one isolated lepton and two isolated leptons can be used in order to determine the branching ratio for the top decay to W , and therefore is sensitive to the presence of a charged Higgs. Indeed, the cross-section for one isolated energetic electron or muon is proportional to $\text{BR}(t \rightarrow W)$ and the cross-section for two isolated energetic electron(s) and/or muon(s) to $[\text{BR}(t \rightarrow W)]^2$.

The ratio is then proportional to $\text{BR}(t \rightarrow W)$ and does not depend on the top production cross-section (which has $\sim 30\%$ uncertainties). To be sensitive to almost all $\tan\beta$ values, we have to determine $\text{BR}(t \rightarrow W)$ at the level of few percents because the branching ratio for the top decay to charged Higgs can be as small as 5 % (for $m_{top} = 200$ GeV, $m_{H^+} \approx m_W$).

This clearly needs a good control of systematic uncertainties, especially in the background subtraction. This is possible only if the backgrounds, which have large uncertainties, are small and therefore in the single isolated lepton channel, we have to require an additional muon from a b decay. Because the uncertainty on $\text{BR}(b \rightarrow \text{lepton})$ is today $\sim 10\%$ ^[57], we have also to require a b decay into muon in the two isolated lepton channels. When this branching ratio will be known with a better precision, it should be then possible to relax this constraint and therefore the statistical error will be smaller (\ddagger) for the numbers quoted below.

To reduce the uncertainties in the acceptance computation, we have also to use as more as possible, the same p_T cuts in both channels to have a cancellation of the uncertainties in the ratio of the acceptances.

In the following, we will give an example of possible cuts which give an error dominated by the statistics for 1 year at $\mathcal{L} = 10^{33} \text{ cm}^{-2} \text{ s}^{-1}$ and dominated by the systematic uncertainties for 1 year at $\mathcal{L} = 10^{34} \text{ cm}^{-2} \text{ s}^{-1}$. For this example, we will assume $m_{top} = 200$ GeV/c² and $m_{H^+} \sim m_W$, in order to have the same acceptance for the muons from b 's if the b comes from a W or a H . This is required only for simplicity and the conclusions do not change if this is relaxed.

(\dagger) We do not consider here the decay $H^+ \rightarrow W^+ h^0$.

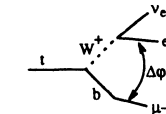
(\ddagger) Of course relaxing this requirement of $b \rightarrow \mu$ in the two isolated $e - \mu$ channel will be always more interesting at low integrated luminosity where the error on the ratio will be dominated by statistics and not by the systematic uncertainty on $B(b \rightarrow \mu)$.

- In the "isolated" $e - \mu$ channel, we require :

$$p_T^e > 75 \text{ GeV}/c$$

$$p_T^\mu > 25 \text{ GeV}/c$$

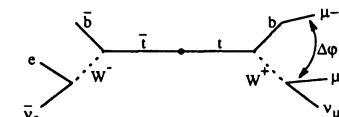
$20^\circ < \Delta\varphi_{(e-\mu)} < 100^\circ$ (to reduce the $b\bar{b}$ background)



$\Delta\varphi$ is the angular separation in the transverse plane.

- In the "isolated" $e - \mu$ channel :

if the muons have opposite signs, we are in this case :



and we require :

$$p_T^{\mu 1} > 75 \text{ GeV}/c$$

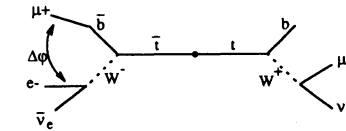
$$p_T^{\mu 2} > 25 \text{ GeV}/c$$

$$20^\circ < \Delta\varphi_{(\mu-\mu)} < 100^\circ$$

$$p_T^\epsilon > 50 \text{ GeV}/c$$

($\mu 1$ is in most of the cases, the isolated muon)

if the muons have the same sign :



we require :

$$p_T^\epsilon > 75 \text{ GeV}/c$$

$$p_T^{\mu 2} > 25 \text{ GeV}/c$$

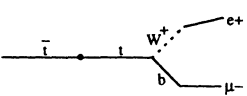
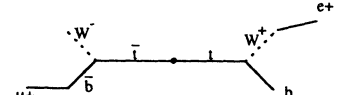
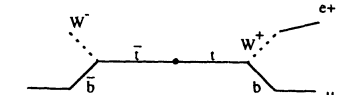
$$20^\circ < \Delta\varphi_{(e-\mu 2)} < 100^\circ$$

$$p_T^{\mu 1} > 50 \text{ GeV}/c$$

In this channel, we use also a $\Delta\varphi$ cut (which is not needed to reduce the background) in order to minimize uncertainties in the ratio of acceptances between both channels.

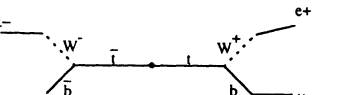
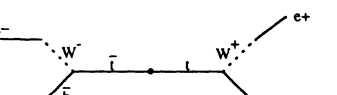
For the computation, we use the $0(\alpha_s^2)$ EUROJET Monte-Carlo program, and we assume for simplicity that H^+ cannot give isolated electrons with $p_T > 75$ GeV/c. We use $BR(b \rightarrow \mu) = \frac{1}{10}$, $BR(W \rightarrow e) = \frac{1}{9}$ (the uncertainty on this number is very small). We define $b = BR(t \rightarrow bW)$.

In the "isolated" e-muon channel we have the following contributions :

<u>Channel</u>	<u>BR</u>	<u>acceptance</u>
	$\frac{9}{10} \frac{1}{10} \left[\frac{2b(1-b)}{9} + \frac{b^2 17}{81} \right]$	$2.51 \cdot 10^{-2}$
	$\frac{9}{10} \frac{1}{10} \left[\frac{2b(1-b)}{9} + \frac{b^2 17}{81} \right]$	$0.51 \cdot 10^{-2}$
	$\frac{1}{100} \left[\frac{2b(1-b)}{9} + \frac{b^2 17}{81} \right]$	$2.27 \cdot 10^{-2}$

We do not need to take into account the two last channels if the electron charge is known. We have "internal top background" in the first channel from $t \rightarrow e$, $\bar{t} \rightarrow \mu$ (with $BR = b^2 \frac{2}{81}$, acceptance = $1.77 \cdot 10^{-2}$). We assume that this contribution is reduced by a factor 10 using isolation. This contribution is taken into account in the following.

We see that, as expected the number of events detected, equal to $\sum BR \times \text{acceptance}$ has a dominant contribution proportional to b . In the "isolated" e^- -isolated μ^- channel the following contributions which are proportional to b^2 are considered([†]).

	$b^2 \frac{2}{81} \frac{1}{10} \frac{9}{10}$	$1.66 \cdot 10^{-2}$
	$b^2 \frac{2}{81} \frac{1}{10} \frac{9}{10}$	$1.66 \cdot 10^{-2}$

where 4 lepton events have been neglected.

(†) In this analysis, some events are "double-counted" in the $e\mu$ and $e\mu\mu$ sets.

From the previous numbers, we can compute the predicted rates for 1 year at $\mathcal{L} = 10^{33}$ $\text{cm}^{-2} \text{s}^{-1}$ (10^4 pb^{-1}), using a global lepton efficiency of .5 in both channels.

for $b = 1$, we find	"isolated" $e - \mu$	2283 events
	"isolated" $e\mu - \mu$	254 events
	<i>ratio</i>	$0.111 \pm 0.007(\text{stat})$

for $b = .95$	"isolated" $e - \mu$	2168 events
	"isolated" $e\mu - \mu$	229 events
	<i>ratio</i>	$0.106 \pm 0.007(\text{stat})$

Therefore, the statistical error on b is .07 for an integrated luminosity of 10^4 pb^{-1} and .022 for 10^5 pb^{-1} .

3. Determination of $BR(t \rightarrow W)$: backgrounds and systematic uncertainties

We will now discuss the possible systematic uncertainties.

* Uncertainty in the energy scale

This effect is minimized by the choice of similar cuts in p_T in both channels. An uncertainty of 1 % in the energy scale gives an error less than 1 % in the ratio of acceptances.

* Uncertainties in the computation of the acceptances (p_T^{top} , higher order uncertainties)

In order to estimate this effect, we have generated events using the tree level $0(\alpha_s^3)$ EUROJET Monte-Carlo with p_T (gluon) > 30 GeV/c (it gives $\sigma(0(\alpha_s^3))$ roughly equal to the total $t\bar{t}$ cross-section) and recomputed the acceptances. The acceptances increase by 30 % but the ratio is unchanged within our statistical error from the Monte-Carlo and we conclude that this uncertainty is smaller than 2 %.

There is no uncertainty from $\sigma_{t\bar{t}}$. The uncertainties on $BR(b \rightarrow \mu)$ and $BR(W \rightarrow e)$ change the ratio by $\lesssim 1$ %.

The last component of the systematic uncertainty on the measurement of $BR(t \rightarrow W)$ is due to backgrounds.

* In the $e - \mu - \mu$ channel, the possible backgrounds estimated by PYTHIA are the following : $WZ \rightarrow e\mu\mu \sim 3$ % of the signal and the uncertainty is estimated to be smaller than 1 % of the signal ; $Wb\bar{b}$ and $Zb\bar{b}$ are also smaller than 1 % (we have assumed a factor 10 of rejection per lepton if we can use isolation). Therefore, the total uncertainty for the background in this channel is around 1 %.

* In the "isolated" $e - \mu$ channel

The WW background is negligible. The dominant backgrounds are $b\bar{b}$ and $Wb\bar{b}/Wc\bar{c}$. The $b\bar{b}$ background is strongly reduced by the $\Delta\varphi$ cut and by a factor 10 from isolation. From PYTHIA, $0(\alpha_s^2) + \text{initial state radiation}$, it is estimated to be ~ 3 % of the signal. In the

$Wb\bar{b}/Wc\bar{c}$ events, the lepton from W is already isolated. This background has been evaluated with PYTHIA and found (\dagger) to be $\sim 8\%$ of the signal. The uncertainty on the $b\bar{b}/Wb\bar{b}/Wc\bar{c}$ backgrounds is difficult to estimate : maybe $\sim 30\%$ of the background value.

In this channel, we have also to take into account the contribution from the Wg -fusion process (see previous section) which gives only one isolated energetic lepton. The contribution from this process (which should be subtracted) is estimated to be 7.7 % on the signal from $t\bar{t}$ (if $BR(t \rightarrow bW) \approx 1$), and with 30 % uncertainties, this gives a uncertainty of 2.3 % (this error will decrease for smaller top masses because the Wg -process contribution decreases).

In both channels there is a contribution of the $gb \rightarrow tW$ process which has to be taken into account. Since the tW cross-section is $\sim 10\%$ of the $t\bar{t}$ cross-section for $m_{top} = 200 \text{ GeV}/c^2$ (see figure 1) and this process contributes to both channels we expect an uncertainty smaller than those computed above ($b\bar{b}/Wb\bar{b}/Wc\bar{c}$).

In conclusion, the total systematic uncertainty is estimated to be $\lesssim 5\%$, and we obtain a total error on $b = BR(t \rightarrow bW)$, $\Delta b \approx 0.05$ for an integrated luminosity of 10^5 pb^{-1} and $\Delta b \approx 0.08$ for 10^4 pb^{-1} . We see in figure 29 that although the total error is small, it is not sufficient to exclude an H^+ of $\sim 130 \text{ GeV}/c^2$ in the top decay ($m_{top} = 200 \text{ GeV}/c^2$) for $2 < \tan\beta < 20$.

We have seen above that the statistical error may decrease if with a better knowledge of $BR(b \rightarrow \mu)$ we would not have to require a b decay into μ for the two isolated leptons channel. It is also clear that the systematic uncertainties will be smaller for smaller top masses and that for specific channels, they can be decreased (asking additional jets for example).

This method can also be used for other exotic top decays. Examples are the decays of the top involving stop \tilde{t} . In this case, an exact computation of acceptance as function of $BR(t \rightarrow bW)$ requires some information on the stop decay (if the stop can give isolated energetic electron or muon, or not, ...).

A general conclusion on this topic is that an observation of the top decay exactly conform to the Minimal Standard Model, can be used to rule out some exotic decay modes.

4. Search for charged Higgs decay into $c\bar{s}$

In this section, we will discuss the charged Higgs search in the electron + jet channel with the same method than in section II.4.

We ask for one top decaying to W , in order to have a lepton for the trigger, and the other top can decay either to W or H^+ . We assume a top mass of $200 \text{ GeV}/c^2$.

The process $t \rightarrow bH^+, H^+ \rightarrow c\bar{s}$ is simulated using the PYTHIA Monte-Carlo program. The same method and the same resolution as in section II.4 are used for this simulation. The

results of the simulation for $m_{H^+} = 130 \text{ GeV}/c^2$ and $m_{H^+} = 100 \text{ GeV}/c^2$ are shown in figure 30 for the case $\tan\beta = 1$ (\dagger). These curves are the 2 jet mass spectrum after the cuts described in section II.4 where $t \rightarrow bW^+$ and $t \rightarrow bH^+$ are added with the branching ratios computed in section V.1.

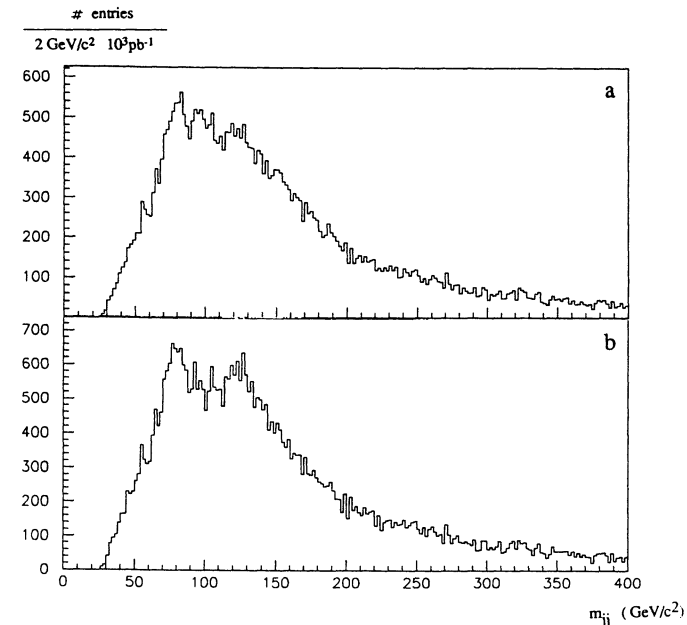


Fig. 30 : Two-jet mass peak (see text) when there is a H^+ with $\tan\beta = 1$ (a) : $m_{H^+} = 100 \text{ GeV}/c^2$; b) : $m_{H^+} = 130 \text{ GeV}/c^2$.

We have already noticed in section V.1 that the H^+ width can become large for $\tan\beta > 10^{-2}$ or $\tan\beta < 10^{-2}$. This is also the case for the top width (for $\tan\beta \sim 10^2$, $m_H \approx 80 \text{ GeV}/c^2$ and $m_{top} \approx 200 \text{ GeV}/c^2$, we have $\Gamma(\text{top}) \approx 14 \text{ GeV}/c^2$).

However in the "preferred" region $1 \leq \tan\beta \leq 20$ these width effects are small both for the H^+ and the top. Figure 30(b) shows that we can see a charged Higgs for $m_{H^+} = 130 \text{ GeV}/c^2$ in the two jet mass spectrum.

To be more quantitative, figure 31 shows an estimate of the statistical significance for 10^3 pb^{-1} (\simeq signal / $\sqrt{\text{combinatorial background}}$) of the charged Higgs mass peak above the combinatorial background and the background from $t \rightarrow bW, W \rightarrow \text{jets}$ for the $\tan\beta$ range $\tan\beta : 10^{-1} \rightarrow 10^2$, and for $m_{H^+} = 100, 130$ and $180 \text{ GeV}/c^2$ ^[58]. For $m_{H^+} = 100 \text{ GeV}/c^2$,

(\dagger) In this case, the Monte-Carlo events $t\bar{t}; t \rightarrow bW, W \rightarrow e\nu, \bar{t} \rightarrow bH, H \rightarrow c\bar{s}$ corresponds to an integrated luminosity of $\sim 1000 \text{ pb}^{-1}$. The $t\bar{t}$ events $t \rightarrow bW, \bar{t} \rightarrow bW$ corresponds now to $\sim 500 \text{ pb}^{-1}$.

(\ddagger) Not counting the background $gb \rightarrow tW; t \rightarrow b$ which gives $Wb\bar{b}$ if we include backward evolution

figure 31 does not take into account the problem of the separation between the H^+ and the W peak.

For the $\tan\beta$ range : $0.1 \rightarrow 1$ most of the phase space can be explored, except if the charged Higgs mass is close to the W mass. ($m_H^+ \leq 110 \text{ GeV}/c^2$). In this case, the separation of the charged Higgs mass peak from the W mass peak is more difficult, and calorimeter resolution effects can be important. One notes that a good knowledge of the resolution and of the background shape may be a help in order to disentangle two nearby mass peaks and that a 2σ effect in the 2-jet mass separation between m_W and m_Z has been observed by UA2 at the CERN $\bar{p}p$ collider^[59]. However figure 30(a) shows how difficult it will be to find a H^+ with a mass of $\sim 100 \text{ GeV}/c^2$. The H^+ peak (seen alone in figure 32) is hidden by the W combinatorial peaks (see figure 7(a)).

In the particular case where $.2 \lesssim \tan\beta \lesssim .5$ the charged Higgs decay dominates the standard $t \rightarrow bW$ decay. (For $\tan\beta \sim .2$, $m_{top} = 200 \text{ GeV}/c^2$, $m_H^+ = 80 \rightarrow 100 \text{ GeV}/c^2$, we have $\text{BR}(t \rightarrow bH^+) \gtrsim 90\%$ and $\text{BR}(H^+ \rightarrow c\bar{s}) > 95\%$). In this case the W mass peak is the more difficult to see (for the very low values of $\tan\beta$ the H^+ peak disappears also because there are no $W \rightarrow e$ to "trigger"). The dominant peak in the 2 jet mass distribution will be the H^+ mass peak and if $m_H^+ \sim m_W$ we would have to rely on the precise mass measurement and on the measurement of $\text{BR}(t \rightarrow bW)$ to see if we have an H^+ .

5. Search for charged Higgs decay into $\tau\nu_\tau$

In the previous section, we have exposed the method to detect the charged Higgs decay into $c\bar{s}$. However in the preferred range of $\tan\beta$: $1.6 \lesssim \tan\beta \lesssim 20$ using the LEP limit in the MSSM framework the only direct method to see the charged Higgs is via the detection of τ , because $\text{BR}(H^+ \rightarrow \tau\nu_\tau)$ dominates ($\geq 90\%$ for $\tan\beta \geq 2$). The failure of the direct $H^+ \rightarrow c\bar{s}$ method is seen in figure 31.

In this channel, we have first to select top events, where one top is requested to decay into a W . This top "tagging" can for example be done using the cuts in the section V.2 which are used to define the top sample with one isolated electron

$$p_T^e > 75 \text{ GeV}/c$$

$$p_T^\mu > 25 \text{ GeV}/c$$

$$20 < \Delta\varphi(e - \mu) < 100^\circ$$

For $\text{BR}(t \rightarrow bW)$ close to 1 we have a sample of $N_{top} \simeq 4000$ top events (if the overall lepton efficiency is $(.9)^2$) with a small ($\simeq 10\%$) background dominated by $Wb\bar{b}$.

A top decay into a charged Higgs will give an excess of taus relative to the standard model where $\text{BR}(t \rightarrow b\tau\nu_\tau) = 1/9$. A useful way to see this excess is to compare the number of isolated muons (N_μ) with the number of isolated taus (N_τ).

$$N_\tau = N_{top} \times \text{BR}(t \rightarrow bW) \times [\frac{1}{9} \text{BR}(t \rightarrow bW) + \text{BR}(H^+ \rightarrow \tau\nu_\tau) \text{BR}(t \rightarrow bH^+)]$$

$$N_\mu = N_{top} \times \text{BR}(t \rightarrow bW) \frac{1}{9} \text{BR}(t \rightarrow bW)$$

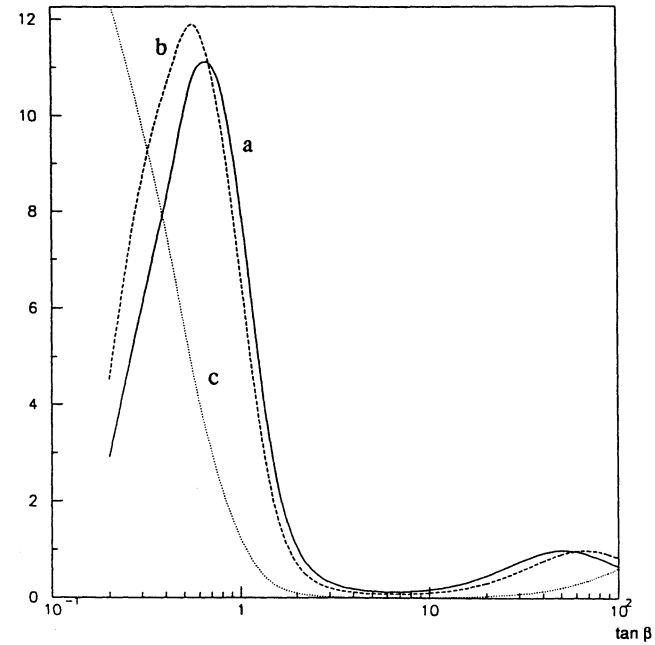


Fig. 31 : a/b/c corresponds to $m_{top} = 100/130/180 \text{ GeV}/c^2$

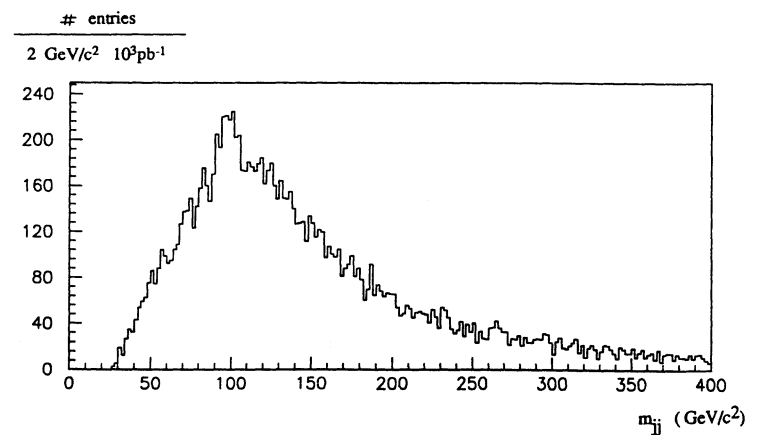


Fig. 32 : Contribution to the jet-jet mass distribution of figure 30 a) of the H^+

If there is no $H^+ \rightarrow \tau\nu$ in top decay $\frac{N_\tau}{N_\mu} = 1$. If there is a H^+ then $\frac{N_\tau}{N_\mu} > 1$. The statistical significance of this excess $(N_\tau - N_\mu)/\sqrt{N_\mu}$ is shown in figure 33 for 1 year at $10^{33} \text{ cm}^{-2} \text{ s}^{-1}$ (for $\mathcal{L} > 10^{33} \text{ cm}^{-2} \text{ s}^{-1}$ the pile-up effects will make the τ identification very difficult) as a function of $\tan \beta$ for various charged Higgs masses.

Fig. 33

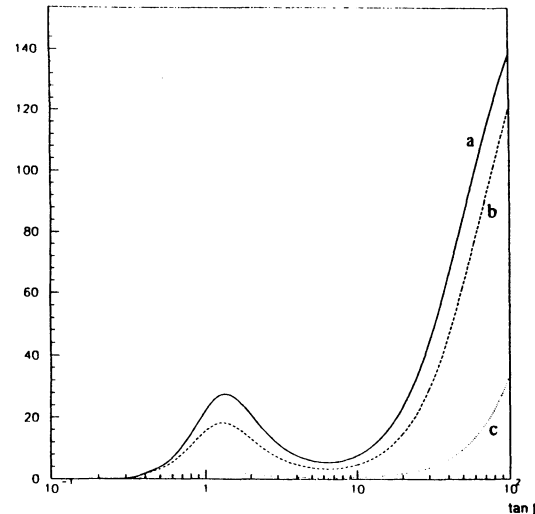
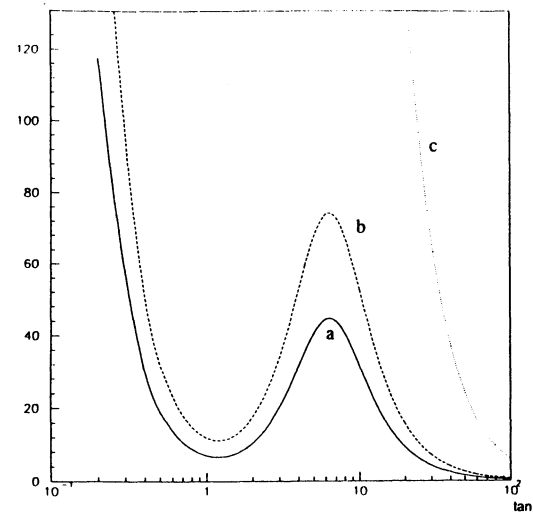


Fig. 34



a/b/c corresponds to $m_{top} = 100/130/180 \text{ GeV}/c^2$

The acceptances and efficiencies for the detection of τ 's are not included. If it is only 10% the $\tan \beta$ range $\tan \beta \approx 3 \rightarrow 15$ cannot be explored even with several 10^4 pb^{-1} ^[60]. Another important problem is the rejection which is needed against jets in the tau identification.

Indeed, we have the jets from W which can fake taus. In figure 34 is shown the ratio between $2.N(t \rightarrow bW, W \rightarrow q\bar{q}')$ and $N(t \rightarrow bH^+, H^+ \rightarrow \tau\nu_\tau)$ which gives the order of the rejection which is needed to see the charged Higgs decay into taus. For $\tan \beta \approx 10$ and $m_{H^+} \approx 130 \text{ GeV}/c^2$ this rejection can be as large as 50, which is difficult to obtain^[61].

6. Conclusion

The study of top decays gives a potential for the discovery of a charged Higgs with $m_{H^+} + m_b < m_{top}$. Depending on the $\tan \beta$ value, two jet masses or tau search have to be used to extract the charged Higgs signal. The charged Higgs effect can also be seen by indirect measurement of $BR(t \rightarrow bW)$ (a precision of $\sim 5\%$ can be reached at the maximum LHC luminosity).

However, it will be difficult to be sensitive to all $\tan \beta$ values for a reasonable range of the charged Higgs mass. This will require at least a very good tau identification at $\mathcal{L} = 10^{33} \text{ cm}^{-2} \text{ s}^{-1}$ and, anyway the $3 < \tan \beta < 10$ zone stays very difficult.

Concerning other exotic decays of the top, the measurement of $BR(t \rightarrow bW)$ can probably be used if the predicted branching ratio are above 5 % (more specific channels can be explored down to much smaller branching ratio).

We have neglected above the $tH^-/\bar{t}H^+$ production. Figure 35 shows the ratio^[62] $\sigma(tH^- + \bar{t}H^+)/[2 \cdot \sigma(t\bar{t}) BR(t \rightarrow H^+)]$ and we see that for most of the $\tan \beta$ values this ratio is much smaller than 1. It was indeed correct to neglect this additional production.

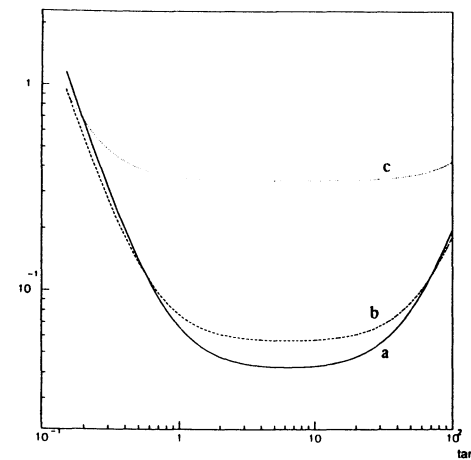


Fig. 35 : a/b/c corresponds to $m_{top} = 100/130/180 \text{ GeV}/c^2$.

CONCLUSIONS

We have shown that, if the top has not been found before its start, the LHC will discover it in all the mass range available within the Standard Model, with low integrated luminosity ($\int \mathcal{L} dt < 10 \text{ pb}^{-1}$), either in the single lepton channel (doing jet masses reconstructions) or in the two lepton channel where a clean top signal can be extracted.

We have also discussed various possibilities to measure the top mass and we have shown that the most precise is the dilepton mass which gives an error on the top mass $\sim 5 \text{ GeV}/c^2$ (for $\int \mathcal{L} dt \sim 10^5 \text{ pb}^{-1}$ and $m_{top} = 200 \text{ GeV}/c^2$) dominated by (theoretical) systematic uncertainties.

We have also shown that using the large top statistics, we are able to study non standard top decays like $t \rightarrow bH^+$. In this case depending on detector performances, a significant part of the parameters space can be explored.

ACKNOWLEDGEMENTS

We thank all our colleagues of the ECFA-LHC Top working group, in particular the conveners D. Denegri, E. Reya and P. Zerwas. We are in particular grateful to D. Froidevaux and T. Sjostrand for many helpful discussions and suggestions.

REFERENCES

- [1] K. Sliwa (CDF Coll.), presented at the XXVth Rencontres de Moriond, Les Arcs, France, March 4-18 1990, Fermilab-Conf. 90/93-E
see also
F. Abe et al. (CDF Coll.), Phys. Rev. Lett. **64** (1990) 142, 147
T. Akesson et al. (UA2 Coll.), Z. Phys. **C46** (1990) 179
C. Albajar et al. (UA1 Coll.), Z. Phys. **C48** (1990) 1
- [2] G.S. Abrams et al. (Mark II Coll.), Phys. Rev. Lett. **63** (1989) 2447
M.Z. Akrawy et al (OPAL Coll.), Phys. Lett. **B236** (1990) 364
P. Abreu et al (DELPHI Coll.), Phys. Lett. **B242** (1990) 536
- [3] see for instance :
J. Ellis, G. Fogli, Phys. Lett. **B232** (1989) 139 ; **B249** (1990) 543
P. Langacker, Phys. Rev. Lett. **63** (1989) 1920
F. Halzen and D.A. Morris, Phys. Lett. **B237** (1990) 107
D. Decamp et al. (ALEPH Coll.), Z. Phys. **C48** (1990) 365
for more general limits see :
A. Blondel, CERN-EP/90-10 (January 1990)
G. Passarino, Phys. Lett. **B247** (1990) 587
B.W. Lynn and E. Nardi, CERN-TH 5876/90 (September 1990)
- [4] The LHC in the LEP tunnel, CERN 87-05 (May 1987) edited by G. Brianti and K. Hübner
- [5] Large Hadron Collider Workshop, Aachen, 1990
- [6] R.J.N. Phillips, P. Zerwas and J. Zunft, private communication
- [7] P. Nason et al., Nucl. Phys. **B303** (1988) 607
- [8] G. Altarelli et al., Nucl. Phys. **B308** (1988) 724
- [9] W. Beenakker et al., DESY 90/064 (May 1990)
- [10] see also H. Plotzsch-Besch in reference 5 for a study of the cross-section for various structure function sets.
- [11] F.M. Renard and D. Treille, Proceedings of Ecole d'Eté de Physique des Particules "Gif 89", Annecy 1989
- [12] A. Böhm and W. Hoogland (eds.), Proc. ECFA Workshop on LEP 200, Aachen, 1986 (CERN 87-08, ECFA 87/108, Geneva, 1987)
- [13] G. Alexander et al. (eds.), Polarization at LEP, report CERN 88-06 (1988)
- [14] G. Altarelli et al. (eds.), Z. Physics at LEP1, Report CERN 89-08 (1989)
- [15] See for instance :
A. Djouadi and C. Verzegnassi, Phys. Lett. **B195** (1987) 265
B.A. Kniehl, J.H. Kühn and R.G. Stuart in reference 13 p158
B.A. Kniehl, J.H. Kühn in reference 14 volume 1 p55
- [16] A. Ali, B. Van Eijk, Proc. 5th Top. Workshop on Proton-Antiproton Coll. Phys., St Vincent, Aosta Italy (1985)
B. Van Eijk, CERN-EP/85-121 (1985)
A. Ali et al., CERN-TH 4523/86 (1986)
A. Ali et al., Nucl. Phys. **B292** (1987) 1
- [17] E. Eichten et al., Rev. Mod. Phys. **56** (1984) 579 ; **58** (1986) 1065 E
- [18] H. Bengtsson and T. Sjostrand, The Lund Monte-Carlo for Hadronic Processes, LUTP 87-3, UCLA-87-001
T. Sjostrand and M. Bengtsson, The Lund Monte-Carlo for Jet Fragmentation and $e^+ e^-$ Physics, LUTP 86-22 (1986)
- [19] T. Sjostrand, private communication
- [20] P. Nason, private communication
see also P. Nason et al., Nucl. Phys. **B327** (1989) 49 and reference 9
- [21] see B. Aubert et al., CERN/DRDC/90-31 DRDC/P5 (August 1990) for the effect of the time response of a Liquid Argon calorimeter on the pile-up
- [22] J. Allison et al., Comp. Phys. Comm. **47** (1987) 55
R. Brun et al., GEANT 3, Report DD/EE/84-1, CERN (1989)
R. Brun, private communication
- [23] S.D. Ellis, R. Kleiss, W.J. Stirling, Phys. Lett. **B154** (1985) 435
F.A. Berends et al., Phys. Lett. **B224** (1989) 237

- [24] This Monte-Carlo was used here with the MRSB set of structure with $\Lambda_{QCD} = 228$ MeV
see :
A.D. Martin, R.G. Roberts and W.J. Stirling, Phys. Lett. **B206** (1988) 327 ;
Mod. Phys. Lett. **A4** (1990) 1135
- [25] see also :
F. Cavanna, D. Denegri, T. Rodrigo and G. Sajot in Reference 5
- [26] F.A. Berends, W.T. Giele, H. Kuijf, Nucl. Phys. **B333** (1990) 120
We thank P. Lubrano for communicating this program to us
- [27] see for instance :
T. Sjostrand in reference 5
It has been noted that one may consider that what is important here for pile-up is not the change of transverse momentum of the jet but the r.m.s. of this change which is also very important in particular in the case of Ionization Chamber calorimeters where the signal is integrated over several bunch crossings.
- [28] D. Froidevaux in : Physics in Collision, 1985, eds. B. Aubert and L. Montanet (éditions Frontières) p 3
- [29] A. Nisati in reference 5
- [30] K. Eggert et al., in Proceedings of the ECFA-CERN workshop on the LHC in the LEP tunnel, ECFA 84/85 CERN 84-10 (september 1984)
- [31] There is an additional 4-jet cross-section due to two times two jets. This additional cross-section increases more rapidly than \mathcal{L} and the corresponding additional trigger rate more rapidly than \mathcal{L}^2 due to pile-up minimum bias (see section II.2)
- [32] see for instance :
H. Baer et al., Phys. Rev. **D38** (1988) 3467
- [33] R. Ansari et al. (UA2 Coll.), Phys. Lett. **B186** (1987) 452
- [34] J. Alitti et al. (UA2 Coll.), CERN-PPE/90-105 (July 1990)
- [35] The PYTHIA/JETSET parameters changed from their default values are :
 $MSTJ(11) = 3$, $PARJ(54) = -.07$, $PARJ(55) = -.055$, $PARJ(56) = -10^{-6}$
- [36] C. Peterson et al., Phys. Rev. **D27** (1983) 105
- [37] B. Adeva et al. (L3 Coll.), Phys. Lett. **B241** (1990) 416
D. Decamp et al. (ALEPH Coll.), Phys. Lett. **B244** (1990) 551
- [38] B. Mele and P. Nason, Phys. Lett. **B245** (1990) 635
- [39] The parameter $PARJ(55)$ was changed from $-.055$ to $-.09$.
- [40] The parameters $PARP(67)$ and $PARP(71)$ are changed from 4. (their default values) to 1.
- [41] Using special routines in order i) to improve the efficiency of having $b\bar{b}$ pairs in the parton shower and ii) to force b into leptons ; T. Sjostrand, private communication
- [42] See for instance I. ten Have, A. Nisati and T. Sjostrand in reference 5

- [43] See also D. Froidevaux in reference 5
- [44] R. Kauffman, presented at Snowmass 1990. We thank K. Wacker for communicating this to us.
- [45] Experiments, detectors, and experimental areas for the supercollider, Berkeley, California, 1987, edited by R. Donaldson and M.G.D. Gilchriese (World Scientific).
- [46] A very similar method was suggested by K.J. Foley et al. in reference 45 p 701.
- [47] These numbers are obtained with EUROJET where the b fragmentation is too hard (see section II.4.). Therefore, the $m_{\mu^+\mu^-}$ is probably scaled by $\sim .9$ and the statistical error should increase by $\sim 10 \%$.
- [48] In particular, even if the energies are the same, the gluon bremsstrahlung of an LHC b may be different of the one of a LEP b (different colour environments). It means the extrapolation of b fragmentation from LEP to LHC is not so simple. We thank P. Zerwas for pointing this argument to us.
- [49] S.S.D. Willenbrock and D.A. Dicus, Phys. Rev. **D34** (1986) 155
- [50] This "tagging" is similar to the tagging of the quarks that emitted W's which will produce heavy Higgs in WW fusion.
see :
R.N. Cahn, S.D. Ellis, R. Kleiss and W.J. Stirling, Phys. Rev. **D35** (1987) 1626
- [51] C.P. Yuan, Phys. Rev. **D41** (1990) 42
- [52] T. Moers, D. Rein, H. Reithler, P. Zerwas and J. Zunft in reference 5
- [53] J.F. Gunion, H.E. Haber, G.L. Kane and S. Dawson ; The Higgs Hunter's Guide (Benjamin 1990)
- [54] See for instance :
F. Richard LAL 90-51 (July 1990) ; Invited talk at the Xth Int. Conf. on Physics in Collision, Durham, USA, 21-23 June 1990
- [55] See also M. Felcini in reference 5
- [56] J.F. Gunion, H.E. Haber, S. Komamiya, H. Yamamoto and A. Barbaro-Galtieri in reference 45 p 110
- [57] K.R. Schubert in : Review of B-meson decay results, 1989, Intern. Symp. on Heavy quark physics, eds. P.S. Drell and D.L. Rubin, AIP Conf. Proc., Vol. 196 (American Institute of Physics, New York, 1989) p 79
- [58] The curve for $m_H = 180$ GeV/c² have been obtained by extrapolation of the previous curves by taking into account the variation of the branching ratios, and therefore is pessimistic because the acceptance is expected to be larger for jets from a heavy charged Higgs and because the background decreases at large two jet masses.
- [59] J. Alitti et al. (UA2 Coll.) CERN-PPE/90-105 (July 1990)
- [60] For this study maybe we can relax some of the cuts used (at the price of increasing a little bit the background) like the p_T^e or the $\Delta\varphi(e - \mu)$ cut, and increase N_{top} by a factor ≥ 3

[61] In fact what really matters are the uncertainties on the τ efficiency and τ rejection ; see reference 55.

[62] The $tH^-/\bar{t}H^+$ cross-section have been calculated using PYTHIA renormalised with the SSC cross-sections of reference 53.

M. Felcini

Physics Dept., University of Boston, Boston (USA)

If a charged Higgs exists which is lighter than $m_t - m_b$, for a t -quark mass $m_t > M_W + m_b$ the on-shell decays $t \rightarrow W^+ b$ and $t \rightarrow H^+ b$ are both allowed and their branching ratios depend on m_t , m_{H^+} and $\tan\beta$. The two branching ratios were shown as functions of $\tan\beta$ in the theoretical part of this report. For values of $\tan\beta$ larger than 1 the relative rate of $t \rightarrow H^+ b$ to $t \rightarrow W^+ b$ is expected to be not larger than 20 %. On the other hand, for these $\tan\beta$ values, the charged Higgs would decay with a large rate into $\tau\nu_\tau$ so that it could induce lepton universality violation in t -quark decays by enhancing the $t \rightarrow \tau^+\nu_\tau b$ mode over the $t \rightarrow \mu(e)\nu_{\mu(e)} b$ mode. The ‘degree’ of lepton universality violation, induced by a charged Higgs in t -quark decays, can be quantified by the ratio

$$R_{\tau\mu} = \frac{BR(t \rightarrow \tau^+\nu_\tau b)}{BR(t \rightarrow \mu^+\nu_\mu b)} = 1 + \frac{BR(t \rightarrow H^+ b)}{BR(t \rightarrow W^+ b)} \frac{BR(H^+ \rightarrow \tau^+\nu_\tau)}{BR(W^+ \rightarrow \tau^+\nu_\tau)} \equiv 1 + \delta R_{\tau\mu} \quad (4.1)$$

(we neglect the contribution to the $t \rightarrow \mu^+\nu_\mu b$ rate given by the muons from leptonic decays of the τ 's in $t \rightarrow \tau^+\nu_\tau b$ which, for the cuts used here, we estimate to be less than 1 % even for τ 's from a charged Higgs of 150 GeV/c²). $\delta R_{\tau\mu}$ must be equal to 0 if lepton universality holds. In Fig.1 the ratio $R_{\tau\mu}$ is shown as function of $\tan\beta$, for three $[m_t, m_{H^+}]$ mass combinations (the branching ratios, appearing in the equation above, have been calculated with the formulae given in Refs.[1] and [2]).

Thus, if the ratio $R_{\tau\mu}$ is measured to be larger than 1, it would be evidence of a charged Higgs in t -quark decays.

We have investigated the possibility of measuring the rate of $t \rightarrow \tau^+\nu_\tau b$ decays at LHC, using $t\bar{t}$ events generated with the ISAJET Monte Carlo program [3]. We start with a sample of ‘tagged’ t -quark events, namely an $e\mu$ sample which, because of the hard p_T^T cuts on the leptons $p_e^T > 75$ GeV/c and $p_\mu^T > 25$ GeV/c, is an almost pure $t\bar{t}$ sample (see the previous section). In this sample we can identify events in which the second t -quark decays via $t \rightarrow \mu^+\nu_\mu b$, as described for the measurement of $BR(t \rightarrow \mu^+\nu_\mu b)$, and via $t \rightarrow \tau^+\nu_\tau b$. The ratio of the rate of (*isolated e - μ*) - *isolated τ*) events $N_{e\mu\tau}$ to the rate of (*isolated e μ*) - *isolated μ*) events $N_{e\mu\mu}$ is directly related to the quantity $\delta R_{\tau\mu}$

$$\frac{N_{e\mu\tau}}{N_{e\mu\mu}} = \frac{BR(\tau \rightarrow hadrons) \epsilon_{W \rightarrow \tau}}{\epsilon_{W \rightarrow \mu}} \left[1 + \frac{\epsilon_{H \rightarrow \tau}}{\epsilon_{W \rightarrow \tau}} \delta R_{\tau\mu} \right] \quad (4.2)$$

We indicate with $\epsilon_{H \rightarrow \tau}$ and $\epsilon_{W \rightarrow \tau}$ the probability of identifying, in the tagged t -quark sample, the $\tau \rightarrow hadrons$ decay in events in which the τ , from the second t -quark, comes from the

decay of the charged Higgs and from the decay of the W , respectively; $\epsilon_{W \rightarrow \mu}$ is the probability of identifying the $t \rightarrow \mu^+ \nu_\mu b$ decay of the second t -quark. We have studied $\tau \rightarrow \text{hadrons}$ identification in t -quark tagged events. The main background to the signal of the $t \rightarrow \tau^+ \nu_\tau b$ decay comes from events in which the second t -quark decays hadronically and one of the hadronic jets is misidentified as a τ -jet. In the Standard Model the rate of hadronic t -quark decays is six times larger than that of the t -quark decay into τ and the branching ratio of $\tau \rightarrow \text{hadrons}$ is 64.4 %. So we have to reduce a background which is at most a factor 6/0.644 larger than the signal. To achieve this, we have applied the following cuts: we ask each jet in the hemisphere opposite to the tagged t -quark (*i.e.* the azimuthal angle difference between the jet and the isolated electron has to be larger than 90 degrees) to have a transverse energy larger than 30 GeV. In addition we ask the number of charged tracks N_{ch} in a cone $\Delta R < 0.1$ around the jet axis to be less than 3 and the sum of the transverse energy in the calorimeter cells (the distance between the centers of two contiguous calorimeter cells is assumed to be $\Delta R = 0.04$), outside a cone $\Delta R = 0.1$ and within a cone $\Delta R = 0.4$ around the jet axis, to be less than 5 GeV. If there is no charged Higgs in the t -quark decay, starting from a sample of 2389 $e\mu$ tagged t -quark events collected in 1 year LHC running at a luminosity of $10^{33} \text{ cm}^{-2} \text{ s}^{-1}$ for $m_t = 200 \text{ GeV}/c^2$, we get after the ' τ ' cuts 123 $e\mu\tau$ events of which 94 have a real τ and 29 have a fake τ . Thus, the acceptance of the set of cuts mentioned above for events with $200 \text{ GeV}/c^2$ t -quark is 55% for events with a τ from W and 1.8 % for events with the second t -quark decaying in hadrons. From the same $e\mu$ sample, asking an additional muon with $p_\mu^T > 50 \text{ GeV}/c$, leaves 248 $N_{e\mu\mu}$ events so that $\epsilon_{W \rightarrow \mu}$ is $\sim 94\%$. In addition we find that $\epsilon_{H \rightarrow \tau} / \epsilon_{W \rightarrow \tau}$ is 1.5 for τ 's from a charged Higgs of $150 \text{ GeV}/c^2$. The measured quantity $R_{\tau\mu}^{\text{meas}}$ is affected by a statistical error and a systematic error. The statistical error is

$$\left[\frac{\Delta R_{\tau\mu}^{\text{meas}}}{R_{\tau\mu}^{\text{meas}}} \right]_{\text{stat}} = \frac{1}{\sqrt{N_{e\mu\mu}}} \left(1 + \sqrt{\frac{\epsilon_{W \rightarrow \mu}}{BR(\tau \rightarrow \text{hadrons}) \epsilon_{W \rightarrow \tau}}} \right) = 17\% \quad (4.3)$$

Experimental systematic uncertainties, like the error on the tracking efficiency (which affects the number of detected charged tracks) and the energy resolution of the calorimeter (which affects both the measurements of the jet energy and of the jet 'isolation'), affect the number of detected (real and fake) τ 's. To evaluate these systematic experimental uncertainties, more work is needed (no detector effects were considered here). An additional contribution to the systematic error comes from the uncertainty of the Monte Carlo prediction for the background of 'fake' τ 's: there is an uncertainty on the predicted number of jets, in the $t\bar{t} \rightarrow \text{hadrons}$ events, which affects the calculated background rejection efficiency (conversely, the larger the number of jets in the event, the higher the probability for one of them to fake a τ). This uncertainty comes from the imperfect knowledge of gluon radiation processes and from the approximations used in the Monte Carlo to simulate the higher order QCD processes. On the other hand, the relative transverse energy cut (30 GeV) should reduce effectively the Monte Carlo uncertainty. From ISAJET, we evaluated that in $t\bar{t} \rightarrow \text{hadrons}$ events about 10% of the fake τ 's come from gluon radiation processes. Assigning 100% error to this prediction, we get a 10% Monte Carlo prediction error on the number of fake τ 's (which is $10\% \times 29 = 2.9$ events): this is 3% of the expected number of real τ 's. In summary, it seems evident that if the systematic error can be reasonably controlled, statistics is the major limitation of this method, since τ identification is probably not feasible at higher luminosity.

In Fig. 2 we show the ratio $R_{\tau\mu}^{\text{meas}}$, defined by

$$R_{\tau\mu}^{\text{meas}} = \left[1 + \frac{\epsilon_{H \rightarrow \tau}}{\epsilon_{W \rightarrow \tau}} \delta R_{\tau\mu} \right] \quad (4.4)$$

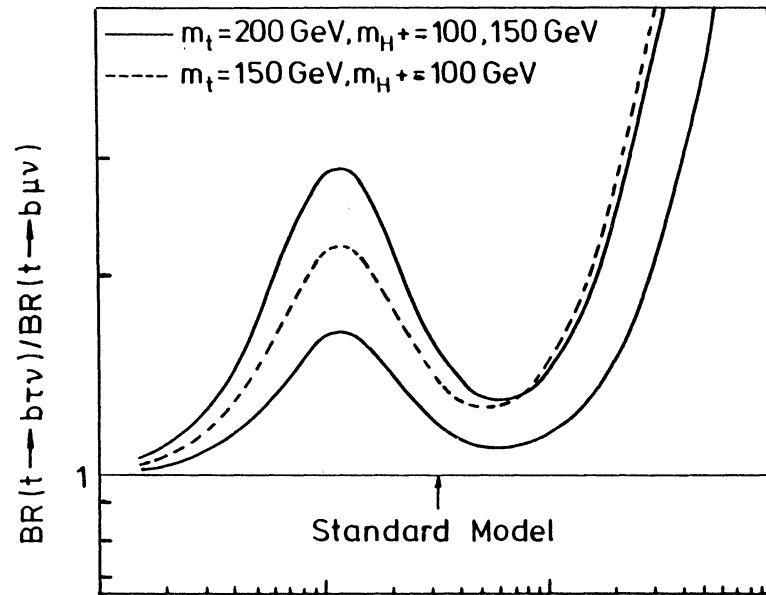


Fig. 1

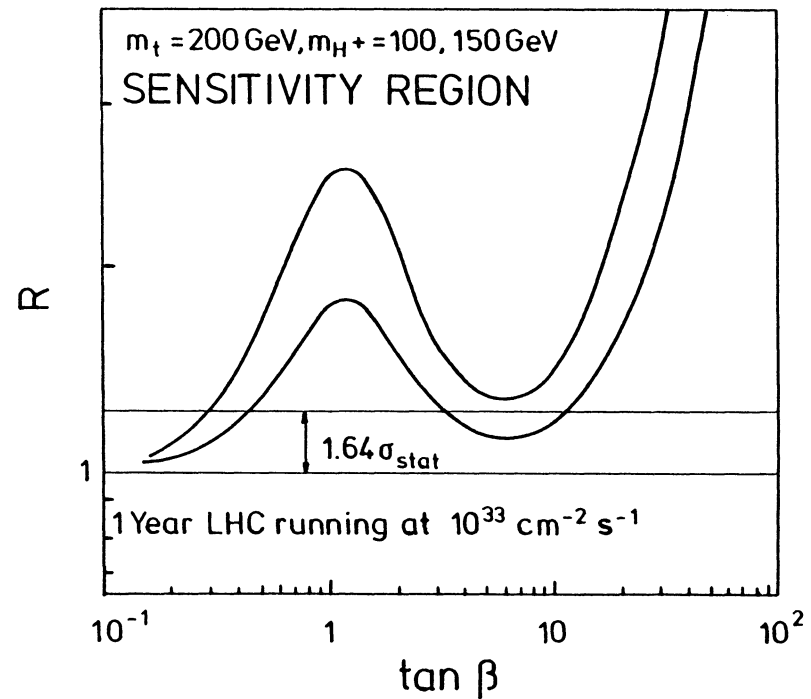


Fig. 2

[see (3.2)] as a function of $\tan\beta$ for $m_t = 200 \text{ GeV}/c^2$ and $m_{H^\pm} = 150$ and $100 \text{ GeV}/c^2$. Shown is also the line where the deviation from the $R_{\tau\mu}$ value of the Standard Model is 1.64 times the statistical error. This line gives an indication of the sensitivity to $t \rightarrow H^+ b \rightarrow \tau\nu_\tau b$ that can be reached by utilizing the method outlined above.

We conclude that τ identification in t -quark events can be feasible, if the detector is equipped with a tracking device and a well segmented calorimeter, but only at low luminosities (*i.e.* $\leq 10^{33} \text{ cm}^{-2} \text{s}^{-1}$) so that the largest uncertainty affecting the measurement would be the statistical error. Nonetheless, it has been shown that with the data collected in one year LHC running at a luminosity of $10^{33} \text{ cm}^{-2} \text{s}^{-1}$ a large region of the parameter space [$\tan\beta, m_{H^\pm}$] could be explored, for a t -quark masses up to about $200 \text{ GeV}/c^2$.

REFERENCES

- [1] I. Bigi, Y. Dokshitzer, V. Khoze, J. Kühn and P. Zerwas, Phys. Lett. B 181 (1986) 157.
- [2] V. Barger and R.J.N. Phillips, Phys. Rev. D 41 (1990) 884.
- [3] F. Paige and S.D. Protopopescu, ISAJET Monte Carlo, BNL 38034 (1986).

Single Top Production: Wg Fusion and Top Mass

T. Moers, R. Priem, D. Rein and H. Reithler

III. Physik. Institut, RWTH Aachen, D-5100 Aachen (FRG)

Introduction

Interest in leptonic decays from the *single top* production via “ Wg fusion” (Fig.1) has two evident experimental motivations: by comparison with $t\bar{t} \rightarrow l\ell\nu\bar{\nu}$ production, this process becomes more copious for top masses above 300 GeV, and the simpler kinematics is likely to allow a more unambiguous reconstruction of the top mass. Since there is only one neutrino involved, its transverse momentum is directly measurable. As a further argument, it was pointed out [1] that the bottom quark from the top decay can be kinematically tagged (experimental resolution was however not taken into account in [1]).

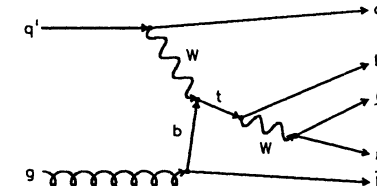


Figure 1: Mechanism of single top production in pp collisions, called “ Wg fusion” or $Wg \rightarrow t\bar{b}$. The top mass has to be reconstructed from its decay products b_t , ℓ , and ν . To stress that it is the b quark from the top decay, we label it b_t .

We focussed our investigation on the main experimental issues related to the measurement accuracy of m_t , namely (a) tagging of b_t from the observable jets, (b) determination of the neutrino longitudinal momentum, and (c) behavior and reduction of the main background.

For this purpose, a detector with large angular coverage $|\eta| < 5$, thus with the possibility to measure the missing transverse momentum $p_{T,\text{miss.}}$, was assumed. Events were generated with the Pythia [2] V5.4 Monte Carlo package for $\sqrt{s} = 16 \text{ TeV}$ pp collisions. As a basic signature, a charged lepton μ (or e) from top decay, and ≥ 3 jets with $E_T(\text{Jet}) > 20 \text{ GeV}$ are required.

Tagging of the Partons

The scattered partons q and \bar{b} should have a larger pseudorapidity η than the parton b_t , which is emitted in the decay of the very massive t . Since the x distribution of quarks is harder than that of gluons, the quark-gluon system will move along the direction of the incoming quark, and the scattered q should have larger η (and momentum) than the \bar{b} . This is confirmed in Fig.2a): *the q has the largest η* . Furthermore, in most events the \bar{b} is emitted in the hemisphere opposite to that of the q .

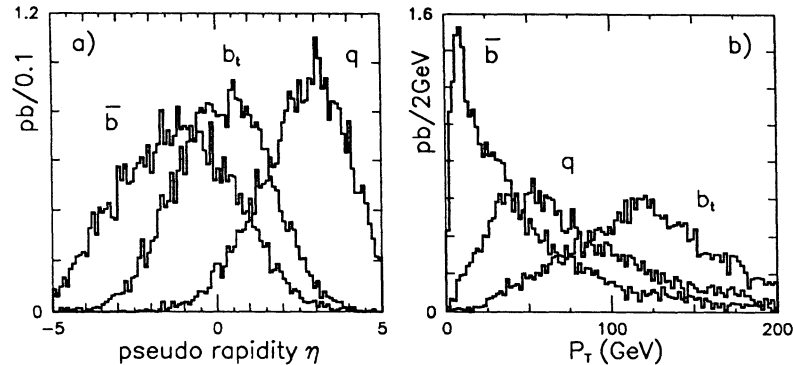


Figure 2: Pseudorapidity η a) and transverse momentum p_T distribution b) of final state quarks q , \bar{b} , and b_t from Wg fusion, for $m_t = 300$ GeV and $W \rightarrow \mu\nu$ decay. To make asymmetries more apparent, the incoming quark is coming from the beam with $\eta > 0$ only.

To distinguish the other two quarks, we look at the transverse momentum distribution. For the b_t , one would expect the maximum of this distribution to be around $m_t/2$ if $m_t \gg m_W$, or slightly below for non-negligible m_W . Much lower transverse momenta of the order of m_b are expected from the gluon splitting into $b\bar{b}$, as demonstrated by Fig.2b). Thus, having already tagged q by its large pseudorapidity, one distinguishes \bar{b} and b_t by noting that \bar{b} has the lowest p_T . The third quark is then the b_t .

Jet vs. Parton Tagging

It is evident from the overlap of the three curves in Fig.2 that the b_t tagging cannot be perfect. In real life the quark's \vec{p} and η have to be inferred from reconstructed jets, thus with additional uncertainties which worsen the tagging.

In our simulation we assume a calorimeter structure with 50 (48) subdivisions in $\eta(\varphi)$, thus having 2400 cells in the range $|\eta| < 5$. The jet algorithm makes a search around a seed of $E_T > 10$ GeV and sums energy depositions (μ excluded) within $\Delta R \equiv \sqrt{(\Delta\eta)^2 + (\Delta\varphi)^2} < 0.4$. Charged particles with $p_T < 1$ GeV are assumed to be trapped by the magnetic field and thus discarded. Jets are required to have $E_T > 20$ GeV.

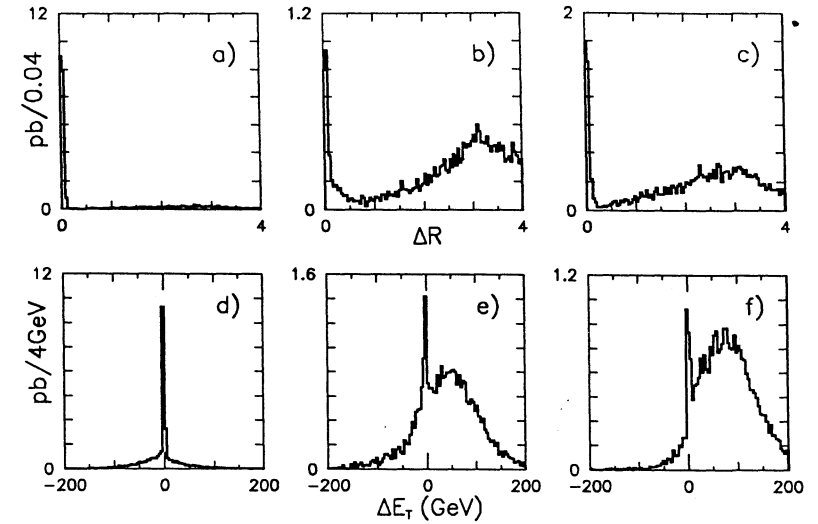


Figure 3: Comparison of jet tagged as “ b_t ” with original quarks b_t (a and d), q (b and e), and \bar{b} (c and f), for $m_t = 300$ GeV. Upper row is ΔR , lower row is ΔE_T . Note the differences in the vertical scales within each row, for the same total number of entries. This jet indeed matches the b_t quark within $\Delta R < 0.2$ in most of the events, but sometimes the other jets also do so.

Some events may turn out to have more than three jets; in such cases we consider the three jets with highest E_T . The quality of the b_t tagging is best shown by plotting ΔR (ΔE_T) between the tagged jet and the quarks, Fig.3. In most cases the correct quark is within $\Delta R < 0.2$, but sometimes the other quarks do match as well. In some cases there is no quark within this limit. To quantify this tagging efficiency, we count how often the b_t jet axis is indeed within $\Delta R < 0.2$ of the b_t quark, see Table 1. It is apparent that this tagging is only effective for large m_t , where the improvement w.r.t. a random choice is a factor 2. An increase of the E_T threshold for the q and b_t jets from 20 to 40 GeV, as probably needed for background reduction, leaves the tagging efficiency of Table 1 unchanged.

m_t (GeV)	150	200	300
tagged b_t jet	33%	47%	60%
random choice	26%	29%	31%

Table 1: Tagging efficiency of b_t jet, as the fraction of events with the axis of the selected jet within $\Delta R < 0.2$ of the b_t quark. For comparison, the efficiency for a random choice of the jet is also given.

The tentative tagging of the b_t jet has a further advantage: when reconstructing the top

mass from its decay products one obtains a distribution which is narrower than for a random choice of the jet. It would therefore be useful to elaborate more on this jet tagging, e.g. with the method of neural networks, once the detector design is settled.

Reconstruction of Neutrino Momentum

The neutrino transverse momentum is well measured by the observed $p_{T,\text{miss.}}$. Since the neutrino originates in the decay $W \rightarrow \mu\nu$, we use the W mass as constraint to determine p_L . The two solutions from the quadratic equation are equivalent for the neutrino, but drastically different for the reconstruction of m_t , see Fig.4. It turns out that in $\approx 65\%$ of the events the solution with the lowest value of p_L is the correct one. The same applies for the heavier top. In the following, we will always select the lowest p_L .

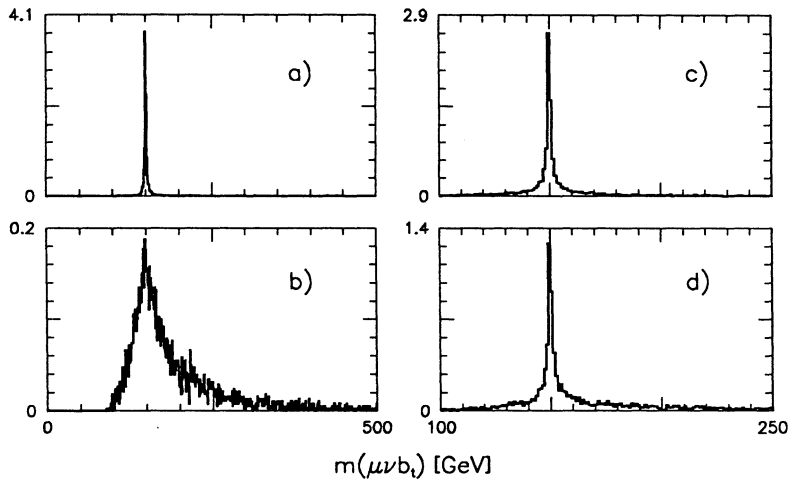


Figure 4: Influence of the ambiguity in the determination of the neutrino longitudinal momentum on the reconstructed top mass, for an ideal detector. a) The correct solution, b) the wrong solution for p_L . A possible experimental criterion is to separate into solution with c) low value p_L , and d) high value of p_L . The low p_L is the correct solution in 65% of the cases.

It should be noted that the “correct solution” has at least an uncertainty reflecting the width of the W mass. The difference between the actual value of the W mass and the central value used in the reconstruction also causes about 8% of the events to have no real solution for p_L (when all other values are error free). Measurement errors in E_J (E_μ) cause further 14% (4%) to be non solvable. First attempts indicate that this total of $\approx 26\%$ may be rescued by appropriate corrections, but we will not use them here.

Reconstruction of Top Mass: Resolution vs. Background

Energy measurement errors were taken into account with a width of $50\%/\sqrt{E} \oplus 5\%$ (E in GeV) for the jets, and of 10% for the muons. The width of $15\%/\sqrt{E} \oplus 1\%$ (E in GeV) for electrons would be much smaller. For the neutrino, each component of the transverse momentum was scaled with the ratio of the corresponding sum over the jets (and the muon) with and without smearing. No smearing was taken for the muon direction of flight, which is accurately known. For the jet axis and for the neutrino, the main uncertainties are built in through the calorimeter cell granularity and the algorithm used.

Events with a muon and at least 3 jets with $E_T > 20$ GeV were generated for the following processes:

Signal of Wg fusion $Wg \rightarrow t\bar{b}; t \rightarrow b_t W; W \rightarrow \mu\nu$ type, amounting to 14 pb (8 pb) for $m_t = 150$ GeV (300 GeV). For the purpose of measuring m_t , the $t\bar{t}$ process $t\bar{t} \rightarrow W\bar{W}bb$ with one $W \rightarrow \mu\nu$ and one $W \rightarrow q\bar{q}$ decays also has to be considered as signal, provided the mass distribution is not much worse than for Wg fusion. It contributes with 378 pb (17 pb) for $m_t = 150$ GeV (300 GeV).

Background becomes hardly reducible when a $W \rightarrow \mu\nu$ decay and jets are present, as e.g. from $q\bar{q} \rightarrow Wg$, or $qg \rightarrow Wq$, or $\bar{q}g \rightarrow W\bar{q}$. This $W + nJ$ background delivers the dominant contribution of 978 pb. By comparison, the correct WW signature from $pp \rightarrow WWX$, having only 0.9 pb, can be neglected.

The top mass distributions resulting from the reconstructed $\mu\nu b_t$ system are shown in Figs.5, 6. For the signal, the shape of the mass distribution has wide tails reflecting the effect of quark tagging and neutrino reconstruction uncertainties. The measurement errors affect mainly the shape of the narrower peak around m_t . Although the event treatment was devised for Wg fusion, the $t\bar{t}$ events also deliver a clear (but somewhat wider) mass peak. The mass peak of the signal follows precisely the value of m_t . As expected, the background displays no mass peak, but a falling distribution with maximum near 120 GeV. In Fig. 6a), the mass distribution of the “wrong jet” $\mu\nu\bar{b}$ system is also shown (dotted line): here, not even a bump is visible around m_t . This is an impressive demonstration of the usefulness of the b_t tagging. As a next step, we try to discard as much as possible from the huge amount of background.

Reduction of Background

Further cuts are needed, to reduce the background level. The most effective handle is shown in Fig.7: The number of jets (with $E_T > 20$ GeV) per event is unfortunately similar for the Wg signal and for the background, but in clear contrast to the $t\bar{t}$ signal. We thus require at least 5 jets in the event, and obtain a signal to background ratio above 5 for $m_t = 150$ GeV (where it is most needed) and above 1 for $m_t = 300$ GeV, see Table 2. This should be sufficient for a good measurement of m_t .

Another interesting possibility is to require $E_T > 60$ GeV, instead of 20 GeV, for the jet with highest rapidity (the jet tagged as “ q ”). The signal to background ratio improves by a factor of about 3, but there is still much background left.

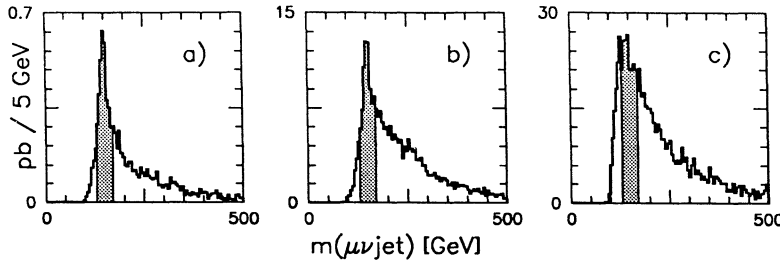


Figure 5: Top mass distribution, as reconstructed from the $\mu\nu b_t$ system, for $m_t = 150$ GeV. a) Wg signal, b) $t\bar{t}$ signal, c) main background $W + nJ$. The mass band of 20 GeV around m_t is shaded.

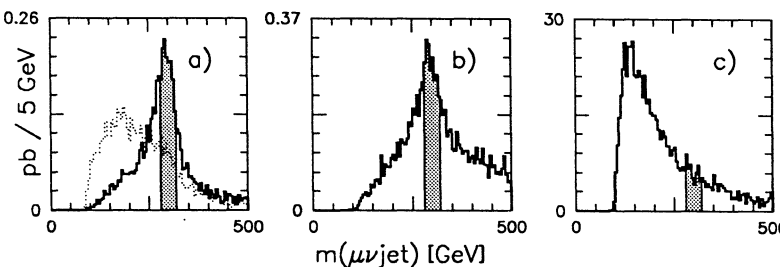


Figure 6: Top mass distribution, as reconstructed from the $\mu\nu b_t$ system, for $m_t = 300$ GeV. a) Wg signal, b) $t\bar{t}$ signal, c) main background $W + nJ$. The dotted line in a) is for the $\mu\nu b$ system and shows the impact of quark tagging.

An isolation requirement for the muon will be unable to distinguish our signal from the $W + nJ$ background, since the muon originates from a W decay in both cases. However, its use is implied here, as we do not take $b\bar{b}$ background sources into account. We also did not restrict the opening angle between two jets.

If one intends to obtain a pure sample of single top events from Wg fusion, i.e. free of contributions from $t\bar{t}$, an adequate choice of cuts may be ≤ 3 jets with $E_T > 25$ GeV, one jet with $|\eta| > 2$ and $E_T > 50$ GeV, a further jet with $E_T > 50$ GeV, $p_{T,\text{miss.}} > 40$ GeV and the charged lepton with $p_T > 40$ GeV and $|\eta| < 2$. A relative contribution $Wg/t\bar{t} \approx 4$ is achieved, but the ratio signal/background ≈ 0.1 is still very poor, see Tab. 2.

Conclusion

A rather background free sample of events with one $t \rightarrow Wb \rightarrow \mu\nu b$ decay can be prepared and the mass of the $\mu\nu b$ system can well be measured. The signal comes from Wg fusion and from $t\bar{t}$ production. The treatment studied for Wg fusion events is also effective for $t\bar{t}$ events. The cuts intended to reduce the $W + nJ$ background, reduce the Wg fusion signal as well.

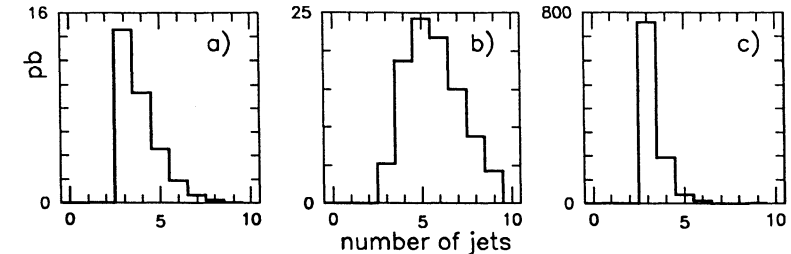


Figure 7: Number of jets (with $E_T > 20$ GeV) per event, for a) Wg signal, b) $t\bar{t}$ signal, c) main background $W + nJ$. Here $m_t = 300$ GeV was used; these distributions remain mainly unchanged when $m_t = 150$ GeV is used, or when the E_T threshold for the first two jets is raised from 20 to 40 GeV.

Further cuts	m_t (GeV)	Signal		Background	signal background (%)
		Wg (pb)	$t\bar{t}$ (pb)	$W + nJ$ (pb)	
—	150	3.5	74.5	184.5	42
	300	1.6	2.2	50.2	8
$E_T(J_q) > 60$ GeV	150	1.4	43.3	40.7	110
	300	0.9	2.1	10.5	29
≥ 5 jets with $E_T > 20$ GeV	150	0.41	38.2	7.2	536
	300	0.33	1.7	≈ 1.7	119
≤ 3 jets with $E_T > 25$ GeV, ... to reject $t\bar{t}$; see text.	200	0.25	0.07	2.8	11
Full mass range 0–500 GeV	150	9.0	263.	700.	39
	300	4.8	9.7	700.	2

Table 2: Summary of expected cross sections for events with one μ , and ≥ 3 jets ($E_T > 20$ GeV) within $|\eta| < 5$, for reconstruction of the top mass. Further cuts as indicated in the table. The cross sections quoted are for events in the mass band $m_t \pm 20$ GeV. Uncertainties from energy measurement, jet reconstruction, quark tagging and neutrino reconstruction are included. Further detection efficiencies are taken as unity. A signal to background ratio in excess of 5 can be achieved.

Hence the final signal is mainly from $t\bar{t}$. For the measurement errors assumed here, the wide component of the mass distribution has a rather combinatorial origin: ambiguities and errors in tagging the b_t quark and in reconstructing the neutrino momentum. Future studies should try to improve on this, since a considerable improvement in final resolution may possibly be achieved without any change in the assumed energy resolution of the detector. Optimization is then to be done mainly for the dominant $t\bar{t}$ contribution.

REFERENCES

- [1] C.-P. Yuan, Phys. Rev. D41 (1990) 42.
- [2] H. Bengtsson and T. Sjöstrand, PYTHIA [CERN Computer Library; V5.4 with amendments for single top production].

A5: HIGGS PHYSICS**The Standard Model Higgs at LHC:
Branching Ratios and Cross-Sections**

Z. Kunszt
 Theoretical Physics, ETH,
 Zurich, Switzerland,

and

W.J. Stirling
 Departments of Physics and Mathematical Sciences,
 University of Durham,
 Durham, England.

Abstract

The Standard Model Higgs boson is studied in the context of 16 TeV proton-proton collisions. Branching ratio calculations are updated, paying attention to the effect of QCD corrections on the $H \rightarrow b\bar{b}$ partial width and to threshold effects in the $H \rightarrow WW, ZZ$ partial widths. A variety of production mechanisms are reviewed, and the associated uncertainties in the theoretical predictions are discussed. Recent theoretical developments concerning the next-to-leading order corrections and the background calculations are briefly summarized. Event rates for the important discovery channels are presented.

1 Introduction

One of the aims of the theoretical study in the Higgs Working Group was to update and refine predictions for the branching ratios and production cross-sections for the Standard Model Higgs boson (H) [1], and to review briefly the most recent theoretical developments concerning the calculation of higher order corrections and background processes. The purpose of this report is to document the results of this study.

Another objective of the theoretical study was to investigate the role of the LHC if, prior to its construction, a scalar boson with properties similar to those of the standard model Higgs was discovered at LEP. This would motivate the investigation of some realistic alternatives to the SM Higgs sector. The two-doublet Higgs sector of the Minimal Supersymmetric Standard Model (MSSM) is generally considered to be the simplest, theoretically most attractive alternative which is also phenomenologically acceptable. At LEP energies, the Higgs sector of this model is experimentally indistinguishable from the SM Higgs sector in a large region of the relevant parameter space. It is therefore interesting to investigate the potential of the LHC to test the MSSM Higgs sector as well. The results of such a study are presented in a separate contribution [2].

In general, the search for the Higgs boson(s) at the LHC is made difficult by the large backgrounds. In order to understand how to reject these backgrounds, detailed simulation work is needed. Much of the effort of the Higgs Working Group was devoted to simulations of the Higgs signal in the mass range $m_Z < m_H < 1$ TeV. The results are summarized in the experimental review by Froidevaux [3], and are presented in separate contributions.

2 Input parameters

Although the branching ratios and production cross-sections of the SM Higgs boson have been calculated before [1,4], there is a need to update these predictions, in view of recent improvements in our knowledge of various Standard Model parameters [5] and parton distributions [6].

Some of the discrepancies in the values of branching ratios and cross-sections in the literature arise simply from different choices of input parameters. For this reason, it is important to list first the parameter values that will be used in the present study:

$$\begin{aligned} M_Z &= 91.16 \text{ GeV}, & M_W &= 80.0 \text{ GeV}, \\ \sin^2 \theta_W &= 0.230, & \alpha \equiv \alpha(M_Z) &= \frac{1}{128}, \\ \Lambda_{\overline{\text{MS}}}^{(5)} &= 125 - 150 \text{ MeV}, & 90 \text{ GeV} < m_t < 200 \text{ GeV}. \end{aligned} \quad (1)$$

For parton distributions, we use the recent HMRS(B) set [7], which have been obtained from a global ‘best fit’ to deep inelastic scattering, prompt photon and Drell-Yan data. The effect of the uncertainty in the parton distributions on Higgs cross-sections will be briefly discussed.

The availability of a high-luminosity option at the LHC ($\mathcal{L} \sim 10^{34} \text{ cm}^2 \text{s}^{-1}$ compared to the standard $\mathcal{L} \sim 10^{33} \text{ cm}^2 \text{s}^{-1}$) demands a reassessment of various channels previously considered of little use. Consequently, one new feature of the present study is our focus on several ‘rare’ production and decay modes.

It is convenient to identify two distinct Higgs mass regions: a ‘heavy’ Higgs is defined as one with $M_H > O(200) \text{ GeV}$, while an ‘intermediate-mass’ Higgs has $O(80) \text{ GeV} < M_H < O(200) \text{ GeV}$. The lower limit of 80 GeV represents the conservative limit of discovery at LEP200 [8].

3 Branching Ratios

A complete discussion of the various Higgs partial decay widths – together with the relevant formulae – can be found in reference [4]. For the present study we have updated the numerical results. Two partial widths have been considered in some detail. First, we have re-analysed the Higgs partial width into $b\bar{b}$, including the effects of higher order QCD corrections and, in particular, the effects of the running b quark mass. The suppression of the partial width that this induces is significant not because the exact value for the decay rate into $b\bar{b}$ is important *per se*, but rather because it can affect the branching ratios of rarer decay modes. In particular we find that the $H \rightarrow \gamma\gamma$ branching ratio is about a factor of two *higher* than the values indicated in the corresponding figures in reference [4], where, however, it was noted that the running b -quark mass effect is expected to be significant. This has important positive implications for searches for the intermediate-mass Higgs in this channel [9].

The partial decay width of the Higgs boson into heavy quarks has recently been calculated to $O(\alpha_S^2)$ [10]. Assuming five active flavours the result in the $\overline{\text{MS}}$ scheme can be summarized as

$$\begin{aligned} \Gamma(H \rightarrow b\bar{b}) &= \frac{3\sqrt{2}}{8\pi} G_F M_H \bar{m}_b^2 \left(1 - \frac{4\bar{m}_b^2}{M_H^2}\right)^{\frac{3}{2}} [1 + 1.803\alpha_S + 2.953\alpha_S^2] \\ &\times \left[1 + O\left(\frac{\bar{m}_b^2}{M_H^2}\right)\right], \end{aligned} \quad (2)$$

where G_F is the Fermi coupling constant, α_S is the QCD coupling constant evaluated at $\mu = M_H$, and the running b -quark mass for five flavours is given by

$$\bar{m}_b = \hat{m}_b \left(\frac{23\alpha_S}{6\pi}\right)^{\frac{12}{23}} [1 + 0.3742\alpha_S + 0.1521\alpha_S^2]. \quad (3)$$

The numerical value of the integration constant \hat{m}_b is 8.23 GeV, assuming $\Lambda_{\overline{\text{MS}}}^{(5)} = 150 \text{ MeV}$ and using the central value of m_b [11]:

$$m_b = 4.25 \pm 0.10 \text{ GeV}, \quad (4)$$

where m_b is defined by the condition $\bar{m}_b(m_b) = m_b$.

The main impact of the running b -quark mass on the $H \rightarrow \gamma\gamma$ branching ratio is in the $100 - 150 \text{ GeV}$ Higgs mass region. The factor of two enhancement in the branching ratio comes simply from the factor $\bar{m}_b^2(M_H = 150 \text{ GeV})/\bar{m}_b^2(m_b) \simeq 0.47$ which reduces the $H \rightarrow b\bar{b}$ partial width from the fixed m_b result.

Very recently the effect of QCD corrections on the $H \rightarrow \gamma\gamma$ partial decay width has been evaluated [13] and found to be small in the mass region of interest.

Typically, the correction varies between -2% and +3%. We note that the remaining uncertainties in the partial decay width due to $\Lambda_{\overline{\text{MS}}}$, m_b are estimated to be smaller than 10%.

The second partial width that we have re-analysed is $H \rightarrow W^{(*)}W^{(*)}$ (and the related $H \rightarrow Z^{(*)}Z^{(*)}$) (see also [12]). For Higgs masses far above threshold the decay width can be calculated assuming on-shell weak bosons. Very recently the electroweak radiative corrections have been evaluated [14]. The corrections are rather small. Since the result has been obtained only very recently, and the corrections become significant only above $M_H = 800$ GeV, these corrections are not included in our figures. The finite-width effects are also negligible for the region $M_H \ll 2M_W$, where one W can be taken on-shell, and the other far-off-shell. The threshold region is more problematic, in that finite W -width effects become important. The correct way to proceed is to calculate the full partial width for, say, $H \rightarrow l\bar{\nu}_l l'\bar{\nu}_{l'}$, from which the width to any other WW final state can be extracted. Thus we have

$$\Gamma(H \rightarrow l\bar{\nu}_l l'\bar{\nu}_{l'}) = \frac{1}{2M_H} \int d\Phi_4 |M|^2(H \rightarrow l\bar{\nu}_l l'\bar{\nu}_{l'}) \quad (5)$$

where the matrix element is

$$|M|^2(H \rightarrow l(p_1)\bar{\nu}_l(p_2)\bar{l}(p_3)\nu_{l'}(p_4)) = \frac{M_W^2 e^6}{\sin^6 \theta_W} \times \frac{p_1 \cdot p_3 p_2 \cdot p_4}{((p_1 + p_2)^2 - M_W^2)^2 + M_W^2 \Gamma_W^2 ((p_3 + p_4)^2 - M_W^2)^2 + M_W^2 \Gamma_W^2}. \quad (6)$$

The phase space integral can be reduced to an integral over the two W boson virtualities which can be performed numerically.

Our results are summarised in Figs. 1-3. Figs. 1 and 2 show the branching ratios of the intermediate-mass Higgs for two top masses: $m_t = 90$ GeV and $m_t = 200$ GeV. Apart from very close to the $t\bar{t}$ threshold, there is virtually no dependence of the other branching ratios on m_t .

Note that (i) the $\gamma\gamma$ branching ratio attains a maximum value of just over 2×10^{-3} at $M_H \sim 125$ GeV, and (ii) there is interesting structure in the $H \rightarrow Z^*Z^*$ branching ratio around $M_H = 150$ GeV, caused by the onset of the WW threshold. The position and height of the local maximum and minimum depend quite sensitively on the way this threshold is handled.

Fig. 3 shows the important branching ratios for the heavy Higgs mass range, again for the two top quark masses. The dominant decays are to WW and ZZ , in the approximate ratio 2:1. The heavier top has a slight impact on these branching ratios, particularly around the threshold region, $M_H = 2m_t$.

Finally, for completeness, we show in Fig. 4 the total Higgs width for the intermediate- and heavy-mass ranges.

4 Cross-sections

There are only a limited number of production mechanisms which give cross-sections large enough to be relevant to LHC physics. Each makes use of the Higgs' preference to couple to heavy particles. A detailed review – with a complete list of references – can be found, for example, in reference [4]. Here we summarise the most important features.

4.1 Gluon-gluon fusion

Except possibly for very heavy Higgs, the dominant production mechanism is $gg \rightarrow H$ via an intermediate top quark loop, Fig. 5(a). The matrix element summed/averaged over spins/colours is [15]

$$|M|^2(gg \rightarrow H) = \frac{\alpha_s^2(M_H^2) G_F M_H^4}{288\sqrt{2}\pi^2} \left| I\left(\frac{m_t^2}{M_H^2}\right) \right|^2 \quad (7)$$

where $I(x)$ is a dimensionless function given by:

$$I(x) = 3x[2 + (4x - 1)F(x)]$$

$$F(x) = \theta(1 - 4x) \frac{1}{2} \left[\log\left(\frac{1 + \sqrt{1 - 4x}}{1 - \sqrt{1 - 4x}}\right) - i\pi \right]^2 - \theta(4x - 1)2 \left[\sin^{-1}(1/2\sqrt{x}) \right]^2 \quad (8)$$

The factor $|I|^2$ vanishes as $x \rightarrow 0$, attains a maximum value of about 3.3 at $x \sim 0.2$ and then decreases to the constant value of 1 as $x \rightarrow \infty$. The cross-section for Higgs production via the gluon fusion mechanism in 16 TeV pp collisions is shown in Fig. 6, as a function of M_H for the three values $m_t = 100, 150, 200$ GeV. The cross-section increases with increasing m_t for fixed large M_H , is approximately independent of m_t for $M_H \sim 400$ GeV and is larger for smaller top masses in the intermediate-mass Higgs region.

4.2 WW , ZZ fusion

When the top quark was believed to be relatively light, the mechanism that received the most attention was Higgs production by WW or ZZ fusion, Fig. 5(b). If the Higgs width is not large compared to its mass, the cross-section is calculated from the $2 \rightarrow 3$ process: $q\bar{q} \rightarrow Hq\bar{q}$. The spin/colour summed/averaged matrix elements are, for WW fusion [16]:

$$|M|^2(q(p_1)q(p_2) \rightarrow q(p_3)q(p_4)H) = \frac{512M_W^8 G_F^3}{2\sqrt{2}} \times \frac{p_1 \cdot p_2 p_3 \cdot p_4}{((p_3 - p_1)^2 - M_W^2)^2((p_4 - p_2)^2 - M_W^2)^2}$$

$$|M|^2(q(p_1)\bar{q}(p_2) \rightarrow q(p_3)\bar{q}(p_4)H) = \frac{512M_W^8 G_F^3}{2\sqrt{2}} \times \frac{p_1 \cdot p_4 p_2 \cdot p_3}{((p_3 - p_1)^2 - M_W^2)^2((p_4 - p_2)^2 - M_W^2)^2} \quad (9)$$

and for ZZ fusion [16]:

$$|M|^2(q(p_1)q'(p_2) \rightarrow q(p_3)q'(p_4)H) = (v_q + a_q)^2(v_{q'} + a_{q'})^2 \frac{M_W^8 G_F^3}{8\cos^8 \theta_W \sqrt{2}} \times \frac{p_1 \cdot p_2 p_3 \cdot p_4}{((p_3 - p_1)^2 - M_Z^2)^2((p_4 - p_2)^2 - M_Z^2)^2}$$

$$|M|^2(q(p_1)\bar{q}'(p_2) \rightarrow q(p_3)\bar{q}'(p_4)H) = (v_q + a_q)^2(v_{q'} - a_{q'})^2 \frac{512 M_W^8 G_F^3}{8 \cos^8 \theta_W \sqrt{2}} \frac{p_1 \cdot p_4 p_2 \cdot p_3}{((p_3 - p_1)^2 - M_Z^2)^2 ((p_4 - p_2)^2 - M_Z^2)^2} \quad (10)$$

with the quark vector and axial couplings given by

$$\begin{aligned} v_u &= \frac{1}{2} - \frac{4}{3} \sin^2 \theta_W, & a_u &= \frac{1}{2} \\ v_d &= -\frac{1}{2} + \frac{2}{3} \sin^2 \theta_W, & a_d &= -\frac{1}{2}. \end{aligned} \quad (11)$$

Convolution with the appropriate quark distribution functions gives the cross-section shown in Fig. 6. As all the electroweak parameters are well-determined, and the quark distributions are sampled in an x range where they are constrained by deep inelastic scattering data, there is very little uncertainty in these predictions, apart from unknown higher order perturbative QCD corrections (see below).

There is a complication, however, at large M_H where the large Higgs width becomes an important factor and the s -channel narrow-resonance approximation is no longer valid. In this case the effective W approximation – where the full $V_L V_L$ scattering amplitude is included – appears to be the most appropriate to use [19]. We note, however, that if $\Gamma_H \approx M_H$, the amplitude for $V_L V_L$ scattering receives unitarization corrections. Recently, a full calculation of the $q\bar{q} \rightarrow qqVV$ process, including all the diagrams at leading order in g_{weak} , has been performed [17,18]. Away from the resonance region the additional background diagrams not appearing in the effective W approximation are clearly relevant. In the resonance region at large M_H , however, the actual expansion parameter is $g_{\text{weak}} M_H^2/M_W^2$ and therefore additional higher order diagrams involving the splitting of the gauge boson lines are in principle important. Fortunately, the $SU(2)_R$ custodial symmetry of the Higgs sector implies that these corrections do not destroy the validity of the effective W approximation [19,20]. Note, however, that in this region a ‘full’ Born level calculation does not necessarily represent the most important subleading corrections. The effective W approximation would presumably still provide the correct framework to extract the behaviour of the $V_L V_L$ cross-section even if the Higgs sector of the standard model were completely wrong.

In view of the ambiguities arising from the large Higgs width it is more appropriate to consider the production rate in the context of the most important final states being studied, with the help of the available event generators [3].

4.3 Associated production with W, Z bosons

The cross-sections for Higgs production in association with W and Z bosons are not large, but may be useful for detecting an intermediate-mass Higgs using the high luminosity option, since the Higgs can be ‘tagged’ by triggering on the weak boson. The production mechanisms are $q\bar{q} \rightarrow WH$, $q\bar{q} \rightarrow ZH$, and the corresponding Feynman diagrams are shown in Fig. 5(c). The spin/colour summed/averaged matrix elements are [21]:

$$|M|^2(q\bar{q} \rightarrow WH) = \frac{\pi^2 \alpha^2}{9 \sin^4 \theta_W \hat{s}}$$

$$\begin{aligned} &\times \frac{\hat{s}^2 + M_W^4 + M_H^4 - 2\hat{s}(M_H^2 - 5M_W^2) + M_W^2 M_H^2}{(\hat{s} - M_W^2)^2} \\ |M|^2(q\bar{q} \rightarrow ZH) &= (v_q^2 + a_q^2) \frac{\pi^2 \alpha^2}{9 \sin^4 \theta_W \cos^4 \theta_W \hat{s}} \\ &\times \frac{\hat{s}^2 + M_Z^4 + M_H^4 - 2\hat{s}(M_H^2 - 5M_Z^2) + M_Z^2 M_H^2}{(\hat{s} - M_Z^2)^2}. \end{aligned} \quad (12)$$

As for the WW, ZZ fusion mechanism, these cross-sections are well-determined theoretically. In fact this is the only production mechanism for which the next-to-leading order QCD corrections are known: the ‘K-factor’ being identical to that for the production for a single massive off-shell W or Z . The cross-sections are therefore increased by $O(20\%)$ by the higher order QCD corrections.

The (lowest-order) production cross-sections are shown in Fig. 6. The WH cross-section is uniformly a factor of about 2 higher than the ZH cross-section. The rate for several decay channels of particular interest for the high-luminosity LHC will be discussed in Section 4.

4.4 Associated production with $t\bar{t}$

In the same spirit as the previous mechanism, a Higgs boson can be radiated off a heavy top quark produced in gluon-gluon or quark-antiquark fusion: $gg \rightarrow t\bar{t}H$, $q\bar{q} \rightarrow t\bar{t}H$ [22]. Some of the relevant Feynman diagrams are shown in Fig. 5(d). Not surprisingly, the cross-section depends quite sensitively on the top quark mass. Although the top quark-Higgs coupling is large for large m_t , this is counterbalanced by the parton distribution suppression of the correspondingly heavier $t\bar{t}H$ final state. The cross-sections for $m_t = 100$ GeV and 200 GeV are shown in Fig. 6. The lighter top quark cross section is larger over most of the M_H range, by a factor between one and three.

Unfortunately, the $t\bar{t}H$ channel is overwhelmed by QCD backgrounds in the dominant Higgs and top quark decay channels: $t \rightarrow b\bar{q}\bar{q}$, $H \rightarrow b\bar{b}, W^+W^-$, ZZ . The only relatively clean channels, involving top quark semi-leptonic decays and Higgs boson leptonic or photonic decays, occur at much too low a rate to be observable. The $b\bar{b}$ channel, however, becomes important in the Supersymmetric Standard Model at large values of the parameter $\tan \beta$ [2].

4.5 Theoretical uncertainties in the cross-sections

Apart from the obvious dependence of some of the production mechanisms on the top mass, there are two sources of theoretical uncertainty in the cross-sections discussed above. The first comes from higher order perturbative QCD corrections. These are completely unknown for the dominant $gg \rightarrow H$ and WW and ZZ fusion processes. In practice this uncertainty is reflected in the scale choice ambiguity in the leading-order cross-sections. For the $gg \rightarrow H$ cross-section, it is natural to choose $\mu = M_H$ in the parton distributions and in α_S . For the WW and ZZ fusion processes the curves in Fig. 6 have been calculated using $\mu = M_W$ in the parton distributions. This is clearly the physical scale if the $V_L V_L$ scattering contribution is dominant ($M_H > 500$ GeV) [19]. At smaller values of M_H the sensitivity to the scale choice is larger, at least in principle, due to the larger contribution from transversely polarized gauge boson exchanges. On the other hand, the allowed

range of scales is smaller, and in any case the contribution from the gauge boson fusion mechanism becomes marginal. Knowledge of the next-to-leading order QCD corrections would of course lead to greater stability with respect to the scale choice.

As mentioned above, the K-factors for the WH and ZH production mechanisms can be inferred from those for Drell-Yan production of a massive W and Z . The net effect is an increase of about 20% in the Higgs mass range where the mechanisms are relevant.

Since only a partial set of 'K-factors' are known for the production processes – and even fewer are known for the background processes – it seems wise to ignore them for the present, particularly when considering the *relative* size of signals and backgrounds. Possible K-factors of order $\pm 30\%$, say, on signals and backgrounds are not likely to dramatically change any of the conclusions derived from using only leading-order expressions.

The second major source of theoretical uncertainty is the uncertainty in the quark and gluon distribution functions. For the former, current deep inelastic data give reasonably tight constraints – of order 10% or less – for x values down to about 0.03. Global parton distribution fits extrapolate smoothly to smaller x values using theoretical prejudices for the $x \rightarrow 0$ behaviour. However the effect of different small- x behaviour only really becomes manifest at x values below $O(10^{-3})$ [23]. Since for Higgs physics at LHC we have $x \sim M_H/\sqrt{s} > O(10^{-2})$, the uncertainties in the *quark* distributions are relatively insignificant. The same cannot be said for the gluon distribution, whose small x behaviour is more uncertain. There have been attempts recently to gauge this uncertainty using distributions which are deliberately chosen to span a wide range of behaviours at small x [24]. In Fig. 7 the Higgs production cross-section given by the gluon fusion mechanism is calculated with various sets of parton densities [6]. In the intermediate-mass region where the sensitivity to the gluon density is the largest the cross-section values differ at most by a factor ≈ 2 .

5 Event Rates for Selected Channels

Signals and backgrounds for a wide variety of production and decay channels have been studied (see the numerous contributions of the Higgs working group). Three channels, however, stand out from the others in that they appear to provide the 'best' chance for discovery of the Higgs at LHC. These are (i) $gg \rightarrow H \rightarrow \gamma\gamma$, (ii) $gg \rightarrow H \rightarrow Z Z^{(*)} \rightarrow l^+l^-l^+l^-$, and (iii) $q\bar{q} \rightarrow WH \rightarrow l\nu\gamma\gamma$. (With (iii) we can include also $q\bar{q} \rightarrow ZH \rightarrow l^+l^-\gamma\gamma$, although very high luminosity would be needed to render this observable.)

Figs. 8-10 show the cross-sections times branching ratios for these channels. For those processes ((i) and (iii)) involving the $\gamma\gamma$ branching ratio, we see that the effect of a rising branching ratio combined with a falling cross-section yields a signal which is remarkably constant as a function of M_H in the intermediate-mass region. Only for Higgs masses of order 140 – 150 GeV and above do both signals start to fall away rapidly. In both cases, the backgrounds tend to increase rapidly as the Higgs mass decreases, making a detection of a 'light' intermediate-mass Higgs difficult. Further details of the $H \rightarrow \gamma\gamma$ channel can be found in the contribution of Seez [9].

The $H \rightarrow 4l^\pm$ rate as a function of M_H (Fig. 9) shows an interesting structure. At the low mass end, the rate falls very sharply to zero below about $M_H = 150$ GeV – a reflection of the behaviour of the branching ratio shown in Figs. 1 and 2.

At the high mass end, the dominant feature is the strong dependence on the top quark mass. It is clear that the four-lepton channel will offer the possibility of discovery in a Higgs mass region bounded from above *and* below, the exact window depending on the available luminosity, the top mass, and the experimental acceptance. A discussion of the experimental possibilities can be found in the accompanying review by Froidevaux [3].

6 Progress in the Evaluation of Backgrounds

As a result of the LHC workshop activity, there has been significant progress in the evaluation of the large background processes which afflict Higgs searches in almost every channel. Since the details of these background analyses are presented in the individual contributions of the Working Group – and are also summarised in the report by Froidevaux – we restrict our attention here to the calculations which are new.

In the intermediate Higgs mass region the $\gamma\gamma$ and $l\nu\gamma\gamma$ final states can be faked by ordinary jet production ($jet \rightarrow \pi^0 \rightarrow \gamma$) and bottom quark production ($b \rightarrow l\nu X$). In addition there are, of course, Standard Model processes which give rise to an identical final state, for example $q\bar{q} \rightarrow \gamma\gamma$ and $q\bar{q}' \rightarrow W\gamma\gamma$.

In this context there have been several new developments. A detailed ISAJET simulation of the $jet - jet$, $jet - \gamma$ and $\gamma\gamma$ signal and background has been performed by Seez and Virdee [9]. In the case of the $WH \rightarrow l\nu\gamma\gamma$ channel, the irreducible background from $q\bar{q} \rightarrow l\nu\gamma\gamma$ has been recently calculated [25]. Many Standard Model processes such as $b\bar{b}g$, $b\bar{g}\gamma$, $b\gamma\gamma$, $W + 1,2$ jets etc. can also fake the same final state. The new cross-section calculations for $b\bar{g}\gamma$ and $b\gamma\gamma$ production [26] have been included in the background analysis carried out by DiLella [9]. We have already stressed the importance of the four lepton final state in the intermediate mass region. One of the most important backgrounds is from $Zb\bar{b} \rightarrow 4l^\pm$. The cross-section has been evaluated during the workshop by Kleiss and has been included in the PYTHIA MC event generators [27]. We note also the analysis of $t\bar{t}$ production and decay as an important reducible background to this channel [28].

In the high-mass Higgs region the QCD radiative corrections have been recently obtained by Mele *et al.* [29]. It has been found that the corrections are of the order of +20%. Important simulation work has been performed by Seymour for Higgs tagging, using the HERWIG event generator [30]. Three recent theoretical results of relevance are: (i) the calculation by Berends *et al.* [31] of the exact matrix elements for $W + 4$ jet production, which can fake $Hqq \rightarrow W(\rightarrow l\nu)W(\rightarrow q\bar{q}')qq$; (ii) the calculations by Baur and Glover of the complete set of tree-level diagrams for $WWqq'$, $WZqq'$ and $ZZqq'$ production [32]; (iii) the calculation by Catani and Trentadue of the Higgs p_T distribution from the process $gg \rightarrow HX$, including a smooth interpolation between the small p_T 'Sudakov' form factor and the large p_T hard tail [33].

We note in closing that although the most important background calculations are now available, more work is still needed, for example, to include some of the recently calculated matrix elements in event generators.

Acknowledgements. ZK thanks B. Kniehl and M. Drees for helpful correspondence. WJS is grateful to the Theoretical Physics Group, ETH, Zurich, and to the University of Washington, Seattle, for financial support during the completion of this work.

References

- [1] G. Altarelli, in Proceedings of the Workshop on Physics at Future Accelerators, La Thuile, edited by J. H. Mulvey, CERN 87-07 (1987), Vol.1.
- [2] Z. Kunszt and F. Zwirner, this volume.
- [3] D. Froidevaux, this volume.
- [4] S. Dawson, J.F. Gunion, H.E. Haber and G.L. Kane, *The Higgs Hunter's Guide*, Addison-Wesley (1990).
- [5] See for example G. Altarelli, rapporteur talk given at the Neutrino-90 Conf., Geneva, Switzerland, June 10-15, 1990, preprint CERN-TH-5834/90, August 1990.
- [6] For reviews see H. Plothow-Besch, this volume, and Wu-Ki Tung, FERMILAB-Conf-90-172-T (1990), to appear in the Proceedings of the Workshop on Hadron Structure Functions and Parton Distributions, Batavia, April 26-28, 1990.
- [7] P.N. Harriman, A.D. Martin, R.G. Roberts and W.J. Stirling, Phys. Rev. **D42** (1990) 798.
- [8] S.L. Wu *et al.*, ECFA Workshop on LEP200, eds. A. Böhm and W. Hoogland, Vol. II (1987).
Z. Kunszt and W.J. Stirling, Phys. Lett. **242B** (1990) 507.
N. Brown, Rutherford Appleton Laboratory preprint RAL-90-059 (1990).
- [9] C. Seez, this volume.
- [10] S.G. Gorishny, A.L. Kataev, S.A. Larin and L.R. Surguladze, Tata Institute preprint TIFR/TH/90-9 (1990) and earlier references therein.
- [11] J. Gasser and H. Leutwyler, Phys. Rep. **87** (1982) 78;
See also the recent discussion by Narison, Phys. Lett. **216B** (1989) 191.
- [12] G. Pancheri, this volume.
V. Barger, G. Bhattacharya, G. Han and B.A. Kniehl, University of Wisconsin, Madison preprints MAD-PH-571,609 (1990).
- [13] A. Djouadi, M. Spira, J.J. van der Bij and P.M. Zerwas, Aachen preprint PITPA 90/24 (1990).
- [14] D.Yu. Bardin, B.M. Vilnskij and P.Ch. Christova, Sov. Yad. Phys. **53**(1991) 240; and preprint JINR, R2-90-287, Dubna (1990).
B. Kniehl, University of Wisconsin preprint MAD-PH-578 (1990) and references therein.
- [15] H. Georgi, S.L. Glashow, M.E. Macaheek and D.V. Nanopolous, Phys. Rev. Lett. **40** (1978) 692.
- [16] R.N. Cahn and S. Dawson, Phys. Lett. **B136** (1984) 196.
- [17] D.A. Dicus and R. Vega, Phys. Rev. **D37** (1988) 2474.
- [18] U. Baur and E.W.N. Glover, preprint FERMILAB-PUB-90/75-T (1990).
- [19] Z. Kunszt and D.E. Soper, Nucl. Phys. **B296** (1988) 253.
- [20] M. Einhorn and J. Wudka, Phys. Rev. **D39** (1989) 2758.
- [21] S.L. Glashow, D.V. Nanopolous and A. Yildiz, Phys. Rev. **D18** (1978) 1724.
- [22] Z. Kunszt, Nucl. Phys. **B247** (1984) 339.
See also J.F. Gunion, H.E. Haber, F.E. Paige, Wu-Ki Tung and S.S.D. Willenbrock, Nucl. Phys. **B294** (1987) 621; D.A. Dicus and S. Willenbrock, Phys. Rev. **D39** (1989) 751.
- [23] J. Kwiecinski, A.D. Martin, R.G. Roberts and W.J. Stirling, Rutherford Appleton Laboratory preprint RAL-90-053 (1990), to be published in Phys. Rev.
- [24] P.N. Harriman, A.D. Martin, R.G. Roberts and W.J. Stirling, Phys. Lett. **243B** (1990) 421.
- [25] R. Kleiss, Z. Kunszt and W.J. Stirling, ETH Zurich preprint ETH-TH/90-29 (1990), to be published in Phys. Lett.
- [26] Z. Kunszt and W.J. Stirling, unpublished.
- [27] R. Kleiss, this volume.
- [28] A. Nisati, this volume.
- [29] B. Mele, P. Nason and G. Ridolfi, preprint CERN-TH 5890/90 (1990).
- [30] M. Seymour, this volume.
- [31] F.A. Berends, W.T. Giele, H. Kuijf and B. Tausk, preprint FERMILAB-PUB-90/213-T (1990).
- [32] U. Baur and E.W.N. Glover, this volume, and U. Baur and E.W.N. Glover, preprint FERMILAB-PUB-90/189 (1990).
- [33] S. Catani and L. Trentadue, in preparation.

Figure Captions

- Fig.1 Branching ratios of the Higgs boson for $m_t = 90$ GeV in the mass range $50 \text{ GeV} < M_H < 200 \text{ GeV}$, for decay modes (a) $b\bar{b}, c\bar{c}, \tau^+\tau^-$, gg and $t\bar{t}$, (b) W^+W^- , Z^+Z^- , $\gamma\gamma$ and $Z\gamma$.
- Fig.2 The same as in Fig. 1 but for $m_t = 200$ GeV.
- Fig.3 Branching ratios of the Higgs boson for (a) $m_t = 90$ GeV, (b) $m_t = 200$ GeV in the high-mass region $200 \text{ GeV} < M_H < 1 \text{ TeV}$.
- Fig.4 Total Higgs width as a function of M_H for $m_t = 90$ GeV and $m_t = 200$ GeV.
- Fig.5 Representative Feynman diagrams describing the main mechanisms of Higgs production: (a) gluon-gluon fusion, (b) WW or ZZ fusion, (c) associated production with weak gauge bosons, and (d) associated production with top quark pairs.
- Fig.6 Total cross-sections for H production at LHC as a function of the Higgs mass M_H , as given by the four production mechanisms illustrated in Fig. 5. Upper solid lines: $gg \rightarrow H$ for $m_t = 100, 150, 200$ GeV; dotted line: gauge boson fusion; lower solid lines: associated production with top quarks for $m_t = 100, 200$ GeV; dashed lines: associated production with weak gauge bosons.
- Fig.7 Higgs production cross-sections from gluon-gluon fusion calculated with seven different sets of parton distributions [6].
- Fig.8 Total cross-sections for Higgs production times the branching ratio for the decay mode $H \rightarrow \gamma\gamma$ at LHC and SSC energies, as a function of the Higgs mass M_H for three values of the top quark mass $m_t = 100, 150, 200$ GeV in the low-mass range.
- Fig.9 Total cross-sections for Higgs production times the branching ratio for the decay mode $H \rightarrow l^+l^-l^+l^-$ ($l = e, \mu$) at LHC and SSC energies, as a function of the Higgs mass M_H for three values of the top mass $m_t = 100, 150, 200$ GeV in the low mass range.
- Fig.10 Total cross-sections for WH and ZH production times the branching ratios for the decay modes $H \rightarrow \gamma\gamma$ and $W^\pm \rightarrow l\nu, (l = e, \mu)$ at LHC and SSC energies, as a function of the Higgs mass M_H in the low-mass range.

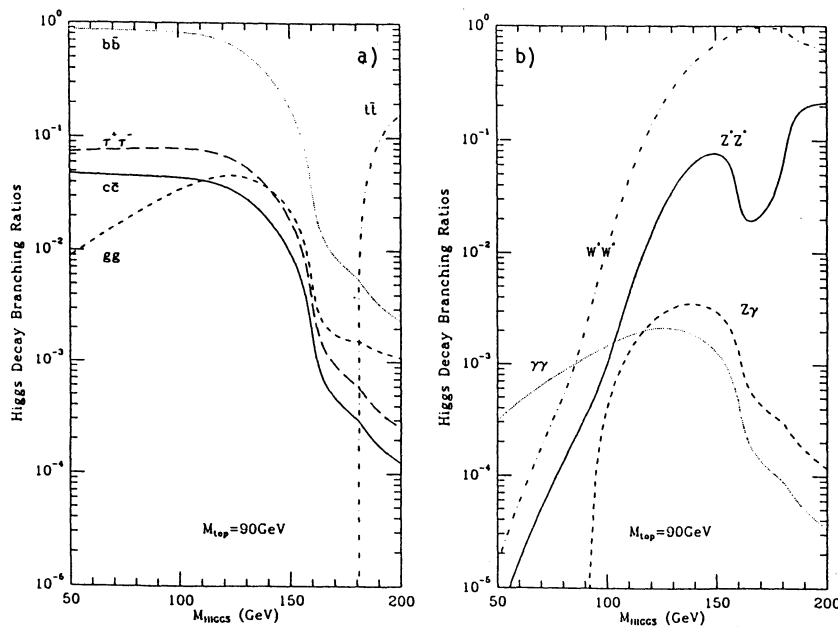


Fig. 1

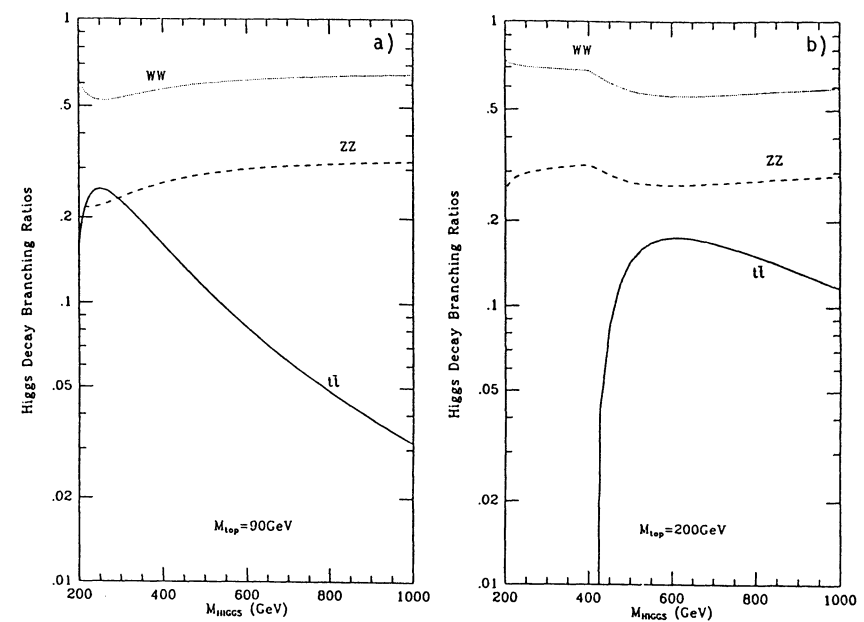


Fig. 3

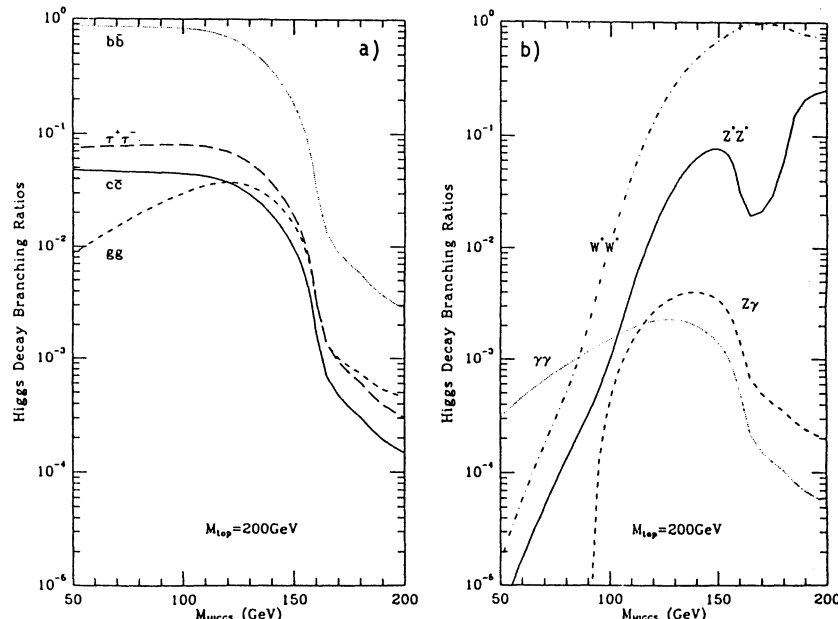


Fig. 2

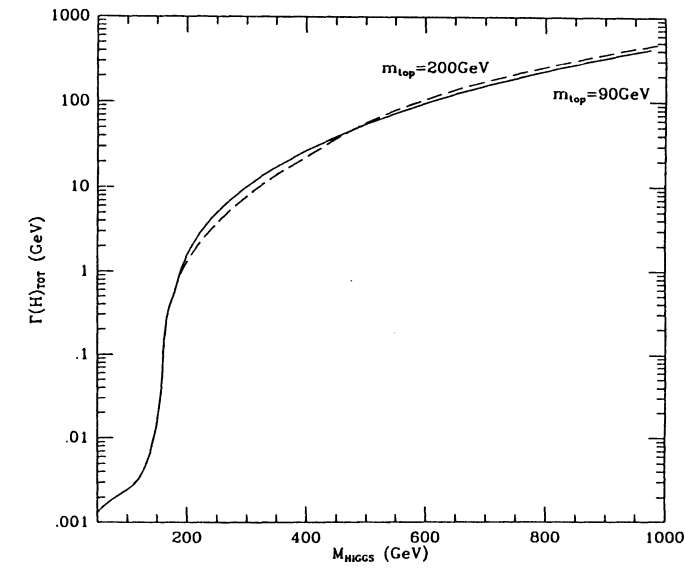


Fig. 4

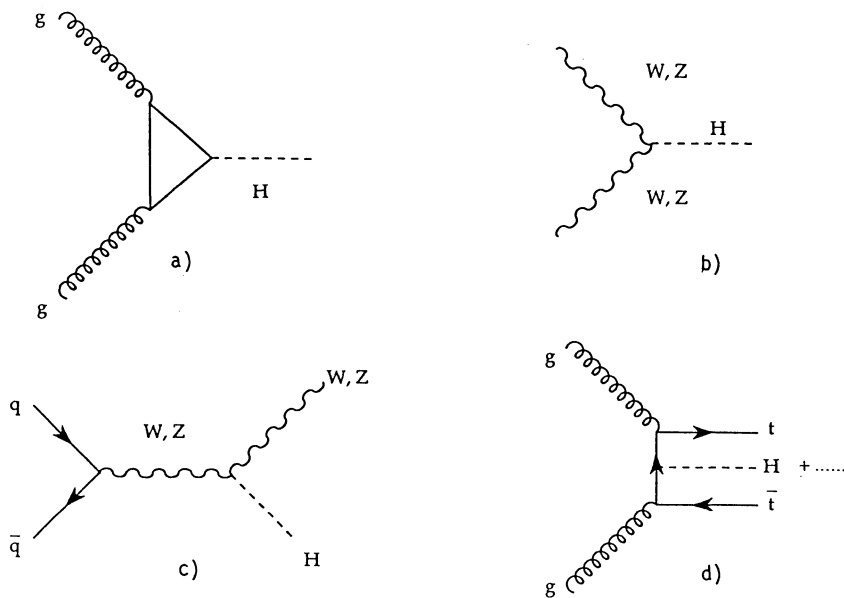


Fig. 5

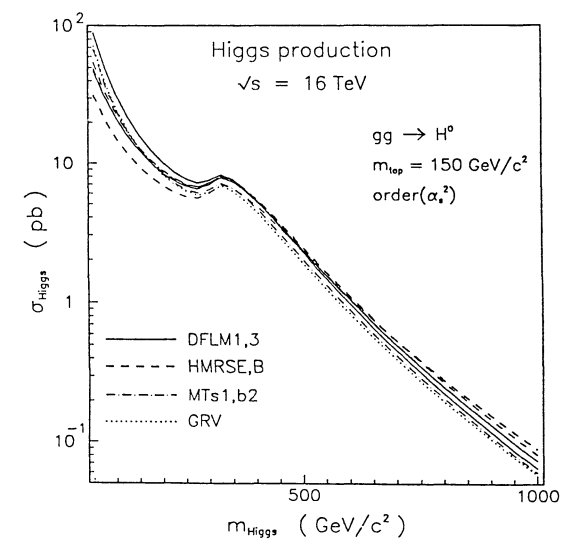


Fig. 7

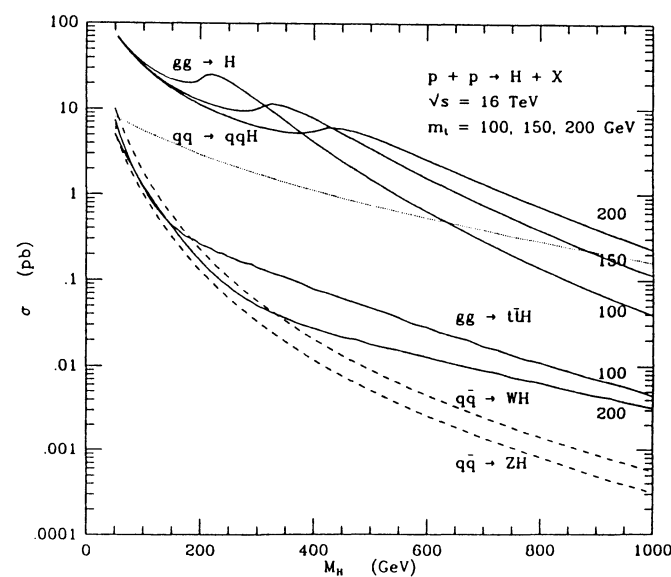


Fig. 6

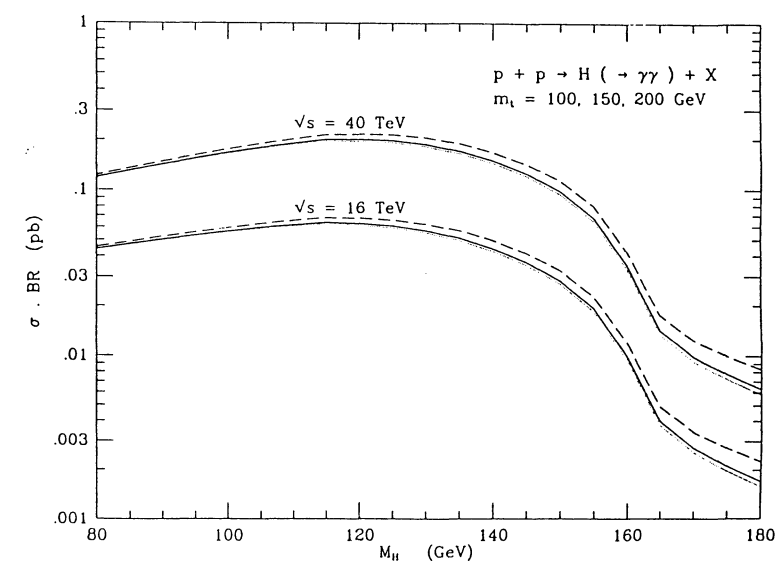


Fig. 8

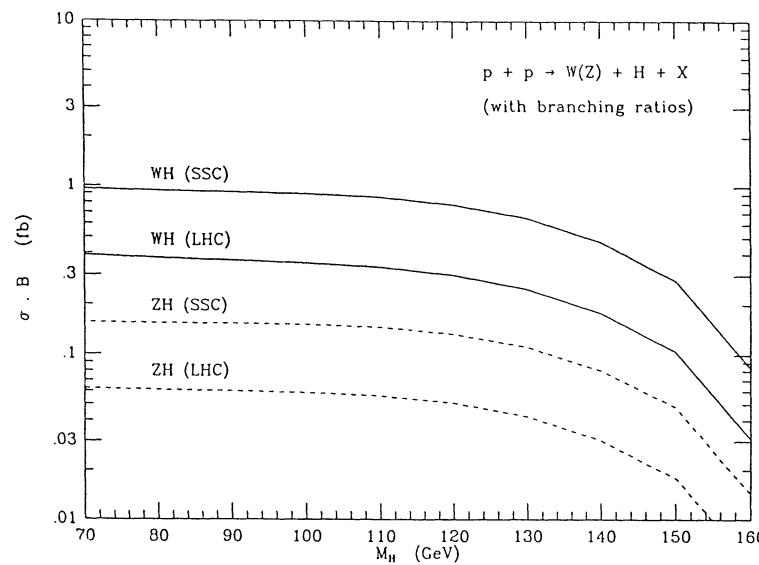


Fig. 9

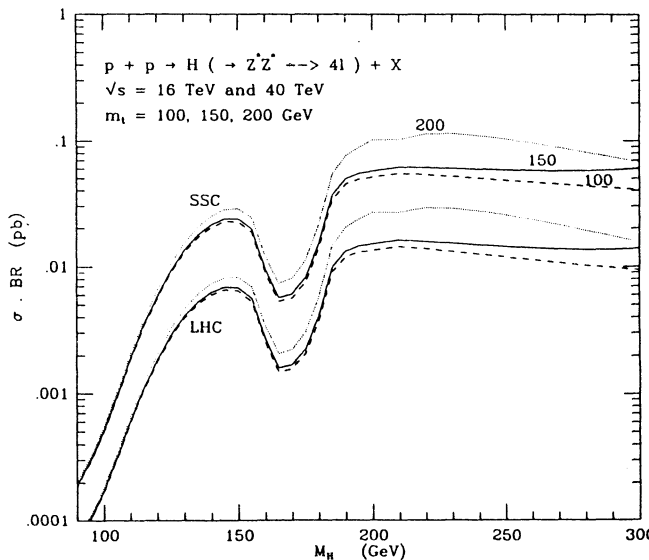


Fig. 10

EXPERIMENTAL REVIEW OF THE SEARCH FOR THE HIGGS BOSON

Daniel Froidevaux

This review will limit its scope to the search for the Standard Model Higgs boson, H , at the LHC, for $\sqrt{s} = 16 \text{ TeV}$. Integrated luminosities of 10^5 pb^{-1} per year of running will be used throughout, unless otherwise stated.

The search for charged Higgs bosons will be covered by the top physics working group [1], and the search for scalar or pseudoscalar neutral Higgs bosons from the Minimal Supersymmetric Standard Model has been summarised in a theoretical overview [2], since no detailed experimental simulations have yet been carried out in this context.

This review would not have been possible without the work of many people, theorists and experimentalists, who have participated in the Higgs working group studies for the Aachen workshop over a relatively short period of about 9 months. It will be divided into four main chapters :

1. $H \rightarrow ZZ, Z^*Z^* \rightarrow 4 \text{ leptons}$

M. Della Negra, D. Froidevaux, K. Jakobs, R. Kinnunen, R. Kleiss, A. Nisati and T. Sjöstrand

2. Intermediate mass Higgs

- a) $H \rightarrow \gamma\gamma$, WH with $W \rightarrow \ell\nu$, $H \rightarrow \gamma\gamma$, and ZH with $Z \rightarrow \ell\ell$, $H \rightarrow \gamma\gamma$
L. DiLella, A. Djouadi, R. Kleiss, Z. Kunszt, G. Panzeri, C. Seez, W.J. Stirling and T. Virdee

This topic is reviewed in detail in the summary given by C. Seez [3]. Only the main conclusions will be discussed here.

- b) $H \rightarrow \tau\tau$

F. Anselmo, K. Bos, L. DiLella and B. Van Eijk

- c) WH with $W \rightarrow \ell\nu$, $H \rightarrow jj$ or bb and ZH with $Z \rightarrow \ell\ell$, $H \rightarrow jj$ or bb
L. Poggiali

3. $H \rightarrow ZZ \rightarrow \ell\ell vv, H \rightarrow ZZ \rightarrow \ell\ell jj, H \rightarrow WW \rightarrow \ell v jj$ for m_H large U. Baur, D. Froidevaux, E.W.N. Glover and M.H. Seymour

4. Impact on detectors

In this section the impact of all these physics studies on the various detector subgroups will be summarised : trigger rates, muon resolution, lepton acceptance in p_T (transverse momentum) and η (pseudorapidity), jet rejection for electron and photon identification, electromagnetic calorimetry resolution, segmentation and granularity, hadron calorimeter performance, calorimeter coverage and forward calorimetry.

Finally the last section will give the conclusions of this working group.

I. $H \rightarrow ZZ, Z^*Z^* \rightarrow 4 \text{ leptons}$

This is the so-called gold-plated channel for Higgs detection at LHC or SSC, since the signal appears as a peak in the invariant 4-lepton mass distribution above a background which previous studies have shown to be small. A full background calculation has not been carried out so far, however, and the aim of this section is to present the results of a study as complete and precise as possible, of all background sources which lead to final states containing four leptons. Particular attention has been paid to a complete evaluation of the inclusive 4-lepton final states originating from $t\bar{t}$ production [4], and, in the case of the intermediate mass Higgs ($m_H < 2m_Z$), to 4-lepton final states originating from Zbb production [5].

In the following, rates for the Higgs signal will always be normalised to the cross-sections and branching ratios discussed in Ref. 6. Unless otherwise stated, 4-lepton final states contain four electrons, four muons or two electrons and two muons. An overall efficiency factor of $0.9^4 = 65.6\%$ has been applied to all the rates in this section, to introduce a somewhat arbitrary (but possibly optimistic) lepton identification efficiency.

I.1 $m_H \geq 2m_Z$

We shall only briefly discuss this channel here, since it has been discussed almost ad nauseam in many previous studies. Yet another study is reported in detail in Ref. 4, warranted for mainly two reasons :

- a) it turns out that background from inclusive four-lepton final states from $t\bar{t}$ decay is not negligible compared to the ZZ continuum background, if $m_H = 200$ GeV and the Z-mass resolution is poor
- b) there has been some debate about the importance of good muon momentum resolution for $H \rightarrow ZZ \rightarrow \mu\mu\mu\mu$ decays.

The study, described in Ref. 4, has therefore mainly concentrated on the decay $H \rightarrow ZZ \rightarrow \mu\mu\mu\mu$, where the muons are reconstructed in an iron toroid spectrometer, with a resolution $\Delta p/p \approx 13\%$, constant and dominated by multiple scattering up to momenta of ≈ 400 GeV. The Z mass is reconstructed with a resolution of about 8 GeV, and therefore all events are considered, with two reconstructed dimuon masses within ± 16 GeV of the Z mass. The momenta of the muons can then be rescaled to constrain each dimuon mass to the Z mass, leading to a spectacular improvement on the reconstructed Higgs mass resolution, as illustrated in Fig. 1, for $m_H = 200$ GeV, where the Higgs signal is shown on top of the ZZ continuum background. After this Z-mass constraint, the Higgs mass resolution is about 4 GeV for $m_H = 200$ GeV. As m_H increases, the natural width of the Higgs begins to take over, and, for $m_H > 400$ GeV, the effect of the Z-mass constraint cannot be seen any more.

Fig. 2 shows, for $m_{top} = 200$ GeV and for $m_H = 200$ GeV, the Higgs signal above the full background, as estimated in Ref. 4. The level of the non-resonant $t\bar{t}$ background varies like $(\Delta m)^2$, where the dimuon mass is required to be within $\pm \Delta m$ of m_Z . As quoted above, a value of $\Delta m = 16$ GeV was chosen, adapted to the resolution of an iron toroid spectrometer. Even in this case, the ZZ continuum background is the dominant one, a feature which can be enhanced by requiring lepton isolation (at least two of the leptons are non-isolated in the $t\bar{t}$ background), or by requiring a large transverse momentum for both reconstructed Z bosons, as expected from Higgs decay. Other backgrounds, such as Zbb or Ztt are negligible in this Higgs mass range.

Fig. 3 shows, for $m_H = 600$ and 800 GeV, the expected Higgs signal above the continuum ZZ background, for a total integrated luminosity of 10^5 pb $^{-1}$. The 4-lepton invariant mass is plotted for all leptons with $p_T > 20$ GeV/c and $|\eta| < 3$. An additional cut, $p_T^{Z1} + p_T^{Z2} > 300$ GeV, is required to reduce the ZZ continuum background, which was simulated from $qq \rightarrow ZZ$ matrix elements only, and scaled up by a factor 1.5 to account for the $gg \rightarrow ZZ$ contribution [7]. It has been pointed out that this procedure is pessimistic because it tends to underestimate the significance of a Higgs signal for large values of m_H [8]. Fig. 4 illustrates this fact with slightly different cuts on the final state particles. The exact result in the presence of the Higgs boson, using the full matrix elements, is shown, for $m_H = 800$ GeV, to yield about 50% more event rate than the s-channel approximation used in most Monte-Carlo generators, in particular for Fig. 3, and to shift the peak to lower values of the reconstructed ZZ mass.

In conclusion, the channel $H \rightarrow ZZ \rightarrow \ell\ell\ell\ell$ would provide a clear signal for the presence of a Higgs boson, in the mass range, $2m_Z \leq m_H \leq 800$ GeV, for $\int L dt = 10^5$ pb $^{-1}$ at LHC. This range would be reduced to $2m_Z \leq m_H \leq 500$ GeV for $\int L dt = 10^4$ pb $^{-1}$. The dominant background is the ZZ continuum (but the background from $t\bar{t}$ production cannot be neglected for $m_H = 200$ GeV, in the case of poor muon momentum resolution).

I.2 $m_H < 2m_Z$

This channel, $H \rightarrow Z^*Z^* \rightarrow \ell\ell\ell\ell$, has been suggested in the literature [9] as one of the most promising ones for searching for the intermediate mass Higgs. Only recently has the partial width $\Gamma(H \rightarrow Z^*Z^*)$ been fully calculated [6]. Previous background studies have indicated that the background from $qq \rightarrow Z^*Z^*$, $\gamma^*\gamma^*$ is quite small [9], but that the background from $gg \rightarrow Zbb$ could be very large [10]. However, to our knowledge, no complete calculation of the backgrounds to this channel exists, and we have therefore performed it for this workshop. We refer the reader to Ref. 5 for the details of this study, and only briefly discuss the salient points here.

The detector simulation used was the following :

- a) Electron energies were smeared, according to $\sigma_E/E = 0.15/\sqrt{E} + 0.02$
- b) Muon momenta were smeared, according to $\Delta p/p = 0.15$. This worst case muon momentum resolution was used to address the important question whether lepton resolution is essential to extract the Higgs signal in this channel, since we are studying a Higgs mass range, where the detector performance determines the width of the observed Higgs signal.
- c) Even though the full calculation for $H \rightarrow Z^*Z^*$ decays was used in the simulation, most $H \rightarrow Z^*Z^*$ final states contain one Z boson on mass shell. We therefore restricted ourselves to the events where one of the Z bosons is on mass shell, requiring a reconstructed dilepton mass, $m_{\ell\ell} = m_Z \pm 10$ GeV with $p_T^\ell > 20$ GeV and $|\eta_\ell| < 3$.
- d) The other two leptons were required to have an invariant mass larger than 12 GeV and $p_T^\ell > 10$ GeV, $|\eta_\ell| < 3$. The effects of lepton p_T -threshold and η -acceptance are discussed in section IV, where the importance of low p_T -threshold and large η -acceptance will be stressed for this particular channel. The cut on the invariant mass of these two leptons does not affect the signal in the mass range of interest, but strongly reduces the backgrounds from $q\bar{q} \rightarrow \gamma^*Z^* \rightarrow \ell\ell\ell\ell$ and, more importantly, from $gg \rightarrow Zbb \rightarrow \ell\ell\ell\ell$, where these two leptons originate from cascade decay of one of the b-quarks.
- e) The 4-lepton invariant mass is then reconstructed, with a resolution, σ_H , ranging from 2 to 3 GeV for $H \rightarrow eeee$ and from 5 to 11 GeV for $H \rightarrow \mu\mu\mu\mu$, with $\Delta p/p = 0.15$. In this last case, the Z-mass constraint considerably improves the resolution, even though it can only be applied to the lepton pair, corresponding to the Z boson on mass shell. Fig. 5 shows the expected rates for the reconstructed signal as a function of m_H , for m_H between 120 and 180 GeV, and for $m_{\ell\ell\ell\ell} = m_H \pm 2\sigma_H$.

The backgrounds are discussed below in decreasing order of importance :

- a) $t\bar{t} \rightarrow 4$ leptons
This background is obtained as described in Ref. 4. About 30% of the 4 lepton final states contain 4 non-isolated leptons from first and second generation b-decays. The remainder contain 2 isolated leptons from W decay. As discussed in the previous section, this background varies as Δm , where Δm is the window around m_Z allowed for the largest dilepton mass. Fig. 6 shows the invariant 4-lepton mass distribution obtained for $m_{top} = 130$ GeV and 200 GeV.
- b) $Zbb \rightarrow 4$ leptons
 Zbb production is dominated by $gg \rightarrow Zbb$ at LHC energies [11]. The exact calculation for $gg \rightarrow Zbb$, with massive b-quarks, has been recently redone [12] and implemented in the LDW [13] and PYTHIA [14] Monte-Carlo programs. Contrary to the case of massless quarks, the calculation is finite and provides a good benchmark to compare the matrix element Monte-Carlo program (ME) to various parton shower Monte-Carlo programs (ISAJET [15] and PYTHIA). We refer the reader to Ref. 5 for more details, and we shall just comment here that the ME results, as shown in Fig. 6 for the 4-lepton reconstructed mass, give larger background estimates, due to the fact that the parton shower Monte-Carlo programs, using $gb \rightarrow Zb$ matrix elements for massless b-quarks and backward evolution, yield a too soft p_T -spectrum for the b-quark. As in the case of the $t\bar{t}$

- background, the 2 leptons from b-decay are non-isolated. Contrary to the $t\bar{t}$ case, however, this background cannot be reduced by decreasing the 10 GeV window used around m_Z , since it contains one real Z boson in the final state.
- c) $q\bar{q} \rightarrow Z^*Z^*, \gamma^*\gamma^* \rightarrow 4 \text{ leptons}$
 This irreducible background has been simulated using the most recent version of the PYTHIA Monte-Carlo program and is also shown in Fig. 6.

Fig. 7 shows the 4-lepton reconstructed mass distribution for the sum of all backgrounds shown in Fig. 6, and also shows how the signal from $H \rightarrow Z^*Z^* \rightarrow 4\text{-leptons}$ would appear above this background, for $m_H = 130, 150$ and 170 GeV, and assuming $\sigma_E/E = 0.15/\sqrt{E} + 0.02$ for all leptons (electrons and muons). Since there are rather large uncertainties in some of the background estimates, it is not clear that a Higgs signal would easily be seen above the background.

Finally, Fig. 8 shows the signals and backgrounds of Fig. 7 after lepton isolation cuts. As discussed in Ref. 5, the efficiency for isolated leptons and the rejection against non-isolated leptons of energy isolation cuts depend strongly on the magnitude of pile-up effects in the calorimeter, the granularity of the electromagnetic calorimeter, the presence or absence of a central magnetic field, but also on the b-quark p_T -spectrum. A study done using a GEANT simulation of a fine-grained electromagnetic + hadronic calorimeter has led to the conclusion that a rejection $R_b^2 = 50$ with efficiency $\epsilon_e^2 = 0.7$ can be obtained with isolation cuts applied on the two leptons accompanying the reconstructed Z. The rejection R_b^2 was applied to the $t\bar{t}$ and $Zb\bar{b}$ backgrounds, and the efficiency ϵ_e^2 was applied to the $Z^*Z^*, \gamma^*\gamma^*$ background and to the Higgs signal.

Fig. 8 clearly shows that with these cuts, a Higgs signal will clearly appear above the background for $130 \leq m_H \leq 2m_Z$. In the case of poor muon momentum resolution ($\Delta p/p = 0.15$), the significance of the signal seen in Fig. 8 is only reduced by $\approx 20\%$, due to the fact that 75% of the events contain at least two well measured electrons. This point will be further discussed in section IV.

In conclusion, the channel $H \rightarrow Z^*Z^* \rightarrow \ell\ell\ell\ell$ would provide a clear signal for the presence of a Higgs boson, in the mass range, $130 \leq m_H \leq 2m_Z$, for $\int L dt = 10^5 \text{ pb}^{-1}$. This channel could not be seen with only 10^4 pb^{-1} . The dominant backgrounds from $t\bar{t}$ and $Zb\bar{b}$ can be handled with emphasis on lepton isolation cuts and/or on lepton momentum resolution, depending upon the exact detector one has in mind.

II. INTERMEDIATE MASS HIGGS

The search for the intermediate mass Higgs, $m_Z \leq m_H \leq 2m_Z$, has turned out to be one of the most difficult goals for experimental searches at the LHC or SSC. Many channels have been proposed and studied [16], especially in the context of SSC. In this workshop, a lot of effort was also devoted to this subject, with special focus on the problems linked with the higher luminosity at LHC.

We have seen in the previous section, that, for $130 \leq m_H \leq 2m_Z$, the Higgs boson can be detected in the channel $H \rightarrow Z^*Z^* \rightarrow \ell\ell\ell\ell$, provided the detector can identify low energy isolated electrons and muons. In the following we shall describe the conclusions of our working group on the other possible channels in this mass range.

II.1 $H \rightarrow \gamma\gamma$, WH with $W \rightarrow \ell\nu$, $H \rightarrow \gamma\gamma$, and ZH with $Z \rightarrow \ell\ell$, $H \rightarrow \gamma\gamma$

The search for the Higgs in its $\gamma\gamma$ decay mode, whether produced singly (mainly through gg fusion in this mass range) or in association with a W or Z boson, subsequently decaying leptonically, is reviewed in detail in these proceedings [3]. We shall only briefly summarise the main conclusions here.

The channel $H \rightarrow \gamma\gamma$ would allow discovery of the Higgs boson at LHC within the mass range, $m_Z \leq m_H \leq 150$ GeV if the following conditions are satisfied :

- 1) The available integrated luminosity is at least 10^5 pb^{-1} .
- 2) The diphoton signal from a narrow Higgs resonance can be extracted from the irreducible continuum $\gamma\gamma$ background. As discussed in detail in Ref. 3, this implies that the resolution, uniformity, and stability of the electromagnetic calorimeter are very good, and that the direction of the photons can be measured to better than ≈ 10 mrad, using the longitudinal segmentation in the electromagnetic calorimeter.
- 3) The potentially overwhelming background from electromagnetic jets, containing one or several leading π^0 's can be reduced well below the $\gamma\gamma$ continuum background. This has been estimated possible if one achieves a rejection of the order of 10^4 per jet, which implies that close-by photon showers from π^0, η decay can be separated down to angles of about 5 mrad, using for example a highly segmented position detector after about four radiation lengths in the electromagnetic calorimeter.

Whether these conditions can only be fulfilled with a dedicated detector is a subject for further study, with detailed simulations of specific electromagnetic calorimeters.

The channel WH, with $W \rightarrow \ell\nu$ and $H \rightarrow \gamma\gamma$ yields rates of at best 20 events per 10^5 pb^{-1} integrated luminosity, as discussed in Ref. 3. There are many sources of potentially overwhelming backgrounds ($b\bar{b}g, b\bar{b}\gamma, b\gamma\gamma, Wjj$), which can only be reduced to the adequate level if the detector has similar performances to those discussed above for $H \rightarrow \gamma\gamma$. If this is indeed the case, then the signal can be seen above the irreducible $W\gamma\gamma$ background, providing an important confirmation of a signal in the $H \rightarrow \gamma\gamma$ channel, especially for Higgs masses close to m_Z .

Finally, the potentially cleaner channel ZH with $Z \rightarrow \ell\ell$ and $H \rightarrow \gamma\gamma$ does not yield enough rate, even for integrated luminosities of 10^5 pb^{-1} , to provide a viable signal.

II.2 $H \rightarrow \tau\tau$

This channel has been proposed in the literature, with the suggestion to improve the $\tau\tau$ mass resolution by triggering on high- p_T pairs [17]. Studies of the $H \rightarrow \tau\tau$ channel at LHC, using acolinear $e\mu$ pairs to obtain good $\tau\tau$ mass resolution are reported in Ref. 18, with the following conclusions :

- 1) The $H \rightarrow \tau\tau$ decay cannot be searched for at the highest LHC luminosities of more than $10^{34} \text{ cm}^{-2} \text{ s}^{-1}$, because both the τ hadronic jet identification with respect to normal QCD jets and the good missing p_T resolution, needed to reconstruct the $\tau\tau$ invariant mass, are heavily affected by pile-up effects.
- 2) For luminosities of $\approx 10^{33} \text{ cm}^{-2} \text{ s}^{-1}$, corresponding to an integrated luminosity of 10^4 pb^{-1} per year, a total of $\approx 70 H \rightarrow \tau\tau \rightarrow e\mu + X$ decays can be reconstructed with a mass resolution of ≈ 13 GeV, for $m_H = 140$ GeV. They are however overwhelmed by the large background from $t\bar{t} \rightarrow e\mu + X$ (about 30 000 events) in the same mass region for the reconstructed $\tau\tau$ mass.

The overall conclusion is that the detection of $H \rightarrow \tau\tau$ decays at LHC seems very difficult. The studies of Ref. 18 have however turned out to be very useful for the case of SUSY Higgs decays into $\tau\tau$ pairs, where a signal can probably be seen above the background in some region of parameter space [2].

II.3 WH with $W \rightarrow \ell\nu$ and $H \rightarrow jj, b\bar{b}$ and ZH with $Z \rightarrow \ell\ell$ and $H \rightarrow jj, b\bar{b}$

The detection of the intermediate mass Higgs through associated production with a W boson and subsequent Higgs decay into $b\bar{b}$ has often been reported as quite promising in previous SSC studies [19]. A study of WH and ZH production, with $H \rightarrow jj$ or $b\bar{b}$ decay has been performed for this workshop [20].

Despite the optimism of previous SSC studies, the channel WH, with $W \rightarrow \ell\nu$ and $H \rightarrow b\bar{b}$, appears to be totally hopeless because of the $t\bar{t}$ background, which, on top of being overwhelmingly larger than any potential signal, also contains b-quarks in the final state, thus rendering b-tagging useless :

- For $m_H = 120 \text{ GeV}$, $\sigma. B(WH, W \rightarrow \ell\nu \text{ and } H \rightarrow b\bar{b}) \approx 0.18 \text{ pb}$
- For $m_{top} = 130 \text{ GeV}$, $\sigma. B(t\bar{t} \rightarrow WWb\bar{b} \text{ with } W \rightarrow \ell\nu) \approx 2 \text{ nb}$

A more detailed study was done for the channel ZH , with $Z \rightarrow \ell\ell$ and $H \rightarrow jj$ or $H \rightarrow b\bar{b}$. For $m_H = 120 \text{ GeV}$, $\sigma. B(ZH, Z \rightarrow \ell\ell \text{ and } H \rightarrow jj) \approx 0.033 \text{ pb}$, corresponding to 3300 events produced for 10^3 pb^{-1} . The backgrounds have turned out to be numerous and overwhelming in this case also :

$$\begin{aligned}\sigma. B(ZZ, Z \rightarrow \ell\ell \text{ and } Z \rightarrow jj) &\approx 1.4 \text{ pb} \\ \sigma. B(ZW, Z \rightarrow \ell\ell \text{ and } W \rightarrow jj) &\approx 1.4 \text{ pb} \\ \sigma. B(Zjj, Z \rightarrow \ell\ell, p_T > 30 \text{ GeV}, |\eta| > 20^\circ) &\approx 210 \text{ pb} \\ \sigma. B(Zbb, Z \rightarrow \ell\ell, p_T > 30 \text{ GeV}) &\approx 2.7 \text{ pb}\end{aligned}$$

Even with very good b-tagging ($\epsilon_b = 90\%$ and $R_{jet} = 10$), the potential Higgs signal is well below the roughly equal contributions from Zjj and Zbb backgrounds (after requiring 2 tagged b-quark jets).

In conclusion, a potential signal from an intermediate mass Higgs boson, produced in association with a W or Z boson and decaying into jj or bb, cannot be extracted from the background, neither at LHC, nor at SSC.

II.4 Conclusions on intermediate mass Higgs, for $m_Z \leq m_H \leq 130 \text{ GeV}$

With an integrated luminosity of 10^5 pb^{-1} , a signal from $H \rightarrow \gamma\gamma$ decays can be observed at LHC, for $80 \leq m_H \leq 150 \text{ GeV}$, through a combination of the $H \rightarrow \gamma\gamma$ and WH , with $W \rightarrow \ell\nu$ and $H \rightarrow \gamma\gamma$, decay modes. This however imposes severe constraints on the detector design (see Ref. 3 and section IV).

None of the other possible channels, which have been studied, provides any hope to discover the Higgs in this mass range. However, as discussed in Ref. 2, $t\bar{t}$ decays of SUSY Higgs bosons seem to provide a promising signature in some region of parameter space.

III. SEARCH FOR A VERY HEAVY HIGGS BOSON

In this section, we shall review the most promising decay channels, which would allow to extend the search for the Higgs boson above the mass range accessible through the $H \rightarrow ZZ \rightarrow \ell\ell\ell\ell$ decay mode, which corresponds to $m_H \approx 800 \text{ GeV}/c^2$ for 10^5 pb^{-1} , and $m_H \approx 500 \text{ GeV}/c^2$ for 10^4 pb^{-1} , as discussed in section I.

The most interesting decay modes, which remain are :

- $H \rightarrow ZZ \rightarrow \ell\ell\nu\nu$, discussed in section III.1.
- $H \rightarrow ZZ \rightarrow \ell\ell jj$ and $H \rightarrow WW \rightarrow \ell\nu jj$, discussed in section III.2 and Ref. 21.

Previous studies have shown other channels to be overwhelmed by background, e.g. $H \rightarrow WW \rightarrow \ell\nu\ell\nu$ [22].

III.1 $H \rightarrow ZZ \rightarrow \ell\ell\nu\nu$

The motivation to study this channel arises from the fact that $B(H \rightarrow ZZ \rightarrow \ell\ell\nu\nu) \approx 8.6 \cdot 10^{-3}$ is 6 times larger than $B(H \rightarrow ZZ \rightarrow \ell\ell\ell\ell)$. However, we cannot reconstruct the Higgs mass in this channel, and the signal will appear as a broad Jacobian peak in the transverse momentum distribution, p_T^Z , of the reconstructed $Z \rightarrow \ell\ell$ decay, or in the transverse mass distribution, m_T , defined as :

$$m_T^2 = 2 p_T^Z p_T^\nu (1 - \cos\Delta\phi_{Z\nu}), \text{ where}$$

p_T^Z is the total missing transverse momentum, and $\Delta\phi_{Z\nu}$, the azimuthal angle between \vec{p}_T^Z and \vec{p}_T^ν .

The irreducible background to this channel is of course the ZZ continuum, but a potentially very large background arises from $Z + \text{jet}$ production, with $Z \rightarrow \ell\ell$, and even from $t\bar{t}$ production with $t\bar{t} \rightarrow \ell\ell + X$. As discussed in section IV, these backgrounds can only be reduced below the ZZ continuum background, if the calorimeter provides extensive coverage and good hermeticity. For these reasons, a full calorimeter simulation was performed, using the GEANT package, assuming a calorimeter coverage of $|\eta| < 5$ and including the effect of pile-up at luminosities of $10^{34} \text{ cm}^{-2} \text{ s}^{-1}$ on the measurement of p_T .

Fig. 9 shows, for $\int L dt = 10^4 \text{ pb}^{-1}$, the expected signal from $H \rightarrow ZZ \rightarrow \ell\ell\nu\nu$, for $m_H = 500 \text{ GeV}$, above the background from $ZZ \rightarrow \ell\ell\nu\nu$. The events are required to contain two electrons (or muons), with $p_T > 40 \text{ GeV}$, $|\eta| < 2$, $|m_Z \ell - m_Z| < 10 \text{ GeV}$, and $p_T^Z > 150 \text{ GeV}$. A final cut, $p_T^\nu > 150 \text{ GeV}$, is necessary to get rid of the $Z + \text{jet}$ background, which is potentially about 1000 times larger than the signal. Fig. 9 shows, in particular for the m_T -distribution, that the expected 87 signal events can be seen above the 48 remaining background events.

Fig. 10 shows the same distributions for $m_H = 800 \text{ GeV}$ and $\int L dt = 10^5 \text{ pb}^{-1}$. With somewhat tighter cuts, $p_T > 60 \text{ GeV}$, $p_T^Z > 250 \text{ GeV}$ and $p_T^\nu > 250 \text{ GeV}$, 166 signal events are expected above a background of 115 events from $ZZ \rightarrow \ell\ell\nu\nu$. The signal appears as an excess in the tail of reconstructed high p_T $Z \rightarrow \ell\ell$ decays, and such an excess could only be interpreted as a Higgs signal, if the theory would predict precisely (i.e. to better than 20 - 30%) the magnitude and shape of high p_T Z's from the ZZ continuum.

In conclusion, the channel $H \rightarrow ZZ \rightarrow \ell\ell\nu\nu$ may significantly improve the Higgs mass range, which can be explored at LHC, allowing to extend it to $m_H \approx 700 \text{ GeV}$ for 10^4 pb^{-1} and to $m_H \approx 1 \text{ TeV}$ for 10^5 pb^{-1} . This can only be achieved, if the calorimeter coverage extends to at least ± 4 units of rapidity, and if the calorimeter hermeticity is good enough that the p_T^ν cut reduces the backgrounds from $Z + \text{jets}$ and $t\bar{t}$ to a negligible level. More details on these last points, including a description of previous work on the subject and of the simulations performed for this workshop, can be found in section IV.

III.2 $H \rightarrow WW \rightarrow \ell\nu jj$ and $H \rightarrow ZZ \rightarrow \ell\ell jj$

The motivation for studying these decay modes is quite obvious : for example $B(H \rightarrow WW \rightarrow \ell\nu jj)$ is about 150 times larger than $B(H \rightarrow ZZ \rightarrow \ell\ell\ell\ell)$, corresponding to about 3000 events produced for $m_H = 1000 \text{ GeV}$ and $\int L dt = 10^5 \text{ pb}^{-1}$. The study of these decays would allow a search for the Higgs boson in the TeV mass region, where the WW fusion production mechanism becomes dominant. This mechanism results in a final state containing two vector bosons and two high energy quark jets at forward rapidities [23]. This would be characteristic of such events, whether from Higgs production or from a possible strongly interacting vector boson sector, which would be expected to manifest itself in the TeV mass region if the Higgs boson were not found at lower masses [24].

Preliminary and approximate studies [25] have shown that this “jet tagging” at large rapidities provides hope to reduce the enormous backgrounds to a potential signal from $H \rightarrow WW \rightarrow \ell\nu jj$. The magnitude of these backgrounds is illustrated in Fig. 11, which shows that, at LHC energies, the production of $(\ell\nu jj)$ final states, with $m_{jj} = m_W \pm 10 \text{ GeV}$, through Wjj and $t\bar{t}$ production, is about 4 orders of magnitude larger than that expected from a Higgs signal in the TeV range. Contrary to what has often been said, the Wjj and $t\bar{t}$ backgrounds are similar in magnitude.

Previous experimental studies [22] have shown that the $H \rightarrow WW \rightarrow \ell\nu jj$ signal cannot be isolated from these backgrounds, with kinematical and topological cuts alone. Despite the optimism suggested by recent SSC studies [26], we felt it important to study more thoroughly the jet tagging technique, as the only really promising means to extract a signal in the $H \rightarrow WW \rightarrow \ell\nu jj$ decay mode. A study of the $H \rightarrow ZZ \rightarrow \ell\ell jj$ mode has yielded similar conclusions, namely that kinematic cuts alone will not allow one to extract the Higgs signal from the background [27]. This decay channel suffers from about 6 times

less rate than $H \rightarrow WW \rightarrow \ell\nu jj$, but has the advantage of providing an unambiguous reconstruction of the Higgs mass, and being unaffected by the $t\bar{t}$ background.

We shall now summarise the salient features of the study presented in Ref. 21, and then draw some preliminary conclusions, based on this study, some results from earlier work [25], and some reasonable assumptions. The impact of this study on a detector design will be discussed in section IV.

III.2.1 Simulation of $qq \rightarrow Hqq \rightarrow WWqq \rightarrow \ell\nu jj qq$

The HERWIG Monte-Carlo [28] was used to generate the Higgs signal and the $W + 4$ jet background. The HERWIG results for $W + 3$ jet events were compared to the exact matrix element calculation contained in the LDW Monte-Carlo program [13], and the jet p_T and η spectra were found to be in rough agreement with the exact calculation. The central part of the events was required to satisfy the usual kinematic cuts :

- $m_{jj} = m_W \pm 10$ GeV
- $\Delta R_{jj} < 0.7$, where $\Delta R_{jj} = \sqrt{\Delta\phi^2 + \Delta\eta^2}$ is the distance in (ϕ, η) space between the two central jets. This cut is equivalent to requiring that p_T^j is large, as expected from Higgs decay.
- $m_{\ell\nu jj} \geq 700$ GeV. This cut assumes that the neutrino is reconstructed, but is mainly meant to select the Wjj background events, which cannot be distinguished from the signal without using jet tagging.

After these simple cuts, the signal to background is about 1/40. The remaining events are then required to contain one tag jet on each side, i.e. one in the forward direction and one in the backward direction. In the results presented below, a tag jet will be defined as a jet with $2 < |\eta_j| < 4.5$ and $E_j > 600$ GeV. Fig. 12 shows the energy spectrum of the lower energy tag jet for the Higgs signal, compared to the $W +$ jet (QCD) background. Fig. 13 shows the improvement in significance of the signal as a function of the cut on E_j . The efficiency of these cuts is about 22% for the signal, and the Wjj background is rejected by a factor ≈ 150 .

The cuts described above may provide a large improvement in the signal to background ratio, but they obviously have a tremendous impact on the forward part of the calorimeter, which will be discussed in section IV. Here we would like to point out that HERWIG was used in this simulation, in order to understand whether the tag jets survive hadronisation. Fig. 14 shows the energy profile around the jet axis, in a plane transverse to the beam, situated at 16 m from the interaction, for tag jets at $|\eta_j| = 4$. Due to the small scale ($p_T \approx m_W$) at which these jets are produced, they do not radiate gluons as much as would be expected from normal TeV energy jets, and therefore their energy profile after hadronisation is smaller than the energy spread, which will arise from hadron showering in the calorimeter.

III.2.2 Pile-up effects

A major worry in this study is the effect of pile-up at high luminosity, which could lead to large energy deposits from spectator fragments near the beam. This was studied in a preliminary way in Ref. 25 and we recall the results here. The difficulty here is in predicting the energy flow from spectators at large rapidities. Fig. 15 shows the energy flow predicted in minimum bias events at LHC, for $3 < \eta < 5$ by a dual parton string model [29], which turned out to be in reasonable agreement with that obtained using the ISAJET Monte-Carlo with a mixture of minimum bias and hard QCD interactions [30]. Also shown in Fig. 15 is the energy reconstructed in jets, with $\Delta R = \sqrt{\Delta\phi^2 + \Delta\eta^2} = 1$, in the same rapidity interval. For total spectator energies above 500 GeV, the probability to find this energy in a such a large cone is 1.5%, reducing to $\leq 0.4\%$ for a cone with $\Delta R = 0.5$, which is adapted to a coarse-grained forward calorimeter. The probability to get two tag jets from minimum bias pile-up can now be compared to the Wjj rejection, $R = 150$, achieved with the tag jet cuts. This probability is $P = (0.004 \cdot n)^2$, where n is the average number of minimum bias events per trigger interaction. At luminosities exceeding $10^{34} \text{ cm}^{-2} \text{ s}^{-1}$, P becomes larger than $1/R$, and Wjj events with one or two tag jets from pile-up will dominate the background to the Higgs signal.

In the following, we have taken these pile-up effects to be negligible at luminosities of $10^{33} \text{ cm}^{-2} \text{ s}^{-1}$, and to introduce an additional background equal to the physical background at luminosities of $10^{34} \text{ cm}^{-2} \text{ s}^{-1}$.

III.2.3 Additional assumptions

The $t\bar{t}$ background to WW final states has not yet been studied, so we made the simple assumption that it is rejected in the same way as the Wjj background. We have conservatively used the lower value of m_{top} , $m_{top} = 130$ GeV, as in Fig. 11. The Wjj background has therefore been enhanced by a factor 2. This simple rule of thumb will of course be checked with a proper simulation in the future, since differences might arise with respect to the Wjj background, due to the different production mechanism and scale for $t\bar{t}$ and to the additional b-quarks present in the final state (though it is very unlikely that they would pass the jet tagging cuts quoted above). A preliminary study of the $t\bar{t}$ background is reported in Ref. 21 and concludes that the rejection of the tagging cuts is ~ 3 times worse than for Wjj , mainly because $t\bar{t}$ pairs are dominantly produced through gg fusion. It is hoped that this factor 3 can be recovered by suitable cuts applied to the central part of the events.

The $H \rightarrow ZZ \rightarrow \ell\ell jj$ decays have not been simulated and we have therefore extrapolated from the $H \rightarrow WW \rightarrow \ell\nu jj$ case. The $H \rightarrow ZZ \rightarrow \ell\ell jj$ rates used were taken to be a fraction $F = 12\%$ of the corresponding $H \rightarrow WW \rightarrow \ell\nu jj$ rates, where $F = 0.156$ (branching ratios). 0.9 (efficiency to detect second lepton). 0.9 (efficiency of a cut $m_{\ell\ell} = m_Z \pm 10$ GeV, which gets rid of potential $t\bar{t}$ background). The background from Zjj events, with $Z \rightarrow \ell\ell$, is about a factor 10 below the Wjj background, with $W \rightarrow \ell\nu$.

III.2.4 Results and conclusions

Table 1 shows, with and without tagging cuts, the significance of a possible Higgs signal, for $m_H = 1$ TeV, in the $H \rightarrow WW \rightarrow \ell\nu jj$ and $H \rightarrow ZZ \rightarrow \ell\ell jj$ channels, for integrated luminosities of 10^4 pb^{-1} and 10^5 pb^{-1} . The backgrounds are subdivided into three categories : background from vector boson + jet and $t\bar{t}$ production, background from vector boson + jet and $t\bar{t}$ production where the tag jets originate from pile-up (only at high luminosity), and, for completeness, the irreducible vector boson pair background.

For 10^4 pb^{-1} , the signal is marginal at best, for $H \rightarrow WW \rightarrow \ell\nu jj$ with jet tagging. However, for 10^5 pb^{-1} , the signal, both from $H \rightarrow WW \rightarrow \ell\nu jj$ and $H \rightarrow ZZ \rightarrow \ell\ell jj$, would appear as an excess of events above the background. The s/B ratio is worse for $H \rightarrow WW \rightarrow \ell\nu jj$ (0.12) than for $H \rightarrow ZZ \rightarrow \ell\ell jj$ (0.39), but the larger rate more than compensates for this.

In conclusion, we would like to stress that we have learned a lot with the study discussed in Ref. 21, and that the results are promising :

- 1) Jet tagging may work even at luminosities as high as $10^{34} \text{ cm}^{-2} \text{ s}^{-1}$.
- 2) Despite the very large backgrounds from $W +$ jets and $t\bar{t}$, the decay mode $H \rightarrow WW \rightarrow \ell\nu jj$ may allow discovery of the Higgs boson for $m_H = 1$ TeV, even with integrated luminosities significantly less than 10^5 pb^{-1} . However, the lack of a true resonance structure in this Higgs mass range implies that it will be very difficult to identify such a statistically significant excess of events as the signal from a Higgs boson of mass 1 TeV (see Fig. 8 of Ref. 21).
- 3) We now have all the Monte-Carlo tools and theoretical input needed to do a full simulation of this channel, which in addition certainly warrants a realistic assessment of forward calorimetry at LHC (see section IV).

IV. IMPACT OF HIGGS PHYSICS SIMULATION ON DETECTORS

IV.1 Trigger rates [31]

In this section, we will briefly show that triggering on the interesting standard model Higgs decay modes is not a problem at LHC, even at luminosities exceeding $10^{34} \text{ cm}^{-2} \text{ s}^{-1}$. We will concentrate on the decay modes containing electrons, which are

dominated at the trigger level by electromagnetic jets, whereas the muon rates are expected to be dominated by prompt muons [32] and are therefore much lower. Calorimeter studies with GEANT [33] have shown that a rejection R_j of 100 to 1000 can be obtained against jets, with an efficiency for electrons of at least 90%, which includes effects due to pile-up and speed of response. We conservatively use a value $R_j = 100$ in the following.

We first consider the decay $H \rightarrow WW \rightarrow evjj$, which is of interest for $m_H \geq 800$ GeV. The acceptance is above 85%, for $p_T^e > 100$ GeV and $|\eta_e| < 2$. Given the dijet cross-section of $1.4 \mu\text{b}$ at $\sqrt{s} = 16$ TeV, for two jets with $p_T^j > 100$ GeV and $|\eta_j| < 2$, we estimate a rate of about 3000 Hz for inclusive jets, with $p_T^j > 100$ GeV and $|\eta_j| < 2$, at $L = 10^{33} \text{ cm}^{-2} \text{ s}^{-1}$. This results in a trigger rate, after calorimeter rejection, of 30 Hz at $L = 10^{33} \text{ cm}^{-2} \text{ s}^{-1}$, which increases to ≈ 800 Hz at $L = 10^{34} \text{ cm}^{-2} \text{ s}^{-1}$, faster than the luminosity because of pile-up effects in the calorimeter. The rate expected from real electrons is small in comparison, ≈ 2 Hz at $L = 10^{34} \text{ cm}^{-2} \text{ s}^{-1}$, dominated by electrons from W and b-quark decay. Such trigger rates are not considered to be a problem by the DAQ/trigger studies [31].

All the other Higgs decays studied, including $H \rightarrow \gamma\gamma$, have a good acceptance for $p_T^{\gamma\gamma} > 20$ GeV and $|\eta_{\gamma\gamma}| < 2$, for a pair of electrons or photons. So we shall consider that the trigger rate in this case is to be computed using the cross-section for observing 2 jets with $p_T^j > 20$ GeV, $|\eta_j| < 2$, which is $\approx 330 \mu\text{b}$. We thus obtain a trigger rate of ≈ 30 Hz at $L = 10^{33} \text{ cm}^{-2} \text{ s}^{-1}$, which increases to ≈ 1000 Hz at $L = 10^{34} \text{ cm}^{-2} \text{ s}^{-1}$. The rate expected from real electrons is about 5 Hz, dominated by $Z \rightarrow ee$ decays.

IV.2 Muon resolution

Even though good muon momentum resolution is always desirable for the detector performance, the studies done for this workshop have shown that this is not a crucial issue in the Higgs sector. A muon spectrometer based on magnetised iron toroids, resulting in momentum resolutions of the order of 10 - 15% up to momenta of about 400 GeV, is not adequate for finding a signal from $H \rightarrow Z^*Z^* \rightarrow \mu\mu\mu\mu$, even if isolation cuts are applied to the background (Fig. 16). A good muon detector, with a resolution $\Delta p_T/p_T = 0.2$ p_T (p_T in TeV), is almost adequate for finding a signal from $H \rightarrow Z^*Z^* \rightarrow \mu\mu\mu\mu$, before isolation cuts are applied (Fig. 17). We would like to stress, however, that, given the limited statistics available, the large uncertainties on the background rates of Figs. 16 and 17, and the difficulty of identifying low energy leptons, it is desirable to identify both electrons and muons, in order to find a possible signal from $H \rightarrow Z^*Z^* \rightarrow \ell\ell\ell\ell$ decays, for $130 \leq m_H \leq 2m_Z$. For $m_H \geq 2m_Z$, the Z-mass constraint more or less results in a Higgs mass resolution, which is independent of the muon momentum resolution. In addition, for even larger Higgs masses, the natural width of the Higgs is the dominant factor, and therefore muon momentum resolution is not an issue.

IV.3 Lepton acceptance in p_T and η

The desired lepton acceptance in p_T and η has obviously a major impact on detector design. We discuss in this section the requirements to be met for the decay mode $H \rightarrow Z^*Z^* \rightarrow \ell\ell\ell\ell$, the only one which imposes severe constraints on the detector design. As a matter of fact, for $m_H \geq 300$ GeV, a lepton acceptance of $|\eta_\ell| \leq 2$ and a $p_T^{\ell\ell}$ -threshold of 20 - 30 GeV are perfectly adequate to search for a possible Higgs signal. In contrast, as shown in Table 2, the acceptance for lower mass Higgs bosons decaying into four leptons, varies quite steeply with the lepton detector η -coverage, and even more so with the lepton p_T threshold. Table 2 also shows that, even for $m_H = 120$ GeV, the trigger acceptance, as discussed in section IV.1, for $p_T^{\ell\ell} > 20$ GeV (1 and 2 are the two highest p_T leptons) and $|\eta| < 3$, is almost 90%. Applying the same cuts to the two remaining leptons reduces the acceptance to 20%, a reduction factor mostly due to the $p_T^{\ell\ell}$ -threshold, as expected at these low Higgs masses. Fig. 18, illustrating the numbers shown in Table 2, shows the expected numbers of detected $H \rightarrow eeee$ (or $\mu\mu\mu\mu$) events per 10^5 pb^{-1} , for a range of Higgs masses, and as a function of the detector η -acceptance and the $p_T^{\ell\ell}$ threshold.

In conclusion, a good detector acceptance in η and p_T is only important for $130 \leq m_H \leq 200$ GeV. At least two of the leptons would have to be identified at transverse energies as low as 10 GeV, and at rapidities as large as 3. It will clearly be a challenge at high luminosity to design a detector, which can efficiently identify electrons and muons in this η and p_T range.

IV.4 Rejection of jets for electron/photon identification

Clearly photon identification for $H \rightarrow \gamma\gamma$ decays imposes stringent requirements on the calorimeter [3]. The main goals are a good electromagnetic calorimeter resolution and a rejection of about 10^4 against jets. Both these goals can only be achieved with calorimetry, which sets a very difficult task for the detector design.

For electron identification, despite the very small expected cross-sections for some of the signals discussed in the previous sections, the situation is easier, and we will take two examples to demonstrate this :

a) $H \rightarrow Z^*Z^* \rightarrow eeee$

As shown in section II and Ref. 5, the cross-section for this decay mode, containing four electrons in the final state, is about 0.2 fb for $130 \leq m_H \leq 2m_Z$. Within the same acceptance, the background from 4-jet events at $L = 10^{34} \text{ cm}^{-2} \text{ s}^{-1}$ corresponds to a cross-section of about 1 mb = 10^{12} fb, including pile-up effects which considerably increase the cross-section at low p_T . From these numbers, it appears that a rejection of 3000 per jet is sufficient to bring this background to a level smaller than 10% of the signal. The other background to be considered is that from $Z + \text{jets}$ with $Z \rightarrow ee$, where two jets fake the electron selection criteria. As mentioned in section IV.1, the inclusive cross-section for $Z \rightarrow ee$, within the trigger acceptance, is about 500 pb, and here again a rejection of 3000 per jet appears sufficient to suppress this background to the $H \rightarrow Z^*Z^* \rightarrow eeee$ signal.

This example shows that a moderate jet rejection, which however cannot be achieved by calorimetry alone [33], and which has to be achieved at transverse momenta as low as 10 GeV, is sufficient to suppress backgrounds from jets faking electrons.

b) $H \rightarrow WW \rightarrow evjj$

In this case, where $m_H \geq 800$ GeV, we have seen (section IV.1) that the inclusive electron cross-section (~ 200 pb) is much smaller than the trigger cross-section, corresponding to jets of $p_T > 100$ GeV. Before additional kinematic and topological cuts are applied, a rejection against jets of 10^5 to 10^6 is needed to reduce the fake electron background to a level of 10% of the signal from real electrons, which in turn is a formidable background to the Higgs signal in this channel, as discussed in section III.2 and Ref. 21.

Such large rejections against jets have been achieved in present hadron colliders, in detectors as different as UA1, UA2 or CDF. It is of course not yet clear whether this can be achieved in the much more difficult conditions prevailing at LHC or SSC.

IV.5 Electromagnetic calorimeter resolution and segmentation

The resolution of the electromagnetic calorimeter is not crucial for electrons (see the discussion on muon resolution in Section IV.2), but is very relevant for the decay mode $H \rightarrow \gamma\gamma$. We refer the reader to Ref. 3 once again for a detailed discussion on this point.

A good lateral granularity of the electromagnetic calorimeter can provide a powerful tool against backgrounds to channels containing electrons :

- a) Lepton isolation has been shown to be an important asset for the search for $H \rightarrow Z^*Z^* \rightarrow \ell\ell\ell\ell$ [5]. To achieve the rejections needed against non-isolated leptons from b-decay, a granularity of $\approx 0.03 \times 0.03$ in $\Delta\phi \times \Delta\eta$ is necessary.

- b) The accuracy of the position measurement of an electromagnetic shower depends strongly on this granularity [33]. A good position measurement with the calorimeter will clearly help to reject the backgrounds from jets faking electrons (see Section IV.4).

Finally, the longitudinal segmentation of the electromagnetic calorimeter obviously has to be balanced against the lateral segmentation, which appears to be more important, in terms of cost and number of channels. Some longitudinal segmentation is clearly desirable to help electron identification at 10 GeV. The implications of a position detector after ≈ 4 radiation lengths for $H \rightarrow \gamma\gamma$ clearly deserve further study.

IV.6 Performance of the hadron calorimeter

In the framework of this working group, a study was done of the possible cases, where hadron calorimeter resolution could be of importance [20]. This is an important point, since a good resolution on reconstructed jet-jet masses can only be achieved with a careful design of the overall calorimeter.

IV.6.1 ZH with $Z \rightarrow \ell\ell$ and $H \rightarrow jj$, $m_H = 120$ GeV

Even though this channel appears to be hopelessly swamped by the background from $Z +$ jets, independently of the resolution on the reconstructed Higgs mass, we have studied the resolution on the reconstructed dijet mass for all jets with $|\eta_j| < 3$ and $p_T^j > 40$ GeV. Before any detector smearing is included, the resolution on the reconstructed Higgs mass is about 11 GeV, due to b-quark fragmentation effects. This point was not studied further, once it became clear that, even with b-tagging at $L = 10^{34} \text{ cm}^{-2} \text{ s}^{-1}$, the signal can still not be extracted from the background.

IV.6.2 ZW, ZZ continuum with $Z \rightarrow \ell\ell$ and $W,Z \rightarrow jj$

A by-product of the study of a possible signal in the ZH mode was a study of the resonant backgrounds to this channel, arising from continuum pair production of ZZ and ZW pairs with $Z \rightarrow \ell\ell$. These channels can be seen above the large background from $Z +$ jets, as discussed in Ref. 20, even at luminosities as high as $4 \cdot 10^{34} \text{ cm}^{-2} \text{ s}^{-1}$, where pile-up effects dominate any possible effects from calorimeter resolution. Fig. 19 shows the summed signal from ZW and ZZ production, where the $W \rightarrow jj$ and $Z \rightarrow jj$ peaks merge due to fragmentation effects and to the jet algorithm used (energies are collected in a cone of $\Delta R = \sqrt{\Delta\phi^2 + \Delta\eta^2} = 0.4$). The r.m.s width of the reconstructed peak is ≈ 6.5 GeV, as shown in Fig. 19a, where a jet energy smearing of $\sigma_E/E = 0.30/\sqrt{E} + 0.01$, corresponding to a very good hadron calorimeter, was included. Such a hadron calorimeter resolution does not affect the intrinsic width of the signal. However, a poorer jet energy resolution, $\sigma_E/E = 1.0/\sqrt{E} + 0.04$, results in an r.m.s. width of ≈ 11 GeV, as shown in Fig. 19b.

The distributions shown in Fig. 19 do not include any pile-up effects, which are summarised in Fig. 20, for the ZZ continuum process alone. Fig. 20a shows, for $p_T^j > 40$ GeV, $|\eta_j| < 3$, and a cone size $\Delta R = 0.4$, the reconstructed dijet mass distribution for all combinations in the event, at $L = 10^{33} \text{ cm}^{-2} \text{ s}^{-1}$ (no pile-up). The reconstructed Z mass is 86.5 GeV with an r.m.s. of 5.1 GeV. The efficiency of the acceptance cuts and the jet algorithm is $\epsilon_{jj} = 43\%$, and an average of 1.7 dijet combinations are found per event. This last number depends of course upon the Monte-Carlo simulation of the spectator hadrons (PYTHIA 5.4 was used in this study).

If the same procedure is applied at $L = 4 \cdot 10^{34} \text{ cm}^{-2} \text{ s}^{-1}$, the $Z \rightarrow jj$ signal disappears below the combinatorial background in the signal events themselves. This is due to the fact that 6.5 dijet combinations are found per event, once the pile-up from 40 additional minimum bias events has been included in the simulation. However, as shown in Fig. 20b, the signal can be recovered by reducing the size of the cone to $\Delta R = 0.3$ in the jet algorithm. The number of dijet combinations is thus reduced to 2.8 per event, and the reconstructed mass peak is found at 103 GeV with an r.m.s. width of 12.0 GeV. This result, though significantly worse than at $L = 10^{33} \text{ cm}^{-2} \text{ s}^{-1}$, is sufficient to see the ZZ continuum signal, with $Z \rightarrow \ell\ell$ and $Z \rightarrow jj$, above the $Z +$ jet background, even at $L = 4 \cdot 10^{34} \text{ cm}^{-2} \text{ s}^{-1}$. We refer the reader for further details to Ref. 20.

IV.6.3 $H \rightarrow ZZ \rightarrow \ell\ell jj$ or $H \rightarrow WW \rightarrow \ell v jj$, $m_H = 800$ GeV

This is the most interesting case, with the feature that the W,Z decays, which one has to reconstruct, now correspond to boosted $W,Z \rightarrow jj$ bosons from heavy Higgs decay, with energies of several hundred GeV. Previous studies [22] have already pointed out the need for good hadron calorimeter granularity to separate the two jets from boosted W,Z decays. This is necessary because, if one were not to explicitly require two reconstructed jets, then the background from W,Z bosons accompanied by one jet would be the dominant one to these Higgs decay modes, due to the intrinsically large mass of a jet at these scales [34]. Fig. 21 illustrates the need for good granularity with the example of $m_H = 800$ GeV, $H \rightarrow WW \rightarrow \ell v jj$: the efficiency, at the parton level, for finding the two jets from the W decay is plotted as a function of the energy of this W boson, assuming that two jets can be separated provided their angular separation, θ_{jj} , is larger than 10° , 20° , and 30° . To achieve an average efficiency of $\approx 50\%$, the hadron calorimeter granularity clearly has to be better than 0.2×0.2 in $\Delta\phi \times \Delta\eta$.

Finally, for those events where two jets are reconstructed after hadronisation, Fig. 22 shows the reconstructed dijet mass, for $H \rightarrow ZZ \rightarrow \ell\ell jj$ with $m_H = 800 \text{ GeV}/c^2$, $|\eta_j| < 3$ and $p_T^j > 40$ GeV. The resolution on this mass is ≈ 11 GeV, an effect due to the fact that the two jets are quite close to each other in space, resulting in a certain amount of mixing between fragmentation products and, possibly, larger effects from uncertainties on jet directions than for normal back-to-back dijet events. Further studies are needed to understand whether this resolution can be improved with a jet algorithm better adapted to this specific case.

IV.7 Calorimeter coverage

Many studies in this workshop have converged towards the somewhat unwelcome fact that calorimeter hermeticity at LHC energies requires calorimeter coverage up to at least $|\eta| = 4$, more probably $|\eta| = 5$. For the specific case of the Higgs boson, calorimeter coverage has been recognised to be crucial for two channels :

- 1) $H \rightarrow ZZ \rightarrow \ell\ell vv$, to reject the potentially very large background from $Z +$ jets. This is illustrated in Fig. 23, which shows, for 10^5 pb^{-1} , the expected number of events with missing transverse momentum, p_T^V , larger than some threshold as a function of this threshold, for a variety of physics processes with a reconstructed $Z \rightarrow \ell\ell$ decay, such that $p_T^{\ell\ell} > 100$ GeV. Fig. 23 shows the expected rates for the $H \rightarrow ZZ \rightarrow \ell\ell vv$ signal ($m_H = 500$ and 800 GeV) and the ZZ continuum background ($ZZ \rightarrow \ell\ell vv$). More importantly, Fig. 23 also shows a parton level study of such rates from $Z +$ jet events, where one or more jets are outside the calorimeter coverage chosen ($|\eta_{calo}| = 2, 3$ or 4). These rates completely overwhelm the background, if $|\eta_{calo}| < 3.5$. They were computed using the LDW Monte-Carlo program, to generate $Z + 1$ jet and $Z + 2$ jet events, properly normalised to the full $0(\alpha_3)$ calculation of Ref. 35. The hashed bands indicate the size of the remaining theoretical uncertainties in this computation, estimated e.g. using $Z + 3$ jet production. It is important to note that fragmentation effects, hadron shower size, calorimeter resolution and cracks, certainly will result in the need for an extra rapidity unit in the calorimeter coverage.

An interesting attempt [36] was made to evaluate the effect of calorimeter cracks, potentially the most dangerous source of tails at large p_T^V . The conclusions from this study, which used the measured response of the CDF detector to jets in cracks, was, quite optimistically, that the $Z +$ jet and $t\bar{t}$ backgrounds can be suppressed below the level of the irreducible $ZZ \rightarrow \ell\ell vv$ continuum background, as shown in Fig. 24. This was, however, also a parton level study, and this crucial point for the $H \rightarrow ZZ \rightarrow \ell\ell vv$ decay mode should be clarified better.

- 2) $H \rightarrow WW \rightarrow \ell v jj$ and $H \rightarrow ZZ \rightarrow \ell\ell jj$

The need for forward calorimetry, to reject the very large backgrounds to these channels, has been clearly explained in Ref. 21 and section IV.2. This calorimeter should provide a crude measurement of the energies of the tag jets, but also of their

directions, for $H \rightarrow WW \rightarrow \ell v jj$, since the accuracy of the measurement of p_T^V relies upon a reasonably accurate measurement of p_T^H .

In the following, we summarise the challenges posed by the need for such a calorimeter :

- The main challenge is of course due to radiation. In a normal LHC intersection [37], the low- β quadrupoles will be approximately 20m away from the interaction point. As a consequence, a forward calorimeter, which could contain hadronic showers from TeV energy jets, could be situated, at the furthest, 16 to 17 m from the interaction point, and would then have to act as a shield for these low- β quadrupoles. From present estimates using a spherical geometry [38], the dose, integrated over $4 < |\eta| < 5$, would be ~ 8 Mrad per year of running at $L = 10^{34} \text{ cm}^{-2} \text{ s}^{-1}$ at LHC ($\int L dt = 10^{41} \text{ cm}^{-2}$). This dose varies very rapidly at such large rapidities, and a more realistic calculation, i.e. with the correct geometry, will soon be performed. An important effect of such large doses is that such a forward calorimeter will become radioactive, and therefore probably inaccessible to human intervention.
- Another challenge, which should not be underestimated, is the integration of such a calorimeter, which by necessity is as far away as possible from the interaction point, into the overall design of a detector. Cracks between different calorimeters always cause problems for missing transverse momentum measurements and should therefore be minimised.
- Finally the last challenge is to actually build such a calorimeter. A granularity of $30^\circ \times 0.5$ in $\Delta\phi \times \Delta\eta$ should be sufficient to reconstruct with reasonable accuracy the energy of the tag jets with tolerable pile-up levels up to luminosities of $10^{34} \text{ cm}^{-2} \text{ s}^{-1}$. More studies are certainly warranted to understand how to measure the direction and time of occurrence of these tag jets.

In conclusion, we would like to point out that several other fields of physics require such a forward calorimetry, which has never, up to now, been considered seriously enough to evaluate its impact on a global detector design at LHC or SSC. If one accounts for jet fragmentation and hadronic shower size, a rapidity coverage of ± 4.5 to 5 units (resp. ± 5.5 to 6 units) is desirable at LHC (resp. SSC).

V CONCLUSIONS

The channel $H \rightarrow Z^{(*)}Z^{(*)} \rightarrow 4 \text{ leptons}$ remains as gold-plated as ever. For the first time, a complete calculation of all possible backgrounds to this channel was performed for this workshop, and the conclusion is that, for $130 \leq m_H \leq 800 \text{ GeV}$, the Higgs boson can be discovered at LHC with $\int L dt = 10^5 \text{ pb}^{-1}$ (or at SSC with $\int L dt = 10^4 \text{ pb}^{-1}$, but with more difficult signal to background conditions for $130 \leq m_H \leq 2m_Z$). This conclusion is only valid if one detects both electrons and muons with good geometrical acceptance and efficiency for transverse momenta as low as 10 GeV.

For the range $80 \leq m_H \leq 130 \text{ GeV}$, the only channels which have survived our experimental studies are $H \rightarrow \gamma\gamma$ and WH with $W \rightarrow \ell v$, $H \rightarrow \gamma\gamma$. They may allow a signal from Higgs decay to be seen above the backgrounds, but pose severe demands on the electromagnetic calorimetry. More detailed studies are needed to understand whether a dedicated detector is needed in this case. The potential significance of a signal in this channel is better at LHC with 10^5 pb^{-1} than at SSC with 10^4 pb^{-1} , but the high luminosity at LHC is obviously more demanding on the detector.

For Higgs masses larger than 800 GeV, the channels $H \rightarrow ZZ \rightarrow \ell\ell vv$ (with some worries still present concerning the level of residual background from $Z + \text{jets}$ in a realistic detector design and simulation) and $H \rightarrow WW \rightarrow \ell v jj$ and $H \rightarrow ZZ \rightarrow \ell\ell jj$ may allow us to reach Higgs masses in the TeV range. In particular we have learned at this workshop, that jet tagging, to select WW/ZZ fusion processes, which might be interesting even in the absence of a Higgs boson, does not seem impossible, even at luminosities of $10^{34} \text{ cm}^{-2} \text{ s}^{-1}$, but poses severe demands on detector design. Firmer conclusions await a thorough and realistic study of forward calorimetry (up to $|\eta| \approx 4.5$ to 5 at LHC, $|\eta| \approx 5.5$ to 6 at SSC).

Last but not least, we believe that the impact of the Higgs physics sector on LHC detectors is now clear. The years to come will not be too many to solve the numerous technical challenges ahead of us to go from the Monte-Carlo studies done here to the first data analysis in an LHC experiment.

I would like to conclude with a renewal of my thanks to all my theoretical and experimental colleagues, who, by their work and enthusiasm during this workshop, have helped made this Higgs study group a success.

$m_H = 1 \text{ TeV}, qq \rightarrow qqH$ $\varepsilon_\ell = 0.9, \varepsilon_{m_Z} = 0.9$		$H \rightarrow WW \rightarrow \ell v jj$		$H \rightarrow ZZ \rightarrow \ell\ell jj$	
		No tagging	With tagging	No tagging	With tagging
Signal $S, \int L dt = 10^5 \text{ pb}^{-1}$		1580	350	206	45
Backgrounds B	- $V + \text{jets}, t\bar{t}$	230000	1480	8450	55
	- Pile-up	-	1480	-	55
	- Irreducible VV	3060	80	130	4
Significance $S/(S+B)^{1/2}$		3.3	6.0	2.2	3.6
Signal $S, \int L dt = 10^4 \text{ pb}^{-1}$		158	35	21	4.5
Backgrounds B	- $V + \text{jets}$	23000	148	845	5.5
	- Irreducible VV	306	8	13	0.4
Significance $S/(S+B)^{1/2}$		1.0	2.5	0.7	1.4

Table 1 Search for high mass Higgs boson using jet tagging

		$p_T^{12} > 20 \text{ GeV}$	$p_T^{\text{all leptons}} > 20 \text{ GeV}$	$p_T^{\text{all leptons}} > 10 \text{ GeV}$
$m_H = 120 \text{ GeV}$	$ \eta < 2$ $ \eta < 3$	0.61 0.87	0.02 0.04	0.20 0.32
$m_H = 170 \text{ GeV}$	$ \eta < 2$ $ \eta < 3$	0.72 0.93	0.28 0.41	0.45 0.71
$m_H = 200 \text{ GeV}$	$ \eta < 2$ $ \eta < 3$	0.73 0.94	0.38 0.56	0.48 0.76
$m_H = 500 \text{ GeV}$	$ \eta < 2$ $ \eta < 3$	0.82 0.98	0.57 0.80	0.62 0.88
ZZ continuum	$ \eta < 2$ $ \eta < 3$	0.50 0.76	0.22 0.34	0.27 0.50

Table 2 Acceptances in η and p_T for $H \rightarrow \ell\ell\ell\ell$ and $ZZ \rightarrow \ell\ell\ell\ell$

REFERENCES

1. L. Fayard, E. Reya and P. Zerwas, top study group, these proceedings.
2. Z. Kunszt and F. Zwirner, Higgs study group, these proceedings.
3. C. Seez, Higgs study group, these proceedings.
4. A. Nisati, Higgs study group, these proceedings.
5. M. Della Negra et al., Higgs study group, these proceedings.
6. Z. Kunszt and W.J. Stirling, Higgs study group, these proceedings.
7. E.W.N. Glover and J.J. Van der Bij, Phys. Lett. 219B (1989) 488, and Nucl. Phys. B321 (1989) 561.
8. U. Baur and E.W.N. Glover, FERMILAB-PUB-90/154-T, MAD/PH/577, submitted to Phys. Rev. D;
- U. Baur and E.W.N. Glover, Higgs study group, these proceedings.
9. J.F. Gunion, G.L. Kane and J. Wudka, Nucl. Phys. B299 (1988) 239.
10. E.M. Wang et al., in proceedings of the 1988 Snowmass Summer Study on High Energy Physics in the 1990's, edited by S. Jensen (World Scientific, Singapore, 1989), p. 109.
11. S. Ellis et al., in Supercollider Physics, edited by D. Soper (World Scientific, Singapore, 1986).
12. R. Kleiss and B. Van Eijk, event generator study group, these proceedings.
13. S.D. Ellis, R. Kleiss and W.J. Stirling, Phys. Lett. 203B (1988) 172;
- F.A. Berends, W.J. Giele and H. Kuijf, Nucl. Phys. B321 (1989) 39.
14. H.V. Bengtsson and T. Sjöstrand, Comp. Phys. Comm. 46 (1987) 43.
15. F. Paige and S.D. Protopopescu, in Physics of the Superconducting Super Collider, 1986, eds. R. Donaldson and J. Marx (1987), p. 320.
16. See e.g. J.F. Gunion et al., The Higgs Hunter's Guide, Frontiers in Physics (1990), p. 162, and references therein.
17. R.K. Ellis et al., Nucl. Phys. B297 (1988) 221.
18. L. Di Lella, Higgs study group, these proceedings;
- F. Anselmo, K. Bos and B. Van Eijk, Higgs study group, these proceedings.
19. See e.g. J.E. Brau et al., in proceedings of the 1988 Snowmass Summer Study on High Energy Physics in the 1990's, edited by S. Jensen (World Scientific, Singapore, 1989), p. 103.
20. L. Poggiali, Higgs study group, these proceedings.
21. M.H. Seymour, Higgs study group, these proceedings.
22. D. Froidevaux, in proceedings of the Workshop on Physics at Future Accelerators, La Thuile, edited by J.H. Mulvey, CERN 87-07 (1987), vol. 1, p. 61.
23. R.N. Cahn et al., Phys. Rev. D35 (1987) 1626.
24. M. Chanowitz, Ann. Rev. Nucl. Part. Phys. 38 (1988) 323.
25. W.J. Stirling, in The Feasibility of Experiments at High Luminosity at the Large Hadron Collider, edited by J.H. Mulvey, CERN-88-02 (1988), p. 67.
26. J.F. Gunion et al., Phys. Rev. D40 (1989) 2223; see also Ref. 16, p. 174-181.
27. M. Dellanegra, private communication.
28. G. Marchesini and B.R. Webber, Nucl. Phys. B310 (1988) 461;
- S. Catani, G. Marchesini and B.R. Webber, Cavendish-HEP-90/17 (1990).
29. P. Aurenche, private communication.
30. F. Pauss, private communication.
31. See also S. Hellman, DAQ and trigger study group, these proceedings.
32. A. Nisati, muon study group, these proceedings.
33. J-P. Repellin, electron study group, these proceedings.
34. Z. Kunszt, in Proceedings of the Workshop on Physics at Future Accelerators, La Thuile, edited by J.H. Mulvey, CERN-87-07 (1987), vol. 1, p. 123.
35. P.B. Arnold and M.H. Reno, Nucl. Phys. B319 (1989) 37;
- R.J. Gonsalves, J.P. Pawlowski and C.F. Wai, Phys. Rev. D40 (1989) 2245.
36. R.M. Barnett, E.D. Carlson and I. Hinchliffe, LBL-27797 (1989);
R.M. Barnett and I. Hinchliffe, LBL-28773 (1990).
37. L. Leistam, Experimental Area study group, these proceedings.
38. G. Stevenson, Radiation Damage study group, these proceedings.

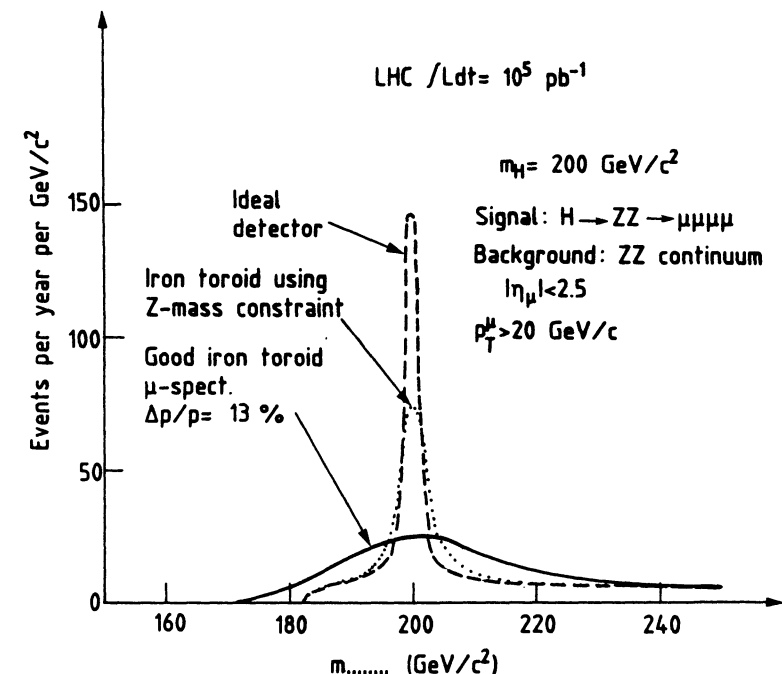


FIG. 1

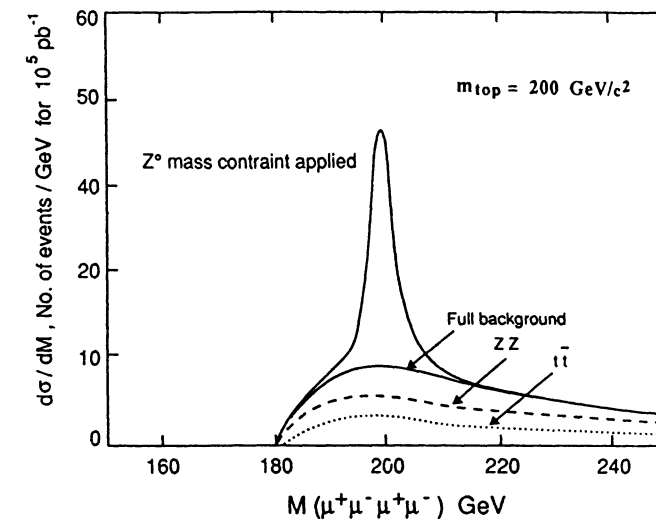


FIG. 2

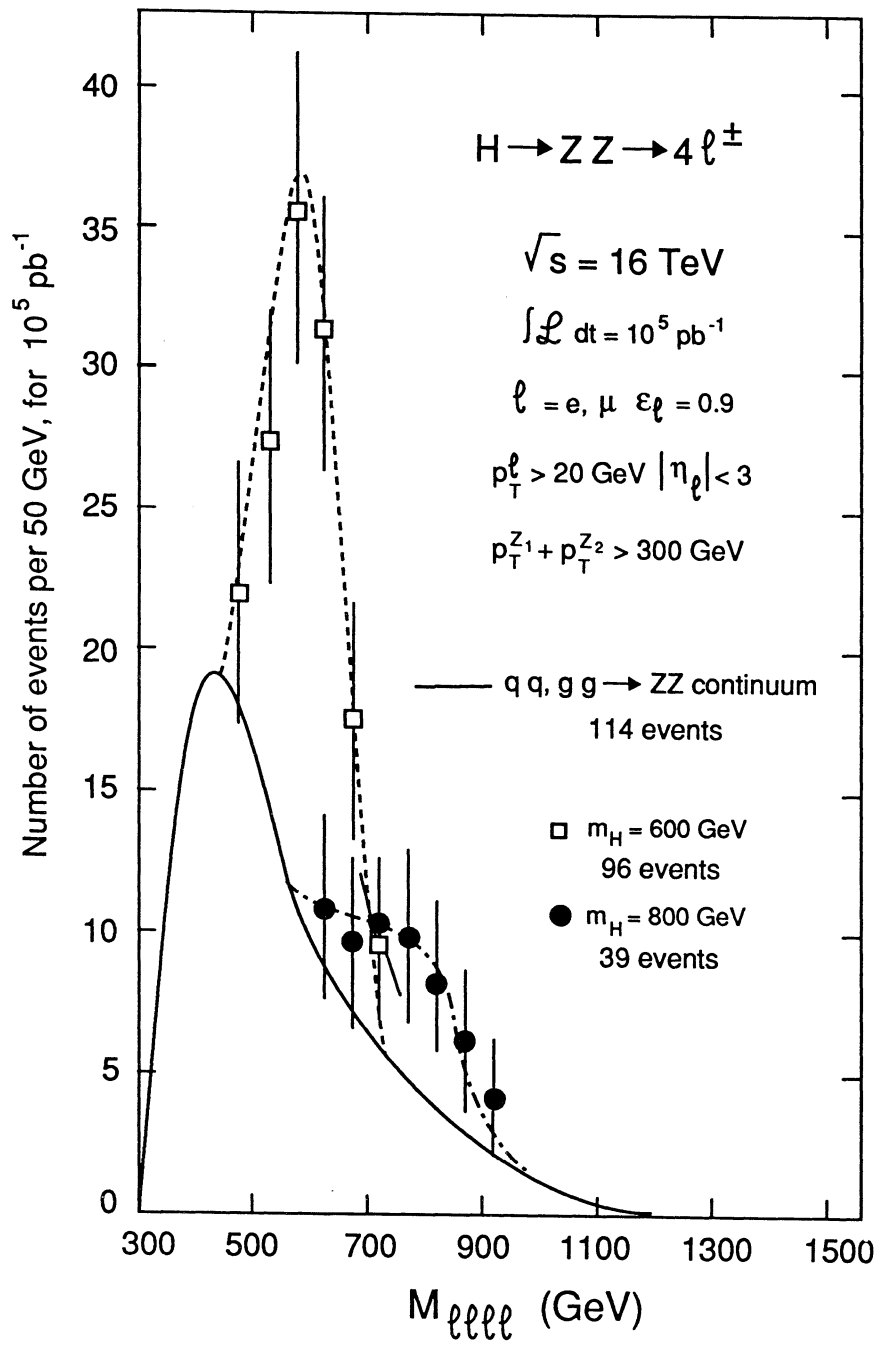


FIG. 3

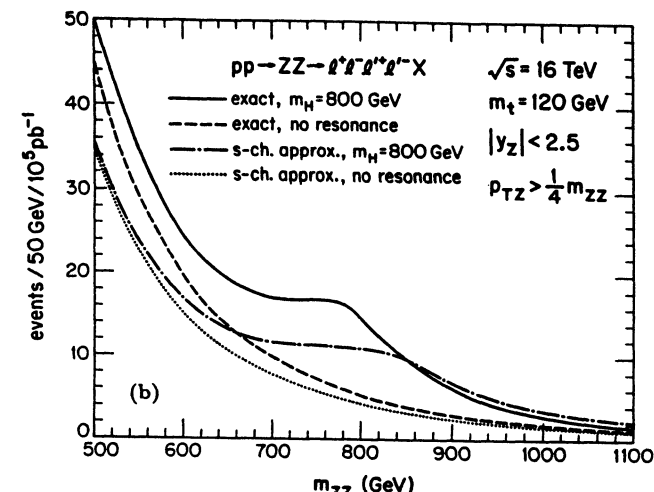


FIG. 4

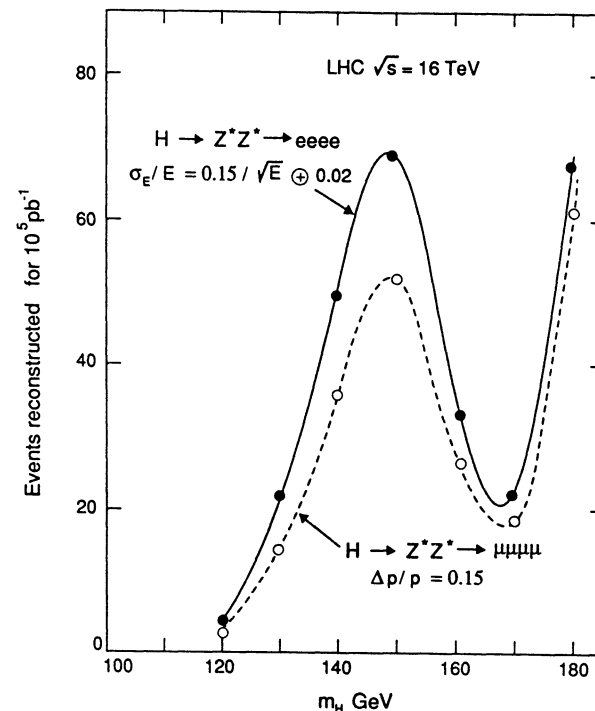


FIG. 5

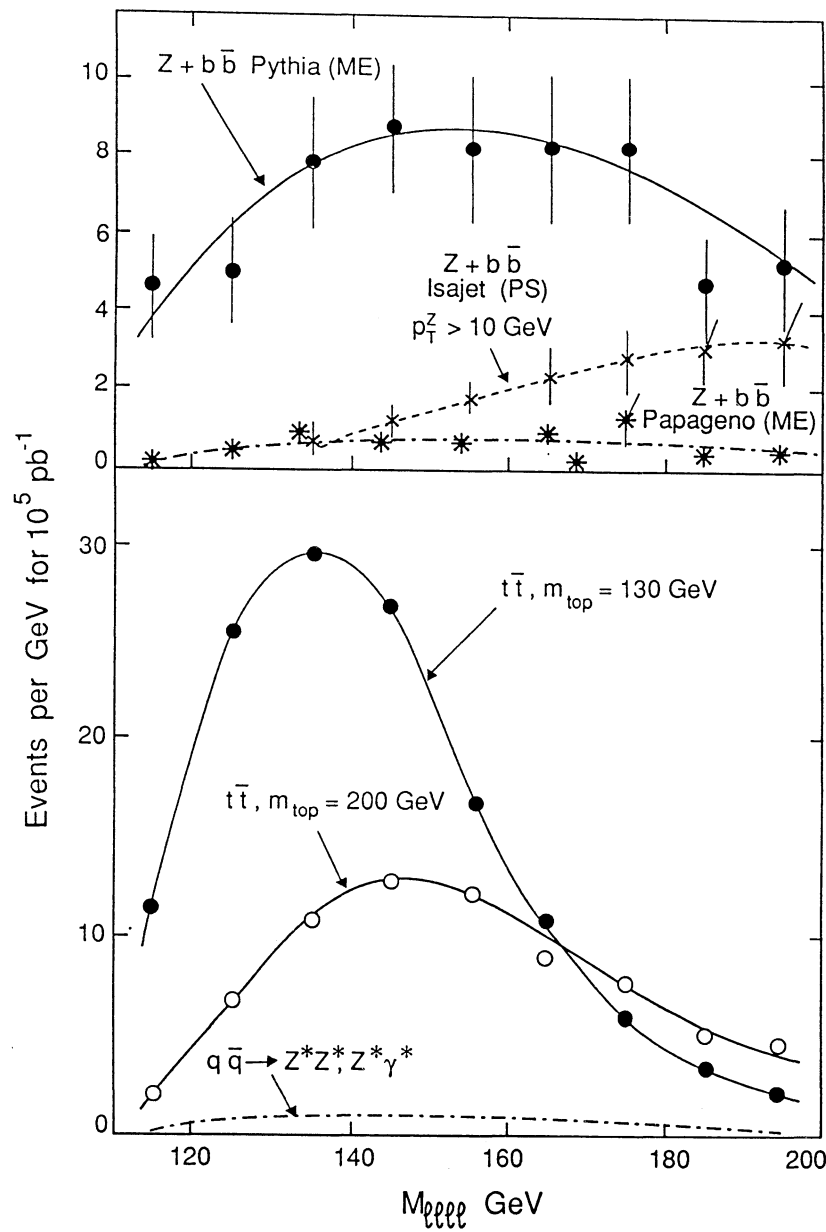


FIG. 6

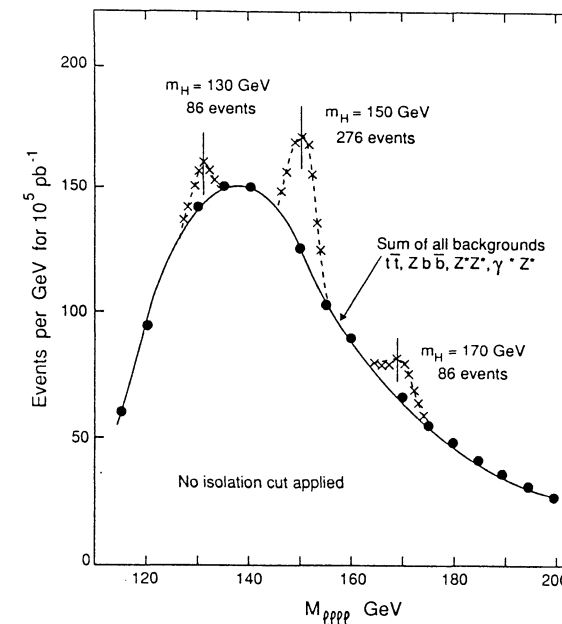


FIG. 7

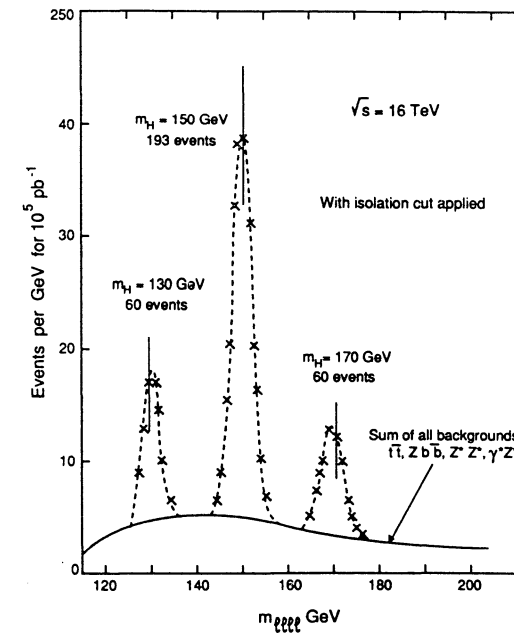


FIG. 8

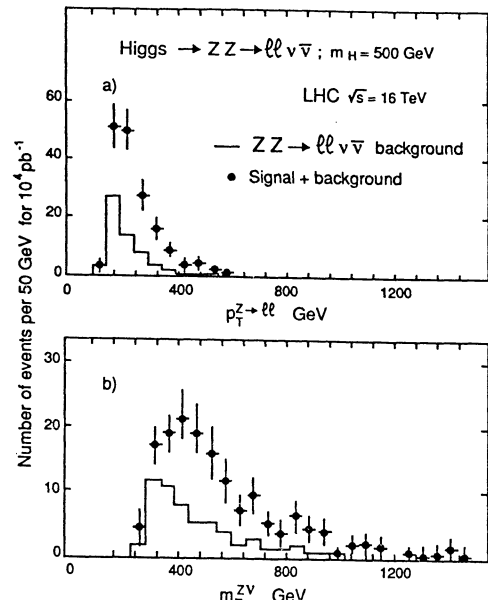


FIG. 9

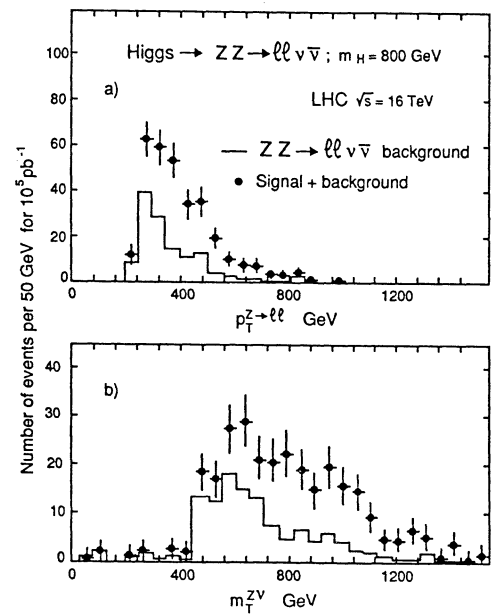


FIG. 10

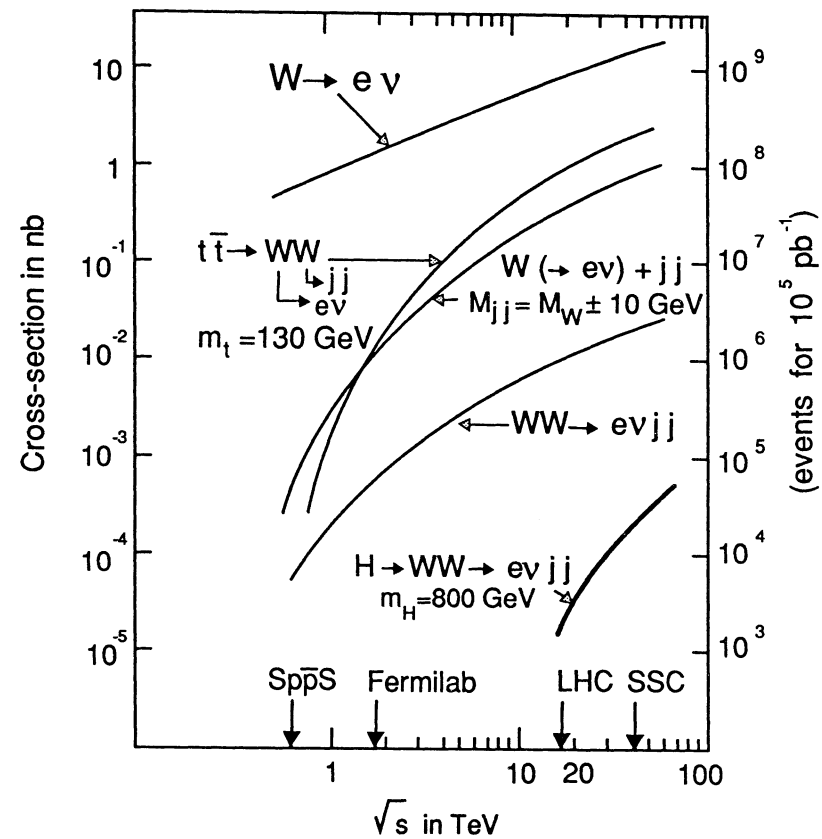


FIG. 11

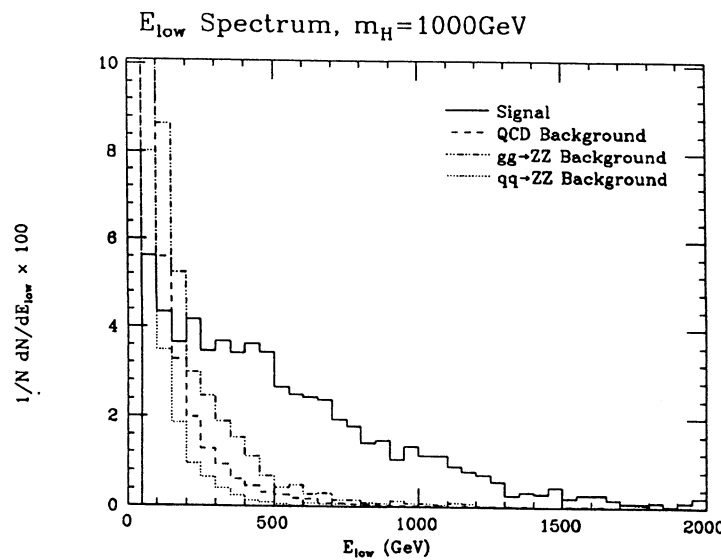


FIG. 12

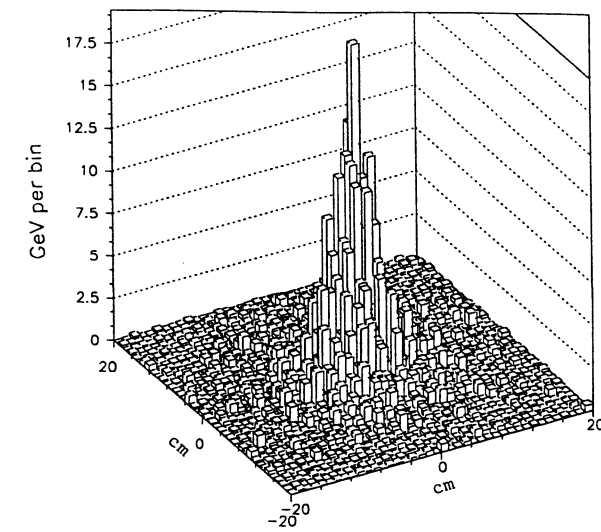


FIG. 14

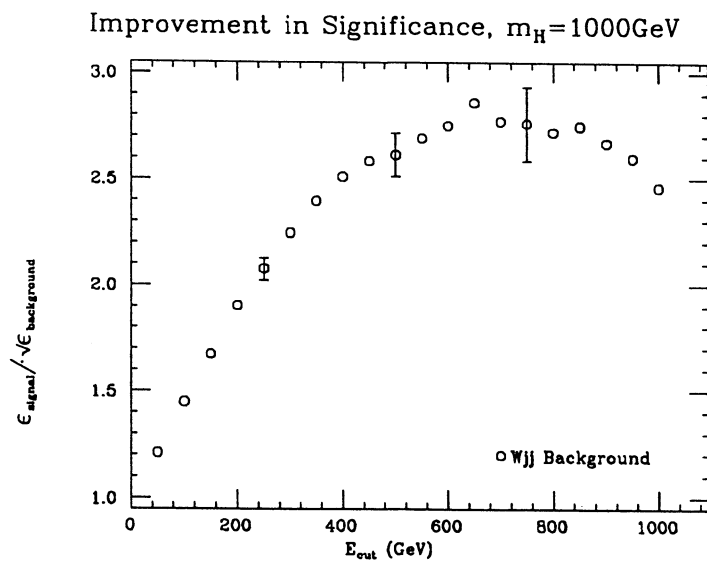


FIG. 13

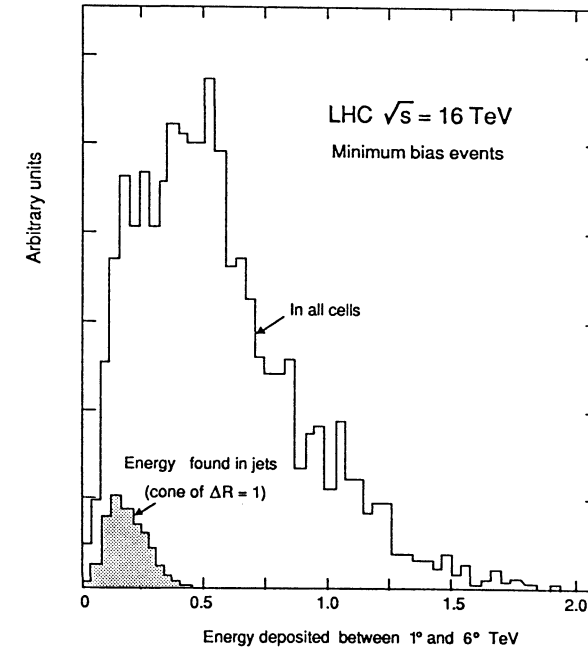


FIG. 15

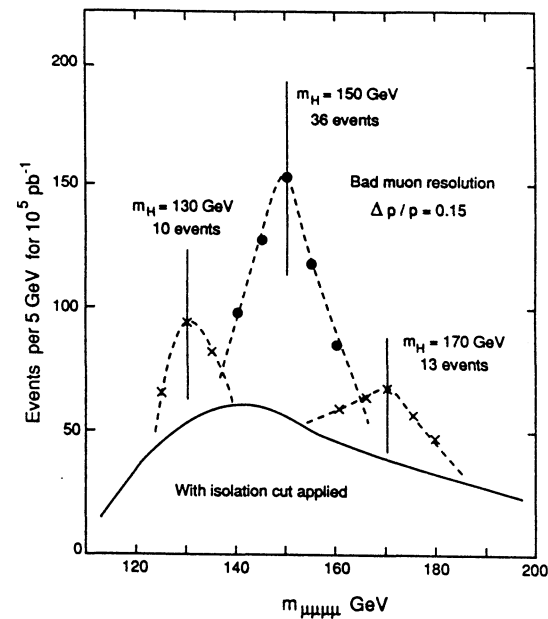


FIG. 16

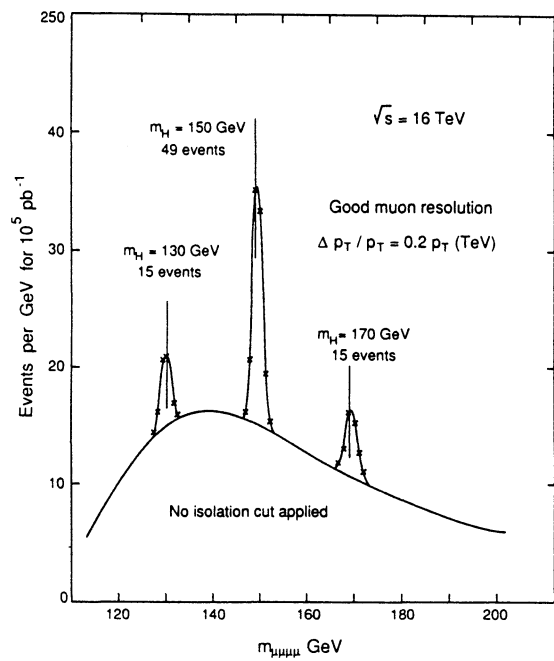


FIG. 17

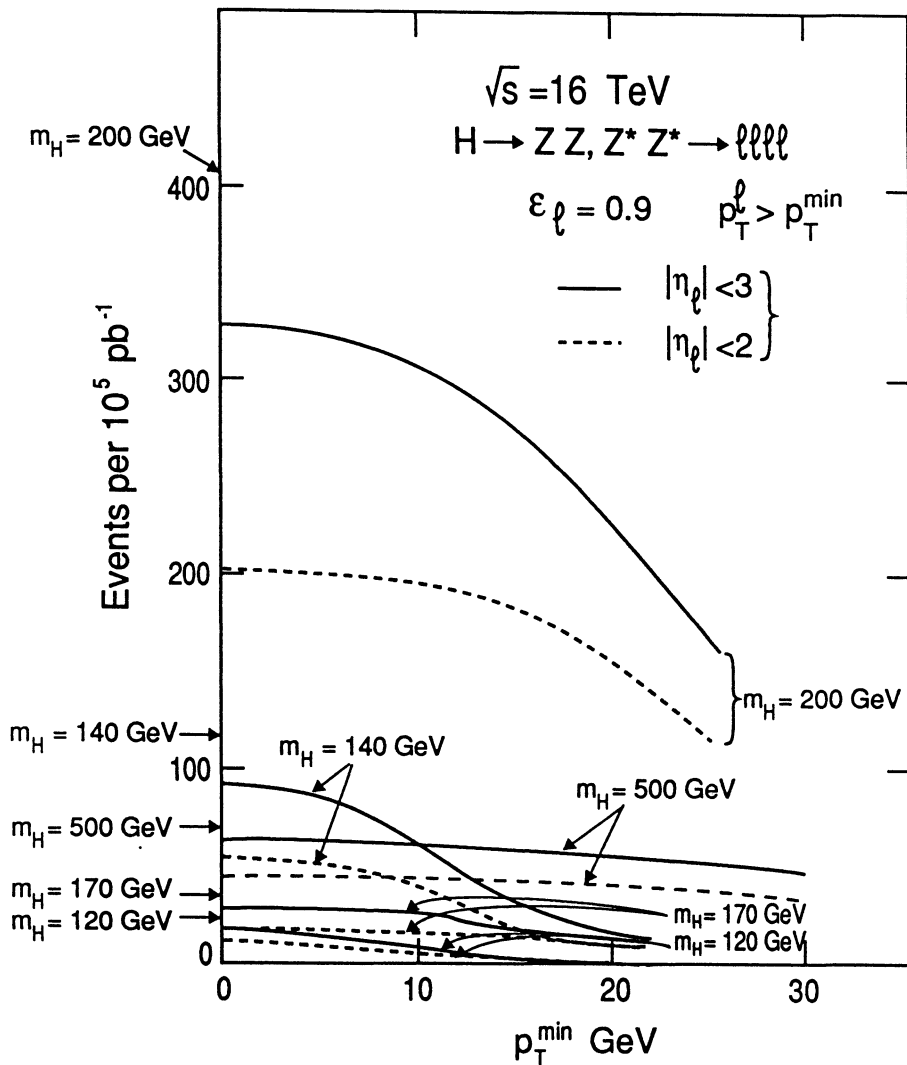


FIG. 18

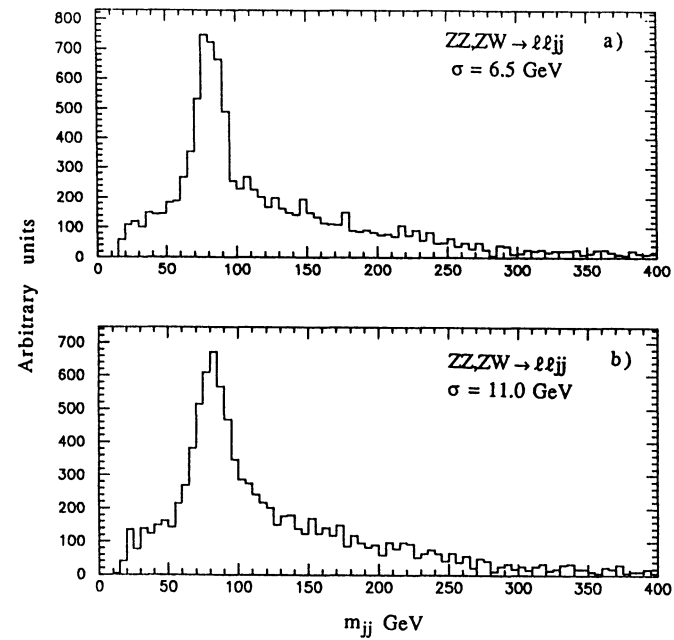


FIG. 19

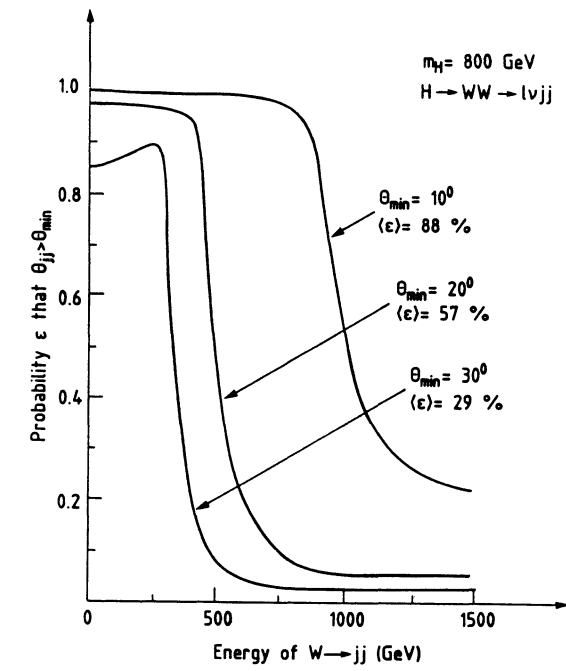


FIG. 21

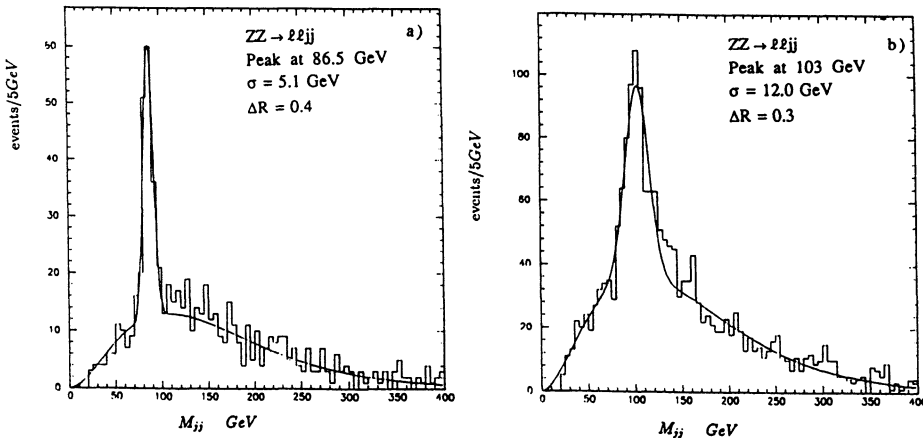


FIG. 20

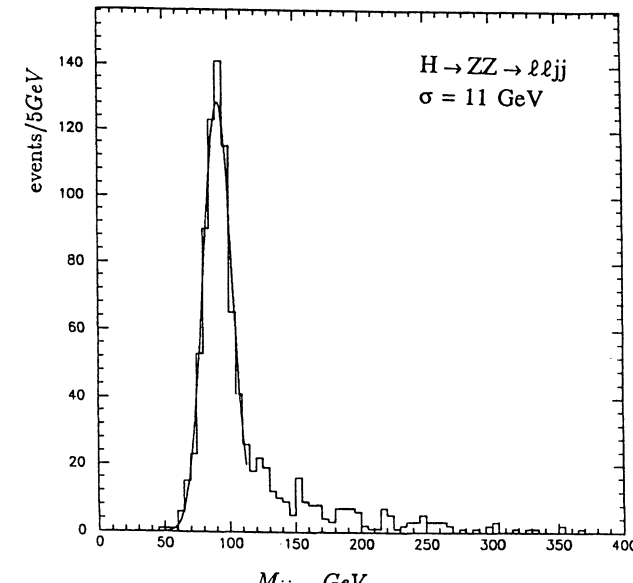


FIG. 22

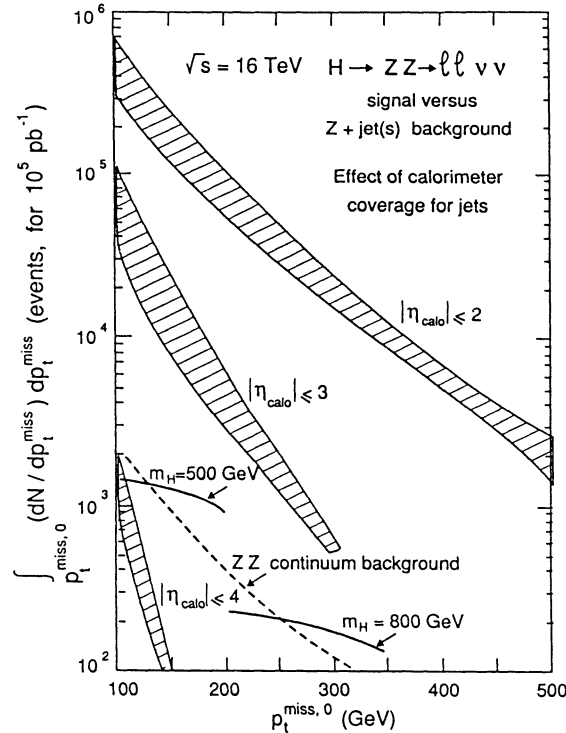


FIG. 23

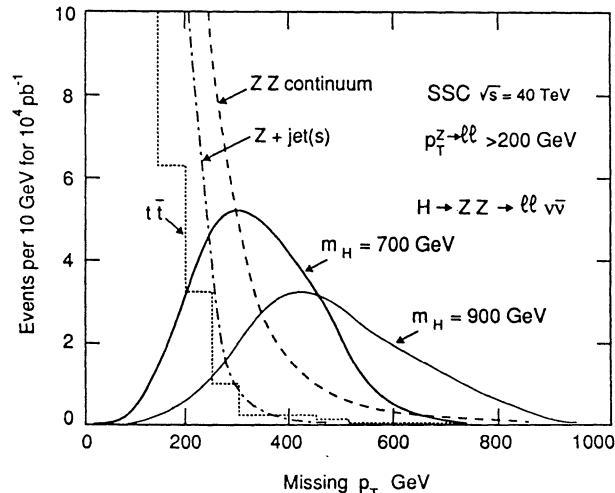


FIG. 24

Photon decay modes of the intermediate mass Higgs

ECFA Higgs working group

C.Seez and T. Virdee

L. DiLella, R. Kleiss, Z. Kunszt and W. J.Stirling

Presented at the LHC Workshop, Aachen, 4 - 9 October 1990
by C. Seez, Imperial College, London.

A report is given of studies of:

- (a) $H \rightarrow \gamma\gamma$ (work done by C. Seez and T. Virdee)
 - (b) $W H \rightarrow \gamma\gamma$ (work done by L. DiLella, R. Kleiss, Z. Kunszt and W. J. Stirling)
- for Higgs bosons in the intermediate mass range ($90 < m_H < 150 \text{ GeV}/c^2$).
The study of the two photon decay mode is described in detail.

Introduction

A Standard Model neutral Higgs boson having a mass above the highest reach of LEP II (around $90 \text{ GeV}/c^2$) [1], and below about $2m_Z$ will be difficult to detect at a hadron collider. The most promising channels for detection are $H^0 \rightarrow \gamma\gamma$, or, for $m_H \geq 130 \text{ GeV}/c^2$, $H^0 \rightarrow ZZ^* \rightarrow e^+e^-e^+e^-$ [2]. As the decay width of the Higgs is about 5.5 MeV at $m_H = 100 \text{ GeV}/c^2$, and 8.3 MeV at $150 \text{ GeV}/c^2$, the width of the reconstructed mass distribution, and hence the signal/background ratio, will be limited by the detector, and in particular by the energy resolution of the electromagnetic calorimeter.

The decay channel $H^0 \rightarrow Z\gamma$ also appears to be potentially attractive, but, after requiring that the Z decay into electrons or muons, the combined branching fraction times cross-section is very small. The intrinsic background (i.e. the background with the same final state as the signal) is large and rules out the possibility of detecting the Higgs boson in this channel.

In this paper a detailed study of the possibility of detecting an intermediate mass Higgs boson in the di-photon channel is reported. Results from another study are also reported in which the same decay is considered but for a Higgs boson produced in association with an intermediate vector boson.

1. $H^0 \rightarrow \gamma\gamma$

Previous studies of $H^0 \rightarrow \gamma\gamma$ [3] concluded that it would probably be possible to find a Higgs of mass $150 \text{ GeV}/c^2$ at the SSC ($\sqrt{s}=40 \text{ TeV}$, and $10^4/\text{pb}$) with an excellent calorimeter, but that it would probably not be possible to obtain a significant signal if the mass was $100 \text{ GeV}/c^2$. The study described here differs from this previous work by:

- a) considering LHC energies and luminosities ($\sqrt{s}=16 \text{ TeV}$, and $10^5/\text{pb}$) and the problems resulting from pileup,
- b) investigating a large range of calorimetric energy resolutions,
- c) including the prompt photon background from bremsstrahlung diagrams, and
- d) making a detailed study of the background from jet processes.

2. Cross-sections

The Higgs production cross-section multiplied by the branching ratio to two photons ($\sigma_{H^0} \cdot \text{Br}_{\gamma\gamma}$) has recently been re-calculated by Kunszt and Stirling [4] for Higgs masses in the

intermediate range, and is shown in figure 1.

The background to the $H^0 \rightarrow \gamma\gamma$ signal may be divided into three categories:

i) prompt di-photon production from the quark annihilation and box diagrams which provides an intrinsic background,

ii) prompt di-photon production from significant higher order diagrams (mainly bremsstrahlung diagrams),

iii) the background from jet processes where an electromagnetic energy deposit results from a quark or gluon jet rather than a prompt photon.

The intrinsic background cross-sections have been calculated using ISAJET [5] as a framework with the matrix elements of Berger, Braaten and Field [6]. For this calculation the HMRSB structure functions [7] were inserted into ISAJET so as to be consistent with the calculation of the Higgs production cross-section.

The bremsstrahlung contribution can be generated with ISAJET. Its cross-section has been fixed by requiring the ratio bremsstrahlung/(quark annihilation+box diagrams) to be that calculated by the direct photon working group [8].

The calculated cross-section for Higgs boson production in the intermediate mass range is insensitive to the choice of top quark mass: for $m_{H^0}=100$ GeV/c 2 it varies by less than 10% for values of top mass ranging from 100 to 200 GeV/c 2 . However, choice of structure functions can vary the calculated cross-sections for both Higgs production and the background processes by $\pm 50\%$, even when the choice is restricted to sets fitting recent BCDMS data [9].

Tables 1 and 2 summarise the cross-sections used. For both signal and background processes Monte-Carlo events have been generated using ISAJET.

m_H (GeV/c 2)	$\sigma \cdot Br(H^0 \rightarrow \gamma\gamma)$ (fb)	
	before cuts	after cuts
80	36.4	9.6
100	46.5	19.0
150	26.5	13.5

Z. Kunszt and W. J. Stirling, HMRSB structure functions, $m_{top}=150$ GeV/c 2
kinematic cuts: $|\eta| \leq 2$, $p_T^1 > 40$, $p_T^2 > 25$ GeV/c, $p_T^1/(p_T^1+p_T^2) < 0.7$

Table 1: The cross-section of the signal

m_γ (GeV/c 2)	qq-> $\gamma\gamma$	gg-> $\gamma\gamma$	Brems- strahlung	Total
80	31.7	84.7	87.5	204.
100	30.8	60.8	61.4	153.
150	12.0	16.1	17.0	45.

$d\sigma/dm_\gamma$ (fb/GeV) of di-photon backgrounds

kinematic cuts: $|\eta| \leq 2$, $p_T^1 > 40$, $p_T^2 > 25$ GeV/c, $p_T^1/(p_T^1+p_T^2) < 0.7$

- qq-> $\gamma\gamma$, gg-> $\gamma\gamma$: ISAJET, using matrix elements of Berger, Braaten and Field, HMRSB structure functions
- Bremsstrahlung: ISAJET, after isolation cut, normalized to analytic calculation (see text)

Table 2: The cross-sections of the prompt di-photon backgrounds

3. The calorimeter, acceptance and cuts

If quantitative and realistic results are to be produced it is necessary to define the properties and characteristics of a detector whose performance can then be simulated.

The model calorimeter used in this study covers a pseudo-rapidity range $-2 \leq \eta \leq 2$, and has an inner radius of 2 metres at $\eta=0$, tapering to 1.5 metres at $\eta=\pm 2$. It is segmented into fully pointing towers, and it is assumed that sufficient lateral shower containment is obtained by reading out an area of 20×20 cm 2 , i.e. photons are reconstructed in an area of $\Delta\phi \times \Delta\eta = 0.1 \times 0.1$. It is assumed that only the energy deposited by the interactions occurring in a single bunch crossing is seen. The cuts placed on the photon transverse momenta are sufficiently high that triggering would pose no problem: $p_T^1 > 40$ and $p_T^2 > 25$ GeV/c (the photons being ordered by p_T).

The photon pairs from bremsstrahlung diagrams tend to be asymmetric in the amount of transverse momentum they carry. A cut on the p_T balance of the photon pair, $p_T^1/(p_T^1+p_T^2) < 0.7$ (where $p_T^1 > p_T^2$), is found to remove about 20% of the bremsstrahlung background remaining after the η and p_T cuts at $m_\gamma=100$ GeV/c 2 while removing only 6.2% of the signal. Since this cut rejects very little of the background contributions from the annihilation and box diagrams the gain in signal significance (measured by $N_S/\sqrt{N_S}$) is, unfortunately, small.

As is described below, an isolation cut is applied to the photons to help reject the jet background. This isolation cut, though only over a small area ($\Delta\eta \times \Delta\phi = 0.1 \times 0.1$), should significantly reduce the remaining hard bremsstrahlung even after the application of the balance cut, as is shown by a semi-analytic calculation [8]. However, the algorithm used in ISAJET to generate photon radiation from quarks during their 'evolution' results in a distribution of the radial separation between radiating quark and photon that is essentially flat, rather than being strongly peaked around $\Delta R=0$. Consequently the isolation cut has little effect on the

bremsstrahlung events generated with ISAJET. We assume that this is incorrect and have corrected the level of the bremsstrahlung background assuming that our isolation cut over an area of $\Delta\eta \times \Delta\phi \approx 0.2 \times 0.2$, after the p_T balance cut, should further reduce it by 50%, as is suggested by the analytic calculation.

The cuts against the bremsstrahlung background could be further optimised. A fairly loose cut on the ΣE_T within a somewhat larger isolation area about the photons, e.g. a circle of radius $\Delta R = 0.3$, should be very effective in reducing the bremsstrahlung background. Since the photons failing the balance cut are, in general, accompanied by harder jets than those passing it, an efficient isolation cut should make the p_T balance cut unnecessary. This deserves to be studied with a realistic simulation taking account of the energy deposited in the isolation cone by pileup.

The limited rapidity range results in a geometric acceptance of around one half (47.1% at $m_H = 80 \text{ GeV}/c^2$, 48.2% at $m_H = 100 \text{ GeV}/c^2$, and 52.6% at $m_H = 150 \text{ GeV}/c^2$). Figure 2 shows the distribution of the absolute rapidity of the photon, in each event, at the highest absolute rapidity, for photon pairs from (a) a Higgs of mass $100 \text{ GeV}/c^2$, (b) the two prompt di-photon background diagrams. In all cases a requirement of $p_T > 40$ and $p_T^2 > 25 \text{ GeV}/c$ has been made on the photons. For the background processes a mass cut of $105 \geq m_{\gamma\gamma} \geq 95 \text{ GeV}/c^2$ has also been made.

The cuts on the transverse momenta of the photons result in very little additional loss of the signal for $m_H > 100 \text{ GeV}/c^2$ and thus the final acceptance is 40.9% for $m_H = 100 \text{ GeV}/c^2$, and 50.8% for $m_H = 150 \text{ GeV}/c^2$. At $m_H = 80 \text{ GeV}/c^2$ the transverse momentum cuts significantly deplete the signal (the final acceptance is 26.4%), however, because the p_T spectra of the intrinsic background is so steep at low p_T , reducing the p_T cuts gives only a small gain in the ratio signal/background. Figure 3 shows the p_T distribution of photons from (a) a Higgs of mass $100 \text{ GeV}/c^2$, (b) $qq \rightarrow \gamma\gamma$ with $105 \geq m_{\gamma\gamma} \geq 95 \text{ GeV}/c^2$, and (c) $gg \rightarrow \gamma\gamma$ with $105 \geq m_{\gamma\gamma} \geq 95 \text{ GeV}/c^2$. In all cases a requirement of $-2 \leq \eta \leq 2$ has been made on the photons.

The significance of the signal could be somewhat improved by extending the coverage of the calorimeter to larger rapidities. For example, for Higgs of mass $100 \text{ GeV}/c^2$, increasing the coverage from $-2 \leq \eta \leq 2$, to $-3 \leq \eta \leq 3$ increases the acceptance, after p_T cuts, by 45%. The background, however, is increased by more than 50%. This results in a gain in the signal significance of about 18%.

Despite many references in the literature to further cuts which enhance the signal with respect to the intrinsic di-photon background we have found no cut which usefully improves the significance of the signal. The cut on large values of $|l\cos\theta^*|$ (the photon scattering angle in the centre-of-mass frame of the two photons) originally advocated by Dicus and Willenbrock [10] (for computational reasons in the absence of η and p_T cuts) and used in most subsequent studies has no power at all after the η and p_T cuts have been applied.

4. Multiple interactions

Taking a mean operating luminosity of $10^{34} \text{ cm}^{-2}\text{sec}^{-1}$ and an inelastic non-single diffractive p-p cross-section of 60mb, one obtains a mean interaction rate of 600 MHz - an average of 9

interactions each crossing for a 15ns bunch spacing. These multiple interactions have a number of effects upon the detection of Higgs di-photon decays.

4.1 energy smearing

Energy may be deposited into the calorimeter cells used to measure a photon's energy from any of the interactions which occur during the cells' effective integration time. This pileup energy smears the signal, and the magnitude of the effect depends upon the size of the area of the calorimeter needed to laterally contain the shower (in our case $\Delta\phi \times \Delta\eta = 0.1 \times 0.1$), the effective integration time (in our case a single bunch crossing), and upon the instantaneous luminosity. The magnitude of this effect has been estimated by Monte-Carlo. Jet events were generated using ISAJET with the jet $p_T > 5 \text{ GeV}/c$. These events were assumed to represent the events accompanying a di-photon trigger. Pileup was then simulated by overlaying a number of these events, the number overlayed being chosen from a Poisson distribution with a mean of 10. All particles were assumed to deposit all their energy in the electromagnetic calorimeter. Figure 4(c) shows the smearing of mass resolution resulting from this pileup alone (i.e. the energy resolution is taken to be otherwise perfect). The broadening of the effective mass peak shown in figure 4(c) may be compared to that caused by a calorimetric resolution of $2\%/\sqrt{E} \oplus 0.5\%$ (where \oplus denotes a quadratic sum) as shown in figure 4(a). It can be seen that the pileup smearing is relatively insignificant.

4.2 signal rejection

As will be discussed below it is necessary to impose an isolation requirement on electromagnetic clusters found in the calorimeter to help reduce the number of such clusters resulting from jet processes. The multiple piled up events increase the probability that the photons from the Higgs decay fail the isolation criteria. Isolation requirements are discussed in more detail below.

4.3 loss of knowledge of the vertex position

Although the transverse location of interactions in an LHC experiment will be known with great precision, the longitudinal position of the interactions will, because of the length of the bunches, be distributed with an r.m.s. spread of 5-6 cm. If it is not known to which vertex the photons belong the reconstructed mass is smeared by the resulting uncertainty on the angle between the photons. The effect on the width of the reconstructed effective mass for a Higgs of mass $100 \text{ GeV}/c^2$ is shown in figure 4(d), where it can be seen that the broadening of the mass peak is of similar magnitude to that resulting from a calorimetric resolution of $7\%/\sqrt{E} \oplus 1.0\%$ shown in figure 4(b). With our chosen geometry a knowledge of the longitudinal vertex position to a precision of about 1 cm results in a smearing of the reconstructed effective mass which is small compared to that caused by even an superb calorimeter.

It may be possible, by measuring the shower position at two depths, to obtain the necessary angular information from the photon showers themselves. Some results are shown below for the case where such a capability is assumed to exist.

A charged particle tracking device will find many vertices per crossing, and it will sometimes be possible to determine which vertex corresponds to the interaction in which the Higgs was produced, by, for example, counting the number of high p_T tracks associated with each vertex. This has been studied by Monte-Carlo. It does not seem possible to make the determination with sufficient efficiency for it to be very useful when there are on average 10 interactions per bunch crossing.

5. The jet background

In the kinematic region being considered the di-jet cross-section is about seven orders of magnitude larger than the di-photon cross-section. A very large rejection of the possibility of any di-jet event faking a di-photon event is needed if the jets are not to be the source of a formidable background. Two tools can be used to reject the jet background:

- Isolation: the photons from Higgs decay are isolated whereas the electromagnetic energy deposits resulting from a jet tend to be accompanied by other jet fragments. Isolation has traditionally been imposed at hadron colliders by cutting on the summed transverse energy within a relatively large cone around the particle to be isolated. Because of the large average ΣE_T deposited into any such cone from the many interactions occurring every bunch crossing at high luminosity such a cut cannot be made very tight. For example: if the mean number of interactions per bunch crossing is 10, then the r.m.s. fluctuation on the ΣE_T deposited in a cone of $\Delta R=0.6$ by the pileup events in a single bunch crossing is about 5 GeV, thus the cut would have to be set at 10 GeV, or more, to avoid the rejection of a significant fraction of the signal (the mean ΣE_T in such a cone is about 12 GeV, but this can be considered to be merely a shift of the zero-point).

A useful rejection factor can be obtained by cutting on relatively small individual energy deposits (or tracks) in a small region around the candidate isolated photons. It is clear that the precise definition of the isolation criteria need to be optimised with a full shower Monte-Carlo for any given detector design. For the results presented here the threshold was taken to be $p>2\text{GeV}/c^2$, and the isolation region was taken to be a square $40\times 40 \text{ cm}^2$ (i.e. $\Delta\phi\times\Delta\eta=0.2\times 0.2$).

- π^0 detection: the jet background is predominantly due to single π^0 's carrying a large fraction of the jet E_T , the decay photons of which are reconstructed as a single electromagnetic energy deposit. The ability to ascertain, with a position detector for example, that there are two photons and not one in an electromagnetic energy deposit is thus a powerful tool to reject the jet background. With the geometry assumed in this study the minimum separation of the photons from the decay of a π^0 with $p_T=20\text{GeV}/c^2$ is 2.7 cm. It has been assumed that a position detector is present that can reliably detect the presence of two showers when they are separated by more than 1cm.

To avoid prohibitive demands on computer time it is necessary to investigate the rejection of single jets, and from this calculate the rejection factor against di-jets.

The uncertainty about the level of the background from jets is large, and arises from the following sources:

- lack of knowledge of the jet cross-section

x3

- lack of knowledge of the hard tail of the fragmentation functions x2²
- inadequacy of the simulation (not full shower simulation), and choice of isolation and π^0 detection algorithms x2²

The second and third items listed above refer to uncertainties on the single jet rejection factor and so enter the di-jet uncertainty squared. Adding these uncertainties quadratically gives a value larger than 5. LEP data allows a check of the quark fragmentation function in the energy range of interest, and the statistical precision in the hard tail will increase over the next few years. A detailed calorimeter design would allow a fuller simulation of the isolation and π^0 detection. Nevertheless it seems clear that the uncertainty on the Monte-Carlo calculation of the jet background will always remain large. It is necessary, therefore, to aim for a large safety margin in rejection power against the jet background. In practice this sets the goal of reducing the jet background to a level well below that of the intrinsic two photon background.

ISAJET (with EHLQ structure functions) was used to generate 100000 jet events in each of 12 bins in p_T^{hard} ($15 \leq p_T^{\text{hard}} \leq 200 \text{ GeV}/c$). The results of the first stage of the investigation are plotted in figure 5. It shows the inclusive cross-sections, as a function of p_T , of jets, π^0 s, isolated π^0 s, and electromagnetic energy deposits originating from π^0 s and not rejected by any cuts. Also shown are the cross-sections of the direct di-photon processes mentioned above. All the cross-sections are shown after a cut of $-2 \leq \eta \leq 2$ has been applied.

The number of γ s originating from π^0 s and not rejected by any cuts has been obtained by decaying each isolated π^0 10 times and finding the resulting separation of the photons in the detector. At low p_T the minimum separation of decay γ s is greater than 1 cm, so it is the asymmetric decays where the separation is such that the lower energy photon falls outside the $40\times 40 \text{ cm}$ isolation boundary which result in the background from unidentified π^0 s. At higher p_T the minimum separation of decay γ s becomes less than 1 cm and the position detector loses its π^0 rejection power.

It can be seen that for $p_T > 25 \text{ GeV}/c$ the spectrum of the remaining γ s is lower than halfway between the jet and the direct di-photon spectra (on the logarithmic scale), suggesting that when the rejection is applied to both jets the di-photon spectrum from di-jet events is below the direct di-photon spectrum.

To obtain a quantitative estimate of this background cross-section the two-dimensional distribution of the p_T of the two jets in each of a series of jet-jet mass bins was obtained, together with the jet cross-section in that bin. The rejection factors as a function of p_T were then applied to obtain the jet background cross-section as a function of mass, which is plotted in figure 6. It can be seen that only after using the π^0 rejection power of the position detector is the background reduced to an insignificant level as compared to the prompt di-photon background.

6. Results

Table 3 shows a summary of the results obtained, for three Higgs masses, assuming the presence of a superb electromagnetic calorimeter. For each mass the table shows the optimum mass bin width, Δm , and the number of signal, N_S , and the number of background events, N_B , counted in a bin of that width for an integrated luminosity of $10^5 /pb$. The last column of the

table shows the significance of the signal seen. The simulations used to obtain the numbers in the table were made with the following conditions:

- The kinematic cuts described previously were applied: $|\eta| \leq 2$, $p_T^1 > 40$, $p_T^2 > 25 \text{ GeV}/c$, $p_T^1/(p_T^1 + p_T^2) < 0.7$

• The electromagnetic calorimeter was assumed to have a resolution function

$$\Delta E/E = 2\%/\sqrt{E} \oplus 0.5\%$$

• It was assumed that the vertex was localized longitudinally with an r.m.s. precision of 1 cm (i.e. an angular precision of about 7 mr on each γ)

• Pileup smearing was included for $\Delta\phi \times \Delta\eta \times \Delta t = 0.1 \times 0.1 \times 1$ crossing (see previous discussion)

• A 7% loss of signal and background due to the isolation cut was included. This value was obtained from a Monte-Carlo simulation taking a mean of 10 piled up events per crossing.

• A 90% reconstruction efficiency on each photon (i.e. a further 19% loss of both signal and background) was assumed.

• It was assumed that the jet background had been reduced to negligible levels (position detector needed).

It can be seen that, by using such an electromagnetic calorimeter, a highly significant signal can be seen at $m_H=100 \text{ GeV}/c^2$ and $m_H=150 \text{ GeV}/c^2$. For Higgs bosons with masses between these two values the situation is even more favorable. However the significance drops away fairly rapidly for Higgs masses below $100 \text{ GeV}/c^2$.

$m_H (\text{GeV}/c^2)$	Δm	N_S	N_B	N_S / N_B
80	1.0	560	15400	4.5
100	1.5	1110	17300	8.4
150	2.0	880	6800	10.7

Table 3: Significance of $H^0 \rightarrow \gamma\gamma$ signal at different masses

Figure 7 presents the results in a slightly different form. A resolution function of the form $\Delta E/E = a/\sqrt{E} \oplus b$, where the two terms are added quadratically, is assumed for the electromagnetic calorimeter. The significance of the signal seen from a Higgs boson of mass $100 \text{ GeV}/c^2$, after accumulating 10^5 pb of data, is plotted as a function of the sampling term, a . It is again assumed that the jet background had been reduced to negligible levels. The 4 lines show the effect on the significance of the mass resolution resulting from:

- the calorimeter resolution alone,
- the calorimeter resolution and the pileup (from a mean of 10 events per crossing as described above),
- the calorimeter resolution, pileup and a longitudinal vertex resolution of 1 cm,
- the calorimeter resolution, pileup and a longitudinal vertex resolution of 5.5 cm.

In figure 7(a) the constant term, b , is taken to be 0.5%, in figure 7(b) it is taken to be 1.0%. These plots emphasise the importance of the constant term, b , and the need for a means to locate the Higgs vertex in order to be able to exploit the power of a calorimeter with such a small sampling term.

7. W $H^0 \rightarrow e(\mu)\gamma\gamma$

The two photon decay mode was also considered for the special case where the Higgs boson is produced in association with an intermediate vector boson which decays leptonically. In these events the presence of a high p_T isolated lepton in the final state provides an additional means of suppressing the hadronic backgrounds.

Table 4 shows the expected number of $\gamma\gamma$ pairs, found in the mass windows specified in the table, resulting from the decay of a Higgs boson and accompanied by an isolated electron or muon from a W. The numbers given assume an integrated luminosity of 10^5 pb , a rapidity coverage of ± 2.5 and a p_T threshold of $20 \text{ GeV}/c$ for both the photons and lepton, with an efficiency of 85% for each γ and 90% for the lepton after isolation cuts. The fraction of the signal falling in the chosen mass windows (about 80%) is taken to be the same as calculated by the simulation of unaccompanied $H \rightarrow \gamma\gamma$ detected by a high resolution calorimeter as described in section 6. In fact, the presence of a charged track, enabling the precise determination of the longitudinal vertex position, might allow a slightly better mass resolution to be achieved.

The rate for Higgs produced in association with Z⁰s is about 6 times lower and thus this channel cannot be considered viable for an integrated luminosity of 10^5 pb .

The background contributions from the following processes were evaluated:

- $W + \gamma\gamma$, the intrinsic or "irreducible" background [11]
- $b\bar{b} + \gamma\gamma$, where one b-quark decays leptonically
- $b\bar{b} + \gamma$, where one b-quark decays leptonically, and the other fakes a photon
- $W + 2\text{jets}$, where the jets fake photons
- $b\bar{b} + \text{gluon}$, where one b-quark decays leptonically and both the other b-quark and the gluon fake photons.

$m_H (\text{GeV}/c^2)$	Signal (GeV/c^2)	Δm (GeV/c^2)	Backgrounds				
			$W\gamma\gamma$	$bb\gamma\gamma$	$b\gamma\gamma$	bbg	$W+2\text{jets}$
80	14.6	1.0	1.8	0.29	0.44	0.20	0.05
100	17.8	1.5	1.7	0.38	0.28	0.18	0.05
140	10.8	2.0	1.4	0.30	0.22	0.17	0.09

Table 4: $W H^0 \rightarrow e(\mu)\gamma\gamma$ signal and backgrounds for 10^5 pb

The study was done at the parton level. It was assumed that a lepton isolation cut gives a factor of 7 rejection against leptons originating from b-quarks. The estimated background

contributions from these processes are shown in table 4, assuming an electromagnetic calorimeter with the same rejection power against jets faking photons as detailed in section 6 above. Because of the large signal to background ratio $N_S/\sqrt{(N_B+N_S)}$ can be used as a crude measure of the statistical significance of the expected signal: 3.5 at $m_H=80 \text{ GeV}/c^2$ and 3.0 at $m_H=140 \text{ GeV}/c^2$. It should be noted that the $b\bar{b}$ background has large uncertainties similar to those associated with the jet background to the unaccompanied $H \rightarrow \gamma\gamma$. Also N_B depends linearly on the width of the mass bin needed to contain the signal. It has recently been brought to our attention [12] that W bosons from the decay of top quarks produced in association with a Higgs (the process $gg \rightarrow t\bar{t}H$) might be expected to more than double the signal.

8. Conclusions

- A superb electromagnetic calorimeter with a resolution of $\Delta E/E = 2\%/\sqrt{E} \oplus 0.5\%$ would be able to detect a very significant signal from standard model Higgs bosons in the mass range $100 < m_H < 150 \text{ GeV}/c^2$ at LHC thus filling the gap between LEP II and $H \rightarrow ZZ^*$ at LHC.

- Unless the jet background can be reduced to an insignificant level any possible signal will be at the mercy of the very large uncertainty on the level of this background. To obtain this rejection it seems that something like a position detector capable of detecting the presence of two photons from π^0 s of transverse momenta up to about $50 \text{ GeV}/c$ is necessary. It will probably be necessary to perform a more detailed Monte-Carlo study of jet rejection for any detector in which it is hoped to detect $H^0 \rightarrow \gamma\gamma$.

- In order to be able to exploit the power of a calorimeter with a small sampling term in the resolution function other factors causing a smearing of the mass resolution need to be controlled. The constant term, usually arising from shower leakage and inhomogeneities, and ultimately limited by intercalibration errors, must be made very small, and the direction of the two photons must be determined with an angular precision of about 7 mrad.

- An electromagnetic calorimeter capable of detecting $H^0 \rightarrow \gamma\gamma$ in the mass range $100 < m_H < 150 \text{ GeV}/c^2$ in conjunction with a reasonable muon detector may also be capable of detecting a signal in the channel $WH^0 \rightarrow \gamma\gamma$ probably with a reach stretching down to even smaller Higgs masses.

References

- [1] See, for example, S. L. Wu, Proceedings of the ECFA workshop on LEP200, vol II, CERN 87-07
Z. Kunszt and W. J. Stirling, Phys. Lett., **242B** (1990) 507
- [2] D. Froidevaux, these proceedings
- [3] C. Barter *et al.*, Proceedings of 1987 Berkeley Workshop
- [4] Z. Kunszt, these proceedings
- [5] F. E. Paige and S. D. Protopopescu, ISAJET version 6.24. ISAJET is a Monte-Carlo event generator using the parton shower technique to simulate QCD and QED topologies beyond leading order.
- [6] E. Berger, E. Bratten and R. Field, Nucl. Phys. **B239** (1984) 52
Of the two diagrams giving large contributions to the prompt di-photon production cross-section in the kinematic region being considered only the quark-antiquark annihilation process is coded in ISAJET 6.24. In order to generate di-photons from the gluon-fusion box diagram we have inserted the matrix element from Berger, Bratten and Field into the relevant ISAJET routine.
- [7] BCDMS fit with $\Lambda=190 \text{ MeV}$, described in P. Harriman, A. Martin, R. Roberts, W. Stirling, preprint DTP 90-04 (April 1990)
- [8] P. Aurenche and L. Camilleri, private communication. The comparison is done using the same structure functions in ISAJET (Duke and Owens) as used by Aurenche *et al.* See also H. Baer and J. Owens, Phys. Lett., **205B** (1988) 377, and M. Werlen, these proceedings.
We have also directly compared the cross-sections for the annihilation and box diagrams obtained using ISAJET with those obtained by Aurenche *et al.* The agreement is excellent.
- [9] See H. Plothow-Besch, these proceedings.
- [10] D. Dicus and S. Willenbrock, Phys. Rev., **37D** (1988) 1801
- [11] Z. Kunszt, these proceedings; also R. Kleiss, Z. Kunszt and W. Stirling, preprint DTP 90-54 and ETH-TH 90-29 (August 1990)
- [12] W. J. Marciano, private communication.

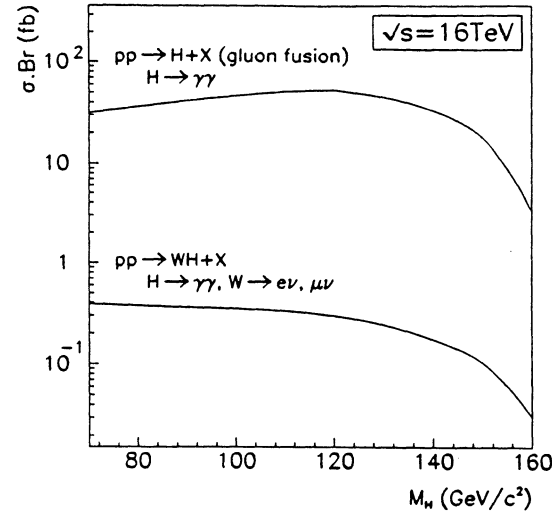


Figure 1: σBr for $H \rightarrow \gamma\gamma$

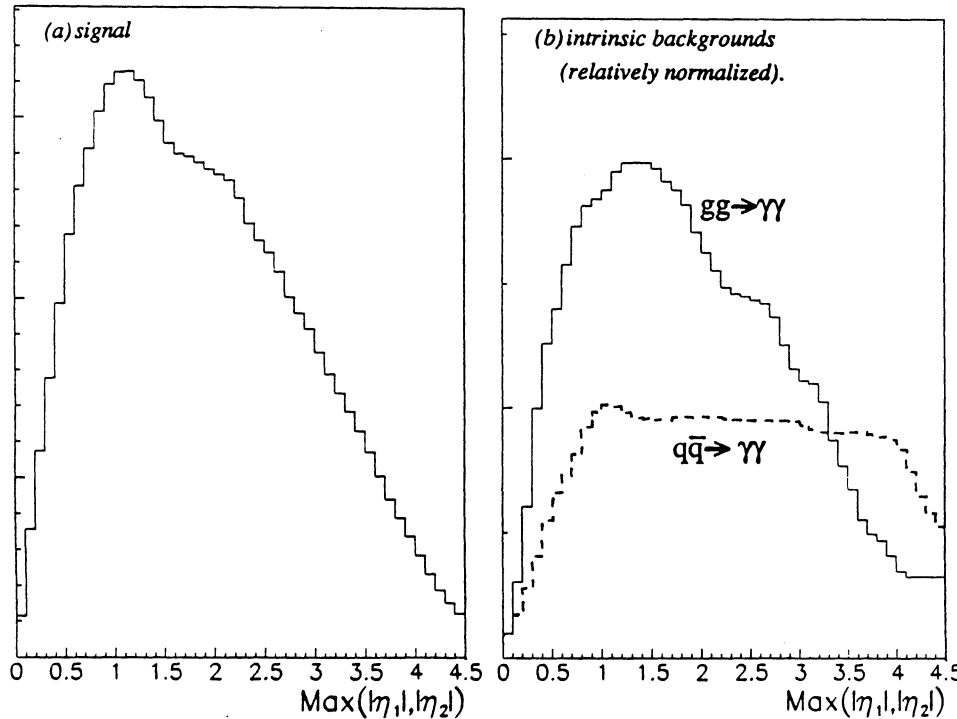


Figure 2: Rapidity of photon with largest absolute rapidity

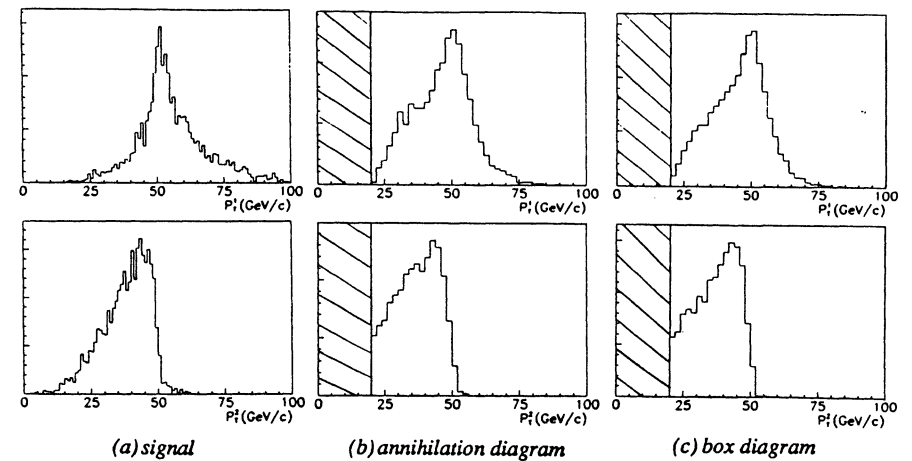


Figure 3: Transverse momentum distributions of photons

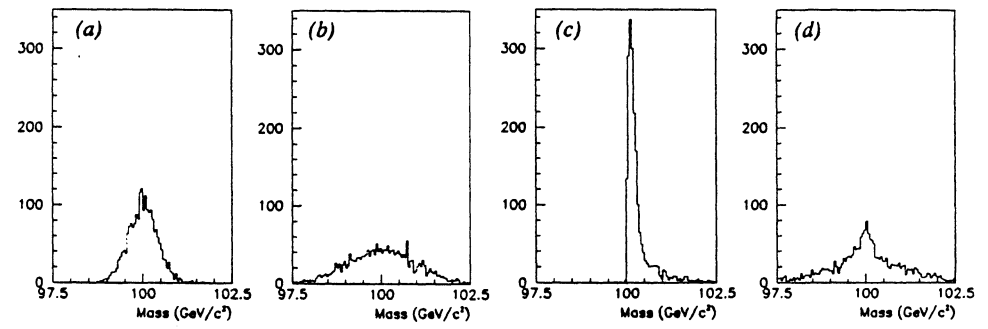
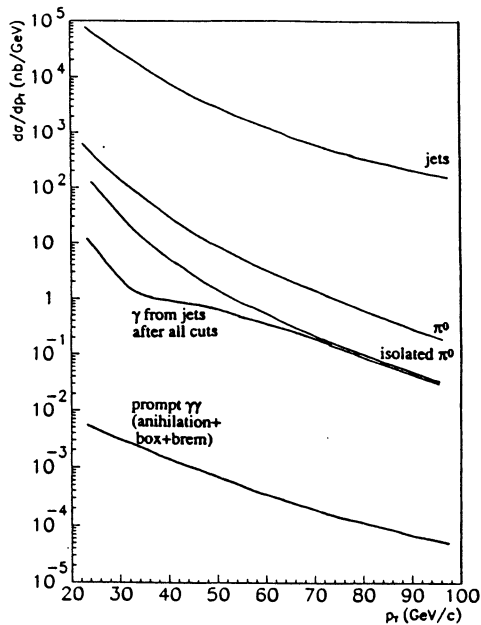
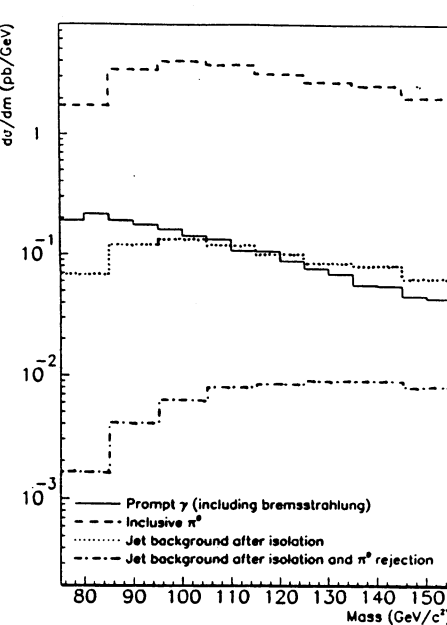
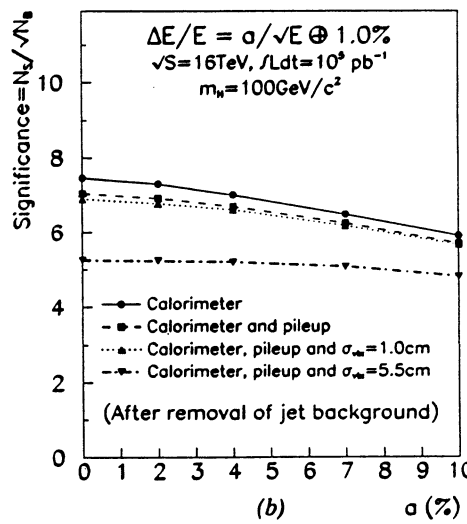
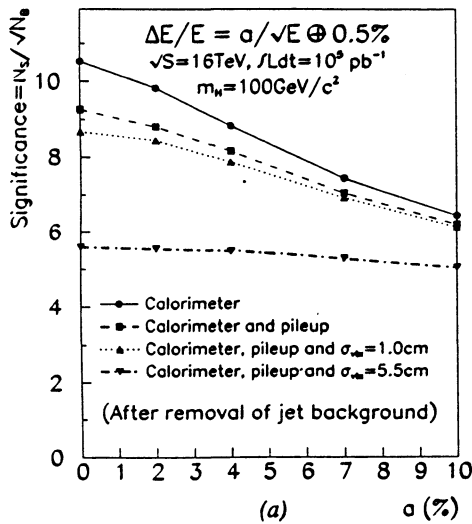


Figure 4: Reconstructed mass plots for Higgs boson, $m_H = 100$ GeV/c²
(a) smeared by: calorimeter energy resolution of $\Delta E/E = 2\%/\sqrt{E} \oplus 0.5\%$
(b) smeared by: calorimeter energy resolution of $\Delta E/E = 7\%/\sqrt{E} \oplus 1.0\%$
(c) smeared by: pileup energy from, on average, 10 interactions
(d) smeared by: loss of knowledge of the vertex position ($\sigma_{v\alpha} = 5.5$ cm)

Figure 5: Inclusive $d\sigma/dp_T (|\eta|<2)$ Figure 6: $d\sigma/dm_{\gamma\gamma}$ after kinematic cutsFigure 7: Significance of signal seen from Higgs boson of mass $100\text{GeV}/c^2$ using calorimeter with resolution function $\Delta E/E = a/\sqrt{E} + b\%$ **$HZ \rightarrow \gamma\gamma l^+l^-$: A Possibility for an Extremely High Luminosity Collider**

A.Grau

Universitat Autònoma de Barcelona, Grup de Física Teòrica, 08193 Bellaterra, Spain

T.Han

Fermi National Accelerator Laboratory, P.O.Box 500, Batavia, IL 60510, USA,

G.Panzeri

INFN, Laboratori Nazionali di Frascati, P.O.Box 13, 00044 Frascati

Abstract

We have considered associated Higgs- Z^0 production at the LHC and calculated the intrinsic background to the signal $HZ \rightarrow \gamma\gamma l^+l^-$. Transverse momentum and invariant mass distributions for double bremsstrahlung from the initial quark legs are presented. It is shown that this background is well below the signal provided a very good mass resolution is obtained. Under normal luminosity conditions, the number of events is not sufficient for discovery, but it can be adequate if an extremely high luminosity is made available, i.e. $L=5 \times 10^{34} \text{ cm}^{-2} \text{ sec}^{-1}$.

In this contribution to the Workshop we address the question of the Higgs search in the light intermediate mass region. For an Intermediate mass Higgs, i.e. one for which $m_Z \leq M_H \leq 2m_W$, there are two mechanisms which have been proposed [1] and which have been the object of extensive study in this workshop [2], i.e. direct Higgs production and decay into virtual Z^0 pairs [3] and $\gamma\gamma$ pairs [4]. For a Higgs boson of mass $M_H \approx m_Z$, the first of these mechanisms however cannot be used for lack of rate and therefore one must rely on the second and on the possibility of building a specialized detector with very high demands on resolution in order to overcome both the background from jets as well as the irreducible intrinsic background from $q\bar{q} \rightarrow \gamma\gamma$. On the other hand, this mass region is probably out of reach by LEP200 and may have to be explored by the Hadron Colliders. Indeed, to exclude or to confirm the existence of a Higgs boson degenerate in mass with the Z^0 is very important from a theoretical point of view. In this note we examine another signature, which is low in rate, but potentially very clean, i.e. associated Higgs- Z^0 production. The probability of finding a Higgs into a Z^0 at the LHC is $10^{-4} \div 10^{-5}$, a not impossibly small number. However, in order to overcome the intrinsic background from Z^0 -pair production, one needs to search for Higgs boson decay modes inaccessible to the Z^0 , i.e. $H\gamma\gamma$, because of Yang's theorem [5]. In addition, if one requires to observe only leptonic decay modes for the associated Z^0 , the event rate becomes very low.

Since the event rate is marginal, special care must be taken to calculate the branching fractions, which become sensitive to virtual and rare channels, as well as to QCD cor-

rections to the b-quark mass [2,6,7]. The decay rate into virtual Z^0 's can be written as [8,9]

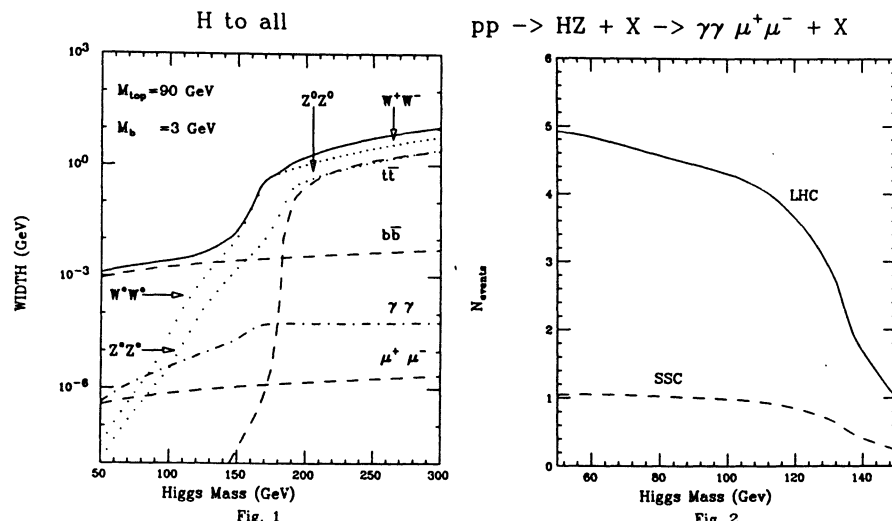
$$\Gamma(H^0 \rightarrow 4\mu) = \int_0^{m_H^2} dQ_1^2 \int_0^{(m_H - Q_1)^2} dQ_2^2 \Gamma(H \rightarrow Z^* Z^*) \cdot \frac{Q_1 \Gamma(Z^* \rightarrow \mu^+ \mu^-)}{\pi [(Q_1^2 - m_Z^2)^2 + (m_Z \Gamma_Z^*)^2]} \frac{Q_2 \Gamma(Z^* \rightarrow \mu^+ \mu^-)}{\pi [(Q_2^2 - m_Z^2)^2 + (m_Z \Gamma_Z^*)^2]} \quad (1)$$

where Γ_Z^* is the total width of a Z_0 of mass Q and $\Gamma(H \rightarrow Z^* Z^*)$ represents the decay of the Higgs boson into a pair of Z_0 's of masses Q_1 and Q_2 and it is given by

$$\Gamma(H \rightarrow Z^* Z^*) = \frac{G_F m_H^3}{16\pi\sqrt{2}} \sqrt{1 + \lambda_1^2 + \lambda_2^2 - 2\lambda_1\lambda_2 - 2\lambda_1 - 2\lambda_2} \cdot [1 + \lambda_1^2 + \lambda_2^2 + 10\lambda_1\lambda_2 - 2\lambda_1 - 2\lambda_2]$$

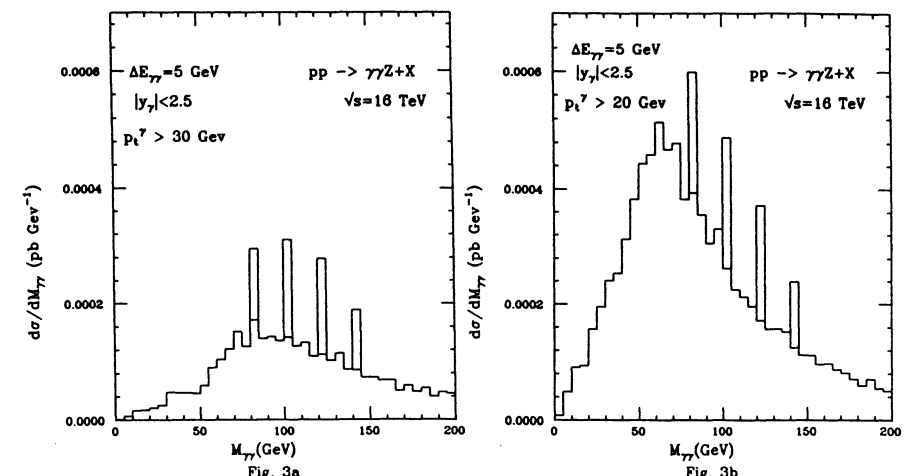
with $\lambda_i = \frac{Q_i^2}{m_H^2}$. It can easily be checked that the above equation reproduces the known expression for $H^0 \rightarrow Z^0 Z^0$ when $Q_1 = Q_2 = m_Z$.

In Fig.1 we show the width of the Higgs boson calculated from eq.(1). Using parton densities from EHLQ, set II [10], we obtain the values shown in Fig.2 for the number of events at LHC and SSC, assuming a nominal integrated LHC luminosity $L = 10^5 pb^{-1}$ for LHC and $L = 10^4 pb^{-1}$ for SSC.

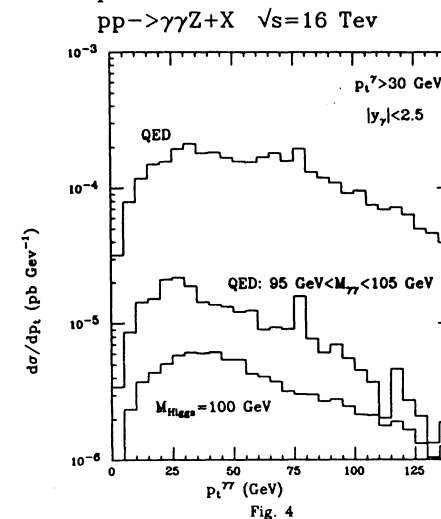


The numbers shown are relative to a single lepton channel for Z^0 decay and nothing more than a rapidity cut, $|y_{H,Z}| \leq 2.5$. To see if the very high luminosity option which

may be available at the LHC could make this process a viable one, one must study the intrinsic background from $Z\gamma\gamma$ and impose realistic cuts. We show in Figs.3a and b the invariant mass distribution of $\gamma\gamma$ pairs produced through QED bremsstrahlung from the initial quark legs annihilating into a Z^0 , [11] summing over the signal $HZ \rightarrow \gamma\gamma Z$, within a 5 GeV bin.



We have chosen two different cuts on the photons transverse momentum, so as to eventually improve statistics. In both cases, the signal is well visible above the background. Clearly, better mass resolution will further sharpen the signal. We show also in Fig.4 the p_t distribution of the signal compared to the QED background for a cut of 30 GeV on the transverse momentum of the photons.



One should also mention that in order to make use of this signal, the detector requirements must be very severe, in order to eliminate, among other things, the dangerous background from $Z + jet + jet$, with the jets faking an isolated photon. If this can be done, then from the intrinsic background analysis, it appears that the signal we have considered here may provide an unmistakable signature, provided the event rate is adequate. Under normal luminosity conditions, this is not the case. If however, the extremely high luminosity option, $L=5 \times 10^{34} \text{ cm}^{-2} \text{ sec}^{-1}$ is available, then the number of events increases and this channel can become a viable one for investigation of a Higgs boson of mass $80 \text{ GeV} \leq M_H \leq 130 \text{ GeV}$.

References

1. C.Rubbia, "Perspectives for a Hadron Collider in the LEP Tunnel", CERN Seminar, November 6th, 1989.
2. Z.Kunszt and J.Stirling, these Proceedings and references therein.
3. M.Della Negra et al., these Proceedings.
4. C.Sez, these Proceedings.
5. C.N.Yang, Phys.Rev. D77, 242(1950).
6. M.Drees and K.Hikasa, Phys. Lett. B240, 455 (1990).
7. S.C.Gorishny, A.L.Kataev, S.A.Larin and L.R.Surguladze, "Corrected three loop QCD correction to the correlator of the quark scalar currents and $\Gamma^{\text{tot}}(H^0 \rightarrow \text{hadrons})$ ", TIFR/th/90-9, Feb. 1990.
8. R.Cahn, Reports on Progr. in Physics 52, 389 (1989).
9. A.Grau, G.Panchari and R.J.N.Phillips, "Contribution of Off-shell-top-quarks to Decay Processes", LNF-90/020, March 1990. To appear in Physics Letters.
10. E.Eichten, I.Hinchcliffe, K.Lane and C.Quigg, Rev. of Modern Phys. 56 (1984) 579
11. V.Barger, T.Han and R.J.N.Phillips, Phys. Rev. D39, 146 (1989) and references therein.

Figure Captions

- Fig.1** Decay width for an intermediate mass Higgs boson decaying into: W^+W^- and Z^0Z^0 pairs *on* and *off* the mass shell (dots), $t\bar{t}$ pairs (dashes), $b\bar{b}$ pairs (dashes), $\gamma\gamma$ pairs (dot-dashes), and $\mu^+\mu^-$ pairs (dashes). The values of $m_{top}=90 \text{ GeV}$ and $m_b=3 \text{ GeV}$ have been used. Full line is the total width.
- Fig.2** Number of events at LHC and SSC. An integrated luminosity $L=10^5 \text{ pb}^{-1}$ for LHC and $L=10^4 \text{ pb}^{-1}$ for SSC has been assumed.
- Fig.3a** Differential cross-section for $pp \rightarrow Z\gamma\gamma + X$ vs. the invariant mass of the $\gamma\gamma$ system at $\sqrt{s}=16 \text{ TeV}$. The signal has been added to the QED background for $M_{Higgs}=80, 100, 120, 140 \text{ GeV}$ assuming a resolution $\Delta M=5 \text{ GeV}$. The cuts $p_t^\gamma \geq 30 \text{ GeV}$ and $|y_\gamma| \leq 2.5$ have been imposed.
- Fig.3b** Same as Fig.3a for $p_t^\gamma \geq 20 \text{ GeV}$.
- Fig.4** Differential cross-section for $pp \rightarrow Z\gamma\gamma + X$ vs. the p_t of the $\gamma\gamma$ system at $\sqrt{s}=16 \text{ TeV}$. Histograms are for the purely QED process, i.e. Z^0 production and double bremsstrahlung from initial quark legs, and for production of a Higgs boson of mass $M_{Higgs}=100 \text{ GeV}$ for a cut on the transverse momentum of the photons $p_t^\gamma \geq 30 \text{ GeV}$ and a rapidity cut $|y_\gamma| \leq 2.5$.

Search for $pp \rightarrow H^0 \rightarrow Z^0Z^0 \rightarrow \mu^+\mu^-\mu^+\mu^-$ at the LHC

Aleandro Nisati

Istituto Nazionale di Fisica Nucleare, Sezione di Roma, Italy.

We analyse the requirements on the lepton momentum resolution in experiments at LHC using as a test bench the detection of the decay of the neutral Higgs boson into four leptons, $H^0 \rightarrow Z^0Z^0 \rightarrow \mu^+\mu^-\mu^+\mu^-$. Many studies on this subject [1] [2] [3] have been done in the past, but contradictory conclusions have been published. In particular the necessity of having a good muon momentum resolution has been often reported [4]. The calculation of all the background sources to this channel is not yet available, apart from the *irreducible* Z^0Z^0 process; in particular the evaluation of the muon production from $pp \rightarrow t\bar{t} + X$ is still missing.

We report in this paper the results of the calculation of the main sources of events with at least four muons in the region $m_{4\mu} > 2m_{Z^0}$; the study of the complementary region $m_{4\mu} < 2m_{Z^0}$ is reported in [5]. After a brief discussion on different muon momentum resolution effects, the possibility of using a "*modest*" resolution of about 10 % together with a simple technique to improve the Higgs mass resolution is reported.

1. Mass resolution for heavy Higgs search.

To determine the adequate momentum resolution two important points have to be taken into account :

- 1) the background to this signature;
- 2) the natural width of the Higgs boson;

The background to the decay $H^0 \rightarrow \mu^+\mu^-\mu^+\mu^-$ can be divided into two classes:

- a) the *resonant* background, for which the four muons come from two $Z^0 \rightarrow \mu^+\mu^-$ decays; the two Z^0 's are produced either in the same event

$$pp \rightarrow Z^0Z^0 + X \rightarrow 4\mu^+X; \quad (Z^0Z^0 \text{ continuum})$$

or in two different events within the detector time resolution Δt (Z^0Z^0 pile-up);

- b) the *non resonant* background, for which at least one $\mu^+\mu^-$ pair does not come from a Z^0 decay:

$$\begin{aligned} pp &\rightarrow t\bar{t} + X \rightarrow 4\mu^+X'; \\ pp &\rightarrow Z^0b\bar{b} + X \rightarrow 4\mu^+X' \\ pp &\rightarrow Z^0t\bar{t} + X \rightarrow 4\mu^+X'; \\ pp &\rightarrow b\bar{b}, c\bar{c} + X \rightarrow 4\mu^+X'; \end{aligned}$$

The background from $b\bar{b}$ and $c\bar{c}$ processes has not yet been calculated; however, this source appears only significant for very low p_T muons [6]. Concerning the $Z^0t\bar{t}$ background it turns out that the total production cross section is very small (1.5 pb for $m_{top}=130 \text{ GeV}/c^2$) compared to that for $Z^0b\bar{b}$ (~100 pb) and therefore can be neglected. Consequently these background sources are not further considered in this study. The Z

pile-up background is negligible as long as the resolution time Δt is of the order of few hundred ns.

The non resonant background can be efficiently reduced by requiring that the invariant mass of both $\mu^+\mu^-$ pairs has to be equal to the Z^0 mass within a tight window. The size of this window is directly related to the experimental dimuon mass resolution $\sigma(m)$ at $m=m_{Z^0}$ and it is limited by the natural width of the Z boson ($\Gamma_{Z^0} = 2.5$ GeV). The better the mass resolution is the stronger the reduction of this background will be.

Concerning the resonant background the dimuon mass cut around m_{Z^0} does not help at all, since it is due to genuine Z^0 decays. However, the Z^0 pair continuum background can be slightly reduced by cutting on the muon p_T , η , ..., and on the p_T of the Z boson. The Z^0 pair background is irreducible and all other backgrounds should be compared to it, and the mass resolution therefore has to be good enough to bring the non-resonant background *reasonably* below the Z^0 pair level. Improvements beyond this may be useful but are not necessary.

Another important reason for good mass resolution is the reconstruction of the $\mu^+\mu^-\mu^+\mu^-$ invariant mass to identify the Higgs resonance as a significant peak on top of the background. However the mass resolution $\sigma(m_H)$ has to be compared with the natural width of the Higgs boson. It increases quickly as the Higgs mass increases (see for instance [7]), following roughly the law $\Gamma=0.5 \times m_H^{-3}$ (Γ and m_H in GeV/c^2). For Higgs masses in the range 200–300 GeV the total width is of the order of a few GeV and a mass resolution of the order of (1+3)% would be matched to it. However it will be shown later that even with a modest muon momentum resolution it is possible to reach a sufficiently good experimental resolution on the Higgs mass.

For larger Higgs masses, the Higgs width is the dominant effect on the four-muon mass reconstruction.

2. Production of $\mu^+\mu^-\mu^+\mu^-$ at the LHC.

The ISAJET Monte Carlo [8] (version 6.24) has been used to calculate at $\sqrt{s} = 16$ TeV. the cross section for $\text{pp} \rightarrow H^0 + X \rightarrow \mu^+\mu^-\mu^+\mu^- + X$ (see table I) and for the various background processes mentioned above. This generator uses the EHLQ structure functions (set I) [9].

Higgs mass GeV/c^2	σ, pb
200	4.31×10^{-3}
300	3.60×10^{-3}
400	2.43×10^{-3}
500	1.04×10^{-3}
600	6.26×10^{-4}
700	3.97×10^{-4}

Table I ISAJET (version 6.24) cross section for $\text{pp} \rightarrow H^0 \rightarrow Z^0 Z^0 \rightarrow \mu^+\mu^-\mu^+\mu^-$. The top mass chosen is $m_{\text{top}} = 150 \text{ GeV}/c^2$.

The calculation of the contribution from $t\bar{t}$ has been done with a modified *ad hoc* version of ISAJET, much more efficient than the standard one. This special implementation is discussed in the Annex I of this report.

Concerning the process $\text{pp} \rightarrow Z^0 Z^0 + X$, the ISAJET Monte Carlo contains only the main subprocess $q\bar{q} \rightarrow Z^0 Z^0$; the contribution from $gg \rightarrow Z^0 Z^0$ has been taken into account following the results of the analytical calculation reported in [10].

The background from $Z^0 b\bar{b}$ was estimated using ISAJET with $gb \rightarrow Z^0 b$ and backward evolution of the initial b-quark, as discussed in [5].

The pile-up contribution from two QCD Z^0 event has been evaluated as in [6].

Fig. 1 shows the $\mu^+\mu^-\mu^+\mu^-$ invariant mass cross section for several processes: $t\bar{t}$ with two values for the top mass: 130 and 200 GeV/c^2 , $Z^0 b\bar{b}$, $Z^0 Z^0$ continuum and Z^0 events pile-up, to be compared with the Higgs peak at various masses: $m_H = 200, 400$ and $700 \text{ GeV}/c^2$. We required $p_T > 5 \text{ GeV}/c$ and $|\eta| < 3.0$ for each muon. For events with more than 4 muons, only the 4 highest in p_T (and with zero total charge) are selected. In this condition the main background comes from $t\bar{t}$, followed by the $Z^0 b\bar{b}$ and the Z^0 pair continuum. The negligible pile-up contribution from single Z^0 events is also shown for $L=10^{34} \text{ cm}^{-2} \text{ s}^{-1}$ and for a resolution time of 15 ns (the bunch crossing period).

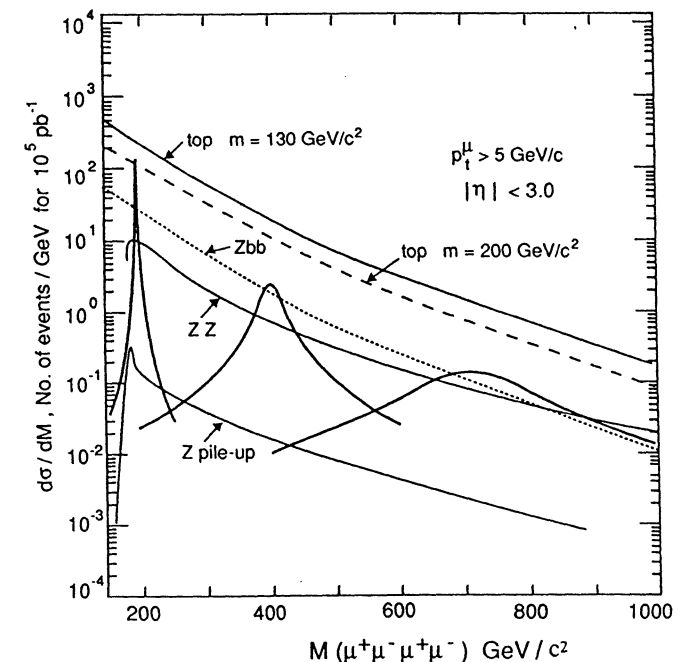


Fig. 1 $\mu^+\mu^-\mu^+\mu^-$ differential cross section $d\sigma/dm$ for several processes; muons have $p_T > 5 \text{ GeV}/c$ and $|\eta| < 3.0$.

The level of the background to the Higgs signal can be efficiently reduced by cutting harder on the muon p_T [6]. Fig. 2 shows the $\mu^+\mu^-\mu^+\mu^-$ invariant mass cross section for $p_T > 20 \text{ GeV}/c$ and $|\eta| < 2.5$.

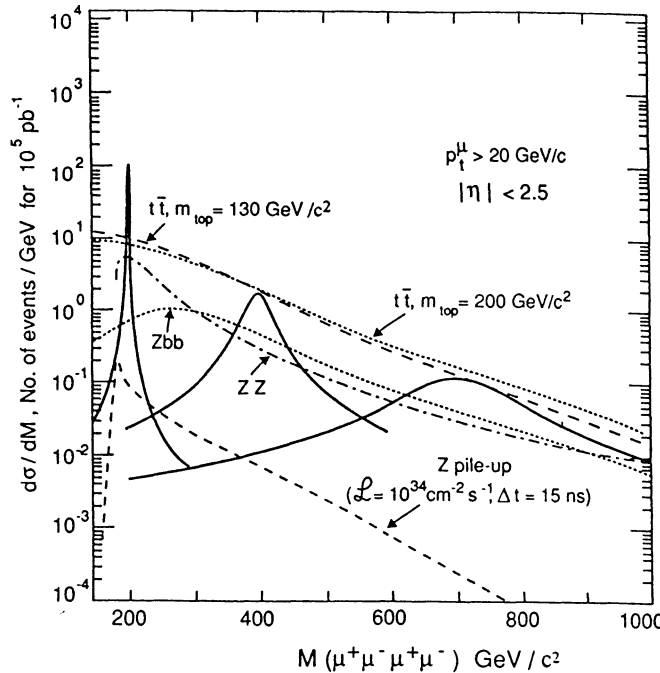


Fig. 2 $\mu^+\mu^-\mu^+\mu^-$ differential cross section $d\sigma/dm$ for several processes; muons have $p_T > 20 \text{ GeV}/c$ and $|\eta| < 2.5$.

The $t\bar{t}$ background is still dominant, independent of the top quark mass. Now, in order to reduce it, we can require that the two $\mu^+\mu^-$ invariant masses are both within a given window around the Z^0 mass. As stated before this window is directly related to the experimental resolution.

3.1 Higgs search with an iron toroid spectrometer.

We simulated the effects of an iron toroid spectrometer with 4 m iron and a uniform magnetic field $B=1.8 \text{ T}$. The momentum of each muon generated by ISAJET has been smeared for the multiple coulomb scattering and the measurement error [11]. The momentum is measured by fitting the muon trajectory with three equidistant points measured with a resolution of $300 \mu\text{m}$. The effects from energy losses [12], muon detection inefficiency and pattern recognition problems [13] have not been taken into account. The momentum resolution of such a spectrometer [14] shows a constant momentum resolution of 12.5 % up to $p \approx 400 \text{ GeV}/c$ due to the multiple scattering in the iron; for higher momenta it is limited by the accuracy on the track measurements and

follows the law $\sigma(p)/p = 3.3 \times 10^{-4} p [\text{GeV}/c]$. The corresponding dimuon invariant mass resolution for the process $Z^0 \rightarrow \mu^+\mu^-$ is then $8 \text{ GeV}/c^2$ for low p_T muons; for high p_T muons the resolution increases up to $10 \text{ GeV}/c^2$.

All the background and signal events have been simulated through such a spectrometer.

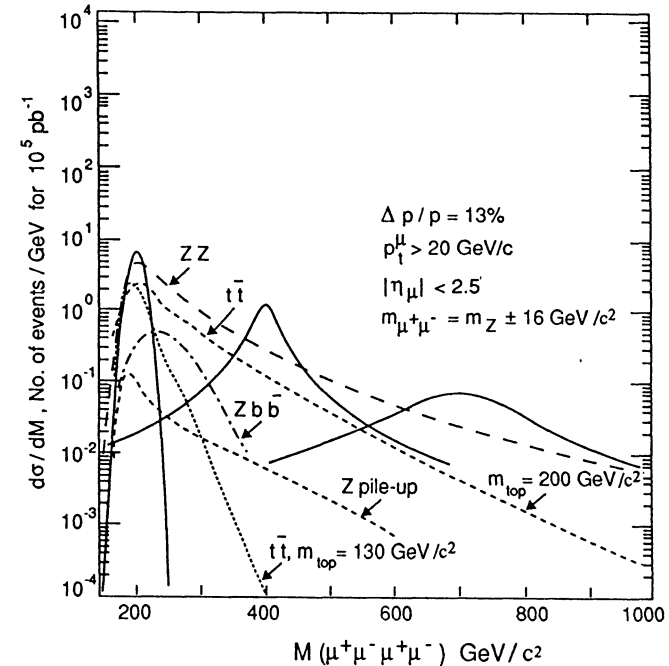


Fig. 3 $\mu^+\mu^-\mu^+\mu^-$ differential cross section $d\sigma/dm$ after detector simulation for several processes; muons are required to have $p_T > 20 \text{ GeV}/c$ and $|\eta| < 2.5$. $\mu^+\mu^-$ invariant mass is equal to the Z^0 mass within $\pm 16 \text{ GeV}/c^2$ for both muon pairs.

Fig. 3 shows the $\mu^+\mu^-\mu^+\mu^-$ differential cross section $d\sigma/dm$ when pairs of unlike-sign muons are selected in order to have dimuon masses equal to the Z^0 mass within $\pm 16 \text{ GeV}/c^2$; this is twice the experimental Z^0 mass resolution and keeps 90 % of the Higgs signal. The $t\bar{t}$ and the $Z^0 b\bar{b}$ background appear now largely reduced and they are significantly below the Z^0 pair background.

Fig. 4 shows the invariant mass distribution of the 4μ system for a Higgs mass of $200 \text{ GeV}/c^2$ on top of the full background ($m_{top} = 130 \text{ GeV}/c^2$). In fig. 5 the result of a simulated experiment with a 10^5 pb^{-1} data sample is shown: it is really hard to isolate the signal from the background. The Higgs mass resolution for $m_H = 200 \text{ GeV}/c^2$ is $\sim 10 \text{ GeV}/c^2$, to be compared with its width $\Gamma = 1.4 \text{ GeV}/c^2$.

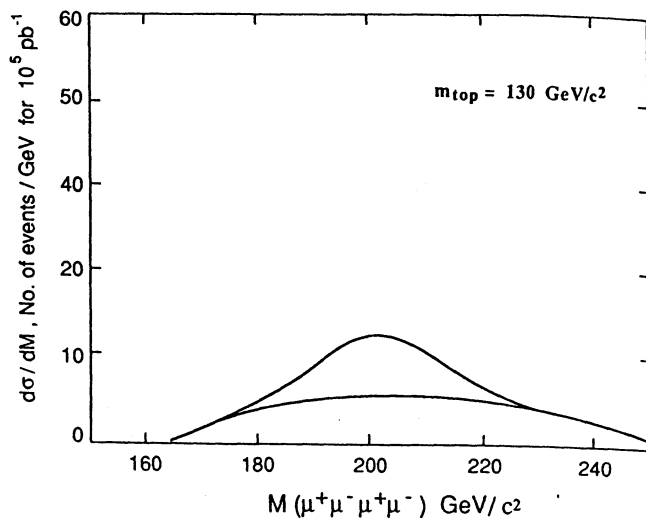


Fig. 4 $\mu^+\mu^-\mu^+\mu^-$ differential cross section $d\sigma/dm$ after detector simulation for the Higgs signal ($m_{H^0} = 200 \text{ GeV}/c^2$) on top of the background. The top mass is $m_{top}=130 \text{ GeV}/c^2$.

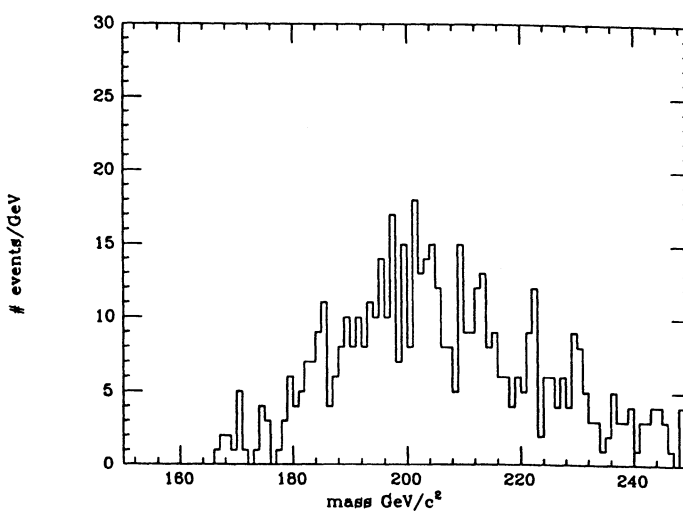


Fig. 5 Example of the Higgs search in the 4 muons channel with an iron toroid spectrometer; $m_{H^0}=200 \text{ GeV}/c^2$, $m_{top}=130 \text{ GeV}/c^2$. $\int L dt = 10^5 \text{ pb}^{-1}$.

In order to improve the Higgs mass reconstruction, the Z^0 mass constraint can be used, as explained in the next section. To use it, however, an unambiguous Z^0 boson identification has to be performed.

3.2 The Z^0 mass constraint.

With four muons $\mu_1^+ \mu_2^- \mu_3^+ \mu_4^-$ two ($\mu^+\mu^-$) pairs are possible: $(\mu_1^+ \mu_2^-)(\mu_3^+ \mu_4^-)$ (1) or $(\mu_1^+ \mu_3^-)(\mu_2^+ \mu_4^-)$ (2). Sometime the events selected by requiring both ($\mu^+\mu^-$) invariant mass pairs equal to m_{Z^0} within a fixed window have both combinations (1) and (2) acceptable. The ambiguity is solved by evaluating for each combination the following χ^2 :

$$\chi^2 = [m(\mu_i^+ \mu_j^-) - m_{Z^0}]^2/\sigma_{ij}^2 + [m(\mu_k^+ \mu_l^-) - m_{Z^0}]^2/\sigma_{kl}^2 \quad (1)$$

where $i=1,j=2,k=3,l=4$ or $i=1,j=3,k=2,l=4$; $m(\mu_m^+ \mu_n^-)$ is the invariant mass of the dimuon $\mu_m^+ \mu_n^-$ with error σ_{kl} . The combination with the minimum χ^2 is selected.

In such an iron toroid spectrometer the smearing effect on the dimuon mass measurement is mainly due to the fluctuation of the absolute value of momentum measurement and is not significantly affected by the direction of the particles ⁽¹⁾. The invariant mass $m_{\mu\mu}$ of two muons is related to the momenta by the relationship

$$m_{\mu\mu}^2 = 2 p_{\mu 1} p_{\mu 2} (1 - \cos \theta_{12}) \quad (2)$$

By constraining $m_{\mu\mu}$ to be equal to m_{Z^0} and keeping the measured value of $\cos \theta_{12}$ we can determine the product $(p_{\mu 1} p_{\mu 2})^{\text{th.}}$:

$$(p_{\mu 1} p_{\mu 2})^{\text{th.}} = m_{Z^0}^2 / 2(1 - \cos \theta_{12}) \quad (3)$$

The quantity $(p_{\mu 1} p_{\mu 2})^{\text{th.}}$ is compared with the experimental value $(p_{\mu 1} p_{\mu 2})^{\text{meas.}}$ and the ratio

$$r^2 = (p_{\mu 1} p_{\mu 2})^{\text{th.}} / (p_{\mu 1} p_{\mu 2})^{\text{meas.}} \equiv (m_{Z^0}^2 / m_{\mu\mu}^2) \quad (4)$$

is used to correct the two muons momentum measurements:

$$p_{\mu 1} \rightarrow p_{\mu 1} \times r_1 = p'_{\mu 1} \quad (5)$$

$$p_{\mu 2} \rightarrow p_{\mu 2} \times r_2 = p'_{\mu 2} \quad (6)$$

such that $r_1 \times r_2 = r^2$.

The correction factors r_1 and r_2 are fixed requiring the minimum value for the expression:

(1) The mass of a pair of muons with $p_T = 0.5 \text{ TeV}$ each and with an opening angle $\alpha = 10^\circ$ is reconstructed with an error $\Delta m/m \sim 10^{-1}$ due to the momentum measurement only, to be compared with $\Delta m/m \sim 6 \times 10^{-3}$ due to the measurement of α .

$$\chi^2 = (p_{\mu 1} - p'_{\mu 1})^2 / \sigma_{p\mu 1}^2 + (p_{\mu 2} - p'_{\mu 2})^2 / \sigma_{p\mu 2}^2 \quad (7)$$

where $\sigma_{p\mu 1}$ and $\sigma_{p\mu 2}$ are the measurement errors on $p_{\mu 1}$ and $p_{\mu 2}$.
The solution of (7), in the approximation of small corrections (i.e. $r_1, r_2 \approx 1$) is:

$$r_1 = r \times \sqrt{(\sigma_{p1} p_{\mu 2} / \sigma_{p2} p_{\mu 1})} \text{ and } r_2 = r \times \sqrt{(\sigma_{p2} p_{\mu 1} / \sigma_{p1} p_{\mu 2})}. \quad (8)$$

In the case of constant momentum resolution, we find of course that $r_1 = r_2$. By applying this technique both to signal and background, we go from the situation shown in fig. 4 to that shown in fig. 6 and from fig. 5 to fig. 7.

As one can see, the situation is very much improved and a clear peak is visible on top of the background. Fig. 8 shows the same distribution for $m_{top} = 200$ GeV/c²: the top background is slightly higher and it shows a longer tail than for $m_{top} = 130$ GeV/c² mass. It is worthwhile to stress that the Higgs mass resolution is now $\sim 2\%$.

As the Higgs mass increases, the Z^0 mass constraint becomes less effective, but improves the resolution up to $m_{H^0} \approx 400$ GeV/c²; for higher masses the natural width is dominant. For $m_{H^0} > 400$ GeV/c² the background is dominated by the Z^0 pair production.

Figs. 9 shows the mass distribution of a simulated experiment for $m_{H^0} = 400$ GeV/c² ($m_{top} = 130$ and 200 GeV/c²); $\int L dt = 10^5$ pb⁻¹. In fig. 10 the Higgs mass is 700 GeV/c² and the additional cut $p_T > 100$ GeV/c has been applied ($m_{top} = 130$ GeV/c²). In this case it is assumed that decays of the Z boson both in muons and electron are detected. $\int L dt = 10^5$ pb⁻¹.

We recall that the muon detection efficiency has been assumed always equal to 1 and we emphasize that all these results do not include any lepton isolation cuts, which would, of course, reduce all the above backgrounds, except that from Z^0 pairs.

The discussion about the discovery limits of the Higgs boson at LHC is given in [15]: in particular it turns out that this particle can be identified for mass values $m_{H^0} < 800$ GeV/c² if both muons and electrons can be detected.

4. Conclusion.

The calculation of the main backgrounds to the processes $pp \rightarrow H^0 + X \rightarrow \mu^+ \mu^- \mu^+ \mu^- + X$ has been reported, for $m_{4\mu} > 2m_{Z^0}$.

After requiring muons with $p_T \geq 20$ GeV/c it turns out that the main background is due to $pp \rightarrow t\bar{t} + X$, followed by the irreducible Z^0 pair contribution. By comparing the Higgs signal with the full background it turns out that a $\sim 13\%$ muon momentum resolution together with the Z^0 mass constraint is adequate to see the signal above the background; a rapidity coverage up to $|y| < 2.5$ is sufficient to this search.

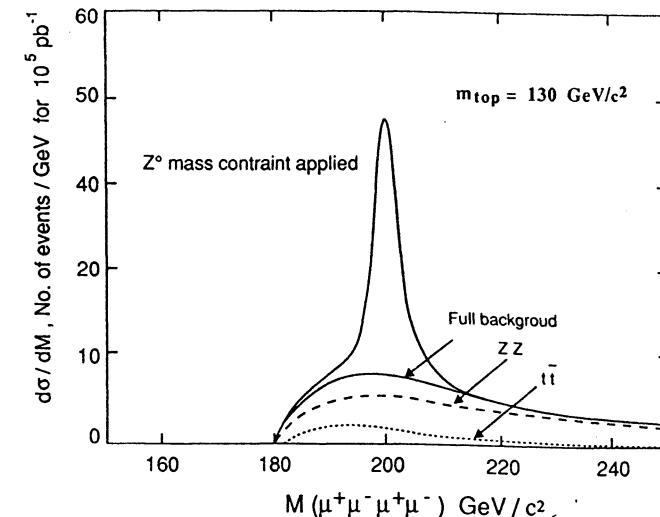


Fig. 6 $\mu^+ \mu^- \mu^+ \mu^-$ invariant mass cross section after detector simulation for the Higgs signal ($m_{H^0} = 200$ GeV/c²) on top of the background. The Z^0 mass constraint is used. The top mass is $m_{top} = 130$ GeV/c².

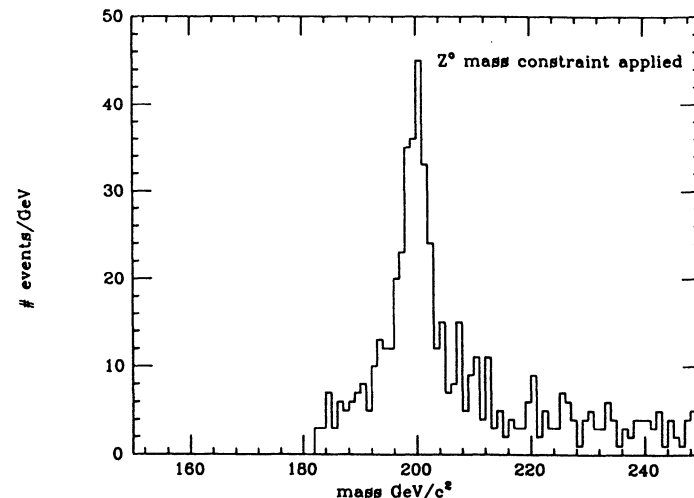


Fig. 7 Example of Higgs search in the 4 muons channel with an iron toroid spectrometer, if the Z^0 mass constraint is used; $m_{H^0} = 200$ GeV/c², $m_{top} = 130$ GeV/c², $\int L dt = 10^5$ pb⁻¹.

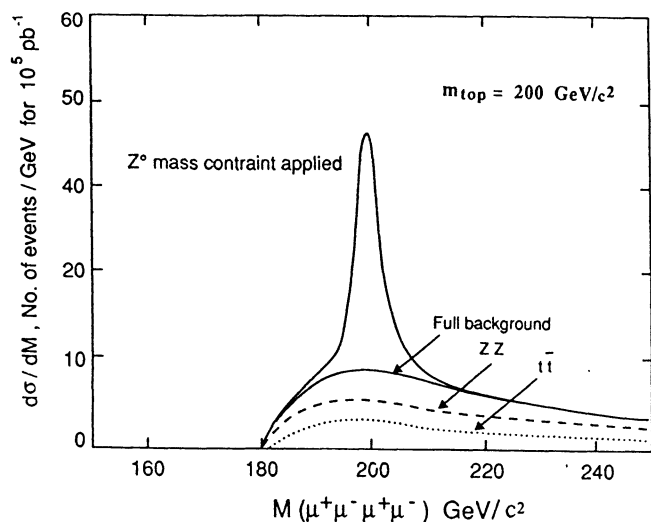


Fig. 8 As in fig. 6. The top mass is $m_{\text{top}}=200 \text{ GeV}/c^2$.

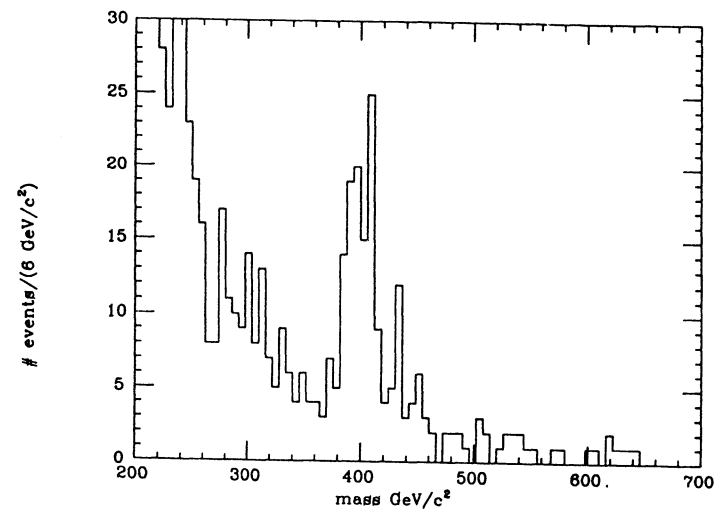


Fig. 9b As in fig. 7; $m_{H^0}=400 \text{ GeV}/c^2$; $m_{\text{top}}=200 \text{ GeV}/c^2$. $\int L dt = 10^5 \text{ pb}^{-1}$.

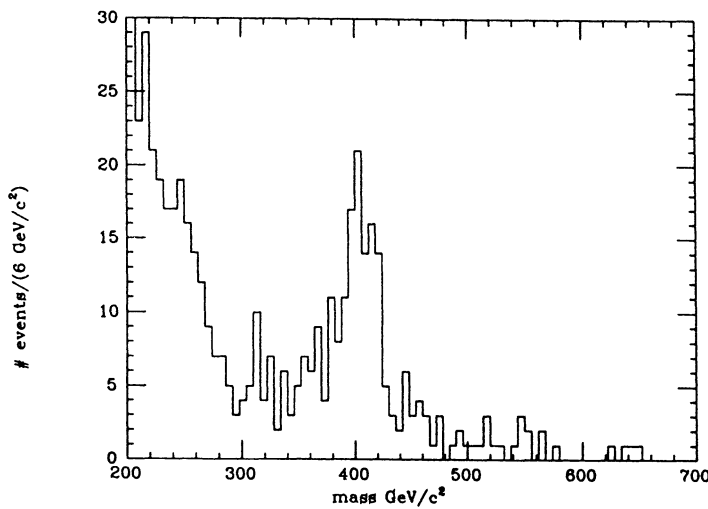


Fig. 9a As in fig. 7; $m_{H^0}=400 \text{ GeV}/c^2$; $m_{\text{top}}=130 \text{ GeV}/c^2$. $\int L dt = 10^5 \text{ pb}^{-1}$.

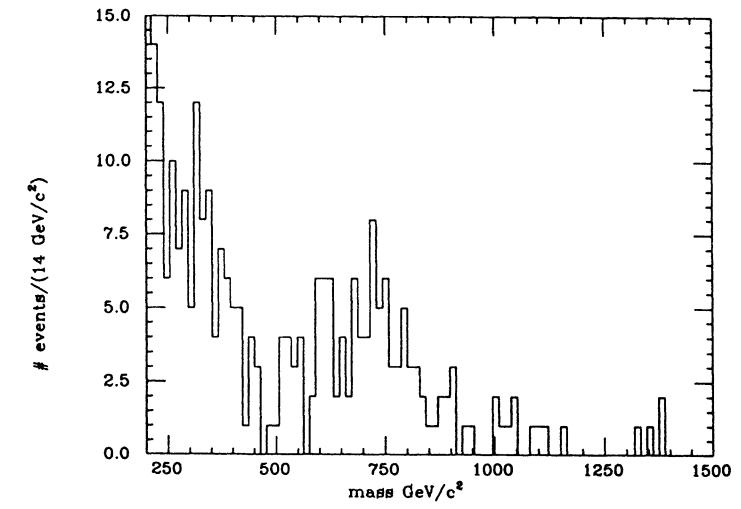


Fig. 10 Example of Higgs search in the 4 leptons channel with an iron toroid spectrometer; $m_{H^0}=700 \text{ GeV}/c^2$, $m_{\text{top}}=130 \text{ GeV}/c^2$. $\int L dt = 10^5 \text{ pb}^{-1}$.

Annex I

The Monte Carlo production of multi-muon events from processes such as $pp \rightarrow t\bar{t} + X$ is a heavy task because of the very low efficiency with which these events are usually generated. This problem is related to the modest branching ratio of the semileptonic decay of heavy flavours: $\sim 10\%$. This means that, following the heavy quark cascade, a $t\bar{t}$ event has a probability of $\sim 2 \times 10^{-3}$ to give four muons in the final state (assuming six muons produced in each event). If muons with $p_T > 5 \text{ GeV}/c$ are selected, then the above probability is much lower than 10^{-4} . Furthermore the decay kinematic routines are applied to all the unstable particles produced after the parton shower and hadronization; for high multiplicity events this procedure is very expensive in terms of CPU time. The production with ISAJET 6.24 of a four muon event with $p_T > 5 \text{ GeV}/c$ from a $pp \rightarrow t\bar{t} + X$ process for a top quark of $130 \text{ GeV}/c^2$ mass for $100 \text{ GeV}/c < p_T^{\text{top}} < 200 \text{ GeV}/c$ takes a time of the order of 10^3 seconds in IBM-168 units. Consequently, the production of a large amount of event appears an impossible job.

For this reason an optimization of the Monte Carlo generator is mandatory. The optimization method implemented consists in three main points:

- 1) The real W coming from t quark (or \bar{t}) decay is always constrained to give a pair $\mu-\nu_\mu$. In this way a factor $[\text{B.R.}(W \rightarrow \mu-\nu_\mu)]^{-2} = 81$ in efficiency is obtained for free. Biases due to this procedure are discussed below.
- 2) The hadrons considered in the decay chains are only those containing at least one heavy quark (t, b, c and related antiquarks). The remaining hadrons are not considered at all since they cannot produce prompt leptons^(A1).
- 3) Finally, after simulation of the parton shower and fragmentation, each event is used several times to simulate the decays of heavy flavour particles. This allows to save some CPU time since the decay section of the Monte Carlo takes much less time than the production of the first hard scattering from which the event evolution starts. The number of decay simulation is such that the mean probability to have at least 4 muons with $p_T > 5 \text{ GeV}/c$ in one event was between 0.5 and 0.9; in this way a given initial hard-scattering is used no more than once.

With this modification installed in ISAJET (6.24) the time required to have a 4-muon event with $p_T > 5 \text{ GeV}/c$ was of the order of a $10+20$ seconds in 168 units, and thus acceptable also for the generation of a large number of events.

Other optimization methods are possible; the important point is that the bias introduced in the physical predictions has to be controlled and has to be as small as possible. In this way a reliable correction can be determined.

In order to verify the level of the bias introduced with this method, a sample of events produced with this "optimized" generator have been compared with those produced relaxing the points 1) and 2) listed above (and having, of course, less events produced). In particular the following distributions have been compared:

(A1) The leptonic decays of the τ lepton are also performed.

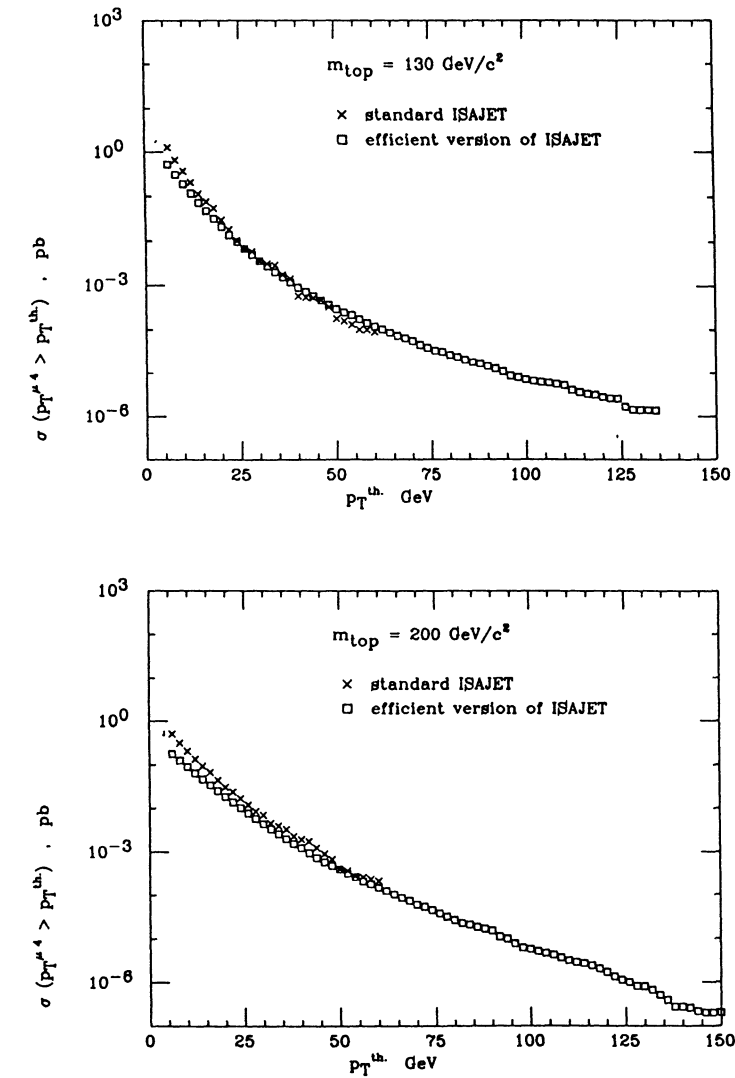


Fig. A1 Four-muon event integral cross section comparison

- i) the four-muon integral cross section as a function of p_T^{th} , $\sigma(p_T^{4\mu} > p_T^{\text{th}})$;
- ii) the $\mu^+\mu^-\mu^+\mu^-$ invariant mass distribution ($p_T^\mu > 5 \text{ GeV}/c$);
- iii) the $\mu^+\mu^-$ invariant mass distribution for events with $m_{4\mu} > 200 \text{ GeV}/c^2$, after having normalised the two distributions to the same cross section. This checks the shape of the dimuon invariant mass.

This comparison has been done for two values of the top mass: 130 and 200 GeV/c^2 .

Fig. A1 shows that the cross section is underestimated by a factor ~ 2.4 for $p_T^\mu > 5 \text{ GeV}/c$ for a 130 GeV/c^2 top mass and 2.9 for a 200 GeV/c^2 top mass. If the threshold is moved to 20 GeV/c then the factors become 1.4 ($m_{\text{top}}=130 \text{ GeV}/c^2$) and 1.6 ($m_{\text{top}}=130 \text{ GeV}/c^2$). For higher p_T^{th} , these factors are very close to 1, as it would be naively expected.

Fig. A2 shows that, as can be expected, the cross section for low invariant 4-muon mass is underestimated; however for masses $m_{4\mu} > 100 \text{ GeV}/c^2$ the ratio between the two curves (for each top mass), does not exceed factors 2 to 3, and they decrease quickly to 1 for larger masses.

An expression of the type

$$R(m_{4\mu}) = [1 + \alpha \exp(-\beta m_{4\mu})] \quad (\text{A1})$$

describes correctly enough this ratio; the parameters α and β are found by fitting the predicted values for the cross section $d\sigma/dm_{4\mu}$.

Figs. A3 shows the comparison mentioned in iii); there is an excellent agreement between the two distributions.

The differential cross sections $d\sigma/dm_{4\mu}$ presented in this report and obtained with this special version of ISAJET have been all corrected following the equation (A1).

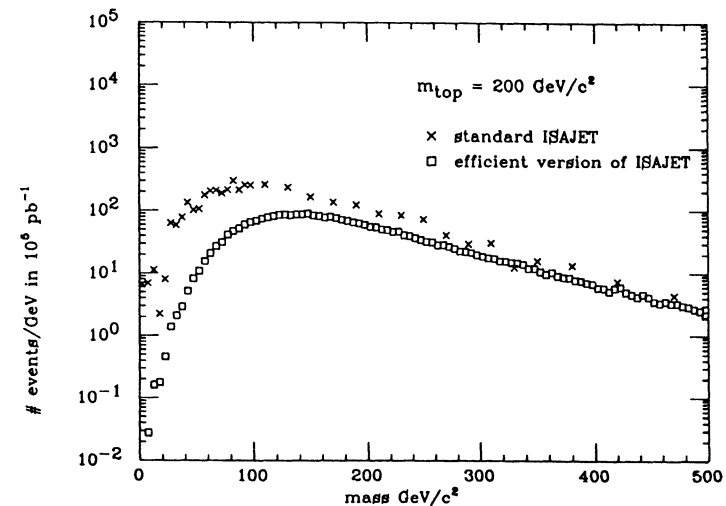
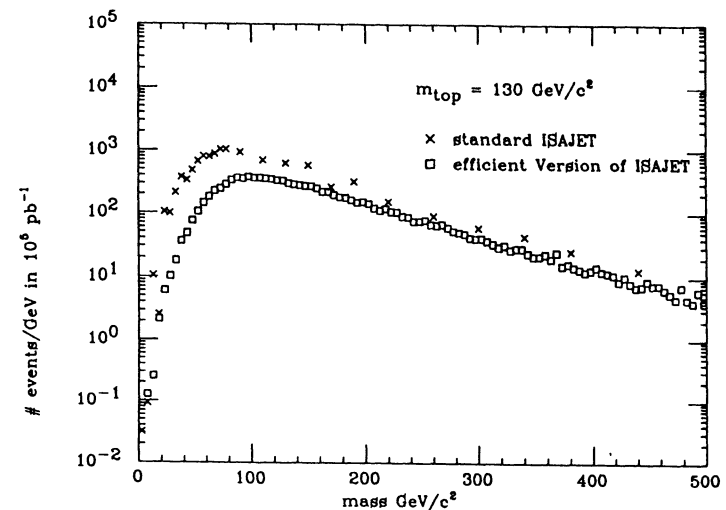


Fig. A2 $\mu^+\mu^-\mu^+\mu^-$ differential cross section comparison

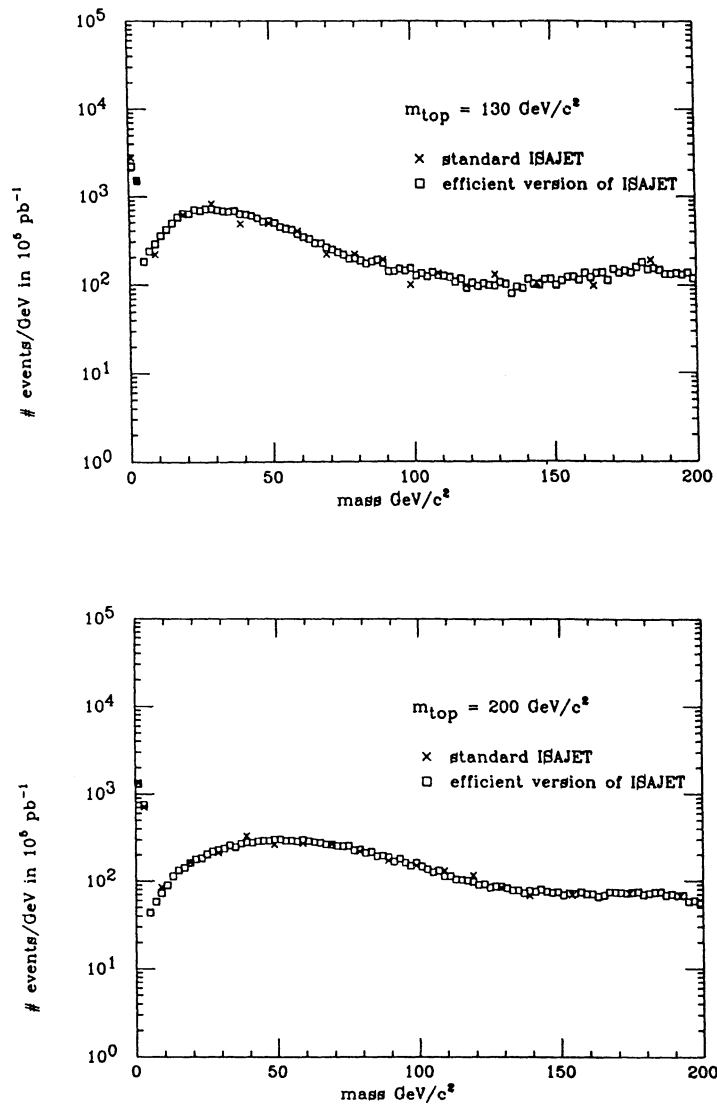


Fig. A3 $\mu^+\mu^-$ differential cross section comparison (after having normalised the two total cross sections to same value)

References

- [1] Proceedings of the ECFA-CERN Workshop , "Large Hadron Collider in the LEP Tunnel", Lausanne , 21-27 March 1984.
- [2] Proceedings of the Workshop on "Experiments, Detectors, and Experimental Areas for the Supercollider", Berkeley, July 7-17 , 1987.
- [3] Proceedings of the Workshop on Physics at Future Accelerators, La Thuile, edit by J. H. Mulvey, 7-87/07 1987.
- [4] see, for instance:
G. Herten "Heavy Top Quark Production as a Background in the Search for the Higgs Boson", published in [2];
M. Chen, E. Nagy and G. Herten, "High p_t weak bosons ...", published in [2].
- [5] M. Della Negra *et al.*, "Search for $H \rightarrow Z^*Z^* \rightarrow 4$ leptons at LHC", these proceedings.
- [6] A. Nisati, "Muon rates at the LHC", these proceedings.
- [7] Z. Kunszt, "Higgs search at LHC. A theory review", these proceedings.
- [8] F.E. Paige and S. Protopopescu, ISAJET Monte Carlo, BNL 38774 (1986);
F.E. Paige and S. Protopopescu, "Physics at the Superconducting ...", eds. R. Donaldson, J. Marx (1987), 320.
- [9] E. Eichten *et al.*, "Supercollider Physics", Rev. Mod. Phys. 56 (1984) 579 and 58 (1985) 1065;
- [10] E.W.N. Glover and JJ Van Der Bij, Phys. Lett. 219B (1989) 400.
E.W.N. Glover and JJ Van Der Bij, Nucl. Phys. B321 (1989) 561.
- [11] R. L. Gluckstern, Nucl. Instr. and Meth. 24, 381 (1963)
- [12] T. Del Prete, "Energy losses", these proceedings.
- [13] M. Della Negra, "Muon Trigger and Identification", these proceedings
- [14] R. Voss and C. Zupancic, "Muon measurement ...", published in [1].
- [15] D. Froidveaux, "Higgs Study Group", these proceedings

SEARCH FOR $H \rightarrow Z^*Z^* \rightarrow 4$ LEPTONS AT LHC

Higgs Study Group

M. Della Negra, D. Froidevaux, K. Jakobs, R. Kinnunen,
R. Kleiss, A. Nisati and T. Sjöstrand

1. Introduction and Motivation

The work reported here was prompted by the need to understand how the gold-plated $H \rightarrow ZZ \rightarrow \ell\ell\ell\ell$ ($\ell = e$ or μ) channel could be extended to Higgs masses below $2m_Z$, and by previous studies which reported possible large backgrounds to this process [1]. Since the observation of the so-called intermediate mass Higgs, $m_H \leq m_H \leq 2m_Z$, is well-known by now to be one of the most difficult experimental challenges for future hadron colliders such as LHC or SSC, we felt that there was really a need for a thorough study of the most promising channel in this Higgs mass range. We have therefore performed a calculation as complete as possible of potential backgrounds to 4-lepton final states in this mass range, and we have studied the effectiveness of good momentum resolution (obviously a problem mainly addressed to muon detection) and lepton isolation (a problem for calorimetry only at luminosities of $10^{34} \text{ cm}^{-2} \text{ s}^{-1}$) at rejecting these backgrounds, which arise mainly from non-resonant and non-isolated multi-lepton final states.

In Section 2, we discuss the simulation of the Higgs signal, and we study the backgrounds from $t\bar{t}$, Zbb and Z^*Z^* , $\gamma^*\gamma^*$, in Section 3. Finally, in Section 4, we present and discuss the results, and we conclude in Section 5.

Throughout the following, we shall quote rates corresponding to one year of running at a luminosity of $10^{34} \text{ cm}^{-2} \text{ s}^{-1}$ at LHC, i.e. an integrated luminosity of 10^5 pb^{-1} . The signals and backgrounds consist of final states containing at least four leptons. For simplicity, we have studied two distinct cases for the detector simulation:

- a) the four leptons are 'electrons', meaning that the generated lepton energies were smeared with a resolution typical of a modest electromagnetic calorimeter, $\sigma_E/E = 0.15/\sqrt{E} + 0.02$, where the energy dependent term and the constant term are summed quadratically.
- b) The four leptons are 'muons', meaning that the generated lepton energies were smeared with a resolution typical of a modest magnetised iron toroid spectrometer, $\Delta p/p = 0.15$.

The rates discussed in the following are therefore either quoted as $eeee$ or $\mu\mu\mu\mu$. We shall consider the mixed $ee\mu\mu$ cases in Section 4, as well as the case of a good muon momentum resolution. Each lepton was assumed to be identified with an efficiency of 90%.

2. Simulation of the Higgs Signal

The Higgs signal was simulated using the PYTHIA 5.4 Monte-Carlo generator [2], properly modified to generate correctly the kinematics of $H \rightarrow Z^*Z^* \rightarrow \ell\ell\ell\ell$ decay. The production cross-section for the Higgs signal and the branching ratio $H \rightarrow Z^*Z^*$ were normalised to the calculations presented in [3], with $m_{top} = 130 \text{ GeV}$ as shown in Table 1, for Higgs masses between 120 and 180 GeV. In this Higgs mass range, the production cross-section is dominated by gg fusion with only a $\pm 10\%$ uncertainty due to m_{top} , but a factor 2 uncertainty from structure functions [3]. Table 1 also shows the branching ratios used for $H \rightarrow Z^*Z^*$, with the characteristic dip around $m_H = 160$ to 170 GeV , due to the opening of the $H \rightarrow WW$ decay [3]. The PYTHIA Monte-Carlo values for the Higgs production cross-section and branching ratios have been checked against the calculations of Ref. 3. The agreement is good for the branching ratios and the gg fusion production cross-section. For the WW fusion production, PYTHIA overestimates the cross-section by a large factor in this Higgs mass range (from a factor 2 for $m_H = 100 \text{ GeV}$ to 20% for $m_H = 200 \text{ GeV}$), a well

known shortcoming of the effective W approximation used in this Monte-Carlo program. Initial state radiation is included in the PYTHIA Monte-Carlo simulation, producing a transverse momentum distribution for the Higgs boson, dominantly produced through gg fusion in this mass range, which has been checked to be in agreement with theoretical predictions [4].

Once the branching ratio of 3.4% for $Z \rightarrow ee$ ($\mu\mu$) decay and the lepton detection efficiency ($\epsilon_\ell = 90\%$ per lepton) are included, Table 1 shows the number of detectable events per 10^5 pb^{-1} at LHC. These numbers vary from ≈ 20 to ≈ 130 events before acceptance cuts, thus already demonstrating the need for detecting both electrons and muons, which increases the rates of Table 1 by a factor 4.

Fig. 1 shows the expected rates for detected $H \rightarrow ZZ$ or $Z^*Z^* \rightarrow eeee$ (or $\mu\mu\mu\mu$) decays for an integrated luminosity of 10^5 pb^{-1} at LHC, as a function of lepton detector rapidity coverage ($|\eta_\ell|$) and lepton p_T -threshold (p_T^{\min}). The horizontal arrows on the vertical axis indicate the expected detectable rate for full acceptance (identical to the corresponding numbers in the third line of Table 1). As expected for large Higgs masses, an acceptance of $|\eta_\ell| < 2$ and $p_T^\ell > 20 \text{ GeV}$ is perfectly adequate, but, for $m_H \leq 200 \text{ GeV}$, a rapidity coverage of $|\eta_\ell| < 3$ and lepton detection down to $p_T^\ell = 10 \text{ GeV}$ would increase the acceptance dramatically, as illustrated by the numbers in Table 2. The first column of Table 2 shows that the acceptance for finding at least two leptons with $p_T^\ell > 20 \text{ GeV}$, $|\eta_\ell| < 3$ is $\approx 90\%$ even for Higgs masses as low as 120 GeV. This is due to the fact that most $H \rightarrow Z^*Z^*$ decays contain one Z on mass shell in the final state, and the trigger rates for such cuts should therefore not pose a problem even at luminosities of $10^{34} \text{ cm}^{-2} \text{ s}^{-1}$ (rates of at most 1000 Hz are expected for a trigger requiring two electromagnetic jets within these acceptance cuts [5]).

We have therefore considered, in this study, a detector which can identify electrons and muons with $|\eta_\ell| < 3$ and $p_T^\ell > 10 \text{ GeV}$. The acceptance for three successive sets of cuts are shown in Table 1, for $120 \leq m_H \leq 180 \text{ GeV}$, as described in the following :

- a) **Cut 1:** in a first step, only those events are kept with at least four leptons with $|\eta_\ell| < 3$ and $p_T^\ell > 10 \text{ GeV}$. The acceptance increases from $\approx 30\%$ for $m_H = 120 \text{ GeV}$ to $\approx 75\%$ for $m_H = 180 \text{ GeV}$. We point out here, that the acceptances of Table 1, obtained using PYTHIA are significantly higher for cut 1 than those obtained using ISAJET. This results from the different Higgs transverse momentum distributions, obtained through initial state radiation for the gg fusion process: for $m_H = 120 \text{ GeV}$, the average Higgs p_T is found to be 30 GeV for ISAJET, compared to 45 GeV for PYTHIA, which also includes an additional 15% contribution from WW fusion, which produces even larger Higgs transverse momenta [6]. The resulting difference in acceptance for cut 1 is $\leq 10\%$ for $m_H \geq 150 \text{ GeV}$, but is as large as 50% for $m_H = 120 \text{ GeV}$.
- b) **Cut 2:** motivated by the trigger rate considerations discussed above, the next step requires that at least one pair of leptons (1,2) satisfies $p_T^{1,2} > 20 \text{ GeV}$ and $|m_{12} - m_Z| < 10 \text{ GeV}$. The acceptances for cut 2 (after cut 1 has been applied) are shown in Table 1 and increase from 54% for $m_H = 120 \text{ GeV}$ to 95% for $m_H = 180 \text{ GeV}$, in the electron case. In the muon case, the acceptance is significantly lower, due to the worse resolution on the reconstructed dilepton mass. This is illustrated in Fig. 2, which shows this reconstructed dilepton mass for all possible lepton pairs, for the electron and muon cases and for $m_H = 140 \text{ GeV}$. Fig. 3 shows the invariant mass distribution for the chosen dilepton combination, closest to the Z mass, where the effect of the 15% muon momentum resolution appears, quite strikingly, as the absence of a clear peak near m_Z .
- c) **Cut 3:** the last cut requires the two remaining leptons to have an invariant mass, $m_{34} > 12 \text{ GeV}$, to reduce some of the backgrounds discussed in Section 3. Obviously, for $m_H \geq 120 \text{ GeV}$, this cut has an efficiency close to 100%.

Table 1 shows the expected rates of observed signal events after all the above cuts have been applied. Clearly, for $m_H < 120 \text{ GeV}$, these rates are too small to hope for the observation of a possible signal in this channel, because of the rapidly falling branching ratio

for $H \rightarrow Z^*Z^*$. The 4-lepton invariant mass can be computed for these remaining events, with or without constraining the dilepton mass, m_{12} , to the Z mass, as illustrated in Fig. 4a (electrons) and Fig. 4b (muons) for $m_H = 140$ GeV. In the case of good resolution, the Z-mass constraint should not be used, as shown in Fig. 4a, since a significant fraction of the events appears in non-Gaussian tails of the 4-lepton invariant mass distribution. On the other hand, the resolution is improved from 8.6 GeV to 6.5 GeV with the Z-mass constraint, in the case of bad muon momentum resolution, as shown in Fig. 4b. Table 1 shows the expected resolution, σ_H , on the reconstructed Higgs mass, as a function of m_H , without (resp. with) the Z-mass constraint for electrons (resp. muons).

Finally, Table 1 shows the expected rates of events with $|m_{\ell\ell\ell\ell} - m_H| < 2\sigma_H$, which we shall now compare to the various possible background rates in the appropriate mass window.

3. Background Simulation

In this study, we have established that there are three main sources of background to the $H \rightarrow Z^*Z^* \rightarrow \ell\ell\ell\ell$ signal, which are, in decreasing order of importance:

- a) A non-resonant reducible background from $t\bar{t} \rightarrow \ell\ell\ell\ell + X$
- b) a semi-resonant reducible background from $Zb\bar{b} \rightarrow \ell\ell\ell\ell + X$
- c) the irreducible background from $Z^*Z^* \rightarrow \ell\ell\ell\ell$.

Other backgrounds, such as $Zt\bar{t} \rightarrow \ell\ell\ell\ell + X$ or $b\bar{b} \rightarrow \ell\ell\ell\ell + X$, are negligible at the LHC. In the following, we shall discuss in turn each one of these background sources, with some emphasis on $Zb\bar{b}$, which was reported to be quite large in a recent study [1].

3.1 Background from $t\bar{t} \rightarrow \ell\ell\ell\ell + X$

This background was simulated using the ISAJET Monte-Carlo program [7], as discussed in detail in Ref. 8. Particular care was taken to simulate as well as possible all inclusive 4-lepton final states from $t\bar{t}$ production in a finite amount of computer time. In the 4-lepton mass range of interest here, the $t\bar{t}$ background turns out to be about twice as large for $m_{top} = 130$ GeV than for $m_{top} = 200$ GeV. In the results discussed in Section 4, we therefore have chosen the value $m_{top} = 130$ GeV to obtain a conservative estimate for this background.

The simulation was done using $t\bar{t}$ events, where both W bosons from t-decay were forced to decay semi-leptonically, which corresponds to a cross-section of 53 pb for $m_{top} = 130$ GeV. To account for 4-lepton final states from $t\bar{t}$, where one or none of the leptons originate from W decay, a correction factor of ≈ 1.5 was estimated, independent of the 4-lepton invariant mass, for $p_T^{\ell} > 10$ GeV, to this cross-section [8].

Table 3 shows the rates and acceptances for the $t\bar{t}$ background, for $m_{top} = 130$ GeV, using the same sequence of cuts as described in Section 2 for the signal. We start off with $\approx 10^5$ events for 10^5 pb $^{-1}$, after accounting for the detection efficiency of $\epsilon_{\ell} = 0.9$ per lepton. This is the inclusive rate of detectable 4-lepton final states from $t\bar{t}$ production, including cascade b-quark semi-leptonic decays. Table 3 shows that $\approx 26\%$ of these events are within the acceptance cuts (cut 1), and that only $\approx 11\%$ of the accepted events contain a lepton pair with a reconstructed mass within ± 10 GeV of the Z mass. Obviously this fraction depends upon this ± 10 GeV cut around m_Z for the non-resonant $t\bar{t}$ background: since the inclusive dilepton mass distribution is approximately flat around m_Z , it is clear that the $t\bar{t}$ background is directly proportional to the window allowed around m_Z , and therefore sensitive to the detector resolution. This point shall be further discussed in Section 4.

Finally, 73% of the events, passing cuts 1 and 2, satisfy the last cut, $m_{34} > 12$ GeV, leading to a total estimated background of ≈ 2200 events for 10^5 pb $^{-1}$. All these events contain at least two non-isolated leptons from b-decay, and, as discussed above, approximately one third of them contain four non-isolated leptons. We shall discuss lepton isolation in Section 4.

Fig. 5 shows the reconstructed 4-lepton invariant mass distribution for the $t\bar{t} \rightarrow eeee$ (or $\mu\mu\mu\mu$) + X background, after all cuts have been applied, for $m_{top} = 130$ and 200 GeV.

3.2 Background from $Zb\bar{b} \rightarrow \ell\ell\ell\ell + X$

This background arises mainly from $gg \rightarrow Zb\bar{b}$, and is potentially dangerous since it contains a Z boson in the final state. In fact, $\approx 90\%$ of the $Zb\bar{b}$ cross-section was estimated to arise from $gg \rightarrow Zb\bar{b}$ [1], and an exact calculation of this process, including a non-zero b-quark mass, has been performed for this Workshop [9].

3.2.1 Rates

The calculation of Ref. 9 has been implemented in the LDW [10] and PYTHIA [2,11] Monte-Carlo programs. We have used LDW to compare rates with those of the PAPAGENO [12] Monte-Carlo program for the same process [1], and with those of Zjj events, to understand what fraction of these events contain b-quark pairs. All the cross-sections quoted in the following include a branching ratio of 3.4% for $Z \rightarrow ee$.

We first compare rates with those quoted in Table 1 of Ref. 1, corrected for the branching ratio $Z \rightarrow ee$. The numbers below are quoted at $\sqrt{s} = 40$ TeV, for $p_T^Z > 100$ GeV:

$$\begin{aligned} \sigma(gg, q\bar{q} \rightarrow Zb\bar{b}) &= 6.9 \text{ pb} && \text{PAPAGENO [1]} \\ \sigma(gg \rightarrow Zb\bar{b}) &= (5.9 \pm 0.5) \text{ pb} && \text{LDW [9,10].} \end{aligned}$$

The LDW result was obtained using the MRSB [13] structure functions, and is in reasonable agreement with the PAPAGENO result of Ref. 1. This result can be compared to the total $Z +$ jet cross-section, using the complete $O(\alpha_s^2)$ calculation of Ref. 14, for $p_T^Z > 100$ GeV, and also using the LDW Monte-Carlo:

$$\begin{aligned} \sigma(Z + \text{jets}, p_T^Z > 100 \text{ GeV}) &= 160 \text{ pb} && \text{obtained using [14]} \\ \sigma(Z + 1 \text{ jet}, p_T^Z > 100 \text{ GeV}) &= 108 \text{ pb} && \text{LDW} \\ \sigma(Z + 2 \text{ jets}, p_T^Z > 100 \text{ GeV}, p_T^j > 40 \text{ GeV}, \omega_{jj} > 20^\circ) &= 83 \text{ pb} && \text{LDW} \end{aligned}$$

From these rates, we conclude that the fraction of $Z +$ jet events which contain a $b\bar{b}$ pair is $\approx 3.7\%$ at $\sqrt{s} = 40$ TeV, for $p_T^Z > 100$ GeV. This fraction is less than that quoted in Ref. 1. However, if we restrict ourselves to the Zjj final states, estimated above using the LDW Monte-Carlo program, where cuts on the jet transverse momentum, $p_T^j > 40$ GeV, and on the angle between the two jets, $\omega_{jj} > 20^\circ$, are applied to obtain a finite cross-section, we find that Zjj production at these energies is flavour-democratic:

$$\begin{aligned} \sigma(q\bar{q} \rightarrow Zjj) &= 13.1 \text{ pb} \\ \sigma(qg \rightarrow Zjj) &= 62.1 \text{ pb} \\ \sigma(gg \rightarrow Zjj) &= 7.6 \text{ pb} \\ \sigma(gg \rightarrow Zb\bar{b}, p_T^{b\bar{b}} > 40 \text{ GeV}, \omega_{b\bar{b}} > 20^\circ) &= (1.6 \pm 0.1) \text{ pb}. \end{aligned}$$

This last cross-section increases to 1.7 pb if the b-quark mass is set to 0 in the calculation. The ratio $(gg \rightarrow Zb\bar{b})/(gg \rightarrow Zjj)$ is $\approx 22\%$, in agreement with the value for $\Gamma(Z \rightarrow b\bar{b})/\Gamma(Z \rightarrow \text{hadrons})$.

We can now compare $Zb\bar{b}$ production rates with Zjj production rates at LHC, in a kinematic region, which corresponds more to that of the background to the signal from $H \rightarrow Z^*Z^* \rightarrow \ell\ell\ell\ell$. For this comparison, we require $p_T^j > 10$ GeV and $\omega_{jj} > 10^\circ$:

$$\begin{aligned} \sigma(gg \rightarrow Zb\bar{b}, m_b = 5 \text{ GeV}) &= (8.2 \pm 0.4) \text{ pb} \\ \sigma(gg \rightarrow Zb\bar{b}, m_b = 0) &= (9.0 \pm 0.4) \text{ pb} \\ \sigma(gg \rightarrow Zjj) &= 48 \text{ pb} \\ \sigma(qg \rightarrow Zjj) &= 442 \text{ pb} \\ \sigma(q\bar{q} \rightarrow Zjj) &= 116 \text{ pb}. \end{aligned}$$

At these much lower p_T -values for the produced jets, flavour democracy no longer holds fully and the $Zb\bar{b}$ rate is only $\approx 1.4\%$ of the total Zjj rate. We should bear in mind however

that the computation of $Z + \text{jet}$ rates at LHC/SSC, with such low p_T -thresholds on the jets, is subject to very large theoretical uncertainties.

This is not the case for $Zb\bar{b}$ production, for which the calculation remains finite without any cuts on the final state partons. This process therefore provides a good benchmark to compare the correct (but CPU time consuming) matrix element (ME) simulation, with the approximate (but much less CPU time consuming) parton shower (PS) simulations. Table 3 shows the cross-sections for $Zb\bar{b} \rightarrow \text{eeee} + X$ at $\sqrt{s} = 16 \text{ TeV}$, estimated with various Monte-Carlo generators, with the EHLQ structure functions (set 1) [12], which yield a larger rate by $\approx 50\%$ for the $Zb\bar{b}$ background than the MRSB structure functions used above. The reference cross-section is 0.39 pb, obtained with the calculation of Ref. 9, for inclusive $Zb\bar{b} \rightarrow \text{eeee} + X$ production. If both b-quarks are required to have $p_T > 10 \text{ GeV}$, the cross-section decreases to 0.24 pb. The PAPAGENO Monte-Carlo which corresponds to a matrix element calculation, gives a smaller cross-section of 0.24 pb, as compared to the calculation of Ref. 9. The parton shower simulations can be done in several ways, after selecting the appropriate flavour, contrary to the claim in Ref. 1:

- a) $gb \rightarrow Zb$, where a cut is required on p_T^Z , because the b-quarks are taken to be massless, both in ISAJET and PYTHIA. With a cut $p_T^Z > 10 \text{ GeV}$, the cross-sections are sizeably different for the two Monte-Carlo programs (such a large difference is not surprising: the chosen Q^2 -scale and the treatment of the $gb \rightarrow Zb$ matrix element divergence for $p_T^Z \rightarrow 0$ are different between the two Monte-Carlo programs). The b-quark is produced through $g \rightarrow b\bar{b}$ branching in the backward evolution of the incoming b-quark, a standard feature of these parton shower Monte-Carlo programs.
- b) $b\bar{b} \rightarrow Z$, with no cut necessary on p_T^Z in this case, and two backward evolutions of the initial b-quarks, to produce the final state $b\bar{b}$ pair. The total cross-section obtained with PYTHIA is in surprising agreement with the ME cross-section, as shown in Table 3.

3.2.2. Comparison of b-quark and lepton spectra

Before comparing the $Zb\bar{b}$ background estimates with the different Monte-Carlo programs, we can first check how good is the agreement between them for some of the generated distributions. Fig. 6 shows a comparison of the Z transverse momentum distribution, p_T^Z , for PYTHIA (ME), PAPAGENO and ISAJET, which agree to about a factor 2 for $10 \leq p_T^Z \leq 200 \text{ GeV}$.

A better test of possible differences between the different Monte-Carlo programs is obtained by comparing the larger and smaller b-quark transverse momentum distributions. In fact, the most sensitive distribution to possible differences between ME and PS is that of the smaller p_T b-quark, since it will almost always be the one generated through backward evolution in the PS case. Fig. 7 shows both distributions for PYTHIA (ME), PAPAGENO and ISAJET (PS). As expected, the distribution for the smaller p_T b-quark, obtained from the PS simulation, is softer, a fact also observed in the PYTHIA (PS) simulations. Apart from the overall normalisation, the distributions obtained from PYTHIA (ME) and PAPAGENO are in good agreement.

Finally, Fig. 7 also shows the corresponding spectra for the leptons from first-generation decay of the considered b-quark, including the semi-leptonic branching ratio. This tests the fragmentation models used in the various Monte-Carlo programs. Given the observed differences between the parent b-quark p_T -spectra, the lepton p_T -spectra are in reasonable agreement between PYTHIA (ME) and ISAJET. On the other hand, the fragmentation model used in the PAPAGENO Monte-Carlo clearly produces a much softer p_T -spectrum for the leptons from b-decay. We also point out that the default fragmentation used for b-quarks in PYTHIA 5.4 has been found to be too hard, with respect to recent observations from LEP data. We therefore conclude that the estimates obtained using

PYTHIA (ME) are probably conservative, though the uncertainties on the b-quark fragmentation have not been included in the estimates of Table 3.

3.2.3. Rates after acceptance cuts

We can now come back to Table 3 for a comparison of the $Zb\bar{b}$ background rates after acceptance cuts. The acceptance for cut 1, requiring 4 leptons with $p_T^l > 10 \text{ GeV}$ and $|\eta_l| < 3$, displays already some marked differences between the different simulations:

- a) The acceptances for PYTHIA (ME) and PAPAGENO are very different, due to the too soft fragmentation of b-quarks in PAPAGENO, as discussed above.
- b) The acceptances for ISAJET (PS) and PYTHIA (PS) are also much lower than the reference simulation using PYTHIA (ME). This is certainly due to the too soft p_T -spectrum obtained for the smaller p_T b-quark, generated through backward evolution, as illustrated in Fig. 7. This is confirmed by the fact that a double backward evolution, using the matrix element for $b\bar{b} \rightarrow Z$ with PYTHIA (PS), results in the smallest acceptance of all.

The acceptances for cut 2 are similar for the various Monte-Carlo programs. Those for cut 3, $m_{34} > 12 \text{ GeV}$, vary however over a wider range. Particular attention should go to the ISAJET (PS) acceptance of only 33% for cut 3. This is due to the fact that this simulation, and the one using PAPAGENO, were the only ones including also second-generation b-quark decays, which often result in very low-mass dilepton pairs, originating from the same b-quark. Cut 3 is thus shown to be very useful to eliminate this part of the $Zb\bar{b}$ background, leaving events dominated by first-generation b-quark semi-leptonic decays.

Finally, Table 3 displays the expected $Zb\bar{b}$ background rates after all cuts. The largest estimate is in fact obtained for the exact calculation interfaced to the PYTHIA Monte-Carlo program for proper b-quark fragmentation. Table 3 shows that applying a cut, $p_T^{b\bar{b}} > 10 \text{ GeV}$, at generation, results in an underestimation of the background by a factor ≈ 1.5 . The PS results tend to give significantly lower estimates, especially if one were to normalise their generated cross-sections to the reference value of 0.39 pb.

Fig. 5 shows the 4-lepton mass distribution obtained from the various Monte-Carlo programs. We have chosen the estimate from PYTHIA (ME) to evaluate the total background to the Higgs signal in the results discussed in Section 4.

3.3 Background From Z^*Z^* , γ^*Z^*

This background turns out to be small, but cannot be neglected since it is the only one which cannot be reduced by isolation cuts. The appropriate $q\bar{q} \rightarrow Z^*Z^*$ and γ^*Z^* matrix elements, including interference terms, have been recently implemented in PYTHIA 5.4, which was used to simulate this background. Given the cuts used in the analysis, the events were generated, requiring $80 < m_{12} < 100 \text{ GeV}$ and $12 < m_{34} < 80 \text{ GeV}$, yielding a cross-section of 0.039 pb for final states containing four electrons.

Table 3 shows what fraction of the events survive the successive cuts, and Fig. 8 shows the distribution of m_{34} , the second dilepton mass, which despite the generation cuts, displays peaks near the photon and Z poles. Finally, Fig. 5 shows the reconstructed 4-lepton mass distribution for the 58.8 events (per 10^5 pb^{-1}), which survive the acceptance cuts.

4. Discussion of Results

We shall now use the signal and background estimates discussed in the previous sections, to study to what extent a Higgs signal can be seen above the background in this Higgs mass range. In particular, we shall discuss the effects of lepton isolation and energy resolution on the signal to background ratio.

4.1 Signal versus Background before Lepton Isolation

Table 4 summarises, in its first five lines, the results of the previous Sections. For $120 \leq m_H \leq 180$ GeV, the expected signal rates are given, for electron and muon resolutions as discussed in Section 2. Also shown are the contributions from each background process, summed over $m_H \pm 2\sigma_H$, and the total background, which can then be compared to the signal in the following way:

- Case 1: all leptons are considered to be well measured, with an energy resolution taken to be $\sigma_E/E = 0.15/\sqrt{E} + 0.02$, for the sake of simplicity.
- Case 2: electrons are considered to be well measured, with the above resolution, and muons are considered to be badly measured, with $\Delta p/p = 0.15$.

The last two lines of Table 4 are then an attempt to quantify crudely the signal significance for Case 1 and Case 2. Note that the computed significance, if S_e (resp. S_μ) are the number of expected 4-electron (resp. 4-muon) reconstructed events, quoted on the first line of Table 4, is:

- for Case 1, $S/(S+B)^{1/2} = 2S_e/(S_e+B_e)^{1/2}$, where the factor 2 accounts for the gain, when using all possible $H \rightarrow Z^*Z^* \rightarrow l\bar{l}l\bar{l}l\bar{l}$ channels,
- for Case 2, $S/(S+B)^{1/2} = [2 S_e^2/(S_e+B_e) + 2 S_\mu^2/(S_\mu+B_\mu)]^{1/2}$, where we have assumed, again for simplicity, that the $H \rightarrow Z^*Z^* \rightarrow ee\mu\mu$ events behave like $H \rightarrow Z^*Z^* \rightarrow eeee$ (resp. $\mu\mu\mu\mu$) events if $m_{\mu\mu}$ (resp. m_{ee}) is close to m_Z , because of the Z -mass constraint.

Before any isolation cuts are applied, Table 4 shows that the significance of a Higgs signal will be marginal, yielding at best a 7σ effect for $m_H = 150$ GeV and for Case 1. However, this somewhat crude estimate of the significance is clearly pessimistic, for two reasons:

- Fig. 9 shows, for $m_H = 130, 150$ and 170 GeV, the signal expected for Case 1, above the sum of all background contributions. Clearly a more proper statistical analysis, than that using the excess event rate observed over $m_H \pm 2\sigma_H$, would yield much better results, if in particular one would fit a Gaussian peak on top of the background.
- The backgrounds in Table 4 are dominated by the non-resonant $t\bar{t}$ background. The magnitude of this background is directly proportional to the window Δm , around the Z -mass, allowed for the first dilepton pair. A value $\Delta m = \pm 10$ GeV was used for Table 4, which clearly can be reduced, depending on the lepton energy resolution. A somewhat extreme example is shown in Fig. 10, for the case of a muon momentum resolution of $\Delta p_t/p_t = 0.2$ pt (pt in TeV) [15], for $|\eta_\mu| < 3$, where the chosen value is $\Delta m = \pm 2.5$ GeV. The $t\bar{t}$ background is reduced by a factor 4 but not, of course, the $Zb\bar{b}$ background, and only the rates for final states containing four muons are considered here. Nevertheless, Fig. 10 shows that there is some hope to extract a signal from $H \rightarrow Z^*Z^* \rightarrow \mu\mu\mu\mu$ alone, if a very good muon momentum resolution of this type can be achieved over the rapidity range $|\eta| < 3$ and for muon momenta as low as 10 GeV.

However, we would like to stress that the uncertainties on the $t\bar{t}$ and $Zb\bar{b}$ background rates are quite large, and that it will certainly be very difficult to identify with high efficiency and measure with high precision, leptons, be they electrons or muons, of transverse momentum ≈ 10 GeV and at large rapidities, at luminosities of $\approx 10^{34} \text{ cm}^{-2} \text{ s}^{-1}$. From these considerations, we conclude that it is highly desirable to increase by a factor 4 the potential rates for a Higgs signal in this mass range, by detecting electrons and muons.

4.2 Signal versus Background with Lepton Isolation

Most of the background events contain at least two non-isolated leptons from b -decay. Lepton isolation has been an efficient tool at present hadron colliders in searches for isolated leptons, and has also been studied by several other working groups at this Workshop

[16]. All these studies were done at particle level, however, though lepton isolation appears to be one of the cases, where full calorimeter simulations using GEANT would be more reliable and worth the large CPU time required.

We have therefore performed such a GEANT simulation of lepton isolation in b -decays, taking the electrons as the most difficult case, since the energy deposited by the electron cannot as easily be separated from that of accompanying hadrons. We used a 'fast' and crude simulation of a very granular calorimeter, with cells of $\Delta\phi \times \Delta\eta = 0.02 \times 0.02$, with one electromagnetic compartment of 25 radiation lengths, and a total of 10 absorption lengths, including the electromagnetic compartment. This calorimeter was of a projective cylindrical geometry, with an inner radius of 1m. To estimate the rejection against non-isolated leptons from b -quark decay, the $Zb\bar{b}$ background events of Fig. 6 (PYTHIA ME) were run through this calorimeter simulation using GEANT. The electromagnetic showers were smeared with a resolution, $\sigma_E/E = 0.15/\sqrt{E}+0.02$, and the hadronic ones with a resolution, $\sigma_E/E=0.50/\sqrt{E}+0.02$. The effect of pile-up at high luminosity was simulated by overlaying each event with 10 minimum bias events generated with PYTHIA. A nonet of cells was used to define the electron energy, corresponding to a cone of $\Delta R = 0.06 \times 0.06$. The nonet electromagnetic transverse energy was required to be larger than 10 GeV. The isolation cut was defined by computing the total energy measured in a cone of $\Delta R = 0.18 \times 0.18$ around the electron, and requiring that this energy minus that of the electromagnetic nonet be less than 10 GeV. Only 15% of the $Zb\bar{b}$ events of Fig. 5 passed this cut. Only 10% of them satisfy the requirement that the generated electron energy be larger than 80% of the measured nonet energy, a Monte-Carlo cut which crudely simulates experimental cuts which would compare the electron track impact on the calorimeter to the measured energy pattern in the nonet and would thus discriminate further between isolated and non-isolated electrons.

The efficiency for isolated electrons, including effects of pile-up, calorimeter speed etc., has been studied in detail in Ref. 17. Energy isolation cuts of about 10 GeV in a cone of $\approx 0.2 \times 0.2$ in $\Delta\eta \times \Delta\phi$ (where the inner cone of 0.06×0.06 is excluded due to the electron energy measurement), can be applied up to luminosities of $2 \cdot 10^{34} \text{ cm}^{-2} \text{ s}^{-1}$ with less than 10% loss of isolated electrons.

We therefore conclude from these studies that a reasonable value for the overall rejection of lepton isolation cuts, applied to the two leptons called 3 and 4 in the previous sections, would be $R_b^2 = 50$ (corresponding to a rejection of ≈ 7 per lepton), with an overall efficiency, $\epsilon_g^2 = 0.70$ (corresponding to an efficiency of ≈ 0.85 per isolated lepton), for isolated leptons from $H \rightarrow Z^*Z^* \rightarrow l\bar{l}l\bar{l}l\bar{l}$ decays. We have chosen to be conservative in these estimates, because these values depend strongly on the magnitude of pile-up effects in the calorimeter, the granularity of the electromagnetic calorimeter (at least 0.03×0.03 is needed to achieve the desired goals), the presence or absence of a central magnetic field, and also on the b -quark p_t -spectrum and the chosen lepton p_t -threshold.

In Table 4, the rejection R_b^2 has been applied to the $t\bar{t}$ and $Zb\bar{b}$ backgrounds, and the efficiency ϵ_g^2 has been applied to the Z^*Z^* , γ^*Z^* background and the Higgs signal. The significance of the signal is computed crudely as discussed above for Case 1 and Case 2, and we note that now the signal emerges clearly above the background, for $130 \leq m_H \leq 180$ GeV. Fig. 11 shows, for Case 1, the sum of all backgrounds after the isolation cut has been applied, and the signal for $m_H = 130, 150$ and 170 GeV. Clearly lepton isolation will be a powerful tool to reject the dominant backgrounds in this mass range.

Fig. 12 shows, after isolation cuts, that a muon momentum resolution of $\Delta p/p = 0.15$ will be marginal to extract a Higgs signal in this channel, using the $H \rightarrow Z^*Z^* \rightarrow \mu\mu\mu\mu$ decay alone. However, as shown in Table 4, such a performance combined with that of a modest electron resolution detector (Case 2), will only be $\approx 20\%$ worse than a detector with good energy resolution for all 4-lepton final states (Case 1), in terms of statistical significance of the observed signal.

5. Conclusions

We have performed a detailed study of the signal properties for the $H \rightarrow Z^*Z^* \rightarrow \ell\ell\ell\ell$ decay channel, for $m_H \leq 2m_Z$. We have also carefully estimated the various background contributions, which are dominantly from $t\bar{t}$ and $Zb\bar{b}$ before lepton isolation cuts are applied. Good lepton energy resolution can significantly reduce the potentially dangerous non-resonant background from $t\bar{t}$.

The low rates expected, even with good lepton acceptance, $p_T^{\ell} > 10$ GeV and $|\eta_{\ell}| < 3$, lead to the conclusion, that a clear observation of a possible Higgs signal in this channel requires identification of both electrons and muons. Lepton isolation cuts have also been carefully studied and proven to yield sufficient rejection against non-isolated leptons from b -quark decay, to reduce the $t\bar{t}$ and $Zb\bar{b}$ backgrounds to the level of the irreducible Z^*Z^* , γ^*Z^* background. The Higgs signal would then clearly appear above background, for a total integrated luminosity of 10^5 pb $^{-1}$ and for $130 \leq m_H \leq 2m_Z$.

References:

- [1] I. Hinchcliffe and E.M. Wang, in Proceedings of the 1988 Snowmass Summer Study on High Energy Physics in the 1990's, edited by S. Jensen (World Scientific, Singapore, 1989), p. 119.
- [2] H.V. Bengtsson and T. Sjöstrand, Comp. Phys. Comm. 46 (1987) 43.
- [3] Z. Kunszt and W. J. Stirling, Higgs study group, these proceedings.
- [4] M. Greco, Phys. Lett. 156B (1985) 109;
R.K. Ellis et al., Nucl. Phys. B297 (1988) 221;
I. Hinchcliffe and S. Novaes, Phys. Rev. D38 (1988) 3475.
- [5] D. Froidevaux, Higgs study group, these proceedings;
S. Hellman, DAQ and trigger study group, these proceedings.
- [6] R.N. Cahn et al., Phys. Rev. D35 (1987) 1626;
- [7] F. Paige and S. Protopopescu, in 'Physics of the Superconducting Super Collider 1986', eds. R. Donaldson, J. Marx (1987), p. 320.
- [8] A. Nisati, Higgs study group, these proceedings.
- [9] R. Kleiss, event generator study group, these proceedings.
- [10] S.D. Ellis, R. Kleiss and W.J. Stirling, Phys. Lett. 203B (1988) 172;
F.A. Berends, W.T. Giele and H. Kuijf, Nucl. Phys. B321 (1989) 39.
- [11] The subprocess to be selected is 131 in PYTHIA 5.4. We will refer to it as PYTHIA ME (matrix element) as opposed to PYTHIA PS (parton shower).
- [12] E. Eichten, I. Hinchcliffe, K. Lane and C. Quigg, Rev. Mod. Phys. 56 (1984) 579.
- [13] A.D. Martin, R.G. Roberts and W.J. Stirling, Phys. Lett. 206B (1988) 327; Mod. Phys. Lett. A4 (1989) 1135.
- [14] P.B. Arnold and M.H. Reno, Nucl. Phys. B319 (1989) 37;
R.J. Gonsalves, J.P. Pawlowski and C.F. Wai, Phys. Rev. D40 (1989) 2245.
- [15] M. Della Negra, muon study group, these proceedings.
- [16] See for example, L. Fayard et al., top study group, and T. Rodrigo, Strong electroweak symmetry breaking study group, these proceedings.
- [17] J.P. Repellin, electron study group, these proceedings.

m_H GeV	120	130	140	150	160	170	180
gg fusion	26.3	23.7	21.6	20.0	18.6	17.6	17.0
σ pb	4.9	4.6	4.3	4.0	3.8	3.6	3.4
Total	31.2	28.3	25.9	24.0	22.4	21.2	20.4
BR ($H \rightarrow Z^*Z^*$)	0.98%	3.15%	5.94%	7.41%	3.37%	2.14%	6.17%
Events per 10^5 pb $^{-1}$, $\epsilon_{\ell} = 0.9$	23.2	67.6	116.7	134.9	57.3	34.4	95.5
ACCEPTANCE							
$ \eta_{\ell} < 3$	e^{\dagger}	0.32	0.43	0.54	0.62	0.65	0.71
$p_T^{\ell} > 10$ GeV	μ^{\dagger}	0.31	0.42	0.53	0.59	0.65	0.70
ACCEPTANCE							
$i_2^{12} > 20$ GeV	e	0.54	0.74	0.78	0.83	0.89	0.89
$ m_Z - m_{12} < 10$ GeV	μ	0.40	0.51	0.58	0.66	0.73	0.76
$m_{34} > 12$ GeV	e	4.0	21.6	49.0	69.0	32.9	21.6
Events per 10^5 pb $^{-1}$	μ	2.8	14.4	35.8	51.7	26.9	18.0
Reconstructed 4-lepton mass resolution	e	1.9 GeV	2.0 GeV	2.1 GeV	2.2 GeV	2.4 GeV	2.5 GeV
	μ	3.7 GeV	5.2 GeV	6.5 GeV	7.5 GeV	10.0 GeV	11.1 GeV
Observed signal	e	3.8	20.5	46.5	65.6	31.3	20.5
$m_{\text{sig}} = m_H \pm 2\sigma_H$	μ	2.7	13.7	34.0	49.1	25.6	17.1

Table 1: $H \rightarrow Z^*Z^* \rightarrow eeee$ or $\mu\mu\mu\mu$ rates and acceptances (only decays into one lepton type considered)
†: the numbers shown correspond to an energy resolution, $\sigma_E/E = 0.15/\sqrt{E} + 0.02$ for e , and a momentum resolution, $\Delta p/p = 0.15$ for μ .

Table 2Acceptances in η and p_T for $H \rightarrow \ell\ell\ell\ell$ and $ZZ \rightarrow \ell\ell\ell\ell$

		$p_T^{12} > 20 \text{ GeV}$	$p_T^{\text{all leptons}} > 20 \text{ GeV}$	$p_T^{\text{all leptons}} > 10 \text{ GeV}$
$m_H = 120 \text{ GeV}$	$ \eta < 2$	0.61	0.02	0.20
	$ \eta < 3$	0.87	0.04	0.32
$m_H = 170 \text{ GeV}$	$ \eta < 2$	0.72	0.28	0.45
	$ \eta < 3$	0.93	0.41	0.71
$m_H = 200 \text{ GeV}$	$ \eta < 2$	0.73	0.38	0.48
	$ \eta < 3$	0.94	0.56	0.76
$m_H = 500 \text{ GeV}$	$ \eta < 2$	0.82	0.57	0.62
	$ \eta < 3$	0.98	0.80	0.88
ZZ continuum	$ \eta < 2$	0.50	0.22	0.27
	$ \eta < 3$	0.76	0.34	0.50

Background process	$\sigma_B \text{ pb}$	Events per 10^5 pb^{-1} $\varepsilon_{\ell\ell} = 0.9$	ACCEPTANCE $ \eta_{\ell\ell} < 3$ $p_T^{\ell\ell} > 10 \text{ GeV}$	ACCEPTANCE $p_T^{12} > 20 \text{ GeV}$ $ m_{Z-Z} < 10 \text{ GeV}$	ACCEPTANCE $m_{34} > 12 \text{ GeV}$	Events accepted $\text{per } 10^5 \text{ pb}^{-1}$
$\bar{b} \rightarrow cccc + X$ $m_{top} = 130 \text{ GeV}$ ISAJET	80.1	106000	0.26	0.11	0.73	2220
$Zb\bar{b} \rightarrow cccc + X$ Kleiss† + PYTHIA	0.39	25900	0.10	0.80	0.60	1240 ± 130
$Zb\bar{b} \rightarrow cccc + X$ $p_T^{Zb} > 10 \text{ GeV}$ Kleiss† + PYTHIA	0.24	15500	0.09	0.73	0.68	700 ± 100
$Zb\bar{b} \rightarrow cccc + X$ PAPAGENO†	0.24	15700	0.02	0.81	0.66	135
$Zb\bar{b} \rightarrow cccc + X$ $gb \rightarrow Zb, p_T^Z > 10 \text{ GeV}$ ISAJET††	0.80	52500	0.03	0.83	0.33	360
$Zb\bar{b} \rightarrow cccc + X$ $gb \rightarrow Zb, p_T^Z > 10 \text{ GeV}$ PYTHIA††	0.48	31500	0.05	0.77	0.72	780 ± 53
$Zb\bar{b} \rightarrow cccc + X$ $b\bar{b} \rightarrow Z$ PYTHIA††	0.43	28200	0.01	0.78	0.81	180 ± 20
$Z^*Z^* \rightarrow cccc$ $80 < m_{12} < 100$ $12 < m_{34} < 80$ PYTHIA†	0.0039	256	0.27	0.87	0.99	58.8

Table 3: Background rates and acceptances for $cccc$ ($\mu\mu\mu\mu$) final states

† Matrix element generation; †† Parton shower generation (b-quarks are considered to be massless)

m_H GeV	120		130		140		150		160		170		180	
	e	μ	e	μ	e	μ	e	μ	e	μ	e	μ	e	μ
Events within $m_H \pm 2\sigma_H$	3.8	2.7	20.5	13.7	46.5	34.0	65.6	49.1	31.3	25.6	20.5	17.1	64.2	57.9
Background from $t\bar{t}$ ($m_{top}=130$ GeV)	144.2	203.5	227.4	561.6	241.0	701.6	195.2	643.3	130.6	593.6	81.9	434.7	50.2	276.8
Background from $Z h \bar{b}$	38.2	38.1	57.2	97.1	70.0	154.2	76.4	191.3	82.6	273.2	81.5	191.8	78.1	310.2
Irreducible background from $Z^* Z^*, \gamma^* Z^*$	2.0	2.7	2.9	6.5	4.2	8.6	4.5	10.4	4.6	13.6	4.8	14.7	4.8	14.4
Total background	184.4	244.3	287.5	665.2	315.2	864.4	276.1	845.0	217.8	880.4	168.2	641.2	133.1	601.4
No lepton isolation	2.7	1.9	14.4	9.6	32.6	23.8	45.9	34.4	21.9	17.9	14.4	12.0	44.9	40.5
Total signal with lepton isolation	5.0	6.7	7.7	17.7	9.2	23.1	8.6	24.0	7.4	26.9	6.6	22.8	5.9	21.8
s/s+B	No isol.	0.6	2.3		4.9		7.1		4.0		3.0		9.1	
Case 1	With isol.	1.9	6.1		10.1		12.4		8.1		6.3		12.6	
s/s+B	No isol.	0.5	1.8		3.8		5.5		3.1		2.3		7.2	
Case 2	With isol.	1.7	5.1		8.7		10.9		6.8		5.3		11.5	

Table 4: $H \rightarrow Z^* Z^* \rightarrow 4$ Leptons: Signal vs Background

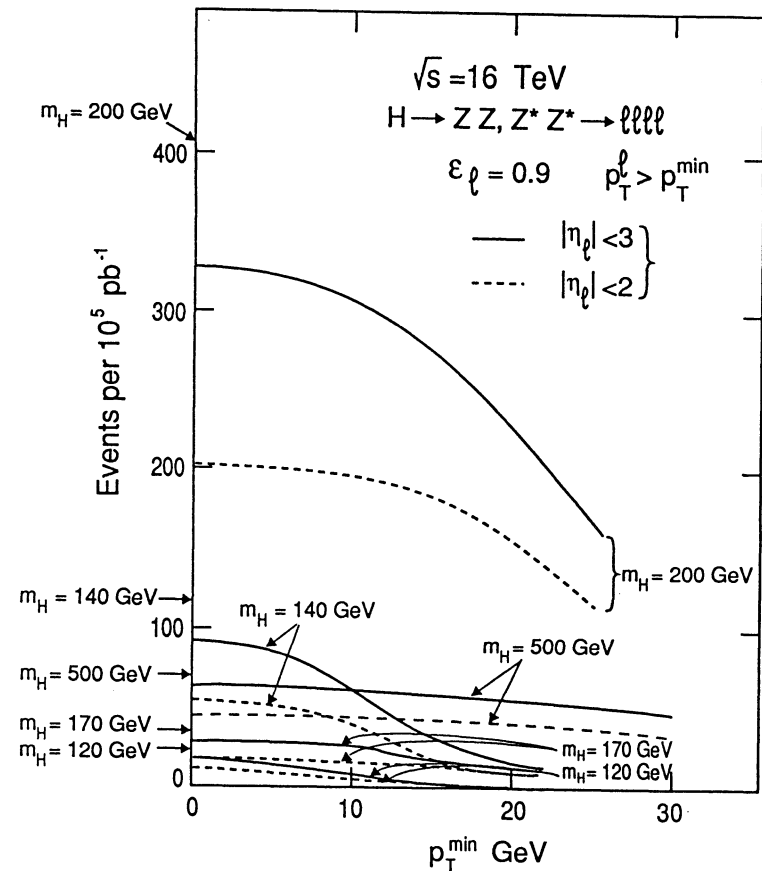


Fig. 1

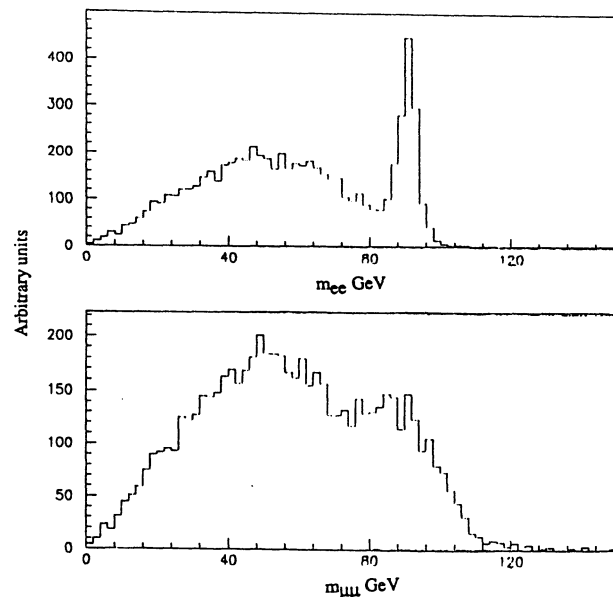


Fig. 2 : Dilepton mass for all combinations

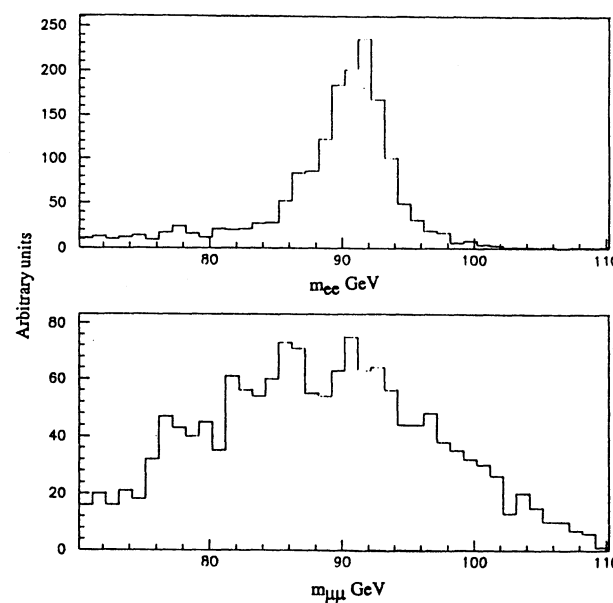


Fig. 3 : Dilepton mass for best combination

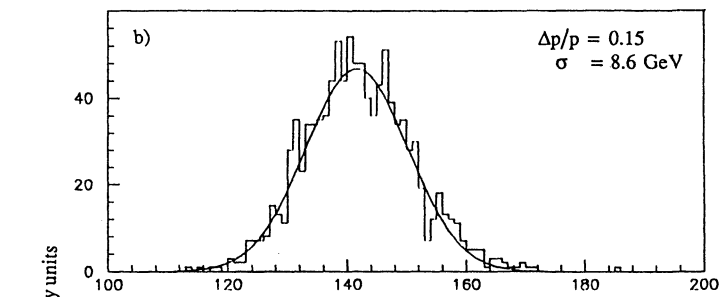
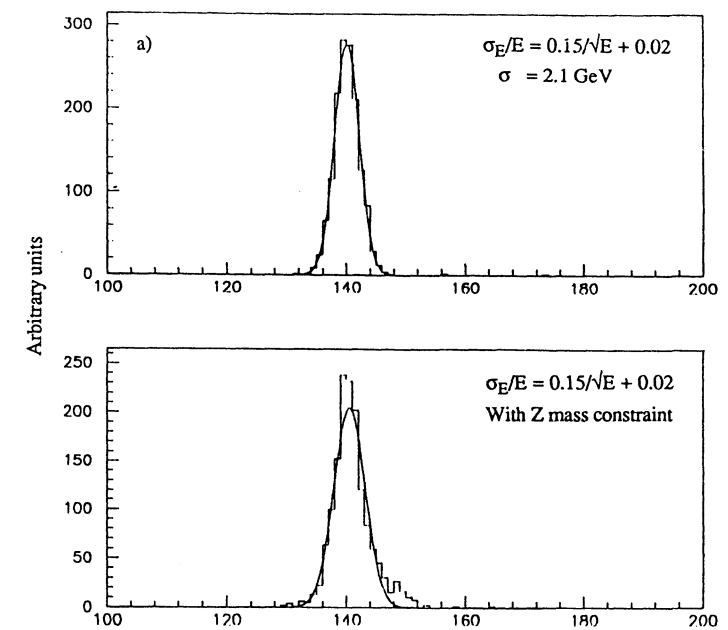


Fig. 4

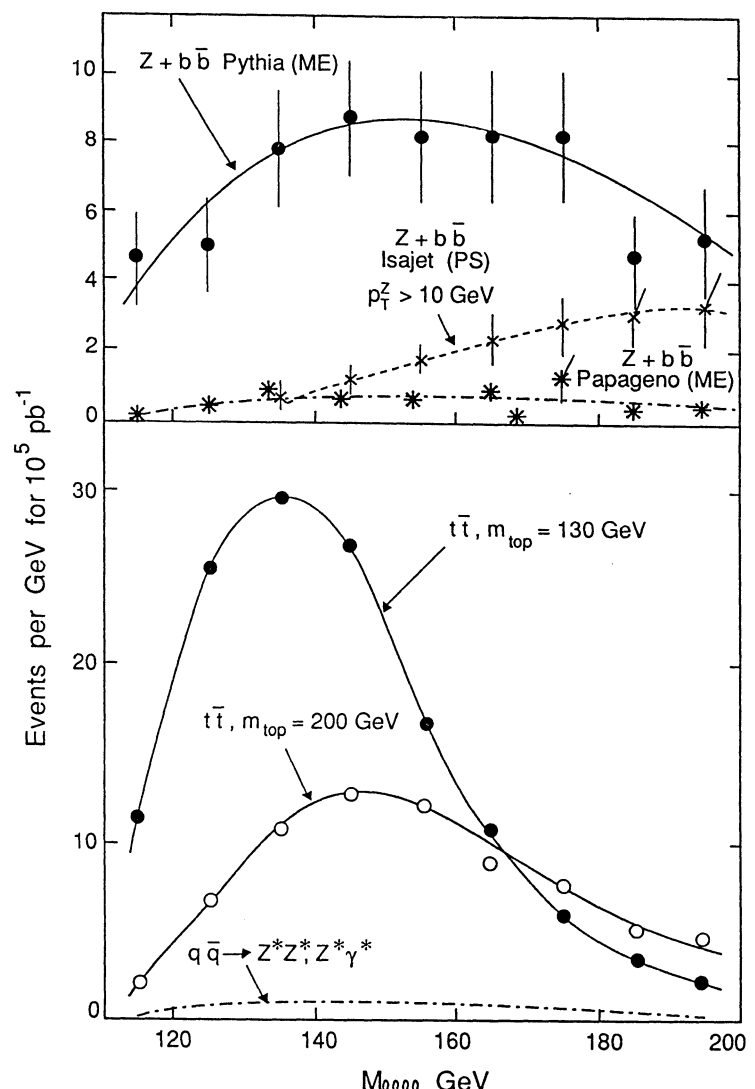


Fig. 5

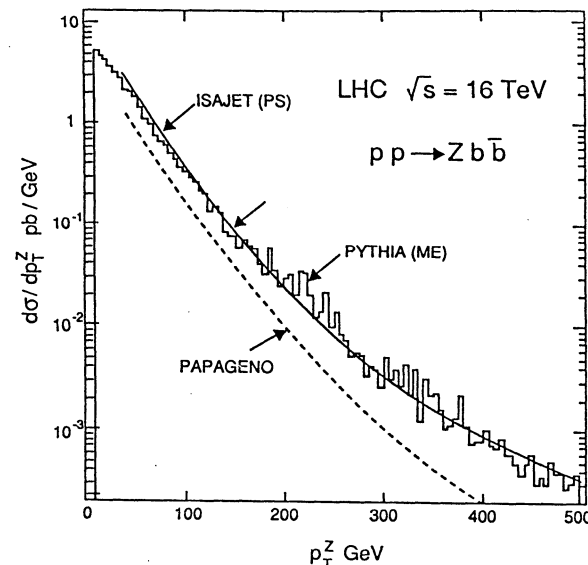


Fig. 6

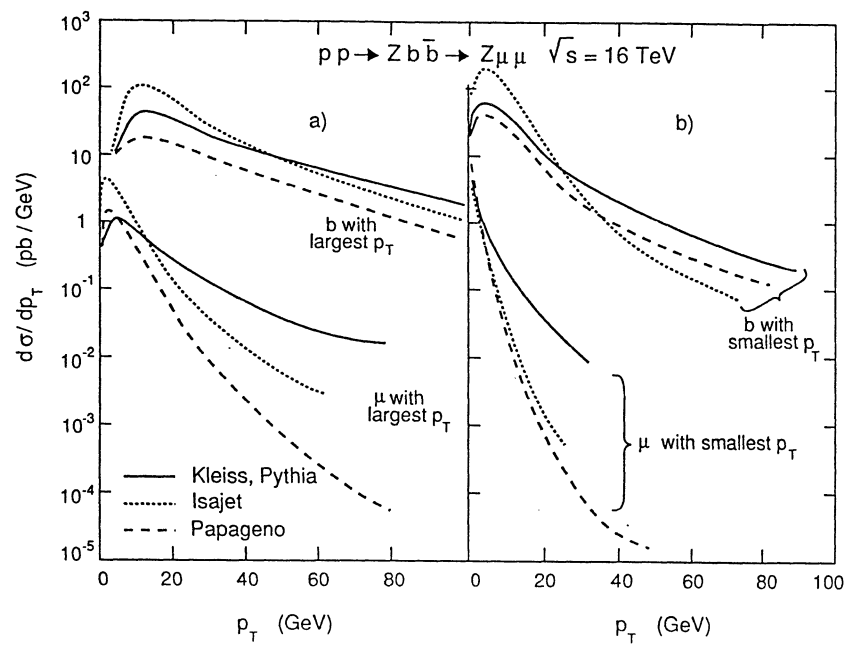


Fig. 7

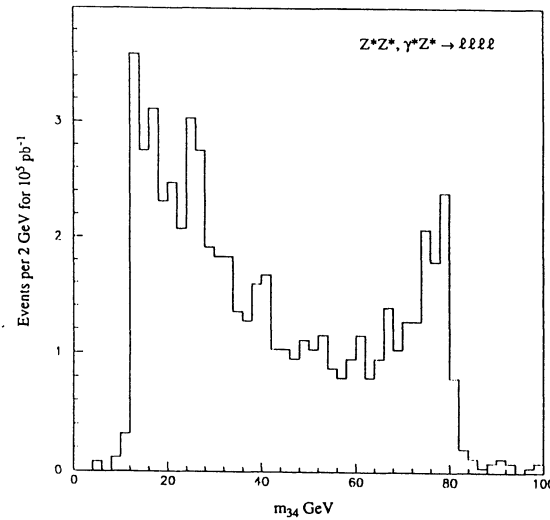


Fig. 8

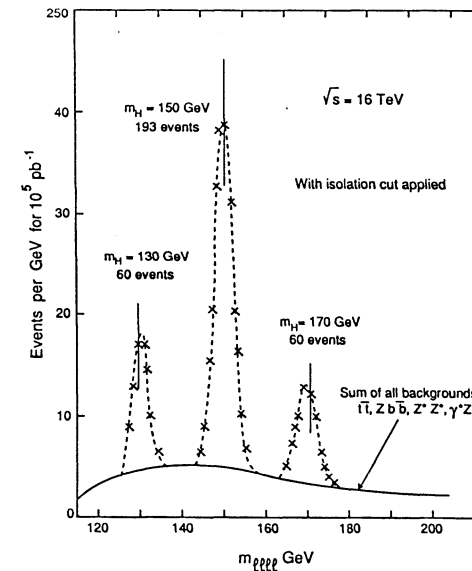


Fig. 10

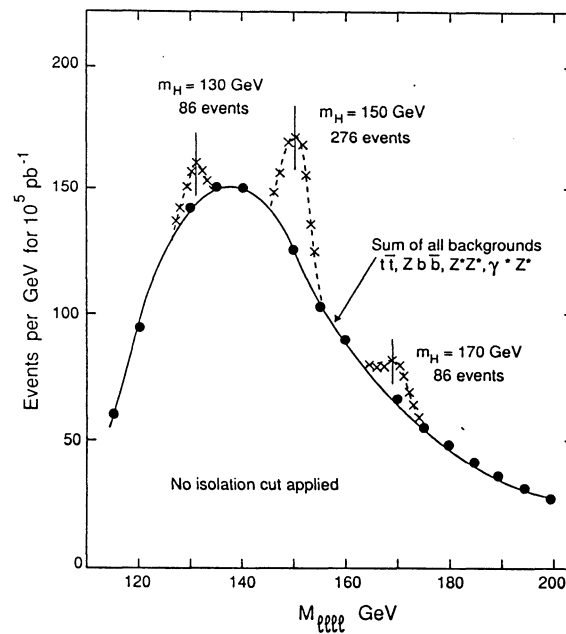


Fig. 9

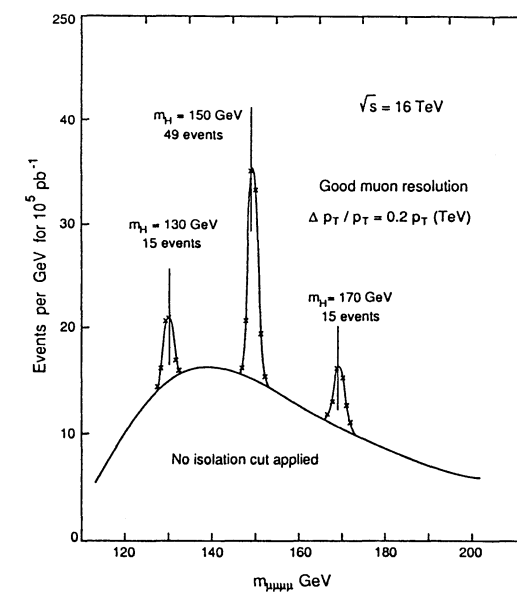


Fig. 11

L. DiLella

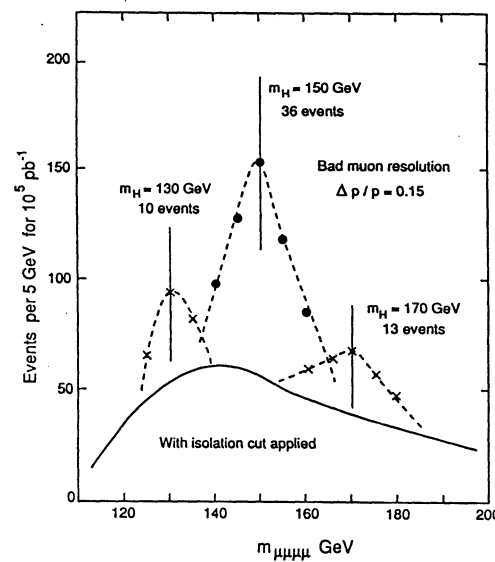


Fig. 12

1. INTRODUCTION

The detection of the decay $H \rightarrow \tau^+\tau^-$ is interesting for the intermediate Higgs mass (m_H) region, $m_Z < m_H < 140$ GeV, because of the large branching ratio ($\sim 6\%$). Because of the very high background expected in the case of hadronic final states, we only consider $e^\pm\mu^\mp$ events resulting from the leptonic decay of both τ 's (6.3% of all $\tau^+\tau^-$ pairs).

Despite the presence of four invisible neutrinos in the final state, the $\tau^+\tau^-$ invariant mass can be reconstructed if the total transverse momentum of the $\tau^+\tau^-$ is large [1]. In the approximation $m_\tau = 0$ one can write

$$p_T(v_1) \vec{u}_1 + p_T(v_2) \vec{u}_2 = \vec{p}_T^{\text{miss}}, \quad (1)$$

where $p_T(v_1)[p_T(v_2)]$ is the total transverse momentum carried by the $v\bar{v}$ pair from the decay of the first [second] τ , \vec{u}_1 (\vec{u}_2) is the measured direction of the charged lepton from the decay of the first (second) τ in the transverse plane and \vec{p}_T^{miss} is the measured missing transverse momentum. Eq. (1) can be solved in $p_T(v_1)$ and $p_T(v_2)$ if the two unit vectors \vec{u}_1 , \vec{u}_2 are not collinear [in this case Eq. (1) represents a system of two independent linear equations].

2. SIMULATION

The PYTHIA generator (version 5.40) is used to generate $H \rightarrow \tau^+\tau^-$ events as well as the background events discussed in Section 4. The effects of energy and momentum resolution are taken into account and simple acceptance and threshold cuts are applied to all detectable particles in the final state. The main parameters of the detector simulation are as follows (the sign \oplus denotes quadratic convolution) :

- Electron identification :
 - Rapidity coverage $|\eta| < 3$;
 - Energy resolution : $\sigma_E/E = A/\sqrt{E} \oplus B$ with $A = 0.15$, $B = 0.01$ (E in GeV);
 - Detection threshold $p_T = 10$ GeV;
 - Detection efficiency 100% above threshold.
- Muon identification :
 - Rapidity coverage $|\eta| < 3$;
 - Momentum resolution $\sigma_p/p = A \oplus B p$ with $A = 0.15$, $B = 1.5 \times 10^{-4}$ (p in GeV);
 - Detection threshold $p_T = 10$ GeV;

Detection efficiency 100% above threshold.

- Central calorimeter:

Rapidity coverage $|\eta| < 3$;

Granularity : $\Delta\phi \times \Delta\eta = 0.0628 \times 0.06$ (10^4 cells);

Energy resolution : $\sigma_E/E = A/\sqrt{E} \oplus B$ with $A = 0.15$, $B = 0.01$ (electromagnetic showers) and $A = 0.5$, $B = 0.02$ (hadronic showers) (E in GeV).

- Forward calorimeters:

Rapidity coverage $3 < |\eta| < 5$;

Granularity $\Delta\phi \times \Delta\eta = 15^\circ \times 0.1$ (2×480 cells);

Energy resolution : $\sigma_E/E = A/\sqrt{E} \oplus B$ with $A = 0.15$, $B = 0.01$ (electromagnetic showers) and $A = 0.8$, $B = 0.03$ (hadronic showers) (E in GeV).

3. RESULTS

Fig. 1 shows the reconstructed $\tau^+\tau^-$ invariant mass for $m_H = 100$ and 140 GeV for $e^\pm\mu^\mp$ pairs with $|cos\Delta\phi(e-\mu)| < 0.8$. The distribution of $cos\Delta\phi(e-\mu)$ is shown in Fig. 2.

The spectra shown in Fig. 1 are obtained by determining \vec{p}_T^{miss} from the energy depositions in all calorimeter cells. If the cells with $|\eta| > 3$ are ignored, these distributions become considerably broader (Fig. 3). The same is true if \vec{p}_T^{miss} is determined using $\sum \vec{p}_T^{\text{jet}}$ where the sum extends to all jets above a given threshold (Fig. 4).

The need to determine \vec{p}_T^{miss} from the energy deposition in all calorimeter cells limits the search for $H \rightarrow \tau^+\tau^-$ to luminosities not higher than $10^{33} \text{ cm}^{-2} \text{ s}^{-1}$. At higher luminosities the presence of multiple interactions deteriorates considerably the measurement of \vec{p}_T^{miss} , whose magnitude is only ~ 50 GeV on average (see Fig. 5).

To calculate the expected number of observed events, we integrate the distribution of Fig. 1 over the $m_{\tau\tau}$ mass intervals $80 < m_{\tau\tau} < 120$ GeV and $120 < m_{\tau\tau} < 160$ GeV for $m_H = 100$ and 140 GeV, respectively. For a total integrated luminosity of 10^{40} cm^{-2} we obtain 169 events for $m_H = 100$ GeV and 68 events for $m_H = 140$ GeV, corresponding to detection efficiencies of 0.061 and 0.143, respectively. The Higgs production cross-sections and branching ratios have been normalised to the calculations of Ref. 2.

4. BACKGROUNDS

We have considered the following sources of $e^\pm\mu^\mp$ events :

- $t\bar{t}$ production;
- Drell-Yan production of $\tau^+\tau^-$ pairs by γ or Z exchange ;
- the production of gauge boson pairs.

For all of these processes the PYTHIA event generator (version 5.40) has been used and the events have been processed using the same detector simulation as for the $H \rightarrow \tau^+\tau^-$ signal.

Fig. 6 shows the $m_{\tau\tau}$ distributions for the three background processes. In the case of $t\bar{t}$ a top mass of 130 GeV has been used. The distribution of Fig. 6b is unbiased for $m_{\tau\tau} > 100$ GeV (only events above this value were generated to obtain a reasonable number of events at high mass with a reasonable amount of computer time. A second run, unbiased for $m_{\tau\tau} > 50$ GeV, was made to estimate the Drell-Yan background in the interval $80 < m_{\tau\tau} < 120$ GeV).

Table I shows the expected numbers of events from the signal and from the three background processes for the two $m_{\tau\tau}$ intervals. It should be noted that an independent simulation of $t\bar{t}$ production using the EUROJET program gives results in good agreement with PYTHIA. The uncertainties given in Table I reflect the statistical errors of the simulation programs.

Table I shows that the $H \rightarrow \tau^+\tau^-$ signal is overwhelmed by the $t\bar{t}$ background for both $m_H = 100$ and 140 GeV. Furthermore, the background from Drell-Yan production of $\tau^+\tau^-$ pairs becomes comparable to the $t\bar{t}$ background in the lower mass interval because of the effect of the near-by Z pole.

TABLE I
Expected numbers of events for $L = 10^{40} \text{ cm}^{-2}$

Process	$m_{\tau\tau}$ interval	
	$80 < m_{\tau\tau} < 120$ GeV	$120 < m_{\tau\tau} < 160$ GeV
$H \rightarrow \tau^+\tau^-$ ($m_H = 100$ GeV)	169 ± 15	-
$H \rightarrow \tau^+\tau^-$ ($m_H = 140$ GeV)	-	68 ± 6
$t\bar{t}$ production ($m_{\text{top}} = 130$ GeV)	$(3.2 \pm 0.6) \times 10^4$	$(2.6 \pm 0.6) \times 10^4$
Drell-Yan	$(1.6 \pm 0.2) \times 10^4$	420 ± 100
Production of two gauge bosons	$(2.3 \pm 0.9) \times 10^3$	$(1.3 \pm 0.6) \times 10^3$

5. CONCLUSIONS

We conclude that the detection of the Standard Model Higgs decay $H \rightarrow \tau^+\tau^-$ in the intermediate m_H region is impossible because of overwhelming physical backgrounds. However, it has been shown that, in the case of non-standard Higgs scenarios, such as in the Minimal Supersymmetric Standard Model, this channel may be used to discover the pseudo-scalar Higgs, A^0 , in a similar mass range [3].

REFERENCES

- [1] R.K. Ellis, et al., Nucl. Phys. **B297** (1988) 221.
- [2] Z. Kunszt and W.J. Stirling, Higgs study group, these proceedings.
- [3] Z. Kunszt and F. Zwirner, Higgs study group, these proceedings.

FIGURE CAPTIONS

1. Invariant mass distribution for $\tau^+\tau^-$ pairs from $H \rightarrow \tau^+\tau^- \rightarrow e^\pm\mu^\mp 2\nu 2\bar{\nu}$ for $m_H = 100$ GeV (a) and 140 GeV (b). The normalization is arbitrary.
 2. Distribution of $\cos\Delta\phi(e\text{-}\mu)$, the azimuthal separation between electron and muon from $H \rightarrow \tau^+\tau^- \rightarrow e^\pm\mu^\mp 2\nu 2\bar{\nu}$ with $m_H = 140$ GeV.
 3. Invariant mass distribution for $\tau^+\tau^-$ pairs from $H \rightarrow \tau^+\tau^- \rightarrow e^\pm\mu^\mp 2\nu 2\bar{\nu}$ with $m_H = 140$ GeV using only the central calorimeter ($|\eta| < 3$).
 4. Invariant mass distribution for $\tau^+\tau^-$ pairs from $H \rightarrow \tau^+\tau^- \rightarrow e^\pm\mu^\mp 2\nu 2\bar{\nu}$ with $m_H = 140$ GeV for the case $\vec{p}_T^{\text{miss}} = -\vec{p}_T(e^\pm) - \vec{p}_T(\mu^\mp) - \sum \vec{p}_T^{\text{jet}}$.
 - a) $p_T^{\text{jet}} > 10$ GeV ; b) $p_T^{\text{jet}} > 20$ GeV. Jets are reconstructed using a cone algorithm with $R = \sqrt{\Delta\eta^2 + \Delta\phi^2} = 0.4$.
 5. Missing transverse momentum distribution, as expected for $m_H = 140$ GeV using the energy deposition in all calorimeter cells.
 6. Invariant mass distribution for $\tau^+\tau^-$ pairs reconstructed from $e^\pm\mu^\mp$ pairs produced in background processes.
 - a) $t\bar{t}$ production with $m_{\text{top}} = 130$ GeV;
 - b) Drell-Yan production of lepton pairs with invariant mass above 100 GeV;
 - c) Production of gauge boson (γ, W^\pm, Z) pairs.
- The normalizations are arbitrary.

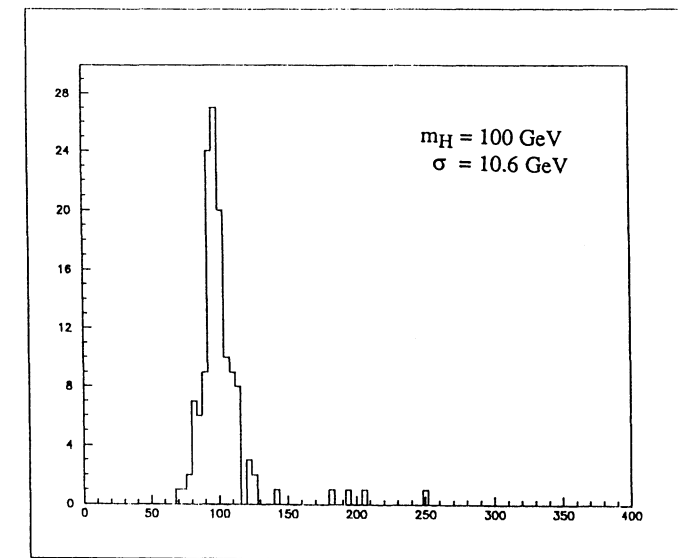


Fig. 1a

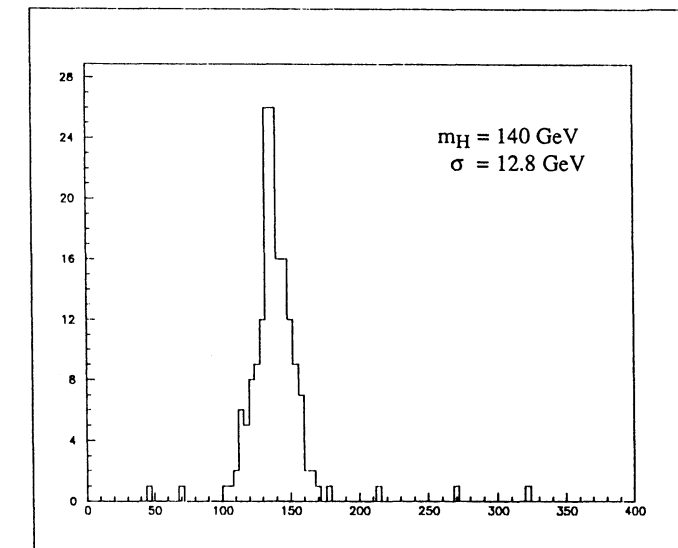


Fig. 1b

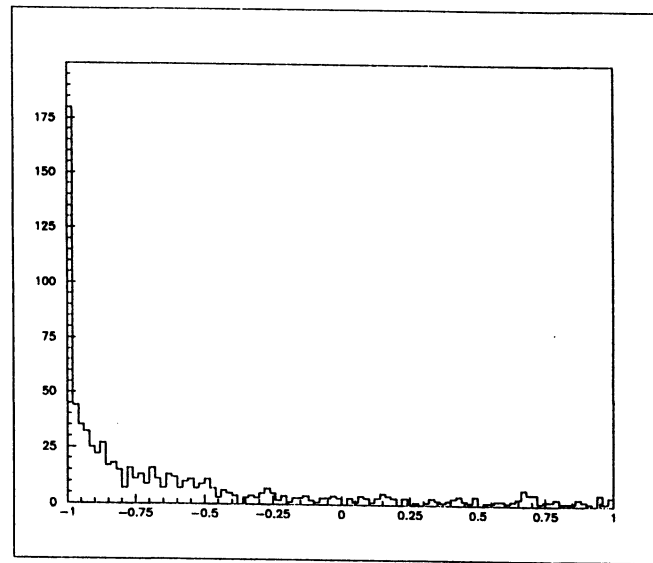


Fig. 2

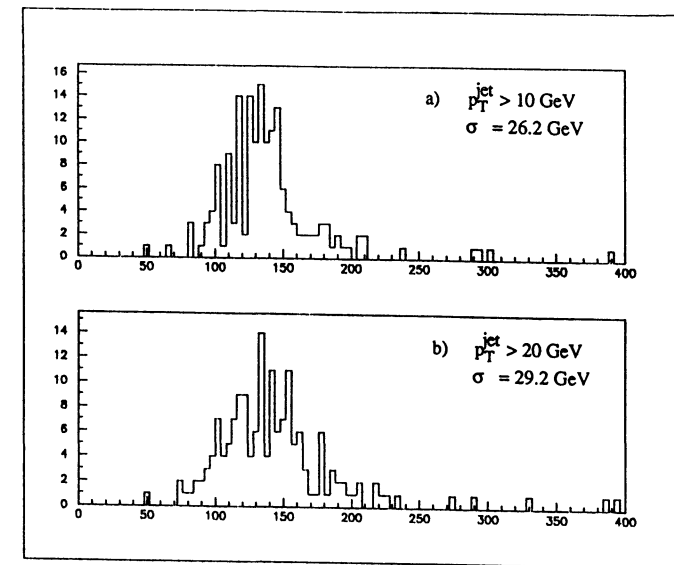


Fig. 4

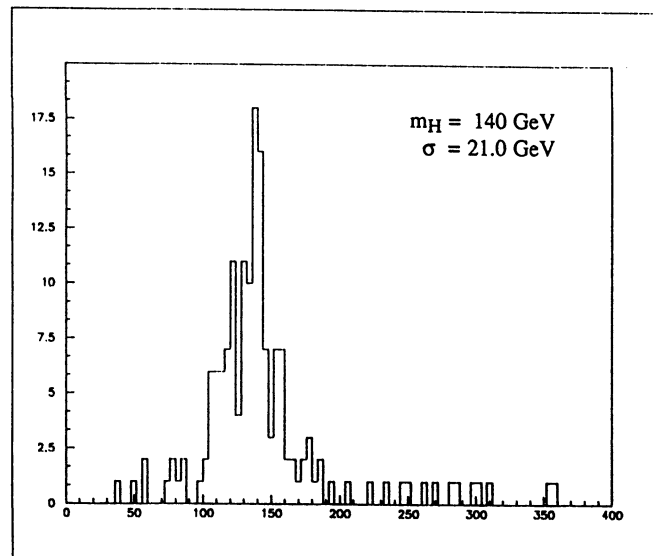


Fig. 3

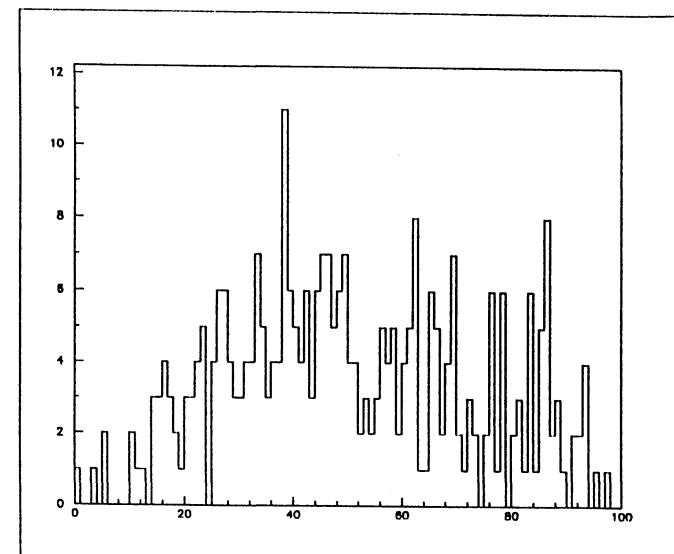


Fig. 5

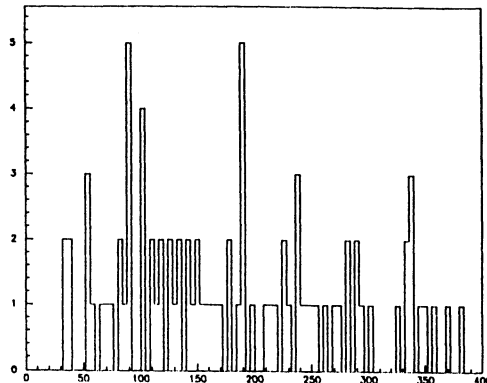


Fig. 6a

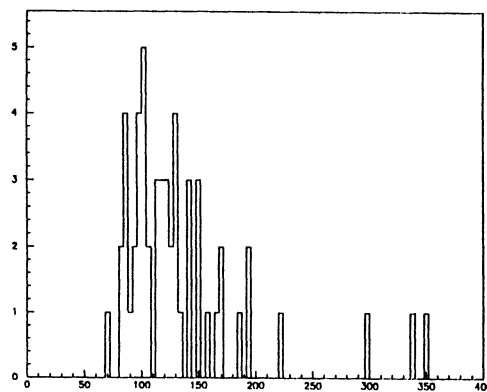


Fig. 6b

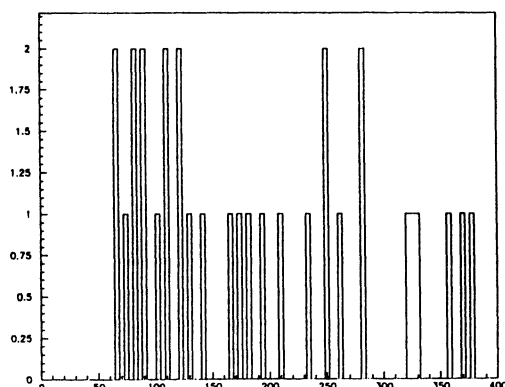


Fig. 6c

$H^0 \rightarrow \tau^+ \tau^-$ Detection at the LHC

K. Bos, NIKHEF-H, Amsterdam, The Netherlands
F. Anselmo* and B. van Eijk**^{***}, CERN, Geneva, Switzerland

1. Introduction

In the search for the intermediate mass Higgs ($M_W \leq m_H \leq 2M_W$), two Higgs decay channels are particularly interesting. Although the branching ratio for $H^0 \rightarrow \gamma\gamma$ is relatively small (0.1 - 0.2 %), the signature of this channel is rather distinct and as it seems, estimates for the signal to background ratio show that this decay channel has a chance to be disentangled from its backgrounds [1]. The second channel on the contrary, has a relatively large branching ratio ~ 6.5 % (depending on the Higgs mass) and has a distinct signature as well: $H^0 \rightarrow \tau^+ \tau^-$. In the following the reaction $pp \rightarrow H^0 X \rightarrow \tau^+ \tau^- X$ is studied for the case that each tau decays semileptonically into a muon or electron plus two neutrinos. The branching ratio for a tau to decay into electron or muon is ~ 18 %. Detection of both electrons and muons therefore doubles the branching ratio and hence increases the signal by a factor four if one allows for combinations like $e^+ \mu^-$ etc.. Thus, the events to look for contain two (opposite !) charged isolated leptons plus missing energy caused by the escaping 4 neutrinos.

In the analysis presented in this paper we limit ourselves to one of the main backgrounds, that is events originating from $t\bar{t}$ (for a more detailed study, we refer the reader to ref. [2]), where both top quarks decay into a W plus a bottom quark and subsequently the W s decay semileptonically into lepton (e, μ) plus neutrino. Such events also have at least two (often isolated) charged leptons and missing energy in the final state but, in addition, will contain two bottom quark jets with energies strongly dependent on the value of the top quark mass. Additional jets will occur in both signal and background processes due to initial state gluon emission. Therefore, signal and background event topologies will differ in jet multiplicity mainly due to the presence of bottom quark jets in the background process.

The branching ratio for the $H^0 \rightarrow \tau^+ \tau^-$ channel rapidly decreases when the mass of the Higgs exceeds $125 \text{ GeV}/c^2$. This drop in rate is the result of the growing importance of the decay $H^0 \rightarrow W f\bar{f}$, where the $f\bar{f}$ results from the decay of a virtual W [3]. Initially, for this study we set the mass of the Higgs to $110 \text{ GeV}/c^2$. Such a low value for the Higgs mass also makes its production cross-section relatively high compared to the one for larger Higgs masses. A still lower value than $110 \text{ GeV}/c^2$ moves the H^0 into the (Breit-Wigner) tail of another serious background, namely, direct production of Z^0 gauge bosons in which case it becomes extremely difficult to distinguish the two observable leptons in the Higgs decay from the two leptons originating from $Z^0 \rightarrow \tau^+ \tau^-$ decays. The large rate and similar event topology for this type of background, will clearly overwhelm the signal.

A larger value for the top quark mass also favours the case for the $H^0 \rightarrow \tau^+ \tau^-$ channel for several reasons. First, a large top quark mass reduces the background cross-section $pp \rightarrow t\bar{t} X$ considerably. Secondly, the b-jet from the decay of the top quark will become harder, which will make it easier to select $t\bar{t}$

* Cern/LAA Project, Geneva, Switzerland.

** Supported by the 'Netherlands Organization for Scientific Research (NWO)', The Netherlands.

events. For this study, we have chosen the most 'favourable' scenario, $m_t = 200 \text{ GeV}/c^2$.

The outline for this paper is as follows. In section 2 we discuss the method of reconstructing the Higgs mass from the experimental observables. We present a comparison between different parton shower models and an exact $O(\alpha_s^3)$ calculation for the main production process (gluon - gluon fusion) and estimate the contributions from boson - boson fusion mechanisms. The third section discusses the implications which the different models will have on the distributions of the experimental observables. We discuss detailed cross-section estimates before and after cuts on event topologies together with background calculations. Finally, we present some preliminary conclusions and make some general remarks about future work that we plan to do in this field.

2. Higgs at large p_t

Only semileptonic tau decays into an electron or muon are considered here. The Feynman diagram for this decay process is depicted in the figure below:

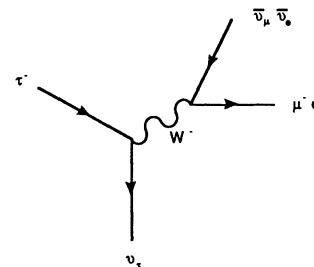


Fig. 1: Feynman diagram for the semileptonic (weak) decay of the τ -lepton.

Due to the large Higgs mass, the mass of the tau is small compared to its energy. Lepton masses will be irrelevant as well. Given the large Lorentz boost which the taus receive in the Higgs decay, the direction of each tau can be well approximated by the direction of the charged lepton. Along the same line of argument, the direction of the missing energy in the transverse plane will be the resultant vector of the neutrinos from each tau decay, which also point in the direction of the charged leptons. In the limit where all particle masses ~ 0 , one is now able to reconstruct the individual transverse components of the neutrino momenta ($p_{\nu_i}^\perp$) provided the two charged leptons are not collinear.

$$\begin{aligned} p_t^{\nu_1} \frac{p_x^{\nu_1}}{|p_t^{\nu_1}|} + p_t^{\nu_2} \frac{p_x^{\nu_2}}{|p_t^{\nu_2}|} &= p_x^{\text{miss}} \\ p_t^{\nu_1} \frac{p_y^{\nu_1}}{|p_t^{\nu_1}|} + p_t^{\nu_2} \frac{p_y^{\nu_2}}{|p_t^{\nu_2}|} &= p_y^{\text{miss}} \end{aligned} \quad (1)$$

When the Higgs has no or only little transverse momentum, the opening angle between the two tau leptons will in general be large due to the isotropic decay of the scalar Higgs. An invariant mass reconstruction will therefore be impossible. Thus for a Higgs produced at large transverse momentum the mass can be rather accurately reconstructed. In [4, 5] it is argued that a resolution of order $10 \text{ GeV}/c^2$ is needed in the tau pair invariant mass to distinguish the signal from the background continuum. After all, for the quoted Higgs mass range, the full width half maximum is relatively small.

In figure 2 the two lowest order (QCD type of) diagrams are given on which the Isajet [6] and Pythia [7] event generators base their calculation of the cross-section for the signal.

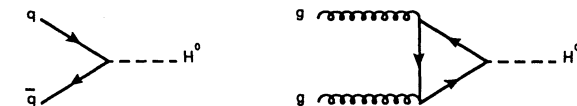


Fig. 2: Feynman diagrams for the lowest order contributions to Higgs production in hadronic interactions. The gluon fusion mechanism gives by far the largest contribution.

Both programs introduce initial state gluon radiation by reconstructing parton cascades after the hard scattering process is treated. At each branching, the partons may obtain a transverse momentum which finally results in an overall transverse motion of the hard scattering process.

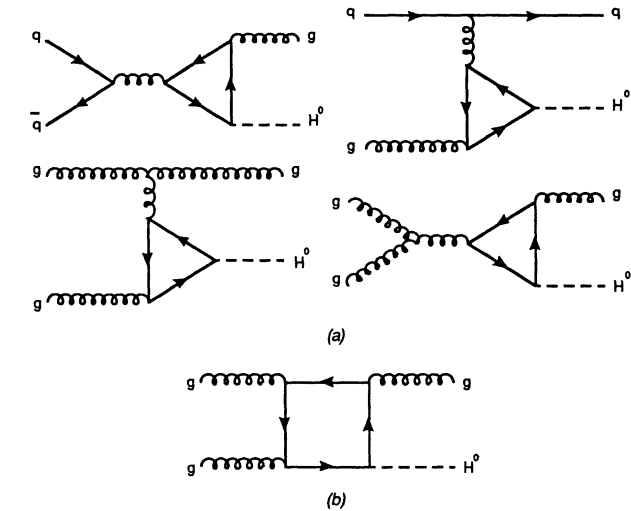


Fig. 3: Feynman diagrams ('crossed' diagrams are not shown) for the next to leading order contributions to Higgs production in hadronic interactions. Again, the gluon fusion mechanism dominates in most kinematical regions.

In order to test this approach, which is known to work quite well in the limit where partons are emitted collinearly, we have introduced the fixed order QCD calculation for the next to leading order contribution to the cross-section [5] in Eurojet [8]. Contributing Feynman diagrams are presented in figure 3^a and 3^b. Note that the class of box diagrams (3^b) can not so easily be implemented in a parton shower approach. Apart from the Higgs production processes described above, we have investigated the relevance of the boson - boson fusion mechanisms to our signal. Pythia includes an approximate description (reasonably accurate for very large Higgs masses) for these processes, which overestimates the cross-section for our choice of parameters by a factor ~ 2 . Nevertheless, we do not expect that event topologies are very sensitive to whether or not one uses exact or approximate formulae. Moreover, the magnitude of this mechanism is relatively small for a Higgs of 110 GeV/c² with a transverse momentum less than 100 GeV/c as illustrated in figure 4.

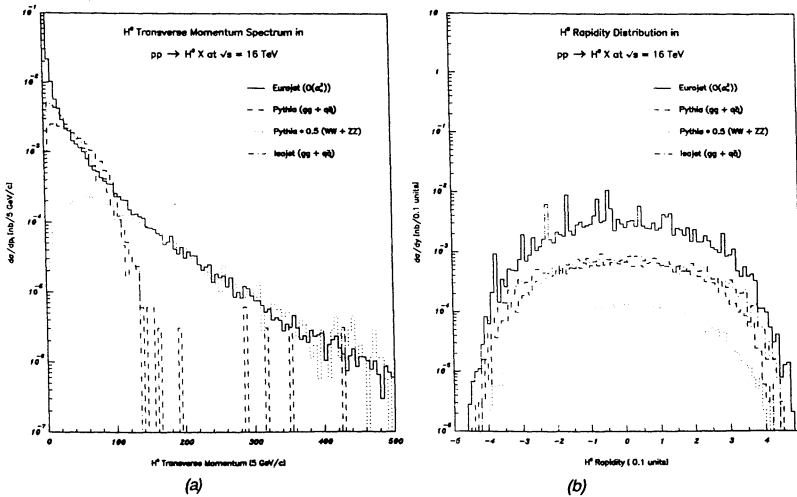


Fig. 4: Comparison of Higgs transverse momentum (a) and Higgs rapidity (b) distributions from Eurojet (drawn line), Pythia (dashed line), Pythia boson - boson fusion (dotted line, scaled by a factor .5 in order to obtain the correct cross-section) and Isajet (dotted - dashed line).

In all calculations the EHLQ (set 1, $\Lambda = 290$ MeV) [9] structure functions were selected. The scale at which α_s and the structure functions are evaluated was set to \sqrt{s} . For the Eurojet calculation (note that we did not include the boson - boson fusion mechanism here!) this choice is rather arbitrary (conservative) and can only be verified when the $O(\alpha_s^4)$ calculation becomes available [5]. The Eurojet distribution (4^a) shows a quite different behaviour at large $p_t^{H^0}$. At small transverse momentum the resummation of soft gluons is lacking which is however, not relevant for our further analysis as will be demonstrated later. The differences

between Pythia and Isajet for the qq , gg production processes are most likely the result of different implementations and phenomenology of the individual parton shower algorithms. The rapidity distributions do not show any significant differences. We conclude that at very large p_t , the parton shower algorithms should be used with care, while the boson - boson fusion mechanism becomes competitive at relative large $p_t^{H^0}$.

3. Background, lepton distributions and mass reconstruction

The most important background to the $H^0 \rightarrow \tau^+ \tau^-$ channel is $t\bar{t}$ production where each top quark decays into a b quark and a W and subsequently, the W decays semileptonically into a lepton plus a neutrino. Due to the relatively large mass of the top quark (200 GeV/c²), the W is likely to be produced close to its mass shell giving rise to isolated leptons. The cross-section for $t\bar{t}$ production at the LHC is ~ 0.5 nb. [8, 10], an order of magnitude larger than the Higgs cross-section ($\sigma \sim 30$ pb.). The semileptonic branching ratio for t - quarks into electrons or muons and neutrinos is in the parton model approximation $\sim 11.2\%$. This leads to a dilepton cross-section (before any cuts) of $\sigma * (BR)^2 \sim 6$ pb, which in turn gives a signal to background ratio of ~ 0.01 . The Eurojet calculation for $t\bar{t}$ uses the same set of structure functions (EHLQ-1) whereas the scale was chosen to be $Q^2 = p_t^2 + m_t^2$.

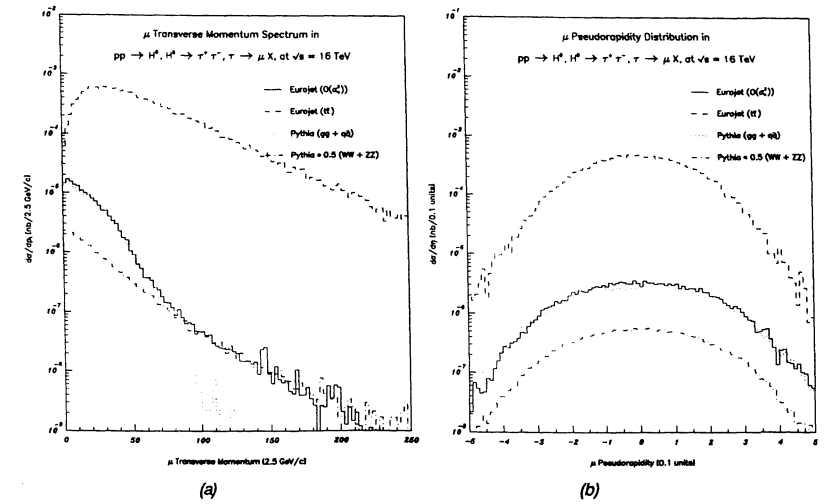


Fig. 5: Comparison of the muon transverse momentum (a) and pseudorapidity (b) distributions for the signal, Eurojet (drawn line), Pythia (dotted line), Pythia boson - boson fusion (dotted - dashed line, scaled by a factor .5 in order to obtain the correct cross-section) and one of the main backgrounds: $pp \rightarrow t\bar{t} X$.

The muon transverse momentum and pseudorapidity distributions for both background and signal are shown in figure 5. For Eurojet, we have introduced a cut of 10 GeV/c on the transverse momentum of the Higgs in order to keep the matrix elements well behaved (and thus excluding the region where the resummation of soft gluons becomes important). The program was interfaced with Eurodec [11] for parton fragmentation and particle decays. Both Eurojet and Pythia (and Isajet) give good agreement for p_t^H up to ~ 60 GeV/c. At larger p_t^H , the fixed order calculation and boson - boson fusion mechanism again become important. For completeness, we have calculated the opening angle (ϕ) between the muons in the transverse plane (fig. 6), requiring $p_t^H > 10$ GeV/c.

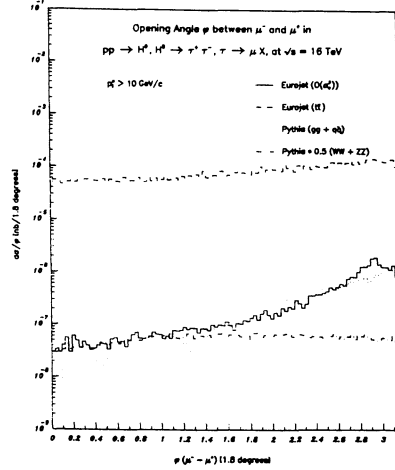


Fig. 6: Opening angle ϕ between the muons from the decaying taus and the two fastest muons in $pp \rightarrow t\bar{t} X \rightarrow \tau^+ \tau^- X$ demanding $p_t^H > 10$ GeV/c.

The missing transverse energy distributions are plotted in figure 7^a and look quite similar to the muon p_t distributions for the signal as presented in fig. 5^a. The background however, peaks at larger missing energies. An accurate measurement of missing transverse energy can only be achieved when the probability for pile-up of energy in the calorimeter due to multiple interactions remains relatively small (luminosities less than 10^{33} cm 2 s $^{-1}$). Figure 7^b shows the Higgs invariant mass distribution after applying minimal cuts on the muons (or electrons) $p_t^H > 10$ GeV/c and the missing energy, $E_t^{\text{miss}} > 10$ GeV. The clear resonance structure in the signal is overwhelmed by the background continuum by an order of magnitude.

The event topology of the background is quite different from the signal as demonstrated by analyzing the jet multiplicity distributions as given in figure 8. The first distribution (8^a) represents the jet multiplicity assuming a jet to have at least 25 GeV transverse energy in a cone of $\Delta R = 0.7$ (defined in the plane of pseudorapidity - azimuthal angle). The distribution in 8^b is obtained requiring a jet transverse energy of at least 50 GeV.

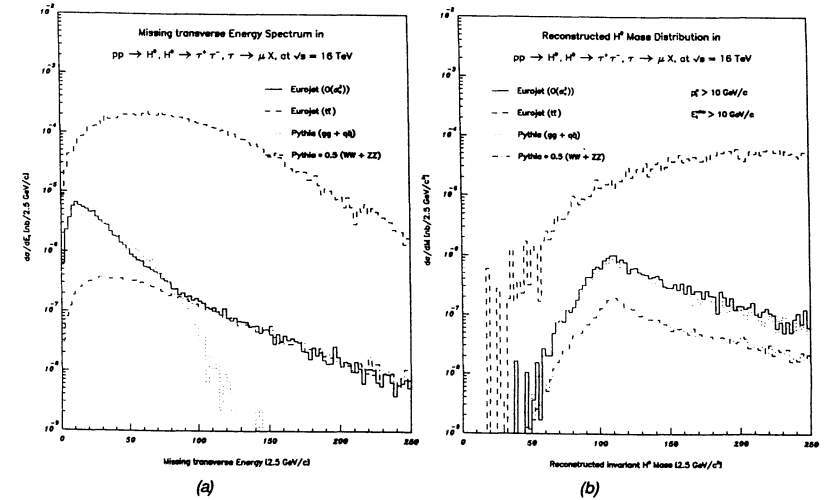


Fig. 7: Missing transverse energy distributions for signal and background (a) and reconstructed invariant Higgs mass (b) requiring $p_t^H > 10$ GeV/c and $E_t^{\text{miss}} > 10$ GeV.

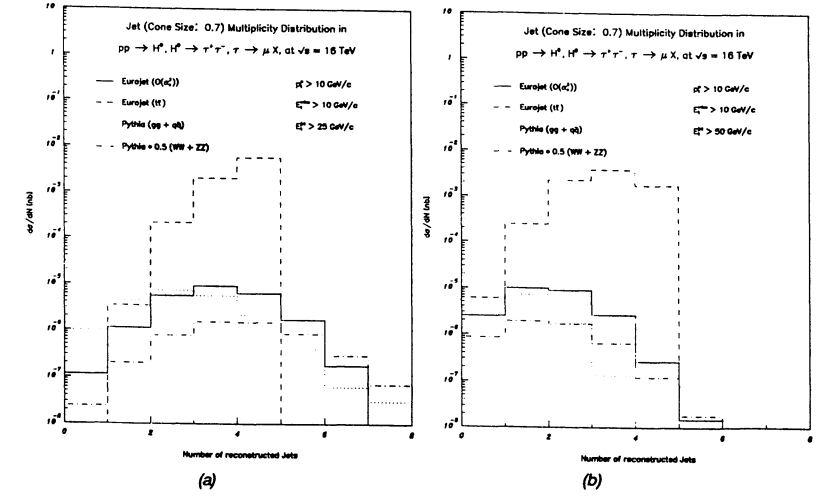


Fig. 8: Jet multiplicity (cone size in $\Delta R = 0.7$) demanding $E_t^{\text{jet}} > 25$ GeV (a) and the number of reconstructed jets with $E_t^{\text{jet}} > 50$ GeV (b).

We used a modified 'LUCELL' jet finding algorithm [12], for which we introduced a calorimeter with 10000 cells (2π coverage in ϕ , ± 3 units in pseudorapidity). The minimum transverse energy for a cell to be considered as a potential jet initiator has been set to 1.5 GeV. A jet was required to have at least a total transverse energy of 15 GeV. No smearing effects (experimental resolutions) are included.

Depending on the jet energy, the first two bins (8^{th}) or the first bin (8^{th}) indicate a huge background reduction by a simple cut on the event topology. One should be aware that both Eurojet distributions are conservative estimates since for the signal (background) only the $O(\alpha_s^3)$ ($O(\alpha_s^2)$) contributions have been included. The reconstructed invariant Higgs mass distributions demanding only 1 jet with $E_t > 25$ GeV or only 1 jet with $E_t > 50$ GeV/c are displayed in fig. 9^a and 9^b respectively.

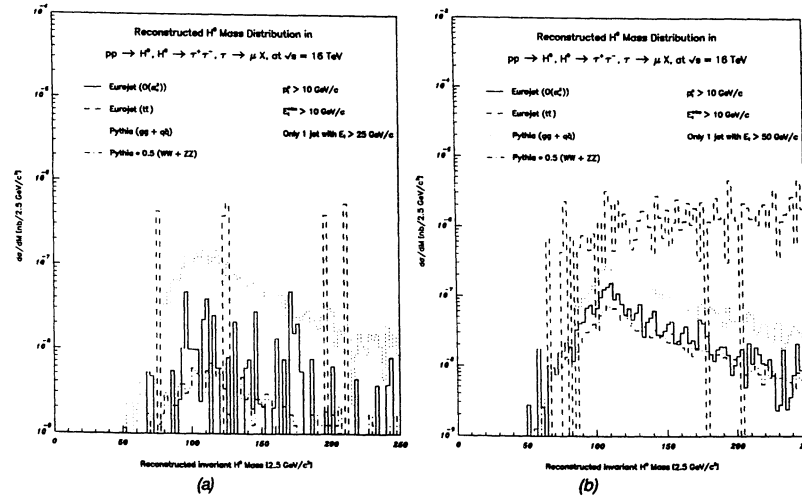


Fig. 9: Reconstructed invariant Higgs mass distributions ($p_t^H > 10$ GeV/c and $E_t^{\text{miss}} > 10$ GeV) requiring one single jet with: $p_t^{\text{jet}} > 25$ GeV/c (a) or 1 jet with: $p_t^{\text{jet}} > 50$ GeV/c (b).

Comparison of these plots with the distributions presented in fig. 7^b show (for both jet conditions) a considerable reduction in background. An increase of the minimum jet energy to 50 GeV or demanding two jets with $E_t > 25$ GeV each (not plotted), show a similar trend, however, less pronounced. Larger statistics should be obtained for $t\bar{t}$ and a careful tuning of topology cuts remains to be done, but nevertheless, results appear to be encouraging.

4. Conclusions

Except for the tail of the Higgs transverse momentum distribution, both parton shower programs, Pythia and Isajet, compare well with the exact calculation by J.J. van der Bij et al. as implemented in the Eurojet program.

With a minimal set of cuts ($p_t^H > 10$ GeV/c, $E_t^{\text{miss}} > 10$ GeV and demanding only 1 jet with $E_t > 50$ (25) GeV) we find for one year of running at the moderate luminosity of 10^{33} cm^{-2} and assuming a liberal (favourable ?) choice of as yet experimentally undetermined quantities ($m_t = 200$ GeV/c 2 , $m_H = 110$ GeV/c 2), about 5 (10) dimuon events, with a strong reduction of the dominant $t\bar{t}$ background. If we allow for e - μ and e - e combinations, this sample increases to ~ 20 (40) events per year. A more detailed study of the backgrounds, including $Z^0 \rightarrow \tau^+ \tau^- \rightarrow e \mu$ and $W W \rightarrow e \mu$, is reported on in ref. [2].

In our analysis we have not yet explored the application of any explicit isolation criterion on the leptons. Whether this may increase the signal to background ratio without cutting away too much of the signal remains to be seen. However, the main result of this study shows that the dominant background from $t\bar{t}$ events to the $H^0 \rightarrow \tau^+ \tau^-$ decay can be considerably reduced by jet energy and jet multiplicity cuts.

References

- [1] C. Seez, Higgs study group, these proceedings,
R. Kleiss, Z. Kunszt and J. Stirling, Durham Report DTP/90/54, Zürich Report ETH-TH/90-29 (1990).
- [2] F. Anselmo, K. Bos and B. van Eijk, NIKHEF Report NIKHEF-H/91-01, in preparation,
L. Di Lella, Higgs study group, these proceedings.
- [3] Z. Kunszt and W.J. Stirling, Higgs study group, these proceedings.
- [4] J. J. van der Bij, private communication.
- [5] R.K. Ellis, I. Hinchliffe, M. Soldate, J.J. van der Bij, Nucl. Phys. B297 (1988) 221.
- [6] Isajet Version 6.35, F. Paige, S. D. Protopopescu, BNL-38774 (1986).
- [7] Pythia Version 5.4, H.U. Bengtsson and T. Sjöstrand, Comp. Phys. Comm. 46 (1987) 43.
- [8] Eurojet Version 3.1, F. Anselmo and B. van Eijk, Cern Program Library Long Write-Up W5048 (in preparation),
A. Ali, B. van Eijk and I. ten Have, Nucl. Phys. B292 (1987) 1.
- [9] E. Eichten et al., Rev. Mod. Phys. 56 (1986) 579
- [10] E. Reya, Top study group, these proceedings.
- [11] Eurodec Version 3.1, B. van Eijk, Cern Program Library Long Write-Up W5048.
- [12] Jetset Version 7.3, T. Sjöstrand and M. Bengtsson, Comp. Phys. Comm. 43 (1987) 367.

Intermediate mass Higgs search

$$\text{pp} \rightarrow \text{ZH} ; \text{WH}$$

Resolution and pile-up studies

Higgs Study Group

L. Poggioli

We report on the search for an intermediate mass Higgs (decaying into 2 jets), when produced in association with a Z (decaying into a lepton pair), or a W (decaying into lepton+neutrino). The case of b -tagging is investigated.

We then study the influence of the resolution of the hadronic calorimeter on the dijet mass resolution. In particular we investigate the effects of pile-up at high luminosity. And finally we study the boson pair production (ZZ or ZW where one Z decays into a lepton pair and the other boson decays into 2 jets). This study then concludes on the relevance of hadronic calorimeter resolution in the Higgs physics sector at LHC.

1 Intermediate mass Higgs search

1.1 Basics

In the range of mass $M_Z \leq M_H \leq 2M_Z$ the Higgs boson decays predominantly into 2 jets. To be able to trigger on this process, especially when running at high luminosity, but also and mainly to have a chance to extract a hadronic Higgs decay from the huge QCD background, one selects the associate production of a Z decaying into 2 leptons. The case of an associated W decaying into lepton+neutrino is far more difficult to trigger on and can probably only be investigated at low luminosity ($10^{33} \text{ cm}^{-2} \text{s}^{-1}$). One can also study ZZ or ZW production, which are potentially very useful channels for calibrating the calorimeter.

1.2 Cross-sections

For the ZH production, we choose, as an example, $M_H = 120 \text{ GeV}/c^2$, which is not too close to the Z and W masses. We thus have $\sigma(pp \rightarrow ZH) = 0.6 \text{ pb}$ [1]. Including the branching ratios of H in 2 jets (81%), and Z into 2 leptons (6.8%), one gets $\sigma * B(pp \rightarrow ZH) = 0.033 \text{ pb}$.

For the ZZ production, taking into account $qq \rightarrow ZZ$ and $gg \rightarrow ZZ$, one has [2] $\sigma(pp \rightarrow ZZ) = 14.4 \text{ pb}$. Including the branching ratios, one obtains $\sigma * B(pp \rightarrow ZZ) = 1.37 \text{ pb}$.

For the ZW production, starting from a cross-section of 30 pb , and accounting for the branching ratios, one obtains $\sigma * B(pp \rightarrow ZW) = 1.36 \text{ pb}$.

The major source of background comes from $Z + 2jet$ production. Using the EKS Monte-Carlo program [3] one obtains :

$$\sigma(Z + 2\text{jets}, Z \rightarrow l^+l^-, P_T^j \geq 30 \text{ GeV}/c, \omega_{jj} \geq 20^\circ) = 212 \text{ pb}$$

where P_T^j is the minimum transverse momentum of the outgoing jets, and ω_{jj} is the minimum angle between the 2 jets produced. The uncertainty on this cross-section is of course very large due to the low threshold on P_T^j .

Another potentially important source of background when combined with pile-up at high luminosity ($\geq 10^{34} \text{ cm}^{-2} \text{s}^{-1}$), is the $Z + 1jet$ production. The cross-section (for $P_T^j \geq 30 \text{ GeV}/c$) is in this case 526 pb .

1.3 Procedure

For the generation of events we used the PYTHIA 5.4 Monte-Carlo program for ZH, ZZ, ZW [4]. For the background processes the EKS Monte-Carlo program has been used.

The study was done at the particle level without any GEANT simulation. We considered a calorimeter covering the rapidity range $|\eta| \leq 3$, and 2π in azimuth. It was divided in cells of size $\Delta\eta * \Delta\phi = .06 * .126$. For reconstructing jets we used a standard jet algorithm collecting energies in cells around a local maximum within a cone $\Delta R^{\text{cone}} = \sqrt{\Delta\eta^2 + \Delta\phi^2} = 0.4$. The efficiency for lepton identification was assumed to be 90%. Electrons were smeared in energy according to $\sigma/E = 13\%/\sqrt{E} \oplus 1\%$. For jets, different hadron responses were studied, as discussed in the following.

For the event selection we used 3 cuts :

1. We required the two final state leptons to be isolated, i.e. that their distance to any reconstructed jet, $\Delta R_{l,jet} \geq 0.4$.
2. We required the two final state leptons to be produced within $|\eta| \leq 3$ and with $P_T \geq 20 \text{ GeV}/c$, and the invariant lepton mass to match the Z mass within $\pm 5 \text{ GeV}/c^2$.
3. We finally required at least 2 reconstructed jets within $|\eta| \leq 3$ and with $P_T^j \geq P_T^{\text{cut}}$. The value of P_T^{cut} will be discussed later.

The effects of these cuts are summarized in Fig. 1.

1.4 Results

We will first discuss the results for an integrated luminosity of 10^4 pb^{-1} (1 year of running at $10^{33} \text{ cm}^{-2} \text{s}^{-1}$). With the choice $P_T^{\text{cut}} = 30 \text{ GeV}/c$, the reconstructed dijet mass M_{jj} is displayed in Fig. 2, assuming an ideal resolution for the calorimeter. One sees that the reconstructed Z mass is found to be $105 \text{ GeV}/c^2$, and that the distribution is quite broad ($\sigma = 10.9 \text{ GeV}/c^2$). These two effects come from energy escaping the chosen cone due to the soft fragmentation of the b-quarks and neutrinos. We therefore computed the expected signal and background in a mass bin of $105 \pm 30 \text{ GeV}/c^2$.

We obtain, after all cuts, a signal S for ZH and a background B from Z+2jets (in events per year):

$S(ZH) = 55$ and $B(Z + 2\text{jets}) = 124000$ yielding a significance $S/\sqrt{B} = 0.16$. We conclude from this that, even in the best of cases, i.e. for 10^5 pb^{-1} and ignoring pile-up effects, the observation of a Higgs signal in this channel is hopeless.

An interesting possibility, but presumably only at low luminosity ($\simeq 10^{33} \text{ cm}^{-2} \text{s}^{-1}$), would be b-quark tagging, since 90% of the jets from Higgs decay are b-quarks. If we introduce a tagging efficiency ϵ_b , and a misidentification factor R_b , we can compute new values S' and B' for S and B :

$$S' = S * B(H \rightarrow b\bar{b}) * \epsilon_b^2$$

$$B' = B(Zb\bar{b}) * \epsilon_b^2 + B(Zjj)/R_b^2$$

where the cross-section for $B(Zb\bar{b})$ has been computed using the calculation of [5], $\sigma(Zb\bar{b}) = 2.7 \text{ pb}$. Assuming optimistic values of $\epsilon_b = .9$ and $R_b = 10$, one gets $S' = 40$, and $B' = 2800$, which gives $S'/\sqrt{B'} = 0.75$, still a hopeless situation, even at higher luminosities. We note that it does not help much to improve the rejection factor R_b since B' is dominated by $Zb\bar{b}$ production.

We have also studied the WH channel, where the W decays into lepton+neutrino. This channel is much more difficult to trigger on than the ZH channel, and can probably only be investigated at low luminosity. Compared to the ZH case, the signal is increased by a factor 6, while the Wjj background is 10 times larger than $B(Zjj)$, which yields a significance $S/\sqrt{B} = 0.3$, still a hopeless situation.

It seems in this case that b-tagging would improve the situation a lot, mainly because $B(Wb\bar{b}) = B(Zb\bar{b})$. With the same notations as for the ZH case, we find $S' = S * 6$

$$B' = B(Wb\bar{b}) * \epsilon_b^2 + B(Wjj)/R_b^2,$$

with $B(Wb\bar{b}) = B(Zb\bar{b})$ and $B(Wjj) = 10 * B(Zjj)$. In this case larger values of R_b would help, but unfortunately one has to account for the top background. One has $\sigma(t\bar{t}, m_t = 130 \text{ GeV}/c^2) = 4.4 \text{ nb}$, with top decaying into Wb [6]. This yields $\sigma(t\bar{t} \rightarrow WWb\bar{b}X) = 2 \text{ nb}$, with $W \rightarrow l\nu$, which means that the irreducible background from $Wb\bar{b}$ final states (i.e. first term in the B' expression) is overwhelming, leading to a significance S/\sqrt{B} of 0.25. The situation remains hopeless.

2 Resolution studies

We now study the effect of the resolution of the hadronic calorimeter on the dijet mass reconstruction. We have seen in the previous section that the intrinsic resolution on M_{jj} for $H \rightarrow jj$ is of the order of $11 \text{ GeV}/c^2$ due to b-quark fragmentation effects (Fig. 2).

We now study the mass spectrum for W and Z decays into 2 jets for ZW and ZZ production with one Z decaying into 2 leptons. As shown in Fig. 3, assuming a calorimeter with ideal resolution, the r.m.s. of each reconstructed peak is of the order of $3 \text{ GeV}/c^2$. However, even before including detector resolution the two signals merge, and the resulting σ is $6.5 \text{ GeV}/c^2$ (Fig. 4). This value increases

slightly to $7 \text{ GeV}/c^2$ for a very good calorimeter (i.e. $\sigma/E = 30\%/\sqrt{E} \oplus 1\%$) and goes up to $11 \text{ GeV}/c^2$ for a very crude calorimeter (i.e. $\sigma/E = 100\%/\sqrt{E} \oplus 4\%$).

We have also investigated the case of the production of a heavy Higgs ($M_H = 800 \text{ GeV}/c^2$), decaying into ZZ , with $Z \rightarrow l^+l^-$ and $Z \rightarrow jj$. We first required $P_T^j \geq 100 \text{ GeV}/c$ which results in an acceptance of 60% for this large Higgs mass. As it can be seen in Fig. 5, the 2 quarks coming from the Z hadronic decay are nearby in space due to the large boost of the Z . We have therefore applied a cut $\Delta R^{jj} \leq 1.2$ (Fig. 6), to reduce the combinatorial background from other jets in the signal events (see also [7]).

One can see on Fig. 7 that the intrinsic width of the reconstructed Z hadronic decay is quite broad, $\sigma = 11.9 \text{ GeV}/c^2$. This is due to the fact that the jets are close in space and the fragmentation products thus mix. More sophisticated jet algorithms may possibly improve this result. The calorimeter resolution only slightly deteriorates the result ($\sigma = 13.1 \text{ GeV}/c^2$ for a crude calorimeter of resolution $\sigma/E = 100\%/\sqrt{E} \oplus 4\%$).

Obviously, a good granularity is needed to separate the 2 jets, but taking into account the high energy of the jets produced, a good granularity in the electromagnetic compartment is probably sufficient. More studies are needed to understand what is the optimum resolution one can hope for in this specific channel.

In conclusion, hadron calorimeter resolution does not seem crucial for the processes studied in this section.

3 Pile-up studies

The pile-up has been treated using minimum bias events generated by PYTHIA. The particle energies from the appropriate number of such events, depending on luminosity, were added to the cell energies for the signal. The results are presented in the following tables. The first column gives the number of expected events per year, the second one evaluates the relative importance of the combinatorial background, the third one the efficiency for seeing events in the peak around the Z mass. This peak is defined according to the mean value μ and the width σ of the dijet mass distribution. We have studied the influence of P_T^{cut} and ΔR^{cone} on the jet-jet mass resolution for two of the channels studied in the previous section :

First case : $H(800 \text{ GeV}/c^2) \rightarrow ZZ$

$\int L dt (\text{pb}^{-1})$	ΔR^c	# evts	$\frac{\# \text{ combinations}}{\# \text{ cuts}}$	$\frac{\# \text{ evts in peak}}{\# \text{ evts}}$	$\mu(\text{GeV})$	$\sigma(\text{GeV})$
10^4	.4	93	1.18	0.67	91.5	10.9
10^5	.4	1000	1.20	0.62	93.8	11.3
$4 \cdot 10^5$.4	4670	1.30	0.36	102.7	14.3
$4 \cdot 10^5$.3	4260	1.22	0.52	96.8	13.1

Second case : ZZ continuum

$\int L dt (pb^{-1})$	ΔR^c	# evts	# combinations # cuts	# cuts in peak # cuts	$\mu(GeV)$	$\sigma(GeV)$
10^4	.4	1600	1.74	0.43	86.5	5.13
10^5	.4	22560	1.96	0.42	96.0	11.0
$4 \cdot 10^5$.4	179700	6.54	-	-	-
$4 \cdot 10^5$.3	113400	2.80	0.38	102.9	12.0

We observe in both cases a shift in the dijet mass and a degradation in the resolution due to pile-up, as luminosity increases. These effects are smaller in Table 1 due to the high value of P_T^{cut} .

In the second case, as can be seen by comparing Fig. 8 (no pile-up) with Fig. 9 (with pile-up), the effect of pile-up is very striking : for $\Delta R^{cone} = 0.4$ the combinatorial background becomes very large and the signal disappears so one definitely needs to reduce the cone to a value of 0.3 (Fig. 9 and Table above).

Clearly pile-up effects deteriorate the resolution, which reinforces the conclusion of the previous section that the hadronic calorimeter resolution is not crucial.

4 Final study of $ZZ + ZW$ production

In this section we present results as a function of luminosity, for the reconstructed $ZZ + ZW$ signal.

$\int L dt (pb^{-1})$	ΔR^c	$P_T^{cut} GeV$	Mass bin GeV/c^2	S($ZZ + ZW$)	B($Z2j$)	B($Z1j$)	S/B	S/\sqrt{B}
10^4	.4	30	70 – 100	2120	60400	0	.035	8.6
10^5	.4	35	75 – 120	21900	$1.22 \cdot 10^6$	444000	.017	17.0
$4 \cdot 10^5$.3	40	75 – 120	105000	$9.92 \cdot 10^6$	$7.58 \cdot 10^6$.0067	25.0

We note that the relative contribution of $Z + 1jet$ compared to $Z + 2jets$ increases with luminosity (due to pile-up). But nevertheless, even at the highest luminosity, the signal is observable with, however, a signal to background ratio 5 times worse than at $10^{33} cm^{-2}s^{-1}$. We also note that despite the small signal to background ratio, the ZW and ZZ signals should nevertheless be observable at LHC, as has been demonstrated in similar conditions at the CERN $p\bar{p}$ collider [8]. Fig. 10 shows the signal and background distributions for the reconstructed dijet mass for one year of running at a luminosity of $10^{34} cm^{-2}s^{-1}$ (the ZH signal has been included for completeness).

5 Conclusions

The observation of an intermediate mass Higgs via ZH or ZW is impossible at LHC or SSC. This remains true even with b-quark tagging.

The resolution of the hadronic calorimeter is not crucial in the standard model Higgs sector.

A signal from ZZ or ZW pair production, with $Z \rightarrow l^+l^-$ and $W, Z \rightarrow jj$, is observable above background at LHC, even at the highest luminosity, and could provide a useful signal to study the hadron calorimeter performance with real data.

Acknowledgements

From providing generated 4-vectors to correcting the draft, Daniel Froidevaux had been supervising this study. I am deeply indebted to him for his constant help.

References

- [1] Z. Kunszt and W.J. Stirling, Higgs study group, these proceedings.
- [2] E.W.N. Glover and J.J. Van der Bij, Phys. Lett. **219B** (1989), 488, and Nucl. Phys. **B321** (1989), 561.
- [3] S.D. Ellis, R. Kleiss and W.J. Stirling, Phys. Lett. **203B** (1988), 172.
- [4] H.V. Bengtsson and T. Sjöstrand, Comp. Phys. Comm. **46** (1987), 43.
- [5] R. Kleiss, event generator study group, these proceedings;
see also M. Della Negra et al., Higgs study group, these proceedings.
- [6] L. Fayard et al., top study group, these proceedings.
- [7] M.H. Seymour, Higgs study group, these proceedings.
- [8] UA2 Coll., J. Alitti et al., CERN-PPE/90-105, to be published in Z. Phys. C.

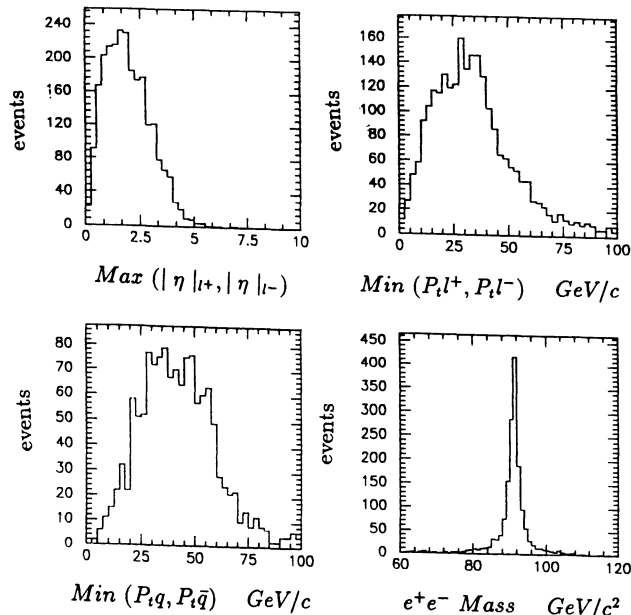


FIG. 1 Acceptance cuts shown for the ZH signal.

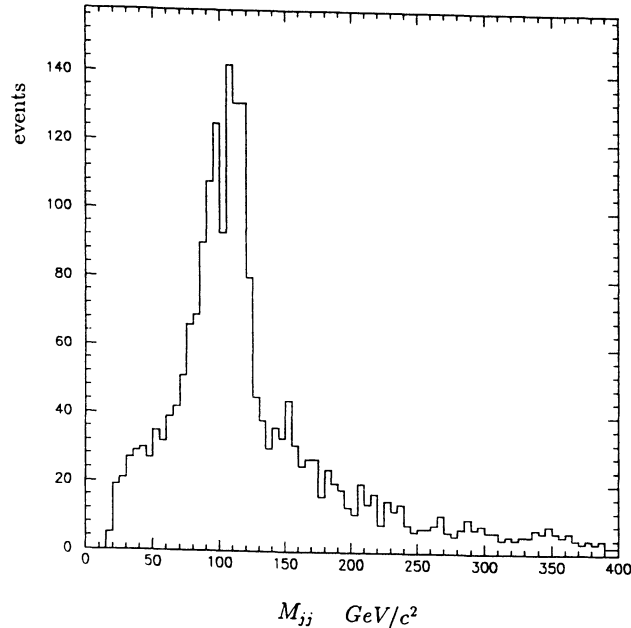


FIG. 2 Dijet mass spectrum for Z production in the ZH channel. The mean value is at $105 \text{ GeV}/c^2$, and the r.m.s. is $\sigma = 10.9 \text{ GeV}/c^2$.

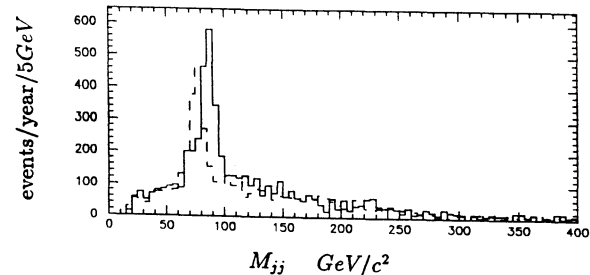


FIG. 3 Dijet mass spectrum for ZZ (solid line) and ZW (dashed line) for a luminosity of 10^4 pb^{-1} . The W mass peaks at $77 \text{ GeV}/c^2$ and the Z one at $87 \text{ GeV}/c^2$.

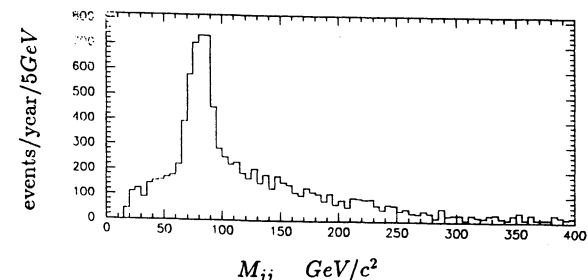


FIG. 4 Same as above with the W and Z signals merged, $\sigma = 6.5 \text{ GeV}/c^2$.

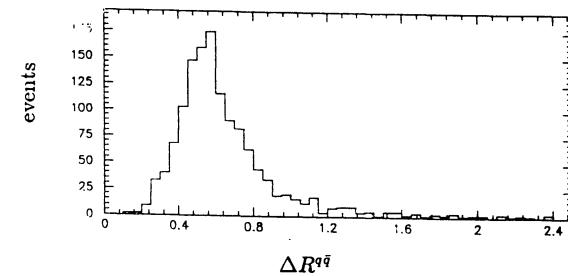


FIG. 5 Heavy Higgs production. ΔR between the 2 quarks coming from the Z decay.

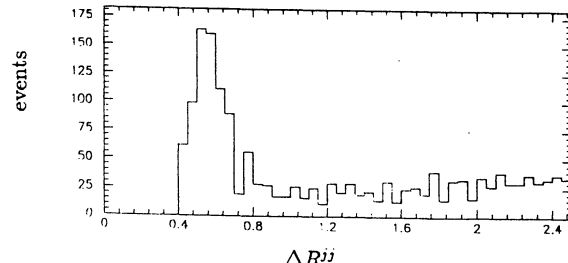


FIG. 6 Same as above for reconstructed jets in the final state.

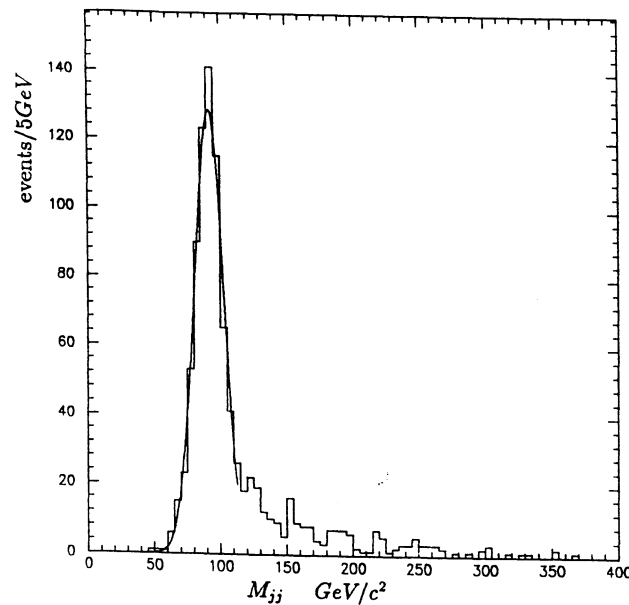


FIG. 7 $H \rightarrow ZZ \rightarrow lljj, M_H = 800 \text{ GeV}/c^2$. Dijet mass spectrum after a cut $\Delta R^{jj} \leq 1.2$. The mean value is $91.5 \text{ GeV}/c^2$ and $\sigma = 10.9 \text{ GeV}/c^2$.

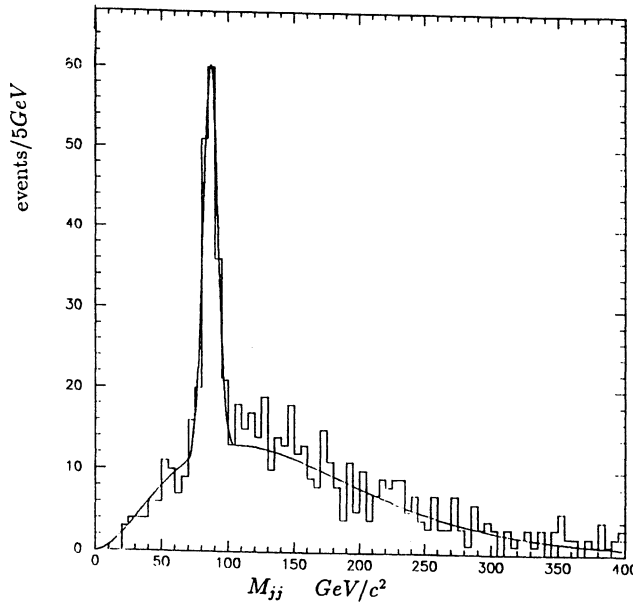


FIG. 8 Dijet mass spectrum in the ZZ channel, without pile-up. The mean value is $86.5 \text{ GeV}/c^2$ and $\sigma = 5.1 \text{ GeV}/c^2$.

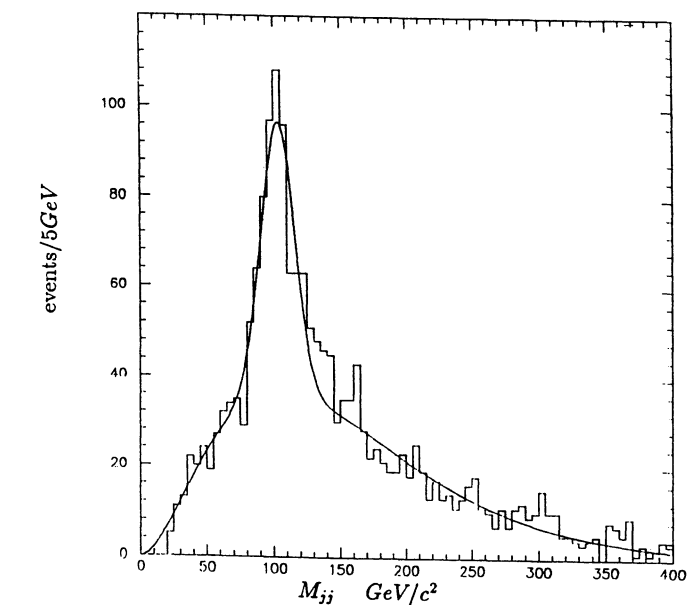


FIG. 9 Same as Fig. 8, with 40 minimum bias events added, and $\Delta R^{\text{cone}} = 0.3$. The mean value is $102.9 \text{ GeV}/c^2$ and $\sigma = 12.0 \text{ GeV}/c^2$.

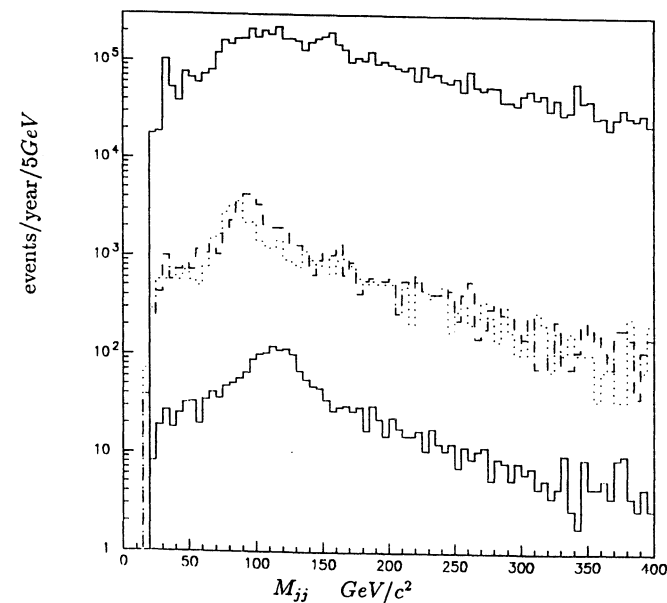


FIG. 10 Dijet mass spectrum for an integrated luminosity of 10^5 pb^{-1} . Are shown the distributions from ZH (bottom), ZW (dotted), ZZ (dashed) and the background $Z\ 2jet + Z\ 1jet$ (top).

Tagging A Heavy Higgs Boson

M.H. Seymour

Cavendish Laboratory, University of Cambridge,
Madingley Road, Cambridge CB3 0HE, U.K.

Abstract

Applications of small-angle detectors to the search for a heavy Higgs boson are discussed, with particular reference to the tag jets (ie. high-energy, small-angle jets) expected from the WW fusion mechanism. It is found that the technique can be used to enhance the semi-leptonic channel $H \rightarrow WW \rightarrow \ell\nu jj$, and can produce a 6σ effect for a Higgs mass of $m_H = 1000$ GeV, an integrated luminosity of $\int \mathcal{L} = 10^5 \text{ pb}^{-1}$, and a centre-of-mass energy of $\sqrt{s} = 16$ TeV.

1. Introduction

In this talk I present preliminary results from a study into jet tagging of WW events, using the parton shower program HERWIG. The latest version of this program contains the full s -channel matrix element for the WW fusion Higgs production mechanism, and simulates W plus multijet production using a parton shower algorithm, using the W + 1jet matrix element as a starting point. Broadly speaking the results confirm the earlier parton level studies[1,2].

I begin by reviewing the motivation for searching for a heavy Higgs boson, and the need for forward jet tagging, before presenting the results of the present study. Finally I consider the effect that more realistic detector parameters might have on the results.

2. Motivation

If the Higgs boson of the Standard Model is heavy ($m_H > 2m_W$), its principal decays are expected to be to W pairs ($\sim \frac{2}{3}$) and Z pairs ($\sim \frac{1}{3}$). The dominant production mechanisms are expected to be gluon fusion and vector boson fusion (see Fig. 1). The latter is referred to as WW fusion, which should be understood to include the much smaller ZZ contribution. For the mass ranges of interest to the present study ($m_{top} \approx 130$ GeV, $m_H \approx 600$ –1000 GeV) the rates are approximately equal. If the Higgs boson is very heavy ($m_H \gtrsim 1$ TeV), then WW scattering would become non-perturbative, and tree-level unitarity would be violated. In the absence of new physics, the Higgs boson must have a mass of less than about 1 TeV, and it is vital that a Higgs search extends all the way to this value at future hadron colliders.

If we wish to reconstruct the Higgs mass from its decays then the cleanest channel is the four charged lepton decay

$$H \rightarrow ZZ \rightarrow \ell^+ \ell^- \ell^+ \ell^-$$

where ℓ, ℓ' are electrons or muons[3]. This is in fact the only channel with no neutrinos or jets, and has the advantage of uniquely specifying the final state, so the only significant background is the irreducible ZZ continuum. However it suffers from having a low branching fraction ($\frac{1}{3} \times (6.6\%)^2 = 1.5 \times 10^{-3}$), and so can only be used if many thousands of Higgs bosons are produced. For the LHC with 10^5 pb^{-1} of data, this channel is useful for Higgs masses up to about 800 GeV.

The two neutrino channel

$$H \rightarrow ZZ \rightarrow \ell^+ \ell^- \nu \bar{\nu}$$

also gives a good signal, since the transverse mass distribution gives a strong Jacobean peak at the Higgs mass[4], and has a higher branching fraction ($2 \times \frac{1}{3} \times 6.6\% \times 20\% = 8.8 \times 10^{-3}$). This channel may extend the reach up to about 1 TeV, but it depends critically on the detector being hermetic, and can easily be eroded by detector problems such as dead cells or calorimeter cracks, which need to be studied more fully. The leptonic WW final state is extremely difficult to reconstruct due to the presence of two neutrinos, and suffers from prohibitively large backgrounds[5].

The semi-leptonic channels

$$\begin{aligned} H \rightarrow WW &\rightarrow \ell\nu q\bar{q} \\ H \rightarrow ZZ &\rightarrow \ell^+ \ell^- q\bar{q} \end{aligned}$$

benefit from having larger branching ratios ($2 \times \frac{2}{3} \times \frac{2}{9} \times \frac{2}{3} = 20\%$ and $2 \times \frac{1}{3} \times 6.6\% \times 70\% = 3\%$ respectively), but suffer from having a large QCD background from W/Z + 2jet processes. After a cut on the jet transverse energy at $E_{T,\min} = 10$ GeV, a reasonable detector resolution allows a resolution on the mass of the hadronic W of about 10 GeV[6], and so a cut on the 2jet mass of $|m_{jj} - m_W| < 10$ GeV reduces the background by a large factor, without affecting the Higgs signal significantly. A further cut is desirable to separate the dynamics of the W decays (almost 100% longitudinally polarized) from the QCD jet background. In previous studies, various cuts on the energy correlations between the jets have been used, but it is believed that realistic energy resolution renders these techniques ineffective. However, since longitudinal polarization favours decays with the two jets close together, an alternative cut is possible on the angular separation of the two jets. This effect has been studied, and the jet separation distribution is shown in Fig. 2, for the Higgs signal and the W + 2jet background. A cut of $\Delta R_{jj} < 0.7$ is seen to pass 89% of the signal, and 22% of the background. Also shown are the signal and background events remaining after a $p_{T,jj}$ cut, which is seen to have a similar effect to the ΔR_{jj} cut.

The W-finder used in this study utilizes this cut by running a jet-finder twice, with cone sizes of $\Delta R = 0.75$ and $\Delta R = 0.25$, and then demands a big jet containing two small jets, with $|m_{jj} - m_W| < 10$ GeV. This set of cuts still leaves the background a factor of ≈ 75 larger than the signal, and without further cuts the situation is hopeless.

The WW fusion mechanism is unusual in having outgoing jets which have radiated a W boson, so have a transverse momentum of $\sim m_W$, but have rather large longitudinal momentum, typically of a TeV or more at the LHC. Their rapidity, η , distribution is shown in Fig. 3, and is seen to peak at $\eta \approx 3.5$, with almost all contained in $\eta \lesssim 5$. These forward jets are the so-called tag jets which, it is hoped, will help identify the $qq \rightarrow qqH$ process. Of course background processes can fake these jets by QCD bremsstrahlung, but this should naively be suppressed by $\sim \alpha_s^2$.

The technique of tagging on these jets has the further advantage that once the Higgs boson is discovered, it can be used to separate gluon fusion from WW fusion events, and can thus increase our knowledge of the entire Higgs sector, and of WW scattering processes in particular—an important area for the study of mass generation.

A parton-level study[2] used the WW fusion matrix element, together with a ‘toy’ model for the background to estimate that a cut on the tag jets of $3 < |\eta| < 5$ and $E > 1$ TeV could improve the signal/background ratio to better than 1/1. The main new tool used in the present study is HERWIG’s parton shower algorithm, which should give more reliable background estimates than the leading order bremsstrahlung model used earlier. This can also be used to study the properties of the tag jets after parton showering and hadronization.

From the detection point of view, these jets have a rather nice property: because they have emitted a W, their QCD scale is $\sim m_W$, so they look something like LEP jets, except that they have a large longitudinal momentum, so they are highly Lorentz boosted. This is expected to result in a rather tight jet, and Fig. 4 shows the typical jet size after parton showering, for 1000 events with a jet energy close to 1 TeV, and a rapidity close to 4. It can be seen that at a distance of 16m from the interaction point (the largest allowed by current designs for the LHC interaction regions[7]) the jet size is smaller than the typical spreading due to hadronic showering. Thus a calorimeter would see it as a single ‘particle’ with the full jet energy.

A preliminary study revealed that the optimum point at which to cut on the tagging rapidity is $\eta \approx 4.5$. To make sure of catching the full shower from these jets, the calorimeter should extend about 20cm beyond this, which corresponds to an edge rapidity of $\eta = 5$. At 16m from the interaction point, this means that the edge of the detector will be 21.5cm from the beam line, which is quite a challenge to experimental designers! In particular the average radiation dose beyond $\eta = 4$ is expected to be ~ 730 krad yr^{-1} , even at $\mathcal{L} = 10^{33} \text{ cm}^{-2} \text{ s}^{-1}$.²

²It has been questioned whether it is meaningful to discuss the average dose, when the incident radiation increases vastly across the rapidity interval, but in fact hadronic showering smears this variation considerably. I thank G. Stevenson of the Radiation Damage Study Group for clarifying this point, and for calculating the quoted dose[8].

3. Detailed Study

To study the effects of jet tagging, I have used the parton shower program **HERWIG**[9] which uses the exact s -channel matrix element to simulate the WW fusion mechanism. The full gauge-invariant set of diagrams for $WW + 2\text{jet}$ production has been calculated[10], and used to test the validity of the s -channel approximation[11]. It was found that the s -channel tag jets are concentrated at slightly higher rapidities than for the full process, which is not expected to affect my results significantly. The same reference also studied cutting on the transverse momentum of the tagging jets, and found that it is not very advantageous over the non-resonant $WW + 2\text{jet}$ background. This is believed to be because the p_T cut does not utilize fully the unique nature of the tagging jets—their large longitudinal momentum. A recalculation[12] cutting on the jet energy shows that a cut of less than 1–1.5 TeV on the tag energy leaves the s -channel Higgs signal above the non-resonant background. As we shall see, this means that it is not the most significant background, and thus will not degrade the results presented.

To study the tagging of $W + 2\text{jet}$ events, a $W + 4\text{jet}$ event generator is needed, but although the matrix elements for these processes have been calculated[13], the CPU-time required to generate unweighted events is prohibitively large. In [14] the possibility of using a “ $W + 1\text{jet}$ ” hard sub-process and **HERWIG**’s parton shower algorithm to simulate $W + n\text{jet}$ events was investigated. This approach was shown to reproduce the matrix element results for the final state distributions to within 10–20%, but an empirical factor is required to normalize the cross-section. The **HERWIG** events were then fed into a generic calorimeter simulator and jet-finder[15] which was initialized to have a granularity of 0.05×0.05 in $\eta \times \phi$, a perfect energy resolution, and an $E_{T,\min}$ of 10 GeV for the jet-finder.

Even using the above approach, the CPU-time required to generate sufficient numbers of tagged fake Higgs events is unreasonable, so the following approach was used. Start by simulating the central detection of the fake Higgs, and run enough events to get good statistics on these cross-sections. Then, rerun the program generating central $W + 1\text{jet}$ events with the same mass distribution as the fake Higgs events, and measure the proportion of these which survive a given tagging cut. Finally rescale the number of tagged events to correspond to the central detection of Higgs-like events. This is valid only in the approximation where the central and tagging regions decouple, ie. if the tagging probability is a function only of the mass of the central system, and not its exact structure. This has been checked with necessarily loose selection criteria for Higgs events, and a loose tagging cut, and is valid to at least 10%.

A further decision must be made about the definition of the tagging energy: is it the highest jet energy in the tagging region, or the total energy of all jets in the tagging region? The present study considered both, and found that they give very similar maximum efficiencies. The former was used, in the hope that it is slightly less susceptible to pile-up problems. The tagging region used was $2 < |\eta| < 4.5$. Fig. 5 shows the energy spectrum of these tagging jets for two representative Higgs masses for the signal and some of the important backgrounds. The quantity plotted, E_{low} , the lower of the two tag energies, is the important quantity for optimizing the cut energy, since it corresponds to the cut which will just accept this event. The proportion of events passing the cut is shown in Fig. 6, where we see what we had hoped for: that the background is reduced by a far larger factor than the signal. Note also that the event numbers surviving the cut do not vary much with Higgs mass.

In optimizing the cut energy, the important quantity is the improvement in $S/\sqrt{S+B}$, the statistical significance of the signal, and this is shown in Fig. 7. Against the QCD background, the optimum cut energy is seen to be $E_{cut} \approx 600$ GeV, which can improve the statistical significance by a factor of 2–2.5. Against the gg background, the tagging cut is seen to give a smaller statistical improvement, and against the $q\bar{q}$ background a larger improvement. This would be expected from the fact that both bremsstrahlung processes which leave a gluon in the hard sub-process have singularities when the radiated particle’s momentum is large, but neither of those which leave a quark have them. The QCD background is dominated by $q\bar{q}$ processes, so would be expected to be between the two.

Before looking at the effect of the tagging cuts on the event rates, I begin by quoting the numbers of signal and background events expected for each of the main channels at the LHC with an integrated luminosity of 10^5 pb^{-1} (Table 1). The cuts on the leptonic channels are taken from [16], and are $|y_Z| < 2.5$, $p_T^Z > \frac{1}{4}m_Z$, $m_Z > m_{min}$, where

Channel		$m_H = 600 \text{ GeV}$	$m_H = 800 \text{ GeV}$	$m_H = 1000 \text{ GeV}$
$\ell\ell\ell\ell$	Signal	140	45	19
	Background	110	50	31
$\ell\ell\nu\nu$	Signal	650	240	50
	Background	400	180	150
$\ell\nu jj$	Signal	4 490	2 660	1 580
	Background	410 000	215 000	115 000
	Irreducible B/ground	4 950	3 600	3 060

Table 1: Numbers of events before jet tagging, for $\int \mathcal{L} = 10^5 \text{ pb}^{-1}$

$E_{cut}(\text{GeV})$	0	50	100	150	200
Signal	45	24	19	16	14
Background	50	14.5	9.3	6.8	5.2
S/\sqrt{B}	6.4	6.3	6.2	6.1	6.1

Table 2: Numbers of events in the $\ell\ell\ell\ell$ channel, for various tagging energy cuts, with $m_H = 800 \text{ GeV}$.

$E_{cut}(\text{GeV})$	0	50	100	150	200
Signal	240	128	101	85	75
Background	180	55	39	31	25
S/\sqrt{B}	17.9	17.3	16.2	15.3	15.0

Table 3: Numbers of events in the $\ell\ell\nu\nu$ channel, for various tagging energy cuts, with $m_H = 800 \text{ GeV}$.

m_{min} is optimized for each m_H value, and is $\sim m_H - \frac{1}{2}\Gamma_H$ for large Higgs masses. The leptons are assumed to be measured with 100% efficiency. For the semi-leptonic channel the cuts are $|y_W| < 2.5$, $\Delta m_{jj} < 10 \text{ GeV}$, $m_{Wjj} > m_{min}$, the lepton is assumed detectable with 90% efficiency, and the leptonic-W momentum is assumed reconstructable. The semi-leptonic background shown is purely the QCD $W + 2\text{jet}$ background, but there is a further background from $t\bar{t}$ production, where both the top quarks decay to real Ws. This is known to be 100–150% of the size of the $W + 2\text{jet}$ background[17], but is not included in the present study. So all that can be done at present is to multiply the background shown by a factor ≈ 2 , and assume that it passes the tagging cut in the same way as the $W + 2\text{jet}$ events³. The semi-leptonic signal shown is purely that from WW fusion, in anticipation of the fact that almost all of the gg -produced events will be lost in the cut. The irreducible background shown is the WW continuum.

Everything necessary to study the effect of tagging cuts on these event rates is now assembled. For a representative value of $m_H = 800 \text{ GeV}$ I show the numbers of events and statistical significance for various values of E_{cut} for the $\ell\ell\ell\ell$ channel (Table 2) and the $\ell\ell\nu\nu$ channel (Table 3). It can be seen that in both cases it is never profitable in terms of statistical significance to use tagging cuts. The reasons for this are that only about half of the signal is from WW fusion, and more importantly, that about 10% of the background is from WW annihilation which gets tagged in the same way as the WW-produced signal. So we must conclude that forward jet tagging is *not useful* for enhancing the leptonic channels. The reader is reminded however that the $\ell\ell\nu\nu$ channel relies on having a detector to at least $\eta = 4.5$ to efficiently suppress the large $Z + \text{jet}$ background with a missing transverse momentum cut, as discussed in [4].

The semi-leptonic background does not contain a significant proportion of WW-initiated events, and so it is hoped that tagging this channel is more successful. As can be seen in Table 4, this is in fact the case. For all Higgs masses considered, the tagging cut is seen to roughly double the statistical significance of the data, and bring the signal/background ratio to within a factor of two or three.

A number of points should be noted about this data. The background shown is still only the $W + 2\text{jet}$ background, without the $t\bar{t}$ data, and so should be multiplied by ~ 2 . Note that with this factor of 2 in the background, running with

³See Section 5 for a fuller discussion of this point.

	$m_H(\text{GeV})$	600	800	1000
BEFORE	Signal	4 490	2 660	1 580
	Background	410 000	215 000	115 000
	Irreducible B/ground	4 950	3 600	3 060
	$S/\sqrt{S+B}$	6.9	5.7	4.6
AFTER	Signal	750	520	350
	Background	2 420	1460	740
	Irreducible B/ground	110	90	80
	$S/\sqrt{S+B}$	13.1	11.4	10.2

Table 4: Numbers of $\ell\nu jj$ events, for a cut of $E_{tag} > 600 \text{ GeV}$, with $\int \mathcal{L} = 10^5 \text{ pb}^{-1}$.

$\int \mathcal{L} = 10^5 \text{ pb}^{-1}$ yields 9.9σ , 8.8σ , and 8.0σ effects for the three Higgs masses considered. Thus even with below full luminosity, a Higgs boson of 1 TeV should be discoverable. Finally, note that after the tagging cuts, the background is still dominated by the reducible QCD background, and so it is important that the approximations used in simulating it are reasonable. In particular it is clearly a high priority to switch to generating the $t\bar{t} \rightarrow WW$ background process.

Although I have demonstrated that a Higgs boson of mass 1 TeV can give a statistically significant signal, we must question whether it can really be identified as such, due to the lack of a true resonance structure. As shown in Fig. 8 the Higgs signal is observed as a broad shoulder on the background distribution, and to separate the two would require an accurate knowledge of the shape of the background. However, the figure also shows that the background near the Higgs ‘peak’ is dominated by QCD $W + 2\text{jet}$ production, whereas at lower values of m_{WW} , it is dominated by $t\bar{t}$, which would make it difficult to normalize the background from the low mass data. It must be concluded that although a Higgs signal is *in principle* observable for $m_H = 1 \text{ TeV}$, we would have a hard time convincing the community that the backgrounds are well-known, without some independent cross-check.

Although I have not studied it in detail, I end this section with a brief analysis of the ZZ semi-leptonic mode. This mode has the disadvantage of a six times smaller branching fraction, but wins back a lot of this loss because the $Z + 2\text{jet}$ background is smaller than the $W + 2\text{jet}$ by a factor of ten, does not have the $t\bar{t}$ background, and has a final state with no neutrinos. The extrapolation of the $W + 2\text{jet}$ study to $Z + 2\text{jet}$ is tabulated in D. Froidevaux’s summary talk, I will not repeat it here but simply state the conclusion—that there are not enough events for this channel to be useful. However it could provide an important cross-check once a potential signal is seen in the $W + 2\text{jet}$ channel.

4. Realistic Forward Detectors

Thus far, the study has assumed an idealized forward calorimeter with perfect energy resolution, and fine granularity. It is clearly important to study whether the above results are significantly affected by more realistic assumptions about the detector used. While this has not been studied to date, I indicate in this section some reasons for optimism in this area.

Energy resolution is not crucial to this problem. If the uncertainty in the energy is written in the usual form $\Delta E/E = A/\sqrt{E} \oplus B$ it can be seen that even if $A = 100\%$, this results in an error of less than 4% for $E > 600 \text{ GeV}$. Small errors from the normalization term are insignificant, since the performance of the cut does not depend critically on the value of the cut-off energy.

It is pointless to build a detector with cell sizes significantly smaller than the hadronic shower size, which is expected to be $\sim 20 \text{ cm}$. At 16m , and a rapidity of $4-5$, this corresponds to cells of around $0.5 \times 30^\circ$ in $\eta \times \phi$. I remind the reader that this is also roughly the size expected of the tag jets. Fig. 9 shows the typical dimensions of such a calorimeter. Clearly the biggest problem with such a detector is the radiation damage.

Another problem faced by the tag-jet method at the LHC is pile-up. Running at $\mathcal{L} = n \times 10^{33} \text{ cm}^{-2} \text{ s}^{-1}$ there are expected to be an average of n interactions per crossing. Pile-up has two effects which may give problems. The first is the soft ‘spray’ of particles expected from minimum-bias events, which could add to tag jets and boost their energy above the cut-off. This is not expected to be a large problem for the high-energy jets under consideration. The second problem is another event providing either two tag jets, or one tag jet with one from the Higgs-like event. This can be studied by considering the proportion of these events which contain a jet in the tagging region, with energy greater than 600 GeV , for a cone size of $\Delta R = 0.5$. This has been done independently using both the dual parton string model of Aurenche et al. and with the ISAJET minimum-bias + hard QCD event model[18–20]. Both give a proportion $\approx 0.5\%$ of events containing tag jets. To study when this effect becomes important, note that $\approx \frac{1}{150}$ of the background events have two tag jets, and $\approx \frac{1}{10}$ have one. Thus the pile-up tagging and genuine tagging are equal when

$$(n \times 0.5\%)^2 \sim \frac{1}{150} \Rightarrow n = 16 \Rightarrow \mathcal{L} = 1.6 \times 10^{34} \text{ cm}^{-2} \text{ s}^{-1},$$

or when

$$\frac{1}{10}(n \times 0.5\%) \sim \frac{1}{150} \Rightarrow n = 13 \Rightarrow \mathcal{L} = 1.3 \times 10^{34} \text{ cm}^{-2} \text{ s}^{-1}.$$

So even at $\mathcal{L} = 1-2 \times 10^{34} \text{ cm}^{-2} \text{ s}^{-1}$ this will only reduce the statistical significance by a factor of $\sqrt{2}$ or so. In particular, for one year of running at $\mathcal{L} = 10^{34} \text{ cm}^{-2} \text{ s}^{-1}$, the statistical significancies shown earlier are reduced to 7.3σ , 6.5σ , and 6.0σ respectively. Thus I conclude that jet pile-up is not a problem at a low-luminosity LHC option, and is beginning to become a problem, though not an insurmountable one, at high luminosities.

5. The $t\bar{t} \rightarrow WW$ Background

Since the bulk of this paper was completed, work has begun on studying the $t\bar{t} \rightarrow WW$ background, and the preliminary results indicate that the assumptions made in Section 3 are over-optimistic. I have considered only one top mass ($m_t = 130 \text{ GeV}$) so far, and with fairly low statistics, but it appears that the $t\bar{t}$ background does not pass the tagging cut in the same way as $W + 2\text{jets}$.

In the central region, the $t\bar{t}$ background behaves very similarly to the QCD $W + 2\text{jet}$ background, in particular it is reduced by the ΔR_{jj} cut by a similar, but slightly larger, factor. This results in a number of background events which is $1.07(\pm 0.09)$ times larger than the $W + 2\text{jet}$ background.

However when these events are tagged, the tag jet energy distribution is much harder than from the $W + 2\text{jet}$ background, and the distributions roughly follow the $gg \rightarrow ZZ$ curves of Figs. 5–7. This corresponds to the fact that the $t\bar{t}$ process is dominated by gg events, and that the tagging region is not very sensitive to the exact structure of the central region—only the energy and type of the incoming partons. Thus the proportion of $t\bar{t}$ events passing a tagging cut of 600 GeV is $\sim 2\%$ rather than the $\sim 0.6\%$ assumed earlier.

The combined effect of these two results is to increase the number of $t\bar{t}$ events after tagging by a factor ~ 3 . It is of course hoped that the top mass will be known, and the top quark final states better understood before attempting this analysis, and that this factor of 3 is pessimistic.

6. Conclusion

I conclude by repeating my earlier remarks on jet tagging:

- Tagging is not good for the leptonic channels.
- Tagging is good for the semi-leptonic WW channel.
- It can produce a 6σ effect for $m_H = 1 \text{ TeV}$ in a run with $\int \mathcal{L} = 10^5 \text{ pb}^{-1}$ in the semi-leptonic channel, and a statistically significant signal at lower luminosities.
- Pile-up does not kill this method, even at $\mathcal{L} = 10^{34} \text{ cm}^{-2} \text{ s}^{-1}$.
- The radiation dose is very large: $0.75 \text{ Mrad yr}^{-1}$, even at $\mathcal{L} = 10^{33} \text{ cm}^{-2} \text{ s}^{-1}$.
- At this level of study, the calorimeter does not seem to need great sophistication.

and by listing the areas in which work is still in progress:

- The $t\bar{t} \rightarrow WW$ background.
- The effects of more realistic detector assumptions (both central and forward).
- More understanding of the effects of pile-up.

Finally I stress once again the result presented by many of the Physics Working Groups in Aachen: If it is possible to build a detector to $\eta = 5$, good physics will come from it.

Acknowledgments

I would like to thank Bryan Webber, Daniel Froidevaux, Nigel Glover, James Stirling, and the Higgs Working Group for many useful discussions on jet tagging and Higgs detection.

References

- [1] R.H. Cahn, S.D. Ellis, R. Kleiss and W.J. Stirling, Phys. Rev. D 35 (1987) 1626.
- [2] R. Kleiss and W.J. Stirling, Phys. Lett. 200B (1988) 193.
- [3] A. Nisati, Muon Study Group, these proceedings.
M. Dellanegra et al., Higgs Study Group, these proceedings.
See also D. Froidevaux's summary talk.
- [4] D. Froidevaux, Higgs Study Group, these proceedings.
- [5] D. Froidevaux, in 'Proceedings of the Workshop on Physics at Future Accelerators', La Thuile, 1987.
- [6] L. Poggiali, Higgs Study Group, these proceedings.
- [7] L. Leistam, Experimental Area Study Group, these proceedings.
- [8] G. Stevenson, Radiation Damage Study Group, these proceedings.
- [9] HERWIG version 4.6, I.G. Knowles, G. Marchesini, M.H. Seymour and B.R. Webber, available from the authors.
G. Marchesini and B.R. Webber, Nucl. Phys. B310 (1988) 461.
S. Catani, G. Marchesini and B.R. Webber, Cambridge preprint Cavendish-HEP-90/11.
- [10] U. Baur and E.W.N. Glover, FERMILAB-PUB-90/75-T.
- [11] U. Baur and E.W.N. Glover, FERMILAB-PUB-90/189-T.
- [12] U. Baur and E.W.N. Glover, Higgs Study Group, these proceedings.
- [13] F.A. Berends, W.T. Giele, H. Kuijf and B. Tausk, FERMILAB-PUB-90/213-T/Leiden Preprint.
- [14] W.T. Giele, T. Matsuura, M.H. Seymour and B.R. Webber, Cambridge preprint Cavendish-HEP-90/17.
- [15] F. Paige, CALSIM and GETJET, from the ISAJET simulation package.
- [16] U. Baur and E.W.N. Glover, FERMILAB-PUB-90/154-T.
- [17] D. Froidevaux, in 'Proceedings of the Workshop on Physics at Future Accelerators', La Thuile, 1987.
P. Colas and D. Denegri, Phys. Lett. 195B (1987) 295.
- [18] P. Aurenche, F.W. Bopp, J. Ranft, in 'Proceedings of the Workshop on Physics at Future Accelerators', La Thuile, 1987.
- [19] ISAJET, F. Paige and S. Protopopescu, in 'Supercollider Physics', Proc. Oregon Workshop, Super High Energy Physics (World Scientific, Singapore, 1986), p.41.
- [20] W.J. Stirling, in 'The Feasibility of Experiments at High Luminosity at the LHC', CERN-88-02 (1988), p.67.
P. Aurenche, F. Pauss, private communications.

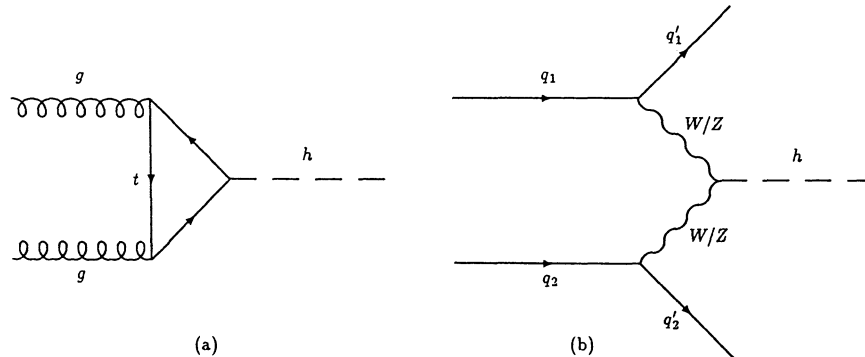


Figure 1: The principal production mechanisms for a heavy Higgs boson: a) gluon fusion, and b) WW fusion.

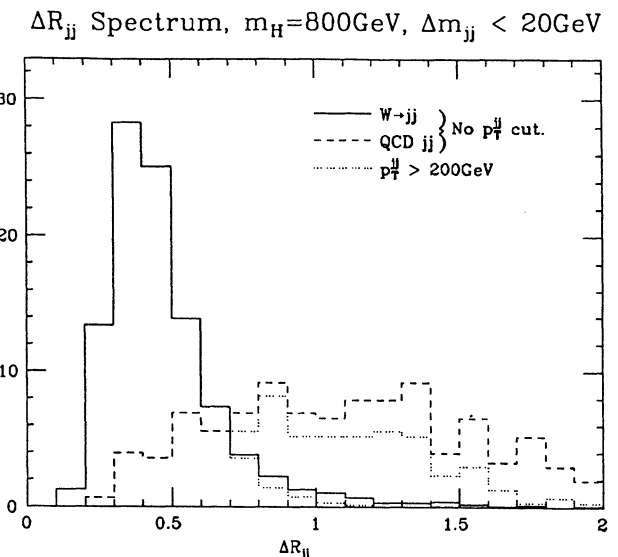


Figure 2: Distribution of ΔR_{jj} , the separation in η, ϕ of the two jets which combine to give $m_{jj} \approx m_W$, for Higgs signal (solid line), QCD background (dashed line), and each after a cut on the transverse momentum of the reconstructed W (dotted lines). All graphs are scaled to 100 initial events. The m_{jj} cut was set to 20 GeV to increase the number of events accepted.

Jet Rapidity Distribution

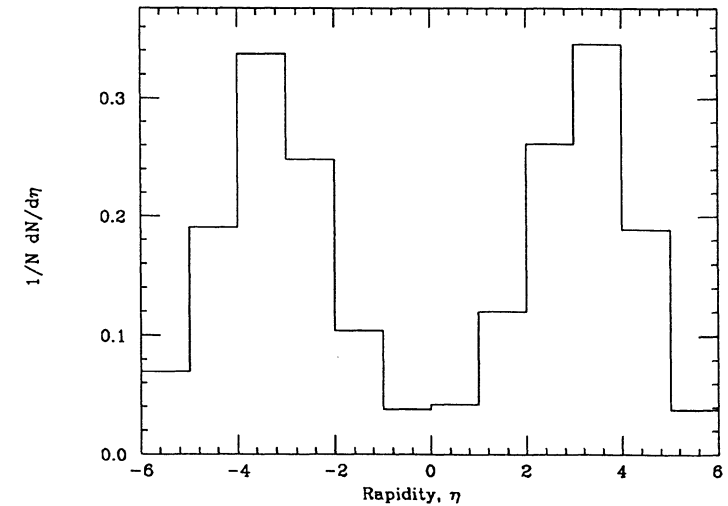


Figure 3: Jet rapidity distribution from WW fusion.

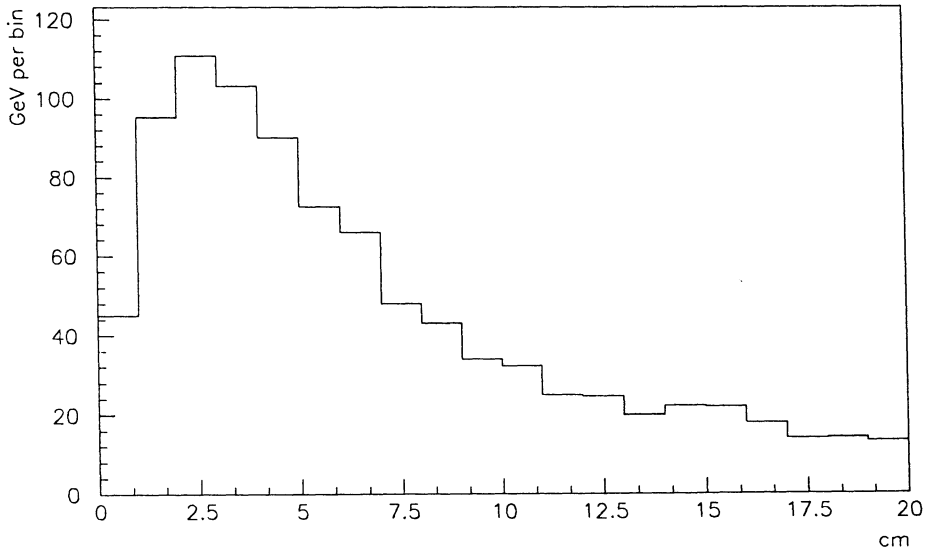


Figure 4: Typical energy flow in tag jets with $E \approx 1$ TeV from WW fusion after parton showering. a) Lego plot with bin size equivalent to 1 cm^2 at 16m from the interaction point. b) Graph of energy flow vs. distance (in cm at 16m) from centre of the jet. The vertical scale in both cases is GeV per bin.

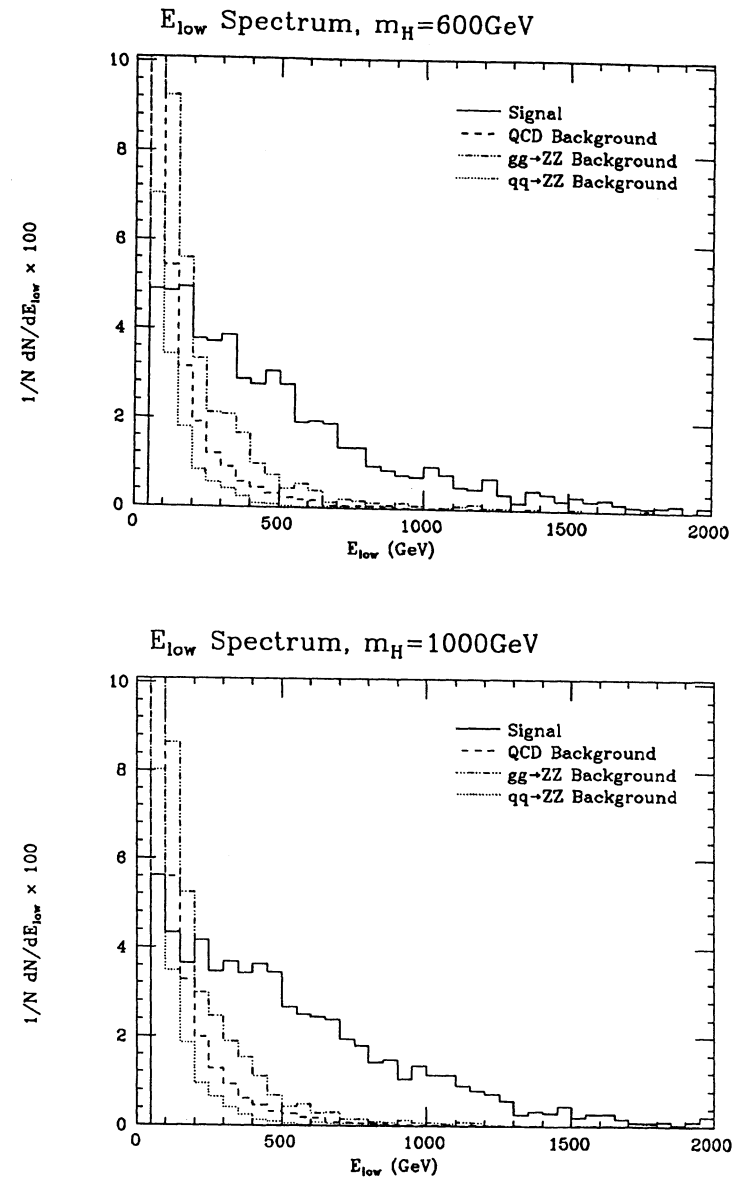
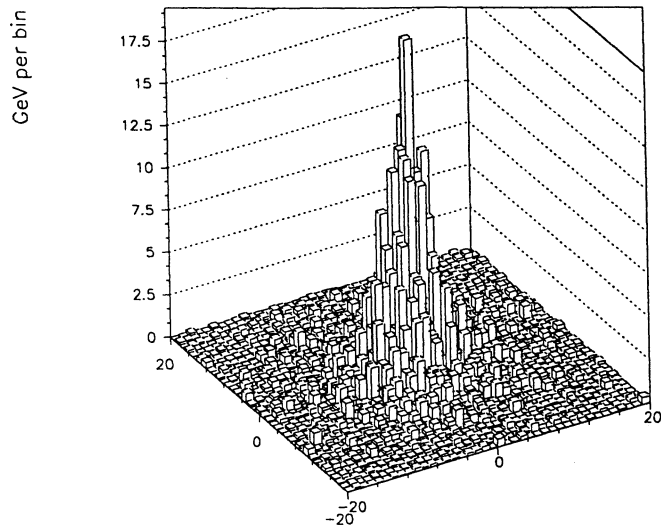


Figure 5: Spectrum of tag jet energy, where tag jets are defined to be the jets with largest energy in $2 < |\eta| < 4.5$. The variable E_{low} is the lower energy of the two directions. Data is for $qq \rightarrow qqH$ (solid line), QCD $W+2jet$ background (dashes), $q\bar{q} \rightarrow ZZ$ continuum background (dotted), and $gg \rightarrow ZZ$ continuum (dot-dashed), with a) $m_H = 600$ GeV, and b) $m_H = 1000$ GeV.

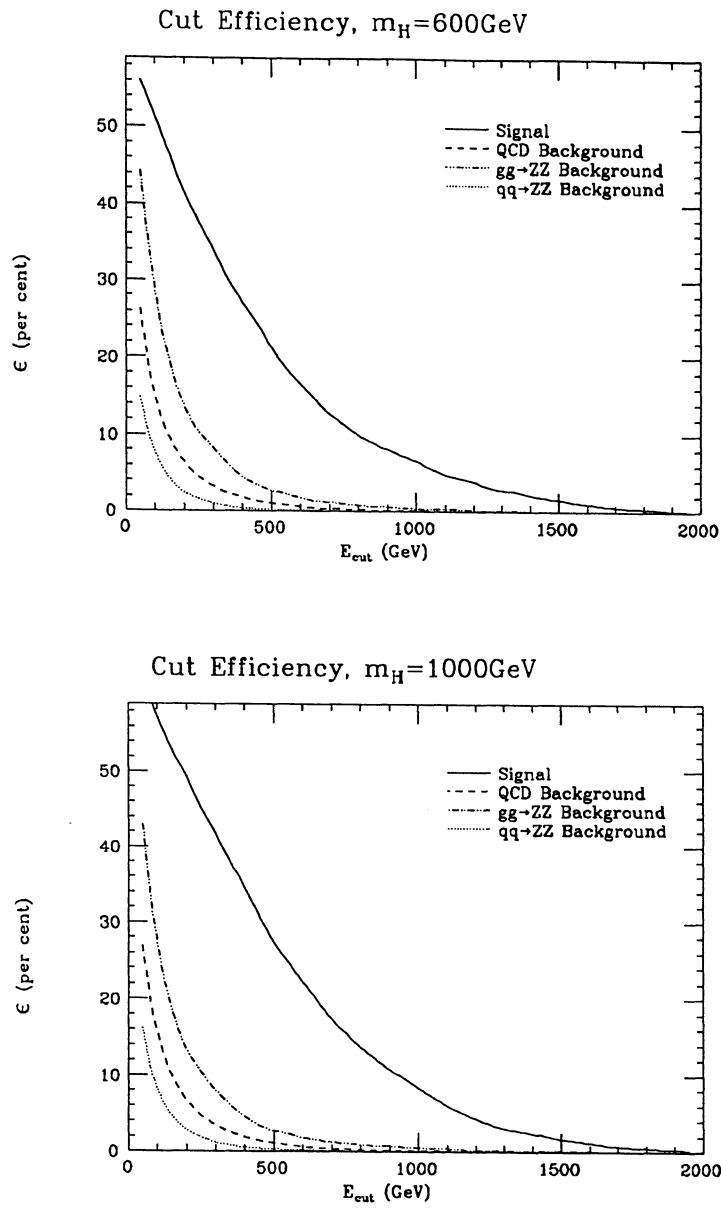


Figure 6: Proportion of events surviving cuts on E_{low} for a) $m_H = 600$ GeV, and b) $m_H = 1000$ GeV. Curves are as in Fig. 5.

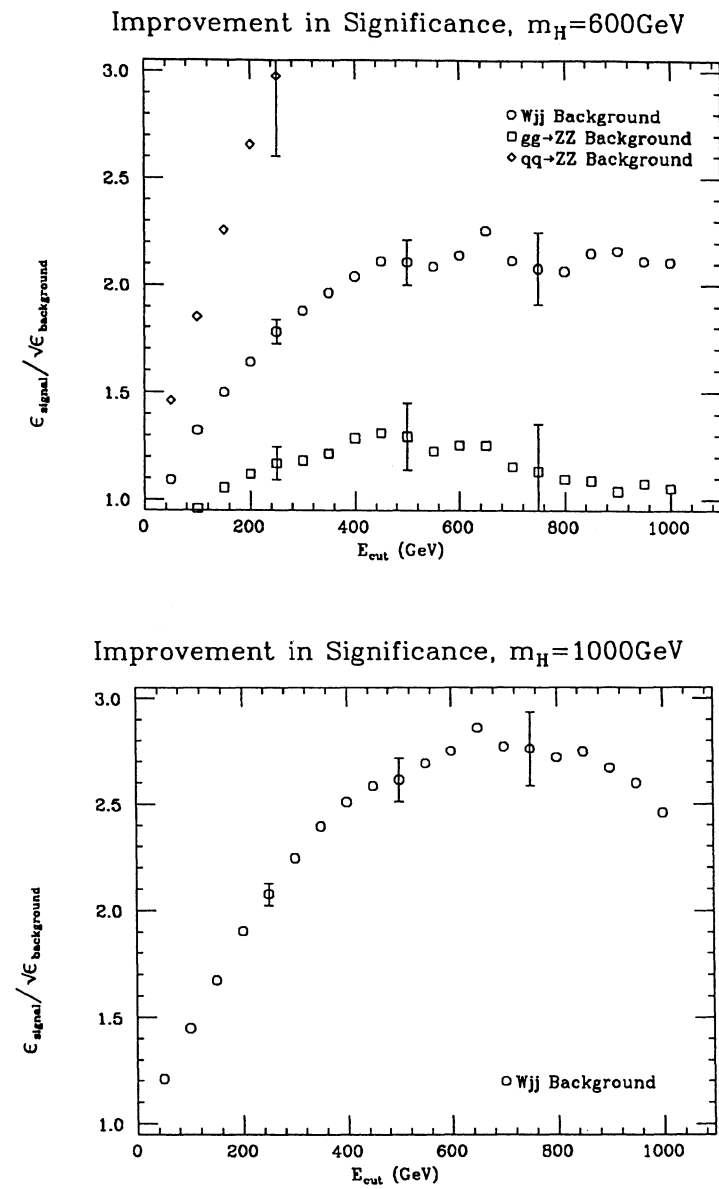


Figure 7: Statistical improvement in signal, for various backgrounds, with a) $m_H = 600$, and b) $m_H = 1000$ GeV. Error bars shown are purely statistical.

A Comparison of Exact and Approximate Calculations of Higgs Boson Production at the LHC

U. BAUR*

Physics Department, University of Wisconsin, Madison, WI 53706, USA

E. W. N. GLOVER*

Fermi National Accelerator Laboratory, P. O. Box 500, Batavia, IL 60510, USA

ABSTRACT

A comparison between exact and approximate calculations of Higgs boson production at the LHC is presented. Interference effects between resonant and non-resonant $gg \rightarrow ZZ$ and $qq \rightarrow qqZZ$ diagrams significantly enhance the $pp \rightarrow ZZX$ cross section in the resonance region for large Higgs boson masses. Non-resonant $qq \rightarrow qqW^+W^-$ diagrams represent a significant background in the jet tagging region, $2.5 < |\eta_j| < 4.5$, for a Higgs boson with mass of $\mathcal{O}(1 \text{ TeV})$.

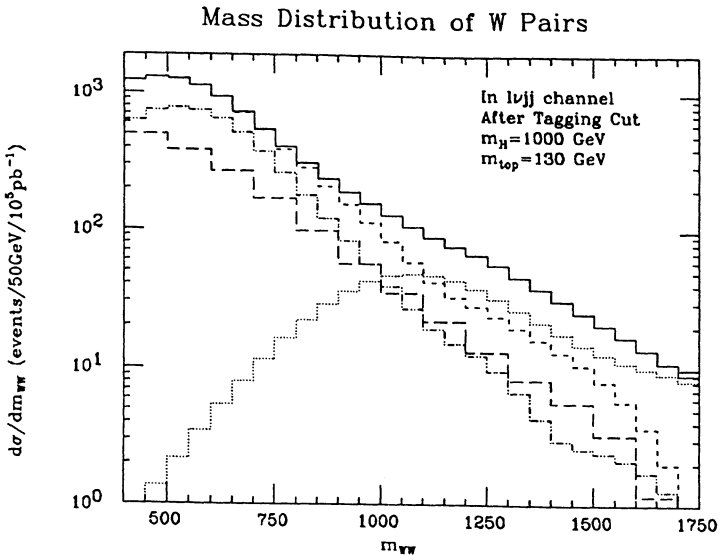


Figure 8: Mass distribution of W pairs after jet tagging, from Higgs signal (dotted line), QCD background (long-dashed line), $t\bar{t} \rightarrow WW$ background (dot-dashed line), total background (short-dashed line) and total signal + background (solid line).

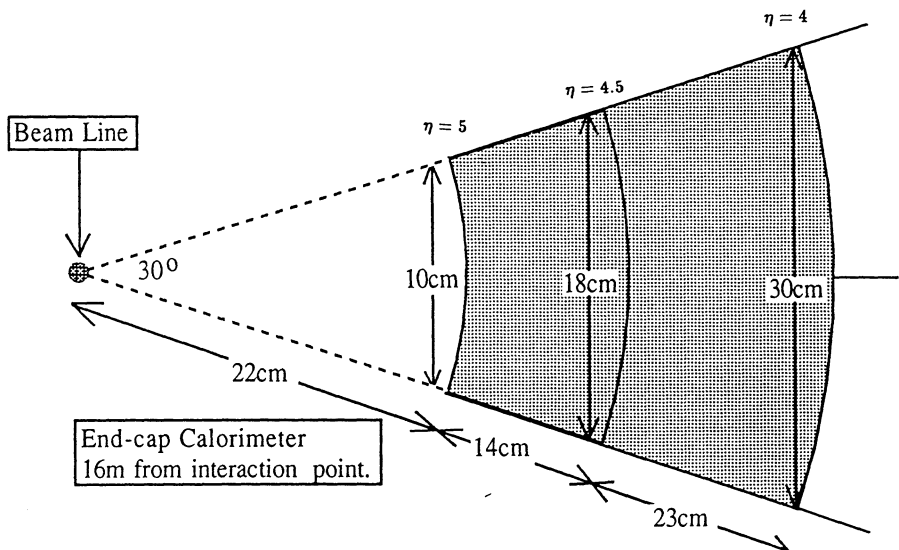


Figure 9: Diagram of typical calorimeter size required for jet tagging.

One of the major goals of the LHC is to search for the standard model Higgs boson in the mass range,

$$2M_W, 2M_Z \leq m_H \leq \mathcal{O}(1 \text{ TeV}).$$

For such heavy Higgs bosons, the dominant decays are $H \rightarrow W^+W^-$ and $H \rightarrow ZZ$, so that one has to examine the $pp \rightarrow VVX$ channel where $V = W^\pm$ or Z in order to find evidence of the Higgs boson. There are two important mechanisms for the production of Higgs bosons in hadron supercolliders; ‘gluon fusion’,^{1–4)}

$$gg \rightarrow H \rightarrow VV, \quad (1)$$

and ‘vector boson fusion’,^{5–8)}

$$qq \rightarrow qqH \rightarrow qqVV. \quad (2)$$

In the gluon fusion process, the gluons couple to the Higgs boson via a top quark loop. Because of the top quark Yukawa coupling with the Higgs boson, the gluon fusion process depends strongly on the top quark mass. In contrast, the vector boson fusion process depends only on the coupling of the Higgs boson with the W and Z and directly probes the electroweak symmetry breaking sector; the incoming quarks radiate vector bosons which annihilate into a Higgs boson.

* SSC Fellow

In addition to the Higgs exchange graphs, both of these processes receive contributions from non-resonant graphs. The full matrix elements for the $gg \rightarrow ZZ^3)$, and $qq \rightarrow qqVV^{6,8)}$ processes have been computed, however, they have not been incorporated into any of the existing shower Monte Carlos. On the other hand, the s -channel Higgs exchange graphs alone lead to relatively simple expressions and are available as an approximation to the Higgs boson signal.

It is well known that the s -channel graphs violate unitarity at large energies, $m_{VV} \gg m_H$, due to the growth of the amplitudes for longitudinally polarised V bosons. This bad high energy behaviour is only cured when all of the non-resonant graphs are included. The interference effects at $m_{VV} \gg m_H$ are therefore destructive and reduce the differential cross section beneath the unitarity allowed limit. At smaller invariant masses, $m_{VV} \ll m_H$, the interferences change sign (due to the Higgs boson propagator, $(m_{VV}^2 - m_H^2 + i m_H \Gamma_H)^{-1}$), and are constructive. Since the contribution from the non-resonant graphs is steeply falling, the net effects of the interferences from either side of the resonance do not cancel and can lead to a sizeable increase in the overall event rate, particularly when the Higgs boson is massive and has a large total width. As a consequence, the position of maximum $d\sigma/dm_{ZZ}$ tends to shift to smaller m_{ZZ} .

Furthermore, the non-resonant graphs lead to the same event topology as the Higgs signal and form an irreducible background. For example, it has been proposed to tag Higgs boson events by identifying the energetic quark jets produced at small angles in (2). Existing studies⁹⁾ have been based on the s -channel approximation and have neglected the effect of the non-resonant graphs.

In this contribution, we make a comparison between the exact matrix elements and the s -channel approximation to the matrix elements in two specific regions. First of all, we examine the ‘gold-plated’ $pp \rightarrow ZZX \rightarrow \ell^+\ell^-\ell^+\ell^-X$ ($\ell, \ell' = e, \mu$) channel and find that the exact matrix elements lead to an enhancement of as much as 50% in $d\sigma/dm_{ZZ}$ for $m_H = 800$ GeV compared to the s -channel approximation. Secondly, we examine the production of W^+W^- pairs via the vector boson fusion process when both quark jets are identified by forward hadronic calorimeters. We find that the non-resonant graphs dominate when the quark jets are very energetic while the Higgs boson signal is more important at smaller energies.

Throughout this contribution, we use the parton level Monte Carlos described in Refs. 3, 6 and 8 with the following standard model parameters, $m_t = 120$ GeV, $\alpha = \alpha(M_Z) = 1/128$, $m_Z = 91.1$ GeV, $\sin^2 \theta_W = 0.23$ and $M_W = M_Z \cos \theta_W = 80$ GeV. With these input parameters, the width of an 800 GeV Higgs boson is given by $\Gamma_H = 258.8$ GeV. Furthermore, we use the parton distributions of

Duke and Owens (set 1)¹⁰⁾ evaluated at momentum scale $Q^2 = \hat{s}/4$. Since both the exact and approximate calculations use the same input, our comparisons are essentially independent of the choice of scales, *etc.*

First of all, let us focus on the $pp \rightarrow ZZX \rightarrow \ell^+\ell^-\ell^+\ell^-X$ process. As in Ref. 11, we assume a lepton identification efficiency of 100% and simulate the finite rapidity coverage of future LHC experiments with a rapidity cut on the parent Z boson of,

$$|yz| < 2.5,$$

which approximately corresponds to $|y_\ell| < 3.0$. Furthermore, we improve the signal to background ratio by making a cut on the transverse momentum of the Z boson,^{3,12)}

$$p_{TZ} > \frac{1}{4} m_{ZZ}.$$

All other cuts are as described in Ref. 11. The main background is $q\bar{q} \rightarrow ZZ^{13})$ while for the exact calculation we also include the effect of the non-resonant graphs. To do this, we use the exact matrix elements in the limit $m_H \rightarrow 0$. The unitarity violating contributions arising in both Higgs and non-Higgs graphs then cancel completely leaving a unitarity respecting distribution. In the s -channel approximation, there is no background from either gluon fusion or vector boson fusion, and the background is given by the $q\bar{q} \rightarrow ZZ$ process alone.

Fig. 1 shows the expected event rates as a function of m_{ZZ} at the LHC for (a) $m_H = 500$ GeV and an integrated luminosity of $\int \mathcal{L} dt = 10^4 \text{ pb}^{-1}$ and (b) $m_H = 800$ GeV and $\int \mathcal{L} dt = 10^5 \text{ pb}^{-1}$. The ‘exact’ result in the presence of the Higgs boson using the full matrix elements (solid line) should be compared with the ‘exact’ background containing the perturbative non-resonant $m_H \rightarrow 0$ contribution (dashed line), while the s -channel approximation signal (dot-dashed line) is to be compared with the $q\bar{q} \rightarrow ZZ$ background (dotted line). The general features are clear. For $m_{ZZ} < m_H$, the non-resonant graphs significantly increase the expected number of events. Interference effects between Higgs and non-Higgs diagrams are constructive below the Higgs resonance and thus enhance the event rate compared to the background. Furthermore, they cause the Higgs peak to shift to smaller values of m_{ZZ} . This is particularly evident for $m_H = 800$ GeV where only a shoulder is observed and the event rate is increased by about 50% over quite a large range of m_{ZZ} . At larger m_{ZZ} , the approximate signal shows the unitarity violating nature of the s -channel approximation and dominates over the ‘exact’ result.

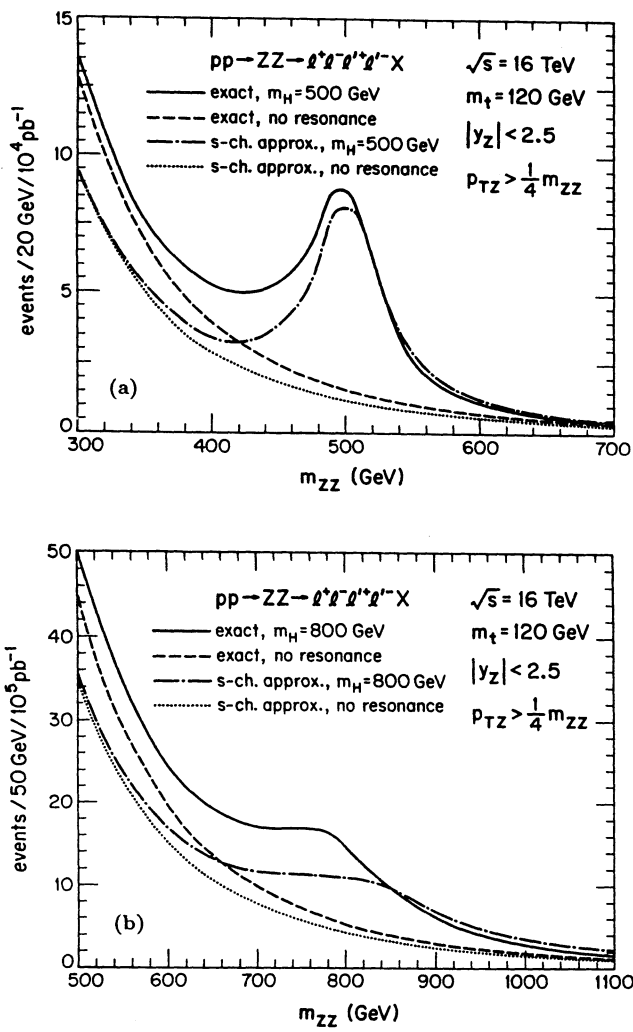


Fig. 1: Expected event rates for $pp \rightarrow ZZX \rightarrow \ell^+\ell^-\ell^+\ell^-X$ at the LHC as a function of m_{ZZ} for (a) $m_H = 500$ GeV per 20 GeV bin and $\int L dt = 10^4 \text{ pb}^{-1}$ and (b) $m_H = 800$ GeV per 50 GeV bin and $\int L dt = 10^5 \text{ pb}^{-1}$. The solid (dot-dashed) line shows the effect of the Higgs boson computed using the exact (*s*-channel approximation) matrix elements, while the dashed line shows the background computed using the exact matrix elements with $m_H \rightarrow 0$. The *s*-channel approximation background ($q\bar{q} \rightarrow ZZ$) is shown dotted. Both Z bosons are required to have rapidity, $|y_Z| < 2.5$, and transverse momentum, $p_{TZ} > 0.25 m_{ZZ}$.

Table 1 displays the expected event rates both in the presence of the Higgs boson and the background alone for $pp \rightarrow ZZX \rightarrow \ell^+\ell^-\ell^+\ell^-X$ from various sources in the resonance region,

$$m_H - \Gamma_H < m_{ZZ} < m_H + \Gamma_H.$$

For $m_H = 500$ GeV, there is little difference in the total event rate between the exact and approximate calculation, principally because of the small Higgs boson width which concentrates the signal in a small range of m_{ZZ} . Although the dominant background source is clearly $q\bar{q} \rightarrow ZZ$, the non-resonant $gg \rightarrow ZZ$ and $qq \rightarrow qqZZ$ diagrams increase the total background by about 30%. As shown by Fig. 1, this increase mainly occurs at m_{ZZ} close to $m_H - \Gamma_H$. The real signal is clearly the difference between the total event rate and the background and this is dominated by gluon fusion at these masses with vector boson fusion contributing only about 15%. On the other hand, for $m_H = 800$ GeV, vector boson fusion accounts for approximately 33% of the signal. Furthermore, because of strong constructive interference effects for $m_{ZZ} < m_H$, the overall event rates in the presence of the Higgs boson are about 30% larger than those calculated in the *s*-channel approximation.

The main motivation for studying the jet tagging region is to exploit the large $H \rightarrow W^+W^- \rightarrow \ell\nu q\bar{q}$ branching fraction. In this case, however, there is a sizeable background from both $pp \rightarrow t\bar{t}X \rightarrow W^+W^-b\bar{b}X$ and $W + n$ jet production where two of the QCD jets have an invariant mass close to M_W and ‘fake’ the hadronic W decay.¹⁴⁾ To reduce these backgrounds, it has been proposed to make use of the quark jets naturally present in the $qq \rightarrow qqW^+W^-$ signal to ‘tag’ the event. Calculations at the parton level^{8,9)} suggest that the optimal tagging region at the LHC is $2.5 < |\eta_j| < 4.5$. To fully contain the hadronic shower, it may be necessary to extend the coverage out to $|\eta_j| < 5.0$. As discussed in Ref. 15, the fake QCD background can be controlled by requiring that each tagging jet be very energetic. Clearly, the ‘fake’ QCD and top quark backgrounds dominate. Nevertheless, there is also an irreducible background from the non-resonant graphs and the question we wish to address here is *What is the background contribution from the non-resonant graphs?* To do this we remain at the level of the W bosons and restrict them to the central region,

$$|y_W| < 2.5.$$

Furthermore, to emphasize the region of interest, we consider only the resonance region, $m_H - \Gamma_H < m_{WW} < m_H + \Gamma_H$ and ignore potential problems in recon-

Table 1

Event rate both in the presence of the Higgs boson and from the background alone from various sources for $pp \rightarrow ZZX \rightarrow \ell^+\ell^-\ell^+\ell^-X$ at the LHC in the resonance region, $m_H - \Gamma_H < m_{ZZ} < m_H + \Gamma_H$ for $m_H = 500$ GeV and $\int \mathcal{L} dt = 10^4 pb^{-1}$, and $m_H = 800$ GeV and $\int \mathcal{L} dt = 10^5 pb^{-1}$. A lepton identification efficiency of 100% is assumed. The results of calculations using the exact $gg \rightarrow ZZ$ and $qq \rightarrow qqZZ$ matrix elements are compared with those using the s -channel approximation.

source	$m_H = 500$ GeV		$m_H = 800$ GeV	
	events per $10^4 pb^{-1}$	exact	events per $10^5 pb^{-1}$	s -ch. appr.
total	35.6	32.1	142.9	107.7
$q\bar{q} \rightarrow ZZ$	7.6	7.6	69.1	69.1
$gg \rightarrow ZZ$	23.8	20.2	51.3	24.3
$qq \rightarrow qqZZ$	4.3	4.3	22.5	14.4
total bgd.	10.1	7.6	87.7	69.1
$q\bar{q} \rightarrow ZZ$	7.6	7.6	69.1	69.1
$gg \rightarrow ZZ$	2.2	-	14.8	-
$qq \rightarrow qqZZ$	0.3	-	3.8	-

structuring m_{WW} from experimental observables. Other cuts to regulate the exact matrix elements are as discussed in Ref. 8.

In Fig. 2, we show the energy distribution of the tagged jet with the lowest energy, $d\sigma/dE_j^{Lo}$, when both jets are observed in the tagging region, $2.5 < |\eta_j| < 4.5$, for (a) $m_H = 800$ GeV and (b) $m_H = 1000$ GeV at the LHC. The solid line shows the full result including the effect of the Higgs boson and using the exact matrix elements of Ref. 8, while the non-resonant background (dashed line) is obtained using the $m_H \rightarrow 0$ limit of the exact matrix elements. We also show the s -channel Higgs contribution as a dotted line. The non-resonant graphs eventually dominate at large E_j^{Lo} , while the ‘signal’ events tend to accumulate at smaller energies. For $m_H \leq 800$ GeV, the resonant graphs dominate for $100 \text{ GeV} < E_j^{Lo} < 1600 \text{ GeV}$, however, due to the large Higgs boson width, the non-resonant graphs are important for all E_j^{Lo} and are generally of about the same size as the Higgs signal for $m_H \approx 1 \text{ TeV}$.

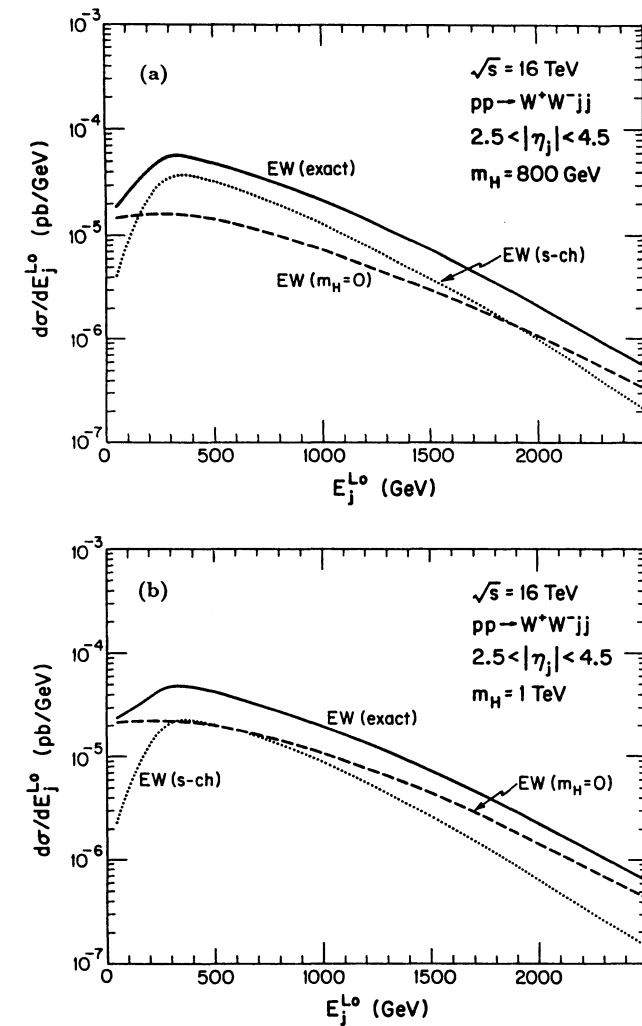


Fig. 2: Distribution of the minimum jet energy, E_j^{Lo} , in $pp \rightarrow W^+W^-jj$ for $2.5 < |\eta_j| < 4.5$ for (a) $m_H = 800$ GeV and (b) $m_H = 1000$ GeV at the LHC in the Higgs resonance region, $m_H - \Gamma_H < m_{WW} < m_H + \Gamma_H$. The solid line shows the exact result from $qq \rightarrow qqW^+W^-$. The dotted curve represents the result in the s -channel Higgs approximation, while the dashed line shows the perturbative $m_H \rightarrow 0$ background from the non-resonant electroweak $qq \rightarrow qqW^+W^-$ diagrams. Both W bosons are required to have rapidity, $|y_W| < 2.5$, and a $\Delta R_{jj}, \Delta R_{Wj} > 0.7$ separation cut is imposed.

In conclusion, we have compared the exact matrix elements for $pp \rightarrow VVX$ with the s -channel approximation to the Higgs signal, $pp \rightarrow HX \rightarrow VVX$, in two specific regions at LHC energies. In general, the non-resonant graphs provide an additional background which, in the case of jet tagging, can be sizeable. On the other hand, because of interference effects between Higgs and non-Higgs graphs, the event rate around the resonance in the ‘gold plated’ $pp \rightarrow ZZ \rightarrow \ell^+\ell^-\ell^+\ell^-$ mode can be significantly increased for heavy Higgs bosons - by around 50% for $m_H = 800$ GeV. Finally, although we have not shown results for the SSC, similar conclusions apply.

Acknowledgements

We thank D. Froidevaux and M. Seymour for fruitful discussions. This research was supported in part by the University of Wisconsin Research Committee with funds granted by the Wisconsin Alumni Research Foundation, by the U. S. Department of Energy under contract DE-AC02-76ER00881, and by funds awarded by the Texas National Research Laboratory Commission.

References

1. H. Georgi, S. L. Glashow, M. E. Machacek and D. V. Nanopoulos, Phys. Rev. Lett. **40**, 692 (1978).
2. D. A. Dicus, C. Kao and W. W. Repko, Phys. Rev. **D36**, 1570 (1987); D. A. Dicus, Phys. Rev. **D38**, 394 (1988).
3. E. W. N. Glover and J. J. van der Bij, Phys. Lett. **219B**, 488 (1989), and Nucl. Phys. **B321**, 561 (1989).
4. D. A. Dicus and C. Kao, University of Texas at Austin preprint DOE-ER 40200-232 (October 1990).
5. D. A. Dicus, S. L. Wilson and R. Vega, Phys. Lett. **192B**, 231 (1987).
6. U. Baur and E. W. N. Glover, Nucl. Phys. **B347**, 12 (1990).
7. D. A. Dicus and R. Vega, Phys. Rev. **D37**, 2474 (1988).
8. U. Baur and E. W. N. Glover, FERMILAB-PUB-90/189-T, MAD/PH/590, preprint (September 1990), to appear in Phys. Lett. **B**.
9. R. N. Cahn, S. D. Ellis, R. Kleiss and W. J. Stirling, Phys. Rev. **D35**, 1626 (1987); R. Kleiss and W. J. Stirling, Phys. Lett. **200B**, 193 (1988); W. J. Stirling, CERN 88-02 report (1988) ed. J. H. Mulvey, p. 73.
10. D. Duke and J. Owens, Phys. Rev. **D30**, 49 (1984).
11. U. Baur and E. W. N. Glover, FERMILAB-PUB-90/154-T, MAD/PH/577, preprint (August 1990), to appear in Phys. Rev. **D**.
12. V. Barger, T. Han and R. J. N. Phillips, Phys. Lett. **206**, 339 (1988).
13. R. W. Brown and K. O. Mikaelian, Phys. Rev. **19**, 922 (1979).
14. S. D. Ellis, R. Kleiss and W. J. Stirling, Phys. Lett. **163B**, 261 (1985); J. F. Gunion, Z. Kunszt and M. Soldate, Phys. Lett. **163B**, 389 (1985).
15. M. H. Seymour, these proceedings.

Testing the Higgs Sector of the Minimal Supersymmetric Standard Model at LHC

Z. Kunszt
Theoretical Physics, ETH,
Zurich, Switzerland

and

F. Zwirner¹
Theory Division, CERN,
Geneva, Switzerland

Abstract

The Higgs sector of the Minimal Supersymmetric Standard Model is studied in the context of 16 TeV proton-proton collisions. Present and future constraints from the LEP experiments are briefly discussed. Emphasis is given to the region of the parameter space corresponding to a neutral Higgs similar to the Standard Model one and with mass within the LEP reach. The relevant branching ratios and production rates for the neutral Higgs particles h , H and A are calculated. Event rates for the important discovery channels are presented. Promising physics signatures are given by the $\gamma\gamma$, $\tau^+\tau^-$ and four lepton decay modes.

¹On leave from INFN, Sezione di Padova, Italy.

1 Introduction

One of the goals of the Higgs working group [1] [2] was to investigate the role of LHC if, prior to its construction, a Higgs boson were discovered at LEP, and, within the limited experimental precision, it showed properties similar to those of the standard model Higgs. In this case, one has to investigate whether at LHC one can test some realistic alternatives to the SM Higgs sector, which at LEP might not be distinguishable from the SM case. For a phenomenological study, the most attractive alternative is the two doublet Higgs sector of the Minimal Supersymmetric Standard Model (MSSM) [3]. At LEP, in a large region of the parameter space, the Higgs sector of the MSSM is experimentally indistinguishable from the SM one. The purpose of this contribution is to discuss, in the above spirit, searches for the neutral Higgs bosons of the MSSM at LHC. The charged Higgs boson of the MSSM is studied in [4].

2 Parametrization, Couplings

Since there are no consistent supersymmetric extensions of the SM with only one Higgs doublet, the MSSM has a two doublet Higgs sector. The physical spectrum of the Higgs sector consists of two CP-even neutral bosons, h and H , one CP-odd neutral boson, A , and one charged boson H^\pm . In the MSSM and in the Born approximation, the Higgs boson masses and couplings are fully determined in terms of two independent parameters: we shall use here the mass of the CP-odd neutral boson, m_A , and $\tan\beta \equiv v_2/v_1$ (where v_1 gives mass to charged leptons and quarks of charge $-1/3$ and v_2 gives mass to quarks of charge $2/3$). The remaining mass values and the mixing angle α , required to diagonalize the mass matrix in the CP-even neutral sector, are obtained from the tree level relations

$$m_{H^\pm}^2 = m_W^2 + m_A^2, \quad (1)$$

$$m_{H,h}^2 = \frac{1}{2} \left(m_A^2 + m_Z^2 \pm \sqrt{(m_A^2 + m_Z^2)^2 - (2m_A m_Z \cos 2\beta)^2} \right) \quad (2)$$

and

$$\cos 2\alpha = -\cos 2\beta \frac{m_A^2 - m_Z^2}{m_H^2 - m_h^2}, \quad -\frac{\pi}{2} < \alpha \leq 0. \quad (3)$$

These relations imply the inequalities

$$m_h < (\min\{m_A, m_Z\}) |\cos 2\beta| < m_Z \quad (4)$$

and

$$m_h < m_A < m_H, \quad m_A < m_{H^\pm}, \quad m_Z < m_H. \quad (5)$$

In the MSSM, as defined for example in [5], the allowed range of $\tan\beta$ is given by

$$1 < \tan\beta < \frac{m_t}{m_b}. \quad (6)$$

We stress that, if the top quark mass is sufficiently heavy, radiative corrections can significantly modify the above tree level relations [6]. These radiative corrections appear to be important for the discussion of SUSY Higgs searches at LEP200. They are less significant at LHC.

The couplings of the three neutral physical Higgs bosons are easily obtained from the standard model Higgs couplings if we multiply them with the α and β dependent factors summarized in Table 1.

	$b\bar{b}$	$t\bar{t}$	VV
h	$\frac{-\sin\alpha}{\cos\beta}$	$\frac{\cos\alpha}{\sin\beta}$	$\sin(\beta - \alpha)$
H	$\frac{\cos\alpha}{\cos\beta}$	$\frac{\sin\alpha}{\sin\beta}$	$\cos(\beta - \alpha)$
A	$-i\gamma_5 \tan\beta$	$-i\gamma_5 \cot\beta$	0

Table 1.

The variation of the relevant coupling constant factors and mass values can be conveniently shown as contour plots in the $(m_A, \tan\beta)$ plane. Figs. 1 a-d show plots for m_h , m_H and the couplings of h to gauge boson pairs and to $b\bar{b}$. We note that, if m_A and $\tan\beta$ are large then $m_h \approx m_Z$, and if $m_h \approx m_A$ then $m_H \approx m_Z$.

The presently allowed region of the $(m_A, \tan\beta)$ plane is restricted by the LEP data. In Fig. 2, the excluded regions are obtained from the present experimental limits [7] on the processes $e^+e^- \rightarrow h + Z^*$ and $e^+e^- \rightarrow h + A$ at $\sqrt{s} \approx m_Z$. From Fig. 2 we obtain the lower limits $m_A > 40$ GeV, $\tan\beta > 1.6$, $m_h > 33$ GeV.

Our discussion concerning the constraints which may be obtained at LEP200 can only be tentative (for previous studies, see [8]). This subject is in rapid development at the moment: presumably highly efficient b-tagging will be possible [9]; furthermore, even a relatively modest shift in the mass values due to radiative corrections [6] can lead to important modifications in the conclusion. Since no complete study is available yet, in Figs. 3a-c we show only contour plots of the production cross section $\sigma(e^+e^- \rightarrow h\bar{l}\bar{l})$, $\sigma(e^+e^- \rightarrow H\bar{l}\bar{l})$, $\sigma(e^+e^- \rightarrow hA)$, at $\sqrt{s} = 190\text{GeV}$ and where $\bar{l}\bar{l}$ denotes the sum of the contributions from e^+e^- , $\mu^+\mu^-$ and $\nu\bar{\nu}$ (3 families). The contour lines correspond to constant values of the cross sections in picobarns. In Fig. 3d a contour plot for the sum of the first two processes is shown.

We stress two features of the cross section values depicted in Figs. 3a-d. First, if at LEP200 high luminosity and effective b-tagging will be achieved, then all the parameter space can be tested: at least one Higgs boson has to be found or the MSSM is ruled out. Unfortunately, this conclusion is rather sensitive to the above mentioned radiative corrections, since the machine energy is close the threshold energies of ZZ, Zh and ZH production, so that even a small shift in the mass values can have a large effect on the rates.

Secondly, in a rather large region of the parameter space ($m_A > 100\text{ GeV}$ or so) the MSSM predicts a Higgs boson h with mass smaller than m_Z , and with production and decay properties very similar to those of the SM Higgs within the expected experimental errors (see the contour plots in Fig. 1c and Fig. 1d). The decay into $b\bar{b}$ will remain the dominant decay channel, but the SUSY Higgs will have a smaller branching ratio into charmed particles than the SM Higgs. It is unlikely, however, that this property can be tested experimentally with the required accuracy. It is especially interesting to explore the potential of LHC for testing the Higgs sector of the MSSM in such a case.

3 Branching Ratios and Widths

The production and decay properties of the Higgs bosons show a rather strong dependence on the masses and couplings of the supersymmetric particles, if these are light. This is due to new open decay channels and new thresholds. At LHC, the discovery of squarks and/or gluinos in the mass

range below 1 TeV seems feasible [5]. On the other hand, LHC will not be able to improve dramatically the LEP200 limits on sleptons, charginos and neutralinos [5]. One should therefore take into account, in principle, the possible existence of supersymmetric decay modes for the neutral Higgses H and A . A complete analysis would involve many parameters and would go beyond the aim of the present report. We will assume instead, for simplicity, that squarks, gluinos, sleptons, charginos and neutralinos are all significantly heavier than H . This would correspond to the case where the first evidence for supersymmetry might be found via the Higgs sector. Even when they are heavier than all SUSY Higgses, supersymmetric particles still give non-trivial contributions to the branching ratios into two gluons or two photons, via the loop diagrams depicted in Fig. 4. A subset of those diagrams also determines the production cross sections of the gluon gluon fusion mechanism. Investigating the couplings of supersymmetric particles to photons and gluons, we can easily see that the squark contribution is the most important one. The decay amplitude from the triangle diagrams with internal squark loop will approach a finite limit for infinitely heavy squark masses. We shall present branching ratios and production cross sections assuming that all the squarks are degenerate and have a mass of 1 TeV, a value which, to a good approximation, can be considered asymptotically large. These considerations are relevant only for h and H , since the two gluon and two photon decay amplitudes of the CP-odd Higgs A receive no contributions from squark loops in the limit of negligible mixing. For the top mass we assumed the value $m_t = 150\text{ GeV}$.

In Fig. 5a, the branching ratios for h are shown as a function of m_h , assuming $\tan\beta = 3$. In Fig. 5b, the same branching ratios are shown without the squark contributions. We can see that the squark contribution is rather important for the gg and $\gamma\gamma$ channels. In Fig. 6a-b, the same curves are shown, but for $\tan\beta = 10$. There is a rather strong dependence on the value of $\tan\beta$. The behaviours of the gg and $\gamma\gamma$ curves are strikingly different. This is due to the fact that the $\gamma\gamma$ decay amplitude receives contributions also from W^\pm and H^\pm loops. In the SM, the contribution of the W^\pm loop is strongly dominant. In the MSSM and at low values of m_A , the W^\pm loop contribution is suppressed and it can be partially cancelled by the b-quark contribution (see Fig. 1d). Except if $m_A \gg m_Z$ (which corresponds to a small interval at the end points (see also Fig. 1a) of the $\gamma\gamma$ curves in Figs. 5-

6), the branching ratio for the $\gamma\gamma$ decay channel is much smaller than in the SM. We note, however, that the small range in m_h where the branching ratio is substantial corresponds to the large region of the $(m_A, \tan\beta)$ plane where h has at LEP a signature similar to the standard model Higgs. The effect of the squarks is to reduce the branching ratio even in this region. Fortunately this effect, as we shall see later, is compensated by an enhanced production cross section.

The branching ratios of H for $\tan\beta = 3$ and including the squark contribution are shown in Figs. 7 a-b as a function of m_H . The same curves for $\tan\beta = 10$ are shown in Figs. 8a-b. At relatively large mass values many channels are open. In particular the opening of the hh channel is significant. For $\tan\beta = 3$, the hh mode is dominant below the $t\bar{t}$ threshold. We note that the $\gamma\gamma$ branching ratio is very small if $m_H > 130$ GeV. If $2m_Z < m_H < 2m_t$, the ZZ channel contributes significantly for low values of $\tan\beta$. As we can see from Fig. 7b, in this mass interval at $\tan\beta = 3$ the ZZ branching ratio is only about 8 times smaller than the corresponding branching ratio of the SM Higgs [1]. We also note that at large values of $\tan\beta$, contrary to the standard model, the decay to $\tau^+\tau^-$ has an almost constant branching ratio of 0.09 even above the WW, ZZ and $t\bar{t}$ thresholds. In contrast to the SM Higgs, $t\bar{t}$ (for moderate $\tan\beta$) and $b\bar{b}$ (for very large $\tan\beta$) are the dominant decay modes in the region of large H masses.

In Figs. 9a-b the branching ratios of the CP-odd boson A are plotted at $\tan\beta = 3$ and $\tan\beta = 10$, respectively. A does not couple to vector boson pairs, so it cannot decay into WW or ZZ . We note that in a large region of the parameter space the branching ratio of the two photon decay is above 10^{-4} . We shall see that the production is strongly enhanced at high values of $\tan\beta$ and intermediate values of m_A . Therefore, even if the branching ratio is small, the $\gamma\gamma$ final state can give a measurable signal at high values of $\tan\beta$. Because of this significant enhancement in the production cross section, the $\tau^+\tau^-$ and Zh decay modes may also become important.

Finally, we note that, in contrast to the SM Higgs, the total widths of the heavy bosons H, A approach constant values less than 2 GeV as m_H and m_A increase (see Fig. 10).

4 Production Cross Sections

There are two dominant production mechanisms for the neutral Higgs bosons of the MSSM :

i) Gluon - gluon fusion (see Fig. 4)

ii) Associated production with b-quarks ($gg \rightarrow b\bar{b}\phi$, $\phi = h, H, A$)

In both cases the production cross section can be obtained from the SM values [1] by changing the coupling constants appropriately (see Table 1). In the case of the gg -fusion mechanism, the squarks give important positive contributions, which can enhance the production cross section of H . The enhancement for h is significant at large values of $\tan\beta$ and m_A .

In the case of the associated production with b-quarks, the leading order QCD prediction [10] is modified by corrections due to running b-quark mass values and to collinear gluon emissions from the b-quark line [11]. A complete treatment is not yet available. Since the two effects, if considered separately, tend to cancel each other, we used the Born approximation assuming $m_b=5$ GeV. The QCD corrections can change these values by a factor of 2 or more.

In Fig. 11 we show the total cross section for the production of h at $\tan\beta = 3$ and 10. The individual contributions from $b\bar{b}h$ production (dashed lines), and the cross section for the production of the SM Higgs, are also shown. The cross section is larger than the SM cross section in the whole parameter space. At small values of m_h and large values of $\tan\beta$, there is a strong enhancement due to $b\bar{b}h$ production. At higher values of m_h the enhancement is given by the squark contribution. The enhanced production cross sections can partially compensate the suppression seen in the $\gamma\gamma$ decay mode.

The production cross section of the heavier neutral Higgs H is shown in Fig. 12. At low values of m_H , we can observe an enhancement due to $b\bar{b}H$ production. In the region $2m_Z < m_H < 2m_t$, the cross section is comparable to the SM value. Therefore there is a potential, but marginal signal in the decay mode $H \rightarrow ZZ \rightarrow 4l$ (see the discussion of the branching ratios above). At higher values of m_H the production cross section is smaller than the SM value, therefore the prospects for discovery are grim.

Finally, in Fig. 13 we show the total cross section for A production. For low values of m_A and for $\tan\beta = 10$ there is a very strong enhancement

due to $b\bar{b}A$ production and to the enhanced coupling to b-quarks. Above the top threshold the rate becomes smaller than for the SM Higgs. We note that for $\tan \beta = 30$ the cross section is further enhanced by an additional factor of more than 10, compared to $\tan \beta = 10$.

5 Observable Signals

5.1 Decays into $\gamma\gamma$

a) $h \rightarrow \gamma\gamma$

In Fig. 14 we have plotted the production cross sections of all three neutral Higgs bosons, with subsequent decay into $\gamma\gamma$, as a function of m_A for $\tan \beta = 3$ and 10. In Fig. 15 the same curves are shown for $\tan \beta = 2$ and 30. The large region of parameter space of Figs. 14 and 15 corresponds to a rather small interval for $m_h < m_Z$ (see Fig. 1a). In the mass range $m_h = 80 - 90$ GeV in the SM, the production cross section times branching ratio is 0.05 pb [1]. As discussed in [12], such a signal is observable only for $\int L dt \geq 10^5 \text{ pb}^{-1}$ and poses some demands on the detector. Under these conditions, signals would be observable for $m_A > 200$ GeV and $\tan \beta > 2$. In this region, h will have SM model properties at LEP, but its discovery there would be difficult since m_h is close to its upper bound m_Z . In this sense we see a complementarity between LEP and LHC. We note that the associated production Wh , with the subsequent decays into $l\nu\gamma\gamma$ final states[13,12], will have the same significance as in the SM, since in this region $\sin^2(\beta - \alpha) \approx 1$. This result, namely that there is a large region of parameter space in which h could be discovered at LHC, may become even more important if radiative corrections shift the value of m_h significantly above m_Z [6], in which case the discovery at LEP will become impossible.

b) $H \rightarrow \gamma\gamma$

From Figs. 14 and 15 we can also read that H will be observable at LHC in the region $m_A < 70$ GeV and $\tan \beta > 3$, where $m_h \approx m_A$ and $m_H \approx m_Z$. Similarly to the case of h , in this region the couplings of H to gauge boson pairs are approximately the same as in the SM. This region is difficult at LEP since the production of h is strongly suppressed and $m_H > m_Z$. We see again the complementarity: the region promising for observation at LHC

is the difficult region for discovery at LEP. Since in this region $\cos^2(\beta - \alpha) \approx 1$, again the associated production of WH will have approximately the same rate as in the SM.

We conclude that via the $\gamma\gamma$ decay mode LHC will provide crucial improvement to the potential of LEP to discover either h or H but not both. Therefore it is interesting to establish under which condition we can find the CP-odd boson A .

c) $A \rightarrow \gamma\gamma$

In Figs. 14 and 15 we can see that A can be observed at LHC in the $\gamma\gamma$ decay mode only if $\tan \beta \gtrsim 13$ in a mass interval for m_A around 100 GeV which increases for increasing $\tan \beta$. For $\tan \beta = 30$ the region of m_A where we have an observable rate extends to the large interval $m_A \approx 90 - 400$ GeV. We note that, at high values of m_A , the total width of A remains below 2 GeV in all the relevant region of the parameter space, and the background is smaller. Therefore at large m_A and large $\tan \beta$ the production of A gives a clear narrow peak in the $\gamma\gamma$ final state. The region $m_A > 200$ GeV, $\tan \beta > 20$ is particularly interesting, since in this region of the parameter space both h and A could be discovered at LHC.

5.2 Decays into ZZ

In the region $\tan \beta < 3$ and $2m_Z < m_H < 2m_t$, the decay mode $H \rightarrow ZZ \rightarrow 4$ leptons can give an observable signal. The production rate for this channel is shown in Fig. 16. With integrated luminosity 10^5 pb^{-1} the total number of events is ≈ 100 or more, therefore even after cuts and efficiency losses one can still see a narrow peak over a small background. Again the total width of H remains less than 1 GeV even at asymptotically large values of m_H , with the possible consequence that good lepton momentum resolution may be important, in contrast to the SM Higgs case. We note that in this region of the parameter space the neutral Higgs h is expected to be found at LEP200 with SM properties. Furthermore, this region of the parameter space is disjoint from the one where A can be discovered in the $\gamma\gamma$ decay mode.

5.3 Decays into $\tau^+\tau^-$

The detection of A in this channel, contrary to the SM Higgs case, may become possible because the production cross section for A is strongly enhanced for high values of $\tan\beta$ (see Fig. 13), while the branching ratio is about the same ($\approx 8\%$, see Fig. 7). A study of the SM case has been performed in [14]. Only the $e^\pm\mu^\mp$ events have been considered, since the QCD backgrounds to hadronic τ decays are overwhelming. These events come from the leptonic decays of both τ 's (6.3% of all τ pairs). The invariant mass of the τ pair can be reconstructed if the Higgs is produced with large transverse momentum, but it requires also the measurement of the total missing transverse momentum. This can be done only at lower luminosity and with good detector coverage. The MC study [14] has shown that, in the mass region $80 - 160\text{GeV}$, about $10 - 15\%$ mass resolution can be achieved. For the standard model Higgs with 10^{-4}pb^{-1} integrated luminosity, in the mass range $120 - 160\text{GeV}$, we get 62 events above a huge number of 32000 background events, dominated by top production¹. At the same mass value and at $\tan\beta = 10$, however, the production rate of the CP-odd neutral Higgs boson of the MSSM, A is ≈ 50 times higher giving 4500 events at $m_A = 140\text{GeV}$. Assuming 10% mass resolution, one obtains a clear signal with 20 standard deviation significance over the broad background from top production, as shown in Fig. 17. The number of signal events increases rapidly for increasing $\tan\beta$ and becomes about 50 times larger at $\tan\beta = 30$ extending the region of discovery up to 400GeV . At $m_{\tau\tau} \approx m_Z$ the most important background comes from Z production. Furthermore, at lower mass values the measurement of the missing transverse momentum is problematic. Therefore it will be more difficult to find a signal in the $\tau^+\tau^-$ decay mode below $\approx 90\text{GeV}$. We conclude that the region of discovery in $\tau^+\tau^-$ decay mode is comparable to the one found for the $\gamma\gamma$ channel, however, it extends to smaller values of $\tan\beta$. The disadvantage of this mode is that it requires the measurement of the missing transverse energy. In the $\tau^+\tau^-$ mode at very high values of $\tan\beta$ a marginal signal of H production may also be seen around $m_H = 100\text{GeV}$.

¹Conservatively, we have taken from ref. [14] the lower estimate of the signal and the upper estimate of the background.

5.4 Other decay modes

It is unlikely that other decay modes could be useful. In the case of H , at moderate values of $\tan\beta$ there is a large branching ratio for the decay into hh . However, h will decay predominantly to $b\bar{b}$, and the background to this signal is too large for detection. The $\tau^+\tau^-$ decay mode of h is useless since the rate is too low, given the bad mass resolution and the large background. In the case of A , the Zh mode has a sizeable branching ratio at moderate values of $\tan\beta$. The production cross section, however, is smaller than the SM cross section. Furthermore, the decay of Z into $l\bar{l}$ and the decay of h into $\gamma\gamma$ have too small branching ratios to give an observable signal.

6 Conclusion

LHC can play a key role in testing the Higgs sector of the MSSM. A tentative summary of the scenario which emerged from our study is presented in Fig. 18. We can classify the different regions of the $(m_A, \tan\beta)$ plane into 'standard', 'good' and 'difficult'.

The 'standard' regions are those where only one Higgs boson can be found in the $\gamma\gamma$ decay mode with SM model properties ($\tan\beta > 3$, $m_A < 70\text{ GeV}$ and $m_A > 200\text{ GeV}$). It should be added that the part of this region corresponding to small values of m_A and large values of $\tan\beta$ could possibly give an observable signal in $t \rightarrow b H^+$ decays [4].

The 'good' regions are the regions where one of the heavy partners of the light Higgs, possibly found at LEP, can be found at LHC. These are:

- discovery regions for A
 - i) in the $\gamma\gamma$ decay mode ($\tan\beta > 15$, with a broadening interval in m_A as $\tan\beta$ increases);
 - ii) in the $\tau^+\tau^-$ decay mode ($\tan\beta > 10$, with a broadening interval in m_A as $\tan\beta$ increases);
- and discovery regions for H
 - iii) in the four lepton final state ($\tan\beta < 3$, $2m_Z < m_H < 2m_t$).

For the $\tau^+\tau^-$ signal, lower luminosity has been assumed. For high values of $\tan\beta$ the signal from $A \rightarrow \gamma\gamma$ should be spectacular.

The ‘difficult’ region is the remaining one ($\tan \beta = 2-10$ and $m_A = 70-200$ GeV), not covered by the ‘standard’ and ‘good’ regions. In the ‘difficult’ region we could not find any measurable physics signal. Fortunately at LEP this is an ‘easy’ region for the discovery of the light Higgs h .

We recall that our conclusions have been reached using several assumptions. We did not consider radiative corrections to the mass relations and we used simplifying assumptions on the spectrum of the supersymmetric partners of the known particles. Further work is needed in these directions.

The test of the MSSM Higgs sector at LHC is rather demanding on the detectors. It requires a very good photon spectroscopy and possibly the measurement of the missing transverse momentum, that is large coverage in rapidity [2].

Acknowledgements

We are grateful to G. Altarelli for many discussions and for insisting that we should carry out this study. We also thank J. Ellis, D. Froidevaux and G. Ridolfi for their important contributions and R. Barbieri for useful discussions.

References

- [1] Z. Kunszt and J.W. Stirling, contribution to the Higgs working group, these Proceedings.
- [2] D. Froidevaux, contribution to the Higgs working group, these Proceedings.
- [3] For a review on supersymmetric Higgs bosons and further references see, e.g., J.F. Gunion, H.E. Haber, G.L. Kane and S. Dawson, *The Higgs Hunter’s Guide*, Addison-Wesley, 1990.
- [4] E. Reya, P. Zerwas et al., summary report of the Top Physics working group, these Proceedings.
- [5] G.G. Ross, F. Zwirner et al., summary report of the Supersymmetry working group, these Proceedings.
- [6] J. Ellis, G. Ridolfi and F. Zwirner, preprint CERN-TH.5946 (1990); H.E. Haber and R. Hempfling, preprint SCIPP-90/42 (1990); Y. Okada, M. Yamaguchi and T. Yanagida, Tohoku University preprint TU-360 (1990).
- [7] D. Decamp et al. (ALEPH Collaboration), Phys. Lett. B236 (1990) 233, B237 (1990) 291, preprints CERN-EP/90-16, CERN-EP/90-70, CERN-PPE/90-101; P. Abreu et al. (DELPHI Collaboration), preprints CERN-EP/90-44, CERN-EP/90-60; B. Adeva et al. (L3 Collaboration), preprints L3-10, L3-15 and L3-19; M.Z. Akrawy et al. (OPAL Collaboration), Phys. Lett. B236 (1990) 224, preprints CERN-EP/90-100, CERN-PPE/90-116, CERN-PPE/90-150.
- [8] A. Bartl, W. Majerotto and N. Oshimo, Phys. Lett. B237 (1990) 229; Z. Kunszt and W.J. Stirling, Phys. Lett. B242 (1990) 507. Other recent works on the subject are: J. Kalinowski, B. Grzadkowski and S. Pokorski, Phys. Lett. B241 (1990) 534; N. Brown, preprint RAL-90-059 (1990); H. Pois, T.J. Weiler and T.C. Yuan, Nucl. Phys. B347 (1990) 461; J.F. Gunion and L. Roszkowski, preprint UCD-90-26 (1990); V. Barger and K. Whisnant, preprint MAD/PH/616 (1990).
- [9] Proceedings of the Cogne meeting of the LEP Experiments Committee, September 24-29, 1990.
- [10] Z. Kunszt, Nucl. Phys. B247 (1984) 339.
- [11] D.A. Dicus and S. Willenbrock, Phys. Rev. D39 (1989) 751.
- [12] C. Seez, contribution to the Higgs working group, these Proceedings.
- [13] R. Kleiss, Z. Kunszt and W.J. Stirling, preprint DTP/90/54, ETH-TH/90-29 (1990).
- [14] L. Di Lella, contribution to the Higgs working group, these Proceedings.

Figure Captions

Fig.1: Contours in the $(m_A, \tan \beta)$ plane of: a) m_h (GeV); b) m_H (GeV); c) $\sin^2(\beta - \alpha)$; d) $(\sin \alpha / \cos \beta)^2$.

Fig.2: Present LEP limits in the $(m_A, \tan \beta)$ plane: the horizontal line corresponds to the process $e^+e^- \rightarrow Z^* h$, the vertical line to $e^+e^- \rightarrow h A$.

Fig.3: Contours of cross-sections (in pb) at $\sqrt{s} = 190$ GeV for the processes ($l = e, \mu, \nu_e, \nu_\mu, \nu_\tau$): a) $e^+e^- \rightarrow h l \bar{l}$; b) $e^+e^- \rightarrow H l \bar{l}$; c) $e^+e^- \rightarrow h A$; d) $e^+e^- \rightarrow \phi l \bar{l}$ ($\phi = h, H$).

Fig.4: Loop diagrams with one external Higgs line $\phi = h, H, A$ and two external photon [(a) and (b)] or gluon [(a)] lines. X can be fermions, sfermions, W , charged Higgs or charginos, Y can be W or charged Higgs.

Fig.5: Branching ratios of the lighter neutral Higgs h for $m_t = 150$ GeV and $\tan \beta = 3$: a) assuming $m_{\tilde{q}} = 1$ TeV; b) neglecting the squark contributions in the loop diagrams.

Fig.6: The same as in Fig.5 but for $\tan \beta = 10$.

Fig.7: Branching ratios of the heavier CP-even neutral Higgs H for $m_t = 150$ GeV, $m_{\tilde{q}} = 1$ TeV and $\tan \beta = 3$.

Fig.8: The same as in Fig.7 but for $\tan \beta = 10$.

Fig.9: Branching ratios of the CP-odd neutral Higgs A for $m_t = 150$ GeV and: a) $\tan \beta = 3$; b) $\tan \beta = 10$.

Fig.10: Total widths of H and A as a function of their mass, in the absence of decay modes into supersymmetric partners of the SM particles.

Fig.11: Total cross-sections for h production at LHC (solid lines), for the representative values $\tan \beta = 3$ and $\tan \beta = 10$. The dashed lines correspond to h production in association with $b\bar{b}$.

Fig.12: Total cross-sections for H production at LHC (solid lines), for the representative values $\tan \beta = 3$ and $\tan \beta = 10$. The dashed lines correspond to H production in association with $b\bar{b}$.

Fig.13: Total cross-sections for A production at LHC (solid lines), for the representative values $\tan \beta = 3$, $\tan \beta = 10$ and $\tan \beta = 30$. The dashed lines correspond to h production in association with $b\bar{b}$.

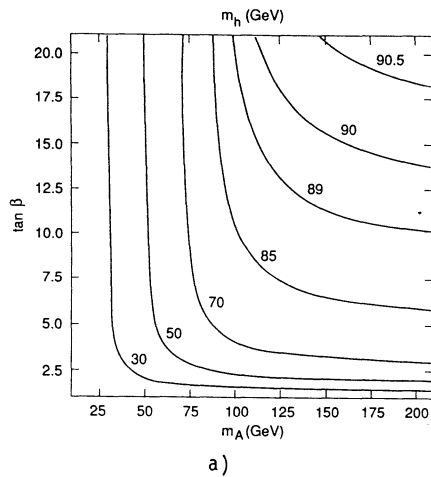
Fig.14: Cross-sections for $pp \rightarrow \phi(\rightarrow \gamma\gamma) + X$ at LHC, for $\tan \beta = 3$, $\tan \beta = 10$ and $\phi = h, H$ or A . The cross-sections are plotted as functions of m_A : the corresponding values of m_h and m_H can be read off Figs.1a and 1b.

Fig.15: The same as in Fig.13 but for $\tan \beta = 2$ and $\tan \beta = 30$.

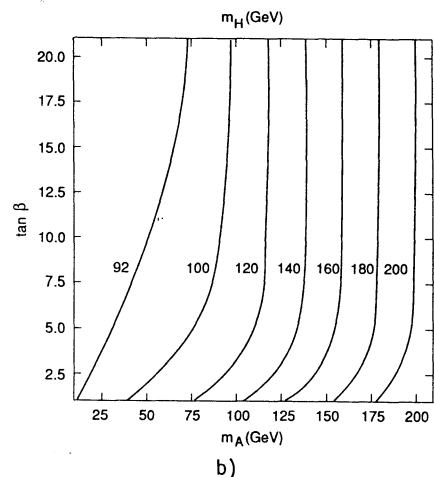
Fig.16: Cross-sections for $pp \rightarrow H(\rightarrow 4l) + X$ at LHC, for $\tan \beta = 2$ and $\tan \beta = 3$. The corresponding value for the standard model Higgs is also shown for comparison.

Fig.17: Signal for $A \rightarrow \tau^+\tau^-$ versus the background from $t\bar{t} \rightarrow \mu e + X$. The background has been evaluated for the conservative value $m_t = 130$ GeV.

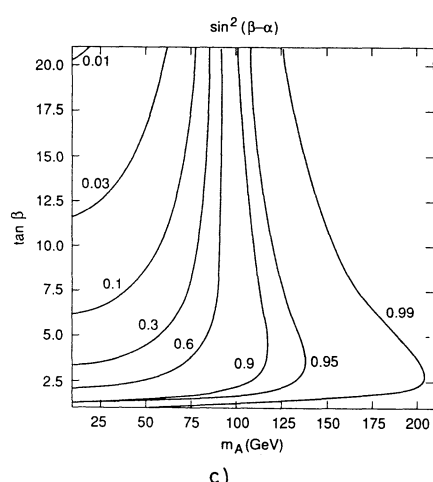
Fig.18: Artist's representation of the 'standard' (dotted), 'good' (hatched) and 'difficult' (empty) discovery regions in the $(m_A, \tan \beta)$ plane.



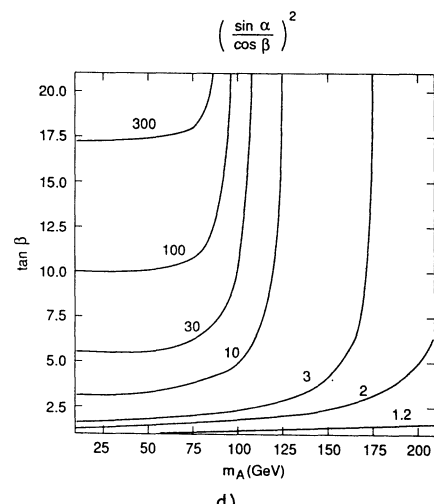
a)



b)



c)



d)

Fig. 1

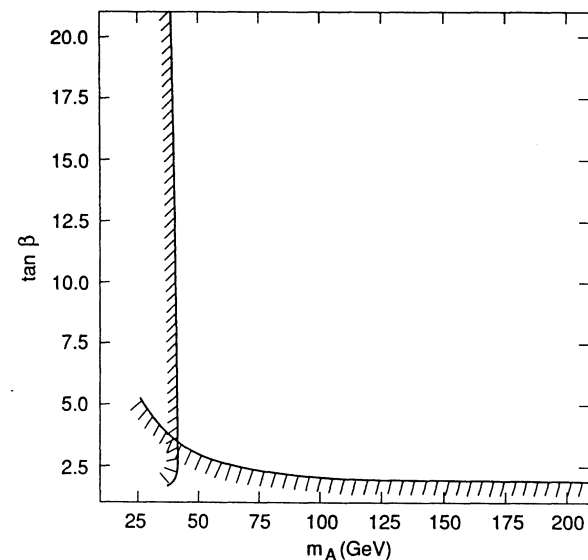
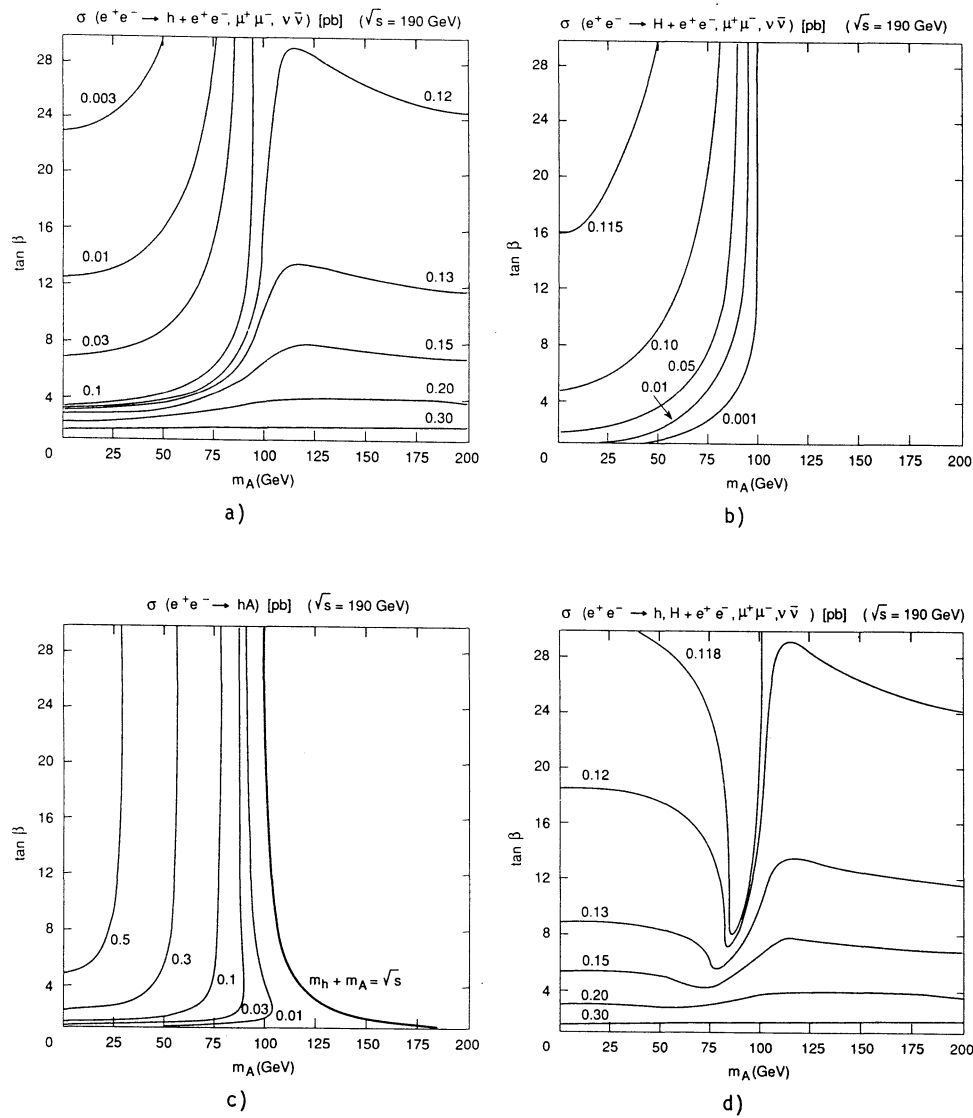
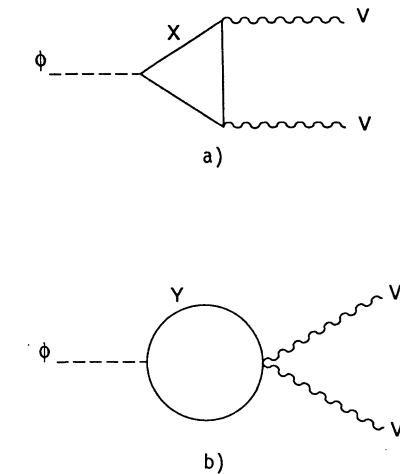


Fig. 2

**Fig. 3****Fig. 4**

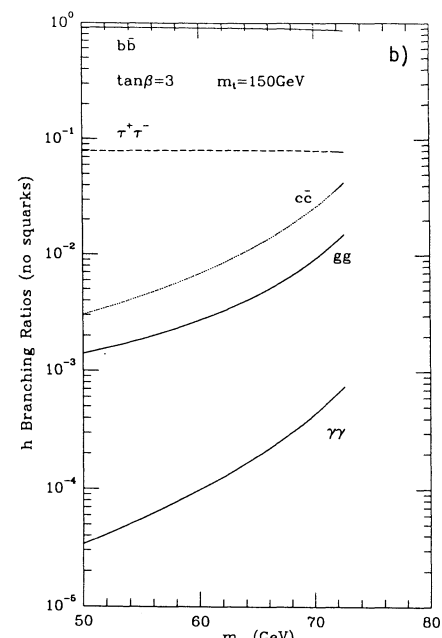
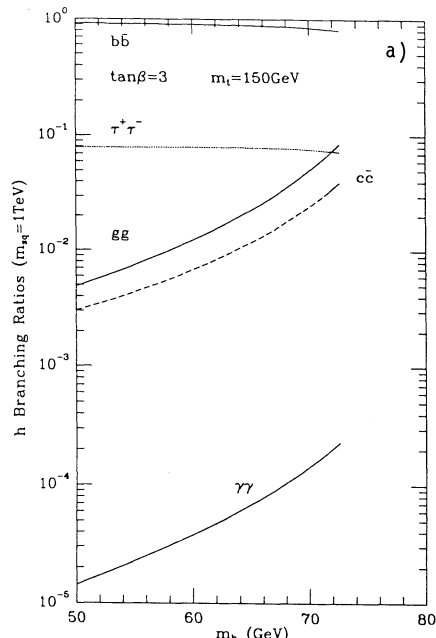


Fig. 5

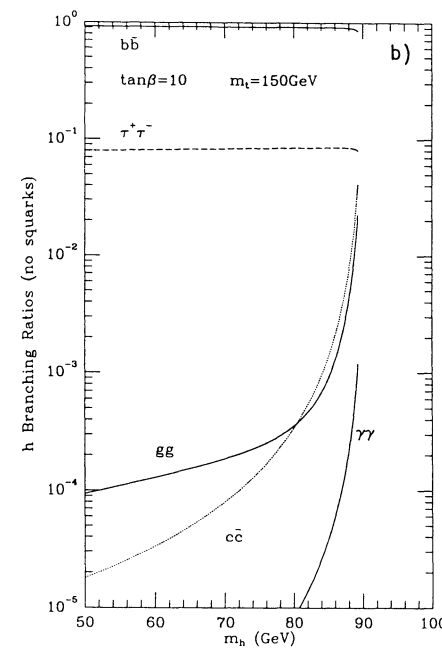
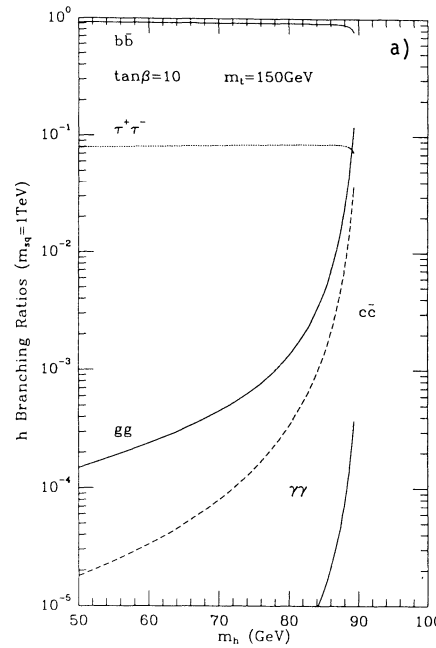


Fig. 6

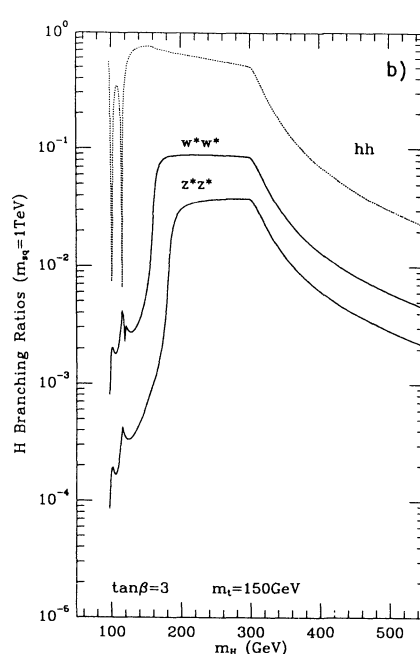
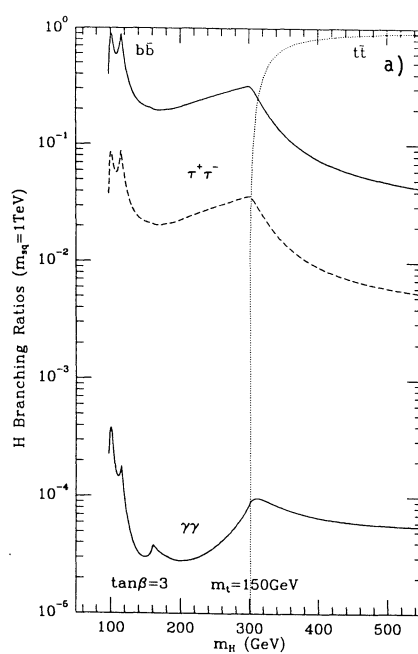


Fig. 7

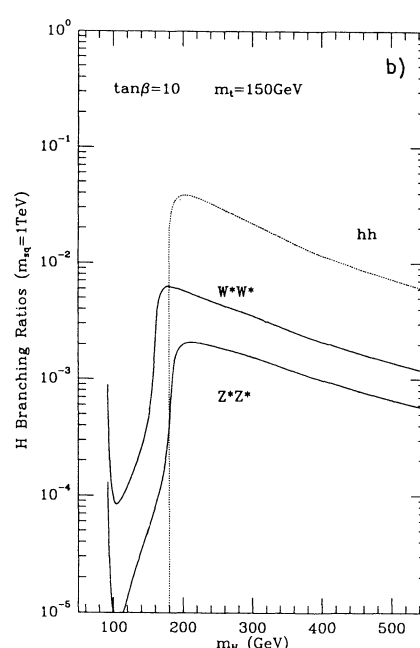
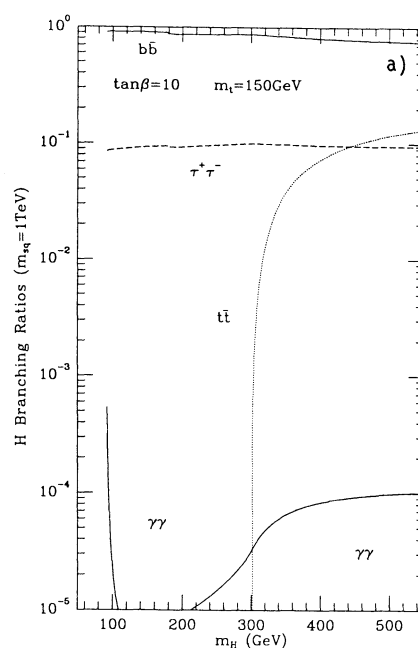


Fig. 8

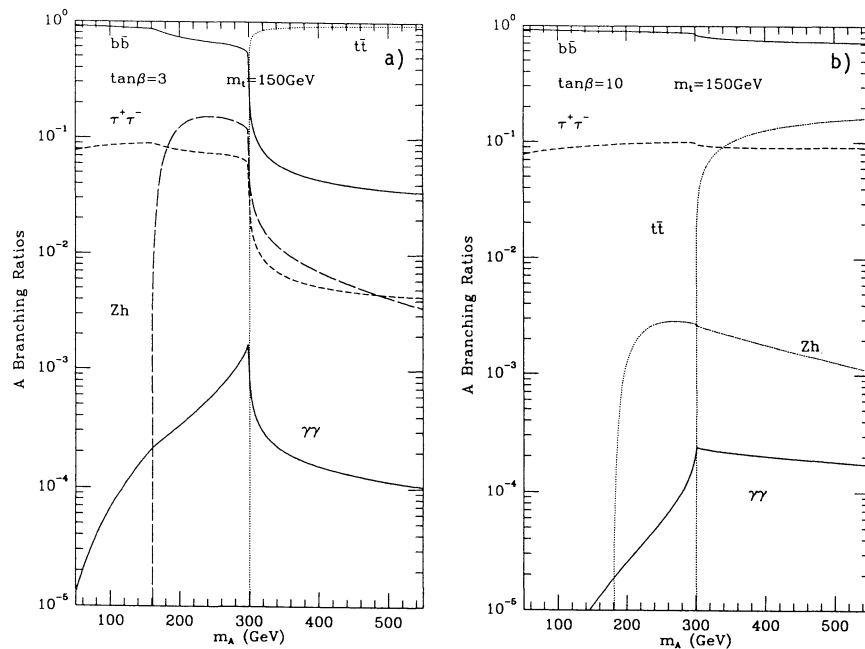


Fig. 9

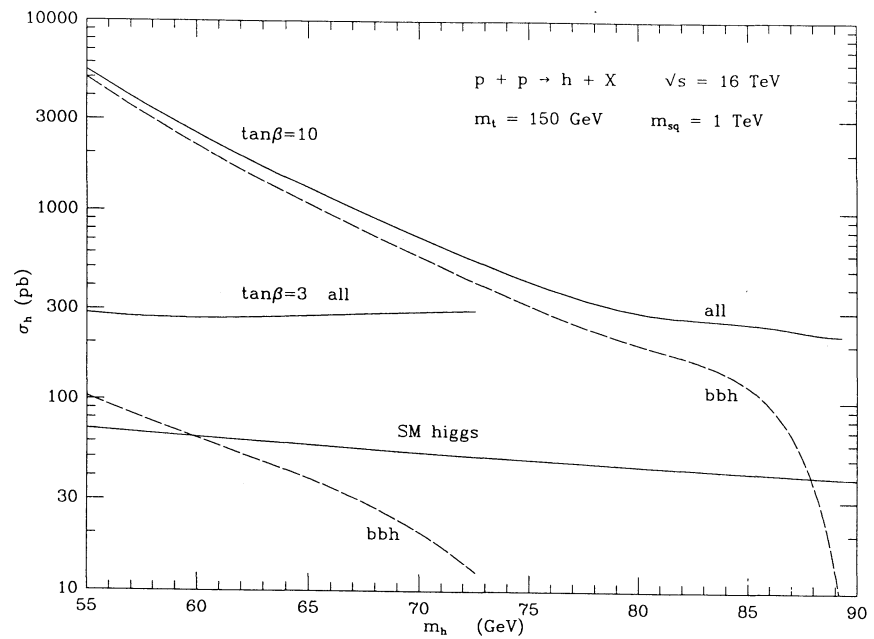


Fig. 11

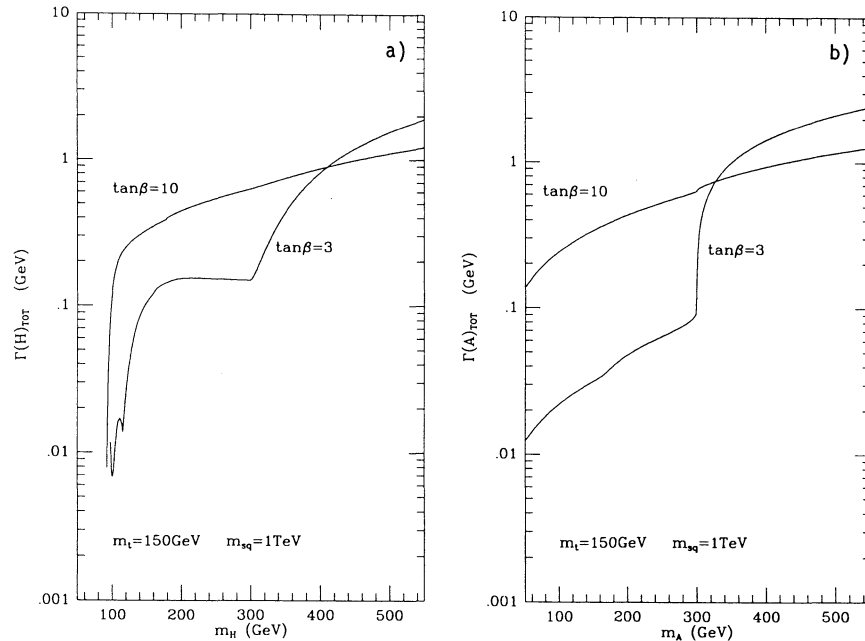


Fig. 10

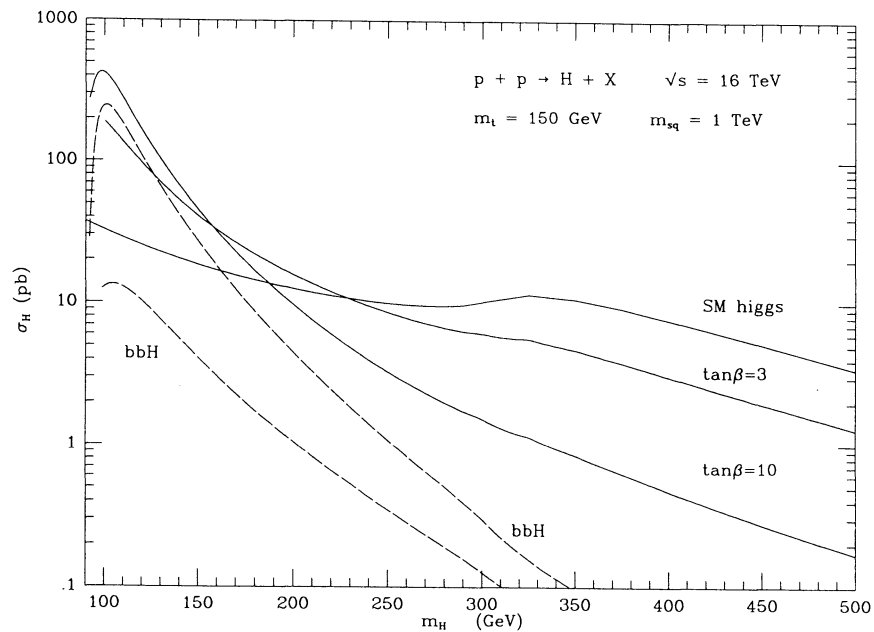


Fig. 12

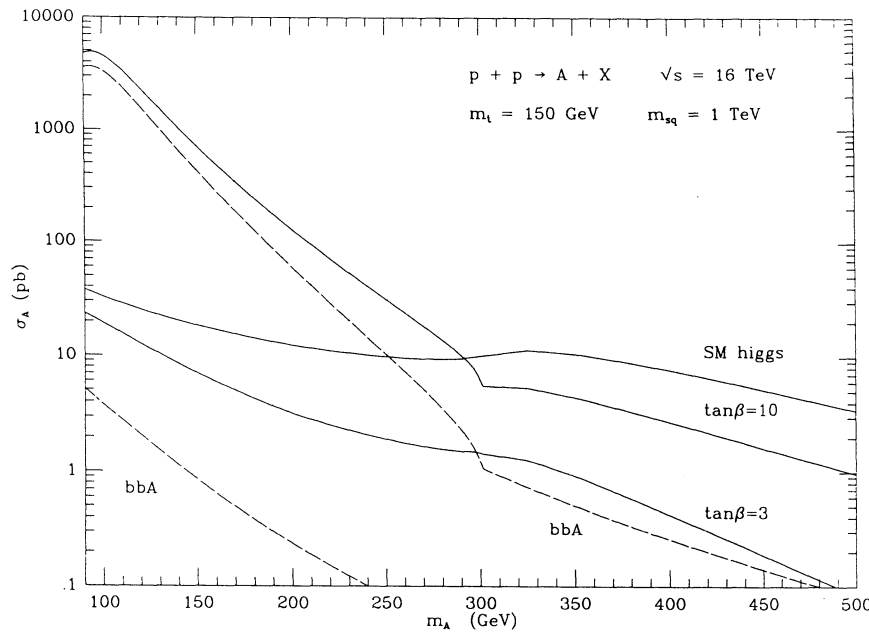


Fig. 13

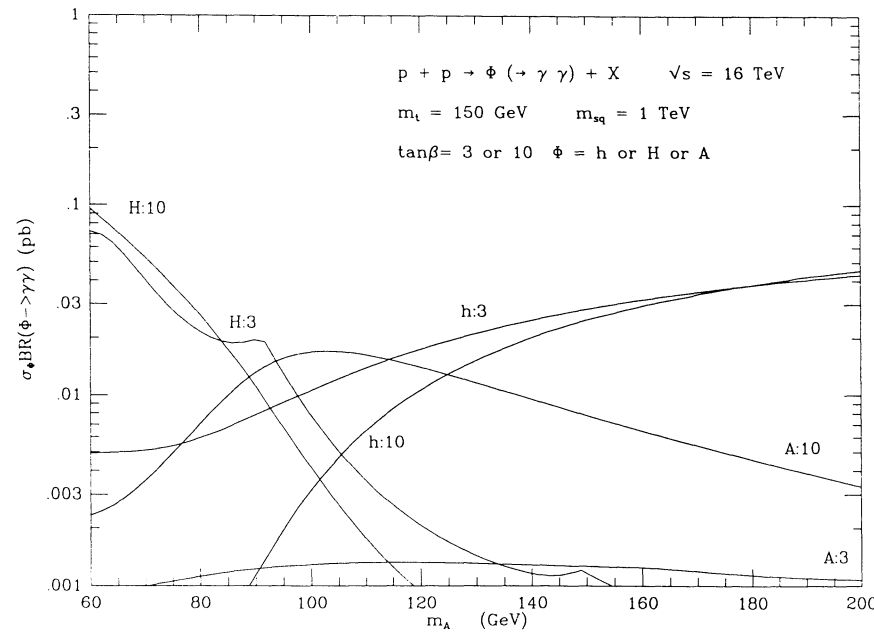


Fig. 14

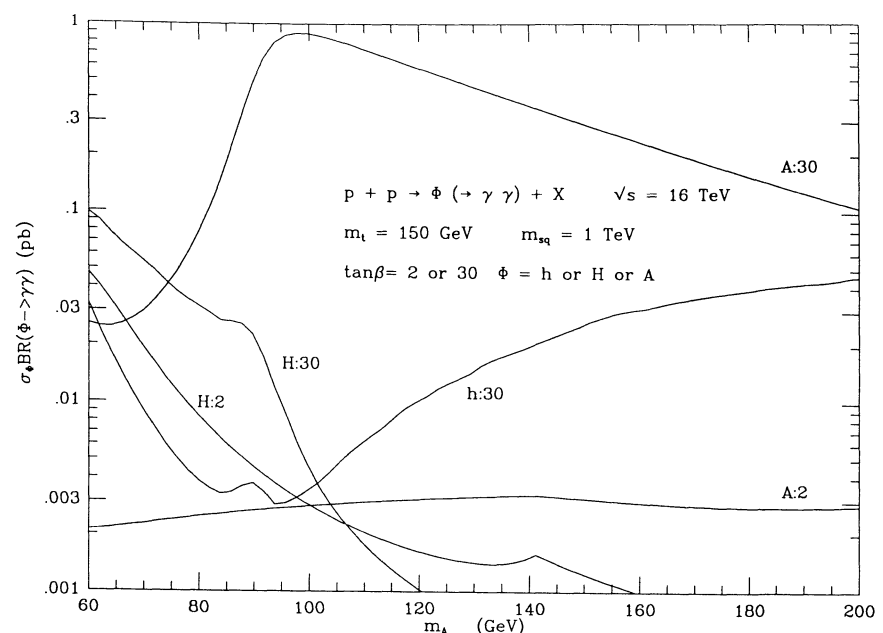


Fig. 15

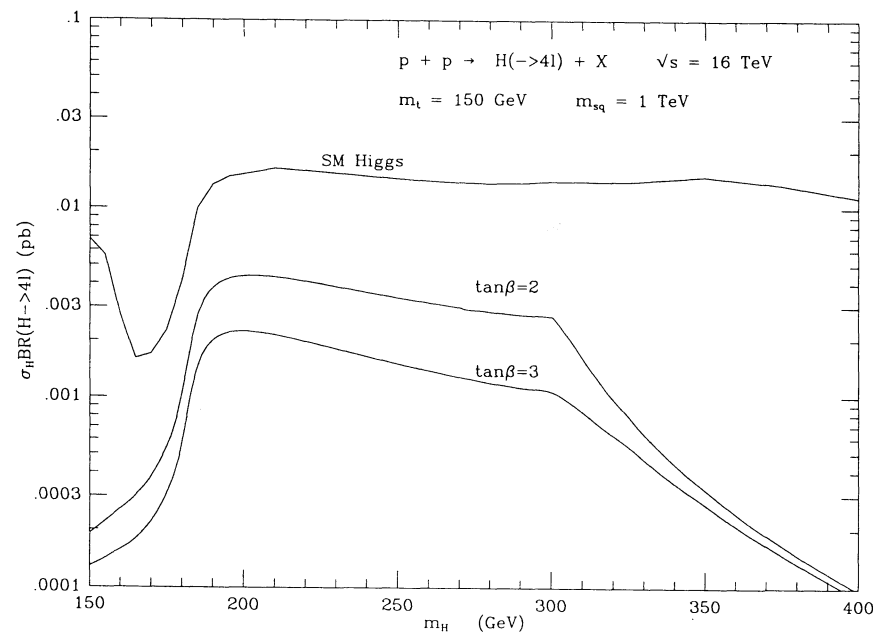


Fig. 16

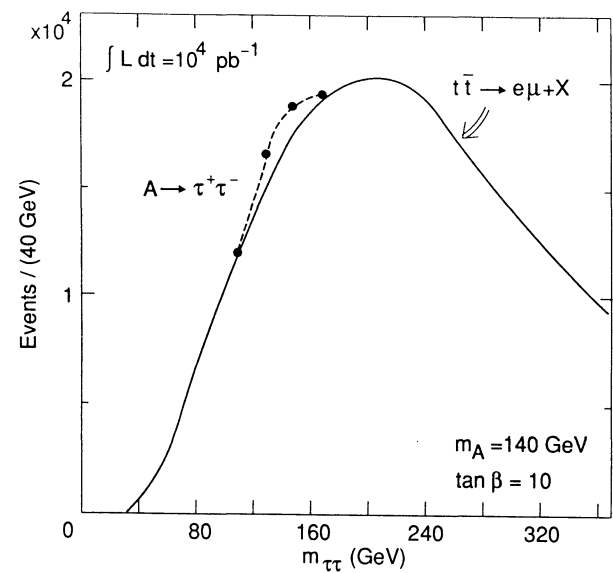


Fig. 17

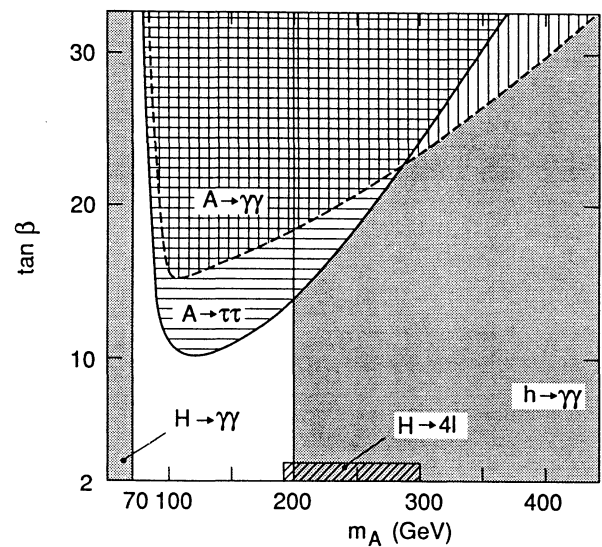


Fig. 18

Convenors:

G.G. Ross¹ and F. Zwirner^{2,3}

Contributors:

C. Albajar⁴, Ll. Amettler⁵, H. Baer⁶, R. Barbieri^{7,8}, A. Bartl⁹, P. Binetruy¹⁰,
F. Caravaglios^{7,8}, F. Del Aguila¹¹, S. Dimopoulos¹², M. Drees¹³, H. Dreiner¹,
D. Dzalo-Karatas¹⁴, J. Ellis², M. Frigeni^{7,8}, C. Fuglesang¹⁵, S. Hellman¹⁵, V. Jain¹⁶,
C. Llewellyn Smith¹, S. Lola¹, W. Majerotto¹⁷, M. Mangano^{8,18}, A. Martin¹⁹,
J. Mc Curry¹, B. Mele², B. Mösslacher¹⁷, E. Nagy²⁰, N. Oshimo^{17,21}, F. Pauss¹⁵,
G. Polesello¹⁵, M. Quirós²², G. Ridolfi²³, P. Sphicas¹⁵, S. Stippel⁹, X. Tata²⁴,
J.W.F. Valle²⁵, J. Woodside²⁶.

A6: SUPERSYMMETRY

¹Dept. of Theor. Physics, Univ. of Oxford, Oxford, United Kingdom

²Theory Division, CERN, Geneva, Switzerland

³INFN, Sezione di Padova, Padua, Italy

⁴Univ. Autonoma de Madrid, Madrid, Spain

⁵Dept. de Fisica i Eng. Nuclear, Univ. Polit. de Catalunya, Barcelona, Spain

⁶Physics Dept., Florida State University, Tallahassee, USA

⁷Dip. di Fisica, Univ. di Pisa, Pisa, Italy

⁸INFN, Sezione di Pisa, Italy

⁹Inst. für Theor. Physik, Univ. Wien, Vienna, Austria

¹⁰Div. de Physique Theorique, Univ. de Paris-Sud, Orsay, France

¹¹Dept. de Fisica Teorica y del Cosmos, Univ. de Granada, Granada, Spain

¹²Physics Dept., Stanford Univ., Stanford, USA

¹³Theory Group, DESY, Hamburg, Fed. Rep. of Germany

¹⁴Physics Dept., Univ. of Texas, Austin, USA

¹⁵PPE Division, CERN, Geneva, Switzerland

¹⁶Max Planck Institut, Munich, Fed. Rep. of Germany

¹⁷Inst. für Hochenergiephysik, Ost. Akad. der Wissenschaften, Vienna, Austria

¹⁸Scuola Normale Superiore, Pisa, Italy

¹⁹Dept. of Physics, Univ. of Durham, Durham, United Kingdom

²⁰CPPM, Marseille, France

²¹Centro de Fisica da Materia Condensada, Lisbon, Portugal

²²Inst. de Estructura de la Materia, Madrid, Spain

²³INFN, Sezione di Genova, Genoa, Italy

²⁴Dept. of Physics and Astronomy, Univ. of Hawaii, Honolulu, USA

²⁵Dept. de Fisica Teorica, Univ. de Valencia, Valencia, Spain

²⁶Physics Dept. and Ames Lab., Iowa State Univ., Ames, USA

Contents

1. Introduction
2. Cascade Decays of Gluinos and Squarks
3. Experimental Aspects of Gluino and Squark Searches
4. Neutralino and Chargino Production in Association with Gluinos and Squarks
5. Charginos and Neutralinos
6. Sleptons
7. Broken R-parity
8. Detection of Heavy Stable Exotics
9. Signals for a Superlight Gravitino

1 Introduction

Contributors: G. Ridolfi, G.G. Ross and F. Zwirner

1.1 The Minimal Supersymmetric Standard Model

The only known theoretical framework which can naturally accommodate elementary spin-0 particles such as the Higgs boson of the Standard Model (SM) is low-energy supersymmetry [1.1], effectively broken in the vicinity of the electroweak scale $G_F^{-1/2} \sim 300$ GeV (for reviews, see, for example, ref. [1.2]). The simplest phenomenological model which implements this idea is the Minimal Supersymmetric Standard Model (MSSM), defined by the following properties:

1. Minimal Gauge Group

As in the SM: $G \equiv SU(3)_C \times SU(2)_L \times U(1)_Y$.

2. Minimal Particle Content

The spin-1 gauge bosons of the SM, plus their spin- $\frac{1}{2}$ superpartners, the *gauginos*; the spin- $\frac{1}{2}$ quarks and leptons of the SM, plus their spin-0 superpartners, the *squarks* and the *sleptons*; two ¹ spin-0 Higgs doublets, $H_1 \equiv (H_1^0, H_1^-)$ and $H_2 \equiv (H_2^+, H_2^0)$, plus their spin- $\frac{1}{2}$ superpartners, the *higgsinos*.

3. Exact R-parity

To enforce baryon- and lepton-number conservation in renormalizable interactions, one imposes a multiplicative discrete symmetry called R-parity, defined as $R \equiv (-1)^{3B+L+2S}$, where S is the spin quantum number: in practice, $R = +1$ for SM particles and Higgs bosons, $R = -1$ for their supersymmetric partners, often called *sparticles*. The existence of an exact R-parity has important phenomenological implications: i) sparticles can only be produced in pairs, ii) sparticle decays always involve an odd number of sparticles in the final state, iii) the lightest supersymmetric particle (LSP) is absolutely stable.

4. Unification conditions

Supersymmetry breaking is parametrized by adding to the globally supersymmetric part of the Lagrangian, \mathcal{L}_{susy} , a collection of explicit supersymmetry breaking terms, \mathcal{L}_{soft} , including gaugino and scalar mass terms and trilinear scalar couplings². The most general form of \mathcal{L}_{soft} would contain a huge number of free parameters, and could lead to phenomenological problems with flavour-changing neutral currents. Motivated by the existing realizations of spontaneous supersymmetry breaking in supergravity and superstrings, one can parametrize all soft supersymmetry-breaking terms via a universal gaugino mass $m_{1/2}$, a universal scalar mass m_0 , and two other parameters assigned at the grand-unification scale³ M_U . The low-energy values of the parameters in \mathcal{L}_{soft} can then be obtained, in terms of the boundary conditions at M_U , by solving the renormalization group equations.

¹In supersymmetric models, at least two Higgs doublets are necessary to give masses to all quarks and charged leptons and to avoid gauge anomalies.

²These terms are called ‘soft’ because they preserve the good ultraviolet properties of global supersymmetry, namely the absence of dangerous quadratic divergences.

³Incidentally, one must remark that, in contrast to minimal $SU(5)$ grand unification, supersymmetric grand unification predicts a value of $\sin^2 \theta_W$ in excellent agreement with the measured one.

The assumptions which define the MSSM are plausible but not compulsory. Relaxing one of them (or more) leads to non-minimal supersymmetric extensions of the SM, with more parameters. For example, relaxing assumption 1 would imply the existence of new vector bosons: the phenomenology of these models is studied in ref. [1.3], both with and without supersymmetry. Assumption 2 can be relaxed in several different ways: one popular departure is the introduction of an extra singlet Higgs; another one is the introduction of extra matter multiplets such as the exotic states contained in the fundamental representation of E_6 . Assumption 3 is of crucial importance, since relaxing it can drastically modify the phenomenological signatures of supersymmetry: alternative models with broken R-parity are discussed in section 7. Finally, assumption 4 is theoretically and phenomenologically well-motivated, so there are not many reasons for relaxing it apart from generality.

1.2 The particle spectrum of the MSSM

In the R-even sector, the only new feature of the MSSM with respect to the SM is its extended Higgs sector, with two independent vacuum expectation values, $v_1 \equiv \langle H_1^0 \rangle$ and $v_2 \equiv \langle H_2^0 \rangle$, which can be taken to be real and positive without loss of generality. Quarks of charge $\frac{2}{3}$ have masses proportional to v_2 , quarks of charge $-\frac{1}{3}$ and charged leptons have masses proportional to v_1 . The W and Z masses are proportional to $\sqrt{v_1^2 + v_2^2}$, which is therefore fixed by their measured values. The remaining freedom is conveniently parametrized by $\tan \beta \equiv v_2/v_1$, whose allowed range of variation in the MSSM is

$$1 < \tan \beta \lesssim \frac{m_t}{m_b}. \quad (1.1)$$

The physical states of the MSSM Higgs sector are three neutral bosons (two CP-even, h and H , and one CP-odd, A) and a charged boson, H^\pm . It is important to realize that, at the tree level, all Higgs masses and couplings can be expressed in terms of two parameters only: a convenient choice is, for example, $(m_A, \tan \beta)$. Radiative corrections to the Higgs masses, however, depend on the top and squark masses and can be large [1.4], [1.5]: this has to be taken into account in phenomenological analyses. The neutral Higgses of the MSSM are discussed in detail in ref. [1.6], the charged ones in ref. [1.7].

In the R-odd sector of the MSSM, the spin-0 fields are the squarks and the sleptons. Neglecting intergenerational mixing, and leaving aside the stop squarks for the moment, their masses can easily be calculated in terms of the fundamental parameters m_0 , $m_{1/2}$, and $\tan \beta$:

$$m_{\tilde{f}}^2 = m_f^2 + m_{soft}^2(\tilde{f}) + m_D^2(\tilde{f}), \quad (1.2)$$

$$m_{soft}^2(\tilde{f}) = m_0^2 + C(\tilde{f})m_{1/2}^2, \quad (1.3)$$

$$m_D^2(\tilde{f}) = m_Z^2 \cos 2\beta (T_{3L}^f - \sin^2 \theta_W Q^f), \quad (1.4)$$

where, omitting generation indices, $f = [q \equiv (u, u^c, d, d^c), l \equiv (\nu, e), e^c]$ and $C(\tilde{q}) \sim 5 - 8$, $C(\tilde{l}) \simeq 0.5$, $C(\tilde{e}^c) \simeq 0.15$. In the case of the stop squarks, the mixing between \tilde{t}_L and \tilde{t}_R is proportional to the top-quark mass, so it cannot always be neglected, as will be discussed in more detail in section 3. Among the spin- $\frac{1}{2}$ particles one finds the strongly interacting gluinos, \tilde{g} , which have mass directly related to $m_{1/2}$ by

$$m_{\tilde{g}} \simeq \frac{\alpha_S(m_{\tilde{g}})}{\alpha_U} m_{1/2} \sim 2.75 m_{1/2}, \quad (1.5)$$

where α_U is the gauge coupling strength at the grand unification scale. The weakly interacting spin- $\frac{1}{2}$ particles are the $SU(2) \times U(1)$ gauginos ($\tilde{W}^\pm, \tilde{W}^0, \tilde{B}^0$) and the higgsinos ($\tilde{H}^\pm; \tilde{H}_1^0, \tilde{H}_2^0$). These interaction eigenstates mix non-trivially via their mass matrices: the two charged mass eigenstates, called *charginos*, are denoted by $\tilde{\chi}_i^\pm$ ($i = 1, 2$), and the four neutral mass eigenstates, called *neutralinos*, by $\tilde{\chi}_k^0$ ($k = 1, 2, 3, 4$). All masses and couplings in the chargino-neutralino sector can be described in terms of the three parameters $m_{1/2}$ [which determines the $SU(2) \times U(1)$ gaugino masses via relations analogous to eq.(1.5)], μ (a supersymmetric Higgs-Higgsino mass term which can be positive or negative), and $\tan \beta$. It should be noted that $\tilde{\chi}_1^0$, often denoted simply as $\tilde{\chi}$, is the favourite candidate for being the LSP. An alternative candidate is the tau sneutrino, but it is actually the LSP for a much smaller range of parameter space. Notice also that, contrary to what is often done in phenomenological analyses, there is no particular reason to assume that $\tilde{\chi}$ is a pure photino.

To summarize, the particle spectrum of the MSSM can be approximately described in terms of five basic parameters:

- the mass m_A of the CP-odd neutral Higgs boson (or any other Higgs mass),
- the ratio of VEVs, $\tan \beta \equiv v_2/v_1$,
- the universal gaugino mass $m_{1/2}$, or equivalently the gluino mass $m_{\tilde{g}}$,
- the universal scalar mass m_0 , or equivalently an average squark mass $m_{\tilde{q}}$,
- the supersymmetric Higgs-Higgsino mass μ .

Of course, the top quark mass is undetermined as in the SM. Moreover, some more subtleties have to be introduced for the description of the stop squark system, as will be done in sections 2 and 3.

1.3 Present limits and expectations

In order to set the stage for the discussion of supersymmetry searches at the LHC, it is useful to review first the present limits and the expected discovery potential of LEP II and of the Tevatron.

The Higgs sector of the MSSM is discussed in detail in ref. [1.6]. Here we just recall that from the present LEP data [1.8]

$$m_h > 33 \text{ GeV}, \quad m_A > 40 \text{ GeV}, \quad (95\% CL). \quad (1.6)$$

Using tree-level formulae, the present LEP limits can be translated into a lower bound on one of our basic low-energy parameters: $\tan \beta > 1.6$. However, it was recently shown in ref. [1.4] that, after inclusion of radiative corrections, values of $\tan \beta$ arbitrarily close to 1 are still allowed. Similar considerations apply to LEP II: using tree-level formulae, one could say that the MSSM can be completely tested at LEP II via its Higgs sector [1.6]: however, this is no longer true after inclusion of radiative corrections [1.4],[1.5].

The best limits on strongly interacting sparticles, squarks and gluinos, are obtained at hadronic colliders: they are usually presented in the $(m_{\tilde{q}}, m_{\tilde{g}})$ plane, but can be easily translated into the $(m_{1/2}, m_0)$ plane, which allows comparison with the limits on weakly interacting supersymmetric particles. Within the MSSM, the present data [1.9] tell us that

$$m_{\tilde{q}} > 150 \text{ GeV} \quad (90\% CL) \quad \text{for } m_{\tilde{g}} > m_{\tilde{q}}, \quad (1.7)$$

$$m_{\tilde{g}} > 100 \text{ GeV} \quad (90\% \text{ CL}) \quad \text{for } m_{\tilde{q}} > m_{\tilde{g}}. \quad (1.8)$$

Notice that the limits get stronger as gluino and squark masses get closer, and that the case $m_{\tilde{g}} \gg m_{\tilde{q}}$ is disfavoured by the MSSM. Future runs at the Tevatron collider should be sensitive to gluino and squark masses up to about 200 GeV. It should be stressed, however, that the above limits are derived assuming 6 degenerate squark flavours, and direct decays into a LSP of negligible mass: they do not apply, for example, to the case of a stop squark significantly lighter than the other squarks. More model-independent limits come from LEP, which is able to exclude squarks with masses less than about half of the Z mass [1.10]. In the future, LEP II should be sensitive to squark masses up to at least 80 GeV or so [1.11].

The present limits on weakly interacting sparticles are dominated by the LEP data. Direct searches [1.12] and precision measurements of the Z properties [1.13] exclude charged sleptons and sneutrinos with masses less than about $m_Z/2$. LEP II will not significantly improve the present limits on sneutrinos, but should be able to bring the limits on charged sleptons up to roughly 80 GeV [1.11]. In the chargino-neutralino sector, the present limits come from direct searches [1.14] and from precision measurements of the Z properties [1.13]: charginos with mass less than about $m_Z/2$ are excluded, whereas the lightest neutralino could still be very light for small values of $\tan \beta$. LEP II should be sensitive to chargino masses up to about 80 GeV, with weaker sensitivity to neutralinos [1.11].

The present experimental limits on supersymmetric particles, and the corresponding expectations after the conclusion of the LEP and Tevatron programmes, are summarized schematically in figs. 1.1 and 1.2. Figure 1.1 shows μ -independent limits in the $(m_0, m_{1/2})$ plane, for the representative values $\tan \beta = 2, 10$. Figure 1.2 shows m_0 -independent limits in the $(\mu, m_{1/2})$ plane, for the same representative values of $\tan \beta$. The figures also show some contours of the relevant sparticle masses in the range of interest for the LHC.

1.4 Overview

The present report is organized as follows.

The first part studies ‘standard’ signals for supersymmetry, in the framework of the MSSM. Sections 2 and 3 deal with searches for strongly interacting sparticles. In section 2, cascade decays of gluinos and squarks into lighter sparticles are studied: a correct treatment of the sparticle branching ratios is essential for the assessment of the LHC discovery limits. Section 3 discusses in great detail the experimental aspects of gluino and squark searches. Different and complementary signals are considered, and the case of a light stop squark is discussed separately. The conclusion is that gluinos and squarks up to masses $O(1 \text{ TeV})$ have excellent prospects for being discovered at the LHC. Also a stop squark sufficiently lighter than the top quark should give an identifiable signal. Section 4 discusses the production of weakly interacting sparticles (charginos and neutralinos) in association with the strongly interacting ones (gluinos and squarks): these processes could give useful complementary signals in the case of relatively light gluinos and squarks. Finally, sections 5 and 6 discuss the possible signals from Drell-Yan production of weakly interacting sparticles. Section 5 studies charginos and neutralinos originating multileptonic final states: the conclusion is that LHC can go significantly beyond the LEP II limits if the top quark mass is heavy enough. Section 6 studies the case of charged and neutral sleptons, and reaches similar conclusions. In both cases, a more detailed simulation of signal and background should be performed before the conclusions can be considered as final.

The second part of this report deals with non-minimal models of low-energy supersymmetry. Section 7 discusses the case in which R-parity is broken, so that the LSP is no longer stable and single sparticle production can occur. As a result the missing energy signals of the MSSM corresponding to LSP production are changed into visible energy of the LSP decay products. In some cases, signals of supersymmetry with broken R-parity could be quite spectacular and unmistakeable. In other cases the missing energy may be converted into hadronic energy but even in these cases we find observable signals for a large range of the parameter space although it is important to look for characteristic signals other than missing energy. More exotic possibilities, like a charged or coloured LSP and a superlight gravitino, are discussed in sections 8 and 9.

References

- [1.1] L. Maiani, Proc. Summer School on Particle Physics, Gif-sur-Yvette, 1979 (IN2P3, Paris, 1980), p. 1;
M. Veltman, Acta Physica Polonica B12 (1981) 437;
E. Witten, Nucl. Phys. B188 (1981) 513;
S. Dimopoulos and H. Georgi, Nucl. Phys. B193 (1981) 150;
N. Sakai, Z. Phys. C11 (1982) 153.
- [1.2] H.-P. Nilles, Phys. Rep. 110 (1984) 1;
H.E. Haber and G.L. Kane, Phys. Rep. 117 (1985) 75;
G.G. Ross, in ‘Supersymmetry: A Decade of Development’ (P.C. West ed.), p.374;
R. Barbieri, Riv. N. Cim. 11 (1988) 1;
F. Zwirner, preprint CERN-TH.5968/90.
- [1.3] P. Chiappetta and M. Greco, summary report of the New Vector Bosons study group, these Proceedings.
- [1.4] J. Ellis, G. Ridolfi and F. Zwirner, preprint CERN-TH.5946/90, GEF-TH-26/1990.
- [1.5] H.E. Haber and R. Hempfling, University of Santa Cruz preprint SCIPP-90/42 (1990);
Y. Okada, M. Yamaguchi and T. Yanagida, Tohoku University preprint TU-360 (1990) and Erratum.
- [1.6] Z. Kunszt and F. Zwirner, contribution to the Higgs study group, these Proceedings and preprint CERN-TH.5994/90, ETH-TH/90-49.
- [1.7] E. Reya, P. Zerwas et al., summary report of the Top Physics study group, these Proceedings.
- [1.8] D. Decamp et al. (ALEPH Collaboration), Phys. Lett. B236 (1990) 233, Phys. Lett. B237 (1990) 291, preprints CERN-EP/90-16, CERN-EP/90-70, CERN-PPE/90-101;
P. Abreu et al. (DELPHI Collaboration), preprints CERN-EP/90-44, CERN-EP/90-60 and CERN-PPE/90-163;
B. Adeva et al. (L3 Collaboration), preprints L3-10, L3-15 and L3-19;
M.Z. Akrawy et al. (OPAL Collaboration), Phys. Lett. B236 (1990) 224, preprints CERN-EP/90-100, CERN-PPE/90-116, CERN-PPE/90-150.

- [1.9] J. Alitti et al. (UA2 Collaboration), Phys. Lett. B235 (1990) 363;
F. Abe et al. (CDF Collaboration), Phys. Rev. Lett. 62 (1989) 1825;
G.P. Yeh (CDF Collaboration), preprint Fermilab-Conf-90/138-E.
- [1.10] P. Abreu et al. (DELPHI Collaboration), preprint CERN-EP/90-79.
- [1.11] Proceedings of the ECFA Workshop on LEP 200 (A. Böhm and W. Hoogland eds.),
Aachen-1986, report CERN 87-08, ECFA 87/108 (1987).
- [1.12] D. Decamp et al. (ALEPH Collaboration), Phys. Lett. B236 (1990) 86;
P. Abreu et al. (DELPHI Collaboration), preprints CERN-EP/90-80;
B. Adeva et al. (L3 Collaboration), Phys. Lett. B233 (1990) 530;
M.Z. Akrawy et al. (OPAL Collaboration), Phys. Lett. B240 (1990) 261.
- [1.13] E. Fernandez, preprint CERN-PPE/90-151 and references therein.
- [1.14] D. Decamp et al. (ALEPH Collaboration), Phys. Lett. B236 (1990) 86, preprint
CERN-EP/90-63;
P. Abreu et al. (DELPHI Collaboration), preprints CERN-EP/90-80;
B. Adeva et al. (L3 Collaboration), Phys. Lett. B233 (1990) 530;
M.Z. Akrawy et al. (OPAL Collaboration), Phys. Lett. B240 (1990) 261, preprint
CERN-PPE/90-95.

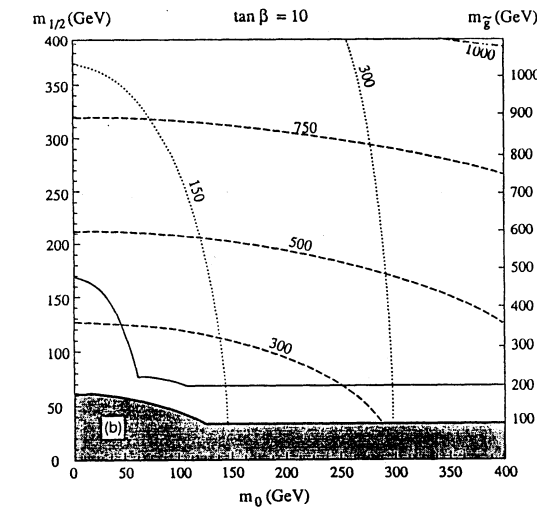
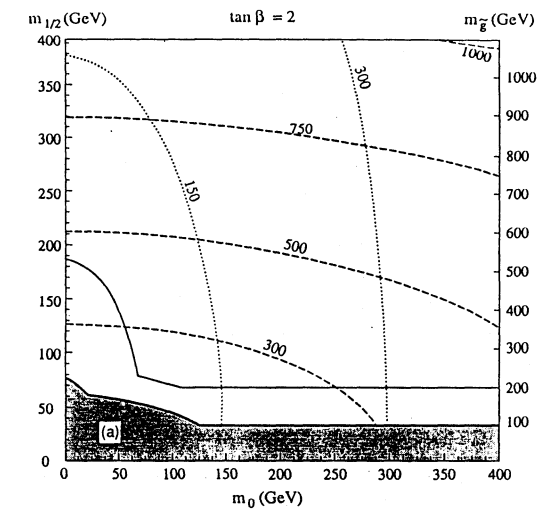


Fig. 1.1: Present limits and future sensitivity in the $(m_0, m_{1/2})$ plane, for the representative values $\tan \beta = 2, 10$ and using μ -independent constraints. The shaded area is excluded by the present data, whereas the solid lines correspond to the estimated discovery potential of the complete LEP and Tevatron programs. Dashed lines correspond to fixed values of an 'average' squark mass, defined by the relation $m_{\tilde{q}} = \sqrt{m_0^2 + 5.5m_{1/2}^2}$. Dotted lines correspond to fixed values of the mass of the lightest charged slepton (\tilde{e}^\pm), as given in the text. The values of the gluino mass as given by eq. (1.5) are also shown.

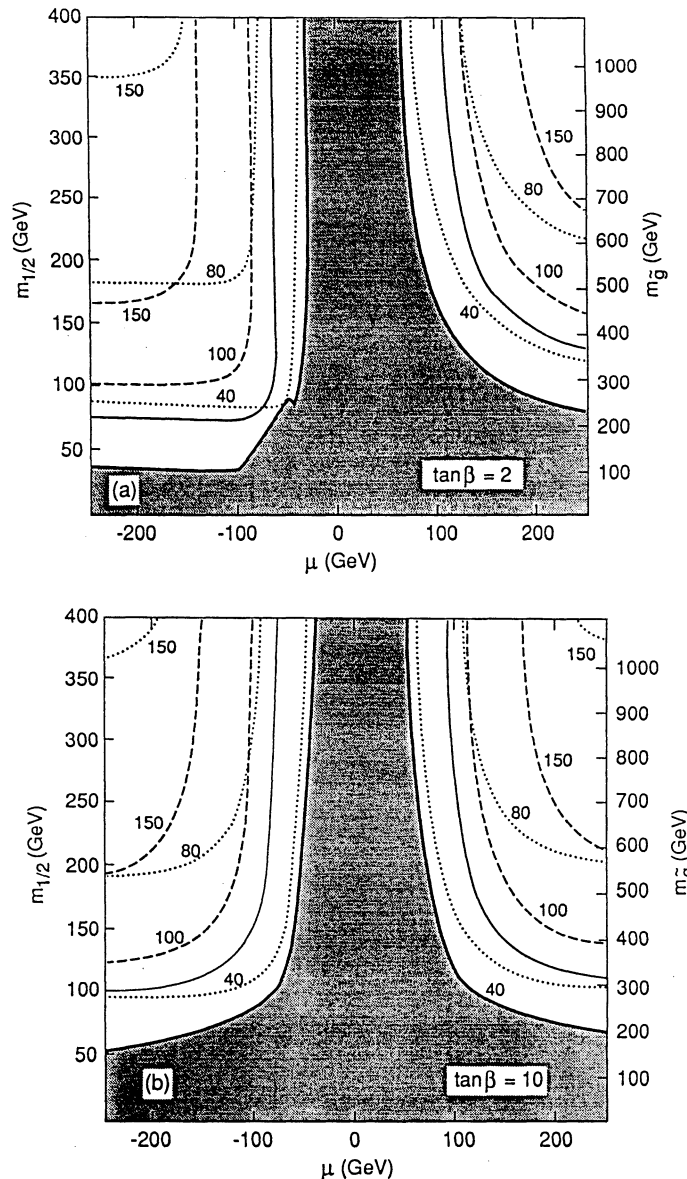


Fig. 1.2: Present limits and future sensitivity in the $(\mu, m_{1/2})$ plane, for the representative values $\tan \beta = 2, 10$ and using m_0 -independent constraints. The shaded area is excluded by the present data, whereas the solid lines correspond to the estimated discovery potential of the complete LEP and Tevatron programs. Dashed and dotted lines correspond to fixed values of the lightest chargino and neutralino mass, respectively. The values of the gluino mass as given by eq. (1.5) are also shown.

2 Cascade Decays of Gluinos and Squarks

Contributors: A. Bartl, W. Majorotto, B. Mösslacher, N. Oshimo and S. Stippel

For the actual detection of gluinos and squarks it is crucial to consider all their possible decay modes. If squarks are heavier than gluinos then the gluinos decay into

$$\tilde{g} \rightarrow q + \bar{q} + \tilde{\chi}_i^0, \quad (2.1)$$

$$\tilde{g} \rightarrow q + \bar{q}' + \tilde{\chi}_i^\pm, \quad (2.2)$$

$$\tilde{g} \rightarrow g + \tilde{\chi}_i^0. \quad (2.3)$$

The charginos and neutralinos in turn decay according to ($H_1^0 \equiv H$, $H_2^0 \equiv h$, $H_3^0 \equiv A$)

$$\tilde{\chi}_i^0 \rightarrow Z^0 + \tilde{\chi}_k^0, W^\pm + \tilde{\chi}_k^\mp, H_l^0 + \tilde{\chi}_k^0, H^\pm + \tilde{\chi}_k^\mp, \quad (2.4)$$

$$\tilde{\chi}_i^\pm \rightarrow Z^0 + \tilde{\chi}_k^\pm, H_l^0 + \tilde{\chi}_k^\pm, W^\pm + \tilde{\chi}_k^0, H^\pm + \tilde{\chi}_k^0, \quad (2.5)$$

if kinematically allowed. If the mass differences are too small, such that the two-body decays are forbidden, the decays $\tilde{\chi}_i^\pm \rightarrow l^\pm + \nu + \tilde{\chi}_k^0$, $q + \bar{q}' + \tilde{\chi}_k^0$, $\tilde{\chi}_i^0 \rightarrow l^+ + l^- + \tilde{\chi}_k^0$, etc. may become important. This will, in general, lead to cascade decays of squarks and gluinos. They end when the lightest supersymmetric particle $\tilde{\chi}_1^0$ is reached. If gluinos are heavier than squarks, then the squarks, have the following decay modes

$$\tilde{q}_{L,R} \rightarrow q + \tilde{\chi}_i^0 \quad (2.6)$$

$$\tilde{u}_{L,R} \rightarrow d + \tilde{\chi}_i^\pm \quad (2.7)$$

$$\tilde{d}_L \rightarrow u + \tilde{\chi}_i^- . \quad (2.8)$$

The neutralinos and charginos again decay as described above. Also here a variety of cascade decays is possible until the lightest neutralino is produced.

In the following we shall present a systematic study of all possible gluino- and squark-decay modes. We shall investigate the whole supersymmetry parameter space relevant for the LHC. We have extended the results of previous studies [2.1] in various ways. In our calculation of the decay widths for $\tilde{g} \rightarrow t + \bar{t} + \tilde{\chi}_i^0$, $\tilde{g} \rightarrow t + \bar{b} + \tilde{\chi}_i^-$, $\tilde{g} \rightarrow b + \bar{t} + \tilde{\chi}_i^+$ we have fully taken into account the top Yukawa coupling as well as all top mass terms. In comparison with Ref. [2.2] we have found that they are important. Furthermore, we have included the loop decay $\tilde{g} \rightarrow g + \tilde{\chi}_i^0$, Eq. (2.3). In discussing squark decays it is also important to include the top Yukawa coupling in the decays $\tilde{t}_{L,R} \rightarrow t + \tilde{\chi}_i^0$, $\tilde{t}_R \rightarrow b + \tilde{\chi}_i^+$, $\tilde{b}_L \rightarrow t + \tilde{\chi}_i^-$. A more comprehensive discussion of gluino and squark decays into heavy top quarks is given in Ref. [2.3].

As will be shown here, despite the complexity of the decay patterns of gluinos and squarks it is possible to find suitable signatures for detecting these particles.

2.1 Discussion of gluino decays

At the LHC gluinos in a mass range up to ~ 1 TeV can be explored. In this section we shall assume that the gluinos are lighter than the squarks. In the numerical examples given below

we shall take $m_{\tilde{q}_L} = m_{\tilde{q}_R} = 2m_{\tilde{g}}$, $\tan \beta = 2$, $M'/M = 5/3 \tan^2 \theta_W$, $M/m_{\tilde{g}} = \alpha_2/\alpha_s$, $m_{\tilde{g}} \simeq 0.3m_{\tilde{g}}$, $\alpha_s = 0.1$, $\sin^2 \theta_W = 0.23$, and $m_t = 150$ GeV. Considering first gluino decays into light quarks, $\tilde{g} \rightarrow q + \bar{q} + \tilde{\chi}_i^{0,\pm}$, then for $|\mu| \leq m_{\tilde{g}}/3$ mainly the heavy chargino and the heaviest neutralino would be produced, whereas for $|\mu| \geq m_{\tilde{g}}/3$ the decays into the light chargino and the second lightest neutralino would dominate. This decay pattern is changed if the transitions $\tilde{g} \rightarrow g + \tilde{\chi}_i^0$ are also included, and in the decays $\tilde{g} \rightarrow t + \bar{t} + \tilde{\chi}_i^0$, $t + \bar{b} + \tilde{\chi}_i^0$, $b + \bar{t} + \tilde{\chi}_i^+$ the top mass is fully taken into account. In Fig. 2.1a we show the branching ratios for these decays into top quarks as a function of μ for a gluino mass $m_{\tilde{g}} = 1000$ GeV. Contrary to the light-quark case, in the parameter domain $|\mu| \leq m_{\tilde{g}}/3$ the dominant transition is that into the light chargino.

As to the loop decays $\tilde{g} \rightarrow g + \tilde{\chi}_i^0$, their branching ratios can go up to about 20%. The branching ratios for $\tilde{g} \rightarrow \tilde{\chi}_i^0 + q + \bar{q}$ (or g) and $\tilde{g} \rightarrow \tilde{\chi}_i^\pm + q + \bar{q}'$, summed over all quark flavours, are shown in Fig. 2.1b. Owing to the Yukawa coupling of the top quark there are appreciable transition rates into the light chargino and the light neutralinos for $|\mu| < m_{\tilde{g}}/3$. For $|\mu| > m_{\tilde{g}}/3$ the decays into the light chargino and the second lightest neutralino are the most important ones. Notice that the branching ratio for the decay into the lightest neutralino which leads to the classical signature for supersymmetry (large missing energy plus jets) is about 15 percent. It is smaller than that of the decay into $\tilde{\chi}_2^0$. The decay into $\tilde{\chi}_3^0$ occurs owing to $\tilde{g} \rightarrow g + \tilde{\chi}_3^0$.

We shall now discuss the interesting signatures for gluino production $p + p \rightarrow \tilde{g} + \tilde{g} + X$. As a result of the chargino and neutralino decays [2.4], Eqs. (2.4) and (2.5), the final state in general contains Z^0 , W^\pm , Higgs particles, jets, leptons, neutrinos, and $\tilde{\chi}_1^0$'s. Of particular interest is the case where the gluino decays directly into $\tilde{\chi}_1^0$. Figure 2.2a shows the probability that only one of the gluinos decays directly into $\tilde{\chi}_1^0$ or both, for $m_{\tilde{g}} = 500$ GeV. The probability for one direct $\tilde{\chi}_1^0$ is about 30 %, for two direct $\tilde{\chi}_1^0$ a few per cent, only weakly dependent on μ . We also indicate the region in μ which will be covered by searching for charginos and neutralinos in the full energy range of LEP. For heavier gluinos we have found smaller values of these branching ratios (within a factor of 3) and a stronger dependence on μ .

Another way to search for gluinos could be to look for Z^0 's in the final state. We have calculated the branching ratio for $\tilde{g} + \tilde{g} \rightarrow 2Z^0 + \text{anything}$. It is shown in Fig. 2.2b for $m_{\tilde{g}} = 1000$ GeV (taking a charged Higgs mass $m_{H^\pm} = 500$ GeV). The branching ratio is a few per cent. In the case of $m_{\tilde{g}} = 500$ GeV the $2Z^0$ branching ratio becomes very small for $|\mu| > 300$ GeV because of phase space.

For detecting gluinos the rate of events with isolated leptons will be important. In Fig. 2.2b we show the branching ratios $\tilde{g} + \tilde{g} \rightarrow 4\mu$, 5μ , and 6μ . Here we have summed over all events with μ 's coming from Z^0 , W^\pm , and three-body decays of charginos and neutralinos, and from t -quark decays into bW . For $m_{\tilde{g}} = 1000$ GeV the 4μ rate is about 10^{-4} and the 5μ rate between 10^{-5} and 10^{-6} . In the case where $m_{\tilde{g}} = 500$ GeV these branching ratios depend more strongly on $\tan \beta$. For $\tan \beta = 10$ the 4μ branching ratio is about 10^{-4} and the 5μ branching ratio between 10^{-5} and 10^{-7} , whereas for $\tan \beta = 2$ the corresponding values are much smaller.

2.2 Discussion of squark decays

In this section we consider the case where the squarks are lighter than the gluinos. At the LHC a squark mass range up to ~ 1 TeV can be explored. In the following we shall always assume $m_{\tilde{q}} = 1.5m_{\tilde{g}}$, $m_{\tilde{q}_L} = m_{\tilde{q}_R}$.

If the quarks in the final state of Eqs. (2.6)–(2.8) are light, right squarks decay only into neutralinos, for $|\mu| > m_{\tilde{g}}/3$ to practically 100 percent into $\tilde{\chi}_1^0$, and for $|\mu| < m_{\tilde{g}}/3$ to more than 90 percent into $\tilde{\chi}_3^0$. Left squarks decay dominantly into charginos as can be seen in Fig. 2.3a, where we plot the branching ratios of $\tilde{u}_L \rightarrow d + \tilde{\chi}_i^+$, $u + \tilde{\chi}_i^0$ for $m_{\tilde{q}} = 500$ GeV. For $|\mu| > m_{\tilde{g}}/3$ ($|\mu| < m_{\tilde{g}}/3$) the transition into the lighter (heavier) chargino has the largest branching ratio. The decays into $\tilde{\chi}_2^0$ ($\tilde{\chi}_4^0$) have appreciable rates for $|\mu| > m_{\tilde{g}}/3$ ($|\mu| < m_{\tilde{g}}/3$). A qualitatively similar pattern holds for \tilde{d}_L decays.

Taking into account the top-quark mass again changes the picture just described. The \tilde{t}_R now dominantly decays into charginos. For $|\mu| \leq m_{\tilde{g}}/3$ the transition into the lighter chargino accounts for approximately 50% of all \tilde{t}_R decays. In the decays of the \tilde{t}_L the essential changes due to the top mass occur in the region $|\mu| \leq m_{\tilde{g}}/3$ (see Fig. 2.3b). Now the decays into $\tilde{\chi}_1^0$, $\tilde{\chi}_2^0$, $\tilde{\chi}_3^0$ become important, as can be seen by comparing Figs. 2.3a and 2.3b. Also the decays of \tilde{b}_L are substantially influenced by the top-quark mass terms [2.3].

We have calculated the probabilities that the squarks produced decay directly into exactly one or two $\tilde{\chi}_1^0$, i.e. $\tilde{q} + \bar{q} \rightarrow \tilde{\chi}_1^0 + X$ and $\tilde{q} + \bar{q} \rightarrow \tilde{\chi}_1^0 + \tilde{\chi}_1^0 + X$ (where X does not contain another $\tilde{\chi}_1^0$). We have averaged over left and right squarks and all flavours. The results are shown in Fig. 2.4a for $m_{\tilde{q}} = 500$ GeV. It is remarkable that over a large range of μ the branching ratio into $2\tilde{\chi}_1^0$ is almost an order of magnitude larger than that of producing only one $\tilde{\chi}_1^0$. This implies that about 40% of the events coming from squark production will have a large missing energy. The reason is that for $|\mu| \geq m_{\tilde{g}}/3$ the right squarks (except \tilde{t}_R) almost exclusively decay into $\tilde{\chi}_1^0$. This feature is also quite independent of $\tan \beta$.

On the other hand, the squarks may decay in cascades until the lightest supersymmetric particle is produced. We show in Fig. 2.4b the rate for $\tilde{q} + \bar{q} \rightarrow 2Z^0 + \text{anything}$ for $m_{\tilde{q}} = 750$ GeV (taking a charged Higgs mass $m_{H^\pm} = 500$ GeV). Depending on μ this rate can go up to a few per cent. Figure 2.4b also shows the rate of multimuon events, i.e. $\tilde{q} + \bar{q} \rightarrow 4\mu$, 5μ , 6μ , including all μ 's coming from Z^0 , W^\pm , and three-body decays of neutralinos and charginos as well as from t -quark decay $t \rightarrow Wb$.

References

- [2.1] H. Baer, V. Barger, D. Karatas and X. Tata, Phys. Rev. (1987) 96; R.M. Barnett, J.F. Gunion and H.E. Haber, Phys. Rev. Lett. **60** (1988) 401; Phys. Rev. **D37** (1988) 1892; R. Barbieri, G. Gamberini, G. Giudice and G. Ridolfi, Nucl. Phys. **B301** (1988) 15
- [2.2] H. Baer, X. Tata and J. Woodside, Phys. Rev. **D42** (1990) 1568.
- [2.3] A. Bartl, W. Majerotto, B. Mösslacher, N. Oshimo and S. Stippel, HEPHY-PUB-538/90, UWThPh-1990-47.
- [2.4] J.F. Gunion and H.E. Haber, Phys. Rev. **D37** (1988) 2515; H. Baer, A. Bartl, D. Karatas, W. Majerotto and X. Tata, Int. Journ. Mod. Phys. **A4** (1989) 4111.

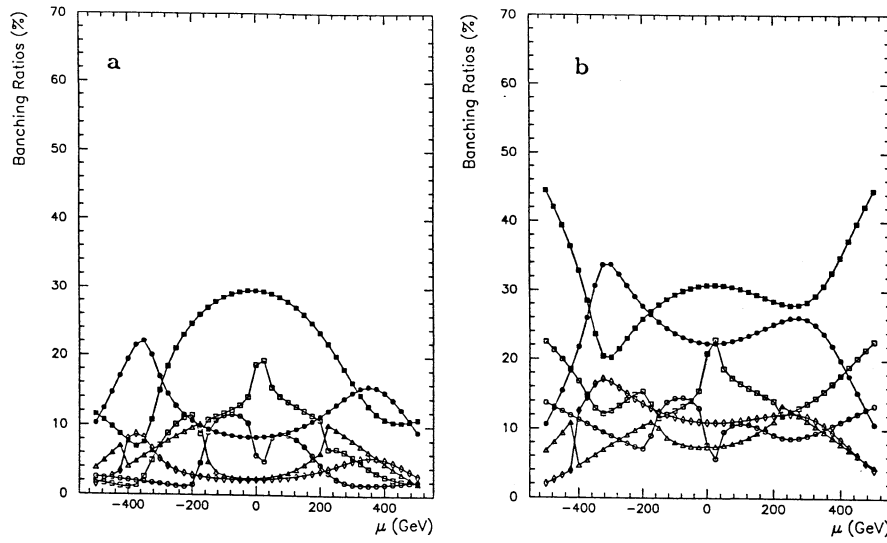


Fig. 2.1: Branching ratios for a) $\tilde{g} \rightarrow \tilde{\chi}_i^0 + \bar{t} + t$, $\tilde{\chi}_i^- + \bar{b} + t$, $\tilde{\chi}_i^+ + \bar{t} + b$; b) $\tilde{g} \rightarrow \tilde{\chi}_i^0 + q + \bar{q}$, $\tilde{\chi}_i^0 + g$, $\tilde{\chi}_j^\pm + q + \bar{q}$ (summed over all flavours). Decays into $\tilde{\chi}_1^\pm$ (\blacksquare), $\tilde{\chi}_2^\pm$ (\bullet), $\tilde{\chi}_1^0$ (\circ), $\tilde{\chi}_2^0$ (\square), $\tilde{\chi}_3^0$ (\triangle), and $\tilde{\chi}_4^0$ (\diamond), for $m_{\tilde{g}} = 1000$ GeV, $\tan \beta = 2$.

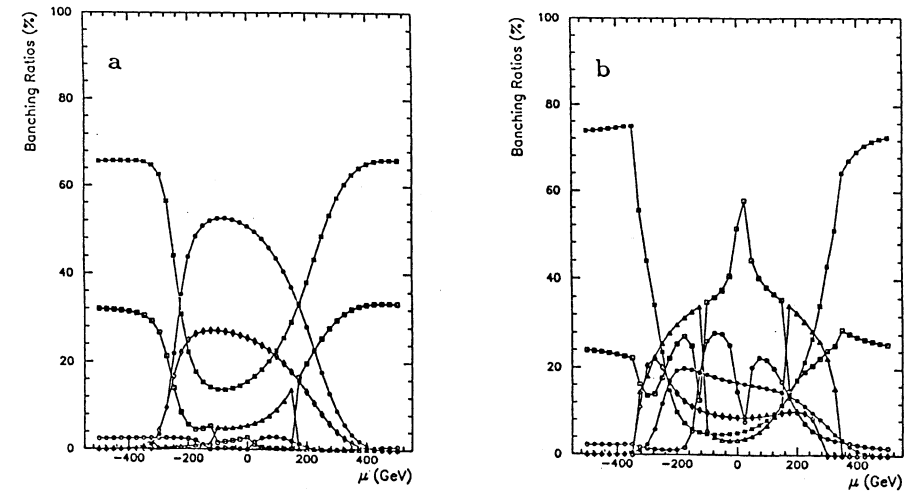


Fig. 2.3: Branching ratios for a) $\tilde{u}_L \rightarrow \tilde{\chi}_i^0 + u$, $\tilde{\chi}_i^+ + \bar{d}$; b) $\tilde{i}_L \rightarrow \tilde{\chi}_i^0 + t$, $\tilde{\chi}_i^+ + \bar{b}$, for $m_{\tilde{g}} = 500$ GeV and $\tan \beta = 2$. The symbols are as in Fig. 2.1.

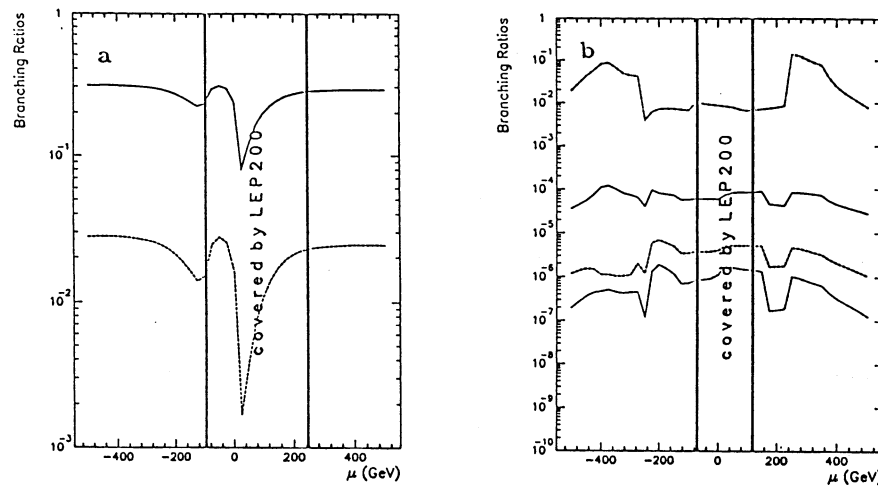


Fig. 2.2: Branching ratios for $\tan \beta = 2$ for a) $\tilde{g} + \tilde{g} \rightarrow \tilde{\chi}_1^0 + X$ (solid line), $2\tilde{\chi}_1^0 + X$ (dash), for $m_{\tilde{g}} = 500$ GeV; b) $\tilde{g} + \tilde{g} \rightarrow 2Z^0 + X$ (dot dash), $4\mu + X$ (solid), $5\mu + X$ (dash), $6\mu + X$ (dot), for $m_{\tilde{g}} = 1000$ GeV.

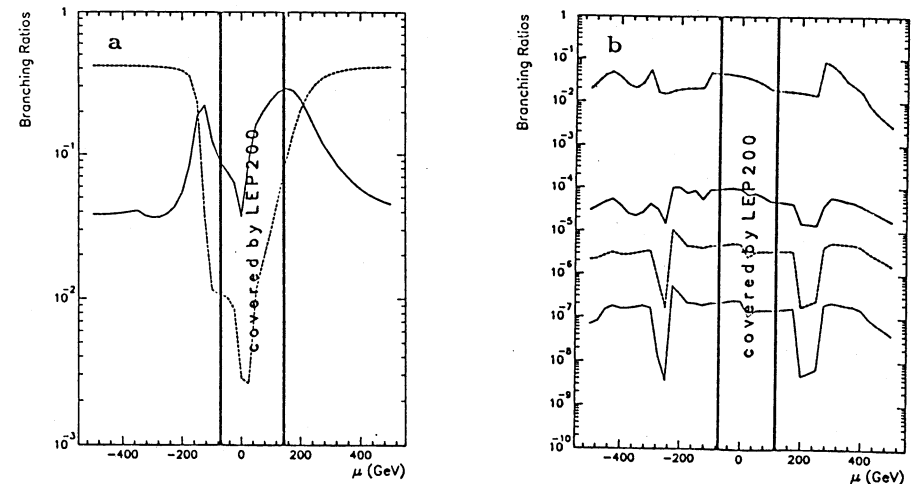


Fig. 2.4: Branching ratios for $\tan \beta = 2$ for a) $\tilde{q} + \tilde{q} \rightarrow \tilde{\chi}_1^0 + X$ (solid), $\tilde{\chi}_1^0 + \tilde{\chi}_1^0 + X$ (dashed), for $m_{\tilde{g}} = 500$ GeV; b) $\tilde{q} + \tilde{q} \rightarrow 2Z^0 + X$ (dash dotted), $4\mu + X$ (solid), $5\mu + X$ (dashed), $6\mu + X$ (dotted), for $m_{\tilde{g}} = 750$ GeV.

3 Experimental Aspects of Gluino and Squark Searches

Contributors: C. Albajar, C. Fuglesang, S. Hellman, E. Nagy, F. Pauss, G. Polesello and P. Sphicas

3.1 Introduction

The experimental signatures for the detection of squark and gluino production at hadron colliders have in recent years been the subject of intense investigation (see, for example, Refs. [3.1,3.2]). Developments in the field include detailed studies of gluino and squark decay patterns, including decays via charginos and neutralinos, the calculation of the decay $\tilde{g} \rightarrow g\tilde{\chi}_1^0$ which occurs at 1-loop, and the effect of the top-quark Yukawa coupling, as well as the t-quark mass term [3.3,3.4]. Instead of having sparticles decaying directly into partons and the lightest supersymmetric particle (LSP), as often assumed in previous studies, the supersymmetric particle produced in this primary decay can be a mixed state of heavier gauginos and higgsinos, which in turn will decay till the LSP is reached. The LSP has a very small interaction cross-section and therefore escapes detection. In the Minimal Supersymmetric Standard Model (MSSM), the branching ratios for the different decay modes and the mass values for the different mass eigenstates in the gaugino–higgsino sector (i.e. the charginos and neutralinos) are a function of a few basic parameters (see section 1 for a more detailed discussion).

The effect of this scenario on the experimental signatures can be summarized as: a softening of the E_T^{miss} distributions, owing to the fact that the LSP very often appears only at the end of a complicated decay chain, a higher number of jets in the final state, and more isotropic event topologies. In addition new decay channels become available, in particular including vector bosons, which provide potentially interesting signatures.

Several studies have been performed earlier to assess the potential discovery limits for supersymmetric particles at supercolliders [3.1,3.2]. The work reported on here updates and complements these earlier studies in two respects.

We have implemented the cascade decays in two Monte Carlo generators, using the calculations of gluino and squark branching ratios presented in Ref. [3.4]. We have thus been able to study the sparticle signatures for different regions of parameter space, taking into account the full complexity of their decays. The two main items addressed have been the investigation of the effect of the softened E_T^{miss} distribution due to the cascade decays and the study of a new signature, utilizing the Z bosons produced in the cascade decays. The last signature complements the ‘standard’ one in certain regions in parameter space, and can be exploited to confirm a possible signal.

The second feature specific to the present study is the inclusion of an explicit Monte Carlo evaluation of experimental effects when investigating the signatures for sparticle pair production. Such effects include a finite detector resolution, a parametrization of particle responses in the calorimeter, the presence of insensitive regions in the detector (cracks), and pile-up of minimum bias events when running at high luminosity. The last effect was already included in one of the previous studies [3.2], with a slightly different approach.

Moreover we investigated the effect, on the cross-section for sparticle production, of varying the structure functions and the definition of the Q^2 scale. All the predictions for the numbers of produced supersymmetric particles used for the present study have been obtained with the EHLQ I [3.5] structure functions set and $Q^2 = \hat{s}$. In Fig. 3.1 the cross-section for

gluino production as a function of gluino mass is shown for different choices of Q^2 scale; the scale we have used gives the lowest predicted cross-section. In Fig. 3.2 the gluino-production cross-section is shown for different choices of structure functions sets; as an example, one sees that the predicted cross-section for gluinos of 1 TeV can be a factor 50% lower or higher than the ones on which the conclusions of this study are based. An uncertainty of the same order of magnitude applies to the cross-sections of the various backgrounds studied.

3.2 Simulation tools

The simulation of supersymmetric processes for the experimental analysis presented below has been done using three different Monte Carlo programs. Two different generators, UA2SUSY and ISAJET [3.6] were used for simulating the production of supersymmetric particles in pp interactions. In order to investigate the effect of more realistic experimental conditions on the detectability of supersymmetric signals, a simple detector simulation was interfaced with the output of the UA2SUSY generator.

UA2SUSY is a parton-level Monte Carlo, with the possibility to easily vary the theoretical parameters. In this ‘toy’ Monte Carlo a particularly important feature is a modular and flexible implementation of the possible decay channels for gluinos. The simulation of the non-perturbative part of the event is reduced to the bare minimum necessary to allow a meaningful assessment of the experimental signatures. A basic advantage of a ‘toy’ is the full control of all the parameters of the simulation, and the ease with which the program can be modified to keep pace with theoretical developments.

ISAJET, extensively used and tuned at present collider energies, generates a complete pp interaction, including the effect of spectator particles. Such an approach implies the modelling of the ‘soft’ part of the hadronic interaction, and the attempt to account for the various multiple radiation phenomena occurring in QCD through a ‘parton shower’ approach (see, for example, Ref. [3.7]). In the following, some details are given on the implementation of the two generators and of the detector simulation program.

3.2.1 The UA2SUSY Monte Carlo

This Monte Carlo is a development of a program originally written by the Orsay UA2 group and used for the search for SUSY particles in UA2. In the following we summarize the main characteristics of this program.

The leading-order matrix elements for sparticle production are taken from Ref. [3.8]. The produced gluinos are fragmented according to the prescription given in Ref. [3.9], and decayed according to phase-space kinematics down to the LSP and ordinary partons. The decay chain is implemented in a flexible way, allowing for all relevant decay chains present in the theory. The masses of the gaugino–higgsino mass eigenstates as well as the branching fractions into the different modes can be selected. The final-state partons are then fed into EURODEC [3.10], which performs fragmentation and hadronization. In particular, track is kept of the quark flavours involved in the gluino decays, so that EURODEC can apply the appropriate prescriptions for heavy-quark decays, important for the correct simulation of the final-state lepton spectrum.

A large set of structure functions (SF), from DO [3.11] and EHLQ [3.5] to the more recent DFLM [3.12] and MRSE/B [3.13] sets, are implemented in the generator, thus allowing a direct comparison with background calculations using the same SF parametrizations. The program does not simulate in full detail the global event structure. In particular, initial-state

radiation is not included, and no attempt is made to simulate the underlying ‘soft’ event. The possibility of superimposing any number of minimum bias events on the generated events at the particle level makes the simulation of the ‘soft’ part unnecessary. This flexibility in the choice of the parametrization of the minimum bias events allows a comparison of the effects of using different parametrizations, in particular in the case of many interactions superimposed in one single bunch crossing.

More important is the omission of initial-state radiation, which for hard radiated gluons can significantly alter both the jet multiplicity in the event and the kinematics of the gluino-gluino system. The use of the approximate model is justified by the desire to concentrate on the essential features of the hard-scattering event, which are used to isolate the supersymmetric signal from the QCD background, with no dependence on the phenomenological models usually employed to simulate the non-perturbative part of the event. The underlying hypothesis is that, for the production of heavy particles, the effect of the approximations in the UA2SUSY generator is not expected to influence in an appreciable way the conclusions of the analysis. Such a hypothesis can be, and has indeed been, checked by comparing the final-state distributions with the ones produced by ISAJET, since this contains a fairly complete parametrization of all the effects not included in the UA2SUSY generator.

The program can be used to generate full events, with the particle coding conventions adopted by the UA2 Collaboration, to be fed into a detector simulation. Alternatively, it can be used to calculate a cross-section value for any given choice of the relevant parameters; an example of this is given in Figs. 3.1 and 3.2.

3.2.2 Simulation of signal and background with ISAJET

ISAJET is based on perturbative QCD, and the hard scattering process is calculated using the leading order $2 \rightarrow 2$ matrix elements. Gluon bremsstrahlung from initial- and final-state partons (including squarks and gluinos) is included via parton shower evolution. Matrix elements from Ref. [3.8] are used for sparticle production. However, no decay modes are specified since these are strongly dependent on the SUSY parameters chosen. For a given set of parameters, gluino and squark signatures have been evaluated using the theoretical branching ratios of Ref. [3.4], which have been implemented in ISAJET. Squarks and gluino decays were then computed according to two- or three-body phase space, and quarks (gluons) from these decays were fragmented according to an independent fragmentation model.

To investigate the dominant background contributions to gluino and squark signals, the following SM processes have been simulated:

- i) $W \rightarrow e\nu, \mu\nu$ and $\tau\nu$
- ii) $Z \rightarrow \nu\nu$
- iii) $t\bar{t}$ production, using $m_t = 150$ GeV.

In the last case a cut on $E_T^{miss} > 75$ GeV was required already at the generation level. A total of 75000 background events were generated and about 7000 events for each of the signals.

3.2.3 Effects of detector resolution and pile-up

We have investigated the effect of finite detector resolutions and pile-up from multiple interactions by using a simple detector model. After the events were generated up to particle level, they were subjected to detector modelling, and the quantities used in the analysis were

compared with the ones computed without any detector modelling. This procedure has been applied to both signal and background events in order to investigate the importance of these effects.

Detector resolution. To model the finite calorimeter resolution, both in energy and space, the calorimeter was represented by a grid in space extending over $|\eta| < 5$. The full pseudorapidity coverage was used for E_T^{miss} calculations, whereas jets and electrons were reconstructed only within $|\eta| < 3$.

The calorimeter was divided into towers of size $\Delta\phi \times \Delta\eta = 0.05 \times 0.05$. Each tower was separated into one electromagnetic and one hadronic cell. The electromagnetic compartments were assumed to have energy resolution $\Delta E/E = 10\%/\sqrt{E} \oplus 1\%$, whereas the hadronic compartments were assumed to have $\Delta E/E = 50\%/\sqrt{E} \oplus 2\%$ (E in GeV).

In these towers electrons and photons deposit all their energy in **one** electromagnetic cell whilst hadrons deposit their energy in **one** tower, i.e. one electromagnetic cell and the hadronic cell immediately behind it. The longitudinal sharing of the energy deposited by hadrons in the two compartments has been parametrized by using test-beam data from the UA2 end-cap calorimeters. The sharing between the $24X_0$ deep electromagnetic compartment and the following hadronic compartment for 10 GeV charged pions has been used as a model. There is no transverse smearing in the model. This simplification can be justified by the following considerations.

For electrons the cell size used is large enough to contain the shower laterally. Certainly the energy will be shared between more than one such cell when an electron or photon impinges close to an intercell boundary. The important point is that although such showers are reconstructed by summing over several cells, the lateral extension of the shower is still small. By ascribing exactly one electromagnetic cell to each electromagnetic shower, we are thus not, in practice, changing the lateral extension of the shower. One does however deteriorate the mass resolution by a small amount, since this procedure in practice forces each electromagnetic shower to be centred on the centre of a cell⁴. Since for jets the energy is collected in cones of $\Delta R < 0.4$ one primarily depends on the fragmentation to assure a realistic distribution of the jet energy between the interior and exterior of this cone. Exactly how the energy inside the cone is shared between the towers is less important.

Muons deposit energy corresponding to a minimum ionizing particle in both compartments of the calorimeter. In addition, their energy and position is assumed to be measured in an external device with a precision of $\Delta p_T = 10\% \times p_T$ (p_T in GeV). This energy is then retained at the analysis stage.

The missing transverse energy is defined as $E_T^{miss} = -\sum_i E_T^i \cdot \hat{n}$, where \hat{n} is a unit vector in the transverse plane from the interaction vertex to the cell centre and the sum ranges over all transverse cell energies, E_T^i , within $|\eta| < 5$.

Pile-up. At high luminosities, detectors will see a large number of minimum bias interactions superimposed on the hard scattering events. We have investigated this effect on signal, as well as on background events. This study was performed by adding, at the particle level, PYTHIA [3.14] generated minimum bias events. The number of such superimposed events was chosen at random from a Poisson distribution. We have considered two cases, with the

⁴In addition there is a small effect, when two electromagnetically interacting particles fall within the same cell. In this model they are by definition seen as one cluster, whilst in a more realistic model it might in some cases be possible to distinguish that there are two showering particles.

average of the Poisson distribution equal to 2 and 15. The former is supposed to represent the underlying event for the case of the UA2SUSY Monte Carlo, which generates only the hard-scattered partons. The latter case corresponds to one bunch-crossing at a luminosity of $1.5 \times 10^{34} \text{ cm}^{-2}\text{s}^{-1}$.

Effect of cracks, and limited η -acceptance. All signatures for supersymmetry considered here contain E_T^{miss} as one characteristic component. Previous hadron collider experience has shown that an important source of E_T^{miss} is due to instrumental effects. Since in some of the cases one will use cuts on E_T^{miss} as low as 300 GeV, it is important to estimate the contribution from instrumental effects such as jet mismeasurement, cracks, and incomplete pseudorapidity coverage.

To attempt such an estimation, multijet⁵ events were generated [3.15] using the PAPAGENO [3.16] Monte Carlo. This Monte Carlo generates parton-level events, using the correct matrix elements for 3, 4, and 5 jets. Examining the effect of calorimeter cracks calls for the use of jets with a spatial extension, rather than infinitesimally narrow parton jets. To this effect a large number of jets were generated using ISAJET. From these the energy flow around the jet axis was parametrized as a function of E_T of the jet and distance from the jet axis. Using these parametrizations, the parton-level jets from PAPAGENO were ‘dressed’ to spatially extended jets. This procedure was used because a simulation on the particle level is not possible owing to the prohibitively large CPU time required.

To simulate the effect of cracks, the resulting jets were sent into a calorimeter with pointing geometry (CDF geometry and granularity, see Ref. [3.17]). The fraction of the energy flow in the jet which fell into the calorimeter cells was smeared by fluctuating both the overall jet energy and the jet direction via cell-to-cell fluctuations. The fraction of the jet energy which fell into a crack region was considered to be completely lost⁶.

A second source of E_T^{miss} is multi-jet events, where one or more of the jets is completely lost owing to limited pseudorapidity coverage. To investigate this effect, 4-jet events were generated with the PAPAGENO Monte Carlo. The E_T^{miss} spectra from events where one or more of the jets fall outside the angular acceptance of the calorimeter have been estimated by varying the calorimeter acceptance. It was found that a calorimeter coverage extending to $|\eta| > 4.5$ ensures an effect smaller than, or similar to, the one caused by cracks for the calorimeter model discussed above.

3.2.4 Criteria for jet and lepton detection

Jets. The jet algorithm used in this study was designed with two objectives in mind; it should be robust against pile-up from minimum bias events at high luminosities and it should be applicable in a similar manner both at particle level and after calorimeter simulation. To initiate a jet, the particle or calorimeter cell with highest transverse energy ($E_T > 10 \text{ GeV}$) is used as a seed. All particles or cells within a radius $\Delta R = \sqrt{\Delta\phi^2 + \Delta\eta^2} < 0.4$ from the seed are joined into the jet, provided that their transverse energy exceeds 1 GeV. The jet direction is defined by the direction from the event vertex to the energy weighted c.o.g. of the particles/cells forming the jet, and the p_T of the jet by the (scalar) sum of particle/cell

⁵Since this study explicitly excludes the most abundant source of E_T^{miss} , i.e. mismeasured di-jet events, that particular topology has to be explicitly excluded for the conclusions drawn here to remain valid.

⁶This is a conservative estimate, since in most geometries lateral shower extensions will be larger than the width of cracks, hence energy deposited in cracks will ‘leak’ back into the sensitive medium.

transverse energies. This procedure is then repeated as long as seed particles/cells above 10 GeV can be found.

Lepton detection. At particle level, electrons and muons were considered to be detected as isolated leptons if the total additional transverse energy in a cone with $R = 0.2$ centred on the lepton direction did not exceed 5 GeV.

After detector simulation the same isolation cut was applied to both electrons and muons. In addition, electrons were subjected to a leakage cut: it was required that less than 20% of the total transverse energy of the electron was detected in the hadronic compartment of the calorimeter.

3.3 Gluino searches

Gluino pairs are copiously produced at supercolliders (see Fig. 3.1). Searches for possible signals have therefore received a lot of attention in various physics studies [3.1,3.2]. Signatures from direct decays into the LSP (e.g. $\tilde{g} \rightarrow q\bar{q}\tilde{\chi}_1^0$) resulting in $(E_T^{\text{miss}} + n \text{ jet})$ final states have been evaluated in detail. However, as pointed out before, the decay into heavier charginos and neutralinos, which in turn decay into lighter charginos and neutralinos until the LSP is reached, become more important with increasing gluino mass. In general, transitions from heavier to lighter neutralinos proceed via a Z and/or h^0 (the lightest neutral Higgs boson), and transitions from and to charginos occur via W’s. Since for any possible decay of the gluino there will always be a LSP in the final state, E_T^{miss} should still remain a characteristic gluino signature. On the other hand, if gluinos cascade via Z particles one expects a very distinct event signature containing 4 leptons in the final state from $\tilde{g}\tilde{g} \rightarrow ZZ + X \rightarrow 4 \text{ leptons} + X$. In the following we will discuss the possible observation of a gluino signal in the $(E_T^{\text{miss}} + n \text{ jet})$ and 4 lepton channel.

3.3.1 The missing transverse energy signal

For the $(E_T^{\text{miss}} + n \text{ jet})$ channel we have chosen two different gluino mass values: $m_{\tilde{g}}=300 \text{ GeV}$ and $m_{\tilde{g}}=1000 \text{ GeV}$. It is important to establish a signal for the lower mass value, in order to ensure that a mass spectrum down to a region accessible to experiments before the turn-on of the LHC is covered. The gluino decay modes have been evaluated choosing the following parameters within the MSSM, taking into account present limits and future expectations from LEP [3.4,3.18]: $\tan \beta = 2$ and 10, $\mu = -440 \text{ GeV}$, $m_{H^\pm} = 500 \text{ GeV}$, and $m_{\tilde{q}} = 2m_{\tilde{g}}$. The two $\tan \beta$ values chosen allow the study of a possible difference in the event signature, which could come from the different decay channels in the two cases. Taking for μ an asymptotic value rather than a value which is more optimistic in terms of event rates for direct decay into the LSP, is a conservative assumption for this parameter. The branching ratios for the above set of parameters were taken from Ref. [3.4]. The decay modes included in the simulation are given in Tables 3.1 and 3.2, the corresponding neutralino, chargino and h^0 masses are given in Table 3.3.

For $m_{\tilde{g}}=300 \text{ GeV}$, as can be seen in Tables 3.1 and 3.3, only decays into $\tilde{\chi}_1^0$, $\tilde{\chi}_2^0$ and $\tilde{\chi}_j^\pm$ are possible, owing to the low gluino mass. Small contributions from loop decays have been neglected for $\tan \beta = 10$. In the case of $m_{\tilde{g}}=1000 \text{ GeV}$, decays into all $\tilde{\chi}_i^0$ and $\tilde{\chi}_j^\pm$ are possible. For $\tan \beta = 2$ only the largest branching ratios have been included in the

Table 3.1: Branching fractions used in the simulation for $m_{\tilde{g}} = 300$ GeV and $\mu = -440$ GeV. All quarks flavours have been included ($q = u, d, s, c, b, t$), and $m_t = 150$ GeV was used [3.4].

Decay	$\tan \beta = 2$	$\tan \beta = 10$
$\tilde{g} \rightarrow q\bar{q} \tilde{\chi}_1^0$	0.19	0.17
$\tilde{g} \rightarrow q\bar{q} \tilde{\chi}_2^0$	0.31	0.31
$\tilde{g} \rightarrow q\bar{q} \tilde{\chi}_1^\pm$	0.50	0.50
total	1.0	0.98
$\tilde{\chi}_2^0 \rightarrow Z \tilde{\chi}_1^0$	-	1.0 ^a
$\tilde{\chi}_3^0 \rightarrow h^0 \tilde{\chi}_1^0$	1.0	-
$\tilde{\chi}_3^0 \rightarrow W \tilde{\chi}_1^\pm$	1.0 ^a	1.0 ^a

^a) Only three-body decay via a virtual vector boson is kinematically possible.

Table 3.2: Branching fractions used in the simulation for $m_{\tilde{g}} = 1000$ GeV and $\mu = -440$ GeV, from Ref. [3.4].

Decay	$\tan \beta = 2$	$\tan \beta = 10$
$\tilde{g} \rightarrow q\bar{q} \tilde{\chi}_1^0$	0.12	0.035
$\tilde{g} \rightarrow q\bar{q} \tilde{\chi}_2^0$	0.19	0.07
$\tilde{g} \rightarrow g \tilde{\chi}_1^0$		0.015
$\tilde{g} \rightarrow g \tilde{\chi}_2^0$		0.11
$\tilde{g} \rightarrow g \tilde{\chi}_3^0$		0.20
$\tilde{g} \rightarrow g \tilde{\chi}_4^0$		0.32
$\tilde{g} \rightarrow q\bar{q} \tilde{\chi}_1^\pm$	0.36	0.15
Total	0.67	0.90
$\tilde{\chi}_2^0 \rightarrow Z(h^0) \tilde{\chi}_1^0$	0.47 (0.53)	0.27 (0.73)
$\tilde{\chi}_3^0 \rightarrow Z(h^0) \tilde{\chi}_1^0$		0.20 (0.06)
$\tilde{\chi}_3^0 \rightarrow Z \tilde{\chi}_2^0$		0.17
$\tilde{\chi}_3^0 \rightarrow W \tilde{\chi}_1^\pm$		0.56
$\tilde{\chi}_4^0 \rightarrow Z(h^0) \tilde{\chi}_1^0$		0.05 (0.12)
$\tilde{\chi}_4^0 \rightarrow Z(h^0) \tilde{\chi}_2^0$		0.02 (0.19)
$\tilde{\chi}_4^0 \rightarrow W \tilde{\chi}_1^\pm$		0.62
$\tilde{\chi}_1^\pm \rightarrow W \tilde{\chi}_1^0$	1.0	1.0

Table 3.3: Neutralino, chargino and h^0 masses for $\mu = -440$ GeV, from Ref. [3.4]

	$m_{\tilde{g}} = 300$ GeV		$m_{\tilde{g}} = 1000$ GeV	
	$\tan \beta = 2$	$\tan \beta = 10$	$\tan \beta = 2$	$\tan \beta = 10$
$m_{\tilde{\chi}_1^0}$ (GeV)	53.21	51.08	171.11	168.15
$m_{\tilde{\chi}_2^0}$ (GeV)	110.78	101.40	340.61	323.27
$m_{\tilde{\chi}_3^0}$ (GeV)	442.42	449.29	447.11	446.76
$m_{\tilde{\chi}_4^0}$ (GeV)	453.78	449.44	450.07	464.11
$m_{\tilde{\chi}_1^\pm}$ (GeV)	110.43	101.46	340.97	323.45
$m_{\tilde{\chi}_2^\pm}$ (GeV)	452.29	454.39	453.32	465.98
m_{h^0} (GeV)	54.07	89.23	54.07	89.23

simulation, i.e. the decays $\tilde{g} \rightarrow g \tilde{\chi}_i^0$ have not been taken into account. However, for $\tan \beta = 10$, loop decays into neutralinos contribute about 65% and have therefore been included. It is obvious from Table 3.2 that the total predicted event rate for the channels considered will be larger for $\tan \beta = 10$. However, this choice of decay modes for the two $\tan \beta$ values will allow the study of a possible difference in event topology for $m_{\tilde{g}} = 1000$ GeV. The cross-sections used were 640 pb and 0.52 pb for $m_{\tilde{g}} = 300$ GeV and $m_{\tilde{g}} = 1000$ GeV, respectively.

Characteristics of signal and background. The missing transverse energy distribution is shown in Figs. 3.3a and b for gluino masses of 300 GeV and 1000 GeV, respectively. No significant difference between $\tan \beta = 2$ and 10 is observed for the shape of these spectra. As expected, the average E_T^{miss} increases by about a factor of 3 when increasing the gluino mass from 300 GeV to 1000 GeV. Because of the addition of cascade decays, the E_T^{miss} spectrum is softer compared with the distributions obtained for the direct decays into the LSP in Ref. [3.2]. Also shown in Figs. 3.3 a,b is the total background contribution from the Standard Model processes discussed in Section 3.2.2. Table 3.4 summarizes the total signal and background event rates expected for 10^4 pb^{-1} (1 year running at $L = 10^{33} \text{ cm}^{-2} \text{s}^{-1}$). The background cross-sections have been obtained from ISAJET. Figure 3.3c shows the individual background contributions to the E_T^{miss} spectrum, where the process $Z(\rightarrow \nu\bar{\nu}) + \text{jets}$, i.e. Z 's produced at large transverse momentum, dominates at large E_T^{miss} . Before any selection cuts the gluino signals always remain below the background.

The background can be reduced by exploiting the expected difference in topology of signal and background events. Isotropic multijet events with large jet transverse momenta are characteristic of a gluino signal, whereas background events have low jet multiplicity (e.g. $Z \rightarrow \nu\bar{\nu}$ decays) and/or softer jet spectra (e.g. $t\bar{t} \rightarrow WWbb$). To study this difference in topology the following quantities are defined: i) jet multiplicity N_{jet} , ii) circularity C , computed from the transverse projection of the calorimeter jets ($E_T > 10$ GeV) and the E_T^{miss} vector, defined as $C = \frac{1}{2} \min(\sum E_T \cdot \hat{n})^2 / (\sum E_T^2)$, and iii) $\Delta\phi_{12}$, the azimuthal angle between the two highest-transverse-energy jets in the event. A comparison of these distributions is shown in Fig. 3.4 for $m_{\tilde{g}} = 300$ GeV. A threshold of 100 GeV has been placed on E_T^{miss} , and for $\Delta\phi_{12}$ at least 3 jets have been required ($E_T^{jet} > 200$ GeV). The same quantities are plotted in Fig. 3.5 for $m_{\tilde{g}} = 1000$ GeV. The expected differences in event topology for signal

Table 3.4: Total expected event rate for signal and background for 10^4 pb^{-1} .

Process	$\tan \beta = 2$	$\tan \beta = 10$
$\tilde{g}\tilde{g}(m_{\tilde{g}}=300 \text{ GeV})$	6.4×10^6	6.2×10^6
$\tilde{g}\tilde{g}(m_{\tilde{g}}=1000 \text{ GeV})$	2.3×10^3	4.2×10^3
$Z \rightarrow \nu\bar{\nu}$	1.4×10^8	
$W \rightarrow l\nu$	8.1×10^8	
$t\bar{t} (m_t=150 \text{ GeV})^a$	1.2×10^7	

^{a)}A cut at $E_T^{\text{miss}} > 75 \text{ GeV}$ has been used on the generation level.

Table 3.5: Expected event rate for signal and background after selection cuts, for 10^4 pb^{-1} .

The quoted errors are the statistical errors from the Monte Carlo generation.

Process	$E_T^{\text{miss}} > 300 \text{ GeV}$		$E_T^{\text{miss}} > 400 \text{ GeV}$	
	$\tan \beta = 2$	$\tan \beta = 10$	$\tan \beta = 2$	$\tan \beta = 10$
$\tilde{g}\tilde{g} (m_{\tilde{g}} = 300 \text{ GeV})$	410 ± 300	420 ± 290	44 ± 20	33 ± 16
$\tilde{g}\tilde{g} (m_{\tilde{g}} = 1000 \text{ GeV})$	114 ± 7	190 ± 12	56 ± 5	87 ± 8
$Z \rightarrow \nu\bar{\nu}$	1		1	
$W \rightarrow l\nu$	3		1.5	
$t\bar{t} (m_t=150 \text{ GeV})$	27		7.5	
total background	31 ± 12		10 ± 3	

and background are clearly seen in each case, more pronounced for $m_{\tilde{g}} = 1000 \text{ GeV}$. No significant difference in event topology is observed for the two $\tan \beta$ values.

A comparison of the E_T^{miss} distribution for gluino pair production and for the total background is shown in Figs. 3.6 a and b, for one possible selection requiring $N_{\text{jet}} \geq 3$ ($E_T^{\text{jet}} > 200 \text{ GeV}$), $\Delta\phi_{12} < 130^\circ$ and $C > 0.2$. The individual background contributions after these cuts are shown in Fig. 3.6 c, $t\bar{t}$ being the dominant background source. The error bars represent the statistical errors from the Monte Carlo generation. The corresponding numbers of signal and background events are given in Table 3.5, for an integrated luminosity of 10^4 pb^{-1} , after applying a cut on E_T^{miss} of 300 GeV and 400 GeV, respectively.

For $m_{\tilde{g}} = 1000 \text{ GeV}$ and $E_T^{\text{miss}} > 400 \text{ GeV}$ one obtains $S/\sqrt{B} \approx 27$ (10) for $\tan \beta = 10$ (2). The difference in the number of selected events for the two $\tan \beta$ values can mostly be attributed to the smaller $\sigma \cdot BR$ used for $\tan \beta = 2$, since no significant difference in event topology was observed (see Fig. 3.4). For $m_{\tilde{g}} = 300 \text{ GeV}$ and $E_T^{\text{miss}} > 300 \text{ GeV}$ one obtains $S/\sqrt{B} \approx 75$; however, there is a large statistical error, indicating that only very few of the generated events survive the selection cuts. Therefore for low gluino masses a lower E_T^{miss} cut would be desirable, in order to avoid sensitivity to fluctuations in the tail of the signal E_T^{miss} distribution. Lowering the E_T^{miss} cut, however, imposes a much stronger requirement on the understanding of instrumental effects and contributions from other possible SM background should be taken into account as well (e.g. heavy-flavour production and IVB pair production).

The signal-to-background ratio does not improve for the above selection if events containing isolated leptons with $p_T > 25 \text{ GeV}$ are removed. This was expected because isolated leptons from W and Z decay are also present in the gluino cascades. However, further improvements in signal-to-background ratios are certainly possible. For example, quantities such as $\Delta\phi$, the difference in azimuthal angle between the E_T^{miss} direction and the direction of the highest- p_T jet, or x_{out} , the component of the E_T^{miss} perpendicular to the circularity axis, can be used for background rejection [3.2]. Figure 3.7 shows the $\Delta\phi$ distribution for events with $E_T^{\text{miss}} > 300 \text{ GeV}$, $N_{\text{jet}} \geq 3$ and $C > 0.2$ for $m_{\tilde{g}} = 1000 \text{ GeV}$. In this case, a signal cross-section of $0.0356 \pm 0.0027 \text{ pb}$ ($0.0217 \pm 0.0009 \text{ pb}$) is obtained for $\tan \beta = 10$ (2). The corresponding total background cross-section is $0.0086 \pm 0.0023 \text{ pb}$. For 10^4 pb^{-1} and applying a cut on $20^\circ < \Delta\phi < 140^\circ$ results in a signal of 162 (109) events for $\tan \beta = 10$ (2), the total background contribution amounts in this case to 9 events for 10^4 pb^{-1} . However the background numbers are based on a rather small sample of Monte Carlo events left after these cuts, resulting in a 50% statistical error. Nevertheless, the above distribution indicates that the background could probably be further reduced, while keeping a large fraction of the signal events.

It should be noted that the calculation of background event rates for IVB production is sensitive to the knowledge of the IVB production cross-section as well as to the topology at large p_T^{IVB} . A similar systematic uncertainty has to be attributed to the predicted $t\bar{t}$ background rates. Taking these uncertainties in the signal and background evaluation into account, gluino masses up to about 1 TeV can be explored with an integrated luminosity of 10^4 pb^{-1} .

Detector effects. The event selection discussed above should allow extrapolation to high-luminosity running, thus extending the expected gluino mass reach. In order to check that in this case the conclusions are not altered, we have studied the effect of calorimeter smearing and pile-up.

The effect of resolution smearing turns out to be minor, as could be expected for the relatively high p_T of interest in this analysis. As an example, we show in Fig. 3.8 the p_T distribution of the hardest jet in the sample before and after resolution smearing. In Figs. 3.9 and 3.10 we show the effect of pile-up on the reconstructed energy of jets and electrons. The generated energy of the jet or electron is compared with the one reconstructed in the calorimeter after resolution smearing and superposition of, on an average 15 minimum bias events. The widths of the distributions are compatible with the ones expected by folding the generated p_T distributions with the resolution functions.

The shift in the distributions demonstrates the shift in reconstructed transverse energy. For electrons we find an average increase of 370 MeV, whilst for jets the shift is on an average 1.6 GeV. Since these jets typically have transverse momenta of several hundred GeV, this demonstrates that the jet algorithm chosen is rather insensitive to pile-up, as intended.

We have also verified that the other quantities used to define analysis cuts are only marginally affected by pile-up and smearing. In particular, the distribution of E_T^{miss} remains largely unchanged by pile-up effects, see Fig. 3.11. Also the circularity distribution, defined in Section 3.3.1, is only marginally effected by pile-up, as can be seen in Fig. 3.12.

For reasons of CPU time limitations the investigation of the effect of detector resolution and pile-up on the variables used in the analysis was made only for one particular set of SUSY parameters. After verifying that these variables are unaffected by smearing and pile-

up, the analysis for the various choices of SUSY parameters presented above was performed on the particle level.

Also the effect on the E_T^{miss} distribution due to jet mismeasurements in the presence of calorimeter cracks (see Section 3.2.3) turns out to be small. In Fig. 3.13 we show the E_T^{miss} distribution, when demanding the presence of three jets, all with $E_T > 150$ GeV, for three different calorimeter resolutions: $\Delta E/E = K/\sqrt{E}$ with $K = 20\%$, 40% and 80% . We note that requiring the presence of three jets with high p_T does not substantially reduce the event rate for large E_T^{miss} .

The E_T^{miss} distributions thus obtained have a much steeper slope compared with the E_T^{miss} distributions of the gluino signal and background displayed in Fig. 3.3 before selection cuts. Therefore, one can expect that after selection cuts the background from jet mismeasurement will be substantially reduced (as is the case for physics backgrounds), provided the calorimeter has a coverage of at least $|\eta| = 4.5$. Cracks clearly play an important role; however their effect can only be studied in detail given a specific design for a detector at the LHC.

3.3.2 The 4-lepton signature

The chain decay of a heavy gluino involves the decay of heavier gauginos (or more precisely gaugino–higgsino mixed states) into their lighter counterparts. These decays are either between gauginos of the same charge, in which case either a Z or h^0 is produced, or between gauginos of different charges, in which case a W is produced [3.4]. An example of the former type of decay is $\tilde{g} \rightarrow g \tilde{\chi}_4^0$ followed by $\tilde{\chi}_4^0 \rightarrow \tilde{\chi}_1^0 Z$ or alternatively $\tilde{\chi}_4^0 \rightarrow h^0 \tilde{\chi}_1^0$.

In the cases where two gluinos in one event decay via cascades containing Z particles there is a possible new signature for supersymmetry, complementary to the ($E_T^{\text{miss}} + n$ jets) signature described in Section 3.3.1. This new signature consists of four high- p_T leptons, reconstructing two Z 's, several hard jets and E_T^{miss} .

Different values for the assumed SUSY parameters will give different mass relations between the $\tilde{\chi}_i^0$ and $\tilde{\chi}_j^\pm$. In addition, the parameter values will define the mixture of higgsino and gaugino in a given $\tilde{\chi}_i^0$ or $\tilde{\chi}_j^\pm$, and hence also their couplings to other particles. Consequently, the inclusive branching ratio for $\tilde{g} \rightarrow Z + X$ will depend critically on the exact choices of the parameters, although it will always increase with increasing $m_{\tilde{g}}$.

To study the 4-lepton signature we have chosen the following parameters: $\tan \beta = 2$, $\mu = -300$ GeV, $m_{\tilde{g}} = 750$ GeV, and $m_{\tilde{q}} = 1.5$ TeV. In Fig. 3.14 we show the inclusive branching ratio for $\tilde{g}\tilde{g} \rightarrow ZZ + X$ for these parameter values, and $m_t = 150$ GeV. Clearly there is a very strong dependence on the μ parameter. The value chosen is not the one corresponding to the absolutely largest branching ratio, but it is admittedly one of the most favourable choices possible for this channel.

Given this set of parameters, and assuming $m_{H^\pm} = 500$ GeV, one obtains (see Ref. [3.4]): $m_{\tilde{\chi}_1^0} = 129.5$ GeV, $m_{\tilde{\chi}_2^0} = 251.9$ GeV, and $m_{\tilde{\chi}_4^0} = 314.2$ GeV. We have considered the following dominant decay modes: i) $\tilde{g} \rightarrow q\bar{q} \tilde{\chi}_2^0$, $\tilde{\chi}_2^0 \rightarrow Z \tilde{\chi}_1^0$ with a combined branching ratio of 14.3%, ii) $\tilde{g} \rightarrow g \tilde{\chi}_2^0$, $\tilde{\chi}_2^0 \rightarrow Z \tilde{\chi}_1^0$ with a combined branching ratio of 2.4%, and iii) $\tilde{g} \rightarrow g \tilde{\chi}_4^0$, $\tilde{\chi}_4^0 \rightarrow Z \tilde{\chi}_1^0$ with a combined branching ratio of 3.4%. These decays represent 20.1% of the gluino decays for these particular parameter values.

The main backgrounds to this signal will be ZZ continuum production, followed by leptonic decays of the Z bosons and $t\bar{t}$ production followed by semileptonic decays of the t and b quarks. Before cuts the combined $\sigma \cdot BR$ into four electrons are 16×10^{-5} pb for $\tilde{g}\tilde{g}$,

16×10^{-3} pb for ZZ continuum production, and 36×10^{-2} pb for $t\bar{t}$ production (a top mass of 150 GeV was assumed).

We have used the UA2SUSY Monte Carlo to generate signal events, PYTHIA for the ZZ -continuum background and EUROJET for the $t\bar{t}$ background. In all cases the detector response was modelled and pile-up from minimum bias events was added as described in Section 3.2.3.

In Fig. 3.15 we show the E_T^{miss} distribution, correctly normalized, for signal and backgrounds before applying cuts. Clearly the large $t\bar{t}$ background can be substantially reduced by requiring two reconstructed Z 's in the event. Asking for two combinations within $81 \text{ GeV} < m_{ee} < 101 \text{ GeV}$ the $t\bar{t}$ background is reduced by a factor of 50, while being 67% efficient for the signal, in the presence of 15 minimum bias events superimposed on the signal event. No sign requirement was imposed on the electron candidates. An additional factor of 5 of rejection against the $t\bar{t}$ background is obtained by requiring that the 4-lepton mass is larger than 250 GeV. The final cut utilizes the large- E_T jets produced in the gluino decays. In Fig. 3.16 we show the distribution of E_T for the hardest jet in the event has $E_T > 200$ GeV, and that the second hardest has $E_T > 100$ GeV.

Considering the small $\sigma \cdot BR$ for the signal one would clearly need the highest possible integrated luminosity for this search. We therefore assume a total integrated luminosity of 10^5 pb^{-1} . After superimposing on an average 15 minimum bias events, the combined effect of these cuts is to reduce the signal from 15.8 produced events to 4, the ZZ background from 1570 events to 1.6, and $t\bar{t}$ background from ~ 36000 events to 13.3. Because of the large rejection factor, there is a substantial uncertainty in the expected number of surviving $t\bar{t}$ events, both statistical and systematic. In addition to these events in the 4-electron channel there will also be a similar contribution from the 4- μ channel, and twice as much from the 2e2 μ channel. Just the rate of events surviving the cuts described above will very likely not be sufficient to establish a signal from gluino pair production.

There is, however, one additional handle when disentangling signal from background: in Fig. 3.17 we show the E_T^{miss} spectra for signal and background after cuts. There is a clear excess of signal events at high E_T^{miss} . The Monte Carlo generations do indicate a difference in E_T^{miss} spectra between signal and background even more pronounced than that shown in Fig. 3.17: no background event has $E_T^{\text{miss}} > 40$ GeV. Still we have chosen, because of the large uncertainties referred to above, to present in Fig. 3.17 the distributions in bins of 100 GeV.

The conclusion is that for a favourable set of SUSY parameters, a signal in the 4-lepton channel can be detected if one requires in addition high- E_T jets and large E_T^{miss} , provided an integrated luminosity of at least 10^5 pb^{-1} , and that data can be used to understand the E_T^{miss} spectrum from the background sources.

3.4 Squark searches

In this section we will assume that the squarks are lighter than the gluinos and that pair-production of squarks is the dominating SUSY sparticle source at the LHC. For any given quark flavour in the MSSM there are two spin-0 partners (\tilde{q}_L , \tilde{q}_R), corresponding to the two chiralities of the associated fermions. Left-right mixing can be neglected for the first five squark flavours and one assumes that they are degenerate in mass. Since the couplings of \tilde{q}_L and \tilde{q}_R are different, one expects different decay modes for the two cases. The scalar

partner of the top quark is an exception, because the stop mass matrix contains a potentially large off-diagonal term, proportional to the top quark mass. It is therefore not excluded that the stop could be lighter than the top and $m_t \ll m_{\tilde{q}}$. The special case of the stop quark will be discussed in Section 3.4.3.

A systematic study of all possible \tilde{q}_L , \tilde{q}_R decay modes can be found in Ref. [3.4]. We have studied \tilde{q}_L , \tilde{q}_R signatures choosing the following example for the SUSY parameters: $m_{\tilde{q}} = 1000$ GeV, $\tan \beta = 10$, $\mu = -440$ GeV, and $m_{\tilde{g}} = 1500$ GeV. As in the case for gluino pair production we have assumed $m_t = 150$ GeV and $m_{H^\pm} = 500$ GeV for the branching ratio evaluation.

3.4.1 Right-handed squarks: \tilde{q}_R

For the SUSY parameter values in our example, \tilde{q}_R decays into a quark and the lightest neutralino with $BR(\tilde{q}_R \rightarrow q\tilde{\chi}_1^0) \approx 99\%$, except for \tilde{t}_R , if the t -quark mass and t -quark Yukawa coupling are fully taken into account. In a previous study of squark searches at the LHC (La Thuile 1987 [3.2]) it was assumed that $BR(\tilde{q}_R \rightarrow q\tilde{\chi}_1^0) = 100\%$ and $m_{\tilde{g}} = 5m_{\tilde{q}}$. Thus for the first five squark flavours we refer to those results, but scale down the signal by a factor of 0.6 to account for the change in production cross-section and the fact that we only consider \tilde{q}_R . Fig. 3.18 shows the E_T^{miss} distribution obtained in the La Thuile analysis after selection cuts, i.e. requiring $N_{jet} \geq 3$ ($E_T^{jet} > 250$ GeV) and $C > 0.25$. For 10^4 pb $^{-1}$ and demanding $E_T^{miss} > 800$ GeV one obtains a \tilde{q}_R signal of 84 ± 13 events and a total SM background of 10.6 ± 2.2 events.

3.4.2 Left-handed squarks: \tilde{q}_L

Left-handed squarks decay dominantly into charginos for the above assumed parameters. The main decay modes for \tilde{u}_L and \tilde{d}_L are $\tilde{u}_L \rightarrow d\tilde{\chi}_1^\pm$ (45%) and $\tilde{d}_L \rightarrow u\tilde{\chi}_1^\pm$ (37%) with the subsequent decay of $\tilde{\chi}_1^\pm \rightarrow W\tilde{\chi}_1^0$. Here up-squarks include \tilde{u}_L , \tilde{c}_L , down-squarks include \tilde{d}_L , \tilde{s}_L , and $m_{\tilde{\chi}_1^0} = 385.6$ GeV, $m_{\tilde{\chi}_1^\pm} = 209.8$ GeV. The \tilde{b}_L and \tilde{t}_L decays are different if the top Yukawa coupling and the top-mass term are taken into account.

The \tilde{u}_L and \tilde{d}_L decays have been simulated using ISAJET with the above branching ratios for $m_{\tilde{q}} = 1000$ GeV. The total $\sigma \cdot BR$ is 0.113 pb, corresponding to 1130 events for 10^4 pb $^{-1}$ (one year running at 10^{33} cm $^{-2}$ s $^{-1}$). The E_T^{miss} distribution for the signal is shown in Fig. 3.19. The spectrum for \tilde{q}_L is harder ($\langle E_T^{miss} \rangle \sim 385$ GeV) than the corresponding distribution for gluino pair production of the same mass ($\langle E_T^{miss} \rangle \sim 300$ GeV). The total background contribution (the same as for the gluino case) is also shown in Fig. 3.19 and remains always above the signal.

The difference in event topology for signal and background is shown in Fig. 3.20, where circularity C , jet multiplicity $N_{jet}(E_T^j > 250$ GeV), and the transverse energy distribution for the highest- E_T jet in the event is plotted. In all cases $E_T^{miss} > 75$ GeV is required, and the distributions are normalized to 1. In comparison with the gluino signal (for $m_{\tilde{g}} = 1000$ GeV), there are fewer but more energetic jets owing to the two-body decay into W and $\tilde{\chi}_1^0$ in the \tilde{q} case. The circularity distribution is therefore also more peaked at smaller values.

The E_T^{miss} distribution for squark pair production and total background is shown in Fig. 3.21a for one possible selection requiring $N_{jet} \geq 3$ ($E_T > 250$ GeV), $E_T^{miss} > 400$ GeV and $C > 0.25$. The individual background contributions are shown in Fig. 3.21b, $t\bar{t}$ being the dominant background source. The corresponding signal and background events are given in Table 3.6, for an integrated luminosity of 10^5 pb $^{-1}$ and requiring $E_T^{miss} > 300$ GeV.

Table 3.6: Expected event rate for signal and background after selection cuts, for 10^5 pb $^{-1}$. The quoted errors are the statistical errors from the MC generation

Process	$E_T^{miss} > 300$ GeV
$\tilde{q}\tilde{q}$ ($m_{\tilde{q}} = 1000$ GeV)	350 ± 200
$Z \rightarrow \nu\bar{\nu}$	2
$W \rightarrow l\nu$	30
$t\bar{t}$ ($m_t = 150$ GeV)	154
Total background	185 ± 41

No improvement in the signal-to-background ratio is obtained by removing events with isolated leptons of $p_T > 25$ GeV. This was expected because the signal contains isolated leptons from the $\tilde{q}_L \rightarrow q\tilde{\chi}_1^\pm \rightarrow qW\tilde{\chi}_1^0$ decay chain.

The effect of pile-up, calorimeter resolution, and rapidity coverage has not been separately studied for the squark signatures discussed above. Since this analysis is very similar to the one done for the ($E_T^{miss} + n$ jet) channel in the gluino case, the conclusions of Section 3.3 are expected to apply to the squark search as well. To obtain a mass-reach estimate for squarks (\tilde{q}_L , \tilde{q}_R), one can combine all possible decay modes. Taking into account the uncertainties involved in signal and background evaluation, a squark mass reach of about 1000 GeV should be possible for an integrated luminosity of 10^4 pb $^{-1}$.

3.4.3 The case of a light \tilde{t}

In the MSSM, one of the supersymmetric partners of the top quark, the lighter stop mass eigenstate \tilde{t}_1 , could be significantly lighter than the other squarks and possibly also lighter than the top quark [3.19]. Such a scenario presents several distinct features which justify a separate study.

The pair production cross-section of \tilde{t}_1 under these conditions has been computed using the UA2SUSY Monte Carlo, and is in the range 0.1–1.0 nb, for $m_{\tilde{t}_1}$ of 50 to 200 GeV. Thus \tilde{t}_1 would be copiously produced even at rather moderate luminosities. The decay of \tilde{t}_1 will, provided that $m_{\tilde{t}_1} > m_{\tilde{\chi}_1^\pm} + m_b$, look very similar to the decay of the SM top: $\tilde{t}_1 \rightarrow \tilde{\chi}_1^\pm b$ followed by $\tilde{\chi}_1^\pm \rightarrow W^*\tilde{\chi}_1^0$. In addition there is a possibility that $m_{\tilde{t}_1} < m_t - m_{\tilde{\chi}_1^0}$, in which case \tilde{t}_1 will be produced also in the decay $t \rightarrow \tilde{t}_1 \tilde{\chi}_1^0$. Since $\sigma(t)$ is almost an order of magnitude larger than $\sigma(\tilde{t}_1)$ [3.20] larger event rates are expected in this case.

We give here analytic expressions for the widths of supersymmetric top decays, as computed by G. Ridolfi. The width for the top decay into a fermion f and a spin-0 scalar S , with masses m_f and m_S respectively, can be written as

$$\Gamma(t \rightarrow fS) = \frac{1}{8\pi} \frac{p}{m_t^2} \mathcal{A}, \quad (3.1)$$

where

$$p = \frac{\sqrt{[m_t^2 - (m_S + m_f)^2][m_t^2 - (m_S - m_f)^2]}}{2m_t} \quad (3.2)$$

and

$$\mathcal{A} = (\alpha^2 + \beta^2)(m_t^2 + m_f^2 - m_S^2) + 2(\alpha^2 - \beta^2)m_t m_f. \quad (3.3)$$

The first case of interest is $f \equiv \tilde{\chi}_i^0, S \equiv \tilde{t}_1$. In this case

$$\begin{aligned} \alpha &= \frac{g}{\sqrt{2}} \left[\frac{m_t}{2m_W \sin \beta} N_{i4} + \frac{2}{3} \sin \theta_W N'_{i1} + \frac{1}{\cos \theta_W} \left(\frac{1}{2} - \frac{2}{3} \sin^2 \theta_W \right) N'_{i2} \right] \cos \theta_t \\ &\quad + \frac{g}{\sqrt{2}} \left[\frac{m_t}{2m_W \sin \beta} N_{i4} - \frac{2}{3} \sin \theta_W N'_{i1} + \frac{1}{\cos \theta_W} \left(\frac{2}{3} \sin^2 \theta_W \right) N'_{i2} \right] \sin \theta_t \end{aligned} \quad (3.4)$$

$$\begin{aligned} \beta &= \frac{g}{\sqrt{2}} \left[-\frac{m_t}{2m_W \sin \beta} N_{i4} + \frac{2}{3} \sin \theta_W N'_{i1} + \frac{1}{\cos \theta_W} \left(\frac{1}{2} - \frac{2}{3} \sin^2 \theta_W \right) N'_{i2} \right] \cos \theta_t \\ &\quad + \frac{g}{\sqrt{2}} \left[\frac{m_t}{2m_W \sin \beta} N_{i4} + \frac{2}{3} \sin \theta_W N'_{i1} - \frac{1}{\cos \theta_W} \left(\frac{2}{3} \sin^2 \theta_W \right) N'_{i2} \right] \sin \theta_t \end{aligned} \quad (3.5)$$

where $\tilde{t}_1 = \tilde{t}_L \cos \theta_t + \tilde{t}_R \sin \theta_t$. For the case $f \equiv \tilde{\chi}_i^+, S \equiv \tilde{b}$ we find

$$\alpha = \frac{g}{2} \left(U_{i1} - \frac{m_t}{\sqrt{2} m_W \sin \beta} V_{i2} \right) \quad (3.6)$$

$$\beta = \frac{g}{2} \left(U_{i1} + \frac{m_t}{\sqrt{2} m_W \sin \beta} V_{i2} \right). \quad (3.7)$$

Finally, for $f \equiv b, S \equiv H^+$ we have

$$\alpha = \frac{g}{2\sqrt{2} m_W} \left(m_b \tan \beta + \frac{m_t}{\tan \beta} \right) \quad (3.8)$$

$$\beta = \frac{g}{2\sqrt{2} m_W} \left(m_b \tan \beta - \frac{m_t}{\tan \beta} \right) \quad (3.9)$$

All the quantities involved are defined as in Ref. [3.21].

Three possible cases can be distinguished:

— $m_{\tilde{t}_1} > m_t$. In this case only direct production of \tilde{t}_1 is possible. We have investigated the case $m_t = 110$ GeV, $m_{\tilde{t}_1} = 200$ GeV. The branching ratio for $\tilde{t}_1 \rightarrow t \tilde{\chi}^0$ was assumed to be 100%, which tends to maximize the signal.

— $m_{\tilde{t}_1} \approx m_t$. Also in this case only direct production of \tilde{t}_1 is possible. We have investigated the case $m_t = m_{\tilde{t}_1} = 110$ GeV, $\tilde{\chi}^\pm = 90$ GeV, and the combined branching ratio for $\tilde{t}_1 \rightarrow \tilde{\chi}^\pm b$ followed by $\tilde{\chi}^\pm \rightarrow W^* \tilde{\chi}^0$ equal to 100%.

— $m_{\tilde{t}_1} < m_t$. In this case \tilde{t}_1 can also be produced in the decay of t . Two possibilities were investigated: a) $m_t = 110$ GeV, $m_{\tilde{t}_1} = 50$ GeV, and $m_{\tilde{\chi}^0} = 43$ GeV. In this case the limited phase space only allows for the decay $\tilde{t}_1 \rightarrow \tilde{\chi}^0 c$. b) $m_t = 190$ GeV, $m_{\tilde{t}_1} = 110$ GeV, and $m_{\tilde{\chi}^0} = 61$ GeV. Here the stop squark decays as for the case of $m_{\tilde{t}_1} \approx m_t$. The branching ratio for $t \rightarrow \tilde{t}_1 \tilde{\chi}^0$ is 38% in case (a) and 11% in case (b).

The signal was generated using a modified version of ISAJET, with the production cross-section rescaled to agree with the one obtained from the UA2SUSY Monte Carlo. The hadronic energy was deposited in a calorimeter grid covering rapidities out to 3, with a granularity of $\Delta\phi \times \Delta\eta \approx 0.09 \times 0.075$. The energy was smeared with a resolution function corresponding to $\sigma(E)/E = 55\%/\sqrt{E}$. Jets were defined as in Section 3.2.4, except that the radius cut was $\Delta R < 0.32$. Leptons were taken directly from the generator, without smearing. Lepton isolation was implemented by requiring that there be no jet ($E_T > 10$ GeV) closer than $\Delta R = 0.32$.

ISAJET was also used to generate the most important sources of background, i.e.: $t\bar{t}$ production with $BR(t \rightarrow Wb) = 100\%$, $b\bar{b}$ production, W and Z production from Drell-Yan processes, and WZ pair production.

To isolate the signal from background the following cuts were applied:

- An isolated e or μ with $p_T > 50$ GeV was required. This serves to assure a manageable prompt trigger rate, and to suppresses background from $b\bar{b}$.
- The angle between E_T^{miss} and p_T of the hardest lepton, $p_t^{\ell 1}$, was required to be larger than 90°, this cut suppresses background from W and Z .
- The ratio $(|p_t^{\ell 1}| - |E_T^{miss}|) / (|p_t^{\ell 1}| + |E_T^{miss}|)$ is required to be smaller than 0.75. This cut mainly serves to suppress background from Z .

In Fig. 3.22 we show the distribution for E_T^{miss} for the four cases considered after these cuts. As can be seen, the only case where one can obtain a signal-to-background ratio larger than one is when $m_{\tilde{t}_1} < m_t$. In particular, the case (a) would yield 9000 signal events with $E_T^{miss} > 300$ GeV over a SM background of 1200 events, for an integrated luminosity of 10^4 pb $^{-1}$. For the case (b) the signal reduces to 3000 events, still significantly above background. We thus conclude that if the stop squark is lighter than the top quark there are good prospects of finding it at the LHC even for relatively modest integrated luminosities.

Finally, we note that the case of a light stop would not significantly modify the expected top signal. We have applied the so-called ‘top1’ and ‘top2’ cuts from Ref. [3.22] to the cases with and without the presence of the light stop. In no case was there a significant signal. The ‘standard top’ selection criteria are therefore not adequate to establish the existence of a light stop.

3.5 Conclusions

Within the framework of the Minimal Supersymmetric Standard Model, representative points in the parameter space have been chosen in order to study the discovery potential for gluino and squarks at the LHC. The full complexity of the different decay channels has been taken into account, i.e. cascade decays via charginos and neutralinos have been included in the Monte Carlo simulations. Effects of finite detector resolution and pile-up at high luminosity were also investigated.

Given the uncertainties involved for signal and background, it is difficult to quote ‘exact’ discovery limits. In the gluino case acceptable event rates are obtained for masses up to about 1 TeV in the $(E_T^{miss} + n \text{ jet})$ channel, for an integrated luminosity of 10^4 pb $^{-1}$. Using the same signature, the study was extended down to $m_g = 300$ GeV. To establish a signal for low gluino masses, it is important to understand the contribution to the E_T^{miss} signature from jet mismeasurements and limited calorimeter rapidity coverage, because of the softer E_T^{miss} spectrum expected for the signal. Our studies indicate that this additional background can be kept small, provided the calorimeter covers $|\eta| \geq 4.5$.

We have investigated the possibility of a four-lepton signature, emanating from cascade decays of gluinos containing Z bosons. For a favourable set of SUSY parameters at $m_g = 750$ GeV a signal emerges for luminosities $\geq 10^{34}$ cm $^{-2}$ s $^{-1}$. The expected event rates are small, but with negligible background.

It should be noted that other possible gluino signals make use of the distinctive feature of gluinos being Majorana fermions, thus decaying with equal probability into fermions and antifermions. In this case a like-sign dilepton signature is expected. We have not investigated

this channel; however it should be included in a more complete survey of interesting gluino signatures.

Squark signatures have been investigated separately for \tilde{q}_R , $\tilde{q}_L(m_{\tilde{g}} = 1000 \text{ GeV})$, and for a light \tilde{t} . In the case of \tilde{q}_R , results from an earlier study of squark signatures in the ($E_T^{miss} + n \text{ jet}$) channel can be used. After rescaling the signal to take into account the changes in cross-section and branching ratios, a signal is still observable. Decays of supersymmetric partners to the left-handed quarks have been simulated. In this case cascade decays have been included in the simulation. For squark pair production (combining \tilde{q}_R and \tilde{q}_L) acceptable event rates are expected for the proposed selection; thus a mass reach of about 1 TeV is possible for an integrated luminosity of 10^4 pb^{-1} .

The case of a stop squark substantially lighter than other squarks has been investigated. We have shown that, in the case when $m_{\tilde{t}} < m_t$, a signal is detectable after dedicated cuts. Standard top cuts do not reveal a stop signal.

The effect of pile-up has been studied for the gluino signatures. Very small effects on the proposed selections have been observed. Extrapolation to high-luminosity running is therefore feasible, thus extending the above quoted gluino and squark discovery limits to higher masses.

References

- [3.1] See for instance: J. Mulvey (ed.), Proc. of the Workshop on Physics at Future Accelerators, La Thuile, 1987 (CERN 87-07, Geneva, 1987) vols. I & II.
R. Donaldson and M. Gilchriese (eds.), Proc. Workshop on Experiments, Detectors and Experimental Areas for the Supercollider, Berkeley, 1987 (World Scientific, Singapore, 1988).
S. Jensen (ed.), Proc. 1988 Summer Study on High-Energy Physics in the 1990's, Snowmass, Colorado, 1988 (World Scientific, Singapore, 1989).
- [3.2] J. Mulvey (ed.), The Feasibility of Experiments at High Luminosity at the Large Hadron Collider (CERN 88-02, Geneva, 1988) p. 79.
- [3.3] H. Baer, V. Barger, D. Karatas and X. Tata, Phys. Rev. **D36** (1987) 96.
R.M. Barnett, J.F. Gunion and H.E. Haber, Phys. Rev. Lett. **60** (1988) 401, Phys. Rev. **D37** (1988) 1892.
R. Barbieri, G. Gamberini, G. Giudice and G. Ridolfi, Nucl. Phys. **B301** (1988) 15.
H. Baer, X. Tata and J. Woodside, Phys. Rev. **D41** (1990) 1568.
- [3.4] A. Bartl, W. Majerotto, B. Mösslacher, N. Oshimo and S. Stippel, HEPHY-PUB-538/90, UWTh Ph-1990-47.
A. Bartl, W. Majerotto, B. Mösslacher and N. Oshimo, HEPHY-PUB-545/90, UWTh Ph-1990-55.
A. Bartl, W. Majerotto, B. Mösslacher, N. Oshimo and S. Stippel, this volume.
- [3.5] E. Eichten et al., Rev. Mod. Phys. **56** (1984) 579 & **58** (1986) 1065E.
- [3.6] F. Paige and S.D. Protopopescu, ISAJET Monte Carlo, BNL 38034 (1986).
- [3.7] B.R. Webber, Ann. Rev. Nucl. Part. Sci. **36** (1986) 253.
- [3.8] S. Dawson, E. Eichten and C. Quigg, Phys. Rev. **D31** (1985) 1581.
- [3.9] A. De Rújula and R. Petronzio, Nucl. Phys. **B261** (1985) 587.
- [3.10] CERN 89-08, p. 226, and references therein.
- [3.11] D.W. Duke and J.F. Owens, Phys. Rev. **D39** (1984) 49.
- [3.12] M. Diemoz et al., Z. Phys. **C39** (1988) 21.
- [3.13] A.D. Martin et al., Phys. Rev. **D37** (1988) 1161, Phys. Lett. **B206** (1988) 327.
- [3.14] T. Sjöstrand, Int. J. Mod. Phys. **A3** (1988) 75.
- [3.15] A. Fucci and P. Sphicas, using stage 3 of PPCS (Parallel Processing Computer Server), joint study project between CERN and IBM Böblingen, Germany.
- [3.16] I. Hinchliffe, PAPAGENO Monte Carlo, see Ref. [3.1], Snowmass 88, p. 119.
- [3.17] F. Abe et al., Nucl. Instrum. Methods Phys. Res., **A271** (1988) 387.
- [3.18] Z. Kunszt and F. Zwirner, see report of the Higgs Working Group, this volume.
- [3.19] See for instance H. Baer et al., Phys. Lett. **220B** (1989) 303.
- [3.20] P. Nason, S. Dawson and R.K. Ellis, Phys. Rev. Lett. **64** (1990) 142.
G. Altarelli et al., Nucl. Phys. **B308** (1988) 724.
- [3.21] H.E. Haber and G.L. Kane, Phys. Rep. **117** (1985) 75.
- [3.22] L. Fayard and G. Unal, LAL preprint 90-66.

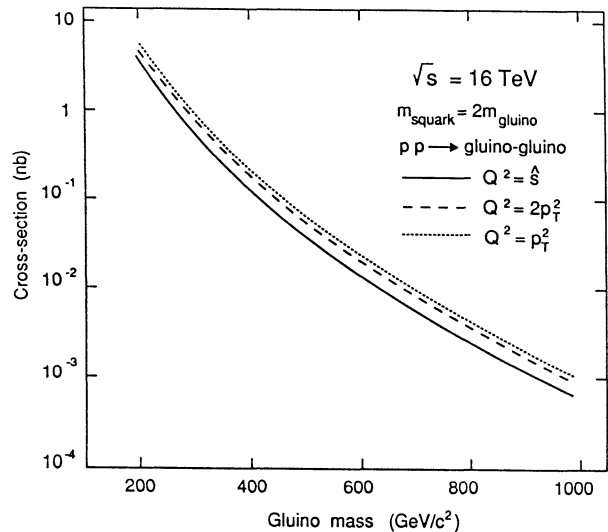


Fig. 3.1: Cross-section, from UA2SUSY Monte Carlo, for gluino pair production at 16 TeV as a function of gluino mass for different choices of Q^2 scale.

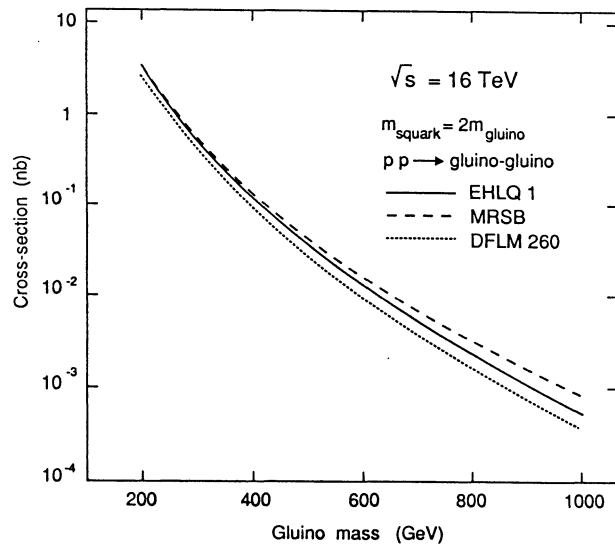


Fig. 3.2: Cross-section, from UA2SUSY Monte Carlo, for gluino pair production at 16 TeV as a function of gluino mass for different choices of structure functions, taken from Refs. [3.5, 3.12, 3.13].

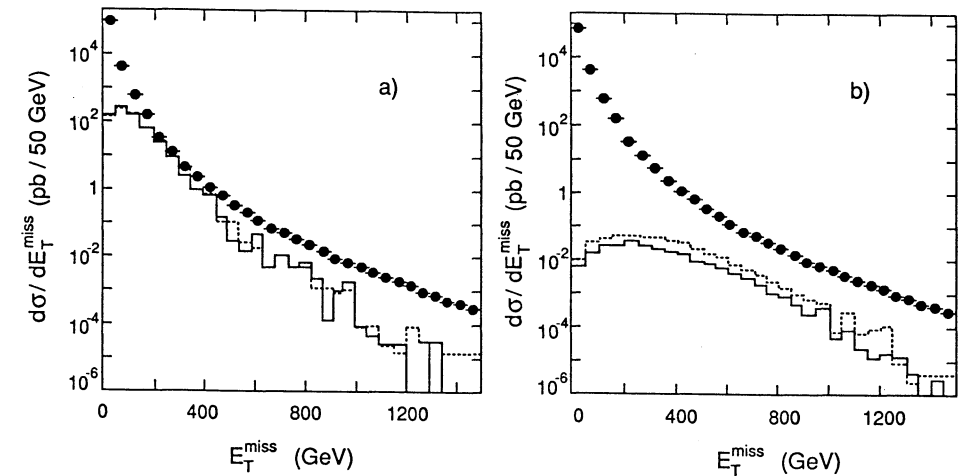
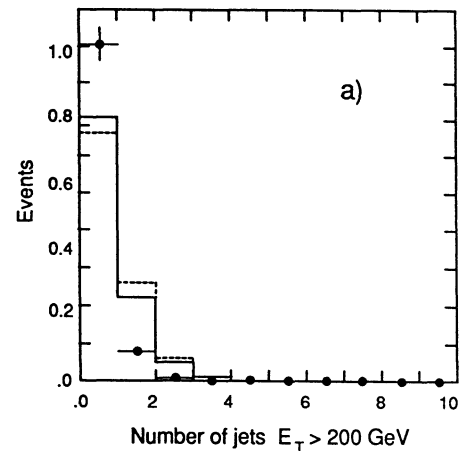
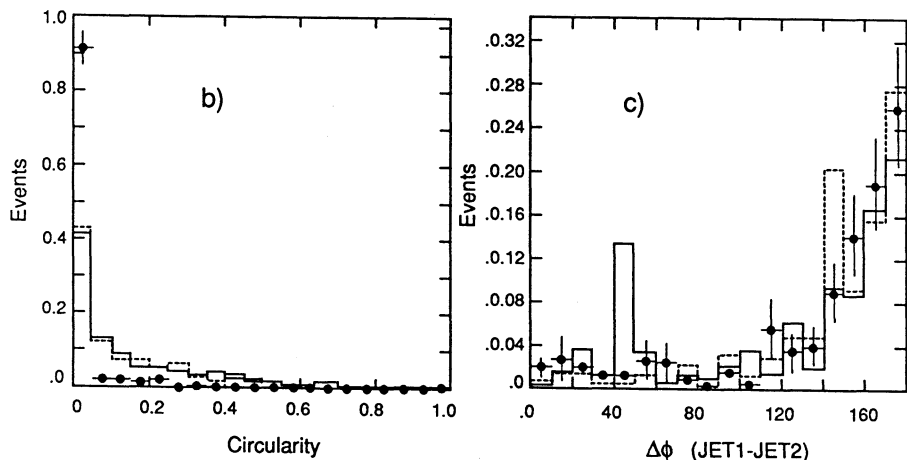


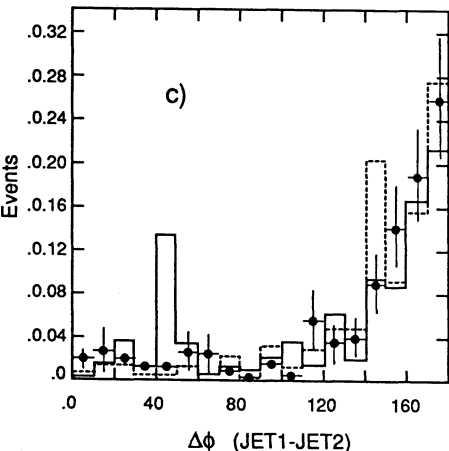
Fig. 3.3: Inclusive E_T^{miss} distribution for $\tilde{g}\tilde{g}$ pair production from ISAJET for a) $m_{\tilde{g}} = 300 \text{ GeV}$ and b) $m_{\tilde{g}} = 1000 \text{ GeV}$; the solid (dashed) line corresponds to $\tan \beta = 2 (10)$. The points with error bars show the total Standard Model background contribution. In c) the individual background contributions are shown.



a)

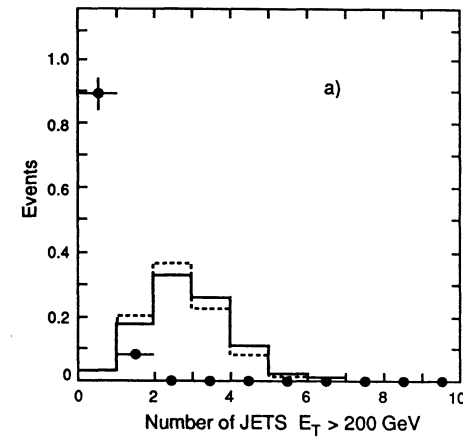


b)

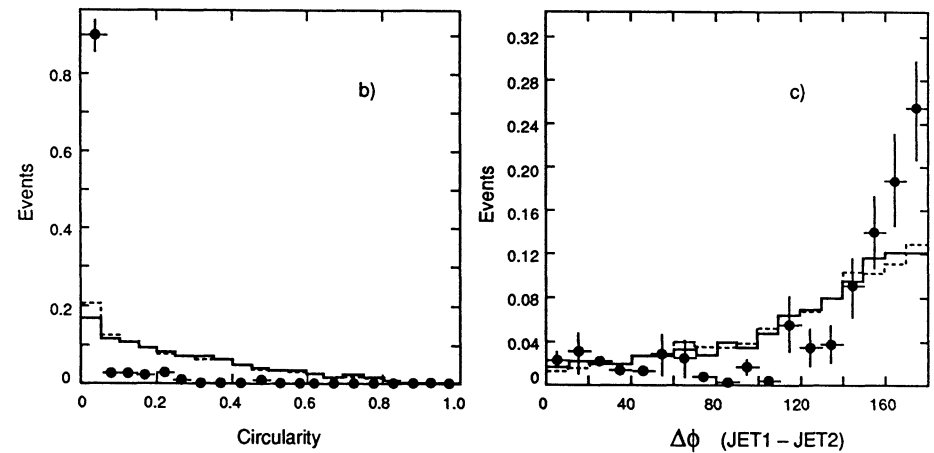


c)

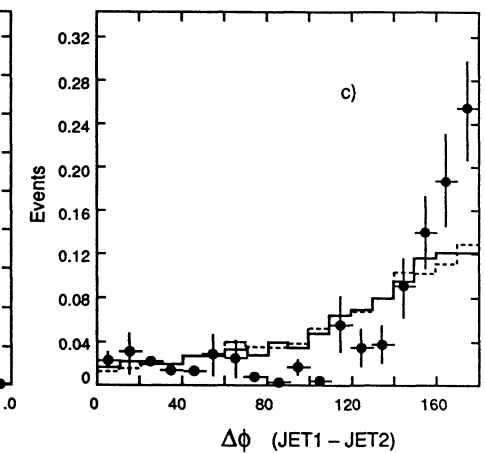
Fig. 3.4: Distribution of a) $N_{jet} \geq 3$ for $E_T^{jet} > 200$ GeV, b) circularity C , and c) $\Delta\phi_{12}$ from ISAJET for gluino pair production of 300 GeV mass for $\tan\beta = 2$ (solid histogram) and $\tan\beta = 10$ (dashed histogram), compared with Standard Model background (points with error bars). $E_T^{miss} > 100$ GeV has been required and the distributions are normalized to 1.



a)



b)



c)

Fig. 3.5: As Fig. 3.4 for $m_{\tilde{g}} = 1000$ GeV.

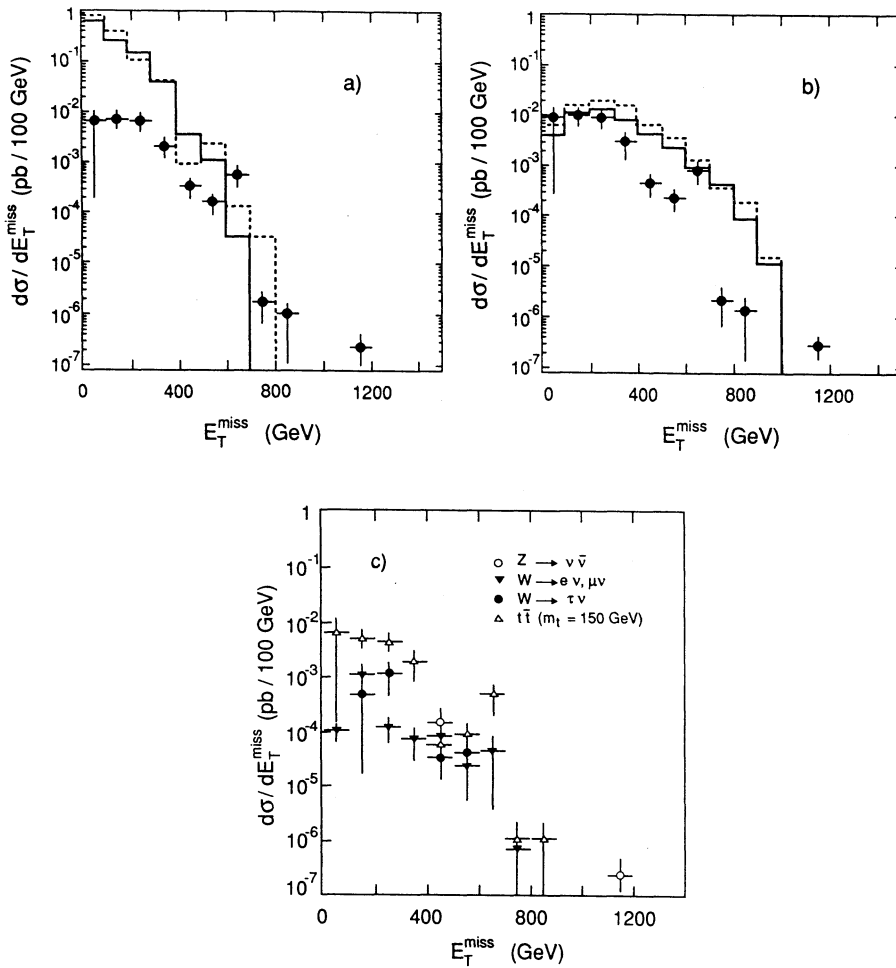


Fig. 3.6: E_T^{miss} distribution from ISAJET after selection cuts for a) $m_{\tilde{g}} = 300 \text{ GeV}$ and b) $m_{\tilde{g}} = 1000 \text{ GeV}$; the solid (dashed) line corresponds to $\tan \beta = 2 (10)$. The points with error bars show the total Standard Model background contribution. In c) the individual background contributions are shown for $t\bar{t}$, $W \rightarrow e\nu, \mu\nu$, $W \rightarrow \tau\nu$ and $Z \rightarrow \nu\nu$.

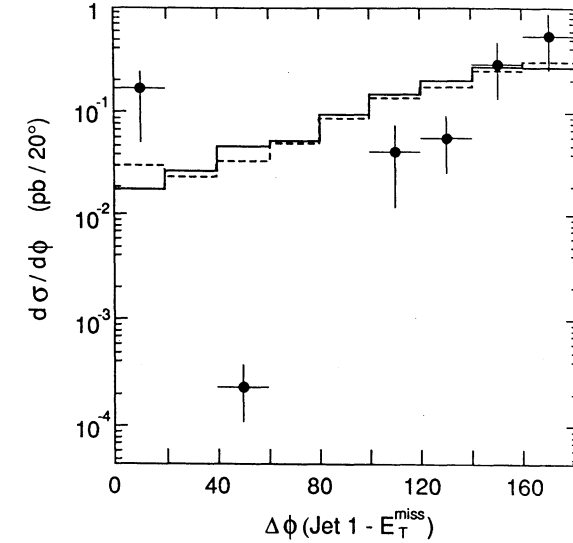


Fig. 3.7: Azimuthal angle difference between the highest transverse energy jet and the E_T^{miss} vector, from ISAJET, for $m_{\tilde{g}} = 1000 \text{ GeV}$ after selection cuts; the solid (dashed) line corresponds to $\tan \beta = 2 (10)$. The points with error bars show the total Standard Model background contribution.

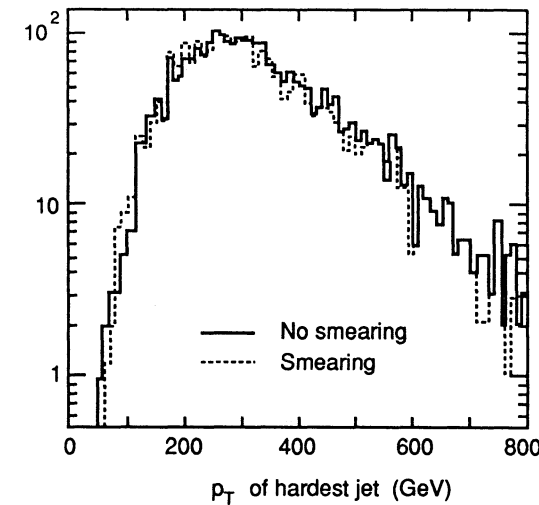


Fig. 3.8: Transverse energy distribution for the highest E_T jet for $m_{\tilde{g}} = 1000 \text{ GeV}$ at particle level (solid) and after calorimeter smearing (dashed), obtained with UA2SUSY.

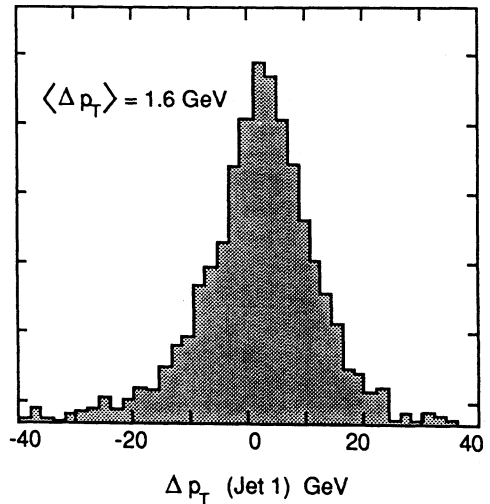


Fig. 3.9: Effect of pile-up and of resolution smearing on the highest transverse energy jet in the event, from UA2SUSY, simulated by superimposing an average of 15 minimum bias events, generated by PYTHIA.

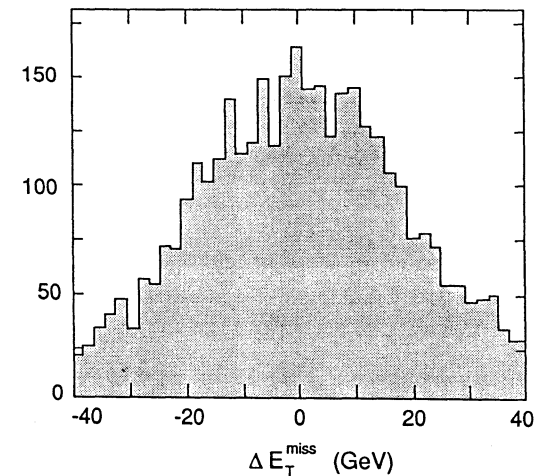


Fig. 3.11: Effect of pile-up on the E_T^{miss} of the event, from UA2SUSY, simulated by superimposing an average of 15 minimum bias events, generated by PYTHIA.

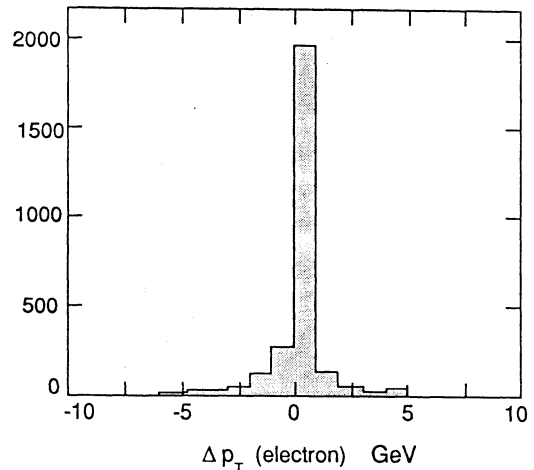


Fig. 3.10: Effect of pile-up and of resolution smearing on the highest transverse energy electron in the event, from UA2SUSY, simulated by superimposing an average of 15 minimum bias events, generated by PYTHIA.

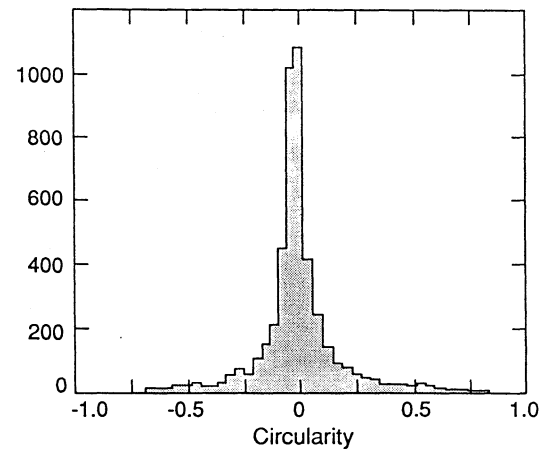


Fig. 3.12: Effect of pile-up and of resolution smearing on the circularity C of the event, from UA2SUSY, simulated by superimposing an average of 15 minimum bias events, generated by PYTHIA.

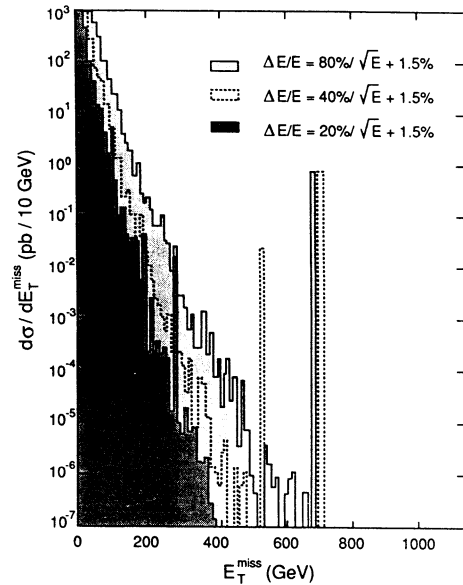


Fig. 3.13: E_T^{miss} distribution for three-jet events, from PAPAGENO, after calorimeter smearing and simulation of cracks, as explained in the text.

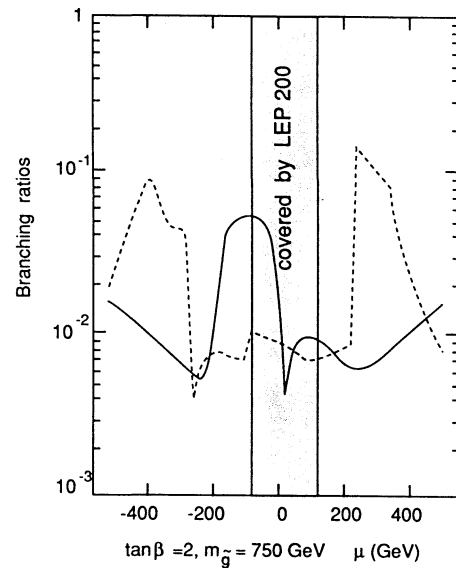


Fig. 3.14: Branching ratios for $\tilde{g}\tilde{g} \rightarrow \tilde{\chi}_1^0 \tilde{\chi}_1^0 + X$ (solid line) and $\tilde{g}\tilde{g} \rightarrow ZZ + X$ (dashed line), as a function of μ for $m_{\tilde{g}} = 750$ GeV and $\tan \beta = 2$. The μ range covered by LEP 200 is also shown.

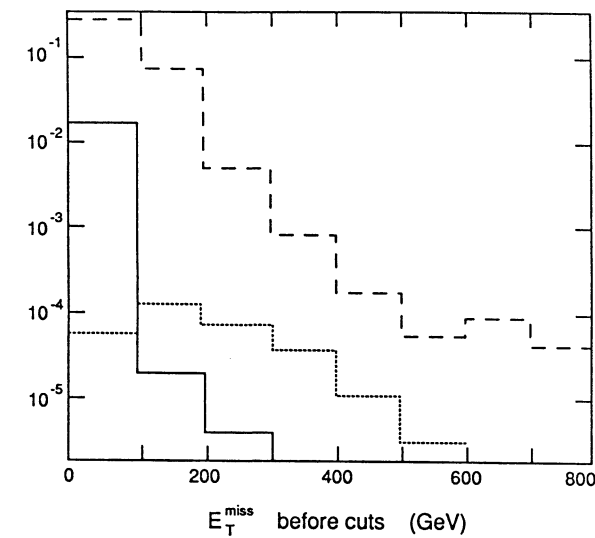


Fig. 3.15: E_T^{miss} distribution before selection cuts for $\tilde{g}\tilde{g} \rightarrow ZZ + X \rightarrow 4e + X$ for $m_{\tilde{g}} = 750$ GeV from UA2SUSY, and for ZZ background from PYTHIA and $t\bar{t}$ background from EUROJET.

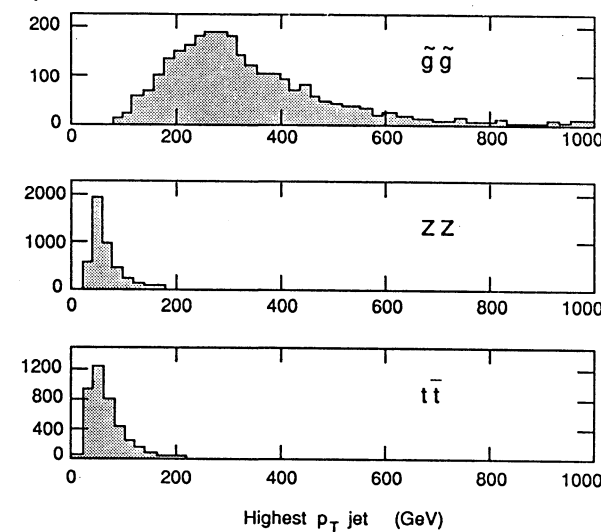


Fig. 3.16: Transverse energy distribution of leading jet before selection cuts for $\tilde{g}\tilde{g} \rightarrow ZZ + X \rightarrow 4e + X$ for $m_{\tilde{g}} = 750$ GeV from UA2SUSY, and ZZ background from PYTHIA and $t\bar{t}$ background from EUROJET.

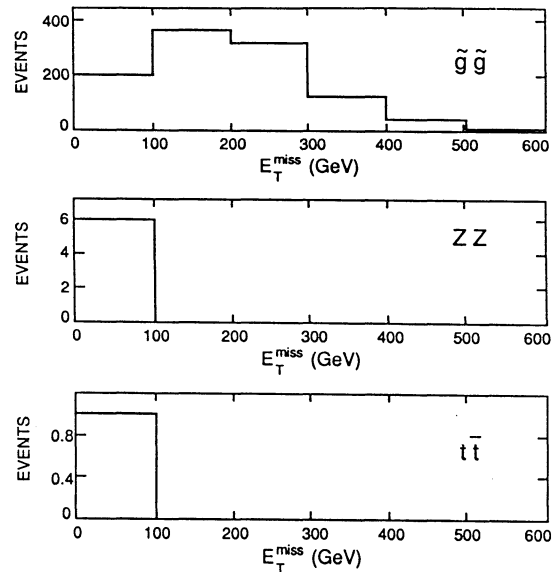


Fig. 3.17: E_T^{miss} distributions after selection cuts for $\tilde{g}\tilde{g} \rightarrow ZZ + X \rightarrow 4e + X$ for $m_{\tilde{g}} = 750$ GeV from UA2SUSY, and ZZ background from PYTHIA and $t\bar{t}$ background from EUROJET.

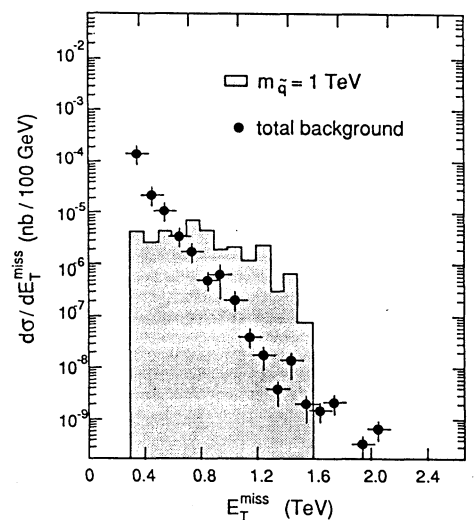


Fig. 3.18: E_T^{miss} distribution for squark pair production of $m_{\tilde{q}} = 1$ TeV (solid histogram) and for the total background contribution (points with error bars) after selection cuts, taken from Ref. [3.2].

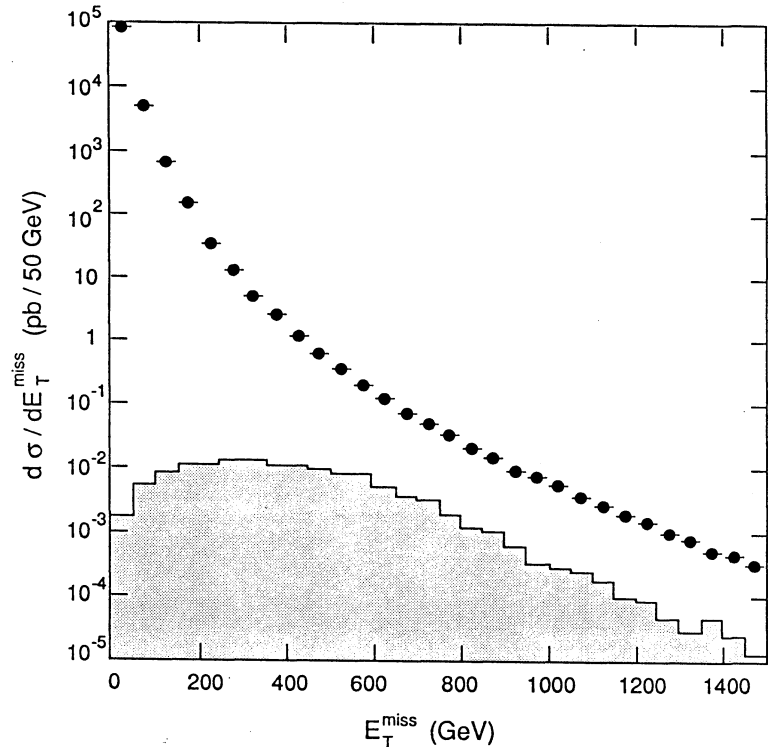


Fig. 3.19: E_T^{miss} distribution from ISAJET after selection cuts for a \tilde{q}_L pair production of 1000 GeV mass. The points with error bars show the total background contribution.

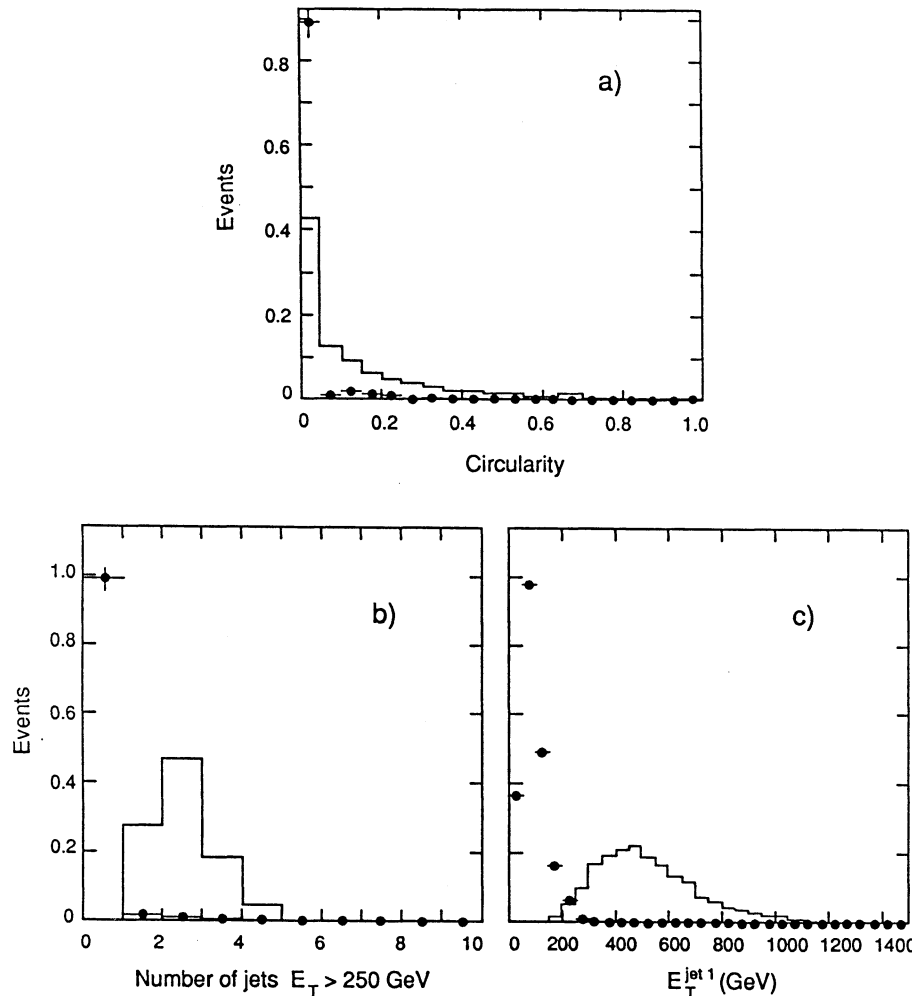


Fig. 3.20: Distribution of a) circularity C , b) N_{jet} for $E_T^{\text{jet}} > 250 \text{ GeV}$, and c) E_T^{jet1} for the hardest jet in the event from ISAJET for \bar{u}_L and \bar{d}_L pair production of 1000 GeV mass (solid histogram) compared to Standard Model background (points with error bars) for $E_T^{\text{miss}} > 75 \text{ GeV}$. The distributions are normalized to 1.

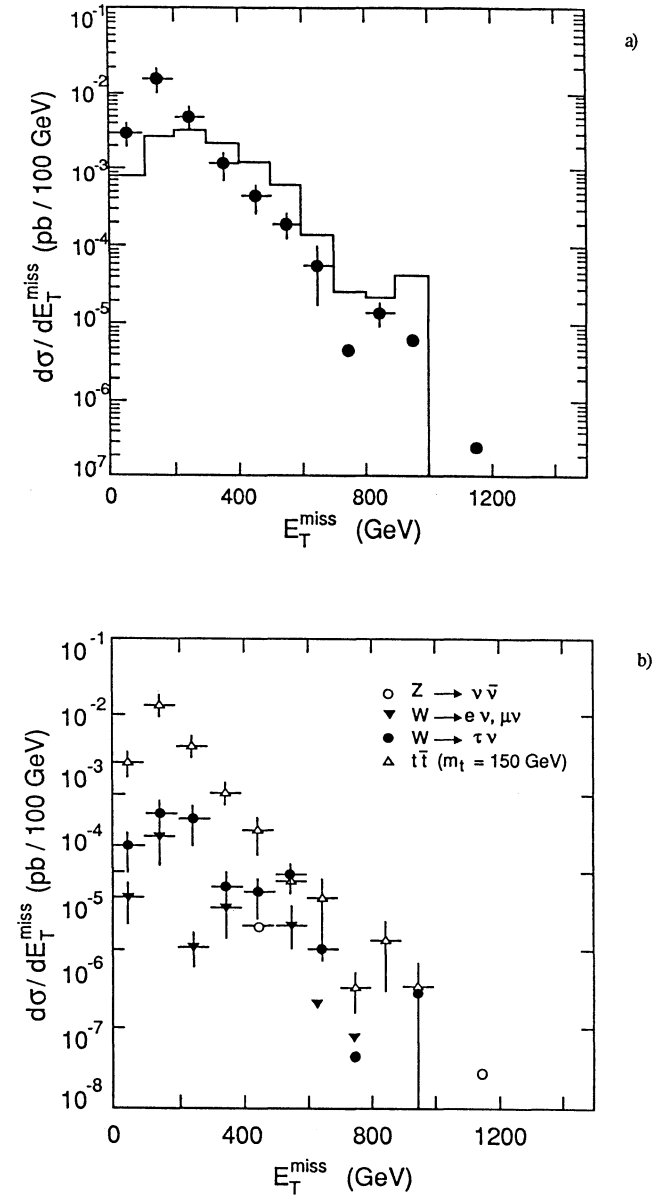


Fig. 3.21: E_T^{miss} distribution from ISAJET after selection cuts for a) \bar{u}_L and \bar{d}_L pair production of 1000 GeV mass. The points with error bars show the total background contribution. In b) the separate background contributions are shown for $t \bar{t}$, $W \rightarrow e \nu$, $W \rightarrow \tau \nu$ and $Z \rightarrow \nu \bar{\nu}$.

4 Neutralino and Chargino Production in Association with Gluinos and Squarks

Contributors: H. Baer, D. Dzalo-Karatas and X. Tata

The cross-section for the production of charginos ($\tilde{\chi}_i^\pm$) or neutralinos ($\tilde{\chi}_j^0$) (collectively denoted by \tilde{G}) in association with strongly interacting sparticles (squarks and gluinos) is smaller than that for $\tilde{q}\tilde{q}$ and $\tilde{g}\tilde{g}$ pair production for two reasons: the basic subprocess is semiweak so that its cross-section is suppressed by $\alpha(\text{weak})/\alpha(\text{strong})$, and associated production cannot occur via gluon fusion. It is, nevertheless, worth studying these processes as they can potentially lead to striking event topologies via which a search for SUSY can be made.

$\tilde{q}\tilde{G}$ production occurs by qg fusion both via annihilation as well as squark exchange diagrams, whereas only squark exchanges contribute to $\tilde{g}\tilde{G}$ production which takes place by $q\bar{q}$ fusion. Unlike squark or gluino production cross-sections, which are completely determined in terms of their masses by QCD, associated production cross-sections depend on the details of the mixings between the higgsinos and the electroweak gauginos. In the following we have used the Minimal Supersymmetric Standard Model (MSSM) as a guide to the masses and couplings. Within this framework, there are two charginos and four neutralinos. All the cross-sections are determined in terms of the four SUSY parameters, which we take to be the squark mass, the gluino mass (this is also assumed to determine the soft SUSY-breaking electroweak gaugino masses), the supersymmetric higgsino mass (denoted by μ), and the ratio $\tan\beta = v_2/v_1$ of the vacuum expectation values (vevs) of the two Higgs fields of SUSY (the Higgs mass bound from the LEP experiments requires at tree level that $\cot\beta < 0.77$, if we assume that it cannot be larger than unity as is the case in all known models).

The results for the total cross-sections, which we have obtained using the matrix elements given in Ref. [4.1], are shown in Fig. 4.1, where we have convoluted them with the EHLQ1 structure functions, and taken $Q^2 = \hat{s}$. In Figs. 4.1a and b we have shown these as a function of $m_{\tilde{g}}$ ($= m_{\tilde{q}}$) for $-\mu = m_w$ whereas in Figs. 4.1c and d we have shown them as a function of $-\mu$ for $m_{\tilde{g}} = m_{\tilde{q}} = 300$ GeV. Throughout, we have fixed $\tan\beta = 1.5$, though none of our results are sensitive to this choice. We see that, depending on sparticle masses, the total cross-sections at the LHC vary from 0.01 to over 100 pb, corresponding to 100 to 10^6 events per year for the lower luminosity case. As shown in Ref. [4.1], the higher energy of the SSC leads to a larger cross-section by a factor of 3–10.

The signatures for the processes depend on how the sparticles decay. One potentially interesting class of events is when \tilde{G} has no hadronic decay products so that such an event contains n leptons recoiling against a system of hard jets from the decay of the gluino (or squark) together with missing p_T . The number n of leptons can be quite large, particularly if the parent gaugino is heavy and decays via a series of cascades into lighter \tilde{G} 's (which can decay leptonically) until the cascade ends in the LSP. The decay patterns of \tilde{G} are also fixed by the SUSY parameters discussed above along with the charged Higgs mass (this fixes the Higgs sector of the MSSM). As long as this mass is large (> 200 GeV) the branching fractions of the charginos and neutralinos are insensitive to its choice. Here, we have nominally fixed it to be 0.5 TeV, a typical value for a generic scalar mass in SUSY models.

The cross-section for such events at the LHC is shown in Fig. 4.2 for a typical choice of SUSY parameters for 0–4 leptons from the decay of \tilde{G} (and no hadrons from its decay).

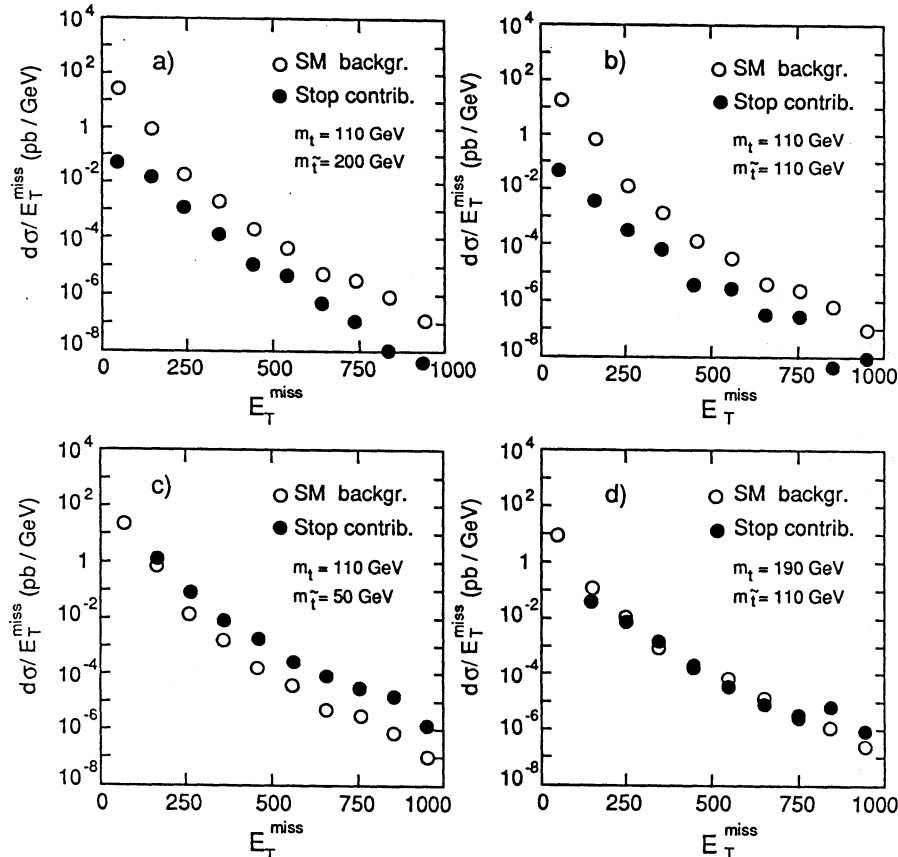


Fig. 3.22: E_T^{miss} spectra, from ISAJET, after cuts as described in text for four combinations of m_t and $m_{\tilde{t}}$. Full circles show the spectra in presence of a stop-quark, open circles for standard model processes only.

Frequently, these leptons are isolated and fairly hard. Since only $O(100)$ trilepton events and $O(1000)$ dilepton events are expected annually, SM backgrounds must be carefully evaluated before any conclusions can be drawn regarding their observability. If the parent \tilde{G} is produced with a large transverse momentum, its decay products are all boosted so that the leptons will be hemispherically separated from the hadronic system. Whether or not this separation is sufficient to result in an identifiable signature requires detailed Monte Carlo studies, which are beyond the scope of this report.

One especially interesting case is $n = 0$, corresponding to the case where \tilde{G} is itself the LSP or is another neutralino which subsequently decays into neutrinos and the LSP. One may hope then that if the event was indeed hemispherically separated, it may be possible to reconstruct the mass of the strongly interacting sparticle that is recoiling against missing p_T (\not{p}_T). The hemispheric separation is maximum if the neutralino is very hard, ie. \not{p}_T is very large. To eliminate SM backgrounds from heavy-flavour (including t -quark) production, we further require the \not{p}_T vector to be well separated from the jets (which are defined to be parton clusters with $p_T > 30$ GeV, where partons have been coalesced if $\Delta R < 0.5$). Towards this end, we further require $\not{p}_T > 400$ GeV and $\Delta\phi(jet, \not{p}_T) > 135^\circ$.

These very hard cuts eliminate the top quark background since it is difficult to get a configuration where the quark is boosted enough to have a very large \not{p}_T and yet no jet within 135° in azimuth. For the same reason, gluino (squark) pair production, which occurs at a much larger rate, is cleanly separated from the data sample [4.1]. The leading background then comes from $Z +$ multijet production, where the Z decays into neutrinos.

The distribution of the invariant mass of the jets (from $\tilde{g}\tilde{G}$ production only) in the hemisphere opposite to the \not{p}_T vector is shown in Fig. 4.3, for three values of the gluino mass. Here, we have taken $m_{\tilde{q}} = m_{\tilde{g}}$, $-\mu = 400$ GeV, with the other SUSY parameters fixed as before. The cross-sections for other values of parameters can be estimated by scaling the cross-sections from Fig. 4.1. Also shown is the contribution from $Z + 2$ jets, for which we have used the program of Ref. [4.2]. We see that within our parton-level calculation, the signal for associated production sticks out well above the background, at least for $m_{\tilde{g}} < 300 - 400$ GeV. Note that our estimate of the signal is conservative, since the contribution of $\tilde{q}\tilde{G}$ production has not been included. If $m_{\tilde{q}} > m_{\tilde{g}}$, as is the case in many models, then the squark would effectively act as a source of gluinos, with the additional quark jet from its decay being rather soft if the two are roughly degenerate. Note also that the peak is only slightly below $m_{\tilde{g}}$ and that the distributions do cut off fairly sharply at $m_{\tilde{g}} - m_{\tilde{\chi}_1^0}$. However, there are only a few hundred events that satisfy our requirements. In view of this, it is not clear to us whether these features will survive when more realistic calculations, including jet broadening, fragmentation, an underlying event, and QCD radiation (which may spoil the strong isolation that we have imposed), etc. are performed. Nevertheless, we feel that this is worthy of further investigation as it may lead to a potential method for measuring the gluino mass (if $m_{\tilde{g}} < 300 - 400$ GeV) at a hadron supercollider such as the LHC.

References

- [4.1] H. Baer, D. Dzalo-Karatas and X. Tata, Phys. Rev. D42, 2259 (1990).
- [4.2] V. Barger, T. Han, J. Ohnemus and D. Zeppenfeld, Phys. Rev D40, 2888 (1990).

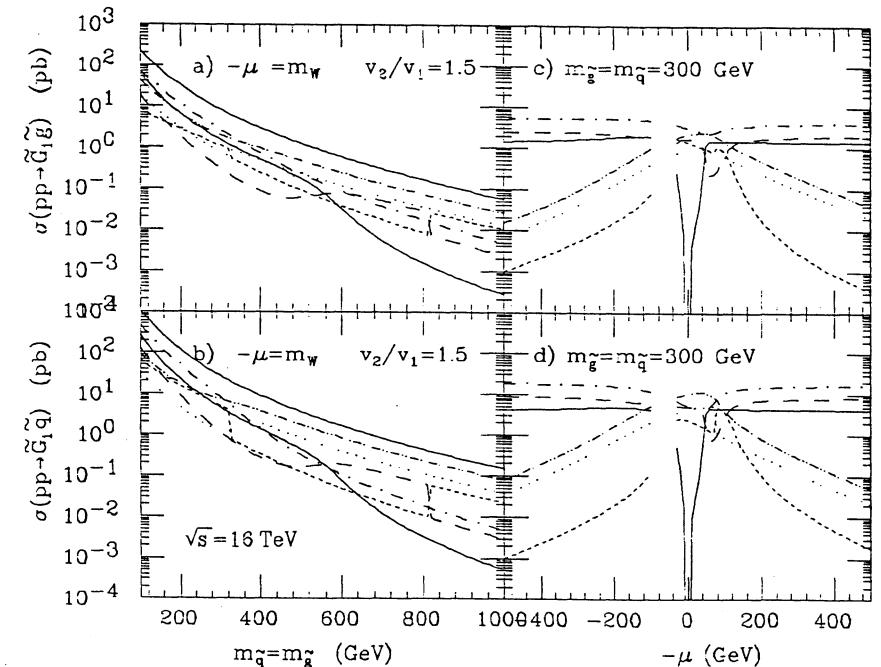


Fig. 4.1: The total cross-sections in pb for the various associated production processes discussed in the text, for pp collisions at $\sqrt{s} = 16$ TeV. In this figure, $-\mu = M_W$ and $\tan\beta = 1.5$ fix the parameters in the chargino and neutralino mass matrices. The different curves are labelled in a) in the following way: $\tilde{g}\tilde{\chi}_2^\pm$ (double dot-dash), $\tilde{g}\tilde{\chi}_1^\pm$ (dot-dash), $\tilde{g}\tilde{\chi}_4^0$ (dots), $\tilde{g}\tilde{\chi}_3^0$ (short dashes), $\tilde{g}\tilde{\chi}_2^0$ (long dashes), and $\tilde{g}\tilde{\chi}_1^0$ (solid). In b), we plot the $\tilde{q}\tilde{G}$ cross-sections, where the curves associated with various \tilde{G} are labelled as in a). The uppermost solid line in a) and b) denotes the sum of all modes. In c) and d) we show the variation in σ with respect to $-\mu$ for $m_{\tilde{g}} = m_{\tilde{q}} = 300$ GeV.

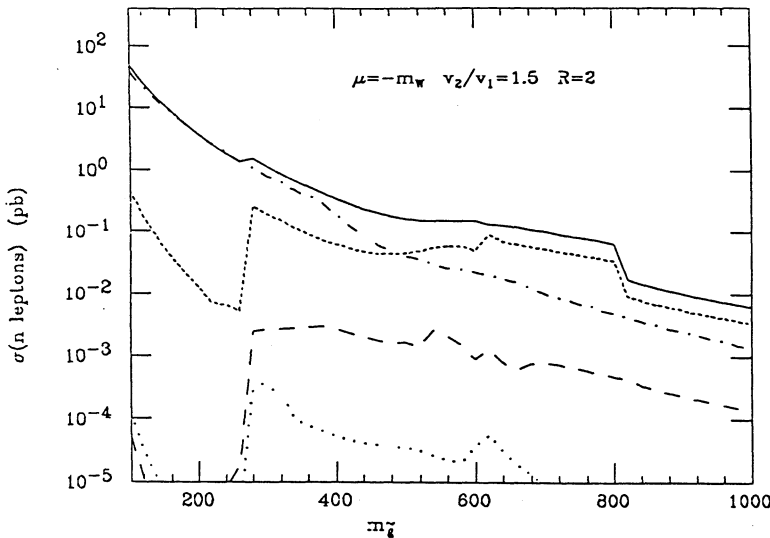


Fig. 4.2: Cross-sections for events where charginos or neutralinos only decay to leptons plus invisible neutrals plotted against $m_{\tilde{g}}$ for $-\mu = M_W$, $\tan \beta = 1.5$ and $R \equiv m_{\tilde{q}}/m_{\tilde{g}} = 2$. Along with additional cuts to select high- p_T sparticles, these could result in hemispherically-separated multi-lepton plus jet events.

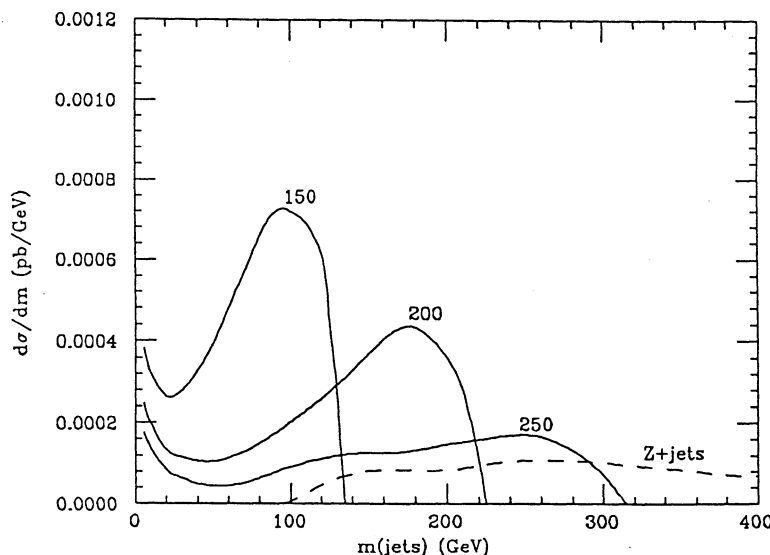


Fig. 4.3: Distribution in mass of jets in the hemisphere opposite \vec{p}_T , after the isolation cut and \vec{p}_T cut described in the text, for $m_{\tilde{q}} = m_{\tilde{g}}$. The plot is for $m_{\tilde{g}} = 150, 200$, and 250 GeV, where $-\mu = 400$ GeV, and $\tan \beta = 1.5$.

5 Charginos and neutralinos

Contributors: R. Barbieri, F. Caravaglios, M. Frigeni and M. Mangano

5.1 Introduction

The fermionic partners of all electroweak gauge and Higgs bosons, usually called charginos and neutralinos, are an essential component of the supersymmetric particle spectrum. As colourless fermions, these particles are in fact likely to be among the lighter fragments of this spectrum. The search for their production in high-energy colliders is therefore one of the most promising tests of supersymmetry.

As it well known, in supersymmetric models with a minimum number of particles, one has four neutralinos ($\chi_1^0, \chi_2^0, \chi_3^0, \chi_4^0$) and two charginos (χ_1^\pm, χ_2^\pm). With a unification hypothesis for the $SU(3) \times SU(2) \times U(1)$ gaugino masses, the mass spectrum and the interactions of all these particles are specified in terms of 2 parameters with dimension of mass (μ, M) and the ratio v_2/v_1 of the vacuum expectation values (VEVs) of the two Higgses [5.1]. For vanishing μ or M the lightest neutralino (χ) is massless, whilst the lighter chargino mass is less than m_W . The gluino mass $m(\tilde{g})$ is proportional to M : $m(\tilde{g}) \simeq 3.5M$. Table 5.1 gives the neutralino and chargino masses in a few representative points of the (μ, M) space for $v_2/v_1 = 2$. All these points are outside the domain explorable at LEP II. On the other hand, they are representative points in the ‘natural’ region of parameter space for the Minimal Supersymmetric Standard Model (MSSM).

Table 5.1: Neutralino and chargino masses (in GeV) for $v_2/v_1 = 2$

μ GeV	M GeV	χ_1^0	χ_2^0	χ_3^0	χ_4^0	χ_1^\pm	χ_2^\pm
-80	100	51.2	72.0	118	141	90.5	145
-150	100	51.2	108	166	178	111	182
-80	200	72.3	104	108	225	94.1	224
-150	200	96.4	144	172	225	155	226

The lightest neutralino is assumed to be the lightest stable supersymmetric particle. We also assume the quark and lepton scalar partners to be heavy enough so that the decays of the heavier neutralinos and charginos are dominated by the chain decays

$$\chi^\pm \rightarrow W^\pm \chi, Z \chi^\pm$$

$$\chi \rightarrow W^\pm \chi^\mp, Z \chi$$

into the lighter components of the spectrum. Depending on phase space, the W and Z bosons may be real or virtual. As mentioned above, the branching ratios to the different final states are specified by the same (μ, M) parameters which determine the spectrum. The most salient features of the various couplings are determined by the fact that the gaugino components of the neutralinos do not couple to the Z -boson and by the absence of mixed gaugino-higgsino couplings both to the W and to the Z .

5.2 Study of the signal

At a hadron collider chargino–neutralino pairs ($\chi\chi$, $\chi\chi^\pm$, $\chi^\pm\chi^\mp$) are mainly produced via the Drell–Yan mechanism with a typical electroweak cross-section. In turn the decays of the ‘excited’ states, all but the lightest neutralino, will produce a number of W and Z bosons, most of the time virtual, and a few (≥ 2) unseen neutralinos. To look for a visible signal we concentrate on final states with leptons only. The number of charged leptons in the final state can vary from 1 ($\chi\chi^\pm \rightarrow \chi\chi l^\pm\nu$) up to 6/7, from chain decays of the heavier states. In the following, we concentrate on the final states with 3 or 5 charged leptons (electrons or muons), since the corresponding signals, in view of the various backgrounds, look more promising than in the other cases.

Table 5.2: Multi-lepton production cross-sections (in pb)
at $\sqrt{s} = 16$ TeV and $v_2/v_1 = 2$

μ (GeV)	M GeV	3 leptons	5 leptons	$\mu^\pm\mu^\pm e^\mp$
-80	100	1.5×-1	27×-4	5.6×-3
-150	100	2.2×-1	0.55×-4	0.65×-3
-80	200	0.3×-1	1.8×-4	0.73×-3
-150	200	0.61×-1	7.6×-4	1.4×-3

Corresponding to a few representative points in parameter space, Table 5.2 contains the pp cross-sections at $\sqrt{s} = 16$ TeV for 3 and 5 leptons in the final states. In both cases we require all the leptons to be central – $|\eta| < 2.5$ – and we require the two leading leptons (*i.e.* the *trigger* leptons) to be harder than a minimum p_T threshold which, depending on their flavour, we choose to be: $p_T^e > 20$ GeV and $p_T^\mu > 15$ GeV. The additional leptons have $p_T > 10$ GeV, regardless of their flavour. Somewhat stronger or weaker cuts may be applied as well, without dramatically changing the values of the cross-sections. More complete information for the 3 lepton cross-section is given in Fig. 5.1, where we show its contour plot in the (μ, M) plane with the same cuts as above. Out of the 3 lepton cross-sections one can isolate the component with 2 muons of the same charge (Table 5.2). These final states take advantage of the Majorana nature of the neutralinos. For example, they arise through the chain

$$pp \rightarrow \chi^+ \chi' \chi^+ \rightarrow \mu^+ \nu \chi \chi' \rightarrow \chi^+ e^- \bar{\nu} \rightarrow \mu^+ \nu \chi e^- \bar{\nu}$$

These equal-sign dileptons may constitute a significant fraction of the 3-lepton events produced in the decay of the heavier chargino–neutralino pairs. On the other hand, for many values of the parameters they represent a fraction of the overall 3-lepton supersymmetric events too small to be interesting when the background-to-signal ratio is considered.

5.3 Study of the background

The only source of irreducible backgrounds to these multileptonic final states comes from the production and decay of multiple gauge bosons, such as:

$$\begin{aligned} pp &\rightarrow WZ \rightarrow l\nu l'\bar{l}, \\ &\quad \rightarrow l\nu\tau\bar{\tau} \rightarrow ll'l'' + \nu's, \\ pp &\rightarrow WWW \rightarrow ll'l'' + \nu's, \\ pp &\rightarrow WZZ \rightarrow l\nu l'\bar{l}l''\bar{l}''. \end{aligned}$$

We calculated the effect of these backgrounds on the 3-lepton signal and verified that they never exceed the level of a $\text{few} \times 10^{-2}$ pb, which is smaller or comparable with the signal for the range of parameters considered here. For example, $\sigma(pp \rightarrow WWW \rightarrow 3l) \simeq 4 \times 10^{-3}$ pb and $\sigma(pp \rightarrow WZ \rightarrow ll'\tau\bar{\tau} \rightarrow 3l) \simeq 2 \times 10^{-2}$ pb, both values obtained without applying the above cuts on the final-state leptons. Furthermore, requiring the absence of ll' pairs with an invariant mass within a few GeV of the Z mass does not affect the signal in a significant way, whilst it reduces backgrounds with one pair of leptons coming directly from the decay of a real Z to practically zero. Therefore the WZZ process will not interfere with the observation of the 5-lepton supersymmetric signal. (The signal rates given in Table 5.2 and Fig. 5.1 were calculated rejecting events with leptons coming from real Z decays.)

As a matter of fact, the main source of background comes from the production of *top* quark pairs. The semileptonic decay of the $t\bar{t}$ and of the heavy quarks generated in the weak decay chain ($t \rightarrow b \rightarrow c$) might lead to final states with a large number of leptons. With $t\bar{t}$ cross-sections largely exceeding the level of the nanobarn (depending on the *t* mass) and a 3-lepton BR larger than 1%, it is easy to see that unless proper cuts are applied this process will totally hide the signal. The variables that can help us to discriminate between *top* events and signal are the *lepton isolation* and the presence of additional hadronic activity in the event. We will now briefly discuss these cuts.

While the first two leptons coming from the decay of the real *W*'s will be hard and isolated, the additional leptons coming from the decay of a *b* or *c* quark will be surrounded by the hadrons produced either during the acceleration of the quark, or during its semileptonic decay. Therefore the leptons coming from the *b* or *c* will not be isolated, contrarily to the leptons of the signal. For the signal, in fact, the only possible contribution to non-isolation comes from the presence of the initial-state radiation and beam fragmentation, plus the possible presence of additional overlapping pp interactions, depending on the beam luminosity. We therefore required that the hadronic energy present in a cone of radius 0.2 units in η – ϕ space around each lepton must not exceed 2 GeV. Our study of the structure of the underlying event in high-mass Drell–Yan processes indicates that for luminosities of the order of $10^{33} \text{ cm}^{-2}\text{s}^{-1}$ this cut is highly efficient for the signal, while it significantly helps to reduce the background. In particular, because of isolation, we found no background to the 5-lepton channel at the level of 10^{-5} pb.

This luminosity is sufficient to observe more than a few hundred signal events in the 3-lepton channel in one year of operation. Trying to detect the 5-lepton signal will require higher luminosities, and the isolation cuts might need to be loosened, therefore possibly bringing in some background. The study of the effect of looser isolation cuts is under way.

In addition to the lepton isolation, in the case of the 3-lepton signal a useful distinguishing feature of *t* events is the presence of hard hadronic activity in the final-state. This is mostly due to the *b*-jet (from the *b* which does not decay semileptonically), but also to the hadrons from the weak decays and from the final-state radiation. In the case of the signal, this additional hadronic activity is due to initial-state radiation. We studied the spectrum of jets emitted from the initial state in Drell–Yan events at large mass and concluded that cutting on the presence of a jet with p_T less than 50 GeV (30 GeV) leaves about 75% (60%) of the signal. The effect of cutting on the p_T of the jet present in *t* events is shown in Table 5.3, where we give the background cross-sections for two values of m_{top} ($m_{top} = 150, 200$ GeV) as a function of the maximum jet p_T . The p_T distribution of the *b*-jet in events passing the 3-lepton cuts is shown in Fig. 5.2. Once again, running at very high luminosity might require

choosing higher cuts, because of the pile-up of energy within the jet cones and because of the possible presence of additional soft jets from overlapping events.

Table 5.3: Three-lepton cross-sections (in pb) from $t\bar{t}$ production at $\sqrt{s} = 16$ TeV and for different values of applied cuts.

b-jet cut	$m_{top}=200$ GeV	$m_{top}=150$ GeV
-	0.24	1.8
50 GeV	4.1×10^{-2}	0.67
30 GeV	1.0×10^{-2}	0.25

In the case of the heavier *top* the signal is observable with standard luminosity in one year of running and for all the choices of μ and M chosen here. In the case of the 150 GeV *top* additional work is necessary to isolate the signal from the background. Possible ways are the following: first of all our study of the effect of isolation cuts is rather conservative, as we generated events at the parton level and we have not accounted for the effects of gluon radiation in the final state. Our only source of non-isolation was the *c* quark from the *b* decay. Therefore a more complete study of the *b* fragmentation process will yield higher rejection factors because of the requirement of lepton isolation. Furthermore, the energy lost by the *b* during the fragmentation itself will give rise to a softer lepton spectrum, so that the p_t cuts will be more efficient in reducing the background. Secondly, one might hope that some detector for LHC will enjoy *b*-tagging capabilities, thus making it possible to reject the *top* events with higher efficiency.

In conclusion, we have shown that purely multileptonic decays of excited neutralinos and charginos are, in principle, observable at LHC for a large range of supersymmetry parameters. In the 3-lepton channel several hundred events can be observed within one year with a standard luminosity. The most serious background to this channel comes from the production and semileptonic decay of *t* quarks. We have indicated that this background can be reduced below the signal for $m_{top} > 150$ GeV, whilst in the case of a lighter *top* more work is necessary. The 5-lepton channel is above background, but requires running at a higher luminosity, where some of the cuts used here to eliminate the *t* background might have to be softened. More details on this analysis, as well as the results for $\sqrt{s} = 8, 40$ TeV, will be given in a forthcoming paper.

References

- [5.1] R. Barbieri et al. in: G. Altarelli et al. (eds.) ‘Z physics at LEP I’, CERN 89-08, vol.2, p.114.

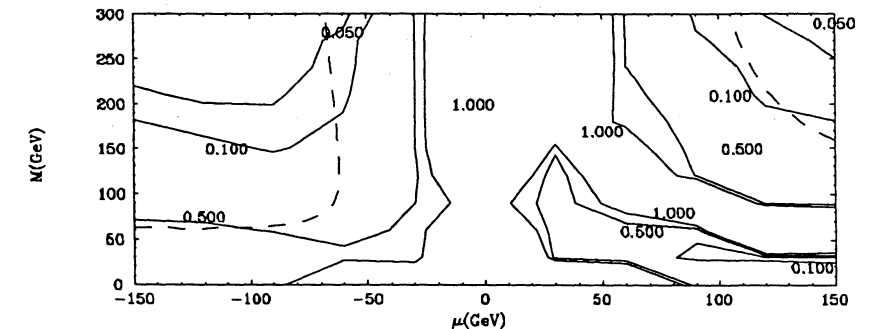


Fig. 5.1: Contour plot of the cross-section for $pp \rightarrow \chi^\pm \chi' \rightarrow 3\text{lept.} + \text{inv.}$ (pb) in (μ, M) space, for $v_2/v_1 = 2$; the dashed lines delimit the region where $m_{\chi^\pm} < m_W$, which is open to exploration by LEP II.

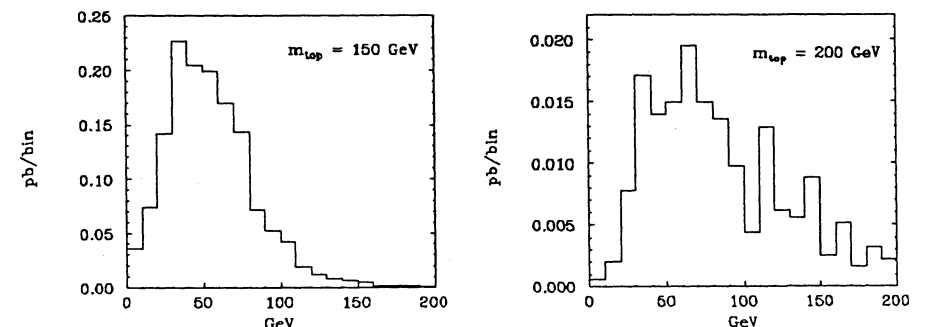


Fig. 5.2: p_T distribution of the b-jet in $t\bar{t}$ events passing the 3-lept. on cuts described in the text, for two values of m_{top} .

6 Sleptons

Contributors: F. del Aguila, Ll. Ametller and M. Quirós

6.1 Introduction

If new particles with strong and/or electroweak couplings do exist in the TeV range, they must be produced at LHC. Their detection, however, is not guaranteed. This requires a sizeable production cross-section and a relatively clean signature. Here we discuss the prospects for slepton detection [6.1].

6.2 Signals and backgrounds

Sleptons can be produced by pairs or in gaugino decays. Among the three standard mechanisms for slepton pair production at LHC, Drell-Yan (DY) quark annihilation, electroweak gauge boson fusion (WW) and gluon fusion (gg), DY gives the largest, although small, cross-section [6.1]. For $\tilde{e}_L \bar{\tilde{e}}_L$ production we show in Fig. 6.1 the DY production (solid), WW fusion (dashed), and gg fusion (dotted), as a function of the slepton mass. We also show the electroweak background $WW \rightarrow e\bar{e}\nu\bar{\nu}$ (dotted-dashed). (We have imposed no cut.) Hence we will concentrate on DY production, in particular on $\tilde{e}_L \bar{\tilde{e}}_L$ production. (The $\tilde{e}_L \bar{\tilde{e}}_L$ cross-section is larger than the $\tilde{e}_L \bar{\tilde{e}}_L$ cross-section, and its irreducible electroweak background $WZ \rightarrow e\nu\bar{\nu}$ is smaller than the $\tilde{e}_L \bar{\tilde{e}}_L$ one, $WW \rightarrow e\bar{e}\nu\bar{\nu}$. However, in this case, the only relevant kinematical variable is the charged lepton transverse momentum. This reduces the number of actual cuts, and then the discovery limit [6.1].) We assume that \tilde{e} decays into $e\tilde{\gamma}$, where $\tilde{\gamma}$ is the photino, and that R -parity is conserved. The signal for $\tilde{e}_L \bar{\tilde{e}}_L$ is two leptons of opposite charge and missing transverse momentum. Heavy quark production, in particular $t\bar{t} \rightarrow WWq\bar{q} \rightarrow e\bar{e}\nu\bar{\nu}jj$, where both jets are misidentified or missing, gives also *a priori* a large background. In Fig. 6.2a we show the p_t^e distribution. The crosses (dashed line) correspond to the signal for $m_{\tilde{\gamma}} = 50$ GeV and $m_{\tilde{e}} = 100$ (300) GeV. We require $p_t^e, p_t^{missing} > 40$ GeV and the pseudorapidities of the charged final particles $|\eta| < 2$. The $pp \rightarrow WW \rightarrow e\bar{e}\nu\bar{\nu}$ background is also plotted (diamonds). The upper (lower) solid line represents the $t\bar{t} \rightarrow q\bar{q}e\bar{e}\nu\bar{\nu}$ background with $m_t = 150$ (200) GeV. Further cuts are imposed, in this case, on the distance in the lego plot $\Delta R_{qe} = \sqrt{(\Delta\phi)^2 + (\Delta\eta)^2} > 0.75$ (for isolation) and on $p_t^q < 40$ GeV (for misidentified and/or missed quarks). In Fig. 6.2b we give the corresponding ϕ distribution, where ϕ is the angle between both charged leptons in the transverse plane ($\phi = \pi$ corresponds to opposite transverse momenta.) Figures 6.2c shows the same distribution but for $p_t^e > 100$ GeV. The former figures translates into a discovery limit for charged sleptons of 250 GeV at LHC, requiring 10 events with $p_t^e, p_t^{missing} > 40$ GeV, $p_t^e > 100$ GeV, $|\eta^e| < 2$, and $\phi < 1.6$ rad, and assuming an integrated luminosity of 10^4 pb^{-1} . (We work at the parton level with no radiation, although we have also done a real top background simulation for testing the quality of our estimate. The p_t^e distribution agrees with the corresponding one in Fig. 6.2, but it is several orders of magnitude larger if no very demanding cuts on isolation etc., are imposed. However, if we associate a suppression factor of at least one order of magnitude for each misidentified bottom, we recover our estimate in Fig. 6.2.)

In specific models sleptons can also decay through large cascades. A striking signal would be $pp \rightarrow \tilde{e}\bar{e} \rightarrow e\tilde{Z}\bar{e}\tilde{Z} \rightarrow e\bar{e}ZZ\tilde{\gamma}\tilde{\gamma} \rightarrow e\bar{e}\mu\bar{\mu}q\bar{q}\tilde{\gamma}\tilde{\gamma}$. The cross-section for $p_t^{lepton} > 25$ GeV

and $p_t^{missing} > 100$ GeV is $2 \times 10^{-5} \text{ pb}$ (we have also required a not very significative cut of 50 GeV on $p_t^{Z \rightarrow q\bar{q}}$), assuming $m_{\tilde{e}} = 200$ GeV and a Zino mass $m_{\tilde{Z}} = 150$ GeV, and the unknown branching ratios equal to one. This cross-section is negligible and comparable with the corresponding top background. Hence cascading sleptons must be difficult to observe at LHC.

Sleptons can be also produced in gaugino decays. Signals and cross-sections depend on the gaugino branching ratios and then on the model. Production cross-sections and decay rates are discussed elsewhere in these proceedings.

6.3 Summary

In most models, among the plethora of new supersymmetric particles, sleptons are expected to be the lightest (charged) superpartners. This makes them more interesting because a relatively low bound on their mass stands for a relatively stringent bound on all the supersymmetric spectrum. At hadron colliders, however, sleptons have small cross-sections, since they do not have strong interactions, and relatively large backgrounds. Pair-produced sleptons with a mass up to 250 GeV could be detected at LHC.

References

- [6.1] F. del Aguila and Ll. Ametller, UAB-FT-243/90, and references therein.

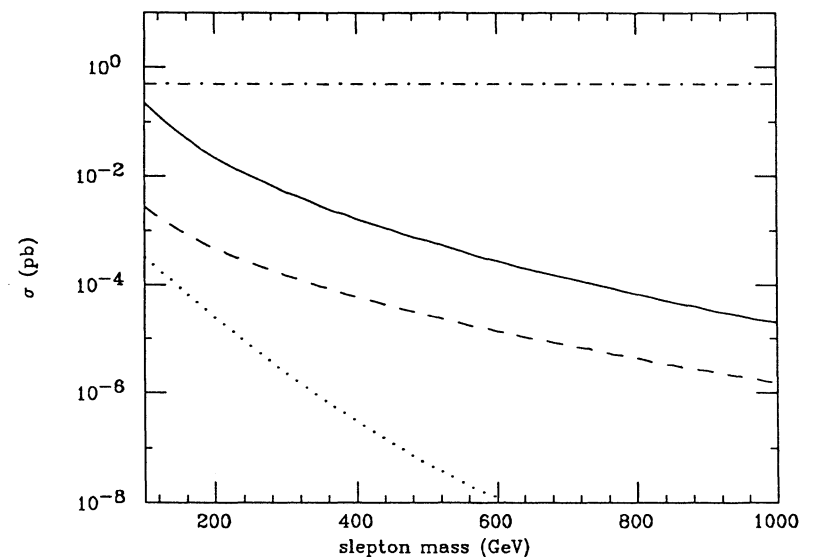


Fig. 6.1: Total cross-section for $\tilde{e}_L \bar{\tilde{e}}_L$ production at LHC as a function of the selectron mass. The solid line corresponds to the Drell-Yan mechanism, the dashed line to the WW fusion for $m_h = m_Z$ and $m_{\tilde{e}} - m_{\tilde{\nu}} = m_W/2$ and the dotted line to the gg fusion for $m_h = m_Z$. The dotted-dashed line gives the $pp \rightarrow W^+ W^- \rightarrow e^+ e^- \nu \bar{\nu}$ production cross section.

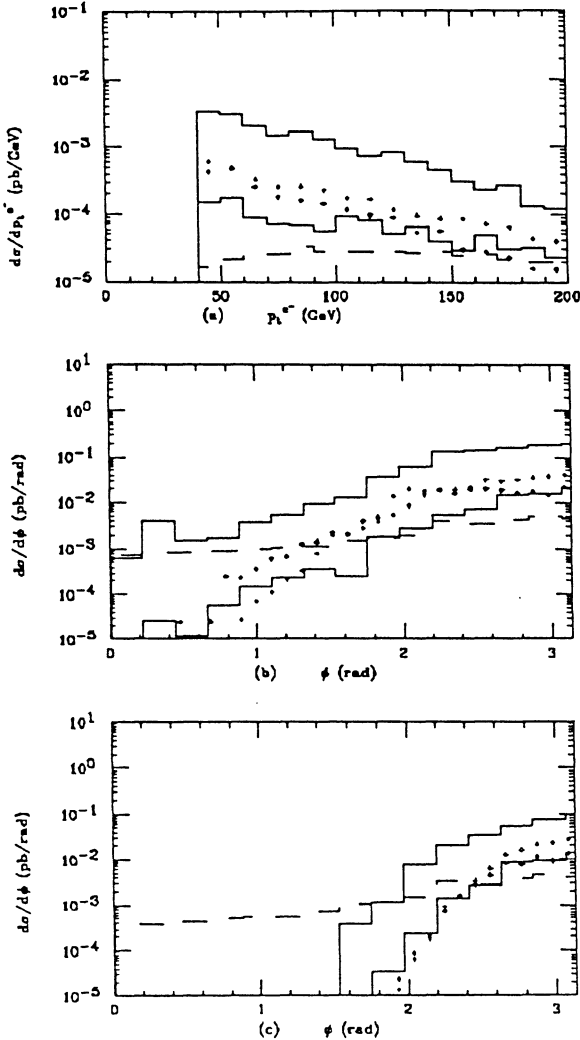


Fig. 6.2: a) Electron transverse momentum distribution for $\tilde{e}_L \bar{\tilde{e}}_L$ (DY) production at LHC, assuming that $\tilde{e} \rightarrow e\tilde{\gamma}$ is the unique decay mode, $m_{\tilde{\gamma}} = 50$ GeV and $m_{\tilde{e}} = 100$ (crosses), 300 (dashed) GeV. The $pp \rightarrow W^+W^- \rightarrow e^+e^-\nu\bar{\nu}$ background (rectangles) is also plotted. $p_t^e, \not{p}_t > 40$ GeV and the pseudorapidities of the charged final particles $|\eta| < 2$. The other p_t^e -distributions correspond to $t\bar{t} \rightarrow q\bar{q}e^+e^-\nu\bar{\nu}$ production. Further cuts are imposed in this case on $\Delta R_{qe} > 0.75$ (for isolation) and on $p_t^q < 40$ GeV (upper and lower solid lines corresponding to $m_q = 150$ and 200 GeV, respectively). b) The corresponding ϕ distributions, ϕ being the angle in the transverse plane between the two charged leptons. c) Same as (b) but for $p_t^e > 100$ GeV.

7 Broken R-Parity

Contributors: P. Binetruy, H. Dreiner, V. Jain, S. Lola, C.H. Llewellyn Smith, J. McCurry, F. Pauss, G.G. Ross, J.W.F. Valle

7.1 Introduction

The vast bulk of supersymmetric phenomenology assumes the “Minimal Supersymmetric Standard Model” (MSSM), which conserves what is known as R-parity [7.1]. As discussed in Section 1.1, in this model all the new states, the superpartners of the SM states, are R-parity odd whilst all the SM states are R-parity even. As a result, the new supersymmetric states can only be produced in pairs, and a supersymmetric state cannot decay only to conventional states. This has a profound effect on the phenomenology of such states; in particular, all experimental searches for the new supersymmetric states rely on pair production and most searches involve missing energy as a signal for the production of the “LSP” the lightest supersymmetric state which must be stable and neutral (for cosmological reasons).

However R-parity need not be conserved in supersymmetric extensions of the Standard Model; indeed, as we shall discuss, such models arise quite naturally in superstring unification schemes. Thus it is important to consider the possible phenomenology associated with such non-standard models in case the LHC supersymmetry simulations should miss important channels. The approach followed here is to survey the dominant signals to be expected in such schemes. We find that R-parity-broken models lead to signals that are at least as visible as in the MSSM, but that it is important in many cases to look in different channels or to impose different cuts if the supersymmetric states are to be identified.

7.2 R-parity-broken models.

The MSSM is built using the minimal particle content (see section (1.1)) and adding the Yukawa and associated scalar-particle couplings needed to give masses to the quarks and leptons. These come from the superpotential terms

$$[h_{ik} L_i H_2 \bar{E}_k, h'_{ik} Q_i H_2 \bar{D}_k, h''_{ik} Q_i H_{7,1} \bar{U}_k]_F \quad (7.1)$$

where L and E (Q and $\bar{U}\bar{D}$) are the left-handed components of lepton doublet and antilepton singlet (quark doublet and antiquark singlet) chiral superfields respectively and $H_{1,2}$ are Higgs superfields. The terms of eq. (7.1) gives rise to the Yukawa couplings involving the component states. For example, the first term gives

$$h_{ik} (\tilde{L}_i \tilde{H}_2 \bar{E}_k + \tilde{L}_i H_2 \overline{\bar{E}_k} + \tilde{L}_i \tilde{H}_{2j} \overline{\bar{E}_k}) , \quad (7.2)$$

where we denote by a supertwiddle the scalar partners to the quarks and leptons, namely the squarks and sleptons. Note that the supersymmetric states only occur in pairs in eq. (7.2), consistent with the R-parity of the model. The terms in eqs. (7.1), and (7.2) are, of course, allowed by the $SU(3) \otimes SU(2) \otimes U(1)$ gauge invariance but they are not the only such terms. The most general trilinear terms consist of those in eq. (7.1) together with the terms (operators)[7.2]

$$[\lambda_{ijk} L_i L_j \bar{E}_k + \lambda'_{ijk} L_i Q_j \bar{D}_k + \lambda''_{ijk} \bar{U}_i \bar{D}_j \bar{D}_k]_F . \quad (7.3)$$

The first term gives rise to the Yukawa couplings

$$\lambda_{ijk}(L_i L_j \bar{E}_k + L_i \bar{L}_j \bar{E}_k + \bar{L}_i L_j \bar{E}_k), \quad (7.4)$$

The terms of eq. (7.3), violate baryon and lepton number and, if present in the Lagrangian, they generate an unacceptably large amplitude for proton decay suppressed only by the inverse squark mass squared. For this reason, a discrete symmetry called matter parity was introduced which forbids these terms [7.3]. Under this symmetry the quark and lepton superfields appearing in the superpotential change sign, whilst the Higgs superfields are left invariant. Thus the terms of eq. (7.3) change sign under this symmetry and are forbidden whilst the terms of eq. (7.1) are invariant and allowed. Using this symmetry the couplings of the MSSM are the only ones allowed and [cf. eq. (7.2)] the new supersymmetric states only couple in pairs in accordance with the R-parity of the model.

However, the origin of the discrete matter parity is not clear at the level of the MSSM; presumably it comes from the underlying unified theory. It is encouraging that in string theories just such discrete symmetries emerge [7.4] but they do show that the MSSM is not the only viable way to construct a minimal supersymmetric extension of the SM. In particular, provided at least one of the last two baryon- or lepton-number violating vertices of eq. (7.3) is absent the nucleon will be stable. It is easy to write down alternative symmetries to matter parity which allow for a different set of couplings. For example, if only the quark superfields change sign then only the last (baryon-number violating) term in eq. (7.3) is forbidden. This gives a new model in which [cf. eq. (7.4)] a single supersymmetric state, a slepton or sneutrino, can couple to SM states breaking R-parity.

Before the advent of string theory it was thought likely that quarks and leptons would transform in the same way in a Grand Unified extension of the SM and this suggested that imposition of matter parity was the most reasonable way to supersymmetrize the SM. However, string theories do not, in general, have discrete symmetries which treat quarks and leptons in the same way. This observation suggests that equally reasonable are alternative minimal supersymmetric models in which any subset of the terms of eq. (7.3) which does not give rise to nucleon decay is included. (It is also possible that R-parity is broken spontaneously [7.5] through a sneutrino vacuum expectation value(VEV), but we do not explore this possibility here.)

7.3 R-parity breaking at the LHC

Since we must allow for the most general family structure in terms of eq. (7.3) there are a very large number of possible R-parity broken schemes. In order to survey the new signals for supersymmetry that may be expected in such schemes, we are forced to consider some simplifying assumptions which, however, we think are the most reasonable possibilities: i) The first assumption is that, of the allowed couplings consistent with no nucleon decay, only one dominates. This is perhaps the most likely circumstance as the new couplings are of the same character as the normal Yukawa couplings responsible for quark and lepton masses and these show a vast difference in magnitude. ii) The second assumption is that a neutralino will be the LSP. It is no longer necessary for the LSP to be neutral in these models for the LSP is unstable and so the cosmological bounds do not apply. However, making this assumption makes the analysis of manageable size and is motivated by (model-dependent) estimates of the superparticle spectrum. If this LSP is lighter than 300 MeV it will decay outside the apparatus and lead to the usual missing-energy signals. Thus we further assume

the (most-likely) case that the LSP is heavier than 300 MeV (In fact we choose a lower bound of m_c to further simplify the analysis, cf. Table 7.2.)

Even with these simplifying assumptions there are 45 different, models to consider, corresponding to the 45 different terms appearing in eq. (7.3). However, as we will see, it is now straightforward to detail the phenomenology of all these models. (The phenomenology of R-parity breaking in high-energy colliders has also been studied in Refs [7.6,7.7].) The coefficients of the operators are limited in size by purely conventional (non-supersymmetric) processes, for the addition of a new interaction may affect these processes by virtual exchange. In Table 7.1 we present these bounds [7.6]–[7.10].

Table 7.1: Limits on the R-parity violating parameters [7.2, 7.8–7.10] from some physical processes

LLĒ		LQD̄		UDD̄	
ijk	$\lambda_{ijk} <$	ijk	$\lambda'_{ijk} <$	ijk	$\lambda''_{ijk} <$
121	0.04 ^(a)	111	0.01 ^(g)	112	$10^{-8(i)}$
122	0.04 ^(a)	112	0.03 ^(a) X		
123	0.04 ^(a)	113	0.03 ^(a) X		
131	0.10 ^(b)	121	0.26 ^(e)		
132	0.10 ^{(b)(c)} X	122	0.45 ^(c)		
133	0.01 ^(h)	123	0.26 ^(c)		
231	0.09 ^(b) X	131	0.26 ^(e)		
232	0.09 ^(b) X	133	0.01 ^(h)		
233	0.09 ^(b) X	211	0.09 ^(b)		
		212	0.09 ^(b)		
		213	0.09 ^(b)		
		221	0.22 ^(f) X		
		231	0.22 ^(f) X		

(a)charged-current universality; (b) $e\mu\tau$ universality; (c)forward-backward asymmetry; (e)atomic parity violation; (f) ν_μ deep-inelastic scattering; (g)neutrinoless double-beta decay; (h)neutrino masses; (i) $|\Delta B| = 2, \Delta L = 0$ transitions. The superscript X denotes that the corresponding number is at the 2σ level, and is excluded at the 1σ level.

Note that not all operators are so constrained, for example there is only one bound for the $\bar{U}\bar{D}\bar{D}$ operators.

We now turn to a determination of the decay patterns of the supersymmetric states. These are given in Table 7.2 for both the LSP and the heavier states. From this table a clear pattern emerges. The LSP decays in all but one case to the non-supersymmetric components of the states of the operator of eq. (7.3). The states heavier than the LSP typically decay as in the MSSM rather than via modes generated by the new (R-parity violating) operator. Thus the decay pattern of a supersymmetric state will involve its conventional cascade decay followed by a non-standard conversion of the LSPs produced to non-supersymmetric states.

Using this structure we may now determine the signals to be expected for the R-parity breaking models following from conventional pair production of supersymmetric states. These are presented in Table 7.3. In this table it may be seen that missing energy is

converted into visible energy changing the signal from that of the MSSM. In the case of the operators $LQ\bar{D}$ and LLE this leads to signals more visible than in the MSSM as there are always channels involving additional charged leptons. In the worst case of the $\bar{U}\bar{D}\bar{D}$ operators the missing energy is converted into visible energy in the form of quark jets and does not lead to a more distinctive signal.

It was not possible to carry out an exhaustive study of these new signals but a case study was undertaken to establish whether conversion of missing energy to visible states involving charged leptons indeed produces a better signal. The process studied was gluino pair production with the decay mode of Table 7.3, column 2, corresponding to the $LL\bar{E}$ operator causing the LSP to decay to $e^+\mu^-\nu$. For $m_{\tilde{g}} = 300$ GeV, $\tan\beta = 2$, $\mu = -440$ GeV with $m_A = 53.2$ GeV, the branching ratio for $\tilde{g} \rightarrow q\bar{q}\Lambda$ is 17% and the cross section for gluino pair production followed by multilepton production is 1.665 pb. A particularly useful distribution proves to be the differential cross-section with respect to the angle between one of the two muons and an electron. In Figs. 7.1 and 7.2 we show these differential cross-sections with cuts imposed to enhance the signal compared with the background coming principally from $t\bar{t}$. It is a very distinctive signal and much more visible than the normal gluino signal in the MSSM.

Unfortunately not all R-parity violating models lead to such distinctive signals. As noted above, the worst case occurs when a $\bar{U}\bar{D}\bar{D}$ operator causes the LSP to decay to quark jets, changing missing energy to visible energy. Even in this case, however, there are visible signals occurring through the normal cascade decays of the gluino. For example, the four-lepton decay channel analysed for the MSSM in Section 3 will still be present at the same level but with no missing energy. In order to detect this signal over background it will be necessary to change the cuts to ones, such as circularity, which do not rely on missing energy. We have not studied this in detail, but a preliminary investigation suggested the signal would still be visible at the LHC for the range of parameters discussed in Section 3.

The discussion has so far involved conventional pair production followed by unconventional decay produced by the R-parity violating operators. However, there is also the possibility of *single* sparticle production via R-parity violating terms leading to novel signatures for supersymmetry. The advantage of such signals is that they allow for production of the supersymmetric state with mass up to the full energy of the LHC. However, the production cross-section is proportional to the square of the R-violating coupling and so for some of the allowed range of couplings will be small. For this reason, it is necessary to consider both types of signal following from single and pair production. The single sparticle production processes are shown in Fig. 7.3. The dominant production mechanism, if allowed, is the slepton or squark production of Fig. 7.3a which occurs through the $LQ\bar{D}$ or $\bar{U}\bar{D}\bar{D}$ terms [7.6,7.7]. If the squark or slepton decays via the same R-parity violating operator it produces two jets with a characteristic resonance at the slepton or squark mass. Unfortunately, this is not a signal to gladden an experimentalist's heart and at first sight the process looks unpromising. However, provided the coupling associated with this operator is not much larger than the gauge couplings, there will be competing cascade decays of the produced squark or slepton which will produce more visible signals. As an example, we consider slepton production followed by the decay of the slepton to a neutralino and a lepton. The neutralino, if it is the LSP, will decay as in Table 7.2, for example to $\tilde{\chi}^0 Z$. Finally, the Z will have a decay into charged leptons and the LSP will decay to $LQ\bar{D}$ giving a four-charged-lepton-plus-jets

final state. The rate for this can be large. From refs. [7.6,7.7], we have the single slepton production cross-section

$$\sigma(p\bar{p} \rightarrow \tilde{\nu} X \rightarrow f) = \frac{4\pi^2 \Gamma_{u\bar{d}} \Gamma_f}{9m\Gamma_t} [\frac{\tau dL}{\hat{s}d\tau}] \quad (7.5)$$

$$\tau \frac{dL}{d\tau} = \frac{\tau}{1 + \delta_{i,j}} \int_\tau^1 dx [f_i^a(x) f_j^b(\tau/x) + (a,i) \leftrightarrow (b,j)]/x. \quad (7.6)$$

At 16 TeV for slepton masses of 50, 100, and 250 GeV and the choice of $\lambda'_{lqd}=0.03$, consistent with the bound of Table 7.1, this gives a cross-section of 10, 1.7, and 0.12 nb respectively. Even for the highest slepton mass for 10^4 pb $^{-1}$ this gives 10^3 events, considerably above the background coming from $t\bar{t}$ of 10^2 events (cf. Section 3).

Although the picture of Fig. 7.3a provides the dominant single sparticle production mechanism, for some of the 45 operators the graph vanishes and it is necessary to consider the contribution from the other graphs of Fig. 7.3. The contribution of Fig. 7.3c has the advantage that any of the 45 possible operators will contribute because the virtual Z creates all flavours of quarks and leptons. In section 4 the Drell-Yan pair production of sleptons at the LHC was found to be small in multilepton channels. The contribution of Fig. 7.3c involves a three-particle final state and consequently, even for large R-parity violating couplings, the production cross-section will be smaller, so it seems that these contributions will not provide observable signals at the LHC. The contributions of Fig. 7.3b have also been analysed. They can lead to interesting signals, for example $q + \bar{q} \rightarrow \tilde{\Lambda} + \nu$ leading, on decay of the LSP to lepton plus jets plus missing energy. Unfortunately, the cross-section proves to be too small to overcome the background (which principally comes from the $t\bar{t}$ channel) and so we will not present the analysis here.

7.4 Conclusions

In the light of the form of unified models based on string theories we think that R-parity violating versions of supersymmetry deserve to be considered on an equal footing with the MSSM. We have surveyed the characteristic signals to be expected in this class of supersymmetric models and found that, owing in part to the important role that cascade decays are likely to play, there are signals visible at the LHC in all cases. However, it is essential, if supersymmetry is to be discovered in these alternative models, that a search is made of channels other than those relying on conventional missing energy signals for the LSP decays converting missing into visible energy. In many cases these involve multilepton production and are more visible than expected in the MSSM, but the class of R-parity violating models involving just the $\bar{U}\bar{D}\bar{D}$ operators convert the missing energy into jets and consequently they lead to signals requiring more involved cuts than needed in the MSSM if the signal is to be observed.

Table 7.2: Dominant Decay Modes and Branching Ratios. Notation: As a decay product \mathcal{O} refers to the $R_\theta = +1$ particle content of an operator from eq.(1) (for $L_1 Q_1 D_1$, $\mathcal{O} = eud$ or $\nu d\bar{d}$). In \mathcal{O}_W in addition one of the particles is $SU(2)$ rotated. (For $L_1 Q_1 D_1$, $\mathcal{O}_W = \nu ud$ or $e d\bar{d}$.) In \mathcal{O}_{mix} (\mathcal{O}_{2mix}) one (two) particle is replaced by a particle it (Kabayashi-Maskawa) mixes with; θ_i are the mixing angles. c_F is a color factor which is 1(LLE), 1(LQD, l^\pm), $\frac{1}{3}(LQD, \nu)$, $\frac{2}{3}(UDD)$. U_C, V_C (U_W, V_W) are the unitary matrices which diagonalize the chargino (neutralino) mass matrix. Γ_s is given in ref [11]

LSP $\tilde{\Lambda}$	$\mathcal{O} = \overline{TBD}_i$	$M_{\tilde{\Lambda}} > m_t$ $m_t > M_{\tilde{\Lambda}} > m_b$ $m_b > M_{\tilde{\Lambda}}$	$\tilde{\Lambda} \rightarrow \mathcal{O}, \overline{\mathcal{O}}$ $\tilde{\Lambda} \rightarrow \mathcal{O}_{mix}, \overline{\mathcal{O}}_{mix}$ $\tilde{\Lambda} \rightarrow \mathcal{O}_{2mix}, \overline{\mathcal{O}}_{2mix}$	$\Gamma_1 = \frac{\alpha \lambda^2}{256\pi^2} \frac{M_{\tilde{\Lambda}}^2}{m_t^4} c_F$ $\Gamma = \Gamma_1 \sin^2 \theta$ $\Gamma = \Gamma_1 \sin^2 \theta_1 \sin^2 \theta_2$
	$\mathcal{O} = \overline{U}_i \overline{D}_j \overline{B}; \quad i, j \neq 3$ $\mathcal{O} = L_i Q_j \overline{B}; \quad j \neq 3$ $\mathcal{O} = L_i Q_3 \overline{D}_j; \quad j \neq 3$	$M_{\tilde{\Lambda}} > m_b$ $M_{\tilde{\Lambda}} < m_b$	$\tilde{\Lambda} \rightarrow \mathcal{O}, \overline{\mathcal{O}}$ $\tilde{\Lambda} \rightarrow \mathcal{O}_{mix}, \overline{\mathcal{O}}_{mix}$	$\Gamma = \Gamma_1$ $\Gamma = \Gamma_1 \sin^2 \theta$
	$\mathcal{O} = L_1 Q_3 \overline{b}$	$M_{\tilde{\Lambda}} > 2m_b$ $M_{\tilde{\Lambda}} < 2m_b$	$\tilde{\Lambda} \rightarrow \mathcal{O}, \overline{\mathcal{O}}$ $\tilde{\Lambda} \rightarrow \gamma\nu, \gamma\bar{\nu}$	$\Gamma = \Gamma_1$ $\Gamma_2 = \frac{9\alpha^2 \lambda^2}{64\pi^2} \frac{m_b^2 M_{\tilde{\Lambda}}^2}{m_b^4} \left[\frac{3}{2} + 2 \ln\left(\frac{m_b}{m_{\tilde{\Lambda}}}\right) \right]^2$
	$\mathcal{O} = LQD$ -Rest; LLE		$\tilde{\Lambda} \rightarrow \mathcal{O}, \overline{\mathcal{O}}$	$\Gamma = \Gamma_1$
Chargino $\tilde{\chi}^\pm$	$\mathcal{O} = LLE; LQD; UDD$	$M_{\tilde{\chi}^\pm} > m_W + M_{\tilde{\Lambda}}$	$\tilde{\chi}^\pm \rightarrow W^\pm \tilde{\Lambda}$	$\Gamma_3 = \frac{\alpha(U_L^2 + V_L^2)}{8} \frac{M_{\tilde{\chi}^\pm}^2}{M_W^2} (1 - 3 \frac{M_W^2}{M_{\tilde{\chi}^\pm}^2})$
		$M_{\tilde{\chi}^\pm} < m_W + M_{\tilde{\Lambda}}$	$\begin{cases} \tilde{\chi}^\pm \rightarrow \mathcal{O}_W \\ \tilde{\chi}^\pm \rightarrow \tilde{\Lambda} l^\pm \nu \end{cases}$	$\Gamma_4 = \frac{\alpha \lambda^2 (U_L^2 + V_L^2)}{128\pi^2 \sin^2 \theta_W} \frac{M_{\tilde{\chi}^\pm}^2}{m_t^4}$ $\Gamma_5^{(*)}$
Neutralino $\tilde{\chi}^0$	$\mathcal{O} = LLE; LQD; UDD$	$M_{\tilde{\chi}^0} > M_{\tilde{\Lambda}} + \min(m_{H^0}, m_Z)$	$\tilde{\chi}^0 \rightarrow \tilde{\Lambda} Z$ $\tilde{\chi}^0 \rightarrow \tilde{\Lambda} H^0$	$\Gamma_6 = \frac{\alpha(U_L^2 + V_L^2)}{8 \sin^2 \theta_W \cos^2 \theta_W} \frac{M_{\tilde{\chi}^0}^2}{m_Z^2} (1 - 3 \frac{m_{\tilde{\chi}^0}^2}{M_{\tilde{\chi}^0}^2})$ $\Gamma_7 = \frac{\alpha(U_L^2 + V_L^2)}{16 \sin^2 \theta_W \cos^2 \theta_W} M_{\tilde{\chi}^0} (1 - \frac{m_{\tilde{\chi}^0}^2}{M_{\tilde{\chi}^0}^2})^2$
		$M_{\tilde{\chi}^0} < M_{\tilde{\Lambda}} + \min(m_{H^0}, m_Z)$	$\tilde{\chi}^0 \rightarrow \mathcal{O}, \overline{\mathcal{O}}$ $\tilde{\chi}^0 \rightarrow \tilde{\Lambda} l^+ l^-$	Analogous to LSP discussion. $\Gamma = \Gamma_5$

Table 7.2 (cont.) Dominant Decay Modes and Branching Ratios. Notation: $\mathcal{O}(\tilde{l})$ refers to the content of the operator without the argument, i.e. for $L_1 Q_1 D_1$, $\mathcal{O}(\tilde{e}) = ud$. (*)Provided \tilde{l} (\tilde{q}) is included in the operator.

Glino \tilde{g}	$\mathcal{O} = LLE$	$\tilde{g} \rightarrow q\bar{q}\tilde{\Lambda}$	$\Gamma_8 = \frac{\alpha \alpha_s \epsilon_q^2}{48\pi^2} \frac{M_{\tilde{g}}^2}{m_q^4}$
	$\mathcal{O} = L_{1,2} Q_1 \overline{D}_i, L_1 Q_3 \overline{D}_3$	$\tilde{g} \rightarrow q\bar{q}\tilde{\Lambda}$	$\Gamma = \Gamma_8$
	Rest	$\begin{cases} \tilde{g} \rightarrow q\bar{q}\tilde{\Lambda} \\ \tilde{g} \rightarrow \mathcal{O}, \overline{\mathcal{O}} \end{cases}$	$\Gamma = \Gamma_8$ $\Gamma_9 = \frac{\alpha \lambda^2}{256\pi^2} \frac{M_{\tilde{g}}^2}{m_q^4}$
S-Lepton \tilde{l}^\pm	$\mathcal{O} = L, L, \overline{E}_k$	$\tilde{l} \rightarrow l\tilde{\Lambda}$	$\Gamma_{10} = \frac{1}{2} \alpha m_l$
	$\mathcal{O} = L_{1,2} Q_1 \overline{D}_i, L_1 Q_3 \overline{D}_3$	$\tilde{l} \rightarrow l\tilde{\Lambda}$	$\Gamma = \Gamma_{10}$
	$\mathcal{O} = LQD$ -Rest	$\begin{cases} \tilde{l} \rightarrow l\tilde{\Lambda} \\ \tilde{l} \rightarrow \mathcal{O}(\tilde{l}) \end{cases}$	$\Gamma = \Gamma_{10}$ $\Gamma_{11} = \frac{3\lambda^2}{16\pi^2} m_l \quad (*)$
	$\mathcal{O} = U_i D_j \overline{D}_k$	$\tilde{l} \rightarrow l\tilde{\Lambda}$	$\Gamma = \Gamma_{10}$
S-Quark \tilde{q}	$\mathcal{O} = LLE$	$\tilde{q} \rightarrow q\tilde{\Lambda}$	$\Gamma_{12} = \frac{1}{2} \alpha e_q^2 m_{\tilde{q}}$
	$\mathcal{O} = LQD; UDD$	$\begin{cases} \tilde{q} \rightarrow q\tilde{\Lambda} \\ \tilde{q} \rightarrow \mathcal{O}_{LQD}(\tilde{q}) \\ \tilde{q} \rightarrow \mathcal{O}_{UDD}(\tilde{q}) \end{cases}$	$\Gamma = \Gamma_{12}$ $\Gamma_{13} = \frac{3\lambda^2}{16\pi^2} m_{\tilde{q}} \quad (*)$ $\Gamma_{14} = \frac{\lambda^2}{8\pi^2} m_{\tilde{q}} \quad (*)$
	$\mathcal{O} = UDD$	$\tilde{q} \rightarrow \tilde{\Lambda}\nu$	$\Gamma = \Gamma_{15}$
S-Neutrino $\tilde{\nu}$	$\mathcal{O} = LLE$	$\tilde{\nu} \rightarrow \tilde{\Lambda}\nu$	$\Gamma_{15} = \frac{\alpha \sin^2 \theta}{8 \cos^2 \theta_W \sin^2 \theta_W} m_{\tilde{\nu}}$
	$\mathcal{O} = LQD$	$\begin{cases} \tilde{\nu} \rightarrow \tilde{\Lambda}\nu \\ \tilde{\nu} \rightarrow \mathcal{O}(\tilde{\nu}) \end{cases}$	$\Gamma = \Gamma_{15}$ $\Gamma = \Gamma_{11}$
	$\mathcal{O} = UDD$	$\tilde{\nu} \rightarrow \tilde{\Lambda}\nu$	$\Gamma = \Gamma_{15}$

Table 7.3: Dominant decay patterns in the associated production of supersymmetric particles. The notation is as in Table 7.2. In addition $(e, \mu, \tau) \otimes (e, \mu)$ refers to the possible signals: ee , $e\mu$, $e\tau$, $\mu\mu$, and $\mu\tau$.

PHYSICAL PROCESS	LL \overline{E}	LQ \overline{D}	UDD
$i^+ l^- \rightarrow i^+ l^- + 2\tilde{\Lambda}$ $\rightarrow i^+ l^- + 2\gamma\nu$	$\not{p}_T + i^+ l^- + 2(e, \mu, \tau)^\pm \otimes (e, \mu)^\mp$ —	$i^+ l^- + 2(e, \mu, \tau)^\pm + 4 \text{ jets}$ $i^+ l^- + 2\gamma\nu$	$i^+ l^- + 2(e, \mu, \tau)^\pm + 6 \text{ jets}$ —
$g\bar{g} \rightarrow 2q\bar{q} + 2\tilde{\Lambda}$ $\rightarrow \mathcal{O}\mathcal{O}, \mathcal{O}\overline{\mathcal{O}}, \overline{\mathcal{O}}\overline{\mathcal{O}}$	$2q\bar{q} + \not{p}_T + 2(e, \mu, \tau)^\pm \otimes (e, \mu)^\mp$ —	$2q\bar{q} + (e, \mu, \tau)^\pm + 4 \text{ jets}$ $2(e, \mu, \tau)^\pm + 4 \text{ jets}$	$2q\bar{q} + 6 \text{ jets}$ 6 jets
$\tilde{q}\bar{q} \rightarrow qq' + 2\tilde{\Lambda}$ $\rightarrow \mathcal{O}(\tilde{q})\mathcal{O}(\tilde{q}')$	$qq' + \not{p}_T + 2(e, \mu, \tau)^\pm \otimes (e, \mu)^\mp$ —	$qq' + 2(e, \mu, \tau)^\pm + 4 \text{ jets}$ $(l, \nu) \otimes (l, \nu) + 2 \text{ jets}$	$qq' + 6 \text{ jets}$ 4 jets
$\tilde{\chi}^+ \tilde{\chi}^0 \rightarrow \begin{cases} W^+ + Z^0 + 2\tilde{\Lambda} \\ l^+ l^- l^+ + 2\tilde{\Lambda} \end{cases}$ $\rightarrow \mathcal{O} + \begin{cases} u + \mathcal{O}(\tilde{d}) \\ d + \mathcal{O}(\tilde{u}) \end{cases}$ $\rightarrow \mathcal{O} + \begin{cases} \nu + \mathcal{O}(\tilde{e}) \\ e + \mathcal{O}(\tilde{\nu}) \end{cases}$	$\not{p}_T + l^+ l^- l^+ + 2(e, \mu, \tau)^\pm \otimes (e, \mu)^\mp$ —	$l^+ l^- l^+ + 2(e, \mu, \tau)^\pm + 4 \text{ jets}$ $l^+ l^- + 4 \text{ jets}$	$l^+ l^- l^+ + 6 \text{ jets}$ 6 jets
		$\not{p}_T + 5l^\pm$	—

References

- [7.1] For reviews see H.P. Nilles, Phys. Rep. 110 (1984) 1; G.G. Ross, Grand Unified Theories, Benjamin Cummings (1985); H.E. Haber and G.L. Kane, Phys. Rep. 117 (1985) 75.
- [7.2] L.J. Hall and M. Suzuki, Nucl. Phys. B231 (1984) 419.
- [7.3] S. Weinberg, Phys. Rev. D26 (1982) 287. N. Sakai and T. Yanagida, Nucl. Phys. B197 (1982) 83. S. Dimopoulos, S. Raby and F. Wilczek, Phys. Lett. 112B (1982) 133.
- [7.4] M. Bento, L.J. Hall and G.G. Ross, Nucl. Phys. B292 (1987) 400.
- [7.5] C. Aulakh and R. Mohapatra, Phys. Lett. B119 (1983) 136. G.G. Ross and J.W.F. Valle, Phys. Lett. B151 (1985) 375. J. Ellis et al., Phys. Lett. B150 (1985) 142; S. Dawson, Nucl. Phys. B261 (1985) 297. R. Barbieri et al., Phys. Lett. B238 (1990) 86. A. Santamaria and J.F.W. Valle, Phys. Lett. B195 (1987) 423; Phys. Rev. Lett. 60 (1988) 397; Phys. Rev. D39 (1989) 1780. M.C. Gonzalez-Garcia and J.F.W. Valle, preprint CERN-TH.5861/90.
- [7.6] S. Dimopoulos and L.J. Hall, Phys. Lett. B207 (1987) 210.
- [7.7] S. Dimopoulos, R. Esmailzadeh, L.J. Hall and G.D. Starkman, Phys. Rev. D41 (1990) 2099.
- [7.8] V. Barger, G.F. Giudice and T. Han, Phys. Rev. D40 (1989) 2987
- [7.9] F. Zwirner, Phys. Lett. B132 (1983) 103. R. Barbieri and A. Masiero, Nucl. Phys. B267 (1986) 679.
- [7.10] R. Mohapatra Phys. Rev. D34 (1986) 3457
- [7.11] H. Baer et al. Physics at LEP Vol. 1, CERN 86-02, p. 372

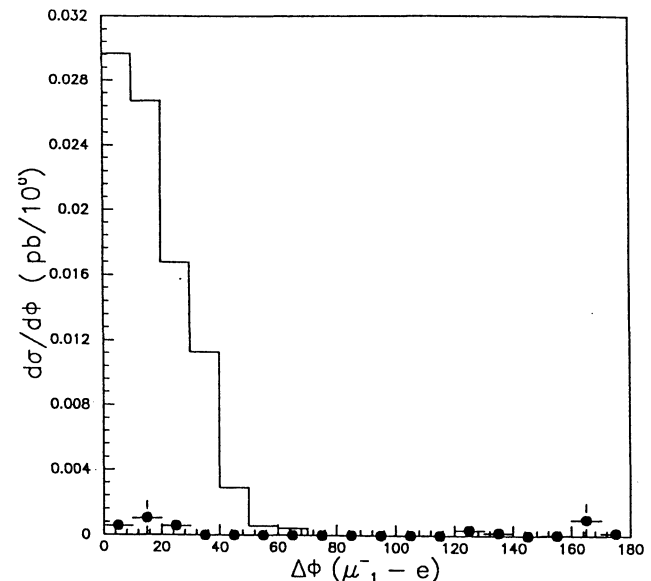


Fig. 7.1: Plot of $d\sigma/d\phi_{(\mu_1^- - e)}$ with the following cuts imposed: $2e: p_\perp > 20\text{GeV}$ (no sign); $2\mu: p_\perp > 10\text{GeV}; N_J \geq 3, E_J^J > 100\text{GeV}; |\eta_e|, |\eta_{jet}| < 3$. The background, coming principally from $t\bar{t}$, is given by the solid circles.

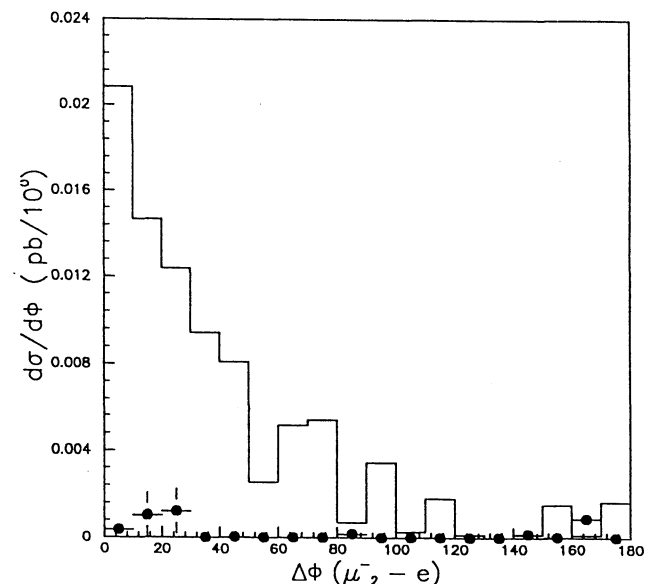


Fig. 7.2: Plot of $d\sigma/d\phi_{(\mu_1^- - e)}$ with the same cuts as in Figure 7.1.

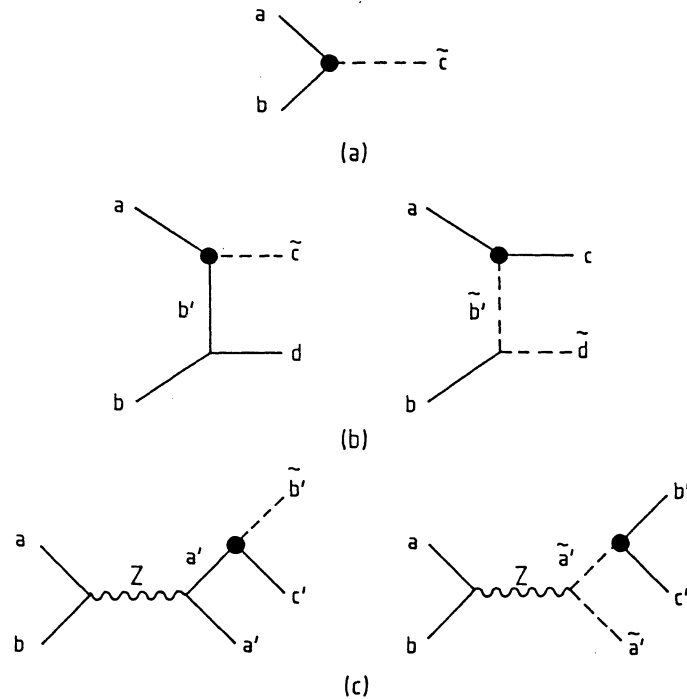


Fig. 7.3: Partonic sub-processes giving sparticle production via R-parity violating terms. The solid circles refer to the interactions coming from the appropriate operators of eq. (7.3).

8 Detection of Heavy Stable Exotics

Contributors: M. Drees and X. Tata

8.1 Prelude and motivation

Many extensions of the SM allow for (quasi)-stable heavy exotics. For our purposes, these are new particles that live long enough to travel several metres before they decay. If these particles interact via strong or electromagnetic forces, they would be abundantly produced at high-energy colliders provided their masses are in the kinematically accessible range; unlike most heavy particles, which decay almost instantly on production, these exotics decay (if at all) outside the detector so that their presence is not signalled by a large shower of energy in the electromagnetic or hadronic calorimeters. We report on the prospects of detecting these particles either at a general-purpose detector at the LHC or by using a specialized, low-cost spectrometer designed for this purpose.

The (quasi)-stable nature of these exotics can be generally traced to either a new (almost) conserved quantum number or, in some special cases, to the smallness of the phase space available for its decay. Here, we consider four candidates for an exotic, each of which can be accommodated in one of the popular extensions of the SM: i) a charge 1 colour singlet scalar (\tilde{e}_R), ii) a charge 1 colour singlet fermion (\tilde{W}), iii) a colour triplet scalar (\tilde{t}), and iv) a colour triplet fermion (D). The first three denote the supersymmetric partner of the electron, the chargino, and the t-quark, whereas the fourth one is an exotic quark (with odd R-parity) as may be present, for example in gauge models based on E(6). If R-parity is conserved, and the only R-odd particle lighter than our exotic candidate is the gravitino, the exotic can only decay gravitationally and so is stable as far as collider experiments are concerned. We have also checked that the lifetimes can be short enough (\ll age of the Universe) so as not to cause cosmological problems. Our choices of illustrative examples has been motivated by today's views of the mass spectra of SUSY models, but it should be clear that our conclusions are not particular to these examples.

8.2 Energy loss of exotics in matter

In order to understand what these exotics look like in the experimental apparatus, we have to study how they lose energy in going through matter. The basic processes are: i) ionization, ii) elastic collisions with electrons and nuclei, iii) inelastic nuclear collisions (only for strongly interacting exotics). We consider each of these in turn.

As is well known, the specific ionization dE/dx depends only on the speed of the particle and not its mass. Thus the fractional energy loss by ionization is much smaller for a heavy particle; as a result, if ionization is the dominant mechanism of energy loss, heavy particles penetrate much deeper. This is illustrated in Fig. 8.1 for particles traversing a block of iron. Note that for $\beta > 1/2$, the range of a particle with $m > 100$ GeV exceeds several metres in iron. The strategy to search for such exotics then is to look for very penetrating particles with β significantly smaller than unity. This requires the ability to time the arrival of the exotic relative to that of the remaining ultrarelativistic debris. It can be shown [8.1] that the hadronic energy losses for strongly interacting particles do not significantly change the penetration depth for $\beta \lesssim 0.7$, corresponding to a range in iron of 10 m for a 100 GeV particle; the same strategy therefore applies for coloured exotics. This basically follows from

the observation that such particles can only transfer $O(1 \text{ GeV})$ of energy to a nucleon in any collision, i.e. a fairly small fraction of their total energy.

Note, however, that if F is rather relativistic, and strongly interacting, it will rapidly lose energy by hadronic interactions until it slows down to $B = 0.6$ or 0.7 . After that, it will be a very penetrating particle, much like the muon. This could lead to an interesting calorimetric signature.

8.3 Signatures of exotics

The Mark II [8.2] and CDF [8.3] experiments have already searched for stable exotics produced at the SLC or the Tevatron. Since we are interested in the LHC, we will follow the CDF study. Their analysis, which was based on the very small data sample of 25nb^{-1} , could not exclude any of the four exotics we have considered, but did put mass limits on coloured particles in higher representations of colour for which the production cross-sections are larger. Apart from geometrical cuts specific to their apparatus, they required

- i) A time delay cut, $\beta < \beta_{\max}$,
- ii) A “soft muon suppression” cut, $p_T > p_{T\min}$,
- iii) A penetration dept cut, $L > d_{Fe}$ which guarantees that F can penetrate into the muon chambers (d_{Fe} is the penetration depth in iron).

Here, we attempt a similar analysis for a general-purpose detector as well as a specialized spectrometer that may be especially suitable for a high luminosity LHC. The computation of the production cross-sections for each of the representative cases is straightforward. For the selectron, the cross-section is fixed by $SU(2) \times U(1)$, whereas for the top squark and D quark, it is fixed by QCD. For the chargino case, it depends on the details of the gaugino-higgsino mixing; here, we have conservatively included only its (model-independent) QED contribution. The QCD cross-section has to be further corrected for hadronization effects. It is generally accepted that for very heavy particles, the meson carries almost all the heavy-quark momentum, so that there is no correction required on those grounds. However, since only charged mesons lose energy by ionization (recall we argued that hadronic energy losses were not important except perhaps for a possible calorimetric signature) and since half (assuming strange meson formation is small compared with the non-strange meson formation) the mesons are electrically neutral, we have to reduce this rate by a factor of 2. Furthermore, since inelastic charge-exchange reactions can cause a charged meson to become neutral in traversing the calorimeter material (resulting in loss of signature), there is a further reduction of the “observable” cross-section. This depends on the charge exchange mechanism as well as the depth of the material to be traversed. We estimate this to be a factor of between 1 and 2, depending on our model for charge exchange.

Shown in Figs. 8.2 and 8.3 are our estimates of the various cross-sections at the LHC and, for comparison, at the SSC, for a general-purpose detector and a specialized, low-cost spectrometer whose arms cover 10° in azimuth as discussed at the Berkeley Workshop on Supercolliders [8.4]. For the hadrons, the reduction factors discussed above have not been included. The detectors are defined by the following cuts:

Our choice of the d_{Fe} for the “generic” detector is obtained by doubling the size of the CDF detector (which we consider conservative); this also allows us a gain in β_{\min} for the same

	General-Purpose Detector	Spectrometer
$p_T >$	50 GeV	50 GeV
$\beta <$	0.85	0.95
$d_{Fe} >$	2 m	3.2 m
$\cos \theta$	< 0.9	< 0.174

timing resolution. The parameters for the spectrometer are from the Berkeley Proceedings. In these figures, at least one of the exotics is required to pass the cuts.

We see from Fig. 8.2 that the low-luminosity LHC should be able to probe exotic masses almost all the way up to 300 GeV, for all the cases that we have considered, after about a year of running, whereas SSC would be able to do a similar job in perhaps just under half that time, assuming that five events would be an observable signal. Note that we have restricted our attention to a mass range below 0.3 TeV, a range we consider reasonable if the “new physics” invoked to guarantee the stability of the electroweak scale has to give a model which is technically natural.

Notice that the search for exotics is difficult to perform at a high luminosity LHC, since the time between consecutive interactions becomes smaller than the time taken by the exotic to traverse the detector; this would obviously interfere with the time-of-flight measurements. At such luminosities, a low-acceptance detector, such as the spectrometer discussed above, would be more suitable. The expectations for the exotic cross-sections are shown in Fig. 8.3. We see that if the luminosity exceeds a few $\times 10^5 \text{ pb}^{-1}$ per year it should be possible to probe this whole mass range at the LHC, whereas at the SSC \tilde{e}_R may escape detection unless it is sufficiently light or the SSC is operated for about 3 years.

8.4 Distinguishing various exotics

One obvious way to distinguish the various candidates is from the total rate. Whereas this would be adequate to distinguish between the strongly and non-strongly interacting exotics, the absolute normalization of our calculated rate might not be believable enough to distinguish stops from D quarks. Toward this end, we have studied the angular and momentum distribution of the exotic. Unfortunately, the differences in the distributions are not spectacular. It may, however, be possible to distinguish \tilde{e}_R from the chargino since its p-wave production ensures a harder momentum distribution as well as favours production at large angles.

Hadronic exotics may also be distinguishable from their non-hadronic counterparts by studying the energy deposition of candidates in matter. Fast hadrons could deposit several GeV of energy in a single “soft” collision with a nucleon. The spectrometer with its large range of acceptable β is the best detector to see this. Note also that the track may disappear and again reappear (owing to charge exchange already discussed). Whether or not the calorimeter will have fine enough segmentation to see this depends on its final design.

Finally, the large amount of iron in the spectrometer makes it possible to look for a novel signature for the exotic hadron, i.e. when it gets stuck in the iron before it can penetrate to the muon chamber. The cross-section for this is shown by the lower curves in Fig. 8.3. Further, we see from Fig. 8.1 that a trapped particle deposits $O(1 \text{ GeV})$ of energy in the last centimeter of its track if $m > 100 \text{ GeV}$.

References

- [8.1] M. Drees and X. Tata, CERN preprint CERN-TH.5811/90 (to appear in Phys. Lett. B).
- [8.2] E. Soderstrom et al., Stanford preprint SLAC-PUB-5192 (1990).
- [8.3] F. Abe et al., Phys. Rev. Lett. **63**, 1447 (1989).
- [8.4] A.M. Litke et al., Proc. Workshop on Experiments, Detectors and Experimental Areas for the Supercollider, Berkeley 1987, eds. R. Donaldson and M.G. Gilchriese (World Scientific, Singapore, 1988), p.853.

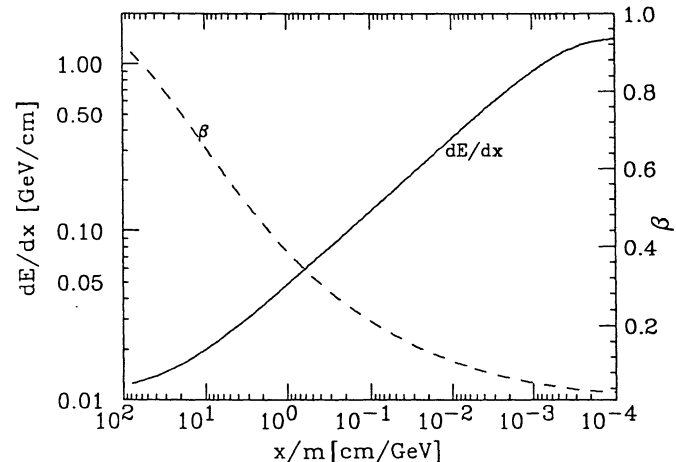


Fig. 8.1: The energy loss through ionization dE/dx and the velocity β of a particle with mass m and unit charge as a function of the rescaled distance x/m from the point where the particle will be stopped in iron. Notice that x/m is independent of m .

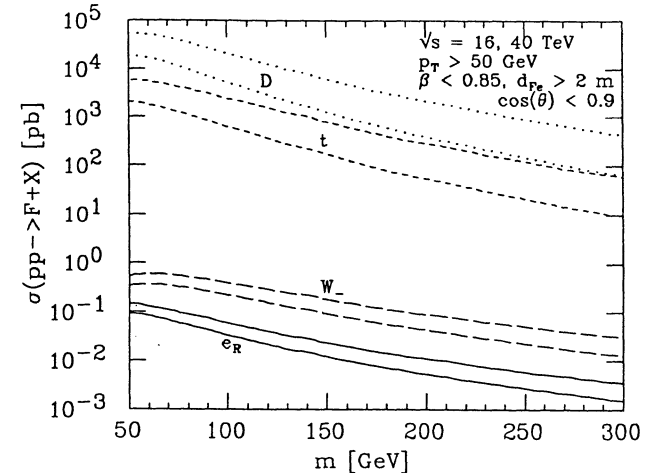


Fig. 8.2: Total signal cross-section after cuts at pp supercolliders as a function of the mass m of the long-lived particle for a general-purpose detector. The different textures correspond to different types of particles: \tilde{e}_R (solid) is a spin-0 $SU(2)$ and colour singlet, \tilde{W}_- a spin- $\frac{1}{2}$ colour singlet, \tilde{t} a spin-0 colour triplet, and D a spin- $\frac{1}{2}$ colour triplet. Note that only one particle of the produced pair needs to pass the cuts. The cross-sections for \tilde{t} and D have to be divided by an additional factor between 1.5 and 4 owing to hadronization effects, as discussed in the text. The upper curves correspond to the higher value of \sqrt{s} .

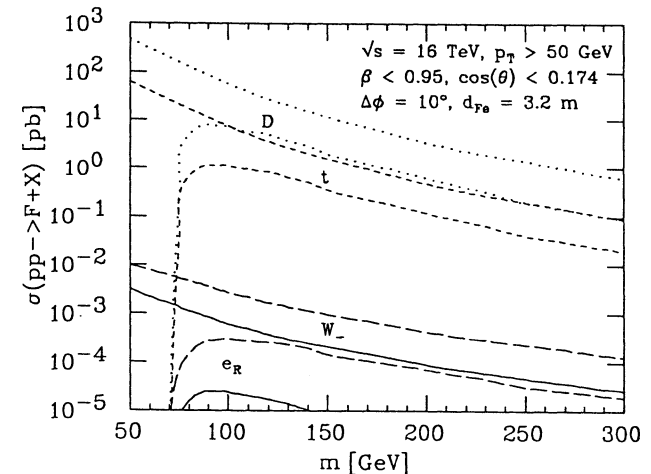


Fig. 8.3: The same as Fig. 8.2 but for the specialized spectrometer discussed in the text. Note that this covers only 20° in both θ and ϕ . The upper (lower) curves are for particles that penetrate (are absorbed in) the calorimeter.

9 Signals for a Superlight Gravitino

Contributors: M. Drees and J. Woodside

The gravitino is the spin 3/2 superpartner of the graviton which is present in local SUSY. In this report we study models where the mass [9.1] of the gravitino, $m_{\tilde{G}}$, is $< 10^{-10}$ GeV (0.1 eV). Since this is the first study ever for gravitino signals at pp supercolliders [9.2], we focus on the most promising process (gluino production) and the simplest signal (n -jets plus missing transverse momentum, \not{p}_T). We include gluino-gluino ($\tilde{g}\tilde{g}$) production via the usual supersymmetry QCD diagrams as well as via exchange of the gravitino, \tilde{G} , and associated $\tilde{g}\tilde{G}$ production via s-channel gluon and t-channel gluino exchange. For the decay of the \tilde{g} the usual decay channels into $q + \bar{q}(\tilde{q}') +$ gaugino are included, as well as the loop decays $\tilde{g} \rightarrow g +$ neutralino [9.3] and the new decay $\tilde{g} \rightarrow g\tilde{G}$.² To fix the gaugino masses and couplings relevant to the first two sets of decays one must specify several parameters, which we take to be the gluino mass, $m_{\tilde{g}}$; the ratio of up to down type Higgs VEVs, $\tan \beta \equiv v_2/v_1$; the Higgsino mass mixing parameter, μ ; and m_t , the top quark mass [9.3], [9.4]. Notice that the width for the decay $\tilde{g} \rightarrow g\tilde{G}$ is proportional to $m_{\tilde{g}}^5/(M_P m_{\tilde{G}})^2$, where $M_P = 2.4 \times 10^{18}$ GeV is the Planck mass, while if $m_{\tilde{g}} \gg m_{\tilde{G}}$, which we will assume throughout, the decays to $q\bar{q}(\tilde{q}')$ + gaugino go like $m_{\tilde{g}}^5/m_{\tilde{q}}^4$. Consider, as well, that the loop decays to gluon-neutralino are at most of the same order as these conventional decays to $q\bar{q}(\tilde{q}')$ + gaugino [9.3]. The result is that the new 2-body mode to gluon-gravitino becomes clearly dominant if

$$m_{\tilde{G}} < 10^{-12} \text{ GeV} \times \left(\frac{m_{\tilde{g}}}{1 \text{ TeV}} \right)^2. \quad (9.1)$$

This behaviour is illustrated in Fig. 9.1 in which $B(\tilde{g} \rightarrow g\tilde{G})$ is plotted against $m_{\tilde{G}}$ for various combinations of gluino and squark masses. The signal for gluino pairs is thus dependent on gravitino mass. If $m_{\tilde{G}}$ is well above the value given in Eq. (9.1) the conventional \tilde{g} decays dominate; moreover, the cross section for $\tilde{g}\tilde{G}$ production, which goes like $m_{\tilde{G}}^{-2}$, is very small here. As a result, we essentially recover the normal \tilde{g} signatures that usually contain many jets due to complicated cascade decays. However, as $m_{\tilde{G}}$ approaches the value in Eq. (9.1), the new 2-body decay of the gluino takes over and the total signal is now dominated by 2-jet events. Most of the monojet events in this region are due to the coalescence of jets or to one jet being too soft to be identified as such. Finally, for $m_{\tilde{G}} < 10^{-13}$ GeV, the \tilde{G} exchange diagrams as well as $\tilde{g}\tilde{G}$ production become important, causing a steep increase of the signal at even lower $m_{\tilde{G}}$. This is demonstrated in Fig. 9.2, where we show the n -jet cross-section for $m_{\tilde{g}} = 750$ GeV for a representative set of parameters, and where realistic jet identification cuts have been applied. (The decrease of the total signal for $m_{\tilde{G}} > 10^{-11}$ GeV is due to these cuts, since events with many jets are less likely to pass.) The cross-section is 2 pb even before \tilde{G} exchange and $\tilde{g}\tilde{G}$ production become important, and for $m_{\tilde{g}} = 500$ GeV, this cross-section is about ten times larger. Figure 9.3 shows the \not{p}_T distribution for a typical gravitino mass at which the 2-jet signal dominates. We generally find that the distribution is peaked at $\not{p}_T = \frac{2}{3}m_{\tilde{g}}$, which will allow for fairly strong cuts on \not{p}_T (we have used $\not{p}_T > 280$ GeV in Fig. 9.2).

We conclude that the presence of a superlight gravitino, $m_{\tilde{G}} < 10^{-11}$ GeV, would make it considerably easier to discover SUSY at the LHC. However, we have to keep in mind that

in this experimentally favourable scenario, tree-level unitarity breaks down at an energy of $\sqrt{288\pi m_{\tilde{G}} M_P}/m_{\tilde{g}} < 7 \times 10^6$ GeV for $m_{\tilde{g}} > 100$ GeV and $m_{\tilde{G}} < 10^{-11}$ GeV; theorists would prefer that this happen only at Planckian energies, which implies $m_{\tilde{G}} > m_{\tilde{g}}/25$.

References

- [9.1] The theory of superlight gravitino masses is considered by J. Ellis, K. Enqvist, and D. V. Nanopoulos, Phys. Lett. **B147** (1984) 99; **B151** (1985) 357.
- [9.2] A study of superlight gravitino signals at Tevatron energies is given in D. A. Dicus, S. Nandi, and J. Woodside, Phys. Rev. **D41** (1990) 2347.
- [9.3] H. Baer, X. Tata, and J. Woodside, Phys. Rev. **D42** (1990) 1568.
- [9.4] Reviews may be found in articles by P. Nieuwenhuizen, Phys. Rep. **68** (1981) 189; R. A. Arnowitt, P. Nath, and A. Chamseidene, *Applied N = 1 Supergravity* (ICTP Series in Theoretical Physics, Vol. 1) (World Scientific, Singapore, 1984); H. P. Nilles, Phys. Rep. **110** (1984) 1; H. E. Haber and G. L. Kane, Phys. Rep. **117** (1985) 75; A. B. Lahanas and D. V. Nanopoulos, Phys. Rep. **145** (1987) 1.

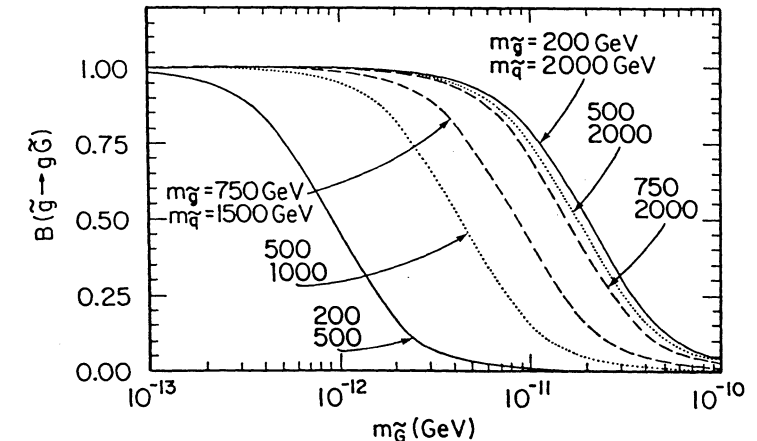


Fig. 9.1: The branching ratio $B(\tilde{g} \rightarrow g\tilde{G})$ plotted against gravitino mass, $m_{\tilde{G}}$, for various values of gluino mass, $m_{\tilde{g}}$, and squark mass, $m_{\tilde{q}}$. We have chosen $\mu = -100$ GeV, $\tan \beta = 2$, and $m_t = 150$ GeV.

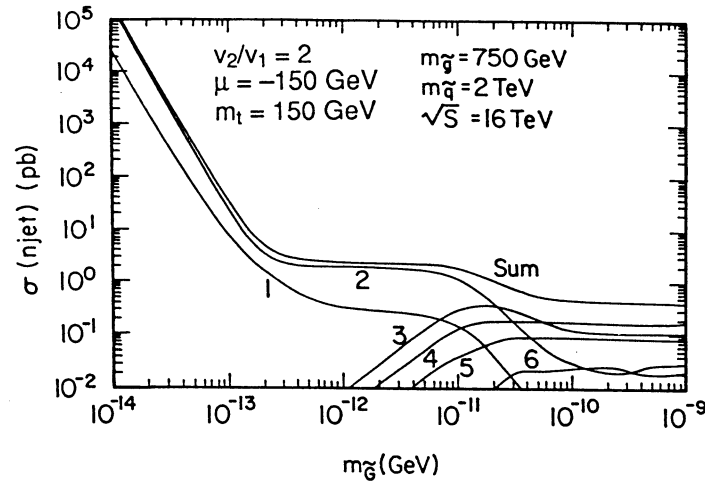


Fig. 9.2: The cross-section for n -jets plus missing transverse momentum, $\sigma(n\text{-jet})$, for $pp \rightarrow \tilde{g}\tilde{g}, \tilde{g}\tilde{G}$ events, at $\sqrt{s} = 16$ TeV for a gluino mass, $m_{\tilde{g}}$, of 750 GeV plotted against gravitino mass, $m_{\tilde{G}}$. Jets are defined by $p_T(j_i) > 25$ GeV, $\Delta R(j_i, j_j) > 0.7$, and $|\eta(j_i)| < 2.5$. Cuts on the signal are $|\eta(j_1)| < 1$, $\Delta\phi(j_1, j_i) < 150^\circ$, and $p_T > 280$ GeV.

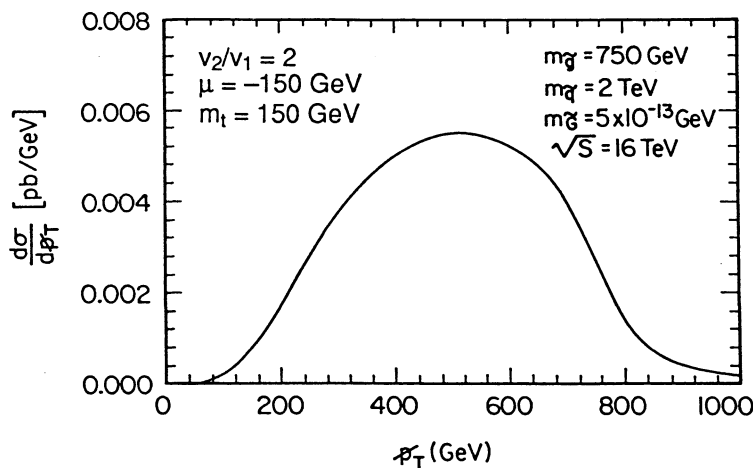


Fig. 9.3: Missing transverse momentum (p_T) distribution for $pp \rightarrow \tilde{g}\tilde{g}, \tilde{g}\tilde{G}$ events at $\sqrt{s} = 16$ TeV for specific values of gluino mass, $m_{\tilde{g}}$, squark mass, $m_{\tilde{q}}$, and gravitino mass, $m_{\tilde{G}}$.

NEW VECTOR BOSONS AT LHC

Conveners : P. Chiappetta¹ and M. Greco².

Contributors : F. Del Aguila³, F. Aversa², S. Bellucci², F. Botterweck⁴, P. Camarri⁵, R. Casalbuoni^{6,7}, V. Cavasinni⁵, D. Cocolicchio⁸, P. Colangelo⁹, M.C. Cousinou¹⁰, S. De Curtis¹¹, F. Feruglio^{6,12}, G.L. Fogli^{9,13}, L.L. Garrido¹⁴, M.C. Gonzalez-Garcia¹⁵, R. Gatto⁶, J.L. Kneur¹⁶, S. Larbi¹⁷, T. Medcalf¹⁸, J.P. Merlo¹⁹, J. Moreno²⁰, G. Moutaka¹⁷, G. Nardulli⁹, J.P. Pansart¹⁹, M. Quiros²⁰, J. Terron²¹, J.W. Valle¹⁵, C. Verzegnassi^{22,23}, C-E. Wulz.²⁴

A7: NEW VECTOR BOSONS

CONTENTS

- I. Introduction
- II. New vector bosons from extended gauge models
- III. New vector bosons from alternative symmetry breakings
- IV. Conclusions

- 1: CPT,CNRS Luminy Case 907 F-13288 MARSEILLE Cedex 9
- 2: INFN FRASCATI P.O. Box 13 I-00044 FRASCATI
- 3: Departamento de Fisica Teorica y del Cosmos,Universita de GRANADA, E-18071 GRANADA
- 4: Univeristy of NIJMEGEN, NL-6525 NIJMEGEN
- 5: Dipartimento di Fisica and sezione INFN, PISA
- 6: Departement de Physique Theorique,Universite de GENEVE,CH-1211 GEN-EVE 4
- 7: Dipartimento di Fisica and sezione INFN, I-73100 LECCE
- 8: Universita di POTENZA ,POTENZA ITALY
- 9: Dipartimento di Fisica and sezione INFN, I-70126 BARI
- 10: Universite d'AIX-MARSEILLE II and CPPM-IN2P3, Luminy,F-13288 MARSEILLE Cedex 9
- 11: INFN, sezione di FIRENZE, I-50125 FIRENZE
- 12: Universita di PADOVA, I-35100 PADOVA
- 13: CERN, CH-1211 GENEVE 23
- 14: Universita Autonoma de BARCELONA, BELLATERRA, E-08193 BARCELONA
- 15: Departamento de Fisica Teorica, Universita de VALENCIA, E-46100 BUR-JASSOT,VALENCIA
- 16: Fakultat fur Physik,Universitat BIELEFELD,FRG BIELEFELD
- 17: Laboratoire de Physique Mathematique,USTL,F-34060 MONTPELLIER
- 18: Royal Holloway and Bedford New College,Egham Hill,SURREY, UK
- 19: DPHPE, CEA SACLAY ,B.P. 2, F-91191 GIF-SUR-YVETTE
- 20: Instituto de Estructura de la Matiera, SERRANO,E-28006 MADRID
- 21: Departamento de Fisica Teorica,Universita Autonoma de MADRID, E-28049 MADRID
- 22: LAPP, B.P.110, F-74941 ANNECY-LE-VIEUX Cedex
- 23: On leave of absence from Dipartimento di Fisica Teorica,Universita di TRIESTE and sezione INFN, TRIESTE ITALY
- 24: Inst. f. Hochenergiephysik.d.Osterr. Akad.d.Wissenschaft., VIENNA,AUSTRIA

I. INTRODUCTION

The existence of new neutral or charged vector bosons is a common feature of many extensions of the standard model (SM), all motivated by attempts to solve its major puzzles. Indeed well known, in spite of its impressive success it is very unsatisfactory, since it is not expected to be valid far above the Fermi scale and leaves many fundamental questions unanswered : gauge problem, hierarchy problem, number of generations, origin of parity and CP violation, incorporation of gravity, All these extensions of the SM can be divided into two main categories : minimal extensions, attempting to unify interactions - E_6 models, left-right models, ... characterized by elementary Higgses, or more drastic ones involving a different mechanism for the electroweak symmetry breaking -BESS model, technicolor, models with composite W and Z bosons - all of them having as a common feature the expectation of some new physics at a scale of $0(1\text{TeV})$. We have considered the possibilities offered by various scenarios, all leading to the existence of new heavy vector bosons accessible at LHC and SSC energies. In particular the models we will study are the following :

— E_6 models, based on ideas of grand unification, aimed to solve the gauge problem, i.e. the existence of three different gauge coupling constants associated with the gauge groups $SU(3)_C, SU(2)_L$ and $U(1)$. Since the unification scale is not far from the Planck scale, it seems natural to unify these interactions with gravity. An attractive possibility is offered by superstring theories from which E_6 may emerge as the low energy (compared to the Planck scale) grand unified group. Since the breaking of E_6 into the SM is accompanied by at least one extra $U(1)_Y$ ($E_6 \rightarrow SU(3)_C \times SU(2)_L \times U(1)_Y \times U(1)_Y$) one expects the existence of a heavy neutral boson which can mix with the ordinary Z . E_6 superstring inspired models are quite constrained since the breaking pattern of E_6 is specified.

— Left-right (LR) models based on the gauge group $SU(2)_L \times SU(2)_R \times U(1)_{B-L}$ are attractive since they provide a hint for solving the origin of parity violation and small neutrinos masses. In minimal LR models where parity invariance is spontaneously broken one predicts the existence of an additional neutral boson and two charged W_R^\pm bosons which mix with left-handed W 's. Low energy phenomenology and especially $K_L - K_s$ mass difference already constrain the mixing angle ξ and the W_R mass. A possible way to evade the mixing is to consider alternative left right models (ALRM) from E_6 superstring theory.

— The BESS model offers a mechanism of possible strong breaking of the electroweak symmetry, and the Higgs is no more a physical particle. Here the principle of local $SU(2)_L \times U(1)$ gauge invariance is maintained but the breaking of electroweak symmetry is realized in a non linear way. Weak interactions are described by an effective lagrangian which is $SU(2)_L \times SU(2)_V \times U(1)$ invariant. The existence of a triplet of spin one resonances, analogue of the ρ in hadron physics, associated to $SU(2)_V$ gauge group is predicted. This model can be viewed as a generalization of technicolor which assumes that this Higgs particle is a composite object made of technifermions.

— Composite models have not reached so far the level of sophistication and predictivity of extended gauge models. Nevertheless we have taken seriously into account the possibility that the W and Z are not elementary and considered a specific model where the low energy features of SM are incorporated into an effective lagrangian which is invariant under a global $SU(2)$ weak isospin symmetry and satisfies local $U(1)$ QED-like gauge invariance. The (W^\pm, Z) triplet is coupled

to fermions in a invariant way with strength g_w , whereas in analogy to vector meson dominance, its neutral component couples to the photon with strength λ_w such that $e = \lambda_w g_w$. In this model one expects a rich spectrum of new heavy bosons. We will limit our study to a simple structure of an isoscalar weak boson, taken to be a singlet under $SU(2)_{W_I}$ -the analogue of the ω meson in hadron physics- and the first excited isotriplet (W^*, Z^*) which is the analogue of the ρ' .

— Finally we consider a simple reference model obtained by taking for the heavy W'^\pm and Z' gauge bosons the same coupling to fermions as ordinary W^\pm and Z . Concerning the trilinear couplings WWZ and $Z'WW$ one can assume either that they are a direct transcription of the correponding standard vertices or that they arise through a mixing between the new and the standard vector bosons.

Our aim is a general study of the signatures and backgrounds for the production of new heavy vector bosons at LHC and a comparison of the discovery limits with the SSC expectations. Heavy spin one resonances can be observed in the usual leptonic channel ($Z' \rightarrow l^+l^-, W' \rightarrow l\nu$) but also in the mode $W' \rightarrow WZ$. The decay mode $Z' \rightarrow WW$ is no more observable because of the top background. Most of the models have been incorporated into Pythia Monte Carlo and a calorimeter simulation has been performed. The problem of identifying the origin of a new neutral vector boson, if eventually found, will also be addressed by studying the forward backward asymmetry. Before LHC operation Fermilab's Tevatron collider will certainly improve the existing bounds for new states. Moreover, since the neutral vector resonance mixes with the ordinary Z , LEP will already put bounds on the mixing angle to $\sim 1\%$ and LEP 200 will push Z' mass limits in the TeV range if no deviations from the SM will be found within the planned accuracy. The plan of this written contribution is the following. We will first study discovery limits for Z' and W' from extended gauge models in section 2. The case of extensions involving a different symmetry breaking mechanism is discussed in section 3. Finally in section 4 we draw our conclusions.

II. NEW VECTOR BOSONS FROM EXTENDED GAUGE MODELS

II.1 NEUTRAL E_6 GAUGE BOSONS AT LHC^{*}

Contributors : M.C. GONZALEZ-GARCIA and J.W.F VALLE

1 E_6 Models

In E_6 gauge models, of the type that may arise from string theories [1,2], there may be an additional gauge boson Z' at the TeV scale, coupling to a combination of the ψ and χ symmetries in $E_6/SO(10)$ and $SO(10)/SU(5)$, respectively. The model space is a continuum labelled by an angle β that specifies the hypercharge to which the Z' couples, i.e.,^{*}

$$Y(\beta) = \cos \beta Y_\chi + \sin \beta Y_\psi. \quad (1)$$

The corresponding hypercharge quantum numbers can be found in ref. [1]. However, when the additional $U(1)$ symmetry at low energies arises from a *superstring* model, the pattern of symmetry breaking starting from the original E_6 is such that the angle β can take on only two possible values,

$$\cos \beta = \sqrt{3/8} \quad \sin \beta = -\sqrt{5/8} \quad (2)$$

corresponding to the situation where E_6 is broken all the way in one step and

$$\cos \beta = 1 \quad (3)$$

corresponding to the case where E_6 is broken first by an abelian flux factor and then subsequently, at an intermediate scale, by the Higgs mechanism. These two possibilities lead, respectively, to the η model of ref [4] and to the χ model described in ref [5]. A special role is played by models where the Z' mixing angle is related to its mass. Examples are the *superstring models*, because their Higgs sector only includes Higgses in the 27, leading to an important restriction in the diagonalization of the neutral gauge boson mass matrix. Models other than these are called *unconstrained*.

In all E_6 gauge models with an extra Z one defines an electroweak mixing angle by $\tan \theta_W = g'/g$, where g is the $SU(2)_L$ gauge coupling constant, and the standard hypercharge gauge coupling constant at low energy is related to the constant g_1 that corresponds to the properly normalized E_6 generator by $g' = \sqrt{3/5} g_1$. This identifies the massless combination of the three weak eigenstate neutral gauge bosons which corresponds to the photon field.

The 2×2 matrix describing the massive neutral gauge bosons in these models may always be written as

$$\begin{pmatrix} M_{Z_0}^2 & \mu^2 \\ \mu^2 & M^2 \end{pmatrix} \quad (4)$$

where $M_{Z_0}^2$ would be the Z mass in the absence of mixing with the extra gauge boson. The mass eigenstates following from eq. (4) are given by

$$\begin{aligned} Z &= \cos \theta' Z_0 - \sin \theta' Z'_0 \\ Z' &= \sin \theta' Z_0 + \cos \theta' Z'_0 \end{aligned} \quad (5)$$

in terms of the weak eigenstate gauge fields Z_0 and Z'_0 .

There is a basic structural formula

$$M_{Z_0}^2 = \frac{M_W^2}{\cos^2 \theta_W \rho_0}. \quad (6)$$

relating the Z^0 mass M_{Z_0} in the standard model, with the W mass and the radiatively corrected electroweak mixing angle

$$\sin^2 \theta_W = \frac{A^2}{M_W^2 (1 - \Delta r)} \quad (7)$$

where the various contributions to the gauge boson self-energies are encoded in the quantity Δr and

$$A^2 = \frac{\pi \alpha}{\sqrt{2} G_F} \simeq (37.281 \text{ GeV})^2. \quad (8)$$

The parameter ρ_0 measuring the ratio between the strength of charged to neutral currents is equal to one in our renormalization scheme, if there are only doublet and singlet Higgs bosons.

The mixing parameter μ^2 is in general arbitrary. However, in *superstring* models it is given by

$$\mu^2 = M_{Z_0}^2 \sin \theta_W \left[\frac{\sqrt{10}}{3} (1 - 2 \xi) \sin \beta - \sqrt{2/3} \cos \beta \right] \quad (9)$$

depending on the chosen model through the angle β and also through the dynamical model-dependent parameter ξ , defined as

$$\xi = \frac{v_d^2}{v_u^2 + v_d^2} \quad (10)$$

where v_d, v_u are the VEVs responsible for electroweak breaking. The parameter M^2 is another model-dependent parameter related to the symmetry breaking scale of the extra $U(1)$.

In all these models the Z' squared mass is given by

$$M_{Z'}^2 = M_{Z_0}^2 + \frac{\mu^4}{M_{Z_0}^2 - M_Z^2} \quad (11)$$

From the equations above we determine the Z' mixing angle according to

$$\sin \theta' = - \sqrt{\frac{M_{Z_0}^2 - M_Z^2}{M_{Z'}^2 - M_Z^2}} \quad (12)$$

Eq. (11) and eq. (12) imply a relationship between $M_{Z'}$ and θ' that may be used to eliminate θ' . This is strictly true only in the case of the χ model while, for the η model this would be approximately true given the narrow range of variation in eq. (12) when the parameter ξ varies over its allowed range [0.04, 0.5].

There are correlated limits on $M_{Z'}$ and the mixing angle θ' that follow from laboratory [6,7] as well as cosmological considerations [9]. Here we concentrate on existing laboratory mass limits, which are directly relevant in order to compare with Z' discovery limits at a pp collider.

2 Z' Mass Limits

The weak neutral current and the measurements of the gauge boson masses at hadron colliders [11] and LEP/SLC [12] have provided a quantitative test of the standard $SU(2) \otimes U(1)$ electroweak theory, over a wide range of energies. A combined fit of the data to the standard model parameters is in good agreement with the standard model [10,7,8]. These constraints depend sharply on the model. For *constrained* E_6 *superstring* models the limits are very sensitive to a good knowledge of the W mass M_W (or, equivalently, the electroweak weak mixing angle θ_W), the top quark mass m_t and to a lesser extent, also to the Higgs mass, m_H [6,7].

Fig. 1a and 1b show the combined laboratory limits on $M_{Z'}$ as a function of the top mass for the χ and η models. The rising, upper curves refer to *constrained* models while the flat, lower curves apply to *unconstrained* models.

In addition to the laboratory limits on *constrained* models being stronger, these string inspired models are often constrained by Big Bang Nucleosynthesis considerations. The corresponding limits have been studied in ref. [9].

^{*}It is reasonable to neglect the possible effect of additional angles that might be present [3].

3 Z' Production and Decay Signatures at LHC

In what follows we neglect the small $Z - Z'$ mixing angle θ' because its effect on the Z' production cross section at a pp collider, as well as on its decay branching ratios is very small.

3.1 Differential cross section $pp \rightarrow e^+e^-X$

The production and decays of a new Z' gauge boson are described by the Lagrangian

$$L = \sum_{i,n} \bar{\psi}^i \gamma_\mu (v_n^i + a_n^i \gamma_5) \psi^i Z_n^\mu \quad (13)$$

where i runs over the different fermions and $n = 0, 1, 2$ labels the photon, standard Z , and Z' , respectively. The vector and axial couplings for the different fermions can be directly derived from the hypercharge assignments and are given in ref. [15].

At hadron colliders such as LHC the main production mechanism of a new neutral gauge boson is the Drell-Yan mechanism $pp \rightarrow e^+e^-X$. In the quark-parton model the basic interaction describing the process is the annihilation of one quark in one of the protons with an antiquark of the sea of the other proton. If we label a and b the colliding protons, the differential cross section of the process is given by

$$d\sigma(a+b \rightarrow e^+e^-X) = \sum_{i,j} \int dx_a dx_b f_i^a(x_a, M^2) f_j^b(x_b, M^2) d\sigma(i+j \rightarrow e^+e^-) \quad (14)$$

where x_a and x_b are the momentum fraction carried by the interacting partons in the protons a and b respectively. M is the e^+e^- invariant mass, the functions $f_{i,j}^{a,b}(x_{a,b}, M^2)$ are the parton distribution functions describing the probability of finding the parton $i(j)$ in the proton $a(b)$ with momentum fraction $x_{a(b)}$. We will use the set 1 parton distribution functions given by Duke and Owens [13]. It is reasonable to extrapolate them to the energy available at the LHC ($\sqrt{s} = 16 \text{ TeV}$) [14]. Using the standard expression for the differential cross section of the elementary process $q\bar{q} \rightarrow e^+e^-$ and using the rapidity variable y verifying $x_{a,b} = \frac{M}{\sqrt{s}} e^{\pm y}$ we have

$$\frac{d\sigma}{dM dy d\cos\theta} = K(M^2) \frac{M}{48\pi} \sum_q \left[g_q^S(y, M) S_q(M)(1 + \cos^2\theta) + 2g_q^A(y, M) A_q(M) \cos\theta \right] \quad (15)$$

where

$$g_q^{S,A}(y, M) = x_a x_b \left[f_q^a(x_a, M^2) f_{\bar{q}}^b(x_b, M^2) \pm f_{\bar{q}}^a(x_a, M^2) f_q^b(x_b, M^2) \right] \quad (16)$$

and

$$S_q = \sum_{n,m} \frac{(M^2 - M_n^2)(M^2 - M_m^2) + \Gamma_n M_n \Gamma_m M_m}{[(M^2 - M_n^2)^2 + (\Gamma_n M_n)^2][(M^2 - M_m^2)^2 + (\Gamma_m M_m)^2]} (v_n^q v_m^q + a_n^q a_m^q) (v_n^q v_m^q + a_n^q a_m^q) \quad (17)$$

$$A_q = \sum_{n,m} \frac{(M^2 - M_n^2)(M^2 - M_m^2) + \Gamma_n M_n \Gamma_m M_m}{[(M^2 - M_n^2)^2 + (\Gamma_n M_n)^2][(M^2 - M_m^2)^2 + (\Gamma_m M_m)^2]} (v_n^q a_m^q + a_n^q v_m^q) (v_n^q a_m^q + a_n^q v_m^q) \quad (18)$$

θ is the scattering angle in the parton system. $K(M^2)$ factorizes the QCD radiative corrections and is given by

$$K(Q^2) = \exp \frac{2}{3} \pi \alpha_s(Q^2)$$

$$\alpha_s(Q^2) = \frac{12\pi}{33 - 2n_f} \frac{1}{\log \frac{Q^2}{\Lambda^2}} \quad (19)$$

where $n_f = 6$ is the number of flavours and $\Lambda = 0.2 \text{ GeV}$. $M_0 = \Gamma_0 = 0$, $M_1 = 91.16 \text{ GeV}$ and $\Gamma_2 = 2.5 \text{ GeV}$.

3.2 Z' Decay Branching Ratios

For the new neutral boson Z_2 the width will depend on the hypercharge determining its couplings to the matter fields and on the number of channels kinematically available for its decay. In general its decay rate to fermions and sfermions is given by [3]

$$\begin{aligned} \Gamma(Z' \rightarrow f\bar{f}) &= \frac{M_{Z'}}{12\pi} \sqrt{(1-4\beta)} c_f \left[v_2^{f^2} (1+2\beta) + a_2^{f^2} (1-2\beta) \right] \\ \Gamma(Z' \rightarrow \tilde{f}_{L,R} \bar{\tilde{f}}_{L,R}) &= \frac{M_{Z'}}{48\pi} \sqrt{(1-4\beta)^3} c_f \left[v_2^f \pm a_2^f \right]^2 \end{aligned} \quad (20)$$

where $\beta = \frac{m_f^2}{M_{Z'}^2}$ and $c_f = 1(3)$ for the colour singlets (triplets). We consider two limit cases:

a) Z' decaying only to the known fermions (including top)

$$\Gamma_2 = \frac{M_{Z'}}{4\pi} \sum_f c_f \left[v_2^{f^2} + a_2^{f^2} \right] \quad (21)$$

b) Z' decaying into three families of 27 fermions and sfermions with negligible masses

$$\Gamma_2 = \frac{3M_{Z'}}{8\pi} \sum_f c_f \left[v_2^{f^2} + a_2^{f^2} \right] = \frac{15M_{Z'}}{16\pi} \frac{e^2}{\cos\theta_W^2} \quad (22)$$

In the second case the decay width is independent of the model, due to the hypercharge normalization condition (neglecting phase space factors). In Fig. 2 and 3 we plot the Z' width and the branching ratio to e^+e^- , respectively, as a function of the model, for the two cases discussed above.

3.3 Cross Section on the Z' Peak and Discovery Limits

We define the cross section on the Z' peak as

$$\sigma(pp \rightarrow Z'X \rightarrow e^+e^-X) = \sigma(pp \rightarrow Z'X) Br(Z' \rightarrow e^+e^-) \quad (23)$$

where

$$\sigma(pp \rightarrow Z'X) = \frac{\pi}{3M_{Z'}^2} \sum_q (v_2^{q^2} + a_2^{q^2}) \int_{\ln \frac{M_{Z'}}{\sqrt{s}}}^{\ln \frac{M_{Z'}}{\sqrt{s}}} dy g_q^S(y, M_{Z'}^2) \quad (24)$$

The number of events N will be given by

$$N = \sigma(pp \rightarrow Z'X \rightarrow e^+e^-X) L \quad (25)$$

where L is the integrated luminosity. At LHC the luminosity should lie in range $10^{33} - 5 \times 10^{34} \text{ cm}^{-2}\text{s}^{-1}$ giving an integrated luminosity of $10^4 - 5 \times 10^5 \text{ pb}^{-1}$ in 10^7 s . If we assume that at least $N \geq 10$ events are needed in order to identify the Z' signal, we can then derive the corresponding discovery limits. These limits will depend on the model and on the channels of decay kinematically available. In Fig. 4 we plot the discovery limits for the two extreme cases defined above and for the two values of the luminosity. As we already pointed out, we have neglected the ZZ' mixing angle. In the presence of a nonzero mixing, a new Z' decay channel opens up, i.e., $Z' \rightarrow W^+W^-$. This would dilute the branching into the easily detectable leptonic decay channel, thus worsening the limits. For a quantitative treatment of this question one needs to know the limits that apply on the mixing. A global fit to all the existing data pertaining to the weak neutral current, W, Z masses and Z widths allows values of this mixing up to $| \sin\theta' | \lesssim 0.1$, as shown in Fig. 5, taken from ref. [8]. The effect that this could have upon the discovery limits is studied in ref. [15].

3.4 Asymmetries

In $pp \rightarrow e^+e^-X$ collisions we can define an asymmetry parameter by

$$A(M) = \frac{\left(\int_0^{\ln \frac{M}{\sqrt{s}}} - \int_{\ln \frac{M}{\sqrt{s}}}^0 \right) dy \left(\int_0^1 - \int_{-1}^0 \right) d\cos\theta \frac{d\sigma}{dM dy d\cos\theta}}{\int_{\ln \frac{M}{\sqrt{s}}}^{\ln \frac{M}{\sqrt{s}}} dy \int_{-1}^1 d\cos\theta \frac{d\sigma}{dM dy d\cos\theta}} \quad (26)$$

This quantity is in general nonzero and sensitive to the details of the model in question. In Fig. 6 we plot the value of the asymmetry for the χ and η model as a function of the invariant mass. The asymmetry presents a minimum around the value $M = M_{Z'}$ but the depth of the minimum depends on the model. In Fig. 7 we plot the value of the asymmetry for $M = M_{Z'}$ as a function of the model.

References

- [1] For recent reviews see J Hewett, T Rizzo, *Phys. Rep.* **C183** (1989) 193; J W F Valle, *Nucl. Phys. B (Proc. Suppl.)* **11** (1989) 118.
- [2] P Candelas *et al.*, *Nucl. Phys.* **B258** (1986) 85; G Ross, *et al.*, *Phys. Lett.* **B192** (1987) 111; *Nucl. Phys.* **B278** (1986) 667; J P Derendinger *et al.*, *Nucl. Phys.* **B267** (1986) 365; F del Aguila *et al.*, *Nucl. Phys.* **B272** (1986) 413; R Mohapatra, J W F Valle, *Phys. Rev.* **D34** (1986) 1642; J W F Valle, *Phys. Lett.* **B186** (1987) 73
- [3] F del Aguila *et al.*, *Nucl. Phys.* **B307** (1988) 571; *Nucl. Phys.* **B284** (1987) 530.
- [4] J Ellis *et al.*, *Mod. Phys. Lett.* **A1** (1986) 57.
- [5] J W F Valle, *Phys. Lett.* **B196** (1987) 157; M. C. Gonzalez-Garcia, J. W. F. Valle, CERN-TH.5861/90.
- [6] M. C. Gonzalez-Garcia, J. W. F. Valle, *Phys. Rev.* **D41** (1990) 2355 and *Phys. Lett.* **B236** (1990) 360.
- [7] M. C. Gonzalez-Garcia, J. W. F. Valle, *Nucl. Phys.* **B345** (1990) 312;
- [8] M. C. Gonzalez-Garcia, J. W. F. Valle, FTUV/90-45.
- [9] M. C. Gonzalez-Garcia, J. W. F. Valle, *Phys. Lett.* **B240** (1990) 163 and references therein.
- [10] U Amaldi *et al.*, *Phys. Rev.* **D36** (1987) 1385; L Durkin, P Langacker, *Phys. Lett.* **B166** (1986) 436; G Costa *et al.*, *Nucl. Phys.* **B297** (1988) 244.
- [11] L Nodulman, talk at EPS Conference on High Energy Physics, Madrid, 1989; V Barger, J Hewett, T Rizzo, *Phys. Rev.* **D42** (1990) 152; UA2 collaboration, *Phys. Lett.* **B241** (1990) 150; CDF collaboration, ANL-HEP-PR-90-71.
- [12] F Dydak, talk at the HEP Conference, Singapore, August 1990; E Fernandez, talk at the Neutrino 90 Conference, Geneva, June 1990
- [13] D W Duke and J F Owens *Phys. Rev.* **D30** (1984) 49
- [14] E Eichten, I Hinchliffe, G Kane and C Quigg, *Rev. Mod. Phys.* **56** (1984) 579.
- [15] M. C. Gonzalez-Garcia, J. W. F. Valle, in preparation.

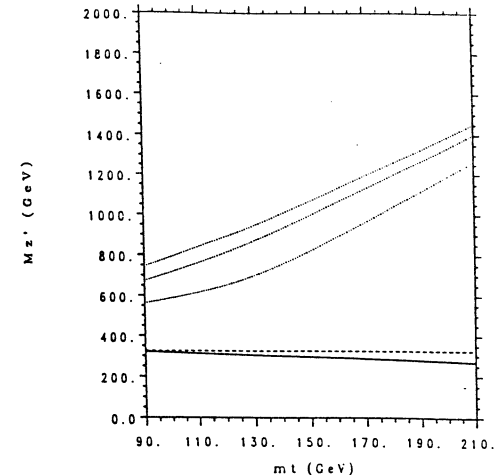


Fig. 1a :

90% CL lower limit on $M_{Z'}$ versus m_t for the χ model. The solid line corresponds to the constrained model and the dashed line to the unconstrained one. In these two cases the dependence on m_H is very weak so we plot only for $m_H = 100 \text{ GeV}$. As explained in ref [7] the dependence on m_t is very weak. The dotted lines correspond to the constrained or superstring model, for $m_H = 1000 \text{ GeV}$ (lower), $m_H = 100 \text{ GeV}$ (central), and $m_H = 10 \text{ GeV}$ (upper).

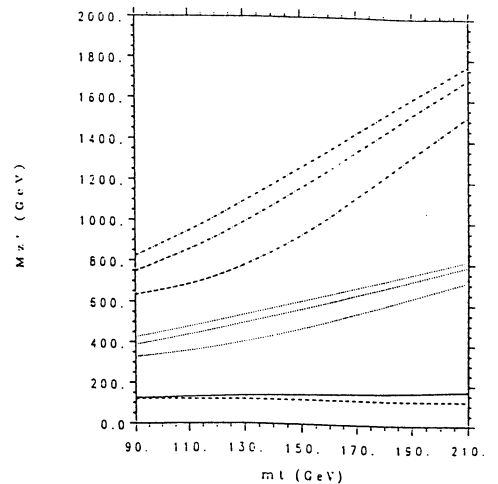


Fig. 1b :

Same as Fig. 1a for the case of the superstring η model. The dotted lines correspond to $\xi = 0.5$ and the dash-dotted ones to $\xi = 0.04$. The lines are plotted for the same Higgs mass values as (1a).

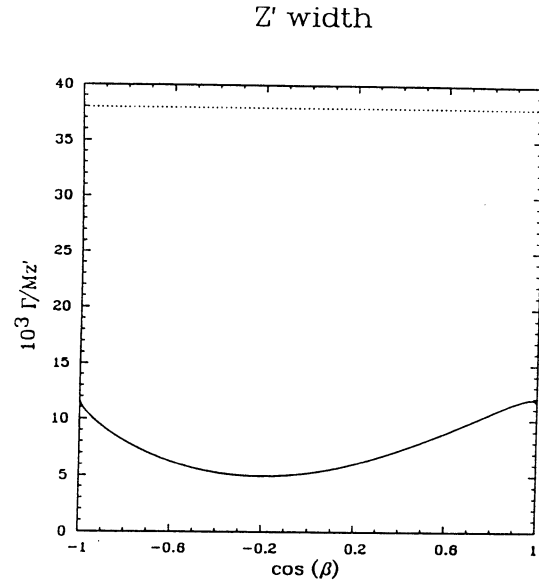


Fig. 2 :
Z' width versus $\cos\beta$ for the two extreme cases: Z' decaying only to the known fermions, including top (solid line) and Z' decaying to three families of the 27 fermions and sfermions (dotted line).

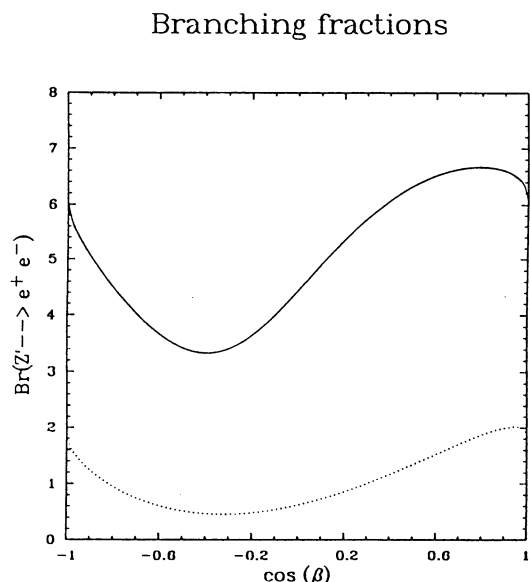


Fig. 3 :
Branching fraction $B(Z' \rightarrow e^+e^-)$ for the different models and for the two cases discussed in the text.

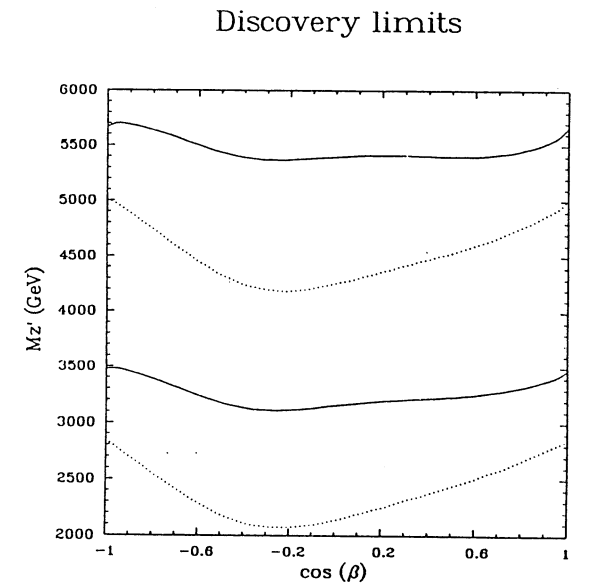


Fig. 4 :
Discovery limits for $N = 10$ events as a function of the model. The lower lines correspond to an integrated luminosity of $10^4 (pb)^{-1}$ and the upper lines to an integrated luminosity of $5 \times 10^5 (pb)^{-1}$. The solid and dotted corresponds to the two extreme cases for the Z' decay as above.

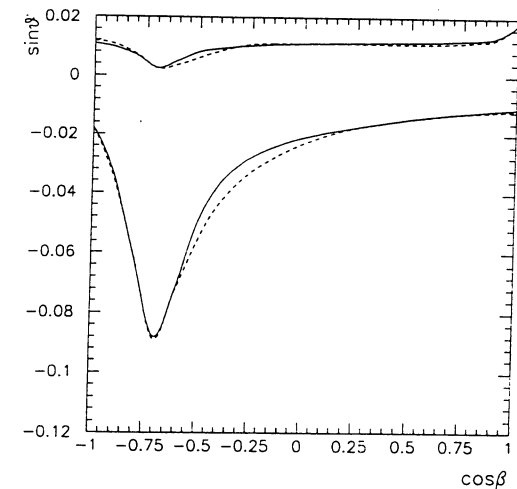


Fig. 5 :
Allowed range (at 90 % CL) on $\sin\theta'$ versus $\cos\beta$ for $m_t = 100 GeV$, $m_H = 100 GeV$ and $\alpha_s = 0.12$. The solid line corresponds to the models where $\rho_0 = 1$ and the dashed line to the models where ρ_0 is left free.

Asymmetry χ and η models

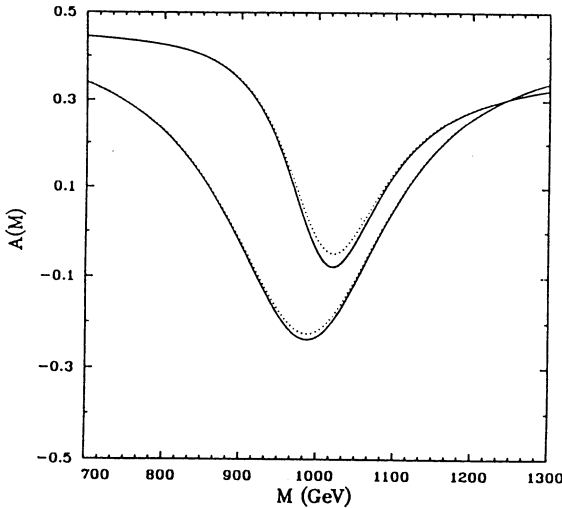


Fig. 6 :

The asymmetry of eq. (26) as a function of the invariant mass M for the η model (upper lines) and χ model (lower lines), for $M'_Z = 1 \text{ TeV}$. The solid line corresponds to a Z' decaying only to the known fermions (including top) and the dotted line correspond to a Z' decaying to three families of the 27 fermions and sfermions.

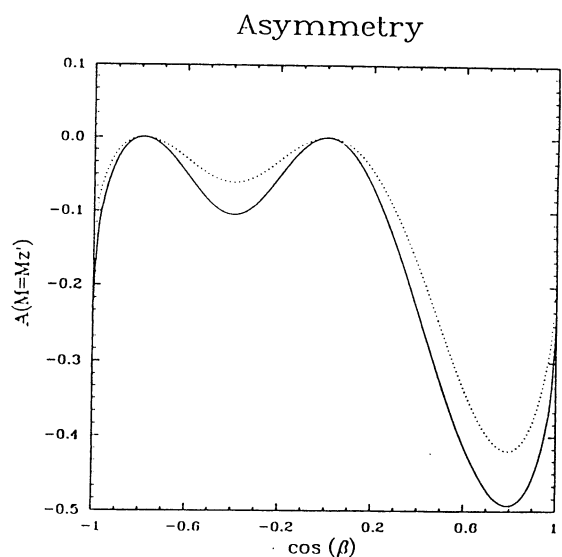


Fig. 7 :

Asymmetry $A(M = M_{Z'})$ plotted versus $\cos \beta$ for $M_{Z'} = 1 \text{ TeV}$ (solid line) and $M_{Z'} = 5 \text{ TeV}$ (dotted line).

II.2 Z' FROM SUPERSTRING-INSPIRED E_6 MODELS

Contributors: F. del Aguila, J. Moreno and M. Quiros.

Introduction

In this summary we present results concerning the capabilities at LHC for detecting extra neutral gauge bosons in extended electroweak models contained in E_6 . We will restrict ourselves to models with one single extra $U(1)$ at low energy. We first introduce the general parametrization and couplings, and a sampling of models that will be used to illustrate the numerical results. Then we analyze the three standard channels into colorless particles where the Z' can be detected: $Z' \rightarrow \ell^+ \ell^-$, $W^+ W^-$ and ZH .

General parametrization

The neutral current lagrangian of extended electroweak models with an extra $U(1)$ can be parametrized in terms of four new parameters [1]: three angles $(\theta_1, \theta_2, \theta_3)$ and a ratio of coupling constants λ . It can be written as

$$\begin{aligned} \mathcal{L}_{NC} &= e J_{EM}^\mu A_\mu + \frac{e}{s_W c_W} (J_Z^\mu Z_\mu + J_{Z'}^\mu Z'_\mu), \\ J_{EM} &= J_1 + \sqrt{\frac{5}{3}} J_2, \\ J_Z &= c_3 J_{Z^o} - s_3 J_{Z'^o}, \\ J_{Z'} &= s_3 J_{Z^o} + c_3 J_{Z'^o}, \\ (J_{Z^o}) &= J_1 - s_W^2 J_{EM}, \\ (J_{Z'^o}) &= \sqrt{\frac{5}{3}} s_W [s_1 c_1 (\lambda - \frac{1}{\lambda}) J_2 - (s_1^2 \lambda + \frac{c_1^2}{\lambda}) J_e], \end{aligned} \quad (1)$$

where $s_i(c_i) = \sin \theta_i(\cos \theta_i)$, $s_W(c_W) = \sin \theta_W(\cos \theta_W)$ (the electroweak angle), e is the electromagnetic constant and J_i are the currents associated with the E_6 orthogonal generators ($T_i = (T_{3L}, Y, Y', Y'', Y^e)$ given in Table 1. θ_2 gives the direction of the intermediate breaking, defining the conserved hypercharge as $Y^e = c_2 Y' - s_2 Y''$ (in superstrings $s_2 = 0, \pm \sqrt{\frac{5}{8}}$). θ_1 is a remnant of $\text{Tr}(YY^e) \neq 0$ at high energy and θ_3 is the $Z^o Z'$ -mixing angle, whereas $\lambda \equiv \frac{g_Y}{g_{Y^e}}$.

Different models will be characterized by different values of $(\theta_1, \theta_2, \theta_3, \lambda)$. The mixing θ_3 behaves like $(M_Z/M_{Z'})^2$ and so is expected to be very small. We can neglect it in the couplings for Z' production at LHC, since the bounds obtained this way are not essentially modified for small θ_3 values. (Of course θ_3 cannot be neglected in the comparison of precision measurements with the electroweak theory neither in $Z' W^+ W^-$ production, which is proportional to s_3 .) For illustration we will use in our numerical estimates a sampling of models [2] characterized by the parameters $(\theta_1, \theta_2, \lambda)$ given in Table 2.

FIELD	T_3^L	$\sqrt{\frac{5}{3}}Y$	$\sqrt{\frac{5}{3}}Y'$	Y''	$\sqrt{\frac{8}{5}}Y^e$
$\begin{pmatrix} u \\ d_1 \end{pmatrix}_L$	$\begin{pmatrix} +\frac{1}{2} \\ -\frac{1}{2} \end{pmatrix}$	$\frac{1}{6}$	$\frac{1}{3}$	0	$\frac{1}{5}$
d_{2L}	0	$-\frac{1}{3}$	$-\frac{2}{3}$	0	$-\frac{2}{5}$
u_L^c	0	$-\frac{2}{3}$	$\frac{1}{3}$	0	$\frac{1}{5}$
d_{1L}^c	0	$\frac{1}{3}$	$-\frac{1}{6}$	$\frac{1}{2}$	$-\frac{3}{5}$
d_{2L}^c	0	$\frac{1}{3}$	$-\frac{1}{6}$	$-\frac{1}{2}$	$\frac{2}{5}$
$\begin{pmatrix} \nu_1 \\ e_1 \end{pmatrix}_L$	$\begin{pmatrix} +\frac{1}{2} \\ -\frac{1}{2} \end{pmatrix}$	$-\frac{1}{2}$	$-\frac{1}{6}$	$\frac{1}{2}$	$-\frac{3}{5}$
$\begin{pmatrix} \nu_2 \\ e_2 \end{pmatrix}_L$	$\begin{pmatrix} +\frac{1}{2} \\ -\frac{1}{2} \end{pmatrix}$	$-\frac{1}{2}$	$-\frac{1}{6}$	$-\frac{1}{2}$	$\frac{2}{5}$
$\begin{pmatrix} e_2^c \\ \nu_3 \end{pmatrix}_L$	$\begin{pmatrix} +\frac{1}{2} \\ -\frac{1}{2} \end{pmatrix}$	$\frac{1}{2}$	$-\frac{2}{3}$	0	$-\frac{2}{5}$
e_{1L}^c	0	1	$\frac{1}{3}$	0	$\frac{1}{5}$
ν_{4L}	0	0	$\frac{5}{6}$	$-\frac{1}{2}$	1
ν_{5L}	0	0	$\frac{5}{6}$	$\frac{1}{2}$	0

Table 1. Action of $(T_{3L}, Y, Y', Y'', Y^e)$ on the $\underline{27}$ of E_6 . Y^e is the extra hypercharge for $s_2 = \sqrt{5/8}$ (superstring models).

The $Z' \rightarrow \ell^+\ell^-$ channel

We have used for the reaction $pp \rightarrow Z'X \rightarrow \ell^+\ell^-X$ the EHLQ structure functions, a scale independent K -factor $K = 1.3$, an integrated luminosity $L = 10^3, 10^4$ and $10^5 pb^{-1}$, a discovery limit of ten events, and a Z' width corresponding to the minimal matter content of the standard model.

We have computed the total cross section $\sigma(\ell^+\ell^-)$ and the forward-backward asymmetry as a function of the rapidity $A(y)$ at the peak and as a function of the $\ell^+\ell^-$ invariant mass $A(M)$. In Fig. 1 we present the total cross section $\sigma(\ell^+\ell^-)$ as a function of $M_{Z'}$ for the models in Table 2. The narrow band for $300 GeV < M_{Z'} < 700 GeV$ corresponds to present bounds for the corresponding models from precision electroweak

measurements (LEP+neutral current data) [3], roughly similar to those that will be obtained for an upgraded Tevatron [2], for $L = 10^2 pb^{-1}$. From Fig. 1 we can read the discovery limits at LHC, depending on the value of L . They are $\sim 2, 3, 4.5 TeV$ for $L = 10^3, 10^4, 10^5 pb^{-1}$. We can compare these values with those obtained for the SSC (with $\sqrt{s} = 40 TeV$ and $L = 10^4 pb^{-1}$). For the considered models and $M_{Z'} = 5 TeV$ the range of the cross-sections at LHC is $2.5 \times 10^{-5} < \sigma(\ell^+\ell^-) < 7 \times 10^{-5}$. This range is shifted at SSC to $1.5 \times 10^{-3} < \sigma(\ell^+\ell^-) < 3 \times 10^{-3}$, which translates into a discovery limit $\sim 5.5 TeV$ for the SSC.

Forward-backward asymmetries could be useful to distinguish between models. In Fig. 2 we present the asymmetry as a function of the rapidity $A(y)$ at the peak for models in Table 2 and $M_{Z'} = 1 TeV$. No detector simulation has been attempted. We can see from Fig. 2 that some models (e.g. B3 and LR) would be very easily differentiated by their asymmetries, while others (e.g. ψ and η) would not.

MODEL	$\theta_2 \in [-\frac{\pi}{2}, \frac{\pi}{2}]$	$\lambda \geq 1$	$\theta_1 \in [-\frac{\pi}{2}, \frac{\pi}{2}]$
$Z_X^{(b)}$	$\arcsin \sqrt{\frac{5}{8}}$	1	-
Z_ψ	$\arcsin \sqrt{\frac{3}{8}}$	1	-
$Z_\eta^{(a)}$	0	1	-
Z_{LR}	$\arcsin \sqrt{\frac{5}{8}}$	1.877	$\arcsin \sqrt{\frac{2}{5}}$
$Z_{X'}^{(c)}$	$-\arcsin \sqrt{\frac{5}{8}}$	1	-
Z_{B3}	$\arcsin \sqrt{\frac{5}{8}}$	1.371	1.195
Z_{B4}	$\arcsin \sqrt{\frac{5}{8}}$	1.179	-1.019
Z_{B7}	$\arcsin \sqrt{\frac{5}{8}}$	1.080	1.174
Z_{B8}	$\arcsin \sqrt{\frac{5}{8}}$	1.227	-0.686
$Z_{C1...C5,D}$	$\arcsin \sqrt{\frac{5}{8}}$	1.045	-0.886

Table 2. Sampling of models used in Fig. 1.

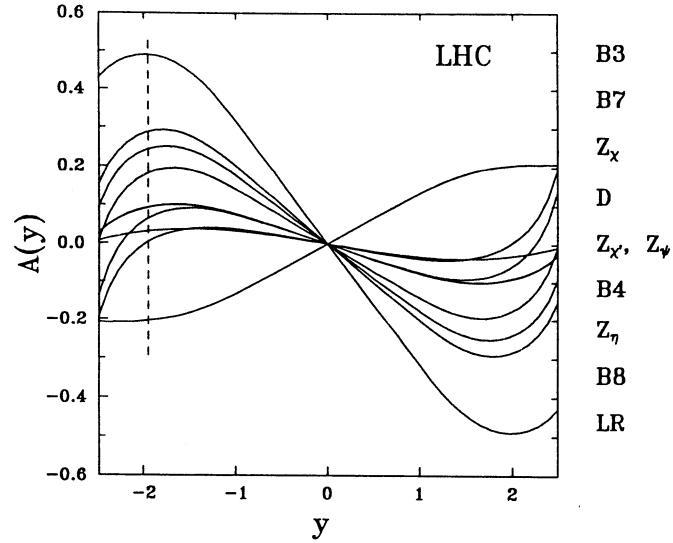


Figure 1. $\sigma(\ell^+\ell^-)$ in pb for models in Table 2.

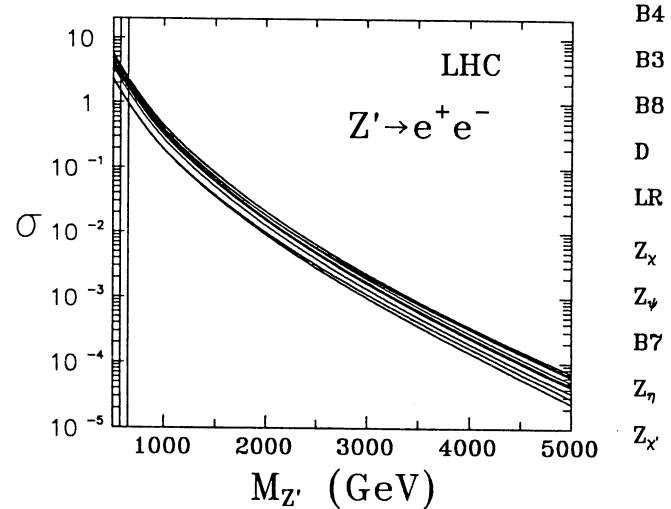


Figure 2. Forward-backward asymmetries for models in Table 2 and $M_{Z'} = 1 \text{ TeV}$. Labelling of models corresponds to the vertical dashed line.

The $Z' \rightarrow W^+W^-$ channel

The coupling $Z'W^+W^-$ is obtained through the Z^0Z' mixing and is, therefore, suppressed by $s_3 \sim (M_{Z'}/M_Z)^2$. However there is a kinematical enhancement factor in the decay rate $\sim (M_{Z'}/M_Z)^4$, which makes the W^+W^- -production cross-section similar to that for $\ell^+\ell^-$ [4]. The plot of $\sigma(W^+W^-)$ as a function of $M_{Z'}$ is very similar to that of Fig. 1, but shifted downward. In particular for $M_{Z'} = 5 \text{ TeV}$, the models in Table 2 cover the range $10^{-5} < \sigma(W^+W^-) < 4 \times 10^{-5}$. However this channel is ruled out for Z' -detection. For the leptonic channel $W^\pm \rightarrow e^\pm\nu$, the cross section is penalized by a factor 10^{-2} and the peak cannot be reconstructed. The only hope for detection is therefore via the channel $WW \rightarrow \ell\nu jj$. However in this case the QCD Wjj background [5] (not to say the $t\bar{t}$ background) would kill the signal .

The $Z' \rightarrow ZH$ channel

This channel could be interesting to detect Z' and/or a *heavy* Higgs [6]. There is no suppression factor in the coupling $ZZ'H$ since it comes from the vertex $Z^0Z^0H < H >$. However there is no kinematical enhancement factor in the decay rate $Z' \rightarrow ZH$. In fact, neglecting phase space factors η_H, η_Z, η_W ($\eta_a = (M_a/M_{Z'})^2$) one can write the relation

$$\sum_i \Gamma(Z' \rightarrow ZH_i) = \Gamma(Z' \rightarrow W^+W^-) \quad (2)$$

for models with several Higgs doublets. [In particular, in the minimal supersymmetric model, with two neutral Higgses, the ratios of their decay rates to $\Gamma(Z' \rightarrow W^+W^-)$ are proportional to $\cos^2(\beta - \alpha)$ and $\sin^2(\beta - \alpha)$]. For a single heavy Higgs ($m_H > 500 \text{ GeV}$) the dominant channels for H -decay are W^+W^- and ZZ , with branching ratios $\sim \frac{2}{3}$ and $\frac{1}{3}$, respectively. We have computed the total cross section $\sigma(ZH)$ for minimal models with one Higgs doublet. Anyhow, our resulting cross-sections are an upper bound for the case of non-minimal models, according to Eq. (2).

For the $B3$ model in Table 2 we find $\sigma(ZH \rightarrow ZWW) \sim 0.14 \text{ pb}$ (0.028 pb) and $\sigma(ZH \rightarrow ZZZ) \sim 0.07 \text{ pb}$ (0.014 pb) for $M_{Z'} = 1 \text{ TeV}$ (1.5 TeV). Leptonic decay channels are penalized by small branching ratios. The branching ratio for the best channel, $ZZZ \rightarrow e^+e^-\nu\bar{\nu}jj$, is $\sim 2.8 \times 10^{-2}$, where we have used the values (valid for $m_t = 100 \text{ GeV}$) $\sum_i B(Z \rightarrow \nu_i\bar{\nu}_i) = 0.2$, $B(Z \rightarrow e^+e^-) = \frac{1}{30}$ and $\sum_i B(Z \rightarrow jj) = 0.7$. For $L = 10^5 \text{ pb}^{-1}$ there would be ~ 200 events (40 events) for $M_{Z'} = 1 \text{ TeV}$ (1.5 TeV). The signature for those events would be a very large missing energy plus e^+e^- reconstructing the Z mass. In other models the value of $\sigma(ZH \rightarrow ZZZ)$ could be possibly increased (by a typically small factor). Other channels with similar signals involving $W \rightarrow e\nu$ do not reconstruct $M_{e^+e^-} \sim M_Z$.

Although work is still in progress, it looks difficult to us to detect a Z' and/or a Higgs in the $Z' \rightarrow ZH$ channel for the cross-sections are too small for the leptonic modes, and the backgrounds are too large for the hadronic ones.

References

- [1] F. del Aguila, M. Quiros and F. Zwirner, *Nucl. Phys.* **B287** (1987) 419.
- [2] F. del Aguila, J.M. Moreno and M. Quiros, *Phys. Rev.* **D40** (1989) 2481 and **D41** (1990) 134; (E) **D42** (1990) 262.
- [3] F. del Aguila, J.M. Moreno and M. Quiros, IEM-FT-16/90 (to appear in *Phys. Lett. B*); IEM-FT-12/90 (1990) and IEM-FT-33/90 (1990).
- [4] F. del Aguila, M. Quiros and F. Zwirner, *Nucl. Phys.* **B284** (1987) 530.
- [5] F. del Aguila, Ll. Ametller, R. Field and Ll. Garrido, *Phys. Lett.* **221B** (1989) 408.
- [6] J.F. Gunion, H.E. Haber and L. Roszkowski, *Phys. Lett.* **189B** (1987) 409; *Phys. Rev.* **D38** (1988) 105.

APPENDIX: Constraints from future LEP data

Contributor : C. VERZEGNASSI

LEP 1 on Z peak will mainly constrain the angle θ_M which characterizes the $Z - Z'$ mixing. By combining information on leptonic width, invisible width, final τ polarization, hadronic width, forward backward asymmetry for b quarks and also M_Z and M_W masses (see ref.[1]) one can set a limit of roughly 1% for the mixing angle of a Z' of E_6 or left right origin. At LEP 200, since the Z' interference with γ and Z generates a term that depends on Z' mass one starts to be sensitive to Z' mass. By combining information from muonic forward backward asymmetry and from the ratio between hadronic width and muonic width one will exclude masses between 500 GeV and 1 TeV.

Reference

- [1] J. Layssac, F.M. Renard and C. Verzegnassi, preprint LAPP-TH-290/90 (1990)

II.3 Z' into Leptons

Paolo Camarri, Vincenzo Cavasinni, Claudia-Elisabeth Wulz

1 Introduction

One or more new neutral heavy vector bosons are required by many theories attempting to extend the Standard Model. The following is a non-complete list of possible models (see also references in the general introduction):

- E_6 -models [1]
- left-right symmetric models [2]
- models with Standard-Model-like Z' -couplings [3]
- models with electroweak symmetry breaking by a strongly interacting sector (BESS) [4]
- composite models [5]

Once a new vector boson is discovered, the question arises how to uniquely determine its fermion-couplings in order to distinguish between those models. We will concentrate on the process $Z' \rightarrow e^+e^-$ within the first three models, but will give some perspectives for the muon channel as well. The BESS and composite models are discussed in contribution III.3 of these proceedings.

The Z' -couplings to fermions were modified in the hadron Monte Carlo program PYTHIA 5.4 [6] which was used to generate the signal and the backgrounds.

In the following chapter the production of lepton pairs from Z' and from backgrounds is described and the discovery limits for a Z' -particle are derived. Chapter 3 deals with the distinction between typical classes of models by a rapidity-analysis of forward-backward asymmetries at the Z' mass peak.

2 Z' -Discovery in the two-lepton channel

In order to study Z' -production we considered three different classes of models: E_6 -models, a left-right symmetric (LR), an alternative left-right symmetric model (ALR) and two special extended gauge models. These models differ by their Z' -couplings to fermions. With the Lagrangian of the form $\mathcal{L} = g(Z') [\bar{f}\gamma^\mu (g_v - \gamma_5 g_a) f] Z'_\mu$ tables 1, 2 and 3 define the axial (g_a) and vector couplings (g_v) to u-like and d-like quarks, charged leptons and neutrinos. Exotic fermions are not considered. For E_6 -type rank 5 and effective rank 5 models g is $g(Z') = \frac{1}{\sqrt{288}} \frac{\alpha_{em}}{\cos \theta_w}$, for the left-right symmetric and the alternative left-right symmetric model g is $g(Z') = \frac{1}{12} \frac{\alpha_{em}}{\sin \theta_w \cos \theta_w} \frac{1}{\sqrt{1-2 \sin^2 \theta_w}}$. x_w denotes $\sin^2 \theta_w$.

We studied the Z' production cross-section in the two-electron channel for the E_6 -model with two different angles ($\sin \theta = 0$ and $\sin \theta = -\sqrt{\frac{5}{8}}$), for the left-right and alternative left-right symmetric models as well as for two models with Standard-Model-like Z' -couplings [3]. These two models are called "extended gauge model" and "reference model" in ref. [3]. They only differ by the couplings of the Z' to ordinary vector bosons. In the extended gauge model Z' -couplings to ordinary W and Z are suppressed by a mixing factor $\zeta = c \left(\frac{m_W^2}{m_{W',Z'}^2} \right)$ where c is of the order 1. This leads to a total Z' -width

that increases linearly with the mass of the Z' and branching ratios into fermions similar to those of ordinary Z into fermions. For the reference model the Z' -width increases with $m^5(Z')$, however. The total Z' -width Γ_{tot} in the extended gauge model is about 3% of the Z' -mass. E_6 -models and left-right symmetric models yield widths of the order of 1% to 3% of the Z' -mass (fig.1). The reference model is not included in the figure since at a Z' -mass of 1 TeV its total width would be in the order of 10 TeV. The $Z' \rightarrow e^+e^-$ production cross-sections for the considered models is plotted in fig.2 as a function

Z' coupling to fermion	g_v	g_a
u	0	$-2\sqrt{3}\cos\theta$
d	$-4\sqrt{3}\cos\theta$	$2\sqrt{3}\cos\theta + \sqrt{5}\cos\theta$
ν	$3\sqrt{3}\cos\theta + \sqrt{5}\sin\theta$	$3\sqrt{3}\cos\theta + \sqrt{5}\sin\theta$
e	$4\sqrt{3}\cos\theta$	$2\sqrt{3}\cos\theta + 2\sqrt{5}\cos\theta$

Table 1: E_6 -model

Z' coupling to fermion	g_v	g_a
u	$3-8x_w$	$-3+8x_w$
d	$-3+4x_w$	$3-6x_w$
ν	$3x_w$	$3x_w$
e	$-3+12x_w$	$3-6x_w$

Table 2: Left-right symmetric model

of the Z' -mass. The alternative left-right model yields the highest cross-section, the E_6 -model with $\sin\theta = -\sqrt{\frac{5}{8}}$ lies about a factor 5 lower. In order to establish a discovery limit for the LHC we performed a simple detector simulation assuming rapidity coverage up to $|y_{max}| = 2$ and an electron resolution of $\frac{\Delta E}{E} = \frac{0.15}{\sqrt{E}} + 0.02$. Fig.3 shows the invariant e^+e^- mass spectra from Z' (extended gauge model) and its backgrounds. All electron-pairs in a range of $\pm 2\Gamma_{tot}(Z')$ around the Z' mass peak have been included. For the analysis we used the two highest- p_T electrons of an event, irrespective of their charges. A very conservative p_T -cut of 15 GeV was applied to both electrons. No significant difference between the thus obtained experimental mass-spectra and the spectra obtained from the two opposite charge Z' -electrons in the Monte Carlo could be found. At $M(Z') = 1$ TeV we can expect more than 30,000 Z' -events per LHC year with $10^5 pb^{-1}$ integrated luminosity. If we require at least 20 $Z' \rightarrow e^+e^-$ events, the LHC has a discovery potential up to a Z' -mass of about 4 TeV. $10^4 pb^{-1}$ would yield 2 events at 4 TeV in one LHC-year. The Drell-Yan background is two orders of magnitude below the signal at all considered Z' -masses. For masses greater than 500 GeV the heavy flavour backgrounds are well below the Drell-Yan background and therefore completely negligible. For the SSC ($\sqrt{s} = 40$ TeV) the discovery limit will be about 5 TeV for one year of running with $10^4 pb^{-1}$ integrated luminosity and under the same experimental conditions.

In order to get feeling for the dependence of the discovery limit on the total width of the Z' we estimated the minimal $Z' \rightarrow e^+e^-$ cross-section required to detect a signal at a statistical significance of at least 5σ as a function of the width normalized to the mass of the Z' . Increasing the width from 3% to 20% for a 1 TeV Z' increases the minimal cross-section by less than a factor 2. An interesting possibility arises if one considers Z' -masses above 5 TeV. For these masses less than 0.1 physics background events are expected so that one event could be significant in the absence of instrumental background.

Let us now take a closer look at the experimental cuts. From the rapidity-distribution of the electrons coming from a Z' of 1 TeV mass in fig.4 it is clear that not much can be gained by extending the detector far beyond $y = 2$. The p_T -spectrum of 10000 electrons and positrons from Z' for different

Z' coupling to fermion	g_v	g_a
u	$3-8x_w$	$3-6x_w$
d	x_w	$-3x_w$
ν	$3-6x_w$	$-3+6x_w$
e	$-6+15x_w$	$-3x_w$

Table 3: Alternative left-right symmetric model

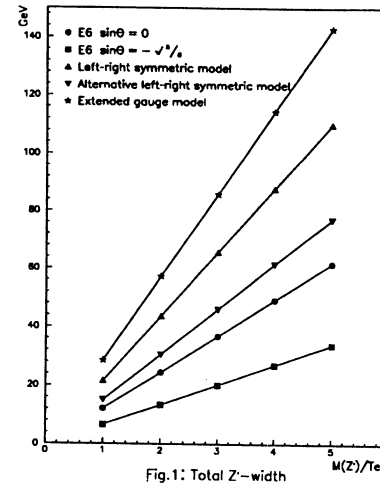


Fig.1: Total Z' -width

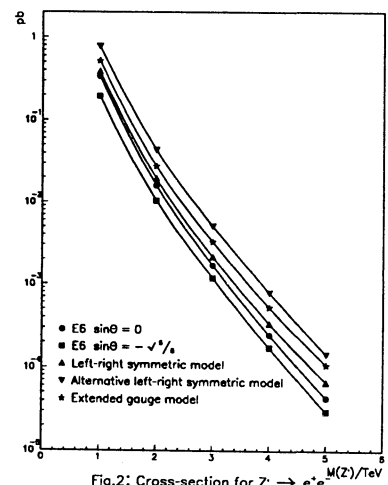


Fig.2: Cross-section for $Z' \rightarrow e^+e^-$

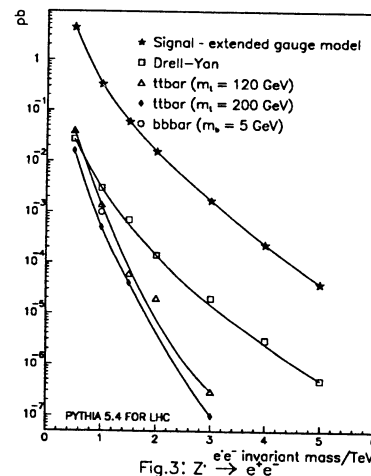


Fig.3: $Z' \rightarrow e^+e^-$

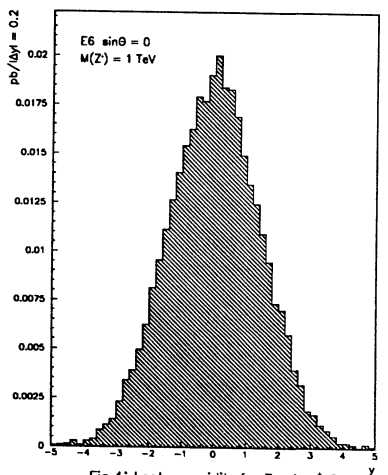
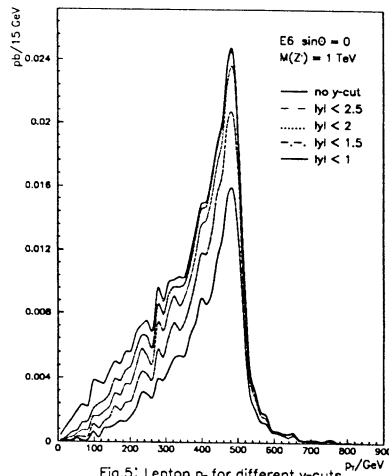
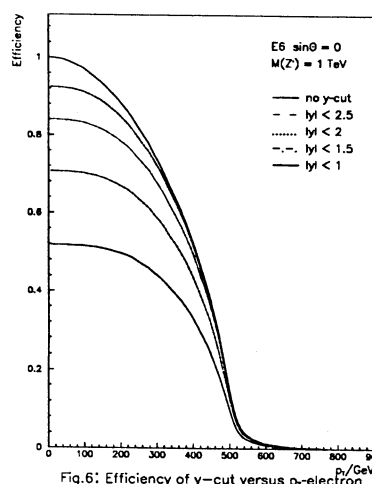


Fig.4: Lepton rapidity for $Z' \rightarrow e^+e^-$

Fig.5: Lepton p_T for different y -cutsFig.6: Efficiency of y -cut versus p_T -electron

y -cuts is plotted in fig.5. Fig.6, which shows the efficiency of the rapidity-cut as a function of the electron p_T -cut, illustrates that one can safely apply a transverse momentum cut of more than 100 GeV and at the same time have a restricted rapidity coverage $|y| < 2$ without being less than about 80% efficient in detecting the electrons and positrons from the Z' . Considering that the background calculation in fig.3 was done with a p_T -cut of 15 GeV and a y -cut of 2 one can easily see that even only slightly stricter cuts could further reduce the background. An isolation cut could also be envisaged.

In the muon channel matters seem somewhat worse. For a constant muon momentum resolution of 10%, which is maybe optimistic at high momenta, the discovery limit does not go down significantly. We also used a typical resolution of a muon toroid proposed for the LHC where the value of $\frac{\Delta P}{P}$ depends on the momentum and the θ angle of the μ . For example when $\theta = 10^\circ$, $\frac{\Delta P}{P}$ runs from 12.6% to 22.6% for muons having momenta between 100 GeV and 1000 GeV. If $\theta = 90^\circ$ it runs from 14.9% to 38%. With these assumptions one can see from fig.7 that a clear muon peak can still be detected at 1 TeV Z' mass. At 3 TeV the peak gets very broad so that we can only expect to discover a Z' up to about 3 TeV at most.

3 Forward-backward asymmetries

The rapidity dependence of the forward-backward asymmetry differs from model to model. If enough Z' -events with electron-positron invariant masses close to the Z' -mass and with large Z' -rapidities are available, distinction between the models or, at least, between different classes of models, should be easy. We will take the example of a Z' at 1 TeV mass to illustrate how many Z' will be needed to uniquely determine the Z' -couplings to fermions. With these couplings one obtains the asymmetries plotted in fig.8. Only events within $\pm 2\Gamma_{\text{tot}}$ of the Z' invariant mass peak are taken into account. The rapidity bins are 0.2 units wide. The errors are the expected errors for one year of LHC running at 10^5 pb^{-1} . Within these errors, the theoretical predictions [7], where available, agree well with the PYTHIA 5.4 data points. One can see that models that differ significantly from each other can be distinguished provided that charge determination is possible for tracks up to the TeV momentum range. It will be very difficult, if not impossible, for Z' -masses larger than about 1 TeV. For statistical reasons it seems impossible to perform off-peak asymmetry studies which could enlighten the interference of Z' and ordinary Z .

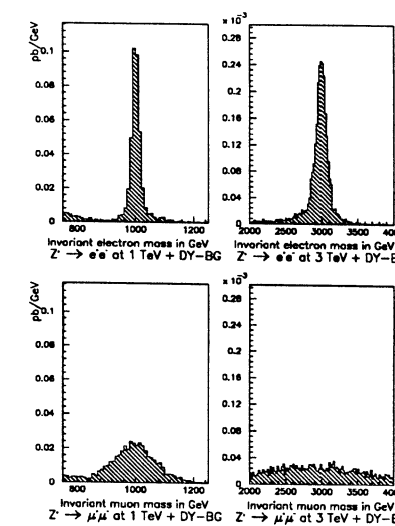


Fig.7: Inv. mass for electrons and muons

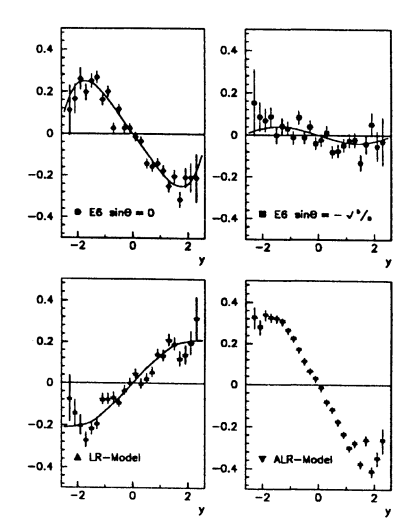


Fig.8: Forward-Backward Asymmetry

4 Conclusions

At a pp-collider with $\sqrt{s} = 16$ TeV it is possible to discover a hypothetical Z' -particle in its e^+e^- -decay channel up to a mass of about 4 TeV within one year of running at the highest luminosity. Even with very conservative experimental resolutions and cuts backgrounds are negligible. The muon channel, however, will need excellent resolution to achieve the same results.

Provided that charge can be measured with great accuracy asymmetry studies may be used to determine the correct model for Z' -production.

5 References

- [1] e.g. J.L. Hewett, T. Rizzo, Phys. Rep. 183 (1989) 193
- [2] e.g. F. Feruglio, L. Maiani, A. Masiero, Phys. Lett. 233B (1989) 512
- [3] G. Altarelli, B. Mele, M. Ruiz-Altaba, Z. Phys. C45 (1989) 109
- [4] R. Casalbuoni, P. Chiappetta, D. Dominici, F. Feruglio, G. Gatto, Nucl. Phys. B310 (1989) 181
- [5] M. Kuroda, D. Schildknecht, K.H. Schwarzer, Nucl. Phys. B261 (1985) 432
W. Baur, D. Schildknecht, K.H. Schwarzer, Phys. Rev. D35 (1987) 297
- [6] T. Sjöstrand, Int. Journ. of Mod. Phys. A3 (1988) 75 and on-line documentation of PYTHIA
- [7] F. del Aguila, M. Quiros, F. Zwirner, Nucl. Phys. B287 (1987) 419
F. del Aguila, J. Moreno, M. Quiros, these proceedings

II.4 Z' INTO JETS

Jean-Pierre Pansart

$pp \rightarrow Z' \rightarrow qq(g)$ events have been generated with the default version of PYTHIA 5.4 at $\sqrt{s} = 16$ TeV, and at Z' masses of 1 and 3 TeV/c^2 . These Z' have the same couplings to the known fermions as the ordinary Z , and no coupling to new fermions or WW pairs, giving widths of 28.5 and 95 GeV/c^2 for Z' masses of 1 and 3 TeV/c^2 respectively. An E6 Z' would have a production cross section about 3 to 5 times smaller, depending on the mixing angle. The γ^*Z' interference was included.

The particles are propagated in a central volume, and leave their energy in a pseudo-calorimeter with perfect compensation and the following resolutions:

$$\text{Electromagnetic part: } \frac{\Delta E}{E} = \frac{0.20}{\sqrt{E}} + 0.01$$

$$\text{Hadronic part: } \frac{\Delta E}{E} = \frac{0.40}{\sqrt{E}} + 0.01$$

These resolutions are very optimistic, but the aim is to show that, even with such an excellent calorimeter, the situation is difficult.

Jets are reconstructed using LUCELL (from JETSET) and another algorithm. The parameters of these algorithms were chosen to give the best results although no fine tuning was done. Both methods give very similar results, and the figures shown were obtained with LUCELL.

Fig. 1 shows the number of events obtained with an integrated luminosity of 10^{41}cm^{-2} , as a function of the mass of the 2 most energetic jets (in the pseudorapidity interval [-2.5, 2.5]). A cut has been applied to the transverse momenta of both jets, at 300 (1200) GeV/c for $M(Z') = 1 (3) \text{TeV}/c^2$ respectively. The figure also shows the QCD backgrounds, with the corresponding p_T -cuts. These backgrounds are not shown in the whole kinematical region allowed by the p_T -cuts for computation time reasons, they are just meant to give the level of the background in the interesting region.

As a check, $pp \rightarrow WZ$ events have been generated at $\sqrt{s} = 630 \text{ GeV}$. A 3% to 4% effect at jet masses of about 80 GeV/c^2 was obtained, in good agreement with the UA2 results (no fine tuning of the jet reconstruction was done, it was a first order check).

Although the QCD background is very large, an effect could be visible with an integrated luminosity of 10^{41}cm^{-2} . Nevertheless, a realistic calorimeter would lower the Z' peak by a factor 1.5, and the trigger rate with a p_T -cut of 300 GeV/c on both jets would be about 70 Hz at $L = 10^{34} \text{ cm}^{-2}\text{s}^{-1}$, which is unacceptable. Under these conditions, a Z' with 1 TeV/c^2 mass would be very difficult to observe in the jet-jet channel.

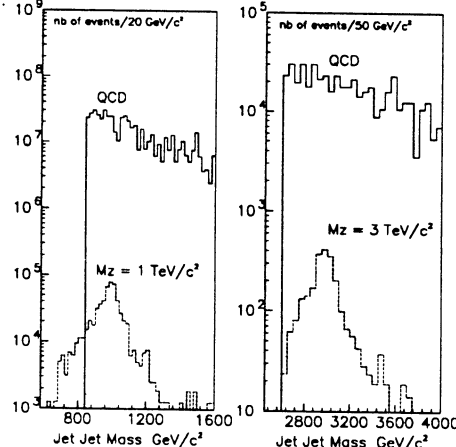


Figure 1: Jet-Jet Mass

II.5 WZ PAIR PRODUCTION IN THE LEFT-RIGHT MODELS

Contributors: D. Cocolicchio, F. Feruglio, G.L. Fogli and J. Terron

In this report we will study the production at LHC of W_R , the charged, heavy gauge vector boson of the left-right (LR) extensions [1] of the standard model (SM). In LR models parity is an exact symmetry at the lagrangian level, spontaneously broken by the vacuum expectation value of some scalar field. At the same time the presence of the right-handed neutrino ν_R , which has no counterpart in the SM, and of a suitable Higgs structure, allows for the so called see-saw mechanism [2] to occur, naturally accounting for the smallness of the left-handed neutrino masses.

As we shall see, at the LHC energies one can produce and detect a W_R with a mass up to several TeV's. As soon as the $W_L - W_R$ mixing angle is different from zero, the W_R decays into a WZ pair [3]. The study of this signature is the main topic of the present note. WZ pair production comes about in a variety of physical situations relevant to the LHC phenomenology, such as the possible presence of anomalous trilinear gauge couplings [4] or the production of technirho-like resonances [5]. In the case of the LR models, the WZ channel could be of particular interest if the ν_R is so heavy to suppress completely or in part the $e\nu_R$ decay mode.

We consider here the model based on the gauge symmetry $SU(2)_L \otimes SU(2)_R \otimes U(1)_{B-L}$, with the symmetry breaking induced by two Higgs triplets Δ_L and Δ_R , transforming as (1,0,2) and (0,1,2), respectively, and one multiplet $\Phi = (1/2, 1/2, 0)$. The following vacuum expectation values (VEVs) are assumed:

$$\langle \Delta_L^0 \rangle = v_L \quad , \quad \langle \Delta_R^0 \rangle = v_R \quad , \quad \langle \Phi \rangle = \begin{pmatrix} v & 0 \\ 0 & v' \end{pmatrix} \quad , \quad (1)$$

where $\Delta_{L,R}^0$ stands for the neutral component of the corresponding triplet. We further assume the usual hierarchy among the VEV's: $v_R \gg v, v' \gg v_L \sim 0$, which reflects the expectation $M_{W_R}, M_{Z_R} \gg M_W, M_Z$ and the absence of large deviations from the SM relation $\rho = M_W^2/M_Z^2 \cos^2 \theta = 1$. The relative size of v and v' is an important parameter of our analysis. By defining:

$$\tan \alpha = v'/v \quad , \quad (2)$$

the $W_L - W_R$ mixing angle ξ is given by:

$$|\xi| \sim |\sin 2\alpha| \left(\frac{M_W}{M_{W_R}} \right)^2 \quad . \quad (3)$$

In the following we choose to work with a positive $\sin 2\alpha$.

We first briefly discuss the limits of the model coming from the experiments. The present data require an upper bound on $|\xi|$ in the range $10^{-2} - 10^{-3}$ [6], even though the most stringent existing bounds are not free from theoretical uncertainties and/or model dependent assumptions (for a review see [7]). Fig. 1 shows the limitations coming from $|\xi| < 10^{-2}$ in the $(\sin 2\alpha, M_{W_R})$ plane. Another constraint shown in Fig. 1 comes from the measurements of M_Z at LEP and M_W/M_Z at UA2 and CDF [8], using the recent values $M_Z = 91.173 \pm 0.031 \text{ GeV}$ [9] and $M_W/M_Z = 0.8808 \pm 0.0036$ [10].

Other limitations on M_{W_R} are derived from the analysis of the $K_S - K_L$ mass difference [11]: $M_{W_R} > 1.6$ TeV, assuming the so-called manifest or pseudomanifest left-right symmetry, which implies a specific relation between the Kobayashi-Maskawa mixing matrices of the left and the right sectors. Finally, the direct search of W' at the Tevatron collider gives the bound $M_{W'} > 478$ GeV [12], looking at the conventional $e\nu$ decay channel and assuming W' couplings equal to the SM's ones.

In the present analysis we will consider the W_R in the mass range from 750 GeV up to several TeV's. The dominant production mechanism at LHC is the usual $q\bar{q}$ annihilation. If the ν_R were light, one could look for W_R decaying into $e\nu_R$. This channel, neglecting the ν_R mass, has a branching ratio (BR) of about 8%. A year (10^7 sec) run at $\sqrt{s} = 16$ TeV with a total integrated luminosity of 10^5 pb^{-1} would lead to 10 $e\nu_R$ events for $M_{W_R} = 6$ TeV*. In the following we will mainly investigate the discovery limits for a W_R through the WZ decay mode. We will also briefly comment about the W higgs (Wh) channel.

In the range of W_R masses we are considering the partial width of W_R into WZ can be well approximated by the limit of massless W and Z ,

$$\Gamma(W_R \rightarrow WZ) = \frac{g^2}{192\pi} M_{W_R} \sin^2 2\alpha \quad : \quad (4)$$

it follows that a preliminary condition to be met in order to have a sizeable WZ signal is a non vanishing and possibly not too small value of $\sin 2\alpha$. On the other hand, this requirement should not contradict the experimentally established smallness of ξ , discussed above.

M_{W_R}	750 GeV	1000 GeV	1000 GeV	2000 GeV	2000 GeV	2500 GeV
$\sin 2\alpha$	0.25	1	0.25	1	0.25	1
ξ	0.003	0.006	0.0016	0.0016	0.0004	0.001
$\Gamma_T(W_R)$ (GeV)	19.4	27	26	53	52	67
$BR(W_R \rightarrow WZ)$	0.0020	0.029	0.0019	0.027	0.0017	0.026
$BR(W_R \rightarrow Wh)$	0.0012	0.021	0.0014	0.025	0.0016	0.025
$\sigma(W_R^+)$	109 pb	37.2 pb	37.2 pb	1.9 pb	1.9 pb	0.59 pb

Table I - For the indicated values of M_{W_R} and $\sin 2\alpha$, one reads the $W_L - W_R$ mixing angle ξ , the total W_R width $\Gamma_T(W_R)$, the branching ratios into WZ and Wh (for $M_h < 200$ GeV) and the total cross section for W_R^+ production via $q\bar{q}$ annihilation at a pp collider with $\sqrt{s} = 16$ TeV. The total cross section has been evaluated with DFLM parton densities ($\Lambda_{QCD} = 260$ MeV) and a K -factor of approximately 1.25 has been included [14].

In Table I we list a number of illustrative cases realizing this compromise. From eq. (3) one sees that a large M_{W_R} already leads to acceptable ξ values,

* This number should not be taken as a discovery limit, since the $e\nu_R$ channel deserves a separate study of the appropriate experimental distributions [13].

without requiring a small value for $\sin 2\alpha$. For instance, at $M_{W_R} = 1$ TeV and $\sin 2\alpha = 1$ one has $|\xi| = 0.006$, of the order of the present upper bound. Table I shows that the largest value for $BR(W_R \rightarrow WZ)$, obtained for $\sin 2\alpha = 1$, is essentially independent from M_{W_R} and amounts approximately to 3%, which is comparable to the BR of the fermionic channels (the BR's were computed assuming a heavy ν_R , but they are not much sensitive to this assumption). Table I also shows that the production cross section for W_R^+ at $\sqrt{s} = 16$ TeV is relatively large, ranging from ~ 109 pb for $M_{W_R} = 750$ GeV, to about ~ 0.6 pb at $M_{W_R} = 2500$ GeV. For the cases considered in Table I, we can conclude that LHC, assuming an integrated luminosity of 10^5 pb^{-1} , could produce a considerable number of WZ pairs.

To further analyze the potentiality of LHC we have selected the completely leptonic decay mode ($3l + \nu$, $l = e, \mu$) of the produced WZ pair and we have studied the corresponding background. This includes an irreducible part coming from the WZ continuum electroweak production. Different production mechanisms contribute to this continuum: $q\bar{q}$ annihilation, γW and WZ fusion. Of these, the first two have been fully included in our analysis. We find that the ratio of the $q\bar{q}$ contribution to the γW one is approximately 5 to 1. The WZ contribution is estimated [5] to be comparable to the γW one.

Another source of background is the production of a $t\bar{t}$ pair, which, through its decay chain, could lead to a final state containing 3 charged leptons plus missing energy, i.e. to the signature we are looking for. This background has been studied in detail in ref. [15] in relation to the WZ production from technirho-like resonances, in kinematical configurations similar to those considered here. The conclusion of ref. [15] is that this background can be rejected at an acceptable level by imposing the constraint coming from the Z mass reconstruction, a suitable cut on the Z transverse momentum p_T^Z and the requirement of lepton isolation.

The background coming from the electroweak $q\bar{q}$ and γW continuum were generated, together with the signal, by a Montecarlo program.

		$(p_T^Z)_{cut}$	$(M_{WZ})_{cut}$	S	B	(S/\sqrt{B})
$M_{W_R} = 750$ GeV	$\sin 2\alpha = 0.25$	300	(500,1000)	166	51	23
$M_{W_R} = 1000$ GeV	$\sin 2\alpha = 1$	240	(750,1250)	1145	89	121
$M_{W_R} = 1000$ GeV	$\sin 2\alpha = 0.25$	360	(750,1250)	65	29	12.1
$M_{W_R} = 2000$ GeV	$\sin 2\alpha = 1$	420	(1750,2250)	58	3	33.6
$M_{W_R} = 2000$ GeV	$\sin 2\alpha = 0.25$	720	(1750,2250)	3	.5	4.8
$M_{W_R} = 2500$ GeV	$\sin 2\alpha = 1$	540	(2200,2800)	19	1	19

Table II - Number of $3l + \nu$ events ($l = e, \mu$) from W_R (signal S) and from the electroweak continuum $q\bar{q}$ and γW (background B) for LHC at $\sqrt{s} = 16$ TeV and $L = 10^5 \text{ pb}^{-1}$, after cuts. Only W^+Z events have been considered. S and B include a branching ratio of 0.015 for the decay of WZ into leptons of the first two generations. A common cut $|y_{W,Z}| < 2.5$ has been applied. Cuts for $(p_T^Z)_{cut}$ and $(M_{WZ})_{cut}$ are expressed in GeV. In the M_{WZ} distribution, the events outside the window indicated have been cut. No K -factor has been included.

Table II compares the signal S and the background B for the cases listed in Table I, after imposing suitable kinematical cuts. A BR of 1.5%, corresponding to the

decay of the WZ pair into leptons of the first two generations, has been included in the quoted numbers. For the cases considered in Table II we have also studied the distributions in the invariant mass M_{WZ} and in the Z transverse momentum p_T^Z . As an example in fig. 2 we show the M_{WZ} distribution for $M_{W_R} = 2$ TeV and $\sin 2\alpha = 1$. The signal appears as a very narrow peak above the electroweak continuum. This feature should be compared to the analogous distribution from a technirho-like resonance which, at least for masses larger than 1.5 TeV, usually exhibits a much broader resonant behaviour [5]. In the p_T^Z distribution, shown in fig. 3 for $M_{W_R} = 2$ TeV and $\sin 2\alpha = 1$, the signal is peaked at a very high Z transverse momentum where the background from the electroweak continuum is very small.

Taking into account the background mentioned above, discovery limits were studied in the plane ($\sin 2\alpha, M_{W_R}$), for both LHC and SSC. Fig. 4 shows the reaches of the two colliders for W_R^+ , assuming for LHC(SSC) $\sqrt{s} = 16(40)$ TeV and an integrated luminosity of $L = 10^5(10^4)$ pb $^{-1}$. We have asked for more than 15 leptonic ($3l + \nu + X$) events, explicitly checking that, by applying suitable cuts, a ratio $S/\sqrt{B} > 3$ can always be obtained. In the conditions simulated here, the reaches of the two machines are very similar. For $\sin 2\alpha = 1$ a discovery limit of 2.8 TeV on M_{W_R} could be obtained. This value drops down if lower values for $\sin 2\alpha$ are considered. For $\sin 2\alpha = 0.2$ a W_R mass of 1.5(1.2) TeV could still be tested at LHC(SSC).

Finally we add some comment about the Wh decay channel. The Φ multiplet of eq. (1) consists of two $SU(2)_L$ doublets. One linear combination of these doublets has vanishing VEV. The orthogonal one corresponds to the usual SM doublet and we identify h with the real part of its neutral component. From Table I one sees that, for a light higgs ($M_h < 200$ GeV) and a M_{W_R} in the TeV range, the $\text{BR}(W_R \rightarrow Wh)$ is similar to the $\text{BR}(W_R \rightarrow WZ)$.

Therefore a production rate comparable to the previous case is expected. However, the further identification of the Wh pair reveals much more problematic.

The signature Wjj has huge QCD and $t\bar{t}$ backgrounds. Even in the most optimistic case of $\sin 2\alpha = 1$, which maximizes also the Wh BR, we obtain a peak value for $d\sigma/dM_{Wjj}$ of approximately $2 \cdot 10^{-2}(5 \cdot 10^{-4})$ pb GeV $^{-1}$ for $M_{W_R} = 1(2)$ TeV. Assuming $m_t = 150$ GeV, the $t\bar{t}$ production leads to $d\sigma/dM_{Wjj} = 2 \cdot 10^{-2}(3 \cdot 10^{-4})$ pb GeV $^{-1}$ at $M_{Wjj} = 1(2)$ TeV [16] and is comparable to the signal. The decay $Wh \rightarrow l\nu\gamma\gamma$ could be used in the mass range $100 \text{ GeV} < M_h < 150 \text{ GeV}$, but due to the very small BR of approximately $2 \cdot 10^{-4}$, it would be effective only in extreme cases (for $M_{W_R} = 1$ TeV and $\sin 2\alpha = 1$ we get 15 events at LHC with $L = 10^5$ pb $^{-1}$). The same consideration applies to $Wh \rightarrow WZZ \rightarrow 5l + \nu$ in the range $M_h > 2M_Z$, which has a BR of approximately 10^{-4} . Finally, for $M_h > 2M_W$, the decay $Wh \rightarrow 3W \rightarrow 3l + 3\nu$ has a BR of about 10^{-2} . However, as in the WZ case, the same signature can be attributed to a non negligible fraction of the $t\bar{t}$ produced at LHC, and a detailed study of the achievable level of rejection, which goes beyond the purpose of this report, would be required.

REFERENCES

- [1] J.C. Pati and A. Salam, Phys. Rev. **D10** (1974) 275;
R.N. Mohapatra and J.C. Pati, Phys. Rev. **D11** (1975) 566 and *ibid.* 2559;
- [2] J. Senjanović and R.N. Mohapatra, Phys. Rev. **D12** (1975) 152;
G. Senjanović, Nucl. Phys. **B153** (1979) 334.
- [3] M. Gell-Mann, P. Ramond and R. Slansky, Supergravity, eds. P. van Nieuwenhuizen and D. Freedman (North-Holland, 1980); T. Yanagida, Proceedings of the Workshop on Unified Theory and Baryon Number in the Universe, eds. O. Sawada and A. Sugamoto (KEK, 1979).
- [4] N.G. Deshpande, J.A. Grifols and A. Méndez, Phys. Lett. **B208** (1988) 141; F. Feruglio, L. Maiani and A. Masiero, Phys. Lett. **B233** (1989) 512.
- [5] See the contributions by U. Baur, S. D. Willenbrock and D. Zeppenfeld, these proceedings.
- [6] R. Casalbuoni, P. Chiappetta, S. De Curtis, F. Feruglio, R. Gatto, B. Mele and J. Terron, these proceedings; A. Dobado, M. Herrero and J. Terron, these proceedings.
- [7] I.I. Bigi and J.M. Frère, Phys. Lett. **B110** (1982) 225; J. Donoghue and B.R. Holstein, Phys. Lett. **B113** (1982) 382; L. Wolfenstein, Phys. Rev. **D29** (1984) 2130.
- [8] P. Langacker and S. Uma Sankar, Phys. Rev. **D40** (1989) 1569.
- [9] D. Cocolicchio, F. Feruglio, G.L. Fogli and J. Terron, preprint CERN-TH.5909/90
- [10] F.Dydak, in Proceedings of the Twenty-Fifth International Conference in High Energy Physics, Singapore, August 1990.
- [11] L.Pondrom, in Proceedings of the Twenty-Fifth International Conference in High Energy Physics, Singapore, August 1990.
- [12] G. Beall, M. Bander and A. Soni, Phys. Rev. Lett. **48** (1982) 848. See also P. Colangelo and G. Nardulli, these proceedings.
- [13] J. Freeman, in Proceedings of the Twenty-Fifth International Conference in High Energy Physics, Singapore, August 1990.
- [14] F. Botterweck, these proceedings.
- [15] M. Diemoz, F. Ferroni, E. Longo and G. Martinelli, Z. Phys. **C39** (1988) 21.
- [16] T. Rodrigo, these proceedings.
- [17] C. Rubbia, seminar given at CERN, 2 November 1989.

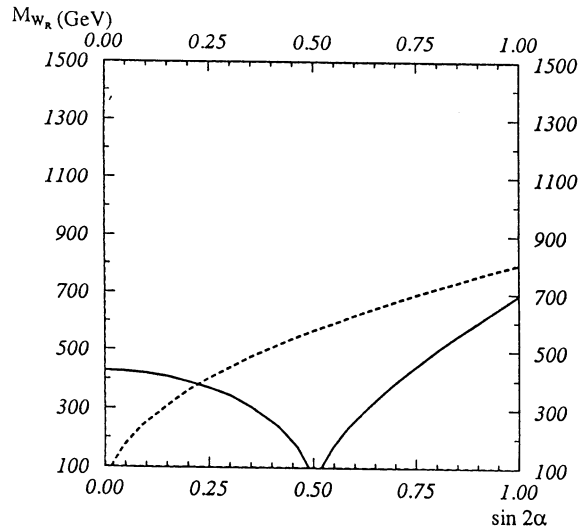


Fig 1 – Regions of the $(\sin 2\alpha, M_{W_R})$ plane allowed (above the corresponding line) from i) $|\xi| < 10^{-2}$, and ii) from the measurements of M_W/M_Z at $p\bar{p}$ colliders (UA2 and CDF experiments) and of M_Z at LEP, assuming $m_t = 150$ GeV. The two limits i) and ii) are represented by the dashed and the continuous line, respectively.

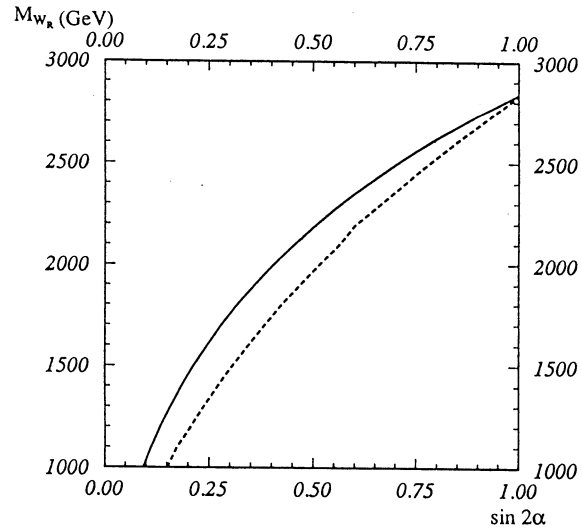


Fig 2 – Number of W^+Z pairs produced per year at LHC as a function of the WZ invariant mass M_{WZ} , for $M_{W_R} = 2$ TeV, $\sin 2\alpha = 1$ and an integrated luminosity of 10^5 pb^{-1} . The lower continuous line represents the background from $q\bar{q}$ and γW and the upper one is the sum of signal and background. For the cuts applied see Table II.

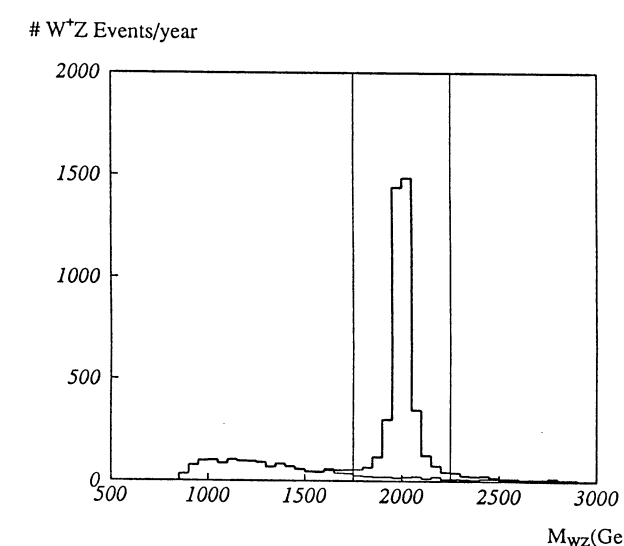


Fig 3 – Number of W^+Z pairs produced per year at LHC as a function of the Z transverse momentum p_T^Z , for $M_{W_R} = 2$ TeV, $\sin 2\alpha = 1$ and an integrated luminosity of 10^5 pb^{-1} . The lower continuous line represents the background from $q\bar{q}$ and γW and the upper one is the sum of signal and background. For the cuts applied see Table II.

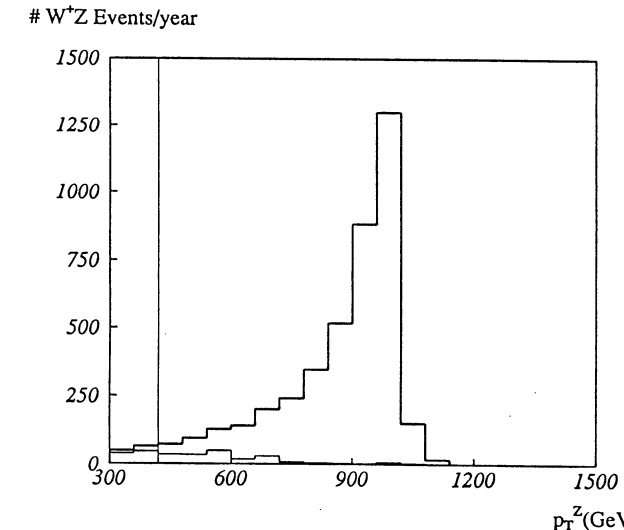


Fig 4 – Discovery limits of the W_R^+ in the WZ channel at LHC ($\sqrt{s} = 16$ TeV, $L = 10^5 \text{ pb}^{-1}$) (continuous line) and SSC ($\sqrt{s} = 40$ TeV, $L = 10^4 \text{ pb}^{-1}$) (dashed line). The region under the curves corresponds to more than 15 leptonic ($3l + \nu$, $l = e, \mu$) events with $S/\sqrt{B} > 3$.

II.6 PRODUCTION OF W_R AND W_I BOSONS FROM SUPERSTRING-INSPIRED E_6 MODELS

CONTRIBUTORS: F. AVERSA, S. BELLUCCI, P. CHIAPPETTA and M. GRECO

We study now the production of two gauge bosons, W_R and W_I , associated with the low-energy groups arising from the breaking of E_6 superstring. The first model is the so-called alternative left-right model (ALRM), where the normal bounds on the W_R mass do not apply, as in the standard $SU(2)_L \times SU(2)_R \times U(1)_{L-R}$ model, because of the absence of mixing with the usual W_L . In the second model the additional $SU(2)_I$ subgroup of E_6 which is obtained at relatively low energy has generators that commute with the electric charge [1]. The corresponding flavour-changing non hermitian gauge bosons W_I , W_I^\dagger couple the conventional fermions to their exotic partners of the 27 representation of E_6 . For both models we only focus on the flavour changing bosons W_R and W_I production and our results, reported in greater detail in ref. [2], show the similarity of the expected effects from the two classes of models, with discovery limits up to masses of 1.2 – 2.5 TeV, for both *SSC* and *LHC* colliders. We also compare with previous studies of the production cross sections and, in particular, we get larger results than those obtained in ref. [3].

Within the context of all possible left-right symmetric realizations of the E_6 superstring, the quantum numbers of the ALRM are uniquely determined from assigning the usual fermions $(\nu_e)_L$, e_L , d^c_L to that part of the 27 representation which transforms as a 10 under $SO(10)$ and a 5 under $SU(5)$, whereas the exotic counterpart of these fields, i.e. the heavy fermions $(\nu_E)_L$, E_L , h^c_L , are assigned to the (16, 5) term in the decomposition of the 27 of E_6 into $SO(10)$ and $SU(5)$ subgroups. Then, in this model, the W_R has negative R -parity and nonvanishing lepton number. This means that there cannot be any mixing of the W_R with the usual W_L . The W_R boson does not couple to the d^c_L quark nor the ν^c field. Hence, the usual arguments from low-energy phenomena do not constrain the mass of the charged W_R boson of the ALRM model. The W_R is coupled instead to the h^c_L leptoquark and the n field, in addition to the usual u^c_L and e^c particles. The coupling of W_R to fermions reads

$$\mathcal{L} = \frac{1}{\sqrt{2}} g_R W_R^\mu \left(\bar{h}^c \gamma_\mu u^c_L + \bar{E}^c \gamma_\mu \nu_L + \bar{e}^c \gamma_\mu n_L + N \bar{e}^c \gamma_\mu e_L \right) + h.c..$$

where $g_R = g_L = g$, denoting the usual $SU(2)_L$ coupling constant. The exotic fermions h , E , N_E and the boson W_R obtain masses from the same scale. These particles are heavy compared to the n mass, which is expected to be of a few GeV order. This fact has important consequences for the W_R decay modes. The dominant W_R production mechanisms are $g + u \rightarrow W_R^+ + h$ and $g + \bar{u} \rightarrow W_R^- + \bar{h}$. Note that the quantum numbers of W_R and the conservation of R -parity imply that the production of W_R from $u\bar{d}$ scattering in hadronic collisions cannot take place. The production of W_R -pairs via the decay of a Z' is forbidden as well, owing to kinematical reasons, i.e. $2M_{W_R} > M_{Z'}$. Finally, production of the W_R boson via $u\bar{h}$ scattering is suppressed, owing to the smallness of the h , \bar{h} sea.

Our results are reported in Fig. 1, where have used the distribution functions from ref. [4] with $\Lambda_{QCD} = 160$ MeV. The parton densities of Duke and Owens [5] with $\Lambda_{QCD} = 200$ MeV, lead to results differing by less than 10% from those plotted in Fig. 1. Note that with a typical branching ratio (BR) of about 1%, obtained by estimating the individual BR for the h and W_R particles into an observable final state to be of order 10%, we can give discovery limits for the W_R mass. Assuming the minimum value for the observed cross-section at *LHC* to be $\sigma_{obs} \sim 10^{-4} pb$, then the W_R^+ could be detected up to a mass of about 2 – 2.5 TeV, and the W_R^- would be observable in the range below $M_{W_R^-} = 1 - 1.5$ TeV (see Fig. 1), depending on the leptoquark mass. The W_R discovery limits at *SSC* with a luminosity of order $10^{33} cm^{-2} sec^{-1}$ are not dramatically higher than those given above for *LHC* with luminosity of about $10^{34} cm^{-2} sec^{-1}$. This is summarised in Table 1. We substantially agree with the results of ref. [6].

Next, we turn our attention to the possible final state signatures. The decay modes of the leptoquark h depend on the superpotential. If the N_e^c is given negative R -parity, then the possible final state signatures are [6]: jet + $l^+ l^- + \bar{\nu}_T$, jet + $e^- + \bar{\nu}_T$, obtained from the decay modes: $h \rightarrow d + \bar{\nu}$, $h \rightarrow u + \bar{e}^-$, which dominate, in the assumption that sleptons are much lighter than squarks. If one assigns positive

R -parity to the N_e^c , then the decay $h \rightarrow d + \bar{N}_e$ is also possible. The W_R decay modes depend on the mass of the n . This is expected to be smaller than the mass scale of the W_R , h , E and N_E by at least one order of magnitude [6,8]. Hence, the largely dominant decay mode is expected to be $W_R^+ \rightarrow e_L^+ + n_R$, with an estimated branching ratio for this mode larger than 10%. This yields the possible final state signatures: $W_R^+ \rightarrow e^+ + \gamma + \bar{\nu}_T(\tilde{\gamma})$, if the *LSP* is, for example, the photino $\tilde{\gamma}$ and the n decays before leaving the detector, or $W_R^+ \rightarrow e^+ + \bar{\nu}_T(n)$, if n is a mass eigenstate and either it is the *LSP* and hence it is stable, owing to R -parity conservation, or it has a mean-life long enough to escape the detector before it decays. Clearly the mixing of n with $\tilde{\gamma}$ and the remaining neutralinos is needed. Combining the h -decay and the W_R -decay gives rise to a final state with a very large invariant mass. Taking $M_{W_R} = 2$ TeV, together with the experimental value $M_{W_L} = 80$ GeV, one gets $\Gamma_{tot}(W_R) = 62$ (144) GeV for $n_g = 0$ (3).

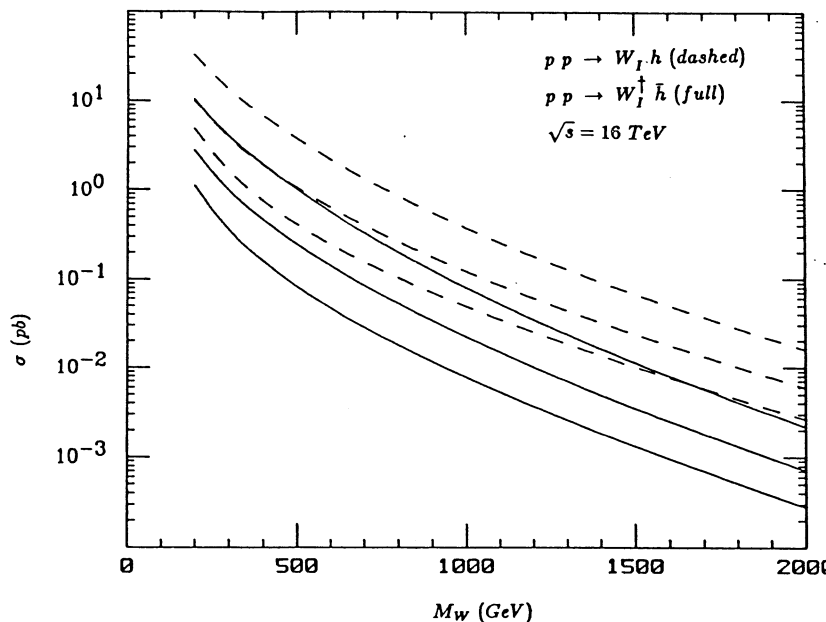
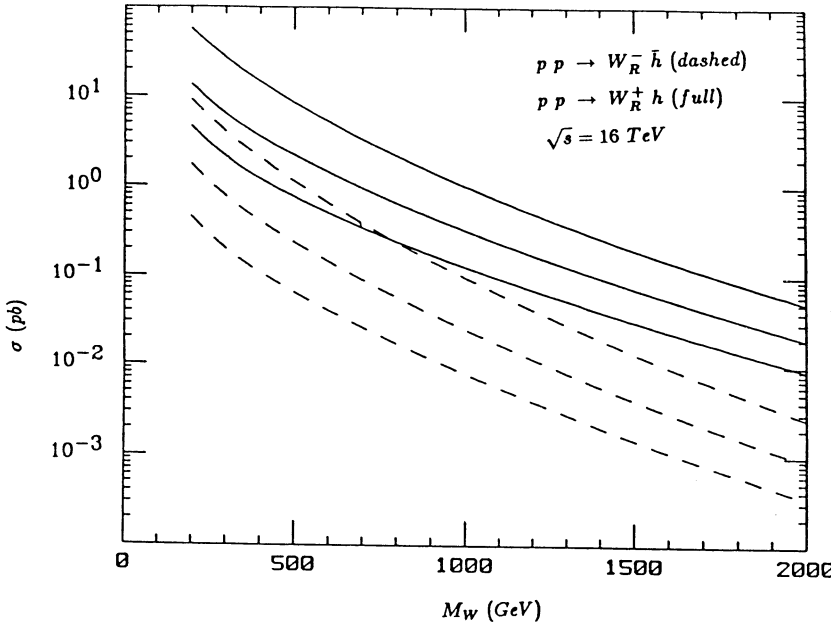
We consider now the flavor-changing gauge boson W_I arising from the $SU(2)_L \times U(1)_Y \times SU(2)_I$ model [3]. The dominant W_I production mechanisms are $g + d \rightarrow W_I + h$ and $g + \bar{d} \rightarrow W_I^\dagger + \bar{h}$. As it is easier to find a d -quark, rather than a \bar{d} -quark in the proton, we expect for the production cross-sections $\sigma(W_I) > \sigma(W_I^\dagger)$. This is clearly seen in our explicit numerical results which also confirm the similarity of the results for W_I production with the cross-section for W_R (see Fig. 2). The signature of the final state is obtained combining the decay of the leptoquark with the decay of the W_I boson, as in the previous case of W_R production. The decay of h proceeds in the same way, whereas the decay of W_I yields several charged leptons, in addition to missing p_T originating from photons and neutrinos, in the final state. Using an estimated BR of 1%, we get the discovery limits for the flavor-changing gauge bosons summarized in Table 1. We find that, at both hadron colliders, W_I will be observable up to a mass of 1.5-2 TeV, whereas for W_I^\dagger the discovery limit is given by a mass of about 1-1.5 TeV, depending on the leptoquark mass.

	W_R^+	W_R^-	W_I	W_I^\dagger
LHC	2 - 2.5 TeV	1 - 1.5 TeV	1.5 - 2.2 TeV	1 - 1.5 TeV
SSC	2.5 - 3 TeV	1.2 - 2 TeV	2 - 2.5 TeV	1.2 - 2 TeV

Table 1

References

- [1] D. London and J.L. Rosner, Phys. Rev. D34 (1986) 1530; J.L. Rosner, Comments Nucl. Part. Phys. 15 (1986) 195.
- [2] F. Aversa, S. Bellucci, P. Chiappetta and M. Greco, Preprint LNF-90 /081(PT) to appear in Phys. Lett. B.
- [3] T.G. Rizzo, Phys. Rev. D38 (1988) 71.
- [4] M. Diemoz, F. Ferroni, E. Longo and G. Martinelli, Z. Phys. C39 (1988) 27.
- [5] D. Duke and J. Owens, Phys. Rev. D30 (1984) 49.
- [6] J.F. Gunion, J.L. Hewett, E. Ma and T.G. Rizzo, Int. J. Mod. Phys. A2 (1987) 1199.
- [7] V. Barger, N.G. Deshpande and J.F. Gunion, in Proceedings of the Summer Study on the Physics of the Superconducting Super Collider, Snowmass, Colorado, 1986, eds. R. Donaldson and J. Marx (New York, 1987)
- [8] E. Ma, Phys. Rev. D36 (1987) 274; D.S. Babu, X-G. He and E. Ma, ibid. 878.



APPENDIX:Limits on the W_R mass and on the mixing angle

Contributors: P.Colangelo and G.Nardulli

The most stringent limit on the W_R mass arises from the $K_L - K_S$ mass difference Δm_K , where, in addition to the usual box diagram describing the short distance contribution to Δm_K , one gets an additional term with exchanges of a W_L and a W_R . By assuming that the matrix element of the left-right effective Hamiltonian does not exceed the Standard Model prediction one obtains

$$8\beta \left| \left(1 + \ln \frac{m_c^2}{M_L^2} \right) \frac{c_1 \mathcal{M}_{LR}^1 + c_2 \mathcal{M}_{LR}^2}{\eta \mathcal{M}_{LL}} \right| \leq 1 \quad (1)$$

where $\beta = (M_L/M_R)^2$, m_c is the charm mass, η , c_1 , c_2 are QCD coefficients ($\eta \simeq 1$, $c_1 \simeq 1.2$, $c_2 \simeq 0.08$) and

$$\mathcal{M}_{LR}^1 = \langle \bar{K}^0 | O_{LR}^1 | K^0 \rangle = \langle \bar{K}^0 | \bar{s}(1 - \gamma_5) d | K^0 \rangle \quad (2)$$

$$\mathcal{M}_{LR}^2 = \langle \bar{K}^0 | O_{LR}^2 | K^0 \rangle = \langle \bar{K}^0 | \bar{s}\gamma^\mu(1 - \gamma_5) d | K^0 \rangle \quad (3)$$

$$\mathcal{M}_{LL} = \langle \bar{K}^0 | O_{LL} | K^0 \rangle = \langle \bar{K}^0 | \bar{s}\gamma^\mu(1 - \gamma_5) d | K^0 \rangle \quad (4)$$

A recent evaluation of these matrix elements [1] by using three-point function QCD Sum Rules gives the results that are reported in Table I together with the vacuum saturation approximation (VSA) results.

Table I

	VSA	QCD Sum Rules
$\mathcal{M}_{LR}^1 (\text{GeV}^4)$	10.0×10^{-2}	$(2.0 \pm 0.7) \times 10^{-2}$
$\mathcal{M}_{LR}^2 (\text{GeV}^4)$	-8.0×10^{-2}	$-(2.0 \pm 0.7) \times 10^{-2}$
$\mathcal{M}_{LL} (\text{GeV}^4)$	1.7×10^{-2}	$(1.7 \pm 0.7) \times 10^{-2}$

The result of this analysis is that, whereas in the case of the left-left operators the vacuum saturation approximation seems to work well, no enhancement of the left-right operators as predicted by the factorization (VSA) hypothesis is found. In other terms the three matrix elements \mathcal{M}_{LR}^1 , \mathcal{M}_{LR}^2 , \mathcal{M}_{LL} have comparable sizes when computed by QCD sum rules.

The limit for W_R mass obtained using Eq.(1) is:

$$M_R \geq 700 \text{ GeV}. \quad (5)$$

This limit holds for the economic model of pseudo-manifest left-right symmetry, where the Kobayashi-Maskawa matrices for left and right handed sectors: U_L and

U_R are related: $U_L = U_L K^*$, where K is a diagonal unitary matrix. In more general models one can obtain less stringent limits, but only for a limited range of parameters [3].

There are a few other processes that give limits on M_R : $B^0 - \bar{B}^0$ mixing, b decays, neutrinoless double β decays; however, the bounds obtained by these processes are less stringent than Eq.(5).

W_L and W_R can mix together by an angle ζ to form mass eigenstates W_1 and W_2 :

$$\begin{aligned} W_L^\pm &= \cos \zeta W_1^\pm - \sin \zeta W_2^\pm \\ W_R^\pm &= e^{i\omega} (\sin \zeta W_1^\pm + \cos \zeta W_2^\pm). \end{aligned} \quad (6)$$

There are several constraints on ζ . From the theoretical bound [4]

$$|\zeta| \leq (M_1/M_2)^2 \quad (7)$$

and from Eq.(5) one obtains $|\zeta| \leq 10^{-2}$. Limits of the same size come from weak universality [5] and from $K_{\pi 3}$ decay [6], provided the CP-violating phases in U_R are large. On the other hand, for small phases, one gets for $|\zeta|$ an upper limit of 2.5×10^{-3} [3].

REFERENCES

- [1] P. Colangelo and G.Nardulli, Report BARI TH/90-67, to appear in Phys. Lett. B.
- [2] G. Beall, M. Bander and A. Soni, Phys. Rev. Lett. **48** (1982) 848.
- [3] P. Langacker and S. Uma Sankar, Phys. Rev. **D40** (1989) 1569.
- [4] E. Masso, Phys. Rev. Lett. **52** (1984) 1956.
- [5] L. Wolfenstein, Phys. Rev. **D29** (1984) 2130.
- [6] J.F. Donoghue and B.R. Holstein, Phys. Lett. **B113** (1982) 382.

II.7 W' SIGNAL AND BACKGROUND AT LHC

F.Botterweck

1 Introduction

Presented here is a feasibility study for W' production at LHC energies. The theoretical aspects of W' as well as Z' are already extensively discussed in these proceedings. The model used in this work is the Extended Gauge model of Altarelli et al. as described in ref. [1], and as implemented in the Pythia Monte Carlo by T.Sjöstrand [2]. Because of the difficulties expected in detecting hadronic decay channels of W' (very high luminosity and event pile up), in this work only leptonic channels are studied. In this analysis the electron decay channels are chosen. Switching to muons does not affect the branching ratios, but requires different detector smearing simulation.

The W' channels and their backgrounds are the following:

- the one electron channel $W' \rightarrow e\nu$ with background from $W \rightarrow e\nu$ and from the heavy top decay $t\bar{t} \rightarrow (Wb)X \rightarrow (e\nu b)X$.
- the three electron channel $W' \rightarrow WZ \rightarrow (e\nu)(ee)$ where the continuum background $WZ \rightarrow (e\nu)(ee)$ and the top decay chain $t\bar{t} \rightarrow (Wb)(Wb) \rightarrow (e\nu e\nu)(e\nu b)$ play an important role.

Before studying the processes in more detail, some remarks on the assumptions made in this analysis are listed in the next sections.

2 Detector aspects and general remarks

All processes have been studied under internally agreed assumptions on detector acceptance and smearing.

- Acceptance in pseudorapidity η is assumed to be $-2 < |\eta| < 2$, for all particles.
- The electron resolution has been assumed to be $\Delta E/E = 0.15/\sqrt{E} + 0.02$.
- For the missing energy, reconstructed from the unsmeared momentum of the "detected" particles, $\Delta E/E = 0.7/\sqrt{E}$ has been used.

Cross sections have been converted to event rates assuming a luminosity $\mathcal{L} = 10^{34} \text{ cm}^{-2} \text{ s}^{-1}$. This is equivalent to $\mathcal{L} = 10^5 \text{ pbarn}^{-1} \text{ year}_{\text{LHC}}^{-1}$ (with a year of 10^7 seconds of running).

The top quark mass is chosen to be $120 \text{ GeV}/c^2$. This allows a top-hadron to decay into a real W and a bottom-hadron. The electron coming from the leptonic W decay is then as isolated as one originating from the W' . So, the single electron background cannot be reduced by applying an isolation cut. On the other hand it is shown that the three electron background from $t\bar{t}$ can be almost eliminated, since one of the electrons has to come from b -hadron decay. This electron will be surrounded by other particles, and can usually not fulfill the isolation requirement.

The Monte Carlo programs used are Pythia5.4 with Jetset7.3.

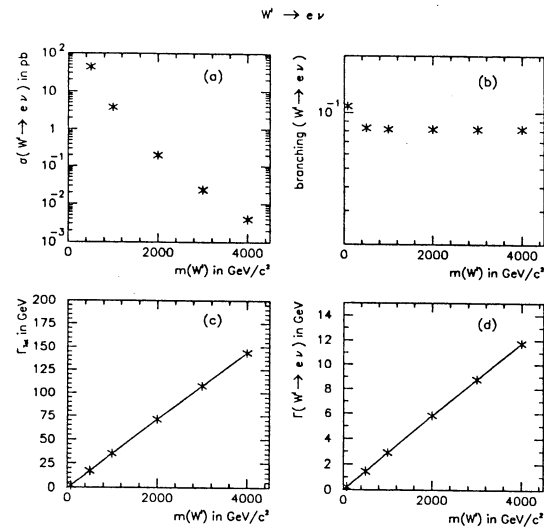


Figure 1: (a) : cross section times branching ratio, (b) : branching ratio, (c) : total and (d) : partial width as a function of the W' mass.

3 The process $p\bar{p} \rightarrow W' \rightarrow e\nu$

In figure 1 some W' characteristics are summarized. It is worthwhile noting that even for a very heavy W' ($4 \text{ TeV}/c^2$) the event rate is still 400, in the case of the high luminosity option for LHC. Furthermore it can be verified from figure 1 c and d that the total (and partial) width of the W' (first point) lies nicely on the straight line connecting the W' data. This is a consequence of the fact that in the Extended Gauge model the W' and Z' couple in the same way to leptons as the W and Z in the Standard Model.

3.1 Efficiency of η and p_T cuts

Since the detector has limited acceptance, and it may be necessary to apply transverse momentum cuts on electrons, it is instructive to look at the signal loss caused by these limitations. The efficiency as function of a minimum transverse electron momentum has been calculated, as follows:

$$\text{Eff}(p_T^{\min}) = \int_{p_T^{\min}}^{\infty} \frac{d\sigma}{dp_T} dp_T / \int_0^{\infty} \frac{d\sigma}{dp_T} dp_T. \quad (1)$$

Of all electrons in an event only the one with the largest p_T has been taken. No cut on missing momentum has been applied, but it should be noted that in the next section we do cut on missing p_T , so the efficiency will be lower there, as we shall see. The efficiency is shown in figure 2 as a function of p_T^{\min} for a W' of $500 \text{ GeV}/c^2$ and $1 \text{ TeV}/c^2$, for 4π detection, with and without standard rapidity cut. It is encouraging to see that even after a $200 \text{ GeV}/c$ cut about 80 % of the signal remains for the 1 TeV W' . Also the limited η region does not reduce the signal too much. The heavier the W' the better the efficiency, but for a light W' ($m = 500 \text{ GeV}/c^2$) the efficiency drops to 40 % for a minimum electron p_T of $200 \text{ GeV}/c$.

3.2 The backgrounds considered

As already mentioned in the introduction, there are two serious background sources. The most obvious one is $W \rightarrow e\nu$. Since it is now generally assumed that the top quark mass should be at least 120

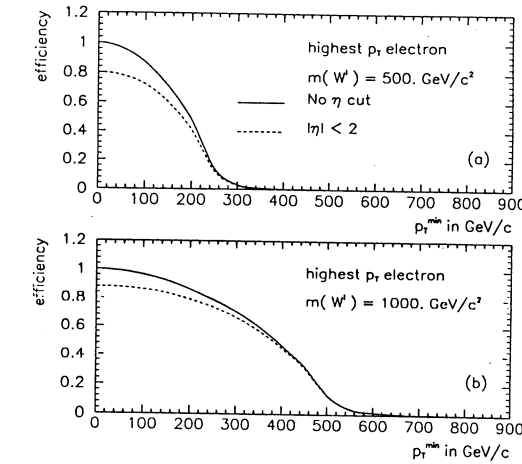


Figure 2: Efficiency as a function of minimum electron p_T , for mass of W' as indicated.

GeV/c^2 , this means that a top hadron decays into a real W and a bottom hadron. At LHC energies, the production cross section for a $t\bar{t}$ pair is rather large (5.8 nb , Pythia5.4), so the background coming from an electron of one of the W 's, is non-negligible. Electrons coming from the b-hadrons have not been considered, since they will be surrounded by many particles, and are not isolated, so can be easily cut out.

Generating $t\bar{t}$ background turned out to be (computer)time consuming. To speed up the procedure, each generated $t\bar{t}$ event has been used ten times for further decay. In addition to that, several runs have been performed with different initial kinematical cuts (the invariant mass of the $t\bar{t}$ pair, and the range of allowed p_T of hard $2 \rightarrow 2$ processes *) to be able to reach the outer regions of phase space (which otherwise could be reached only by generating orders of magnitude more events). Finally the distributions of these runs have been combined, such that in each interval of e.g. transverse mass, only the statistically most relevant sample is taken. This yields as envelope the dotted line as shown in figure 3. For the $W \rightarrow e\nu$ background the same trick of kinematical cuts has been applied and also in that case each distribution is an envelope of many different ones. In figure 3 a the differential cross section as a function of the transverse mass of the electron and the missing momentum is shown. The numbers on top of the nice Jacobian peaks of the signal indicate the mass of the W' . The backgrounds are also shown, and it is clear that a light W' suffers severely from $t\bar{t}$ production. The importance of the other background, $W \rightarrow e\nu$, grows with $m_{W'}$ compared to $t\bar{t}$, but for the heavier W' 's there is no serious background problem anymore, as shall become clear from the numbers in table 1. In this table 1 the following is listed :

The mass of the W' , the production cross section times branching ratio ($\sigma \cdot BR$) and the latter after the standard cut $|\eta| < 2$ (indicated by $\sigma_{|\eta| < 2}$). The expected numbers of events per pbarn per LHC year ($\mathcal{L} = 10^{34} \text{ cm}^{-2} \text{ s}^{-1}$) are listed, for signal, as well as for both backgrounds. The indicated transverse mass cut is the value where the largest background signal cuts the W' signal. In addition a transverse momentum cut is applied, indicated by $+p_T > 100$. This cut holds for the electron and the missing transverse momentum. For the $2, 3$ and 4 TeV W' masses, the signal, nor background changes when a p_T cut is applied, so here only one row is presented.

*variables CKIN(1) and CKIN(3) in Pythia5.4 see [2]

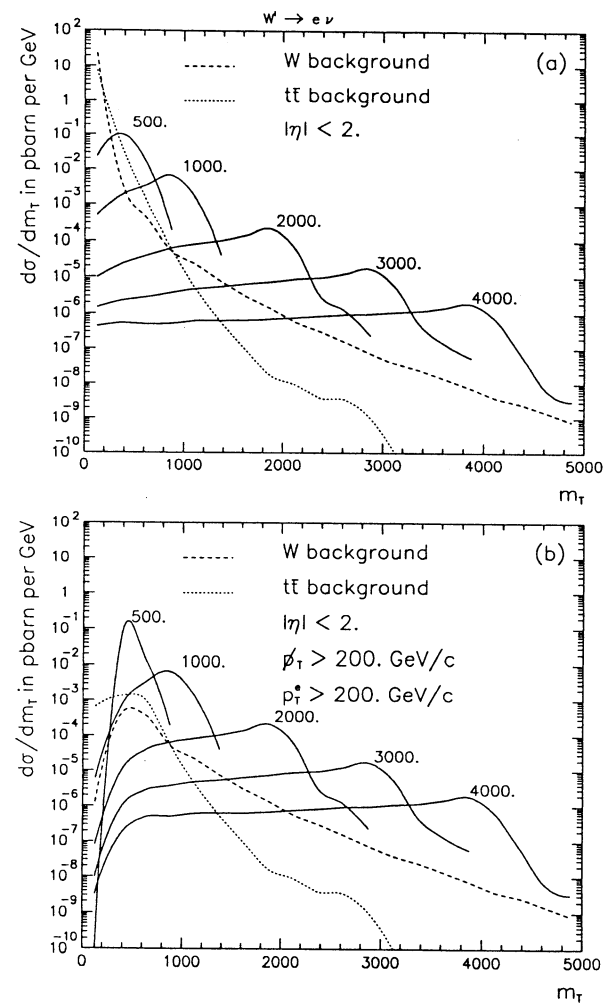


Figure 3: Signal and Backgrounds for a: only η cut, b: η cut plus p_T cuts as indicated.

$m_{W'} = 500 \text{ GeV}/c^2$	$\sigma \cdot BR = 43.1 \text{ pb}$	$\sigma_{ \eta <2} = 34.5 \text{ pb}$	
$m_T > 300$	# $W' \rightarrow e\nu$	# $W \rightarrow e\nu$	# $t\bar{t}$
	$25.6 \cdot 10^5$	$0.519 \cdot 10^5$	$4.85 \cdot 10^5$
$+p_T > 100$	$25.6 \cdot 10^5$	$0.516 \cdot 10^5$	$4.34 \cdot 10^5$
$+p_T > 200$	$14.8 \cdot 10^5$	$0.208 \cdot 10^5$	$0.60 \cdot 10^5$
$m_{W'} = 1000 \text{ GeV}/c^2$	$\sigma \cdot BR = 3.68 \text{ pb}$	$\sigma_{ \eta <2} = 3.34 \text{ pb}$	
$m_T > 550$	# $W' \rightarrow e\nu$	# $W \rightarrow e\nu$	# $t\bar{t}$
	$2.66 \cdot 10^5$	$8.4 \cdot 10^3$	$1.61 \cdot 10^4$
$+p_T > 100$	$2.66 \cdot 10^5$	$8.4 \cdot 10^3$	$1.60 \cdot 10^4$
$+p_T > 200$	$2.65 \cdot 10^5$	$8.4 \cdot 10^3$	$1.53 \cdot 10^4$
$m_{W'} = 2000 \text{ GeV}/c^2$	$\sigma \cdot BR = .196 \text{ pb}$	$\sigma_{ \eta <2} = .183 \text{ pb}$	
$m_T > 900$	# $W' \rightarrow e\nu$	# $W \rightarrow e\nu$	# $t\bar{t}$
	$1.57 \cdot 10^4$	$1.35 \cdot 10^3$	$3.26 \cdot 10^2$
$m_{W'} = 3000 \text{ GeV}/c^2$	$\sigma \cdot BR = 0.0239 \text{ pb}$	$\sigma_{ \eta <2} = 0.0222 \text{ pb}$	
$m_T > 1450$	# $W' \rightarrow e\nu$	# $W \rightarrow e\nu$	# $t\bar{t}$
	$1.74 \cdot 10^3$	$1.63 \cdot 10^2$	$3.59 \cdot 10^2$
$m_{W'} = 4000 \text{ GeV}/c^2$	$\sigma \cdot BR = 0.0039 \text{ pb}$	$\sigma_{ \eta <2} = 0.0036 \text{ pb}$	
$m_T > 2000$	# $W' \rightarrow e\nu$	# $W \rightarrow e\nu$	# $t\bar{t}$
	$2.49 \cdot 10^2$	30.	.5

Table 1: Event rates for signal and background at one year running with $\mathcal{L} = 10^{34} \text{ cm}^{-2} \text{ s}^{-1}$.

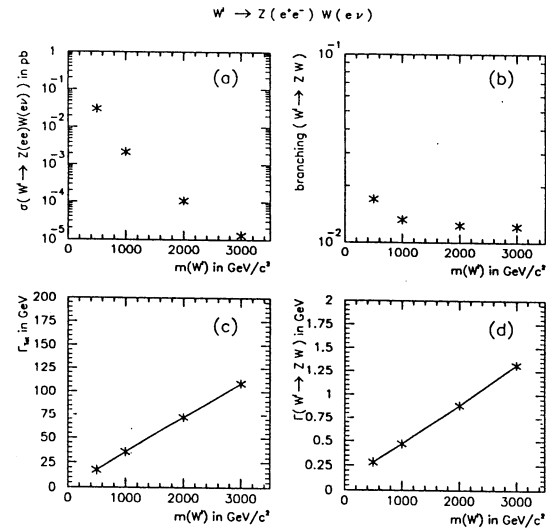


Figure 4: (a) : cross section times branching ratio, (b) : branching ratio, (c) : total and (d) : partial width as function of W' mass.

4 The process $p\bar{p} \rightarrow W' \rightarrow WZ \rightarrow (e\nu)(ee)$

From a comparison of figure 1 and figure 4 it can be concluded that there is much less signal in this channel. A 500 GeV W' still gives 3000 events in an LHC-year, but it decreases rapidly with the increasing mass, and a 2 TeV W' triggers only 10 times. It should be stressed that in the study of this channel, the charge of the leptons has not been used, so when speaking about electrons, both electrons and positrons are meant.

4.1 Efficiency of η and p_T cuts

Also for the 3 electron channel the efficiency has been plotted as a function of the p_T of the 3 highest p_T electrons. From figure 5 b it can be seen that more than 20% of the signal is lost after the rapidity cut for a W' mass of $1 \text{TeV}/c^2$. On the other hand, the loss due to an electron p_T cut of 25 GeV/c (which turns out to be a severe cut for the background) is negligible. For a W' mass of 500 GeV/c^2 the efficiency after applying the same cuts is only about 60 %.

4.2 The backgrounds

It has been mentioned previously that there are two important backgrounds. The WZ continuum producing three electrons is a clear case and needs no further explanation. The $t\bar{t}$ case is more difficult since there are many ways to obtain 3 electrons. Considered here is only the decay chain :

$$t\bar{t} \rightarrow W^+ (\rightarrow e^+ \nu) b (\rightarrow e^- \bar{\nu}) c W^- (\rightarrow e^- \bar{\nu}) \bar{b} (\rightarrow X) \quad (2)$$

Thus, only one electron comes from a b-hadron. The reason for leaving out the other possibilities, is that a cut on isolation would kill them anyway.

The electron isolation can be defined as the sum over the p_T of all particles within a cone ΔR of 0.2 around the electron (the latter not used):

$$\sum_{\Delta R < 0.2} p_T < 5 \text{ GeV}/c \quad (3)$$

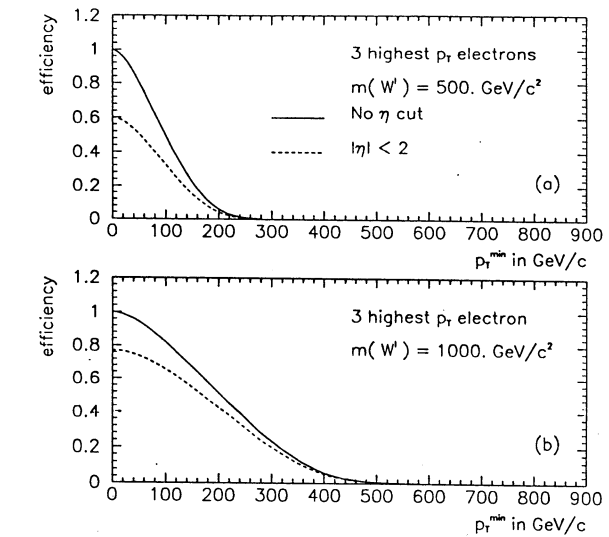


Figure 5: Efficiency as a function of minimum electron p_T for W' masses as indicated.

$$\Delta R = \sqrt{\Delta\phi^2 + \Delta\eta^2}. \quad (4)$$

Another way to get rid of the $t\bar{t}$ background, is to look at the invariant mass of all three two electron combinations. If the pair with mass closest to the Z mass does not lie in the interval:

$$m_Z - 3 \cdot \Gamma_{\text{Tot}}(Z) < m_{ee} < m_Z + 3 \cdot \Gamma_{\text{Tot}}(Z) \quad (5)$$

the event is rejected. This puts an enormous constraint on $t\bar{t}$ events, while the W' signal, and the WZ background are hardly affected. In figure 6 the differential cross section is plotted as a function of p_T^Z . In all cases the "Z" momentum is reconstructed from the electron pair with mass closest to the Z mass. It is clear from figure 6 that the $t\bar{t}$ background is enormous when no cuts are applied, but that it drastically decreases after the electron p_T cut and the invariant mass cut. The numbers corresponding to the different cuts can be found in table 2. In each successive line the quoted cut is applied in addition to that of the previous lines. Thus in the fifth line all above mentioned cuts are applied. The cut on the invariant "Z" mass is clearly not sufficient to get rid of the background. It's influence on $t\bar{t}$ background is large as can be expected, but not enough to kill it. The extra cut on the electron p_T is a good choice for both backgrounds, but the situation can be improved by imposing the isolation cut, and in addition a cut on the p_T of the "Z". The value of the p_T^Z cut is chosen in the same way as has been done for the transverse mass cut in table 1.

5 Conclusion

From tables 1 and 2 it can be seen that both channels are worthwhile studying, though for high mass W' 's the leptonic decay channel is the only possibility. Background is in both cases far less than the signal.

References

- [1] G.Altarelli, B.Mele, M.Ruiz-Altaba ,Z.Phys. C45 (1989) 109
- [2] T.Sjöstrand : Int.Journ.of Mod.Phys. A3 (1988) 75 and Pythia54 and Jetset73 on-line manual.

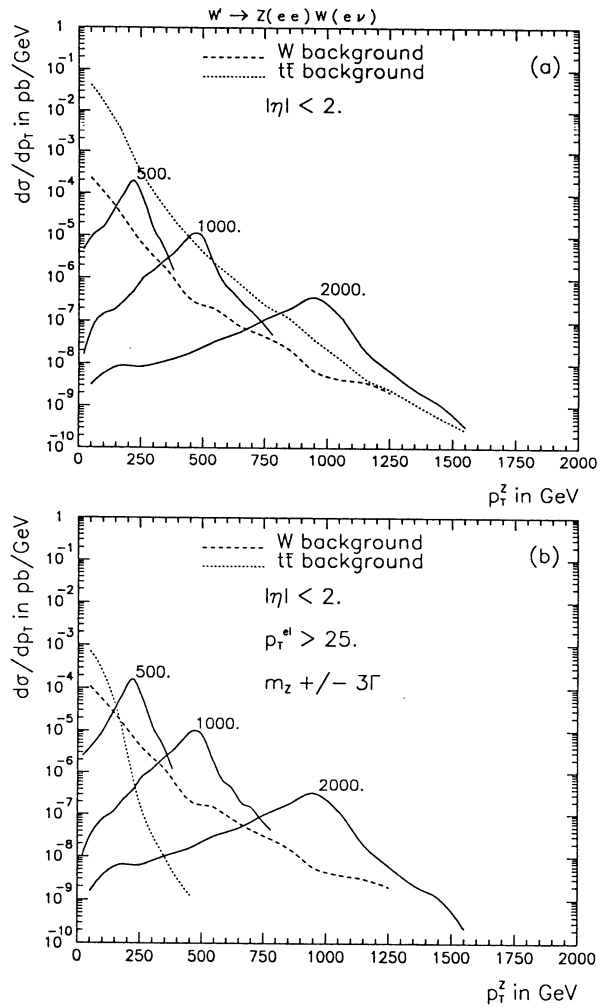


Figure 6: Signal and backgrounds for cuts as indicated.

$m_{W'} = 500. \text{ GeV}/c^2$	$\sigma \cdot BR = 0.030 \text{ pb} \quad \sigma_{ \eta <2} = 0.0181 \text{ pb}$		
cuts:	# $W' \rightarrow WZ$	# WZ	# $t\bar{t}$
$ \eta < 2.$	$1.81 \cdot 10^3$	$2.85 \cdot 10^3$	$4.76 \cdot 10^5$
$+ m_Z \pm 3 \cdot \Gamma$	$1.64 \cdot 10^3$	$2.55 \cdot 10^3$	$6.29 \cdot 10^4$
$+ p_T^e > 25$	$1.40 \cdot 10^3$	$1.41 \cdot 10^3$	$7.42 \cdot 10^3$
+isolation	$1.36 \cdot 10^3$	$1.38 \cdot 10^3$	132
$+ p_T^Z > 160$	1200	110	-

$m_{W'} = 1000. \text{ GeV}/c^2$	$\sigma \cdot BR = 0.0022 \text{ pb} \quad \sigma_{ \eta <2} = 0.0017 \text{ pb}$		
cuts:	# $W' \rightarrow WZ$	# WZ	# $t\bar{t}$
$ \eta < 2.$	167	$2.85 \cdot 10^3$	$4.76 \cdot 10^5$
$+ m_Z \pm 3 \cdot \Gamma$	149	$2.55 \cdot 10^3$	$6.29 \cdot 10^4$
$+ p_T^e > 25$	143	$1.41 \cdot 10^3$	$7.42 \cdot 10^3$
+isolation	137	$1.38 \cdot 10^3$	132
$+ p_T^Z > 320$	127	12	-

Table 2: Event rates for signal and background at one year running with $\mathcal{L} = 10^{34} \text{ cm}^{-2} \text{ s}^{-1}$.

III. NEW VECTOR BOSONS FROM ALTERNATIVE SYMMETRY BREAKINGS

III.1 PRODUCTION OF VECTOR BOSONS IN THE BESS MODEL

Contributors: R.Casalbuoni, P.Chiappetta, M.C.Cousinou, S.De Curtis, F.Feruglio and R.Gatto

1. The BESS model

Aim of this report is to study the production at LHC [1] of vector resonances arising from a strongly interacting electroweak sector. The production mechanism is $q\bar{q}$ annihilation followed by the leptonic decays $V^0 \rightarrow \ell^+\ell^-$ and $V^\pm \rightarrow \ell^\pm\nu$. The BESS model has been fully described in refs. [2,3]. It describes vector resonances V , which are bound states of a strongly interacting sector and somewhat analogous to ordinary ρ vector mesons of strong interactions or to the techni- ρ of technicolor theories [4]. We will only recall here the physical meaning of the parameters of the BESS model. The theory describes 6 massive gauge bosons (W^\pm, Z, V^\pm, V^0) and the photon. Besides the ordinary gauge coupling constants g and g' there is an additional coupling g'' . The bosons V mix with W and Z , the mixing angles being of the order of g/g'' . The V particle is coupled to fermions through mixing, but in addition there may be a direct coupling specified by the parameter b . A complete list of the couplings of mass eigenstates to quarks and leptons can be found in ref. [3].

Table I : Total width and branching ratio of V^0 boson for several values of BESS parameters

$(M_V(\text{GeV}), g'', b)$	$\Gamma_{\text{tot}}(\text{GeV})$	$\text{BR}(V^0 \rightarrow \ell^+\ell^-)$	$\text{BR}(V^0 \rightarrow W^+W^-)$
(500,6.5,-0.02)	2.4	0.0175	0.703
(500,13,-0.02)	1.5	0.035	0.286
(500,6.5,0)	1.9	$0.77 \cdot 10^{-2}$	0.895
(500,13,0)	0.48	$0.76 \cdot 10^{-2}$	0.897
(1000,6.5,-0.02)	48.1	$0.17 \cdot 10^{-2}$	0.969
(1000,13,-0.02)	14.1	$0.75 \cdot 10^{-2}$	0.841
(1000,6.5,0)	47.6	$0.62 \cdot 10^{-3}$	0.991
(1000,13,0)	12.1	$0.61 \cdot 10^{-3}$	0.992
(1500,6.5,-0.02)	343	$0.36 \cdot 10^{-3}$	0.993
(1500,13,-0.02)	89.8	$0.18 \cdot 10^{-2}$	0.962
(1500,6.5,0)	345	$0.13 \cdot 10^{-3}$	0.998
(1500,13,0)	87.7	$0.13 \cdot 10^{-3}$	0.998

The parameter space is given by (g, g', v, M_V, g'', b) . Since the first three parameters are known from (α_{em}, G_F, M_Z) we are left with (M_V, g'', b) . Present LEP 1 data [5] combined with CDF/UA2 [6] M_W/M_Z measurements restrict the allowed region in the plane $(b, g/g'')$ for M_V fixed. In Fig. 1 we show the allowed region, for $m_t = 150 \text{ GeV}$, $\alpha_s = 0.12$ and $M_V = 1.5 \text{ TeV}$, as coming from

the LEP data which are more restrictive for the BESS model: $\Gamma_h = 1764 \pm 16 \text{ MeV}$, $\Gamma_Z = 2496 \pm 16 \text{ MeV}$, and from the weighted average from CDF and UA2: $(M_W/M_Z)^2 = 0.773 \pm 0.006$. The allowed domain depends weakly from the top mass in the range $100 \leq m_t \leq 200 \text{ GeV}$ and from M_V . For increasing values of m_t , α_s , and M_V , the allowed region shifts towards the left part of the figure and gets slightly enlarged. We have focused on some illustrative sets of parameters for M_V ranging from 0.5 TeV to 2 TeV , g'' from 6.5 to 13 , and b from -0.02 to 0.00 , well inside the present allowed domain. Future LEP data for unpolarized beams will put the value $b = -0.02$ closer to the border of physical region if no deviations from standard model expectations will be observed.

For heavy V bosons the dominant branching ratios are $V^0 \rightarrow W^+W^-$ and $V^\pm \rightarrow W^\pm Z$ in analogy with $\rho \rightarrow \pi\pi$. As an illustration we give in Table I the total width and several branching ratios for V^0 particle. Since the fermionic branching ratios are smaller than in Standard Model by roughly one to two orders of magnitude the production rates will be depressed compared to gauge boson pair production. Nevertheless since the process $pp \rightarrow W^+W^- + X$ is expected to suffer from a very severe background coming from $pp \rightarrow t\bar{t} + X$ because $m_t > M_W$, the discovery of V^0 from lepton pair production is a priori the cleanest channel.

2. V production

At hadron colliders lepton pair production from a V resonance is described by a $q\bar{q}$ mechanism at Born level. The expressions for the differential cross section $d\sigma/(dm dy d\cos\theta^*)$ where m is lepton pair mass, y its rapidity and θ^* the scattering angle of the lepton in the partonic center of mass frame and for its parity conserving, σ^{pc} , and parity violating parts, σ^{pv} , were given in ref. [7]. Effects due to soft gluon radiation from partonic legs were taken into account through the K factor (see ref. [8]) leading to an increase of the Born cross section by roughly 25% for a scale of about 1 TeV . The two observables we will study are the mass dependence of lepton pair production and the rapidity dependence of forward backward asymmetry [7]. The background due to γ^* and Z has been taken into account. The contribution from $t\bar{t}$ production is smaller than the previous background for $m > .8 \text{ TeV}$ [9] and therefore ignored. We fix $g'' = 13$ and choose two values for $b : b = -0.02$ and $b = 0$. The range of M_V values explored runs from 500 GeV to 2 TeV . The assumed parameters for LHC are $\sqrt{s} = 16 \text{ TeV}$ with a luminosity of $10^{34} \text{ cm}^{-2} \text{ sec}^{-1}$ and for SSC $\sqrt{s} = 40 \text{ TeV}$ with a luminosity of $10^{33} \text{ cm}^{-2} \text{ sec}^{-1}$. Typically a cross section of 10^{-5} pb corresponds to 1 event/year at LHC. In our calculation we have used the DFLM set of structure functions [10] for $\Lambda = 160 \text{ MeV}$. Another choice of structure functions like EHLQ [11] or DO1 [12] would affect our results by less than 10%, also the results are not very sensitive to the precise choice of Λ . The Pythia Monte Carlo [13] is used to generate samples of signal and background. A rough simulation of the calorimeter allowing a detailed study of statistical significance both at LHC and SSC is described elsewhere in this book [14].

We give in Fig. 2 the differential cross section $d\sigma/dm$ for three values of V masses : $.5, 1$, and 1.5 TeV . For $b = 0$ (dashed curves) the presence of V resonance of 500 GeV manifests as a narrow peak in $d\sigma/dm$ (since $\Gamma_V < 1 \text{ GeV}$), whereas for $M_V = 1 \text{ TeV}$ one just observes a small bump around the mass of resonance. The presence of a V boson of 1.5 TeV is not visible. The case $b = -0.02$ (full curves) is more favourable since, as could have been inferred from Table I, the couplings to fermions are enhanced. A discovery limit of 1.5 TeV seems reachable. One can

also show that at SSC energy with planned luminosity of $10^{33} \text{ cm}^{-2} \text{ sec}^{-1}$ the LHC discovery limit is not increased.

Due to the smallness of the V^0 width below the TeV scale, compared to the mass resolution of the calorimeter, it is not possible to detect a V^0 boson lighter than 1 TeV . For $b = 0$ the production rate above 1 TeV is too small to observe a signal over Standard Model background. For $b = -0.02$ the discovery limit both at LHC and SSC energies is around 1.5 TeV . For $b = -0.01$ a signal is still observable for $M_V = 1 \text{ TeV}$.

We have done numerical calculations of the forward-backward asymmetry $A_{FB}(y)$ for a number of cases. Already for $M_V = 1 \text{ TeV}$, even for negative b , the deviations from standard γ^* and Z production in $A_{FB}(y)$ appear too small to be detected. Only for such low masses as $M_V = 0.5 \text{ TeV}$, $A_{FB}(y)$ comes out to sensibly deviate, at large rapidities, from Standard Model expectations ($\approx 25\%$ for $y \approx 2$ when $M_V = 0.5 \text{ TeV}$, $g'' = 13$ and $b = 0$).

We have studied also V^+ and V^- production followed by the leptonic decays $V^\pm \rightarrow e^\pm \nu$. The observable we deal with is the transverse momentum distribution of the lepton $d\sigma/dP_T^l$. The processes $pp \rightarrow V^+, V^-$ are generated in Pythia Monte Carlo and the decay modes $V^\pm \rightarrow e^\pm \nu_e$ selected. The relevant backgrounds are the tail of inclusive W production, $pp \rightarrow t\bar{t}$, $pp \rightarrow WW$ and $pp \rightarrow \gamma^*, Z$. As can be inferred from Table II the number of events per year expected for a charged V of 1 TeV is small due to the smallness of fermionic couplings. The calculations have been done for LHC for $M_V = 1 \text{ TeV}$, $g'' = 13$, and several b values and it turns out that the discovery of V^\pm from leptonic final state is very difficult. Although we have not tried more appropriate cuts the best channel for V^\pm discovery seems to remain $pp \rightarrow W^\pm Z \rightarrow l^\pm \nu l^+ l^-$ allowing for a discovery limit of 2.5 TeV [15], as illustrated in Fig. 3.

Table II : Total width and branching ratios of V^+ boson for $M_V = 1 \text{ TeV}$ and $g'' = 13$

b	$\Gamma_{V^+} (\text{GeV})$	$BR(V^+ \rightarrow e\nu)$	$BR(V^+ \rightarrow ud)$	$BR(V^+ \rightarrow WZ)$
0	12.5	$0.62 \cdot 10^{-3}$	$0.18 \cdot 10^{-2}$	0.993
-0.01	12.4	$0.57 \cdot 10^{-3}$	$0.17 \cdot 10^{-2}$	0.993
-0.02	13.9	$0.51 \cdot 10^{-2}$	$0.15 \cdot 10^{-1}$	0.938

3. Discussion and conclusions

In conclusion, discovery of V at LHC or SSC through its production and subsequent decay into lepton pairs appears problematic if there is no direct coupling of V to fermion pairs. The situation is however quite different if there is a small direct coupling to fermions as allowed by present LEP and CDF/UA2 data, and also by future precision measurements at LEP with unpolarized beams assuming no deviation emerges from the Standard Model within the foreseen experimental accuracies. For the small direct couplings we find here a discovery limit for the mass of the V^0 around 1.5 TeV after detector simulation. On the other hand, as far as V^\pm production is concerned, the WZ pair production channel, extensively studied in [15], looks much more promising than the leptonic final state discussed in this note, leading to a discovery limit of about 2.5 TeV .

REFERENCES

- [1] Large Hadron Collider in the LEP Tunnel, ed. G. BRIANTI et al. CERN 84/10.
- [2] R. Casalbuoni, S. De Curtis, D. Dominici and R. Gatto, Phys. Lett. B155 (1985) 95 ; Nucl. Phys. B282 (1987) 235.
- [3] R. Casalbuoni, P. Chiappetta, D. Dominici, F. Feruglio and R. Gatto, Nucl. Phys. B310 (1988) 181.
- [4] S. Weinberg, Phys. Rev. D13 (1976) 974; D20 (1979) 1277; L. Susskind, Phys. Rev. D20 (1979) 2619; S. Dimopoulos and L. Susskind, Nucl. Phys. B155 (1979) 237; E. Fahri and L. Susskind, Phys. Rep. 74 (1981) 277.
- [5] F. Dydak, Summary Talk at Singapore Conference, Singapore, August 1990.
- [6] L. Pondrom, Summary Talk at Singapore Conference, Singapore, August 1990.
- [7] R. Casalbuoni, P. Chiappetta, M.C. Cousinou, S. De Curtis, F. Feruglio, R. Gatto, Preprint CPT-90/P.2429, UGVA/DPT 1990-08-690.
- [8] P. Chiappetta, T. Grandou, M. Le Bellac and J.L. Meunier, Nucl. Phys. B207 (1982) 251.
- [9] C.E. Wulz and V. Cavasinni, these proceedings.
- [10] M. Diemoz, F. Ferroni, E. Longo and G. Martinelli, Z. Phys. C39 (1988) 21.
- [11] E. Eichten, I. Hinchliffe, K. Lane and C. Quigg, Rev. Mod. Phys. 56 (1984) 579 ; Erratum Rev. Mod. Phys. 58 (1986) 1065.
- [12] D.W. Duke and J.F. Owens, Phys. Rev. D30 (1984) 49.
- [13] T. Sjostrand, Int. Journ. of Mod. Phys. A3 (1988) 75.
- [14] P. Chiappetta and M.C. Cousinou, these proceedings.
- [15] R. Casalbuoni, P. Chiappetta, S. De Curtis, F. Feruglio, R. Gatto, B. Mele, J. Terron, Phys. Lett. B249 (1990) 130.

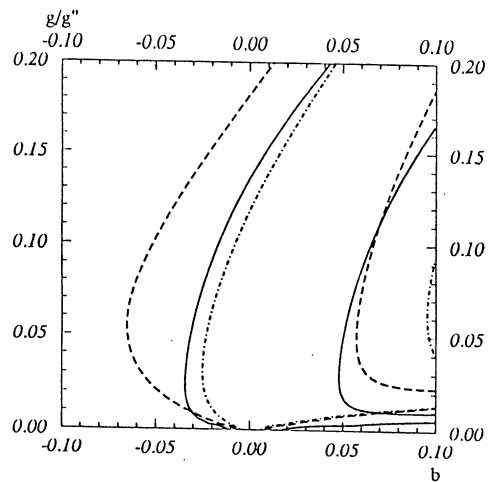


Fig. 1 - Allowed region (90% C.L.) in the $(b, g/g'')$ plane for $M_V = 1500 \text{ GeV}$, $m_t = 150 \text{ GeV}$ and $\alpha_s = 0.12$ from M_W/M_Z (continuous line), Γ_Z (dashed line) and Γ_h (dashed-dotted line).

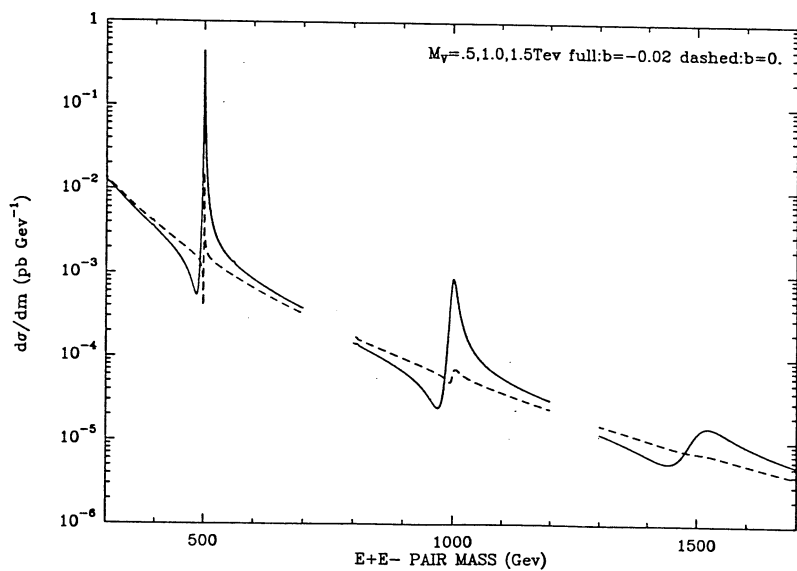


Fig. 2 - Invariant mass distribution of lepton pairs at LHC for $M_V = 0.5, 1.0$ and 1.5 TeV . Full curves : $b = -0.02, g'' = 13$. Dashed curves : $b = 0, g'' = 13$

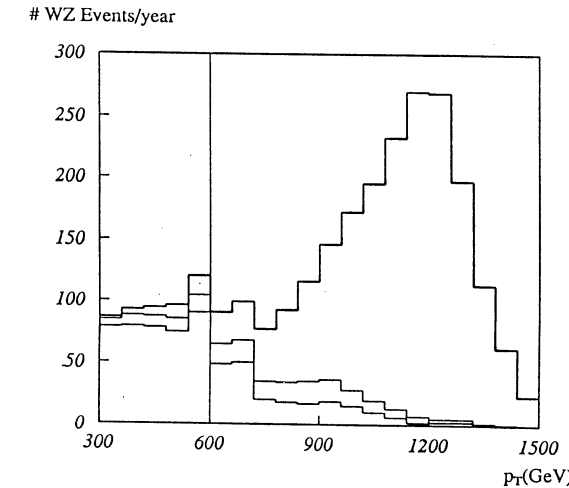


Fig. 3 - $(p_T)_Z$ distribution from $W^+Z + W^-Z$ pairs produced per year at LHC for $M_V = 2.5 \text{ TeV}$, $g/g'' = 20$ and $b = -0.01$ for a luminosity of $10^{34} \text{ cm}^{-2} \text{ sec}^{-1}$. The applied cuts are : $|y_{W,Z}| < 2.5, (p_T)_Z > 600 \text{ GeV}$ and $M_{WZ} > 1800 \text{ GeV}$. The lower, intermediate and higher histograms refer to the background, background plus fusion signal and background plus fusion signal plus $q\bar{q}$ annihilation signal, respectively.

III.2 ISOSCALARS AND EXCITED BOSONS AT LHC

Contributors :J.L. Kneur and G. Moultaka.

Although recent results from LEP I¹⁾ are in impressive agreement with the electroweak standard theory predictions, theoretical motivations to go beyond the standard model (SM) remain as strong as ever. Various present theoretical considerations (supersymmetry, substructure²⁾,...) have all in common a strong prejudice that "something new" might happen around the Fermi scale ($\Lambda_F \simeq 300$ GeV). This is indeed one of the motivations, apart from standard Higgs search, to construct very high energy hadron colliders (LHC, SSC,...) able to reach the multi-TeV scale in the parton CM frame.

Effective models for the $Y(Y_L)$ ³⁾ and W^* ⁴⁾ have been constructed in the framework of vector dominance (VD)⁵⁾, in analogy with the $\omega, \phi, \rho, \rho^*$...vector mesons of strong interactions. In the single W -dominance model^{3,6)}, the essential difference with the SM is that one starts from a basic $SU(2)_{WL}$ invariant theory, broken down explicitly to $U(1)_{em}$ via the mixing of the photon with the neutral W_3 member of the $SU(2)_{WL}$ triplet. One can also obtain the Yang-Mills structure for the W self-interactions as a consequence of VD^{5,6)}, and the effective Lagrangian coincides with the $SU(2)_L \times U(1)_Y$ SM Lagrangian in the unitary gauge, but without a Higgs scalar. This picture is then supplemented essentially by either γ - Y mixing in the $Y(Y_L)$ model, or γ - W_3^* mixing in the W^* model. Possible signatures and some phenomenological properties of the $Y(Y_L)$ and W^* models have been discussed several years ago^{4,7)}. However, some extensions of these studies, as well as an up-dating of existing constraints on parameters of these models, taking into account the recent LEP precision measurements, is at present necessary. Discovery limits of the Y and Y_L particles at the LHC will be significantly improved, (compare ref.7).

The $Y(Y_L)$ model.

The coupling of the isoscalar boson to the hypercharge current ($j_{\mu R}^Y$) can be either vector (Y -boson), or chiral (Y_L -boson)³⁾. The Y_L case would correspond to a composite scenario where right-handed fermions remain elementary, and thus a direct, pointlike coupling of the (primordial) photon a_μ to $j_{\mu R}^Y$ is necessary in order to recover consistently vector QED. In both Y and Y_L cases, the mixing with a_μ and the (VD) requirement imply

$$g_W \lambda_W = e = g_Y \lambda_Y , \quad (1)$$

where g_W and g_Y are the (initial) couplings of W and Y to fermions, λ_W and λ_Y being the mixing strengths of the photon respectively to W^3 and $Y(Y_L)$. A mass m_W for the degenerate $SU(2)_L$ triplet W_μ^i and m_Y for the isoscalar Y_μ are also introduced, such that the mixing in the neutral sector is to be diagonalized, leading to the neutral mass eigenvalues $M_Y = 0$, M_{Z_0} and M_Y . Diagonalization also implies that the physical Y -boson couples to W^+W^- due to the initial $W^3W^+W^-$ coupling in the W non-Abelian kinetic term. The form of the YW^+W^- coupling is thus of the Yang-Mills type, with its precise strength fixed by the diagonalization. Note that there is no YZZ , $Y\gamma\gamma$ or $YZ\gamma$ couplings, from $SU(2)$ local invariance. Similarly it is straightforward to derive the physical Y and Y_L couplings to fermions $Y(Y_L)f\bar{f}$ resulting from diagonalization.

Before studying possible signatures, it is important to clearly determine the freedom in the 5-parameter space introduced so far. Actually only λ_Y and m_Y are free parameters, whereas g_W , λ_W and m_W are kept at their SM values, (ex. $\lambda_W^2 \equiv \sin^2\theta_W$). Now there are constraints on λ_Y and M_Y from present (or near future) data. At LEP 1 the lower bound on the Y_L mass ranges from 400 GeV to 600 GeV^{8,13)}, depending on the unknown value of the parameter λ_Y^2 . The same conclusion applies for the Y model, but only for $\lambda_Y^2 \leq 0.6$. We will take these mass lower bounds as a starting point for our study at LHC. One should also note that LEP 2 will give impressive limits on isoscalars composite bosons. For Y_L (as shown in fig.1 taken from ref.13) the bounds are beyond 1 TeV over the full λ_Y^2 range whereas for Y boson the bounds depend strongly on the mixing parameter but can reach a few TeV.

Now the recent precision measurements of the Z_0 mass and $\sin^2\theta_W$ at LEP I¹⁾ yield an upper bound on λ_Y as a function of M_Y , that we have systematically taken into account in our analysis. For illustration, we get $\lambda_Y^{2,max} \simeq 0.34(0.70)$ for $M_Y \simeq 800$ GeV(3 TeV). Also the Y and Y_L fermionic couplings actually increase for small λ_Y , and consequently there exists lower bounds on

λ_Y (for given M_Y), coming essentially from the present constraints on the neutral-current (NC) parameters $\delta\rho$ (≤ 0.02 ¹⁾) and C (≤ 0.01 ⁹⁾). For M_Y above $\simeq 800$ GeV, those lower bounds are not very sensitive to M_Y , and lie into the range $0.05 - 0.01$ for $M_Y \simeq 800$ GeV to a few TeV, respectively⁷⁾.

As a first hint of the possible signatures of these models, we have computed the various allowed decay modes. We give in fig. 2a, 2b the resulting branching ratios for Y and Y_L respectively, as a function of λ_Y^2 for fixed M_Y . One can see that the production of W^+W^- pairs from Y or Y_L is largely suppressed, and becomes competitive with the fermionic decays only for large values of $\lambda_Y^2 > 0.5$, which however could be reached only if M_Y is sufficiently large, according to the upper bounds $\lambda_Y^{max}(M_Y)$ discussed above. Moreover, the SM $t\bar{t}$ background to W^+W^- production¹⁰⁾ dominates largely the isoscalar signal by a factor of 20 on the resonance (for a top of 100 GeV). In contrast, the Drell-Yan process $q\bar{q} \rightarrow Y(Y_L) \rightarrow \mu^+\mu^-$ is a particularly promising way of revealing such particles at the LHC or SSC. An important property which is not clearly reflected in fig. 2a,b because of the ratios, is that the fermionic decays are very sensitive to λ_Y . Both Y and Y_L fermionic couplings are large for small λ_Y (i.e. strong g_Y), but for large λ_Y (i.e. $\simeq \lambda_Y^{max}(M_Y)$) one finds that the Y coupling to fermions is very small compared to the Y_L one. This different behaviour of Y and Y_L for large λ_Y is essentially due to the additional direct coupling of the photon to $j_{\mu R}^Y$ in the Y_L case, which leads through diagonalization to a large non-vanishing Y_L fermionic coupling even for small $g_Y = e/\lambda_Y$.

We have thus studied¹¹⁾ the $\mu^+\mu^-$ invariant-mass distribution $d\sigma/dm(q\bar{q} \rightarrow Y(Y_L) \rightarrow \mu^+\mu^-)$ at LHC energy, as a function of M_Y and λ_Y in the relevant range. For most λ_Y values one obtains prominent non-standard signals, with net resonance peaks. When requiring the Y or Y_L signals (integrated over an energy bin of $\Delta E = 20$ GeV around the peak, and for a one-year integrated luminosity of $\mathcal{L} = 10^3 pb^{-1}$) to exceed by 20 events the SM background, we got the mass discovery limits of Y and Y_L given in Table 1 (together with the discovery limit of the W^* -model, to be discussed next). These limits reflect the differences between Y and Y_L : the highest limit ($M_Y \simeq 4.1$ TeV) is obtained for small λ_Y in the Y case, due to the corresponding large g_Y coupling, while in the Y_L case, $M_Y \simeq 4.3$ TeV is reached for $\lambda_Y = \lambda_Y^{max}(M_Y) \simeq 0.73$, due to the net increase of the $Y_L \rightarrow u\bar{u}$ branching ratio with λ_Y (see Fig. 2a). However it is interesting to note that the discovery limits are not as much sensitive to λ_Y as expected, since e.g. the Y_L discovery limit varies between $M_Y \simeq 3.8$ TeV to $M_Y \simeq 4.3$ TeV in the allowed λ_Y range. In Table 1 we also give for comparison the corresponding discovery limits at the SSC (for $\mathcal{L} = 10^4 pb^{-1}$). Finally, we briefly mention the interesting possibility, to be discussed in details elsewhere¹¹⁾ of distinguishing Y and Y_L by studying the forward-backward $A_{FB}(y)$ asymmetry as a function of the rapidity y , which is very sensitive to λ_Y only in the Y_L case. For illustration, some values of $\Delta A_{FB}(y) \equiv A_{FB}(y) - A_{FB}^{SM}(y)$ are given for a few typical λ_Y^2 values in Table 2.

The W^* model.

The W^* would correspond to the first radial excitation of the weak W -triplet in composite models. The essential difference with the Y -model is that VD takes a different form due to the $SU(2)_L$ -triplet nature of such an excited state. Accordingly W^* couples to the weak isospin fermionic current j_μ^3 with a strength g_W^* , and after introducing an arbitrary γ - W^* -mixing λ_{W^*} , the VD requirement takes the form

$$g_W \lambda_W + g_{W^*} \lambda_{W^*} = e . \quad (2)$$

Comparing to the Y case, where the VD requirements (1) gave two constraints on the parameters, with (2) we end up with six intrinsic parameters $\{g_W, \lambda_W, m_W, g_W^*, \lambda_{W^*}, m_{W^*}\}$, where m_{W^*} is the mass of the initially degenerate W^* -triplet. To reduce further this parameter space, it has been assumed⁴⁾ a duality¹²⁾ relation, in analogy with the known strong interaction dynamics, which give the additional constraint

$$\lambda_{W^*} = \lambda_W \frac{m_W}{m_{W^*}} . \quad (3)$$

Another essential difference with the Y -model is that all charged and neutral-current parameters satisfy "sum rules" like (2). It results that there is not much room left for the W^* parameters, as

¹see also the contribution of Chiappetta and Cousinou in section 3.3

compared to the Y case. From such sum rules together with the constraint (3), one can express all W^* -parameters in terms of the measured quantities a , G_F , $\sin \theta_W$, m_W plus one single free parameter, chosen as m_W^* . Actually, the W-parameters g_W , λ_W , m_W , deviate very slightly from their minimal SM values, due to the presence of W^* , and present accuracy data give bounds on the W^* -parameters (like in the Y-models case) rather than fixed values. However, for studying signatures of the W^* at LHC or SSC, such refinements are not very useful².

As to the bosonic sector, keeping only dimension-four effective terms, one considers the $SU(2)_L$ and electromagnetic invariant Lagrangian⁴⁾

$$L_{eff} = g_1 \mathbf{W}^{*\mu\nu} \cdot (\mathbf{W}_\mu \times \mathbf{W}_\nu) + g_2 \mathbf{W}^{\mu\nu} \cdot (\mathbf{W}^*{}_\mu \times \mathbf{W}_\nu) + i\kappa F^{\mu\nu} (W_\mu^- W_\nu^+ - W_\mu^+ W_\nu^-), \quad (4)$$

where g_1 , g_2 , and the anomalous magnetic moment, κ , are given⁴⁾ in terms of the basic parameters. Within the assumptions of $\lambda_W^* \ll \lambda_W$, and $|g_W^*| \leq |g_W|$, in good agreement with present experimental data, one obtains approximately⁴⁾ $g_1 \simeq \frac{1}{2} \frac{\lambda_W^*}{\lambda_W} g_W$, $g_2 \simeq -g_W^*$, $\kappa \simeq -(\lambda_W g_W^* + \lambda_W^* g_W)$. Note also that due to the smallness of the λ_W^* mixing parameter, Z_0^* is practically degenerate with W_\pm^* , and their fermionic coupling strengths are of order g_W^* .

With this in mind, we can compute the various possible decay modes of W_\pm^* or Z_0^* , and we give the corresponding branching ratios in Fig. 3. The decays of W^* or Z^* into boson pairs are the dominant ones, and behave like $(m_{W^*}/m_W)^5$ for $m_{W^*} \gg m_W$. This also means, unfortunately, that the widths of such particles become rapidly very large.

Now as the couplings in (4) are not of the Yang-Mills type, one should expect some characteristic signatures of this model in the decays $Z_0^* \rightarrow W^+ W^-$, $W^*{}^{+(-)} \rightarrow W^*{}^{+(-)} Z_0$, and $W^*{}^{+(-)} \rightarrow W^*{}^{+(-)} \gamma$, at energies $s \simeq m_W^2$ well above the W or Z_0 peaks, where the SM amplitudes show a rapid decrease due to the well-known high-energy unitary behaviour in the Yang-Mills type models. However the rapid increase of the W^* or Z_0^* width with their mass makes it extremely hard to identify W^* and Z_0^* as true resonances. The invariant mass distribution $d\sigma/dm$ converted into number of events per bins of 20 GeV is given in Fig. 4 for the WZ_0 final state (the $W\gamma$ final state shows¹¹⁾ very similar properties). Note the large excess of events over a wide range in the invariant mass, however the resonance becomes fairly broad (0.5 TeV) already for a bosons of 1 TeV. Above this mass the identification of such particles would be very difficult. The same conclusion holds for SSC. The other, a priori interesting, WW and $\mu^+\mu^-$ final states are not considered here, as the first one is largely dominated by the $t\bar{t}$ background, while the Drell-Yan process can be seen to be of the same order as the SM contribution¹¹⁾. Finally note that LEP 1 will put a bound of 600 GeV whereas LEP 2 will reach the limit of 980 GeV for the Z^* mass¹³⁾.

LHC		SSC	
Y	$M_Y = 3.8 \text{ TeV } (\lambda_Y^2 \simeq 0.73)$	$M_Y = 4.3 \text{ TeV } (\lambda_Y^2 \simeq 0.74)$	
	$M_Y = 4.1 \text{ TeV } (\lambda_Y^2 \simeq 0.03)$	$M_Y = 5 \text{ TeV } (\lambda_Y^2 \simeq 0.03)$	
Y_L	$M_Y = 4.3 \text{ TeV } (\lambda_Y^2 \simeq 0.74)$	$M_Y = 5 \text{ TeV } (\lambda_Y^2 \simeq 0.74)$	
	$M_Y = 3.8 \text{ TeV } (\lambda_Y^2 \simeq 0.03)$	$M_Y = 4.2 \text{ TeV } (\lambda_Y^2 \simeq 0.03)$	
	$M_{W^*} \simeq M_Z^* \simeq 1 \text{ TeV at LHC and SSC}$		

Table 1: Y , Y_L and W^* discovery limits, at LHC for $\mathcal{L} = 10^5 \text{ pb}^{-1}$ and SSC for $\mathcal{L} = 10^4 \text{ pb}^{-1}$.

λ_Y^2	0.03	0.05	0.11	0.42
$\Delta A_{FB}(y)$, Y	0.217	0.217	0.218	0.222
$\Delta A_{FB}(y)$, Y_L	-0.096	-0.017	+0.35	+0.128

Table 2: $\Delta A_{FB} = A_{FB} - A_{FB}^{SM}$ for Y and Y_L at LHC (for a rapidity of $y = -2.5$).

References

1. ALEPH Collaboration, D. Decamp et al., preprint CERN-EP/90-104 (1990)
DELPHI Collaboration, P. Abreu et al., preprint CERN-EP/90-32
L3 Collaboration, B. Adeva et al., Phys. Lett. B237 (1990) 136.
OPAL Collaboration, M. Z. Akrawy et al., Phys. Lett. B240 (1990) 497
2. For a review see e.g. H. Fritzsch in Proc. 22nd Int. School of Subnuclear Physics (Erice 1984), ed. A. Zichichi and Plenum Press, p.135.
3. R. Kögerler and D. Schildknecht, CERN-TH preprint 3231 (1982) unpublished;
M. Kuroda, D. Schildknecht, and K. H. Schwarzer, Nucl. Phys. B261 (1985) 432.
4. M. Kuroda and D. Schildknecht, Phys. Lett. B121 (1983) 173;
U. Baur, D. Schildknecht, and K. H. Schwarzer, Phys. Rev. D35 (1987) 297.
5. N. Kroll, T. D. Lee, and B. Zumino, Phys. Rev. 157 (1967) 1376;
T. D. Lee and B. Zumino, Phys. Rev. 163 (1967) 1667.
6. M. Kuroda, F. M. Renard, and D. Schildknecht, Phys. Lett. B183 (1987) 366.
7. U. Baur and K. H. Schwarzer, Phys. Lett. B180 (1986) 163;
U. Baur, M. Lindner, and K. H. Schwarzer, Nucl. Phys. B291 (1987) 1.
8. Cern Report 89-08, "Z Physics at LEP 1", ed. G. Altarelli, R. Kleiss and C. Verzegnassi, p. 185.
9. S. L. Wu, Phys. Reports 107 (1984) 59.
10. P. Colas and D. Denegri, Phys. Lett. B195 (1987) 295.
11. J. L. Kneur and G. Moutaka, in preparation.
12. A. Bramon, E. Etim and M. Greco, Phys. Lett. B41 (1972) 609.
J. J. Sakurai, Phys. Lett. B46 (1973) 207.
13. J. Layssac, F.M. Renard and C. Verzegnassi, preprint LAPP-TH-290/90 (June 1990).

²In contrast to the Y-models where we used the freedom on λ_Y given by present experimental uncertainty, to cope with the sensitivity of the model to λ_Y , due to the form of the constraint (1).

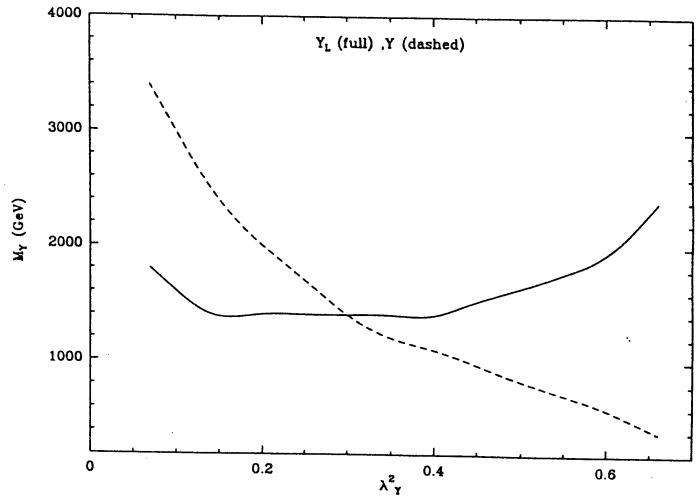


Fig. 1: Mass limits versus λ_Y^2 for Y_L and Y at LEP200

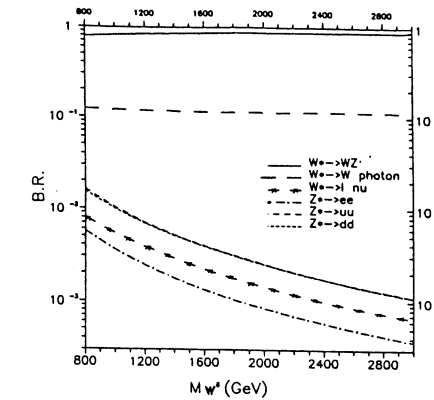


Fig. 3: The W^* and Z_0^* branching ratios.

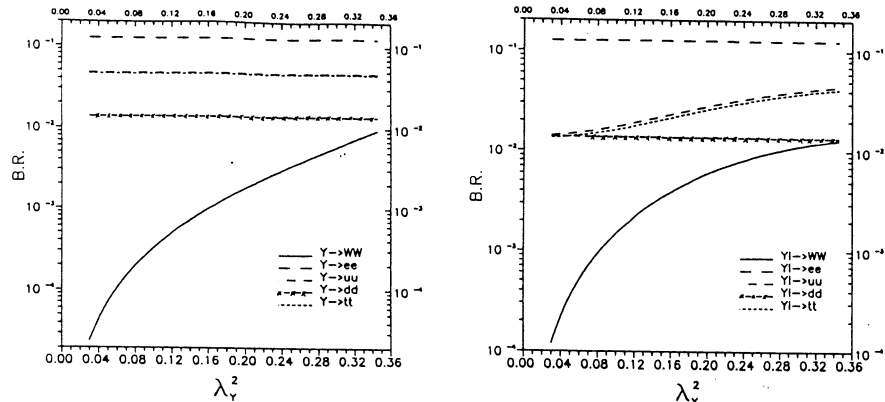


Fig. 2: Branching ratios versus λ_Y^2 , for $M_Y = 800$ GeV.
Fig. 2a (Y)
Fig. 2b (Y_L)

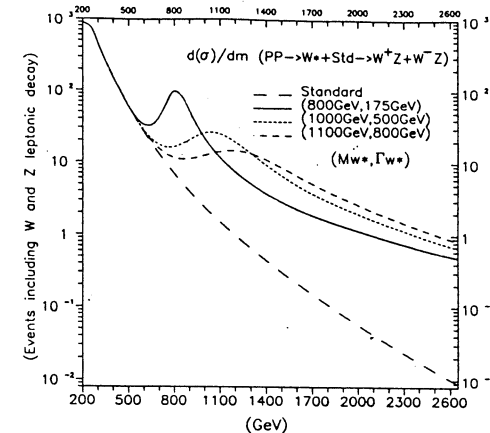


Fig. 4: $d\sigma/dm(m)$ for $q\bar{q} \rightarrow W^*(Z_0^*) \rightarrow WZ_0$.

III.3 MASS DISCOVERY LIMITS FOR NEW NEUTRAL GAUGE BOSONS FROM ALTERNATIVE SYMMETRY BREAKINGS

Contributors: P. Chiappetta and M.C. Cousinou

The aim of this report is to determine up to which mass new neutral gauge bosons could be detected at LHC [1]. Two models are used: we study the production of vector resonances arising from a strongly interacting electroweak sector (BESS model) and from compositeness of gauge bosons.

In each case the detection of the neutral boson is performed from its e^+e^- decay mode using the same experimental technique to select the events.

1 Detector simulation

The PYTHIA Monte Carlo (version 5.4) [2] is used to generate samples of signal and background. In this version of PYTHIA the couplings of new bosons to fermions and to ordinary W pairs can be exactly implemented. To study Z' production the processes $PP \rightarrow \gamma, Z, Z'$ have been generated and the decay mode $Z' \rightarrow e^+e^-$ selected. The Duke and Owens set of structure functions [3] (set 1) has been used.

A rough simulation of a calorimeter is then performed. It covers a range of ± 3 in rapidity and is segmented in pseudorapidity-azimuthal angle space in cells of: $\Delta\eta \times \Delta\phi = 0.06 \times \frac{2\pi}{100}$. The energy of each particle entering the calorimeter is smeared according to: $\frac{\Delta E}{E} = \frac{15\%}{\sqrt{E}} \oplus 2\%$ for electrons and photons and $\frac{\Delta E}{E} = \frac{50\%}{\sqrt{E}} \oplus 4\%$ for hadrons.

Then using the transverse energy E_T deposited in each cell of the calorimeter (summed over all particles inside this cell) a search for clusters with $E_T > 10\text{GeV}$ within a clustering radius $\Delta R = \sqrt{\Delta\eta^2 + \Delta\phi^2} < 0.5$ is performed. An electron (or positron) is then selected as a narrow jet with $\Delta R < 0.1$.

2 BESS model

The BESS model has been fully described in refs [4,5]. It describes 6 massive gauge bosons (W^\pm, Z, V^\pm, V^0) and the photon. Besides the ordinary gauge coupling constants g and g' there is an additional coupling g'' . The V particle is coupled to fermions through its mixing with W and Z, but in addition there may be a direct coupling specified by the parameter b .

Due to the smallness of the V^0 width below the TeV scale it is not possible to detect a V^0 boson lighter than 1 TeV with this type of calorimeter resolution. For $b = 0$ the production

rate above 1 TeV is too small to observe a signal over Standard Model background. Our main results are presented in fig. 1 in terms of number of events per year, a year being 10^7 seconds of running of the colliders. We assume a luminosity of $10^{34}\text{cm}^{-2}\text{s}^{-1}$ at LHC and of $10^{33}\text{cm}^{-2}\text{s}^{-1}$ at SSC. The efficiency of finding electrons after jet reconstruction in the calorimeter is around 60% as inferred by comparing the shaded area to the full one. For $b = -0.02$ the discovery mass limit both at LHC or SSC energies is around 1.5TeV. A signal is still observable up to $M_V = 1\text{TeV}$ when $b = -0.01$.

We give in fig. 2 the forward backward asymmetry for $M_V = 1\text{TeV}$ $g''=13$ and $b = -0.02$. The procedure used to define the asymmetry is the following: we first identify an electron or a positron as a cluster size $\Delta R < 0.1$. The trimomenta \vec{P}_{e^-} and \vec{P}_{e^+} are then computed from the energy deposited in the calorimeter cell and the direction of the cell's center. We perform a Lorentz boost from PP center of mass frame to the V^0 reference frame. For positive rapidities we define θ^* as the angle between the electron and the V^0 original direction whereas for negative rapidities θ^* is the angle between the positron and the V^0 . The squares in fig. 2 represent the theoretical values obtained from PYTHIA without detector simulation taking a rapidity interval of $\Delta y = 0.2$ whereas the points with error bars have been obtained after jets reconstruction. The errors plotted are calculated using the number of events expected after one year of LHC running. The discrepancy with Standard Model expectations is too tiny to be detectable.

3 Composite models

A signature for compositeness of vector bosons and Higgs particles would be a spectrum of new particles around the TeV scale. We limit our study to an isoscalar weak boson - the analogue of ω meson in hadron physics - and the first excited isotriplet which is the analogue of ρ'

3.1 Weak isoscalar vector bosons

In particular the first model [6,7] predicts a weak isoscalar vector boson which would couple or to the weak hypercharge current(to both left and right handed currents): Y , or only to lefthanded current : Y_L

The cross sections and widths depend strongly of the mass of the vector boson and of the mixing parameter λ_Y^2 . In tables 1 and 2 we give the discovery mass limits for the Y and Y_L computed as follows : For each (M_Y, λ_Y^2) set we plot the e^+e^- mass distribution for one year of LHC running. We count the number of events within $M_Y \pm 2\Gamma$ and estimate, inside the same cuts, the Drell Yan background. The value of Γ is computed using the natural width of the Y together with the experimental resolution.

In figures 3 and 4 are shown some distributions $\frac{dN}{dM_{e^+e^-}}$ for Y_L and Y respectively. The forward backward asymmetries for Y_L and Y bosons are plotted on fig. 5 and 6. The sensitivity of the asymmetry shape to the value of the mixing parameter is very important for the Y_L case , but weak for the Y case.

To see how the previous limits change at SSC energy (with a luminosity of $10^{33}\text{cm}^{-2}\text{s}^{-1}$)

λ_Y^2	$M(Y)_{TeV}$	$\Gamma(Y)_{GeV}$	$N_{events}/Year$	# σ
0.03	2.0	780	10617	37
0.1	4.2	445	488	8
0.2	4.7	210	84	7
0.4	4.2	62	67	6.5
0.68	3.2	11	38	5.5

Table 1: Y mass discovery limits

λ_Y^2	$M(Y_L)_{TeV}$	$\Gamma(Y_L)_{GeV}$	$N_{events}/Year$	# σ
0.03	4.7	368	60	4.6
0.1	4.1	95	52	5.5
0.2	4.1	55	39	5.0
0.4	4.5	76	40	5.7
0.68	4.5	438	123	5.7

Table 2: Y_L mass discovery limits

we generate Y events with $\lambda_Y^2 = 0.68$ and obtain exactly the same mass limit than at LHC energy: $M_Y = 3.2TeV$. Generating Y_L events with $\lambda_Y^2 = 0.2$ we obtain a better mass limit of 5 TeV (compared to 4.1 TeV at LHC energy)

3.2 Excited Z

In this model higher isovector excitations to the known weak intermediate bosons W and Z are expected . The main observable effects will derive from the least massive excited vector boson (W^* or Z^*). The same procedure has been used to estimate discovery limits for an excited Z [8]. The main limitation comes from the rapid increase of the width Γ_{Z^*} with the mass M_{Z^*} . As an illustration $\Gamma_{Z^*} \simeq 750GeV$ for $M_{Z^*} = 1.3TeV$. In this range of mass we have still to face with an important Drell Yan background. Therefore we estimated the discovery mass limit to be around 1 TeV as shown in fig. 7. Fig. 8 gives the forward backward asymmetry for $M_{Z^*} = 1TeV$. Deviations from Standard Model are not detectable.

4 Observability of Z' decaying in $\mu^+\mu^-$

To estimate how the previous discovery limits change if we detect these new gauge bosons from their decay mode $\mu^+\mu^-$, we choose to use the isoscalar boson Y with 2 different values of the coupling strength.

We simulate two kinds of momentum resolution for the muons . The first one (called in

the figure 9 resolution A) has been taken from an Iron Toroid simulation [9] presented to this workshop. The value of $\frac{\Delta P}{P}$ depends on the momentum value and the θ angle of the μ .For example when $\theta = 10^\circ$, $\frac{\Delta P}{P}$ runs from 12.6% to 22.6% for muons having a momentum between 100 GeV and 1000 Gev. If $\theta = 90^\circ$ it runs from 14.9% to 38%. The second one (referenced in the figure as resolution B) is a very crude simulation of the momentum resolution presented also in this workshop [10] for a Compact Muon Solenoid. In this case we assume that the $\frac{\Delta P}{P}$ does not depend neither on the muon momentum nor on its angle. We take $\frac{\Delta P}{P} = 8\%$.

In fig. 9 are shown four distributions $\frac{dN}{dM_{\mu^+\mu^-}}$ for an isoscalar Y generated with different mass values. Three of them correspond to a simulation using the resolution A for the muon's momentum. No signal is visible for the values : $M_Y = 4.7TeV$ and $\lambda_Y^2 = 0.2$ which correspond to the discovery limit in the decay mode e^+e^- obtained with a poor electron resolution. With this type of muon resolution the discovery mass limits are of the order of 2.5 TeV only. When we use the resolution B, we obtain discovery mass limits comparable to those we get in the e^+e^- channel.

References

- [1] Large Hadron Collider in the LEP tunnel, ed. G. Brianti et al CERN 84/10.
- [2] T.Sjostrand, Int. Journ. of Mod. Phys. A3(1988)75.
- [3] D.W. Duke and J.F. Owens, Phys. Rev. D30(1984)49.
- [4] R. Casalbuoni, S. De Curtis , D. Dominici and R. Gatto Phys. Lett. B155(1985) 95; Nucl. Phys. B282(1987) 235.
R. Casalbuoni, P. Chiappetta , D. Dominici F. Feruglio and R. Gatto Nucl. Phys. B310(1988) 181
- [5] R. Casalbuoni, P. Chiappetta , M.C. Cousinou, S. De Curtis, F. Feruglio and R. Gatto in these proceedings
- [6] M. Kuroda, D. Schildknecht, K.H Schwarzer Nucl. Phys. B261 (1985) 432
- [7] J. L. Kneur, G. Moutaka in these proceedings
- [8] U. Baur, D. Schildknecht, K.H Schwarzer Phys. Rev. D35(1987) 297
- [9] G. Carboni Iron Toroid in these proceedings
- [10] K. Eggert CMS in these proceedings

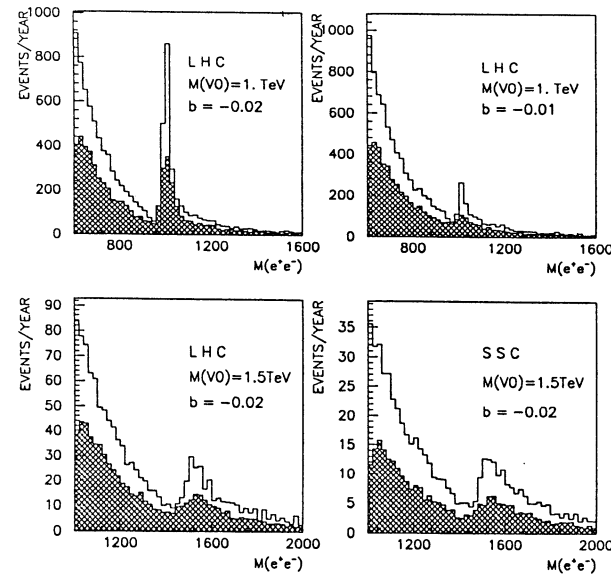


Fig.1: Invariant mass distribution of e^+e^- pairs for several values of BESS parameters. The full histogram refers to PYTHIA events without detector simulation whereas the shaded area gives the number of events/year after jets reconstruction

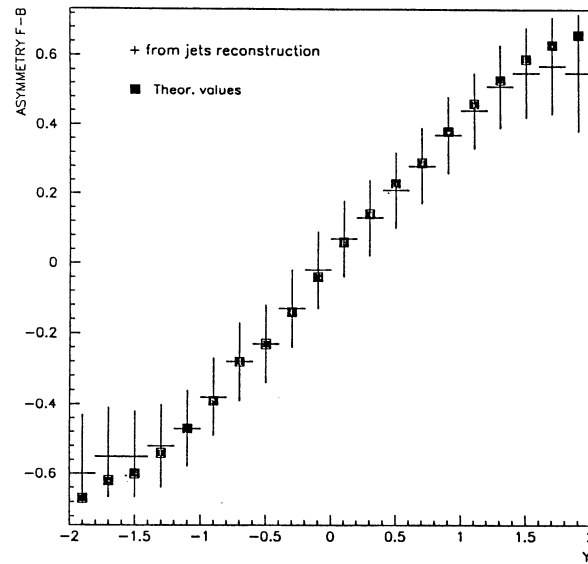


Fig.2: Rapidity dependence of forward backward asymmetry before and after jets reconstruction. BESS model with $M_V = 1\text{TeV}$, $b = -0.02$, $g'' = 13$ at LHC

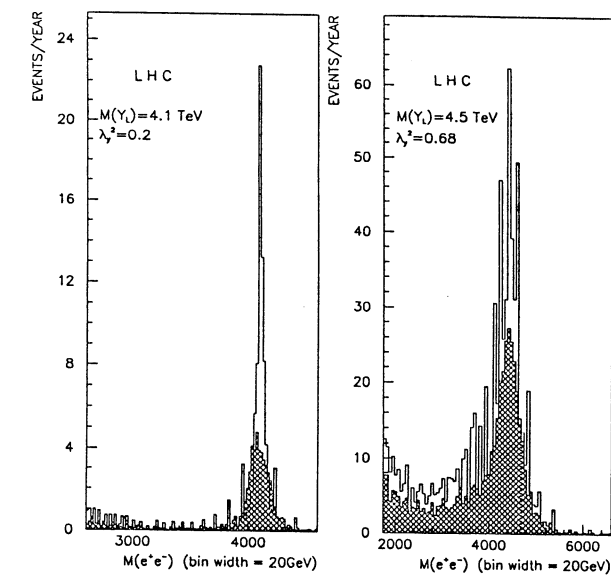


Fig.3: Invariant mass distribution of e^+e^- pairs for isoscalar vector boson Y_L

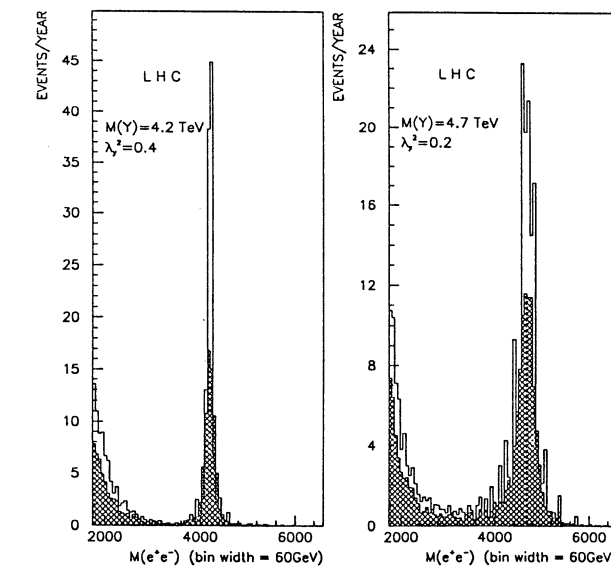


Fig.4: Invariant mass distribution of e^+e^- pairs for isoscalar vector boson Y

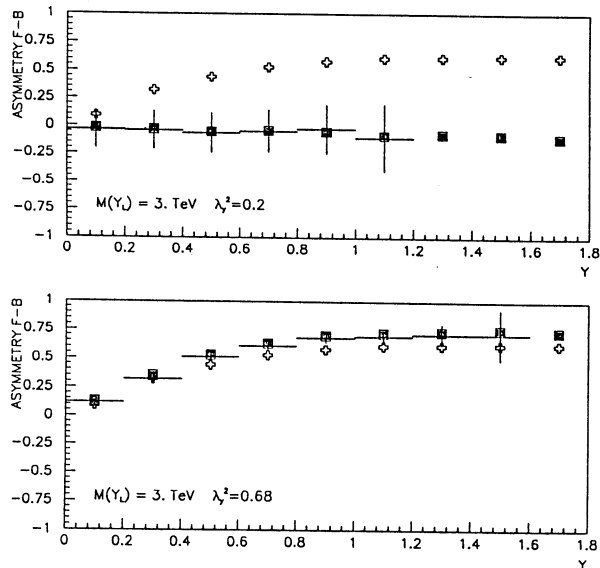


Fig.5: Rapidity dependence of forward backward asymmetry for isoscalar vector boson Y_L

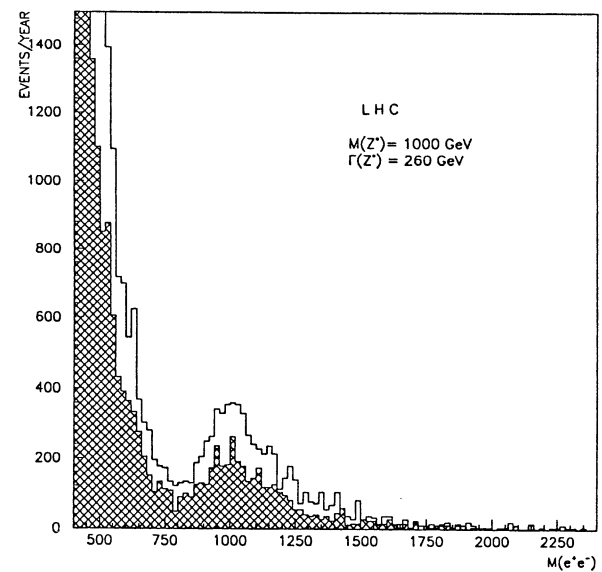


Fig.7: Invariant mass distribution of e^+e^- pairs for Z^*

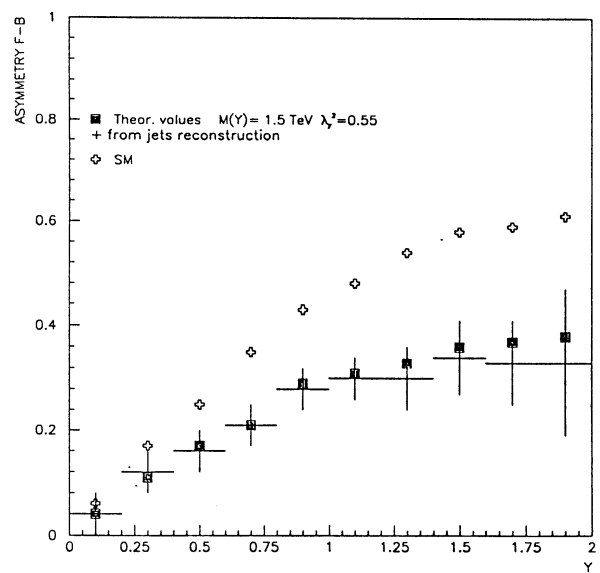


Fig.6: Rapidity dependence of forward backward asymmetry for isoscalar vector boson Y

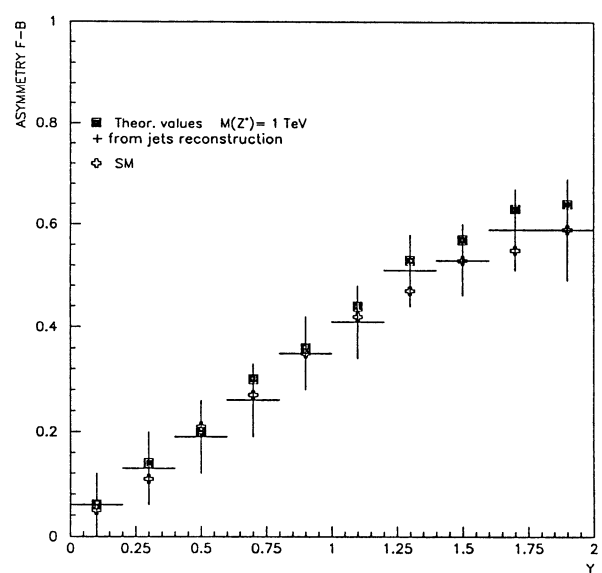


Fig.8: Rapidity dependence of forward backward asymmetry for excited Z boson

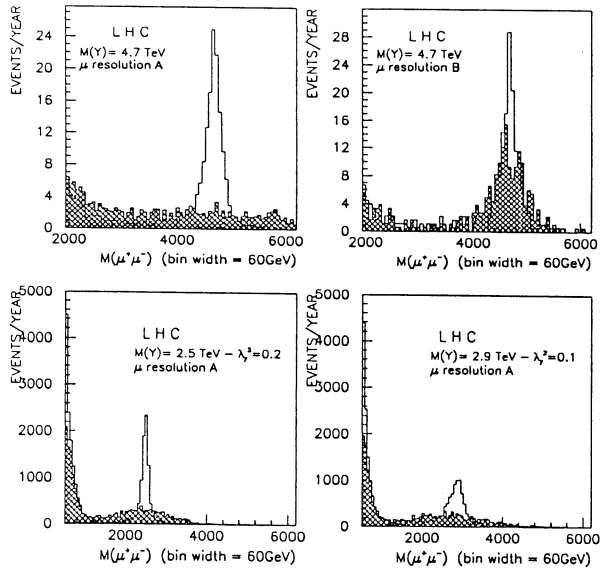


Fig.9: Invariant mass distribution of $\mu^+\mu^-$ pairs for isoscalar vector boson Y

III.4 COMPOSITENESS OF Z^0, Z' AT THE LHC

T Medcalf

1 Introduction

If the Z^0 or the Z' (or Z'' etc.) is composite, with coloured constituents, then it will be formed together with a photon, via a lower order diagram, involving a preonic loop, through gluon fusion, at a rate much greater than in the standard model, where this production is dominated by quark fusion. Leurer, Harari and Barbieri [1] calculated the enhancement due to this mechanism for experiments at the SpS and Tevatron. Here the prediction is extended to the LHC, and an estimate made of the observability of the reaction.

2 Monte Carlo Simulation

Renard [2],[3] gives for the cross-section

$$\frac{d\sigma}{d\Omega}(g + g \rightarrow Z^0 + \gamma) = \frac{4\pi\alpha_s^2\alpha}{9s} (F_W/M_W)^2 [(s - M_Z^2)/2s](3 + \cos^2\theta)(\langle Q_s^2 Q \rangle)^2$$

where (F_W/M_W) has a greatest reasonable value of 1.6 (but could be much smaller for particular models of compositeness) and $(\langle Q_s^2 Q \rangle)^2$ is of order 1 in most models. This formula with the above values was installed as a new process within PYTHIA 5.4 [5]. In order to evaluate the process, gluon distribution functions have to be assumed, and quark distributions are also required for the standard model comparisons. [1] used those of Baier et al [6], but these are not available within PYTHIA 5.4, so the two distributions EHLQ1 and EHLQ2 [4] were used and compared. [1] used Λ_{QCD} values of 0.4 and 0.1 GeV with the same functions; here each set was used with its optimum value, 0.2 and 0.29 GeV respectively. Following [1] and [7] the minimum value of \sqrt{s} was set to $1.05M_{Z^0}$ ($1.05M_{Z'}$ in section 5). This ensures that none of the cross-section relating to the production of photons above 5 GeV in the case of Z^0 or photons above 25 GeV in the case of a 500 GeV Z' is omitted, whilst avoiding the singularity at $\sqrt{s} = M_Z$.

3 Detector Simulation for the LHC

In order to estimate the real observability of the events generated, the following detector simulation was used: a tracker/electromagnetic calorimeter with energy resolution $15\%/\sqrt{E} + 2\%$ and charged/neutral discrimination, and a muon chamber with resolution 10%. Coverage of ± 2 in pseudorapidity was assumed, with angular resolution of 1° in θ and ϕ . Degradation of the angular resolution to 2° was also investigated but results were not distinguishable. Signals used for Z^0 reconstruction were required to be each > 10 GeV.

4 Comparison With Earlier Calculations at SpS and Tevatron

In general agreement with [1] the enhancement of the composite process compared with the standard model is greater for large values of the transverse momentum of the photon $P_{T,\gamma}$. Table 1 shows the relative production rate for $Z^0 + \gamma$ where $P_{T,\gamma} > 10$ GeV, of the processes $g + g$ in a generic composite model and $q + q'$ in the standard model, for the two experiments and various simulation conditions described above.

	[1] $\Lambda_{QCD} = 0.4$	[1] $\Lambda_{QCD} = 0.1$	EHLQ1	EHLQ2
SpS	20	7	7.4	7.3
Tevatron	170	40	134	111

Table 1: Relative rates $(g + g \rightarrow Z^0 + \gamma)/(q + q' \rightarrow Z^0 + \gamma)$

The systematic error between EHLQ1 and EHLQ2 is very small at the lower energy and smaller than, but consistent with, the error of the older distribution functions at the higher energy. The agreement of the EHLQ sets with the older $\Lambda_{QCD} = .1$ GeV result for the SpS is obviously fortuitously exact, but the general consistency is satisfactory.

5 Z^0 at the LHC

At the higher energies and much higher expected backgrounds of the LHC, it is unrealistic to expect consistent identification of photons of $P_{T,\gamma} \sim 10$ GeV. Results are presented for $P_{T,\gamma} > 60$ GeV and 100 GeV. However the motion of Z^0 itself may be expected to be relativistic, and so results have also been calculated for the scalar sum of the transverse momenta of the photon and the Z^0 , $|P_{T,z_0}| + |P_{T,\gamma}| > 100$ GeV. The enhancement of the composite process with respect the standard model is always very large (~ 3300 for the data in the last column of table 2) but this merely represents the undetectability of the standard model process with these cuts. Table 2 shows events/year for the generic composite model, assuming 100 running days at a luminosity of $4 \times 10^{34} m^{-2}s^{-1}$. For the low luminosity LHC option these numbers should be divided by 40. Both total numbers and ‘goldplated event’ numbers are shown where the gold-plated event is defined as a Z^0 decay to e^+e^- or $\mu^+\mu^-$ with both leptons and the photon within pseudorapidity ± 2 . Allowance was made for detection efficiency and reconstruction efficiency for the Z^0 mass through the detector simulation described in section 3. The efficiency for the Z^0 reconstruction given by this simulation was 8.8%. When the PYTHIA 5.4 simulation of multiple interactions [5] was switched on, there was no significant event loss. Only EHLQ2 results are shown, as EHLQ1 values are the same within 10%.

	$P_{T,\gamma} > 60$	$P_{T,\gamma} > 100$	$ P_{T,z_0} + P_{T,\gamma} > 100$ GeV
All events	7×10^4	3×10^4	2×10^5
Goldplated	420	180	1200

Table 2: Events/year ($g + g \rightarrow Z^0 + \gamma$)

The expected numbers of events are more than adequate to detect compositeness of the Z^0 , although goldplated events would be rather few in the low luminosity option. Using the last column and assuming that 10 events/year is sufficient for reliable detection, the maximum value of (F_W/M_W) can be reduced by a factor ~ 10 , using only goldplated events. Fig 1 shows the distributions for (a) $P_{T,\gamma}$ and (b) $|P_{T,z_0}| + |P_{T,\gamma}|$.

6 $Z'(500GeV)$ at the LHC

With the same general simulation procedure (PYTHIA 5.4, new process with a cross-section given by the same formula), a hypothetical Z' may be simulated, essentially by specifying the mass $M_{Z'}$ (taken to be 500 GeV) in place of M_Z . In the composite context such a particle might be an excited variant of the Z^0 , or a Z' arising from some other physics, below which there is still an underlying compositeness. Results from the EHLQ2 distributions are given and EHLQ1 results are < 7% different. Fig 2 shows the distribution of $P_{T,\gamma}$ from which it can be seen that the requirement $P_{T,\gamma} > 100$ GeV is satisfied for most events. The event-rate predicted is 2.7×10^5 events/year in the LHC high luminosity option, making no allowance for new knowledge (for instance of the result of the search described in section 5). If the branching ratios of $Z' \rightarrow e^+e^-, \mu^+\mu^-$ are the same as those of the Z^0 , then goldplated events, $P_{T,\gamma} > 100$ GeV, photon and both leptons within pseudorapidity ± 2 , and successful reconstruction of the Z' by the same tracker/calorimeter described above, is predicted to be 1270/year (with no loss due to multiple interactions), more than adequate to identify the particle as composite.

References

- [1] M. Leurer, H. Harari and R. Barbieri, Phys. Letts. 141B (1984), 455
- [2] F. M. Renard, Phys. Letts. 116B (1982), 269
- [3] F. M. Renard, Phys. Letts. 132B (1983), 450
- [4] E. Eichen,I. Hinchliffe,K. Lane and C. Quigg, Rev. Mod. Phys. 56 (1984), 579
- [5] H.-U. Bengtsson and T. Sjöstrand, Computer Phys. Comm. 46 (1987) 43
T. Sjöstrand, Private Communication
- [6] R. Baier,J. Engels and B. Petersson, Z. Phys. C2 (1979),265
- [7] R. W. Brown, D. Sahdev and K. O. Mikaelian, Phys. Rev. D20 (1979),1164

Pt Plots

20/11/90 17.00

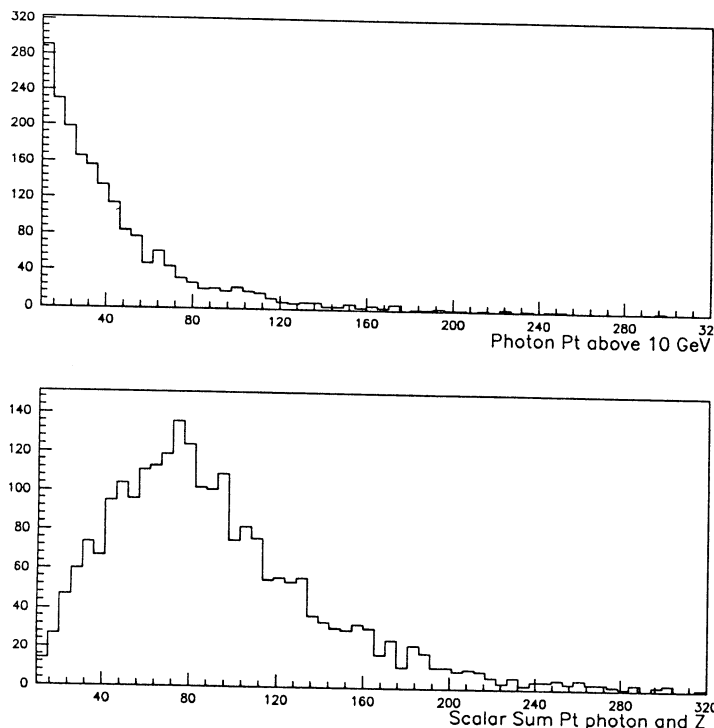


Fig. 1

Pt Plots

20/11/90 16.53

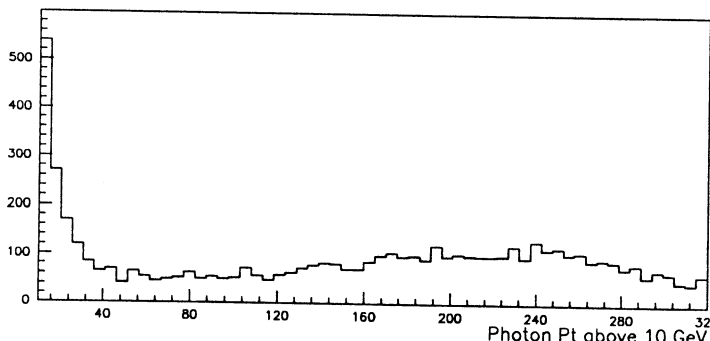


Fig. 2

IV. CONCLUSIONS

LHC is ideal to discover new heavy vector bosons. Concerning neutral gauge boson the observable channel is $Z' \rightarrow l^+l^-$ since the W^+W^- one is overwhelmed by top production. For an integrated luminosity of $10^5 pb^{-1}$ the discovery limits for Z' of E_6 origin or isoscalar composite bosons are around $4 - 5 TeV$, i.e. in a range comparable to SSC which can reach $5 - 6 TeV$ for an integrated luminosity of $10^4 pb^{-1}$. Discovery of the neutral gauge boson V^0 expected in BESS model is more difficult due to the weakness of its coupling to fermions. In the most optimistic case one can reach the limit of $1.5 TeV$ at LHC, that SSC will not improve. A neutral excited composite isovector Z^* will be hardly detectable above $1 TeV$ due to the broadness of the resonance, a limit that LEP 200 can reach. Forward backward asymmetries could be useful to pin down the origin of a neutral Z' . Since differentiations appear at large rapidities huge statistics and good detector resolution -with identification of the charge of the lepton- are mandatory.

Concerning heavy charged vector bosons expected in minimal left right models and in BESS model the most promising channel is $W' \rightarrow WZ$ followed by leptonic decays of W and Z since the most dangerous background from top production can be rejected at an acceptable level. Discovery limits are around $2 TeV$ at LHC and $2.5 TeV$ at SSC. If W' is of E_6 superstring origin it will be produced in association with a leptoquark. The discovery limits, which depend on leptoquark mass, lie in the $2 TeV$ range. If a new heavy W' , having the same couplings to fermions as ordinary W and tri-linear ones arising through mixing, exists it can be observed in its leptonic channel up to $4 TeV$.

Alternative Symmetry Breaking and Exotica

CONVENORS: S. Dimopoulos^{1,2,3}, M. Lindner¹

A8: ALTERNATIVE SYMMETRY BREAKING AND EXOTICA

CONTRIBUTORS: E. Argyres⁴, U. Baur^{5*}, R. Casalbuoni^{6,7}, P. Chiappetta⁸, S. De Curtis⁹, A. Dobado^{1,10}, J. Ellis¹, F. Feruglio^{7,11}, R. Gatto⁷, M. Herrero^{1,12}, I. Josa¹, V.A. Khoze^{1,13}, B. Mele¹, C. Papadopoulos⁴, F. Pauss¹, M. Perrottet⁸, A. Ringwald¹, T. Rodrigo¹, F. Schrempp¹⁴, M. Spira¹⁵, J. Terron¹², S. Vlassopoulos¹⁶, C. Wetterich¹⁴, P. Zerwas¹⁵

Contents

- I. Electroweak Symmetry Breaking and the *TeV* Scale
- II. $V_L V_L$ Scattering : Chiral Lagrangian Approach
- III. WZ Production from the BESS Model
- IV. $W_L^\pm Z_L^0$ Production at the LHC from the Strongly Interacting Symmetry Sector – Experimental Aspects
- V. Compositeness
- VI. Signatures for Geometrical Flavour Interactions and $B + L$ Violation at LHC
- VII. Summary

- 1) CERN, 1211 Geneva 23, Switzerland
- 2) permanent address: Stanford University, Stanford, CA 94305, USA
- 3) Boston University, Physics Dept., 590 Commonwealth Ave., Boston, MA 02215, USA
- 4) Institute of Nucl. Phys. NRCPS Democritos, GR-153 10 Athens Greece
- 5) University of Wisconsin, Physics Dept., 1150 Univ. Ave., Madison, WI 53706, USA
- 6) Dipartimento di Fisica and Sezione INFN, I-73100 Lecce, Italy
- 7) Dept. de Phys. Theor., Univ. de Geneve, 1211 Geneva 4, Switzerland
- 8) CPT CNRS LUMINY Case 907, 13288 Marseille, Cedex 9, France
- 9) I.N.F.N., Sezione di Firenze, I-50125 Firenze, Italy
- 10) Dep. de Fisica Teorica de la Univ. Complutense de Madrid, 28040 Madrid, Spain
- 11) Univ. of Padova, I-35100, Italy
- 12) Dep. de Fisica Teorica de la Univ. Autonoma de Madrid, 28049 Madrid, Spain
- 13) Leningrad Inst. for Nucl. Phys., 188350 Gatchina, USSR
- 14) DESY, Notkestraße 85, 2000 Hamburg 52, Germany
- 15) Rhein.-Westf. Tech. Hochschule, Physikzentrum, 5100 Aachen, Germany
- 16) Department of Physics, Nat. Tech. Univ., GR-157 73 Zografou, Athens, Greece

*SSC Fellow

One of the main motivations to build a machine like LHC is to try to get a deeper understanding of the mechanism of electroweak symmetry breaking. This question is so important to our understanding of what may lie ahead in particle physics that the aim of this working group was mostly to see how much we can expect to learn about this problem and how this can be done. In section I we recall the arguments which make the TeV scale special. These arguments are so central and stand behind the expectation that something essential can be learned about symmetry breaking that it is worth to give a short survey here. Sections II and III contain two contributions which model in different ways a strongly interacting Higgs sector corresponding to rather general dynamical symmetry breaking scenarios. Section IV deals with the experimental aspects of the detection of WZ production as expected by a strongly interacting Higgs sector. In section V we have some contributions on compositeness which do not fall under ‘excited gauge bosons’ which have been studied by a different working group. Section VI is a contribution discussing the possible implications of baryon number violating processes with possibly spectacular consequences for new experiments in the multi TeV area. Finally in section VII we summarize the main results of this working group.

I. ELECTROWEAK SYMMETRY BREAKING AND THE TeV SCALE

Contributors: S. Dimopoulos and M. Lindner

I.1. Introduction

So far the Standard Model (SM) with Spontaneous Symmetry Breaking (SSB) describes all data perfectly and no direct evidence of the Higgs sector or anything equivalent has been seen. We will illustrate why the $O(TeV)$ scale is under all circumstances special and that it is guaranteed that something connected inherently to electroweak symmetry breaking must show up before that scale. This could be a fundamental Higgs, a composite Higgs, a ρ -like state corresponding to Technicolor scenarios or something else which we did not even think of before depending on the mechanism of symmetry breaking. But it must show up and thus machines like the LHC are very important probes into the symmetry breaking mechanism.

Theoretically there are a number of reasons to believe that SSB with a fundamental scalar field may only be a technical step required by a consistent, renormalizable gauge invariant theory. In all but supersymmetric theories we have good reasons [1] not to like fundamental scalars and the way to avoid SSB with a fundamental Higgs particle is to replace it by a dynamical mechanism. Very attractive ideas in this direction were inspired by QCD when the longitudinal components of the W and Z bosons are identified with some sort of pions of a new interaction. This obviously requires a corresponding rescaling of all dimensionfull quantities of QCD and would after rescaling automatically imply strong interactions in the TeV range. As a consequence W_L - W_L should (like pion-pion) be strongly coupled. If the Higgs particle of the SM is very heavy then the SM by itself also has rather strongly coupled W 's and Z 's. But the result of a W_L - W_L scattering experiment will look different if a strongly coupled dynamical symmetry breaking mechanism with a nontrivial boundstate spectrum is at work. Therefore one of the key tasks of machines like the LHC will be to measure W_L - W_L scattering and to see if deviations from the SM pointing towards strongly coupled dynamical symmetry breaking in the TeV range can be found. Since QCD like confining gauge theories are just one out of many

thinkable alternative symmetry breaking mechanisms it is necessary to study the problem in a very general manner. Since individual scenarios have been discussed in detail (see e.g. [2] and references therein) we would like to recall the essence of the arguments which arise if one tries to avoid anything beyond the known fermions and the weak gauge bosons and we will see how this makes the TeV scale unavoidably special.

I.2. Substitutes for a Fundamental Higgs Particle

Looking at the Higgs mechanism one realizes immediately that it contains unavoidable essential elements and ugly features at the same time. If the SM Higgs field is split in a nonlinear way into Higgs modes η and Goldstone modes π_i then

$$\Phi = U \cdot \phi; \quad U = \exp\left(\frac{i\pi_i \tau_i}{v}\right); \quad \phi = \begin{pmatrix} 0 \\ v + \eta \end{pmatrix}; \quad v \simeq 175 \text{ GeV} \quad (1)$$

and we have $\Phi^\dagger \Phi = \phi^2$ so that the Higgs potential does not depend on the Goldstone bosons in U :

$$V(\Phi^\dagger \Phi) = V(\phi^2) = V(\eta) = \frac{m_H^2}{2} \eta^2 + \frac{m_H^2}{2v} \eta^3 + \frac{m_H^2}{8v^2} \eta^4 \quad (2)$$

The Goldstone degrees of freedom π_i reappear however with derivative couplings through the kinetic energy term

$$|\partial\Phi|^2 = |\partial\eta|^2 + \frac{v^2}{2} \text{Tr}(\partial_\mu U^\dagger \partial^\mu U) + O(\eta \cdot \partial U, \partial\eta \partial U) \quad (3)$$

It is nicely seen that the Higgs mechanism needs only the ‘rotational’ π fields in order to work properly. In ‘radial’ direction a fixed, nonvanishing vacuum expectation value (VEV) is required and the oscillations η around this VEV are in some sense obsolete. This observation makes it very tempting to remove the η degrees of freedom from the theory by sending $m_H \rightarrow \infty$ (while v is fixed) and thus freezing out the physical Higgs field. The result is the nonlinear σ -model limit of the SM with two problems. First this limit corresponds to a nonrenormalizable theory. This means that (at least perturbatively) one cannot make much sense out of this model by itself beyond tree level while on the other hand some loop effects (radiative corrections) of the SM have already been seen [3]. If no miracles occur then the only way to cure the associated problems is to invent a cutoff Λ which controls the loop expressions. Physically such a cutoff would correspond to new physics at Λ which in this case is certainly not many orders of magnitude above M_W . Therefore we see that if we remove the Higgs modes η that we are forced to reinvent something new instead of it. This corresponds nicely to the second problem of the $m_H \rightarrow \infty$ limit of the SM. After η has been frozen out one finds that Goldstone boson scattering amplitudes grow like [4]

$$A(W^+ W^- \rightarrow ZZ) \simeq \frac{-m_H^2}{v^2} (1 + \frac{m_H^2}{s - m_H^2}) \xrightarrow{m_H \rightarrow \infty} \frac{s}{v^2} \quad (4)$$

and violate tree unitarity between 1 and 2 TeV [2]. Therefore some additional state must come in and dampen the amplitudes. Both problems of the $m_H \rightarrow \infty$ limit require that some Higgs substitute must cure the associated problems. If we are willing to accept a wealth of new states in the TeV area then the renormalizability of the SM or modifications does not mean much and we just need to restore tree unitarity so that only one problem is left over.

One obvious solution is going back to the starting point of a not too heavy fundamental Higgs scalar. But this is not desired due to the problems associated with fundamental scalars

[1]. A second solution to both problems could in principle lie in loop effects. This is because the limiting procedure $m_H \rightarrow \infty$ could give a different answer if performed in the fully renormalized theory with loop effects included. Large m_H with fixed v implies large λ and therefore strong loop effects might just cure the tree level unitarity problems so that the limiting procedure of the quantum theory could be better behaved. But this is not the case as is well known from so called ‘‘triviality’’ studies [5,6]. The underlying general consistency requirements show that for $m_H \gtrsim 200 \text{ GeV}$ even the renormalized SM cannot live without new physics at some scale $\Lambda \lesssim M_W \cdot \exp[\text{const} \cdot M_W / (m_H - 200 \text{ GeV})]$. If the Higgs mass is increased then Λ becomes significantly smaller until $\Lambda \simeq m_H \simeq O(\text{TeV})$ requires immediately new additional physics beyond the SM. So one cannot send the Higgs mass to infinity in the renormalized SM and the old unitarity problem is recovered even after loop effects are included. Finally a whole class of solutions to the unitarity problem is given by dynamical symmetry breaking scenarios which anyway seem to be an attractive alternative to the static Higgs mechanism with fundamental scalars. The best known example is scaled QCD or Technicolor [7] where the π fields of eq. (1) are then the ‘‘pions’’ of a new interaction and a new ρ meson solves the unitarity problems. Also a wealth of states (‘‘Techni-mesons’’, ‘‘Techni-baryons’’) would be expected to be found in the TeV area.

But note that for the mentioned problems minimally only one new state is required to cure the unitarity problems and that both the quantum numbers of this state(s) and the remaining part of the new spectrum are not fixed and entirely due to the assumed dynamics. If we scale QCD then we make a choice on the dynamics motivated by history and we expect a Techni- ρ meson and many other new states in the TeV area. But we should be openminded and think of all possible dynamical scenarios. As an example we will illustrate below that there are dynamical mechanisms which are in a certain sense the extreme opposite of QCD like dynamics. They predict only one composite scalar state in the TeV area and allow to put the remaining spectrum arbitrarily high in energy.

The fact that the tree amplitudes grow up to the point where a Higgs substitute shows up leads to the so called ‘‘no lose corollary’’ ([2] and references therein). The ‘‘no lose corollary’’ says in short simply that the higher in energy the unitarization of amplitudes sets in the stronger it has to be to avoid unitarity problems. Within the SM this means that either the Higgs is light enough to be discovered directly or it will be so heavy that λ is so big as to imply strongly interacting $W_L - W_L$. For dynamical symmetry breaking schemes the statement is very similar and again either something new shows up directly or strong $W_L - W_L$ scattering is required. Therefore a certain success of machines like LHC seems guaranteed. But note that once unitarization is taken care of nothing else is required immediately. Especially there is no per se reason that the whole spectrum of a dynamical breaking scheme is settled in the TeV range as suggested by QCD-like scenarios. A perfect example of such a situation is given further down and has been called Minimal Dynamical Symmetry Breaking.

I.3. Simulation Methods for Alternative Symmetry Breaking

Two different approaches for simulations were used in this working group. The first method used in section II is based on Chiral Perturbation Theory and rests on the observation that in the limit $m_H \rightarrow \infty$ only the term

$$\frac{v^2}{2} \text{Tr}(\partial_\mu U^+ \partial^\mu U) \quad (5)$$

is left over from the Higgs sector. From the previous chapter we know that this Higgs-less limit is not viable by itself and one must therefore add at least $O(p^4)$ terms. Unlike the leading $O(p^2)$ term of eq. (5) these new $O(p^4)$ terms are not fixed by the low energy symmetries. Therefore the most general terms with initially free new dimensionful couplings are added

$$\mathcal{L} = \frac{v^2}{2} \text{Tr}(\partial_\mu U^+ \partial^\mu U) + M \text{Tr}(\partial_\mu U \partial^\mu U^+) \cdot \text{Tr}(\partial_\nu U \partial^\nu U^+) + N \text{Tr}(\partial_\mu U \partial_\nu U^+) \cdot \text{Tr}(\partial^\mu U \partial^\nu U^+) \quad (6)$$

Since these new terms correspond to additional multi-pion dynamics it is possible to choose the dimensionful couplings M and N so that different dynamical situations are emulated as closely as possible. The addition of these new terms does not unitarize the amplitudes and in addition a unitarization procedure must be chosen. Two different methods are used for comparison. The first is the K-matrix method which has a saturation behaviour and is not very abrupt. The other method is the Pade approximation which mimics in some approximation a resonance. Even though this general chiral approach allows to simulate many different dynamical scenarios as seen from low energies it is also clear that there are limitations. Especially the development of all new resonances can only be done approximately. Since e.g. a new ρ -like resonance turns out to be extremely important for the predictions it has been included explicitly in addition. This is especially important for scaled QCD or Technicolor scenarios where the ρ particle produces big effects via the $W - \rho$ mixing.

The second method used for simulations in section III is the so called BESS approach. There some dynamics which develops a new ρ -like vector resonance is assumed and this new state is included by hand with the most general parameters. Also a possible direct $\rho - f\bar{f}$ coupling is included. This is of course inspired by and especially good for QCD-like electroweak symmetry breaking. Due to this analogy the most interesting situations arise when all details of QCD are scaled by F_π/f_π (scaled QCD) and additionally rescaled to an arbitrary number of colors by large N_C arguments (Technicolor).

I.4. Radiative Consistency and the TeV Scale

We discussed above that at least one extra state is needed (and guaranteed) in the $m_H \rightarrow \infty$ limit to solve the tree unitarity problems in the TeV area. Here we will show that more is required to show up at another scale if we ask for consistency beyond tree level. As already indicated above the fact that the SM is a well defined theory does not imply automatically that this remains so once radiative corrections are included. If one or more of the running effective coupling constants grows with energy scale then typically there is a scale Λ at which the couplings will begin to diverge into a Landau Singularity (LS). Such a blow up is (if not an artifact of perturbation theory) inconsistent with the required functional form on pure dimensional grounds. A dimensionless coupling should (away from mass thresholds) run only logarithmically while a LS implies a power law. A theory is called ‘‘trivial’’ if the only way to avoid such problems is to restrict it to the non-interacting free case. For example for a single scalar with a quartic interaction term $\lambda \Phi^4$ triviality has been established rather reliably. Since there are hints that the problem is very common one should take every LS even in perturbation theory as a serious possible source of such inconsistencies. The way to avoid these problems in the SM is to anticipate a scale of new physics Λ and to demand that the parameters of the theory are chosen so that all couplings are well behaved (i.e. no blowup) in the physical region up to Λ :

$$g(\mu), \lambda(\mu) < \infty \quad \text{for } \mu \in [m_H, \Lambda] \quad (7)$$

In general the range of couplings is thus with a finite range of validity (i.e. up to Λ) in mind “restricted” as a function of Λ . If a theory is restricted to $\lambda \equiv 0$ in the limit $\Lambda \rightarrow \infty$, i.e. only the free version of the theory is consistent, then it is “trivial”.

Another problem besides triviality is that the Higgs potential can become unstable under radiative corrections for large top masses and a moderate Higgs mass [8]. To one-loop precision the effective potential for the Standard Model single Higgs doublet is given by:

$$V(\phi) = -\mu^2 \phi^2 + \frac{a}{16\pi^2 v^2} \phi^4 \ln(\phi^2/M^2); \quad a = 3 \sum_V M_V^4 - 4m_t^4 + m_H^4 \quad (8)$$

where V runs over the vector bosons, W^\pm, Z and the sum over fermions counts each quark color separately. Here μ and M are constants which are implicitly determined by specifying the Higgs particle mass and by demanding that the potential must have an absolute minimum at $\langle \phi \rangle / \sqrt{2} = 246$ GeV. The potential becomes unstable since the induced one loop radiative corrections to λ include a graph with a top loop proportional to $g_t^4 = m_t^4 \cdot v^4$. This contribution has a minus sign due to statistics and tends to drive λ negative. If the initial value of $\lambda = m_H^2 / 2v^2$ is small and $g_t = m_t/v$ is big then the sign of λ can change. If we look at eq. (8) then we see that the region of a stable potential is limited by a balance between the negative term from the top mass and a positive term from the Higgs mass. This can be crudely approximated to be

$$m_t \lesssim 90 \text{ GeV} + \frac{4}{7} m_H \quad (9)$$

though, for a more precise statement of the limits we refer to [9]. In the spirit of above we need only be concerned about such problems if the sign change occurs in the physical region up to Λ and therefore finite embedding scales were included in the analysis of ref. [9].

The limitations from both consistency requirements are summarized in Figs. 1) and 2) for different values of Λ . The strongest constraints for m_H and m_t arise for the highest values of Λ . So if LHC finds nothing than new lower limits on m_H and m_t , then these limits will be so high that the highest values for Λ are excluded. When the window closes only the highest allowed Higgs masses are left over and imply the lowest scale of new physics which is of order TeV again. Therefore from this point of view it would be better if e.g. the Higgs particle or its equivalent were heavy since this implies that the Standard Model cannot be taken to be valid at arbitrarily high energies. If the Higgs mass were at its highest allowed value of order TeV then new physics *beyond* the SM is guaranteed to show up in the TeV range.

Note that these kind of statements come essentially from the fact that with higher Higgs and top mass λ and g_t get bigger and the stronger loop effects lead to instabilities in the running coupling constants. In short the bounds on Λ are stronger if the initial coupling is bigger and therefore the instability is reached faster. This statement has probably an equivalent of much more general scope. If we would substitute the Higgs particle then very often a similar situation is expected. If the state which ensures unitarity is of the order of 1 - 2 TeV then this is (since the unitarity problem is solved only shortly before one arrives at an inconsistency and strong effects are needed to avoid this) a sign of a strongly interacting Higgs sector. If we would try to take this model with a Higgs substitute serious by itself then the strong couplings involved tend to produce “accidents” in the running couplings when loop effects are included. These “accidents” could then in general be interpreted as the need for new physics beyond the SM. By this handwaving argument we expect that the heavier the unitarizing particle is the more likely it will be that physics beyond the SM must show up earlier.

I.5. Extreme Examples of Dynamical Symmetry Breaking

As indicated above tree unitarity guarantees that at least one state which is connected inherently to the breaking of the electroweak symmetry must show up in the few TeV area. If one thinks that dynamical symmetry breaking mechanisms are more attractive than static mechanisms with fundamental scalars then one immediately recalls the similarities between the pions of QCD and the W and Z bosons. This has led to the development of scaled QCD or Technicolor [7] theories based on new Techni-fermions which carry a new confining Technicolor. In its simplest version there is one Techni-doublet (U,D) in analogy to the existing quarks and leptons and the boundstates of this doublet give rise to a set of Goldstone bosons as desired. Bigger models use more fermions like full generations or even more generations. But most models which use more than a minimal doublet of Techni-quarks are nowadays barely acceptable since they would predict extra pseudo Goldstone bosons with masses typically up to M_W or M_Z and most of the allowed range is already experimentally excluded. There are also limits on the number of new bosonic and fermionic fields in Technicolor scenarios from the analysis of precision data of radiative corrections to the SM [10]. Roughly speaking very big colour groups and very large numbers of fermions as well as technifermion mass splittings would lead to virtual effects that would already show up as deviations from the SM.

There is however one common feature to all Technicolor ideas. Since they are based on QCD scaled by F_π/f_π or additionally rescaled to any number of colors by large N_C arguments there is not much freedom in the spectrum. From radiative corrections [10] N_C is already restricted to be not too big and the Techni-meson to Techni-baryon mass ratios are only changed by N_C factors which implies that the Techni-baryons cannot be many orders of magnitude above the Techni-mesons. Therefore it seems as if a wealth of new states is unavoidably predicted in the multi TeV range. Another common feature of Technicolor scenarios is that the dampening of the amplitudes of the Higgs-less SM is always done by a Techni-rho.

To show that both the expectation of a wealth of states as well as the nature of the state that ensures unitarity are determined by the unknown dynamics we would like to contrast the Technicolor expectations with what has been called ‘Minimal Dynamical Symmetry Breaking’ [11]. There the fact that the top quark is very heavy is translated into a model where top quark condensation breaks the electroweak symmetry. One assumes that there is no fundamental Higgs field and that new four fermi interactions are added to the SM instead of it. The four fermi term is thought to be produced by new physics at Λ which has been integrated out so that one arrives at

$$\mathcal{L}_{(\mu=\Lambda)} = \mathcal{L}_{g,f} + \frac{g^2}{\Lambda^2} \bar{L} t_r \bar{t}_r L; \quad L = (t_l, b_l) \quad (10)$$

where $\mathcal{L}_{g,f}$ refers to the part of the Lagrangian which contains only gauge fields, fermions and no scalars. If the coupling g is chosen suitable [11] as to fulfill a gap equation like in BCS theory then the normal SM Higgs Lagrangian can be derived as an effective Lagrangian where the Higgs field is now a $t\bar{t}$ boundstate. The heaviness of the top quark would thus be linked to the non fundamental nature of the Higgs field.

Besides reproducing *effectively* the Higgs field which was thrown out one obtains relations between m_t , m_H and M_W . In its simplest and most elegant form the preferred values for the Higgs and top mass are $m_H \simeq 250$ GeV and $m_t \simeq 225$ GeV. This value of m_t is somewhat high when compared with the preferred range from the analysis of radiative corrections [3]. But even if the simplest version of this mechanism should not be acceptable on phenomenological grounds one can still start to build extensions which agree with experiment and have the same sort of dynamics. The important point is that the breaking of the electroweak symmetry by

top condensation can lead to situations very different from Technicolor ideas. The particle which ensures unitarity is a composite Higgs particle which is a $t\bar{t}$ boundstate with *exactly* the same properties as the fundamental Higgs field that was eliminated. Additionally unlike in Technicolor where mass ratios are rather inflexible here the ratio between the mass of this composite Higgs and the scale of new physics can be tuned to become *arbitrarily small*. Since the Higgs mass has to be somewhere in the TeV area this means that new physics besides this tight composite Higgs particle can be placed arbitrarily high. This would mean that we could find a Higgs particle where we are experimentally unable to tell if it is composite or fundamental since it is a very tight bound state and nothing else within reasonable energies accessible to any thinkable accelerator.

So even if the simplest version of top condensation turns out not to be realized it is still a good example which shows how dynamics determines the properties of the state which ensures unitarity and where the remaining spectrum is settled.

I.6. Cosmological Arguments for the TeV Scale: Dark Matter and Stable Particle Searches at LHC

The LHC and SSC are designed to unravel the mechanism of electroweak symmetry breaking. In this section we argue that these accelerators have a good chance to discovering much more. We point out that any perturbative new physics with cosmologically stable remnants has to occur below a few TeV . The single ingredient from which these conclusions follow is the cosmological requirement that the density of the universe does not exceed its critical value. This requirement implies that any perturbatively coupled cosmologically stable elementary particle must be lighter than the geometric mean of the Planck mass and the cosmic background radiation temperature of $2.7 K$ [12].

$$m \lesssim \sqrt{M_{Pl} \times 2.7 K} \simeq \text{few } TeV \quad (11)$$

By a remarkable coincidence this is of the order of a few TeV and thus implies that any stable electroweak particles must be energetically accessible to the LHC.

The list of theoretically motivated stable particles is long and distinguished.

(1) The Dark Matter of the Universe. Since it is most probably electrically neutral [13] and colorless it may be searched for via missing energy type experiments. They can also be searched by looking for the decays of their heavy electroweak partners which, if any, are necessarily charged [14].

(2) Technibaryons. They typically weigh $2 TeV$ and carry fractional electric charge; they can be colorless or colorfull depending on the theory [15].

(3) Lightest Superparticle (LSP). It is expected to be charge and color neutral; thus, it can be searched for by missing momentum measurements just like dark matter searches. In fact the LSP could eventually be true dark matter.

(4) Fractionally charged particles. These can occur in superstring theories [16]. They may be searched for by looking for sub (or super) -minimum ionizing particles. To measure their mass one needs time of flight experiments or/and magnetic fields.

References

- [1] K. Wilson, unpublished; E. Gildener and S. Weinberg, Phys. Rev. **D13**(1976)3333; L. Susskind, Phys. Rev. **D20**(1979)2619.
- [2] M. Chanowitz and M.K. Gaillard, Nucl. Phys. **B261**(1985)379.
- [3] For a recent analysis see e.g. P. Langacker, Univ. of Pennsylvania preprint UPR-0435T, Aug. 1990.
- [4] M. Veltman, Acta Phys. Pol. **B8**(1977)475; B.W. Lee, C. Quigg and H. Thacker, Phys. Rev. **D16**(1977)1519.
- [5] L.Maiiani, G.Parisi and R. Petronzio, Nucl. Phys. **B136**(1978)115; N. Cabibbo et al., Nucl. Phys. **B158**(1979)295; R. Dashen and H. Neuberger, Phys. Rev. Lett. **50**(1983)1847.
- [6] M. Lindner, Z. Phys. **C31**(1986)295.
- [7] L. Susskind, Phys. Rev. **D20**(1979)2619; S. Dimopoulos and L. Susskind, Nucl. Phys. **B155**(1979)237; E. Eichten and K. Lane, Phys. Lett. **B90**(1980)125.
- [8] P.Q. Hung, Phys. Rev. Lett. **42**(1979)873; H.D. Politzer and S. Wolfram, Phys. Lett. **B82**(1979)242.
- [9] M. Lindner, M. Sher and H. Zaglauer, Phys. Lett. **B228**(1989)139.
- [10] B. Lynn, M.E. Peskin and R.G. Stuart, CERN Yellow Book on Physics at LEP, ed. by J. Ellis and R. Peccei, CERN 86-02 report; M. Peskin and T. Takeuchi, Phys. Rev. Lett. **65**(1990)964.
- [11] W. Bardeen, C. Hill and M. Lindner, Phys. Rev. **D41**(1990)1647.
- [12] S. Dimopoulos, Phys. Lett. **B246**(1990)247 and references therein.
- [13] S. Dimopoulos et al., Phys. Rev. **D41**(1990)2388; R.S. Chivukula et al., Phys. Rev. Lett. **65**(1990)957; G. Starkman et al., Phys. Rev. **D41**(1990)3594.
- [14] S. Dimopoulos et al., "TeV Dark Matter", to be published in Nucl. Phys. B.
- [15] R. Chivukula and T. Walker, Nucl. Phys. **B 329**(1990)445.
- [16] G. Athanasiou et al., Phys. Lett. **B214**(1988)55.

Figure Captions

Fig. 1: Upper bounds on the top and Higgs mass from triviality and vacuum stability arguments for different values of Λ (taken from [6]).

Fig. 2: Lower limits on the Higgs mass from vacuum stability as a function of the top and Higgs mass and the scale of new physics (taken from [9]).

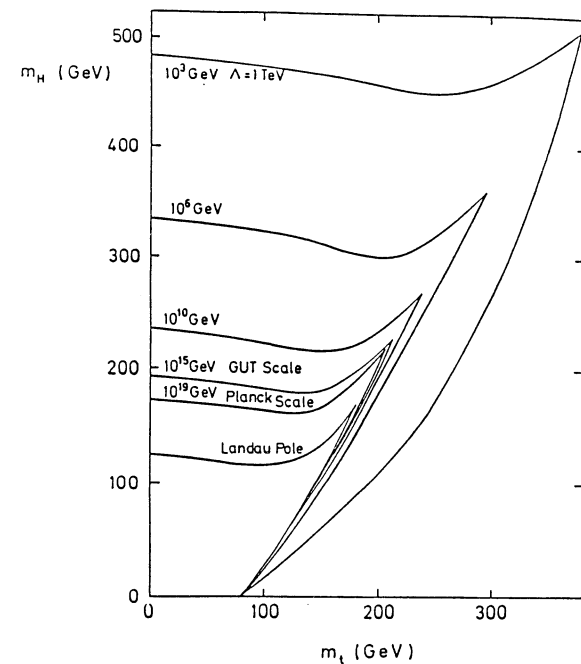


Fig. 1

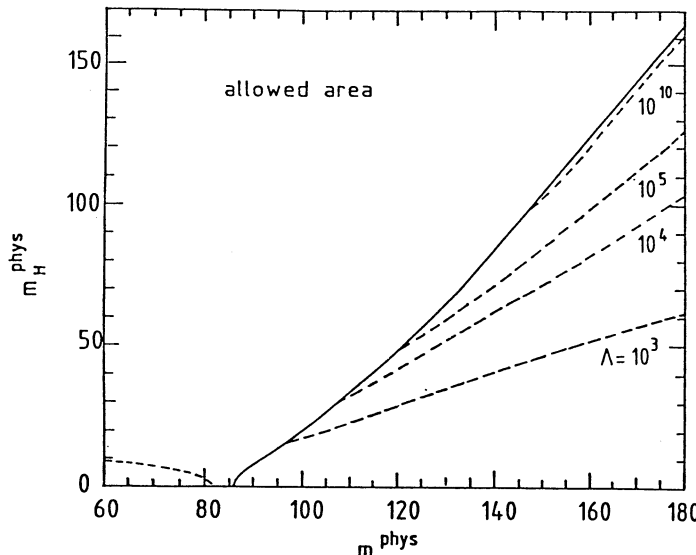


Fig. 2

II. $V_L V_L$ SCATTERING : CHIRAL LAGRANGIAN APPROACH

Contributors: A. Dobado, M.J. Herrero and J. Terron

II.1. Introduction

One of the main goals of the LHC is to clarify the origin of the Symmetry Breaking Sector (SBS) of the Standard Model (SM). Either the Higgs particle will be found at LHC (or SSC) with a mass below 1 TeV or some manifestation of the strongly interacting system to which the longitudinal components of the gauge bosons, W_L^\pm and Z_L , belong must show up in the TeV energy regime [1]. Generally speaking, the **Strongly Interacting Symmetry Breaking Sector (SISBS)** hypothesis simply means *the absence of any physical state belonging to the SBS well below 1 TeV other than the Longitudinal Weak Bosons (LWB) themselves*. In that case, the relative low masses of the gauge bosons as compared to the TeV energy domain, where the emerging resonances are expected to occur, may be understood on the basis of an approximate global symmetry of the SBS which is spontaneously broken and the LWB being the associated Nambu-Goldstone bosons. If experimentally achievable, the scattering of the LWB, $V_L V_L$ ($V_L = W_L^\pm$ or Z_L), at the TeV energy scale [2] will provide the clue to fully understand the nature of the SBS. Why this must be so?

First of all, in the case of a SISBS the scattering of the longitudinal degrees of freedom at high energies (say for $\sqrt{s} \gg M_W$) dominates over the scattering of the transverse components. Secondly, the Equivalence Theorem tells us that by measuring the $V_L V_L \rightarrow V_L V_L$ scattering at high energies ($\sqrt{s} \gg M_W$) what is really being measured is the scattering of the corresponding Nambu-Goldstone bosons and, consequently, the strength of the interactions in the SBS. Thirdly, it is precisely the energy scale of about 1 TeV where perturbative unitarity in $V_L V_L$ scattering is broken down. This has two important consequences. One is that the V_L 's self-interactions cannot be treated perturbatively. The other and probably the most interesting consequence concerning the phenomenological implications at LHC is the fact that there must be a system that is responsible for restoring unitarity in the $V_L V_L$ scattering at the TeV energy scale [3]. This system could be the Higgs particle itself as in the SM (H), a composite vector boson as for instance the technirho (ρ_{TC}^\pm and ρ_{TC}^0) of Technicolor theories or the isotriplet (V^\pm and V^0) of the BESS model, a composite scalar system resembling the Higgs particle , or it could even be a more exotic system with higher isospin and/or spin quantum numbers not even proposed yet.

The aim of this report is to set up the typical signatures of a SISBS at LHC and, for comparison, at SSC that come from different scenarios for the SBS as those just quoted above. In order to be able to deal with different physical situations for the SISBS on the same grounds and without loss of generality we choose the Chiral Lagrangian formalism and the Chiral Perturbation Theory (ChPT) techniques [4] that have been proven to be quite satisfactory in the context of low energy hadron physics.

The nicest feature of the Chiral Lagrangian approach when applied to the SISBS problem [5], besides of being completely general, is that it relies just on three simple requirements: 1) The global symmetry pattern for the building-up of this Chiral Lagrangian must be compatible with the symmetries of the SM, $SU(2)_L \times U(1)_Y \rightarrow U(1)_{em}$, 2) The ρ parameter must be close to one, and, 3) The value of the dimension-full parameter that plays the role of f_π in low energy hadron physics is fixed here to $v = 246\text{GeV}$. These three requirements lead us to adopt

the following chiral symmetry breaking pattern: $SU(2)_L \times SU(2)_R \rightarrow SU(2)_V$ with $SU(2)_V$ being the so-called custodial symmetry, and W_L^\pm , Z_L being the three Nambu-Goldstone bosons associated to this global symmetry breaking. All what rests is provided by the machinery of ChPT and the $V_L V_L$ scattering may, in fact, be described in formal analogy to $\pi\pi$ scattering. In the latter case the isospin symmetry plays the same role as the custodial symmetry does in the former case. More specifically, ChPT gives an expansion of the $V_L V_L$ scattering amplitudes in powers of $s/(4\pi v)^2$ and it is valid in the energy range $M_W \ll \sqrt{s} \ll \min(4\pi v, M_R)$, with M_R being the mass of the (unknown) lowest resonance belonging to the SISBS.

The $V_L V_L$ scattering amplitudes computed by means of ChPT do not respect unitarity for energies larger than about 1.5 TeV [5]. The problem of getting unitary answers for the scattering amplitudes is treated here by supplementing the Chiral Lagrangian approach with a unitarization prescription (we call it **Unitarized-ChPT**) [6]. In particular we use the following procedures: the Padé approximant method and the K-matrix one.

In our search for typical signatures of a SISBS at LHC (and SSC) we have been systematic: 1) we have looked at the four different final states in pair boson production, $W^+ W^-$, ZZ , $W^\pm Z$ and $W^\pm W^\pm$ and, 2) we have made predictions for three characteristic scenarios: Scaled-QCD, $SU(N_{TC})$ Technicolor and a Higgs-like scenario. Notice, however, that our study could be extended to more exotic scenarios as for instance those containing a system with isospin and electric charge equal to two that would resonate in the $W^+ W^+$ or $W^- W^-$ channels. For a more detailed description of the ChPT approach for $V_L V_L$ scattering see refs. [5], [7] and [8]. Some of the results presented in this report are contained in [7].

II.2. Cross-sections for strongly interacting signals

In order to compute the cross-section for the process $pp \rightarrow (V_1^L V_2^L \rightarrow V_3^L V_4^L) + X$, we have used the effective W -approximation [9] that allows us to derive it in terms of the cross-section for the subprocess $V_1^L V_2^L \rightarrow V_3^L V_4^L$, where the initial longitudinal gauge bosons are taken to be real. More precisely, it is given by:

$$\sigma = \sum_{ij} \int \int d\tau d\eta f_i(x_1, Q^2) f_j(x_2, Q^2) \int \int d\hat{\tau} d\hat{\eta} \left(\frac{d^2 \mathcal{L}}{d\hat{\tau} d\hat{\eta}} \right)_{V_1 V_2} \times \int_{-1}^1 d\cos\theta \frac{d\hat{\sigma}}{d\cos\theta} \quad (1)$$

where, f_i and f_j are the distribution functions of the quarks i and j , respectively, inside the proton; the variables τ and η are related to the momentum fractions of the quarks by $x_{1,2} = \sqrt{\tau} e^{\pm i\eta}$; the variables $\hat{\tau}$ and $\hat{\eta}$ are related to the momentum fractions of V_1, V_2 respect to q_i, q_j , \hat{x}_1 and \hat{x}_2 , by $\hat{x}_{1,2} = \sqrt{\hat{\tau}} e^{\pm i\hat{\eta}}$; $(\frac{d^2 \mathcal{L}}{d\hat{\tau} d\hat{\eta}})$ is the luminosity function for the gauge boson pair $V_1^L V_2^L$ to be radiated from the quark pair $q_i q_j$; and $\frac{d\hat{\sigma}}{d\cos\theta}$ is the differential cross-section for the subprocess $V_1^L V_2^L \rightarrow V_3^L V_4^L$ given by:

$$\frac{d\hat{\sigma}}{d\cos\theta} = \frac{|T(V_1^L V_2^L \rightarrow V_3^L V_4^L)|^2}{32\pi M_{VV}^2}. \quad (2)$$

For final states with identical particles an additional factor of 1/2 must be included.

The scattering amplitudes for the various signal subprocesses $T(V_1^L V_2^L \rightarrow V_3^L V_4^L)$ are given in ChPT to $O(p^4)$ by [5]:

$$T(W_L^+ W_L^- \rightarrow W_L^+ W_L^-) = A(s, t, u) + A(t, s, u), \quad T(W_L^+ W_L^- \rightarrow Z_L^0 Z_L^0) = A(s, t, u)$$

$$T(Z_L^0 Z_L^0 \rightarrow Z_L^0 Z_L^0) = A(s, t, u) + A(t, s, u) + A(u, t, s)$$

$$\begin{aligned} T(W_L^\pm Z_L^0 \rightarrow W_L^\pm Z_L^0) &= A(t, s, u), \quad T(W_L^\pm W_L^\pm \rightarrow W_L^\pm W_L^\pm) = A(t, s, u) + A(u, t, s) \\ A(s, t, u) &= \frac{s}{v^2} + \frac{4}{v^4} \left(2M_R(\nu)s^2 + N_R(\nu)(t^2 + u^2) \right) \\ &+ \frac{1}{(4\pi)^2 v^4} \left[-\frac{1}{12}(3t^2 + u^2 - s^2) \log \frac{-t}{v^2} - \frac{1}{12}(3u^2 + t^2 - s^2) \log \frac{-u}{v^2} - \frac{1}{2}s^2 \log \frac{-s}{v^2} \right] \end{aligned} \quad (3)$$

and, $M_R(\nu)$, $N_R(\nu)$ are the two renormalized parameters appearing in the $O(p^4)$ terms of the Chiral Lagrangian. The values of M_R and N_R have to be chosen properly for each different scenario of the SISBS one is interested to mimic. The $O(p^2)$ terms in (3) are independent of the underlying dynamics and correspond to the well known Universal Low Energy Theorems results [10].

For the numerical computations we have introduced the above expressions into a parton level Monte Carlo program (VEGAS) that besides of calculating the total cross section it generates all the relevant distributions with the required cuts. The various background contributions were also computed by the same Monte Carlo program. The signal processes for the three scenarios considered here were also introduced into the PYTHIA Monte Carlo program and some of them were studied parallelly by another subgroup [11].

We have used the EHLQ structure functions set II [12] (the choice done for Q^2 will be discussed separately for each process), and the following parameters for LHC and SSC were assumed: $LHC, \sqrt{s} = 16\text{TeV}, L = 4 \times 10^{34}\text{cm}^{-2}\text{sec}^{-1}$ and $SSC, \sqrt{s} = 40\text{TeV}, L = 10^{33}\text{cm}^{-2}\text{sec}^{-1}$. Some comments will also be done for a lower luminosity at the LHC of $L = 10^{34}\text{cm}^{-2}\text{sec}^{-1}$ (unless it is said explicitly the highest luminosity with the factor 4 included will be assumed). All the numbers of events presented in this report correspond to a running time of 10^7sec .

Our starting "raw events" are those obtained after applying the following set of minimal cuts: $0.5\text{TeV} < M_{VV} < 10\text{TeV}$, $|p_{TV}| > 10\text{GeV}$, $|y| < 1.5$ or 2.5 . Here M_{VV} is the invariant mass of the final gauge boson pair, p_{TV} is their transverse momentum and y is their rapidity. Notice that the lower cut on the invariant mass is necessary for the computation of the signal rates since we are using the Equivalence Theorem that assumes $M_{VV} \gg M_V$. In order to improve the observability of the signal over the background processes we apply more stringent cuts than the minimal cuts. These are obtained from a optimization procedure that is based on making cuts simultaneously on M_{VV} and p_{TV} . Depending on the kind of the signal, we adopt one of the two following strategies:

(A) Whenever there is a wide resonance or there is an excess of events over the continuum we look for the cuts (we call them **optimal cuts**) that maximize the function

$$F((p_{TV})_c, (M_{VV})_c) = \frac{n_s(p_{TV} > (p_{TV})_c, M_{VV} > (M_{VV})_c)}{\sqrt{n_T(p_{TV} > (p_{TV})_c, M_{VV} > (M_{VV})_c)}} \quad (4)$$

where $n_s(\dots)$ ($n_T(\dots)$) is the number of events in the signal (total = signal + background) that satisfy the cuts indicated. The notation used in the tables for the optimal cuts is: $((p_{TV})_c, (M_{VV})_c)$. Note that F measures the statistical significance of the signal.

(B) Whenever there is a narrow resonance we choose a window on the M_{VV} variable and search for the cut on p_{TV} that makes $F(p_{TV})$ maximal. The notation used in the tables for the optimal cuts is $((p_{TV})_c)$.

II.3. Scenarios for the SISBS

In order to study the phenomenological implications at LHC we have considered three scenarios [7]: Scaled-QCD, $SU(N_{TC})$ Technicolor and a Higgs-like scenario.

II.3.1. Scaled-QCD

This scenario is based on transferring the low energy phenomenology of QCD from the energy domain of several hundreds MeV to the region of several hundreds GeV. The LWB are really the pions of this Scaled-QCD scenario. In particular, the $V_L - V_L$ scattering is a replica of the $\pi - \pi$ scattering data (including the broad enhancement in the I=J=0 channel and the appearance of the ρ resonance in the I=J=1 channel) that have been scaled up in energy by a factor of $v/f_\pi = 2600$. We do this rescaling by means of Unitarized-ChPT.

The physical parameters of the ρ -like resonance of this Scaled-QCD scenario are the following: $M_{\rho_{QCD}} = 2\text{TeV}$, $\Gamma_{\rho_{QCD}} = 480\text{GeV}$.

II.3.2. $SU(N_{TC})$ Technicolor

In this scenario, $SU(N_{TC})$ Technicolor [13], we assume there is a vector resonance I=J=1 in the spectrum. Using large N_{TC} arguments one expects that the mass of the vector resonance goes like [13] $M_{\rho_{TC}} \approx M_\rho \frac{v}{f_\pi} (\frac{3}{N_{TC}})^{\frac{1}{2}}$, where $M_\rho = 770\text{MeV}$. Increasing N_{TC} implies a lighter resonance as compared to the resonance in the QCD-like scenario that would correspond in this context to $N_{TC} = 3$. By assuming the KSFR relation [14] holds in $SU(N_{TC})$ theories as it (approximately) does in QCD, more specifically $\Gamma_{\rho_{TC}} = \frac{M_{\rho_{TC}}^3}{96\pi v^2}$, then the larger N_{TC} is, the narrower turns out to be the resonance. In this way one can study the experimental possibilities for detecting vector resonances over a wide range of mass values, based on some general assumptions. In particular, the existence of a lighter resonance increases considerably the production rates of $W^\pm Z^0$ pairs and, thus, the observability of these resonances. The way one has to choose M and N in order to reproduce the low energy behaviour of these $SU(N_{TC})$ scenarios is the following one:

$$M_R^{TC}(\frac{v}{f_\pi}(\frac{3}{N_{TC}})^{\frac{1}{2}}) = \frac{N_{TC}}{3} M_R^{QCD}(\nu) ; \quad N_R^{TC}(\frac{v}{f_\pi}(\frac{3}{N_{TC}})^{\frac{1}{2}}) = \frac{N_{TC}}{3} N_R^{QCD}(\nu) \quad (5)$$

where M_R^{QCD} and N_R^{QCD} are the parameters of the $O(p^4)$ terms in the chiral Lagrangian of low energy QCD.

In order to take into account properly the contribution of the I=J=1 resonance (the technirho) in the computations, we have chosen the Padé unitarization method. The reason is that it provides a resonant behaviour in the I=J=1 channel with the particularity of fulfilling automatically the KSFR relation. In particular, it is known to reproduce very well the $\pi - \pi$ scattering data in the three channels, I=J=0, I=J=1 and I=2,J=0 [15].

In order to study a wide range of signatures we have considered two technicolor scenarios: 1) $M_{\rho_{TC}} = 1.0\text{TeV}$, $\Gamma_{\rho_{TC}} = 55\text{GeV}$ and 2) $M_{\rho_{TC}} = 1.5\text{TeV}$, $\Gamma_{\rho_{TC}} = 185\text{GeV}$. They correspond to $N_{TC} = 12$, and $N_{TC} = 5$ respectively.

II.3.3. Higgs-like

We define the Higgs-like scenario in two steps. First, we choose the parameters of the effective Lagrangian to $O(p^4)$, M and N [5], so as to reproduce the LWB scattering amplitudes in the SM to one loop order and in the limit $m_H^2 \gg s$ [16]. Thus, with this first step we are simulating the effect at low energies of a very heavy Higgs boson in the SM to one loop level. The way one has to choose the parameters M and N is the following:²

$$M_R(\nu) = \frac{1}{8}(c_1 - \frac{1}{2}c_2) + \frac{1}{12(4\pi)^2} \log \frac{M_H}{\nu} ; \quad N_R(\nu) = \frac{c_2}{8} + \frac{1}{6(4\pi)^2} \log \frac{M_H}{\nu} \quad (6)$$

where, $c_1 = \frac{1}{(4\pi)^2}(\frac{9\pi}{2\sqrt{3}} - \frac{76}{9})$, $c_2 = -\frac{4}{9}\frac{1}{(4\pi)^2}$ and M_H is the renormalized Higgs mass as defined in the first ref. of [16].

The second step involves the unitarization of the LWB scattering amplitudes obtained in the first step. We remind that, in their present form, they violate unitarity at about 1.5 TeV [5] and they should not be used without a unitarization prescription for the event rates computation at LHC or SSC [17]. The two unitarization methods used here give partial waves that verify $\text{Im } a_{IJ} = |a_{IJ}|^2$. Besides, they are characterized by:

**** K-matrix method:** It stops the increase with energy of the a_{IJ} partial waves (particularly the a_{00} partial wave in this Higgs-like scenario) and gives a saturation behaviour.

**** [1,1]-Padé-approximant method:** It also stops the increase with energy of the a_{IJ} partial waves but instead of saturating all of them it develops a resonant behaviour in the a_{00} channel. The scalar resonance S of the Higgs-like scenario shows up at a mass scale which is given by the position of the pole in the unphysical sheet of the $a_{00}^{[1,1]}(s)$ function [18]. More precisely, M_S is given by the solution to the equation:

$$M_S^2 = \frac{4v^2}{\frac{1}{3}(22c_1 + \frac{1}{4}c_2) + \frac{100}{9(4\pi)^2} \log \frac{M_H}{M_S}}. \quad (7)$$

We define the Higgs-like scenario in this case as the one having the scalar resonance at $M_S \sim 1\text{TeV}$. It is worth to mention that, as pointed out in [19], the features obtained by the Padé method when applied to the SM case (in particular the appearance of the so called "Higgs Remnant" corresponding in our case to the scalar resonance S) are in qualitative agreement with the ones obtained by the large N expansion of the O(N) model [20].

II.4. Numerical Results

In view of the present controversy about the question of whether such a high luminosity as that planned for LHC and SSC will allow to disentangle SISBS signals by studying the hadronic decays of the weak bosons or not, we have considered in this report only their *LEPTONIC DECAYS*.

²Strictly speaking, there would be an additional contribution to M_R that comes from the tree level and is given by $M_{tree} = \frac{v^2}{8M_H^2}$ [8]. We thank G.Valencia for making us this remark. However, we do not consider this term here since it is completely negligible in the limit we are concerned with, $v^2 \ll s \ll M_H^2$.

II.4.1. W^+W^- Channel

This channel looks potentially very interesting in terms of signal rates and signal patterns as it would give resonant behaviour in all the three scenarios considered here. However, in view of the present lower bounds for the top quark mass, $m_t > 89$ GeV [21], already above the W -boson mass, it turns out that the dangerous background $pp \rightarrow t\bar{t}X$ with the top (anti-top) quarks decaying into real W^+ 's (W^- 's) overwhelms completely the signal. In view of that we have not considered this channel here.

II.4.2. ZZ Channel [7]

This channel offers a potential good probe for the Higgs-like scenario and in general for any scenario containing a scalar- isoscalar resonance. The reason is that it couples dominantly to the $I=J=0$ channel and therefore, in principle, it could produce either a bump or in the worst case an enhancement in the invariant mass distribution of the gold-plated events, $l^+l^-l^+l^-$ with $l = \mu$ or e , over the continuum background.

**** Leptonic branching ratio:** $BR(ZZ \rightarrow l^+l^-l^+l^-) = 0.4\%$

**** Signal processes:** The total rates for the signal correspond to the sum of the following separate contributions: 1) $W_L^+W_L^- \rightarrow Z_LZ_L$ and 2) $Z_LZ_L \rightarrow Z_LZ_L$. The Q^2 scale used in the distribution functions of the quarks is $Q^2 = M_W^2$.

**** Background processes:** The total background is the sum of the following separate contributions (in parenthesis it is written the percentage relative to the total background for both LHC and SSC and for top masses ranging from 100 GeV to 180 GeV): 1) $q\bar{q} \rightarrow Z^0Z^0$ (80%-70% at LHC) (65%-55% at SSC) and 2) $gg \rightarrow Z^0Z^0$ (20%-30% at LHC) (35%-45% at SSC). The Q^2 scale used in the distribution functions of quarks and gluons (and in $\alpha_s(Q^2)$) is $Q^2 = \hat{s}$. Here (and in the rest of the report) \hat{s} is center-of-mass-energy squared of the parton-parton system.

**** Results and comments:** The results for the signal-to-background ratios, S/B, of the final leptonic $l^+l^-l^+l^-$ events ($l = \mu$ or e) after applying the optimal cuts are collected in table 1. We have chosen here two among the three scenarios: The Higgs-like and the Scaled-QCD scenarios.

Figs. 1a and 1b show the invariant mass distribution M_{ZZ} (no leptonic-BR has been included in the figs.) of the ZZ reconstructed events (it assumes 100% efficiency in the reconstruction). From these numerical results one can conclude that the search of SISBS signals in this channel seems difficult. The signal-to -background ratio is always less than one and there is no apparent bump in the M_{ZZ} -invariant mass distribution. The most favourable case is the Higgs-like scenario where the best S/B-ratio that can be got at LHC with the highest luminosity is 33/75. The S/B-ratio at SSC is slightly larger (8/11) but it is poor in statistics. The results with the K-matrix method (not shown in table 1) give comparable signal rates for the Scaled-QCD scenario and slightly smaller rates (about a factor 2/3) for the Higgs-like scenario.

The curves show a small enhancement in the high- M_{ZZ} region of the M_{ZZ} -invariant mass distribution over the continuum. This enhancement is clearly larger in the Higgs-like scenario than in the Scaled-QCD one and, in general, the corresponding total signal rates are in a ratio of 2 to 1 respectively. Finally, whether it will be possible to discern this small enhancement from the continuum or not is a question strongly dependent on the accuracy in the calibration of this continuum along the whole invariant mass range.

II.4.3. $W^\pm Z$ Channels [7]

These channels are a good probe for the Scaled- QCD and Technicolor scenarios and, in general, for any scenario containing a ρ -like vector resonance (for instance the V^\pm resonances of the BESS model [22]). This resonance couples dominantly to the $I=J=1$ channel and therefore can give rise to a resonant behaviour in $W^\pm Z$ production at LHC and SSC. The final $l^\pm\nu_l l^\pm l^-$ leptonic events (with $l = \mu$ or e) produced from the decay chain $\rho^\pm \rightarrow W^\pm Z \rightarrow l^\pm\nu_l l^\pm l^-$ will present typical signatures and distributions characterized by the physical parameters (the mass and the width) of this resonance.

**** Leptonic branching ratio:** $BR(W^\pm Z \rightarrow l^\pm\nu_l l^\pm l^-) = 1.5\%$

**** Signal processes:** Here we distinguish the Higgs-like scenario from the other ones, i.e., the Scaled-QCD and the Technicolor scenarios.

Higgs-like: There is just one type of signal process: 1) $W_L^\pm Z_L \rightarrow W_L^\pm Z_L$.

Scaled-QCD and Technicolor: There are two kind of processes that contribute to the signal, that is to $W_L^\pm Z_L$ production: 1) $W_L^\pm Z_L \rightarrow W_L^\pm Z_L$, and 2) $q\bar{q} \rightarrow W^\pm \rightarrow \rho_{TC} \rightarrow W_L^\pm Z_L$. The first mechanism is the so-called WZ fusion process and gives a generic SISBS signal since it is present in all the SISBS scenarios. The choice done for the Q^2 scale is $Q^2 = M_W^2$. The second mechanism where $q\bar{q}$ annihilates into ρ_{TC} via $\rho_{TC} - W$ mixing is not present in the Higgs-like scenario but it is always present in any SISBS scenario containing a vector resonance with the quantum numbers of the W gauge boson. This is for instance the case of the Scaled-QCD scenario, Technicolor and the BESS model. For the two scenarios we are concerned with, we will assume as a reasonable working hypothesis that this second mechanism is well described in terms of Vector Meson Dominance (VMD) [23],[12]. The choice for the Q^2 scale here is $Q^2 = \hat{s}$.

**** Background processes:** We have taken into account the following background processes: 1) $q\bar{q} \rightarrow W^\pm Z$. This is the main background. We have used the formulas of [12]; 2) $\gamma W^\pm \rightarrow W^\pm Z$. We have calculated the amplitudes for this process in the Standard Model and checked the expressions of [24]. The ratio of the production rates is $\gamma W_L^\pm \rightarrow W^\pm Z / \gamma W_T^\pm \rightarrow W^\pm Z = 0.04$ for both the LHC and the SSC; 3) $W^\pm Z \rightarrow W^\pm Z$ This background is defined as the contribution from all the polarization channels in WZ elastic scattering as predicted in the SM without the Higgs contribution and without the configuration $W_L^\pm Z_L \rightarrow W_L^\pm Z_L$. The latter is considered by us as the signal and is described by means of the effective chiral Lagrangian. We have obtained the following relations for the production rates: $W_T^\pm Z_T \rightarrow W^\pm Z : W_T^\pm Z_L + W_L^\pm Z_T \rightarrow W^\pm Z : W_L^\pm Z_L \rightarrow W^\pm Z = 1 : 0.1 : 0.003$ for both the LHC and the SSC for the 2.5 rapidity cut. The relative contributions respect to the total background are the following:

	LHC	SSC
$q\bar{q}$	65%	45%
γW^\pm	15%	20%
$W^\pm Z$	20%	35%

The Q^2 scale used in each case is: $Q^2 = M_W^2$ for the WZ and γW processes and $Q^2 = \hat{s}$ for the $q\bar{q}$ process.

There is an additional potentially dangerous background that we have not included here. It is the $t\bar{t}$ production with subsequent top decays into real W 's. This process fakes our signal when both W 's decay leptonically and one of the bottom quarks decays semileptonically. Although the rate for this process at the starting point is huge as compared to the signal, a careful study done by M.I.Josa, F.Pauss and T.Rodrigo [11] indicates that there exists a set of feasible cuts that diminishes this background to a level comparable or even lower to the backgrounds considered here.

**** Results and comments:** The results for the signal-to-background ratios, S/B, of the final leptonic $l^\pm \nu l^\pm l^-$ events ($l = \mu$ or e) after applying the optimal cuts are collected in table 2. Predictions were made for the three scenarios: Scaled-QCD, Technicolor and the Higgs-like scenario. In looking for the optimal cuts we have used strategy A for the Higgs-like scenario and strategy B for the Scaled-QCD and Technicolor scenarios. We took: 950-1050 GeV, 1400-1550 GeV, 1500-2500 GeV as the windows in M_{WZ} for $M_\rho = 1.0, 1.5, 2.0$ TeV respectively.

We have also computed the signal that would be produced in the Standard Model at tree level with a heavy Higgs boson of $m_H = 1$ TeV (SMH), in order to compare the results with our Higgs-like scenario results (HIGGS) that in contrast include the one loop corrections and a unitarization procedure. The analytic expressions in the SMH case were calculated for all possible configurations of polarizations (TT, TL, LT, LL, T for transverse and L for longitudinal). The formulae are too long to be included here and will be published elsewhere. As we have found some errors in the expressions for the $W_L^\pm Z_L \rightarrow W_L^\pm Z_L$ amplitudes published in the literature [25], the corrected formulae were included explicitly in [7] and incorporated into PYTHIA. In comparing the SMH and the Higgs-like scenario we find, as expected, comparable rates. The differences in S/B ratios of table 2 are due to the differences in the applied optimal cuts. As it is clear from the results in table 2, the S/B ratios are too low to be observable in either the Higgs-like scenario or in the SMH.

The situation is completely different in the Scaled-QCD and Technicolor scenarios where there are actual possibilities of observing the signal over the background with the total S/B ratios being always larger than one (see table 2). The contributions to the signal coming from the WZ fusion process and the $q\bar{q}'$ annihilation process via $\rho_{TC} - W$ mixing are presented separately in table 2. We would like to emphasize here that the S/B ratios obtained by considering just the WZ fusion contribution to the signal represent the most general and conservative expectations for the SISBS signals at LHC and SSC, and are already (for all the cases considered here) larger than one. The WZ fusion mechanism gives a generic SISBS signal and does not involve any assumption on the couplings between the fermionic sector and the SBS. The relative percentages of the WZ fusion contribution to the total signal are:

M_ρ	rap.cut	1.0TeV	1.5TeV	2.0TeV
LHC	(2.5)	9%	24%	45%
SSC	(2.5)	22%	50%	72%

An increase in M_ρ results in a larger contribution from WZ fusion process, which reveals itself as the most efficient mechanism in probing the SISBS for large enough values of M_ρ . This fact is clearly reflected in figures 2a and 2b. It is interesting to point out that the contribution of the fusion process is even more important at the SSC than at the LHC, due to the higher energy available at the subprocess level. The comparison of these mechanisms in technicolor theories was first discussed by Chivukula in [23] in the context of the SSC.

In figures 3a (LHC) and 3b (SSC) the M_{WZ} invariant mass distributions of the different background processes are displayed and for reference we have also included the spectrum of the WZ fusion signal process (with the optimal cuts).

As it is clearly manifested in figures 2 and 3 and in table 2 the results are encouraging for both LHC and SSC and for all the three values of M_ρ considered. Special mention must be given to the technicolor models where there is a large and clear signal in the M_{WZ} spectrum. In both cases, the Scaled-QCD and Technicolor scenarios, masses up to 2 TeV will be reachable at LHC. (See [11] for more details on this channel).

II.4.4. $W^\pm W^\pm$ Channels [26]

These channels are called exotic channels since they produce 2 like-sign leptons in the final state ($l^\pm \nu l^\pm \nu$ with $l = \mu$ or e) that are not easily produced by means of standard physics. Any potential signal in these channels will compete with a less prominent background than in the other channels. For instance, the important qq' background in W^+W^- , ZZ and $W^\pm Z$ channels is not present in $W^\pm W^\pm$ channels. Unfortunately, the latter are not good probes for any of the scenarios considered here in the sense that these do not contain any doubly charged resonance with $I=2$ that could resonate in the $W^\pm W^\pm$ channels. However, it is precisely its singular nature what makes this channel an interesting landmark especially adequate to probe new unexpected resonances. For the scenarios we are concerned with, the expected SISBS signal will be an enhancement in the large invariant mass M_{WW} that, unfortunately, is hard to translate into physical leptonic variables. These channels will serve at best as a test-confirmation of compatibility with whatever is seen in the ZZ and/or $W^\pm Z$ channels.

**** Leptonic branching ratio:** $BR(W^\pm W^\pm \rightarrow l^\pm \nu l^\pm \nu) = 5\%$

**** Signal processes:** $W_L^\pm W_L^\pm \rightarrow W_L^\pm W_L^\pm$. The Q^2 scale chosen here was $Q^2 = \hat{s}$.

**** Background processes:** These have been studied in detail by Barger et al. in [26]. The numerical results used in this report for the various background processes were taken from that reference. The main background processes in the W^+W^+ case are the following:

1) $qq' \rightarrow qq'W^+W^+$ (weak): This takes place through electroweak interactions and produces mainly $W_T^+W_T^+$ pairs. The exact calculation was presented in [26]. We will refer to this background as $W_T^+W_T^+$. 2) $qq' \rightarrow qq'W^+W^+$ (semi-weak): This takes place through gluon exchange. It will be referred to as gluon exchange. 3) $q\bar{q} \rightarrow W^+t\bar{t}$: This process fakes the leptonic signal when the quark top decays into a real W^+ , both W^+ 's decay semileptonically and the remaining bottom and anti-top quarks decay hadronically. Its contribution depends crucially on the top mass value. The values $m_t = 100$ GeV and 200 GeV were chosen here. 4) $W^+W^+ + 3$ -jets-QCD: One contributing process is for instance, $qq' \rightarrow qq'W^+W^+g$. It will be called 3 jets QCD. The relative contributions of the various backgrounds respect to the total for $M_{WW} > 0.8$ TeV and $|y_W| < 1.5$ are as follows:

Process	LHC ($m_t =$)	LHC 100GeV	SSC 200GeV	SSC 100GeV	SSC 200GeV
$W_T^+W_T^+$	31%	36%	43%	46%
gluon exchange	14%	15%	19%	19%
3 jets QCD	12%	13%	17%	16%
$W^+t\bar{t}$	43%	36%	21%	19%

It has also been checked (by explicit computation) in [26] that a cut on the W-boson variables given by $M_{WW} > 0.8$ TeV and $|y_W| < 1.5$ is approximately equivalent to the following cuts on the leptonic variables (this is for both the total signal and the total background): $m_{ll} > 0.5$ TeV, $|y_l| < 2.0$ and $p_T(l) > 25$ GeV.

**** Results and comments:** The results for the signal-to-background ratios, S/B, of the final $l^\pm \nu l^\pm \nu$ events ($l = \mu$ or e), for various choices of the invariant mass cut are shown in table 3. The corresponding rates for the $l^- \nu l^- \nu$ events (not shown in the table) are approximately 1/3 of those in table 3. The results from a tree level calculation in the SM with a Higgs boson of $m_H = 1$ TeV (SMH) are also included for comparison with our Higgs-like scenario (HIGGS). From these numerical results one can conclude that the search of SISBS signals coming from the kind of scenarios considered in this report will be very hard in these channels. The S/B ratio is always less than one and the M_{WW} distribution of the signal shows no singular behaviour.

From figs. 4a and 4b it is clear that for the energy range of interest the total background is well above the signal. In ref.[26] it is claimed that by using central jet vetoing techniques one can notably improve the S/B ratios. Since the signal in this report is computed by means of the Effective W approximation, that assumes zero transverse momentum for the WW system and the remaining jet-jet system, these jet vetoing techniques cannot be implemented properly here. We leave this work for a Monte Carlo level simulation.

II.4.5. Multiple V_L Production

Another probe to test the nature of the Symmetry Breaking Sector is the multiple production of LWB [27]. In the case of a SISBS, the multiple production of LWB is not suppressed by powers of the weak coupling constant as it occurs in weakly interacting SBS. We consider here the production of four LWB, $V_L V_L \rightarrow V_L V_L V_L V_L$, in the context of the effective Chiral Lagrangian approach³. We first calculate the amplitude for this process at the tree level, that is to $O(p^2)$ in ChPT. Thus, as long as these results are universal (fixed just by the scale v) they constitute a conservative estimate of the rates and they serve to test the nature of the SBS, but not the underlying dynamics.

As these amplitudes increase with the energy, it is necessary to study the question of unitarity. In fact, the $2 \rightarrow 4$ amplitudes are expected to violate unitarity at the same scale as the $2 \rightarrow 2$ channels, namely $O(1\text{-}2 \text{ TeV})$. This implies that the effects of higher order corrections must be taken into account in order to restore unitarity. As we have already seen for the case of pair production, one way of incorporating these effects is through the use of a unitarization procedure. In order to obtain conservative estimates, we consider the K-matrix method (a more detailed presentation of these computations will be given in [28]). Comparing the non-unitarized amplitudes with the unitarized ones, it results that they begin to differ from each other by about 20% (in units of (amplitude)²) for $M_{VV} \sim 1.5\text{-}2 \text{ TeV}$. As we have skipped the Chiral expansion via a unitarization procedure we have no information about the scale that controls the range of validity of the unitarized amplitudes. It is expected the unitarized amplitudes to be reliable up to, at least, 2 TeV, although their validity is doubtful beyond $4\pi v \sim 3 \text{ TeV}$ (the scale that controls the original chiral expansion).

In table 4 the results after unitarization and for various upper cuts on M_{VV} (the invariant mass of the initial pair) of 2 TeV, 3 TeV and no cut, are presented. They include in addition the following cuts: a lower cut on M_{VV} of $M_{VV} > 1 \text{ TeV}$, cuts on the rapidity and transverse momentum of each final state bosons, $|y| < 2.5$, $p_T > 10 \text{ GeV}$, and in the separation of the final state boson, $\Delta R_{VV} > 0.7$. The results without unitarizing and without applying any upper cut on M_{VV} are also given (in parenthesis) for comparison. As it is clearly seen, the effects of unitarization are very important in the total number of events, meaning that one should only trust the results obtained after unitarization. In particular, the two first numbers of table 4, corresponding to a cut of $M_{VV} < 2 \text{ TeV}$ and 3 TeV respectively, give the most realistic lower bound to the total number of expected events.

On the other hand, in order to have a detectable experimental signal with acceptable rates it is necessary to consider the hadronic decay channels of the LWB, and consequently the background from QCD needs to be computed. It is expected a large suppression of the QCD background relative to the signal when a very stringent cut on the transverse momentum of the jets is applied. The jets coming from the signal have a very large p_T of $p_T \sim 0.5\text{-}1 \text{ TeV}$ for the

³Notice that processes like $V_L V_L \rightarrow V_L V_L V_L$ are not allowed due to the symmetry breaking pattern assumed here, $SU(2)_L \times SU(2)_R \rightarrow SU(2)_V$.

LHC(SSC).

From this preliminary study we conclude that if there is a SISBS, about a total number of $100 V_L V_L V_L V_L$ events will be produced at LHC. They will provide events with multiple jets with the particularity of having very high p_T . However, given the fact that this kind of SISBS probe relies on the spectroscopy of jets, it is still premature to conclude anything more precise until a more detailed analysis including the QCD background is done [28].

II.5. Conclusions

We have studied the $V_L V_L$ scattering at LHC and SSC in the Chiral Lagrangian formalism that incorporates all the facts that are known about the symmetry breaking sector of the SM and has the appealing feature of treating the SISBS problem within a general framework (a feature always desirable given the controversial nature of the subject). It allows to simulate different possible scenarios for the SISBS. We have studied in this report the phenomenological implications of three of them: Scaled-QCD, Technicolor and a Higgs-like scenario. This study was done in a systematic way for the three relevant channels: ZZ , $W^\pm Z$ and $W^\pm W^\pm$, and, in order to be conservative, we have considered just the leptonic decays of the gauge bosons.

Our main conclusions can be summarized as follows:

1.- If the SBS behaves at the TeV energy scale as the Higgs-like scenario or as the Standard Model with a heavy Higgs boson of $M_H = 1 \text{ TeV}$, it will be difficult to disentangle any signal from the background at LHC (and SSC). The most favourable channel is ZZ where a small enhancement in the $O(1 \text{ TeV})$ M_{ZZ} region of the spectrum of the gold plated events is found. The S/B ratios are always less than one and there is lack of statistics in the signal. The best ratio found is $S/B = 33/75$ and it corresponds to the highest integrated luminosity option for LHC of $L = 4 \times 10^5 \text{ pb}^{-1}$.

2.- If the SBS behaves at the TeV energy scale as the Scaled-QCD or Technicolor scenarios, characterized by the existence of a ρ -like vector resonance, there are actual possibilities of observing the signal over the background in the $W^\pm Z$ channels. A clear resonance shape will show up in the M_{WZ} and p_T^Z spectra. If the highest luminosity option for LHC is achieved, masses up to $M_\rho \sim 2 \text{ TeV}$ will be tested. The WZ fusion mechanism contributes about 50% (70%) to the total signal at LHC (SSC) for $M_\rho = 2 \text{ TeV}$. It will provide by itself generic SISBS signals that involve just the interactions in the SBS and not the interactions of the SBS with the fermionic sector.

For ρ -like particles lighter than 2 TeV (1.5 TeV) the qq' annihilation mechanism where qq' annihilates into ρ via $\rho - W$ mixing starts being the dominant signal contribution at LHC (SSC). The rates computed with the VMD assumption show that there will be sizeable S/B ratios with also sizeable statistical significance (see table 2).

3.- It is not found any clear SISBS signal in the $W^\pm W^\pm$ channels for any of the three scenarios studied here. However, this channel offers itself as an ideal laboratory to search for new exotic resonances. Will LHC show up new unexpected physics in the Symmetry Breaking Sector of the SM?

Acknowledgments: We would like to thank S.Dimopoulos for encouragement and stimulating discussions. A.D and M.J.H thank T.Truong for providing them information about the unitarization procedures and for interesting discussions. M.J.H thanks M.K.Gaillard for reading a preliminary version of this work and for stimulating her interest for this subject.

References

- [1] D.A.Dicus, V.Marthur, Phys.Rev. **D7**(1973)3111; J.M. Cornwall,D. N. Levin and G. Tiktopoulos, Phys. Rev. **D10** (1974)1145; B. W. Lee, C. Quigg and H. Thacker, Phys. Rev. **D16**(1977)1519; M. Veltman, Acta Phys. Pol. **B8**(1977)475; M. S. Chanowitz and M. K. Gaillard, Nucl. Phys. **B261**(1985)379.
- [2] R.N.Cahn and S.Dawson, Phys.Lett.**136B**(1984)196; **138B(E)**(1984)464.
- [3] For a recent review of the field and many further references see M. S. Chanowitz, Ann. Rev. Nucl. Part. Sci. **38**(1988)323.
- [4] S. Weinberg, Physica **96 A**(1979)327;
J. Gasser and H. Leutwyler, Ann. of Phys. **158**(1984)142.
- [5] A.Dobado and M.J. Herrero, Phys.Lett.**B228**(1989)495; **B233**(1989)505; J.F.Donoghue and C.Ramirez, Phys.Lett.**B234**(1990)361.
- [6] T.N.Truong, Phys.Rev.Lett. **61**(1988)2526; A.Dobado, M.J.Herrero and T.N.Truong, Phys.Lett.**B235** (1990)129, and 134.
- [7] A. Dobado, M.J. Herrero, J. Terron, CERN preprint CERN-TH.5670/90 to appear in Z.fur Phys. C (1990); A. Dobado, M.J. Herrero, J. Terron, CERN preprint CERN-TH.5813/90. Submitted to Z.fur Phys.C.
- [8] G.Valencia and S.Dawson, preprint BNL-45194, to appear in Nucl.Phys.B(1990).
- [9] S. Dawson, Nucl. Phys. **B249**(1985)42.
- [10] M. Chanowitz, M. Golden and H. Georgi, Phys. Rev. **D36**(1987)1490.
- [11] M.I.Josa, F.Pauss, T.Rodrigo. Contribution to these proceedings.
- [12] E.Eichten et al., Rev.Mod.Phys.**56**(1984)579.
- [13] E.Farhi and L.Susskind, Phys.Rep.**74**(1981)277; S.Dimopoulos, L.Susskind, Nucl.Phys. **B155**(1979)237.
- [14] K.Kawarabayashi and M.Suzuki, Phys.Rev.**16B**(1966)225; Riazuddin and Fayazuddin, Phys.Rev.**147**(1966)1071.
- [15] A. Dobado, M.J. Herrero, T.N. Truong, Phys.Lett. **B235** (1990) 129.
- [16] S.Dawson, S.Willenbrock, Phys.Rev.**D40**(1989)2880; M.Veltman, F.J.Yndurain,Nucl. Phys.**B325** (1989) 1. A one loop computation of the logarithmic terms was previously done in an effective Lagrangian approach in: O.Cheyette, M.K.Gaillard, Phys.Lett. **B197** (1987) 205.
- [17] The problem of unitarization in LWB scattering has been discussed recently by a number of authors: O.Cheyette, M.K.Gaillard in [16]. D.A.Dicus and W.Repko, Phys. Lett. **B228** (1989) 503; S. Dawson, S. Willenbrock, Phys. Rev. Lett. **62** (1989) 1232; A.Dobado et al in [5], [6] and [7]; A.Dobado, Phys.Lett. **B237** (1990) 457; D.A. Dicus, W.W. Repko, preprint MSUTH 89/06; R.Rosenfeld, preprint EFI-89-54.

- [18] A.Dobado et al. in [6].
- [19] A.Dobado in [17]; S.Willenbrock, preprint BNL-44955 (1990).
- [20] M.B. Einhorn, Nucl.Phys.**B246** (1984)75; R. Casalbuoni, R. Dominici, R. Gatto, Phys. Lett. **147B**(1984)419. See also, Lee et al. in [1].
- [21] CDF collaboration, F.Abe et al., Phys.Rev.Lett.**64**(1990)142.
- [22] R.Casalbuoni et al. Contribution to these proceedings.
- [23] J.J. Sakurai, *Currents and Mesons*, University of Chicago Press,1969; R. Rosenfeld, J.L. Rosner Phys. Rev.**D38** (1988)1530; R.S. Chivukula, preprint BUHEP-88-16.
- [24] B.Mele, Proceedings of the Workshop on Physics at Future Accelerators, La Thuile, CERN report 87-07, Vol.2, p.13 (1987).
- [25] M.C. Bento, C.H. Llewellyn Smith, Nucl. Phys. **B289** (1987)36.
- [26] V.Barger et al., preprint MAD-PH-556(1990); J.Terron, Doctoral Thesis (Univ. Autonoma de Madrid), unpublished.
- [27] M.S.Chanowitz, M.K.Gaillard, Phys.Lett.**B142** (1984)85.
- [28] A. Dobado, M.J. Herrero and J. Terron, in preparation.

Figure Captions

- Fig. 1: ZZ-events distribution with respect to the invariant mass M_{ZZ} for SISBS signals at LHC. No leptonic BR has been included. The top mass value chosen is $m_t = 100\text{GeV}$. The LWB scattering amplitudes were unitarized with the Padé method. Solid histograms are the total rates, signal plus background. Dashed histograms are the background contribution alone. (a) Predictions for the Higgs-like scenario. (b) Predictions for the Scaled-QCD scenario.
- Fig. 2: (a) WZ invariant mass distribution of the signal and background processes with the optimal cuts for the LHC (the 2.5 rapidity cut has been chosen). No leptonic BR has been included. The results for the Scaled-QCD and Technicolor scenarios are displayed: lower solid histogram represents WZ fusion signal process and dotted histogram represents qq' annihilation signal process. The total background is the dashed histogram and the total background plus total signal is the upper solid histogram. (b) Same for the SSC.
- Fig. 3: (a) WZ invariant mass distribution for the WZ fusion signal process (solid histogram) and for the background processes (dashed histogram for qq' , dotted histogram for γ W fusion and dash-dotted histogram for WZ fusion background process) of the Scaled-QCD scenario for the LHC (the 2.5 rapidity cut has been chosen). No leptonic BR has been included. (b) Same for the SSC.
- Fig. 4: Like-sign WW invariant mass distribution for the various SISBS scenarios and for the total background. Rates are for $W^+W^+ + W^-W^-$. No leptonic BR has been included. The short-dashed line is for the Scaled-QCD scenario and the lower solid

line is for the Higgs-like scenario. The upper solid curve corresponds to the unitarized Low Energy Theorems results taken from [26]. The SM rates for $M_H = 1\text{TeV}$ (SMH) are also shown for comparison (dot-dashed line). The long dashed lines are the results for the total background taken from [26]. The upper line is for $m_t = 100\text{GeV}$. The lower line is for $m_t = 200\text{GeV}$.

Table Captions

Table 1: ZZ channel: Number of $l^+l^-l^+l^-$ events for SISBS signals in two scenarios, and for the total background. Rates are presented in the form of S/B-ratios for both LHC and SSC. Two different rapidity cuts and two values of the top quark mass were chosen. The numbers in parenthesis are the optimal cuts.

Table 2: WZ channel: Number of $l^+\nu l^+l^- + l^-\nu l^+l^-$ events for the total SISBS signal in various scenarios and for the total background at LHC and SSC. Rates are presented in the form of S/B-ratios. The rates for both processes contributing to the signal in Scaled-QCD and Technicolor scenarios: WZ-fusion (WZ) and qq' annihilation (qq') are also shown separately for comparison. The optimal cuts are shown in parenthesis.

Table 3: W^+W^+ channel: Number of $l^+\nu l^+\nu$ events for SISBS signals in various scenarios at LHC and SSC. Rates are presented in the form of S/B-ratios.

Table 4: $V_L V_L V_L V_L$ channels: Partial and total SISBS signal rates. The results are after unitarization and for $M_{VV} < 2\text{TeV}, 3\text{TeV}$ and *no* M_{VV} cut respectively. In parenthesis the non-unitarized results without any upper cut on M_{VV} are shown for comparison.

Table 1:

Scenario	LHC (1.5) $m_t = 100\text{GeV}$	LHC (2.5) $m_t = 100\text{GeV}$	SSC (1.5) $m_t = 100\text{GeV}$	SSC (2.5) $m_t = 100\text{GeV}$
HIGGS	27/48 (300,750)	33/75 (300,750)	5/6 (240,750)	8/11 (240,750)
QCD	9/36 (360,750)	15/90 (300,700)	2/3 (360,800)	3/6 (360,800)
	LHC (1.5) $m_t = 180\text{GeV}$	LHC (2.5) $m_t = 180\text{GeV}$	SSC (1.5) $m_t = 180\text{GeV}$	SSC (2.5) $m_t = 180\text{GeV}$
HIGGS	25/57 (300,750)	39/111 (240,750)	5/8 (240,750)	8/14 (240,750)
QCD	12/69 (300,700)	15/102 (300,700)	2/6 (300,800)	3/12 (300,750)

Table 2:

Scenario	LHC (1.5)	LHC (2.5)	SSC (1.5)	SSC (2.5)
TECHN 1.0	1713/71 161 (WZ) 1552 ($q\bar{q}'$) (10)	2628/213 318 (WZ) 2310 ($q\bar{q}'$) (180)	142/7 26 (WZ) 116 ($q\bar{q}'$) (10)	263/24 59 (WZ) 204 ($q\bar{q}'$) (180)
TECHN 1.5	136/16 33 (WZ) 103 ($q\bar{q}'$) (360)	197/43 59 (WZ) 138 ($q\bar{q}'$) (300)	18/2 8 (WZ) 10 ($q\bar{q}'$) (300)	33/6 17 (WZ) 16 ($q\bar{q}'$) (300)
QCD 2.0	53/25 23 (WZ) 30 ($q\bar{q}'$) (480)	65/31 29 (WZ) 36 ($q\bar{q}'$) (540)	11/4 7 (WZ) 4 ($q\bar{q}'$) (480)	21/12 15 (WZ) 6 ($q\bar{q}'$) (420)
HIGGS	20/434 (300,500)	27/786 (300,500)	3/17 (420,500)	5/34 (420,500)
SMH	29/907 (240,500)	39/1744 (240,500)	5/87 (240,500)	7/196 (240,500)

Table 3:

$m_t = 100 \text{ GeV}$	LHC (1.5)		SSC (1.5)			
Scenario	$M_{WW} > 0.8 \text{ TeV}$	1.0 TeV	1.2 TeV	$M_{WW} > 0.8 \text{ TeV}$	1.0 TeV	1.2 TeV
QCD	32/212	20/96	12/150	8/26	5/14	4/8
HIGGS	22/212	13/96	7/50	5/26	3/14	2/8
SMH	30/212	16/96	9/50	6/26	4/14	2/8
$m_t = 200 \text{ GeV}$	LHC (1.5)		SSC (1.5)			
Scenario	$M_{WW} > 0.8 \text{ TeV}$	1.0 TeV	1.2 TeV	$M_{WW} > 0.8 \text{ TeV}$	1.0 TeV	1.2 TeV
QCD	32/154	20/71	12/38	8/21	5/11	4/7
HIGGS	22/154	13/71	7/38	5/21	3/11	2/7
SMH	30/154	16/71	9/38	6/21	4/11	2/7

Table 4:

Channel	LHC	SSC
$W^+W^- \rightarrow W^+W^-W^+W^-$	7-17-25 (54)	3-9-78 (331)
$W^+W^- \rightarrow W^+W^-Z^0Z^0$	6-9-12 (56)	3-14-24 (347)
$W^+W^- \rightarrow Z^0Z^0Z^0Z^0$	5-7-7 (59)	2-3-3 (366)
$Z^0Z^0 \rightarrow W^+W^-W^+W^-$	6-8-8 (69)	2-3-4 (430)
$Z^0Z^0 \rightarrow W^+W^-Z^0Z^0$	2-4-5 (18)	1-2-6 (111)
$Z^0Z^0 \rightarrow Z^0Z^0Z^0Z^0$	2-4-6 (0)	1-2-6 (0)
$W^+Z^0 \rightarrow W^+Z^0W^+W^-$	7-16-22 (57)	2-6-27 (356)
$W^-Z^0 \rightarrow W^-Z^0W^+W^-$	3-7-9 (19)	1-3-12 (116)
$W^+Z^0 \rightarrow W^+Z^0Z^0Z^0$	5-11-15 (37)	2-6-17 (229)
$W^-Z^0 \rightarrow W^-Z^0Z^0Z^0$	2-4-6 (13)	1-2-7 (79)
$W^+W^+ \rightarrow W^+W^+W^+W^-$	11-25-34 (108)	3-9-27 (665)
$W^-W^- \rightarrow W^-W^-W^+W^-$	2-4-5 (12)	1-2-4 (78)
$W^+W^+ \rightarrow W^+W^+Z^0Z^0$	3-7-9 (27)	1-2-12 (168)
$W^-W^- \rightarrow W^-W^-Z^0Z^0$	1-1-1 (3)	0-0-2 (19)
Total	62-124-164 (532)	23-63-229 (3295)

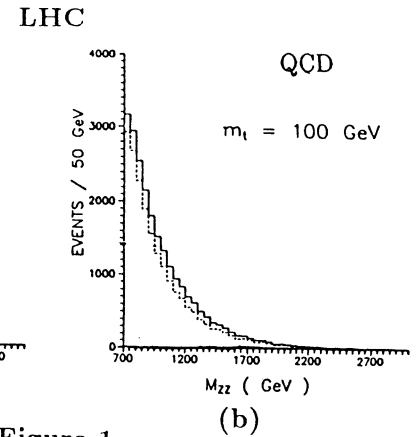


Figure 1

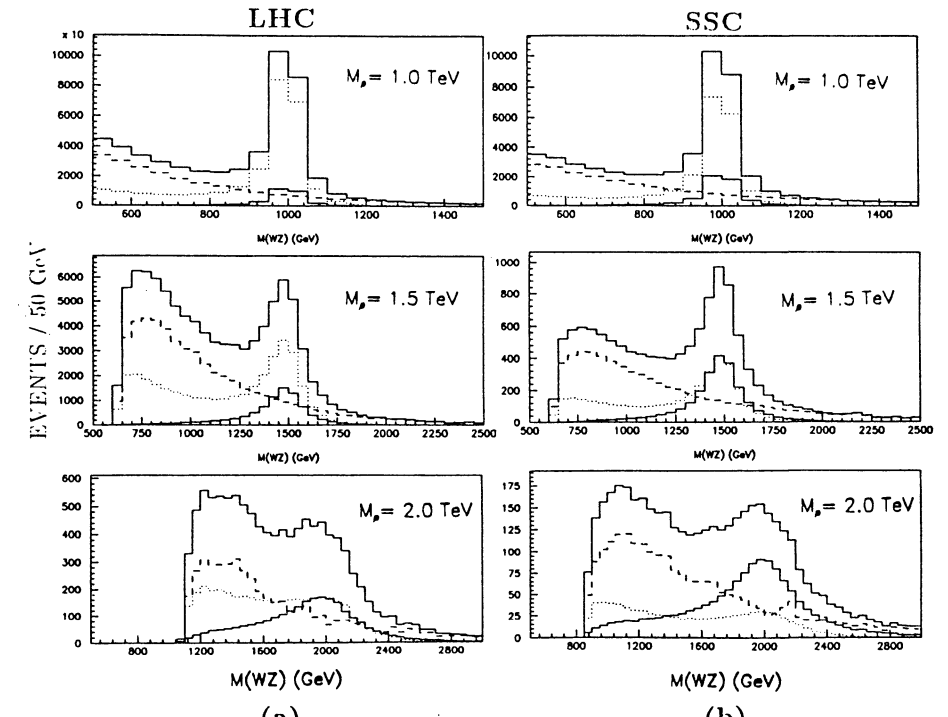


Figure 2

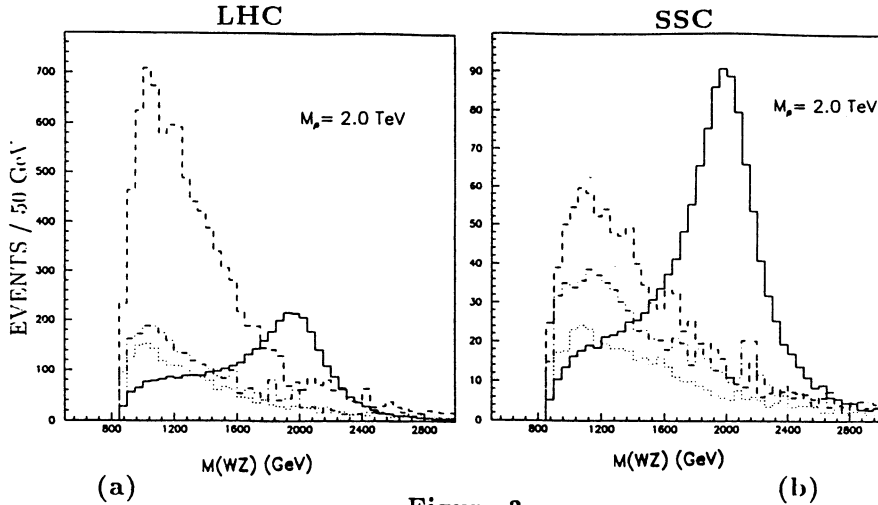


Figure 3

III. WZ PRODUCTION FROM THE BESS MODEL

Contributors: R.Casalbuoni, P.Chiappetta, S.De Curtis, F.Feruglio, R.Gatto, B.Mele and J.Terron

III.1. Introduction

In this report we shall examine the capability of LHC [1] to explore a possible strong sector responsible for electroweak symmetry breaking. A comparison with SSC [2] will also be made.

Our analysis will be carried out within the BESS model (BESS standing for Breaking Electroweak Symmetry Strongly) [3]. The BESS model is at the same time very simple and it hopefully contains the most relevant elements of a possible strong electroweak breaking. The model has no Higgs particle. In addition to W and Z it contains a triplet of new massive vector bosons V . In BESS the electroweak symmetry breaking is described in a non-linear way. A local "hidden" $SU(2)$ symmetry is implicit in the description and the bosons V are indeed the associated gauge bosons. It is explicitly assumed that they constitute effective dynamical degrees of freedom. The bosons V mix with W and Z . The existing data of CDF/UA2 [4] and of LEP [5] already imply certain restrictions on BESS parameters. To remain on the safe, we shall take into account not only these restrictions, but also possible stronger restrictions from future LEP data, assuming no deviations will be observed from the standard model within the foreseen experimental precision [6].

III.2. The BESS model

The vector resonances of the BESS model are bound states of a strongly interacting sector. In this sense they are similar to ordinary ρ vector mesons, or to the techni- ρ particle of technicolor theories [7]. Due to their composite nature, the V particles are then expected to mix to the photon and to the W and Z vector bosons. From this, a non trivial behaviour under the electromagnetic gauge group $U(1)_{em}$ is expected (see ref. [8]). Using this fact and the requirement that the electroweak ρ -parameter be equal to 1 at tree level, one can easily construct the most general mixing term of the V -particles with the ordinary vector bosons. By defining

$$\mathcal{V}_\mu = \sum_{i=1}^3 i g'' \frac{\tau^i}{2} \tilde{V}_\mu^i, \quad \mathcal{W}_\mu = \sum_{i=1}^3 i g \frac{\tau_i}{2} \tilde{W}_\mu^i, \quad \mathcal{B}_\mu = i g' \frac{\tau_3}{2} \tilde{B}_\mu \quad (1)$$

one has

$$\mathcal{L}_M = -\frac{v^2}{4} [\text{tr}(\mathcal{W} - \mathcal{B})^2 + \alpha \text{tr}(\mathcal{W} + \mathcal{B} - 2\mathcal{V})^2] \quad (2)$$

where v and α are free parameters. The first term is nothing but the usual mass term for the Weinberg-Salam fields, whereas the second one is the only mixing term compatible with the properties we have just discussed. The lagrangian (2) must then be supplemented by kinetic Yang-Mills terms for all the three vector boson fields, with a gauge coupling g'' for the field \tilde{V} . As far as the interactions with fermions are concerned, one must specify the current \vec{J} to which the new triplet of states \tilde{V} couples. If we assume $\vec{J} = \vec{J}_L$ (see ref. [3] for a more general discussion), the $U(1)_{em}$ gauge invariance requires the interaction lagrangian to be

$$\mathcal{L} = \frac{g}{1+b} \tilde{W} \cdot \vec{J}_L + g' \tilde{B} J_Y + \frac{1}{2} \frac{b}{1+b} g'' \tilde{V} \cdot \vec{J}_L \quad (3)$$

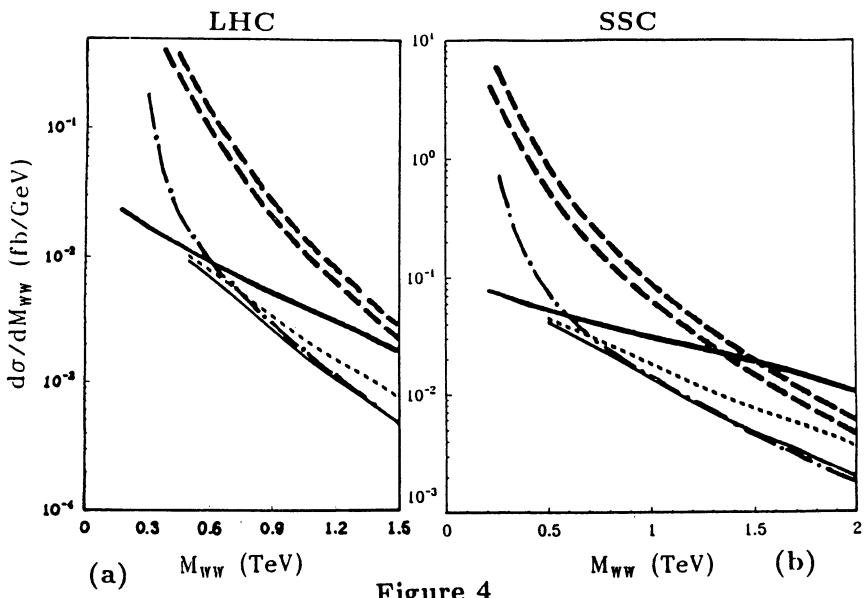


Figure 4

The parameter b specifies a possible direct coupling of the fermions to the new gauge vector bosons. However, it must be stressed that also when $b = 0$ a coupling of the physical V -particles to fermions is present due to their mixing with the physical Weinberg-Salam vector bosons. At the zeroth order in the weak couplings the V mesons are degenerate in mass and

$$M_V^2 = \frac{1}{4} v^2 \alpha g''^2 \quad (4)$$

The complete list of couplings to fermions can be found in refs. [3,6]. Here we will only be concerned with the couplings to the charged currents:

$$(h_W W_\mu^i + h_V V_\mu^i) T_L^i, \quad i = 1, 2 \quad (5)$$

where the coupling of V^\pm is given by

$$h_V = \frac{1}{1+b} \left(g \sin \varphi + \frac{1}{2} g'' b \cos \varphi \right) \quad (6)$$

The parameter space of the model is given by (g, g', v, M_V, g'', b) . We trade off (g, g', v) for (α_{em}, G_F, M_Z) and therefore we remain with (M_V, g'', b) . In turn, the parameter v can be reexpressed in terms of M_W , and the expressions of (g, g', M_W) in terms of (α_{em}, G_F, M_Z) can be found in ref. [6]. In order to get the physical region for the parameters (M_V, g'', b) we have considered the envelope of the 90% C.L. curves obtained from the observables related to the Z -line shape measured at LEP1, and from the ratio M_W/M_Z measured at CDF and UA2. The most restrictive observables turn out to be Γ_{had} , Γ_Z and M_W/M_Z . The experimental values we have used come from the LEP1 combined data [5], $\Gamma_h(MeV) = 1764 \pm 16$, $\Gamma_Z(MeV) = 2496 \pm 16$, and from the CDF and UA2 combined data [4], $(M_W/M_Z)^2 = 0.773 \pm 0.006$. As an example we give in Fig. 1 the allowed region in the plane $(b, g/g'')$ for $M_V = 1500$ GeV. We have taken $m_{top} = 150$ GeV and $\alpha_s = 0.12$. For increasing m_{top} and/or M_V the area of the allowed region has only a small increase. Notice that the origin of the plane (standard model limit) lies inside the allowed region.

III.3. Gauge boson pair production in the BESS model

At hadron colliders, as far as detection of a signal from a strongly interacting symmetry breaking sector is concerned, vector boson pair production is particularly relevant. In the BESS model there are two main mechanisms which compete for the production of a pair of ordinary gauge vector bosons at a pp collider: $q\bar{q}$ annihilation, and WW (WZ, ZZ) fusion.

In the first mechanism a quark-antiquark pair annihilates into a V vector boson, which in turn decays into a pair of ordinary gauge vector bosons. We stress the fact that this process is always operating in BESS independently of the existence of a direct coupling of V to fermions. In fact, the mixing of V with W and Z always induces a well determined coupling of order g/g'' between the mass eigenstates V and the fermions, even if the original, unmixed, states \tilde{V} were not coupled to matter. We further observe that, at least in the range of masses for V we are interested in (few TeVs), the decay of V 's is dominated by the WW , WZ channels, due to the large coupling, (of order $\alpha g''$), for $V^0 W_L^+ W_L^-$ and $V^\pm W_L^\mp Z_L$ (L stands for the longitudinal components). On this basis we expect (and we shall verify quantitatively) that, even in the case $b = 0$, the $q\bar{q}$ mechanism remains efficient in producing a W/Z pair. We have evaluated the $q\bar{q}$

contribution in the context of the parton model along the lines described in ref. [6], and the relevant expressions are given in ref. [9].

Another mechanism to produce W/Z pairs is the rescattering of a pair of ordinary gauge vector bosons, each being initially emitted from a quark or antiquark leg. In the so-called effective- W approximation the initial W/Z 's are assumed to be real and the cross section for producing a W/Z pair is obtained by a double convolution of the cross section for the rescattering (or fusion) process with the luminosities of the initial W/Z 's inside the quarks and the structure functions of the quarks inside the proton [10]. The relevance of this mechanism is then related to the strength of the fusion process. In the standard model of electroweak interactions such a fusion process is expected to be weak. The potentially large amplitudes, those among the longitudinally polarized W/Z 's, are in fact asymptotically constant (for large energy), once the whole set of lowest order diagrams is taken into account. However such a constant depends on the Higgs mass m_H and for a sufficiently large value of m_H the asymptotic value of the amplitude violates the perturbative unitarity requirement. The speculations on a possible strongly interacting regime for the standard model [11,3] are based on this observation. In BESS the rescattering process is naturally strong. In fact the scattering of two longitudinally polarized W/Z 's proceeds via the exchange of a V vector boson with large couplings (of order $\alpha g''$) at each vertex. If some W/Z 's is taken to be transverse, the corresponding amplitude is strongly depressed and will be neglected in our analysis. We have computed the scattering amplitudes among longitudinal W/Z 's in BESS, by making use of the equivalence theorem [12]. Such amplitudes approach the ones among the corresponding goldstone bosons as the value of the energy increases, the difference being of order (M/\sqrt{s}) ($M = M_W$ or M_Z), or, in other words, they verify the low-energy theorems [13]. The full expressions for the corresponding amplitudes can be found in ref. [9]. Here we will give only the expression for the width of the V particle

$$\Gamma_V = \frac{G_F^2 M_V^5}{24\pi g''^2} \quad (7)$$

which is valid in the limit $M_V \gg M_W, M_Z$, and where we have neglected the fermionic decays.

III.4. Discussion of the results

In hadronic collisions the $pp \rightarrow W^\pm Z + X$ reaction appears to be the most interesting one in the framework of the BESS model. The process $pp \rightarrow W^+ W^- + X$ is expected to suffer from a very severe background coming from $pp \rightarrow t\bar{t} + X$, with t and \bar{t} both decaying into W , which should be the dominant mode for $m_{top} > M_W$. Final leptonic configurations from $t\bar{t}$ production might also simulate configurations from $W^\pm Z$, but the Z mass reconstruction should protect the signal from such a background. The ZZ mode has not been considered because it does not proceed via an s -channel contribution in BESS.

Comparing the two channels $W^+ Z$ and $W^- Z$, we find that $W^- Z$ is roughly one half of the $W^+ Z$. Finally we remark that the final states observed at LHC and SSC will be demanded to contain leptons. Our results will be given in terms of numbers of produced $W^\pm Z$ pairs. For both bosons decaying leptonically one has to multiply by the branching factor $B(Z \rightarrow \ell^+ \ell^-) \cdot B(W^\pm \rightarrow \ell^\pm \bar{\nu}_\ell) \approx 1.5\%$, for $(\ell = e, \mu)$.

The relevant backgrounds are the standard model production of $W^\pm Z$ through quark-antiquark annihilation [14], γW^\pm fusion [15], and $W_T^\pm Z_T$ fusion. In our calculation we have

made use of the DFLM structure functions [16], for $\Lambda_{QCD} = 260$ MeV. We have also run the computer programs by using the EHLQ1 structure functions [17] obtaining very similar results (actually the DFLM structure functions give a number of events which is about 6-8% lower than for EHLQ1). In the case of the fusion process, we have used a value of Q^2 inside the structure functions equal to the square of the invariant mass of the produced gauge boson pair. The K-factor coming from soft gluon resummation is not known for all the processes considered here, and we have decided not to introduce it. As a consequence the number of events we have evaluated is probably underestimated by about 20-30% (in fact, where the K-factor is known, as in the case of the V -production through $q\bar{q}$ [18], it has a value of about 1.3).

Our results were obtained through a Monte Carlo simulation which allowed to study the details of the various final state distributions. They are summarized in Tables 1-2. Tables 1 and 2 refer to the process $W^+Z + W^-Z$ at LHC and at SSC respectively. The assumed energy parameters for LHC and SSC are 16 TeV and 40 TeV respectively. The luminosities we have assumed are $10^{34} \text{ cm}^{-2} \text{ sec}^{-1}$ for LHC, and $10^{33} \text{ cm}^{-2} \text{ sec}^{-1}$ for SSC, and all the numbers refer to one effective year = 10^7 sec of running of the colliders. In the Tables we have considered a very extensive choice of parameters. A first cut on the rapidity $y_{W,Z}$ of the final W and Z , $|y_{W,Z}| \leq 2.5$ was applied to all cases. Then we applied a lower cut in M_{WZ} (the invariant mass of the WZ -pair), approximately corresponding to the beginning of the resonance at the left of the peak. An upper cut has been fixed once for all at $M_{WZ} = 3$ TeV, where in all the practical cases considered here the resonance tail is already extinguished. Finally a cut in p_T (the transverse momentum of the Z) has been obtained from the requirement of maximizing the statistical significance of the signal, $S/(S+B)^{1/2}$, S being the signal and B the background, which in our case includes the continuum standard WZ -pair production both from $q\bar{q}$ annihilation and γW fusion.

For a better understanding of the results we have exhibited in Tables 1 and 2 the different contributions, fusion and $q\bar{q}$ annihilation, to the signal. We have also given the number of events from the background and the total number of events. The range of M_V values we have explored runs from 1 TeV up to 2.5 TeV. The last value can be probably considered as a limiting value for discovery at both machines. About this point notice that in order to have a decent number of events at LHC, say more than 10 leptonic events/year and a good statistical significance S/\sqrt{B} , for $M_V = 2500$ GeV, one have to run LHC at a luminosity of about $3.5 \times 10^{34} \text{ cm}^{-2} \text{ sec}^{-1}$ at least, for $b \approx 0$.

The values chosen for g'' and b are well inside the region allowed from LEP1, and CDF/UA2 data (see Fig. 1). Furthermore (see ref. [6]) they will be inside the allowed region also after precision measurements of forward-backward asymmetry and of tau-polarization will be made at LEP1, if we make the hypothesis that no deviation from the SM is observed within the expected experimental precision. For instance, from ref. [6] in the more restrictive case of $M_V = 250$ GeV one gets $g/g'' < 0.1$ at $b = 0$ both from A_{FB} and from A_τ . For the values of g'' that we have considered, one has a width for the V (see eq. (7)) of 11 GeV for $M_V = 1000$ GeV, 84 GeV for $M_V = 1500$ GeV, whereas we have $\Gamma_V = 353$ GeV for $M_V = 2000$ GeV (notice that this case corresponds almost exactly to a techni- ρ obtained by scaling from QCD), and $\Gamma_V = 455$ GeV for $M_V = 2500$ GeV. For smaller g'' the resonance becomes broader. In the computation of Γ_V we have ignored the contribution from the fermionic channels because it turns out to be completely negligible. Notice that the $b = 0$ case corresponds, in practice, to the most pessimistic situation, since in general allowing for a direct coupling ($b \neq 0$) a much larger signal from production via $q\bar{q}$ annihilation is predicted. Direct couplings of techni- ρ to fermions emerge in extended technicolor theories (for calculations at SSC energies see ref. [19]).

Table 1 : Events per year in $pp \rightarrow (W^+Z + W^-Z) + X$ at LHC from BESS.

(M_V, g'', b)	$(p_T)_c$	$(M_{WZ})_c$	Fusion	$q\bar{q}$	Signal	Backgr.	Total
(1000,13,0)	360	850	858	10089	10947	4786	15733
(1500,13,0)	480	1250	498	1929	2427	1121	3548
(2000,13,.02)	540	1400	339	3863	4202	608	4810
(2000,13,0)	600	1600	241	443	684	310	994
(2000,13,-.01)	540	1400	339	4186	4525	608	5133
(2500,20,0)	600	1400	212	57	269	430	699
(2500,20,-.01)	600	1800	141	1807	1498	211	2159

Table 2 : Events per year in $pp \rightarrow (W^+Z + W^-Z) + X$ at SSC from BESS.

(M_V, g'', b)	$(p_T)_c$	$(M_{WZ})_c$	Fusion	$q\bar{q}$	Signal	Backgr.	Total
(1000,13,0)	300	800	1280	3969	5249	3963	9212
(1500,13,0)	420	1250	895	1030	1925	1063	2988
(2000,13,.02)	480	1600	671	2814	3485	462	3947
(2000,13,0)	480	1600	671	339	1010	462	1472
(2000,13,-.01)	480	1400	772	3119	3891	636	4527
(2500,20,0)	540	1500	486	54	540	428	968
(2500,20,-.01)	600	1800	360	1721	2081	211	2292

From the Tables we see that the fusion signal increases going from LHC to SSC, whereas the signal from $q\bar{q}$ decreases (of course the decreasing in the luminosity by a factor 10 has to be considered). This is expected on the basis of the different ratio of LHC and SSC values for $q\bar{q}$ and $W_L W_L$ luminosities [20]. In particular, for $b = 0$, at LHC the $q\bar{q}$ annihilation dominates for low V masses up to $M_V = 2$ TeV, whereas at SSC the two mechanisms are already comparable at $M_V = 1500$ GeV. However for $b < 0$ the situation changes and, increasing $|b|$, the $q\bar{q}$ annihilation will overcome again the fusion contribution.

We have also made an extensive study of the $(p_T)_Z$ and M_{WZ} distributions. Here we give examples in Figs. 2-9 of the two distributions both at LHC (Figs. 2, 3, 4 and 5) and SSC (Figs. 6, 7, 8 and 9) in the case of $M_V = 1500$ GeV, $g'' = 13$, $b = 0$ and $M_V = 2000$ GeV, $g'' = 13$, $b = 0$ (for a case with $b \neq 0$, see ref. [21] in this volume).

The figures show that, even after multiplying by the branching factor corresponding to selecting only leptonic decays of W and Z , one is left with a statistically significant signal having quite well distinguished features both in M_{WZ} and $(p_T)_Z$ distributions. The vertical lines in the graphs indicate where the lower cuts in M_{WZ} and p_T have been put for the illustrated cases (see corresponding entries in Tables 1-2). We emphasize that the statistical significance of the signal versus the background is very good practically in all the cases we have considered in this note.

III.5. Conclusions

We have studied WZ pair production at LHC and SSC within the BESS model, which is simple and probably contains the dominant features of a strong electroweak breaking. To extrapolate to

possible future scenarios, we have restricted the BESS parameters below the expected limitations from future LEP data, assuming these come out not to deviate, within the expected precision, from the standard model prediction. The new conclusion of our work is the generally dominant role, particularly at LHC, of production through $q\bar{q}$ annihilation, as compared to the extensively studied boson pair fusion mechanism. The increase of gauge boson pairs, resulting from the $q\bar{q}$ mechanism, as expected in the BESS model, together with its distinguished features in the p_T and invariant mass distributions, suggests an important role of LHC and SSC in the exploration of a possible strong electroweak symmetry breaking sector.

Figure Captions

Fig. 1 - Allowed region (90% C.L.) in the $(b, g/g'')$ plane for $M_V = 1500 \text{ GeV}$, $m_{top} = 150 \text{ GeV}$ and $\alpha_s = 0.12$, from M_W/M_Z (continuous line), Γ_Z (dashed line) and Γ_{had} (dashed-dotted line). The origin (corresponding to the standard model limit) is inside the allowed region.

Fig. 2 - Invariant mass distribution of the $W^+Z + W^-Z$ pairs produced per year (1 year = 10^7 sec) at LHC for $M_V = 1500 \text{ GeV}$, $g'' = 13$ and $b = 0$, with a luminosity of $10^{34} \text{ cm}^{-2} \text{ sec}^{-1}$. The applied cuts are: $|y_{W,Z}| < 2.5$, $(p_T)_Z > 480 \text{ GeV}$ and $M_{WZ} > 1250 \text{ GeV}$. The lower, intermediate and higher histograms refer to the background, background plus fusion signal and background plus fusion signal plus $q\bar{q}$ annihilation signal, respectively.

Fig. 3 - $(p_T)_Z$ distribution from the $W^+Z + W^-Z$ pairs produced per year at LHC for $M_V = 1500 \text{ GeV}$, $g'' = 13$ and $b = 0$, for a luminosity of $10^{34} \text{ cm}^{-2} \text{ sec}^{-1}$. The applied cuts are: $|y_{W,Z}| < 2.5$, $(p_T)_Z > 480 \text{ GeV}$ and $M_{WZ} > 1250 \text{ GeV}$. The lower, intermediate and higher histograms refer to the background, background plus fusion signal and background plus fusion signal plus $q\bar{q}$ annihilation signal, respectively.

Fig. 4 - Invariant mass distribution of the $W^+Z + W^-Z$ pairs produced per year at SSC for $M_V = 1500 \text{ GeV}$, $g'' = 13$ and $b = 0$, for a luminosity of $10^{33} \text{ cm}^{-2} \text{ sec}^{-1}$. The applied cuts are: $|y_{W,Z}| < 2.5$, $(p_T)_Z > 420 \text{ GeV}$ and $M_{WZ} > 1250 \text{ GeV}$. The lower, intermediate and higher histograms refer to the background, background plus fusion signal and background plus fusion signal plus $q\bar{q}$ annihilation signal, respectively.

Fig. 5 - $(p_T)_Z$ distribution from the $W^+Z + W^-Z$ pairs produced per year at SSC for $M_V = 1500 \text{ GeV}$, $g'' = 13$ and $b = 0$, for a luminosity of $10^{33} \text{ cm}^{-2} \text{ sec}^{-1}$. The applied cuts are: $|y_{W,Z}| < 2.5$, $(p_T)_Z > 420 \text{ GeV}$ and $M_{WZ} > 1250 \text{ GeV}$. The lower, intermediate and higher histograms refer to the background, background plus fusion signal and background plus fusion signal plus $q\bar{q}$ annihilation signal, respectively.

Fig. 6 - Invariant mass distribution of the $W^+Z + W^-Z$ pairs produced per year at LHC for $M_V = 2000 \text{ GeV}$, $g'' = 13$ and $b = 0$, with a luminosity of $10^{34} \text{ cm}^{-2} \text{ sec}^{-1}$. The applied cuts are: $|y_{W,Z}| < 2.5$, $(p_T)_Z > 600 \text{ GeV}$ and $M_{WZ} > 1600 \text{ GeV}$. The lower, intermediate and higher histograms refer to the background, background plus fusion signal and background plus fusion signal plus $q\bar{q}$ annihilation signal, respectively.

Fig. 7 - $(p_T)_Z$ distribution from the $W^+Z + W^-Z$ pairs produced per year at LHC for $M_V = 2000 \text{ GeV}$, $g'' = 13$ and $b = 0$, for a luminosity of $10^{34} \text{ cm}^{-2} \text{ sec}^{-1}$. The applied cuts are: $|y_{W,Z}| < 2.5$, $(p_T)_Z > 600 \text{ GeV}$ and $M_{WZ} > 1600 \text{ GeV}$. The lower, intermediate and higher histograms refer to the background, background plus fusion signal and background plus fusion signal plus $q\bar{q}$ annihilation signal, respectively.

Fig. 8 - Invariant mass distribution of the $W^+Z + W^-Z$ pairs produced per year at SSC for $M_V = 2000 \text{ GeV}$, $g'' = 13$ and $b = 0$, for a luminosity of $10^{33} \text{ cm}^{-2} \text{ sec}^{-1}$. The applied cuts are:

$|y_{W,Z}| < 2.5$, $(p_T)_Z > 480 \text{ GeV}$ and $M_{WZ} > 1600 \text{ GeV}$. The lower, intermediate and higher histograms refer to the background, background plus fusion signal and background plus fusion signal plus $q\bar{q}$ annihilation signal, respectively.

Fig. 9 - $(p_T)_Z$ distribution from the $W^+Z + W^-Z$ pairs produced per year at SSC for $M_V = 2000 \text{ GeV}$, $g'' = 13$ and $b = 0$, for a luminosity of $10^{33} \text{ cm}^{-2} \text{ sec}^{-1}$. The applied cuts are: $|y_{W,Z}| < 2.5$, $(p_T)_Z > 480 \text{ GeV}$ and $M_{WZ} > 1600 \text{ GeV}$. The lower, intermediate and higher histograms refer to the background, background plus fusion signal and background plus fusion signal plus $q\bar{q}$ annihilation signal, respectively.

References

- [1] C. Rubbia, seminar given at CERN on November 2, 1989; "Large Hadron Collider in the LEP Tunnel", ed. G. Brianti et al., CERN 84/10.
- [2] "Superconducting Super Collider Conceptual Design", Central Design Group, SSC Report SR-2020, March 1986.
- [3] R. Casalbuoni, S. De Curtis, D. Dominici and R. Gatto, Phys. Lett. **B155** (1985) 95; Nucl. Phys. **B282** (1987) 235.
- [4] L. Pondrom, Summary Talk presented at the Singapore Conference, Singapore, August 1990.
- [5] F. Dydak, Summary Talk presented at the Singapore Conference, Singapore, August 1990.
- [6] R. Casalbuoni, P. Chiappetta, D. Dominici, F. Feruglio and R. Gatto, Nucl. Phys. **B310** (1988) 181.
- [7] S. Weinberg, Phys. Rev. **D 13** (1976) 974; **D 20** (1979) 1277; L. Susskind, Phys. Rev. **D 20** (1979) 2619; for extended technicolor, see: S. Dimopoulos and L. Susskind, Nucl. Phys. **B155** (1979) 237. See also the review by E. Fahri and L. Susskind, Phys. Rep. **74** (1981) 277.
- [8] G. Altarelli, R. Casalbuoni, D. Dominici, F. Feruglio and R. Gatto, Nucl. Phys. **B342** (1990) 15.
- [9] R. Casalbuoni, P. Chiappetta, S. De Curtis, F. Feruglio, R. Gatto, B. Mele and J. Terron, Phys. Lett. **B249** (1990) 130.
- [10] S. Dawson, Nucl. Phys. **B249** (1985) 42. G.L. Kane, W.W. Repko and W.B. Rolnick, Phys. Lett. **148B** (1985) 367; M.S. Chanowitz and M.K. Gaillard, Phys. Lett. **142B** (1984) 85.
- [11] M. Veltman, Acta Phys. Polon. **B8** (1977) 475; B.W. Lee, C. Quigg and H.B. Thacker, Phys. Rev. **D 16** (1977) 1519; see also the review by M.S. Chanowitz, Ann. Rev. Nucl. Part. Sc. **38** (1988) 363.
- [12] J.M. Cornwall, D.N. Levin and G. Tiktopoulos, Phys. Rev. **D 10** (1974) 1145. C.G. Vayonakis, Lett. N. Cimento **17** (1976) 17; M.S. Chanowitz and M.K. Gaillard, Nucl. Phys. **B261** (1985) 379; G.J. Gounaris, R. Kögerler and H. Neufeld, Phys. Rev. **D 34** (1986) 3257.

- [13] S. Weinberg, *Physica* **96A** (1979) 327; M.S. Chanowitz, M. Golden and H. Georgi, *Phys. Rev. D* **36** (1987) 1490; *Phys. Rev. Lett.* **57** (1986) 2344.
- [14] R.W. Brown, D. Sahdev and K.O. Mikaelian, *Phys. Rev. D* **20** (1979) 1164; K.O. Mikaelian, M.A. Samuel and D. Sahdev, *Phys. Rev. Lett.* **43** (1979) 746.
- [15] B. Mele, Proceedings of the Workshop on Physics at Future Accelerators, La Thuile and Geneva, ed. J.H. Mulvay, CERN report 87-07, vol. 2, p. 13, Geneva (1987)
- [16] M. Diemoz, F. Ferroni, E. Longo and G. Martinelli, *Z. Phys* **C39** (1988) 21.
- [17] E. Eichten, I. Hinchliffe, K. Lane and C. Quigg, *Rev. Mod. Phys.* **56** (1984).
- [18] P. Chiappetta, T. Grandou, M. Le Bellac and J.L. Meunier, *Nucl. Phys.* **B207** (1982) 251.
- [19] R.S. Chivukula, Proc. of the 12th Johns Hopkins Workshop, Baltimore June 1988, eds. G. Domokos and S. Kövesi-Domokos, World Scientific, Singapore (1988).
- [20] Z. Kunszt, Proceedings of the Workshop on Physics at Future Accelerators, La Thuile and Geneva, ed. J.H. Mulvay, CERN report 87-07, vol. 1, p. 123, Geneva (1987).
- [21] R. Casalbuoni, P. Chiappetta, M.C. Cousinou, S. De Curtis, F. Feruglio and R. Gatto, preprint CPT-90/P.2429 and UGVA/DPT 1990-08-690.

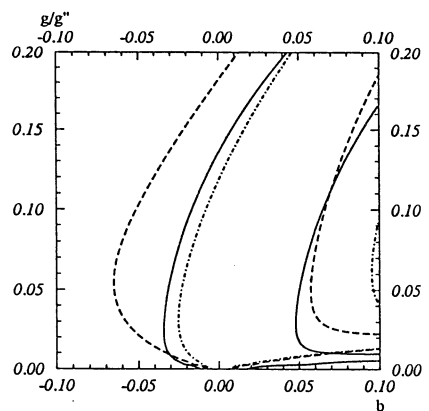


Fig. 1

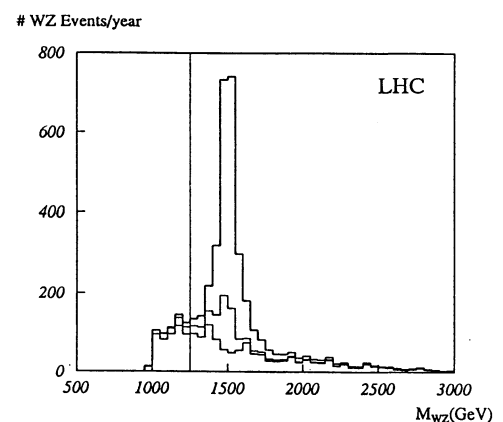


Fig. 2

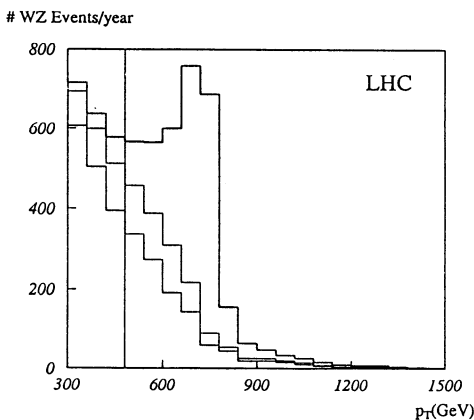


Fig. 3

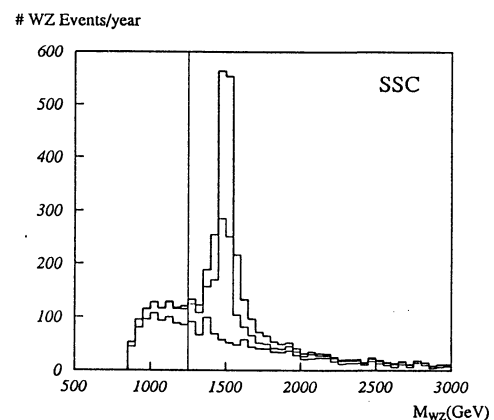


Fig. 4

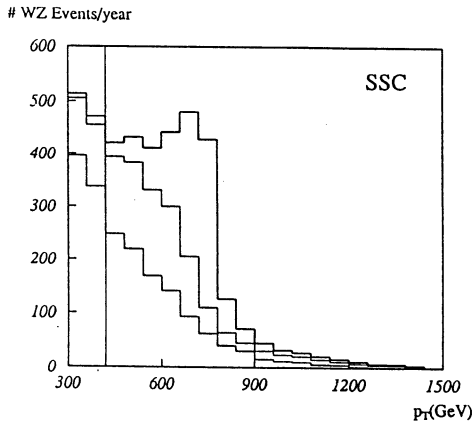


Fig. 5

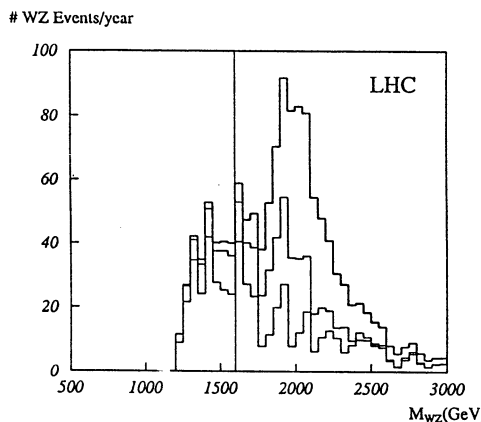


Fig. 6

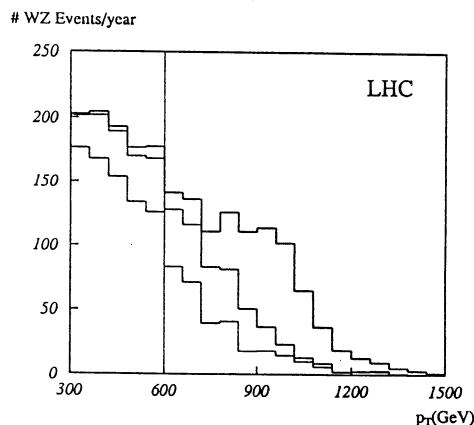


Fig. 7

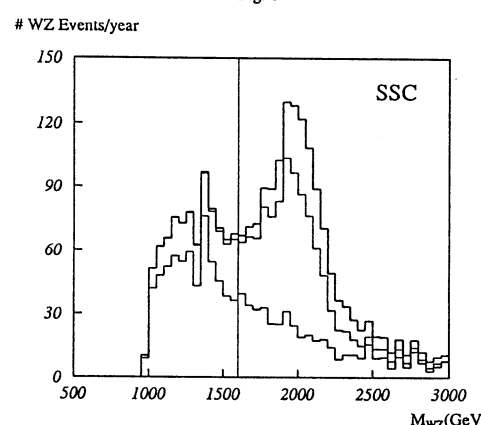


Fig. 8

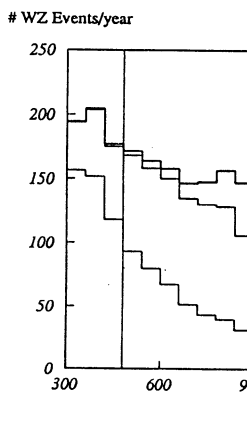


Fig. 9

IV. $W_L^\pm Z_L^0$ PRODUCTION AT THE LHC FROM THE STRONGLY INTERACTING SYMMETRY BREAKING SECTOR – EXPERIMENTAL ASPECTS

Contributors: Isabel Josa, Felicitas Pauss and Teresa Rodrigo

IV.1. Introduction

We study the $W_L^\pm Z_L^0$ production at $\sqrt{s} = 16$ TeV in the presence of a strongly interacting symmetry breaking sector (SISBS) using two different approaches: the DHT model [1] (DHT stands for Dobado, Herrero and Terron) and the BESS model [2] (BESS stands for Breaking Electroweak Symmetry Strongly).

In the DHT model the SISBS is treated within a chiral perturbation theory, supplemented by a unitarization procedure [1]. Within this general approach to $V_L V_L$ scattering three different scenarios have been considered: a) a unitarized Standard Model with heavy Higgs boson to one-loop (Higgs-like scenario); b) a scenario based on scaling the low-energy phenomenology of QCD to the TeV region (QCD-like scenario); in this case one expects the appearance of a vector resonance in analogy with the existence of the ρ resonance in QCD; and c) a SU(N) gauge theory in the spirit of Technicolor with the possibility of changing the number of Technicolors N_{TC} , thus allowing the study of the vector resonance production over a wide range of mass values:

$$m_{\rho_{TC}} \sim 2 \times (3/N_{TC})^{1/2} \text{ TeV} \quad \text{and} \quad \Gamma_{\rho_{TC}} \sim 480 \times (3/N_{TC})^{3/2} \text{ GeV.}$$

In the case of $N_{TC} = 3$, $\rho_{TC} \equiv \rho_{QCD}$, and for example, for $m_{\rho_{QCD}} = 2$ TeV one expects a width of $\Gamma_{\rho_{QCD}} \sim 480$ GeV. The different scenarios can be simulated by choosing the parameters of the effective Lagrangian accordingly. In the SU(N) Technicolor case it is possible to incorporate the additional mechanism for $W_L^\pm Z_L^0$ production via $q\bar{q}$ annihilation: $q\bar{q} \rightarrow W^\pm \rightarrow W_L^\pm Z_L^0$, where $W - \rho_{TC}$ mixing is assumed to be described in terms of Vector Meson Dominance.

In the BESS model [2] the electroweak symmetry breaking is described in a non-linear way. The model has no Higgs particles and contains a triplet of new massive vector bosons, V^\pm, V^0 , which are bound states of a strongly interacting sector. They are similar to the ordinary ρ vector mesons, or the Techni- ρ particle of Technicolor theories. The V bosons are produced through $q\bar{q}$ annihilation and intermediate vector boson (IVB) fusion. The process $q\bar{q} \rightarrow V$ depends on the direct coupling of the V to fermions, but is still present even in the absence of this direct coupling. The fusion process, where two longitudinally polarized IVB's are rescattered, proceeds through the exchange of a V boson. The decay of V is dominated by $V \rightarrow WW$ or WZ .

The relation to Technicolor theories is obtained for a limited set of values of the parameter space of the BESS model: $\alpha = 2$, $g'' > 5.4$ ($N_{TC} \leq 14$) and $b = 0$. The parameter b specifies a possible direct coupling of the fermions to the new gauge vector bosons, g'' is the additional gauge coupling and α is a free parameter.

Signals from $W_L Z_L$ production at the Large Hadron Collider (LHC) are discussed in Ref.[3] for the DHT model and in Ref.[4] for the BESS model. In order to understand the experimental requirements for observing a possible signal above background in the WZ channel, a Monte Carlo simulation is performed on the particle level. The signal is evaluated using the PYTHIA Monte Carlo program [5], where the $q\bar{q}$ annihilation and the WZ fusion process have been included. The parameters of the models are chosen such that the result of the simulation can

be applied to both model predictions discussed above. We have generated 15000 events for two different mass values of the ρ_{TC} vector resonance: $m_\rho = 1$ TeV, $\Gamma_\rho \simeq 55$ GeV and $m_\rho = 2$ TeV, $\Gamma_\rho \simeq 480$ GeV. The first case corresponds to $N_{TC} = 12$ and the second one to $N_{TC} = 3$ in SU(N) Technicolor. In the context of the BESS model the corresponding set of values are $\alpha = 2$, $g'' = 5.9$ and $\alpha = 2$, $g'' = 11.7$. No direct coupling to fermions has been assumed, i.e. $b = 0$, which leads to a more conservative rate estimate.

PYTHIA allows the two different production mechanisms involved in $W_L^\pm Z_L^0$ production to be studied separately: $W_L Z_L$ fusion (taken from the DHT model) and $q\bar{q}$ annihilation (taken from the BESS model). Expected event rates are evaluated for an integrated luminosity of 4×10^5 pb $^{-1}$, i.e. one year of running at a high luminosity of $L = 4 \times 10^{34}$ cm $^{-2}$ s $^{-1}$.

IV.2. $W_L^\pm Z_L^0$ production properties and background evaluation

A signal in the $W_L Z_L$ channel is studied considering only the leptonic decays of W and Z. Using the PYTHIA Monte Carlo we predict the following cross-sections:

- a) for $m_\rho = m_V = 1$ TeV, $\Gamma \simeq 55$ GeV the cross-section $\sigma(pp \rightarrow W_L Z_L) \times BR(W \rightarrow \ell\nu) \times BR(Z \rightarrow \ell\ell) = 1.321 \times 10^{-2}$ pb, where $q\bar{q}$ annihilation contributes 84% and the fusion process contributes 16% to the total cross-section.
- b) for $m_\rho = m_V = 2$ TeV, $\Gamma \simeq 480$ GeV the cross-section $\sigma(pp \rightarrow W_L Z_L) \times BR(W \rightarrow \ell\nu) \times BR(Z \rightarrow \ell\ell) = 0.809 \times 10^{-3}$ pb; here the dominant contribution (78%) comes from the fusion process, while $q\bar{q}$ annihilation contributes 22% to the total cross-section.

The transverse momentum spectrum of the final-state leptons are shown in Fig. 1a for the new vector resonance of 1 TeV mass. Leptons produced via the $q\bar{q}$ annihilation mechanism have a harder spectrum than those coming from VV fusion. Figure 1b shows the lepton acceptance for both production mechanisms as a function of the lepton p_T . A cut on $p_T^\ell > 20$ GeV results in an acceptance of $\geq 85\%$ for VV fusion and $q\bar{q}$ annihilation. Rapidity distribution and acceptance as a function of the rapidity coverage are shown in Figs. 2a and b respectively. More than 95% of the leptons are contained in $|\eta| < 3$. With these cuts on p_T and η full acceptance efficiency is obtained for both kinds of production mechanism, and will be used in this analysis.

The backgrounds from the Standard Model to $pp \rightarrow W_L^\pm Z_L^0 \rightarrow 3$ leptons include the production of WZ through quark-antiquark annihilation, γW fusion, and $W_T Z_T$ fusion as well as $t\bar{t}$ production. We have used the ISAJET Monte Carlo program [6] to generate the dominant background contributions expected from WZ production through quark-antiquark annihilation and $t\bar{t}$ production. A top mass of 200 GeV has been used in the simulation. A total of about 15000 background events have been generated.

The cross-sections of Table 1 are obtained with ISAJET after requiring $|\eta^\ell| < 3$ and $p_T^\ell > 20$ GeV : $\sigma(pp \rightarrow t\bar{t} \rightarrow 3 \text{ leptons} + X) = 7.25$ pb and $\sigma(pp \rightarrow WZ \rightarrow 3 \text{ leptons}) = 0.077$ pb.

IV.3. Discussion of results

For an integrated luminosity of 4×10^5 pb $^{-1}$ and requiring the leptons to have $p_T > 20$ GeV and $|\eta| < 3$, one expects a total of 4829 (277) events from a signal $pp \rightarrow W_L Z_L \rightarrow 3$ leptons for $m_\rho = m_V = 1$ TeV (2 TeV) respectively. The background from $t\bar{t}$ production amounts to 2.9×10^6 events and 3.1×10^4 events are expected from Standard Model WZ production.

$\Delta p/p$ [%]	$W_L Z_L$ [%]	$t\bar{t}$ ($m_t = 200$ GeV) [%]
2	78	15
5	91	39
10	96	64

Table 1: Z^0 selection efficiency as a function of lepton resolution for signal and $t\bar{t}$ background, using $(m_Z \pm 3\sigma)$.

In order to reduce the background coming from $t\bar{t}$ production we first require a Z^0 mass constraint, considering all possible two-lepton combinations (no charge requirement is used). The dilepton mass spectrum obtained for signal and background is shown in Fig. 3, assuming a lepton resolution of $\Delta p/p = 5\%$. Retaining events with $m_Z \pm 3\sigma$ (with $\Delta p/p = 5\%$) results in a reduction factor for top events of ~ 2.3 and the selection efficiency for events containing a real Z^0 is $\sim 91\%$. The dependence on the reduction of the background as a function of lepton resolution is given in Table 1. A gain of a factor ~ 4 in background rejection is possible if one uses a resolution of $\Delta p/p = 2\%$ instead of $\Delta p/p = 10\%$. Charge information would further improve the background rejection for $t\bar{t}$ events.

In order to further reduce the background from $t\bar{t}$ and WZ production, the differences in the topology of signal and background events can be exploited. The signal is expected to have a much harder p_T^Z distribution than that of the background processes. Figures 4a and b show the transverse momentum distribution of the reconstructed Z^0 boson for $m_\rho = m_V = 1$ TeV and 2 TeV respectively, together with the total background prediction. These distributions were obtained by imposing a constraint on the lepton-pair mass, $m_{ll} = m_Z \pm 3\sigma$, using a lepton resolution of $\Delta p/p = 5\%$ and requiring that $p_T^l > 20$ GeV and $|\eta_l| < 3$. A clear signal is observed for $m_\rho = m_V = 1$ TeV, coming mostly from $q\bar{q}$ annihilation. Requiring $p_T^Z > 400$ GeV results in a signal of 2579 ± 671 events for 4×10^5 pb $^{-1}$, where the fusion process only contributes 6% to the signal. For a 2 TeV vector resonance, no clear signal is visible. For $p_T^Z > 400$ GeV one expects 113 ± 29 events, where 56% of the signal comes from the fusion process. The total background, shown in Figs. 4a and b, is dominated by $t\bar{t}$ production. For $p_T^Z > 400$ GeV the total background contribution amounts to 590 ± 230 events, where 524 ± 250 events come from $t\bar{t}$, whereas Standard Model WZ production has been reduced to 66 ± 20 events after imposing the above cuts.

The $t\bar{t}$ background can be further reduced by imposing an isolation cut on all three leptons. The signal is expected to have three isolated leptons, whereas in the $t\bar{t}$ case the third lepton has to come from b- or c-quark decay and is therefore not expected to be isolated. Figure 5 shows the lepton isolation distribution, where $\sum E_T$ in $\Delta R = 0.2$ ($\Delta R = \sqrt{\Delta\eta^2 + \Delta\phi^2}$) around the lepton is plotted for the signal and both backgrounds. As expected, leptons from $t\bar{t}$ are less isolated. The efficiency of reducing the $t\bar{t}$ background via isolation requirements increases with increasing lepton p_T . Figure 6 shows the average p_T of the leptons from $t\bar{t}$ production as a function of the reconstructed p_T^Z . For $p_T^Z > 400$ GeV one expects $< p_T^\ell > \simeq 200$ GeV. The isolation of leptons coming from b-jets was studied separately using a high statistics Monte Carlo sample of $b\bar{b}$ events. A rejection factor from lepton isolation as a function of lepton transverse momentum was calculated, requiring that leptons of $p_T = 10$ to 15 GeV yield a rejection factor of about 10, achieved at present Collider experiments. Figure 7 shows the thus obtained rejection factor as a function of p_T for leptons comming from b-jets. However, applying an isolation cut on all three

leptons in $t\bar{t}$ events did not leave enough Monte Carlo statistics to obtain a reliable estimate for the $t\bar{t}$ background contribution – a well-known problem when dealing with cut efficiencies $\ll 1\%$. Therefore a conservative $t\bar{t}$ background reduction of a factor of 50 was used after requiring $p_T^Z > 400$ GeV, based on Figs. 6 and 7. For the signal and for the WZ background only about 5% of the events are removed if lepton isolation is required.

The result, after imposing a cut of $p_T^Z > 400$ GeV and applying the reduction factor from lepton isolation, is shown in Figs. 8a and b for $m_\rho = m_V = 1$ TeV and 2 TeV as well as for the total background. For an integrated luminosity of $4 \times 10^5 \text{ pb}^{-1}$, one expects a signal of 2450 ± 637 (107 ± 27) events for $m_\rho = m_V = 1$ TeV (2 TeV). The total background amounts to 74 ± 30 events (64 events from WZ and 10 events from $t\bar{t}$). For the 2 TeV vector resonance, an improvement in signal-to-background ratio is obtained by applying a harder p_T^Z cut. For $p_T^Z > 600$ GeV a signal of 67 ± 17 events is expected over a total background of 15 ± 3 events (13 events from WZ and 2 events from $t\bar{t}$). Thus the background can be reduced sufficiently to observe a signal from new vector resonances with masses up to 2 TeV, provided the integrated luminosity exceeds 10^5 pb^{-1} . It should be noted that the stringent cuts on p_T^Z are imposed to obtain the final signal-to-background ratios. However, the full p_T^Z range has to be measured experimentally, in order to see a clear Jacobian peak (see Fig. 4a) or an excess at high p_T^Z (see Fig. 4b) over the Standard Model background.

We have not studied the effect of pile-up due to multiple interactions present at high-luminosity ($L > 10^{34} \text{ cm}^{-2}\text{s}^{-1}$) running, which should however be taken into account for a 2 TeV mass reach. The effect of pile-up on electron identification has been studied, for example in Ref.[7].

The possibility of forward jet ($|\eta^{\text{jet}}| > 3$) tagging, perhaps possible at the LHC [8], could allow further separation of the fusion process from background. This additional background rejection could be important for large masses of the new vector resonance, where the fusion process becomes the dominant production mechanism.

IV.4. Conclusions

We have studied the feasibility of detecting a signal above background in the $W_L^\pm Z_L^0 \rightarrow \ell^\pm \nu \ell^+ \ell^-$ channel if the underlying dynamics contains a new vector resonance as present in the BESS model or in SU(N) Technicolor theories. A clear signal for a 1 TeV vector resonance can be expected in the Jacobian peak of the p_T^Z distribution. To reach a 2 TeV mass scale, a luminosity of $L > 10^{34} \text{ cm}^{-2}\text{s}^{-1}$ is required in order to observe the expected enhancement at a high transverse momentum of the p_T^Z spectrum. In this case a good lepton-detection capability is crucial. Electrons and muons have to be detected up to $|\eta| = 3$, with a resolution of ~ 5 to 10%, and lepton-isolation requirements are necessary in order to reduce the large $t\bar{t}$ background.

With the high-luminosity option at the LHC we can explore a possible strongly interacting symmetry breaking sector if the underlying dynamics contains a vector resonance up to a mass of about 2 TeV.

Acknowledgement: We like to thank T. Sjöstrand for many discussions and his help in using the PYTHIA Monte Carlo program.

References

1. A. Dobado and M.J. Herrero, Phys. Lett. **228B** (1989) 495 and **233B** (1989) 505.
2. A. Dobado, M.J. Herrero and J. Terrón, preprints CERN TH 5670/90 to appear in Z. für Physik C, and CERN TH 5813/90.
3. R. Casalbuoni, S. de Curtis, D. Dominici and R. Gatto, Phys. Lett. **155B** (1985) 95, Nucl. Phys. **B282** (1987) 235.
4. R. Casalbuoni, P. Chiappetta, D. Dominici, F. Feruglio and R. Gatto, Nucl. Phys. **B310** (1988) 181.
5. R. Casalbuoni, P. Chiappetta, S. De Curtis, F. Feruglio, R. Gatto, B. Mele and J. Terrón, preprint CERN TH 5814/90.
6. A. Dobado, M.J. Herrero and J. Terrón, these proceedings.
7. R. Casalbuoni, P. Chiappetta, S. De Curtis, F. Feruglio, R. Gatto, B. Mele and J. Terrón, these proceedings.
8. T. Sjöstrand, Int. J. Mod. Phys. **A3** (1988) 75, and on-line documentation of PYTHIA, version 5.4.
9. F. Paige and S.D. Protopopescu, BNL 38034 (1986), ISAJET Monte Carlo, version 6.36.
10. C. Albajar, C. Fuglesang, S. Hellman, F. Pauss and G. Polesello, these proceedings.
11. M. Seymour and D. Froidevaux, these proceedings.

Figure Captions

Fig. 1 a) Transverse momentum distribution of final-state leptons from $pp \rightarrow W_L^\pm Z_L^0 \rightarrow 3 \text{ leptons}$ ($m_\rho = m_V = 1$ TeV) for the fusion mechanism (full line) and the $q\bar{q}$ annihilation mechanism (dotted line). The upper full line represents the total $W_L^\pm Z_L^0$ production (fusion + $q\bar{q}$ annihilation); b) acceptance as a function of the p_T^Z threshold for the fusion mechanism (open circles) and for the total $W_L^\pm Z_L^0$ production (full circles).

Fig. 2 a) Rapidity distribution of final-state leptons and b) acceptance as a function of $|\eta|$ coverage from $pp \rightarrow W_L^\pm Z_L^0 \rightarrow 3 \text{ leptons}$ ($m_\rho = m_V = 1$ TeV). Same notation as in Fig.1.

Fig. 3 Dilepton mass spectrum for $p_T^Z > 20$ GeV and $|\eta^\ell| < 3$. From top to bottom, the histograms show the backgrounds from $t\bar{t}$ and WZ, and the signals from the decay chain $pp \rightarrow V/\rho_T \rightarrow W_L Z_L \rightarrow \ell\nu\ell\ell$, for masses of 1 and 2 TeV.

Fig. 4 Transverse momentum distribution of the reconstructed Z^0 boson for a signal from $pp \rightarrow V/\rho_T \rightarrow W_L Z_L \rightarrow \ell\nu\ell\ell$, for a) $m_\rho = m_V = 1$ TeV and b) $m_\rho = m_V = 2$ TeV. The solid histogram represents the total signal, the dashed histogram shows the contribution from WZ fusion only. The stars show the total background from $t\bar{t}$ and WZ production.

Fig. 5 Lepton isolation ($\sum E_T$ in $\Delta R = 0.2$) for $W_L^\pm Z_L^0$ events (shaded histogram), $t\bar{t}$ events (full line), and $W^\pm Z^0$ background events (dotted line).

Fig. 6 Average p_T of leptons from $t\bar{t}$ production as a function of the reconstructed p_T^Z .

Fig. 7 Reduction factor for leptons from b-jets after isolation requirement.

Fig. 8 The same distributions as in Fig. 4, but after the final selection cuts have been applied.

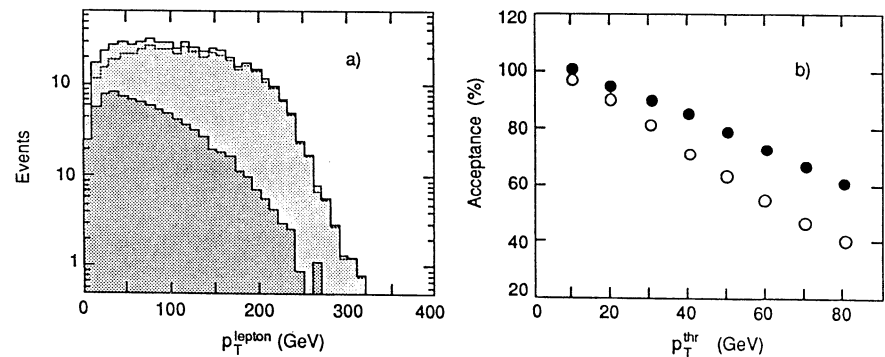


FIG. 1

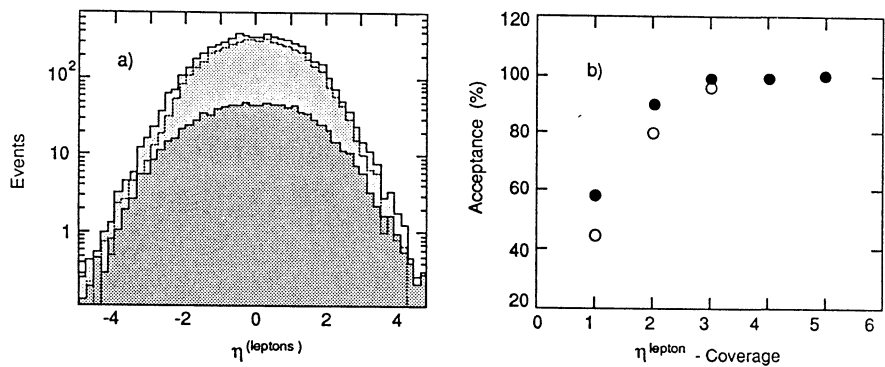


FIG. 2

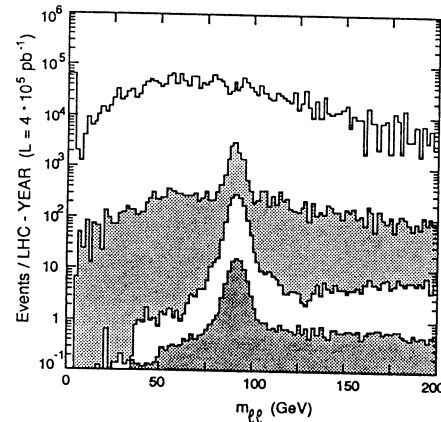


FIG. 3

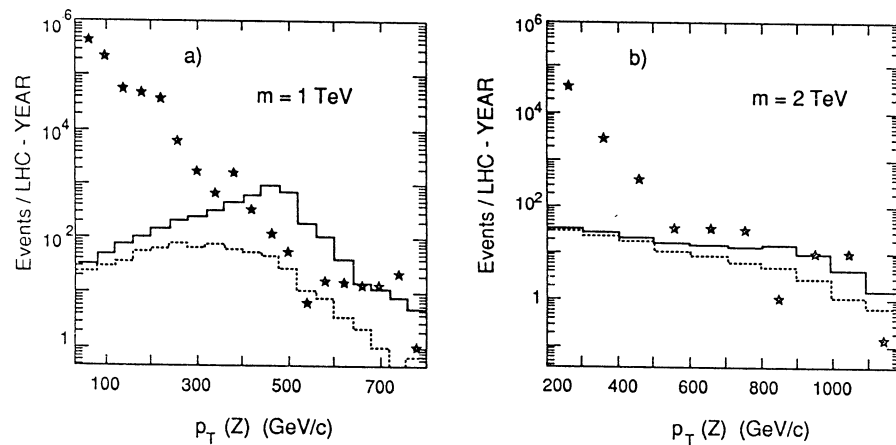


FIG. 4

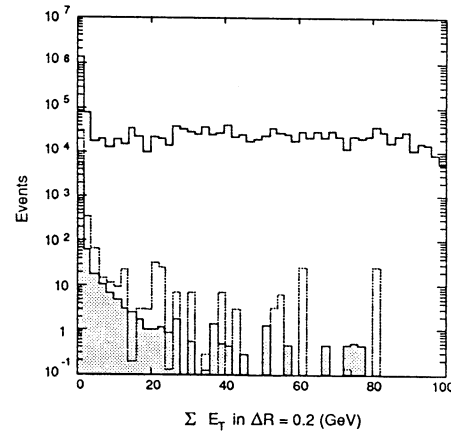


FIG. 5

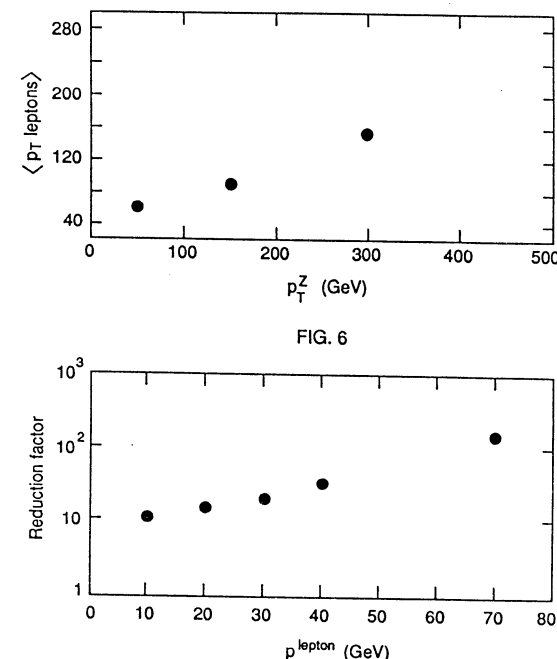


FIG. 6

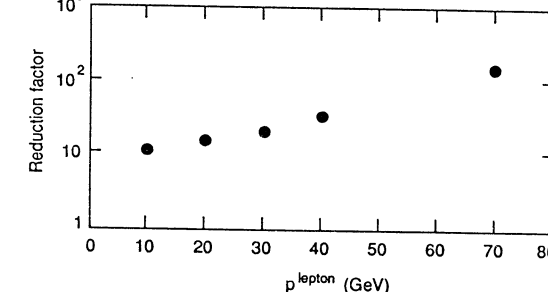


FIG. 7

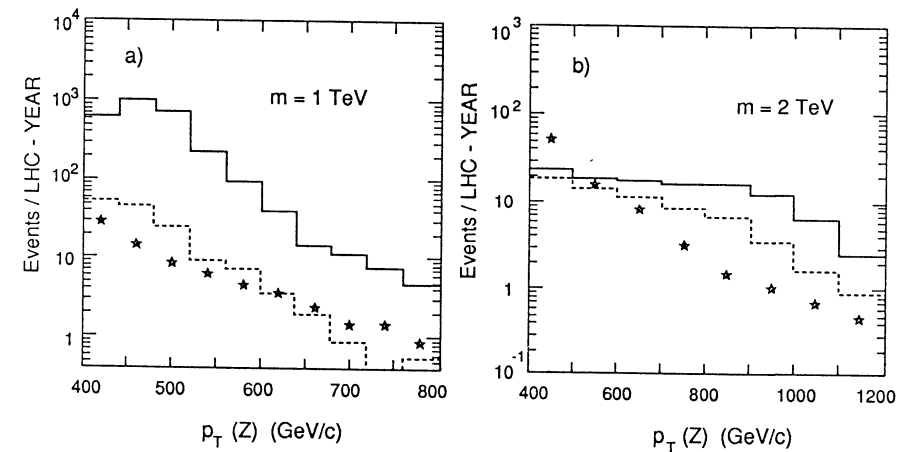


FIG. 8

V. COMPOSITENESS

Contributors: E.N. Argyres, U. Baur, P. Chiappetta, C.G. Papadopoulos, M. Perrottet
M. Spira, S.D.P. Vlassopoulos, P. Zerwas

V.1. Introduction

The proliferation of quarks and leptons and their mysterious deep relations among each other are suggestive indications for substructures of these particles [1]. No satisfactory theoretical model has been developed so far, in which the light masses of quarks and leptons could be reconciled with their small radii $< \mathcal{O}(10^{-16} \text{ cm})$ corresponding to a compositeness scale of 1 TeV and beyond. However, the quark model of hadrons has taught us very clearly in the past that theorists' puzzles cannot force Nature not to realize physically novel concepts. The compositeness scale may be anywhere between the $\mathcal{O}(1 \text{ TeV})$ range and the Planck scale. A high-energy collider like the LHC will be able to either discover preonic substructures or to improve the limits on quark radii down to $\mathcal{O}(10^{-17} \text{ cm})$ in a model independent way, an order of magnitude more than accessible now.

(i) Quark radii can be measured or bounded by studying jet production at large transverse momenta [2]. A surplus of scattering events over the predictions from standard QCD would be observed at transverse momenta $p_T \sim \mathcal{O}(R^{-1})$ where the cross section would begin to be dominated by the non-pointlike quark radius R .

(ii) A unique signal for the substructure of quarks and leptons would be the discovery of excited states [3] towering over the lepton and quark ground states: $\ell, \ell^*, \ell^{**}, \dots$ and q, q^*, q^{**}, \dots . The masses m^* of excited fermions are generally expected to be of the order of the compositeness scale Λ .

We will not discuss a specific model in the following, but we will elaborate the experimental consequences of these two rather general physical points for the LHC. The main results of this study may be summarized in limits of $\sim 20 \text{ TeV}$ for the compositeness scale probed in quark-quark scattering, and mass limits of 5 to 10 TeV for the production of excited leptons and quarks.

Other signatures of compositeness — strongly produced multi-lepton final states, leptoquarks, colored leptons and other novel particle types — have been discussed frequently in the literature, see e.g. [1].

Compositeness of gauge bosons and Higgs particles can stabilize the Higgs mass. The natural scale of this sector is the Fermi scale $\sim 250 \text{ GeV}$. Substructures of these particles would manifest themselves through excited W^* and Z^* bosons and isoscalar partners which have been described elsewhere in this report. Anomalous production of gauge boson pairs due to non-standard trilinear self-couplings is another signal of substructures at distances of $\mathcal{O}(10^{-16} \text{ cm})$.

V.2. Bounds on Quark and Lepton Radii

Contributors: P. Chiappetta and M. Perrottet

The aim of this report is to study some effects of contact terms due to composite quarks and leptons on inclusive jet production and on massive dilepton production [4].

V.2.1. Inclusive jet production.

We first compute the effect of the 4 quark contact term of dimension 6 [5]

$$\mathcal{L}_{qqqq} = \frac{\eta g^2}{2\Lambda_q^2} \bar{\psi}_q^L \gamma^\mu \psi_q^L \bar{\psi}_q^L \gamma_\mu \psi_q^L \quad (1)$$

on the inclusive one jet production at $\sqrt{s} = 16 \text{ TeV}$ (LHC) and $\sqrt{s} = 40 \text{ TeV}$ (SSC). Here η is a sign (± 1), g a strong interaction coupling constant such that $g^2 = 4\pi$ and Λ_q is the compositeness scale associated with the effective 4 quark operator of eq. (1). ψ_q^L is the usual $SU(2)_L$ doublet made out of up- and down-type quarks. Note that the current in the current-current interaction (1) is a color- and isospin-singlet. More precisely, we study the deviations due to (1), with respect to the lowest order QCD predictions, on the differential cross section

$$\frac{d^2\sigma}{dp_T dy} \Big|_{y=0} \quad (2)$$

where p_T is the jet transverse momentum and y is rapidity. The contact term (1) modifies the various elementary two-body quark cross sections. Because we disagree with some of the results published by other authors [5,7], we give below a list of our own formulas

$$q_i \bar{q}_j \rightarrow q_i \bar{q}_j : |\mathcal{M}|^2 = \frac{4}{9} \frac{\hat{u}^2 + \hat{s}^2}{\hat{t}^2} + \hat{u}^2 C^2 \quad (3)$$

$$q_i q_j \rightarrow q_i q_j : |\mathcal{M}|^2 = \frac{4}{9} \frac{\hat{u}^2 + \hat{s}^2}{\hat{t}^2} + \hat{s}^2 C^2 \quad (4)$$

$$q_i \bar{q}_i \rightarrow q_j \bar{q}_j : |\mathcal{M}|^2 = \frac{4}{9} \frac{\hat{u}^2 + \hat{t}^2}{\hat{s}^2} + \hat{u}^2 C^2 \quad (5)$$

$$\bar{q}_i \bar{q}_j \rightarrow \bar{q}_i \bar{q}_j : |\mathcal{M}|^2 = \frac{4}{9} \frac{\hat{u}^2 + \hat{s}^2}{\hat{t}^2} + \hat{s}^2 C^2 \quad (6)$$

$$q_i q_i \rightarrow q_i q_i : |\mathcal{M}|^2 = \frac{4}{9} \left\{ \frac{\hat{s}^2 + \hat{u}^2}{\hat{t}^2} + \frac{\hat{s}^2 + \hat{t}^2}{\hat{u}^2} - \frac{2\hat{s}^2}{3\hat{u}\hat{t}} \right\} + \frac{8}{9} \hat{s}^2 \left(\frac{1}{\hat{t}} + \frac{1}{\hat{u}} \right) C + \frac{8}{3} \hat{s}^2 C^2 \quad (7)$$

$$q_i \bar{q}_i \rightarrow q_i \bar{q}_i : |\mathcal{M}|^2 = \frac{4}{9} \left\{ \frac{\hat{u}^2 + \hat{s}^2}{\hat{t}^2} + \frac{\hat{u}^2 + \hat{t}^2}{\hat{s}^2} - \frac{2\hat{u}^2}{3\hat{s}\hat{t}} \right\} + \frac{8}{9} \hat{u}^2 \left(\frac{1}{\hat{t}} + \frac{1}{\hat{s}} \right) C + \frac{8}{3} \hat{u}^2 C^2 \quad (8)$$

$$\bar{q}_i \bar{q}_j \rightarrow \bar{q}_i \bar{q}_j : |\mathcal{M}|^2 = \frac{4}{9} \left\{ \frac{\hat{s}^2 + \hat{u}^2}{\hat{t}^2} + \frac{\hat{s}^2 + \hat{t}^2}{\hat{u}^2} - \frac{2\hat{s}^2}{3\hat{u}\hat{t}} \right\} + \frac{8}{9} \hat{s}^2 \left(\frac{1}{\hat{t}} + \frac{1}{\hat{u}} \right) C + \frac{8}{3} \hat{s}^2 C^2 \quad (9)$$

The indices i and j refer to quark flavors. \hat{s} , \hat{t} and \hat{u} are the usual Mandelstam variables. C is directly related to the compositeness scale Λ_q through

$$C = \frac{\eta}{\alpha_s(Q^2)\Lambda_q^2} \quad . \quad (10)$$

Finally, the differential cross sections $d\sigma/d\hat{t}$ which enter into the computation of eq. (2) are given by

$$\frac{d\sigma}{d\hat{t}} = \frac{\pi}{\hat{s}^2} \alpha_s^2(Q^2) |\mathcal{M}|^2 \quad (11)$$

where the argument Q^2 of the effective QCD coupling constant is p_T^2 . In order to obtain results which are little sensitive to the choice of structure functions and mass scales, we have studied the ratio

$$D = \frac{\frac{d^2\sigma}{dp_T dy} \Big|_{y=0} (\text{QCD} + \text{CT}) - \frac{d^2\sigma}{dp_T dy} \Big|_{y=0} (\text{QCD})}{\frac{d^2\sigma}{dp_T dy} \Big|_{y=0} (\text{QCD})} \quad (12)$$

where CT means contact term. The discovery limits for the compositeness scale Λ_q that we will give below correspond to a deviation from the QCD prediction larger than 100%, namely $D \geq 1$ (theoretical uncertainties including higher order corrections are of the order of 40% [8]). With $\Delta p_T = 100\text{GeV}/c$, we would like to have at least ten events per year in the standard model. Considering the expected luminosities $\mathcal{L}_{\text{LHC}} = 10^{34}\text{cm}^{-2}\text{s}^{-1}$ and $\mathcal{L}_{\text{SSC}} = 10^{33}\text{cm}^{-2}\text{s}^{-1}$, one can reach for the cross section (2) $x_T \equiv \frac{2p_T}{\sqrt{s}} \cong 0.5$ for LHC, and $x_T \cong 0.3$ for SSC. These discovery limits are displayed in table 1 for LHC and SSC, using two sets of distribution functions, DFLM set of ref. [9] with $\Lambda_{\text{QCD}} = 160\text{ MeV}$, and set 1 of Duke-Owens [10]. As expected, there is little sensitivity to the choice of structure functions, typically a few percent. It should be noted that the difference in luminosities compensates to a large extent the gap in energy between LHC and SSC. We have checked that another choice of the mass scale ($Q^2 = p_T^2/4$) changes the discovery limits by a few percent only.

Table 1

	qqqq CT		qqgg CT	
	$\eta = +1$	$\eta = -1$	Vector	Axial
LHC Duke-Owens	20 TeV	28 TeV	4.6 TeV	4.6 TeV
	20 TeV	27 TeV	4.3 TeV	4.4 TeV
LHC Diemoz et al.	27 TeV	33 TeV	7.6 TeV	7.7 TeV
	27 TeV	32 TeV	7.4 TeV	7.5 TeV
SSC Duke-Owens	27 TeV	33 TeV	7.6 TeV	7.7 TeV
	27 TeV	32 TeV	7.4 TeV	7.5 TeV

Obviously discovery limits depend on luminosity and the value of required deviation from QCD prediction. As an example if we assume $\mathcal{L}_{\text{LHC}} = 10^{33}\text{cm}^{-2}\text{sec}^{-1}$ and a deviation larger than 200 % we get a discovery limit of 13 TeV for $\eta = +1$. We have also computed the effect

of a contact term between transverse gluons considered as true gauge particles and composite quarks. Several CP- and chirality-conserving operators can be written [11] but for the present study we have selected the one of the lowest dimension. It is called N_{TT}^2 in ref. [11] and can be written as [12]

$$\mathcal{L}_{\text{qqgg}} = i \frac{\alpha_s}{\Lambda_g^4} \bar{\psi}_q \{ (\gamma^\mu \partial_\rho + \gamma_\rho \partial^\mu) (C_V - C_A \gamma_5) \psi_q \} G_{\mu\nu} G^{\nu\rho} \quad (13)$$

where Λ_g is the compositeness scale associated with the dimension 8 operator, $C_V(C_A)$ the vector (axial) part of the lagrangian. For completeness, we give below the contribution of (13) to the relevant processes [6]

$$q_i \bar{q}_i \rightarrow gg : |\mathcal{M}|^2 = \frac{8}{3} (\hat{u}^2 + \hat{t}^2) \left\{ \frac{4}{9\hat{u}\hat{t}} - \frac{1}{\hat{s}^2} \right\} + \frac{4}{3} \frac{\hat{u}^2 + \hat{t}^2}{\Lambda_g^4} \left\{ \frac{2}{3} C_V + \frac{\hat{u}\hat{t}}{\Lambda_g^4} (C_V^2 + C_A^2) \right\} \quad (14)$$

$$q_i g \rightarrow q_i g : |\mathcal{M}|^2 = -(\hat{u}^2 + \hat{s}^2) \left\{ \frac{4}{9\hat{u}\hat{s}} - \frac{1}{\hat{t}^2} \right\} - \frac{1}{2} \frac{\hat{u}^2 + \hat{s}^2}{\Lambda_g^4} \left\{ \frac{2}{3} C_V + \frac{\hat{u}\hat{s}}{\Lambda_g^4} (C_V^2 + C_A^2) \right\} \quad (15)$$

$$gg \rightarrow q_i \bar{q}_i : |\mathcal{M}|^2 = \frac{3}{8} (\hat{u}^2 + \hat{t}^2) \left\{ \frac{4}{9\hat{u}\hat{t}} - \frac{1}{\hat{s}^2} \right\} + \frac{3}{16} \frac{\hat{u}^2 + \hat{t}^2}{\Lambda_g^4} \left\{ \frac{2}{3} C_V + \frac{\hat{u}\hat{t}}{\Lambda_g^4} (C_V^2 + C_A^2) \right\} \quad . \quad (16)$$

We have assumed that the color structure in the contact term is the same as that of the QCD amplitude. The differential cross section $d\sigma/d\hat{t}$ is still given by eq. (11). Since QCD is a vector theory, the interference term between QCD and the contact interaction (13) is simply proportional to the vector coupling C_V . To set discovery limits for the compositeness scale Λ_g , we used the same approach as for interaction (1). These limits are given in Table 1. There is little difference between the vector case ($C_V = 1, C_A = 0$) and the axial one ($C_V = 0, C_A = 1$). Of course, the operator (13) being of higher dimension than (1), the discovery limits are much lower and will be completely hidden by the presence of the contact term (1) if one assumes that Λ_g is of the order of Λ_g .

V.2.2. Massive lepton pair production

Finally, we have similarly analyzed the influence of a contact term between quarks and leptons on massive dilepton production through the Drell-Yan mechanism. The effective contact interaction is similar to (1)

$$\mathcal{L}_{\text{qqll}} = \frac{\eta g^2}{4\Lambda_{lq}^2} \bar{\psi}_l \gamma^\mu (1 - \eta_l \gamma_5) \psi_l \bar{\psi}_q \gamma_\mu (1 - \eta_q \gamma_5) \psi_q \quad (17)$$

with $\eta = \pm 1, \eta_l = \pm 1, \eta_q = \pm 1, g^2 = 4\pi$ and Λ_{lq} is the compositeness scale associated to the dimension 6 operator of eq. (17). We will use the same criteria as described previously to define the discovery limits, namely deviations with respect to the QCD predictions larger than 100%.

We will concentrate on the differential cross section $\frac{d\sigma}{dM_{l+l^-}}$ where M_{l+l^-} is the invariant mass of the lepton pair. Then the deviation to study is

$$\tilde{D} = \frac{\frac{d\sigma}{dM_{l+l^-}}(\text{QCD} + \text{CT}) - \frac{d\sigma}{dM_{l+l^-}}(\text{QCD})}{\frac{d\sigma}{dM_{l+l^-}}(\text{QCD})} \quad (18)$$

where CT is now the contribution from the interaction (17). Keeping in mind a rate of at least 10 events per year from the standard model with $\Delta M = 100\text{GeV}$, a direct computation shows that one can reach $M_{l+l^-} \cong 2.05\text{TeV}$ at LHC and $M_{l+l^-} \cong 2.15\text{TeV}$ at SSC. For illustration, we have considered the two extreme chirality cases $\eta_l = \eta_q = 1$ (left-left, or LL) and $\eta_l = \eta_q = -1$ (right-right or RR). The corresponding discovery limits are displayed in Table 2 for LHC and SSC with the structure functions of ref. [9]. One can see that the difference in luminosity between LHC and SSC compensates exactly the difference in energy. We can also notice that for a given overall sign of the contact interaction (17), the discovery limits depend very little on the choice of chirality (LL or RR).

Table 2

	$\eta = +1$		$\eta = -1$	
	LL	RR	LL	RR
LHC	15 TeV	16 TeV	25 TeV	25 TeV
SSC	15 TeV	16 TeV	24 TeV	24 TeV

V.2.3. Conclusion

To conclude, it is interesting to make a comparison between our results and the corresponding limits at Hera and at the Tevatron. For Hera, the LL 2quark- 2lepton contact term (17) leads to a discovery limit of about 5 TeV [13], to be compared with the 15 TeV limit of Table 2. Concerning the 4 quark contact term (1), LHC and SSC will improve the expected Tevatron limit (2 to 3 TeV) [14] by roughly one order of magnitude.

V.3. Testing Contact Interactions of Quarks and Gluons at Future pp Colliders

Contributors: E.N.Argyres, C.G.Papadopoulos and S.D.P.Vlassopoulos

New interactions at an energy scale Λ of the order of a few TeV will manifest themselves at energies below this scale, through deviations from the Standard Model (SM), described by an effective non-renormalizable $SU(3) \otimes SU(2) \otimes U(1)$ invariant lagrangian. Such interactions may arise either as low-energy tails of heavy exotic particle exchange (e.g. non-minimal Higgses, E_6 -diquarks, extra neutral currents, etc) or as a manifestation of quark and gluon substructure. It is therefore, interesting to search for deviations from the SM predictions at future accelerators, like LHC and SSC, which will provide us with the highest available center of mass energies, $\sqrt{s}=16\text{TeV}$ and 40TeV , respectively.

In this work we calculate the effect of qq,qg,gg contact interactions, described by [15]

$$\mathcal{L}_{eff} = g_1 f_{ABC} G_\mu^{A\nu} G_\nu^{B\lambda} G_\lambda^{C\mu} \quad (19a)$$

$$+ ig_2 \bar{q} \lambda^A \gamma_\mu D_\nu q G^{A\mu\nu} \quad (19b)$$

$$+ ig_3 \bar{q} \gamma_\mu q \bar{q} \gamma^\mu q \quad (19c)$$

$$+ ig_4 \bar{q} \lambda^A \gamma_\mu q \bar{q} \lambda^A \gamma^\mu q \quad (19d)$$

in the 2- and 3-jet cross sections. The dimensionful coupling constants, g_i , are given by $g_i = \eta_i \frac{4\pi}{\Lambda^2}$, where $\eta_i = \pm 1$ and we have assumed a common scale Λ . More explicitly we calculate

$$\sigma(pp \rightarrow n \text{jets} + X) = \int \sum_{a,b} dx_a dx_b \mathcal{F}_a(x_a, Q) \mathcal{F}_b(x_b, Q) |\mathcal{M}_{ab}|^2 d\mathcal{L}ips^{(n)} \quad (20)$$

where \mathcal{F}_a are the quark and gluon distributions and \mathcal{M}_{ab} the helicity amplitudes, calculated using the "E-product" [16] formulation of the well known spinor-product technique [17]. Notice that in the case $n = 2$ the full lagrangian (19) has been used, whereas in the case $n = 3$ only the operator (19c) has been employed⁴. In both cases we use $\eta_i = +1$.

In order to compare the theoretical predictions with experimental data we have to impose appropriate cuts on the momenta of the produced jets, quarks and gluons, which, neglecting all hadronization effects, are simply

$$|\eta_{jet}| \leq 2.5 \quad (21a)$$

$$\cos(\theta_{ij}) \leq 0.766 \ (\theta_{min} = 40^\circ) \quad (21b)$$

where η_{jet} is the pseudorapidity and θ_{ij} the angle between the 3-momenta of the jets i and j . We use $Q = \sqrt{\hat{s}}$, $\hat{s} = x_a x_b s$ and the structure-function parametrization EHLQ II [18] with $\Lambda_{QCD} = 0.29\text{GeV}$.

Since we are interested in enhancing the signal of the new interactions, we impose the supplementary cuts

$$M_{njets} \geq 6.4(12)\text{TeV} \quad (22a)$$

$$p_T \geq 0.4(1)\text{TeV} \quad (22b)$$

for $\sqrt{s} = 16(40)\text{TeV}$, where M_{njets} is the invariant mass of the produced jets [19] and p_T the transverse momentum. These cuts have the effect to suppress the QCD background, whereas the contact interaction contribution remains almost unaffected. Notice that the cuts (22a) and (22b) are necessary in the case $n = 3$, since a quark-quark contact interaction signal can be detectable only if we suppress the gg initial state contribution [19]. We focus our attention to the normalized χ distribution,

$$\frac{1}{\sigma} \frac{d\sigma}{d\chi}$$

where

$$\chi = \frac{1 + \cos \theta^*}{1 - \cos \theta^*} \quad (23)$$

⁴The details of the calculation will be given elsewhere

and θ^* is the c.m. angle of the beam and the produced jet momentum, in the 2-jet case, and the angle of the beam with the fastest jet, in the 3-jet case.

Figs.(1a) and (1b) show the 2-jet cross section for $\sqrt{s} = 16$ and 40 TeV respectively. As we can see, the contact interaction prefers to accumulate events at smaller values of χ (spherical events), whereas the QCD background is almost flat. If one assumes a statistical error

$$\frac{\delta\sigma}{\sigma} = \sqrt{\frac{1}{\sigma L}} \quad (24)$$

where L is the luminosity, a χ^2 analysis gives that (at 95% C.L.):

$$\Lambda \geq 40 \text{TeV} (\sqrt{s} = 16 \text{TeV}) \quad (25a)$$

$$\Lambda \geq 50 \text{TeV} (\sqrt{s} = 40 \text{TeV}) \quad (25b)$$

where we have used $L = 400 \text{fb}^{-1}$ at LHC and $L = 10 \text{fb}^{-1}$ at SSC [20].

In figs.(2a) and (2b) we show the results for the three-jet cross section. The corresponding bounds are:

$$\Lambda \geq 15 \text{TeV} (\sqrt{s} = 16 \text{TeV}) \quad (26a)$$

$$\Lambda \geq 10 \text{TeV} (\sqrt{s} = 40 \text{TeV}) \quad (26b)$$

The bound for the SSC is smaller than for the LHC, due to the smaller luminosity of the SSC and to the fact that the 3-jet χ -distribution of QCD is not flat.

Although there are other quantities which are sensitive to contact interactions, like the p_T spectrum, the normalized χ distribution offers the very advantage of being relatively free of the uncertainties due to the small- x behaviour of the gluon distribution and the higher order QCD corrections (in particular, choice of the scale Q^2 and the jet-cone size) [8], which are expected not to be strongly dependent on χ .

Comparing the bounds in all cases, one can state, that the luminosity L is a crucial parameter in order to probe the contact interactions. Especially for the quark-quark contact interactions, LHC seems to be more sensitive than SSC.

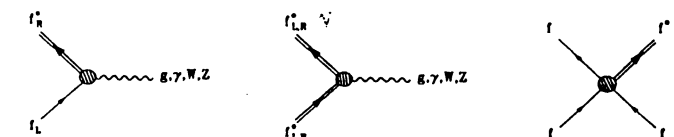
V.4. Excited Quarks and Leptons

Contributors: U. Baur, M. Spira and P. Zerwas

Spin and isospin of the excited fermions will be set to 1/2 in order to restrict the number of parameters to be introduced in this study [3]. The assignment of left- and right-handed components to isodoublets, e.g. for the first generation

$$\begin{bmatrix} \nu_e \\ e^- \end{bmatrix}_L \quad \begin{bmatrix} \nu_{eR} \\ e_R^- \end{bmatrix} \quad \begin{bmatrix} \nu_e^* \\ e^{*-} \end{bmatrix}_L \quad \begin{bmatrix} \nu_e^* \\ e^{*-} \end{bmatrix}_R \quad \text{and} \quad \begin{bmatrix} u \\ d \end{bmatrix}_L \quad \begin{bmatrix} u_R \\ d_R \end{bmatrix} \quad \begin{bmatrix} u^* \\ d^* \end{bmatrix}_L \quad \begin{bmatrix} u^* \\ d^* \end{bmatrix}_R$$

allows for non-zero masses prior to $SU(2) \times U(1)$ symmetry breaking, and it protects $(g-2)_e$ quadratically in the mass ratio $(m_e/m^*)^2$. The coupling of excited fermion states to the chiral Standard Model particles consists of three interaction types:



the first being the standard fermion-gauge boson interaction; the second being a gauge invariant magnetic type coupling between ground state and excited state; the third describing the strong excitation of fermions through contact interactions mediated, for instance, by preon interchange. Throughout this analysis we put $m^* = \Lambda$, for the sake of simplicity, and we neglect [minor] form factor effects.

Decay. Heavy excited fermions will decay into light fermions plus gauge bosons, but also, through preon-pair creation, into bunches of quarks and leptons

$$f^* \rightarrow f + V \quad \text{and} \quad f^* \rightarrow f + f' \bar{f}'$$

with $V = g, \gamma, Z, W$. Assuming $m^* \gg m_{W,Z}$ and neglecting light quark masses, the partial widths for the various gauge decay channels lead to the branching ratios listed in Table 3.

Table 3

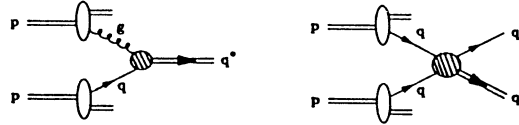
	$\sum_V \Gamma(f^* \rightarrow fV)/m^*$ [$m^* = \Lambda$]							
	e^*	B_G	ν^*	B_G	u^*	B_G	d^*	B_G
ν^*	$6.5 \cdot 10^{-3}$		νZ	0.39	ug	0.85	dg	0.85
e^*	$6.5 \cdot 10^{-3}$		eW	0.61	$u\gamma$	0.02	$d\gamma$	0.005
u^*	$3.9 \cdot 10^{-2}$				uZ	0.03	dZ	0.05
d^*	$3.9 \cdot 10^{-2}$				dW	0.10	uW	0.10

Contact interactions widen the excited states such that excited leptons and quarks would have comparable widths as expected from strong preon interactions. Results are shown in Table 4.

Table 4

	Γ_{tot}/m^*	Γ_G/Γ_{tot}	Γ_{CT}/Γ_{tot}	leptonic decays/all
ν^*	$8.9 \cdot 10^{-2}$	0.07	0.93	100%
e^*	$8.9 \cdot 10^{-2}$	0.07	0.93	100%
u^*	$1.2 \cdot 10^{-1}$	0.32	0.68	16.3%
d^*	$1.2 \cdot 10^{-1}$	0.32	0.68	16.3%

q^* production. Excited quarks can be produced in pp collisions through a variety of mechanisms. The dominant processes are the gluonic excitation of quarks $g + q \rightarrow q^*$ [3,21,22] and the excitation through contact interactions $qq \rightarrow qq^*$ [3,21].



The cross section for the gluonic excitation of quarks, $qg \rightarrow q^*$, at pp colliders is shown in Fig. 3. Assuming gauge interactions to dominate over contact interactions, the signals for singly produced excited quarks are large transverse momentum jj , $j\gamma$, jZ or jW pairs with an invariant mass peaking at m^* . The jj mass distributions of the QCD background is integrated over twice the q^* width. The mass distributions for pp collisions at $\sqrt{s} = 16$ TeV are shown in Fig. 4 for various values of m^* . At LHC the q^* signal stands out clearly. Similar results are obtained for $j\gamma$, jW and jZ final states.

If contact interactions contribute significantly to the decay rate of excited quarks they may be a bubbling source for excited quarks q^* at hadron colliders. Excited quarks can be produced through contact interactions in qq collisions and $q\bar{q}$ annihilation together with an ordinary quark. Excited quark decays, mediated either by gauge or contact interactions lead to final states that consist of three or four jets, two jets and a photon, or two jets and a lepton pair. The qq^* production cross sections for LHC energies are shown in Fig. 5. The background to the qq^* signal, the q^* decaying into three jets via contact interactions, are four-jet final states. In addition to pure QCD processes the contact interactions are a second important source of four-jet background events. All these background cross sections however are significantly smaller than the signal, as demonstrated in Fig. 5. This is also the case for the background from diagrams involving both QCD and contact interactions, with gluons in either the initial or the final state. The combinatorial background arising from the wrong three-jet combination in the jjj mass distribution is of the same order as the signal.

ℓ^* production. The possibility to create leptons copiously through contact interactions in pp collisions is one of the most exciting phenomena expected in composite models in which quarks and leptons have common constituents [5]. In this case also excited leptons could be produced in large numbers either singly via $q\bar{q} \rightarrow \ell\bar{\ell}^*$, $\ell^*\bar{\ell}$, or pairwise via $q\bar{q} \rightarrow \ell^*\bar{\ell}^*$ ($\ell = e, \nu$), Fig. 6. Background reactions to these channels are very rare in the Standard Model, and purely leptonic decays would provide very clear signatures for the experimental identification of excited electrons.

Summary. Excited quarks and leptons are produced with large cross sections in pp collisions once the threshold energy has been reached. This observation can be condensed in a few numbers by deriving the maximum excited quark and lepton masses accessible at the pp collider. As the discovery criterion we require that at least 100 signal events be observed within cuts. The discovery limits are summarized in the following table. For the LHC we considered two options: an integrated luminosity of 10^4 pb^{-1} and a “high luminosity” option with $4 \cdot 10^5 \text{ pb}^{-1}$.

pp colliders turn out to be well suited for the search of excited quarks. Single q^* production is expected to be much larger than q^*q^* production. Clean and simple experimental signatures with small background are predicted for excited quarks which are produced via qg fusion and which decay via gauge interactions. Contact interactions may substantially enhance the q^* production cross section. This is reflected by the discovery limits for the LHC summarized in

Table 5

$\int \mathcal{L} dt$	LHC 10^4 pb^{-1}	LHC $4 \cdot 10^5 \text{ pb}^{-1}$
$q^* [G]$	6.5 TeV	9.0 TeV
$q^* [\text{CT}]$	7.0 TeV	8.9 TeV
$\ell^* [\text{CT}]$	4.0 TeV	5.6 TeV

the preceding table. If quarks and leptons share common subconstituents, even excited leptons could be produced copiously at this machine, producing spectacular lepton final states at very high rates.

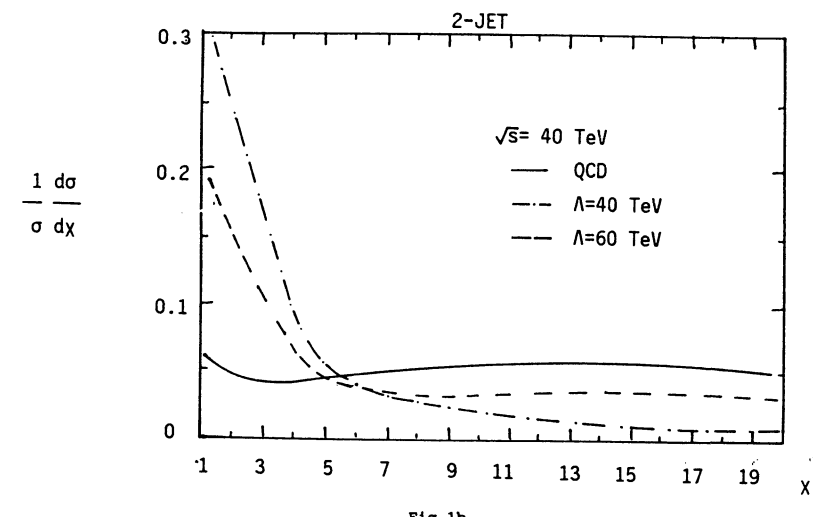
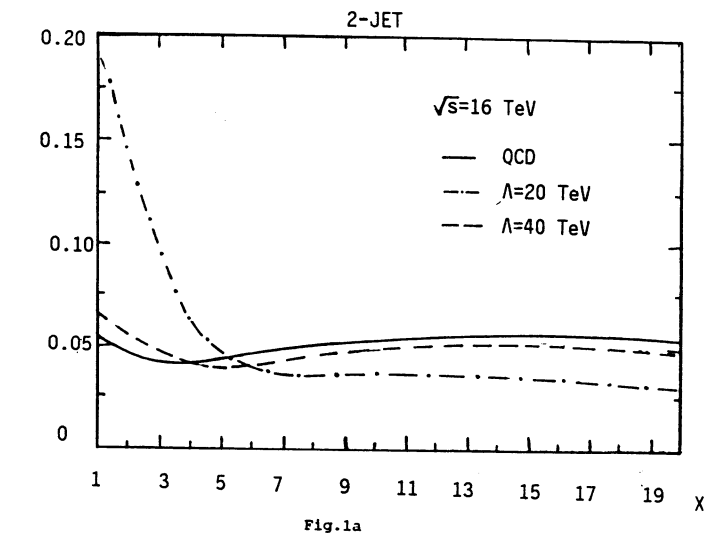
Figure Captions

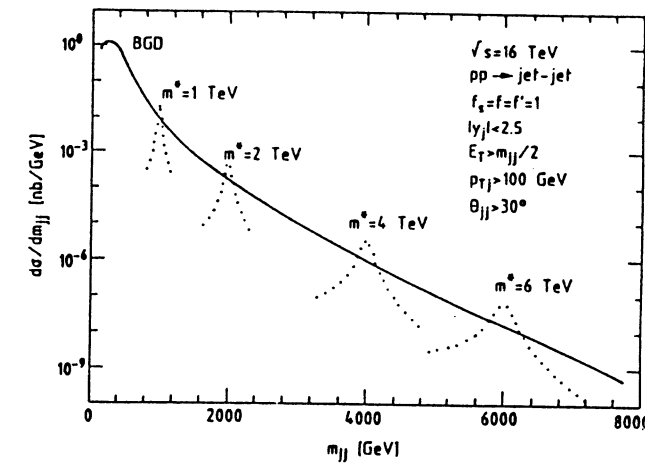
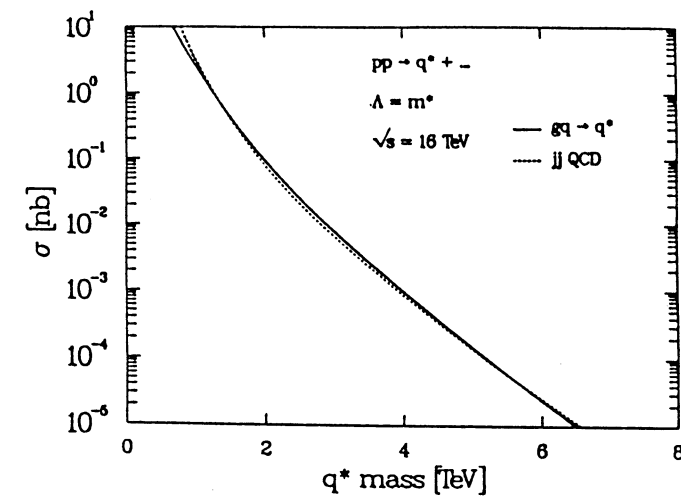
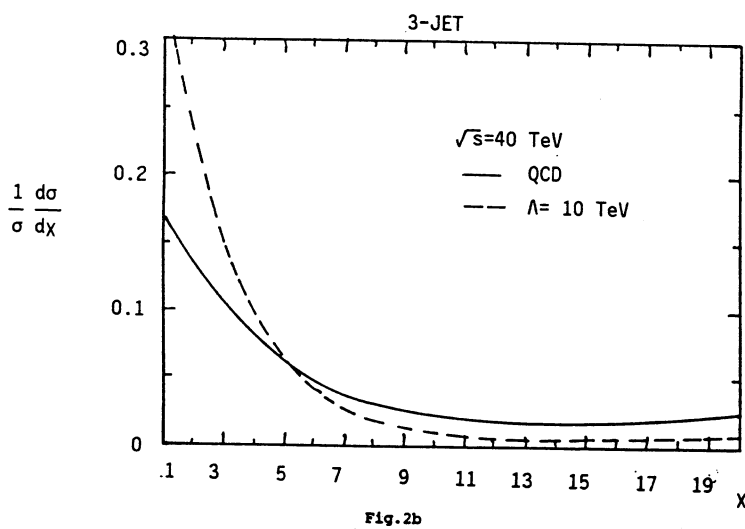
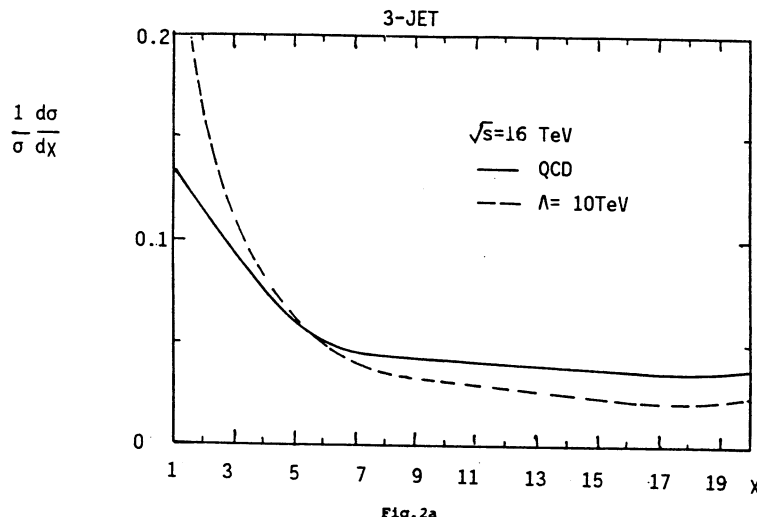
- Fig. 1: Normalized x -distributions for 2 jet cross sections at LHC (a) and SSC (b).
- Fig. 2: Normalized x -distributions for 3 jet cross sections at LHC (a) and SSC (b).
- Fig. 3: Cross section for the production of excited quarks in quark-gluon fusion (solid line). The 2-jet QCD background is shown by the dashed line.
- Fig. 4: Invariant mass distributions of excited quarks in the jj decay channel for various values of m^* (dotted lines). The solid curve represents the QCD jj background.
- Fig. 5: Cross section for the associated production of excited and ordinary quarks (solid line) with subsequent decay of the excited quark into three jets (contact interactions). The other curves show the four-jet background from QCD, contact interactions and diagrams involving both QCD and contact interactions.
- Fig. 6: Cross sections for the associated production of ordinary and excited electrons (solid line) and e^* pair production (dashed line).

References

- [1] H. Harari, Proceedings of the 1984 Scottish Universities Summerschool, St. Andrews, Scotland.
- [2] E. J. Eichten, K. D. Lane and M. I. Peskin, Phys. Rev. Lett. **50** (1983) 811.
- [3] U. Baur, M. Spira and P. M. Zerwas, Phys. Rev. **D42** (1990) 815.
- [4] P. Chiappetta and M. Perrottet, Preprint Marseille CPT-90/P.2440 (September 1990) to appear in Phys. Lett. B
- [5] E. Eichten, I. Hinchliffe, K. Lane and C. Quigg, Rev. Mod. Phys. **56** (1984) 579.
- [6] C. Bourrely, F.M. Renard, J. Soffer and P. Taxil, Phys. Rep. **177** (1989) 319.

- [7] E.N. Argyres, C.G. Papadopoulos and S.D.P. Vlassopoulos, Nucl. Phys. **B324** (1989) 91.
- [8] F. Aversa, P. Chiappetta, M. Greco and J.-Ph. Guillet, Phys. Rev. Lett. **65** (1990) 401; S.D. Ellis, Z. Kunszt and D.E. Soper, Phys. Rev. Lett. **64** (1990) 2121.
- [9] M. Diemoz, F. Ferroni, E. Longo and G. Martinelli, Z. Phys. **C39** (1988) 21.
- [10] D.W. Duke and J.F. Owens, Phys. Rev. **D30** (1984) 49.
- [11] P. Méry, M. Perrottet and F.M. Renard, Z. Phys. **C36** (1987) 249.
- [12] P. Méry, S.E. Moubarik, M. Perrottet and F.M. Renard, Z. Phys. **C46** (1990) 229.
- [13] R. Rückl, in the Proceedings of the ECFA Workshop on LEP 200, CERN 87-08 (1987), Vol. II, p.453.
- [14] P. Jenni, in the Proceedings of the ECFA Workshop on LEP 200, CERN 87-08 (1987), Vol. II, p.486.
- [15] W.Buchmüller & D.Wyler, Nucl.Phys.**B268**(1986)621.
- [16] E.N.Argyres & C.G.Papadopoulos: "Testing 3-boson couplings in the Standard Model via single W production at LEP", NCSR "Democritos" preprint, July 1990.
- [17] R.Kleiss and W.J.Stirling, Nucl.Phys. **262**(1985)235.
- [18] E.Eichten et al., Rev.Mod.Phys.**56**(1984)579; **58**(1986)1065(E).
- [19] E.N.Argyres, C.G.Papadopoulos & S.D.P. Vlassopoulos, Nucl.Phys.**B324**(1989)91.
- [20] U.Baur & E.W.N.Glover, Nucl. Phys. **B347**(1990) 12.
- [21] R. Kleiss and P. Zerwas, Proceedings, Workshop "Physics at Future Accelerators", La Thuile/CERN 1987.
- [22] U. Baur, I. Hinchliffe and D. Zeppenfeld, Proceedings, Workshop "From Colliders to Supercolliders", Madison (Wisconsin) 1987; Int. J. Mod. Phys. **A2** (1987) 1285.





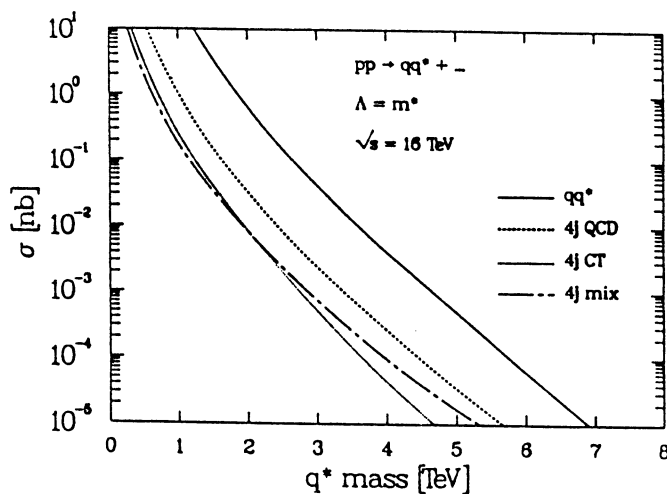


Fig. 5

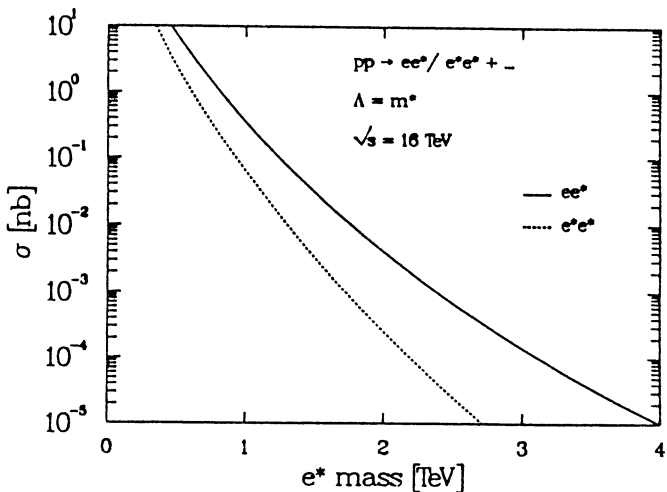


Fig. 6

VI. SIGNATURES FOR GEOMETRICAL FLAVOUR INTERACTIONS AND B+L VIOLATION AT THE LHC

Contributors: J. Ellis, V.A. Khoze, A. Ringwald, F. Schrempp, C. Wetterich

VI.1. Introduction

It has recently been suggested that there may be a large non-perturbative cross-section for electroweak interactions at high energies [1 – 4]. This suggestion originated from the observation that the s-wave cross-section for electroweak baryon (B) and lepton (L) number violating interactions [5] rises rapidly with energy [1, 2], and could become large at energies comparable to the sphaleron [6] energy $M_{sp} \simeq 10$ TeV. Instanton calculations suggest [1 – 3] a sharp threshold for strong flavour interactions at $E \sim M_{sp}$, with a high mean multiplicity of weakly-interacting particles $\bar{n}_w \simeq \pi/\alpha_w = \mathcal{O}(100)$, which would be produced quasi-isotropically close to threshold. At higher energies, the s-wave amplitude would then be bounded by unitarity and other partial waves as well as (B+L)-conserving amplitudes would become strong, inducing large forward-peaked cross-sections at asymptotic energies $E \gg M_{sp}$ [3].

There remain considerable theoretical uncertainties in these non-perturbative estimates, notably whether the rapidly-rising (B+L)-violating cross-section flattens out at some energy below M_{sp} , and whether it ever reaches a sizeable fraction of the unitarity limit. Nevertheless, there is by now a consensus that analogous (B+L)-violating effects are important in a hot plasma [7], and the consequences of large non-perturbative electroweak interactions are so far-reaching and dramatic⁵, that we believe our experimental colleagues should include this contingency in their planning for the LHC.

There may even be deeper analogies between the electroweak interactions and QCD at very high energies, as both are non-Abelian gauge theories with similar infrared divergences [4] and topological features. These analogies refer not only to the scattering of a few particles at large angles, which is well described by (parton model) perturbation theory, but also to the large, logarithmically-rising, total inelastic cross-section, where perturbation theory presumably fails. In this note we adopt the following working hypotheses, motivated by the above considerations [3, 4, 8]:

- 1) At high parton cm energies $\sqrt{\hat{s}}$ the total weak inelastic cross-section becomes approximately energy-independent

$$\sigma_w = 4\pi c_w m_w^{-2} \approx 0.1 \text{ nb} - 10 \mu\text{b}, \quad (1)$$
where c_w is a logarithmically-varying coefficient;
- 2) the asymptotic behaviour sets in abruptly above a certain threshold energy of the order of a few TeV to about 20 TeV;
- 3) the mean constituent multiplicity is high, typically of order $1/\alpha_w \sim 30$;
- 4) there is a substantial contribution of (B+L)-violating events to the total weak cross-section;

⁵For a detailed discussion of the expected phenomenology see ref. [8].

- 5) the inclusive differential cross-sections decrease rapidly for transverse momenta exceeding a characteristic value of order m_w .

We call processes with these characteristics Geometric Flavour Interactions (GFI) [8].

VI.2. Cross-Sections and Production Rates

We start from the working hypothesis that the parton cross-section $\sigma_w(\hat{s})$ becomes almost constant above the threshold E_w^{crit} , with a size of order $\sigma_w^0 \simeq 0.1 \text{ nb} - 10 \mu\text{b}$ [4,8]. In particular, let us assume in this paper a relatively sudden onset of geometrical QFD cross-sections for $\sqrt{\hat{s}} \geq E_w^{\text{crit}}$ and approximate $\sigma_w(\sqrt{\hat{s}}) = \sigma_w^0 \theta(\sqrt{\hat{s}} - E_w^{\text{crit}})$. After folding σ_w with the parton distributions (no gluons) we obtain the event rate for the production of many weakly interacting particles in proton-proton collisions, see fig. 1. The limit of detectability should be around 100 events per year. We conclude that GFI events can be seen for $E_w^{\text{crit}} < 11 \text{ TeV}$ for the LHC if σ_w^0 is around 1 nb.

VI.3. Critical Energy and Multiplicity

Weakly-interacting particles produced by geometrical flavour interactions at high energies comprise W and Z bosons, photons, Higgs bosons, leptons, and quarks. Quarks will appear as jets and we count jets as particles.

We explore the notion that GFI events set in abruptly once the energy is high enough to produce a critical number n_w^{crit} of weakly interacting particles. These phenomena are presumably related to the breakdown of perturbation theory for large particle numbers, namely when $n_w \alpha_w$ becomes large. We therefore, assume $n_w^{\text{crit}} \alpha_w = \nu_w$ with ν_w some constant of order one. The threshold energy can then be roughly guessed by requiring that $\sqrt{\hat{s}}$ must be large enough to produce n_w^{crit} particles with mass m_w without a strong phase space suppression. We therefore parametrize

$$E_w^{\text{crit}} = f_w n_w^{\text{crit}} m_w = f_w \nu_w m_w / \alpha_w. \quad (2)$$

Both, instanton estimates [1 – 3] as well as a comparison with QCD [4,8] suggest values of n_w^{crit} and E_w^{crit} in the range $n_w^{\text{crit}} \simeq 30 - 100$, $E_w^{\text{crit}} \simeq (3.5 - 20) \text{ TeV}$. We use a conservative value $n_w = 30$ for the remainder of this paper: all results can be rescaled easily for the experimentally even more advantageous case of higher multiplicity.

VI.4. Transverse Momentum and Energy

At very high parton energies the characteristic transverse momentum of the weakly interacting particles produced in GFI events presumably corresponds to the geometrical size R_w of the cloud of gauge bosons and scalars around the quarks [3,8]. Exploiting the analogy to hadronic cross-sections, we take the (inclusive) distribution $d\sigma_w/dp_t \sim p_t \exp(-R_w \sqrt{m^2 + p_t^2})$, $R_w \simeq \sqrt{2} \cdot \pi / m_w$, for the transverse momentum of a "geometrically" produced particle with mass m [8]. This gives an average transverse momentum for a produced W, $\bar{p}_t \simeq 48 \text{ GeV}$ ⁶.

⁶Throughout this paper we denote by \bar{A} the average of a quantity A for events with given parton kinematics, whereas $\langle A \rangle$ denotes averages in pp scattering with the (anti) quark distributions in the proton folded in. In particular one has $\langle p_t \rangle = \bar{p}_t$.

The W, Z bosons, Higgs scalars and top quarks will not be directly observable in the detectors of future pp colliders. They decay into jets and leptons. Let l_w denote the number of light quarks and leptons produced in GFI events, i.e. those particles with mass much smaller than $\langle p_t \rangle$, including the bottom quark. We expect $l_w/n_w \simeq 1.5 - 2$. Due to the decay of the heavy particles the average transverse momentum per light fermion will be somewhat smaller than the average transverse momentum of a produced W, namely $\bar{p}_t^l \simeq 36 \text{ GeV}$ [8]. The average total transverse energy per GFI event (for l_w between 45 and 60) is $\bar{E}_t^{\text{tot}} = l_w \cdot \bar{p}_t^l \simeq (1.6 - 2.2) \text{ TeV}$.

VI.5. Event Topology

We estimate in fig. 2 the fraction $\langle l_{\text{centr.}}/l_w \rangle$ of the number of light particles in a central range of pseudo-rapidities, $|\eta| < \eta_0 \simeq 2.5$, corresponding to $10^\circ < \vartheta < 170^\circ$, as a function of the dimensionless quantity $\sqrt{s}/\bar{E}_t^{\text{tot}}$ for three values of $E_w^{\text{crit}}/\sqrt{s}$. We assume for an individual light fermion an essentially constant rapidity distribution in the parton cms (for more details see ref. [8]). In order to provide an impression of the angular distribution of the light fermions in a GFI event, we plot in fig. 3 the relative number of particles in the angular region $\vartheta_0 < \vartheta < 180^\circ - \vartheta_0$ as a function of ϑ_0 for a fixed value $\bar{E}_t^{\text{tot}} = 2 \text{ TeV}$. We find that the average "centrality" of the events depends strongly on the parton threshold energy E_w^{crit} . This effect arises since the average gets a large contribution from partons with "threshold kinematics" for which the "centrality" of the events essentially depends on f_w [8]. If f_w is near one, very little longitudinal momentum is available. In this case we expect important activity at scattering angles around or even above 35° .

VI.6. Charged Lepton Multiplicity

The cleanest signature of these events is probably the expected high number of isolated charged leptons in each event. We expect [8] $R_L \equiv \langle \# \text{ charged leptons} / n_w \rangle \simeq 1/8 - 1/3$, leading to a mean lepton multiplicity larger than 4 – 10 for $n_w \geq 30$. Assuming that at least one third of the produced particles are gauge bosons and at most one fifth are scalars one finds (for $n_w = 30$) $R_L > 0.16$, $\langle \# \text{ charged leptons} \rangle > 5$. Similarly, one finds [8] $\langle N_{e,\mu} / l_w \rangle \simeq 1/20 - 1/25$, giving an average of 2.4 - 3 electrons and 2.4 - 3 muons for $l_w = 60$.

VI.7. Missing Transverse Momentum and Energy

The mean number of neutrinos is comparable to that of charged leptons. For $n_w = 30$ we thus expect around 5-9 neutrinos, each with an average transverse momentum $\sim 30 - 40 \text{ GeV}$. We expect that the total missing transverse momentum and the total missing energy are given by $\langle \not{p}_t^{\text{tot}} \rangle \simeq \sqrt{\langle N_\nu \rangle \bar{p}_t^l} \simeq 100 \text{ GeV}$ and $\langle \not{E}_t^{\text{tot}} \rangle \simeq 1 \text{ TeV}$, respectively.

VI.8. Jet Activity

We expect [8] $\langle \# \text{jets} / l_w \rangle \approx 3/4 - 5/6$. For $l_w = 60$, a typical event contains the enormous number of 45 – 50 jets with a total charged hadron multiplicity ~ 500 . These numbers are so high that it becomes hard to resolve all the jets individually if much of the activity is in the forward direction.

Within the range of the central detector ($\eta < 2.5$), however, there should be a good chance to resolve almost all jets. The number of jets in this region can be found from fig. 2, using $\#$ central jets = $\#$ jets $\langle l_{\text{centr.}}/l_w \rangle$. We see that more than 20 central jets are expected, yielding more than ~ 200 charged hadrons in the central detector. If there are too many jets in the central region one may simply watch out for an impressive "jet-fireball topology" in the central region.

VI.9. Signal and Background

The main background [8] comes from the tails of strong interaction processes where leptons are produced from semi-leptonic decays of heavy quarks. Near the threshold of detectability, the effective cross section is only of order 10^{-2} pb. At the LHC, the QCD cross section for 6 widely separated jets ($\theta_{jj} > 50^\circ$) with $p_t > 20$ GeV exceeds this value by seven orders of magnitude [9].

In order to reduce this huge QCD background we propose [8] to use criteria based on total transverse energy deposition and on the expected characteristics of GFI events in the central and forward/backward regions.

Typical cuts are in the total transverse energy ($E_t^{\text{tot}} > 700$ GeV) and the total missing transverse momentum ($\vec{p}_t^{\text{tot}} > 50$ GeV). Another possible cut would select events containing more than two clearly isolated charged leptons with $p_t > 25$ GeV in the central region. One would also require 200 charged hadrons or more in the range $5^\circ < \vartheta < 175^\circ$.

These selection criteria reduce the background from strong interaction events considerably without affecting much the GFI event rate. Subsequently, the detailed leptonic and hadronic structure of the events has to be analyzed in the central region. This strategy should result in a clean distinction from QCD events, and we conclude that GFI events stand a very good chance to be seen, even if the rate is near the threshold of detectability.

VI.10. Violation of Baryon and Lepton Number

If B+L violation becomes strong in the TeV range [1 – 3], the topology of the (B+L)-violating events will, presumably, resemble roughly the one corresponding to generic GFI events described above (for f_w not much bigger than one). It will be rather central close to the threshold energy and increasingly forward-oriented as the parton energy increases beyond the threshold. A search for B+L violation should therefore directly concentrate on quantum numbers [8] (see also ref. [10]). A (B+L)-violating interaction [5, 1] $q + q \rightarrow 7\bar{q} + 3\bar{l} + X$ produces on average more positrons and μ^+ than electrons and μ^- . Thus one should measure the average lepton charge asymmetries, $\langle N_{e^+(\mu^+)} - N_{e^-(\mu^-)} \rangle / (N_{e^+(\mu^+)} + N_{e^-(\mu^-)})$, for isolated electrons and muons (with $p_t > 20$ GeV) in the central region. The asymmetry vanishes, in principle, for L-conserving GFI events and gives, therefore, a direct measure of the relative strength of (B+L)-violating interactions. In addition, one expects the primary e^+ 's and μ^+ 's from a (B+L)-violating interaction to be more energetic than the decay products of the associated gauge bosons. This leads to an asymmetry in the mean energy of the fastest anti-lepton as compared to that of the fastest lepton. However, only L violation that is large compared to the (B+L)-conserving GFI background can be detected by a measurement of these asymmetries.

VI.11. Conclusions

We have discussed strategies to detect possible signals of geometrical flavour production (see points 1)-5) in the introduction) in the TeV regime. The corresponding events are characterized by the production of many $\mathcal{O}(\alpha_w^{-1}) \approx 30$ weakly-interacting particles. We have concentrated on light fermions of mass smaller than the transverse momentum, which may be produced both promptly and as decay products of W, Z bosons, etc. The associated jets and charged leptons are directly accessible experimentally.

We find the following characteristic features of "geometrical flavour interaction" (GFI) events (for $n_w = 30$):

- 1) For parton kinematics near the threshold ($\sqrt{s} \approx E_w^{\text{crit}}$), the events look rather central, i.e. jets and charged leptons are distributed over the whole angular range. Only partons with energies much above E_w^{crit} produce more forward-oriented events. At the LHC most of the activity will be in the central detector ($10^\circ < \vartheta < 170^\circ$).
- 2) The average transverse momentum per light particle is estimated to be $\vec{p}_t \approx 35$ GeV, and the total transverse energy is large: $\langle E_t^{\text{tot}} \rangle \approx 1.6 - 2.2$ TeV.
- 3) We expect on average at least 3.5 "isolated" electrons or muons per event.
- 4) A similar number of neutrinos is responsible for an average missing transverse momentum $\langle \vec{p}_t^{\text{miss}} \rangle \approx 100$ GeV.
- 5) More than 20 jets/event, corresponding to ~ 200 charged hadrons, should be seen in the central detector.
- 6) In addition, we expect many events with a high charged hadron multiplicity ($n_h > 100$) in the forward and/or backward detectors ($|\eta| > 2.5$).
- 7) If B+L violation is relatively strong in comparison to the (B+L)-conserving GFI processes, it may be possible to observe the L violation by measuring average lepton charge asymmetries and/or $\langle E_{e^+, \mu^+} \rangle > \langle E_{e^-, \mu^-} \rangle$.

We conclude that there is essentially no background for these events. Even with a parton cross-section $\sigma_w^0 \approx 1$ nb they should be detected at the LHC if the threshold energy E_w^{crit} is below 11 GeV.

Acknowledgement: We thank W. Bartel, G. Schuler and J. Vermaseren for useful discussions.

Figure Captions

Fig. 1: Number of GFI events per second as a function of the (parton) threshold energy E_w^{crit} (taken from ref. [8]). We assume a constant cross section $\sigma_w^0 = 1$ nb for weakly interacting partons with energies above E_w^{crit} and a pp luminosity of $\mathcal{L} = 10^{33} \text{ cm}^{-2}\text{sec}^{-1}$.

Fig. 2: Fraction of the number of light particles in the angular region, $10^\circ < \vartheta < 170^\circ$, of a typical central detector, displayed versus $\sqrt{s}/E_t^{\text{tot}}$ for three representative values of $E_w^{\text{crit}}/\sqrt{s}$ [8]. The values for a fixed number of light fermions, $l_w = 60$, are marked by solid circles ($\sqrt{s} = 16$ TeV) and square ($\sqrt{s} = 40$ TeV).

Fig. 3: Relative number of light particles in the angular region $\theta_0 < \vartheta < 180^\circ - \theta_0$ versus θ_0 for fixed total transverse energy $\bar{E}_t^{\text{tot}} = 2 \text{ TeV}$ and the same values of E_w^{crit} and \sqrt{s} as in fig. 2 [8].

References

- [1] A. Ringwald, Nucl. Phys. B330 (1990) 1.
- [2] O. Espinosa, Nucl. Phys. B343 (1990) 310.
- [3] L. McLerran, A. Vainshtein and M. Voloshin, Phys. Rev. D42 (1990) 171.
- [4] A. Ringwald and C. Wetterich, DESY 90-067.
- [5] G. 't Hooft, Phys. Rev. D14 (1976) 3432.
- [6] F. Klinkhamer and N. Manton, Phys. Rev. D30 (1984) 2212.
- [7] V. Kuzmin, V. Rubakov and M. Shaposhnikov, Phys. Lett. 155B (1985) 36; P. Arnold and L. McLerran, Phys. Rev. D36 (1987) 581; A. Ringwald, Phys. Lett. 201B (1988) 510.
- [8] A. Ringwald, F. Schrempp and C. Wetterich, DESY 90-127.
- [9] Z. Kunszt, in Proc. "Physics at Future Accelerators", La Thuile, 1987, CERN 87-07, Vol 1.
- [10] G. Farrar and R. Meng, DESY 90-099.

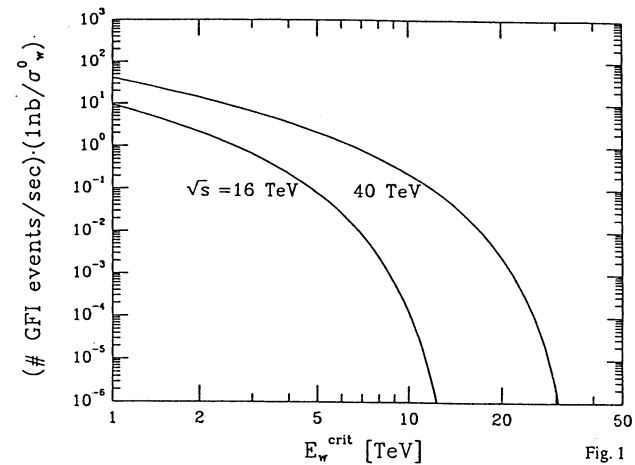


Fig. 1

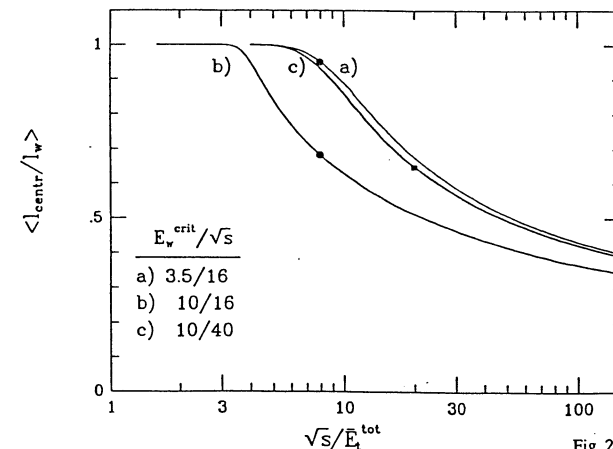


Fig. 2

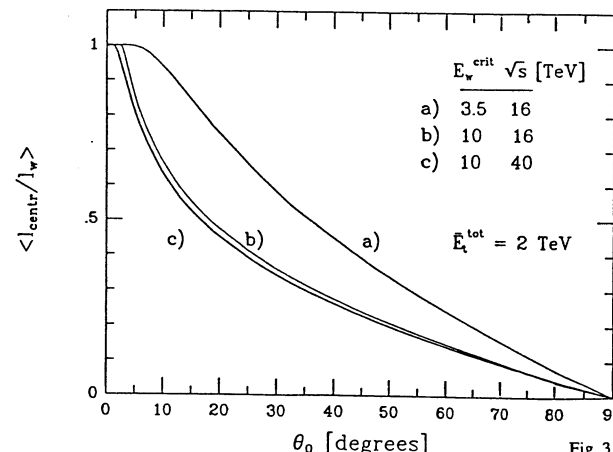


Fig. 3

VII. SUMMARY

In summary a main effort of this working group was to study how one can learn something about electroweak symmetry breaking at machines like LHC. The main result is that a ρ -like object as expected in QCD-like or Technicolor scenarios can be seen in the $W^\pm Z$ channel via leptonic decays if it has a mass up to $O(2\text{ TeV})$. The luminosity will determine the highest reachable mass. With $\mathcal{L} = 10^{34}\text{ cm}^{-2}\text{s}^{-1}$ LHC should be able to detect such a state below 2 TeV where good lepton detection capabilities are assumed. If this ρ -like object is however heavier then more luminosity will be essential. To surpass 2 TeV and maybe even reach 2.5 TeV the full luminosity of $4.0 \cdot 10^{34}\text{ cm}^{-2}\text{s}^{-1}$ is required. Both simulation methods (see section II and III) give comparable consistent results. The dominance of the contributions from qq' annihilation via mixing for masses $m_\rho < 2\text{ TeV}$ particularly at LHC parameters was nicely emphasized by the BESS group and also included in the DHT approach.

The DHT approach allows to simulate more general dynamical cases such as Higgs-like dynamics for which the ZZ channel is most promising. The signal to background ratio is however not as good as in the QCD/Technicolor case. Correspondingly the limits on a Higgs like state will be weaker. For a Higgs particle a lower limit up to about 800 GeV (see Higgs group) will arise. Since consistency requirements limit the Standard Model Higgs to values below this limit it will be possible to cover the full window of allowed masses of the Standard Model. If no Higgs is found then the normal (simplest) Higgs scenario is ruled out and alternatives must be sought. In this context it is important that the search for ρ -like objects will be possible up to 2 or 2.5 TeV which is precisely the range where scaled QCD or Technicolor would predict it to be. Therefore the LHC can fully cover the two simplest scenarios of symmetry breaking. Note that the limits for a scalar or ρ -like object are a direct consequence of its mass and the underlying mass to width relations. Therefore any nonstandard width can make the corresponding signal more or less visible. If the widths are for whatever reason wider than normal then the limits get weaker.

Comparing the LHC and SSC one finds roughly the same physics potential. With the chosen parameters both machines are good at finding a ρ -like state in the $W^\pm Z$ channel up to masses $O(2\text{ TeV})$. The signal to background ratio is typically slightly better for the SSC but with a smaller number of events. The ability to reach the design parameters and to build such demanding detectors will therefore decide which machine is better.

The LHC will be able to put very strong limits on the scale of compositeness. Typically these limits are $\sim 20\text{ TeV}$. Excited leptons and quarks can be limited to be heavier than $5 - 10\text{ TeV}$.

Consequences of baryon number violating processes have been described in section VI. Some of the ingredients involved are still disputed and are hopefully fully clarified within the next years. If this mechanism is relevant and if the threshold energy is below 11 TeV then this will be important at LHC any may be one out of many new things that could show up when we make such a big step forward towards higher energies.

B: ELECTRON-PROTON COLLISIONS

Kinematics and Resolution at LEP \times LHC

J. Blümlein, J.Feltesse and M. Klein

IHEP, Zeuthen, Germany and DPhPE, CEN-Saclay, France

Abstract

Limitations due to resolution and kinematics are discussed of the (Q^2, x) range accessible in deep inelastic scattering of 50 GeV electrons from LEP and 2-8 TeV protons from LHC.

1 Introduction

The deep inelastic inclusive scattering cross section σ depends on two kinematic variables, besides the energy $s = 4E_l E_p$. In the experiment the polar angle $\theta_e(\theta_j)$ of the scattered electron e (the current jet j , resp.) and the secondary energies E_e (and E_j) are measured. The four-momentum transfer Q^2 , the relative energy transfer y and the Bjorken variable x can be calculated from the measured quantities as follows:

$$\begin{aligned} Q^2 &= 4E_l E_e \sin^2(\theta_e/2) \\ y &= 1 - E_e \cos^2(\theta_e/2)/E_l \\ Q^2 &= E_j^2 \sin^2(\theta_j)/(1-y) \\ y &= E_j \sin^2(\theta_j/2)/E_e \end{aligned} \quad (1)$$

where x is given as Q^2/sy . Note that the angles θ are defined between the directions of the outgoing electron and the electron beam (θ_e) and between the jet and the proton beam (θ_j). In the tree approximation, both kinematic sets have to agree. This offers important cross calibration possibilities in the regions where both the electron and the hadronic jet measurements can be used. The accessible kinematic range is restricted due to angular coverage, finite detector resolution and calibration uncertainties. This study comes to conclusions which were similarly reached for HERA [1].

2 Accessible (x, Q^2) range

Lines of constant energy and angle of the scattered electron and the current jet are located differently in the (Q^2, x) plane because of the relations:

$$\begin{aligned} Q^2(x, E_e) &= sx(1 - E_e/E_l)/[1 - xE_p/E_l] \\ Q^2(x, E_j) &= sx(1 - E_j/xE_p)/[1 - E_l/(xE_p)] \\ Q^2(x, \theta_e) &= sx/[1 + xE_p \cot^2(\theta_e/2)/E_l] \\ Q^2(x, \theta_j) &= sx/[1 + E_l \cot^2(\theta_j/2)/xE_p] \end{aligned} \quad (2)$$

A first limitation of the kinematical range is introduced by the beam pipe which will exclude angles below a few degrees, i.e. about 3° for the electrons. This introduces a cut at small momentum transfers, $Q^2(x, \theta_e) \simeq (2E_l \tan^2(\theta_e/2))^2 \simeq 7\text{GeV}^2$, in most of the x region, except the extremely small x values. The jet measurement can be extended down to about 5° provided single tracks are caught

at even lower angles (down to 10 mrad). One easily derives from (2) that this excludes the higher x region ($x \geq 0.01$), the borderline being linear in a double log plot, i.e. $Q^2(x, \theta_j) \simeq (2E_p x \tan^2(\theta_j/2))^2$. Thus at $E_p = 8\text{TeV}$ the minimum Q^2 is about $5000x^2$ at a minimum angle of 5° . Note that the extension of the kinematic range for the jet measurement towards larger x at LEPxLHC (and as well at HERA) relies only on lowering the proton-beam energy. In particular, it is independent of the electron-beam energy. It is not difficult to see the effect of varying the angular cut to lower or higher values, the principle conclusions, however, stay.

In addition to simple kinematics one has to study resolution effects in order to define the accessible region. A straightforward calculation yields the uncertainties in x and Q^2 given those for the polar angle and the secondary energy electrons:

$$\begin{aligned}\delta x/x &= 1/y \times \delta E_e/E_e \\ &\quad + [(1-y)/y \times \tan(\theta/2) + \cot(\theta/2)]\delta\theta \\ \delta Q^2/Q^2 &= \delta E_e/E_e + \cot(\theta/2)\delta\theta\end{aligned}\quad (3)$$

jet:

$$\begin{aligned}\delta x/x &= 1/(1-y) \times \delta E_j/E_j \\ &\quad + [-2\cot(\theta) \\ &\quad + (1-2y)/(1-y) \times \cot(\theta/2)]\delta\theta \\ \delta Q^2/Q^2 &= (2-y)/(1-y) \times \delta E_j/E_j \\ &\quad + [2\cot(\theta) + y/(1-y) \times \cot(\theta/2)]\delta\theta\end{aligned}\quad (4)$$

For the electrons, the main problem results from the coefficient $1/y$ for the x resolution. Thus the region of good cross-section measurements using the scattered electron is limited by a y cut around 0.05 and the line of minimum accessible scattering angle θ_e . This has been verified by performing a Monte-Carlo calculation of the smearing correction defined as the ratio of the generated cross section to the reconstructed one in a given bin. We have applied a Gaussian smearing to the electron energy and angle assuming

$$\delta E_e/E_e = 0.01 + 0.1/\sqrt{E_e/\text{GeV}} \quad \delta\theta_e = 1\text{mrad} \quad (5)$$

The effect of finite angular resolution is smaller than the energy resolution effect. One should realize that the $1/y$ behaviour represents a severe limitation, i.e. if one wanted to extend the electron region one would be forced to think of a very accurate calorimetric measurement.

The hadronic jet measurement can be simulated similarly. We have assumed

$$\delta E_j/E_j = 0.02 + 0.4/\sqrt{E_j/\text{GeV}} \quad \delta\theta_j = 10\text{mrad} \quad (6)$$

The smearing correction is large where the energy E_j becomes small resulting in curved bounds at lower Q^2 [2]. The uncertainty of the angular measurement should be kept below about 10 mrad in order to avoid a further increase of the minimum jet angle covered. Furthermore, it is clear from (4) that the jet measurement is less accurate at high y because the resolutions vary as $1/(1-y)$. The kinematic and resolution considerations are summarized in fig.1 showing the ranges accessible with electron (a) and current jet measurements (b). Note that we have combined the low and high energy options for LEPxLHC (i.e. 50×2000 and $50 \times 8000 \text{ GeV}^2$) and HERA (30×820 and $15 \times 300 \text{ GeV}^2$). Thus fig.1a gives a clear impression of how the ep colliders are going to extend the fixed target measurements with scattered leptons. As discussed above, the collider electron measurements are limited mainly by the beam-pipe cut at low Q^2 and the y cut at about 0.05.

Apart from early measurements of the x dependence in neutrino scattering at CERN and Fermilab there have been no deep inelastic structure function measurements based on the current jet. Fig.1b

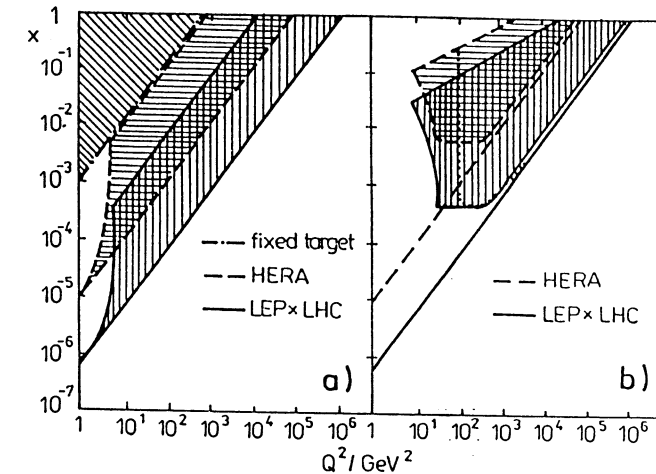


Figure 1: Kinematical range accessible in fixed target and ep -collider experiments. a) lepton measurement; b) current jet measurement

shows the (Q^2, x) range to be covered at HERA (dashed) and LEPxLHC. For the neutral current measurement the ranges are limited at high x due to the beam pipe (and angular resolution) and at low Q^2 and low x due to energy resolution as the jet energies become small in that region. Very roughly, the x_{min} value is somewhat below $x = E_l/E_p$ because the energies become small at lower x . Thus LEPxLHC extends the jet measurements of HERA towards smaller x .

For charged currents one has another limitation of the range, as the charged current events have to be distinguished from the many NC events. This requires a minimum transverse energy cut. As a dotted curve we have shown in fig.1b the line $p_\perp = 10 \text{ GeV}$, ($p_\perp^2 = (1-y)Q^2$), indicating the narrowing of the CC jet measurement relatively to the NC case.

3 Calibration

Besides kinematics and resolution effects, severe limitations are caused by energy calibration uncertainties. Using the following formulae one can calculate the effect of systematic energy shifts on the cross section:

$$\begin{aligned}\hat{x}_\epsilon &= \frac{x}{1-\epsilon_\epsilon/(1+\epsilon_\epsilon)y} & \hat{x}_j &= x \frac{(1+\epsilon_j)(1-y)}{1-y(1+\epsilon_j)} \\ \hat{Q}_\epsilon^2 &= Q^2(1+\epsilon_\epsilon) & \hat{Q}_j^2 &= Q^2 \frac{(1+\epsilon_j)^2(1-y)}{1-y(1+\epsilon_j)} \\ \hat{y}_\epsilon &= y - \epsilon_\epsilon(1-y) & \hat{y}_j &= y(1+\epsilon_j)\end{aligned}\quad (7)$$

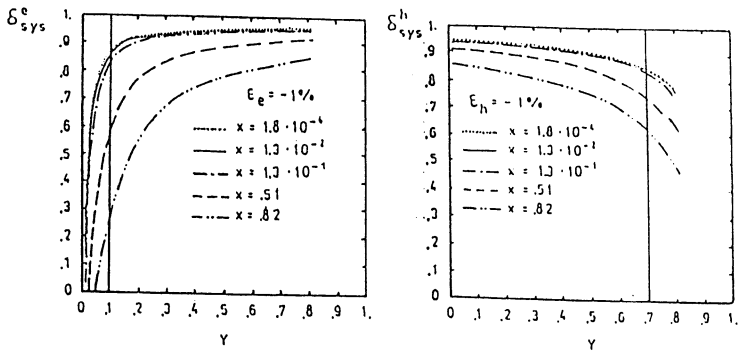


Figure 2: Systematic shifts of the neutral current cross sections for the electron and hadron flow measurement

It follows, as before, that \hat{x}_e/x becomes large for $y \rightarrow 0$ whereas \hat{x}_j/x and \hat{Q}_j^2/Q^2 grow with $y \rightarrow 1$. Fig.2 shows a calculation of the systematic shifts of the cross section by a 1% change of the scattered electron and jet energy, resp. As for HERA, the absolute energy calibration has to be managed at the per cent level. Since the electron and jet measurements are sensitive to miscalibrations in different regions of y , one has the possibility to reduce the energy uncertainty effect by cross calibrating the electron and jet measurements in the regions of overlap, see fig. 1. In a very wide region, the Q^2 as determined from the electrons is very precise, see (3). This may be used to replace or cross check the Q^2 measurement with the hadronic jets.

4 Conclusion

LEP \times LHC will extend the kinematic domain compared to HERA by about one order of magnitude towards higher Q^2 and lower x . It will have enough overlap with the HERA range if the low E_p option of the LHC will be realized. As for HERA, the calorimetric measurements are very demanding, i.e. they have to cover the smallest possible angles and be calibrated to better than 1%.

References

- [1] J.Feltesse, *Proceedings of the DESY Workshop on Physics at HERA*, DESY, Hamburg, 1988, Vol.1, p.33.
- [2] J.Blümlein, M.Klein PHE 90-19 (1990)

LEP+LHC Deep Inelastic Scattering: Structure Functions and Final States

G. Ingelman

Dept. of Radiation Sciences, Uppsala University
Box 535, S-751 21 Uppsala, Sweden

Abstract: Some basic issues of deep inelastic scattering are discussed for the option of electron-proton collisions using LEP and LHC. The electroweak cross-sections and the expected event rates are given and the problems of kinematics reconstruction are considered. Estimates of the precision for measurements of various quark densities and structure functions are presented based on approximate and exact unfolding from measurable differential cross-sections. The salient features of the hadronic final state, such as multiplicities, jets and rapidity distributions, are also discussed.

1 Introduction

The proton substructure is most directly measured by deep inelastic lepton scattering. In particular, the quark momentum distributions can be obtained and the predictions of QCD evolution tested. In electron-proton scattering at very high energies, i.e. at ep colliders, the weak effects in the cross-section become important and hence the electro-weak theory can be experimentally tested. High energies and momentum transfers also leads to possibilities of observing new particles, interactions and smaller scale structures which could provide a window for physics beyond the standard model. These different aspects of ep collider physics using LEP+LHC are reviewed in ref. [1].

The technical aspects of achieving collisions between electrons (positrons) in LEP and protons in LHC are discussed in refs. [2,3]. It is here sufficient to summarize the attainable energies, luminosities and the expected statistics of event samples obtained in a years running time.

Table 1: Energies and luminosities

	E_e [GeV]	E_p [TeV]	\sqrt{s} [TeV]	\mathcal{L} [cm $^{-2}$ s $^{-1}$]	$\int_{\sim 1 \text{ year}} dt \mathcal{L}$ [fb $^{-1}$]
LEP	100	8	1.79	$2 \cdot 10^{31}$	0.1
\oplus	50	8	1.26	$2 \cdot 10^{32}$	1
LHC	50	2	0.63	$2 \cdot 10^{32}$	1
HERA	30	0.82	0.31	$2 \cdot 10^{31}$	0.1

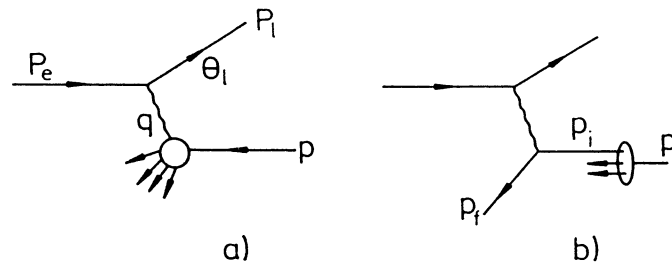


Figure 1: Deep inelastic scattering in general (a) and in the quark-parton model (b).

2 Kinematics and cross-sections

The inelastic scattering process $e + p \rightarrow \ell + H$, where ℓ is the scattered lepton and H the final hadron system, is illustrated in Fig. 1a. The exchanged vector boson is a γ/Z^0 for neutral current (NC) interactions and a W^\pm for charged current (CC) interactions. The deep inelastic scattering is characterized by the following kinematic variables

$$ep \text{ cms energy } \sqrt{s} : s \equiv (p_e + P)^2 \simeq 4E_e E_p \quad (1)$$

$$\text{momentum transfer} : Q^2 \equiv -q^2 = -(p_e - p_\ell)^2 \simeq 4E_e E_\ell \sin^2 \frac{\theta_\ell}{2} \quad (2)$$

$$\text{energy transfer } \nu : m_p \nu \equiv P \cdot q \simeq 2E_p(E_\ell - E_\ell \cos^2 \frac{\theta_\ell}{2}) \quad (3)$$

$$\text{Bjorken-}x : x \equiv \frac{Q^2}{2P \cdot q} = \frac{Q^2}{2m_p \nu} \simeq \frac{E_e E_\ell \sin^2 \frac{\theta_\ell}{2}}{E_p(E_\ell - E_\ell \cos^2 \frac{\theta_\ell}{2})} \quad (4)$$

$$\text{scaling variable} : y \equiv \frac{P \cdot q}{P \cdot p_e} = \frac{2P \cdot q}{s} = \frac{\nu}{\nu_{max}} \simeq \frac{E_\ell - E_\ell \cos^2 \frac{\theta_\ell}{2}}{E_\ell} \quad (5)$$

$$\text{hadronic mass } W : W^2 \equiv (q + P)^2 = Q^2 \frac{1-x}{x} + m_p^2 \quad (6)$$

Here, p_e , p_ℓ , P denote the four-momenta of the incoming and scattered lepton and the incoming proton, respectively, and E_ℓ , θ_ℓ is the energy and angle of the scattered lepton. The ‘ \simeq ’ sign corresponds to neglecting the masses of the electron, proton and scattered lepton.

For the overall event kinematics, i.e. when the structure of the hadronic final state H is not considered, there are only two independent variables which are usually chosen as (x, y) or (x, Q^2) , although one may prefer (E_ℓ, θ_ℓ) which are directly measurable in NC events. The transformation between any two sets is obvious from the above relations. The kinematics can in principle be reconstructed from either the scattered lepton, i.e. E_ℓ and θ_ℓ , or from the four-momentum p_H of the total hadron system (due to energy-momentum conservation in the process). One should note that no assumption about the structure of the proton or about the final hadronic state has been made so far. In the quark-parton model, where the current couples to a quark (Fig. 1b), the Bjorken- x variable can be interpreted as the energy-momentum fraction of the proton carried by the struck quark (cf. [4]). For a more detailed account of kinematical relations in ep collisions see [4,5].

For the following analysis we use the inclusive NC and CC cross-sections in lowest order of the electroweak couplings and leading order QCD. Since we will primarily consider large Q^2 one can neglect power corrections in $1/Q^2$ such as target proton mass and primordial transverse momenta of the partons as well as higher twist effects. Threshold effects from heavy quarks can also be neglected and it is here sufficient to consider four massless quark flavours (u, d, s, c) [6]. The complete cross-section formulae for polarized electron (positron) scattering, with details of electroweak couplings, structure functions etc, can be found in [4]. Here, we only consider unpolarized beams for our study.

The differential cross-section for unpolarized NC scattering, $ep \rightarrow eX$, is given by

$$\frac{d\sigma_{NC}(e^\mp)}{dx dy} = \frac{4\pi\alpha^2 s}{Q^4} \left[y^2 x F_1(x, Q^2) + (1-y) F_2(x, Q^2) \pm (y - \frac{y^2}{2}) x F_3(x, Q^2) \right] \quad (7)$$

$$F_2(x, Q^2) = 2x F_1(x, Q^2) = \sum_{f=u,d,s,c} A_f(Q^2) [x q_f(x, Q^2) + x \bar{q}_f(x, Q^2)] \quad (8)$$

$$x F_3(x, Q^2) = \sum_{f=u,d,s,c} B_f(Q^2) [x q_f(x, Q^2) - x \bar{q}_f(x, Q^2)]$$

The NC structure functions $F_i(x, Q^2)$ are here given in terms of the quark (antiquark) density distributions q_f (\bar{q}_f), with standard Q^2 -evolution in leading-log QCD, and the flavour-dependent coefficients

$$\begin{aligned} A_f(Q^2) &= e_f^2 - 2e_f v_f v_f P_Z + (v_f^2 + a_f^2)(v_f^2 + a_f^2) P_Z^2 \\ B_f(Q^2) &= -2e_f a_f a_f P_Z + 4v_f v_f a_f a_f P_Z^2 \end{aligned} \quad (9)$$

where e_f, v_f, a_f is the electric charge, the vector and axial vector couplings to the Z^0 boson of a fermion f . From the appearance in eq. (9) of the factors $P_Z = Q^2/(Q^2 + m_Z^2)$, denoting the ratio of the Z and γ propagators, one can easily recognize the individual contributions from γ exchange, Z exchange and $\gamma - Z$ interference.

Similarly, the differential cross-section for unpolarized CC scattering, $ep \rightarrow \nu X$, takes the form

$$\frac{d\sigma_{CC}(e^\mp)}{dx dy} = \frac{G_F^2 s}{4\pi} \left(1 + \frac{Q^2}{m_W^2} \right)^{-2} x \left\{ \begin{array}{l} u + c + (1-y)^2(\bar{d} + \bar{s}) \\ \bar{u} + \bar{c} + (1-y)^2(d + s) \end{array} \right\} \quad (10)$$

where G_F is the Fermi constant, m_W the W boson mass and $u = u(x, Q^2)$ etc.

Higher order QCD corrections, which modify the evolution equations and give a non-zero longitudinal structure function ($F_L = F_2 - 2x F_1$), are not expected to be large enough to influence the results of the following study, in similarity with earlier investigations for HERA [6,7]. In contrast, higher order electroweak corrections are important [8], but being known they can be taken into account such that the above formalism can be used for a structure function analysis.

The numerical values resulting from the above cross-sections are shown in Fig. 2. Here, and in the following, we have used the parametrization EHLQ set 1 [9] for the quark densities and the values $\alpha = 1/137$, $\sin^2 \theta_W = 0.226$ and $m_W, m_Z = 81.4, 92.5$ GeV for the electroweak parameters. The typical event rates at LEP+LHC, obtained by multiplication with the integrated luminosities in Table 1, are quite large. Useful

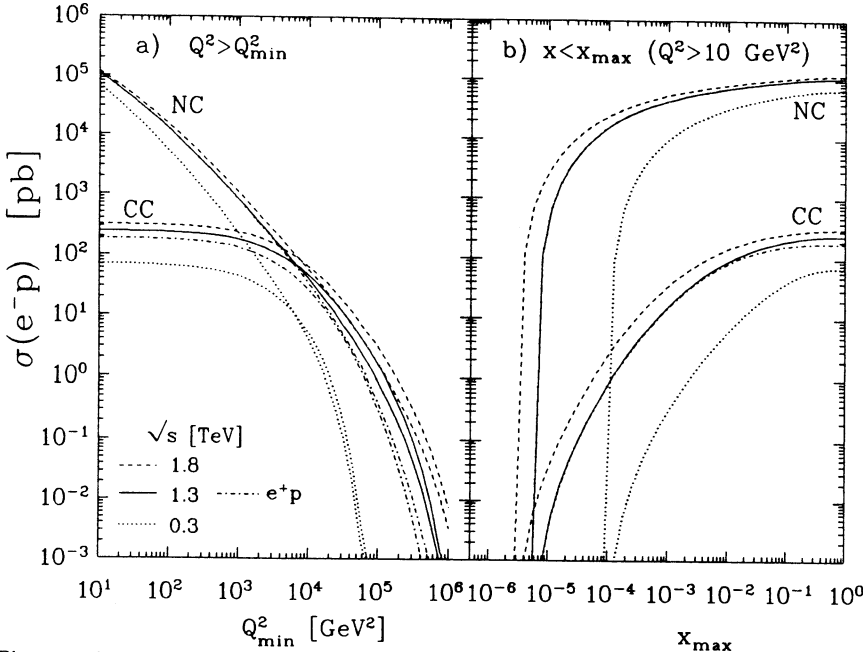


Figure 2: Integrated DIS cross-sections versus (a) a lower cut-off in Q^2 and (b) an upper cut-off in x . Charged and neutral current interactions are compared for different $e^- p$ cms energies corresponding to LEP+LHC and HERA; only one $e^+ p$ energy for clarity.

statistics extend up to $Q^2 \approx 5 \cdot 10^5 \text{ GeV}^2$, i.e. about ten times higher than at HERA. Similarly, more than an order of magnitude is gained in the small- x region (Fig. 2b). The sharp fall at small x_{\max} is, however, due to the cut-off $Q^2 > 10 \text{ GeV}^2$ imposed to define the DIS region.

The large difference between the electron and proton beam energies in ep colliders give rise to a very elongated phase space for the scattered lepton and quark, as shown in Fig. 3. The considerably larger imbalance between the beam energies in LEP+LHC as compared to HERA accentuate this effect. In the HERA lab frame, the ep cms moves with a velocity $\beta = 0.929$ giving a γ -factor of 2.7, whereas the corresponding numbers for LEP+LHC are $\beta = 0.988$ and $\gamma = 6.4$. The events are therefore more asymmetric at LEP+LHC, which puts even stronger requirements on the detector capabilities in the very forward proton direction and forces the the machine quadrupole to be as far from the interaction point as possible [3].

In NC events the kinematics can be reconstructed from the energy and angle of the scattered electron using eqs. (2,4). A detailed discussion on the influence of experimental errors ($\delta E_t, \delta \theta_t$) are given in [11]. The most important feature is the increased error at small y , $\delta x/x \propto 1/y \cdot \delta E_t/E_t$. The resulting effect can be illustrated by the typical error $\delta E_t/E_t = 0.1/\sqrt{E_t} \oplus 0.01$ in a good electromagnetic calorimeter where, at $y \approx 0.1$, the first term (smearing) results in a 20% error in x and the second term (calibration) gives a 10% systematic uncertainty of the differential cross-section. Thus, a lower limit $y_{\min} = 0.05 - 0.1$ is obtained for the useful kinematical region.

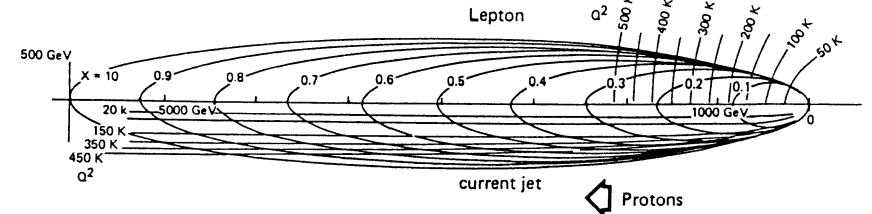


Figure 3: Phase space diagram for the kinematics of the scattered lepton (upper part) and quark (lower part) at LEP+LHC (60 GeV e on 8 TeV p) with lines of constant x and Q^2 , from [10]. The lab momentum vector is given by a line from the origin to the relevant x, Q^2 point, i.e. longitudinal and transverse momenta can be read off at the axes and the lab angle directly seen. Compare the much less elongated phase space of HERA in fig. 2 of [4].

In CC events the kinematics has to be reconstructed from the total hadron flow and in NC events this may be used as an alternative. The relations [12,13] $y = \sum_h (E_h - p_{zh})/2E_e$ and $Q^2 = |\sum_h \vec{p}_{\perp h}|^2/(1-y)$ are then used, since they minimize the sensitivity to particles lost in the beam pipe along the proton (+z) direction. Nevertheless, the resulting uncertainty in y and Q^2 depends on these losses, as illustrated in Fig. 4. Since the errors are large for configurations where the current jet is close to the beam pipe, the strong boost effect at LEP+LHC accentuate this problem which must be studied in great detail.

Lacking such a study, one can get the general trends from current jet kinematics. A detailed study of the propagation of the expected jet measurement errors in a hadronic calorimeter with $\delta E_j/E_j = 0.4/\sqrt{E_j} \oplus 0.02$ and a jet angle resolution $\delta \theta_j = 10 \text{ mrad}$ has been made in [11]. It can here be summarized in terms of a region for ‘safe’ kinematics reconstruction, and thereby limited systematic shifts of the differential cross-sections, as shown in Fig. 5a. The limit at small- x is due to poor x and Q^2 resolution from this error propagation. As mentioned above, reconstruction problems occur when the current jet is close to the beam hole giving another limit, as marked, for θ_{jet} somewhere between 5° and 10° relative the proton direction. Finally, the lower limit in Q^2 at 10^2 GeV^2 originates from a trigger requirement of a minimum transverse energy in CC events.

For NC measurements, the region accessible via the scattered electron can be added resulting in Fig. 5b. The lower limit in y , discussed above, is here seen to be a major restriction. The combination of a Q^2 measurement from the electron and an x measurement from the hadrons adds the ‘nose’ which is cut off at a minimum electron angle of 2°. For both CC and NC the large- x region is limited by small event statistics. One should also note in Fig. 5 the small overlap with the similar ‘safe’ kinematical regions at HERA [12]. A larger overlap can be obtained by a lower proton beam energy in LHC, e.g. 2 TeV keeping the same luminosity [2], since this would essentially move the shaded areas in Fig. 5 towards the upper left corner, i.e. smaller Q^2 and larger x .

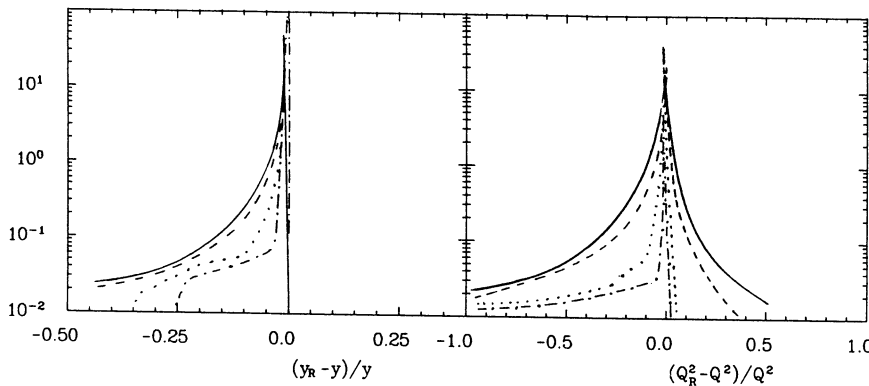


Figure 4: Relative error on y and Q^2 reconstruction due to particle losses at LEP+LHC with $Q^2, W^2 > 3 \cdot 10^4 \text{ GeV}^2$. The curves correspond to different MC models [18] for generating the hadronic final state and varying angular coverage of an ideal detector. Dash-dotted: simple quark-parton model scattering and string hadronization, full angular coverage (tail due to neutrinos from charm etc. decays). Dotted: same model, but 70 mrad beam hole. Dashed (full): QCD effects added using first order matrix elements (parton showers), 70 mrad beam hole.

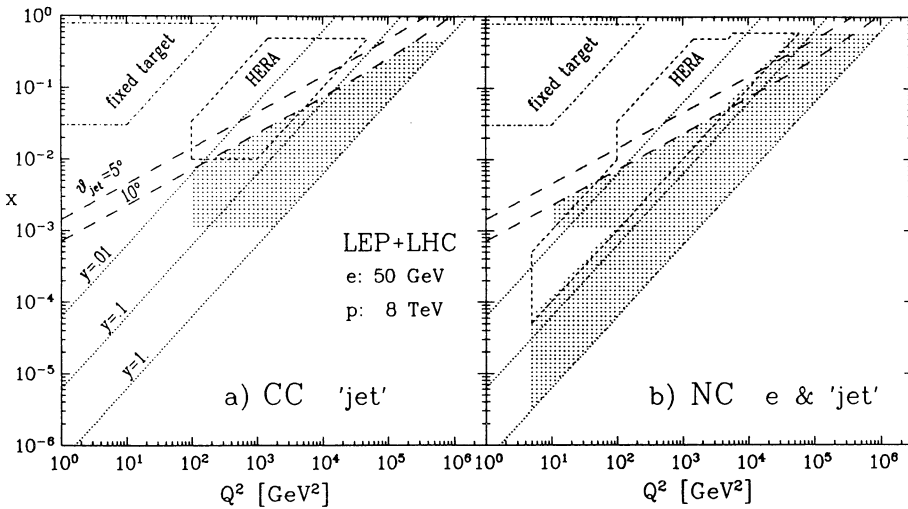


Figure 5: Experimentally acceptable regions (shaded areas) for kinematics reconstruction at LEP+LHC using (a) charged current events and (b) neutral current events. Lines of constant y are shown as well as lines of fixed angle of scattered quark jet with respect to the proton beam. For comparison, regions accessible to HERA and fixed target experiments are indicated.

3 Extraction of quark distributions

Single quark distributions or some combinations, i.e. structure functions, can be extracted from the differential cross-sections using either approximate or exact unfolding methods. The first has the advantage of being simpler since a single, suitably scaled cross-section (or maybe combination of two) directly represents the desired function, but is restricted to a limited region of applicability of the approximation. An exact unfolding, although better in principle, has the disadvantage that all four cross-sections have to be combined which imply more data taking and possible problems of relative normalization of the different data sets. Both ways have been studied extensively with respect to the theoretical strategies and the prospects of results at HERA [6].

The extraction methods are tested using the Monte Carlo generator LEPTO 5.2 [14], which is based on the cross-sections and parameters given in section 2. Event samples are simulated and binned in x and y or Q^2 and then fed into the unfolding relations giving the extracted structure function with a statistical error obtained by error propagation. When concentrating on the shape in x of these distributions the other free variable is averaged over. Specifically for LEP+LHC we consider the scattering of 50 GeV e^\pm on 8 TeV protons and event samples corresponding to 1 fb^{-1} per lepton beam. Since the interest is here focused on the deep inelastic region, the cut $Q^2 > 100 \text{ GeV}^2$ is applied which also make power corrections negligible. The cut $x > 10^{-3}$ is made to avoid the region of very small x where the leading log evolution of the applied quark distributions [9] may be inadequate [15]. In addition, the cut $y > 0.01$ is imposed for experimental reasons as discussed above.

Considering first approximate extraction from the NC cross-sections it is convenient to factor out the dominant Q^2 dependence to obtain

$$\tilde{\sigma}_{NC}(e^\mp) \equiv \frac{Q^4}{2\pi\alpha^2 s Y_+} \frac{d\sigma_{NC}(e^\mp)}{dx dy} = F_2(x, Q^2) \pm \frac{Y_-}{Y_+} x F_3(x, Q^2) \quad (11)$$

where $Y_\pm \equiv 1 \pm (1 - y)^2$. By adding or subtracting the $e^- p$ and $e^+ p$ cross-sections one can separate the structure functions F_2 and $x F_3$. For sufficiently small values of Q^2 , Z -exchange can be neglected relative to γ -exchange and consequently $x F_3$ vanishes, while F_2 approaches the electromagnetic structure function F_2^{em} . As shown in [6], the best approximation of F_2^{em} is given by $\tilde{\sigma}_{NC}(e^+)$ due to a partial cancellation of the Z -contributions in F_2 and $x F_3$. This still holds at LEP+LHC energy, but the region of validity of the approximation

$$F_2^{em} \equiv \sum_f e_f^2 (x q_f + x \bar{q}_f) \approx \tilde{\sigma}_{NC}(e^+) \quad (12)$$

is actually more restricted as demonstrated in Fig. 7.

This has important consequences for studies of QCD scaling violations since the Q^2 effects in $\tilde{\sigma}_{NC}(e^+)$ from the Z propagator dominate over the logarithmic scaling violations in most of the experimentally accessible kinematical region as clearly shown in Fig. 6a. (Compare fig. 3 in [7] for HERA where this is not the case.) Thus, at LEP+LHC energies one can no longer use the simple QCD evolution equations for a structure function, such as F_2^{em} , but must instead use a QCD formalism for the

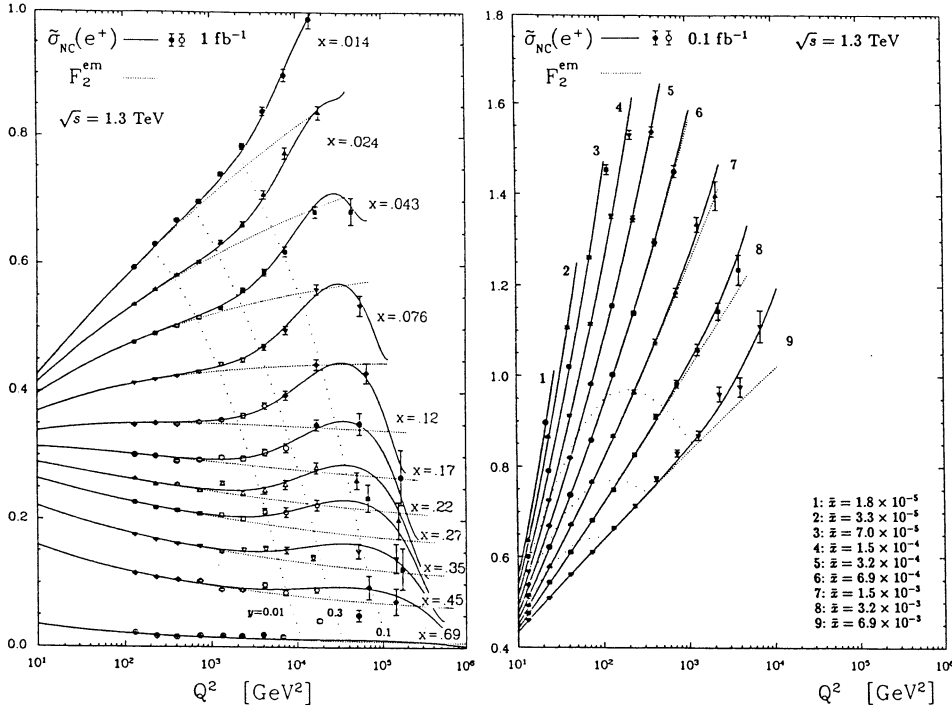


Figure 6: Q^2 dependence of the scaled differential NC e^+p cross-section at LEP+LHC for (a) $x > 10^{-2}$ and (b) $10^{-5} < x < 10^{-2}$. The full curves correspond to $\tilde{\sigma}_{NC}(e^+)$, also represented by the MC data, while the dotted curves represent F_2^{em} , i.e. pure photon exchange, and show the pure QCD scaling violations. The full (open) MC data symbols are with (without) the restriction to the experimentally acceptable phase space region shown in Fig. 5.

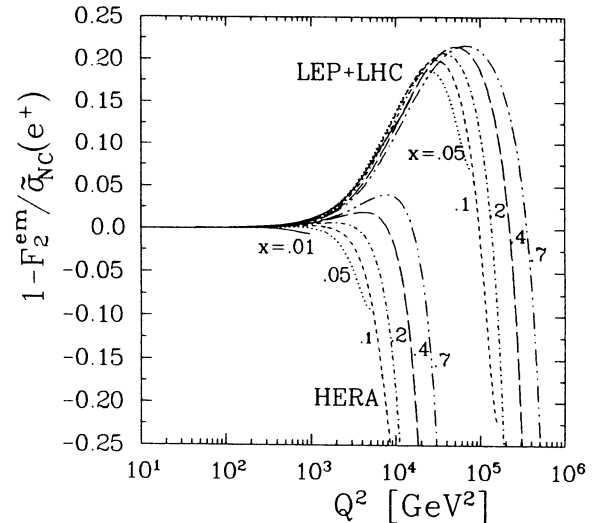


Figure 7: Relative deviation of the structure function F_2^{em} from the measured quantity $\tilde{\sigma}_{NC}(e^+)$ at LEP+LHC and HERA.

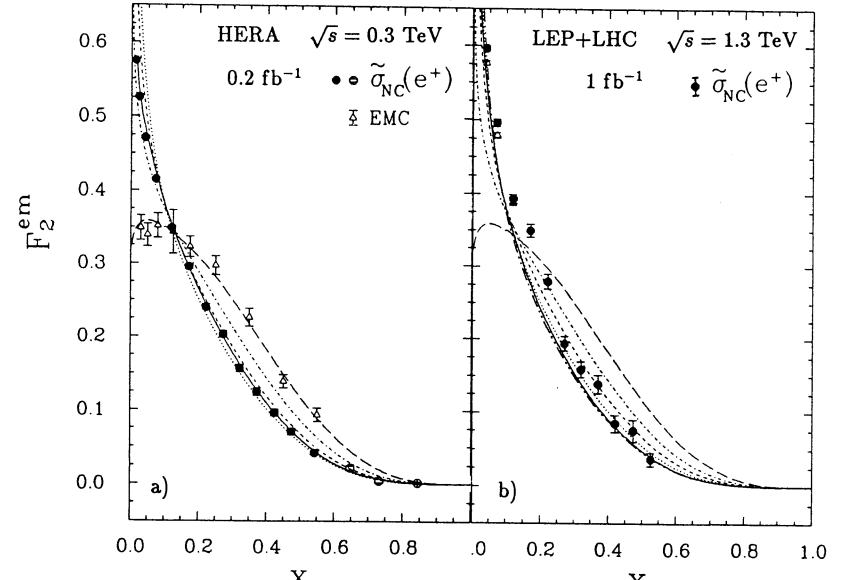


Figure 8: Measurement of $\tilde{\sigma}_{NC}(e^+)$ at HERA and LEP+LHC, averaged over $0.03 < y < 0.3$ and imposing the restriction of Fig. 5b. Via approximation (12) this represents the electromagnetic structure function F_2^{em} , shown at the same Q^2 (full curve) and at fixed $Q^2 = 10$ (long-dashed), 10^2 (dash-dotted), 10^3 (dashed), 10^4 (dotted), 10^5 GeV^2 (dot-dot-dashed) and measured by EMC (open triangles).

complete cross-section where the weak corrections are taken into account [16]. In the small- x region, on the other hand, the weak effects can usually be neglected as shown in Fig. 6b. In addition, the cross-section is here very large giving good statistics already with a lower luminosity. Together with the stronger scaling violations this opens new possibilities for QCD tests, but one has to worry about small- x corrections in QCD [15].

The breakdown of the approximation in eq. (12) at large energies (Fig. 7) also leads to systematic shifts in the x -shape of F_2^m at LEP+LHC, whereas a very good measurement can be obtained at HERA, as shown in Fig. 8. In addition, the statistical precision at LEP+LHC is worse, in spite of five times larger integrated luminosity, due to the shift of the accessible kinematical region to larger Q^2 (Fig. 5b) where the cross-sections are smaller. In view of Fig. 6b, however, LEP+LHC should give a useful measurement of F_2^m for $x < 10^{-2}$.

The parton densities in the CC cross-section, eq. (10), can easily be separated by dividing out the prefactor with the W propagator giving the scaled cross-sections $\tilde{\sigma}_{CC}(e^\pm)$ [6]. From the sum and difference of the CC cross-sections one then gets

$$\tilde{\sigma}_{CC+} \equiv \tilde{\sigma}_{CC}(e^-) + \tilde{\sigma}_{CC}(e^+) = x(U + (1-y)^2 D) \quad (13)$$

$$\tilde{\sigma}_{CC-} \equiv \tilde{\sigma}_{CC}(e^-) - \tilde{\sigma}_{CC}(e^+) = x(u_v - (1-y)^2 d_v) \quad (14)$$

where $U \equiv u + \bar{u} + c + \bar{c}$ and $D \equiv d + \bar{d} + s + \bar{s}$. For small y , this provides the approximation $x(u_v - d_v) \approx \tilde{\sigma}_{CC-}$ and access to the singlet structure function which is best approximated when only sea quarks are neglected

$$F_s \equiv xU + xD = \sum_f x(q_f + \bar{q}_f) \approx \tilde{\sigma}_{CC}(e^-) + \tilde{\sigma}_{CC}(e^+)/(1-y)^2. \quad (15)$$

These approximations hold in the same y -regions as at HERA [6]. Finally, at large x one obtains the valence approximations

$$xu_v \approx \tilde{\sigma}_{CC}(e^-), \quad xd_v \approx \tilde{\sigma}_{CC}(e^+)/(1-y)^2. \quad (16)$$

An exact unfolding of structure functions can be obtained from the electroweak cross-sections. This can be seen as a matrix equation relating the four differential cross-sections (e^\pm and NC,CC) to any basis of four structure functions via a four-by-four matrix given by the kinematical variables, electroweak propagators and couplings. Although these quantities are known, the inversion of this matrix equation is only possible in some cases. A convenient basis is provided by the valence quark densities u_v and d_v , and the structure functions U and D . The solutions are of the form $u_v = f_{NC}^{u_v} \tilde{\sigma}_{NC-} + f_{CC}^{u_v} \tilde{\sigma}_{CC-}$ and $xU = f_{NC}^U \tilde{\sigma}_{NC+} + f_{CC}^U \tilde{\sigma}_{CC+}$ where the f 's are functions of the kinematical variables and the electroweak coefficients in eq. (9). The behaviour of these functions and thereby the applicability of this unfolding method is essentially the same as found in a study [6] for HERA, to which we refer for details.

The expected quality of various quark distributions extracted through both approximations and exact unfolding are demonstrated in Figs. 8 to 10. Although the valence up-quark distribution can be easily obtained from the CC cross-section eq. (16), the result depends strongly on how well the kinematics can be reconstructed in configurations where the current jet is close to the proton beam directions as shown in Fig. 9a. Exact

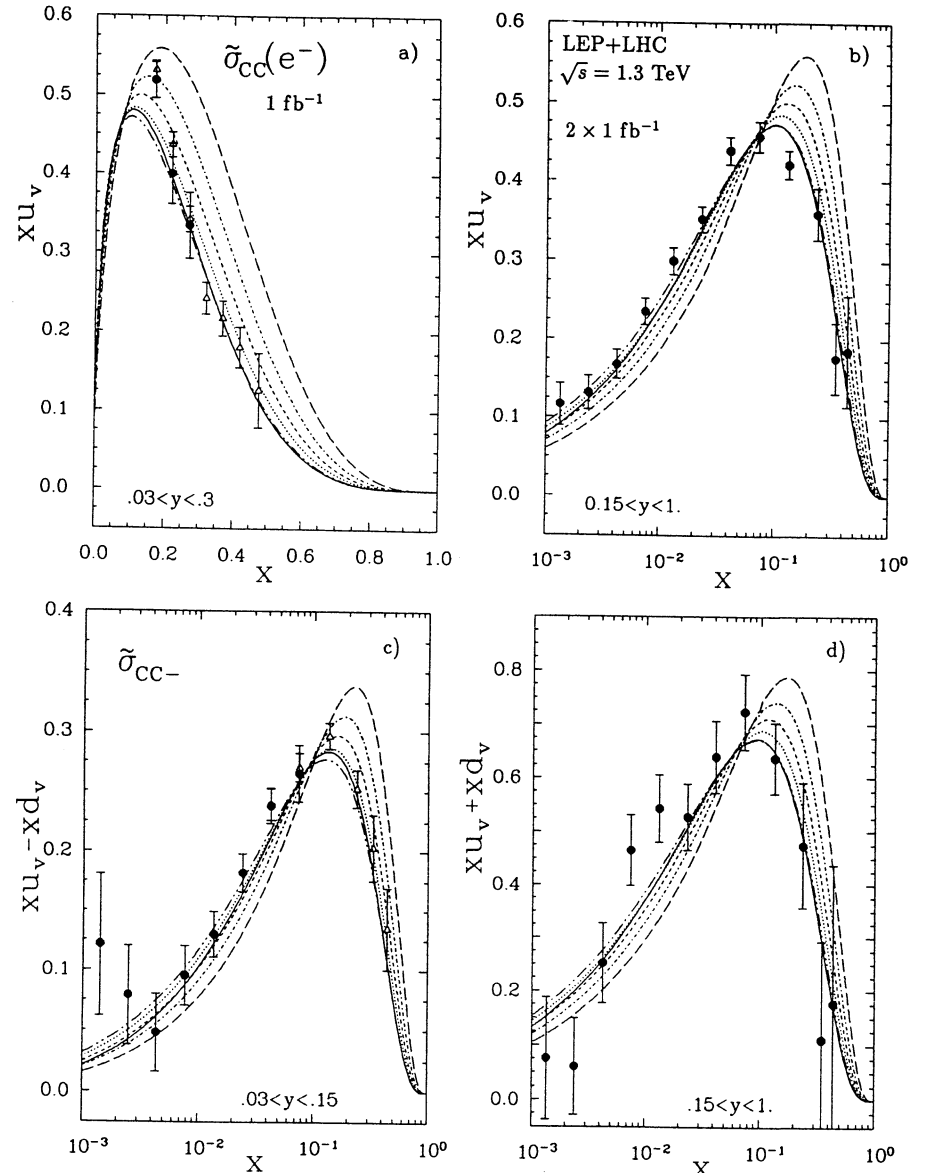


Figure 9: The valence up-quark distribution (a,b), and difference, sum (c,d) of the valence quark distributions obtained through approximation (a,c) and exact unfolding (c,d), averaging over y and restricting to the experimentally accessible region, Fig. 5, assuming a 5° (open symbols) and 10° (full symbols) effective lower cut-off for the current jet angle. The lines represent the functions at the same Q^2 as the MC data (full curve) and at fixed $Q^2 = 10^2, 10^3, 10^4, 10^5$ GeV 2 (cf. Fig. 8).

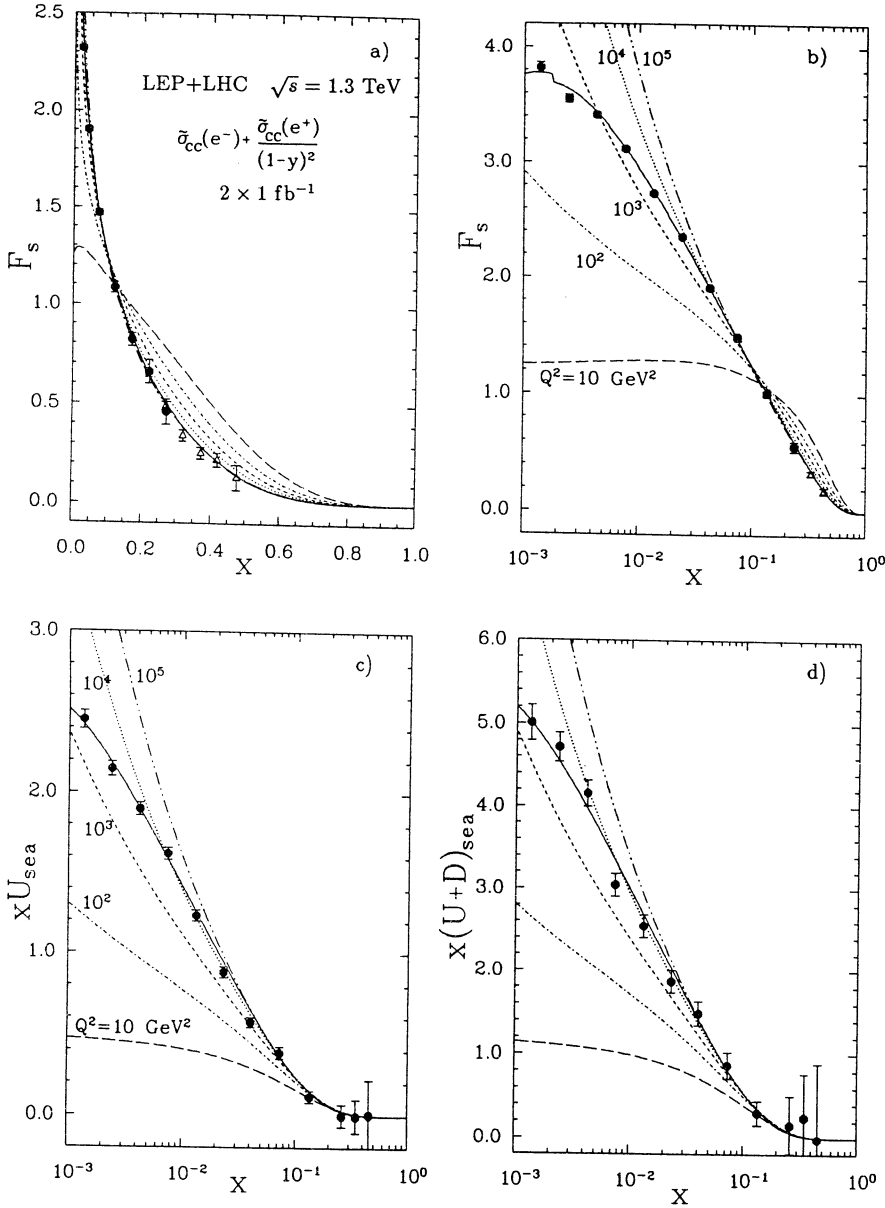


Figure 10: The singlet structure function, in two x -regions (a,b), from CC data via approximation (15), averaging over $0.03 < y < 0.3$. Exact unfolding of the up-type sea quarks (c) and the total sea (d) from NC and CC $e^\mp p$ cross-sections, averaging over $0.65 \leq y \leq 1$. Accessible region imposed and meaning of curves as in Fig. 9.

unfolding provides a very good measurement, except at large x , of u_v at a very large Q^2 scale, varying between 10^3 and 10^5 GeV^2 (Fig. 9b). In comparison with HERA (fig. 8 in [6]), the result is worse at large x but improves in the small- x region. The valence down-quark distributions cannot be measured well [6], but the combinations $u_v \pm d_v$ can be obtained with a precision that is still useful, see Fig. 9cd.

The flavour singlet structure function can be quite well measured both through the approximation (15) and exact unfolding. Since the approximation holds very well this method is preferable; it is both simpler, requiring less data, and still gives somewhat smaller statistical error bars. As shown in Fig. 10a, the large- x region again suffers from problems of the current jet being close to the beam pipe due to the more strongly boosted ep system as compared to HERA where smaller errors are expected in spite of the lower luminosity (cf. fig. 13 in [6]). On the other hand, the measurement of F_s at small x , Fig. 10b, is of very high quality. Finally, sea quark distributions can be measured quite well in the small- x region (Fig. 10cd) using the exact unfolding method, in spite of its necessary restriction to a limited region of large y -values.

Although proper QCD tests cannot be made with these Q^2 -averaged distributions, one can in some cases clearly see an evolution in Q^2 when comparing with the same function obtained at lower energies and thus obtain a qualitative check of QCD.

4 Hadronic final state structure

Detailed predictions of the structure of the hadronic final state must be based on Monte Carlo models such as LEPTO [14]. Starting from the cross-sections for the basic electro-weak scattering, QCD corrections can be included at different levels of sophistication and finally hadronization performed using, e.g., the Lund string model. Although the simple quark-parton model (QPM), where QCD effects are neglected, is expected to be inadequate it is useful as comparison to show the effect when including QCD effects. This can be made using first order exact matrix elements (ME), for the two processes $\gamma^* q \rightarrow qg$ and $\gamma^* g \rightarrow q\bar{q}$, or using parton showers (PS) which include higher orders but only in the leading log approximation. A systematic study of these models, with some extensions to LEP+LHC energy, is given in [13].

Hadronic final states in lepton production has been studied experimentally up to $W \simeq 25 \text{ GeV}$ only. It is therefore an enormous extrapolation of the models when making predictions for LEP+LHC, as illustrated in Fig. 11a. In addition, the theoretical uncertainties in these models are larger than in the case of simulating e^+e^- annihilation, since the ep system is more complicated in several ways. First, there is a proton target remnant which influences the hadronic system strongly as seen in Fig. 11b. The QCD matrix elements are more complicated with more processes and are so far only implemented to first order and without virtual corrections. The parton shower approach is more difficult to match with exact matrix elements and has additional problems related to a not well-defined virtuality scale and the separation of initial and final state radiation. Moreover, constraints must be imposed to guarantee a proper evolution of structure functions and in the small- x region, which is of importance at LEP+LHC, this connects to the small- x problem in QCD [15]. Nevertheless, the parton shower model is

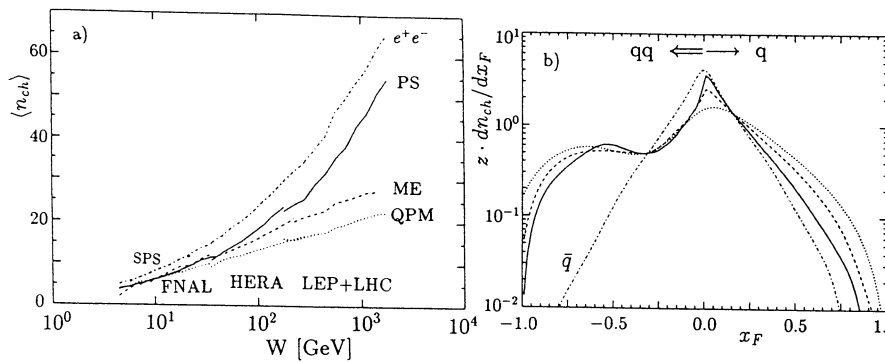


Figure 11: (a) Average charged multiplicity as a function of the hadronic mass in NC events; leftmost SPS, thereafter FNAL, HERA and LEP+LHC. (b) Energy-weighted distribution of scaled longitudinal momenta, for charged particles in the hadronic CM frame of HERA events with $Q^2, W^2 > 10^3$ GeV 2 ($x_F > 0$ for the current jet and < 0 for the beam jet). Curves for different models: QPM (dotted), ME (dashed), PS (full) and for comparison e^+e^- events of same energy using parton showers (dash-dotted).

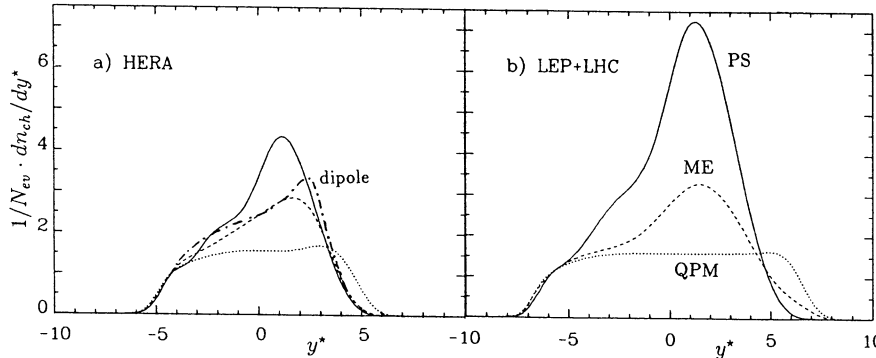


Figure 12: Charged particle rapidity distribution in the hadronic CM frame of (a) HERA events with $Q^2, W^2 > 10^3$ GeV 2 and (b) LEP+LHC ones with $Q^2, W^2 > 3 \cdot 10^4$ GeV 2 using the QPM (dotted), ME (dashed), PS (full) and dipole (dash-dotted) models.

expected to be the most realistic one and give reasonable predictions provided x is not too small.

There is a substantial increase in the hadronic activity (hadron and jet multiplicity) due to QCD radiation, in particular in the PS case where higher orders are included, see Figs. 11–13. It is still smaller, however, than in e^+e^- events at the same mass of the hadronic system. The reason is partly that the proton remnant jet is treated as a spectator and give no parton radiation, resulting in a much harder particle spectrum (Fig. 11b). Further, the initial state radiation is suppressed [13] and is not located so far out in rapidity along the incoming quark (i.e. target remnant direction), but

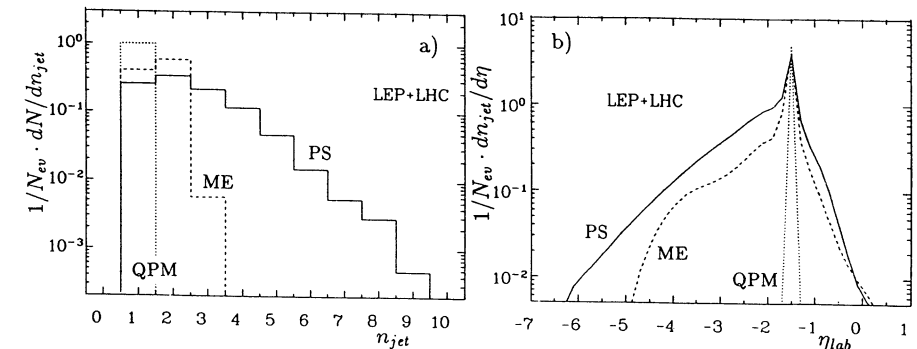


Figure 13: Multiplicity and lab pseudorapidity distributions of jets (reconstructed with UA1-type algorithm $\Delta R < 0.5, E_{\perp jet} > 5$ GeV) in fixed kinematics events $x = 0.1, y = 0.3$ using the QPM (dotted), ME (dashed) and PS (full) models [13].

is more central in the hadronic cms. These effects cause the clear forward-backward asymmetry in Fig. 12. The increased PS radiation at LEP+LHC compared to HERA, seen in Fig. 12, may be an overestimate related to the problems mentioned above. The Lund dipole model [17], which generate higher order gluon emission based on radiation from the string seen as an extended colour dipole, predicts substantially less radiation as shown in Fig. 12a. This illustrates the uncertainties that exist, but also the potential to gain understanding by distinguishing between models based on different physics ideas.

Fig. 13b shows the distribution of jet pseudorapidity in the lab frame for events with fixed kinematics, i.e. with the current jet at a fixed angle in the naive QPM model. Even if the current jet is rather central there are additional jets, in particular in the forward region. Some of these radiated jets may be (partly) lost in the beam hole and their recoil taken by other jets, including the struck quark, causing shifts in the kinematical variables reconstructed from the observable hadronic system as discussed above.

5 Conclusions

The ep cms is very strongly boosted in the LEP+LHC lab frame causing most particles to appear at small angles relative to the proton beam. This has severe consequences for the experimentation and limits the x, Q^2 -region where the conventional DIS kinematics can be safely reconstructed to give differential cross-sections with acceptable systematic uncertainties. The useful region is thereby pushed to larger y , i.e. larger Q^2 , where the cross-sections are smaller resulting in a smaller effective statistics than naively expected from the large luminosity. Fortunately, the large- Q^2 frontier is not so much affected by these problems, giving access to an order of magnitude larger Q^2 compared to HERA, but as usual this region is limited by small cross-sections. In addition, a new domain at very small x -values will become accessible.

Structure function analysis based on NC cross-sections in the accessible region is, in the conventional x -region, strongly influenced by weak Z -exchange making QCD tests more involved than at HERA. The main interest is likely to be focused on the small- x region, where statistics is high and weak corrections are small, in order to investigate novel QCD effects [15]. In particular, LEP+LHC will here go beyond HERA to cover the region $3 \cdot 10^{-6} < x < 10^{-4}$. Concerning quark distributions from CC data, there is a danger of loosing the region $x \gtrsim 0.2$ due to particle losses in the beam hole or at least having smaller statistical precision compared to HERA for $x \gtrsim 0.1$. However, a new small- x region between 10^{-3} and 10^{-2} is accessible also in this case. Better results in the region of conventional x -values could be obtained by lowering the proton beam energy, whereas the normal beam energies in LEP+LHC give the best prospects for structure function physics in the small- x region.

References

- [1] R. Rückl, these Proceedings, CERN 90-10, Vol. I, p. 229
- [2] A. Verdier, these Proceedings, CERN 90-10, Vol. III, p. 820
- [3] W. Bartel, these Proceedings, CERN 90-10, Vol. III, p. 824
- [4] G. Ingelman et al., proc. HERA workshop 1987, Ed. R.D. Peccei, Vol. 1, p. 3
- [5] B. Campbell, V. Elias, W.R. Frisken, Can. J. Phys. 59 (1981) 1742
E. Lohrmann, K.-H. Mess, DESY HERA 83/08 (1983)
- [6] G. Ingelman, R. Rückl, Z. Phys. C44 (1989) 291
- [7] J. Blümlein, G. Ingelman, M. Klein, R. Rückl, Z. Phys. C45 (1990) 501
- [8] H. Spiesberger, these Proceedings, CERN 90-10, Vol. II
- [9] E. Eichten et al., Rev. Mod. Phys. 56 (1984) 579, ibid. 58 (1986) 1047
- [10] W. Bartel, CERN 87-07, Vol. I, p. 303
- [11] J. Feltesse, these Proceedings, CERN 90-10, Vol. I, p. 219
J. Blümlein, J. Feltesse, M. Klein, these Proceedings, CERN 90-10, Vol. II
- [12] J. Feltesse, proc. HERA workshop, Hamburg 1987, Ed. R.D. Peccei, Vol. 1, p. 33
- [13] M. Bengtsson, G. Ingelman, T. Sjöstrand, Nucl. Phys. B301 (1988) 554
- [14] G. Ingelman, LEPTO 5.2 program manual, unpublished
- [15] J. Bartels, G.A. Schuler, these Proceedings, CERN 90-10, Vol. II
- [16] J. Blümlein, these Proceedings, CERN 90-10, Vol. II
- [17] B. Andersson, G. Gustafson, L. Lönnblad, U. Petterson, Z. Phys. C43 (1989) 625

Structure Function Measurement and QCD-Tests at $LEP \otimes LHC$

J. Blümlein

Institut für Hochenergiephysik, Zeuthen, O-1615, Germany

Abstract

A study is presented on the possibilities to measure the neutral and charged current structure functions F_2 , xG_3 , W_2 , xW_3 and $R = \sigma_L/\sigma_T$ using both proton and deuteron targets. A QCD analysis is performed for a combination of neutral current cross sections. Possible measurements of the gluon distribution both from F_L and from the QCD analysis are discussed.

1 Introduction

Deep inelastic lepton-nucleon scattering has been proven to be one of the most direct possibilities to study the nucleon structure [1]. So far the kinematical range $x \gtrsim 10^{-2}$ and $Q^2 \lesssim 300\text{GeV}^2$ has been probed. At HERA this range will be extended to $x \gtrsim 10^{-4}$ and $Q^2 \lesssim 2 \cdot 10^4\text{GeV}^2$ in the near future [2,3]. The study of deep inelastic $e^\pm N$ -scattering at $LEP \otimes LHC$ would extend this range further to $x \gtrsim 10^{-5}$ and $Q^2 \lesssim 10^5\text{GeV}^2$.

In this way a detailed study could be performed of the behaviour of structure functions at extremely small x and very high Q^2 . Compared to HERA the accessible Q^2 -range at small x will be extended to larger values which allows to compare the data with theoretical predictions [4] in a broad range in Q^2 . Particularly, it will be important to unfold the gluon and sea-quark distributions in this range, because any prediction of reaction cross sections at the future pp -colliders depends on these distributions. In the range of high Q^2 the measurement of the deep inelastic scattering cross section can be used to search for new interactions and a possible substructure of quarks and leptons [5].

In this paper a study is performed on the potential to measure different nucleon structure functions, the gluon distribution and of the running coupling constant $\alpha_s(Q^2)$ in a QCD-analysis at $LEP \otimes LHC$. If not mentioned differently we use the cuts given in [6] and refer to the cms-energies and integrated luminosities of $\sqrt{s} = 1265\text{GeV}$, $\mathcal{L} = 1\text{fb}^{-1}$ for $LEP1 \otimes LHC$ and $\sqrt{s} = 1789\text{GeV}$, $\mathcal{L} = 100\text{pb}^{-1}$ for $LEP2 \otimes LHC$ and use the parton distributions of ref. [7]. In section 2 possibilities are discussed to measure neutral and charged current structure functions using both $p-$ and $d-$ targets. Section 3 deals with the measurement of the longitudinal structure function, R and an unfolding of the gluon distribution at small x . In section 4 a QCD-analysis of neutral current cross sections is performed and section 5 contains the conclusions.

2 Neutral and Charged Current Structure Functions

The deep inelastic scattering cross sections of neutral current $e^\pm N$ reactions $d^2\sigma_{NC}^\pm/dxdQ^2$ are determined by the five structure functions F_2 , G_2 , H_2 , xG_3 and xH_3 [8] in lowest order perturbation

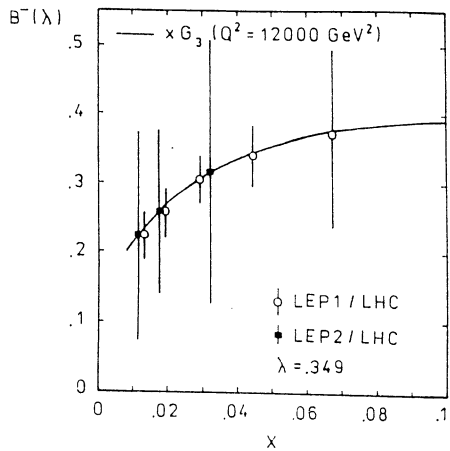


Figure 1: Possible measurement of $B^- \propto xG_3(x)$.

theory¹. Because only two differential cross sections can be measured experimentally only two sets of combinations between this structure functions can be determined. The sum and the difference of the differential cross sections yields the following combinations.

$$\begin{aligned} B_+(x, Q^2) &= \frac{1}{2} \left[\frac{d^2\sigma^-}{dx dQ^2} + \frac{d^2\sigma^+}{dx dQ^2} \right] \frac{xQ^4}{2\pi\alpha^2 Y_+} \\ &= F_2(x, Q^2) + \kappa_Z(-v + \lambda a) G_2(x, Q^2) + \kappa_Z^2(v^2 + a^2 - 2\lambda av) H_2(x, Q^2) \end{aligned} \quad (1)$$

and

$$\begin{aligned} B_-(x, Q^2) &= \frac{1}{2} \left[\frac{d^2\sigma^-}{dx dQ^2} - \frac{d^2\sigma^+}{dx dQ^2} \right] \frac{xQ^4}{2\pi\alpha^2 \kappa_Z(a - \lambda v) Y_-} \\ &= xG_3(x, Q^2) + \kappa_Z \frac{\lambda(a^2 + v^2) - 2va}{a - \lambda v} xH_3(x, Q^2) \end{aligned} \quad (2)$$

Here, $Y_{\pm} = 1 \pm (1 - y)^2$, $\kappa_Z(Q^2) = Q^2/(Q^2 + M_Z^2)/(4 \sin^2 \theta_W \cos^2 \theta_W)$, v and a are the vector and axial coupling of the electron and λ denotes the lepton beam polarization. The structure functions may be rewritten in the parton picture in terms of quark distributions by

$$\begin{aligned} (F_2, G_2, H_2) &= x \sum_q (e_q^2, 2e_q v_q, v_q^2 + a_q^2)(q + \bar{q}) \\ (xG_3, xH_3) &= 2x \sum_q (e_q a_q, v_q a_q)(q - \bar{q}) \end{aligned} \quad (3)$$

For $Q^2 \ll M_Z^2$ $B_+(x, Q^2)$ is represented by the structure function $F_2(x, Q^2)$. At higher Q^2 the Q^2 -dependence due to the Z -propagator becomes visible and can be well resolved within the statistical

¹We assume, that the electro-weak radiative corrections have been carried out already [9]. The longitudinal structure functions emerging at $\mathcal{O}(\alpha_s)$ will be dealt with in sect. 3.

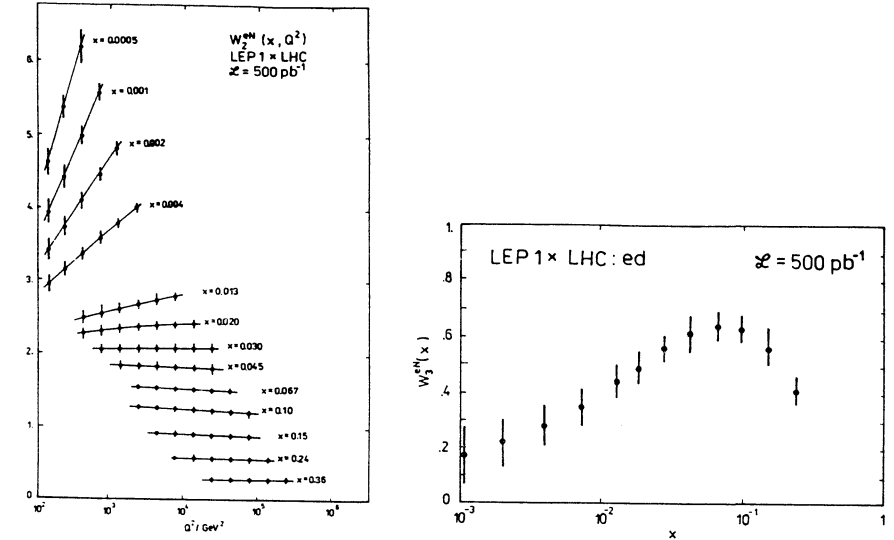


Figure 2: Statistical precision of charged current structure functions in deep inelastic ed -scattering. a: $W_2^{eN}(x, Q^2)$, ($N = (p + n)/2$); b: $xW_3^{eN}(x)$

precision. This has been illustrated in [10]. For $Q^2 \gtrsim 10 \text{ GeV}^2$, $y > 0.1$ [6] $F_2(x, Q^2)$ can be measured down to $x \sim 2 \cdot 10^{-5}$ with high precision. Because of the dominance of the photon propagator for $Q^2 \ll M_Z^2$ one may use even one of the differential cross sections instead of B_+ to measure F_2 .

The combination $B_-(x, Q^2)$ can be used to determine the structure function xG_3 . This is illustrated in fig. 1 for a measurement of B_- averaging over Q^2 . Within the statistical precision the effect of the structure function xH_3 can not be resolved and B_- represents $xG_3(x)$. The measurement covers only rather small values of x . Compared to a similar measurement at HERA (cf. [3]) the accessible x range is shifted by one order of magnitude to lower values of x but is still limited by $x \sim 0.01$.

In ep -reactions the charged current structure functions $W_2^\pm(x, Q^2)$ and $xW_3^\pm(x, Q^2)$ can not be unfolded, since only cross sections are measured and the flavour-contents of the proton does not allow a separation of the Y_+ - and Y_- -terms. This, however, is possible in charged current ed -scattering due to the isospin symmetry of the deuteron. The charged current cross sections are given by

$$\frac{d^2\sigma^\pm}{dx dQ^2} = \frac{2\pi\alpha^2}{x(Q^2 + M_W^2)^2} \frac{1}{16 \sin^4 \theta_W} [Y_+ W_2^\pm(x, Q^2) \mp Y_- xW_3^\pm(x, Q^2)] \quad (4)$$

Here, $W_2^\pm(x, Q^2) = \Sigma(x, Q^2)$ and $xW_3^\pm(x, Q^2) = x(u_v(x, Q^2) + d_v(x, Q^2)) \pm 2x(s(x, Q^2) + b(x, Q^2) - c(x, Q^2))$. From the sum of the differential cross sections σ^- and σ^+ one can measure

$$W_2(x, Q^2) = \Sigma(x, Q^2) - \frac{Y_-}{Y_+} 4x(s(x, Q^2) + b(x, Q^2) - c(x, Q^2)) \quad (5)$$

and from the difference of the cross sections the valence distribution

$$W_3(x, Q^2) = x(u_v(x, Q^2) + d_v(x, Q^2)) \quad (6)$$

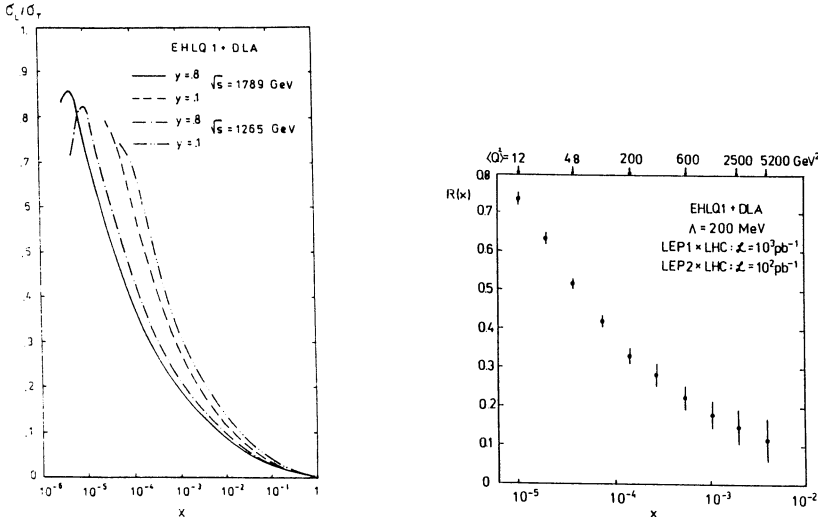


Figure 3: (a) Dependence of R from x and y ; (b) Statistical precision of a possible measurement of $R(x)$, see text.

Both distributions are illustrated in fig. 2, where we have assumed that a correction for the second term in (5) is possible taking this distribution from other measurements and assuming an integrated luminosity of $\mathcal{L} = 500 \text{ pb}^{-1}$ [11]. W_2^{gN} can be measured with sufficient precision down to $x \sim 5 \cdot 10^{-3}$ for $Q^2 \geq 100 \text{ GeV}^2$, which has to be applied because of trigger conditions [6]. Compared to HERA [3] the kinematical range is shifted by half an order of magnitude to lower x . The structure function xW_3 can be determined as a function of x only. Again, the measurement is shifted by nearly one order of magnitude to lower x , which is a kinematical effect due to the higher values of s at $LEP1 \otimes LHC$.

3 Measurement of R and $xG(x, Q^2)$

The measurement of the structure function $F_2(x, Q^2)$ at small x requires to determine also the longitudinal structure function $F_L(x, Q^2)$, because this structure function may become rather large and cannot be considered as a known correction. In lowest order QCD $F_L(x, Q^2)$ is given by

$$F_L(x, Q^2) = \frac{4\alpha_s(Q^2)}{3\pi} \int_x^1 \frac{dy}{y} z^2 \left[F_2(y, Q^2) + \frac{5}{3}(1-z)yG(y, Q^2) \right] \quad (7)$$

with $z = x/y$ and $N_f = 4$ [12]. Because $xG(x, Q^2)$ becomes rather large at small x also F_L grows in this range. This behavior is illustrated by $R = F_L/2xF_1$ in Fig. 3a. Here, $2xF_1 = \sum_{i=1}^{N_f} e_i^2 x(q_i + \bar{q}_i)$. For the numerical calculation we used the parton distributions [7] and its DLA-extrapolation (cf.[13]) for $x \leq 10^{-4}$. To determine F_L in a model independent way the neutral current cross section $\hat{\sigma}_N = d^2\sigma_{NC}/dx dQ^2$ has to be measured at different values of y in the same (x, Q^2) -bin. This can be achieved measuring $\hat{\sigma}_{NC}$ at different \sqrt{s} . In the present analysis we will combine the samples $\sqrt{s} = 1265 \text{ GeV}$, $\mathcal{L} = 1 \text{ fb}^{-1}$ and $\sqrt{s} = 1789 \text{ GeV}$, $\mathcal{L} = 100 \text{ pb}^{-1}$. R is determined from $r = \hat{\sigma}_{NC}(s_1)/\hat{\sigma}_{NC}(s_2)$. The statistical error, δR , is obtained by

$$\delta R = r \frac{(1+R)^2(Y_2 - y_2^2 R/(1+R))^2}{|Y_1 + y_2^2 - Y_2 + y_1^2|} \sqrt{\frac{1}{N_1} + \frac{1}{N_2}} \quad (8)$$

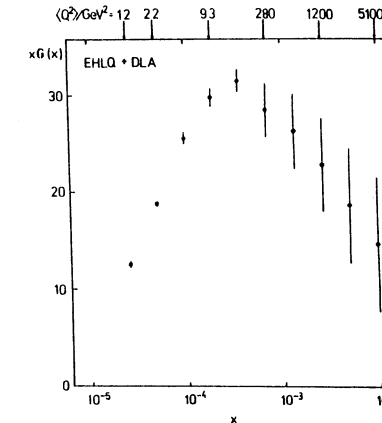


Figure 4: Statistical precision of a possible measurement of $xG(x)$

where N_1 and N_2 are the event rates in the (x, Q^2) -bin at y_1 and y_2 resp. In Fig. 3b the precision of a possible measurement of R is illustrated. In the range $x \leq 10^{-2}$ the x dependence of R can be determined with high precision. This measurement is correlated with Q^2 . For $x \leq 2 \cdot 10^{-2}$ even the Q^2 dependence could be measured in a limited range. Compared to HERA [3] the range for a R -measurement is extended by more than one order of magnitude to lower x .

According to (7) a measurement of $F_L(x, Q^2)$ can be used to determine $xG(x, Q^2)$ (cf. [14]). At very small x the contribution due to F_2 can be neglected against the second term in (7) and one may use the relation

$$xG(x, Q^2) \simeq 1.77 \frac{3\pi}{2\alpha_s(Q^2)} F_L(0.4x, Q^2) \quad (9)$$

to determine the gluon distribution. The statistical precision of a possible measurement of $xG(x)$ corresponding to the measurement of R (Fig. 3a) is shown in Fig. 4. In the range $x \geq 2 \cdot 10^{-2}$ only the shape of $xG(x)$ can be measured, but for lower x even the Q^2 -dependence of xG might be unfolded.

4 QCD-Tests

Deep inelastic scattering provides one of the cleanest possibilities to test QCD. The measurement of the scaling violations of structure functions allows to determine Λ_{QCD} in a combined fit of the initial distributions $\Sigma(x, Q_0^2) = \sum_{i=1}^{N_f} x(q_i(x, Q_0^2) + \bar{q}_i(x, Q_0^2))$, $\Delta(x, Q_0^2) = \sum_{j=1}^{N_f} x(u_j(x, Q_0^2) + \bar{u}_j(x, Q_0^2) - d_j(x, Q_0^2) - \bar{d}_j(x, Q_0^2))$ and the gluon distribution $xG(x, Q_0^2)$ using the evolution equations. In the energy range of $LEP \otimes LHC$ we view a more complicated situation. The neutral current structure function $F_2(x, Q^2)$ can not be measured directly and one has to use the cross section combination $B_+^{sp}(\lambda; x, Q^2)$ for the QCD-analysis instead. As illustrated in [10] this quantity is well measurable, however, it contains aside the structure function $F_2(x, Q^2)$ also terms induced by the $\gamma - Z$ -interference and Z -exchange³. These terms can not be neglected at high Q^2 because the

²A similar analysis is given in [15].

³A direct analysis of either σ^- or σ^+ requires the fit of more initial distributions at Q_0^2 which leads to a larger statistical error of α_s .

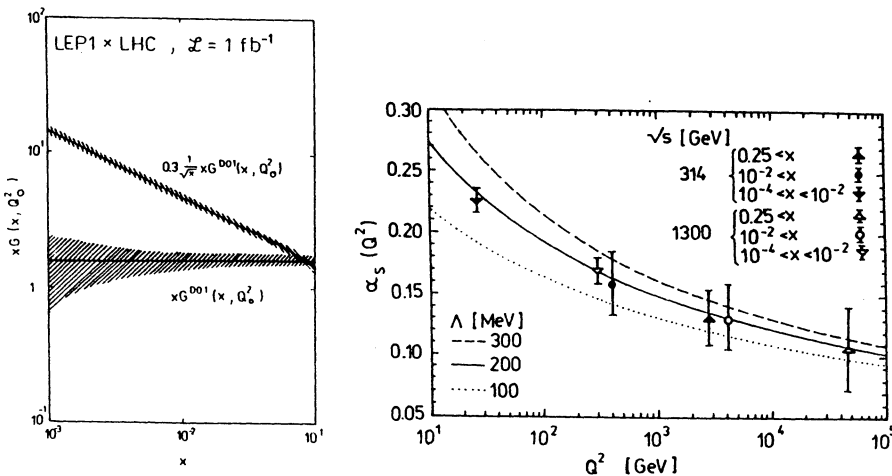


Figure 5: (a) Constraints on $xG(x, Q_0^2)$ from a QCD-analysis of $F_2(x, Q^2)$ for $10^{-4} \leq x \leq 10^{-2}$ assuming two different initial distributions; (b) Statistical precision of α_s in different ranges of Q^2 . A comparison to similar possible measurements at *HERA* [16] is given.

Q^2 -dependence due to the propagator terms $\kappa_Z(Q^2) \sim Q^2/(Q^2 + M_Z^2)$ is much stronger than the Q^2 -behaviour due to QCD evolution⁴.

B_+^{ep} , as a linear combination of three genuine structure functions⁵ F_2 , G_2 and H_2 , can be used for a QCD-fit directly. One may rewrite B_+^{ep} as

$$B_+^{ep}(x, Q^2) = C_\Sigma(Q^2)\Sigma(x, Q^2) + C_\Delta(Q^2)\Delta(x, Q^2) \quad (10)$$

The Q^2 -evolution of Σ and Δ [17] can be expressed by three evolution operators [18] which yields the representation

$$\begin{aligned} B_+^{ep}(x, Q^2) &= C_\Sigma(Q^2) [E_{qq}(x, Q^2) \otimes \Sigma(x, Q_0^2) + E_{qG}(x, Q^2) \otimes xG(x, Q_0^2)] \\ &+ C_\Delta(Q^2) E_{NS}(x, Q^2) \otimes \Delta(x, Q_0^2) \end{aligned} \quad (11)$$

Here, the operator \otimes denotes the Mellin-type convolution. Similar to the limit $Q^2/M_Z^2 \rightarrow 0$, where $C_\Sigma \rightarrow 5/18$ and $C_\Delta \rightarrow 1/6$ three input distributions at Q_0^2 have to be fitted, but the coefficients $C_{\Sigma,\Delta}$ are Q^2 -dependent. In the valence range, $x \geq 0.25$, two initial distributions remain (e.g. xu_v and xd_v) because of the different Q^2 -dependence of C_Σ and C_Δ contrary to the case $Q^2/M_Z^2 \rightarrow 0$, where only one input distribution has to be determined.

In the subsequent analysis we have carried out the QCD-fits deviating the accessible x -range into different intervals. Because x and Q^2 are correlated due to the fixed cms-energy a determination of α_s at different values of $\langle Q^2 \rangle$ is implied. The values of α_s given refer to an assumed value of $\Lambda_{MS}^{(4)} = 200 \text{ MeV}$ [19]. The analysis showed, that only the measurement of $B_+(x, Q^2)$ at *LEP1* \otimes *LHC* for $\mathcal{L} = 1 \text{ fb}^{-1}$ allows a QCD-test, but the statistics at *LEP2* \otimes *LHC* is too small to perform a QCD-analysis.

⁴A way out of this situation could be provided by studying ed -scattering, cf. eq.(5).

⁵Here, we assume that the measurement of the longitudinal structure functions (cf. sect. 3) has been carried out and B_+ is already corrected for this contribution.

In the valence range $x \geq 0.25$ a value of $\alpha_s = 0.108 \pm 0.060$ at $\langle Q^2 \rangle = 5 \cdot 10^4 \text{ GeV}^2$ is obtained for a fit of the non-singlet form of (11). Here, we assumed that the jet-measurement will be possible down to $\theta_J = 5^\circ$. For the whole range $x \geq 10^{-2}$ one obtains for a combined singlet and non-singlet fit of eq. (11) $\alpha_s = 0.130 \pm 0.054$ at $\langle Q^2 \rangle = 4.4 \cdot 10^3 \text{ GeV}^2$.

In the range $10^{-4} \leq x \leq 10^{-2}$ we analyzed the scaling violations of $B_+^{ep}(x, Q^2)$ as predicted by the Altarelli-Parisi evolution equations and obtained $\alpha_s = 0.170 \pm 0.010$ for $\langle Q^2 \rangle = 290 \text{ GeV}^2$. As a result of the singlet-fit also an error-band for $xG(x, Q_0^2)$ is derived. This is illustrated in fig. 5a assuming the gluon distribution [20] $xG^{DO}(x, Q_0^2)$ and $0.3x^{1/2}G^{DO}(x, Q_0^2)$ at $Q_0^2 = 4 \text{ GeV}^2$, which have the same normalization. Within the statistical precision a QCD-fit can distinguish between both initial distributions, which will be very important for the understanding of the low- x behaviour of the gluon distribution.

A summary of the values of α_s determined is given in fig. 5b. If one compares these results with expectations for similar measurements at *HERA* [16] one finds the measurements in a given bin in x for *LEP1* \otimes *LHC* shifted by one order of magnitude towards higher Q^2 , but at similar precision. One should note, that the luminosity at *LEP1* \otimes *LHC* is a factor of five higher than that used in the estimates for *HERA*, however. An interesting measurement could be provided in the range $10^{-4} \leq x \leq 10^{-2}$ comparing the results between *HERA* and *LEP1* \otimes *LHC*. Because of the different range of Q^2 probed one might unveil the influence of higher order screening corrections experimentally.

The analysis in the range $10^{-4} \leq x \leq 10^{-2}$ has merely to be understood as a response on the Altarelli-Parisi evolution. As pointed out in [4] this is probably only partially justified, because screening effects due to higher twist diagrams may start to influence the evolution of $B_+^{ep}(x, Q^2)$ in this range already. Otherwise, the Q^2 values are still rather high. Nevertheless, a full analysis including the relevant higher order terms is required, since these terms influence the evolution in a non-linear way. These contributions are not yet completely worked out and further theoretical work is required. This applies of course also for still smaller x -values, as far as a perturbative treatment will be possible.

5 Conclusions

The study of deep inelastic scattering at *LEP1* \otimes *LHC* will allow to investigate the nucleon structure in a new kinematical range. Compared to *HERA* both the accessible ranges in x and Q^2 will be extended by one order of magnitude. This will allow particularly a detailed study of the behaviour of neutral current structure functions down to $x \sim 10^{-5}$. Whereas a combination of neutral current structure functions, $B_+^{ep}(x, Q^2)$, and at $Q^2 \ll M_Z^2$ also F_2^{ep} can be measured with high precision in a wide range of x and Q^2 the structure function $xG_3(x)$, which originates from $\gamma - Z$ mixing, can only be determined as a function of x at lower x values. Using deuterons also the charged current structure functions W_2^{ed} and xW_3^{ed} can be unfolded. Again, W_2 can be measured in both x and Q^2 but for xW_3 only a shape measurement in x is possible.

Using data from both *LEP1* \otimes *LHC* and *LEP2* \otimes *LHC* one can measure the longitudinal structure function F_L and $R(x)$ down to $x \sim 10^{-5}$. Because of the relation of F_L and the gluon density also $xG(x)$ can be measured down to $x \sim 2 \cdot 10^{-5}$. In the lower part of this range even the Q^2 dependence may be determined.

Possibilities have been considered to determine $\alpha_s(Q^2)$ from $B_+^{ep}(x, Q^2)$ considering fixed bins in x . α_s can be measured at similar precision as estimated for *HERA*, but the according values are shifted by one order of magnitude towards higher $\langle Q^2 \rangle$. For the complete understanding of the QCD-evolution at small x still more theoretical work is required.

Acknowledgement

For discussions during the workshop I would like to thank J. Feltesse, G. Ingelman, M. Klein and R. Rückl.

References

- [1] F. Eisele, Rep. Progr. Phys. **49** 233 (1986); M. Diemoz, F. Ferroni, E. Longo, Phys. Rep. **130** 293 (1986); T. Sloan, G. Smadja, R. Voss, Phys. Rep. **162** 45 (1988).
- [2] J. Feltesse, Proc. HERA Workshop, ed. R.D. Peccei, DESY, 1988, p.33.
- [3] J. Blümlein, M. Klein, T. Naumann, T. Riemann, Proc. HERA Workshop, ed. R.D. Peccei, DESY, 1988, p.67.
- [4] L.V. Gribov, E.M. Levin, M.G. Ryskin, Phys. Rep. **100** 1 (1983); J. Collins, J. Kwiecinski, Nucl. Phys. **B335** 89 (1990); J. Bartels, J. Blümlein, G. Schuler, DESY 90-091, PHE 90-10, Nucl. Phys. Proc. Suppl. and Z. Phys. C in press.
- [5] H.U. Martyn, these proceedings.
- [6] J. Blümlein, J. Feltesse, M. Klein, these proceedings.
- [7] E. Eichten et al., Rev. Mod. Phys. **56** 579 (1984) and Erratum **58** 1065 (1986).
- [8] M. Klein, T. Riemann, Z. Phys. **C24** 151 (1984).
- [9] H. Spiesberger, these proceedings;
J. Blümlein, these proceedings.
- [10] G. Ingelman, these proceedings.
- [11] W. Bartel, private communication.
- [12] E. Reya, Phys. Rep. **69** 195 (1980) and references therein.
- [13] C. Quigg, M.H. Reno, T.P. Walker, Phys. Rev. Lett. **57** 774 (1986).
- [14] Y.L. Dokshitser, D.I. Dyakonov, S.I. Troyan, Phys. Rep. **58** 269 (1980); A. Cooper-Sarkar et al., Z.Phys. **C39** 281 (1988).
- [15] N. Magnussen, G. Schuler, these proceedings.
- [16] J. Blümlein, G. Ingelman, M. Klein, R. Rückl, Z. Phys. **C45** 501 (1990).
- [17] G. Altarelli, G. Parisi, Nucl. Phys. **B126** 298 (1977).
- [18] W. Furmanski, R. Petronzio, Nucl. Phys. **B195** 237 (1982).
- [19] G. Altarelli, Ann. Rev. Nucl. Part. Sci. **39** 357 (1989).
- [20] D.W. Duke, J.F. Owens, Phys. Rev. **D30** 49 (1984).

Extracting the gluon density from the longitudinal structure function

N. Magnussen^a and G. A. Schuler^b

^aBergische Universität-Gesamthochschule Wuppertal, FRG

^bII. Institut für Theoretische Physik ¹, Universität Hamburg, FRG

Abstract

We discuss measurements of the longitudinal structure functions at small x in ϵp collisions at LEP/LHC energies. We outline how such measurements can be used to extract the gluon distribution. Statistical and experimental systematic errors are estimated and machine requirements for the measurements are outlined. We find that the gluon density can be probed in a range $6.3 \times 10^{-5} < x < 1.5 \times 10^{-3}$ at $25 < Q^2 < 150 \text{ GeV}^2$ accurately enough to distinguish between different gluon distributions.

¹Supported by Bundesministerium für Forschung und Technologie, 05 4HH 92P/3, Bonn, FRG.

Constraining the gluon distribution is one of the central themes of structure function measurements. The interest in the glue at future hadron colliders lies in the fact that gluon initiated subprocesses become more and more dominating as the cm energies of colliders increase. Then parton distribution functions are also being probed at smaller and smaller x values. The theoretical interest arises from the fact that starting from edges (modest values of x) which can be probed by perturbative means, one will eventually (as $x \rightarrow 0$) enter the nonperturbative regime which is the large Q^2 continuation of the Regge limit. It consists of dense partonic systems at weak coupling (Q^2 sufficiently large such that $\alpha_s(Q^2)$ is small) where, however, the effective interactions are strong due to the high numbers of partons involved. First estimates indicate that HERA might already enter the transition region between perturbative and nonperturbative physics, and possibly also the nonperturbative region at low Q^2 . One of the central virtues of the $e\mu$ option LEP/LHC is certainly its power of exploring the small x physics. In this note we investigate possible measurements of the longitudinal structure function F_L at small x and the prospects of extracting the gluon density.

We argue here that the gluon distribution can be measured in a range $6.3 \times 10^{-5} < x < 1.5 \times 10^{-3}$ at $25 < Q^2 < 150 \text{ GeV}^2$ in neutral current (NC) $e\mu \rightarrow eX$ collisions at the LEP/LHC collider. This optimism is based on the leading twist calculation of the inclusive (NC) $e\mu$ cross section to $O(\alpha_s)$ in the one-photon exchange approximation:

$$\frac{d^2\sigma}{dx dQ^2} = \frac{2\pi\alpha^2 Y_+}{x Q^4} \left\{ 2x F_1(x, Q^2) + \frac{2(1-y)}{Y_+} F_L(x, Q^2) \right\} \quad (1)$$

where $Y_+ = 1 + (1-y)^2$. We are interested in the very small x region but at still deep inelastic Q^2 (say, $Q^2 > 25 \text{ GeV}^2$). Then QCD at leading twist can be used to calculate the cross section². Furthermore, at small x values ($x < 10^{-3}$) weak contributions can safely neglected [3] since kinematics restricts Q^2 to small values as well, $Q^2 = xys$ with $y < 1$. In this approximation the longitudinal structure function in (1) is given by [2]

$$F_L(x, Q^2) = \frac{\alpha_s(Q^2)}{4\pi} \left[\frac{16}{3} I_F + 8 \sum_i \epsilon_i^2 I_G \right] \quad (2)$$

where I_F and I_G specify the contributions from the quark and gluon operators, respectively, and $\sum_i \epsilon_i^2$ represents a flavour sum over quark charges.

The crucial observations are now [4]:

- the dominant contribution to F_L comes from I_G at small x ;
- the integral I_G (I_F) is essentially proportional to the gluon distribution $g(x, Q^2)$ (the structure function $F_2(x, Q^2)$) at a rescaled value of x :

$$\begin{aligned} I_F &= \int_x^1 \frac{dz}{z} \left(\frac{x}{z} \right)^2 F_2(z, Q^2) \approx \frac{1}{2} F_2(2x) \\ I_G &= \int_x^1 \frac{dz}{z} \left(\frac{x}{z} \right)^2 \left(1 - \frac{x}{z} \right) G(z, Q^2) \approx \frac{1}{\theta} G\left(\frac{x}{\xi}\right) \end{aligned} \quad (3)$$

²We assume standard QCD evolution [2] to be valid over the whole considered range. Possible modifications at small x are discussed in [1].

where $G(x, Q^2) = xg(x, Q^2)$, $\xi = (1+\delta)/(3+\delta)$, $\theta = (3+\delta)(2+\delta)\xi^t$, and δ is a free parameter ($0 < \delta < 1$). We compare in Fig. 1 the exact and approximate expressions for I_G and I_F (3) for $\delta = 0.4$ using the parametrization B1 of [5]. We find excellent agreement over the whole x range $10^{-5} < x < 10^{-3}$. The approximation is, in fact, only slightly dependent on δ . Furthermore we can clearly see the dominance of I_G over I_F . Using the approximations (3) in (1) we can solve for the gluon density (assuming four flavour)

$$G(x, Q^2) = \frac{3}{5} \cdot 5.9 \left[\frac{3\pi}{4\alpha_s} F_L(0.4x, Q^2) - \frac{1}{2} F_2(0.8x, Q^2) \right] \quad (4)$$

Therefore the gluon distribution at small x can be extracted provided that the structure functions F_L and F_2 can be measured at somewhat smaller x values [4]. More precisely, two measurements of the cross sections at x and $2x$ yield the gluon density at $2.5x$. Thus the range where the gluon density can be extracted does not coincide with the exploratory range for F_2 : in the (x, Q^2) plane it is shifted towards larger values of x by the factor 5/2.

In order to extract $G(x, Q^2)$ at fixed x and Q^2 we must disentangle F_L and F_2 from the measurement of the inclusive cross section (1). Thus we have to vary y in (1) which via $Q^2 = xys$ implies we have to combine cross section measurements at different values of the cm energy \sqrt{s} . It is convenient to introduce the transverse and longitudinal cross sections $\sigma_{T,L}$ and to rewrite (1) as

$$\Gamma^{-1} \frac{d^2\sigma}{dx dQ^2} = \sigma_T(x, Q^2) + \epsilon \sigma_L(x, Q^2) \equiv \Sigma(x, Q^2) \quad (5)$$

where Γ is a kinematical factor representing the virtual photon flux. The resulting precision of separating σ_L from σ_T in (5) depends on the lever arm in the polarization ϵ of the exchanged virtual photon, $\epsilon \equiv 2(1-y)/Y_+$. Our choice of different machine setups is in addition determined by the kinematical restriction $0 < \epsilon < 1$, the requirement to minimize the number of different cm energies, and a cut $\epsilon > 0.32$ which we apply to avoid a region where radiative corrections are rapidly varying³. We assume that LEP/LHC can be operated with proton beam energies from 2 TeV to 8 TeV and with electron energies between 40 and 50 GeV. We take four different machine setups as specified in Table 1. The integrated luminosities listed in Table 1 for the three non standard machine setups can be accumulated in one month each at nominal LEP/LHC running conditions. For a given value of Q^2 we choose four subsequent x bins which differ by exactly a factor two (remember (4)) where the smallest x bin is determined by kinematics. With these we can extract the gluon distribution at three different x values.

Experimentally the cross section (5) is determined in bins of x and Q^2 through measurements of the scattered electron. The bin widths (see Tables 2 and 3) have to be chosen according to the achievable detector resolution. At LEP/LHC the energy resolution for the measured electrons will be at least as good as at HERA due to their higher energies. Thus if we choose the relative bin widths as in ref. [4] we can use their result for the resolution dependent point to point errors as a conservative estimate of the systematic errors of 3% achievable at LEP/LHC. Since the cross sections to be measured are steeply falling functions

³This is of course a crude approximation. A more complete treatment should rather include the radiative corrections. This is, however, beyond the scope of this study.

of the measured quantities x and Q^2 we choose the bin widths exponentially asymmetric with respect to the bin centers. The bin widths and the respective cross sections σ (1) and Σ (5) obtained for two different parton density parametrizations (set B1 and B2 of [5]) are listed in Tables 2 and 3. The quoted statistical errors were derived using the integrated luminosities of Table 1 and are small compared to the systematic uncertainties.

It is now straightforward to extract the gluon distributions from Tables 2 and 3. We summarize our results in Table 4 and Fig. 2. Our results are for the two Q^2 values $Q^2 = 50 \text{ GeV}^2$ and 100 GeV^2 . Similar results can be obtained in a range $25 < Q^2 < 150 \text{ GeV}^2$ with correspondingly shifted values of x . The statistical error and systematic error due to finite resolution are given separately in Table 4, and are added in quadrature in Fig. 2. In addition to this there is an overall luminosity error. Since measurements at various s values are combined, differing luminosity errors are potential sources of large point to point errors. However, as shown in [4], this uncertainty can be eliminated by normalising different s runs at higher x , where the cross section for a particular x, Q^2 is independent of the value of $F_L(x, Q^2)$ and very nearly independent of s . As a consequence the luminosity error introduces only an overall normalization error in the extracted gluon distribution, but does not introduce any error in its shape. In conclusion we find that accurate measurements of the longitudinal structure function at small x can be obtained, and hence we can expect to discriminate between different gluon distributions very well.

References

- [1] *Proceedings of the Small- x Workshop*, held at DESY, May 1990 (to be published in *Nucl.Phys.*, ed.A.Ali and J.Bartels).
- [2] V.N. Gribov and L.N. Lipatov, *Sov. Journ. Nucl. Phys.* **15**, 438 and 675 (1972); G.Altarelli and G.Parisi, *Nucl.Phys.* **126**, 297(1977); Yu.L.Dokshitser, *Sov.Phys.JETP* **46**, 641(1977).
- [3] G. Ingelman, *Structure function measurements at LEP/LHC*, these proceedings.
- [4] A.M. Cooper-Sarkar et al., *Z. Phys.* **C39** (1988) 281, and in proceedings of the HERA workshop, DESY, Hamburg 1987.
- [5] J.G. Morfin and Wu-Ki Tung, Fermilab-Pub-90/74 (1990).

Figure captions

Figure 1 Integrals I_F and I_G (3) versus x at $Q^2 = 50 \text{ GeV}^2$ for the parton density parametrization B1 of ref.[5].

Figure 2 The gluon distributions B1 and B2 of ref.[5] superimposed on the measurements expected at LEP/LHC, for $Q^2 = 50 \text{ GeV}^2$. The error bars shown indicate the size of the systematic and statistical errors expected for the integrated luminosities given in Table 1.

$\vec{p}_p \times \vec{p}_e$ [GeV/c x GeV/c]	Polarization ϵ of the exchanged virtual photon								$\int L dt$ [pb $^{-1}$]	
	$Q^2 = 50$ [GeV 2]		$Q^2 = 100$ [GeV 2]		$Q^2 = 50$ [GeV 2]		$Q^2 = 100$ [GeV 2]			
	$x = 0.00005$	$x = 0.0001$	$x = 0.0001$	$x = 0.0002$	$x = 0.0002$	$x = 0.0004$	$x = 0.0004$	$x = 0.0008$		
8000 x 50	0.6575		0.9337		0.9857		0.9967		1000	
6000 x 50	0.3243		0.8705		0.9733		0.9940		100	
4000 x 50			0.6575		0.9337		0.9857		100	
2000 x 40					0.4175		0.8887		100	

Table 1: Polarization ϵ of the virtual photon exchanged at LEP/LHC for the given proton and electron beam momenta at the specified values for Q^2 and x . The integrated luminosities are the values used in the calculations.

$Q^2 = 50 \text{ GeV}^2$	$x = 0.00005$		$x = 0.0001$	
	Low s , $\epsilon = 0.3243$	High s , $\epsilon = 0.6575$	Low s , $\epsilon = 0.6575$	High s , $\epsilon = 0.9337$
x-bin	$(4.5 - 5.56) \cdot 10^{-5}$	$(4.25 - 5.88) \cdot 10^{-5}$	$(0.85 - 1.18) \cdot 10^{-4}$	$(0.85 - 1.18) \cdot 10^{-4}$
Q^2 -bin	$(47 - 53.2) \text{ GeV}^2$	$(45 - 55.6) \text{ GeV}^2$	$(45 - 55.6) \text{ GeV}^2$	$(45 - 55.6) \text{ GeV}^2$
$xg(x, Q^2)$	B1 B2	B1 B2	B1 B2	B1 B2
$\Delta\sigma$ in this bin	73.7 pb 401.2 pb	250.5 pb 1276.0 pb	222.1 pb 909.7 pb	318.8 pb 1246.0 pb
statistical error on Σ	1.2%	0.5%	0.2%	0.9%
systematic error on Σ	3.0%	3.0%	3.0%	3.0%
$\Sigma(10^{-3} \text{ GeV}^{-2})$	6.00 32.95	7.05 35.83	6.16 25.54	6.93 27.09
	$x = 0.0002$		$x = 0.0004$	
	Low s , $\epsilon = 0.4175$	High s , $\epsilon = 0.9857$	Low s , $\epsilon = 0.8887$	High s , $\epsilon = 0.9967$
x-bin	$(1.8 - 2.22) \cdot 10^{-4}$	$(1.7 - 2.35) \cdot 10^{-4}$	$(3.4 - 4.71) \cdot 10^{-4}$	$(3.4 - 4.71) \cdot 10^{-4}$
Q^2 -bin	$(47 - 53.2) \text{ GeV}^2$	$(45 - 55.6) \text{ GeV}^2$	$(45 - 55.6) \text{ GeV}^2$	$(45 - 55.6) \text{ GeV}^2$
$xg(x, Q^2)$	B1 B2	B1 B2	B1 B2	B1 B2
$\Delta\sigma$ in this bin	62.2 pb 214.6 pb	333.6 pb 1048.1 pb	228.8 pb 594.9 pb	320.1 pb 821.0 pb
statistical error on Σ	1.3%	0.7%	0.2%	0.1%
systematic error on Σ	3.0%	3.0%	3.0%	3.0%
$\Sigma(10^{-3} \text{ GeV}^{-2})$	5.01 17.29	6.24 19.61	5.34 13.89	5.54 14.21

Table 2: Bin-widths, cross sections, statistical and systematic errors on Σ and the values for Σ for the two different parton density parametrizations B1 and B2 of ref.[5] for $Q^2 = 50 \text{ GeV}^2$.

$Q^2 = 100 \text{ GeV}^2$	$x = 0.0001$				$x = 0.0002$			
	Low $s, \epsilon = 0.3243$		High $s, \epsilon = 0.6575$		Low $s, \epsilon = 0.6575$		High $s, \epsilon = 0.9337$	
x-bin	$(0.9 - 1.11) \cdot 10^{-4}$		$(0.85 - 1.18) \cdot 10^{-4}$		$(1.7 - 2.35) \cdot 10^{-4}$		$(1.7 - 2.35) \cdot 10^{-4}$	
Q^2 -bin	$(94 - 106.4) \text{ GeV}^2$		$(90 - 111.1) \text{ GeV}^2$		$(90 - 111.1) \text{ GeV}^2$		$(90 - 111.1) \text{ GeV}^2$	
$xg(x, Q^2)$	B1	B2	B1	B2	B1	B2	B1	B2
$\Delta\sigma$ in this bin	43.6 pb	163.7 pb	144.0 pb	513.1 pb	125.6 pb	367.4 pb	177.0 pb	500.7 pb
statistical error on Σ	1.5%	0.8%	0.3%	0.1%	0.9%	0.5%	0.2%	0.1%
systematic error on Σ	3.0%	3.0%	3.0%	3.0%	3.0%	3.0%	3.0%	3.0%
$\Sigma(10^{-3} \text{ GeV}^{-2})$	3.58	13.15	4.08	14.45	3.53	10.31	3.87	10.91
	$x = 0.0004$				$x = 0.0008$			
	Low $s, \epsilon = 0.4175$		High $s, \epsilon = 0.9857$		Low $s, \epsilon = 0.8887$		High $s, \epsilon = 0.9967$	
x-bin	$(3.6 - 4.44) \cdot 10^{-4}$		$(3.45 - 4.71) \cdot 10^{-4}$		$(6.8 - 9.41) \cdot 10^{-4}$		$(6.8 - 9.41) \cdot 10^{-4}$	
Q^2 -bin	$(94 - 106.4) \text{ GeV}^2$		$(90 - 111.1) \text{ GeV}^2$		$(90 - 111.1) \text{ GeV}^2$		$(90 - 111.1) \text{ GeV}^2$	
$xg(x, Q^2)$	B1	B2	B1	B2	B1	B2	B1	B2
$\Delta\sigma$ in this bin	35.3 pb	88.0 pb	181.6 pb	424.7 pb	123.1 pb	243.8 pb	171.1 pb	335.7 pb
statistical error on Σ	1.7%	1.1%	0.2%	0.2%	0.9%	0.6%	0.2%	0.2%
systematic error on Σ	3.0%	3.0%	3.0%	3.0%	3.0%	3.0%	3.0%	3.0%
$\Sigma(10^{-3} \text{ GeV}^{-2})$	2.84	7.09	3.40	7.94	2.87	5.69	2.96	5.81

Table 3: Bin-widths, cross sections, statistical and systematic errors on Σ and the values for Σ for the two different parton density parametrizations B1 and B2 of ref.[5] for $Q^2 = 100 \text{ GeV}^2$.

$Q^2/[GeV^2]$	Input $xg(x, Q^2)$	$x = 0.000125$	$x = 0.00025$	$x = 0.0005$	$x = 0.001$
50	B1	$17.7 \pm 1.4 \pm 0.6$	$15.8 \pm 1.1 \pm 0.5$	$12.8 \pm 0.7 \pm 0.4$	
	B2	$46.0 \pm 3.2 \pm 1.6$	$31.0 \pm 1.9 \pm 1.1$	$24.0 \pm 1.4 \pm 0.8$	
100	B1		$18.3 \pm 2.3 \pm 0.6$	$15.2 \pm 1.8 \pm 0.5$	$12.9 \pm 1.2 \pm 0.4$
	B2		$34.7 \pm 4.5 \pm 1.3$	$26.4 \pm 2.7 \pm 0.9$	$19.3 \pm 2.0 \pm 0.6$

Table 4: Values of $xg(x, Q^2)$ extracted at the specified values for Q^2 and x for the two different input gluon distributions according to the parametrizations B1 and B2 of ref.[5]. The errors given are the statistical error, using the integrated luminosities given in table 1, and the estimated systematic error due to finite detector resolution, respectively.

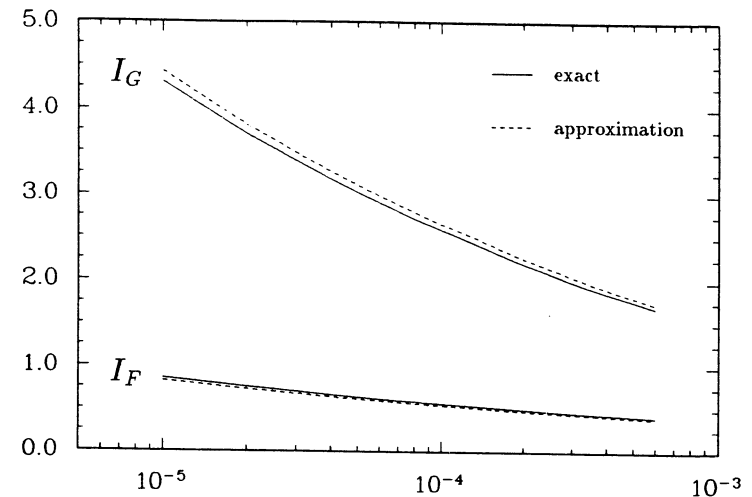


Fig. 1

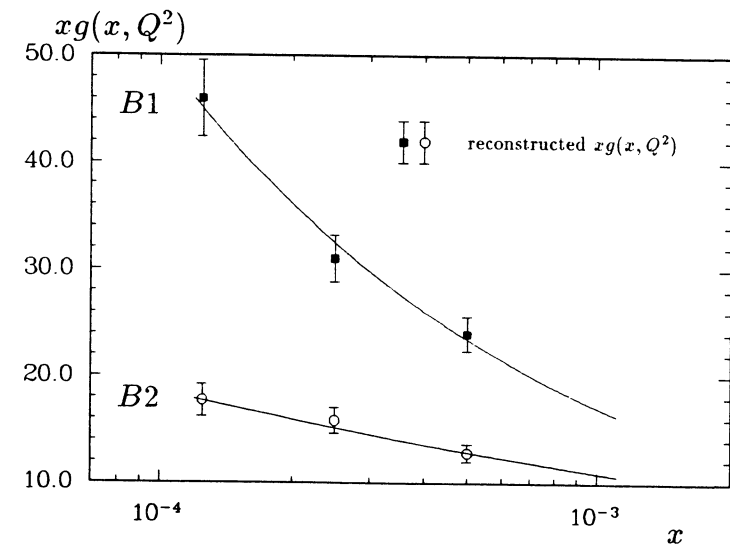


Fig. 2

Small-x Physics at LEP/LHC

J. Bartels and G. A. Schuler¹

II. Institut für Theoretische Physik, Universität Hamburg, Germany

ABSTRACT

The small- x behavior of deep inelastic structure functions in QCD is discussed. After a brief review of theoretical ideas we describe numerical estimates which show that LEP/LHC will be extremely useful for distinguishing between "standard QCD" and "new" physics in the low- x region. We also discuss which measurements will be useful for unravelling the new features of small- x physics.

1 Theoretical Ideas

Deep Inelastic scattering of electrons on protons (DIS) provides the classical test of our parton picture of hadrons and, hence, of QCD at short distances. With the advent of HERA (anticipated for the summer of 1991) we are entering new kinematical regions in both $Q^2 = -q^2$ and Bjorken- $x = Q^2/(2pq)$. LEP/LHC will further increase the kinematically accessible region by more than an order of magnitude. This talk will focus on the small- x region, and we shall try to answer the question to what extent LEP/LHC will see new physics in this region (for a collection of related papers see [1]).

Fig. 1 shows the connection between different high energy limits, in particular the Bjorken limit ($Q^2 \rightarrow \infty$, $x_{\text{Bjorken fixed}}$) and the Regge limit ($s \rightarrow \infty$, $Q^2 \approx Q_0^2$ fixed). The small- x region above the Bjorken limit is not far from the Regge limit: it is the continuation of the Regge limit towards large Q^2 , and one therefore expects ultimately to face the same dynamics as in the Regge limit. For the discussion of the small- x limit of DIS scattering it is useful to use the variables ($\beta_0 = (11N_C - 2n_f)/3$):

$$\xi = \ln \ln \frac{Q^2}{\Lambda^2}, \quad y = \frac{8N_c}{\beta_0} \ln \frac{1}{x}. \quad (1.1)$$

¹Supported by Bundesministerium für Forschung und Technologie, 05 4HH 92P/3, Bonn, FRG.

The theoretical situation of these high energy limits can be summarized as follows. The Bjorken limit (in the horizontal direction of Fig. 1) is dominated by the light cone behavior of operator products and can therefore reliably be described by perturbation theory [2]. In particular, the renormalization group equation predicts [3,4,5] the Q^2 dependence of the moments of the structure functions. The Regge limit (in the vertical direction of Fig. 1 at low Q_0^2), on the other hand, has a strong nonperturbative component: for small momentum transfer scattering of hadrons is dominated by large transverse distances (impact parameter) and, hence, sensitive to the behavior of QCD at large distances. For the moment, no final solution to the behavior of QCD in this limit is at hand, although important work has been done [6,7,8,9,10,11,12]. In between these two regions lies the small- x limit of deep inelastic scattering (marked by the shaded area in Fig. 1): it probes the transition from the perturbative Bjorken limit to the nonperturbative region which extends the Regge limit towards large Q^2 , and it thus provides the opportunity to test theoretical ideas about the onset of nonperturbative dynamics in QCD, the change from the language of quarks and gluons to that of composite hadrons. The theoretical issue to be discussed in this talk is the question how much and what we know about this transition region.

Let us first recapitulate what goes wrong with the standard QCD evolution program when x is taken to be very small. The small- x behaviour of F_2 is dominated by gluon production, and it is of the form:

$$F(x, Q^2) \approx \frac{\exp(\sqrt{2(\xi - \xi_0)y})}{\sqrt{2\pi}\sqrt{2(\xi - \xi_0)}} \quad (1.2)$$

From this it follows that the total cross section for the scattering of a virtual photon off the proton would rise faster than any power of $\ln \frac{1}{x} \approx \ln \frac{s}{Q^2}$. Unitarity, on the other hand, requires that the growth cannot be faster than the square of the hadron radius:

$$\sigma_{tot}^{\gamma^*} = \frac{4\pi^2\alpha}{Q^2} F(x, Q^2) \leq 2\pi R(s)^2, \quad R(s) \approx const \cdot \ln s. \quad (1.3)$$

Somewhere in the small- x region, therefore, the standard QCD description has to become invalid.

That something new has to come in at small values of x can be seen rather easily within the parton picture [13]. The standard QCD-evolution framework can be viewed as a cascade of partonic decay processes inside the nucleon: the photon picks a quark with momentum fraction x and virtuality Q^2 (which is approximately equal to the transverse momentum squared or the inverse square of the transverse radius). Such a quark represents the final result of a chain of subsequent decay processes, in course of which the partons become slower and, at the same time, gain a larger virtuality. This picture is nothing but a space-time interpretation of the QCD-ladder diagrams shown in Fig. 2a. In the transverse (impact parameter) plane the same situation is illustrated in Fig. 3: partons at the lower end of the ladder have still a rather low momentum scale and hence appear as "fat" in Fig. 3a. Partons at the upper end have larger virtuality and are much "thinner" (Fig. 3b and c). The number (or density) of the partons is determined by the structure

functions: according to eq.(1.2) which represents the "standard QCD evolution", the number of small- x partons increases very fast. Hence, in the transverse plane their density becomes high and it becomes more and more probable that they will interact among each other. In the standard QCD framework only one type of interaction has been taken into account, namely decay processes which cause the parton density to increase. It therefore appears to be extremely suggestive to expect also other interaction processes, e.g. recombination or annihilation processes which might balance the number of partons or even decrease their density. A simple argument (Fig. 4) may illustrate how such partonic annihilation processes will modify the QCD evolution equations. In the standard scenario (Fig. 4a) a change of parton densities is obtained by a splitting of the incoming parton into two outgoing partons. Such a change δF is proportional to the probability of finding the initial parton, i.e. we have a linear evolution equation. Recombination processes (Fig. 4b), on the other hand, must be proportional to the probability of finding two incoming partons. Most naively, this probability could be assumed to be proportional to the square of the probability of having one parton: one then obtains the nonlinear term indicated in Fig. 4b. The strength of this nonlinear term also depends upon the descent of the two incoming partons: if they originate from one common "parent" parton (e.g. one valence quark), it seems more likely that they have a chance to recombine again than for the case where they come from different valence quarks which are spatially separated. In the first case, the strength would be proportional to the inverse square of the quark radius, in the latter to that of the hadron.

A possible result of these creation and annihilation processes could be a "saturation" as shown in Fig. 5: the "true" QCD structure function no longer increases at small x , it approaches a constant value (up to powers of $\ln \frac{1}{x}$). Such a behaviour would also match the observed slow increase of the hadronic total cross section at low Q_0^2 in the Regge limit. Strong-field calculations within QED and QCD [14] indeed point into this direction.

This very qualitative description of small- x physics allows, in fact, a first estimate of the boundary between perturbative and nonperturbative physics in the ξ, y plane (Fig. 1). Consider the quantity

$$W(x, Q^2) = \frac{\alpha_s(Q^2)}{Q^2} \frac{F(x, Q^2)}{R^2} \approx \frac{\text{const}}{Q^2 \ln Q^2} \frac{\exp \sqrt{2\xi} y}{y^2} \quad (1.4)$$

which measures the probability of partons to interact with each other. In order that the standard QCD cascade picture works, this probability should be less than one: neglecting all nonleading terms, this condition can be approximated by

$$y \leq \text{const} \cdot \exp 2\xi \quad (1.5)$$

which is a very crude approximation to the upper border line of the transition region in Fig. 1.

In order to make these ideas more quantitative, one has to analyse sets of QCD Feynman diagrams. According to Gribov, Levin, and Ryskin [13] and Mueller and Qiu [15] who have done such an investigation ten years ago, the first corrections to the standard QCD ladder diagrams (Fig. 2a) are diagrams of the type shown in Fig. 2b (so-called fan diagrams). The upper ladder branches into two ladders which

at the lower end couple to the nucleon (in our picture only one quark line is shown; other possibilities include the coupling to two different quarks). The branching vertex (triple-ladder vertex) consists of the sum of several (nonplanar) diagrams, only one of which is shown. Taking the energy discontinuity of this set of diagrams in all possible ways, one obtains, among other contributions, the recombination process shown in Fig. 4b. However, since this set of diagrams allows for other energy cuts, the recombination process in Fig. 4 must necessarily be accompanied by other contributions. A careful analysis of all these terms leads to the well-known Abramowski-Gribov-Kancheli rules (AGK-rules) [16]. In particular, the sum of all terms carries a minus sign, relative to the ladder diagrams which correspond to the standard evolution equations. Clearly, this minus sign is highly desirable to fight the strong increase of the structure function at small x .

In the approximation where only leading powers in both $\ln Q^2$ and $\ln \frac{1}{x}$ are kept (DLA approximation), the behavior of Fig. 2 is rather simple. If we denote by $F_0(y, \xi)$ the expression for the left part of Fig. 2, then the first correction is given by:

$$- \text{const} \int^y dy_1 \int^\xi d\xi_1 F_0(y - y_1, \xi - \xi_1) V(\xi_1) F_0^2(y_1, \xi_1) \quad (1.6)$$

where

$$V(\xi) = \frac{3\pi^2 Q_0^2}{4\beta_0 \Lambda^2} \exp\{-e^\xi - \xi\} \equiv C \exp\{-e^\xi - \xi\} \quad (1.7)$$

stands for the triple ladder vertex.

In order to proceed further, Gribov, Levin, and Ryskin made an assumption concerning the coupling of $n \geq 2$ ladders to the hadron: this coupling is assumed to be proportional to the n -th power of the single-ladder coupling. As a consequence, the probability of finding two gluons (at low momentum Q_0^2) with momentum fractions x_1 and x_2 is proportional to $g(x_1, Q_0^2) \cdot g(x_2, Q_0^2)$. This assumption then allows to find an equation for the sum of all fan diagrams, the GLR equation. It is a nonlinear integro-differential equation. In its simplest form, the DLA approximation, it is obtained by generalizing eq.(1.6) and performing the sum over all ladders:

$$F(y, \xi) = F_G(y, \xi) - \int_0^y dy' \int_{\xi_0}^\xi d\xi' F_0(y - y', \xi - \xi') C \exp(-e^{\xi'} - \xi') F^2(y', \xi'). \quad (1.8)$$

where C stands for the constant factors of (1.7), and F_G denotes the sum of QCD ladder diagrams with some initial distribution $G(y)$. The more accurate form of the equation is given as:

$$\frac{\partial \phi(x, q^2)}{\partial \ln \left(\frac{1}{x} \right)} = \int \hat{K}(q^2, q'^2) \phi(x, q'^2) \frac{4N\alpha_s(q'^2)}{4\pi} dq'^2 - \frac{1}{4\pi R^2} \left(\frac{\alpha_s(q^2)}{4\pi} \right)^2 V \phi^2(x, q^2). \quad (1.9)$$

Here $\phi = \frac{\partial F}{\partial Q^2}$, R denotes the transverse radius of the hadron (or quark), and V stands for the triple ladder vertex, evaluated more accurately than in (1.7), namely in the semiclassical approximation.

Among the few features that are known [13,17] about analytic solutions to these nonlinear equations, we only mention one, namely the existence of a well-defined line in the x, Q^2 plane which marks the beginning of the nonperturbative

regime. It is approximately of the form

$$y = \frac{1}{4} \left(\ln \frac{Q^2}{\Lambda^2} \right)^2 + \text{const}, \quad (1.10)$$

and in Fig. 1 it is the upper boarder line of the transition region. The exact position of this "critical" line depends upon the initial conditions and can be determined only numerically. Above this line, the GLR equation is no longer valid, and the dynamics is expected to be very similar to that of the Regge limit.

2 Numerical Estimates

In the context of LEP/LHC (and also HERA) one of the most important question seems to be: where in the (x, Q^2) -plane lies the transition region, i.e. that region for which the GLR equation should replace the standard QCD evolution scheme? To answer this one has to solve the GLR-equations numerically. So far there exist two calculations [17,19]. They both solve the DLA approximation (1.8), but inside the QCD gluon ladders they use the full Altarelli-Parisi splitting functions for the rungs.

As we have explained before, the numerical solution depends upon two input quantities, the initial y -distribution at some low Q_0^2 and the strength C of the nonlinearity. [17] therefore uses two different input distributions, and both papers vary the parameter C by a factor of 10 or 2.5, respectively. Predictions for the (momentum weighted) gluon distribution are shown in Figs. 7 and 8, for F_2 in Fig. 9. In Fig. 7, the full curves correspond to the nonlinear evolution: the upper ones to the (steeper) Morfin-Tung initial [20] distribution, the lower ones to the (almost flat) Eichten-Hinchcliffe-Lane-Quigg [21] distribution. The dashed and the dotted curves show the corresponding results of the standard (linear) evolution programs for two different values of C : the lower curves belong to the larger value eq. (1.7), for the upper ones C is divided by ten. The main point to be emphasized is the fact that e.g. for $Q^2 = 10 \text{ GeV}^2$, deviations are visible already at x close to 10^{-2} . For the larger of the two C -values this effect is, of course, more pronounced than for the smaller one. Fig. 6 shows an approximate estimate of the transition region. The critical curve which marks the boundary between the perturbative and the nonperturbative domains can be written as

$$Q_c^2(x) = Q_0^2 + \Lambda^2 \exp \left(c_1 \sqrt{\ln \frac{x_0}{x}} \right). \quad (2.11)$$

Levin and Ryskin [22] estimated $\Lambda = 52 \text{ MeV}$, $Q_0^2 = 2 \text{ GeV}^2$, $c_1 = 3.56$, and $x_0 = 1/3$, whereas in [17] the parameters are $\Lambda = 212 \text{ MeV}$, $Q_0^2 = 0$, $c_1 = 3.39$, and $x_0 = 1/15.9$. The two estimates are shown as curves 1 and 2 in Fig. 6, respectively. The region of validity of the standard evolution is estimated to lie below the tangent in the (y, ξ) -plane to the boundary line at $\xi = \xi_0$. This line is shown as curve 3 in Fig. 6.

Figs. 8 and 9 show results of [19] for $xg(x, Q^2)$ and $F_2(x, Q^2)$, respectively. In this case the input distribution is again a rather steeply rising function in y ; its analytic form has been motivated by the analysis of [24]. Deviations between the linear and the nonlinear evolution start at x between 10^{-2} and 10^{-3} , quite

in agreement with the findings of [17]. [19] also presents results for F_2 : it is, however, not clear whether this calculation takes into account certain difficulties which have been pointed out in [25]: once the gluon structure function has been calculated from the GLR-equation, the quark loop which couples the gluons to the deep inelastic photon, can no longer be used in the leading- Q^2 approximation.

The important message of these two papers seems to be that, provided the x -distribution at low Q^2 is as steeply rising as it was assumed in most of these calculations, already HERA will enter the region where the "new" physics is at work (to be more precise, since at these relatively small values of $Q^2 \approx 10 \text{ GeV}^2$ the "intermediate" region between perturbative and nonperturbative QCD is very narrow, HERA not only enters this transition region but also reaches into the domain of nonperturbative QCD). However, this does not necessarily imply that it will be possible to conclude from HERA measurements of structure functions beyond any doubt, whether one sees this new physics or not. Due to our ignorance of the correct x -distribution at low Q_0^2 which always enters the calculation as an input, it is possible that the measurement of some flat structure function can be described very well by the standard evolution, using some modified input function. Conversely, a continuing rise of the structure function at low x is not necessarily a reliable indication that the "new physics" is not yet at work. The best way to distinguish is the comparison of evolution in Q^2 : linear and nonlinear evolution equations predict different Q^2 -dependence. In order to extract this from data we need a range in Q^2 as large as possible: this is the point where LEP/LHC will be most powerful. By offering, at, say, $x = 10^{-4}$, a substantially larger range in Q^2 than HERA, it will be possible to distinguish much better between "standard" and "new" physics than at HERA.

It will still be desirable to look for experiments which are specially designed to probe the "new physics". So far, two such measurements have been proposed. The one is due to A.Mueller [14] and refers to the "hot spots", the other one uses the diffractive dissociation of the photon and has been proposed by Ryskin [22]. Returning to the discussion on "saturation" in Part I of this talk, the density of gluons in the transverse plane may not be uniform, i.e. there may be regions inside the nucleon (Fig. 3) which are more densely populated by soft gluons than others. Since the structure function F_2 ("total photon hadron cross section") measures the parton density, averaged over the full size of the hadron, one needs to look at exclusive final states which measure the distribution of partons inside limited subregions of the hadron (Fig. 3b). Such an experiment is illustrated in Fig. 10: measure the cross section of jets which carry the momentum fraction x (not to be confused with the usual Bjorken x_B which belongs to the photon at the upper end) and the momentum scale (transverse momentum squared) k_\perp^2 . The latter should be not much smaller than Q^2 , the mass of the photon: $R_{\text{parton}}^2 \approx \frac{1}{Q^2}$ is the transverse radius of the parton struck by the photon, and $R_{\text{jet}}^2 \approx \frac{1}{k_\perp^2}$ is the square of the average transverse distance, by which the jet is separated from this parton. If $k_\perp^2 \leq Q^2 \ll Q_0^2$, then $R_{\text{parton}}^2 \leq R_{\text{jet}}^2 \ll R_{\text{hadron}}^2$, and this process explores the parton cloud of diameter R_{jet} around the struck parton. The cross section should be measured as a function of the ratio $\frac{x_B}{x}$, and the region of interest is defined as

$x_B \ll x$. The cross section for this process is, in the QCD-parton model, given by:

$$\frac{k_\perp^2 x d(\nu W_2)}{dx dk_\perp^2} = C \alpha(Q^2) \left(x g(x, k_\perp^2) + \frac{4}{9} (x q(x, k_\perp^2) + x \bar{q}(x, k_\perp^2)) \right) F\left(\frac{x_B}{x}, Q^2, k_\perp^2\right) \quad (2.12)$$

where C is a normalization factor, $g(x, q^2)$ and $q(x, q^2)$ are the quark and gluon distribution functions, resp., and $F\left(\frac{x_B}{x}, Q^2, k_\perp^2\right)$ stands for the sum of QCD ladders above the jet, evaluated in the limit $\frac{x_B}{x} \rightarrow 0$ (this is one of the places where the so-called "Lipatov Pomeron" [10] could be tested). This formula predicts a steep rise as $\frac{x_B}{x}$ becomes small:

$$F\left(\frac{x_B}{x}, Q^2, k_\perp^2\right) \approx C \frac{\exp\left(\frac{12\alpha(Q^2)}{\pi} \ln 2 \ln \frac{x_B}{x}\right)}{\sqrt{\ln \frac{x}{x_B}}} \quad (2.13)$$

and a deviation from this would be indicative of "local saturation", i.e. the existence of a "hot spot". Corrections to this formula can (and should) be calculated: these are not fan-diagrams but reggeon diagrams, since both Q^2 and k_\perp^2 are of the same order.

Another strong prediction based upon the existence of such "hot spots" has been made by Ryskin [26]. Instead of the "one-jet inclusive cross section" of Fig. 10 one considers the photon diffractive dissociation processes shown in Fig. 11 (its connection with the Pomeron structure function [28,29,30] has been discussed in [27]): there is a rapidity gap between the proton at the lower end and the missing mass cluster above. As an example, this missing mass final state could consist of three jets, originating from $q\bar{q}g$. The final states are further restricted by the requirement that the jet in the direction of the Pomeron should have a controllable k_\perp . It is then the dependence upon this k_\perp which differentiates between "saturation" and "standard" QCD behavior: with saturation the cross section should be substantially smaller, and for the integrated cross section there could be a difference up to a factor of one hundred!

There are clearly more measurements that might be suitable to test the presence of the "new physics" described in the this talk: this will not be discussed here and should be a topic of further theoretical work.

3 Measurements at small- x

In this section we report about the prospects to actually measure structure functions and parton distribution functions at LEP+LHC in the small- x region. We will discuss measurements of F_2 as well as various ways to extract the gluon densities. All analyses performed so far use the conventional approach in the evolution of the parton densities. This is certainly sufficient to estimate the limits on the explorable regions in x and Q^2 for a given reaction. Our compilation of the various kinematic ranges allows an overview of the overlaps and the gaps in the determination of parton distributions. Furthermore, first estimates on prospects to observe new physics can be drawn, e.g. one can find how much of the evolution in Q^2 may be seen at a given values of x . Clearly, new calculations of cross sections and differential distributions based on the improved evolution scenario are necessary to eventually set limits on the quantities parametrizing the new effects.

We start by discussing the structure function F_2 which is obtained in inclusive lepton scattering from a measurement of the differential cross section $d^2\sigma/dxdQ^2$. Assuming the validity of the standard evolution one predicts large rates for (neutral current) deep inelastic ep scattering in the small- x region at LEP/LHC[31]. At small- x the kinematical variables x and Q^2 and thereby $d^2\sigma/dxdQ^2$ can well be reconstructed via a measurement of the scattered electron. The kinematic region accessible to (possible) experiments is investigated in detail in ref.[32]. Here we show in Fig. 12 (label F_2) the region which is accessible in inclusive DIS via measurements of the scattered electron, if LEP/LHC is run with 50 GeV electrons on 8000 GeV protons. Changes of the beam energies will shift the accessible region accordingly[32]. As one can see from Fig. 12, LEP/LHC at $\sqrt{s} = 1.26$ TeV allows measurements down to $x \approx 6 \times 10^{-6}$ at still high Q^2 ($Q^2 > 10$ GeV 2). At a given value of x about one order of magnitude in Q^2 can be covered. This range is extended if LEP/LHC is run at lower and higher cms energies. From the relation $Q^2 = xyz$ with $y < 1$ it becomes clear that small- x values imply also small values for Q^2 . Thus for $x < 10^{-3}$ weak effects can be neglected[31] and the measurements at small- x are then sensitive to the electromagnetic structure function $F_2^{em} = \sum_f e_f^2 [q_f(x, Q^2) + \bar{q}_f(x, Q^2)]$. Thus it is the total quark sea which is being probed. The prospects of unfolding individual components of the (sea) quark distributions are studied in [31].

An ep collider offers several ways to measure the gluon density. Inclusive electron scattering is sensitive to the gluon either via the Q^2 evolution of a (singlet) structure function or via the longitudinal structure function $F_L(x, Q^2)$. Among the exclusive processes heavy quark production appears most promising to extract the gluon density. The interest in the gluon distribution arises not only from its increasingly importance for predicting cross sections and distributions at hadron colliders at higher energies. As mentioned above, screening corrections are expected to set in earlier in x for the gluon density than for the quark densities. Moreover, it is the gluon which "drives" the evolution equations at small- x .

There are several problems in the determination of the gluon density from the Q^2 evolution of F_2 : (i) the restricted Q^2 -range at fixed- x (c.f. Fig. 12); (ii) the unknown value of Λ_{QCD} which has to be fitted together with the gluon density (see e.g. [33]); and (iii) the validity of the evolution equations. It is well known that DIS data alone do not allow to fix the parameters of the gluon distribution very precisely (even if the standard evolution is assumed to be valid), and Drell-Yan data (and possibly direct-photon data) are usually added to obtain more severe constraints (see e.g. [34]). If screening corrections are taken into account then the use of an improved evolution equation requires the fit of at least one more parameter (e.g. the quantity C in eq. 1.7). Further development of computer algorithms for the nonlinear evolution equations is needed before reliable estimates on gluon determination from this method can be made. Extrapolating present day limits [34] we can crudely estimate a range

$$0.0005 < x < 0.03 \quad , \quad Q_0^2 \approx 5 \text{ GeV}^2 \quad (3.14)$$

in which the gluon distribution $G(x, Q_0^2)$ at an input scale Q_0^2 might be determined. This range is shown as dashed line labeled $\partial F_2 / \partial \ln Q^2$ in Fig. 12.

Another way of determining the gluon density makes use of data in the $25 \lesssim Q^2 \lesssim 150$ GeV 2 region[33]. At small- x , the ratio $R = \sigma_L/\sigma_T$ in DIS is expected to

be relatively large due to the contribution to the longitudinal structure function F_L from the glue: the gluon initiated contribution I_G dominates over the quark contribution I_F in $F_L(x, Q^2) = 4\alpha_s(Q^2)/(3\pi)[I_F + 5/3 I_G]$. In fact, at small- x , the value of F_L is essentially proportional to the gluon distribution at a re-scaled value of x [35]. An accurate measurement of F_L in this region is thus a direct probe of the gluon distribution. Experimentally, F_L can be disentangled from the differential cross section at fixed x and Q^2 by combining measurements at various cms energies. Thus this method yields the gluon density $G(x, Q^2)$ differential in x and Q^2 . The corresponding study for LEP/LHC was performed in [36]. The exploratory kinematic range was estimated to

$$\begin{aligned} 6.3 \times 10^{-5} < x < 2.5 \times 10^{-4} & \quad \text{at} \quad Q^2 = 25 \text{ GeV}^2 \\ 3.8 \times 10^{-4} < x < 1.5 \times 10^{-3} & \quad \text{at} \quad Q^2 = 150 \text{ GeV}^2 \end{aligned} \quad (3.15)$$

and is shown in dash-dots labeled F_L in Fig. 12. Within this region different gluon parametrizations should clearly be distinguishable. This is illustrated in Fig. 13 which shows two different gluon distributions superimposed on measurements expected at LEP/LHC. The error bars include both statistical and systematic errors. To arrive at the region (3.15), it was assumed in [36] that LEP/LHC is run at four different machine set ups, ranging from $E_p \times E_e = 2000 \times 40 \text{ GeV}^2$ to $8000 \times 50 \text{ GeV}^2$ with an integrated luminosity of 100 pb^{-1} each.

Parton densities can also be measured in exclusive final states. Here one faces two problems. First, in contrast to lepton inclusive scattering, the (momentum) scale argument μ of the parton densities is not uniquely defined. In quasi-real photoproduction, for example, Q^2 is much smaller than 1 GeV^2 . The scale μ that governs high p_T reactions is then \hat{s} or p_T^2 rather than Q^2 . Second x_p , the momentum fraction of the struck parton is no longer equal to Bjorken- x , $x_p > x$ in general. The procedure to measure a specific parton density is then the following one: First one has to isolate those events which are sensitive to the desired distribution. Then one tries to reconstruct kinematical variables which constraint x_p and μ .

Thus far only the prospects of measuring the gluon density have been considered [37]. Because of the large rates, the clean (leptonic) signatures, and the fact that the leading order production mechanism is photon-gluon fusion, the production of heavy quarks looks most promising. In [37] a systematic investigation of gluon extraction from heavy quark production in ep collisions has been performed. Here it is shown that the gluon density can successfully be reconstructed from heavy quark production in ep collisions. The analysis is based on complete (signal and background) events and, in the case of J/Ψ , it includes a full detector simulation. The reconstruction of the event kinematics is outlined, in particular uncertainties due to insufficient known fragmentation properties of the proton remnants and photon spectator jet are discussed. Higher order corrections on the event topology are approximately taken into account by multiple gluon radiation in a parton cascade approach. Only information obtainable from a main detector is used. In a previous study on gluon extraction from J/Ψ events at HERA[38] the information on the scattered electron coming from a luminosity monitor measurement has been used. This is not done in [37] since it is not clear whether such a device will work with the high rates expected at LEP/LHC. Furthermore it was found that with the main detector a much larger range in x is accessible, including the range

reachable via the luminosity measurement. The outcome is that one will obtain measurements of $d\sigma/dx_g$ which are accurate enough to extract the gluon density, and hence to distinguish between different parametrizations.

In general, unknown higher order corrections introduce systematical (theoretical) uncertainties. For the purpose of extracting the gluon density along the lines of [37] it is necessary to have available the full one-loop corrections of the di-heavy quark invariant mass and rapidity distributions, or even better the fully differential cross section evaluated at next-to-leading-order (NLO). Such a calculation needs in addition a correct treatment of the bound state system to that order for J/Ψ events. A consistent NLO calculation requires the inclusion of the resolved photon processes with appropriate caveats of double counting the collinear contributions. Thus the results of [37] have to be interpreted as the extraction of the leading order gluon density. A determination accurate to NLO would require the implementation of the above mentioned corrections.

With these caveats in mind let us discuss the result of the analysis in [37]. In J/Ψ production the gluon density may be determined at an average scale in a range of:

$$3 \times 10^{-5} < x < 1 \times 10^{-2} \quad \text{at} \quad Q^2 \approx 25 \text{ GeV}^2 \quad (3.16)$$

This is shown as solid line in Fig. 12. The scale Q is identified with the invariant mass \sqrt{s} of the subsystem and not to be confused with the (almost zero) virtuality of the exchanged photon. For open heavy quark production the average scale of the gluon density increases with x_g . Here one finds

$$6 \times 10^{-5} < x < 5 \times 10^{-2} \quad \text{at} \quad Q^2(x_g) \approx \sqrt{x_g} 10^4 \text{ GeV}^2 \quad (3.17)$$

which is shown as dashed line in Fig. 12. The larger lower limit of x_g arises from the fact that harder cuts are necessary to trigger and identify open heavy quark events. The rates are large enough to allow a binning in the scale. Thus actually a range in both x and Q^2 (full line labeled $Q\bar{Q}$ in Fig. 12) can be probed:

$$\begin{aligned} 400 < \mu^2 < 1600 \text{ GeV}^2 & \quad \text{at} \quad x_g = 0.001 \\ 2300 < \mu^2 < 7800 \text{ GeV}^2 & \quad \text{at} \quad x_g = 0.020 \end{aligned} \quad (3.18)$$

opening the prospects of observing the evolution of the gluon density in open heavy quark production at LEP/LHC. The discriminative power is illustrated in Figs. 14 and 15 where two different gluon distributions superimposed on measurements expected at LEP/LHC are shown. The error bars include the statistical and (experimental) systematic errors.

In comparing the different kinematic regions of Fig. 12 we find that the J/Ψ and F_L measurements partly overlap. The smallest value in x of the gluon density can probably be obtained through measurements of J/Ψ events. Open heavy quark production extends the x region towards higher x and scale Q values. The heavy quark results are obtained assuming that LEP/LHC is run solely at a fixed cms energy ($\sqrt{s} = 1.26 \text{ TeV}$). Data at different cms energies are highly desirable also in this case. This will not only allow to check the theoretical predictions and to put the description of the events on a firmer basis. Since there is strong correlation between the average scale and the cms energy in the case of open heavy flavour production runs of LEP/LHC at various cms energies would allow measurements

of the gluon density over an extended $\{x, Q^2\}$ region, bridging the gap between the F_L and the $Q\bar{Q}$ measurements of the glue. If we finally compare the kinematic ranges of Fig. 12 with predictions for the boundary lines in fig. 6 then we find that LEP/LHC can clearly probe the transition region better than HERA (and also better than hadron colliders). Furthermore the nonperturbative regime will be entered with a comfortable range in Q^2 allowing a study of the dynamical behaviour of this new region.

4 Summary

The ep option LEP/LHC will enable us to explore a new domain in deep inelastic scattering, namely the region of very small Bjorken- x . Measurements will extend down to $x < 10^{-5}$ for, say, $Q^2 \geq 10 \text{ GeV}^2$, i.e. for values of Q^2 where α_s is small. From the theoretical viewpoint, this kinematic region is interesting since it lies at the interface between perturbative and nonperturbative QCD: for moderate (i.e. not too small) x -values, we have the well-tested QCD evolution equations of Gribov, Lipatov, Altarelli, and Parisi, whereas in the extreme small- x limit one reaches the nonperturbative Regge limit which we do not yet fully understand. Generally one expects that the "true" structure functions at small x are smaller than the extrapolation of the standard QCD evolution equation. One attractive possibility is "saturation", i.e. a flattening of the structure function.

In between these two domains lies a transition region, where one might hope to see, still using perturbative QCD, the beginning of the transition to nonperturbative physics. For this region Gribov, Levin and Ryskin suggested a new, nonlinear evolution equation. It results from a careful analysis of large classes of Feynman diagrams (and also relies upon a certain assumption), and investigations of solutions (both analytically and numerically) have only been started. Although the validity of this equation in the x - Q^2 plane is limited and does not extend into the nonperturbative region, its predictions for this region are consistent with unitarity and, in particular, with the idea of "saturation".

Existing numerical estimates indicate that HERA and even more LEP/LHC will not only enter this transition region but also reach the nonperturbative regime. The advantage of LEP/LHC over HERA is the possibility to observe the small- x behavior over a much larger range in Q^2 , i.e. to distinguish between the Q^2 evolution à la Alfarelli-Parisi and Gribov, Lipatov, and Ryskin.

So far effects of the nonlinear evolution have been calculated only for the inclusive distributions F_2 and the gluon structure function. So practically all existing estimates of possible measurements at small- x assume the validity of the standard (linear) evolution and have to be redone, taking into account the effects of the "new" physics. Particular attention has to be given to special measurements which are sensitive to the onset of the "new" physics. Examples are the "hot spots" or photon diffractive dissociation.

Moreover we feel it necessary to further develop new computer programs based on the improved evolution equations. Analytic studies of the GLR-equation have shown several aspects which have to be taken into account when using these equations. One is the fact that the input distributions at fixed Q_0^2 should be prescribed only for a finite x -interval. Second, it may be useful to analyse the data along

particular lines in the x - Q^2 plane, the so called "classical paths". This may be the best way to distinguish between "standard" and "new" physics and also determines the boundary line between perturbative and nonperturbative physics.

As to practical measurements, at small- x the contribution of the gluon density to the cross sections becomes more and more important. Measurements of the longitudinal structure function F_L are estimated to be precise enough to extract the gluon density down to $x = 6.3 \times 10^{-5}$ (at $Q^2 = 25 \text{ GeV}^2$). Additional information on the gluon distribution in a somewhat different part of the small- x region can be obtained from heavy quark production.

Let us finally emphasise the importance of running LEP/LHC at various cms energies. First, this will enlarge the Q^2 range accessible to F_2 measurements at fixed x . This clearly increases the resolution power for new physics. A larger lever arm in Q^2 also increases the sensitivity to the glue as well as allows a better determination of Λ . Second, several cms energies are necessary to extract the gluon density via measurements of F_L , theoretically the most appealing method. Last not least the range accessible to gluon measurements in heavy quark production is extended. Even more important, this allows for tests of the production mechanisms of heavy quarks and thus to control the theoretical systematic errors.

References

- [1] *Proceedings of the Small-x Workshop*, held at DESY, May 1990 (to be published in *Nucl.Phys.*, ed.A.Ali and J.Bartels).
- [2] For general reviews on perturbative QCD see, e.g.:
H.D.Politzer, *Phys.Rep.* **14C**, 129(1974);
C.H. Llewellyn Smith, Schladming Lectures 1987, *Acta Phys. Austr. Suppl. XIX*, 331(1978);
Yu. Dokshitzer, D.I. Dyakonov, S.I. Troyan, *Phys.Rep.* **58**, 269(1980);
E.Reya, *Phys.Rep.* **69**, 195(1981); A.H.Mueller, *Phys.Rep.* **73**, 237(1981);
G.Altarelli, *Phys.Rep.* **81**, 1 (1982).
- [3] V.N. Gribov and L.N. Lipatov, *Sov. Journ. Nucl. Phys.* **15**, 438 and 675 (1972).
- [4] G.Altarelli and G.Parisi, *Nucl.Phys.* **126**, 297(1977).
- [5] Yu.L..Dokshitser, *Sov.Phys.JETP* **46**, 641(1977).
- [6] E.A.Kuraev, L.N.Lipatov, V.S.Fadin, *Sov.Phys.JETP* **44**, 443(1976).
- [7] E.A.Kuraev, L.N.Lipatov, V.S.Fadin, *Sov.Phys.JETP* **45**, 199(1977).
- [8] Ya.Ya.Balitzky, L.N.Lipatov *Sov.Jour.Nucl.Phys.* **28**, 822(1978).
- [9] Ya.Ya.Balitzky, L.N.Lipatov *JETP Letters* **30**, 355(1979).
- [10] L.N.Lipatov, *Sov.Phys.JETP* **63**, 904(1986) and references therein.
- [11] J.Bartels, *Nucl.Phys.* **B151**, 293(1979); *Nucl.Phys.* **175**, 365(1980); *Acta Phys.Pol.* **B11**, 281(1980); unpublished.

- [12] A.R.White, ANL-HEP-PR-90-28 and references therein.;
- [13] L.V.Gribov, E.M.Levin, and M.G.Ryskin, *Phys. Rep.* **100**, 1 (1982)
- [14] A.H.Mueller, *Nucl.Phys.* **B307**, 34 (1988); *Nucl.Phys.* **B317**, 573(1989); preprint Columbia Univ. CU-TP-441.
- [15] A.H.Mueller and J.Qiu, *Nucl.Phys.* **B268**, 427 (1986).
- [16] V.A. Abramovsky, V.N. Gribov, O.V. Kancheli, *Sov. Journ. Nucl. Phys.* **18**, 595(1973).
- [17] J. Bartels, J. Blümlein and G.A. Schuler, DESY 90-91 and to appear in *Zeitschrift für Physik C*.
- [18] A.H.Mueller, to appear in the *Proceedings of the Small-x Workshop*, held at DESY, May 1990 (to be published in *Nucl.Physics*, ed.A.Ali and J.Bartels);
- [19] J. Kwiecinski, A.D. Martin, W.J. Stirling, and R.G. Roberts, Rutherford Preprint RAL-90-053
- [20] J.Morfin and Wu-Ki Tung, preprint Fermilab-Pub 90/74 (1990).
- [21] E. Eichten et al., *Rev. Mod. Phys.* **56** (1984) 579 and Erratum **58** (1986) 1065.
- [22] M.G.Ryskin, *Sov.Journ.Nucl.Physics* **47**, 230 (1988).
- [23] J.Collins and J.Kwiecinski, *Nucl.Phys.* **B316**, 307 (1988).
- [24] J.Collins and J.Kwiecinski, *Nucl.Phys.* **B335**, 89 (1990).
- [25] E.M.Levin and M.G.Ryskin, Frascati Preprint April 1990.
- [26] M.G.Ryskin, DESY 90-050 and to appear [1].
- [27] J.Bartels, G.Ingelman, *Phys.Lett.* **235B**, 175 (1990).
- [28] G.Ingelman and P.Schlein, *Phys.Lett.* **152B**, 256(1985).
- [29] H.Fritsch and H.H.Streng, *Phys.Lett.* **154B**, 391(1985).
- [30] E.L.Berger, J.C.Collins, D.E.Soper, G.Sterman, *Nucl.Physics* **B286**, 704 (1987).
- [31] G. Ingelman, *LEP/LHC deep inelastic scattering: structure functions and final states*, these proceedings.
- [32] J. Feltesse, *Experimentation at LEP/LHC*, these proceedings.
J. Blümlein, J. Feltesse and M. Klein, *Kinematics and reconstruction at LEP/LHC*, these proceedings.
- [33] A.D. Martin, R.G. Roberts and W.J. Stirling, *Phys. Rev.* **D37** (1988) 1161.
- [34] J.G. Morfin, Fermilab-Conf-90/155, and in proceedings of the workshop on hadron structure functions and parton distributions, Batavia, Illinois, April 1990.
- [35] A.M. Cooper-Sarkar et al., *Z. Phys.* **C39** (1988) 281, and in proceedings of the HERA workshop, DESY, Hamburg 1987.
- [36] N. Magnussen and G.A. Schuler, *Extracting the gluon density from the longitudinal structure function F_L* , these proceedings.
- [37] K.J. Abraham, H. Jung, G.A. Schuler and J.F. de Trocóniz, *Gluon extraction from charm and bottom production at LEP/LHC*, these proceedings.
- [38] S.M. Tkaczyk, W.J. Stirling and D.H. Saxon, in proceedings of the HERA workshop, DESY, Hamburg 1987.

Figure Captions

Fig. 1: Different High Energy Limits.

Fig. 2: QCD ladders (a) and the first correction (fan diagram, b).

Fig. 3: Partons in the transverse plane (impact parameter plane).

Fig. 4: Partonic subprocesses: (a) splitting of partons, (b) partonic recombination process.

Fig. 5: Small- x behavior of the structure function: standard QCD evolution versus "true QCD" evolution. Labels A, B, and C denote the region of perturbative QCD, the transition region and the nonperturbative region, respectively.

Fig. 6: The transition region in the (x, Q^2) plane. The lines are defined in the text, eq. (2.11) and below.

Fig. 7: x -distributions of $xg(x, Q^2)$ for the model of [17] for different values of Q^2 . The full lines always belong to the linear equation ($C = 0$), the dashed ones to the nonlinear case with C of eq.(2.3), and the dotted ones to the nonlinear case with $\frac{1}{10}C$.

Fig. 8: x -distributions of $xg(x, Q^2)$ for different values of Q^2 (from [19]): the solid line belongs to the linear evolution. The dashed and the dot-dashed lines are the results of the nonlinear evolution; in the second case the nonlinearity parameter is increased by a factor of 2.5, compared to the first one.

Fig. 9: x -distributions for $F_2(x, Q^2)$ (from [19]): for the upper three curves the notation is the same as for Fig.8. The dotted curve corresponds to another input distribution (which is flat for $x \rightarrow 0$).

Fig. 10: A final state configuration which probes the "Hot spot".

Fig. 11: Final state configuration for photon diffractive dissociation.

Fig. 12: Kinematic region in x and Q^2 explorable at LEP/LHC.

Fig. 13: Measurement of the gluon distribution from the longitudinal structure function F_L [36]. Two different gluon distributions are superimposed on the measurements expected for data at LEP/LHC. The error bars indicate the size of the (combined) statistical and systematic errors.

Fig. 14: Measurement of the gluon distribution from inelastic J/Ψ production[37]. Two different gluon distributions are superimposed on the measurements expected for data at LEP/LHC. The error bars indicate the size of the (combined) statistical and (experimental) systematic errors.

Fig. 15: Measurement of the gluon distribution from open heavy quark production[37]. Two different gluon distributions are superimposed on the measurements expected for data at LEP/LHC. The error bars indicate the size of the (combined) statistical and (experimental) systematic errors.

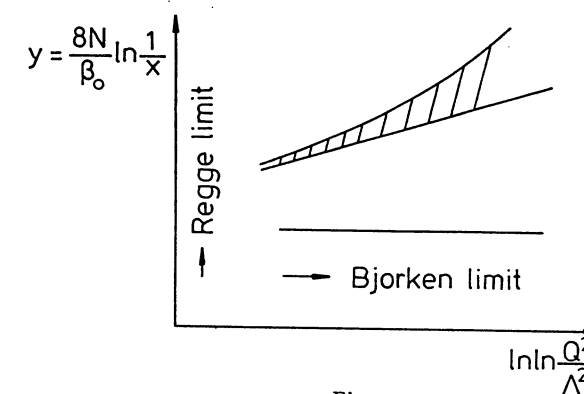


Fig. 1

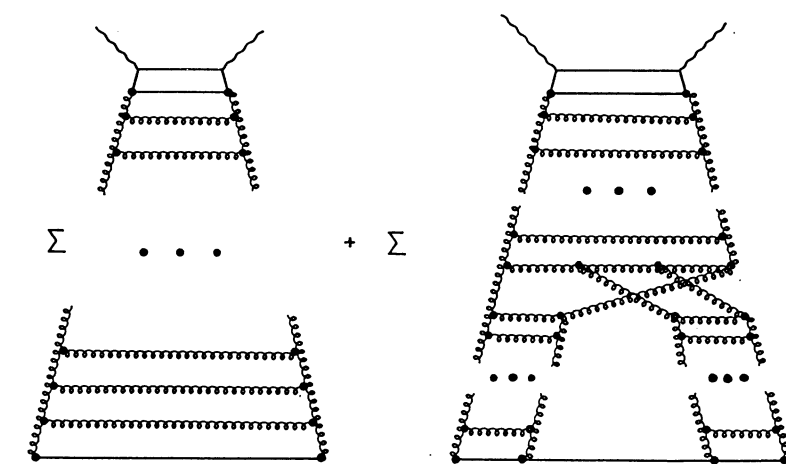


Fig. 2

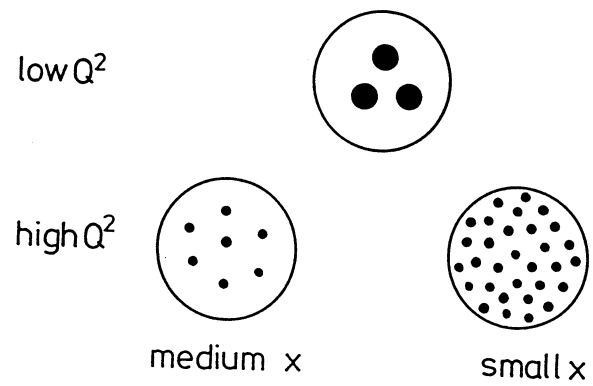


Fig. 3

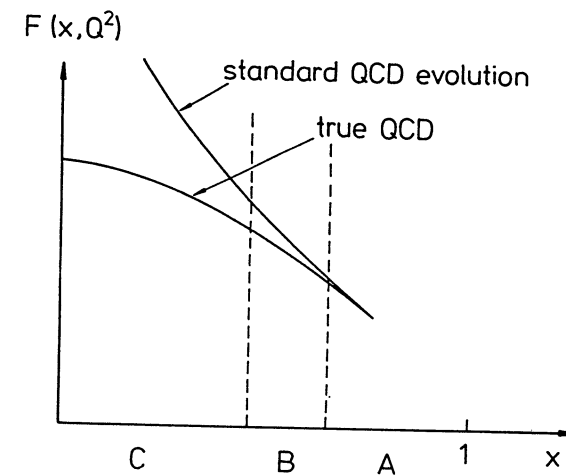


Fig. 5

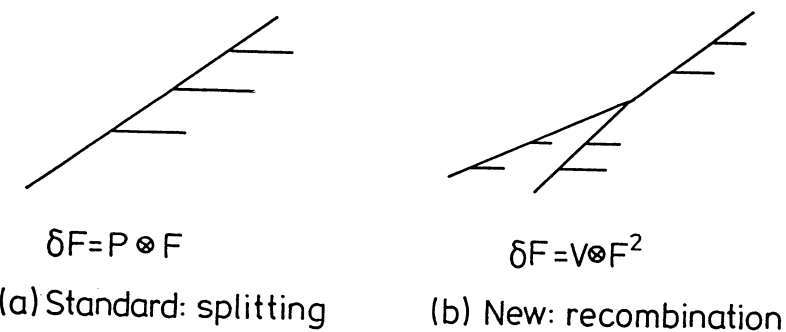


Fig. 4

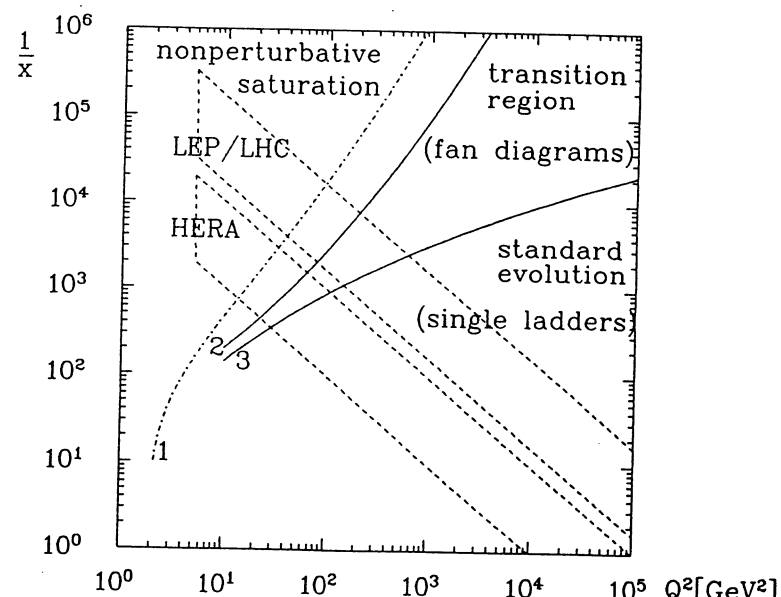


Fig. 6

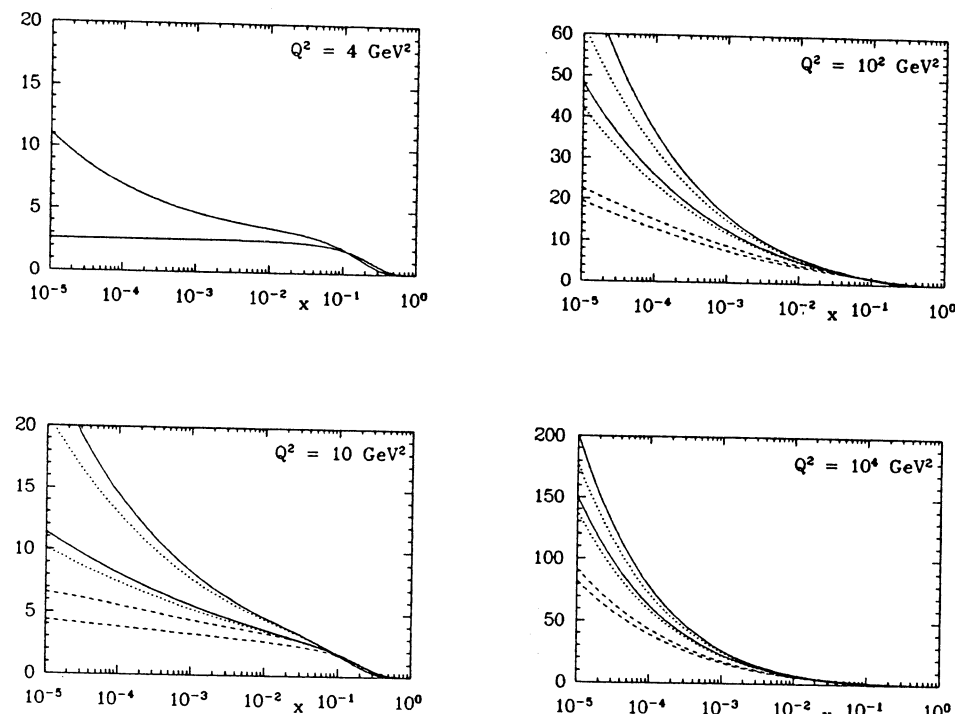


Fig. 7

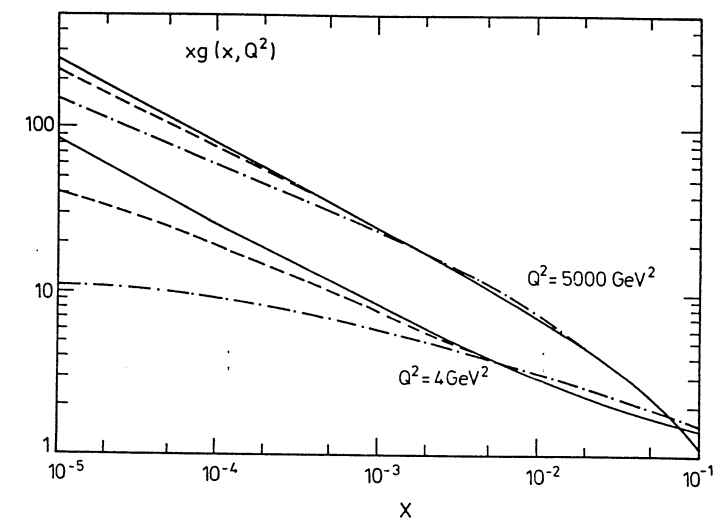


Fig. 8

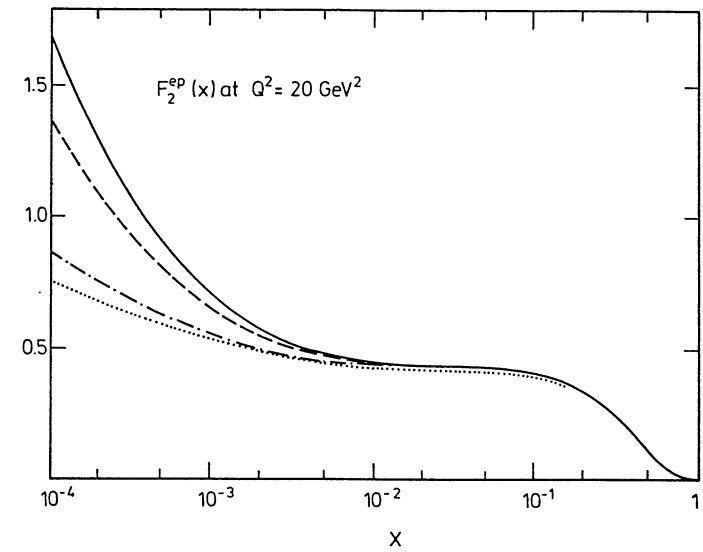


Fig. 9

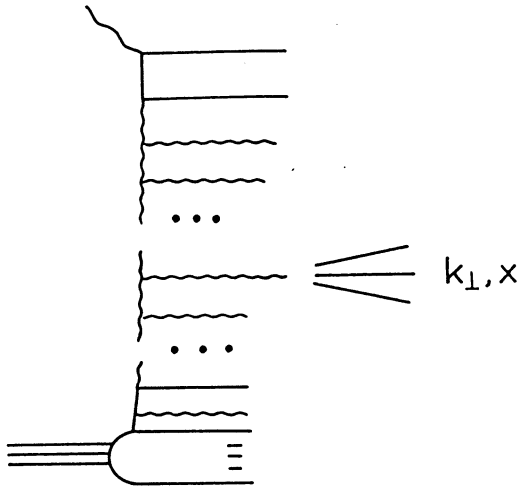


Fig. 10

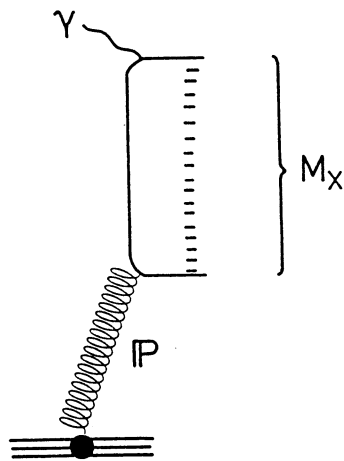


Fig. 11

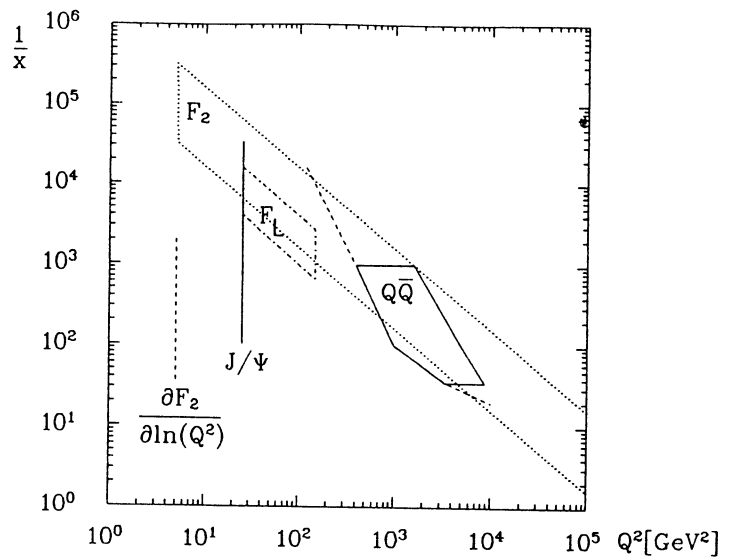


Fig. 12

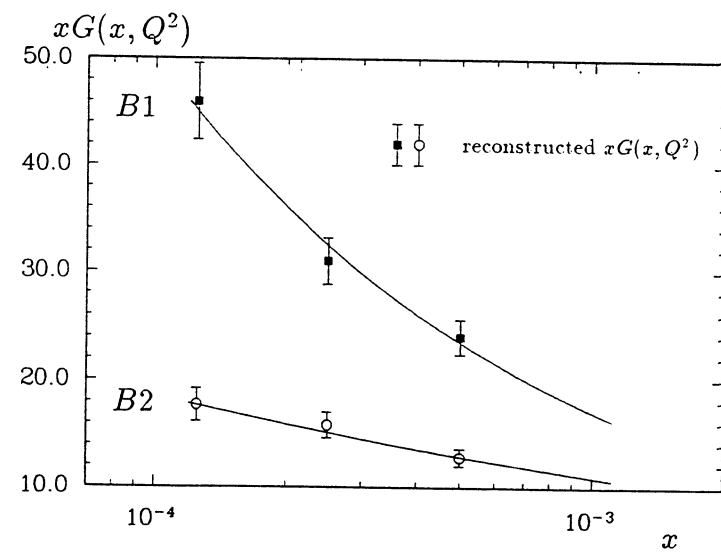


Fig. 13

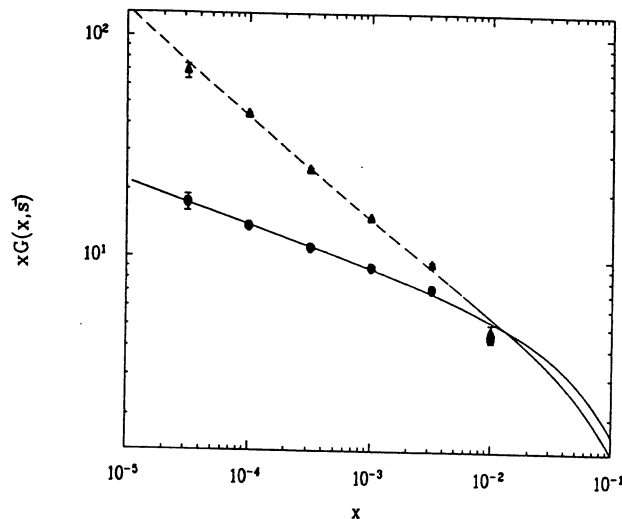


Fig. 14

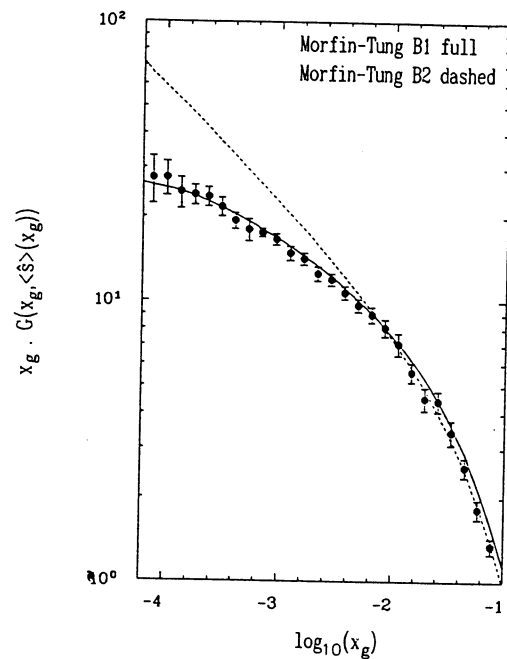


Fig. 15

Electroweak Radiative Corrections at LEP + LHC

H. Spiesberger*

II. Institut für Theoretische Physik der Universität Hamburg
Luruper Chaussee 149, 2000 Hamburg 50, FRG

Abstract

We give a review of the $\mathcal{O}(\alpha)$ electroweak radiative corrections in deep inelastic electron proton scattering at LEP+LHC. These corrections include one-loop contributions and single-photon bremsstrahlung. A major contribution to the radiative corrections is due to real photon bremsstrahlung $ep \rightarrow e\gamma X$. The Monte Carlo event generator HERACLES is used to study event distributions and the observability of radiative events is discussed.

1 Introduction

The knowledge of the detailed features of electroweak radiative corrections is indispensable for the interpretation of any high energy experiment. For HERA it is known that these corrections can be very large for large y and small x [1,2]. We will show that these large corrections are due to the emission of hard photons, mainly from the lepton line. If these potentially visible events could be excluded from the data sample used for a physics analysis, the remaining corrections which are due to unidentified radiative events would be smaller. After cutting out radiative events, standard unfolding procedures could be applied over a larger range of x and y than one could have expected from a study of the fully inclusive bremsstrahlung corrections.

2 Inventory of Radiative Corrections for $ep \rightarrow eX$

We are not going to present the complete set of formulas for the $\mathcal{O}(\alpha)$ radiative corrections. They can be found *e.g.* in [1,2]. Instead we only discuss some important features:

- The Born cross section for eP scattering is expressed as a sum over quark flavors and over the type of the exchanged boson. Each contribution gets different corrections. They depend on both the external quark line and on the type of the exchanged boson. The $\mathcal{O}(\alpha)$ -corrected cross section has the general form

$$\frac{d^2\sigma}{dx dy} \Big|_{eP \rightarrow eX} = \sum_f \sum_{B=\gamma, \text{Int}, Z} (1 + \delta_{f,B}) \sigma_{f,B}^{\text{Born}}(x, y) + \int d^3 P S(\vec{k}) R_{f,B}(x, y, \vec{k}) \hat{\sigma}_{f,B}^{\text{Born}}(\hat{x}, \hat{y}). \quad (1)$$

*Supported by Bundesministerium für Forschung und Technologie, 05 5HH 91P(8), Bonn, FRG

The factorized part $\delta_{f,B}$ contains virtual one-loop contributions and soft photonic corrections. The hard bremsstrahlung part results from a convolution of the Born cross sections $\delta_{f,B}^{Born}(x,y) = d^2\sigma/dx dy \delta_{f,B}^{Born}(x,y)$ taken at rescaled kinematic variables \hat{x}, \hat{y} which are functions of the photon momentum k with radiation functions $R_{f,B}(x,y,\vec{k})$.

The various contributions to $\delta_{f,B}$ and $R_{f,B}$ can be further separated according to gauge invariant subsets of diagrams, namely into:

- i) the leptonic corrections that are described by diagrams containing an additional photon attached to the lepton line, i.e. the photonic correction to the lepton gauge boson vertex, the photonic contribution to the self energies of the external fermion lines, and the photon emission from the lepton line.
- ii) the quarkonic corrections described by diagrams with an additional photon at the quark line analogous to i).
- iii) The lepton-quark interference part consisting of the $\gamma\gamma$ and γZ box diagrams and the interference of leptonic and quarkonic bremsstrahlung.
- iv) the purely weak corrections consisting of all the other diagrams that do not contain an additional photon. This part is IR finite and contains the diagonal γ and Z self energies, the γZ mixing, the weak lepton and quark vertex corrections, and the boxes with two heavy gauge bosons.
- The self energy diagrams contain loop diagrams that are built with all particle degrees of freedom that couple to the gauge bosons. Therefore they contain information on the whole theory. They depend on the top mass, the Higgs mass, and on the masses and couplings of eventually existing other unknown particles.

• The self energies are dominated by the fermion loops. This contribution is sometimes referred to as a QED part. The photon self energy can be accounted for by the use of the running fine structure constant $\alpha(Q^2) = \alpha(0)/(1 - \Pi^\gamma(Q^2))$, where $\alpha(0) = 1/137.036$ and Π^γ is the vacuum polarization. At $Q^2 \simeq M_Z^2$ its value is $\Pi^\gamma \simeq 0.06$. The prescription to use the running fine structure constant together with the leptonic QED corrections (discussed below) gives the $\mathcal{O}(\alpha)$ corrected cross section already with a precision of a few %. The Z self energy can be included approximately by normalizing the Z exchange part with the help of the μ decay constant.

Radiation from the lepton line. Numerical results for the leptonic corrections show a very pronounced increase at small x and large y and can become also large but negative for small y and large x . This behaviour can be understood from the following observations:

- i) The order of magnitude is determined by the factor

$$\frac{\alpha}{\pi} \ln \frac{Q^2}{m_e^2} \simeq (0.24\%) \times 25 \simeq 6\%.$$

This number is multiplied by logarithms of ratios of the maximal photon energy and the center of mass energy which can also become large for small values of x and large y .

ii) The emission of an energetic photon can shift the value of the momentum transfer \hat{Q}^2 seen from the quark line to very small values. x, y and $Q^2 = -(p_e - p_{e'})^2 = xyS$ are determined from the momenta p_e and $p_{e'}$ of the incoming and outgoing electron. But $\hat{Q}^2 = -(p_e - p_{e'} - k)^2$ is also determined by the momentum

k of the emitted photon and \hat{Q}^2 can be very small compared to Q^2 if the emitted photon takes away a large energy. In this case the bremsstrahlung contribution gets enhanced through the photon propagator $1/\hat{Q}^4$. This effect is similar to the radiative tail effect above the peak of a resonant cross section. It is responsible for the large increase of the corrections at large y .

iii) At small values of y and large x the photon phase space volume shrinks and for $x \rightarrow 1$ and $y \rightarrow 0$ the virtual and soft real corrections dominate and lead to large negative contributions.

- **Radiation from the quark line.** The quarkonic corrections contain mass singularities due to the initial quark masses. These can be factorized from the cross section and absorbed into the definition of the distribution functions. The only effect of the photonic quark line corrections is to introduce an additional Q^2 dependence which can be described in complete analogy to the Q^2 dependence arising from gluonic corrections, e.g. with the help of the Altarelli-Parisi equations. Numerically the corrections are then at most of the order of 2% in the range of x and Q^2 accessible at LEP + LHC. In addition to these leading logarithmic corrections there are also non-logarithmic contributions. But they are even smaller and can be neglected if one aims at not more than an accuracy of 1 %.

- **The lepton-hadron interference** contributions do not contain a logarithmic dependence neither on the lepton nor on the quark mass and therefore remain numerically small except at extreme values of x and y . They also can safely be neglected if one contents oneself with a precision at a few percent level.

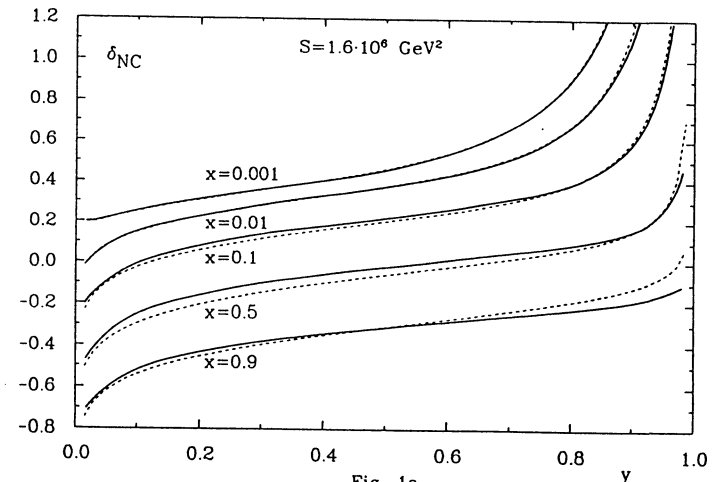


Fig. 1a

Fig. 1a shows a comparison of numerical results of a calculation including the complete $\mathcal{O}(\alpha)$ electroweak corrections except the quarkonic QED part (full

lines) with an approximation which includes the leptonic QED contributions in the leading logarithmic approximation [3] and the photon and Z boson self energies (dashed lines). Based on this approximation we have calculated contours of constant radiative corrections $\delta_{NC}(x, Q^2) = \text{const}$ for the neutral current process at LEP + LHC in the x - Q^2 plane. The results in Fig. 1b show that requiring the corrections to stay below 50 % would mean to restrict the x - Q^2 region considerably. We will show now that the accessible region can be enlarged if radiative events are identified and rejected from event samples used for a physics analysis.

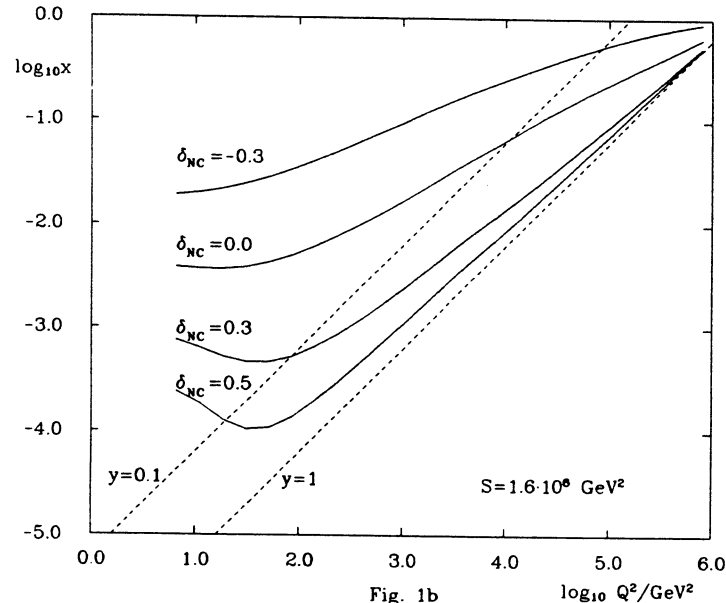


Fig. 1b

3 Results of a Monte Carlo Study

The event generator HERACLES [4], originally designed for deep inelastic scattering at HERA, was used to study the characteristics of radiative events in $e p$ collisions at LEP+LHC. HERACLES includes the leptonic corrections as well as the complete one-loop virtual corrections and is thus able to give a good description of the neutral current reaction, including radiative effects. The event generation is performed on the parton level and the events are described by the 4-momenta of the final state particles electrons, quarks, and photons (and the flavor of the scattered quark), but the hadronic final state is not generated.

Fig. 2a shows the distribution of events with $0.75 \times 10^{-2} \leq x \leq 1.25 \times 10^{-2}$, $0.85 \leq y \leq 0.90$, $E_\gamma \geq 2 \text{ GeV}$ versus the emission angle of the photon θ_γ , which is measured with respect to the electron direction. In the figure one recognizes three peaks:

- Events with $\theta_\gamma \simeq 0$, i.e. events where the photon is emitted collinearly with the

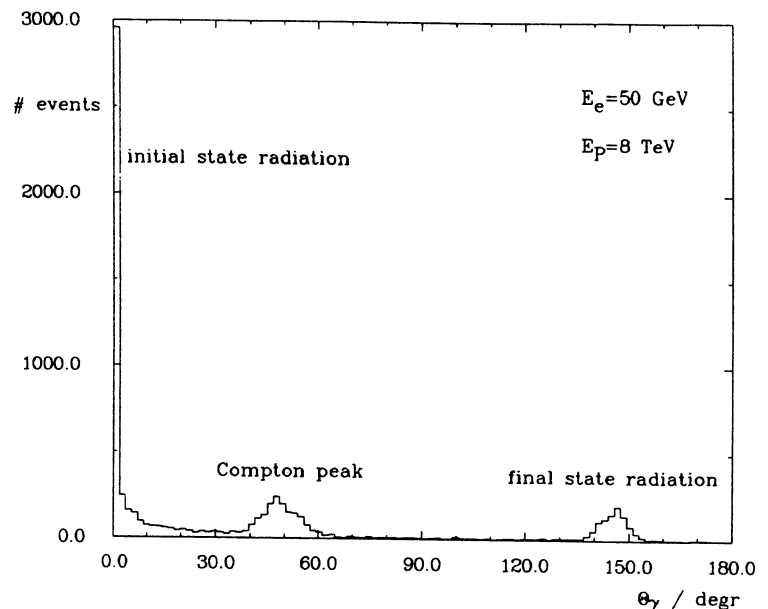


Fig. 2a

incoming electron (initial state radiation). Events of this type are the main source of the large corrections at small x and large y .

- Events with $\cos \theta_\gamma \simeq \cos \theta'_e$, i.e. events where the photon is emitted collinearly with the scattered electron (final state radiation); the scattering angle of the electron is determined by

$$\cos \theta'_e = \frac{(1-y)E_e - xyE_P}{(1-y)E_e + xyE_P}. \quad (2)$$

(E_e and E_P are the energies of the incoming electron and of the proton. Fermion masses have been neglected here). In the (x, y) bin considered here the electron scattering angle varies from 138° to 154° . Consequently also the peak from final state emission is smeared out over this range.

- A third peak is due to events with $\hat{Q}^2 \simeq 0$. The condition $\hat{Q}^2 = 0$ fixes the energy and the emission angle of the photon as functions of x and y :

$$E_\gamma^C = yE_e + x(1-y)E_P, \quad \cos \theta_\gamma^C = \frac{yE_e - x(1-y)E_P}{yE_e + x(1-y)E_P}. \quad (3)$$

These expressions are identical to the relations determining the energy $E_{q'}^0$ and the angle $\theta_{q'}^0$ of the final quark from x and y in the case of non-radiative scattering, i.e. for the $2 \rightarrow 2$ process $e q \rightarrow e q$. From eq. (3) one finds that for $\hat{Q}^2 \simeq 0$ the transverse momentum of the photon and of the electron are balanced: $k_T^C = p'_{e,T}$. This third contribution to the bremsstrahlung cross section is called the Compton part because it can be viewed as resulting from the emission of a quasireal photon from the quark line with subsequent Compton scattering $e\gamma \rightarrow e\gamma$. This peak is more pronounced for smaller values of x and large values of y but disappears at

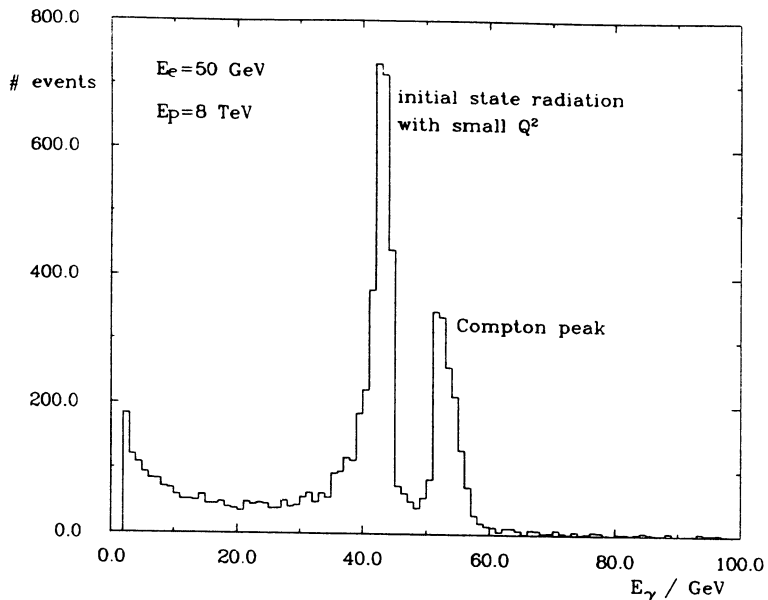


Fig. 2b

large x and small y . It is also visible in fig. 2b which shows the same sample of events distributed over the energy of the photon E_γ . The soft photon peak at $E_\gamma = 0$ is cut at the lower end of the spectrum by the condition $E_\gamma \geq 2 \text{ GeV}$. In addition to these peaks one finds also an accumulation of events with energies E_γ between 40 and 45 GeV. This enhancement of the cross section at a rather large photon energy is due to the combined effect of the factors $1/kp_e$ and $1/Q^2$ in the differential cross section. Its position is determined by the maximal photon energy allowed for emission parallel to the incoming electron:

$$E_\gamma^{\max}(\theta_\gamma = 0) = y \frac{1-x}{1-xy} E_e. \quad (4)$$

The aim of the following discussion is to present first ideas of how radiative events could eventually be identified and radiative corrections be reduced thereby. A complete investigation would have to start with a Monte Carlo which also simulates hadronization effects in order to include photons occurring during the evolution of the quark cascade, photons from hadron bremsstrahlung and hadron decays, as well as broadening of the current jet and systematic shifts of the angle and energy of the original parton from which the current jet is emerging. Eventually, it will also be necessary to perform a detector simulation. This was not done here and the results shown below should be understood as showing up directions for further studies.

Photons can be identified if they have enough energy and if they are emitted with an angle being large enough. Our Monte Carlo study showed that cutting out the phase space region characterized by $6^\circ \leq \theta_\gamma \leq 174^\circ$ and $E_\gamma \geq 2 \text{ GeV}$ would reduce the corrections already by typically 30 % to 50 % except at small y where the

corrections are dominated by soft photons. At $x \approx 10^{-2}$ for instance the corrections would reach 50 % only above $y \geq 0.9$ (without cut for $y \geq 0.7$). Somewhat smaller reductions could be reached by leaving out events with $\theta_\gamma \geq 2 \text{ mrad}$ and $E_\gamma \geq 2 \text{ GeV}$. It might be possible that events of this type can be identified with the help of a luminosity monitor.

In addition to directly identifying a bremsstrahlung photon there is also the possibility to observe a photon indirectly because the emission of momentum by a photon disturbs the relation of energies and scattering angles of the electron and the hadron jet as it would be expected for events without (or only soft) photons.

A cross-check of this kinematical relation could be performed by comparing the results of the electron measurement of the scaling variables x_e, y_e with the values x_h, y_h which are obtained by using the Jaquet-Blondel method via the measurement of the total hadron flow. We assume that the difference of the polar angles between the actually emitted quark q' and that of the expected quark q'_0 as it is calculated from the electronic measurement of x and y using non-radiative kinematics eq. (3) is a measure of $|x_e - x_h|$ and $|y_e - y_h|$.

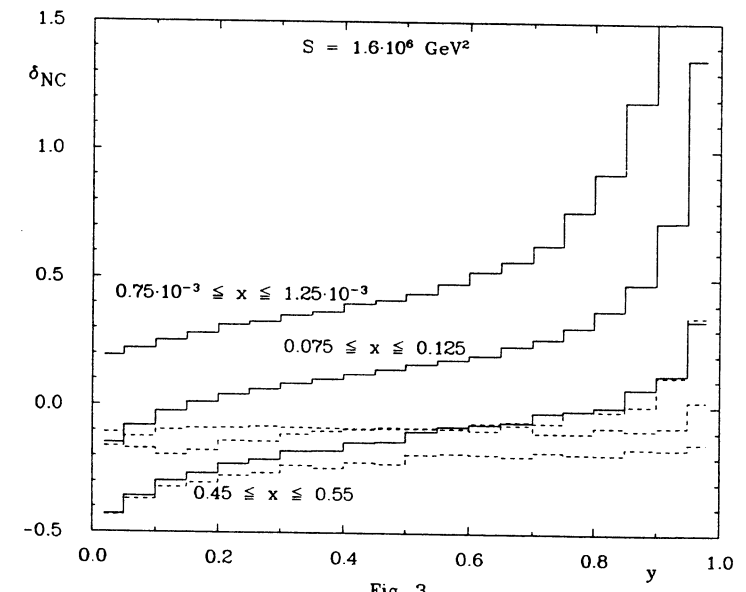


Fig. 3

In Fig. 3 the effect of a cut is shown which combines the possibility of cross-checking the electronic and the hadronic measurements via $\theta_{q'}$ with that of directly observing a photon. The cut is defined by the conditions

- (i) $E_\gamma \geq 1 \text{ GeV}$ and $50 \text{ mrad} \leq \theta_\gamma \leq \pi - 150 \text{ mrad}$,
but $\angle(\vec{k}, \vec{p}_e) \geq 150 \text{ mrad}$,
 - (ii) $E_\gamma \geq 5 \text{ GeV}$ and $\theta_\gamma \leq 5 \text{ mrad}$,
 - (iii) $|\theta_{q'} - \theta_{q'_0}| \geq 10^\circ$.
- (5)

Results are shown for the fully inclusive corrections, *i.e.* without any cut (full lines) and for the corrections that remain after applying the cut (5). We find huge reductions down to values below 0% even at very large y . The results for the corrections after cut don't depend very strongly on the actual minimal value of $|\theta_{q'} - \theta_q^0|$ which means that a good accuracy of the jet angle measurement is not essential. Note, that we did not use the energy of the scattered quark for the cross-checking of kinematics. An additional cut on $\Delta E_{q'} = |E_{q'} - E_q^0|$ could lead to a further reduction of the radiative corrections. The results obtained here with the help of a Monte Carlo treatment of the exact $\mathcal{O}(\alpha)$ leptonic corrections are in good agreement with a leading-log calculation [5].

As a prerequisite of the applicability of a cut on the jet angle, the jet has of course to come out with an energy big enough so that it can be identified as a jet. This is the case for larger values of x . Requiring a minimal jet energy of 20 GeV would not change the results shown in Fig. 3b essentially. Only in the last bin $0.95 \leq y \leq 0.98$ and for $x \simeq 10^{-3}$ the corrections would be bigger by a few % than without this additional condition. For smaller values of x however, the jet energies are generally smaller and the additional condition $E_{q'} \geq E_{q',\min}$ prevents from reaching similarly big reductions.

The experimental feasibility of these cuts is due to the fact that many events have a hard bremsstrahlung photon which turns the scattered quark into the central region of the detector so that radiative events can be identified because they have a clearly visible jet although from the electron measurement there was none expected. Also, photon emission allows for scattering with larger cms-energy and therefore higher energetic outgoing quarks are also possible.

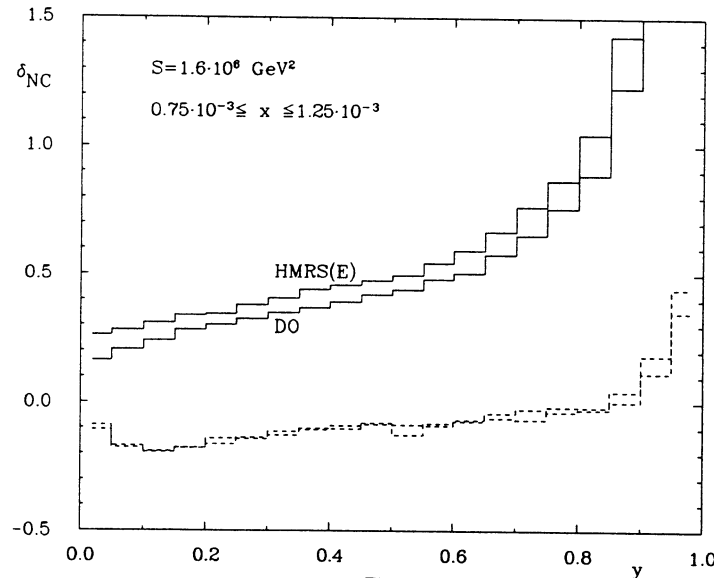


Fig. 4

Radiative corrections should not be seen as a source of theoretical uncertainties but rather as a generic ingredient in the calculation of reliable predictions from theory. However, as is the case for Born level calculations, they are subject to uncertainties from the parton distribution functions. Fig. 4 shows results of a comparison of two different input distributions. We have applied the cut (5) on two samples of events in the same x -region $0.75 \times 10^{-3} \leq x \leq 1.25 \times 10^{-3}$. For the first sample the parton parametrizations of [6] (set E) is used, while for the second we took the parton distributions of [7] as input. The total corrections are clearly distinct. The results for the corrections after cutting out observable radiative events, however, are very similar to each other. This fact should simplify the physics analysis of experimental data considerably. In turn it also means that the observable radiative events themselves have a potential for obtaining information on the structure functions.

Finally, we would like to comment on the influence of higher order corrections. $\mathcal{O}(\alpha^2)$ corrections in the leading logarithmic approximation have been calculated in [5] also for LEP + LHC. Only at extremely large y and at small x these corrections can reach a level of several percent.

Acknowledgment

I want to thank J. Blümlein, G. Kramer, W. Krasny, J. Kripfganz, A. Kwiatkowski, H.-J. Möhring, G. Schuler and T. Riemann for helpful discussions.

References

- [1] D. Yu. Bardin, C. Burdik, P. Ch. Christova, T. Riemann, Dubna preprint E2-87-595, E2-88-682, and Z. Phys. C 42 (1989) 679.
- [2] M. Böhm, H. Spiesberger, Nucl. Phys. B294 (1987) 1081.
Proceedings of the HERA Workshop, Hamburg 1987, ed. R. D. Peccei, Vol. 2, p. 577.
- H. Spiesberger, DESY-89-175, 13th International School of Theoretical Physics, Szczyrk, Poland, 1989.
- [3] W. Beenakker, F. A. Berends, W. L. van Neerven, Proceedings of the Ringberg Workshop on "Radiative Corrections for e^+e^- Collisions", Ringberg 1989, ed. J. H. Kühn, p.3.
J. Blümlein, Z. Phys. C 47 (1990) 89.
- [4] A. Kwiatkowski, H.-J. Möhring, H. Spiesberger, DESY-90-041 and DESY-90-145.
- [5] J. Kripfganz, H.-J. Möhring, H. Spiesberger, DESY 90-096, to appear in Z. Phys. C .
- [6] P. N. Harriman, A. D. Martin, W. J. Stirling, R. G. Roberts, Phys. Rev. D42 (1990) 798.
- [7] D.W. Duke, J.F. Owens, Phys. Rev. D30 (1984) 49.

Leading Log Radiative Corrections to Deep Inelastic Scattering at LEP \otimes LHC

J. Blümlein

Institut für Hochenergiephysik, Zeuthen, O-1615, Germany

Abstract

Numerical results are presented for the $\mathcal{O}(\alpha)$ neutral and charged current deep inelastic $e p$ -scattering cross section comparing corrections obtained using lepton or jet measurement. The influence of the non-perturbative low Q^2 behaviour of parton densities is discussed.

Deep inelastic $e p$ -scattering at LEP \otimes LHC will offer the possibility to measure structure functions down to $x \simeq 10^{-6}$. In the low- x range, which was not yet probed, the electro-weak radiative corrections (RCs) are particularly large [1, 2], if the measurement of the scattered lepton is used to define the kinematical variables. To isolate the structure functions a detailed quantitative understanding of the RCs is required in this range. The dominant contributions to the RCs are the QED-corrections. They can be calculated in the leading log formalism at a precision of a few per cent [2, 3]. Since for neutral current reactions in a wide kinematical range, $0.01 < y < 0.1$, and in the case of charged current reactions only the jet measurement can be used to determine the kinematical variables, the RCs have been calculated also for this case [3]. Moreover it appears to be feasible, that from a comparison of the RCs for both lepton and jet measurement in the overlap-range [4] for neutral current scattering also large corrections may be controlled.

In the case of lepton measurement the neutral current RCs arise in a physical gauge from initial and final electron bremsstrahlung and the collinear emission of the intermediary photon with respect to the initial quark line [2, 5], which is also called the Compton-contribution. Contrary to this, only initial state bremsstrahlung contributes in the case of jet measurement. Because Q^2 is measured at the hadronic vertex and demanded to be larger than some Q_{\min}^2 , characterizing the deep inelastic range, the Compton term does not contribute. Due to the Kinoshita-Lee-Nauenberg theorem there is also no contribution due to final lepton bremsstrahlung.

In Fig. 1a the corrections $\delta_{NC} = \sigma_{NC}^{1,QED}/\sigma_{NC}^0$ are shown for the case of lepton and jet measurement resp. using the parton distributions [6]. Contrary to the RCs for lepton measurement, which are rather large particularly at small x and high y , the RCs for jet measurement are far smaller, show a flat behaviour in y and depend on x only logarithmically. This difference is mainly due to the different Q^2 -rescaling of the Born cross sections for initial and final state bremsstrahlung for lepton ($Q^2 = zQ^2(Q^2/z)$ resp.) and jet measurement ($\hat{Q}^2 = Q^2(1-y)/(1-y/z)$). Applying the radiative corrections both for lepton and jet measurement in the overlap-region [4] could lead to a cross-control determining the Born cross section due to the different behaviour of the RCs.

A similar behaviour of the RCs for jet measurement is obtained for charged current scattering [2b,3] (Fig. 1b). Only at smaller x values δ_{CC} deviates from δ_{NC} but agrees completely at higher x . The latter property is due to the factorization of the soft-bremsstrahlung corrections and the fact that the hard contributions vanish as $x \rightarrow 1$.

In the case of lepton measurement the initial state bremsstrahlung can give rise to rather small values of $\hat{Q}^2 = zQ^2$ for the Born cross section. Because these values may be smaller than a minimum value of Q^2 typical for perturbative QCD one can no longer refer to the Q^2 behaviour as determined for the parton distributions by Altarelli-Parisi evolution [7], but has to account for non-perturbative terms at small Q^2 yielding the behaviour $xq_i(x, Q^2) \propto (Q^2/(Q^2 + M_i^2))^{\alpha_i}$ as $Q^2 \rightarrow 0$ [8]. In Fig. 1c this effect is illustrated matching both descriptions at $Q_0^2 = 4\text{GeV}^2$. In the range of small x and lower y the usual parton densities (e.g. [7]) would result into a rising behaviour of δ_{NC} while the description accounting for non-perturbative terms resembles the soft-peak behaviour at low y , known from higher x .

In summary, we have calculated the Leading log radiative corrections to deep inelastic scattering at LEP \otimes LHC both for lepton and jet measurement. The flat behaviour in y of the RCs using the jet measurement can be used to cross control the RCs in the case of lepton measurement in the overlap-range. Care has to be taken in the simulation of initial state bremsstrahlung at low x , where non-perturbative terms determine the Q^2 -behaviour of parton distributions.

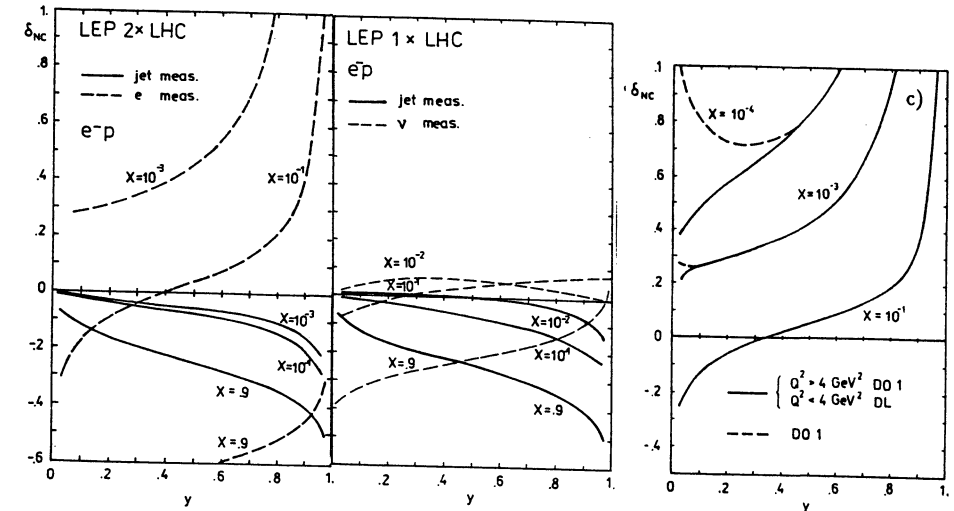


Figure 1: Comparison of the RCs to $e^- p$ using the lepton or jet measurement: a) neutral current; b) charged current; c) Effect of the non-perturbative behaviour of quark distributions at low \hat{Q}^2 (full line). The dashed line illustrates the extrapolation using the distributions [7].

References

- [1] M. Böhm, H. Spiesberger, Nucl. Phys. **B294** 1081 (1987); H. Spiesberger, DESY-89-175; D.Y. Bardin, C. Burdik, P.C. Christova, T. Riemann, Z.Phys. **C47** 89 (1990).
- [2] W. Beenakker, F.A. Berends, W.L. van Neerven, Proc. Ringberg Workshop, Springer, Berlin, 1989, p.3; J. Blümlein, Z.Phys. **C47** 89 (1990).
- [3] J. Blümlein, PHE 90-06.
- [4] J. Blümlein, J. Feltesse, M. Klein, these proceedings; J. Blümlein, M. Klein, Proc. Snowmass Workshop, 1990, in press and PHE 90-19.
- [5] J. Blümlein, G. Levman, H. Spiesberger, Proc. Snowmass-Workshop, 1990, in press; PHE 90-20.
- [6] E. Eichten et al., Rev. Mod. Phys. **56** 579 (1984) and Erratum **58** 1065 (1986). We set $xq_i(x, Q^2) = xq_i(x, 4\text{GeV}^2)$ for $Q^2 \leq 4\text{GeV}^2$.
- [7] D.W. Duke, J.F. Owens, Phys. Rev. **D30** 49 (1984).
- [8] A. Donnachie, P.V. Landshoff, Nucl. Phys. **B244** 322 (1984); Phys. Lett. **207B** 319 (1988).

Gluon Extraction from Charm and Bottom Production at LEP/LHC

K. J. Abraham^a, H. Jung^b, G. A. Schuler^c, J. F. de Trocóniz^{d1},

^a*Nikhef-H, Amsterdam, The Netherlands*

^b*III. Phys. Institut, Lehrstuhl B, RWTH Aachen, FRG*

^c*II. Institut für Theoretische Physik², Universität Hamburg, FRG*

^d*Dpto. de Física Teórica, Universidad Autónoma de Madrid, Spain*

Abstract

We discuss heavy quark production in ep collisions at LEP/LHC energies. The various production mechanisms as well as background processes are studied. We succeed in separating the direct photon-gluon fusion channel, and show how to measure the gluon density in both open and hidden heavy quark production at LEP/LHC. We specify the explorable ranges in x and Q^2 and estimate the errors with which the gluon density may be reconstructed at LEP/LHC.

1 Introduction

The primary source of information on parton distributions comes from structure functions measured in deep inelastic scattering experiments. Taking appropriate combinations of charged current and neutral current events, combining e^+p and e^-p data, and choosing suitable kinematic ranges, it is possible to unfold individual quark distributions at LEP/LHC[1]. Inclusive lepton scattering, however, is not directly sensitive to the gluon distribution. A dependence on the glue (simultaneously with a dependence on Λ) arises through the Q^2 evolution of (singlet) structure functions or through contributions from the longitudinal structure function $F_L(x, Q^2)$ (see [2,3] for corresponding studies at LEP/LHC). In this note we investigate the prospects of determining the gluon density from exclusive processes, namely open and hidden heavy flavour production. Previous attempts to extract the gluon distribution from heavy quark production can be found in [4,5]. The new methods we develop in this first systematic study could also be used at the HERA experiments.

At ep colliders, heavy quarks are mainly produced via exchange of quasi-real photons ($Q^2 \approx 0$). The scattered electron is typically lost into the beam pipe. Heavy quark production at ep colliders can thus be viewed as a continuation of photoproduction experiments up to higher cms energies. The leading order production mechanism of heavy quarks is photon gluon fusion

$$\gamma + g \rightarrow c + \bar{c}, b + \bar{b} \quad (1)$$

$$\gamma + g \rightarrow J/\Psi + g. \quad (2)$$

For the following reasons heavy quark production looks well suited for a measurement of the gluon density: (i) the direct sensitivity to the gluon density, (ii) the comfortable rates, and (iii) the clean signatures.

Cross section estimates for (1,2) depend rather heavily on the values of the mass scales in the strong coupling constant α_s , and the gluon density. In contrast to lepton inclusive ep scattering the scale μ in (1,2) is not uniquely defined. According to QCD factorization μ has to be of order of the heavy quark mass. We identify mass and renormalization scales and take $\mu = \sqrt{s}$, the partonic cms energy. Furthermore we use throughout this paper the one-loop formula for α_s , with four flavours and take $\Lambda_{QCD} = 200$ MeV. If not otherwise stated the parton density parametrization set B1 of Morfin and Tung[6] is used.

The rather strong dependence on the choice of the scale indicates that higher order corrections are important. For open heavy flavour production these corrections can be calculated perturbatively. Since we shall require a substantial invariant mass for the heavy quark pair in our analysis, corrections from quark initiated subprocesses, $\gamma + q \rightarrow q + g (\rightarrow Q\bar{Q})$, will be greatly reduced. But the remaining corrections are gluon initiated, exactly as the leading contribution (1). Furthermore it is expected that these corrections can be described by a rather constant K -factor[7]. Thus we generate events according to (1) and assume $K(c\bar{c}) = K(b\bar{b}) = 2$. We do, however, include effects of multiple gluon emission on the event topology by using the event generator AROMA[8] where they are

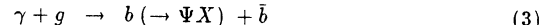
¹Partially supported by the exchange programme CICYT-Kfz., Karlsruhe.

²Supported by Bundesministerium für Forschung und Technologie, 05 4HH 92P/3, Bonn, FRG.

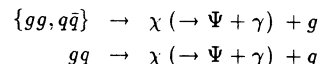
included in a parton cascade approach. Higher order corrections to J/Ψ production are more difficult to estimate since the calculations assume the validity of the non relativistic quarkonium model. In [9] it was shown that this model describes differential distributions well, if $z < 0.8$ and $p_T > 1 \text{ GeV}$. We shall therefore apply these cuts later when reconstructing the quantities z and p_T . However, there is a problem with absolute normalisation, a K -factor of about two seems to be required to fit the data. For simplicity we take $K=1$.

2 J/Ψ analysis

The subprocesses contributing to J/Ψ production in addition to (2) are:



and



Additional background events may come from the production of light quark events with subsequent decays into leptons. Our analysis is based on the leptonic decay, $J/\Psi \rightarrow l^+l^-$, where l is either an electron or a muon. By restricting the lepton invariant mass to the J/Ψ mass these background events can be rejected. We thus do not consider these events any further. Corrections given by the hadronic component of the photon (4,5) are known to be large[10]. These resolved photon contributions give rise to $q\bar{q}$, qg , gq , and gg initial states. A K -factor of about two is required in the analyses of J/Ψ production at the SPS and the Tevatron where at high enough energies the dominant contributions come from gluon-gluon fusion to χ states [11,12]. Assuming that the K -factors for (4,5) will be similar, the K -factors for the resolved and direct processes will be roughly the same. Hence we use uncorrected Born level cross sections ($K=1$ also for (4,5)) in order to optimise cuts.

The p_T distributions of the various J/Ψ production mechanisms are shown in fig. 1 with the labels: solid line: direct production (2), dashed line: resolved photon contributions (5), and dashed-dotted line: b -decays (3). The curves show the Monte Carlo p_T^Ψ distributions where no cut was applied. The subprocess (4) can only produce J/Ψ 's with small transverse momentum and is therefore omitted. At high p_T values ($p_T \gtrsim 5 \text{ GeV}$) the bottom production mechanism (3) dominates. Yet, for $p_T \lesssim 4 \text{ GeV}$ it can safely be neglected. J/Ψ 's from b -decays could further be reduced by requiring them to be isolated. The other two processes, (2) and (5), are about equally large. They have similar p_T distributions and can thus not be discriminated by a cut in p_T .

Direct photon (2) and resolved photon (5) contributions do, however, differ in the laboratory polar angle distribution of the J/Ψ . In fig. 2 we show $d\sigma/d\cos\theta$

for both subprocesses. Again, the distributions are Monte Carlo results without applying any cut except $p_T > 1 \text{ GeV}$. We find a rather flat distribution for the direct process whereas the resolved photon process is strongly peaked at $\cos\theta \equiv (\vec{p}_\Psi \cdot \vec{p}_p)/(|\vec{p}_\Psi| \cdot |\vec{p}_p|) = 1$, i.e., in the direction of the outgoing proton remnant³. A cut in $\cos\theta$ will therefore be very effective in suppressing the latter reaction.

For our analysis we now generate complete event samples for both processes. The hadronization is implemented using the LUND string fragmentation. The events are then passed through a detector of H1 type[13]. The J/Ψ momenta are reconstructed in the tracking system via their decay leptons. Due to the geometrical acceptance this implies a cut of $|\cos\theta| < 0.98$ on the (reconstructed) polar angle. Referring to fig. 2 it is clear that this diminishes the resolved photon contribution quite a lot compared to the “signal events” (2). We now apply a cut on the transverse J/Ψ momentum, $p_T^\Psi > 1 \text{ GeV}$, in order to select events where (2) is a reliable description of J/Ψ production. After the two requirements, (i) the J/Ψ 's can be reconstructed in the tracking device, and (ii) $p_T^\Psi > 1 \text{ GeV}$, we find a signal-to-background ratio $S/B \approx 5$, i.e. the direct contribution (2) is approximately a factor five larger than the resolved one (5).

In order to improve the signal to background ratio we consider the distribution in z : the ratio of energie-plus-longitudinal-momentum of the J/Ψ to the photon in the laboratory frame:

$$z = \frac{p_p \cdot p_\Psi}{p_p \cdot p_\gamma} \underset{\text{Lab}}{\sim} \frac{(E + p_L)_\Psi}{(E + p_L)_\gamma} . \quad (6)$$

The momenta are labelled as proton p_p , photon p_γ , and J/Ψ p_Ψ . As argued in ref.[14], J/Ψ 's carry almost all of the incident energy when the proton and photon couple directly but only a small fraction when they couple indirectly, i.e. via the partons in the photon. This is a consequence of the soft parton distribution in the photon. This is quantified in fig. 3 where we show the z -distributions of the two processes as they are obtained from the Monte Carlo. The direct channel peaks at $z \rightarrow 1$, whereas the resolved photon contributions accumulate near $z = 0$. A cut in z will therefore substantially improve S/B provided z can well be reconstructed.

Experimentally, z in (6) has to be reconstructed from a measurement of the momentum of the exchanged photon. The photon momentum is determined by the variable y defined by

$$y = \frac{p_p \cdot p_\gamma}{p_p \cdot p_e} \underset{\text{Lab}}{\sim} \frac{(E + p_L)_\gamma}{(E + p_L)_e} \quad (7)$$

where p_e is the incoming electron momentum. As stated above, the exchanged photon is almost real in J/Ψ production. In the collinear approximation, $Q^2 = 0$, we obtain $E_\gamma = (p_L)_\gamma$ or $p_\gamma = y p_e$. Independent of this approximation, z is now reconstructed by (neglecting the electron mass):

$$z_{\text{rec}} = \frac{(E + p_L)_\Psi}{2 y_{\text{rec}} E_e} . \quad (8)$$

³Our positive z -axis is defined by the direction of the incoming electron.

We reconstruct y from the calorimeter measurement

$$y_{rec} = \sum_h \frac{(E + p_L)_h}{2E_e} \quad (9)$$

where the sum runs over all particles measured in the calorimeter except the scattered electron⁴. We show in figs. 4a and b the correlation y vs. y_{rec} for J/Ψ production via the direct process (2) and the resolved photon process (5). The reconstructed z distributions can be found in fig. 3 where they are plotted together with the Monte Carlo results. From fig. 4a we find that y can very well be reconstructed over the whole y range using (9) for the direct production channel. Here also the reconstructed z distribution approximates the true (Monte Carlo) distribution very well over the whole z range except near $z = 0$. For J/Ψ 's produced via the hadronic component of the photon this method does not work the reason being the spectator jet of the photon. In fact, we have to distinguish the following cases for the resolved photon contributions:

- The photon remnants are fully contained in the calorimeter. Then the measurement (9) reconstructs y (7), the energy fraction carried by the photon. Also (8) approximates z as defined in (6). Thus the reconstructed z distribution follows the exact one. This is the region z close to zero in fig. 3.
- The photon remnants are completely lost into the beam pipe. Then (9) gives the energy fraction carried by that parton p^γ within the photon which participated in the hard interaction, $y_{rec} \approx y_p$ with

$$y_p = \frac{(E + p_L)_{p^\gamma}}{2E_e} = x_p y. \quad (10)$$

Here x_p denotes the momentum fraction of the photon carried by the parton. Since $0 < x_p < 1$ we have $y_{rec} \approx y_p < y$. Consequently a parton- z_p is reconstructed

$$z_p = \frac{p_p \cdot p_\Psi}{p_p \cdot p_{p^\gamma}} = \frac{(E + p_L)_\Psi}{(E + p_L)_{p^\gamma}} = \frac{z}{x_p} > z. \quad (11)$$

This creates the peak at $z = 0.9$ in fig. 3 and yields even values $z > 1$. In this case the seen (reconstructed) subprocess is actually one initiated by a parton inside the *electron* plus a parton inside the proton. If the latter parton is the gluon, then these events are really signal events as (2).

- The photon remnants are only partly be reconstructed. Then (9) yields a value y_{rec} with $y_p < y_{rec} < y$. Correspondingly (8) yields a value z_{rec} with $z < z_{rec} < z_p = z/x_p$. This fills the region $0.2 \lesssim z \lesssim 0.6$ in fig. 3.

Which of the above mentioned situations occurs depends on the acceptance of the calorimeter and the details of the fragmentation of the photon structure function which are far from being understood. In fig. 4b and c we compare for the resolved

⁴We do not include information on the scattered electron energy coming from a luminosity monitor measurement since it is not clear whether the latter will work with the high rates expected at LEP/LHC.

photon contributions y_{rec} versus y and y_p , respectively. It seems that at least in our simulation there is a good correlation between the reconstructed and the partonic y 's. Note also, that the photon remnants are usually flying backwards (i.e. keeping the direction of the incoming electron) in contrast to the proton remnants which follow the incoming proton direction.

Despite of the fact that z cannot be reconstructed over its entire region, we apply a cut $z > 0.2$ in order to diminish the resolved photon contributions. Furthermore we require $z < 0.8$ to stay away from elastic and diffractive J/Ψ production. Then we end up with a total J/Ψ cross section of $\sigma(J/\Psi) \times BR(J/\Psi \rightarrow l^+l^-) = 0.3$ nb. At an integrated luminosity of 1 fb^{-1} per year this corresponds to about 3×10^5 events. Among these events are then only 13% J/Ψ 's coming from resolved photon contributions (5).

We did not attempt to improve further the S/B ratio. In principle one could further discriminate at least against the background from χ production by tagging on the photon in the decay, on the lines of [12]. However, present knowledge of the fragmentation of the spectator jet from the photon is inadequate for the purposes of completely eliminating backgrounds from pion decay.

When trying to measure the gluon density one has to find observables which on the one hand side constraint x_g , the momentum fraction of the proton carried by the gluon, and which, on the other hand, can actually be measured experimentally. We determine x_g from the following relation:

$$x_g = \frac{\hat{s} + Q^2}{y s} \quad (12)$$

where \sqrt{s} is the total cms energy and $\sqrt{\hat{s}}$ the partonic cms energy. As mentioned above, the photon virtuality is very small so that we can approximate it by

$$Q^2 \approx Q_{rec}^2 = 0. \quad (13)$$

The partonic cms energy $\sqrt{\hat{s}}$ can well be measured in J/Ψ events through measurements of $p_T(l\bar{l}) = p_T(\Psi)$ and $z(l\bar{l}) = z(\Psi)$ using the relation

$$p_T^2 = z(1 - z)\hat{s} - (1 - z)m_\Psi^2. \quad (14)$$

The measurement of y as given in (9) completes the x_g determination from (12). The quality of this reconstruction for J/Ψ events is shown in fig. 5 where we plot x_g vs. x_g^{rec} (5a and b) and the distribution in the resolution $(x_g - x_g^{rec})/x_g$ (5c). We find that x_g can be determined with good quality (FWHM = 0.12, fig. 5c) over the whole range

$$3 \times 10^{-5} < x_g < 1 \times 10^{-2} \quad \text{at} \quad <\mu^2> \sim 25 \text{ GeV}^2 \quad (15)$$

where the average value of $\mu \equiv \sqrt{\hat{s}}$ is rather independent of x_g .

Having reconstructed x_g we now proceed to determine the input gluon density. It is related to the measured distribution $d\sigma/dx_g$ via

$$g(x_g, \mu^2(x_g)) = \frac{d\sigma(x_g)/dx_g|_{exp}}{f(x_g)|_{MC}} \quad (16)$$

where $f(x_g)|_{MC} = 1/g(x_g)|_{MC} d\sigma/dx_g|_{MC}$ is determined by the Monte Carlo program. We find that the systematic error is rather small. The reconstructed gluon density is shown in fig. 6. The statistical errors for an integrated luminosity of $50 pb^{-1}$ (corresponding to ~ 1 month running) are shown by the vertical error bars in fig. 6. We also show the gluon density as obtained from set B2 of Morfin-Tung. We find that our method can clearly discriminate between these different parametrizations and provides an excellent way of measuring the gluon density in ep collisions at LEP/LHC energies.

3 $c\bar{c}$ and $b\bar{b}$ analysis

The signatures we want to exploit to identify the “signal” reactions (1) are based on the semileptonic decays of the heavy quarks. Specifically, we require two opposite sign leptons, electrons or muons. For our analysis we generate complete event samples using a modified version of the event generator AROMA both for signal events (1) as well as for the other processes discussed below. AROMA[8] contains gluon emission from the $Q\bar{Q}'$ system in a parton cascade approach and hadronization according to the LUND string model and heavy flavour decay. We assume a beam pipe of opening angle of 100 mrad. We require a minimal total transverse energy in the calorimeter for triggering purpose. In order to be measurable we demand a minimal transverse momentum p_T for the two leptons. Thus we have:

$$\sum E_T > 10 \text{ GeV} , \quad p_T(l^\pm) > 1 \text{ GeV} , \quad \theta_{\text{beam}} = 100 \text{ mrad}. \quad (17)$$

After these cuts we obtain the following cross sections at $\sqrt{s} = 1.265 \text{ TeV}$ (including the K -factors stated in chapter 1):

$$\sigma(c\bar{c}) = 1.5 \text{ nb} , \quad \sigma(b\bar{b}) = 1.0 \text{ nb}. \quad (18)$$

Corrections given by the hadronic component of the photon to (1) are important. For open heavy quark production the leading order contributions are $q\bar{q} \rightarrow Q\bar{Q}$ and $gg \rightarrow Q\bar{Q}$. We studied the question of y reconstruction in detail following the lines in the previous section. We reconstruct y from all stable particles outside the beam pipe using (9). Again we find that y can very well be reconstructed for the signal events (1). For resolved photon events the photon remnants are mostly lost into the beam pipe. Thus (9) yields y_p (10) to a rather good accuracy. Since the gluon initiated subprocess is by far dominating the resolved photon contribution will depend on the gluon density in the proton in just the same way as the direct channel does. Both samples could therefore be added. Let us emphasize that the results depend on details of the fragmentation of the photon spectator jet and the detector acceptance. More work is needed to settle the question of reconstructing the kinematics of resolved photon processes. For the subsequent analysis we omit the resolved contribution, assuming that it either behaves like signal events or can be discriminated via the photon remnants by suitable detectors in the backward direction.

Background events come from the production of light quark events with subsequent decays into leptons. As was shown in [15] already weak isolation requirements on the leptons kill practically all background events without significant losses of charm and bottom events. The background is also reduced to a negligible level by a cut on the invariant mass of the lepton pair. For background events $m(l^+l^-)$ peaks at small values, whereas signal events have a rather wide distribution. We thus imposed the cut $m(l^+l^-) > 1 \text{ GeV}$. A discrimination of charm and bottom events is not necessary. The cut (17) on $\sum E_T$ implies a rather strong cut on \hat{s} (remember $\sqrt{\hat{s}_{\min}} = 2m_Q$). In fact, the average $\sqrt{\hat{s}}$ is about 11 GeV in the smallest x_g -bin and rises to about 100 GeV at large x_g . Hence we can combine charm and bottom events.

In open heavy quark production it is more difficult to find observables which can be measured experimentally and are related to x_g . We did not find a satisfying way to measure \hat{s} . Among the variables we tried are $\sum E_T$, the total visible energy, the invariant mass of the lepton pair, and transverse energies combined with polar angle information obtained from the leptons. In [15] two of us proposed another way to determine x_g which is based on the rapidity \hat{y} of the partonic system:

$$\hat{y} = \frac{1}{2} \ln \left[\frac{y E_\epsilon}{E_p(x_g - Q^2/s)} \right] \quad (19)$$

The crucial point is now that \hat{y} can well be approximated by the rapidity of the lepton pair. This is documented in fig. 7 where we plot y_{ll} vs. \hat{y} . As in the case of J/Ψ production we approximate Q^2 by zero. We reject events at high Q^2 by requiring that the scattered electron cannot be identified. Combining the y and \hat{y} measurements we find the following kinematic range explorable in heavy quark production at LEP/LHC:

$$6.3 \times 10^{-5} < x_g < 0.05 \quad \text{at} \quad <\mu^2> \approx x_g^{0.46} 10^4 \text{ GeV}^2 \quad (20)$$

The kinematic range is limited by statistics, the range in \hat{y} , and the total transverse energy cut in (17). Note that the average scale increases with x_g . The quality of the x_g determination is only slightly worse than in the J/Ψ case. In fig. 8 we show the probability that $x_g = 10^{-3}$ is reconstructed as x_g^{rec} . We find that the distribution peaks at the input value.

Systematic errors on event number enter since the measured values, x_g^{rec} , differ from the true x_g values and the number of events seen $\mathcal{L} \Delta x_g d\sigma/dx_g(x_g)|_{\text{exp}}$ in a bin of width Δx_g will differ from the true number $\mathcal{L} \Delta x_g d\sigma/dx_g(x_g)|_{MC}$ (at a given integrated luminosity \mathcal{L}). We use the Monte Carlo to correct for these effects using (16). The systematic error on this correction was estimated by varying the Monte Carlo functions $f|_{MC}$ using different gluon distribution functions. We adopted the bin sizes Δx_g at the edges of $d\sigma/dx_g$ such that migrations out and into the bins remained small. The result of this is shown in fig. 9 where the error bars indicate the systematical and statistical uncertainties. In fact, the statistical errors are very small. To guide the eye we have included the input density evaluated at the average $<\mu> = <\mu(x_g)>$. We also show the gluon density as obtained from set B2 of Morfin-Tung. We see that we can expect to discriminate between different

gluon distributions very well. The discrimination power clearly improves for lower x values.

Since the rates for open heavy flavour production are so large, we tried to reconstruct the gluon density at two different values of the scale argument. As stated above, the measurement of \hat{s} is poor. Also the reconstruction from (19) is not particularly useful. We thus impose a larger cut in $\sum E_T$, $\sum E_T > 35 \text{ GeV}$. This increases the average μ^2 by about a factor four to five almost uniformly over the entire x_g range. The reconstructed gluon density for this sample with $\sum E_T > 35 \text{ GeV}$ is shown in fig. 10 together with the input gluon density at the corresponding average values of $\mu = \mu(x_g)$. Even when applying such a high cut in $\sum E_T$ the statistical error remains small. Also the systematical error is small enough in order to allow a discrimination against the gluon density evaluated at the lower scale values corresponding to the sample with $\sum E_T > 10 \text{ GeV}$. We thus conclude that it seems possible to measure the gluon density in open heavy quark production over the wide range specified in (20) at an average scale and in an somewhat reduced range even as a function of the scale:

$$\begin{aligned} 400 < \mu^2 < 1600 \text{ GeV}^2 &\quad \text{at} \quad x_g = 0.001 \\ 2300 < \mu^2 < 7800 \text{ GeV}^2 &\quad \text{at} \quad x_g = 0.020. \end{aligned} \quad (21)$$

4 Discussion and Summary

In this work we investigated the prospects of extracting the gluon density from open and hidden heavy quark production in $e\gamma$ collisions at LEP/LHC energies. The analysis is based on complete (signal and background) events and, in the case of J/Ψ , it includes a full detector simulation. The reconstruction of the event kinematics is carefully outlined, in particular uncertainties due to unsufficient known fragmentation properties of the proton remanants and photon spectator jet are discussed. Higher order corrections on the event topology are approximately taken into account by multiple gluon radiation in a parton cascade approach. Only information obtainable from a main detector is used. In a previous study on gluon extraction from J/Ψ events at HERA[4] the information on the scattered electron coming from a luminosity monitor measurement has been used. This is not done here since it is not clear whether such a device will work with the high rates expected at LEP/LHC. Furthermore it was found that with the main detector a much larger range in x is accessible, including the range reachable via the luminosity measurement.

The outcome is that one will obtain measurements of $d\sigma/dx_g$ which are accurate enough to extract the gluon distribution at small- x , and hence to distinguish between different parametrizations, even if LEP/LHC is run at 10% of the design integrated luminosity (1 fb^{-1} per year) only. The successful reconstruction of the glue from open heavy quark production is demonstrated here for the first time. We estimate the explorable ranges to be $3 \times 10^{-5} < x_g < 1 \times 10^{-2}$ at an average scale of $\mu^2 \approx 25 \text{ GeV}^2$ for J/Ψ production, and $6.3 \times 10^{-5} < x_g < 5 \times 10^{-2}$ at an average scale of $\mu^2 \approx \sqrt{x_g} 10^4 \text{ GeV}^2$ for $c\bar{c}$ and $b\bar{b}$ production. The larger lower

limit of x_g for the latter case arises from the fact that harder cuts are necessary to trigger and identify open heavy quark events. Though the distribution in the invariant mass $\sqrt{\hat{s}}$ of the $Q\bar{Q}$ subsystem is steeply falling, events at high \hat{s} will copiously be produced due to the large rates expected at LEP/LHC. Cuts in the total transverse energy define samples with different average values of the scale argument μ of the gluon density which we took to be $\mu = \sqrt{\hat{s}}$. Hence we expect the evolution of the gluon density with μ to be observable in open heavy quark production at LEP/LHC. The explorable range is estimated in (21).

Systematical uncertainties arise due to unknown higher order corrections. The strong scale dependence of the cross sections as well as the expected large K factors indicate the importance of such corrections. The full one-loop corrections to the photoproduction of heavy flavours are known for the one heavy quark inclusive distributions[7]. For the purpose of extracting the gluon density along the lines discussed here it is necessary to have available the analogous calculation of the di-heavy quarks invariant mass and rapidity distributions, or even better the fully differential cross section evaluated at next-to-leading-order (NLO). Such a calculation needs in addition a correct treatment of the bound state system to that order for J/Ψ events. Consistent NLO calculations require the inclusion of the resolved photon processes with appropriate caveats of double counting the collinear contributions. It is clear that our results have to be interpreted as the extraction of the leading order gluon density. A determination accurate to NLO would require the implementation of the above mentioned corrections. Let us add that at the high cms energies at LEP/LHC a description based on fixed order QCD calculations (even with the inclusion of the NLO corrections) might not be adequate due to large logarithmic terms[16] like m_{TQ}^2/s where $m_{TQ}^2 = p_{TQ}^2 + m_Q^2$. It would be very useful to compare with an alternative description where such terms are resummed to all orders.

With the very small values of x reachable at LEP/LHC one will likely enter a region where the standard QCD evolution à la Dokshitser, Gribov, Lipatov, Altarelli, and Parisi[17] ceases to be valid. Screening corrections are expected to become sizeable[18]. The analyses presented here use the conventional approach[17] in the evolution of the parton densities. New calculations of cross sections and differential distributions based on the improved evolution scenario are necessary and eagerly awaited.

All of the above results are obtained assuming that LEP/LHC is run solely at a fixed cms energy ($\sqrt{s} = 1.26 \text{ TeV}$). Data at different cms energies are highly desirable to check the theoretical predictions and to put the description of the events on a firmer basis. Changes of \sqrt{s} will also move the accessible x_g ranges accordingly. The value of the scale $\mu = \sqrt{\hat{s}}$ is not expected to be affected for J/Ψ production since the rate is relatively low and thus the steeply falling \hat{s} -distribution is probed essentially at $\hat{s}_0 = (m_\Psi + 2p_T)^2 \approx 25 \text{ GeV}^2$, roughly independent of \sqrt{s} . In the case of open heavy flavour production, however, there is strong correlation between the average scale and the cms energy. Here runs of LEP/LHC at various cms energies would clearly allow measurements of the gluon density over a wide $\{x, Q^2\}$ region.

References

- [1] G. Ingelman, *Structure function measurements at LEP/LHC*, these proceedings.
- [2] J. Blümlein, *QCD tests at LEP/LHC*, these proceedings.
- [3] N. Magnussen and G. A. Schuler, *Extracting the gluon density from the longitudinal structure function*, these proceedings.
- [4] S.M. Tkaczyk, W.J. Stirling and D.H. Saxon, in proceedings of the HERA workshop, DESY, Hamburg 1987.
- [5] G. D'Agostini and D. Monaldi, DESY preprint, DESY 90-015 (1990).
- [6] J.G. Morfin and Wu-Ki Tung, Fermilab-Pub-90/74 (1990).
- [7] R. K. Ellis and P. Nason, Nucl. Phys. B312 (1989) 551;
W. Beenakker, W. L. van Neerven, R. Meng, G. A. Schuler and J. Smith, DESY preprint DESY 90-064, Nuclear Physics B in press;
G. A. Schuler, DESY-89-019 and in Proceedings of the 5th workshop of the INFN Eloisatron Project, Erice, Italy 1988, Editor: A. Ali.
- [8] G. Ingelman and G. A. Schuler, Z. Phys. C40 (1988) 299.
- [9] R.Baier and R.Rückl, Nucl. Phys. B201 (1982) 1.
- [10] Z. Kunszt and W.J. Stirling, Phys. Lett. B217 (1989) 563;
R.S. Fletcher, F.Halzen and R.W.Robinett, Phys. Lett. B225 (1989) 1.
- [11] C. Albajar et al., Phys. Lett. B200 (1988) 381;
E.W.N.Glover, F.Halzen and A.D.Martin, Phys. Lett. B185 (1987) 441;
E.W.N.Glover, A.D.Martin and W.J. Stirling, Z. Phys. C38 (1988) 473.
- [12] B. van Eijk and R.Kinnunen, Z. Phys. C41 (1988) 489.
- [13] Technical Proposal for the H1 detector, H1 Collaboration (1986).
- [14] K.J. Abraham, Nikhef Preprint 91-02.
- [15] G. A. Schuler and J. F. de Trocóniz, DESY preprint in preparation.
- [16] S. Catani, M. Ciafaloni and F. Hautmann, Phys. Lett. B242 (1990) 97.
- [17] Yu.L..Dokshitser, Sov.Phys.JETP 46, 641(1977);
V.N.Gribov and L.N.Lipatov, Sov.Journ.Nucl.Phys. 15, 438 and 675 (1972);
G.Altarelli and G.Parisi, Nucl.Phys. 126, 297(1977).
- [18] *Proceedings of the Small-x Workshop*, held at DESY, May 1990 (to be published in *Nucl.Physics*, ed.A.Ali and J.Bartels).

Figure captions

- Figure 1 p_T distributions of the various J/Ψ production mechanisms: direct production (solid line, eq. (2)), resolved photon contributions (dashed line, eq. (4)), and b decays (dashed-dotted line, eq. (3)). The curves show the Monte Carlo p_T^Ψ distributions where no cut was applied.
- Figure 2 Monte Carlo distributions in the polar angle in the Lab system, $d\sigma/d\cos\theta$, of J/Ψ 's produced via the direct process (solid line) and the hadronic component of the photon (dashed line). Only a cut $p_T^\Psi > 1$ GeV was applied.
- Figure 3 Distributions in the variable z (eq. 6) for J/Ψ 's events after demanding that they can be reconstructed in the tracking system and after a cut $p_T^\Psi > 1$ GeV. Monte Carlo results for the direct process as solid line, for the hadronic component of the photon in dashes. Distributions in the reconstructed z_{rec} (eq. 8) in dash-dots for the direct channel and in dots for the resolved photon one.
- Figure 4 The correlation y vs. the reconstructed y_{rec} (eqs. 7 and 9) for J/Ψ production via the direct process (a) and the hadronic component of the photon (b). Correlation y_p vs. y_{rec} (eq. 10) in Fig. 4c.
- Figure 5 The correlation x_g vs. the reconstructed x_g^{rec} for J/Ψ 's production via the direct process (a) and the hadronic component of the photon (b). The resolution of the reconstructed x_g^{rec} (c).
- Figure 6 The reconstructed gluon density from J/Ψ production with statistical error bars corresponding to an integrated luminosity of $50 pb^{-1}$ for set B1 and $20 pb^{-1}$ for set B2 (upper points). Also shown are the input gluon densities set B1 and B2 (dashed line) of ref.[6].
- Figure 7 The correlation y_{ll} vs. \hat{y} (eq. 19) for open heavy quark production.
- Figure 8 Probability distribution that the true $x_g = 10^{-3}$ is reconstructed as x_g^{rec} for open heavy quark production.
- Figure 9 The reconstructed gluon density for open heavy quark production including systematic and statistical errors. Also shown are the input gluon density (set B1 of ref.[6]) and the gluon density B2 of ref.[6] both evaluated at the average scale $\langle \mu^2 \rangle = \langle \hat{s} \rangle (x_g)$.
- Figure 10 The reconstructed gluon density for open heavy quark production including systematic and statistical errors for the sample with $\sum E_T > 10$ GeV and for the sample with increased cut $\sum E_T > 35$ GeV (upper points). Also shown is the input gluon density (set B1 of ref.[6]) evaluated at the respective average scales $\langle \mu^2 \rangle = \langle \hat{s} \rangle (x_g)$ corresponding to the two samples $\sum E_T > 10$ GeV and $\sum E_T > 35$ GeV.

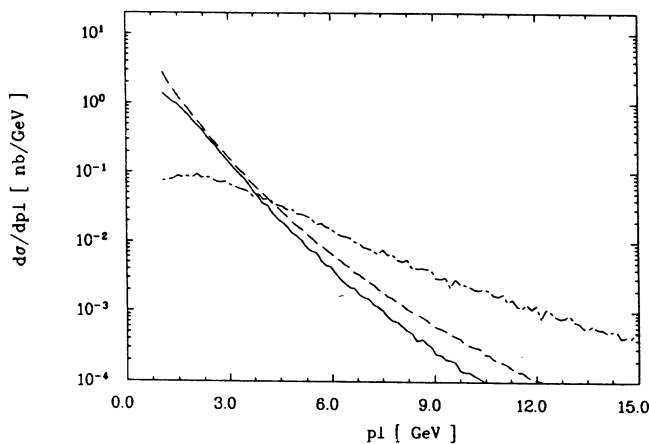


Fig. 1

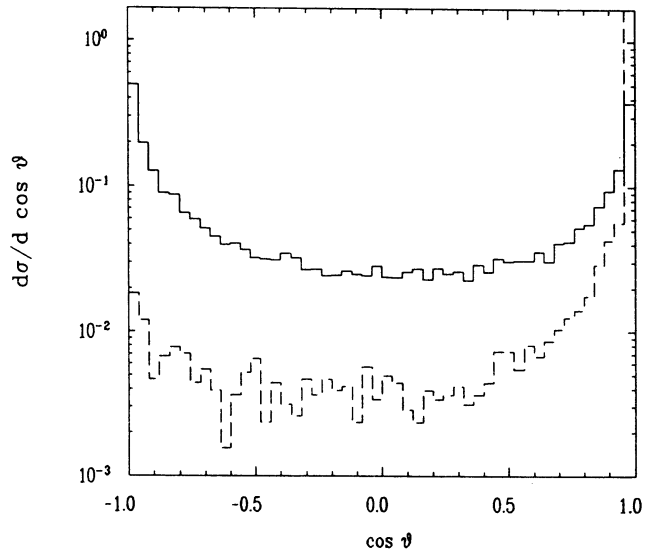


Fig. 2

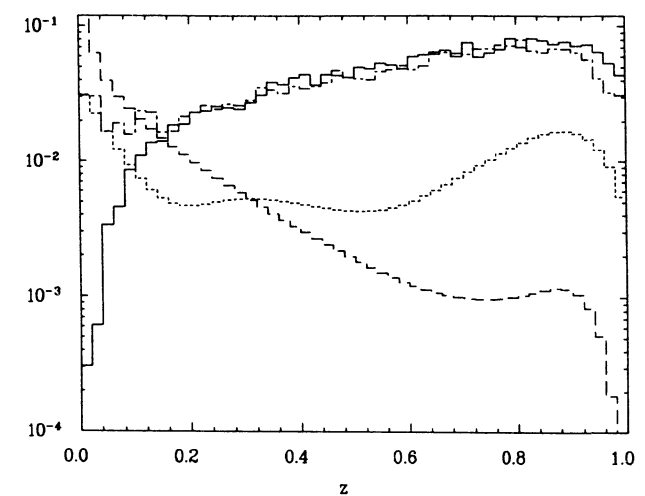


Fig. 3

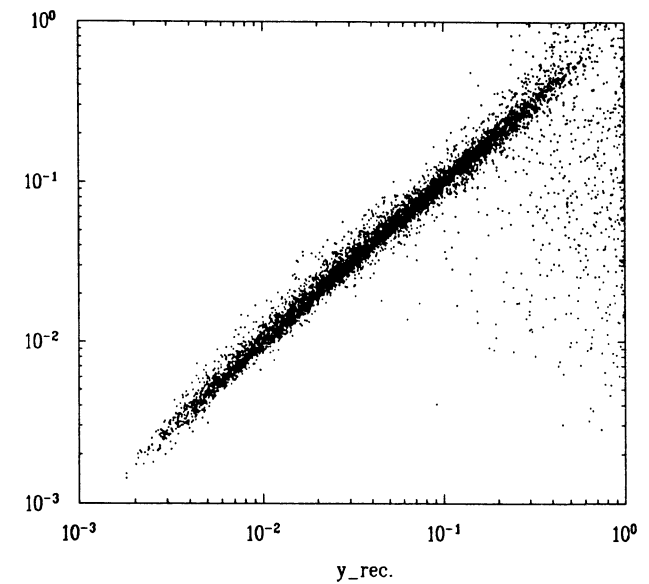


Fig. 4 a

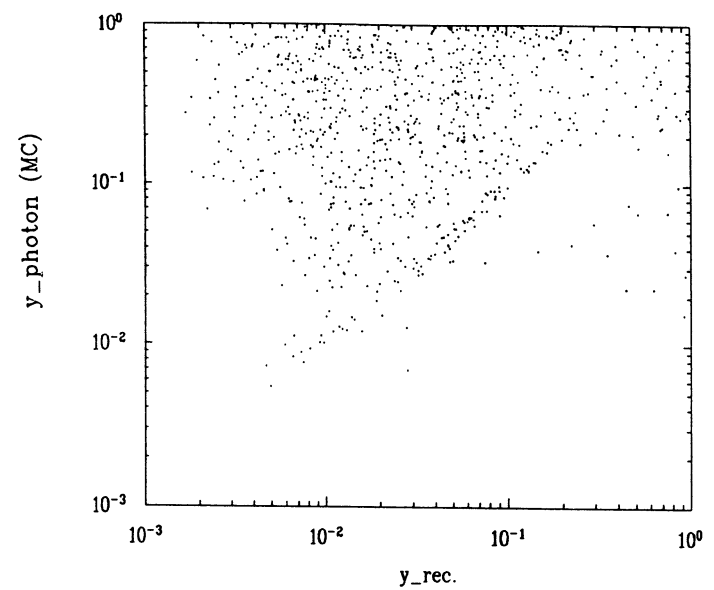


Fig. 4 b

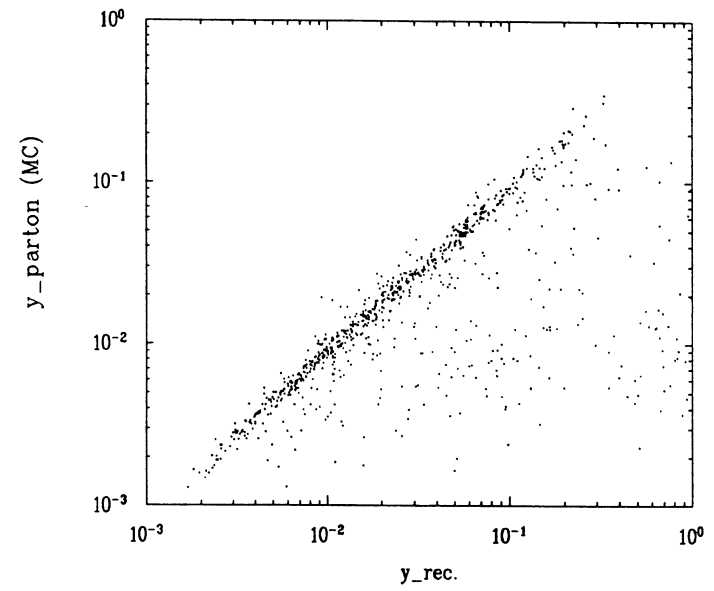


Fig. 4 c

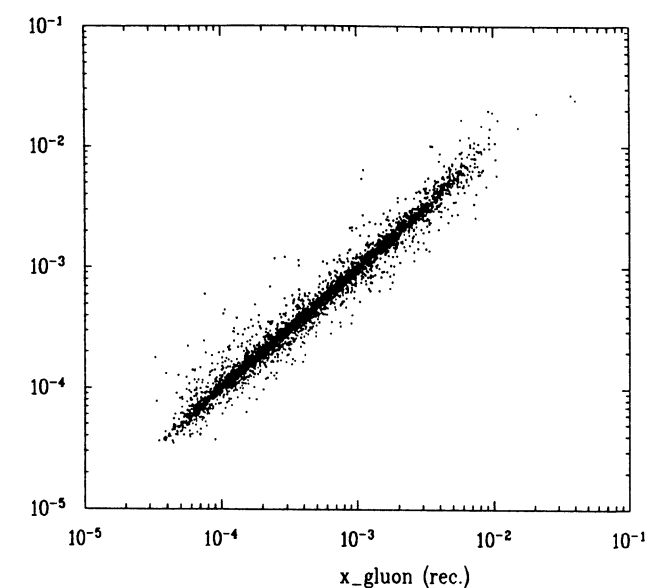


Fig. 5 a

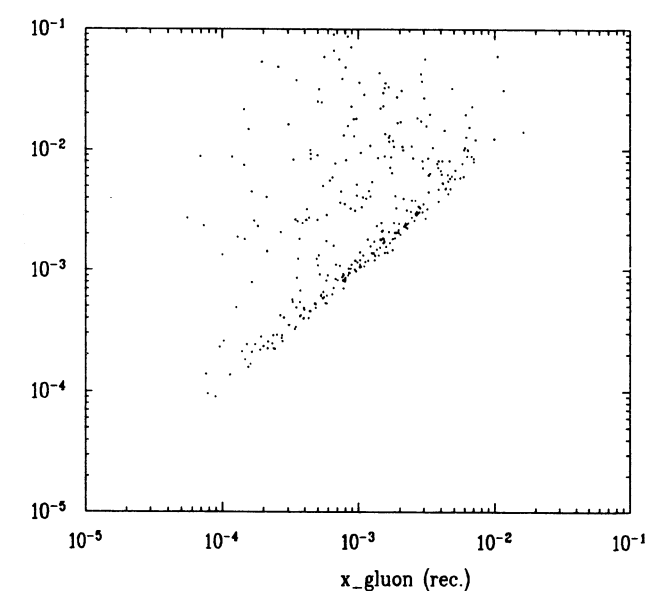


Fig. 5 b

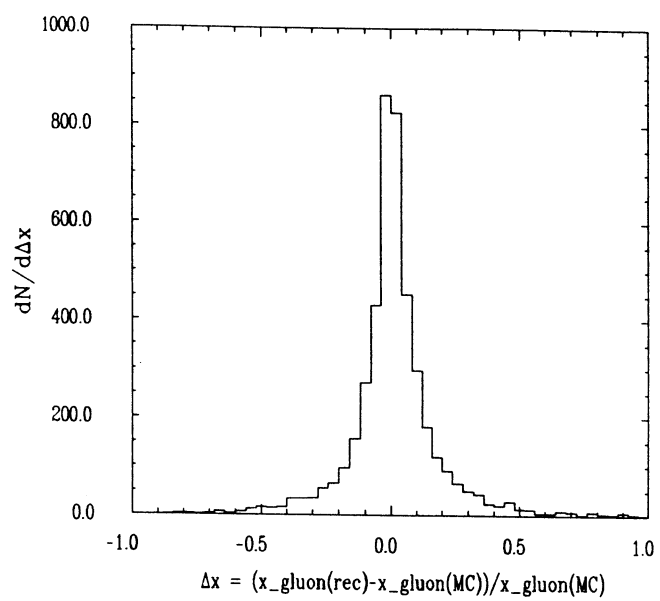


Fig. 5 c

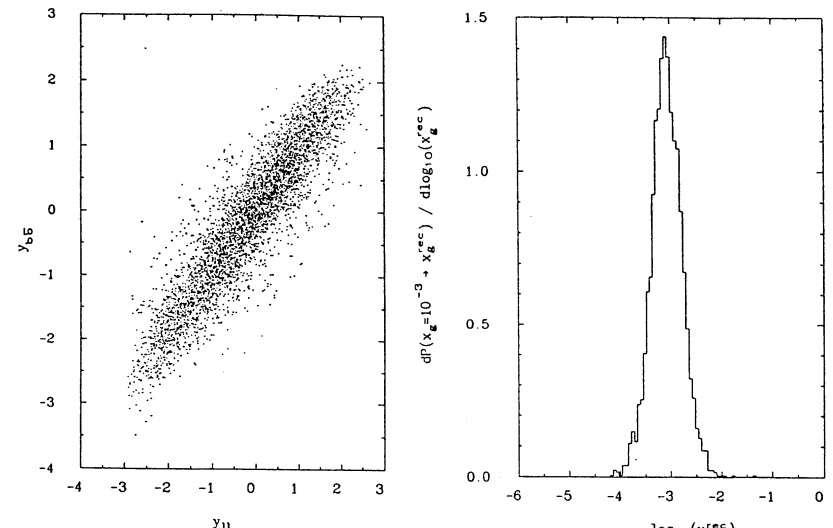


Fig 7

Fig 8

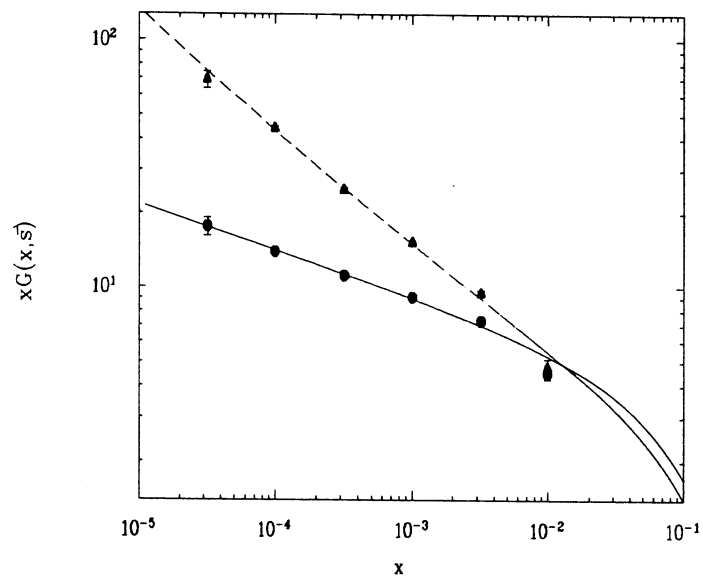


Fig. 6

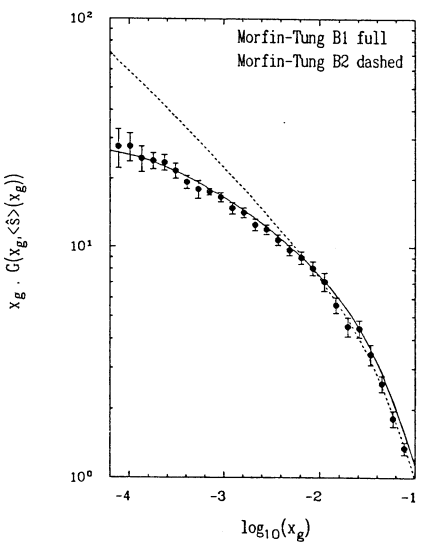


Fig 9

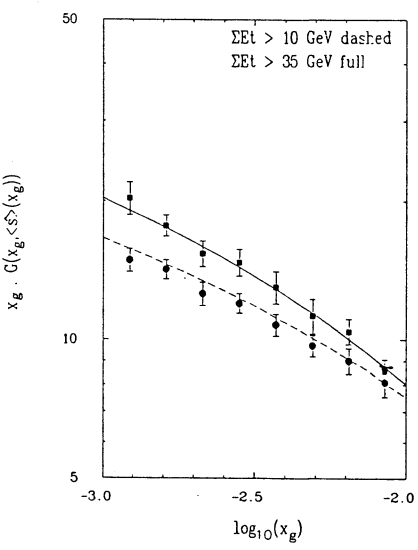


Fig 10

Heavy Quark Physics in ep Collisions at LEP+LHC

Abstract

A. Ali

Deutsches Elektronen Synchrotron DESY
Hamburg, Fed. Rep. Germany

F. Barreiro, J.F. de Trocóniz

Universidad Autónoma de Madrid, Madrid, Spain

G.A. Schuler

II Inst. f. Theor. Phys. der Universität Hamburg
Hamburg, Fed. Rep. Germany

J.J. van der Bij

Inst. voor Theor. Fysica, Univ. van Amsterdam
Amsterdam, The Netherlands

We study electroweak production of heavy quarks- charm, beauty, and top- in deep inelastic electron-proton collisions at the proposed LEP+LHC collider at CERN. The assumed energy for the collisions is $E_e = 50 \text{ GeV}$, $E_p = 8000 \text{ GeV}$, providing an ep center of mass energy, $\sqrt{s} \simeq 1.26 \text{ TeV}$. We invoke the boson-gluon fusion model to estimate theoretical cross sections and distributions for the heavy quarks. Higher order QCD corrections are only approximately taken into account, by assuming a (normalization) K-factor of 2 for the charm and beauty quark production rates and incorporating the parton shower cascades. With these assumptions and the parametrization of Eichten et al. for the structure functions (EHLQ, set 1), we find the following cross sections: $\sigma(ep \rightarrow c + X) \simeq O(3 \mu b)$, $\sigma(ep \rightarrow b + X) \simeq O(40 nb)$, and $\sigma(ep \rightarrow t + X) \simeq 4 pb$ for $m_t = 120 \text{ GeV}$, decreasing to $0.5 pb$ for $m_t = 250 \text{ GeV}$. These cross sections would provide $O(6 \times 10^9)$ charmed hadrons, $O(8 \times 10^7)$ beauty hadrons, and $O(10^3)$ top hadrons, for an integrated ep luminosity of 1000 pb^{-1} . The heavy quark rates in ep collisions are considerably smaller than the corresponding rates in pp collisions at LHC, with $\sqrt{s} = 16 \text{ TeV}$. This gives a clear advantage to pp collisions for top searches. However, for the charmed and beauty quarks only a tiny fraction of the cross sections in $p + p \rightarrow Q + X$ can be triggered in comparison to the corresponding cross sections in $e + p \rightarrow Q + X$, resulting in comparable number of measured heavy quark events in the ep and pp mode. We sketch the energy-momentum profile of heavy quark events in ep collisions and illustrate the kind of analyses that experiments at the LEP+LHC collider would undertake to quantitatively study heavy quark physics. In particular, prospects of measuring the particle-antiparticle mixing parameter $x_s = \Delta M/\Gamma$ for the $B_s^0 - \bar{B}_s^0$ meson system are evaluated, and search strategies for the top quark in ep collisions are presented.

1 Introduction

Heavy flavour physics is one of the central themes of high energy colliders. It is fair to say that Quantum Chromodynamics (QCD) provides an adequate account of heavy quark production at present colliders [1]. These comparisons will become more quantitative in the forthcoming experiments at Tevatron ($p\bar{p}$) and HERA (ep). The interest in the charmed and beauty physics at future colliders lies mainly in the hopes that the anticipated high rates could be advantageously used to do high precision physics, including rare decays and possibly CP violation. In exploring the potential of c- and b- quark physics at the LEP+LHC collider we have, therefore, concentrated on those aspects which could be characterized as search for new phenomena which may possibly be studied in ep collisions.

The situation with the top quark is, however, quite different with the top quark becoming more and more conspicuous due to its continued absence. Hence the primary goal is to find the top quark and measure its mass with a reasonable accuracy. Unfortunately, the present lower bound on the top quark mass, $m_t \geq 91$ GeV [2], and indirect mass estimates from the electroweak radiative corrections yielding $m_t = 140 \pm 40$ GeV [3]–[6], have pushed the top quark discovery threshold beyond the reach of the presently operating and about to be commissioned accelerators in Europe. This list includes the CERN colliders, $SppS$, LEP(I), LEP(II), and the ep collider HERA at DESY. In the foreseeable future the Fermilab $p\bar{p}$ collider is best poised for bagging the top quark [7]. Future pp colliders, SSC and LHC, have robust rates for even (unrealistically) heavy quarks [1], [8]–[12], and hence hadron colliders are the most natural habitat of the elusive top quark. The potential of an ep collider, such as LEP+LHC, is of exploratory nature as far as top quark physics is concerned.

We argue here that a top quark with a mass less than or equal to 200 GeV can be produced and discovered in ep collisions at the LEP+LHC collider. This optimism is based on theoretical calculations for the two relevant production mechanisms $e + p \rightarrow \nu + \bar{t} + b + X$ and $e + p \rightarrow e - t + \bar{t} + X$, shown in Fig. 1. The integrated cross sections for the two processes and their sum as a function of the top quark mass are shown in Fig. 2. They have been calculated for ep collisions with $E_e = 50$ GeV and $E_p = 8000$ GeV, giving $\sqrt{s} \simeq 1.26$ TeV. With an integrated luminosity of 1000 pb^{-1} these cross sections yield ~ 3500 top quark events for $m_t = 120$ GeV, with the rate decreasing to ~ 500 events for $m_t = 250$ GeV. Top quarks in the standard model decay mainly via $t \rightarrow b + W^+$, giving rise to the dominant final state $e + p \rightarrow \nu + b + \bar{b} + W^- + X$, involving a W boson and a pair of $b\bar{b}$ quarks. With the above mentioned rate estimates, we undertake two complementary analyses based on the decay $\bar{t} \rightarrow \bar{b} + W^-$, followed by the leptonic decay $W^- \rightarrow l^- + \nu_l$ and the hadronic decay $W^- \rightarrow q + \bar{q}'$. The former decay would give rise to the final state containing a (b-quark)-jet, an l^- , and large missing transverse momentum, \not{p}_\perp . We shall call this analysis the semileptonic top quark analysis. The latter decay mode of the top quark would give rise to multijet final states, emanating from the 3-parton decay $t \rightarrow b + W^+ \rightarrow b + q + \bar{q}'$, and we call this the hadronic top quark analysis.

An estimate of the number of background events in ep collisions at the LEP+LHC collider at $\sqrt{s} \simeq 1.26$ TeV for an assumed luminosity of 1000 pb^{-1} is given in Table 1 (section 2). Though the background from the deep inelastic charged current CC and neutral current NC processes (both low and high Q^2), as well as from the c- and b- quark production is huge in comparison with the expected number of top quark events, this can be brought down to a tolerable level by imposing a series of topological and kinematic cuts, which are detailed

in the text. We remark that the hardest background in both the semileptonic and hadronic analysis emerges from the processes in which a W^\pm is radiated off the lepton or the quark line. The production of a real W^- boson, with or without additional jet(s), gives rise to event topologies in which the top quark signals are being sought. Not surprisingly, the real W-events directly produced (background) and the ones emerging as secondary particles in top quark decays (signal) behave qualitatively similarly.

To improve the signal to background (S/B) ratio, one may have to demand b-quark tagging as the top quark production always leads to $W^- + b + \bar{b}$ or $W^+ W^- + b + \bar{b}$ events. Since the directly produced $W^\pm X$ background events are expected to be poor in b-quark, b-tagging is going to play a crucial role for top quark searches. In the analyses presented below, we impose b-tagging by demanding a charged lepton inside a jet (i.e., not isolated lepton) having $p_\perp > 5$ GeV. This improves the S/B ratio, but at a considerable cost of top quark events. This reduction in rate could be overcome if one could use a microvertex detector, which, for instance in the context of photoproduction of charmed hadrons, has so successfully been used to suppress the dominant background due to the light quarks at lower energies [13]. In Tables 3 and 4 we take the reader through a myriad of kinematic cuts, to suppress the background in top quark searches. It is clear from these tables, that the LEP+LHC collider would have a sensitivity (at $\geq 5\sigma$ level) to the top quark for $m_t \leq 200$ GeV. The hadronic analysis provides a good estimate of the top quark mass through the invariant mass of the 3-jets coming from top decays, where the jets have been defined by a typical algorithm, such as the one used by the UA1 collaboration. To simulate experimental conditions, we have smeared the invariant mass distributions of the jets with a Gaussian function of width $\Delta m_t = 15$ GeV. The resulting distributions still allow to observe the invariant mass peak due to the top quark.

We now turn to the discussion of charmed and beauty quark physics in ep collisions at the LEP+LHC collider. To simulate their production and decays we have used the Monte Carlo programme AROMA [14], which was developed for heavy flavour studies at HERA. We caution that there are considerable uncertainties in the theoretical underpinning of the event generator being used and hence in the projections presented here. They pertain in part to the gluon density, which would be probed at HERA and LEP+LHC colliders at very small x-values. There are good arguments to expect that the gluon density at small-x would show a certain saturation behaviour due to the QCD non-linear evolution effects [15]–[18]. This behaviour is hard to quantify at this stage and we have used the conventional approach in the evolution of the parton densities [19], [20]. In part, the uncertainties are also due to the presence of large logarithm terms like $(\alpha_s \log(4m_Q^2/s))^n$ in $\sigma(ep \rightarrow Q + X)$ [21], [22], which will have to be resummed in all orders –something which has not yet been accomplished. We also remark that colour coherence influences the attendant partonic radiation accompanying the $Q\bar{Q}$ pair in $e + p \rightarrow Q + X$ events [23], an effect which has still to be incorporated in the programme being used.

We content ourselves here with incorporating the QCD corrections by an effective K-factor, which increases the $e + p \rightarrow Q + X$ cross section, evaluated in the lowest non-trivial order, by $K=2$ for both $\sigma(ep \rightarrow c + X)$ and $\sigma(ep \rightarrow b + X)$. For the structure functions we use the EHLQ (set 1) parametrization [24], with the number of quark flavours $n_f = 5$ in both the parton evolution and α_s . With these inputs we determine : $\sigma(ep \rightarrow c + X) = 2.8 \text{ } \mu\text{b}$, $\sigma(ep \rightarrow b + X) = 40 \text{ nb}$ at $\sqrt{s} \simeq 1.26$ TeV. These rates should be contrasted with the corresponding estimated rates $\sigma(ep \rightarrow c + X) \sim 1 \text{ } \mu\text{b}$ and $\sigma(ep \rightarrow b + X) \sim 10 \text{ nb}$, at HERA with $\sqrt{s} = 314$ GeV [25]. The estimated increase in cross sections between the HERA and

LEP+LHC energies is a factor ~ 3 for $\sigma(ep \rightarrow c + X)$, and a factor ~ 4 for $\sigma(ep \rightarrow b + X)$. With an integrated luminosity of 1000 pb^{-1} , one would have $\sim 6 \times 10^9$ charmed hadrons and $\sim 8 \times 10^7$ beauty hadrons in ep collisions at LEP+LHC. These potentially large rates could be put to good use if one has a dedicated ep detector, having good particle identification, energy momentum resolution, and a functional microvertex detector.

Note that the cross-sections for producing the charmed and beauty hadrons in ep collisions at the LEP+LHC collider though large are no where close to the corresponding cross-sections in $p+p \rightarrow Q+X$ at LHC, which are estimated to be: $\sigma(pp \rightarrow c+X) \sim O(1 \text{ mb})$ and $\sigma(pp \rightarrow b+X) \sim O(100 \mu\text{b})$. Thus, the rates in ep collisions at LEP+LHC are typically 3-4 orders of magnitude smaller than at LHC(pp) with $\sqrt{s} = 16 \text{ TeV}$. The large rates in the pp mode are not necessarily an advantage, since rates of $\sim 10 \text{ MHz}$ for the charmed hadrons and $\sim 1 \text{ MHz}$ for the beauty (for a luminosity of $10^{34} \text{ cm}^{-2} \text{ s}^{-1}$ in pp collisions) can not possibly be triggered. So, only charmed and beauty hadron events with large transverse momentum will actually be measured in pp collisions. Since the cross sections at LEP+LHC are smaller and the intended ep luminosity typically $10^{32} \text{ cm}^{-2} \text{ s}^{-1}$, the charmed and beauty quark events in ep collisions will have a frequency of $\sim 300 \text{ Hz}$ and $\sim 4 \text{ Hz}$, respectively, which are probably measurable without much data reduction. We expect that the trigger conditions may lead to comparable measured cross sections for the charmed and beauty hadrons in the ep (LEP+LHC) and the pp (LHC) modes.

Production of heavy quarks in ep collisions would allow a very precise measurement of the gluon structure function, in particular at very small values of the x_g -variable, where x_g is the fractional energy of the proton that a gluon carries. Because of the impending interest in the small- x_g region, it would be worthwhile to use the charm and beauty hadrons as sensitive probes of the new QCD dynamics. We calculate the rates for some useful heavy quark final states in ep collisions and find that a trigger, based on the transverse hadron energy of say 10 GeV measured in the pseudorapidity interval $|\eta| \leq 3$, would make x_g -values as small as 10^{-5} accessible at the LEP+LHC collider. If in addition, a charged lepton (electron or muon) having $p'_\perp \geq 1 \text{ GeV}$ is required as a heavy quark tag, then still x_g -values as small as $\sim 6 \cdot 10^{-5}$ would be reachable. Likewise, the process $e + p \rightarrow J/\psi + X$ has rather large cross-section. Using the dileptons from J/ψ decays to trigger on heavy quarks, it has been estimated in an accompanying report, that x_g -values as small as $3 \cdot 10^{-5}$ could be measured in ep collisions at LEP+LHC [26]. These issues will be studied at HERA with the view of measuring the gluon saturation effects. The larger energy at LEP + LHC would allow to probe the gluon structure function at an order of magnitude smaller x_g -values.

There is one specific issue that we have investigated for the process $e + p \rightarrow b + X$, namely the decay length distributions of the beauty hadrons and the prospects of measuring oscillation length for the $B_s^0 - \bar{B}_s^0$ transition. We recall here that the ratio $x_d = \Delta M/\Gamma$ for the $B_d^0 - \bar{B}_d^0$ system has already been measured by the ARGUS and CLEO collaborations [27], [28] with the result: $x_d = 0.65 \pm 0.13$. This is a landmark measurement in b-physics. The corresponding ratio for the $B_s^0 - \bar{B}_s^0$ transition, x_s , is expected to be very large, with present expectations dispersed in the range $3 \leq x_s \leq 30$. Measuring x_s is going to be a hard nut to crack, not only for experiments at the ep colliders but at any collider [29]–[35]. It is now generally agreed that the measurement of x_s may require at least $O(10^7)$ beauty hadrons, which is attainable in ep collisions at the LEP+LHC collider with an integrated luminosity of 1000 pb^{-1} . The real question is how many of these events will survive the trigger conditions, and how many of the B_s^0 -hadrons can actually be identified and/or reconstructed.

We recall that at present only time integrated information on the mixing measures $x_i = x_i^2/2(1+x_i^2)$, $i=d,s$, is available. The weighted mixing average $\chi = \chi_d P_d + \chi_s P_s$ (with P_d and P_s being the branching ratios for $b \rightarrow B_d$ and $b \rightarrow B_s$, respectively) has been measured in a number of $\epsilon^+\epsilon^-$ annihilation and $p\bar{p}$ collision experiments. Some representative measurements of χ are [36]:

$$\chi = 0.160 \pm 0.040 \pm 0.020 \quad (\text{UA1})$$

$$\chi = 0.130 \pm 0.045 \quad (\text{ALEPH})$$

$$\chi = 0.178 \pm 0.049 - 0.040 \quad (\text{L3})$$

In particular, the L3 collaboration has quoted a lower bound: $\chi_s > 0.14$ at 90% confidence level [37]. These measurements will very likely be improved at LEP [43], Tevatron [38] and HERA [25]. The improvement of the statistical errors in χ may allow to check the expectations in the standard model $\chi_s \sim 0.5$, but it may not allow a meaningful determination of the quantity x_s , partly due to the model dependent branching ratios P_d, P_s , but more importantly due to the (theoretically expected) large value of x_s , for which deviations from perfect mixing, $\propto (1/2 - x_s^2/2(1+x_s^2))$, become quadratically insensitive to x_s . One may be forced to measure the time-dependent oscillation phenomena, i.e. oscillation lengths, to be able to determine x_s . The oscillation lengths of a hadron may be defined as:

$$\lambda_{osc} = (2\pi/c)\gamma\beta c\tau \quad (1)$$

where γ and β are the Lorentz factors, and $c\tau = 300 \mu\text{m}$ for beauty hadrons. Note that λ_{osc} is inversely proportional to the mixing ratio $x_i, i = d, s$, in contrast to the quadratic dependence of χ_i on x_i . The only measurable oscillating component in the decay lengths is expected to be due to the $B_s^0 - \bar{B}_s^0$ transition. The point is that the oscillation length for the $B_d^0 - \bar{B}_d^0$ transition is just too long to be measurable; all other B-hadrons (except B_s) decay exponentially. So, one has to measure the small but characteristic sinusoidal (oscillating) component against a large and (almost) exponentially falling background. In doing this, one has to separate the time evolution of the right-sign meson, i.e. $B_s \rightarrow B_s$, and the wrong-sign meson, $B_s \rightarrow \bar{B}_s$, since otherwise no deviation from the background would be seen. This would require B_s -tagging in some functional form. We have not investigated the all important question of the efficiency of B_s -meson tagging and the resulting precision on the B_s hadron energy, which are the real limiting factors in estimating the error on the proper time resolution. A detector-oriented detailed study has to follow our first estimates here to ascertain whether or not the $O(10^7)$ $e + p \rightarrow b + X$ events anticipated at the LEP+LHC collider are sufficient to measure x_s , and the attainable accuracy.

The final states which we have analysed here are the same in which most of the mixing phenomena in the $B^0 - \bar{B}^0$ sector todate have been observed in time integrated experiments, namely the same sign and opposite sign dileptons. The differential (in length) distributions for the processes $e + p \rightarrow b + \bar{b} + X \rightarrow l^\pm l^\pm + X$ and $e + p \rightarrow b + \bar{b} + X \rightarrow l^\pm l^\mp + X$, after subtraction of the background, should show the sinusoidal behaviour characteristic of the $B_s^0 - \bar{B}_s^0$ oscillation. For this study we have assumed a (Gaussian distributed) resolution of $100 \mu\text{m}$ in the reconstruction of decay length - a requirement which a microvertex detector should easily be able to meet. Since the error on proper time arises also from the error on the B-hadron momentum, this has to be measured with a reasonable accuracy (say 10%). The result for the opposite sign dileptons with the (assumed) indicated B-hadron energy binning and $x_s = 10$ is shown in Fig. 23. The main difficulty in determining x_s via dilepton final states is the (anticipated) large error in the determination of the B-hadron energy and

it is very likely that the experimental distributions would be smeared over a much larger energy range than what we have assumed in our study, thereby degrading the nice oscillating patterns being shown here. Consequently, the relative error $\Delta x_s/x_s$, that one could get from this method could be rather large. Nevertheless, it will be a determination of x_s . Of course, at some point all the sensitivity will be lost if x_s is very large, say $x_s \geq 15$, since the oscillations would become too fine grained to be resolved.

The paper is organized as follows. Section 2 describes the estimates of the heavy quark cross sections in ep collisions at the LEP+LHC collider. Strategies for the top quark search using the semileptonic and hadronic final states are also presented in this section. Section 3 contains an energy momentum profile of the charmed and beauty hadrons at the LEP+LHC collider, including estimates of the decay lengths for the beauty hadrons and (x_s)-dependent oscillation lengths. The measurements of the gluon density at very small values of x_g using inclusive lepton final states is also taken up in this section; the inclusive J/ψ -production in this context is being discussed elsewhere [26]. We conclude with a summary in section 4.

2 Top Quark Searches at LEP(I)+LHC

2.1 Estimates of cross sections

In QCD, the leading order contribution to heavy quark production is due to the boson-gluon mechanism shown in Fig. 1 [39]–[42]:

$$CC : W^- + g \rightarrow \bar{t} + b; \bar{c} + s, \dots \quad (2)$$

$$NC : \gamma/Z + g \rightarrow \bar{t} + t; \bar{b} + b; \bar{c} + c \quad (3)$$

giving rise to the processes

$$e(l_e) + p(P) \rightarrow \nu_e(l') + \bar{Q}(p'_f) + Q'(p_f) + X \quad (4)$$

$$e(l_e) + p(P) \rightarrow e(l') + \bar{Q}(p'_f) + Q(p_f) + X \quad (5)$$

where the 4-momenta of the particles are indicated. The definition of the kinematic variables follows the standard notation:

$$\hat{s} = (p_f + p'_f)^2 \quad (6)$$

$$Q^2 = -q^2 = -(l_e - l')^2 \quad (7)$$

$$W^2 = (P + q)^2 \quad (8)$$

$$x = \frac{Q^2}{2P \cdot q} \quad (9)$$

$$y = \frac{P \cdot q}{p \cdot l_e} \quad (10)$$

with the obvious relations

$$Q^2 = xys \quad (11)$$

$$W^2 = Q^2 \frac{(1-x)}{x} + m_p^2 \quad (12)$$

NC	CC	νW^-	$e W^-$	$c\bar{c}$	$b\bar{b}$
$4.3 \cdot 10^9$	$2.4 \cdot 10^5$	960	$2.8 \cdot 10^4$	$2.8 \cdot 10^9$	$4 \cdot 10^7$

Table 1: Expected number of background events in ep collisions at the LEP+LHC collider with an integrated luminosity of $1 fb^{-1}$. The cuts are explained in the text.

$$\hat{s} = Q^2 \frac{(x_g - x)}{x} \quad (13)$$

and x_g has been defined earlier. Note that $x_g \gg x$, in general.

The Monte Carlo generator AROMA [14], used in the calculations, is based on leading order QCD calculation for the production and weak decays of heavy quarks. The NC and CC processes (for both low and high Q^2) have been simulated using the event generators AROMA [14] and LEPTO [48]. As already stated in the introduction, higher order QCD corrections have been only approximately taken into account by using the K-factors: $K(b\bar{b}) = K(c\bar{c}) = 2$, and implementing the parton shower cascades. Note, that we have set $K(b\bar{t}) = K(t\bar{t}) = 1$. Furthermore, the DIS events have been generated with the cuts $Q^2 \geq 5 GeV^2$, $x \geq 10^{-4}$ and $W^2 \geq 5 GeV^2$; and the light quark production at low Q^2 has been incorporated using the processes: $\gamma/Z + g \rightarrow q\bar{q}$; $\gamma/Z + q \rightarrow qg$, with the cuts $(p_{\perp})_q > 1 GeV$, $Q^2 < 5 GeV^2$.

The calculations presented here are rather similar to the ones undertaken for heavy quark studies at HERA [25] –with obvious differences. These lie in the higher energy at the LEP+LHC collider ($E_e = 50 GeV$, $E_p = 8 TeV$, $\sqrt{s} \simeq 1.26 TeV$) compared to HERA ($\sqrt{s} = 0.314 TeV$), and in the decay pattern of the top quark, which with $m_t \geq m_W$ now decays via $t \rightarrow b + W^+$, giving rise to a 2-body state, as compared to the 3-body decays $t \rightarrow (q\bar{q}, l^+\bar{\nu}_l) + b$, which were assumed for the top quark searches at HERA. The events at the LEP+LHC collider involving top quark decay products would then have the final state configurations:

$$ep \rightarrow e W^+ W^- b\bar{b} X \quad (14)$$

$$ep \rightarrow \nu W^- b\bar{b} X \quad (15)$$

Consequently, one has to take into account real W^\pm production including parton cascades and fragmentation to estimate this background. Estimated rates for the heavy quarks, charm and beauty, and the background events for the NC, CC and real W^- production processes, νW^- and $e W^-$, are shown in Table 1, for an integrated luminosity of $1 fb^{-1}$. These numbers correspond to the assumed value of the electromagnetic fine structure constant $\alpha^{-1} = 127$, quark masses $m_c = 1.5 GeV$, $m_b = 5.0 GeV$, and ep energy $\sqrt{s} \simeq 1.26 TeV$.

The expected numbers of top quark events for the same integrated luminosity for some representative values of the top quark mass are shown in Table 2.

The cross section $\sigma(ep \rightarrow \bar{t}X)$ for the top quark mass range $120 GeV \leq m_t \leq 250 GeV$ is plotted in Fig. 2, where the separate contributions from the NC process (γ/Z) and the CC process (W^-) are also shown. It is clear from Fig. 2 that for the plotted m_t range, the CC process $W^- + g \rightarrow \bar{t}b$ dominates, due to the (larger) available phase space, as compared to the NC process $\gamma/Z + g \rightarrow \bar{t}t$. For the central value $m_t = 140 GeV$ (hinted by the electroweak data analysis), $\sigma(ep \rightarrow \bar{t}X) = 2.5 pb$, becoming approximately $0.5 pb$ for $m_t = 250 GeV$.

In what follows, we outline top quark search strategies for an assumed top quark mass, $m_t = 150 GeV$, for which we expect 2000 events/ fb^{-1} . The analyses presented here are based

$m_t(GeV)$	120	150	175	200	225	250
number of events	3500	2050	1380	950	670	475

Table 2: Expected number of top quark events in ep collisions at the LEP+LHC collider with an integrated luminosity of $1 fb^{-1}$.

Cuts	CC	W^-	$c\bar{c}$	$b\bar{b}$	$top(150)$	$top(200)$	$top(225)$
$\Sigma E_\perp > 20 GeV$	$2.3 \cdot 10^5$	$2.6 \cdot 10^4$	$2.4 \cdot 10^7$	$4.0 \cdot 10^6$	1971	937	662
$p_\perp^l > 8 GeV$	1810	7170	$9.16 \cdot 10^4$	$9.17 \cdot 10^4$	833	429	303
$E_{acc}(0.4) < 1 GeV$	—	6275	—	$1.37 \cdot 10^4$	444	204	144
$\not{p}_\perp > 15 GeV$	—	6050	—	3	415	193	137
$N_{jet}(\eta < 2) \geq 1$	—	1925	—	1	325	141	96
$p_\perp^l > 5 GeV$	—	21	—	—	82	44	31

Table 3: Expected number of background events from the indicated processes and top quark events for an integrated luminosity of $1 fb^{-1}$, decaying semileptonically at the LEP+LHC collider with $\sqrt{s} \simeq 1.26 TeV$. The kinematic cuts on the events are indicated and the successive cuts are cumulative. The background from the NC process is completely removed by demanding a lepton with $p_\perp^l > 8 GeV$, and hence not shown here.

on both the CC top quark production process, $e + p \rightarrow \nu + \bar{t} + b + X$, and the NC process, $e + p \rightarrow e + t + \bar{t} + X$. However, we note that $\sigma(\bar{t}b) \gg \sigma(\bar{t}t)$. The top quark decays via $\bar{t} \rightarrow W^- + \bar{b}$, followed by either $W^- \rightarrow l^- + \nu_l$, giving rise to the jet + $l^- + \not{p}_\perp$ configuration, or by the hadronic decay $W^- \rightarrow q + \bar{q}$, giving rise to 3-jet events.

We shall make use of various cuts to enhance the S/B ratio, which are specific to each search strategy. Note, that in all the analyses we have assumed the beam pipe cut to be 100 mrad, and in the analysis of the NC background, a cut on Q^2 , $Q_{NC}^2 \leq 10 GeV^2$, is assumed, which is also applied to the $t\bar{t}$ production, which, of course, does not significantly reduce the top rate. The latter cut has been chosen, since for larger values of Q^2 , the scattered electron will be detected, allowing the subtraction of such events. A cut in the visible transverse energy $\Sigma E_\perp \geq 20 GeV$ is also imposed, which suppresses the background without significantly compromising the top signal.

2.2 Semileptonic Analysis for Top Quark Search

Here the charged lepton (e^- or μ^-) with the largest p_\perp is used as the top quark tag. The large energy release in top quark decay contributes to events with high p_\perp^l , with p_\perp^l measured w.r.t. the beam axis. We find that a cut on p_\perp^l of the hardest lepton in the event, $p_\perp^l \geq 8 GeV$, completely removes the NC(light quark) background and reduces the contribution from the CC events, $c\bar{c}$ and $b\bar{b}$ events by one to two orders of magnitude. However, this cut affects the real $W^- \rightarrow l^- + \nu_l$ events and top quark sample more or less in a similar way. This is shown in Fig. 3 and the numbers of events surviving this cut are displayed in Table 3.

In order to further suppress the $c\bar{c}$, $b\bar{b}$ and CC events we invoke a lepton isolation cut, which

is defined by introducing a cone centred around the lepton momentum in the pseudorapidity η and azimuthal angle ϕ space. Defining

$$\Delta R \equiv \sqrt{(\Delta\eta)^2 + (\Delta\phi)^2} \leq R_c \quad (16)$$

a lepton is considered as isolated if the transverse energy within the cone of size R_c is less than a given number. Our isolation criterion is: $E_\perp^{acc}(R_c = 0.4) \leq 1 GeV$. This cut completely removes the $c\bar{c}$ and CC events, with the $b\bar{b}$ events reduced to about 15%. Understandably, the lepton isolation cut leaves the $W^- \rightarrow l^- + \nu_l$ events practically intact and removes about 50% of the top events. At this stage, the $b\bar{b}$ and W-event samples constitute the largest background, as shown in Table 3.

The cut that is most effective in removing the $b\bar{b}$ events is the one on the missing transverse energy, \not{p}_\perp^{cut} . The point is that the dominant source of top events is the CC process, $e + p \rightarrow \nu + \bar{t} + b + X$. Thus for the signal, there are three sources of \not{p}_\perp , namely the scattered neutrino, the neutrino coming from the t decays and the beam pipe cut. In contrast, $b\bar{b}$ events are produced by the neutral current process $\gamma/Z + g \rightarrow b\bar{b}$, and for these events the distribution in \not{p}_\perp falls off very sharply. We find that $< 10 b\bar{b}$ events survive for $\not{p}_\perp^{cut} = 15 GeV$. At this point the only background that remains is from the real W-boson production processes but unfortunately it is very large, giving an S/B ratio of 415/6050!

The S/B ratio can be brought to a significant level if one demands a jet, i.e. looks for the configuration $l^- + \not{p}_\perp + jet(s)$. Defining the jets using the UA1 jet algorithm with the jet-cone size $R_{jet}(\Delta\eta, \Delta\phi) = 0.7$ and having a minimal transverse energy $\Sigma E_\perp \geq 7 GeV$, the jet multiplicity in the pseudorapidity interval $|\eta_j| < 2$, for the $t\bar{t}$, $b\bar{t}$, $b\bar{b}$ and W^-X events is shown in Fig. 4. One should draw attention to the very appreciable differences in the pseudorapidity distributions of the $e + p \rightarrow t + X$ and real W-production processes, due to the central production mechanism of the former and the fact that in the latter, the W-boson is radiated mainly from a quark line, which produces the W-bosons preferentially in the forward (i.e. proton-) direction. This effect can be seen quantitatively in Fig. 5, where we show the pseudorapidity distributions in the interval $|\eta| < 3$ for the topology of interest involving one-jet events. Demanding $N(jets) \geq 1$, with the jet(s) contained in the pseudorapidity interval of $|\eta_j| < 2$ would remove about 2/3 of the W^-X events, whereas $\sim 80\%$ of the top quark events would survive, resulting in the ratio $\frac{S}{B} = \frac{325}{1925}$, for $m_t = 150 GeV$.

The final improvement of the S/B ratio can now be achieved if one requires b-quark (jet) tagging, since the top production and decay processes involve $W^+W^-b\bar{b}$ and $W^-b\bar{b}$ states. A useful (though by no means very efficient) b-tagging can be achieved by looking for lepton(s) inside a jet. This amounts to searching for the top quark in the dilepton final states, where one of the leptons is from the W-decay and the second one from the b-quark decay. Demanding that the second lepton satisfies a p_\perp^l -cutoff of 5 GeV, the S/B ratio becomes 82/21 for $m_t = 150 GeV$, becoming 44/21 for $m_t = 200 GeV$, as shown in Table 3. This would be sufficient to establish the existence of the top quark, but unfortunately the semileptonic analysis does not allow a very meaningful determination of m_t , for which we turn to the hadronic analysis.

¹In the ep group summary report of these proceedings by R. Rückl (vol. 1), the preliminary conclusions about top quark searches were drawn from an analysis in which the eW-production background was not adequately taken into account. As shown here, this is the most significant background to top searches in ep collisions and hence additional kinematic cuts and analyses had to be done to reduce it. This has resulted in smaller S/B ratios (substantially for the semileptonic analysis but also for the hadronic), which are given in Tables 3 and 4 here.

Cuts	CC	W^\pm	$c\bar{c}$	$b\bar{b}$	$top(150)$	$top(200)$	$top(225)$
$\Sigma E_\perp > 120 \text{ GeV}$	$3.6 \cdot 10^4$	$1.4 \cdot 10^4$	$1.6 \cdot 10^4$	3300	1110	675	505
$S_{cm} > 0.25$	1046	2716	935	230	668	267	150
$N(jets) \geq 3$	701	2394	928	228	650	255	142
$p_\perp > 30 \text{ GeV}$	680	690	30	7	500	190	110
$N_{jet}(\eta < 3) = 3$	540	500	15	3	190	90	50
$N_{jet}(\eta < 3) = 4$	115	170	12	3	192	76	42
$p_\perp > 5 \text{ GeV}$	30	65	6	3	166	80	45

Table 4: Expected number of background events from the indicated processes and top quark events, decaying hadronically, at the LEP+LHC collider at $\sqrt{s} \simeq 1.26 \text{ TeV}$ and an integrated luminosity of 1 fb^{-1} . The kinematic cuts on the events are indicated and the successive cuts are cumulative. The NC process has been removed by the cuts: $S_{cm} > 0.25$, $\Sigma E_\perp > 120 \text{ GeV}$, $p_\perp > 30 \text{ GeV}$ and hence not shown. The last cut corresponds to the minimal b-tagging, discussed in the text.

2.3 Hadronic Analysis for Top Quark Search

Searches for the top quark in this section are based on the hadronic decays of the top quark

$$ep \rightarrow \nu \bar{t} b X \Rightarrow q \bar{q}' b \bar{b} X \quad (17)$$

$$ep \rightarrow e \bar{t} t \rightarrow e W^+ W^- b \bar{b} X \Rightarrow q \bar{q}' q'' \bar{q}''' b \bar{b} X \quad (18)$$

leading to 4-parton and 6-parton configurations, respectively. The hadronic analysis for the top search is complementary to the semileptonic analysis discussed in the previous section, in that for the former we demand that there are no isolated high- p_\perp leptons present in the event sample. Hence the two sets of events can be added to increase the top signal. Clearly, the number of jets seen experimentally depends on the jet definition and the efficiency of the particular algorithm. Like in the previous section we use a UA1-like jet algorithm to define jets; $R_{jet}(\Delta\eta, \Delta\phi) = 0.7$ and $E_{\perp,jet} \geq 7 \text{ GeV}$ with $\Delta\phi = 12^\circ$ and $|\eta| \leq 3$.

To reduce the background from the NC, CC and $W^\pm X$ events, we impose the cuts $\Sigma E_\perp \geq 120 \text{ GeV}$, and $S_{cm} \geq 0.25$, where S_{cm} is the sphericity defined in the hadronic c.m. system. The sphericity distributions from the top quark events and the background processes are shown in Fig. 6. The jet-multiplicity distributions from the NC, CC and $t\bar{b}$ events are shown in Fig. 7. We see that the 4-parton state (from the $t\bar{b}$ events) translates itself into 3-, 4- and 5-jet configurations due to the definition of jets. Based on Fig. 7, we impose a cut on the number of jets, $N(jets) \geq 3$, and will concentrate mostly on the 3-jet and 4-jet configurations. We remark that at this stage the $\frac{S}{B}$ ratio is $\frac{650}{4250}, \frac{255}{4250}$ and $\frac{142}{4250}$ for $m_t = 150, 200, 225 \text{ GeV}$, respectively. The quality of the top signal can be improved by demanding a cut on the missing p_\perp , $p_\perp \geq 30 \text{ GeV}$, which effectively removes the NC background (but not the CC and W^\pm events) giving a $\frac{S}{B}$ ratio of $\frac{500}{1410}, \frac{190}{1410}$ and $\frac{110}{1410}$ for $m_t = 150, 200, 225 \text{ GeV}$, respectively.

At this stage, an attempt can be made to reconstruct the top quark mass. We do this for the 3-jet and 4-jet event samples separately. Fig. 8 shows the invariant mass $m(jjj)$ distribution for the background and signal plus background event samples, with the indicated cuts and $m_t = 150 \text{ GeV}$. The corresponding distributions for $m_t = 200 \text{ GeV}$ are shown in

Fig. 9. The S/B ratios corresponding to these configurations are shown in Table 4. For the 4-jet sample, one expects that the b-jet produced in the process $e + p \rightarrow \nu + \bar{t} + b + X$ is the softest. Thus, ordering the jets in transverse energy $E_\perp^1 \geq E_\perp^2 \geq E_\perp^3 \geq E_\perp^4 \simeq E_\perp^b$, the $\frac{S}{B}$ ratio can be improved. We show the invariant mass distributions $m(j_1 j_2 j_3)$ for the background and signal plus background event samples in Fig. 10 for $m_t = 150 \text{ GeV}$; the corresponding distributions for $m_t = 200 \text{ GeV}$ are shown in Fig. 11. This gives: $\frac{S}{B} = \frac{190}{300}, \frac{76}{300}, \frac{42}{300}$ for $m_t = 150, 200, 225 \text{ GeV}$, respectively.

Finally, we show that the $\frac{S}{B}$ ratio can be significantly enhanced (albeit at the cost of rates!) if one demands some minimal b-tagging. In Fig. 12, we show the inclusive cross section for the process $e + p \rightarrow (\geq 3) - jets + l^\pm + X$ (with non-isolated lepton) at $\sqrt{s} \simeq 1.26 \text{ TeV}$, as a function of the transverse lepton energy cut-off ($p_\perp^l \geq p_\perp^{cut}$). We incorporate the requirement of b-tagging by demanding at least one lepton, with $p_\perp^l \geq 5 \text{ GeV}$. The $\frac{S}{B}$ ratio becomes in this case $\frac{166}{104}, \frac{79}{104}, \frac{45}{104}$ for $m_t = 150, 200, 225 \text{ GeV}$, respectively, for the (≥ 3)-jet sample. Invariant mass distributions for $m_t = 150$ are shown in Figs. 13. For the 4-jet sample, with the additional minimal b-tagging requirement mentioned above, the top enriched sample has the $\frac{S}{B}$ ratios of $\frac{71}{18}, \frac{32}{18}$ and $\frac{19}{18}$ for the three m_t values 150, 200 and 225 GeV, respectively, allowing a good determination of m_t , certainly up to $m_t = 200 \text{ GeV}$. The resulting $m(jjj)$ distributions are shown in Figs. 14 and 15 for $m_t = 150 \text{ GeV}$ and 200 GeV , respectively.

We would like to conclude this section by summarising the main results. The semileptonic decays of the top quark would allow to search for the top quark in the range of present theoretical interest, namely $100 \text{ GeV} \leq m_t \leq 200 \text{ GeV}$. This analysis should be able to confirm top quark signals, which probably would have been seen in the pp mode. The hadronic decays of the top quark allow a proper mass reconstruction in terms of the t-quark decay products (jets). Using a UA1-type jet algorithm, top topologies can be gleaned clearly in the 3-jet and 4-jet samples. Since decays of the top quark (almost) always imply the presence of beauty quark, some minimal b-tagging would be helpful. We find that the hadronic analysis (augmented by b-tagging) allows the reconstruction of the top quark in the mass range $100 \text{ GeV} \leq m_t \leq 200 \text{ GeV}$.

3 Charmed and Beauty Quark Physics at LEP(I)+LHC

We have presented the estimates for the heavy quark production cross sections in ep collisions at $\sqrt{s} \simeq 1.26 \text{ TeV}$ in the previous section (see Tables 1 and 2). The cross sections $\sigma(ep \rightarrow c + X)$ and $\sigma(ep \rightarrow b + X)$, in contrast to the top quark cross section $\sigma(ep \rightarrow t + X)$, are completely dominated by the NC process, $\gamma + g \rightarrow Q\bar{Q}$, in which the photon is almost real ($Q^2 \sim 0$). Consequently, the scattered electron will be lost in the beam pipe for most of charmed and beauty quark events. So, charmed and beauty hadron events in ep collisions, though basically NC processes, will have to be triggered through the (heavy quark) jet characteristics, namely the associated transverse energy and/or the leptons in the jet(s). The processes, $e + p \rightarrow c + X$ and $e + p \rightarrow b + X$ provide a very long handle on the minimum values of the variables, Q^2 and Bjorken-x, which can be measured experimentally. This is illustrated in Fig. 16, where we display the $\log(Q^2) - \log(x)$ scatter plot for the process, $e + p \rightarrow c + X$ at LEP+LHC, with $\sqrt{s} \simeq 1.26 \text{ TeV}$. Clearly, the limits in (x, Q^2) reachable in this figure are of theoretical interest only, since the actual accessibility would be much more restricted due to the trigger conditions, which we shall discuss in a while.

3.1 Profiles of charm and beauty hadrons in ep collisions

In this section, we present an energy-momentum profile of the charmed and beauty hadrons produced in ep collisions and their subsequent decays. We have used the LUND symmetric fragmentation function [49] for the fragmentation of heavy quarks.

$$f(z) = \frac{(1-z)^a}{z} \exp \frac{-bm^2}{z} \quad (19)$$

This gives an increasingly harder spectrum for heavy hadrons, in agreement with data. In addition, the standard V-A matrix elements have been used for the heavy quark decays. We start by showing the correlation between the heavy hadron energy and its polar angle, measured w.r.t. the beam axis with the proton direction being along $\theta = 180^\circ$, for the charmed ($D, D_s, \equiv F$)-mesons and B-mesons. As expected, the most energetic hadrons are along the beam and hence lost. To show this effect quantitatively, we plot in Figs. 17 the energy and polar angle distributions for the charmed hadrons, charged leptons l^\pm and kaons produced in their decays, at $\sqrt{s} \simeq 1.26 \text{ TeV}$. The effects of the beam pipe cut on the energy distributions are shown by the shaded histograms. The corresponding distributions for the NC beauty production process $e + p \rightarrow b + X$ are shown in Figs. 18. The beam pipe cut in this case also removes the fastest hadrons, which are preferentially produced along the beam direction, though the effect on the cross-sections themselves is not as drastic. We estimate that about 50 % of the $e + p \rightarrow c + X$ and 70 % of the $e + p \rightarrow b + X$ will survive the stated beam pipe cut. Thus, we expect that at $\sqrt{s} \simeq 1.26 \text{ TeV}$, $O(10^9) e + p \rightarrow c + X$ and $O(10^7) e + p \rightarrow b + X$ events per 1000 pb^{-1} would be produced in the fiducial volume of a detector in ep collisions, with detection capability over the range $|\eta| \leq 3$.

Returning to our discussion of triggers for heavy quark events in ep collisions, we evaluate the effect of successive cuts on the inclusive charmed and beauty hadron production rates. To that end we plot the distribution $\frac{d\sigma}{d\log x_g}$ for NC production of heavy quarks at $\sqrt{s} \simeq 1.26 \text{ TeV}$ for the process $e + p \rightarrow c + X$ (Fig. 19 (a)) and $e + p \rightarrow b + X$ (Fig. 19 (b)). The successive cuts used are:

- a) Transverse energy cut on the hadrons inside the fiducial volume of the detector ($E_{\perp}(\text{had.}) \geq 10 \text{ GeV}$, $|\eta(\text{had.})| \leq 3$)
- b) Non-isolated lepton(s): $N(l^\pm) \geq 1$, with $p'_\perp \geq 1 \text{ GeV}$.

With these cuts, we estimate that $\sim 1.3\%$ of the $e + p \rightarrow c + X$ and $\sim 23\%$ of the $e + p \rightarrow b + X$ events can be measured in the fiducial volume of a detector. This would correspond to a trigger rate of $\sim 3 \text{ Hz}$ and $\sim 1 \text{ Hz}$, respectively, for the charmed and beauty hadron events at LEP+LHC, with a luminosity of $10^{32} \text{ cm}^{-2} \text{ s}^{-1}$ in the ep mode. Obvious measurements here include determination of the gluon densities at very small- x_g values, via the inclusive lepton final states and/or J/ψ production, from the dominant process $e p \rightarrow c\bar{c} + X \rightarrow J/\psi + X$ as well as from the b decays, $e + p \rightarrow b + X \rightarrow J/\psi + X$. Concentrating on the inclusive lepton state, and using the cutoffs on $\Sigma E_{\perp}(\text{had.})$ and/or p'_\perp given above, one can read the accessible x_g -values from Fig. 19. We estimate that x_g -values as small as $6 \cdot 10^{-5}$ will be accessible from the inclusive lepton measurements. The corresponding minimum value of x_g , reachable through the final states $e p \rightarrow c\bar{c} + X \rightarrow J/\psi + X$, has been estimated to be $x_g(\text{min.}) \simeq 3 \cdot 10^{-5}$ in an accompanying report [26].

This highly enriched charmed and beauty hadron data set can be analysed to search for rare and new phenomena. In particular, searches for the flavour changing neutral current

processes in the charmed and beauty hadron decays are topics of obvious interest. Experimental goals here include, among others, measurements of the transitions $D^0 \rightarrow l^+ l^-$; $D^0 - \bar{D}^0$ oscillations, measured through, for example, the doubly Cabibbo-suppressed decays or $e + p \rightarrow l^\pm l^\pm + X$, with only $c \rightarrow s$ decay vertices; and, as noted already, the $B_s^0 - \bar{B}_s^0$ oscillation, measured via $e + p \rightarrow l^\pm l^\pm + X$, with secondary vertices which would come from the $b \rightarrow c \rightarrow s$ decays. The quantity χ , defined earlier, can be measured by the (time integrated) inclusive same-sign to opposite-sign dilepton rates. We shall exemplify this class of phenomena through the analysis geared to measure $B_s^0 - \bar{B}_s^0$ oscillation parameter, x_s .

3.2 Prospects of x_s - measurements at LEP(I)+LHC

Since the mixing ratio for the $B_d^0 - \bar{B}_d^0$ is known, a measurement of the corresponding ratio x_s for the $B_s^0 - \bar{B}_s^0$ could be used in a model independent way (up to SU(3) breaking effects) to determine the Cabibbo-Kobayashi-Maskawa (CKM) matrix element ratio $|V_{ts}/V_{td}|^2$, via the relation [50]:

$$\frac{x_s}{x_d} = \left| \frac{V_{ts}}{V_{td}} \right|^2 (1 + \Delta) \quad (20)$$

where $\Delta \sim O(\text{SU}(3) \text{ breaking}) \sim 0.2 - 0.5$. The above measurement can be combined with the unitarity constraint, $|V_{ts}| = |V_{bc}| \sim 0.04$, to provide a very good measurement of the (otherwise difficult to measure) CKM matrix element, V_{td} . We shall use the present measurement of $x_d \sim 0.65$, and the anticipated value $|V_{td}| \sim \sin(\theta_c)|V_{ts}| \simeq 0.01$, and $\Delta = 0.2$, to get a ball park estimate of x_s . This gives $x_s \sim 24$ $x_d \sim 15$. Such a large value of x_s is also expected for $m_t \sim 140 \text{ GeV}$, a value hinted upon by the recent electroweak analysis, and theoretical expectations that the pseudoscalar coupling constant for the B-mesons has a value $\geq 200 \text{ MeV}$ [51]. A value of x_s that large would not lend itself to be culled from time integrated experiments, such as the ones which measure χ_s , and one may have to resort to measurements of the oscillation lengths to determine the mixing ratio $x_s = \Delta M/\Gamma$, for the $B_s^0 - \bar{B}_s^0$ oscillations, to which we now turn.

We recall that the time-dependent measurements of the yield of the “right-sign” and “wrong-sign” components follow the distributions:

$$\tau \frac{dN}{dt}(B^0 \rightarrow B^0) \equiv |f_+(t)|^2 = e^{-t/\tau} \cos^2 \omega t \quad (21)$$

$$\tau \frac{dN}{dt}(B^0 \rightarrow \bar{B}^0) \equiv |f_-(t)|^2 = e^{-t/\tau} \sin^2 \omega t \quad (22)$$

with $\omega = \frac{\pi}{2\tau}$. The oscillation period is given by $T_{osc} = \frac{\pi}{\omega} = \frac{2\pi\tau}{\pi}$. So, using our ball-park estimate we expect sinusoidal oscillations with periods:

$$(T_{osc})_s \sim 0.4 \text{ psec} \quad (23)$$

$$(T_{osc})_d \sim 10.0 \text{ psec} \quad (24)$$

The cross-section for $e + p \rightarrow b + X$ will not be sufficient to measure the oscillation length in the $B_d^0 - \bar{B}_d^0$ sector, but measuring $(T_{osc})_d$ should be possible if proper time resolution of $O(0.1 \text{ psec})$ could be attained. Therefore, for all practical purposes, one could treat only the $B_s^0 - \bar{B}_s^0$ and $B_d^0 - \bar{B}_d^0$ decay length distributions as sinusoidal, with all others essentially falling exponentially. The oscillation lengths themselves depend on the Lorentz boost and

lifetime, as indicated in Eq. (1). Thus, for $x_s = 15$, $\gamma = 10$, one expects $(\lambda_{osc})_s \sim 1.3$ mm for the $B_s^0 - \bar{B}_s^0$ oscillation, with the corresponding number for the $B_d^0 - \bar{B}_d^0$ oscillation being ~ 3.3 cm. There are three requirements to carry out these kind of measurements:

1. A functional microvertex detector
2. Flavour-tagging B_s^0 and \bar{B}_s^0 through hadronic or semileptonic decays
3. A determination of the B_s^0 (or \bar{B}_s^0) momentum, as already indicated by the dependence $\lambda_{osc} \sim |p_B|/M_B$.

The resolution of the proper decay time can be considered as resulting from addition of the following errors in quadrature:

$$\left(\frac{\sigma_t}{\tau}\right)^2 = \left(\frac{\sigma_d}{d}\right)^2 + \left(\frac{\sigma|p_B|}{|p_B|}\right)^2 \quad (25)$$

The error on $(\frac{\sigma_t}{\tau})^2$ has to be brought to the level of a few per cent, in order to well measure the quantity $(T_{osc}/\tau)_s^2 = O(0.1)$. It is also clear that the larger the value of x_s , the smaller is (T_{osc}/τ) and the better is the resolution required on proper time measurements. Here, $\frac{\sigma_d}{d}$ depends (essentially) on the details of the vertex detector, and $\frac{\sigma|p_B|}{|p_B|}$ on the method to measure the B-hadron momentum.

With the (simulated or assumed) proper time resolution and B_s -tagging efficiency, of course, the number of B-hadrons needed to determine a certain x_s can be easily evaluated. The possibility of measuring x_s at future experimental facilities where large beauty hadron rates are anticipated, and where detectors either already exist or a detector design has been assumed, has been taken up in a number of studies [43]–[47]. Perhaps these numbers are representative for the ep experiments as well, if appropriate detectors can be built for these collisions. We show in Fig. 20 the end result of one such recent studies, which states that for a proper time resolution $\sigma_t/\tau \leq 0.1$, and B_s tagging efficiency of $O(10^{-3})$, at least $O(10^7)$ beauty hadrons will be required to measure $x_s \leq 10$. These requirements on the detectors are necessary conditions to measure x_s . That these are also sufficient depends upon the actual value of x_s , as can be seen in the analysis of Defoix [46].

The oscillation lengths can be obtained by convoluting the functions $(|f_+(t)|^2, |f_-(t)|^2)$ with the energy distributions of the B-hadrons, which have been obtained from the programme AROMA [14]. Since, as discussed earlier, the oscillation period for the $B_d^0 - \bar{B}_d^0$ transitions is very large as compared to the lifetime, we do not show it here. The decay length distribution $\frac{d\sigma}{dt}(\epsilon + p \rightarrow e\bar{b} \rightarrow B_s + X)$ are shown in Fig. 21 for the right-sign meson (i.e. $\propto |f_+|^2$) for $x_s = 10$, and the assumed B-hadron energy bins indicated on the figures. The corresponding distributions for the wrong-sign B_s meson (i.e. $\propto |f_-|^2$) are shown in Fig. 22.

Next, we concentrate on the processes $\epsilon + p \rightarrow b + \bar{b} + X \rightarrow l^\pm l^\mp + X$ and $\epsilon + p \rightarrow b + \bar{b} + X \rightarrow l^\pm l^\mp + X$ involving dilepton final states, and study their yield as a function of the decay length. As stated earlier, the only oscillating components in these distributions are the ones coming from the $B_s^0 - \bar{B}_s^0$ and $B_d^0 - \bar{B}_d^0$ transitions. They can be separated by subtracting an exponential background, an assumption that has been checked with the help of the Monte Carlo programme. To estimate the smearing effect due to the imprecise measurement of the B_s -hadron energy, we again assume certain B_s -energy bins, hoping that such a precision can be reached experimentally in the dilepton final state. To crudely estimate the effect of

the $\frac{\sigma_d}{d}$ term in Eq. (25), we have convoluted the decay length distributions with a vertex resolution of 100 μm , distributed as a Gaussian. The resulting decay length distributions for the process $e + p \rightarrow b + \bar{b} + X \rightarrow l^\pm l^\mp + X$, assuming a beam pipe cut of 100 mrad are shown in Fig. 23. Thus, if the B-hadron energy could be experimentally determined with the assumed accuracy, then the oscillation lengths for the $B_s^0 - \bar{B}_s^0$ can be measured. Again, we reiterate that this pattern rapidly vanishes if either the B-hadron resolution worsens and/or the value of x_s becomes large.

4 Summary

We have discussed at some length the production of heavy quarks in the processes $e + p \rightarrow Q + X$ at the LEP+LHC collider assuming $\sqrt{s} \simeq 1.26$ TeV. The rates for c- and b-hadrons in these collisions are rather robust. With a luminosity of $10^{32} \text{ cm}^{-2} \text{ s}^{-1}$, we estimate a measurable rate of ~ 3 Hz, and ~ 1 Hz for the charmed and beauty hadron events, respectively, assuming that events with $\Sigma E_\perp (\text{had.}) > 10 \text{ GeV}$ and having a charged lepton with $p_\perp^l > 1 \text{ GeV}$, can be triggered over the pseudorapidity interval $|\eta| < 3$. These trigger rates are probably manageable, so that no big data reduction may be necessary. This would make the ep collisions an attractive possibility to do high precision c- and b- physics. We have argued here that the inclusive lepton events, as well as J/ψ -production are very well suited to measure the gluon structure function in very small- x_g region –an area of obvious theoretical interest. As an example of the kind of new phenomena which could be studied at the LEP+LHC collider, we have presented profiles of oscillation lengths associated with the $B_s^0 - \bar{B}_s^0$ transition. The experimental prerequisites for carrying out such measurements have been discussed, and it is argued that a proper time resolution of $O(0.1)$ and an effective B_s -tagging should enable one to measure x_s in the vicinity of ~ 10 .

The potential of the ep collider in studying the physics of the top quark is mostly of exploratory nature, since the cross sections for $e + p \rightarrow t + X$ are typically in the range of $(5 - 0.5) \text{ pb}$, for the top quark in the mass range $(100 - 250) \text{ GeV}$, providing $\sim (5000 - 500)$ top quark events. To be able to detect these events and construct the top quark mass, we have done two complementary analyses here. In the case of the semileptonic decays of the top quark, the dominant background is due to the production and decays of real W-boson. To suppress this background, one may have to require an additional b-quark tagging, which discriminates the direct W-production (background). This should allow top searches for up to $m_t = 200 \text{ GeV}$, and to higher mass if the secondary vertices of the b-quark could be measured with the help of a vertex detector. For the hadronic decay modes of the top quark, the main background is both due to the CC process and the real W-production. Here again, an additional b-tagging would be very helpful. The hadronic events allow the reconstruction of the top quark mass, using the 3-jet decays of the top quark. We estimate that searches of the top quark, certainly up to $m_t = 200 \text{ GeV}$, could be successfully undertaken in ep collisions.

Acknowledgements

F.B. would like to thank the Alexander v. Humboldt-Stiftung for supporting his stay at DESY during summer 1990. J.J.vd Bij wants to thank DESY for its hospitality and support

during his stay at DESY, where most of this work was done. J.F.T. would like to thank the binational exchange programme— CICYT, Madrid-KFZ, Karlsruhe— for partially supporting his stay at DESY. We would also like to acknowledge useful discussions with Paweł Krawczyk and Herbert Steger on aspects of b-physics, and thank A. Ghinculov for his help with the computer programme for one of the top-backgrounds. This work has partially been supported by BMFT, Bonn, FRG.

References

- [1] For a recent review see, for example, Heavy Flavors and High Energy Collisions in the 1-100 TeV Range, Ettore Majorana Int. Science Series, Vol. 44 (1989), A. Ali and L. Cifarelli (Eds.) (Plenum Press, N.Y., 1989).
- [2] G.W. Brandenburg (CDF Collaboration), Talk presented at the 5th. Yukawa Memorial Symposium, Nishinomiya, Japan (Oct. 25-28, 1990).
- [3] F. Dydak, Talk presented at the XXV Int. Conf. on High Energy Physics, Singapore(August 1990).
- [4] D. Haidt, in EPS-High Energy Physics '89, Madrid, Spain(1989), Nucl. Phys. B (Proc.Suppl.)16(1990) 294, F. Barreiro et al. (Eds.).
- [5] J. Ellis and G.L. Fogli, CERN Report TH-5817(1990).
- [6] P. Langacker, Phys. Rev. Lett. 63(1989) 1920.
- [7] N.J. Nodulman, in EPS-High Energy Physics '89, Madrid, Spain(1989), Nucl. Phys. B (Proc.Suppl.)16(1990) 40, F. Barreiro et al. (Eds.).
- [8] W. Beenakker et al., DESY Report 90-064(1990).
- [9] D. Denegri, in ref. [1].
- [10] F. Cavanna et al.— These Proceedings.
- [11] T. Rodrigo et al.— These Proceedings.
- [12] P. Zerwas et al.— These Proceedings.
- [13] J.C. Anjos et al., Phys. Rev. Lett. 60(1988) 1239.
- [14] G. Ingelman and G.A. Schuler, Z. Phys. C40(1988) 299.
- [15] L.V. Gribov, E.M. Levin and M.G. Ryskin, Phys. Rep. 100(1983) 1.
- [16] E.M. Levin and M.G. Ryskin, LNPI-Report 1316(1987).
- [17] E.M. Levin and M.G. Ryskin, in Proc. of Workshop on Small-x Behaviour of Deep Inelastic Structure Functions in QCD, DESY, Hamburg, FRG(May 1990); to appear in Nucl. Phys. B (Proc. Suppl.) A. Ali and J. Bartels (Eds.).
P.N. Harriman et al., ibid;
- [18] J. Bartels, G.A. Schuler and J. Blumlein, DESY Report 90-091(1990).
- [19] V.N. Gribov and L.N. Lipatov, Sov. J. Nucl. Phys. 15(1972) 78.
- [20] G. Altarelli and G. Parisi, Nucl. Phys. B126(1977) 298.
- [21] S. Catani, M. Ciafaloni and F. Hautmann, Cavendish Lab., Cambridge Report-HEP 90/13(1990).
- [22] J.C. Collins and R.K. Ellis in [17].
- [23] G. Abbiendi and L. Stanco, DESY Report 90-112(1990).
- [24] E. Eichten, C. Quigg, I. Hinchliffe and K. Lane, Rev. Mod. Phys. 56(1984) 579.
- [25] A. Ali et al., in Proc. of HERA Workshop, DESY, Hamburg, FRG, Vol.1 (1988) 393; R.D. Peccei(Ed.).
- [26] K.J. Abraham, H. Jung, G.A. Schuler and J. F. de Trocóniz —These proceedings.
- [27] M. Danilov, in Proc. of the 1989 Int. Symp. on Lepton and Photon Interactions at High Energies, Stanford, USA, M. Riordan (Ed.) (World Scientific, Singapore, 1989) p. 139.
- [28] D. Kreinick, in Proc. of the 1989 Int. Symp. on Lepton and Photon Interactions at High Energies, Stanford, USA, M. Riordan (Ed.) (World Scientific, Singapore, 1989)p. 129.
- [29] The Physics Program of a High Luminosity Asymmetric B Factory at SLAC, D. Hitlin, SLAC Report 353(1989).
- [30] Feasibility Study for a B-meson Factory in the ISR Tunnel, CERN Report 90-02(1990), PSI Report PR-90-08(1990), T. Nakada (Ed.).
- [31] G.J. Feldman et al., in Proc. of the Summer Study on High Energy Physics in the 1990s, Snowmass, Colorado, USA , S. Jensen (ed.) (World Scientific, Singapore, 1989); R.H. Siemann et al., ibid;
D. Cline and C. Pellegrini, ibid.
- [32] Proc. of Workshop on Detectors for an Asymmetric B Factory, Max-Planck Institut- Heidelberg Internal Report, MPI-H/1990-V6(1990).
- [33] The Design of the Electron-Positron Source for Novosibirsk Phi and B Factories and VEPP-3.4, A.V. Novokhotski, SLAC-AAS-NOTE-56(1990).
- [34] B-factories with e^+e^- Colliders,
G. Coignet- Talk at the KEK Topical Conf. on e^+e^- Collision Physics, Tsukuba, Japan, and LAPP-Annecy Report LAPP-EXP-89-09(1989).

- [35] An Asymmetric B-factory at KEK,
T. Nozaki, KEK Report 90-68(1990).
- [36] J. Tuominiemi (UA1 Collaboration);
R.P. Johnson (ALEPH Collaboration);
J.G. Branson (L3 Collaboration);
Talks presented at the XXV Int. Conf. on High Energy Physics, Singapore(August 1990).
- [37] L3 Collaboration (B. Adeva et al.), L3 Preprint # 20 (Nov. 1990).
- [38] T. Rohaly, Talk presented at the XXV Int. Conf. on High Energy Physics, Singapore(August 1990).
- [39] U. Baur and J.J. van der Bij, Nucl. Phys. B304(1988) 451, and in Proc. of the HERA Workshop, DESY, Hamburg(1988) R.D. Peccei (Ed.).
- [40] M. Glück, R.M. Godbole and E. Reya, Z. Phys. C38(1988) 441, Erratum C39(1988)590.
- [41] R.A. Eichler and Z. Kunszt, Nucl. Phys.B299(1988) 1.
- [42] G. A.Schuler, Nucl. Phys. B299(1988) 21.
- [43] P. Roudeau, Orsay Reports, LAL-89-21(1989); LAL-90-47 (1990).
- [44] M. Reidenbach, in ref. [32].
- [45] L.P. Chen et al., SLD Physics Studies, SLAC Report -354(1989).
- [46] C. Defoix, College de France Preprint LPC 90-41(1990) and in CERN Yellow Report:
LEP at High Luminosity, CERN(1990).
- [47] D. Treille, CERN Report EP/90-30(1990).
- [48] G. Ingelman, DESY Report (to be published).
- [49] B. Andersson, G. Gustafson and M. Söderberg, Z. Phys. C20(1983) 317.
- [50] A. Ali and Z.Z. Aydin, Nucl. Phys. B148(1979) 165.
- [51] G. Martinelli, Univ. of Rome & INFN-Sezione di Roma Preprint # 754(1990).
- [52] G. Fidacaro -These proceedings.
- [53] F. Grancagnolo -These proceedings.

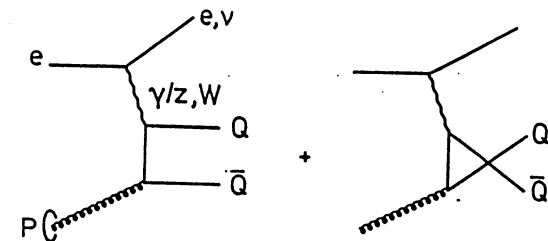


Figure 1

Lowest order boson-gluon fusion diagrams for heavy quark production processes $e + p \rightarrow Q + X$.

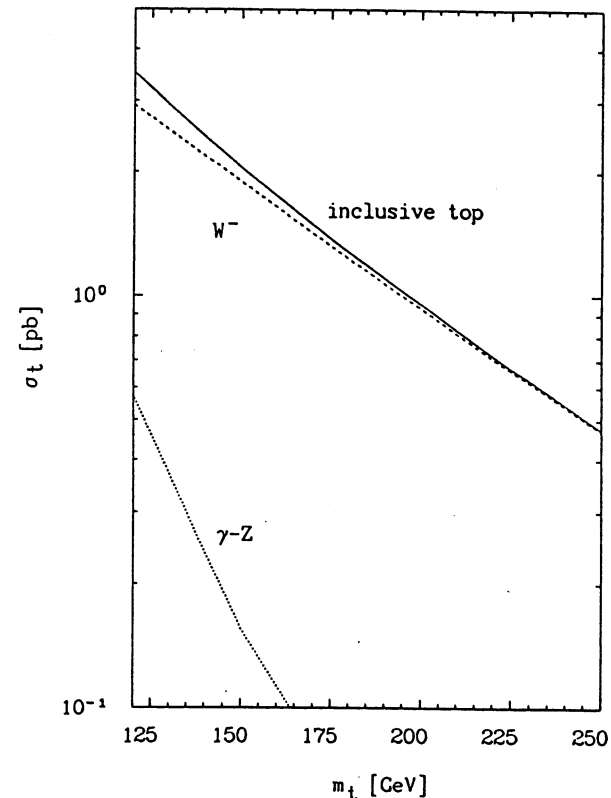


Figure 2

Top quark production cross sections in ep collisions at $\sqrt{s} \sim 1.26 \text{ TeV}$; contribution from the NC process $e + p \rightarrow e + t + \bar{t} + X$ (dotted curve), from the CC process $e + p \rightarrow \nu + \bar{t} + b + X$ (dashed curve), and the sum (solid curve), are shown separately.

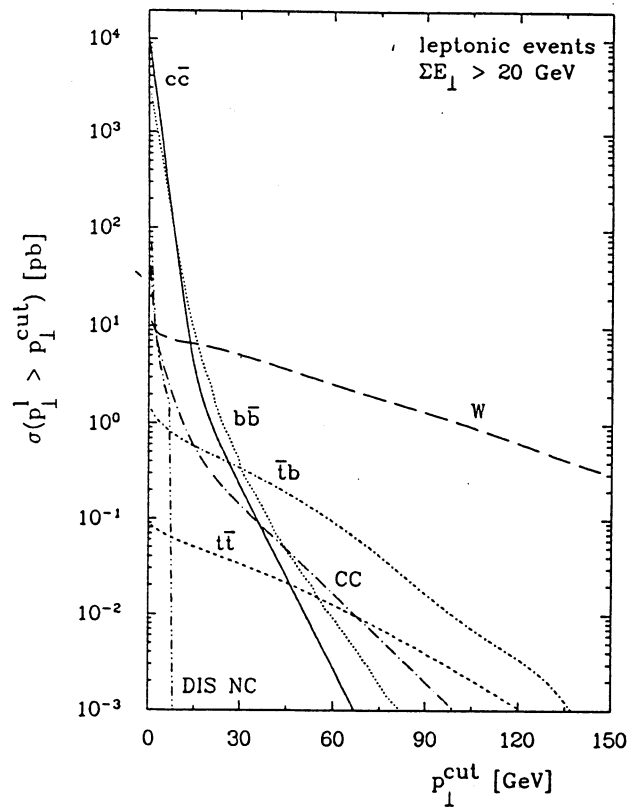


Figure 3

Inclusive semileptonic cross-sections for the process $e + p \rightarrow l^\pm + X$ with ΣE_\perp (hadrons) ≥ 20 GeV as a function of the transverse lepton energy cutoff p_\perp^l , at $\sqrt{s} \sim 1.26$ TeV. The contributions from the top quark (for $m_t = 150$ GeV) and the backgrounds (dominated by NC production of W^\pm) are shown individually.

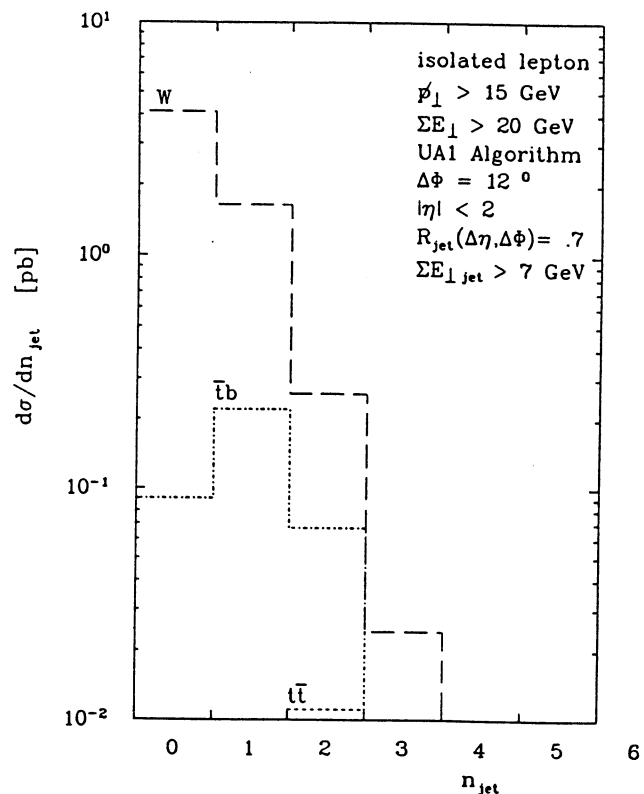
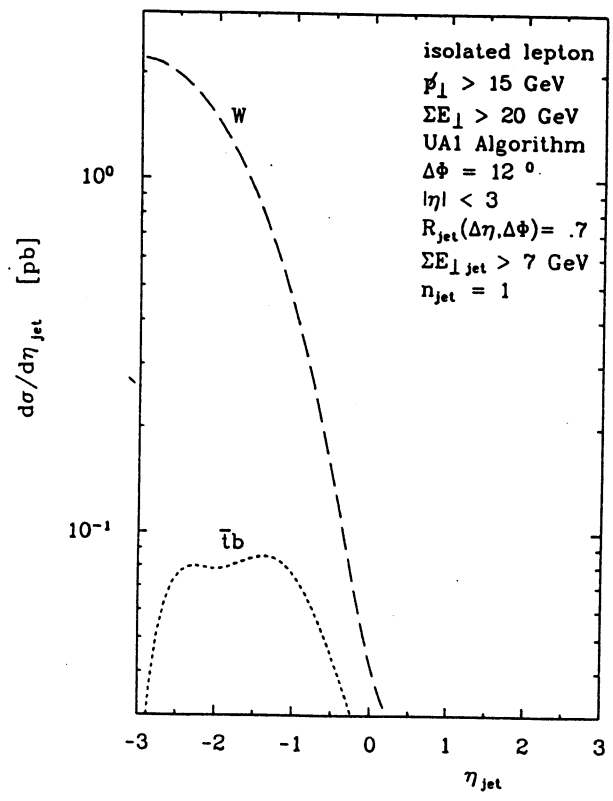
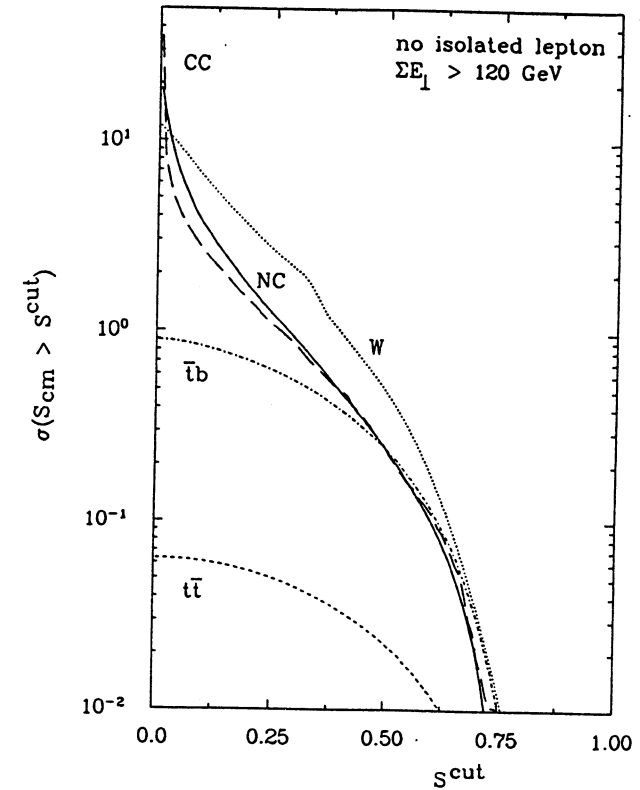


Figure 4

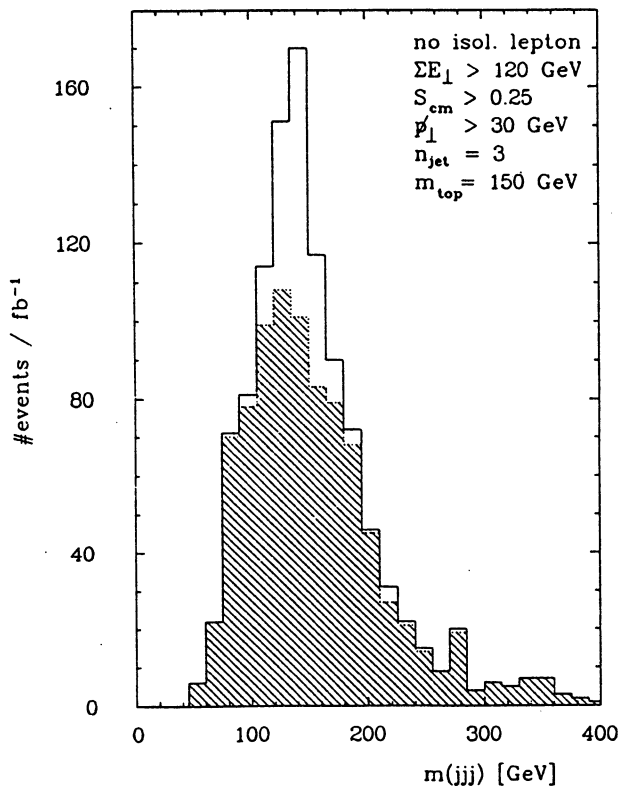
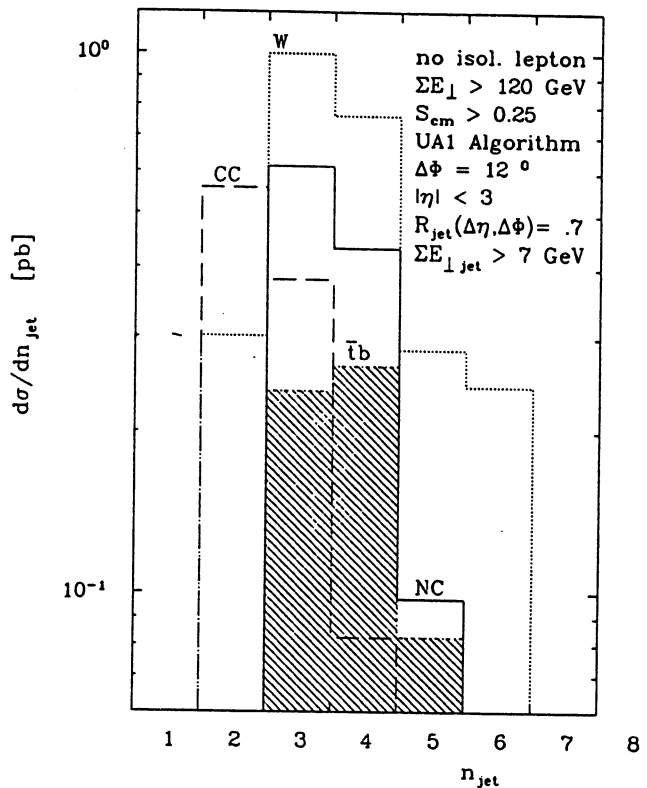
Jet multiplicity distributions in the process $e + p \rightarrow l^- + p_\perp + jet(s) + X$ at $\sqrt{s} \sim 1.26$ TeV. The definition of jets and additional cuts on the event topology are indicated and $m_t = 150$ GeV is assumed.

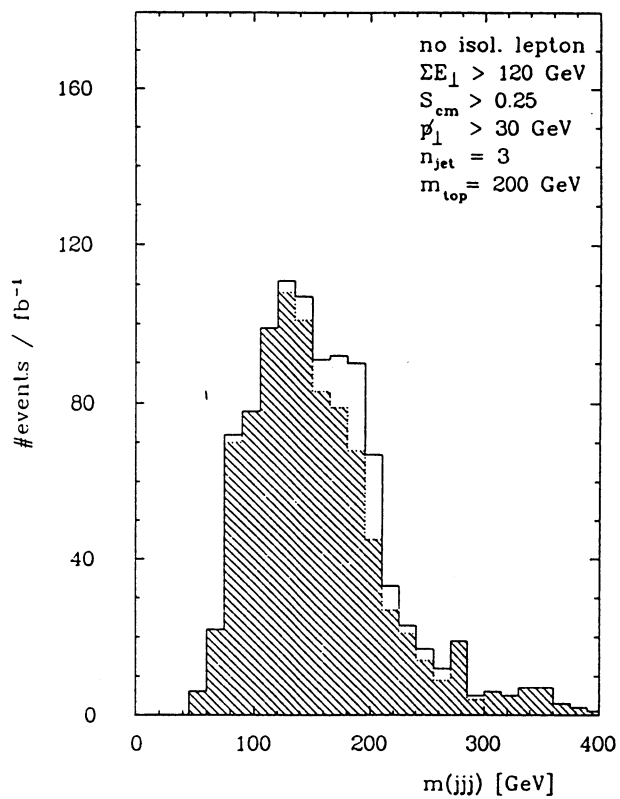
**Figure 5**

Pseudorapidity distributions for the process $e + p \rightarrow l^- + \not{p}_T + jets + X$, for $|\eta_{jet}| \leq 3$ from the top quark process (dotted curve) and the dominant background from the NC production of W^- (dashed curve).

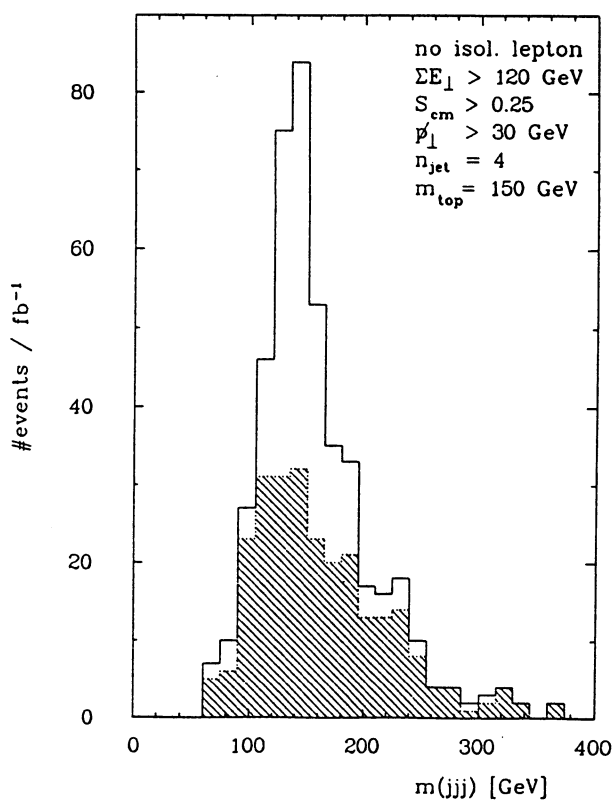
**Figure 6**

Sphericity distributions for the processes $ep \rightarrow jets + X$, with no isolated lepton at $\sqrt{s} \sim 1.26 \text{ TeV}$ and $\Sigma E_T(\text{had.}) \geq 120 \text{ GeV}$. The top quark contribution ($t\bar{t}$ and $t\bar{b}$) and background processes are shown.



**Figure 9**

Same as Fig. 8, with $m_t = 200 \text{ GeV}$.

**Figure 10**

Invariant jet-mass, m_{jjj} , distributions for the process $e + p \rightarrow 4 - jets + X$, including the top quark contribution (for $m_t = 150 \text{ GeV}$), and the indicated cuts on the event topology, at $\sqrt{s} \sim 1.26 \text{ TeV}$. The jets are ordered in transverse energy and the three most energetic jets have been used to define m_{jjj} . The shaded distribution denotes the background, and the unshaded signal + background.

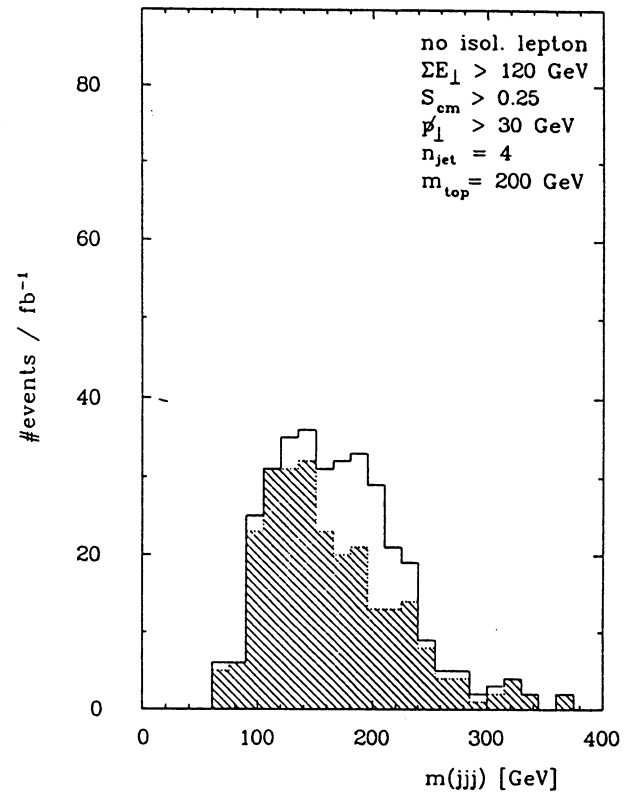


Figure 11

Same as Fig. 10, with $m_t = 200 \text{ GeV}$.

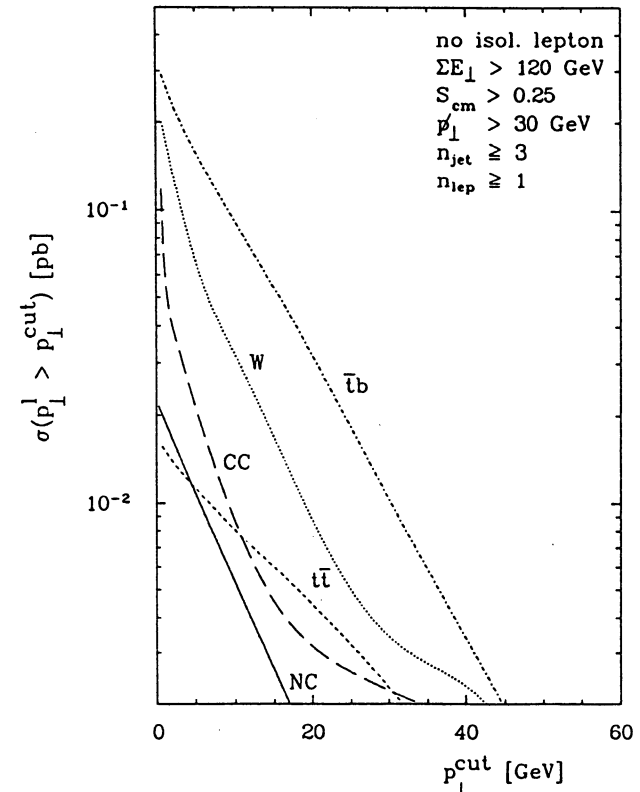
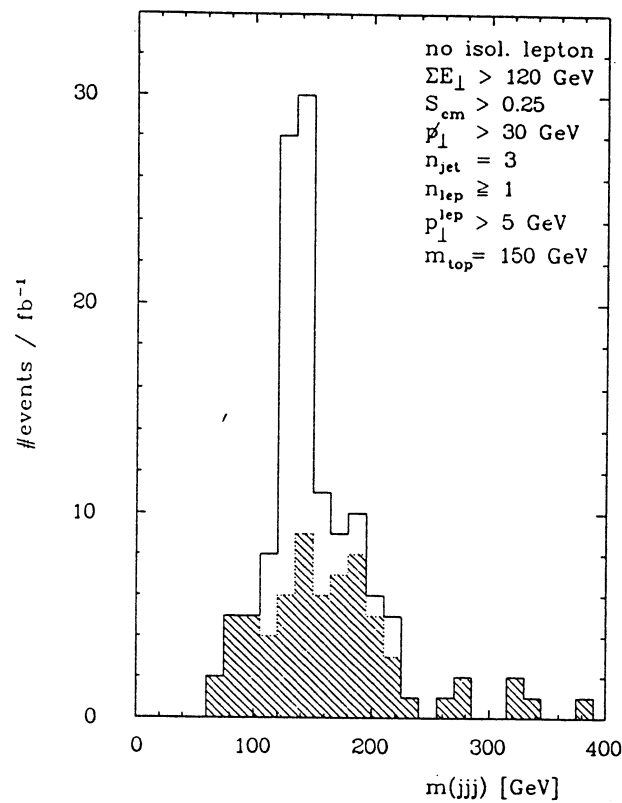
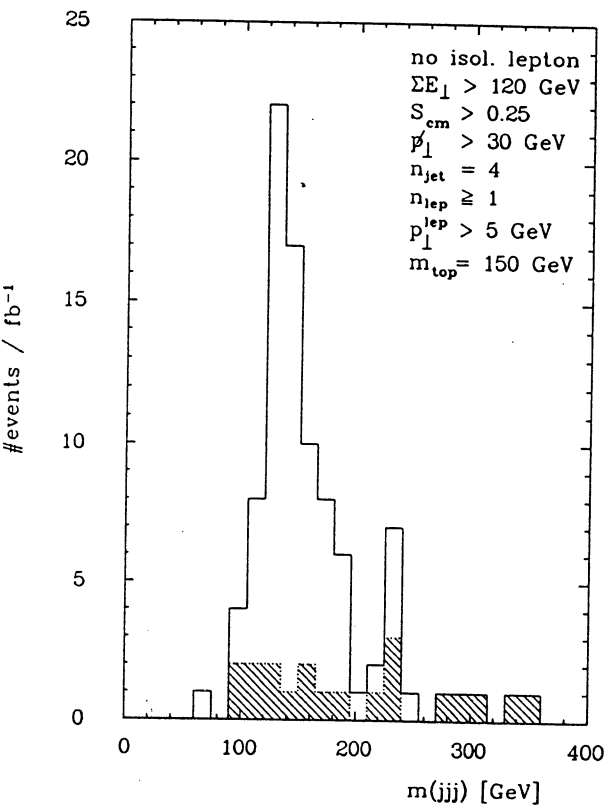


Figure 12

Inclusive cross section for the process $e + p \rightarrow (\geq 3) - \text{jets} + l^\pm + X$ (with non-isolated lepton) at $\sqrt{s} \simeq 1.26 \text{ TeV}$, as a function of the transverse lepton energy cut-off ($p'_\perp \geq p'_\perp^{\text{cut}}$). Additional cuts on the event topology are indicated and $m_t = 150 \text{ GeV}$.

**Figure 13**

Invariant jet-mass, m_{jjj} , distributions for the process $e + p \rightarrow 3 - \text{jets} + l^\pm + X$, including the top quark contribution (for $m_t = 150 \text{ GeV}$) at $\sqrt{s} \simeq 1.26 \text{ TeV}$. The lepton(s) satisfy $p_T^l \geq 5 \text{ GeV}$ and is(are) not isolated; additional topological cuts are indicated.

**Figure 14**

Invariant jet-mass, m_{jjj} , distribution for the process $e + p \rightarrow 4 - \text{jets} + l^\pm + X$ at $\sqrt{s} \simeq 1.26 \text{ TeV}$. The jets are ordered in transverse energy and the three most energetic jets have been used to define m_{jjj} . The lepton(s) satisfy $p_T^l \geq 5 \text{ GeV}$ and $m_t = 150 \text{ GeV}$.

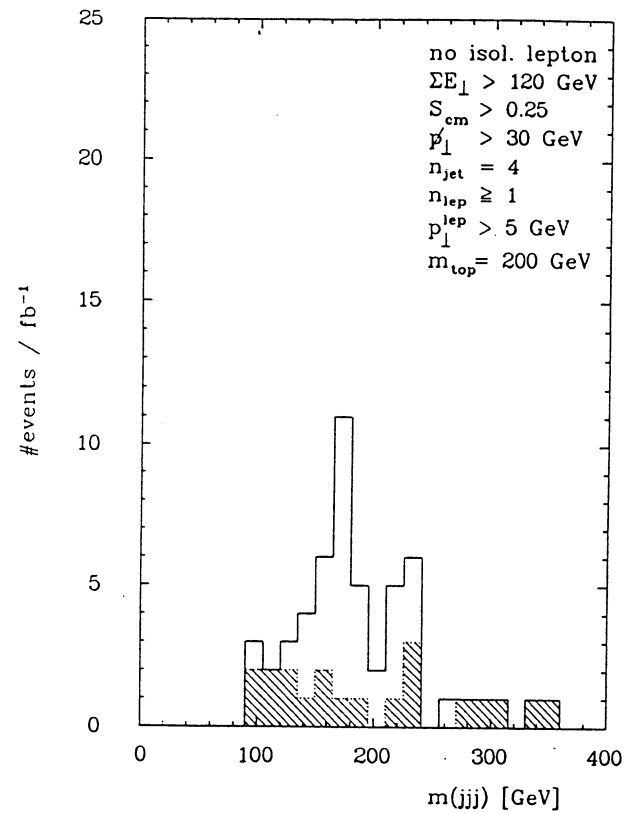


Figure 15

Same as Fig. 14, with $m_t = 200$ GeV.

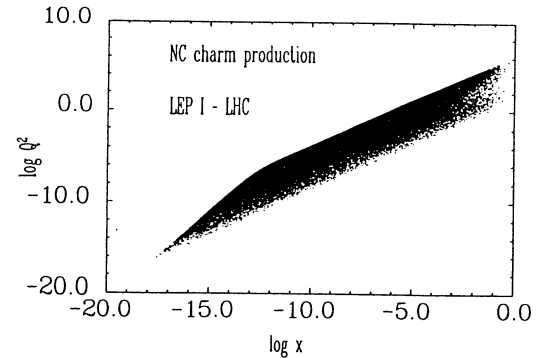


Figure 16

$\log Q^2 - \log x$ scatter plot for the process $e + p \rightarrow c + X$ at $\sqrt{s} \sim 1.26$ TeV.

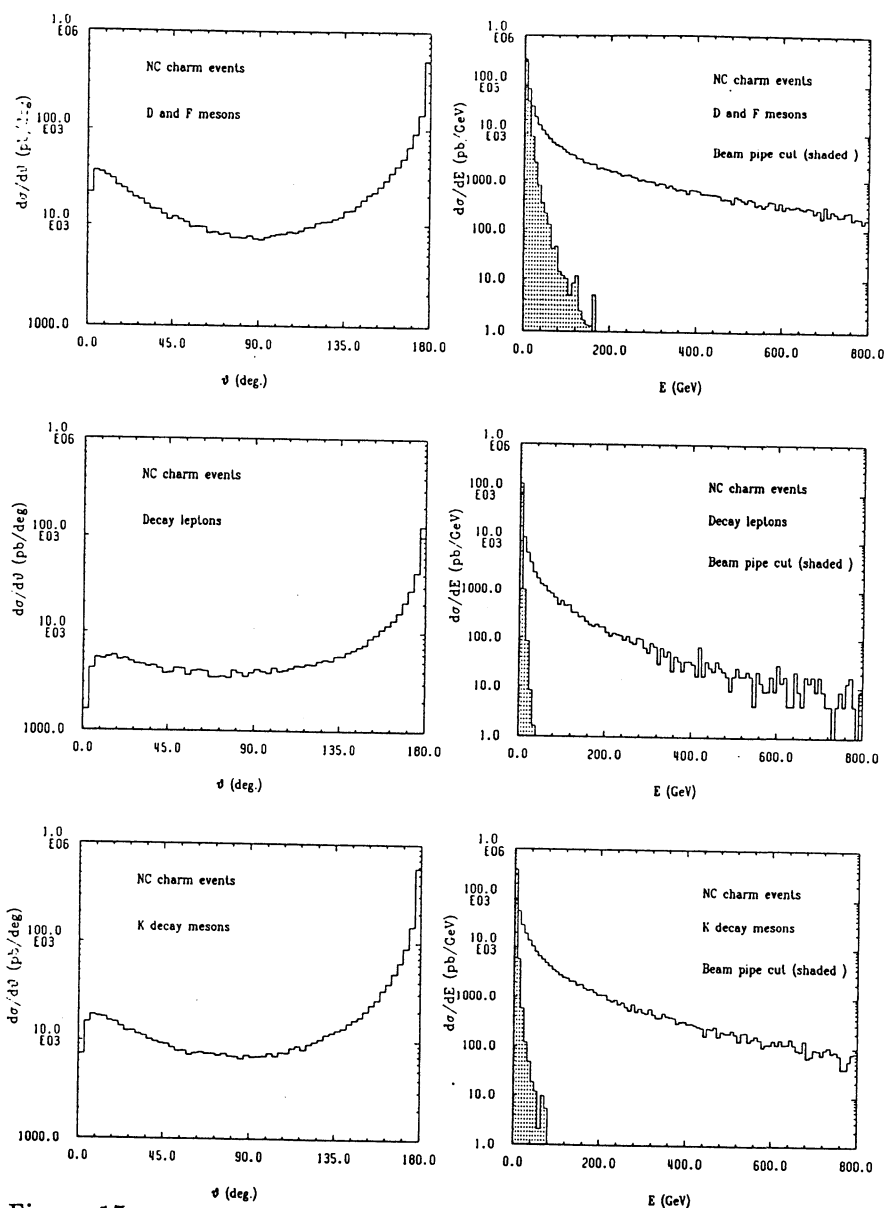


Figure 17

Energy- and Polar angle- distributions for the charmed hadrons D and F ($\equiv D_s$), kaons and charged leptons, produced in the NC process $e + p \rightarrow c + X$ at $\sqrt{s} \sim 1.26$ TeV and subsequent fragmentation and decays. The energy distributions resulting after imposing a beam pipe cut of 100 mrad are shown by shaded areas.

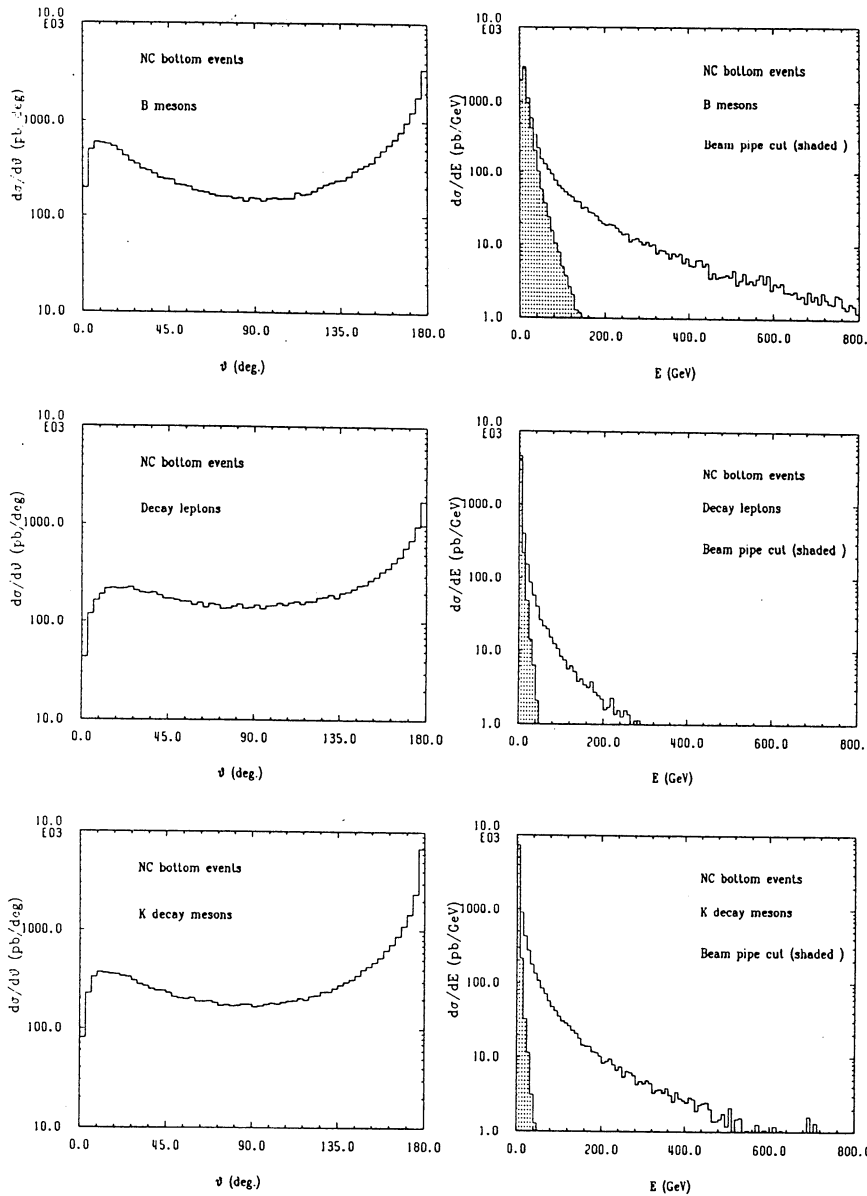


Figure 18

Same as Fig. 17 but for the NC process $\epsilon + p \rightarrow b + X$ and involving the B-mesons, kaons and charged leptons.

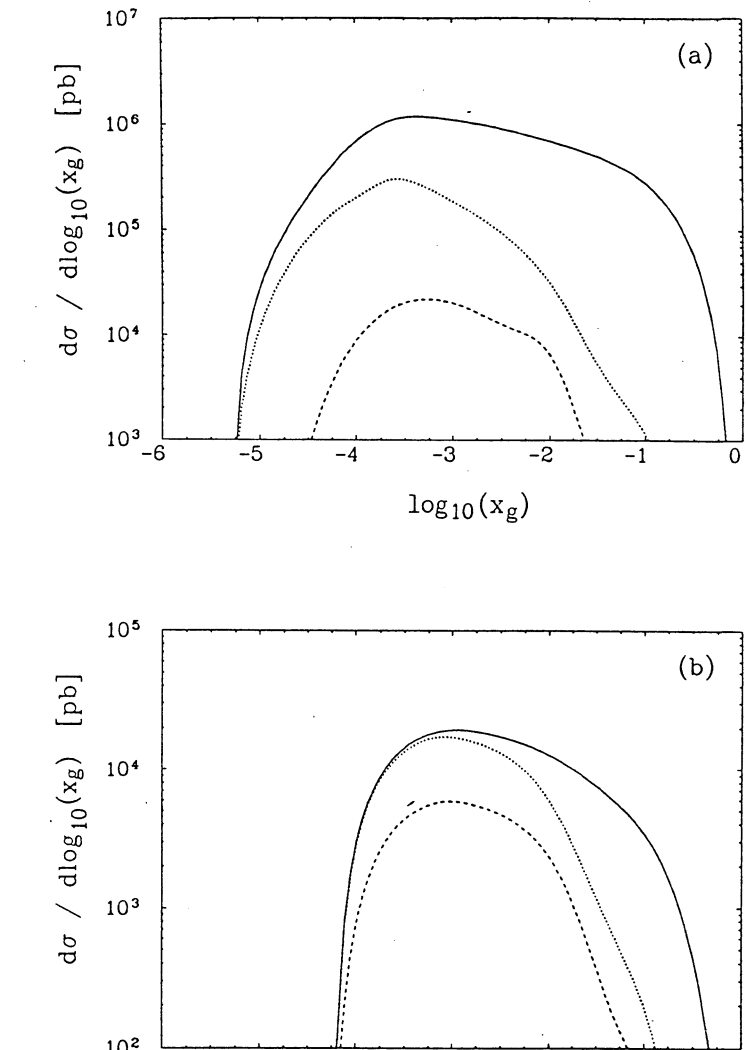


Figure 19

The distribution $\frac{d\sigma}{d\log x}$ for NC production of heavy quarks at $\sqrt{s} \sim 1.26 \text{ TeV}$: (a) $\epsilon + p \rightarrow c + X$ and (b) $\epsilon + p \rightarrow b + X$. The legends are: No cuts (solid curve), $\Sigma E_{\perp} (\text{had.}) \geq 10 \text{ GeV}$ (dotted curve), $\Sigma E_{\perp} (\text{had.}) \geq 10 \text{ GeV}$ and $p_{\perp}^l \geq 1.0 \text{ GeV}$ (dashed curve), where the lepton is from the semileptonic decay of the charmed and beauty hadrons.

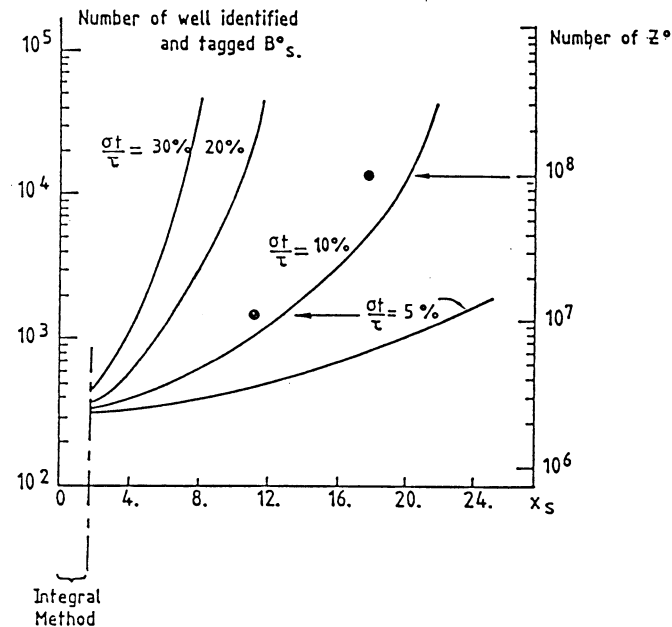


Figure 20

The number of well identified and tagged B_s^0 mesons required versus the measurable value of x_s , with the assumed proper time resolutions indicated on the curves. The black spots correspond to 10^7 and 10^8 Z^0 events, which would be required at LEP(I) to measure x_s . The required number of B_s^0 mesons for the time integrated method are also indicated. Figure taken from ref. [42].

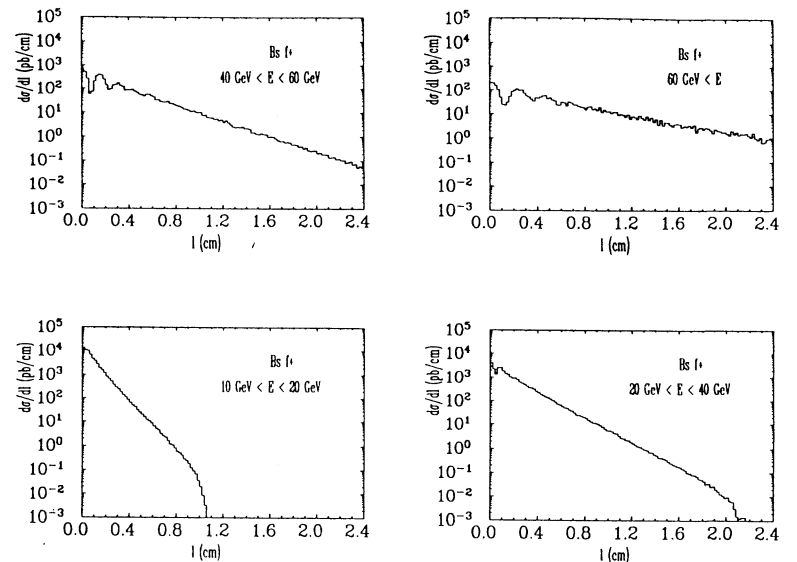


Figure 21

B_s^- -meson decay length distributions, $\frac{d\sigma}{dl}$ (l in cm) for the right-sign meson transition $B_s^0 \rightarrow B_s^-$ in the process $c + p \rightarrow b + X$ at $\sqrt{s} \approx 1.26$ TeV. An x_s -value of 10 has been assumed and the B_s^- -meson energy bins are indicated.

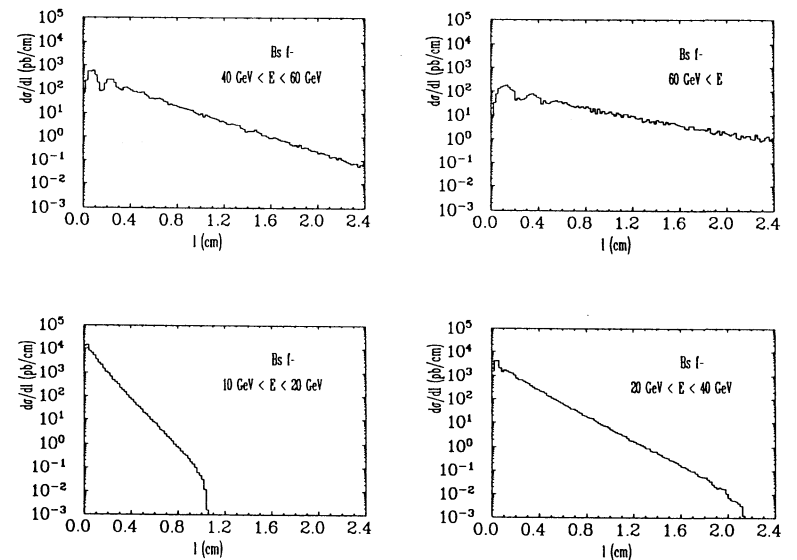


Figure 22

B_s^- -meson decay length distributions, $\frac{d\sigma}{dl}$ (l in cm) for the wrong-sign meson transition $B_s^0 \rightarrow B_s^-$ in the process $c + p \rightarrow b + X$ at $\sqrt{s} \approx 1.26$ TeV. An x_s -value of 10 has been assumed and the B_s^- -meson energy bins are indicated.

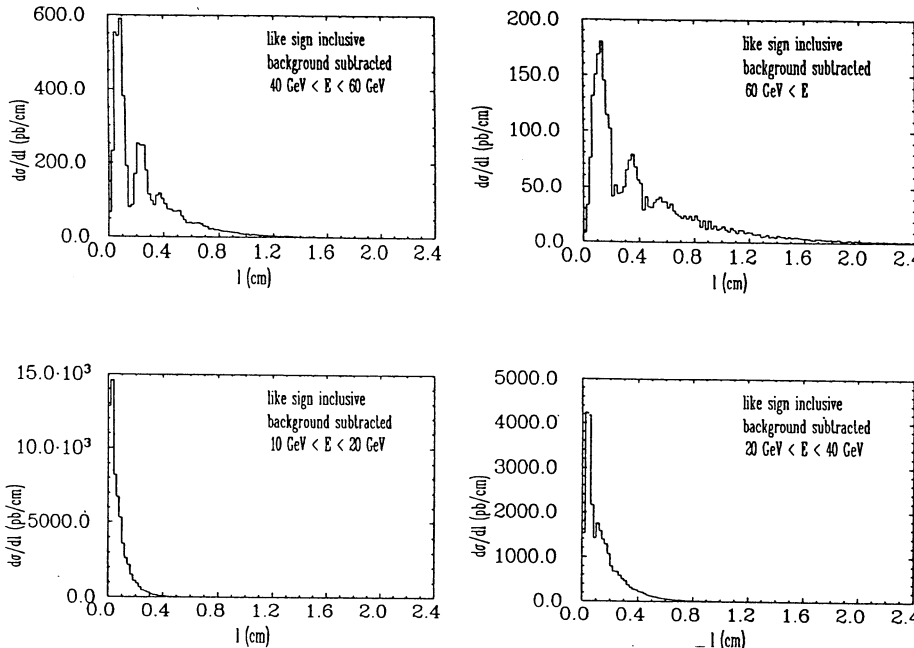


Figure 23

Differential cross section $\frac{d\sigma}{dl}$ (l in cm) for the opposite-sign dilepton process $e + p \rightarrow b + \bar{b} + X \rightarrow l^\pm l^\mp + X$ cm) at $\sqrt{s} \sim 1.26 \text{ TeV}$, after subtracting an exponential background and assuming a vertex resolution of $100 \mu\text{m}$. The indicated energy bins on the B_s -mesons are indicated, and a value $x_s = 10$ has been used.

Single W and Z Production at LEP/LHC

U. BAUR^{1*}, B. A. KNIEHL¹, J. A. M. VERMASEREN², AND D. ZEPPENFELD¹

¹Physics Department, University of Wisconsin, Madison, WI 53706, USA

²NIKHEF-H, P.O. Box 41882, NL-1009 DB Amsterdam, The Netherlands

ABSTRACT

Single W and Z production at LEP/LHC is investigated. Standard Model predictions for $ep \rightarrow eW^\pm X$, $ep \rightarrow \nu W^- X$, $ep \rightarrow \nu W^- p$, and $ep \rightarrow \nu ZX$ are presented. Possibilities to test the gauge theory structure of the $WW\gamma$ and WWZ vertex are explored. It is found that at LEP/LHC the $WW\gamma$ (WWZ) vertex can be measured with 10–40% (20–100%) accuracy after one year of running.

1. Introduction

The main task of LEP/LHC will be to extend measurements of deep inelastic scattering to higher values of Q^2 and smaller values of x than is possible at HERA.¹⁾ Of no lesser importance for our understanding of the Standard Model (SM) is the study of weak boson production. Six different processes contribute to single W and Z production in ep collisions,

$$ep \rightarrow eW^\pm X, \quad ep \rightarrow \nu W^- X, \quad ep \rightarrow \nu W^- p, \quad ep \rightarrow \nu ZX, \quad (1.1)$$

and,

$$ep \rightarrow eZX, \quad ep \rightarrow eZp. \quad (1.2)$$

The production of W and Z bosons at LEP/LHC provides an interesting physics signal as well as an important background to a number of processes indicating the presence of new physics. The primary interest in production of weak bosons in high energy ep collisions is the measurement of the $WW\gamma$ and WWZ vertices,^{2–6)} but they are also a potentially dangerous background to supersymmetry signals,⁷⁾ Higgs boson⁸⁾ and top quark production.⁹⁾

In the following we shall concentrate on the four processes enumerated in (1.1). They depend on the $WW\gamma$ and/or WWZ couplings, whereas the reactions shown in (1.2) do not involve any three vector boson vertices. In Section 2 we shall present SM predictions for the processes shown in (1.1). We investigate in Section 3 how well the $WW\gamma$ and WWZ couplings can be measured in those reactions. Section 4 contains our conclusions.

* SSC Fellow

Table 1

Standard model cross sections for $ep \rightarrow eW^\pm X$, $ep \rightarrow \nu W^- X$, $ep \rightarrow \nu W^- p$, and $ep \rightarrow \nu ZX$ for $E_e = 55$ GeV and $E_e = 100$ GeV, and $E_p = 8$ TeV. To regulate the u -channel pole in $ep \rightarrow eW^\pm X$ a $p_{Tj} > 5$ GeV cut is imposed on the transverse momentum of the jet originating from the scattered quark.

process	$E_e = 55$ GeV, $E_p = 8$ TeV σ [pb]	$E_e = 100$ GeV, $E_p = 8$ TeV σ [pb]
$eW^+ X$	9.6	14.9
$eW^- X$	7.8	12.2
$\nu W^- X$	1.5	2.5
$\nu W^- p$	0.66	0.97
νZX	0.52	0.91

In all our calculations we use EHLQ (set 1)¹⁰⁾ parton structure functions, evaluated at $Q^2 = -(p_q - p_{q'})^2 > 5$ GeV² where p_q ($p_{q'}$) is the four momentum of the initial (final) state quark, and the following SM parameters, $\alpha = \alpha(M_Z) = 1/128$, $M_Z = 91.1$ GeV, $\sin^2 \theta_W = 0.23$, and $M_W = M_Z \cos \theta_W = 80$ GeV. Our analysis is based on the calculation of helicity amplitudes for the complete $2 \rightarrow 4$ processes as *e.g.* depicted in Fig. 1. In particular it includes subsequent W or Z decays. Apart from anomalous $WW\gamma$ and WWZ couplings we assume the SM to be valid. All calculations are performed at the parton level.

2. Standard Model Cross Sections

The SM cross sections for the processes we consider are summarized in Table 1 for two different electron energies, $E_e = 55$ GeV and $E_e = 100$ GeV. The cross section typically varies by 50 – 75% between the two energies. Henceforth we take $E_e = 55$ GeV and $E_p = 8$ TeV ($\sqrt{s} \approx 1.3$ TeV), where the luminosity of LEP/LHC is expected to peak at $\mathcal{L} \approx 10^{32}$ cm⁻² s⁻¹¹¹⁾. For $E_e = 100$ GeV the expected luminosity is about one order of magnitude smaller, resulting in a correspondingly smaller yearly event rate. Clearly, $eW^\pm X$ production is the major source of W boson production at LEP/LHC. At the parton level the reaction $ep \rightarrow eW^\pm X$ proceeds via the Feynman diagrams shown in Fig. 1. The dominant contribution arises from photon exchange in Fig. 1a, which at the level of the $\gamma q \rightarrow Wq'$ subprocess is a u -channel quark exchange. The associated u -channel pole leads to strong peaking of the cross section at small transverse momenta of the hadronic jet, p_{Tj} , originating from the scattered quark, q' . However, in the low p_{Tj} region, QCD corrections are expected to be large and W production can be thought of as $q\bar{q} \rightarrow W$ where one of the quarks is regarded as a constituent of the photon.

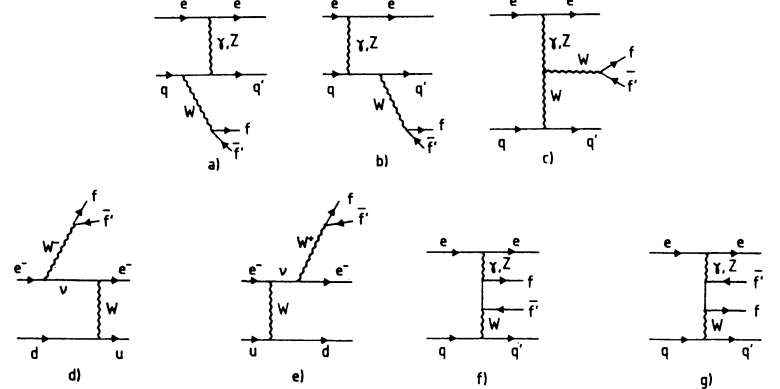


Fig. 1: Feynman graphs for the parton level processes contributing to $ep \rightarrow eW^\pm X$, including the subsequent decay $W \rightarrow f\bar{f}'$. Diagrams (f) and (g) have to be included for off-shell W 's, in order to preserve electromagnetic gauge invariance.

Thus contact is made with parton structure functions inside the photon and a careful merging of the two pictures is required.¹²⁾ To avoid the complications of the small p_{Tj} region, we have imposed a transverse momentum cut of $p_{Tj} > 5$ GeV in $ep \rightarrow eW^\pm X$ in Table 1.

Deep inelastic νW^- production, $ep \rightarrow \nu W^- X$, is described by a set of Feynman diagrams similar to those shown in Fig. 1, but with the incoming electron and quark interchanged. Since the photon does not couple to a neutrino, the u -channel pole is absent in $ep \rightarrow \nu W^- X$, and the cross section is significantly smaller than for $eW^\pm X$. In our calculation of inelastic νW^- production we only take into account the region $|t| > 5$ GeV², t being the square of the photon momentum transfer, where the EHLQ set 1 structure functions are valid. The rate for elastic νW^- production, $ep \rightarrow \nu W^- p$, is approximately 40% of the $\nu W^- X$ cross section. The diagrams contributing to $ep \rightarrow \nu W^- p$ are similar to those for $ep \rightarrow \nu W^- X$, with only photon exchange contributing and the initial and final state quarks replaced by a proton. The cross section for elastic νW^- production is obtained by using the electric and magnetic form factors,

$$G_E(t) = (1 - t/0.71 \text{ GeV}^2)^{-2}, \quad G_M(t) = 2.79 \cdot G_E(t), \quad (2.1)$$

and agrees well with the result obtained using the modified Weizsäcker-Williams approach of Ref. 13. Finally, the reaction $ep \rightarrow \nu ZX$ proceeds exclusively via W exchange and thus is suppressed with respect to the W production processes.

The structure of the Feynman diagrams contributing to each process is directly reflected in the p_T spectrum of the jet originating from the scattered quark which

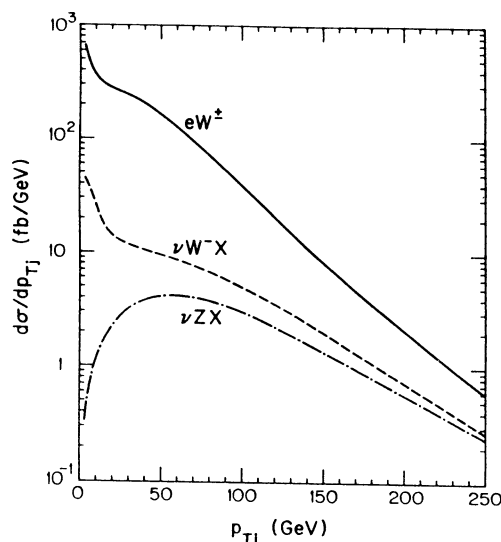


Fig. 2: Transverse momentum distribution, $d\sigma/dp_{Tj}$, of the jet originating from the scattered quark for $ep \rightarrow eW^\pm X$ (solid line), $ep \rightarrow \nu W^- X$ (dashed line), and $ep \rightarrow \nu ZX$ (dash-dotted line) at LEP/LHC.

is shown in Fig. 2. Due to the u -channel fermion singularity and/or the $1/t$ pole induced by the photon propagator, the p_{Tj} distributions for $eW^\pm X$ and $\nu W^- X$ production sharply peak at small values of p_{Tj} , while the jet transverse momentum distribution in $ep \rightarrow \nu ZX$ has a broad maximum at $p_{Tj} \approx 50$ GeV.

The scattered proton in elastic νW^- production typically has a very small transverse momentum of a few hundred MeV only. Since it loses only about 4% of its energy in the scattering process on average, it will remain inside the beam pipe. Nevertheless, it may be possible to tag the scattered protons by installing special proton spectrometers after the first group of dipole magnets, where they will receive a slightly larger deflection than the unscattered protons in the bunch.

The hadronic decays of W and Z bosons at LEP/LHC will, in general, be difficult to observe, due to the large two and three jet QCD background.¹⁴⁾ In the following we shall therefore consider only the leptonic W and Z decay modes, $W \rightarrow \ell\nu$ and $Z \rightarrow \ell^+\ell^-$ with $\ell = e, \mu$. Fig. 3 shows the p_T spectrum of the charged lepton from W and Z decays (Fig. 3a) and the missing transverse momentum, \not{p}_T , distribution (Fig. 3b). To regulate the u -channel singularity in $ep \rightarrow eW^\pm X$ we have imposed a $p_{Tj} > 5$ GeV cut. eW^\pm events with a jet transverse momentum smaller than 5 GeV mostly contribute for $p_{T\ell}, \not{p}_T < 50$ GeV only. The high $p_{T\ell}$ and \not{p}_T tail thus is not affected by the p_{Tj} cut we impose.

The $p_{T\ell}$ distributions show the familiar jacobian peak at $p_T \approx \frac{1}{2} M_W, \frac{1}{2} M_Z$,

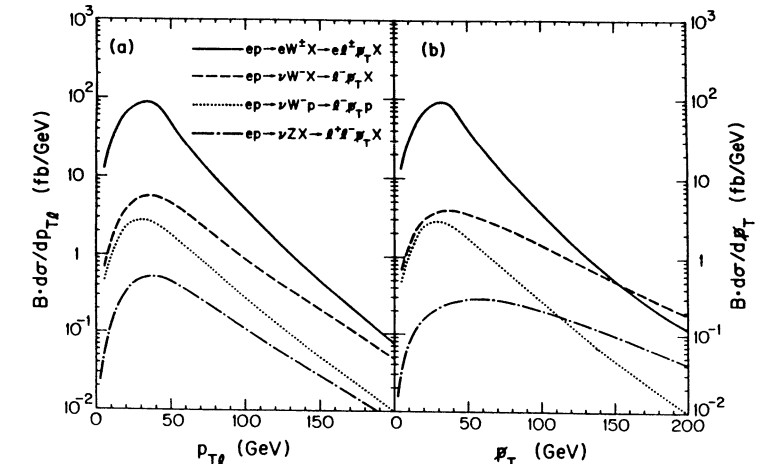


Fig. 3: (a) Transverse momentum spectrum of the charged lepton from W and Z decays, and (b) \not{p}_T distribution for $ep \rightarrow eW^\pm X$ (solid line), $ep \rightarrow \nu W^- X$ (dashed line), $ep \rightarrow \nu W^- p$ (dotted line), and $ep \rightarrow \nu ZX$ (dash-dotted line).

smeared by the W/Z transverse momentum. For $\nu W^- X$ and νZX production the $p_{T\ell}$ distribution is slightly harder than for the other two processes, due to the relatively larger average jet transverse momentum in these processes. The p_T of the ℓ^+ and the ℓ^- in νZX production are almost identical, and therefore only one of the distributions is shown.

While the \not{p}_T spectrum for $eW^\pm X$ and $\nu W^- p$ is very similar to the $p_{T\ell}$ spectrum, it is much harder for the other two processes. This can be easily understood. Since the dominant contribution to the $ep \rightarrow eW^\pm X$ cross section originates from the exchange of an almost real photon, the scattered electron tends to have small p_T . The same is true for the scattered proton in $ep \rightarrow \nu W^- p$. Hence both processes are governed by $2 \rightarrow 2$ kinematics, $\gamma q \rightarrow W^\pm q'$ and $e\gamma \rightarrow \nu W^-$, which makes it hard for the decay neutrino in the first case or the decay lepton in the second to pick up large p_T .

3. Testing the $WW\gamma$ and WWZ Vertex

All four W and Z production processes depend on the $WW\gamma$ or WWZ couplings, which enter via Feynman graphs similar to the one shown in Fig. 1c for $ep \rightarrow eW^\pm X$. Since both the virtual and the decaying on-shell W or Z couple to essentially massless fermions, the tensor structure of the WWV vertex, $V = \gamma, Z$, is restricted to allow for seven free parameters,^{15,16)} $g_1^V, \kappa^V, \lambda^V, g_4^V, g_5^V, \tilde{\kappa}^V$, and $\tilde{\lambda}^V$. g_4^V, κ^V and $\tilde{\lambda}^V$ violate CP . Within the SM, at tree level, the only nonzero couplings are

$$g_1^V = 1, \quad \kappa^V = 1. \quad (3.1)$$

Electromagnetic gauge invariance puts an additional constraint on $g_1^\gamma - 1$, g_4^γ and g_5^γ : for on-shell photons these anomalous couplings are forbidden.⁵⁾ Computing the cross sections for $ep \rightarrow eW^\pm X$, $\nu W^- X$, and $\nu W^- p$, one integrates over the squared momentum transfer t . Due to the $1/t$ pole induced by the photon propagator, the dominant part of the cross section arises from very small $|t|$ -values and $g_1^\gamma - 1$, g_4^γ , and g_5^γ effectively vanish.

Considering leptonic W decay modes only, the signal for $ep \rightarrow eW^\pm X$ is

$$ep \rightarrow \ell^\pm + \text{jet} + \not{p}_T (+e). \quad (3.2)$$

Because the dominant contributions to the cross section arise from the exchange of an almost real photon, the scattered electron will quite often be lost in the beam pipe. For elastic and deep inelastic νW^- production the signals are

$$ep \rightarrow \ell^- + \not{p}_T (+p), \quad \text{and} \quad ep \rightarrow \ell^- + \not{p}_T (+\text{jet}). \quad (3.3)$$

In the first case the scattered proton will always remain in the beam pipe. Elastic νW^- events with the W decaying leptonically thus will be rather spectacular: they consist of a single e^- or μ^- at large p_T , and are completely quiet hadronically. For deep inelastic νW^- production, on the other hand, one in general expects hadronic activity, or an observable jet, to accompany the $\ell^- \not{p}_T$ signature. Finally, the signal for $ep \rightarrow \nu ZX$ is

$$ep \rightarrow \ell^+ \ell^- + \not{p}_T + \text{jet}. \quad (3.4)$$

Due to the hard p_T distribution of the scattered quark in this reaction (see Fig. 2), there usually is an observable hadronic jet.

In order to assess the observability of anomalous couplings, we must take into account the finite acceptance of detectors. We require that the charged lepton pseudorapidity is $|\eta_\ell| < 3.5$. Furthermore, we impose a $p_{T\ell} > 15$ GeV and $\not{p}_T > 20$ GeV cut. In $ep \rightarrow eW^\pm X$ ($ep \rightarrow \nu ZX$) we ask for an observable jet with $p_{Tj} > 15$ GeV (20 GeV), $|\eta_j| < 3.5$ (4.5), and a jet-lepton separation of $\Delta R_{j\ell} > 0.7$. The separation cut helps to remove backgrounds from heavy quark (*c, b*) semileptonic decays. No cuts on the final state hadrons are imposed in deep inelastic νW^- production.

Due to the dominance of photon exchange graphs, the process $ep \rightarrow eW^\pm X$ is quite insensitive to anomalous WWZ couplings, and subsequently we shall only consider anomalous contributions to the $WW\gamma$ vertex in this reaction. The p_T distribution of the jet in eW^\pm production, shown in Fig. 4a, turns out to be

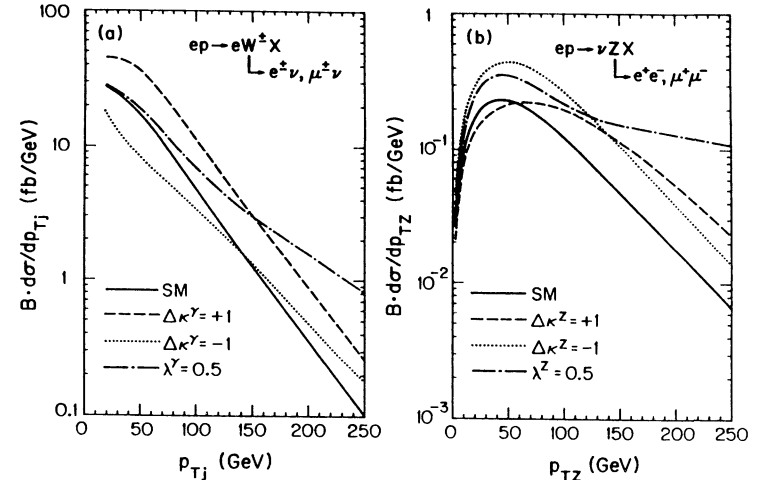


Fig. 4: Transverse momentum distribution of (a) the jet in $ep \rightarrow eW^\pm X$, and (b) the Z boson in $ep \rightarrow \nu ZX$ for the SM (solid line) and various values of anomalous $WW\gamma$ and WWZ couplings. The cuts imposed are described in the text.

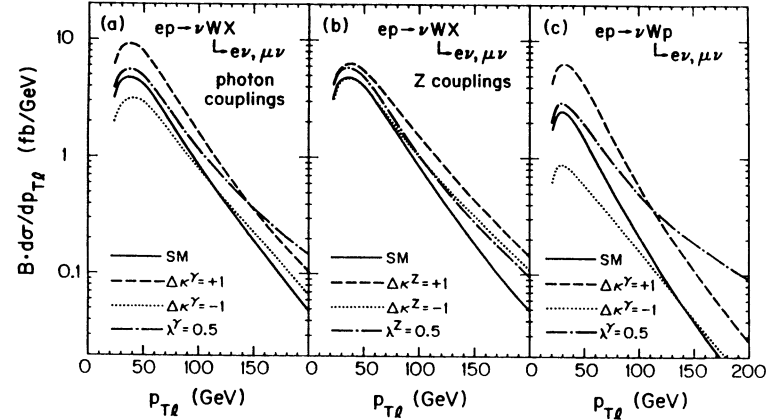


Fig. 5: Transverse momentum distribution of the charged lepton in $ep \rightarrow \nu W^- X$, $W \rightarrow \ell\nu$, (a) for various anomalous $WW\gamma$ couplings and (b) for some anomalous WWZ couplings. The $p_{T\ell}$ spectrum for elastic νW^- production is shown in (c) for the SM (solid line) and several anomalous $WW\gamma$ couplings. The cuts imposed are described in the text.

rather sensitive to anomalous $WW\gamma$ couplings.⁵⁾ On the other hand, since only W -exchange graphs contribute to νZ production, $ep \rightarrow \nu ZX$ is only sensitive to anomalous WWZ couplings. Fig. 4b shows the p_T distribution of the Z boson for some anomalous values of $\Delta\kappa^Z = \kappa^Z - 1$ and λ^Z . It is obvious that the p_{TZ} spectrum is very sensitive to anomalous couplings.

Due to the absence of the u -channel fermion exchange pole in deep inelastic νW^- production, Z -exchange diagrams play a non-negligible role, and $ep \rightarrow \nu W^- X$ is sensitive to both anomalous $WW\gamma$ and WWZ couplings. In elastic νW^- production, however, only photon exchange contributes, and $ep \rightarrow \nu W^- p$ therefore only probes anomalous $WW\gamma$ couplings. It turns out that the charged lepton p_T spectrum is the quantity most sensitive to anomalies of the three vector boson vertices in the νW^- case. Figs. 5a and 5b show the $p_{T\ell}$ distributions assuming anomalous $WW\gamma$ and WWZ vertices, respectively, for deep inelastic νW^- production. Fig. 5c displays the $p_{T\ell}$ spectrum of $ep \rightarrow \nu W^- p$ for anomalous $WW\gamma$ couplings. It is obvious that $ep \rightarrow \nu W^- X$ is less sensitive to anomalous $WW\gamma$ and WWZ couplings than $ep \rightarrow eW^\pm X$ and $ep \rightarrow \nu ZX$, while νW^- production via elastic ep collisions looks promising.

These qualitative statements may be substantiated by deriving those values of $\kappa^V - 1, \dots, \tilde{\lambda}^V$ which would give rise to a deviation from the SM at the 90% confidence level (CL) in the distributions shown in Fig. 4 or 5. Here statistical errors only are considered assuming an integrated luminosity of $\int \mathcal{L} dt = 1 \text{ fb}^{-1}$. $\tilde{\kappa}^\gamma$ is omitted subsequently since the electric dipole moment of the neutron places an upper limit of $\mathcal{O}(10^{-3})$ on $|\tilde{\kappa}|$.¹⁷⁾ $g_1^\gamma - 1$, g_4^γ and g_5^γ are, as mentioned above, not probed in single W production in ep collisions.

An important point in such an analysis is the potentially dangerous background to $ep \rightarrow \nu W^- X$ originating from top quark production, $ep \rightarrow \nu \bar{t}bX \rightarrow \nu W^- \bar{b}bX$, in particular if flavor identification is not possible at LEP/LHC. However, the $p_{T\ell}$ distribution for leptons originating from top decays drops much faster than that of leptons from $ep \rightarrow \nu W^- X$. This is shown in Fig. 6, where we compare the p_T distribution of the charged lepton from W decays in $ep \rightarrow \nu W^- X$ (solid line) with that resulting from $\bar{t}b$ production assuming a top quark of mass $m_t = 100 \text{ GeV}$ (dashed line) and $m_t = 200 \text{ GeV}$ (dotted line). Although no cuts on the final state hadrons are imposed, which could further suppress the top quark background, νW production clearly dominates for $p_{T\ell} > 80 \text{ GeV}$, independently of m_t . Since anomalous couplings mostly affect the lepton transverse momentum spectrum at large values of $p_{T\ell}$, the sensitivities which one can achieve are only little affected by the top quark background.

Top quark production also represents a background for $ep \rightarrow eW^- X$ when the scattered electron is lost in the beam pipe, which is expected for more than half of the signal events. This is illustrated by the dash-dotted line in Fig. 6 which represents the $p_{T\ell}$ spectrum from $ep \rightarrow eW^- X$ for scattered electrons with $|\eta_e| > 4$. However, since the top quark background affects only part of the $eW^- X$ signal, the combined sensitivity limits from $ep \rightarrow eW^\pm X$ and $ep \rightarrow eW^- X$ are again only marginally altered. The other three processes, $ep \rightarrow eW^+ X$, $ep \rightarrow \nu ZX$, and elastic νW^- production, are essentially background free.

The resulting minimal anomalous couplings, which would give rise to a 90% CL

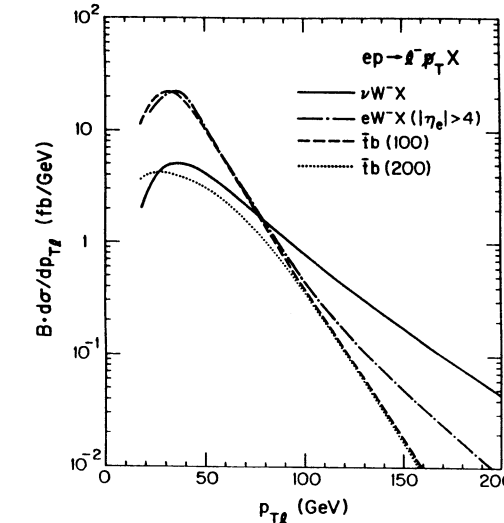


Fig. 6: Transverse momentum distribution of the charged lepton ℓ^- in $ep \rightarrow \ell^- p_{T\ell} X$ from $\bar{t}bX$ production with $m_t = 100 \text{ GeV}$ (dashed line) and $m_t = 200 \text{ GeV}$ (dotted line), SM $\nu W^- X$ production (solid line), and SM $eW^- X$ production with $|\eta_e| > 4$. A $p_{T\ell} > 20 \text{ GeV}$, $p_{Tj} > 15 \text{ GeV}$ cut is imposed. To regulate the u -channel singularity, $p_{Tj} > 5 \text{ GeV}$ has been required in the eW^- case, whereas no jet cuts are imposed for the other processes.

effect are given in Table 2 for $WW\gamma$ couplings and in Table 3 for WWZ couplings. In order to derive realistic limits we allow for a normalization uncertainty $\Delta\mathcal{N}$ of the SM cross sections of $\Delta\mathcal{N} = 30\%$. For $ep \rightarrow \nu W^- X$ we include the top quark background for $m_t = 100 \text{ GeV}$. No cuts on the final state hadrons in $\nu W^- X$, which may further reduce the top quark background, are imposed.

Tables 2 and 3 demonstrate that LEP/LHC can measure the $WW\gamma$ and WWZ vertex with 10 – 40% and 20 – 100% accuracy, respectively, with an integrated luminosity of 1 fb^{-1} if the normalization of the SM rate is known to better than 30%. $eW^\pm X$ and elastic νW^- production are most sensitive to κ^γ , λ^γ , and $\tilde{\lambda}^\gamma$, whereas $ep \rightarrow \nu ZX$, although its rate is very small, yields the most useful bounds on anomalous WWZ couplings.

4. Conclusions

Single W and Z production processes at LEP/LHC provide both an interesting physics signal as well as potentially important background sources. eW^\pm , νZ , and elastic and inelastic νW^- production provide an opportunity to measure the $WW\gamma$ and WWZ vertices. The sensitivity bounds which we have summarized in Tables 2 and 3 have of course to be compared with the limits which can be

Table 2

Sensitivities achievable at the 90% CL for the anomalous $WW\gamma$ couplings $\Delta\kappa^\gamma = \kappa^\gamma - 1$, λ^γ and $\tilde{\lambda}^\gamma$ in $ep \rightarrow eW^\pm X$, $ep \rightarrow \nu W^- X$ and $ep \rightarrow \nu W^- p$ for $\int L dt = 1 fb^{-1}$. Only one coupling at a time is assumed to be different from the SM value.

coupling	$ep \rightarrow eW^\pm X$	$ep \rightarrow \nu W^- X$	$ep \rightarrow \nu W^- p$
$\Delta\kappa^\gamma$	+0.4	+0.7	+0.4
	-0.4	-1.3	-0.5
λ^γ	+0.12	+0.35	+0.25
	-0.12	-0.35	-0.25
$\tilde{\lambda}^\gamma$	+0.12	+0.4	+0.26
	-0.12	-0.4	-0.26

Table 3

Sensitivities achievable at the 90% CL for the anomalous WWZ couplings in $ep \rightarrow \nu W^- X$ and $ep \rightarrow \nu ZX$ for $\int L dt = 1 fb^{-1}$. Only one coupling at a time is assumed to be different from the SM value.

coupling	$ep \rightarrow \nu ZX$	$ep \rightarrow \nu W^- X$	coupling	$ep \rightarrow \nu ZX$	$ep \rightarrow \nu W^- X$
$\Delta\kappa^Z$	+0.8	+0.7	g_1^Z	+0.3	+0.5
	-0.8	-0.8		-0.6	-0.9
λ^Z	+0.3	+0.5	g_4^Z	+0.35	+0.8
	-0.2	-0.4		-0.35	-0.8
$\tilde{\kappa}^Z$	+1.0	+1.4	g_5^Z	+0.5	+0.8
	-1.0	-1.4		-0.5	-0.7
$\tilde{\lambda}^Z$	+0.24	+0.5			
	-0.24	-0.5			

achieved at LEP II and with the LHC pp mode.

W pair production at LEP II is expected to yield limits which, in general, are expected to be quite similar or somewhat better than those obtained from single W and Z production at LEP/LHC.¹⁶⁾ All bounds on anomalous contributions to the $WW\gamma$ and WWZ vertices depend in principle on the form factor assumed to regularize the unitarity violating behaviour of the anomalous couplings¹⁸⁾ in the multi-TeV range, and its scale Λ . Since the available center of mass energy at LEP II and LEP/LHC does not exceed a few hundred GeV, the limits obtained from $e^+e^- \rightarrow W^+W^-$ and single W and Z production in ep collisions are completely insensitive to the form factor and the scale Λ chosen. On the other hand, bounds from $W\gamma$ and WZ production at the LHC or SSC depend quite strongly on Λ , due to the much larger center of mass energy of these machines. For $\Lambda \approx 1$ TeV the $pp \rightarrow W\gamma$ and $pp \rightarrow WZ$ limits are typically a factor 2 – 3 more stringent,

whereas for $\Lambda \gg 1$ TeV they are up to one order of magnitude better^{19,20)} than those listed in Tables 2 and 3. Nevertheless, the measurement of the anomalous $WW\gamma$ and WWZ couplings in single W and Z production at LEP/LHC would be a useful complement to the results obtained at LEP II and the LHC.

Acknowledgements

We would like to thank Ch. Berger, J. J. van der Bij, M. Böhm and A. Ghinoculov for useful discussions. This research was supported in part by the University of Wisconsin Research Committee with funds granted by the Wisconsin Alumni Research Foundation, by the U. S. Department of Energy under contract DE-AC02-76ER00881, and by funds awarded by the Texas National Research Laboratory Commission.

References

1. J. Feltesse, these proceedings;
R. Rückl, these proceedings.
2. K. Neufeld, Z. Phys. C17, 145 (1983).
3. E. Gabrielli, Mod. Phys. Lett. A1, 465 (1986).
4. M. Böhm and A. Rosado, Z. Phys. C42, 479 (1989).
5. U. Baur and D. Zeppenfeld, Nucl. Phys. B325, 253 (1989).
6. D. Atwood *et al.*, MAD/PH/591 preprint, to appear in the Proceedings of the 1990 Snowmass Summer Study on “Research Directions for the Decade”, Snowmass, Colorado, June 25 – July 13, 1990.
7. G. Altarelli, *et al.*, Nucl. Phys. B262, 204 (1985).
8. D. Zeppenfeld, these proceedings;
G. Grindhammer *et al.*, these proceedings.
9. G. Schuler and J. F. de Troconiz, these proceedings.
10. E. Eichten, I. Hinchliffe, K. Lane and C. Quigg, Rev. Mod. Phys. 56, 579 (1984), erratum 58, 1065 (1986).
11. G. Brianti, these proceedings.
12. J. Blümlein and G. Schuler, PHE 90-04 preprint, 1990.
13. B. A. Kniehl, MAD/PH/595 preprint, to appear in Phys. Lett. B.
14. H. Baer, J. Ohnemus and D. Zeppenfeld, Z. Phys. C43, 675 (1989); see however the analysis for LEP/LHC energies in Ref. 8.
15. K. Gaemers and G. Gounaris, Z. Phys. C1, 259 (1979).
16. K. Hagiwara *et al.*, Nucl. Phys. B282, 253 (1987).
17. W. J. Marciano and A. Queijo, Phys. Rev. D33, 3449 (1986).
18. U. Baur and D. Zeppenfeld, Phys. Lett. 201B, 383 (1988).
19. U. Baur and D. Zeppenfeld, Nucl. Phys. B308, 127 (1988).
20. S. Willenbrock and D. Zeppenfeld, Phys. Rev. D37, 1775 (1988).

Searching for the Higgs in ep collisions at LEP/LHC

G. Grindhammer,¹⁾ D. Haidt,²⁾ J. Ohnemus,³⁾ J. Vermaseren,⁴⁾ and D. Zeppenfeld⁵⁾

¹⁾MPI für Physik, Föhringer Ring 6, 8000 München 40, Germany

²⁾DESY, Notkestr. 85, 2000 Hamburg 52, Germany

³⁾Florida State University, Tallahassee, FL 32306, USA

⁴⁾NIKHEF-H, Postbus 41882, 1009 DB Amsterdam, the Netherlands

⁵⁾Department of Physics, University of Wisconsin, Madison, WI 53706, USA

Abstract

We investigate the possibility to observe an *intermediate mass* Higgs in ep collisions at LEP/LHC. We find that such a particle can be observed once a reasonable level of flavor identification is available to separate efficiently the $b\bar{b}$ decay mode of the Higgs from most of the background.

1. Introduction

This study tries to assess the visibility of a Higgs particle in ep-collisions at LEP/LHC in the mass range from 80 GeV to about 140 GeV, the so called intermediate mass range of the Higgs boson. We chose to investigate this restricted mass range for practical reasons. If the Higgs is lighter than 80 GeV the high energy phase of LEP is expected to find it. If it is heavier than 140 GeV its main decay mode is into two vector bosons of which one may be virtual when the mass of the Higgs is still less than twice the vector boson mass. This decay mode is easily searched for via the leptonic decay modes of the resulting Z bosons. Because of the relatively small branching ratio of $Z \rightarrow l^+l^-$ it is important to have a very high production rate for the Higgs. This is the case for the SSC and for the LHC itself and the chances are favorable that *e.g.* the LHC will find the Higgs if its mass is in the range from about 130 GeV to 800 GeV [1]. This leaves open the ‘intermediate mass range’ in which the Higgs decays predominantly into a pair of b -quarks. To see a resonance in a dijet spectrum one has to deal with a background that consists of regular QCD two jet production. Even with perfect flavor identification this is a difficult task because b -quarks are also pair produced by means of QCD mechanisms. Currently it is believed that the intermediate mass Higgs cannot be found via its $b\bar{b}$ decay mode at either the SSC or the LHC in its pp mode.

While QCD processes play an important role in ep collisions as well, they have to be initiated via electroweak boson exchange and are thus much less severe as backgrounds to electroweak physics than at hadron colliders. In addition the cleanliness of the electron part of the interaction provides for additional leverage to distinguish signal from background. The subject of our study was hence to understand the characteristic signature of ‘intermediate mass’ Higgs production in ep collisions and the features of the main background processes in this environment.

As we shall see below the signal can be characterized as a 3-jet event with a substantial amount of missing transverse momentum (\not{p}_T), when we look for Higgs production via WW fusion. Backgrounds arise from a variety of processes. Multijet production due to charged current (CC) processes has to be considered and there are neutral current (NC) events in which the electron escapes detection but the missing transverse momentum of the neutrino is simulated by a very hard jet that stays inside the beam pipe [2]. A jet of 2 TeV with a rapidity of 5 for instance has a transverse momentum of 27 GeV.

In addition there are backgrounds due to Z and W production. If the Higgs happens to have a mass that is close to the mass of the Z there is an irreducible background from the Z decaying into b -quarks. The relevance of the W background depends crucially on the quality of the flavor detection. An additional possible background from top production and decay must be considered. At present the background due to the top contains large uncertainties because its mass is not known yet. In principle the production of a top involves also a b -quark as a spectator. The decay is predominantly into a W and a b -quark and the W can decay again into a quark pair that shows as one or more additional jets. Hence there are various ways to mimic the signal and they have to be estimated.

While the main properties of these backgrounds can be discussed at the parton level, fragmentation will also influence reaction features. Hence there are additional background effects from hadronization, which must be studied separately. Systematic uncertainties in our numbers arise because radiative correction calculations are available neither for the signal nor for most of the background reactions. Radiative corrections can give extra contributions to the production of heavy objects that are estimated to be between 25% and 75%. This holds both for the signal and for the W , Z and top backgrounds. The size of the radiative corrections to the QCD backgrounds is even more uncertain. We estimate them to be roughly a factor two. None of these corrections have been applied to our numbers.

All our calculations are done for 60 GeV on 8 TeV ep collisions, assuming a luminosity of $\mathcal{L} = 10^{32} \text{cm}^{-2}\text{s}^{-1}$. With an effective running time of 10^7 sec/year this corresponds to 1fb^{-1} per year. Under these assumptions we will first discuss the signal in Section 2. Next we will address the various parton level backgrounds in Section 3, assuming that there is no flavor detection. The additional background rejection which is possible with flavor identification will be addressed in Section 4. Finally, in Section 5 we discuss hadronization effects and in particular the $b\bar{b}$ mass resolution. Because this last investigation was largely done with event generators of the evolution type we will address also some of the problems that we encountered when using these ‘standard’ event generators. We end with an evaluation of the results in Section 6.

2. The Signal

The main production mechanisms for Higgs particles in ep collisions [3, 4] are WW and ZZ fusion as shown in Fig. 1. The contribution from WW fusion turns out to dominate over ZZ fusion by about a factor 5. This is partially due to the heavier mass of the exchanged Z and partially to its smaller coupling to fermions. Because the Z -induced signal defines a final state different from the W -induced signal, and because NC processes have potentially larger backgrounds we will only look at the WW fusion signal. In the intermediate mass range the decay of the

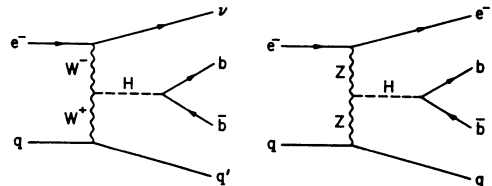


Figure 1: Feynman graphs for Higgs production in ep collisions via WW and ZZ fusion.

Higgs is predominantly into $b\bar{b}$ pairs until the decay into a real and a virtual W takes over. The relevant branching ratios [5] are given in Table 1. The numbers include the 1-loop QCD corrections to the $H \rightarrow b\bar{b}$ decay width and in particular the running of the b -quark mass.

mass(GeV)	$b\bar{b}$	$c\bar{c}$	gluons
80	0.860	0.055	0.019
90	0.854	0.054	0.025
100	0.844	0.053	0.031
110	0.815	0.052	0.036
120	0.741	0.047	0.040
130	0.603	0.038	0.039
140	0.413	0.026	0.031
150	0.219	0.014	0.019

Table 1: Hadronic branching ratios of the Higgs

In Fig. 2 we have summarized the total Higgs production cross sections from WW and ZZ fusion together with the result for $\sigma(ep \rightarrow \nu H X) B(H \rightarrow b\bar{b})$ at LEP/LHC. Since the total Higgs production rate is of order 100 events per year, one has to search in the dominant decay channel. Thus the precise characteristics of the $ep \rightarrow H\nu$ jet, $H \rightarrow b\bar{b}$ events have to be understood.

For the calculation of the signal cross section we have used a parton level Monte Carlo program based on the complete $2 \rightarrow 4$ processes shown in Fig. 1. Agreement with previous calculations at LEP/LHC energies [6] was confirmed. The statistical errors of the Monte Carlo are always considerably less than one percent when they refer to total cross sections and about 1 percent or slightly larger when they refer to a differential distribution (mostly for backgrounds). They are negligible hence compared to the QCD uncertainties, but the errors give useful information when comparing results. We have used Eichten et al. structure functions [7] (set 1, version of April 1990) throughout this work and the following values for the weak boson masses and widths: $M_W = 80.15$ GeV, $M_Z = 91.18$ GeV, $\Gamma_W = 2.1$ GeV, and $\Gamma_Z = 2.5$ GeV. The electroweak couplings were then obtained either by fixing the QED value of α ($1/128.5$) and setting $\sin^2 \theta_W = 0.23$ or by using G_F , M_Z , and $\sin^2 \theta_W = 0.226$ as input parameters. These two sets of coupling constants lead

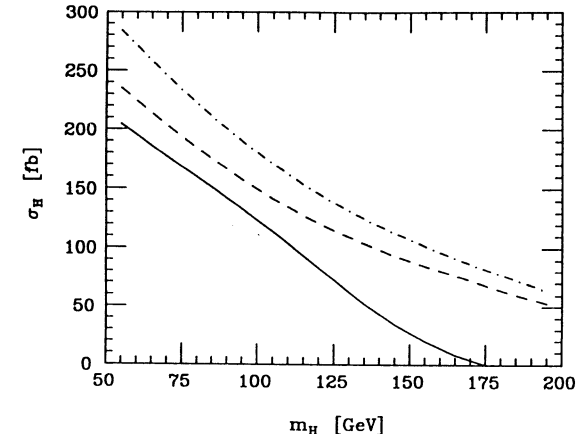


Figure 2: Total Higgs production cross-section from $WW + ZZ$ fusion (dash-dotted line), WW fusion only (dashed line), and WW fusion including the branching ratio for $H \rightarrow b\bar{b}$ (solid line) at LEP/LHC.

to cross section differences at the percent level only and are completely negligible compared to the QCD uncertainties. The value of the strong coupling constant, which influences the signal rate via the $H \rightarrow b\bar{b}$ branching ratio, was fixed to $\alpha_S = 0.12$.

The principle characteristics of the WW fusion signal are two b jets with an invariant mass equal to the parent Higgs, a spectator jet, and p_T due to the escaping neutrino. In order to judge their visibility in an actual experiment we have plotted in Fig. 3 the transverse momentum and rapidity distributions of the individual partons. Already for the 100 GeV Higgs shown in Fig. 3 the two b jets are relatively hard, $\langle p_T(b) \rangle = 55$ GeV, and, what is even more important, the b jets are quite central. The spectator quark, on the other hand, tends to be relatively forward with respect to the proton direction, with an average rapidity of 3.5, but it carries away a substantial amount of transverse momentum as well. As is apparent from the symmetry of the fusion processes in Fig. 1 and because the W couples identically to quarks and leptons, the unobserved neutrino has a p_T distribution which is identical to the one of the spectator quark. The relatively large p_T of the signal events will be crucial in eliminating NC backgrounds.

Because of the isotropic decay of the scalar Higgs the b jets will in general deposit a large amount of transverse energy in the detector. Combined with the substantial transverse energy of the spectator jet, the Higgs events are characterized by a large deposit of total transverse energy. The E_T spectrum for a 100 GeV Higgs is shown in Fig. 4. For a heavier Higgs the peak in the E_T spectrum shifts to even higher values. NC or CC induced multijet events of comparable invariant mass usually favor smaller jet transverse momenta due to the presence of infrared and collinear singularities. Hence an E_T cut is a safe and efficient way to reduce these backgrounds (see below).

The characteristics of the signal shown in Fig. 3 suggest the following set of minimal cuts to define the phase space region for the Higgs search:

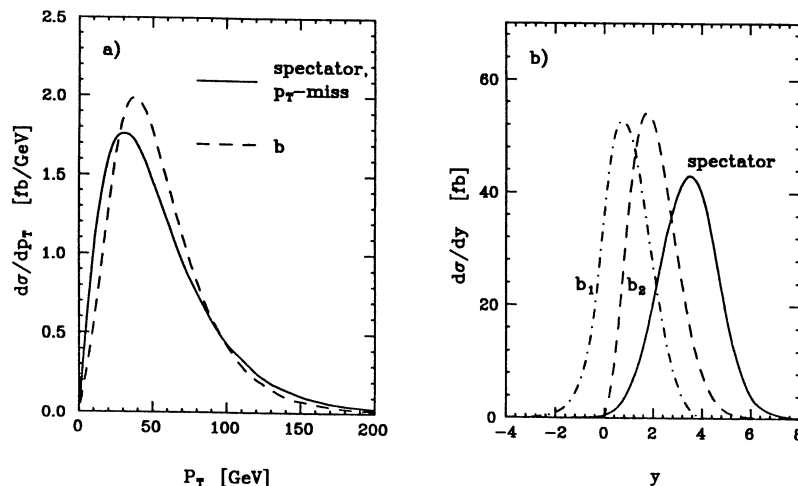


Figure 3: Characteristics of the signal arising from a 100 GeV Higgs boson. Shown are a) the p_T spectra of the spectator jet and the missing neutrino (solid line) and of the 2 b jets. In b) the rapidity distributions of the b jets and of the spectator jet are shown. b_1 denotes the b jet with the lowest rapidity and b_2 the one with the highest rapidity.

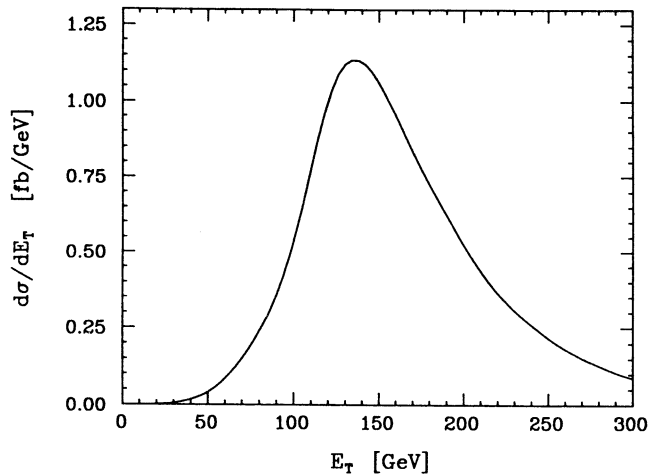


Figure 4: Total transverse energy distribution of the three partons in the production of a 100 GeV Higgs boson from WW fusion.

- Missing transverse momentum of at least 20 GeV.
- Two or three jets with rapidity less than 4.5.
- Each of the jets has a transverse energy of at least 20 GeV.

Here we have assumed a calorimeter coverage down to about 1 degree, which is a necessary requirement of a LEP/LHC detector anyway in order to be well suited for the measurement of deep inelastic scattering processes.

Obviously the two b jets have to be observed in order to reconstruct a Higgs invariant mass peak. Imposing the above jet-cuts on the Higgs decay products only, one obtains the signal rates marked '2-jet inclusive' in Table 2. Many of these events exhibit a third jet, the spectator jet, which satisfies all of the above requirements and which is well separated from the decay jets, *i.e.*,

- all three jets are well separated in the rapidity – azimuthal angle plane fulfilling the requirement $R_{jj} = \sqrt{\Delta y^2 + \Delta\phi^2} > 1$. R_{jj} is the distance of the jets in the Lego plot.

The resulting signal rates are marked '3-jet' in Table 2. One finds that about 2/3 of the '2-jet inclusive' Higgs events contain a well visible spectator jet. Because most backgrounds are substantially reduced by requiring the presence of a third jet (see next Section) we will not consider the search for the Higgs in the 2-jet sample any further.

mass(GeV)	2-jet incl.	3-jet	3-jet (all cuts)	bb only
80	108	71.9	60.1	55.3
90	105	71.0	60.4	55.3
100	99.5	68.0	58.3	53.0
110	91.1	62.4	53.8	48.5
120	77.1	52.8	45.4	40.7
130	58.0	39.5	34.1	30.3
140	36.3	24.6	21.2	18.7
150	17.7	12.0	10.4	9.0

Table 2: Two jet and three jet Higgs signal. All cross sections are given in fb in this and all subsequent tables, *i.e.*, the entries correspond to # events/year.

In the 3-jet sample the problem arises which two jets to identify with the Higgs decay products. From Fig. 3 one finds that the transverse momenta of the jets do not constitute a good separation criterion. However, in about 90% of all Higgs events the spectator jet has the highest rapidity. Hence the combinatorial background is largely eliminated by searching for an invariant mass peak among the two lowest rapidity jets only. There is typically only about 0.3% pollution in the form of events that contain the spectator jet as one of the two jets with the smallest rapidity, if one requires that the mass reconstruction should be within 5 GeV of the input mass, which corresponds to an optimistic estimate of the eventual experimental mass resolution. We will come back to this in Section 5.

Together with the transverse energy considerations discussed before, this leads to the remaining two requirements for a signal candidate:

- Visible transverse energy of at least 100 GeV.
- The two Higgs decay jets are the two jets with the smallest rapidities.

The remaining signal rate for Higgs masses between 80 and 150 GeV is given in the column labeled ‘3-jet (all cuts)’ in Table 2. These rates combine all hadronic decay channels of the Higgs: $c\bar{c}$, $b\bar{b}$, and gg final states. The final 3-jet sample restricted to the $H \rightarrow b\bar{b}$ decay mode is listed as ‘ $b\bar{b}$ only’.

In order to get a reliable estimate of the signal we should know how stable these numbers are when varying the values of the cut parameters. In reality there will be a fragmentation process which in combination with experimental resolution problems leads to an effective smearing of the cut values. A strong sensitivity to these parameters would indicate a large uncertainty in the size of the observed signal. From Figs. 3 and 4 this is clearly not the case. The exact value of the rapidity cut influences only the spectator jet. Still the rapidity cut on the spectator jet is the major single source of loss of data. Also the transverse momentum distributions are relatively flat and hence changes of a few GeV in the cuts do not lead to dramatic changes in signal rate. As a result fragmentation and the experimental resolutions should not change the signal rate very much. Another important point is that the actual cut values are not critical in retaining a sizeable signal. The cut values can still be optimized according to the dominant backgrounds which will be discussed in the next Section.

3. Background Processes

Whether or not the rate of clean 3-jet signal events, being of order 50 events per year, will suffice to detect the intermediate mass Higgs, is purely a function of the background rejection which can be achieved. In order to have a fair comparison of signal and backgrounds we have modeled all backgrounds with parton level Monte Carlo programs which are based on the full QCD/electroweak tree level matrix elements. The background processes which we have considered are the following.

i) Photoproduction of multijet events.

More generally, NC production of multijet events where the e^- is lost in the beam pipe can give rise to a \not{p}_T signature due to mismeasurement/cracks in the calorimeter or because of very energetic particles which are lost due to the detector acceptance (beam pipe). Because of the huge photoproduction cross-section of dijet events, $\sigma_{NC}(\text{dijet}) = 1.5 \text{ nb}$ within the acceptance cuts described in Section 2, this is a potentially dangerous background [6].

We have modeled the NC induced 3-jet + \not{p}_T background by calculating photoproduction of 4 parton final states in the Weizsäcker-Williams approximation, using the amplitudes for these processes given in Ref. [8]. In order to estimate the \not{p}_T signal arising from energy mismeasurement the cross sections for 3 parton final states are used. For the equivalent photon flux we have taken

$$f_\gamma(z) = \frac{\alpha}{2\pi} \frac{1 + (1 - z)^2}{z} \log(q_{\max}^2/q_{\min}^2), \quad (1)$$

with $\alpha = 1/137$. Here q_{\min}^2 is given by the kinematic limit and q_{\max}^2 is determined by requiring the electron to vanish in the beam hole which was assumed to have a

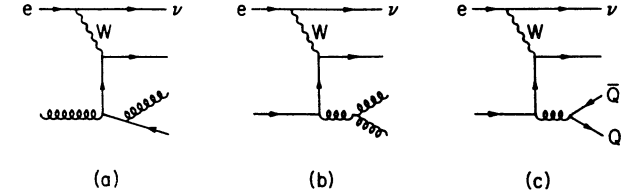


Figure 5: Typical Feynman graphs for CC induced 3-jet production. a) W -gluon fusion, b) quark-gluon-gluon production, and c) production of heavy quark pairs.

size of 2 degrees. The scale of the strong coupling constant α_s and of the structure functions was chosen as the geometric mean of the p_T 's of the 4 jets. Of these 4 jets one is required to disappear in the proton beam pipe, i.e., to have $|y_j| > 4.5$ thus giving rise to missing transverse momentum. All soft singularities are eliminated by the $p_T > 20 \text{ GeV}$ cuts on the visible jets and by requiring a finite amount of \not{p}_T due to the forward jet. Collinear singularities in the matrix elements are avoided by imposing $\Delta R_{jj} > 1$ for all 4 jets.

Because of the size of the photoproduction rate and because this background was considered to make the intermediate mass Higgs unobservable in previous investigations [6], we will discuss its reduction in more detail below.

ii) CC multijet production.

Typical Feynman graphs contributing to CC 3-jet production are shown in Fig. 5. Contributions from 8 different Feynman graphs for the processes in Fig. 5a) and b) and for 2 graphs for 3 quark production (Fig. 5c)), including interference effects, were calculated using the algebraic manipulation program FORM [9]. The resulting parton level cross sections were then summed over all contributing subprocesses. Although having a smaller rate, $\sigma_{CC}(\text{dijet}) = 56 \text{ pb}$, these events exhibit a generic \not{p}_T signature and are hence more difficult to suppress. On the other hand $b\bar{b}$ pair production only occurs via the subprocess indicated in Fig. 5c) and the resulting heavy flavor rate is quite small. Hence flavor identification will be particularly useful in fighting the CC background.

iii) Single W or Z production with subsequent hadronic decay.

These processes have been considered in detail in Ref. [10]. Production cross sections are in the pb-range:

$$\begin{aligned} \sigma(ep \rightarrow eWj) \text{ Br}(W \rightarrow jj) &\approx 10 \text{ pb} \\ \sigma(ep \rightarrow eZj) \text{ Br}(Z \rightarrow jj) &\approx 2 \text{ pb} \\ \sigma(ep \rightarrow \nu Wj) \text{ Br}(W \rightarrow jj) &\approx 1 \text{ pb} \\ \sigma(ep \rightarrow \nu Zj) \text{ Br}(Z \rightarrow jj) &\approx 0.4 \text{ pb} \end{aligned} \quad (2)$$

Single weak boson production will be an important background if the Higgs is degenerate with the W or the Z . Most troublesome are νW and νZ production with their generic \not{p}_T signature.

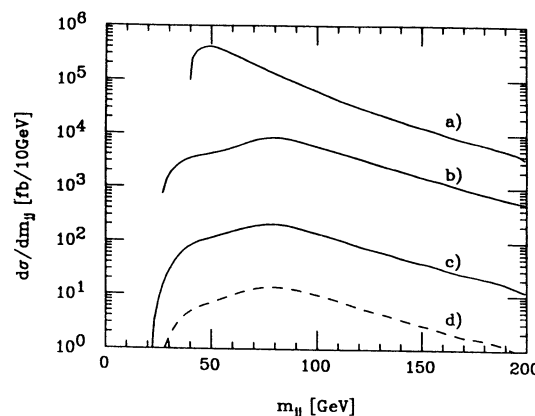


Figure 6: Invariant mass distribution of the 2 jets with the smallest rapidity for multijet events from photoproduction. a) All dijet events, b) 3-jet events with $E_T > 100$ GeV, c) requiring $p_T > 20$ GeV, and d) events satisfying all of the above which contain a $b\bar{b}$ pair.

iv) Top production.

The level of the background process $ep \rightarrow \nu\bar{t}bX$, $\bar{t} \rightarrow \bar{b}jj$ depends critically on the as yet unknown top mass. For $m_t = 160$ GeV one finds $\sigma(ep \rightarrow \nu\bar{t}bX) \approx 2$ pb [11]. Because these events almost always contain a $b\bar{b}$ pair, top production is a dangerous background even if good b -identification is available.

As an example for the background reduction which is obtained by applying the acceptance cuts described for the signal, let us consider the background with the largest rate, photoproduction of multijet events.

In order to find the Higgs signal we are searching for a peak in the invariant mass distribution of the two jets with the lowest rapidity. Photoproduction will lead to a large number of high invariant mass dijet events, either via photon-gluon fusion or via the mixed QED-QCD Compton process, analogous to the processes depicted in Fig. 5a) and b), respectively. For the jet acceptance cuts discussed in Section 2 the resulting dijet invariant mass distribution is given by curve a) in Fig. 6. Even in a relatively narrow mass bin of 10 GeV only, this dijet rate is 10^3 times larger than the Higgs signal listed in Table 2. However we have not used the additional characteristics of the Higgs signal yet. Requiring the presence of a spectator jet ($p_T > 20$ GeV, $|y_j| < 4.5$) and imposing the transverse energy requirement on the 3-jet system of $E_T > 100$ GeV reduces the background rate by an order of magnitude, to curve b) in Fig. 6.

A further strong reduction is achieved by requiring $p_T > 20$ GeV. Energy measurement in the detector has been simulated by Gaussian smearing of the parton momenta with an optimistic resolution of $\delta E/E = 0.35/\sqrt{E} \oplus 1\%$ and with a conservative one of $\delta E_T = 0.5\sqrt{E_T}$. The resulting p_T distributions for 3 parton events are shown in Fig. 7a). A more effective way to generate missing transverse momentum is from very energetic particles lost in the beam pipe [2]. The 4-jet Monte Carlo

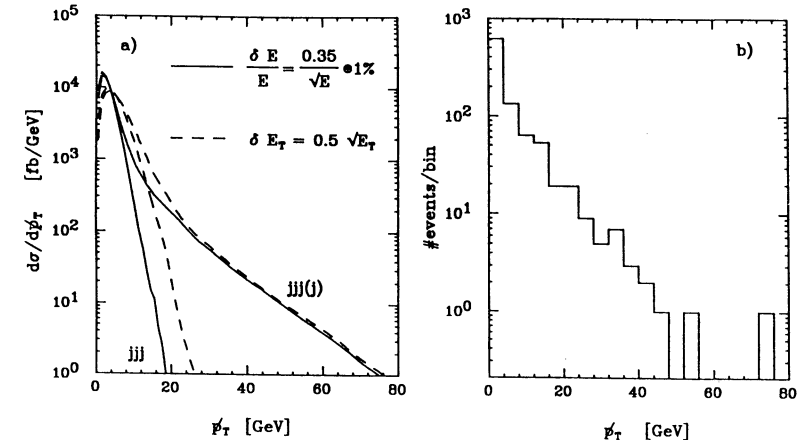


Figure 7: p_T distribution of a) parton level photoproduction events with 3 jets inside the detector and b) $b\bar{b}$ events generated with the AROMA Monte Carlo. The curves labeled jjj allow for energy mismeasurement only, while for the $jjj(j)$ curves a fourth jet of finite p_T is lost inside the proton beam pipe.

described before was used for this purpose and one of the jets was required to disappear in the proton beam pipe ($y_j > 4.5$). The p_T distributions arising from this lost jet are shown in Fig. 7a) for both energy resolutions. They probably overestimate losses in the beam pipe because in the simulation one single parton carries away the transverse momentum while in reality it will be shared by several hadrons with ensuing cancellations of \vec{p}_T .

Requiring $p_T > 20$ GeV leads to a further reduction of the photoproduced 3-jet events by a factor ~ 40 . This reduction factor was confirmed by studying fully hadronized NC events generated with the AROMA Monte Carlo [12]. In Fig. 7b) we show the p_T spectrum for AROMA generated $b\bar{b}$ events. 48 out of 932 generated events survive the $p_T > 20$ GeV cut, i.e., even in the presence of neutrinos from semileptonic b decays one still obtains a reduction factor of about 20. The resulting dijet invariant mass distributions for all photoproduction processes and for true $b\bar{b}$ events are given as curves c) and d) in Fig. 6.

While the background level after the p_T cut is still critical, flavor identification promises to reduce the NC background well below the signal level. The NC background without flavor identification, curve c) in Fig. 6, is also listed as column ‘NC’ in Table 3. The table also gives the background contributions from CC multijet production, νW and νZ production, and from the production of a 160 GeV top quark. The numbers in this table are differential cross sections integrated over a 10 GeV bin around the central value (± 5 GeV), so they can be compared with the signal directly. It is clear that these backgrounds are much larger than the signal, but a close comparison shows that the signal is about a one to three sigma effect. Hence this way the Higgs is just barely not visible. Note that Z production causes many events outside the resonance region. The computation took the finite width of the Z into account and worked with the entire Breit-Wigner. But this is not the main cause for the events outside the peak. These events are mainly due to a

mass(GeV)	CC	NC	Z	W	160 Gev top	sum	signal
80	182	199	11.0	239	247	880	60.1
90	211	176	147	19.4	60	613	60.4
100	160	135	16.8	8.3	59	379	58.3
110	136	106	5.9	5.9	57	311	53.8
120	123	82	4.3	4.5	51	265	45.4
130	108	65	3.1	3.5	38	218	34.1
140	76	49	2.6	2.7	12.4	143	21.2
150	67	38	2.0	2.2	7.6	116	10.4

Table 3: Three jet backgrounds from various sources, no flavor separation. The background cross sections are given in fb and are integrated over a 10 GeV mass bin in this and the following tables.

‘wrong identification’ of the jets: the spectator jet is not the jet with the largest rapidity. Since the Z can also be radiated off the fermion lines in Fig. 1b), this effect is considerably larger than for the Higgs.

The backgrounds due to the Z and the W can be used to gauge the experiment. These particles give a peak in the mass distributions, and because they have a larger production cross section than the Higgs this peak should be visible. This can be considered as a good test of the various uncertainties. First it gives a test of the experimental possibilities. Second it gives a test of the various K-factors. The K-factors for W and Z production are expected to be comparable to those for Higgs production. More detailed higher order calculations should show whether this conjecture is true.

The first test of the stability of these results concerns their dependence on the cuts. If we define x as the fraction of the original cuts (transverse momenta and energies) we can see the results in Table 4: The last numbers ($x = 0.25$) correspond

x	Charged Current	Neutral Current	signal (120 GeV Higgs)
1.5	0.58 pb	0.087 pb	0.023 pb
1.0	2.0 pb	1.55 pb	0.040 pb
0.5	9.7 pb	96 pb	0.052 pb
0.25	24 pb	3000 pb	0.055 pb

Table 4: Backgrounds and signal cross sections for cuts scaled by a factor x .

to a missing transverse momentum of 5 GeV and a transverse energy of 25 GeV. Such small values for the cuts are outside the region where one can trust the tree level perturbative calculations. Higher order corrections are expected to be large here. They show us, however, that only the neutral current cross section rises by more than one order of magnitude under these extreme circumstances. This large variation of the NC cross section is due to the large number of potential divergencies when the cuts are removed.

The strong variation of the photoproduction cross section with changing x implies that it is very difficult to make a precise prediction of the total background cross

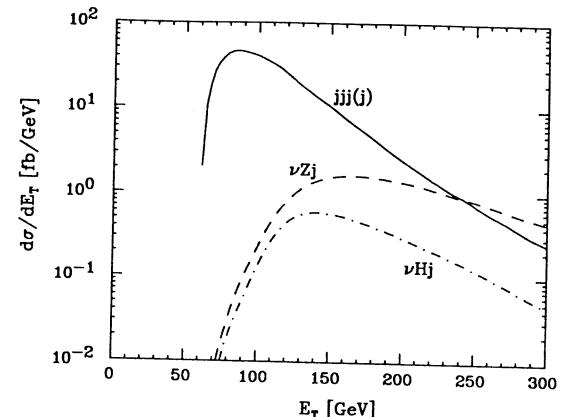


Figure 8: Total transverse energy distributions for the photoproduction cross section (solid line), νZ production (dashed line) and the WW fusion signal of a 90 GeV Higgs (dash-dotted line). All the cuts of Section 2 are applied except for the E_T cut.

section, one needs to know the correspondence between parton level variables like p_T and quantities measured in the calorimeter like cluster transverse energy to do so. On the other hand the very weak dependence of the signal on the scaling factor x means that the final experimental cuts can be adjusted to minimize the continuum background and thus maximize the significance of signal.

We should point out that in the present study we have not optimized the acceptance cuts for maximal S/\sqrt{B} . One reason is that such an optimization will depend on the Higgs mass region in which one is searching. This can be seen for example by inspecting the total transverse energy distributions of signal and backgrounds. In Fig. 8 we show the E_T spectra of the photoproduction background, the νZ background, and the signal for a 90 GeV Higgs boson. One finds that the dominant background for the 90 GeV Higgs, which is single Z production, has an even harder E_T spectrum than the signal. Hence the 100 GeV E_T cut that we always impose should not be increased in this case, even though it would improve the significance of the signal with respect to the NC background. Rather one might contemplate imposing an upper bound on the allowed transverse energy.

For a considerably heavier Higgs on the other hand νZ production is a negligible background (see Table 3), and increasing the E_T cut will enhance the signal to background ratio. When considering all the other background processes also, optimization of the Higgs signal becomes a complex task, which we have not yet attempted.

4. Flavor Identification (2b or not 2b)

The above backgrounds were all computed under the assumption that all jets must be treated equal regardless of their flavor. Using a detector with vertex information it is possible to see whether a jet contains a particle that has a small decay path. The practicality of this is a very strong function of the region of phase space

in which the detector has to operate. In our case we are interested in the two jets that come from the Higgs particle. These are mainly b -jets and they emerge in the region of phase space that has a rapidity of less than 3.5. This corresponds very much to the region in which LEP operates. There are more similarities, because the mass of the Higgs we are looking for is very much the same as the energy range of LEP. The only complication lies in the fact that at LEP the decay products would constitute the entire final state, while in our case there are extra hadrons. As a result our decay jets are not necessarily back to back.

Because of the similarities with LEP physics we base our assumptions on flavor detection possibilities on the vertex detector of DELPHI. An analysis of the possible flavor identification capabilities of DELPHI, using information from the vertex detector and general event shape variables, is described in Ref. [14]. They arrive at the numbers listed in Table 5.

input	seen as light jet	seen as c -jet	seen as b -jet
light jet	0.87	0.11	0.009
c -jet	0.30	0.62	0.07
b -jet	0.02	0.09	0.89

Table 5: Projected DELPHI flavor recognition efficiencies. Each horizontal line gives the probabilities that a jet pair of the given type is identified as a dijet system of the column type.

Notice that the last column is by far the most important one because we are only interested in how many b -quarks are observed. The numbers in the table include the fact that b quarks are produced pairwise at LEP while this assumption cannot be made for the two jets of lowest rapidity in which we are interested for the Higgs search. On the other hand studies are performed [13] to identify jet types with neural networks, and these techniques may improve upon the above results.

In the following we will use a reliability of 80% to correctly identify a b -jet as a b -jet, while we use a 25% chance that a single c -jet is seen as a b -jet, and a 10% chance that a light quark or gluon jet is identified as a b -jet. When squared these numbers roughly reproduce the dijet misidentification probabilities in the last column of Table 5. If one would assume that the DELPHI numbers are the results of two totally uncorrelated measurements one would arrive at slightly less favorable numbers for the efficiency to correctly identify the b jets. For example $0.89 \simeq 1 - (1 - 0.7)(1 - 0.7)$ and the single b efficiency would be about 70%. This can however not be the case, because there would be conflicts between one jet being recognized as one type of quark and the other as another type with no known physics process producing the two simultaneously. Hence the 70% should be an absolute lower limit and 80% seems more reasonable, especially with 10 years of development still ahead of us.

In order to present our results as independently of the precise flavor identification assumptions as possible, Table 6 lists the separate flavor contributions to the total background which was given in Table 3. With the help of this table alternate flavor identification efficiencies can easily be explored. We have not included the top contribution due to the uncertainty of its mass.

The top background is however not to be ignored because it is rather easy for the top events to produce b -quarks inside our acceptance cuts. About half of the

mass(GeV)	l-l	l-c	l-b	c-c	c-b	b-b	b-b signal
80	367	191	6.9	55.2	0.34	15.2	55.3
90	360	72	6.6	72.2	0.31	43.4	55.3
100	199	64	5.0	40.3	0.27	12.5	53.0
110	162	49	4.3	30.0	0.24	8.0	48.5
120	141	41	3.5	23.3	0.19	6.1	40.7
130	119	33	2.8	18.4	0.17	4.8	30.3
140	84	28	2.2	14.1	0.12	3.7	18.7
150	72	21	1.9	10.8	0.10	2.8	9.0

Table 6: The background split into the various flavor combinations for the two jets that should recombine into the Higgs. l, c, and b stand for light, charm, and bottom partons, respectively. No top contributions are included.

top events will pass our general acceptance cuts described in Section 2 and about 1/3 of those will give $b\bar{b}$ pairs inside the two jets of lowest rapidity. Because the fraction of $b\bar{b}$ events is so high we give this contribution in Table 7 for various values of the top mass. Notice in Table 6 that the total $b\bar{b}$ background is much smaller

mass(GeV)	$m_t = 120$ GeV	$m_t = 160$ GeV	$m_t = 200$ GeV
80	13.3	5.0	1.5
90	11.6	4.4	2.0
100	8.6	6.1	1.6
110	6.8	4.7	2.1
120	5.6	5.3	2.1
130	4.8	5.3	2.0
140	3.6	3.5	1.8
150	3.1	3.3	2.2

Table 7: $b\bar{b}$ background due to the top for three representative top masses.

than the original backgrounds without flavor recognition. It comes mainly from the photoproduction background, the Z resonance and possibly the top quark. It is now very easy to combine the results of the Tables 6 and 7 with our assumptions about flavor recognition. In Fig. 9 we have plotted the contribution from all backgrounds including a 160 GeV top and the non-top background separately. The dijet invariant mass spectrum is given in units of $\text{fb}/10$ GeV. Assuming a mass resolution of 10 GeV it can hence be directly compared with the total Higgs signal which is given in the figure in units of fb as a function of Higgs mass. For a 10 GeV mass resolution the Higgs would hence be seen as an additional peak on top of the background with a height roughly equal to the signal level. A level of flavor identification which is comparable to the DELPHI projections would allow to find the Higgs if it has an ‘intermediate mass’. The main problem occurs in the vicinity of the Z peak. The Z signal is rather similar to the Higgs signal, which should come as no surprise. Vector particles usually enjoy a slightly larger production cross section, but then the Z has a smaller branching ratio into b -quarks. The top backgrounds will be better known

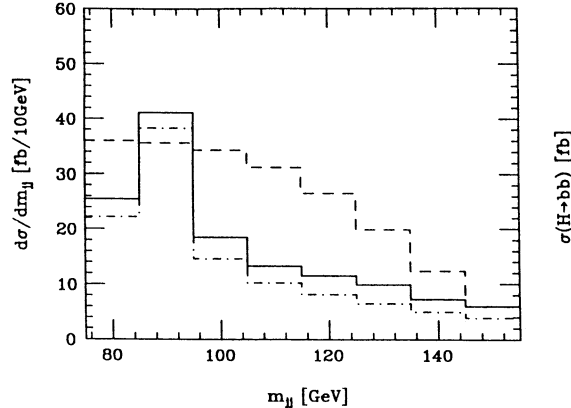


Figure 9: Comparison of signal (dashed line) and total background (solid line), including a 160 GeV top quark, after flavor identification. Also shown is the the background without the top contribution (dash-dotted line).

once the mass of the top has been measured. It may then also be possible to obtain a more efficient set of cuts.

The use of the Tables 5 and 6 will allow the designer of a vertex detector to check quickly whether his detector is sufficient to see the Higgs.

5. Experimental Considerations and Event Generation

For a realistic analysis of signal and background events the final state partons have to be evolved into hadrons and reconstructed from the detector information. The detector consists of a calorimeter covering the full azimuthal range, while the rapidity range extends up to 4.5, thus avoiding the beam hole. The cell structure is assumed to be $\Delta\phi \times \Delta y = 0.1 \times 0.1$ and provides an adequate granularity for the jet reconstruction. Resolution effects include the intrinsic calorimeter granularity and typical energy measurement uncertainties. The detector design should allow for vertex detection. Signal events have been generated with PYTHIA 5.4 [16]. The event shapes in the relevant quantities agree with the corresponding parton calculations. An example is shown in Fig. 10. The fraction of accepted events is about 30 — 40 %, depending of the parameter choice for the jet definition, and is somewhat smaller than at the partonic level. The Higgs particle is reconstructed from the two central jets. The LUCELL algorithm [17] with jet cone $R = 1$, $p_{T,\text{init}} = 3$ GeV and $p_{T,\text{jet}} = 20$ GeV leads to a line shape as shown in Fig. 11a). Events consisting of the wrong jet combination cause a small and broad tail to both sides of the peak. Missing particles, notably neutrinos, and the systematics of the jet algorithm applied to the cells with energy deposition lead to a shift of the peak towards smaller masses by about 10 % as well as a broadening of the natural line width ($\ll 1$ GeV) to typically 10 — 12 GeV. An important contribution to the low mass wing of the peak comes from missing neutrinos (semileptonic B-meson decays) and from Higgs decays involving gluon radiation. A variation of the LUCELL parameters does not change

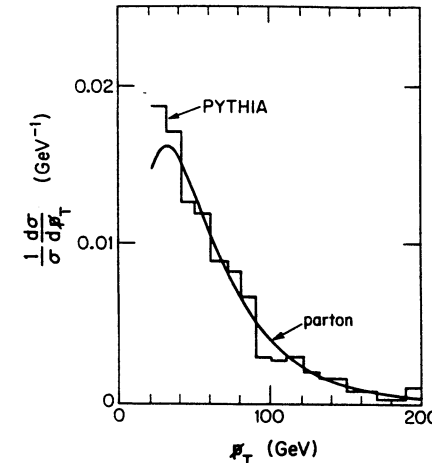


Figure 10: Comparison of the normalized p_T spectrum for a 120 GeV Higgs as obtained with parton level cross sections (solid line) and by using the PYTHIA Monte Carlo (histogram).

dramatically the peak structure. Also another jet algorithm based upon invariant masses [18] has been applied giving comparable results.

Neutral current and charged current background events have been generated with LEPTO 5.2 [15] and AROMA 1.2 [12]. The application of the LEPTO Monte Carlo program was not straightforward, since its range of validity, established for $Q^2 \geq 4$ GeV 2 and $x \geq 0.01$, must be extended to very small values of x for use at LEP/LHC. This is uncrical for CC events. For NC events, on the contrary, the cross section rises steeply for decreasing values of x . The problem lies in the fact that the description of a higher order process, here three jets in the final state, involves necessarily the definition of the mass scale relevant for the hadronization. Instead of the extreme scales given by W^2 (W being the invariant mass of the entire hadronic system) and Q^2 , an intermediate scale adequate for invariant masses in the range of the Higgs masses considered has been chosen. Under this condition the results of LEPTO and AROMA compare favorably. AROMA needs only compute processes which are one order higher in the coupling constant.

The stability of the cuts has been verified by comparing events generated with the same program once with and without hadronization. Missing particles in NC events act in opposite ways : firstly they reduce the visible jet momentum, secondly they contribute to the missing transverse energy of the event. In the first case the requirement $p_T(\text{jet}) \geq 20$ GeV is more difficult to meet, in the second case the requirement $p_T \geq 20$ GeV is more easily fulfilled. The net effect is only a small dependence on missing particles. For the signal events as well as for most of the charged current background events both effects are small.

Making use, however, of the actual topological event structure it was possible to obtain a sharp line without tail (see Fig. 11b)). This procedure, at the present stage, reduces statistics by about a factor of three. The visual inspection of the

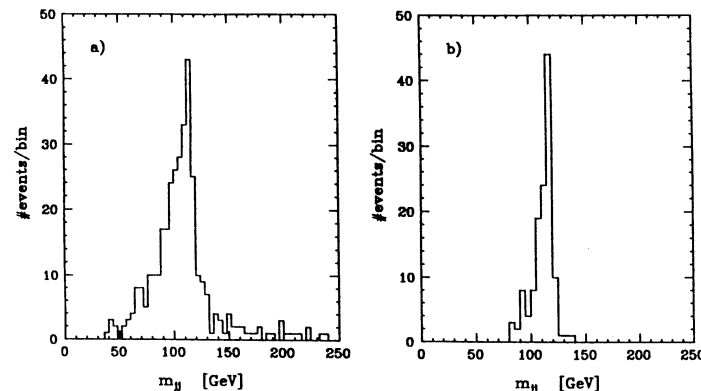


Figure 11: Invariant mass distribution of the dijet system originating from a 120 GeV Higgs after hadronization effects and missing particles are taken into account. a) Minimal jet reconstruction requirements. b) After some optimization for an improved dijet mass resolution.

events in the tail indicated suggestions for improving the jet algorithm (left for future investigations). In this study no use has been made of flavor tagging. Once vertex information is available a strong reduction of background (rejection of wrong jet combination) and a refinement of the algorithm in collecting the particles belonging to the b -jets may be expected.

6. Discussion of the Results

The search for the Higgs in ep collisions at LEP/LHC, if its mass is in the intermediate range, looks very promising. We have studied in detail the signatures of Higgs production via WW fusion and its subsequent decay into a $b\bar{b}$ pair, and find that the characteristics of the signal are sufficiently different from all the backgrounds, that a suppression of the background rates below the signal level should be possible.

For the single largest background, photoproduction of multijet events, this is achieved by making use of the substantial missing transverse momentum which is inherent in the signal, its 3-jet topology with large average transverse energy, and finally the fact that the Higgs mostly decays into a pair of b -quark jets. In a similar fashion the flavor content and the 3-jet topology distinguish the signal from backgrounds arising from CC multijet production, W and Z production and their subsequent hadronic decay, and top production.

In order to make use of the differences between signal and background processes, an excellent detector is indispensable. Of particular importance are good energy resolution and in particular excellent coverage in the forward region. If the coverage extends further than the rapidity of 4.5 which we have assumed, it becomes less likely that particles disappear in the proton beam hole and hence the suppression of backgrounds due to the $\not{p}_T > 20$ GeV requirement becomes more powerful. As

a side benefit the signal rate would also increase because the spectator jet is more easily observed. With the limited rate available at LEP/LHC a detector which is to search for the intermediate mass Higgs must have excellent b -identification capabilities, comparable to the projected performance of the DELPHI detector at LEP [14].

Whether the required level of b -identification will be achievable for an ep-detector requires further dedicated studies. Another experimental question which needs further investigation is the mass resolution which is possible for the dijet system which results from the $H \rightarrow b\bar{b}$ decay. Preliminary studies which we have performed indicate that a 10% mass resolution may be possible.

Among the theoretical uncertainties of our analysis we should mention that the exact normalization of the cross sections which we have studied is not known. All numbers which were presented are lowest order perturbative computations, so higher order corrections will change them by some factor. These numbers (K-factors) may be as large as 2 for the backgrounds. For the signal they may be somewhat smaller (like 1.5). However this would not affect the significance of the signal, S/\sqrt{B} . In addition we chose a small scale and hence a large value of α_S in the dominant photoproduction background which enters at order α_S^3 . If anything this choice is conservative also. Hence we believe that the normalization as we present it should not be wrong by very much and the signal to background ratio is expected to be correct within a factor 1.5.

Taken at face value and assuming a mass resolution of 10%, the results presented in Fig. 9 lead to a significance of the Higgs signal in the 5 to 7 standard deviation range. While such an excellent mass resolution may be possible only with loss of some statistics, thus reducing the significance of the Higgs signal, there is still ample room for improvements in our analysis which may well overcompensate losses from hadronization and resolution effects. We should stress again that in our analysis we have only used some rather loose cuts to define the phase space region containing the signal and optimization of these cuts or even a multidimensional analysis of signal and backgrounds should lead to a considerable improvement.

The search for the intermediate mass Higgs at LEP/LHC is a challenge mainly because of the relatively small usable production rate of ≈ 50 events per year. If experiments in the ep mode can collect substantially more than the 1 fb^{-1} which we have assumed throughout, LEP/LHC can discover the intermediate mass Higgs even with modest flavor identification capabilities.

Valuable discussion with the other members of the ‘ep working group’ and with M. Drees are greatfully acknowledged. This research was supported in part by the University of Wisconsin Research Committee with funds granted by the Wisconsin Alumni Research Foundation, and in part by the U. S. Department of Energy under contract DE-AC02-76ER00881.

References

- [1] See e.g. D. Denegri, these proceedings.
- [2] J. J. Engelen, in *Proceedings of the Workshop on Experimentation at HERA*, Amsterdam 1983, p.241.
- [3] T. Han and H. C. Liu, *Z. Phys. C28* (1985) 295; D. A. Dicus and S. Willenbrock, *Phys. Rev. D32* (1985) 1642.
- [4] K. J. F. Gaemers, R. M. Godbole, and M. van der Horst, in *Proceedings of the HERA Workshop, 1987*, ed. by R. D. Peccei, vol. 2, p. 739.
- [5] J. F. Gunion, H. E. Haber, G. Kane, and S. Dawson, *The Higgs Hunter's Guide*, Addison-Wesley (1990).
- [6] G. Altarelli, in *Proceedings of the Workshop on Physics at Future Accelerators*, La Thuile, 1987, CERN 87-07, vol. 1, p. 36.
- [7] E. Eichten, I. Hinchliffe, K. Lane and C. Quigg, *Rev. Mod. Phys.* **56**, (1984) 579, erratum **58**, (1986) 1065.
- [8] K. Hagiwara and D. Zeppenfeld, *Nucl. Phys.* **B313** (1989) 560.
- [9] J.A.M. Vermaseren (to be published). The manual and the program can be obtained by means of anonymous ftp from nikhef.nikhef.nl.
- [10] U. Baur, B. A. Kniehl, J. A. M. Vermaseren, and D. Zeppenfeld, these proceedings.
- [11] U. Baur and J. J. van der Bij, *Nucl. Phys.* **B304** (1988) 451.
- [12] G. Ingelman, and G. Schuler, AROMA 1.2 program manual, unpublished; G. Ingelman, and G. Schuler, *Z. Phys. C40* (1988) 299.
- [13] L. Lonnblad, C. Peterson and T. Rognvaldsson, Lund preprints LU-TP-90-3 and LU-TP-90-8.
- [14] Ch. de la Vaissière and S. Palma-Lopes, note DELPHI 89-32 PHYS 38 (1989).
- [15] G. Ingelman, LEPTO 5.2 program manual, unpublished; M. Bengtsson, G. Ingelman, and T. Sjostrand, *Nucl. Phys.* **B301** (1988) 554.
- [16] H.-U. Bengtsson, and T. Sjostrand, *Computer Phys. Comm.* **46** (1987) 43.
- [17] T. Sjostrand, JETSET 7.3 (July 1990) ; LUCELL is a subroutine of the JETSET package.
- [18] S. Bethke et al., *Phys. Lett.* **B213** (1988) 235.

Contact Interactions and New Vector Bosons at LEP/LHC

Fernando Cornet, University of Granada
Hans – Ulrich Martyn , RWTH Aachen

November 22, 1990

Abstract

We study the sensitivity of deep inelastic e p scattering experiments at LEP / LIIC to electron–quark contact interactions and several models of new neutral and charged vector gauge bosons. It is shown that longitudinally polarised leptons will considerably improve the detectable mass scales.

1 Introduction

One of the most important tasks of new accelerators is to search for effects of ‘new physics’ beyond the Standard Model (SM). These effects can be either the production of new, exotic particles or just small deviations from the SM predictions. This is the case for deep inelastic scattering in the presence of a four-fermion contact interaction or new gauge bosons.

Assume that ‘new physics’ sets in at a scale $\Lambda \sim \mathcal{O}(TeV)$. This could be compositeness or any kind of new, heavy particle. If the available center of mass energy $\sqrt{s} \geq \Lambda$ spectacular effects would appear, e.g. on mass shell production of new particles. However, at $\sqrt{s} \ll \Lambda$ the ‘new physics’ would manifest itself as a residual contact interaction modifying the SM predictions.

A more definite possibility is to enlarge the electroweak gauge group $SU(2) \times U(1)$, which has often been considered in the frame work of grand unified or left-right symmetric theories. In all these cases additional gauge bosons are expected and some of them could be light enough to provide observable effects at LEP/LIIC.

In this paper we investigate the inclusive neutral and charged current reactions

$$e^\pm p \rightarrow e^\pm X \quad (1)$$

$$e^\pm p \rightarrow \nu X \quad (2)$$

with unpolarised and longitudinally polarised leptons under reasonable experimental conditions. The strategy to search for new phenomena is to analyse the data in terms of the SM at low Q^2 and to look for any deviation from the SM at high Q^2 . The assumptions are that the structure functions and radiative corrections are well known. The interpretation is of course subject to the model under investigation and not always unambiguous. We show that polarised leptons are very useful to distinguish between different models. Possible deviations from the SM are parametrised in terms of electron–quark contact interactions, in several E_6 models with new Z' bosons, and in a left-right symmetric model with a new Z' and a right-handed W' .

2 Contact interactions

2.1 Formalism of contact interactions

Consider the deep inelastic neutral current reaction (1) with helicity conservation at each vertex. Possible contact interactions [1], [2] modify the SM Lagrangian through interference of the γ and Z fields with the ‘new’ current. The effective Lagrangian reads in an obvious notation

$$\mathcal{L}^{eff} = \mathcal{L}^{SM} + \mathcal{L}' \quad (3)$$

$$\mathcal{L}^{SM} = e \sum_f \left(\bar{f} \gamma^\mu Q^f f A_\mu + \frac{1}{\sin \theta_W \cos \theta_W} \bar{f} \gamma^\mu (v^f - a^f \gamma_5) f Z_\mu \right) \quad (4)$$

$$\begin{aligned} \mathcal{L}' = & \pm \sum_q \frac{g^2}{\Lambda_\pm^2} \{ \eta_{LL} (\bar{e}_L \gamma^\mu e_L) (\bar{q}_L \gamma^\mu q_L) + \eta_{RR} (\bar{e}_R \gamma^\mu e_R) (\bar{q}_R \gamma^\mu q_R) \\ & + \eta_{RL} (\bar{e}_R \gamma^\mu e_R) (\bar{q}_L \gamma^\mu q_L) + \eta_{LR} (\bar{e}_L \gamma^\mu e_L) (\bar{q}_R \gamma^\mu q_R) \}. \end{aligned} \quad (5)$$

The electron-quark contact interaction is conveniently described by assuming a ‘strong’ coupling $g^2 = 4\pi$, thus Λ_\pm is the only free parameter. The indices L and R denote left-handed and right-handed currents. Restricting the coefficients η to values of 0 or ± 1 allows to construct 6 different chirality structures times 2 signs for positive \oplus or negative \ominus interference, as shown in the following table:

Coupling	η_{LL}	η_{RR}	η_{RL}	η_{LR}
LL	1	0	0	0
LR	0	0	0	1
RL	0	0	1	0
RR	0	1	0	0
VV	1	1	1	1
AA	1	1	-1	-1

As input to the theory we choose $\sin^2 \theta_W = 0.230$, $M_Z = 91.16 \text{ GeV}$ [3] and the structure function set I of Eichten *et al.* [4].

It should be noted that the phenomenological ansatz (5) for contact interactions could not only be used to test the originally proposed compositeness scale, but is rather general applicable to inclusive searches for all types of new phenomena by proper adjustment of the coupling strength g^2 and the coefficients η .

2.2 Experimental conditions and analysis procedure

The following Machine Conditions at LEP I/LHC are assumed:

electron beam	50 GeV
proton beam	8 TeV
cms energy	$\sqrt{s} = 1.26 \text{ TeV}$
integrated luminosity per data set	$\int \mathcal{L} dt = 500 \text{ pb}^{-1}$
lepton polarisation	$\vec{P} = 80 \%$

We further assume that the full integrated luminosity is available for each kind of lepton, i.e. e^- , e_L^- , e_R^- , e^+ , e_L^+ , e_R^+ , which corresponds to about half a year of running per data set.

Measurable Quantities are

1. differential cross sections

$$\frac{d^2\sigma}{dx dQ^2}$$

or

$$R(Q^2) = \frac{d\sigma^{CI}/dQ^2}{d\sigma^{SM}/dQ^2}$$

2. asymmetries between various lepton charges c , c' and polarisation states P , P'

$$A_P^{cc'} = \frac{d\sigma(e_P^c) - d\sigma(e_{P'}^{c'})}{d\sigma(e_P^c) + d\sigma(e_{P'}^{c'})}$$

for unpolarised leptons

charge asymmetry A^{-+}

for polarised leptons

polarisation asymmetries A_{LR}^{-+} A_{LR}^{++}

charge asymmetries A_{LL}^{-+} A_{RR}^{-+}

mixed asymmetries A_{LR}^{-+} A_{RL}^{-+}

The differential cross section measurements rely on a precise knowledge of the detector acceptance, the absolute normalisation and the underlying SM to compare with. The advantage of using asymmetries is that common systematic errors (like luminosity, acceptance, assumptions on structure functions, radiative corrections, ...) partially cancel. The disadvantage is that often data with less information content are combined and one has larger statistical errors by subtracting data samples of similar sizes. Note that only 4 out of the 6 asymmetry combinations for polarised beams are independent from each other.

For the Analysis Procedure we assume that the data are corrected for resolution smearing and radiative effects. Choosing ‘safe’ kinematic regions where (i) the smearing due to the experimental resolution in bins of the $x - Q^2$ plane is below 10% and (ii) the radiative corrections are ‘reasonably’ small and under control [5], [6] the following kinematical cuts are applied:

$$\begin{aligned} 0.01 < x &< 0.50 \\ 0.075 < y &< 0.80 \\ 1.2 \cdot 10^3 < Q^2 &< 6.4 \cdot 10^5 \text{ GeV}^2 \end{aligned}$$

Remind that all kinematic quantities are derived from the scattered electron alone, for which a resolution of $\Delta E_e/E_e = 0.10/\sqrt{E_e}(\text{GeV}) \oplus 0.01$ and $\Delta \theta_e = 1 \text{ mrad}$ is assumed.

The cross sections are computed in $x - Q^2$ bins as function of Λ_\pm applying the above kinematic cuts

$$\sigma_i(x, Q^2, \Lambda_\pm) = \int_{Q_i^2}^{Q_i^2 + \Delta Q_i^2} \int_{x_i}^{x_i + \Delta x_i} \frac{d^2\sigma}{dx dQ^2} dx dQ^2$$

and then compared to the SM predictions performing a χ^2 analysis

$$\chi^2 = \sum_i \left(\frac{\sigma_i^{SM} \cdot f_{norm} - \sigma_i^{CI}(\Lambda_\pm)}{\Delta\sigma_i^{SM} \cdot f_{norm}} \right)^2 + \left(\frac{f_{norm} - 1}{\Delta f_{norm}} \right)^2.$$

The errors include statistics according to the integrated luminosity and a systematic uncertainty on the normalisation of $\Delta f_{norm} = \pm 5\%$. Each data set is treated independently, i.e. no correlated errors in combined or asymmetry analyses are considered. Limits are given at 95% confidence level for each lepton beam separately and for combined results assuming $\int \mathcal{L} dt = 500 \text{ pb}^{-1}$ per data set.

2.3 Results

The results on the most sensitive limits from polarised and unpolarised lepton beams are summarised in Tables 1 and 2. Possible deviations from the SM are shown in Figs. 1 and 2 for the unpolarised cross sections normalised to the SM and in Fig. 3 for asymmetry measurements, always for the 95% detection limits. As expected the sensitivity rises with Q^2 . Note, however, that the deviations are not always continuously below or above the SM, but some distributions show a cross over at some value of Q^2 . This emphasises the importance of exploiting the full Q^2 range, in particular the low Q^2 region for normalisation to the SM.

Table 1: Best lower limits (95% c.l.) on $\Lambda_+(\text{TeV})$ for \oplus interference from differential cross section and asymmetry measurements

Coupling	unpolarised	polarised	asymmetry
+ LL	e^- 13.1	e_L^- 16.1	A_{LR}^{--} 10.4
+ LR	e^+ 11.9	e_R^+ 14.2	A_{RR}^{++} 11.8
+ RL	e^+ 11.8	e_L^+ 16.0	A_{LR}^{++} 13.4
+ RR	e^- 12.6	e_R^- 17.8	A_{LR}^{--} 14.7
+ VV	e^+ 19.3	e_L^+ 20.8	A_{LL}^{+-} 13.1
+ AA	e^- 16.4	e_R^- 17.2	A_{RR}^{+-} 13.8

The following conclusions can be drawn:

- One observes a higher sensitivity to \oplus interference than to \ominus interference.
- Polarised beams increase the sensitivity by about 1 to 5 TeV. Since there is a close correspondence of $e_L^- \leftrightarrow e_R^+$ and $e_R^- \leftrightarrow e_L^+$, other choices than those quoted in the tables may result in very similar numbers.
- Asymmetries generally provide less stringent limits on Λ than differential cross sections (see comment above), an exception being A_{RR}^{+-} for AA coupling with Θ interference.
- Mass scales up to $\Lambda \simeq 20 \text{ TeV}$ can be explored depending on the chirality structure.

Table 2: Best lower limits (95% c.l.) on $\Lambda_-(\text{TeV})$ for Θ interference from differential cross section and asymmetry measurements

Coupling	unpolarised	polarised	asymmetry
- LL	e^- 11.1	e_L^- 14.6	A_{LR}^{--} 9.4
- LR	e^+ 7.4	e_R^+ 8.6	A_{RR}^{++} 7.2
- RL	e^+ 7.9	e_L^+ 12.6	A_{LR}^{++} 9.8
- RR	e^- 10.3	e_R^- 16.4	A_{LR}^{--} 13.7
- VV	e^- 17.8	e_R^- 19.6	A_{LR}^{++} 11.6
- AA	e^- 13.4	e_R^- 14.2	A_{RR}^{+-} 15.5

- The sensitivity rises with max. Q^2 or s and luminosity as $\Lambda \propto (s \cdot \int \mathcal{L} dt)^{\frac{1}{2}}$. Therefore LEP II/LHC ($\sqrt{s} = 1.79 \text{ TeV}$, $\int \mathcal{L} dt = 100 \text{ pb}^{-1}$) is expected to be less sensitive by $\sim 20\%$ than LEP I/LHC.

Case study for polarisation

Lepton polarisation and asymmetry measurements are very important to differentiate the chirality couplings in the presence of a signal, i.e. a deviation from the SM. In order to investigate the importance of polarisation further, suppose a positive signal is observed for the LR model and one wants to know which Λ^{LR} values can be discriminated against LL, RR, ... models? More than one distribution is needed to find a minimum χ^2 at the same Λ value. The most sensitive distributions are $d\sigma(e_R^+)/dQ^2$, A_{RR}^{+-} and $d\sigma(e_L^-)/dQ^2$. The most competitive model is LL with the same helicity structure at the electron vertex. The LL model can be excluded at 95% c.l. for $\Lambda > 12$ (9) TeV for \oplus (\ominus) interference. The RR model can be excluded far beyond the detection limits of 14 (9) TeV due to the opposite behaviour of the charge asymmetry at high Q^2 . All other models are completely ruled out.

Typical mass resolutions as obtained from $d\sigma(e_R^+)/dQ^2$ are

coupling	input	fit
+ LR	$\Lambda_+^{LR} = 10.0 \text{ TeV}$	$\Lambda_+^{LR} = 10.0^{+1.1}_{-0.6} \text{ TeV}$
+ LR	$\Lambda_+^{LR} = 12.0 \text{ TeV}$	$\Lambda_+^{LR} = 12.0^{+2.5}_{-1.4} \text{ TeV}$
- LR	$\Lambda_-^{LR} = 8.0 \text{ TeV}$	$\Lambda_-^{LR} = 8.0^{+1.2}_{-0.3} \text{ TeV}$

2.4 Limits from other experiments

So far the only measured limits on electron-quark contact interactions come from $e^+e^- \rightarrow q\bar{q}$ at PETRA [7]. They may be improved by LEP experiments running above the Z^0 pole with an expected sensitivity gain over PETRA of $\sim 1.33 \cdot (\int \mathcal{L} dt / 100 \text{ pb}^{-1})^{\frac{1}{2}}$. Table 3 shows a comparison between PETRA and $e^- p$ scattering at HERA ($\sqrt{s} = 0.314 \text{ TeV}$, $\int \mathcal{L} dt = 100 \text{ pb}^{-1}$) and LEP/LHC, where limits from the sum of both unpolarised e^+ and e^- are given. The experiments at LEP/LHC will extend the accessible mass scales considerably, by a factor of 5 – 10 over present limits and by a factor of 3 – 4 over HERA,

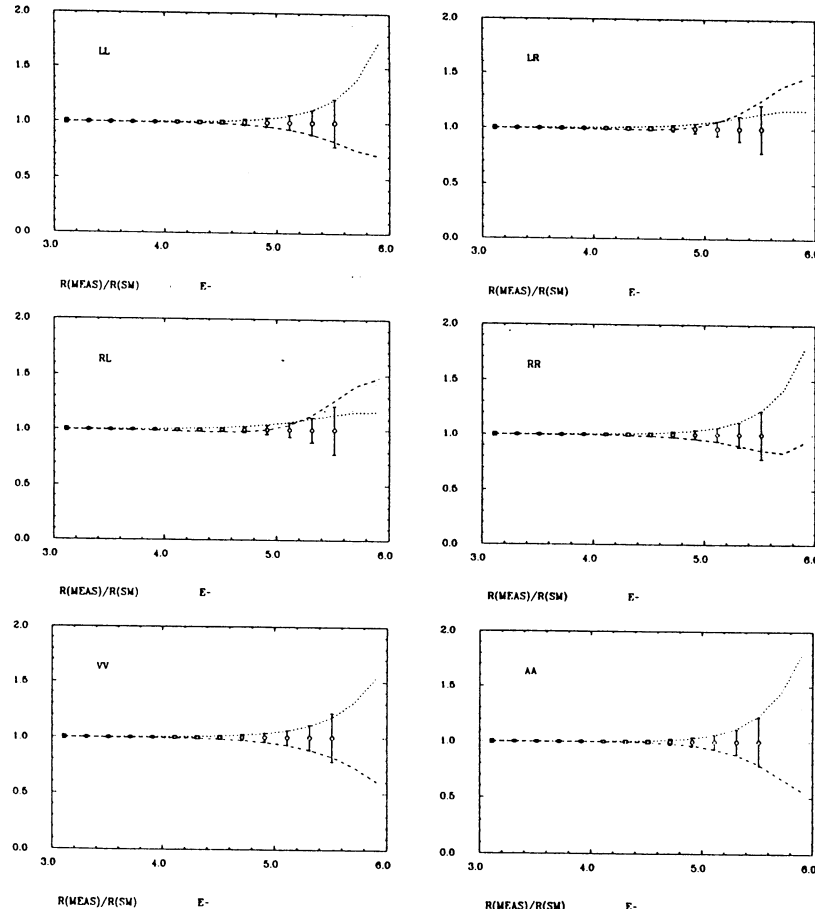


Figure 1: Differential cross sections for e^- scattering normalised to the SM as function of Q^2 . The curves show the detection limits for \oplus interference (dotted) and \ominus interference (dashed). The errors correspond to $\int \mathcal{L} dt = 500 pb^{-1}$

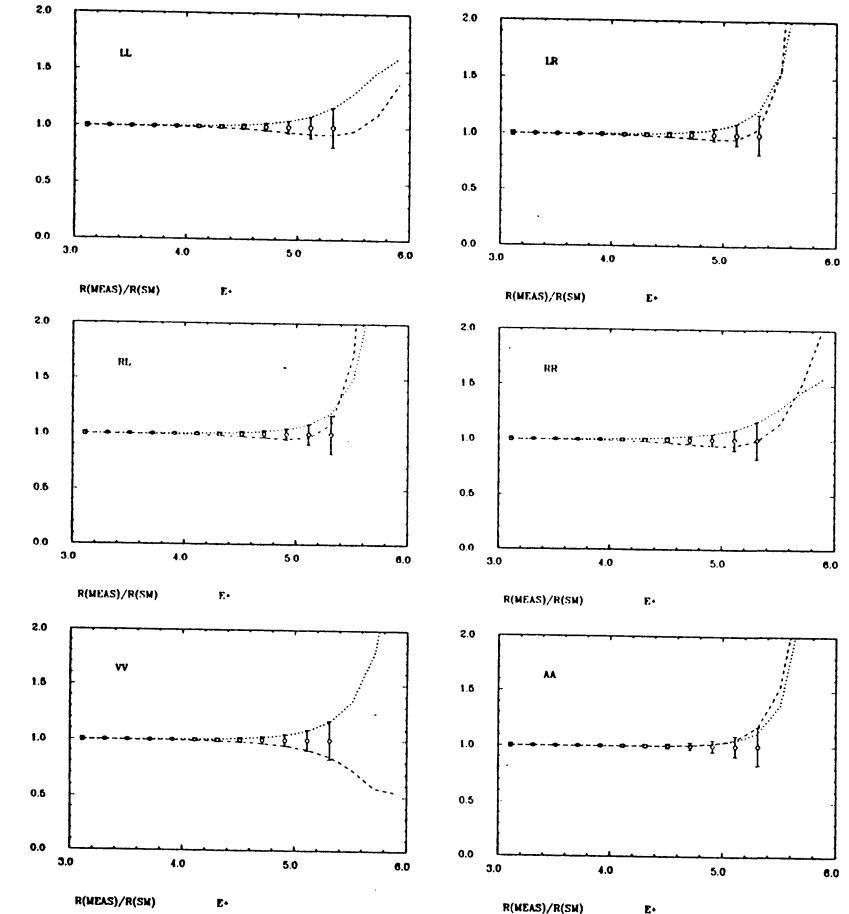


Figure 2: Differential cross sections for e^+ scattering normalised to the SM as function of Q^2 . The curves show the detection limits for \oplus interference (dotted) and \ominus interference (dashed). The errors correspond to $\int \mathcal{L} dt = 500 pb^{-1}$

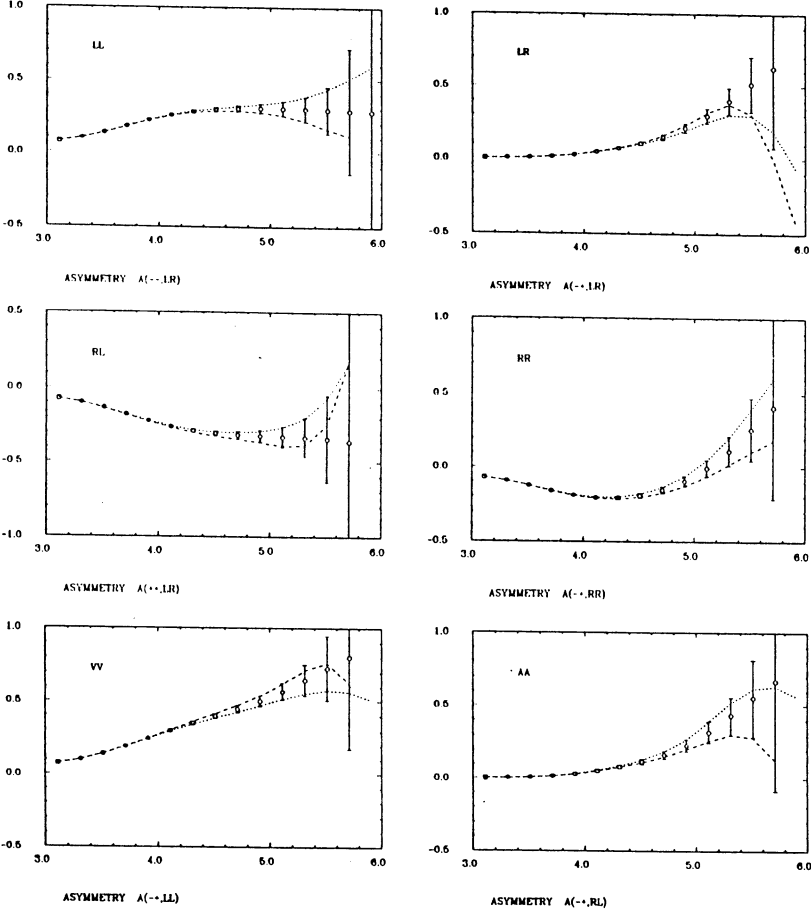


Figure 3: Asymmetries from polarised leptons as function of Q^2 . The curves show the detection limits for \oplus interference (dotted) and \ominus interference (dashed). The errors correspond to $\int \mathcal{L} dt = 500 \text{ pb}^{-1}$

depending on the helicity structure. At the LHC Drell – Yan production $p p \rightarrow e^+ e^- X$ might set limits of e.g. $\Lambda_{eq}^{VV} \approx 20 \text{ TeV}$.

Table 3: Comparison of lower limits on $\Lambda_\pm (\text{TeV})$ from PETRA, HERA and LEP/LHC

Coupling	PETRA		HERA		LEP/LHC	
	Λ_+	Λ_-	Λ_+	Λ_-	Λ_+	Λ_-
LL	1.2	1.8	4.2	3.3	13.8	11.9
LR	2.1	2.1	4.1	2.9	12.1	7.5
RL	1.1	1.9	4.1	2.9	12.0	8.0
RR	3.4	2.7	4.0	2.9	13.3	11.3
VV	5.1	3.9	6.9	6.3	21.7	20.9
AA	1.7	2.4	5.5	5.6	16.6	15.7

3 Additional Z'

The electroweak sector of the standard model $SU(2)_L \times U(1)_Y$ may be enlarged by another group $U(1)_{Y'}$ or $SU(2)$, thus introducing additional neutral and charged gauge bosons. Examples of extensions of the SM are E_6 and left-right symmetric models [8]. New non-gauge vector bosons are considered in the BESS model [9].

The coupling of the γ , Z and a new Z' to fermions is described by the effective NC Lagrangian

$$\mathcal{L}_{NC}^{eff} = e J_{em}^\mu A_\mu + \frac{g}{\cos \theta_W} J_Z^\mu Z_\mu + g' J_{Z'}^\mu Z'_\mu . \quad (6)$$

The mass eigenstates are in general a mixture of Z and Z'

$$\begin{aligned} Z_1 &= Z \cos \theta + Z' \sin \theta \\ Z_2 &= -Z \sin \theta + Z' \cos \theta . \end{aligned} \quad (7)$$

The low mass Z_1 is usually identified with the observed Z ($m_{Z_1} = 91.16 \text{ GeV}$), which is lighter than the SM value of m_Z

$$m_Z^2 = m_{Z_1}^2 \cos^2 \theta + m_{Z_2}^2 \sin^2 \theta \geq m_{Z_1}^2 .$$

Consistency with experiments requires $\theta \rightarrow 0$ as $m_{Z_2} \rightarrow \infty$. The weak mixing angle now becomes

$$\sin^2 \theta_W \equiv 1 - \frac{m_W^2}{m_{Z_1}^2} \leq 1 - \frac{m_W^2}{m_Z^2} \equiv \sin^2 \theta_W ,$$

At this stage the theory has four free parameters: g' , $\sin^2 \theta_W$, m_{Z_2} and θ . In order to reduce the number of free parameters we assume $\rho = 1$ (i.e. symmetry breaking by Higgs doublets or singlets). This implies $\sin^2 \theta_W = f(m_Z, m_{Z_1}, \theta)$ and we are left with two free parameters: θ and m_{Z_2} .

3.1 E_6 models with one low mass Z'

In general the group E_6 contains the SM and two additional $U(1)$ groups

$$E_6 \subset SU(3)_C \times SU(2)_L \times U(1)_Y \times U(1)_X \times U(1)_\psi.$$

In the minimal low energy extension of the SM this reduces to

$$E_6 \subset G = SU(2)_L \times U(1)_Y \times U(1)_{Y'}.$$

The effective $U(1)_{Y'}$ gauge coupling is chosen as

$$g' = \sqrt{\frac{5}{3}} \frac{e}{\cos \theta_W}.$$

The group $U(1)_{Y'}$ can be represented as a linear combination of $U(1)_X$ and $U(1)_\psi$ and the corresponding Z' field is a superposition of

$$Z'^\mu = Z_\psi^\mu \cos \alpha + Z_X^\mu \sin \alpha$$

The angle α specifies a particular model, convenient choices are:

model A (η)	$\cos \alpha = \sqrt{\frac{5}{8}}$	$\sin \alpha = \sqrt{\frac{3}{8}}$
model B (χ)	$\cos \alpha = 0$	$\sin \alpha = 1$
model C	$\cos \alpha = -\sqrt{\frac{15}{16}}$	$\sin \alpha = -\sqrt{\frac{1}{16}}$

Fig. 4 shows the expected asymmetries of the 3 models for a particular set of parameters at a specific kinematic region. As can be seen the model C will only provide poor limits on $m_{Z'}$.

3.2 Left-right symmetric model

The simplest left-right symmetric model is based on the group

$$G = SU(2)_L \times SU(2)_R \times U(1)_{B-L}$$

with a triplet field $W'_{1,2,3}$ associated to $SU(2)_R$ and a singlet field associated to $U(1)_{B-L}$. After symmetry breaking 3 additional massive vector bosons Z' and W'^{\pm} are generated. The mass eigenstates generally mix with the ordinary gauge bosons, for the Z and Z' as in (7). The left-handed and right-handed couplings are assumed to be identical

$$g = g' = \frac{e}{\cos \theta_W}. \quad (8)$$

3.3 Results

The analysis for the models A, B, C, and L-R is done in the same way as for contact interactions. The 95% c.l. contours are evaluated in the $m_{Z_2} - \theta$ plane and are shown in Fig. 5 for the most sensitive unpolarised cross sections and polarisation asymmetries.

Again polarised leptons improve the mass limits considerably (models A and L-R) and constrain the mixing angles to $\theta \lesssim \pm 1^\circ$. The best mass limits of $\mathcal{O}(1 \text{ TeV})$ are obtained

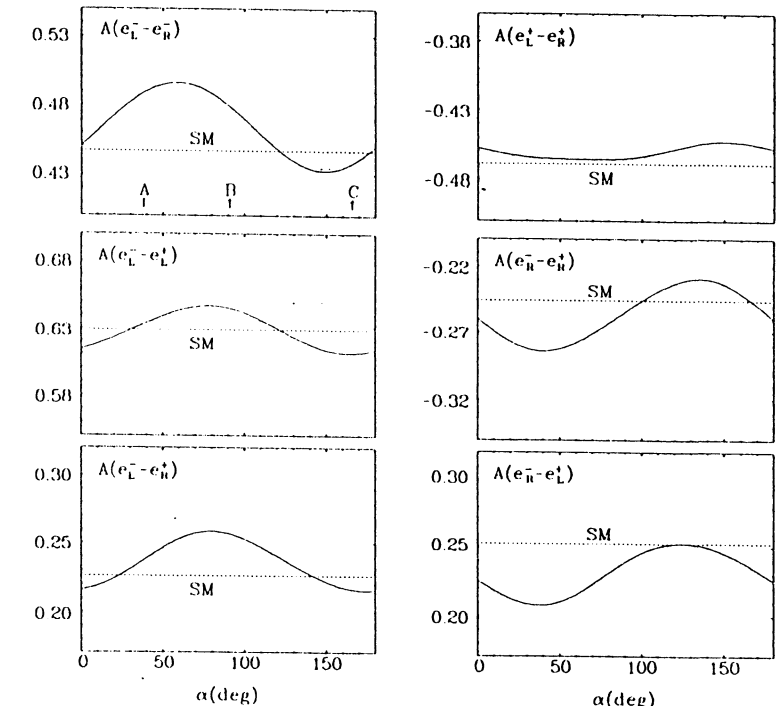


Figure 4: Expected deviations from the SM (dotted) for asymmetries in the E_6 models A, B and C. $x = 0.05$, $Q^2 = 7 \cdot 10^4 \text{ GeV}^2$, $\theta = 0$ and $m_{Z'} = 300 \text{ GeV}$

for the left-right symmetric model. As expected the model C gives only poor bounds even with polarisation.

The lower limits on m_{Z_2} assuming a mixing angle $\theta = 0$ from differential cross section and asymmetry measurements are summarised in Table 4 together with present [3, 10] and HERA [8] (only statistical errors) limits. Substantial improvements can be expected from LEP/LHC. LEP experiments running at the Z^0 resonance are not able to put more stringent bounds on m_{Z_2} and θ when the relation between these quantities is left free (as done in our analysis) [10] because they are too close to m_{Z_1} and not sensitive to the interference terms.

Table 4: Best lower limits (95% c.l.) on m_{Z_2} (GeV) at $\theta = 0$ from differential cross section and asymmetry measurements, present and HERA limits

model	unpolarised	polarised	asymmetry	present limit	HERA
A (η)	e^- 210	e_R^- 500	A_{LR}^- 400	180	200
B (χ)	e^+ 390	e_R^+ 450	A_{LR}^+ 340	310	300
C	e^+ 130	e_L^+ 180	A_{LL}^+ 140	—	130
L-R	e^- 730	e_R^- 1190	A_{RR}^- 1120	426	470

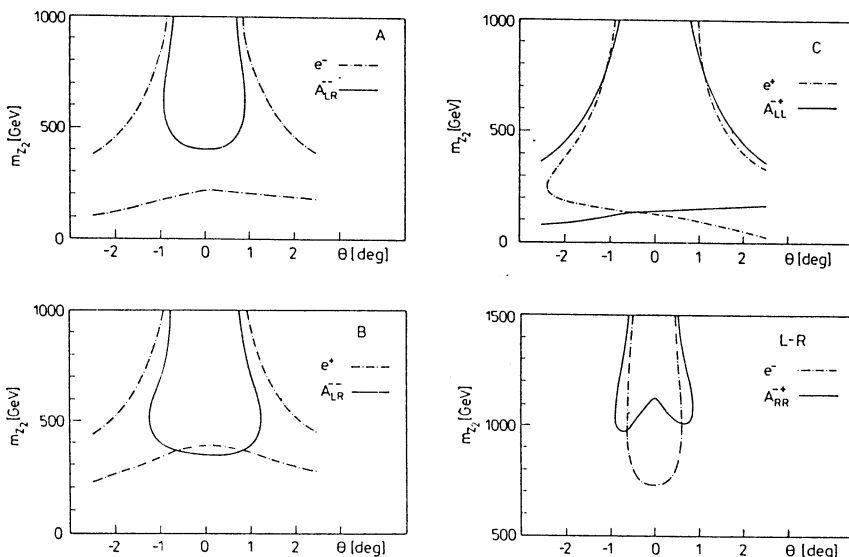


Figure 5: Allowed regions (95% c.l.) contours for the models A, B, C and L-R from unpolarised cross section and asymmetry measurements

It is interesting to note the correspondence to the couplings defined in contact interactions. Since here weak couplings are involved, the mass scales are much lower, i.e. $m_{Z_2} \ll \Lambda^{CI}$. The chirality structure translates into

$$\begin{aligned} \text{model A} &= -\frac{1}{30} (LA + 2RA) \\ \text{model B} &= -\frac{1}{40} (3LA + RA) \\ \text{model C} &= \frac{1}{40} (2LA - RA) \end{aligned}$$

It is probably the negative interference of the amplitudes in model C which causes the low sensitivity to an additional Z' .

4 Right-handed W'

Consider a right-handed W'_R which induces the charged current reaction

$$e^- p \rightarrow \nu_R X ,$$

where the right-handed ν_R is assumed to be light. The effective CC Lagrangian in the presence of an additional W' is

$$\mathcal{L}_{CC}^{eff} = \frac{g}{2\sqrt{2}} J_W^\mu W_\mu + \frac{g'}{2\sqrt{2}} J_{W'}^\mu W'_\mu + c.c..$$

In a left-right symmetric model the couplings g and g' are assumed to be identical. The mass eigenstates of W^\pm and W'^\pm in general mix

$$\begin{aligned} W_1 &= W \cos \zeta + W' \sin \zeta \\ W_2 &= -W \sin \zeta + W' \cos \zeta \end{aligned}$$

We choose the mixing angle $\zeta = 0$, which is already limited to small values by other experiments. Thus we are left with 1 free parameter: m_{W_2} .

4.1 Analysis procedure

The analysis is done in a similar way as for contact interactions. The cuts chosen for ‘safe’ kinematic regions are

$$\begin{aligned} 0.01 < x &< 0.25 \\ 0.05 < y &< 0.80 \\ 1.0 \cdot 10^3 < Q^2 &< 3.2 \cdot 10^5 \text{ GeV}^2 \end{aligned}$$

Remind that the kinematic quantities are calculated from jets/hadrons, for which a resolution of $\Delta E_h/E_h = 0.35/\sqrt{E_h \text{ (GeV)}} \oplus 0.02$ is assumed.

Obviously the most sensitive probes for a right-handed current are e_R^- and e_L^+ . If both e_L^- and e_R^- were available with a degree P of polarisation, the following ratio is very sensitive

$$\begin{aligned} R_{e^-}(Q^2) &= \frac{d\sigma(e_R^-)/dQ^2}{d\sigma(e_L^-)/dQ^2} \\ &= \frac{(1+P)\sigma(e_R^-) + (1-P)\sigma(e_L^-)}{(1+P)\sigma(e_L^-) + (1-P)\sigma(e_R^-)} \\ &\xrightarrow{\text{SM}} \frac{1-P}{1+P}. \end{aligned}$$

This quantity is independent of any structure function assumptions, systematic detector uncertainties cancel and it is a constant in the SM, where no right-handed current exists. Similar arguments hold for $R_{e^+}(Q^2) = d\sigma(e_L^+)/d\sigma(e_R^+)$.

4.2 Results

The lower limits on m_{W_2} from unpolarised and polarised cross section measurements are summarised in Table 5 together with present and HERA limits. As expected, polarised leptons improve the mass limits considerably, since the polarisation can be chosen to be maximally sensitive to a right-handed current. A polarisation of $P = 60\%$ reduces the mass limits by $\sim 100 \text{ GeV}$.

Table 5: Lower limits (95% c.l.) on $m_{W_2} (\text{GeV})$ from differential cross section measurements, present and HERA limits

e^-	e^+	e_R^-	R_{e^-}	e_L^+	R_{e^+}	present limit	HERA
490	390	770	780	630	640	478	400

5 Conclusions

LEP/LHC will provide a very clean environment to search for electron-quark contact interactions or compositeness and will allow to extend the limits on mass scales considerably up to $\Lambda_{eq} \sim 20 \text{ TeV}$, depending on the helicity structure. This corresponds to a sensitivity gain by a factor $\sim 5 - 10$ over present limits and by a factor $\sim 3 - 4$ over HERA limits. Polarised leptons give further improvements up to a factor of ~ 1.5 compared to unpolarised beams and are vital to disentangle the chirality structure in case of a deviation from the standard model.

Several models with an additional Z' gauge boson can be considerably constrained in mass limits and mixing angles, in particular if polarised leptons are available. Right-handed electrons provide detection limits in a left-right symmetric model up to $m_{Z'} > 1.2 \text{ TeV}$, which is a factor ~ 3 over the present limit. For unpolarised leptons, however, the mass limits on new Z' bosons are comparable to those set by present or future Tevatron experiments.

An additional W' gauge boson in a left-right symmetric model can be detected if it is not heavier than $m_{W'_R} > 780 \text{ GeV}$ with right-handed polarised electrons. For unpolarised electrons the mass limits are comparable to the existing ones.

References

- [1] E.J. Eichten, K.D. Lane and M.E. Peskin, *Phys. Rev. Lett.* **50** (1983) 811
- [2] R. Rückl, *Phys. Lett.* **129B** (1983) 368 and *Nucl. Phys.* **B234** (1984) 91
- [3] Particle Data Group, *Phys. Lett.* **239B** (1990) 1
- [4] E.J. Eichten *et al.*, *Rev. Mod. Phys.* **56** (1984) 247 and *Rev. Mod. Phys.* **58** (1986) 1065
- [5] H. Spiesberger, Contribution to these Proceedings
- [6] J. Blümlein and T. Riemann, Contribution to these Proceedings
- [7] H.-U. Martyn, Proceedings of the HERA Workshop, vol 2, p. 801, Hamburg, October 1987
- [8] F. Cornet and R. Rückl, Proceedings of the HERA Workshop, vol 2, p. 771, Hamburg, October 1987 and Proceedings of the Workshop on Physics at Future Accelerators, vol 2, p. 190, La Thuile, January 1987
- [9] D. Dionisi, Contribution to these Proceedings
- [10] F. del Aguila, J.M. Moreno and M. Quiros, preprints UAB-FT-227/90 and IEM-FT-12/90

ELECTROWEAK SYMMETRY BREAKING BY A STRONG SECTOR AT LEP/LHC

Contributors: D. Dominici and F. Feruglio

1. INTRODUCTION

In this report we will consider the sensitivity of the $e - p$ option of LHC to a standard model (SM) extension containing one triplet of extra gauge bosons V . The model corresponds to a breaking of the electroweak symmetry due to a strongly interacting sector: breaking electroweak symmetry strongly (BESS) [1,2]. In this case the electroweak symmetry breaking is obtained via a non-linear realization and no Higgs particles are present. The new gauge bosons V mix with the ordinary W and Z .

We assume the existence of a scale Λ below which the approximate $SU(2)_L \otimes SU(2)_R$ symmetry is non linearly realized. A non linear σ -model describes the breaking $SU(2)_L \otimes SU(2)_R \rightarrow SU(2)_{diag}$. This scheme include the standard model when $M_H \gg 1$ TeV [3] and also technicolor models with one doublet of technifermions [4]. In this case the scalar lagrangian becomes an effective lagrangian containing the gauge vector bosons associated to $SU(2)_L \otimes U(1)_Y$ and the related goldstone bosons. In such a situation the partial wave analysis of the longitudinal W and Z scattering amplitudes indicates the occurrence of strong interactions and suggests the formation of resonances (not only in the $J = 0$ but also $J = 1$ channel)[5]. For instance in technicolor theories one expects a techni- ρ meson. The BESS model describes 6 massive gauge bosons (the usual W^\pm and Z , plus three new ones to be denoted by V^\pm and V^0), and the photon.

The direct production $ep \rightarrow eVX$, via one photon exchange, gives a marginal contribution even for light V masses. This is due to the smallness of the V couplings to the fermions. Therefore we have concentrated on the deep inelastic $e - p$ scattering process, considering the additional effect of the V^0 , V^\pm exchange. We have considered cross section and asymmetry measurements, assuming 100% longitudinal polarization and, given a certain experimental accuracy, we have studied the bounds on the parameter space of the model.

For future reference we collect the couplings of the gauge vector bosons to the fermions. In the neutral sector one has

$$Z_\mu^0(AT_L^3 + BQ_{em}) + V_\mu^0(CT_L^3 + DQ_{em}) + eQ_{em}A_\mu \quad (1.1)$$

with

$$e = g \sin \theta \cos \psi \quad (1.2)$$

$$A = \frac{G}{1+b} \cos \xi \left[1 + b \frac{g'^2}{G^2} \left(1 - \frac{g \tan \xi}{g' \sin \psi} \right) \right] \quad (1.3)$$

$$B = -\frac{g'^2}{G} \cos \xi \left(1 - \frac{g}{g'} \tan \xi \sin \psi \right) \quad (1.4)$$

$$C = \frac{G}{1+b} \sin \xi \left[1 + b \frac{g'^2}{G^2} \left(1 + \frac{g \cot \xi}{g' \sin \psi} \right) \right] \quad (1.5)$$

$$D = -\frac{g'^2}{G} \sin \xi \left(1 + \frac{g}{g'} \cot \xi \sin \psi \right) \quad (1.6)$$

where ξ , ψ and θ are the angles coming from the diagonalization of the neutral gauge boson mass matrix. Their expressions are given by:

$$\xi = -\frac{g^2 - g'^2}{g''G} \frac{1}{1 - (\frac{M_W}{M_V})^2 \frac{1}{\cos^2 \theta}}, \quad \psi = \frac{2gg'}{g''G}, \quad \sin \theta = \frac{g'}{G} \quad (1.7)$$

Here $G = (g^2 + g'^2)^{1/2}$ and g'' is the gauge coupling associated to the new triplet of gauge bosons. The mixing angles are evaluated for $g'' \gg g$. The parameter b specifies a possible direct coupling of the fermions to the new gauge vector bosons. The limit $g'' \rightarrow \infty$ and $b = 0$ corresponds to the SM with decoupled V particles.

In the charged sector one has

$$(h_W W_\mu^i + h_V V_\mu^i) T_L^i, \quad (i = 1, 2) \quad (1.8)$$

where

$$h_W = \frac{1}{1+b} \left(g \cos \varphi - \frac{1}{2} g'' b \sin \varphi \right) \quad (1.9)$$

$$h_V = \frac{1}{1+b} \left(g \sin \varphi + \frac{1}{2} g'' b \cos \varphi \right) \quad (1.10)$$

and the mixing angle is given by

$$\varphi = -\frac{g}{g''} \frac{1}{1 - (\frac{M_W}{M_V})^2} \quad (1.11)$$

The model can be parametrized by the usual SM parameters (α_{em}, G_F, M_Z) and (M_V, g'', b) . M_V represents the common mass of the new vector boson triplet.

The parameter space of the model is already bounded from the present experimental data. In particular the Z -line shape measured at LEP1 and the ratio M_W/M_Z measured at CDF and UA2 provide strong restrictions on (M_V, g'', b) . In order to assess the sensitivity of further limitations coming from future $e-p$ measurements, in the following we will take into account the existing bounds.

2. DEEP INELASTIC $e - p$ SCATTERING

We will consider deep inelastic scattering process $ep \rightarrow lX$ where $l = e, \nu$. We adopt the usual kinematical variables: the momentum transfer Q^2 , the Bjorken variables x and y and the squared total c.m. energy s . The cross section for the deep inelastic process $ep \rightarrow eX$ is given by [6]

$$\frac{d\sigma_{NC}(e_{L,R}^-)}{dx dQ^2} = \frac{2\pi\alpha^2}{xQ^4} \left[(1 + (1-y)^2) F_2^{L,R}(x, Q^2) + (1 - (1-y)^2) x F_3^{L,R}(x, Q^2) \right] \quad (2.1)$$

The functions $F_2^{L,R}$ and $x F_3^{L,R}$ are given by

$$F_2^{L,R} = \sum_f [xq_f(x, Q^2) + x\bar{q}_f(x, Q^2)] \bar{F}_{2f}^{L,R}(Q^2) \quad (2.2)$$

$$xF_3^{L,R} = \sum_f [xq_f(x, Q^2) - x\bar{q}_f(x, Q^2)] \bar{F}_{3f}^{L,R}(Q^2) \quad (2.3)$$

Here $q_f(x, Q^2)$ and $\bar{q}_f(x, Q^2)$ are the quark and antiquark structure functions. In the calculations we use the DFLM structure functions corrected up to next to leading order with $\Lambda_{QCD} = 260$ MeV [7]. Furthermore

$$\begin{aligned} \bar{F}_2^{L,R}(Q^2) &= Q_f^2 + \sum_{i=1,2} [(v_{ie} \pm a_{ie})^2 (v_{if}^2 + a_{if}^2) P_i^2 - 2Q_f(v_{ie} \pm a_{ie}) v_{if} P_i] \\ &\quad + 2(v_{1e} \pm a_{1e})(v_{2e} \pm a_{2e})(v_{1f}v_{2f} + a_{1f}a_{2f}) P_1 P_2 \\ \bar{F}_{3f}^{L,R}(Q^2) &= \pm 2[\sum_{i=1,2} ((v_{ie} \pm a_{ie})^2 v_{if} a_{if} P_i^2 - Q_f(v_{ie} \pm a_{ie}) a_{if} P_i) \\ &\quad + (v_{1e} \pm a_{1e})(v_{2e} \pm a_{2e})(v_{1f}a_{2f} + a_{1f}v_{2f}) P_1 P_2] \end{aligned} \quad (2.4)$$

where

$$P_1 = \frac{Q^2}{Q^2 + M_Z^2}, \quad P_2 = \frac{Q^2}{Q^2 + M_V^2} \quad (2.5)$$

The coefficients v_{if}, a_{if} , $i = 1, 2$ can be reexpressed in terms of A, B, C, D of eqs.(1.3-1.6) according the following relations

$$\begin{aligned} v_{1f} &= \frac{1}{2e} (T_{3f}A + 2Q_fB) & a_{1f} &= \frac{1}{2e} T_{3f}A \\ v_{2f} &= \frac{1}{2e} (T_{3f}C + 2Q_fD) & a_{2f} &= \frac{1}{2e} T_{3f}C \end{aligned} \quad (2.6)$$

In evaluating the various observables we have considered a range of Q^2 from $Q_{min}^2 = 10^4$ GeV 2 to $Q_{max}^2 = 5 \cdot 10^5$ GeV 2 . This range has been divided into 5 bins, constant on a \log_{10} scale. Taking into account the kinematical cuts in Table I, for each bin we have computed the following quantities

$$d\sigma_{NC}(e_{L,R}^\pm) = \int dQ^2 \int dx \frac{d\sigma_{NC}}{dx dQ^2}(e_{L,R}^\pm) \quad (2.7)$$

where the integration limits refer to the chosen bin. Using the integrated cross sections given in eq. (2.7) one can immediately evaluate the relevant physical observables. In the neutral current (NC) case, we have restricted our analysis to the unpolarized cross section $d\sigma_{NC} = \frac{1}{2} (d\sigma_{NC}(e_L^-) + d\sigma_{NC}(e_L^+))$, the polarized one $d\sigma_{NC}(e_L^-)$ and the left-right asymmetry A_{LR}^{--} defined as

$$A_{LR}^{--} = \frac{d\sigma_{NC}(e_L^-) - d\sigma_{NC}(e_R^-)}{d\sigma_{NC}(e_L^-) + d\sigma_{NC}(e_R^-)} \quad (2.8)$$

This last observable and the polarized cross section give bounds which are more stringent or of the same order of the ones we may get from asymmetries containing the positron cross section.

We have also studied the charged current (CC) process $ep \rightarrow \nu X$. In this case the cross section is given by

$$\frac{d\sigma_{CC}(e_L^-)}{dx dQ^2} = \frac{1}{32\pi Q^4} A_L \sum_f [u_f(x, Q^2) + (1 - y^2)\bar{d}_f(x, Q^2)] \quad (2.9)$$

with

$$A_L = (h_W^2 P_1 + h_V^2 P_2)^2 \quad (2.10)$$

where h_W and h_V are given in eqs.(1.9-1.10). The analogous cross section for right-handed electron is zero because the model considered does not have right-handed charged currents *.

We will also consider the cross section corresponding to $e^+ p$ scattering

$$\frac{d\sigma_{CC}(e_R^+)}{dx dQ^2} = \frac{1}{32\pi Q^4} A_L \sum_f [\bar{u}_f(x, Q^2) + (1 - y^2)d_f(x, Q^2)] \quad (2.11)$$

and the ratio R defined as

$$R = \frac{d\sigma_{CC}(e^+)}{d\sigma_{CC}(e^-)} \quad (2.12)$$

where $d\sigma_{CC}(e^\pm)$ are integrated cross sections computed for a given bin of Q^2 with the procedure outlined above.

	NC	CC
x_{min}	0.01	0.01
x_{max}	0.5	0.25
y_{min}	0.075	0.05
y_{max}	0.8	0.8

Table I : cuts on the x and y variables for NC and CC. They define kinematical domains where the systematic errors are assumed to be kept under 10%.

To get the bounds in the parameter space of the model for each observables we have considered the χ^2 defined as

$$\chi^2 = \sum_{bins \text{ in } Q^2} \left(\frac{O(SM) - O(BESS)}{\delta O_{st}} \right)^2 \quad (2.13)$$

where O denotes a generic observable and δO_{st} is the statistical error associated. In the case of the unpolarized cross section measurements we have also defined

$$\chi^2 = \sum_{bins \text{ in } Q^2} \left(\frac{\sigma(SM)f_n - \sigma(BESS)}{\delta\sigma_{SM}f_n} \right)^2 + \left(\frac{f_n - 1}{\delta f_n} \right)^2 \quad (2.14)$$

where we have included a factor f_n to equally normalize the two total cross sections and a systematic uncertainty $\delta f_n = 0.05$.

Bounds have been obtained for fixed values of M_V in the plane $(b, g/g'')$. They are given by 90% CL contours defined by $\chi^2 = 4.61$.

* Right-handed charged currents can be introduced in the BESS model [1,2]. However, as shown in ref.[1,8] they are strongly suppressed with respect to the left-handed ones.

3. DISCUSSIONS OF THE RESULTS

In this section we present our results. We have assumed a center of mass energy $\sqrt{s} = 1265 \text{ GeV}$ and an integrated luminosity of 500 pb^{-1} for both unpolarized and polarized measurements.

In fig. 1 we present limitations from NC measurements at $M_V = 1 \text{ TeV}$ and $m_t = 150 \text{ GeV}$. On the same figure we have superimposed the region allowed by the present data on hadronic Z width Γ_h and the ratio M_W/M_Z . We have taken $\Gamma_h = 1764 \pm 16 \text{ MeV}$ [9] and $M_W/M_Z = 0.8801 \pm 0.0037$ [10]. In the fit we have assumed $\alpha_s = 0.12$ and the region displayed has a CL of 90%. From fig. 1 one can see that the measurements of the unpolarized NC cross section could provide only a small improvement with respect to the existing limitations, excluding a part of the region of small and positive b and g/g'' . This improvement becomes even more modest when one includes a 5% systematic error for the cross section. A substantial improvement of the bounds, still concerning mainly the region of small and positive b and g/g'' , could be obtained by polarized measurements. Taking into account only the statistical errors, $d\sigma_{NC}(e_L^-)$ and A_{LR}^{--} give rise to comparable limitations. Fig. 1 shows that these limitations are similar to those obtainable from a measurement of M_W/M_Z at LEPII with an absolute precision of $2 \cdot 10^{-3}$. The bounds depend only very weakly on the value of M_V . Contrary to what happens in conventional gauge extensions of the SM, deviations from SM expectations do not vanish for large M_V . On the contrary, as soon as M_V is larger than few times M_W , these deviations are essentially independent from M_V .

In fig. 2 we consider again limitations from NC measurements in the plane $(b, g/g'')$ at $M_V = 1 \text{ TeV}$. A top mass of 200 GeV has been assumed in this case. This has the effect of shifting the present allowed region towards negative b values. Also in this case the unpolarized cross section provides no significant additional bounds. Polarized measurements now are effective in a different region of $(b, g/g'')$ plane: at fixed b they lower the existing upper bound on g/g'' .

Finally fig. 3 shows the limitations from CC measurements in the $(b, g/g'')$ plane at $M_V = 1 \text{ TeV}$ and $m_t = 150 \text{ GeV}$. With respect to the NC case the unpolarized cross section appears to be more sensitive. However, also in this case, the inclusion of a 5% systematic error greatly reduces the effectiveness of this measurement. On the other hand, the measurement of the ratio R does not give rise to any appreciable limitation.

In conclusion the measurements of the unpolarized NC and CC cross sections will not significantly improve the already existing limitations on the BESS parameter space. NC polarized measurements, for instance the A_{LR}^{--} asymmetry, could lead to sizable improvements of the existing bounds in regions of the parameter space which depend on the actual value of m_t . Such improvements are nevertheless comparable to those reachable, probably much sooner, with future LEPII data on M_W/M_Z .

FIGURE CAPTIONS

Fig 1: 90% CL contours for $M_V = 1 \text{ TeV}$ and $m_t = 150 \text{ GeV}$ from the unpolarized NC cross section $d\sigma_{NC}$ with only statistical error (thin continuous line), $d\sigma_{NC}$ including a 5% systematic error (thick continuous line), polarized NC cross section $d\sigma_{NC}(e_L^-)$ (dashed-dotted line), and the asymmetry A_{LR}^{--} (dashed-double dotted line). The dotted line contours the region allowed by Γ_h and M_W/M_Z present data. The dashed line defines the 90% CL bound obtainable by measuring M_W/M_Z with an error $2 \cdot 10^{-3}$.

Fig 2: same as fig. 1 with $m_t = 200 \text{ GeV}$.

Fig 3: 90% CL contours for $M_V = 1 \text{ TeV}$ and $m_t = 150 \text{ GeV}$ from the unpolarized CC cross section $d\sigma_{CC}$ with only statistical error (thin continuous line), $d\sigma_{CC}$ including a 5% systematic error (thick continuous line), the ratio $R = d\sigma_{CC}(e^-)/d\sigma_{CC}(e^+)$ (dashed-dotted line). The dotted line contours the region allowed by Γ_h and M_W/M_Z present data.

REFERENCES

- [1] R. Casalbuoni, S. De Curtis, D. Dominici and R. Gatto, Phys. Lett. **B155** (1985) 95; Nucl. Phys. **B282** (1987) 235.
- [2] R. Casalbuoni, P. Chiappetta, D. Dominici, F. Feruglio and R. Gatto, Nucl. Phys. **B310** (1988) 181.
- [3] T. Appelquist and C. Bernard, Phys. Rev. **D 22** (1980) 200; C. Longhitano, Phys. Rev. **D 22** (1980) 1166.
- [4] S. Weinberg, Phys. Rev. **D 13** (1976) 974; **D 20** (1979) 1277; L. Susskind, Phys. Rev. **D 20** (1979) 2619.
- [5] M. Veltman, Acta Phys. Polon. **B8** (1977) 475; B.W. Lee, C. Quigg and H.B. Thacker, Phys. Rev. **D 16** (1977) 1519; P. Q. Hung and H. B. Thacker, Phys. Rev. **D 31** (1985) 2866.
- [6] F. Cornet and R. Rückl, Proceedings of the Hera Workshop, ed. R. D. Peccei, 1987 vol. II, pp. 771-794.
- [7] M. Diemoz, F. Ferroni, E. Longo and G. Martinelli, Z. Phys **C39** (1988) 21.
- [8] H. Neufeld, Nucl. Phys. **B 291** (1987) 629.
- [9] F. Dydak, in Proceedings of the Twenty-Fifth International Conference in High Energy Physics, Singapore, August 1990.
- [10] L. Pondrom, in Proceedings of the Twenty-Fifth International Conference in High Energy Physics, Singapore, August 1990.

1007

1008

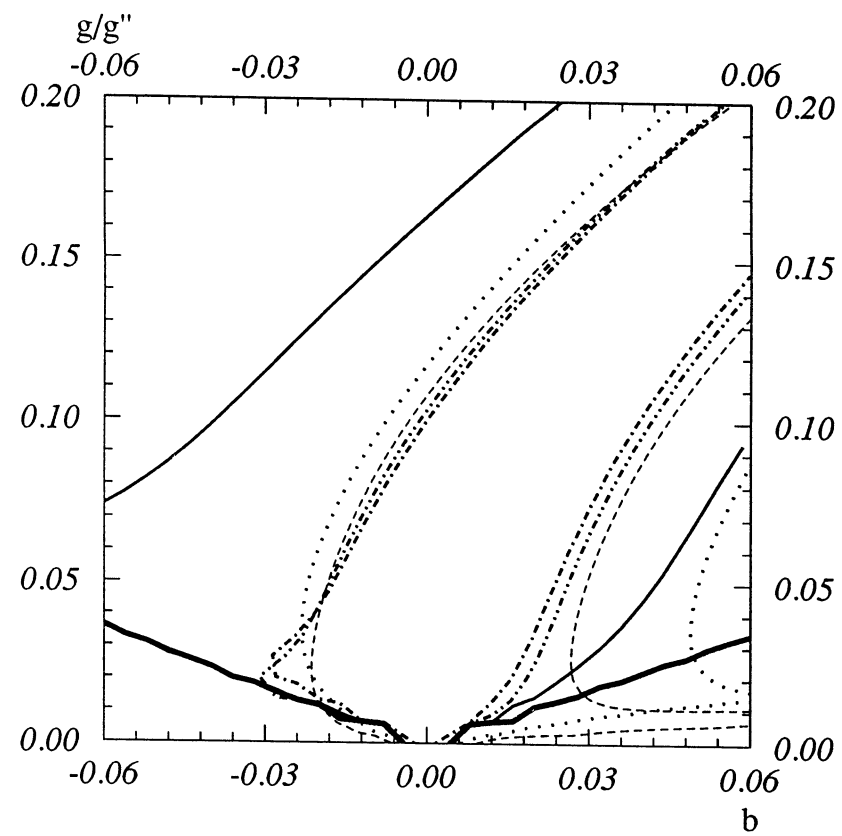


Fig. 1

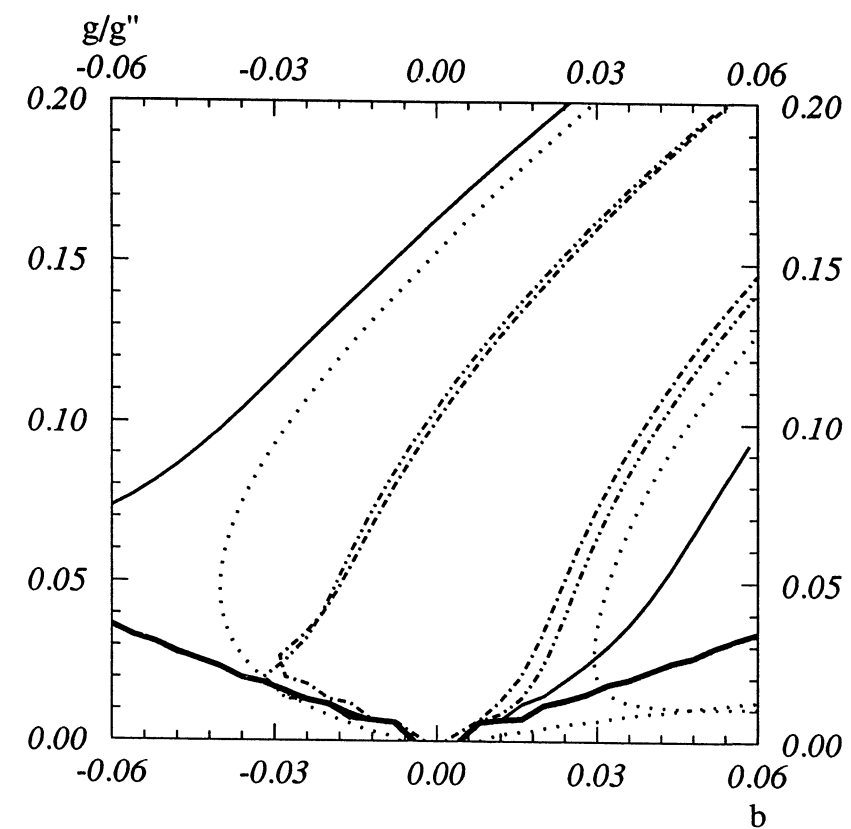


Fig. 2

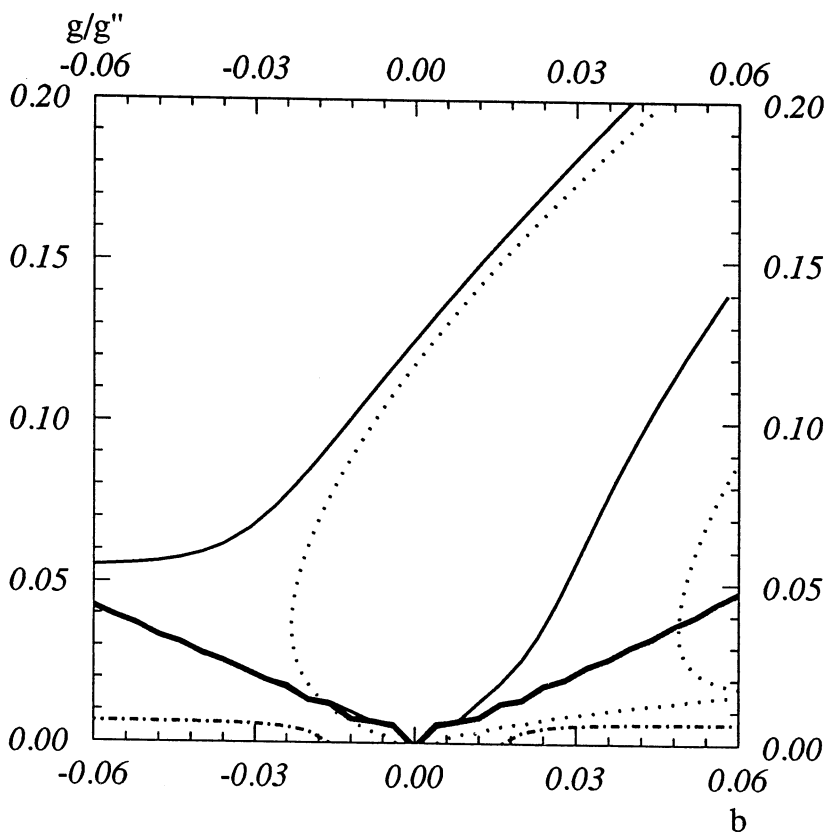


Fig. 3

Radiative Corrections to Deep Inelastic Scattering in the Presence of an Additional Z' at $LEP \times LHC$

J. Blümlein, A. Leike, T. Riemann
 Institut für Hochenergiephysik, Platanenallee 6, D-1615 Zeuthen, Germany

Abstract

The study of ep-scattering at $LEP \times LHC$ offers an interesting opportunity to search for additional heavy neutral gauge bosons. We study the influence of radiative corrections, especially of the potentially large QED contributions, to the expected cross sections. These corrections are typically of the same order as the effect searched for or even larger and have to be taken into account properly.

1 Formulation of the Problem

Neutral current scattering of electrons and protons proceeds via the exchange of photons and Z bosons. If there exist additional heavy gauge bosons in Nature, these would also give some contribution to the cross section. So, they could be detectable at the $LEP \times LHC$. The experimental sensitivity of the reaction

$$e^- p \longrightarrow (\gamma, Z, Z') \longrightarrow e^- X \quad (1)$$

to details of the Z' model has been studied earlier ([1] and refs. quoted therein) and also in a contribution to this workshop [2]. It is well-known that the Born cross section may be modified strongly by radiative corrections of the standard model. These effects have to be under definite control. For the annihilation channel, the problem has been solved in [3] where some of the notations used may be found. Here, we calculate the weak and QED corrections to reaction (1) in presence of an additional heavy gauge boson Z' .

The Born cross section may be denoted as follows:

$$\frac{d\sigma_0}{dx dy} = 2\pi\alpha^2 \frac{s}{Q^4} [\sigma(\gamma, \gamma) + 2\sigma(\gamma, Z) + \sigma(Z, Z) + 2\sigma(\gamma, Z') + 2\sigma(Z, Z') + \sigma(Z', Z')] \quad (2)$$

In a compact notation, the six contributions are:

$$\sigma(B_i, B_j) = \chi_i(Q^2)\chi_j(Q^2)[Y_+ \mathbf{V} + Y_- \mathbf{A}] \quad (3)$$

$$\chi_n(Q^2) = \frac{g_n^2}{4\pi\alpha} \frac{Q^2}{Q^2 + M_n^2}, \quad Y_{\pm} = [1 \pm (1 - y)]^2, \quad (4)$$

$$\mathbf{V} = [C_V(e) + \lambda Q_e C_A(e)] \times [C_V(u)(u + \bar{u}) + C_V(d)(d + \bar{d})], \quad (5)$$

$$\mathbf{A} = -[Q_e C_A(e) + \lambda C_V(e)] \times [C_A(u)(u - \bar{u}) + C_A(d)(d - \bar{d})], \quad (6)$$

$$C_V(f) = v_f(i)v_f(j) + a_f(i)a_f(j), \quad C_A(f) = v_f(i)a_f(j) + a_f(i)v_f(j). \quad (7)$$

The couplings in the standard theory are:

$$g_0 = e, \quad g_1 = \sqrt{\sqrt{2}G_\mu M_Z^2}, \quad v_f(0) = Q_f, \quad a_f(0) = 0, \quad v_f(1) = I_3^L - 2Q_f \sin^2 \theta_W, \quad a_f(1) = I_3^L. \quad (8)$$

Here, $i = 0, 1$ are photon and Z boson with $Q_e = -1$, $I_3^L(e) = -1/2$.

We now discuss the inclusion of the QED corrections. For the standard theory, for the $\gamma Z'$ interference, and for the pure Z' contribution, this may be done following e.g. [4] correct to order $O(\alpha)$ or e.g. [5] in the leading log approximation (LLA). The term to be determined additionally is the ZZ' interference. We have calculated the bremsstrahlung corrections in LLA which is known to agree with the exact calculation within about 1 % or better. We took into account all the contributions which are discussed in [5] where also the notational details may be found. The general form of the bremsstrahlung terms is:

$$d\sigma_{QED} = \frac{\alpha}{2\pi} \ln \frac{Q^2}{m_e^2} \int_0^1 dz \frac{1+z^2}{1-z} \left\{ \theta(z-z_0) \frac{y}{\hat{y}} \frac{1}{z^a} \frac{d\sigma_0}{dx dy} |_{z=\hat{z}, y=\hat{y}, s=\hat{s}} - \frac{d\sigma_0}{dx dy} \right\}. \quad (9)$$

Finally, the weak loop corrections of the standard theory are taken into account using the form factor approach [4]. This leads to an introduction of finite renormalisation factors for the Fermi constant from muon decay and for the weak mixing angle as being defined in the on mass shell renormalisation scheme:

$$G_\mu \rightarrow G_\mu \rho(s, Q^2, \alpha, M_Z, M_H, m_t, \dots), \quad \sin^2 \theta_W \rightarrow \sin^2 \theta_W \kappa(s, Q^2, \alpha, M_Z, M_H, m_t, \dots). \quad (10)$$

In the effective Born cross section, we also use a running $\alpha_{QED}(Q^2)$. Leaving out the complex details of weak loop effects, we quote only the leading, universal t-quark mass effects [6]:

$$\rho \approx \frac{1}{1 - \delta \bar{\rho}}, \quad \kappa \approx 1 + \frac{\cos^2 \theta_W}{\sin^2 \theta_W} \delta \bar{\rho}, \quad \delta \bar{\rho} = 3 \frac{G_\mu}{\sqrt{2}} \frac{m_t^2}{8\pi^2} \left[1 + \frac{G_\mu}{\sqrt{2}} \frac{m_t^2}{8\pi^2} (19 - 2\pi^2) \right]. \quad (11)$$

2 Extra Z bosons

We study the interaction of photon, standard Z boson and one extra Z boson Z' with fermions:

$$\mathcal{L} = e A_\mu J_\gamma^\mu + g_1 Z_\mu J_Z^\mu + g_2 Z'_\mu J_{Z'}^\mu, \quad (12)$$

where the currents are of the form

$$J_n^\mu = \sum_f \bar{f} \gamma^\mu [v_f(n) + \gamma_5 a_f(n)] f, \quad n = \gamma, Z, Z'. \quad (13)$$

The physical mass eigenstates Z_1 and Z_2 are the result of a mixing between Z and Z' . From experimental data the corresponding mixing angle is known to be very small, $\cos \theta_M \approx 0$.

We now investigate numerical consequences of extra Z bosons arising from a grand unified theory based on the E_6 group [7]:

$$E_6 \rightarrow \dots \rightarrow SU(3)_c \times SU(2)_L \times U(1)_Y \times U(1)_X \times U(1)_\psi. \quad (14)$$

The following linear combination of the two extra Z bosons Z_X of $U(1)_X$ and Z_ψ of $U(1)_\psi$ is assumed to be light [8]:

$$Z' = \cos \theta_E Z_X + \sin \theta_E Z_\psi. \quad (15)$$

We consider three models which differ in their phenomenological consequences considerably as has been studied in [2]: model A (B, C) with $\theta_E = -0.9117$ (0., 1.3181). The relation to the mixing angle α of ref. [2] is: $\theta_E = \alpha - \pi/2$.

3 Results

We discuss radiative corrections in presence of a Z' for parameters and observables as used in [2]:

$$A_{LR}^{-+} = \frac{d\sigma(e_L^-) - d\sigma(e_R^-)}{d\sigma(e_L^-) + d\sigma(e_L^+)}, \quad A_{LL}^{-+} = \frac{d\sigma(e_L^-) - d\sigma(e_L^+)}{d\sigma(e_L^-) + d\sigma(e_L^+)}, \quad A_{RR}^{-+} = \frac{d\sigma(e_R^-) - d\sigma(e_R^+)}{d\sigma(e_R^-) + d\sigma(e_R^+)}, \quad (16)$$

where the degree of polarisation has been chosen to be $\lambda = 0.8$.

At small y , where also the energy scale set by Q^2 is small, both the left-right asymmetries and the corrections to them are small since the symmetric pure photon exchange dominates. Although the largest cross section corrections are due to bremsstrahlung (especially at large y), being followed by those due to the running α , this is not true for asymmetries as is seen best from figs. 1 and 2. There, the loop corrections dominate over bremsstrahlung. Further, a closer inspection shows that the influences from a running α and the weak form factor effects are of the same size and have equal sign. For comparison, the curves from the standard model predictions are also shown. They are corrected by LLA bremsstrahlung, by effects due to running α_{QED} and the weak form factors. As may be seen they behave such that a distinct experimental signal from a Z' deserves a careful analysis of data.

We conclude that in the analysis of experimental asymmetries all different origins of radiative corrections have to be carefully taken into account. This is even more important for the charge asymmetries as shown in figs. 3 and 4.

References

- [1] F. Cornet, R. Rückl, in: Proc. of the HERA workshop, Hamburg, Oct 1987, ed. R. D. Peccei (DESY, Hamburg, 1988), Vol. 2, p. 771.
- [2] F. Cornet, H. Martyn, contribution to this workshop.
- [3] A. Leike, T. Riemann, M. Sachwitz, Phys. Letters **B241** (1990) 267;
A. Leike, T. Riemann, Zeuthen prepr. PHE 90-27 (1990), subm. to Z. Physik C.
- [4] D. Bardin, C. Burdik, P. Christova, T. Riemann, Z. Physik **C42** (1989) 679.
- [5] J. Blümlein, Z. Physik **C47** (1990) 89.
- [6] D. Bardin, W. Hollik, T. Riemann, München prepr. MPI-PAE/PTh 32/90 (1990), to appear in Z. Physik C, and references quoted therein.
- [7] D. London, J. L. Rosner, Phys. Rev. **D34** (1986) 1530.
- [8] L. S. Durkin, P. Langacker, Phys. Letters **B166** (1986) 436.

Excited Leptons at LEP/LHC

Ch. Berger¹, P. Fuhrmann¹, F. Raupach¹, M. Spira² and P. Zerwas²

¹ I. Physik Institut, RWTH Aachen, D-5100 Aachen (FRG)

² Inst. Theor. Physik, RWTH Aachen, D-5100 Aachen (FRG)

The search for excited electrons e^* has a long tradition in ep scattering experiments. In fact, one of the first publications [1] from the newly built DESY accelerator reported limits on the coupling and mass of such a particle. Although the LEP/LHC machine allows to search for all sorts of excited fermions, we concentrate in this paper on e^* production. We assume a total cm energy $\sqrt{s} = 1.26$ TeV to be produced by 50 GeV electrons colliding with 8 TeV protons. Production rates are in general based on an integrated luminosity of $\int \mathcal{L} = 10^3 pb^{-1}$.

In the context of composite models the existence of excited fermions is a generic prediction of this picture. The present limit on the compositeness scale Λ is of $\mathcal{O}(1$ TeV) [2]. At LEP/LHC excited leptons and quarks can be produced up to masses of approximately 1 TeV, i.e. in the range of the compositeness scale itself.

For the following study we adopted the standard magnetic moment type coupling [3,4] of the normal fermions f and their excited spin 1/2 partners f^* to the γ, W^\pm, Z field strengths. This gauge field interaction is described by the Lagrangian

$$\mathcal{L}_G = \sum_{V=\gamma, W, Z} \frac{e}{2\Lambda_G} \bar{f}^* \sigma_{\mu\nu} (c_V - d_V \gamma_5) f V_{\mu\nu} + h.c. \quad (0.1)$$

Choosing $c_V = d_V$ we restrict the interactions to left-handed light fermions coupled to right-handed excited fermions. This assumption assures that $(g-2)_\ell$ is protected quadratically to order $(m_\ell/\Lambda)^2$. Defining the electromagnetic couplings to be

$$c_V = d_V = \frac{1}{2}$$

gauge symmetry fixes the W and Z interactions,

$$c_W = d_W = \frac{1}{2\sqrt{2} \sin \theta_W} \quad c_Z = d_Z = \frac{I_{3f} - e_f \sin^2 \theta_W}{\sin 2\theta_W}$$

Beside these gauge field interactions, excited fermions can also be coupled to light fermions through contact interactions [5] which may be generated by preon interchange. The interaction density is generally chosen as an effective current-current product [of left-handed particles] locally confined to the compositeness radius $\sim \Lambda_{CT}^{-1}$:

$$\mathcal{L}_{CT} = \frac{4\pi}{\Lambda_{CT}^2} j_\mu j_\mu \quad (0.2)$$

Decay and production properties of excited leptons and quarks are rather different in both approaches, and we will describe them for the LEP/LHC collider subsequently. Since the scales Λ_G and Λ_{CT} need not coincide, we shall assume, for the sake of simplicity, that only one type of interaction be operative effectively for a time.

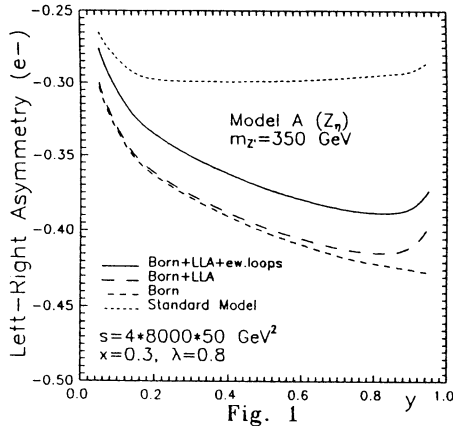


Fig. 1

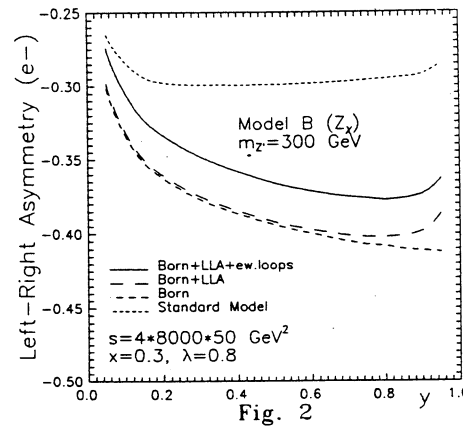


Fig. 2

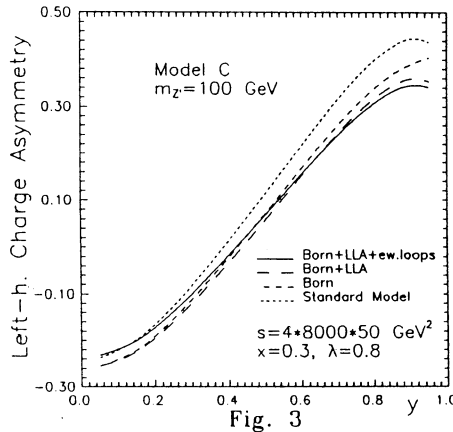


Fig. 3

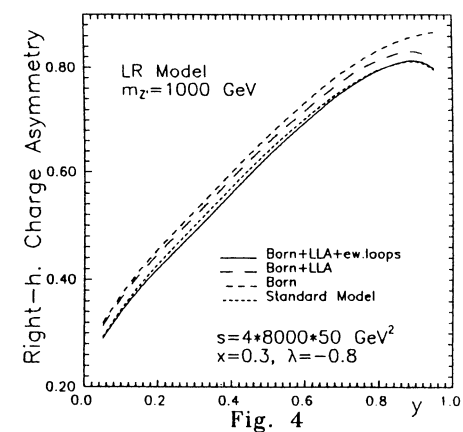


Fig. 4

1. Gauge interactions

Heavy excited fermions decay into light fermions plus gauge bosons:

$$\begin{aligned} e^* &\rightarrow e + \gamma, \quad e + Z \text{ and } \nu + W \\ \nu^* &\rightarrow \nu + Z \text{ and } e + W \end{aligned}$$

[In a slight extension of the present analysis, ν^* may also deexcite by γ emission [6]]. The decay widths for the masses m_* sufficiently above the W, Z masses,

$$\begin{aligned} \Gamma(e^* \rightarrow e\gamma) &= \frac{\alpha}{4} \frac{m_*^3}{\Lambda_G^2} & \Gamma(\nu^* \rightarrow \nu Z) &= \frac{\alpha}{4 \sin^2 2\theta_W} \frac{m_*^3}{\Lambda_G^2} \\ \Gamma(e^* \rightarrow eZ) &= \frac{\alpha}{4 \tan^2 2\theta_W} \frac{m_*^3}{\Lambda_G^2} & \Gamma(\nu^* \rightarrow eW) &= \frac{\alpha}{8 \sin^2 \theta_W} \frac{m_*^3}{\Lambda_G^2} \quad (1.3) \\ \Gamma(e^* \rightarrow \nu W) &= \frac{\alpha}{8 \sin^2 \theta_W} \frac{m_*^3}{\Lambda_G^2} \end{aligned}$$

are small and the states are quite narrow. For $m_{e^*} = 600$ GeV and $\Lambda_G = 1$ TeV the partial width $\Gamma(e^* \rightarrow e\gamma)$ is less than 400 MeV. The sum of the partial widths for the various gauge decays and the corresponding branching ratios are collected in the following table.

Table 1:

	$\sum_V \Gamma(f^* \rightarrow fV) \Lambda_G^2 / m_*^3$	e^*	B_G	ν^*	B_G
e^*	6.5×10^{-3}	$e\gamma$	0.28	νZ	0.39
ν^*	6.5×10^{-3}	eZ	0.11	νW	0.61
		νW	0.61		

Excited electrons and neutrinos can be produced in electron-photon and electron- W collisions

$$e + \gamma \rightarrow e^* \quad \text{and} \quad e + W \rightarrow \nu^* \quad (1.4)$$

The cross section for e^* production may be written in the narrow width approximation as

$$\sigma(e\gamma \rightarrow e^*) = \frac{8\pi^2}{m_*} \Gamma(e^* \rightarrow e\gamma) \delta(\hat{s} - m_*^2) \quad (1.5)$$

and analogously for ν^* production, $\sqrt{\hat{s}}$ being the invariant energy of the $(e\gamma)$ system. Z exchange is negligible because the e^* rate is completely dominated by low q^2 photon-electron interactions. The [gauge] cross sections for ep collisions have been discussed in Ref.[7]. Adjusted to LEP/LHC kinematics, they are presented in Fig.1 for the mass range m_* below 1.2 TeV.

1.1 Elastic e^* production

For a more detailed study of excited fermions and the background from standard physics we have chosen e^* production, especially

$$e + p \rightarrow e^* + p \rightarrow (e\gamma) + p \quad (1.6)$$

This elastic channel accounts for half of the total production cross section [7] and provides a very clear signature. The elastic cross section may either be calculated directly or by folding

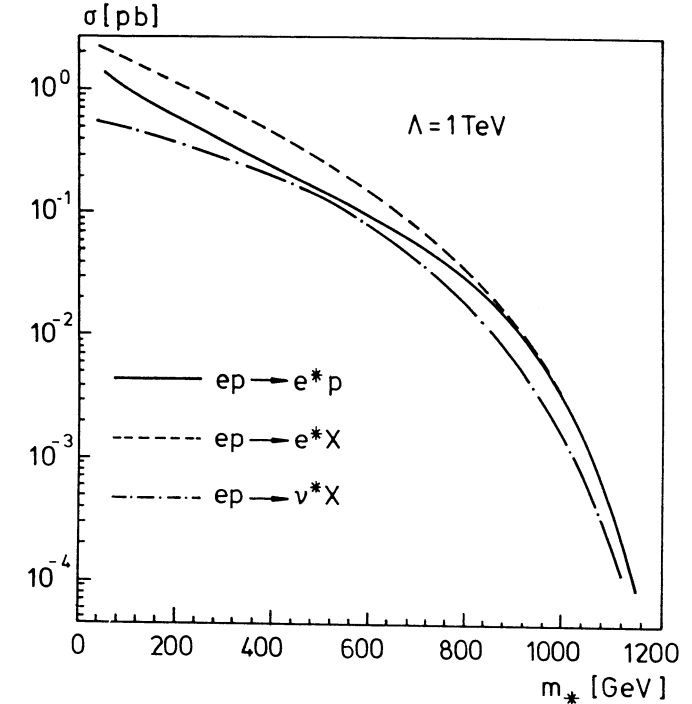


Fig.1. Cross section for the production of excited electrons and neutrinos in elastic and deep inelastic ep scattering processes for the LEP/LHC energy.

eq.(1.5) with the flux of Weizsäcker-Williams photons from the proton source. Due to the proton form factor the flux is nearly independent of the proton energy. This simple method reproduces the exact calculation [7] at the percent level*. The final result has been shown by the full line in Fig.1.

The event generator [9] is based on the formulae of Ref.[7] but includes the decay branching ratios of excited electrons into $e\gamma$, eZ and νW given in Table 1, and the decay angular distribution in the e^* rest frame

$$\frac{1}{\Gamma} \frac{d\Gamma}{d \cos \theta} = \frac{1 + \cos \theta + \kappa(1 - \cos \theta)/2}{2 + \kappa} \quad (1.7)$$

where $\kappa = m_V^2/m_*^2$.

The only background process to the $e^* \rightarrow e\gamma$ decay channel is γ bremsstrahlung,

$$e + p \rightarrow e + p + \gamma \quad (1.8)$$

*We disagree with the formula for the photon flux in Ref.[8] (Ch. Berger et al., in preparation).

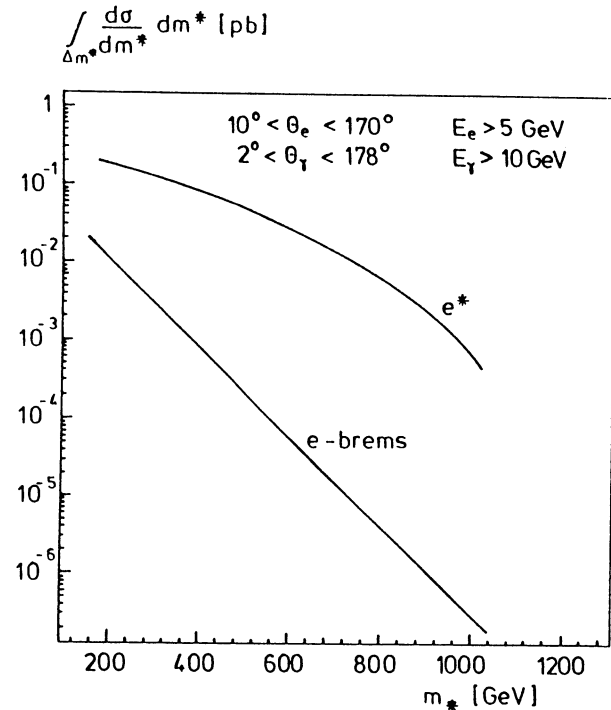


Fig.2a) Signal and background for elastic production of excited electrons.

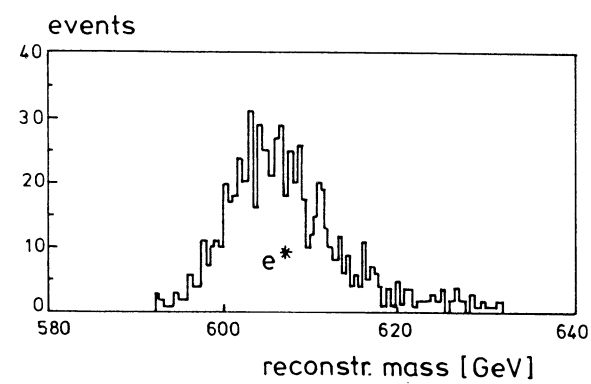


Fig.2b) Reconstruction of the e^* mass in $(e\gamma)$ final states.

The photons are emitted either from the electrons or from the protons. While the amplitude for γ radiation off the electrons is straightforward to calculate, we estimate the bremsstrahlung off the proton by a quark model calculation in a quasielastic approximation by requesting the outgoing quarks to be emitted within a cone of aperture $1/2^\circ$ around the incoming proton direction.

Signal and background were subjected to a detector simulation. The main detector parameters were a momentum resolution of $0.003 p[\text{GeV}]$, an electromagnetic energy resolution of $0.10/\sqrt{E[\text{GeV}]}$ and a hadronic energy resolution of $0.45/\sqrt{E[\text{GeV}]}$. The cuts applied

$$10^\circ < \theta_e < 170^\circ \quad \text{and} \quad E_e > 5 \text{ GeV}$$

$$2^\circ < \theta_\gamma < 178^\circ \quad E_\gamma > 10 \text{ GeV}$$

reduced the signal by a few percent only. The result for $\int \frac{d\sigma}{dm_*} dm_*$ is shown in Fig.2a. The bin width Δm_* was taken from the simulation of the signal, e.g. 16 GeV for an excited electron mass of 600 GeV[†]. As can be seen from the figure the bremsstrahlung cross section is well below the e^* signal. We also found, that the bremsstrahlung from the proton is completely negligible for $m^* > 300$ GeV. The signal in Fig.2b corresponds to $\Lambda_G = 1$ TeV.

1.2 Inelastic e^*, ν^* production

The inelastic cross sections

$$e + p \rightarrow e^*, \nu^* + X \quad (1.9)$$

have been presented in Fig.1 by the dashed curves. Set I of EHLQ Ref.[10] has been adopted for the parametrization of the quark distributions. We calculated the cross section (1.9) by folding the differential cross section $d\sigma/d\hat{t}$ for $eq \rightarrow e^*q$ with the quark distributions at the scale \hat{t} . It is evident from Fig.1 that about 50% of the e^* production cross section is deep inelastic.

2. Contact interactions

If contact interactions are operative [5] they naturally dominate the decay and production mechanisms. They reflect the onset of a new physical force which is strong *sui generis*.

The decay modes of excited leptons through contact interactions

$$\begin{aligned} e^* &\rightarrow eee, e\mu\mu, ejj \dots \\ \nu^* &\rightarrow \nu ee, \nu\mu\mu, ejj \dots \end{aligned}$$

predict spectacular signatures. Summing up the partial widths

$$\Gamma(f^* \rightarrow f + f' \bar{f}')_{CT} \sim \frac{m_*}{96\pi} \left(\frac{m_*}{\Lambda_{CT}} \right)^4 \quad (2.10)$$

the total widths of the excited leptons increase to

$$\Gamma(e^*, \nu^*)_{tot} = 8.9 \times 10^{-2} m_* \quad (2.11)$$

[†]The slight shift of the reconstructed mass is an artifact of the simulation routine used, the fast simulation program of the H1 detector. This program tries to match the track detector and calorimeter momentum determination.

where $\Lambda_{CT} = \Lambda_G = m_*$ has been assumed for definiteness. The excited states then decay almost exclusively

$$\Gamma(e^*, \nu^*)_{CT}/\Gamma_{tot} \sim 93\% \quad (2.12)$$

to 3-particle [and jet] final states.

The e^* [and ν^*] production cross section has been presented in Ref.[11],

$$\sigma(ep \rightarrow e^*q) = \frac{\pi}{\hat{s}} \left(\frac{\hat{s}}{\Lambda_{CT}^2} \right)^2 \left[1 - \frac{m_*^2}{\hat{s}} \right]^2 \quad (2.13)$$

By folding this cross section with the quark distributions in the proton we derive the total e^*, ν^* production cross section in ep collisions. The cross section is displayed in Fig.3 versus the mass m_* of e^* or ν^* .

Since excited electrons which are produced by contact interactions, decay mainly into electrons plus a fermion-antifermion pair through the same mechanism, the branching ratio into $e\gamma$ is only a few percent. Taking also account of the large width, one has therefore to search for rather broad enhancements in $e\mu\mu$ or ejj final states. By just counting color and flavor degrees of freedom we get a crude estimate of 4% for the branching ratio in the $e\mu\mu$ channel. On the other hand, this channel should have a small background. We calculated the visible cross section for this final state in two-photon interactions to be less than 10^{-3} pb in the $e\mu\mu$ mass range from 550 to 650 GeV. This moves the Λ_{CT} values up to 8 TeV at 95% CL.

3. Conclusions

From the cross sections reported above it is straightforward to derive the 95% CL area in the $[\Lambda, m_*]$ plane that can be probed at LEP/LHC. The result for the gauge interactions is shown in Fig.4. A similar analysis for contact interactions shifts the accessible Λ_{CT} value up to ~ 8 TeV at a mass of the excited lepton of 600 GeV.

The figure demonstrates that bounds expected from HERA can be extended by a factor of $\sim 2 - 5$. The LEP/LHC collider approaches the magic 1 TeV limit of possible phenomena beyond the Standard Model.

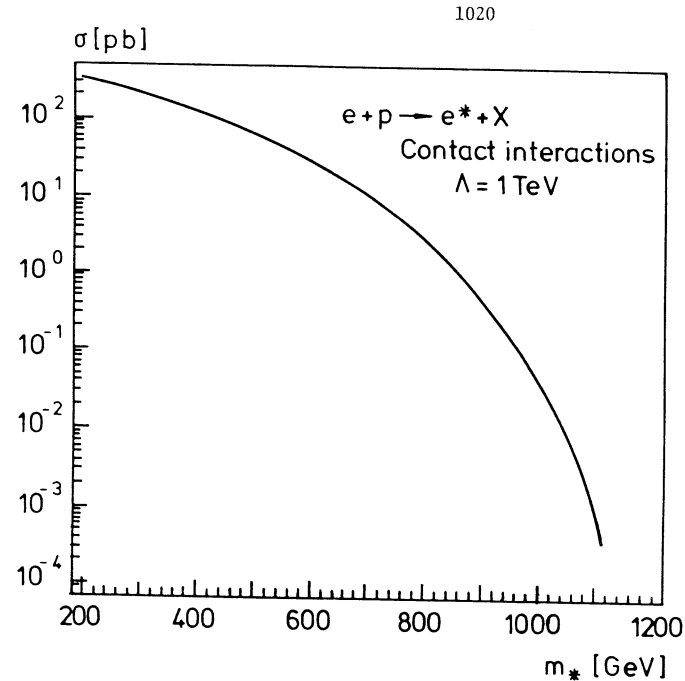


Fig.3. Cross section for the production of excited electrons through contact interactions.

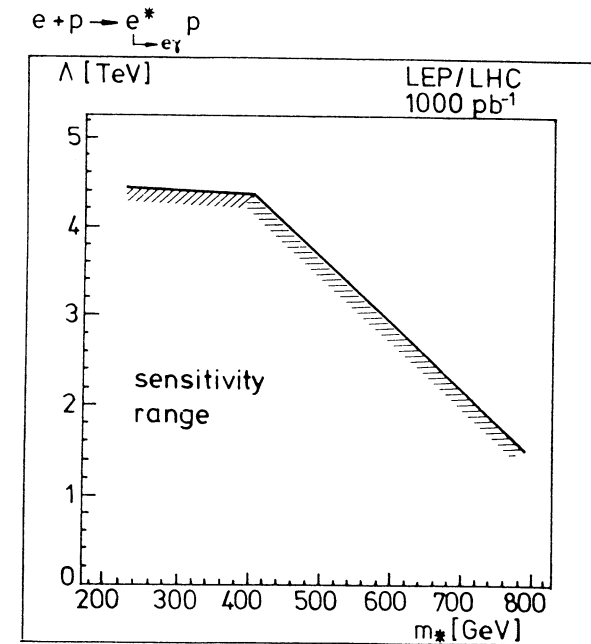


Fig.4. 95% CL area in the $[\Lambda, m_*]$ plane that can be probed at LEP/LHC.

REFERENCES

- [1] H. J. Behrend, F. W. Brasse, J. Engler, E. Ganssauge, H. Hultschig, S. Galster, G. Hartwig and H. Schopper, Phys. Rev. Lett. **15** (1965) 900.
- [2] Particle Data Group, Phys. Lett. **239B** (1990) 1.
- [3] F. Low, Phys. Rev. Lett. **15** (1965) 900.
- [4] F. M. Renard, Phys. Lett. **116B** (1982) 264 and Phys. Lett. **139B** (1984) 449; N. Cabibbo, L. Maiani and Y. Srivastava, Phys. Lett. **139B** (1984) 459; A. DeRújula, L. Maiani and R. Petronzio, Phys. Lett. **140B** (1984) 253; J. Kühn and P. Zerwas, Phys. Lett. **147B** (1984) 189; J. Kühn, H. D. Tholl and P. Zerwas, Phys. Lett. **158B** (1985) 270.
- [5] R. Kleiss and P. Zerwas, Proceedings, Workshop "Physics at Future Accelerators", La Thuile/CERN 1987, CERN 87-07.
- [6] F. Boudjema and A. Djouadi, Phys. Lett. **240B** (1990) 485.
- [7] K. Hagiwara, S. Kornamiya and D. Zeppenfeld, Z. Phys. **C29** (1985) 115.
- [8] V. M. Budnev, I. F. Ginzburg, G. V. Meledin and V. Serbo, Phys. Rep. **C15** (1975) 181.
- [9] Th. Köhler, Diplomarbeit, RWTH Aachen.
- [10] E. Eichten, I. Hinchliffe, K. Lane and C. Quigg, Rev. Mod. Phys. **56** (1984) 579.
- [11] U. Baur, M. Spira and P. Zerwas, Phys. Rev. **D42** (1990) 815.

LEPTOQUARK PRODUCTION AT THE LHC/LEP $e - p$ COLLIDER

N. Harnew

Department of Nuclear Physics, University of Oxford,
Keble Road, Oxford, OX1 3RH, U.K.

ABSTRACT

Experimental signatures for leptoquark production at the LHC/LEP $e - p$ collider are described. These signatures are striking; leptoquarks manifest themselves as s -channel resonances in electron-quark collisions. By considering background processes, discovery limits are presented as a function of leptoquark mass and coupling strength. The importance of beam energy and luminosity is investigated and finally comparisons are made with discovery limits attainable at HERA.

1. INTRODUCTION

This paper considers experimental signatures for leptoquark production at the LHC/LEP $e - p$ collider using Monte Carlo methods. It extends the study presented in the proceedings of the La Thuile workshop⁽¹⁾. Leptoquarks have been proposed to mediate quark-lepton transitions in unified models such as SU(5) and also in superstring motivated theories⁽²⁾. An $e-p$ machine is a natural place to look for these states since their production is characterised by s -channel resonances of electron and quark. By considering background processes, experimental discovery limits have been calculated as a function of leptoquark mass and coupling strength. Throughout this paper three centre of mass energies have been considered, (i) 30 GeV electrons on 820 GeV protons, (ii) 50 GeV electrons on 8.0 TeV protons, and (iii) 100 GeV electrons on 8.0 TeV protons. Case i) corresponds to HERA, cases ii) and iii) correspond to proposed energies of $e p$ collisions in the LEP tunnel. The integrated luminosities are taken to be 200pb^{-1} , 1000pb^{-1} and 100pb^{-1} respectively and correspond to approximately one year of running at each centre of mass energy⁽³⁾.

2. LEPTOQUARK PRODUCTION

Leptoquark event rates are based on the production cross sections of Buchmüller, Rückl and Wyler⁽⁴⁾ and the diagrams considered for their production and decay are shown in figure 1(a). Only the production and decay of the scalar leptoquark, labelled S , is considered in these studies. The differential cross section for the process $S \rightarrow eu$ is given in reference 2 as

$$\frac{d^2\sigma}{dx dQ^2} (e_{L,R}^\pm p) = \frac{1}{16\pi^2 x^2 s^2} \sum_{\text{quarks}} \{ |A_\gamma + A_Z|_{L,R}^2 + 2\text{Re}(A_\gamma + A_Z) A_{LQ}^* \\ + |A_{LQ}|_{L,R}^2 \} q(x, Q^2) \quad (1)$$

where Q^2 is the momentum transfer in the event $Q^2 = (p_e - p_{e'})^2$, s is the centre of mass energy squared, $s = (p_e + p_p)^2$ and x is the quark fractional momentum (Bjorken scaling variable). The first term in formula (1) corresponds to the squared amplitude for the neutral current process (γ and Z° exchange), the third term is the amplitude squared for leptoquark production and the second term is the interference of the two. The $q(x, Q^2)$ are the quark densities in the proton, ie structure functions. A similar expression holds for the neutrino decay mode of the S leptoquark (ie $S \rightarrow \nu d$) but in this case the neutral current is replaced by the charged current amplitude.

The width of the leptoquark is given in terms of the left handed and right handed coupling strengths, λ_L and λ_R , by $\Gamma_s = \frac{1}{16\pi} (2\lambda_L^2 + \lambda_R^2)m_s$, where m_s is the leptoquark mass. The amplitude has a Breit-Wigner form given by

$$|A_{LQ}|_{L,R}^2 = \frac{1}{2} \frac{\lambda_{L,R}^2 (\lambda_L^2 + \lambda_R^2) \hat{s}^2}{(\hat{s} - m_s^2) + m_s^2 \Gamma_s^2}$$

where $\hat{s} = sx$.

Note that leptoquark decay $S \rightarrow \nu d$ can only proceed if the left handed coupling λ_L is non zero while the decay $S \rightarrow eu$ can proceed via both left and right handed amplitudes. Also, we define the relative coupling strengths

$$F_L = \{\lambda_L^2/4\pi\}/\alpha_{em}, \quad F_R = \{\lambda_R^2/4\pi\}/\alpha_{em}$$

where, if $F_L = 1$, the coupling is just the EM coupling, similarly for F_R .

Production rates will clearly depend on the relative coupling strengths chosen, however in these studies F_L is variable and F_R fixed at zero. Hence in this case the decays $S \rightarrow eu$ and $S \rightarrow \nu d$ contribute equally in the final state.

Figure 2 shows the event rates per year for the scalar leptoquark, S , produced at the centre of mass energies (and integrated luminosities) given above, for two values of F_L namely $F_L = 1.0$ (electromagnetic coupling), and $F_L = 0.01$. It can be clearly seen that the event rates are extremely dependent on the couplings, varying by a factor 100 over these chosen F values.

2-1 Kinematics

Shown in figure 1 are the diagrams for a) leptoquark production and b) deep inelastic scattering (DIS), charged and neutral current interactions. It can be seen that the leptoquark and DIS events look exactly alike in their final states and hence identical in their kinematics. Hence the only serious backgrounds to leptoquark production are DIS neutral current interactions and DIS charged current interactions to the $S \rightarrow eu$ and $S \rightarrow \nu d$ channels, respectively.

Leptoquark decay is isotropic (spin zero). This decay gives a flat Q^2 distribution and hence a flat y distribution, where y is the scaling variable, $y = Q^2/sx$. This contrasts sharply with DIS interactions which go as $1/Q^4$ (or $1/y^2$). Leptoquark events are produced at constant x ,

$$\text{ie} \quad x = m_s/s.$$

Hence the signature for leptoquark production is a peak in the x (or m_s) distribution. Note that the x of the event can be calculated from the electron alone, the quark alone or the effective mass of the electron quark system. In the case of $S \rightarrow d\nu$, the quark alone must be relied upon to provide the only measurement of x . Hence good jet energy resolution is paramount for this channel. Note that a measurement of BOTH the $S \rightarrow ue$ and $S \rightarrow d\nu$ channels provides a measurement of both the F_L and F_R couplings in the absence of a polarized beam.

Because of the different y dependence of leptoquark and DIS events, selecting events with high y (or Q^2) will greatly enhance leptoquark events from DIS background. In the limit of uniform detector acceptance the flat y nature of leptoquark events will lead to an efficiency which scales with the magnitude of the cut. In addition, the angular distributions of the lepton and quark in the laboratory will look very different when comparing leptoquark and DIS events. However, for a given x , an angular cut will be kinematically equivalent to a y cut, but the efficiency of the cut will not scale.

2-2 The Monte Carlo Program

For the purpose of event generation, DIS events and leptoquark events were distributed according to the formulae given in reference 4. As seen in equation 1, DIS-leptoquark interference is explicitly included. String fragmentation of the current quark and proton di-quark was incorporated *à la* Lund⁽⁵⁾. The stable particles from the fragmentation process were tracked through a realistic detector simulation. At HERA beam energies the ZEUS detector⁽⁶⁾ configuration was assumed. At LHC/LEP beam energies the detector configuration of Bartel⁽⁷⁾ was adopted.

For the electron, perfect angular precision was assumed (since the electron direction is measured by tracking chambers). The electron energy was calculated directly from the calorimeter cluster assigned to the electron track, appropriately smeared. For the jet, the parton direction was reconstructed from weighted energy deposits in the calorimeter towers which had been assigned to the jet cluster (again appropriately smeared). This gave a jet angular resolution slightly worse than 10 mrad at all energies. A 4π detector without cracks was assumed, however tracks with polar angles of less than 2° to the beam were rejected (note that this also defines the electron angular cut). Jets with reconstructed polar angles less than 7.5° to the beam were rejected in order to ensure a well contained energy cluster.

For the electronic and hadronic energy resolutions a combination of $10\%/\sqrt{E} + 1\%$ (electromagnetic) and $40\%/\sqrt{E} + 2\%$ (hadronic) was taken. These studies have shown that the \sqrt{E} term is important at HERA, however at LHC/LEP energies the constant term in the resolution is dominant (except at the lowest leptoquark masses). Therefore it is important for the calorimeter to have controlled systematic uncertainties in order to reduce this constant term to a minimum.

Throughout this study unpolarized electron and proton beams were assumed. Note that this is contrary to reference 1 where a 100% electron polar-

ization was adopted (which increases the statistics by a factor of two at a given integrated luminosity).

At each of the three centre of mass energies leptoquark events were generated independently at discrete mass values and coupling strengths F_L (with $F_R = 0$) up to the kinematic limit. The leptoquarks were decayed isotropically in the centre of mass system of the incoming lepton and quark according to reference 4 (the quark x value on resonance being defined by the leptoquark mass). For the $S \rightarrow eu$ decay mode, the x , y and Q^2 of the event can be calculated i) from the electron alone, ii) from the jet alone and iii) from the electron and jet (by calculating the effective mass of the electron and jet). For the $S \rightarrow eu$ decay mode, the x of the event was calculated from electron and jet, however for the $S \rightarrow \nu d$ decay mode one has to rely on jet information alone for the calculation of the kinematic variables.

The marked difference in the signature of leptoquark events and DIS events is shown in figure 3 for a 500 GeV leptoquark produced at LHC/LEP I (50 GeV e on 8.0 TeV p beam). Here is shown the y distribution with $y > 0.05$ for events on the leptoquark mass peak (taken as 20 MeV about the mean mass value) compared to events off the mass peak. It can be seen from figure 3 that leptoquark events have a flat y distribution (in contrast to the NC events go which go as $1/y^2$). It turns out that a y cut of 0.5 is optimal in achieving best signal to noise.

Shown in figures 4 and 5 are the x distributions that would be observed experimentally from the decay of a 500 GeV leptoquark into eu and νd respectively at the 50 GeV electron on 8.0 TeV proton machine. The plots correspond to 1 fb^{-1} , ie approximately 1 year's running. The leptoquark coupling strength chosen in these figures is $F_L = 0.1$, ie 10% of the EM coupling (with $F_R = 0$). It can be seen that the leptoquark signals can be cleanly seen above the DIS background. The effect of a y cut (> 0.5) is clearly seen to significantly improve the signal to noise.

2-3 Discovery Limits

To calculate the discovery limits for leptoquark production, the following criteria were chosen :-

- i) Require the number of signal events (after y cuts) to be $N_{signal} > 25$ events AND
- ii) Require a 5 sigma signal, ie $N_{signal} > 5/\sqrt{(\text{background})}$.

The DIS backgrounds to $S \rightarrow eu$ and $S \rightarrow \nu d$ were calculated by fitting a Gaussian resolution function to the leptoquark mass peak, superimposed on top of a smooth background function. Clearly the discovery limits are dependent on the y cut chosen. There is a trade off between improved signal to noise with a loss of events as the y cut is increased. Studies have shown that the optimal y cut is 0.5, independent of mass, except at masses very close to the kinematic limit where the number of signal events fall rapidly.

Shown in figure 6 are the discovery limits after one years running for $S \rightarrow eu$ and $S \rightarrow \nu d$ at the three centre of mass energies as a function of leptoquark mass and coupling strength F_L ($F_R = 0$). The discovery of leptoquarks will be possible if F_L values are greater or equal to the values shown by the curves in

the figure. It can be seen that discovery of leptoquarks is possible for masses almost up to the kinematic limit if coupling strengths are comparable with α_{em} . Also it can be seen that the higher energy electron beam (100 GeV) does not improve the discovery limits compared to a 50 GeV electron beam except at leptoquark masses above 1.0 TeV; the factor 10 lower luminosity hurts.

3. CONCLUSIONS

The conclusions are summarized below :-

- i) At $e - p$ colliders, leptoquarks are produced as s -channel resonances and hence have very clean signatures, however the event rates are extremely dependent on coupling strengths. Background rates from DIS charged and neutral current interactions are manageable and can be substantially reduced by a y or Q^2 cut.
- ii) Leptoquarks can be discovered with masses almost up to the kinematic limit for leptoquark couplings comparable with α_{em} . In particular it is possible to probe masses up to approximately a) 270 GeV at Hera, b) 1.1 TeV at LHC/LEP I, and c) 1.3 TeV at LHC/LEP II.
- iii) The higher electron energy (100 GeV compared to 50 GeV) does not help in the discovery of leptoquarks except for masses above 1.0 TeV; the factor 10 lower luminosity hurts. However the LHC offers substantial improvement over HERA, increasing the mass discovery range by a factor of 4.
- iv) There are no special detector requirements for leptoquark discovery, however high resolution calorimetry helps.

ACKNOWLEDGEMENTS

The author is indebted to R.Rückl for invaluable discussions and consultations.

REFERENCES

- (1) N.Harnew, Experimental Signatures for Leptoquark Production at Future ep Colliders. Proceedings: La Thuile Workshop CERN 87-07
- (2) V.D.Angelopoulos *et al*, *Nucl. Phys.* **B292** (1987) 59
- (3) See G.Brianti. These proceedings.
- (4) W.Buchmüller, R.Rückl and D.Wyler, *Phys. Lett.* **191B** (1987) 442
- (5) G.Ingelman, The LEPTO52 Monte Carlo Generator (unpublished).
- (6) The ZEUS Detector Status Report. DESY PRC/87-02.
- (7) See W.Bartel. These proceedings.

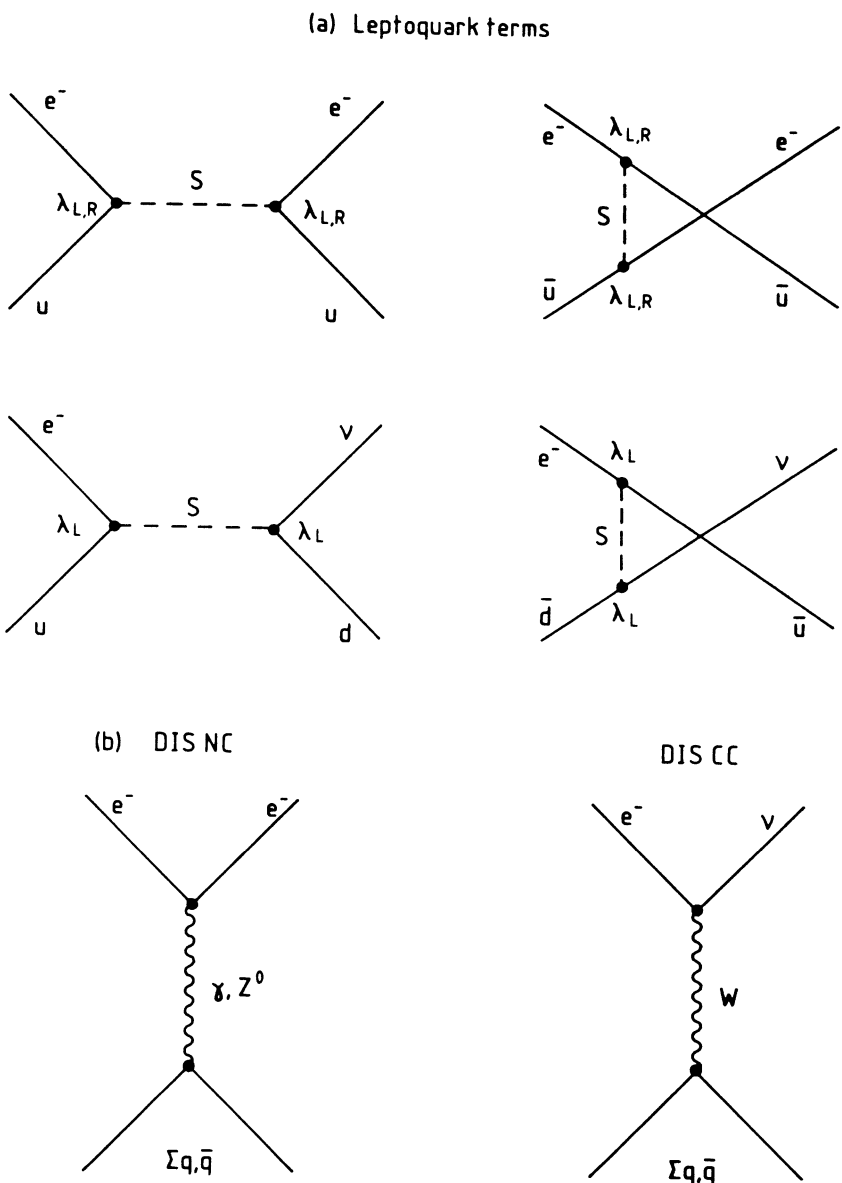


Figure 1. Diagrams contributing to the neutral and charged current process $e^- p \rightarrow e^- X$.

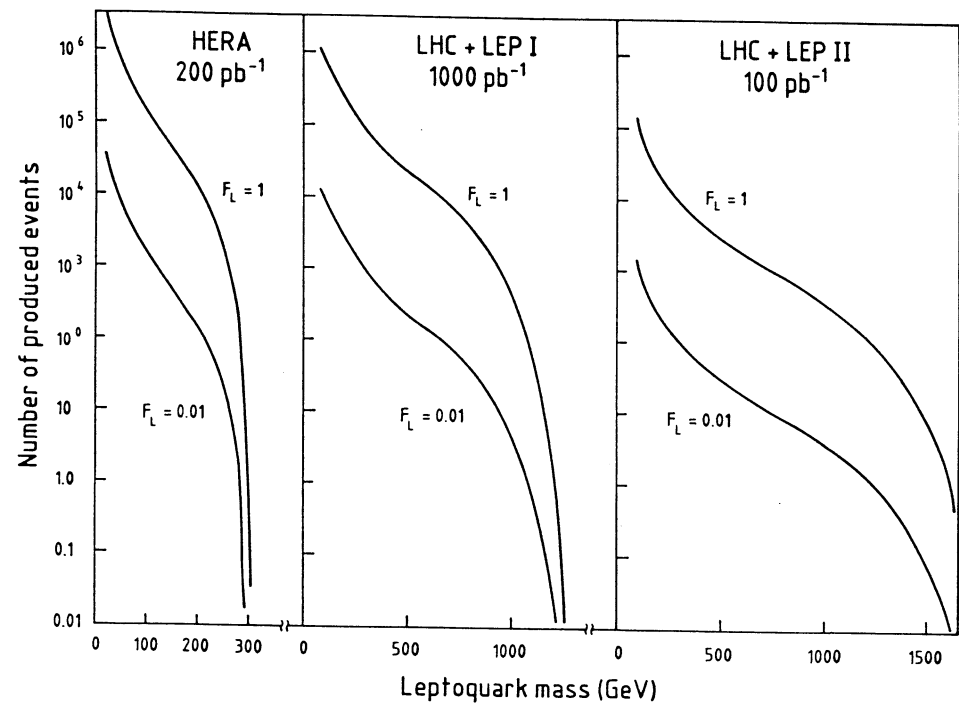


Figure 2. Event rates per year as a function of leptoquark mass and beam energy
(a) $F_L = 1.0$ (EM coupling), and (b) $F_L = 0.01$.

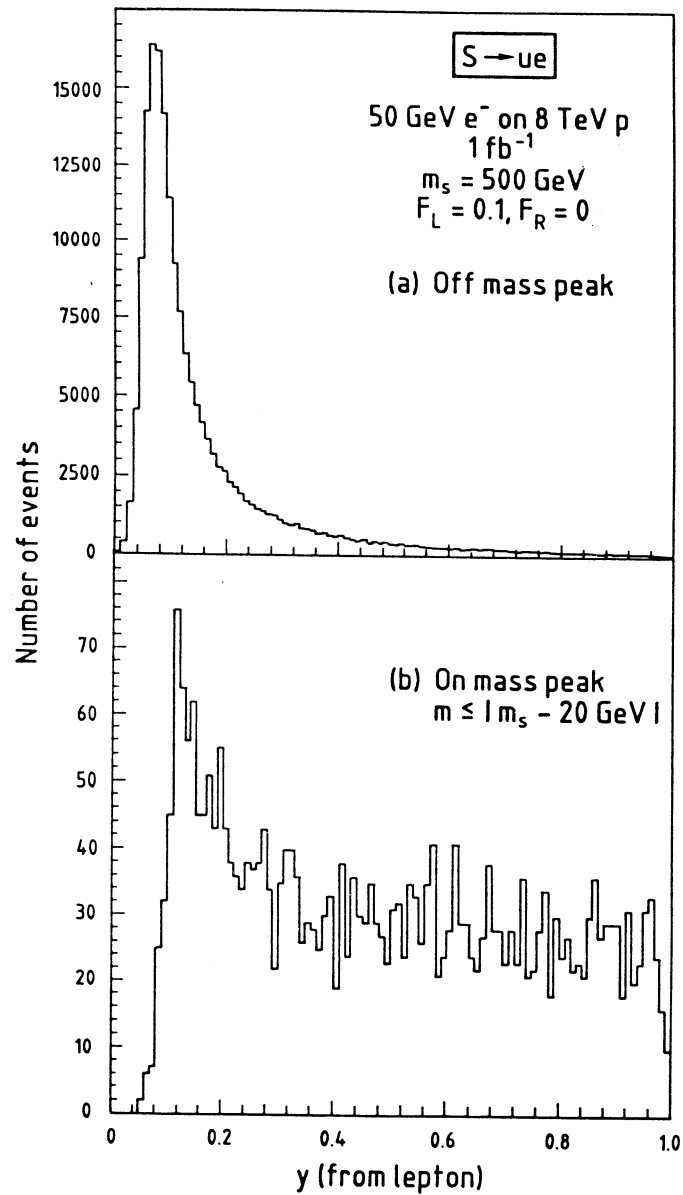


Figure 3. Comparison of y distributions with $y > 0.05$ for (a) events off the leptoquark mass peak and (b) events on the leptoquark mass peak.

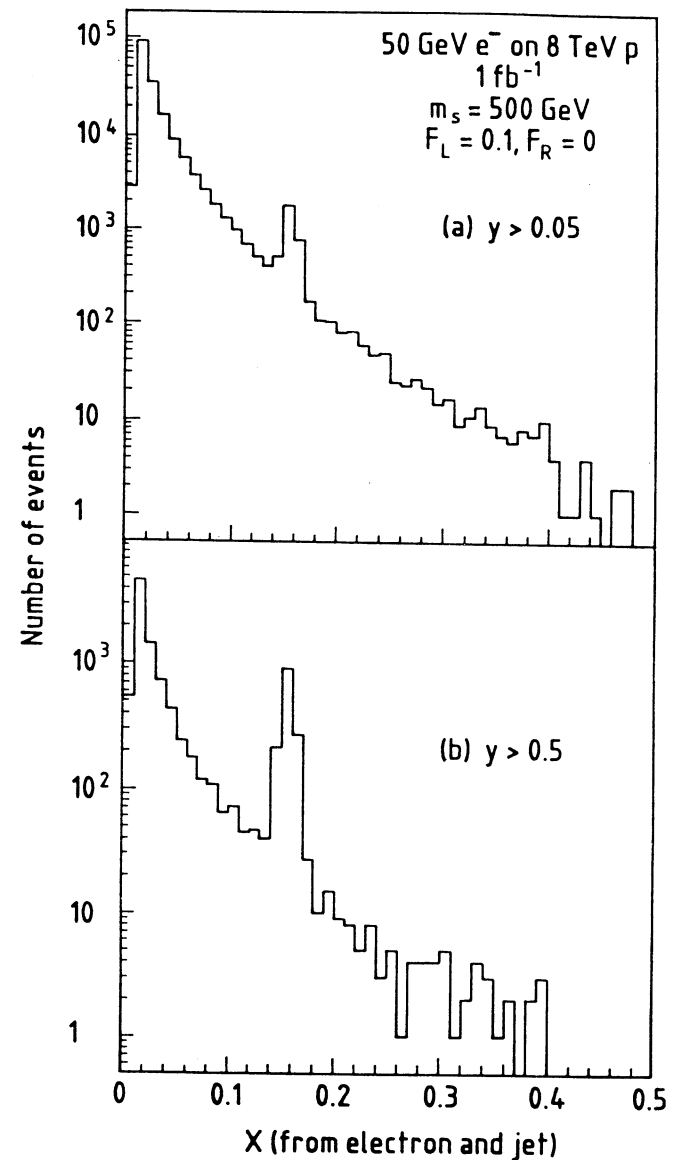


Figure 4. x distributions for the decay of a 500 GeV leptoquark $S \rightarrow eu$ with couplings $F_L = 0.1, F_R = 0$ (a) $y > 0.05$, and (b) $y > 0.5$.

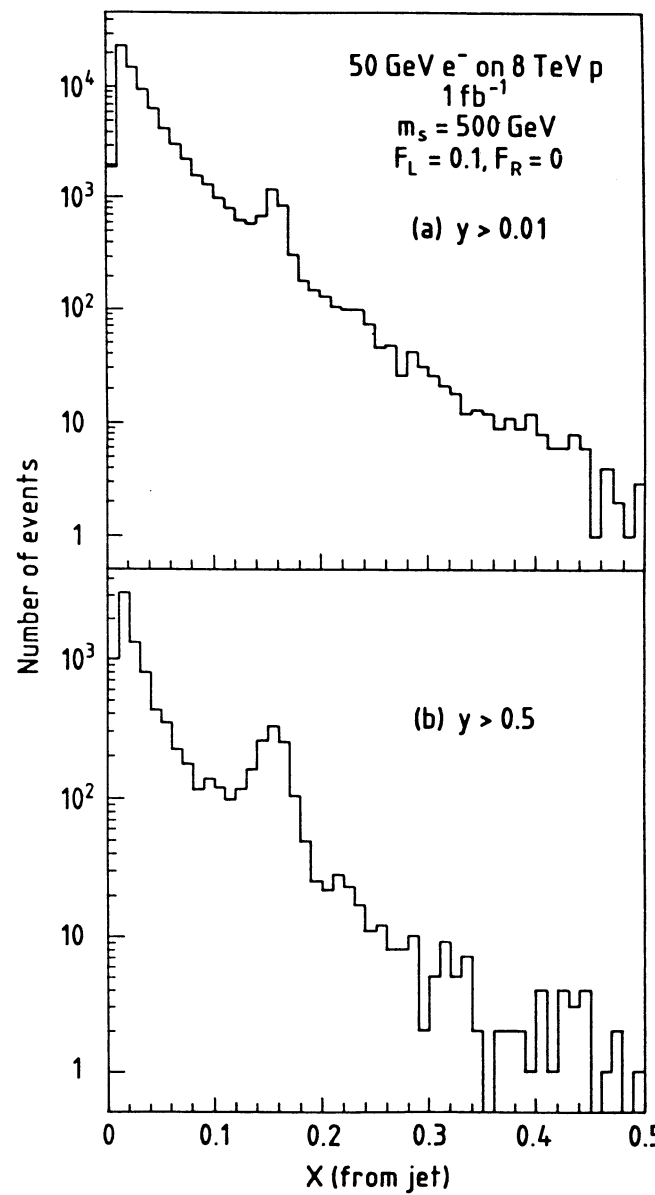


Figure 5. x distributions for the decay of a 500 GeV leptoquark $S \rightarrow \nu d$ with couplings $F_L = 0.1, F_R = 0$ (a) $y > 0.01$, and (b) $y > 0.5$.

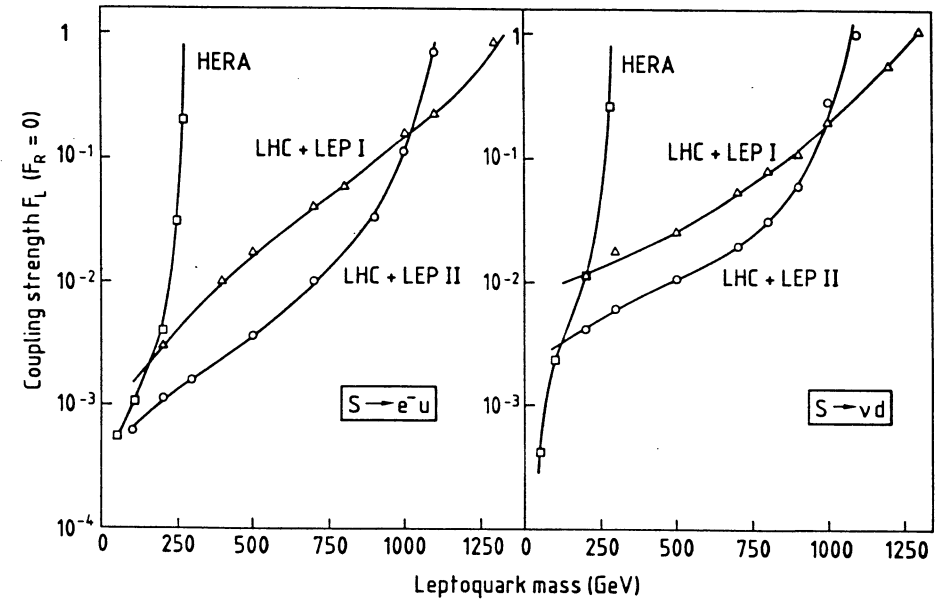


Figure 6. Leptoquark discovery limits assuming one years' running vs leptoquark mass and coupling strength (a) $S \rightarrow e^- u$ and (b) $S \rightarrow \nu d$.

Slepton–Squark Production and Decay in ep Collisions

A. Bartl¹, W. Majorotto², B. Mösslacher², N. Oshimo^{2,3} and S. Stippel¹

¹Institut für Theoretische Physik, Universität Wien, Vienna, Austria

²Institut für Hochenergiephysik, Österreichische Akademie der Wissenschaften, Vienna, Austria

1 Introduction

In ep collisions the most promising processes to search for supersymmetric particles are [1,2,3]

$$e + p \rightarrow \tilde{e}_{L,R} + \tilde{q}_{L,R} + X \quad (1)$$

$$e + p \rightarrow \tilde{\nu}_L + \tilde{q}_L + X, \quad (2)$$

where $\tilde{e}_{L,R}$, $\tilde{\nu}_L$, and $\tilde{q}_{L,R}$ are the selectron, sneutrino and squark, respectively. These processes proceed via t -channel neutralino (chargino) exchange (Feynman diagrams in Fig. 1). The produced particles $\tilde{e}_{L,R}$, $\tilde{\nu}_L$, and $\tilde{q}_{L,R}$ decay in the following way:

$$\tilde{e}_{L,R} \rightarrow e + \tilde{\chi}_i^0, \quad \tilde{e}_L \rightarrow \nu + \tilde{\chi}_k^- \quad (3)$$

$$\tilde{\nu}_L \rightarrow \nu + \tilde{\chi}_i^0, \quad e^- + \tilde{\chi}_k^+ \quad (4)$$

$$\tilde{q}_{L,R} \rightarrow q + \tilde{\chi}_i^0, \quad \tilde{q}_L \rightarrow q' + \tilde{\chi}_k^-, \quad (5)$$

where $\tilde{\chi}_i^0$, $i = 1, \dots, 4$, are the neutralinos and $\tilde{\chi}_k^\pm$, $k = 1, 2$ are the charginos. (Here we assume that the gluinos are heavier than the squarks.)

The neutralinos and charginos are the mass eigenstates of the gauge and Higgs fermion system. The lightest neutralino $\tilde{\chi}_1^0$ is usually assumed to be the lightest supersymmetric particle and gives rise to missing energy in experiment. The charginos and the neutralinos decay in various modes until $\tilde{\chi}_1^0$ is reached:

$$\tilde{\chi}_i^0 \rightarrow Z^0 + \tilde{\chi}_k^0, \quad W^\pm + \tilde{\chi}_k^\mp, \quad H_l^0 + \tilde{\chi}_k^0, \quad H^\pm + \tilde{\chi}_k^\mp \quad (6)$$

$$\tilde{\chi}_i^\pm \rightarrow Z^0 + \tilde{\chi}_k^\pm, \quad H_l^0 + \tilde{\chi}_k^\pm, \quad W^\pm + \tilde{\chi}_k^0, \quad H^\pm + \tilde{\chi}_k^0, \quad (7)$$

³present address: Centro de Física da Matéria Condensada, Av. Prof. Gama Pinto 2, P-1699 Lisbon Cedex, Portugal

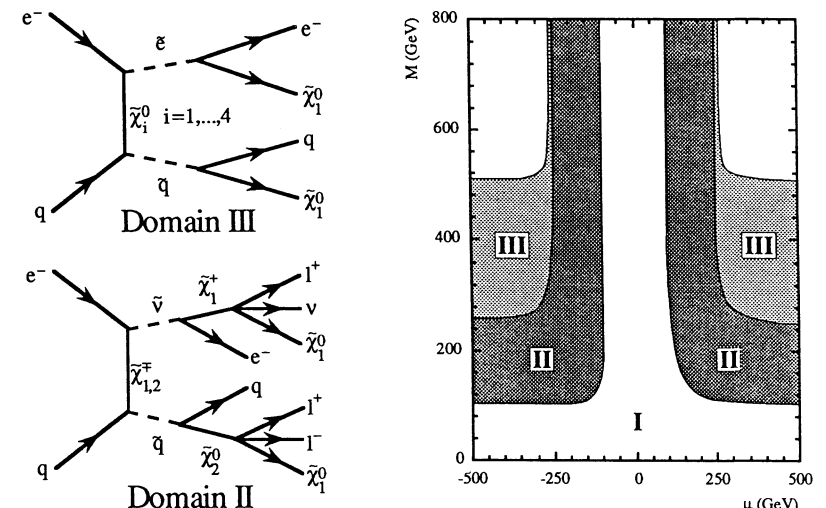


Figure 1: Domains in (M, μ) plane for typical decay patterns of a squark or slepton with a mass of 250 GeV, for $\tan \beta = 4$. Domain I: Explored by LEP 200. Domain II: Cascade decays possible. Domain III: Only decays into $\tilde{\chi}_1^0$ possible. Also shown typical Feynman diagrams for $e + q \rightarrow \tilde{e} (\tilde{\nu}) + \tilde{q}$ and subsequent decays.

where H_a^0 , $a = 1, 2, 3$, and H^\pm represent the neutral and charged Higgs bosons, respectively. If these two-body decays are kinematically forbidden, then the following three-body decays will be important:

$$\tilde{\chi}_i^\pm \rightarrow l + \bar{l} + \tilde{\chi}_k^\pm, \quad q + \bar{q} + \tilde{\chi}_k^\pm, \quad l^\pm + \overset{(-)}{\nu} + \tilde{\chi}_k^0, \quad q + \bar{q}' + \tilde{\chi}_k^0. \quad (8)$$

$$\tilde{\chi}_i^0 \rightarrow l + \bar{l} + \tilde{\chi}_k^0, \quad q + \bar{q} + \tilde{\chi}_k^0, \quad l^\mp + \overset{(+)}{\nu} + \tilde{\chi}_k^\pm, \quad q + \bar{q}' + \tilde{\chi}_k^\pm. \quad (9)$$

We shall work within the minimal supersymmetric extension of the standard model based on $N = 1$ supergravity [4,5]. The parameters describing the basic production process $e + q \rightarrow \tilde{l} + \tilde{q}$ and the slepton and squark decays, Eqs. (3 – 5), are the masses of the sleptons and squarks, $m_{\tilde{e}}$ and $m_{\tilde{q}}$, the mass parameters of the $SU(2)$ gauge and Higgs fermions, M and μ , and the ratio of the vacuum expectation values of the two Higgs doublets, $v_2/v_1 (\equiv \tan \beta)$. We shall fix the mass parameter of the $U(1)$ gauge fermion by $M'/M = (5/3)\tan^2 \theta_W$. The mass of the charged Higgs boson m_{H^\pm} is also a parameter for the decays of the neutralinos and charginos [6], Eqs. (6 – 7).

In this article we shall study slepton and squark production and decay in ep collisions at $\sqrt{s} = 1.4$ TeV, the CMS energy of LEP/LHC. At LEP/LHC the masses of the produced slepton and squark can be as large as several hundred GeV. For such a heavy sfermion

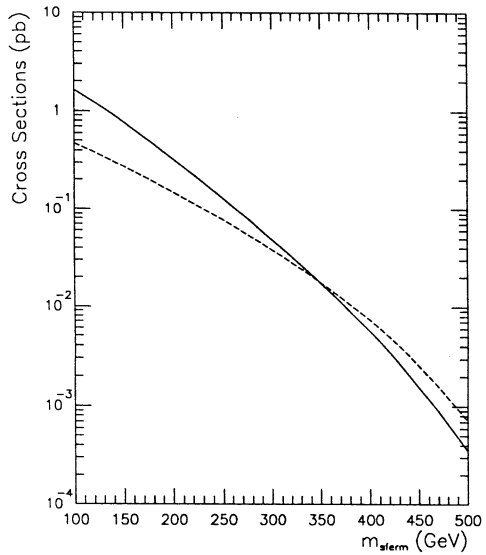


Figure 2: Cross sections for $e + p \rightarrow \sum(\tilde{l} + \tilde{q} + X)$ at $\sqrt{s} = 1.4$ TeV, where the sum goes over all slepton and squark species, as a function of $m_{\tilde{l}}$, for $m_{\tilde{\epsilon}} = m_{\tilde{\nu}} = m_{\tilde{q}} = m_{\tilde{f}}$, $\tan \beta = 4$, and $\mu = -400$ GeV. $M = 200$ GeV (—), $M = 800$ GeV (---).

the dominant decay will not necessarily be the simplest one, $\tilde{f} \rightarrow f + \tilde{\chi}_1^0$. In general, one has a more complex decay pattern due to cascade decays involving heavier neutralinos and charginos, Eqs. (3–9). A systematic analysis of the whole process of production and decay is necessary in order to work out suitable signatures. For illustration we show in Fig. 1 the domains in the (M, μ) plane (for $\tan \beta = 4$) where, for a squark or a slepton with a mass of 250 GeV, cascade decays are kinematically possible (domain II), or where only transitions into the lightest neutralino are allowed (domain III).

2 Numerical analysis and discussion

For simplicity, we assume in the following that the sleptons and squarks have the same mass, which is theoretically reasonable [5]. Due to the existing experimental bounds it is sufficient to consider the mass range $m_{\tilde{l}} = m_{\tilde{q}} > 150$ GeV. In the numerical examples we shall take $\tan \beta = 4$. We shall not consider the supersymmetry parameter region corresponding to a chargino mass lower than 100 GeV (see domain I in Fig. 1) as this will be explored by LEP.

We first discuss the production process, Eqs. (1–2). The formulae for the cross sections are given in [1] and [2]. We show in Fig. 2 the cross section of $e + p \rightarrow \sum \tilde{l} + \tilde{q} + X$, summed over all possible pairs of sleptons and squarks, as a function of the sfermion mass for

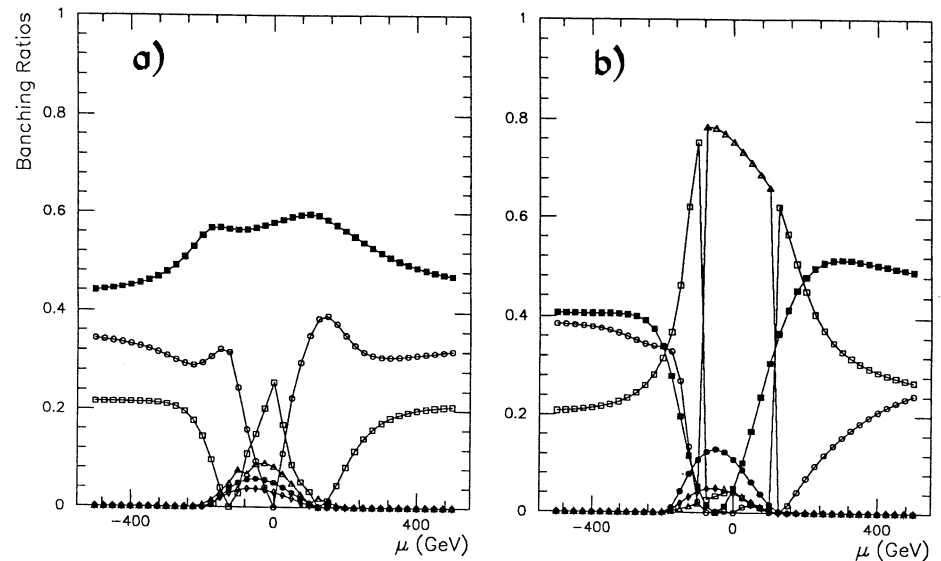


Figure 3: Branching ratios for a: $\tilde{\nu}_L \rightarrow \tilde{\chi}_1^0 + \nu$, $e + \tilde{\chi}_k^+$; b: $\tilde{e}_L \rightarrow \tilde{\chi}_1^0 + e$, $\nu + \tilde{\chi}_k^-$, for $m_{\tilde{\epsilon}} = m_{\tilde{\nu}} = 250$ GeV, $M = 200$ GeV, $\tan \beta = 4$. Decays into $\tilde{\chi}_1^\pm$ (■), $\tilde{\chi}_2^\pm$ (●), $\tilde{\chi}_1^0$ (○), $\tilde{\chi}_2^0$ (□), $\tilde{\chi}_3^0$ (△), and $\tilde{\chi}_4^0$ (◇).

$\mu = -400$ GeV, $M = 200$ GeV and $M = 800$ GeV. This cross section is larger than 0.1 pb for $m_{\tilde{f}} \leq 300$ GeV. Assuming an integrated luminosity of 500 pb $^{-1}$, this would give between 50 and 1000 events per year. The cross section shows almost no variation with μ and depends moderately on M . However, the individual production cross sections for different slepton and squark species are very different from each other. Since in general the charginos couple more strongly to the sleptons and squarks than the neutralinos, $e + p \rightarrow \tilde{\nu}_L + \tilde{d}_L + X$ has the largest cross section. Moreover, in a wide range of the parameters M , μ and $\tan \beta$ the cross section depends essentially on the sum $m_{\tilde{l}} + m_{\tilde{q}}$, and not on $m_{\tilde{l}}$ and $m_{\tilde{q}}$ separately.

In the following discussion of the decays of sleptons and squarks we shall take $m_{\tilde{\epsilon}_L} = m_{\tilde{\epsilon}_R} = m_{\tilde{\nu}_L} = m_{\tilde{\nu}_R} = m_{\tilde{q}_L} = m_{\tilde{q}_R} = 250$ GeV. The formulae for the decay widths are taken from [2]. For $M < 250$ GeV, in a wide range of μ , the masses of the second lightest neutralino $\tilde{\chi}_2^0$ and the lighter chargino $\tilde{\chi}_1^\pm$ are in this case smaller than the mass of the sfermions. Then each sfermion can decay in several modes (domain II in Fig. 1). In Fig. 3a and b the branching ratios of $\tilde{\nu}_L$ and \tilde{e}_L are shown as a function of μ . The most important decay modes of $\tilde{\nu}_L$ and \tilde{e}_L are those into the lighter chargino (except $|\mu| \leq 100$ GeV for \tilde{e}_L). In Fig. 3a and b the branching ratios become practically independent of μ for $|\mu| \geq 500$ GeV. Also \tilde{u}_L and \tilde{d}_L most dominantly decay into lighter charginos [7,8]. It should be noted that for all left scalar particles the direct decay into the lightest neutralino, $\tilde{f}_L \rightarrow f + \tilde{\chi}_1^0$, is

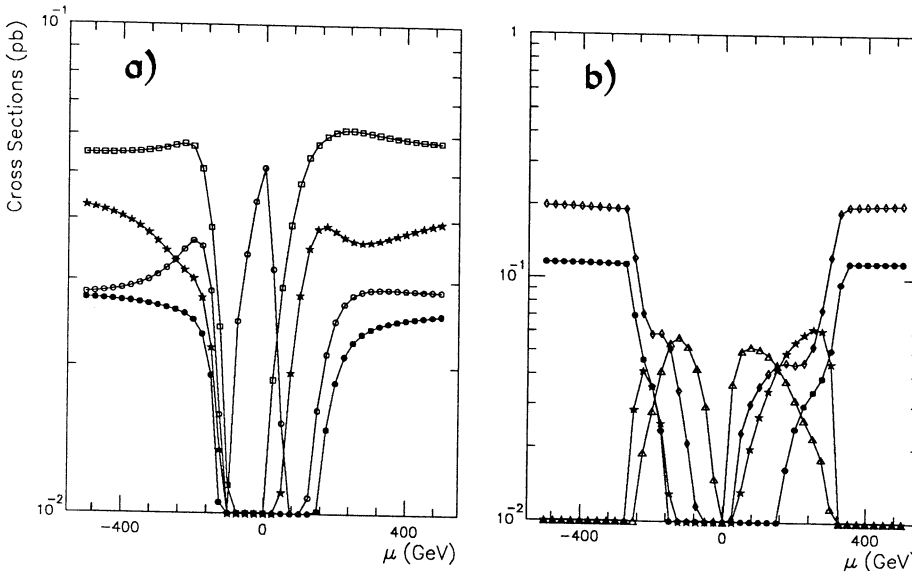


Figure 4: Cross sections (at $\sqrt{s} = 1.4$ TeV) for various final states for $m_{\tilde{f}} = m_{\tilde{q}} = 250$ GeV and $\tan \beta = 4$ **a:** $M = 200$ GeV; **b:** $M = 300$ GeV. The curves correspond to the following processes: $ep \rightarrow eu\tilde{\chi}_1^0\tilde{\chi}_1^-X + ed\tilde{\chi}_1^0\tilde{\chi}_1^-X$ (\bullet), $ep \rightarrow \nu u\tilde{\chi}_1^0\tilde{\chi}_1^-X$ (*), $ep \rightarrow ed\tilde{\chi}_1^+\tilde{\chi}_1^0X$ (\circ), $ep \rightarrow eu\tilde{\chi}_1^+\tilde{\chi}_1^-X$ (\square), $ep \rightarrow \nu d\tilde{\chi}_1^0\tilde{\chi}_1^-X$ (\diamond), and $ep \rightarrow ed\tilde{\chi}_1^+\tilde{\chi}_1^0X$ (Δ).

not the dominant one. For $\tilde{\nu}_L \rightarrow \nu + \tilde{\chi}_1^0$ and $\tilde{e}_L \rightarrow e + \tilde{\chi}_1^0$ the branching ratio is between 20 and 40 percent. For \tilde{u}_L and \tilde{d}_L the branching ratio into $\tilde{\chi}_1^0$ is less than 10 percent, and in the region $|\mu| \geq 100$ GeV it is even much smaller than that into $\tilde{\chi}_2^0$. Among the decays of the right scalar fermions \tilde{e}_R , \tilde{u}_R , and \tilde{d}_R , the decay into $\tilde{\chi}_1^0$ has the largest branching ratio, $B(\tilde{f}_R \rightarrow f + \tilde{\chi}_1^0) \sim 1$, except for $|\mu| \leq 100$ GeV. For $M > 250$ GeV, only the lightest neutralino has a mass smaller than 250 GeV in a wide range of μ (domain III of Fig. 1), yielding $B(\tilde{f}_{L,R} \rightarrow f + \tilde{\chi}_1^0) = 1$.

For discussing the signatures it is necessary to perform a combined analysis of the individual production processes together with the various decay modes of the produced particles. In Fig. 4a and b we show the sum of the cross sections for $ep \rightarrow \sum \tilde{e}_a \tilde{u}_b X \rightarrow eu\tilde{\chi}_1^0\tilde{\chi}_1^-$ and $ep \rightarrow \sum \tilde{e}_a \tilde{d}_b X \rightarrow ed\tilde{\chi}_1^0\tilde{\chi}_1^-$, where both the slepton and the squark directly go into the lightest supersymmetric particle $\tilde{\chi}_1^0$. This would give rise to large missing energy in the final state, the "classical" signature for supersymmetry. For $M = 200$ GeV and $|\mu| \geq 200$ GeV (Fig. 4a), this cross section is $0.02 - 0.03$ pb, mainly due to the reactions $ep \rightarrow \tilde{e}_R \tilde{q}_R X$ and $\tilde{f}_R \rightarrow f \tilde{\chi}_1^0$. It is smaller than the total cross section $\sigma(ep \rightarrow \sum \tilde{e}\tilde{q}X)$ by one order of magnitude. As also shown in Fig. 4a the largest cross section in this parameter region is obtained for the process $ep \rightarrow \tilde{\nu}_L \tilde{d}_L X \rightarrow eu\tilde{\chi}_1^+\tilde{\chi}_1^-X$. Also $\sigma(ep \rightarrow \tilde{\nu}_L \tilde{d}_L X \rightarrow ed\tilde{\chi}_1^+\tilde{\chi}_1^0X)$ is equal to or even larger than $\sigma(ep \rightarrow eu\tilde{\chi}_1^0\tilde{\chi}_1^-X + ed\tilde{\chi}_1^0\tilde{\chi}_1^-X)$. Since both $\tilde{\chi}_1^\pm$

	Cross Section
$e + p \rightarrow Z + X + p_{\text{miss}}$	$4.8 \cdot 10^{-2}$ pb
$e + p \rightarrow W + X + p_{\text{miss}}$	$2.2 \cdot 10^{-1}$ pb
$e + p \rightarrow H_2^0 + X + p_{\text{miss}}$	$9.3 \cdot 10^{-1}$ pb
$e + p \rightarrow (e)_{\text{l.s.}} + X + p_{\text{miss}}$	$6.1 \cdot 10^{-2}$ pb
$e + p \rightarrow (e + \text{jets})_{\text{l.s.}} + X + p_{\text{miss}}$	$7.4 \cdot 10^{-2}$ pb
$e + p \rightarrow l^+l^- + X + p_{\text{miss}}$	$3.9 \cdot 10^{-2}$ pb

Table 1: Cross sections for various final states coming from $e + p \rightarrow \tilde{e} + \tilde{q} + X$ and $e + p \rightarrow \tilde{\nu} + \tilde{q} + X$ at $\sqrt{s} = 1.4$ TeV for $M = 200$ GeV, $\mu = -500$ GeV, $\tan \beta = 4$. The subscript "l.s." means "lepton side".

and $\tilde{\chi}_2^0$ dominantly decay into two quarks and $\tilde{\chi}_1^0$, events with an electron and jets in the lepton hemisphere and jets in the hadron hemisphere provide another important signature for supersymmetry. As an example we give in Table 1 the cross sections for several final states for $M = 200$ GeV and $\mu = -500$ GeV. (For the mass of the charged Higgs boson we have taken $m_{H^\pm} = 500$ GeV, leading to $m_{H_2^0} = 80$ GeV for $\tan \beta = 4$.) Due to the large mass differences between $\tilde{\chi}_1^0$ and $\tilde{\chi}_2^0$ or $\tilde{\chi}_1^\pm$, the Z -boson, W^\pm -boson, and neutral Higgs boson H_2^0 are produced in the $\tilde{\chi}_2^0$ and $\tilde{\chi}_1^\pm$ decays.

In Fig. 4b we show the situation for $M = 300$ GeV. For $|\mu| \geq 300$ GeV only decays into the lightest supersymmetric particle $\tilde{\chi}_1^0$ are kinematically allowed. The cross section of $ep \rightarrow eu\tilde{\chi}_1^0\tilde{\chi}_1^-X + ed\tilde{\chi}_1^0\tilde{\chi}_1^-X$ is ~ 0.1 pb, being higher than in the previous case for $M = 200$ GeV. For $|\mu| < 250$ GeV, also here cascade decays are possible.

3 Conclusions

We have studied the production of sleptons and squarks and their decays in ep collisions at LEP/LHC. If the sum of the masses of slepton and squark is smaller than 600 GeV, the production cross section (summed over all possible pairs) becomes larger than ~ 0.1 pb.

The signature of slepton and squark production decisively depends on the supersymmetry parameters. In a certain region, mainly $|\mu| > m_{\tilde{f}}$, $M > m_{\tilde{f}}$, $M' < m_{\tilde{f}}$, indicated as domain III in Fig. 1, the slepton (squark) can only decay into the lightest neutralino plus a lepton (quark). The signature in this case is an isolated electron (on the lepton side) and jets (on the hadron side) with large missing momentum in the final state.

If either M or $|\mu|$ is smaller than $m_{\tilde{f}}$ (domain II in Fig. 1), then many configurations are possible for the final state and some of them have cross sections larger than 10^{-1} pb. The final state containing an electron coming from the decay $\tilde{\nu}_L \rightarrow e + \tilde{\chi}_1^\pm$ has a cross section up to $\sim 10^{-1}$ pb. This electron is accompanied by jets or another charged lepton.

In order to decide which is the best signature for slepton and squarks it will, however, be necessary to perform detailed Monte Carlo studies taking into account the background [9].

Acknowledgements

We gratefully acknowledge useful discussions and correspondence with M. Besançon and R. Rückl. S. St. thanks for financial support by the Austrian Ministry of Science and Research.

References

- [1] S.K. Jones and C.H. Llewellyn Smith, Nucl. Phys. B217 (1983) 145; P.R. Harrison, Nucl. Phys. B249 (1985) 704; J.A. Bagger and M.E. Peskin, Phys. Rev. D31 (1985) 2211; H. Komatsu and R. Rückl, Proceedings of the Workshop on Physics at Future Accelerators, La Thuile and Geneva, 1987, CERN 87-07, Vol. II, p. 132; Nucl. Phys. B299 (1988) 407; J. Bartels and W. Hollik, Z. Phys. C39 (1988) 433
- [2] A. Bartl, H. Fraas and W. Majerotto, Nucl. Phys. B297 (1988) 479; Z. Phys. C41 (1988) 475
- [3] R. Rückl, these Proceedings
- [4] H.E. Haber and G.L. Kane, Phys. Rep. 117 (1985) 75
- [5] H.P. Nilles, Phys. Rep. 110 (1984) 1
- [6] J.F. Gunion and H.E. Haber, Nucl. Phys. B272 (1986) 1
- [7] Contribution of the SUSY- pp -Working Group, these Proceedings
- [8] A. Bartl, W. Majerotto, B. Mösslacher, N. Oshimo and S. Stippel, HEPHY-PUB-538/90, UWThPh-1990-47
- [9] M. Besançon, these Proceedings

PROSPECTS OF SUPERSYMMETRY SEARCHES AT LEP/LHC

Marc Besançon

Weizmann Institute, Rehovot, Israel
and Dphpe, Saclay, France

Abstract

We present a Monte-Carlo study of the signal coming from sleptons and squarks produced via supersymmetric lepto production in the ep collisions of the LHC. We show how the supersymmetric signal can be extracted from the background due to standard processes and particularly the important background due to the heavy top quarks produced via weak boson and gluon fusion and the background due to the production of single W bosons.

1 Introduction and model

The LHC has the unique feature of being able to run not only in the pp or in the ion-ion collider mode but, also in the ep collider mode with 50 GeV electrons and 8 TeV protons at a luminosity of $10^{32} \text{ cm}^{-2} \text{ s}^{-1}$ i.e. 1000 pb^{-1} for a one year running. The standard and exotic physics potentials of this LEP/LHC collider are large [1] and in the following we discuss the possibilities of searching for supersymmetry assuming these machine parameters.

Selectron-squark and sneutrino-squark productions, $eq \rightarrow \tilde{e}\tilde{q}, \tilde{\nu}\tilde{q}$ are the most probable supersymmetric processes that can occur in the ep collisions of LEP/LHC. The Feynmann diagrams and the formulae for the cross sections are known from the literature, see references in [2].

The study of the signals coming from the sleptons \tilde{l} and squarks \tilde{q} and the study of the background reduction are performed with the help of Monte Carlo simulations. We present the analysis according to the three following steps.

In a *first step* we have chosen to look at supersymmetric lepto production for one example of the equal masses case $m_{\tilde{l}} = m_{\tilde{q}}$ in two different points of the parameter space M, μ (which are respectively the mass parameter of the SU(2) gauginos and the mass parameter of the higgsino, both taken from minimal low energy supergravity theories MLES) consistent with the present LEP excluded region [3], see table 1.

The choice of these two points is motivated by the fact that they are leading to two different phenomenologies, i.e. gauginos masses, cross sections (resp. tables 1,2) and, above all, decays of scalars and fermions [2] which determine the signature of the supersymmetric events.

As far as the decays are concerned, for the point 1 of the mass parameter space, the scalars have the simplest decay into their fermionic partners and the lightest supersymmetric particle LSP whereas for the point 2 cascade decays can occur [2]. In this example, the choice of the masses of $\tilde{e}, \tilde{\nu}, \tilde{u}$ and \tilde{d} is 250 GeV which is typical for the LEP/LHC accessible range.

The study of this example will allow us to find a simple set of cuts that reduces the background at a reasonable level. Moreover, the study of the cascade decays for one example of $m_{\tilde{l}}$ and $m_{\tilde{q}}$ is instructive enough to show that these decays are actually complicating the signatures and the detection of the supersymmetric processes.

In a *second step*, in order to find the detection limits, we extend the study to a wider range of selectrons and squarks masses in the equal masses case $m_{\tilde{e}} = m_{\tilde{q}}$, but assuming only the simplest decay: $\tilde{e}, \tilde{q} \rightarrow e, q \tilde{\chi}_1^0$ with a 100 % branching ratio and $\tilde{\chi}_1^0$ being the lightest neutralino considered as the LSP.

The study of the detection limits of the supersymmetric signal for a wide range of $m_{\tilde{l}}$ and $m_{\tilde{q}}$ in the case of cascade decays is more complicated because the channels and the branching ratios are changing with $m_{\tilde{l}}$ and $m_{\tilde{q}}$ and with the different parameters of the previous parameter space, see [2]. Implementing and working out the present example for the cascade decays at $m_{\tilde{l}} = m_{\tilde{q}} = 250 \text{ GeV}$ taught us that this study can be a tedious and very long one. Nevertheless, such a study remains to be done.

In a *third step*, we examine the case of unequal masses $m_{\tilde{l}} < m_{\tilde{q}}$. The study of the detection limits for $m_{\tilde{e}}$ and $m_{\tilde{q}}$ in this case is done assuming once again only the simplest decay. The same previous arguments can be here repeated for the study of the unequal masses case with cascade decays. One additional feature of the unequal masses case is that a slepton can also be produced in the cascade decay of a squark and this slepton can have in turn its own cascade decay.

The supersymmetric events generator used is described in [4]. It has been upgraded in order to include all the previous masses and cross sections as well as the full description of the decays especially the cascade decays. The events generators for the background study is described in [5].

Finally a detector is crudely simulated by:

- beam pipe 100 mrad
- Hadron energies are fluctuating with a dispersion $\frac{0.5}{\sqrt{E}} + 0.02$
- Electron energies are fluctuating with a dispersion $\frac{0.1}{\sqrt{E}} + 0.01$

2 The equal mass case at 250 GeV

2.1 Point 1 of the parameter space: simple decays

In the point 1 of the parameter space previously defined, the \tilde{l} and \tilde{q} have the following 100 % branching ratio simple decay:

$$\tilde{e}, \tilde{\nu}, \tilde{q} \rightarrow e, \nu, q \tilde{\chi}_1^0$$

for the scalar partners of both left and right handed fermions.

In consequence, for the charged current supersymmetric process $\tilde{C}\tilde{C}$ where $\tilde{\nu}, \tilde{q}$ are produced (see the cross section in table 2), the signature of the event is jets and large missing energy due to the two undetected LSPs and the neutrino.

The main background is due to the charged current deep inelastic scattering (CC DIS) process which has the same signature.

By looking at the distribution of the missing transverse momentum P_t^{miss} w.r.t the beam axis for both kinds of events showed in fig. 1, we conclude that CC and $\tilde{C}\tilde{C}$ processes cannot be distinguished. With the simplest decay yielding no isolated charged lepton in the signature, the detection of $\tilde{C}\tilde{C}$ is hopeless.

In the supersymmetric neutral current case $\tilde{N}\tilde{C}$, where \tilde{e}, \tilde{q} are produced (see the cross sections in table 2), the signature is one electron, jets and a large amount large missing energy due to the two undetected LSPs.

One of the most serious background is likely to be the production of a single heavy top quark t with the decays $t \rightarrow W b$, where the W is real, and $W \rightarrow e \nu$ giving rise to the same signature. Single tops are produced via the fusion of a W and a gluon going into t and b quarks. The cross sections have been computed for various top masses by J.v.d Bij and G. Schuler from the heavy flavour working groups [6] and we concentrated here on three top masses namely 100,150 and 200 GeV.

Fig. 2a to Fig. 5a show respectively the pseudorapidity η of the electron, the accompanying energy E_{acc} as defined in [7] (i.e. the total transverse energy within a cone around the electron momentum defined in the azimuthal angle and η space), the transverse momentum of the electron w.r.t the beam axis P_t^e and P_t^{miss} of the $\tilde{N}\tilde{C}$ events whereas Fig. 2b to Fig. 5b show respectively the same quantities for the previous tb background events for a top mass of 150 GeV.

The two electrons coming from the $\tilde{N}\tilde{C}$ signal and from the tb background are equally well isolated i.e. more than 80 % of the events have $E_{acc} < 1 \text{ GeV}$, and they have comparable pseudorapidities.

With $E_{acc} < 1 \text{ GeV}$ (electron isolation), $P_t^{miss} > 50 \text{ GeV}$ and $P_t^e > 80 \text{ GeV}$ we obtain 60 events for $\tilde{N}\tilde{C}$ with the cross section of table 2 and of the order 10 tb of background events for the 3 previous top masses considered.

The most efficient cut is $P_t^e > 80 \text{ GeV}$ which helps to reduce the tb background at an acceptable level. Going to a lower P_t^e cut, affects drastically the signal to background ratio.

The same previous set of cuts reduces completely the other possible sources of background, such as NC DIS, CC DIS with an electron coming from a secondary decay and c and b production with one electron in the signature.

The background coming from the single W production $ep \rightarrow eWX$, with one electron in the signature of the event, is a possible source of background. From [8], the number of single W events, with one electron in the signature, passing the previous cuts on P_t^e and on P_t^{miss} is expected to be small i.e. of the order of 3 events. The case of the single W production $ep \rightarrow \nu WX$ followed by the decay $W \rightarrow e\nu$ is also a source of background. From [9], after applying the previous set of cuts, the number of background events is found to be of the order of 25. Nevertheless, more detailed simulations are needed for the study of this source of background.

2.2 Point 2 of the parameter space: cascade decays

In the point 2 of the parameter space, cascade decays occur. \tilde{l} and \tilde{q} have decays into l and q respectively plus heavy neutralinos or charginos. These neutralinos and charginos have in turn their own decays into quarks or leptons and lighter neutralinos or charginos. These cascade decays continue until the LSP is produced. The signature for this type of events will be multi-(charged)leptons, jets, and missing energy.

In our particular example, 6 different decay channels are possible for each $\tilde{e}_L, \tilde{\nu}_L, \tilde{u}_L$ and \tilde{d}_L . The dominant ones are [2]:

$$\tilde{e}_L \rightarrow e \tilde{\chi}_1^0 \quad 0.5168, \quad \tilde{u}_L \rightarrow d \tilde{\chi}_1^+ \quad 0.5793$$

$$\tilde{\nu}_L \rightarrow e \tilde{\chi}_1^- \quad 0.4713, \quad \tilde{d}_L \rightarrow u \tilde{\chi}_2^\pm \quad 0.3306$$

Where the numbers correspond to the branching ratios. The partners of the right handed fermions have the simplest decay with 100 % branching ratio. Then, afterwards, the decays of the charginos and the heavy neutralinos occur (in our example, 10 channels for $\tilde{\chi}_1^\pm$, 8 for $\tilde{\chi}_2^\pm$, 10 for $\tilde{\chi}_2^0$, 24 for $\tilde{\chi}_3^0$, and 23 for $\tilde{\chi}_4^0$). The dominant ones for $\tilde{\chi}_1^\pm$ are [2]:

$$\tilde{\chi}_1^\pm \rightarrow \nu e \tilde{\chi}_1^0 \text{ 0.0966}$$

$$\tilde{\chi}_1^\pm \rightarrow q q' \tilde{\chi}_1^0 \text{ 0.7062}$$

where $q, q' = u, d$ and c, s . The numbers correspond to the branching ratios. For our particular example, the following observations can be made:

- \tilde{e} still decays dominantly into e and the LSP.
- $\tilde{\nu}$ dominantly decays into e and chargino $\tilde{\chi}_1^\pm$. This is very different from the situation in point 1 in which $\tilde{\nu}$ decays into ν and the LSP, both being undetected. Now, the presence of a charged lepton in the decay of $\tilde{\nu}$ allow us to detect the $\tilde{C}\tilde{C}$ processes. $\tilde{C}\tilde{C}$ can also be detected through cascade decays on the \tilde{q} side.
- \tilde{q} has also dominant decays into $q \tilde{\chi}^\pm$.
- $\tilde{\chi}_1^\pm$ decays dominantly into quarks and LSP. The branching ratio of its decay into charged leptons e, μ and LSP is of the order of 19 %.
- $\tilde{\chi}_2^\pm$ has three comparable dominant decays into higgs H_2^0 or W and neutralinos.
- $\tilde{\chi}_2^0$ decays dominantly into q or ν pairs and the LSP.
- $\tilde{\chi}_3^0$ and $\tilde{\chi}_4^0$ decay dominantly into the H_2^0 higgs and $\tilde{\chi}^0$.

It follows that, in our example, when all the channels of the cascade decays are taken into consideration, the dominant signature for both $\tilde{N}\tilde{C}$ and $\tilde{C}\tilde{C}$ processes is again one electron, jets and missing energy. Due to the cascade decay, $\tilde{C}\tilde{C}$ processes can now be detected but, in this example, they do not distinguish from $\tilde{N}\tilde{C}$.

The most serious background of such events is the same as the previous one i.e. tb events with one electron coming from the top side and the single W production $ep \rightarrow \nu W X$ followed by the decay $W \rightarrow e\nu$.

And for example, Figs. 6a-6d show the distributions of P_t^e , η , E_{acc} of the electron and the P_t^{mis} distribution of the $\tilde{N}\tilde{C}$ process with the dominant decay for \tilde{e} , with $\tilde{q} \rightarrow q \tilde{\chi}_1^\pm$, and with the dominant decay for the $\tilde{\chi}_1^\pm$ giving rise to a signature with one electron.

Figs. 7a-7d show the distribution of the same quantities for $\tilde{C}\tilde{C}$ process with the dominant decay for $\tilde{\nu}$ and the same decays for \tilde{q} and $\tilde{\chi}_1^\pm$ as above giving also rise to a signature with one electron.

Due to slightly lower P_t^e and P_t^{mis} , this $\tilde{C}\tilde{C}$ process is more affected by the previous set of cuts than the $\tilde{N}\tilde{C}$ process. Consequently, the sample of supersymmetric events is simply enhanced by the contribution of the $\tilde{C}\tilde{C}$ process.

Taking both $\tilde{N}\tilde{C}$ and $\tilde{C}\tilde{C}$ processes with the cross sections of table 2, taking also into consideration all the channels of the cascade decays and considering the previous signature with one electron, we obtain of the order of 45 events with the same previous set of cuts (the background remains off course unchanged).

Cascade decays of supersymmetric particles are also responsible for signatures with multi (charged)leptons (plus jets and missing energy). In our present example, the signature with multi-leptons is not the dominant one. Nevertheless $\tilde{N}\tilde{C}$ and $\tilde{C}\tilde{C}$ events with,

for example, the signature in 2e, jets and missing energy or with the signature in e, μ , jets and missing energy (in which the charged leptons may come not only from sleptons but also from charginos or neutralinos of the cascade decay) may have less background. The most serious background is likely to be again tb events in which 2e or e, μ are coming from the t and b.

With $E_{acc} < 1 \text{ GeV}$ and $P_t^l > 5 \text{ GeV}$ for charged leptons and requiring $P_t^l > 45 \text{ GeV}$ for the hardest charged lepton, and with $P_t^{mis} > 50 \text{ GeV}$, we obtain less than 1 event of tb background for a top mass of 150 GeV for each of the two signatures.

Taking our example of cascade decays, without making any distinctions between $\tilde{N}\tilde{C}$ and $\tilde{C}\tilde{C}$ (with the cross section of table 2), considering events with the signature in 2e or in e, μ , we obtain of the order of 10 events.

3 Detection limits in the equal mass case

The total cross section for $m_{\tilde{e}} = m_{\tilde{q}} = 325 \text{ GeV}$ is of the order of $2.5 - 3.0 \cdot 10^{-2} \text{ pb}$, see [2].

We assume the simplest decays for \tilde{e}, \tilde{q} into e, q and the LSP $\tilde{\chi}_1^0$ giving the signature e, jets and missing energy.

Fig. 8a. shows the percentage of events that pass the set of cuts defined in 2.1 for two different masses of $\tilde{\chi}_1^0$. For $m_{\tilde{e}} + m_{\tilde{q}} > 600 \text{ GeV}$ this percentage reaches a plateau at a value of the order of 70 - 75 % with few differences between the two LSP masses considered. The attainable mass is limited by the cross sections around 325 GeV. Above this limit, the ratio $signal/\sqrt{background}$ begins to be smaller than 3.

4 Detection limits in the unequal mass case

\tilde{q} may have a higher mass than the \tilde{e} . We take the cross sections from [2] and we assume again the simplest decays for \tilde{e}, \tilde{q} into e, q and the LSP.

Taking the set of cuts of 2.1, fig. 8b shows the contours in the $m_{\tilde{e}}, m_{\tilde{q}}$ plane inside which we obtain more than 20 events (i.e. $signal/\sqrt{background}$ greater than 3) for two different masses for the LSP.

The attainable masses in the domain $m_{\tilde{e}}, m_{\tilde{q}}$ above 250 GeV is limited by the cross sections.

Although the cross sections are higher for smaller $m_{\tilde{e}}$ and $m_{\tilde{q}}$ (respectively of the order of 150 GeV and 200 to 300 GeV), the cut on P_t^e affects the accessible \tilde{e} mass region below 200 GeV, in the case of a LSP mass of 100 GeV.

5 Conclusion

The detection of the supersymmetric signal that comes from the production of \tilde{l} and \tilde{q} at the LEP/LHC looks promising.

In one example at $m_{\tilde{e}} = m_{\tilde{q}} = 250 \text{ GeV}$ of the equal masses case, assuming the simplest decay, we obtain of the order of 60 events for the signal and 10 events for the tb events, with top masses between 100 and 200 GeV, and 25 events for the $ep \rightarrow \nu W X$ events. Assuming the cascade decays in this particular example, we obtain of the order of 45 events for the dominant signature with one electron.

Nevertheless, detailed simulations are needed for the study of the background coming from the single W production $ep \rightarrow \nu W X$ followed by the decay $W \rightarrow e\nu$.

Cascade decays allow signatures with more than one charged leptons. In our example, although the signature with, for example, 2 electrons is not the dominant one, we expect very little background from tb events i.e. less than 1 event for $m_t = 150 \text{ GeV}$.

As far as the detection limits are concerned, the equal masses case assuming the simplest decay would allow to set a limit of the order of 650 GeV for the sum of the masses. This limit is 550 - 600 GeV in the case of unequal \tilde{e} and \tilde{q} masses, assuming the simplest decay into a light LSP.

Acknowledgements

Its a pleasure to thank A.Bartl, W.Majerotto, N.Oshimo and B.Mösslacher for a fruitful collaboration and active help in providing me all the necessary ingredients for this Monte Carlo study. I wish also to thank J.v.d. Bij for having provided me with the cross-section of single top production and G.Schuler for the relevant top events generator. I am also grateful to U.Baur who has accepted to run his Monte Carlo program for the single W events, with my set of cuts, in order to have a quick estimation of the reduction of this background, and to J.Vermaseren in providing me with the number of the $ep \rightarrow \nu WX$ events passing my acceptance conditions.

References

- [1] R.Rückl and also J. Feltesse these proceedings.
- [2] A.Bartl, W.Majerotto, B.Mösslacher N.Oshimo and S.Stippel, these proceedings.
The numerical values for the masses of the charginos and neutralinos, cross sections and branching ratios for the two points of the parameter space considered have been provided by this group.
- [3] D.Decamp et al., (ALEPH Coll.),CERN-EP/90-63 submitted to Phys.lett.B.
- [4] G.D'agostini et al., Internal Report 854 (1985), Univ. di Roma "La Sapienza".
- [5] G.Ingelman and G.Schuler 1990 AROMA 1.2 DESY, in preparation.
- [6] J.v.d.Bij, G.Schuler, J.F.d Troconiz these proceedings.
- [7] A.Ali et al, Heavy quarks physics at HERA, DESY preprint 88-119.
- [8] U.Baur, private communication.
- [9] J.Vermaseren, private communicaton. See also these proceedings.

Table 1
The gaugino masses

$v_2/v_1 = 2$	Point 1	Point 2
M	250 GeV	200 GeV
μ	-600 GeV	-150 GeV
$m_{\tilde{\chi}_1^\pm}$	255.0 GeV	155.3 GeV
$m_{\tilde{\chi}_2^\pm}$	608.7 GeV	226.8 GeV
$m_{\tilde{\chi}_1^0}$	124.2 GeV	100.6 GeV
$m_{\tilde{\chi}_2^0}$	255.0 GeV	143.9 GeV
$m_{\tilde{\chi}_3^0}$	602.3 GeV	172.3 GeV
$m_{\tilde{\chi}_4^0}$	609.2 GeV	225.7 GeV

Table 2
The cross sections

Point 1	Point 2
$\sigma(ep \rightarrow \tilde{\nu}_L \tilde{q}_L) = 2.111 \cdot 10^{-1} pb$	$\sigma(ep \rightarrow \tilde{\nu}_L \tilde{q}_L) = 1.660 \cdot 10^{-1} pb$
$\sigma(ep \rightarrow \tilde{e}_L \tilde{q}_L) = 8.811 \cdot 10^{-2} pb$	$\sigma(ep \rightarrow \tilde{e}_L \tilde{q}_L) = 7.716 \cdot 10^{-2} pb$
$\sigma(ep \rightarrow \tilde{e}_R \tilde{q}_R) = 3.377 \cdot 10^{-2} pb$	$\sigma(ep \rightarrow \tilde{e}_R \tilde{q}_R) = 2.200 \cdot 10^{-2} pb$
$\sigma(ep \rightarrow \tilde{e}_R \tilde{q}_L) = 9.493 \cdot 10^{-3} pb$	$\sigma(ep \rightarrow \tilde{e}_R \tilde{q}_L) = 1.000 \cdot 10^{-2} pb$
$\sigma(ep \rightarrow \tilde{e}_L \tilde{q}_R) = 3.224 \cdot 10^{-3} pb$	$\sigma(ep \rightarrow \tilde{e}_L \tilde{q}_R) = 3.400 \cdot 10^{-3} pb$

Figure captions

Fig. 1a: P_t^{mis} in GeV for $\tilde{C}\tilde{C}$ events for the point 1 of the parameter space.

Fig. 1b: P_t^{mis} in GeV for CC DIS events.

Fig. 2a: Pseudorapidity of the electron from the \tilde{e} decay for $\tilde{N}C$ events for the point 1 of the parameter space.

Fig. 2b: Pseudorapidity of electron from the real W of the top decay for a top mass of 150 GeV.

Fig. 3a: E_{acc} in GeV of the electron from the \tilde{e} decay for $\tilde{N}C$ events for the point 1.

Fig. 3b: E_{acc} in GeV of the electron from the real W of the top decay for a top mass of 150 GeV.

Fig. 4a: P_t^{mis} in GeV for $\tilde{N}C$ events for the point 1.

Fig. 4b: P_t^{mis} in GeV of top events for a top mass of 150 GeV.

Fig. 5a: P_t^e in GeV of the electron from the decay \tilde{e} for the point 1.

Fig. 5b: P_t^e in GeV from the real W of the top decay for a top mass of 150 GeV.

Fig. 6a: P_t^e in GeV of the electron from the \tilde{e} decay for the point 2.

Fig. 6b: Pseudorapidity of the electron from the \tilde{e} decay for the point 2 of the parameter space and one channel of the cascade decay.

Fig. 6c: E_{acc} in GeV of the electron from the \tilde{e} decay for the point 2.

Fig. 6d: P_t^{mis} in GeV for $\tilde{N}C$ for point 2.

Fig. 7a: P_t^e in GeV of the electron from the $\tilde{\nu}$ decay for the point 2.

Fig. 7b: Pseudorapidity of the electron from the $\tilde{\nu}$ decay for the point 2.

Fig. 7c: E_{acc} in GeV of the electron from the $\tilde{\nu}$ decay for the point 2.

Fig. 7d: P_t^{mis} in GeV for $\tilde{C}\tilde{C}$ events for point 2.

Fig. 8a: Percentage of events passing the set of cuts of section 2.1 vs $m_{\tilde{e}} + m_{\tilde{q}}$ in GeV assuming the simplest decays for \tilde{e} and \tilde{q} produced in $\tilde{N}C$, and assuming two LSP masses i.e. 0 GeV and 100 GeV.

Fig. 8b: Detection limits in the $m_{\tilde{e}}, m_{\tilde{q}}$ plane for $\tilde{N}C$ assuming the simplest decay ($m_{\tilde{q}}$ in GeV on the vertical axis and $m_{\tilde{e}}$ in GeV on the horizontal axis). Taking the set of cuts of section 2.1, the lines show the contours, for two LSP masses, in the $m_{\tilde{e}}, m_{\tilde{q}}$ plane inside which we obtain more than 20 events, i.e. $signal/\sqrt{background} > 3$.

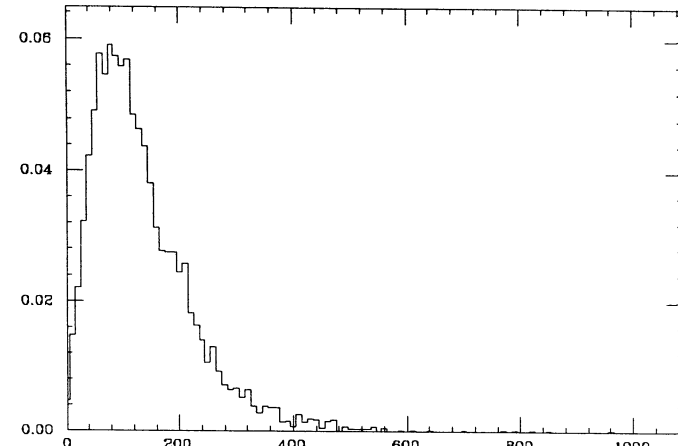


Fig. 1a

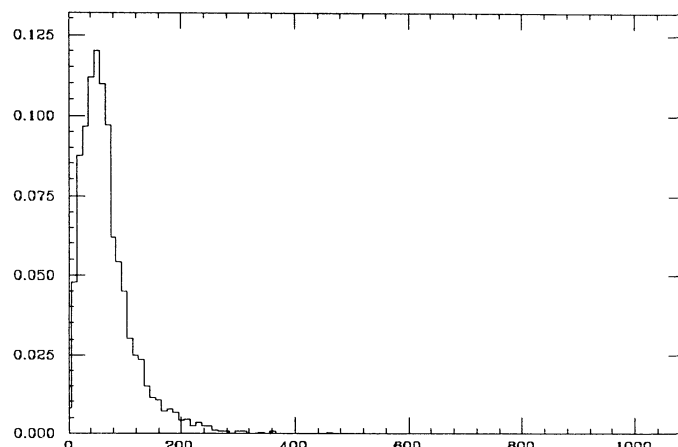


Fig. 1b

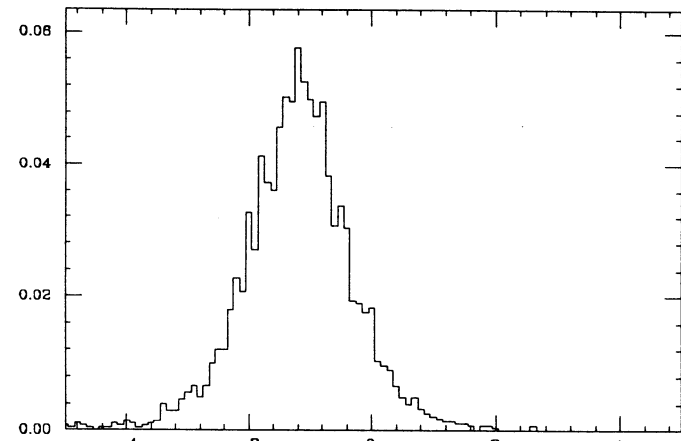


Fig. 2a

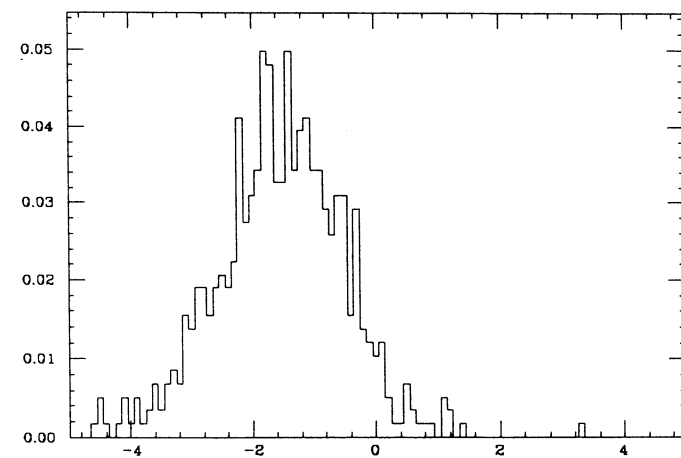


Fig. 2b

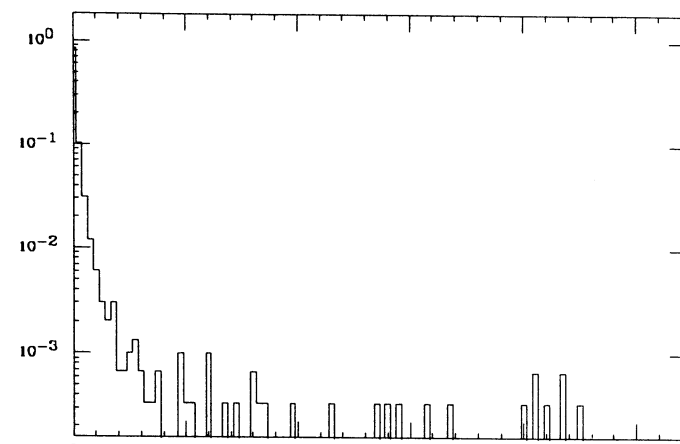


Fig. 3a

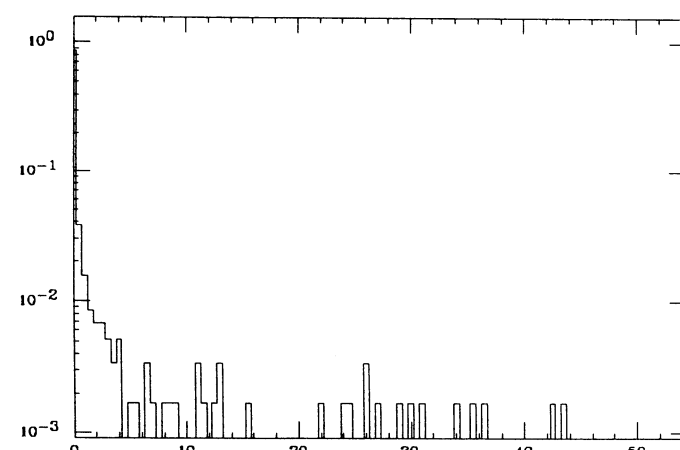


Fig. 3b

1051

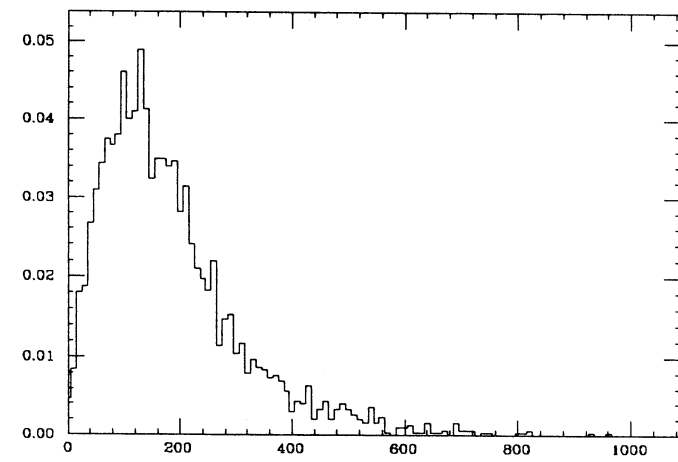


Fig. 4a

1052

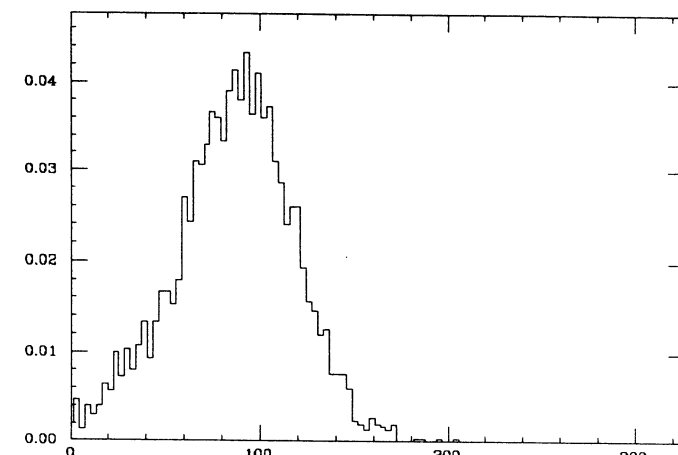


Fig. 5a

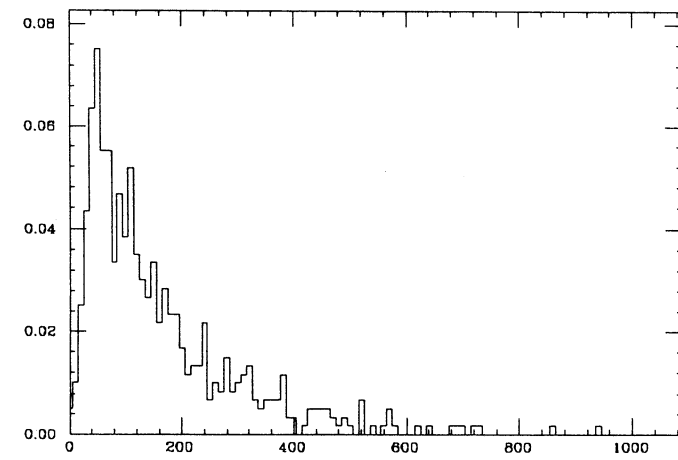


Fig. 4b

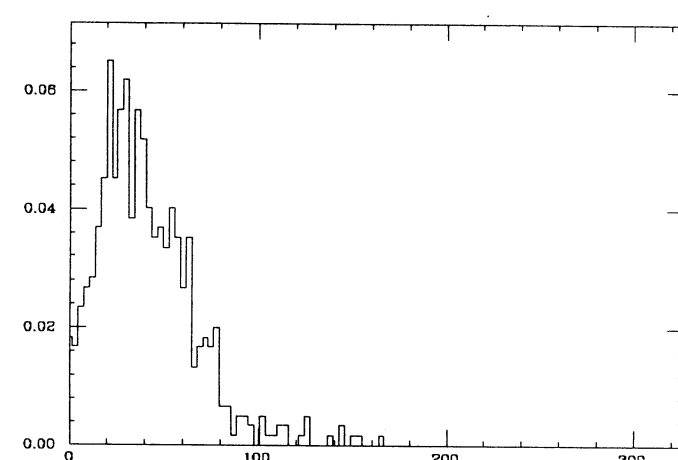


Fig. 5b

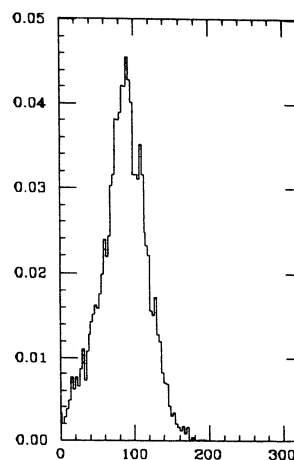


Fig. 6a

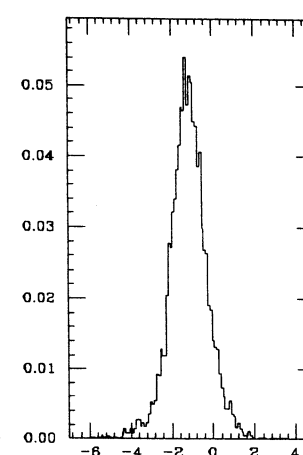


Fig. 6b

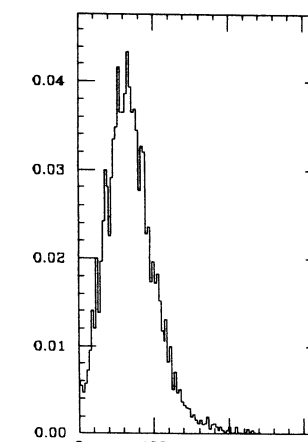


Fig. 7a

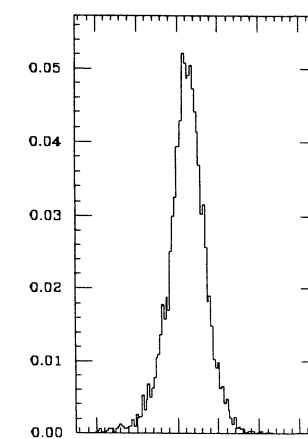


Fig. 7b

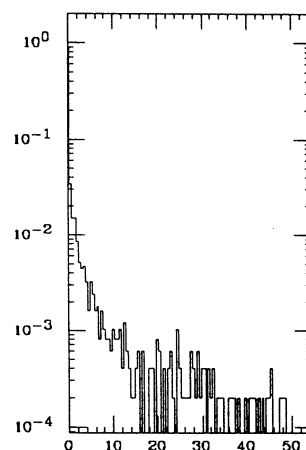


Fig. 6c

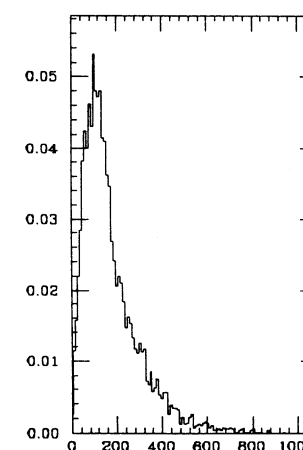


Fig. 6d

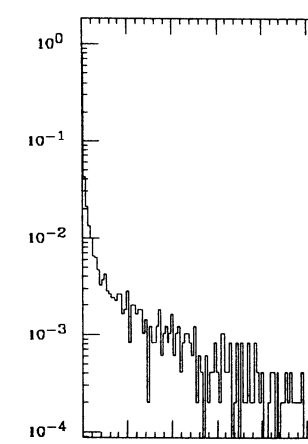


Fig. 7c

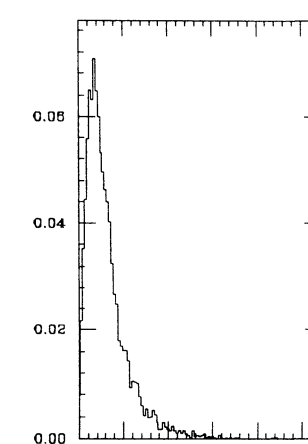


Fig. 7d

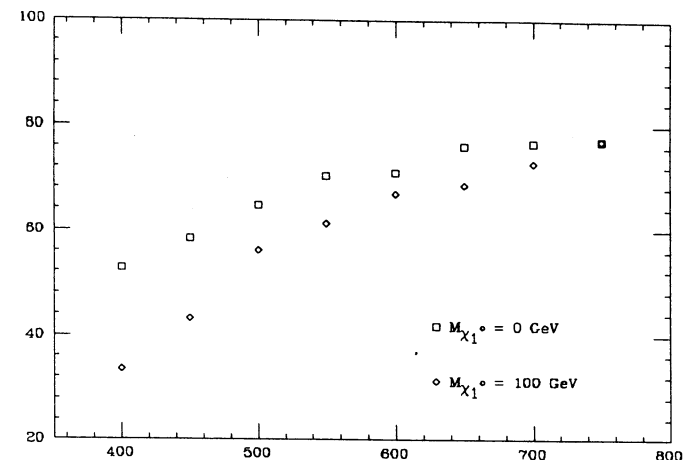


Fig. 8a

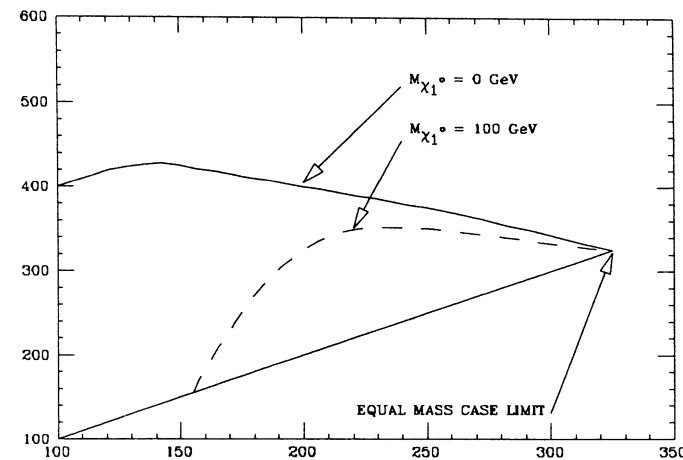


Fig. 8b

C: HEAVY-ION COLLISIONS

LATTICE QCD PREDICTIONS FOR VERY HOT NUCLEAR MATTER.

Bengt PETERSSON

Fakultät für Physik, Universität Bielefeld, Postfach 8640, 4800 Bielefeld 1, F.R.G.

C1: THEORETICAL ASPECTS

Abstract: In this report we review the predictions of lattice QCD for the parameters of the finite temperature phase transition, which is expected to be seen in ion-ion collisions at the LHC. In particular we present the results on the critical temperature and the order. Furthermore some expected properties of the quark-gluon plasma phase are discussed.

1. INTRODUCTION

In this report I will discuss the lattice results which may be most relevant for planning the ion-ion experiments at the LHC. These are the value of the critical temperature T_c in physical units, the order of the transition, and some properties of the plasma phase. For a more detailed review I refer to my talk at Quark Matter 90¹.

The present calculations show that these results are quite sensitive to the number of nearly massless dynamical (sea) quark flavours N_f . This is in contrast to e.g. the mass spectrum, which seems within errors to be insensitive to N_f . Therefore the mass spectrum has mostly been calculated in the quenched approximation ($N_f = 0$), which corresponds to the pure gluon theory. Calculations with dynamical quarks are at least a factor of 10^3 slower, because of the fermionic determinant. Such calculations have, however, been performed for N_f between 2 and 4 degenerate flavours. With four flavours one has a manageable exact algorithm², for the more physical case of $N_f = 2$ further approximations and assumptions must be made. Because the values of the parameters characterizing a possible phase transition can be expected to be sensitive to the number of nearly massless quarks, it is important to perform both finite temperature and mass calculations consistently, including dynamical quarks. Such calculations have recently been performed, e.g. by the MT_c -collaboration³.

The physical values of the temperature T and the value V are related to the lattice parameters by

$$T = 1/N_\tau a$$

$$V = (N_\sigma a)^3$$

where a is the lattice spacing on an $N_\tau \times N_\sigma^3$ lattice. In the full theory, at present, the calculations have been restricted to systems, where the ultraviolet cut off $1/a \approx 1$ GeV, and the length of the box $N_\sigma a \approx 3$ fermi.

In the quenched case ($N_f = 0$), one has been able to push to $1/a \approx 2 \text{ GeV}$. As will be discussed below, some important physical ratios seem not to be very sensitive to this variation of the ultraviolet cut off. Thus one may hope the properties determined on the rather coarse-grained lattices might be at least indicative of what happens in the real world.

In section II I will present the results for the critical temperature. In section III the order of the transition is discussed, in section IV the thermodynamics of the plasma phase, and in section V some conclusions are drawn.

2. T_c IN MEV

It is quite important to determine the critical temperature T_c in physical units with some precision, because we expect the energy density ϵ needed in the experiments to create the quark-gluon plasma to behave like

$$\epsilon \sim T_c^4 \quad (1)$$

and thus to be very sensitive to T_c .

The phase transition is signalled by a discontinuity (at a first order transition) or a sharp change in the value of the Polyakov loop and/or the chiral condensate. The Polyakov loop L is related to the free energy of a static quark, and is an exact deconfinement order parameter for $N_f = 0$ ⁴. The chiral condensate $\langle \bar{\psi}\psi \rangle$ becomes an exact order parameter for the restoration of chiral symmetry for all N_f when $m_q a = 0$. Other physical quantities measured are e.g. the energy density ϵ , the pressure p , the entropy density s and the Debye screening length r_D . For their precise definitions I refer to Ref. 5. At a first order transition the energy density and the entropy density should have a discontinuity, related to the latent heat.

In a finite temperature lattice calculation one obtains primarily a possible phase transition at a particular value of the bare coupling $g = g_c(N_\tau, N_f, m_q a)$. We assume N_σ so big that there is little dependence on N_σ . The temperature in physical units can only be obtained by setting the scale by another physical quantity. There exist new measurements of g_c for $N_f = 0$ by the Columbia group⁶, for $N_f = 2$ by Gottlieb et al.⁷ and by the Grand challenge collaboration⁸ and for $N_f = 4$ by the MT_c collaboration². The Grand challenge group is a collaboration of universities in the US, and the MT_c collaboration is centered around the German universities of Aachen and Bielefeld and the supercomputer-center HLRZ at Jülich.

One possibility to set the scale for T_c is by using asymptotic scaling to relate it to $\Lambda_{\overline{MS}}$. The famous formula is

$$\frac{T_c}{\Lambda_{\overline{MS}}} = \frac{1}{N_\tau a \Lambda_{\overline{MS}}} = \frac{1}{N_\tau} c(g_c)^{b_1/4b_0^2} e^{\frac{1}{2b_0 s_c}} (1 + O(g^2)) \quad (2)$$

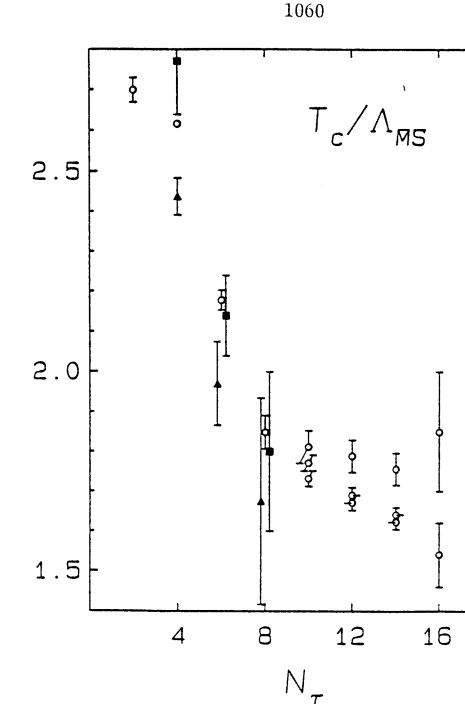


Fig. 1: $T_c/\Lambda_{\overline{MS}}$ as a function of the temporal lattice extent N_τ . Open dots refer to $N_f = 0$, filled triangles to $N_f = 2$, and filled squares to $N_f = 4$. Data are from refs. 6-9.

where

$$\begin{aligned} b_0 &= \frac{1}{16\pi^2} \left(11 - \frac{2}{3} N_f \right) \\ b_1 &= \frac{1}{(16\pi^2)^2} \left(102 - \frac{38}{3} N_f \right) \end{aligned} \quad (3)$$

and c is also a known constant depending on N_f . This formula is valid for $g \rightarrow 0$ and in the limit when the bare quark mass $m_q a = 0$. In fig. (1) T_c is shown as a function of N_τ . For $N_f = 0$ asymptotic scaling may have been reached for $N_\tau \geq 8$. The two different values plotted are due to different estimates of the critical couplings, which are systematic uncertainties due to the finite size of the system. One must also be aware that higher order corrections are expected to be proportional to g^2 , which varies only by 5 % for N_τ between 8 and 16. For $N_f = 2$ and 4 the data follow the scalebreaking trend from $N_f = 0$. It is not clear if the asymptotic scaling regime has been reached for $N_\tau = 8$.

Another possibility to extract T_c in physical units is to assume scaling but not necessarily asymptotic scaling. Then one measures e.g. the hadron masses at the critical value of the

T_c (MeV)

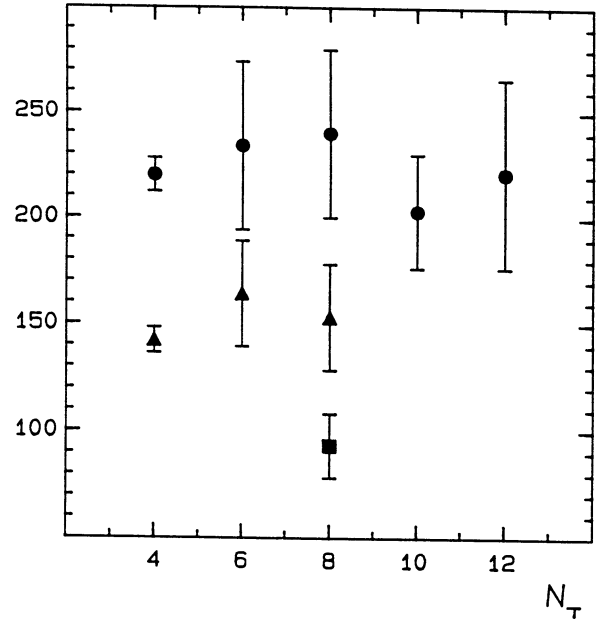


Fig. 2: T_c in MeV as function of N_τ . Symbols are explained in the text. Data are from refs. 6-12.

coupling constant but on a lattice with large time extent, i.e. at temperature zero. One has then

$$T_c = \frac{1}{N_\tau a(g_c) M_H} M_H^{exp} \quad (4)$$

where aM_H is the hadron mass in lattice units. The goal of the MT_c collaboration is to do just this with four flavours of dynamical fermions. The results show that T_c in QCD with four degenerate flavours is only about half as big as in the $N_f = 0$ case, if one assumes the masses to be independent of N_f . A similar tendency of lower T_c was already seen for $N_f = 2$ ⁷. In fig. (2) we show the available estimates for T_c , normalized to m_ρ for $N_f = 0$ (circles), $N_f = 2$ (triangles) and $N_f = 4$ (square). For $N_f = 0$ we use the masses which have been measured by the APE group⁹ and Gupta et al.¹⁰, for $N_f = 2$ by Gottlieb et al.⁷ and the Grand Challenge Collaboration⁸, and

for $N_f = 4$ by the MT_c collaboration^{2,12}. One can see that there is approximate scaling in T_c for $N_f = 0$ down to $N_\tau = 4$, in contrast to the asymptotic scaling which is strongly broken between $N_\tau = 4$ and 8. There is also, as was mentioned above, a clear dependence

on N_f in the data; T_c decreasing as N_f increases. Normalizing to other physical quantities gives a similar picture. The main uncertainty is, if scaling for $N_f = 2$ and 4 will be as good as seems to be the case for $N_f = 0$. To check this, considerably larger lattices are needed, which demands a new generation of computers. For the moment, the only independent support for the decreasing values of T_c in the presence of dynamical quarks found in the lattice calculations is the rather handwaving argument that more degrees of freedom should lead to more screening.

3. THE ORDER OF THE TRANSITION

Apart from the direct determination of the order of the finite temperature phase transition there exist universality arguments relating the field theory to simpler three dimensional spin models¹³. For $N_f = 0$ the deconfinement is characterized by the behaviour of the Polyakov loop L . More precisely, an $SU(N)$ theory has a global Z_N symmetry under which L transforms non-trivially.

A spontaneous breakdown of this symmetry is possible. The dynamics near the transition may be governed by a (local) Z_N theory. Then one has the prediction that e.g. $SU(3)$ in $d = 3+1$ dimensions is related to Z_3 in $d = 3$. For this latter theory only first order transitions are known. Thus $SU(3)$ should have a first order transition. This is not a complete proof, however, because e.g. the hypothesis of locality may be violated. For $SU(2)$ the corresponding model is Z_2 in $d = 3$, one example of which is the Ising model, which has a second order transition. It is thus expected that if $SU(2)$ has a second order transition it has the same critical indices as the Ising model. This has in fact been confirmed¹⁴.

For $N_f > 0$, $m_q = 0$, there is similarly an effective model of the chiral symmetry restoration. QCD with N_f dynamical flavours in $d = 3+1$ should be related to a $U(N_f) \times SU(N_f)$ σ -model in $d = 3$. As was discussed by Pisarski and Wilczek some time ago, the transition in this model is expected to be first order for all $N_f > 2$ ¹⁵.

A summary of the present situation as regards the pure gauge theory ($N_f = 0$) can be made as follows. For detailed review of the results see ref. 16.

- (a) The transition is first order for $N_\tau = 4$. All groups now agree on this. An increase in computer speed of more than a factor of 1000 is probably needed to repeat these calculations for N_τ in the asymptotic scaling regime. This has to wait for a new generation of computers.
- (b) All Z_3 -models investigated show first order behaviour. There were earlier some evidence pointing to a second order transition for certain admixtures of ferromagnetic and antiferromagnetic couplings. This again has been shown to be a transient effect for small volumes. The fact that all Z_3 -models have first order transitions does of course not prove that $SU(3)$ has a first order transition. It still has to be shown that $SU(3)$ in the asymptotic scaling region is equivalent to a Z_3 -model with only local couplings.

- (c) The transition is weak in the sense that the latent heat $\Delta\epsilon$ is small compared to the discontinuity predicted by inserting the Stefan-Boltzmann value ϵ_{SB} for an ideal gluon gas. In fact

$$\Delta\epsilon \approx \frac{\epsilon_{SB}}{4}. \quad (5)$$

Furthermore the string tension σ is small compared to its value at zero temperature,

$$\sigma(T_c) \approx .1\sigma(0) \quad (6)$$

and the Debye screening length r_D is big compared to its value further above the transition

$$r_D(T_c) \approx 3r_D(1.2T_c). \quad (7)$$

Because of computer time limitations, it has not been possible to study QCD with dynamical quarks in the same detail. Still there have been several investigations of QCD with $N_f = 4$. In table 1 is given a list of the results obtained. The general conclusion is that there is a first order transition when $m_q \leq .1T_c$. The fact that the transition appears only for small masses indicates that it is connected to the restoration of chiral symmetry. The results for $N_f = 2$ and $N_f = 2 + 1$ are collected in table 2 and 3. In contrast to indications in some earlier calculations there seems to be no evidence for a first order transition for $N_f = 2$. For $N_f = 3$ the first order nature reappears. The physical case seems to be just on the borderline between a discontinuous and a smooth transition. As was mentioned in the introduction the implementation of the $N_f = 2$ or $N_f = 2 + 1$

Table 1: $N_f = 4$

Reference	lattice size	m_q/T_c	order
Columbia ¹⁷	4×16^3	4.0	cont
	4×16^3	2.0	cont
	4×16^3	0.2	1 st
Karsch et al. ¹⁸	4×8^3	0.1	1 st
Kyoto-Tsukuba ¹⁹	$4^4 - 4 \times 12^3$	0.1	1 st
Columbia ¹⁷	4×16^3	0.1	1 st
	4×16^3	0.04	1 st
Columbia ¹⁷	6×16^3	0.15	cont
	6×16^3	0.06	1 st
	8×12^3	0.2	cont
$MT_c^{3,20}$	8×16^3	0.08	1 st

Table 2: $N_f = 2$

Reference	lattice size	m_q/T_c	order
Irbäck et al. ²¹	$4^4 - 4 \times 12^3$.4	cont.
Gottlieb et al. ²²	$4 \times 8^3 - 12^3$.4	cont.
Kyoto-Tsukuba ¹⁹	$4^4 - 4 \times 12^3$.1	cont.?
Columbia ¹⁷	4×16^3	.1	cont.
	4×16^3	.04	cont.

Table 3: $N_f = 2 + 1$

Results from Columbia¹⁷, lattice size 4×16^3

m_{u-d}/T_c	m_s/T_c	order
.1	2.0	cont
.1	.4	cont
.1	.2	1 st ?
.1	.1	1 st

flavours contain some systematic errors, both in the algorithm and in the realization of the fermionic determinant, especially since the transition has been studied only at rather strong coupling. Still there seems to be two distinct regions in an $m_q - N_f$ parameter space, one connected with deconfinement in the sense of the Z_3 -symmetry breaking, near $N_f = 0$ and/or large quark mass and one connected with chiral symmetry breaking, for $N_f > 2$, and small quark mass. If the chiral transition separates the hadron phase from a phase that behaves essentially like a free quark-gluon gas, or if there are hadronic excitations in the chirally symmetric phase has still to be established. In all cases known, the deconfinement order parameter has a discontinuity at the same value of the temperature as the chiral order parameter.

4. THE EQUATION OF STATE

A simple model giving the equation of state is the bag model. In this model the thermodynamics of the quark-gluon phase is given by

$$\epsilon = \kappa \frac{\pi^2}{30} T^4 + B \quad (8)$$

$$p = \kappa \frac{\pi^2}{90} T^4 - B$$

where

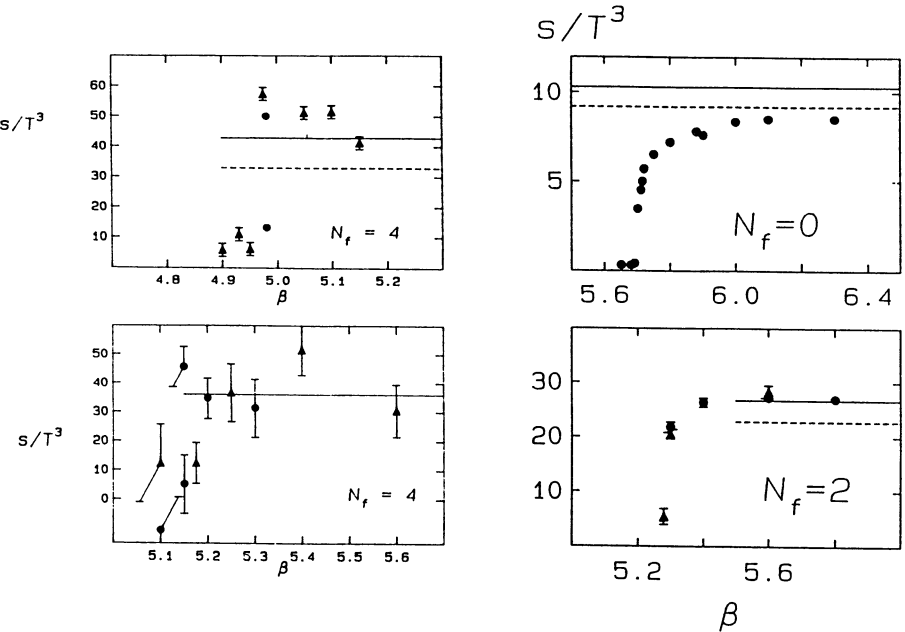


Fig. 3a: s/T^3 as a function of β for $N_f = 0, N_\tau = 4$. $T = 2T_c$ corresponds approximately to $\beta = 6.0$. The full line is the free gas value, the dashed line includes g^2 -corrections. Data are from refs. 23,24.

Fig. 3b: The same for $N_f = 2$. Data are from ref. 25.

Fig. 3c: The same for $N_f = 4$. Data are from refs. 18 (triangles) and 17 (dots).

Fig. 3d: The same for $N_f = 4$ but $N_\tau = 8$. Data from refs. 3, 20.

$$\kappa = 2\left(8 + \frac{21}{4}N_f\right) \quad (9)$$

counts the effective number of degrees of freedom, and B is the bag pressure. In this model the entropy density

$$s = \frac{\epsilon + P}{T} = \frac{4}{3}\kappa \frac{\pi^2}{30} T^3 \quad (10)$$

does not involve B , but has the free gas value. The hadronic phase may be described as a pion gas, i.e. by the above formulae, but with $\kappa = 3$ and $B = 0$. The bag model is certainly too simple to give a completely correct description of the nonperturbative effects. It predicts a first order phase transition, where the entropy density has a jump from its value for the free pion gas to a free quark-gluon gas. It turns out that the entropy density is also the easiest quantity to measure on the lattice, because it does not require a subtraction of the $T = 0$ value. In fig. 5 is shown s/T^3 as a function of the coupling $\beta = 6/g^2$ for various values of N_f . Also the temperature scale is indicated. For $N_f = 0$ the discontinuity is only about a quarter of the Stefan-Boltzmann value thus indicating a "weak first order transition". It

reaches the perturbative regime for $T \geq 2T_c$. For $N_f = 2$ the phase transition is presumably continuous, but the entropy density goes fairly quickly to its free gas value.

For $N_f = 4$ there is a clear discontinuity, as measured by the Columbia group for $N_\tau = 4^{17}$ and by the MT_c -collaboration for $N_\tau = 8^2$. Again, the upper value agrees with a free quark-gluon gas.

The data on energy and pressure are less precise, in particular for $N_f > 0$. The energy density is near its perturbative value, while the pressure, which has to be continuous at T_c , contains large non-perturbative effects for $T \lesssim 2T_c$.

Measurements of correlation functions in the plasma give information about screening lengths, and possibly about the relevant excitation modes. The latter information is, however, rather indirect, because one can measure only static correlation functions. A serious problem with most of these measurements is that they have been restricted to rather short distances $r \lesssim 1/T$.

It is possible that most of the data can be explained by perturbation theory in an essentially free quark-gluon gas²⁶. There is, however, some evidence for a rather short Debye radius, which would mean that also heavy resonances like the J/ψ may dissolve in the plasma¹. Furthermore, there seem to be non-perturbative effects in the $\pi - \sigma$ channel, signalling perhaps a massive chirally symmetric $\pi - \sigma$ multiplet^{27,28}. The physical values of the screening lengths seem to be rather independent of N_f . More careful investigations of these interesting results are needed.

5. CONCLUDING REMARKS

- (i) Calculations with dynamical quarks give $T_c < 200$ MeV, if normalized to the hadron masses. If $T_c \approx 150$ MeV in the physical case, the energy density of the quark-gluon plasma just above the phase transition would be only around 1 GeV/fermi³.
- (ii) For the pure gluon theory, $N_f = 0$, the phase transition is first order, at least for the lattice sizes investigated. For $N_f = 4$ there is also a first order transition for sufficiently small quark masses, thus related to the restoration of chiral symmetry. For $N_f = 2$, however, no discontinuity is observed. The physical case may be a borderline case. Thus we don't know if the phase transition in the real world is first order with a latent heat and possible bubble formation. It seems to be the case, however, that for all values of N_f , investigated, there is a sharp change in entropy from a low value in the hadronic phase to the Stefan-Boltzmann value in the quark-gluon plasma, within a narrow interval in temperature. This means that the signal for the phase transition in a plot of the mean transverse momentum versus multiplicity, proposed by van Hove, should be apparent in the experimental data.

- (iii) Free gas behaviour seems to set in in all thermodynamical quantities at least for $T \geq 2T_c$. For $T \leq 2T_c$ there may be a modification especially of low momentum modes, which especially modifies the pressure.
- (iv) Although the phase transition for $N_f = 0$ is related to deconfinement of static quarks, and for $N_f = 4$ to restoration of chiral symmetry, the properties of the high temperature phase seem to be very similar, in the sense that $\epsilon/\epsilon_{SB}, s/ssB, r_D$ and other screening lengths are essentially independent of N_f . The experimentally most relevant indications coming from the lattice results on the screening lengths is that the Debye screening length may be short enough, so that heavy resonances like the J/ψ may not be bound in the plasma phase, and that the hadronic screening lengths indicate the presence of a massive chirally invariant pion-sigma multiplet in the plasma. More detailed studies of these nonperturbative properties has to be performed, to confirm these interesting results, in particular by extending them to larger distances and larger sizes of the system.
- (v) To be able to perform calculations in the asymptotic scaling regime especially for QCD with dynamical quarks a new generation of computers with performances of at least 10^3 times the present ones are needed. Such projects are, however, realistic and under study. Taking the pure gluon theory as a guide, many of the results obtained up to now in QCD with dynamical quarks may not change very much when we move into the asymptotic scaling regime. Still, in 3-4 years we will know this better.

ACKNOWLEDGEMENT

For valuable discussions I thank in particular S. Gupta, A. Irbäck, F. Karsch and H. Satz.

REFERENCES

- 1) B. Petersson, Rapporteur's talk at the VIIth International Conference on Ultrarelativistic Nucleus-Nucleus Collisions "Quark Matter '90", Preprint BI-TP 90/28.
- 2) S. Duane, A.D. Kennedy, B.J. Pendleton and D. Roweth, Phys. Lett. B195 (1987) 216.
- 3) R.V. Gavai, S. Gupta, A. Irbäck, F. Karsch, S. Meyer, B. Petersson, H. Satz and H.W. Wyld, Phys. Lett. B241 (1990) 567.
- 4) A.M. Polyakov, Phys. Lett. 72B (1978) 447;
L. Susskind, Phys. Rev. D20 (1979) 2610;
L. McLerran and B. Svetitsky, Phys. Lett. 98B (1981) 195.
- 5) F. Karsch, Preprint CERN-TH-5498/89 (1989).
- 6) N.H. Christ, Nucl. Phys. B17 (Proc. Suppl.) 267.
- 7) S. Gottlieb, W. Liu, R.L. Renker, R.L. Sugar and D. Toussaint, Phys. Rev. D38 (1988) 2245.
- 8) S. Gottlieb et al., Nucl. Phys. B17 (Proc. Suppl.) (1990) 173.
- 9) S. Cabasino et al., Nucl. Phys. B (Proc. Suppl.) 17 (1990) 431.
- 10) R. Gupta, Nucl. Phys. B (Proc. Suppl.) 17 (1990) 59.
- 11) K.M. Bitar et al., Florida State Univ. preprint FSU-SCRI 90-98.
- 12) E. Laermann et al., Nucl. Phys. B (Proc. Suppl.) 17 (1990) 59.
- 13) B. Svetitsky and L.G. Yaffe, Nucl. Phys. B210 [FS6] (1982) 423.
- 14) See e.g. J. Engels, J. Fingberg, M. Weber, Nucl. Phys. B332 (1990) 737 and reference therein.
- 15) R.D. Pisarski and F. Wilczek, Phys. Rev. D29 (1984) 338.
- 16) A. Ukawa, Nucl. Phys. B17 (Proc. Suppl.) (1990) 118.
- 17) F.R. Brown et al., Columbia University Preprint CU-TP-470 (1990) and priv. comm. from N.H. Christ.
- 18) F. Karsch, J.B. Kogut, D.K. Sinclair and H.W. Wyld, Phys. Lett. B188 (1987) 353.
- 19) M. Fukugita, H. Mino, M. Okawa and A. Ukawa, University of Tsukuba Preprint UTHEP-204 (1990).
- 20) R.V. Gavai et al., Phys. Lett. B232 (1989) 491.
- 21) A. Irbäck, F. Karsch, B. Petersson and H.W. Wyld, Phys. Lett. B216 (1989) 177.
- 22) S. Gottlieb et al., Phys. Rev. D35 (1987) 3972;
S. Gottlieb, in Proceedings of Lattice 89, Capri, Nucl. Phys. B (Proc. Suppl.) in press.
- 23) F.R. Brown, N.H. Christ, Y. Deng, M. Gao and T.Y. Woch, Phys. Rev. Lett. 61 (1988) 2058.
- 24) N. Attig, F. Karsch, B. Petersson, H. Satz and M. Wolff, unpublished.
- 25) F. Karsch and H.W. Wyld, Phys. Lett. B213 (1988) 505.
- 26) B. Petersson and T. Reisz, Bielefeld Preprint BI-TP 90/18, Nucl. Phys. in press.
- 27) C. DeTar and J.B. Kogut, Phys. Rev. D36 (1987) 2828
- 28) A. Irbäck, Bielefeld Preprint and MT_c -collaboration, work in progress.

CHIRAL PHASE TRANSITION AT FINITE TEMPERATURE AND DENSITY

Contributors: A.Barducci, R.Casalbuoni, S.De Curtis, R.Gatto and G.Pettini

1. Introduction

Relativistic heavy ions collisions are expected to produce a hot and baryon-rich fireball. Thus, besides thermal effects, the theoretical modeling has to take into account also the chemical potential (μ) dependence (mainly associated to the u, d quarks) of the relevant quantities (condensates, decay constants etc.), in order to reproduce the effects of the net baryon charge. On the lattice, there are difficulties to take into account the finite density dependence, since the chemical potential enters as a pure imaginary term into the euclidean partition function, leading to a complex fermion determinant.

Although there are few QCD results derived at finite density even within analytical approaches [1-4], the aim of this brief report is to resume which are those available at present. We shall compare the QCD phase transitions description with lattice results for what concerns the temperature dependence as well [1-10].

Up to now no reliable result about the deconfinement transition has been derived starting from the fundamental QCD Lagrangian and applying analytical methods. Current literature rather deals with the chiral phase transition.

Thus we start with the description of the chiral phase diagram in the (μ, T) plane, as derived within the different models and only at the end we shall discuss some connection with deconfinement. We will discuss also possible effects of quantum anomalies on the order of the phase transition, and finally the pion decay constant and the pion mass will be analyzed at finite temperature and density.

We refer here mostly to QCD or QCD-related models, considering phenomenological models (Gross-Neveu, Nambu Jona-Lasinio etc.) only where there is lack of QCD results (for instance in discussing axial and scale anomaly).

2. The chiral symmetry phase diagram

A general requirement which holds for spontaneously broken theories with fermions (but not for bosons, see ref. [11]) is the lowering of the critical temperature for symmetry restoration, for increasing chemical potentials. Qualitatively a similar structure has indeed been found since the first attempts to simulate QCD at finite temperature and density both in effective models (Nambu Jona-Lasinio, Gross-Neveu etc.) and in QCD-like gauge theories to which we are hereby referring [1-4].

The main points which still remain to be clarified are the following: the first is the determination of the critical values for chiral symmetry restoration and the corresponding values of energy and baryon densities, and the second is the order of the transition and the "speed" of it (critical exponent for a second order phase transition or latent heat for a first order one) both in temperature and in chemical potential. The answers to these questions coming from QCD-like models [1-10] are not always in agreement.

A common feature of refs. [1-10] is that, owing to the fact that gluons are expected to play a predominant role in the deconfinement mechanism rather than in the restoration of chiral symmetry, only the QCD fermion sector and the formation of fermion bound states is considered through the Schwinger-Dyson equation for the dynamical quark mass at the level of a single gluon exchange. Then the formalism is extended at finite T [6-10] and μ [1-5] by using standard equilibrium

techniques and some approximate scheme is adopted in order to guess the behaviour of the quark condensate. The gap equation sometimes is directly solved numerically [1-3], [6-10] and in other studies by means of variational methods [4,5,7]. Nevertheless, even if the central point is quite always the same in the studies of refs. [1-10], they differ for other features, such as the gauge chosen to perform calculations, which deserves particular comments. Thus in the following we shall describe separately the results of the various models by specifying which are the main assumptions within which they have been derived.

We start with refs. [2,3] where the chiral phase diagram in the (μ, T) plane is derived in the Coulomb gauge and the Schwinger-Dyson equation for the fermion self-energy is considered within the Hartree-Fock approximation (i.e. by taking bare vertex and gluon propagator).

The fact that the use of a non-covariant gauge leads to a preferred Lorentz frame is not really a serious disadvantage at finite temperatures and densities since one has to specify the rest frame of the hot system anyhow. On the other hand, the advantage of using the Coulomb gauge, investigated first in refs. [12], is that the gap equation for the generated quark mass allows for the use of $q\bar{q}$ potentials similar to those used in potential theory treatments for heavy-quark bound states. Since these potentials are static (nonrelativistic), which amounts to ignoring the effect of transverse gluons on the $q\bar{q}$ Bethe-Salpeter (BS) kernel, the gap equation at finite temperatures and densities can still be reduced to a one-dimensional nonlinear integral equation. This equation can be solved numerically fairly readily for various potentials. The general expression for the fermion self-energy in these papers is

$$\Sigma(p) = C_F \int_k \tilde{V}(p - k) \gamma^0 S(k) \gamma^0 \quad (2.1)$$

where C_F is the Casimir operator in the fundamental representation of the gauge group and $S(k) = (\hat{k} - \Sigma(k))^{-1}$ is the fermion propagator, whereas \int_k reminds that the imaginary-times formalism is used, where the integration over the time component $k_0 = i\omega_n + \mu$ is replaced by a discrete sum over antiperiodic frequencies ω_n . Finally $\tilde{V}(k)$ is the Fourier transform of the potential, which the authors have chosen of various types, in order to simulate the quark-gluon interaction and depending only on the three-momentum transfer k due to the instantaneous approximation used. The authors of ref. [3], who have generalized the previous work of ref. [2], have considered several shapes for $\tilde{V}(k)$ among which the most interesting cases are a Coulomb potential with running coupling to simulate asymptotic freedom and a Coulomb plus linear confining potential. In fact, as discussed by Adler and Davis [12], the $q\bar{q}$ BS kernel can be approximated by a static potential in single-gluon exchange and specifically, to be consistent with the Ward identities, by $\tilde{V}(k) = \alpha/k^2$. In higher loops, renormalization group improvements make α a running function of k^2 at high momentum, thus exhibiting features of asymptotic freedom, namely $\tilde{V}(k) = g/k^2 \ln(k^2/\Lambda_{QCD}^2)$ where the value of the coupling g is chosen above a critical value g_c in order to have chiral symmetry breaking at $T = 0$. Furthermore it is shown [13] that multiple longitudinal gluon exchange produces an additional confining-potential contribution to make \tilde{V} in coordinate space of the form $\tilde{V}(r) = \sigma r - 4\alpha/3r$, where σ is the string tension. In eq. (2.1) the self-energy is decomposed in the following way, $\Sigma(p) = a_p + b_p \gamma \cdot p + c_p \gamma_0$ and thus a system of three coupled nonlinear integral equations for the functions a_p, b_p and c_p has to be solved after having easily got the frequency summation

in eq. (2.1) since a_p, b_p and c_p depend only on \mathbf{p} . The numerical study of these equations, performed in refs. [2,3], shows that chiral symmetry restoration occurs always through a second order phase transition both in temperature and in chemical potential. A special case is when the linear confining term mentioned above is added. In fact it has been found in ref. [2] that this term allows a critical chemical potential at $T = 0$, whereas chiral symmetry never restores at any finite temperature if $\mu = 0$. A more complete study shows that, in order to restore the symmetry for increasing temperatures, below the critical density, an additional temperature dependence in the string tension, $\sigma(T) = \sigma_0 \{1 - [T/T_D]^2\}^{1/2}$ (for $T < T_D$), has to be added. In this case the symmetry is restored at the temperature T_D where the string tension vanishes, namely at the deconfinement temperature [3].

One of the problems of the Coulomb gauge approaches is the difficulty to reproduce the known phenomenology. For instance, at $T = \mu = 0$ in the confining case, in ref. [12] a pion decay constant of only $10 \div 20$ MeV is found. Analogously, for the case of a Richardson potential considered in ref. [14], the value for f_π turns out to be 50 MeV for a scale of about 500 MeV. If one tries to increase the typical scales in order to increase f_π one runs into the problem of having pion masses too large or having quark masses too small. As a result of this situation the typical values for the critical temperature and chemical potential turn out to be very small. For instance, the authors of refs. [2,3], in the Coulomb case, get $T_c = 35$ MeV at $\mu = 0$, and $\mu_c = 28$ MeV at $T = 0$. For the confining potential, the result is $\mu_c = 45$ MeV at $T = 0$.

The previous problem can be overcome in the Landau gauge approach, as shown in refs. [1,4,8].

In ref. [1] chiral symmetry restoration has been studied in its temperature dependence and partially also in its μ -dependence. The gap equation for the dynamical fermion mass has been considered in the Landau gauge, and an approximate value $T_c \simeq 180$ MeV for the critical temperature has been found using a relation similar to the one found in a BCS-type gap equation. The inclusion of the chemical potential leads to a $T = 0$ critical value $\mu_c \simeq 450$ MeV (again for a second order phase transition).

We conclude this section on the structure of the chiral phase diagram in the (μ, T) plane for a QCD-like gauge theory with the study in ref. [4]. Therein the behaviour with T and μ of the fermion condensate is derived by generalizing a composite operator formalism previously developed at $T = \mu = 0$ [15]. The method of ref. [15] consists in choosing a suitable ansatz on the momentum dependence of the scalar fermion self-energy (coming from a preliminary analysis of the Schwinger-Dyson equation), by parametrizing it in terms of a variational field χ and then by determining the value of χ at the absolute minimum of the effective potential for composite operators, V (evaluated at the two loops level) [15,16]. The generalization at $T, \mu \neq 0$ has been worked out for three flavours in the chiral limit, performing calculations for imaginary-times. The fermion self-energy test function is chosen to be

$$\Sigma(p^2, T, \mu) = \chi(T, \mu) \frac{M^3}{(p^2 + M^2)} \quad (2.2)$$

where all the dependence on T, μ is in the dimensionless field χ , M is a mass scale which is a parameter of the model (see later), and the momentum dependence of Σ is consistent with the OPE analysis (neglecting logarithmic corrections). When

the absolute minimum of the effective potential is located out of the origin, chiral symmetry is dynamically broken by the formation of a condensate

$$\langle \bar{\psi} \psi \rangle_{T, \mu} = \frac{3M^3}{g^2(T, \mu)} \bar{\chi}(T, \mu) \quad (2.3)$$

where $\bar{\chi}$ is the value at the absolute minimum of V . In eq. (2.3)

$$g^2(T, \mu) = g^2/[1 + \ln(1 + \xi T^2/M^2 + \zeta \mu^2/M^2)g^2/2b] \quad (2.4)$$

($b = 24\pi^2/(11N_c - 2N_f)$ where N_c and N_f are respectively the number of colors and flavors) takes phenomenologically into account the evolution of the gauge coupling with T and μ . $g^2 = 2b/(\ln(M^2/\Lambda_{QCD}^2))$ is the gauge coupling constant fixed at the scale M . Finally, the two parameters ξ and ζ are let free to study how the dynamics is influenced by changes in the relative weight of the coupling in T and μ . In the $T = \mu = 0$ case, the only parameters of the model (in the chiral limit) are M and Λ_{QCD} . From a phenomenological fit to the meson masses and decay coupling constant, following the procedure outlined in refs. [4,15], one finds $M = 282$ MeV and $\Lambda_{QCD} = 220$ MeV. As a result one gets $\langle \bar{\psi} \psi \rangle(1 \text{ GeV}) \simeq -(257 \text{ MeV})^3$.

The phase diagram which originates from the effective potential [4] shows the existence of a tricritical point $t \equiv (\mu_t, T_t)$ (see Fig. 1), dividing the critical line in two parts L_{II} and L_I : by crossing them chiral symmetry is restored through a second order or a first order phase transition respectively. In particular, in the $\mu = 0, T \neq 0$ case, the symmetry is restored continuously at the point $(0, T_c)$, whereas in the opposite limit one always finds (for any value of $\zeta \neq 0$) a first order phase transition at the point $(\mu_c, 0)$. The other two curves in Fig. 1 are nothing but the lines where the second derivative of V vanishes at the origin (γ) and the ending line of metastable phases (δ). In Fig. 1 $\xi = \zeta = 0.6$, although the same structure holds for the other values of ξ, ζ ($\zeta \neq 0$).

The critical values depend weakly on ξ and ζ , except for μ_c and μ_δ which sensibly grow for $\zeta < 0.5$. As an example, the coordinates of the point $t \equiv (\mu_t, T_t)$ vary from (82 MeV, 107 MeV) for $\xi = 0, \zeta = 0.1$ to (73 MeV, 81 MeV) for $\xi = 1.5, \zeta = 1.2$ [4].

The behaviour of the condensate versus T for various values of the chemical potential, below, above, and at the tricritical point is given in Fig. 2. We see that the condensate vanishes steeply when crossing the line L_{II} and this can be analytically justified. In fact V can be expanded *à la Landau* in a Taylor series in χ^2 , around any point lying on L_{II} (including t). The coefficients of the expansion are free from IR divergences, namely the finite T and μ contributions cancel out the IR divergences which are present in the $T = \mu = 0$ case (we recall that for $\chi = 0$ the fermions become massless in the chiral limit). This is consistent with recent analysis showing that the generalization of the Kinoshita-Lee-Nauenberg theorem holds at finite temperature in QCD at two loops level [17]. This allows to conclude that the critical exponents which describe the behaviour of the condensate (they are the same of the field $\bar{\chi}(T, \mu)$, see eq. (2.3)) are 0.5 by approaching any point lying on L_{II} excluding t , and 0.25 around t , moving along orthogonal directions in the phase diagram of Fig. 1. A similar result in the Coulomb gauge has been obtained numerically in ref. [9].

For $\mu = 0$ and $T \rightarrow 0$, the one-loop correction to the $T = 0$ effective potential is exponentially suppressed, whereas the two loops term (which has the same

functional dependence on χ as in the $T = 0$ case) depends on T through the gauge coupling given in eq. (2.4). Thus it is easy to find, for $T \rightarrow 0$, the following behaviour for the condensate

$$\langle\bar{\psi}\psi\rangle_T \simeq \langle\bar{\psi}\psi\rangle_0 [1 - B\xi(T/f_0)^2] \quad (2.5)$$

where $B \simeq 0.206$ ($N_f = 3$) and $f_0 \simeq 91$ MeV is the value of the pion decay constant at $T = \mu = 0$ in the chiral limit [18]. Since the same leading behaviour for low temperatures has been found in the literature [19] (by using a quite different approach), we get a possible determination of the parameter ξ by equating the coefficient of T^2 in eq. (2.5) and in the corresponding expression of ref. [19]. The result is $\xi \simeq 1$. For arbitrary values of N_f one finds $B = 1.78(f_0/\mu)^2\pi^2/b$ and comparing again with ref. [19] one gets $B\xi \simeq (N_f^2 - 1)/(12N_f)$. Because fixing ξ is equivalent to fix the critical temperature, one finds that for $N_f = 2, 3, 4, 5$ the critical temperature is given by $T_c(\text{MeV}) = 108, 101, 96, 93$, decreasing but not as fast as in the case of ref. [19].

A phase diagram in the (μ, T) plane with a structure similar to ref. [4], till now has been found in other theories such as in the Gross-Neveu model [20], but not in QCD. Recently the main features have been confirmed also in the study of ref. [5], where using strong coupling expansion in lattice QCD, the restoration of chiral symmetry has been analyzed analytically finding second order chiral phase transitions at $\mu = 0$ and first order chiral phase transition at $\mu = \mu_c$ and at any low temperature. We conclude by observing that in the limiting case of $\mu = 0, T \neq 0$, all the approaches considered here have found a second order phase transition. To compare with lattice results one should keep in mind that on the lattice a single phase transition is observed, and it is possible that it is the deconfinement transition which drives the chiral one. We remember also that on the lattice the jump in the order parameter depends strongly on the number of flavors and on the fermion masses and it seems that it has to be small in the most realistic situation.

Regarding the gauge dependence of these approaches, nothing is known at T and $\mu \neq 0$. We will summarize the results for zero temperature and chemical potential. It is known that in the case of a dynamical generation of the self-energy the Ward identities are not generally satisfied if one makes use of the free quark-gluon vertex. A notable exception is the Landau gauge. In ref. [21] Atkinson et al. and Curtis et al. have shown that the dynamical mass is gauge independent if one chooses appropriately the vertex in the non-Landau gauges, confirming indirectly the validity of the results in the Landau gauge. A similar conclusion has been found by Mitani et al. [21] by studying the independence from the gauge choice of the minima of the effective potential.

3. Effects of explicit $U(1)_A$ breaking on the chiral phase transition

We know that the QCD Lagrangian in the chiral limit possesses a flavor symmetry group $\mathcal{G} = U(N_f)_L \otimes U(N_f)_R$. The chiral symmetry is not realized linearly in the hadron spectrum. Indeed it is spontaneously broken to $SU(N_f)_V \otimes U(1)_V$ with the appearance of $N_f^2 - 1$ Goldstone bosons. For $N_f = 3$ these are the light pseudoscalar mesons π, K, η . Notice that the hadron spectrum does not show a ninth pseudoscalar Goldstone boson related to the breaking of the $U(1)_A$ symmetry. This problem has been solved by 't Hooft via instanton interactions [22].

In all the calculations we have so far reported on, the $U(1)_A$ problem has been neglected. A way to break explicitly the unwanted $U(1)_A$ symmetry, proposed by

't Hooft [22], is to introduce in the Lagrangian a $2N_f$ -fermion effective interaction (the 't Hooft determinant), representing the instanton dynamics of QCD.

The problem has been studied in the framework of particular models because it is too difficult to implement it directly in QCD. For instance, the case of the linear σ -model has been analyzed by Pisarski and Wilczek [23]. By using renormalization group arguments, these authors conclude that the anomaly should change the chiral second order phase transition into a first one for $N_f \geq 3$. This has been confirmed recently by explicit calculations for $N_f = 3$ by Frei and Patkos [24]. However, analogous studies made in the Nambu Jona-Lasinio model show no such effects [25].

A similar problem arises for the scale symmetry in QCD which is broken (as well as the axial anomaly) by quantum effects. A study of the effects of such an anomaly on the chiral and deconfinement transitions, in the context of a nonlinear σ -model, has been done recently by Campbell, Ellis and Olive [26].

4. Pion properties: f_π, m_π

In ref. [15] a set of Feynman rules was derived to evaluate pion amplitudes. Using the extension of these rules to finite temperature and density (ref. [18]) it is possible to evaluate the pion decay constant and to show that for small quark masses the Adler-Dashen relation still holds

$$m_\pi^2(T, \mu) f_\pi^2(T, \mu) = -2m_q \langle\bar{\psi}\psi\rangle_{T, \mu} \quad (4.1)$$

where m_q is the quark mass. A similar result has been shown also in refs. [6,9]. In Fig. 3 we give the behaviour of f_π versus T at various values of the chemical potential, showing the same behaviour of the condensate, that is a first order transition above and a second order phase transition below the tricritical point [18]. Following the analysis *à la Landau* discussed previously, it has been found that f_π has the same critical exponent as $\langle\bar{\psi}\psi\rangle_T$. Again at $\mu = 0$ for $T \rightarrow 0$ one finds $f_\pi(T)/f_0 \simeq (1 - A\xi(T/f_0)^2)$ with $A \simeq 0.157$ for $N_f = 3$. Comparison with the results of ref. [19] gives again $\xi \simeq 1$ in agreement with the analysis from the condensate.

From the Adler-Dashen relation we see that the critical exponent for the pion mass is the one of the condensate multiplied by the factor $-1/2$. Therefore, at $\mu = 0, T \rightarrow T_c$ the pion mass increases as $(1 - T/T_c)^{-1/4}$, signalling that the pion is loosing its Goldstone boson nature.

5. Deconfinement phase transition

A very central problem in QCD at non zero temperature is the knowledge of its phase transitions [27]. For infinite quark masses one is lead to the choice of the thermally averaged Polyakov loop as a significant order parameter. The study of its T -dependence informs us directly on the deconfinement transition which, at some critical temperature T_d , separates the hadronic phase of confined quarks and gluons from the unconfined ones.

In the opposite limit, of vanishing quark masses, the expectation values of the quark bilinears act as order parameters for the chiral transition, at a temperature T_c beyond which chiral symmetry is restored. In this case it is the underlying symmetry, chiral symmetry, which suggests the choice of the order parameter.

In the realistic situation of QCD with quarks of finite mass, it has not been possible, so far, to conclusively decide on the phase structure. Both deconfinement and chiral symmetry restoration are expected to be present at large temperature,

but, it has not yet been possible to decide whether they occur at the same temperature or not.

Let us consider the various possibilities:

- 1) $T_c < T_d$. In this case one would have an intermediate phase of massless baryons (for massless quarks) and massive pions, corresponding to the abnormal matter discussed by Lee and Wick [28]. Casher and Pisarski [29] have argued against the stability of this phase concluding that this situation should not be verified in nature.
- 2) $T_c > T_d$. In the intermediate phase we have deconfinement, but there should be a sufficient residual interaction such as to produce pion as massless bound states (for massless quarks).
- 3) $T_c = T_d$. Recent lattice calculations with dynamical fermions [30] and our initial discussion about confining potentials suggest strongly this possibility. A further argument in favor of this case comes from Finite Energy Sum Rules (FESR) at finite temperature. In this context an effective threshold S_0 separating hadronic resonances from the QCD continuum is introduced. If one increases the temperature starting from $T = 0$, one expects that the resonances become broader and broader going into the continuum. As a result the threshold gets lower and lower going to zero for $T = T_d$. Therefore one can characterize the deconfinement temperature requiring $S_0(T_d) = 0$ [31]. Using the correlator for two axial currents it is possible to obtain a relation between $f_\pi(T_d)$ and T_d , allowing us to express a relation between chiral and deconfinement temperature. The relation one gets is $f_\pi(T_d) = T_d/\sqrt{6}$. This equation is solved graphically in Fig. 4 by intersecting $f_\pi(T)/f_0$ with the straight line $T_c/(\sqrt{6}f_0) \times (T/T_c)$. For $\xi = 1$ we get $T_d/T_c = 0.978$ [32]. The almost equality we get for the two temperatures is strictly related with the very steep behaviour of f_π around the critical point, which is a consequence of the value of the critical exponent. For instance, in the case of ref. [19] one would get $T_d/T_c = 0.55$. The result is a further indication that $T_c = T_d$.

FIGURE CAPTIONS

- Fig. 1 Phase diagram in the (μ, T) plane for $\xi = \zeta = 0.6$.
- Fig. 2 Behaviour of the condensate versus T for different values of μ : $\mu_1 = 113$ MeV, $\mu_t = 76$ MeV and $\mu_2 = 0$ MeV.
- Fig. 3 Behaviour of f_π versus T for different values of μ : $\mu_1 = 113$ MeV, $\mu_t = 76$ MeV, and $\mu_2 = 0$ MeV.
- Fig. 4 Plot of $f_\pi(T)/f_0$ and $\alpha T/T_c$ ($\alpha = T_c/\sqrt{6}f_0$) versus T/T_c for $\xi = 1$ (corresponding to $T_c \approx 102$ MeV).

REFERENCES

- [1] D.Bailin, J.Cleymans and M.D.Scadron, Phys. Rev. **D31**, 164 (1985)
- [2] A.Kocic, Phys. Rev. **D33**, 1785 (1986)
- [3] V.Galina and K.S.Viswanathan, Phys. Rev. **D38**, 2000 (1988)
- [4] A.Barducci, R.Casalbuoni, S.De Curtis, R.Gatto and G.Pettini, Phys. Lett. **B231**, 463 (1989) and Phys. Rev. **D41**, 1610 (1990)
- [5] S.I.Azakov and E.S.Aliev, Miramare-Trieste, Preprint IAEA-ICTP IC/90/71
- [6] A.C.Davis e A.H.Matheson Nucl. Phys. **B246**, 203 (1984)
- [7] P.Castorina, Nuovo Cimento **A93**, 125 (1986)
- [8] J.Cleymans, A.Kocic and M.D.Scadron, Phys. Rev. **D39**, 323 (1989)
- [9] R.Alkofer, P.A.Amundsen and K.Langfeld, Z. Phys. **C42**, 199 (1989)
- [10] T.F.Treml, Ottawa, Canada, Preprint DTJ414 D15/J (June 1990)

- [11] B.J.Harrington and A.Yildiz, Phys. Rev. Lett. **33**, 324 (1974); H.E.Haber and H.A.Weldon, Phys. Rev. **D25**, 502 (1982)
- [12] J.Finger and J.Mandula, Nucl. Phys. **B199**, 168 (1982); S.Adler and A.Davis, Nucl. Phys. **B244**, 469 (1984)
- [13] A.Le Yaouanc, L.Oliver, O.Pène and J.Raynal, Phys. Rev. **D29**, 1233 (1984)
- [14] R.Alkofer, P.A.Amundsen, Nucl. Phys. **B306**, 305 (1988)
- [15] A.Barducci, R.Casalbuoni, S.De Curtis, D.Dominici and R.Gatto, Phys. Rev. **D38**, 238 (1988)
- [16] M.Cornwall, R.Jackiw and E.Tomboulis, Phys. Rev. **D10**, 2428 (1974)
- [17] R.Baier, B.Pire and D.Schiff, Phys. Rev. **D38**, 2814 (1988); T.Altherr, P.Aurenche and T.Becherrawy, Nucl. Phys. **B315**, 436 (1989); T.Altherr and T.Becherrawy, Nucl. Phys. **B330**, 174 (1990); T.Altherr and P.Aurenche, Z. Phys. **C45**, 99 (1990); Y.Gabellini, T.Grandou and D.Poizat, Ann. of Phys. (N.Y.) **202**, 436 (1990)
- [18] A.Barducci, R.Casalbuoni, S.De Curtis, R.Gatto and G.Pettini, Phys. Lett. **B240**, 429 (1990); Phys. Rev. **D42**, 1757 (1990)
- [19] J.Gasser and H.Leutwyler, Phys. Lett. **B184**, 83 (1987) and **B188**, 477 (1987)
- [20] U.Wolff, Phys. Lett. **B157**, 303 (1985)
- [21] D.Atkinson, P.W.Johnson and K.Stam, Phys. Lett. **B201**, 105 (1988); N.Mitani, T.Muta and H.-L.Yu, Phys. Rev. **D41**, 1296 (1990); D.C.Curtis, M.R.Pennington and D.A.Walsh, Univ. of Durham, U.K., Preprint DTP-90/38 (May 1990)
- [22] G.'t Hooft, Phys. Rev. Lett. **37**, 8 (1976); Phys. Rep. **142**, 357 (1986)
- [23] R.D.Pisarski and F.Wilczek, Phys. Rev. **D29**, 338 (1984)
- [24] Z.Frei and A.Patkos, Phys. Lett. **247**, 381 (1990)
- [25] S.Klimt, M.Lutz and W.Weise, Univ. of Regensburg preprint, TPR-90-34 (1990)
- [26] B.A.Campbell, J.Ellis and K.A.Olive, Nucl. Phys. **B345**, 57 (1990).
- [27] For general reviews see: H.Satz, H.J.Specht and R.Stock, "Quark Matter 87", Z. Phys. **C38**, 1 (1988); M.Jacob, "Quark Matter 88", Nucl. Phys. **498A**, 1 (1989); F.Karsch, Nucl. Phys. (Proc. Suppl.) **B9**, 357 (1989); L.Van Hove, preprint CERN, CERN-TH-5489/89 (1989); F.Karsch, preprint CERN, CERN-TH-5498/89 (1989)
- [28] T.D.Lee and G.Wick, Phys. Rev. **D9**, 2291 (1974)
- [29] A.Casher, Phys. Lett. **B83**, 395 (1979); R.D.Pisarski, Phys. Lett. **B110**, 155 (1982).
- [30] R.V.Gavai, S.Gupta, A.Irbäck, F.Karsch, S.Meyer, B.Petersson, H.Satz and H.W.Wyld, Phys. Lett. **B241**, 567 (1990)
- [31] A.I.Bochkarev and M.E.Shaposhnikov, Phys. Lett. **B145**, 276 (1984), and Nucl. Phys. **B268**, 220 (1986); A.I.Bochkarev, Sov. J. Nucl. Phys. **45**, 517 (1987); C.A.Dominguez and M.Loewe, Phys. Lett. **B233**, 201 (1989)
- [32] A.Barducci, R.Casalbuoni, S.De Curtis, R.Gatto and G.Pettini, Phys. Lett. **B244**, 311 (1990)

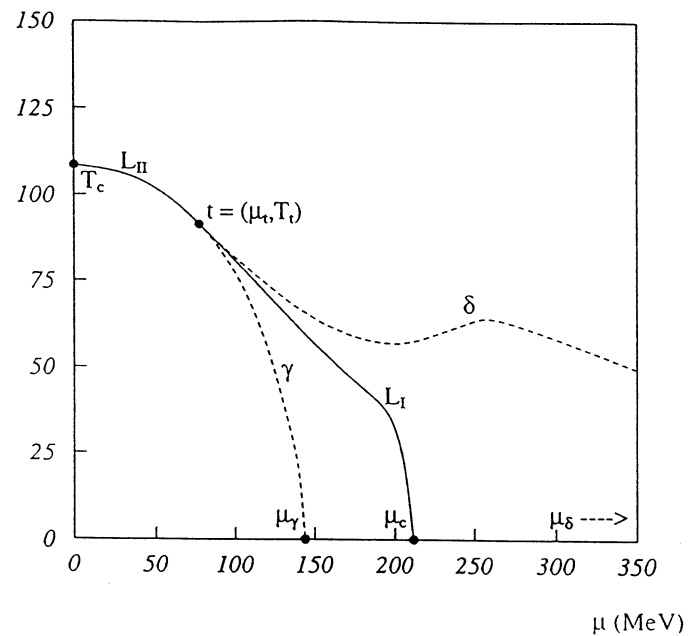


Fig. 1

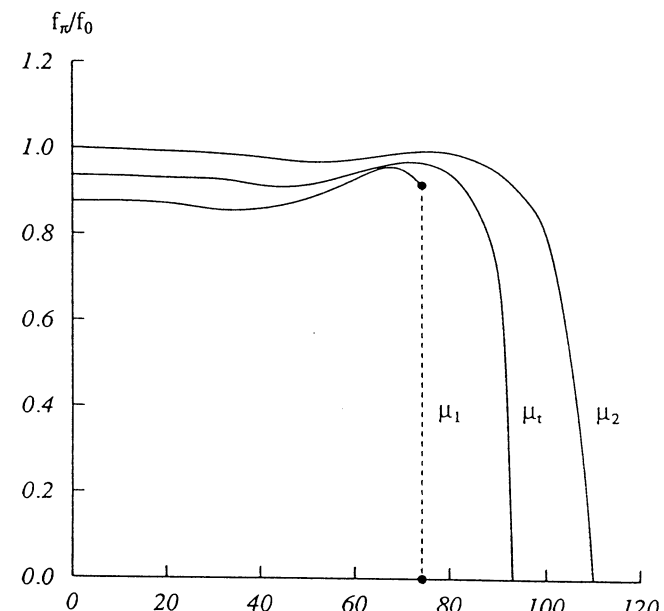


Fig. 3

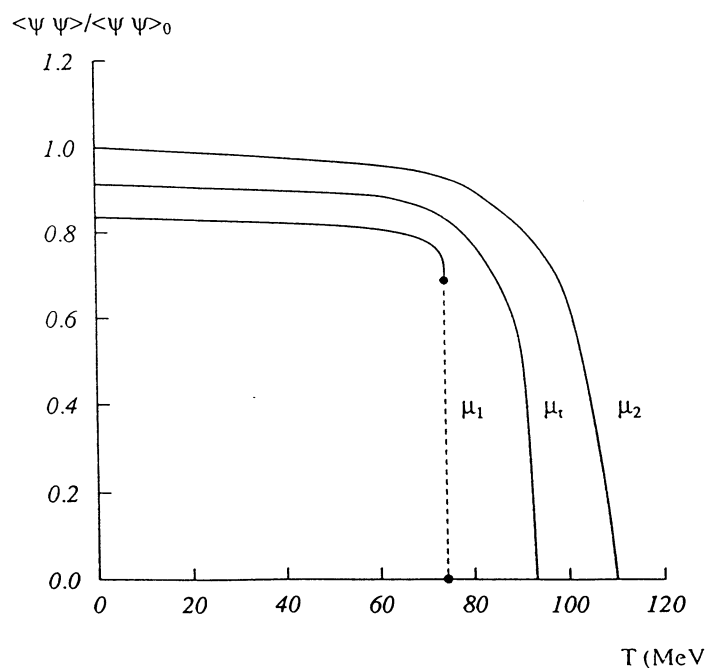


Fig. 2

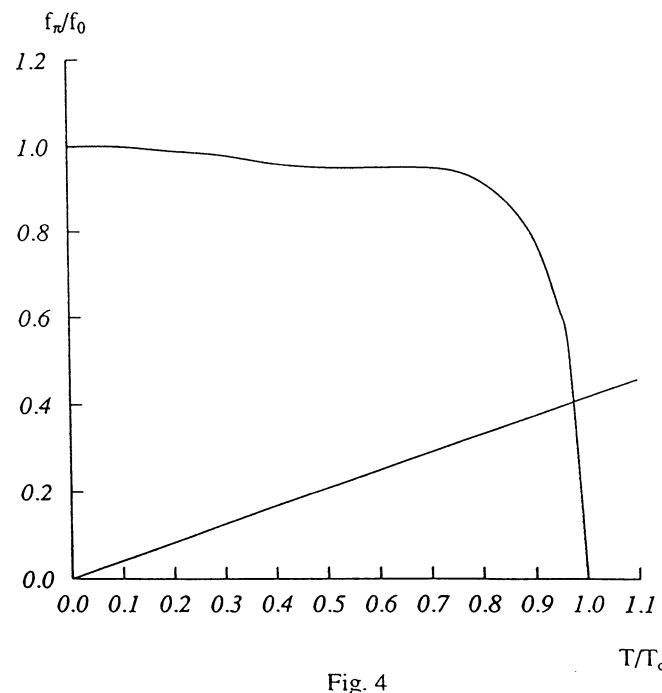


Fig. 4

General Conditions in Heavy Ion Collisions at the LHC

U. Heinz and P. Koch (Regensburg)
B. Friman (GSI)

Introduction. Discussions on possible heavy-ion experiments at the LHC need as an input rough estimates on the general conditions achievable in such collisions. These in turn require considerable extrapolations from existing experimental knowledge, since the LHC will really open up a new ball-park for nuclear physics experiments. In this contribution we will try to give such estimates to the best of our present knowledge. We will try to stay conservative and avoid overly optimistic speculations. The history of discussions on heavy ion experiments at RHIC has taught us that extrapolations based on purely theoretical input are liable to suffer major revision after experimental data become available. In this respect we are now in a better position discussing LHC physics than we were 5 years ago when planning for the first RHIC experiments: recent data from nuclear collisions at the CERN SPS and from $\bar{p}p$ collisions at the Tevatron Collider have already delivered some of the input needed to constrain our freedom when extrapolating to even higher energies and to even larger nuclei.

Basic parameters. We will base our discussion on collisions with Pb beams ($A_p = A_t = 208$) at an energy of 3.125 A TeV on 3.125 A TeV, *i.e.* a c.m. energy per nucleon pair of $\sqrt{s} = 6.25$ TeV. This corresponds to beam/target rapidities $y_{\max} = \pm \ln(\sqrt{s}/m_N) = \pm 8.8$ units in the c.m. frame, *i.e.* the collider spans a total rapidity gap of $y_p - y_t = 17.6$ units.

LHC is assumed to deliver a luminosity of $L = 10^{27}$ cm $^{-2}$ s $^{-1}$. We estimate the $A+A'$ reaction cross section by

$$\sigma_{AA'}^{\text{inel}} \simeq \pi r_0^2 (A^{1/3} + A'^{1/3})^2 , \quad (1)$$

where πr_0^2 with $r_0 = 1.2$ fm is the average transverse area covered by a nucleon in a nucleus. For $A=A'=\text{Pb}$ we obtain $\sigma_{\text{PbPb}}^{\text{inel}} \simeq 45\text{mb} \times 140 \simeq 6.3$ barn. Taking for central collisions a fraction of order 1% of the total cross section, we thus estimate *about 100 central collisions/sec.*

The decay products from these collisions will fill the rapidity gap between target and projectile. Due to the limited stopping power of a Pb-nucleus which on average decelerates a nucleon passing it with relativistic energies by only $\Delta y \simeq 2 - 2.5$ units of rapidity [2] (a shift of about 1 - 1.5 units of rapidity by sulphur nuclei has been observed in S+S collisions at CERN [3]), essentially none of the projectile and target nucleons are expected to end up at the c.m. rapidity: they will be distributed in a window of width $\sim 2\Delta y$ below target and projectile rapidity, leaving us with a clean baryon-free central region at least 8 units wide. In this region one expects to find only produced matter (mesons and baryon-antibaryon pairs), with no baryon number excess. This is one of the points where LHC provides essentially different conditions from RHIC: there the total rapidity gap is only about 10 units, such that very little room (max. 2 units) for a clean baryon free central region remains.

The existence of such a region at LHC-type energies is supported by recent data from the CØ experiment at Fermilab at $\sqrt{s} = 1.8$ TeV. The Tevatron collider spans a total rapidity gap of 15 units, and the baryon-free region is expected to be at least 5-6 units wide. CØ find no evidence for different p and \bar{p} production in the pseudorapidity window $-3.25 \leq \eta \leq 3.25$ [4]. – The possible observation of a discrepancy from this expectation in the case of heavy-ion collisions, on the other hand, would be sensational by itself, because it would shatter basic theoretical beliefs on the relativistic kinematics and the quantum mechanics of secondary particle formation.

The baryon free region provides a favorable arena for antibaryon and antinucleus production, due to the lack of final-state absorption on projectile and target nucleons and of suppression via a non-zero chemical potential. On the other hand, the large size of the central rapidity gap robs us of our chances to observe the formation of strange matter droplets (“strangelets”) in the collider mode, since strangelet formation (if it occurs at all [5]) requires the mechanism of “strangeness distillation” which only works in an environment of finite net baryon number [6]. These issues will be discussed in more detail in the following contribution.

Multiplicity densities. In our discussion we will always work with total rather than charged multiplicities, and all numbers will refer to central rapidity $y_{cm} = 0$. At SPS energies (\sqrt{s} always in GeV) one finds with minimum bias trigger (see, e.g., ref. 3, Fig. 1a)

$$\frac{dN}{dy} \Big|_{pp}^{\sqrt{s}=20} \simeq 2.4 . \quad (2)$$

Extrapolation to larger \sqrt{s} : Based on data from the $S\bar{p}pS$ collider by the UA5 collaboration [7] and from CDF data at the Tevatron [8] (both taken with a non-single-diffractive (NSD) trigger which selects for higher multiplicities than minimum bias) one finds the parametrization [8]

$$\frac{dN}{dy} \Big|_{pp}^{\text{NSD}} = \frac{3}{2} (0.023 \ln^2 s - 0.25 \ln s + 2.5) . \quad (3)$$

At $\sqrt{s} = 1800$ this reproduces the CDF value of ~ 6 for the total multiplicity density. For $\sqrt{s} = 20$ this extrapolates to $dN/dy = 2.74$ for NSD events instead of (2) for minimum bias events. Scaling eq. (3) down by a factor 2.4/2.74 and extrapolating to LHC energies, we find for minimum bias trigger

$$\frac{dN}{dy} \Big|_{pp}^{\sqrt{s}=6250} \simeq 6.8 . \quad (4)$$

By going into the tail of the multiplicity distribution, it is possible [4] to get 5 times larger multiplicity densities ($dN/dy|_{pp}^{\sqrt{s}=6250} \rightarrow 35$). As an aside, the numbers for the nominal pp collision energy in the LHC are $dN/dy|_{pp}^{\sqrt{s}=16000} = 8.3$ for minimum bias trigger, with densities > 40 in the tails of the distribution.

The last value corresponds to an energy density of about 4.5 GeV/fm 3 (see below) for the most violent pp collisions in the LHC. The only way to obtain larger energy densities than this (even if not by a huge margin) is by using heavy ions. Although in

nuclear collisions one cannot make very effective use of the tail in the pp multiplicity distribution (not all of the NN collisions can be simultaneously more violent than in minimum bias events), the growths with A (as we will show below, ϵ scales like $A^{1/3+\alpha}$ with $\alpha \geq 0$) eventually makes up for this disadvantage. For Pb nuclei the multiplicative factor is > 6 (*i.e.* even larger than for the highest multiplicity bin in pp), but it now corresponds to about a 1% fraction of the total cross section (rather than 10^{-4} in the case of pp). Also the high density region is much larger and lives longer, reducing the influence of surface effects.

Extrapolation to larger nuclei: This extrapolation is much less certain than the one in \sqrt{s} , because the only available data are from the recent SPS heavy ion experiments (*i.e.* at low \sqrt{s}) and for small nuclei (up to ${}^{32}S$). The streamer chamber collaboration has made a comparison between central (*i.e.* full overlap) S+S and minimum bias pp collisions. They find [9] that in central S+S events (7% of total cross section) 54-58 nucleons participate, *i.e.* 27-29 times as many as in pp collisions, and that at the same time the total multiplicity is a factor 33 times larger. The rapidity distribution is about 10% narrower, and the central rapidity density a factor 36 higher in S+S than in $p + p$. Thus dN/dy appears to scale like $A_{\text{part}}^{1+\alpha}$, with $\alpha = 0.05$. The fact that $\alpha > 0$ is attributed to rescattering [9] which, however, in this small collision system can only affect about 50% of the participants. For larger nuclei at the same SPS energy α may thus be about twice as large, $\alpha \geq 0.1$.

We thus expect (and the Pb-beam project at CERN will test this conjecture) that at SPS energies

$$\frac{dN}{dy} \Big|_{AA}^{\sqrt{s}=20} = A^{1+\alpha} \frac{dN}{dy} \Big|_{pp}^{\sqrt{s}=20} \quad \text{with} \quad 0 \leq \alpha \leq 0.1 , \quad (5)$$

yielding for Pb+Pb the estimate

$$\frac{dN}{dy} \Big|_{\text{PbPb}}^{\sqrt{s}=20} = 500 \cdot f \quad \text{with} \quad 1 \leq f \leq 1.7 . \quad (6)$$

However, it is completely unknown how α will behave as a function of \sqrt{s} . There are arguments (see K. Eskola's talk) that at higher energies hard phenomena (mini-jets) should become increasingly important for the production of multiplicity, and such phenomena are expected to scale like $A^{4/3}$, corresponding to $\alpha = 1/3$. (This is very likely a safe upper limit on α .) As a result, for the LHC our estimate is less certain:

$$\frac{dN}{dy} \Big|_{\text{PbPb}}^{\sqrt{s}=6250} = 1400 \cdot f \quad \text{with} \quad 1 \leq f \leq 6 . \quad (7)$$

If the upper limit on f were exhausted at LHC energies, experiments would have to cope with up to 8000 particles per unit rapidity for Pb beams, and up to 10000 for U beams. However, based on our present knowledge from heavy ion experiments at the SPS, considerably smaller densities are not unlikely.

We summarize our results (2-7) on the multiplicity densities with ${}^{208}\text{Pb}$ beams in the following table (LHB="Large Hadron Beam" denotes fixed target mode operation of the LHC, and the numbers in brackets are \sqrt{s} in GeV):

	SPS(17)	LHB(77)	RHIC(200)	LHC(6250)
dN/dy	500 - 850	560 - 1000	670 - 2000	1400 - 8000
α	0 - 0.1	0 - 0.1	0 - 0.2	0 - 0.3

The range of the uncertainty interval for dN/dy is given by the factor $f = A^\alpha$ (with $A=208$) whose upper limit depends on the unknown energy dependence of α . In the lower row we give our guess for a reasonable range for α which we used to calculate the upper row. A similar range of uncertainty is reflected in the predictions from various event generators (discussed later in these proceedings).

Energy and entropy densities in the central region. In contrast to SPS energies, at LHC energies the Bjorken picture of boost-invariant longitudinal expansion [10] is likely to be applicable over a large rapidity range around y_{cm} . Based on this scenario, there exist two formulas to extract initial state information from the final multiplicity densities:

$$(i) \quad \epsilon = \frac{1}{\pi(1.2A^{1/3})^2} \frac{1}{\tau_0} \langle m_T \rangle \frac{dN}{dy} \quad (\text{Bjorken [10]}) \quad (8)$$

$$(ii) \quad s = \frac{3.6}{\pi(1.2A^{1/3})^2} \frac{1}{\tau_0} \frac{dN}{dy} \quad (\text{Hwa \& Kajantie [11]}) \quad (9)$$

(i) assumes free-streaming expansion without work done by the pressure, and τ_0 is the formation time of the particles. Unless the particles are also thermalized at τ_0 , ϵ from (8) cannot be used to estimate a temperature; on the other hand, if τ_0 is taken to be the thermalization time scale, (8) is inconsistent because it neglects work done by the thermal pressure during the expansion. However, at least transverse collective flow can be taken into account effectively by increasing $\langle m_T \rangle$.

(ii) assumes longitudinally boost-invariant *hydrodynamical* expansion at constant entropy, and thus includes the work done by the pressure when extrapolating from final state densities to initial conditions. In this case τ_0 is the time scale for local equilibration. (9) uses an ideal gas equation of state for massles quarks and gluons or massles pions and neglects entropy production during expansion by viscosity or shocks.

For the same τ_0 , (9) yields higher initial temperatures than (8), see below.

With our estimates (7) on dN/dy for Pb-beams we obtain from (8,9)

$$\epsilon = 3.5 \left(\frac{1\text{fm}/c}{\tau_0} \right) \left(\frac{\langle m_T \rangle}{0.4\text{GeV}/c^2} \right) f \text{ GeV/fm}^3 \quad (10)$$

$$s = 32 f \left(\frac{1\text{fm}/c}{\tau_0} \right) \text{ fm}^{-3} \quad (11)$$

To estimate $\langle m_T \rangle$ in (10) we use the result [4,12] that minimum bias events at $\sqrt{s} = 1.8$ TeV show $\langle p_T \rangle = 0.46 \pm 0.01$ which, using the measured K/π , \bar{p}/π , Λ/π ratios [4], translates into $\langle m_T \rangle \simeq 0.53$. This is $\sim 20\%$ higher than at SPS energies. Due to the increasing importance of mini-jets at higher energies, $\langle m_T \rangle$ may grow some more for LHC.

The time scale τ_0 is only known to be of the order of $1 \text{ fm}/c$ and could well be a factor 2 larger or smaller; it is very hard to make a better prediction. In some

models [13] it depends on A like $A^{-1/6}$ which would buy us a factor 2.4 in initial state densities for Pb-beams. We will assume $\tau_0 = 1 \text{ fm}/c$, hoping that at least for Pb-beams this is a conservative estimate.

We thus obtain from (10,11)

	SPS(17)	LHB(77)	RHIC(200)	LHC(6250)
$\epsilon (\text{GeV}/\text{fm}^3)$	1.6 - 2.7	1.8 - 3.1	2.1 - 6.3	4.4 - 25
$s (\text{fm}^{-3})$	11 - 19	13 - 23	15 - 45	32 - 180

Note that these estimates refer to *average* central collisions; for estimates on the variance of ϵ we refer to the contributions on event generators. While the upper limits on ϵ and s are rather uncertain, we believe the lower limits to be safe conservative estimates. These lower estimates exceed for all four machines the critical energy density of $\sim 1 \text{ GeV}/\text{fm}^3$ (corresponding to a critical temperature of 150 MeV) which seems to be favored by the latest lattice QCD calculations including dynamical fermions (see B. Petersson's talk). However, only for the LHC they also exceed the threshold $\epsilon \simeq 5 \epsilon_{\text{cr}}$ (corresponding to $T \simeq 1.5 T_{\text{cr}}$) above which the QGP should behave more or less as an ideal gas.

Initial temperatures in the central region. We now use an ideal gas equation of state for non-interacting massless quarks (3 flavors, zero chemical potential) and gluons, to convert these numbers into estimates for the initial temperature of an equilibrated quark-gluon plasma. When using Bjorken's formula (8) as a basis, we first have to subtract the vacuum energy density $B \simeq 0.4 \text{ GeV}/\text{fm}^3$ due to the outside bag pressure. From

$$\epsilon = \frac{\pi^2}{30} \left(2 \times 8 + \frac{7}{8} 2 \times 3 \times 3 \times 2 \right) \frac{T^4}{(\hbar c)^3} + B \quad (12)$$

(the numbers denote spin, color, flavor and particle-antiparticle degeneracies) we thus obtain

$$T_{\text{Bj}} = \left(\frac{\epsilon - B}{1953} \right)^{1/4} \quad (T \text{ in GeV}, \epsilon \text{ in } \text{GeV}/\text{fm}^3) \quad (13)$$

From the analogous ideal gas expression for s we obtain on the basis of (9) the temperature estimate

$$T_{\text{HK}} = \left(\frac{s}{2605} \right)^{1/3} \quad (T \text{ in GeV}, s \text{ in } \text{fm}^{-3}) \quad (14)$$

The results are summarized in the following table:

	SPS(17)	LHB(77)	RHIC(200)	LHC(6250)
T_{Bj} (MeV)	157 - 185	164 - 193	172 - 234	213 - 335
T_{HK} (MeV)	162 - 194	171 - 207	179 - 259	231 - 410

For comparison between free-flowing and isentropic hydrodynamical expansion we quote for LHC the energy densities corresponding to these temperatures:

$$\epsilon_{\text{Bj}} \simeq 4.4 - 25 \text{ GeV}/\text{fm}^3; \quad (15)$$

$$\epsilon_{\text{HK}} \simeq 6.0 - 56 \text{ GeV}/\text{fm}^3. \quad (16)$$

For smaller values of τ_0 this difference grows like $(1\text{fm}/c\tau_0)^{4/3}$ while the temperature T_{HK} itself grows very weakly like $\tau_0^{-1/3}$.

While the temperatures that can be reached with LHC are thus safely above the expected critical temperature for the phase transition ($\sim 150 \text{ MeV}$), it appears very difficult to exceed temperatures of 350-400 MeV. This will be of great relevance for the prospects of observing thermal dileptons from the quark-gluon plasma stage in these collisions (see the appropriate contributions).

Conditions in the fragmentation regions. Due to the large central rapidity gap in the baryon density it will be experimentally all but impossible to study, with LHC in the collider mode, the projectile and target fragmentation regions of the colliding nuclei. Such a study would be only possible by running LHC in a fixed target mode which would, however, correspond to very much smaller \sqrt{s} . Therefore it is important to ask: are we missing anything of crucial interest?

Fortunately, the answer is "no". Due to the limited stopping power of even very large nuclei, there is only a limited maximum rapidity shift for the nucleons in the fragmentation regions of order $\Delta y \sim 2 - 2.5$. According to [14] this leads to a kinematical compression of baryon density in those regions by a factor

$$\frac{\rho}{\rho_0} = \frac{1}{\Delta\gamma - \sqrt{\Delta\gamma^2 - 1}} = 7.5 - 12 \quad (17)$$

where $\Delta\gamma = \cosh \Delta y \sim 3.7 - 6.1$ is the change in the Lorentz-contraction factor induced by $\Delta y \sim 2 - 2.5$. Any further compression requires collective effects (compression shocks, density waves, etc.) which are excluded in the ultrarelativistic regime from the target fragmentation region due to their intrinsic retardation.

It is also not easily possible to trap inside the fragmentation region a large fraction of the energy produced by collisionally exciting the target and projectile nucleons. In [14] for $\sqrt{s} = 100 \text{ GeV}$ the excitation energy of the target fireball is estimated to be

$$M_{\text{FB}} \simeq 3.5 \text{ GeV/nucleon}, \quad (18)$$

with a very weak rise as a function of \sqrt{s} ($\sim \ln \ln \sqrt{s}$). Thus one expects that for $\sqrt{s} = 6250 \text{ GeV}$

$$M_{\text{FB}} \leq 5 \text{ GeV/nucleon}. \quad (19)$$

Combining this with the kinematical compression (17) of the fireball we thus estimate for the fragmentation regions

$$3.9 \text{ GeV}/\text{fm}^3 \leq \epsilon \leq 9 \text{ GeV}/\text{fm}^3. \quad (20)$$

This does not lead to energy densities which by themselves would be more interesting than those obtained in the central region. Also, these estimates have a very weak \sqrt{s} -dependence. The kinematical compression effect (17) can thus be studied nearly as effectively at lower energies (SPS, RHIC), using large nuclei. To search for a baryon-rich quark-gluon plasma in the target fragmentation regions, the SPS with Pb-beams thus appears to be much better suited than LHC.

Lifetime and size of the collision zone, transverse flow. In this section we estimate the expansion timescales of a hot quark-gluon plasma formed in the central

rapidity region of a nucleus-nucleus collision at LHC energies, assuming hydrodynamic expansion and taking the transverse flow into account. We also discuss the transverse momentum spectra in such a model, in light of our above estimates of the initial energy densities.

In order to obtain simple estimates, we shall assume, that the system is described by the Bjorken model [10], extended to take the transverse flow into account [15,16]. Thus, after some formation and equilibration time τ_0 , the system is assumed to be in a deconfined quark-gluon plasma phase in local thermodynamic equilibrium. (Since the above estimates for the initial ϵ and T cannot be reasonably reconciled with an equilibrium hadron resonance gas, we shall not consider a pure hadronic scenario.) Thereafter, the system expands hydrodynamically in *both* the longitudinal and the transverse direction. Along the beam axis, the initial conditions for the hydrodynamic expansion are assumed to be translationally invariant, while in the transverse direction different initial conditions are possible, with the initial transverse size of the system roughly given by the radius R_A of the colliding nuclei.

The early stages of the hydrodynamic expansion are dominated by the fast longitudinal expansion. The typical timescale for the transverse expansion is given by the time it takes a sound wave to travel from the surface to the center of system, $\tau_T \approx R_A/c_s$, where c_s is the velocity of sound in the plasma ($\simeq 1/\sqrt{3}$). Thus, for a central collision of two ^{208}Pb nuclei $\tau_T \simeq 10 \text{ fm}/c$. Consequently, for time scales $\ll 10 \text{ fm}/c$, the transverse expansion can be neglected.

Lifetimes. The lifetime of the pure plasma phase can be estimated by taking into account only the longitudinal expansion. For boost invariant initial conditions, corresponding to a plateau in rapidity, the solution to the hydrodynamic equations remains boost invariant. Thus the thermodynamic quantities are, at a given proper time $\tau = \sqrt{t^2 - z^2}$, independent of the rapidity $y = \frac{1}{2} \ln((t+z)/(t-z))$. In ideal hydrodynamics, the entropy is conserved during the expansion, which for the longitudinal expansion implies $s\tau = s_0\tau_0$, where the s_0 is the initial entropy density. Since the entropy density in the plasma is proportional to T^3 , this implies that the transition temperature T_{tr} is reached at the proper time

$$\tau_1 = \left(\frac{T_0}{T_{\text{tr}}} \right)^3 \tau_0. \quad (21)$$

For $T_{\text{tr}} = 150 \text{ MeV}$ and we obtain from the table of temperatures above the following table for the lifetime of the plasma phase:

	SPS(17)	LHB(77)	RHIC(200)	LHC(6250)
τ_1/τ_0	1.15 - 2.1	1.3 - 2.6	1.5 - 5.1	2.9 - 20

In all cases except the most optimistic upper temperature limit for LHC, this time is short enough to allow to neglect transverse expansion.

At $\tau > \tau_1$ the plasma coexists with the hadronic phase, until the hadronization is finished. Hence, the lifetime of the plasma is effectively longer than τ_1 . In determining the lifetime of the coexistence phase the transverse expansion can no longer

be neglected. Still, to obtain a rough estimate, let us first only consider longitudinal expansion. Then entropy conservation implies

$$s_{\text{pl}}(T_{\text{tr}}) \tau_1 = s_{\text{had}}(T_{\text{tr}}) \tau_2. \quad (22)$$

Here τ_2 denotes the completion of the hadronization process, and $s_{\text{pl}}(T_{\text{tr}})$, $s_{\text{had}}(T_{\text{tr}})$ are the entropy densities of the plasma and hadronic phase, respectively, at the transition temperature. If the phase transition is strongly first order, with a large jump in the entropy density due to gluon deconfinement, τ_2 can thus be much larger than τ_1 . Lattice calculations have not yet converged on a verdict as to the order of the QCD phase transition, but in any case indicate a drop of the entropy density by nearly an order of magnitude in a rather narrow region around T_{tr} . For purely longitudinal expansion, we would thus expect a rather long lifetime of the coexistence region.

Transverse expansion shortens this estimate to a certain extent; details depend on the properties of the equation of state near the phase transition, a subject still under intensive study by the lattice people. The solution to the hydrodynamic equations for the coupled longitudinal and transverse flow can only be obtained numerically [17]. For $T_0 = 250 \text{ MeV}$ and $T_{\text{tr}} = 200 \text{ MeV}$ as above, and using a simple bag model equation of state for the QGP while approximating the hadron phase by an ideal gas of massless pions, the transverse rarefaction wave reaches the center at $\tau \approx 30 \text{ fm}/c$ for a central collision of two Uranium nuclei. The unexpectedly large timescale for the transverse expansion is due to the small sound velocity in the coexistence region. In fact, the hydrodynamic solution involves a rarefaction shock propagating into the coexistence region from the surface [15,18]. The slow expansion of the coexistence region has been confirmed in [19] where a system of quark-gluon plasma globs interacting with pions was studied in a cascade model. Still, shorter lifetimes are expected to result if a more realistic equation of state, including resonances in the hadron phase and interactions in the QGP [20], is used which reproduces the somewhat weaker discontinuity in s as indicated by the lattice results.

Once the rarefaction wave has reached the center and the system is completely hadronized, the expansion is effectively three-dimensional [17]. Thus the system cools very fast in the hadronic phase and freezes out almost immediately. Consequently, the expected total lifetime of a hot equilibrated system is on the order of 30 fm/c.

We note at this point, that a pure hadronic scenario would live shorter; since the sound velocity does not become small the transverse expansion timescale is then of the order of 10 fm/c [17].

Transverse size at freeze-out. Due to transverse expansion, the transverse size of the fireball at decoupling is expected to be larger than R_A . First results from HBT interferometry with pions from nuclear collisions at the AGS and SPS [21] strongly support this expectation. One finds that the transverse freeze-out radius R_f scales like $(dN/dy)^\beta$, with β in the range $1/3 \leq \beta \leq 1/2$. This behaviour is not yet entirely understood theoretically, because it is not easy to estimate the freeze-out volume without a detailed understanding of the expansion dynamics. Assuming [22] isentropic expansion of the collision zone, an initial slice of size $V_0 = \pi R_A^2 \tau_0$ would grow in volume to $V_f = (V_0 s_0)/s_f = (3.6/s_f) dN/dy$, where we have inserted the

relation (9) for the initial state, and where s_f is the entropy density at freeze-out. At this point the transverse radius of the slice will be $R_f > R_A$, and its longitudinal dimension will have grown by boost-invariant expansion with the velocity of light to a size $\tau_{TC} \simeq (R_f/c_s)c \simeq \sqrt{3}R_f$ (which is the time it takes a sound wave to travel from the surface to the center): $V_f = \sqrt{3}\pi R_f^3$.

To determine s_f we need a freeze-out criterium. We can either assume that freeze-out occurs immediately after the end of hadronization, in which case we have to calculate the entropy density of a hadron gas at the transition temperature $T_f = T_{tr} \simeq 150$ MeV. In this case we obtain

$$R_f^{(1)} = 1.05 \text{ fm} \left(\frac{dN}{dy} \right)^{1/3}, \quad (23)$$

where the coefficient corresponds to the assumption of a massless pion gas in the final state.

The other possibility is to calculate pion freeze-out by asking when the pion mean free path exceeds the size of the system, $R_f = \lambda_\pi$. In this case an additional temperature dependence enters through the strongly energy dependent $\pi\pi$ cross section (which nearly vanishes at zero momentum) [23]: $\lambda_\pi \simeq 12f_\pi^4/T_f^5$ where $f_\pi = 93$ MeV is the pion decay constant. Eliminating T_f from the freeze-out condition and the final volume, again employing an ideal massless pion gas, we obtain this time

$$R_f^{(2)} = 0.86 \text{ fm} \left(\frac{dN}{dy} \right)^{5/12}. \quad (24)$$

Finally, if one includes also the effect of interactions among the pions and of resonances on the hadron gas equation of state, which according to [24] can be parametrized by using, instead of the ideal gas expression, $s = (4/3)T^5/T_c^2$ with $T_c = 100$ MeV, we find

$$R_f^{(3)} = 0.46 \text{ fm} \left(\frac{dN}{dy} \right)^{1/2}. \quad (25)$$

All three expressions are compatible with the available data [22], and we will need experiments with Pb-beams at the SPS to distinguish between them. Extrapolating into the region of dN/dy reached by LHC and using $R_A = 7$ fm for Pb-beams, we obtain the following table:

	SPS(17)	LHB(77)	RHIC(200)	LHC(6250)
$R_f^{(1)}/R_A$	1.2 - 1.4	1.2 - 1.5	1.3 - 1.9	1.7 - 3.0
$R_f^{(2)}/R_A$	1.6 - 2.0	1.7 - 2.2	1.8 - 2.9	2.5 - 5.2
$R_f^{(3)}/R_A$	1.5 - 1.9	1.6 - 2.1	1.7 - 2.9	2.5 - 5.9

Thus at LHC with Pb-beams we will be able to produce fireballs as big as several 10^4 fm^3 at the point of freeze-out; this will be our best chance ever to produce locally equilibrated excited hadronic matter *in bulk!*

Transverse momentum spectra. If the deconfinement transition is of first order, a characteristic correlation between multiplicity and $\langle p_T \rangle$ is predicted [25]. The basic idea is that the temperature and pressure, which determine the average transverse

momentum of the particles, remain roughly constant during the hadronization transition, while the entropy, which is proportional to the multiplicity density, changes.

This problem has been studied in [17]. The initial average transverse momentum, before the onset of transverse flow, indeed shows a plateau for initial conditions corresponding to the coexistence region, and a sharp rise when the plasma phase starts being probed. The effect of the subsequent hydrodynamic evolution is to convert some thermal energy into collective transverse flow, and the amount of flow at freeze-out increases with the initial entropy density. Thus even in the coexistence region, where T is constant, $\langle p_T \rangle$ due to its increasing flow component keeps growing as a function of $dN/dy(\sim s)$, thereby drastically smoothing out [17] the structure in $\langle p_T \rangle$. What remains is a decrease in the slope of $\langle p_T \rangle$ as a function of dN/dy which for reasonable model parameters lies in the range $3 \lesssim (1/A)(dN/dy) \lesssim 50$. For multiplicity densities beyond $50A$, a smooth rise of the average transverse momentum again sets in. This threshold should come down somewhat if instead of $T_{cr} = 200$ MeV [17] the more realistic value $T_{cr} = 150$ MeV were used in the calculation.

According to our above estimates for average Pb+Pb events one can expect a multiplicity density of at most 8000 charged particles, which corresponds to $(1/A)(dN/dy) \approx 40$. Thus, although the energy density reached in such collisions is probably well inside the plasma domain, the average transverse momentum may still be fairly unspectacular, and we will not be able to deeply probe into the “asymptotic rise region”.

The detailed shape of transverse momentum spectra may be useful for identifying collective flow. The idea is that particles of different mass, travelling with the same collective velocity v , have different momenta $p = mv$. Thus, a heavy particle receives a higher transverse momentum from the collective flow than a lighter one. This affects both the average, $\langle p_T \rangle$ [17], and the p_T -distribution [26]. In Ref. 17 it was found (using the Bjorken geometry) (that for $(1/A)(dN/dy) \approx 10$ the average p_T of pions is $\simeq 400$ MeV, while that of nucleons is $\gtrsim 1$ GeV. This difference corresponds to a radial velocity at decoupling of $v_r/c \approx 0.6$, and it increases with dN/dy . A tendency for such a behaviour, with numbers for $\langle p_T^{\pi,p} \rangle$ of the given order, was observed in the recent study [4] at the Tevatron. An analysis [26] of heavy ion data from Brookhaven and the SPS indicates somewhat smaller expansion velocities, $v_r/c \approx 0.45$, at these lower energies. A similar analysis at LHC would be very interesting. It requires clean particle identification and high statistics data on the momentum distributions of various particle species, spanning the p_T -range from 0 to several GeV/c.

Conclusions. At LHC energies we expect a large baryon-free central rapidity gap, at least 8 units wide, which is filled with produced matter at high initial density. Extrapolating from existing “low”-energy heavy-ion and high-energy $\bar{p}p$ data, we conclude that LHC will be the first machine to safely exceed in average central Pb-Pb collisions the critical energy density for quark matter formation, even in the most conservative estimates. To exceed these lower limits by a considerable margin it is necessary that semi-hard mechanisms (like minijet production), for which the produced multiplicity density scales like $A^{4/3}$ rather than A , begin to dominate at higher energies the production mechanisms which are at work in present day

experiments. In this case the use of very heavy ions could pay doubly off, by maximizing the size and lifetime of the high-density region *and* by considerably increasing its initial density.

The combination of high initial energy densities and large nuclei leads to sizes and lifetimes of the hot collision zone which are unique and without precedents. Fireballs with volumes of the order of several 10^4 fm^3 and lifetimes of several $10 \text{ fm}/c$ will provide a unique chance for observing locally equilibrated hot hadronic matter, allowing the use of simple thermodynamic concepts for its description.

However, even in the most optimistic extrapolation scenarios it appears to be difficult to reach initial plasma temperatures above 350-400 MeV. This will be sufficient to fully equilibrate strangeness (see next contribution), but may make it difficult to see the emission of thermal dileptons from the QGP or to observe the asymptotic rise in the average p_T as discussed above.

With LHC in the collider mode, the target fragmentation regions are virtually out of experimental reach. However, due to relativistic kinematic effects and the resulting transparency of the colliding nuclei, the conditions in the target fragmentation regions are only very weakly energy dependent in the relevant domain. It is thus possible and much more advisable to study them under not too dissimilar conditions at lower beam energies with the SPS Pb-beam, rather than sacrificing another interaction region at LHC for a dedicated fixed target experiment.

Acknowledgements: The authors thank the other members of the working subgroup (E. Quercigh, H. Ströbele, and O. Villalobos) and H. Satz for the fruitful discussion meetings and their input to this presentation. U. H. gratefully acknowledges a useful exchange with K. Kajantie on the influence of minijets. This work was supported in part by BMFT.

References:

1. E-710 Coll., N. A. Amos *et al.*, *Phys. Lett.* **B243** (1990), 158, Fig. 3
2. W. Busza and A. Goldhaber. *Phys. Lett.* **B139** (1984) 235
3. NA35 Coll., H. Ströbele *et al.*, in: "The Nuclear Equation of State", W. Greiner and H. Stöcker (eds.), p. 85, NATO ASI Series, Vol. 216B, Plenum, New York, 1990
4. E-735 Coll., T. Alexopoulos *et al.*, *Phys. Rev. Lett.* **64** (1990) 991
5. H. W. Barz, B. Friman, J. Knoll, and H. Schulz, *Phys. Lett.* **B242** (1990) 328
6. U. Heinz, K. S. Lee, and M. Rhoades-Brown, *Mod. Phys. Lett.* **A2** (1987) 152;
C. Greiner, P. Koch, and H. Stöcker, *Phys. Rev. Lett.* **58** (1987) 1825
7. UA5 Coll., G. J. Alner *et al.*, *Z. Phys.* **C33** (1986) 1
8. CDF Coll., F. Abe *et al.*, *Phys. Rev.* **D41** (1990) 2330
9. NA35 Coll., H. Ströbele *et al.*, talk at "Quark Matter '90", *Nucl. Phys.* **A**, in press
10. J. Bjorken, *Phys. Rev.* **D27** (1983) 140
11. R. Hwa and K. Kajantie, *Phys. Rev.* **D32** (1985) 1109
12. E-735 Coll., T. Alexopoulos *et al.*, *Phys. Rev. Lett.* **60** (1988) 1622
13. M. Gyulassy and A. Iwazaki, *Phys. Lett.* **B165** (1985) 157;
A. Kerman, T. Matsui, and B. Svetitsky, *Phys. Rev. Lett.* **56** (1986) 219
14. R. Anishetty, P. Köhler, and L. McLerran, *Phys. Rev.* **D22** (1980) 2793
15. G. Baym, B. L. Friman, J.-P. Blaizot, M. Soyeur and W. Czyż, *Nucl. Phys.* **A407** (1983) 541
16. H. von Gersdorff, L. McLerran, M. Kataja and P. V. Ruuskanen, *Phys. Rev.* **D34** (1986) 794
17. M. Kataja, P. V. Ruuskanen, L. D. McLerran and H. von Gersdorff, *Phys. Rev.* **D34** (1986) 2755;
K. Kajantie, M. Kataja, L. McLerran and P. V. Ruuskanen, *Phys. Rev.* **D34** (1986) 811
18. B. L. Friman, K. Kajantie and P. V. Ruuskanen, *Nucl. Phys.* **B226** (1986) 468
19. G. Bertsch, M. Gong, L. McLerran, V. Ruuskanen, and E. Sarkkinen, *Phys. Rev.* **D37** (1988) 1202
20. U. Heinz, P. R. Subramanian, H. Stöcker, and W. Greiner, *J. Phys.* **G12** (1986) 1237
21. W. Zajc, rapporteur talk given at "Quark Matter '90", *Nucl. Phys.* **A**, in press
22. The following arguments are a modified version of the ones given in R. Stock, IKF Frankfurt preprint IKF90-3, to be published in *Annalen der Physik*
23. J. L. Goity and H. Leutwyler, *Phys. Lett.* **B228** (1989) 517
24. E. V. Shuryak, *Phys. Rep.* **61** (1980) 71
25. L. van Hove, *Phys. Lett.* **B118** (1982) 138
26. K. S. Lee, U. Heinz, and E. Schnedermann, *Z. Phys.* **C48**, in press

Strangeness and Antimatter Production at the LHC

P. Koch and U. Heinz (Regensburg)
 B. Friman (GSI)

Introduction. It is known that in e^+e^- , ep , and pp collisions the ratio of produced strange over produced light quark pairs, $\lambda_s = (\bar{s}s/\frac{1}{2}(\bar{u}u + \bar{d}d))_{\text{produced}}$, is about 0.2 [1] to 0.3 [2] and is nearly independent of \sqrt{s} all the way from a few times the threshold energy to collider energies (see e.g. Fig. 1). Only at Tevatron energies there appears to be a significant (10–20%) rise above this value [1,3], due to a strong rise by about 50% of the K/π ratio in very high multiplicity $p\bar{p}$ events [3]. The definition of λ_s does not include secondary $\bar{u}u$ and $\bar{d}d$ pairs which stem from resonance decays. Thus the experimentally observed ratio of strange to non-strange quark pairs (extracted from particle ratios like K/π , Λ/p , etc.) is even smaller (since resonance decays in general do not produce additional strangeness) and has to be corrected for resonance contributions in order to extract the “primordial” s/u -ratio. The smallness of λ_s shows that strangeness production is suppressed in collisions between elementary particles. Its constancy over the whole energy range in hadronic collisions would make a possible deviation in nuclear collisions, even if only by a factor 2 or so, a clear signal for new physics.

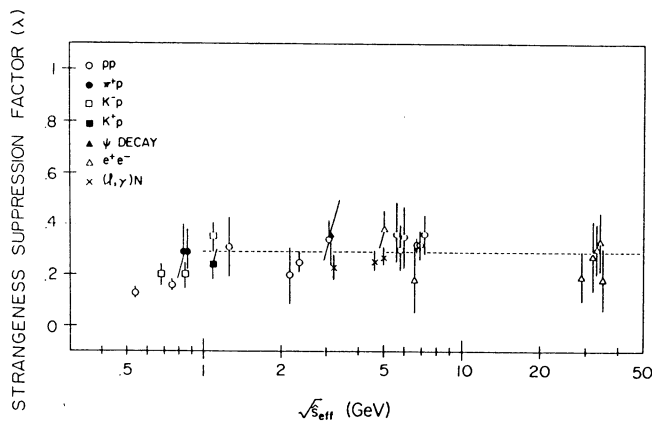


Fig. 1: Strangeness suppression factor λ_s as a function of the effective c.m. energy [2].

In contrast to this feature of pp phenomenology, in an equilibrated quark-gluon plasma with temperature $T > m_s \approx 150 - 200$ MeV and $\mu_B = 0$, one has $(s/u) = 2(\bar{s}s/\bar{q}q) \simeq 0.9 - 1.0$ (where $\bar{q}q \equiv \frac{1}{2}(\bar{u}u + \bar{d}d)$), which is much larger than the value of λ_s observed in pp collisions. Thus, at first sight, it might appear that QGP formation in collisions between nuclei should manifest itself in a strong rise of the factor λ_s , by about a factor 3. (Additional effects, like the particular enhancement of the (\bar{s}/\bar{u}) -ratio that occurs in baryon-rich systems due to the chemical suppression of light antiquarks [4], need not be considered here, because LHC experiments will have access primarily to the baryon-free central region.)

However, the large number of gluons in the QGP strongly influences the hadronization process and thus λ_s . This will be discussed in the first part of this contribution. In the second part we will discuss antibaryon production in nuclear collisions and some possible anomalies in this context associated with QGP formation.

Strangeness production. Based on the estimates in our preceding contribution, the initial temperature and plasma lifetime should be ample to equilibrate strangeness well before the plasma begins to hadronize [4]. We can thus begin our considerations with an (s/u) -ratio close to 1. As the plasma expands and cools, the equilibrium ratio will begin to drop slightly below 1 when the temperature decreases below m_s . However, due to the cooling, the $\bar{s}s$ -annihilation processes become slower at the same time so that the new, somewhat lower equilibrium value will be approached more slowly and from above. We can thus safely assume that at the onset of hadronization (at $T_{cr} \approx 150$ MeV) the (s/u) -ratio is still in the region 0.8-1.0, and we will take it to be 1 to simplify our estimates.

The complications begin with the hadronization process. It is a simple matter of counting degrees of freedom to see that in the plasma phase the gluons carry about 1/3 of the total entropy:

$$\frac{S_g}{S_{u\bar{u}d\bar{d}s\bar{s}}} = \frac{2 \times 8}{\frac{7}{8} \times 2 \times 2 \times 3 \times 3} \simeq \frac{1}{2}. \quad (1)$$

With each gluon carrying 3.6 units of entropy, while each (anti-)quark contributes 4.2 units, this translates into the following ratio of particle numbers ($N_q \equiv N_u + N_d$):

$$\frac{N_g}{N_q + N_{\bar{q}} + N_d + N_{\bar{d}}} \simeq 0.6. \quad (2)$$

The easiest way to carry the initial condition $\lambda_s \simeq 1$ over into the final state (thus producing a clear QGP signal) would be to assume that during hadronization these quarks and antiquarks simply combine to form hadrons while the gluons just vanish without trace. However, in this way the number of degrees of freedom is severely reduced, which creates the problem that total entropy can only be conserved if the final state has a very large entropy per particle. What this means can be seen by studying the expression for S/N in a Boltzmann-gas [5] ($u = m/T$ is fixed by the hadronization temperature):

$$\frac{S}{N} = 4 + \frac{u K_1(u)}{K_2(u)} + \ln \left(\frac{V T^3}{2\pi^2 N} u^2 K_2(u) \right). \quad (3)$$

In order for S/N to exceed the value 4 by a considerable amount, the last term has to become big; since the number of particles is fixed by the number of available quarks, this means that the volume has to grow exponentially [4] such that the final state becomes very dilute, with densities by orders of magnitude below chemical equilibrium.

No dynamical scenario is known which would produce such a state; rather, the system will avoid the problem by creating new degrees of freedom via gluon fragmentation [4], thereby reducing the entropy per particle in the final state to a reasonable

value. Since gluon fragmentation can go into light and into strange quark pairs, it can change the value of λ_s . Thus, it is not clear to what extent the fully hadronized state still remembers the initial value $\lambda_s \simeq 1$.

Let us assume that during hadronization each gluon, before it vanishes, produces f_q additional light quark pairs and f_s additional strange quark pairs. Then, using (2), we can compute the number of quark pairs at the end of hadronization:

$$\begin{aligned} (N_s + N_{\bar{s}})^{\text{final}} &= (N_s + N_{\bar{s}})^{\text{QGP}} + f_s N_g^{\text{QGP}} \\ &= (1 + 0.6f_s)(N_s + N_{\bar{s}})^{\text{QGP}} + 0.6f_s(N_q + N_{\bar{q}})^{\text{QGP}} \end{aligned} \quad (4)$$

$$\begin{aligned} (N_q + N_{\bar{q}})^{\text{final}} &= (N_q + N_{\bar{q}})^{\text{QGP}} + f_q N_g^{\text{QGP}} \\ &= (1 + 0.6f_q)(N_q + N_{\bar{q}})^{\text{QGP}} + 0.6f_q(N_s + N_{\bar{s}})^{\text{QGP}} \end{aligned} \quad (5)$$

Using that initially in our QGP $N_u = N_{\bar{u}} = N_d = N_{\bar{d}} \simeq N_s = N_{\bar{s}}$, this is easily solved for the strange-to-nonstrange ratio at the end of hadronization:

$$\lambda_s = \frac{N_s^{\text{final}}}{N_u^{\text{final}}} = \frac{1 + 1.8f_s}{1 + 0.9f_q}. \quad (6)$$

We can now discuss various possibilities:

(i) If gluons fragment with equal probability into $s\bar{s}$, $u\bar{u}$, and $d\bar{d}$ pairs (complete $SU(3)_{\text{flavor}}$ symmetry), *i.e.* if $f_q = f_u + f_d = 2f_s$, then $\lambda_s = 1$, *i.e.* the unusual chemical composition of the QGP is completely carried over into the final hadronic state, leaving us with a clear difference to pp phenomenology and thus providing us with an unambiguous QGP signal.

(ii) A more cautious estimate would assume that strangeness production from gluon fragmentation is suppressed by the same factor as observed in pp collisions (in line with the view of the QGP hadronization process as a sequence of string-breaking processes [6]), *i.e.*

$$\frac{f_s}{f_u} = \frac{f_s}{f_d} = \frac{2f_s}{f_q} = 0.3. \quad (7)$$

In this case we find

$$\lambda_s = \frac{1 + 0.27f_q}{1 + 0.9f_q}. \quad (8)$$

For $0 \leq f_q \leq \infty$ we thus have $1 \geq \lambda_s \geq 0.3$. As discussed above, the lower limit on f_q (no gluon fragmentation) is unrealistic; in the other limit all memory of the initial QGP composition is lost, and the final state only remembers the features of the gluon fragmentation dynamics which dominates hadron production.

The minimum fragmentation rate f_q which ensures entropy conservation depends now on the details of the assumed quark recombination mechanism. In Ref. [4], for example, a combinatoric recombination mechanism was studied, and it was found that in this case a value of f_q of order 1-2 was sufficient to guarantee that the final state did not have less entropy than the initial one. This mechanism produces a final state in which the hadrons are not in chemical equilibrium, and in which in particular multiply strange hadrons are enhanced above their equilibrium value. From (6) we would conclude that the results in [4] correspond to $0.67 \geq \lambda_s \geq 0.55$, *i.e.* a factor 2 above the pp value. The nice thing is that also in this scenario the

pp value for λ_s is approached from above, leaving hope to see some clear signal of the unusual QGP chemistry even in the final state.

(iii) The most pessimistic scenario assumes that gluons do fragment, but do not produce any strange quarks: $f_s = 0$. Now λ_s could become arbitrarily small as $f_q \rightarrow \infty$. However, even in this case $f_q \geq 2.6$ is needed to push λ_s below its pp -value, and this appears to be more than what is required by entropy conservation [4]. We don't think that scenario (iii) is very realistic.

(iv) One final possibility is that gluon fragmentation and other microscopic processes of similar type are so effective that they keep the system at every step in chemical equilibrium, thereby generating an equilibrated hadron resonance gas at the end of hadronization [7,6]. In this case λ_s depends only on the transition temperature: For $T_{\text{tr}} = 200$ MeV $\lambda_s = 0.45$, while for $T_{\text{tr}} = 150$ MeV $\lambda_s = 0.35$.

Altogether it appears very likely that QGP formation will leave an (at first sight not very strong but) significant trace even in the overall strange-to-nonstrange ratio λ_s . To determine λ_s requires a detector that is capable of identifying strange and non-strange hadrons, in order to be able to extract a complete set of particle ratios. This will also then allow to check the degree of chemical equilibration in the final state and thereby provide valuable hints as to the microscopic hadronization mechanism (*i.e.* similarities and differences compared with string hadronization in pp collisions).

In addition, there is always the chance that particular strange channels (for example multiply strange hadrons or strange antibaryons) show much stronger deviations from pp phenomenology than the average total strangeness yield. There is an extensive literature on predictions along these lines (*e.g.* [4,6]), but these depend much more on the details of the hadronization model employed and can only be tested by experiment.

The fact that the primordial QGP has such an unusual chemical composition should certainly be sufficient motivation for an experimental investigation of this question. Some very interesting results on enhanced $\bar{\Lambda}$ -production in nucleus-nucleus collisions at $\sqrt{s} = 20$ GeV [8] and the observation of an unusually large number of events, in which pairs of Λ 's were produced, in \bar{p} -nucleus collisions at $\sqrt{s} = 3$ GeV [9] have so far not found a convincing "conventional" explanation and give further momentum to a continuation of such studies. The baryon-free central region at LHC, which minimizes the problem of \bar{K} and $\bar{\Lambda}$ final state absorption, should provide a particularly clean environment, allowing for a complete determination of the strangeness balance and thereby facilitating the theoretical analysis of the data.

Production of baryon-antibaryon pairs and small (anti-)nuclei. In this section we will review data on (strange and nonstrange) antibaryon production in pp and $\bar{p}p$ collisions at collider energies, extrapolate them to the LHC energy and compare them with a thermal hadron gas model and various QGP hadronization models. We will also shortly comment on the production of small antinuclei.

The baryon-free central region is a preferred environment for antibaryon creation, due to the absence of projectile nucleons which, through the Pauli principle or, in thermodynamic language, via a non-vanishing baryon chemical potential, suppress

antibaryon production. This antibaryon suppression in the fragmentation regions is clearly seen in ISR data (see [10], Fig. 7.10) even if, on the other hand, the central region there (at energies below $\sqrt{s} = 50$ GeV) does not yet appear to be baryon-free, since p and \bar{p} production at y_{cm} are still different by a factor 2 or so. Thus, for effective antibaryon production in nuclear collisions, a baryon-free region near y_{cm} is essential, making RHIC or LHC the machine of choice for such studies.

The UA5 collaboration (see [11], in particular Table 2 on p. 460 in [11], and references therein) determined in $p\bar{p}$ collisions at $\sqrt{s} = 546$ GeV for the central pseudorapidity range $|\eta| < 5$ an antibaryon-to-charged ratio of

$$\frac{\langle \bar{B} \rangle}{\langle n_{ch} \rangle} = \frac{\bar{N} + \bar{\Lambda} + \bar{\Sigma} + \bar{\Xi}}{\langle n_{ch} \rangle} \simeq 0.1. \quad (9)$$

At 546 GeV all ingredients to this balance equation have been measured; in [11] these data were successfully compared with a simulation which was then also used to predict production rates at $\sqrt{s} = 200$ and 900 GeV, with the conclusion that the ratio (9) does not change in this energy interval.

It may be worth to note some interesting strange antibaryon ratios from this UA5 work, for later comparison with heavy ion data:

$$\frac{\bar{\Sigma}^\pm}{\bar{\Lambda} + \bar{\Sigma}^0} \simeq \frac{1}{2}; \quad \frac{\bar{\Lambda} + \bar{\Sigma}^0}{\bar{p} + \bar{n}} \simeq 0.12; \quad \frac{\bar{\Xi}^0 + \bar{\Xi}^+}{\bar{\Lambda} + \bar{\Sigma}^0} \simeq 0.37. \quad (10)$$

Clearly, there is a suppression of strange antibaryons; the $\bar{\Xi}$'s appear to be less suppressed relative to the antihyperons than the latter are relative to antinucleons.

The E-735 collaboration at the Tevatron collider ($\sqrt{s} = 1800$ GeV) determined [11]

$$\frac{\langle \bar{\Lambda} + \bar{\Sigma} \rangle}{\langle n_{ch} \rangle} = 0.023; \quad \frac{\langle \bar{p} + \bar{n} \rangle}{\langle n_{ch} \rangle} = 0.06. \quad (11)$$

Guessing $\langle \bar{\Xi} \rangle / \langle n_{ch} \rangle \simeq 0.005$ (as at the SPS collider [11]), we again obtain an antibaryon-to-charged ratio of order 10%:

$$\frac{\langle \bar{B} \rangle}{\langle n_{ch} \rangle} \simeq 0.09. \quad (12)$$

It is expected that this number will not change drastically up to LHC energies.

These values are not inconsistent with a naive hadron resonance gas estimate. For the latter we obtain, using $\mu_B = 0$ and free-space baryon masses as input:

$$0.06 \leq \frac{\langle \bar{B} \rangle}{\langle n_{ch} \rangle} \leq 0.13 \quad \text{for} \quad 160 \text{ MeV} \leq T \leq 200 \text{ MeV}. \quad (13)$$

However, the various particular ratios (10,11) are not easily reproduced by such a hadron gas picture in the grand canonical framework. Perhaps inclusion of conservation laws for strangeness, baryon number, and isospin into the theory via a canonical treatment [12] can help here, but on the other hand it is not clear why a hadron gas picture should be expected to work at all for such a small system.

The formation of a hot equilibrated hadron gas or of QGP in *nuclear* collisions should have various consequences for the ratios discussed above. In the framework of effective chiral Lagrangians to simulate QCD at low energies it was discussed [13,14] that (anti-)baryons should be strongly affected by effective mass corrections which occur as a precursor phenomenon indicating the restoration of chiral symmetry at the transition to quark matter. Based on these ideas, in [14] a modified hadron gas estimate was given for a system close to the phase transition:

$$0.35 \leq \frac{\langle \bar{B} \rangle}{\langle n_{ch} \rangle} \leq 0.40 \quad \text{for} \quad 160 \text{ MeV} \leq T \leq 200 \text{ MeV}. \quad (14)$$

Since not only the baryon effective masses themselves, but also the mass splittings in the baryon octet are reduced by this mechanism, the suppression of strange antibaryons is reduced [14] compared to the naive estimate used in (13).

Reduced effective masses lead to a faster chemical equilibration of antibaryons via hadronic processes such that larger antibaryon rates than observed in $p\bar{p}$ collisions may be attainable in nuclear collisions even in the absence of a transition to QGP. However, if a QGP is formed (as expected at LHC energies), then the chiral models discussed in [14] suggest a particular topological hadronization mechanism which naturally leads to large antibaryon formation rates (compatible with the estimate (14)). In this picture, antibaryons form from the QGP as topological defects in the chiral condensate as it develops during the spontaneous breaking of chiral symmetry associated with the phase transition. A simple combinatoric estimate [14] yields a formation rate for topological defects with winding number -1 which translates into the prediction

$$\frac{\langle \bar{B} \rangle}{\langle n_{ch} \rangle} \simeq \frac{1}{3} \quad (15)$$

from topological hadronization of a QGP. This formation of topological defects is entirely flavor blind, and thus the formation of strange antibaryons should not be suppressed.

As a final comment we wish to point out the relevance of this for the production of antinuclei. In pA collisions at 70 GeV/c [15] and 200 GeV/c [16], respectively, antimatter clusters with mass A are suppressed by 4-5 orders of magnitude per unit of A . This can be understood in terms of a coalescence model, where antinuclei appear through the coalescence of antinucleons in the final stages of the collision [17,18]: about three orders of magnitude per nucleon are due to the coalescence probability for the antinucleons [18] while the last order of magnitude is due to the smallness of the number of antinucleons per collision. If the above predictions are correct, this last number may rise by a factor of 3 or more in nuclear collisions, leading, for example, to a relative gain of 2 orders of magnitude for anti- α production. Furthermore, the absence of strangeness suppression in the topological hadronization scenario may provide a unique opportunity to allow the formation of exotics like the H -dibaryon and its antiparticle via coalescence of hyperons [19].

Acknowledgements: The authors thank the other members of the working subgroup (E. Quercigh, H. Ströbele, and O. Villalobos) for their input to this presentation through the discussion meetings. This work was supported in part by BMFT.

References:

1. A. Wroblewski, *Acta Phys. Pol.* **B16** (1985) 379; and contribution to the XXV Conference on High Energy Physics, Singapore, 1990
2. P. K. Malhotra and R. Orava, *Z. Phys.* **C17** (1983) 85
3. E-735 Coll., T. Alexopoulos *et al.*, *Phys. Rev. Lett.* **64** (1990) 991
4. P. Koch, B. Müller, and J. Rafelski, *Phys. Rep.* **142** (1986) 167
5. W. Greiner, L. Neise, and H. Stöcker, "Thermodynamik und Statistische Mechanik", Verlag H. Deutsch, Frankfurt, 1987, p. 245, eq. (121)
6. H. W. Barz, B. Friman, J. Knoll, and H. Schulz, *Nucl. Phys.* **A484** (1988) 661
7. K. S. Lee, U. Heinz, and M. Rhoades-Brown, *Phys. Rev.* **C37** (1988) 1452
8. NA35 Coll., J. Bartke *et al.*, *Z. Phys.* **C**, in press
9. K. Miyano *et al.*, *Phys. Rev.* **C38** (1988) 2788
10. G. Giacomelli and M. Jacob, *Phys. Rep.* **55** (1979) 1
11. UA5 Coll., G. J. Alner *et al.*, *Nucl. Phys.* **B291** (1987) 445
12. R. Hagedorn and K. Redlich, *Z. Phys.* **C27** (1985) 541;
B. Müller and J. Rafelski, *Phys. Lett.* **B116** (1982) 274
13. V. Bernard and U.-G. Meißner, *Phys. Lett.* **B227** (1989) 465
14. J. Ellis, U. Heinz, and H. Kowalski, *Phys. Lett.* **B233** (1989) 223
15. Yu. M. Antipov *et al.*, *Phys. Lett.* **B34** (1971) 164
16. W. Bozzoli *et al.*, *Nucl. Phys.* **B144** (1978) 317
17. T. F. Hoang and H. J. Crawford, *Z. Phys.* **C43** (1989) 215
18. C. Dover, U. Heinz, E. Schnedermann, and J. Zimányi, Regensburg preprint,
to be published
19. C. Dover, P. Koch, and M. May, *Phys. Rev.* **C40** (1989) 115

The VENUS Model for Heavy Ion Collisions at LHC Energies

K. Werner

Institut für Theoretische Physik der Universität Heidelberg
6900 Heidelberg, Germany

P. Cerello and P. Giubellino

INFN Torino, 10125 Torino, Italy

We report on upgrades of the string model VENUS to allow simulations of p - p and ion-ion collisions up to LHC energies. Multiple parton-parton scattering is taken into account in a simplified fashion. In p - p collisions the rise of the rapidity plateau as well as the mean p_t with increasing energy is reproduced. We discuss for ion-ion collisions the mass number and energy dependence of the rapidity plateau height and of the energy density.

1 Introduction

What do we gain by colliding heavy ions at LHC with 3.15+3.15 TeV per nucleon, compared to present SPS energies ($\sqrt{s_{pp}} = 20$ GeV)? An important parameter concerning plasma formation is the central energy density, and clearly this energy will increase by increasing the beam energy. However, since we know that ultrarelativistic p - p collisions are partly transparent it is by no means clear to what extent the large increase in beam energy manifests itself in a large increase in energy density. We are going to investigate this question.

We briefly introduce the string model VENUS, an event generator successfully used already to describe data from SPS heavy ion experiments. We discuss multiple parton scattering, and realize that this can be simulated by making two parameters energy dependent: the average number of colour exchanges (\bar{k}) and the average p_t of partons (\bar{p}_t^q).

We use this updated VENUS model to discuss energy and mass number dependence of the central rapidity height and of energy densities for ion-ion collision from p - p to Pb-Pb and for energies from the SPS to the LHC range.

2 The string model VENUS

The model consists of four independent building blocks: Nuclear geometry, string formation, string fragmentation and rescattering. We sketch these points in the following, for a detailed discussion see [1].

Nuclear Geometry. At this stage the parton structure of nucleons is ignored. Hard spheres representing nucleons are distributed in projectile and target randomly according to standard nuclear density distributions. The two nuclei penetrate each other, displaced by a random impact parameter \bar{b} . Whenever two nucleons come closer than $\sqrt{\sigma}/\pi$ a collision occurs. In this way we obtain a sequence of nucleon-nucleon collisions.

String Formation. Each nucleon-nucleon interaction is realized via colour exchange (CE) (like in the Dual Parton Model [2]). The dominant one-CE contribution for $p-p$ collisions is

$$(q_1 q_1 q_1) + (q_2 q_2 q_2) \xrightarrow{CE} (q_1 q_1 q_2) + (q_1 q_2 q_2) \quad (1)$$

where q_1 denotes projectile and q_2 target quark, the bracket () stands for singlet coupling. So eq.(1) means that two quarks exchange colour with the consequence that new colour singlets occur consisting of quarks from different original nucleons. The quarks are assumed to keep their momenta, so the new singlets consist of two partons (qq and q), moving, in the $p-p$ cms, with high momentum into opposite directions. These singlets are identified with strings (yo-yo's).

We also consider contributions, where a quark or antiquark from a colour singlet $q-\bar{q}$ pair is involved in the colour exchange:

$$(q_1 q_1 q_1)(\bar{q}_1 q_1) + (q_2 q_2 q_2) \xrightarrow{CE} (q_1 q_1 q_1) + (\bar{q}_1 q_2) + (q_1 q_2 q_2). \quad (2)$$

Here a qqq singlet from the projectile survives (like a spectator), a colour exchange occurs between the projectile $q-\bar{q}$ singlet and the target, leaving a $q-\bar{q}$ string and like before a $qq-q$ string. We also consider antiquark colour exchange ([4]).

Multiple colour exchange means applying single colour exchange several times like

$$\begin{aligned} (q_1 q_1 q_1)(\bar{q}_1 q_1) &+ (q_2 q_2 q_2)(\bar{q}_2 q_2) \\ \xrightarrow{CE} &(q_1 q_1 q_1) + (\bar{q}_1 q_2) + (q_2 q_2 q_2) + (\bar{q}_2 q_1) \\ \xrightarrow{CE} &(q_1 q_1 q_2) + (\bar{q}_1 q_2) + (q_1 q_2 q_2) + (\bar{q}_2 q_1) \end{aligned} \quad (3)$$

where two colour exchanges provide two $q-\bar{q}$ and two $qq-q$ strings. The whole contribution is a superposition

$$\sum_k w(k) C_k \quad (4)$$

of k -CE contributions C_k with a k -CE probability

$$w(k) \sim \left(\frac{\bar{k}}{\bar{k} + 1} \right)^k \quad (5)$$

with a (so far) energy independent parameter \bar{k} .

String fragmentation. We use an “area law” procedure [3]. The general method may be characterized by two requirements. Firstly, strings evolve according to classical string theory (Nambu action). This implies that once a breakpoint is known on the string surface, the evolution of the substrings is completely fixed. The second requirement determines the breakpoint: the probability dP for a break to occur within a small surface element d^2A is proportional to d^2A :

$$dP \sim d^2A \quad (6)$$

This determines the fragmentation procedure up to details like for example the weights for $u\bar{u}$, $d\bar{d}$, and $s\bar{s}$ breakups.

Secondary interactions. Since in general strings or string segments do not get too long (they break) we consider strings pointlike for the sake of rescattering of strings (including the final “strings” = hadrons) among themselves and with spectator nucleons. Whenever two tracks come close, the corresponding “objects” fuse, which means we form an intermediate object by adding momenta and additive quantum numbers. If the object corresponds to some particle in the resonance table, it gets the corresponding life time τ_R , otherwise always $\tau = 1fm$. For a dense system we have therefore the possibility of producing “blobs” of many quarks and antiquarks.

3 Multiple parton scattering

Multiple parton scattering [5] has been mainly investigated to study high p_t phenomena ($p_t >> p_t^{soft}$), however, one may use multiple parton scattering ideas to get consistent description for soft and (semi) hard scattering [6]. We demonstrate in the following that one might get a model quite similar to our model described in section 2. The $p-p$ cross section due to parton scattering may be written as

$$\frac{\partial \sigma}{\partial p_t^2} = \sum_{ijk} \int dx_1 dx_2 dt f_i(x_1) f_j(x_2) \frac{d\sigma_{ij}^k}{dt} (st) \delta(p_t^2 - p_t^2(stu)) \quad (7)$$

with elementary parton-parton cross sections $\frac{d\sigma_{ij}^k}{dt}$. We may define a “QCD cross section” σ_{QCD} as

$$\sigma_{QCD} = \int_{(p_t^f)^2}^{s/4} \frac{d\sigma}{dp_t^2} dp_t^2 \quad (8)$$

Since $d\sigma/dp_t^2$ behaves typically as p_t^{-4} the cross section σ_{QCD} becomes easily (for small enough cutoff p_t^f and large enough \sqrt{s}) larger than the inelastic cross section

σ_{in} – which simply means multiple parton scattering. An average number \bar{k} of parton scatterings may be defined as

$$\begin{aligned}\bar{k} &= \frac{\sigma_{QCD}}{\sigma_{in}} = \int_{(p_t^c)^2}^{s/4} \frac{d\sigma}{dp_t^2} dp_t^2 \\ &= \frac{1}{\sigma_{in}} \sum_{ijk} \int dx_1 dx_2 f_i(x_1) f_j(x_2) \int dt \frac{d\sigma_{ij}^k}{dt}(st)\end{aligned}\quad (9)$$

if the t -dependence of the distribution functions f is ignored. If for $x \rightarrow 0$ the t -integration remains finite, and taking $f \sim x^{-1}$ for small x , we get due to the lower limit m/\sqrt{s} of the x -integration, in the limit of large \sqrt{s} :

$$\bar{k} = \bar{k}(\sqrt{s}) = a + b \ln \sqrt{s} + c(\ln \sqrt{s})^2, \quad (10)$$

so we expect a quadratic increase of the mean number of parton–parton scatterings in $\ln \sqrt{s}$. How does the average p_t depend on \sqrt{s} ? We get for $d\sigma/dp_t \sim p_t^{-4}$

$$\begin{aligned}\bar{p}_t^2 &= \int \frac{d\sigma}{dp_t^2} p_t^2 dp_t^2 / \int \frac{d\sigma}{dp_t^2} dp_t^2 \\ &= \int p_t^{-2} dp_t^2 / \int p_t^{-4} dp_t^2\end{aligned}\quad (11)$$

with some cutoff $(p_t^c)^2$ as lower and $s/4$ as upper limit. So we get for large s

$$\bar{p}_t^2 = a + b \ln \sqrt{s}, \quad (12)$$

so not only more partons scatter at higher energy (eq.(10)), the partons also acquire higher p_t .

In the following we discuss singlet construction. Before the interaction we consider the nucleons as singlets consisting of a diquark (d), a quark (q) and a gluon

$$N = (dqg)_1 = (dq)_8 g_8)_1 \quad (13)$$

where $(\cdot)_i$ denotes an SU(3) colour multiplet. A $gg \rightarrow gg$ scattering leads to a system of 4 octets

$$N + \bar{N} \rightarrow (dq)_8 g_8 \bar{g}_8 (\bar{d}\bar{q})_8. \quad (14)$$

There are 8 independent possibilities to couple to an overall singlet, one of these is

$$(d\bar{q})_1 (q\bar{d})_1 (g_8 \bar{g}_8)_1. \quad (15)$$

Since a gluon can be written as $(3\bar{3})_8$, the gg singlet corresponds to two $(3\bar{3})_1$ singlets and thus eq.(15) corresponds to the two colour exchange process in eq.(3). In this sense the mean number of colour exchanges (minus one) corresponds to the mean number of parton scatterings (eq.(10)) and the average quark p_t^2 (related to \bar{p}_t^2) corresponds to the mean parton p_t^2 given in eq.(12). As a first step to include (semi)hard parton scattering we therefore introduce a quadratic dependence of the parameters \bar{k} and \bar{p}_t^2 as a function of $\ln \sqrt{s}$. We use for both \bar{k} and \bar{p}_t^2 a parametrization $a + b \ln \sqrt{s} + c(\ln \sqrt{s})^2$, the parameters we obtained by comparing with pp data from ISR, SPS and Tevatron [7].

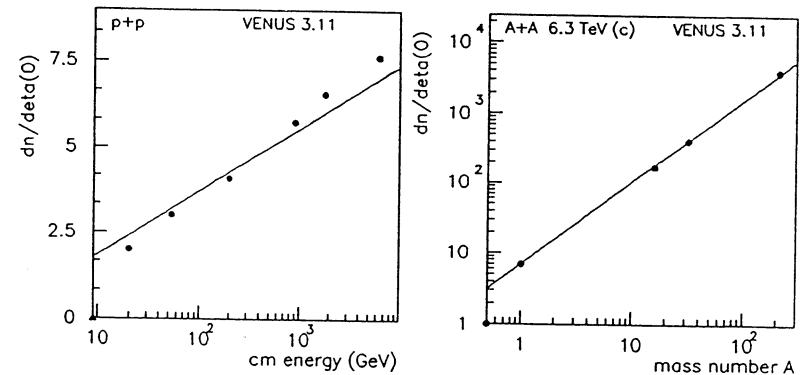


Figure 1: Energy dependence of the central pseudorapidity $dn/d\eta(0)$ for $p-p$ collisions. Points are VENUS results, the line is a parametrization of data

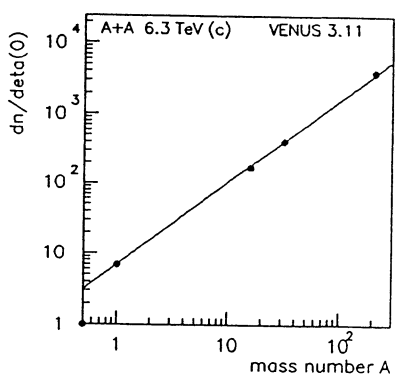


Figure 2: Mass number dependence of the central pseudorapidity $dn/d\eta(0)$ for ion–ion collisions. The points are VENUS results, the line is the best fit to these points of the form aA^α (with $\alpha = 1.17$).

4 Results

First of all we want to study the energy (\sqrt{s}) and mass number (A) dependence of the rapidity plateau height $dn/d\eta(0)$ at $\eta = 0$. In fig. 1 we show VENUS results for $dn/d\eta(0)$ for $p-p$ collisions as a function of \sqrt{s} together with a fit to data of the form

$$\frac{dn^{pp}}{d\eta}(0) = 0.8 \ln \sqrt{s} \quad (16)$$

which also provides a good fit to the VENUS points. In fig. 2 we show VENUS results for ion–ion collisions of $dn/d\eta(0)$ versus the nuclear mass number A together with a fit of the form

$$\frac{dn^{AA}}{d\eta}(0) = \frac{dn^{pp}}{d\eta}(0) A^\alpha \quad (17)$$

with $\alpha = 1.17$ corresponding to the best fit. Such an A dependence is easily understood: VENUS provides two types of strings: $qq-q$ strings and $q-\bar{q}$ strings, the number of $qq-q$ strings being equal to the number N_p of participants and the number of $q-\bar{q}$ strings being proportional to the number N_c of binary collisions. Because of $N_p \sim A$ and $N_c \sim A^{4/3}$ we expect an A^α dependence with $1 < \alpha < 4/3$.

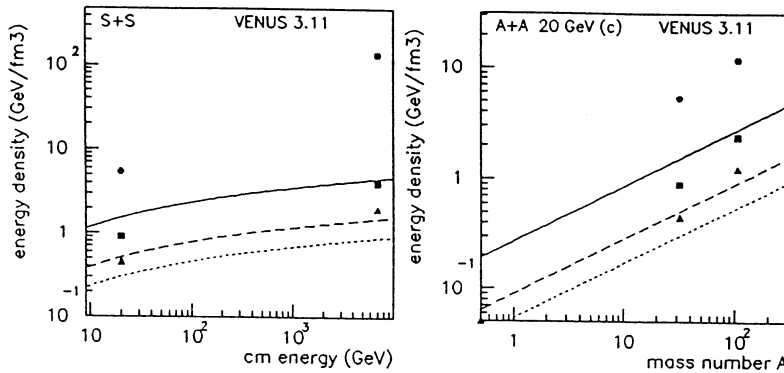


Figure 3: Energy dependence of the central energy density for S-S collisions. The points are direct VENUS results, the lines are calculated from Bjorken's formula with $\tau = 1, 3, 5$ fm/c from top to bottom, using the parametrizations of figs. 1,2 as input.

In the following we want to discuss energy densities. Bjorken's formula

$$\epsilon_{Bj} = \frac{dn^{AA}}{dy}(0) \frac{\bar{m}_t}{\pi R^2 \tau} \quad (18)$$

relates the energy density ϵ at an early time τ to the rapidity density dn/dy as seen in the detector, by assuming free streaming from a pointlike source. Using eq.(16) and eq.(17) and setting $R = 1.2A^{1/3}$ and $\bar{m}_t = 0.5$ GeV we get (we use $y = \eta$)

$$\epsilon_{Bj} = \epsilon_{Bj}(\tau, A, s) = \frac{0.09}{\tau} \sqrt{A} \ln \sqrt{s}. \quad (19)$$

In fig. 3 we show the \sqrt{s} dependence for fixed A (S-S) for $\tau = 1, 3, 5$ fm/c (from top to bottom). We observe for $\tau = 1$ an increase of ϵ_{Bj} from SPS energy ($\sqrt{s} = 20$ GeV) to LHC energy ($\sqrt{s} = 6.3$ TeV) from 1.5 to 4.5, or more generally we obtain for any τ an increase by a factor of 3. In fig. 4 we show ϵ_{Bj} for fixed energy ($\sqrt{s} = 20$ GeV) as a function of the mass number A . Here we observe an increase from the highest presently achievable mass number $A = 32$ (for symmetric collisions) to $A = 207$ from 1.5 to 3.9, being an increase by a factor of 2.6 for any τ . So we gain a similar factor by going from S-S to heavy nuclei and by increasing the energy from SPS to LHC.

A different approach to determine energy densities is discussed in the following. The points in figs. 3 and 4 are central energy densities calculated from VENUS simulations as

$$\epsilon_V = U_\mu T^{\mu\nu} U_\nu \quad (20)$$

with a hydrodynamic velocity U and an energy momentum tensor T , these quantities being determined from a superposition of N VENUS events as

$$T_{\mu\nu} = \frac{1}{N \Delta V} \sum \frac{p_\mu p_\nu}{p_0} \quad (21)$$

$$U_\mu = \gamma v_\mu \equiv (1 - v_i v_i)^{-1/2} v_\mu \quad (22)$$

$$(23)$$

with

$$v_i = \sum p_i / \sum p_0 \quad (24)$$

where the sum \sum means summing over all events and all particles inside a volume element ΔV (the results for ϵ_V are preliminary since we were using still energy independent parameters, updated calculations will provide larger numbers). The covariant quantity ϵ_V (the energy density in the local rest frame) is a function of space time: $\epsilon_V = \epsilon_V(x) = \epsilon_V(t, \vec{x})$. Here we are only considering $\vec{x} = 0$: the three points in figs. 3 and 4 for given \sqrt{s} or given A correspond to $\epsilon_V(t, \vec{0})$ for $t = 1, 3, 5$ fm/c from top to bottom. Since $t = \tau$ for $x = 0$ the three points correspond to the three lines obtained from Bjorken's formula, however, the points (ϵ_V) are considerably above the lines (ϵ_{Bj}), especially for $\sqrt{s} = 6.3$ TeV we find ϵ_V being two orders of magnitude larger than ϵ_{Bj} , although both numbers are based on VENUS simulations. To calculate ϵ_V , however, we consider particles in a general sense, meaning that at an early time we are counting strings as massive pointlike objects. At LHC energies we obtain easily objects heavier than a TeV. The high value of ϵ_V at $\tau = 1$ is due to such massive objects rather than multiplicity. After breaking most of this energy leaves the central rapidity bin (around $y = 0$) and will appear as particles covering the whole rapidity range ($-9 < y < 9$). This behaviour is very different to Bjorken's picture where energy is conserved in a rapidity bin. Nevertheless ϵ_{Bj} is a useful quantity since it measures the energy available for particle production subtracting the energy producing simply longitudinal kinetic energy.

5 Summary

Observing some correspondence between multiple parton scattering and multiple colour exchange in VENUS we simulate the former by assuming an energy dependence as $a + b \ln \sqrt{s} + c (\ln \sqrt{s})^2$ for the following two parameters in VENUS: the average number \bar{k} of colour exchanges and the average parton transverse momentum \bar{p}_t^q . The experimentally observed increase with energy of $dn/d\eta(0)$ and of $\langle p_t \rangle$

can be reproduced. The A and \sqrt{s} dependence for $dn/d\eta$ of VENUS simulations can be parametrized as

$$\frac{dn^{AA}}{d\eta}(0) = 0.8 A^{1.17} \ln \sqrt{s} \quad (25)$$

which leads to an energy density à la Bjorken of

$$\epsilon_{Bj} = \frac{0.09}{\tau} \sqrt{A} \ln \sqrt{s}. \quad (26)$$

This increases by a factor of 3 by increasing the energy from 20 GeV to 6.3 TeV, another increase of a factor of 2.6 is obtained by going from S-S to Pb-Pb. The energy density calculated microscopically from VENUS is much larger than ϵ_{Bj} since it contains a lot of energy later on leaving the central rapidity region (going mainly into longitudinal kinetic energy).

References

- [1] K. Werner, Z. Phys. C42 (1989) 85
- [2] A. Capella, U. Sukhatme and J. Tran Thanh Van, Z. Phys. C3 (1980) 329
- [3] K. Werner and P. Koch, Z. Phys. C47 (1990) 215
- [4] K. Werner, Phys. Rev. Lett. 62, 2460 (1989)
- [5] L. Durant and H. Pi, Phys. Rev. Lett. 58 (1987) 303; K. Kajantie, V.P. Landshoff and J. Lindfors, Phys. Rev. Lett. 59 (1987) 2527
- [6] T. Sjöstrand and M. van Zijl, Phys. Rev. D36 (1987) 2019
- [7] P. Cerello, P. Giubellino and K. Werner, these proceedings.

RESULTS FROM VENUS 3.11 AT LHC ENERGIES

Piergiorgio Cerello and Paolo Giubellino

INFN Torino , Italy

Klaus Werner

Inst. f. Theor. Physik der Univ. Heidelberg , Germany

The VENUS 3.11 generator has been tuned to reproduce proton- proton and Ion-Ion experimental distributions up to the highest available energies and then extrapolated to generate p-p and A-A events at 3.15+3.15 Tev per nucleon. Distributions describing the global features of the events are presented.

1. INTRODUCTION

The ECFA Working Group on Heavy Ion Physics at the Large Hadron Collider has as a goal the evaluation of the physics potential of this machine when operated with colliding beams of Heavy Ions (up to Pb on Pb).

One of the first tasks the Working Group has focused on is the definition of the general conditions of such collisions, providing estimates of rapidity distributions, particle composition and spectra of transverse momentum. This knowledge is needed both to assess the overall experimental conditions, such as the occupancy of detectors and so on, and to evaluate the general physics conditions needed as input for theoretical considerations on plasma formation and detection. To generate the events, we chose to use the Venus model, which is one of the most successful ones in describing Nucleus-Nucleus collisions at SpS energies [1,2].

2. TUNING OF THE EVENT GENERATOR

The VENUS 3.11 event generator, a multistring model specifically developed to describe nucleus-nucleus interactions, will not be discussed here, since it is described elsewhere in these proceedings [3]. We will limit ourselves to a sketch of the procedure we followed to adapt the code to LHC energies. As described in more detail in [3], we assumed that the energy dependence in the model could be described by making energy-dependent two parameters, which control the average number of colour exchanges (QMUST) and the average p_T of the partons (PTQ). Varying these two parameters, we tuned the code to reproduce the main features of present collider data, namely those of UA5 [4] at the CERN ISR, those of UA5 [4] and UA1 [5] at the CERN $p\bar{p}$ collider, and E735 [6] and CDF [7] at the FNAL Tevatron. Next, we performed a fit to the energy dependence of the parameters,

thus obtaining a new set for each of the energies, plus an extrapolation to the energy of LHC. The set of tuned parameters is shown in Fig. 1 and 2 together with a quadratic fit in $\ln s$ (solid line). The choice of the fitting function was a sensible guess [3], but does involve some arbitrariness, which translates in an uncertainty in the values chosen for LHC. The dashed line in the figures shows an exponential fit in $\ln s$: the predicted multiplicities and transverse momenta at LHC are different by about one percent only. Other fitting functions, which would give more relevant differences, reproduced the data very poorly and were disregarded. In Fig. 3a-3d are shown the comparisons of the rapidity distributions of experimental data with the ones obtained from VENUS using the fitted parameters. The agreement, given the simple energy dependence which we have introduced, is quite satisfactory. In Fig. 4-6 we show the comparison between VENUS and the experiments for the average transverse momentum, the multiplicity at $\eta=0$ and the multiplicity for $|\eta| < 2.5$. Again, the simulation done using the fitted parameters nicely describes the available data. Somewhat unexpected is the saturation of $\langle p_T \rangle$ at high energies as seen from Fig. 7, where we plot the energy dependence of $\langle p_T \rangle$ in different rapidity regions; however one has to keep in mind that an increase of PTQ only increases the p_T of the endpoints of the string whereas inner particles acquire only p_T from string break (which is energy independent). Since at higher energies we have more inner particles, we have therefore a mechanism which reduces $\langle p_T \rangle$ and compensates the increase due to the endpoints.

3. EVENT SAMPLES

With the choice of parameters described above, we generated the following samples of events at 3.15+3.15 TeV per nucleon:

- p-p min bias 10000 events
- O-O min bias 4000 events
- S-S min bias 1500 events
- O-O central 4000 events
- S-S central 1500 events
- Pb-Pb central 50 events

We define central events the ones generated with zero impact parameter; these correspond to about 3% of the cross section, as can be seen from Fig. 8, in which the multiplicity distributions for minimum bias and central events are superimposed (normalized to each other).

4. GLOBAL FEATURES OF THE EVENTS

In Fig. 9 we show the mean particle composition for central S-S events, integrated over the whole rapidity range. The charge asymmetry of the kaons reflects

the associated production with the $\bar{\Lambda}$. Fig. 10a and 10b, respectively, show the pseudorapidity and rapidity distributions of some particles species in central Pb-Pb events. They are characterized by a very wide plateau, of up to 10 units for the pions; the distributions of Λ 's and antiprotons, which are centrally produced, are much narrower, but still extend over more than six units. On the plateau, the multiplicity of charged particles reaches the impressive value of ≈ 2000 per unit of rapidity, which, at 10 cm distance, would require a detector to handle 3 particles per square centimeter in a typical central event.

5. A- AND ENERGY DEPENDENCE

In Fig. 11 we show the rapidity distribution of the net baryon number for Pb-Pb and p-p interactions at 3.15+3.15 TeV/ Λ (the lead curve is divided by Λ). It is clear from this plot that in this model the degree of stopping is quite high. While the rapidity shift for p-p is only half a unit more than the one predicted by PYTHIA [8], the one for Pb-Pb events is substantially larger. This result stresses the importance of a real simulation of Ion-Ion interaction vs. the mere superposition of p-p events, which would inevitably lead to an underestimate of the energy deposition in the central region. We fitted with gaussians the peaks of the net baryon number distributions at different energies for p-p interactions and for different Λ at the LHC energy: the variation of the peak position of the fits with both energy and mass of the projectile are given in Fig. 12 and 13, with the vertical bars indicating the peak widths. The change going from proton-proton to nucleus-nucleus is quite dramatic. Fig. 14 shows the Λ -dependence of the rapidity density at $\eta=0$ for different particle species, with fits of the form Λ^α . The Λ -dependence is clearly different for different particles, going from $\alpha=1.16$ for pions to $\alpha=1.42$ for antiprotons and antilambdas. Obviously, a superposition of p-p interactions would not show any such difference. Finally, in Fig. 15a, 15b and Fig. 16a, 16b we present the Λ and energy dependence of the mean transverse momentum for the different particle species, averaged over the whole rapidity or in the central region. The saturation effect mentioned before is clearly visible in the restricted rapidity region. It should also be stressed that the $\langle p_T \rangle$ of the pions shows a modest change with both energy and mass number, while most of the energy dependence has to be attributed to baryons, and mostly to the ones produced outside the central region.

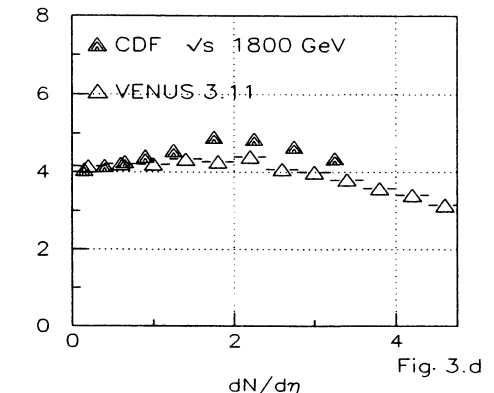
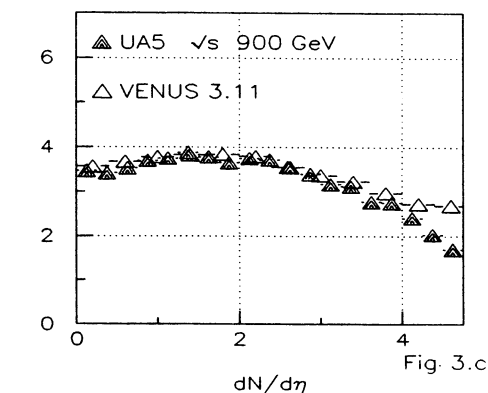
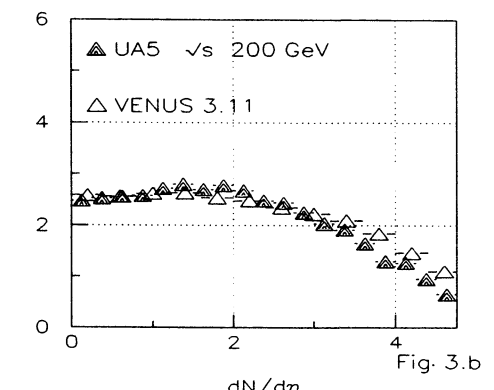
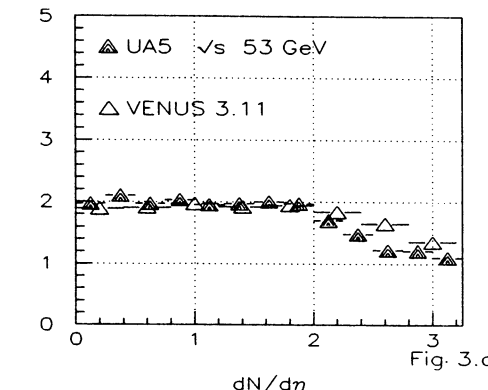
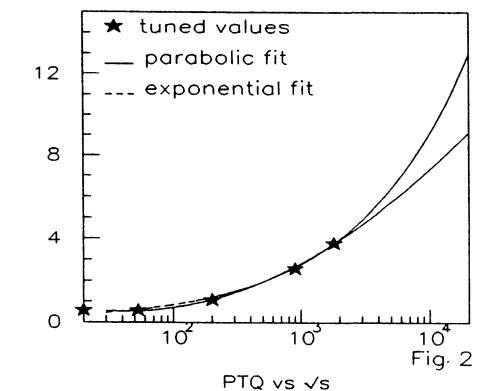
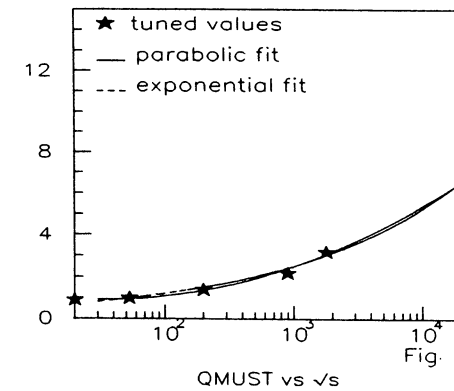
6. CONCLUSION

The VENUS model has been tuned to generate Λ - Λ interactions at the energy of LHC, and a first survey of the characteristics of the events has been performed. Global distributions have been presented, which indicate a high level of stopping,

and general features which differ significantly from what one would obtain superimposing proton-proton events.

REFERENCES

- 1) K. Werner, Z. Phys. C42(1989)85.
- 2) K. Werner and P. Koch, Z. Phys. C47(1990)215.
- 3) K. Werner, P. Cerello and P. Giubellino, these proceedings.
- 4) G.J. Alner et al., Z. Phys. C33 (1986) 1.
- 5) C. Albajar et al., Nucl. Phys. B335 (1990) 261.
- 6) T. Alexopoulos et al., Phys. Rev. Lett. 60 (1988) 1622.
- 7) F. Abe et al., Phys. Rev. Lett. 61 (1988) 1819, and Phys. Rev. D41 (1990) 2330.
- 9) M. Masera, L. Ramello, these proceedings.



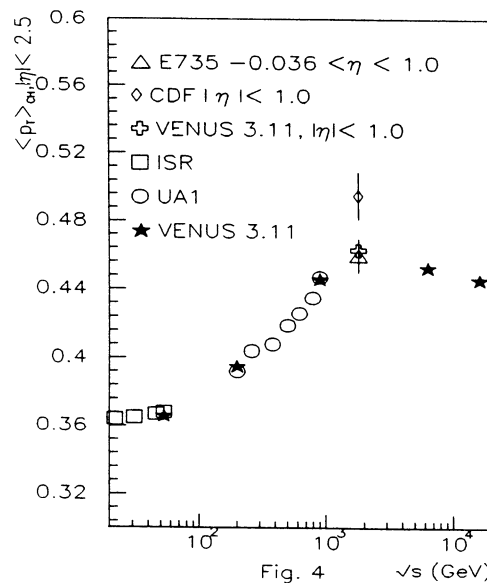


Fig. 4

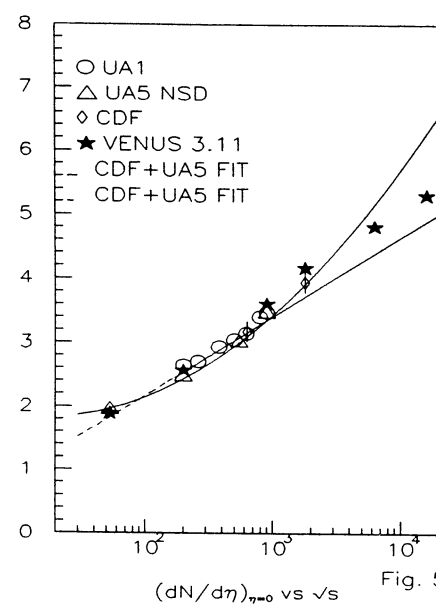


Fig. 5

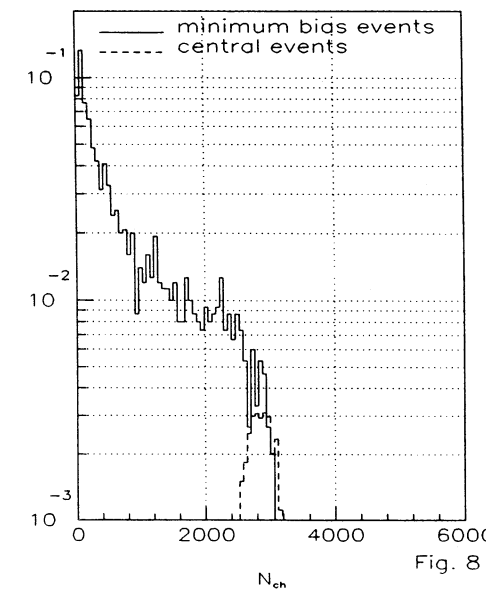
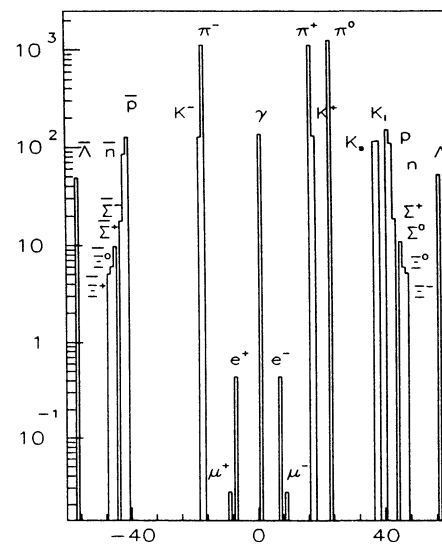


Fig. 8



Particle type Fig. 9

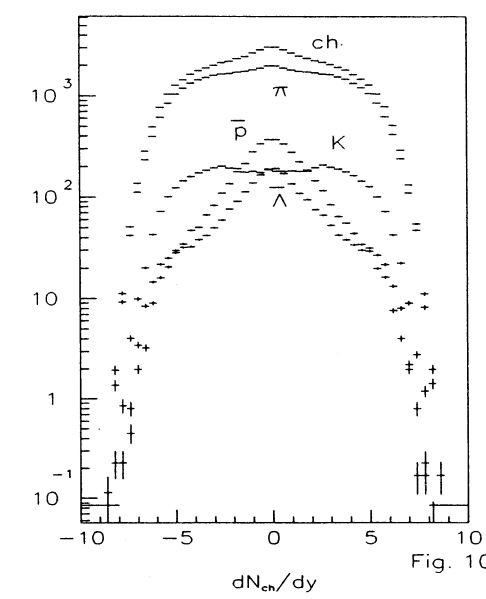


Fig. 10.a

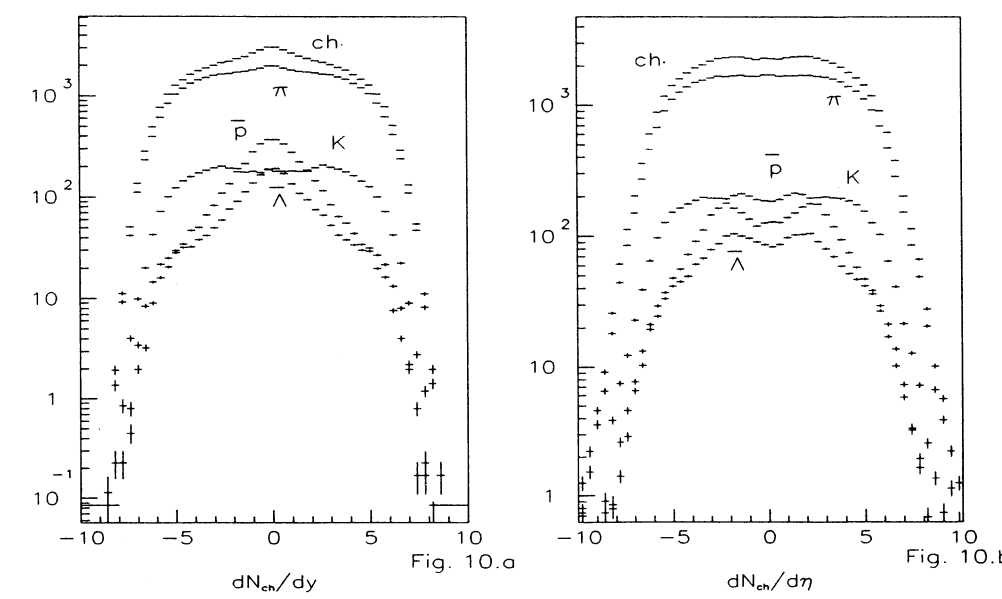


Fig. 10.b

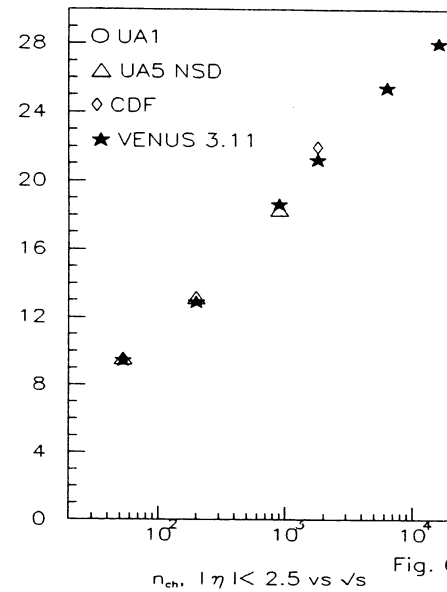


Fig. 6

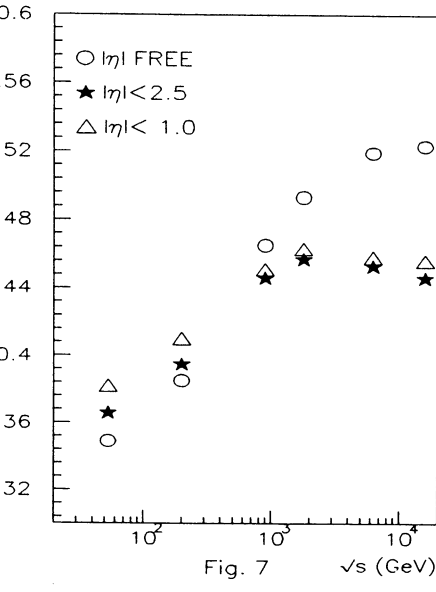


Fig. 7

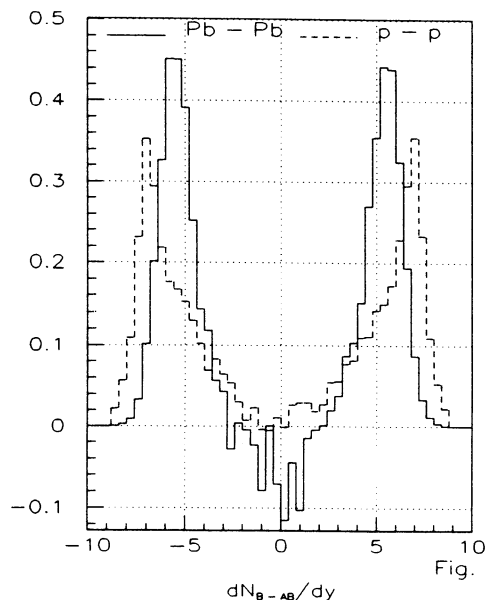


Fig. 11

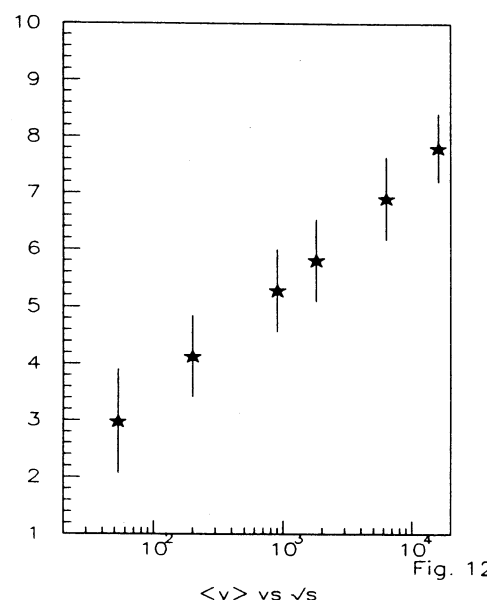


Fig. 12

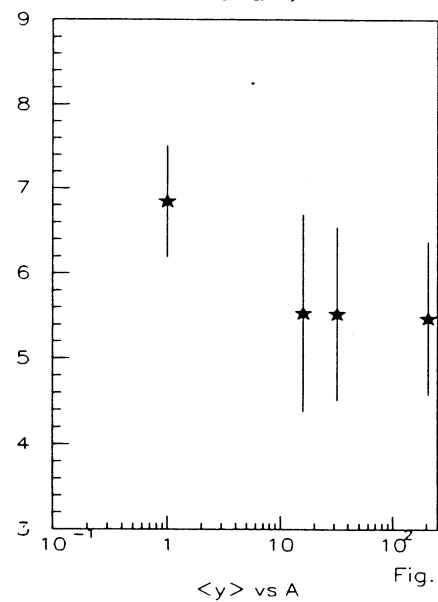


Fig. 13

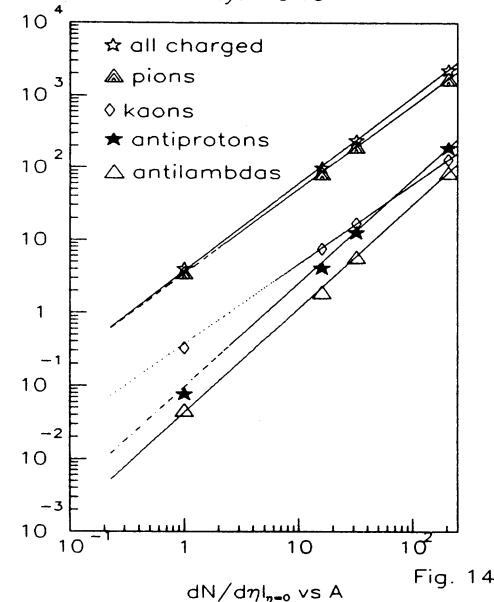
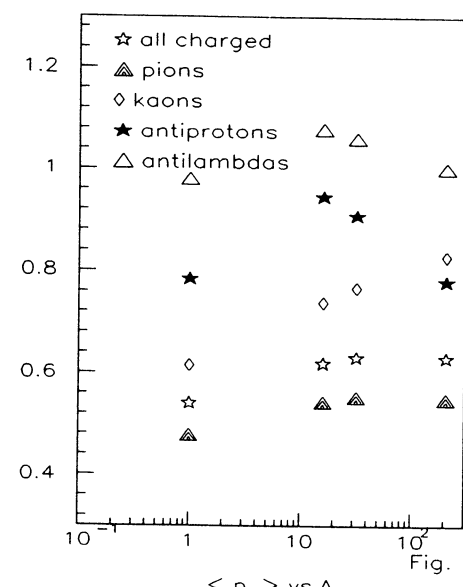
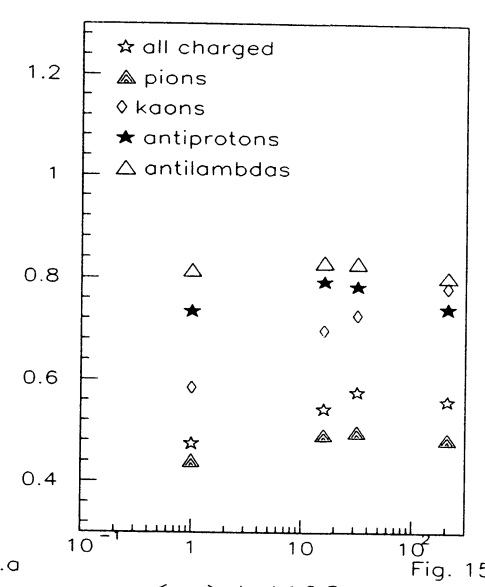
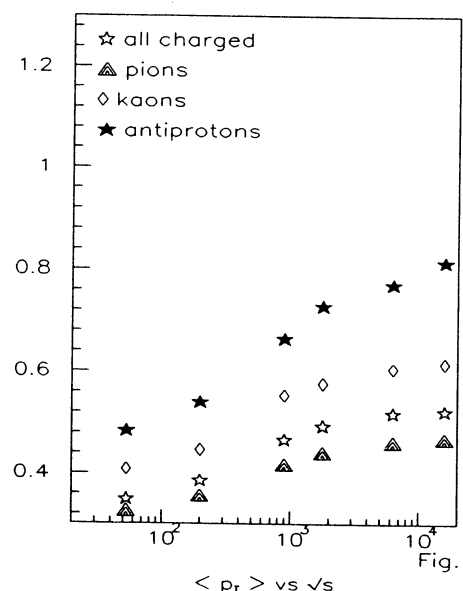
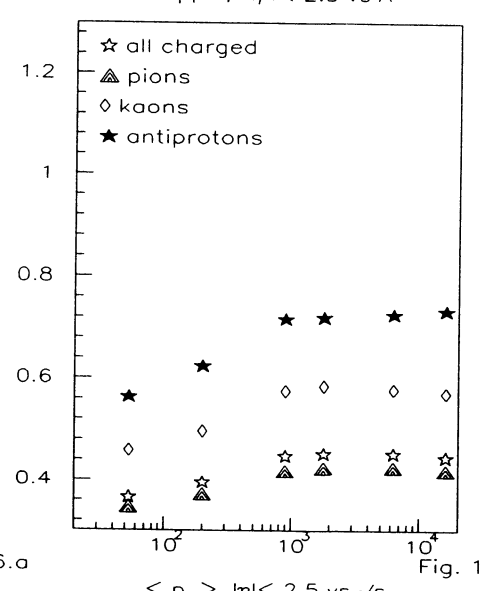


Fig. 14

<p_t> vs A<p_t>, |eta| < 2.5 vs A<p_t> vs sqrt(s)<p_t>, |eta| < 2.5 vs sqrt(s)

RESULTS FROM PYTHIA AT LHC ENERGIES

Massimo Masera, Luciano Ramello

Dipartimento di Fisica Sperimentale dell'Università and INFN, Via P. Giuria 1,
I-10125 Torino, Italy

Minimum bias proton-proton events at LHC energies (3.15+3.15 TeV per nucleon for A-A, 8+8 TeV per nucleon for p-p) have been generated using PYTHIA, which was tuned to existing $SppS$ and Tevatron data. A simple convolution has been made to build minimum bias and central A-A events, up to Pb-Pb. Rapidity and p_T distributions for several particle species are presented.

1. INTRODUCTION

The purpose of the ECFA Working Group on Heavy Ion Physics at the Large Hadron Collider is to evaluate the physics potential of this machine with colliding beams up to lead at a nucleon-nucleon center of mass energy of about 6.3 TeV.

More specifically, event generators are needed to simulate the general conditions of such collisions, providing estimates of (among other things) particle densities and transverse momentum spectra. The general conditions are needed both to estimate the energy densities and temperatures which could be reached, and to evaluate backgrounds from conventional physics to the interesting observables which could signal the formation of quark-gluon plasma (among them, dilepton invariant mass spectra).

The basic idea of the present work is to use a well established event generator (PYTHIA) to simulate minimum bias p-p events at LHC energy, and then to use a simple convolution rule for extrapolation to minimum bias or central A-A collisions.

2. PYTHIA FOR p-p COLLISIONS

The Lund Monte Carlo program PYTHIA, originally developed to describe high p_T hadronic physics, has been extended to cover also low p_T interactions; a picture in which hadronic events contain a variable number of parton-parton interactions, depending on the impact parameter, has been developed [1].

Recently, PYTHIA was tuned [2,3] to reproduce the main features of present collider data, namely those of UA5 [4] and UA1 [5] at the CERN $p\bar{p}$ collider, and E735 [6] and CDF [7] at the FNAL Tevatron.

Specifically, the observed average charged multiplicity $\langle N_{CH} \rangle$ was used to fix the value of p_{T0} , the scale for the transition from perturbative QCD hard scattering to low p_T interactions ($p_{T0}=1.9$ GeV). The correlation between $\langle p_T \rangle$

and N_{CH} was used to fix the structure of the secondary (non-hardest) parton-parton interactions (10% $q\bar{q}$ scattering, 81% gg scattering with minimal string length and 9% gg scattering with maximal string length).

We have used the above parameter values to generate p-p events at \sqrt{s} of 6.3 TeV (LHC ion-ion) and 16 TeV (LHC proton-proton). PYTHIA 5.3 has been used together with JETSET 7.2 for the fragmentation. In addition, events at \sqrt{s} of 53, 200, 900 and 1800 GeV have been generated for comparison with existing data.

Some features of charged particle distributions as a function of \sqrt{s} are presented in fig. 1-3. The linear increase of $\langle N_{CH} \rangle$ in a restricted pseudorapidity interval ($|\eta| \leq 2.5$) with $\ln s$ is reproduced by PYTHIA and extended up to LHC energies (fig. 1).

A linear increase with $\ln s$ of $(dN_{CH}/d\eta)_{\eta=0}$ is predicted by PYTHIA (fig. 2), in good agreement with the linear fit of CDF to their data and UA5 data [7] ($0.27 \ln s - 0.32$, dashed line) and in contrast with the quadratic fit [7] ($0.023 \ln^2 s - 0.25 \ln s + 2.5$, full line) which would predict higher pseudorapidity densities.

The $\langle p_T \rangle$ of charged particles in $|\eta| \leq 2.5$ is also reasonably well reproduced by PYTHIA (fig. 3). The $dN_{CH}/d\eta$ distributions of CDF data and PYTHIA at $\sqrt{s}=1800$ GeV are compared in fig. 4.

The $dN/d\eta$ distributions of charged particles, π , K and \bar{p} for minimum bias p-p events at \sqrt{s} of 6.3 TeV are presented in fig. 5. The dN/dy distribution for the net baryon number is presented in fig. 6. The average rapidity shift of the protons is $\Delta y=1.28$. The baryon free region, defined as the available rapidity gap minus four times the shift, is 12.5 units (the available rapidity gap is $\Delta y=17.6$).

The transverse momentum distributions of produced charged particles, π , K and \bar{p} are shown for the full η range in fig. 7, and for $|\eta| \leq 2.5$ in fig. 8. The average particle composition of an event and the $\langle p_T \rangle$ of the various particles are listed in table 1 (note that all hyperons have been allowed to decay).

Particle	$\langle N \rangle$	$\langle p_T \rangle$ GeV/c	$\langle p_T \rangle$ $ \eta \leq 2.5$
charged	68.2	.445	.507
π^\pm	56.3	.413	.466
K^\pm	5.95	.598	.724
p	3.28	.624	.947
\bar{p}	2.09	.724	.931

Table 1

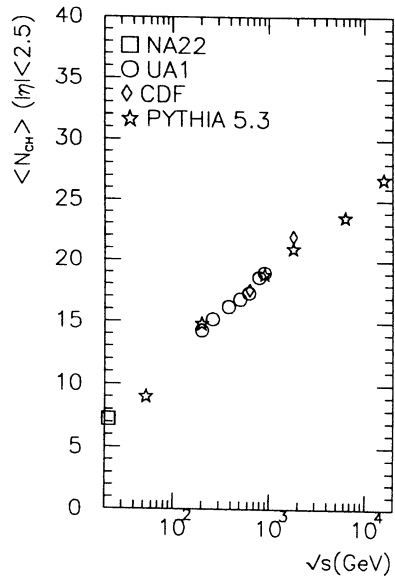


Fig. 1

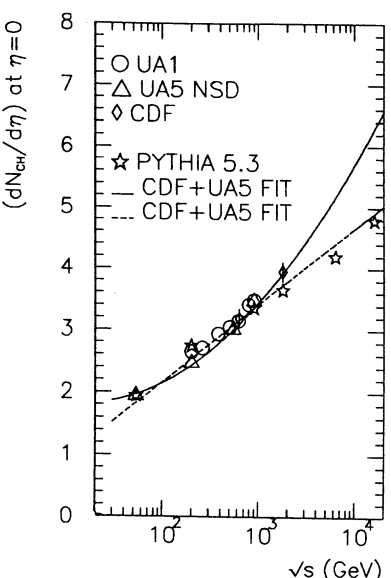


Fig. 2

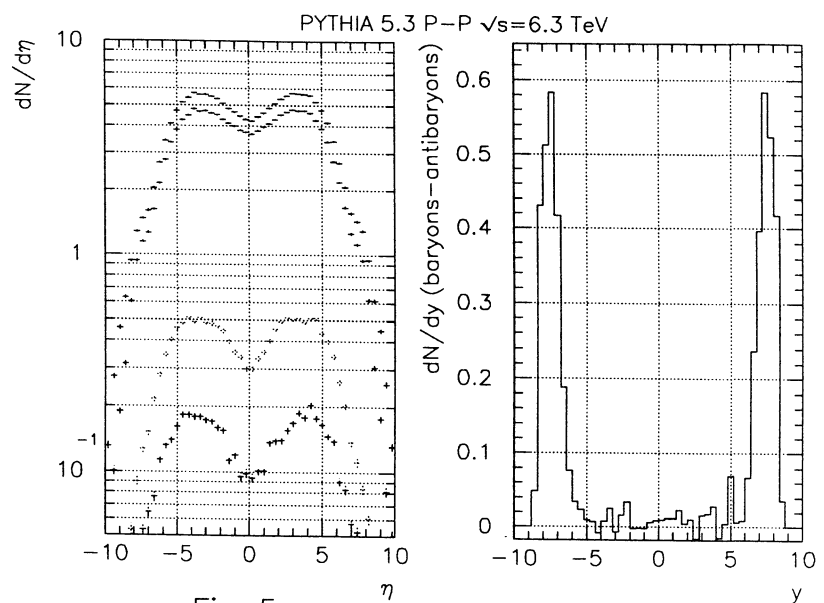


Fig. 5

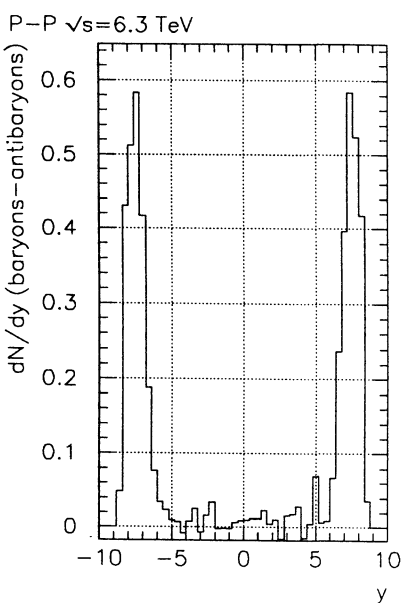


Fig. 6

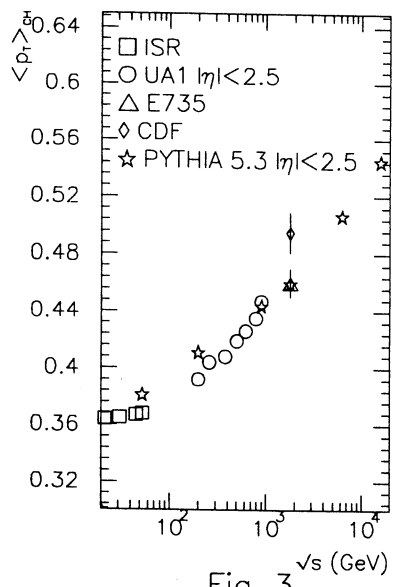


Fig. 3

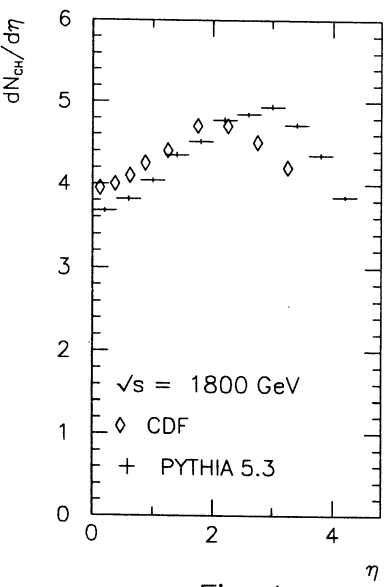


Fig. 4

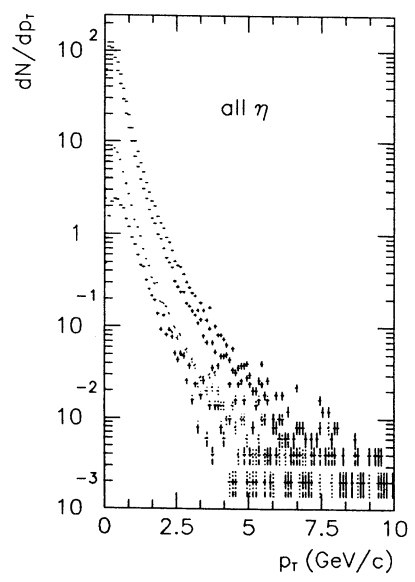


Fig. 7

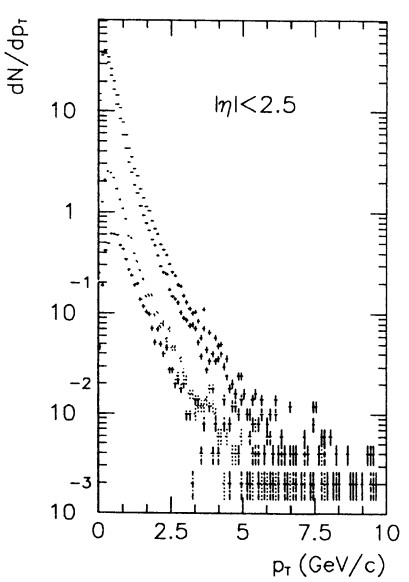


Fig. 8

3. CONVOLUTION OF p-p COLLISIONS

A simple scaling law was found to hold for the average charged multiplicity in proton-emulsion experiments as a function of the average charged multiplicity in p-p collisions [8]:

$$\langle N_S \rangle_{pEm} = 2.34 \langle N_{CH} \rangle_{pp} - 4.12 \quad (E_{LAB} = 1 - 800 \text{ GeV}) \quad (1)$$

($\langle N_S \rangle$ is the average shower particle multiplicity), and a similar law was later found for oxygen-emulsion experiments [9]:

$$\langle N_S \rangle_{OEm} = 10.1 \langle N_{CH} \rangle_{pp} - 16.6 \quad (E_{LAB} = 2.1 - 200 \text{ GeV/N}) \quad (2)$$

Adamovich et al. [9] found that eq. (2) can be reproduced by multiplying eq. (1) by a suitable weighted average between the ratio of participants oxygen-emulsion/proton-emulsion (which is expected to be relevant if the formation time is long and individual nucleons fragment independently) and the ratio of binary collisions (which is expected to be relevant for short formation times):

$$R_{OEm} = \frac{2}{3} \frac{P_{OEm}}{P_{pEm}} + \frac{1}{3} \frac{C_{OEm}}{C_{pEm}} \quad (3)$$

The number of participant nucleons (from projectile and target) $P = P_P + P_T$ and the number of binary nucleon-nucleon collisions C , averaged over impact parameter, are given from simple geometrical considerations by:

$$P_P = \frac{A_P \sigma_{pAt}}{\sigma_{ApAt}}, \quad P_T = \frac{A_T \sigma_{pAp}}{\sigma_{ApAt}}, \quad C = \frac{A_P A_T \sigma_{pp}}{\sigma_{ApAt}} \quad (4)$$

This scaling law seems to indicate that the energy dependence of particle production is the same for p-p, p-A and A-B collisions. We may extend this approach to arbitrary A-B collisions, defining a ratio R_{AB} in analogy with R_{OEm} in eq. (3), and then writing:

$$\langle N_S \rangle_{AB} = R_{AB} \langle N_S \rangle_{pEm} = \left(\frac{2}{3} \frac{P_{AB}}{P_{pEm}} + \frac{1}{3} \frac{C_{AB}}{C_{pEm}} \right) \langle N_S \rangle_{pEm} \quad (5)$$

where $\langle N_S \rangle_{pEm}$ is given by eq. (1).

The number of p-p interactions to be convoluted to reproduce the average multiplicity of an A-B collision, \mathcal{N}_{AB} , is obtained by requiring $\langle N_S \rangle_{AB} = \mathcal{N}_{AB} \langle N_{CH} \rangle_{pp}$:

$$\mathcal{N}_{AB}(\sqrt{s}) = R_{AB} \frac{2.34 \langle N_{CH} \rangle_{pp} (\sqrt{s}) - 4.12}{\langle N_{CH} \rangle_{pp} (\sqrt{s})} \quad (6)$$

(the \sqrt{s} dependence of \mathcal{N}_{AB} is weak for high $\langle N_{CH} \rangle_{pp}$).

System	P	C	\mathcal{N}_{AB}	dN_{ch}/dy $y=0$	$A^\alpha (dN_{ch}/dy)_{pp}$ $\alpha = 1.$	$A^\alpha (dN_{ch}/dy)_{pp}$ $\alpha = 1.1$
pp	2	1	-	5.25	(5.25)	(5.25)
pEm	3.66	2.66	-	-	-	-
OO mb	8.66	8	6	31.5		
OO c	32	37	24	126	84	111
SS mb	16.3	18	12	63		
SS c	64	93	53	278	168	237
PbPb mb	105	199	100	525		
PbPb c	414	1126	493	2588	1087	1852

Table 2

We computed \mathcal{N}_{AB} for minimum bias collisions using the definitions (4) with inelastic cross-sections parametrized as [9]:

$$\begin{aligned} \sigma_{pp} &= 32.3 \text{ mb}, & \sigma_{pA} &= 38.17 A^{0.719} \text{ mb}, \\ \sigma_{AB} &= 109.2 (A^{0.29} + B^{0.29} - 1.39)^2 \text{ mb} \end{aligned}$$

For central collisions \mathcal{N}_{AB} was estimated using the number of participants $P_{AB} = A + B$, and the number of binary collisions C as calculated from the overlap integral. Some $1.5 \cdot 10^5$ p-p events at \sqrt{s} of 6.3 TeV were then convoluted to simulate O-O, S-S and Pb-Pb events. The numbers used for the convolution and the charged rapidity densities obtained are summarized in table 2. Other systems can easily be treated using the same method.

The values of $(dN_{CH}/dy)_{y=0}$ obtained for central collisions are considerably higher than those extrapolated from the p-p value assuming an A^α dependence [10] with $\alpha=1.0$ without rescattering (column 6 in table 2) or $\alpha=1.1$ with rescattering (column 7). In fact, a fit to such a dependence using the value of $(dN_{CH}/dy)_{y=0}$ from the convoluted events (column 5) gives $\alpha \simeq 1.16$.

The $dN_{CH}/d\eta$ distributions for central and minimum bias S-S and Pb-Pb events at \sqrt{s} of 6.3 TeV are presented in fig. 9 and 10. More detailed information can be extracted from figures 5-8 (proton-proton distributions) by taking into account the convolution factors \mathcal{N}_{AB} from table 2.

The picture of an ion-ion collision as a straight superposition of a number of p-p collisions is certainly too naïve. For example, the stopping is most probably higher in A-A collisions. A more realistic simulation should include at least a proper treatment of the nuclear geometry. This would require using PYTHIA to describe multiple collisions of a nucleon, at lower and lower values of \sqrt{s} .

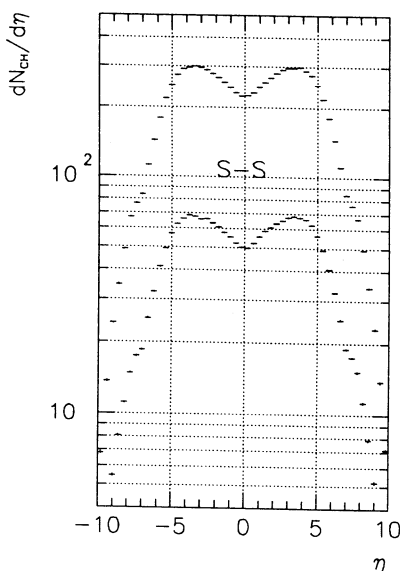


Fig. 9

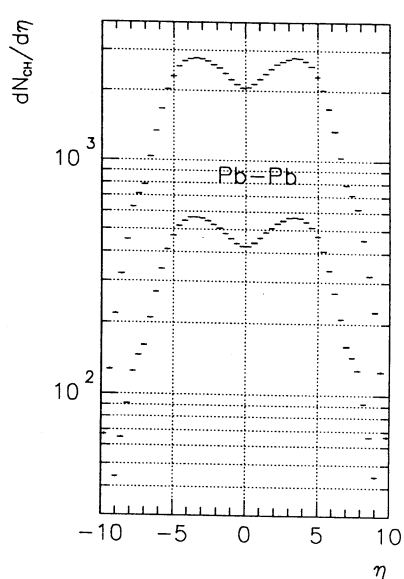


Fig. 10

4. CONCLUSIONS

We have used a phenomenological convolution rule to simulate ion-ion events by superposition of proton-proton events generated with PYTHIA at \sqrt{s} of 6.3 TeV.

Since PYTHIA was tuned to existing $p\bar{p}$ and $p\bar{p}$ data up to \sqrt{s} of 1.8 TeV, we believe that these event samples can provide a useful starting point for the estimation of general conditions and backgrounds in Pb-Pb collisions at LHC. In particular, it will be interesting to compare our results with those of generators which contain the full nuclear geometry, like for example VENUS [11].

ACKNOWLEDGEMENT

We gratefully acknowledge very useful discussions with A. Di Ciaccio, M. Mon-
teno and T. Sjöstrand.

REFERENCES

- 1) T. Sjöstrand and M. van Zijl, Phys. Rev. D36 (1987) 2019.
- 2) G. Ciapetti and A. Di Ciaccio, Minimum bias models, these proceedings.
- 3) T. Sjöstrand, Summary of pp working group on event generators, these pro-
ceedings.
- 4) G.J. Alner et al., Z. Phys. C33 (1986) 1.
- 5) C. Albajar et al., Nucl. Phys. B335 (1990) 261.
- 6) T. Alexopoulos et al., Phys. Rev. Lett. 60 (1988) 1622.
- 7) F. Abe et al., Phys. Rev. Lett. 61 (1988) 1819, and Phys. Rev. D41 (1990)
2330.
- 8) B. Andersson et al., Phys. Lett. 84B (1979) 469.
- 9) M.I. Adamovich et al., Mod. Phys. Lett. 5A (1990) 169.
- 10) U. Heinz, General Conditions in Heavy Ion Collisions at LHC, these proceed-
ings.
- 11) P. Cerello, P. Giubellino and K. Werner, Results from VENUS at LHC energies,
these proceedings.

Results of the Event Generator FRITIOF

Ulrich Goerlach
CERN, Geneva, Switzerland

Abstract

The possible use of the event generator FRITIOF (version 1.6) to calculate global event parameters of heavy-ion collisions such as rapidity and p_T distributions at LHC energies, is discussed. It is argued that this version of the code, although broadly and successfully used at SPS energies, is not appropriate at the high energies of LHC. It fails to reproduce charged multiplicities and p_T distributions already at Tevatron energies. The origin of these discrepancies is the simplified treatment of gluon bremsstrahlung radiation of excited hadronic strings. Substantial upgrades of the code are necessary to overcome this limitation. A tentative evaluation of the baryon distribution at LHC seems to indicate the possible presence at central rapidities of baryon rich tails originating from the projectile region. However the code is not reliable anymore at this \sqrt{s} .

The Lund Fritiof model [1] has been used to simulate the global event properties of proton-proton and highly relativistic heavy-ion collisions up to $\sqrt{s} = 20$ GeV at the SPS. The apparent success of the model suggested that it could also be used to obtain some ideas about the event characteristics of heavy ion collisions at the LHC. However, the use of the code at these very high energies and for the heaviest elements is obstructed in several ways.

First, there are technical problems concerning the size of the common blocks used within the code and the JETSET library. These, however, have been overcome by simple modifications [2] that extended the range of the code up to a total multiplicity of 10000 produced particles. This is not sufficient for central Pb+Pb collisions at the LHC. The heaviest calculable system is Nb+Nb ($A = 93$). In order to extend the program to the heaviest systems, a more substantial correction of the FRITIOF and JETSET code is necessary.¹

The more serious and, as we will see later, prohibitive difficulties are based on the treatment of the gluon bremsstrahlung radiation of excited hadronic strings. As pointed out in Ref. [3], charged multiplicity and p_T distributions are very sensitive to the detailed treatment of this radiation. The authors report that up to the energy range of the ISR the final-state string masses are sufficiently small to simplify the code including only one gluon emission in each string, but nevertheless achieving a numerically satisfying result. However, at higher energies at the collider, and in particular for nucleus-nucleus collisions, higher string masses are obtained and it is necessary to include multiple gluon emission. Single-gluon radiation underestimates the tail of the multiplicity distribution and gives too large transverse momenta. It is shown how multiple gluon radiation can be implemented into the model. Furthermore, hard-scattering processes have been included

¹Calculations using an extended version of the code are at present carried out at the University of Lisbon by Carlos Lourenço.

without violating infrared stability. Data from the CERN p \bar{p} Collider are well reproduced after these modifications of the model. Unfortunately, there is at present no authorized version of the Lund FRITIOF model available for nucleus-nucleus collisions, which includes these important modifications. The standard FRITIOF version 1.6 includes only single-gluon radiation. Therefore it should NOT be used at high energies.

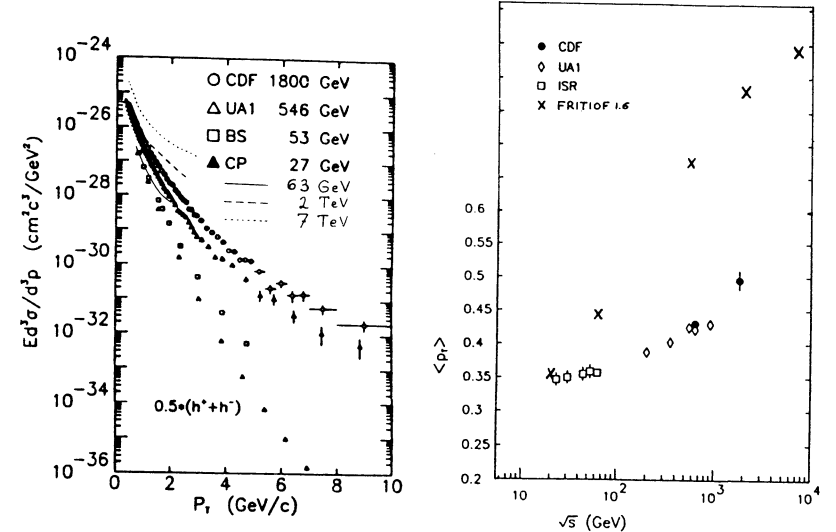


Figure 1: a) The p_T distribution at the ISR, p \bar{p} Collider and the Tevatron compared with the FRITIOF(1.6) prediction (lines) b) The average p_T as a function of \sqrt{s} . The crosses refer to FRITIOF(1.6).

To demonstrate the unsuitability of this version, we present in Fig. 1a, taken from ref. [4], a comparison of the p_T distributions measured at the ISR, the p \bar{p} Collider, and at the Tevatron, together with the FRITIOF prediction at these and at LHC energies. Here, we only want to compare the shape of the distributions, therefore data and calculations are normalized arbitrarily. Only the transverse-momentum range below 1 GeV/c is described correctly by this simulation code. Above 1 GeV/c, already at ISR energies a clear deviation is obvious. In this regime, where hard parton scattering plays an important role, the code overestimates the cross-section by a large factor, although hard scattering is not implemented. In Fig. 1b we show the average p_T at central rapidity, i.e. $|\eta| \leq 1.0$, as a function of \sqrt{s} . Clearly, FRITIOF does not reproduce the trend and the magnitude of the data, except at \sqrt{s} around 20 GeV where data and calculation coincide. At higher energies the average transverse momentum is significantly overestimated.

Similarly, FRITIOF underestimates the central charged rapidity densities: whereas the central charged multiplicity per unit of rapidity scales like $0.54 \cdot \ln \sqrt{s} - 0.32$ up to Tevatron energies [5], FRITIOF gives a value of 2.2, increasing only by 18% from the ISR to the LHC.

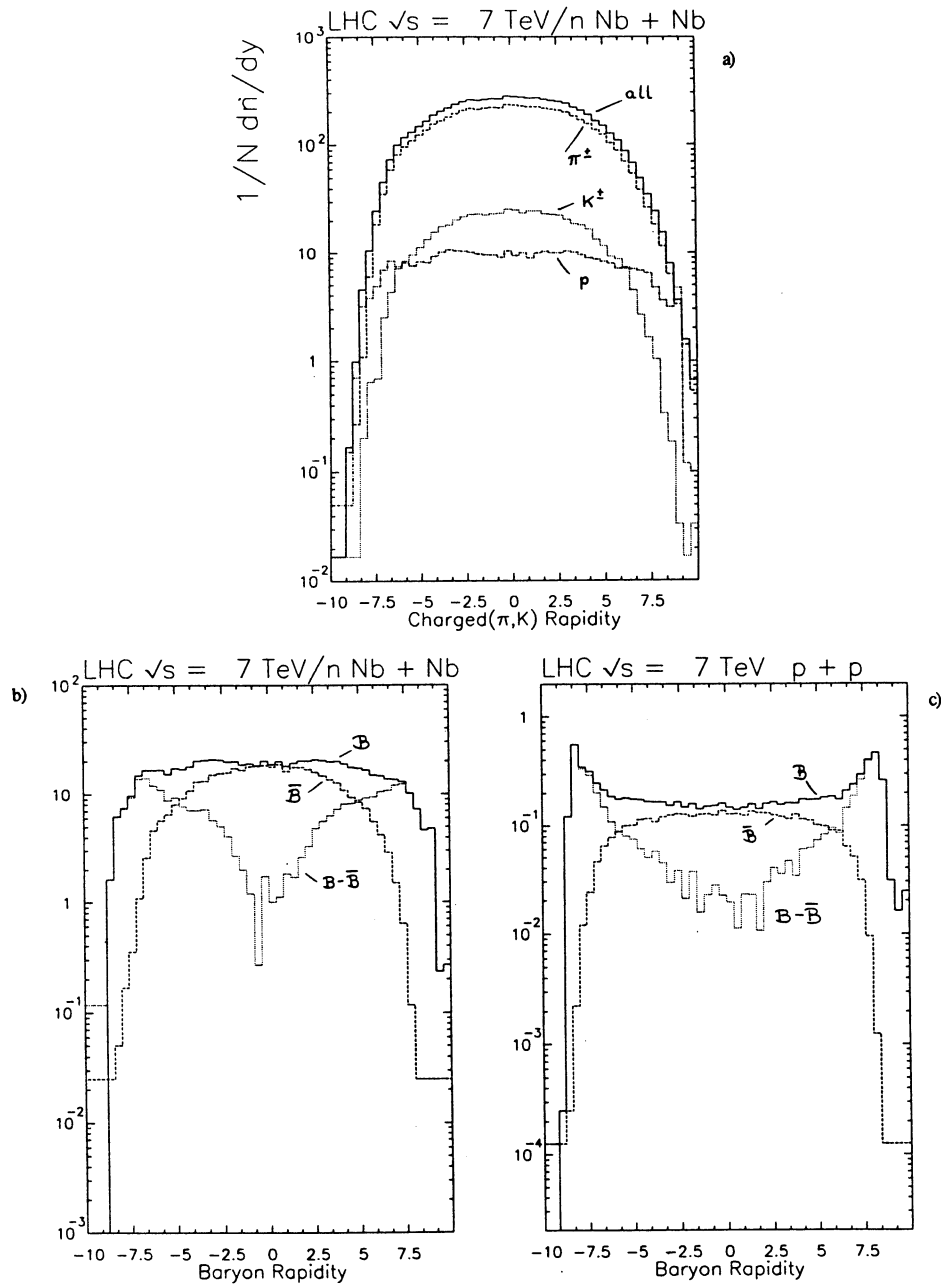


Figure 2: a)The charged rapidity distribution for Nb-Nb at $\sqrt{s}=7$ TeV/nucleon. according to FRITIOF(1.6).

b and c)The baryon(B) and antibaryon(\bar{B}) rapidity distribution and the baryon Excess($B - \bar{B}$) for Nb-Nb and p-p collisions, respectively

One of the most interesting questions concerning heavy-ion collisions at the LHC is the distribution of baryons and antibaryons in rapidity. It has been argued frequently that there should be no significant baryon excess in the central region. Despite the imperfection of the present FRITIOF version 1.6, we present in Fig. 2a and b the rapidity distributions of all charged particles and of all baryons, respectively.

In Fig. 2b also the baryon excess is plotted, showing a dip of very low baryon density (one per unit of rapidity) about 2 units wide. The tails of the two baryon-rich regions around the two projectiles are long and reach the central region. For comparison, in Fig. 2c the same distribution is plotted for pp collisions at the same \sqrt{s} , showing a clearer but not complete separation of the projectile regions.

At present, there are no experimental data on identified charged particles available, covering a wide rapidity interval at the p-p or the Tevatron collider. Measurements at central rapidity ($|\eta| \leq 1.0$) [6] are consistent with a baryon-free central region ($p/\pi \approx 0.07$), but they do not allow to determine its width.

In summary we may conclude that version 1.6 of the FRITIOF code used at present is only of very limited help to extrapolate to the energies of the LHC. The improvements [3] that have been developed for pp collisions have to be made available for the simulation of heavy-ion collisions. So far the charged multiplicity is heavily underestimated, whereas the p_T distributions are too hard.

The obtained baryon distribution seems to indicate that the central region may not be completely baryon-free. However, this tentative result should be taken with considerable caution, as it may be caused by the simplified treatment of the gluon radiation of strings of very high masses.

Acknowledgement: I would like to thank G. Gustafson for explaining to me the limitations of the FRITIOF version 1.6.

References

- [1] B. Andersson, G. Gustafson and B. Nilsson-Almqvist, Nucl. Phys. B281 (1987) 289.
- [2] E. Stenlund, private communication.
- [3] B. Andersson, G. Gustafson and B. Nilsson-Almqvist, Preprint University of Lund, LU TP 87-6 (1987).
- [4] F. Abe et al. (CDF), Phys. Rev. Lett. 61 (1988) 1819.
- [5] F. Abe et al. (CDF), Phys. Rev. D41 (1990) 2330.
- [6] T. Alexopoulos et al. (E735), Phys. Rev. Lett. 64 (1990) 991.

HADRON PRODUCTION IN NUCLEUS-NUCLEUS COLLISIONS AT LHC ENERGIES IN THE DUAL PARTON MONTE-CARLO MODEL DTUNUC

J. Ranft
Leipzig

1. Introduction, the new Monte-Carlo Dual Parton Model event generator DTUNUC

The model used will be described in more detail elsewhere[1]. DTUNUC uses the Glauber model cascade in the formulation of Zadorozhnyi et al. [2]. The multiparticle chains are fragmented using the BAMJET independent chain decay code[3].

After the production of fast hadrons in the Glauber-cascade we continue with the full (multi-generation) formation zone intranuclear cascade[4] in the target and projectile nuclei. In [4] only the first generation formation zone cascade in the target nucleus was considered.

DTUNUC can be used to sample hadron-hadron, hadron-nucleus and normal and central nucleus-nucleus collisions according to the Dual Parton Model. Only the naive two-chain per collision (single Pomeron exchange) Dual Parton Model is used. Multiple Pomeron exchange and minijets resulting from hard perturbative QCD collisions will be included in DTUNUC in the future. Central nucleus-nucleus collisions in the model are understood as collisions, where for projectile nuclei with mass numbers smaller than the ones of the target nuclei all projectile nucleons and wherer in collisions of identical nuclei more than 93 percent of the projectile nucleons take part in the collision.

Increasing the collision energy is a severe test for a Monte-Carlo model of the type considered. One problem is the large number of produced chains and particles. This requires a drastic increase of the storage requirement of the code. A second problem is the requirement of numerical stability for all kinematical calculations, which becomes more difficult to maintain with growing collision energy.

First results obtained with DTUNUC and comparison to data on hadron production in hadron-nucleus collisions have been presented at the Meeting *Quark Matter 90* at Menton[5]. Here we present only results at energies beyond the energies of presently existing heavy ion accelerators.

2. DTUNUC results for heavy ion collisions at the energies of future heavy ion colliders up to LHC

In the calculations reported, we use the naive two-chain-per-collision Dual Parton Model at energies, where in reality multi-pomeron exchange contributions become important and where furthermore a second component (the production of minijets due to parton-parton collisions as described by perturbative QCD) becomes important. These modifications to the model are presently understood in the case of hadron-hadron collisions at the energies of present and future hadron-hadron colliders[6]. It will take some time until all of this is also implemented for the nuclear collisions considered here.

In the calculations reported, we also neglect the formation time intranuclear cascade. This is reasonable for central collisions, where all nucleons of the colliding nuclei interact, but not completely realistic for normal noncentral collisions.

Besides multipomeron exchange and the formation of minijets, there are two more reasons for the multiplicity and the rapidity plateau of heavy ion collisions to rise with the collision energy in the Dual Parton Model.

(i) At low energies, many of the sea-sea collisions demanded by the Glauber cascade are suppressed kinematically. This suppression disappears with rising energy.

(ii) The cross-sections of nucleon-nucleon collisions, which have to be used as input for the Glauber cascade rise strongly with the collision energy. This leads to a slow rise of the nucleus-nucleus collision cross-sections with rising energy and to a rather rapid rise of the total number of elementary collisions in central nucleus-nucleus interactions. This number of collisions in central Au-Au collisions doubles approximately between the RHIC energy (200 GeV in the nucleon-nucleon cms.) and the LHC energy of 6300 GeV per nucleon-nucleon cms. Correspondingly, we get such a rise of the rapidity plateau.

Table 1. Results of the Glauber model cascade for Au-Au collisions at the energies of future heavy ion colliders.

Collision	\sqrt{s} (GeV)	$\sigma_{pp,tot}$ (mb)	n	n_a	n_b	σ_{Au-Au} (b)
central	200	52	1278	197	197	6.821
normal	200	52	314	64	64	6.821
central	630	63	1446	193	193	6.977
normal	630	63	299	56	57	6.977
central	2000	77	1697	195	195	7.134
normal	2000	77	352	56	59	7.134
central	7000	93	2027	197	196	7.313
normal	7000	93	362	50	57	7.313

We consider only gold (Au) nuclei as typical heavy projectiles and targets. In Table 1 we give the average number of collisions (n), the average number of interacting projectile nucleons (n_a) and the average number of interacting target nucleons (n_b) in normal and central Au-Au collisions as obtained from the Glauber model cascade. The input total p-p cross-section and the output gold-gold inelastic cross section are also given. Some of the numbers in the Table have large statistical errors because of the small number of events sampled. From the numbers given and similar calculations for other hadron-nucleus and nucleus-nucleus

collisions (we use in addition p-O, p-Ar, p-Xe and O-O, Ar-Ar and Xe-Xe) we can study the general behaviour of the inelastic output cross-sections and of the number of elementary collisions, which at high energies should be proportional to the central rapidity plateau obtained after the hadronization. We obtain from a fit to the cross-sections between $\sqrt{s} = 20$ GeV and 6300 GeV calculated in our Monte-Carlo calculation for proton-nucleus collisions

$$\sigma_{p-A} = 18 \cdot \sigma_{pp,tot}^{0.34} A^{0.61}$$

and for collisions of two identical nuclei

$$\sigma_{A-A} = 71 \cdot \sigma_{pp,tot}^{0.29} A^{0.63}.$$

The A-dependence corresponds closely to the one expected in the Glauber model as recently summarized by Kaidalov [7]. The dependence on $\sigma_{pp,tot}$ contradicts the naively expected proportionality of the nucleus-nucleus cross-section to the input nucleon-nucleon cross-section. The reason is, that we are in an energy region with $\sigma_{pp,tot}$ between 39 and 93 mb, where the nucleus-nucleus cross sections approach the geometrical value, which rises slowly only due to contributions from the periphery of the colliding nuclei.

A similar fit is performed to the calculated product of σ_{p-A} or σ_{A-A} with n , where n is the number of elementary collisions in the p-A or A-A collision. The number of collisions n is at high energies above all threshold effects proportional to the central rapidity plateau. We obtain in the fit a A^α dependence with $\alpha = 0.99$ for p-A collisions and $\alpha = 1.98$ for minimum bias A-A collisions. These α -values correspond closely to the expectation ($\alpha_{p-A} = 1$ and $\alpha_{A-A} = 2$) in the Glauber-model [7]. For n the fit gives the behaviour

$$n_{p-A} = 0.095 \sigma_{pp,tot}^{0.49} A^{0.38}$$

and for minimum bias nucleus-nucleus collisions

$$n_{A-A, \text{minimum bias}} = 0.043 \sigma_{pp,tot}^{0.43} A^{1.35}.$$

The A-dependence corresponds completely to the expectations [7], while the dependence on the input nucleon-nucleon cross-section is again modified by the effects as discussed already above.

In central nucleus-nucleus collisions we found another unexpected result, which is maybe not so surprising. We obtain an A^α -dependence with an α above the value 1.33 expected and obtained in minimum bias collisions. The behaviour depends certainly on the definition of *central collisions*. Our definition already given above is, that more than 93 percent of both the target and projectile nucleons are involved in the collision. We obtain in the fit

$$n_{A-A, \text{central}} = 0.074 \sigma_{pp,tot}^{0.51} A^{1.47}.$$

The $\alpha_{A-A, \text{central}} = 1.47$ together with the large A of gold explains the fact, that our model gives in central collisions of heavy nuclei rapidity plateaus larger than the ones reported from other models at this meeting.

Table 2. Average multiplicities calculated with DTUNUC for normal and central Au-Au collisions at energies up to LHC (7 TeV cms energy per nucleon-nucleon collision).

Collision	\sqrt{s} (GeV)	n_{tot}	n_{ch}	n_{π^-}	n_p
central	200	18476	10677	4592	115
normal	200	5233	3020	1296	32
central	630	31109	18041	7740	216
normal	630	7100	4110	1758	51
central	2000	48434	28148	12053	357
normal	2000	10743	6225	2655	81
central	6300	71592	41525	17833	571
normal	6300	13824	8012	3420	108

In Table 2 we give average multiplicities obtained from the DTUNUC runs and in Table 3 we give central rapidity densities obtained from the same Monte-Carlo runs. Again, we stress, that the statistical errors at the highest energies might be large due to the limited statistics in the Monte-Carlo runs.

Table 3. Central rapidity densities calculated with DTUNUC for normal and central Au-Au collisions at energies up to LHC (7 TeV cms energy per nucleon-nucleon collision).

Collision	\sqrt{s} (GeV)	$\frac{dn_{tot}}{dy}_{max}$	$\frac{dn_{ch}}{dy}_{max}$	$\frac{dn_{\pi^-}}{dy}_{max}$
central	200	3460	1960	829
normal	200	928	526	224
central	630	4830	2740	1150
normal	630	1040	586	247
central	2000	6320	3590	1510
normal	2000	1340	770	323
central	6300	8130	4660	1960
normal	6300	1490	848	346

We are shure, that the multiplicities and rapidity distributions will be modified by the effects discussed above, which have not yet been implemented into DTUNUC.

The effect of taking multi-pomeron exchange into account will be a rise of the rapidity distribution. From proton-antiproton collisions, we know, that this rise at the energy of 6.3 TeV will be approximately a factor of two. The minimal rise to be expected in nucleus-nucleus collisions is this factor two for the valence-valence chains, there is one pair of valence-valence chains for each interacting projectile nucleon. The maximum possible rise is the same factor as for proton-antiproton collisions.

The effect of taking minijets into account is more difficult to understand. We expect in nucleus-nucleus collisions as compared to hadron-hadron collisions much larger numbers of minijets, but shadowing effects will modify this contribution significantly.

At high energies we get in minimum bias and central Au-Au collisions a central rapidity region with vanishing Baryon number density. The total width in rapidity of this region is still $\Delta y = 0$ at $\sqrt{s} = 200$ GeV and it rises to $\Delta y = 3$ at $\sqrt{s} = 630$ GeV and $\Delta y = 6$ at $\sqrt{s} = 6300$ GeV.

REFERENCES

1. H.-J.Möhring and J.Ranft, to be published.
2. A.M.Zadorozhnyi, W.W.Uzhinskii and S.Yu.Shamakov, Dubna preprint P2-86-361 (1986) unpublished.
3. S. Ritter and J. Ranft, Acta Phys. Polonica B11, 259 (1980); S. Ritter, Z. Phys. C6, 27 (1982); Comp. Phys. Commun. 31, 393 (1984).
4. J.Ranft, Phys. Rev. D37, 1842 (1988); J.Ranft, Z.Phys. C 43, 439 (1989).
5. H.J.Möhring et al., presented by J.Ranft, to be published in the Proceedings of Quark Matter 90, Menton, France, 1990.
6. J.Ranft, Proceedings Multiparticle Dynamics 1988, D.Schiff and J.Tran Thanh Van (ed.), Editions Frontiers, 1988, p. 331. ; J.Ranft, P.Aurenche, F.Bopp, A.Capella, K.Hahn, J.Kwiecinski, M.Maire and J.Tran Thanh Van, SSC report SSC-149, (1987); K.Hahn and J.Ranft, Phys. Rev. D41, 1463 (1990); papers by the same authors to be published and the write-up for the DTU-JET code.
7. A.Kaidalov, CERN-preprint ERN-TH.5781/90 (1990).

BACKGROUND STUDIES FOR DILEPTON EXPERIMENTS AT THE LHC

Piergiorgio Cerello

INFN, Torino, Italy.

First results from a detector simulation for a heavy ion experiment at the LHC, concerning the combinatorial background of lepton pairs, are presented. The study has been carried out using two samples of 1000 O - O and 1500 S - S central events, obtained from the VENUS 3.11 generator. The framework for future, more detailed studies is described.

1. INTRODUCTION

The present work has been started with the final aim of evaluating the feasibility of a dilepton experiment with heavy ion beams at the LHC.

The first step has been the optimization of the model VENUS [1,2], to get event samples to be used in the simulation. The second step, still in progress, is the development of a detector simulation program, in order to provide a tool for the design of a dilepton experiment. This tool shall be able to estimate backgrounds from conventional sources, and to reproduce the detector response in different experimental configurations.

2. DETECTOR SIMULATION

For the detector simulation, it has been decided to use the GEANT package [3], which has the advantage of a simple definition of the setup, but takes a large amount of CPU time, especially for heavy ion central collisions at the LHC energy, where, before any decay, the total charged multiplicity ranges from 2500 (O-O) to 30000 (Pb-Pb).

The result of the propagation through a boron carbide absorber of a proton-proton event at $\sqrt{s} = 6300$ GeV is shown in fig. 1, while fig. 2 shows the propagation in air of the primary particles produced in an oxygen-oxygen interaction.

3. BACKGROUNDS TO DILEPTON EXPERIMENTS

3.1 MUONS FROM DECAYS OF PIONS AND KAONS

The starting points for the computation of the number of decays are the pseudorapidity and momentum distributions of pions and kaons at generation. Fig. 3.a and 3.b show respectively $dN/d\eta dp$ and $dN/d\eta dp_T$ distributions for kaons in

O - O interactions. On the other hand, the definition of the absorber material, shape and position is essential, since it fixes the mean free path of pions and kaons before they undergo an interaction.

The inner shape of the absorber is chosen so that the decay probability be independent of the angle. In particular, for each particle, the mean path x before the decay is computed as

$$x = \beta \gamma \tau_0 \ln \frac{1}{(1 - pr)} = \frac{p}{m} \tau_0 \ln \frac{1}{(1 - pr)}$$

where p , m , τ_0 and pr represent respectively the momentum, the rest mass, the lifetime in the rest frame and the decay probability of the particle (which is kept fixed). Then the mean value of this path is computed in different pseudorapidity regions, and the distance of the absorber from the interaction point is given by the difference between this path and one interaction length: so its value depends on the absorber material. The simulation has been carried out for 3 different materials (B_4C , Al_2O_3 and Cu), but can be repeated with little effort for other materials. By the way, from here on, the inner shape of the absorber is assumed to be a cylinder.

The absorber position, in principle, should be chosen in order to minimize the number of decays: this of course means that it has to be as close to the interaction point as possible. The absorber has been put at a distance of half an interaction length of B_4C from the beam axis (16.3cm). This value is quite reasonable, keeping in mind that in any case the beam pipe radius is of the order of a few centimeters and that the decay path into the absorber would already be dominant with respect to the one in air.

For each particle the decay probability can now be computed as

$$pr = 1 - \exp\left(-\frac{x}{\beta \gamma \tau_0}\right) = 1 - \exp\left(-\frac{mx}{p \tau_0}\right)$$

where both the momentum p and the path x depend on the emission angle θ . In particular, x is given by the sum of two terms: the free path in air and the mean path before the particle interacts in the absorber (one interaction length). As a function of the emission angle:

$$x = \lambda_{B_4C} + \frac{0.5 \lambda_{B_4C}}{\sin \theta}$$

Given the branching ratios for the decay channels:

$$\pi \rightarrow \mu + \nu_\mu$$

$$K \rightarrow \mu + \nu_\mu$$

the number of decay muons per event and, from kinematics, their 4-momenta are obtained.

At this point, it is possible to impose some cuts on the kinetic energy and on the transverse momentum of the muons, and to get the combinatorial mass spectrum from all the possible opposite sign pairs. Namely, assuming an absorber thickness of 8 interaction lengths, an energy loss of $1.86 MeV cm^2/g(B_4C)$, $1.867 MeV cm^2/g(Al_2O_3)$, $1.67 MeV cm^2/g(Cu)$, and a magnet momentum kick of $0.6 GeV$, all the muons with a kinetic energy below $1.223 GeV(B_4C)$, $1.474 GeV(Al_2O_3)$, $1.820 GeV(Cu)$ and a transverse momentum below $0.6 GeV$ are cut away.

The resulting mass distributions for dimuons are shown in fig. 4 for S-S collisions and a boron carbide absorber (full line). It is evident that the high mass tail of the spectrum is significant. But, looking at the correlation of the pair mass ($M_{\mu\mu}$) with the pseudorapidity interval between the two muons ($\Delta\eta_{\mu\mu}$), one sees that all the high mass dimuons have a large value of $\Delta\eta_{\mu\mu}$ (fig. 5, S-S interactions). Now, looking only at the pseudorapidity region $2 < \eta < 3.5$, which is a suitable candidate for a muon spectrometer, the mass spectrum, with the previous cuts, is shown in fig. 4 (dashed line). The mass region of the J/ψ and of the Υ are completely free from this kind of background.

The muons pseudorapidity distributions, after cuts on kinetic energy and transverse momentum, are shown in fig. 6 for different absorbers (O-O interactions).

3.2 OTHER BACKGROUNDS

The hadrons which, coming out after the absorber, simulate a muon in the spectrometer are the second main source of problems for a dimuon experiment. These particles, generally referred to as punch through particles, have a very steep dependence on the thickness of the absorber (fig. 7). The requirement of a low level of punch through is in direct conflict with the need of a short absorber for this kind of experiment, to guarantee optimum mass resolution. Therefore, presently available parametrizations, like the one in ref. [4], are not particularly suitable for this purpose, since they are optimized for very thick absorbers and high energy particles. So, it has been decided that a specific simulation should be developed to evaluate the punch through probability for low energy particles and short absorbers: this work is in progress, and we hope to be able to make sensible estimates within a short time scale.

In parallel, we are trying to set up an evaluation of backgrounds also for e^+e^- pairs. In fig. 8 a preliminary estimate of the background from Dalitz decays of π^0 's in O-O interaction is shown. The full line represents the mass spectrum over the whole pseudorapidity range, while the dashed line refers to the pairs in the

interval $-0.5 < \eta < 0.5$. There are no cuts on the momentum. This work is also still in progress.

4. CONCLUSIONS

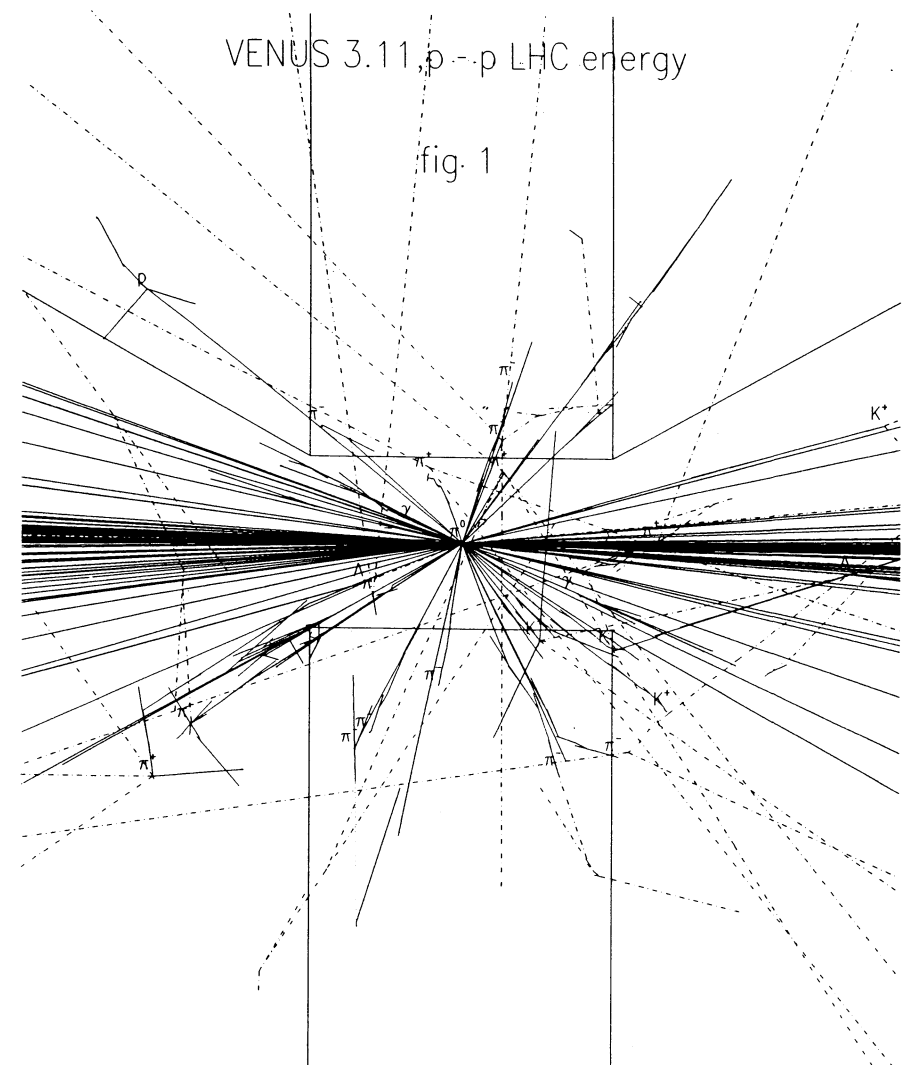
A program to perform detector simulations for ion-ion interactions at the LHC energy has been set up. This tool will be used to extensively study the various problems connected to the design of a detector for this kind of experiments. As a first step the background to the dimuon spectrum from decays of pions and kaons has been estimated. We are presently working on the problems of punch through and of the combinatorial background for electron pairs. Future developments shall include studies of effects such as the albedo and the lateral leakage from the muon absorber.

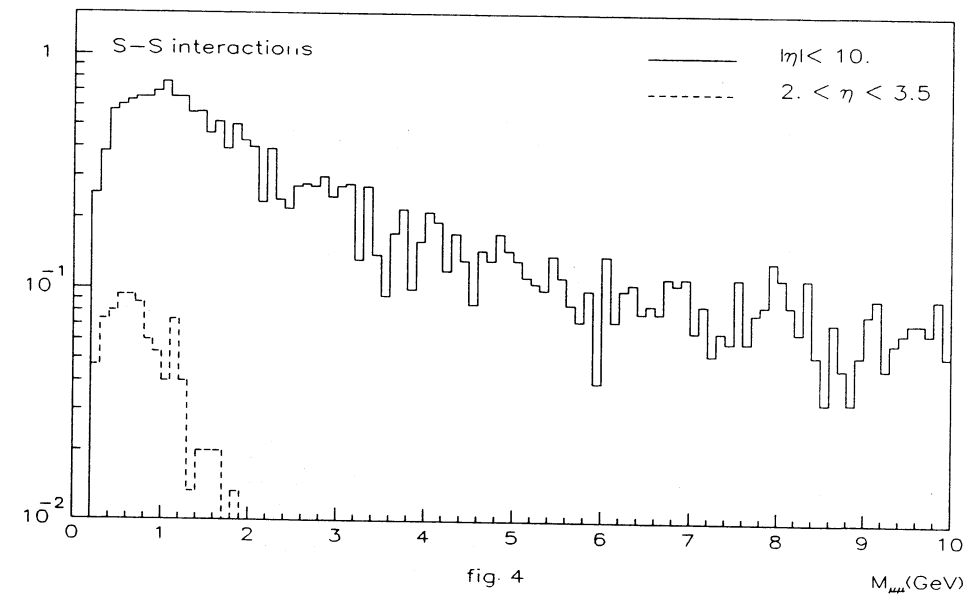
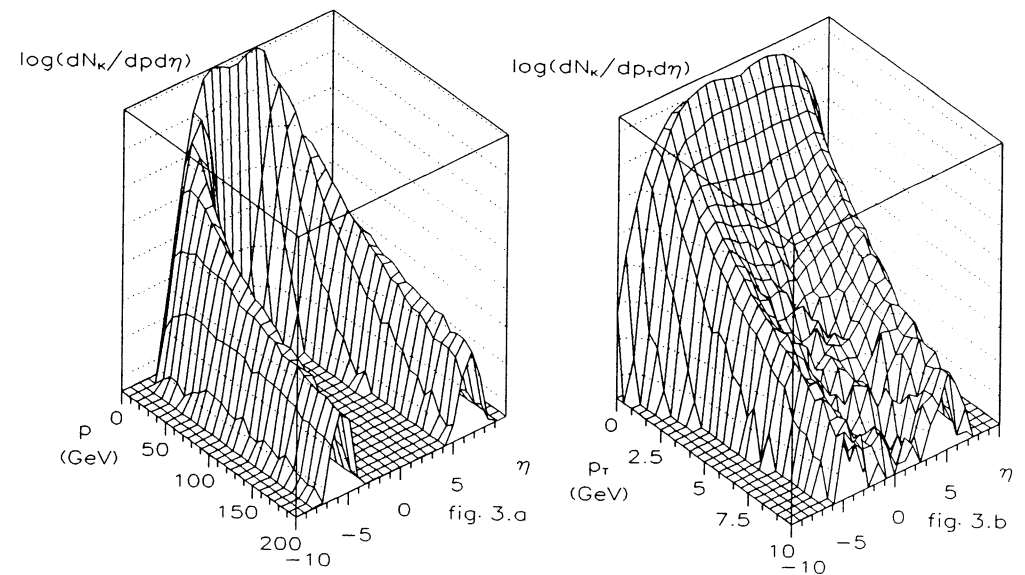
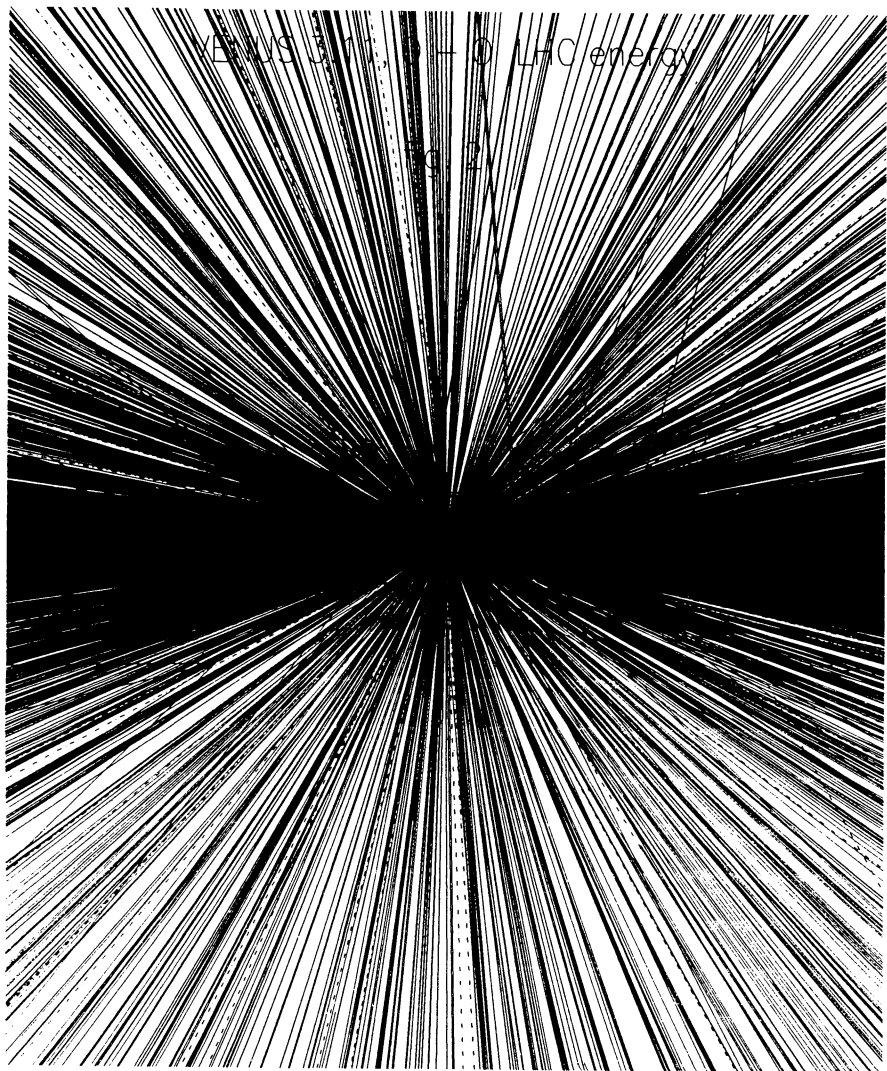
ACKNOWLEDGEMENTS

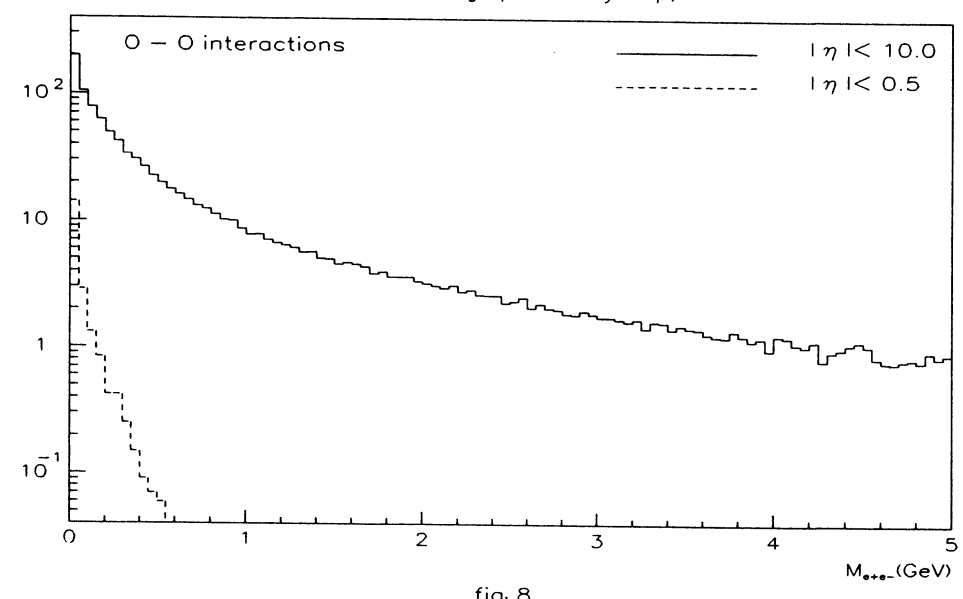
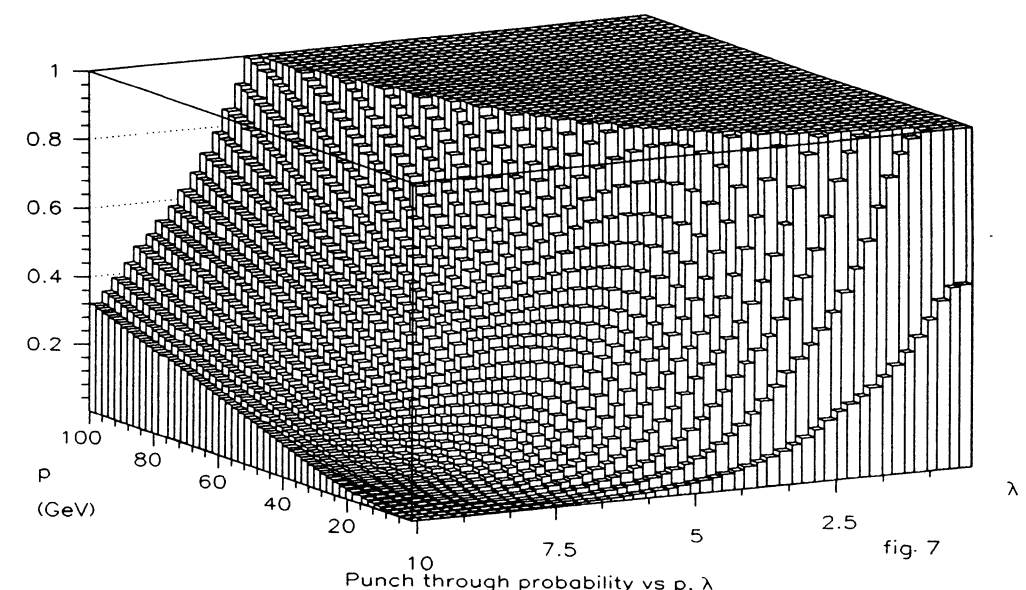
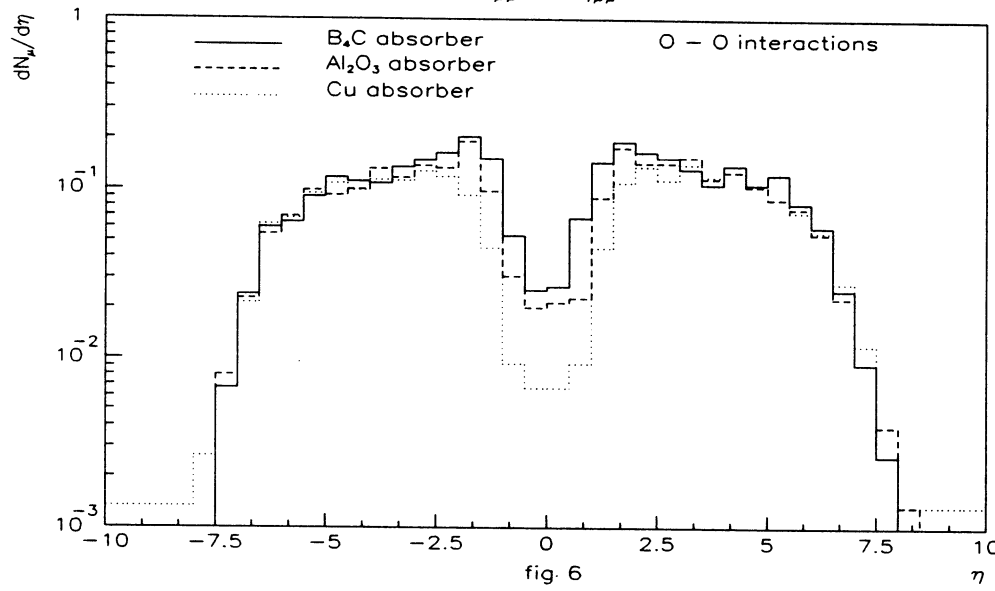
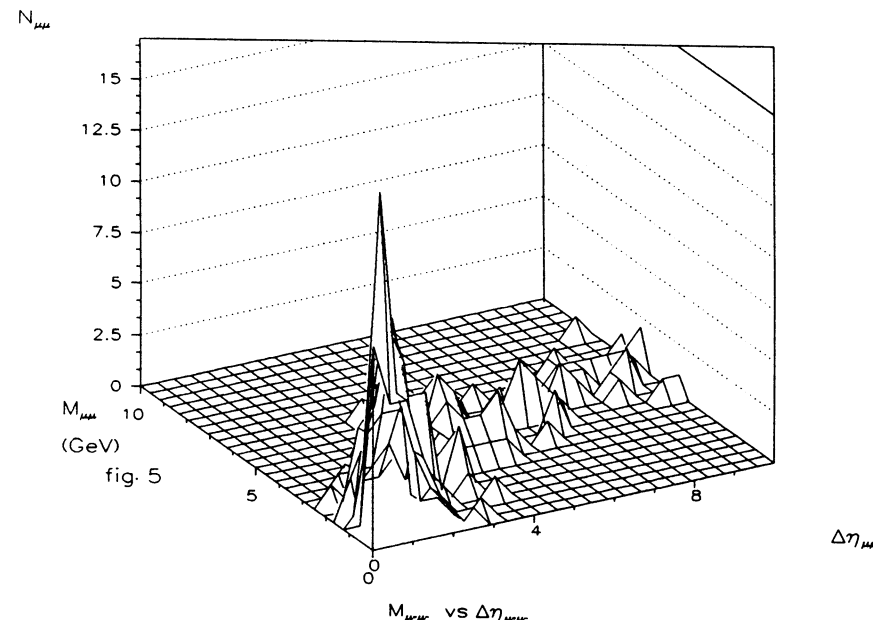
Dr. P. Giubellino, Prof. L. Kluberg and Prof. P. Sonderegger are gratefully acknowledged for their guidance and useful discussions.

REFERENCES

- 1) K. Werner, Z. Phys. C42(1989)85.
- 2) K. Werner and P. Koch, Z. Phys. C17(1990)215.
- 3) R. Brun et al, GEANT3, CERN DD/EE/84-1.
- 4) F. Lacava, these proceedings.







HEAVY QUARK RESONANCES IN HEAVY ION COLLISIONS: FROM SPS TO LHC

FRITHJOF KARSCH
Fakultät für Physik, Universität Bielefeld
D-4800 Bielefeld 1, F.R.G.

ABSTRACT

The experimentally observed suppression of J/ψ production in $O-U$ and $S-U$ collisions at the SPS can be understood in terms of screening in a quark gluon plasma as well as absorption in a hadron gas combined with initial state rescattering of quarks and gluons. We extrapolate predictions of these models to $Pb-Pb$ collisions at SPS and future colliders like RHIC and LHC. We extend these models to study the suppression pattern of other $c\bar{c}$ and $b\bar{b}$ resonances.

1. Introduction

The existence of a phase transition from hadronic matter at low temperatures and/or densities to a quark gluon plasma is theoretically well established. Detailed numerical investigations of the parameters of the transition suggest a critical temperature, $T_c \simeq 150$ MeV, for QCD with two massless flavours¹. It is, however, far more difficult to detect this transition experimentally, i.e. to prepare suitable thermal equilibrium conditions in an experiment, that would allow a clean observation of the QCD phase transition. It has been suggested that one possible way to observe a quark-gluon plasma would be the study of hadronic matter formed in ultra-relativistic heavy ion experiments². It is expected that at high enough energies a quark-gluon plasma (QGP) can form in such collisions. For a short time the system would then stay in the QGP phase, it would undergo a rapid cooling and finally should go back into the hadronic gas (HG) phase via a phase transition.

One of the most promising signatures for the existence of the QGP-phase in early stages of a nucleus-nucleus collision is the suppression of heavy quark resonances³. It has been argued that due to the strong *screening of the heavy quark potential* in the plasma phase⁴, it will be impossible to form $q\bar{q}$ bound states in a QGP already at temperatures slightly above T_c ^{5,6}. The finite lifetime of the QGP-phase, as well as its finite spatial extent, will lead to a characteristic

dependence of the suppression pattern on the transverse momentum of the $q\bar{q}$ -resonances and the total transverse energy of the event⁷.

The production of heavy quark resonances in heavy ion collisions is usually discussed in terms of the relative yields, $N_x(E_T)$, which give the number of resonances of type x in events with a total transverse energy E_T relative to the corresponding yield of Drell-Yan pairs. In addition the relative rates of resonances with a given transverse momentum, p_T , are studied. Here one compares the p_T spectra in various E_T -bins with those in a reference system, which usually is taken to be the lowest E_T -bin available:

$$S_x(p_T) = \frac{N_x(E_T \text{ high}, p_T)}{N_x(E_T \text{ low}, p_T)} \quad (1)$$

The presence of a QGP in early stages of a nucleus-nucleus collision would lead to a decrease of $N_x(E_T)$ with increasing E_T ³ and an increase of $S_x(p_T)$ with increasing p_T ⁷. These qualitative features of the resonance suppression pattern expected in a QGP have been observed in the first heavy ion experiments with O^{16} , S^{32} beams and U^{238} -targets at the SPS⁸. The experimentally observed suppression of J/ψ resonances⁸ can, however, also be understood in terms of *absorption in a dense nuclear medium*, i.e. a resonance gas⁹. It even seems to be possible to understand the suppression pattern within the framework of the dual parton model, i.e. without assuming the existence of a thermalized system¹⁰. An additional mechanism that will contribute to the observed p_T -dependence of the J/ψ -suppression pattern is *initial state parton scattering*¹¹; quarks and gluons may rescatter in a nuclear medium several times before giving rise to a $q\bar{q}$ -resonance in a hard scattering process.

In Fig. 1 we show the data for the momentum and transverse energy dependence of the J/ψ -suppression pattern in $S-U$ collisions together with predictions from a QGP-model as well as a HG-model with and without initial state rescattering of gluons. Clearly there are differences in the model predictions, in particular at large p_T . However, with the present statistics this regime cannot be studied and it thus is not possible to get a reliable estimate for the relevance of initial state scattering effects from the $S-U$ data. In order to disentangle the p_T -dependence due to initial state rescattering from that arising from the presence of a QGP one should go to a p_T -regime where the plasma model would predict no influence on the p_T -spectra of J/ψ .

As various models lead to qualitatively similar predictions for the suppression pattern of heavy quark resonances in heavy ion collisions one is forced to perform a detailed quantitative analysis of the predictions and look for systematic differences in the predictions when comparing data for different target and projectile nuclei as well as different energies. What are the predictions of the existing models for the $q\bar{q}$ -resonance suppression pattern for nucleus-nucleus collisions with heavier nuclei and/or at larger CMS-energies? Will this lead to an easier distinction between the various proposed mechanisms? An answer to these questions is of particular

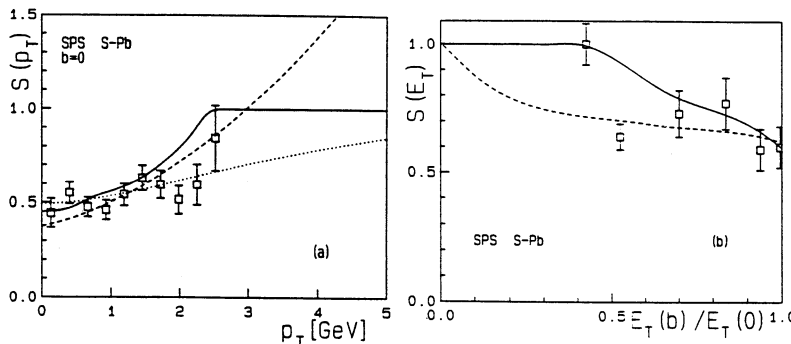


Figure 1: The fraction of $c\bar{c}$ -pairs leaving the hot interaction region in a $S-U$ collision as J/ψ resonances versus transverse momentum (fig. 1a) and transverse energy (fig. 1b). Data are from ref. [12]. Data have been normalized to the lowest E_T bin. They are compared with predictions from a quark-gluon plasma model (solid line) and a hadron gas model with (dashed line) and without (dotted line) initial state rescattering. In the model calculations the transverse energy is taken to be proportional to the number of participants (see Eq. 6) through which it is related to the impact parameter b of the collision.

importance in view of the planned $Pb-Pb$ experiments at the SPS as well as for future heavy ion experiments at RHIC and LHC.

In the following sections we discuss the extrapolation of predictions of the QGP model as well as the hadron gas model with initial state rescattering effects to heavier nuclei and larger energies. In section 2 we give a brief summary of the basic parameters in the hydrodynamical model on which these extrapolations are based. Sections 3 and 4 deal with the p_T -dependence of the suppression pattern in the QGP-model and in models which incorporate initial state rescattering effects, respectively. In section 5 we discuss the expected overall suppression predicted by the QGP and HG models for various $c\bar{c}$ and $b\bar{b}$ resonances. Section 6 contains our conclusions.

2. Initial Conditions

The idea to search for the formation of a quark-gluon plasma in nucleus-nucleus ($A-B$) collisions is based on the hope that during the collision of two heavy nuclei a dense system of hadronic matter is formed in the overlap volume of target and projectile nuclei. It is expected that this dense system of matter thermalizes after some initial time, $t_i \simeq 1\text{fm}$, and afterwards undergoes an isentropic hydrodynamic expansion during which the system cools down again. This cooling is mainly due to the rapid longitudinal expansion of the system. It is controlled by the condition for entropy conservation,

$$s(\vec{r}, t) | t = s(\vec{r}, t_i) | t_i , \quad (2)$$

which relates the entropy density $s(\vec{r}, t)$ at time t and position \vec{r} in the interaction region to the initial entropy density $s(\vec{r}, t_i)$ at thermalization time.

The average initial entropy density obtained in a $A-B$ collision with impact parameter b can be related to the experimentally observed particle multiplicity in a central rapidity interval

$$s_i(b) = \frac{3.6 dN(b)/dy}{S_{eff}(b)t_i} , \quad (3)$$

where S_{eff} denotes the overlap area in a $A-B$ collision at impact parameter b as shown in fig. 2.

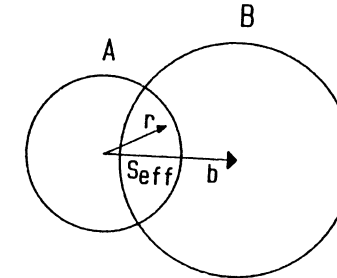


Figure 2: Geometrical parameter in a $A-B$ collision at impact parameter b .

The crucial parameter, which determines the initial entropy density and its dependence on the CMS-energy, \sqrt{s} , as well as the nuclei A and B is the particle multiplicity dN/dy . In the following we will assume that this can be approximated by

$$\frac{dN}{dy}(b) = \frac{1}{2} N_{AB}(b) \left(\frac{dN}{dy} \right)_{pp} , \quad (4)$$

with

$$\left(\frac{dN}{dy} \right)_{pp} = 0.8 \ln \sqrt{s} \quad (5)$$

denoting the multiplicity in $p-p$ collisions at \sqrt{s} and $N_{AB}(b)$ being the number of participants in a $A-B$ collision at impact parameter b ,

$$N_{AB}(b) = \frac{3}{2\pi} \int_{S_{eff}} d^2r \left[R_A \left(1 - \left(\frac{\vec{r}}{R_A} \right)^2 \right)^{1/2} + R_B \left(1 - \left(\frac{(\vec{r} - \vec{b})}{R_B} \right)^2 \right)^{1/2} \right] , \quad (6)$$

with $R_A = 1.2A^{1/3}$. From eqs. (3) - (6) we find for the entropy density in central $A-A$ collisions

$$s_i(0) \simeq 0.8A^{1/3} \ln \sqrt{s} . \quad (7)$$

These are our basic relations which determine the initial conditions in $A-B$ collisions at SPS and LHC energies. We note that the above assumptions for dN/dy are

rather conservative, as we did not take into account a possible increase of dN/dy in A - B collisions due to final state rescattering effects. In fact, results from S - S collisions indicate that dN/dy rises somewhat faster than $A^{1/3}$. For a discussion of this see for instance ref. [13].

Using as an input the observed multiplicities in S - U collision at the SPS, $dN/dy \simeq 150^2$, we obtain from Eq. (4)

$$\left(\frac{dN}{dy}\right)_{Pb-Pb, LHC} \simeq 1600 , \quad (8)$$

for the multiplicity in central Pb - Pb collisions at LHC energies. We further note that

$$(s_i(0))_{Pb-Pb, LHC}^{1/3} \simeq 1.8 (s_i(0))_{S-U, SPS}^{1/3} . \quad (9)$$

The entropy density is proportional to T^3 , at least at high enough temperature, where one can assume approximate ideal gas behaviour of the QGP. Eq. (9) thus reflects roughly the expected rise of the initial temperature when going from SPS to LHC energies.

3. p_T -Dependence of the Suppression Pattern in a QGP Model

There are two quite different mechanisms, which may lead to a strong p_T -dependence of the rates of $q\bar{q}$ resonances relative to the Drell-Yan background. On the one hand such a p_T -dependence may arise from the rescattering of partons in the initial state, i.e. already before the formation of the $q\bar{q}$ pair, which leads to the formation of a resonance. We will discuss this aspect in the next section. On the other hand, a strong p_T -dependence is also induced through the screening of the heavy quark potential in a QGP.

In a QGP $q\bar{q}$ -pairs with large transverse momenta are less suppressed because they form at a late time in the plasma rest frame. The plasma cools rapidly according to Eq. (2) and at the time of resonance formation, τ_x ⁷, the temperature may have dropped already below the critical value needed to provide a sufficiently screened heavy quark potential that prohibits resonance formation⁵. A characteristic feature of the QGP-model is the existence of a critical momentum, $p_{c,x}$, for each resonance x , such that $q\bar{q}$ -pairs in this channel with momentum $p_T > p_{c,x}$ are not suppressed. The critical momentum is given by⁷

$$p_{c,x} = M_x \sqrt{\left(\frac{t_{f,x}}{\tau_x}\right)^2 - 1} = M_x \sqrt{\left(\frac{t_i s_i}{\tau_x s_x}\right)^2 - 1} , \quad (10)$$

where we have used Eq. (2) to obtain the last equality. The various resonance parameters like the resonance mass M_x and formation time τ_x are given in Table 1 for some $c\bar{c}$ and $b\bar{b}$ resonances⁶. The plasma lifetime for a given resonance is obtained again from Eq. (2) as

$$t_{f,x} = t_i \left(\frac{T_i}{T_x^d}\right)^3 , \quad (11)$$

States :	ψ	ψ'	χ_c	Υ	Υ'	χ_b
M_x	3.1	3.7	3.5	9.6	10.0	9.9
r_x	0.45	0.88	0.70	0.23	0.51	0.41
τ_x	0.89	1.5	2.0	0.76	1.9	2.6
μ_x	0.70	0.36	0.34	1.57	0.67	0.56
T_x^d/T_c	1.17	1.0	1.0	2.62	1.12	1.0
σ_x	0.1	0.37	0.24	0.025	0.13	0.08

Table 1

Bound state masses M_x [GeV], radii r_x [fm], formation times τ_x [fm], critical screening masses μ_x [GeV], dissociation temperatures T_x^d and break-up cross sections σ_x [fm²], for $c\bar{c}$ and $b\bar{b}$ states. The dissociation temperatures are given in terms of the deconfinement temperature $T_c = 150$ MeV; the cross sections were obtained using geometric arguments (ref. 6) and $\sigma_\psi = 0.1$ fm² = 1 mb.

with T_x^d denoting the dissociation temperature needed to prohibit formation of the resonance x .

We note that the critical momenta $p_{c,x}$ are well approximated by

$$p_{c,x} \simeq M_x \frac{t_i}{\tau_x} \frac{s_i}{s_x} \simeq M_x \frac{t_i}{\tau_x} \left(\frac{T_i}{T_x^d}\right)^3 , \quad T_i > T_x^d . \quad (12)$$

From the scaling relation for the entropy density, Eq. (7), we thus deduce the corresponding scaling behaviour of the critical momenta in the plasma model,

$$p_{c,x} \sim A^{1/3} \ln \sqrt{s} . \quad (13)$$

In fig. 3 we show the resulting suppression pattern for directly produced J/ψ 's in Pb - Pb collisions at various collider energies which clearly reflects the shift of $p_{c,x}$ to larger values with increasing \sqrt{s} . Fig. 4 displays the suppression pattern for various $c\bar{c}$ and $b\bar{b}$ resonances at LHC-energies. We note that even at this high energies screening of the heavy quark potential is not sufficient to prohibit the formation of Υ -resonances in a QGP.

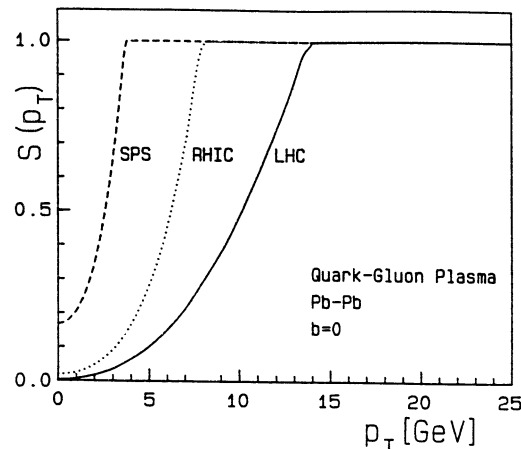


Figure 3: $S(p_T)$ of directly produced ψ 's versus transverse momentum at CMS energies $\sqrt{s} = 20$ GeV (SPS), 200 GeV (RHIC) and 6400 GeV (LHC).

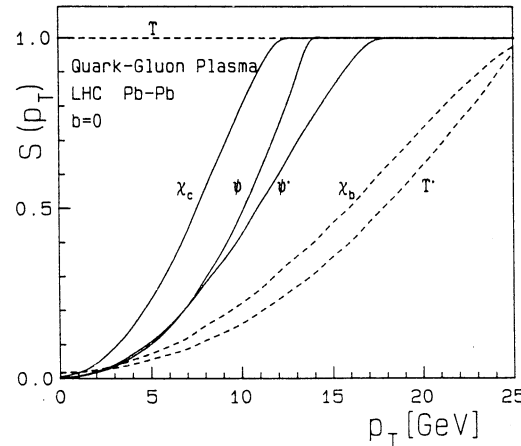


Figure 4: $S(p_T)$ versus transverse momentum p_T at $\sqrt{s} = 6400$ GeV for various $c\bar{c}$ and bb resonances.

4. Initial State Effects

A further mechanism leading to a strong p_T -dependence of $S_x(p_T)$ is the initial state rescattering of partons, which after a few soft collisions in a nucleus form a $q\bar{q}$ -resonance in a final hard collision¹¹. This leads to a broadening of the p_T -distribution of $q\bar{q}$ -resonances, i.e. some of the low p_T $q\bar{q}$ -pairs get shifted to larger p_T . Such a p_T -broadening has been observed in p -A collisions¹⁴. For the average

p_T^2 in a A - B collision one expects on the basis of various rescattering models

$$\langle p_T^2 \rangle_{AB}^x = \langle p_t^2 \rangle_{pp}^x + (\Delta p_T^2)_{x,AB}, \quad (14)$$

where $(\Delta p_T^2)_{x,AB}$ is related to the average number of soft collisions of the participating partons, the cross-section σ_{xN} for such collisions and the average p_T transfer,

$$(\Delta p_T^2)_{x,AB} \sim \langle p_T^2 \rangle_x \sigma_{xN}(A^{1/3} + B^{1/3}). \quad (15)$$

With this we obtain for the contribution of initial state effects to the momentum dependence of $S_x(p_T)$,

$$S_x(p_T) = f_x(p_T)(1 - \alpha_{AB})^2 \exp \left\{ \frac{2p_T}{\langle p_T \rangle_{pp}^x} \alpha_{AB} \right\}, \quad (16)$$

with

$$\alpha_{AB} = 1 - \frac{\langle p_T \rangle_{pp}^x}{\langle p_T \rangle_{AB}^x}. \quad (17)$$

Here $f_x(p_T)$ parametrizes the remaining p_T dependence which either arises from the absorption in a hadron gas or the screening in a quark-gluon plasma. We note that the parameter α_{AB} is independent of \sqrt{s} , if one assumes that the parton transverse momenta show the same \sqrt{s} -dependence as resonances, i.e. $\langle p_T \rangle_x \sim \langle p_T \rangle_{pp}^x$. In that case we find

$$\begin{aligned} \alpha_{x,AB} &\simeq \frac{1}{2} \frac{(\Delta p_T^2)_{AB}}{\langle p_T^2 \rangle_{pp}^x} \\ &\simeq 1.2 \cdot \frac{9}{32\pi} \sigma_{xN}(A^{1/3} + B^{1/3}). \end{aligned} \quad (18)$$

The entire \sqrt{s} -dependence of $S(p_T)/f(p_T)$ thus enters through $\langle p_T \rangle_{pp}^x$.

From Eq. (13) we find that the critical momentum $p_{c,x}$ changes by a factor 3-4 when going from SPS to LHC energies. A similar change has been found for $\langle p_T \rangle_{pp}$ of Drell-Yan pairs¹⁵ and it is to be expected that this is also true for resonances, i.e. for $\langle p_T \rangle_{pp}^x$. This would also lead to a broadening of the p_T -distribution due to initial state effects. Modifications of the p_T -dependence of the suppression pattern due to changes of \sqrt{s} thus seem to be similar in the QGP-model and in models with initial state rescattering effects. The A -dependence on the other hand follows an opposite trend. With increasing A the number of collisions increases and the rescattering models thus predict a steeper rise in p_T , whereas in the QGP-model $p_{c,x}$ is shifted again to larger values and one would thus expect a weaker p_T -dependence. This is illustrated in fig. 5, where we compare the p_T -dependence obtained from QGP and rescattering models for S - Pb and Pb - Pb collisions, respectively. It is clear from this that both models lead to a similar functional form of the normalized p_T -distribution despite the different mechanisms leading to it and despite the difference in the A -dependence discussed above.

In fig. 6 we show the suppression pattern expected for the J/ψ 's in $Pb-Pb$ collisions at the SPS. This should be compared with fig. 1a. One sees that the QGP model leads to a somewhat stronger A -dependence of the total suppression rate; in the QGP model $S(0)$ decreases from 0.45 in $S-Pb$ collisions to 0.2 in $Pb-Pb$ collisions while in a hadron gas model with initial state rescattering it only drops from 0.4 to 0.28. However, it remains to be seen whether such subtle differences will become visible in $Pb-Pb$ collisions. In any case a careful comparison with $S-Pb$ and also $S-S$ data will be needed to clarify the underlying mechanisms for the p_T -dependence.

5. E_T Dependence of the Suppression Pattern

So far we have only discussed the transverse momentum dependence of the resonance suppression pattern and its extrapolation to heavier nuclei and larger energies. As illustrated in fig. 1 it is also of interest to look at the E_T dependence of the suppression pattern. In order to make predictions for this we should integrate the functions $S_x(p_T)$ over p_T . However, even if we assume an exponential p_T -distribution for the resonances we have to know the \sqrt{s} dependence of the average transverse momentum for the resonances. Reasonable assumptions can be made for this⁶. For our present discussion it will, however, be sufficient to approximate the total suppression rate by the value of $S_x(p_T)$ at $p_T = 0$. This allows to illustrate the general features of the A - and \sqrt{s} -dependence of the suppression pattern in the QGP- and HG-models, respectively.

At $p_T = 0$ resonances are produced at rest in the plasma rest frame (we assume $p_L = 0$). In a QGP-model it will then only be possible to form resonances in the cooler, outer regions of the overlap region S_{eff} of a nucleus-nucleus collision. Given a temperature profile $T(\vec{r}, b) \sim s^{1/3}(\vec{r}, b)$, with the entropy density $s(\vec{r}, b)$ being proportional to the integrand of Eq. (6), one can estimate $S_x(p_T = 0)$ as

$$S_x(p_T = 0) = 1 - \left(\frac{R_x}{R_A} \right)^2 . \quad (19)$$

Here R_x denotes the transverse radius at which the temperature drops below T_x .

The suppression in a hadron gas, on the other hand, is due to absorption in the entire overlap region S_{eff} and thus depends only on the initial conditions of the collision. We thus obtain the standard relation of absorption models⁹

$$S_x(p_T = 0) \sim e^{-c_x A^{1/3} \ln \sqrt{s}} , \quad 20$$

with c_x depending on the initial conditions as well as the cross-section for the absorption of resonances of type x . Some results for the suppression pattern as a function of the transverse energy E_T are shown in fig. 7. One sees also here that with increasing energy and/or for heavier nuclei the number of heavy quark resonances reduces faster in a QGP due to screening effects than in a HG due

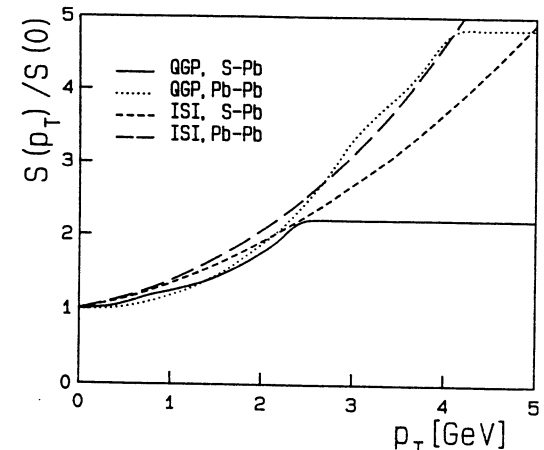


Figure 5: $S(p_T)/S(0)$ versus p_T for J/ψ 's produced in $S-Pb$ and $Pb-Pb$ collisions at SPS energies. Shown is a comparison of the p_T -dependence emerging from suppression in a QGP and a hadron gas with initial state rescattering, respectively.

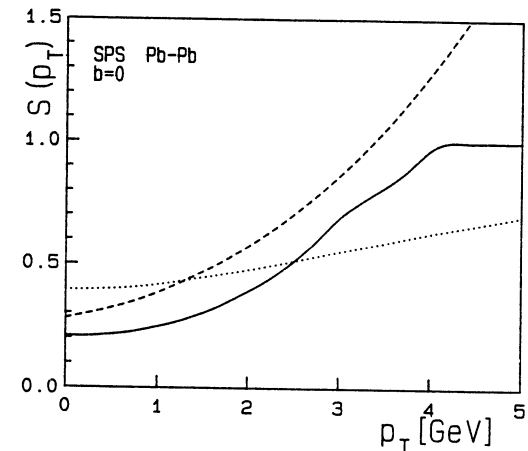


Figure 6: $S(p_T)$ versus p_T for J/ψ production in $Pb-Pb$ collisions at SPS energies. Notations are as in fig.1a.

to absorption. We also note that at LHC energies the Υ -resonance is still not suppressed in a QGP while there is substantial absorption in a HG. Any reduction of the absolute rate of Υ 's in $Pb-Pb$ collisions relative to $S-S$ collisions at LHC energies can thus only be due to absorption in a HG.

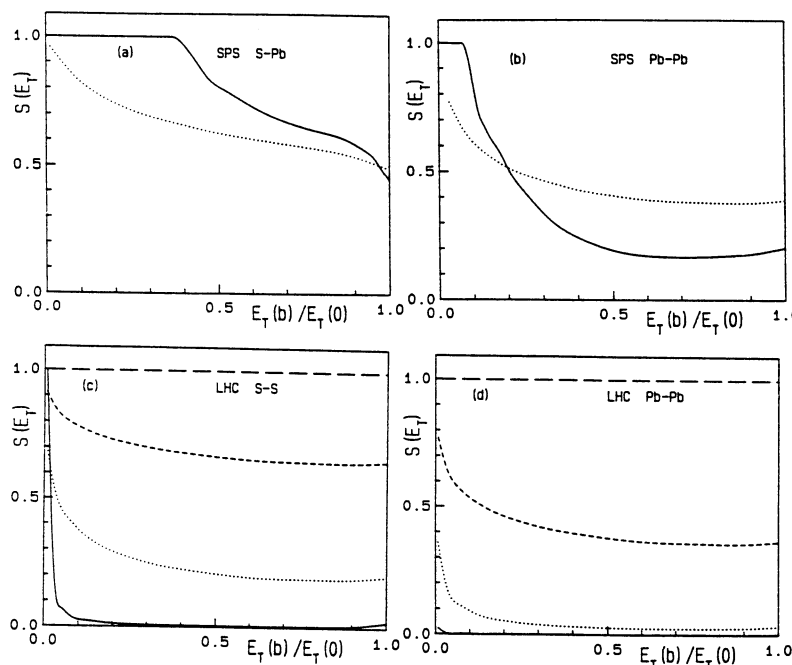


Figure 7: $S(p_T = 0)$ versus $E_T(b)/E_T(0)$ for ψ and Υ production in $S\text{-}Pb$, $S\text{-}S$ and $Pb\text{-}Pb$ collisions at SPS and LHC energies. Shown are results for suppression of ψ in a QGP (solid curve) and HG (dotted curve). At LHC energies we also show predictions for Υ suppression in a QGP (long dashes) and HG (short dashes).

6. Discussion and Conclusions

We have seen that similar resonance suppression patterns arise from the screening of the heavy quark potential in a quark gluon plasma and from absorption in a hadron gas combined with rescattering of partons in the initial state, i.e. before any hard scattering. A distinction between these different mechanisms can only come through a detailed quantitative comparison of the suppression pattern for various resonances at different energy densities (which may be achieved by varying A as well as \sqrt{s}).

Let us finally mention a further complication that has to be taken care of, once a detailed quantitative comparison with data will become possible: The experimentally observed resonances are not always directly produced but arise as decay products of other resonances. For instance, when discussing the suppression pattern for the J/ψ , we have to take into account that already at SPS energies about 40 % of the observed J/ψ 's originate from χ -decays¹⁶. This fraction

increases with increasing \sqrt{s} . At LHC energies centrally produced J/ψ 's are completely dominated by B -meson decays¹⁷. Moreover, one has to be aware of the fact that the contribution of different decay channels is strongly p_T -dependent at LHC energies¹⁸.

The large number of possible decay channels will make the analysis of $c\bar{c}$ -resonances at the LHC very complicated. Most promising seems to be here the $b\bar{b}$ -system, where the hadron gas and quark-gluon plasma models lead to quite different predictions for Υ suppression. Although this may, to some extent, be difficult to detect due to the strong contamination from Υ' -decays.

References

- for a recent review of lattice results see for instance: F. Karsch, *Simulating the Quark-Gluon Plasma on the Lattice*, in: *Quark-Gluon Plasma*, ed. R.C. Hwa, Advanced Series on Directions in High Energy Physics, Vol. 6, (World Scientific 1990).
- for recent experimental results see: Proceedings of *Quark Matter '90*, to be published in *Nucl. Phys. A*.
- T. Matsui and H. Satz, *Phys. Lett.* **178B** (1986) 416.
- F. Karsch and H.W. Wyld, *Phys. Lett.* **B213** (1988) 505.
- F. Karsch, M.T. Mehr and H. Satz, *Z. f. Phys.* **C37** (1988) 617.
- F. Karsch and H. Satz, *The Spectral Analysis of Strongly Interacting Matter*, CERN Preprint, CERN-TH 5900/90, 1990.
- F. Karsch and R. Petronzio, *Phys. Lett.* **193B** (1987) 105 and *Z. f. Phys.* **C37** (1988) 627; J. Blaizot and J.Y. Ollitrault, *Phys. Lett.* **199B** (1987) 499.
- M.C. Abreu et al. (NA 38), *Z. f. Phys.* **C38** (1988) 117; C. Baglin et al. (NA38) *Phys. Lett.* **B220** (1989) 471.
- see for instance: J. P. Blaizot, *Nucl. Phys.* **A498** (1989) 273.
- A. Capella, C. Merino, J. Tran Thanh Van, C. Pajares and A. Ramallo, *Phys. Lett.* **B243** (1990) 144.
- S. Gavin and M. Gyulassy, *Phys. Lett.* **B214** (1988) 241; J. Hüfner, Y. Kurihara and H.J. Pirner, *Phys. Lett.* **B215** (1988) 218; J. Blaizot and J.Y. Ollitrault, *Phys. Lett.* **B217** (1989) 386.
- O. Drapier, *Ph.D. thesis*, Université Claude Bernard-Lyon 1, (May 1990).
- U. Heinz, *General Conditions in Heavy Ion Collisions at the LHC*, to appear in the Proceedings of the LHC-workshop.
- for a review see: S. Gavin, contribution to the proceedings of the LHC-workshop.
- S. Gupta, contribution to the proceedings of the LHC-workshop.
- Y. Lemoigne et al., *Phys. Lett.* **113B** (1982) 509.
- E.W.N. Glover, A.D. Martin and W.J. Stirling, *Z. f. Phys.* **C38** (1988) 473.

18. L. Bergström, R. W. Robinett and L. Weinkauf, *Aspects of ψ and Υ Production at Supercollider Energies*, Pennsylvania State University Preprint, PSU / TH / 63, 1990.

INITIAL STATE SCATTERING IN NUCLEAR DRELL-YAN AND J/ψ PRODUCTION

Sean Gavin

Research Institute for Theoretical Physics
Siltavuorenpuisto 20 C, SF-00170 Helsinki, FINLAND

INTRODUCTION

Nuclear effects discovered in the transverse momentum spectra of Drell-Yan dimuons by experiment NA10 [1] have been attributed to initial state parton scattering [2-4]. Similar phenomena occur to a progressively greater extent in J/ψ production in hadron-nucleus [5,6] and nucleus-nucleus collisions at 200 AGeV [7]. The realization that the $AB \rightarrow J/\psi$ and Drell-Yan effects can have the same cause has taught us that quark gluon plasma detection at the SPS is not easy — the p_T pattern of J/ψ suppression thought to be the signature of quark gluon plasma production can be forged [8-11]. But “can be” is not the same as “is”. In this report I examine the degree to which the systematics of Drell-Yan and J/ψ hadroproduction establish initial state scattering. Extending Satz’s recent work [12], I study the confidence level of our extrapolation to ion-beam experiments, focusing on the new precision measurements from the 800 GeV $p + A$ experiment E772 at Fermilab [13]. I then speculate about the energy dependence of initial state scattering and discuss experiments that can help to pin down the present theoretical uncertainties.

As at the SPS, J/ψ suppression in LHC ion-ion collisions is likely to prove a very complex phenomenon. To conclude, I briefly discuss various additional nuclear and dense matter contributions and speculate about their relative importance at the LHC.

INITIAL STATE SCATTERING

The strong influence of initial-state parton scattering on the p_T dependence of hard processes such as J/ψ formation in nuclear targets is suggested by recent Drell-Yan dimuon data. NA10 [1] found a broadening of the p_T distribution in $\pi^- + {}^{184}W \rightarrow \mu^+ \mu^-$ relative to $\pi^- + {}^2H$ corresponding to an increase of the p_T dispersion of $\langle p_T^2 \rangle_{\pi W \rightarrow \mu^+ \mu^-} - \langle p_T^2 \rangle_{\pi H \rightarrow \mu^+ \mu^-} = 0.15 \pm 0.06 \text{ GeV}^2$. Such an increase can only arise from initial-state interactions, since the final-state in the Drell-Yan production of high-mass pairs does not interact strongly. In fact, the effect had been predicted [2,3] due to the quasielastic scattering of the sea quark and antiquark before their annihilation. Scattering adds to the $\langle p_T^2 \rangle$ of the resulting dimuons but does not reduce the p_T -integrated dimuon yield, because it directs the beam momentum transversely without changing the net parton flux. The absence of an absorptive component of initial-state interactions is supported by the $A^{1.00 \pm 0.02}$ dependence of the p_T -integrated cross section.

As the pion crosses the nucleus, the quark (or antiquark) suffers a number of elastic collisions before its annihilation that is proportional to $(\bar{n}_A - 1)/2$, where \bar{n}_A is the average number of inelastic π -nucleon collisions. This random walk increases the p_T dispersion of the dimuon from the intrinsic Drell-Yan value $\langle p_T \rangle_0 \approx \langle p_T \rangle_{\pi p}$ to

$$\langle p_T^2 \rangle_{\pi A} \approx \langle p_T^2 \rangle_0 + \delta_q^2 \{\bar{n}_A - 1\}. \quad (1)$$

The mean number of collisions grows with the target length, which is roughly $\propto A^{1/3}$. The NA10 data implies that the effective p_T transfer per quark-nucleon collisions is $\delta_q \approx 0.24 \text{ GeV}$, since \bar{n}_A is roughly 3.7 in $\pi + W$. The small magnitude of δ_q suggests that initial state scattering occurs at soft scales.

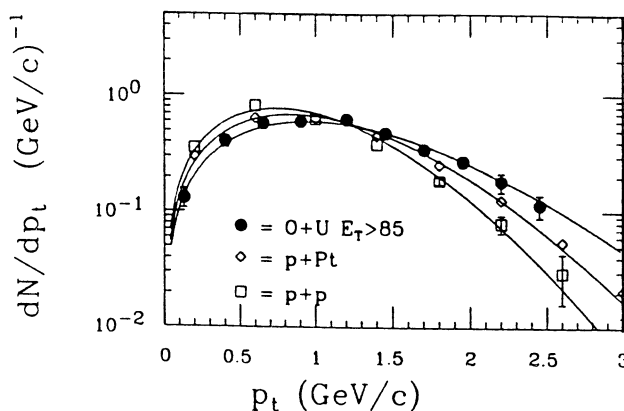


Fig. 1. Measured p_T spectra in $p + p$, $p + Pt$ and $O + Au \rightarrow J/\psi$ display a broadening trend at 'low' energies which can be attributed to initial state scattering. Data from NA3 [5] and NA38 [7] are compared to model extrapolations in Ref. 8.

Gyulassy and I, along with many others, observed that a similar initial-state scattering of gluons can occur in J/ψ production prior to the formation of the $c\bar{c}$ pair, and such scattering can in fact account [8-11] for much of the p_T dependence seen by NA38 [7]. NA3 [5] studied $p + A \rightarrow J/\psi + X$ at 200 GeV for Pt and 2H targets, and I show their measured p_T distributions in Fig. 1 together with the distribution for central $O + U$ from NA38. The normalized distribution $N_\psi^{-1}dN_\psi/dp_T$ for Pt is broader than that for H , and that the $O + U$ distribution is broader still. NA3 found that $\langle p_T^2 \rangle_{pP} = 1.57 \pm 0.03 \text{ GeV}^2$ and $\langle p_T^2 \rangle_{pp} = 1.23 \pm 0.05 \text{ GeV}^2$, so that $\delta_g^2 \approx (0.36 \text{ GeV})^2$ for gluon-nucleon collisions, which is $\approx 9\delta_q^2/4$ as expected from perturbative QCD arguments [8,9]. The $p + A$ spectra in Fig. 1 are fit by taking $dN_\psi/d^2p_T \propto \exp\{-\alpha(p_t^2 + m_\psi^2)^{1/2}\}$, where we use $\langle p_T^2 \rangle$ to relate the slope parameter α to the measured dispersion [8].

In a nucleus-nucleus collision, the number of initial-state interactions depends on impact parameter. The p_T dispersion is increased by the scattering of both target partons in the projectile and projectile partons in the target, so that $\langle p_T \rangle_{AB} \approx \langle p_T \rangle_{pA} + \langle p_T \rangle_{pB}$, for $\langle p_T \rangle_{pA}$ of the form (1). Glauber theory implies $\bar{n}_O + \bar{n}_U \approx 8$ in a central $O + U$ collision. The p_T dependence of the NA38 data in Fig. 1 is accounted for essentially by (1), together with a 20% contribution from the final-state interactions (details are discussed in [8]).

Despite the circumstantial evidence offered by NA10 and NA3, the case for initial state interactions in hard processes is far from closed. Satz has emphasized that the random-walk increase of $\langle p_T^2 \rangle$ with the number of collisions \bar{n} is not demonstrated by NA10 and NA3: These groups studied only two targets, so that the linear rise of $\langle p_T^2 \rangle$ with $A^{1/3}$ implicit in (1) was not checked. Another potential test of (1) is the centrality dependence of the p_T shift for NA38's dimuon continuum. One expects $\langle p_T^2 \rangle$ to increase with increasing total transverse energy E_T (the larger is E_T , the more central is the event). So far, NA38 has not resolved the expected dependence, perhaps due to their limited statistics compared to NA10 as discussed by Varela [7].

Recently, the E772 experiment at FNAL has reported measurements of $p + A \rightarrow \mu^+ \mu^-$

at 800 GeV for several nuclear targets with high statistics comparable to NA3 and NA10. This experiment focused on EMC-type nuclear modification of parton structure functions, so that great care was taken to minimize the relative errors in the different targets. Although their p_T acceptance was somewhat limited, ratios of the production rates in C , Ca , Fe , and W relative to deuterium are available. Preliminary results show a clear p_T shift that increases with increasing A for both Drell-Yan and J/ψ production. To exhibit the A dependence of $\langle p_T^2 \rangle$ indicated by this data, I have fit the measured ratios assuming gaussian distributions $dN/d^2p_T \propto \exp\{-p_t^2/\langle p_T^2 \rangle\}$. Figure 2 shows the extracted $\langle p_T^2 \rangle$ vs. A . The fitting errors shown were estimated using the standard jackknife procedure. I emphasize that much of the data from which $\langle p_T^2 \rangle$ was constructed is preliminary, and no attempt was made to compensate for E772's experimental biases. Quantitative results must be interpreted accordingly.

In Fig. 2, I compare the extracted A dependence of $\langle p_T^2 \rangle$ to the random walk form (1) for $\bar{n} \approx A^{1/3}$,

$$\langle p_T^2 \rangle_{\text{random}} \approx \langle p_T^2 \rangle_0 + c(A^{1/3} - 1), \quad (2)$$

and also with a saturating form,

$$\langle p_T^2 \rangle_{\text{sat}} \approx \langle p_T^2 \rangle_0 + c'(1 - A^{-1/3}), \quad (3)$$

proposed in [12]. Both forms are 'correct' with equal probability. This fact is very important because the saturating form (3) does not account for the added broadness of central $O + U \rightarrow J/\psi$ compared to $p + Pt$ evident [12].

Saturation – if verified experimentally – would imply that a new mechanism is behind the NA10 and E772 p_T broadening. Initial state scattering generally leads to the random-walk increase of $\langle p_T^2 \rangle$ for increasing A . To stress the generality of this result, I derive (1) in more detail than is perhaps necessary. In typical events at NA10 and E772 energies, the successive interactions of a parton with different nucleons are essentially incoherent, so that Glauber theory implies

$$\langle p_T^2 \rangle = \frac{\langle p_T^2 \rangle_0 P_0 + \langle p_T^2 \rangle_1 P_1 + \dots}{P_0 + P_1 + \dots} = \frac{\langle p_T^2 \rangle_0 + \langle p_T^2 \rangle_1 L/\lambda + \dots}{1 + L/\lambda + \dots}, \quad (4)$$

where $\langle p_T^2 \rangle_k$ is the dispersion after k initial state interactions, $P_k = (L/\lambda)^k \exp(-L/\lambda)/k!$ is the probability that k such interactions occur, λ is the parton's mean free path and L is the distance traveled through the nuclear medium. Note that (1) is then the average of (4) over the target geometry. If the mean free path is longer than the average path length $\bar{L} \propto A^{1/3}$, then I can take $\langle p_T^2 \rangle \approx \langle p_T^2 \rangle_0 + (\langle p_T^2 \rangle_1 - (\langle p_T^2 \rangle_0)L/\lambda + \dots)$, which gives the random-walk A -dependence (1). For a general λ , I must allow for any number of collisions. Poisson statistics again implies (1), since the average kick $\langle p_T^2 \rangle_k - \langle p_T^2 \rangle_{k-1} \approx \delta^2$ is roughly independent of k (the fitted δ 's are much smaller than the beam momenta).

I remark that the mean free path is roughly $\lambda = (\rho \sigma_{qN})^{-1}$, where ρ is the nuclear matter density and σ_{qN} is the effective parton-nucleon cross section. If initial state interactions occur at soft scales in accord with our expectations, then σ_{qN} is likely in the several millibarn hadronic range so that $\lambda \ll R$ [8]. For interactions at hard perturbative scales, I expect the $\lambda \gg R$ regime to be relevant, since both σ_{qN} and δ^2 are then $\propto \alpha_s$ [14].

Historically [3,12], the saturating result (3) was first obtained from (4) in the $\lambda \ll R$ regime by truncating the multiple-scattering series after one collision. Such a truncation is incorrect from the standpoint of perturbative QCD, but may mimic nonperturbative effects that cut off the possible number of initial state interactions [12]. Alternatively, a saturating A dependence can arise if the source of p_T enhancement is an entirely new mechanism such as the EMC effect [15].

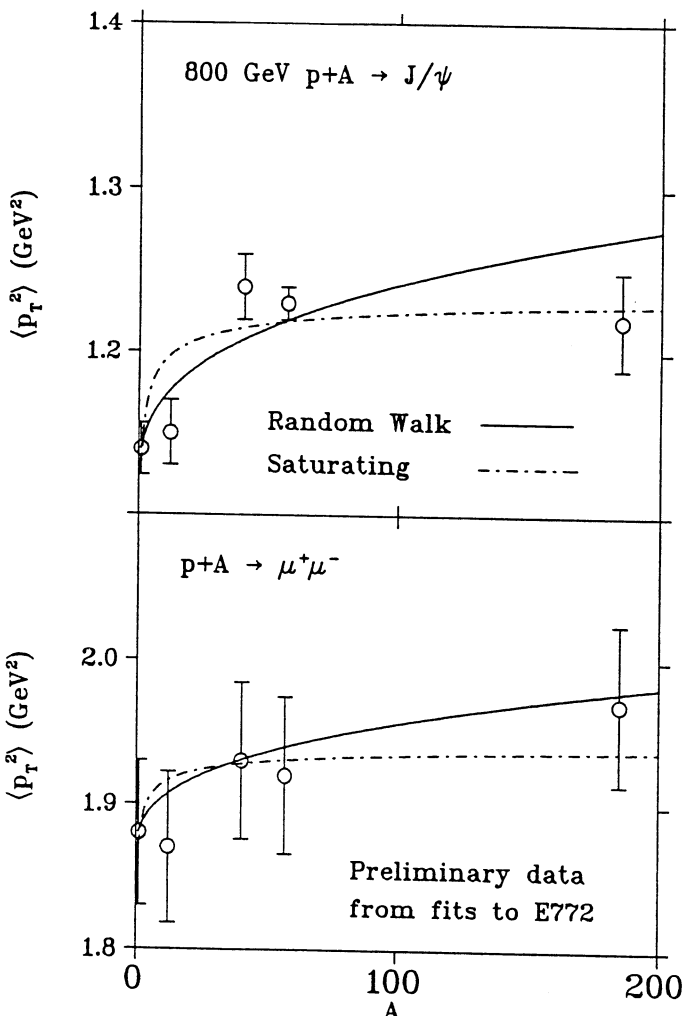


Fig. 2. The target mass dependence of $\langle p_T^2 \rangle$ from gaussian fits to preliminary E772 J/ψ and Drell-Yan data compared to fits using random-walk and saturating parametrizations, eqs. (2) and (3) respectively.

In deriving (4), initial state interactions were taken to be incoherent and independent of the hard Drell-Yan or gluon fusion processes. Coherence is expected only in the extreme kinematic regime where the target parton in the hard process has a momentum fraction x_2 smaller than $\sim 0.05 - 0.1$. There the wavelength of a parton exceeds the nucleon size of ~ 1 fm, so that successive initial state interactions can interfere both with the hard process and possibly with each other. Brodsky and Lu [16] have recently proposed that *destructive interference* can explain the shadowing phenomena discussed phenomenologically by Castorina in these proceedings. If the interference is indeed destructive, then I expect the p_T shift (4) to be reduced in the deeply shadowing regime. The E772, NA3, and NA10 signals originate mostly from ‘unshadowed’ target and projectile partons of roughly equal x ’s satisfying $x > M/\sqrt{s} \gtrsim 0.1 - 0.15$, since Drell-Yan and J/ψ production is peaked at mid-rapidity (the EMC effect can be important at these energies, see Ref. 15). One can extract information on the shadowing regime, however, by triggering on rare events at high Feynman x_F corresponding to low x_2 . In principle, E772 has p_T information for high x_F events, although it is not clear that statistically meaningful spectra can be constructed from present data [17]. In contrast with present experiments, typical LHC events will come from shadowing regime, as emphasized in Eskola’s and Castorina’s talks. High x_F data from E772 will not only help to distinguish models of the controversial shadowing effect, but will be essential in making convincing LHC predictions.

Experiments at different beam energies suggest that the nuclear broadening of p_T spectra is reduced at higher beam energies for a given dimuon mass. Specifically, the comparison of NA10 140 GeV $\pi + A$ and E772 800 GeV $p + A$ data in fig. 3 for $4 < M_{\mu\mu} < 9$ GeV imply that the relative p_T shift becomes less pronounced as the beam energy is increased. The first hint of this ‘flattening’ trend is seen by comparing 286 and 140 GeV NA10 data, although the demonstration of the trend is marginal within the errors. The onset of flattening at the moderate NA10 energies implies that this trend is not associated with the shadowing regime, but has a more commonplace origin.

I argue that this flattening is a consequence of the well known rise of the intrinsic $\langle p_T^2 \rangle_0$ for dimuon production for increasing energy; Karsch has proposed a similar interpretation at this workshop. To illustrate how the flattening arises, I assume Gaussian p_T spectra and write the ratio

$$\frac{(d\sigma/dp_\perp)_W}{(d\sigma/dp_\perp)_H} \propto \exp\{p_T^2(\langle p_T^2 \rangle_D^{-1} - \langle p_T^2 \rangle_W^{-1})\}. \quad (5)$$

Equation (1) implies that the scale over which the ratio rises is $\approx \langle p_T^2 \rangle_D \langle p_T^2 \rangle_W / (\langle p_T^2 \rangle_W - \langle p_T^2 \rangle_D) \propto (\langle p_T^2 \rangle_0 / \delta)^2$. The intrinsic dispersion $\langle p_T^2 \rangle_0$ grows with energy due to the increase in phase space for Compton and other high-order contributions to dimuon production at finite p_T , as discussed by Gupta in these proceedings. The ratio becomes flatter in a fixed p_T range as in Fig. 3, as long as the p_T kick δ_q grows more slowly with energy than $\langle p_T^2 \rangle_0$. My fit to E772 and NA10 data gives $\delta_q = 0.24$ GeV independent of energy, in agreement with prediction [2] (see above).

J/ψ production exhibits a similar flattening at high energy. NA3 studied $\pi + A \rightarrow J/\psi$ at the beam energies 140, 200 and 280 GeV and reported the p_T dispersion explicitly. Figure 4 shows the measured increase of $\langle p_T^2 \rangle$ as a function of energy \sqrt{s} . Observe that the difference between the P_T and 2H data is roughly independent of energy, while the dispersions separately rise as $\log s$. These observations support our Drell-Yan picture, although it must be emphasized that the transverse momentum distribution in J/ψ can be influenced by final as well as initial state effects.

Bold extrapolation to the LHC range using these estimated energy dependencies implies that the p_T shift due to initial state interactions will be negligible for $p_T < 3$ GeV. For

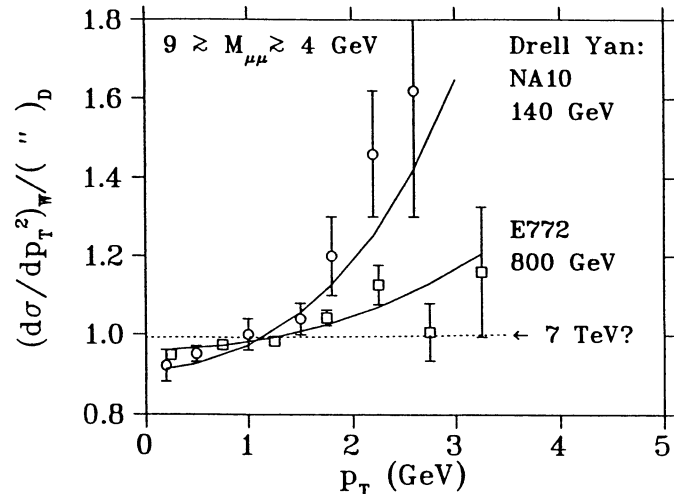


Fig. 3. W -to- 2H ratio for Drell-Yan production from 140 GeV $\pi + A$ [1] and 800 GeV $p + A$ [13] may suggest that the effects initial state scattering are less important as the beam energy is increased. Expectations at LHC energy are indicated by the dashed curve.

example, if I assume a value $\langle p_T^2 \rangle_0 \approx 10 \text{ GeV}^2$ as suggested by Gupta, then the calculated p_T ratio is as shown in Fig. 3. Only the bravest among us would believe such an estimate, since experimental information is very limited, and the present models are quite primitive.

Additional experimental information is needed to establish the systematics of initial state interactions in energy and target mass. In terms of planned experiments, we can follow the continuation of E772, E789, and look forward to pA or ${}^2H + A$ experiments at RHIC. Ideally, one would like to see measurements of $\pi + A \rightarrow$ Drell-Yan and J/ψ using an E772-like multiple target setup down to the lower NA3 energies where the p_T shift is strongest. A goal of these experiments should be to determine the p_T broadening as a function of A to fix the mechanism behind the p_T shift. Measurement of the x_F dependence of $\langle p_T^2 \rangle$ into the shadowing region for several nuclei would have important implications for LHC energies, as I have argued above. Of course, to calibrate quark-matter studies at the LHC, it is best to have pA input from LHC experiments! While it is perhaps not feasible to study asymmetric systems like pA at the LHC, Drell-Yan studies in AA collisions will provide some information. However, it is preferable to have a direct handle on gluon initial state interactions in isolation from other effects in order to calibrate the nuclear J/ψ p_T shift. Gupta and I realised that these interactions can also be studied in $AA \rightarrow$ direct photons; this possibility merits further study.

OTHER COMPETING EFFECTS

Initial state scattering is one of several suspected contributions to J/ψ suppression in nucleus-nucleus collisions. The complex scenario discussed in [18] (see also [23]) has emerged from a consideration of the NA38 data together with the data on nuclear effects in J/ψ photo and hadroproduction, Drell-Yan production, and deep inelastic scattering. The formation of a particular $c\bar{c}$ bound state such as the J/ψ can be influenced by a variety of final state

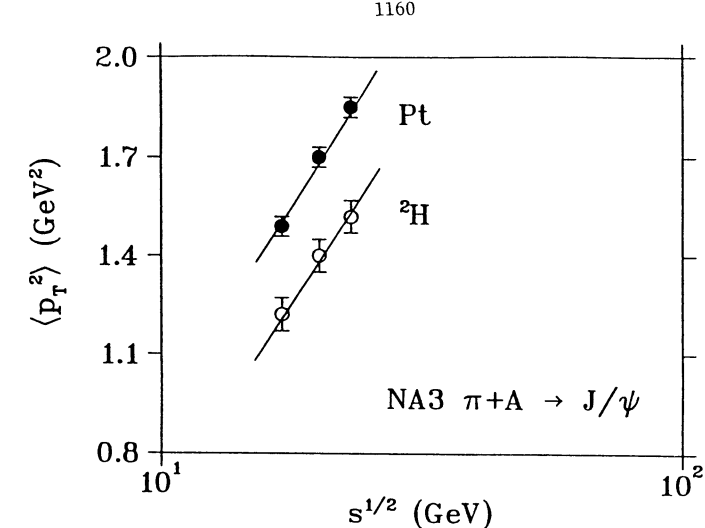


Fig. 4. Energy dependence of $\langle p_T^2 \rangle$ for $p + Pt$ and $p + {}^2H \rightarrow J/\psi$ [3].

interactions at both the quark and the hadronic level. In addition, the production of the $c\bar{c}$ pairs in the mid-rapidity dense matter region can be influenced by various nuclear effects, of which initial state scattering is only one. A few of these effects are described in Fig. 5. I must stress that our present knowledge is far from complete, and some contributions may be ruled out as experimental and theoretical work continues.

The following contributions to J/ψ production and suppression can be important at the LHC:

1. Medium Effects: color screening and self energy effects in the quark gluon plasma alters J/ψ abundance by inhibiting bound state formation. Hadron liquid effects are also possible [19].
2. Co-mover Scattering: scattering with co-moving secondaries (produced quarks and antiquarks) can alter the final J/ψ abundance through dissociation, e.g. $\rho\psi \rightarrow D\bar{D}$, and chemical reactions, e.g. $\rho\chi \rightarrow \pi\psi$. Analogous quark-level processes exist in the plasma [20].
3. Shadowing: Nuclear modification of the structure function in the relevant small x regime alters $c\bar{c}$ production, see Castorina's talk.
4. Minijets: new production processes appear as discussed in Gupta's talk.

Scattering and medium effects are important both at SPS and LHC energy, while shadowing is a new effect that is likely to become very important at LHC.

Further effects thought to be important at SPS and FNAL energies are expected to be effectively absent at the LHC. Firstly, scattering with nucleons (valence quarks), which dissociate $c\bar{c}$ at low energies as demonstrated in photoproduction experiments [21], can be inhibited at higher energies due to color transparency [22]. Support for this hypothesis comes from the successful account of E772 800 GeV J/ψ , ψ' , and ν data [13] by color-transparency-based model calculations [23] using parameters fit from lower energy data [6,7]. Secondly,

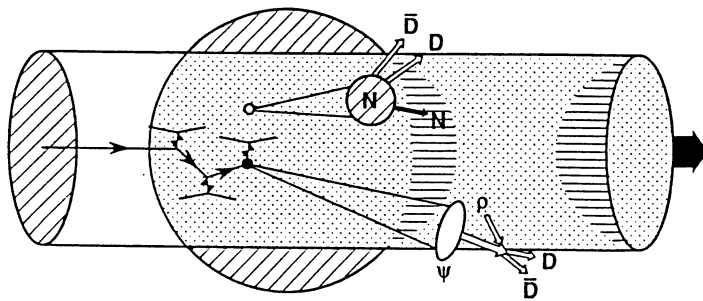


Fig. 5. A schematic representation of J/ψ suppression in an ultrarelativistic collision viewed in the target frame. A parton in the projectile (hadron or nucleus) scatters quasielastically until the hard collision occurs that produces the $c\bar{c}$ pair. The pair then separates to form a J/ψ in the central region provided that it does not scatter with the target nucleons or with co-moving secondaries. It can be dissociated through interactions within the nucleus (the upper event) or by scattering with co-movers (the lower event).

J/ψ formation from a conjectured pre-existing intrinsic charm component in the nucleon can suffer an enhanced nuclear absorption [24]. This mechanism can describe the curiously strong J/ψ absorption found at moderate and high x_F 's [24]. However, one expects the domain where this mechanism is important to move to inaccessibly high rapidities at a $\sqrt{s} = 7$ TeV collider, since the measured effect scales with $x_F \approx M_{\psi} e^{2y} / \sqrt{s}$.

The very difficult problem of distinguishing medium and scattering effects is explored by Karsch in these proceedings. For simplicity he assumes that quark-matter screening and hadron-gas scattering are *exclusive*, alternative mechanisms, and asks how systematics such as the p_T dependence can be exploited to identify the correct one. It is crucial to remember that this formulation is an idealization — one cannot say *ab initio* whether or not these mechanisms are exclusive. The experimental problem is not to decide between distinct alternatives but, rather, to use experimental systematics to distinguish an emerging plasma component from the hadronic background. As in initial state scattering, one can use photo and hadroproduction data in nuclear targets to study final state scattering in the absence of plasma, and then extrapolate to heavy ion collisions. Vogt and I begin to apply this approach at SPS and E772 energies in Refs. [23]. No attempt was made to include plasma formation, however, so there is much work remaining. Blascke *et al.* are working in that direction [25].

Sorting through the various contributions to J/ψ suppression is a theoretical and experimental imperative. The analysis of other heavy-ion probes such as pion interferometry are similarly — if not more greatly — complicated. J/ψ production offers the theoretical

advantage that it is directly sensitive to the deconfining nature of quark gluon plasma. The SPS light ion experiments have already yielded convincing evidence of strong nuclear effects in J/ψ production, while the other clues of interesting physics remain at the one or two sigma level. Moreover, one has identified the crucial uncertainties, and can now plan a workable experimental program to establish the *modus operandi* of the alleged plasma forgery.

I am grateful to P. L. McGaughey for a glimpse of the preliminary E772 data, L. Kärkkäinen and K. Rummukainen for help with the analysis of that data, and S. Brodsky, K. Eskola, S. Gupta, V. Ruuskanen, H. Satz and R. Vogt for many helpful discussions.

REFERENCES

1. P. Bordalo *et al.*, Phys. Lett. **B193** (1987) 373.
2. G. T. Bodwin, S. J. Brodsky, and G. P. Lepage, Phys. Rev. Lett. **47** (1981) 1799.
3. C. Michael and G. Wilk, Z. Phys. **C10** (1981) 169.
4. P. Chiappetta and H. J. Pirner, Nucl. Phys. **B291** (1987) 765.
5. J. Badier *et al.*, Z. Phys. **C20** (1983) 101.
6. S. Kastanevas *et al.*, Phys. Rev. Lett. **60** (1988) 2121.
7. C. Baglin *et al.* (NA38 Collab.), Phys. Lett. **220B** (1989) 471; J. Y. Grossiord *et al.*, Nucl. Phys. **A498** (1989) 477c; J. Varela, in Quark Matter '90, Proc. Seventh Int. Conf. on Ultrarelativistic Nucleus-nucleus Collisions, J.-P. Blaizot, C. Gerschel, B. Pire, and A. Romana, eds., to appear Nucl. Phys. A.
8. S. Gavin and M. Gyulassy, Phys. Lett. **214B** (1988) 241.
9. J. Hüfner, Y. Kurihara, and H. J. Pirner, Phys. Lett. **215B** (1988) 218.
10. J.-P. Blaizot and J.-Y. Ollitrault, Phys. Lett. **217B** (1989) 392.
11. K. S. Lee and U. Heinz (unpublished).
12. H. Satz, Phys. Lett. **242B** (1990) 107.
13. D. M. Alde *et al.* (E772 Collab.), Phys. Rev. Lett. **64** (1990) 2479; J. M. Moss, in Quark Matter '90, *ibid.*; "The A -Dependence of J/ψ and ψ' Production at 800 GeV/c", Los Alamos preprint, to appear in Phys. Rev. Lett.
14. G. Altarelli, G. Parisi, and R. Petronzio, Phys. Lett. **76B** (1978) 351.
15. R. V. Gavai and S. Gupta, in Quark Matter '90, *op. cit.*; Phys. Lett. **227B** (1989) 161.
16. S. J. Brodsky and H. J. Lu, Phys. Rev. Lett. **64** (1990) 1342.
17. P. L. McGaughey, private communications.
18. H. Satz, in "Quark Gluon Plasma", Advanced Series in *Directions in High Energy Physics*, R. Hwa, ed. (World Scientific, Singapore); J.-P. Blaizot and J.-Y. Ollitrault, *ibid.*
19. F. Grassi and G. Baym, in Quark Matter '90, *op. cit.*
20. R. Vogt, M. Prakash, P. Koch, and T. H. Hansson, Phys. Lett. **B 207** (1988) 263; J. Milana, Phys. Rev. Lett. **62** (1989) 2921.
21. M. D. Sokoloff *et al.*, Phys. Rev. Lett. **57** (1986) 3003.

22. S. J. Brodsky and A. H. Mueller, Phys. Lett. **B206** (1988) 685.
23. S. Gavin and R. Vogt, Nucl. Phys. **B345** (1990) 104; R. Vogt and S. Gavin, Preprint HU-TFT-90-57, in Quark Matter 90, *op. cit.*
24. S.J. Brodsky and P. Hoyer, Phys. Rev. Lett. **63** (1989) 1566.
25. D. Blascke, G. Röpke, and H. Schulz, Phys. Lett. **B233** (1989) 434; D. Blascke in Quark Matter 90, *op. cit.*

RATES OF THERMAL PHOTONS AND LEPTON PAIRS
IN HEAVY ION COLLISIONS AT LHC

P.V. Ruuskanen

Department of Physics
University of Jyväskylä
PL 35, SF-40345 Jyväskylä
FINLAND

ABSTRACT

Thermal production rates of lepton pairs and photons are estimated for central nucleus-nucleus collisions and compared with dominant background sources. The cross sections of basic processes in quark-gluon plasma are calculated in lowest order perturbation theory. For dileptons also the contribution from hadron gas is included assuming that the hadron gas consists of pions only. Hydrodynamics is used to describe the thermal evolution. Initial conditions are determined using proper nuclear geometry and a parametrization, which permits to explore the mass number and energy dependence of production process locally in transverse variable. The possibility to experimentally observe the thermal signals depends crucially on the multiplicity of produced hadrons.

1. INTRODUCTION

Thermal emission of photons and lepton pairs from a hot and dense matter, which is produced in the nucleus-nucleus collisions at energies much larger than the rest energies of the nuclei [1] may provide a probe to study the evolution and the properties of the produced system. At densities, which are considered possible in these collisions, the mean free paths of electromagnetically interacting quanta are still larger than the nuclear size. For this reason lepton pairs and photons carry information from the conditions and the properties of the dense, strongly interacting system as it evolves after the collision.

The extraction of information from the thermal electromagnetic signals is complicated by the contributions from several other sources and slightly also by the profound changes the system undergoes during the period of thermal emission. If the initial density of produced matter is high enough, a high-temperature plasma of quarks and gluons is expected to form first. When the matter expands and cools, hadrons start to form when the temperature and the density drop to their critical values. Since the number of degrees of freedom in plasma is larger than in hadron phase, the hadronization stage, when temperature stays constant or changes little [2], may last long. After complete transfer to hadrons, the matter can still emit thermally, but finally it becomes so dilute that collisions cease to occur. At the same time as the temperature drops, a transverse collective motion builds up. This will not affect the mass spectrum of thermal dileptons, but changes the transverse momentum dependence of distributions [3,4].

To observe the thermal emission and to measure its properties, the other sources of lepton pairs and photons must be thoroughly studied and well understood and the thermal signal must be comparable in strength with these sources. Since the thermal signal is cut off exponentially, the hard primary partonic processes with power-law behaviour will always dominate at high values of mass or transverse momentum. The cross-over region

of thermal and hard processes is expected to be around 2-5 GeV. At low masses and transverse momenta soft hadronic backgrounds are large and may overwhelm the thermal emission. The other production mechanisms are studied in several contributions to these Proceeding and will only be mentioned here.

Lepton pairs receive a large background from the uncorrelated leptonic decays of pions and kaons and at low masses also from the Dalitz decays. This background dominates in the mass region $M \lesssim 2$ GeV and the ability to subtract the uncorrelated pairs depends on the details of experimental setup [5]. Vector mesons, ρ , ω , ϕ , as well as the J/ψ and Υ and their excited states, have a decay branch to lepton pairs. The importance of heavy vector mesons [6] is discussed in detail by Karsch [7]. In general, the observation of resonance peaks in dilepton spectra gives information on the abundances of these mesons in nuclear collisions.

The primary interactions among the partons of colliding nuclei lead to lepton pair formation in different ways. In hadron-hadron collisions the best known is the Drell-Yan process, $q\bar{q} \rightarrow l^+l^-$, which is well understood when the mass or the transverse mass is large enough for the QCD perturbation theory to apply [8]. Problems in extrapolating to nuclei and to very high collision energies are discussed in S. Gupta's contribution [9].

In the hadron-hadron collisions, also the decays of heavy-flavour mesons lead to correlated pairs. Their fraction in the dilepton continuum below the J/ψ mass is sizable [10]. In central nucleus-nucleus collisions at large energies, several $c\bar{c}$ pairs can be produced [11], leading also to uncorrelated pairs. Background from charm can be considerably reduced due to their different angular distribution by applying proper cuts. If very high temperatures are reached in the collision, also the thermal production of charm becomes significant, but the resulting dileptons have a softer mass distribution than those from electromagnetic pair production [11].

Photon spectrum for transverse momenta $k_T \lesssim 3$ GeV gets a major contribution from the decays of neutral mesons, π^0 , η , η' , and ω . This contribution can be estimated once the hadron spectra are known [12]. In a dedicated experiment it is also possible to determine the fraction of decay photons for $k_T \gtrsim 1.5$ GeV with high accuracy [13]. For very small transverse momenta, $k_T \lesssim 10 - 20$ MeV, hadronic bremsstrahlung becomes important. However, the soft photon contributions both from plasma and the hadronic gas are not well understood and could turn out to be large. Here, I will concentrate on the semi-hard thermal photons from plasma and ignore the k_T region below 1 GeV.

At transverse momenta of order or greater than several GeV's, the spectrum will be dominated by direct photons from the $gq(\bar{q}) \rightarrow \gamma q(\bar{q})$ and $q\bar{q} \rightarrow \gamma g$ and related higher order processes among the incoming partons. In estimating the direct production, QCD perturbation theory can be applied for large enough transverse momenta. At very high collision energies a large part of the higher order contributions in the transverse momentum range of few GeV, which is important when considering the thermal signal, comes from the fragmentation of minijets into collinear photons [14]. The situation in nucleus-nucleus collisions is qualitatively different from that in hadron-hadron collisions, where direct photons can be isolated from jets [15].

2. BASIC CROSS SECTIONS AND THERMAL RATES

Lepton pairs: The thermal production of pairs from plasma proceeds through the same basic QCD processes as in the primary interactions of incoming partons. The thermal counterpart of Drell-Yan mechanism is the annihilation of quarks and antiquarks in thermal collisions. In calculating the rates, the basic parton level cross section is folded

with the incoming parton distributions (structure functions) for the Drell-Yan case, and with the thermal distribution functions and the thermal history of the matter for thermal production [16,17]. Similar relation between the primary and thermal production holds also for the charm channel [11]. In this case the analysis is more complicated, however, since the formation of hadrons takes place as an intermediate step before the decay of charm into leptons.

For thermal rates, the lowest order cross section [18] for $q\bar{q} \rightarrow l^+l^-$ is used. Second order corrections in a finite temperature matter have been studied [19]. They are found to be small and have not been here included in the numerical calculations. For the Drell-Yan pair production at LHC energy, the results by S. Gupta [9], which include second order corrections, are used. Nuclear shadowing [20], the decrease of quark densities at small x , has not been included in the calculations. The neglect of higher orders in thermal rates and nuclear shadowing in Drell-Yan means that thermal rate is somewhat underestimated relative to Drell-Yan especially at higher energies where the shadowing (small- x region) becomes more important.

In the hadronic phase the most important pair production process is the $\pi^+\pi^-$ annihilation into a lepton pair, which has no direct counterpart in the primary collision. This annihilation cross section is dominated by the ρ meson pole in the pion form factor and the process can be interpreted as a formation of ρ meson and its subsequent decay. As was mentioned above, dileptons result also from the decays of vector mesons which form in the hadronization of plasma or directly in the primary collision. Thermal pairs from $\pi^+\pi^-$ annihilations in hadron gas will essentially enhance the ρ region. Thermal collisions will also change the abundances of other vector mesons [22] in a way which, in addition to the collision dynamics also depends on the density and lifetime of the matter. It is important to notice that dileptons give a means of measuring these abundances also in the high multiplicity events of nucleus-nucleus collisions where direct observation of resonances through hadronic decay products is not possible.

As a probe, the dileptons from ρ decays differ from lepton pairs from other vector mesons. The reason is the short lifetime of ρ meson, $\tau_\rho \sim 1.3$ fm/c, as compared to the lifetimes of ω (23 fm/c) and ϕ (50 fm/c). We expect, both from the results of pion interferometry and from theoretical estimates, that the interactions among the final particles last longer than 1-2 fm/c. This means that ρ 's decay and re-form continuously during the evolution, making the size of the ρ peak in the dilepton spectrum a direct measure of the size and the lifetime of hadron gas. On the other hand the ω and the ϕ mesons decay mainly after the freeze-out. Their abundances give information about hadronization dynamics and the processes in the hadron gas [22,23]. Since the collective motion of the final hadronic matter may change between hadronization and freeze-out, the transverse mass dependence of ρ on one hand and ω and ϕ on the other could be different leading to a change in $\rho/(\omega + \phi)$ ratio with increasing transverse mass.

Photons: The lowest order partonic processes to produce real photons are the gluon-to-photon Compton scattering off (anti)quarks and the crossed reaction of quark-antiquark annihilation to photon and gluon.

Assuming Boltzmann statistics, the thermal photon emission rate for these reactions can be written in the limit $\omega T/m^2 \gg 1$ as [24,12,21]

$$\frac{dN}{d^4x d^3k/\omega} = \sum Q_f^2 \frac{4}{\pi^4} \alpha \alpha_s(T) \ln\left(\frac{4\omega T}{m_q^2}\right) T^2 e^{-\omega/T}, \quad (1)$$

where $k = (\omega, \mathbf{k})$ is the momentum of the photon and m_q is the quark mass. The important feature in this equation is the presence of quark mass which comes from the singularity

in the quark propagator. Renormalization of quark mass at finite temperature leads to a temperature dependent mass term [25],

$$m_q = \frac{1}{6} g_s^2 T^2 = \frac{2}{3} \pi \alpha_s(T) T^2. \quad (2)$$

From lattice results $\alpha_s(T)$ can be parametrized as [26],

$$\alpha_s(T) = \frac{6\pi}{(33 - 2n_f) \ln(\kappa T/T_c)}, \quad (3)$$

with $\kappa \simeq 8$, which gives $\alpha_s(T_c) \simeq 0.3$. Thus the quark mass is essentially of order of the temperature. This is considerably higher than the current masses of the light quarks.

Bremstrahlung processes, which diagrammatically are higher order in QCD perturbation theory, turn out to be of the same order (modulo logarithmic terms) in α_s , as Compton scattering and $q\bar{q}$ -annihilation [25]. They have a steeper transverse momentum dependence than the latter and will be neglected since the main emphasis is here in the upper k_T range of thermal photons.

When the thermal emission rate, eq. (1) is integrated over the thermal evolution to obtain the transverse momentum distribution of emitted photons, it turns out that in the argument of logarithm, ω can be replaced by the transverse momentum k_T . The azimuthal and longitudinal integrals can then be calculated analytically and the remaining transverse and time integrals, similar to the those for dilepton spectra, are performed numerically.

3. PRODUCTION AND THERMAL EVOLUTION OF FINAL MATTER

In order to calculate the number of pairs per nucleon-nucleon collision, the thermal rates must be folded with the thermal evolution of the final state matter. The details of how the thermal evolution is described, can be found e.g. in refs. 16 and 21 and will not be repeated here. Let me, however, remind of some of the uncertainties one encounters in such a description: The thermalization assumption itself is a strong assumption. It has been studied for longitudinally expanding pion system [27]. The results show, that in an expanding system thermalization is never complete but it gets the better the denser the system. Since thermal lepton pairs and photons can probably be observed only in the highest multiplicity events, thermalization assumption seems justified here. Another problem connected with thermalization, is the contribution from the early collisions which thermalize the system. This uncertainty is connected with the problem of how to fix the thermalization time, which is just one of the uncertainties of the hydrodynamic description to be discussed next.

In the hydrodynamic description of expansion [16,28] the longitudinal expansion is assumed to be invariant under Lorentz boosts and the transverse expansion is solved numerically using the Bag Model equation of state with $T_c = 160$ MeV [2]. Once this prescription to calculate the evolution is fixed, the remaining major uncertainty comes from the initial conditions. Since the thermal rates depend exponentially on temperature through the thermal distribution functions, small changes in initial conditions lead to large changes in final results, especially in the high mass or transverse mass region. For this reason the details of the parametrization for the extrapolations of initial conditions in mass number and collision energy become important [17,21].

In NN-collisions the dependence on the collision energy is known over a large range of energies [29]. On the mass number dependence we still have very little information at higher energies. Results from the present SPS heavy ion experiments at CERN seem to

indicate that at this energy the multiplicity, dN/dy , grows slightly faster than linearly with the mass number [30]. Some production models lead to a faster growth [31] even approaching an $A^{4/3}$ dependence. In the parametrization used for these calculations for central collisions, production rate per unit transverse area is assumed to be proportional to a power $1 + \beta$ of nuclear thickness at that location [17,21]. Thus $\beta = 0$ leads to a linear mass number dependence of hadron multiplicity, dN/dy , and $\beta = 1$ to $A^{4/3}$ behaviour if the effects of energy conservation are neglected. These limiting cases of $\beta = 0$ and 1 can be considered to give reasonable estimates of the lower and upper limits of the multiplicity.

This parametrization [17,21] gives the total transverse energy deposition per unit rapidity and unit transverse area. Given the thermalization time τ_i , the local energy density can be calculated. Finally through the use equation of state, all other thermodynamic quantities are obtained. Under the usual assumption of (near) isentropic expansion, the initial conditions fix the multiplicity of the collision.

Usually, $\tau_i = 1$ fm/c is used as the thermalization time in estimating the initial densities. For high multiplicity events, production and thermalization may proceed faster and satisfy $\tau_i T_i = 1$ [32]. The later evolution of matter is not changed by earlier thermalization time, but even a short time interval at higher temperature makes a large difference in thermal emission, as will be seen below, when results for $\tau_i = 1$ fm/c and $\tau_i T_i = 1$ are compared.

For $\beta > 0$ each nucleon collides several times in central collisions. E.g. for lead $T_{\text{Pb}}(0) \simeq 2/\text{fm}^2$ which for $\sigma_{\text{in}}^{\text{NN}} \sim 3 \text{ fm}^2$ gives ~ 6 collisions/nucleon near the collision axis in the limiting case $\beta = 1$. Energy conservation reduces then the amount of transverse energy which is deposited on the average in these collisions. This is taken into account through a reduced average collision energy in the calculation of initial conditions by assuming that a nucleon loses a fixed fraction of energy (rapidity loss $\Delta y \sim 0.7$) in each collision. The effect of energy conservation is a severe constraint at present CERN energies for the $\beta = 1$ case.

4. RESULTS

At the present CERN energy, $\sqrt{s} = 20$ GeV for NN pair, the choice $\beta = 1$ gives a total pion multiplicity (all charge states) $dN/dy = 110$ in a central S+S collision. This is slightly higher than the highest observed multiplicity. For a lead-lead collision a similar calculation gives $dN/dy = 1110$ corresponding to $\alpha = 1.16$ for the A^α parametrization of multiplicity. The emission from plasma is always below the Drell-Yan production for such collisions. However, both the region of low-mass vector mesons and the production of J/ψ can still be of great interest even at the present CERN energies.

In fig. 1 dilepton spectra are shown for central Pb+Pb collisions at three different collision energies, which are taken to be the present CERN SPS energy (10 GeV + 10 GeV for NN in center of mass frame) and the projected Brookhaven Relativistic Heavy Ion Collider (100+100), and CERN LHC (3200+3200) energies. In all three cases $\beta = 1$ and $\tau_i = 1$ fm/c in the parametrization of initial conditions and the multiplicities which are obtained from these calculations are 1110, 1710, and 3830 for SPS, RHIC, and LHC, respectively. As was mentioned in the discussion of initial conditions, $\beta = 1$ should be considered to give a reasonable upper limit for the multiplicity. The result for the contribution from plasma at SPS is probably too high because 1 fm/c is used for thermalization time also in this case. For this reason the difference between the SPS and RHIC energies is probably bigger than these results show.

obtained. The mass distribution of Drell-Yan pairs is from a second order calculation [9].

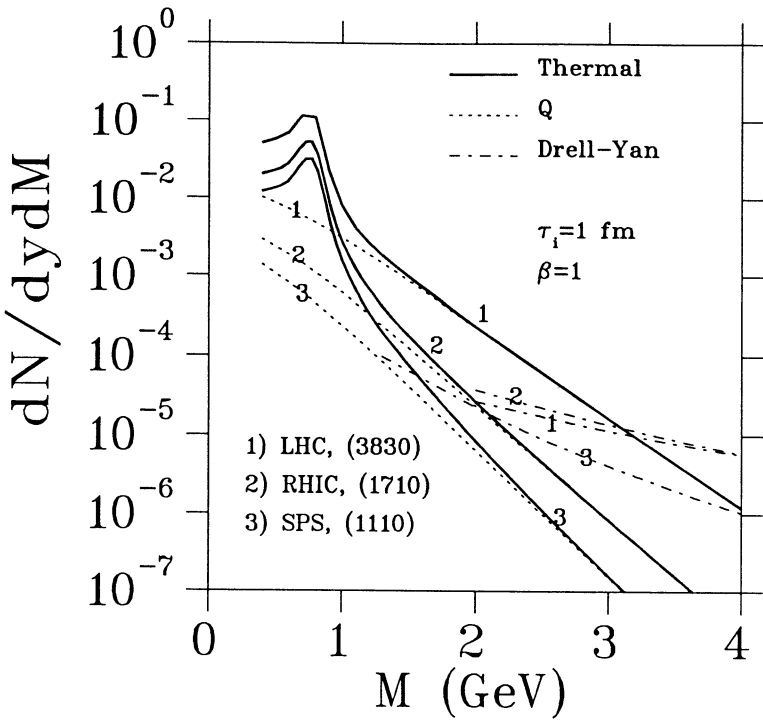


Fig. 1. Dilepton spectra for central Pb+Pb collisions at SPS, RHIC, and LHC energies. Q indicates pure plasma above the critical temperature T_c .

The Drell-Yan spectrum has also been plotted at each energy. For SPS the curve is obtained from a first order calculation with K -factor, $K = 2$, using the structure functions of Duke and Owens [33]. For RHIC and LHC the curves show the second order results by S. Gupta [9]. At RHIC energy the crossing with thermal spectrum occurs around 2 GeV and at LHC energy around 3 GeV. Changes in thermalization time and/or in multiplicity can move the crossover region either way as will be discussed in more detail for the LHC energy. Before that let us notice that collision energy enters the calculation only through the initial conditions. Different choices of β at different energies can lead to very similar initial conditions. The results of fig. 1 can then be as well interpreted as giving the dilepton rates as a function of multiplicity, independent of collision energy. Should it turn out that multiplicities up to 3700 are reached at RHIC, curves labeled with 1 would give the predicted thermal rates.

In fig. 2 results are shown for calculations with $\beta = 1$ and $\beta = 0$ at the CERN LHC energy for two different assumptions on the thermalization time. (Initial temperature $T_i(r, \tau_i)$ is plotted in ref. 21.) The thick curves were obtained by assuming a fixed thermalization time $\tau_i = 1$ fm/c. If the thermalization time is assumed to be correlated with the temperature through $T_i \tau_i = 1$ [32], distributions described by the thin curves are

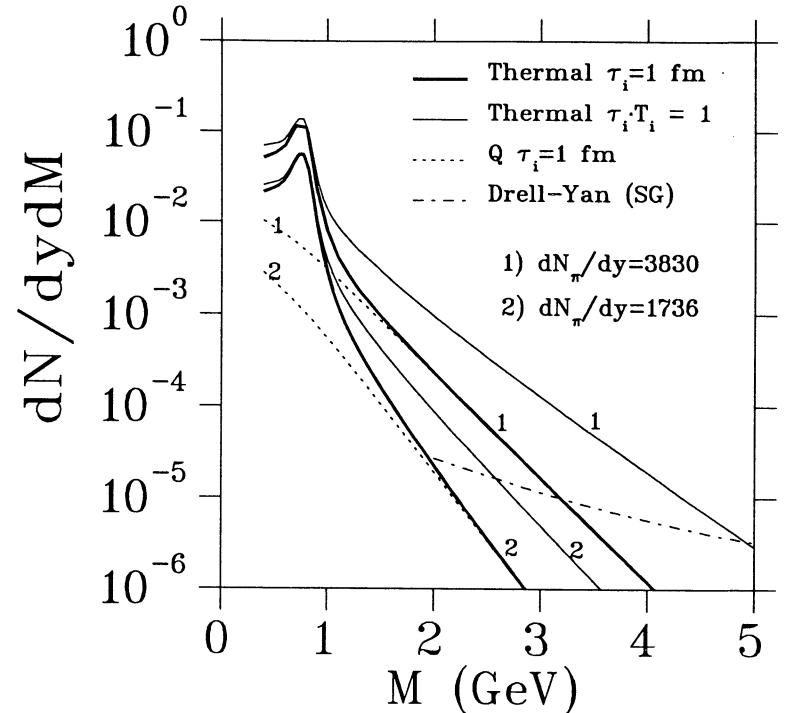


Fig. 2. Dilepton spectra for central Pb+Pb collisions at LHC energy for two hadron multiplicities and two different assumptions on thermalization time as indicated in the figure.

The first thing to notice is the large variation in the different estimates. As the multiplicity goes up from 1736 to 3830, the rate at $M = 3$ GeV increases by more than an order of magnitude. The change in thermalization time can lead to another order of magnitude change at this mass value. As long as we lack reliable information, either theoretical or experimental, on the production and thermalization dynamics, it is difficult to reduce this gap which covers the cases of having almost no chances of observing the thermal pairs from the plasma to an abundant thermal signal even above the J/ψ mass region.

Should the case of high multiplicities and abundant thermal emission be the one realized in the collisions, a way to identify the thermal component would be through the transverse mass distribution. High temperatures imply also high transverse momenta which increase with mass and temperature [17,21,35]. For high mass thermal pairs from plasma, $\langle p_T^2 \rangle \sim 2T_i M$.

Transverse momentum distributions of thermal pairs with $M = 4$ GeV are shown in fig. 3 for the case $\beta = 1$, $dN_\pi/dy = 3730$, together with a parametrization which reproduces the experimental distribution for Drell-Yan pairs hadron-nucleus collisions [34]. The p_T

distribution of thermal pairs has smaller slope than the one measured for Drell-Yan pairs on the p_T scale of $\sqrt{2T_i M}$. At larger p_T 's the thermal component cuts off exponentially and the distribution will be dominated by Drell-Yan pairs. The onset of thermal emission should then lead to a clear change in the shape of the p_T -distribution in the range of the order $\sqrt{2T_i M}$.

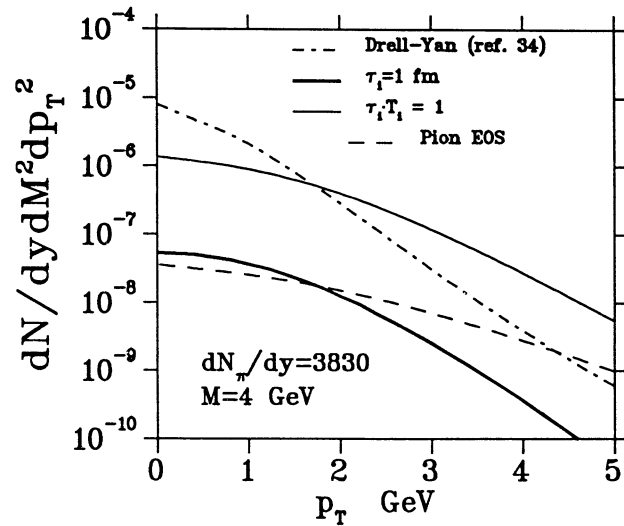


Fig. 3. Transverse momentum spectrum of lepton pairs for central Pb+Pb collisions at LHC energy for the case $\beta = 1$, $\tau_i T_i = 1$ and $\tau_i = 1$ fm/c.

The (lowest order) results on the transverse momentum spectrum of thermal photons in a central Pb+Pb collision are shown in fig. 4 together with an estimate of decay photons and lowest order calculation of direct photons from the gluon-to-photon Compton process. Initial conditions are as in fig. 2 with $\tau_i = 1$ fm/c. For the decay photons Neubert's calculation at $\sqrt{s} = 20$ GeV [12], normalized to the appropriate multiplicity, is used. Even though the total number of decay photons in this estimate is probably quite reliable, the shape of the spectrum does not take into account the expected broadening of the hadronic p_T -distributions which can increase the high k_T tail considerably. For the direct photons the $q\bar{q}$ -annihilation in lowest order is expected to be smaller than the Compton contribution and will not change the lowest order background qualitatively.

At high energies that part of bremsstrahlung from a (semi)hard quark from initial parton interactions, which correspond to collinear fragmentation of the quark into photon, will become increasingly important. It will dominate at LHC energy over the Compton and the annihilation contributions by a factor of 10 or more [24,9] in the few GeV transverse momentum region which is relevant from the point of view of thermal photons. The k_T dependence of this contribution like that of Compton and annihilation parts is shallow compared to the thermal spectrum. This seems to leave a possible window for the observation of thermal photons in the $k_T \sim 2$ GeV region, where thermal photons could still dominate over the direct photons and be large enough a fraction to be separated from the decay photons [13].

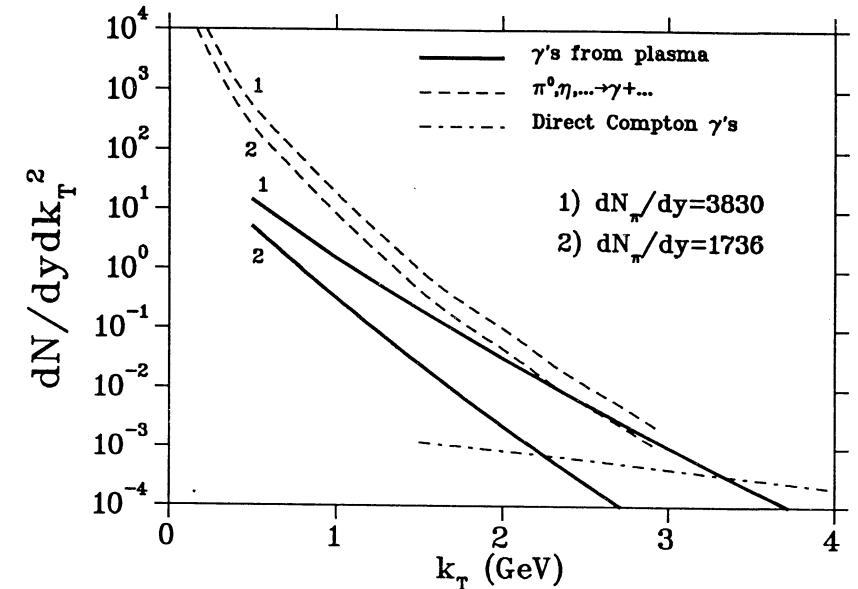


Fig. 4. Transverse momentum spectrum of photons for central Pb+Pb collisions at LHC energy for two hadron multiplicities. Thermalization time is assumed to be 1 fm/c. See the text below about the direct photons.

5. SUMMARY

Thermal rates of photons and lepton pairs were estimated for central collisions between lead nuclei at different energies and compared with several background sources. At LHC the uncertainties in the thermal rate of lepton pairs was seen to be as large as two orders of magnitude for pair masses around 3 GeV. The uncertainty in photon rate can be expected to be as large. The large range of the estimates comes from the uncertainty in the values of multiplicity and thermalization time.

At LHC energy the hadron multiplicities of central collisions are estimated to be ~ 1700 or more [36]. In the least favourable case the thermal rate from plasma is larger than that of Drell-Yan pairs for masses less than 2 GeV. In this region lepton pairs from charm decays can be a large background [11]. If multiplicities approaching 4000 occur, observation of thermal leptons from plasma becomes feasible and if production and thermalization proceeds very fast, thermal pairs can become an important source also in the J/ψ mass region. Similar conclusions hold for thermal photons. In the estimates presented here, neither the effects of thermalization being reached earlier than at 1 fm/c nor higher order contributions were considered. These could considerably enhance the thermal photon rate.

REFERENCES

1. For an overview see the Proceedings of Quark Matter '90, to appear Nucl. Phys. A.
2. B. Petterson in ref. 1.
3. P. Siemens and S.A. Chin, Phys. Rev. Lett. **55**, 1266 (1985);
4. K. Kajantie, M. Kataja, L. McLerran, and P.V. Ruuskanen, Phys. Rev. **D34**, 811 (1986).
5. H. Specht, Plenary talk in this Workshop, Proceedings Vol. I
6. T. Matsui and H. Satz, Phys. Lett. **B178**, 416 (1986).
7. F. Karsch, Report to this Workshop, Proceedings Vol. III
8. G. Altarelli, Ann. Rev. Nucl. Part. Sci. **39**, 357 (1989).
9. S. Gupta, Report to this Workshop, Proceedings Vol. III
10. H.G. Fisher and W.M. Geist, Z. Phys. **C19**, 159 (1983); S.N. Ganguli, A. Gurtu, and R. Raghaven, Phys. Rev. **D32**, 1104 (1985).
11. A. Shor, Phys. Lett. **B215**, 375 (1988); Phys. Lett. **B233**, 231 (1989) and in Proceedings of the International Workshop on Quark Gluon Plasma Signatures, (W. Geist ed.) 1990.
12. M. Neubert, Z. Phys. **C42**, 231 (1989).
13. H. Gudbrod, Report to this Workshop, Proceedings Vol. III
14. S. Gupta, Phys. Lett. **B248**, 453 (1990).
15. P. Aurenche, R. Baier, and M. Fontannez, Phys. Rev. **D42**, 1440 (1990).
16. P.V. Ruuskanen in "QUARK-GLUON PLASMA - Advanced Series on Directions in High Energy Physics Vol. 6", ed. R. Hwa, World Scientific, Singapore, 1990;
17. P.V. Ruuskanen in ref. 1.
18. K. Kajantie, J. Kapusta, L. McLerran, and A. Mekjian Phys. Rev. **D34**, 2746 (1986).
19. T. Altherr and P. Aurenche, Z. Phys. **C45**, 99 (1989).
20. M. Arneodo et al., Phys. Lett. **B211**, 493 (1988); P. Castorina and A. Donnachie, Z. Phys. **C45**, 141 (1989).
21. P.V. Ruuskanen, Proceedings of The International Workshop on Quark Gluon Plasma Signatures, Strasbourg, France, September 1990.
22. P. Koch, U. Heinz, and J. Pišút, Phys. Lett. **B243**, 149 (1990).
23. J. Varela in ref. 1.
24. R. Hwa and K. Kajantie, Phys. Rev. **D32**, 1109 (1985).
25. V.V. Klimov, Yad. Fiz. **33**, 1734 (1981); Sov. J. Nucl. Phys. **33**, 934 (1981); K. Kajantie and P.V. Ruuskanen, Phys. Lett. **B121**, 352 (1983).
26. F. Karsch, Z. Phys. **C38**, 147 (1988).
27. S. Gavin, preprint HU-TFT-90-50 (August, 1990), to appear in Nucl. Phys. **B**
28. J.-P. Blaizot, Proceedings of The International Workshop on Quark Gluon Plasma Signatures, Strasbourg, France, September 1990.
29. C. Albajar et al., UA1 Collaboration, Nucl. Phys. **B335**, 261 (1990)
30. J.W. Harris, Nucl. Phys. **A498**, 133c (1989).
31. A. Capella in ref. 1; J. Ranft, Report to this Workshop, Proceedings Vol. III
32. H. von Gersdorff, L. McLerran, M. Kataja, and P.V. Ruuskanen, Phys. Rev. **D34**, 794 (1986); A. Bialas and W. Czyż in "QUARK-GLUON PLASMA - Advanced Series on Directions in High Energy Physics Vol. 6", ed. R. Hwa, World Scientific, Singapore, 1990.
33. D.W. Duke and J.F. Owens, Phys. Rev. **D30**, 49 (1984).
34. J.S. Conway et al., Phys. Rev. **D39**, 92 (1989).
35. B. Kämpfer and O.P. Pavlenko, CERN preprint TH-5771/90.
36. U. Heinz, Report to this Workshop, Proceedings Vol. III
37. E. Braaten, R.D. Pisarski, and T.C. Yuan, Phys. Rev. Lett. **64**, 2242 (1990).

Dimuon Backgrounds to Thermal Signatures in Heavy Ion Collisions

Sourendu Gupta

Theory Division, CERN, CH-1211 Geneva, Switzerland

ABSTRACT

The major characteristics of the standard dimuon rates from known physics are estimated at masses of interest for quark gluon plasma search in heavy ion collisions at the LHC and RHIC. Limits of uncertainties in these rates due to various effects are listed.

1. INTRODUCTION

Dimuons are important probes of quark gluon plasma formation in heavy ion collisions. Dissolution of certain quarkonium resonances in the plasma, leading to a fall in the resonance cross section in the dimuon channel as compared to the continuum, may be a signal of plasma formation [1]. Furthermore, the shape of the continuum at invariant masses below the J/ψ may yield information on the temperature of a fireball, if it is formed [2]. Presented here are initial estimates of the continuum spectrum in the mass region from just below the J/ψ to just above the Υ , computed in perturbative QCD without assuming plasma formation. This is the baseline prediction against which signals have to be compared.

The computations presented here have been made using the order α_s corrections to the Drell-Yan process [3], and using standard structure function parametrisations [4-6]. Possible effects due to nuclear mass dependence of structure functions have been estimated in Ref. 7. Dimuon rates from heavy quark decays have been computed in Ref. 8. These uncertainties are taken into account, as mentioned later. Higher order corrections to the Drell-Yan cross sections are now available [9], but have not yet been included in these computations.

2. CROSS SECTIONS AND DENSITIES

The dimuon cross section differential in the invariant mass M and the pair rapidity y , including first order QCD corrections are very well known. One can write symbolically

$$\frac{d^2\sigma}{dM^2dy} = \int_{x_1^0}^1 dx_1 \int_{x_2^0}^1 dx_2 [H(x_1, x_2)f(x_1, x_2) + K_1(x_1, x_2)h(x_1, x_2) + K_2(x_1, x_2)h(x_2, x_1)],$$

where

$$x_1^0 = \sqrt{\tau}e^y, \quad x_2^0 = \sqrt{\tau}e^{-y}, \quad \text{and} \quad \tau = \frac{M^2}{S},$$

and the functions $f(x_1, x_2)$ and $h(x_1, x_2)$ contain the results of the order α_s computation after cancellation of singularities from the real and virtual diagrams. The parton density combinations can be written in terms of quark and gluon densities as

$$\begin{aligned} H(x_1, x_2) &= \sum_f e_f^2 [q_f(x_1)\bar{q}_f(x_2) + \bar{q}_f(x_1)q_f(x_2)], \\ K_1(x_1, x_2) &= g(x_1) \sum_f e_f^2 [q_f(x_2) + \bar{q}_f(x_2)], \\ K_2(x_1, x_2) &= g(x_2) \sum_f e_f^2 [q_f(x_1) + \bar{q}_f(x_1)]. \end{aligned}$$

There are two sources of large corrections to the Drell-Yan cross section in the formula above. The first arises from the fact that the parton densities are measured in deep inelastic scattering where the photon is spacelike, and applied to the Drell-Yan process where it is timelike. The second is through distributions like $1/(x_1 - x_1^0)$ and $\log(x_1 - x_1^0)/(x_1 - x_1^0)$ (and the equivalents in x_2) in the function $f(x_1, x_2)$. These arise from soft and collinear gluon emissions from quark lines. There are no large parts to the processes involving a gluon in the initial state, *i. e.*, in the function $h(x_1, x_2)$.

The input parton distributions can be characterised in terms of the parton luminosities for species i and j —

$$\tau \frac{dL_{ij}}{d\tau} = \tau \int_\tau^1 dx f_i(x) f_j(\tau/x).$$

These are plotted for the combinations H and $K_1 + K_2$ in Fig. 1 at the scale $M^2 = 9 \text{ GeV}^2$ for the different sets used here. It should be noted that at LHC

($\sqrt{S}=7 \text{ TeV}$) the value of $\sqrt{\tau}$ near the J/ψ mass is less than 10^{-3} . It is seen that most of the densities plateau at values of $\sqrt{\tau}$ much lower than this. Hence one is led to expect similar plateaus in the cross section as a function of \sqrt{S} . Differences between these parametrisations show up strongly at LHC energies, and arise out of the fact that the distributions are not measured down to values of x of relevance here. Hopefully the situation will improve with the HERA experiments, allowing a more reliable computation.

3. MASS AND RAPIDITY DISTRIBUTIONS

The agreement between data and the results of the first order QCD corrected predictions for the mass and rapidity distributions of lepton pairs upto ISR energies is excellent. It is worth noting that at $\sqrt{S} = 38.8 \text{ GeV}$, nuclear effects in the cross section are less than 5%. Since the cross section as a function of mass varies by several orders of magnitude, it requires extremely high statistics to isolate such effects with precision.

The mass distributions at zero rapidity are shown for both RHIC and LHC energies in Fig. 2. These cross sections have been extrapolated down to $M = 2 \text{ GeV}$, where they may not be reliable. The effect of changing the structure function set is seen in this figure. Note that the cross sections, specially at low mass are not significantly different at these two energies. This saturation with \sqrt{S} is shown in Fig. 3 for two fairly small values of M .

The rapidity distributions at LHC energies are shown for a series of masses in Fig. 4. It can be seen that the distribution is flat. Shifting detectors in rapidity, over this range, does not yield any changes in this cross section.

4. TRANSVERSE MOMENTUM DISTRIBUTIONS

The p_T distribution of dimuon pairs can be reliably computed in perturbation theory by exponentiating the soft and collinear corrections to any given order [10]. These distributions at different energies and the same mass are compared in Fig. 5. It is seen that the main effect of going to large values of \sqrt{S} is to enhance the large p_T perturbative tail of the distribution. Taken along with the fact that the integrated cross section remains constant, this implies that the cross section in a low p_T bin falls with energy at very high \sqrt{S} .

The average $p_T(\langle p_T \rangle)$ can be computed from this fully exponentiated formalism. This has been done at lower energies in Ref. 11. It is seen that at fixed $\sqrt{\tau}$,

the complete computation is necessary at small energies. At larger values of \sqrt{S} it is sufficient to take the first-order corrected value of $\langle p_T^2 \rangle$. These values are shown in Fig. 6 for the mass range of interest. It should be noted that the values obtained from this computation are strong underestimates of the true numbers at \sqrt{S} less than about 60 GeV. A full computation restores agreement with data even at these energies [11].

5. REMAINING UNCERTAINTIES

The major sources of remaining uncertainties and their probable effects (where estimated) are given below.

- 1) Higher order corrections: These are now available, but have not been used in this computation. Their main effect should be in the p_T distributions. For better control over this process, however, they must eventually be taken into account.
- 2) Muons from heavy quark decays: These have been estimated in [8,12]. Since they mimic lepton pairs only through accidental coincidences of oppositely charged leptons from independent decays, their effect is mainly in the low mass region. After suitable cuts, the irreducible background is seen to be about 2–3 times the Drell-Yan cross section near $M = 2$ GeV.
- 3) Structure function saturation: The effects of possible nonlinearities in the QCD evolution equations at small x might tend to depress the dimuon cross section. Very simple estimates show a probable factor 2 suppression at about $M = 2$ GeV. In any case, this is an yet unmeasured effect, and should be taken into account after measurements at, for example, HERA or the LHC operating in ep mode.
- 4) Nuclear effects on densities: These have been investigated in Ref. 7. Shadowing of parton densities (which is related to saturation effects) may give upto factor 3 depression of the cross section at $M = 2$ GeV.

6. CONCLUSIONS

The dimuon cross section from standard (non-plasma) sources is seen to be comparable to, or larger than, the thermal cross section already at $M = 2$ GeV (Fig. 7). Taking into account possible uncertainties in the cross section does not change this number very much, due to the relative steepness of the thermal cross section. A larger multiplicity at LHC would shift this limiting mass further out.

However, in view of the fact that the standard background is not very well fixed, it seems difficult to disentangle the thermal signal from the continuum.

REFERENCES

- 1 F. Karsch, report at this Workshop, Vol III.
- 2 V. Ruuskanen, report at this Workshop, Vol III.
- 3 G. Altarelli, R. K. Ellis and G. Martinelli, *Nucl. Phys.* B157 (1979) 461; J. Kubar, M. le Bellac, J. L. Meunier and G. Plaut, *Nucl. Phys.* B175 (1980) 251.
- 4 M. Diemoz, F. Ferroni, E. Longo and G. Martinelli, *Z. Phys.* C39 (1988) 21.
- 5 D. W. Duke and J. F. Owens, *Phys. Rev.* D30 (1984) 49.
- 6 M. Glück, E. Hoffmann and E. Reya, *Z. Phys.* C13 (1982) 1.
- 7 P. Castorina, report at this Workshop, Vol III.
- 8 A. Shor, talk delivered at the Strasbourg meeting on Quark Gluon Plasma Signatures, Oct. 1–4, 1990.
- 9 T. Matsuura, S. C. van der Marck and W. L. van Neerven, *Nucl. Phys.* B319 (1989) 570; T. Matsuura, R. Hamberg and W. L. van Neerven, *Nucl. Phys.* B345 (1990) 337.
- 10 G. Altarelli, R. K. Ellis, M. Greco and G. Martinelli, *Nucl. Phys.* B246 (1984) 12.
- 11 G. Altarelli, R. K. Ellis and G. Martinelli, *Phys. Lett.* 151B (1985) 457.
- 12 S. Gupta, *Phys. Lett.* B248 (1990) 453.

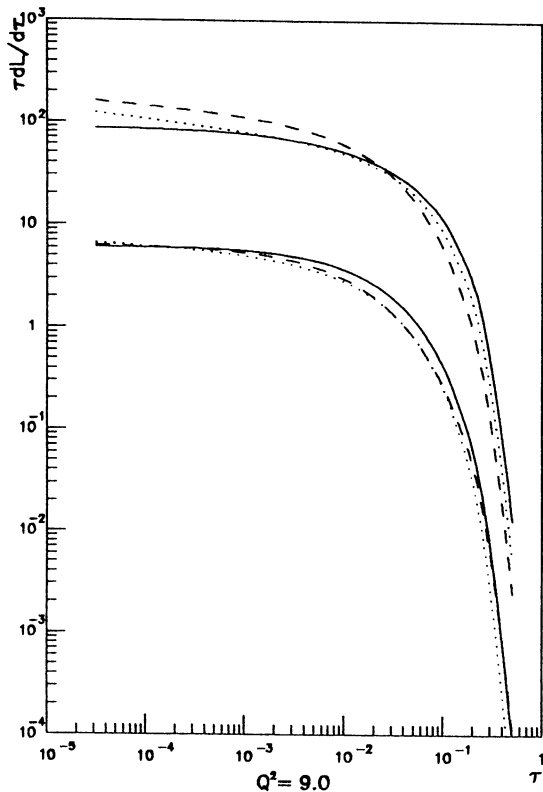


Figure 1. The parton luminosities from different structure function parametrisations evaluated at a scale of 9 GeV². The full line corresponds to the GHR structure functions[6], the dashed to the DFLM [4] and the dotted to the Duke-Owens set I [5]. Note that the qg luminosity at small τ is about an order of magnitude larger than the $q\bar{q}$ luminosity.

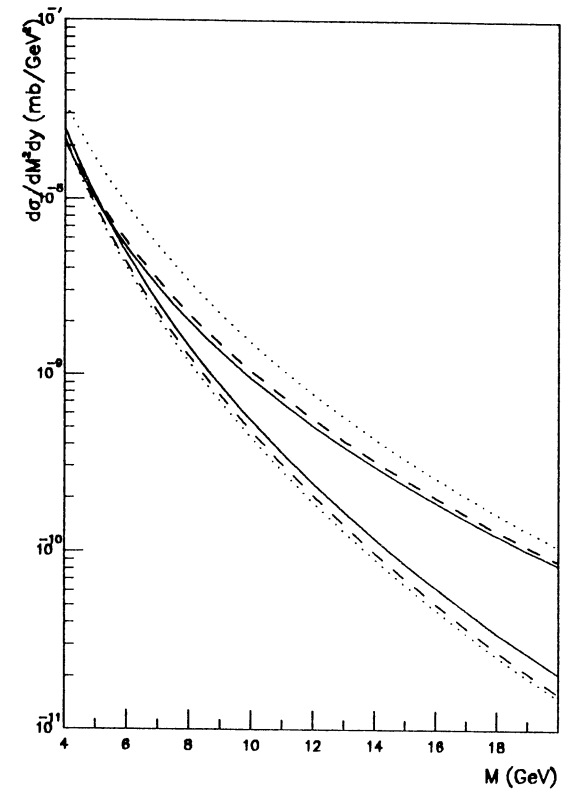


Figure 2. The inclusive dimuon cross section at LHC and RHIC energies at $y = 0$. The coding of line styles is explained in the caption to Fig. 1.

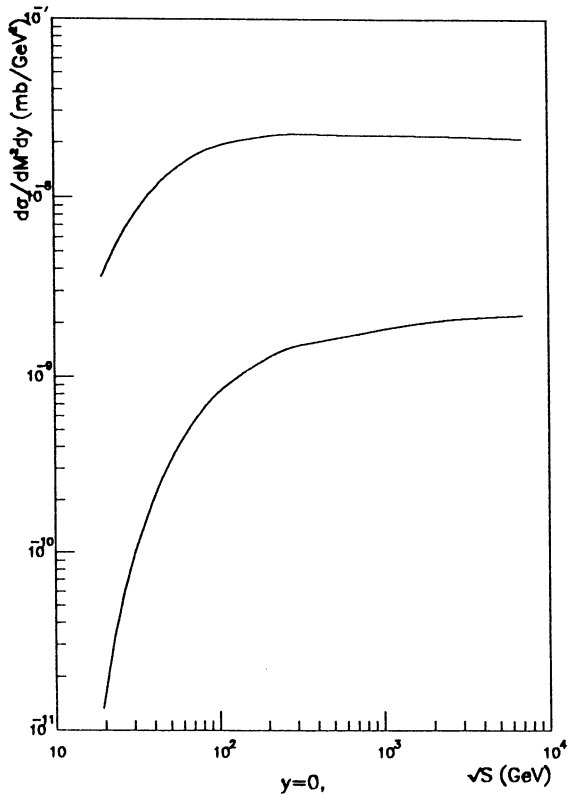


Figure 3. The \sqrt{S} dependence of the cross section at fixed mass (the larger cross section is for $M=4$ GeV, and the other for $M=8$ GeV) and $y = 0$, evaluated with the DFLM structure functions.

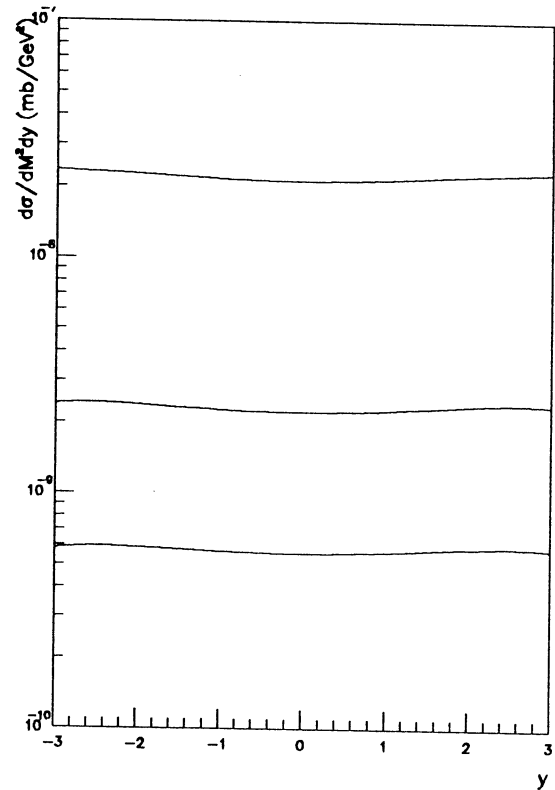


Figure 4. The rapidity distributions for dimuons at $\sqrt{S}=7$ TeV. The three lines correspond to $M=4$, 8 and 12 GeV, in decreasing order of cross sections. The DFLM structure functions have been used. Other structure functions also yield a flat distribution.

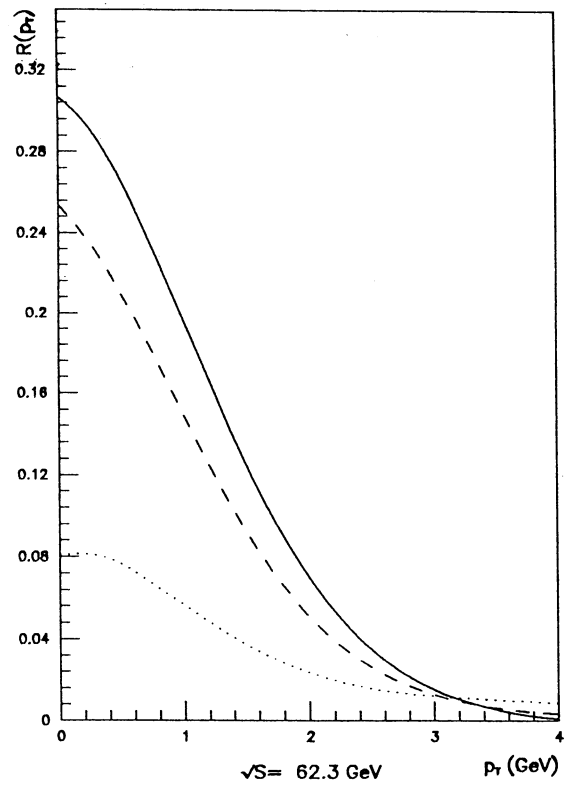


Figure 5. The p_T distribution of dimuon pairs (normalised to the cross section integrated over p_T) for $M=6$ GeV and $y=0$. The full line is for $\sqrt{S}=63.3$ GeV, the dashed line for $\sqrt{S}=200$ GeV, and the dotted line for $\sqrt{S}=7$ TeV. Note the flattening of the curve at larger values of \sqrt{S} .

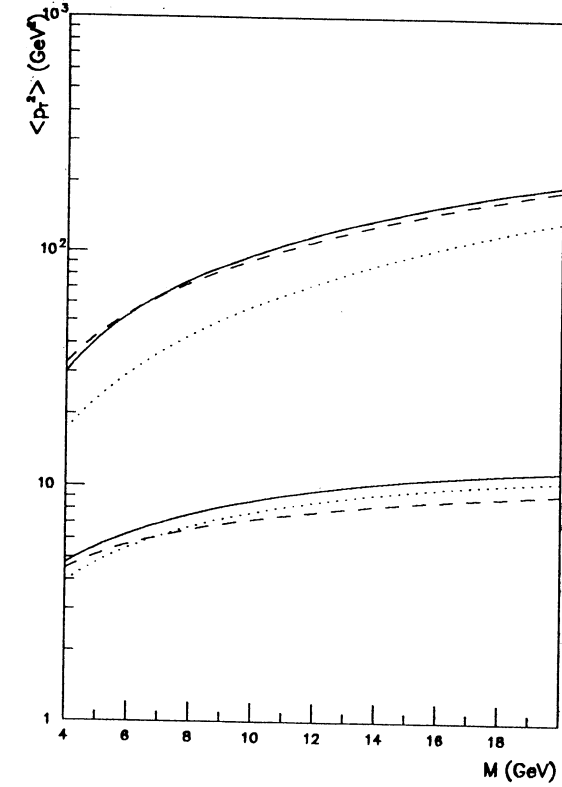


Figure 6. $\langle p_T^2 \rangle$ as a function of mass at $y = 0$ for LHC and RHIC energies. The higher values of $\langle p_T^2 \rangle$ are obtained at the larger energy. The different line styles code for the structure function set as explained in the caption for Fig. 1.

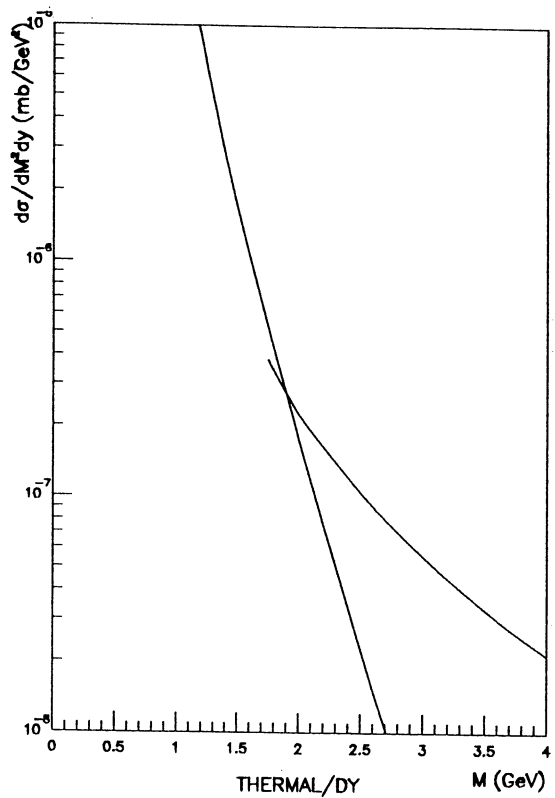


Figure 7. Comparison between the Drell-Yan cross section at $\sqrt{S}=7$ TeV and the thermal dimuon rate obtained in Ref. 2. Limits on uncertainties due to structure function and other non-thermal sources (as mentioned in the text) are shown by the horizontal lines at $M=2$. The thermal dimuon rate is smaller than the non-thermal rate for $M > 2$ GeV.

SHADOWING EFFECT IN HEAVY ION COLLISIONS AT LHC ENERGY

P.CASTORINA

Dipartimento di Fisica, Università di Catania,Catania,Italy

Istituto Nazionale Fisica Nucleare
Sezione di Catania,Catania,Italy

and

A.DONNACHIE

Department of Physics, University of Manchester,Manchester,U.K.

ABSTRACT

The effect of the modification of the structure functions of the nucleon in a nuclear environment on lepton pairs production is discussed. In particular, it is shown that the shadowing effect gives a strong suppression of Drell-Yan cross section for heavy ions collisions at LHC energy.

1. INTRODUCTION

The transition to a new phase of matter, predicted by non perturbative analysis of QCD at finite temperature ^(1,2), has many interesting and, in principle, clear signatures, such as the well known J/Ψ suppression. However, in relativistic heavy ion collisions, where at the LHC energy it is surely possible to reach the conditions for the phase transition, the phenomenological consequences of the new phase are not easily separable from more standard effects.

As discussed by Ruuskanen ⁽³⁾, the production of lepton pairs in heavy ion collisions is a signal of thermal effects and it is essential to have a control of the other sources of dileptons to clarify if the thermal contribution can be unambiguously observed at the LHC energy. One of the most important processes of production of dileptons is the standard Drell-Yan mechanism. By defining the dilepton mass, M , the dilepton Feynman variable, x_F , and the c.m. energy \sqrt{s} , the usual variables x_1 , x_2 and $\sqrt{\tau}$ are given by

$$\begin{aligned}\tau &= \frac{M^2}{s} \\ x_{1,2} &= \frac{1}{2}[\pm x_F + \sqrt{x_F^2 + 4\tau}]\end{aligned}$$

and the Drell-Yan cross section per nucleon at $x_F = 0$ (i.e. zero rapidity of dilepton) is

$$\frac{d\sigma}{dMdx_F} \Big|_{x_F=0} = \frac{8\pi\alpha^2}{9} \frac{1}{2\sqrt{\tau}M^3} K(\sqrt{\tau}) \left[\sum_f e_f^2 q^A(x) \bar{q}^A(x) + (1 \rightarrow 2) \right] \quad (1)$$

In this expression the sum is over the quarks flavours u,d,s, $K(\sqrt{\tau})$ is the rescaling factor in QCD given in ref.(4), and $q^A(x)$ and $\bar{q}^A(x)$ are the quark and anti-quark distributions per nucleon in the nucleus.

A reliable calculation of cross section (1) at the LHC energy requires informations on the parton distributions per nucleon in a region of very small Bjorken x . Indeed, for $x_F = 0$, $M \sim 3$ GeV, $\sqrt{s} = 6300$ GeV, one has $x_1 = x_2 = \sqrt{\tau} \sim 5 * 10^{-4}$ and in this x region there is, so far, no available experimental information on $q^A(x)$ and $\bar{q}^A(x)$. From the theoretical point of view the analysis of the small x behaviour of the structure functions is an interesting problem because a simple extrapolation of the perturbative QCD calculations from the region of moderately small value of x ($\sim 10^{-2}$), where the parton picture has been successfully applied, is not correct. In fact the QCD linear evolution equations for parton distributions have to be modified because, at low x , the density of gluons and quarks is very large and the contribution of parton recombination becomes important ^(5,6,7). Moreover, in the limit of very small value of x there are non perturbative effects related to the Regge behaviour.

For heavy ion collisions one has to take into account also the modification of structure functions in a nuclear environment. Deep inelastic scattering data show three effects :

- i) For values of $x > 0.2$ the structure function of the bound nucleon is less than that of the free nucleon. This is the original "EMC effect" ;
- ii) For values of $x < 0.1$ the structure function of the bound nucleon is again depleted relative to that of the free nucleon. The term "shadowing" is usually applied to this region, although the effect is known to persist out to large Q^2 ;
- iii) For $0.1 < x < 0.2$ antishadowing occurs, i.e. the structure function of the bound nucleon is enhanced relative to that of the free nucleon.

In this contribution to the Workshop I shall discuss the role of the shadowing in the

Drell-Yan production at LHC.

2. DRELL-YAN PRODUCTION ON HEAVY NUCLEI

Before discussing the implications at $\sqrt{s} = 6300 \text{ GeV}$ one has to verify that nuclear target effects are present in the available data on Drell-Yan. In ref.(8) the data of Badier et al. ^(9,10) for $d\sigma/dMdx_F$ in p-Pt collision at $\sqrt{s} = 27.4 \text{ GeV}$ have been analyzed. A satisfactory description of the data and the explanation of the apparent variation of the rescaling factor K , with respect to the proton-proton case, have been obtained by including at partonic level, according to the model in ref.(11), shadowing, anti- shadowing and the EMC effect. On the other hand, the recent data by Alde et al.⁽¹²⁾ for p-Fe scattering at $\sqrt{s} = 38.8 \text{ GeV}$ for $d\sigma/dM$ seem to show no dependence on the nuclear target in the region $4 < M < 9 \text{ GeV}$. However, in my opinion, there is no contradiction between these experimental results because to obtain $d\sigma/dM$ from $d\sigma/dMdx_F$ one integrates over x_F in the kinematical range fixed by the experimental cuts. In doing this integration, at fixed M , one gets contributions from parton distributions in the target from very different region of the Bjorken x and then, in some range of $\sqrt{\tau}$, the nuclear effects could be washed out. I would like to support this observation in a more quantitative way by a very simple phenomenological analysis, inspired to the model of shadowing proposed in ref.(11).

Let us assume that:

- 1) shadowing is only due to the suppression at small x of the sea distribution $x\bar{q}^A(x)$ per nucleon in the nucleus with respect to the sea distribution for the free nucleon $x\bar{q}^N(x)$;
- 2) the momentum sum rule is maintained and then, due to point 1) there is an anti-shadowing region.

The EMC effect is taken into account by the x -rescaling mechanism ⁽¹³⁾ and the Q^2 dependence of the parton distributions in the nuclear target , which is weak for shadowing ⁽⁶⁾ , has been neglected. By using the parametrization by Diemoz et al. ⁽¹⁴⁾ for the parton distributions in the free nucleon, the nuclear sea distribution is now fitted, with the constraints (1)-(2), in such a way to reproduce the data on $d\sigma/dMdx_F|_{x_F=0}$ by Brown et al ⁽¹⁵⁾ for p-Cu collisions at $\sqrt{s} = 38.8 \text{ GeV}$.

In fig.(1a) is shown the ratio $x\bar{q}^A(x)/x\bar{q}^N(x)$ which gives the fit of Brown et al. data of fig.(1b). It is clear that there are strong nuclear effects which, without any optimization procedure, reproduce the data in the mass region $6 < M < 10 \text{ GeV}$ (the discrepancy at large M is due to the approximation of neglecting the Q^2 -evolution for the parton distribution in the target). With the ratio $x\bar{q}^A(x)/x\bar{q}^N(x)$ of fig.(1a) it is possible to evaluate the ratio of structure functions F_2^A/F_2^D and fig.(2) is the comparison with the result from Drell - Yan data by Alde et al.⁽¹²⁾. The cross section $d\sigma/dM$, given in fig.(3), evaluated with the strong nuclear effects in the ratio $x\bar{q}^A(x)/x\bar{q}^N(x)$, is almost flat in the region $4 < M < 9 \text{ GeV}$ and , by considering that the analysis is not optimized and neglects the evolution of the structure functions in the target, is in reasonable agreement with data by Alde et al..

Then one can conclude that the modifications of quark distributions in nuclear environment observed in deep inelastic scattering are also present in Drell-Yan data as shown in ref.(8) and by the above simple analysis for $d\sigma/dMdx_F$. On the other hand, the integrated cross section $d\sigma/dM$ can apparently show only a weak dependence on nuclear target in some range of $\sqrt{\tau}$.

Let us now discuss the shadowing effect on the ratio

$$R = \frac{\frac{d\sigma}{dMdx_F}|_{x_F=0}^{D-D}}{\frac{d\sigma}{dMdx_F}|_{x_F=0}^{P^t-P^t}} \quad (2)$$

at the LHC energy in the range $2 < M < 6 \text{ GeV}$.

Many models ⁽¹⁶⁾ are able to explain the observed shadowing in deep inelastic scattering, however, in the kinematical region of small x , ($\sim 10^{-4}$), the points (1)-(2) of the previous phenomenological fit are, in my opinion, quite reasonable. In ref.(8) the analysis of Badier et al. data has been performed by following the same strategy with the further information that the suppression

$$S = \frac{x\bar{q}^A}{x\bar{q}^N}|_{x=0}$$

is calculable in the model and depends on the overlap of the nucleons in the nucleus ($S^{Pt} \sim 0.55$). A good fit of the data is obtained for a sea distribution per nucleon of the form

$$x\bar{q}^{Pt} = 0.25S(1-x)^{8.5}[1 + \alpha x^\beta(1-x)^\gamma] \quad (3)$$

with $\beta = 2.0, \gamma = 15$ and α fixed by the momentum sum rule. By using eq.(3), which is also compatible with the data by Brown et al. for Cu at $\sqrt{s} = 38.8 \text{ GeV}$ ⁽¹⁵⁾, it is straightforward to estimate the ratio R at $\sqrt{s} = 6300 \text{ GeV}$. Fig. (4) shows that in the range $2 < M < 6 \text{ GeV}$ the ratio R is about 3 and then there is a strong suppression in Drell-Yan due to shadowing effects in heavy nuclei. By combining the above result with the QCD calculation for Drell-Yan ⁽¹⁷⁾, one has an extrapolation of dilepton cross section at LHC energy completely consistent with the low energy data.

REFERENCES

- 1) For a review see B.Peterson: Deconfinement and chiral symmetry restoration in Lattice QCD, ECFA LHC-WORKSHOP,Aachen,Oct. 90.
- 2) For a review see R.Casalbuoni: Deconfinement and chiral symmetry restoration in Effective Lagrangian Theories, ECFA LHC-WORKSHOP, Aachen,Oct. 90.
- 3) V.Ruuskanen : Thermal dileptons and photons,ECFA LHC-WORKSHOP, Aachen,Oct. 90.
- 4) P.Chiappetta and M.J.Pirner, Nucl.Phys.B291(1987)765.
- 5) L.V.Gribov, E.M.Levin, M.G.Ryskin, Phys. Rep. 100,1(1982)
- 6) A.H.Mueller and J.Qiu, Nucl. Phys. B268(1986)427.
J.Qiu, Nucl. Phys. B291(1987)746.
- 7) J.Bartels,J.Blumlein,G.A Schuler,Desy-preprint 90-091.
- 8) P.Castorina and A.Donnachie, Z.Phys.C Part. and Fields 45,(1989)141.
- 9) J.Badier et al., Zeits.Phys.C26(1985)489.
- 10)J.Badier et al., Zeits.Phys.C28(1985)9,15.
- 11)P.Castorina and A.Donnachie, Phys. Lett.B215(1988)589.
- 12)D.M.Alde et al., Phys. Rev. Lett.64,(1990)2479.
- 13)S.V.Akulichev,S.A.Kulagin and G.M.Vagradov, Phys. Lett. B158(1985)485
- 14)M.Diemoz,F.Ferroni,E.Longo and G.Martinelli, Zeit. Phys. C39(1988)21.
- 15)C.N.Brown et al., Phys. Rev. Lett.63,(1989)2637.

- 16) For a review see R.J.M.Covolan and E.Predazzi, Univ. di Torino preprint
 DFTT 11/90. See also N.N.Nikolaev and B.G.Zakharov, OUTP-90.23.P ;
 S.J.Brodsky and H.J.Lu, Phys. Rev. Lett. 64,(1990)1342.
- 17) S.Gupta: Drell-Yan production , ECFA LHC-WORKSHOP,Aachen,Oct. 90.

FIGURE CAPTIONS

Fig.1) (a)The ratio $x\bar{q}^A(x)/x\bar{q}^N(x)$ which gives the fit of fig.1b); (b) Fit of $d\sigma/dM dx_F|_{x_F=0}$ of Brown et al. data obtained with the phenomenological analysis described in the text.

Fig. 2) The ratio F_2^A/F_2^D compared with result from Drell-Yan by Alde et al.

Fig. 3) The cross section $d\sigma/dM$, evaluated by using the ratio $x\bar{q}^A(x)/x\bar{q}^N(x)$ in fig.1b, compared with exerimental data by Alde et al.

Fig. 4) The prediction for the ratio R, see text, at LHC energy.

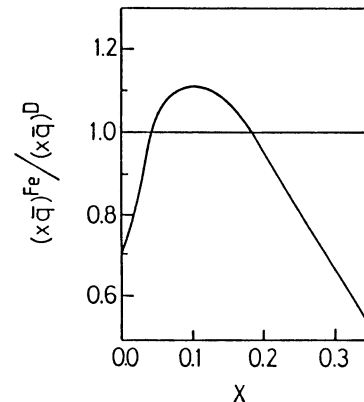


Fig. 1a

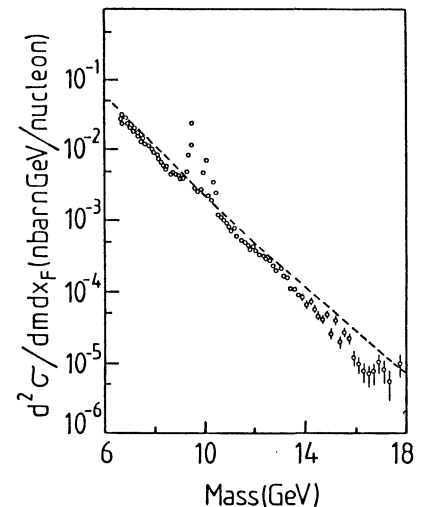


Fig. 1b

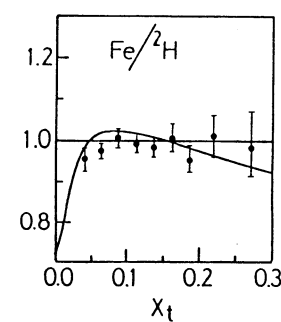


Fig. 2

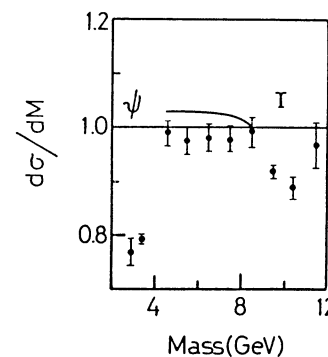


Fig. 3

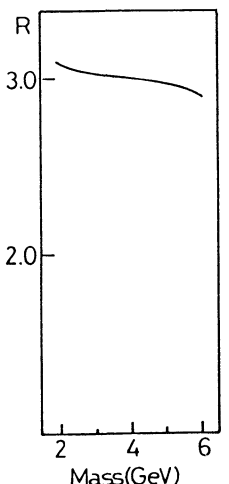


Fig. 4

MINIJET PRODUCTION IN A+A AT THE LHC

K. J. Eskola

Department of Theoretical Physics, University of Helsinki
Siltavuorenpuisto 20 C, 00170 Helsinki, Finland
kjeskola@finuhcb.bitnet

We calculate the transverse energy distribution $d\sigma/dE_T$ of quarks and gluons produced in a U+U and Pb+Pb collision at the proposed RHIC and LHC energies by including both soft and hard QCD contributions. At $\sqrt{s} = 7000$ AGeV the E_T distribution is clearly dominated by hard processes while soft processes are important until $\sqrt{s} \sim 200$ AGeV. We also study the effects of varying the smallest p_T -scale of the hard partons as well as give an estimate of the effects of nuclear shadowing.

Minijets are abundant in nucleus-nucleus collisions at high energies but due to the large multiplicity of the soft E_T background one cannot observe them. Nevertheless, hard QCD quanta contribute to the evolution of the system the more the higher the energy is [1-2]. In this talk we shall concentrate on the transversal energy distribution $d\sigma/dE_T$ of quarks and gluons produced in an $A+B$ collision at proposed RHIC and LHC energies. We use the standard nuclear collision geometry and apply first order QCD perturbation theory for computation of the needed hard cross sections. A hard parton (= minijet) is defined here to be a quark or a gluon with $p_T \geq p_0$, where p_0 is the scale above which perturbative QCD can be applied. We shall take $p_0 \approx 2$ GeV [1].

Let us first consider (mini)jets in pp-collisions. The 2-jet inclusive cross section in the QCD improved parton model is given by

$$\frac{d\sigma_h}{dp_T^2 dy_1 dy_2} = x_1 f(x_1, p_T^2) x_2 f(x_2, p_T^2) \frac{d\sigma^{gg}}{dt}, \quad (1)$$

where the various partonic subprocesses are approximated by the effective structure function $f = g + \frac{4}{9} \sum [q_f + \bar{q}_f]$ and by using the $gg \rightarrow gg$ differential cross section [3]. In our numerical calculations we use the Duke-Owens soft gluon structure functions with $\Lambda_{QCD} = 200$ MeV and the scale $Q = p_T$ [4]. From this we calculate the 1-jet inclusive cross section at central rapidity by integrating over y_2 and setting $y_1 = 0$. This is shown in fig. 1 at the Tevatron and LHC energies. As is well known, this perturbative computation reproduces well the data [5] (for the two-jet inclusive cross section, see [6]). Here we apply only the Born level perturbative QCD and neglect the higher order corrections (i.e. $K = 1$). The α_s^3 terms to jet production in pp have been calculated in [7] and they are expected to be significant. However, the definition of the K -'factor' depends on the jet definition, on the scale used and on the structure function choice. It is thus non-universal

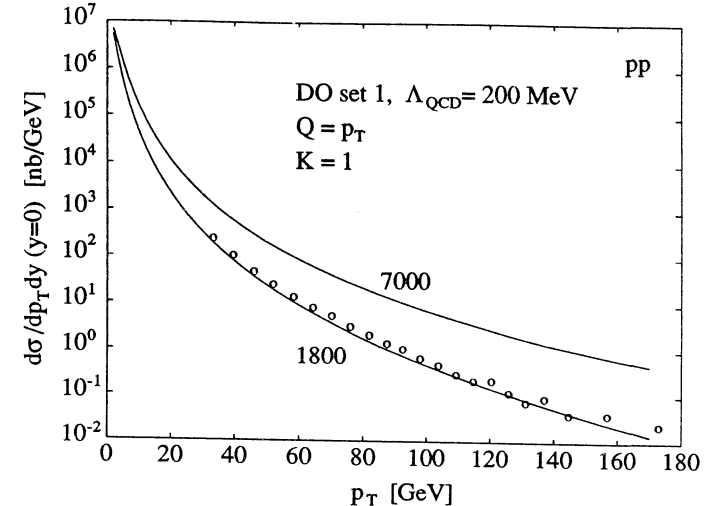


Fig. 1. The lowest order QCD prediction for the single jet inclusive cross section in a pp collision for $\sqrt{s} = 1800$ GeV and 7000 GeV. The Tevatron data (o) from ref. [5] is also sketched in the figure. As seen in the figure, most of the jet cross section (2) is from the extrapolation to small p_T region. Here the smallest value of p_T is 2 GeV.

and cannot be generally given. For example if one wishes to reproduce the UA1 minijet data [8] at $p_T > 5$ GeV at $\sqrt{s} = 200$ GeV one needs $K \sim 2.5$ [1].

Next we define the jet cross section in a pp-collision as

$$\sigma_h^{pp}(p_0) = \int_{p_0} dp_T^2 dy_1 dy_2 \frac{1}{2} \frac{d\sigma_h}{dp_T^2 dy_1 dy_2}, \quad (2)$$

where we have assumed the 2-jet dominance. This cross section for producing jets at any rapidity and with $p_T \geq p_0$ is displayed at different energies in fig. 2. We plot σ_h^{pp} as a function of p_0 , so that the effect of choosing p_0 is seen. The choice of this hard scale and its dynamical significance is discussed in refs. [9]. Note that when going towards higher energies, the uncertainty caused by p_0 decreases, since the differential cross sections do not drop as rapidly in p_T than at lower energies.

Next we shall proceed to the nucleus-nucleus level. The average number of hard collisions that one nucleon experiences when going through a nucleus A at a transversal location s , is given by $T_A(s)\sigma_h^{pp}$, where T_A is the nuclear thickness function. In the independent collision picture the average number of hard collisions in an $A+B$ collision at a fixed impact parameter b is given by

$$\bar{N}_{AB}(b) = T_{AB}(b)\sigma_h^{pp}(p_0), \quad (3)$$

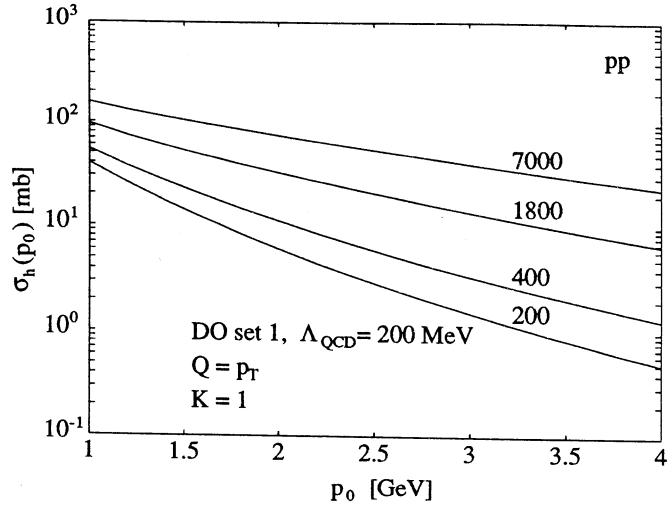


Fig. 2. The hard cross section σ_h^{pp} for producing jets in a pp collision with $p_T \geq p_0$ and any rapidity as a function of p_0 . The cross section is computed from eq. (2) in the first order QCD for $\sqrt{s} = 200, 400, 1800, 7000$ GeV. The value for 1800 GeV and $p_0 = 2$ GeV coincides with the prediction of [15].

where $T_{AB}(\mathbf{b}) = \int d^2s T_A(s) T_B(\mathbf{b} - s)$ is the nuclear overlap function (see the app. of [1]). Since there are dominantly two jets coming from each hard subcollision, the average number of jets at any rapidities is simply given by $2\bar{N}_{AB}(\mathbf{b})$, see table 1. In order to estimate how many (mini)jets on the average fall e.g. in $|y| \leq 0.5$ range, we impose cuts to the rapidity integrals of (2) and take into account of how many jets are inside the detected kinematical region. The resulting numbers are given in table 1 for a central Pb-Pb collision at $\sqrt{s} = 7A$ TeV. Note that the reason for the large numbers is basically the $A^{4/3}$ scaling of T_{AB} . The value of T_{AB} for Pb-Pb is 31.7 mb^{-1} .

average #jets in Pb+Pb at $\mathbf{b} = 0$		
p_0/GeV	all y	$ y \leq 0.5$
2	4500	400
3	2400	240
4	1380	150

Table. 1. The average number of jets in a central ($\mathbf{b} = 0$) Pb-Pb collision at $\sqrt{s} = 7A$ TeV . The numbers for all rapidities as well as the central rapidities accepted are shown as functions of p_0 .

The hard E_T spectrum of the produced partons can be obtained by folding together the E_T distributions from N independent hard collisions. Each subcollision

brings an amount of 0, p_T or $2p_T$ to the total E_T , depending whether neither of the jets, either one of them, or both jets fall inside the detector. Thus the hard E_T spectrum is given by

$$\frac{d\sigma_h^{AB}}{dE_T} = \int d^2\mathbf{b} \sum_1^\infty \frac{[\bar{N}_{AB}(\mathbf{b})]^N}{N!} \exp[-\bar{N}_{AB}(\mathbf{b})] \cdot \int \prod_1^N dE_{Ti} \frac{1}{\sigma_h^{pp}} \frac{d\sigma_h^{pp}}{dE_{Ti}} \delta(E_T - \sum_1^N E_{Ti}). \quad (4)$$

The E_T distribution from a single QCD subprocess is given by

$$\frac{d\sigma_h^{pp}}{dE_T} = \int dp_T dy_1 dy_2 \delta(E_T + (\epsilon_1 + \epsilon_2)p_T) \frac{1}{2} \frac{d\sigma_h}{dp_T dy_1 dy_2}, \quad (5)$$

where $\epsilon_i \equiv \epsilon(y_i, \phi_i)$ gets the value 1(0) if the jet i is inside(outside) the detector. The first moment of the distribution (5) is plotted in fig. 3.

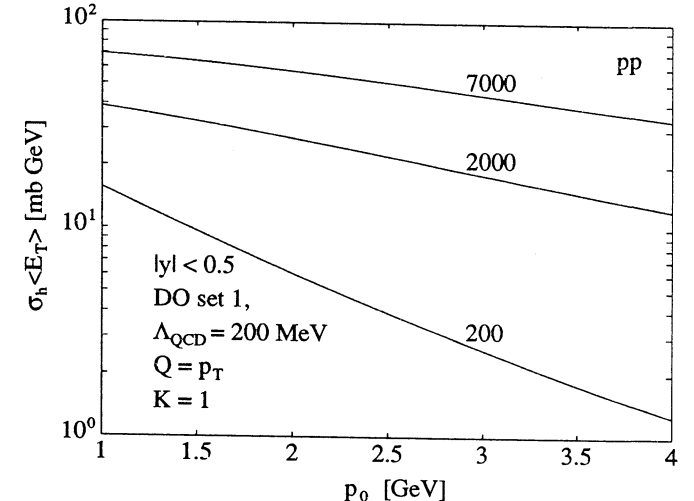


Fig. 3. The first moment of the hard E_T distribution, computed from eq. (5). The acceptance functions ϵ_1 and ϵ_2 accept two back-to-back jets with $p_T \geq p_0$ and $|y_i| \leq 0.5$. The respective estimate for the soft component is 15 mbGeV.

For $E_T > 0$ the spectrum (4) is approximated by a gaussian distribution. The soft component is then included on the basis of a CERN heavy ion experiment [10]. We simply add soft contributions to the first and second E_T -moments of the pp collision. Furthermore, we assume the soft component to be energy independent. Thus the final, semi-inclusive E_T spectrum becomes [1,2]

$$\frac{d\sigma_h^{AB}}{dE_T} = \int d^2\mathbf{b} \frac{1}{\sqrt{2\pi\sigma^2(\mathbf{b})}} \exp \left\{ -\frac{[E_T - \bar{E}_T^{AB}(\mathbf{b})]^2}{2\sigma^2(\mathbf{b})} \right\}, \quad (6)$$

where

$$\bar{E}_T^{AB}(\mathbf{b}) = T_{AB}(\mathbf{b})[\sigma_h^{pp}(p_0) < E_T >_h^{pp} + 15 \text{ mbGeV}] \quad (7)$$

$$\sigma^2(\mathbf{b}) = T_{AB}(\mathbf{b})[\sigma_h^{pp}(p_0) < E_T^2 >_h^{pp} + 50 \text{ mbGeV}^2]. \quad (8)$$

We have plotted the final E_T spectrum in a Pb+Pb collision at different energies in fig. 4. Of the hard minijets those with $p_T \geq p_0 = 2 \text{ GeV}$ and $|y| < 0.5$ (all ϕ) were considered. Until $\sqrt{s} \sim 200 \text{ AGeV}$ the soft part is dominant, while at 2000 and 7000 AGeV the hard minijets clearly carry the dominant part of the total E_T . Note that we may slightly overestimate the A scaling of the soft component in (7-8), but at high energies, the correction due to this should be negligible. In the same figure we also show the effect of varying p_0 from 1 GeV up to 3 GeV, and conclude that at LHC energies, where the hard part is dominant, changing p_0 from 2 GeV to 3 GeV results a 20 % decrease in the total E_T .

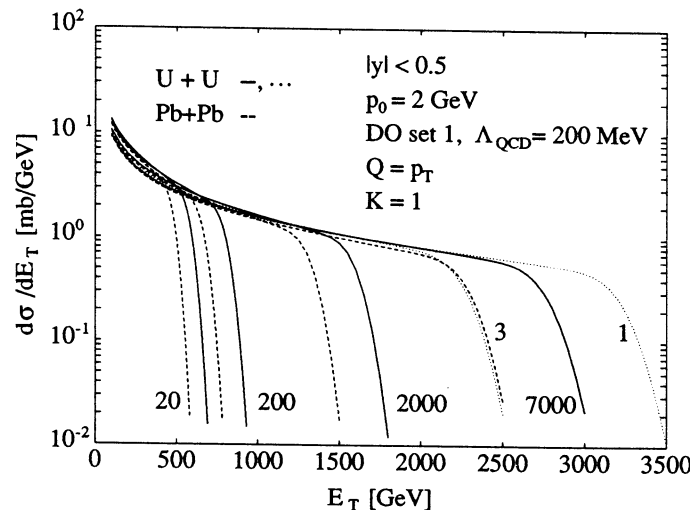


Fig. 4. The distribution of transverse energy within $|y| < 0.5$, all ϕ , in U+U and in Pb+Pb collisions at $\sqrt{s} = 20, 200, 2000$ and 7000 AGeV . The solid curves are for U+U and the dashed ones for Pb+Pb with the smallest QCD scale p_0 set to 2 GeV. The effect of varying p_0 from 1 GeV to 3 GeV in U+U at $\sqrt{s} = 7000 \text{ AGeV}$ is shown by the dotted lines.

The nuclear overlap function T_{AB} is normalized to AB , which means that calculating the average number of jets in an $A + B$ collision as in (3) is equivalent to writing the average nuclear structure functions simply as $f_A(x, p_T^2) = Af(x, p_T^2)$. This in turn means that we have above totally neglected the nuclear effects to the

parton densities. The main contribution to the E_T -distribution at high energies comes from the minijets with $p_T \sim p_0$, i.e. from partons at low x . Typical x values for processes producing $y = 0$ jets in a pp collision at $\sqrt{s} = 200 \text{ GeV}$ are of the order 0.01 and for $\sqrt{s} = 7000 \text{ GeV}$ they are less than 0.001. This is why we shall here briefly study only the effects of nuclear shadowing, i.e. the depletion of the structure functions at small x relative to Af [11]. The EMC data [12] shows a clear depletion for quarks and antiquarks, but unfortunately we do not have the respective data for gluonic structure functions in a nucleus. The very small x region is still uncertain, but one expects the saturation of the depletion when $x \rightarrow 0$. We want to get a first estimate on the magnitude of the shadowing effects, therefore it is enough for us to take the following ansatz for a 'shadowing function':

$$S_A(x) \equiv \frac{f_A(x)}{Af(x)} = \begin{cases} 1, & x \geq x_N; \\ 1 - K_A \ln(x/x_N)/\ln(x_A/x_N), & x_N > x > x_A; \\ 1 - K_A, & x_A \geq x, \end{cases} \quad (9)$$

where we simply assume that nuclear shadowing starts at $x_N \equiv 1/2m_N r_N \approx 0.1$ and is complete at $x_A \equiv 1/2m_N R_A$. The parameter K_A describes the amount of shadowing in the complete shadowing region. This kind of an ansatz was made in ref. [13], although in (9) the analytic form of $S_A(x)$ in the $x_N > x > x_A$ region was motivated by the F_2 data. Here we shall neglect a possible scale dependence of S_A , which was studied in [13], and furthermore, we shall assume that the depletion is of the same form and of the same magnitude for gluons and quarks. The ansatz (9) negligibly violates the momentum sum rule but we shall ignore this, too.

In fig. 5 we have computed the final E_T distribution in U+U collision with the shadowed nuclear structure functions. Curves are shown for $\sqrt{s} = 200$ and 7000 AGeV and for $K_U = 0, 0.3, 0.5$. The corrections due to nuclear shadowing in this simple picture are then at most 20% for $\sqrt{s} = 200 \text{ AGeV}$ and even 50% for 7000 AGeV . This difference can be easily understood since the complete shadowing region for U begins at $x_U \approx 0.014$ and hence at 7000 AGeV there is more contribution from the complete shadowing region. Also the soft contribution is more important at RHIC energies than at LHC energies, which decreases the relative effect caused by shadowing at RHIC energies. Finally, we note that shadowing effects depend also on the impact parameter, i.e. the structure functions are different in central and in peripheral collisions. This, as well as the effects of more realistic shadowing functions [11], will be studied in [14].

In conclusion, we have computed the E_T -distribution $d\sigma/dE_T$ in very high energy Pb-Pb and U-U collisions by including both hard and soft interactions. The production of hard quarks and gluons is computed in first order perturbative QCD

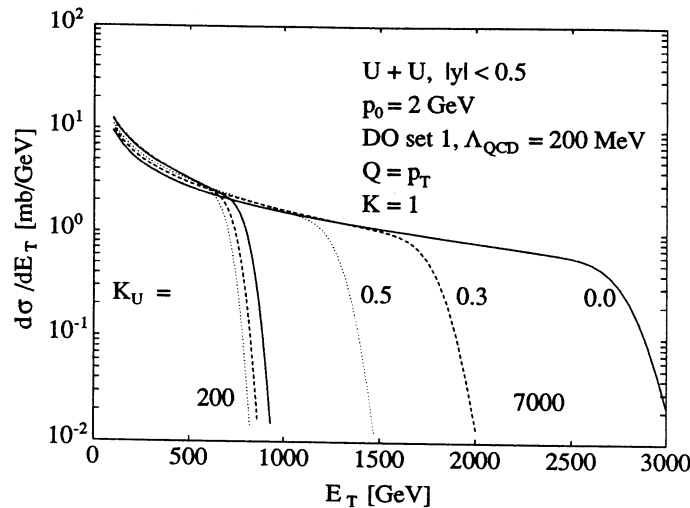


Fig. 5. Effects of nuclear shadowing to the E_T -distributions according to the simple ansatz of eq. (9). The curves represent U+U collisions at 200 and 7000 AGeV. The parameter K_U was varied from 0 to 0.5.

while the soft component is added on the basis of a CERN heavy ion experiment. In these heavy ion collisions the soft component dominates until $\sqrt{s} = 200$ AGeV but at 7000 AGeV the main contribution comes from the hard QCD quanta (see also [1], the effect of the K -factor). The main uncertainties are the higher order terms in jet production cross sections, the choice of the hard QCD scale p_0 and the modifications to the nuclear structure functions, caused by e.g. nuclear shadowing. Higher order corrections tend to increase the E_T whereas nuclear shadowing has an opposite effect. Nuclear shadowing effects in U+U are studied within a simple model and it is found that at large energies the corrections due to the two competing effects can be of the same order.

References

- [1] K.J. Eskola, K. Kajantie and J. Lindfors, Nucl. Phys. B323 (1989) 37. Note the following corrections: The curves in Fig. 3 should be scaled down by a factor 2; two lines after eq. (2.10) replace 'partons per collision' by 'collisions'. We thank Dr. Xin-Nian Wang, LBL, for pointing this out.
- [2] K. Kajantie, P.V. Landshoff and J. Lindfors, Phys Rev. Lett. 59 (1987) 2527; K.J. Eskola, K. Kajantie and J. Lindfors, Phys. Lett. B214 (1989) 613.
- [3] B.L. Combridge and C.J. Maxwell, Nucl. Phys. B239 (1984) 429;
- F. Halzen and P. Hoyer, Phys. Lett. B130 (1983) 326.
- [4] D.W. Duke and J.F. Owens, Phys. Rev. D30 (1984) 49.
- [5] F. Abe et al., Phys. Rev. Letters 62 (1989) 613.
- [6] F. Abe et al., Phys. Rev. Letters 64 (1990) 157.
- [7] S. Ellis, Z. Kunszt and D. Soper, Phys. Rev. Letters 64 (1990) 2122.
- [8] UA1 collaboration, C. Albajar et al., Nucl. Phys. B309 (1988) 405.
- [9] J.-P. Blaizot and A.H. Mueller, Nucl. Phys. B289 (1987) 847; L.V. Gribov, E.M. Levin and M.G. Ryskin, Phys. Reports 100 (1983) 1; E.M. Levin and M.G. Ryskin, Nucl. Phys. B304 (1988) 805; T. Sjöstrand and M. van Zijl, Phys. Rev. D36 (1987) 2019.
- [10] A.D. Jackson and H. Bøggild, Nucl. Phys. A470 (1987) 669; HELIOS collaboration, T. Åkesson et al., Phys. Lett. B214 (1988) 295.
- [11] P. Castorina and A. Donnachie, Z. Phys. C45 (1989) 141 and references therein; L.L. Frankfurt, M.I. Strikman and S. Liuti, Phys. Rev. Letters 65 (1990) 1725.
- [12] M. Arneodo et al., Nucl. Phys. B333 (1990) 1.
- [13] Jianwei Qiu, Nucl. Phys. B291 (1987) 746.
- [14] K.J. Eskola, in preparation
- [15] I. Sarcevic, S. Ellis and P. Carruthers, Phys. Rev. D40 (1989) 1446.

INTERMITTENCY: AN UPDATE WITH LHC IN VIEW

J. Seixas*

CERN - Geneva

ABSTRACT

Present status of intermittency, both theoretical and experimental, is reviewed. Possible scenarios for LHC are also discussed.

I- Introduction

It is a known fact that large local fluctuations appear in multiparticle rapidity distributions (see Fig. 1). Since large fluctuations normally tend to be damped in a statistical system, one can indeed ask what might be the reason for these unusual fluctuations to persist. Two views can be adopted:

- 1) They are just an indication of insufficient statistics *i.e.*, increasing the number of events they would be diluted;
- 2) They have a truly dynamical origin and stem from the characteristics of the underlying dynamics.

No matter which of the hypothesis is correct, it is clear that the first step consists in extracting these fluctuations from the “normal” smooth background in order to study them more carefully. This can be achieved by constructing filters that are only sensitive to spikes like those appearing in Fig. 1. These filters are the so-called factorial moments.

Let us be more precise. Suppose we have a certain region \mathcal{R} of length \mathcal{L} and that N objects are falling in that region. Let us put a grid on \mathcal{R} composed of M bins of length l , and measure the probability for objects to fall in each of those bins. For bin m with k_m objects this is ^{#1}

$$p_m = \frac{k_m}{N} \quad (1)$$

and, taking into account all the bins

$$\begin{aligned} \langle p_m \rangle &= \frac{1}{M} \sum_{m=1}^M \frac{k_m}{N} \\ \langle p_m^n \rangle &= \frac{1}{M} \sum_{m=1}^M \left(\frac{k_m}{N} \right)^n \quad (n = 1, 2, \dots) \end{aligned} \quad (2)$$

If the distribution $\mathcal{P}_{\mathcal{R}}$ of the N objects over \mathcal{R} is uniform, then $k_m \sim \frac{N}{M}$ and the quantity

$$F_n = \frac{\langle p_m^n \rangle}{\langle p_m \rangle^n} = M^{n-1} \frac{\sum_{m=1}^M k_m^n}{\left(\sum_{m=1}^M k_m \right)^n} \quad (3)$$

will behave like

$$F_n \xrightarrow{n \rightarrow \infty} 1 \quad (4)$$

that is, F_n is independent on l ^{#2}. On the other hand, in the extreme case of all the objects falling into one single bin,

$$F_n \sim M^{n-1} = \left(\frac{\mathcal{L}}{l} \right)^{n-1} \quad (5)$$

^{#1} This is of course only true when $N \rightarrow \infty$. When this is not the case, one has to make an assumption on the effect of insufficient statistics.¹

^{#2} Note that if $\mathcal{P}_{\mathcal{R}}$ is smooth then k_m is in any case proportional to l for sufficiently small l , which in turn implies that in that case $F_n \cong \text{constant}$.

* Also Departamento de Física, IST, Lisbon, Portugal

The quantities F_n defined in (3) are thus very sensitive to the existence of spikes in the distribution \mathcal{P}_R and therefore can be taken as the filters we were looking for. As stated previously, (cf. footnote #1 on page 1) insufficient statistics will, however, introduce noise in our determination of the probabilities p_m . Therefore the F_n have to be modified in order to filter *also* this noise. Different assumptions on noise will give different forms for the modified F_n ; assuming, for instance, Poisson noise one gets the expression

$$F_n = \frac{\langle \frac{1}{M} \sum_{m=1}^M k_m (k_m - 1) \dots (k_m - n + 1) \rangle_{events}}{\langle (\frac{1}{M} \sum_{m=1}^M k_m) \rangle_{events}^n}$$

first introduced by Bialas and Peschanski¹. These are the usually called factorial moments. Notice that when $N \rightarrow \infty$ this expression will tend to the form (3).

If fluctuations are purely statistical, then intuitively the smaller the size of a bin the less probable is to have a big concentration of objects inside it: everything will look more and more uniform and thus $F_n \rightarrow cst.$ as the bin size is reduced. If, on the other hand, the probability to encounter spikes is independent of the scale (bin size) we choose to look at the system

$$F_n \xrightarrow{\text{def}} M^{f_n} = \left(\frac{\mathcal{L}}{l}\right)^{f_n} \quad (6)$$

Systems obeying (6) are called intermittent and the exponents f_n are called the intermittency indices. Usually one writes f_n in the form

$$f_n = (n - 1)D_n \quad (7)$$

where D_n is the fractal dimension of order n . If all the D_n can be expressed in terms of $D_2 = D_F$ we say we have a simple fractal, D_F being the fractal dimension. If this is not possible the system is said to be multifractal.

We have thus found a way of characterizing strong local fluctuations. It still remains, of course, to find physical systems which can produce them. These systems are known, however: those obeying non-linear laws. They have been found in dynamical systems, fluid mechanics, statistical mechanics (critical systems), astronomy, etc.. No wonder if most models for intermittency in multiparticle production have been taken from these sources.

II- One-dimensional intermittency

The first model for intermittency – and, to a large extent, still one of the most important – was proposed by Bialas and Peschanski¹. This model, the so-called α -model, was taken from the theory of fully developed turbulence², and is characterized by a self-similar cascade process for multiparticle production: each multiparticle event is described as a series of steps in which the initial rapidity interval Y is repeatedly divided into n parts. To obtain the normalized particle density at step ζ in each of the n bins one multiplies

the normalized density in step $\zeta - 1$ by a particular value of a random variable W , with probability distribution $\mathcal{P}(W)$. Without loss of generality one assumes that

$$\langle W \rangle = \int \mathcal{P}(W) dW = 1 \quad (8)$$

According to the recipe above, the normalized density after ζ steps in bin m will be

$$Z_m = W_1 W_2 W_3 \dots W_\zeta \quad (m = 1, 2, \dots, M) \quad (9)$$

where the number M of bins in step ζ will be n^ζ and each bin will have a length Y/M . If we admit that the steps of the cascade are statistically independent,

$$\langle Z^i \rangle = \langle W^i \rangle^s = \left(\frac{Y}{d}\right)^{\log(W_i)/\log d} \quad (10)$$

which, according to (3) and (8) shows that the α -model is indeed intermittent. Some comments are in order:

- i) The α -model is just a toy model. Its results depend on the distribution $\mathcal{P}(W)$ assumed. Different distributions give different results.
- ii) As stated here, the α -model is a one-dimensional model (we just look at what happens in rapidity) and this, as we shall see below is an incomplete description of the experimental data.

Dynamical systems is also a traditional place to look at intermittency. This lead Dias de Deus³ to propose that intermittency in multiproduction proceeds much in the same way as in interval mappings. If one assumes that we are close to a tangent bifurcation point⁴ and that particles produced are associated with the number of iterations of the interval mapping, then we see that as we approach the “narrow channel” close to the tangent bifurcation point we will have a lot of particles produced (laminar flow). This will be followed by a zone of only few produced particles, since eventually the map will have to leave this “narrow channel” (chaotic or turbulent flow). Of course, it will return to it after a certain number of iterations.

Although the connection with interval mappings is not a straightforward one, the experimental data contains many of the characteristics predicted by the model, as has been shown by the NA22 collaboration⁵. The success of the model can perhaps be attributed to the fact that it corresponds to the situation of a system approaching a critical point, thus showing that intermittency could be related to the existence of a phase transition.

Naturally, before embarking on any considerations concerning the “new physics of intermittency”, it remains to be seen whether data could be explained by conventional means. This implies, incidentally, that spikes are just statistical noise and that known forms of the two-particle distribution (or correlation) function can reproduce the observed trend of the factorial moments. A Gaussian form⁶,

$$\rho_2(y_1, y_2, Y) = C_2(Y) e^{-((y_1 - y_2)/\xi_2)^2} \quad (11)$$

has been used to calculate the factorial moments, yielding the result

$$F_i(\delta y, Y) = \frac{\int_0^{\delta y} dy_1 \dots \int_0^{\delta y} dy_i \rho_i(y_1, y_2, \dots, y_i, Y)}{\left(\int_0^{\delta y} dy \rho_1(y) \right)^i} = K_i(Y) [\Phi(\delta y/\xi_i(Y)) / \delta y]^{i-1} \quad (12)$$

where $\Phi(x)$ is the error function and δy the bin size. The form (12) seems to be in good agreement with the data, and furthermore shows that the generalized dimensions D_i are of the form

$$D_i = 1 - \frac{\partial^i \log \Phi(\delta y/\xi)}{\partial \delta y^i} \quad (13)$$

Eq. (13) has an important consequence, *viz.* that the intermittency exponents become scaling functions of $\eta = \delta y/Y$ as $Y \rightarrow \infty$ and $\delta y \rightarrow 0$. Real intermittency would thus only be achieved at infinite \sqrt{s} , where the gaussian form (11) would have been transformed into a singular function.

Another possibility would be to try to explain the observed behaviour of the factorial moments using only short range correlations. This implies that⁷

$$\rho_2(y_1, y_2, Y) \sim C_2 e^{(-|y_1 - y_2|/\xi)} \quad (14)$$

which again has been shown to be in good agreement with the data, if exceptional events like the ones observed in NA22 (total charged multiplicity 26 with 10 particles in a bin $\delta y = .1$, cf. Fig. 1) were excluded.

A well known source of short range correlations is the Hanbury Brown-Twiss effect⁸. It would seem thus possible that the observed behaviour of the factorial moments could be due to this; the effect would then be bigger for like sign particles than for opposite sign ones⁹. In fact experimentally this is not the case and HBT seems to contribute very little, if anything, to the observed effect.

Implicitly or explicitly most models assume that the n -particle distribution functions can be expressed as weighted products of two-particle distributions functions. This question has been analysed more carefully by Carruthers *et al.*¹⁰, which have shown on quite general grounds that the assumption is quite powerful. In particular, if one assumes that negative binomial is a good description for the multiparticle distribution function, all the weights are fixed. While it is clear that this approach is consistent with data, the reason *why* it should work is still obscure. However, like the α -model it is a good benchmark to study distributions.

Attempts were made also to include both short range correlations and the presence of exceptional events. In its most recent form¹¹ one assumes that the n -particle distribution function is a sum of two components

$$\rho(y_1, y_2, \dots, y_p) = \lambda_c \rho_c(y_1, y_2, \dots, y_p) + (1 - \lambda_c) \rho_s(y_1, y_2, \dots, y_p) \quad (15)$$

where ρ_c comes from collective effects (production of a Feynman-Wilson fluid) and ρ_s stems from conventional short range production. This model has a certain number of definite predictions:

- i) Existence of a minimal rapidity interval δ_0 below which intermittency disappears (namely for large p if $\delta_0 \ll .1$) (see Fig. 2).
- ii) At large scales the system obeys KNO scaling.
- iii) Interaction is long range which according to the authors shows the possibility of a phase transition.

Two comments are in order. First, the assumed breakdown of the intermittent behaviour below δ_0 is an effect competing with the known breakdown due to "empty bin effect" (insufficient number of particles in the smallest bins in order to study higher moments). This means that the first prediction is very difficult to test experimentally. Second, strictly speaking, in one-dimensional systems there are in general no phase transitions at non-zero temperature, except if the range of the interaction is infinite¹², which is certainly not the case here. In fact, as has been shown numerically and analytically¹³, in a one-dimensional Ising system one can very well be misled when studying the intermittent behaviour of one-dimensional systems. In any case, the model of Ref. [11] has the merit of being one of the few trying to give a unified description of data.

All these "fitting models" have, however, the drawback of not showing precisely where intermittent behaviour is coming from in a QCD environment. Phrased otherwise, is intermittency coming from parton cascading, hadronization or both? Definite steps to solve this question have been taken by the Lund group¹⁴, which was able to show in the dipole approximation how intermittency could appear. On the other hand, Chiu and Hwa¹⁵ have tried QCD inspired branching models with different splitting functions in order to study their influence on intermittent behaviour. Last, but not least, van Hove¹⁶ proposed the existence of a new state of hadronic matter (Cold Quark Gluon Plasma) in order to explain both the anomalous production of soft photons and strong intermittency at low p_T as has been observed in UA1¹⁷ and NA22 experiments⁵. The existence of cold QGP is a consequence of overproduction of gluons in the QCD cascade, with the consequence that it could overshoot the zone of normal hadronization via $q\bar{q}$ fusion. Although a very appealing model, it still requires, of course, confirmation either by Monte-Carlo¹⁸ or analytic QCD calculations.

III- Intermittency in higher dimensions

The need to put intermittency in a QCD framework lead several authors to argue that the relevant variables to look at should be the invariant mass and relative angles (which are strongly ordered) in the QCD cascade^{14,19}. Consequently, intermittency should be much bigger in the rapidity/azimuthal angle (y, φ) plane. This has now been confirmed in many experiments^{5,17,20,21} (cf. Fig. 3). Naturally, p_T is also a relevant dynamical variable and therefore should also be included: this lead Ochs²² to test the effect of projections onto two ((y, φ) plane) and one (y) dimensions in the context of a three-dimensional generalization of the α -model. The result is that projection reduces or even kills the effect. The same conclusion was reached independently by Bialas and Seixas²³ using a two-particle distribution function in momentum space.

$$\rho_2(p_1, p_2) = [|p_1 - p_2|^2 + m_{cul}^2]^{-\alpha/2} e^{-(m_{T1} + m_{T2})/\beta} \quad (16)$$

which was shown to be consistent with the recent DELPHI data²¹. Notice that reducing the size of the total interval in p_T when integrating (16) over p_T increases also the intermittent behaviour. This shows that the already referred p_T anomaly could be just a consequence of the existence of a singular distribution function in momentum space.

IV- Heavy Ions

Recently Bialas and Hwa²⁴ have proposed to use intermittency as a signal to detect the formation of quark-gluon plasma in heavy ion collisions. The basic idea behind this proposal stems from the observation that the generalized fractal dimensions behave quite differently when one goes from e^+e^- collisions to heavy ion collisions (see Fig. 4). Clearly in the latter case there seems to be *only one* generalized dimension ($D_2 = D_F$) which is indicative of a simple fractal and, by renormalization group arguments²⁵, a second order phase transition. However, one should notice that this study has been performed using only one-dimensional (rapidity) projections where intermittency, as we have seen in the last section, is drastically reduced. Also, a further reduction comes from superposition of sources as has first been remarked by Buschbeck, Lipa and Peschanski²⁶ and confirmed by several experiments (see Fig. 5). On the other hand, it assumes that the transition from normal hadronic matter to QGP is a second order one, which is certainly dangerous. This shows the importance of studying intermittency for systems exhibiting first-order phase transitions and of further studies of phase transitions in cascading models.²⁷

V- Conclusions and prospects for LHC

At the time of writing this (short) review, the status of intermittency can be summarized in the following points:

- i) e^+e^- data (at LEP energies) is consistent with Lund Parton Shower and Herwig Monte-Carlo results.²¹
- ii) The same cannot be said for $h-h$, $h-A$ and $A-A$ collisions: there is a permanent discrepancy between experimental data and existing Monte-Carlos.²⁸
- iii) There seems to be indications that intermittency studies can be used as QGP formation signal.
- iv) HBT seems to contribute very little to the observed effect.
- v) Intermittency has a three-dimensional origin and projection onto subspaces of lower dimension reduces or even kills the effect.

The first point implies that the origin of intermittency can soon be disclosed in e^+e^- if the present situation is maintained. As for the second point, LHC is certainly going to be an excellent laboratory. The reason is twofold: first, as has been shown by other working groups contributing to this Workshop (cf. report of the Monte-Carlo event generator subgroup), multiplicity is certainly going to be very large, with the consequence that all statistical errors due to insufficient number of particles will be greatly reduced. One can even envisage an event by event analysis – perhaps a way of checking the existence of a first order phase transition. Second, if the major contribution to intermittency in $h-h$

collisions comes from QCD evolution and branching then one can have a very good insight on the underlying physics by comparing intermittency results on the SpS collider and LHC. Also, minijets are expected to give an overwhelming contribution to the QCD cross-section at LHC energies, and thus their contribution in intermittency studies has to be taken into account. Preliminary results in this area have already been obtained²⁹, but their crudeness asks for a more complete analysis in the near future.

The third and fourth points are somewhat subtle. In fact the heavy ion program at LHC will probably bring forth clear signals of QGP formation. Therefore, one will have the possibility of looking at an extended blob of QGP, and thus one should expect a definite contribution of HBT to the observed results. As was shown by Buggild in this Workshop, the situation of HBT is still somewhat unclear. Could intermittency help to estimate its contribution? This question will certainly have to be dealt with in the future.

Last, but not least, the whole consequences of the fifth point still remain to be drawn. In particular, in what concerns factorial moments and correlators a clear relation between them seems to point to a much more profound description of the fractal singularity or of the cascading process³⁰. Also, it shows that in order to have a much bigger signal of intermittency one *should not* have detectors with a $\pm\pi$ angular coverage, and as for maximal rapidity resolution $\delta y=1$ is probably good enough, provided one can neglect track miscounting.

All in all, LHC will certainly contribute in intermittency as in any other area of High Energy interactions to a much better understanding of all the problems still unsolved.

Acknowledgements

I would like to thank A. Bialas, J. Alberty, S. Gupta, A. de Angelis and I. Sarcevic for very interesting discussions and comments. Special thanks are due to R. Peschanski for reading the present manuscript (and for useful criticism!) and W. Kittel for a thorough discussion of the experimental data concerning correlators.

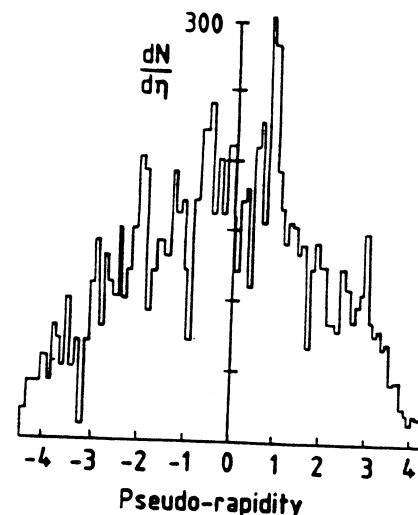
References

- 1- A. Bialas and R. Peschanski, *Nucl. Phys.* **B273** (1986) 703 and *Nucl. Phys.* **B308** (1988) 857.
- 2- G. Paladin and A. Vulpiani, *Phys. Rep.* **156** (1987) 148 and references therein.
- 3- J. Dias de Deus *Phys. Lett.* **B194** (1987) 297.
- 4- P. Maneville and Y. Pomeau, *Phys. Lett.* **A120** (1987) 1; Y. Pomeau and P. Maneville, *Commun. Math. Phys.* **74** (1980) 189.
- 5- I.V. Ajinenko *et al.* (NA22), *Phys. Lett.* **B222** (1989) 306 and **B235** (1990) 373; W. Kittel (NA22), proc. of the Santa Fe Workshop on Intermittency in High Energy Collisions.
- 6- J. Dias de Deus and J. Scixas, *Phys. Lett.* **B229** (1989) 402.
- 7- A. Capella, K. Fialkowski and A. Krzywicki, *Phys. Lett.* **B230** (1989) 271; *Festschrift L. Van Hove*, eds. A. Giovannini and W. Kittel, World Scientific, 1989, pg. 413; K. Fialkowski, proc. Santa Fe Workshop on Intermittency in High Energy Collisions.
- 8- R. Hanbury Brown and R.Q. Twiss, *Phil. Mag.* **45** (1954) 663.

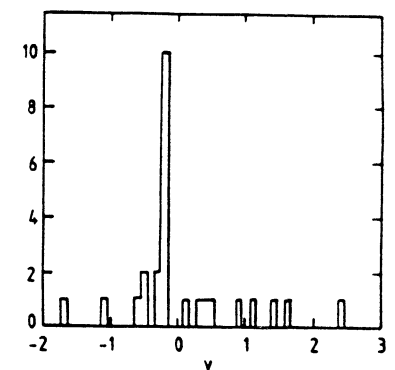
- 9- P. Carruthers, E.M. Friedlander, C.C. Shih and R.M. Weiner, *Phys. Lett.* **B222** (1989) 487; M. Gyulassy, *Festschrift L. Van Hove*, eds. A. Giovannini and W. Kittel, World Scientific 1990, pg. 479.
- 10- P. Carruthers and I. Sarcevic, *Phys. Rev. Lett.* **63** (1989) 1562; P. Carruthers *et al.*, preprint AZPH-TH/90-9 (1990); P. Carruthers *et al.*, preprint AZPH-TH/90-16B (1990); E.A. De Wolff, preprint HSNO379-301X, to be published in *Acta Phys. Pol.*; E.A. De Wolff, private communication.
- 11- N.G. Antoniou *et al.*, *Phys. Lett.* **B245** (1990) 619; N.G. Antoniou *et al.*, preprints CERN-TH.5798/90 and CERN-TH.5815/90.
- 12- F. Dyson, *Commun. Math. Phys.* **12** (1969) 212.
- 13- J. Dias de Deus and J. Seixas, *Phys. Lett.* **B246** (1990) 506; J. Seixas, proc. of the Santa Fe Workshop on Intermittency in High Energy Collisions.
- 14- P. Dahlqvist, G. Gustafson and B. Andersson, *Nucl. Phys.* **B328** (1989) 76; B. Andersson *et al.*, preprint LUTP 90-4; G. Gustafson and A. Nilsson, preprint LUTP 90-7; G. Gustafson and C. Sjögren, *Phys. Lett.* **B248** (1990) 430.
- 15- C.B. Chiu and R. Hwa, *Phys. Lett.* **B326** (1990) 466.
- 16- L. Van Hove, *Annals of Physics* **192** (1989) 66; see also A. Giovannini and L. Van Hove, preprint CERN-TH.5885/90.
- 17- C. Albajar *et al.* (UA1), *Nucl. Phys.* **B345** (1990) 1; B. Bushbeck (UA1), *Festschrift L. Van Hove*, eds. A. Giovannini and W. Kittel, World Scientific 1990 and preprint IHEPHY-PUB 535/90.
- 18- M. Jedrzejczak, *Phys. Lett.* **B228** (1989) 259 (who was in fact the first to test intermittency in the environment of a real QCD Monte-Carlo); W. Kittel, Nijmegen preprint IHEN-335/90; I. Sarcevic, private communication.
- 19- W. Ochs and J. Wosiek, *Phys. Lett.* **B214** (1988) 617 and **B232** (1989) 271.
- 20- R. Holynski *et al.* (KLM), *Phys. Rev. Lett.* **62** (1989) 733 and *Phys. Rev.* **C40** (1989) R2449.
- 21- P. Abreu *et al.* (DELPHI), *Phys. Lett.* **B247** (1990) 137; A. de Angelis, preprint CERN-PPE/90-129 (to appear in *Mod. Phys. Lett. A*).
- 22- W. Ochs, *Phys. Lett.* **B247** (1990) 101 and preprint MPI-PAE/PTh 63/90; see also W. Ochs, proc. of the Santa Fe Workshop on Intermittency in High Energy Collisions.
- 23- A. Bialas and J. Seixas, *Phys. Lett.* **B250** (1989) 161.
- 24- A. Bialas and R. Hwa, preprint CERN-TH.5751/90.
- 25- J. Wosiek, *Acta Physica Polon.* **B19** (1988) 863 and Cracow preprint TPJU 2/89 (1989); H. Satz, *Nucl. Phys.* **B326** (1989) 613.
- 26- B. Bushbeck, P. Lipa and R. Peschanski, *Phys. Lett.* **B215** (1988) 788; P. Lipa and B. Bushbeck, *Phys. Lett.* **B223** (1988) 465.
- 27- P. Brax and R. Peschanski, Saclay preprint SPhT/89-203 and SPhT/90-044.
- 28- X.-N. Wang, preprint LBL-28789.
- 29- For a review of the present status W. Kittel in Ref. [18]; W. Kittel and R. Peschanski, *Nucl. Phys.* **B16** (1990) 445; A. Bialas, proc. "Quark Matter '90" (1990).
- 30- R. Peschanski and J. Seixas, CERN preprint CERN-TH.5894/90.
- 31- T.H. Burnett *et al.* (JACEE), *Phys. Rev. Lett.* **50** (1983) 2062.
- 32- M.I. Adamovitch *et al.* (EMU01), *Phys. Lett.* **B201** (1988) 307

Figure captions

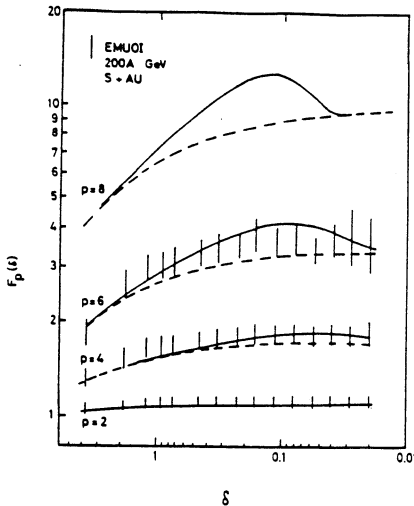
- 1- (a) JACEE event³¹ and (b) NA22 exceptional event.⁵
- 2- Model of Ref. [11] compared with EMU01 data SF Au (200GeV/nucleon).³²
- 3- P_η in O-Ag,Br collisions, (η, φ) distributions.²⁰
- 4- D_i for various types of collisions.²¹
- 5- Comparison of f_2 for pp and nuclear collisions.²⁰



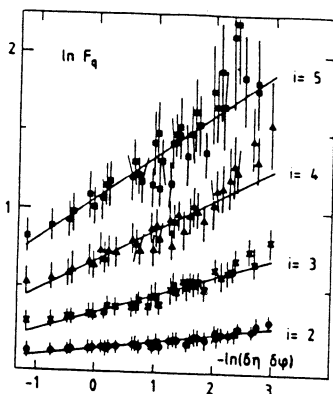
- Fig. 1a -



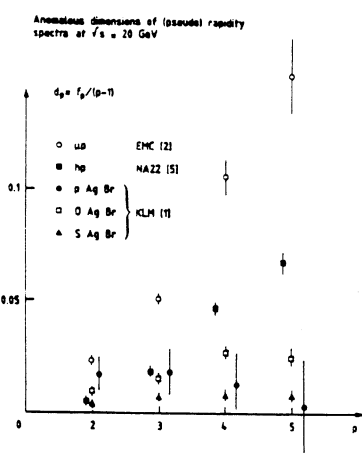
- Fig. 1b -



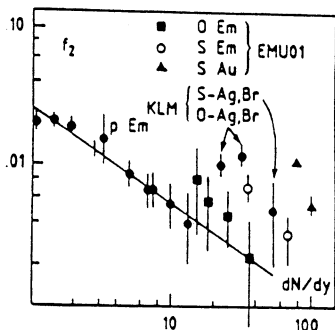
- Fig. 2 -



- Fig. 3 -



- Fig. 4 -



- Fig. 5 -

CASCADING AND INTERMITTENCY

Ina Sarcevic

*University of Arizona
Physics Department
Tucson, AZ 85721*

ABSTRACT: We discuss self-similar cascading as a new mechanism for multiparticle production in high energy hadronic and nuclear collisions. We find that this new pattern leads to the universal power law behavior of the normalized multiplicity moments. All UA5 data show very good agreement with the predicted behavior. We extrapolate our results to higher energies and propose further tests at Tevatron and LHC energies. We also discuss a generalization of the 1-dimensional self-similar cascade model to higher dimensions.

1. INTRODUCTION

The unusually large multiplicity fluctuations in variable rapidity intervals (the so-called "intermittency" phenomenon) have been observed in leptonic, hadronic and nuclear collisions [1]. The dynamical origin of these fluctuations has not been completely understood. The conventional Monte Carlo programs for the simulation of high energy data, which were very successful in describing many global features of the multiparticle production, do not account for the observed effect. The possibility that intermittency could be a signal of some new, exotic phenomenon has created new excitement in the field of multiparticle production. Several theoretical studies have shown that the random cascading process leads to intermittency [2], suggesting that the scale-invariant QCD cascade might be a new mechanism for particle production at very high energies. For example, in e^+e^- collisions, the perturbative QCD cascade seems to be the origin of the observed fluctuations. However, in hadronic and heavy-ion collisions most of the particles are produced via soft interactions and presently there is very little theoretical understanding of these interactions. Thus, by studying intermittency phenomena, we could get useful information about the role of QCD branching in soft collisions. Furthermore, recent theoretical studies show that by measuring intermittency exponents one can distinguish between the cascading process and a second-order phase transition [3]. This particular result could be important at LHC energies, where one hopes to find an unambiguous signal of quark-gluon plasma formation.

The study of intermittency was first proposed by Bialas and Peschanski [3]. They argued that the power-law behavior of the bin-averaged factorial moments, F_i , defined as

$$F_i = \frac{\langle \frac{1}{M} \sum n_m (n_m - 1) \dots (n_m - i + 1) \rangle}{\langle \frac{1}{M} \sum n_m \rangle^i}, \quad (1)$$

where n_m is the number of particles in a rapidity bin m and M is a total number of bins in the interval ΔY ($\delta y = \Delta Y/M$), in the small δy region (i.e. $F_i(\delta y) \sim (\delta y)^{-\nu_i}$), is a signal of dynamical “intermittent” behavior and is analogous to phenomena accompanying the onset of turbulence in hydrodynamics. Subsequently, several experimental groups reported the observation of intermittency in leptonic, hadronic and nuclear collisions [1].

2. ONE-DIMENSIONAL SELF-SIMILAR CASCADES

In our previous work we have shown that the increase of these one-dimensional factorial moments with decreasing rapidity bin size in the small δy region is due to conventional short-range correlations [4]. On the other hand, in the large δy region, outside the usual resonance formation region ($\delta y \geq 1 - 2$), it is possible to discern a signal of intermittency or self-similar structure [5]. Clearly, at very high energies the phase space available for particle production becomes large enough to develop a self-similar cascade with many branches. Thus, this new mechanism for multiparticle production has some threshold energy. At energy $\sqrt{s} = 20 \text{ GeV}$ because the maximum rapidity available ($Y \equiv \ln s$) is only slightly above the resonance formation threshold the cascade has only a few branches. In contrast, at CERN Collider energies, $Y \geq 10$ and a self-similar cascade with many branches can develop. We find that the threshold energy for this self-similar cascade mechanism is of the order of a few hundred GeV. Since we expect that at these energies the application of perturbative QCD is well-justified, this self-similar cascade should be related to low- p_T jet production. Support for this conjecture is found in the recent observation of “minijets” [6], which indicates that the fraction of “semi-hard” events responsible for low- p_T jet production increases with energy very quickly. For example, at $\sqrt{s} \sim 20 - 50 \text{ GeV}$ this fraction is only a few percent, while at CERN Collider energies it is about 15 – 17%. Keeping this in mind, we construct a simple self-similar cascade model [5], in which a collision takes place in several steps. First, a “heavy mass particle” is created (this could be a jet, for example). Then, this particle decays into two lighter particles of mass m_1 , which is related to the initial particle of mass m_0 by energy conservation

($m_0^2 = 4(m_1^2 + p_1^2)$). This decay cascade continues until the initial mass is reduced to the mass of the resonance ($m_{\pi\pi} \sim 0.5 \text{ GeV}$). This happens after r steps and, therefore, $m_{\pi\pi} \equiv m_r = (1/\alpha)m_{r-1} = (1/\alpha)^r m_0$, where α is the fraction of the mass which goes into each of the produced particles ($\alpha \leq 2$). For $\alpha = 2$ there would be no kinetic energy in the products of the decay. A schematic drawing of the self-similar cascade is shown on Fig. 1. We note that after r steps there will be $n(r)$ particles produced, each one with mass m_r . These particles will not entirely fill the mass interval between zero and m_0 . Namely,

$$n(r)m_r = 2^r \left(\frac{1}{\alpha}\right)^r m_0 \leq m_0. \quad (2)$$

This will be true even in the $r \rightarrow \infty$ limit. The larger the value of r , the less space is covered. This situation is well known in the theory of fractal structure [7]. Consequently, we can define a generalized fractal dimension [8]

$$d_F = \lim_{r \rightarrow \infty} \left| \frac{\ln n(r)}{\ln(m_0/m_r)} \right| = \frac{\ln 2}{\ln \alpha}. \quad (3)$$

The number of particles produced after r steps is then given by

$$n(r) = (m_0/m_r)^{d_F} \quad (4)$$

Clearly, for $\alpha = 2$ the whole space is covered and $d_F = 1$ (or $n(r) = m_0/m_r$). We note that the $r \rightarrow \infty$ limit can be taken either by fixing m_0 and letting $m_r \rightarrow 0$ or by fixing m_r and letting $m_0 \rightarrow \infty$. The first option corresponds to an infinite decay cascade of the fixed mass m_0 , while the second option corresponds to fixing the final-state mass while increasing the initial mass m_0 . The latter will turn out to be the relevant case for multiparticle production at very high energies.

Now we apply these ideas to multiparticle production in high-energy collisions. Since the multiplicity of a jet is proportional to the rapidity, we identify mass with rapidity, so that $m_0 = Y = \ln s$ and $m_r = \delta y$. Eq. (4) can then be written as

$$n(r) = (Y/\delta y)^{d_F}. \quad (5)$$

The normalized multiplicity moments are defined by

$$C_l(\delta y) = \left\langle \frac{1}{M} \sum_{m=1}^M n_m^l / \left(\frac{1}{M} \sum_{m=1}^M n_m \right)^l \right\rangle, \quad (6)$$

where n_m is the number of particles in the m th bin and $\langle \dots \rangle$ denotes the average over the events. Since $\sum n_m = N$ and $M = Y/\delta y$, we can rewrite Eq. (6) in the

following form:

$$C_l(\delta y) = (Y/\delta y)^{l-1} \left\langle \sum_{m=1}^M P_m^l \right\rangle. \quad (7)$$

Here P_m is the probability of finding a particle in bin m ($P_m \equiv n_m/N$). In a high-energy collision, the probability P_m fluctuates greatly from bin to bin and it is difficult to extract meaningful information concerning this quantity. However, we can map this one-dimensional self-similar cascade onto a d_F -dimensional ($d_F \leq 1$) fractal space where the probability distribution is “smooth” and is proportional to the inverse of the number of produced particles in a given rapidity bin ($P_m = 1/n_m$). Thus, using Eq. (5), the multiplicity moments given by Eq. (7) can be cast in the following form:

$$C_l = (Y/\delta y)^{(l-1)(1-d_F)}. \quad (8)$$

This implies that the plot of $\ln C_l$ versus $\ln(Y/\delta y)$ is a straight line with a slope given by

$$\lambda_l \equiv (l-1)(1-d_F). \quad (9)$$

Strictly speaking, the derived power-law should hold in the $Y/\delta y \rightarrow \infty$ limit. In the discussion of the cascade of Fig. 1, we have seen that this limit could be taken either by fixing Y and letting $\delta y \rightarrow 0$, or by fixing δy and letting $Y \rightarrow \infty$. Since the self-similar cascade exists only in the region outside the resonance formation region, we consider the latter limit. This implies that the straight line behavior of $\ln C_l$ versus $\ln(Y/\delta y)$ will flatten out at the point where the short-range correlations take over. By increasing the energy, the cascade will be “longer” and the flattening will move to higher values of $\ln(Y/\delta y)$. In the limit of infinite energy ($Y \rightarrow \infty$), there should be no deviation from the straight line. This is schematically presented in Fig. 2.

Now, we apply our theory of multiparticle production to the experimental data. We consider the UA5 measurements of the normalized multiplicity moments $f_l(\delta y)$, defined as

$$f_l(\delta y) \equiv F_l(\delta y)/F_l(Y), \quad (10)$$

where

$$F_l = \frac{\langle n_0(n_0 - 1) \dots (n_0 - l + 1) \rangle}{\langle n_0 \rangle^l}, \quad (11)$$

and n_0 is the number of particles in the central rapidity bin. We find that the UA5 data at energies $\sqrt{s} = 200, 546$ and 900 GeV follow the predicted universal

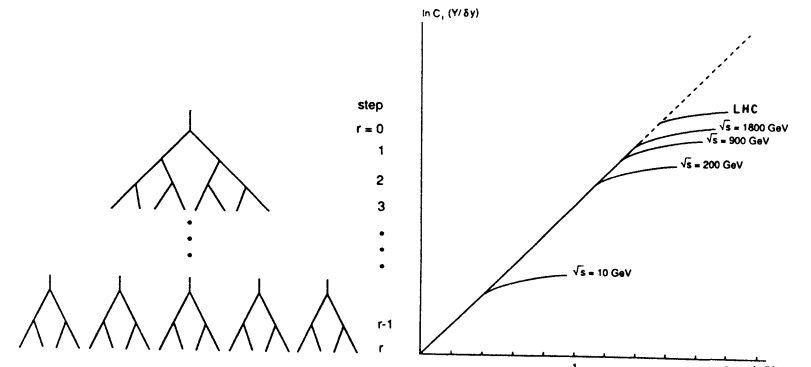


Figure 1: The self-similar cascade.

Figure 2: Schematic illustration of the multiplicity moments $C_l(Y/\delta y)$ for fixed i and $\delta y_0 = 1.8$ for the energies $\sqrt{s} = 22 \text{ GeV}$, 200 GeV , 900 GeV and 1800 GeV . The dashed line represents moments C_l in the limit $\sqrt{s} \rightarrow \infty$.

power-law behavior (Figs. 3-6), with the slopes having the following values [5]:

$$\lambda_2 = 0.140 \pm 0.008, \quad (12a)$$

$$\lambda_3 = 0.172 \pm 0.009, \quad (12b)$$

$$\lambda_4 = 0.203 \pm 0.013, \quad (12c)$$

$$\lambda_5 = 0.228 \pm 0.016. \quad (12d)$$

In a simple fractal picture, the ratio of the slopes should be constant ($\lambda_l/\lambda_{l+1} = (l-1)/l$). From Eqs. (12) we note that the data require the fractal dimension d_F has an additional l dependence of the This is the well-known case of “multifractals” [8]. Furthermore, from Figs. 3-6 it is apparent that the data show the expected deviation from straight-line behavior at the point where short-range correlations come in ($\delta y_0 \sim 1.8$). This point corresponds to $\ln(Y/\delta y) = 1.2$ at $\sqrt{s} = 200 \text{ GeV}$, $\ln(Y/\delta y) = 1.3$ at $\sqrt{s} = 546 \text{ GeV}$ and $\ln(Y/\delta y) = 1.4$ at $\sqrt{s} = 900 \text{ GeV}$.

From these considerations the multiplicity moments $C_l(\delta y)$ at Tevatron and LHC energies are predicted to follow the universal power-law behavior found in the UA5 data. The deviation from straight-line behavior will start at a slightly higher value of $\ln(Y/\delta y)$.

3. MULTIDIMENSIONAL CASCADES

The flattening of the one-dimensional factorial moments in the small-rapidity region (see Figs. 3-6) is a characteristic of all the experimental data, including the data from leptonic and nuclear collisions. Recently, it has been pointed out that this could be a consequence of dimensional reduction [10]. Specifically, there is a possibility that intermittency or self-similar structure is present in three dimensions (for the full range of scales), but that the lower dimensional projections have reduced fluctuations (or show no intermittency). We illustrate with three examples: the α model, a scale-invariant branching model, and a QCD parton cascade model with cluster hadronization [10].

In the α -model, at each step of a cascade, the density is proportional to the initial full rapidity density and the independent random variable ω . In the simplest case, at each step ω can take only two values, ω_1 and ω_2 with probabilities p_1 and p_2 . The results for the two- and one-dimensional factorial moments in the α -model are presented on Figs. 7a and 7b, respectively. We note that even though there is strong intermittency in two dimensions, the one-dimensional projection shows slow saturation in the small-rapidity region. In Figs. 7, the comparison with TASSO data is only for illustration.

The second example is a self-similar cascade with virtual mass degradation. In this model, the initial mass splits into two states with masses m_1 and m_2 with distribution function $dn/d\mu_1 d\mu_2 = F(\mu_1, \mu_2)$, where μ_j is the scaled mass ($\mu_j = m_j/m$). This decay pattern continues until the final state mass is $2m_\pi$. The factorial moments for the scale-invariant model are presented in Fig. 8. The qualitative behavior depicted in Fig. 8 is very similar to that found in the α model: three-dimensional moments show power law behavior, while two- and one-dimensional projections flatten in the small parameter region.

Finally, we consider the QCD parton cascade with cluster hadronization model as implemented into the HERWIG Monte Carlo program. From Fig. 9 we note that when hadronization is turned off, the parton cascade in three dimensions gives almost power-law behavior. The scaling violation is very small and it is due to the running α_s and the quark masses. Once the hadronization is included there is an additional source of scale violation that comes at the hadronization scale cutoff. Again, projection to lower dimension shows faster saturation at small bin sizes.

As Figure 10 show, the experimental data on two-dimensional moments in

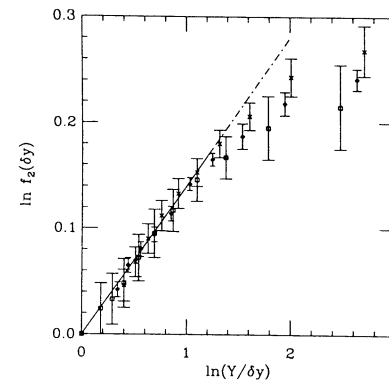


Figure 3: Experimental data on multiplicity moments $\ln f_2(\delta y)$ ($f_2(\delta y) \equiv F_2(\delta y)/F_2(Y)$) as a function of $\ln(Y/\delta y)$ for energies $\sqrt{s} = 200\text{GeV}$ (squares), $\sqrt{s} = 546\text{GeV}$ (diamonds) and $\sqrt{s} = 900\text{GeV}$ (crosses) and the straight line fit to the data at large δy .

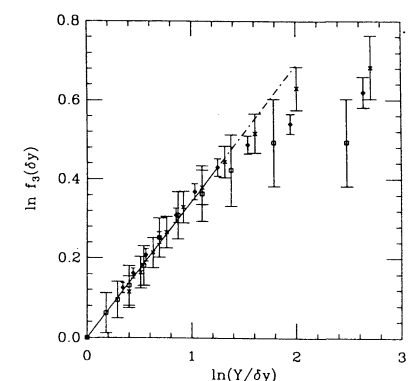


Figure 4: Same as Figure 3, but for $\ln f_3(\delta y)$ ($f_3(\delta y) \equiv F_3(\delta y)/F_3(Y)$).

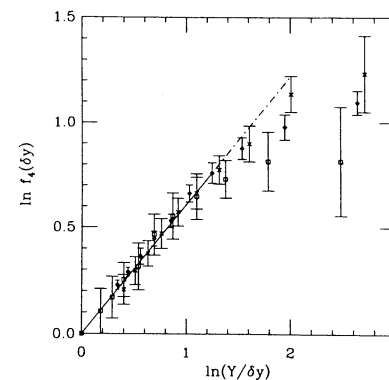


Figure 5: Same as Figure 3, but for $\ln f_4(\delta y)$ ($f_4(\delta y) \equiv F_4(\delta y)/F_4(Y)$).

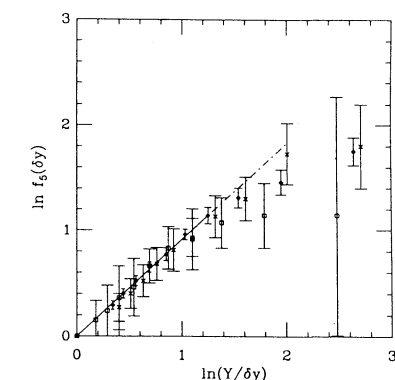


Figure 6: Same as Figure 3, but for $\ln f_5(\delta y)$ ($f_5(\delta y) \equiv F_5(\delta y)/F_5(Y)$).

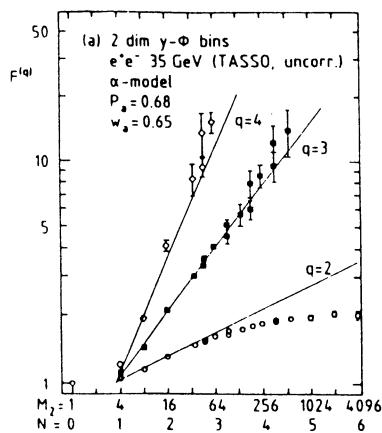


Figure 7a: Two-dimensional factorial moments in the α model compared with the TASSO data, from Ref. 10.

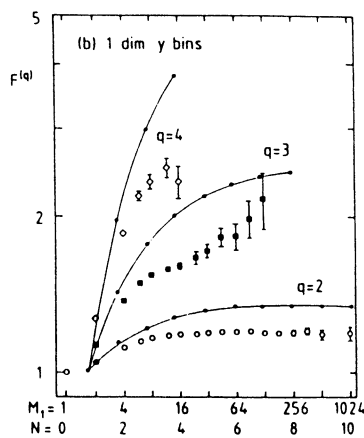


Figure 7b: One-dimensional projection of the factorial moments in the α model compared with the TASSO data, from Ref. 10.

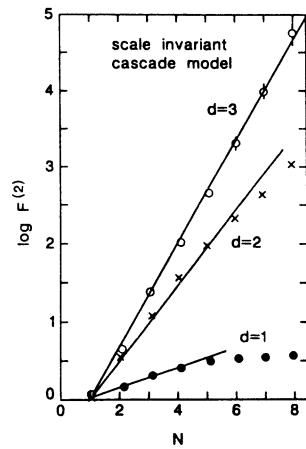


Figure 8: The three-, two- and one-dimensional factorial moment $F^{(2)}$ in the scale-invariant model, from Ref. 10.

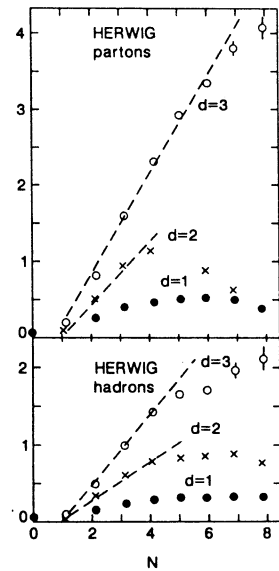


Figure 9: Same as Figure 8, but for the HERWIG Monte Carlo model: a) parton cascade only, b) hadronization included; from Ref. 10.

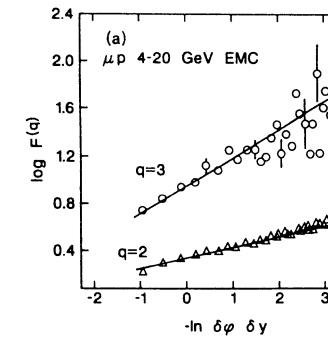


Figure 10a: The EMC data on two-dimensional factorial moments in μp collisions, from Ref. 10. The solid lines represent straight-line fit to the data.

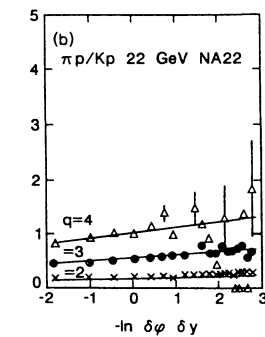


Figure 10b: The NA22 data on two-dimensional moments in $\pi p/Kp$ collisions, from Ref. 10. The solid lines represent straight-line fit to the data.

leptonic and hadronic collisions are in qualitative agreement with the predicted behavior. Recent DELPHI results on factorial moments in e^+e^- collisions at LEP energies are in good agreement with the existing shower Monte Carlo predictions [11]. This is consistent with our picture that the parton cascade is responsible for the intermittent behavior of the moments. At these energies, the cascade is long and the hadronization has very little effect on the shape of the multiplicity distribution. In hadronic collisions, the situation is different. Higher-dimensional moments show stronger intermittency (there is already power-law behavior in two dimensions), but no existing Monte Carlo can successfully describe it. Here, the remaining theoretical challenge is to construct a QCD-based cascade for hadronic collisions. Such a microscopic model should in principle be able to predict the values of the slopes of the multidimensional moments.

Another interesting theoretical study has shown that specific values of the intermittency exponents might signal the formation of a quark-gluon plasma (QGP) [3]. The claim is that the dependence of the slopes λ_q on the index q is different for the cascading process and the second-order phase transition. For example, if $\lambda_q/\lambda_2 = (q^\mu - q)/(2^\mu - 2)$, where μ is an arbitrary parameter, then the system is

cascading. However, if $\lambda_q/\lambda_2 = (q - 1)$, the system is at the critical temperature of a second-order phase transition. Even though it is premature to use the existing heavy-ion data to conclude much about a QGP, it is important to perform further theoretical and experimental studies of this sort.

It will also be important to study intermittency at the LHC, both in hadronic and nuclear collisions. Measurements of the multiplicity moments in different rapidity bins in hadronic and nuclear collisions at LHC energies could reveal one of the most interesting properties of hadronic matter, the formation of quark-gluon plasma. Furthermore, we might be able to learn about soft physics and find a microscopic description of the nonperturbative self-similar cascades. Understanding the scaling feature of this type of cascade might shed some light on our rather limited knowledge of the nonperturbative regime of the strong interaction.

ACKNOWLEDGEMENTS

Part of the work presented here was done in collaboration with H. Satz whom I also thank for many useful discussions. This work was supported in part by the United States Department of Energy, Division of High Energy and Nuclear Physics and a NATO Research Collaboration Grant.

REFERENCES

- 1) For a review, see W. Kittel and R. Peschanski, talk presented at the *EPS Conference*, Madrid, Sep. 6-13, 1989, Saclay preprint Saclay PhT/89-143 and J. Seixas, these proceedings.
- 2) A. Bialas and R. Peschanski, *Nucl. Phys.* **B273** (1986) 703; *ibid.* **B308** (1988) 857.
- 3) R. Brax and R. Peschanski, Saclay preprints Saclay SPhT-90-44 and SphT-90-102.
- 4) P. Carruthers and I. Sarcevic, *Phys. Rev. Lett.* **63** (1989) 1562.
- 5) I. Sarcevic and H. Satz, *Phys. Lett.* **233B** (1989) 251.
- 6) UA1 Collaboration, C. Albajar et al., *Nucl. Phys.* **B309** (1988) 405.
- 7) B. Mandelbrot, *The fractal geometry of nature* (Freeman, San Francisco, 1982).
- 8) F. Hausdorff, *Math. Ann.* **79** (1919) 157.
- 9) W. Ochs and J. Wosiek, *Phys. Lett.* **232B** (1989) 271, G. Gustafson, in Proceeding of XXIVth Rencontres de Moriond, pg. 161 (1989).
- 10) W. Ochs, *Phys. Lett.* **B247** (1990) 101 and Max-Planck Institute preprints MPI-PAE/PTh 35/90 and MPI-PAE/PTh 63/90.
- 11) DELPHI Collaboration, P. Abreu et al., *Phys. Lett.* **B247** (1990) 137.

Coherent Processes in Heavy Ion Collisions at the LHC

K. J. Abraham,¹⁾ M. Drees,²⁾ R. Laterveer,¹⁾ E. Papageorgiu,³⁾ A. Schäfer,⁴⁾ G. Soff,⁵⁾ J. Vermaseren,¹⁾ D. Zeppenfeld⁶⁾

¹⁾NIKHEF-H, Postbus 41882, 1009 DB Amsterdam, the Netherlands

²⁾DESY, Notkestr. 85, 2000 Hamburg 52, Germany

³⁾RAL, Chilton, Didcot, OX11 0QX, England

⁴⁾MPI für Kernphysik, Postfach 103980, 6900 Heidelberg, Germany

⁵⁾GSI, Postfach 110 552, 6100 Darmstadt, Germany

⁶⁾Department of Physics, University of Wisconsin, Madison, WI 53706, USA

Abstract

The strong electromagnetic fields in relativistic heavy ion collisions lead to sizable photon-photon scattering cross sections. We study the production of the intermediate mass Higgs boson, W pairs and new charged particles. For a Higgs search the $\gamma\gamma \rightarrow b\bar{b}$ background is important. Higgs production via diffractive collisions is also studied.

1. Introduction

Relativistic heavy ion collisions in the LHC tunnel are being contemplated as a means to study strong interaction thermodynamics [1]. At the same time the very strong electromagnetic fields around the ions provide for high photon fluxes which can be used to study two photon physics. More precisely the coherent coupling of the photons to nuclei of atomic number Z provides for an enhancement factor of Z^4 as compared to equivalent cross sections in proton-proton scattering. It has been suggested to use the resulting large two-photon cross sections to search for new particles, like the Higgs boson or charged superpartners of the known quarks and leptons, or to study W^+W^- pair production [2-13].

In this report we address the question to what extent the discovery potential of the LHC in the high energy domain can be enhanced by two-photon physics in heavy ion scattering. More precisely we have investigated the reach of lead-lead collisions with a center of mass energy of 1312 TeV (3.2 TeV/nucleon for ^{206}Pb), assuming a heavy ion luminosity of $10^{28} \text{ cm}^{-2}\text{s}^{-1}$.

The main emphasis has been on the production of an intermediate mass standard model Higgs boson. If $m_H \leq 80$ GeV, the Higgs will presumably be discovered at LEP. For Higgs masses above ~ 130 GeV Higgs production via gluon fusion at the LHC and/or the SSC will allow the detection of the decay mode $H \rightarrow ZZ$ (with one of the Z 's possibly being virtual) [14]. This leaves the interesting intermediate mass range between 80 GeV and 130 GeV where a search at a heavy ion collider would have to be performed in the dominant $H \rightarrow b\bar{b}$ decay mode. Production cross sections in heavy ion collisions, event characteristics, and irreducible physics backgrounds (from $\gamma\gamma \rightarrow b\bar{b}$) to this search will be discussed in Section 2. In Section 3 we discuss production cross sections for heavy charged particles like the W boson or charged superpartners of the quarks, leptons and gauge bosons. Finally in Section 4 diffractive production processes are addressed.

2. Higgs Production

The basic Higgs production and decay process we are interested in here is

$$Pb Pb \rightarrow Pb Pb H, H \rightarrow b\bar{b}, \quad (1)$$

which proceeds via two-photon collisions and is depicted in Fig. 1. Because of the small production rate one must search for the hadronic decay mode of the Higgs in a background from generic heavy ion collisions, which is many orders of magnitude larger. Clearly one must fully exploit the cleanliness of generic two-photon events, *i.e.* only such events will be useful where the parent nuclei do not break up. At the same time this is a necessary condition for the coherent coupling of the photons to the parent nuclei.

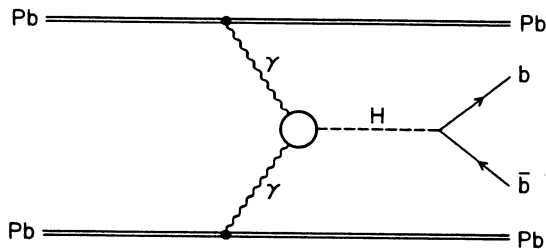


Figure 1: Feynman graph for coherent Higgs production in $Pb Pb$ collisions.

When calculating the Higgs production cross section the coherence requirement can be implemented by using form factors for the coupling of the photons as determined from elastic electron nucleus scattering [5]. This form factor is precisely the Fourier transform of the charge distribution of the parent nucleus. For lead nuclei a Gaussian form factor

$$F_{Pb}(Q^2) = e^{-Q^2/2Q_0^2} \quad (2)$$

with $Q_0 = 60$ MeV gives a good approximation [12]. The form factor limits the virtuality $q^2 = -Q^2$ of the exchanged photons to very small values compared to the Higgs mass and hence reasonable results are obtained by using a Weizsäcker Williams approximation (WWA). In the WWA the production cross section is given by folding the subprocess cross section $\hat{\sigma} = \hat{\sigma}(\gamma\gamma \rightarrow X)$ with the photon flux $f_{\gamma/Pb}(z)$,

$$\sigma(Pb Pb \rightarrow Pb Pb X) = Z^4 \int dz_1 dz_2 f_{\gamma/Pb}(z_1) f_{\gamma/Pb}(z_2) \hat{\sigma}(z_1 z_2 s) \quad (3)$$

where the photon flux is given in terms of the elastic form factor by

$$f_{\gamma/Pb}(z) = \frac{\alpha}{\pi} \int_{zM^2}^{\infty} dQ^2 \frac{|F_{Pb}(Q^2)|^2}{Q^2} \left(\frac{1}{z} - \frac{M^2}{Q^2} z \right). \quad (4)$$

Here M is the mass of the lead nucleus.

The cross section of Eq. 3 does not correspond to the rate of clean two photon events, as was first noted by Cahn [7]. When producing massive objects X of order

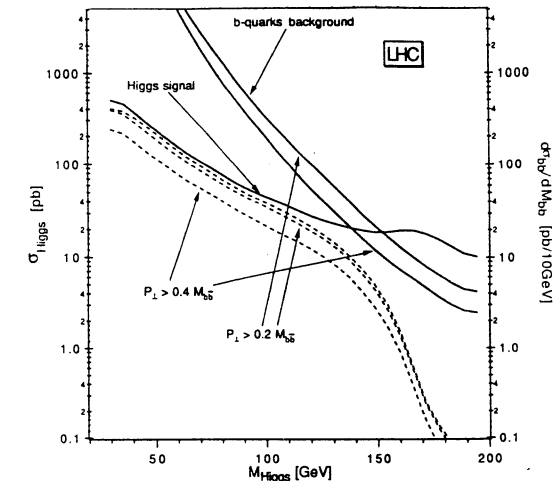


Figure 2: The $b\bar{b}$ rates for Higgs signal and background arising from two photon fusion in $Pb Pb$ scattering at the LHC. An impact parameter cut has been imposed already. Note that the $b\bar{b}$ background is in units of $pb/10\text{GeV}$. From Ref. [12].

100 GeV a substantial fraction of the collisions occurs at small lead-lead impact parameters where the two nuclei overlap and are subject to strong interactions in addition to the two-photon process. The strong interaction effects will almost always lead to a breakup of the parent nuclei thus spoiling the cleanliness of the events.

In a black disk approach to the nuclear interactions the requirement of no residual strong breakup is equivalent to a cut on the relative impact parameters $\vec{b}_1 - \vec{b}_2$ of the two nuclei

$$|\vec{b}_1 - \vec{b}_2| > 2R \quad (5)$$

with $R \approx 7$ fm the nuclear radius. This cut can either be imposed in the WWA by performing a Fourier transformation of the transverse heavy ion momenta, which implicitly enter in the Q^2 integrals of the photon flux functions $f_{\gamma/Pb}(z)$ in Eq. (3) [8, 10, 11], or it can be imposed in a calculation of the complete $Pb Pb \rightarrow Pb Pb H$ process [9, 13]. An alternative approach was followed in Ref.[12], where the cut was directly imposed on the relative transverse momenta $q_{1\perp}$ and $q_{2\perp}$ of the final state lead nuclei:

$$\frac{1}{4}(q_1 - q_2)_\perp^2 < \frac{1}{4R^2}. \quad (6)$$

Depending on the procedure to implement the absence of nuclear scattering on top of Higgs production, one finds reduction factors of 2–5 compared to the Higgs production cross section given by Eq. (3). Using Eq. (6) one finds a reduction factor ≈ 4 and the resulting cross sections at the LHC are plotted in Fig. 2 for both the Higgs signal and the $b\bar{b}$ background.

For the Higgs signal we show both the total Higgs production cross section (solid line) and 3 curves for the signal $b\bar{b}$ cross sections (dashed lines). The strong

suppression of the latter for Higgs masses above 120 GeV arises because the Higgs decay into one real and one virtual W starts to become important. Already at $m_H = 140$ GeV this new channel dominates over the $b\bar{b}$ mode.

For backgrounds we only show the irreducible physics background arising from $\gamma\gamma \rightarrow b\bar{b}$, more precisely we show the $b\bar{b}$ invariant mass distribution in units of pb/10 GeV. Assuming a $b\bar{b}$ mass resolution of 10 GeV the signal total cross section and the background mass distribution can thus be compared directly. As was already noted in [5], the signal to background ratio can be improved substantially by imposing a cut on the transverse momentum, $p_T > \eta m_{b\bar{b}}$, of the produced b jets. While the signal is produced in a pure s -wave, many partial waves contribute to the background which results in a much softer transverse momentum spectrum for a given $b\bar{b}$ invariant mass. Because the Higgs is produced with essentially zero transverse momentum this cut is equivalent to a cut on the rapidity difference of the two b quark jets [5].

In Fig. 2 both signal and background are plotted for p_T cuts with $\eta = 0.2$ and 0.4 respectively. Even for the last more stringent p_T cut the signal to background ratio is never better than 1 : 3, assuming an experimental mass resolution of 10 GeV. Notice that this statement is unaffected by the uncertainties of our calculation: changing the usable two photon luminosities will affect signal and background rates in the same manner.

In order to detect the Higgs as a peak in the $b\bar{b}$ invariant mass distribution one would probably like to see at least a 4σ signal. Denoting by N_S and N_B the number of signal and background events and requiring $N_S/\sqrt{N_S + N_B} \geq 4$, we find that in the mass range $80 \text{ GeV} < m_H < 140 \text{ GeV}$ an integrated luminosity of between 5 and 15 pb^{-1} is required to obtain a 4σ signal. Note that these estimates are highly optimistic since no efficiency factors have been included for e.g.

- i) b quark identification. The background due to $c\bar{c}$ pairs is 16 times larger than the b quark dijet background.
- ii) Vetoing against the $b\bar{b}$ background which arises from gluon gluon fusion events [5, 15].

On the other hand it has been argued that a luminosity in Pb Pb collisions at the LHC beyond $10^{28} \text{ cm}^{-2} \text{s}^{-1}$ is very difficult if not impossible to achieve [16]. Already at this luminosity the very large electromagnetic dissociation and electron capture cross sections of order 100 barns or more lead to beam life times of only a few hours. Assuming 10^7 sec of running time per year, a luminosity in excess of $10^{30} \text{ cm}^{-2} \text{s}^{-1}$ would be required at the LHC in order to establish a Higgs signal in the $b\bar{b}$ decay mode, according to our previous optimistic criteria.

It appears that a Higgs search in the $H \rightarrow b\bar{b}$ decay mode is not a feasible experiment in heavy ion collisions in the LHC tunnel.

3. Charged Particle Production within and beyond the Standard Model

Apart from searches for the Standard Model minimal Higgs, efforts at present and future colliders focus on the production and detection mechanisms of the new particles that Supersymmetry and other theories beyond the Standard Model predict.

The production of electrically charged exotic particles in two-photon collisions is interesting because the couplings are fixed to lowest order and thus the production

rates of exotic particles with a certain mass are given in a model-independent way. Therefore the first question to be addressed is whether the mass range that heavy-ion collisions at the LHC can cover will exceed that of LEP2. A rough estimate for the maximum two-photon invariant mass yields: $W_{\max} \sim \gamma/R \simeq 200 \text{ GeV}$ assuming a Lorentz contraction factor $\gamma \simeq 3500$ and a nuclear radius $R \simeq 7 \text{ fm}$, but at a luminosity of $\mathcal{L} = 10^{28} \text{ cm}^{-2} \text{s}^{-1}$ the event rate might not be significant. While the cross sections grow mainly with some power of the logarithm of the heavy-ion energy, which is typical for the two-photon subprocesses, light particles are boosted in the direction of the beam and escape detection as the beam energy is increased. Hence detection is easiest at the upper end of the mass spectrum where, however, the usable two-photon flux is most uncertain when one requires exclusion of events with residual strong interactions.

The other interesting point will be to look for the pair-production of W^+W^- via photon-photon collisions. A test of the four-boson vertex via this process would supplement the LEP2-tests of the nonabelian gauge structure of the electroweak theory.

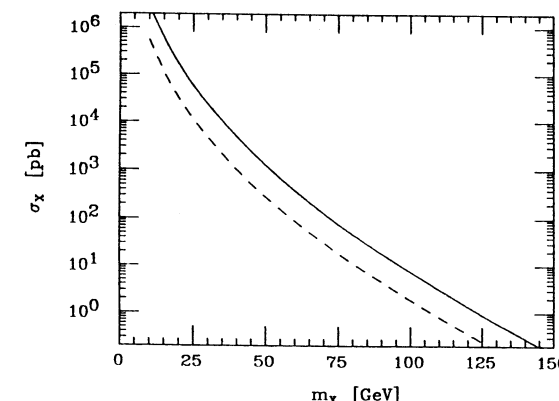


Figure 3: The cross section for the production of a pair of fermions (solid line) and a pair of scalars (dashed line) in lead on lead collisions at the LHC as a function of the particle's mass. Adapted from Ref. [11].

The cross section for the production of a pair of fermions, which can be a pair of quarks, leptons or a pair of winos (the supersymmetric partner of the W -boson), out of two real photons is given by [17]:

$$\sigma(\gamma\gamma \rightarrow f\bar{f}) = \frac{4\pi\alpha^2 q_f^4}{W^2} \left[2 \left(1 + y - \frac{1}{2}y^2 \right) \ln \left(\frac{1}{\sqrt{y}} + \sqrt{\frac{1}{y} - 1} \right) - (1+y)\sqrt{1-y} \right], \quad (7)$$

where q_f and M_X are the charge and mass of the fermion and $y = 4M_X^2/W^2$. The integration over the two-photon invariant mass W is performed using an equivalent-photon luminosity which excludes nuclear absorption effects in a sharp-cut off model. For particle masses $M_X \geq 100 \text{ GeV}$ the total cross sections are $\leq 10 \text{ pb}$ at the LHC operating with lead beams [11], as is shown in Fig. 3. This means that with a

luminosity of $10^{28} \text{cm}^{-2}\text{s}^{-1}$ the discovery range of the LHC does not exceed that of LEP2. Earlier results which were obtained by allowing the nuclei to overlap in impact parameter space were enhanced by an overall factor of ten [6], while the low-frequency approximation had pushed the 10 pb mass threshold from 100 GeV down to 50 GeV [4].

For charged scalars like squarks, sleptons, or charged Higgs bosons the total production cross section is given by [18]

$$\sigma(\gamma\gamma \rightarrow S^+S^-) = \frac{2\pi\alpha^2}{W^2} \left[(1+y)\sqrt{1-y} - 2y \left(1 - \frac{y}{2}\right) \ln \left(\frac{1}{\sqrt{y}} + \sqrt{\frac{1}{y}-1} \right) \right], \quad (8)$$

and is even smaller than the one for fermion pairs [11], Fig. 3.

The two-photon cross section of W^+W^- pairs is given by [19]

$$\sigma(\gamma\gamma \rightarrow W^+W^-) = \frac{8\pi\alpha^2}{W^2} \left[\frac{1}{t} \left(1 + \frac{3}{4}t + 3t^2 \right) \beta - 3t(1-2t) \ln \left(\frac{1+\beta}{1-\beta} \right) \right], \quad (9)$$

with

$$t = \frac{M_W^2}{W^2} \quad \text{and} \quad \beta = \sqrt{1-4t}. \quad (10)$$

This leads to the production of $\simeq 40$ W^+W^- pairs per year at the LHC operating again with beams of lead at a luminosity of $\mathcal{L} = 10^{28} \text{cm}^{-2}\text{s}^{-1}$. The resulting W^+W^- invariant mass spectrum is shown in Fig. 4.

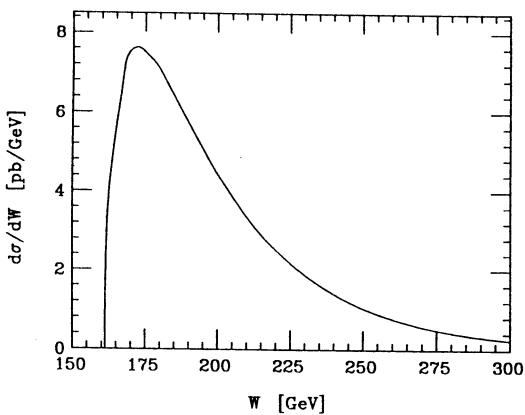


Figure 4: The invariant mass spectrum for the production of W^+W^- pairs in lead-on-lead collisions at the LHC.

Since the number of pairs is small their identification above the four-jet and the two-jet plus lepton background becomes crucial. Assuming that the background originates only from other competing two-photon processes one can try to estimate the order of magnitude of the signal to background ratio. From Fig. 2 one finds that only few $\gamma\gamma \rightarrow b\bar{b}$ events with high $p_T(\text{jet})$ and an invariant mass larger than 150 GeV will be produced. Even though the production rate for all light flavors is a factor $\Sigma(e_q/e_b)^4 = 34$ larger, one is still left with a dijet rate which is comparable to the W

pair rate. The rate for 4 well-separated jets is then suppressed by 2 powers of the strong coupling constant $\alpha_s \sim 0.15$ and hence there will be a small background only to the double hadronic decay of the two W 's. The two-jet plus lepton plus missing p_T and double leptonic decay signals for W^+W^- will be virtually background-free.

The above remarks assume, however, that a near perfect veto against the presence of beam jets is possible, which occur in all hard QCD background reactions, *i.e.* that it is possible to identify the quiet two-photon events in the huge background of hard QCD processes. Additional studies are needed to assess the validity of this assumption.

4. Production of Higgs particles in diffractive collisions

In order to observe the two-photon processes which we have discussed so far one will have to trigger on soft collisions in which the nuclei stay intact. Such reactions are not distinguishable from diffractive strong interactions, which are described by pomeron exchange. Therefore we have analysed Higgs production via Pomeron exchange as an example for diffractive production processes [20]. We present this analyses for proton proton collisions for which it might be promising. It is then easy to see why it is not of interest for heavy ion collisions.

Two processes can contribute, the inclusive ($p + p \rightarrow p + p + H + X$) and the exclusive ($p + p \rightarrow p + p + H$) one. The inclusive process is fairly straightforward to estimate using the methods developed for ‘hard diffraction’ [21–23].

The incoming protons produce an equivalent flux of pomerons which in turn produce a flux of gluons (G) which can produce a Higgs by GG fusion. Using the formulae of [23] the differential number of pomerons from the protons is given by

$$dn_{Pom}(E_i, \omega_i, |t_i|) = \frac{9\beta^2}{4\pi^2} [F_1(t_i)]^2 \left(\frac{\omega_i}{E_i} \right)^{1-2\alpha(t_i)} d\left(\frac{\omega_i}{E_i} \right) d|t_i| \quad (11)$$

Here $E_i = p_i^0$, $\omega_i = k_i^0$, $t_i = (p_i - p_i')^2$, $i = 1, 2$, $\beta = 1.8 \text{ GeV}^{-1}$, $\alpha(t) = 1.085 + \alpha't$, $\alpha' = 0.25 \text{ GeV}^{-2}$, and $F_1(t)$ is the isoscalar electromagnetic nucleon form factor

$$F_1(t) = \frac{4M_N^2 - 2.8t}{4M_N^2 - t} (1 - t/0.7 \text{ GeV}^2)^{-2} \quad (12)$$

where M_N is the nucleon mass. According to Ref. [23] Eq. 11 should be valid for $\omega_i/E_i \leq 0.1$. We therefore cut the pomeron spectrum off at $0.1E_i$ by requiring each proton to suffer at most an energy loss of 10 percent.

For the flux of gluons in a pomeron we use the Ingelman-Schlein distribution function [21]

$$G_{Pom}(x) = \frac{6}{x}(1-x)^5. \quad (13)$$

Putting everything together we find for the total cross section of diffractive Higgs production in the inclusive case :

$$\begin{aligned} \sigma(p + p \rightarrow p + p + H + X) &= \frac{\pi^2}{32} \frac{\Gamma(H \rightarrow GG)}{m_H} \int dn_G(E_1, \omega'_1) \\ &\times \int dn_G(E_2, \omega'_2) \delta(m_H^2/4 - \omega'_1 \omega'_2) \end{aligned} \quad (14)$$

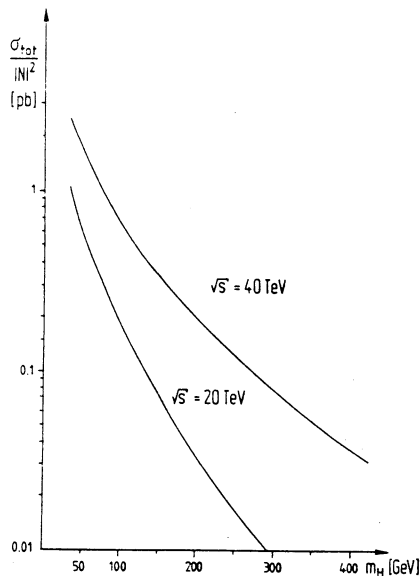


Figure 5: Total diffractive Higgs production cross section modulo $|N|^2$ as a function of the Higgs mass in pp collisions of 20 TeV and 40 TeV. From Ref. [20].

Here $\Gamma(H \rightarrow GG)$ is the two-gluon width of the Higgs which is dominated by the t quark loop, and thus approximately given by

$$\Gamma(H \rightarrow GG) = G_F \sqrt{2} \frac{m_H^3 \alpha_s^2}{72\pi^3} |N|^2 \quad (15)$$

where $|N|^2$ is a numerical factor between 1 and 2 depending on the top mass. In Fig. 5 we show the resulting $\sigma/|N|^2$ as function of m_H for $\sqrt{s}=20$ TeV and 40 TeV. Although the obtained cross sections are very small, the large luminosity expected for the LHC leads to counting rates of ≈ 10 per hour already for $\mathcal{L}=10^{34} \text{ cm}^{-2} \text{ s}^{-1}$, orders of magnitudes more than what can be expected from heavy ion experiments.

After having discussed the nucleon-nucleon process let us now turn to the problem of Higgs production in heavy ion collisions. Here we have to insert the nucleus formfactor instead of the nucleon and have to multiply with the coherence factor $A^{8/3}$. As the integration over the formfactor leads to a factor $1/R_{\text{nuc}}^4 \sim A^{-4/3}$ the effective gain factor is at most $A^{4/3}$ which is too small to balance the difference in luminosity. Thus if one wants to look for diffractive Higgs production one should do so in proton-proton collisions, not in heavy-ion collisions.

Diffractive processes could, however, produce additional background for heavy-ion collisions. Müller and Schramm [24] concluded that this is no problem if one requires that both heavy ions stay completely intact. For a more realistic trigger this still has to be investigated. An additional, probably much more severe background problem is due to photon-gluon fusion [25]. Thus heavy ion collisions with the

presently discussed luminosities are not promising for Higgs searches, neither in the two-photon nor in the diffractive production channel.

The idea of Higgs production by diffractive pomeron-pomeron interactions has been criticised as it uses a proton-proton collider of 16 TeV center of mass energy effectively as a 1 TeV pomeron-pomeron collider with comparable luminosity, which seems like a waste of energy. While this is true it misses the point. The pomeron interactions are a subset of all hadronic interactions, namely the ‘silent’ ones. Looking for the weak signals of Higgs decays it seems very reasonable to investigate this class of events. What has been done in Ref. [20] is to calculate how many Higgs particles are produced in such events and it appears that this rate is high enough to make such an analysis interesting.

Valuable discussion with the other members of the ‘Heavy Ion Group’ and with R. Cahn, K. Eggert, J. Ellis, and M. Traseira are greatly acknowledged.

References

- [1] H. Satz, *Heavy ion physics at very high energies*, these proceedings.
- [2] M. Grabiak, B. Müller, W. Greiner, G. Soff, and P. Koch, *J. Phys. G* **15** (1989) L25; G. Soff, J. Rau, M. Grabiak, B. Müller, and W. Greiner, GSI preprint 89-55.
- [3] E. Papageorgiu, *Phys. Rev. D* **40** (1989) 92.
- [4] E. Papageorgiu, MPI-Report 68/89.
- [5] M. Drees, J. Ellis, and D. Zeppenfeld, *Phys. Lett. B* **223** (1989) 454.
- [6] J. Rau, B. Müller, W. Greiner, G. Soff, *J. Phys. G: Nucl. Part. Phys.* **16** (1990) 211.
- [7] R. N. Cahn, In *Proceedings of the 1989 International Symposium on Lepton Photon Interactions at High Energies*, Stanford 1989, ed. by M. Riordan, p.60; R. N. Cahn and J. D. Jackson, LBL-28592 (1990).
- [8] G. Baur and L. G. Ferreira Filho, Jülich preprint 90-0313 (1990); G. Baur and L. G. Ferreira Filho, Jülich preprint, (1990).
- [9] J. Wu, C. Bottcher, M. Strayer, and A. Kerman, Oak Ridge preprint ORNL/CCIP/90/02 (1990).
- [10] B. Müller and A. Schramm, DUKE preprint DUK-TH-90-7
- [11] E. Papageorgiu, *Phys. Lett. B* **250** (1990) 155.
- [12] K. J. Abraham, R. Laterveer, J. A. M. Vermaseren, and D. Zeppenfeld, CERN preprint CERN-TH-5835/90.
- [13] M. Greiner, M. Vidovic, J. Rau, and G. Soff, GSI preprint GSI-90-59 (1990).

- [14] See e.g. D. Denegri, these proceedings.
- [15] G. Altarelli and M. Traseira, *Phys. Lett.* **B245** (1990) 658.
- [16] D. Brandt, SPS/AMS/Note/89-6 (1989).
- [17] V. M. Budnev, I. F. Ginzburg, G. V. Meledin, and V. G. Serbo, *Phys. Rep.* **C15** (1975) 181.
- [18] I. S. Choi, B. H. Cho, B. R. Kim, R. Rodenberg, *Phys. Lett.* **B200** (1988) 200.
- [19] M. Katuya, *Phys. Lett.* **B124** (1983) 421.
- [20] A. Schäfer, O. Nachtmann, R. Schöpf, *Phys. Lett.* **B249** (1990) 331.
- [21] G. Ingelman, P. Schlein, *Phys. Lett.* **B152** (1985) 256.
- [22] H. Fritzsch and K.-H. Streng, *Phys. Lett.* **B164** (1985) 391.
- [23] A. Donnachie and P. V. Landshoff, *Nucl. Phys.* **B303** (1988) 634.
- [24] B. Müller and A. Schramm, DUKE preprint DUK-TH-90-8.
- [25] Ch. Hofmann, W. Greiner, A. Schäfer and G. Soff, to be published.

**EXPERIMENTAL ASPECTS OF HEAVY ION
PHYSICS AT LHC ENERGIES**

Hans J. Specht

Physikalisches Institut der Universität Heidelberg
D-6900 Heidelberg, Germany

C2: EXPERIMENTAL ASPECTS

1. Introduction

The physics motivations of nuclear collisions at the LHC have been extensively dealt with by H. Satz elsewhere in this volume [1]. The discussions in the various subgroups have indeed largely concentrated on the *physics* assessment, and *experimental* aspects have thus far only played a minor role. A few general points, including first ideas on a universal dedicated detector, have nevertheless been brought up, and it is the purpose of this report to shortly summarize them. They are based on the experience gained in the first generation fixed-target experiments at CERN and at BNL with light ion beams in the years 1986/87, but are also influenced by the planning for the future Pb-beams at CERN and, in particular, by the planning for the 100+100 GeV/u collider RHIC at BNL, for which several detector workshops with strong European participation have been held in the past [2-5], and a number of Letters-of-Intent have just been submitted [6]. Contributions to the Aachen workshop concerning selected experimental issues of heavy ion physics are contained in Volume II of these Proceedings [7-12].

In the following, we will discuss the physics observables in general terms (section 2), the experimental boundary conditions (section 3), some specific problems associated with lepton pair detection (section 4), and finally two concepts for a general purpose heavy ion/min. bias pp detector for the LHC (section 5).

2. Physics Observables and Detector Strategy

The preceding physics assessment by H. Satz has led to a long list of physics observables which need to be measured to fully explore the different facets of nuclear collisions at very high energies:

- (i) transverse energy distributions $d\sigma/dE_T$, both electromagnetic and hadronic
- (ii) charged multiplicities $d\sigma/dn_{ch}$, dn_{ch}/dy
- (iii) transverse momentum distributions $d\sigma/dp_T$ of identified hadrons (π , K , p ...)
- (iv) strangeness production (K^+ , K^- , hyperons, ϕ ...)
- (v) identical-particle interferometry with identified pairs ($\pi\pi$, KK ...), if possible event-by-event; speckle interferometry
- (vi) vector mesons with low mass (ρ , ω , ϕ) and with high mass (J/ψ , ψ' , Y , Y' ...)
- (vii) continuum lepton pairs (e^+e^- and/or $\mu^+\mu^-$)
- (viii) continuum direct photons
- (ix) high-transverse-momentum jets

The discussion of the experimental aspects of these observables has followed, as usual, two distinct lines, one associated with the principal feasibility (rates, background etc.), the other with the technical realization.

On the principal side, many of the observables have already been investigated at SPS energies with some success, and no really serious difficulties in the extrapolation to LHC energies are expected for items (i)-(iv). This may also be true for interferometry (v), although some problems associated with the very large freeze-out radii (20-40 fm) and correspondingly small momentum differences are not yet solved [1, 10, 13]. Vector mesons (vi) and continuum lepton pairs (vii) have received particular attention in the working group discussions, and since principal obstacles (like irreducible background) do exist in these cases, a special section (4) is devoted to them. The isolation of direct photons (viii) from the overwhelming background of π^0 -and η -decays seems extremely difficult, and the prospects for successful experimentation largely depend on the (ambiguous) size of the signal [14], given the anticipated level of systematic uncertainties of 5-10% [9]. Jet physics (ix) has so far only been discussed in connection with RHIC experiments [6].

On the technical side, a general consensus exists that the (characteristically) *low- p_T nature of the physics* of this field requires dedicated experimental techniques. The use of one of the planned LHC pp-detectors for selected observables (notably Y -mesons, possibly high-mass continuum lepton pairs and jets) may be viable or even attractive, but cannot fulfill the needs for the bulk of the programme. LEP detectors, which may become available for other uses towards the end of the decade, may directly - or after modifications - also be suitable for some aspects (to be more closely investigated), but an optimal outcome is far from obvious. However, given the constraints of probably only one interaction region for nuclear collisions at the LHC, only one really dedicated detector can, at least initially, be foreseen. The conceptual design of such a general

purpose detector with perfect capabilities for all observables within one set-up appears, on first sight, as a nearly unsolvable task. Historically, ion experiments have, in fact, both within the CERN fixed-target programme and in the planning for RHIC [6] evolved in the opposite direction - towards specialization, optimized for a narrow group of observables (due, of course, to the horrendous particle multiplicities). An extremely important, although still very preliminary outcome from the discussion in the study group has been that an appropriate detector concept could actually be developed. A generally accepted compromise, consistent with the physics assessment [1], is a rather limited rapidity coverage around the central region (see section 5).

3. Experimental Conditions

Luminosity

With a design luminosity of $L = 2 \cdot 10^{27} \text{ cm}^{-2}\text{s}^{-1}$ [15] and a total inelastic cross section for $\text{Pb} + \text{Pb}$ of $\sigma_{in} = 5.6 \text{ b}$, the total interaction rate is only 11000 s^{-1} . Since collisions with partial rather than complete nuclear overlap are of limited interest, rate estimates for any observables are based on the upper 20% of the $d\sigma/E_T$ - or $d\sigma/dn_{ch}$ -distribution, i.e. a "central collision" rate of 2200 s^{-1} . The selection is done, like usual, by multiplicity detectors, e.g. Si-counters close to the vertex, but outside of the main detector acceptance. The low rate of 2200 s^{-1} implies that only rather loose triggers are required for further selection. For the integrated luminosity per year, the equivalent of one month of $\text{Pb} + \text{Pb}$ running in the LHC is assumed per year. For the investigation of minimum bias pp collisions, only luminosities matched to the ion detector rate capabilities are usable, i.e. values several orders of magnitude below the standard pp running mode.

Particle Multiplicities

A comparison between the approximate charged particle rapidity densities for different reactions, referred to central collisions, is contained in the following table:

reaction	SPS (fixed target)		LHC
	S + Pb	Pb + Pb	Pb + Pb
$\sqrt{s} (\text{GeV})$	20	17	6300
$(dn_{ch}/dy)_{\text{centr}}$	160	~550	~2000
$(Y_{\text{lab}})_{\text{centr}}$	2.5	2.9	0
$(dn_{ch}/d\Omega)_{\text{centr}} (\text{sr}^{-1})$	1000	~7000	~300

Depending on the rapidity acceptance, an LHC detector would have to handle a total of 2000-6000 charged particles, a huge flow of information, but still only a factor of 3 above what is expected for Pb + Pb running at the SPS. In terms of spatial particle densities, the situation is actually eased at the LHC.

Momentum Resolution

From the list of physics observables in the preceding section, the most stringent requirement on the momentum resolution in the limit of low momenta is posed by identical particle interferometry. In view of source size radii of 20-40 fm, a momentum-difference resolution of $\delta Q \leq 2 \text{ MeV}/c$ is desirable, leading to

$$\delta p/p \leq 5 \cdot 10^{-3} \text{ for } p < 1 \text{ GeV}/c$$

This is consistent with the multiple-scattering limit, if a field integral of 0.8...1 T·m is assumed for the magnet (equivalent to a momentum kick of $\Delta p_m = 240 \dots 300 \text{ MeV}/c$), and if the total amount of material is kept on a level of $\leq 2\%$ of a radiation length.

In the limit of high momenta, the most severe requirement is a sufficiently good mass resolution in lepton pair measurements to resolve the different Y-states (Y, Y', Y'...). With $\delta M \leq 100 \text{ MeV}/c^2$ at $M = 10 \text{ GeV}/c^2$, roughly $\delta p/p \leq 10^{-2}$ at $p = 5 \text{ GeV}/c$ or

$$\delta p/p^2 \leq 2 \cdot 10^{-3} \text{ for } p \geq 5 \text{ GeV}/c$$

is necessary. This should be achievable for the field integral quoted, using tracking chambers with good spatial resolution and sufficient lever arm. Combining the two limiting regions gives

$$\delta p/p = [(5 \cdot 10^{-3})^2 + (2 \cdot 10^{-3}p)^2]^{1/2}$$

which has been used to estimate the mass resolution for the vector mesons in the next section.

4. Vector Mesons and Continuum Lepton Pairs

The numerous sources for lepton pair production in nuclear collisions have been extensively discussed in [1]. An attempt has been made for this report to summarize all these sources in one figure (Fig. 1), including the expected level of combinatorial background. The figure is a modified and updated version from a contribution to this

workshop [16]. It shows the production rates and integrated number of detected pairs/month, resp., as a function of the dilepton mass. The conversion from one scale to the other is done using the numerical input from section 3, i.e. $L = 2 \cdot 10^{27} \text{ cm}^{-2} \text{ s}^{-1}$, $\sigma = 5.6 \text{ b}$, upper 20% of $d\sigma/dE_T$ for central collision selection; in addition, a mass-independent pair detection efficiency of 0.1, referred to production in $\Delta y = 1$, is assumed (corresponding roughly to the acceptance of Fig. 4). For the source and background estimates, $dn_{ch}/dy = 2000$ has been used (except where noted otherwise). The details of the estimates are the following:

Vector Mesons

The cross sections for the low mass mesons ρ , ω and ϕ have been scaled up from $\sqrt{s} = 20 \dots 60 \text{ GeV}$ pp data to Pb + Pb at the LHC by keeping the ratio of the respective rapidity density to the total charged multiplicity density constant. The cross sections for the high mass mesons J/ψ and Y are based on a new systematics (Fig. 2), contained in a contribution to this workshop [8]. The values of 100nb and 3nb, resp., for a p_T -cut of $\geq 2 \text{ GeV}/c$ from Fig. 2 are extrapolated to $p_T = 0$ with a factor of 4 and 2, resp., and converted from pp to Pb + Pb with $(A_1 A_2)^{0.9}$, resulting in 6 mb and 90 μb , resp. For the ρ , ω , ϕ , J/ψ and Y, resp., the resonances are plotted with resolution widths (rms) of 65 (natural w.), 6, 6, 20 and $120 \text{ MeV}/c^2$, resp., and the sample-sizes/month are about $8 \cdot 10^6$, $4 \cdot 10^6$, $2 \cdot 10^6$, $6 \cdot 10^5$, and 10^4 , resp. (without suppression in a deconfined state).

Drell-Yan Pair Continuum

Drell-Yan pair production at LHC energies in the mass region of interest corresponds to very small values of $\sqrt{\tau} = M/\sqrt{s}$; at $M = 6 \text{ GeV}/c^2$, $\sqrt{\tau} = 10^{-3}$. For the associated small x-values, the quark and gluon structure functions are not yet known. Higher order QCD corrections, i.e. scaling violations tend to increase the K-factor [18], while nuclear shadowing at small x reduces it [19]. Assuming approximate cancellation of these effects, the rates have been estimated using a simple scaling form for pp collisions [17] and converting to Pb + Pb with $(A_1 A_2)^{1.0}$.

Thermal Pair Continuum

At low masses, thermal pair emission is mainly determinated by the total space-time volume of the system. In the high mass region, on the other hand, it is rather the highest temperature which is decisive for the rate (via $e^{-M/T}$), allowing experimental access to the temperature $T > T_c$ of a deconfined state. The curves (1) and (2), taken from thermal model calculations for Pb + Pb at LHC energies [14], correspond to volume-averaged initial temperatures of 270 and 350 MeV, resp., reached at total particle multiplicity densities of $dn/dy = 1700$ and 3800, resp. ($dn_{ch}/dy = 1200$ and 2600, resp.).

An excess above Drell-Yan exists in both cases, but the higher temperature is obviously more favourable. Somewhat surprisingly, the yield of the ρ from this calculation corresponds exactly to the simple multiplicity scaling used above for the ρ rate estimate.

Anomalous Pair Continuum

In the mass region below the ρ/ω , a pair continuum is observed in hadron collisions with a rate exceeding by far what is expected from Drell-Yan [20]. Its origin is still mysterious. The most common interpretation is the "soft $q\bar{q}$ -annihilation" model [21-23], associated with a quadratic multiplicity dependence [23] analogous to what is expected for thermal pairs. Preliminary data on a non-linear multiplicity dependence have been reported [24], but remain thus far unconfirmed. To be conservative, the pair continuum has therefore been scaled up linearly from pp to Pb + Pb, and the input cross sections [20] have been reduced by a factor of 2, following preliminary evidence from a new experiment [25]. Also, a p_T -cut of ≥ 0.2 GeV/c is applied to the *single* leptons to cope with the combinatorial background (see below). A feature not drawn in Fig. 1 is the speculative possibility of structure at $2m_\pi = 280$ MeV/c²; pair creation from pion annihilation is excluded below $2m_\pi$, while pair creation from quark annihilation would still exist, allowing to disentangle these processes and study the relative fractions of pions and quarks in the system as a function of energy density. The region of very low masses may be of additional interest in view of certain plasma effects proposed recently on the basis of finite temperature perturbation theory [26, 27].

Combinatorial Background

A combinatorial background occurs both in measurements of e^+e^- - and of $\mu^+\mu^-$ -pairs. In the case of e^+e^- , it originates from unrecognized partners of low mass Dalitz and conversion pairs, while in the case of $\mu^+\mu^-$, it is due to pion and kaon decays in flight before their first interactions in the hadron absorber. Since it also exists as like-sign pairs, it can be determined separately and subtracted as long as it does not dominate the signal. For e^+e^- , the upper limit of this background is reached in a detector which does not recognize *any* of the Dalitz and conversion pairs (if, e.g., a strong magnetic field always sweeps away one partner, and no measurement is done before the magnet). Assuming a total amount of material equivalent to 3% of a radiation length, this limit has been estimated on the basis of Monte Carlo simulations done for the CERES/NA45 experiment at CERN [28], and is plotted as line (1) in Fig. 1. For $\mu^+\mu^-$, assuming a mean decay distance of 0.4 m and a rapidity range for a possible spectrometer of $2.0 < \eta < 3.4$, a rough background estimate gives results rather similar, to within a factor of ~ 2 , to line (1). Both simulations so far use pion p_T -spectra as measured at $\sqrt{s} = 20...60$ GeV; the situation would still be more severe if $\langle p_T \rangle$ would strongly increase with \sqrt{s} . It is evident that all lepton pair sources below the J/ψ cannot

realistically be measured under these circumstances. However, the e^+e^- -case can much be improved by recognizing and rejecting the low mass Dalitz and conversion pairs as effectively as possible. If this is done in an optimized set-up under conditions equivalent to [28] (material 1% of a radiation length, 95% track efficiency, rejection before opening through a magnet), line (2) in Fig. 1 is obtained (see [16, 29] for more details). Further improvements are possible by applying p_T -cuts to the *single* leptons: lines (3) and (4) correspond to $p_T \geq 0.2$ and ≥ 0.3 GeV/c, resp. Still higher cuts would also start reducing (1), but this would eventually affect the physics sources in the mass region ≤ 1 GeV/c² in an unacceptable way. The net result of a superior background situation in the e^+e^- -case is ultimately due to the much softer p_T -spectrum of the decay electrons compared to the decay muons [28].

Conclusion

Two main conclusions can be drawn from this still very simplified and preliminary feasibility study of lepton pair detection at LHC energies:

- (i) The mass region below the J/ψ appears to be essentially unaccessible to a $\mu^+\mu^-$ -experiment because of combinatorial background. An e^+e^- -experiment may have a chance, but would still be extremely difficult (except for the narrow resonances ω and ϕ).
- (ii) In one month of running time, enough data could be accumulated in the Y -region to make a meaningful search for vector meson suppression.

5. Detector Concepts

This part of the report is quite naturally least developed. As stressed before, the need to condense the measurement of all observables of interest into one dedicated set-up, has presented a great challenge to the discussion group, and the first ideas presented below are far from matured. A rather clear consensus was reached on the general principle of an open axially symmetric spectrometer magnet, along the lines of the former AFS magnet at the ISR (now used in OBELIX at LEAR), or of an enlarged derivative proposed in a Letter-of-Intent for RHIC (OASIS [7]), or of Helmholtz-coil type magnets with field-free inner regions as previously discussed for RHIC either without [29] or with [30] iron. The prime advantage of such a magnet is its flexibility for the use of different detectors, the possibility for long flight paths where needed, the simple integration of special spectrometers viewing through "ports" [30] etc. Such magnets can also be focussing to some extent [7], but this is not decisive.

Concept I

Fig. 3 shows a central detector based on such an open field magnet in conjunction with a forward μ -spectrometer. The magnetic field, created by two pairs of coils on conical pole tips, is maximal at the vertex. The momentum kick Δp_m does not need to exceed 300 MeV/c to fulfill the resolution requirements of section 3. More than that is, in fact, undesirable to avoid spiralling of low p_T particles. The total rapidity acceptance for charged hadrons is $\Delta\eta = \pm 0.55$. Tracking is done only outside the field, using either a TPC or a set of tracking chambers with a high segmentation in 2 dimensions like parallel plate pad detectors [28] or parallel plate chambers with optical readout [31] or a combination of TRD (for electron identification at $p \geq 1$ GeV/c) and thin TPC [7]. Hadron identification is done by time-of-flight with a highly granular scintillator array arranged in a "picket-fence" geometry (phototubes attached to both scintillator ends). With a flight path of 6 m and a time resolution of 50-80 ps as has been achieved in E802 at BNL and in NA44 at CERN, π/K separation up to > 3 GeV/c and K/p separation up to > 5 GeV/c is possible (4σ). However, the costs of such an array will be enormous, and cheaper alternatives for high resolution TOF with a very high granularity are among the most urgent R&D projects of this field for the future (relevant also for Pb + Pb fixed target experiments at the SPS). Finally, a nearly hermetic electromagnetic calorimeter encloses all the other detectors. Part of this could be a high-resolution array of a homogeneous calorimeter like BGO for the measurement of direct photons [9]. Simulations done for RHIC [32] indicate that in such a device π^0 -reconstruction is still possible above the $\gamma\gamma$ combinatorial background for transverse momenta above 1 GeV/c.

The forward μ -spectrometer views the vertex through a hole in the magnet yoke which is filled with an optimized hadron absorber. The principal design with a toroidal field follows the layout of the NA38 experiment at CERN, but with a much improved mass resolution to achieve $\delta M \leq 100$ MeV/c² at $M = 10$ GeV/c². The rapidity acceptance is $2 < \eta < 3.4$, pushed as close as possible to $\eta = y = 0$. On the other hand, additional rapidity coverage at larger values like $4 < \eta < 5$ (with a different design or a second arm on the other side?) would also be of interest to disentangle direct c-production from b → c production (c has a wider y-distribution than b; see [8] for a more detailed discussion). Extensive simulations will be necessary to arrive at a solid design and study also problems like the emission of secondary hadrons from the absorber in the middle of the central detector.

Concept II

Another variant of a central axially symmetric detector with an open magnetic field is shown in Fig. 4. Here, two concentric pairs of Helmholtz coils with different inner and outer coil diameter create a radially localized field. The region inside the small pair is kept field-free by proper compensation of the contributions from the two pairs; in the

region in between, the field is maximal, providing a momentum kick Δp_m of again ~ 300 MeV/c; outside the large pair, the field drops rapidly, helped by the flux return yoke (in contrast to air coils; see [29] for field mapping and ray-tracing). To avoid excessive bulging of the field lines between the coils, the polar opening angle has to be somewhat limited (like $\Delta\Theta = \pm 22.5^\circ$), restricting the rapidity acceptance for charged particles to $\Delta y = \pm 0.4$. Hadrons are tracked and identified outside the field, using a TPC or parallel plate chambers together with a TOF-system completely analogous to concept I. The same applies to direct photons and electromagnetic (and hadronic) calorimetry. Lepton pair measurements, on the other hand, are done in this concept via electron pairs. An axially symmetric ring image Cerenkov detector (RICH), placed in the field-free inner region and operated with a gas radiator of a sufficiently high Cerenkov threshold (like $\gamma_{th} \sim 30$), serves both to locally identify electrons and to reject Dalitz and conversion pairs by angular cuts before they are opened by the magnetic field - a technique developed for and presently under test in CERES/NA45 [28]. In the geometry drawn (see also [16, 29]), the Cerenkov mirrors are parts of spherical surfaces such that the centers of the spheres lie on the beam axis, but are symmetrically displaced from $z = 0$ along the axis. This assures unsplit images (except at 90°), and allows to retract the RICH UV-detectors out of the electron paths to keep the total material on a level of $\leq 1\%$ of a radiation length. The UV detectors could, e.g., be parallel plate counters with pad readout [28]. The total number of charged particles traversing the chambers would be ~ 2000 , but with a density of still only $\sim 1/\text{ring area}$; a He-based gas mixture could assure a sufficiently low ionization per particle. An additional microvertex detector, consisting of some planes of microstrip or micropixel Si- or gas counters, has been proposed [11] as the proper tool for hyperon identification (by decay vertices); the field-free region would certainly be helpful here. This detector could also form part of the general tracking scheme, determining, e.g., the centers of the electron Cerenkov rings.

The following table serves to illustrate the charged particle area densities in the different detector components, assuming $dn_{ch}/dy = 2000$:

Radius (cm)	Detector	dn_{ch}/dS (cm ⁻²)	dn_{ch}/dS
5	microvertex	13	$0.005/(200 \mu\text{m})^2$
60	RICH UV	0.09	$0.008/(2.6 \text{ mm})^2$
300	TPC (average)	$4 \cdot 10^{-3}$	$0.014/(2 \text{ cm})^2$
400	TOF	$2 \cdot 10^{-3}$	$0.1/1 \cdot 50 \text{ cm}^2$
450	EM calorimeter	$1.6 \cdot 10^{-3}$	$0.05/(6 \text{ cm})^2$

The reference areas in the last column are specific to the respective detector component: a pixel size of 200 μm in the microvertex, a pad size of 2.6 mm in the UV detector, a double-track resolution of 2 cm in the TPC, a scintillator element of $1 \cdot 50 \text{ cm}^2$, and a fiducial element of 6 cm in, e.g., a BGO calorimeter. It is seen that none of the occupancy values is excessive.

A specific problem for all charged particle detectors may arise from the intense production of e^+e^- pairs via the very strong electromagnetic fields carried by the high-Z ion beams (see, e.g. [15]). In concept I, the magnetic field will presumably curl up the majority of these electrons, but for concept II (and in any use of microvertex detectors close to the beam), a detailed investigation of the problem is clearly desirable.

Detector Research and Development

As a follow-up to the ECFA discussion group, a special study group for a heavy ion detector at the LHC should soon be set up to

- (i) agree on a principal design
- (ii) make a more detailed technical study
- (iii) define the areas for detector research and development

Although much development work is carried out at present in connection with future Pb-beam experiments at the SPS (and, of course, with p-experiments at the LHC), some dedicated further work for ion experiments at the LHC will definitely be necessary. Among the items identified are tracking at high track density (TPC's, pad chambers, microvertex detectors, high-resolution muon chambers), particle identification (large TOF-systems with 50 ps resolution at reasonable costs, RICH detectors), and data acquisition systems capable of handling the huge flow of information expected.

Acknowledgements

This report is, to a large extent, based on the work of the ECFA discussion group "Heavy Ion Physics at the LHC". I am grateful to all the participants, and in particular to P. Glässel, H. Gutbrod, L. Kluberg, J. Schukraft and P. Sonderegger, for their contributions towards a first detector concept.

References

- [1] H. Satz, Plenary Talk at this Workshop, Proceedings Vol. I
- [2] P. Haustein and C. Woody, eds., Proc. BNL Workshop on Experiments and Detectors for a Relativistic Heavy Ion Collider, BNL 51921 (1985)
- [3] H.G. Ritter and A. Shor, eds., Proc. Second Workshop on Experiments and Detectors for a Relativistic Heavy Ion Collider, LBL 24604 (1988)
- [4] B. Shivakumar and P. Vincent, eds., Proc. Third Workshop on Experiments and Detectors for a Relativistic Heavy Ion Collider (RHIC), BNL 52185 (1988)
- [5] M. Fatyga and B. Moskowitz, eds., Proc. Fourth Workshop on Experiments and Detectors for a Relativistic Heavy Ion Collider, BNL 52262 (1990)
- [6] T. Ludlam, Plenary Talk at this Workshop, Proceedings Vol. I
- [7] D. Lissauer, Report at this Workshop, Proceedings Vol. II
- [8] P. Sonderegger, Report at this Workshop, Proceedings Vol. II
- [9] H. Gutbrod, Report at this Workshop, Proceedings Vol. II
- [10] H. Bøggild, Report at this Workshop, Proceedings Vol. II
- [11] E. Quercigh, Report at this Workshop, Proceedings Vol. II
- [12] P. Seyboth, Report at this Workshop, Proceedings Vol. II
- [13] R. Stock, priv. communication (1990)
- [14] V. Ruuskanen, Report at this Workshop, Proceedings Vol. II
- [15] D. Brandt, Report at this Workshop, Proceedings Vol. II
- [16] P. Glässel, Report at this Workshop, Proceedings Vol. II
- [17] N.S. Craigie, Phys. Rep. 47 (1978) 2
- [18] S. Gupta, Report at this Workshop, Proceedings Vol. II
- [19] P. Castorina and A. Donnachie, Z. Phys. C45 (1989) 141, and P. Castorina, Report at this Workshop, Proceedings Vol. II
- [20] K.J. Anderson et al., Phys. Rev. Lett. 36 (1976) 237, and many other references; see R. Stroynowski, Phys. Rep. 71 (1981) 1 or H.J. Specht, in Quark Matter 1984, Helsinki, ed. K. Kajantie, Lecture Notes in Physics 221 (1985) 221 for reviews
- [21] J. D. Bjorken and H. Weisberg, Phys. Rev. D13 (1976) 1405
- [22] V. Cerny et al., Phys. Rev. D24 (1981) 652
- [23] V. Cerny, P. Lichard, J. Pisut, Z. Phys. C31 (1986) 163; P. Lichard, CERN-TH 4805/87, and later references
- [24] T. Åkesson et al., Phys. Lett. 192B (1987) 463, and V. Hedberg, thesis, Univ. Lund, LUNFD6/NFFL-7037 (1987)

- [25] CERN-experiment NA34-1, P. Nevski, Contrib. to the Pittsburgh Workshop on Soft Lepton Pair and Photon Production (1990), and other preliminary data (unpublished)
- [26] E. Braaten, R. Pisarski and T.C. Yuan, Brookhaven Preprint BNL 43882 (1990)
- [27] H.A. Weldon, Contrib. to the Quark Matter Conf., Menton (1990)
- [28] CERES/NA45; "Study of Electron Pair Production in Hadron and Nuclear Collisions at the CERN SPS", Proposal P237 to the SPSC (1988)
- [29] P. Glässel and H.J. Specht, in Ref. [3] p. 107
- [30] M. Albrow et al., in Ref. [3] p. 21
- [31] H. Gutbrod, private communication, and Proposal P252 to the SPSC (1990)
- [32] T. Awes et al., ORNL, discussed in [9]

Figure Captions

- Fig. 1 Production rates for lepton pairs as a function of the dilepton mass M at $y_{CM} = 0$ for central collisions of $Pb + Pb$ at the LHC. The thermal model predictions (1) and (2) [14] correspond to charged particle rapidity densities of 1200 and 2600, resp. The combinatorial background estimates refer to $\mu^+\mu^-$ (1) and to e^+e^- without low mass pair rejection (1), and to e^+e^- with best possible pair rejection and various cuts (2-4). More details are given in the text.
- Fig. 2 Production cross sections for the vector mesons J/ψ and Υ as a function of \sqrt{s} [8]. The experimental points (solid) contain a large letter denoting the respective experiment; in case of a p_T -cut, the corresponding cut-value (> 2 or > 5 GeV/c) follows the letter. The points R are new CDF-data which have not yet been acceptance-corrected. The dashed line represents the J/ψ "standard fit" [17]. The dashed points containing small letters are values from recent QCD calculations (also with p_T -cuts). The references to the letters are given in [8].
- Fig. 3 Concept I for a universal heavy ion detector at LHC. Hadrons are measured in the central detector, consisting of an open axially symmetric magnet with maximal field at the vertex, of tracking chambers (TC), and of a highly segmented time-of-flight system (TOF). Photons are measured in a high-resolution subsection of the surrounding electromagnetic calorimeter. Muon pairs (in the mass region $M \gtrsim 2$ GeV/c 2) are measured in an additional forward spectrometer viewing the vertex through a hole in the magnet yoke filled with the hadron absorber.
- Fig. 4 Concept II for a universal heavy ion detector at LHC. Two pairs of Helmholtz coils with different diameters create an axially symmetric, radially localized magnetic field with a zero-field region in the center. Hadrons are tracked and identified with the microvertex detector, tracking chambers (TC), and a highly segmented time-of-flight system (TOF); the microvertex also identifies hyperon decays. Electron pairs (whole mass region of interest) are measured with the ring-image Cerenkov detector (RICH) in conjunction with the microvertex and the tracking chambers. Photons are measured in a high-resolution subsection of the surrounding electromagnetic calorimeter. Si-detectors in the forward region provide a multiplicity trigger.

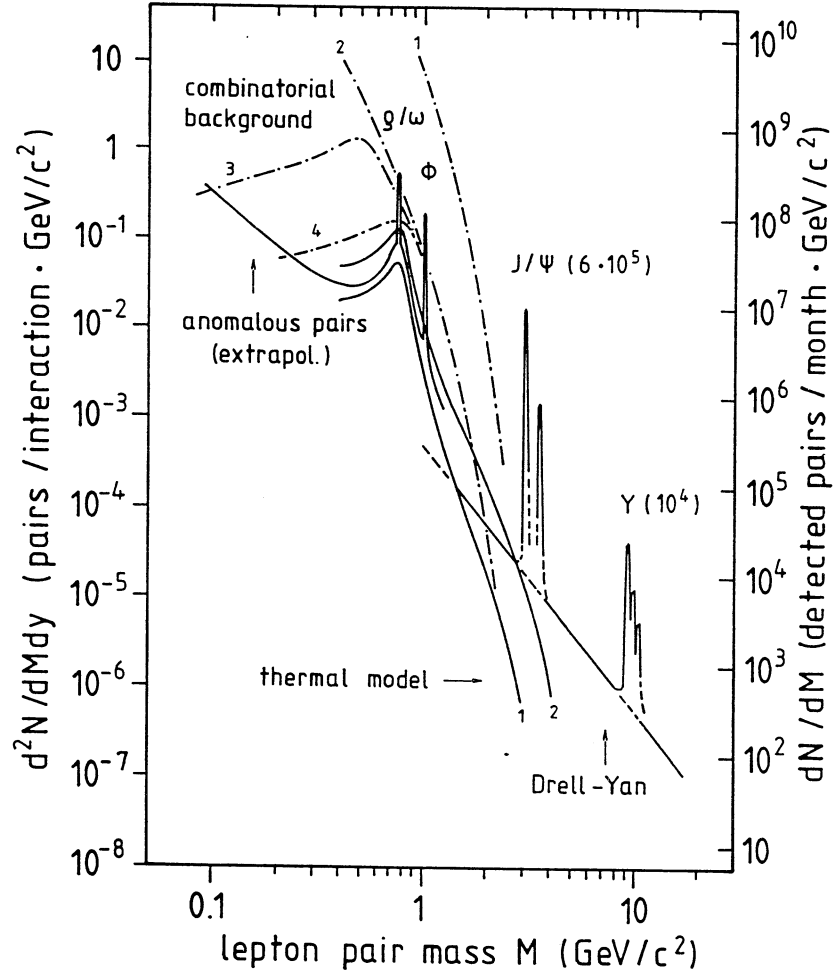


Fig. 1

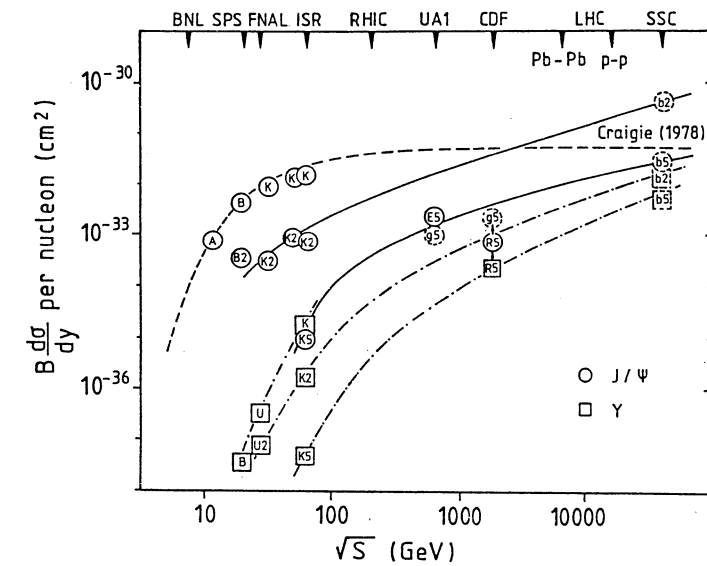


Fig. 2

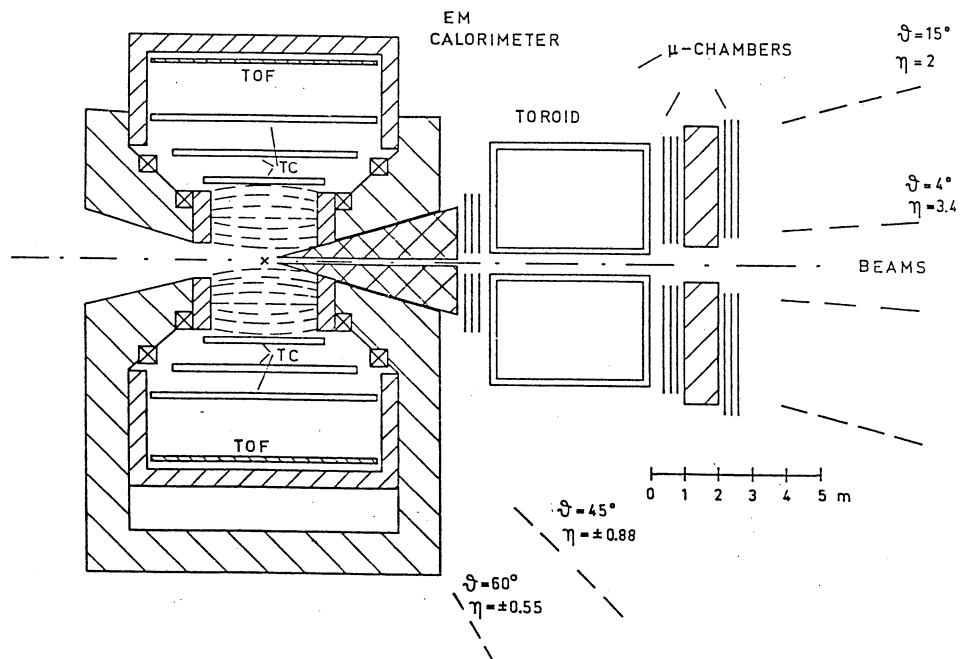


Fig. 3

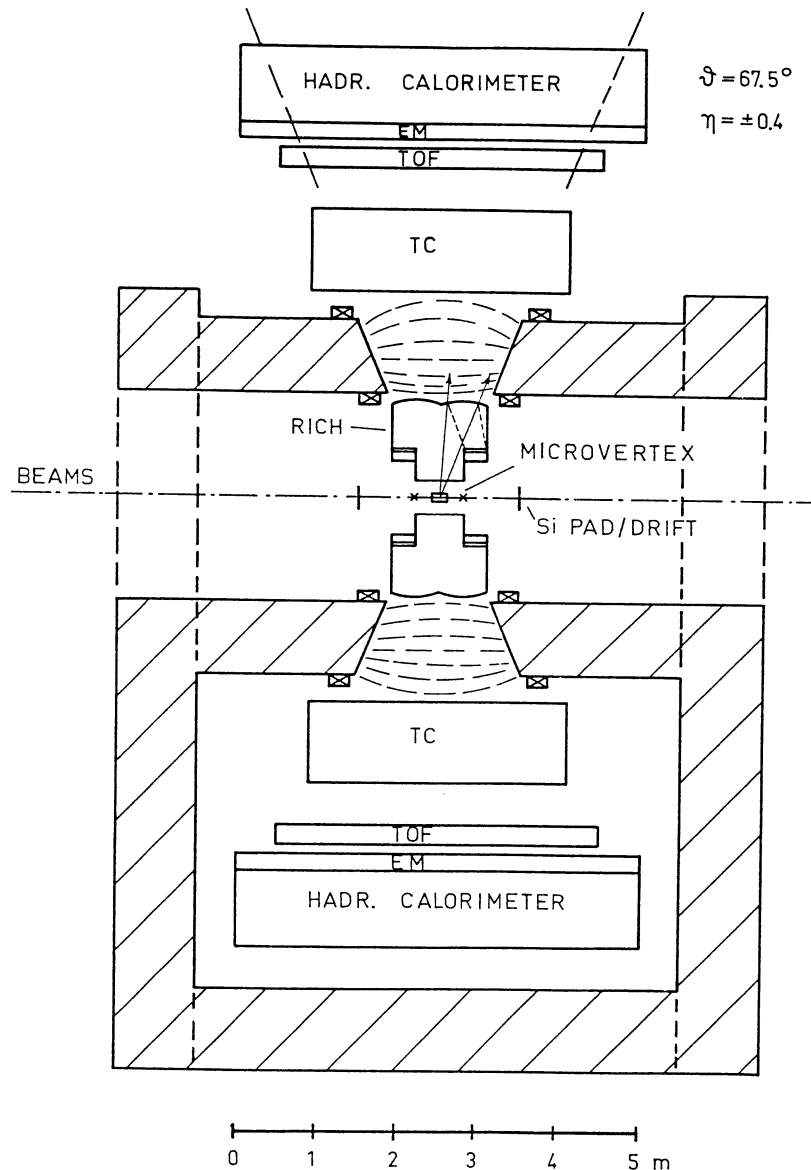


Fig. 4

DILEPTON PHYSICS WITH IONS AT LHC

P. Sonderegger, CERN

Abstract

Recent progress in theoretical understanding has led to a reassessment of the dilepton road towards the physics of the Quark-Gluon Plasma. Thermal dileptons (and photons) reflect the early, hot stages of the collisions; they are not prominent when large latent heat keeps the QGP initial temperature low. The Debye colour screening can be studied not so much on charmonium, since most J/Ψ 's produced at LHC originate from B decay, than on the Υ 's, whose production rate is orders of magnitude higher at LHC than at RHIC.

1 Introduction and Acknowledgments

This report is mainly based on the findings of the LHC/Ions/Dileptons Working Group which met five times to prepare the Aachen Workshop [Aud90]. In addition to the contributions by P. Castorina, S. Gavin, S. Gupta, F. Karsch and V. Ruuskanen, which are published in this Volume, I wish to acknowledge the related work of D. Blaschke and of B. Kämpfer, the help of co-convenor F. Karsch, and fruitful exchanges with H. Satz, J. Schukraft and H. Specht; also, I am indebted to F. Pauss and D. Treille for making available to me new material from UA1 and CDF. The physics scope is **studying the Quark-Gluon Plasma**; other topics, such as the EMC effect, do not concern us here. The accent is on the theoretical developments, not so much because the concerned experimentalists were absorbed by this summer's ^{32}S ion run, but because the areas of priority had to be identified prior to designing an experiment. Indeed, both space and running time will be scarce for ion collisions at LHC, excluding from the start the policy chosen for RHIC, where a beautiful stand-alone dimuon detector of widest acceptance was designed (including even J/Ψ 's at rest) [You90], leaving the physics choices essentially open until the time of running. Some of my remarks will be deliberately provocative, out of the desire to provoke further work on some of the new and not yet confirmed findings.

Before addressing our two major topics, the thermal dileptons in Section 3 and the vector mesons in Section 4, we discuss the dilepton background in Section 2, in which we include the Drell-Yan mechanism. In Section 5 we conclude.

2 Continuum, Drell-Yan pairs

The main physics interest of Drell-Yan dileptons produced by ion collisions would be the study of the EMC effect, which is not our concern here. We need

however to understand the background under the thermal and vector meson dileptons addressed in the following sections. The Drell-Yan cross sections up to LHC energies have been calculated both for p-p [Gup90] and A-A [Cas90]. The following results are relevant for our purposes:

- QCD calculations cover dilepton masses above a few GeV, and are done for $p_T > 2 \text{ GeV}/c$, and tentatively extrapolated to $p_T = 0$;
- the average p_T^2 increases strongly with \sqrt{s} , reaching some 20 $(\text{GeV}/c)^2$ at LHC [Gup90]; in fact, the cross section is still expected to peak around $p_T = 1 \text{ GeV}/c$, but the higher order QCD terms greatly enhance the cross section at large p_T ;
- The production of $D\bar{D}$ and $B\bar{B}$ pairs followed by semileptonic decays of both mesons leads to dilepton rates comparable to the Drell-Yan mechanism and can in principle be calculated in a similar way.

A measurement of the amount of admixture of $D\bar{D}$ and $B\bar{B}$ decays in the dilepton continuum, say, at masses below the J/Ψ and above the ψ' , has been attempted for p-p reactions in three ways:

1. by reconstructing *both mesons* of the $D\bar{D}$ resp. $B\bar{B}$ states (see in particular 17 $D\bar{D}$ events fully reconstructed in EHS [Agu88]),
2. via the missing energy associated to the dilepton [Wil83], and
3. by measuring $e - \mu$ pairs [Wil83].

These studies are notoriously difficult for p-p collisions, and look close to impossible for ion collisions, respectively

1. because of the rate limitations of the emulsion approach, the only one to have addressed $D\bar{D}$ production in ion collisions (using a statistical analysis of white stars [Aok89]);
2. because the ratio missing/total (transverse) energy goes as $1/A$ for A-A collisions and ceases to be measurable for fairly light nuclei; and
3. because of the conflicting layout requirements of measuring the electrons at a distance large and growing with A , but still before the hadron absorber whose distance should be small and diminish when A grows.

In practice, this means that in the p_T range open to QCD calculations both Drell-Yan pairs and $D\bar{D}$ and $B\bar{B}$ pairs should be computed together, and that at low p_T one is left with an a priori unknown continuum, to be determined by experiment, assuming however that its p_T or ϵ dependence resembles that of Drell-Yan pairs.

3 Thermal Dileptons and Photons

Updated calculations by V. Ruuskanen [Ruu90] show thermal dilepton emission when QGP is formed, with the separated contributions for each emitting phase, and also dilepton emission in the absence of QGP, assuming a hot and dense pion gas is formed instead.

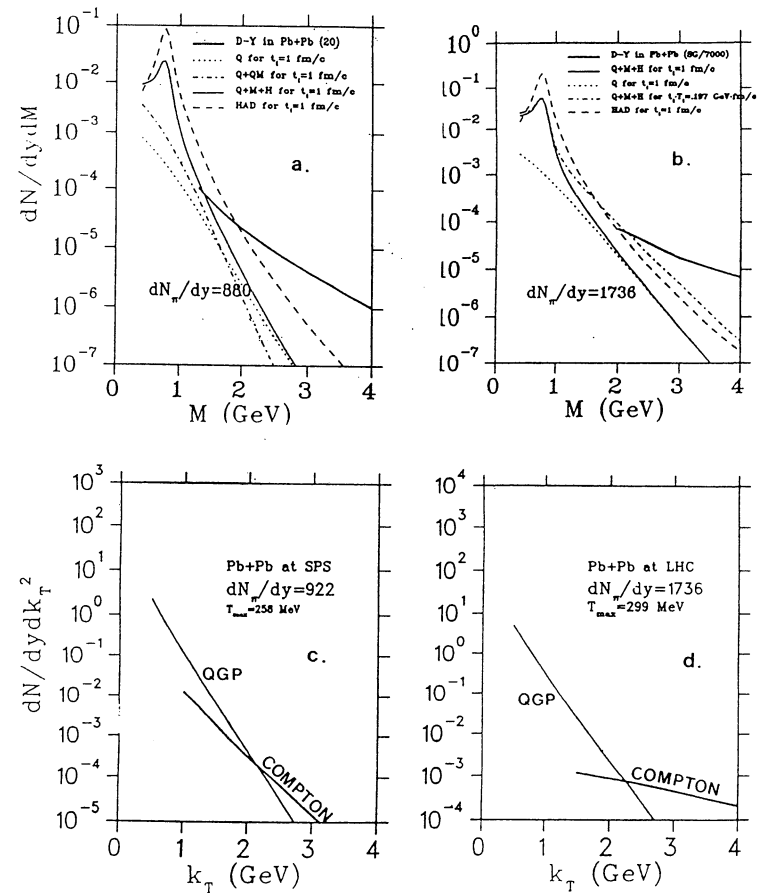


Figure 1: Top: Rates for thermal dileptons in central Pb-Pb collisions (a. SPS, b. LHC) [Ruu90]. A hadron gas gets hotter and emits more thermal dileptons than the QGP phase (Q, dotted lines; the solid lines include the less significant contributions of the mixed (M) and hadronic (H) phases). The thick lines show the Drell-Yan contribution. Bottom: Direct thermal photon emission by QGP (thin lines, c. SPS, d. LHC), compared with the Compton QCD photons (thick lines), from [Ruu90]. The (much more abundant) photons from hadron decay are not shown.

From the results shown in Fig. 1a and 1b, and an analysis of the underlying physics, we draw the following conclusions:

1. a degree of **model dependence** is unavoidable, so that virtual and real thermal photons are a signal in a qualitative rather than a quantitative sense;
2. they signal the highest temperatures attained, and are therefore relatively reduced when QGP is formed, since part of the available energy goes then into latent heat;
3. the signal, even in the most favourable mass region between the ϕ and the J/Ψ , is
 - tiny, especially when QGP is formed, and only marginally more prominent at the LHC than at the SPS,
 - not much different from the continuum from which it must be separated (see previous section for uncertainties in the latter),
 - not easy to interpret in terms of the history of the emitting system.

Ways of separating a thermal signal from the (as we have seen, a priori unknown) dilepton Continuum on the grounds of the differing E_T (or ϵ) behaviour have been discussed [Kam89]. Fig. 1c and 1d show predictions for thermal direct photons, computed [Rau90] using Neubert's method [Neu89], and shown to exceed QCD Compton photon production again over a sizeable domain of the variable which is now k_T . A detailed discussion of the relative merits and problems of dimuons, dielectrons and direct photons at the three levels of counting rate, distinguishability from the continuum, and subtraction of the decay background ($\pi \rightarrow \mu\nu$ vs. $\pi^0 \rightarrow e^+e^-\gamma$ vs. $\pi^0 \rightarrow 2\gamma$), is necessary, and has not been done. The absence of meaningful results from the AGS and SPS programs is a handicap.

In spite of all these difficulties, it remains true that **thermal emission** of real or virtual photons is the best, possibly the **only signal** capable of carrying information from the **early phases of high energy nuclear collisions**, be they QGP or not. Such promise is enough to warrant a stronger involvement both in experimental searches of thermal photons and dileptons, and in assessing the interpretability of the observed spectra.

4 The Vector Mesons

We will first inspect the physics interest and feasibility of the light vector mesons, then turn to the J/Ψ and Ψ' , and finally to the Υ 's.

The Λ (or ϵ) dependence of the **light vector meson production** (ρ , ω and ϕ) production has two foci of clear physics interest:

- the ϕ is a privileged **strangeness enhancement detector** [Bal89],[Koc90], [Bar90], possibly (i.e. in the limit of exclusive production via $s\bar{s}$ or $K\bar{K}$ recombination) proportional to the square of the strangeness fraction: $\phi/\omega \sim (K/\pi)^2$;
- The interest of the ρ stems from the fact that the **intensity of its dilepton peak measures effectively the duration of the final state interaction**.

Indeed, ρ 's and π 's will live in dynamical equilibrium; while the observed hadron spectrum will consist of the mesons formed at freezeout time τ_f , each preceding generation of ρ 's will have had its own chance to decay into a lepton pair, and the *observed* leptonic decay fraction will be enhanced, e.g. with respect to the long lived ω 's, as [Hei90]

$$\frac{\rho \rightarrow \mu^+\mu^-}{\omega \rightarrow \mu^+\mu^-} = \frac{\rho \rightarrow \mu^+\mu^-}{\omega \rightarrow \mu^+\mu^-} [p - p] \cdot \frac{\tau_f - \tau_c}{\tau_\rho}$$

where τ_c is the hadronization time and τ_ρ the ρ lifetime.

But what are the **chances of experimental observation** of the light vector mesons at LHC? In a dimuon setup, they will be buried in a combinatorial background of π and K decay muons which could well outnumber them by two orders of magnitude in, say, central Pb-Pb collisions. The possibility of subtraction of such a huge background, albeit very precisely monitored by the like-sign muon pairs, is unlikely and demands a major simulation study. A dielectron experiment will be plagued by a comparable amount of Dalitz pairs and photon conversions, but the mass resolution should be much better and allow a glimpse of the narrow peaks (ϕ and possibly ω) [Spe90].

We now turn to the J/Ψ and Ψ' which, if produced as $c\bar{c}$ bound states, are predicted [Kar90,Gav90] to be considerably more suppressed by Debye colour screening at the LHC than at the SPS, and up to much higher p_T . However, at LHC energies most J/Ψ 's and all Ψ' are expected to originate from B 's which decay far away from the interaction region, and hence, to carry no information on the conditions in the interaction volume. UA1 found that 31 ± 12 % of the wealth of J/Ψ 's measured at $\sqrt{s}=630$ GeV for $p_T > 5$ GeV/c come from B decays, on the grounds of a statistical analysis of the charged tracks accompanying the J/Ψ , and comparison to a sophisticated simulation [Alb90]. CDF found, at $\sqrt{s}=1800$ GeV and again $p_T > 5$ GeV/c, that 61 % of all J/Ψ 's originate from B decays [Roh90]. Here, this fraction is determined by postulating that all Ψ' come from B decays, and that the relative branching fraction of the B 's to J/Ψ and Ψ' is the same as measured at CLEO.

The production of J/Ψ via the different mechanisms (including via production and decay of χ 's and of the Ψ') has been computed by Glover et al. [Glo88], using QCD, for the energies of the two experiments and $p_T > 2$ GeV/c. Fig. 2 shows their results for the SPS together with an extrapolation of their results to the LHC ventured by the author. Direct production of charmonium is seen to dominate even at LHC at low p_T , but not in the region where one would like to study the transition from J/Ψ suppression to non-suppression, which is just where production via B decay takes over. There is a particularly interesting rapidity region from, say, $y=4$ to $y=6$ where b production fades away while $c\bar{c}$ production persists for another unit of rapidity; unfortunately any experimental exploration into this region seems to be utterly excluded.

While its connection with the B renders the J/Ψ almost useless for QGP study at LHC, the Υ does not plague the Υ 's in any comparable way. The Υ family is well suited for the study of final state interactions [Kar90], provided it is produced in sufficient abundance. We will now attempt to estimate both the J/Ψ and the Υ production cross sections at LHC by using, as shown in Fig. 3, both representative available experimental data and recent QCD calculations.

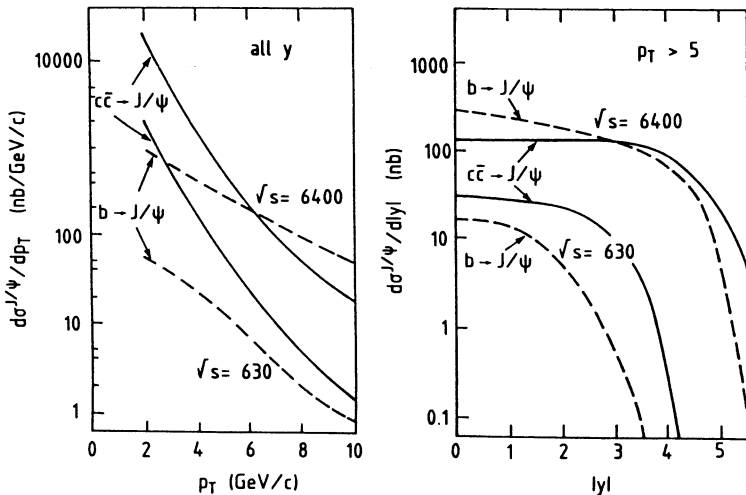


Figure 2: J/ψ production cross section, vs. p_T (left) and y (right), at $SPPS$ and at LHC, via b production and decay (dotted lines), and via $c\bar{c}$ (the solid lines are the sum over production and decay of the χ 's, the Ψ' , and direct J/ψ production) ([Glo88]).

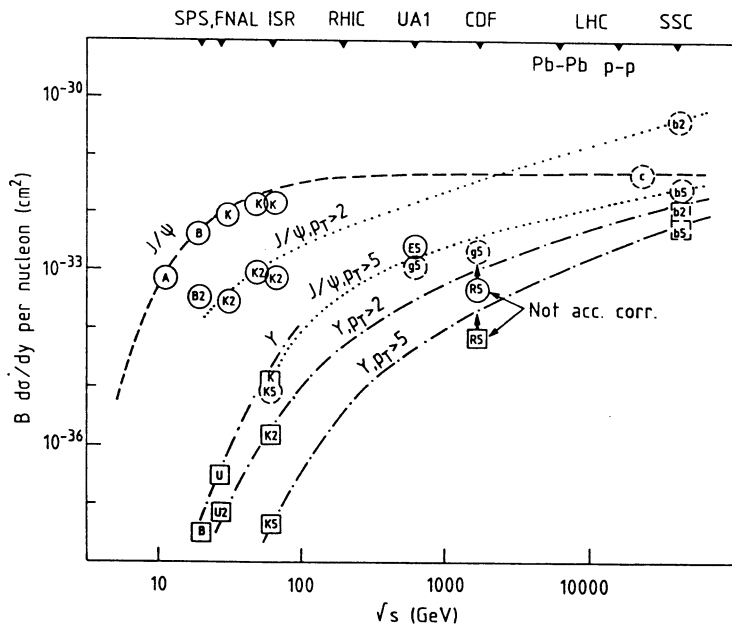


Figure 3: Cross sections for J/ψ (circles) and Υ (squares) decaying to dileptons, vs. energy. Labels refer to the references given in the text, and if appropriate, give the p_T cut value in GeV/c . Data points are solid, QCD calculations dashed. All lines except Craigie's fit (c) are meant to guide the eye.

The QCD predictions of Glover et al. [Glo88] and Bergström et al. [Ber90] extend from the $SPPS$ to the SSC , and are shown for $p_T > 5 \text{ GeV}/c$ and, when available, for $p_T > 2 \text{ GeV}/c$. The experimental data come from Serpukhov, [Ant76], the $SPPS$ [Bad79, Bad83] and FNAL [Uen79], the ISR [Kou80], the $SPPS$ [Alb90] and the Tevatron (CDF) [Roh90], the latter not yet corrected for acceptance. Whenever possible, data for the p_T cuts of the QCD calculations have been extracted. One notices that

- the widely used parametrization introduced by Craigie [Cra78] which reads for the J/ψ

$$B \cdot d\sigma/dy = 50 \cdot \exp(-14.7M/\sqrt{s}) \text{ nb}$$

and reaches rapidly a plateau, is at variance with modern QCD calculations, which rise practically linearly with \sqrt{s} up to SSC energies;

- the QCD calculations are not in contradiction with the data, although there is not much overlap (note the agreement between UA1 data [Alb90] and calculations [Glo88]);
- for $Pb-Pb$ collisions at the LHC, at a luminosity of 10^{27} and using a $A^{2.95}$ behaviour of the Υ cross section, $\approx 1000 \Upsilon$ per day and unit rapidity interval are expected;
- the Υ rate is a clear bonus of the LHC with respect to RHIC, being three orders of magnitude higher (two from the cross section, one from the luminosity).

Karsch [Kar90] has contributed a complete comparison, covering all J/ψ and Υ vector mesons, between suppression from Debye screening in a QGP and suppression by hadronic rescattering (with initial state scattering to solve the p_T problem). Both models are tuned to reproduce the p -nucleus data basis. The differences are not as large as one might have hoped. The largest difference is seen for the Υ which is fairly suppressed in the hadronic scenario, and not at all in the QGP model, mainly because of its large formation time: it is born outside the plasma volume. Unlike UA1 and CDF, ion beam experiments at LHC will in all probability not be able to identify any of the resonances, in particular the χ 's and the χ_c 's, whose decays produce a majority of the observed J/ψ 's and Υ 's. The model will have to incorporate this feature.

To conclude these short remarks about meaningfulness of future results, we insist on the crucial importance to develop further broadly constructed and comprehensive models in the line of Karsch's, in order to provide us with research tools at the time of planning LHC experiments.

5 Towards Experimentation; Conclusions

No experimental layout has been drafted yet. The goals of dilepton experiments are however in the process of being defined: measuring the Υ family with good acceptance and a resolution sufficient to separate the different states; striving at a realistic methodology to measure some or all light mesons; checking one last time the unlikely possibility of accessing that large y region where c production still subsists while b production vanishes.

The running strategy has been discussed elsewhere [Son90]. Varying the energy density is the experimental approach to QGP physics. At LHC this will be done by varying the atomic number Λ of the colliding ions, and, to a lesser extent, their energy.

The first large p-p detectors for LHC are being drafted and must be closely analyzed in view of their applicability for the main ion beam tasks.

Above all, the phenomenology of the *signatures* has outgrown the days when effects of a dense final state were attributed to QGP for lack of alternatives: we need now a degree of sensitivity to the early hot stages of fireball explosions that will allow us to identify the QGP and measure its properties. Here, the significance of heavy meson survival and the thermal photon hunt (real and virtual) are among the first tasks.

References

- [Agu88] M. Aguilar-Benitez et al., Z.Phys. C40 (1988) 321.
- [Alb90] C. Albajar et al., CERN Preprint, CERN-PPE/90-154 (Oct. 1990); see also Phys.Lett. B200 (1988) 380.
- [Ant76] Yu.M. ANTIPOV et al., Phys.Lett. 60B (1976) 309.
- [Aok89] S. Aoki et al., Phys. Lett. B224 (1989) 441.
- [Aud90] LHC/Ions/Dileptons Working Group; the complete collection of the Minutes can be obtained from the author or via e-mail from RMAUDRIA@CERNVM.
- [Bad83] J. Badier et al., Z.Phys. C20 (1983) 101.
- [Bad79] J. Badier et al., Phys.Lett. 86B (1979) 98.
- [Bal89] A. Baldissari et al., Annecy Preprint LAPP-EXP-89-15 and Proc. Internat. Conf. on High Energy Physics, Madrid (1989), and private communication from D. Jonan.
- [Bar90] H.W. Barz et al., Darmstadt GSI 90-55 (Sept. 1990).
- [Ber90] L. Bergström et al., PSU/TII/63 and USITP-90-03.
- [Cas90] P. Castorina, Contribution to the Aachen Workshop, these Proceedings, this Vol.
- [Cra78] N.S. Craigie, Phys.Rep. 47 (1978), 2.
- [Gav90] S. Gavin, Contribution to the Aachen Workshop, these Proceedings, this Vol.
- [Glo88] E.W.N. Glover et al., Z.Phys. C38 (1988) 473.
- [Gup90] S. Gupta, Contribution to the Aachen Workshop, these Proceedings, this Vol.
- [Kar90] F. Karsch, Contribution to the Aachen Workshop, these Proceedings, this Vol.
- [Hei90] The formula is basically due to U. Heinz to whom I am indebted for a discussion.
- [Kam89] B. Kämpfer et al., "Correlations between Dilepton Yields and Pion Multiplicities", Darmstadt, GSI 89-23 (1989).
- [Koc90] P. Koch et al., Univ. Regensburg Preprints TPR-90-7 and TPR-90-8 (Feb. 1990).
- [Kou80] C. Kourkoumelis et al., Phys.Lett. 91B (1980) 481.
- [Neu89] M. Neubert, Z.Phys. C42(1989)231.
- [Roh90] T.F. Rohaly, Contribution to the Singapore Conference on High Energy Physics (Aug. 1990).
- [Ruu90] V. Ruuskanen, Contribution to the Aachen Workshop, these Proceedings, this Vol.
- [Son90] P. Sonderegger, Ion Collisions at LHC, Experimental Areas section, these Proceedings, Vol. III.
- [Spe90] H. Specht, Ion-Ion Collisions at LHC (Experiment), Plenary Talk, these Proceedings, Vol. II.
- [Uen79] K. Ueno et al., Phys.Rev.Lett. 42 (1979) 486.
- [Wil83] NA34/IHELOS: W. Willis et al., Lepton Production, CERN SPSC/83-51/P189. Analysis both of missing energy and of e- μ pairs is under way (private communication from J. Schukraft).
- [You90] G. Young et al., RHIC Letter of Intent, 30 Sept. 1990.

REMARKS ON HYPERON DETECTION AT LHC

E. Quercigh, CERN

These remarks stem from several discussion had within our strangeness working group (B. Fritman, U. Heinz, P. Koch, E. Quercigh, H. Stroebele and O. Villalobos-Baillie) and with P. Jarron, H. Heijne and M. Campbell who are well known experts in microdetectors. Useful remarks from P. Giubellino and J. Schukraft are gratefully acknowledged.

1 Why Hyperons ?

The study of hyperon production in central heavy ion collisions has been proposed (see for instance: P. Koch, B. Muller and J. Rafelski, Phys. Rep. 142 (1986) 167) as a useful diagnostic tool for the onset of a Quark-Gluon Plasma (QGP) phase in the early stages of the reaction; the formation of a QGP could give rise to an enhancement of hyperon and antihyperon yields with respect to normal hadronic reactions.

Enhancements of Λ and $\bar{\Lambda}$ yields relative to pions have been observed, in 200 · Λ GeV/c sulphur-sulphur and sulphur-tungsten central collisions, by the NA35 and WA85 experiments at the CERN SPS. Data on the production of Ξ^- and $\bar{\Xi}^-$, which are necessary to understand the nature of the $\Lambda/\bar{\Lambda}$ enhancements, are now forthcoming and plans are being made to pursue the study of hyperon production with heavier projectile nuclei using a Pb ion beam at 160 · Λ GeV/c from the CERN SPS. It seems therefore natural to look now into the physics interest and the technical feasibility of hyperon detection in Pb + Pb collisions at the future LHC.

The physics case for hyperons at LHC energies has been neatly summarized by U. Heinz at this Workshop. I shall therefore concentrate on the experimental aspects of their detection.

2 Hyperon detection in Pb+Pb collisions at LHC.

In a central Pb + Pb collision at $\sqrt{S} = 1300$ TeV, one may expect about 3000 particles (charged + neutrals) to be produced per unit rapidity interval: amongst these one should find, extrapolating from existing CERN and Fermilab data, about 100 hyperons. We shall consider the possibility of detecting them at central rapidity i.e.

in one unit pseudorapidity interval centered at zero which corresponds to production angles between 60 and 120 degrees with respect to the beam axis.

Hyperons can undergo strong decay [all hyperons from the higher SU3 multiplets and the Σ (1385), Ξ (1530) from the $JP = 3/2 +$ decuplet], electromagnetic decay [Σ^0] or weak decay [Λ, Σ, Ξ from the $JP = 1/2 +$ octet and Ω^- from the $JP = 3/2 +$ decuplet]. It seems unlikely that charged particle identification alone, i.e. without decay vertex reconstruction, would be sufficient to detect them. A possible exception is the $\Lambda(1520)$ which may have a chance to be detected above the combinatorial background through its decay into proton + K^- (B.R. = 45%) because of its narrow width (15.6 MeV/c); such a possibility will not be further investigated here.

In what follows we consider only those hyperons which decay weakly; since these have an average decay length of a few centimeters per GeV of momentum ($\Lambda : 7.1$ cm/GeV; $\Xi^- : 3.7$ cm/GeV; $\Omega^- : 1.5$ cm/GeV), a measurement of both production and decay vertices to better than 1 millimeter in space permits to isolate the decay tracks from all the other secondaries; these hyperon could therefore be identified without having to handle a prohibitively large combinatorial background. We furthermore exclude those decays which have neutral pions or neutrons amongst the decay products because of the difficulty of reconstructing their momenta in a high multiplicity environment.

We are then left with three species of hyperons carrying one, two and three units of strangeness respectively: Λ , Ξ^- and Ω^- . We shall therefore look for the decay of the Λ into proton + π^- and of the Ξ^- (Ω^-) into $\Lambda + \pi^-$ (K^-).

In a central Pb + Pb event we could expect (without QGP) about 50 Λ 's, 5 Ξ^- and 0.5 Ω^- (antiparticles included) per rapidity unity. To illustrate the main features of these events, in Fig.1 is sketched the decay of a central rapidity ($Y=0$) low transverse momentum ($PT=0.5$ GeV/c) Ξ^- , into a π^- and a Λ which in turn decays into a π^- and a proton. Both decay planes have been chosen to coincide with the plane of the figure. The Ξ^- and Λ have average decay lengths and both decays have their most likely configuration i.e. they correspond to the Jacobian peak (90 degrees in the c.m. with respect to the line of flight). All tracks are drawn as straight lines i.e. there is no magnetic field (in a magnetic field of two Kgauss which seems adequate for momentum measurement on the decay tracks, these would still look rather straight since all sagittas would be smaller than 1 millimeter).

The reconstruction of the decay vertices requires extrapolation of low momentum (few hundred MeV/c) tracks. Because of multiple scattering errors, the requirement of an accuracy of 1 millimeter in space on the vertex position seems difficult to meet if the distances over which one extrapolates were to exceed 10-20 centimeters. As a consequence one needs a detector near the interaction point i.e. in a region where the maximum track density through a cylindrical surface around the beam axis exceeds 1 track per cm^2 . Such track densities are larger than what most practical detectors can handle.

A possible way out could however be offered by the use of a high resolution,

multi-layer silicon detector situated near the interaction point to provide vertex reconstruction, together with more conventional tracking devices situated at a safe distance, to provide momentum measurement in a magnetic field.

R & D work on high resolution Si-pixel detectors has started and the status of these developments is described in a paper presented by H. Heijne at this Workshop. A starting point for a simulation study of an hyperon detector inspired by the technical developments described in H. Heijne's paper, could be given by the following example:

The fine-grained multi-layer detector consists of 5 cylindrical layers of silicon pixel detectors, coaxial to the beam with radii from 5 to 9 centimeters and an azimuthal coverage of 180 degrees. In Fig.1 the intersection of these layers with a plane perpendicular to the beam axis are shown superimposed to the decay. A possible choice for the pixel size is (200 micron)². The pixel detectors are hybrid devices with on-chip signal processing and sparse data readout. The detector material seen by a particle crossing it at 90 degrees should not exceed 0.6% of an interaction length and 2% of a radiation length. Assuming a length of 30 centimeters ($\pm 2 \sigma$'s on the LHC bunch length), the detector has a total surface of about 0.33 square meters, and it consists of 8.25 millions of pixels. The total power dissipation would be of about 250 watt.

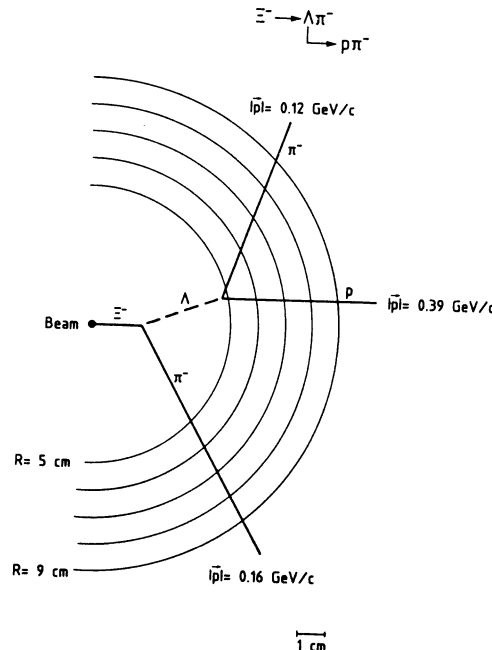


FIG. 1

BOSON INTERFEROMETRY at RHIC and LHC (I)

Physics, Experimental Difficulties and Possible Solutions

Daniel Ferenc¹ and Guy Paic^{1,2}

(1) Rudjer Boskovic Institute, P.O.B.1016,41001 Zagreb,
Republic of Croatia, Yugoslavia
(2) GSI Darmstadt, Germany

Abstract

The expected signature of the first order QCD phase transition is a very long lifetime of the system created by the ultrarelativistic nuclear collision. On the other hand, without phase transition, the hadronic gas is expected to reach a very large transverse size (considerably larger than in case of the phase transition). The present public opinion seems to be that the expected very large lifetimes and transverse sizes ($t, R > 20$ fm), hence the correspondingly very narrow two-pion correlation functions, cannot be measured, because of the insufficient momentum resolution and some other related problems. However, we recall here that, due to the same kinematical rules which enable one to extract important information about the internal motion (hydrodynamics) of the rapidly expanding system by interferometry, the effective measured size may be (under certain conditions) much smaller than the real size. The point is that one is therefore able to measure very large sizes or lifetimes with pion and kaon interferometry indirectly, by measuring much shorter, and therefore measurable effective sizes (the "short ruler method"). The procedure is proposed specifically for the measurement of the expected very long (normally unmeasurable) lifetime, being the signature of the phase transition. Finally, a minimal set of characteristics for the detector capable of doing the proposed sort of analysis is listed.

1. Introduction

In the ultrarelativistic nuclear collisions at RHIC and LHC one hopes to be able to study physics of the extremely hot matter at very high energy density. The QCD phase transition is expected to take place under such conditions. The space-time development of the system created in the collision strongly depends on the actual dynamical scenario. However, the pion interferometry may yield unique information about the space-time development of the system [1,2,10], and is therefore of crucial importance for the future studies at nuclear colliders. In this article, we shall first discuss the global expectations on the size and lifetime of the system, both in case of the first order phase transition, and in case without phase transition. After that we shall discuss the ability of the pion interferometry to measure the expected magnitudes. For instrumental reasons the pion interferometry is probably not capable of measuring the expected very large magnitudes. The crucial point of this article is to demonstrate how pion interferometry may still, thanks to a slightly changed approach, yield very important information. Namely, simple kinematical considerations show that one can measure the proper lifetime of the system indirectly, by measuring the effective longitudinal size, which has (under certain conditions) a shorter natural scale and therefore can be measured.

This work was supported in part by the US-YU Fund JF858 (DOE)

2. The expected magnitudes of the lifetime and the transverse size

Global expectations for the size and the lifetime of the system shall be discussed, both in case of the first order phase transition, and in case without phase transition. Let us first discuss what has to be expected if there is no phase transition. Hadronic gas is created during the formation process, and multiple collisions among the created hadrons take place until the system reaches the freezeout conditions (the mean free path becomes gradually longer than the system size). Calculations [3] show that at rapidity density expected at the LHC, the hadronic gas should reach a very large transverse size, $R_T > 20$ fm at the freezeout time. The important input parameter in this calculation [3] is the total cross section of pion-pion scattering, which was assumed to be about 20 mb. However, a very strong dependence of the cross section on temperature (and pion chemical potential) has been reported recently [4,5,6]. It turns out that the mean time between two collisions t_{coll} depends on temperature T as T^{-5} . Therefore [4], e.g. at $T = 200$ MeV, t_{coll} is only 0.7 fm, while at $T = 100$ MeV, t_{coll} is even 25 fm! The transverse size therefore strongly depends on the actual temperature, and might be much larger, or much smaller than the value of 20 fm, already for a small variation of temperature.

Let us now discuss the other physical scenario, when the first order phase transition takes place. The fundamental difference between the quark-gluon and the hadronic phase, is a large difference in the entropy densities, or the numbers of degrees of freedom. Namely, the ratio of the numbers of degrees of freedom is more than 10 in favour of the quark-gluon phase. The other interesting feature is the existence of the mixed phase. The velocity of sound in the mixed phase is vanishing, or in other words, there is no pressure gradient in the system; the pressure is constant. It was suggested [7,8,10] that a shock wave moves radially from the periphery of the cylinder-like system towards the center, and the pure hadronic phase is created on its front. The shock wave speed is lower than the speed of sound in hadronic phase, which is considerably lower than the speed of light. Transverse rarefaction is therefore very slow, and the system cools faster by the rapid longitudinal expansion. According to the simple one-dimensional (longitudinal) hydrodynamics, the lifetime of the system is proportional to the ratio of the numbers of degrees of freedom in both phases. This ratio being large the lifetime is correspondingly very long: e.g. $t > 20$ fm. In fact, all different theoretical assumptions about the initial conditions etc. (e.g. fluid dynamics, Bjorken Scaling Hydrodynamics - considered above, Landau Hydrodynamics, droplet models etc.) come to the same conclusion: the lifetime has to be much longer in case of the first order phase transition, than without phase transition.

The transverse size of the system in case of the first order transition might well be much smaller than without phase transition. Due to a very long lifetime, the hadronic phase is created at a much slower rate and consequently along a much larger longitudinal range, than in case of the fast direct formation (without phase transition) of a dense hadronic gas. Therefore, rescattering in the hadronic phase is weak. On top of that, the mixed phase does not expand much radially, because there is no pressure gradient, or in other words, the equation of state is "soft", and there is no transverse flow. The signature for that must also come from the single particle spectra, in the form of a plateau in the $\langle P_T \rangle$ vs dN/dY -plot [4]. Other, more violent modes of decay of the mixed phase are also possible, particularly if the initial energy density significantly exceeds that needed for the quark gluon plasma formation [4,7]. Then a strong transverse flow is possible.

3. Pion and Kaon Interferometry at LHC and RHIC

The lifetime of sources of bosons may be conveniently measured by the study of the two boson correlation function, as a function of the energy difference corresponding to

boson pairs. An example of this approach is the parametrization suggested by Kopylov and Podgoretskii [9]. Recently, a very similar approach was suggested [8,10], according to which a specific cylindrical symmetry, instead of a spherical symmetry, was assumed. The source was supposed to be cylindrically shaped, and subject to the Bjorken Scaling Hydrodynamics, and in [10] also to a general hydrodynamic space-time development. Scaling hydrodynamics means that the physics of the system does not depend on rapidity, but depends only on the proper time. A plateau in rapidity distribution is the obvious consequence, and the other, very important for pion interferometry (that shall be explained latter in some more detail), is a direct proportionality between the longitudinal speed of a local source element, and its longitudinal space coordinate. Kinematic variables in [8] were defined as follows. Difference of the two pions' transverse momentum vectors, which is invariant to boosts along the collision axis, may be decomposed into two components: one perpendicular to the sum of the two transverse momentum vectors, called $Q_{T\text{side}}$, and the other parallel to the transverse momentum sum vector, called $Q_{T\text{out}}$. The following parametrization of the correlation function was used in [8]:

$$C(Q_{T\text{out}}, Q_{T\text{side}}, Q_L) = 1 + \lambda \exp(-Q_L^2 R_L^2/2) \exp(-Q_{T\text{side}}^2 R_{T\text{side}}^2/2) \exp(-Q_{T\text{out}}^2 R_{T\text{out}}^2/2). \quad (1)$$

In order to measure the lifetime, one investigates the two-pion correlation function as a function of the $Q_{T\text{out}}$ component, effectively at very small $Q_{T\text{side}}$ and very small Q_L . In other words, one considers only pion pairs of nearly parallel momentum vectors, perpendicular to the collision axis. Since the other components of the momentum difference vector are small, $Q_{T\text{out}}$ component is nearly equal to the energy difference (particularly for $P_T \gg$ pion mass), which demonstrates the analogy with Kopylov-Podgoretskii method.

Confronted with the experimental difficulties linked with the required resolution, we propose to give up the traditional "long ruler" concept of pion interferometry, based on the ambition to measure the total length or lifetime of the system "completely at once". Instead of that, the "short ruler" concept is introduced, by recalling some very simple relativistic kinematics arguments. It turns out that, under realistic conditions, relativistic kinematics prevents us from measuring the "real" longitudinal size of the system, but on the other hand helps us to measure both, the parameters of the space-time development of the system (hydrodynamic regime etc.), and the proper lifetime of the system [1,2,10]. We want to point out the importance of both aspects, particularly of the latter one as a possible unique technical help in solving the problems arising from the narrowness of the correlation function accompanied by a limited experimental resolution.

The space-time development of the system may be (approximately) described by the Bjorken Scaling Hydrodynamics [11], in which the source is supposed to rapidly expand along the collision axis during the emission of particles. There is a strong correlation between the space-time coordinate of an elementary local source (fluid element) and its longitudinal velocity. Like the galaxies in the Universe, all the elementary sources move (but here only longitudinally) away from each other the faster, the larger the distance between them. Due to a sort of the red shift effect, it is hard to find two pions with equal longitudinal momenta, which originate from two distant local sources. Pion interferometry, which needs pions of almost equal momentum vectors, measures therefore only that short section of the whole source, which is short enough to be capable of radiating pions with similar momenta from "both ends" of the short section. It was shown, for a general hydrodynamic system (not only

Scaling) [10], that the effective section length is sufficient to determine the total proper lifetime of the system! If one assumes that the momentum spectrum of radiated pions in the rest frame of the local source is thermal and isotropic, then the effective segment length measured by the pion interferometry (in a "sliding observer" reference frame [12], in which the total longitudinal momentum of each pion pair is zero) equals [10]:

$$R_L(y, m_T) = (2T_f/m_T)^{1/2} t(y), \quad y = (y_1 + y_2)/2 \quad (2)$$

where T_f is the freezeout temperature, m_T is the transverse mass and $t(y)$ is the proper lifetime of the system.

It is important to note the specific dependence of the apparent length R_L on the transverse mass m_T in Equ.2. We shall try to explain that behavior in a qualitative way (for details, see [1,2,10]). Since the spectrum of the radiated pions is nearly thermal and isotropic in the rest frame of the corresponding local source, the total momentum of each pion is practically limited in its magnitude. Therefore when we select only pions with very high transverse momenta, it is very unlikely that their momentum vectors could point along the collision axis, since the total momenta should be almost completely contained in their transverse components. Consequently, when two rapidly receding local sources radiate pions of very high transverse momenta, and therefore of very small longitudinal momenta, due to the strong relativistic boost of the two longitudinal momenta in the opposite directions, it is very unlikely or even impossible that the two pions could ever have nearly equal momentum vectors in any reference frame (e.g. in the one symmetric with respect to both local sources). Since the pion interferometry needs close momentum vectors, it is not going to work for high- P_T particles, unless the relative speed of the two receding local sources is very small so that the relativistic boost of momenta is negligible. Since there is a strong correlation between the longitudinal space coordinate and the longitudinal velocity for each local source, the requirement for a small relative speed is equivalent to the condition of small relative longitudinal distance between the two sources. Therefore, by selecting only particles of high transverse momenta, one measures much shorter effective longitudinal distances, than by selecting only low- P_T particles. The "short ruler" concept is based on our ability to reduce the effective measured longitudinal size, by selecting bosons of relatively high transverse masses (high transverse momentum, and/or high rest mass). From the experimental point of view, it is essential that the corresponding width of the correlation function as a function of Q_L becomes much wider and therefore less sensitive to resolution problems.

Since the values for all parameters in Equ.2. should be known (at least approximately) and R_L could be measured, one should be able to determine the proper lifetime t , our main goal in detecting the phase transition by pion interferometry. It was shown [10] that the study of the effective longitudinal size as a function of both, rapidity and transverse momentum, has a unique power in distinguishing different dynamical space-time scenarios, like the Landau Hydrodynamics, Bjorken Scaling Hydrodynamics, or no hydrodynamics (spherical static fireball). For any hydrodynamic system, dependence of the effective length on m_T in Equ.2. is characteristic, while different hydrodynamic regimes may be distinguished from the $t(y)$ -dependence (e.g. $t(y)=\text{const}$ for the Scaling regime). For the first preliminary experimental results on that subject see [12]. Therefore, before extracting the lifetime from Equ.2., one has to insure that the hydrodynamic regime is relevant, and the only way to do that is to check whether the m_T -dependence from Equ.2. holds. The single particle spectra must have certain

characteristics too, like e.g. a plateau in dN/dy spectrum if the Scaling Hydrodynamics is relevant, or a bell-shaped spectrum if the Landau Hydrodynamics is relevant etc.. Generally, dN/dy has a similar shape like $t(y)$, see [10].

In case of a phase transition the transverse size could stay relatively small [7,8], for reasons explained above. It means that the $Q_{T\text{side}}$ component from Equ.1., which measures the spatial transverse size of the system, may be normally measured, since the corresponding width of the correlation function would be large enough.

In case that in any physical scenario a strong transverse flow is present, a reasoning similar to that applied to the longitudinal component, applies also to the transverse component [1,2,10]. The "short ruler" method then applies also to the measurement of the transverse size.

Let us now discuss some conceptual difficulties. When all the variables are measurable, one fits the correlation function in the $(Q_L, Q_{T\text{out}}, Q_{T\text{side}})$ momentum space to Equ.1., and gets the corresponding radii for each component. On the other hand, one may also project all the experimental data to any single coordinate, e.g. to Q_L . Then a lot of information is averaged out, and the apparent correlation intensity is too weak. However, a sort of compromise seems to work very well on the existing data [12], namely one projects the data onto one of the momentum axes, but only that momentum space volume is projected which contains the most of the interferometric information. Since the effect is contained in the low relative momentum region, when projecting data e.g. to the Q_L axis, one has to apply a cut on the other two variables, like $(0 < Q_{T\text{side}} < Q_{\text{cut}}, 0 < Q_{T\text{out}} < Q_{\text{cut}})$. The width of the projected correlation function (i.a. the source size) seems to be rather insensitive to the applied Q_{cut} value, only the effective correlation intensity drops down considerably with increasing Q_{cut} . Insufficient experimental resolution would smear out the correlation function in $Q_{T\text{out}}$ variable, making it much wider and distorted. But the correlated pairs are still within few times the original width in $Q_{T\text{out}}$, and one is free to cut e.g. at a Q_{cut} value equal to several times the original width, thus incorporating a large part of the region containing the correlated pairs on one hand, and not too many uncorrelated pairs on the other hand. Another very important difficulty is the problem of corrections for Coulomb repulsion of the like-sign pions. Instead of the usual Gamow correction, a completely different approach is possible. One should consider both positive and negative pions in the same event, and measure the Coulomb attraction. By measuring the Coulomb attraction between the oppositely charged pions in the same variable (Q_L) and under the same kinematical and acceptance conditions used for the like sign pions in interferometry, one is able to get a much more realistic correction in a single variable (Q_L) of interest. Of course, the effects of smearing, differences in acceptance of close like sign and opposite sign pions, etc. have to be carefully studied for a particular detector.

Still, the problem of hadronic resonances [13] remains. The presence of some long lived resonances causes serious ambiguities in the interpretation of the interferometric results, because it is not clear e.g. whether the long measured lifetime comes from the real long lifetime of the source, or it comes from a large yield of long lived resonances. The measurement of the yields of the resonances would therefore be very helpful.

4. Detector

A global set of requirements for the future detector system suitable for pion and kaon interferometry at LHC or RHIC, follows.

1. A large acceptance tracking detector which covers at least four units of rapidity (out of e.g. eighteen at LHC), and measures both charges, is needed for the following reasons:
 - (i) for the event preselection on a single-event basis (in order to trigger "off line" on single-event temperature parameter), because high statistics is necessary for single-event temperature measurement, and because the fluctuations in the single-event measured temperature parameter, coming from a limited phase space, or from considering a single charge, tend to spoil the selection.
 - (ii) different (hydro)dynamical scenarios may be distinguished in a study of the effective longitudinal size as a function of both, rapidity and transverse momentum; also the single particle spectra are needed for that in a wide phase space range
 - (iii) Coulomb correction could be done by the measurement of the Coulomb attraction between the oppositely charged pions, therefore one needs particles of both charges from the same event, in the same acceptance.
2. Since in the "short ruler" method one uses high- P_T particles, the momentum resolution should be accordingly optimized.
3. The measurement of yields of the hadronic resonances would be very helpful.
4. Good particle identification is needed, at least for two reasons:
 - (i) First, the "short ruler" method needs bosons of high transverse masses, which means large transverse momentum and/or large rest mass. Accordingly, kaons should be identified in order to be used in the interferometry. Besides that, kaons are less sensitive to the difficulties coming from the long living resonances [13].
 - (ii) When pions are considered, one should ideally have a pure pion sample, i.e. one should not mix kaons, electrons and other particles with pions.

References:

1. S.Pratt, Phys.Rev. D33(1986)1314
2. B.Andersson and W.Hofmann, Phys.Lett. B169(1986),364
Y.Hama and S.Padula, Phys.Rev. D37(1988)3237
3. R.Stock, "Pion Interferometry in High Energy Hadron and Nuclear Collisions: Radial Expansion and Freeze-out", to be published in Annalen der Phys.
4. E.V.Shuryak, Report BNL-44859, to be published in Nucl.Phys. A
5. P.Gerber and H.Leutwyler, "Kinetics of an Expanding Pion Gas",
Report BUTP-90/16
6. G.Bertsch, M.Gong, L.McLerran, V.Ruuskanen and E.Sarkkinen, Phys.Rev D37,(1988)1202
7. B.L.Friman, K.Kajantie and P.V.Ruuskanen, Nucl.Phys. B266(1986)468
8. G.Bertsch, M.Tohyama and M.Gong, Phys.Rev. C37(1988)1986
9. G.I.Kopylov and M.I.Podgoretskii, Sov.J.Nuc.Phys. 15(1972)219
10. A.N.Makhlin and Yu.M.Sinyukov, Z.Phys. C39(1988)69
Yu.M.Sinyukov, Nucl.Phys. A 498(1989)151c
Yu.M.Sinyukov, V.A.Avarchenkov and B.Lorstad, LUNDFD6/(NFFL-7055)1990
11. M.I.Gorenstein, Yu.M.Sinyukov, V.I.Zhdanov, Phys.Lett. B71(1977)199
J.D.Bjorken, Phys.Rev. D27(1983)140
12. D.Ferenc et.al., R.Boskovic Inst. Report IRB-FEP 01-90, Talk at CAMP workshop,
Marburg, May 1990., (World Scientific Pub. 1990.)
D.Ferenc, Talk at XXV Rencontres de Moriond, Les Arcs, March 1990., (Editions
Frontieres 1990.)
13. S.S.Padula, M.Gyulassy, Talk at QM 90., Menton, to appear in Nucl.Phys. A

D: ADDITIONAL PAPERS FOR VOLUME III

Vacuum Microelectronics

G. H. Grayer (RAL)

D2: SIGNAL PROCESSING

Introduction

The last few years have seen references in scientific and economic literature to research and development taking place on "vacuum microelectronics", but few in the particle physics community seem to know more than these brief, second hand reports, mostly written for a non-scientific readership. The interest of these devices is obvious when it is realised that one of the driving forces for this R. and D. is the military need for electronic components which can withstand very high doses of radiation, which is endemic in experiments involving the new generation of hadron particle accelerators (the SSC in Texas, and the proposed LHC near Geneva). The author therefore arranged to visit one of the centres of research on these components, and the information obtained there formed the principle source material for this summary.

What is Vacuum Microelectronics?

Vacuum microelectronics (abbreviated as VM in this text) is based on the control of electrons in a vacuum by electrostatic and possibly magnetic fields. Only in this respect does it resemble the technology of thermionic vacuum devices, which have now largely been superceded by semiconducting solid state components. In contrast with "valves" (referred to as "tubes" in the U.S.A.), which involved structures between 1 and 10 cm approximately, the "micro" prefix shows that these devices are very small, involving structures measuring only a few micrometres, a scaling down of no less than 10^4 . Their fabrication involves similar techniques to those used in the semiconductor industry. The other major difference is that electrons are not obtained by thermionic emission involving a heated cathode, but by the emission of electrons in an intense electric field (field emission). This is one of the undesirable features of the characteristics of the thermionic valve, which manifested itself as an increase in anode current (I_a) with increasing anode volts (V_a), normally after saturation of thermal emission had been realised (fig.1). Under these conditions, very high voltages are required to obtain measurable field emission; the aim of VM is to develop high

fields at moderate voltages, relying on the enhancement of the electric field around sharp structures.

Advantages of Vacuum Microelectronics

The primary attraction of VM for applications in particle physics experiments is its extreme resistance to the effects of any kind of ionizing radiation, in view of the high levels of radiation which are expected in the forthcoming generation of accelerators. Since the flow of electrons is through vacuum and not through any matter, there is no danger of damage to the electronic properties of the device. The ultimate limit is presumably when the dose received is such that the structure fails mechanically, or when the flux of radioactive charged particles (of internal or external origin) become sufficient to disrupt the electronic functioning of the device through modifying potentials.

Compared with thermionic vacuum devices, there is a saving in power, heat, and number of connections through the use of field emitting cathodes. The development of these devices depends critically on being able to achieve a rugged, reliable, and long-lived field emitting structure.

The property of small size is obviously essential in achieving competitiveness with modern semiconductor devices. Together with the high mobility of electrons in vacuum and the low capacitance due to the low permittivity of vacuum and small size, this will result in extremely fast devices.

Sources of Information

The principle vehicle for the exchange of information on VM is an annual series of conferences. The last one for which proceedings are presently available (October 1990) was that in Bath, England last year [1]. The third such Conference was held in Monterey, USA in July 1990.

Research Centres

The active research which is known to the author consists of the following. The Stamford Research Institute (SRI) and the Sandia Laboratories, California, USA, are probably the most advanced, other development taking place at the Naval Research Laboratory and elsewhere. There is certainly some activity in Japan, though little seems known about it. In Europe, Thomson-CSF in collaboration with LETI, Grenoble, France, and in England the GEC Hirst Research Centre (HRC) at Wembley and the Thorn-EMI Research Centre in Hayes are known to be active. The research taking place falls into three principal categories: (i) fundamental research, mainly directed at understanding the factors which control field emission; (ii) development of practical cathode structures which satisfies the requirements of high

emission and longevity; and (iii) the identification of the most suitable applications in terms of devices suitable for fabrication in VM. Although these may be carried out as separate activities, obviously to a large extent (ii) depends on (i), and (iii) on (ii). I will now treat each of these areas one at a time.

Fundamental Research

Since the essential and novel aspect of VM devices is the field emitting cathode, understanding this effect to a level where design and prediction can be carried out is obviously very important. This is being studied on both a theoretical and experimental basis [2].

Field emission is basically a tunneling effect as shown in fig. 2. Attempts are being made to obtain agreement between the calculated field emission and that measured experimentally. There are some interesting theoretical aspects of this problem; for example, when the electron is outside the material, it sees an image charge in the metal which results in electrostatic repulsion, increasing the energy of the electron. Since the quantum mechanical wave-function which describes the tunneling effect has a finite value outside the material, the question exists as to the amount this increases the probability of escape of the electron inside the material.

Apart from thinking about such problems as these, on the experimental side the HRC group is attempting to measure the shape of the surface barrier. It is doing this by shining light onto the surface of the material; this can be absorbed by an electron in the conduction band and elevated to an excited state. The probability that this electron tunnels through the barrier gives some measure of its width (fig. 3).

Cathode Development

As mentioned above, the cathode development programme is aimed at producing high emission, reproducible, and reliable cathodes. The emission depends of course on the material forming the surface of the cathode. High emission also implies a strong field, which is obtained by forming a very sharp structure. The fabrication of this depends on the material used and the method of forming the point. Investigations, both theoretical and practical, are being made into the formation of the pointed cathode by etching and abrasion [1]. Computer models of these processes are being used in this study.

A typical cathode structure is shown in fig. 4. Approximate dimensions are a few micrometres, as shown. The radius of the point itself lies in the range 5 to 50 nm, the smallest being only a few molecules across, hence not resolvable even with an

electron microscope. The "grid" structure near the cathode - in reality a very small hole through which the point of the cathode appears - is to enhance the field at the cathode. Various materials are being tried for fabrication of the cathode structure, included coated structures and liquids [1]. Though the overall basic structure will be fabricated from silicon, as the technology for the manipulation of this material is most advanced, it is not expected to be a good material for the cathode structure. Metals seem to be the most promising candidates. Typically, currents of a few tenths of a microampere are obtained from these structures with potentials of a few hundred volts.

Device Characteristics

Because the probability of an electron tunneling through the surface potential barrier decreases rapidly with increasing width, the electrons emitted all tend to come from the upper energy level in the conduction band. The electron spectrum is thus a fairly tight distribution around the Fermi energy (fig. 5a), in contrast with thermionic devices which show a large spread in electron energy. This results in (fig. 5b) a very steep dependance of anode current on grid voltage (I_a/V_g), implying a high amplification factor. The operating point, however, would seem to be difficult to control. It is anticipated that multi-grid structures will be utilised in amplifying or logic devices, in order to stabilise the emission. These extremely small structures can, of course, easily be damaged by too much current flowing, and suitable protection must be arranged. However, it may be that space charge may itself be sufficient to stabilize emission. This may also limit the noise which tends to occur from irregularities in the emission from field effect cathodes.

Device Identification

Apart from military requirements, the most important incentive at the present time is the development of a flat screen television display, which would obviously reduce enormously the bulk, weight, and power consumption of a television receiver. Working prototypes have been demonstrated. Once practical, reliable field emission cathode structures can be fabricated with a good yield, they can be expected to replace thermionic cathodes in conventional macroscopic devices. This will be most useful in situations where power consumption is critical, e.g. for travelling wave tubes in satellites [2]. Obviously longevity is an important criterion in this application. Arrays of at least 10^6 VM cathodes will be required for macroscopic tubes, but the emission per unit area actually exceeds that of a conventional thermionic emitter.

The first genuine VM devices are almost certain to be digital, since the V/I curve favours this approach, and digital devices are likely to be much more tolerant of changes in emission. Eventually, amplifying devices can be expected. It is these

which are perhaps most interesting for the particle physics community, since the innermost detector system in the experiments on the generation of high intensity accelerators which are just being commenced are in an extremely high radiation environment, and will almost certainly require local amplification. The detectors themselves are somewhat problematic, needle chambers relying on the same micron sized point technology being under development. Gallium-arsenide diode detectors are another possibility, though doubts have been expressed that they are significantly better than silicon detectors.

Conclusion

It is expected that viable cathode structures will be produced within the next two years. Allowing for subsequent device development and production plant to be set up, I would be surprised to see devices on the market in less than five years. Moreover, the first devices will probably not be of interest to particle physics. Thus we can probably assume that these devices are unlikely to be available for the first round of super-collider experiments. However, these experiments will probably not be able to exploit the full intensity capability of the accelerators, and for subsequent generations of experiments these devices could well be the only solution for local (on detector) electronics.

The question then arises whether we can help in the development of these devices. It seems to me that, with only limited resources, a long term time scale, and other commercial incentives for industry, we need not at the moment need to consider participation. The situation might seem different in a few years when the devices are shown to be practicable, and development of types suited to our requirements is necessary.

References

- [1] Proceedings of the Second International Conference on Vacuum Microelectronics, Bath, 24-26 July 1989; ed. R. E. Turner (IOP 1989).
- [2] N.A. Cade and R.A. Lee, "Vacuum Microelectronics", GEC Journal of Research 7, 3, pp.129-138 (1990).

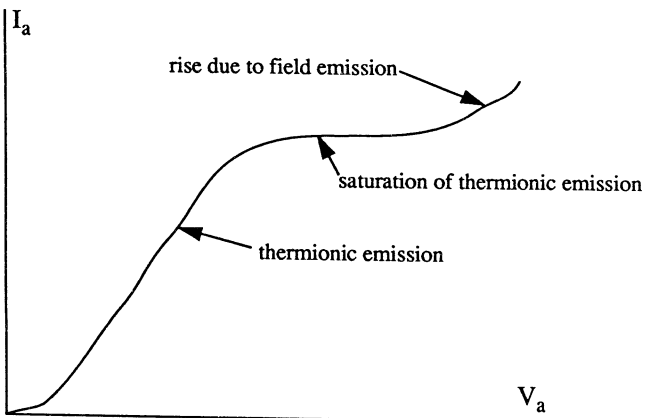


Fig. 1. The effect of field emission on “typical” thermionic valve characteristics.

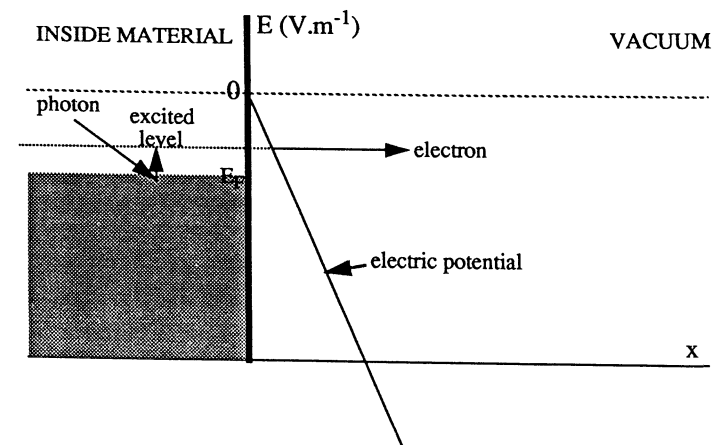


Fig. 3. Measurement of the surface barrier shape by photo-excitation of electrons into an excited state, and measuring their probability of escape.

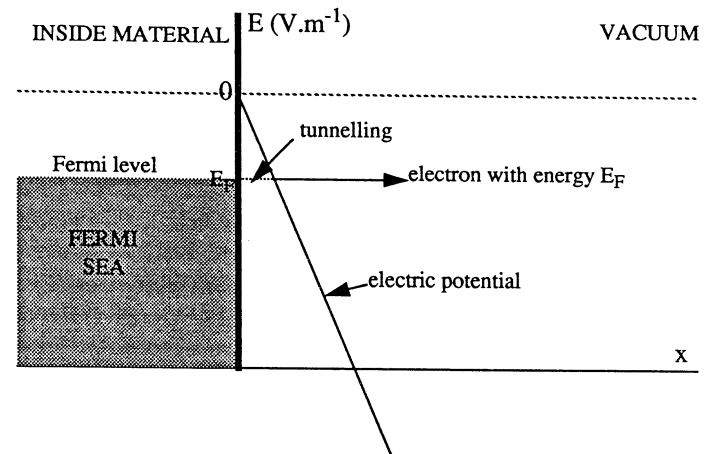


Fig. 2. Field emission of electrons is by tunnelling through the surface barrier. Electrons emerge with an energy close to the Fermi surface.

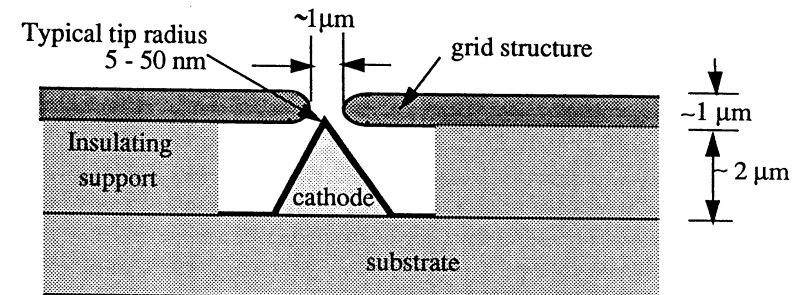


Fig. 4. Typical grid structure and dimensions surrounding a field emission cathode.

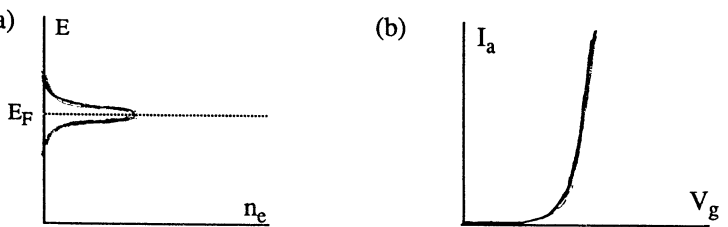


Fig. 5 (a) Energy distribution of emitted electrons; (b) I_a/V_g characteristics.

The Role of Analogue Circuitry in LHC/SSC Triggering

G. H. Grayer (RAL)

Introduction

For the first generation of collider experiments, the advantages and disadvantages of digital and analogue trigger circuitry were strongly debated. This was epitomized in the differing approaches to triggering of the UA1 and UA2 experiments. I think it is fair to claim that the balance of opinion came out on the side of digital processors, and this has been obvious from the second and third generation of collider experiments (CDF and D0 at the Tevatron collider, and the LEP experiments). However, the next generation of machines (SSC and LHC) will have to operate under very much more arduous conditions in speed and complexity, and this re-opens the question whether analogue circuitry has a major role to play. I will first review the conventional wisdom, and then look how this might differ in the new regime.

Analogue vs. Digital

Here is a brief summary of the general arguments put forward in favour of one technique or the other, though their validity depends greatly on the application:

- **Speed.** Analogue used to be used where speed was a priority. Now however this argument can hardly be sustained. Digital circuits have become faster and faster, and at the same time power consumption reduced. Although there is always the overhead of digitization, this can be reduced to nanoseconds where necessary by the use of flash ADCs. This of course takes power, but analogue circuitry is also power-hungry when high speeds are required.

- **Power.** The simplest analogue circuitry is passive, but as soon as active circuits are included, analogue circuitry can consume very large amounts of power. This is because most devices have to support a standing current even in the presence of no signal, in order to retain linearity. Large dynamic ranges require high currents to represent them with fixed precision, as do high speed (fast slew rate) amplifier/buffers. Digital circuits, on the other hand, by using their devices as switches which are either off (no current) or turned fully on (low resistance) limit their I^2R dissipation. The final comparison of power budgets for doing the same task with the two kinds of circuitry finally depends largely on the complexity, precision, and speed required, and must be evaluated in individual cases.

- **Accuracy; precision; stability.** For limited precision (as is often sufficient for trigger systems) analogue circuitry can sometimes offer a much simpler solution. As soon as high precision and accuracy is required, circuitry becomes much more complex and power consumption increases. Cost also increases as components must satisfy closer tolerances. Long term stability, due to the hostile environment found in particle physics experiments, is likely to make performance deteriorate. Digital circuitry, on the other hand, has a precision and accuracy which is exactly determinable, and can be expanded to any desired level. Also correctly designed digital circuitry has immunity to quite large changes in environment (temperature and supply voltage) and ageing. In addition, they possess considerable noise immunity, which is also important in the environment of a particle physics experiment.

- **Design; programming.** Digital circuitry is simple to design compared with analogue. Its results are completely predictable and manipulable, using Boolean algebra, as long as the individual elements operate within their performance specification. Control and programming is more natural, since these will involve digital techniques. Digital storage is easy and accurate; indeed, the usual technique for programming analogue circuitry is by a digital register followed by a DAC.

After these very general remarks, I will now go on to consider in detail the possibilities of analogue circuitry in two of the three main divisions of detectors: calorimeters, tracking devices, and particle identification devices (see Fig. 1). I do not know of any suggested applications to particle

identification devices at the LHC or SSC. Furthermore, I consider only its use at the first or quasi-first level, since this is the critical regime where analogue trigger circuitry could play a part.

Calorimeter Triggers

Although later stages of calorimeter trigger processors tend to be digital, many of the schemes for SSC and LHC experiments plan to retain the raw data in analogue form while a first level trigger is being performed, this being more economical in terms of circuitry, an important factor in view of the large number of channels involved. This does not necessarily imply that the trigger itself is using analogue circuitry, however.

Most trigger systems use a reduced number of channels for the first level calorimeter trigger. The simplest way to achieve this would seem to be a simple passive analogue addition of signals, such as has been done in almost all large collider experiments, from UA1 to the ZEUS liquid argon calorimeter. However Goggi and Löfstedt [1] have pointed out that this can conflict with the optimisation of a system. Briefly, the reasoning is that with the high energies involved, a very large dynamic range (typically 15 bits, or 90 dB!) is required for the calorimetry, but the precision can be significantly less (9 to 10 bits, for the trigger even less), because of the intrinsic resolution of the calorimeter. In view of the large number of channels involved, and the need to reduce the electronics to a minimum, it makes sense to compress the dynamic range in some way. They considered the optimum transfer function, which is here irrelevant; what is not, however, is where this compression is applied to the data. There are three ways to apply this:

- 1) Linear pre-amp and non-linear ADC; this has two difficulties. A non-linear pre-amp with 90 dB dynamic range is extremely difficult to construct, and implies high current consumption. In addition, a non-linear ADC is not an obvious device.
- 2) A non-linear pre-amplifier and a linear ADC; this seems much easier, and accurate logarithmic amplifiers can be constructed which are a good approximation to the optimum.
- 3) A non-linear pre-amp and non-linear ADC; this approach has some advantages and is favoured by the authors.

Only the first approach results in linear signals at a level suitable for addition, and as pointed out this is a very unattractive solution.

Another problem of an analogue addition of channels for trigger purposes is that of noise. For example, the transverse energy trigger adds calorimeter cells over a large part of the experiment. If these are a simple addition, the

resulting noise is obtained by the usual sum of squares over all these channels. A better solution would be to put a threshold on each channel before they entered the sum. An output gated by a discriminator operating on the signal present would be necessary.

Tracking Triggers

The principle difficulty with first level tracking triggers is the number of interconnections which must be made in all three dimensions in order to reconstruct tracks. Even if this is done with local logic, this can be mechanically very difficult. Therefore some coding of position using analogue signals with a single wire have been proposed. However, the problem is one of occupancy; multiple hits could be difficult to handle.

An example is the trigger proposed by R. Nickerson [2] for the silicon tracker on the SSC experiment on the SSC. Each output is weighted by a different value resistor, and the result summed. A linear addition of the outputs is also made, and divided into the other sum. This normalises the result, which is proportional to the centroid of the track in the case of several adjacent hits (see Figs. 2,3,4,5).

Neural Networks etc.

An introduction was given at CERN to the LHC Trigger Group by C. Peterson of Lund University [3]. As background, I refer you to [4]. Since the classic neural network involves feedback or feedforward proportional to some resistance determined by the data, they must be classified as analogue circuits.

Neural networks have the advantage that they are highly parallel analogue computers, and hence fast. They are especially suited to pattern recognition problems, such as track recognition and cluster finding. Their performance in a particular case depends on the number of intermediate levels between input and output and the number of neurons in these levels, as well as the quantity of data used to train the network, and the number of passes made on this set of data. There is still a lot to be done to understand how to optimise these parameters.

Denby et al. at FNAL have made software simulations of track finding using neural network techniques [5]. They have examined the performance for different numbers of training events and different numbers of passes. Most tracks are found successfully, but there is always a residual of tracks not correctly reconstructed. However, this inefficiency may be acceptable for

trigger purposes. It is planned to test its performance under real conditions in a CERN test beam in tests for the SDC experiment (Belletini et al.) [6].

Fast track finding will require special LSICs to implement the neural network calculations. Neural network ASICs can already be purchased commercially, but they are much too slow for this application. However, the problem remains of the number of connections necessary, how these can be brought on-chip, and made in depth on the detector.

A related, but not classical neural network, has been developed by Bonino and Lautrop at CERN [7]. They have built a two-dimensional network which, applied to calorimeter data, finds clusters, gives their energy, and their area. The algorithm which achieves consists of a transfer of energy from cells to the neighbour with higher energy; this process is iterated until all energy is concentrated in isolated cells. Simulation shows that other (software) methods show that resolution of overlapping clusters is not as good as can be obtained by the best methods, but it is sufficient for triggering. The settling time is a few hundred nanoseconds.

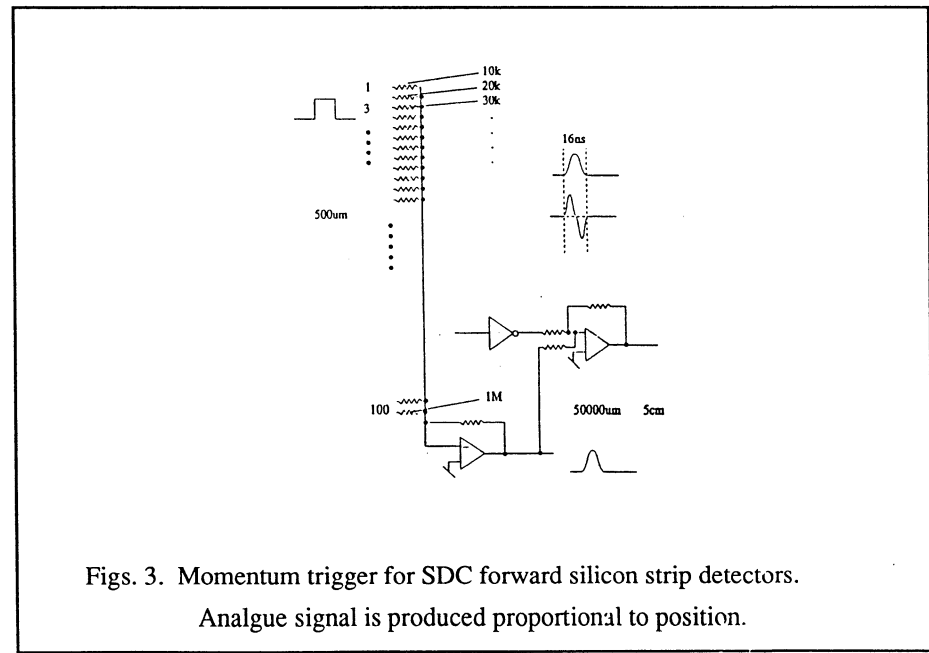
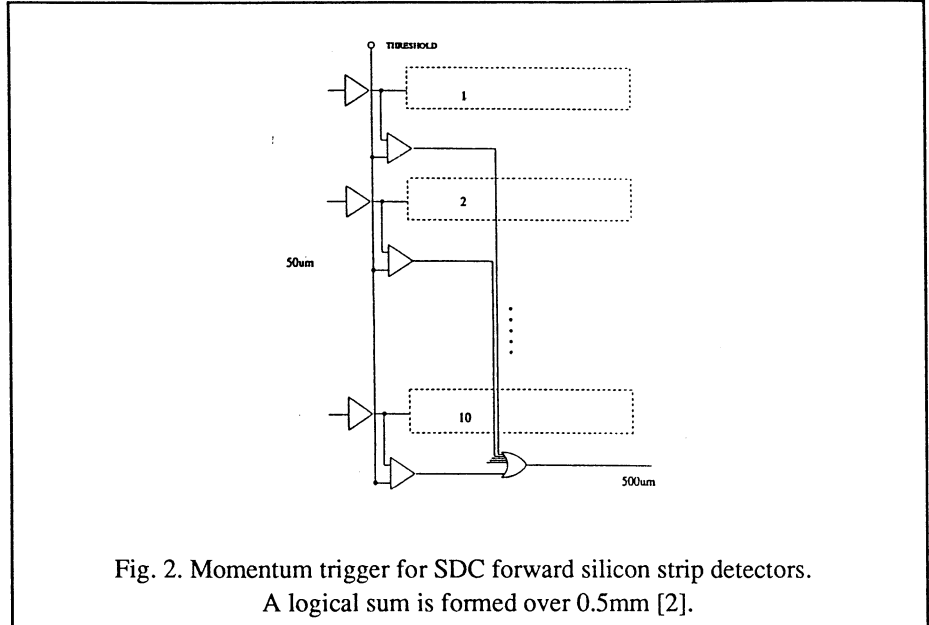
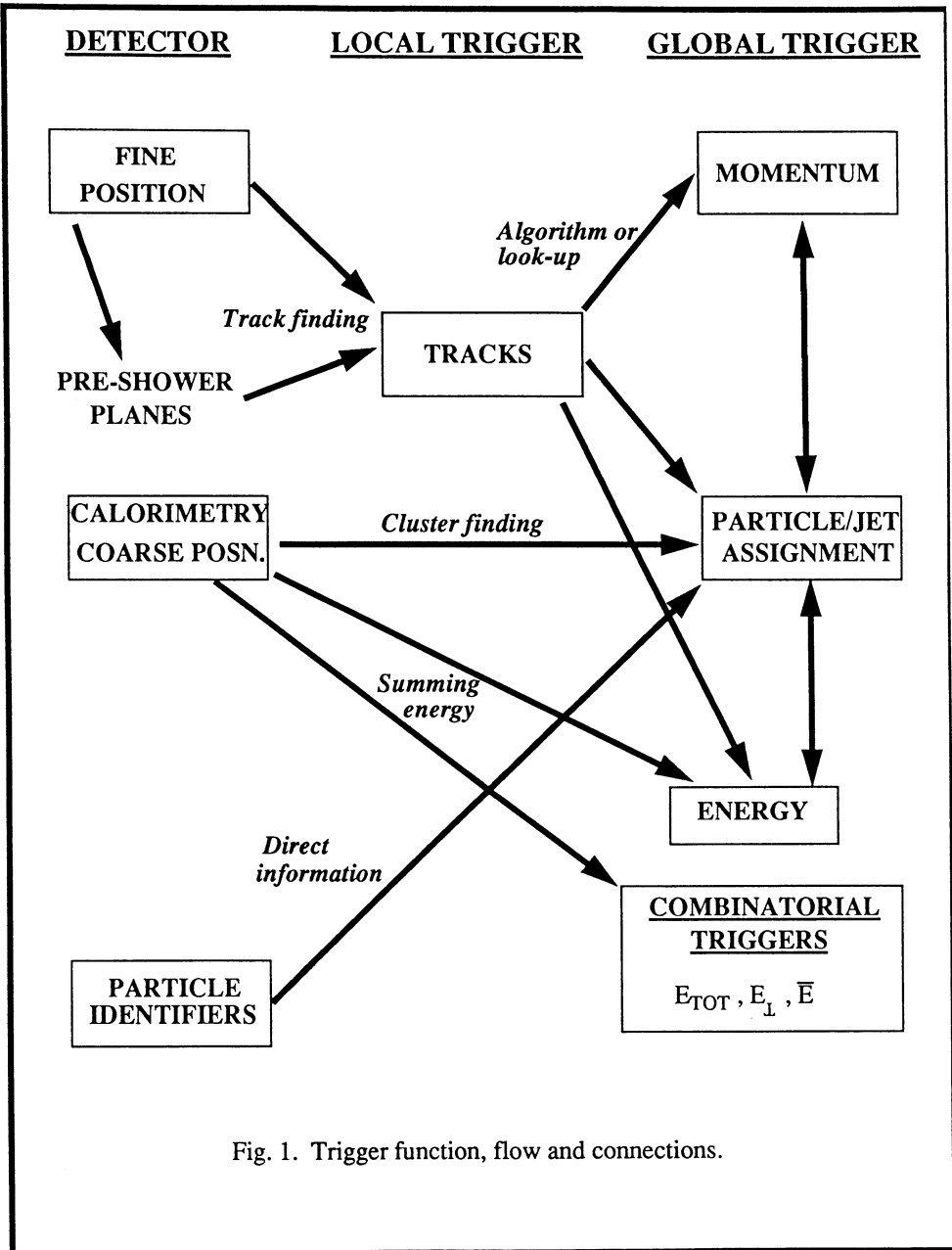
Contiguity processors are the extreme case of a "dumb" network. These may be quite general track finders [8], or may have acceptable tracks predetermined by the wiring [9]. One can argue that these are digital devices, for in their simplest form they just consist of a series of switches. However, one way of dealing with inefficiencies is to have a finite resistance with the switches open, then the inefficiency along a track is proportional to the resistance remaining [10]. This is essentially an analogue summation. An application of this principle to muon chambers was described in this Workshop.

Conclusion

It will be seen from this survey that the days when analogue or digital circuitry was a burning question are long passed. The advantages of digital techniques for most on- and off-line computing are manifest, but specialised techniques, for the most part on a grey area between analogue and digital circuitry, are likely to play an important role. After all, that so-far unequalled computer, the human brain, is a mixture of digital and analogue operations, as the section on neural networks pointed out. As our problems get more complex, we will presumably move towards the way that was pioneered by Nature, which mostly shows us the best way of solving a problem.

References

- [1] G. Goggi, B. Löfstedt, "Digital front end for a calorimeter at LHC", talk given in LHC Trigger /DAQ Working Group, CERN, 26 July 1990.
- [2] R. Nickerson, presentation at UK SDC meeting.
- [3] C. Peterson, talk given in LHC Trigger /DAQ Working Group, CERN.
- [4] See Scientific American (January 1990 issue).
- [5] B. Denby, M. Campbell, F. Bedeschi, N. Chriss, C. Bowers, F. Nesti "Neural Networks for Triggering"; FNAL Conf. 90/20.
- [6] S.R. Amendolia, F.Bedeschi, G.Belletini, S.Galeotti, A.Lusiani, A.Menzione, F.Morsani, D.Passuello, L.Ristori "Study of a fast trigger system on Beauty Events at Fixed Target"; NIM
- [7] F.Bonino; "An Analog Cellular Automaton for Cluster Identification" obtainable from EF Division, CERN.
- [8] The Contiguity Processor - A SIMD Architecture for a 2nd level track trigger"; Proc. Int. Conf. on the Impact of Digital Microelectronics and Microprocessors on Particle Physics, Trieste, 28-30 March 1988, pp.199-212.
- [9] M. Dell'Orso, L. Ristori; "A Highly Parallel Algorithm for Track Finding"; Proc. Int. Conf. on the Impact of Digital Microelectronics and Microprocessors on Particle Physics, Trieste, 28-30 March 1988, pp.292-295.
- [10] G.H. Grayer, "Real Time Track Finding for Future Large Particle Physics Experiments using LSI"; RAL-89-041 (May 1989) available from the author.



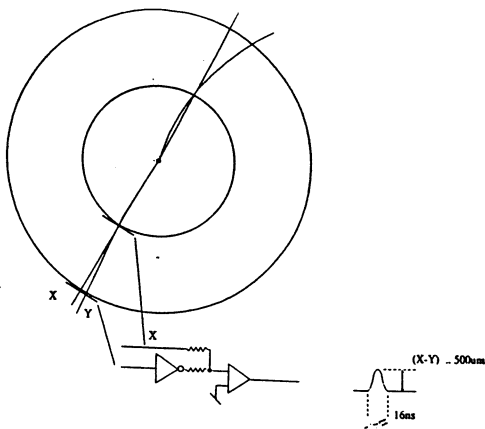
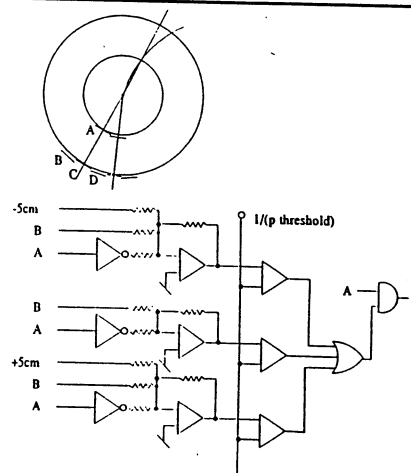


Fig. 4. Momentum trigger for SDC forward silicon strip detectors. A signal is produced proportional to the deviation from a straight line in projection [2].



Figs. 5. Momentum trigger for SDC forward silicon strip detectors. Each sector is tested separately for exceeding the momentum threshold [2]

D7: MUON IDENTIFICATION

MASS RESOLUTION FOR HEAVY HIGGS PARTICLE SEARCH

Th. Moers, R. Priem, H. Reithler, H. Schwarthoff
Phys. Inst. IIIA, RWTH Aachen

4 Oct 1990

Abstract

The dependence of the reconstructed Higgs particle mass resolution on the muon momentum measurement is studied for the $H^0 \rightarrow 2Z^0 \rightarrow 4\mu$ channel. The known mass of the Z^0 is used as a constraint to correct the muon momenta. Results are presented for magnetic spectrometers with any combination of air and iron components.

1 Introduction: Detector Types

The most promising signature for the search of a “heavy” ($m_{H^0} \geq 2m_{Z^0}$) Higgs particle is its decay to four charged leptons, especially

$$H^0 \rightarrow Z^0 + Z^0 \rightarrow \mu^+ + \mu^- + \mu^+ + \mu^- \quad (1)$$

since muons can be identified readily. On the other hand, their momentum measurement, done with a magnetic spectrometer, would require a huge effort if high accuracy at high momentum is needed. Therefore, the question of necessary muon momentum resolution for the Higgs search is at the root of any detector design. The main irreducible background consists of the QCD process $q\bar{q} \rightarrow Z^0 Z^0 X$ with two real Z^0 , which cannot be removed by cuts in $m_{\mu\mu}$, the reconstructed mass of the Z^0 . The Higgs signal must thus show up as a narrow mass peak over a wider background. Hence, the scale for the optimal measurement accuracy is determined by the *natural width* of the Higgs particle itself, which varies as $\sim m_{H^0}^3$ from a few GeV at $m_{H^0} = 200$ GeV to ≈ 250 GeV at $m_{H^0} = 800$ GeV.

A magnetic spectrometer measures the tiny bending of the muon track in the magnetic field. This sagitta is a measurement of $1/p_\mu$, where p_μ is the muon momentum. A detector having a constant resolution for the sagitta measurement has thus a *constant error* $\sigma(1/p_\mu)$, or $\sigma(p_\mu)/p_\mu$ proportional to p_μ . On the other hand, massive spectrometers using magnetized iron have an additional uncertainty arising from multiple scattering of the muon in the iron. Since this random deflection from multiple scattering has the same energy dependence as the magnetic deflection, the effective momentum resolution in a massive magnetized iron spectrometer is nearly a *constant error* $\sigma(p_\mu)/p_\mu$ *independent of energy*.

Other detector designs may feature a mixture of both types of response. This is the case when a part of the magnetic field is in iron and a part in air, or when the magnetic field in iron is raised above its saturation value, thus increasing the magnetic deflection without increase of multiple scattering.

In this work we present the Higgs mass resolution obtainable with any type of spectrometer characterized by the two components of constant $\sigma(1/p_\mu)$ and constant $\sigma(p_\mu)/p_\mu$. This allows a direct appreciation of the detector performance and an objective comparison of basic detector designs. A real detector will very likely have a momentum resolution depending not only on the

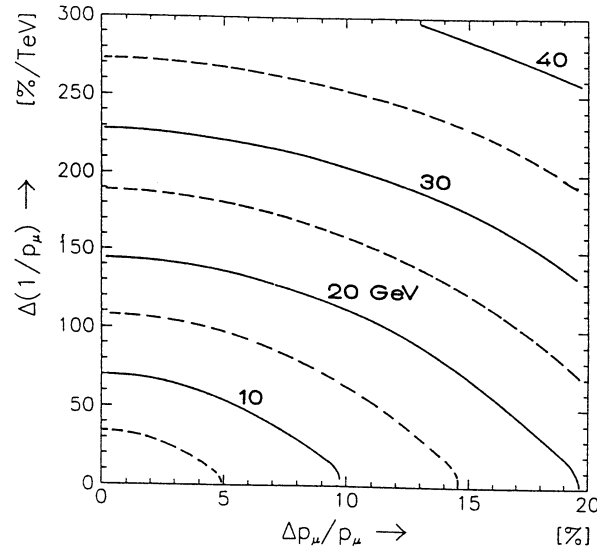


Figure 1: Resolution of the reconstructed Higgs mass, for any combination of muon momentum resolutions $\Delta(p_\mu)/p_\mu$ and $\Delta(1/p_\mu)$. This resolution contains the contribution from measurement errors only, and is significantly larger than the natural width Γ_{H^0} . Here $m_{H^0} = 200$ GeV was used and no fit of the muon momenta was attempted.

momentum, but also on the direction of flight of the muon. Here, for simplicity, the momentum resolution was assumed to be independent of the direction of flight.

2 Generation of Events

Events of reaction (1) were generated for the LHC energy $\sqrt{s} = 16$ TeV. In order to make the effect of the measurement accuracy more apparent, the events were generated for a natural width of the Higgs particle set to zero. Therefore, the mass distributions shown here have a width reflecting the experimental resolution only. The muon momenta were smeared randomly with two gaussian widths $\sigma_1 = \sigma(p_\mu)/p_\mu$ and $\sigma_2 = \sigma(1/p_\mu)$. These errors $\Delta_1 p_\mu$ and $\Delta_2 p_\mu$ were added in quadrature. Since the direction of flight of the muon is well determined it was kept unchanged.

The resulting resolution of m_{H^0} is shown in fig. 1 for $m_{H^0} = 200$ GeV. It displays lines of constant $\sigma(m_{H^0})$, obtained from a gaussian fitted to the reconstructed Higgs mass distribution, as a function of both components of the muon resolution. At first sight it does not look too promising, for e.g. a present central detector featuring $\sigma_2 \approx 0.5\%/\text{GeV} = 500\%/\text{TeV}$, or for an iron spectrometer with $\sigma_1 \approx 17\%$.

3 Fit of Muon Momentum

To improve the measurement accuracy, the condition $m_{\mu\mu} = m_{Z^0}$ was used to correct the observed raw muon momenta. A second condition is needed to fix the two Δp ; we have chosen to require $\sum(\Delta p/\sigma)^2$ minimal. The expected error σ of the muon momentum p was taken to be $\sigma(p) = \sqrt{\sigma_1^2 + \sigma_2^2}$. A fit was done for each muon pair. The effect of this fit on the reconstructed

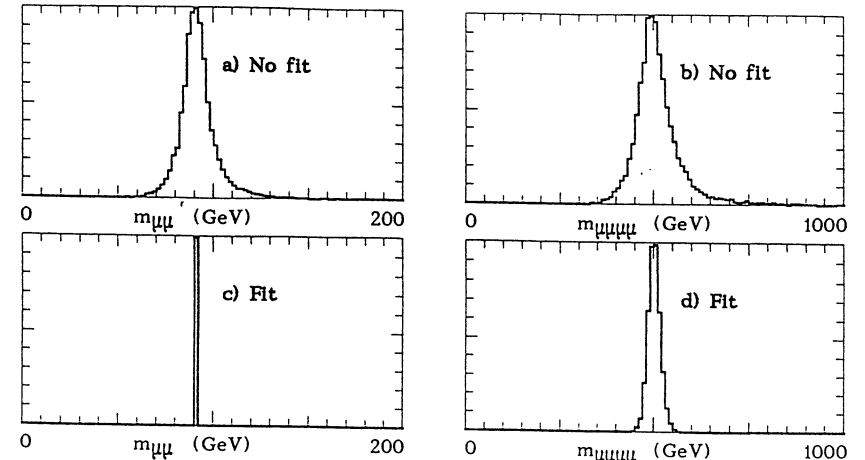


Figure 2: Reconstructed masses for $m_{H^0} = 500$ GeV, $\Gamma_{H^0} = 0$, $\Delta p_\mu/p_\mu = 50\% \times (p_\mu/\text{TeV})$. In a) and b) the raw momenta were used, while in c) and d) the momenta were fitted to match $m_{\mu\mu} = m_{Z^0}$. The fit reduces the experimental width $\sigma(m_{H^0})$ from 46 to 16 GeV.

Z^0 and H^0 mass is illustrated in fig. 2: part a) shows a raw $m_{\mu\mu}$ distribution and the resulting $m_{\mu\mu\mu\mu}$ (part b)), while parts c) and d) show the analogue distributions after $m_{\mu\mu} = m_{Z^0}$ has been fitted for both muon pairs. As expected, the improvement is considerable.

A natural limitation is imposed to this fit by the Z^0 width $\Gamma_{Z^0} \approx 2.5$ GeV itself: since for the fit $m_{\mu\mu} = m_{Z^0}$ one uses the central value of m_{Z^0} , an error of order Γ_{Z^0} is always present. If a detector would have a better resolution, this type of fit should of course be avoided. The effect of the Z^0 width on the H^0 mass, reconstructed with the fit above, is a minimum width of 4, 10, ≈ 20 GeV for $m_{H^0} = 200, 500, 800$ GeV respectively. However, this unavoidable width is much smaller than the natural width of the Higgs particle, except for the lowest value $m_{H^0} = 200$ GeV.

It should be noted that this procedure cannot produce an artificial $m_{Z^0 Z^0}$ mass peak for the QCD background events $q\bar{q} \rightarrow Z^0 Z^0 X$, since their $m_{Z^0 Z^0}$ distribution has no peak.

4 Wrong Pairings

For a high momentum particle the reconstruction of its track might sometimes be poor and just give a lower bound for the momentum, thus leaving the sign of its electric charge unmeasured. When the sign of the electric charge of at least three of the four observed muons is known, there are two possible combinations to form two Z^0 particles from pairs of muons. If less than three charges are known, three such pairings may become possible. Thus there are always (at least) two pairings to be considered.

It turns out that this ambiguity does not spoil the Higgs signal. The invariant mass distribution of $m_{\mu\mu}$ for the wrong pairings is wide (fig. 3a). Here the Z^0 mass fit will not improve the measured muon momenta, but rather distort them further. The resulting $m_{Z^0 Z^0}$ distribution has a maximum always near its lower kinematical limit (fig. 3d). One might thus suspect that inclusion of such wrong pairings becomes disturbing for a Higgs mass near 200 GeV, but even here it will not jeopardize the recognition of the much narrower peak for the correct pairings.

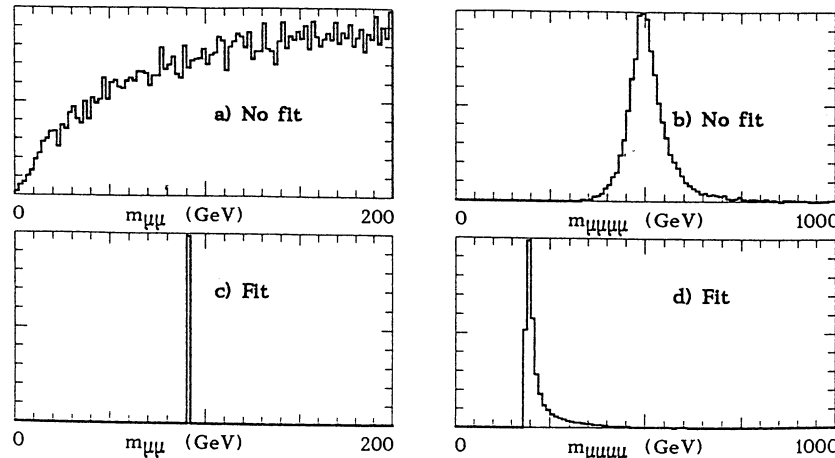


Figure 3: Reconstructed masses for the wrong $\mu\mu$ pairings; same conditions as for fig. 2. The $m_{\mu\mu}$ reconstructed from the raw muon momenta a) are much higher than m_{Z^0} (50% of the events are in the overflow region of this histogram). Therefore, the fit to m_{Z^0} c) would cause the reconstructed four muon invariant mass d) to concentrate at the lower kinematical bound. The wrong pairings (fig. 3d) are thus clearly distinguishable from the correct pairings (fig. 2d).

Furthermore we compared the raw value $\Delta^2 = (m_{\mu_1\mu_2} - m_{Z^0})^2 + (m_{\mu_3\mu_4} - m_{Z^0})^2$ for each pairing. With the very simple rule of choosing the pairing with the lowest Δ^2 , the correct pairing is tagged with about 92% (85%) efficiency for two (three) pairings for a momentum resolution of $100\% \times (p/\text{TeV})$ and $m_{H^0} = 200 \text{ GeV}$. For higher masses this tagging improves; for $m_{H^0} = 500 \text{ GeV}$ this efficiency is 99.5% (99%). This worst case selection (from three possible pairings) was applied to calculate the experimental resolution in m_{H^0} for the final curves in fig. 4–6.

5 Results

The fit procedure, including the “worst case selection” of pairings as described above, was repeated for the full range of detector resolutions. The resulting Higgs mass resolutions are summarized in fig. 4–6 for $m_{H^0} = 200, 500$ and 800 GeV . These curves show, for any mixture of air-type ($\sigma(1/p_\mu) = C^{te}$) and of iron-type ($\sigma(p_\mu)/p_\mu = C^{te}$) spectrometer behaviour, the error on m_{H^0} resulting from measurement errors only. The natural width of the Higgs particle is given for each figure. A good detector should match this resolution, or be slightly better.

It turns out, that a relatively “modest” muon momentum resolution is sufficient to measure the mass peak of the Higgs particle for the whole range of Higgs masses from 200 to 800 GeV considered here. The most stringent requirement is for the lightest Higgs (fig. 4): if one accepts a measurement width of $\sigma(m_{H^0}) \approx 5 \text{ GeV}$, the needed muon momentum resolution is about 14% for an iron-type spectrometer (or 130%/TeV for an air-type spectrometer, or any suitable combination of both spectrometer types).

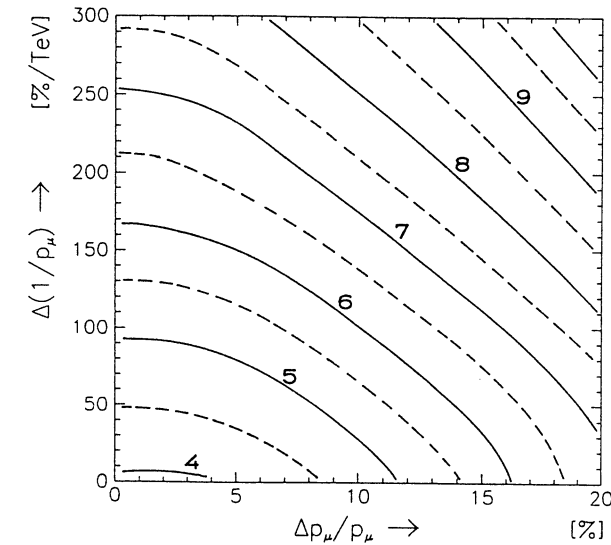


Figure 4: Resolution of the reconstructed Higgs mass, for any combination of muon momentum resolutions $\Delta(p_\mu)/p_\mu$ (massive spectrometer) and $\Delta(1/p_\mu)$ (air spectrometer). As in all figures, the natural width of the Higgs particle is set $\equiv 0$. Hence, the line width shown reflects the contribution from measurement errors alone. The muon momenta were fitted to reproduce m_{Z^0} . Note that for a very good detector (lowest value on picture) a better mass resolution is achieved without the Z^0 mass constraint. A mass $m_{H^0} = 200 \text{ GeV}$ was assumed here. For comparison, the natural width of the Higgs is 1.4 GeV.

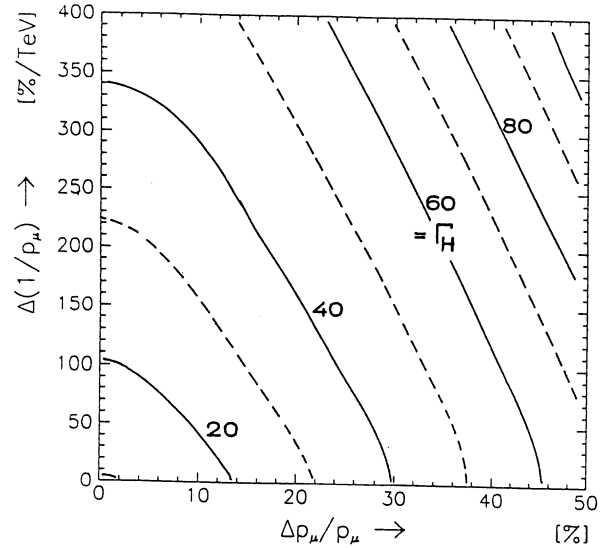


Figure 5: Reconstructed Higgs mass resolution resulting from measurement errors, as in fig. 4, but here for $m_{H^0} = 500$ GeV. The natural Higgs width is $\Gamma_{H^0} = 60$ GeV.

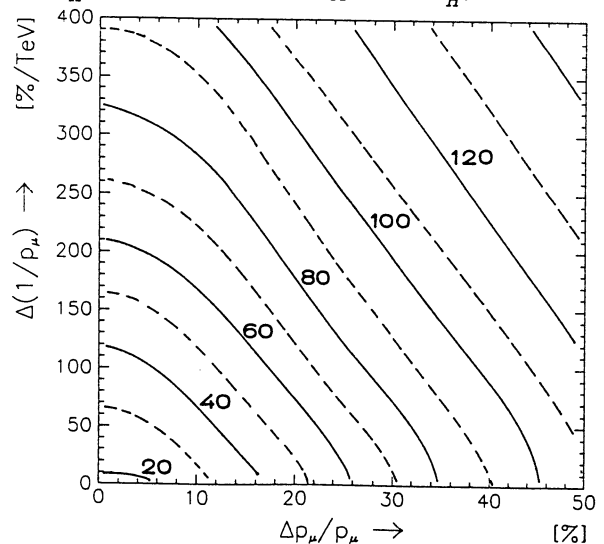


Figure 6: Reconstructed Higgs mass resolution resulting from measurement errors, as in fig. 4, but here for $m_{H^0} = 800$ GeV. The natural Higgs width is $\Gamma_{H^0} = 246$ GeV.

List of CERN Reports published in 1990

CERN 90-01

Billinge, R; Boltezar, E; Boussard, D: et al.
Concept for a lead-ion accelerating facility at
CERN
CERN, 28 Feb 1990. – 40 p

CERN 90-02

Nakada, T [*ed*]
Feasibility study for a B-meson factory in the
CERN ISR tunnel
CERN, 30 Mar 1990. – 96 p

CERN 90-03

CERN, Genève
Turner, S [*ed*]
Proceedings, CAS - CERN Accelerator school ;
Synchrotron radiation and free electron lasers,
Chester, UK, 6-13 Apr 1989
CERN, 2 Apr 1990. – 482 p

CERN 90-04

CERN, Genève
Turner, S [*ed*]
Proceedings, CAS - CERN Accelerator school ;
Third advanced accelerator physics course, Uppsala,
Sweden, 18-29 Sep 1989
CERN, 24 Apr 1990. – 227 p

CERN 90-05

CERN, Genève
Wilson, E J N
Accelerators for the twenty-first century – a
review
CERN, 29 May 1990. – 28 p
Lectures in the Academic Training Programme

CERN 90-06

CERN, Genève
Verkerk, C [*ed*]
Proceedings, 1989 CERN school of computing,
Bad Herrenalb, 20 Aug – 2 Sep 1989
CERN, 29 May 1990. – 347 p

CERN 90-07

CERN, Genève
Turner, S [*ed*]
Proceedings, CAS - CERN Accelerator school ;
Power converters for particle accelerators, Montreux,
26 – 30 Mar 1990
CERN, 23 Jul 1990. – 381 p

CERN 90-08

CERN, Genève
Kuiper, B [*ed*]
Proceedings, Europhysics conference on control
systems for experimental physics, Villars-sur-Ollon,
Switzerland, 28 Sep – 2 Oct 1987
CERN, 12 Oct 1990. – 592 p

CERN 90-09

Telegdi, V L
Mind over matter ; The intellectual content of
experimental physics
CERN, 2 Nov 1990. – 20 p

CERN 90-10 v.1; ECFA 90/133 v.1

CERN, Genève
Jarliskog, G; [*eds*]
Proceedings, v.1, Large Hadron Collider Work-
shop, Aachen,
CERN, 3 Dec 1990. – 634 p

CERN 90-10 v.2; ECFA 90/133 v.2

CERN, Genève
Jarliskog, G; [*eds*]
Proceedings, v.2, Large Hadron Collider Work-
shop, Aachen,
CERN, 3 Dec 1990. – 1306 p

CERN 90-10 v.3; ECFA 90/133 v.3

CERN, Genève
Jarliskog, G; [*ed*]
Proceedings, v.3, Large Hadron Collider Work-
shop, Aachen,
CERN, 3 Dec 1990. – 853 p

CERN 90-10 v.2; ECFA 90/133 v.2

ISSN 0007-8328
ISBN 92-9083-030-1